Malaysian Journal of Analytical Sciences
(MJAS)
Published by Malaysian Analytical Sciences Society

Vol 27 No 1 (2023)

Vol 27 No 2 (2023)

Vol 27 No 3 (2023)

Vol 27 No 4 (2023)

Vol 27 No 5 (2023)

Vol 27 No 6 (2023)

2023

Malaysian Journal of Analytical Sciences Vol 27 No 1 2023

Analytical Method

1. ANALYSIS OF ILLICIT DRUGS IN MUNICIPAL WASTEWATER USING LC-MS/MS: A METHOD VALIDATION STUDY 1
Mohammad Azimuddin Izani, Nurul `Azyyati Sabri, Nurul Nadiah Hamidon, Kooi Yeong Khaw, Iekhsan Othman, Jochen Mueller, and Joo Hui Tay

Nano or Advanced Materials Analysis

2. CHARACTERIZATION OF *Anadara granosa* AS A POTENTIAL SOURCE OF CALCIUM CARBONATE FOR GLASS IONOMER CEMENT FORMULATION 8
Nur Izzah Md Nasir, Norhazlin Zainuddin, and Francis Thoo Voon Wai

Analytical Method

3. SYNTHESIS AND CHARACTERIZATION OF MOLECULARLY IMPRINTED POLYMER IN OLEIC ACID ISOLATION FROM PALM FATTY ACID DISTILLATE WASTES 20
Nurlin Abu Samah, Siti Maizatul Ameera Azhar, and Gaanty Pragas Maniam

Nano or Advanced Materials Analysis

4. EVALUATION OF CARRAGEENAN GEL PROPERTIES AT DIFFERENT CONCENTRATIONS OF CALCIUM CHLORIDE DIHYDRATE SALT 30
Nur Anis Alisya Kamarol Zani, Fatmawati Adam, Nurul Aini Mohd Azman, and Nor Hanuni Ramli

Organic or Inorganic Analysis

5. STUDIES ON THE SYNTHESIS OF β-CARBOLINE AND ITS DERIVATIVES AS POTENTIAL ANTIMALARIAL DRUG COMPONENTS 44
Ruwaida Shamsujunaidi, Aimi Suhaily Saaidin, Muhammad Hazim Abdul Aziz, Mohd Fazli Mohammat, and Noor Hidayah Pungot

Nano or Advanced Materials Analysis

6. HYDROTHERMAL SYNTHESIS OF Co AND Pd DOPED TIN OXIDE NANORODS AND THEIR PHOTOCATALYTIC DEGRADATION OF POLYPROPYLENE 54
Vicinisvarri Inderan, Nur Aina Shahida Ahmad, Nurizyan Amirah Mohd Zaidi, Norain Isa, Wan Zuraida Wan Kamis, Hooi Ling Lee, and Siva Raseetha

Nano or Advanced Materials Analysis

7. THE EFFECT OF NANOFILLERS ON THE FUNCTIONAL PROPERTIES OF PLA AND CHITOSAN BASED FILM 63

Raja Hasnida Raja Hashim, Ahmad Anas Nagoor Gunny, Sam Sung Ting, Nor Helya Iman Kamaludim, and Subash C. B. Gopinath

Analytical Method

8. NOVEL MAGNETIC EGGSHELL MEMBRANE FUNCTIONALIZED WITH WASTE PALM FATTY ACID FOR SELECTIVE ADSORPTION OF OIL FROM AQUEOUS SOLUTION 74
Siti Khalijah Mahmad Rozi, Khairul Muzzammil Berhanundin, Ahmad Razali Ishak, Fairuz Liyana Mohd Rasdi,Nazri Che Dom, Nurul Yani Rahim, Mohd Yusmaidie Aziz, Farah Ayuni Shafie, and Abdul Mujid Abdullah

Analytical Method

9. DETERMINATION OF L-CARNITINE AND COENZYME Q $_{10}$ ACTIVE SUBSTANCE LEVELS IN FOOD SUPPLEMENTS USING HIGH- PERFORMANCE LIQUID CHROMATOGRAPHY 87
Muhaimin, Hilda Andini, and Henry Himawan

Organic or Inorganic Analysis

10. THE EFFECT OF ANTHRACENE GROUP SUBSTITUTION OF DISUBSTITUTED CHALCONE DERIVATIVE FEATURING TEREPHTHALALDEHYDE π-LINKER ON NON-LINEAR OPTICAL (NLO) CHARACTERISTIC 96
Nurul Nabilah Shuaib, Adibah Izzati Daud, Suhana Arshad, Mohamad Aizat Abu Bakar, and Wan M. Khairul

Environmental Analysis

11. SEASONAL VARIATION IN CONCENTRATION OF HEAVY METALS IN TROPICAL RIVER SEDIMENT 108
Nur Amirah Hidayah Madzlan, Suhaimi Suratman, Khairul Nizam Mohamed, and Ong Meng Chuan

Environmental Analysis

12. PRIMORDIAL RADIONUCLIDES CONTENT AND RADIATION RISK ASSESSMENT OF SURFACE SOILS SURROUNDING TEMENGGOR RESERVED FOREST, GERIK, PERAK 119
Nursyairah Arshad, Misbah Hassan, Nor Aizam Adnan, and Rozita Osman

Organic or Inorganic Analysis

13. ACETAL DERIVATIVES OF HYDROXYCITRONELLAL: A REVIEW ON SYNTHESIS, CHARACTERIZATION AND THEIR MOSQUITOE REPELLENT ACTIVITIES 129
Ariff Mahtar and Juliana Jumal

Nano or Advanced Materials Analysis

14. SYNTHESIS AND CHARACTERISATION OF COMPOSITE SILICA, POLY(METHYL METHACRYLATE) (PMMA) AND GOLD-SILVER (Au-Ag) ALLOY VIA CO-CRYSTALLISATION FOR LIGHT MANIPULATION APPLICATIONS 147
Rozaitunmas Jamal, Rabiatul Addawiyah Azwa Tahrin, Mohd Sabri Mohd Ghazali, Sibu C. Padmanabhan, Chan Kiki, and Syara Kassim

Computational Chemistry

15. *In Silico* MODELLING OF DRUG ADSORPTION USING AMINE-FUNCTIONALIZED IRMOF-74-III METAL-ORGANIC FRAMEWORKS 160
Mostafa Yousefzadeh Borzehandani, Emilia Abdulmalek, Mohd Basyaruddin Abdul Rahman, and Muhammad Alif Mohammad Latif

Nano or Advanced Materials Analysis

16. FACILE CHEMICAL SYNTHESIS OF PURE Zn DOPED CeO_2 NANOPARTICLES WITH ENHANCED PHOTOCATALYTIC PERFORMANCE UNDER UV IRRADIATION 174
Swathi Chidaraboyina, Arputharaj Samson Nesaraj, and Manasai Arunkumar

Natural Product Analysis

17. MALAYSIAN MEDICINAL PLANTS (*Euphorbia milii*) AS A DRUG ALTERNATIVE SOURCE FOR ANTI-GOUT THERAPY 189
Nur Syafika Amani Abd. Mutalib, Mohamad Hussin Haji Zain, Asnuzilawati Asari, Maulidiani, Ahmad Nazif Aziz, Norhayati Yusuf, Nurul Huda Abdul Wahab

Nano or Advanced Materials Analysis

18. FORMATION AND STABILITY STUDY OF SILVER NANOPARTICLES REDUCED BY *Murdania Loriformis* EXTRACT FOR ANTIBACTERIAL APPLICATIONS 198
Norain Isa, Nazatul Nabila Mohamad, Ainorkhilah Mahmood, Nor Aziyah Bakhari, Marlina Mohd Mydin, and Norhafiza Mohd Arshad

Analytical Method

19. MULTI-TRACE METALS DETERMINATION OF PENINSULAR MALAYSIA STINGLESS BEE HONEYS FROM DIFFERENT REGIONS AND SEASONS USING INDUCTIVELY COUPLED PLASMA-OPTICAL EMISSION SPECTROMETRY AND CHEMOMETRIC TECHNIQUES 216
Syazwani Dzolin, Wan Aini Wan Ibrahim, Naji Arafat Mahat, Dzulkiflee Ismail, and Aidil Fahmi Shadan

Malaysian Journal of Analytical Sciences (MJAS)
Published by Malaysian Analytical Sciences Society

ANALYSIS OF ILLICIT DRUGS IN MUNICIPAL WASTEWATER USING LC-MS/MS: A METHOD VALIDATION STUDY

(Analisa Dadah Berbahaya dalam Air Sisa Perbandaran Menggunakan LC-MS/MS: Satu Kajian Pengesahan Kaedah)

Mohammad Azimuddin Izani[1], Nurul `Azyyati Sabri[1], Nurul Nadiah Hamidon[1], Kooi Yeong Khaw[2], Iekhsan Othman[3], Jochen Mueller[4] and Joo Hui Tay[1*]

[1]Faculty of Industrial Sciences & Technology,
Universiti Malaysia Pahang,
Lebuhraya Persiaran Tun Khalil Yaacob, 26300 Gambang, Pahang, Malaysia
[2] School of Pharmacy, Monash University Malaysia,
Jalan Lagoon Selatan, 47500 Bandar Sunway, Selangor, Malaysia
[3]Jeffrey Cheah School of Medicine & Health Sciences,
Monash University Malaysia, Jalan Lagoon Selatan, 47500 Bandar Sunway, Selangor, Malaysia
[4]Queensland Alliance for Environmental Health Sciences (QAEHS),
The University of Queensland, 4102, Brisbane, Australia

[*]Corresponding author: tayjoohui@ump.edu.my

Received: 19 September 2022; Accepted: 18 December 2022; Published: 22 February 2023

Abstract

An analytical method based on solid-phase extraction (SPE) liquid chromatography-tandem mass spectrometry (LC-MS/MS) for the determination of five illicit drugs, namely amphetamine (AM), methamphetamine (MA), 3,4-methylenedioxymethamphetamine (MDMA), 3,4-methylenedioxyamphetamine (MDA), and morphine (MOR) in municipal wastewater has been optimized and validated. Sample preparation was performed using Oasis MCX SPE cartridges. LC separation was performed using a Zorbax Eclipse Plus C_{18} RRHD column. The linearity of the calibration curve was between 5 ng/mL and 250 ng/mL, with determination coefficient (R^2) greater than 0.99, except for morphine. The mean recoveries of target analytes ranged from 91.6 to 112%, and the method demonstrated good inter-day repeatability (coefficient of variation, CV ranged from 2 to 19%). The limit of detection (LOD) for AM, MA, MDMA, MDA, and MOR was 0.29, 0.37, 0.86, 1.09 and 7.56 ng/mL, respectively. The method was applied to municipal wastewater samples collected from sewage treatment plants in Kuantan, Pahang, in which AM, MA and MDA were detected in all 3 samples.

Keywords: amphetamine, illicit drugs, LC-MS/MS, methamphetamine, municipal wastewater

Abstrak

Kaedah analisis berdasarkan spektrometri jisim kromatografi-tandem cecair (LC-MS/MS) untuk penentuan lima dadah berbahaya, iaitu amphetamine (AM), methamphetamine (MA), 3,4-methylenedioxymethamphetamine (MDMA), 3,4methylenedioxyamphetamine (MDA), dan morfin (MOR) dalam air sisa perbandaran telah dioptimumkan dan disahkan.

Penyediaan sampel dilakukan menggunakan kartrij SPE Oasis MCX. Pemisahan LC dilakukan dengan menggunakan turus Zorbax Eclipse Plus C_{18} RRHD. Kelinearan keluk tentukuran bagi semua analit sasaran berada di antara 5 ng/mL dan 250 ng/mL, kecuali morfin. Putara pemulihan analit sasaran berjulat antara 91.6 hingga 112%, dan kaedah ini menunjukkan kebolehulangan antara hari yang baik (pekali variasi berkisar antara 2 hingga 19%). Had pengesanan (LOD) bagi AM, MA, MDMA, MDA dan MOR adalah 0.29, 0.37, 0.86, 1.09 and 7.56 ng/mL. Kaedah ini digunakan untuk sampel air sisa perbandaran yang dikumpulkan dari loji rawatan kumbahan di Kuantan, Pahang, di mana AM, MA dan MDA telah ditemui dalam ketiga-tiga sampel.

Kata kunci: amphetamine, dadah berbahaya, LC-MS/MS, methamphetamine, air sisa perbandaran

Introduction

Drug abuse has been identified as a serious public health issue in Malaysia. Despite strict drug trafficking and possession laws, the Malaysian National Anti-drug Agency (AADK) reported 128,325 drug users and addicts in 2020, with Amphetamine-Type Stimulants (ATS) recorded the highest consumption (65.2%), followed by Opiates (30.9%) and Cannabis (2.7%) [1]. These official statistics, which are compiled from drug sweep operations conducted by The Royal Malaysia Police (PDRM) in cooperation with AADK, numerous ministries and governmental agencies as well as the Private Drug Rehabilitation Centers (PDRC), can provide a valuable overall picture of drug use in this country. However, since no extensive surveillance test is done, the actual consumption rates and drug use prevalence at the community, district or national level may be underestimated because these official figures are derived directly from consumers. Administered drugs are excreted as either unchanged parent drugs, conjugated forms or metabolites, flushed down the drain and eventually reach sewage treatment plants (STPs) [2]. By collecting STPs influent samples and quantifying the concentration of drug residues or metabolites in the samples, the population-normalized total consumption of a given drug within the population of a sewage treatment service area could be estimated. This wastewater-based epidemiology (WBE) method has been widely used to objectively monitor population-level drug usage, notably in the Western countries [3-6]. In a recent study conducted in Kuala Lumpur, Malaysia, 14 illicit drug residues with concentrations up to 1640 ng/L were found in municipal sewage samples [7]. This finding suggests that WBE could be used as a complementary monitoring approach in our country to estimate drug consumption.

Current analytical methods for quantifying illicit drugs in sewage commonly include a sample concentration step, such as solid-phase extraction (SPE) with various sorbent materials, followed by instrumental analysis with liquid chromatography-tandem mass spectrometry (LS-MS/MS) [8]. Direct injection and/or large-volume injection to LC-MS/MS (without pre-concentration) are also reported in the literature [9]. Before applying an analytical method to real samples, it is essential to determine whether it is suitable for the intended use. Therefore, in this study, an analytical method for the determination of ATS drugs, namely AM, MA, MDMA and MDA, as well as MOR (one type of opiates drugs) in sewage based on SPE and LC-MS/MS was validated. The method was tested on sewage samples taken from STPs in the Kuantan area to check if it was sensitive enough to detect these substances. The validated method will be used in the future to measure the usage of these drugs by utilizing the WBE approach.

Materials and Methods

Reagents and materials

The reference standards for the target compounds (AM, MA, MDMA, MDA and MOR) (Figure 1) as well as the deuterated internal reference standards used (AM-d_6, MA-d_5, MDMA-d_5, MDA-d_5 and MOR-d_3) were purchased from Lipomed AG (Switzerland) at concentrations of 1 mg/mL and 0.1 mg/mL in methanol (MeOH), respectively. Working solutions with concentrations ranging from 5 ng/mL to 250 ng/mL were prepared in MeOH. LC-grade MeOH and acetonitrile were purchased from Merck (Germany). Analytical grade ammonium hydroxide (NH_4OH) and hydrochloric acid (HCl) were obtained from Merck (Germany). Formic acid (Optima LC/MS) was obtained from Fisher Chemical (UK). Oasis MCX (60 mg, 3 mL) SPE cartridges were purchased from Waters Corporation (Milford, MA, USA). Glass fiber filters (0.7 µm) were obtained from Whatman (UK).

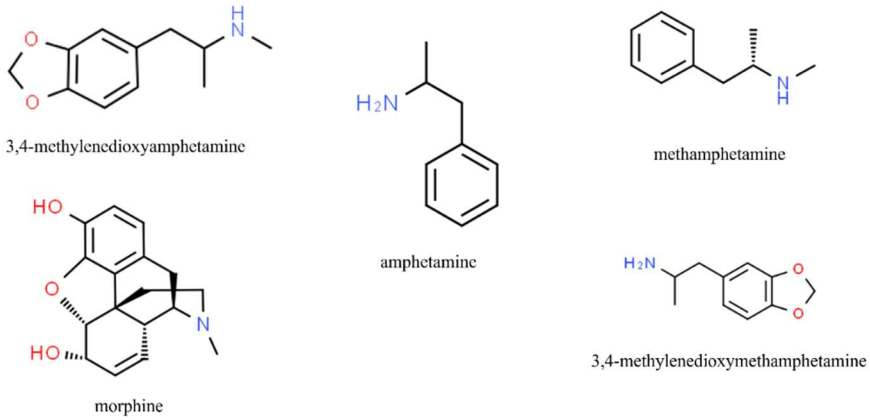


Figure 1. Chemical structures of the investigated of illicit drugs

Sample preparation, extraction, and sampling

A spiking test was used to validate the sample preparation and extraction method used by Kinyua et al. [10]. In brief, 500 mL of deionized (DI) water was spiked with reference standards (both native and deuterated internal standards at three concentration levels: 12.5, 50 and 100 ng/mL) and then analyzed to determine the extraction recovery, inter-day, and intra-day repeatability. For MOR, only 2 levels of spiking (50 and 100 ng/mL) were performed due to its high limit of detection (LOD). The samples were loaded onto Oasis MCX SPE cartridges preconditioned with 6 mL of methanol (MeOH), 4 mL DI water, and 4 mL of DI water at pH 2. After that, the cartridges were washed with 3 mL DI water before drying. The target analytes were eluted with 2 mL MeOH and 2 mL 5% NH_4OH in MeOH, evaporated to dryness under a gentle stream of nitrogen, and reconstituted in 100 µL of DI water containing 5% of acetonitrile and 0.1% formic acid. For each batch of extraction, one procedural blank (solvent blank spiked with internal standards) was included.

Three sewage samples were taken on August 10th, 17th and 24th, 2021, respectively, at the inlet of three STPs in Kuantan (designated STP-A, STP-B and STP-C). One 24-hour composite influent sample was collected at each station using a Watson-Marlow qdos 20 peristaltic pump at a flowrate of 5 mL/min. The samples were brought to pH 2 by adding 2M HCl, and they were then kept at -20 °C until analysis. Prior to extraction, the sewage samples were thawed and filtered through a 0.7 µm glass fiber filter to remove solid particles. For each sample, a 500-mL aliquot of the filtrates was spiked with internal standards at a concentration of 50 ng/mL and subjected to the previously described SPE procedure.

LC-MS/MS analysis

An Agilent 6410B Triple Quadrupole LC-MS/MS with an electrospray ionization (ESI) technique was used to detect and quantify target analytes. LC-MS/MS method used by Lai et al. [11] was adopted and optimized accordingly. In short, the chromatographic separation was performed using a Zorbax Eclipse Plus C18 RRHD column (2.1 × 50mm, 1.8µm). A mobile phase composed of A: 0.1% formic acid in water, and B: 0.1% formic acid in acetonitrile, was applied at a flow rate of 0.35 mL/min. The gradient was as follows: 0-2 min: 92% A, 2-2.1 min: 75% A, 2.1-3 min: 100% B. The total run time, which included column equilibration, was 5 minutes. The column and autosampler temperatures were set to 45°C and 4°C, respectively. The injection volume was set to 1 µL. Other MS parameters included gas temperature of 300°C, gas flow of 11 L/min, nebulizer pressure of 45 psi, and capillary voltage of 4000 V. Multiple reaction monitoring (MRM) was used to quantify the analytes. The mass spectrometer compound dependent parameters are listed in Table 1.

Table 1. LCMS/MS parameters for target drugs for MRM acquisition in positive mode

Drugs	Parent Ion (m/z)	Fragmentor Voltage (V)	Dwell (sec)	Collision Energy (V)	Product Ion (m/z)	Retention Time (min)
AM	136.1	60	160	23, 13	91, 119	1.18
MA	150.1	70	160	29, 17	91, 119	1.33
MDA	180.1	60	160	15, 33	163.1, 105	1.30
MDMA	194.1	80	120	17, 35	163, 105.1	1.40
MOR	286.1	150	160	80, 80	152, 128	0.55

Results and Discussion

LC optimization

During LC optimization, one mix native standard solutions (containing all targeted native compounds at a concentration of 500 ng/mL) and one mix internal standards (IS, deuterated standards at 500 ng/mL) were prepared and analyzed. A longer LC column (Zorbax RRHD Eclipse Plus C18, 2.1 × 150mm, 1.8µm) was initially tested with the LC method used by Lai et al. [11]; however, not all of the target compounds were well retained. A shorter column with the same stationary phase (2.1 × 50mm, 1.8µm) was then chosen due to its good retention and separation capacity for the target compounds. Different injection volumes (1 and 3 µL) were tested. Results showed that injection volume of 1 µL gave the best peak shape for the compounds compared to 3 µL (Figure 2). As all the target compounds eluted within 0.2 to 2 minutes, the gradient of the mobile phase was then modified to shorten the total run time to 5 minutes. An example of a chromatogram of a spiked sample is shown in Figure 3.

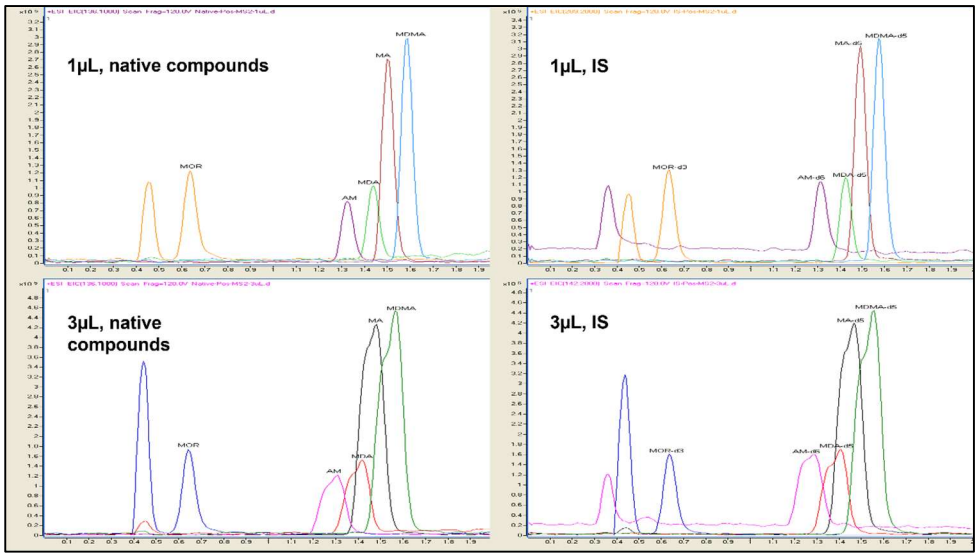


Figure 2. Chromatograms showing the peak shapes for different injection volumes

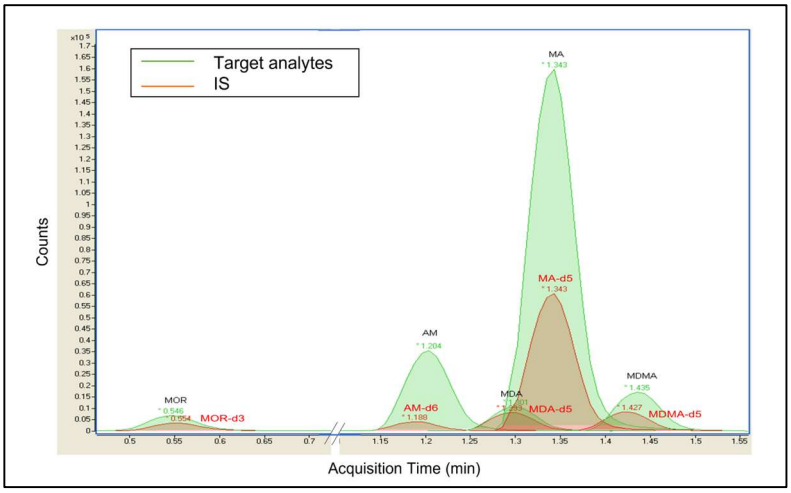


Figure 3. Typical LC-MS/MS chromatogram of a spiked sample

Method validation

The analytical method was validated in terms of linearity, recoveries, inter- and intra-day repeatability, and lower limit of quantification (LLOQ) according to the Bioanalytical Method Validation guidelines provided by the European Medicines Agency (EMEA) [12]. The method validation results were summarized in Table 2 and Table 3. The calibration curves were linear between 1 ng/mL and 250 ng/mL for AM and MA, 5 – 250 ng/mL for MDMA and MDA, and 10 – 250 ng/mL for MOR. The determination coefficients (R^2) for all calibration curves were higher than 0.99, except for MOR. The LOD and LLOQ were calculated based on the lowest concentration of standards with signal-to-noise ratio of 3 and 10, respectively. The mean recovery of spiked standards ranged between 91.6 and 112%, with the coefficient of variation (CV) between 2 and 19%, which was within the acceptable criteria of the EMEA guidelines. Target illicit drugs in all the procedural blanks were below LOD in all batches of extractions.

Table 2. Linear ranges, detection limits and calibration equations for the determination of illicit drugs

Drugs	Linear Range (ng/mL)	LOD (ng/mL)	LLOQ (ng/mL)	Calibration Equation	R^2
AM	1-250	0.29	0.95	y = 10.962427x -0.144109	0.9999
MA	1-250	0.37	1.22	y = 1.773839x + 0.029082	0.9999
MDA	5-250	0.86	2.86	y = 0.925804x + 0.026275	0.9999
MDMA	5-250	1.09	3.64	y = 1.361590x -0.021144	0.9997
MOR	10-250	7.56	25.2	y = 0.949434x + 0.031253	0.9494

Table 3. SPE-LCMS/MS method intra-day and inter-day precision at three spiking concentrations (low = 12.5 ng/mL, medium = 50 ng/mL, high = 100 ng/mL)

Drugs	Intra-day (n=3, 1 day) (mean ±SD) (CV) (%)			Inter-day (n=9, 3 days) (mean ±SD) (CV) (%)		
	Low	Medium	High	Low	Medium	High
AM	99.7±9.10 (9)	100 ±9.97 (10)	99.3±10.6 (11)	91.6±14.0 (15)	97.3 ±13.0 (13)	97.9±9.07 (9)
MA	97.5±17.5 (18)	111 ±6.27 (6)	107±11.1 (10)	98.3±15.1 (15)	106 ±13.0 (12)	105±14.7 (14)
MDA	101±18.8 (19)	97.6 ±5.62 (6)	96.3±12.2 (13)	94.1±18.1 (19)	109 ±10.2 (9)	108±15.8 (15)
MDMA	93.3±9.26 (8)	112 ±9.87 (9)	107±15.3 (14)	106±7.84 (9)	95.5 ±7.68 (8)	107±12.6 (12)
MOR	*	102 ±2.29 (2)	93.6±14.0 (15)	*	99.9 ±5.39 (5)	103±15.6 (15)

*: No data as spiking test for MOR was performed on 2 levels (50 and 100 ng/mL)

Sewage samples

The validated procedure was applied to 3 sewage samples collected from STPs in Kuantan. Results showed that AM, MA, and MDA were detected in all samples at concentrations ranging from 5.27 to 82.2 ng/L (Table 3). MDMA and MOR were below LOD in all sewage samples. This finding is consistent with the AADK official numbers, which show that ATS including AM, MA, MDMA and MDA, are the most commonly used illicit drugs in Malaysia [1]. The absence of MDMA in sewage samples could be explained by MDMA degradation in sewage [13-14]. The levels of AM, MA, MDA detected in this study were within the range of that reported by Du et al. [7] in 2 STPs at Kuala Lumpur. The absence of MOR in this study could indicate a different drug use patterns in different communities. However, due to the limited number of samples, the findings in this preliminary study require further research involving more communities.

Table 3. Concentrations (ng/L) of the target analytes in influent sewage from STPs in Kuantan

STP	Date of sampling	AM	MA	MDMA	MDA	MOR
STP-A	10/8/2021	5.28	82.2	ND	7.21	ND
STP-B	17/8/2021	10.1	423	ND	11.6	ND
STP-C	24/8/2021	11.7	443	ND	20.0	ND

ND: Below LOD

Conclusion

In this study, an analytical method based on SPE–LC-MS/MS was validated for the detection of five illicit drugs (AM, MA, MDA, MDMA and MOR) in municipal wastewater. Results from spiking test indicated satisfactory recoveries and good inter- and intraday repeatability. The validation demonstrates that the established analytical method is applicable for detecting the presence of illegal substances in STPs by providing good LODs, linearities, and recoveries. In the future, this analytical procedure will be applied in a large monitoring program in Kuantan, which aims at calculating the drug consumption from their concentrations in sewage.

Acknowledgement

The authors would like to thank the Ministry of Higher Education for providing financial support under Fundamental Research Grant Scheme (FRGS) No. FRGS FRGS/1/2019/STG01/UMP/02/5 (University reference RDU1901198) and Universiti Malaysia Pahang for laboratory facilities. Ms Nasihah Musa (Monash University Malaysia) is acknowledged for her help with the LC-MS/MS analysis. The staff of the Indah

Water Konsortium Sdn Bhd (IWK) Kuantan is gratefully acknowledged for their sampling support.

References

1. AADK (2020). Buku Maklumat Dadah 2020. https://www.adk.gov.my/buku-maklumat-dadah-2020/ [Access online 21 August 2022].
2. Subedi, B. and B. Loganathan (2016). Environmental emission of pharmaceuticals from wastewater treatment plants in the U.S.A, *in* persistent organic chemicals in the environment: status and trends in the Pacific basin countries II temporal trends. American Chemistry Society, Washington, DC: pp. 181-202.
3. Yargeau, V., Taylor, B., Li, H., Rodayan, A. and Metcalfe, C. D. (2014). Analysis of drugs of abuse in wastewater from two Canadian cities. *Science of the Total Environment* 487: 722-730.
4. Lai, F.Y., O'Brien, J., Bruno, R., Hall, W. Prichard, J., Kirkbride, P., Gartner, C., Thai, P., Carter, S., Lloyd, B., Burns, L. and Mueller, J. (2016). Spatial variations in the consumption of illicit stimulant drugs across Australia: A nationwide application of wastewater-based epidemiology. *Science of the Total Environment* 568: 810-818.
5. Asicioglu, F., Kuloglu Genc, M., Tekin Bulbul, T., Yayla, M., Simsek, S.Z., Adioren, C. and Mercan, S. (2021). Investigation of temporal illicit drugs, alcohol and tobacco trends in Istanbul city: Wastewater analysis of 14 treatment plants. *Water Research* 190: 116729.
6. Bannwarth, A., Morelato, M., Benaglia, L., Been, F., Esseiva, P., Delemont, O. and Roux, C. (2019). The use of wastewater analysis in forensic intelligence: drug consumption comparison between Sydney and different European cities. *Forensic Sciences Research* 4(2): 141-151.
7. Du, P., Liu, X., Zhong, G., Zhou, Z., Thomes, M.W., Lee, C.W., Bong, C.W., Zhang, X., Hao, F., Li, X., Zhang, G. and Thai, P.K. (2020). Monitoring consumption of common illicit drugs in Kuala Lumpur, Malaysia, by Wastewater-Cased Epidemiology. *International Journal of Environmental Research and Public Health*, 17(3): 889.
8. van Nuijs, A.L., Castiglioni, S., Tarcomnicu, I., Postigo, C., Lopez de Alda, M., Neels, H., Zuccato, E., Barcelo, D. and Covaci, A. (2011). Illicit drug consumption estimations derived from wastewater analysis: a critical review. *Science of the Total Environment* 409(19): 3564-3577.
9. Chiaia, A.C., C. Banta-Green, and J. Field. (2008). Eliminating solid phase extraction with large-volume injection LC/MS/MS: Analysis of illicit and legal drugs and human urine indicators in US wastewaters. *Environmental Science & Technology* 42: 8841-8848.
10. Kinyua, J., Covaci, A., Maho, W., McCall, A., Neels, H. and van Nuijs, A.L.N. (2015). Sewage-based epidemiology in monitoring the use of new psychoactive substances: Validation and application of an analytical method using LC-MS/MS. *Drug Testing and Analysis* **7**(9): 812-818.
11. Lai, F.Y., Ort, C., Gartner, C., Carter, S., Prichard, J., Kirkbride, P., Bruno, R., Hall, W., Eaglesham, G. and Mueller, J.F. (2011). Refining the estimation of illicit drug consumptions from wastewater analysis: co-analysis of prescription pharmaceuticals and uncertainty assessment. *Water Research,* 45(15): 4437-4448.
12. EMEA (2015). Guideline on bioanalytical method validation, in EMEA/CHMP/EWP/192217/2009 Rev. 1 Corr. 2**. Committee for Medicinal Products for Human Use (CHMP), European Medicines Agency (EMEA): London, UK.
13. Khan, U. and Nicell, J.A. (2011). Refined sewer epidemiology mass balances and their application to heroin, cocaine and ecstasy. *Environment International* 37(7): 1236-1252.
14. Choi, P.M., Tscharke, B.J., O'Brien, J.W., Grant, S.C., Kaserzon, S.L., Mackie, R., O'Malley, E., Crosbie, N.D., Thomas, K.V. and Mueller, J.F. (2018). Wastewater-based epidemiology biomarkers: Past, present and future. *Trends in Analytical Chemistry* 105: 453-469.

Malaysian Journal of Analytical Sciences (MJAS)
Published by Malaysian Analytical Sciences Society

CHARACTERIZATION OF *Anadara granosa* AS A POTENTIAL SOURCE OF CALCIUM CARBONATE FOR GLASS IONOMER CEMENT FORMULATION

(Pencirian *Anadara granosa* Sebagai Sumber Kalsium Karbonat yang Berpotensi untuk Formulasi Simen Kaca Ionomer)

Nur'Izzah Md Nasir, Norhazlin Zainuddin*, and Francis Thoo Voon Wai

Department of Chemistry, Faculty of Science,
Universiti Putra Malaysia, 43400 Serdang, Selangor, Malaysia

**Corresponding author: norhazlin@upm.edu.my*

Received: 6 October 2022; Accepted: 18 December 2022; Published: 22 February 2023

Abstract

Glass ionomer cements (GIC) are produced via acid-base reaction between calcium fluoroaluminosilicate glass powders and freeze-dried polyacrylic acid powder. Shells from *Anadara granosa* or commonly known as cockle, consist of >90% calcium carbonate ($CaCO_3$), have been utilized as the source of $CaCO_3$ by incorporating it as part of glass components for production of GIC. The main objective of this research is to investigate the effect of *Anadara granosa* shells in setting reaction of GIC using FT-IR spectroscopy. Two types of GIC were synthesized, GIC-A (analytical grade $CaCO_3$) and GIC-B (replacing $CaCO_3$ with the shells). FT-IR spectra showed the setting reaction for both GICs with the occurrence of cross-linking between polyacrylate chain and metal ion from the glass by gradual conversion of COOH at 1690-1700 cm^{-1} into COO^-M^{n+} at 1550-1600 cm^{-1}. For compressive strength, GIC-B showed a lower compressive strength compared to GIC-A at 1-day aging time. However, it reached similar value as GIC-A after 28 days aging time. In conclusion, *Anadara granosa* shells can be utilized for Ca aluminosilicate glass in GIC production where it exhibited similar setting properties and compressive strength as GIC from glass synthesized using commercial $CaCO_3$.

Keywords: *Anadara granosa*, glass ionomer cement, calcium carbonate, calcium fluoroaluminosilicate

Abstrak

Simen kaca ionomer (GIC) dihasilkan melalui tindak balas asid-bes di antara serbuk kaca kalsium fluoroaluminosilikat dan serbuk asid poliakrilik kering sejuk beku. Cengkerang dari *Anadara granosa* atau kebiasaannya dikenali sebagai kerang ini mengandungi >90% kalsium karbonat ($CaCO_3$), telah dimanfaatkan sebagai sumber kalsium karbonat dengan menggabungkannya sebagai sebahagian daripada komponen kaca untuk menghasilkan GIC. Objektif utama kajian ini adalah untuk menyiasat kesan cengkerang *Andara granosa* dalam tindak balas pengerasan GIC menggunakan spektroskopi FT-IR. Dua jenis GIC telah disintesis, GIC-A ($CaCO_3$ gred analisis) dan GIC-B (menggantikan $CaCO_3$ dengan cengkerang). Spektrum FT-IR menunjukkan bahawa tindak balas pengerasan bagi kedua-dua GIC berlaku dengan kehadiran rangkai silang antara rantai poliakrilat dan ion logam daripada kaca dengan pertukaran COOH secara beransur-ansur pada 1690-1700 cm^{-1} kepada COO^-M^{n+} pada 1550-1600 cm^{-1}. Untuk kekuatan mampatan, GIC-B menunjukkan kekuatan mampatan yang lebih rendah berbanding GIC-A pada masa penuaan 1 hari, namun, ia mencapai nilai yang sama seperti GIC-A selepas masa penuaan 28 hari. Kesimpulannya, cengkerang *Anadara granosa* boleh

digunakan untuk kaca Ca aluminosilikat dalam penghasilan GIC di mana ia mempamerkan sifat pengerasan dan kekuatan mampatan yang sama seperti GIC daripada kaca yang disintesis menggunakan $CaCO_3$ komersial.

Kata kunci: *Anadara granosa*, simen kaca ionomer, kalsium karbonat, kalsium floroaluminosilikat

Introduction

Blood cockle is a bivalve marine mollusc from the species *Anadara granosa* which is mostly used as a source of protein-rich food. Countries such as Malaysia, Indonesia, and Thailand are known for their extensive cockle industry [1]. The production of cockle in Malaysia is great and keeps increasing year by year. However, the shells are treated as waste with an unpleasant smell and are often just dumped in landfill or the sea [2-3]. From early 2000 until now, studies on seashells as a source of calcium carbonate, $CaCO_3$ are widely explored, especially in the medical field such as for bone and dental applications [4-11]. $CaCO_3$ in cockle shell consists of three polymorphs known as calcite, aragonite, and vaterite. Researchers are more interested in aragonite polymorph due to its biocompatible properties [12]. Aragonite has osteoregenerative potential and can be used for bone substitution [13]. On the other hand, calcite has good thermodynamic stability. Calcite nanoparticle is considered as an extremely effective material in biomedical due to their shape, non-toxic properties, and it is also easily metabolized by all cells. Calcite with nanostructure could supply calcium sources to retain Ca ions in the supersaturation state in the enamel minerals. Hence, calcite has great potential in preventing tooth erosion thereby it could be used for dental hypersensitive treatment [14]. While vaterite, less commonly occurs in nature because it is the least thermodynamically stable polymorph. Vaterite can rapidly transform into calcite and aragonite in an aqueous solution [15].

In dental applications, calcium hydroxide has been considered the gold standard for pulp capping materials for decades to stimulate the formation of tertiary dentin. Blood cockle shells are expected to be an alternative pulp protective material for initiating dentin tissue deposition so that the healing process can occur by the formation of reactionary dentin [16]. The cockle shell is also claimed to have anti-inflammatory properties as well as good stability due to calcite polymorph [17]. Researchers have also prepared zirconia stabilized by CaO known as calcia-doped zirconia using CaO derived from cockle shells for dental application [18]. The study was done by comparing the CaO from cockle shells with the commercial CaO and the research concluded that the calcia-doped zirconia with the CaO derived from cockle shells may be used as an alternative to the current zirconia available in the market for dental application due to its physical and mechanical properties. Apart from that, their flexural and compressive strength are also comparable with the commercial type. Cockle shell is also being studied as hydroxyapatite paste as a remineralization agent, to which the result showed that it can increase tooth enamel surface hardness with nearly the same effect as CPP-ACP (commercial GC Tooth Mousse®) paste [19]. Another study has applied CaO in the glass formulation derived from clamshell for the production of glass ionomer cement, GIC. The physical and mechanical properties of GIC derived from soda lime glass and clamshell improved with the addition of hydroxyapatite [20].

Even though studies using clamshell as $CaCO_3$ source in GIC had been done previously, the studies only focused on the influence of hydroxyapatite existence. In this study, the GIC was prepared using Ca aluminosilicate glass derived from cockle shell and the setting reaction was thoroughly investigated using FT-IR spectroscopy. A comparison study with a similar formulation of glass ionomer using analytical grade $CaCO_3$ was done to determine the suitability of the cockle shell as the $CaCO_3$ source in the synthesis of GIC for dental application.

Materials and Methods

Materials

Silicon dioxide, SiO_2 and calcium fluoride, CaF_2 were purchased from Sigma-Aldrich Co., US. Aluminium oxide, Al_2O_3, and calcium carbonate, $CaCO_3$ were purchased from Fisher Scientific, US, and phosphorus pentoxide, P_2O_5 from Acros Organics, US. All chemicals were analytical-grade reagents with more than 99% purity. *Anadara granosa* shells were obtained

from a fresh market at Lumut, Perak, Malaysia. These cockle shells were used as an alternative source to $CaCO_3$. A medical-grade freeze-dried poly(acrylic acid) was supplied by Advance Healthcare, Kent, England with a molecular weight of ~30,000. Throughout the experiment, analytical-grade ethanol was used to dehydrate the cement. In addition, liquid nitrogen was employed to terminate the setting reaction in GICs.

Preparation of *Anadara granosa* shells powder

Anadara granosa shells were washed thoroughly and immersed in water to remove surface impurities. The shells were then dried in an oven at 110 ℃. Heat treatment was applied to the shells at 400 ℃ for 2 hours. The shells were then crushed using stainless steel pounder and ball mill for 24 hours. After that, the ground shells were sieved to less than 45 µm particle size.

Preparation of glasses

Two Ca aluminosilicate glasses, glass GIC-A (analytical grade $CaCO_3$) and GIC-B ($CaCO_3$ from *Anadara granosa* shells), with similar formulations were synthesized. Weight percentages of each composition were 16.60% alumina, 16.91% calcium oxide, 37.57% silica, 16.68% phosphorus pentoxide, and 12.24% calcium fluoride. All chemical compositions (SiO_2, Al_2O_3, $CaCO_3$, and CaF_2) were homogenized by using a ball mill unit for 6 hours before melting. Phosphorous pentoxide was only added to the mixture just before the melting process to avoid hydration as it is a highly hygroscopic material. Approximately 30 g of the mixture in an alumina crucible was melted in a furnace at 1500 ℃ for 2 hours. The molten mixture was poured immediately into the water for shock quenching to produce non-crystallized glass frits. The glass obtained was air-dried before placing it in an oven for overnight drying at 37 ℃. It was then ground by dry milling in a rotary ball mill and sieved to ≤45 µm particle size.

Preparation of glass ionomer cement (GIC)

The preparation of GIC was done according to ISO 9917-1:2007 Dentistry Water Based Cements Part 1: Powder/liquid acid-base cements 2007 [21]. The glass powder was mixed with freeze-dried poly (acrylic acid), PAA and distilled water on a glass slab using a stainless-steel spatula in a weight ratio of 3:1:1. The GIC was then inserted into a cylinder mold with a dimension of 4.0 mm x 6.0 mm. Then, the GIC together with the mold was placed in an incubator at 37 ℃ for 1 hour. After that, the samples were transferred into containers with deionized water and left for a certain period according to their aging times studied. The aging time was from 5 minutes to 28 days. Liquid nitrogen and ethanol were applied to the GICs with aging time of less than 1 hour to terminate the setting reaction by dehydrating the GIC.

Setting reaction study of GIC

The setting reaction of GIC was studied at several time intervals: 5 minutes, 15 minutes, 30 minutes, 1 hour, 6 hours, 1 day, 7 days, and 28 days. Samples with time intervals ranging from 5 minutes to 1 hour were set in an incubator at 37°. GICs with aging time of more than 1 hour were placed in the incubator at 37 °C for 1 hour then it was transferred into a sample bottle containing deionized water and kept in the incubator for the remaining aging period. For GICs less than 1 hour of aging time, liquid nitrogen and ethanol were used to terminate the reaction and dehydrate the GICs. The GICs were then ground to a fine powder for the FT-IR analysis.

Characterizations of *Anadara granosa* and GIC

The *Anadara granosa* shell was characterized by energy dispersive x-ray (EDX), thermogravimetric analysis (TGA), and X-ray diffraction (XRD), while GIC samples were characterized using Fourier transform infrared spectroscopy (FT-IR), and compressive strength test.

Energy dispersive X-ray

Elemental analyses of *Anadara granosa* shells in powder form were determined using an energy dispersive X-ray analyzer (FEI-Quanta 200, The Netherlands) directly linked to a scanning electron microscopy, SEM operated with environmental mode at 15 kV and relative humidity of 96%- 99%.

X-ray diffraction

XRD is a non-destructive technique for qualitative analysis. XRD was used to compare the XRD pattern of *Anadara granosa* shells with the analytical grade $CaCO_3$. The analysis was conducted from 4° to 90° by

using a 2θ goniometer X-ray powder diffractometer (PANalytical X'pert-Pro MPD PW 3040), operated at Cu-K α radiation (λ = 0, 15406 nm). The diffractogram was scanned at a scan rate of 2° min^{-1}.

Thermogravimetric analysis

Thermogravimetric analysis (TGA) was used to analyze the thermal decomposition of *Anadara granosa* shells by using Metter-Toledo thermogravimetric analyzer. Shell in powder form with particle size ≤45 μm was placed in a 40 μl alumina crucible and subjected to heating in the range of 25 to 1000 ℃ at 10 °C/min under the flow of nitrogen gas at 50 ml/min.

Fourier transform infrared (FT-IR) spectroscopy

FT-IR Spectroscopy is a non-destructive method for both qualitative and quantitative analysis. In this study, FT-IR was used to study the setting reaction of GIC from aging time of 5 minutes to 28 days. Perkin- Elmer FT-IR spectrometer coupled with UATR accessory was used to record FT-IR transmittance spectra. Approximately 0.001 g of sample was used and scanned within the wavenumber of 280 cm^{-1} to 4000 cm^{-1}.

Compressive strength test of GIC

Compressive strength of the GIC was done according to ISO7489:1986 specifications [22, 23] with the dimension of 6.0mm × 4.0mm cylindrical-shaped cement. GIC samples were tested at 1, 7, and 28 days. The test was performed using Instron 4082 Universal Testing Machine with a 1kN load cell at a crosshead of 1mm/min until the cement fractured. Five specimens of each GIC were tested. The mean compressive strength and standard deviation of GIC were calculated.

Results and Discussion

Energy dispersive X-ray (EDX) of *Anadara granosa* shell

Table 1. shows the weight percentage of the composition of *Anadara granosa* shell. It was found that the major component of the shell was $CaCO_3$ with the presence of a small amount of other metal oxides such as Na_2O, Al_2O_3 and SiO_2. The presence of a small amount of sodium oxide may come from the sodium content of seawater during the *Anadara granosa* growth in the sea [9]. The percentage of $CaCO_3$ in *Anadara granosa* powder was 97.53%. Other oxides were all detected in very small amounts in the sample. Moreover, the result in this study is in good agreement with the findings of previous studies. Previous studies in Malaysia reported that *Anadara granosa* shells were composed of 98.7% $CaCO_3$, 0.05% Mg, 0.9% Na, 0.02% P and 0.2% of other elements (Fe, Cu, Ni, Zn, B, and Si) [24, 25].

Table 1. The weight percentage of *Anadara granosa* shell

Composition	Percentage in Weight (%)
Na_2O	0.73
$CaCO_3$	97.53
Al_2O_3	1.76
SiO_2	0.07

X-ray diffraction analysis

XRD analysis shows that *Anadara granosa* shell exhibited similar XRD patterns as analytical grade calcium carbonate as shown in Figure 1. The diffraction lines for *Anadara granosa* shells were well matched with pure analytical grade $CaCO_3$ and thus indicates that it is suitable to be utilized as a source of CaO in the synthesis of Ca aluminosilicate glass.

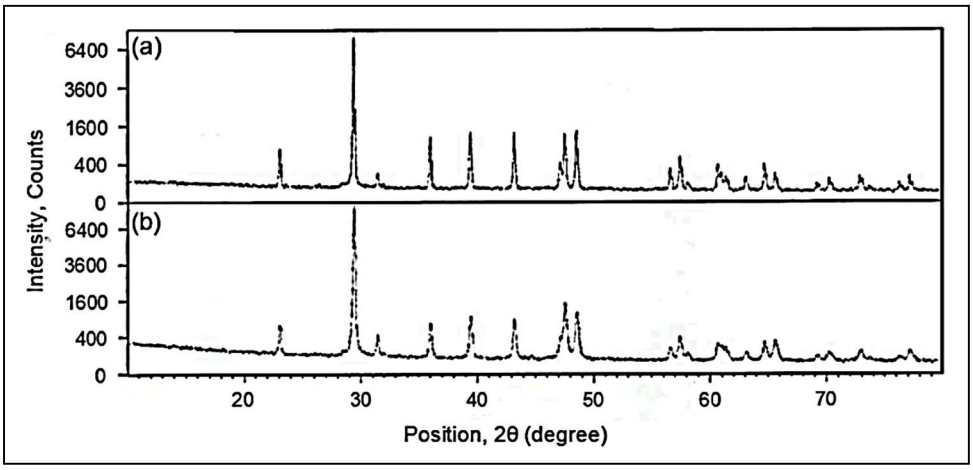


Figure 1. XRD pattern for (a) analytical grade $CaCO_3$; (b) *Anadara granosa* shells powder

Thermogravimetric analysis

From XRD analysis, it is found that the main component of *Anadara granosa* shell is $CaCO_3$. Generally, $CaCO_3$ will undergo thermal decomposition when the heating temperature is more than 550 ℃. In this experiment, the *Anadara granosa* shell was heated up to 1000 ℃, hence the calcium carbonate in *Anadara granosa* shell was expected to decompose to calcium oxide eventually.

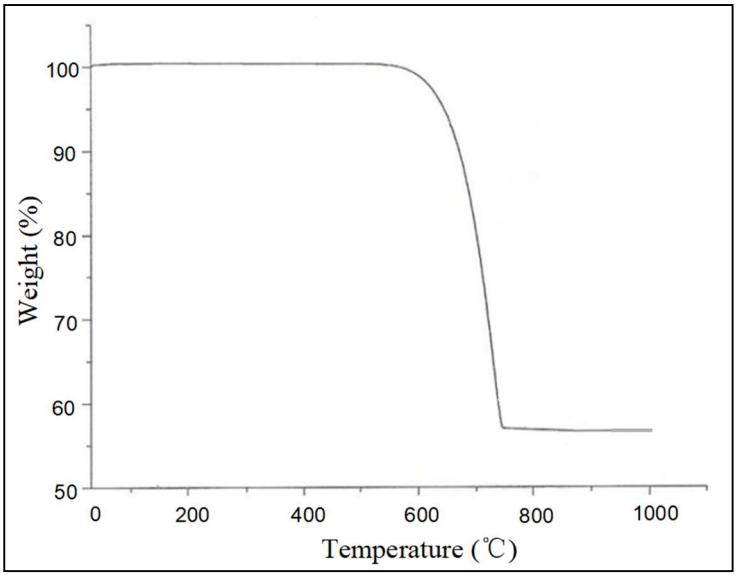


Figure 2. TGA decomposition graph of *Anadara granosa* shell

Based on the thermal decomposition curve in Figure 2, single-stage decomposition with an onset decomposition temperature of 508.6 ℃ was observed. The single decomposition step suggested calcium carbonate only undergoes a reaction in which bound carbon dioxide was released upon heating. At 508.6 ℃, calcium carbonate in *Anadara granosa* shells started to decompose and evolve into carbon dioxide. The offset temperature of 768.3 ℃ indicated the ending of the decomposition process and calcium oxide together with trace metals constituted the residue.

The process of decomposition of $CaCO_3$ to CaO can be presented using the equation shown below:

$$CaCO_3(s) \longrightarrow CaO(s) + CO_2(g) \quad \text{(eq. 1)}$$

Based on the equation, it shows that 1 mol of $CaCO_3$ will produce 1 mol of CaO. The percentage of calcium carbonate in *Anadara granosa* shells can be calculated as below:

$$Percentage(\%)\ of\ CaCO_3\ in\ Anadara\ granosa = \frac{CO_2\ weight\ loss}{Mr\ CO_2} \times \frac{Mr\ CaCO_3}{Mass\ of\ Anadara\ granosa} \quad \text{(eq. 2)}$$

Based on the formula above, 98.68% of calcium carbonate was found in *Anadara granosa*. This result agrees with the percentage of $CaCO_3$ obtained from the EDX analysis. According to a previous study, the total mineral content of cockle shells in west coast Malaysia comprises 98.7% of calcium carbonate and an insignificant amount of trace metals [24]. A high percentage of calcium carbonate in the shells suggested that it is suitable to be utilized as a source of calcium carbonate for the synthesis of Ca aluminosilicate glass.

Setting reaction of GIC-A and GIC-B by using FT-IR spectroscopy

The setting reaction of GIC-A and GIC-B were studied by using FT-IR spectroscopy. Generally, setting reaction in GIC involves the formation of metal polyacrylate and silica gel repolymerization. Figure 3 shows the FT-IR spectra of GIC-A (analytical grade $CaCO_3$), and GIC-B ($CaCO_3$ from shells) in the range of 2000 cm^{-1} to 600 cm^{-1} for setting time from 5 minutes to 28 days. Both GICs show similar trends in FT-IR spectra.

The formation of metal polyacrylate takes place between carboxylic part (-COOH) of polyacrylic acid with metal ions such Al^{3+} and Ca^{2+} from the glass particle. This reaction is known as cross-linking reaction and produced COO^-M^{n+} species in the GIC. In FT-IR spectroscopy, COO^-M^{n+} is assigned as asymmetric vibration of $(COO^-)Ca^{2+}$ and $(COO^-)Al^{3+}$ with respect to Ca^{2+} and Al^{3+} present in the glass [26]. From Figure 3, the absorption band of COOH at wavenumber 1730 cm^{-1} is observed at 5 minutes aging time and at the same aging time, a shoulder peak corresponds to the cross-linking absorption band, COO^-M^{n+} at wavenumber 1620 cm^{-1} also appeared. As the aging time increased, the absorption band of COOH began to disappear and the intensity of the COO^-M^{n+} band increased. The disappearance of COOH band is due to the cross-linking between the PAA and the glass proceeds to a higher extent with aging time. It is also found that the absorption bands of COOH group for GIC-A and GIC-B slightly shifted to lower wavenumbers from 1745 to 1720 cm^{-1}.

As the aging time increased from 5 minutes to 28 days, the intensity of the absorption band of COOH decreased while COO^-M^{n+} absorption band increased gradually. This suggests that the cross-linking of carboxylate group, COO^- by metal cations occurred to a greater extent and corresponded to progressive proton removal from carboxyl groups. At 28 days of aging time, there was still a shoulder band at 1700 cm^{-1} corresponding to the unreacted COOH of PAA. COOH group of PAA did not undergo complete ionization as PAA is generally a weak acid. Furthermore, the remaining protons were strongly attracted by electrostatic forces due to greater ionization of polyacrylate chains as setting reaction continued. Due to strong binding forces, protons on the unionized COOH group were hard to be replaced by metal cations for cross-linking [26].

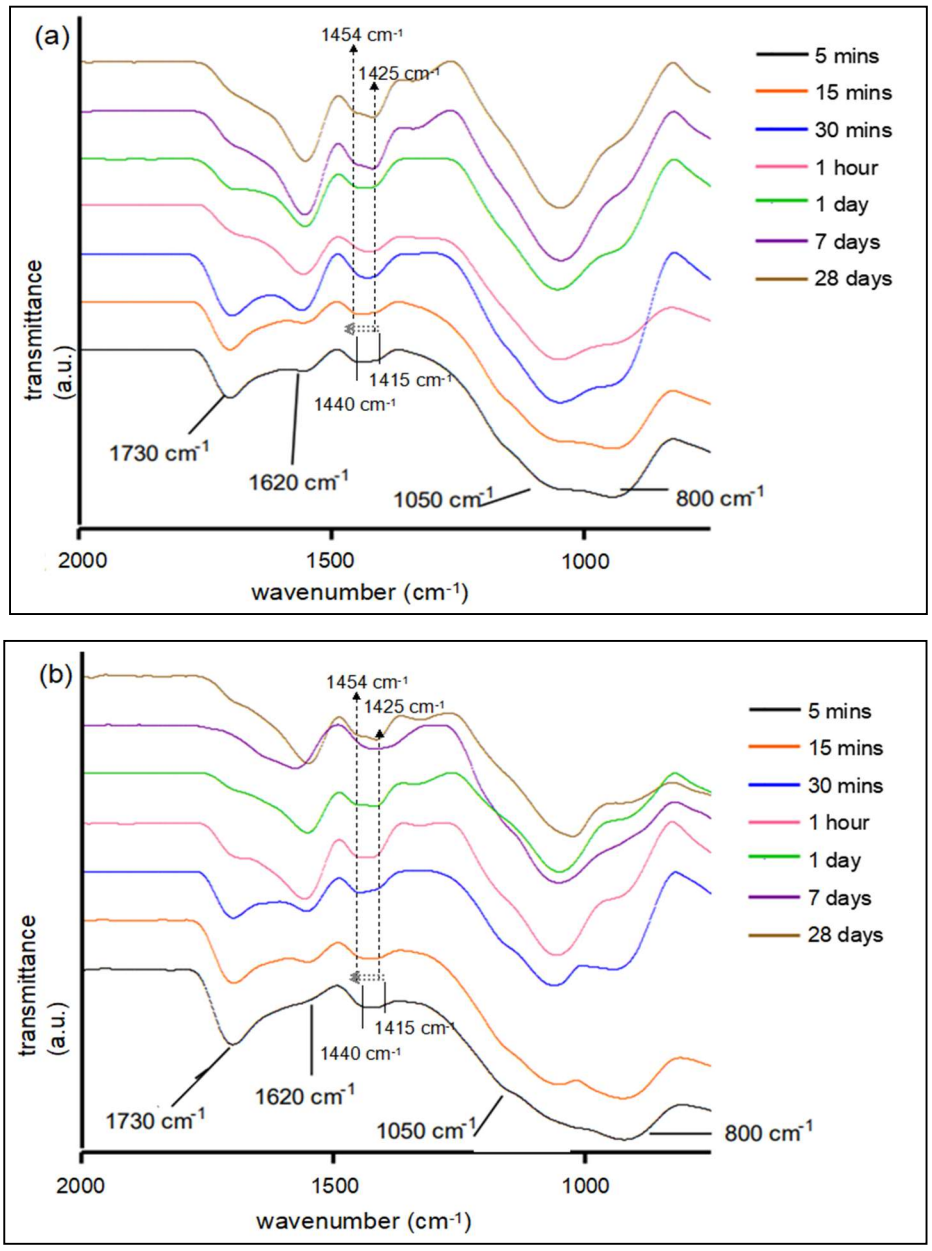


Figure 3. FTIR spectra for (a) GIC-A and (b) GIC-B from 5 minutes to 28 days aging time.

Another reaction in the setting of GIC is repolymerization of silica network of the glass. FT-IR spectra showed changes in the region of 1200 to 800 cm^{-1} which corresponded to the changes from Si-OH (800 cm^{-1}) to Si-O-Si (1050 cm^{-1}). At the early aging time, Si-O-H band from the formation of silica gel was easily observed as compared to Si-O-Si band which remained obscure. This is in line with the setting mechanism which suggests that the proton ionized from COOH group of PAA had displaced metal cations in the silicate network and formed Si-O-H. At a later setting reaction, an absorption band with a shoulder corresponding to Si-O-Si gradually appeared. Meanwhile, the diminishing absorption band of Si-O-H was observed. Next, two weak bands were observed at 1440 cm^{-1} and 1415 cm^{-1} associated with scissors and bending vibrations of $-CH_2$ and -CH-C=O groups respectively. Both bands were slightly shifted to a higher wavenumber from 1440 cm^{-1}

to 1454 cm^{-1} for $-CH_2$ and from 1415 cm^{-1} to 1425 cm^{-1} for CH-C=O. This may be due to the cross-linking reaction where the angle of CH-C=O bonding was altered for calcium ion and aluminum ion to cross-link with the polyacrylic acid on the surface of the glass. This interaction caused the $-CH_2$ bond near the CH-C=O to vibrate and altered the position of $-CH_2$ bending [27]. Due to the higher energy needed to vibrate these species, the absorption bands shifted slightly higher wavenumber in the cement. In conclusion, the study of setting reaction of GICs by using FT-IR spectroscopy indicates that the setting mechanism involves both cross-linking reaction and silica gel repolymerization occur concurrently.

Degree of cross-linking (DCL)

Cross-linking of PAA by metal cations resulted in the formation of cement matrix due to gelation of PAA. The degree of cross-linking (DCL) was calculated according to a previous study by Matsuya et al. [29] using FT-IR spectroscopy. The DCL between polyacids chains was calculated from the formula:

$$\mathrm{DCL} = \frac{Abs(COO^{-}M^{n+})}{Abs(COOH) + Abs(COO^{-}M^{+})} \qquad \text{(eq. 3)}$$

where Abs refer to FTIR absorbance with respect to specific wavenumber.

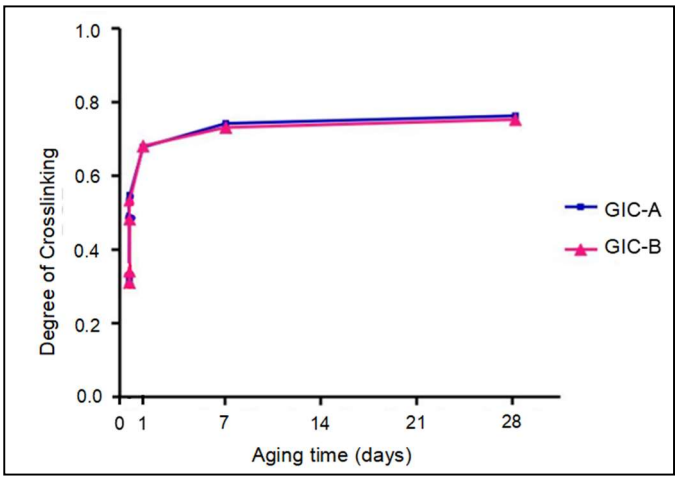


Figure 4. Degree of cross-linking for GIC-A and GIC-B

Figure 4 shows the rapid increment of DCL value within 1 hour followed by gradual increment up to 28 days for both GIC-A and GIC-B. A similar finding was reported previously by Matsuya et al. [29]. The DCL value for GIC-A and GIC-B increased drastically within 1 hour of aging time with DCL values of 0.5473 and 0.5344, respectively. The increase in DCL suggests that a greater extent of the cross-linking reaction occurred between polyacrylate chains and metal cations from the glass. This finding also suggests that there is a high amount of metal cations released during glass degradation where these metal cations then cross-link with the polyacrylate chain. There was only a slight increment in DCL values for longer aging time (7 to 28 days) from 0.7426 to 0.7631 for GIC-A and 0.7316 to 0.7528 for GIC-B. The fact that the DCL still increased up to 28 days suggests that the cross-linking reaction continues with time after the initial setting [30]. This is probably caused by continuous release of ions from the glass and the change in conformation of PAA [31,32]. Change in PAA chain conformation provided accessibility for cross-linking sites at carboxylate group. Previous study by Cattani-

Lorente et al. [33] suggested slow additional cross-linking to be another factor other than the role of silica gel phase which contributed to the strengthening of cement.

In addition, as the setting reaction proceeded, the polyacrylate matrix became rigid and highly viscous which rendered free carboxylic groups from forming ionic bonding with metal cations [27]. Therefore, the intensity of FT-IR absorption bands for COOH and COO^-M^{n+} and DCL values for both cement types were not significantly changed. In conclusion, the setting study of GIC-B which was produced from the *Anadara granosa* shell showed a similar setting mechanism as GIC-A from analytical grade $CaCO_3$.

Compressive strength of GIC

The effect of maturation of cement was examined on compressive strength for GIC-A and GIC-B. Previous studies had reported maturation of cement which involved additional cross-linking between polyacrylate matrices [31, 33]. A minimum aging time of 24 hours is needed as GICs are weak and sensitive to desiccation and moisture contamination at the early setting stage. Loss of water will cause shrinking and crazing of cement surface while hydration will result in the leaching of matrix-forming ions upon disintegration. Figure 5 shows the mean values (MPa) and standard deviations obtained for the compressive strength of GIC-A and GIC-B from 1 day to 28 days of aging time.

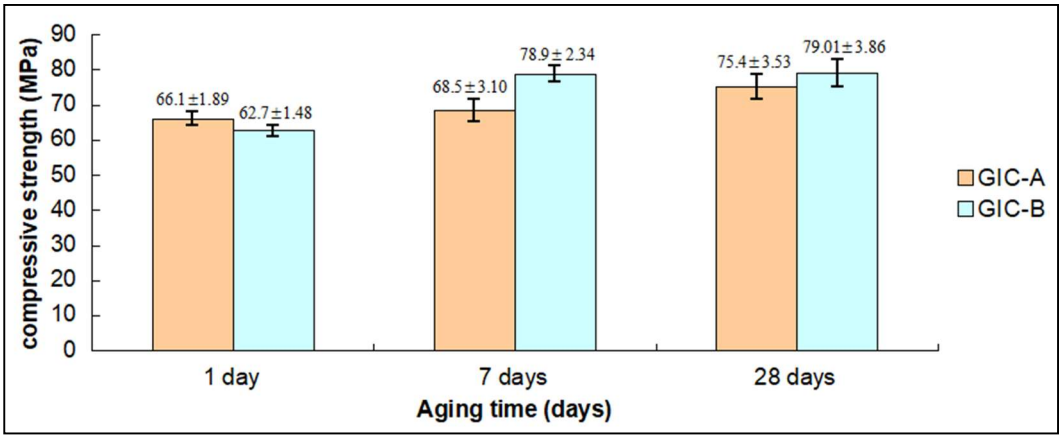


Figure 5. Compressive strength of GIC-A and GIC-B cements at 1 day to 28 days aging time

Figure 5 shows that at 1 day of aging time, GIC-B exhibited slightly lower compressive strength than GIC-A with the value of 62.7 MPa and 66.1 MPa, respectively. The lower compressive strength of GIC-B than GIC-A at 1-day aging time may be due to the presence of sodium in *Anadara granosa* shell in the glass. Lohbauer [34] stated that the incorporation of sodium into glass resulted in an adverse effect on solubility, hydrolytic stability, and mechanical properties of the set cement. The high mobility of sodium in silicate glass increased its tendency to be released from the glass and readily exchanged with protons during the setting reaction [35]. Since sodium was not strongly bound to carboxylate group as COO^-Na^+ hence, it was ionized readily into the aqueous phase.

When aging time increased from 1 day to 7 days, there was an increase in the compressive strength for GIC-B from 62.7 MPa to 78.9 MPa. Previous studies stated that commonly GIC does not reach its maximum strength at 24 hours after setting reaction [36]. For both GICs, the compressive strength increased slightly from 7 days dan 28 days of aging time which is consistent with the findings from FT-IR spectra (Figure 3) as well as DCL (Figure 4). Based on Figure 5, both GICs exhibited almost similar compressive strength at 28 aging time with a value in the range of 75.0 - 79.0 MPa.

Conclusion

In this study, the high percentage of $CaCO_3$ in *Anadara granosa* shells indicates that they can be used as a source of $CaCO_3$ in dental glass. The setting reaction and

compressive strength of GIC made from *Anadara granosa* shells show similar results as GIC from analytical grade $CaCO_3$. Therefore, this study has revealed the potential of *Anadara granosa* shells for dental cement formulation.

Acknowledgments

The authors are grateful for the financial support from the Ministry of Higher Education (MOHE), Malaysia (Fundamental Research Grant Scheme FRGS/1/2013/SG06/UPM/02/2), and the Chemistry Department, Faculty of Science, UPM for the equipment and laboratory.

References

1. Jaji, A.Z., Md Zuki, A.B.Z., Mahmud, R., Yusof, M.L., Mohamad, M.N.H., Isa, T., Fu., W. and Hammadi, N.I. (2017). Synthesis, characterization, and cytocompatibility of potential cockle shell aragonite nanocrystals for osteoporosis therapy and hormonal delivery. *Nanotechnology, Science and Applications,* 10: 23-33.
2. Fu, W., Mohd Noor, M. H., Mohamad Yusof, L., Tengku Ibrahim, T. A., Keong, Y. S., Jaji, A. Z. and Abu Bakar Zakaria, M. Z. (2017). In vitro evaluation of a novel pH-sensitive drug delivery system-based cockle shell-derived aragonite nanoparticles against osteosarcoma. *Journal of Experimental Nanoscience,* 12: 166-187.
3. Summa D., Lanzoni, M., Castaldelli, G., Fano, E. A., & Tamburini, E. (2022). Review: Trends and opportunities of bivalve shells' waste valorization in a prospect of circular blue bioeconomy. *Resources*, 11(48); 1-16
4. Yang, E. I., Yi, S. T., and Leem, Y. M. (2005). Effect of oyster shell substituted for fine aggregate on concrete characteristics: Part I. Fundamental properties. *Cement and Concrete Research,* 35(11): 2175-2182.
5. Ballester, P., Mármol, I., Morales, J., and Sánchez, L. (2007). Use of limestone obtained from waste of the mussel cannery industry for the production of mortars. *Cement and Concrete Research*, 37(4): 559-564.
6. Mohamed, M., Yusup, S., and Maitra, S. (2012). Decomposition study of calcium carbonate in cockle shell. *Journal of Engineering Science and Technology,* 7(1): 1-10.
7. Asmi, D., and Zulfia, A. (2017). blood cockle shells waste as renewable source for the production of biogenic $CaCO_3$ and its characterisation. *IOP Conference Series: Earth and Environmental Science*, 94: 012049.
8. Ghafar, M. S. L., Hussein, M. Z., Rukayadi, Y. and Zakaria, M. Z. A. B. (2017). Synthesis and characterization of cockle shell-based calcium carbonate aragonite polymorph nanoparticles with surface functionalization. *Journal of Nanoparticle*, 2017: 1-12.
9. Mailafiya, M. M.,Abubakar, K., Danmaigoro, A., Chiroma, S. M., Abdul Rahim,E. Mohd Moklas, M. A. and Zakaria, Z. A. B. (2019). Review: Cockle shell-derived calcium carbonate (aragonite) nanoparticles: A dynamite to nanomedicine. *Applied Science*, 9(2897): 1-25.
10. Sainudin, M. S., Othman, N. H., Ismail, N. N., Wan Ibrahim, M. H. and Rahim, M. A. (2020). Utilization of cockle shell (*Anadara granosa*) powder as partial replacement of fine aggregates in cement brick. *The International Journal of Integrated Engineering,* 12(9): 161-168.
11. Syafwandi, and Cerra, R. A. (2021). The effect of substitution of coarse and fine aggregates with shells of blood clams and cement with fly ash and the additional of superplasticizer against the compressive test. *International Journal of Transportation and Infrastucture,* 4(2): 148-156.
12. Chen, J. and Xiang, L. (2009). Controllable synthesis of calcium carbonate polymorphs at different temperatures. *Powder Technology*, 189(1): 64-69.
13. Akilal, N., Lemaire, F., Bercu, N. B., Sayen, S., Gangloff, S. C., Khelfaoui, Y., Rammal, H., Kerdjoudj, H. (2019). Cowries derived aragonite as raw biomaterials for bone regenerative medicine. *Materials Science and Engineering: C,* 94: 894-900.
14. Tram, N. X. T., (2020). Synthesis and characterization of calcite nano-particle derived from cockle shell for clinical application. *ASEAN Engineering Journal,* 10(1): 49-54.

15. Ni, M., and Ratner, B. D. (2008). Differentiation of calcium carbonate polymorphs by surface analysis techniques – an XPS and TOF-SIMS study. *Surface and Interface Analysis,* 40(10): 1356-1361.
16. Praja, H. A., Dhaniar, N., Santoso, R. M., Putri, D., Annisa Salsabila A. P., Veda Sahasika A. N., Soetojo, A. and Saraswati, W. (2022) Calcium carbonate of blood cockle (*Anadara granosa*) shells induced VEGF-A expression in dentin pulp complex an in vivo study. *Malaysian Journal of Medicine and Health Sciences,* 18(SUPP6): 24-30.
17. Al Omari, M. M. H., Rashid, I. S., Qinna, N. A., Jaber, A. M. and Badwan, A. A. (2016). Chapter 2: Calcium carbonate. Book title: Profiles of drug substances, excipients, and related methodology. Elsevier, 41: pp 2-445.
18. Hussein, A. I., Che Mat, A. N., Abd Wahab, N. A. A., Rahman, Husein, A. and Ab-Ghani, Z. (2020). Synthesis and properties of novel calcia-stabilized zirconia (Ca-SZ) with nano calcium oxide derived from cockle shells and commercial source for dental application. *Applied Science*, 10(5751): 1-13.
19. Nugroho, J. J., Natsir, N., Trilaksana, A. C., Rovani, C. A., and Atlanta, M. M. (2019). The increase of tooth enamel surface hardness after application blood cockle shells (*Anadara granosa*) paste as remineralization agent. *International Journal of Applied Pharmaceutics,* 11(4): 26-29.
20. Wan Jusoh, W. N., Matori, K. A., Mohd Zaid, M. H., Zainuddin, N., Ahmad Khiri, M. Z., Abdul Rahman, N. A., Abdul Jalil, R. and Kul, E. (2021). Incorporation of hydroxyapatite into glass ionomer cement (GIC) formulated based on alumino-silicate-fluoride glass ceramics from waste materials. *Materials,* 14(954): 1-14.
21. International Organization for Stadardization (2007). Dentistry-water-based cements Part 1: Powder/liquid acid-base cements (ISO 9917-1:2007). Retrieved from https://www.iso.org/standard/ 45818.html
22. Genebra (1986). International organization for standardization. ISO7489. Dental glass polyalkenoate cements.
23. Mallmann, A., Ataíde, J. C. O., Amoedo, R., Rocha, P. V. and Jacques, L. B. (2007). Compressive strength of glass ionomer cements using different specimen dimensions. *Brazillian Oral Restorative,* 21: 204-208.
24. Awang-Hazmi, A. J., Zuki, A. B. Z., Noordin, M. M., Jalila, A., and Norimah, Y. (2007). Mineral composition of the cockle (*Anadara granosa*) shells of West Coast of Peninsular Malaysia and it's potential as biomaterial for use in bone repair. *Journal of Animal and Veterinary Advances,* 6(5): 591-594.
25. Hoque E, Shehryar M, Islam K. N. (2013). Processing and characterization of cockle shell calcium carbonate ($CaCO_3$) bioceramic for potential application in bone tissue engineering. *Journal Materials Sciences Engineering,* 2(4): 2-6.
26. Tomlinson, S. K., Ghita, O. R., Hooper, R. M. and Evans, K. E. (2007). Investigation of the dual setting mechanism of a novel dental cement using infrared spectroscopy. *Vibrational Spectroscopy*, 45(1): 10-17.
27. Crisp, S., M. A. Pringuer, M. A., Wardleworth, D. and Wilson, A. D. (1974). Reactions in glass ionomer cements: II. An infrared spectroscopic study. *Journal of Dental Research*, 53(6): 1414-1419.
28. Md Nasir, N. I., Zainuddin, N., Wan Yunus, W. M. Z. and Matori, K. A. (2014). The influence of modified sodium montmorillonite as filler on the performance of glass polyalkenoate cement. *Malaysian Journal of Analytical Sciences,* 18(3): 572-583.
29. Matsuya, S., Maeda, T. and Ohta, M. (1996). IR and NMR analyses of hardening and maturation of glass- ionomer cement. *Journal of Dentistry Restorative*, 75(12): 1920-1927.
30. Hill, R. G. (1993). The fracture properties of glass polyalkenoate cements as a function of cement age. *Journal of Materials Science*, 28(14): 3851-3858.
31. Crisp, S. and A. D. Wilson (1974). Reactions in glass ionomer cements: I. Decomposition of the powder. *Journal of Dental Research*, 53(6): 1408-1413.
32. Crisp, S. and A. D. Wilson (1974). Reactions in glass ionomer cements: III. The precipitation reaction. *Journal of Dental Research,* 53(6): 1420-1424.

33. Cattani-Lorente, M. A., Godin, C. and Meyer, J. M. (1994). Mechanical behavior of glass ionomer cements affected by long-term storage in water. *Dental Materials*, 10(1): 37-44.
34. Lohbauer, U. (2010). Dental glass ionomer cements as permanent filling materials? – properties, limitations and future trends. *Materials,* 3(1): 76-96
35. De Barra, E. and Hill, R. G. (1998). Influence of alkali metal ions on the fracture properties of glass polyalkenoate (ionomer) cements. *Biomaterials,* 19(6): 495-502.
36. Cattani-Lorente, M. A., Godin, C. and Meyer, J. M. (1993). Early strength of glass ionomer cements. *Dental Materials*, 9(1): 57-62.

Malaysian Journal of Analytical Sciences (MJAS)
Published by Malaysian Analytical Sciences Society

SYNTHESIS AND CHARACTERIZATION OF MOLECULARLY IMPRINTED POLYMER IN OLEIC ACID ISOLATION FROM PALM FATTY ACID DISTILLATE WASTES

(Sintesis dan Ciri-Ciri Polimer Tercetak Molekul dalam Pengasingan Asid Oleik Daripada Sisa Penyulingan Asid Lemak Kelapa Sawit)

Nurlin Abu Samah*, Siti Maizatul Ameera Azhar and Gaanty Pragas Maniam

Faculty of Industrial Sciences and Technology,
Universiti Malaysia Pahang, 26300, Pahang, Malaysia

**Corresponding author: nurlin@ump.edu.my*

Received: 20 September 2022; Accepted: 23 November 2022; Published: 22 February 2023

Abstract

In this study, molecularly imprinted polymer-oleic acid (MIPOA) was synthesized using oleic acid (OA) as the template via bulk polymerization. The objective of this study was to characterize the MIPOA as an adsorbent for the isolation of OA from palm fatty acid distillate (PFAD) waste, using thermogravimetric analysis (TGA) and Brunauer-Emmett-Teller (BET) analysis. Isolation method of OA from PFAD waste using MIPOA via esterification reaction in methanol and detection of OA by using gas chromatography–mass spectrometry (GC-MS) showed that MIPOA was capable of isolating OA from PFAD waste sample at 99.99% of isolation efficiency. Findings obtained from TGA results showed that MIPOA was less thermally-stable compared to NIP at higher temperature as the percentage weight loss of MIPOA was higher than NIP. At 215 °C, the weight loss of MIPOA (9.36%) was higher compared to NIP (6.55%) as a control due to the less branch of cross-linked polymer was successfully synthesized. Higher surface area in MIPOA compared to NIP was successfully proven in this experiment. In addition, the presence of OA as a template leaves the cavities during MIPOA washing contributes to the increase of the surface contact. Due to its high surface area and ease of degradation by external energy from heating when compared to NIP (which act as control), MIPOA has a high porosity and an abundance of an organic cross-linkage network. From BET analysis, surface area of MIPOA was 390.52 m^2/g and this value was relatively high in isolation efficiency for the isolation of OA methyl ester. MIPOA displays type I isotherms which indicates that the MIPOA was microporous. These results proved that MIPOA can be employed as a potential adsorbent to isolate OA from PFAD waste.

Keywords: molecularly imprinted polymer, oleic acid, palm fatty acid distillate

Abstrak

Dalam kajian ini, polimer tercetak molekul-asid oleik (MIPOA) telah disintesis menggunakan asid oleik (OA) sebagai templat melalui pempolimeran pukal. Objektif kajian ini adalah untuk mencirikan MIPOA sebagai bahan penjerap untuk mengasingkan OA daripada sisa penyulingan asid lemak sawit (PFAD), analisis termogravimetrik (TGA) dan analisis Brunauer-Emmett-Teller (BET). Kaedah pengasingan OA daripada sisa PFAD menggunakan MIPOA melalui tindak balas pengesteran dalam metanol dan pengesanan OA menggunakan kromatografi gas–jisim spektrometer (GC-MS) yang menunjukkan MIPOA mampu mengasingkan

OA daripada sampel sisa PFAD pada 99.99% kecekapan pengasingan. Dapatan diperolehi daripada keputusan TGA menunjukkan MIPOA kurang stabil dari segi haba berbanding NIP pada suhu yang lebih tinggi kerana peratusan kehilangan berat MIPOA adalah lebih tinggi daripada NIP. Pada suhu 215 °C, penurunan berat MIPOA (9.36%) adalah lebih tinggi berbanding NIP (6.55%) kerana kurang bilangan cabang polimer bersilang yang telah berjaya disintesiskan. Luas permukaan yang lebih tinggi dalam MIPOA berbanding NIP telah berjaya dibuktikan dalam eksperimen ini. Di samping itu, kehadiran OA sebagai templat dikeluarkan daripada liang kaviti semasa pencucian MIPOA menyumbang kepada peningkatan permukaan sentuhan. Oleh kerana luas permukaannya yang tinggi dan kemudahan degradasi oleh tenaga luaran daripada pemanasan jika dibandingkan dengan NIP (yang bertindak sebagai kawalan), MIPOA mempunyai keliangan yang tinggi dan kelimpahan rangkaian rantai silang organik. Daripada analisis BET, luas permukaan MIPOA ialah 390.52 m^2/g dan nilai ini agak tinggi dalam kecekapan pengasingan untuk pengasingan OA metil ester. Isoterma jenis paparan MIPOA I yang menunjukkan bahawa MIPOA adalah mikroliang. Keputusan ini membuktikan bahawa MIPOA boleh digunakan sebagai penjerap yang berpotensi untuk mengasingkan OA daripada sisa PFAD.

Kata kunci: Polimer tercetak molekul, asid oleik, sulingan asid lemak sawit

Introduction

Palm Fatty Acid Distillate (PFAD) is a processing residue resulting from the physical refining of crude palm oil (CPO) products. The annual global production of PFAD is estimated at 2.5×10^6 tons, where Malaysia (29%) and Indonesia (58%) are the main contributors [1]. PFAD consists of more than 80% of free fatty acids, primarily palmitic acid, and oleic acid, which can be esterified and added to the biofuel and oleo-chemical industries as feedstock. Free fatty acid (FFA) is an important specification that influences the palm oil quality. According to previous study, PFAD contains roughly 40% of oleic acid (Figure 1), depending on the quality of CPO. Oleic acid (OA) is the most abundant monounsaturated fatty acid in nature which plays important roles in many industries. OA has multiple properties and applications of great value and importance. OA has been used in a variety of industries and sectors that produce many products such as textiles, cosmetics, inks, paints, pharmaceuticals, detergents, and food processing.

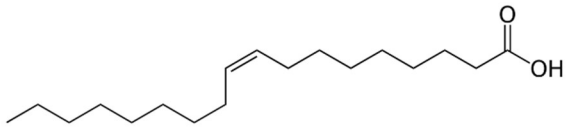


Figure 1. Molecular structure of OA

Throughout the years, different kinds of sorbents were developed to isolate variety of free fatty acids from PFAD waste. Molecularly imprinted polymer (MIP) is one of the sorbents used in research and development which shows great findings. MIP is a synthetic polymer with a predetermined selectivity for a given analyte, or group of structurally related compounds, making them ideal materials to be used in separation processes [2]. For the synthesis of MIP, relevant selection of the template, monomer, crosslinker, and porogen solvent is considered critical to produce high percentage of analyte isolation.

MIPs offer many advantageous features such as simple to synthesize and easy to prepare [3], low cost, and can maintain its performance even if it is stored for several years. They are intrinsically more stable chemically and physically, and robust due to their highly cross-linked polymer nature, which facilitates their application in harsh environments such as in the presence of strong acids or bases, organic solvents, and high temperature and pressures [4]. In this study, the use of MIP as isolation technique of OA from PFAD waste has been proposed to obtain OA from the PFAD waste. The synthesized MIP for oleic acid has been characterized via esterification reaction in methanol with gas chromatography–mass spectrometry (GC-MS), TGA, and BET analysis.

Materials and Methods

Synthesis of MIPOA

The MIP was prepared by following Kugimiya's synthesis method [5]. All ingredients (1.0 mmol oleic acid, 4.0 mmol of allylthiourea, 20 mmol of EGDMA, and 0.12 mmol of AIBN initiators) were dissolved in 4.0 mL of acetonitrile. The solution was then sonicated and purged with nitrogen gas for 5 minutes to remove oxygen gas from the solution. Then, the sealed solution was polymerized at 60 °C in a water bath for 24 hours.

The resulting polymer was washed with methanol/acetic acid (9:1, v/v) using a Soxhlet apparatus to remove oleic acid template. A final washing step using 25 mL of methanol for 3 times washing was carried out and a polymer was centrifuged at 5300 rpm for 3 mins to remove residual of acetic acid. The supernatant methanol was analyzed using a UV spectrophotometer at 280 nm to confirm that there was no OA remains in the cross-linked polymer. Afterwards, the polymer was dried at 60 °C under vacuum overnight and stored at room temperature. Finally, the polymer was ground using mortar and pestle, and sieved to yield particle size between 28 µm and 100 µm. The non-imprinted polymer (NIP) as a control was synthesized using the same procedure described above, with the absence of OA, to evaluate the sorption capacity of the polymer itself and to discriminate from the adsorption of the selective sites of MIP [3].

MIPOA characteristics

Isolation of OA from PFAD waste

The PFAD sample was turned into liquid form at room temperature by esterification process which changed it to fatty acid methyl esters (FAME) [6][7]. Esterification of PFAD was conducted in a flask equipped with reflux condenser and temperature indicator on a hot plate with a magnetic stirrer shown in Figure 2. The mixture of methanol and PFAD was heated to 60ºC under continuous stirring at 500 rpm. The experiment was carried out at around 60ºC-80ºC for a few hours. The volume ratio of methanol to PFAD used was 2:1. The mixture was then separated into six different small jars and left at room temperature. Next, 20 mg of MIPOA and NIP were added and stirred for 1 hour into the mixture solution, respectively (Figure 3). The experiment was carried out in duplicate. After that, the oil-based mixture solution was collected for detection of OA using GC-MS.

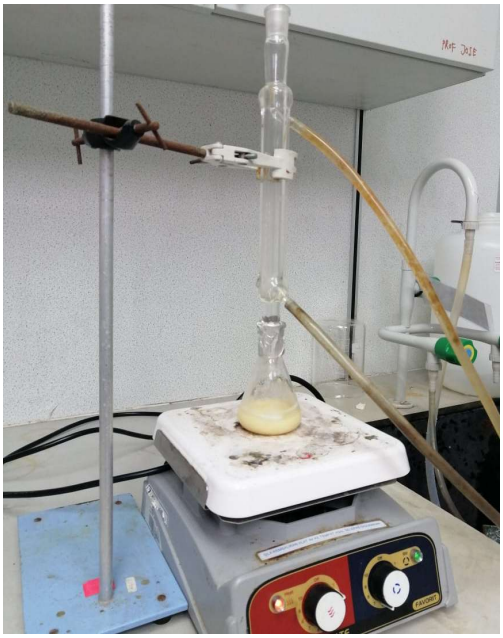


Figure 2. Esterification reaction set-up experiment using PFAD sample

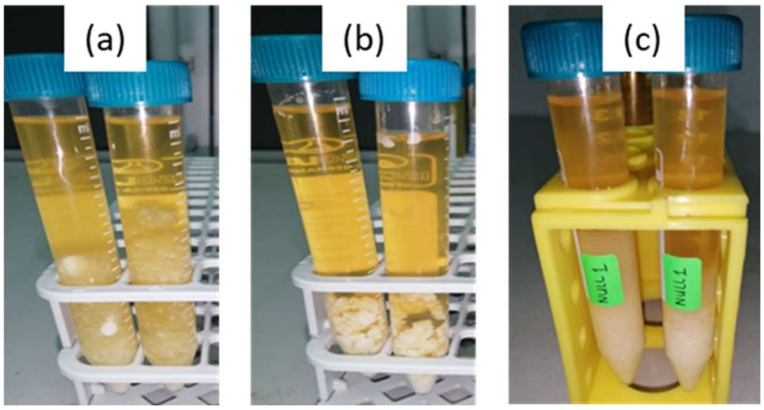


Figure 3. Oil-based mixtures were seen to accumulate solids in different form of yield at room temperature (a) PFAD-methanol after mixed with MIPOA (b) PFAD-methanol after mixed with NIP as a control and (c) PFAD-methanol with absence of any adsorbent.

An Agilent 7890A gas chromatography equipped with a BPX5 capillary column size 30 m × 0.25 mm i.d. (0.25 µm stationary film thickness) was used with helium (purity 99.999%) as carrier gas at a flow rate of 1.2 mL min^{-1}. The initial oven temperature was held at 50 °C for 1 min, and then increased to 280 °C at 20 °C min^{-1}, and held at 280 °C for 1 min. The total analysis run time was 13.5 minutes. The injector temperature was set at 280 °C, and the injection was performed in the splitless mode. The identification of analyte was done by GC retention time (R_t) and by a comparison of the mass spectra of identified substances with those of authentic reference substances.

TGA Analysis of MIPOA

The thermal degradation of different samples for non-isothermal conditions was investigated thermogravimetrically. The calculation of kinetic parameters was carried out under a heating rate of 30 °C min^{-1} in 30-700 °C using a thermogravimetric analyzer (TGA) instrument (model STA7200). In order to minimize the test error, the weight of all the samples in powder form (177 < 210 mm) was identical to be 6 mg to 7 mg. The TGA experiments was carried out in a nitrogen atmosphere (99.99% minimum purity) with a flow rate of 30 mL min^{-1} [8].

BET analysis of MIPOA

In order to determine the MIPOA surface area, an automated gas adsorption analyzer model ASAP2020 (Micromeritics Instrument Corporation, USA) was used with adsorption-desorption isotherms of nitrogen gas temperature sets at -195.89 °C. About 0.05g of sample was used for each analysis. The samples were automatically degassed at 22 °C under nitrogen for at least 24 hours. The specific surface areas of sample were calculated by the BET (Brunauer, Emmett, and Teller) method, while volume of micropore was estimated using the Dubinin Radushkevich (DR) equation. For pore volume, it was directly calculated from the volume of nitrogen held at the highest relative pressure (P/P^o = 0.99).

Results and Discussion

Ability of MIPOA to isolate OA from PFAD waste

Standard solution was Chromatogram of OA standard shows that the R_t for OA occurs at 11.73 mins as a main peak (Figure 4).

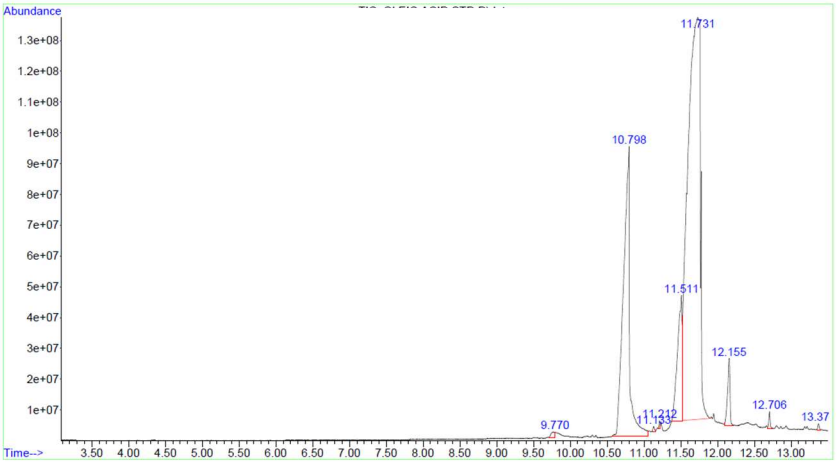


Figure 4. Chromatogram for OA standard using GC-MS

Figure 5 shows the GC-MS chromatogram of the untreated PFAD sample after esterification to produce methyl ester compounds from various free fatty acids. In a PFAD sample with a volume ratio of 1:2 between PFAD and methanol, the composition of certain prominent peaks produced by esterification of free fatty acids is as displayed in Table 1. The fragmentation pattern of the major active compound (R_t = 10.8 mins) was determined as n-Hexadecanoic acid methyl ester or methyl palmitate. OA methyl ester or methyl oleate was

found to be the second higher abundance at the R_t equals to 11.7 mins. Therefore, detection of OA in treated PFAD samples with MIPOA and NIP was observed at R_t around 11.7 mins as mentioned in calibration of OA standard. There was a possibility of peak overlapping occurred at 11.7 mins. However, for the recent findings, it was estimated that OA methyl ester was observed at 11.7 mins by referring to the chromatograms obtained.

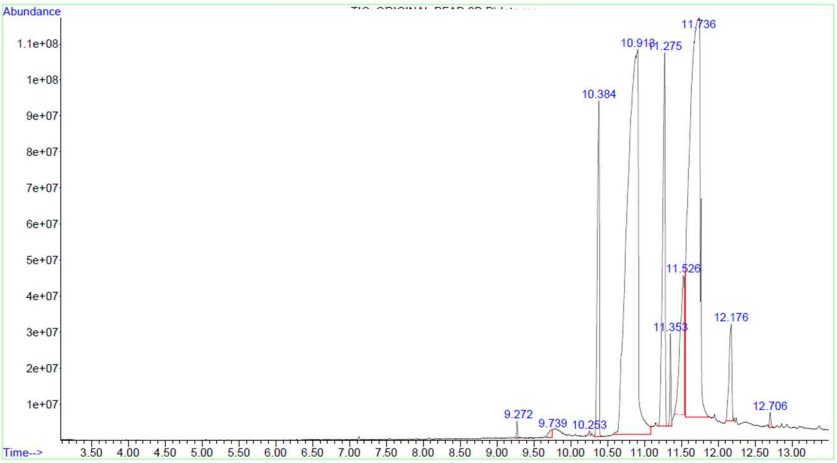


Figure 5. GC-MS chromatogram of PFAD sample in methanol with volume ratio of PFAD to methanol equals to 1:2 with absence of any adsorbent

Table 1. Some major peaks found in untreated PFAD sample

Peak	Retention time, R_t	% Composition	Compound
1	9.2724	0.14	Tridecanoic acid methyl ester
2	9.7389	0.23	Tetradecanoic acid
3	10.2526	0.06	Cyclopentadecanone methyl ester
4	10.9131	38.28	n-Hexadecanoic acid methyl ester/ palmitic acid methyl ester
5	11.2748	8.42	9-Octadecenoic acid methyl ester
6	11.3534	0.83	Octadecanoic acid methyl ester
7	11.7361	38.19	Oleic acid methyl ester

Figure 6 displays the GC-MS chromatogram of treated PFAD sample with MIPOA in methanol. From the results, OA methyl ester was totally isolated with composition left about 0.03% contained in the free oil-based mixture. Palmitic acid methyl ester was not isolated at all as even palmitic acid methyl ester contained about 38.28% in the PFAD samples. The composition of palmitic acid methyl ester was higher after being treated with MIPOA due to the potential of stirring and heating process which caused the increasing in oil viscosity. It was proved that MIPOA was highly selective for the isolation of OA methyl ester. Palmitic acid methyl ester was not isolated at all after being treated with MIPOA. In Table 2, the composition analysis from the chromatogram showed significant peaks of compound present in PFAD samples treated with MIPOA. There was possibility at 11.7 mins that the redundant peaks were determined. However, further study is required to enhance the separation peaks at approximately 11.6 mins until 11.7 mins to identify the ghost peak which was redundant with OA methyl ester peak in the chromatogram.

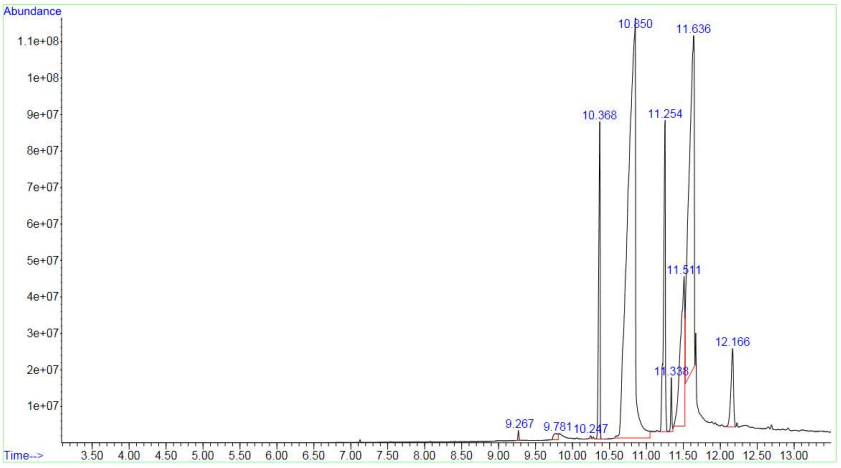


Figure 6. GC-MS chromatogram of PFAD sample after treated with MIPOA as an adsorbent in methanol with volume ratio of PFAD to methanol equals to 1:2.

Table 2. GC-MS analysis in PFAD sample after treated with MIPOA as an adsorbent in methanol

Peak	Retention time, R_t	% Composition	Compound
1	9.2671	0.1361	Tridecanoic acid methyl ester
2	9.7808	0.4017	Tetradecanoic acid
3	10.8502	46.8937	n-Hexadecanoic acid methyl ester
4	11.2538	8.0424	9-Octadecenoic acid methyl ester
5	11.3377	0.7857	Octadecanoic acid methyl ester
6	11.5107	9.2846	Linoleic Acid methyl ester
7	11.7361	0.0300	Oleic acid methyl ester

GC-MS chromatograms of treated PFAD samples with NIP as a control is shown in Figure 7 whereas the significant peaks of compounds present in PFAD samples treated with NIP is shown in Table 3. From the results, at R_t equals to 11.71 mins, the peak for OA methyl ester was presented with composition at 34.53% in free oil-based mixture. The same trend was found when PFAD sample was treated with NIP. The abundance of OA methyl ester was found to be higher compared to the initial condition.

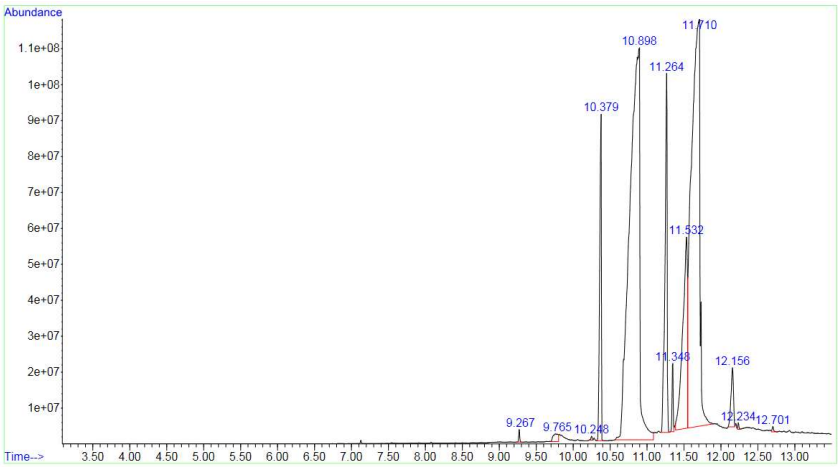


Figure 7. GC-MS chromatogram of PFAD sample after treated with NIP as an adsorbent in methanol with volume ratio of PFAD to methanol equals to 1:2

Table 3. GC-MS analysis in PFAD sample after treated with NIP as an adsorbent in methanol

Peak	Retention time, R_t	% Composition	Compound
1	9.2673	0.128	Tridecanoic acid, 12-methyl-, methyl ester
2	9.7653	0.4011	Tetradecanoic acid
3	10.8975	40.1635	n-Hexadecanoic acid methyl ester
4	11.2645	7.7556	8-Octadecenoic acid, methyl ester
5	11.3483	0.7522	Octadecanoic acid, methyl ester
6	11.7100	34.5268	Oleic Acid methyl ester

The OA methyl ester found at R_t around 11.7 mins in treated sample with MIPOA and NIP respectively are shown in Table 4. The average percentage of oleic acid adsorbed by MIPOA at R_t around 11.7 mins is 99.99%, while the adsorption by NIP samples is 0.88%. This result shows that MIP was capable of isolating oleic acid from PFAD sample. The differences of oleic acid adsorbed by MIPOA and NIP samples are not that high, probably due to some of the template on MIP vanished during crushing and the medium of sample is in oil-based which makes it difficult for MIP to extract because of its high viscosity properties. In addition, using real sample commonly contributes to the unknown compound which is present in the samples due to the matrix effect.

Table 4. % OA methyl ester adsorbed by MIPOA and NIP

Composition of OA methyl ester	MIPOA	NIP
% Initial composition	38.190	38.190
% Final composition	0.002	38.526
% Adsorbed	99.99	0.88

BET analysis

Isotherm linear plot (BET)- N^2 adsorption isotherm in MIPOA

The N^2 adsorption isotherms of the MIPOA is shown in Figure 8. From this figure, MIPOA displays type I isotherms and according to International Union of Pure

and Applied Chemistry (IUPAC) classification, it indicates that the MIPOA is microporous. Usually, Type I isotherm displays a convex curve, and the platform of this type comes out horizontal or virtually horizontal, and the adsorption isotherm directly intersects with the line $P/P^o = 1$ [9]. As seen in the initial stage, the volume adsorbed increased sharply at low relative pressure region ($P/P^o < 0.2$). This means that nitrogen molecules were adsorbed mainly in the microporous structure [9]. Table 5 presents the BET surface area, total pore volume, micropore volume, and average pore diameter of MIPOA that were obtained from N^2 adsorption isotherms. The surface area of MIPOA was 390.52 m^2/g and this value was considered to have potential in adsorbing OA at high isolation efficiency.

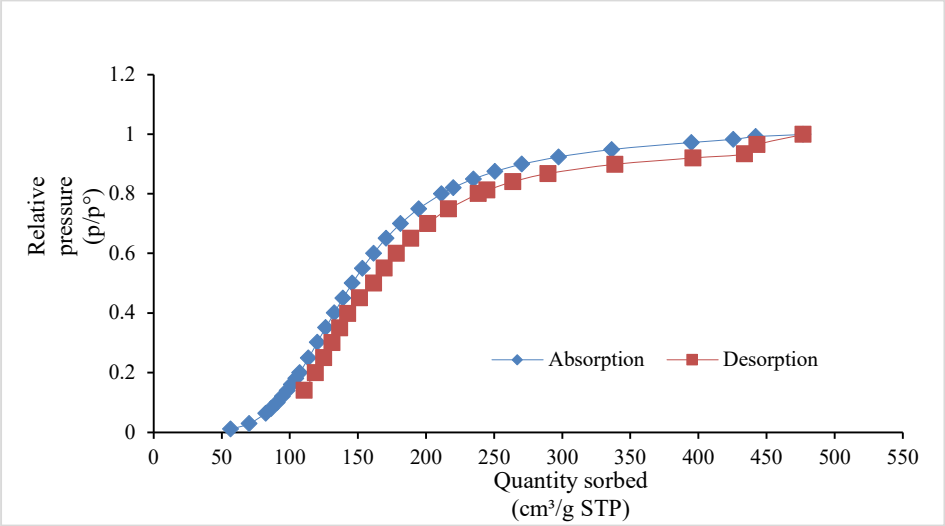


Figure 8. N_2 gas adsorption-desorption isotherms of MIPOA

Table 5. BET surface area, total pore volume, micropore volume and average pore diameter of MIPOA

Sample	BET Surface Area (m^2/g)	Total Pore Volume (cm^3/g)	Micropore Volume (cm^3/g)	Average Pore Diameter (Å)
MIPOA	390.52	0.6106	0.0072	62.55

TGA analysis

During a ramped heating under nitrogen, such as in a TGA experiment, the degradation process usually passes through three stages. In the first and second stage, the less branch cross-linked bonds located at the outer side of the particles were decomposed. Whereas more stable structure polymer which consists of substituted allylthiourea as an active site was degraded in the third stage due to the inner part of the polymer particles contributing to the stability of MIPOA. The final step was the high temperature degradation of these stabilised structures to yield volatile products and a small quantity of carbonaceous char.

The curves for MIPOA display three weight loss stages (DTG maxima at 215 °C, 390 °C and 450 °C) that lead to the formation of a small high temperature residue (9.36 wt.%) (Figure 9). The first DTG peak can be related to the overlapping of less branch of polymer chain (degradation) and char-forming secondary reactions (cross-linking), whereas the second peak corresponds to decomposition of the stabilised allylthiourea structures. The similar temperature range was observed for NIP as a control which led to the formation of a small high temperature residue (6.55 wt.%) (Figure 10).

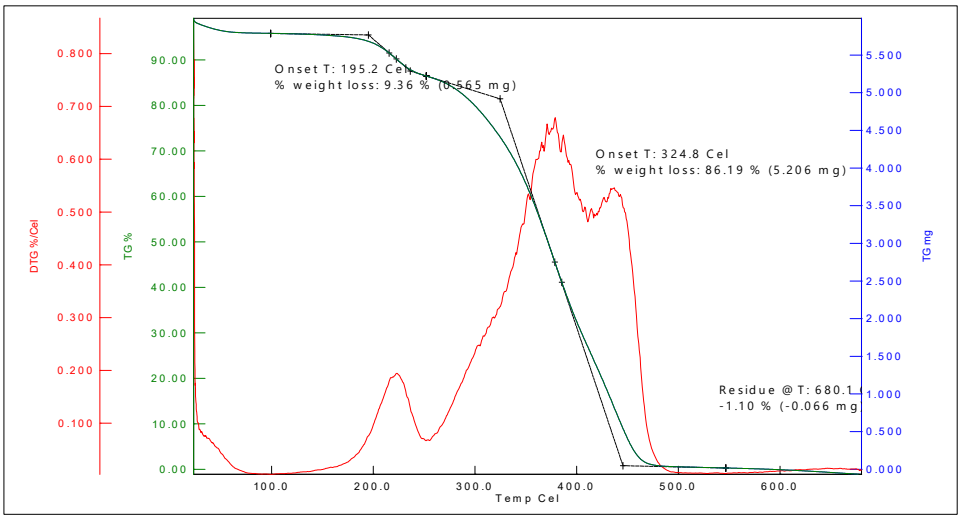


Figure 9. TGA thermogram of MIPOA before isolation

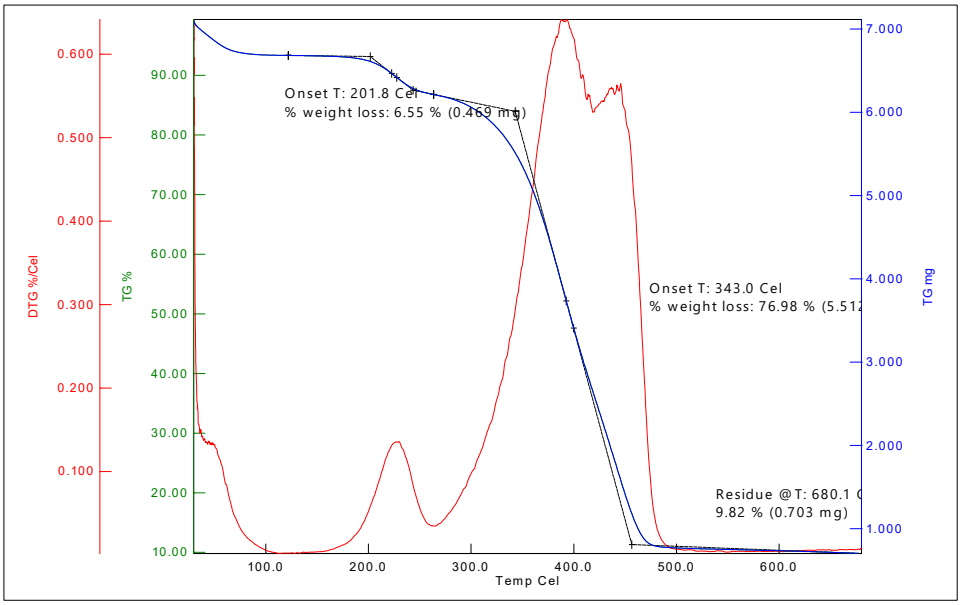


Figure 10. TGA thermogram of NIP as a control

From Table 6, the weight loss due to the degradation was investigated. At 215 °C, the weight loss of MIPOA (9.36%) was higher compared to NIP (6.55%) as a control due to the less branch of cross-linked polymer which was successfully synthesized. Higher surface area in MIPOA compared to NIP was successfully proven in this experiment. In addition, the presence of OA as a template leaves the cavities during MIPOA washing contributes to the increase of the surface contact. At 330 °C, MIPOA (86.19%) also showed higher mass loss compared to NIP (76.98%). In the synthesis of polymer, the cross-linked effect gives benefits in terms of affinity properties as a sorbent and higher surface area of MIPOA.

Table 6. Percentage weight loss of MIPOA and NIP within temperature range of 0 °C to 400 °C

DTG Temperature (°C)	MIPOA (% weight loss)	NIP (% weight loss)
215	9.36	6.55
330	86.19	76.98
680	0.00	9.82

Conclusion

In this research, MIPOA was successfully synthesized using oleic acid as template, acetonitrile as a porogen solvent, allylthiourea as functional monomer, and EGDMA as a cross-linker. Both MIPOA and NIP were synthesized by bulk polymerization technique. The synthesized MIPOA and NIP were successfully characterized by using GC-MS, TGA and BET instruments to understand its sorption ability and thermal properties. Based on GC-MS analysis, the average percentage of oleic acid adsorbed by MIPOA samples at R_t around 11.7 is 99.99%, while by NIP samples is 0.88%. This proves that MIPOA was capable of isolating OA from PFAD sample. BET analysis shows that MIPOA displays type I isotherms and indicates that the MIPOA was microporous. Lastly, TGA data shows that MIPOA was less thermally-stable compared to NIP at higher temperature due to high surface area. The higher % weight loss of MIPOA than NIP ensured the presence of an organic cross-linked network. This study concludes that MIPOA was successfully employed for the effective and selective isolation of oleic acid from PFAD waste.

Acknowledgement

The authors would like to thank the Universiti Malaysia Pahang for laboratory facilities as well as additional financial support under Internal Research grant RDU1903106.

References

1. Xu, H., Lee, U. and Wang, M. (2020). Life-cycle energy use and greenhouse gas emissions of palm fatty acid distillate derived renewable diesel. *Renewable and Sustainable Energy Reviews*, 134: 110144.
2. Turiel, E. and Esteban, A. M. (2019). Molecularly imprinted polymers. In *Solid-Phase Extraction* (pp. 215–233).
3. Samah, N. A., Sánchez-Martín, M. J., Sebastián, R. M., Valiente, M. and López-Mesas, M. (2018). Molecularly imprinted polymer for the removal of diclofenac from water: Synthesis and characterization. *Science of the Total Environment*, 631–632:1534-1543.
4. Gao, S., Wang, W. and Wang, B. (2004). Molecularly imprinted polymers as recognition elements in optical sensors. *Molecularly Imprinted Materials: Science and Technology*, 2004: 701-726.
5. Kugimiya, A. and Takei, H. (2006). Preparation of molecularly imprinted polymers with thiourea group for phosphate. *Analytica Chimica Acta*, 564(2): 179-183.
6. Hidayat, A., Rochmadi, Wijaya, K., Nurdiawati, A., Kurniawan, W., Hinode, H., Yoshikawa, K., & Budiman, A. (2015). Esterification of palm fatty acid distillate with high amount of free fatty acids using coconut shell char based catalyst. *Energy Procedia*, 75: 969-974.
7. Sudibyo, H., Rochmadi, R. and Fahrurrozi, M. (2017). Kinetic study of palm fatty acid distillate esterification with glycerol over strong acidic cation exchanger tulsion 42SM. *Engineering Journal*, 21: 45-61.
8. Abbas-Abadi, M. S., Van Geem, K. M., Fathi, M., Bazgir, H. and Ghadiri, M. (2021). The pyrolysis of oak with polyethylene, polypropylene and polystyrene using fixed bed and stirred reactors and TGA instrument. *Energy*, 232: 121085.
9. Hidayu, A. R., Mohamad, N. F., Matali, S. and Sharifah, A. S. A. K. (2013). Characterization of activated carbon prepared from oil palm empty fruit bunch using BET and FT-IR techniques. *Procedia Engineering*, 68: 379-384.

Malaysian Journal of Analytical Sciences (MJAS)
Published by Malaysian Analytical Sciences Society

EVALUATION OF CARRAGEENAN GEL PROPERTIES AT DIFFERENT CONCENTRATIONS OF CALCIUM CHLORIDE DIHYDRATE SALT

(Penilaian Gel Carrageenan Beraroma Pada Variasi Kepekatan Garam Kalsium Klorida Dihidrat)

Nur Anis Alisya Kamarol Zani, Fatmawati Adam*, Nurul Aini Mohd Azman, Nor Hanuni Ramli

Faculty of Chemical and Process Engineering Technology
Universiti Malaysia Pahang,
Lebuhraya Tun Razak, 26300 Gambang, Kuantan, Pahang, Malaysia

**Corresponding author: fatmawati@ump.edu.my*

Received: 18 August 2022; Accepted: 22 December; Published: 22 February 2023

Abstract

Aromatherapy is an alternative therapy for Complementary and Alternative Medicine (CAM) to relieve mild depression in individuals. This study aimed to evaluate the effect of incorporating calcium chloride dihydrate in carrageenan gel to increase stability property. The gel formulation was produced from a mixture of semi-refined carrageenan, sodium benzoate, alginic acid, polyethene glycol (PEG) and sorbitan monolaurate (Span 20) followed by the inclusion of calcium chloride dehydrate (CCD) at 0%, 0.5%, 1%, 1.5%, and 2% concentrations. The effects of CCD concentration on rheology, gel Bloom strength, morphology, and thermal properties were investigated. The viscosity and shear stress decreased on incorporating of CCD in the carrageenan gel formulation. The highest viscosity of the control gel was 597.84 mPa.s. The intersection of G' and G" at various concentrations of CCD salts in the gel formulation demonstrated that the increment of salt concentration resulted in a faster gelation process in the range 56.6 to 50.43 °C. The gel Bloom strength increased from 830.04 g at 0.5% CCF salt to 1331.39 g at 2% CCD. The highest gel strength of 1324.59 g was achieved with 2% CCD and a melting temperature of 194.4 °C. The weight loss rate for the control gel was 28.88%, the lowest weight loss rate for 2% CCD gel was 11.82%. The residual gel weight was also highest for 2% CCD: 16.74% after 21 days. A high residual gel weight reflects the stability of the carrageenan gel formulation to retain the product and last as aromatherapy gel product. The morphology images showed a highly porous gel structure on addition of CCD salts. In conclusion, CCD salt is capable of forming a strong interaction with the gel matrix to produce a stable gel.

Keywords: aromatherapy, biocomposite, depression, bloom, porosity

Abstrak

Aromaterapi adalah terapi alternatif untuk Perubatan Pelengkap dan Alternatif (CAM) untuk melegakan kemurungan ringan pada individu. Kajian ini bertujuan untuk menilai kesan penggabungan kalsium klorida dihidrat dalam gel karagenan untuk meningkatkan sifat kestabilan. Formulasi gel dihasilkan daripada campuran karagenan separa halus, natrium benzoat, asid alginik, polietilena glikol (PEG) dan sorbitan monolaurat (Span 20) diikuti dengan kemasukan kalsium klorida dehidrat (CCD) pada 0%, 0.5%, 1%, 1.5%, dan 2% kepekatan. Kesan kepekatan CCD pada reologi, kekuatan Bloom gel, morfologi, dan sifat terma telah disiasat. Kelikatan dan tegasan ricih berkurangan apabila pengambilan CCD dalam formulasi gel karagenan. Kelikatan tertinggi gel kawalan ialah 597.84 mPa.s. Persilangan G' dan G" pada pelbagai kepekatan garam CCD dalam rumusan gel menunjukkan

bahawa pertambahan kepekatan garam menghasilkan proses pemeringkatan yang lebih cepat dalam julat 56.6 hingga 50.43 °C. Kekuatan Bloom gel meningkat daripada 830.04 g pada 0.5 % garam CCF kepada 1331.39 g pada 2% CCD. Kekuatan gel tertinggi sebanyak 1324.59 g dicapai dengan 2% CCD dan suhu lebur 194.4 ° C. Kadar penurunan berat badan untuk gel kawalan ialah 28.88%, kadar penurunan berat badan terendah untuk 2% gel CCD ialah 11.82%. Berat sisa gel juga tertinggi untuk 2% CCD: 16.74% selepas 21 hari. Berat sisa gel yang tinggi mencerminkan kestabilan formulasi gel karagenan untuk mengekalkan produk dan kekal sebagai produk gel aromaterapi Imej morfologi menunjukkan struktur gel yang sangat berliang pada penambahan garam CCD. Kesimpulannya, garam CCD mampu membentuk interaksi yang kuat dengan matriks gel untuk menghasilkan gel yang stabil

Kata kunci: aromaterapi, biokomposit, kemurungan, mekar, keliangan

Introduction

Aromatherapy is one of the complementary and alternative medicine (CAM) treatments for patients with depressive symptoms. Aromatherapy is defined as the therapeutic application of plant-derived concentrated essences extracted through distillation. It is a low-cost, non-invasive CAM used to improve psychological and mental wellbeing. Ali et al. concluded that aromatherapy is a natural and noninvasive gift of nature because the whole of the human body is rejuvenated on using aroma from essential oil [1]. Essential oils which contain volatile organic compounds that have a pharmacological effect by penetrating the human body through oral, dermal or olfactory administration are commonly used [2]. An electroencephalograph study concluded that fragrances significantly modulate the activity of different brain waves and are responsible for physiological effects of mood, stress, and working capacity [3]. Several marker compounds represent the characteristics of a fragrance, such as patchoulol as the major compound in patchouli oil scent [4]. Olfactory stimulation related to aromatherapy may result in an immediate reduction in pain as well as changes in physiological parameters such as pulse, blood pressure, skin temperature, and brain activity [5]. Application of essential oil aromatherapy gels is particularly used in the home, office, room, and car. This is because most people nowadays spend their time in a room to rest, in an office to work, or in a car to travel. A gel air freshener made from natural polymer gelatin with lavender essential oil and natural banana aroma has been shown to be tolerable for application compared to commercial ones [6].

Most fragrance-scented gel applications use gelatin or gellan gum as the primary material. Both materials are expensive. Gelatin, for example, is derived from animals and would be a source of concern for Muslim consumers if they used the product. Therefore, this research provides an insight into the potential of using carrageenan in the gelling material for scented gel products. Adam et al. developed a carrageenan–gum Arabic and carrageenan–cellulose for application in hard capsules, demonstrating the compatibility of the components [7]. Carrageenan, by itself, can allow the active volatile ingredient of aromatherapy essential oil to evaporate. The objective of this study is the development of carrageenan gel product made from carrageenan. The incorporation of carboxymethyl cellulose (CMC) and microcrystalline cellulose (MCC) can toughen the bioplastic film and harden capsules made from carrageenan [8]. The effect of alginate gel and $CaCl_2$ (calcium chloride) solution made through the external gelation method may contribute to an increase in gel strength with an increment of $CaCl_2$ [9]. The incorporation of cellulose nanofibers (CNF) with α-tocopherol improves the properties of bioplastic film in active packaging [10]. Carrageenan gel produced via crosslinking with calcium ions followed by incorporation of different concentrations of lavender essential oil shows promising mechanical and thermal properties to be applied in the pharmaceutical industry [11]. Pectin, carrageenan, and gelatin are economically valuable hydrophilic polysaccharides that have broad usage in the food, pharmaceutical, cosmetic, and biotechnology industries as gelling, thickening, stabilizing, and emulsifying agents. These polysaccharides have promising potential in many areas and accelerate global technological breakthroughs in this line of work [12].The sol–gel process, which has been used to create silica-based materials doped with flavor and fragrance, is an efficient alternative to previous microencapsulation methods because it prevents the degradation of the delicate compounds included and has the possibility to provide odorant and

flavored components with new and innovative beneficial properties [13]. The purpose of this study was to evaluate the effect of different concentrations of calcium chloride dehydrate salt on carrageenan gel to make a stable gel for potential of aromatherapy carrageenan gel.

Materials and Methods

Chemicals and materials

Carrageenan was purchased from TACARA, Sabah, Malaysia. Sodium benzoate, calcium chloride dehydrates (CCD), sorbitan monolaurate (Span 20), and polyethylene glycol (PEG) were purchased from Merck, Germany.

Preparation of carrageenan gel solution

In 100 mL of deionized water, 3 g of semi-refined carrageenan and 0.5 g of sodium benzoate were mixed for 1 hour at 75 °C. The solution was stirred until homogeneous. After that, 1.5 g of Span 20, 2 ml of PEG, and 0.02 g alginic acid were added. All materials were mixed in a glass beaker and stirred for 2 hours on a hot plate magnetic stirrer at 75°C. After that, the semi-solid gel was molded and left at room temperature. The same method was repeated but with the concentration of calcium chloride dihydrate manipulated at (0, 0.5, 1, 1.5, and 2 wt.%).

Rheology analysis

The viscosity of carrageenan formulation solutions was measured using a cup and bob rotational measuring block Rheometer (Rheo 3000, Brookfield, USA) equipped with LCT 25 4000010 geometry. Approximately 16.5 mL of solution was programmed at speed of 300 rpm, with 100 MPoints at a constant temperature of 40 °C in duplicate. The dynamic rheology measurement was determined using Kinexus Lab+ Rheometer with a controlled stress rheometer using a parallel-plate geometry (gap 1 mm, diameter 40 mm). Within the linear viscoelastic regime, the values of the strain amplitude were set as 4% for all measurements. Before the heating process, the temperature of the loading platform was raised to 60 °C. The prepared fresh samples at 85 °C were put into the loading platform, and then the temperature of the loading platform was reduced to 20 °C and balanced for 1 h. The temperature ramp tests of mixed gels were conducted during heating from 20 to 95 °C and cooling from 95 to 20 °C. Both processes were carried out at a rate of 5 °C/min.

Weight variation analysis

The evaporation of liquid from the formulated gels was tested by weighing the gel each week for 4 weeks. Carrageenan gel weight loss for each week and a total weight reduction after 4 weeks of storage were calculated. Weight reduction of carrageenan gels was obtained by calculating the difference in weight of the gel at the time of weighing (M_n), with weight of gel at initial time (M_0). The difference in weight is the amount of liquid that evaporates. The percentage of total liquid evaporated and residual gel weight were measured by gravimetry and calculated by the formula:

$$Total\ Liquid\ Evaporation\ Percent = \frac{M_n - M_{n-1}}{M_0} \times 100 \quad \text{(eq. 1)}$$

$$Residual\ Gel\ Weight\ Percent = \frac{M_n}{M_0} \times 100\% \quad \text{(eq. 2)}$$

where M_n is the weight of gel at the time of weighing; M_{n-1} is the weight of the gel in the previous week; and M_0 is the weight of gel at the initial time [14].

Gel bloom strength test

Mechanical and Bloom strength test were conducted using a CT3 Texture Analyzer (Rheo 3000, Brookfield, USA). The texture analyzer was loaded with a 50 kg load cell. An average of at least three measurements was taken for each formulation. A flat-end probe (TA-10) with a diameter of 12.7 mm and a Brookfield bloom jar were used for the analysis. Carrageenan gel was placed on the texture analyzer platform and positioned at the center of the probe. The analyzer was programmed to use the 'compression' testing mode and the 'distance' target option was approximately 4.0 mm. At a speed of

1.0 mm/s, the probe was pressed onto the gel and breaking force was recorded.

Thermal properties

Thermogravimetric analysis (TGA) is a precise method for studying the weight loss, decomposition pattern and thermal characterization of carrageenan gel. A TA Instruments Q 500 series instrument with a TGA heating rate of 10 °C/min for a temperature range of up to 800 °C was used. Nitrogen gas was used as the purge gas at a rate of 10 ml/min. Measurements were taken in triplets, with average values recorded.

The thermal properties of the carrageenan gel formulation solution were analyzed by differential scanning calorimetry, DSC, using a TA-Instrument Q1000 calorimeter. Samples of 8 mg were placed on an aluminum pan and nitrogen gas was purged at a flow rate of 10 mL/min and heating rate of 10 °C/min. The heating range was set between 0 to 350 °C.

Morphology analysis

A scanning electron microscope **(**SEM; TM3030 PLUS, Hitachi, Japan) was used to examine the surface morphology of carrageenan gel. SEM was used to examine the surface of the biocomposite obtained. The carrageenan gel was cut into 1 cm × 1 cm rectangles and applied to the specimen stub. The sample was examined and photographed at a magnification of 300×.

Statistical analysis

The confidence level p-value was calculated using ANOVA with the testing null analysis (H_o) and alternative analysis (H_i) for solution viscosity, shear stress, and gel bloom strength of the gel formulation at different CCD concentrations. For the comparison of rejection values, the level of significance was set at $\alpha = 0.05$.

Results and Discussion

Rheology analysis

Sol–gel transitions are common during the process of aqueous gelling systems, resulting in overly complex rheological behaviour. Several factors such as time, temperature, and concentration frequently cause dramatic changes in viscoelastic behaviour [15]. The viscosity of carrageenan gels with different concentrations of CCD is shown in Figure 1. Viscosity and shear stress decreased on increasing the concentration of CCD from 0 to 2 wt.%. ANOVA test results for the viscosity and shear stress have p-values of 0.00012 and 0.000262 at $\alpha = 0.05$, respectively. In previous studies, a solution of carrageenan blended with *Chlorella vulgaris* lipid had a viscosity value of 245.29 mPa.s [16] and that of carrageenan–gum Arabic solution increased to 1058 mPa.s at a 67% w/w ratio of semi-refined carrageenan to gum Arabic [7].

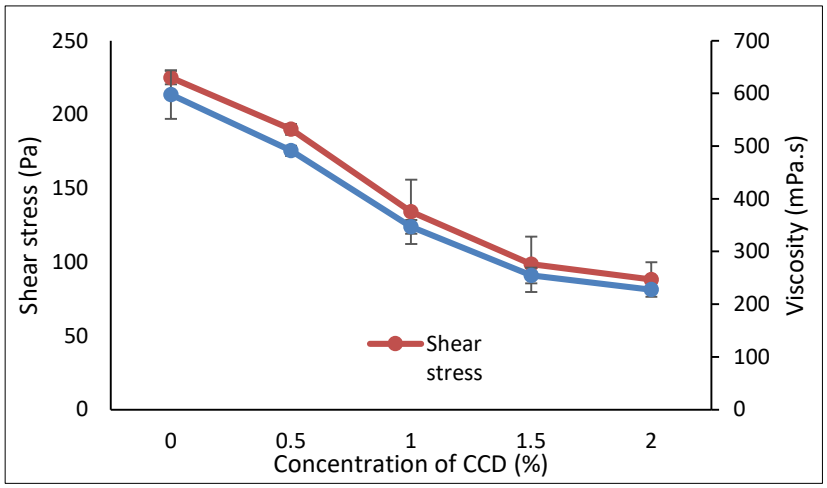


Figure 1. Viscosity and shear stress at different concentrations of CCD

Figure 2 shows the effect of temperature on the sol–gel transition and gel–sol transition for the gel formulations; the analysis is divided into cooling and heating processes. Both G′ and G″ values decreased sharply as temperature increased. During the cooling process, G′ values were always greater than G″ values, and the samples displayed elastic behavior. However, as the temperature increased during the heating process, G′ and G″ values both increased slightly, and G″ gradually surpassed G′, indicating viscous behavior. During the heating process, melting temperature (T_m) was defined as the temperature at which the G′ and G″ values crossed, and the gelling temperature (T_g) was defined likewise for the cooling process. At 0% CCD salt concentration, T_g was 56.66 °C and gradually decreased as the concentration of CCD salt increased, to 50.43 °C at 2% CCD salt. The T_m ranged from 62.17 to 43.88 °C on increasing the concentration of CCD salt. The highest T_m and T_g, 56.66 and 62.17 °C, respectively, were obtained for gels made without 0% CCD salts.

Figure 3 shows the melting and gelling temperature from G' and G'' crossover. The storage modulus of a polymer determines its solid-like properties. The higher the storage modulus, the more difficult it is to degrade the polymer. Loss modulus, which is the inverse of storage modulus, describes a polymer's liquid-like nature. When the storage modulus is large, the loss modulus is small, and vice versa [17]. During the cooling stage, the loss modulus is greater than the storage modulus during the initial cure period. This means that during this stage, the gel's liquid-like (viscous) behavior takes precedence over its solid-like (elastic) character. When G′ = G″, a crossover point is reached, implying that a crosslinking reaction is initiated. This is referred to as the gel point. G′ was much greater than G″ in the final cure stage, meaning that the gel had mostly solidified into an elastic solid. The results for the gelling point, the intersection of G′ and G″, for various concentrations of CCD salts added to the gel formulation demonstrate that increasing the salt concentration resulted in faster gelation (shorter gel point), as shown in Table 1. In a previous study by Cui et al., kappa carrageenan/konjac gum solution with the addition of gellan gum and Ca^{2+}, which remained a gel in the solid state under heating treatment at 85 °C, demonstrated good thermal stability [18], higher than that found in the current study. Here, the highest T_m was 62.17 °C without the addition of CCD salts; this difference is probably due to the addition of gellan gum to the formulation by Cui et al. Gellan gum is insoluble in cold water and must be heated to 90 °C or higher to be completely dissolved [19]. According to Tako et al., in their formulation that consisted of iota-carrageenan and CCD salt, gelation up to 80 °C was observed in the presence of an intermolecular Ca^{2+} bridge with intra- and intermolecular hydrogen bonding and van Der Waals' forces [20]. The higher crossover temperature of iota-carrageenan solution induced with sodium chloride salt indicates a stronger interaction between iota-carrageenan helices and salt ions [21]. The addition of calcium chloride to gelatin extracted from skins of tropical fishes can reduce the G′ and G″ values of the gelatin solution compared to calcium sulphate and magnesium sulphate [22].

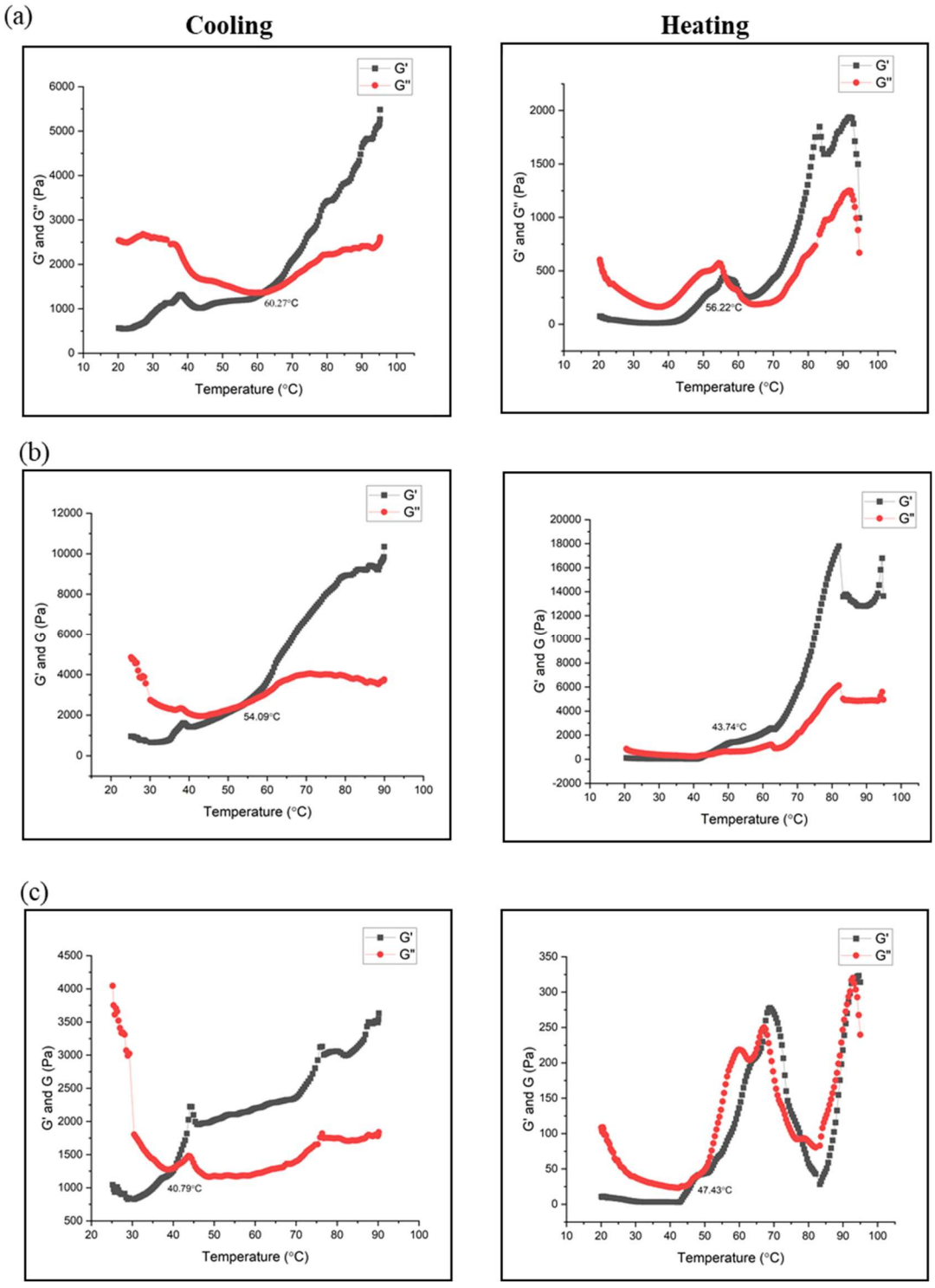


Figure 2. Changes in modulus (G′ and G″) of gels with different concentrations of CCD salts: (a) 0%, (b) 1%, and (c) 2% during heating and cooling

Table 1. Gelling point and melting point of gels with different concentration of CCD salts

Sample (%)	$T_{melting}$ (°C)	$T_{gelling}$ (°C)
0	62.17 ± 1.94	56.66 ± 1.48
0.5	50.53 ± 1.62	56.17 ± 1.75
1	43.90 ± 1.11	56.14 ± 0.54
1.5	48.94 ± 0.57	52.73± 2.61
2	43.88 ± 0.14	50.43 ± 5.45

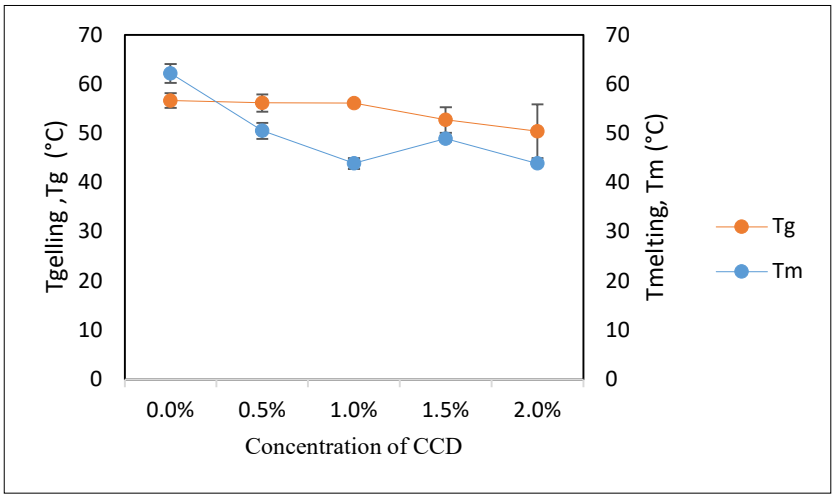


Figure 3. Melting and gelling temperature from G' and G" crossover

Weight variation analysis

Figure 4 (a) and (b) show the weight variation and residual gel weight of the gel air freshener after 4 weeks. The highest residual gel weight percentage was observed for 2% CCD salt concentration, indicating that the formulation solution's ability to prevent evaporation is better for the higher CCD concentration in comparison to lower concentrations. According to Hutagaol, gels made with 3% carrageenan show the ability to maintain the substance to better prevent evaporation [14]. In this study, gels were formulated with 3% carrageenan and different concentrations of CCD salts. Carrageenan gel at 2% shows the ability to maintain its structure at higher concentrations of CCD salts. Figure 4 shows the weight and residual gel weight (%) of the carrageenan gel solution for 45 days. The results obtained in this study support the hypothesis that the greater the resistance of carrageenan gel, the less weight is lost or the greater the weight remaining, meaning less volatile oil and water are evaporated [14].

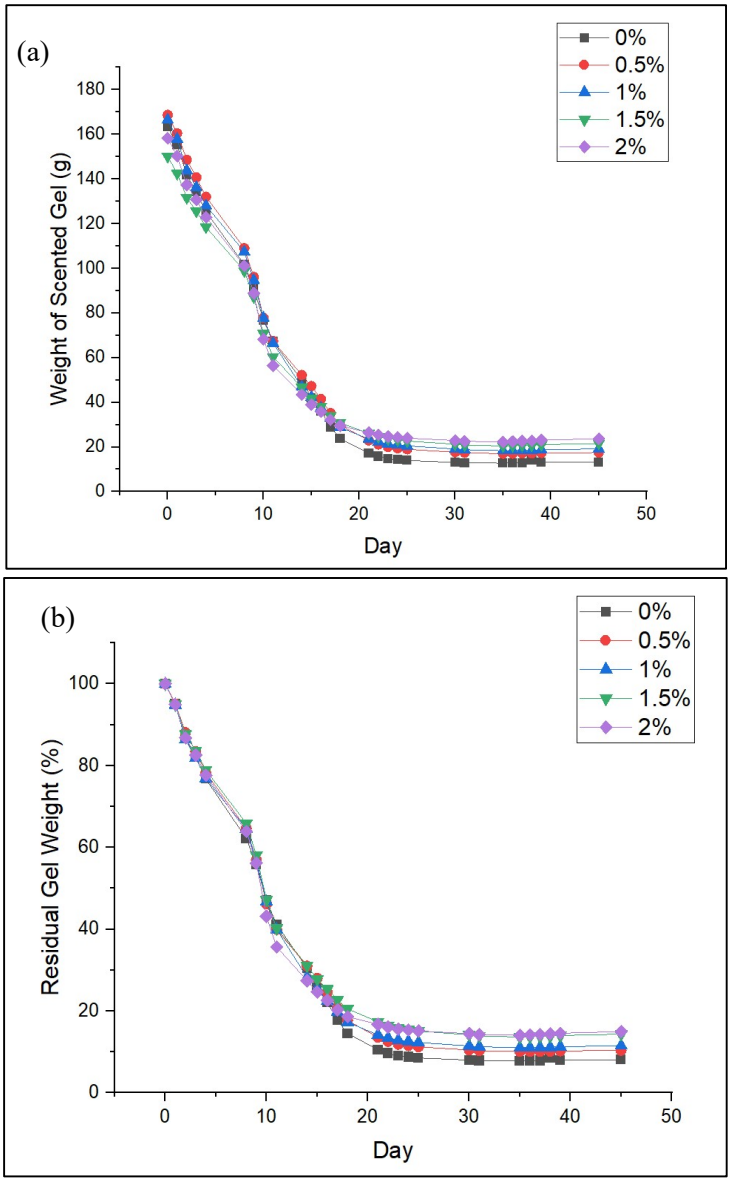


Figure 4. (a) Weight variation (b) residual gel weight

Gel bloom strength test

As shown in Figure 5, the analysis of gel Bloom strength, a commercially important parameter, showed varying values for different samples. The gel formation process is extremely sensitive to the structural and compositional properties of semi-refined carrageenan (SRC). The highest gel Bloom strength, 1331.39 g, was obtained for the carrageenan gel formulation with 2% CCD salt at the lowest viscosity (probability of rejection p-value = 0.00017). The gel Bloom strength has an inverse relationship with viscosity: the higher the gel strength, the lower the viscosity. Formulation solutions containing gellan gum as their gelling agent with the inclusion of calcium ions show decreasing gel strength because of the excessively high concentration of CCD salts. This is because gellan gum molecule relation developed the coagulation state, preventing the stable three-dimensional network structure from being retained [19]. In this study, gel Bloom strength increased with the addition of CCD salts. A better gel strength could also

be attributed to improved carrageenan gelation, as it is believed that chloride salts can improve carrageenan gel strength [23]. In a previous study, the addition of hydroxypropyl methyl cellulose to carrageenan solution increased the viscosity from 172 to 616.5 mPa.s due to the intermolecular interaction between composite chains in the solution which may cause higher mechanical properties [24]. According to Sarbon et al., addition of CCD salts to gelatin solution decreases the gel strength of gelatin but calcium sulphate and magnesium sulphate increase it [22]. This is because of the formulation of a gelatin network in which salt acts as elastic masses for the gelatin. In contrast, in this study, the gel strength increased at higher concentrations of CCD salt. This is probably due to other effects of chemicals such as sodium benzoate and sorbitan monolaurate in the formulation, the effect of which on the gel strength needs to be investigated. Iota-carrageenan hydrogels with various weight percentages of calcium chloride have been successfully developed [25]. Using nanosilica as the carrageenan reinforcement agent increases the mechanical properties of the bioplastic film at a melting temperature of 68 °C [26].

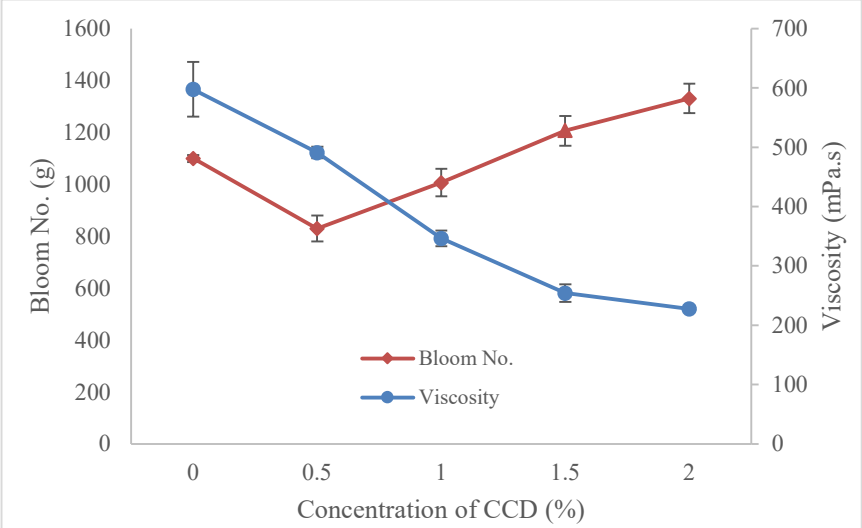


Figure 5. Gel strength test using Bloom gel analysis of carrageenan gel

Thermal properties

TGA was performed to assess the thermal properties of the carrageenan gel formulation. Figure 6(a) and (b) present the relative weight loss from thermogravimetric curves and the weight loss first derivative thermogravimetric (DTG) curves, as functions of temperature in a nitrogen atmosphere, of the carrageenan gels made with various CCD salt concentrations. The results for weight loss obtained from TGA analysis provide an intercorrelation between the variation of CCD salt concentration and weight loss.

Figure 6 (b) shows that the control gel sample had a four-stage weight loss. In the first stage, up to 50 °C, approximately 11.66 % of the weight was lost. This could be attributed to the vaporization of water (absorbed and bound water). The second stage of weight loss began at about 263.4 °C and continued up to 800 °C. At this stage, faster thermal degradation and a weight loss of more than 25% were demonstrated. In the formulation with 2% CCD salts, fewer residues remained at 800 °C and the total weight loss at about 210.2 °C was 11.82%. Carrageenan–poly (vinyl alcohol) composite film heated at 800 °C has shown an increased trend of weight loss with the addition of inorganic ions. This can be explained by the presence of mineral salt produced from the ash [27].

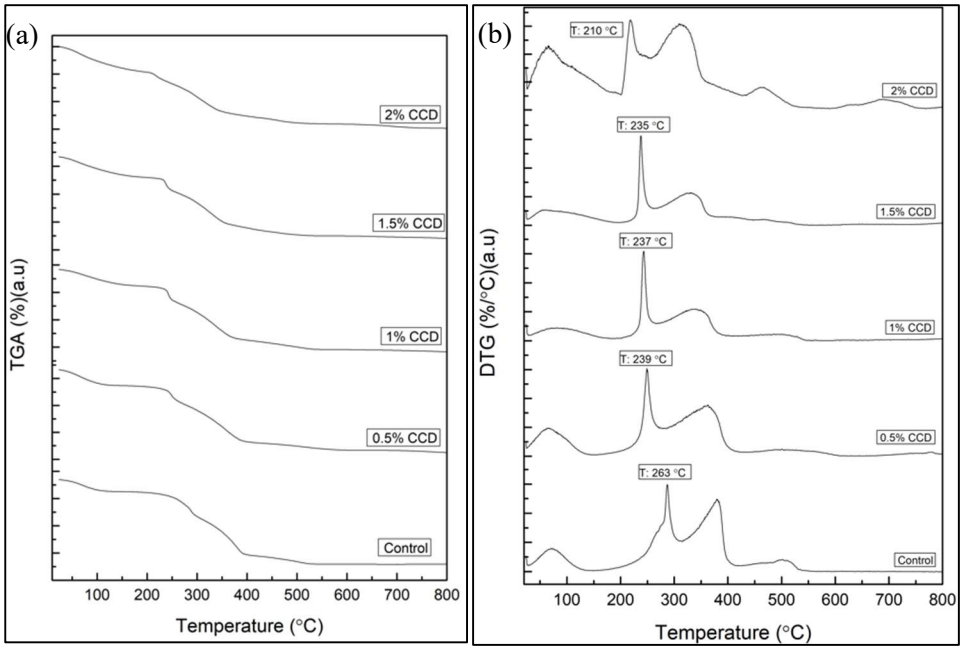


Figure 6. (a) TGA and (b) DTG thermogram for carrageenan gels

Figure 7 and Table 2 shows the DSC analysis on carrageenan gel at different concentrations of CCD salts. The DSC run curve of the control carrageenan gel exhibited an exothermic peak centered at about 185.04 °C corresponding to 323.45 mW of heating. A peak position situated at a higher temperature indicates a stronger interaction with water. Thus, these results suggest that there is an interaction between semi-refined carrageenan and water that may be responsible for the formation of a more stable gel under this condition. According to Figure 7, the DSC results show the enthalpy change during high-temperature heating of samples. In the DSC thermograms, there only one major intense peak was recorded, which was an endothermic transition at temperatures around 185~194 °C. The endothermic transition resulted from the heat absorption for dehydration of water and sample decomposition [28]. Melting temperature decreases with the addition of calcium chloride in bovine gelatin [22].

Table 2. DSC analysis on carrageenan gel at different concentrations of CCD salts

Sample	Sample Mass (mg)	T_m/°C	Heat flow (mW)
0% CCD	7.17	185.04	323.45
0.5% CCD	8.68	184.85	504.06
1% CCD	8.73	188.86	145.78
1.5% CCD	8.39	193.9	154.92
2% CCD	8.89	194.36	415.81

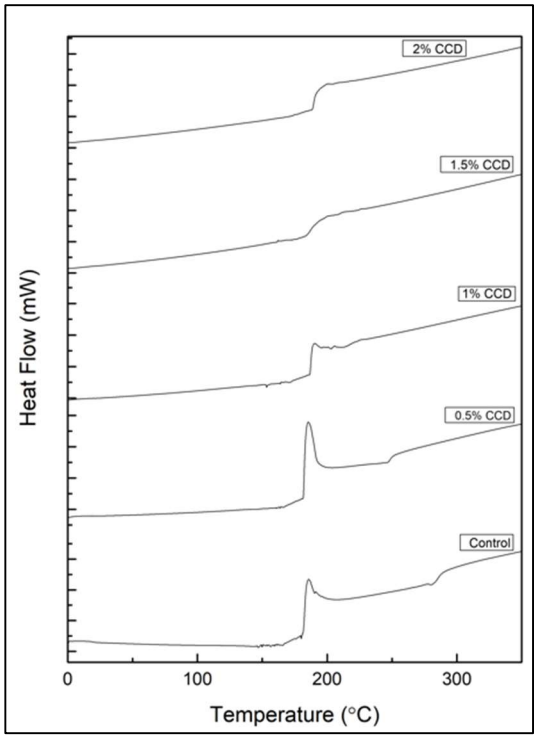


Figure 7. DSC thermograms for carrageenan gels

Morphology analysis

Figure 8 (a) and (b) show SEM images for carrageenan gels from the control sample and 2% CCD salt sample, respectively. Both samples display sponge-like particles with a prominent macroporous structure. In this case, the diameter of the pores seemed to increase at higher calcium chloride concentrations. The images show that the carrageenan gel without salt has a network of smaller and shallow pores. The average diameter of pores at 0% CCD salt was 416.4 μm while at 2% CCD it was 514.1 μm. However, in contrast, the gel produced with the presence of salt displayed larger pores and a higher degree of porosity. The networks became denser by adding CCD salt. This finding is supported by Pan et al., who found that the surface morphology of porcine-myosin–κ-carrageenan mixtures demonstrated large aggregates and cavities at higher calcium chloride concentrations [23]. Adding gellan gum and calcium chloride to surimi gel results in a finer and denser structure compared to surimi gel without the addition of gellan gum and calcium chloride that shows coarser and larger voids due to low breaking force and water-holding capacity [29]. The structure of calcium–ι-carrageenan blended gel has pores that are denser and fragmented; and with addition of glutamic acid, a sheet structure is observed, leading to a weak and open structure [30].

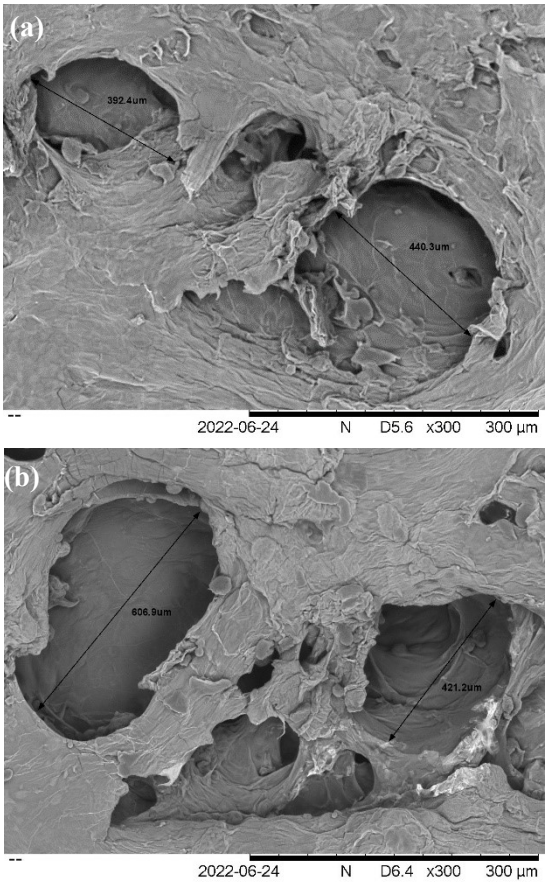


Figure 8. SEM images of surface morphology of carrageenan gel: (a) 0% at 300× and (b) 2% at 300×

Conclusion

In conclusion, the findings in this work provide an important insight into the role of CCD salt to form a strong interaction between gel matrix chemicals to produce stable gel properties. The addition of 2% CCD to the gel formulation manages to increase the residual gel weight from 8% to 15% and improve the mechanical and thermal activities of the gel prepared. This finding suggests the role of CCD salt can be fully utilized in the formulation of a base for aromatherapy scented gel, offering the opportunity to produce a better-quality gel. The mechanical and thermal properties show that the 2% concentration of CCD salts can be used as a base for aromatherapy scented gel, which offers a high gel strength and is expected to enhance the formulation solution of carrageenan scented gel due to the ionic compound of calcium ions.

Acknowledgement

This study was supported by Universiti Malaysia Pahang for the project funding (PDU213218 and PGRS220357) and providing facilities in undertaking this study.

References

1. Ali, B., Al-Wabel, N. A., Shams, S., Ahamad, A., Khan, S. A. and Anwar, F. (2015). Essential oils used in aromatherapy: A systemic review. *Asian Pacific Journal of Tropical Biomedicine*, 5(8): 601-611.
2. Sánchez-Vidaña, D. I., Ngai, S. P.-C., He, W., Chow, J. K.-W., Lau, B. W.-M. and Tsang, H. W.-H. (2017). The effectiveness of aromatherapy for depressive symptoms: A systematic review. *Evidence-Based Complementary and Alternative Medicine*, 2017: 1-21.

3. Sowndhararajan, K. and Kim, S. (2016). Influence of fragrances on human psychophysiological activity: With special reference to human electroencephalographic response. *Scientia Pharmaceutica*, 84(4): 724-751.
4. Adam, F., Abu Bakar, S. H., Yusoff, M. M. and Tajuddin, S. N. (2013). Molecular dynamic simulation of the patchouli oil extraction process. *Journal of Chemical Engineering Data*, 59(2): 183-188.
5. Lakhan, S. E., Sheafer, H. and Tepper, D. (2016). The effectiveness of aromatherapy in reducing pain: A systematic review and meta-analysis. *Pain Research and Treatment*, 2016: 1-13.
6. Bratovcic, A. (2019). Synthesis of gel air freshener and its stability. *Technologica Acta*, 12: 15-21.
7. Adam, F., Jamaludin, J., Abu Bakar, S. H., Abdul Rasid, R. and Hassan, Z. (2020). Evaluation of hard capsule application from seaweed: Gum Arabic-kappa carrageenan biocomposite films. *Cogent Engineering*, 7(1): 1765682.
8. Hamdan, M. A., Ramli, N. A., Othman, N. A., Mohd Amin, K. N. and Adam, F. (2021). Characterization and property investigation of microcrystalline cellulose (MCC) and carboxymethyl cellulose (CMC) filler on the carrageenan-based biocomposite film. *Materials Today: Proceedings*, 42: 56-62.
9. Ramdhan, T., Ching, S. H., Prakash, S. and Bhandari, B. (2019). Time dependent gelling properties of cuboid alginate gels made by external gelation method: Effects of alginate-$CaCl_2$ solution ratios and pH. *Food Hydrocolloids*, 90: 232-240.
10. Wan Yahaya, W. A., Subramaniam, S. D., Mohd Azman, N. A., Adam, F. and Almajano, M. P. (2022). Synthesis of active hybrid films reinforced with cellulose nanofibers as active packaging material. *Chemical Engineering Technology*, 45(8): 1448-1453.
11. Mat Amin, K. A. and Abdul Hadi, T. (2020). Mechanical performance and thermal behaviour of carrageenan gel with lavender essential oil. *IOP Conference Series: Materials Science and Engineering*, 957(1): 012068.
12. Bagal-Kestwal, D. R., Pan, M. H. and Chiang, B.-H. (2019). Properties and applications of gelatin, pectin, and carrageenan gels. In P. M. Visakh, O. Bayraktar and G. Menon (Eds.), Bio monomers for green polymeric composite materials. John Wiley and Sons, Hoboken, NJ, Chichester, UK: pp. 117-140.
13. Ciriminna, R. and Pagliaro, M. (2013). Sol–gel microencapsulation of odorants and flavors: Opening the route to sustainable fragrances and aromas. *Chemical Society Reviews*, 42(24): 9243.
14. Hutagaol, R. (2017). Formulation of air freshener gel with carrageenan as gelling agent, lemon oil as fragrance and patchouli oil as binder. *International Journal of ChemTech Research*, 10(4): 207-212.
15. Osorio, F. A., Bilbao, E., Bustos, R. and Alvarez, F. (2007). Effects of concentration, Bloom degree, and pH on gelatin melting and gelling temperatures using small amplitude oscillatory rheology. *International Journal of Food Properties*, 10(4): 841-851.
16. Mat Yasin, N. H., Othman, N. A. and Adam, F. (2022). Evaluation of the properties on carrageenan bio-films with *Chlorella vulgaris* blending. *Chemical Engineering Communications*: 1-15.
17. Kimbell, G. and Azad, M. A. (2021). 3D printing: Bioinspired materials for drug delivery. In M. Nurunnabi (Ed.), *Bioinspired and Biomimetic Materials for Drug Delivery*. Woodhead Publishing, Oxford, UK: pp. 295-318.
18. Cui, B., Chen, W., Liang, H., Li, J., Wu, D., Ye, S. and Li, B. (2022). A novel κ-carrageenan/konjac gum thermo-irreversible gel improved by gellan gum and Ca2+. *LWT*, 154: 112645.
19. Omoto, T., Uno, Y. and Asai, I. (2000). The latest technologies for the application of gellan gum. In K. Nishinari (Ed.), Physical Chemistry and Industrial Application of Gellan Gum. Progress in Colloid and Polymer Science, vol 114. Springer, Berlin, Heidelberg: pp. 123–126.

20. Tako, M., Sakae, A. and Nakamura, S. (1989). Rheological properties of gellan gum in aqueous media. *Agricultural and Biological Chemistry*, 53(3): 771-776.
21. Elfaruk, M. S., Wen, C., Chi, C., Li, X. and Janaswamy, S. (2021). Effect of salt addition on iota-carrageenan solution properties. *Food Hydrocolloids*, 113: 106491.
22. Sarbon, N. M., Cheow, C. S., Kyaw. Z. W. and Howell, N. K. (2014) Effects of different types and concentration of salts on the rheological and thermal properties of sin croaker and shortfin scad skin gelatin. *International Food Research Journal*, 21(1): 317-324.
23. Pan, T., Guo, H., Li, Y., Song, J. and Ren, F. (2017). The effects of calcium chloride on the gel properties of porcine myosin–κ-carrageenan mixtures. *Food Hydrocolloids*, 63: 467-477.
24. Ramli, N. A., Adam, F., Mohd Amin, K. N., Nor, A. M. and Ries, M. E. (2022). Evaluation of mechanical and thermal properties of carrageenan/hydroxypropyl methyl cellulose hard capsule. *Canadian Journal of Chemical Engineering*, 2022: 6.
25. Mazni, N. Z., Saidin, S. N. and Mobarak, N. N. (2021). Effect of calcium chloride weight percentage on the development of iota-carrageenan based hydrogel. *Journal of Polymer Science and Technology*, 6(2): 27-38.
26. Rane, L. R., Savadekar, N. R., Kadam, P. G. and Mhaske, S. T. (2014). Preparation and characterization of K-carrageenan/nanosilica biocomposite film. *Journal of Materials*, 2014: 1-8.
27. Meng, F., Zhang, Y., Xiong, Z., Wang, G., Li, F. and Zhang, L. (2018). Mechanical, hydrophobic and thermal properties of an organic-inorganic hybrid carrageenan-polyvinyl alcohol composite film. *Composites Part B: Engineering*, 143: 1-8.
28. Jamaludin, J., Adam, F., Rasid, R. A. and Hassan, Z. (2017). Thermal studies on Arabic gum - carrageenan polysaccharides film. *Chemical Engineering Research Bulletin*, 19: 80.
29. Petcharat, T. and Benjakul, S. (2017). Effect of gellan and calcium chloride on properties of surimi gel with low and high setting phenomena. *RSC Advances*, 7(83): 52423-52434.
30. Wen, C., Wang, N., Dong, Y., Tian, J., Song, S. and Qi, H. (2021). Calcium-induced-gel properties for ι-carrageenan in the presence of different charged amino acids. *LWT*, 146: 111418.

Malaysian Journal of Analytical Sciences (MJAS)
Published by Malaysian Analytical Sciences Society

STUDIES ON THE SYNTHESIS OF β-CARBOLINE AND ITS DERIVATIVES AS POTENTIAL ANTIMALARIAL DRUG COMPONENTS

(Kajian Mengenai Sintesis β-Karbolina dan Terbitannya sebagai Komponen Ubat Anti Malaria yang Berpotensi)

Ruwaida Shamsujunaidi[1,3], Aimi Suhaily Saaidin[1,2*], Muhammad Hazim Abdul Aziz[1,3], Mohd Fazli Mohammat[1,3], Noor Hidayah Pungot[1,3]

[1]Organic Synthesis Laboratory,
Institute of Science,
Universiti Teknologi MARA Kampus Puncak Alam,
42300 Bandar Puncak Alam, Selangor, Malaysia
[2]Centre of Foundation Studies,
Universiti Teknologi MARA, Cawangan Selangor, Kampus Dengkil,
43800 Dengkil, Selangor, Malaysia
[3]School of Chemistry and Environment,
Faculty of Applied Sciences,
Universiti Teknologi MARA, 40450 Shah Alam, Selangor, Malaysia

[*]Corresponding author: aimisuhaily@uitm.edu.my

Received: 29 September 2022; Accepted: 17 January 2023; Published: 22 February 2023

Abstract

β-Carboline constitutes a tricyclic pyrido[3,4-b] indole ring structure and is widely recognized for its prevalent biological activities. In recent years, numerous studies have reported on its excellent biological activities, particularly anti-cancer, anti-fungal, anti-malarial agents and many more. Thus, a collective of β-carboline derivatives were synthesized to explore its pharmacological properties. The synthetic approach towards β-carboline derivatives has been constructed in a two-step reaction, including Pictet-Spengler condensation reaction and the iodine-mediated oxidative dehydrogenation reaction. Pictet-Spengler was carried out by treating aldehydes bearing different substituents with tryptamine in the presence of trifluoroacetic acid. The synthesized intermediates were then aromatized to give the desired β-carboline derivatives. All these synthesized intermediates and β-carboline derivatives were analyzed and confirmed by NMR and ATR-FTIR spectroscopy. The working foundation established in this study will be applied in future research and development of new broad-spectrum β-carboline based anti-malarial drugs. Compounds **6**, **9** and **12** synthesized in this work could be promising anti-malaria candidates in this future user.

Keywords: β-carboline, oxidative dehydrogenation reaction, pictet-spengler condensation, tetrahydro-β-carboline, trifluoroacetic acid

Abstrak

β-Karbolina membentuk struktur cincin indol pyrido trisiklik [3,4-b] dan diiktiraf secara meluas untuk aktiviti biologinya yang lazim. Dalam beberapa tahun kebelakangan ini, banyak kajian telah dilaporkan mengenai aktiviti biologinya yang sangat baik terutamanya sebagai agen anti-kanser, anti-kulat, anti-malaria dan banyak lagi. Oleh itu, satu kolektif terbitan β-karbolina telah disintesis untuk meneroka lebih lanjut sifat farmakologinya. Pendekatan sintetik terhadap terbitan β-karbolina telah dibina dalam tindak balas dua langkah yang merangkumi tindak balas pemeluwapan Pictet-Spengler dan tindak balas dehidrogenasi oksidatif pengantara iodin. Pictet-Spengler telah dijalankan dengan merawat aldehid yang mengandungi substituen berbeza dengan triptamina dengan kehadiran trifluoroasetik asid. Perantaraan yang disintesis kemudiannya diaromatis untuk memberikan terbitan β-karbolina yang dikehendaki. Semua perantaraan yang disintesis dan terbitan β-karbolina ini dianalisis dan disahkan oleh spektroskopi NMR dan ATR-FTIR. Asas kerja yang ditubuhkan dalam kajian ini akan digunakan dalam penyelidikan dan pembangunan masa depan ubat antimalaria berasaskan β-karbolina spektrum luas baharu. Kompaun **6**, **9** dan **12** yang disintesis dalam kerja ini boleh menjanjikan calon anti-malaria pada pengguna masa hadapan ini.

Kata kunci: terbitan β-karbolina, tindak balas pendehidrogenan oksidatif, pemeluwapan picter-spengler, tetrahydro-β-karbolina, trifluoroasetik asid

Introduction

In the year 2020, WHO estimated 241 million malaria cases leading to 627 000 deaths, globally [1] whilst based on the annual Commonwealth Malaria Report 2022, the increment of malaria incidences and mortality rates has been reported and ever since the outbreaks of COVID-19. This pandemic disrupted all malaria services and progressed.

Malaria is a global disease induced by apicomplexan parasites derived from plasmodium species [2] where plasmodium falciparum and plasmodium vivax were found to be the most dominant genus contributed to the accession of mortality and morbidity rates [3]. These parasites are carried by female *Anopheles* mosquitoes and infect the human bloodstream upon bloodmeals.

Over the years, multiple treatments and approaches like vector control, vaccines and chemotherapy have been used to combat this infectious disease [4]. The most popular malaria treatments are the common artemisinin-based combination (Fig.1) therapies (ACTs). These first-line treatments comprise artemisinin derivatives such as artesunate-mefloquine (AS-MQ), artesunate-sulfadoxine-pyrimethamine (AS+SP) and artesunate-pyronaridine [5]. The absence of a vaccine and the complexity of these plasmodium species lifecycle triggers the resistance of these strains towards the ACTs [6] and other available drugs [7]. Thus, studies on such artemisinin-based molecules will lead to the potential discovery of new and effective anti-malarial drugs.

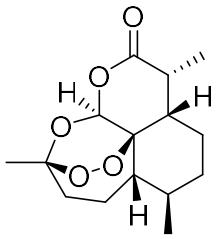


Figure 1. Parent structure of artemisinin

Natural β-carboline alkaloid **1** was found to hold the essential moiety in the exploration of various kinds of drugs due to its excellent biological and pharmacological activities which include anti-plasmodial [8], anti-fungal [9], anti-microbial [10], anti-cancer [11] and more. The scaffolds of β-carboline are extensively distributed in natural products such as plants, insects, marine invertebrates and plant-derived foods [12]. β-Carboline is a part of the indole alkaloid family [13] with a deviating degree of aromaticity [14] of the N-containing six-membered rings. Unsaturated members of β-carboline are known as fully aromatic-β-carbolines (FAβCs). In contrast, the partially saturated and completely saturated rings are known as dihydro-β-carbolines (DHβCs) and tetrahydro-β-carboline (THβCs), respectively (Fig.2).

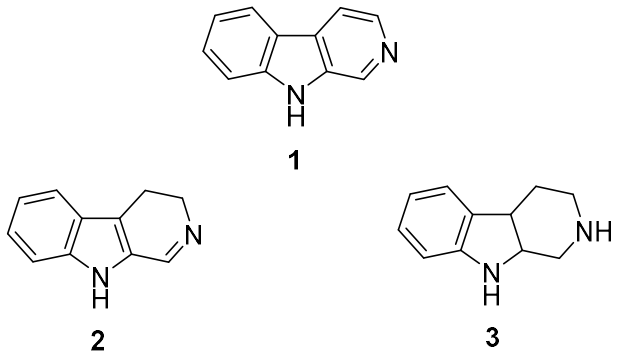


Figure 2. Aromaticity of β-carbolines: (**1**) FAβCs, (**2**) DHβCs, (**3**) THβCs

Yeung et al. (2010) discovered that β-carboline derivatives, spiroindolones or spirotetrahydro β-carbolines possess good anti-malarial activity with in vitro IC_{50} of 90nM. The racemic mixture of spiroazepineindole has been identified to exhibit good efficacy against NF54 and chloroquine-resistant (KI) parasite strains [8]. Additionally, azepineindole (Fig.3) and tetrahydro-β-carboline derivative also (Fig.4) showed a moderate potency towards anti-malarial activity. Tetrahydro-β-carboline (THβCs) and fully aromatic-β-carboline (FAβCs) derivatives such as 5-chloro-tetrahydro-β-carboline [6] exhibit satisfaction activities with low toxicity towards human cells. As for [15], they had reported two guanidine conjugated β-carboline compounds composing excellent activities against malaria strains with IC_{50} values of 0.6 to 1.0 µM.

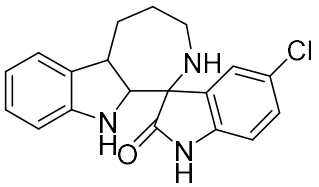


Figure 3. Azepineindole

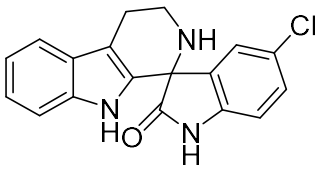


Figure 4. Tetrahydro-*β*-carboline derivative

In line with our interest in finding and developing novel anti-plasmodial agents, we are intrigued to synthesize β-carboline derivatives using tryptamine with various benzaldehyde substituents by applying two facile synthesis reactions. The application of the Pictet-Spengler condensation reaction was the most reported method to synthesize THβCs with the aid of strong Brønsted acids to promote the ring closure of imine. In order to synthesize FAβCs, an oxidative dehydrogenation reaction with iodine was found to be more feasible and convenient [16]. Herein, we report a collection of synthesis results upon applying the Pictet-Spengler reaction catalyzed by trifluoroacetic acid (TFA) and oxidative dehydrogenation reaction.

Materials and Methods

Procedure for the synthesis of compounds 6a-g:
Benzaldehyde (1.0 equiv.) was added to a stirred suspension of tryptamine (1.0 equiv.) and TFA (1.5 equiv.) in DCM. The resulting solution was stirred for 24 hours. The reaction mixture was extracted with EtOAc and dried over anhydrous Na_2SO_4. The combined organic layer was concentrated and purified by silica gel column chromatography with n-hexane, EtOAc (4:1) gradient and 3% triethylamine.

Procedure for the synthesis of compounds 7a-g:
Compound **6(a-g)** (1.0 equiv.) was added to DMSO, iodine, I_2 (0.5 equiv.) and followed by H_2O_2 (1.0 equiv.) and the resulting mixture was stirred at 100˚C for 12 hours. The reaction mixture was poured over cold water extracted with EtOAc and dried over anhydrous Na_2SO_4. The organic layer was evaporated and purified by silica gel column chromatography eluting with a gradient of n-hexane and EtOAc (9:1).

Results and Discussion

4-(2,3,4,9-tetrahydro-1H-pyrido[3,4-b]indol-1-yl)benzonitrile (6a). Yield: 82%, yellow solid. IR *v* cm^{-1}: 3344, 2491, 1659,1449,641cm^{-1}. 1H-NMR (400 MHz, METHANOL-D4) δ 7.86 (dt, J = 8.4, 1.8 Hz, 2H), 7.59-7.54 (m, 3H), 7.29-7.27 (m, 1H), 7.17-7.06 (m, 2H), 6.01 (s, 1H), 3.65-3.53 (m, 2H), 3.23-3.12 (m, 1H). 13C-NMR (101 MHz, METHANOL-D4) δ 139.2, 137.3, 132.9, 130.6, 126.1, 125.8, 122.7, 119.5, 118.0, 117.6, 114.0, 111.2, 108.1, 56.1, 40.8, 18.1.

1-(4-bromophenyl)-2,3,4,9-tetrahydro-1H-pyrido[3,4-b]indole (6b). Yield: 60%, brown oil. IR *v* cm^{-1}: 3067,2174, 1670, 1455, 722 cm^{-1}. 1H-NMR (400 MHz, METHANOL-D4) δ 7.67-7.65 (m, 2H), 7.53 (d, J = 7.8 Hz, 1H), 7.32-7.26 (m, 3H), 7.14-7.07 (m, 2H), 5.89 (s, 1H), 3.28-3.15 (m, 4H). 13C-NMR (101 MHz, METHANOL-D4) δ 137.2, 133.4, 132.3, 131.4, 126.6, 125.9, 124.4, 122.5, 119.4, 117.9, 111.1, 107.9, 56.2, 40.7, 18.2.

1-(3-bromophenyl)-2,3,4,9-tetrahydro-1H-pyrido[3,4-b]indole (6c). Yield: 66%, yellow oil. IR *v* cm^{-1}: 3239, 2179, 1675, 1432, 744 cm^{-1}. 1H-NMR (400 MHz, METHANOL-D4) δ 7.61 (dt, J = 7.6, 1.7 Hz, 1H), 7.55-7.50 (m, 2H), 7.39-7.32 (m, 2H), 7.26 (d, J = 8.2 Hz, 1H), 7.14-7.03 (m, 2H), 5.68 (s, 1H), 3.51-3.38 (m, 2H), 3.12-3.05 (m, 2H). 13C-NMR (101 MHz, METHANOL-D4) δ 138.7, 137.1, 132.6, 132.3, 130.7, 128.2, 128.1, 126.1, 122.7, 122.2, 119.2, 117.8, 111.0, 108.3, 56.3, 41.0, 19.1.

1-(3-nitrophenyl)-2,3,4,9-tetrahydro-1H-pyrido[3,4-b]indole (6d). Yield: 92%, yellow oil. IR *v* cm^{-1}: 3258, 2180,1667, 1135, 667 cm^{-1}. 1H-NMR (400 MHz, METHANOL-D4) δ 8.40-8.37 (m, 1H), 8.32 (t, J = 2.1 Hz, 1H), 7.80-7.73 (m, 2H), 7.56 (d, J = 7.8 Hz, 1H), 7.29 (d, J = 8.2 Hz, 1H), 7.19-7.07 (m, 2H), 6.10 (s, 1H), 3.67-3.58 (m, 2H), 3.24-3.18 (m, 2H). 13C-NMR (101 MHz, METHANOL-D4) δ 148.7, 137.3, 136.2, 135.7, 130.5, 126.1, 125.9, 125.0, 124.5, 122.7, 119.6, 118.1, 111.2, 108.3, 56.0, 41.0, 18.2.

1-(4-(trifluoromethyl)phenyl)-2,3,4,9-tetrahydro-1*H*-pyrido[3,4-*b*]indole (6e). Yield: 90%, yellow solid. IR *v* cm^{-1}: 3055, 1617, 1415, 1321, 742 cm^{-1}. 1H-NMR (400 MHz, METHANOL-D4) δ 7.63 (d, J = 8.2 Hz, 2H), 7.44 (d, J = 8.2 Hz, 3H), 7.20-7.18 (m, 1H), 7.00 (tdd, J = 14.9, 7.0, 1.2 Hz, 2H), 5.23 (s, 1H), 4.07 (q, J = 7.2 Hz, 1H), 3.21 (dt, J = 12.5, 5.4 Hz, 1H), 3.07-3.01 (m, 1H), 2.92-2.78 (m, 2H). 13C-NMR (101 MHz, METHANOL-D4) δ 146.1, 136.7, 132.7, 129.3, 127.0, 125.1, 125.1, 121.1, 118.5, 117.5, 110.7, 109.2, 56.8, 41.2, 21.5.

1-(naphthalen-1-yl)-2,3,4,9-tetrahydro-1*H*-pyridol[3,4-*b*]indole (6f). Yield: 76%, brown oil. IR *v* cm^{-1}: 3055, 1617, 1415, 1321, 742 $cm^{-1.}$ 1H-NMR (400 MHz, CHLOROFORM-D) δ 8.22-8.29 (1H), 7.86-7.93 (1H), 7.80-7.84 (1H), 7.55-7.61 (2H), 7.47-7.53 (1H), 7.33-7.40 (1H), 7.21-7.30 (1H), 7.10-7.18 (2H), 5.85-5.95 (1H), 3.29-3.39 (1H), 3.13-3.22 (1H), 2.84-3.03 (2H). 13C-NMR (101 MHz, METHANOL-D4) δ 147.2, 146.1, 145.7, 138.8, 136.7, 136.7, 132.7, 129.3, 128.3, 127.0, 125.1, 125.1, 121.1, 118.5, 117.5, 110.7, 109.2, 56.8, 41.2, 21.5.

1-(4-isopropylphenyl)-2,3,4,9-tetrahydro-1H-pyrido[3,4-b]indole (6g). Yield: 53%, yellow oil. IR *v* cm^{-1}: 3136, 3057, 1453, 1359, 1710, 744 cm^{-1}. 1H-NMR (400 MHz, CHLOROFORM-D) δ 7.59-7.63 (1H), 7.52-7.55 (1H), 7.18-7.21 (4H), 7.09-7.13 (2H), 5.10-5.15 (1H), 4.08-4.14 (1H), 3.32-3.40 (1H), 3.07-3.15 (1H), 2.86-2.96 (2H), 2.80-2.84 (1H), 1.24-1.25 (3H), 1.22-1.23 (3H). 13C-NMR (101 MHz, CHLOROFORM-D) δ 149.0, 148.7, 141.3, 139.1, 135.9, 134.7, 128.5, 127.5, 126.9, 121.7, 119.4, 118.3, 110.9, 110.2, 57.9, 43.0, 34.0, 24.1, 24.1, 22.6.

4-(9H-pyrido[3,4-b]indol-1-yl)benzonitrile (7a). Yield: 33%, yellow oil. IR *v* cm^{-1}: 3240, 2922, 1670, 1136, 746 cm^{-1}. 1H-NMR (400 MHz, METHANOL-D4) δ 8.42 (dd, J = 5.5, 1.8 Hz, 1H), 8.22 (d, J = 7.8 Hz, 1H), 8.15-8.09 (m, 3H), 7.97-7.93 (m, 2H), 7.61-7.54 (m, 2H), 7.29 (dd, J = 8.2, 6.9 Hz, 1H). 13C-NMR (101 MHz, METHANOL-D4) δ 139.2, 137.3, 132.9, 130.6, 126.1, 125.8, 122.7, 119.5, 118.0, 117.6, 114.0, 111.2, 108.1, 56.1, 40.8, 18.1.

1-(4-bromophenyl)-9H-pyrido[3,4-b]indole (7b). Yield: 71%, yellow solid. IR *v* cm^{-1}: 2983, 1736, 1372, 1233, 1043, 607 cm^{-1}. 1H-NMR (400 MHz,

CHLOROFORM-D) δ 8.54-8.57 (1H), 8.13-8.18 (1H), 7.93-7.97 (1H), 7.81-7.87 (2H), 7.68-7.73 (2H), 7.48-7.59 (2H), 7.29-7.35 (1H). 13C-NMR (101 MHz, METHANOL-D4) δ 137.2, 133.4, 132.3, 131.4, 126.6, 125.9, 124.4, 122.5, 119.4, 117.9, 111.1, 107.9, 56.2, 40.7, 18.2

1-(3-bromophenyl)-9H-pyrido[3,4-b]indole (7c). Yield: 41%, yellow solid. IR *v* cm^{-1}: 3061, 2925, 1231, 742, 673 cm^{-1}. 1H-NMR (400 MHz, ACETONE-D6) δ 8.48 (d, J = 4.8 Hz, 1H), 8.25 (d, J = 7.3 Hz, 1H), 8.20 (t, J = 1.8 Hz, 1H), 8.10-8.05 (m, 2H), 7.64-7.61 (m, 2H), 7.55-7.46 (m, 2H), 7.27 (td, J = 7.5, 0.9 Hz, 1H). 13C-NMR (101 MHz, METHANOL-D4) δ 138.6, 133.1, 132.7, 132.4, 131.6, 126.9, 124.4, 122.5, 117.4, 117.9, 111.3, 104.1, 56.2, 46.7, 19.2

1-(3-nitrophenyl)-9H-pyrido[3,4-b]indole (7d). Yield: 33%, yellow solid. IR *v* cm^{-1}: 3403, 2922, 1348, 729 cm^{-1}. 1H-NMR (400 MHz, ACETONE-D6) δ 8.57-8.47 (m, 3H), 8.41-8.15 (m, 4H), 7.62 (dd, J = 8.2, 0.9 Hz, 1H), 7.57-7.53 (m, 1H), 7.49 (d, J = 8.7 Hz, 0H), 7.29 (td, J = 7.5, 0.9 Hz, 1H). 13C-NMR (101 MHz, METHANOL-D4) δ 148.7, 137.3, 136.2, 135.7, 130.5, 126.1, 125.9, 125.0, 124.5, 122.7, 119.6, 118.1, 111.2, 108.3, 56.0, 41.0, 18.2

1-(4-(trifluoromethyl)phenyl)-9H-pyrido[3,4-b]indole (7e). Yield: 48%, yellow oil. IR *v* cm^{-1}: 3018, 1214, 743, 668 cm^{-1}. 1H-NMR (400 MHz, CHLOROFORM-D) δ 8.58 (d, J = 5.5 Hz, 1H), 8.17 (d, J = 8.2 Hz, 1H), 8.07 (d, J = 7.8 Hz, 2H), 7.98 (d, J = 5.0 Hz, 1H), 7.81 (d, J = 8.2 Hz, 2H), 7.59-7.50 (m, 2H), 7.35-7.31 (m, 1H). 13C-NMR (101 MHz, CHLOROFORM-D) δ 139.8, 136.8, 128.9, 128.6, 128.4, 126.2, 126.2, 125.9, 125.9, 125.6, 125.1, 122.0, 120.8, 120.7, 120.2, 114.6, 112.2, 111.7.

1-(naphthalen-1-yl)-9H-pyrido[3,4-b]indole (7f). Yield: 56%, brown oil. IR *v* cm^{-1}: 3345, 2921, 1625, 741 cm^{-1}. 1H-NMR (400 MHz, CHLOROFORM-D) δ 8.65 (d, J = 5.0 Hz, 1H), 8.20 (t, J = 8.2 Hz, 1H), 8.05 (d, J = 5.5 Hz, 1H), 7.98 (dd, J = 12.8, 8.2 Hz, 2H), 7.77 (dd, J = 7.1, 1.1 Hz, 1H), 7.71 (d, J = 8.2 Hz, 1H), 7.63 (dd, J = 8.0, 7.1 Hz, 1H), 7.54-7.49 (m, 2H), 7.42-7.36 (m, 2H), 7.33-7.29 (m, 1H). 13C-NMR (101 MHz, CHLOROFORM-D) δ 142.4, 140.5, 138.8, 134.7, 134.1, 129.6, 128.9, 128.7, 128.0, 126.9, 126.4, 125.8, 125.5, 122.0, 121.7, 120.4, 114.2, 111.8.

1-(4-isopropylphenyl)-9H-pyrido[3,4-b]indole (7g). Yield: 46%, yellow solid. IR *v* cm^{-1}: 3382, 2956, 1456, 743 cm^{-1}. 1H-NMR (400 MHz, CHLOROFORM-D) δ 8.54 (d, J = 5.5 Hz, 1H), 8.15 (d, J = 7.8 Hz, 1H), 7.91 (d, J = 5.5 Hz, 1H), 7.87 (dd, J = 6.4, 1.8 Hz, 2H), 7.54 (t, J = 1.1 Hz, 1H), 7.49 (s, 1H), 7.42 (d, J = 8.2 Hz, 2H), 7.32-7.28 (m, 1H), 2.99 (t, J = 6.9 Hz, 1H), 1.30 (d, J = 6.9 Hz, 6H). 13C-NMR (101 MHz, METHANOL-D4) δ 139.1, 137.2, 134.4, 132.3, 132.1, 128.6, 125.9, 124.4, 122.5, 120.8, 119.4, 117.9, 116.1, 111.1, 107.9, 74.3, 56.2, 40.7, 17.2.

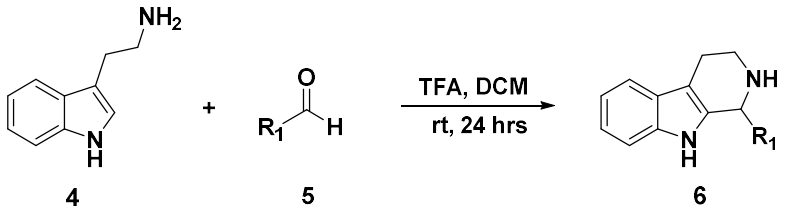
Tryptamine was designated as the model substrate due to its readily synthetic availability. The utilization of benzaldehyde derivatives as the electrophile to undergo condensation with tryptamine commanded most of the initial attention. The Pictet-Spengler reaction was applied to induce the formation of the cyclic ring via C-C bond by the usage of tryptamine as the starting material.

Technically, the Pictet-Spengler reaction expressed the formation of iminium salt upon acid-catalyzed condensation of tryptamine with benzaldehyde derivatives followed by *endo* cyclization between the nucleophilic carbon at the C-2 position and resulting in the intermediate product of N-heterocyclic ring with new C-C bond. Looking at the structure of tryptamine, both carbon-2 and carbon-3 can act as a nucleophile. Spiroindolenine intermediate is produced if the reaction proceeds to attack at carbon-3 before undergoing the 1,2-alkyl shift to yield the tetrahydro-β-carboline (THβCs) intermediates.

In this study, a collective of benzaldehyde derivatives and tryptamine were used to develop a series of tetrahydro-β-carboline (THβCs) and fully aromatic-β-carbolines (FAβCs). Generally, benzaldehyde (**5**) bearing electron-withdrawing group (EWG) provided a higher yield of intermediate THβCs (**6**) compared to those with an electron-donating group (EDG) (Table 1). This can be explained by the inductive and resonance

effects of the substituents. Benzaldehyde with electron-donating groups (EDG) in **6f-g** activated the ring and reduced the electrophilicity of the carbonyl carbon, resulting in weaker reactivity and lower product yields. On the contrary, benzaldehydes bearing electron-withdrawing groups (EWG) in **6a-e** contributed substantially greater yields.

Table 1. Scope of reactions of tryptamine with different substituted benzaldehydes



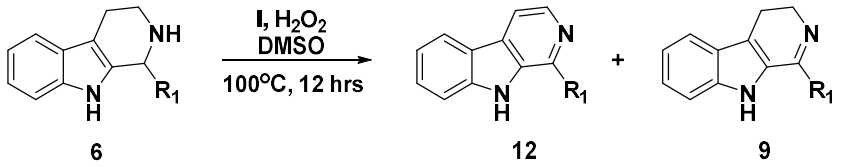
4 5 6

Entry	R_1	Yield (%)
6a	*p*-cyanophenyl	82
6b	*p*-bromophenyl	60
6c	*m*-bromophenyl	66
6d	*m*-nitrophenyl	92
6e	*p*-(trifluoromethyl)phenyl	90
6f	*o*-napthaldehyde	76
6g	*p*-isopropylphenyl	53

Each of the intermediate products, THβCs (**6**) proceeded for aromatization by utilizing the oxidative dehydrogenation reaction with iodine. There are various ways to promote the aromatization and construction of these β-carboline structures. However, a few drawbacks were highlighted. Some procedures such as applying heat with palladium, Pd on carbon, C [17] or sulphur, S [18] or boiling the intermediate THβCs with organic solvents over high temperature with oxidizing agents are not favorable because they require raucous condition. Method utilizing reagents such as chloranil [19], DDQ [20], trichloroisocyanuric acid [21], $PhI(OAc)_2$ [22], N-chlorosuccinimide [23] and IBX [24] could promote aromatization. However, they were reported to suffer from disadvantages of using excess reagents, having massive waste production and affording low yield of target compounds.

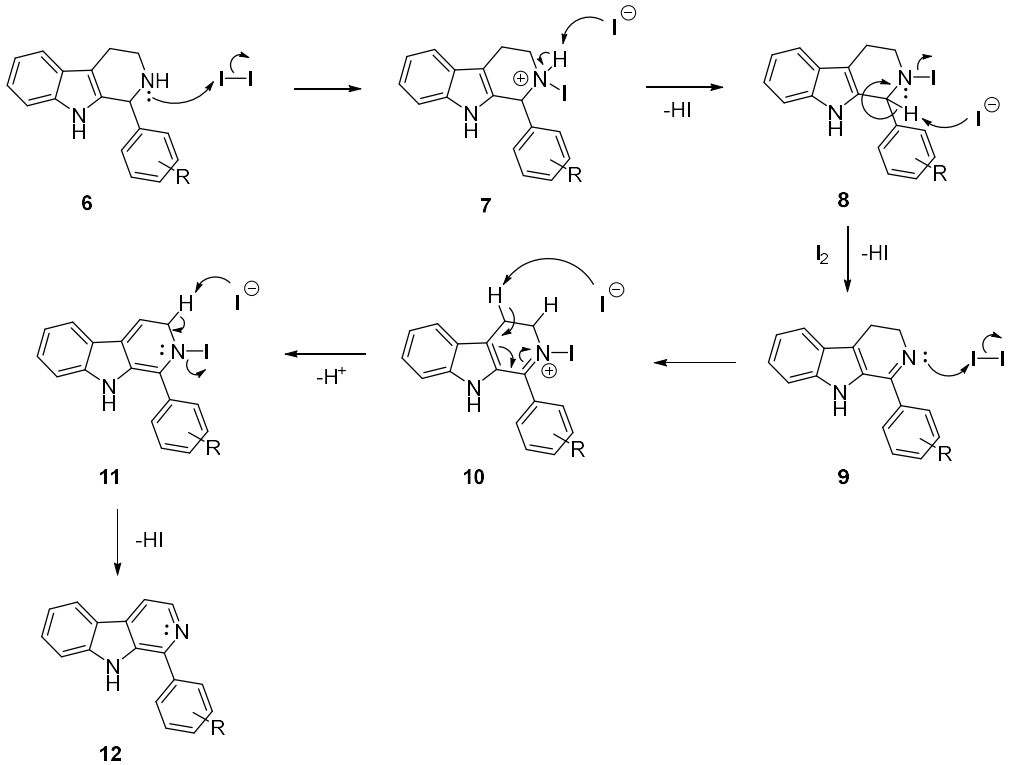
According to Table 2, THβCs with both the electron-withdrawing group (EWG) and electron-donating group (EDG) provided moderate product yields since the electronic effect and activation profile of each of the benzaldehyde substituent does not affect the aromatization of the N-heterocyclic ring. The moderate yields of the target products, FAβCs (**12**) can be explained by the formation of DHβCs (**9)** as the minor products. Alternately, complete aromatization of THβCs could also be achieved by increasing the equivalent amount of H_2O_2 [16],[25].

Table 2. Aromatization of tetrahydro-β-carboline (THβCs) intermediates



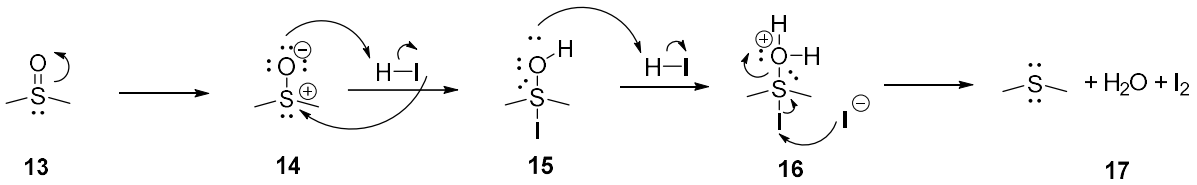
Entry	R_1	Yield (%)
7a	*p*-cyanophenyl	33
7b	*p*-bromophenyl	71
7c	*m*-bromophenyl	41
7d	*m*-nitrophenyl	33
7e	*p*-(trifluoromethyl)phenyl	48
7f	*o*-napthaldehyde	56
7g	*p*-isopropylphenyl	46

The mechanism of oxidative dehydrogenation reaction can be explained by the initial N-iodination of THβCs intermediate (**6**) where the lone pair of the nitrogen attacks the iodine, followed by the formation of imine intermediate, DHβCs (**9**) *via* dehydroiodination process. Next, DHβCs undergo another N-iodination reaction to yield an ammonium intermediate (**10**). Subsequent deprotonation and dehydroiodination upon this intermediate promote aromatization and give our final target product of FaβCs (Scheme 1).



Scheme 1. Mechanism of iodine-mediated oxidative dehydrogenation

The regeneration of iodine, I_2 is crucial to maintain a continuous cycle for this reaction. Dehydroiodination reaction took at least twice to produce HI where its acidic proton will promote the removal of water, reduction of DMSO to dimethyl sulfate (DSM) and regeneration of iodine, I_2 (Scheme 2). H_2O_2 promotes an atmospheric environment to control the reduction activity by oxidizing the DMS to DMSO and catalyzed the reaction activity [26].



Scheme 2. Mechanism on regeneration of iodine, I_2

Conclusion

In conclusion, a series of tetrahydro-β-carboline intermediates were synthesized via Pictet-Spengler reaction from tryptamine and benzaldehydes with different substituents. Benzaldehydes bearing the electron-withdrawing groups (EWG) provided higher yields compared to those with electron-donating groups (EDG). Application of iodine-mediated oxidative dehydrogenation method promoted the aromatization of N-heterocyclic ring of THβCs intermediates into fully aromatized-β-carbolines (FAβCs) as the major products and dihydro-β-carbolines (DHβCs) as the minor products. Further study on the biological properties of the synthesized products toward anti-malaria activities are currently in progress.

Acknowledgement

The authors acknowledge the generous support of Organic Synthesis Research Laboratory, Institute of Science (IOS), Universiti Teknologi MARA in providing required chemicals and instruments, as well as the financial support from Research Management Centre UiTM (grant 600-RMC/GPM LPHD 5/3 (113/2021).

References

1. Health Organization, W. (2022). WHO Guidelines for malaria-3 June 2022. (No. WHO/UCN/ GMP/2022.01 Rev. 2). World Health Organization.
2. Phillips, M. A. and Rathod, P. K. (2010). Plasmodium dihydroorotate dehydrogenase: a promising target for novel anti-malarial chemotherapy. *Infectious Disorders Drug Targets*, 10(3): 226-239.
3. Jaromin, A., Gryzło, B., Jamrozik, M., Parapini, S., Basilico, N., Cegła, M., Taramelli, D. and Zagórska, A. (2021). Synthesis, molecular docking and antiplasmodial activities of new tetrahydro-β-carbolines. *International Journal of Molecular Sciences*, 22(24):13569.
4. Gorki, V., Singh, R., Walter, N. S., Bagai, U. and Salunke, D. B. (2018). Synthesis and evaluation of antiplasmodial efficacy of β-carboline derivatives against murine malaria. *ACS Omega*, 3(10): 13200-13210.
5. World Health Organization. (2018). Artemisinin resistance and artemisinin-based combination therapy efficacy: status report (No. WHO/CDS/GMP/2018.18) World Health Organization.
6. Eagon, S., Hammill, J. T., Bach, J., Everson, N., Sisley, T. A., Walls, M. J., Durham, S., Pillai, D. R., Falade, M. O., Rice, A. L., Kimball, J. J., Lazaro, H., DiBernardo, C. and Kiplin Guy, R. (2020). Antimalarial activity of tetrahydro-β-carbolines targeting the ATP binding pocket of the Plasmodium falciparum heat shock 90 protein. *Bioorganic & Medicinal Chemistry Letters*, 30(21): 127502.

7. Morita, H., Tomizawa, Y., Deguchi, J., Ishikawa, T., Arai, H., Zaima, K., Hosoya, T., Hirasawa, Y., Matsumoto, T., Kamata, K., Ekasari, W., Widyawaruyanti, A., Wahyuni, T. S., Zaini, N. C. and Honda, T. (2009). Synthesis and structure-activity relationships of cassiarin A as potential antimalarials with vasorelaxant activity. *Bioorganic & Medicinal Chemistry*, 17(24): 8234-8240.
8. Yeung, B. K. S., Zou, B., Rottmann, M., Lakshminarayana, S. B., Ang, S. H., Leong, S. Y., Tan, J., Wong, J., Keller-Maerki, S., Fischli, C., Goh, A., Schmitt, E. K., Krastel, P., Francotte, E., Kuhen, K., Plouffe, D., Henson, K., Wagner, T., Winzeler, E. A., … Keller, T. H. (2010). Spirotetrahydro β-carbolines (spiroindolones): A new class of potent and orally efficacious compounds for the treatment of malaria. *Journal of Medicinal Chemistry*, 53(14): 5155–5164.
9. Singh, R., Jaisingh, A., Maurya, I. K. and Salunke, D. B. (2020). Design, synthesis and bio-evaluation of C-1 alkylated tetrahydro-β-carboline derivatives as novel antifungal lead compounds. *Bioorganic & Medicinal Chemistry Letters*, 30(3): 126869.
10. Saify, Z. S., Farhad, J., Mushtaq, N., Noor, F., Akhtar, S., Arif, M., Naqvi, B. S. and Shoaib, M. H. (2005). Antibacterial activity of 1-methyl-7-methoxy-beta-carboline and its phenacyl and coumarine analogues. *Pakistan Journal of Pharmaceutical Sciences*, 18(3): 39-41.
11. Mohamed, H. A., Girgis, N. M. R., Wilcken, R., Bauer, M. R., Tinsley, H. N., Gary, B. D., Piazza, G. A., Boeckler, F. M. and Abadi, A. H. (2010). Synthesis and molecular modeling of novel tetrahydro-β-carboline derivatives with phosphodiesterase 5 inhibitory and anticancer properties. *Journal of Medicinal Chemistry*, 54(2): 495-509.
12. Ferraz, C. A. A., de Oliveira Júnior, R. G., Picot, L., da Silva Almeida, J. R. G. and Nunes, X. P. (2019). Pre-clinical investigations of β-carboline alkaloids as antidepressant agents: A systematic review. *Fitoterapia*, *137*.
13. Yang, M. L., Kuo, P. C., Damu, A. G., Chang, R. J., Chiou, W. F. and Wu, T. S. (2006). A versatile route to the synthesis of 1-substituted β-carbolines by a single step Pictet–Spengler cyclization. *Tetrahedron*, 62(47): 10900-10906.
14. Zhang, J., Li, L., Dan, W., Li, J., Zhang, Q., Bai, H. and Wang, J. (2015). Synthesis and antimicrobial activities of 3-methyl-β-carboline derivatives. *Natural Product Communications*, 10(6): 9-12.
15. Kumar, V., Sachdeva, C., Waidha, K., Sharma, S., Ray, D., Kumar Kaushik, N. and Saha, B. (2021). In vitro and in silico anti-plasmodial evaluation of newly synthesized β-carboline derivatives. *ChemistrySelect*, 6(21): 5338-5342.
16. Ash'ari, N. A. N., Pungot, N. H., Shaameri, Z. and Jani, N. A. (2021). A facile synthesis of n-alkylated daibucarboline a derivatives via pictet-spengler condensation of tryptamine. *Malaysian Journal of Analytical Sciences*, 25(5): 706-715.
17. Soerens, D., Sandrin, J., Ungemach, F., Mokry, P., Wu, G. S., Yamanaka, E., Hutchins, L., DiPierro, M. and Cook, J. M. (1979). Study of the Pictet-Spengler reaction in aprotic media: synthesis of the β-galactosidase inhibitor, pyridindolol10. *Journal of Organic Chemistry*, 44(4): 535-545.
18. Cain, M., Weber, R. W., Guzman, F., Cook, J. M., Barker, S. A., Rice, K. C., Crawley, J. N., Paul, S. M. and Skolnick, P. (1982). β-Carbolines: Synthesis and neurochemical and pharmacological actions on brain benzodiazepine receptors. *Journal of Medicinal Chemistry*, 25(9): 1081-1091.
19. Lippke, K. P., Schunack, W. G., Wenning, W. and Muller, W. E. (1983). β-carbolines as benzodiazepine receptor ligands. 1. synthesis and benzodiazepine receptor interaction of esters of β-carboline-3-carboxylic acid. *Journal of Medicinal Chemistry*, 26(4): 499-503.
20. Jun'ichi, K., Cheng, J. F., Ohizumi, Y., Ohta, T., Nozoe, S. and Sasaki, T. (1990). Eudistomidins B, C, and D: novel antileukemic alkaloids from the okinawan marine tunicate *Eudistoma glaucus*. *Journal of Organic Chemistry*, 55(11): 3666-3670.

21. Yin, W., Sarma, P. V. V. S., Ma, J., Han, D., Chen, J. L. and Cook, J. M. (2005). Synthesis of bivalent ligands of β-carboline-3-carboxylates via a palladium-catalyzed homocoupling process. *Tetrahedron Letters*, 46(37): 6363-6368.
22. Kamal, A., Tangella, Y., Manasa, K. L., Sathish, M., Srinivasulu, V., Chetna, J. and Alarifi, A. (2015). PhI(OAc)2-mediated one-pot oxidative decarboxylation and aromatization of tetrahydro-β-carbolines: synthesis of norharmane, harmane, eudistomin U and eudistomin I. *Organic & Biomolecular Chemistry*, 13(32): 8652-8662.
23. Kamal, A., Sathish, M., Prasanthi, A. V. G., Chetna, J., Tangella, Y., Srinivasulu, V., Shankaraiah, N. and Alarifi, A. (2015). An efficient one-pot decarboxylative aromatization of tetrahydro-β-carbolines by using N-chlorosuccinimide: total synthesis of norharmane, harmane and eudistomins. *RSC Advances*, 5(109): 90121-90126.
24. Panarese, J. D. and Waters, S. P. (2010). Room-temperature aromatization of tetrahydro-β-carbolines by 2-iodoxybenzoic acid: Utility in a total synthesis of eudistomin U. *Organic Letters*, 12(18): 4086-4089.
25. Gaikwad, S., Kamble, D. and Lokhande, P. (2018). Iodine-catalyzed chemoselective dehydrogenation and aromatization of tetrahydro-β-carbolines: A short synthesis of Kumujian-C, Eudistomin-U, Norharmane, Harmane Harmalan and Isoeudistomine-M. *Tetrahedron Letters*, 59(25): 2387-2392.
26. Chu, J. W. and Trout, B. L. (2004). On the mechanisms of oxidation of organic sulfides by H_2O_2 in aqueous solutions. *Journal of the American Chemical Society*, 126(3): 900-908.

Malaysian Journal of Analytical Sciences (MJAS)
Published by Malaysian Analytical Sciences Society

HYDROTHERMAL SYNTHESIS OF Co AND Pd DOPED TIN OXIDE NANORODS AND THEIR PHOTOCATALYTIC DEGRADATION OF POLYPROPYLENE

(Sintesis Hidroterma Nanorod Stanum Oksida Terdop Co dan Pd dan Degradasi Fotokatalitik Polipropilena)

Vicinisvarri Inderan[1,*], Nur Aina Shahida Ahmad[1], Nurizyan Amirah Mohd Zaidi[1], Norain Isa[1], Wan Zuraida Wan Kamis[1], Hooi Ling Lee[2], and Siva Raseetha[3]

[1]*Chemical Engineering Studies,*
College of Engineering,
Universiti Teknologi MARA, Penang Branch,
13500 Permatang Pauh, Penang, Malaysia
[2]*Nanomaterials Research Group,*
School of Chemical Sciences,
Universiti Sains Malaysia, 11800 USM, Penang, Malaysia
[3]*Faculty of Applied Sciences,*
Universiti Teknologi MARA, 40450 Shah Alam, Selangor, Malaysia

[*]*Corresponding author: vicinisvarri@uitm.edu.my*

Received: 6 October 2022; Accepted:17 Jan 2023; Published: 22 February 2023

Abstract

It has been reported that the wastewater treatment processes are unable to remove microplastics (MPs) from wastewater completely and often bypass the treatment plants into water resources. Hence, this study tested cobalt (Co) and palladium (Pd) doped tin oxide SnO_2 nanorods as photocatalysts to degrade the MPs. Co and Pd were selected as dopants due to their high oxidation catalytic characteristics. A dosage of 10 mol% dopants was used to prepare the doped SnO_2 nanorods. The SnO_2 was synthesized using a facile hydrothermal route at a relatively lower temperature, 180 °C. To study the photocatalytic performance of MPs, the reaction was executed on polypropylene (PP) for 72 hours under visible light irradiation. While, the effect of pH was tested at different pH conditions (5,7, and 9). The SnO_2 nanorods were analyzed using X-ray diffraction (XRD), field emission scanning electron microscope (FESEM), Fourier transforms infrared (FTIR) spectrometer, and UV-Vis spectrometer. The broadening of XRD peaks in Pd and Co-doped SnO_2 nanorods signifies a decrease in crystalline size, which is supported by FESEM images with ~15 nm diameter. The performance of the photodegradation of PP is verified by using FTIR analysis. The strong vibration peaks of the carbonyl and hydroxyl bands confirmed that the polymer chain broke down via a photo-oxidation reaction. Cracks and cavities have been found on the surface of PP after the photocatalytic reaction. Overall, 10% Pd-doped and Co-doped SnO_2 have exhibited good performance after 72 hours of photocatalytic reaction at pH 9, and it has a high potential as a photocatalyst for the degradation of MPs.

Keywords: tin oxide, palladium doped, cobalt doped, microplastics, photodegradation

Abstrak

Laporan menunjukkan bahawa proses rawatan air sisa tidak dapat membuang mikroplastik (MP) sepenuhnya yang terkandung dalam air sisa malah sering memintas loji rawatan ke sumber air. Oleh yang demikian, dalam kajian ini kobalt (Co) dan paladium (Pd) terdop stanum oksida (SnO_2) telah diselidik sebagai fotokatalis untuk mendegradasi MP. Co dan Pd telah dipilih sebagai logam dopan disebabkan kedua-dua logam tersebut mempunyai ciri-ciri pemangkin oksida yang tinggi. Sukatan sebanyak 10 mol% dopan telah digunakan untuk menyediakan nanorod SnO_2 terdop. SnO_2 telah disintesis menggunakan laluan hidroterma yang mudah pada suhu yang agak rendah, 180 °C. Untuk mengkaji prestasi fotodegradasi MP, proses fotokatalisis telah dijalankan pada polipropilena (PP) selama 72 jam, di bawah penyinaran cahaya nampak. Manakala, kesan pH pada telah dikaji pada pH yang berlainan (5,7 dan 9). Nanorod SnO_2 yang terhasil telah dianalisis menggunakan pembelauan sinar-X (XRD), mikroskop elektron pengimbasan pancaran medan (FESEM), spektrometer Fourier inframerah transfomasi (FTIR) dan spektrometer UV-Vis. Pelebaran puncak XRD bagi sampel nanorod SnO_2 terdop menunjukkan penurunan dalam saiz kristal, yang disokong oleh imej FESEM dengan diameter ~ 15 nm. Prestasi fotodegradasi PP telah disahkan melalui analisis FTIR. Kehadiran puncak getaran kuat karbonil dan hidroksil mengesahkan rantai polimer terputus melalui tindak balas pengoksidaan foto. Keretakan dan rongga telah ditemui pada permukaan PP yang telah dirawat dengan fotokatalisis. Secara keseluruhan, SnO_2 terdop dengan 10 mol% Co and Pd telah menunjukkan prestasi yang baik selepas 72 jam tindak balas fotokatalitik pada pH 9 dan ia mempunyai potensi tinggi sebagai fotomangkin untuk degradasi mikroplastik.

Kata kunci: stanum oksida, dop palladium, dop kobalt, mikroplastik, penguraian foto.

Introduction

The contamination of water by microplastics (MPs) has emerged as a global environmental and public health issue. In contrast to large plastic waste, the removal of MPs is more difficult due to the microscale size, which is often less than 5 mm and hard to detect with the naked eye [1]. Scientists suspect that wastewater treatment plants are the primary source of MPs in rivers and oceans, despite the fact that MPs break down from larger plastics into smaller pieces and eventually enter the water resources. As MPs' concentration in the environment rises, so does the likelihood of ecosystem exposure. Consequently, there is an increased risk of interaction, ingestion, and adverse effects across food webs [2].

Therefore, in recent years, extensive effort has thus been focused on developing ways to minimize the volume of MPs entering the natural aquatic system using various technologies such as electrocoagulation, magnetic extraction, and photodegradation. Electrocoagulation is a method that utilizes metal electrodes to create coagulation for the removal of MPs. Although this method has a higher MP removal efficiency, the characteristics of the electrode and wastewater, such as density, conductivity, and pH, have a significant impact on the process, making consistency difficult to achieve [3]. On the other hand, in magnetic extraction, MPs bind with iron-based nanoparticles before being separated by external magnetic attraction from the wastewater. This technique normally leads to secondary sludge waste. The photodegradation method usually uses UV light to break the polymer chain of MPs. However, the technique's scalability is limited by its high energy consumption and lengthy reaction time [4].

Visible light photocatalysis using semiconductor nanoparticles is regarded as an environmentally friendly process capable of degrading MPs in less time with less energy consumption. Over the years, various semiconductors nanoparticles, especially titanium dioxide (TiO_2) [5, 6] and zinc oxide (ZnO)[7-9] have been extensively studied in the photocatalysis of MPs in water. In spite of the fact that these materials demonstrated degradation of MPs, complete degradation has not yet been reported. Moreover, their applications were often restricted by the limited absorption of visible light and the short lifetime of electron-hole pairs [10]. Tin oxide is an n-type semiconductor, which is well known for its wide band gap (3.6 eV at 300 K), large exciton binding energy (130 meV), and high electron mobility (100-200 $cm^2\ V^{-1}\ S^{-1}$) [11]. Due to its wide band gap, tin oxide itself exhibits a relatively low photocatalytic effect. However, in comparison to SnO_2 to TiO_2 and ZnO, it is known to be a better electron acceptor due to the presence of a more

positive conductive band (CB). Hence, coupling with other metal oxides or doping with transitional metals or noble metals effectively reduces the photogenerated electrons-holes pairs recombination during the photocatalytic reaction [12].

Our previous study reported on the hydrothermal synthesis of metal doped SnO_2 nanorods and their performance as ethanol gas sensors. The results revealed that doping improves the physiochemical properties of SnO_2 [13, 14]. Thus, in the current study, cobalt (Co) and palladium (Pd) doped tin oxide nanorods were synthesized using the hydrothermal method and tested their photocatalytic performance on polypropylene (PP) sample, which is one of the most widely found microplastic pollutants in wastewater.

Materials and Methods

Chemicals

Tin (IV) chloride pentahydrate ($SnCl_4.5H_2O$), cobalt chloride hexahydrate ($CoCl_2.6H_2O$), and palladium chloride ($PdCl_2$) were purchased from Sigma-Aldrich. All chemical reagents were analytical grade without any further purification. Sodium hydroxide (NaOH) was purchased from Qrec Asia Sdn. Bhd, Malaysia, and absolute ethanol (C_2H_5OH) were procured from HmbG Chemicals. All the solutions were prepared using distilled water. MPs sample was prepared from fully aged Polypropylene (PP), which was obtained from a local home storage manufacturer, ASOTV, Kuala Lumpur.

Synthesis of tin oxide nanorods

The synthesis of doped SnO_2 nanorods using the hydrothermal method is described elsewhere [14]. Briefly, tin oxide, 0.32 mol of tin (IV) chloride pentahydrate ($SnCl_4.5H_2O$) was dissolved in 40 ml absolute ethanol - distilled water solvent (1:1 v/v) while stirring continuously. Co and Pd dopants (10 mol%) were added separately in the solution above. Simultaneously the pH of the reaction solution was adjusted to pH 13 by slowly adding an equal volume of 6 M NaOH aqueous solution and absolute ethanol. The pH was monitored throughout the reaction. The final volume of the reaction mixture was completed to 80 mL by adding in absolute ethanol – distilled water solvent (1:1 v/v). A white slurry for undoped SnO_2, a peach color slurry for Co-doped SnO_2, and a grey color slurry for Pd-doped SnO_2 were obtained at the end of the reaction. The samples were then transferred into a 100 mL Teflon -linen stainless-steel autoclave, sealed, and heated at 180 °C for 24 hrs. After being naturally cooled at room temperature, the product was centrifuged and repeatedly washed with distilled water followed by ethanol and then dried in the oven at 60 °C for 24 hrs. The undoped SnO_2 nanorod sample was prepared similarly but without the dopant. Figure 1 shows the final product produced via the hydrothermal process.

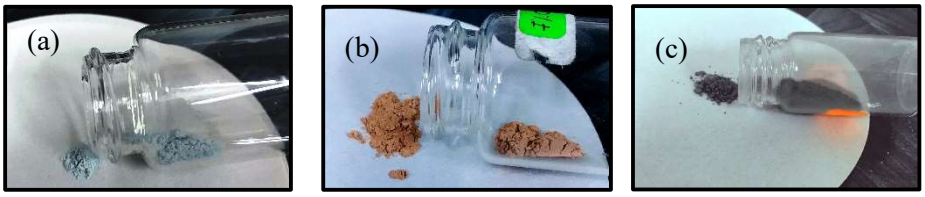


Figure 1. (a) Undoped SnO_2, (b) Co doped SnO_2, and (c) Pd doped SnO_2 powder samples

Photocatalysis reaction setup

The photocatalytic performance of the as-synthesized tin oxide nanorod sample was tested on PP. A known amount of PP microplastics sample (1 g, size particle~125 µm) was suspended in 100 ml distilled water. The photocatalytic reaction was carried out at room temperature under visible light (LED Blu-ray, 18 Watt, λ, 460 -462 nm) irradiation. 0.5 mg of tin oxide nanorods photocatalyst was added to the MPs sample. To obtain a uniform distribution of PP with a photocatalyst, the sample was shaken at the speed of 150 rpm using an orbital shaker for the duration of 72 hrs. To study the effect of pH, doped SnO_2 samples were tested at different pH conditions (5,7, and 9). After the reaction, the PP and photocatalyst were filtered out using a vacuum pump and dried at room

temperature for 24 hours. Figure 2 shows the experimental setup for the photocatalytic reaction.

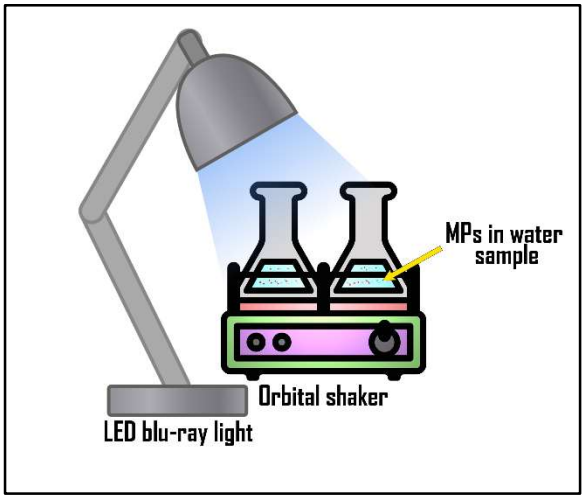


Figure 2. Schematic diagram of photocatalytic reaction under visible light (LED blu-ray) source

Characterization

The morphology and composition of the SnO_2 were determined using HRTEM (high-resolution transmission electron microscopy (HRTEM) (TECNAI G2 20 S-TWIN, FEI, China) and X-ray diffraction technique (PW 3040/60 X'PERT PRO (PANanalytical, Neterland). The X-ray diffraction (XRD) patterns are obtained using Cu Kα radiation (λ=0.1541 nm) in the 2θ range of 20° to 90°. The band gap was calculated using a UV-Vis spectrometer (Perkin Elmer Lambda 35, United States). The photodegradation was verified using Fourier transform Infrared (FTIR) spectrometer (Perkin Elmer's System 2000 FTIR, United States). The infrared spectra were collected in the range of 4000-400 cm^{-1}. For oxidized PP, carbonyl groups were identified in the wide infrared range at 1500-1800 cm^{-1}, with the peak at 2800-2950 cm^{-1} utilized as a reference, which is related to CH bending and CH_3. SEM (HITACHI, TM3030Plus, Japan) was used to observe and determine the morphology of the microplastics with a photocatalyst. The SEM images were taken at a magnification of 600x to 5000x.

Results and Discussion

Figure 3 shows the XRD patterns of undoped SnO_2, Co, and Pd-doped SnO_2 nanorod powder samples. All diffraction peaks could be assigned to the rutile-type tetragonal phase (space group, *P42/mnm*); which was indexed on the basis of ICSD 092552, and no trace of other metallic or metal oxide phases have been detected. The broadening of diffraction peaks shows that the dopants not only reduced the particle size but also lowered the crystallinity of nanoparticles. The prominent reflection of (101), (110), and (211) peaks indicate the preferential crystal planes of the nanostructure [15].

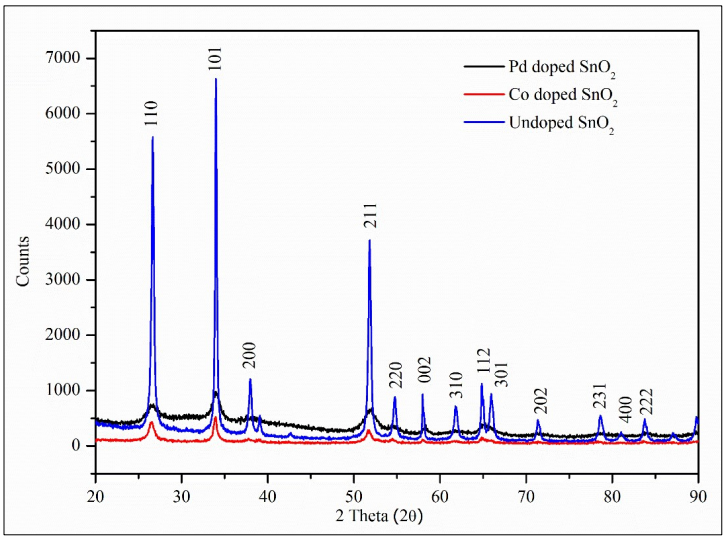


Figure 3. XRD diffraction patterns of undoped and doped SnO_2 nanostructures

The morphology of as-synthesized SnO_2 samples was analyzed by using SEM and HRTEM. Figure 4 exhibits the SEM images of SnO_2 samples. From the SEM images, it can be seen clearly that the SnO_2 are in the form of nanorods. A comparison of the morphology images revealed that the presence of 10% Co and 10% Pd dopants did not affect the shape of the nanorods; However, in comparison to the undoped SnO_2, the size of the nanorods has been significantly reduced. This result suggested that the Co and Pd greatly inhibited SnO_2 grain size, which is in line with XRD data, where the broadening of peaks was observed clearly in doped SnO_2 samples [15].

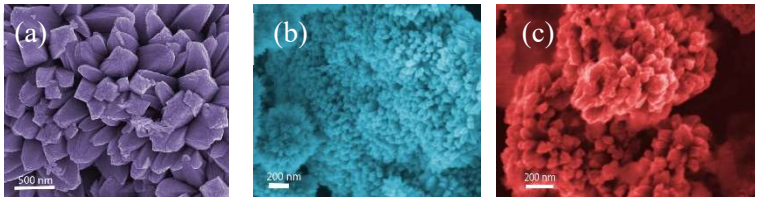


Figure 4. SEM images of (a) undoped SnO_2, (b) Co doped SnO_2 and (c) Pd doped SnO_2 nanorods

Additionally, to study the size and shape of particles, HRTEM analysis was performed on the samples. Figure 5(a) depicts an undoped SnO_2 spear rod-shaped nanorods cluster with an estimated average diameter and length of 23.0 ± 4.2 nm and 152.0 ±7.6 nm, respectively. While Co doped, SnO_2 exhibits needle-like nanorods with an average diameter and length of 14.2± 2.4 nm and 77.2 ± 8.3 nm, respectively (Figure 5 (c)). In contrast, Pd doped SnO_2 formed nanorods with a rounded tip (Figure 5 (c)). The calculated average diameter and length are 8.5 ± 2.9 nm and 43.9 ± 2.7 nm, respectively. The aspect ratio for undoped SnO_2, Co doped SnO_2, and Pd doped SnO_2 changed from 6.6, 5.4 to 5.2, respectively. The result shows that the nanorods formed in the Pd doped SnO_2 sample were the smallest. The drastic decrease in the particle size may be due to the fact that the ionic radii of Co^{2+} (0.72 Å) and Pd^{2+} (0.86 Å) are much bigger than Sn^{4+} (0.69 Å); the introduction of these dopant ions results in lattice strain and a reduction in particle size as well as crystalline size [16].

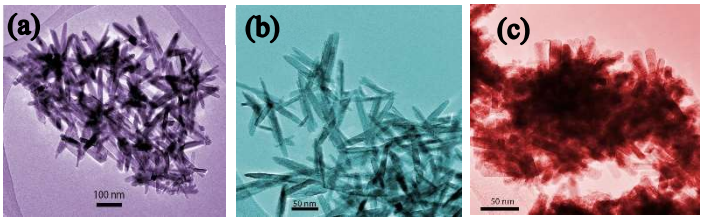


Figure 5. HRTEM images of (a) undoped SnO_2, (b) Co doped SnO_2 and (c) Pd doped SnO_2 nanorods

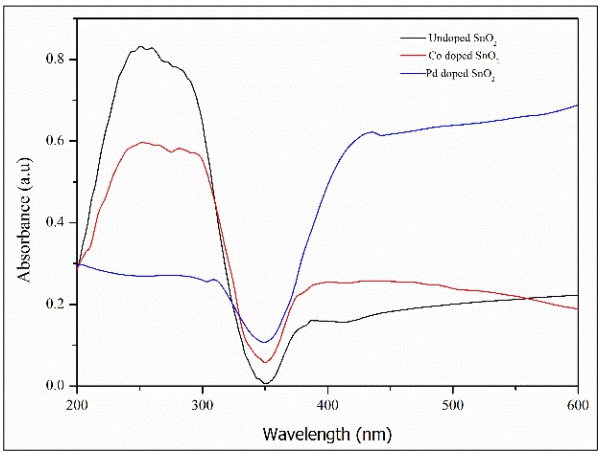


Figure 6: UV-Vis spectra of as-synthesized SnO_2 samples

The UV-Vis absorption spectra of as-synthesized SnO_2 nanorods are shown in Figure 6. The absorption edges of Co-doped SnO_2 and Pd-doped SnO_2 show a redshift (300 -350 nm) which could cause by the high concentration of oxygen vacancies or defects in the SnO_2. The high uptake at the wavelength of 380 nm to 450 nm in Co and Pd doped SnO_2 nanorod samples reveals the sp-d exchange interactions between the band electrons and localized d electrons of dopant ions that replace Sn^{4+} ions in the crystal lattice. Consequently, this finding suggests that the absorption capacity of the Co and Pd doped SnO_2 nanorods is improved from the UV region to the visible region, which is essential for visible light photocatalysis. A similar trend was also obtained in previous studies [17]. The bandgap energy was estimated following Tauc's relation. The bandgap energies of the resulted samples are 3.88 eV, 3.61 eV and 3.55 eV for undoped SnO_2, Co doped SnO_2 and Pd doped SnO_2, respectively, suggest that doping has reduces the bandgap energy [18].

Photodegradation of PP microplastics under visible light

The photocatalytic reactions were conducted for 72 hours under visible light irradiation to test the SnO_2 nanorods as a photocatalyst for degrading the PP MPs in water. The PP residues were filtered and dried before being characterized using an FTIR spectrometer. As can be seen in Figure 7, some chemical reactions occurred during the photocatalytic process. This reaction led to the formation of new functional groups such as carbonyl, hydroperoxide, peroxides, and unsaturated groups, which are assigned to the peaks at 1700-1630 cm^{-1}, 3500-3300 cm^{-1}, 3000-2750 cm^{-1} and 1374 cm^{-1}, respectively. This result is in agreement with previous literature [9]. During the degradation process under visible light, radiation of oxidizing agents, particularly reactive oxygen radical species, would react with PP and eventually produce new functional groups. The combination of visible light irradiation with a chemical attack by reactive oxygen species induced by photocatalysts has

effectively promoted the degradation of PP microplastics [19]. Based on the FTIR spectra, the Co and Pd doped SnO_2 sample exhibit more new peaks than the undoped SnO_2. This may be due to smaller particle size, narrow bandgap, and the presence of oxygen vacancies in Co and Pd-doped SnO_2 nanorods samples.

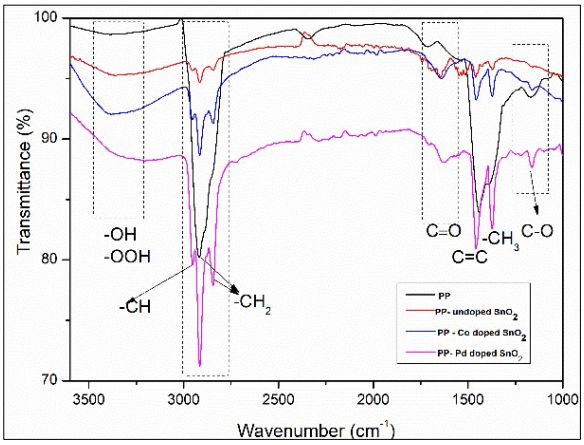


Figure 7. FTIR spectra of PP MPs photodegradation reaction after 72 hours under visible light irradiation

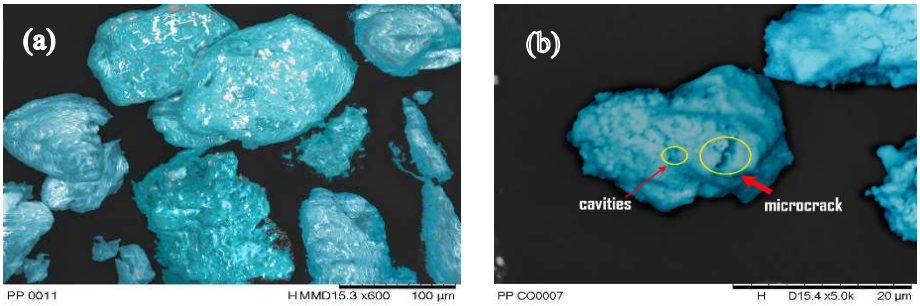


Figure 8. SEM images of PP MPs (a) before the photodegradation reaction (b) after 72 hours of photodegradation under visible light using Pd doped SnO_2 nanorods as the photocatalyst

Further analysis was executed using SEM to investigate the morphology of PP MPs prior to and after photocatalytic reaction; the images are presented in Figure 8. Referring to the figure, the treated PP exhibits surface structural changes such as brittleness, microcracks, and cavities. In conjunction with FTIR findings, the formation of low molecular weight compounds has led to the development of these surface defects, which evidence the degradation process [9]. Generally, in photocatalysis reaction, electron/holes are generated when metal oxide photocatalyst is irradiated by light source that has a higher energy than its bandgap. These pairs migrate to the surface and produce species such as hydroxyl radical (ȮH) and superoxide radical ($\cdot O_2^-$). For SnO_2, it was found that ȮH are the primary active species, this is due to the fact that the conduction band (CB) of SnO_2 (0.2 eV) is more positive than that of ($O_2/\cdot O_2^-$) (-0.05 eV). Hence, when some holes in valence band of SnO_2 reacted with water produced ȮH radicals which subsequently degraded the PP MPs [20, 21] .

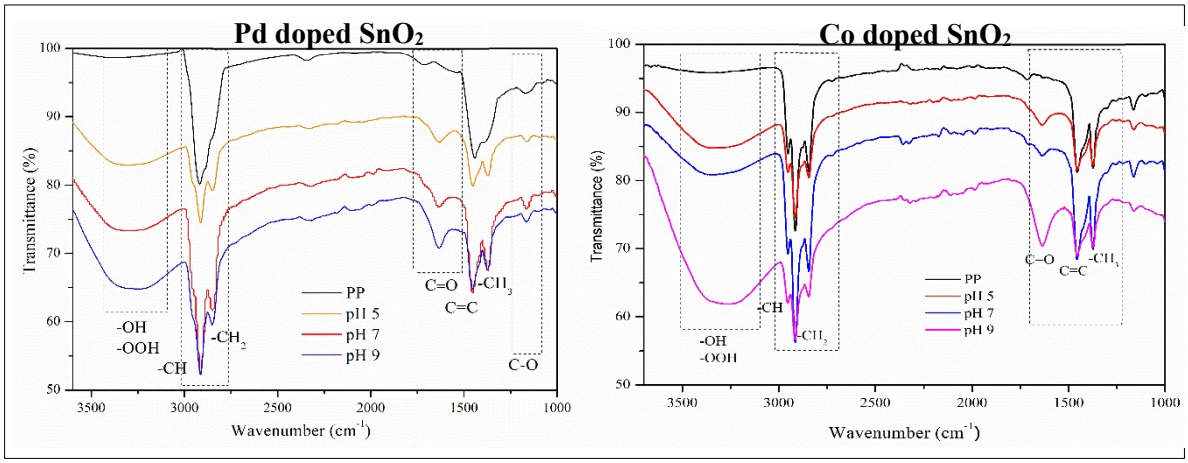


Figure 9. FTIR spectra of PP MPs before and after the 72 hours photodegradation reaction using Pd doped SnO_2 and Co doped SnO_2 as the photocatalysts under different pH conditions.

In order to study the effect of pH, the photocatalytic reaction was performed at different pH (5,7, and 9) using Pd and Co doped SnO_2. Figure 9 depicts the spectra of PP before the treatment and PP MPs residues obtained after 72 hours of photodegradation at various pH under visible light irradiation. The results show for both photocatalysts the intensity of hydroxyl, carbonyl, and peroxide peaks increased when the pH increased. The result suggests that the presence of hydroxide ions increases the degradation of MPs by inducing the formation of more hydroxide radical species [19].

Conclusion

This study successfully demonstrates the degradation of MPs and polypropylene (PP) in water using visible light and hydrothermal synthesized tin oxide nanorods photocatalysts. The photocatalytic reaction led to the formation of low molecular weight compounds such as hydroperoxides, peroxides, carbonyl, and other unsaturated groups, which cause cracks on the surface of PP, and subsequently degrade the MPs. The higher pH of the water sample improves the photodegradation process. In addition, the physical and chemical properties, such as the particle size, bandgap energy, and oxygen vacancies of the photocatalyst, also contribute to enhancing PP degradation. Overall, we conclude that Pd and Co doped SnO_2 nanorods can be applied as an alternative technology to combat global MP pollution.

Acknowledgement

This work is supported by the Malaysia Ministry of Higher Education-Fundamental Research Grant Scheme (FRGS/1/2021/STG05/UiTM/02/9) and Kurita Water and Environment Foundation for Kurita Overseas Research Grant Program 2022 (22Pmy112-T5). The authors also wish to thank Universiti Teknologi Mara Kampus Permatang Pauh, Cawangan Pulau Pinang, for the facility and financial support.

References

1. Issac, M. N. and Kandasubramanian, B. (2021). Effect of microplastics in water and aquatic systems. *Environmental Science Pollution Research,* 28(16):19544-19562.
2. Auta, H.S., Emenike, C. U. and Fauziah, S. H. (2017). Distribution and importance of microplastics in the marine environment: A review of the sources, fate, effects, and potential solutions. *Environmental International,* 102:165-176.
3. Elkhatib, D., Oyanedel-Craver, V. and Carissimi, E. (2021). Electrocoagulation applied for the removal of microplastics from wastewater treatment facilities. *Separation Purification Technology,* 276: 11887.

4. Zhang, Y., Jiang, H., Bian, K. et al (2021). A critical review of control and removal strategies for microplastics from aquatic environments. *Journal Environmental Chemical Engineering,* 9:105463.
5. Ge, J., Zhang, Z., Ouyang, Z., et al (2022). Photocatalytic degradation of (micro)plastics using TiO_2-based and other catalysts: Properties, influencing factor, and mechanism. *Environmental Research*, 209: 112729.
6. Maulana, D. A, Ibadurrohman, M. and Slamet (2021). Synthesis of nano-composite Ag/TiO for polyethylene microplastic degradation applications. *IOP Conference Material Science Engineering,* 1011(1): 012054.
7. Tofa, T. S., Ye, F., Kunjali, K. L. and Dutta, J. (2019). Enhanced visible light photodegradation of microplastic fragments with plasmonic platinum/zinc oxide nanorod photocatalysts. *Catalysts*, 9: 819.
8. Uheida, A., Mejía, H. G., Abdel-Rehim, M., et al (2021). Visible light photocatalytic degradation of polypropylene microplastics in a continuous water flow system. *Journal Hazard Materials*, 406: 124299.
9. Syeed Tofa, T., Karthik, Kunjali, L., et al. (2019). Visible light photocatalytic degradation of microplastic residues with zinc oxide nanorods. *Environmental Chemistry Letters,* 17:1341-1346.
10. Kim, S., Sin, A., Nam, H., et al. (2022), Advanced oxidation processes for microplastics degradation: A recent trend. *Chemical Engineering Journal Advances*, 9:100213.
11. Inderan, V., Lim, S. Y., Ong, T. S., et al. (2015). Synthesis and characterisations of SnO_2 nanorods via low temperature hydrothermal method. *Superlattices Microstructure*, 88: 396-402.
12. Tamez Uddin Md, Nicolas Y, Olivier C, et al. (2012). Nanostructured SnO_2–ZnO heterojunction photocatalysts showing enhanced photocatalytic activity for the degradation of organic dyes. *Inorganic Chemistry,* 51: 7764-7773.
13. Inderan, V., Arafat, M. M., Kumar, S., et al. (2017). Study of structural properties and defects of Ni-doped SnO_2 nanorods as ethanol gas sensors. *Nanotechnology,* 28(26): 265702.
14. Inderan, V., Arafat, M. M., Haseeb, A. S. M. A., et al (2019), A comparative study of structural and ethanol gas sensing properties of pure, nickel and palladium doped SnO_2 nanorods synthesised by the hydrothermal method. *Journal Physical Sciences*, 30:127-143.
15. Epifani, M., Arbiol, J., Pellicer, E., et al. (2008). Synthesis and gas-sensing properties of Pd-doped SnO_2 nanocrystals. A case study of a general methodology for doping metal oxide nanocrystals. *Crystal Growth Design*, 8(5):1774-1778.
16. Medhi, R., Marquez, M. D., Lee, T. R. (2020). Visible-light-active doped metal oxide nanoparticles: Review of their synthesis, properties, and applications. *ACS Applied Nano Materials,* 3(7): 6156-6185.
17. Babu, B., Kadam, A. N., Rao, G. T., et al. (2018). Enhancement of visible-light-driven photoresponse of Mn-doped SnO_2 quantum dots obtained by rapid and energy efficient synthesis. *Journal Luminescence,* 195: 283-289.
18. Liu, Y., Liu, X. and Zhang, X. (2023). Synergy of multi-means to improve SnO_2 lithium storage performance achieved by one-pot solvothermal method. *Electrochimica Acta*, 437:141453.
19. Longo, C., Savaris, M., Zeni, M., et al. (2011). Degradation study of polypropylene (PP) and bioriented polypropylene (BOPP) in the environment. *Material Research,* 14: 442-448.
20. Dai, S. and Yao, Z. (2012). Synthesis of flower-like SnO_2 single crystals and its enhanced photocatalytic activity. *Applied Surface Sciences*, 258: 5703-5706.
21. Kim, S. P., Choi, M. Y. and Choi, H. C. (2016). Photocatalytic activity of SnO_2 nanoparticles in methylene blue degradation. *Materials Research Bulletin,* 74: 85-89.

Malaysian Journal of Analytical Sciences (MJAS)
Published by Malaysian Analytical Sciences Society

THE EFFECT OF NANOFILLERS ON THE FUNCTIONAL PROPERTIES OF PLA AND CHITOSAN BASED FILM

(Kesan Pengisian Nano Kepada Sifat Filem yang Berasaskan Asid Polilatik dan Kitosan)

Raja Hasnida Raja Hashim[1*], Ahmad Anas Nagoor Gunny[1,2], Sam Sung Ting[1], Nor Helya Iman Kamaludim[1], Subash C. B. Gopinath[2,3]

[1]Faculty of Chemical Engineering Technology, Universiti Malaysia Perlis, Kompleks Pusat Pengajian Jejawi 3, Kawasan Perindustrian Jejawi, 02600, Arau, Perlis, Malaysia
[2] Centre of Excellence for Biomass Utilization, Faculty of Chemical Engineering Technology, Universiti Malaysia Perlis, 02600, Arau, Perlis, Malaysia
[3]Institute of Nano Electronic Engineering, Universiti Malaysia, Perlis, 01000 Kangar, Perlis, Malaysia

[*]Corresponding author: ahmadanas@unimap.edu.my

Received: 20 September 2021; Accepted: 13 September 2022; Published: 22 February 2023

Abstract

The aim of this study was to develop poly (lactic acid) and chitosan-based films and to examine the effect of cellulose nanocrystal (CNC) as nanofillers on the properties of the films. The biofilms were prepared by solvent casting method. The physical and mechanical properties of the resulting films were examined. SEM analysis showed that the surface of PLA/Cs films smoother when 1% and 2 % of CNC were added. The results for percent of water absorption of the films increased with increasing amount of CNC in PLA/Chitosan matrix. Tensile test results indicated higher TS value by incorporation of 2% of CNC. However, the PLA/Chitosan-CNC films at 3% and 4% CNC concentration exhibited a decreased TS value. PLA/Chitosan films were improved with the addition of a small amount of CNC resulting in PLA nanocomposite, which will be further evaluated for fruit packaging applications. The data obtained through this research could contribute to the establishment of a biofilms with improved the physical and mechanical properties promising significant advantages in term of longer storage life, maintaining safety, and keeping quality of a product especially in fruit packaging.

.

Keywords: polylactic acid, chitosan, cellulose nanocrystal, films, packaging

Abstrak

Tujuan kajian ini adalah untuk membuat filem berasaskan poli (asid laktik) dan kitosan dan mengkaji kesan kristal nano selulosa (CNC) sebagai pengisi nano pada sifat filem. Biofilm tersebut disiapkan dengan kaedah tuangan pelarut. Sifat fizikal dan mekanikal filem yang dihasilkan diperiksa. Analisis SEM menunjukkan bahawa permukaan filem PLA/Cs lebih licin apabila 1% dan 2 % CNC ditambah.Selanjutnya, peratus penyerapan air filem meningkat dengan peningkatan jumlah CNC dalam matriks PLA/ kitosan. Hasil ujian tegangan menunjukkan nilai TS yang lebih tinggi dengan memasukkan 2% CNC. Walau bagaimanapun, filem PLA / Chitosan-CNC pada kepekatan CNC 3% dan 4% menunjukkan penurunan nilai TS. Filem PLA / kitosan ditambah baik

dengan penambahan sejumlah kecil CNC yang menghasilkan nanokomposit PLA, yang akan dinilai lebih lanjut untuk aplikasi pembungkusan buah. Data yang diperoleh melalui penyelidikan ini dapat menyumbang pada pembentukan biofilm dengan peningkatan sifat sifat fizikal dan mekanikal yang lebih baik yang menjanjikan kelebihan yang ketara dari segi jangka hayat penyimpanan yang lebih lama, mengekalkan keselamatan, dan mengekalkan kualiti produk terutamanya dalam pembungkusan buah-buahan

.

Kata kunci: asid polilaktik, kitosan, selulosa nanokristal, filem, pembungkusan

Introduction

The primary function of food packaging is to preserve the quality and safety of food products during storage and transportation, as well as to extend the shelf-life of food products by preventing undesirable factors such as spoilage microorganisms, chemical contaminants, oxygen, moisture, light, or external force. Many foods packaging currently on the market are made of synthetic polymers that were produced from fossil fuels. This is due to their high mechanical and barrier qualities, as well as their ease of processing and low price. However, there are some disadvantages to this type of material: it requires a lot of energy to recycle, and if it is not properly disposed of, this could pose a risk to the environment because it does not decompose or decomposes slowly in landfills or in the environment, releasing polluting substances. People are currently dealing with rapid climate change as well as the issue of waste disposal that comes with it. As a result, avoiding petroleum-based non-biodegradable polymers such polyethylene (PE), low-density polyethylene (LDPE), and high-density polyethylene (HDPE), as well as polypropylene (PP), which are commonly used in food packaging, is necessary. In recent years, there has been a lot of interest in developing more environmentally acceptable alternatives to the plastics that are currently utilized in the packaging sector. Many natural biopolymer materials, such as chitosan, cellulose, hemicellulose, lignin, pectin, starch, agar, *Eucommia ulmoides* gum, and natural rubbers, have been widely employed to manufacture biodegradable food packaging materials due to their environmentally friendly and biodegradable characteristics.

Chitosan

A chitosan (Cs)-based film has been chosen as an innovative film-forming content. The polysaccharide chitosan is the second most abundant in nature. It has been demonstrated to be biodegradable, non-toxic, biocompatible, and useful [1]. Chitosan is a linear polysaccharide and biodegradable copolymer made up of N-acetyl glucosamine and D-glucosamine. Chitosan is formed by chitin deacetylation, which has the structural element of crustacean exoskeleton, such as crabs and shrimps [2]. Chitosan is a deacetylated product of chitin ß-(1-4)-2-acetamido-2-deoxy-D-glucan. Chitosan has similar characteristics with chitin as the most stable anti-acid and alkali substances, and this portion is also not soluble in ordinary solvents. Most interestingly, it is microbial resistant due to its positively charged amino group, which interacts with negatively charged microbial cell membranes, causing proteinaceous and other intracellular constituents of the microorganisms to leak out [3].

However, the disadvantage of using chitosan-based film is its high cost, which makes it unsuitable for fruit packaging. As a result, it is proposed that chitosan be combined with other biopolymer to form a film in order to produce active fruit packaging [4]. Polylactic acid was chosen to combine with chitosan due to its excellent mechanical properties, which include low flammability, low moisture reversion value, low refraction index, and high UV safety index.

Polylactic acid

Polymers such as polylactic acid (PLA) have attracted the attentions of researchers due to their high strength and modulus. PLA has a proven ability either to substitute traditional petrochemical-based polymers for industrial applications or as a leading biomaterial for a wide range of applications in medicine [5][6]. PLA comes from renewable plant sources, such as starch and sugar. Degradation of PLA can be accomplished by hydrolysis of ester bonds without the need for enzymatic procedure. The use of PLA as food packaging polymer for short shelf-life products with popular applications is growing. In addition, PLA is safe and GRAS is widely

accepted as safe for use in food packages. Indeed, PLA has been known to be ideal for packaging orange juice, yoghurt and dressings [7]. Polylactic acid is a hydrophobic polymer that belongs to a class of biomaterials usually referred to as poly-a-hydroxy acids, poly-a-esters or aliphatic polyesters. It is synthesised from lactic acid (LA; 2 hydroxypropanoic acid) which is a water-soluble monomer with two enantiomeric forms, namely L-(+)-LA and D-(-)-LA. The drawbacks of PLA as it has poor thermal stability, low water vapour or gas barrier properties and inherent brittleness. In order to achieve the films as bioplastics, a filler must be added to improves the mechanical and physical properties of a film.

Cellulose nanocrystal

Cellulose nanocrystal (CNC) has sparked great attention as a potential nano-reinforcement for chitosan films due to its sustainability, abundance, high surface area to volume ratio, lightness, and high mechanical strength among the numerous nanofillers [8]. CNC is a nanometer-sized crystal rod-shaped particle that is formed as a stable aqueous colloidal suspension and is commonly separated from cellulose by acid hydrolysis [9]. Previous researchers have published numerous studies on PLA/ chitosan/CNC bio-composite films [10][11] .There are two ways to obtain nanocellulose. First is mechanical treatment and second is acid hydrolysis. In acid hydrolysis, the separation of cellulose nanocrystals (nanowhiskers) is the product of the difference in solubility between the two regions (amorphous and ordered regions) in the cellulose chain.

Cellulose is a hydrophilic polymer and therefore generally has poor compatibility with hydrophobic synthetic polymers and also poor thermoplastic properties. This constrains the use of nanocellulose, especially cellulose nano crystal, in nanocomposite fabrication [12]. However, according to Sullivan et al. CNC is easily dispersed in water, therefore it can be used as a water-based coating and films for food packaging applications [13].

The use of cellulose nanocrystal as a component in polymeric materials has received a lot of attention. Because of their high crystallinity, good processability, abundance, renewable and biodegradable nature, and outstanding mechanical properties, cellulose-based materials have been the focus of much research. In summary, the combination of cellulose-based fillers to polymer matrices improves material performance in terms of barrier, thermal, and mechanical properties. As reinforcement fillers in polymeric materials, various types of cellulose particles have been used. These cellulose particles can be distinguished by their size, morphology, crystallinity, and crystal structure [14].

Although a number of research efforts aimed at improving the film properties of biopolymer-based packaging films have shown great changes in film properties, their physical & mechanical properties are still not satisfactory and have encountered difficulties in industrial applications [15]. Blending and homogenising cellulose nanocrystals in PLA/Chitosan matrix would result in a new nanocomposite with sufficient mechanical strength suitable for use in food packaging. Therefore, the incorporation of CNC as nanofiller may be useful in improving the mechanical properties of packaging materials. This study evaluates the physical properties and mechanical properties of a new packing material of Poly-lactic acid (PLA)/Chitosan (Cs), Cellulose Nanocrystal (CNC) biopolymer film by using solvent casting technique.

Materials and Methods

Materials

Polylactic acid (PLA) resin of 4032D type used in this study was supplied by Nature Works LLC (USA) with a specific gravity of 1.24, high molecular weight and melt mass flow rate (MFR) of 7 g/10 min at 210°C/2.16 kg. Chitosan (Cs) powder with a degree of deacetylation of 90.5%, molecular weight of >700 kDa, a viscosity of 62 cPs, was purchased from Cleo International Trading (Shanghai)

Isolation of CNC

Microcrystalline cellulose (MCC) is often derived from wood pulp and purified cotton linters. 1g of Micro Crystalline Cellulose was hydrolysed by 10 g of 64% w/w sulphuric acid at 45 °C for 45 min under constant mechanical stirring. The suspension was then diluted with cold deionised water and centrifuged at 4300xg for

15 min. Sodium hydroxide was used in the washing process to neutralize the pH value. After completion of process, the acid was moved by washing with deionized water and centrifuged first, then, 0.5 N of NaOH was applied to neutralizing the suspension followed by washing again by deionised water. The supernatant was removed, and the solid phase was diluted again with deionised water until the milky substance was form and can start to collect (Lim et al., 2021).

Films preparation

Preparation materials Polylactic acid (PLA) and chitosan (Cs) were pre-treated by drying in a vacuum oven at 50 °C for 24 h to eliminate possible absorbed water on the surface of the particles. The PLA and chitosan were dissolved separately in different solvents before blending. PLA (1% by weight) (0.3 g) was dissolved in 30 ml of chloroform and 1 g chitosan in 100 ml of 1% (v/v) acetic acid. Then chitosan solution (1% by weight) was added to the PLA solution and stir until homogenized. After stirring, the solution was modified with glycerol (1% by weight) as plasticizers and stirred for 30 minutes. Then, 1, 2, 3 and 4 wt % of CNC solution were added in PLA/CS solution and stirred until homogenized. Then the solutions were poured on a petri dish, and the solvent used was evaporated at room temperature in fume chamber for 24 h to volatilize the residual solvent. To control film thickness, the quantity of each film-forming solution poured onto a plate was calculated. After that time, films were peeled from the plates and cut to specimens of appropriate sizes for subsequent testing.[9]

Tensile properties

The tensile strength and elongation at break were assessed according to American Society for Testing and Materials (ASTM) method D882 [17]. Specimens were prepared from rectangular film strips (1 cm × 10 cm), dimensions. A universal testing machine, Instron (Model 5569) with 1kN load cell was operated at a crosshead speed of 2 mm/ min. The average value of at least three samples for each composition was reported.

Scanning electron microscopy

The microstructural analysis of the cross-sections of the films was carried out by means of a scanning electron microscope (JEOL JSM-5410, Japan). Film pieces, 0.5 x 0.5 cm^2 in size, were cryofractures from films and fixed on copper stubs, gold coated, and observed using an accelerating voltage of 10 kV. Observations were taken in duplicate for each formulation. [18]

Water absorption

Water absorption was measured using the following procedure. Films with dimensions 2cm x 2cm were placed in a desiccator for 24 h, followed by weighing to measure the dry mass. The films were then immersed entirely in the distilled water in a sealed beaker. The weight gained was monitored until equilibrium was obtained as described by previous findings [19], the percent of water absorption was calculated as follows:

$$\text{Water absorption } \% = \frac{(Ww - Wd)}{Wd} \times 100 \qquad \text{(eq. 1)}$$

Fourier transform infrared spectroscopy

The samples were dried in a desiccator for at least 1 week before analysis. A Nicolet iS10 Fourier transform infrared spectroscopy, with a spectral resolution of 1 $cm^{-1}$was used to recorded infrared spectra of samples. FTIR spectra were collected from 400 cm^{-1} to 4000 cm^{-1}[18].

Statical analysis

All data are shown as a mean ± standard deviation. Analysis of variance (one-way ANOVA; Microsoft Excel 2010) was conducted, utilising a probability level less than 5% ($p < 0.05$). A value of $p < 0.05$ was represented to be statistically significant.

Results and Discussion

Scanning electron microscopy

The results of SEM of the pure PLA/Cs films with (0% - 4%) of CNC are presented in Figure 1. SEM images showed that the surface of PLA/Cs films changed when the concentration of CNC increased. For the pure PLA /Cs film, the surface was seen to be rough and rigid, while the surface of films with CNC content up to 2% was relatively smoother than the pure PLA. For the films containing 1% and 2% of CNC, there is no agglomerations of CNC in the surface of the polymer matrix, which indicated that filler substances were homogeneously dispersed. This might have occurred

because of the processing route of films' preparation [13]. However, for the nanocomposite films with high CNC content (3% & 4%), the presence of agglomerations of CNC in the surface of the PLA matrix was observed. These agglomerations on the surface of the PLA matrix are caused by the hydrophilic nature of cellulose, which encourages strong interactions between the cellulose nanocrystals via hydrogen bonds, resulting in agglomerations on the polymer surface [14].

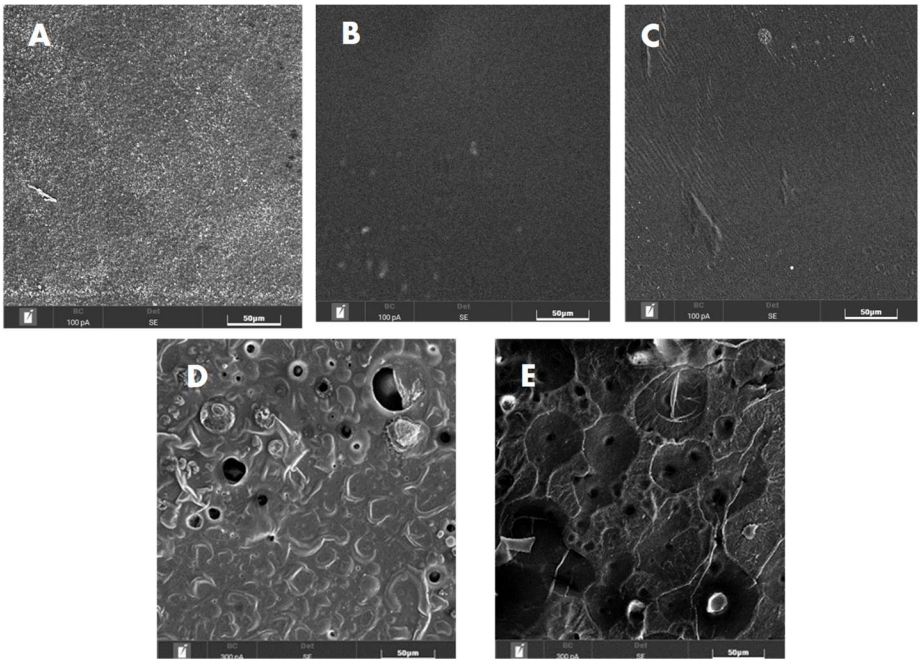


Figure 1. SEM image of the surface of (A) PLA/Cs film, (B) PLA/Cs/CNC 1% film (C) PLA/Cs/CNC 2% film, (D) PLA/Cs/CNC 3% film, (E) PLA/Cs/CNC 4% film

Tensile properties

The obtained results of tensile strength test, elongation at break and young modulus were conducted on the pure PLA/Chitosan film and the nanocomposite films with different content of CNC (0%- 4%). The comparison of the ultimate strength point of the films are presented in Figure 2, Figure 3 and Figure 4. For the pure PLA/Chitosan film without CNC, the yielded TS value (ultimate strength point) was 5.4 MPa. In the case of the film containing 2% of CNC, the TS increased significantly to 13.8 MPa in comparison with the pure PLA/Chitosan film value.

The PLA/Cs films at 3% and 4% CNC concentration exhibited a decreased TS value. The PLA/Cs films at 4% CNC load were more brittle which may be the cause for higher elastic modulus as shown in Figure 4 which is the highest value of young modulus is the films with 4% CNC [20]. The decrease in toughness in nanocomposites has been attributed to large agglomerations of nanofillers has been discussed on the SEM analysis above, the films with high CNC content (3% & 4%) showed the presence of agglomerations of CNC in the surface of the PLA/Cs matrix. Zeyad and Sullivan et al. reported similar results of the tensile strength of their cellulose nanocomposites [13, 21]. These agglomerations can act as stress concentrators, which facilitate the spreading of defects generated at the interface. These defects can grow larger than the critical crack size, resulting in film failure as can be seen on films with 3% and 4% CNC. This suggested that the film containing 2% of CNC was more ductile than the other films since the tensile strength and the elongation break is the highest compared to others [21]. Generally, the

improvement of the mechanical performance of nanocomposite films results from different factors: compatibility between the polymer matrix and the filler, aspect ratios of the filler, and the orientations of the filler. However, in this work, we can hypothesize that the improvement of the tensile strength of the nanocomposite films caused by the stiffness effect of CNC that homogeneously dispersed in the PLA matrix [22].

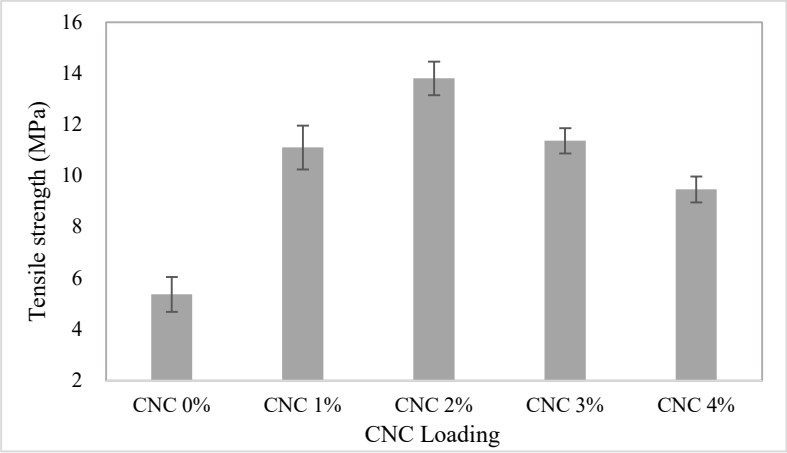


Figure 2. Effect of CNC loading on tensile strength of the film. Values in the figure were significantly different ($p < 0.05$)

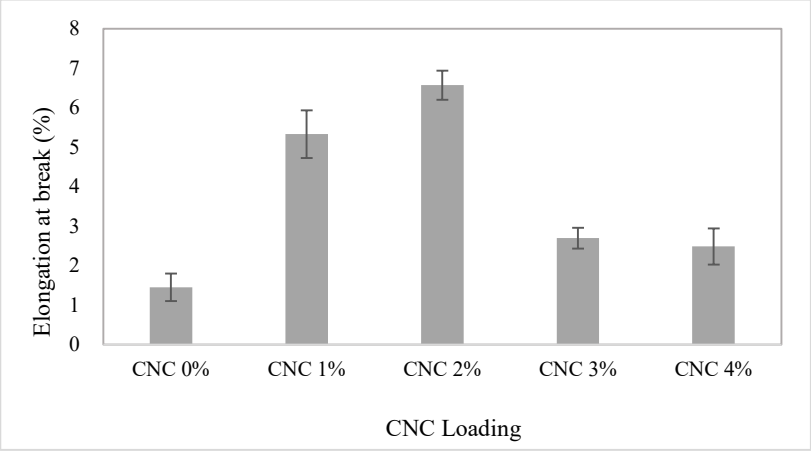


Figure 3. Effect of CNC loading on elongation break of the film. Values in the figure were significantly different ($p < 0.05$)

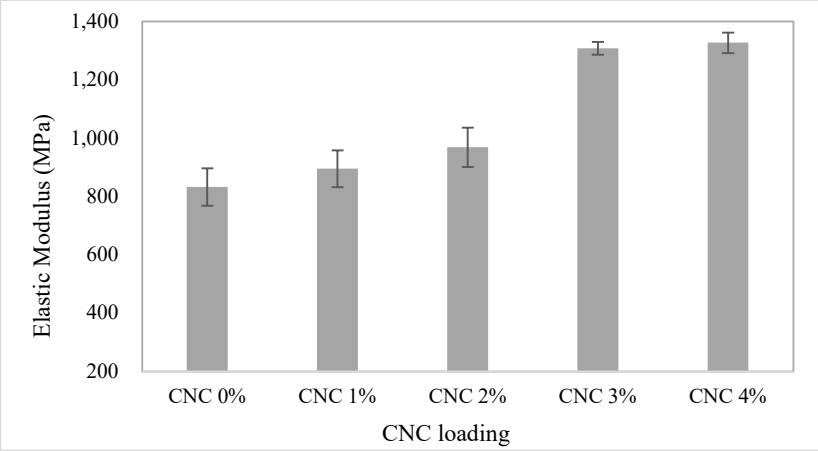


Figure 4. Effect of CNC loading on young modulus of the film. Values in the figure were significantly different ($p < 0.05$)

Water absorption

Water absorption test of pure PLA/Chitosan and PLA/chitosan/CNC films were carried out to investigate water absorption properties by calculating the percentage of water absorption. The water absorption value is shown in Table 2. It can be seen from Figure 5 that the percent of water absorption of the films increased with increasing amount of CNC in PLA/Chitosan matrix. The water absorption of all PLA/Cs/CNC films containing 0, 1, 2, 3 and 4 wt.% CNC increased to 3.02%, 3.77%, 9.82%, and 16.18% after 180 minutes of immersion, respectively. Since PLA is strongly hydrophobic [17] and CNC has hydrophilic nature [21], where hydrogen bonds easily form in water thus increased water absorption [23]. The water absorption of the films is mainly due to the CNC which affect the ability of the film to retain water. The increased water absorption of the film with CNC corresponds to the FT-IR curve, which shows a stronger intensity of the hydrophilic functional group band at 1750 cm^{-1} (reflecting C=O stretching).

Table 1. The initial weight of a films and water absorption of films containing different amount of CNCs

CNC Concentration (%)	Initial Weight (g)	Water Absorption (%)
0	± 0.0218	1.90 ± 0.50
1	± 0.0229	3.02 ± 0.39
2	± 0.0246	3.77 ± 0.29
3	± 0.0136	9.82 ± 0.45
4	± 0.0188	16.18 ± 0.36

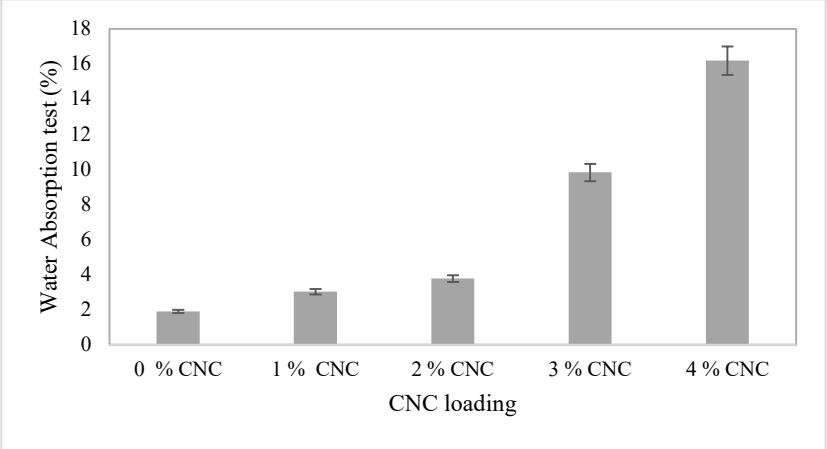


Figure 5. Water absorption test on Films with different concentration of CNC Values in the figure were significantly different ($p < 0.05$)

Fourier transform infrared spectroscopy

FT-IR spectroscopy analysis spectra were recorded to study the differences in the identifying signals of PLA/Cs/CNC films. The infrared spectra of the film with CNC as shown in Figure.6. The absorption peaks of the PLA/Cs/CNC film spectrum are mainly due to the –CH3 stretching vibration at 2,991 cm^{-1}. A strong absorption band was observed at 1,750 cm^{-1} due to the C=O stretching from keto esters [9] According to previously published research, the bending vibrations at 1,452 and 1,382 cm^{-1} are connected to symmetric and antisymmetric deformations of the CH_3 group by [24]. The band at 1261 cm^{-1} are from the antisymmetric and symmetric stretching of C–O–C in esters. The peak at 1,181 cm^{-1} can be attributed to C–O–C stretching of PLA as mentioned in previous studies [9, 12]. The peaks of the chitosan can be found at 1542 cm^{-1} (N-H bending in amide and protonated amino group) which in the agreement of previous study [25]). The peaks at 876 cm^{-1} (β-glycosidic linkage of the cellulose) were observed, associated with typical structures of cellulose [26, 27].

Conclusion

Packaging materials based on PLA and chitosan containing different amount crystal nanocellulose (CNC) were developed to improve the mechanical and physical properties of the films. Cellulose nanocrystal improved the physical properties, tensile strength, percentage elongation breaks and the water absorption. SEM images showed that the surface of PLA/Cs films smoother when 1% and 2% of CNC were added. The addition of 2% CNC enhanced the interactions (e.g., hydrogen bonds and electrostatic interactions) between the PLA/chitosan chains to perform a well-disperse film. FTIR analysis allowed characterizing the molecular interactions occurring after incorporation of Cellulose nanocrystal The set of results indicates that the films with 2% CNC were promising as a filler for PLA/Chitosan based film. However, more work is required in this area of research to maximize the effectiveness of the fillers and also bioactive incorporated agents.

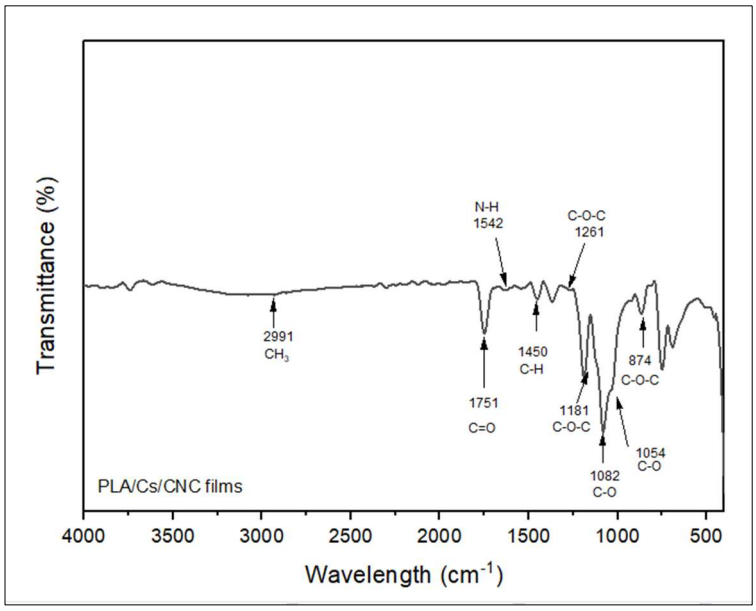


Figure 6. Fourier-transform infrared spectroscopy analysis PLA/Cs//CNC film. Scanning range from 400 to 4000 cm^{-1} is shown.

Acknowledgement

The authors would like to thank the Faculty of Chemical Engineering Technology, Universiti Malaysia Perlis (UniMAP) and Ministry of Education for financing the research under Fundamental Research Grant Scheme FRGS/1/2018/STG01/UNIMAP/03/.

References

1. Jovanovic, G. D., Klaus, A. S. and Niksic, M. P. (2016). Antimicrobial activity of chitosan films with essential oils against listeria monocytogenes on cabbage. *Jundishapur Journal of Microbiology*, 9(9): e34804.
2. Bhuvaneshwari, S., Sruthi, D., Sivasubramanian, V., Niranjana, K. and Sugunabai, J. (2011). Development and characterization of chitosan films. *International Journal of Engineering Research and Applications*, 1(2): 292-299.
3. Priyadarshi, R., Kumar, B., Deeba, F., Kulshreshtha, A. and Negi, Y. S. (2018). Chitosan films incorporated with apricot (*Prunus armeniaca*) kernel essential oil as active food packaging material. *Food Hydrocolloids*, 85: 158-166.
4. Raghav, P. K., Agarwal, N. and Saini, M. (2012). Edible coating of fruits and vegetables: a review. *International Journal of Scientific Research and Modern Education*, 1(1): 188-204.
5. Farah, S., Anderson, D. G. and Langer, R. (2016). Physical and mechanical properties of PLA, and their functions in widespread applications—a comprehensive review. *Advanced Drug Delivery Reviews*, 107: 367-392.
6. Casalini, T., Rossi, F., Castrovinci, A. and Perale, G. (2019). A perspective on polylactic acid-based polymers use for nanoparticles synthesis and applications. *Frontiers in Bioengineering and Biotechnology*, 7: 259.
7. Salmieri, S., Islam, F., Khan, R. A., Hossain, F. M., Ibrahim, H. M., Miao, C. and Lacroix, M. (2014). Antimicrobial nanocomposite films made of poly (lactic acid)–cellulose nanocrystals (PLA–CNC) in food applications—Part B: Effect of oregano essential oil release on the inactivation of listeria monocytogenes in mixed vegetables. *Cellulose*, 21(6): 4271-4285.
8. Wildan, M. W. and Lubis, F. I. (2021). Fabrication and characterization of chitosan/cellulose nanocrystal/glycerol bio-composite films. *Polymers*, 13(7): 1096.

9. Salmieri, S., Islam, F., Khan, R. A., Hossain, F. M., Ibrahim, H. M., Miao, C. and Lacroix, M. (2014). Antimicrobial nanocomposite films made of poly (lactic acid)-cellulose nanocrystals (PLA-CNC) in food applications: part a—effect of nisin release on the inactivation of listeria monocytogenes in ham. *Cellulose*, 21(3): 1837-1850.
10. Yang, W., Fortunati, E., Dominici, F., Giovanale, G., Mazzaglia, A., Balestra, G. M., ... and Puglia, D. (2016). Effect of cellulose and lignin on disintegration, antimicrobial and antioxidant properties of PLA active films. *International Journal of Biological Macromolecules*, 89: 360-368.
11. Zakaria, Z., Islam, M., Hassan, A., Mohamad Haafiz, M. K., Arjmandi, R., Inuwa, I. M. and Hasan, M. (2013). Mechanical properties and morphological characterization of PLA/chitosan/epoxidized natural rubber composites. *Advances in Materials Science and Engineering*, 2013: 629092.
12. Wei, L., Stark, N. M., Sabo, R. C. and Matuana, L. (2016). Modification of cellulose nanocrystals (CNCs) for use in poly (lactic acid) (PLA)-CNC composite packaging products. In: *Proceedings, Forest Products Society International Convention, June 28-29, 2016, Portland, OR.*
13. Sullivan, E. M., Moon, R. J. and Kalaitzidou, K. (2015). Processing and characterization of cellulose nanocrystals/polylactic acid nanocomposite films. *Materials*, 8(12): 8106-8116.
14. Dos Santos, F. A., Iulianelli, G. C. and Tavares, M. I. (2017). Effect of microcrystalline and nanocrystals cellulose fillers in materials based on PLA matrix. *Polymer Testing*, 61: 280-288.
15. Rhim, J. W., Park, H. M. and Ha, C. S. (2013). Bio-nanocomposites for food packaging applications. *Progress in Polymer Science*, 38(10-11): 1629-1652.
16. Lim, W. L., Gunny, A. A. N., Kasim, F. H., Gopinath, S. C., Kamaludin, N. H. I. and Arbain, D. (2021). Cellulose nanocrystals from bleached rice straw pulp: acidic deep eutectic solvent versus sulphuric acid hydrolyses. *Cellulose*, *28*(10), 6183-6199.
17. Zeid, A., Karabagias, I. K., Nassif, M. and Kontominas, M. G. (2019). Preparation and evaluation of antioxidant packaging films made of polylactic acid containing thyme, rosemary, and oregano essential oils. *Journal of Food Processing and Preservation*, 43(10): e14102.
18. Qin, Y., Li, W., Liu, D., Yuan, M. and Li, L. (2017). Development of active packaging film made from poly (lactic acid) incorporated essential oil. *Progress in Organic Coatings*, 103: 76-82.
19. Rosdi, N. and Zakaria, Z. (2016). Biodegradability properties of chitin/polylactic acid composite films. *eProceedings Chemistry*, 1(1): 48-52.
20. Graupner, N. (2008). Application of lignin as natural adhesion promoter in cotton fibre-reinforced poly (lactic acid)(PLA) composites. *Journal of Materials Science*, *43*(15): 5222-5229.
21. Albahr, Z. (2018). Development of polylactic acid (PLA)-based nanocomposite films for smart food packaging applications. Thesis of Master Degree, South Dakhota State University.
22. Orellana, J. L., Wichhart, D. and Kitchens, C. L. (2018). Mechanical and optical properties of polylactic acid films containing surfactant-modified cellulose nanocrystals. *Journal of Nanomaterials*, 2018.
23. Wildan, M. W. and Lubis, F. I. (2021). Fabrication and characterization of chitosan/cellulose nanocrystal/glycerol bio-composite films. *Polymers*, 13(7): 1096.
24. Hossain, K. M. Z., Ahmed, I., Parsons, A. J., Scotchford, C. A., Walker, G. S., Thielemans, W. and Rudd, C. D. (2012). Physico-chemical and mechanical properties of nanocomposites prepared using cellulose nanowhiskers and poly (lactic acid). *Journal of Materials Science*, *47*(6): 2675-2686.

25. Jakubowska, E., Gierszewska, M., Nowaczyk, J. and Olewnik-Kruszkowska, E. (2020). Physicochemical and storage properties of chitosan-based films plasticized with deep eutectic solvent. *Food Hydrocolloids*, 108: 106007.
26. Nikonenko, N. A., Buslov, D. K., Sushko, N. I. and Zhbankov, R. G. (2000). Investigation of stretching vibrations of glycosidic linkages in disaccharides and polysaccarides with use of IR spectra deconvolution. *Biopolymers: Original Research on Biomolecules*, *57*(4): 257-262.
27. El-Sakhawy, M., Kamel, S., Salama, A. and Tohamy, H. A. S. (2018). Preparation and infrared study of cellulose based amphiphilic materials. *Cellulose Chemical Technology*, 52(3-4): 193-200.

Malaysian Journal of Analytical Sciences (MJAS)
Published by Malaysian Analytical Sciences Society

NOVEL MAGNETIC EGGSHELL MEMBRANE FUNCTIONALIZED WITH WASTE PALM FATTY ACID FOR SELECTIVE ADSORPTION OF OIL FROM AQUEOUS SOLUTION

(Novel Magnetik Membran Kulit Telur Berfungsikan dengan Sisa Asid Lemak Sawit untuk Penjerapan Minyak Terpilih daripada Larutan Akueus)

Siti Khalijah Mahmad Rozi[1,2], Khairul Muzzammil Berhanundin[1], Ahmad Razali Ishak[3,*], Fairuz Liyana Mohd Rasdi[3], Nazri Che Dom[3], Nurul Yani Rahim[4], Mohd Yusmaidie Aziz[5], Farah Ayuni Shafie[3], and Abdul Mujid Abdullah[3]

[1] Faculty of Chemical Engineering and Technology,
Universiti Malaysia Perlis,
Kompleks Pusat Pengajian Jejawi 3, 02600 Arau, Perlis, Malaysia
[2]Centre of Excellence for Biomass Utilization,
Universiti Malaysia Perlis, 02600 Arau, Perlis, Malaysia
[3]Centre for Environmental Health and Safety,
Faculty of Health Sciences,
Universiti Teknologi MARA, Puncak Alam Campus,
42300 Kuala Selangor, Malaysia
[4] School of Chemical Sciences,
Universiti Sains Malaysia,
11900 Minden, Pulau Pinang
[5] Integrative Medicine Cluster, Advanced Medical and Dental Institute,
Universiti Sains Malaysia, 13200 Bertam, Kepala Batas, Penang, Malaysia

**Correspondence author: ahmadr2772@uitm.edu.my*

Received: 17 June 2022; Accepted: 14 October 2022; Published: 22 February 2023

Abstract

Emulsified oil in wastewater is a severe problem and requires extensive treatment before it can be disposed of in a manner that meets environmental regulation standards. One strategy to remove emulsified oil is by utilizing the adsorption process. The goal of this study is to synthesis magnetic eggshell membrane (ESM) functionalized with waste palm fatty acid, (MNP@ESM-WPFA) for the adsorption of oils (lubricating oil). The synthesis procedure involves three steps including preparation of ESM, functionalization of ESM with waste palm fatty acid (WPFA) and magnetization of eggshell membrane (ESM) functionalized with waste palm fatty acid (ESM-WPFA) through co-precipitation method to obtain MNP@ESM-WPFA. The novel adsorbent was characterized using SEM, FTIR, and EDX analyses. SEM analysis revealed the magnetic nanoparticles scattered throughout the porous and fibrous network structure of ESM-WPFA, confirming the successful synthesis of the MNP@ESM-WPFA. Further FTIR analysis on MNP@ESM-WPFA adsorbent revealed the appearance of peaks at 2933 cm^{-1} and 2852 cm^{-1} and 630 cm^{-1}, thus

confirming the presence of the alkyl chain of the waste palm fatty acid (WPFA) and Fe-O band on the surface of MNP@ESM-WPFA. The oil adsorption performance of MNP@ESM-WPFA was optimal at pH 7, treatment time of 50 minutes, and adsorbent dosage of 50 mg. The MNP@ESM-WPFA showed the highest oil adsorption capacity (K) for lubricating oil (4.61 mg/mg), followed by olive oil (2.72 mg/mg), and corn oil (2.00 mg/mg). The MNP@ESM-WPFA adsorbent was also reusable, with a sorption capacity that was maintained after five usage-regeneration cycles.

Key words: Eggshell membrane, waste palm fatty acids, magnetic nanoparticles, adsorbents, oil removal

Abstrak

Minyak teremulsi dalam air sisa merupakan satu cabaran yang serius dan memerlukan rawatan yang meluas sebelum ia boleh dilupuskan dengan cara yang memenuhi piawaian peraturan alam sekitar. Salah satu strategi untuk mengeluarkan minyak emulsi adalah dengan menggunakan proses penjerapan. Kajian ini bermatlamat untuk sintesis membran kulit telur (ESM) magnetik berfungsikan dengan sisa asid lemak sawit, (MNP@ESM-WPFA) untuk penjerapan minyak (minyak pelincir). Prosedur sintesis merangkumi tiga langkah termasuk penyediaan ESM, perfungsian ESM dengan sisa asid lemak sawit dan permagnetan membran kulit telur (ESM) berfungsikan dengan sisa asid lemak sawit (ESM-WPFA) melalui kaedah kopresipitasi untuk mendapatkan MNP@ESM-WPFA. Penjerap novel ini telah dicirikan menggunakan analisis SEM, FTIR, dan EDX. Analisis SEM mendedahkan nanopartikel magnetik yang bertaburan di seluruh struktur rangkaian berliang dan berserabut ESM-WPFA, mengesahkan kejayaan sintesis MNP@ESM-WPFA. Selanjutnya, analisis FTIR pada penjerap MNP@ESM-WPFA mendedahkan kemunculan puncak-puncak pada 2933 cm^{-1} and 2852 cm^{-1} and 630 cm^{-1} mengesahkan kehadiran rantai alkil WPFA dan Fe-O pada permukaan MNP@ESM-WPFA. Prestasi penjerapan minyak MNP@ESM-WPFA adalah optimum pada pH 7, masa rawatan 50 minit, dan dos penjerap 50 mg. MNP@ESM-WPFA menunjukkan kapasiti penjerapan minyak (K) tertinggi untuk minyak pelincir (4.61 mg/mg), diikuti minyak zaitun (2.72 mg/mg), dan minyak jagung (2.00 mg/mg). Penjerap MNP@ESM-WPFA juga boleh digunasemula, dengan kapasiti penyerapan yang dikekalkan selepas lima kitaran penjanaan semula penggunaan.

Kata kunci: membran kulit telur, sisa asid lemak sawit, zarah nano magnetik, penjerap, penyingkiran minyak

Introduction

Emulsified oil wastewater is regarded as a widespread pollutant around the world. Large volumes of wastewater containing oil and grease are increasingly produced due to population growth and fast urbanization. The release of oil-containing wastewater into water bodies causes public concern due to toxicological and aesthetic reasons [1]. Oil effluents come from various sources, including petroleum refineries, rolling mills, chemical processing, manufacturing plants, industrial processing, and municipal wastewaters [2-4]. Oily wastewater can contain fats, oil, cutting fluids, lubricants, edible oil, grease, crude oils, diesel oils, and other hydrocarbons [5]. Emulsified oils are difficult to handle and pose a real problem for treatment because of steric interaction or structural barriers and electrostatic repulsion between oil droplets [6]. Oil emulsions can produce an impermeable layer on the water's surface, decreasing oxygen content in the water and retard the photosynthesis process of aquatic plants [7-9].

The removal of residual oil remains a difficult technological challenge. Gravity separation, flotation, coagulation, ultracentrifugation, and membrane filtration are traditional methods for removing oil from industrial oily wastewater [10, 11]. In recent years, several techniques for handling emulsified oil have been developed, including bacterial degradation [12], electrocoagulation [13], emulsion destabilization [14], filtration [15], and adsorption [16-19]. An ideal adsorbent should have a high adsorption capacity, a fast adsorption rate, high selectivity, and be relatively inexpensive. Although the adsorption process is not extensively employed in treating emulsions, it has several benefits, and it does not always necessitate the use of extra chemicals [20]. Even though most commercially available oil sorbents are made of synthetic polymers with high sorption capacities such as polypropylene and polyurethane, their use releases massive amounts of hard to recover, non-biodegradable plastic into the environment [21].

There are three main types of adsorbents commonly used to remove oily pollutants: organic sorbents

(activated carbon, sawdust, straw, butyl rubber, carbon-based product), inorganic sorbents (kieselguhr, organoclay, bentonite, vermiculite), and synthetic sorbents (polyvinyl chloride, polyurethane, nylon fibres) [17]. Recently, biomaterials have attracted a great deal of attention as a prospective adsorbent material due to their abundance, environmental friendliness, and ability to be manufactured from renewable sources [22]. Various studies have been carried out to evaluate the preparation of bio-sorbents (sugarcane bagasse, coffee grounds, eggshell membranes, lignocellulosic material) as well as their properties and efficacy in removing various organic contaminants [22]. One of which, the eggshell membrane (ESM), comprises of a porous network of insoluble fibrous proteins with a high surface area that could be exploited as a sorbent for various types of pollutants in wastewater [23, 24]. ESM contains disulfide bonds, causing it to be impermeable to water, thus giving it an advantage in specific applications [25].However, ESM consists of hydrophilic functional groups such as hydroxyl, amine, and carboxylic acid that limits its use as adsorbent for hydphobic pollutants, especially oil contaminants [26, 27]. To overcome this problem, the surface of ESM can be coated with a hydrophobizing agent.

Waste palm fatty acid can be a potential hydrophobic modifier on the surface of ESM. High amounts of free fatty acids can be produced in waste palm cooking oil through a hydrolytic process that occurs in the presence of oil and water from food. The chemical structure of free fatty acids, which consists of long alkyl chains, makes them an excellent hydrophobizing agent to tune the hydrophilic surface of ESM for selective adsorption of oil from aqueous. Waste palm cooking oil was selected because it is easily available and economically viable.In this study, a novel magnetic eggshell membrane (ESM) functionalized waste palm fatty acid, (MNP@ESM-WPFA) was synthesized for the removal of lubricating oil. Magnetic Fe_3O_4 nanoparticles dispersed onto ESM functionalized with waste palm fatty acid can facilitate the rapid separation of oil from water while boosting the adsorption capability of ESM-WPFA. As the utilization of MNP@ESM-WPFA has not been reported yet for environmental applications, therefore, it is a good idea to explore its potential as adsobent for treatment and decontamination of organic pollutants, particularly oil. Therefore, this work focuses on analyzing the performance of MNP@ESM-WPFA in removing lubricating oil. The influence of adsorbent dosage, pH of the solution and contact time on the removal process was thoroughly investigated. Subsequently, the adsorption capacity and reusability of MNP@ESM-WPFA were evaluated.

Materials and methods

Chemicals

Sulphuric acid was purchased from Fischer Scientific (New Hampshire, USA). Sodium sulphate (anhydrous), while *n*-hexane, ethanol, ammonium iron(II) sulphate and iron trichloride hexahydrate were obtained from Merck (Darmstadt, Germany). All solvents used for the synthesis were of analytical grade. Deionized water was used throughout the study.

Instrumentation

Surface morphological analysis of MNP@ESM-WPFA was carried out using Hitachi SU8220 Scanning Electron Microscopy (Oxford Instrument, Oxford shire, UK) that is equipped with x-ray energy dispersion (Carl-Zeiss, Germany). FTIR spectra were recorded on Perkin Elmer FTIR spectrophotometer (Massachusetts, USA) with a crystal diamond universal ATR sampling accessory at room temperature. All spectra were recorded in the wavenumber range of 4000 to 450 cm^{-1}. Wettability analyses were performed using the Theta Lite 100 and Theta Lite 101 contact angle measurement instruments (Attension, Espoo, Finland).

Preparation of magnetic eggshell membrane functionalized with waste palm fatty acid:

Preparation of ESM

Raw eggshells were collected from a local shop and rinsed with deionized water to minimize the deterioration of the eggshell membrane (ESM). The ESM were then carefully removed from the eggshells and rinsed with deionized water again. This is followed by a drying process for 1 hour at 70 °C in the oven, after which the ESM were crushed and sifted using a 30 nm sieve to produce consistently sized powder particles.

Preparation of ESM-WPFA

The ESM-WPFA was prepared in accordance with a previously reported work by Sathasivam and Haris [28] but with minor modifications. Briefly, 2.00 g of ESM powder was mixed with 8.00 g of free fatty acid from waste palm cooking oil (WPCO) and three drops of concentrated sulphuric acid was used as a catalyst. This mixture was dispersed in 20 mL of *n*-hexane for 15 minutes at 60 °C. The obtained ESM-WPFA was then washed with excess *n*-hexane and air-dried.

Preparation of MNP@ESM-WPFA

The MNP@ESM-WPFA preparation was also slightly modified from the reported work by Rozi et al. [29]. In summary, 2.00 g ESM-WPFA, 3.17 g $FeCl_2.4H_2O$, and 7.57 g $FeCl_3.6H_2O$ were mixed in 320 mL deionized water. The mixed solution was agitated for 1 hour at 80 °C. The reaction mixture was then rapidly infused with 40 mL of aqueous ammonia. The resulting mixture was stirred for another hour before allowed to cool to room temperature. The precipitated MNP@ESM-WPFA was washed five times with hot water until the filtrate becomes neutral, after which it was separated using magnetic decantation.

Batch adsorption studies

A certain amount of MNP@ESM-WPFA was mixed with 3 mL lubricating oil in 20 mL water at room temperature for 30 minutes according to the method of Rozi et al. [29]. Using an external magnet, the MNP@ESM-WPFA was separated from the water surface after several minutes. The procedure is illustrated in Figure 1. The adsorption capacity was determined by weighing the sample before and after introducing it to the lubricating oil. Oil adsorption capacity K was calculated using Equation 1.

$$K = \frac{m_2 - m_1}{m_1} \quad \text{(eq. 1)}$$

Where m_1 represents the weight before adsorption and m_2 represents the weight after adsorption.

In this experiment, several parameters such as contact time, adsorbent dosage, and pH of the solution were investigated for their influence in the removal of lubricating oil. Adsorption experiments were carried out in batches, with different conditions of the parameters which includes adsorbent dosage (10, 20, 30, 40, 50, and 60 mg), contact time (10, 20, 30, 40, 50, and 60 minute), and pH of the solutions (pH 2, 4, 7, 8, and 10). This is to determine the best conditions for the removal of lubricating oil using MNP@ESM-WPFA. The optimum conditions obtained from adsorption of lubricating oil were adopted to examine the performance of MNP@ESM-WPFA for removal of several oils including olive and corn oil. Experiments were performed in triplicate for each parameter. After adsorption, the MNP@ESM-WPFA adsorbent was rinsed with *n*-hexane to desorb the lubricating oil and then dried for 24 hours at 90 °C. The regenerated MNP@ESM-WPFA adsorbent was reused up to 5 times. The oil adsorption capacity of the regenerated adsorbent towards the removal of lubricating oil was again measured to determine its reusability.

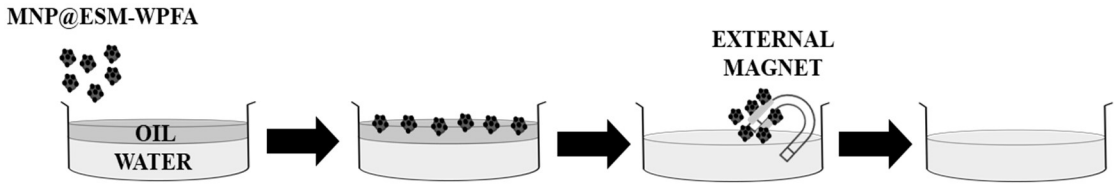


Figure 1. The schematic illustration of oil adsorption using magnetic adsorbent

Results and Discussion

Characterization

The FTIR spectra of ESM, ESM-WPFA, and MNP@ESM-WPFA are illustrated in Figure 2(A-C). Figure 2(A) shows the most significant peaks for ESM at 3429 cm^{-1}, 2933 cm^{-1}, 2852 cm^{-1} and 1647 cm^{-1}. The broad peak at 3429 cm^{-1} can be assigned to the N-H and O-H stretching vibrations. The peaks at 2922 cm^{-1} and 2852 cm^{-1} are attributed to asymmetric and symmetric stretching of a methylene group ($=CH_2$) respectively, while the band at 1647 cm^{-1} represents the stretching of the carbonyl group (C=O). In Figure 2(B), the high intensity of infrared bands at 2925 cm^{-1} and 2855 cm^{-1}

for ESM-WPFA correspond to an alkane stretching, proving that the alkyl chain of the WPFA has been successfully functionalized onto the ESM surface. In Figure 2(C), a new prominent band appears at 630 cm^{-1} due to the Fe-O group confirming the presence of Fe_3O_4 particles in MNP@ESM-WPFA.

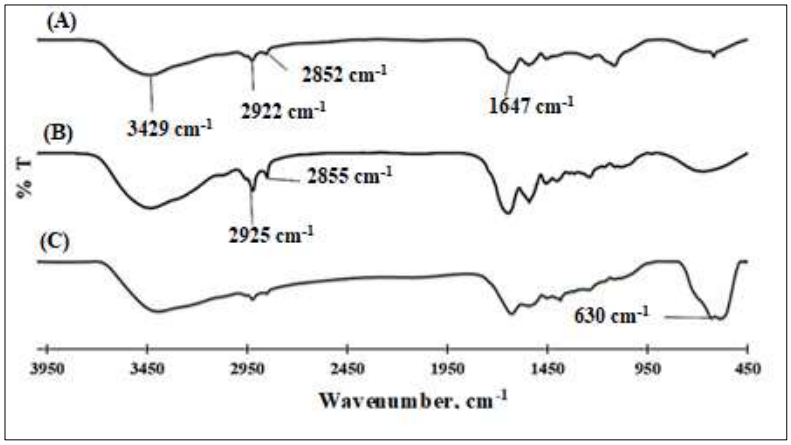


Figure 2. FT-IR spectra of (A) ESM (B) ESM-WPFA and (C) MNP@ESM-WPFA

The morphologies of ESM, ESM-WPFA and MNP@ESM-WPFA (Figure 3(A-C)) was examined by using scanning electron microscopy. The image of ESM shows that the virgin ESM has porous and fibrous surface (as circled in Figure 3(A)). The porous and fibrous structure of ESM-WPFA (Figure 3(B)) was found to be smoother after functionalization of waste palm fatty acid (WPFA). Small particles scattered throughout the structure of ESM-WPFA (Figure 3 (C-D)) are the magnetic nanoparticles proving the successful synthesis of MNP@ESM-WPFA.

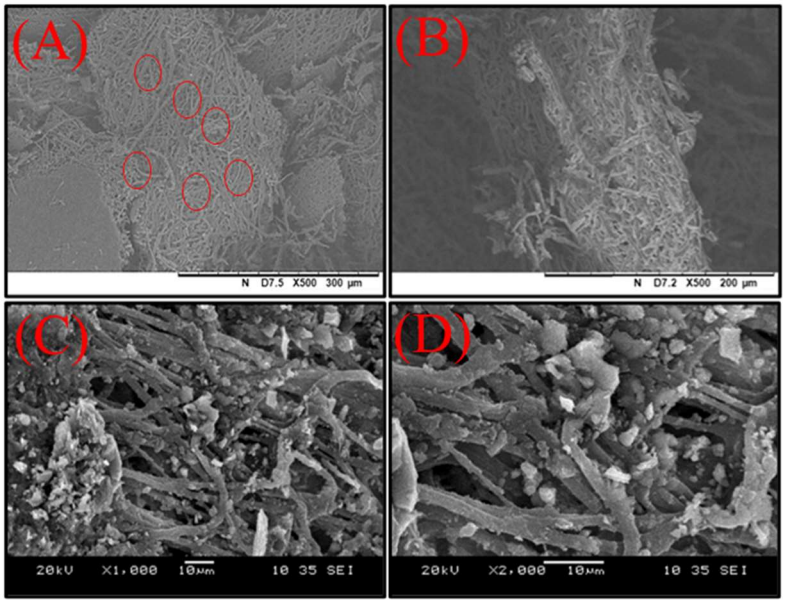
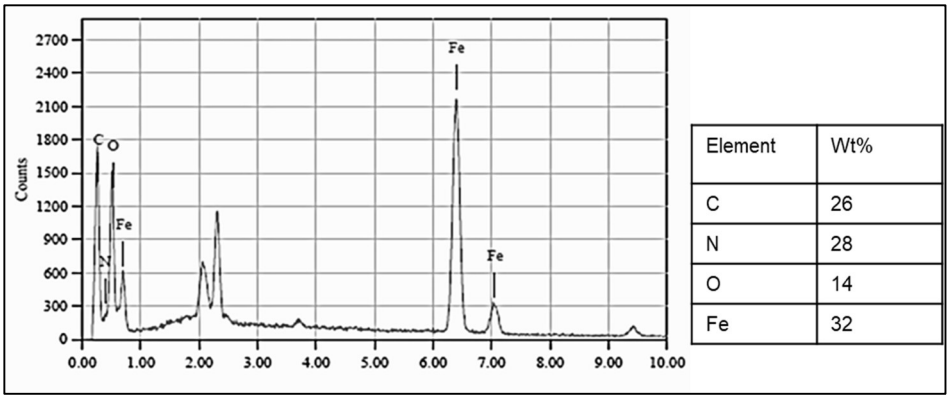


Figure 3. Morphological surface structure of (A) ESM (B) ESM-WPFA under 500× and MNP@ESM-WPFA under magnification of (C) 1000× (D) 2000×

The elemental composition of MNP@ESM-WPFA was examined using energy-dispersive X-ray spectroscopy (EDX) analysis. Figure 4 shows that MNP@ESM-WPFA have an iron (Fe) content of 32%, carbon (C) content of 26%, nitrogen (N) content of 28%, and oxygen (O) content of 14%.



Element	Wt%
C	26
N	28
O	14
Fe	32

Figure 4. EDX spectrum of MNP@ESM-WPFA

The buoyancy of the synthesized nanosorbent was checked by placing it on a surface of water for 24 hours. Remarkably, the MNP@ESM-WPFA was found to float on water (Figure S1 (A) and (B)) , suggesting the fabricated adsorbents possess high buoyancy. In addition, The contact angle (CA) of MNP@ESM-WPFA was measured to be 123.6º (Figure S1 (C)) showing this adsorbent exhibits higly hydrophobic, which may be exploited for the adsorption of oil pollutants on the surface of water.

The optimization of the parameter for efficient oil removal:

Effect of treatment time

The effect of treatment time on oil adsorption using MNP@ESM-WPFA was studied within the range of 10 to 60 minutes. Figure 5(A) shows that the K value increase significantly until 50 minutes, after which it reaches a plateau (at time >50 min). As the treatment time increases, so does the mixing cycle; as the oil droplets have more time to break up and shrink in diameter (emulsification), resulting in a larger interfacial area for adsorption on the MNP@ESM-WPFA [30]. The curve shows that the maximum adsorption capacity was reached at 50 minutes of treatment. The highest K value obtained at 50 minutes of treatment is due to greater existence of interfacial surface of MNP@ESM-WPFA for adsorption, while the K value plateau after 50 minutes is due to the saturation of the surface of MNP@ESM-WPFA. Thus, 50 minutes was chosen as optimum treatment time for subsequent studies.

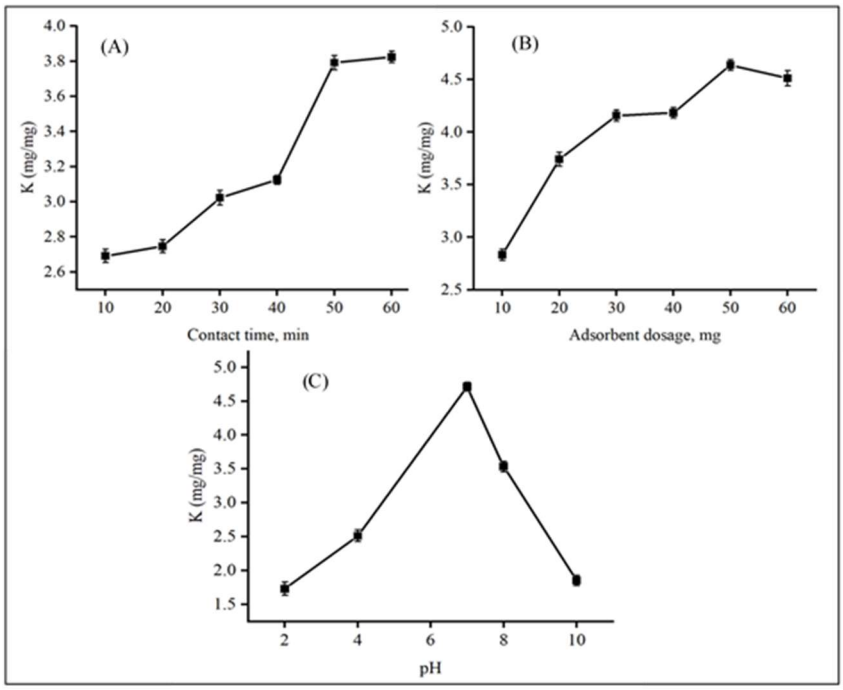


Figure 5. The effect of (A) contact time (B) adsorbent dosage (C) pH on oil adsorption capacity. The error bar represents the relative standard deviations of 3 measurements

Effect of adsorbent dosage

A batch experiment was carried out to determine the effect of adsorbent dosage (10 to 60 mg) on adsorption capacity. Figure 5(B) shows the relationship between adsorption capacity and the MNP@ESM-WPFA adsorbent dosage. Initially, the adsorption capacity increases together with increase of adsorbent dosage from 10 to 50 mg. The maximum adsorption capacity was reached when the dosage was 50 mg. After 50 mg, the adsorption capacity value decreased slightly, likely due to self-aggregation of the adsorbent which reduces the available sites for oil adsorption [31]. The optimum dosage for oil uptake using MNP@ESM-WPFA was thus set at 50 mg.

Effect of pH

The effect of the treatment pH on the oil adsorption process is presented in Figure 5(C). The adsorption process of oil on MNP@ESM-WPFA was found to be highly pH-dependent. The adsorption capacity rapidly increased from 1.73 to 4.71 mg/mg when the solution pH was increased from 2 to 7. However, at pH above7 (pH 8-10), the adsorption capacity slowly decreased until it reaches 1.86 mg/mg at pH 10. This phenomenon can be explained by the changes in the number of free protons in the solution and the stability of the oil emulsion [6]. In acidic conditions, the residual amine, carboxyl, and hydroxyl groups on the surface of MNP@ESM-WPFA becomes protonated, increasing the surface's cationic property and thus improving the adsorbent's hydrophilicity [29]. Additionally, in acidic conditions, as the acidity increased (from pH 7 to pH 2), the oil emulsion began to destabilize, causing clusters to form and larger oil droplets to form [30]. As a result, the interfacial area available for adsorption on MNP@ESM-WPFA decreases. On the other hand, the deprotonation of residual amine, carboxyl, and hydroxyl from ESM-WPFA in alkaline solution causes the adsorbent surface to become more anionic, reducing the oleophilic property of MNP@ESM-WPFA [29] and thus its oil adsorption capability. Thus pH 7 was selected as the optimum pH for oil uptake using MNP@ESM-WPFA.

The adsorption capacity of various oils

The adsorption capacities (K) of MNP@ESM-WPFA for lubricating oil, olive oil and corn oil were also

determined, and the results are shown in Table 1. MNP@ESM-WPFA was found to have the highest K value for lubricating oil, at 4.6 mg/mg, followed by olive oil (2.7 mg/mg) and corn oil (2.0 mg/mg). The difference in oil adsorption capacity is attributed to the difference in the viscosity of the oils [32]. The adsorption capacity increases with oil viscosity due to improved oil adhesion onto the adsorbent surface [33-35].

Table 1. Adsorption capacities and viscosity values for studied oils. (Amount of MNP@ESM-WPFA = 50 mg, contact time = 50 min, and pH = 7)

Type of Oils	K, (mg/mg)	Viscosity, (mm^2/s)	Density, (kg/m^3)	Surface Tension, (mN/m)
Lubricating Oil	4.6	157.7	767.0	30.3
Corn oil	2.0	34.9	918.5	31.6
Olive oil	2.7	43.2	916.0	31.9

Reusability of MNP@ESM-WPFA

For practical application purposes, reusability is a crucial feature of any adsorbent. Here, the reusability study was carried out by repeating the lubricating oil adsorption experiment five times using the same adsorbent. Between each repeated runs, the adsorbent was cleaned with *n*-hexane and dried in an oven at 70 °C for one hour. Each experiment run used 50 mg MNP@ESM-WPFA, pH 7, and 50 min treatment time. The performance for five successive cycles is shown in Figure 6. Evidently, the regenerated MNP@ESM-WPFA can be recycled many times as it can adsorb oil 4.18 times its own weight even after five cycles. Therefore, the synthesized adsorbent MNP@ESM-WPFA can be considered recyclable and stable. The high hydrophobic/oleophilic property also contributes to the excellent recyclability of the adsorbent. This is because when hydrophobicity and oleophilicity are introduced to a sorbent, it tends to concentrate and interact with the oil phase medium, hence, transforming it to a semisolid phase via Van der waals forces [36]. This makes it easier for desorption. This characteristic suggests that as-prepared MNP@ESM-WPFA shows a great potential application in multifunctional wastewater purification.

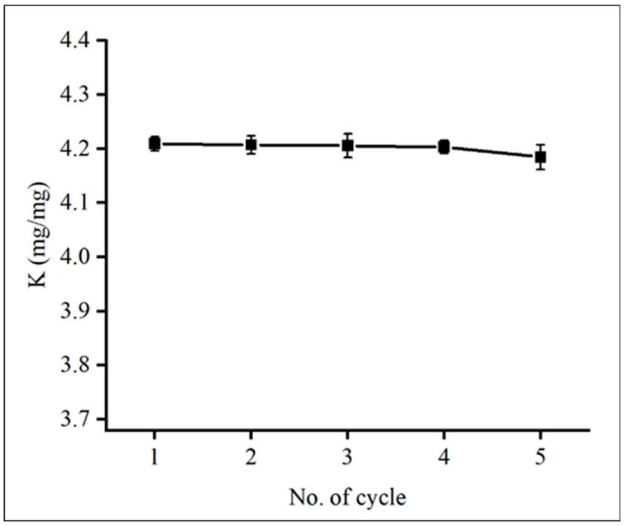


Figure 6. Oil-adsorption capacity of MNP@ESM-WPFA at different cycles. The error bar length accounts for the relative standard deviations for 3 measurements

Analysis of Oil-Loaded MNP@ESM-WPFA

The surface of lubricating oil loaded MNP@ESM-WPFA was evaluated using FTIR, SEM and EDX analyses. Figure 7 depicts the FTIR analysis of MNP@ESM-WPFA with and without oil loading (A-B). When comparing the original MNP@ESM-WPFA (Figure 7(A)) spectrum to the oil loaded MNP@ESM-WPFA spectrum (Figure 7(B)), it is observed that the intensity of -CH_2- group bands at 2853 cm^{-1} and 2923 cm^{-1} are substantially higher for oil loaded MNP@ESM-WPFA. This result proves that a significant amount of oil adsorption occurred at the hydrophobic tails of waste palm fatty acid on the surface of MNP@ESM-WPFA.

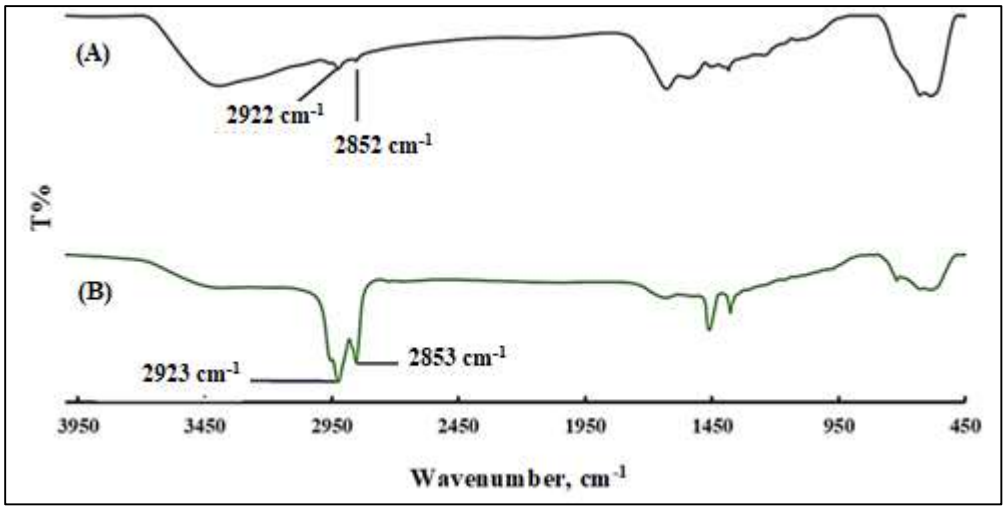


Figure 7. FTIR spectra of (A) MNP@ESM-WPFA and (B) lubricating oil loaded MNP@ESM-WPFA

Figure 8 shows the SEM images of MNP@ESM-WPFA before and after the lubricating oil adsorption process. The SEM images of oil-loaded MNP@ESM-WPFA (Figure 8(C-D)) show substantial differences from the unloaded MNP@ESM-WPFA (Figure 8(A-B)). The oil loaded MNP@ESM-WPFA surface was covered with a layer of oily mud-like material, which is the adsorbed oil molecules.

Elemental analysis reveals that the mass content of C (33%) in the oil-loaded MNP@ESM-PFA (Figure 9(B)) is notably higher than the percentage of C discovered in the unloaded MNP@ESM-WPFA (26%) (Figure 9(A)). These results align with that obtained from the FTIR analysis for oil loaded MNP@ESM-WPFA (Figure 7(B)) indicating that a higher carbon content causes a stronger band intensity for the alkane group in oil-loaded MNP@ESM-WPFA.

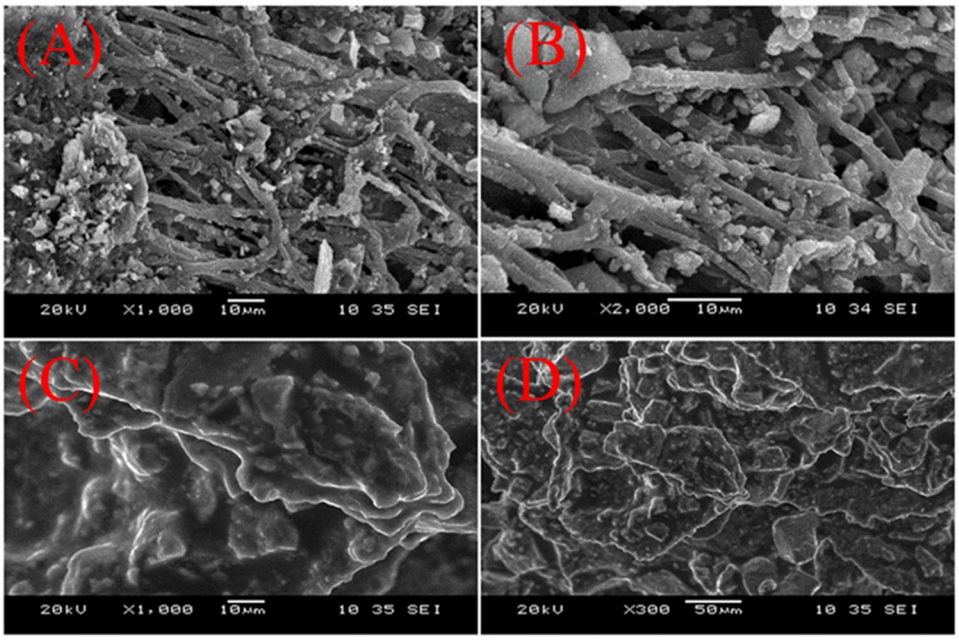
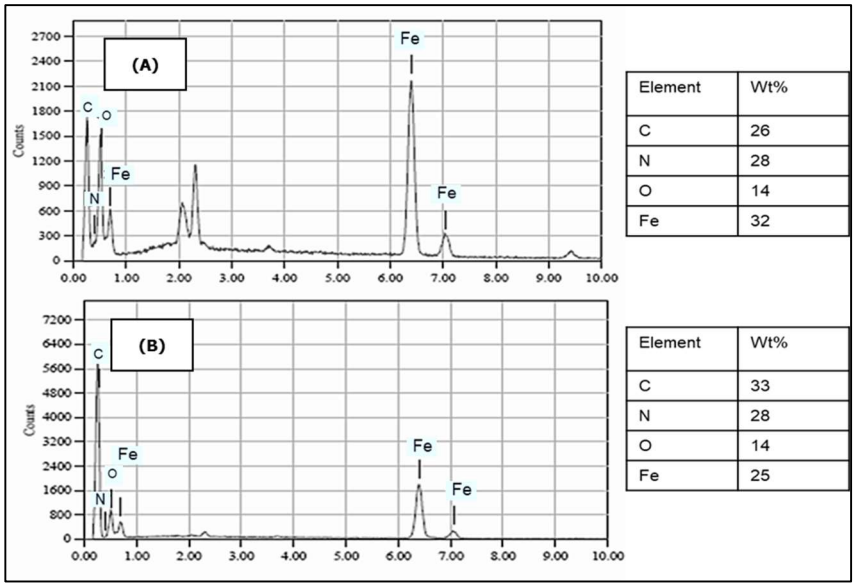


Figure 8. Morphological surface of MNP@ESM-WPFA under different magnifications (A) x 1000 (B) x 2000 and lubricating oil loaded MNP@ESM-WPFA under different magnifications (C) X 1000 (D) X 300



Element	Wt%
C	26
N	28
O	14
Fe	32

Element	Wt%
C	33
N	28
O	14
Fe	25

Figure 9. EDX spectra of (A) MNP@ESM-WPFA and (B) Oil Loaded MNP@ESM-WPFA

Comparison of MNP@ESM-WPFA with other adsorbents

Table 2 summarizes and compares this work with previous works reported in literature. MNP@ESM-WPFA shows the highest adsorption capacity among the published works reported in the table, suggesting the potential of MNP@ESM-WPFA usage in water remediation. Furthermore, the proposed approach offers numerous other benefits, such as simplicity, ease of removal, and operation.

Table 2. Comparison to oil adsorbents from the literature

Adsorbent	Emulsified Oil Studied	Sorption Capacity (mg/mg)	References
MNP-FA	Lubricating oil	3.50	[29]
ACF-PO	Lubricating oil	3.03	[37]
Fe_3O_4@PS	Motor oil	3.00	[38]
Fe_3O_4@PVP	Lubricating oil	3.63	[39]
MNP@ESM-WPFA	**Lubricating oil**	**4.61**	**This study**

Conclusion

This present study shows that the synthesized MNP@ESM-WPFA can be potentially used for the removal of oil from an oil-water system. SEM, FTIR, and EDX analyses confirmed the successful synthesis of MNP@ESM-WPFA. The oil adsorption performance of MNP@ESM-WPFA was optimum at pH 7, 50 minutes treatment time, and 50 mg adsorbent dosage. MNP@ESM-WPFA is versatile as it can adsorb several types of oil, which are, for this study, lubricating oil, corn oil and olive oil. The MNP@ESM-WPFA has an adsorption capacity of 4.6 mg/mg for lubricating oil, 2.0 mg/mg for corn oil, and 2.7 mg/mg for olive oil. The MNP@ESM-WPFA can also be reused up to 5 times without losing efficiency. FTIR, SEM, and EDX analyses proved that the oil was adsorbed by MNP@ESM-WPFA, as evidenced by the intense peaks attributed to the oil in the FTIR spectrum, the mud-like covering seen in the SEM images, and the increase in C content during the EDX analysis. It is suggested that the oil droplets adsorbed on MNP@ESM-WPFA interacts with the hydrophobic tails of waste palm fatty acid via hydrophobic interaction. This study opens new possibilities for developing high-efficiency, recyclable demulsifiers for emulsified oil wastewater.

Acknowledgement

This study was supported by the Special Research Grant (600-RMC/GPK 5/3 (181/2020) from Universiti Teknologi MARA.

References

1. Sanghamitra, P., Mazumder, D., and Mukherjee, S. (2021). Treatment of wastewater containing oil and grease by biological method- a review. *Journal of Environmental Science and Health, Part A*, 56(4): 394-412.
2. Benito, J. M., Pazos, C., Coca J, and Rios G. (1998). Methods for the separation of emulsified oil from water: a state-of-the-art review. *Trends in Chemical Engineering*, 4: 203-231.
3. Lawrence K. W., Jiaping, P. C., Yung-Tse, H., Nazih, K. S. (2008). *Membrane and Desalination Technologies* (Vol. 13). Springer Science+ Business Media, LLC.
4. Quemeneur, M. (1994). Fatty acids and sterols in domestic wastewaters. *Water Research*, 28(5): 1217-1226.
5. Jamaly, S., Giwa, A., and Hasan, S. W. (2015). Recent improvements in oily wastewater treatment: Progress, challenges, and future opportunities. *Journal of Environmental Sciences*, 37: 15-30.
6. Ibrahim, S., Ang, H.-M., and Wang, S. (2012). Adsorptive separation of emulsified oil in wastewater using biosorbents. *Asia-Pacific Journal of Chemical Engineering*, 7: S216-S221.
7. Abass, O. A., Jameel, A. T., Muyubi, S. A., Abdul Karim, M. I., and Alam, A. Md. Z. (1970). Removal of Oil and Grease as Emerging Pollutants of Concern (EPC) in Wastewater Stream. *IIUM Engineering Journal*, 12(4): 161-169.

8. Kundu, P., and Mishra, I. M. (2018). Treatment and reclamation of hydrocarbon-bearing oily wastewater as a hazardous pollutant by different processes and technologies: a state-of-the-art review. *Reviews in Chemical Engineering*, 35(1): 73-108.
9. Fadile, A., El Hassani, F. Z., Aissam, H., Merzouki, M., and Benlemlih, M. (2011). Aerobic treatment of lipid-rich wastewater by a bacterial consortium. *African Journal of Microbiology Research*, *5*(30): 5333-5342.
10. Rajak, V. K., Singh, I., Kumar, A., and Mandal, A. (2016). Optimization of separation of oil from oil-in-water emulsion by demulsification using different demulsifiers. *Petroleum Science and Technology*, *34*(11–12), 1026–1032.
11. Rajak, V. K., Relish, K. K., Kumar, S. and Mandal, A. (2015). Mechanism and kinetics of separation of oil from oil-in-water emulsion by air flotation. *Petroleum Science and Technology*, 33(23-24): 1861-1868.
12. Xu, X., Liu, W., Tian, S., Wang, W., Qi, Q. et al. (2018). Petroleum hydrocarbon-degrading bacteria for the remediation of oil pollution under aerobic conditions: a perspective analysis. *Frontiers in Microbiology*, 9: 1-11.
13. Manilal, A. M., Soloman, P. A. and Basha, C. A. (2020). Removal of oil and grease from produced water using electrocoagulation. *Journal of Hazardous, Toxic, and Radioactive Waste*, 24(1): 04019023.
14. Chawaloesphonsiya, N., Guiraud, P. and Painmanakul, P. (2018). Analysis of cutting-oil emulsion destabilization by aluminum sulfate. *Environmental Technology*, 39(11): 1450-1460.
15. Lobo, A., Cambiella, Á., Benito, J. M., Pazos, C. and Coca, J. (2006). Ultrafiltration of oil-in-water emulsions with ceramic membranes: Influence of pH and crossflow velocity. *Journal of Membrane Science*, *278*(1-2): 328-334.
16. Fallah, Z., and Roberts, E. P. L. (2019). Combined adsorption/regeneration process for the removal of trace emulsified hydrocarbon contaminants. *Chemosphere*, 230: 596-605.
17. Srinivasan, A., and Viraraghavan, T. (2010). Oil removal from water using biomaterials. *Bioresource Technology*, 101(17): 6594-6600.
18. Elanchezhiyan, S. S., Prabhu, S. M. and Meenakshi, S. (2018). Effective adsorption of oil droplets from oil-in-water emulsion using metal ions encapsulated biopolymers: Role of metal ions and their mechanism in oil removal. *International Journal of Biological Macromolecules*, 112: 294-305.
19. Albatrni, H., Qiblawey, H., Almomani, F., Adham, S. and Khraisheh, M. (2019). Polymeric adsorbents for oil removal from water. *Chemosphere*, 233: 809-817.
20. Ji, F., Li, C., Dong, X., Li, Y. and Wang, D. (2009). Separation of oil from oily wastewater by sorption and coalescence technique using ethanol grafted polyacrylonitrile. *Journal of Hazardous Materials*, 164(2–3): 1346-1351.
21. Wu, D., Fang, L., Qin, Y., Wu, W., Mao, C. and Zhu, H. (2014). Oil sorbents with high sorption capacity, oil/water selectivity and reusability for oil spill cleanup. *Marine Pollution Bulletin*, 84(1–2): 263-267.
22. Bessashia, W., Berredjem, Y., Hattab, Z. and Bououdina, M. (2020). Removal of basic fuchsin from water by using mussel powdered eggshell membrane as novel bioadsorbent: equilibrium, kinetics, and thermodynamic studies. *Environmental Research*, 186: 109484.
23. Wang, W., Chen, B., Huang, Y., and Cao, J. (2010). Evaluation of eggshell membrane-based bio-adsorbent for solid-phase extraction of linear alkylbenzene sulfonates coupled with high-performance liquid chromatography. *Journal of Chromatography A*, 1217(36): 5659-5664.
24. Torres, F. G., Troncoso, O. P., Piaggio, F. and Hijar, A. (2010). Structure–property relationships of a biopolymer network: The eggshell membrane. *Acta Biomaterialia*, *6*(9): 3687-3693.
25. Abdulla, R., Sanny, S. A., and Derman, E. (2017). Stability studies of immobilized lipase on rice husk and eggshell membrane. *IOP Conference Series: Materials Science and Engineering*, 206: 012032.

26. Ravi, T, and Sundararaman, S. (2020). Synthesis and characterization of chicken eggshell powder coated magnetic nano adsorbent by an ultrasonic bath assisted co-precipitation for Cr(VI) removal from its aqueous mixture. *Journal of Environmental Chemical Engineering*, 8(4): 103877.
27. Li, J., Ng, D. H. L., Ma, R., Zuo, M., and Song, P. (2017). Eggshell membrane-derived $MgFe_2O_4$ for pharmaceutical antibiotics removal and recovery from water. *Chemical Engineering Research and Design*, 126: 123-133.
28. Sathasivam, K., and Mas Haris, M. R. H. (2010). Adsorption kinetics and capacity of fatty acid-modified banana trunk fibers for oil in water. *Water, Air, & Soil Pollution*, 213(1-4): 413-423.
29. Rozi, S. K. M., Nodeh, H. R., Kamboh, M. A., Manan, N. S. A., and Mohamad, S. (2017). Novel palm fatty acid functionalized magnetite nanoparticles for magnetic solid-phase extraction of trace polycyclic aromatic hydrocarbons from environmental samples. *Journal of Oleo Science*, 66(7): 771-784.
30. Ahmad A, Sumathi, S., and Hameed, B. (2005). Adsorption of residue oil from palm oil mill effluent using powder and flake chitosan: Equilibrium and kinetic studies. *Water Research*, 39(12): 2483-2494.
31. Baharin, S. N. A., Muhamad Sarih, N., Mohamad, S., Shahabuddin, S., Sulaiman, K., and Ma'amor, A. (2016). Removal of endocrine disruptor di-(2-ethylhexyl)phthalate by modified polythiophene-coated magnetic nanoparticles: characterization, adsorption isotherm, kinetic study, thermodynamics. *RSC Advances*, 6(50): 44655-44667.
32. Wu, J., Wang, N., Wang, L., Dong, H., Zhao, Y. and Jiang, L. (2012). Electrospun porous structure fibrous film with high oil adsorption capacity. *ACS Applied Materials & Interfaces*, 4(6): 3207-3212.
33. Kumagai, S., Noguchi, Y., Kurimoto, Y. and Takeda, K. (2007). Oil adsorbent produced by the carbonization of rice husks. *Waste Management*, 27(4): 554-561.
34. Johnson, R. F., Manjreker, T. G. and Halligan, J. E. (1973). Removal of oil from water surfaces by sorption on unstructured fibers. *Environmental Science & Technology*, 7(5): 439-443.
35. Zheng, J., He, A., Li, J., Xu, J. and Han, C. C. (2006). Studies on the controlled morphology and wettability of polystyrene surfaces by electrospinning or electrospraying. *Polymer*, 47(20): 7095-7102.
36. Guan, H., Cheng, Z. and Wang, X. (2018). Highly compressible wood sponges with a spring-like lamellar structure as effective and reusable oil absorbents. *ACS Nano*, 12(10): 0365-10373.
37. Raj, K. G. and Joy, P. A. (2015). Coconut shell based activated carbon–iron oxide magnetic nanocomposite for fast and efficient removal of oil spills. *Journal of Environmental Chemical Engineering*, 3(3): 2068-2075.
38. Chen, M., Jiang, W., Wang, F., Shen, P., Ma, P. et al. (2013). Synthesis of highly hydrophobic floating magnetic polymer nanocomposites for the removal of oils from water surface. *Applied Surface Science*, 286: 249-256.
39. Gu, J., Jiang, W., Wang, F., Chen, M., Mao, J. and Xie, T. (2014). Facile removal of oils from water surfaces through highly hydrophobic and magnetic polymer nanocomposites. *Applied Surface Science*, 301: 492-499.

Malaysian Journal of Analytical Sciences (MJAS)
Published by Malaysian Analytical Sciences Society

DETERMINATION OF L-CARNITINE AND COENZYME Q_{10} ACTIVE SUBSTANCE LEVELS IN FOOD SUPPLEMENTS USING HIGH-PERFORMANCE LIQUID CHROMATOGRAPHY

(Penentuan Kadar Zat Aktif L-Carnitine dan Ko-enzim Q_{10} dalam Suplemen Makanan Menggunakan Kromatografi Cecair Prestasi Tinggi)

Muhaimin[1,*], Hilda Andini [2], and Henry Himawan[3]

[1] Study Program of Chemistry Education,
Department of Chemistry, Islamic University of Indonesian, Indonesia
[2] Diploma Program of Chemical Analysis,
Department of Chemistry, Islamic University of Indonesian, Indonesia
[3] PT. Dipa Pharmalab Intersains,
Majalengka, West Java, Indonesia

**Corresponding author: muhaimin@uii.ac.id*

Received: 23 July 2022; Accepted: 25 October 2022; Published: 22 February 2023

Abstract

This study aimed to determine the active substance levels in L-Carnitine and Coenzyme Q_{10} in dietary supplements using the High-Performance Liquid Chromatography (HPLC)-UV method. They are often found in dietary supplements because these ingredients can be used to maintain heart health. L-Carnitine is an active ingredient belonging to amino acids, while Coenzyme Q_{10} is one of the most significant lipid antioxidants, which prevents the formation of free radicals and modification of proteins, lipids, and DNA. The method used in this study is HPLC-UV because the method has good sensitivity, can use the column and solvent developer many times, the detector varies, the analysis time is generally short, easy to operate, and has relatively high accuracy and precision. The HPLC procedure for determining L-Carnitine used a UV detector with a wavelength of 225 nm using an L1 (4.6 mm x 15 cm; 5 m) column with a flow rate of 0.7 mL/min. Meanwhile, the determination of Coenzyme Q10 using the HPLC procedure used a UV detector with a wavelength of 280 nm using a C_{18} (4.6 mm x 15 cm, 5µm) column with a flow rate of 1.5 mL/minute. This study also reports differences in L-Carnitine and Coenzyme Q10 in dietary supplements (in capsule form) during the mixing and encapsulation processes. The results show the suitability test for the HPLC-UV system in good condition; seen from the %RSD value below 2%. In testing the active substance Coenzyme Q_{10} in the mixing process is 101.07% and encapsulation is 96.77%. While the active substance L-Carnitine in the mixing process is 105.05% and encapsulation is 93.03%. The overall test results fall into the range of requirements, meaning that the product quality is in a good category.

Keywords: l-carnitine, coenzyme Q_{10}, high-performance liquid chromatography, mixing, encapsulation

Abstrak

Penelitian ini untuk mengetahui kadar zat aktif L-Carnitine dan Ko-enzim Q_{10} pada suplemen makanan menggunakan kaedah kromatografi cecair prestasi tinggi (HPLC)-UV. Zat aktif ini sering ditemukan dalam suplemen makanan kerana bahan-bahan ini dapat digunakan untuk menjaga kesihatan jantung. L-Carnitine merupakan bahan aktif yang tergolong ke dalam asid amino, sedangkan Ko-enzim Q_{10} adalah salah satu antioksidan lipid yang paling signifikan, yang mencegah pembentukan radikal bebas dan modifikasi protein, lipid, dan DNA. Kaedah yang digunakan dalam penelitian ini adalah HPLC-UV karena memiliki sensitiviti yang baik, dapat menggunakan turus dan pelarut berkali-kali, pengesan pelbagai, memiliki waktu analisis yang singkat, mudah dioperasikan, dan memiliki ketepatan dan kejituan yang relatif tinggi. Prosedur HPLC untuk penentuan L-Carnitine menggunakan pengesan UV dengan panjang gelombang 225 nm menggunakan turus L1 (4.6 mm x 15 cm; 5 m) dengan kadar aliran 0.7 mL/minit. Sedangkan penentuan Ko-enzim Q_{10} menggunakan prosedur HPLC menggunakan pengesan UV dengan panjang gelombang 280 nm menggunakan turus C_{18} (4.6 mm x 15 cm, 5µm) dengan kadar aliran 1.5 mL/minit. Dalam penelitian ini, kami juga melaporkan perbezaan kadar L-Carnitine dan Koenzim Q_{10} dalam suplemen makanan (dalam bentuk kapsul) selama proses pencampuran dan pengkapsulan. Hasil pengujian menunjukkan bahwa uji kesesuaian sistem HPLC-UV dalam keadaan baik dilihat dari nilai %RSD dibawah 2%. Pada pengujian zat aktif Ko-enzim Q_{10} pada proses pencampuran adalah 101.07% dan pengkapsulan adalah 96.77%. Sedangkan zat aktif L-Carnitine pada proses pencampuran adalah 105.05% dan pengkapsulan adalah 93.03%. Hasil pengujian secara keseluruhan menepati piawaian, memberi maksud produk berada pada kategori baik.

Kata kunci: L-carnitine, ko-enzim Q_{10}, kromatografi cecair prestasi tinggi, pencampuran, pengkapsulan

Introduction

This study aimed to determine the active substance levels in L-Carnitine and Coenzyme Q_{10} in dietary supplements using the High-Performance Liquid Chromatography method. L-Carnitine is a component that is needed by the human body. Where L-Carnitine is an amino acid derivative such as a vitamin, which is an important factor in fatty acid metabolism as an acyltransferase cofactor and in energy production processes, such as interconversion in the regulatory mechanisms of ketogenesis and thermogenesis, and is also used in the treatment of primary and secondary deficiencies, as well as in other diseases [1–3]. L-Carnitine is a zwitterion at pH 3.8. L-Carnitine has a molecular weight of 161.2 g/mol with a solubility of >2500 g/L at a temperature of 20 ºC with the chemical formula $C_7H_{15}NO_3$. The structural formula of L-Carnitine is presented in Figure 1 [4].

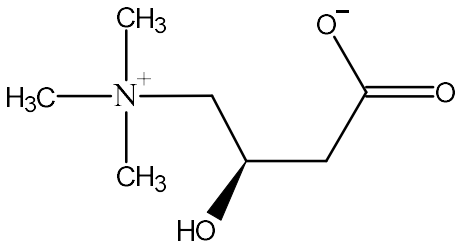


Figure 1. Chemical structure of L-Carnitine [4]

In particular, L-Carnitine among the various forms of Carnitine is also called vitamin B and Carnitine used for food generally means L-Carnitine. L-Carnitine plays a role in helping the breakdown of fat in the human body. Therefore, if it is insufficient, the energy produced in the decomposition of fatty acids is not generated, because the fatty acids do not decompose properly. For this reason, Carnitine is widely used as a drug or food additive to aid diet [5]. L-Carnitine deficiency leads to the accumulation of lipids in the cytosol and impaired energy production of long-chain fatty acids, especially during periods of fasting or stress. L-Carnitine can be found in various foods or medicines such as injections, syrups, tablets, and capsules, which can be used in treating primary and secondary Carnitine deficiency in other diseases such as dyslipoproteinemia and Alzheimer's [6]. Several oral formulations (tablets, capsules, solutions) are commercially available from a wide various of products [7].

The content of L-carnitine in various types of food has been published. Contents vary widely and the highest amounts of L-carnitine are found in meat and dairy products, and a wide variety of fruits and vegetables. In addition to biosynthetic ingredients, L-carnitine can also be found in dietary supplements. Various methods that are sensitive, reliable, relatively simple, inexpensive, and powerful for assessing L-carnitine content are needed to determine the amount of L-carnitine in

various materials [8–10]. Various methods to determine the L-carnitine content in food or other materials have been developed including using high-performance liquid chromatography (HPLC) or gas chromatography (GC), Mass Spectrometric (MS), capillary electrophoresis (CE), TLC-densitometry technique [11–14]. Because L-Carnitine is a polar compound, amphoteric and non-volatile, and does not have a chromophore group [3, 5]. Based on AOAC, the HPLC method can be used to determine L-Carnitine quantitatively [3].

Coenzyme Q_{10} is one of the most significant lipid antioxidants, which prevents forming free radicals and the modifying proteins, lipids, and DNA [15]. Coenzyme Q_{10} is a lipophilic compound consisting of a benzoquinone ring and ten isoprenoid side chain units. [16, 17]. Coenzyme Q_{10} also has poor stability to light and very poor solubility in water. This poor solubility stems from the isoprenoid chain, which is very long in its chemical structure and has a relatively high molecular weight (MW: 864 g/mol) (Figure 2) [18].

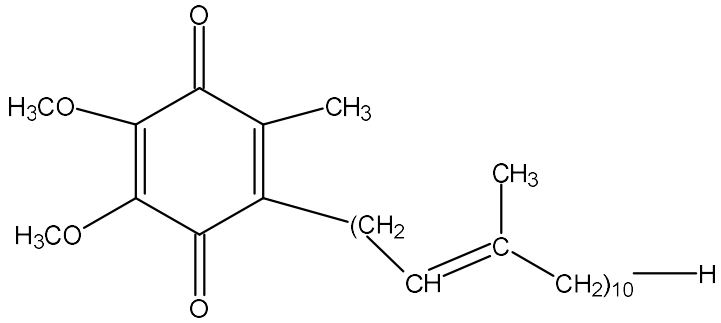


Figure 2. Chemical structure of Coenzyme Q10 [18]

The name Coenzyme Q_{10} comes from its chemical structure, a benzoquinone ring with a side chain of 10 isoprene units. These natural compounds are ubiquitous in nature; thus, it is also known as ubiquinone. There are three types of Coenzyme Q_{10} in the oxidized state the fully reduced form of ubiquinol (CoQ_{10} H_2), the semiquinone radical intermediate (CoQ_{10} H), and the fully oxidized form of ubiquinone (CoQ_{10}) [19–21]. Coenzyme Q_{10} (ubiquinone and its reduced form ubiquinol) can be found in most dairy products, vegetables, fruits, and cereals [22].

Methods of determining Coenzyme Q_{10} in various samples have been carried out such as FT-NIR spectroscopy [23], UPLC/MS-MS [24], ^{1}H NMR Spectroscopy [25], HPLC-ESI-MS/MS [26], HPLC-ECD [27], HPLC with coulometric detection [28], HPLC-UV[17]. Thus, this study discusses the determination of Coenzyme Q_{10} in dietary supplements using HPLC-UV. The HPLC-UV method is an excellent method in all validation parameters (sensitivity, bias, repeatability, intermediate precision, and accuracy profiles) for the determination of Coenzyme Q_{10}. In addition, it allows its widespread use in QC in the pharmaceutical industry [29].

This study reports the determination of L-Carnitine and Coenzyme Q10 in capsules of dietary supplement samples in two manufacturing processes: mixing and filling (encapsulation); the determination will see the levels of L-Carnitine and Coenzyme Q10 from each process. In addition, this test also looks at the precision of the method used which is expressed as Percent Relative Standard Deviation (%RSD).

Materials and Methods

Tools and materials

The tools used in this study include Analytical Balance (Sartorius type B 124 S), Analytical Balance (Shimadzu type ATY124), Disintegrator Tester (Flight type BJ-3), High-Performance Liquid Chromatography (Shimadzu), pH meter (Lovibond type 150), Karl Ficher (Mitsubishi), Spatula, Pro pipette (D&N), Syringe (one road), 0.20 m filter (Phenomenex), 0.4 m filter

(Meissner), Vacuum filter (Duran), Sonification (Elma type S 30 H), Stopwatch (Toto). In contrast the materials used in this research are Acetonitrile 99.9% (JT Backer), phosphoric acid 85%-87% (JT Backer), water for HPLC (JT Backer), Potassium Dihydrogen Phosphate 99% (KH_2PO_4) (JT Backer), 99.5% tetrahydrofuran (JT Backer), 95% N-Hexane (JT Backer), 99.9% Ethanol (JT Backer), L-Carnitine standard, and Coenzyme Q_{10} standard.

Procedure

The research includes two processes: mixing (mixing the capsule's contents) and encapsulation (combining the capsule's contents with the capsule shell, which then becomes a complete capsule. The test is carried out by determining the level of the active substance contained in the supplement, namely L-Carnitine which is a derivative of the active substance L-Carnitine, and also Coenzyme Q_{10} using the high-performance liquid chromatography (HPLC) method.

Instrumentation and optimization of HPLC

The HPLC instrument before being used for the analysis of L-Carnitine and Coenzyme Q_{10} must be optimized first with the specifications in Table 1.

Table 1. Instrumentation and Optimization of HPLC

Description	Condition of HPLC	
	L-Carnitine	**Coenzyme Q_{10}**
Detector	225 nm (UV)	280 nm (UV)
Column	L1 (4.6 mm x 15 cm; 5 µm)	C18 (4.6 mm x 15 cm, 5µm)
Flow rate	0.7 mL/minute	1.5 mL/minute
Injection volume	20 µL	20 L

Preparation of standard solutions of L-Carnitine and Coenzyme Q_{10}

Standard L-Carnitine weighed as much as 100 mg, put into a 50 mL volumetric flask, added solvent to fill 30 mL, sonicated for 5 minutes, then calibrated with solvent to the meniscus mark and homogenized. The standard solution was pipetted as much as 1 mL, put into a 10 mL volumetric flask, diluted with a solvent to the meniscus mark, and homogenized. The standard solution was filtered using a syringe equipped with a 0.20 L filter and inserted into the vial. Then the standard solution was measured using HPLC at a wavelength of 225 nm. The same method was also carried out to determine the Coenzyme standard solution by changing the type of standard used and measuring using an appropriate wavelength of 280 nm for the Coenzyme standard solution.

Determination of the active substance of L-Carnitine by HPLC-UV:

Mobile phase preparation

The mobile phase was made with a mixture of 0.05 M KH_2PO_4 and acetonitrile (4:6), and the pH of the solution was adjusted using phosphoric acid to pH 4.2. The mixture was filtered using a vacuum equipped with a 0.4 L filter and then sonicated for 15 minutes.

L-carnitine analysis using HPLC

The sample was weighed (capsule contents) equivalent to 20 mg of standard, put into a 100 mL volumetric flask, added solvent to fill 50 mL, sonicated for 15 minutes, then calibrated using a solvent to the meniscus mark and homogenized. The sample solution was filtered using a syringe equipped with a 0.20 µL filter and inserted into the vial. Standard solutions were measured using HPLC at a wavelength of 225 nm. This test is repeated in triples.

Determination of the active substance of Coenzyme Q_{10} with HPLC:

Mobile phase preparation

The mobile phase was made with a mixture of acetonitrile: tetrahydrofuran: water (55:40:5). The mixture was filtered using a vacuum equipped with a 0.4 L filter, then sonicated for 10 minutes.

Coenzyme Q_{10} analysis using HPLC

The sample was weighed (capsule contents) equivalent to 100 mg, put into a 50 mL volumetric flask, added solvent to fill 30 mL, sonicated for 5 minutes, and then calibrated with solvent to the meniscus mark and homogenized. 5 mL of the solution was pipetted, put into a 25 mL volumetric flask, diluted with a solvent to the meniscus mark, and homogenized. The sample solution was filtered using a syringe equipped with a 0.20 L filter and inserted into the vial. Standard solutions of Coenzyme Q_{10} were measured using HPLC at a wavelength of 280 nm

Results and Discussion

HPLC system suitability Analysis on L-Carnitine and Coenzyme Q_{10} samples

The system suitability test was carried out using a single standard for six repeated injections, where the %RSD result obtained had to be less than 2%. This value is acceptable because it is below 2% and can be used for quality control of pharmaceutical preparations [6, 30, 31]. Table 2 shows the results of the suitability test for the Coenzyme Q_{10} active substance system.

Table 2. HPLC system suitability test on samples of L-Carnitine and Coenzyme Q_{10}

Description	L-Carnitine				Coenzyme Q_{10}			
	Retention time		Area		Retention time		Area	
	Mixing	Encapsulation	Mixing	Encapsulation	Mixing	Encapsulation	Mixing	Encapsulation
	(minute)		(uAU)		(minute)		(uAU)	
Average test results	1.933	1.995	4378568	4516281	7.827	7.827	3571486	3571486
SD	0.005	0.001	7630	1933	0.0238	0.024	16721	16721
RSD (%)	0.283	0.055	0.174	0.043	0.304	0.304	0.468	0.468

Table 2 shows that the HPLC system suitability test results for L-Carnitine and Coenzyme Q10 standards can be categorized as good. It can be seen from the value of %RSD below 2%. Therefore, this test is feasible for sample analysis in dietary supplements.

Determination of active substance levels in Coenzyme Q_{10} samples

Table 3 shows that the retention time of the sample in the mixing process is longer than the retention time in the encapsulation process. However, this does not affect the results in the separation process using HPLC. Moreover, Table 4 shows that the measurement results are still within the predetermined limits.

Table 3. The retention time of Coenzyme Q_{10}

Description	Retention Time (minute)	
	Mixing	Encapsulation
Sample 1	7.859	7.541
Sample 2	7.827	7.492
Sample 3	7.771	7.457
Average	7.819	7.497

Table 4. Results of the active substance Coenzyme Q_{10}

Process	Description	Area of Sample (uAU)	Area of Standard (uAU)	Standard Concentration %w/v	Content %w/v
Mixing	Sample 1	3635588	3571486	99.62	101.41
	Sample 2	3520627	3571486	99.62	98.20
	Sample 3	3714669	3571486	99.62	103.61
				Average	101.07
				%RSD	2.69
				CV Horwitz	1.9968
Encapsulation	Sample 1	3564557	3571486	99.62	99.43
	Sample 2	3431624	3571486	99.62	95.72
	Sample 3	3411998	3571486	99.62	95.17
				Average	96.77
				%RSD	2.39
				CV Horwitz	2.0099

% w/v is percent weight/volume

Determination of Coenzyme Q_{10} levels using the HPLC method with a UV detector at a wavelength of 280 nm. The use of a UV detector is because the Coenzyme Q_{10} compound has a chromophore group that can absorb wavelengths in the UV region. In addition, the use of the HPLC method uses an inverted phase where the stationary phase in the form of a C18 column is non-polar and the mobile phase used is polar.

Table 4 shows that the results of testing the Coenzyme Q_{10} level in the sample of dietary supplements fall into the required category; the value must be between 90%-115% [32]. Based on the repetition of the sample 3 times, it shows that the precision value seen based on the %RSD shows more than 2%, meaning that the value does not meet the requirements that have been set. Then, the %RSD value was compared with Horwitz's CV value. Because the %RSD value is good if the %RSD obtained is within the acceptable limit, i.e. %RSD is less than 2/3 CV Horwitz [33]. The determination results indicate that the %RSD value is above the CV Horwitz value. Although the %RSD value is greater than the CV Horwitz value, this does not affect the test. The levels obtained in the HPLC test are still within the required range.

Determination of active substance levels in L-Carnitine samples

The results of the retention time of the active ingredient L-Carnitine in Table 5 show that the sample in the mixing process is shorter (1.927 minutes) than the encapsulation process (1.990 minutes). It occurs in HPLC conditions, especially during the test's mobile and stationary phases. The stationary phase is used repeatedly which causes its performance to decrease over time so that it can affect the retention time of the tests performed.

Table 5. The retention time of L-Carnitine levels

Description	Retention Time (minute)	
	Mixing	Encapsulation
Sample 1	1.927	1.989
Sample 2	1.927	1.986
Sample 3	1.928	1.996
Average	1.927	1.990

Table 6. Results of levels of the active substance L-Carnitine

Process	Description	Area of Sample	Area of Standard	Standard Concentration	Content
		(uAU)	(uAU)	%w/v	%w/v
Mixing	Sample 1	4572792	4378568	100	104.44
	Sample 2	4611470	4378568	100	105.32
	Sample 3	4615174	4378568	100	105.40
				Average	105.05
				%RSD	0.51
				CV Horwitz	1.9852
Encapsulation	Sample 1	4175852	4516281	100	92.46
	Sample 2	4185019	4516281	100	92.67
	Sample 3	4243936	4516281	100	93.97
				Average	93.03
				%RSD	0.88
				CV Horwitz	2.0219

%w/v is percent weight/volume

Table 6 shows that the measurement results of L-Carnitine in the sample using the HPLC method in the mixing or encapsulation process have met the specified requirements; the results are in the range of 90%-115%, i.e. 105.05% w/v in the mixing process, and 93, 03 %w/v on the encapsulation process. The sample's precision is determined by repeatability, measuring three times repetition in each process, either in the mixing or encapsulation process. The measurement results obtained that the %RSD value was below the CV Horwitz value. That is, the results of sample precision in each process are in a good category.

Conclusions

The results of the active substance levels in the mixing process of Coenzyme Q_{10} were 103.61% and L-Carnitine was 105.05%, then in the encapsulation process, the results were Coenzyme Q_{10} of 96.77% and L-Carnitine of 93.03%. The internal specifications of the two active substances that have been determined are the same 90%-115%. Based on the comparison of the results obtained with the specifications, the two active substances contained in the supplement meet the range of requirements, meaning that the quality of the chemical test of the product is in a good category.

References

1. Manoharan, G. (2021). Quantitative determination of l-carnitine tablet formulation by a validated stability-indicating reversed-phase HPLC method. *South Asian Research Journal Pharmaceutical Sciences,* 3:46-51.
2. Dąbrowska, M. and Starek, M. (2014). Analytical approaches to determination of carnitine in biological materials, foods and dietary supplements. *Food Chemistry,* 142: 220-232.
3. Park, J. M., Koh, J. H. and Kim, J. M. (2021). Determination of l-carnitine in infant powdered milk samples after derivatization. *Food Science Animal Resource,* 41:731-738.
4. Durazzo, A., Lucarini, M., Nazhand, A., Souto, S. B., Silva, A. M., Severino, P., Souto, E. B. and Santini, A. (2020). The nutraceutical value of carnitine and its use in dietary supplements. *Molecules* 25: 1-19.
5. Ahn, J. H., Kwak, B. M., Park, J. M., Kim, N. K. and Kim, J. M. (2014). Rapid determination of l-carnitine in infant and toddler formulas by liquid chromatography-tandem mass spectrometry. *Korean Journal Food Science Animimal Resource,* 34:749-756.
6. Khoshkam, R. and Afshar, M. (2014). Validation of a stability-indicating RP-HPLC method for

determination of l-carnitine in tablets. *International Scholary Resesearch Notice,* 2014: 1-7.

7. Kakou, A., Megoulas, N. C. and Koupparis, M. A. (2005). Determination of l-carnitine in food supplement formulations using ion-pair chromatography with indirect conductimetric detection. *Journal Chromatography A,* 1069: 209-215.
8. Seline, K. G. and Johein, H. (2007) The determination of l-carnitine in several food samples. *Food Chemistry,* 105:793-804.
9. Gustavsen, H. S. M (2000) Bestimmung von L-carnitin und seiner Ester in Lebensmitteln. Aus dem Physiologischen Institut der Tierärztlichen Hochschule Hannover.
10. Demarquoy, J., Georges, B., Rigault, C., Royer, M. C., Clairet, A., Soty, M., Lekounoungou, S. and Le Borgne F. (2004). Radioisotopic determination of l-carnitine content in foods commonly eaten in western countries. *Food Chemistry*, 86: 137-142.
11. Bene, J., Szabo, A., Komlósi, K. and Melegh, B (2019). Mass spectrometric analysis of l-carnitine and its esters: potential biomarkers of disturbances in carnitine homeostasis. *Current Molecular Medicine*, 20: 336-354.
12. Prokorátová, V., Kvasnička, F., Ševčík, R. and Voldřich, M. (2005). Capillary electrophoresis determination of carnitine in food supplements. *Journal Chromatography A*, 1081: 60-64.
13. He, G.X. and Dahl, T. (2000). Improved high-performance liquid chromatographic method for analysis of l-carnitine in pharmaceutical formulations. *Journal Pharmaceutical Biomedicine Analysis*, 23: 315-321.
14. Dâbrowska, M., Sieczka, E. and Starek, M. (2012). TLC assay of l-carnitine in dietary supplements. *Journal Planar Chromatography - Mod TLC*, 25:450-455.
15. Saxena, J. D., Yadav, P. and Kantharia, N. D. (2011). Coenzyme Q10: The essential nutrient. *Journal Pharmaceutical Bioallied Sciences*, 3: 465-466.
16. Neergheen, V., Chalasani, A., Wainwright, L., Yubero, D., Montero, R., Artuch, R. and Hargreaves, I. (2017). Coenzyme Q_{10} in the treatment of mitochondrial disease. *Journal Inborn Errors Metabolism Screening*, 5: 1-8.
17. Temova Rakuša, Ž., Kristl, A. and Roškar, R. (2020). Quantification of reduced and oxidized coenzyme Q_{10} in supplements and medicines by HPLC-UV. *Analytical Methods*, 12: 2580-2589.
18. Choi, C. H., Kim, S. H., Shanmugam, S., Baskaran, R., Park, J. S., Yong, C. S., Choi, H. G., Yoo, B. K. and Han, K. (2010). Relative bioavailability of coenzyme Q_{10} in emulsion and liposome formulations. *Biomolecule Theraphy*, 18:99-105.
19. Raizner, A. E. (2019). Coenzyme Q_{10}. *Methodist Debakey Cardiovasc Journal,* 15: 185-191.
20. Aaseth, J., Alexander, J. and Alehagen, U. (2021). Coenzyme Q_{10} supplementation – in ageing and disease. *Mechanism and Ageing Development,* 197: 111521.
21. Wang, Y. and Hekimi, S. (2016). Understanding ubiquinone. *Trends Cell Biology*, 26:367-378.
22. Gleize, B, Steib M, André M. and Reboul, E. (2012). Simple and fast HPLC method for simultaneous determination of retinol, tocopherols, coenzyme Q_{10} and carotenoids in complex samples. *Food Chemistry*, 134:2560-2564.
23. Rácz, A., Vass, A., Héberger, K. and Fodor, M. (2015). Quantitative determination of coenzyme Q10 from dietary supplements by FT-NIR spectroscopy and statistical analysis. *Analytical Bioanalytical Chemistry*, 407: 2887-2898.
24. Visconti, G. L., Mazzoleni, L., Rusconi, C., Grazioli, V., Roda, G., Manini, G. and Gambaro, V. (2015). Determination by UPLC/MS-MS of Coenzyme Q10 (CoQ10) in Plasma of Healthy Volunteers before and After oral intake of food supplements containing CoQ_{10}. *Journal Analytical Bioanalytical Technology*, S13:011.
25. Monakhova, Y. B., Ruge, I., Kuballa, T., Lerch, C. and Lachenmeier, D. W. (2013). Rapid determination of coenzyme Q_{10} in food supplements using 1H NMR spectroscopy. *International Journal Vitamamin Nutrional Research,* 83: 67-72.
26. Vass, A., Deák, E. and Dernovics, M. (2015). Quantification of the reduced form of coenzyme $Q_{10,}$ ubiquinol, in dietary supplements with HPLC-ESI-MS/MS. *Food Analytical Methods,* 8: 452-

458.

27. Schou-Pedersen, A. M. V., Schemeth, D. and Lykkesfeldt, J. (2019). Determination of reduced and oxidized coenzyme Q_{10} in canine plasma and heart tissue by HPLC-ECD: Comparison with LC-MS/MS quantification. *Antioxidants* 8(8): 1-14.
28. Tang, P. H. (2006). Determination of coenzyme Q_{10} in over-the-counter dietary supplements by high-performance liquid chromatography with coulometric detection. *Journal AOAC International*, 89: 35-39.
29. Ün, İ., Vatansever, B., Şimşek, A. and Gören, A. C. (2016). Comparison of qNMR and HPLC-UV techniques for measurement of coenzyme Q_{10} in dietary supplement capsules. *Journal Chemical Metrology,* 10:1-10
30. Ermer, J. and Ploss, H. J. (2005) Validation in pharmaceutical analysis: Part II: Central importance of precision to establish acceptance criteria and for verifying and improving the quality of analytical data. *Journal Pharmaceutical Biomedicine Analysis,* 37: 859-870.
31. Chan, C. C., Lam, H., Lee, Y. C. and Zhang, X. (2004). Analytical method validation and instrument performance verification. John Wiley & Sons, Inc., Hoboken, NJ, USA
32. United States Pharmacopeia (2018). The United States Pharmacopeia, USP 41/The National Formulary, NF 36. MD: U.S. Pharmacopeial Convention, Inc., Rockville
33. Ratnawati, N. A., Prasetya, A. T. and Rahayu, E. F. (2019). Validasi metode pengujian logam berat timbal (Pb) dengan destruksi basah menggunakan FAAS dalam sedimen sungai banjir Kanal Barat Semarang. *Indonesian Journal Chemical Sciences,* 8: 60-68.

Malaysian Journal of Analytical Sciences (MJAS)
Published by Malaysian Analytical Sciences Society

THE EFFECT OF ANTHRACENE GROUP SUBSTITUTION OF DISUBSTITUTED CHALCONE DERIVATIVE FEATURING TEREPHTHALALDEHYDE π-LINKER ON NON-LINEAR OPTICAL (NLO) CHARACTERISTIC

(Kesan Penggantian Kumpulan Antrasena Atas Terbitan Kalkon Dualgantian Yang Menampilkan Terephthalaldehid π-Penyambung Keatas Ciri-Ciri Optik Bukan Linear)

Nurul Nabilah Shuaib[1], Adibah Izzati Daud[1*], Suhana Arshad[2], Mohamad Aizat Abu Bakar[3], Wan M. Khairul[4]

[1]Faculty of Engineering and Chemical Technology,
Universiti Malaysia Perlis,
02600 Arau, Perlis, Malaysia.
[2]School of Physics,
Universiti Sains Malaysia, 11800 USM, Pulau Pinang, Malaysia.
[3]Institute of Nano Optoelectronics Research and Technology (INOR),
Universiti Sains Malaysia, 11800 USM, Penang, Malaysia
[4]Faculty of Science and Marine Environment,
Universiti Malaysia Terengganu, 21030 Kuala Nerus, Terengganu, Malaysia.

[*]Corresponding author: adizzati@unimap.edu.my

Received: 22 September 2022; Accepted: 17 January 2023; Published: 22 February 2023

Abstract

In past years, the π-conjugated system has attracted much attention as a promising material for developing and manufacturing the next generation of organic electronics made of synthesised organic compounds. Chalcone, having the π-conjugated systems in their molecular structures and the unique α, β-unsaturated ketone structural, have gained much attraction due to their potential use in optoelectronics applications like organic light emitting diode (OLED). By altering the molecular structure, the physical and chemical properties of chalcone derivatives can be tailored to the application needed. In recent years, chemists have produced many types of π-conjugated molecules to acquire excellent luminescence characteristics from organic compounds, and such structures typically lead to intense colour and excellent photoluminescence. In this study, a disubstituted chalcone derivative featuring terephthalaldehyde (**N1A**) as a π-linker with anthracene as donating group substitution has been synthesised through the Claisen-Schmidt condensation reaction. The synthesised compound has been characterised using Fourier Transform Infrared spectroscopy (FTIR) and UV-Visible analysis. Density functional theory (DFT) computations are executed to evaluate the effect of anthracene as an electron donating substitution on NLO properties of disubstituted chalcone derivative. NLO responses of this disubstituted chalcone derivative disclose that the chalcone molecular framework exhibit an important characteristic for further application as OLED emitting material.

Keywords: chalcone, density functional theory, non-linear optical, spectroscopic

Abstrak

Pada tahun-tahun lepas, sistem π-konjugasi telah menarik banyak perhatian sebagai bahan yang berpotensi untuk dibangunkan dan dikeluarkan sebagai generasi seterusnya elektronik organik, yang dibuat daripada sintesis sebatian organik. Kalkon, yang mempunyai sistem terkonjugasi-π dalam struktur molekulnya serta struktur keton α, β-tak tepu yang unik, telah mendapat banyak tarikan kerana potensi penggunaannya dalam aplikasi optoelektronik seperti diod pemancar cahaya organik (OLED). Dengan mengubah struktur molekul, sifat fizikal dan kimia, terbitan kalkon boleh disesuaikan dengan aplikasi yang diperlukan. Dalam tahun-tahun kebelakangan ini, ahli kimia telah menghasilkan banyak jenis molekul terkonjugasi-π untuk memperoleh ciri kependarkilauan yang sangat baik daripada sebatian organik, dan struktur sedemikian biasanya membawa kepada warna yang terang dan foto pendarcahaya yang sangat baik. Dalam kajian ini, terbitan kalkon tergantian yang menampilkan terephthalaldehid (**N1A**) sebagai penghubung-π dengan antrasena sebagai penggantian kumpulan penderma, telah disintesis melalui tindak balas pemeluwapan Claisen-Schmidt. Sebatian yang disintesis telah dicirikan menggunakan spektroskopi Lembayung Inframerah (FTIR) dan analisa Ultra Lembayung sinar nampak. Pengiraan teori fungsi ketumpatan (DFT) dilaksanakan untuk menilai kesan antrasena sebagai penggantian pendermaan elektron ke atas sifat NLO bagi terbitan kalkon tersubstitusi. Dapatan NLO bagi terbitan dualgantian ini menunjukkan kerangka molekul kalkon mempunyai ciri penting untuk aplikasi seterusnya sebagai bahan pemancar OLED.

Kata kunci: kalkon, teori fungsi ketumpatan, optik bukan linear, spektroskopi

Introduction

Light emitting diode (LED) represents a little solid-state semiconductor device that produces light when current flows through it [1]. The current produced is due to the movement of electrons through a semiconductor. An inorganic semiconductor is commonly used in LED. Haque et al. reported that using inorganic semiconductors in LED has several problems in terms of efficiency, heat management, colour rendering, lifetime, and probably the most significant one is the high cost [2]. In contrast, LED that uses an organic semiconductor is called organic light emitting diode (OLED), which was first revealed by Pope, Kallmann, and Magnante in 1963 [2]. Organic semiconductors are polymers or π-bonded molecules and can conduct electricity when charge carriers are injected into them [3]. Organic semiconductor devices now form the basis of an ongoing revolution in electronics in the twenty-first century. One of the materials used in organic electronics is organic materials that are made up of carbon-based materials. The widely used inorganic materials in semiconductors have caused some disadvantages as it needs high purity and accurate processing under extremely demanding conditions. The problems arising when using inorganic semiconductors have led to extensive semiconductor technology development. Hence, the organic semiconductors are wished for the potential solutions, especially on how the organic compound in these organic semiconductors will affect the OLED performance. Some benefits of using organic semiconductors are infinite variety and tuneable properties by changing the chemical structure, easy shaping, and manufacturing. These benefits came from the great properties of organic materials [4].

Organic materials such as chalcone having π-conjugated materials have become a major interest in OLED applications due to their low cost, tuning ability, structural diversity, favourable chemical modification, flexibility, and ease of fabrication. Chalcone derivatives occur naturally in plants and can also be synthesised using a synthetic approach to produce fluorescent materials. The characteristics of chalcone, particularly having benefits of chemical structure modification, have raised a question on how the modified structure can change the effect chalcone derivatives have on that particularly applied field. Organic materials having well-defined electrical properties are being deployed for optoelectronic devices such as OLED, and these devices are now replacing the use of liquid crystal displays (LCD) in consumer electronics such as cell phones, tablets, and televisions [5]. In past years, the π-conjugated system has attracted much attention as a promising material for developing and manufacturing the next generation of electronics, such as organic electronics. Organic semiconductors possess structural plasticity that allows the molecular design to incorporate functionality [6]. Aside from that, π-conjugated systems in molecular structures have received much attention due to their use in optoelectronics like OLEDs. The

conjugated organic molecules are used in organic electronics. Furthermore, by altering the molecular structure, the physical and chemical properties of organic molecules can be customised to the application's needs. For example, the colour of organic molecules' emission can be changed by increasing or lowering the π-electron conjugation [7]. Over the last 150 years, chemists have produced many types of π-conjugated molecules to acquire excellent luminescence characteristics from organic compounds, and such structures typically lead to intense colour and excellent photoluminescence [8]. In addition, Cho et al. stated that it has recently been discovered that even minor chemical changes can significantly impact luminescence characteristics [9].

It is worth noting that chalcones have a unique structure with an α, β - unsaturated carbonyl framework that helps with structural alterations [10]. By modifying the polarity of aprotic solvents, heteroaryl chalcones containing both electron donor and acceptor groups have been studied, which improves quantum yields and fluorescence intensity via intermolecular charge transfer (ICT) [11]. As a result, the researchers are working on chalcone structural alteration in developing new and unique materials with a wide range of uses. This structural modification also includes the electron donating-withdrawing substituents that will affect the luminescent properties of chalcone derivatives. According to Prabhu et al., it is clear that the electron-donating group significantly influences the optical properties of the chalcones [12]. Therefore, a comprehensive understanding of the relationship between conjugated π-linker and molecular design is a crucial concern for developing efficient luminescent materials in chalcone derivatives for high OLED performance.

In this study, a new disubstituted chalcone derivative; ((2E,2'E)-3,3'-(1,4-phenylene) bis(1-(anthracen-9-yl) prop-2-en-1-one) (**N1A**) has been successfully synthesised. This study aims to characterise and elucidate the disubstituted chalcone derivative using Fourier Transform Infrared spectroscopy (FTIR) and Ultraviolet-Visible (UV-vis) spectroscopy. The nonlinear optical (NLO) properties such as nonlinear refractive (μ), nonlinear absorption (β) and third-order nonlinear susceptibility (χ^3) of the disubstituted chalcone derivative are evaluated through the Z-scan method. Moreover, the density functional theory (DFT) method is computed using B3LYP/6-31G (d, p) basic set to obtain the optimised geometric molecular structure before analysing the NLO response.

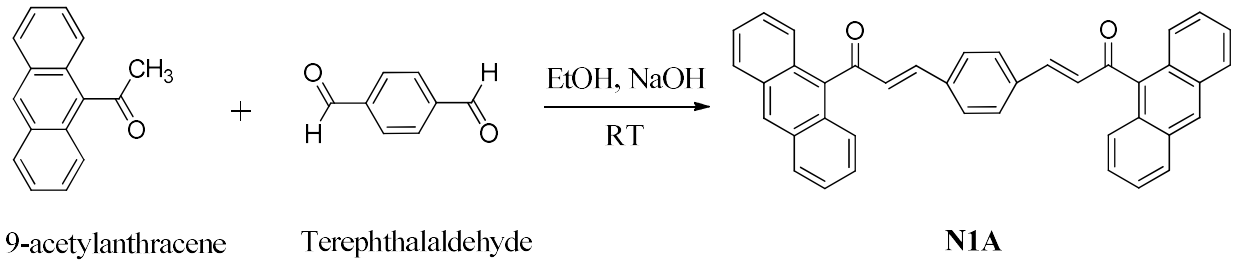
Materials and Methods

Chemical and reagents

All starting chemicals, reagents, and solvents were purchased and used as received from Sigma-Aldrich and Merck which are 9-acetylphenanthrene, terephthalaldehyde, ethanol, sodium hydroxide, acetonitrile, and dichloromethane. All of the chemicals, reagents, and solvents were used as received without further purification.

Experimental details

Disubstituted chalcone is prepared using the Claisen-Schmidt condensation reaction method because it is affordable, simple to use, and not sensitive to oxygen or water, making it simple to operate at room temperature and readily applicable in laboratories [13]. 9-Acetylanthracene (7.5 mmol, 1.6 g) and terepthalaldehyde (3.7 mmol, 0.5 g) were each dissolved in ethanol (10 mL). Both mixtures are mixed before adding ethanol (50-60 mL) until the mixture is completely dissolved. While stirring, a catalytic amount of 20% NaOH was added to the solution dropwise. The reaction mixture was stirred for 5 hours at room temperature. Once adjudged completed, the reaction mixture was poured into cold iced water and left for precipitation. The resultant crude product was filtered. The obtained crude product of **N1A** was recrystallised from acetonitrile by a slow evaporation process to afford the corresponding disubstituted chalcone derivative (**N1A**). Scheme 1 illustrates the synthetic pathway to the synthesis of **N1A**.



9-acetylanthracene Terephthalaldehyde **N1A**

Scheme 1. Synthesis of disubstituted chalcone derivative (**N1A**)

Instrumentation and characterisation

The chemical structure of the **N1A** chalcone is confirmed by recording its FTIR spectra. KBr pellet is used on Perkin Elmer Spectrum Version 10.03.06 to obtain FTIR spectra in the wavenumber range at 4000-650 cm^{-1}, and the infrared values are listed in $\bar{\upsilon}$ units. The UV–Vis absorption spectrum was observed in acetonitrile (CH_3CN) solutions at room temperature respectively on Perkin Elmer Lambda 365 UV–Vis Spectrophotometer in the range of 200-700 nm at a concentration of 10^{-5} mol L^{-1} in 1 cm cuvette.

The third-order NLO properties of **N1A** chalcone are evaluated using the Z-scan technique. The transmittance of a nonlinear medium is measured with this method as a function of the sample position using a single polarised Gaussian laser beam in a tight focus geometry. This single beam, which is propagating in the Z direction, is narrowly concentrated. The sample is moved in the Z direction, and a finite aperture in the far field is used to measure the transmitted intensity as a function of the sample's Z position, measured with reference to the focal plane. Self-focusing or self-defocusing changes the wavefront phase when the sample passes through the beam focus (at Z = 0), changing the observed beam intensity [13]. A continuous wave from a diode-pumped solid-state laser operating at 532 nm is used to analyse the NLO response in the **N1A** chalcone. The sample was kept in a quartz cuvette with a path length of 1 mm, and the beam was sharply focussed with a 20 cm focusing lens. A laser beam profiler measured the beam waist at the focal point [14]. A powdered sample weighing 0.002 g was used for the analysis in 1 mL acetone. The experiments were conducted at room temperature. The sample used in this experiment is $4x10^{-3}$ M of acetone solution of **N1A**. The Z-scan technique measures nonlinear absorption (NLA) and nonlinear reflection (NLR). This technique was used to explore third-order susceptibility (χ^3), nonlinear refractive index (n_2), and nonlinear absorption coefficient (β).

The basic single-beam Z-scan setup is shown in Figure 1 [15]. The normalised transmittance was plotted by Levenberg–Marquardt algorithm to estimate the effective nonlinear absorption β_{eff} value. From the value of nonlinear absorption (β) and nonlinear refractive (n_2), the imaginary and real part of third-order nonlinear susceptibility, $\chi^{(3)}$, can be obtained from the following equation (Eq. 1 – Eq. 3):

$$Re\,\chi^{(3)}\,(\text{esu}) = [10^{-4}(\varepsilon_0 C^2 n_0^2 n_2]/\pi \quad \text{(Eq. 1)}$$

$$Im\,\chi^{(3)}\,(\text{esu}) = [10^{-2}(\varepsilon_0 C^2 \beta\lambda]/\pi \quad \text{(Eq. 2)}$$

$$\chi^{(3)} = [(Re\,\chi^{(3)})^2 + (Im\,\chi^{(3)})^2]^{1/2} \quad \text{(Eq. 3)}$$

where C is the velocity of the light in a vacuum, ε_0 is the permittivity of the free space, and n_0 is the linear refractive index of the sample solution.

The optimisation of the molecular geometries leading to energy minima was achieved using the DFT method with a basic set of B3LYP/6-31G (d, p) level of theory as implemented in the GAUSSIAN 09 program

package. The optimised structural parameters were used to calculate the vibrational wavenumbers [16]. The nonlinear optical properties such as static dipole moments (μ_{tot}), mean polarizability ($<\alpha_{tot}>$), anisotropic polarizability ($\Delta\alpha$) and first hyperpolarizability index (β-V), were computed via B3LYP/6-31G (d, p) level of theory under finite field scheme at $\omega = 0$, and the values obtained were calculated using the following equations (Eq. 4 – Eq. 7):.

$$\mu_{tot} = \left(\mu_x^2 + \mu_y^2 + \mu_z^2\right)^{1/2} \quad \text{(Eq. 4)}$$

$$< \alpha_{tot} > = \frac{1}{3}\left(\alpha_{xx} + \alpha_{yy} + \alpha_{zz}\right) \quad \text{(Eq. 5)}$$

$$\Delta\alpha = \frac{1}{\sqrt{2}}\left[\left(\alpha_{xx} - \alpha_{yy}\right)^2 + \left(\alpha_{yy} - \alpha_{zz}\right)^2 + \left(\alpha_{zz} - \alpha_{xx}\right)^2 + 6\left(\alpha_{xy}^2 + \alpha_{xz}^2 + \alpha_{yz}^2\right)\right] \quad \text{(Eq. 6)}$$

$$\beta - V = \left(\beta_x^2 + \beta_y^2 + \beta_z^2\right)^{1/2} \quad \text{(Eq. 7)}$$

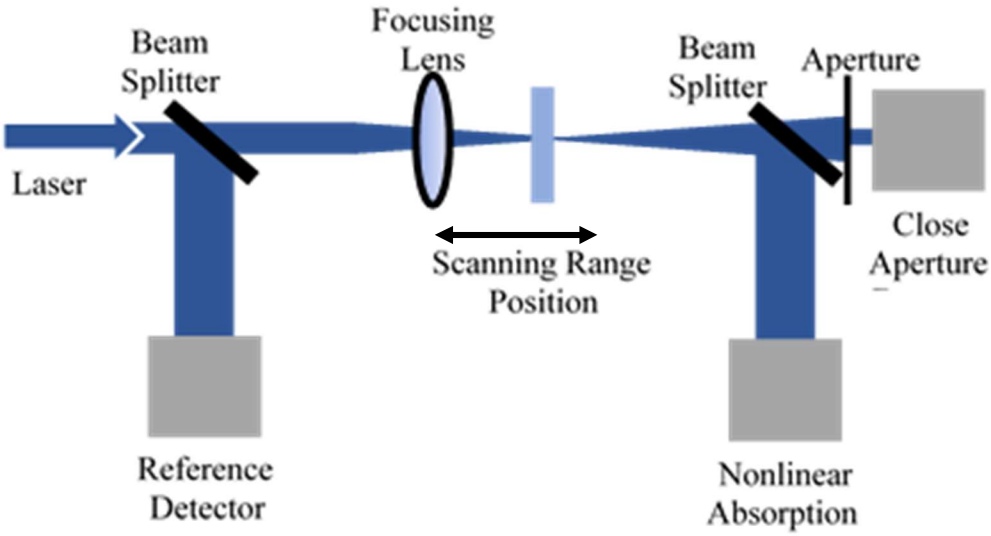


Figure 1. The setup for Z-scan analysis

Result and Discussion

Vibrational analysis

The FTIR spectrum of **N1A** is shown in Figure 2. The stretching frequency of α, β-unsaturated carbonyl compounds usually lie in the range of 1660-1685 cm^{-1}. The stretching frequency of **N1A** gives away characteristics -C=O stretching at 1645 cm^{-1} and -C=C- stretching at 1586 cm^{-1}. The carbonyl group mostly depends on the bond strength, which depends on steric effects, inductive effects, conjugative effects, and oxygen lone pair electrons. This might be the reason for the difference in wavelength in the **N1A** chalcone. However, the wavelength still agrees with the literature value of 1600 cm^{-1}. The C=C stretching vibration is probably around 1667-1640 cm^{-1}. However, C=C is expected around 1600 cm^{-1} when conjugated with C=O. Additional -C=C- stretching and the aromatic C-H in-plane and out-of-plane bending bands of aromatics C-H at 1108 cm^{-1} and 734 cm^{-1}, respectively [17], had established due to the frequent occurrence of aromatic rings in all compounds, especially in **N1A** chalcones. The typical ranges for the C-H in-plane and out-of-plane bending vibrations are 1300-1000 cm^{-1} and 1000-700 cm^{-1}, respectively. The type of substituents has no impact on the bands in this region. Due to the inductive effect that increases the substituent's chain length, all C-H stretching is weak [18]. The vibrational modes for the **N1A** chalcone are presented in Table 1.

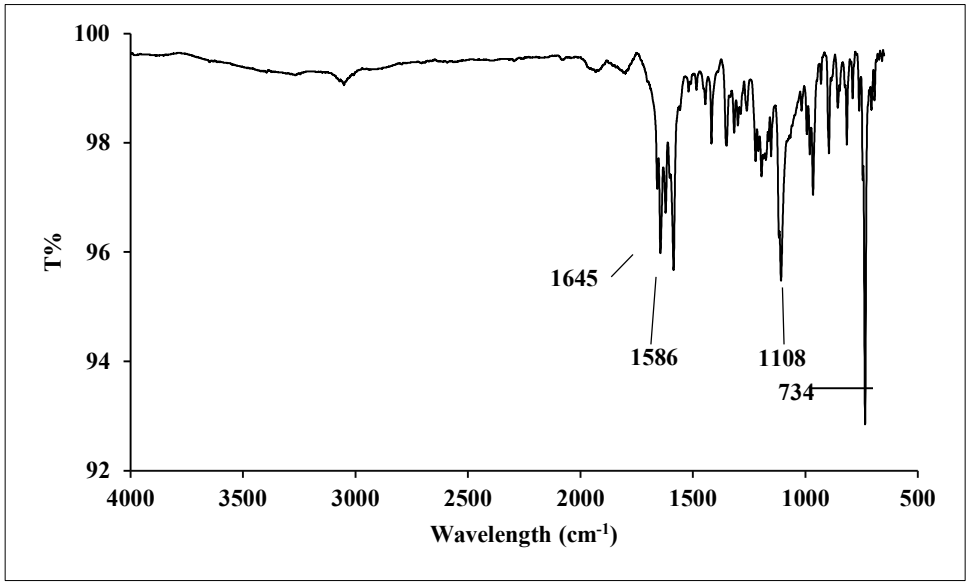


Figure 2. The FTIR spectrum of **N1A**

Table 1. Vibrational Mode for **N1A** chalcone.

Vibrational Mode	N1A
	Wavelength (cm^{-1})
C=O stretch	1645
C=C-C aromatic ring stretch	1586
C-H in-plane band	1108
C-H out-of-plane band	734

Electronic transition analysis

The UV-vis absorption spectrum of **N1A** is shown in Figure 3. It is clear that **N1A** chalones are transparent in the entire visible region and the absorption takes place in the UV region. The absence of absorption in the visible region is a key factor if any compound is to be exploited for NLO applications at room temperature [19]. Most organic compound absorption spectroscopy is based on transitions of n or π-electrons to the π* excited state. As a result, the transition absorption peaks occur within 200–700 nm suitable for experimental investigation. In order to supply the electrons for these transitions, the molecule must have an unsaturated group. α, β-unsaturated carbonyl compounds usually show two absorption bands of the n→π* and π→π* transitions [20]. The absorption and transmission spectra help us to identify the nature of the molecule by analysing the transition of electrons in σ and π orbitals between the ground state and higher excited states with the energy absorbed [21]. The UV-Vis absorption spectra of **N1A** exhibit one absorbance maximum, as shown in Figure 3, at 252 nm. The maximum absorption of **N1A** chalcone at 252 nm is due to the increased conjugation and greater resonance stabilisation. This peak might attribute to π→π* transition since the wavelength is below 300 nm, indicating the presence of a carbonyl group in the compound. The other absorbance bands observed are 341 nm, 367 nm and 384 nm. The absorbance bands observed have an absorption tail stretching to ± 454 nm. The peaks may be attributed to the mixture transition of n→π* and π→π* interband transition and are due to the excitation in the aromatic

rings for wavelengths more than 300 nm. N1A chalcone exhibits a higher maximum wavelength due to its greater amount of benzene rings. The absorption corresponds to the transition from the highest occupied molecular orbital (HOMO) in the ground state to the lowest unoccupied molecular orbital (LUMO) in the excited state [21]. As the molecule is conjugated, the HOMO-LUMO transition implies the transfer of electron charge density throughout the aromatic rings [22].

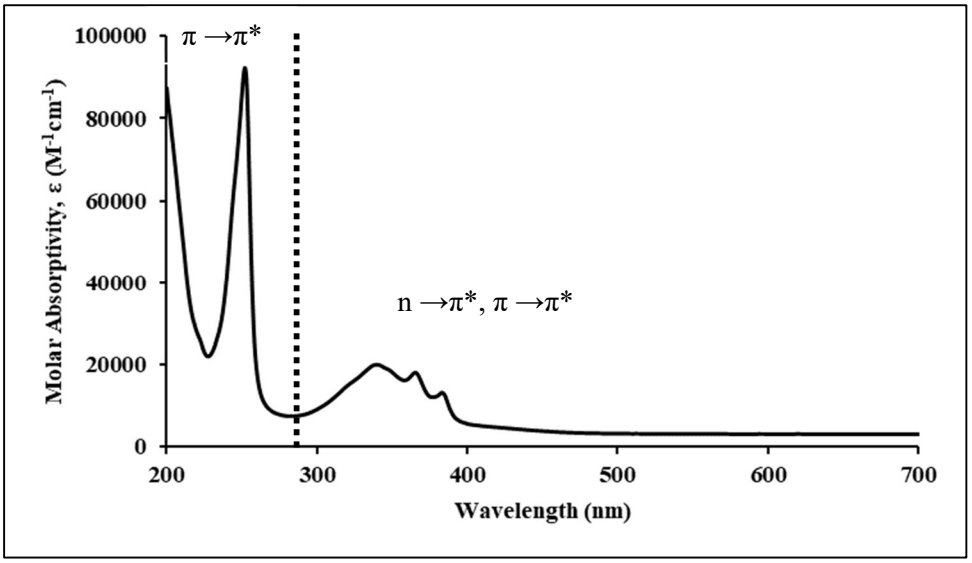


Figure 3. UV-Vis spectrum and electronic transition of **N1A** chalcone

Table 2. electronic transition of **N1A** chalcones

Compound	λ (nm), ε (M^{-1} cm^{-1})	Electronic transition
N1A	252, 92134	π→π*
	341, 19810	n→π*, π→π*
	367, 17381	n→π*, π→π*
	384, 12889	n→π*, π→π*

Optical energy band gap (E_g) analysis

The strongest absorption and smaller energy gap, particularly in the visible region, are important features in the suitability for optoelectronic applications [23]. The purpose of evaluating the energy band gap (E_g) is to calculate the difference in orbital energy between the highest occupied molecular orbital (HOMO) (the top of the valence band) and its lowest unoccupied molecular orbital (LUMO) (the bottom of the conduction band). Since they have a greater capability for electron mobility in the π-conjugated system, compounds with shorter HOMO-LUMO energy gaps are highly preferred because they produce an enlarged energy distribution [24]. The optical band gap was calculated via Tauc's approach (Figure 4) by analysing the UV-vis spectra to determine the absorption coefficient (α) and photon energy ($h\nu$). This technique entails extrapolating the linear stretch of the tail of the lower energy band $(\alpha h\nu)^2$ up to the cut-off value with the abscissa axis, which corresponds to the photon (hν) energy. The absorption coefficient (α) is calculated from the absorbance data, and frequency (ν) is the reciprocal of wavelength, with h being Planck's constant [25]. The optical bandgap for the **N1A** chalcone is 3.16 eV. The optical bandgap plays

an essential role in the enhancement of the NLO properties of the compound. The narrowed bandgap is due to the intermolecular charge transfer (ICT) transition, leading to the high performance of NLO response [26]. Anthracene as donating group substituent, has a greater π-conjugation system, leading to lower optical bandgap energy in the **N1A** chalcone. The optical bandgap was evaluated using the following equation (Eq. 8 – Eq. 10):

$$(\alpha h\nu)^2 = A(h\nu - E_g) \quad \text{(Eq. 8)}$$

$$h\nu = \frac{1240}{\lambda} \quad \text{(Eq. 9)}$$

$$\alpha = 2.303\frac{A}{L} \quad \text{(Eq. 10)}$$

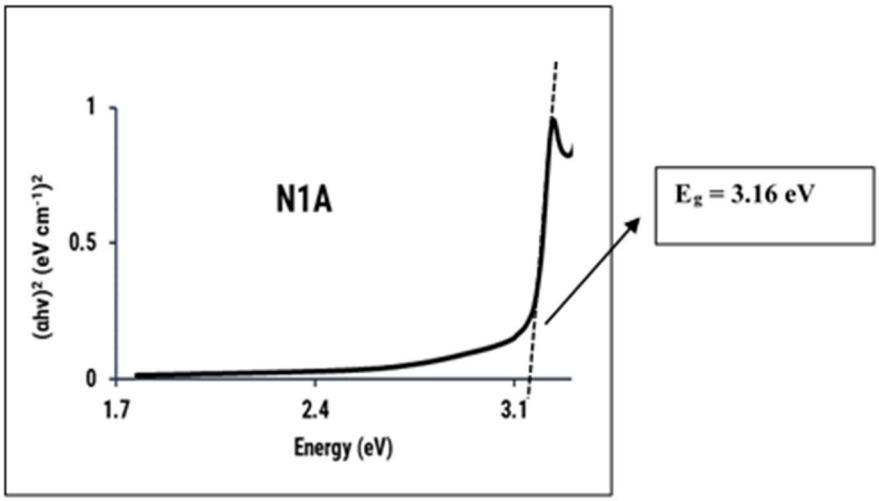


Figure 4. The Tauc's plot for optical energy band gap analysis of **N1A**

Non-linear optical characterisation

The NLO properties were investigated using the Z-scan technique. From Figure 3, the absorption is absent in the region between 500-700 nm which is a key requirement for materials having NLO properties. The linear absorption coefficient, α, of the compound for the 4 x 10^{-3} M was measured to be 0.4604/cm. Figure 5 shows the open (left) and closed aperture (right) transmittance spectra for the **N1A** chalcone. **N1A** chalcone shows a symmetric valley in the open aperture Z-scan spectrum about the focus, indicating positive non-linear absorption in the compound. Maximum absorption typically occurs when the sample is at the focal point of the lens since the on-axial peak irradiance I_0 of the beam is the maximum. The reduction in the transmittance measured with an open aperture is independent of non-linear refraction (NLR) and thus can be used to determine the value of the two-photon absorption (TPA) coefficient (β) by the depth of the valley. By fitting experimental normalised transmission data to the equation described in the literature [27], the value of nonlinear absorption (β) was found to be 2.5 x 10^{-4} cm W^{-1} for **N1A** chalcone. The strong reverse saturable absorption (RSA), which is responsible for the NLO material properties [28], is visible in the sample transmittance profile shown in Figure 5 (right), where the excited state absorption is greater than that for the ground state. This might be due to the effect of the delocalisation of π-electrons in the anthracene group and strong ICT in the compound.

Nonlinear refraction coefficient (n_2) is obtained from the transmittance measurements during close aperture by placing an aperture in front of the detector (closed aperture). The division method is applied to obtain pure nonlinear refraction. The Z-scan spectrum in close aperture is shown in Figure 5. The finding shows a negative nonlinear refraction property in the **N1A** chalcone (defocusing). However, the calculation shows a positive value of nonlinear refraction. The experimental data were fitted with the equation described in the literature, which yields nonlinear refraction, 1.2 x10^{-15} esu. From the value of the imaginary part (Im χ^3) and real part (Re χ^3), the third-order nonlinear susceptibility, $|\chi^3|$, was evaluated to be 2.8 x 10^{-6} esu, which indicates that the material possesses good NLO properties. However, the value is lower due to the donor-pi-donor system compared to the previously reported chalcone derivatives of the D-p-A system [15, 16]. The calculated NLO parameters extracted from Z-Scan curves are shown in Table 3.

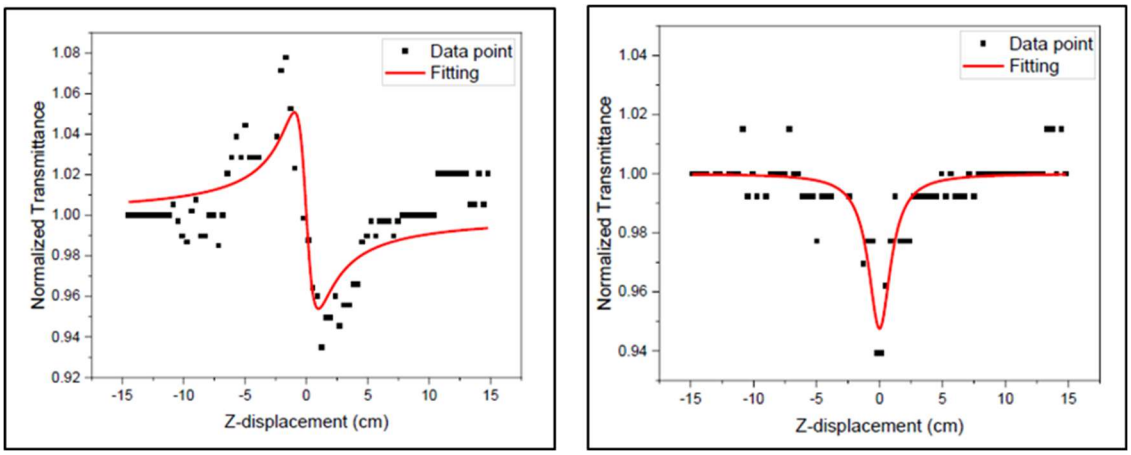


Figure 5. Close (left) and open (right) aperture of Z-scan analysis

Table 3. The calculated NLO parameters extracted from Z-Scan curves

Parameter	Value
Nonlinear absorption [β]	2.5 x10^{-4} cm/W
Nonlinear refraction [n_2]	1.2 x10^{-15} cm^2/W
Imaginary part of third susceptibility [Im $\chi^{(3)}$]	2.8 x10^{-6} esu
Real part of third susceptibility [Re $\chi^{(3)}$]	8.5 x10^{-15} esu
Third-order nonlinear susceptibility [$\chi^{(3)}$]	2.8 x10^{-6} esu

Quantum chemical calculation using density functional theory (DFT)

The nonlinear optical response of a material is strongly correlated with its electric properties, such as its dipole moments, polarizability, and hyperpolarizabilities [29]. When an external field is applied, molecules experience an induced electric dipole moment. This dipole moment is then approximated as the origin to examine microscopic polarizabilities. Additionally, the dipole moment directly affects the hyperpolarizability [30]. In this study, the static dipole moment and polarizability, anisotropic polarizability and hyperpolarizability were computed for the **N1A** chalcone under B3LYP / 6-31G (d, p) method, and the values obtained are presented in Table 4. A higher dipole moment will induce greater polarisation in the field direction. The total dipole moment (μ), mean polarizability (<α>), anisotropy of polarizability (Δα) and hyperpolarizability (β) are found to be 4.49 D, 3.45 x 10^{-23} esu, 3.96 x 10^{-24} esu and 3.53 x 10^{-30} esu, respectively for **N1A** chalcone. The value of

the dipole moment of **N1A** chalcone is higher than the chalcone derivative with anthracene studied by [31] which is 3.18 D. NLO properties can be related to the HOMO-LUMO energy gap and the dipole moment of the molecules. When E_g decreases, NLO properties increase. Smaller E_g allows a higher charge transfer within the electron delocalisation system. Based on Table 4, **N1A** chalcone shows good NLO properties and has the potential in related NLO devices application. DFT study provides a valuable tool for the in-depth examination of new disubstituted chalcone derivative compounds and the electronic property prediction for possible applications.

Table 4. Calculated static dipole moment, polarizability, anisotropic polarizability and hyperpolarizability from DFT data

Compound	Electric dipole moment, μ (debye)	Polarizability, <α> (e.s.u) (x10^{-23})	Anisotropic polarizability, Δα (e.s.u) (x10^{-24})	Hyperpolarizability, β (e.s.u) (x10^{-30})
N1A	4.49	3.45	3.96	3.53

Conclusion

A new chalcone derivative ((2E,2'E)-3,3'-(1,4-phenylene) bis(1-(anthracen-9-yl) prop-2-en-1-one) (**N1A**) was successfully synthesised and characterised for its NLO properties. The functional groups of the C=O carbonyl group, C=C-C aromatic ring, and aromatic C-H of the FTIR spectrum confirmed the structure of chalcone in **N1A** chalcone. The UV-visible study shows that the material is transparent in the visible region with the energy band gap of 3.16 eV and the electron transition analysis revealed the n→π* and π→π* transition of the carbonyl group and the presence of aromatic rings. The NLO response has been explored using a single-beam Z-scan and DFT method. The value of nonlinear absorption (β) and nonlinear susceptibility (χ3) are 2.5 x10^{-4} cmW^{-1} and 2.8 x10^{-6} esu, respectively, while for dipole moment (μ), polarizability (α) and hyperpolarizability (β), the values are found to be 4.49 D, 3.45 x10^{-23} esu and 3.5 x10^{-30} esu, respectively. **N1A** chalcone represents a promising NLO material due to the good NLO response. This NLO characteristic and strong band gap stability of this material are very intriguing for potential use in nonlinear optical devices. In a nutshell, molecular arrangement, the role of donor substituent, and the narrow energy gap may all contribute to the NLO performances.

Acknowledgement

The authors would like to acknowledge the financial support from the Ministry of Higher Education, Malaysia, for the Fundamental Research Grant Scheme (FRGS) FRGS/1/2020/STG05/UNIMAP/02/6, School of Physics and Institute of Nano Optoelectronics Research and Technology (INOR), Universiti Sains Malaysia for assisted in Z-scan analysis, and Universiti Malaysia Perlis for research facilities and support.

References

1. Bagher, A. M. (2017). Quantum dot display technology and comparison with OLED display technology. *International Journal of Advanced Research in Physical Science*, *4*(1): 48-53.
2. Haque, S., Shah, M. S., Rahman, M. and Mohiuddin, M. (2017). Biopolymer composites in light emitting diodes. *Biopolymer Composites in Electronics*, 277-310.
3. Nagar, R., Varrla, E. and Vinayan, B. P. (2018). Photocatalysts for hydrogen generation and organic contaminants degradation. *Multifunctional Photocatalytic Materials for Energy*: pp. 215-236.
4. Chen, F. C. (2018). Organic semiconductors. *Encyclopedia of Modern Optics*: pp. 220-231.
5. Dykstra, E., Fralaide, M., Zhang, Y., Biswas, R., Slafer, W. D., Shinar, J. and Shinar, R. (2022). OLEDs on planarized light outcoupling-enhancing structures in plastic. *Organic Electronics*, 111: 106648.
6. Wang, C., Dong, H., Hu, W., Liu, Y. and Zhu, D. (2012). Semiconducting π-conjugated systems in field-effect transistors: a material odyssey of organic electronics. *Chemical reviews*, 112(4): 2208-2267.

7. Ansari, S. P. and Ali, F. (2018). Conjugated organic polymers for optoelectronic devices. Functional Polymers, edited by MA Jafar Mazumder, H. Sheardown, and A. Al-Ahmed (Springer International Publishing): pp. 1-40.
8. Ahmad, A., Sinha, R. K., Kulkarni, S. D., Lewis, P. M., Bhat, P. and Shetty, N. S. (2022). Synthesis, photophysical properties and DFT studies of chalcones and their 2-methoxy-3-cyanopyridine derivatives. *Journal of Photochemistry and Photobiology A: Chemistry*, 114494.
9. Cho, E., Coropceanu, V. and Brédas, J. L. (2021). Impact of chemical modifications on the luminescence properties of organic neutral radical emitters. *Journal of Materials Chemistry C*, *9*(33): 10794-10801.
10. Rammohan, A., Reddy, J. S., Sravya, G., Rao, C. N. and Zyryanov, G. V. (2020). Chalcone synthesis, properties and medicinal applications: a review. *Environmental Chemistry Letters*, 18(2): 433-458.
11. Pannipara, M., Asiri, A. M., Alamry, K. A., Arshad, M. N. and El-Daly, S. A. (2015). Synthesis, spectral behaviour and photophysics of donor–acceptor kind of chalcones: excited state intramolecular charge transfer and fluorescence quenching studies. *Spectrochimica Acta Part A: Molecular and Biomolecular Spectroscopy,* 136: 1893-1902.
12. Prabhu, A. N., Upadhyaya, V., Jayarama, A. and Bhat, K. S. (2016). Third-order NLO property of thienyl chalcone derivative: Physicochemical analysis and crystal structure determination. *Molecular Crystals and Liquid Crystals,* 637(1), 76-86.
13. Al-Ahmad, A. Y., Shabeeb, G. M., Abdullah, A. Q. and Ziadan, K. M. (2011). Z-scan measurement for the nonlinear absorption and the nonlinear refraction of poly1, 4-diazophenylene-bridged-tris (8-hydroxy-quinoline) aluminum (PDPAlq3). *Optik*, 122(21): 1885-1889.
14. De Araújo, C. B., Gomes, A. S. and Boudebs, G. (2016). Techniques for nonlinear optical characterization of materials: a review. *Reports on Progress in Physics*, 79(3): 036401.
15. Alsaee, S. K., Bakar, M. A. A., Zainuri, D. A., Anizaim, A. H., Zaini, M. F., Rosli, M. M. and Razak, I. A. (2022). Nonlinear optical properties of pyrene-based chalcone:(E)-1-(4′-bromo-[1, 1′-biphenyl]-4-yl)-3-(pyren-1-yl) prop-2-en-1-one, a structure-activity study. *Optical Materials*, 128: 112314.
16. Anizaim, A. H., Arshad, S., Zaini, M. F., Abdullah, M., Zainuri, D. A. and Razak, I. A. (2019). Third order nonlinear optical properties of selected fluorinated chalcone derivatives. *Optical Materials*, 98: 109406.
17. Kumar, P. R., Ravindrachary, V., Janardhana, K. and Poojary, B. (2012). Structural and optical properties of a new chalcone single crystal. *Journal of Crystal Growth*, 354(1): 182-187.
18. Sabina, X. J., Karthikeyan, J., Velmurugan, G., Tamizh, M. M. and Shetty, A. N. (2017). Design and in vitro biological evaluation of substituted chalcones synthesized from nitrogen mustards as potent microtubule targeted anticancer agents. *New Journal of Chemistry*, 41(10): 4096-4109.
19. Chinnasami, S., Manikandan, M., Chandran, S., Paulraj, R. and Ramasamy, P. (2019). Growth, Hirshfeld surfaces, spectral, quantum chemical calculations, photoconductivity and chemical etching analyses of nonlinear optical p-toluidine p-toluenesulfonate single crystal. *Spectrochimica Acta Part A: Molecular and Biomolecular Spectroscopy*, 206: 340-349.
20. Sawant, A. B. and Nirwan, R. S. (2012). Synthesis, characterization and DFT studies of 6, 8-dichloro-2-(4-chlorophenyl)-4H-chromen-4-one. *Indian Journal of Pure and Applied Physics*, 50: 308-313.
21. Costa, J. C., Taveira, R. J., Lima, C. F., Mendes, A. and Santos, L. M. (2016). Optical band gaps of organic semiconductor materials. *Optical Materials*, 58: 51-60.
22. Hegde, H., Sinha, R. K., Kulkarni, S. D. and Shetty, N. S. (2020). Synthesis, photophysical and DFT studies of naphthyl chalcone and nicotinonitrile derivatives. *Journal of Photochemistry and Photobiology A: Chemistry*, 389: 112222.
23. Sánchez-Vergara, M. E., Leyva-Esqueda, E. A., Alvarez, C., López Reyes, M., Miralrio, A. and Salcedo, R. (2016). Influence of TCNQ acceptor on optical and electrical properties of tetrasubstituted allenes films fabricated by vacuum thermal

evaporation. *Journal of Materials Science: Materials in Electronics*, 27(9): 9900-9910.

24. Bureš, F. (2014). Fundamental aspects of property tuning in push–pull molecules. *RSC Advances*, 4(102): 58826-58851.
25. Janardhana, K., Ravindrachary, V., Kumar, P. C., Umesh, G. and Manjunatha, K. B. (2013). Third order optical non-linearity of a novel chalcone derivative through Z scan technique. *Indian Journal of Pure and Applied Physics,* 51: 844-850.
26. Nakum, K. J., Katariya, K. D., Hagar, M. and Jadeja, R. N. (2022). The influence of lateral hydroxyl group and molecular flexibility on the mesogenic behaviour of a new homologous series based on thiophene-chalcone: Synthesis, characterization, crystal structure and DFT study. *Journal of Molecular Structure*, 1261: 132891.
27. Jiang, X., Zhao, S., Lin, Z., Luo, J., Bristowe, P. D., Guan, X. and Chen, C. (2014). The role of dipole moment in determining the nonlinear optical behavior of materials: ab initio studies on quaternary molybdenum tellurite crystals. *Journal of Materials Chemistry C*, 2(3): 530-537.
28. Maidur, S. R., Jahagirdar, J. R., Patil, P. S., Chia, T. S. and Quah, C. K. (2018). Structural characterizations, Hirshfeld surface analyses, and third-order nonlinear optical properties of two novel chalcone derivatives. *Optical Materials*, 75: 580-594.
29. Maidur, S. R., Patil, P. S., Ekbote, A., Chia, T. S. and Quah, C. K. (2017). Molecular structure, second- and third-order nonlinear optical properties and DFT studies of a novel non-centrosymmetric chalcone derivative:(2E)-3-(4-fluorophenyl)-1-(4-{[(1E)-(4-fluorophenyl) methylene] amino} phenyl) prop-2-en-1-one. *Spectrochimica Acta Part A: Molecular and Biomolecular Spectroscopy*, 184: 342-354.
30. Jagadeesh, M., Lavanya, M., Babu, B. H., Hong, K., Ma, R., Kim, J. and Kim, T. K. (2015). Synthesis and detailed spectroscopic characterization of various hydroxy-functionalized fluorescent chalcones: A combined experimental and theoretical study. *Spectrochimica Acta Part A: Molecular and Biomolecular Spectroscopy*, 150: 557-564.
31. Chaudhry, A. R., Irfan, A., Muhammad, S., Al-Sehemi, A. G., Ahmed, R. and Jingping, Z. (2017). Computational study of structural, optoelectronic and nonlinear optical properties of dynamic solid-state chalcone derivatives. *Journal of Molecular Graphics and Modelling*, 75: 355-364.

Malaysian Journal of Analytical Sciences (MJAS)
Published by Malaysian Analytical Sciences Society

SEASONAL VARIATION IN CONCENTRATION OF HEAVY METALS IN TROPICAL RIVER SEDIMENT

(Variasi Bermusim dalam Kepekatan Logam Berat di Dalam Sedimen Sungai Tropikal)

Nur Amirah Hidayah Madzlan[1], Suhaimi Suratman[2], Khairul Nizam Mohamed[3], Ong Meng Chuan[1,2,4*]

[1]Faculty of Science and Marine Environment,
University Malaysia Terengganu, 20130 Kuala Nerus, Terengganu, Malaysia
[2]Institute of Oceanography and Environment,
Universiti Malaysia Terengganu, 21030 Kuala Nerus, Terengganu, Malaysia
[3]Department of Environment,
Faculty of Forestry and Environment,
Universiti Putra Malaysia, 43400 UPM Serdang, Selangor, Malaysia
[4]Ocean Pollution and Ecotoxicology (OPEC) Research Group,
Universiti Malaysia Terengganu, 21030 Kuala Nerus, Terengganu, Malaysia

[*]Corresponding author: ong@umt.edu.my

Received: 23 October 2022; Accepted: 24 November 2022; Published: 22 February 2023

Abstract

Heavy metal contamination has a more significant impact than microbial and organic contaminations as the elements could remain in the aqueous and particulate phases for an extended period. Setiu River, Terengganu, is one of the crucial rivers utilised as sites for aquaculture by the local communities. Generally, the concentrations of lead (Pb), zinc (Zn), copper (Cu), and arsenic (As) were influenced by human activities around river systems. Consequently, the present study investigated the seasonal concentration variations of Pb, Zn, Cu, and As in the surficial sediment of the river. The sediment samples were collected between January and July 2017, corresponding to the wet and dry seasons, from 60 different sampling locations along the river. The samples were subjected to Teflon bomb closed digestion procedures with mixed acid before the concentrations of the metals were determined with inductively coupled plasma mass spectrometry (ICP-MS). Resultantly, the mean concentrations of Pb, Zn, Cu, and As were 19.9 ± 9.89, 68.4 ± 31.8, 1.30 ± 0.66, and 3.05 ± 0.53 µg/g dry weight (wt.), respectively, in the samples gathered in the wet season (January). Alternatively, the samples collected during the dry season (July) contained 16.7 ± 15.1, 68.9 ± 48.5, 14.7 ± 16.9, and 2.46 ± 2.78 µg/g dry wt. mean concentrations of Pb, Zn, Cu, and As, respectively. The sample sediment quality was assessed based on the geoaccumulation index (I_{geo}). Based on the I_{geo}, the area was considered uncontaminated to moderately contaminated as the average values acquired were within Classes 0 and 2. Nevertheless, the pollution load index (PLI) revealed elevated concentrations of the metals, thus indicating anthropogenic sources, particularly in the aquaculture area. Accordingly, the Setiu river was assumed to be slightly polluted as the PLI values were 1.25 ± 0.34 (wet season) and 1.00 ± 1.00 (dry season).

Keywords: heavy metals, tropical river, pollution, index of geoaccumulation, pollution load index

Abstrak

Pencemaran logam logam berat mempunyai kesan yang lebih signifikan berbanding dengan pencemaran mikrob atau organik

kerana unsur–unsur ini dapat dikitar dalam fasa berair dan partikulat untuk jangka masa yang panjang. Sungai Setiu di Terengganu adalah salah satu sungai yang penting sebagai tempat akuakultur bagi masyarakat setempat. Secara amnya, kepekatan plumbum (Pb), zink (Zn), kuprum (Cu), dan arsenic (As) dipengaruhi oleh aktiviti manusia di sekitar system sungai. Oleh itu, kajian ini dilakukan untuk menyelidik variasi bermusim dalam kepekatan logam Pb, Zn, Cu dan As dalam sedimen permukaan sungai. Sampel sedimen dikumpulkan dari 60 lokasi persampelan yang berlainan di sepanjang sungai, di antara Januari dan Julai 2017, selaras dengan musim hujan dan musim kering. Setelah kaedah penghadaman tertutup bom Teflon dengan asid campuran, kepekatan logam ditentukan menggunakan spektrometri jisim plasma gandingan aruhan (ICPMS). Dari keputusan yang diperoleh, kepekatan purata Pb, Zn, Cu dan As adalah 19.9±9.89 µg/g berat kering, 68.4±31.8 µg/g berat kering, 1.30±0.66 µg/g berat kering dan 3.05±0.53 µg/g berat kering. untuk musim hujan (Januari), manakala, 16.7±15.1 µg/g berat kering; 68.9±48.5 µg/g berat kering, 14.7±16.9 µg/g berat kering dan 2.46±2.78 µg/g berat kering untuk musim kering (Julai). Penilaian kualiti sedimen menggunakan indeks geoakumulasi (I_{geo}) menunjukkan bahawa kawasan tersebut masih boleh dianggap tidak tercemar hingga sederhana tercemar kerana nilai purata Igeo dikategorikan dalam Kelas 0 hingga 2. Sementara itu, indeks beban pencemaran (PLI) mendedahkan peningkatan kepekatan logam yang dikaji, menunjukkan sumber antropogenik, terutama di kawasan akuakultur. Sungai Setiu boleh dianggap sedikit tercemar kerana nilai PLI lebih dari 1; 1.25±0.34 (musim hujan); 1.00±1.00 (musim kering). Secara amnya, kepekatan Pb, Zn, Cu dan As telah menunjukkan bahawa logam tersebut dipengaruhi oleh aktiviti manusia di sekitar sistem sungai tersebut.

Kata kunci: logam berat, sungai tropikam pencemaran, indeks geoakumulasi, indeks beban pencemaran

Introduction

Environmental contaminants from human and natural activities are the most severe problems confronting communities today. Industrial and economic growth and the production of various compounds and chemicals pose serious environmental and human health risks [1–3]. Moreover, heavy metal contaminants from human activities accumulate in the environment, most notably in river sediments [4-6]. Nonetheless, river sediments are complex and heterogeneous media. The roles of river sediments as a sink or source of contaminants has yet to be understood entirely, while numerous biogeochemical processes determine the fate of trace metals [7, 8].

The Setiu River is located in the Setiu district in the northern region of Terengganu, on the eastern coast of Peninsular Malaysia. The river possesses a catchment area of 188 km^2 and is approximately 52 km long. The northeast monsoon or the wet season strongly influences the river between November and March, while the southwest monsoon or the dry season occurs from May to September. Consequently, the river is vital to the surrounding communities, and it supplies freshwater to the Setiu Wetland as it flows southeast towards the wetland [9, 10]. Furthermore, water for irrigation and freshwater aquaculture is obtained from the Setiu River [11]. Intake points are also constructed along the riverbanks to extract raw water, providing water for domestic use [11].

Metal contaminants might have a more significant impact compared to organic and microbial contaminations, as metals could cycle between the aqueous and particulate phases over an extended time [12, 13]. Consequently, the current study aimed to determine the concentrations of heavy metals in the surficial sediment of the Setiu River system. The data would be crucial in highlighting the potential threat of the metals to humans and ecosystems. Furthermore, the present investigation aspired to evaluate the seasonal changes in the distribution of selected heavy metals and the Setiu River sediment pollution status.

Materials and Methods

Sample collection and sample analysis

For each season, wet (January) and dry (July), 60 bottom sediment samples were collected by employing Ponar Grab along the Setiu River (see Figure 1). Foreign objects that were not sediment were discarded in the field. The acquired samples were kept in plastic bags, preserved at low temperatures, and transported to the laboratory. Subsequently, the sediment samples were transferred to Petri dishes and oven-dried at 60 °C for several days to complete dryness. The dry samples were then ground into a fine powder with pestle and mortar and stored in polyethylene vials before subjecting the samples to the digestion process.

The heavy metals present in the samples were analysed by employing the Teflon bomb closed digestion method [14–16]. A total of 0.0.5 g of sediment samples were transferred to Teflon beakers. Subsequently, 1.5 mL of HNO_3, HCl, and HF (3:3:1) was added to each beaker. Following that, the samples were digested in the oven for eight hours at 100 ℃. The digested samples were transferred into 10 mL test tubes, and deionised water was added until the volume was 10 mL. Finally, the lead (Pb), zinc (Zn), copper (Cu), and arsenic (As) contents were determined and identified with inductively coupled plasma mass spectrometry (ICP-MS) [14–16].

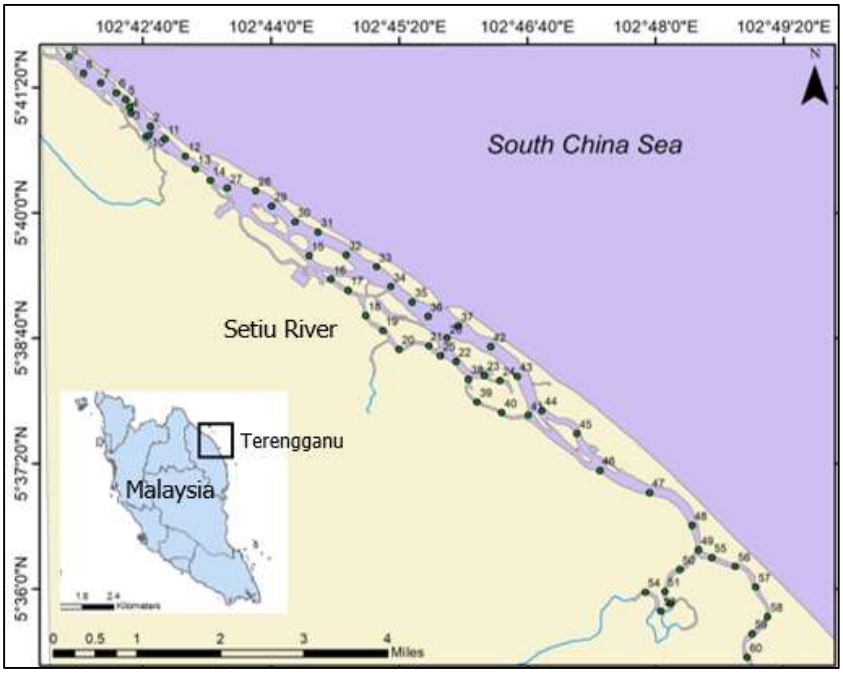


Figure 1. Sampling stations along Setiu River, Terengganu

Index of geoaccumulation (I_{gno})

The contamination of heavy metals in sediments was determined according to the geoaccumulation index (I_{geo}) [17, 18]. Moreover, the I_{geo} assessed the relationship between the geochemical background values of sediments and the measured metals concentrations in the sediment samples. Table 1 lists the sediment contamination categories suggested by Haris et al. [19] and Williams and Antoine [20]. The I_{geo} values of the samples collected in the present investigation were calculated with Equation (1).

Table 1. Sediment contamination categories according to I_{geo} value

Class	I_{geo} value	Sediment Quality
0	$I_{geo}<0$	Practically uncontaminated
1	$0<I_{geo}<1$	Uncontaminated to moderately contaminated
2	$1<I_{geo}<2$	Moderately contaminated
3	$2<I_{geo}<3$	Moderately to heavily contaminated
4	$3<I_{geo}<4$	Heavily contaminated
5	$4<I_{geo}<5$	Heavily to extremely contaminated
6	$I_{geo}>5$	Extremely contaminated

$$\text{Index of geoaccumulation (Igeo)} = \text{Log}_2 \frac{C_n}{1.5B_n} \quad \text{(Eq. 1)}$$

Where C_n is the concentration of the heavy metals in the sediment sample (n), B_n is the background value in the average shale of the metals (n), and 1.5 is the background matrix correction factor due to lithogenic effects.

Pollution Load Index

Pollution load index (PLI) value indicates the number of times the metal content in the sediment surpassed the mean background concentration, serving as an indicator of the overall level of heavy metal toxicity in a given sample. The PLI recommended by Tomlinson et al. [21] was employed to establish the mutual contamination status of the measured metals in the current study. The PLI is calculated as a contamination factor (CF) for each metal in relation to the background value in the sediment sample [22, 23]. The CF value expresses the pollution by a single heavy metal in a sample (Table 2) [24]. The CF was defined by Equation 2, while Equation 3 was utilised to express the PLI. Table 3 demonstrates the contamination status according to the calculated PLI values [21].

Table 2. Contamination factor categories based on CF value

CF Value	Contamination Factor
CF < 1	Low contamination factor
1 ≤ CF ≤ 3	Moderate contamination factor
3 ≤ CF < 6	Considerable contamination factor
CF ≥ 6	Very high contamination factor

$$\text{Contamination Factor (CF)} = \frac{C_{\text{sample}}}{C_{\text{background}}} \quad \text{(Eq. 2)}$$

Where C_{sample} is the metal concentration in the sediment sample and $C_{background}$ represents the background value of the metals.

$$\text{PLI} = (\text{CF1} \times \text{CF2} \times \text{CF3} \times \ldots\ldots \times \text{CF}_n)\ 1/n \quad \text{(Eq. 3)}$$

Where n is the number of metals examined.

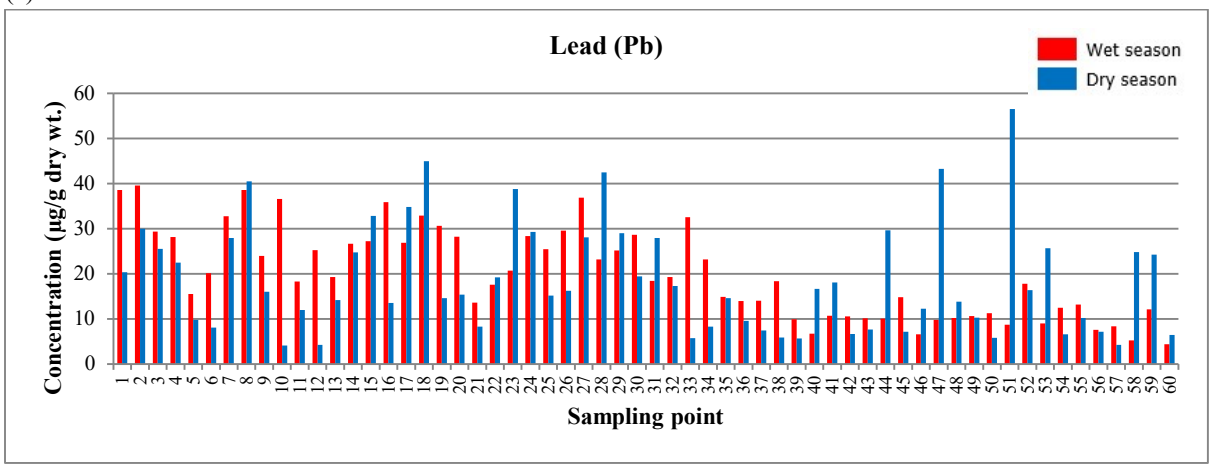
Table 3. Contamination status based on PLI value

PLI Value	Contamination Status
PLI<1.0	No heavy metal contamination occurs
PLI>1.0	Heavy metal contamination occurs

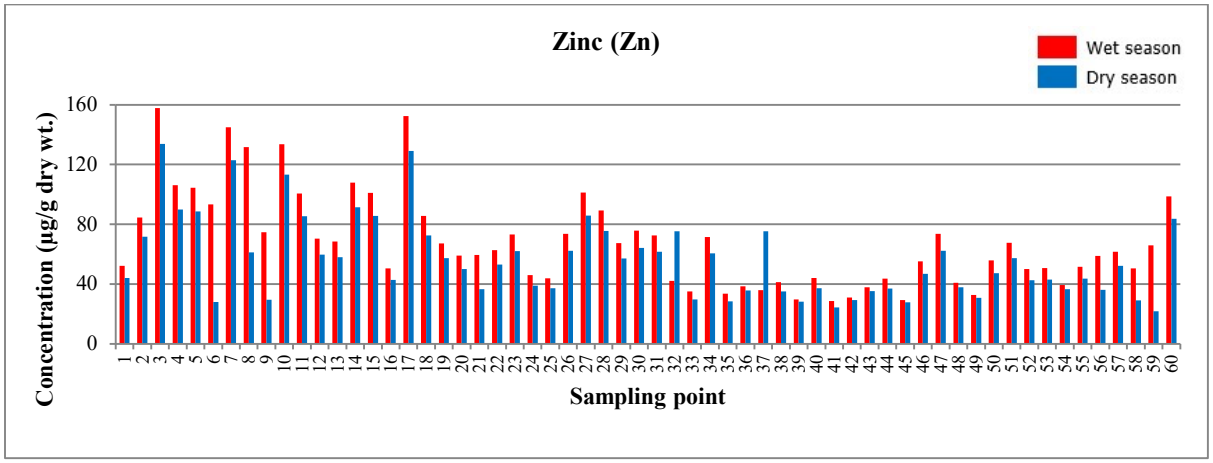
Results and Discussion

The distribution of Pb, Zn, Cu, and As concentrations in the Setiu River during the wet and dry seasons in 2017 are displayed in Figure 2. The concentrations of the studied metals were higher than the estimated average concentrations of shales and crust materials on Earth [25]. Possible sources of contamination of the metals in the sampling area were likely anthropogenic activities, such as boating, aquaculture, agriculture, plantation, sand mining, and discharge of untreated waste into the river system.

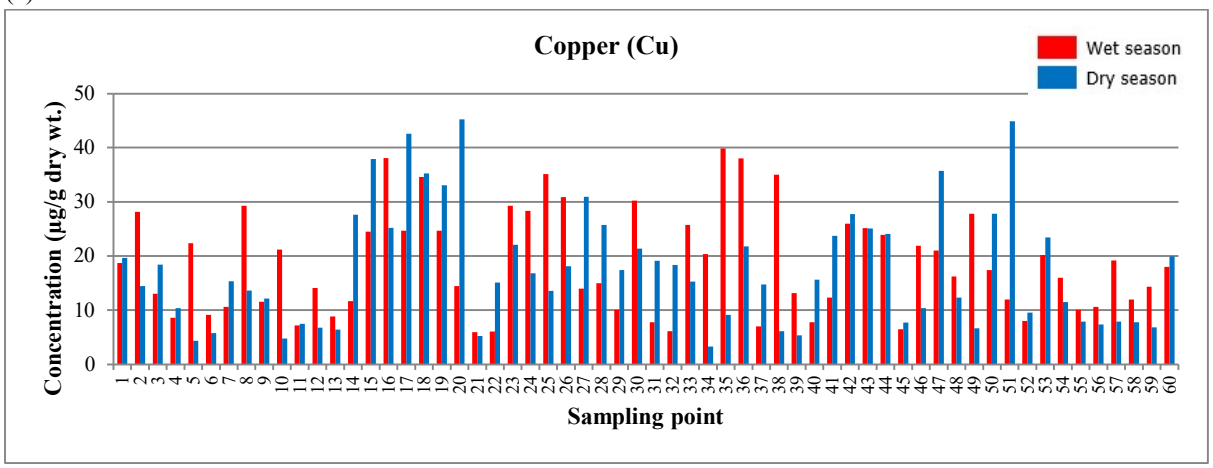
(a)


Lead (Pb)
Wet season
Dry season
Concentration (µg/g dry wt.)
Sampling point

(b)


Zinc (Zn)
Wet season
Dry season
Concentration (µg/g dry wt.)
Sampling point

(c)


Copper (Cu)
Wet season
Dry season
Concentration (µg/g dry wt.)
Sampling point

(d)

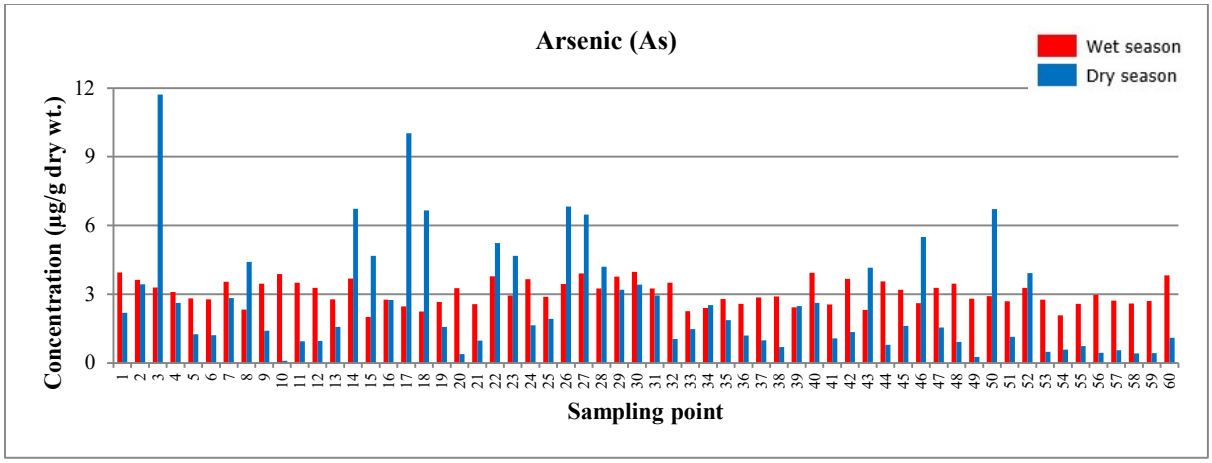


Figure 2. The distribution of (a) Pb, (b) Zn, (c) Cu, and (d) As concentration in the sediment samples from Setiu River during the wet and dry seasons

Lead has been known as poisonous since medieval times [26]. The sources of exposure to Pb vary from country to country, depending on historical and current uses [27]. Environmental Pb is from anthropogenic sources, such as lead-based paints, gasoline, and past and present mining and industrial activities [28]. Figure 2(a) displays the distribution of the concentration of Pb in the Setiu River sediment samples. The highest Pb concentration for the wet season was 39.5 µg/g dry wt., while the lowest was 4.38 µg/g dry wt. with an average of 19.9 ± 9.89 µg/g dry wt., which was considered to be slightly higher compared to the average background level of 17.0 µg/g dry wt.

The sediment with the lowest Pb concentration was obtained from station (St.) 60, while St. 2 contained the highest concentration of Pb. Nevertheless, during the dry season, the highest concentration of Pb concentration was 92.9 µg/g dry wt., recorded by the sample from St. 17, while the lowest concentration was in St. 60 at 1.58 µg/g dry wt. The average concentration for the dry season was 16.7 ± 15.1 µg/g dry wt., which was considered slightly lower than the average background level of 17.0 µg/g dry wt. [25].

Zinc is utilised in various consumer, agricultural, infrastructure, and industrial products [29]. Most importantly, Zn is vital to life as the substance is essential in the biological processes of living organisms, including humans. The chemical is crucial to cell division, protein synthesis, the immune system, and growth [30, 31]. A small part of Zn in soils, rocks, and sediments is constantly moved and transported throughout the environment via natural erosion processes [32].

Figure 2(b) displays the distribution of Zn concentration in the Setiu River sediment samples acquired during the wet and dry seasons of 2017. The highest concentration of Zn for the wet season was 158 µg/g dry wt., while the lowest concentration was 28.6 µg/g dry wt. The average concentration of Zn was 68.4±31.8 µg/g dry wt., which was higher than the average background level at 52.0 µg/g dry wt. The lowest concentration of Zn was from St. 41, while the sample from St. 3 exhibited the highest concentration of Zn. The highest concentration of Zn was 323 µg/g dry wt. from St. 17, while the lowest was from St. 40 at 12.4 µg/g dry wt. during the dry season. The average concentration for the dry season was 65.9 ± 48.5 µg/g dry wt., which was above the average background level of 52.0 µg/g dry wt. [25].

Copper is an essential micronutrient required for the growth of plants and animals [33, 34]. The substance is usually present in drinking water distributed in Cu pipes and additives designed to control algal growth [35]. The highest Cu concentration in the wet season was obtained from St. 35 at 39.9 µg/g dry wt., while the lowest

concentration value was recorded by the sample collected from St. 21 at 5.94 µg/g dry wt. The average value was 18.7 ± 9.48 µg/g dry wt., which was higher than the average background level of 14.3 µg/g dry wt. During the dry season, the highest concentration of Co was exhibited by the sample from St. 17 at 109 µg/g dry wt., while the lowest concentration was 1.05 µg/g dry wt. from St. 56. The average concentration value for the dry season was 14.7±16.9 µg/g dry wt., which was slightly higher than the average background level of 14.3 µg/g dry wt. [25].

Arsenic naturally occurs in the Earth's crust and is found in water, air, and land [36]. The inorganic form of the metal is highly toxic to organisms [37]. The chemical is employed in industrial activities, including as an alloying agent and in textile, glass, paper, wood preservatives, and metal adhesives processing [38]. The highest As concentration for the wet season was 3.98 µg/g dry wt., while the lowest concentration was 2.01 µg/g dry wt. The average value of 3.05 ± 0.53 µg/g dry wt. was considered higher than the background average of 2.0 µg/g dry wt. The lowest concentration of As was in St. 15, while the highest concentration of As was recorded by St. 30. During the dry season, the maximum As concentration was documented in St. 17 at 15.8 µg/g dry wt. and the minimum concentration was demonstrated by the sample from St. 52 with a value of 0.04 µg/g dry wt. The average concentration during the season was 2.45 ± 2.78 dry wt. and appeared to be above the average background concentration of 2.0 µg/g dry wt. [25].

Anthropogenic activities might significantly affect metal contaminations in the sediment of the Setiu River. Based on Figure 1, the concentration of metals is notably well distributed among most of the sampling points during the wet season. The observation might be due to the higher rainfall during the season [39] (November to March), with November being the wettest month of the year. Nevertheless, during the dry season, the concentration of metals was higher, mainly at St. 16 and 17 in July. The conditions might be due to heavy aquaculture and boating activities in the region. Theoretically, the dry season starts in May and ends in September, with June being the driest month [40].

The bottom sediments are the most prominent heavy metals reservoirs in aquatic systems. The metals accumulated in the sediments threaten the entire aquatic ecosystem [41]. Heavy metal contamination was widely distributed in the Setiu River system. Table 4 lists the I_{geo} values of the sediment samples for two seasons, the wet and dry seasons of 2017. Resultantly, all studied metals were classified in Classes 0 to 2, indicating that the sediments were uncontaminated to moderately to heavily contaminated.

Table 4. The I_{geo} value based on the average concentration obtained from the sediment of Setiu river for wet and dry seasons

Metal	Min – Max I_{geo} Value		Average I_{geo} Value		I_{geo} Class	
	Wet Season	Dry Season	Wet Season	Dry Season	Wet Season	Dry Season
Pb	(–2.54) – 0.63	(–4.01) – 1.87	–0.55	–1.11	0–1	0–2
Zn	(–1.44) – 1.02	(–2.66) – 2.05	–0.33	–0.52	0–2	0–3
Cu	(–1.85) – 0.90	(–4.35) – 2.35	–0.40	–1.24	0–1	0–3
As	(–0.58) – 0.41	(–6.36) – 2.40	0.004	–1.26	0–1	0–3

* Class 0 = $I_{geo}<0$ Practically uncontaminated; Class 1 = $0<I_{geo}<1$ Uncontaminated to moderately contaminated; Class 2 = $1<I_{geo}<2$ Moderately contaminated; Class 3 = $2<I_{geo}<3$ Moderately to heavily contaminated

The severity and variation of metal pollution at the 60 sampling points were assessed according to the PLI. Consequently, PLI was employed to determine the contamination status of the measured metals in the present investigation. Resultantly, the CF values for As, Pb, Cu, and Zn in the wet and dry seasons in the studied

areas exceeded 1, as summarised in Table 5. The findings indicated a moderate CF, although the value for Pb in the dry season was less than 1.

Table 5. The CF values of the metals in the sediment samples from Setiu River during the wet and dry seasons of 2017

Metal	Min – Max Value		CF Value		Contamination Factor	
	Wet Season	Dry Season	Wet Season	Dry Season	Wet Season	Dry Season
Pb	0.26–2.33	0.09–5.47	1.18	0.98	Moderate	Low
Zn	0.55–3.03	0.24–6.22	1.32	1.27	Moderate	Moderate
Cu	0.42–2.79	0.07–7.65	1.30	1.03	Moderate	Moderate
As	1.01–1.99	0.02–7.90	1.53	1.23	Moderate	Moderate

The PLI values obtained in the current study were more than 1, thus classifying Setiu River as slightly polluted due to heavy metals contamination (Table 6). Anthropogenic activities along the river contributed to the As, Pb, Cu, and Zn contamination. Fish loading and offloading, cleaning, maintenance practices such as painting, antifouling applications, fuelling activities, and urban runoff could also be the sources of metal pollution. Moreover, the usage of leaded gasoline by fishers led to increased Pb concentration in the region.

Table 6. The PLI values obtained based on the concentration of metals in the sediment samples from Setiu River in the wet and dry seasons of 2017

Min – Max Value		PLI Value		Metal Contamination Status	
Wet Season	Dry Season	Wet Season	Dry Season	Wet Season	Dry Season
0.76–2.00	0.17–6.73	1.25±0.34	1.00±1.0	Polluted	Polluted

Conclusion

Generally, the concentrations of metals in Setiu River sediments were significantly influenced by anthropogenic activities in the surrounding areas. The present investigation proved that heavy metals contamination occurred in the Setiu river system based on the I_{geo} and PLI values. Furthermore, the levels of heavy metals in the samples obtained during the dry season (July) were higher than in the wet season (January). The observations might be due to the dilution of metals in the aquatic system through precipitation. Consequently, comprehensive studies that include other pollutants, such as hydrocarbon, persistent organic pollutants, and microplastics should be conducted to ensure good water quality for aquaculture purposes.

Acknowledgement

This research was conducted with funding from the Ministry of Higher Education Malaysia, under the Niche Area Research Grant Scheme (NRGS) project number NRGS/2015/53131/32. The authors wish to acknowledge their gratitude to the anonymous reviewers who gave freely time and effort, constructive recommendations that enhanced the value of this manuscript. The authors also wish to express their appreciation to Oceanography Laboratory, Faculty of Science and Marine Environment staff for their invaluable assistance and providing the facilities to carry out the research. The authors also would like to thank Mr. Joseph Bidai for his assistant in detecting heavy

metals using ICPMS at the Institute of Oceanography and Environment.

References

1. Shanbehzadeh, S., Dastjerdi, M. V., Hassanzadeh, A. and Kiyanizadeh, T. J. (2014). Heavy metals in water and sediment: a case study of Tembi River. *Journal of Environmental and Public Health*, 2014: 858720.
2. Liang, W. and Yang, M. (2019). Urbanization, economic growth and environmental pollution: Evidence from China. *Sustainable Computing: Informatics and Systems*, 21: 1-9.
3. Rao, C. and Yan, B. (2020). Study on the interactive influence between economic growth and environmental pollution. *Environmental Science and Pollution Research*, 27: 39442-39465.
4. Jia, Y., Wang, L., Qu, Z. and Yang, Z. (2017). Effects on heavy metal accumulation in freshwater fishes: Species, tissues, and sizes. *Environmental Science and Pollution Research*, 25: 7012-7020.
5. Wang, Q., Chen, Q., Yang, D. and Xin, S. (2018). Distribution, ecological risk, and source analysis of heavy metals in sediments of Taizihe River, China. *Environmental Earth Sciences*, 77: 569.
6. Shahmoradi, B., Hajimirzaei, S., Amanollahi, J., Wantalla, K., Maleki, A., Lee, S. M. and Shim, M. J. (2020). Influence of iron mining activity on heavy metal contamination in the sediments of the Aqyazi River, Iran. *Environmental Monitoring Assessment*, 192: 521.
7. Khan, B., Ullah, H., Khan, S., Aamir, M., Khan, A. and Khan, W. (2016). Sources and contamination of heavy metals in sediments of Kabul River: The role of organic matter in metals retention and accumulation. *Soil and Sediment Contamination*, 25(8): 891-904.
8. Li, Y., Chen, H. and Teng, Y. (2020). Source apportionment and source–oriented risk assessment of heavy metals in the sediments of an urban river–lake system. *Science of The Total Environment*, 737: 140310.
9. Suratman, S., Mohd Tahir, N., Lee, C.Y. and Abdul Rashid, S.R. (2006). Monsoon effects on water quality at Besut River Basin, Terengganu. *Malaysian Journal of Analytical Sciences*, 10: 143-148.
10. Suratman, S., Hussein, A. N. A. R., Latif, M. T. and Weston, K. (2014). Reassessment of physico–chemical water quality in Setiu Wetland, Malaysia. *Sains Malaysiana*, 43(8): 1127-1131.
11. Suratman, S. and Talib, M.T. (2015). Reassessment of nutrient status in Setiu Wetland, Terengganu, Malaysia. *Asian Journal of Chemistry*, 27(1): 239-242.
12. Lin, J., Zhang, S., Liu, D., Yu, Z., Zhang, L., Cui, J., Xie, K., Li, T. and Fu, C. (2018). Mobility and potential risk of sediment–associated heavy metal fractions under continuous drought–rewetting cycles. *Science of The Total Environment*, 625: 79-86.
13. Sojka, M., Siepak, M., Jaskula, J. and Wicher–Dysarz, J. (2018). Heavy metal transport in a river–reservoir system: A case study from Central Poland. *Polish Journal of Environmental Studies*, 27(4): 1725-1734.
14. Kamaruzzaman, B. Y., Siti, W. A., Ong, M. C. and Joseph, B. (2010). Spatial distribution of lead and copper in the bottom sediments of Pahang River estuary, Pahang, Malaysia. *Sains Malaysiana*, 39(4): 543-547.
15. Kamaruzzaman, B. Y., Nurulnadia, M. Y., Shazili, N. A. M., Ong, M. C., Saad, S., Chowdhury, A. J. K. and Bidai, J. (2011). Heavy metal concentration in the surface sediment of Tanjung Lumpur mangrove forest, Kuantan, Malaysia. *Sains Malaysiana*, 40(2): 89-92.
16. Ong, M. C., Joseph, B., Shazili, N. A. M., Ghazali, A. and Mohamad, M. N. (2015). Heavy metals concentration in surficial sediments of Bidong Island, South China Sea off the East Coast of Peninsular Malaysia. *Asian Journal of Earth Sciences*, 8(3): 74-82.
17. Barbieri, M. J. (2016). The importance of enrichment factor (EF) and geoaccumulation index (I_{geo}) to evaluate the soil contamination. *Geology & Geophysics*, 5(1): 1000237.
18. Duncan, A. E., de Vries, N. and Nyarko, K. B. (2018). Assessment of heavy metal pollution in the sediments of the River Pra and its tributaries. *Water, Air, & Soil Pollution*, 229: 272.

19. Haris, H., Looi, L. J., Aris, A. Z., Mokhtar, N. F., Ayob, N. A. A., Yusoff, F. M., Salleh, A. B. and Praveena, S. M. (2017). Geo–accumulation index and contamination factors of heavy metals (Zn and Pb) in urban river sediment. *Environmental Geochemistry and Health*, 39: 1259-1271.
20. Williams, J. A. and Antoine, J. (2020). Evaluation of the elemental pollution status of Jamaican surface sediments using enrichment factor, geoaccumulation index, ecological risk and potential ecological risk index. *Marine Pollution Bulletin*, 157: 111288.
21. Tomlinson, D. C., Wilson, J. G., Harris, C. R. and Jeffrey, D. W. (1980). Problems in the assessment of heavy metals levels in estuaries and the formation of pollution index. *Helgoländer Wissenschaftliche Meeresuntersuchungen*, 33: 566-569.
22. Ding, X., Ye, S., Laws, E. A., Mozdzer, T. J., Yuan, H., Zhao, G., Yang, S., He, L., Wang, J. (2019). The concentration distribution and pollution assessment of heavy metals in surface sediments of the Bohai Bay, China. *Marine Pollution Bulletin*, 149: 110497.
23. Joksimović, D., Perošević, A., Castelli, A., Pestorić, B., Šuković, D., Đurović, D. (2020). Assessment of heavy metal pollution in surface sediments of the Montenegrin Coast: A 10–year review. *Journal of Soils and Sediments*, 20: 2598-2607.
24. Nweke, M. O. and Ukpai, S. N. (2016). Use of enrichment, ecological risk and contamination factors with geoaccumulation indexes to evaluate heavy metal contents in the soils around Ameka mining area, South of Abakaliki, Nigeria. *Journal of Geography, Environment and Earth Science International,* 5(4): 1-13.
25. Wedepohl, D. H. (1995). The composition of the continental crust. *Geochima et Cosmochima Acta*, 59(7): 1217-1232.
26. Shukla, V., Shukla, P. and Tiwari, A. (2018). Lead poisoning. *Indian Journal of Medical Specialities*, 9(3): 146-149.
27. Xu, D., Wang, R., Wang, W., Ge, Q., Zhang, W., Chen, L. and Chu, F. (2019). Tracing the source of Pb using stable Pb isotope ratios in sediments of Eastern Beibu Gulf, South China Sea. *Marine Pollution Bulletin*, 141: 127-136.
28. EPA (1990). http://www.atsdr.cdc.gov/toxprofiles/tp13–c6.pdf. [Access online 20 September 2021]
29. Baruah, R. (2018). Towards the bioavailability of zinc in agricultural soils. In role of rhizosperic microbes in soil: pp. 99-136.
30. Cakmak, I., McLaughlin, M. J. and White, P. (2017). Zinc for better crop production and human health. *Plant Soil*, 411: 1-4.
31. Wani, A. L., Parveen, N., Ansari, M. O., Ahmad, M. F., Jameel, S. and Shadab, G. G. H. A. (2017). Zinc: an element of extensive medical importance. *Current Medical Research and Practice*, 7(3): 90-98.
32. Hernández, E., Obrist–Farner, J., Brenner, M., Kenney, W. F., Curtis, J. H. and Duarte, E. J. (2020). Natural and anthropogenic sources of lead, zinc, and nickel in sediments of Lake Izabal, Guatemala. *Journal of Environmental Sciences*, 96: 117-126.
33. Lajayer, H. A., Savaghebi, G., Hadian, J., Hatami, M. and Pezhmanmehr, M. (2016). Comparison of Copper and Zinc Effects on Growth, Micro– and Macronutrients Status and Essential Oil Constituents in pennyroyal (*Mentha pulegium* L.). *Brazilian Journal of Botany*, 40: 379-388.
34. Schneider, L., Maher, W. A., Potts, J., Taylor, A. M., Batley, G. E., Krikowa, F., Adamack, A., Chariton, A. A. and Gruber, B. (2018). Trophic transfer of metals in a seagrass food web: Bioaccumulation of essential and non–essential metals. *Marine Pollution Bulletin*, 113(A): 468-480.
35. Martinez, C. E. and Motto, H. L. (2000). Solubility of lead, zinc and copper added to mineral soils. *Environmental Pollution,* 107: 153-158.
36. Wang, Y., Le Pape, P., Morin, G., Asta, M. P., King, G., Bártová, B., Suvorova, E., Frutschi, M., Ikogou, M., Pham, C. H. C., Vo, P. L., Herman, F., Charlet, L. and Bernier–Latmani, R. (2018). Arsenic speciation in Mekong Delta sediments depends on their depositional environment. *Environmental Science and Technology*, 52(6): 3431-3439.

37. Ma, Z., Lin, L., Wu, M., Yu, H., Shang, T., Zhang, T. and Zhao, M. (2018). Total and inorganic arsenic contents in seaweeds: absorption, accumulation, transformation and toxicity. *Aquaculture*, 497: 49-55.
38. WHO(2012). http://www.who.int/mediacentre/factsheets/fs372/en/. [Access online 20 September 2021].
39. Zaini, N. M., Lee, H. W., Mohamed, K. N., Sabuti, A. A., Suratman, S. and Ong, M. C. (2020). Datasets on spatial and temporal distribution of heavy metals concentration in recent sediment at Merang River system, Terengganu, Malaysia. *Data in Brief*, 31: 105900.
40. Akhir, M. F., Zakaria, N. Z. and Tangang, F. (2014). Intermonsoon variation of physical characteristics and current circulation along the east coast of Peninsular Malaysia. *International Journal of Oceanography*, 2014: 527587.
41. Pradit, S., Noppradit, P., Goh, B. P., Sornplang, K., Ong, M. C. and Towatana, P. (2021). Occurrence of microplastics and trace metals in fish and shrimp from Songkhla Lake, Thailand during the COVID-19 pandemic. *Applied Ecology and Environmental Research*, 19(2): 1085-1106.

Malaysian Journal of Analytical Sciences (MJAS)
Published by Malaysian Analytical Sciences Society

PRIMORDIAL RADIONUCLIDES CONTENT AND RADIATION RISK ASSESSMENT OF SURFACE SOILS SURROUNDING TEMENGGOR RESERVED FOREST, GERIK, PERAK

(Kandungan Radionuklid Primordial dan Penilaian Risiko Radiasi Tanah Permukaan di Sekitar Hutan Rizab Temenggor, Gerik, Perak)

Nursyairah Arshad[1,2], Misbah Hassan[1,2], Nor Aizam Adnan[3] and Rozita Osman[1*]

[1]Faculty of Applied Sciences,
Universiti Teknologi MARA, 40450 Shah Alam, Selangor, Malaysia
[2]Institute of Sciences,
Universiti Teknologi MARA, 40450 Shah Alam, Selangor, Malaysia
[3]Faculty of Architecture, Planning & Surveying,
Universiti Teknologi MARA, 40450 Shah Alam, Selangor, Malaysia

**Corresponding author: rozit471@uitm.edu.my*

Received: 17 September 2022; Accepted: 23 November 2022; Published: 22 February 2023

Abstract

Natural radioisotopes' occurrence on the earth's surface and the crust might raise concerns for the environment in terms of their radiation risk. Their existence in the environment can be measured through the evaluation of soil from the targeted areas. This study aimed to assess the radionuclides content including thorium-232, uranium-238, and potassium-40 in surface soil samples from Temenggor Reserved Forest areas. The radiation assessment of the environment was done by calculating the Radium Equivalent (Ra_{eq}), Absorbed Dose Rate (AD), Outdoor Annual Effective Dose (AED), and External Hazard Index (H_{ex}). The surface soil samples were collected from twelve locations surrounding Temenggor Reserved Forest using a hand auger. The radionuclides content was measured using the Energy Dispersive X-Ray Fluorescence (EDXRF) Spectrometer and was converted to activity concentration for the risk assessment calculation. The activity concentration of ^{232}Th, ^{238}U and ^{40}K was found to be in the range of 28.92-179.92, 32.56-110.10 and 214.45-1083.38 Bq/kg, respectively. The values of Ra_{eq}, AD, AED and H_{ex} that were obtained were in the range of 103.90-312.17 Bq/kg, 49.99-149.65 (nGy/h), 0.06-0.18 mSv/y and 0.29-0.86, respectively. The results showed that the activity concentration and radiation risk were higher than the limit set by the United Nations Scientific Committee on the Effects of Atomic Radiation (UNSCEAR 2000) at certain study locations. However, the AED and H_{ex} were very low compared to the UNSCEAR 2000 limit. The high content of radionuclides might be caused by the types of soils and rocks as well as the anthropogenic sources from past activity in the targeted area.

Keywords: energy dispersive X-ray fluorescence, Perak, radionuclides, risk assessment, surface soil

Abstrak

Kewujudan radionuklid semulajadi di permukaan bumi dan di dalam kerak bumi mungkin menimbulkan kebimbangan kepada alam sekitar dari segi risiko radiasi mereka. Kewujudan mereka di dalam alam sekitar boleh diukur melalui penilaian tanah dari kawasan yang di kenalpasti. Kajian ini menyasarkan untuk menilai kandungan radionuklid termasuk torium-232, uranium-238 dan potasium-40 didalam sampel tanah permukaan di kawasan Hutan Rizab Temenggor. Penilaian risiko radiasi di kawasan sekitar telah dijalankan menggunakan penggiraan *Radium Equivalent (Ra_{eq}), Absorbed Dose Rate (AD), Outdoor Annual Effective Dose (AED) and External Hazard Index (H_{ex})*. Sampel-sampel tanah permukaan telah dikumpulkan dari dua belas (12) lokasi disekitar kawasan Hutan Rizab Temenggor dengan menggunakan gerimit tangan. Kandungan radinuklid telah diukur dengan menggunakan Energy Dispersive X-Ray Fluorescence (EDXRF) Spektrometer dan ditukar kepada aktiviti kepekatan untuk penggiraan risiko radiasi mereka. Aktiviti kepekatan tiga radionuklid ^{232}Th, ^{238}U dan ^{40}K telah direkodkan masing-masing dalam julat 28.92-179.92, 32.56-110.10 dan 214.45-1083.38 Bq/kg. Keputusan aktiviti kepekatan dan risiko radiasi yang direkodkan adalah melebihi had yang telah ditetapkan oleh United Nations Scientific Committee on the Effects of Atomic Radiation (UNSCEAR 2000) di beberapa lokasi kajian. Walaubagaimanapun, keputusan AED dan H_{ex} adalah sangat rendah berbanding had yang ditetapkan oleh UNSCEAR 2000. Kandungan radionuklid yang tinggi mungkin disebabkan oleh jenis tanah dan batu serta sumber antropogenik daripada aktiviti terdahulu di kawasan kajian.

Kata Kunci: energy dispersive x-ray fluorescence; perak; radionuklid, penilaian risiko, tanah permukaan

Introduction

Primordial radionuclides are long-lived radionuclides that are present on earth since their formation [1,2]. These radionuclides exist in various geological formations in the environment including the earth's crust, rocks, soils, plants, water and air. Radionuclides in the ^{238}U and ^{232}Th decay series and non-series of ^{40}K are called primordial radionuclides. Every radionuclide emits radiation at a specific rate, which is calculated as its half-life. Half-life is the time for the half-radionuclides that are present to decay, thus forming another type of radioisotope. Therefore, the radionuclides emit some radiation during this process. Exposure to a high level of radiation can cause acute health effects such as skin burns and acute radiation syndrome as well as long-term effects such as cancer and cardiovascular disease. However, exposure to low-level radiation does not cause immediate health effects but can be a minor contributor to an overall cancer risk [3]. Thus, the activity concentrations of these radionuclides play an important role in environmental public health.

Soils play a vital role in transporting radionuclides into the environment, and act not only as the source but also as a medium to transport radionuclides into other environmental media such as air and water. Thus, from the perspective of radiation protection, the assessment of the level of radionuclides in the environment and the consequent radiation exposure to humans is mostly carried out in soil [1]. However, the distribution of these radionuclides in the soil is not uniform; it varies according to the soil type, mineral content, geological features and geological conditions [4-8]. The types of rock also elevate the concentrations of the radionuclides in the soil. Higher concentrations of radionuclide are mostly found in igneous rocks such as granite whereas the lower concentration is discovered in sedimentary rocks [1, 2]. Moreover, anthropogenic activities in an area can alter the distribution of radionuclides in such an environment.

Many countries around the world have begun to achieve the Sustainability Development Goals (SDGs) that has been launched by the United Nation (UN), whose agenda aims to protect the environment for future generations. Correspondingly, Malaysia is no exception in jointly making the agenda a success. To ensure the sustainability of the environment, early data should be documented to allow other research or appropriate steps to be taken to achieve SDGs. To date, the radionuclides data of Temenggor areas are still not comprehensively available. Thus, this study aims to evaluate the activity concentration of ^{238}U, ^{232}Th and ^{40}K in the surface soil of the surrounding Temenggor Reserved Forest area. Furthermore, Temenggor Reserved Forest is part of Belum-Temenggor Forest Complex (BTFC) [9] which is well known for its nature attractions. During the peak

season, BTFC will be busy with tourists for activities such as bird watching, water activities, fishing and others. Moreover, the Temenggor area has lithosolos and shallow red-yellow podzolic solids with s-types granitoid soil [10, 11]; granite, phosphate and igneous rocks contain a higher concentration of uranium and thorium. Thus, another objective of this study is to estimate their possible radiation risk to the environment in terms of Radium Equivalent (Ra_{eq}), Absorbed Dose Rate (AD), Outdoor Annual Effective Dose (AED), and External Hazard Index (H_{ex}). These predictions allowed the researches to observe and categorised the sampling locations according to their risk exposure to humans. The calculated risk was compared to the limit set by UNSCEAR 2000 as well as other research studies.

Materials and Methods

Study area

Temenggor Reserved Forest is situated in the North part of Peninsular Malaysia. Located in Gerik, Perak, Temenggor Reserved Forest is a part of the bigger Belum-Temenggor Forest Complex (BTFC) and is one of Malaysia's biggest premier ecotourism spots. The main attractions of this ecotourism area include bird watching, Rafflesia tracking and water activities. This reserved forest consists of several small islands such as Pulau Tali Kail, Pulau TNB, and Pulau MARA. Several Orang Asli localities are also located in the surrounding the Temenggor Reserved Forest.

Sampling

The surface soil samples were collected from twelve (12) points surrounding the Temenggor Reserved Forest. The locations were determined based on their accessibility and random judgmental method. The exact sampling sites were marked using the Global Positioning System (GPS) as tabulated in Table 1, and illustrated in a map as shown in Figure 1. About 1 kg of each sample was collected using a hand auger from a 15 cm depth, at the marked sampling site. The samples were collected from a 1 m^2 area of five (5) different holes and mixed in a labelled plastic bag to represent one (1) sample.

Table 1. GPS of 12 sampling sites for soil samples

Location	GPS	
	N	E
S1	05º37'02.7	101º17'44.8
S2	05º35'47.5	101º18'53.6
S3	05º32'58.4	101º21'16.0
S4	05º27'47.1	101º17'34.3
S5	05º29'40.3	101º18'51.1
S6	05º30'37.2	101º21'24.4
S7	05º28'30.0	101º20'51.5
S8	05º28'01.8	101º21'26.4
S9	05º29'46.9	101º23'09.0
S10	05º30'11.4	101º23'17.2
S11	05º31'28.2	101º23'23.5
S12	05º32'55.9	101º22'08.0

Sample preparation and analysis of radionuclides

The wet soil samples were dried in an oven at 60-70°C for about 24-72 hours until they were completely dried. Before drying, unnecessary materials were removed from the soil to avoid contamination. The dried soil was grounded into a powder form using an agate type planetary ball mill and sieved through 250 µm sieves. About 2 g of sample was then placed in a clean pellet mold using a Fluxana Vaneox Technology Pressing machine and pressed with 15 tons pressure. The pellet form samples were stored in a desiccator prior to analysis. The concentration of uranium (U), thorium (Th) and potassium (K) were measured using an Energy Dispersive X-Ray Fluorescence (EDXRF) Spectrometer (Model of EPSILON 3XL by PANalytical), and reported in the unit of mg/kg. The measured concentration was then converted into activity concentration with the unit of Bq/kg using the conversion factors in equations 1-3 [12, 13].

$$^{23}\ \mathrm{Th}\left(\frac{\mathrm{Bq}}{\mathrm{kg}}\right) = 0.246\ \mathrm{ppm\ Th} \qquad \text{(Eq. 1)}$$

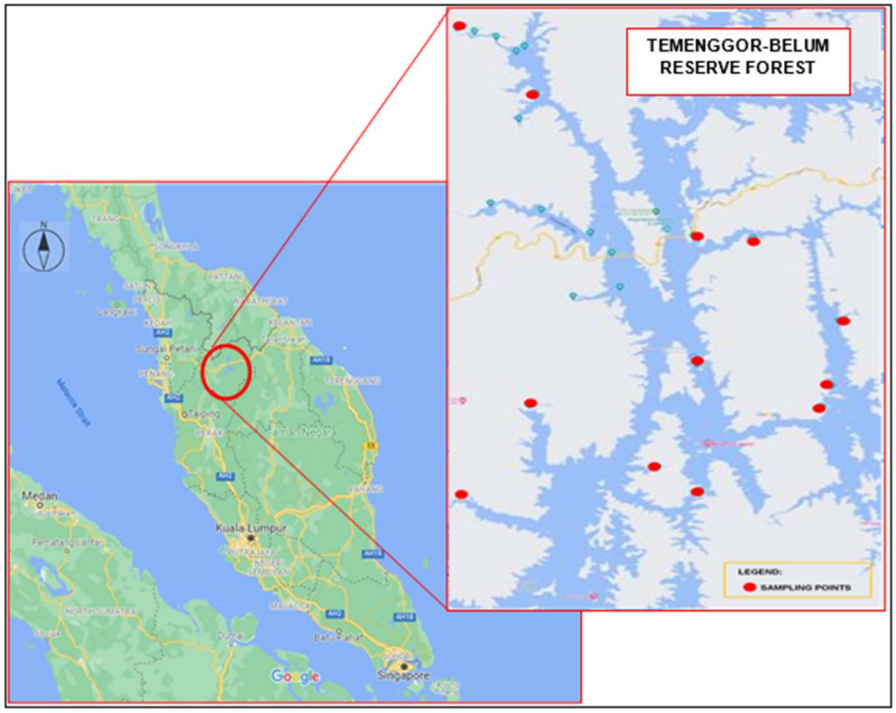


Figure 1. Maps showing the surface soil sampling sites

$$^{238}\mathrm{U}\left(\frac{\mathrm{Bq}}{\mathrm{kg}}\right) = 0.081 \text{ ppm U} \quad \text{(Eq. 2)}$$

$$^{40}\mathrm{K}\left(\frac{\mathrm{Bq}}{\mathrm{kg}}\right) = 32.2 \text{ ppm K} \quad \text{(Eq. 3)}$$

Method validation

The accuracy of the EDXRF was performed by analyzing the standard reference material (JLK-1, SRM 2709a and SO-7) for soil. The results obtained were compared with the established method of ICPMS. For this purpose, the samples were analyzed in the Agensi Nuklear Malaysia laboratory.

Radiology assessment

The content of ^{238}U, ^{232}Th and ^{40}K in soil are not uniformly distributed. The uniformity concerning radiation exposure can be expressed as Radium Equivalent Dose Rate (Ra_{eq}) measured in Bq/kg [14]. This calculation is for the comparison of the specific activity concentration level of constituents including radium, thorium and potassium as a constituent in varying amounts [10]. Before that, the activity concentration of ^{238}U was converted into ^{226}Ra activity concentration using Equation 4. Then, the Ra_{eq} was calculated using Equation 5. In addition, the Annual Effective Dose Rate (AED) is estimated to access the health effects of the absorbed dose. The AED used a conversion coefficient (0.7Sv/Gy) to transform the absorbed dose in the air into the absorbed dose received by humans with an outdoor occupancy factor (0.2) for adults (refer to Equation 7) [14, 15], whereby the absorbed dose rate (D) was calculated using Equation 6. On the other hand, multiple radionuclides contribute to the γ-dose, therefore the radiological hazards are presented as a single quantity that is known as the hazard index [10]. The hazard index is divided into two-internal and external hazard index. This study has only calculated the external hazard index to observe the radiological health risks of this locality since the

exposure to radiation from the soil is externally measured. The external hazard index was calculated using Equation 8 [14, 16, 17];

$$^{226}\mathrm{Ra}\left(\frac{\mathrm{Bq}}{\mathrm{kg}}\right) = 0.76 + 0.84\ (\mathrm{A}_{^{238}\mathrm{U}}) \quad \text{(Eq. 4)}$$

$$\mathrm{Ra}_{\mathrm{eq}}\left(\frac{\mathrm{Bq}}{\mathrm{kg}}\right) = \mathrm{A}_{^{226}\mathrm{Ra}} + 1.43\ \mathrm{A}_{^{232}\mathrm{Th}} + 0.077\ \mathrm{A}_{^{40}\mathrm{K}} \quad \text{(Eq. 5)}$$

$$\mathrm{D\ (nGy/h)} = 0.427\ \mathrm{A}_{^{238}\mathrm{U}} + 0.662\ \mathrm{A}_{^{232}\mathrm{Th}} + 0.0432\ \mathrm{A}_{^{40}\mathrm{K}} \quad \text{(Eq. 6)}$$

$$\mathrm{AED}\left(\frac{\mathrm{mSv}}{\mathrm{yr}}\right) = \mathrm{D}\left(\frac{\mathrm{nGy}}{\mathrm{h}}\right) \mathrm{x}\ 8760\ (\mathrm{h})\ \mathrm{x}\ 0.2\ \mathrm{x}\ 0.7\left(\frac{\mathrm{Sv}}{\mathrm{Gy}}\right) \mathrm{x}\ 10^{-6} \quad \text{(Eq 7)}$$

$$\mathrm{H_{ex}} = \frac{\mathrm{A}_{^{226}\mathrm{Ra}}}{370} + \frac{\mathrm{A}_{^{232}\mathrm{Th}}}{259} + \frac{\mathrm{A}_{^{40}\mathrm{K}}}{4810} \quad \text{(Eq. 8)}$$

where $\mathrm{A}_{^{226}\mathrm{Ra}}$ = Activity concentrations of ^{226}Ra, $\mathrm{A}_{^{238}\mathrm{U}}$ = Activity concentration of ^{238}U, $\mathrm{A}_{^{232}\mathrm{Th}}$ = Activity concentration of ^{232}Th, $\mathrm{A}_{^{40}\mathrm{K}}$ = Activity concentrations of ^{40}K, D (nGy/h) is the total air absorbed dose rate in the outdoors, 8760h is the number of hours in one year; 0.2 is the outdoor occupancy factor (AELB standard); 0.7 Sv/Gy is the conversion coefficient from absorbed dose in the air to the effective dose that is received by adults (AELB standard); 10^{-6} is the conversion factor between nano- and milli measurements.

Results and Discussion

In this study, the EXDRF method was validated using a variety of standard reference materials (SRM) including JLK-1, SRM 2709a and SO-7. Good recoveries were obtained in the range of 87-115%. The accuracy of the EDXRF method was also compared with the inductively coupled plasma-mass spectrometer (ICPMS) in the Agensi Nuklear Malaysia laboratory using similar samples. The results obtained were relatively comparable with the recoveries in the range of 70-136 %, showing the reliability of the EXDRF method that was used for the analysis of elements in the soil samples.

The activity concentrations of three (3) radionuclides of ^{238}U, ^{232}Th and ^{40}K from twelve (12) locations surrounding the Temenggor area are presented in Table 2. The measured concentration from the EDXRF in the unit of mg/kg was converted into activity concentration with the unit of Bq/kg. As tabulated in the table, the activity concentrations ^{238}U, ^{232}Th and ^{40}K were in the range of 32.56-110.10, 28.92-179.92 and 214-1083 Bq/kg with the mean of 52.55, 79.49, and 476 Bq/kg, respectively. The lowest level of ^{238}U was observed at site S05 with a value of 32.56 Bq/kg and the highest was at site S03 (110.10 Bq/kg). Meanwhile, for ^{232}Th the lowest was at site S01 (28.92 Bq/kg) and the highest was at site S11 (179.92 Bq/kg). Site S11 gave the lowest concentration with a value of 214 Bq/kg, while S03 contained the highest activity concentration of ^{40}K (1083 Bq/kg). The difference in concentrations was most probably caused by the type of soil and the surrounding environment of the sampling site. According to Sanusi et al., granite soil has higher radionuclides content compared to other types of soil [11]. Temenggor areas are made up of lithosolos and shallow red-yellow podzolic solids with s-types granitoid soil [10]. Factually, this can explain the high concentrations of radionuclides in this area. Moreover, the additional anthropogenic sources might elevate the natural content of radionuclides. It was found that site S03 was located near the small jetty for a private boat, a site that has become a pickup and drop-off point for goods and other amenities. This site is also a place for small boats to refuel their engine oil. Furthermore, vehicles can also access to this location from the mainland. Thus, radionuclides can be released into the environment

through transportation as radionuclides are one of the burning fuel products [18, 19]. On the other hand, site S11 is located in a place named Tanah Banun (according to local people). This location has an open space which is a habitat for most of the wild animals to roam as well as rest. The transfer of radionuclides from their origin to the environment could be through the food chain. Plants absorb nutrients and other contaminants from the soil and are eaten by animals. Additionally, soil can also be ingested by animals through the licking or preening of their fur, feathers, or offspring [20]. Then, the absorbed radionuclides can be excreted in urine or endogenously excreted in the faeces and absorbed back into the soil of the areas [21]. This might explain the elevated concentrations of radionuclides in location S11. Furthermore, Site S11 is also near one of the Orang Asli localities in the Temenggor area. While samples from other locations have mostly been collected from the small island that has not been occupied anymore.

The standard permissible limit for radionuclides in soil that is reported by the UNSCEAR is 35, 30, and 400 Bq/kg for ^{238}U, ^{232}Th, and ^{40}K, respectively as shown in Table 2. The majority of the sampling sites have higher radionuclides content if compared to the world limit [3]. Additionally, the activity concentrations of the three radionuclides in this study were compared to other reported studies of soil around Malaysia. Mohammad Syazwan et al. [22] studied the influence of geological and soil formation on natural gamma (γ) radiation exposure. The study focused to obtain the baseline data of γ radiation exposure and radioactivity that were associated with soil in the granitic territory in the Western Region of Peninsular Malaysia. The study stated ^{238}U and ^{232}Th activity concentrations to be in the range of 7-554 and 23-1809 Bq/kg, respectively. Temenggor area has lower activity concentrations when compared to the Western Region of Peninsular Malaysia despite having the same soil types [22]. Another reported study of radionuclides from the soil samples that were collected in Bangi by Mei-Wo and Ali showed a different pattern [23]. The activity concentrations of ^{32}Th and ^{40}K are relatively in the range of the Temenggor area but there is a slightly higher range for ^{238}U. The author has stated that the noticeable difference may be attributed to the geochemical composition and origins of the soil types in the particular study areas. Moreover, the higher values of the activity concentrations belong to soil samples that may be attributed to soil types which were probably radioactive-rich granite, phosphate, sandstone, and quartzite [23]. Abdul Aziz and Khoo studied the assessed absorbed dose and radiation hazard index from the soil in Bukit Kledang, Perak [24]. The obtained results were in the lower range than this study for the three radionuclides, as shown in Table 2. The authors stated that the varied values that were obtained varied according to the location. It is most likely to be affected by several factors such as soil type, soil pH, the latitude of area, soil texture, the existence of underground rock, and organic matter [24].

The findings of activity concentrations surround Temenggor area was also compared to some studies from oversea. The vertical distributions of forty-four soil samples from Qatar were studied by Ahmad et al. [7]. The mean concentrations of this study are presented in Table 2 and have lower concentrations compared to this study. The authors agreed that the different levels of radionuclides in the soil depend primarily on the concentration of radionuclides in bedrocks from which the soil originates. Besides, the author said that the natural radionuclides levels (^{226}Ra, ^{232}Th, and ^{40}K) in the soil might be affected by the physiochemical characteristic of the soil [7]. Another reported study of activity concentrations for the three natural radionuclides (^{226}Ra(^{238}U), ^{232}Th, and ^{40}K) using soil samples was carried out in Korea [8]. The in-situ and laboratory γ-ray spectroscopy techniques were compared to evaluate the activity concentration of natural radionuclides in soil. Table 2 shows the results of the in-situ measurement using gamma spectroscopy techniques. The authors reported that all-natural radionuclide concentrations were lower on Jeju Island due to its geological origin of quarternary basalt/trachyte, while they were higher in Chuncheon due to its geological origin of Jurassic granite. Moreover, a strong correlation was observed between the techniques with linear regression lines of 99% for ^{226}Ra and ^{232}Th, whereas for ^{40}K the correlation was 97.5% [8]. All of the reported studies have agreed that the difference and high concentrations of radionuclides

are most likely caused by the original, geochemical, and physiochemical types of the soil itself.

Table 2. The activity concentrations of ^{238}U, ^{232}Th and ^{40}K

Location	Activity Concentrations (Bq/kg)		
	^{238}U	^{232}Th	^{40}K
S01	33.31	28.92	418
S02	70.97	72.59	752
S03	110.10	86.75	1083
S04	46.86	28.95	290
S05	32.56	38.69	263
S06	44.73	102.42	339
S07	51.90	44.43	657
S08	53.86	160.51	411
S09	41.49	41.79	311
S10	51.21	71.67	405
S11	34.50	179.92	214
S12	59.17	97.28	562
Mean	**52.55**	**79.49**	**476**
UNSCEAR 2000 [14]	35	30	400
Western region Peninsula Malaysia [22]	7-554	23-1806	-
Bukit Kledang, Perak [24]	11.98 – 29.93	20.97 – 41.45	5.73 – 59.41
Bangi [23]	17.2-85.4	23.9-89.9	98.4-499.4
Qatar [7]	17	10	201
Korea [8]	13-188	14.6-230	241-1328

Temenggor area has Ra_{eq} values between 103.90 - 312.17 Bq/kg. The Ra_{eq} of the study area is presented in Figure 2. It can be observed that this study has a lower concentration than the limit that is set by UNSCEAR 2000 of 370 Bq/kg. Meanwhile, it is relatively comparable with the reported values of other studies [1,14,22,25,26,27].

The absorbed dose date of radionuclides was calculated in the unit of nGy/h. This is the measurement of presented radionuclides in the air exposed to humans. The absorbed dose rate at sampling sites varies from 49.99 to 149.65 nGy/h (Figure 3). The highest value in the Temenggor area that has been observed at site S03 is about three times higher in value than the world limit (55 nGy/h). However, Temenggor areas have absorbed dose rates in a range comparable with other reported studies [1, 14, 25, 27].

The estimated outdoor absorption of radiation was calculated using the annual effective dose (AED) in the unit of mSv/y. The calculated AED for the Temenggor area was about four times lower than the reported world limit by UNSCEAR 2000 as illustrated in Figure 4. The value was between 0.0621 to 0.1835 mSv/y. The reported value from Nigeria in 2019 [26] has a higher AED than the Temenggor area, while the values in other reported studies were comparable with the study areas [1, 14, 25, 26, 27].

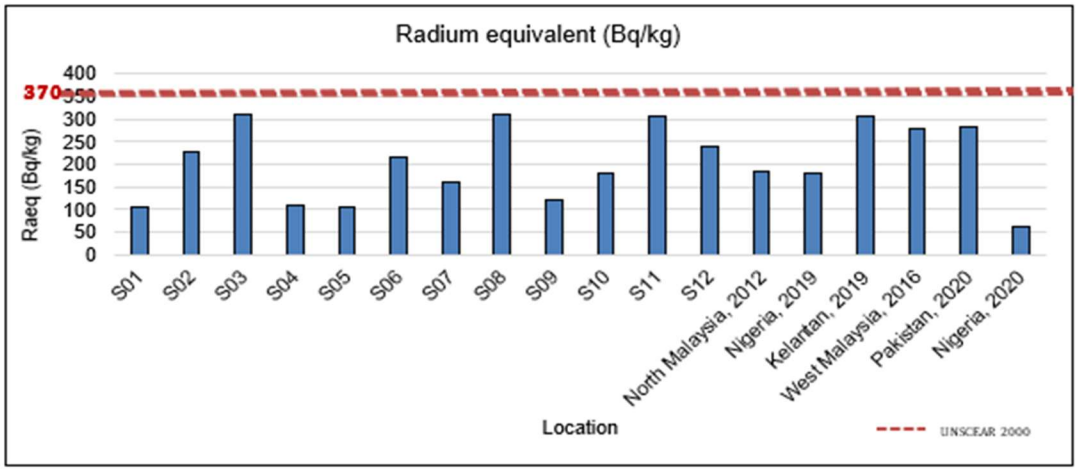


Figure 2. The radium equivalent (Ra_{eq})

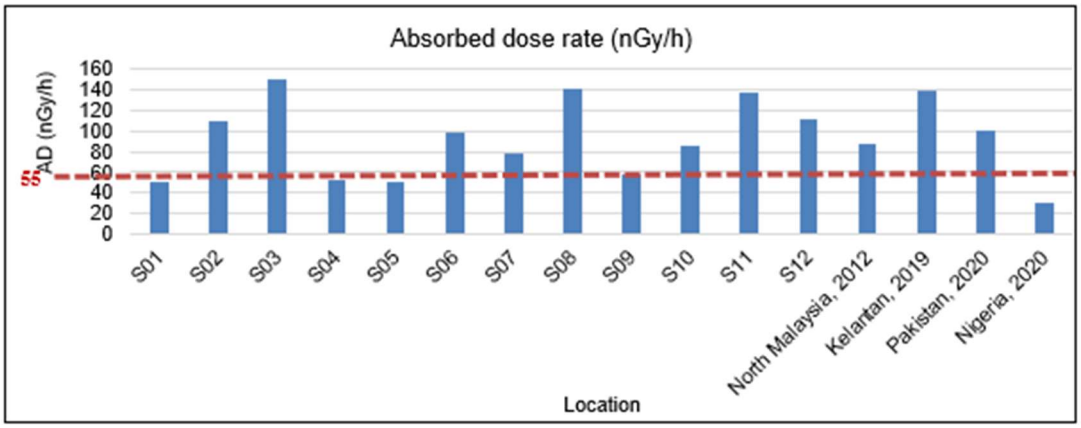


Figure 3. The absorbed dose rate (AD)

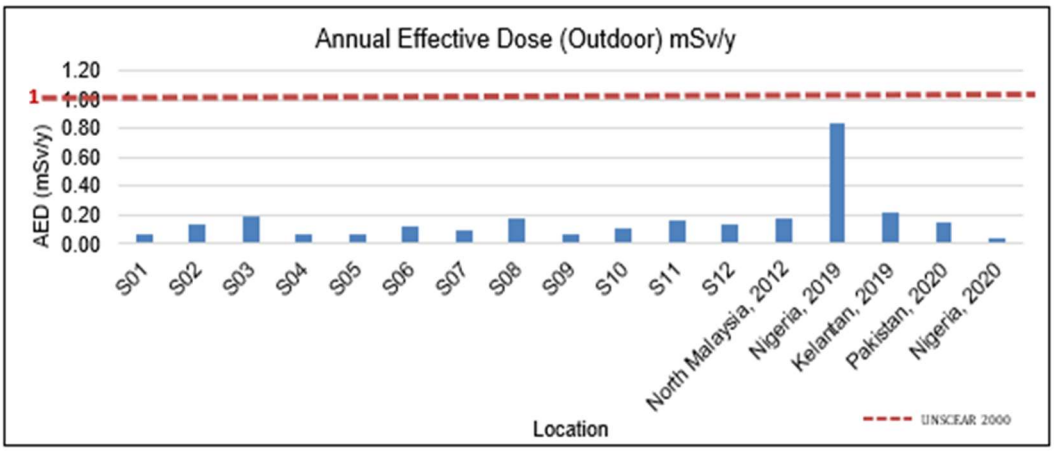


Figure 4. The annual effective dose (AED)

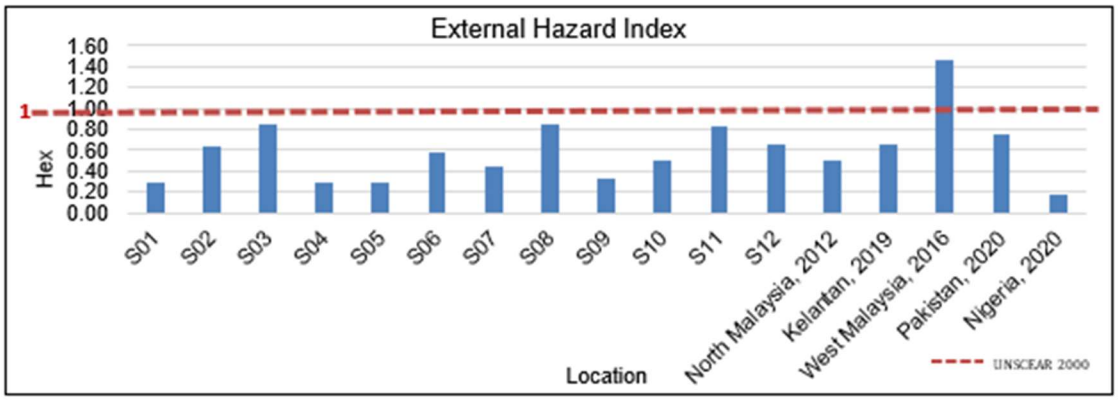


Figure 5. The external hazard index (H_{ex})

The total estimation of γ -dose radiation was calculated using the hazard index. In this study, researchers used the external hazard index since the estimation was based on the radiation in the soil. Figure 5 shows the distribution of the external hazard index for the Temenggor area and a comparison between the world limit and other reported studies. Temenggor area has a hazard index in the range of 0.2885-0.8577. All locations have a lower value than the world limit that is set by UNSCEAR 2000 with the value of 1. This implies that exposure to the gamma radiation from the soil has no significant consequence to health. The other reported values [1, 14, 25, 27] were also in-between the Temenggor area; except for West Malaysia [22] where it has a higher value.

Conclusion

A study to observe the distribution of three radionuclides- including ^{238}U, ^{232}Th and ^{40}K, has been conducted in the Temenggor Reserved Forest area. The mean activity concentrations of ^{238}U, ^{232}Th, and ^{40}K are 52.55, 79.49, and 476 Bq/kg, respectively. Some of the locations have higher activity concentrations than the world limit that is released by UNSCEAR 2000. Comparing the activity concentrations with the reported studies around Malaysia, the Temenggor area has a lower activity concentration. The type of soil in the study area contributes to the high activity concentrations of radionuclides. On the other hand, the radiation risk assessment has shown that the study areas do not pose a significant risk to humans. This is based on the calculation of Radium Equivalent (Ra_{eq}), Absorbed Dose Rate (AD), Outdoor Annual Effective Dose (AED), and External Hazard Index (H_{ex}).

Acknowledgment

The authors would like to thank Jabatan Perhutanan Negeri Perak, Bahagian Hulu Perak, the staff of Pulau Tali Kail Resort, and all individuals who were involved directly or indirectly throughout this study. The appreciation also includes the Institute of Sciences and Faculty of Applied Sciences of Universiti Teknologi MARA (UiTM) Shah Alam for permission to use their laboratory and facilities.

References

1. Esan, D. T., Ajiboye, Y., Obed, R. I., Ojo, J., Adeola, M. and Sridhar, M. K. (2022). Measurement of natural radioactivity and assessment of radiological hazard indices of soil over the lithologic units in Ile-Ife area, South-West Nigeria. *Environmental Health Insights*, 16: 1-13.
2. Al-Khawlany, A., Khan, A. and Pathan, J. (2018). Review on studies in natural background radiation, *Radiation Protection Environment,* 41: 215.
3. United Nations Scientific Committee on The Effects of Atomic Radiation (UNSCEAR) (2000). Sources and biological effects of ionizing radiation, United Nations, New York
4. Araromi, O. I., Ojo, A. O., Olaluwoye, M. O. and Odefemi, O. B. (2016). The concentration of natural radionuclides in soil samples from the practical year agricultural farmland, University of Ibadan, *Journal of Applied Physics*, 8(4): 60-68.
5. Ramli A. T. (1997). Environmental terrestrial gamma radiation dose and its relationship with soil type and radiation isotope and underlying geological formation in Pontian District, Malaysia, *Journal of Applied Radiation and Isotopes*, 48 : 407-412.
6. Florou, H. and Kritidis, P. (1992). Gamma radiation measurements and dose rate in the coastal areas of Island,

Aegean Sea, Greece. *Journal of Radiation protection Dosimetry,* 45: 227-279.

7. Ahmad, A. Y., Al-Ghouti, M. A., and Al-Sadig, I. (2019). Vertical distribution and radiological risk assessment of ^{137}Cs and natural radionuclides in soil samples. *Scientific Report,* (9): 12196.
8. Hassan, N. M., Kim, Y. J., and Jang, J. (2018). Comparative study of precise measurements of natural radionuclides and radiation dose using in-situ and laboratory γ-ray spectroscopy techniques. *Scientific Report,* (8): 14115.
9. Kamal, S. H. S., Suratman, M. N., Khamis, S., Hassan, A. N. N. and Mohammad, M. S. (2021). Host-parasitic relationships between *Tetrastigma rafflesiae* and *Rafflesia azlanii* and *Rafflesia cantleyi* in Belum-Temenggor Forest Complex, Perak, Malaysia, *Pertanika Journal of Tropical Agricultural Science*, 44(4): 755-771.
10. Jabatan Mineral dan Geosains Malaysia (JMG), Malaysia Government Portal.
11. Sanusi, M. S. M., Ramli, A. T., Hassan, W. M. S. W., Lee, M. H., Izham, A., Said, M. N., Wagiran, H., and Heryanshah, A. (2017). Assessment of impact of urbanisation on background radiation exposure and human health risk estimation in Kuala Lumpur, Malaysia, *Environment International,* 104: 91-101.
12. Arshad, N. (2017). The assessment of selected atmospheric pollutant elements using moss (*Leucobryum Aduncum*) as Bio-Monitor, Thesis of Master Degree, Universiti Teknologi MARA.
13. Nuclear Solution Division, (2000). Specific activities. Access from http://www.iem-inc.com/information/tools/specific-activities. [Access online on 3 April 2022]
14. Khan, I. U., Qin, Z., Xie, T., Bin, Z., Li, H., Sun, W. and Lewis, E. (2020). Evaluation of health hazards from radionuclides in soil and rocks of North Waziristan, Pakistan, *International Journal of Radiation Research*, 18(2): 243-253.
15. Alzubaidi, G., Hamid, F. B. and Abdul Rahman, I. (2016). Assessment of natural radioactivity levels and radiation hazards in agricultural and virgin soil in the state of Kedah, North of Malaysia, *Scientific World Journal*, 2016: 6178103.
16. Arshad, N., Hamzah, Z. and Saat, A. (2015). Determination of heavy metals and radionuclides in *Ligumia recta* (Black Sandshell) from Kampung Gajah, Perak. *Malaysian Journal of Analytical Sciences,* 19(5): 911-919.
17. Abdullah, A., Hamzah, Z., Saat, A., Wood, A. K. and Alias, M. (2015). accumulation of radionuclides in selected marine biota from Manjung coastal area, *AIP Conference Proceedings,* 1659: 050009.
18. Ramadhan, H. H. and Kim, J. (2021). Radiological risk assessment of vehicle transport accidents associated with consumer products containing naturally occurring radioactive materials. *Applied Sciences*, 11(18):8719.
19. Obayes, K. H., Mahdi, K. H., Nassif, R. M. and Mansour, H. L. (2019). Determination of radionuclides and heavy elements in the rising dust in the small side of Diwaniyah city due to the movement of wheels and cars. *Journal of Physics,:Conference Series,* 1234: 012046.
20. Brenda, H. (2021). Environmental pathways of radionuclides to animal products in different farming and harvesting systems, nuclear and radiological emergencies in animal production systems, preparedness, response and recovery. Springer, Germany: pp. 53.
21. Victar, S. A. (2021). Measurement of radioactivity, nuclear and radiological emergencies in animal production systems, preparedness, response and recovery, Springer, Germany: pp. 29.
22. Sanusi, M. S. M., Ramli, A. T., Wagiran, H., Lee, M. H., Heryanshah, A. and Said, M. N. (2016). Investigation of geological and soil influence on natural gamma radiation exposure and assessment of radiation hazards in Western Region, Peninsular Malaysia. *Environment Earth Science*, 75: 485.
23. Mei-Wo, Y. and Hasan, A. M. A. (2019). Natural radioactivity in surface soil of malaysian nuclear agency bangi complex and its radiation risk. *Proceedings of the Research and Development Seminar Nuklear Malaysia 2018 Nuclear Technology Towards Sustainable Development, Malaysia*: Malaysian Nuclear Agency.
24. Abdul Adziz, M. I. and Khoo, K. S. (2018). An assessment of absorbed dose and radiation hazard index from soil around repository facility at Bukit Kledang, Perak, Malaysia, *IOP Conference Series: Materials Science and Engineering*, 298: 012001.
25. Almayahi, B. A., Tajuddin, A. A. and Jaafar, M. S. (2012) Radiation hazard indices of soil and water samples in Northern Malaysian Peninsula, *Applied Radiation Isotope*, 70(11): 2652-2660.
26. Joel, E. S., Maxwell, O., Adewoyin, O. O., Olawole, O. C., Arijaje, T. E., Embong, Z. and Saeed, M. A. (2019) Investigation of natural environmental radioactivity concentration in soil of coastaline area of Ado-odo/ota Nigeria and its radiological implications, *Scientific Report,* 9: 4219.
27. Garba, N., Ramli, A., Saleh, M. and Gabdo, H. (2018). Natural radioactivity and associated radiation hazards in soil of Kelantan, Malaysia, *Human and Ecological Risk Assessment*, 25(10): 1707-1717.

Malaysian Journal of Analytical Sciences (MJAS)
Published by Malaysian Analytical Sciences Society

ACETAL DERIVATIVES OF HYDROXYCITRONELLAL: A REVIEW ON SYNTHESIS, CHARACTERIZATION AND THEIR MOSQUITOE REPELLENT ACTIVITIES

(Terbitan Asetal Hidroksisitronelal: Ulasan ke atas Sintesis, Pencirian dan Aktiviti Penghalau Nyamuk)

Ariff Mahtar and Juliana Jumal*

Faculty of Science and Technology
Universiti Sains Islam Malaysia 71800 Nilai, Negeri Sembilan, Malaysia

**Corresponding author: juliana.j@usim.edu.my*

Received: 7 September 2022; Accepted: 20 December 2022; Published: 22 February 2023

Abstract

Mosquitoes represent the deadliest animal species in tropical regions because they can affect human health. Personal protection which is mosquito repellent has been used since 20th century. Mosquito repellent which contains plant-based ingredients has high demand from consumers since its efficacy is as good as synthetic ones. Citronella genus plants are originally extracted to be used in perfumery, then they were used for ingredients of plant-based mosquito repellents as they have repellent properties. Citronellal-based repellent has an effective dose such as *N,N*-diethyl-meta-toluamide dose. However, the oil content has high volatility causing it to reduce its efficacy because the oil evaporates. Recently, the structure of citronellal compound has been modified into hydroxycitronellal by adding some functional groups to reduce the release rate, prolong the protection time and improve the stability of the compound. The release rate properties are affected by functional groups and the molar mass of the compounds. This paper presents a summary of recent catalyst and solvent usage during synthesis, characterization and comparison of mosquito repellents.

Keywords: synthesis, hydroxycitronellal, acetal derivatives, mosquito repellent

Abstrak

Perlindungan diri iaitu penghalau nyamuk telah digunakan sejak abad ke-20. Nyamuk mewakili spesies haiwan yang paling mematikan di kawasan tropika kerana ia boleh menjejaskan kesihatan manusia. Ubat nyamuk yang mengandungi bahan berasaskan tumbuhan mendapat permintaan tinggi daripada pengguna memandangkan keberkesanannya setanding dengan sintetik. Tumbuhan genus *Citronella* pada asalnya diekstrak untuk digunakan dalam minyak wangi, kemudian ia digunakan untuk bahan-bahan penghalau nyamuk berasaskan tumbuhan kerana ia mempunyai sifat penghalau. Penghalau berasaskan sitronelal mempunyai dos berkesan seperti dos *N,N*-dietil-meta-toluamida. Walau bagaimanapun, kandungan minyak mempunyai kemeruapan yang tinggi menyebabkan ia mengurangkan keberkesanannya kerana minyak menyejat. Struktur sebatian sitronel telah diubah suai dengan menambah beberapa kumpulan berfungsi untuk mengurangkan kadar pelepasan, memanjangkan masa perlindungan dan meningkatkan kestabilan sebatian. Sifat kadar pelepasan dipengaruhi oleh kumpulan berfungsi dan jisim molar sebatian. Kertas ini membentangkan ringkasan penggunaan pemangkin dan pelarut terkini semasa sintesis, pencirian dan perbandingan penghalau

nyamuk.

Kata kunci: sintesis, hidroksisitronelal, terbitan asetal, penghalau nyamuk

Introduction

Mosquitoes represent the deadliest animal among other species in the tropical regions as they can affect human health [1]. They can spread the pathogens among human in the regions because of the powerful vectors [1]. Malaria, oestridean parasites which can cause myasis, Japanese and encephatilis and the parasites come from the mosquito themselves [2]. Aedes albopictus is one of the common example of Asian tiger mosquito which can cause several reported severe disease cases [3]. There are many strategies which help to reduce infection by and transmission of vector disease especially in tropical regions, such as chemical control, genetic control and personal protection [4]. The use of insecticides represents the chemical control of mosquitoes in order to kill the adults [5]. There are many ways for environmental controls such as the removal of disused tires, draining of ponds and introducing predatory fish [6]. In addition, genetic control mosquito population can also be implemented by reducing mosquitoes's lifespan [7]. However, personal protection is the best way to protect user from mosquito bites as well as to reduce mosquito-borne disease outbreaks potential of user's surrounding [8].

Personal protection which commonly used by individual is mosquito repellent. Mosquito repellent is a key recommendation of health authorities to reduce the potential of mosquito-borne disease. *N,N*-diethyl-m-toluamide (DEET), picaridin and p-menthane-3,8-diol (PMD) are the most commonly used repellent products. The common repellent products have high demand from users because they have good efficacy since 1950s [9]. One of the repellent products which gains the highest demands from users and commonly commercialized by mosquitos repellent industries is DEET [10]. However, DEET can lead to negative impacts to humans [10]. It is reported that DEET can lead to neurotoxic effects not only to insects but as well as human because it can disturb the acetylcholinesterase's activity which is a key enzyme of synaptic transmission [1]. Besides, it can affect the channels of Na^+ and K^+ which are located at cortical neurons in mammalian and it can cause the pro-angigenic effects to human because DEET acts as an allosteric modulator of M3 mAchR [11]. Picaridin also one of the repellents which can cause dermatitis on our skin [12].

Therefore, there has been an effort to seek for environment-friendly repellent [13]. Plant-based repellents is an alternative mosquito repellent to be used for personal protection [13]. Geranyl acetate, citronellal, 6-methyl-5-hepten-2-one and geranyl acetone [8] give response to odor receptors of mosquito which the receptor also can receive the same respond from the gold-standard repellent DEET [14]. Citronellal is reported to be one of the plant-based repellent which has most effective repellent properties because it is monoterpenoid aldehyde and there is a carbonyl group [13]. On the other hand, the two functional or substituent groups of citronellal contributes to biological interaction towards mosquito receptor as mosquito repellent. On the other side of coin, citronellal has high release rate and high volatility because of the presence of carbonyl group [15] and low molecular weight [16]. The structure of citronellal can be modified by adding a functional group [14] and undergoes an acetalization in order to increase its molecular weight and protection time [15].

Acetal, ketal and their derivatives

Acetal and ketal

Acetal (Figure 1) or ketal (Figure 2) can be formed via the reaction between carbonyl and alcohols, for instance methanol or ethanol (Scheme 1) [7]. The reaction is catalysed by acid catalyst. The formaldehyde or higher aldehydes with diols such as 1,2-diols or 1,3-diols in the presence of an acid catalyst can react to form cyclic acetal (Figure 3) [17]. Usually, carbonyl compound will react with an alcohol and aided by catalyst such as Lewis acid to form acetal or ketal [18]. The reaction is stereotypically undergoes with homogenous catalysis; sulphuric acid and phosphoric acid which are mineral inorganic acids [19]. It is important to choose a suitable azeotropic solvent from ketone or aldehyde solution to aid in the process of water removing. Besides, acetal or cyclic acetal can act as protecting group of carbonyl

group against an attack by reagents, for example, reducing agents, basic, nucleophiles, catalytic and oxidant [20].

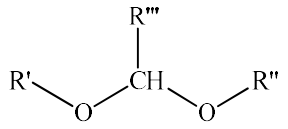


Figure 1. Structure of acetal [21]

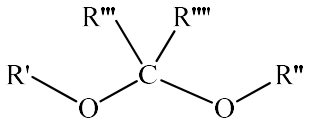
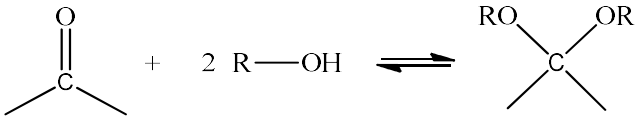


Figure 2. Structure of ketal [21]



Scheme 1. Chemical reaction on synthesizing ketal or acetal [21, 22]

Acetal and ketal can also be synthesized from orthoester carbonyl compound with the presence of glycol and a catalyst [23]. The structures of 1,3-dioxane and 1,3-dioxalane can be formed if the reaction undergoes between polyol and suitable ketone and aldehyde with the used of glycerol in the presence of catalyst [24]. The reaction produces 6 membered ring of 1,3-dioxane or 5 membered ring of 1,3-dioxalane because of the reaction between glycerol and steric blocking of hydrogen atom and radical. The reaction of diol will form a ketal or cyclic ketal (Fig. 4).

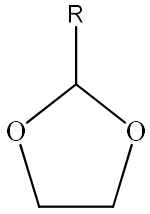


Figure 3. Structure of cyclic acetal [17]

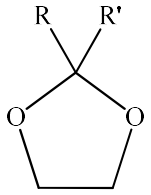


Figure 4. Structure of cyclic ketal [17]

Derivatives of acetal and ketal

Different substituents such as methanol or ethanol have been used in the reaction with aldehyde or ketone to produce our desired acetal or ketal derivatives [25]. The process of acetalization can modify the functional groups of compound in order to provide better efficiency and transformations of subsequent synthetic flexibility [26]. The characteristics of aroma, vapour pressure, flavour and solubility can be modified by using different methods in carbonyl compound conversion, for instance, the compound process is commonly called as attenuation in perfumery industry [23]. Besides, different methods also have been used to synthesize acetal or ketal derivatives by using different catalyst such as β-cyclodextrin. The use of this catalyst has been proven to reduce the release rate, the volatility and to prolong its insect repellent activities [27] in insect repellent industry. On the other hand, the process of synthesizing allysine ethylene acetal (Figure 5) can be simplified using amination method instead of using 8-step process to produce the acetal [28].

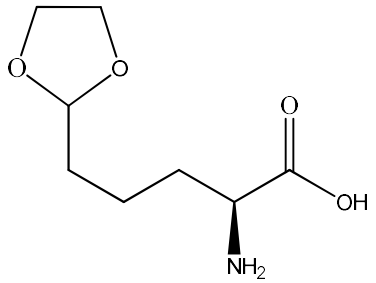


Figure 5. Structure of allysine ethylene acetal [29, 30]

In a view of pharmaceutical industry, the acetal derivatives can improve the activity of anti-inflammatory [31]. The binding of the acetal derivatives to skin which has thiol groups can accumulate in the skin which resulted by the ring-opening of an intermediate of Schiff base. Ethylene ketal derivatives of prostaglandin E2 can also contribute in stability of solid-state improvement. The hydrocortisone 21-acetate spirothiazolidines and hydrocortisone spirothiazolidines have been prepared to be reacted to the substituents of cysteine esters or β-aminothiols and produce the derivatives [31].

Properties of acetal:

Physicochemical properties of acetal

Acetal is an organic compound which has pleasant odor such as earth, nutty, green, sweet [32] and ethereal [33]. The color of acetal in liquid form is colorless at standard state. Acetal has moderate toxicity and narcotic at high concentration [34]. Table 1 lists the physicochemical properties of acetal.

Synthesis:

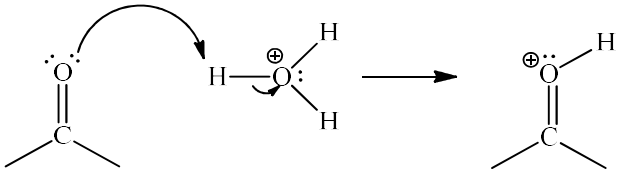
Mechanism of formation of acetal

There are 7 steps of mechanism in the formation of hemiacetal and acetal. Scheme 2 displays the mechanism steps which consist of carbonyl protonation, alcohol's nucleophilic attack, hemiacetal formation through deprotonation, protonation of alcohol, removal of water, alcohol's nucleophilic attack and deprotonation of water [35].

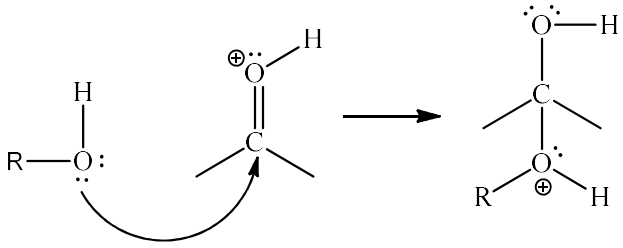
Table 1. Physicochemical properties of acetal

Property	Value	Reference
Molecular Weight	118.17 g/mol	
Density	0.831 g/cm^3	
Melting Point	-80-(-90) °C	
Boiling Point	103-104 °C	[36]
Vapor Pressure	20 mmHg	
Flash Point	-5 °C	
Solubility	Soluble in water	

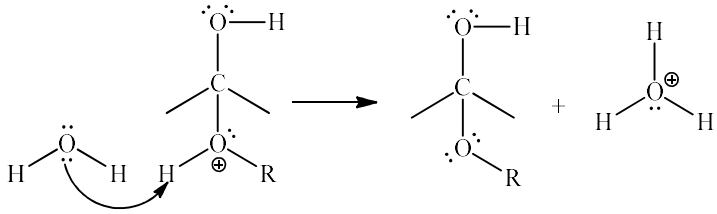
Step 1: Carbonyl Protonation



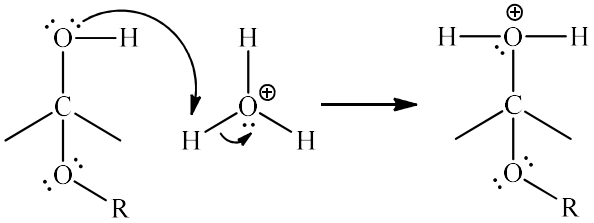
Step 2: Alcohol's Nucleophilic Attack



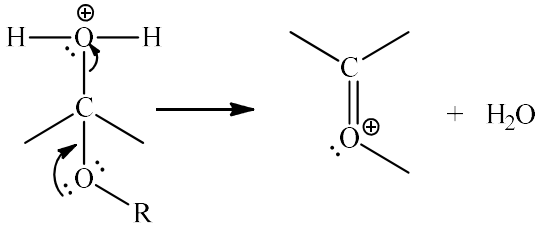
Step 3: Hemiacetal Formation through Deprotonation



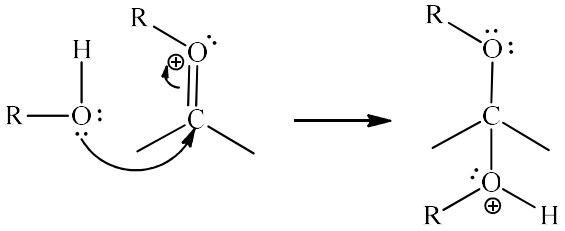
Step 4: Protonation of Alcohol



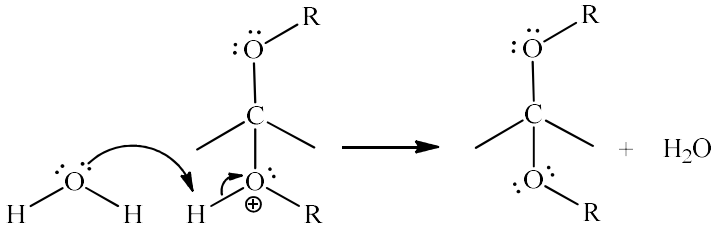
Step 5: Removal of Water



Step 6: Alcohol's Nucleophilic Attack



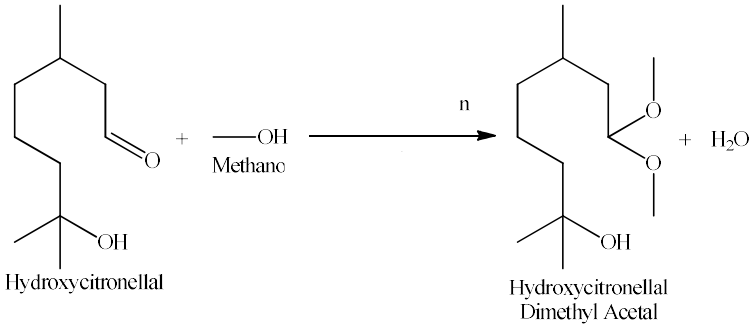
Step 7: Deprotonation of Water



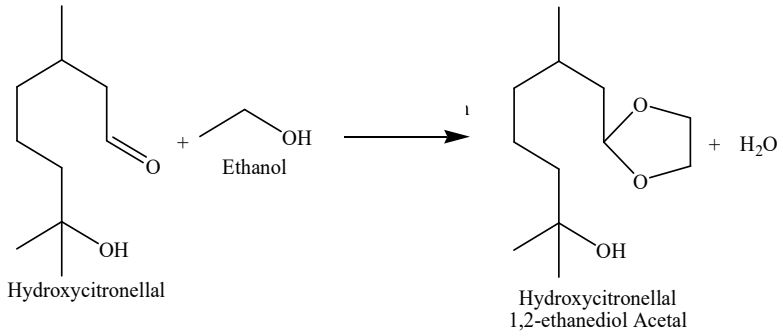
Scheme 2. Mechanism for Hemiacetal and Acetal Formation [35]

Synthesis of hydroxynellal acetal derovatives

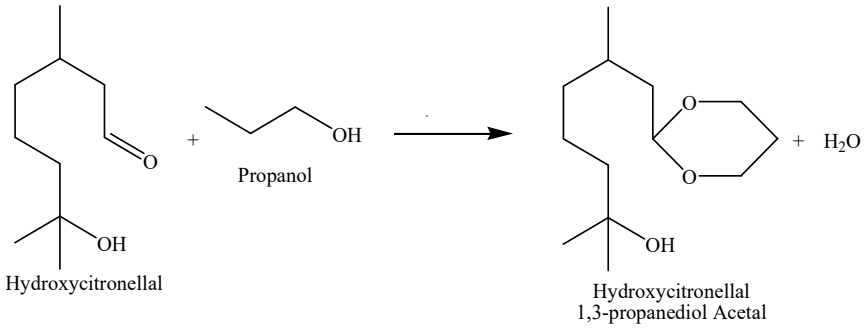
Some plants such as *Cymbopogon* species, to be more specified, *Cymbopogon winterianus* has been traditionally used to repel mosquitoes because it has mosquito repellent properties [37]. The plant can produces a yellow liquid of citronella oil through distillation process of dried Cymbopogon plants [27]. Citronella oil has been approved by United States Environmental Protection Agency (US EPA) to be applied on skin for insect repellent activities [13]. Recently, one of the citronella oil terpenes which are citronellal has been further studied by Zongde [25] by synthesizing hydroxycitronellal acetal derivatives to prolong its protection time . Schemes 3-5 show the synthesis reactions between hydroxycitronellal and its substituents. The overall reactions will be synthesized by using the same type of starting material which is hydroxycitronellal and by using the same methods.



Scheme 3. Synthesis of hydroxycitronellal dimethyl acetal [25]



Scheme 4. Synthesis of hydroxycitronellal 1,2-ethanediol acetal [25]



Scheme 5. Synthesis of hydroxycitronellal 1,3-propanediol acetal [25]

Catalysts usage during synthesis of acetal and acetal derivatives

Hydroxycitronellal is an aldehyde which has been synthesized from citronellal through hydrolysis process. Previously, citronellal acts as starting material, but the repellent properties itself has protection time less than 23 minutes [38] although citronellal has various of effective concentration from 0.05 to 25% (weight/volume) [27]. Then, hydroxycitronellal acts as starting material and has been reacted with a substituent which is methanol and benzene as a solvent [25]. The mixture has been mixed with sulfamic acid that acts as a catalyst. The presence of common acid catalysts such as hydrochloric acid, sulphuric acid, p-toluenesulfonic acid and trifluoroacetic acid [39] in the formation of ketals or acetals by treating aldehydes or ketones with alcohols are corrosive [40]. Alkynes, alkenes, silyl-protected alcohols and N-Boc-protected amines are the subtrates of acid-sensitive groups which are not compatible with acidic condition [41]. Pyridinium salt derivatives [42], dialkyltriazolium salts [43] and imidazolium salts [44] are aprotic salts series which are capable to act as Brønsted acids in chemoselectively acetalization [45]. Ammonium salts also can be employed to the acetalization or ketalization process between aromatic aldehydes or ketones and diols with pentyl methyl ether as solvent in Dean-Stark condition [46]. Mesoporous polymelamine-formaldehyde polymer can be used as catalyst in chemoselectively of aldehydes acetalization [47]. Graphitic-carbon nitride can catalyse the aldehydes or ketones acetalization process with alcohols compound to form acetals or ketal by using light in ambient conditions [48].However, Songkro [27] has found another alternative to control the release rate of desired product by using β-cyclodextrin as a catalyst for the synthesis and can increase the solubility in water [4]. This is because β-cyclodextrin forms an inclusion complex by forming hydroxycitronellal dimethyl acetal-β-cyclodextrin inclusion complex [27]. β-cyclodextrin is a better catalyst to be used in this reaction. Table 2

summarizes the types of catalysts which have been used for acetalization.

Solvent usage during synthesis of acetal and acetal derivatives

Benzene has been used as a solvent in the synthesis of hydroxycitronellal acetal derivatives. However, based on human and animal studies by the International Agency for Research on Cancer (IARC) since 1982, benzene has carcinogenic potential toward both studies [49]. Inhalation is the primary cause of the benzene exposure and the highest amount of the exposure which is 95%-99% can be found in cigarettes [50]. Benzene compound is associated with asthma effect among children [51]. Ferreira [35] has used carbon tetrachloride as one of the solvents to investigate iron (III) porphyrins catalytic activities for acetalization process and the solvent usage shows no product in the reaction because it is non-polar solvent. Besides, carbon tetrachloride also has been observed as chemical that can give liver injury due to its toxic metabolites [52]. Tanaka and co-researchers have found that the usage of dichloromethane as solvent for the regioselectivity ring-opening of benzylidene acetal can produce to 83% of percentage yield [53]. Ethyl acetate also has been used for both processes of preparation of dioxanesldithianes using hydrogen sulphate and deprotection of dioxanesldithianes using hydrogen sulphate [20]. Then, cyclohexane can be considered as an effective and efficient solvent. The usage of the solvent in both process of carbonyl compound as 1,3-dioxalanes protection using indium (III) chloride as catalyst and carbonyl compounds as dialkyl acetals protection using indium (III) chloride as catalyst can give more than 80% of percentage yield [54]. It can create an azeotropic mixture of cyclohexane and water and according to Le Chatelier's Principle, it will favour towards the product [55] if the ratio of the substituent more than starting material. However, the acetalization process does not take place between 2-methylpentanal and 2-methyl-2-propyl-1,3-propanediol at 1:1 ratio using cyclohexane, hexane, heptane and 1,4-dioxane as the solvents. The solubility between the solvents and 2-methyl-2-propyl-1,3-propanediol was low because their dielectric constant values are low [56]. Apart from that, water, glycerol [57] and polyethylene glycol [58] also can be a better option compared to other solvents because of its low toxicity and low risk of hazard [59]. Water can contribute to highest percentage yield of product from acetalization process. Table 3 lists the red solvents and their alternative green solvents for acetalization process.

Characterization

Fourier transform infra-red (FTIR) spectroscopy

The FTIR spectra have shown the absorption of specific chemical groups such as hydroxyl groups, carbonyl groups and alklyl groups [60] which are related to the synthesized acetal derivatives. The FTIR spectra will be recorded in the range of 3040-780 cm^{-1}. The stretching frequency of the C=C group in the aromatic shown at 1400 cm^{-1} and 1460 cm^{-1}. On the other hand, the stretching frequency of C-O in the compound has shown at 1100-1220 cm^{-1}. The peaks of C-H stretching vibration in the benzene ring of the acetal appeared at 759 cm^{-1}, 701 cm^{-1}, 3039 cm^{-1} and 3069 cm^{-1}[61]. Table 4 possess the IR frequency range and band assignment of acetal derivatives.

Proton nuclear magnetic resonance (^{1}H NMR) spectroscopy

The synthesized of hydroxycitronellal dimethyl acetal detected the resonance peak at 3.58 ppm which attributed to hydroxyl group in the acetal compound. On the other hand, result of the ^{1}H NMR showed signal at 4.19 ppm which attributed to methine group. Methyl group can be detected from the peak at 3.50 ppm. ^{1}H NMR chemical shift of hydroxycitronellal acetal derivatives is shown in Table 5.

CHNS elemental analysis

CHNS elemental analysis is a technique to identify the elements namely carbon, hydrogen, nitrogen and sulphur. The analyzed compound will undergo oxidative decomposition [62]. The compound also will undergo reduction of nitrogen and sulfur dioxide. The characteristic of thermal decomposition and the properties of the analyzed compounds that we have synthesized will affect the errors. There is potential of the under oxidation of the compound which will affect the determination of carbon and hydrogen. The speciation of nitrogen in synthesized compound will affect the decomposition of nitrogen-containing

compound [62]. Table 6 show the percentage of the C and H elements.

Mosquito repellent activities

Mosquito repellent

There are variety ways to measure the spread of mosquito disease such as chemical measure, genetic measure, environmental measure and personal protection; mosquito repellents [4]. Chemical measure has been used larvicides and insecticides [71] to kill the larvae and adults. However, the use of the chemicals have contaminated the water source and this measure have not developed to control all mosquito species [63]. The non-biological pesticides have high toxicity which gave severe impact to our environment and wildlife [4]. Environmental measure also has been applied by monitoring or removing the unused tires, draining the ponds; mosquito habitats, putting the predator fish in the ponds and building the water flow system in the pools [6]. Unfortunately, this measure has many difficulties for its maintenance and requires a good cooperation between local people [4]. Genetic measure also has been used by manipulating the mosquitoes genetic, for instance, the lifespan of the mosquito becomes shorter to reduce the transmit rate of malaria [64] and the sterilized males has been released to mate with females but the females cannot fertilize eggs [65]. This measure requires high expense to produce males and only works on the islands because of the variability of genetics is high [4] and the insects are migrate from place to place. The usage of personal protection; mosquito repellents become our first line defense from mosquitoes because this measure has lowered the transmit of malaria above 80% [66]. This reason have brought awareness to use personal protection control [1] to prevent from getting mosquito bites [4]. The synthetic mosquito repellents which have been commercialized are N,N-diethyl-meta-toluamide (DEET) [9] and ethylbutylacetylaminopropionate (IR3535) [67] which are synthetic repellent and citronellal [68], [69] which is essential oil mosquito repellent.

N,N-diethyl-meta-toluamide (DEET)

DEET (Figure 6) has been considered as gold mosquito repellents standard [14] because of its effectiveness [70]. The efficacy of DEET at 15% solution is 7-8 hours of protection time against mosquitoes [71]. However, DEET has been highlighted to has high potential severe effects on human health as well as surrounding [1]. It can cause neurotoxic effects on human and other insects by inhibiting an specific enzyme key activities [72]. In addition, it also can cause effects of pro-angiogenic on human by inhibiting specific ion channels in mammalian cortical neurons [73].

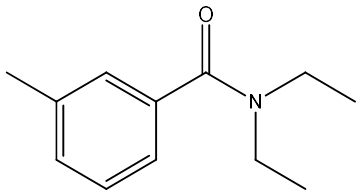


Figure 6. Chemical structure of DEET [1, 14, 70, 71, 72, 73]

Ethylbutylacetylaminopropionate (IR3535)

IR3535 (Figure 7) is one of the efficient repellents against mosquitoes. IR3535 has same effectiveness as DEET, also known as gold standard [1]. IR3535 has 7-10 hours protection times against Culex and Aedes mosquitoes and 3-4 hours protection time against Anopheles mosquitoes [67]. However, it has potential in dermal and oral toxicity [74] after the repellent has been tested on rats. It can cause eye irritation and skin irritation on human [1]. Then, IR3535 also can cause damage to synthetic material [75]. The positive point of IR3535 is this mosquito repellent may not has toxic potential towards life in water and it also not accumulates in our environment [76]. Figure 7 shows the chemical structure of IR3535.

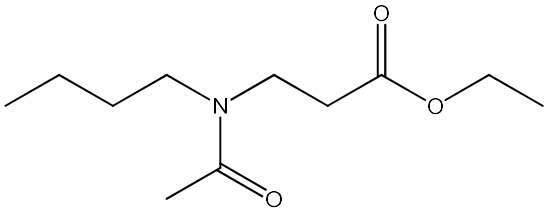


Figure 7. Chemical Structure of IR3535 [1, 67, 74, 75, 76]

Hydroxycitronellal acetal derivatives

Plant-based material have been used for thousand years by human as a personal protection against mosquitoes; a practice which is still widely uses in developing countries [77]. *Cymbopogon winterianus* has been extracted to produce citronellol, citronellal (Figure 8) and geraniol [78]. Citronella oil has been registered as mosquito repellent under United States Environmental Protection Agency (US EPA) [13], [37] because of its efficacy and it has low toxicity on test animal. Although, the gold-standard synthetic repellent DEET [14] can protect against various insect species, but it was reported that the repellent can give negative effect to human as mentioned earlier. Citronella-based repellents can repel in a certain period from mosquitoes. However, the oils rapidly leave the user unprotected because of the citronella itself is chemically has high rate of evaporation property [79]. Thus, Zongde [25] has modified the structure citronellal oil into hydroxycitronellal acetal derivatives (Figure 9) using acetalization process and Songkro [27] has formed inclusion complex [80] which will increase the number of molecules [81]. These efforts can enhance the protection time of the oil against mosquitoes.

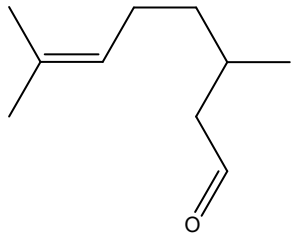


Figure 8. Chemical Structure of Citronellal [82]

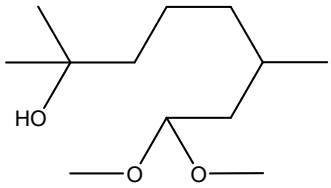


Figure 9. Chemical Structure of hydroxycitronellal dimethyl acetal [25]

Table 2. Catalysts for acetalization

Catalysts	References
Sulfamic acid	[25]
Hydrochloric acid Sulphuric acid p-toluenesulfonic acid Trifluoroacetic acid	[39]
Pyridinium salt derivatives	[42]
Dialkyltriazolium salts	[43]
Imidazolium salts	[44]
Ammonium salts	[46]
Mesoporous-polymelamine-formaldehyde polymer	[47]
Graphitic-C_3N_4	[48]
β-cyclodextrin	[27]

Table 3. Solvents for acetalization

Types of Solvent	Solvents Name	References
Red solvents	Benzene	[25]
	Carbon tetrachloride Chloroform	[35]
	Cyclohexane	[54], [56]
Alternatives solvents	Hexane Heptane 1,4-dioxane	[56]
	Dichloromethane	[53]
	Ethyl Acetate	[20]
Green solvents	Water	[59]
	Glycerol	[57]
	Polyethylene glycol	[58]

Table 4. IR frequency range and band assignment of acetal derivatives

Band Assignment	Wavenumber (cm^{-1})			Reference
	Hydroxycitronellal dimethyl acetal	Hydroxycitronellal 1,2-ethanediol acetal	Hydroxycitronellal 1,3-propanediol acetal	
v(C-O)	1056-1192	1052-1199	1076-1143	[25]
v(C-O-C)	1058-1194	1058-1201	1078-1250	
v(C-H)	1375-1464	2837-2939	1379-1647	
v(OH)	3212-3440	3257-3441	3259-3424	

Table 5. ^{1}H NMR chemical shift range of acetal derivatives

Compounds	Assignment	^{1}H NMR Chemical Shift Range, δ (ppm)	Reference
Hydroxycitronellal dimethyl acetal	δ_H (OH)	3.58-3.65	[25]
	δ_H (Methine)	1.65-4.19	
	δ_H (Methyl)	0.96-3.50	
	δ_H (Methylene)	1.25-1.44	
Hydroxycitronellal 1,2-ethanediol acetal	δ_H (OH)	3.58-3.65	
	δ_H (Methine)	1.65-4.19	
	δ_H (1,3-dioxalane)	4.05-4.89	
	δ_H (Methyl)	0.96-1.24	
	δ_H (Methylene)	1.25-1.40	
Hydroxycitronellal 1,3-propanediol acetal	δ_H (OH)	3.58-3.65	
	δ_H (Methine)	1.65-4.19	
	δ_H (1,3-dioxane)	1.88-4.69	
	δ_H (Methyl)	0.96-1.24	
	δ_H (Methylene)	1.25-1.55	

Table 6. Composition of carbon and hydrogen element in acetal derivatives

Compounds	Element Composition (%)		Reference
	C	H	
Hydroxycitronellal dimethyl acetal	66.06	11.93	[62]
Hydroxycitronellal 1,2-ethanediol acetal	66.67	11.11	
Hydroxycitronella1,3-propanediol acetal	67.83	11.30	

Method of repellency test using human assay

The neutral soap will be used to wash the forearm and hand of a human subject. The forearm and hand will be thoroughly rinsed and dried for 10 min before apply synthesized compound. The hand will be wear a glove to protect against bites [83]. The forearm will be covered using a paper sleeve with a 25 mm circle to expose the skin. 3 mL product will be applied to the skin. The other forearm will be protected with a same paper sleeve without applying any products to the skin as a control. 20 mosquitoes will be placed in 20 × 20 × 20 cm cages. The cage will have a cotton stockinet on the front, clear glass at the back and top, an aluminum sheet bottom and screen on the sides. The test must be 27 °C temperature. Test will be conducted by placing the forearm with the repellent into a test cage for 5 minutes [84]. After 5 minutes of repellent application the stopwatch will be started. Every 30 minutes will be recorded as protection time until the test subject received a mosquito bite. Protection time will be recorded as the period time between repellent application and the observation period until the forearm obtain a bite. If no bites in 90 min, test will be stopped and protection time will be recorded as 90 minutes. It will be considered as a bite if a mosquito attempt to insert its stylets [83]. For the rare case, if there is no mosquito bite on the without repellent application arm during the observation, the trial will be stopped and will be repeated with new mosquito batch. This situation is to make sure that no bites is due to the repellent compound. Every synthesized compound will be used three times on the subject [10]. Each of the product will be tested once a day. Since, there are three different acetal derivatives that will be obtained, so the repellence test will be taken 9 days to complete it. Each of the repellency test will be conducted at night.

Method of repellency test using animal assay

The soap will be used to wash the abdomen of 4 mice and dried the mice for 20 minutes. The fur of mice's abdomen has been shaved in square shape of 2.5 cm x 2 cm. Hydroxycitronellal oil has been applied to first mice on its skin, which acts as controlled mice. Then, the remaining mice's have been applied hydroxycitronellal dimethyl acetal, hydroxycitronellal 1,2-ethandiol acetal and hydroxycitronellal 1,3-propanediol acetal. Then, they have prepared a cylindrical applicator with the diameter 5.5 cm and height of 12 cm with a square opening area of 2 cm x 2 cm at the lower end [25]. The applicator has been filled with 30 mosquitoes. The test has been repeated three times to obtain an average protection time of mice against mosquitoes.

Protection time of mice against mosquitoes

According to result, the first mice which has been applied to hydroxycitronellal oil has the shortest protection time. The last mice which have been applied with hydroxycitronellal 1,3-propanediol acetal has the longest protection time. Table 7 shows the repellence times of synthesized hydroxycitronellal derivatives which are hydroxycitronellal dimethyl acetal, hydroxycitronellal 1,2-ethanediol acetal and hydroxycitronellal 1,3-propanediol acetal.

Table 7. The repellence time of the compounds against mosquitoes

Compounds	Repellence Times (min)			Reference
	Number of Trial			
	1	2	3	
Hydroxycitronellal	10	8	9	[10, 25]
Hydroxycitronellal dimethyl acetal	20	18	29	
Hydroxycitronellal 1,2-ethanediol acetal	30	28	40	
Hydroxycitronellal 1,3-propanediol acetal	60	58	57	

Protection time of human against mosquitoes

According to the result, the first human hand which has been applied to hydroxycitronellal oil has the shortest protection time. The last human hand which has been applied with hydroxycitronellal 1,3-propanediol acetal has the longest protection time. Table 8 lists the repellence times of synthesized hydroxycitronellal derivatives which are hydroxycitronellal dimethyl acetal, hydroxycitronellal 1,2-ethanediol acetal and hydroxycitronellal 1,3-propanediol acetal.

Table 8. The repellence time of the compounds against mosquitoes

Compounds	Repellence Times (min)			Reference
	Number of Trial			
	1	2	3	
Hydroxycitronellal	10	8	9	[10, 25]
Hydroxycitronellal dimethyl acetal	20	18	29	
Hydroxycitronellal 1,2-ethanediol acetal	30	28	40	
Hydroxycitronellal 1,3-propanediol acetal	60	58	57	

Conclusion

DEET, IR3535 and citronellal are initially used for mosquito repellent because of the potential protection time and release rate. However, DEET and IR3535 recently have been reported to have high potential effect towards human health and surroundings. Citronellal oil, plant-based oil has similar efficacy as mosquito repellent compared to the commercial repellents. The green oil undergoes hydrolysis process to produce hydroxycitronellal oil and recently hydroxycitronellal oil undergo acetalization process to produce its derivatives. The modification of functional groups of

green citronellal oil has been take place to improve the protection time and efficacy. During the synthesis process, acid catalysts can improve in protection time. However, by using green catalyst which is β-cyclodextrin, it can form inclusion complex. The complex improves the release rate mosquito repellent. The usage of solvent in acetalization can improve to percentage yield of our desired product. Benzene, carbon tetrachloride, chloroform, toluene, acetone and xylene are listed in red solvents. This is due to one of the solvents which is benzene has carcinogenic potential towards human and animal through primary exposure of benzene which is through inhalation. There are many alternatives solvents which can be used for this reaction such as water, glycerol and polyethylene glycol. The alternatives solvents are not just green solvents but it can contribute to the reaction to obtain products with better percentage yield. Green synthesis of mosquito repellent can be undergoing by wisely selecting potential plant-based starting material, non-hazardous solvent and green catalyst. Apart from that, there are two types of assays to examine our mosquito repellent products which are human assay and animal assay. Acetal derivatives of hydroxycitronellal oils have promising protection time. The derivatives have promising release rate and volatility which affected by their molecular weight and inter-molecular bonding.

Acknowledgment

The authors would like to thank Faculty of Science and Technology, Universiti Sains Islam Malaysia, for all the support given to complete this review.

References

1. Abd-Ella, A., Stankiewicz, M., Mikulska, K., Nowak, W., Pennetier, C., Goulu, M. and Lapied, B. (2015). The repellent DEET potentiates carbamate effects via insect muscarinic receptor interactions: An alternative strategy to control insect vector-borne diseases. *PLoS ONE*, 10(5): 1-20.
2. Abdullah Khan, M., Teixeira, I. F., Li, M. M. J., Koito, Y. and Tsang, S. C. E. (2016). Graphitic carbon nitride catalysed photoacetalization of aldehydes/ketones under ambient conditions. *Chemical Communications*, 52(13): 2772-2775.
3. Ali Ashter, S. (2016). 3 - mechanisms of polymer degradation. In *Introduction to Bioplastics Engineering* (pp. 31–59).
4. Amraoui, F., Pain, A., Piorkowski, G., Vazeille, M., Couto-Lima, D., de Lamballerie, X., … and Failloux, A. B. (2018). Experimental adaptation of the yellow fever virus to the mosquito *Aedes albopictus* and potential risk of urban epidemics in Brazil, South America. *Scientific Reports*, 8(1): 4-11.
5. Azzena, U., Carraro, M., Mamuye, A. D., Murgia, I., Pisano, L. and Zedde, G. (2015). Cyclopentyl methyl ether-NH_4X: A novel solvent/catalyst system for low impact acetalization reactions. *Green Chemistry*, 17(6): 3281-3284.
6. Barnard, D. R. and Xue, R. De. (2004). Laboratory evaluation of mosquito repellents against *Aedes albopictus, Culex nigripalpus,* and *Ochlerotatus triseriatus* (Diptera: Culicidae). *Journal of Medical Entomology*, 41(4): 726-730.
7. Cal, K. and Centkowska, K. (2008). Use of cyclodextrins in topical formulations: Practical aspects. *European Journal of Pharmaceutics* and *Biopharmaceutics*, 68(3): 467-478.
8. Capeletti, M. R., Balzano, L., De La Puente, G., Laborde, M. and Sedran, U. (2000). Synthesis of acetal (1,1-diethoxyethane) from ethanol and acetaldehyde over acidic catalysts. *Applied Catalysis A: General*, 198(1–2): 8-11.
9. Chen, L., Nohair, B. and Kaliaguine, S. (2015). Glycerol acetalization with formaldehyde using water-tolerant solid acids. *Elsevier B.V.*, (10): 1-38.
10. Chen, W. L., Wang, L. Y. and Li, Y. J. (2020). C-H functionalization of amino alcohols by osmium tetroxide/NMO or TPAP/NMO: Protecting group-free synthesis of indolizidines (–)-223AB and 3-Epi-(–)-223AB. *European Journal of Organic Chemistry*, 2020(1): 103-107.
11. Choi-sledeski, Y. M. and Wermuth, C. G. (2015). Designing prodrugs and bioprecursors. *The Practice of Medicinal Chemistry*, 2015: 657-696.
12. Clarensia, V., Kurniawan, J. and Lo, D. (2021). The changes in density, flavor compounds, and sensory description of vanilla extract after expiration. *IOP Conference Series: Earth Environmental Science*, 794: 1-8.

13. Climent, M. J., Corma, A. and Velty, A. (2004). Synthesis of hyacinth, vanilla, and blossom orange fragrances: the benefit of using zeolites and delaminated zeolites as catalysts. *Applied Catalysis A: General*, 263(2): 155-161.
14. Corazza, M., Borghi, A., Zampino, M. R. and Virgili, A. (2004). Allergic contact dermatitis due to an insect repellent : double sensitization to picaridin and methyl glucose dioleate. *Acta Dermato-Venereologica*, 1(1): 264-265.
15. Corby-Harris, V., Drexler, A., de Jong, L. W., Antonova, Y., Pakpour, N., Ziegler, R. and Riehle, M. A. (2010). Activation of akt signaling reduces the prevalence and intensity of malaria parasite infection and lifespan in *Anopheles stephensi* mosquitoes. *PLoS Pathogens*, 6(7): 1-10.
16. Diaz, J. H. (2016). Chemical and plant-based insect repellents: efficacy, safety, and toxicity. *Wilderness and Environmental Medicine*, 27(1): 153-163.
17. Dong, J. L., Yu, L. S. H. and Xie, J. W. (2018). A simple and versatile method for the formation of acetals/ketals using trace conventional acids. *ACS Omega*, 3(5): 4974-4985.
18. dos Reis, E. F., Campos, F. S., Lage, A. P., Leite, R. C., Heneine, L. G., Vasconcelos, W. L., Mansur, H. S. (2006). Synthesis and characterization of poly (vinyl alcohol) hydrogels and hybrids for RMPB70 protein adsorption. *Materials Research*, 9(2): 185-191.
19. Drapeau, J. (2017). Insect repellents based on para-menthane-3,8-diol. *University of Regensburg*, 1(1): 1-194.
20. Eden, W. T., Alighiri, D., Supardi, K. I. and Cahyono, E. (2020). The mosquito repellent activity of the active component of air freshener gel from Java citronella oil (*Cymbopogon Winterianus*). *Journal of Parasitology Research*, 1(1): 1-5.
21. Erlanger, T. E., Keiser, J. and Utzinger, J. (2008). Effect of dengue vector control interventions on entomological parameters in developing countries : A systematic review and meta-analysis. *Medical and Veterinary Entomology*, 22(1): 203-221.
22. Fadeeva, V. P., Tikhova, V. D. and Nikulicheva, O. N. (2008). Elemental analysis of organic compounds with the use of automated CHNS analyzers. *Journal of Analytical Chemistry*, 63(11): 1094-1106.
23. Fradin, M. and Day, J. (2002). Comparative efficacy of insect repellents against mosquitoes. *AAP Grand Rounds*, 8(4): 42-43.
24. Gautam, S. (2020). A call to (green) arms : Synthesis of acetals and cyclic acetals with and without solvents - a comparison. *International Journal of Scientific Development and Research*, 5(2): 416-423.
25. Gillij, Y. G., Gleiser, R. M. and Zygadlo, J. A. (2008). Mosquito repellent activity of essential oils of aromatic plants growing in argentina. *Bioresource Technology*, 99(7): 2507-2515.
26. Goodyer, L. I., Croft, A. M., Frances, S. P., Hill, N., Moore, S. J., Onyango, S. P. and Debboun, M. (2010). Expert review of the evidence base for arthropod bite avoidance. *Journal of Travel Medicine*, 17(3): 182-192.
27. Grabowski, J., Granda, J. M. and Jurczak, J. (2018). Preparation of acetals from aldehydes and alcohols under basic conditions. *Organic and Biomolecular Chemistry*, 16(17): 3114-3120.
28. Grison, C., Carrasco, D., Pelissier, F. and Moderc, A. (2020). Reflexion on bio-sourced mosquito repellents: nature, activity, and preparation. *Frontiers in Ecology and Evolution*, 8(8): 1-14.
29. Gupta, N., Sonu, Kad, G. L. and Singh, J. (2007). Acidic ionic liquid $[B_{mim}]HSO_4$: An efficient catalyst for acetalization and thioacetalization of carbonyl compounds and their subsequent deprotection. *Catalysis Communications*, 8(9): 1323-1328.
30. Hosseini, M. S. and Masteri-Farahani, M. (2020). Fabrication of new magnetite based sulfonic-phosphotungstic dual-acid catalyst for catalytic acetalization of benzaldehyde with ethylene glycol. *Reaction Kinetics, Mechanisms and Catalysis*, 130(2): 979-991.
31. Hsieh, W., Chang, C. and Gao, Y. (2006). Controlled release properties of chitosan encapsulated volatile citronella oil microcapsules by thermal treatments. *Colloids and Surface B: Biointerfaces*, 53(1): 209-214.

32. Johnson, A. A. and Riehle, M. A. (2015). Resveratrol fails to extend life span in the mosquito anopheles stephensi. *Rejuvenation Research*, 18(5): 473-478.
33. Kaetan, G., Ferreira, B., Carvalho, C. and Nakagaki, S. (2019). Studies of the catalytic activity of iron (III) porphyrins for the protection of carbonyl groups in homogeneous media. *Catalysts*, 9(4): 1-14.
34. Kaihara, S., Matsumura, S. and Fisher, J. P. (2007). Synthesis and properties of poly [poly (ethylene glycol)-co-cyclic acetal] based hydrogels. *Macromolecules*, 40(21): 7625-7632.
35. Katz, T. M., Miller, J. H. and Hebert, A. A. (2008). Insect repellents: Historical perspectives and new developments. *Journal of American Academy of Dermatology*, 58(5): 865-871.
36. Kubisa, P. and Vairon, J. P. (2012). Ring-opening polymerization of cyclic acetals. In *Polymer Science: A Comprehensive Reference,* 4: pp. 183-211.
37. Kumar, R., Kumar, D. and Chakraborti, A. K. (2007). Perchloric acid adsorbed on silica gel ($HClO_4$-SiO_2) as an inexpensive, extremely efficient, and reusable dual catalyst system for acetal/ketal formation and their deprotection to aldehydes/ketones. *Synthesis*, 1(2): 299-303.
38. Legeay, S., Clere, N., Hilairet, G., Do, Q. T., Bernard, P., Quignard, J. F. and Faure, S. (2016). The insect repellent n,n-diethyl-m-toluamide (DEET) induces angiogenesis via allosteric modulation of the M3 muscarinic receptor in endothelial cells. *Scientific Reports*, 6(1): 1-13.
39. Lenard, E. J., Botteselle, G. V, Azambuja, F. De, Perin, G. and Jacob, R. G. (2007). Citronellal as key compound in organic synthesis. *Tetrahedron*, 63(803): 6671-6712.
40. Li, X., He, W., Chen, Y., Yang, G., Wan, H., Zhang, L., … and Tao, W. (2017). Discovery of SHR9352: A highly potent g protein-biased μ -opioid receptor agonist. *ACS Omega*, 2(12): 9261-9267.
41. Lindbohm, M. L., Sallmén, M., Kyyrönen, P., Kauppinen, T. and Pukkala, E. (2009). Risk of liver cancer and exposure to organic solvents and gasoline vapors among finnish workers. *International Journal of Cancer*, 124(12): 2954-2959.
42. Lu, P. C. W., Shahbaz, S. and Winn, L. M. (2020). Benzene and its effects on cell signaling pathways related to hematopoiesis and leukemia. *Journal of Applied Toxicology*, 40(8): 1018-1032.
43. Lupi, E., Hatz, C. and Schlagenhauf, P. (2013). The efficacy of repellents against aedes, anopheles, culex and ixodes Spp. - A literature review. *Travel Medicine and Infectious Disease*, 11(6): 374-411.
44. Maia, M. F. and Moore, S. J. (2011). Plant-based insect repellents: A review of their efficacy, development and testing. *Malaria Journal*, 10: 1-15.
45. Manwill, P. K., Kalsi, M., Wu, S., Martinez-Rodriguez, E. J., Cheng, X., Piermarini, P. M. and Rakotondraibe, H. L. (2020). Semi-synthetic cinnamodial analogues: structural insights into the insecticidal and antifeedant activities of drimane sesquiterpenes against the mosquito *Aedes aegypti. PLoS Neglected Tropical Diseases*, 14(2): 1-21.
46. Marina, C. F., Bond, J. G., Hern, K., Valle, J., Ulloa, A., Fern, I. and Liedo, P. (2021). Population dynamics of *Aedes aegypti* and *Aedes albopictus* in two rural villages in Southern Mexico : Baseline data for an evaluation of the sterile insect technique. *Insects*, 12(58): 1-18.
47. Moore, S. J., Hill, N. and Ruiz, C. (2007). Field evaluation of traditionally used plant-based insect repellents and fumigants against the malaria vector anopheles darlingi in Riberalta, Bolivian Amazon. (Bloland 2001): 624-630.
48. Morrison, A. C., Minnick, S. L., Rocha, C., Forshey, B. M., Stoddard, S. T., Getis, A. and Kochel, T. J. (2010). Epidemiology of dengue virus in iquitos, Peru 1999 To 2005: Interepidemic and epidemic patterns of transmission. *PLoS Neglected Tropical Diseases*, 4(5): e670.
49. Moss, G., Smith, P. A. S. and Tavernier, D. (1995). Glossary of class names of organic compounds and reactive based on structure (IUPAC Recommendations 1995). *Pure and Applied Chemistry*, 67: 1307-1375.

50. Myles, L., Gathergood, N. and Connon, S. J. (2013). The catalytic versatility of low toxicity dialkyltriazolium salts: in situ modification facilitates diametrically opposed catalysis modes in one pot. *Chemical Communications*, 49(46): 5316-5318.
51. Myles, L., Gore, R. G., Gathergood, N. and Connon, S. J. (2013). A new generation of aprotic yet brønsted acidic imidazolium salts: low toxicity, high recyclability and greatly improved activity. *Green Chemistry*, 15(10): 2740-2746.
52. Myles, L., Gore, R., Špulák, M., Gathergood, N. and Connon, S. J. (2010). Highly recyclable, imidazolium derived ionic liquids of low antimicrobial and antifungal toxicity: a new strategy for acid catalysis. *Green Chemistry*, 12(7): 1157-1162.
53. Nentwig, G. (2003). Use of repellents as prophylactic agents. *Parasitology Research*, 90(1): 40-48.
54. Nerio, L. S., Olivero-Verbel, J. and Stashenko, E. (2010). Repellent activity of essential oils: A review. *Bioresource Technology*, 101(1): 372-378.
55. Panke, S. and Wubbolts, M. (2005). Advances in biocatalytic synthesis of pharmaceutical intermediates. *Current Opinion in Chemical Biology*, 9(2): 188-194.
56. Park, B. S., Choi, W. S., Kim, J. H., Kim, K. H. and Lee, S. E. (2005). Monoterpenes from thyme (*Thymus vulgaris*) as potential mosquito repellents. *Journal of the American Mosquito Control Association*, 21(1): 80-83.
57. Patel, R. N. (2008). Synthesis of chiral pharmaceutical intermediates by biocatalysis. *Coordination Chemistry Reviews*, 252(5-7): 659-701.
58. Peng, Z., He, M., Zhou, L., Wu, X., Wang, L., Li, N. and Deng, S. (2022). Mosquito repellents: Efficacy tests of commercial skin-applied products in China. *Molecules*, 27(17): 1-13.
59. Perestrelo, R., Silva, C., & Câmara, J. S. (2019). Madeira Wine Volatile Profile. A Platform To Establish Madeira Wine Aroma Descriptors. *Molecules*, *24*(17), 3028.
60. Procuranti, B., & Connon, S. J. (2008). Unexpected catalysis: Aprotic pyridinium ions as active and recyclable brønsted acid catalysts in protic media. *Organic Letters*, 10(21): 4935-4938.
61. Purcaro, G., Moret, S. and Conte, L. S. (2015). Polycyclic aromatic hydrocarbons. In *Encyclopedia of Food and Health*.
62. Qian, S., Liu, X., Emel'Yanenko, V. N., Sikorski, P., Kammakakam, I., Flowers, B. S. and Bara, J. E. (2020). Synthesis and properties of 1,2,3-triethoxypropane: a glycerol-derived green solvent candidate. *Industrial and Engineering Chemistry Research*, 1(1): 1-11.
63. Sastri, V. R. (2014). 7 - Engineering thermoplastics: Acrylics, polycarbonates, polyurethanes, polyacetals, polyesters, and polyamides. In plastics in medical devices *(Second Edition)*: pp. 121-172.
64. Ranu, B. C., Jana, R. and Samanta, S. (2004). A simple, efficient and general procedure for acetalization of carbonyl compounds and deprotection of acetals under the catalysis of indium (III) chloride. *Advanced Synthesis and Catalysis*, 346(4): 446-450.
65. Reinhold, J. M., Lazzari, C. R. and Lahondère, C. (2018). Effects of the environmental temperature on *Aedes aegypti* and *Aedes albopictus* mosquitoes: A review. *Insects*, *9*(4): 1-17.
66. Rowland, M., Downey, G., Rab, A., Freeman, T., Mohammad, N., Rehman, H. and Fayaz, M. (2004). DEET mosquito repellent provides personal protection against malaria: A household randomized trial in an afghan refugee camp in Pakistan. *Tropical Medicine and International Health*, 9(3): 335-342.
67. Sakulku, U., Nuchuchua, O., Uawongyart, N., Puttipipatkhachorn, S., Soottitantawat, A. and Ruktanonchai, U. (2009). Characterization and mosquito repellent activity of citronella oil nanoemulsion. *International Journal of Pharmaceutics*, 372(1-2): 105-111.
68. Scalia, S., Tursilli, R., Bianchi, A., Nostro, P. Lo, Bocci, E., Ridi, F. and Baglioni, P. (2006). Incorporation of the sunscreen agent, octyl methoxycinnamate in a cellulosic fabric grafted with β-cyclodextrin. *International Journal of Pharmaceutics*, 308(1-2): 155-159.

69. Sekerová, L., Spáčilová, M., Vyskočilová, E., Krupka, J. and Červený, L. (2019). Acid catalyzed acetalization of aldehydes with diols resulting into the formation of fragrant cyclic acetals. *Reaction Kinetics, Mechanisms and Catalysis*, 127(2): 727-740.
70. Sheng, D., Xu, F., Yu, Q., Fang, T., Xia, J., Li, S. and Wang, X. (2015). A study of structural differences between liver cancer cells and normal liver cells using FTIR spectroscopy. *Journal of Molecular Structure*, 1099(1): 18-23.
71. Songkro, S., Hayook, N., Jaisawang, J., Maneenuan, D., Chuchome, T. and Kaewnopparat, N. (2012). Investigation of inclusion complexes of citronella oil, citronellal and citronellol with β-cyclodextrin for mosquito repellent. *Journal of Inclusion Phenomena and Macrocyclic Chemistry*, 72(3–4): 339-355.
72. Sparks, J. T., Botsko, G., Swale, D. R., Boland, L. M., Patel, S. S. and Dickens, J. C. (2018). Membrane proteins mediating reception and transduction in chemosensory neurons in mosquitoes. *Frontiers in Physiology*, 9(1309), 1-14.
73. Stephen D., Dini M., Chow-Y. L. (2018). Advances in the biology and management of modern bed bugs. (1st edition). United Kingdom: John Wiley & Sons Ltd.
74. Tan, M. X., Gu, L., Li, N., Ying, J. Y. and Zhang, Y. (2013). Mesoporous poly-melamine-formaldehyde (MPMF)-a highly efficient catalyst for chemoselective acetalization of aldehydes. *Green Chemistry*, 15(5): 1127-1132.
75. Tanaka, N., Ogawa, I., Yoshigase, S. and Nokami, J. (2008). Regioselective ring opening of benzylidene acetal protecting group(s) of hexopyranoside derivatives by DIBAL-H. *Carbohydrate Research*, 343(15): 2675–2679.
76. Teschke, R. (2018). Liver injury by carbon tetrachloride intoxication in 16 patients treated with forced ventilation to accelerate toxin removal via the lungs : a clinical report. *Toxics*, 6(25): 1-32.
77. Trifoi, A. R., Agachi, P. Ş. And Pap, T. (2016). Glycerol acetals and ketals as possible diesel additives. a review of their synthesis protocols. *Renewable and Sustainable Energy Reviews*, 62: 804-814.
78. Von Elert, E., Preuss, K. and Fink, P. (2016). Infodisruption of inducible anti-predator defenses through commercial insect repellents? *Environmental Pollution*, 210(1): 18-26.
79. Ward, R. D. (2008). Parasites & vectors review of "medical entomology for students". *BioMed Central*, 1(12): 1-2.
80. Webb, C. E. and Hess, I. M. R. (2016). A review of recommendations on the safe and effective use of topical mosquito repellents. *Public Health Research and Practice*, 26(5): 8-11.
81. World Health Organization. (2009). Guidelines for efficacy testing of mosquito repellents for human. Access from https://apps.who.int/iris/handle/10665/70072.
82. Yu, L., Lin, C., Liao, C., Zeng, X., Chen, X., Zhu, Z. and Chen, L. (2020). Green chemistry: Efficient acetalization of aldehydes with alcohols using the acid red 52 photocatalyst. *Environmental Chemistry Letters*, 18(4): 1353-1359.
83. Zhang, Y., Wang, Z., Xu, X., Gao, J., Xu, D., Zhang, L. and Wang, Y. (2020). Entrainers selection and vapour-liquid equilibrium measurements for separating azeotropic mixtures (ethanol+n-hexane/cyclohexane) by extractive distillation. *Journal of Chemical Thermodynamics*, 144(1): 106070.
84. Zongde, W., Jinzhu, C., Qian, S. Z., Zhi-wide, J. and Outstanding, S. D. (2010). Synthesis of hydroxycitronellal and acetals repellent activity against mosquitoes. *Acta Entomologica Sinica*, 53(11): 1241-1247.

Malaysian Journal of Analytical Sciences (MJAS)
Published by Malaysian Analytical Sciences Society

SYNTHESIS AND CHARACTERISATION OF COMPOSITE SILICA, POLY(METHYL METHACRYLATE) (PMMA) AND GOLD-SILVER (Au-Ag) ALLOY VIA CO-CRYSTALLISATION FOR LIGHT MANIPULATION APPLICATIONS

(Sintesis dan Pencirian Komposit Silika, Poli(metil metakrilat) (PMMA) dan Aloi Emas-Perak (Au-Ag) Melalui Penghabluran Bersama Untuk Aplikasi Manipulasi Cahaya)

Rozaitunmas Jamal[1], Rabiatul Addawiyah Azwa Tahrin[1], Mohd Sabri Mohd Ghazali[2], Sibu C. Padmanabhan[3,4], Chan Kiki[1], and Syara Kassim[2*]

[1]Faculty of Science and Marine Environment,
Universiti Malaysia Terengganu, 21030 Kuala Nerus, Terengganu, Malaysia
[2]Advanced Nano Materials (ANoMa) Research Group,
Faculty of Science and Marine Environment,
Universiti Malaysia Terengganu, 21030 Kuala Nerus, Terengganu, Malaysia
[3]Advanced Materials and BioEngineering Research (AMBER) Centre,
Trinity College Dublin, Dublin 2, Ireland
[4]School of Chemistry,
Trinity College Dublin, College Green, Dublin 2, Ireland

[*]Corresponding author: syara.kassim@umt.edu.my

Received: 28 June 2022; Accepted: 23 November 2022; Published: 22 February 2023

Abstract

Metallodielectric photonic crystal has emerged as a formidable asset in the realms of light trapping materials. Inverted silica, and alloy noble metal nanoparticles of gold-silver alloy(Au-Ag) exhibited promising light trapping capabilities that have the potential of applications across many fields including solar cell, and biomedical device production. This composite was prepared via self-assembly; a fast, simple, and low-cost method capable of generating photonic crystals of greater surface area. Poly(methyl methacrylate) (PMMA) was used as the crystal template, and hydrolysed tetraethyl orthosilicate (TEOS) as the cementing component. In this study, methyl methacrylate monomer underwent a complete polymerisation reaction to form PMMA due to the absent of C=C bond around 1639.83 cm^{-1} as characterised by IR spectroscopy. Alloy(Au-Ag) nanoparticles displayed good light absorption ability as shown from UV-Vis analysis of the nanoparticles at wavelength of 437nm. SEM imaging revealed that after the removal of PMMA template from Si-Alloy(Au-Ag)-PMMA composite, an inverted structure that possessed a hole skeleton structure was produced. The performance of the inverted Si-alloy(Au-Ag) composite was tested via a dye sensitive solar cell (DSSC) that showed an amplification in voltage reading.

Keywords: nanostructure, photonics, metallo-dielectric, alloy nanoparticles, inverse opal

Abstrak

Kristal fotonik metallodielektrik telah muncul sebagai aset yang menggerunkan dalam bidang bahan perangkap cahaya. Silika songsang, dan aloi nanopartikel logam adi daripada Aloi emas-perak (Au-Ag) mempamerkan keupayaan memerangkap cahaya yang mempunyai potensi aplikasi merentasi banyak bidang termasuk sel solar, dan pengeluaran peranti bioperubatan. Komposit ini disediakan melalui pemasangan sendiri; kaedah yang cepat, mudah dan kos rendah yang mampu menghasilkan kristal fotonik dengan luas permukaan yang lebih besar. Poli(metil metakrilat) (PMMA) digunakan sebagai templat kristal, dan tetraetil orthosilikat terhidrolisis (TEOS) sebagai komponen penyimenan. Dalam kajian ini, monomer metil metakrilat menjalani tindak balas pempolimeran lengkap untuk membentuk PMMA kerana ketiadaan ikatan C=C sekitar 1639.83 cm^{-1} seperti yang dicirikan oleh spektroskopi IR. Nanozarah aloi (Au-Ag) menunjukkan keupayaan penyerapan cahaya yang baik seperti yang ditunjukkan daripada analisis UV-Vis bagi nanozarah pada panjang gelombang 437nm. Pengimejan SEM mendedahkan bahawa selepas penyingkiran templat PMMA daripada komposit Si-Alloy(Au-Ag)-PMMA, struktur songsang yang mempunyai struktur rangka lubang dihasilkan. Prestasi komposit Si-aloi(Au-Ag) songsang telah diuji melalui sel suria sensitif pewarna (DSSC) yang menunjukkan penguatan dalam bacaan voltan.

Kata kunci: struktur nano, fotonik, metalo-dielektrik, zarah nano aloi, opal songsang,

Introduction

Nobel laureate Richard Smalley once pointed out that energy and environmental problems will be the hardest challenges mankind will face in the next 50 years [1]. Solar photovoltaic (PV) technology gained traction as a popular renewable energy source due to its cost effectiveness, easy fabrication, and environmental friendliness [2]. In particular, solar cell devices, which harness sunlight and convert it into usable energy and electricity, became the focal interest of the photovoltaic industries that are ever-expanding due to the increasing prices of fossil fuel and to accelerate the push towards sustainable energy options [3]. Many endeavours had been made in researching and developing thin film materials that are capable of reducing costs of mass producing efficient solar strategies and mechanically flexible devices [4, 5]. Silicon is a prevalent material in solar cells, provided it yields strong low-light performances and is non-toxic [6, 7]. However, a shortcoming of the current silicon thin-film solar cells is the insufficient absorption of the near-bandgap light. The limitation could possibly be overcome by efficient light trapping which points towards the expansion of different light trapping geometries, one of which is the photonic crystal [8-10].

A photonic crystal is a periodic optical nanomaterial that manipulates the movement of the light (photons) directed by their lattice structure [11]. Photonic crystals have different dielectric constants and these materials cause a photonic band gap (PBG) that allows precise control over the flow of light [12]. This unique property has been applied in various advance technological devices such as sensors, photovoltaic and solar concentrators [13-16].

PMMA is used as the crystal template because higher yield of monodispersed particles can be produced [17]. PMMA will be synthesised through free-emulsifier emulsion polymerisation in water. This method is much safer for environment compared to methods that utilise toxic solvents such as toluene, dimethylformamide and dimethyl sulfoxide as medium of reaction. The removal of PMMA template results in inverse opal capable of achieving a complete band gap.

“Bottom up” method is used in the fabrication of film. This simple step reinforces the quality of long range ordered structures with greater strength. “Bottom up” co-crystallisation method is used rather than “top down” as the “top down” approach is complex, involves multi-steps and costly procedures [18–20].

Materials and Methods

Synthesis of PMMA colloidal nanoparticle

PMMA was synthesised through free-emulsifier emulsion polymerisation reaction with potassium persulphate as initiator, methyl methacrylate monomer, and deionised water as dispersion medium under nitrogen condition at 90 $°C$. The reaction was kept

stirring at speed of 350 rpm. Deionised water of 64 ml was bubbled with nitrogen gas and heated for 15 minutes at 90 $°C$. MMA monomer was added and kept stirring for 30 minutes. Lastly, potassium persulphate was added, with the solution kept stirring for another 40 minutes until polymerisation reaction was completed. The milky colloidal was centrifuged and washed for 6 times.

Synthesis of hydrolysed TEOS

Hydrolysed TEOS was prepared utilising the sol-gel method. Tetraethylorthosilicate (TEOS) of 1 ml, 8 ml of ethanol, and 1 ml of HCL were mixed together and stirred at speed of 350 rpm for 1 hour.

Synthesis of alloy(Au-Ag) nanoparticles

Deionised water of 78 ml was heated at 100 $°C$. 1 ml of 0.05M $HAuCl_4$, 1 ml of 0.05M $AgNO_3$ and 8 ml of 0.1M sodium citrate were added and stirred for 15 minutes at 100 $°C$.

Fabrication of inverted silica alloy(Au-Ag) film

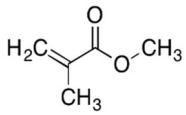
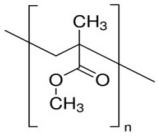
Silica, alloy(Au-Ag), and PMMA film were prepared by utilising vertical deposition of the self-assembly method. A clean glass substrate was placed in the mixture of PMMA+TEOS+Alloy(Au-Ag) with a volume ratio of 50µl:5µl:40µl. Then, the mixture was placed in the oven for 3 days at 60 $°C$. Inverted silica and alloy(Au-Ag) were prepared by soaking the film in acetone and heated on hot plate at 300 $°C$ to remove the PMMA template.

Results and Discussion

Characterisation of PMMA

The synthesised PMMA colloidal nanoparticles were investigated by using Fourier-transform infrared spectroscopy (FTIR). The FTIR spectra (Figure 1), of the synthesised PMMA was compared to MMA to gauge the complete polymerisation reaction of MMA to form PMMA. As shown in Table 1, there is a distinct difference in presence of C=C functional group between MMA and PMMA.

Table 1. Comparison of functional group of MMA and PMMA

Functional Group	Absorbance of MMA(cm^{-1})	Absorbance of PMMA(cm^{-1})
		
O-H	3437.68	3445.11
Sp^3 CH	2969.64-2857.88	2996.14-2843.33
C=O	1748.47	1731.91
C=C	1639.83	-
CH_3	1329.97	1449.45 & 1388.57
C-O	1169.36	1242.77

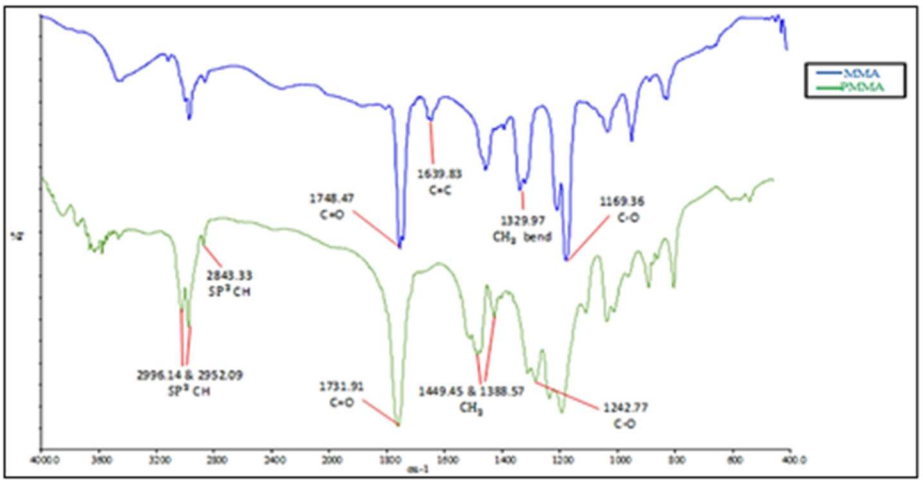


Figure 1. FTIR of methyl methacrylate(MMA) and poly(methyl methacrylate)

From the IR spectra obtained, the synthesised PMMA nanoparticles were concluded to be successful due to the absence of C=C peak at 1639.83 cm^{-1} which would be present should there be incomplete polymerisation leaving residual MMA.

Structural elucidation of the synthesised PMMA was determined by using X-ray diffraction (XRD). Figure 2 shows the XRD diffractogram of synthesised PMMA. PMMA powder was analysed in the range from 0 to 80 of 2θ at a scan speed of 2°/min. Bragg's angle was observed at $2\theta = 13.75^{0}$. Based on the XRD diffractogram, PMMA had a broad peak that suggested a complete amorphous, non-crystalline trait in nature.

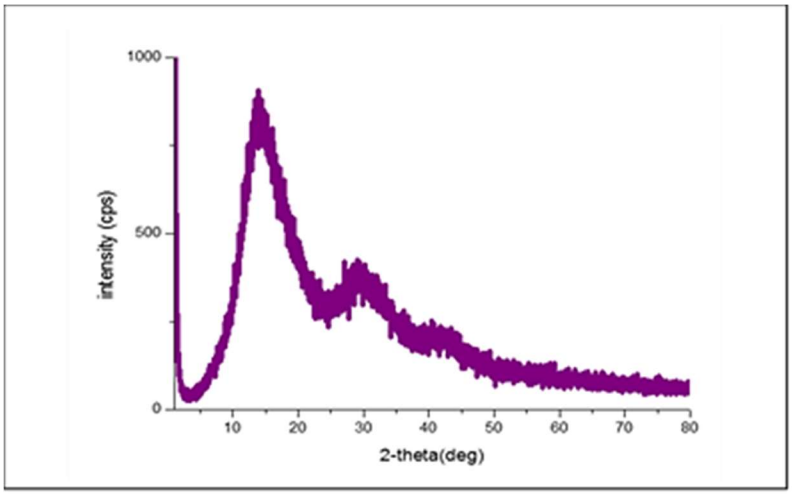


Figure 2. X-ray diffraction of synthesised PMMA

Thermogravimetric analysis (TGA) was used to further probe the purity and composition of the synthesised PMMA. Figure 3 shows the TGA curve, whereby the decomposition of PMMA and mass loss occurred in three stages.

According to Gałka et al. [21], thermal degradation of PMMA involved three stages; the first stage happened due to depolymerisation process that initiated involving head-to-head linkages, second stage involving unsaturated vinyl ends, and the last stage involving

chain scissions. For the synthesised PMMA, first stage of decomposition of PMMA occurred at 264 °C due to the loss of water and weak head-to-head bonds become decomposed. Second stage happened at 339 °C due to the radical transfer to unsaturated chain, which led to the decomposition of unsaturated chain-ends. Last stage of decomposition of PMMA occurred at 422 °C due to the random scission of polymer chains. These results conformed to established thermogravimetric analysis of PMMA thermal stability, suggesting that the success in PMMA synthesis via the method of free-emulsifier emulsion polymerisation reaction, which was the 'greener' option for fabrication.

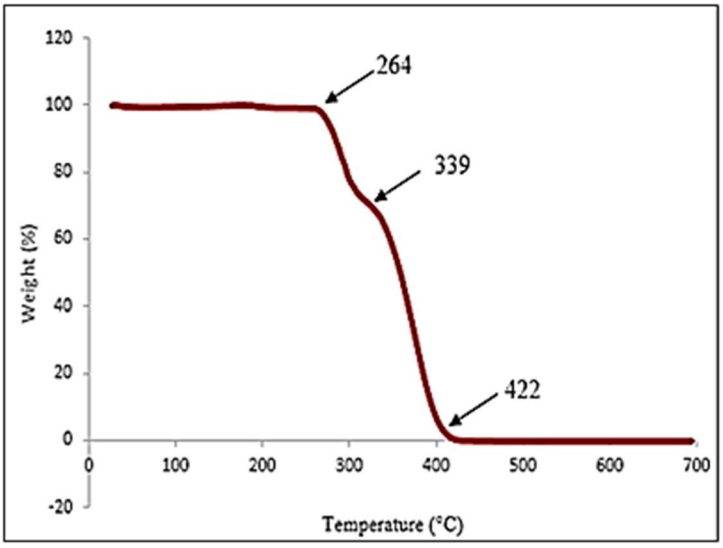


Figure 3. TGA graph of the synthesised PMMA

The surface morphology of PMMA was characterised by using scanning electron microscopic (SEM). Figure 4 shows that the PMMA produced were homogeneous sphere-shaped particles with average size of 495 nm. The homogeneous sphere shape of PMMA was obtained due to the stable control temperature throughout the experiment. Centrifugation also aided in separating PMMA particles based on density and eliminated the small particles of PMMA. The SEM images also shows the formation of well-ordered arrangement of the nanosized particles. The PMMA particles were not aggregated and had good monodispersity, which was fundamental for yielding high quality photonic crystals.

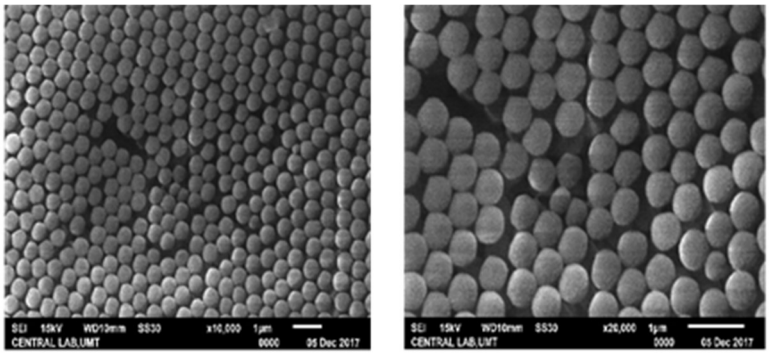


Figure 4. Scanning electron microscopic characterization of synthesised PMMA at 20000x (left) and 10000x (right)

Characterisation of hydrolysed TEOS

Hydrolysed TEOS was prepared utilising sol-gel polymerisation and the functional groups of the TEOS molecule were determined by Fourier-transform infrared spectroscopy (FTIR). The functional groups in the FTIR spectra of the hydrolysed TEOS (Figure 5), is translated into Table 2.

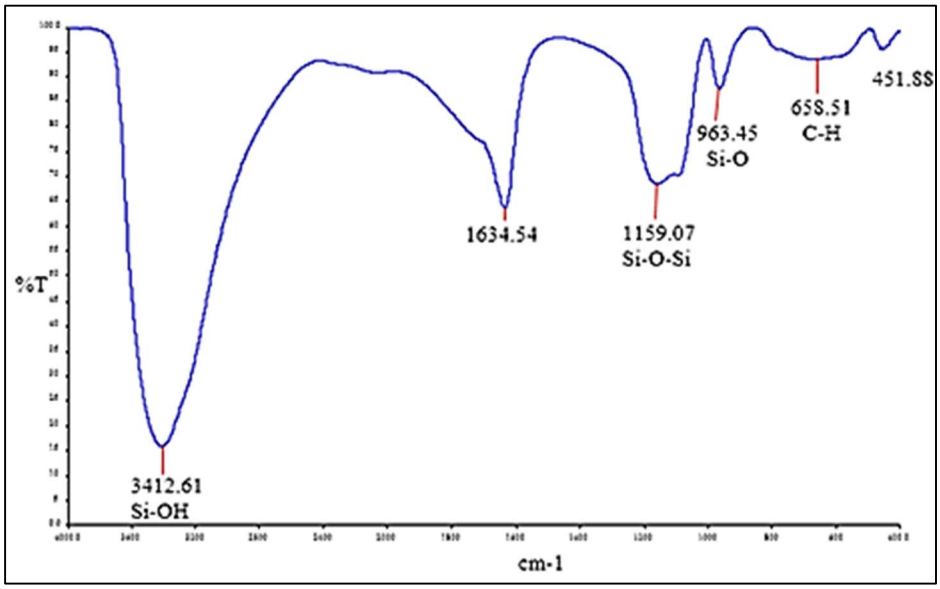
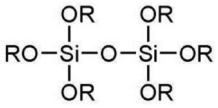


Figure 5. FTIR of hydrolysed TEOS

Table 2. Functional groups of hydrolysed TEOS

Molecular Structure of TEOS



where R is an alkyl chain

Vibrational mode	Hydrolysed TEOS (cm^{-1})
Si-OH	3412.61
Si-O-Si	1159.07
Si-O	963.45
C-H	658.51

A strong peak can be seen at 3412.61 cm^{-1} due to the stretching of Si-OH bond. Peak at 1159.07 cm^{-1} indicated the formation of Si-O-Si bond. A weak peak appeared at 963.45 cm^{-1} due to the Si-O bond. Lastly, C-H peak appeared at 658.51 cm^{-1}. This indicated the successful synthesis of hydrolysed TEOS to be used as the cementing component. The sol-gel polymerisation method involved hydrolysis and condensation

processes. First, TEOS underwent catalytic hydrolysis in the presence of HCL and water. Ethanol was added as a homogenising agent between water and TEOS, which were immiscible, and HCL was added to expediate the hydrolysis process. The condensation reaction took place under acidic condition. The Si became more electrophilic and susceptible to nucleophilic attack, forming a longer polymer network.

Characterisation of alloy(Au-Ag)

Au and Ag can strongly interact with sunlight. Silver is the commonly chosen metal nanoparticle due to its low cost and great absorption. However, silver is not the most stable. On the other hand, gold is much more stable in comparison. According to Al-Azawi et al. [22], the bimetallic nanoparticle (Au–Ag alloy nanoparticle) structure possessed a good stability, a greater ability to absorb light in a wider range of wavelength (broad LSPR peak). Also, capacity to tune the nanoparticle optical properties compared with that originating from individual nanoparticle. These; thus suggested a potential in increasing the effectiveness of a solar cell.

Absorption of alloy(Au-Ag) was determined by using ultra-violet visible spectroscopy. Typical absorption of Au is located at 521 nm, and Ag at 407 nm. Figure 6 shows a single absorption peak at 437 nm, which is the intermediate position between typical absorption of Au and Ag. This broad absorption band strongly indicated the formation of Au–Ag alloy NPs and not simply a mixture of Au and Ag NPs.

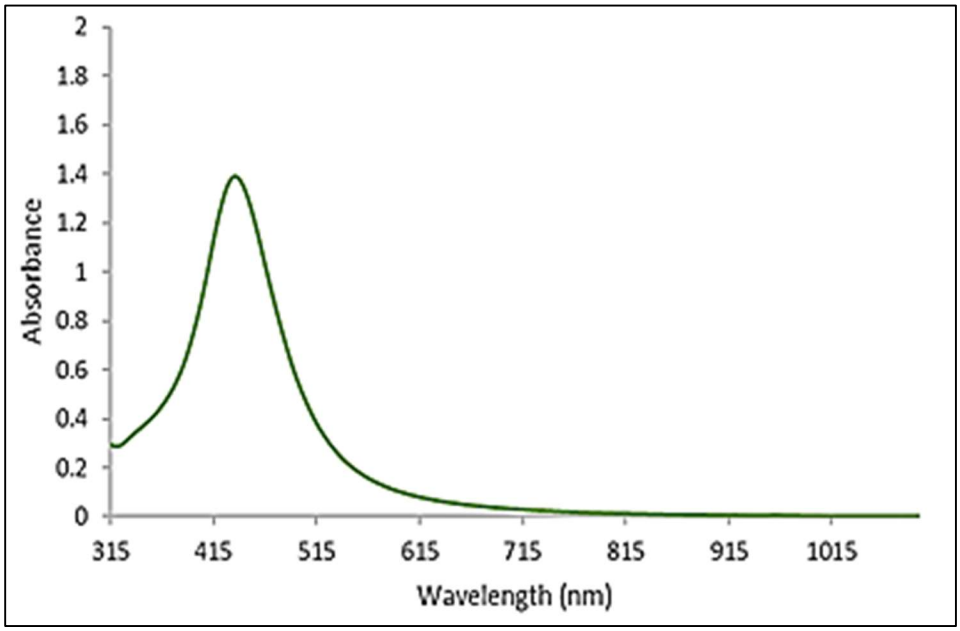


Figure 6. Ultraviolet–visible spectroscopy of alloy(Au-Ag)

Figure 7 shows the morphology of alloy(Au-Ag) characterised by SEM. SEM image revealed the properties of aggregation of alloy(Au-Ag) nanoparticle. Based on SEM image, alloy(Au-Ag) with volume ratio 1:3 had a uniform spherical shape. Au has a tendency to aggregate more than Ag due to its smaller size.

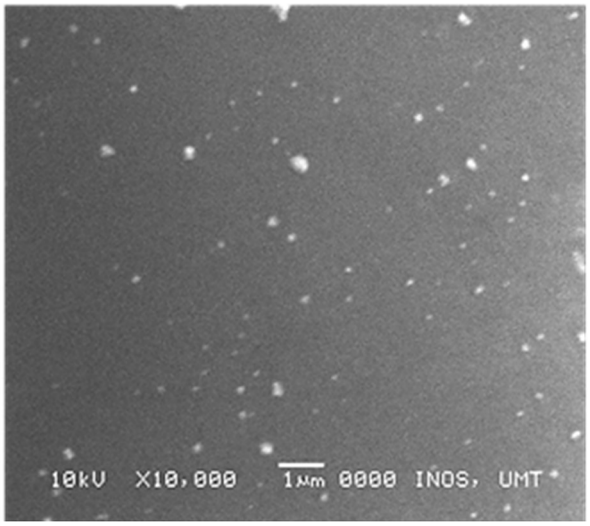


Figure 7. Morphology of alloy(Au-Ag).

Characterisation of inverted silica alloy(Au-Ag) film

The surface morphology of silica-PMMA, inverted silica, PMMA-silica-Alloy(Au-Ag) and inverted silica-alloy(Au-Ag) had been characterised by using scanning electron microscope (SEM) as shown in Figure 8.

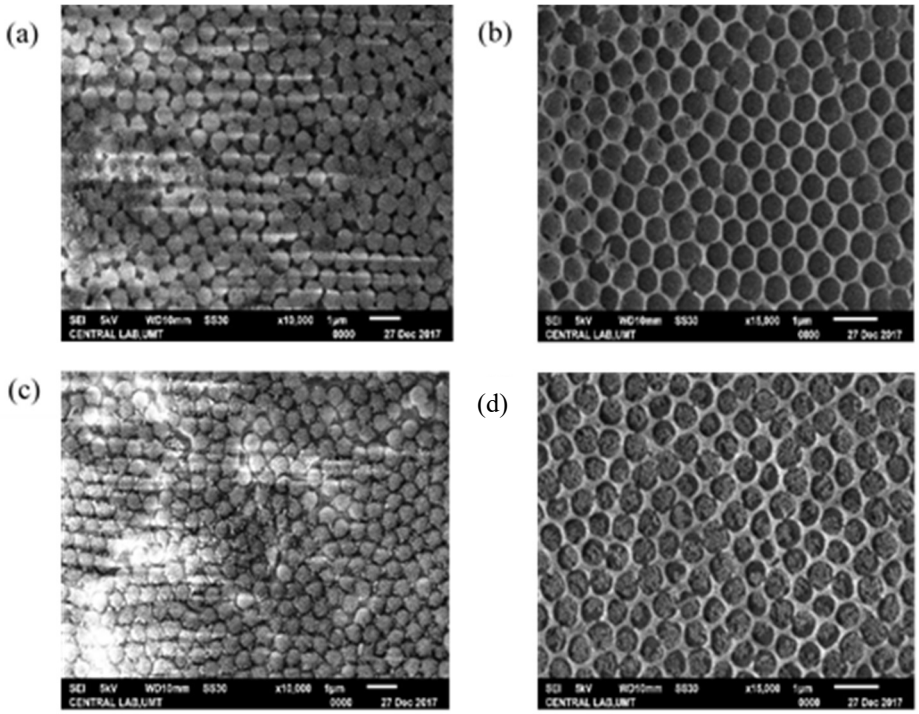


Figure 8. SEM image of silica-PMMA morphology (a), inverted silica morphology (b), silica-PMMA-alloy(Au-Ag) morphology (c), and inverted silica-alloy(Au-Ag) morphology (d)

The morphology of silica-PMMA (a) was sphere-shaped with homogenous structure of the same size. The addition of hydrolysed TEOS held the PMMA structure together and prevented cracking in the film. The structure was packed closely with almost consistently-sized spaces in between. The morphology of the inverted silica (b) showed a skeleton structure of silica after the removal of PMMA. The 'holes' were almost uniform in size and arrangement. With the addition of alloy(Au-Ag) into the solution of silica-PMMA, morphology of PMMA-silica-alloy(Au-Ag) (c) appeared to also possess spherical shape with homogenous structure of the same size, including the presence of alloy(Au-Ag) scattered around the PMMA. The morphology of the inverted silica-alloy(Au-Ag) (d) too had a skeleton structure, similar to the inverted silica (b). However, the inverted silica-alloy(Au-Ag) (d) had a 'grainy' appearance from the successful embedding of the alloy(Au-Ag) within the inverted silica structure. Precise control must be applied to obtain a completely inverted structure by tuning the volume ratio of PMMA suspension, alloy nanoparticles solution and TEOS solution during fabrication. The average diameter of the hole was observed to shrink after the removal of PMMA spheres. However, no silica backbone cracking was observed. This proved that the suitability of hydrolysed silica or TEOS as cementing agent for crack-free inverted structure. This inverted structure with the plasmonic properties of the alloy(Au-Ag) has potential in increasing the light trapping capabilities, particularly in increasing the effectiveness of a solar cell.

Performance of inverted structure towards dye sensitive solar cell (DSSC)

Inverted Si-alloy(Au-Ag) substrate with spherical holes structure contained voids that had the potential in fully trapping light within a solar cell for photovoltaic applications. The performance of inverted Si-alloy(Au-Ag) substrate in DSSC was tested by utilising a multimeter. Figure 9 illustrates the multimeter setup. It was found that the voltage reading of the multimeter increased by 0.4V when the inverted silica-alloy(Au-Ag) was applied. This showed that the inverted structure, possessing plasmonic properties of alloy(Au-Ag), had successfully trapped light and the increased the voltage of the multimeter.

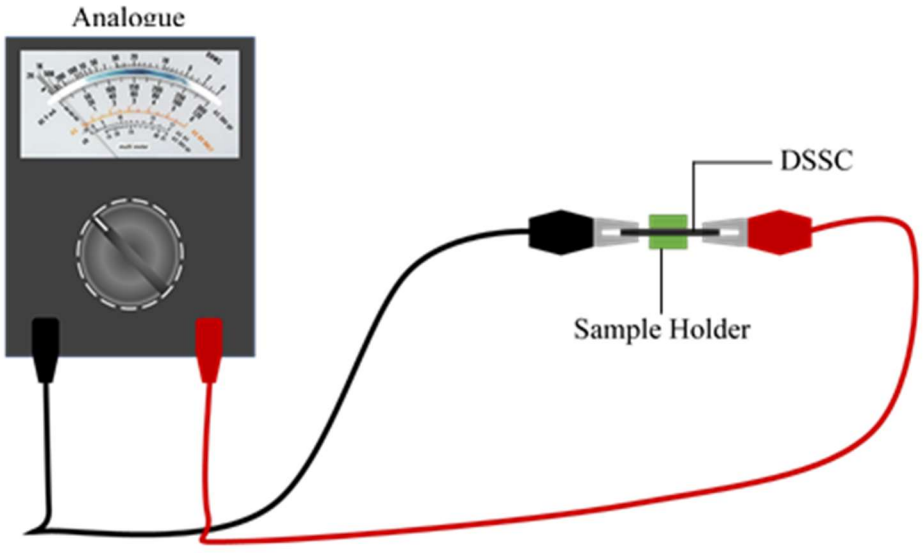


Figure 9. Simplified illustration of the multimeter setup

Conclusion

Photonic crystals or photonic band gap materials have harnessed global interest for the past decades due to the special periodic structure capable of modulating the propagation of electromagnetic waves [23, 24]. Presently, more attention is turned towards adapting inverted opal photonic crystals in light trapping and solar energy harvesting, allowing improvements in the photo-collection efficiency in dye desensitised solar cell (DSSC) and silicon solar cell through enhanced electron transport [13, 24].

In this work, the researchers presented the fabrication and structural, and optical characterisations of inverted Si-alloy(Au-Ag) composite photonic crystal via co-crystallisation method involving tetraethyl orthosilicate (TEOS) solution, poly(methyl methacrylate) (PMMA) spheres, and alloy of gold and silver nanoparticles. Polymer PMMA was synthesised via free-emulsifier emulsion polymerisation and used as template. Free-emulsifier emulsion polymerisation is an environment-friendly method of synthesising PMMA because of the absence of harmful surfactants that negatively impact the environment, particularly wastewater pollution. The reaction utilised water as dispersion medium instead of toxic solvents. The complete polymerisation of PMMA from MMA via this technique was confirmed via the absence of C=C peak at 1639.83 cm^{-1} in the FTIR spectra and further characterised via XRD diffraction analysis, thermogravimetric analysis, which aligned with the established pattern of PMMA TGA curve. Also, SEM analysis that revealed homogeneous sphere-shaped PMMA nanospheres of 495 nm in average size and good monodispersity. TEOS was successfully prepared via sol-gel polymerisation consisting of hydrolysis and condensation reaction. The initial reaction began with the use of an alkoxysilane in ethanol and resulted in a solution of siloxane polymer suitable to be used to produce a crack-free inverted structure. The FTIR spectra of TEOS collated with the molecular structure of hydrolysed TEOS to be used as cementing component. TEOS used in this research is a cheaper and non-toxic alternative to other silica precursors. Gold and silver nanoparticles were alloyed and characterised through UV-vis spectroscopy and SEM analysis. The synthesis of alloy(Au-Ag) was deemed successful as the absorption spectra of the produced alloy nanoparticles was absent of single Au and Ag absorbance peaks, indicating the absence of single Au and Ag species in the solution. Inverted silica alloy(Au-Ag) film was successfully synthesised via co-crystallisation method by implementing 'bottom-up' vertical deposition fabrication method. At each stage of the fabrication process, SEM analysis was conducted. The SEM imaging of silica-PMMA, inverted silica, silica-PMMA-alloy(Au-Ag), and inverted silica-alloy(Au-Ag) compared the 3D nanostructures pre-PMMA removal and post-removal through calcination process, and the absence and presence of the alloy(Au-Ag). The inverted silica-alloy(Au-Ag) film fabricated possessed consistent skeleton hole structure of rough-textured grainy surface appearance, notably ideal for light manipulating functions [25, 26].

In this paper, the researchers also investigated briefly the effect of silica-alloy(Au-Ag) substrate towards DSSC, as it is one of the most common purposes of photonic crystals in solar technology. The two are almost synonymously mentioned in any search. The inverted structure of silica-alloy(Au-Ag) had proven to trap light within a solar cell, consequently increasing its effectiveness. This is due to the skeletal structure of the substrate combined with the plasmonic properties of alloy(Au-Ag) of which increased the multimeter reading by 0.4V once applied.

The systematic light trapping properties of inverted silica-alloy(Au-Ag) nanostructure provide much room for future work in exploring further applications of the material synthesised in this work. Surface-enhanced Raman spectroscopy (SERS) is an excellent vibrational analytical technique for probing minute molecules bound in proximity to plasmonic surfaces [27,28]. The material synthesised in this study allowed for effective light trapping and photon density state, combining with the alloy nanoparticles of Ag that produced impressive SERS signal intensities, and Au that is highly resistant to oxidation [29]. Aside from that, the procedures in synthesising these substantially homogenous inverse silica-alloy(Au-Ag) by using PMMA and environment-friendly surfactant-free dispersion medium and linking agent makes mass producing this material an easier,

cheaper, a 'greener' sustainable approach to SERS substrate. Inverse silica-alloy(Au-Ag) requires a short fabrication time and could be integrated into plasmonic biosensors and point-of-care devices in the studying and monitoring of disease progression. Moreover, the composite could be easily modified or coated to be relatively safe and biocompatible for further study in *in vivo* applications [30,31]. Optical microchips could significantly minimise the power consumption of computers and permits exponentially faster data processing speed. With some fine-tuning, the photonic band gap of 3D silica-alloy(Au-Ag) photonic crystal allows for not just the simple trapping of light but also guiding light beyond the traditional method that is rooted in total internal reflection, such as optical fibres [32]. Incorporation of silica-alloy(Au-Ag) in optoelectronics could be made possible in offering important advantages over 2D electronic chips and expand the class of optical telecommunications in a variety of fields, including engineering and medicine in future studies [33].

Acknowledgement

We would like to express our acknowledgement to the Ministry of Education of Malaysia for Fundamental Research Grant Scheme (FRGS) 59630 (FRGS/1/2020/STG05/UMT/02/4) and Universiti Malaysia Terengganu for research supports and facilities.

References

1. Shakeel Ahmad, M., Pandey, A. K. and Abd Rahim, N. (2017). Advancements in the development of TiO_2 photoanodes and its fabrication methods for dye sensitized solar cell (DSSC) applications. A review. *Renewable and Sustainable Energy Reviews*, 77: 89-108.
2. Wang, Z., Tang, Y., Li, M., Zhu, Y., Li, M., Bai, L., Luoshan, M., Lei, W. and Zhao, X. (2017). Plasmonic enhancement of the performance of dye-sensitized solar cells by incorporating TiO_2 nanotubes decorated with Au nanoparticles. *Journal of Alloys and Compounds*, *C* (714): 89-95.
3. Aberle, A. G. (2009). Thin-film solar cells. *Thin Solid Films*, 517(17): 4706-4710.
4. Andreani, L. C., Bozzola, A., Kowalczewski, P. and Liscidini, M. (2015). Photonic light trapping and electrical transport in thin-film silicon solar cells. *Solar Energy Materials and Solar Cells*, 135: 78-92.
5. Zanotto, S., Liscidini, M. and Claudio Andreani, L. (2010). Light trapping regimes in thin-film silicon solar cells with a photonic pattern. *Optics Express*, 18(5): 4260-4272.
6. Werner, J., Weng, C.-H., Walter, A., Fesquet, L., Seif, J. P., De Wolf, S., Niesen, B. and Ballif, C. (2016). Efficient monolithic perovskite/silicon tandem solar cell with cell area >1 cm^2. *The Journal of Physical Chemistry Letters*, 7(1): 161-166.
7. Eisenlohr, J. (2017). Light trapping in high-efficiency crystalline silicon solar cells. Doctoral dissertation, University of Konstanz, Germany.
8. Cao, D. H., Stoumpos, C. C., Farha, O. K., Hupp, J. T. and Kanatzidis, M. G. (2015). 2D homologous perovskites as light-absorbing materials for solar cell applications. *Journal of the American Chemical Society*, 137(24): 7843-7850.
9. Ouanoughi, A., Hocini, A. and Khedrouche, D. (2016). Enhanced absorption of solar cell made of photonic crystal by geometrical design. *Frontiers of Optoelectronics*, 9(1): 93-98.
10. Li, Y., Chen, Y., Ouyang, Z. and Lennon, A. (2015). Angular matrix framework for light trapping analysis of solar cells. *Optics Express*, 23(24): A1707-A1719.
11. Kassim, S., Mcgrath, J. and Padmanabhan, S. (2015). Preparation and properties of silica inverse opal via self-assembly. *Applied Mechanics and Materials*, 699: 318-324.
12. Chen, W., Meng, Z., Xue, M. and Shea, K. (2016). Molecular imprinted photonic crystal for sensing of biomolecules. *Molecular Imprinting*, 4: 1-12.
13. Lonergan, A., McNulty, D. and O'Dwyer, C. (2018). Tetrahedral framework of inverse opal photonic crystals defines the optical response and photonic band gap. *Journal of Applied Physics*, 124(9): 095106.
14. Armstrong, E. and O'Dwyer, C. (2015). Artificial opal photonic crystals and inverse opal structures – fundamentals and applications from optics to energy storage. *Journal of Materials Chemistry C*, 3(24): 6109-6143.

15. Garín Escrivá, M., Hernández, D., Trifonov, T. and Alcubilla, R. (2014). Three-dimensional metallo-dielectric selective thermal emitters with high-temperature stability for thermophotovoltaic applications. *Solar Energy Materials and Solar Cells*, 134: 22-28.
16. Rout, D. and Vijaya, R. (2017). Role of stopband and localized surface plasmon resonance in raman scattering from metallo-dielectric photonic crystals. *Plasmonics*, 12(5): 1409-1416.
17. Kassim, S. (2014). Polymer and metallodielectric based photonic crystals. Doctoral thesis, University College Cork, Ireland.
18. Kassim, S., Mukhtar, N. A. and Tahrin, R. A. A. (2020). Synthesis and characterization of plasmon-enhanced SERS substrate based on Au-Ag alloy-coated, large-area photonic (methyl methacrylate+styrene) co-polymer. *Materials Science Forum*, 982: 14-19.
19. Kassim, S., Padmanabhan, S. C. and Pemble, M. E. (2021). Bottom-up colloidal synthesis of PMMA@Au core–shell based metallodielectric photonic crystals as substrates for surface-enhanced Raman spectroscopy. *Applied Surface Science*, 569: 151014.
20. Padmanabhan, S.C., Kassim, S. and Pemble, M. (2018). Colloidal co-crystallization: A new route for production of three-dimensional metallodielectric photonic crystals. *Asian Journal of Chemistry,* 30(7): 1613-1616.
21. Gałka, P., Kowalonek, J. and Kaczmarek, H. (2014). Thermogravimetric analysis of thermal stability of poly(methyl methacrylate) films modified with photoinitiators. *Journal of Thermal Analysis and Calorimetry*, 115(2): 1387-1394.
22. Al-Azawi, M. A., Bidin, N., Bououdina, M. and Mohammad, S. M. (2016). Preparation of gold and gold–silver alloy nanoparticles for enhancement of plasmonic dye-sensitized solar cells performance. *Solar Energy*, 126: 93-104.
23. Marichy, C., Muller, N., Froufe-Pérez, L. S. and Scheffold, F. (2016). High-quality photonic crystals with a nearly complete band gap obtained by direct inversion of woodpile templates with titanium dioxide. *Scientific Reports*, 6(1): 21818.
24. Shishkin, I. I., Rybin, M. V., Samusev, K. B., Golubev, V. G. and Limonov, M. F. (2014). Multiple Bragg diffraction in opal-based photonic crystals: Spectral and spatial dispersion. *Physical Review B*, 89(3): 035124.
25. Wang, Z. and Yu, B. (2018). Plasmonic control of refractive index without absorption in metallic photonic crystals doped with quantum dots. *Plasmonics*, 13(2): 567-574.
26. Van Lare, C., Lenzmann, F., Verschuuren, M. A. and Polman, A. (2015). Dielectric scattering patterns for efficient light trapping in thin-film solar cells. *Nano Letters*, 15(8): 4846-4852.
27. Byrne, H. J., Baranska, M., Puppels, G. J., Stone, N., Wood, B., Gough, K. M., Lasch, P., Heraud, P., Sulé-Suso, J. and Sockalingum, G. D. (2015). Spectropathology for the next generation: Quo vadis? *Analyst*, 140(7): 2066-2073.
28. Yang, S., Dai, X., Stogin, B. B. and Wong, T.-S. (2016). Ultrasensitive surface-enhanced Raman scattering detection in common fluids. *Proceedings of the National Academy of Sciences*, 113(2): 268-273.
29. Shukla, R., Bansal, V., Chaudhary, M., Basu, A., Bhonde, R. R. and Sastry, M. (2005). Biocompatibility of gold nanoparticles and their endocytotic fate inside the cellular compartment: A microscopic overview. *Langmuir*, 21(23): 10644-10654.
30. Du, Z., Qi, Y., He, J., Zhong, D. and Zhou, M. (2021). Recent advances in applications of nanoparticles in SERS in vivo imaging. *WIREs Nanomedicine and Nanobiotechnology*, 13(2): e1672.
31. Samanta, A., Maiti, K. K., Soh, K.-S., Liao, X., Vendrell, M., Dinish, U. S., Yun, S.-W., Bhuvaneswari, R., Kim, H., Rautela, S., Chung, J., Olivo, M. and Chang, Y.-T. (2011). Ultrasensitive Near-Infrared Raman Reporters for SERS-Based In Vivo Cancer Detection. *Angewandte Chemie*, 123(27): 6213-6216.
32. Götz, S. and Karst, U. (2007). Recent developments in optical detection methods for microchip separations. *Analytical and Bioanalytical Chemistry*, 387(1): 183-192.

33. Kumar, V. V. R. K., George, A. K., Knight, J. C. and Russell, P. S. J. (2003). Tellurite photonic crystal fiber. *Optics Express*, 11(20): 2641-2645.

Malaysian Journal of Analytical Sciences (MJAS)
Published by Malaysian Analytical Sciences Society

In Silico MODELLING OF DRUG ADSORPTION USING AMINE-FUNCTIONALIZED IRMOF-74-III METAL-ORGANIC FRAMEWORKS

(Pemodelan Penjerapan Ubat menggunakan Rangkaian Logam-Organik IRMOF-74-III Terfungsi-Amina Secara *In Silico*)

Mostafa Yousefzadeh Borzehandani[1,2], Emilia Abdulmalek[1,2], Mohd Basyaruddin Abdul Rahman[1,2,4], and Muhammad Alif Mohammad Latif[1,3,4*]

[1]*Integrated Chemical BioPhysics Research,*
Faculty of Science,
Universiti Putra Malaysia, 43400 UPM Serdang, Selangor, Malaysia
[2]*School Department of Chemistry,*
Faculty of Science,
Universiti Putra Malaysia, 43400 UPM Serdang, Selangor, Malaysia
[3]*Centre of Foundation Studies for Agricultural Science,*
Universiti Putra Malaysia, 43400 UPM Serdang, Selangor, Malaysia
[4]*Institute of Nanoscience and Nanotechnology,*
Universiti Putra Malaysia, 43400 UPM Serdang, Selangor, Malaysia

[*]*Corresponding author: aliflatif@upm.edu.my*

Received: 21 September 2022; Accepted: 30 January 2023; Published: 22 February 2023

Abstract

Metal-organic frameworks (MOFs) have been touted as prospective materials for drug storage and delivery. Functionalizing MOFs with an amine group has proven to be a successful strategy to achieve enhanced drug adsorption. To the best of our knowledge, however, there no report has been published showing the impact of increasing a common functional group such as amine on MOF's performance for drug adsorption. With the aim of exploring this possibility, IRMOF-74-III (IRM3) was functionalized with the amine group in various numbers and positions on the phenyl ring of the organic linker. The ability to adsorb several candidate drugs, including aspirin (Asp), fenbufen (Fen), ibuprofen (Ibu) and naproxen (Nap), were tested using density functional theory calculations and molecular docking. When the number of the amines increased, the MOF's pore polar surface area increased, but the energy gap between the HOMO and LUMO orbitals was reduced. Different pockets on the amine-functionalized IRM3's pore wall were analyzed by electrostatic potential contours, and then further investigated by a docking simulation. Fen@MOF was shown to be the most stable drug@MOF complex system, as demonstrated by the highest binding affinity. Coordinatively unsaturated magnesium sites in the frameworks, as well as hydroxyl and carbonyl groups on the drugs, are crucial for the interactions and charge transfer. This work successfully highlighted that having different numbers and positions of the amine group on the organic linker can affect the drug adsorption behavior of IRM3 MOF.

Keywords: amine-functionalized, anti-inflammatory drug adsorption, IRMOF-74-III, metal-organic frameworks, molecular docking

Abstrak

Rangkaian logam-organik (MOF) telah diketengahkan sebagai bahan prospektif bagi penyimpanan dan penghantaran ubatan. Berkenaan ini, memfungsikan MOFs dengan kumpulan amina adalah strategi yang berjaya bagi menambah baik jerapan ubatan. Walaubagaimanapun, mengikut pengetahuan kami, buat masa kini masih tiada laporan menunjukkan impak penambahan kumpulan berfungsi umum seperti amina terhadap prestasi MOF bagi jerapan ubatan. Dengan tujuan menerokai kemungkinan ini, IRMOF-74-III (IRM3) telah difungsikan dengan kumpulan amina dengan jumlah dan kedudukan yang berbeza pada cincin fenil penyambung organik. Kemampuan untuk menjerap beberapa calon ubat termasuklah aspirin (Asp), fenbufen (Fen), ibuprofen (Ibu) dan naproxen (Nap) telah diuji menggunakan pengiraan teori berfungsi ketumpatan dan pendokkan molekul. Adalah didapati bahawa jika jumlah kumpulan amina meningkat, permukaan berkutub MOF juga meningkat tetapi jurang tenaga di antara orbital HOMO dan LUMO adalah berkurang. Saku berbeza pada dinding rongga IRM3 terfungsi-amina dianalisa menggunakan kontur keupayaan elektrostatik dan disiasat lebih lanjut oleh simulasi pendokkan. Fen@MOF mempamerkan sistem kompleks drug@MOF yang paling stabil dan disahihkan oleh afiniti pengikat tertinggi. Tapak magnesium tak tepu yang terselaras di dalam rangkaian, dan juga kumpulan hidroksil dan karbonil pada ubat adalah penting bagi saling tindakan dan pemindahan cas. Kerja ini berjaya mengetengahkan yang memiliki kumpulan amina pada jumlah dan posisi berbeza pada penyambung organik boleh memberi kesan kepada sifat penjerapan ubatan MOF IRM3.

Kata kunci: terfungsi-amina, penjerapan ubat anti-inflamasi, IRMOF-74-III, rangka logam-organik, pendokkan molekul

Introduction

Metal-organic frameworks (MOFs) are a class of porous materials constructed by a mixture of metal nodes and organic linkers [1]. They have been extensively investigated in numerous applications, such as catalysis [2], gas adsorption and separation [3], biosensing and bioimaging [4], water purification [5], and drug delivery [6]. MOFs with partially coordinated metals, commonly known as coordinatively unsaturated metal sites (CUSs), can be obtained by removing the solvent via the activation step [7, 8]. MOF structures containing CUSs have great potential for drug adsorption. IRMOF-74 is a series of isoreticular MOF-74 that possess a similar topology that was initially synthesized by Yaghi et al. [9]. IRMOF-74 MOFs have become attractive for encapsulating drugs, since the magnesium (Mg) metal ion has low toxicity, and polycarboxylic linkers can be removed under physiological conditions [10].

The IRMOF-74 series comprises a variety of pore sizes such that each MOF can be employed for a specific amount of drug loading. For example, MOF-74-I demonstrated the lowest methotrexate (MTX) and 5-fluorouracil (5-FU) loading at 0.31 and 0.71 $g.g^{-1}$, respectively, primarily due to the smallest pore size among the IRMOF-74 family members [11]. In contrast, IRMOF-74-XI showed 2.78 and 4.24 $g.g^{-1}$ for MTX and 5-FU storage, respectively. Preparing IRMOF-74s comprising CUSs has made them more efficient for drug adsorption. Fairen-Jimenez et al. elucidated that the adsorption of ibuprofen (Ibu) inside MOF-74 pores was influenced by hydrogen bond (HB) interactions among polar hydrogen atoms in Ibu and the oxygen atoms surrounding Mg, and more importantly, the coordination bond between oxygen atoms in Ibu and Mg CUSs (O–Mg) [12].

The intrinsic tunability of pore size and pore wall surface in IRMOF-74-III (Figure 1-a) is achievable by incorporating functional groups on organic linkers via either pre-functionalization [13] or the post-synthetic modification (PSM) method [14]. For example, seven reactions based on the PSM method were carried out for sequential incorporating tripeptides on amine-functionalized IRMOF-74-III [14]. Amine functionalization onto MOFs have been shown to improve drug adsorption [15–17]. Among the frequently investigated amine-functionalized MOFs, however, the effect of increasing the number of amine-functionalized organic linkers on drug adsorption has not been further investigated. Incorporating two amine groups on the phenyl ring in organic linkers as *ortho*, *meta* and *para* positions may potentially generate different dynamic and electronic conditions on the pore wall. Theoretical design and computational explorations are useful tools for a better understanding by reducing the cost of time and chemicals. Moreover, computational strategies provide a conceptual understanding of the physiochemical properties of organic linkers, desirable conformation of drug molecules on the MOF pore

surface, and host-guest interactions. These are crucial factors for rational functionalization, higher drug loading and controlled drug release.

In this work, we utilized computational methods to characterize a variety of amine-functionalized IRMOF-74-IIIs, hereafter referred to as IRM3 (Figure 1-b). Corresponding amine-functionalized IRM3 MOFs were then employed to encapsulate four non-steroidal anti-inflammatory drugs (NSAIDs), including aspirin (Asp), fenbufen (Fen), ibuprofen (Ibu) and naproxen (Nap) (Figure 1-c). NSAIDs are consumed to ease the pain and inflammation by inhibiting the cyclooxygenase enzyme [18]. These drug compounds are frequently used by numerous researchers, as they are cheap and abundantly available in laboratories [19, 20]. Due to the hydrophobic property of NSAIDs, they are poorly-water soluble, which can result in erratic absorption and low bioavailability. Hence, encapsulating NSAID drug molecules within porous solid material such as MOFs is highly recommended to improve drug adsorption and delivery [21, 22].

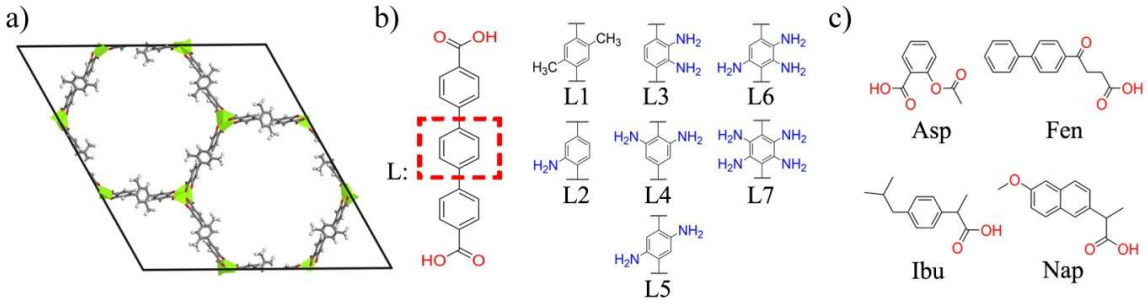


Figure 1. a) Unit cell of IRMOF-74-III, b) parent organic linker (L1) and the amine-functionalized organic linkers (L2-L7), and c) structure of NSAID drugs molecules

Computational Details

Geometry optimization of the organic linkers (L1-L7) was carried out using Gaussian 09 [23]. The structures were optimized at their ground state and gaseous phase. In order to characterize the organic linkers using an accurate level, DFT-B3LYP functional with a basis set of 6-31+G(d) was adopted. This level of computation generates highly accurate electronic properties. The corresponding basis set supports all atom types used in the frameworks (Mg, O, N, C, and H) and drug molecules (O, C, and H). Subsequently, the outputs allow us to analyze frontier molecular orbitals (FMOs), polarizability (α), topological polar surface area (TPSA) and dipole moments (μ) for organic linkers. At the same level of computation, single point energy calculation was carried out for the frameworks derived from the organic linkers to obtain the electrostatic potential (ESP) contours.

All amine-functionalized IRM3s were derived from the crystal structure of Mg-IRMOF-74-III available at the Cambridge Crystallographic Data Centre (CCDC), with deposition code 841643 [9]. The unit cell was extended to 2×2×5, and the supercell model was situated in a vacuum box for docking calculation. Then, the center of the supercell was set for the grid box as 120×90×60 points in the three dimensions for the docking simulation. In addition, a grid spacing of 1.000 Å was set to cover the two central pores of the large frameworks. AutoDock version 4 and AutoDock Vina version 1.1.2 [24] were employed to implement the automated molecular docking calculation of drug molecules inside the MOFs. The Lamarckian genetic algorithm (LGA) combined with a grid-based energy evaluation method were applied to evaluate the grid maps. Gaussian 09 was utilized to calculate the atomic partial charges using the CHarges from ELectrostatic Potentials using a Grid-based (CHELPG) method [25] based on B3LYP/6-31+G(d) level.

The optimal pose of the drug molecules on the MOF surface was considered for natural bond orbital (NBO) analysis. The smaller cluster structures containing drug@MOF were separated from the docking results

and used for single point energy calculation at B3LYP/6-31+G(d) level. NBO version 3.1 [26], available in the Gaussian 09 package, was used for the energy calculation. The second-order perturbation theory from the NBO calculation was then used to identify the electron donor and acceptor between the NSAID drugs and the IRM3 frameworks.

Results and Discussion

Geometry optimization at level DFT-B3LYP/6-31+G(d) was implemented to interpret the physiochemical properties of the organic linkers (L1-L7). FMO analysis described the chemical reactivity of the proposed organic linkers. FMOs were divided into the highest occupied molecular orbital (HOMO) and the lowest unoccupied molecular orbital (LUMO). HOMO orbitals were found to be distributed on the whole of the parent organic linker (L1). However, they were clearly localized on the middle phenyl ring when the methyl groups were replaced by amine groups (L2-L7) (Figure 2). The formation of HOMOs in all types of amine-functionalized linkers followed the number and position of amine groups. Being localized HOMOs in the middle phenyl ring with different formations can be useful for donating electrons to the electrophilic sites in the drug molecules. On the other side, the formation of LUMO orbitals remained almost constant in all organic linkers (L1-L7).

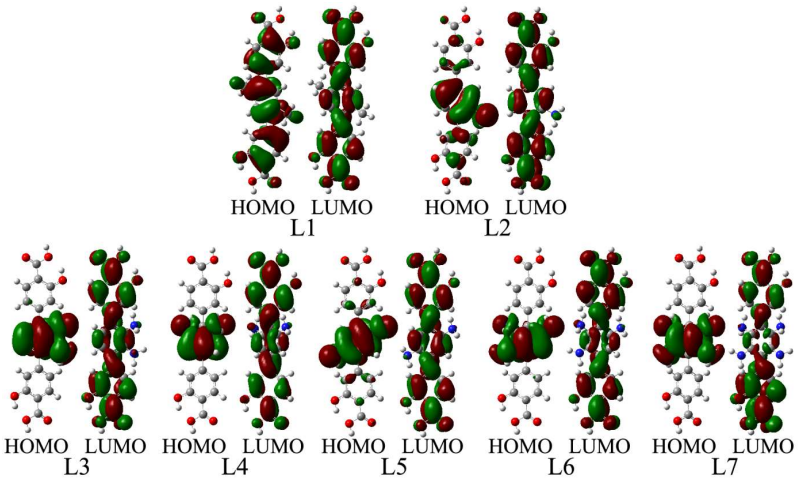


Figure 2. HOMO and LUMO orbitals for all the organic linkers

According to Table 1, the organic linkers demonstrated different values for the energy gap between the HOMO and LUMO orbitals (E_{HL}), polarizability, TPSA and dipole moments. The values of E_{HL} showed that increasing the substitution of the amine functional group on the organic linkers made them more kinetically stable. For example, the large value of E_{HL} in L1 implies difficult electron transfer, whereas a small value of E_{HL} in L7 indicates more facile electron transfer between HOMO and LUMO, as well as easier electrons donating to the electrophilic sites in the drug molecules. Incorporating the amine functional group generally caused the polarizability (α) of the organic linkers to improve. The TPSA parameter determines the overall surface on all polar atoms within the molecular structure. The calculated TPSA confirmed the enhancement of the polar surface by increasing the amine group on linkers. Although the organic linker containing one amine group (L2) had the lowest polarizability (α), it produced a high amount of dipole moments (μ). Dipole moments play an important role in adsorption using MOFs. Srepusharawoot *et al*. studied the capability of four different metal-organic framework-525, namely, M-MOF-525 (M= Ti, V, Zr and Hf) for hydrogen adsorption using first-principles calculations [27]. The authors found that Zr- and Hf-MOF-525 were able to trap the hydrogen molecules on the surface due to stronger dipole moments. Also, zero values of dipole moment for L1 and L5 were obtained from *para* position of the functional groups, which means equal electron distributions on the middle phenyl ring.

Table 1. Physiochemical properties for the organic linkers

Compound	E_{HL} (eV)	α (A^3)	TPSA (A^2)	μ (D)
L1	4.41	46.24	115.1	0.00
L2	3.77	45.84	141.1	1.70
L3	3.58	46.52	167.1	1.29
L4	3.57	46.66	167.1	1.65
L5	3.14	47.59	167.1	0.00
L6	3.12	47.73	193.1	0.86
L7	2.76	48.24	219.1	0.64

In this report, the frameworks derived from the proposed organic linkers (L1-L7) are referred to as IRM3 (L1), IRM3-1 (L2), IRM3-2*o* (L3), IRM3-2*m* (L4), IRM3-*p* (L5), IRM3-3 (L6) and IRM3-4 (L7). The electrostatic potential (ESP) contours for all the frameworks are illustrated in Figure 3. The ESP contours revealed a highly distinguished pattern for each MOF's pore when the functionalized-amine groups were increased or placed in the *ortho*, *meta* or *para* positions. The conversion of the hexagonal ESP pattern in L1 to the trigonal ESP pattern for L2-L7 was attributed to the different symmetry point group of the functional groups. The symmetry point group for the methyl and amine functional groups is C_{3v} and C_{2v}, respectively. Therefore, an R-3 symmetry was detected for the crystal structure of IRM3, whereas an R3 symmetry was observed for all amine-functionalized IRM3s. The EPS contours of the MOF crystals represented by red lines indicate negative potentials on the phenyl rings and the amine groups due to stronger electron distribution. This feature was amplified by increasing the amine groups on the linkers (the most for L7).

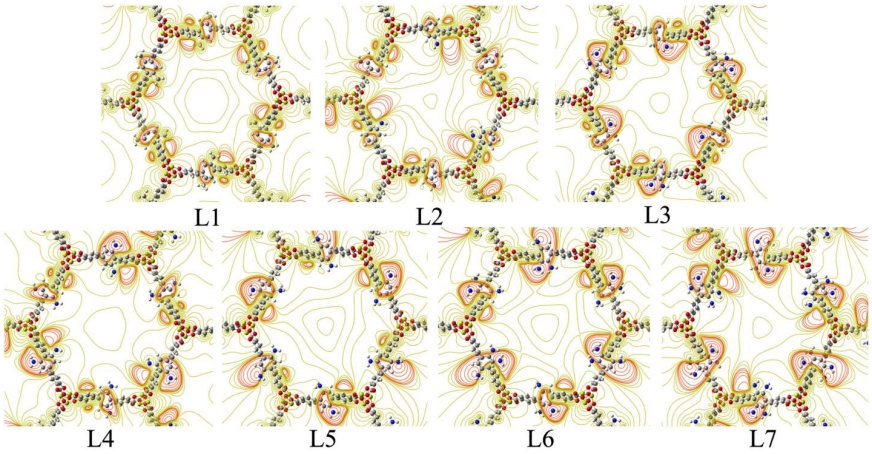


Figure 3. Electrostatic potential (ESP) contour for the frameworks

Overall, the DFT study of the organic linkers (L1-L7) and their corresponding frameworks demonstrated that HOMOs were localized where amine functional groups were incorporated in the middle phenyl ring. These changes were also illustrated by the ESP contour patterns. Middle phenyl rings had a higher electron density as the number of amine groups was increased. In addition, the values of polarizability (α) and TPSA demonstrated that increasing functional groups on IRM3 organic linker enhanced the polarity. It is expected that increasing the number of amine groups on IRM3 organic linkers would activate the MOF pore surface to trap more drug molecules by donating more electrons. All frameworks were further investigated for the adsorption of NSAID drug molecules by means of molecular docking simulation and NBO calculation to determine

the most favorable interaction site and the intensity of electron transmission, respectively. As depicted in Figure 4, all amine functionalized IRM3s produce different pockets (orange color) in the CUSs. This property could also be observed in the EPS contour. In comparison, the tightest pocket in the CUSs tend to be in IRM3-2*o* and IRM3-4, whereas the largest pocket was in IRM3-2*m*. The distance between the amine groups on the linker clearly influence the size of pockets in the CUSs.

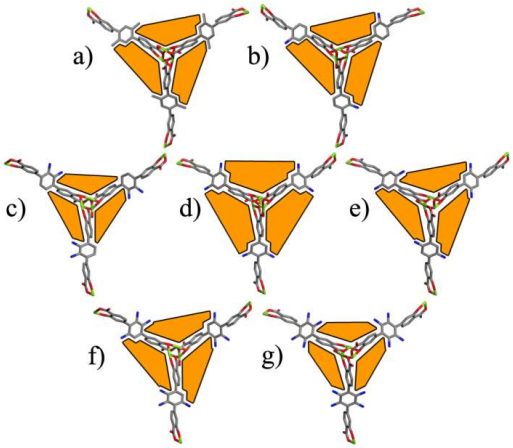


Figure 4. 2D schematic presentation of the pockets in CUSs for a) IRM3, b) IRM3-1, c) IRM3-2*o*, d) IRM3-2*m*, e) IRM3-2*p*, f) IRM3-3 and g) IRM3-4

Binding affinity can be defined as the degree of the binding of the drug molecules in the MOF pores [28]. Docking simulation using Autodock Vina produced nine modes of binding affinity (kcal mol^{-1}) for each drug@MOFs complex system. The first (best) mode value was used to construct Figure 5. The variety of binding affinity values generated by each drug@MOF complex confirmed that the pockets on CUS sites had various spaces and morphologies. The highest binding affinity was produced by the Fen molecule, whereas the lowest binding affinity was exhibited by Asp. This result could be attributed to their molecular size, as Fen and Asp have the largest and the smallest molecular size, respectively. The measured drug molecular size was shown as the order of Asp (10.6 × 8.9 Å) < Ibu (12.9 × 7.8 Å) < Nap (13.6 × 7.9 Å) < Fen (17.2 × 7.5 Å). Being the largest size of Fen led to the strongest fitting into the CUS pockets. In contrast, being the smallest size of Asp made it the least fitting. Moreover, Ibu and Nap docked into the CUS pockets and Asp due to a larger molecular size.

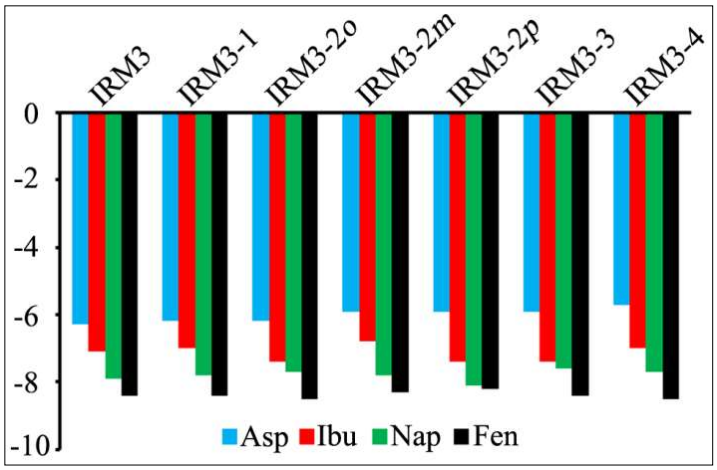


Figure 5. Bar chart derived from the first mode of the binding affinity

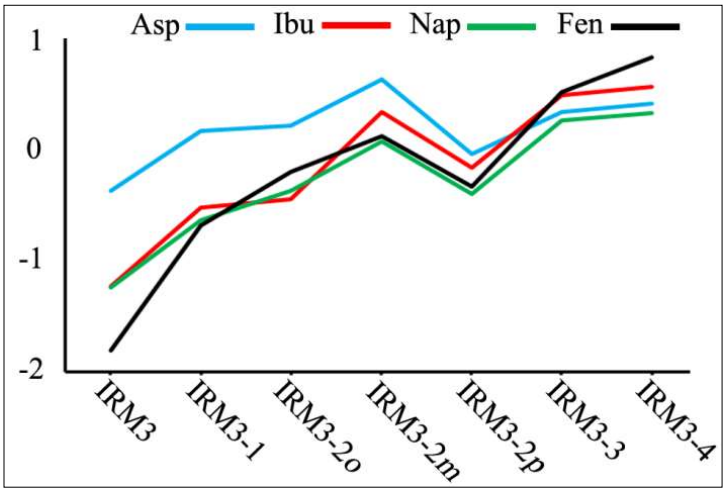


Figure 6. Line chart derived from the first rank of the binding energy

The highest rank of binding energy calculated by AutoDock is presented in Figure 6. The line chart shows a general upward trend for binding energies as the number of functionalized amine groups increase. These results suggest that the strength of the total interactions between the NSAID drug molecules and the frameworks was reduced. Drug molecules had a lower binding energy and stronger interactions when they were complexed in IRM3-2*p* compared to the other two isomers, IRM3-2*o* and IRM3-2*m*. Additionally, among the two isostructures, IRM3 and IRM3-2*p*, which differ only on the type of functional group, the positive charge of magnesium (Mg) (+1.3184) in IRM3 was reduced to +1.3003 in IRM3-2*p*. This change was governed by the inductive effect of the polar functional group such as the amine group [29]. Thus, the binding energies produced by drug@IRM3 complex systems had the lowest values (the strongest interactions). In general, increasing amine groups on organic linkers reduced the strength of interactions in the drug@MOF complex systems.

Using MOF-1 and MOF-4, which have identical pore sizes, Zhang et al. observed reduced drug loading due to weaker interactions between Ibu and the pore surface [30]. It was shown that stronger interactions between the carboxyl group in Ibu and MOF-1 pore surface resulted in a two fold higher loading compared to MOF-4. In addition, the abundance of the secondary interactions such as hydrogen bond (HB), and electrostatic and hydrophobic interactions, play a crucial role in controlled drug release after drug loading [12, 31, 32].

Considering the matter of host-guest interactions, all types of interactions between the frameworks and the drug molecules were collected in Table 2. An analysis of the interactions indicated that the drug molecules mainly built interactions on the CUSs in IRM3, IRM3-1, IRM3-2*m* and IRM3-2*p*. On the other side, NSAID drugs were observed to have amine-based HB interactions when they were complexed in IRM3-2*o*, IRM3-3 and IRM3-4. The presence of two neighboring amine functional groups on the middle phenyl ring seemed dominant to CUS sites, since they provide large enough polar surfaces. Figure 7 shows an example of this behavior. The top three binding modes of Nap indicated that they were preferably placed on CUS sites in IRM3-2*p*. In contrast, they were concentrated on amine functional groups in IRM3-3. By comparing the interaction distances in Table 2, we found that IRM3, IRM3-1, IRM3-2*m* and IRM3-2*p* generally provided abundant and strong interactions with drug molecules on CUSs. Some examples are metal-acceptor interactions ($Mg_{framework} \cdots OC_{drug}$), oxygen-based HB interactions ($O_{framework} \cdots HO_{drug}$), and plenty of hydrophobic (π-based) interactions. In contrast, drug molecules had amine-based HB interactions with IRM3-2*o*, particularly in IRM3-3 and IRM3-4. The results obtained indicate that the functionalizing of MOFs using two neighboring amine groups on organic linkers close to CUS sites would disrupt the capability of CUS for the adsorption of drug molecules.

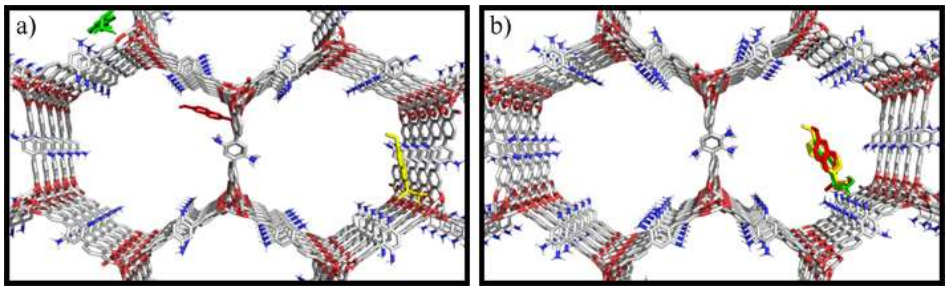


Figure 7. The top three binding modes of Nap in a) IRM3-2*p* and b) IRM3-3

Single point energy calculations allowed us to evaluate the electron transfer between the NSAID drug molecules and the frameworks using NBO analysis. The four highest NBO donor-acceptor interactions between the drug molecules and the frameworks are compiled in Tables 3 to 6. The atomic numbers of NSAID drug molecules are illustrated in Figure 8. The calculated stabilization energies (E_{ij}) indicate that all the drug molecules transferred the most electrons when they were complexed with IRM3. Lone electron pair (LP) of oxygen atoms in the drug molecules and unfilled valence-shell nonbonding (LP*) of Mg in the frameworks played the primary role as the electron donor and the electron acceptor, respectively, in drug@IRM3, drug@IRM3-1, drug@IRM3-2*o*, drug@IRM3-2*m*, and drug@IRM3-2*p*. However, the NBO donor-acceptor interactions derived from drug@IRM3-3 and drug@IRM3-4 complex systems primarily involved the amine functional group, and the corresponding values of stabilization energies (E_{ij}) were relatively poor. This evidence from NBO analysis confirmed that CUSs were the most favorable sites for stronger electron transfer and adsorption of the NSAIDs molecules.

Table 2. Interactions involved in all drug@MOF complex systems

	Asp		Fen		Ibu		Nap	
	Interaction Type	**Distance (Å)**	**Interaction Type**	**Distance (Å)**	**Interaction Type**	**Distance (Å)**	**Interaction Type**	**Distance (Å)**
IRM3	Mg ⋯ OC_{Asp}	1.74	O ⋯ OC_{Fen}	2.36	O ⋯ OC_{Ibu}	2.38	O ⋯ OC_{Nap}	2.54
	O ⋯ OC_{Asp}	2.56	O ⋯ HO_{Fen}	1.77	O ⋯ HO_{Ibu}	1.98	O ⋯ HO_{Nap}	2.21
	π - π Stacked	3.72	Mg ⋯ CO_{Fen}	1.68	Mg ⋯ CO_{Ibu}	1.69	Mg ⋯ OC_{Nap}	1.67
	π ⋯ Alkyl	5.36	π - π T-shaped	5.13	π - π Stacked	4.29	π ⋯ HC_{Nap}	3.40, 3.94
			π ⋯ Alkyl	5.41, 4.61, 4.60	π ⋯ Alkyl	4.36, 4.86, 5.07	π ⋯ Alkyl	4.09, 4.55, 5.04, 5.38
IRM3-1	NH ⋯ O_{Asp}	1.74, 1.76	O ⋯ OC_{Fen}	2.72	O ⋯ OC_{Ibu}	2.76	O ⋯ HO_{Nap}	1.95
	π - π Stacked	3.95	Mg ⋯ OC_{Fen}	1.81	O ⋯ HO_{Ibu}	1.85	Mg ⋯ OC_{Nap}	1.96
			π ⋯ HC_{Fen}	3.67	Mg ⋯ OC_{Ibu}	2.11	π - π Stacked	4.27, 5.31
			π - π Stacked	3.88	π - π T-shaped	5.07	π - π T-shaped	5.07, 5.15
			π - π T-shaped	4.73, 5.44, 5.83	π ⋯ Alkyl	4.28, 4.62, 4.79, 5.22, 5.26, 5.36	π ⋯Alkyl	4.62
IRM3-2*o*	NH ⋯ O_{Asp}	2.09	NH ⋯ HO_{Fen}	2.19	NH ⋯ OC_{Ibu}	2.44, 2.85	NH ⋯ OC_{Nap}	1.95
	O ⋯ OC_{Asp}	2.55	O ⋯ OC_{Fen}	2.48	O ⋯ HO_{Ibu}	2.01	O ⋯ HO_{Nap}	1.67
	Mg ⋯ OC_{Asp}	1.67	Mg ⋯ OC_{Fen}	1.72	Mg ⋯ OC_{Ibu}	1.82	Mg ⋯ OC_{Nap}	1.75
	π - π Stacked	4.04	π - π Stacked	3.92	π ⋯ Anion	4.53	π - π Stacked	4.08, 4.15
				5.46	π - π Stacked	4.49		
					π ⋯Alkyl	4.61, 4.86,		
IRM3-2*m*	NH ⋯ OC_{Asp}	1.70	O ⋯ OC_{Fen}	2.47, 2.74	O ⋯ OC_{Ibu}	2.48, 2.99	O ⋯ OC_{Nap}	2.64, 2.78
	π - π T-shaped	5.33	O ⋯ HO_{Fen}	2.06	O ⋯ HO_{Ibu}	2.04	NH ⋯ O_{Nap}	2.18
			Mg ⋯ OC_{Fen}	1.75	Mg ⋯ OC_{Ibu}	1.95	Mg ⋯ OH_{Nap}	2.15
			π ⋯ Cation	3.77, 4.13	Mg ⋯ OH_{Ibu}	1.85	Mg ⋯ OC_{Nap}	2.00
			π ⋯ Anion	3.43	π - π Stacked	4.66	π - π Stacked	4.21, 4.53
			π - π Stacked	3.96, 4.76	π ⋯Alkyl	4.65	π ⋯ Alkyl	5.47
IRM3-2*p*	O ⋯ OC_{Asp}	2.69, 2.76	O ⋯ OC_{Fen}	2.81, 3.18	O ⋯ OC_{Ibu}	2.60	NH ⋯ O_{Nap}	2.16
	NH ⋯ OC_{Asp}	1.95	O ⋯ HO_{Fen}	2.08	O ⋯ HO_{Ibu}	1.94	O ⋯ OC_{Nap}	2.36, 3.01
	Mg ⋯ OC_{Asp}	1.90	Mg ⋯ OC_{Fen}	1.91	Mg ⋯ OC_{Ibu}	1.70	O ⋯ HO_{Nap}	1.90
	π - π Stacked	3.88	π ⋯ Cation	4.07	π - π T-shaped	5.61	Mg ⋯ OC_{Nap}	1.91
			π ⋯ Anion	3.83			π ⋯ Cation	4.91
							π - π Stacked	4.08, 4.23
							π ⋯ Alkyl	4.57, 5.24
IRM3-3	NH ⋯ O_{Asp}	1.75, 1.84	NH ⋯ O_{Fen}	1.74	NH ⋯ O_{Ibu}	1.72, 1.75	NH ⋯ O_{Nap}	1.74, 1.84
			π - π Stacked	3.64, 5.62				
			π - π T-shaped	5.24				
IRM3-4	NH ⋯ O_{Asp}	1.90, 2.03	NH ⋯ O_{Fen}	1.62, 1.63	NH ⋯ O_{Ibu}	1.76, 1.87	NH ⋯ O_{Nap}	1.62, 1.63

* Atom symbol without subscript belongs to the framework

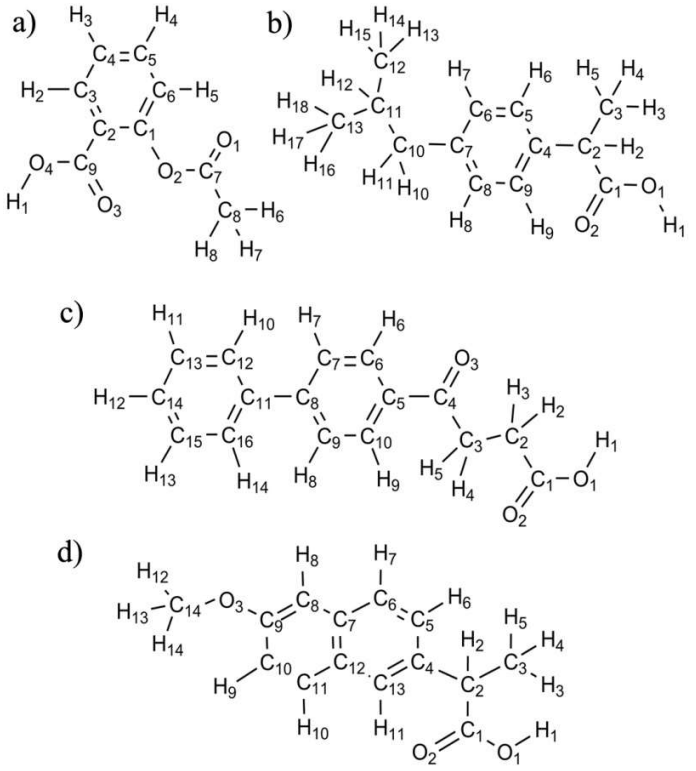


Figure 8. Atomic numbers for a) Asp, b) Ibu, c) Fen and d) Nap used in Tables 3-6

Table 3. The highest four NBO donor-acceptor interactions for Asp@MOF complex systems

Asp@MOFs	**Donor (i) → Acceptor (j)**	***E*$_{ij}$ (kcal/mol)**	**Donor (i) → Acceptor (j)**	***E*$_{ij}$ (kcal/mol)**
Asp@IRM3	1: LP (2) O_4 → LP* (3) Mg	29.53	2: LP (2) O_4 → LP* (2) Mg	9.00
	3: BD (1) $O_4 – H_1$ → LP* (3) Mg	8.19	4: LP (2) O_4 → LP* (1) Mg	6.64
Asp@IRM3-1	1: LP (2) O_2 → LP* (1) Mg	16.19	2: LP (2) O_4 → LP* (1) Mg	11.56
	3: LP (2) O_2 → LP* (3) Mg	11.21	4: BD (1) C_1-O_2 → LP* (1) Mg	4.52
Asp@IRM3-2*o*	1: LP (1) O_3 → LP* (3) Mg	16.24	2: LP (2) O_1 → LP* (2) Mg	12.05
	3: LP (1) O_3 → BD* (1) N-H	5.36	4: LP (1) O_2 → BD* (1) N-H	4.28
Asp@IRM3-2*m*	1: LP (2) O_2 → LP* (1) Mg	14.83	2: LP (2) O_2 → LP* (3) Mg	13.77
	3: LP (2) O_4 → LP* (1) Mg	10.26	4: LP (1) O_4 → LP* (1) Mg	4.88
Asp@IRM3-2*p*	1: LP (1) O_4 → LP* (3) Mg	16.26	2: LP (2) O_2 → LP* (1) Mg	14.31
	3: LP (1) O → BD* (1) O_4-H_1	11.04	4: LP (2) O_2 → LP* (3) Mg	10.60
Asp@IRM3-3	1: LP (1) O_3 → BD* (1) N-H	5.58	2: LP (1) O_4 → BD (1) N-H	4.57
	3: LP (1) O_4 → BD* (2) N-H	3.24	4: BD (1) C_6-H_5 → BD* (1) N-H	0.61
Asp@IRM3-4	1: LP (1) N → BD* (1) O_4-H_1	6.02	2: LP (2) O_4 → BD* (1) N-H	5.42
	3: BD (1) O_4-H_1 → BD* (1) N-H	4.47	4: LP (1) O_4 → BD (1) N-H	3.56

* Atom symbol without subscript is belong to the framework

Table 4. The highest four NBO donor-acceptor interactions for Fen@MOF complex systems

Fen@MOFs	Donor (i) → Acceptor (j)	E_{ij} (kcal/mol)	Donor (i) → Acceptor (j)	E_{ij} (kcal/mol)
Fen@IRM3	1: LP (1) O_1 → LP* (3) Mg	18.63	2: LP (1) O_1 → LP* (2) Mg	15.54
	3: BD (1) O_1-H_1 → LP* (2) Mg	11.57	4: LP* (2) Mg → BD* (1) O_1-H_1	8.91
Fen@IRM3-1	1: LP (2) O_1 → LP* (2) Mg	5.90	2: BD (2) C_{16}-C_{15} → LP* (4) Mg	4.51
	3: BD (1) C_{16}-H_{14} → LP* (2) Mg	3.66	4: LP (1) O_1 → LP* (2) Mg	3.52
Fen@IRM3-2*o*	1: LP (2) O_1 → LP* (3) Mg	29.41	2: BD (1) O_2 → LP* (2) Mg	8.66
	3: LP (1) O_1 → BD* (1) N-H	3.07	4: LP (1) O_3 → BD* (1) N-H	2.87
Fen@IRM3-2*m*	1: BD (2) C_{16}-C_{15} → LP* (4) Mg	4.02	2: LP (2) O_1 → LP* (2) Mg	3.57
	3: BD (1) C_{16}-H_{14} → LP* (2) Mg	3.25	4: BD (2) C_{16}-C_{15} → LP* (3) Mg	2.90
Fen@IRM3-2*p*	1: LP (1) O_1 → LP* (2) Mg	4.00	2: BD (2) C_{13}-C_{12} → LP* (4) Mg	3.59
	3: BD (1) C_{12}-H_{10} → LP* (2) Mg	3.59	4: LP (2) O_1 → LP* (2) Mg	3.37
Fen@IRM3-3	1: LP (1) O_1 → BD* (1) N-H	6.44	2: LP (2) O_3 → BD* (1) N-H	5.07
	3: BD (1) C_{10}-H_9 → BD* (1) N-H	3.87	4: LP (1) O_1 → BD (2) N-H	3.17
Fen@IRM3-4	1: LP (2) O_3 → BD* (1) N-H	4.81	2: LP* (3) N-H → BD* (1) O_1-H_1	4.52
	3: LP (1) O_1 → BD* (1) N-H	3.29	4: LP (1) O_1 → BD* (2) N-H	3.05

* Atom symbol without subscript is belong to the framework

Table 5. The highest four NBO donor-acceptor interactions for Ibu@MOF complex systems

Ibu@MOFs	Donor (i) → Acceptor (j)	E_{ij} (kcal/mol)	Donor (i) → Acceptor (j)	E_{ij} (kcal/mol)
Ibu@IRM3	1: LP (1) O_1 → LP* (3) Mg	26.77	2: LP (2) O_1 → LP* (2) Mg	13.37
	3: BD (1) O_1-H_1 → LP* (3) Mg	9.29	4: BD (1) O_1-H_1 → LP* (2) Mg	6.47
Ibu@IRM3-1	1: LP (1) O_1 → LP* (2) Mg	14.37	2: LP (2) O_1 → LP* (4) Mg	12.56
	3: LP (2) O_1 → LP* (2) Mg	11.25	4: BD (1) O_1-H_1 → LP* (3) Mg	9.91
Ibu@IRM3-2*o*	1: LP (2) O_1 → LP* (3) Mg	17.32	2: LP (1) O_1 → LP* (2) Mg	12.58
	3: LP (1) O_1 → BD (1) N-H	5.10	4: LP (1) O_3 → BD* (2) N-H	3.76
Ibu@IRM3-2*m*	1: LP (1) O_1 → LP* (4) Mg	16.26	2: LP (1) O_1 → LP* (2) Mg	11.36
	3: BD (1) O_1-H_1 → LP* (3) Mg	9.05	4: LP (2) O_1 → LP* (2) Mg	8.22
Ibu@IRM3-2*p*	1: LP (2) O_1 → LP* (2) Mg	13.95	2: BD (1) C_{13}-H_{18} → LP* (4) Mg	8.36
	3: BD (1) C_9-H_9 → LP* (4) Mg	6.04	4: LP (1) O → BD* (1) C_{11}-H_{12}	4.55
Ibu@IRM3-3	1: LP (1) O → BD* (1) C_2-H_2	5.34	2: BD (2) C_1-O_2 → BD* (1) N-H	4.53
	3: LP (1) O_1 → BD (1) N-H	4.19	4: LP (1) O → BD (2) C_2-H_2	3.04
Ibu@IRM3-4	1: LP (3) O → BD* (1) O_1-H_1	4.56	2: LP (1) O_1 → BD* (1) N-H	3.68
	3: LP (1) O_1 → BD (1) N-H	3.16	4: BD (1) N-H → BD* (1) C_8-H_9	2.88

* Atom symbol without subscript is belong to the framework

Table 6. The highest four NBO donor-acceptor interactions for Nap@MOF complex systems

Nap@MOFs	Donor (i) → Acceptor (j)	E_{ij} (kcal/mol)	Donor (i) → Acceptor (j)	E_{ij} (kcal/mol)
Nap@IRM3	1: LP* (4) Mg → BD* (1) O_1-H_1	15.55	2: LP (2) O_1 → LP* (2) Mg	14.67
	3: BD (1) O_1-H_1 → LP* (4) Mg	14.61	4: LP (1) O_1 → LP* (3) Mg	12.00
Nap@IRM3-1	1: LP (1) O_1 → LP* (3) Mg	12.19	2: BD (1) O_1-H_1 → LP* (4) Mg	8.86
	3: LP (1) O_1 → LP* (4) Mg	8.07	4: BD (1) O_1-H_1 → LP* (3) Mg	6.66
Nap@IRM3-2*o*	1: LP (2) O_2 → LP* (3) Mg	13.75	2: BD (1) O_2 → LP* (3) Mg	12.24
	3: BD (1) O_1 → LP* (3) Mg	6.21	4: LP (1) O_1 → BD (1) N-H	4.10
Nap@IRM3-2*m*	1: LP (1) O_1 → LP* (3) Mg	14.03	2: BD (1) O_1-H_1 → LP* (3) Mg	13.04
	3: LP (2) O_1 → LP* (4) Mg	10.70	4: BD (1) C_1-O_1 → LP* (3) Mg	7.41
Nap@IRM3-2*p*	1: LP (1) O_1 → LP* (3) Mg	13.87	2: BD (1) O_1-H_1 → LP* (3) Mg	9.70
	3: BD (1) C_1-O_1 → LP* (3) Mg	7.30	4: BD (1) O_1-H_1 → LP* (4) Mg	5.82
Nap@IRM3-3	1: BD (1) C_{10}-H_9 → BD* (1) N-H	5.55	2: BD (1) N-H → BD* (1) C_{10}-H_9	5.07
	3: LP (1) O_2 → BD* (1) N-H	4.05	4: BD (1) C_{10}-H_9 → BD* (1) N-H	3.91
Nap@IRM3-4	1: LP (1) N → BD* (1) C_3-H_5	4.66	2: LP (1) N → BD* (1) C_3-H_5	3.87
	3: BD (1) C_{10}-H_9 → BD* (1) N-H	3.68	4: LP (1) O_1 → BD (1) N-H	2.21

* Atom symbol without subscript is belong to the framework

Conclusion

In this computational work, a set of amine-functionalized IRM3 was derived from the parent structure (IRMOF-74-III). Initially, all organic linkers (L1-L7) were characterized at the DFT level. The results indicated that the increase of the amine group on organic linkers extended the polarity of the MOF pore surface and decreased the values of E_{HL}. The reduced E_{HL} in the MOFs containing more amine groups indicate their capability to donate electrons to drug molecules during binding. This was corroborated by the evaluation of framework-drug interactions and NBO analysis. NSAID drug molecules were found to prefer accommodating on CUS sites, which resulted in a variety of framework-drug interactions and a stronger electron transfer. In this set of drug@MOF complex systems, NBO analysis revealed that electron transfer from lone pair of electrons on oxygen atoms in the drugs to magnesium CUSs had the highest energy stabilization. Meanwhile, drug molecules were found more on organic linkers, making amine-based HB interactions when two neighboring amine groups were present such as in IRM3-2*o*, IRM3-3 and IRM3-4 MOFs. In addition, it was found that larger NSAID drug molecules had better fit into the CUS sites in the order of Fen > Nap > Ibu > Asp. Our results provide valuable insights on functionalizing MOF containing CUS sites with amine groups to improve drug encapsulation.

Acknowledgements

The authors would like to acknowledge the Ministry of Education (MOE) Malaysia. This research is supported by the Ministry of Education (MOE) Malaysia through Fundamental Research Grant Scheme (FRGS/1/2020/STG04/UPM/02/9).

References

1. Kitagawa, S. (2014). Metal–organic frameworks (MOFs). *Chemical Society Reviews*, 43(16): 5415-5418.
2. Zhu, L., Liu, X. Q., Jiang, H. L. and Sun, L. B. (2017). Metal–organic frameworks for heterogeneous basic catalysis. *Chemical reviews*, 117(12): 8129-8176.
3. Li, J. R., Ma, Y., McCarthy, M. C., Sculley, J., Yu, J., Jeong, H. K. and Zhou, H. C. (2011). Carbon dioxide capture-related gas adsorption and separation in metal-organic frameworks. *Coordination Chemistry Reviews*, 255(15-16): 1791-1823.

4. Wang, H. S. (2017). Metal–organic frameworks for biosensing and bioimaging applications. *Coordination Chemistry Reviews*, 349: 139-155.
5. Feng, M., Zhang, P., Zhou, H. C. and Sharma, V. K. (2018). Water-stable metal-organic frameworks for aqueous removal of heavy metals and radionuclides: A review. *Chemosphere*, 209: 783-800.
6. Lázaro, I. A. and Forgan, R. S. (2019). Application of zirconium MOFs in drug delivery and biomedicine. *Coordination chemistry reviews*, 380: 230-259.
7. Zhang, X., Wang, J., Dong, X. X. and Lv, Y. K. (2020). Functionalized metal-organic frameworks for photocatalytic degradation of organic pollutants in environment. *Chemosphere*, 242: 125144.
8. Zheng, X., Zhang, L., Fan, Z., Cao, Y., Shen, L., Au, C. and Jiang, L. (2019). Enhanced catalytic activity over MIL-100 (Fe) with coordinatively unsaturated Fe^{2+}/Fe^{3+} sites for selective oxidation of H_2S to sulfur. *Chemical Engineering Journal*, 374: 793-801.
9. Deng, H., Grunder, S., Cordova, K. E., Valente, C., Furukawa, H., Hmadeh, M. and Yaghi, O. M. (2012). Large-pore apertures in a series of metal-organic frameworks. *Science*, 336(6084): 1018-1023.
10. Kotzabasaki, M., Galdadas, I., Tylianakis, E., Klontzas, E., Cournia, Z. and Froudakis, G. E. (2017). Multiscale simulations reveal IRMOF-74-III as a potent drug carrier for gemcitabine delivery. *Journal of Materials Chemistry B*, 5(18): 3277-3282.
11. Erucar, I. and Keskin, S. (2017). Computational investigation of metal organic frameworks for storage and delivery of anticancer drugs. *Journal of Materials Chemistry B*, 5(35): 7342-7351.
12. Bernini, M. C., Fairen-Jimenez, D., Pasinetti, M., Ramirez-Pastor, A. J. and Snurr, R. Q. (2014). Screening of bio-compatible metal–organic frameworks as potential drug carriers using Monte Carlo simulations. *Journal of Materials Chemistry B*, 2(7): 766-774.
13. Fracaroli, A. M., Furukawa, H., Suzuki, M., Dodd, M., Okajima, S., Gándara, F. and Yaghi, O. M. (2014). Metal–organic frameworks with precisely designed interior for carbon dioxide capture in the presence of water. *Journal of the American Chemical Society*, 136(25): 8863-8866.
14. Fracaroli, A. M., Siman, P., Nagib, D. A., Suzuki, M., Furukawa, H., Toste, F. D. and Yaghi, O. M. (2016). Seven post-synthetic covalent reactions in tandem leading to enzyme-like complexity within metal–organic framework crystals. *Journal of the American Chemical Society*, 138(27): 8352-8355.
15. Van Tran, T., Nguyen, D. T. C., Le, H. T. N., Vo, D. V. N., Doan, V. D., Dinh, V. P. and Bach, L. G. (2019). Amino-functionalized MIL-88B (Fe)-based porous carbon for enhanced adsorption toward ciprofloxacin pharmaceutical from aquatic solutions. *Comptes Rendus Chimie*, 22(11-12): 804-812.
16. Xu, X. Y. and Yan, B. (2016). Selective detection and controlled release of Aspirin over fluorescent amino-functionalized metal–organic framework in aqueous solution. *Sensors and Actuators B: Chemical*, 230: 463-469.
17. Almáši, M., Zeleňák, V., Palotai, P., Beňová, E. and Zeleňáková, A. (2018). Metal-organic framework MIL-101 (Fe)-NH2 functionalized with different long-chain polyamines as drug delivery system. *Inorganic Chemistry Communications*, 93: 115-120.
18. Smith, S. R., Deshpande, B. R., Collins, J. E., Katz, J. N. and Losina, E. (2016). Comparative pain reduction of oral non-steroidal anti-inflammatory drugs and opioids for knee osteoarthritis: systematic analytic review. *Osteoarthritis and cartilage*, 24(6): 962-972.
19. Juère, E., Florek, J., Bouchoucha, M., Jambhrunkar, S., Wong, K. Y., Popat, A. and Kleitz, F. (2017). In vitro dissolution, cellular membrane permeability, and anti-inflammatory response of resveratrol-encapsulated mesoporous silica nanoparticles. *Molecular Pharmaceutics*, 14(12): 4431-4441.
20. Koç, F. E. and Şenel, M. (2013). Solubility enhancement of non-steroidal anti-inflammatory drugs (NSAIDs) using polypolypropylene oxide core PAMAM dendrimers. *International journal of pharmaceutics*, 451(1-2): 18-22.

21. Rivas, C. J. M., Tarhini, M., Badri, W., Miladi, K., Greige-Gerges, H., Nazari, Q. A. and Elaissari, A. (2017). Nanoprecipitation process: From encapsulation to drug delivery. *International journal of pharmaceutics*, 532(1): 66-81.
22. Shishir, M. R. I., Xie, L., Sun, C., Zheng, X. and Chen, W. (2018). Advances in micro and nano-encapsulation of bioactive compounds using biopolymer and lipid-based transporters. *Trends in Food Science & Technology*, 78: 34-60.
23. Frisch, M. J., Trucks, G. W., Schlegel, H. B., Scuseria, G. E., Robb, M. A., Cheeseman, J. R. and Fox, D. J. (2009). Gaussian 09 Program; Gaussian, Inc. *Wallingford, CT*.
24. Trott, O. and Olson, A. J. (2010). AutoDock Vina: improving the speed and accuracy of docking with a new scoring function, efficient optimization, and multithreading. *Journal of Computational Chemistry*, 31(2): 455-461.
25. Liu, J. Q., Li, X. F., Gu, C. Y., da Silva, J. C., Barros, A. L., Alves-Jr, S. and Soares, T. A. (2015). A combined experimental and computational study of novel nanocage-based metal–organic frameworks for drug delivery. *Dalton Transactions*, 44(44): 19370-19382.
26. Weinhold, F. and Glendening, E. D. (2001). NBO 5.0 program manual: natural bond orbital analysis programs. *Theoretical Chemistry Institute and Department of Chemistry, University of Wisconsin, Madison, WI*, 53706.
27. Suksaengrat, P., Amornkitbamrung, V. and Srepusharawoot, P. (2020). Enhancements of hydrogen adsorption energy in M-MOF-525 (M= Ti, V, Zr and Hf): A DFT study. *Chinese Journal of Physics*, 64: 326-332.
28. Rodrigues, M. O., de Paula, M. V., Wanderley, K. A., Vasconcelos, I. B., Alves Jr, S. and Soares, T. A. (2012). Metal organic frameworks for drug delivery and environmental remediation: A molecular docking approach. *International Journal of Quantum Chemistry*, 112(20): 3346-3355.
29. Pham, T., Forrest, K. A., Nugent, P., Belmabkhout, Y., Luebke, R., Eddaoudi, M. and Space, B. (2013). Understanding hydrogen sorption in a metal–organic framework with open-metal sites and amide functional groups. *The Journal of Physical Chemistry C*, 117(18): 9340-9354.
30. Sun, K., Li, L., Yu, X., Liu, L., Meng, Q., Wang, F. and Zhang, R. (2017). Functionalization of mixed ligand metal-organic frameworks as the transport vehicles for drugs. *Journal of colloid and interface science*, 486: 128-135.
31. Hai, T., Wan, X., Yu, D. G., Wang, K., Yang, Y. and Liu, Z. P. (2019). Electrospun lipid-coated medicated nanocomposites for an improved drug sustained-release profile. *Materials & Design*, 162: 70-79.
32. Hate, S. S., Reutzel-Edens, S. M. and Taylor, L. S. (2020). Influence of drug–silica electrostatic interactions on drug release from mesoporous silica-based oral delivery systems. *Molecular Pharmaceutics*, 17(9): 3435-3446.

Malaysian Journal of Analytical Sciences (MJAS)
Published by Malaysian Analytical Sciences Society

FACILE CHEMICAL SYNTHESIS OF PURE Zn DOPED CeO_2 NANOPARTICLES WITH ENHANCED PHOTOCATALYTIC PERFORMANCE UNDER UV IRRADIATION

(Sintesis Kimia Mudah bagi Nanopartikel CeO_2 Dop Zn Tulen dengan Prestasi Fotokatalitik yang Dipertingkatkan di bawah Penyinaran UV)

Swathi Chidaraboyina[1,3], Arputharaj Samson Nesaraj[1],[2*], Manasai Arunkumar[1]

[1]Department of Applied Chemistry,
Karunya Institute of Technology and Sciences (Deemed to be University),
Karunya Nagar, Coimbatore – 641 114, Tamil Nadu, India
[2]Department of Chemistry,
Kalasalingam Academy of Research and Education (Deemed to be University), Anand Nagar,
Krishnankoil – 626 126, Tamil Nadu, India
[3]Department of Chemistry, Keshav Memorial Institute of Technology, 3-5-1026, Narayanaguda,
Hyderabad – 500 029, Telengana, India

**Corresponding author: samson@klu.ac.in*

Received: 5 August 2022; Accepted: 10 November 2022; Published: 22 February 2023

Abstract

Rhodamine B (RhB) is an organic dye which is generally used in paint, paper and textile industries as a tracer dye. It is found to be highly toxic to living organisms and is expected of having carcinogenic effect. Therefore, the effluents containing RhB dye should be properly treated before releasing into water bodies, such as, rivers, ponds, etc. In this research work, attempts were made to prepare and use zinc doped ceria ($Ce_{1-x}Zn_xO_{2-\delta}$; x = 0, 0.1, 0.2, 0.3, 0.4, 0.5) nanoparticles as photocatalysts to remove RhB dye present in water. These nanoparticles were synthesized by simple wet chemical technique using cheap chemicals. The prepared materials were analyzed by X-ray diffraction (XRD), Fourier transform infra-red (FTIR), Energy-dispersive X-ray spectroscopy (EDX), scanning electron microscope (SEM), ultra violet-visible (UV-Vis) and photo-luminescence (PL) spectroscopy methods. The samples were indexed in face-centered cubic (FCC) crystalline structure. FTIR showed M-O bond in the samples. EDX notified the occurrence of appropriate elements. SEM exhibited smaller and bigger grains in the materials. The λ_{max} was found to be 349 nm by UV-visible analysis. The band gap energy (E_g) was reported in the range of 1.5-3 eV. The photoluminescence spectra for all suspensions were obtained in the range of 390 to 550nm. Then, the photocatalytic elimination of Rhodamine B (Rh B) with the help of $Ce_{1-x}Zn_xO_{2-\delta}$ nano-photocatalysts under UV light was studied. Among the several trials studied, highest photodegradation efficiency (58.71%) was found at pH=11 after 60 minutes irradiation in UV light at room temperature for $Ce_{0.60}Zn_{0.40}O_{2-\delta}$.

Keywords: Zn doped CeO_2 nanoparticles, Rhodamine B, dye removal, photocatalytic degradation, UV irradiation

Abstrak

Rhodamine B (RhB) ialah pewarna organik yang biasanya digunakan dalam industri cat, kertas dan tekstil sebagai pewarna pengesan. Ia didapati sangat toksik kepada organisma hidup dan dijangka mempunyai kesan karsinogenik. Oleh itu, efluen yang

mengandungi pewarna RhB hendaklah dirawat dengan betul sebelum dilepaskan ke dalam badan air, seperti sungai, kolam, dsb. Dalam kerja penyelidikan ini, percubaan telah dibuat untuk menyediakan dan menggunakan ceria terdop zink ($Ce_{1-x}Zn_xO_{2-\delta}$; x = 0, 0.1, 0.2, 0.3, 0.4, 0.5) nanopartikel sebagai fotomangkin untuk menghilangkan pewarna RhB yang terdapat dalam air. Nanopartikel ini telah disintesis dengan teknik kimia basah mudah menggunakan bahan kimia murah. Bahan-bahan yang disediakan telah dianalisis dengan pembelauan sinar-X (XRD), infra merah transformasi Fourier (FTIR), spektroskopi sinar-X penyebaran tenaga (EDX), mikroskop elektron pengimbasan (SEM), Ultra ungu-cahaya nampak (UV-Vis) dan kaedah spektroskopi foto-pendarcahaya (PL). Sampel telah diindeks dalam struktur hablur kubik berpusat muka (FCC). FTIR menunjukkan ikatan M-O dalam sampel. EDX memberitahu berlakunya elemen yang sesuai. SEM mempamerkan butiran yang lebih kecil dan lebih besar dalam bahan. λ_{maks} didapati 349 nm oleh analisis UV-cahaya nampak. Tenaga jurang jalur (Eg) dilaporkan dalam julat 1.5-3 eV. Spektrum foto-pendarcahaya untuk semua suspensi diperoleh dalam julat 390 hingga 550nm. Kemudian, penghapusan fotomangkin Rhodamine B (Rh B) dengan bantuan fotomangkin nano $Ce_{1-x}Zn_xO_{2-\delta}$ di bawah cahaya UV telah dikaji. Antara beberapa ujian yang dikaji, kecekapan fotodegradasi tertinggi (58.71%) didapati pada pH=11 selepas 60 minit penyinaran dalam cahaya UV pada suhu bilik untuk $Ce_{0.60}Zn_{0.40}O_{2-\delta}$.

Kata kunci: nanopartikel CeO_2 terdop Zn, Rhodamine B, penyingkiran pewarna, degradasi fotokatalitik, penyinaran UV

Introduction

Prestigious revolution by nanoscience especially nano metal oxides is being noticed nowadays because of its tremendous application in the fabrication of medical devices [1-4], sensors [5-7], photo catalysts [8-10], etc. The pollutants in particular organic dyes released by the textile industries are affecting the environment seriously. Hence, the elimination of organic dye molecules from the effluent water of textile industry is an urgent issue. Among different organic dyes reported, Rhodamine B is found to be highly harmful when swallowed, with acute oral toxicity, causes serious eye damage or irritation, hazardous to the aquatic environment with long-term side effects [11]. Different technologies, such as, adsorption, ozonation, advanced oxidation process (AOP), membrane filtration, biological methods [12-13] have been tried across the globe for the past two decades to remove the variety of organic dyes present in water. AOP was found to be good in removing different kind of dye molecules and other organic effluents [14-16].

Recently, it was noticed that photocatalysis can also be involved in degrading the organic dyes present in the textile effluents [17]. Metal oxide nanoparticles were found to be effective as photocatalysts [18]. Ceric oxide (CeO_2) is a widely used rare earth oxide material with attractive scientific, technological, energy and environmental applications [19]. The physico-chemical properties, such as, photoluminescence and photocatalytic activity were improved by doping Zn in Ce site of CeO_2 [20]. Further, 1% nickel (Ni) doping was found to retard the band gap of undoped ceria, which could be associated with the reduction of the average crysllite size and therefore, it is considered to be an optimum dopant for ceria [21]. The thermal stability of CeO_2 was improved by doping lanthanum (La) [22]. Iron (Fe) doped CeO_2 nanoparticles exhibited excellent dielectric properties and antimicrobial activity especially in the persistence of bacterial infection [23].

In this research work, to improve the material characteristics of ceria, the metal ion like Zn is doped in cerium lattice of CeO_2 with varying concentration. It was reported that doping Zn into CeO_2 could result in better UV absorptivity [24]. The present study deals with two parts. The first part involves the synthesis and characterization of zinc doped ceria ($Ce_{1-x}Zn_xO_{2-\delta}$; x = 0, 0.1, 0.2, 0.3, 0.4, 0.5) nanoparticles. The second part is about the photocatalytic studies of zinc doped ceria nanomaterials in degrading the Rh B dye found in the water sample under UV light illumination. The obtained experimental results were analyzed in a detailed manner in this research article.

Materials and methods

Chemicals and reagents

Analytical grade of ceric nitrate hexahydrate, zinc nitrate hexahydrate, sodium hydroxide and ethanol were procured and used in this study as such.

Material preparation

Stoichiometric quantities of metal nitrates (cerous nitrate and zinc nitrate) were dissolved in ultra-pure

water. The precipitant solution (NaOH) was mixed drop-wise to the metal nitrate salts solution with constant stirring in a magnetic stirrer. The pH of the solution was kept above pH 9 during the course of the reaction. The resultant precipitate (cerium hydroxide and zinc hydroxide mixture) was filtered-off using Whatman filter paper and cleaned thoroughly without any impurities using the mixture of distilled water and ethanol (9:1 v/v). Then, the precipitate mixture was dried in an air oven and calcined at 600 °C. This resulted as a pure $Ce_{1-x}Zn_xO_{2-\delta}$ (where x = 0, 0.1, 0.2, 0.3, 0.4 and 0.5) nanoparticles. The amount of chemicals used to prepare the materials is indicated in Table 1. The possible reaction mechanism for this preparation is indicated in Equation 1.

$$(1\text{-}x)\ Ce(NO_3)_3 + x\ Zn(NO_3)_2 + 2\ NaOH \rightarrow Ce_{1-x}Zn_xO_{2-\delta} + 2\ NaNO_3 + y\ H_2O \quad \text{(eq. 1)}$$

where x = 0, 0.1, 0.2, 0.3, 0.4 and 0.5

Characterization of materials

X-ray diffraction measurement (XRD) was conducted using X-ray diffractometer (in Shimadzu XRD 6000) at 30 mA current and voltage of 40kV involved the usage of Cukα (K=0.154059nm) radiation with a nickel filter. The 2θ scanning range was 2˚ to 80˚ at a continuous scan mode with a scan speed of 10˚/min. The unit cell parameter was measured by DOS computer programming. The average crystallite size for the samples was determined by Debye –Scherrer's formula. Fourier-Transform infrared (FT-IR) spectra of parent CeO_2 and Zn doped CeO_2 nanoparticles was measured by Shimadzu (IR Prestige 21) FTIR spectrophotometer, using KBr pellet technique in the range of 4000 to 400 cm^{-1}. Scanning electron microscopy (SEM) was performed to detect the surface morphology and the elemental composition of parent CeO_2 and Zn doped CeO_2 nanoparticles (SEM JEOL JSM-6610) equipped with an energy dispersive X-ray (EDAX) spectrophotometer which is operated at 20kV. The band gap of synthesized pure CeO_2 and Zn doped CeO_2 nanoparticles was determined by UV spectrophotometer (Shimadzu 1800). The synthesized samples were loaded into a quartz experimental set-up and the spectrum was recorded using absorbance method.

Table 1. Amount of precursor salts used for the synthesis of CeO_2 and Zn doped CeO_2 nanoparticles [Volume of each solution is 10 mL]

Sample	Weight of $Ce(NO_3)_3$ (g)	Weight of $Zn(NO_3)_2$ (g)	Weight of NaOH (g)
CeO_2	4.342	-	1.6
$Ce_{0.90}Zn_{0.10}O_{2-\delta}$	3.907	0.297	1.6
$Ce_{0.80}Zn_{0.20}O_{2-\delta}$	3.473	0.594	1.6
$Ce_{0.70}Zn_{0.30}O_{2-\delta}$	3.039	0.892	1.6
$Ce_{0.60}Zn_{0.40}O_{2-\delta}$	2.605	1.189	1.6
$Ce_{0.50}Zn_{0.50}O_{2-\delta}$	2.171	1.487	1.6

Photocatalytic experiment

To understand the photocatalytic behavior of Zn doped CeO_2 nanoparticles, Rhodamine B dye was used. For each experiment, 50 mL of RhB dye solution (0.005g of RhB dye was dissolved in one liter of ultra-pure water to make a solution) was mixed with 0.02g of Zn doped CeO_2 nanoparticles and kept in dark for 30 minutes until reach equilibrium. The sample was irradiated to the UV light and the study was carried out at 0, 15, 30, 45 and 60 minutes intervals and centrifuged. 3 mL of the photo reacted solutions was taken for UV-visible spectroscopy measurements at a wavelength of 554 nm. The removal efficiency and percentage of degradation of dye was determined using the Equation 2.

Percentage of degradation of dye = $(C_0-C_t/C_0)*100$ (eq. 2)

where, 'C_o' is the initial absorbance of the dye solution (Rh B solution) and 'C_t' is the absorbance of RhB dye solution after the photodegradation reaction, i.e., after certain time 't'.

Results and Discussion

XRD studies

The crystalline behavior of the prepared materials was analyzed by XRD. The XRD patterns obtained on Zn doped CeO_2 nanoparticles are reported in Figure 1. The resultant XRD results were matched well with the standard CeO_2 data (JCPDS No. 65-5923). The diffraction peaks found at 2θ values of 28.62˚, 33.17˚, 47.59˚, 56.45˚, 59.20˚ and 69.51˚ corresponding to (111), (200), (220), (311), (222) and (400) crystal planes respectively whose hkl values were concurrent with the reported data [25-27]. No impurity peaks relevant to any impurity phases were seen in the XRD diagrams. The crystalline structure of all compositions of CeO_2 was found to be face centered cubic (FCC). The crystallite size, D_x, was calculated by using Debye-Scherrer formula (Equation 3):

$D_x = K\lambda/\beta \cos\theta$ (eq. 3)

where, β is the full width at half maximum (FWHM) of a diffraction peak, K is the shape factor approx. 0.91, λ is the wavelength of the X-ray source that equals 1.54 Å and θ is the Bragg's angle. The calculated crystallite size values of Zn doped CeO_2 are presented in Table - 2. The crystallite size of the samples varied between ranges from 20.47 to 22.04 nm. The theoretical density (D_p) was calculated by using the formula (Equation 4),

$D_p = Z*M/NxV$ $(g.cm^{-3})$ (eq. 4)

where, Z is the number of chemical species in the unit cell, M is the molecular mass of the sample (g/mol), N is the Avogadro's number (6.023×10^{23}) and V is the unit cell volume equals to a^3 which is the lattice constant in cm. From the XRD data, it was found that there is no much variation in the unit cell parameter and unit cell volume of Zn doped CeO_2 samples. The XRD parameters were compared with the Joint Committee on Powder Diffraction Standards (JCPDS) data. Theoretical density values got reduced with regard to the enhancement of dopant concentration as reported in the literature [28].

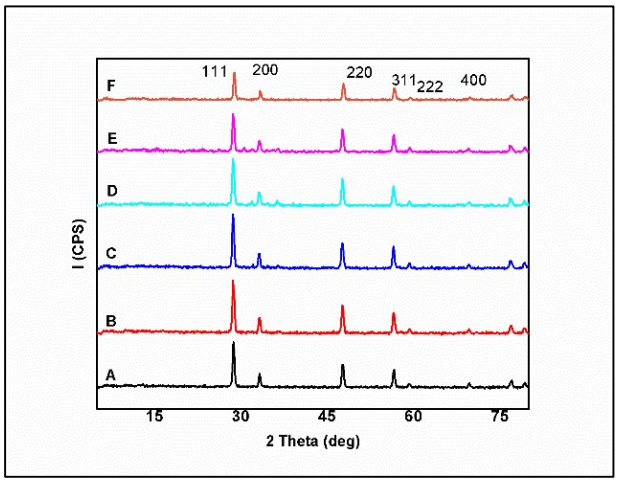


Figure 1. XRD patterns obtained on CeO_2 based nanoparticles a) Pure CeO_2, b) $Ce_{0.90}Zn_{0.10}O_{2-\delta}$, c) $Ce_{0.80}Zn_{0.20}O_{2-\delta}$, d) $Ce_{0.70}Zn_{0.30}O_{2-\delta}$, e) $Ce_{0.60}Zn_{0.40}O_{2-\delta}$, and f) $Ce_{0.50}Zn_{0.50}O_{2-\delta}$

Table 2. Crystallographic parameters obtained on CeO_2 and Zn doped CeO_2 nanoparticles by XRD analysis

Sample	Crystal Structure	Unit Cell Parameter (Å)	Unit Cell Volume ($Å^3$)	Crystallite Size (nm)	Theoretical Density (gcm^{-3})
CeO_2	Cubic (F.C)	5.39	156.59	20.69	7.30
$Ce_{0.90}Zn_{0.10}O_{2-\delta}$	Cubic (F.C)	5.40	157.46	22.13	6.92
$Ce_{0.80}Zn_{0.20}O_{2-\delta}$	Cubic (F.C)	5.40	157.46	20.58	6.60
$Ce_{0.70}Zn_{0.30}O_{2-\delta}$	Cubic (F.C)	5.40	157.46	22.04	6.28
$Ce_{0.60}Zn_{0.40}O_{2-\delta}$	Cubic (F.C)	5.40	157.46	20.47	5.96
$Ce_{0.50}Zn_{0.50}O_{2-\delta}$	Cubic (F.C)	5.40	157.46	20.90	5.65

FTIR studies

The FTIR analysis for all the samples were measured at room temperature. FTIR spectra obtained on Zn doped CeO_2 nanoparticles are shown in Figure 2. The absorption bands observed in the range of 600 cm^{-1} attribute to the stretching vibration modes of M-O [29]. FTIR showed a weak band at 842 cm^{-1} which may be due to the presence of CO_3^{2-} in the sample. Peak appeared at 1384 cm^{-1} may be due to the presence of NO_3^- in the sample. Peak appeared at 1700 cm^{-1} may be due to the presence of carboxylic acid in the sample. The above peaks were reported in the final product because of trace level of organic and inorganic impurities present in the sample as reported [30].

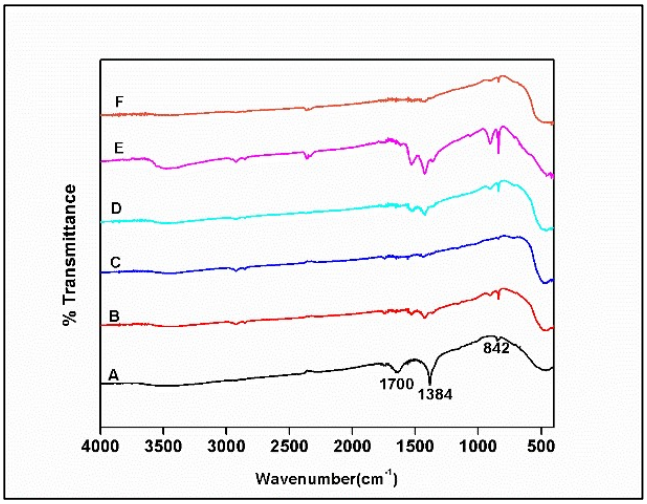


Figure 2. FTIR spectra obtained on CeO_2 based nanoparticles a) Pure CeO_2, b) $Ce_{0.90}Zn_{0.10}O_{2-\delta}$, c) $Ce_{0.80}Zn_{0.20}O_{2-\delta}$, d) $Ce_{0.70}Zn_{0.30}O_{2-\delta}$, e) $Ce_{0.60}Zn_{0.40}O_{2-\delta}$, f) $Ce_{0.50}Zn_{0.50}O_{2-\delta}$

Elemental analysis

The EDX spectra obtained on Zn doped CeO_2 based nanoparticles are shown in Figure 3 and the corresponding data are presented in Table 3. From the data, it was confirmed that appropriate quantities of Ce, Zn and O alone are present in the samples. No impurity elements were seen. So, all the synthesized materials are pure. The product formed is well matched with stoichiometric weight of the corresponding elements.

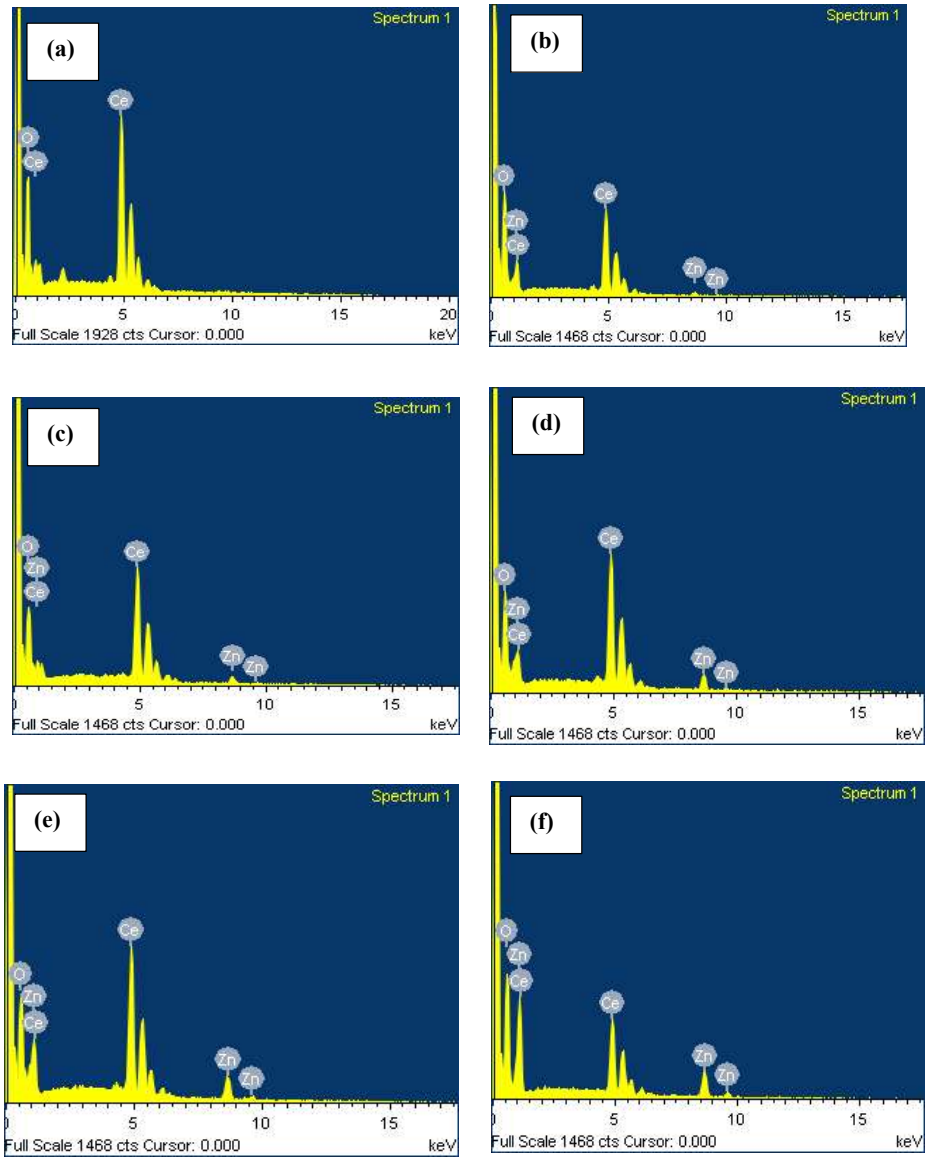


Figure 3. EDAX patterns obtained on CeO_2 based nanoparticles a) Pure CeO_2, b) $Ce_{0.90}Zn_{0.10}O_{2-\delta}$, c) $Ce_{0.80}Zn_{0.20}O_{2-\delta}$, d) $Ce_{0.70}Zn_{0.30}O_{2-\delta}$, e) $Ce_{0.60}Zn_{0.40}O_{2-\delta}$ and f) $Ce_{0.50}Zn_{0.50}O_{2-\delta}$

Morphological study

The SEM photographs of Zn doped CeO_2 nanoparticles are presented in Figure 4. The grain size was found to be 200 to 300 nm. The presence of bigger sized grains in the sample may be due to the agglomeration effect because of high temperature calcination process. Suitable heating rate needs to be followed during calcination which can control the grain growth of the materials [31].

Table 3. Elemental composition data obtained on CeO_2 and Zn doped CeO_2 nanoparticles by EDX analysis

Sample	Cerium		Zinc		Oxygen	
	Atomic %	Weight %	Atomic %	Weight %	Atomic %	Weight %
CeO_2	26.23	75.7	-	-	73.77	24.30
$Ce_{0.90}Zn_{0.10}O_{2-\delta}$	16.92	62.59	1.78	3.08	81.30	34.33
$Ce_{0.80}Zn_{0.20}O_{2-\delta}$	24.00	70.23	4.25	5.80	71.76	23.98
$Ce_{0.70}Zn_{0.30}O_{2-\delta}$	22.05	65.68	7.45	10.35	70.5	23.97
$Ce_{0.60}Zn_{0.40}O_{2-\delta}$	21.61	63.72	9.53	13.10	68.86	23.18
$Ce_{0.50}Zn_{0.50}O_{2-\delta}$	11.51	44.96	11.32	20.63	77.17	34.42

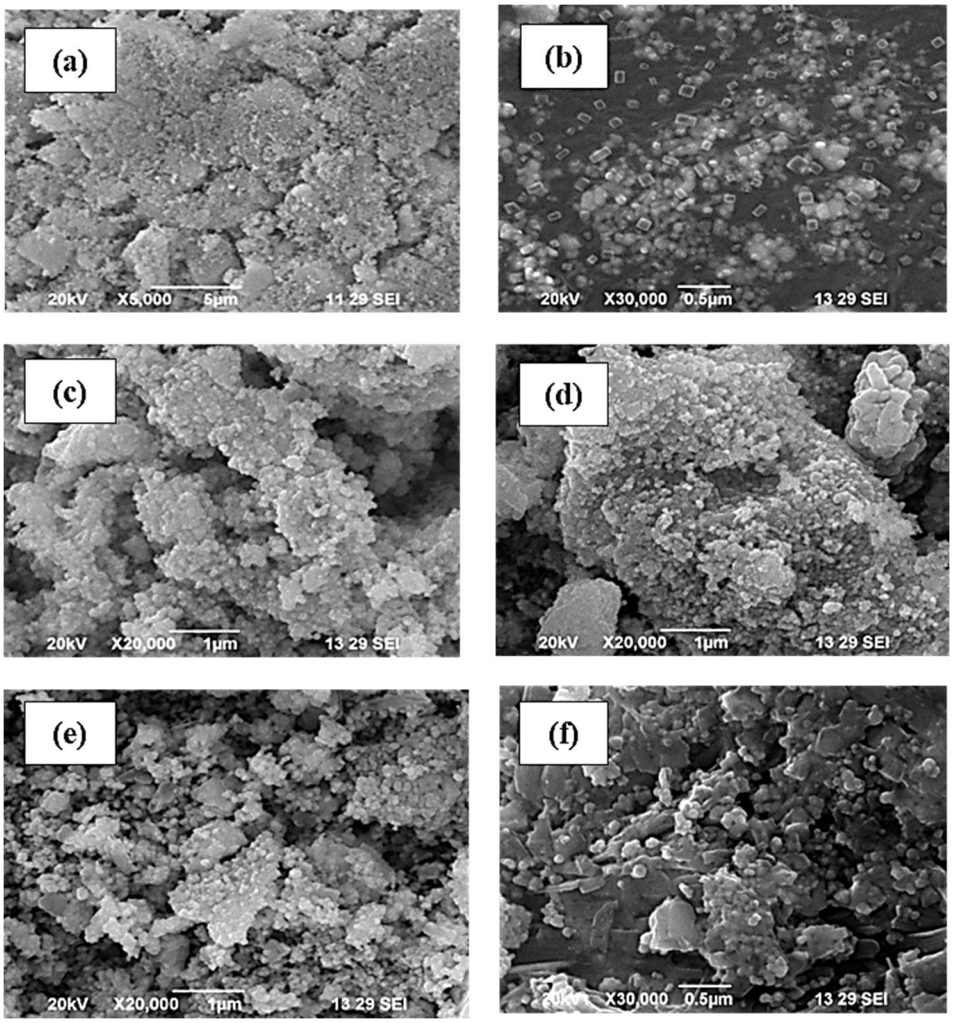


Figure 4. SEM photographs obtained on CeO_2 based nanoparticles a) Pure CeO_2, b) $Ce_{0.90}Zn_{0.10}O_{2-\delta}$ c) $Ce_{0.80}Zn_{0.20}O_{2-\delta}$, d) $Ce_{0.70}Zn_{0.30}O_{2-\delta}$, e) $Ce_{0.60}Zn_{0.40}O_{2-\delta}$ and f) $Ce_{0.50}Zn_{0.50}O_{2-\delta}$

UV studies

To investigate the effect of Zn ion doping on the optical band-gap of the CeO_2 nanoparticles, UV-visible absorption study was carried out. The absorption spectra for undoped and Zn doped CeO_2 nanoparticles were determined in the spectral range of 250nm -350nm as presented in Figure 5. A strong absorption peak is observed at 349nm by the incorporation of Zn ion at Ce

site. The peak shifted towards the lower wavelength side in the doped sample indicated a change in the electronic band structure. Using the absorption data, the energy gap (E_g) of the samples were estimated from Tauc equation [32-33] using the Equation (5)

$$\alpha h\nu)^n = A(h\nu - E_g) \quad \text{(eq. 5)}$$

where 'A' is proportionality constant, 'h' is the Planck's constant, 'ν' is the frequency of vibration, 'hν' is the photon energy, 'α' is the absorption coefficient and 'n' is either 2 for direct band transitions or ½ for indirect band transitions. The absorption coefficient (α) has been calculated using the relation (Equation 6)

$$\alpha = 2.303(A/t) \quad \text{(eq. 6)}$$

where 't' is thickness and 'A' is optical absorbance. The energy band gap (E_g) is estimated by extrapolating the linear region of a plot of $(\alpha h\nu)^2$ *vs* hν shown in the Figure 6. It was observed that the band gap of Zn doped CeO_2 nanoparticles is found to be in the range of 3.0 to 3.19 eV and our results are in close agreement with the reported data [33-34].

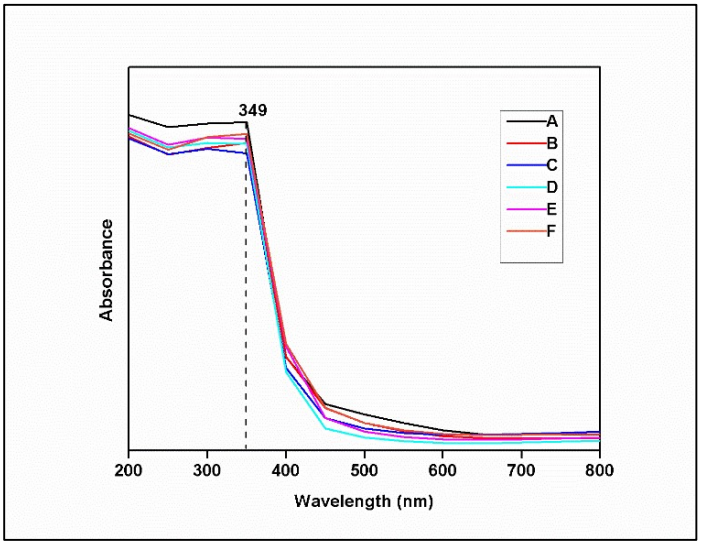


Figure 5. UV-visible spectra obtained on CeO_2 based nanoparticles a) Pure CeO_2, b) $Ce_{0.90}Zn_{0.10}O_{2-\delta}$, c) $Ce_{0.80}Zn_{0.20}O_{2-\delta}$, d) $Ce_{0.70}Zn_{0.30}O_{2-\delta}$, e) $Ce_{0.60}Zn_{0.40}O_{2-\delta}$ and f) $Ce_{0.50}Zn_{0.50}O_{2\delta}$

Photoluminescence studies

The optical, electronic and photochemical properties of the materials can be well studied by photoluminescence (PL) studies [35-36]. PL spectra of Zn doped CeO_2 nanoparticles are reported in Figure 7. This spectra show two emission peaks, one at 395 nm to 425 nm which may correspond to band gap excitonic emission and another one located in between 500 nm to 520 nm which may relate to the presence of surface defects. The occurrence of strong and broad peaks reveals that the fabricated CeO_2 based nanoparticles are pure and crystalline [37]. Based on the above results, UV light source has been utilized for the photodegradation experiments. The best photochemical properties are shown by $Ce_{0.60}Zn_{0.40}O_{2-\delta}$ nanophotocatalyst.

Photocatalytic studies

The photocatalytic activity Zn doped CeO_2 nanoparticles was performed for Rh B dye under UV light illumination. The photodegradation curves obtained the presence of CeO_2 based nanophotocatalysts with Rh B dye and Rh B dye alone without nanophotocatalysts are shown in Figure 8. The results revealed that the optimum photocatalytic efficiency (54.9 %) was shown by $Ce_{0.60}Zn_{0.40}O_{2-\delta}$ after 60 minutes of UV irradiation compared to the other compositions. Thus, the 40 mol% Zn doped CeO_2 nanophotocatalyst

was used as an optimized material to study the photocatalysis with respect to effect of pH and dye concentration. The photocatalytic degradation of the RhB dye can also be understood by plotting a first-order kinetic plot (Figure 9) described by Langmuir and Hinshelwood kinetic model [38]. The rate constant 'k' is calculated by using the Equation 7.

$$\ln C_t/C_0 = -kt \quad \text{(eq. 7)}$$

Where 'C_0' is the concentration at the beginning, 'C_t' is the final concentration and 'k' is the first order rate constant. The rate constant values were found to be 0.08 min^{-1} (CeO_2), 0.005 min^{-1} ($Ce_{0.90}Zn_{0.10}O_{2-\delta}$), 0.007 min^{-1} ($Ce_{0.80}Zn_{0.20}O_{2-\delta}$), 0.012 min^{-1} ($Ce_{0.70}Zn_{0.30}O_{2-\delta}$), 0.016 min^{-1}($Ce_{0.60}Zn_{0.40}O_{2-\delta}$) and 0.012 min^{-1} ($Ce_{0.50}Zn_{0.50}O_{2-\delta}$).

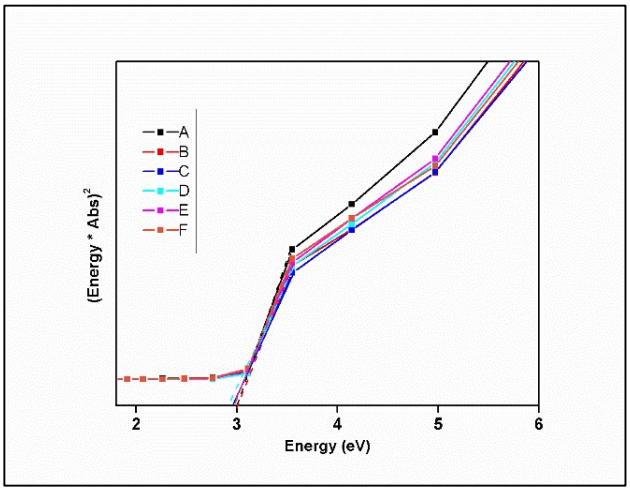


Figure 6. The band gap curves obtained on CeO_2 based nanoparticles a) Pure CeO_2, b) $Ce_{0.90}Zn_{0.10}O_{2-\delta}$, c) $Ce_{0.80}Zn_{0.20}O_{2-\delta}$, d) $Ce_{0.70}Zn_{0.30}O_{2-\delta}$, e) $Ce_{0.60}Zn_{0.40}O_{2-\delta}$ and f) $Ce_{0.50}Zn_{0.50}O_{2-\delta}$

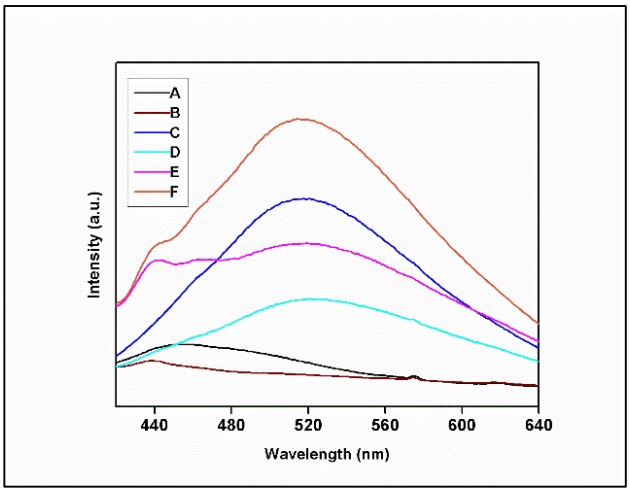


Figure 7. The PL spectra obtained on CeO_2 based nanoparticles a) Pure CeO_2, b) $Ce_{0.90}Zn_{0.10}O_{2-\delta}$, c) $Ce_{0.80}Zn_{0.20}O_{2-\delta}$, d) $Ce_{0.70}Zn_{0.30}O_{2-\delta}$, e) $Ce_{0.60}Zn_{0.40}O_{2-\delta}$ and f) $Ce_{0.50}Zn_{0.50}O_{2-\delta}$

Influence of pH

The most important parameter to control the adsorption process is pH [39]. The pH of the dye solution in the present study was adjusted by the addition of dilute hydrochloric acid and dilute sodium hydroxide. To this study, pH values, such as, 2.5, 4.3, 6.5, 9.0 and 11.0 were fixed and the photodegradation efficiency was measured after irradiation in UV light source for one hour. The influence of pH value on the photocatalytic efficiency of Rh B dye in the presence of $Ce_{0.60}Zn_{0.40}O_{2-\delta}$ (best sample) is shown in Figure 10. The photocatalytic phenomenon is optimum (58.71%) at pH 9 in comparison with other pH values. Generally, the dye removal efficiency is minimal at low pH ranges [40].

Influence of concentration of dye

The photocatalytic efficiency of the best performing material ($Ce_{0.60}Zn_{0.40}O_{2-\delta}$) was further studied at a standardized pH 9 of varying RhB dye concentrations, such as, 0.0025 g/L, 0.005 g/L, 0.0075 g/L and 0.01 g/L after 60 minutes under UV irradiation. Figure 11 shows the influence of RhB dye concentration on the photocatalytic efficiency of $Ce_{0.60}Zn_{0.40}O_{2-\delta}$ (best sample). The results revealed that the optimum photocatalytic efficiency is found at 58.71% for the dye concentration of 0.005g/L at pH 9. It was reported that the photodegradation is highly dependent on the probability of creation of OH radicals on the catalyst surface during the reaction process. If the concentration of dye is very high, it will retard the reaction between the dye molecules and OH radicals. Hence, optimum concentration of dye is required to have better efficiency of photodegradation process [41].

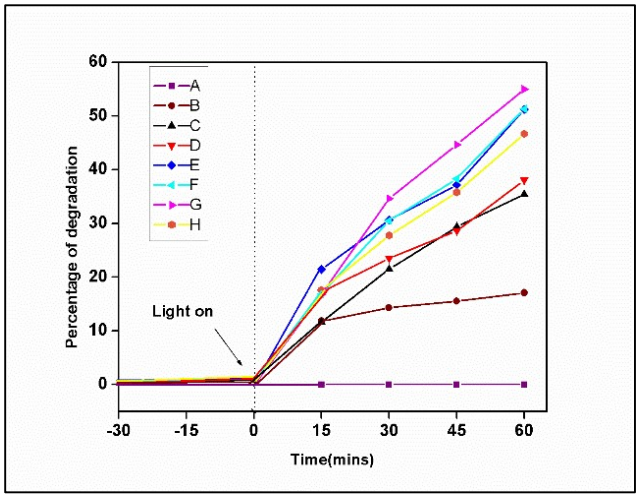


Figure 8. Photodegradation curves obtained in presence of CeO_2 based nanophotocatalysts with RhB dye and RhB dye alone without nanophotocatalysts a) RhB alone in dark, b) RhB alone in light, c) Pure CeO_2, d) $Ce_{0.90}Zn_{0.10}O_{2-\delta}$, e) $Ce_{0.80}Zn_{0.20}O_{2-\delta}$, f) $Ce_{0.70}Zn_{0.30}O_{2-\delta}$, g) $Ce_{0.60}Zn_{0.40}O_{2-\delta}$, h) $Ce_{0.50}Zn_{0.50}O_{2-\delta}$

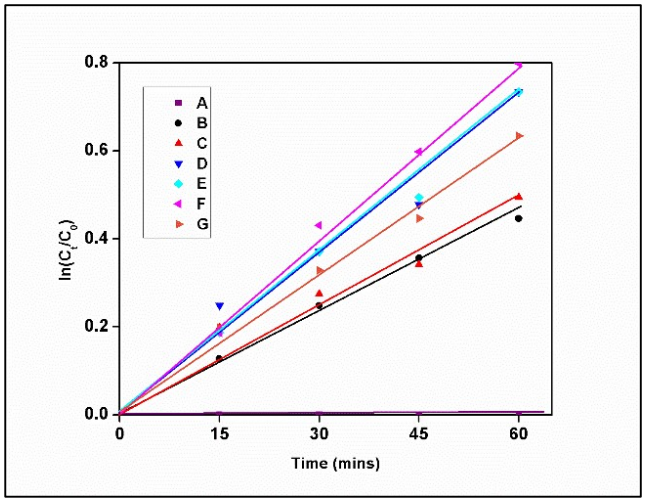


Figure 9. First order kinetic plot of RhB dye using a) RhB alone in the absence of photocatalyst, b) Pure CeO_2; c) $Ce_{0.90}Zn_{0.10}O_{2-\delta}$, d) $Ce_{0.80}Zn_{0.20}O_{2-\delta}$, e) $Ce_{0.70}Zn_{0.30}O_{2-\delta}$, f) $Ce_{0.60}Zn_{0.40}O_{2-\delta}$; G) $Ce_{0.50}Zn_{0.50}O_{2-\delta}$

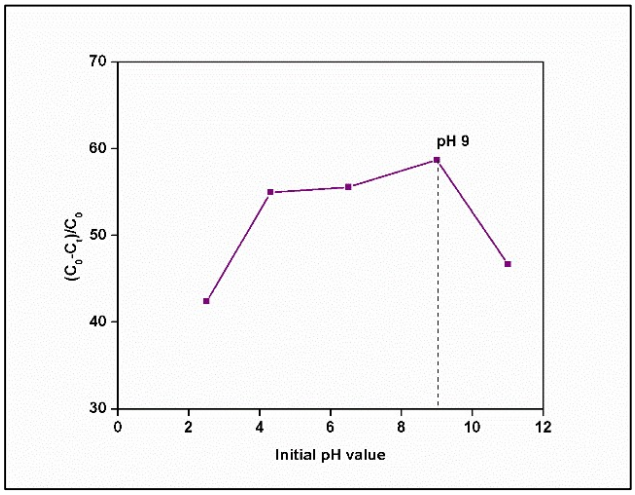


Figure 10. The influence of pH value on the degradation efficiency of RhB in presence of $Ce_{0.60}Zn_{0.40}O_{2-\delta}$ photocatalyst material

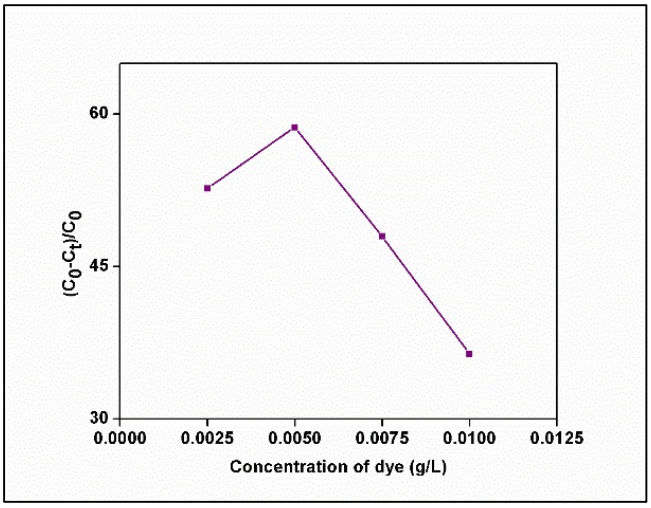


Figure 11. The influence of RhB dye concentration on the photocatalytic efficiency of $Ce_{0.60}Zn_{0.40}O_{2-\delta}$ nanoparticle

Conclusion

Simple wet chemical method was adopted for the preparation of pure CeO_2 and Zn doped CeO_2 ($Ce_{1-x}Zn_xO_{2-\delta}$; where x=0, 0.10, 0.20, 0.30, 0.40 and 0.50) nanoparticles in this research work. All the samples were assigned with cubic (F.C) crystalline structure based on XRD analysis. FTIR data confirmed the presence of M-O bond in the samples. EDX analysis reported the presence of Ce, Zn and O in the powder particles with appropriate concentration. Agglomeration of grains was revealed by SEM. The UV-visible spectra showed strong absorption peak around 349nm (λ_{max}) in all the composition of CeO_2 samples. The E_g of $Ce_{1-x}Cu_xO_{2-\delta}$ was found to be in the range of 3.0eV - 3.19eV. The PL spectra of samples exhibited two peaks, viz., at 420nm (blue emission) and the other at 520 nm (blue emission). The photocatalysts, such as, CeO_2, $Ce_{0.90}Zn_{0.10}O_{2-\delta}$, $Ce_{0.80}Zn_{0.20}O_{2-\delta}$, $Ce_{0.70}Zn_{0.30}O_{2-\delta}$, $Ce_{0.60}Zn_{0.40}O_{2-\delta}$ and $Ce_{0.50}Zn_{0.50}O_{2-\delta}$ delivered a photocatalytic degradation efficiency of 35.46, 38.06, 51.25, 51.30, 54.97 and 46.69 % at pH 4.3 under illumination of UV light after 60 minutes. The parameters like, effect of pH and effect of initial concentration of dye were studied for the best sample $Ce_{0.60}Zn_{0.40}O_{2-\delta}$. At different pH values of 2.5, 4.3, 6.5, 9 and 11, the photocatalytic efficiency for $Ce_{0.60}Zn_{0.40}O_{2-\delta}$ was found to be 42.39, 54.97, 55.59, 58.71 and 46.69% respectively. Therefore, among the different compositions studied, $Ce_{0.60}Zn_{0.40}O_{2-\delta}$ exhibited excellent performance towards elimination of Rhodamine B dye (Rh B) with 58.71% efficiency under UV irradiation. Further, the results revealed that the degradation efficiency was found to be maximum at pH = 9 and at a concentration of 0.005 g/L of RhB under a path route of pseudo-first order kinetic reaction.

Acknowledgements

The authors acknowledge Karunya Institute of Technology and Sciences for providing the research facilities.

References

1. Wasim, M., Ashraf, M., Tayyaba, S. and Nazir, A. (2019). Simulation and Synthesis of ZnO nanorods on AAO nano porous template for use in a MEMS device. *Digest Journal* of *Nanomaterials* and *Biostructures*, 14: 559-567.
2. Liu, H., Liu, J., Xie, X. and Li, X. (2020). Development of photo-magnetic drug delivery system by facile-designed dual stimuli-responsive modified biopolymeric chitosan capped nano-vesicle to improve efficiency in the anesthetic effect and its biological investigations. *Journal* of *Photochemistry* and *Photobiology B*: *Biology*, 202: 111716.
3. Andryukov, B. G., Besednova, N .N., Romashko, R. V., Zaporozhets, T. S. and Efimov, T. A. (2020). Label-free biosensors for laboratory-based diagnostics of infections: Current achievements and new trends. *Biosensors*, 10(2):11.

4. Souza, J. M. T., de Araujo, A. R., de Carvalho, A. M. A., Amorim, A. d. G. N., Daboit, T. C., de Almeida, J. R. d. S., da Silva, D. A. and Eaton, P. (2020). Sustainably produced cashew gum-capped zinc oxide nanoparticles show antifungal activity against *Candida parapsilosis*. *Journal of Cleaner Production*, 247: 119085.
5. Ilager, D., Shetti, N. P., Malladi, R. S., Shetty, N. S., Reddy, K. R. and Aminabhavi, T. M. (2020). Synthesis of Ca-doped ZnO nanoparticles and its application as highly efficient electrochemical sensor for the determination of anti-viral drug, Acyclovir. *Journal* of *Molecular Liquids*, 322:114552.
6. Kulkarni, D. R., Malode, S. J., Prabhu, K. K., Ayachit, N. H., Kulkarni, R. M. and Shetti, N. P. (2020). Development of a novel nanosensor using ca-doped ZnO for antihistamine drug. *Materials Chemistry and Physics*, 246: 122791.
7. Shanbhag, M. M., Shetti, N. P., Kulkarni, R. M. and Chandra, P. (2020). Nanostructured Ba/ZnO modified electrode as a sensor material for detection of organosulfur thiosalicylic acid. *Microchemical* Journal, 159: 105409.
8. Gadisa, B. T., Appiah-Ntiamoah, R. and Kim, H. (2019). *In-situ* derived hierarchical ZnO/Zn-C nanofiber with high photocatalytic activity and recyclability under solar light. *Applied Surface Science*, 491: 350-359.
9. He, J., Zhang, Y., Guo, Y., Rhodes, G., Yeom, J., Li, H. and Zhang, W. (2019). Photocatalytic degradation of cephalexin by ZnO nanowire under simulated sunlight: Kinetics, influencing factors, and mechanisms. *Environment International*, 132: 105105.
10. Messih, M. A., Shalan, A. E., Sanad, M. F. and Ahmed, M. (2019). Facile approach to prepare ZnO@SiO_2 nanomaterials for photocatalytic degradation of some organic pollutant models. *Journal of Materials Science*: *Materials in Electronics*, 30: 14291-14299.
11. Vatchalan, L. and Pandiselvam, S. (2021). Carbon nano particles as better adsorbent against photocatalytic degrader for the rhodamine - B dye. *Journal of Water and Environmental Nanotechnology*, 6(3): 232-240.
12. Deng, Y. and Zhao, R. (2015). Advanced oxidation processes (AOPs) in wastewater treatment. *Current Pollution Reports*, 1: 167-176.
13. Francis, M. H., Sarkar, R., Roy, S., Jaffar, S., Mohan, V. R., Kang, G. and Balraj, V. (2016). Effectiveness of membrane filtration to improve drinking water: A quasi-experimental study from rural Southern India. *American Journal of Tropical Medicine* and *Hygiene*, 95(5): 1192-1200.
14. El Nemr, A., Hassaan, M. A. and Madkour, F. F. (2018). Advanced oxidation process (AOP) for detoxification of acid red 17 dye solution and degradation mechanism. *Environmental Processes*, 5: 95-113.
15. Qi, K., Cheng, B., Yu, J. and Ho, W. (2017). Review on the improvement of the photocatalytic and antibacterial activities of ZnO. *Journal of Alloys and Compounds*, 727: 792-820.
16. Liu, H., Li, L., Guo, C., Ning, J., Zhong, Y. and Hu, Y. (2020). Thickness-dependent carrier separation in $Bi_2Fe_4O_9$ nanoplates with enhanced photocatalytic water oxidation. *Chemical Engineering Journal*, 385:123929.
17. Chong, M. N., Jin, B., Chow, C. W. K. and Saint, C. (2010). Recent developments in photocatalytic water treatment technology: A review. *Water Research*, 44 (10): 2997-3027.
18. Joshi, N.C., Gururani, P. and Gairola, S.P. (2022). Metal oxide nanoparticles and their nanocomposite-based materials as photocatalysts in the degradation of dyes. *Biointerface Research in Applied Chemistry*, 12(5): 6557-6579.
19. Zhang, H., He, X., Zhang, Z., Zhang, P., Li, Y., Ma, Y., Kuang, Y. and Chai, Z. (2011). Nano-CeO_2 exhibits adverse effects at environmental relevant concentrations. *Environmental Science & Technology*, 45(8): 3725-3730.
20. Majeed Khan, M. A., Khan, W., Ahamed, M. and Alhazaa, A. N. (2017). Microstructural properties and enhanced photocatalytic performance of Zn doped CeO_2 nanocrystals. *Scientific Reports*, 7: 12560.

21. Habib, I. Y., Muhammad, M., Yakasai, M. Y. and Abdullahi, A. D. (2021). Structural, morphological and optical properties of Ni-doped CeO_2 nanospheres prepared by surfactant free co-precipitation technique. *Open Journal of Science and Technology*, 4(4): 165-177.
22. Hou, X., Lu, Q. and Wang, X. (2017). Enhanced catalytic properties of La-doped CeO_2 nanopowders synthesized by hydrolyzing and oxidizing $Ce_{46}La_5C_{49}$ alloys. *Journal of Science: Advanced Materials and Devices*, 2(1): 41-44.
23. Kumar, S., Al Omar, S. Y., Kumari, K., Albalwi, F., Kumar, R., Ahmed, F., Ahmed, N., Dwivedi, S. and Alvi, P.A. (2021). Electrical and antibacterial properties of Fe-doped CeO_2 nanoparticles. *Crystals,* 11: 1594.
24. Nurhasanah, I., Sutanto, H. and Futikhaningtyas, R. (2014). Optical properties of Zn-doped CeO_2 nanoparticles as function of Zn content. *Advanced Materials Research*, 896: 108-111.
25. Prabaharan, D. M. D. M., Sadaiyandi, K., Mahendran M. and Sagadevan, S. (2016). Structural, optical, morphological and dielectric properties of cerium oxide nanoparticles. *Materials Research*, 19(2): 478-482.
26. Wang, Z., Quan, Z. and Lin, J. (2007). Remarkable changes in the optical properties of CeO_2 nanocrystals induced by lanthanide ions doping. *Inorganic Chemistry*, 46(13): 5237-5242.
27. Jasmine Ketzial, J. and Samson Nesaraj, A. (2011). Synthesis of CeO_2 nanoparticles by chemical precipitation and the effect of a surfactant on the distribution of particle sizes. *Journal of Ceramic Processing Research*, 12(1): 74-79.
28. Thavarani, M., Charles Robert, M., Pavithra, N., Saravanan, R., Kannan, Y.B. and Balaji Prasath, S. (2022). Effect of Ca^{2+} doping on the electronic charge density and magnetic properties of $ZnFe_2O_4$ spinel ferrites. *Journal of Materials Science: Materials in Electronics*, 33: 4116-4131.
29. Udayakumar, S., Renuga, V. and Kavitha, K. (2012). Synthesis and characterization of Ni - doped ZnO by chemical precipitation method. *International Journal of Recent Scientific Research*, 3: 118-122.
30. Nandiyanto, A. B. D., Oktiani, R. and Ragadhita, R. (2019). How to read and interpret FTIR spectroscope of organic material. *Indonesian Journal of Science & Technology*, 4(1): 97-118.
31. Napitupulu, R. A. M. (2017). Influence of heating rate and temperature on austenite grain size during reheating steel. *IOP Conference Series: Materials Science and Engineering*, 237: 012038.
32. Arunkumar, M. and Samson Nesaraj, A. (2021). One pot chemical synthesis of ultrafine $NiAl_2O_4$ nanoparticles: Physico-chemical properties and photocatalytic degradation of organic dyes under visible light irradiation. *Inorganic and Nano-Metal Chemistry*, 51(6): 910-917.
33. Balogun, S.W., Sansui, Y. K. and Aina, A.O. (2018). Structural and optical properties of titanium dioxide thin film deposited by spin-coating technique. *International Journal of Development Research*, 8(1): 18486-18490.
34. Bhatia, S. and Verma, N. (2017). Photocatalytic activity of ZnO nanoparticles with optimization of defects. *Materials Research Bulletin*, 95: 468-476.
35. Amiri Gharaghani, M. and Malakootian, M. (2017). Photocatalytic degradation of the antibiotic ciprofloxacin by ZnO nanoparticles immobilized on a glass plate. *Desalination and Water Treatment*, 89: 304-314.
36. Chen, X. and Mao, S. S. (2007). Titanium dioxide nanomaterials: Synthesis, properties, modifications, and applications. *Chemical Reviews*, 107(7): 2891-959.
37. Sadiq, M. M. J. and Samson Nesaraj, A. (2013). Effect of surfactants in the synthesis of NiO nanoparticles by colloidal thermal assisted reflux condensation method. *Journal of New Technology Materials*, 3(2): 14-28.
38. Chandraboss, V. L., Natanapatham, L., Karthikeyan, B., Kamalakkannan. J., Prabha, S. and Senthilvelan, S. (2013). Effect of bismuth doping on the ZnO nanocomposite material and study of its photocatalytic activity under UV-light. *Materials Research Bulletin*, 48(10): 3707-3712.

39. Akpan, U. G. and Hameed, B. H. (2009). Parameters affecting the photocatalytic degradation of dyes using TiO_2-based photocatalysts: A review. *Journal of Hazardous Materials*, 170(2-3): 520-529.
40. Anju Chanu, L., Joychandra Singh, W., Jugeshwar Singh K. and Nomita Devi, K. (2019). Effect of operational parameters on the photocatalytic degradation of methylene blue dye solution using manganese doped ZnO nanoparticles. *Results in Physics*, 12: 1230-1237.
41. Jantawasu, P., Sreethawong, T. and Chavadej, S. (2009). Photocatalytic activity of nanocrystalline mesoporous-assembled TiO_2 photocatalyst for degradation of methyl orange mono azo dye in aqueous wastewater. *Chemical Engineering Journal*, 155 (1-2):223-233.

Malaysian Journal of Analytical Sciences (MJAS)
Published by Malaysian Analytical Sciences Society

MALAYSIAN MEDICINAL PLANTS (*Euphorbia milii*) AS A DRUG ALTERNATIVE SOURCE FOR ANTI-GOUT THERAPY

(Tumbuhan Perubatan Malaysia (*Euphorbia milii*) sebagai Sumber Ubat Alternatif untuk Terapi Anti-gout)

Nur Syafika Amani Abd. Mutalib[1], Mohamad Hussin Haji Zain[2], Asnuzilawati Asari[1,3], Maulidiani Maulidiani[1], Ahmad Nazif Aziz[1,3], Norhayati Yusuf[1], Nurul Huda Abdul Wahab[1,3*]

[1]*Faculty of Science and Marine Environment, Universiti Malaysia Terengganu, 21030 Kuala Nerus, Terengganu, Malaysia*
[2]*Center for Foundation Studies in STEM, Universiti Malaysia Terengganu, 21030 Kuala Nerus, Terengganu, Malaysia*
[3]*Advanced Nano Materials (ANoMa) Research Group, Universiti Malaysia Terengganu, 21030 Kuala Nerus, Terengganu, Malaysia*

[*]*Corresponding author: nhuda@umt.edu.my*

Received: 3 July 2022; Accepted: 20 January 2023; Published: 22 February 2023

Abstract

Gout has been detected as amongst the oldest disease since the 5th Century BC and to date it is arising. This disease occurs due to excess production of uric acid that leads to the formation of crystals around the joints. It may become worse when permanent tissue damage is involved. Nowadays, many advance treatments are found. However, it may be very costly. One of the cheapest alternatives is a synthetic drug called allopurinol, which has negative side effect for long term consumption. *Euphorbia milii* (Euphorbiaceae) was chosen as the sample due to various secondary metabolites being reported which might be beneficial for treatment of gout. Quantitative analysis of total phenolic content and xanthine oxidase inhibitory assay were done to the crude extracts of Malaysian *E. milii*, followed by IC_{50} to determine the concentration needed to reduce 50% of uric acid production. The result showed that methanol leaves extract of *E. milii* had the highest total phenolic content (0.77 ± 0.02 mg QAE/g of sample), which made this extract a potent uric acid inhibitor (Half maximal inhibitory concentration, IC_{50} = 0.0864 mM). This value had significantly reduced uric acid production by 65.6%. Therefore, methanolic leaves extract that was subjected to GC-MS and hexadecanoic acid and has anti-gout properties, was discovered in the crude extract. In conclusion, the Malaysian *E. milii* plant has potential to be developed as a new drug which might be beneficial for the treatment of gout.

Keywords: *Euphorbiaceae,* Malaysian plant, quantitative analysis, anti-gout, uric acid

Abstrak

Gout telah dikesan sebagai antara penyakit tertua sejak abad ke-5 SM dan ia terus wujud hingga kini. Penyakit ini berlaku akibat pengeluaran asid urik berlebihan yang menyebabkan pembentukan kristal di sekeliling sendi. Ia mungkin menjadi lebih teruk apabila melibatkan kerosakan kekal pada tisu. Kini, banyak rawatan awal telah ditemui. Walau bagaimanapun, ia mungkin sangat mahal. Salah satu alternatif yang paling murah ialah ubat sintetik bernama allopurinol yang mempunyai kesan sampingan negatif untuk penggunaan jangka panjang. *Euphorbia milii* (Euphorbiaceae) telah dipilih sebagai sampel kerana pelbagai metabolit sekunder yang mungkin bermanfaat untuk rawatan gout telah dilaporkan. Analisis kuantitatif jumlah kandungan fenolik dan ujian perencatan xanthine oxidase telah dilakukan terhadap ekstrak mentah *E. milii* Malaysia diikuti dengan IC_{50} untuk menentukan

kepekatan yang perlu untuk mengurangkan 50% daripada pengeluaran asid urik. Hasilnya, ekstrak metanol daun *E. milii* menunjukkan jumlah kandungan fenolik yang tertinggi (0.77 ± 0.02 mg QAE/g sampel) yang menjadikan ekstrak ini berpotensi sebagai perencat asid urik (Kepekatan perencatan separuh maksimum, IC50 = 0.0864 mM). Nilai ini mengurangkan pengeluaran asid urik dengan ketara sebanyak 65.6%. Oleh itu, ekstrak metanol daun kemudiannya tertakluk kepada GC-MS dan asid heksadekanoik serta mempunyai sifat anti-gout, telah dikenal pasti wujud dalam ekstrak mentah. Kesimpulannya, tumbuhan *E. milii* Malaysia ini berpotensi untuk dibangunkan sebagai satu ubat baru yang mungkin bermanfaat untuk rawatan gout.

Kata kunci: *Euphorbiaceae*, tumbuhan Malaysia, analisis kuantitatif, anti-gout, asid urik

Introduction

Gout has been alarming worldwide and it is now the most common type of inflammatory arthropathy in adults. This disease is caused by excess uric acid levels in blood due to oxidative stress that increases the production of xanthine oxidase incorporation to increase the uric acid production. This condition results in the deposition of urate (as monosodium urate monohydrate) crystals around joints, which causes an acute inflammatory response and induces a permanent tissue damage that is characterized by the appearance of ulceration of the joint cartilage, marginal osteophytosis, erosive lesions and chronic inflammation of synovial membrane [1, 2]. The most common urate lowering treatment is the development of xanthine oxidase (XO) inhibitor. Allopurinol is one of the best and the most widely used as XO inhibitor. However, prolonged usage of Allopurinol can cause negative side effects to the patient such as nephrolithiasis, hypersensitivity reaction, Stevens-Johnson syndrome, renal toxicity, allergic reactions, and fatal liver necrosis [3].

Flavonoids are secondary metabolites that are responsible to give color to plants. In medicinal aspect, it can also act as anti-oxidative, anti-inflammatory, anti-mutagenic, antifungal, antiviral, antibacterial activity and anti-carcinogenic properties coupled with their capacity to modulate key cellular enzyme function [4]. Moreover, flavonoids are known to inhibit a number of enzymes such as phosphodiesterase, Ca^{2+} ATPase, aldosereductase, lipoxygenase, cyclooxygenase [5], and human P450 enzymes. Recently, studies on flavonoids against xanthine oxidase (XO) had become a trend. The study by Yuan et al. [6] revealed that different structure of flavonoids would affect the binding process which affected the inhibition of xanthine oxidase. Research by Suyun Lin et al. [7] proposed that amongst the 20 flavonoids used in their project can be categorized into three groups based on activeness. The first group was composed of the most active flavonoids with low α values (≤10), which were chrysin and genistein (α values of 0.49 and 0.59, respectively). The first group had α values of below 1, which indicated that only compounds in small amount was needed to inhibit XO as compared to allopurinol. Additionally, quercetin (α = 9.76) and kaempferol (α = 5.76) were less active than apigenin (α = 1.20. The second group was referred as flavonoids that expressed intermediate activity ($10 < \alpha \leq 50$). Most of them were flavonols, such as morin, myricetin, diosmetin, isorhamnetin, and hyperin. In the last group ($\alpha > 50$), as compared to rutin (α = 57.29) and baicalin (α = 50.13), naringenin and silybin, exhibited much weaker inhibition (α = 140.4 and 189.6, respectively). Nonetheless, phloretin, curcumin, and epicatechin did not even show XO inhibition activity [8, 9].

Therefore, this study is designed to identify potential xanthine oxidase inhibitor properties contained in *Euphorbia milii* Malaysian species as it is rich in natural bioactive compound. *Euphorbia milii* Des Moul. *ex* Boiss var. *hislopii* is a decorative, cactus-like plant that contains milky sap and the branches and stems are covered with thick sharp black thorns. This plant is native to Inselberge, which is located in the central Plateau of Madagascar, Africa and it is also found in tropical and subtropical countries [10]. Phytochemical studies of methanolic extract of *E. milii* by Delgado et al. [11] revealed the presence of β-sitosterol, cycloartenol, β-amyrin acetate, lupeol, euphol, and flavonoid. Meanwhile, there were two triterpenoids (Taraxerol and 28-hydroxyfriedelan-1, 3-dione-29-oic acid), one flavone (Quercetin 3-O-(2”-O-galloyl)-a-L-arabinofuranoside) and two phenolic compounds (7 7’-dihydroxy, 8, 6’-bicoumarin and 9-acetyl-3’4’ dimethoxy dehydroconiferyl-3-alcohol) from the red flowers of *E. milii* that were isolated by Kamurthy et al. [12]. Based on literature review, *E. milli* was expected to show positive results towards the XO inhibitor properties which might give benefits as a safer approach for the prevention and treatment of gout [13]. Table 1 shows the taxonomic hierarchy of *E. milii* and its origin. Meanwhile, Figure 1 shows the *E. milii* plant used.

Table 1. Taxonomic hierarchy of *Euphorbia milii* [13]

Kingdom	**Plantae**
Phylum	Trachephyta
Class	Magnoliopsida
Family	Euphorbiaceae
Genus	*Euphorbia*
Scientific Name	*Euphorbia milii Des Moul*
Others Name	Christ plant, Christ thrown (Brazil) Chrown of Thorn (Malaysia)
Origin	Plateau of Madagascar, Africa



Figure 1. *Euphorbia milii* plant (flowers and leaves)

Materials and Methods

Plant identification

Plant material (flowers and leaves) were collected from Kota Tinggi, Johor and identified by Tuan Haji Muhamad Razali Salam, a senior lab assistant of Biological laboratory, Faculty of Science and Marine Environment, Universiti Malaysia Terengganu.

Sample preparation

Each sample was washed and dried at room temperature until it was completely dried. About 40 g of dried flower samples and 40 g of dried leaf samples were ground and extracted by using three different solvents with increasing polarities (hexane, ethyl acetate, and methanol) at room temperature. Then, each extract was concentrated by using a rotary evaporator to obtain the crude extracts.

Determination of total phenolic content

This test was performed by using Folin–Ciocalteu method that was developed by Chun and his teams with some modifications in 2013 [14]. A calibration curve was established by using gallic acid (0.01 to 0.05 mg/ mL) as standard references plotted. TPC was revealed as mg GAE/ g sample [15].

Preparation of calibration curve of standard uric acid

Standard uric acid (1 mM) was prepared by dissolving 1.69 mg of uric acid with a few drops of 0.2 M sodium hydroxide (NaOH) and added with distilled water until the calibration mark of 10 mL volumetric flask. Then, a series of concentrations of uric acid solution were prepared (0.01 mM to 0.2 mM) and the absorbance was recorded by using UV-Vis spectrophotometer (Shimadzu, UV- Vis 1800) at a wavelength of 295 nm.

Xanthine oxidase inhibitory activity

This test was carried out by referring to the method reported by Boumerfeg et al. [16] with some modification. The reaction mixture consisted of 1500 µL phosphate buffer solution, 300 µL of distilled water, 300 µL of 0.1 mg/mL extract solution and 300 µL of enzyme solution. After 5 min of incubation, 600 µL of xanthine solution was added to the mixture. The absorbance of the kinetic assay was measured immediately by using UV-Vis spectrophotometer (Shimadzu, UV- Vis 1800) at 295 nm at an interval of 2 min for 30 min. The blank was prepared by using the same method but the enzyme was replaced with a buffer solution.

A standard reaction mixture was prepared in the same way as the sample reaction mixture. However, the extracts solution was replaced with 0.1 mg/mL of

positive control of Allopurinol. Meanwhile, for negative control (blank) the extracts solution was replaced with distilled water. The percentage of XOI assay was calculated by using the following formula:

Concentration of uric acid produced for every 2 min of reaction (G),

$$(G) = \frac{(D-E)}{F} \quad \text{(eq. 1)}$$

where, D is absorbance of each sample, E is blank absorbance of each sample and F is slope from the calibration curve of standard uric acid.

Production rate of uric acid (activity of enzyme) (A) is,

$$(A) = \frac{B}{2} \quad \text{(eq. 2)}$$

where, B is slope (gradient) from G for 30 min of reaction.

Percentage of inhibition is,

$$\%\ inhibition = (1 - \left(\frac{C}{A}\right) \times 100 \quad \text{(eq. 3)}$$

where, A is absorbance of control at 30 min and C is absorbance of sample at 30 min.

IC_{50} evaluation for methanol leaves extract on XOI activity

The sample and positive control of Allopurinol were repeated as the xanthine oxidase inhibitory activity method. However, five different concentrations (0.02 mg/mL - 0.1 mg/mL) were used to evaluate the inhibitory percentage at 50%. The equation was calculated by using natural Log dose inhibition curve.

Gas chromatography - mass spectroscopy (GC-MS) analysis

Methanolic leaves extract of *E. milii* was subjected to GC-MS analysis by using GCMS-QP2010 Ultra (Shimadzu Co., Japan) equipped with SLB ™ – 5ms (Fused Silica Capillary Column; 30m x 0.25mm x 0.25µm film). Electron impact mode of 70 electron volt (eV) was used for ionization in the GC-MS analysis. The analysis was carried out by injecting 1µL of sample with split ratio of 10 with inert helium gas (99.99%) as carrier gas. The initial oven temperature was maintained at 50°C for 1 min, then increased up to 320 °C and held for 5 min. The injection was performed on the split-less mode with the injector port temperature maintained at 300 °C. The chromatograms were recorded at range 50 600 m/z MS - 600 m/z MS scan mode and the compounds were identified by comparing the molecular weight, intensity of peak and peak mass with NIST library and HMDB library.

Results and Discussion

In this research, the flowers and leaves of *Euphorbia milii* were selected as samples and underwent an extraction method by using three different solvents (hexane, ethyl acetate and methanol) to obtain the crude extracts. Then, the crude extracts underwent a total phenolic content test to determine the presence of phenolic compounds from the crude extracts.

Methanol leaves extract had the highest phenolic content (0.77 ± 0.02 mg GAE/g of sample), followed by methanol flowers extract (0.51 ± 0.03 mg GAE/g of sample), ethyl acetate leaves extract (0.17 ± 0.00 mg GAE/g of sample) and ethyl acetate flowers extract (0.07 ± 0.00 mg GAE/g of sample). Nonetheless, the lowest phenolic content was discovered in the hexane extracts; leaves (0.04 ± 0.01 mg GAE/g of sample) and flowers (0.05 ± 0.00 mg GAE/g of sample). Another study which used *E. splendida* also revealed that the methanolic extract showed the highest total phenolic content, which was 270.74 ± 0.005 mg GAE / g as compared to ethyl acetate extract (208.54 0.005 mg GAE / g sample) [17].

Referring to the plant parts, the highest phenolic content was contributed by leaves with 0.98 mg QAE/g of sample and followed by flowers (0.0.63 mg GAE/g of sample). A significant result was reported by Abu Arra et. al. [18], in which the leaves extract of *E. hirta* showed the highest amount of phenolic content (206.17 ± 1.95 mg GAE/g) as compared to flowers, roots and stems crude extracts. Figure 2 summarizes the estimation of phenolic contents in different crude extracts of *E. milii*.

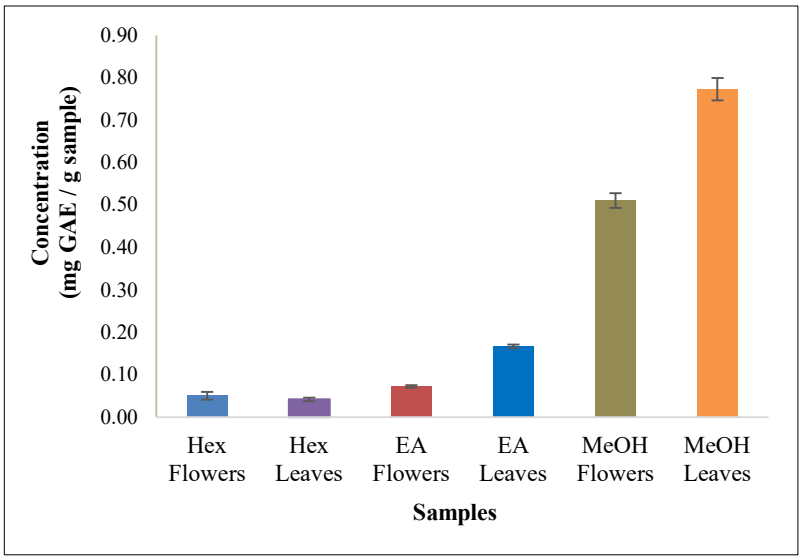


Figure 2. Estimation of total phenolic content in different crude extracts of *E. milii*

Xanthine oxidase inhibitor was tested on the ethyl acetate and methanol crude extracts which contain the highest phenolic and flavonoid content to identify the behavior of crude extracts in reducing the uric acid production [19, 20]. The reducing potential was measured by calculating the percentage of xanthine oxidase inhibition by using the absorbance recorded by UV-Vis spectrophotometer at wavelength 295 nm. Methanolic leaves extract showed the highest percentage of xanthine oxidase inhibition (66.5 ± 0.4%), followed ethyl acetate leaves (33.3 ± 4.3%), methanol flowers (29.3 ± 4.5%) and lastly ethyl acetate flowers (12.2 ± 1.4%). The standard allopurinol had 98.3 ± 1.3% XO inhibition. The results obtained were equivalence with the total phenolic and flavonoids content in *E. milii*. This result was in agreement with other researchers, in which it indicated that XO inhibition activity could be linked to the content and nature of flavonoids and phenolic compounds present in the extract [21]. Figure 3 shows the percentage of xanthine oxidase inhibition of the four crude extracts of *E. milii* and standard allopurinol.

Based on the result obtained, methanolic leaves extract and allopurinol were chosen to undergo IC_{50} test by using different concentrations (0 µg/mL - 100 µg/mL). The value of IC_{50} was obtained by using natural Log dose inhibition curve of a series of different sample concentrations against percent inhibition. Methanolic leaves extract showed a significant XO inhibitory activity with an IC_{50} value of 86.7 µg/mL (Figure 3). However, its activity was low and remained not as good as allopurinol with IC_{50}, 4.18 µg/mL. The obvious gap of activity between the extract and allopurinol due to the concentration of active flavonoid and phenolic compounds in the extract was very low as compared to the mass of pure allopurinol compound.

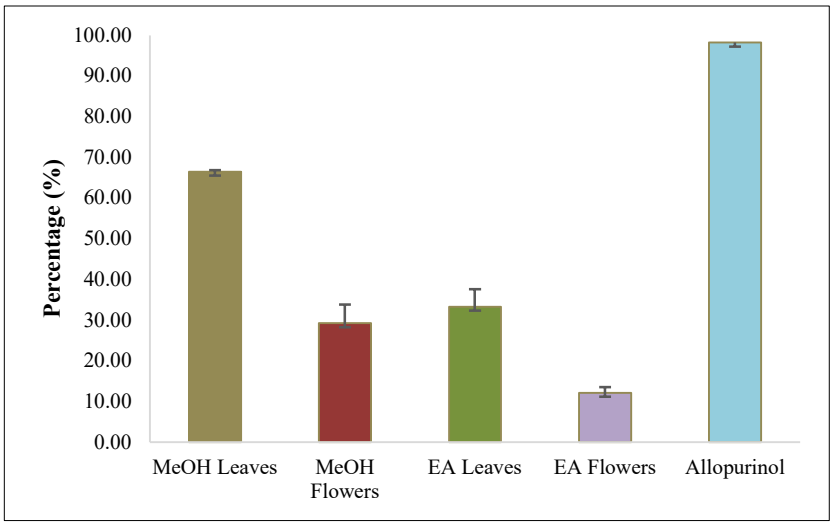


Figure 3. Percentage of xanthine oxidase inhibition of the four crude extracts of *E. milii* and the standard allopurinol

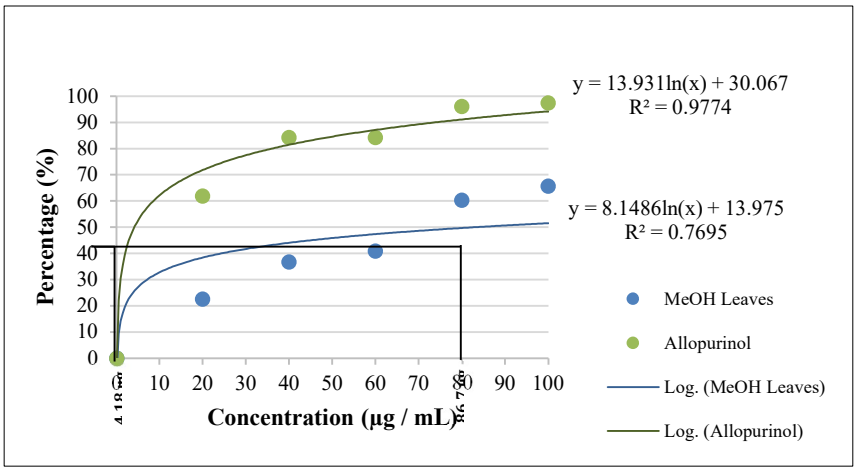


Figure 4. Percentage inhibition of IC_{50}

Therefore, methanolic leaves extract of *E. milii* was subjected to GC-MS in order to trace or identify phytocompounds that exist in the sample. The chromatogram obtained (Figure 5) revealed the presence of hexadecanoic acid [RT: 32.923, Peak Area (%): 14.79%, Molecular Formula: $C_{17}H_{34}O_2$] that possess anti-gout behavior. Hexadecanoic acid (Figure. 6) or also known as palmitic acid is one of the most common saturated fatty acid chains that can be found naturally in plant. Various studies had proven that hexadecanoic acid can act as an antifungal, antioxidant, antimalarial or a potent antimicrobial agent and inhibit the production of uric acid [22, 23]. According to Li and his team [24], oxidative stress played a crucial role in the pathogenesis of gout and the effective treatment was by lowering the oxidative stress. This was supported by Zamudio-Cuevas et al. [25], monosodium urate (MSU) crystals were shown to induce renal cell apoptosis through a mechanism which involved reactive oxygen species (ROS) generation and led to loss of cartilage repair and tissue damage observed in gouty patients. In part of that, Trevisan et al. [26], suggesting that oxidative stress (OS) was responsible for acute gout attack due to overproduction of OS traced. In fact, Masuoka et al. [27], have identified the possible mechanism pathway which relate the compounds that are superoxide radical antioxidants and XO activity inhibitor. Hexadecanoic acid was identified as able to induce the formation of hydrogen peroxide, H_2O_2 (source of oxygen-derived free radical) [28, 29]. In referring to Euphorbia species, the

leaves of *E. cuneata* [30], essential oil from dried leaves of *E. hirta* Linn [31, 32] and the culture cell of *E. tirucalli* and *E. milii* showed the presence of hexadecanoic acid as one of their phytocompounds. Table 2 shows a summary of the data obtained from the GC-MS and biological activity of hexadecanoic acid.

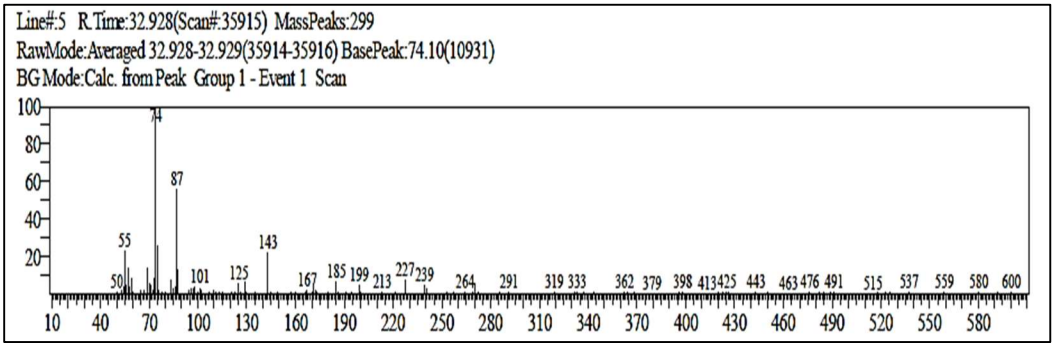


Figure 5. Mass spectra of hexadecanoic acid contained in methanolic leaves extract of *E. milii*

Figure 6. The molecular structure of hexadecanoic acid

Table 2. Name, retention time, percentage area, molecular weight, molecular formula, and biological activity of hexadecanoic acid

No	Name of Compound	Retention Time	Percentage Area (%)	Molecular Weight	Molecular Formula	Biological Activity
1.	Hexadecanoic acid	32.923	23.88	270	$C_{17}H_{34}0_2$	Antifungal, antioxidant, antimalarial, potent antimicrobial agent, inhibit production of uric acid [22, 23]

Conclusion

This study revealed that the methanolic leaves extract of *E. milii* possess anti-gout properties because it significantly reduced uric acid production and had higher xanthine oxidase inhibitor as compared to other crude extracts. Moreover, the estimation of phenolic contents contained in the methanolic leaves extract was the highest amongst others. Therefore, the methanolic leaves extract of *E. milii* had higher potential to be used as a new medicine in the treatment of gout.

Acknowledgement

The authors would like to express appreciation to the Faculty of Science and Marine Environment, Universiti Malaysia Terengganu for providing laboratory facilities and UMT-TAPE-RG (Vote:55159) for the financial support.

References

1. Corrado, A., D'Onofrio, F., Santoro, N., Melillo, N. and Cantore, F. P. (2006). Pathogenesis clinical findings and management of acute and chronic gout. *Minerva Medicine,* 97: 495-509.
2. Elzahar, K. (2022). Remedial action of yoghurt enriched with watermelon seed milk on renal injured hyperuricemic rats. *Fermentation,* 8: 41.
3. Abu Bakar, F. I, Abu Bakar, M. F, Rahmat, A., Abdullah, N., Sabran, S. F. and Endrini S. (2018) Anti-gout potential of malaysian medicinal plants. *Frontier Pharmacology,* 9: 261.
4. Panche, A. N., Diwan, A. D. and Chandra, S. R. (2016). Flavonoids: an overview. *Journal of Nutritional Science*, 5: e47.

5. Ibrahim, S. R. M., Mohamed, G. A., Alshali, K. Z., Al Haidari, R. A., El-Kholyf, A. A. and Zayed, M. F. (2018). Lipoxygenase inhibitors flavonoids from *Cyperus rotundus* aerial parts. *Revista Brasileira de Farmacognosia*, 23(3); 320-324.

6. Yuan, M., Yi, L., Xiao, A., Leng, J. L., Liping, M., Lei, L. and Liang, L. (2019). The interaction of dietary flavonoids with xanthine oxidase: *In vitro*: Molecular property-binding affinity relationship aspects. *RSC Advances*. 9: 10781-10788.

7. Suyun L., Zhang, G., Liao, Y., Pan, J. and Gong, D. (2015). Dietary flavonoids as xanthine oxidase inhibitors: Structure–affinity and structure–activity relationships. *Journal of Agricultural and Food Chemistry*, 63(35): 7784-7794.

8. Li, J., Gong, Y., Li, J. and Fan, L. (2022). In vitro inhibitory effects of polyphenols from Tartary buckwheat on xanthine oxidase: Identification, inhibitory activity, and action mechanism. *Food Chemistry*, 379: 132100.

9. Trivedi, D., Sureja, D., Sanghvi, K., Shah, A. and Seth, D. (2016). Integrated health sciences extract of *Euphorbia milii* flower: A natural indicator in acid-base titration. *Journal of Integrated Health Sciences*, 4 (2): 2-6.

10. Kartesz, J. T. (1994). A synonymized checklist of the vascular flora of the United States, Canada, and Greenland. 2nd edition. 2 vols. Timber Press, Portland.

11. Delgado, I. F., De-Carvalho, R. R., De- Oliveira, A. C., Kuriyama, S. N., Oliveira-Filho, E. C., Souza, C. A. and Paumgartten. F. J. (2003). Absence of tumor promoting activity of *Euphorbia milii* latex on the mouse back skin. *Toxicology Letters,*145(2): 175-180.

12. Kamurthy, H., Dontha, S. and Rajani, K. (2015). Phytochemical screening on *Euphorbia milii* red flowers – isolation of terpenoids, flavone and phenols. *American Journal of Ethnomedicine, 2*(6): 322.

13. Pokhrel, B., Nilling, J. J., Ete, T. and Bharti, A. (2017). Green synthesis of stable silver nanoparticles using *Euphorbia milii* extract and study of its antimicrobial activity against *Escherichia coli*. *International Journal of Chemical Studies*. 5: 1124-1128.

14. Chun, O. K., Kim, D. O. and Lee, C. Y. (2013). Superoxide radical scavenging activity of the major polyphenols in fresh plums. *Journal of Agriculture Food Chemistry*, 51: 8067-8072.

15. Fattahi, S., Zabihi, E., Abedian, Z., Pourbagher, R., Ardekani, A. M., Mostafazadeh, A. and Akhavan-Niaki, H. (2014). Total phenolic and falvonoid contents of aqueous extract of stinging nettle and in vitro antipoliferative effect on hela and BT-474 cell lines. *International Journal of Molecular and Cellular Medicine*, 3(2): 102-107.

16. Boumerfeg, S., Baghiani, A., Djarmouni, M., Ameni, D., Adjadj,M. , Belkhiri, Charef, N., Khennouf, S., and Arrar, L. (2012). Inhibitory activity on xanthine oxidase and antioxidant properties of *Teucrium polium* L. extracts. *Chinese Medicine,* 3: 30-41.

17. Kefayati, Z., Motamed, S.M., Shojaii, A., Noori, M. and Ghods, R. (2017). Antioxidant activity and phenolic and flavonoid content of the extract and subfraction of *Euphorbia splendida* Mobayen. *Pharmacognosy Research*, 9(4): 362-365.

18. Abu Arra B., Zakaria, Z., Latha, L. Y. and Sasidharan, S. (2011). Antioxidant activity and phytochemical screening of the methanol extracts of *Euphorbia hirta* L. *Asian Pacific Journal of Tropical Medicine,* 4(5): 386-390.

19. Sasidharan, S., Braganza, C., Soundararajan, V., S, S., Subramaniam, S., Boon Yin, K., Thaarani, S., Ng, M. L., Venugopal, K., Lee, Y. T., Chen, Y., Ratheesh M., Oon, C. (2021). Green anticancer therapy: Revisiting the Role of medicinal plants as a future anticancer medicine. *Wulfenia,* 28: 107-131.

20. Mutalib, N. S. A., Yusuf, N., Asari, A., Aziz, A. N. and Wahab, N. H. A. (2020). Qualitative and quantitative analysis of Malaysian *Euphorbia milii* (Euphorbiaceae) and its antioxidant activities. *Malaysian Applied Biological*, 49(4): 233-239.

21. Isa, S. S. P. M., Ablat, A. and Mohamad, J. (2018). The antioxidant and xanthineoxidase inhibitor activity of *Plumeria rubra* flowers. *Molecules*, 23(2): 400.

22. Igwe, K. K., Madubuike, A. J., Akomas, S. C., Otuokere, I. E. and Ukwueze, C. S. (2016). Studies of the medicinal plant *Euphorbia hirta* methanol leaf extract phytocomponents by GCMS analysis. *International Journal of Scientific and Technical Research in Engineering,* 1(4): 9-16.

23. Kotteswari M, Rao M. R. K, Kumar S, Prabhu K, Sundaram R. L, Dinakar S. (2018). GC-MS analysis of one ayurvedic preparation 'Aswagandharishtam'. *Biomedicine Pharmacology Journal,* 11(2): 1061-1072.

24. Li, S., Li, L., Yan, H., Jiang, X., Hu, W., Han, N. and Wang, D. (2019). Anti-gouty arthritis and anti-hyperuricemia properties of celery seed extracts in rodent models. *Molecular Medicine Reports*, 20: 4623-4633.

25. Zamudio-Cuevas, Y., Martinez-lores, K. and Fernandez-Torres, J. (2016). Monosodium urate crystals induce oxidative stress in human synoviocytes. *Arthrities Research and Therapy*, 18: 117.
26. Trevisan, G., Hoffmeister, C., Rossato, M. F., Oliveira, S. M. and Silva, C. R. (2014). TRPA1 receptor stimulation by hydrogen peroxide is critical to trigger hyperalgesia and inflammation in a model of acute gout. *Free Radical Biology and Medicine*, 72: 200-209.
27. Masuoka, N., Matsuda, M. And Kubo, I. (2012). Characterization of antioxidant activity of flavonoids. *Food Chemistry*, 131: 541-545.
28. Mohamed Isa, S., Ablat, A. and Mohamad, J. (2018). The antioxidant and xanthine oxidase inhibitory activity of *Plumeria rubra* flowers. *Molecules (Basel, Switzerland)*, 23(2): 400.
29. Gehrmann, W., Wurdemann, W., Plotz, T., Jorns, A., Lenzen, S. and Elsner, M. (2015). Antagonism between saturated and unsaturated fatty acids in ROS mediated lipotoxicity in rat insulin-producing cells. *Cell Physiology Biochemistry*, 36(3): 852-865.
30. Soliman, M., Abdella, A., Khidr, Y. A., Hassan, G., Al-Saman, M. A. and Elsanhoty, R. M. (2021). Pharmacological activities and characterization of phenolic and flavonoid compounds in methanolic extract of *Euphorbia cuneata* vahl aerial parts. *Molecules (Basel, Switzerland)*, 26(23): 7345.
31. Ogunlesi, M., Okiei, W., Ofor, E. and Osibote, A. (2009). Analysis of the essential oil from dried leaves of *Euphorbia hirta Linn* (Euphorbiaceae), a potential medication for asthma. *African Journal of Biotechnology*, 8: 7042-7050.
32. Salehi, B., Iriti, M., Vitalini, S., Antolak, H., Pawlikowska, E., Kregiel, D., Sharifi-Rad, J., Oyeleye, S. I., Ademiluyi, A. O. and Czopek, K. (2019). Euphorbia-derivative natural products with potential for use in health maintenance. *Biomolecules*, 9: 337.

Malaysian Journal of Analytical Sciences (MJAS)
Published by Malaysian Analytical Sciences Society

FORMATION AND STABILITY STUDY OF SILVER NANOPARTICLES REDUCED BY *Murdania Loriformis* EXTRACT FOR ANTIBACTERIAL APPLICATIONS

(Kajian Pembentukan dan Kestabilan Nanopartikel Perak yang Diturunkan oleh Ekstrak *Murdania Loriformis* untuk Aplikasi Antibakteria)

Norain Isa[1,2*], Nazatul Nabila Mohamad[1], Ainorkhilah Mahmood[3,] Nor Aziyah Bakhari[3], Marlina Mohd Mydin[4] and Norhafiza Mohd Arshad[5]

[1]*Chemical Engineering Studies,*
College of Engineering,
Universiti Teknologi MARA, Cawangan Pulau Pinang,
Permatang Pauh Campus, 13500 Pulau Pinang, Malaysia
[2]*Waste Management and Resource Recovery (WeResCue) Group,*
Chemical Engineering Studies,
College of Engineering,
Universiti Teknologi MARA, Cawangan Pulau Pinang,
Permatang Pauh Campus, 13500 Pulau Pinang, Malaysia
[3]*Department of Applied Sciences,*
Universiti Teknologi MARA, Cawangan Pulau Pinang,
Permatang Pauh Campus, 13500 Pulau Pinang, Malaysia
[4]*Faculty of Health Sciences,*
Universiti Teknologi MARA,
Cawangan Pulau Pinang Kampus Bertam, 13200 Kepala Batas,Pulau Pinang, Malaysia
[5]*Centre for Research in Biotechnology for Agriculture,*
Universiti Malaya, 50603 Kuala Lumpur, Malaysia

[*]*Corresponding author: norain012@uitm.edu.my*

Received: 21 September 2022; Accepted: 30 January 2023; Published: 22 February 2023

Abstract

The aggregation of silver nanoparticles (AgNPs) is a serious problem in their applications. This article describes the synthesis of AgNPs using $AgNO_3$ as a metal precursor and *Murdannia loriformis* extract (MLE) as a reducing agent. The effect of MLE concentration, $AgNO_3$ concentration, reaction time, and pH on the synthesis of AgNPs was studied using the absorbance of the surface plasmon resonance (SPR) band. From the TEM image, highly scattered AgNPs with a spherical shape and an average particle size of around 12.60 nm ± 2.83 nm were observed for synthesized AgNPs at optimized conditions (pH 8, 100% MLE concentration, 2 mM of $AgNO_3$ and 24 hr reaction time). The stability of synthesized AgNPs was initially studied using a different initial concentration (5 and 10 mM) of the metal precursor. The aggregation process was evaluated by the zeta potential and UV-

vis spectra measurements and finally confirmed by TEM. For an antibacterial performance, the disk diffusion method was applied. It was observed that the synthesized AgNPs showed enhanced antibacterial activity depicting the inhibition zone between 18.27 and 22.09 mm reported against *Escherichia coli* (*E. coli*) compared to *Staphylococcus aureus* (*S aureus)*, which has an inhibition zone between 9.11 and 10.99 mm. The significance of this study showed that the AgNPs synthesized in this process were found to have efficient antibacterial activity against bacteria *E. coli*. Additionally, the increasing metal precursor concentrations exhibited a reduction in the stability of AgNPs.

Keywords: *Murdannia loriformis*, silver nanoparticles, stability, *Escherichia coli, Staphylococcus aureus*

Abstrak

Penggumpalan nanopartikel perak (AgNPs) adalah masalah serius dalam aplikasinya. Artikel ini menerangkan sintesis AgNPs menggunakan $AgNO_3$ sebagai prekursor logam dan ekstrak *Murdannia loriformis* (MLE) sebagai agen penurunan. Kesan kepekatan MLE, kepekatan $AgNO_3$, masa tindak balas, dan pH ke atas sintesis AgNPs telah dikaji menggunakan penyerapan jalur resonans plasmon permukaan (SPR). Daripada imej TEM, AgNPs yang tersebar adalah dalam bentuk sfera dan saiz zarah purata sekitar 12.60 nm ± 2.83 nm di sintesis pada keadaan optimum (pH 8, 100% kepekatan MLE, 2 mM $AgNO_3$ dan 24 jam masa tindak balas). Kestabilan AgNPs pada mulanya dikaji menggunakan kepekatan awal prekursor logam yang berbeza (5 dan 10 mM). Proses penggumpalan dinilai oleh potensi Zeta dan ukuran spektrum UV/vis dan akhirnya disahkan oleh TEM. Untuk prestasi antibakteria, penyebaran cakera dilaksanakan. Diperhatikan bahawa AgNPs menunjukkan aktiviti antibakteria yang dipertingkatkan yang menggambarkan zon perencatan antara 18.27 dan 22.09 mm yang dilaporkan terhadap *Escherichia coli* (*E. coli*) berbanding *Staphylococcus aureus* (*S aureus*), yang mempunyai zon perencatan antara 9.11 dan 10.99 mm. Kepentingan kajian ini menunjukkan bahawa AgNPs yang disintesis dalam proses ini didapati mempunyai aktiviti antibakteria yang cekap terhadap bakteria *E. coli*. Di samping itu, didapati bahawa peningkatan kepekatan prekursor logam menunjukkan pengurangan kestabilan AgNPs.

Kata kunci: *Murdannia loriformis*, nanopartikel perak, kestabilan, *Escherichia coli, Staphylococcus aureus*

Introduction

This article describes the synthesis, stability and antibacterial study of AgNPs synthesized using $AgNO_3$ as a metal precursor and *Murdannia loriformis* extract (MLE) as a reducing agent. *Murdannia loriformis* (Hassk.) (*M. loriformis*) is an Indian plant that belongs to the Commelinaceae family. The plant species are found throughout the forests and grassy slopes of Asia, especially in China and Thailand [1]. This plant is gaining popularity in Malaysia due to its therapeutic potential for conditions such as psoriasis and dermatitis [2]. *M. loriformis* is one of Thailand's most popular folk medicines for cancer and diabetes patients. It is thought to slow cancer progression as well as provide symptomatic relief from contemporary therapy [3]. *M. loriformis* is also a traditional Chinese remedy for detoxifying respiratory tract problems [4]. *M. loriformis* is known as “Beijing grass,” or “Angel grass” in English, “Rumput Cina,” “Rumput Beijing,” and Rumput Siti Khatijah in Malay and “Ya Pak King” in Thailand (Figure 1). The phytochemical analysis of *M. loriformis* found that the plant's extract contains phenolics, flavonoids, condensed tannin, carbohydrates, protein, and plant membrane lipids [2, 5, 6]. Several scientific reports support the traditional use of *M. loriformis* in treating different ailments. From the kinds of literature, *M. loriformis* extract possesses numerous pharmacological properties, including antioxidant, antimutagenicity, anticancer, anti-inflammatory, immunomodulatory effects, antipyretic, analgesic, antimicrobial, antibacterial, and gastroprotective activity, which support its traditional use [2]. Due to the phytochemicals and properties of *M. loriformis*, this plant is selected as a potential reducing agent for synthesis of AgNPs.

The scientific world has recently given special attention to the use of bioresources in nanotechnology due to their eco-friendly properties, availability, and low cost, and *M. loriformis* has a promising future in this regard [7]. Nanomaterials have piqued the interest of the scientific community due to their unique properties and diverse biomedical and environmental remediation applications [7–11]. Nanomaterials, such as silver nanoparticles (AgNPs), have numerous possible applications, such as medical diagnostics, imaging, medication delivery,

identification of biological samples, solar cells, catalysis, photovoltaics, and digital data storage [12]. The most famous application of AgNPs is their usage in environmental cleaning. Due to the use of benign phytochemicals and the elimination of dangerous molecules that would have been employed in chemical synthesis, the green synthesis of nanoparticles has earned considerable favor [13]. This technique utilizes bio-extracts as reducing agents, making them relatively less expensive, quicker, and easier than alternative processes. Controlling the size, shape, and structure of AgNPs is crucial due to the close correlation between these features and their optical, electrical, and catalytic properties [14].



Figure 1. Murdannia loriformis plant

In this study, AgNPs were synthesized using silver nitrate as a metal precursor and *Murdannia loriformis* extract (MLE) as a reducing agent. The stability of synthesized AgNPs was investigated and characterized by a variety of characterization techniques. Then, the antibacterial properties were studied against *Escherichia coli* (*E. coli*) and *Staphylococcus aureus* (*S. aureus*) using the disc diffusion method.

Materials and Methods

Materials

Silver nitrate, 99.8%, and sodium hydroxide, 99%, were purchased from QReC. Sulphuric acid, 95-97%, was acquired from Supelco. The aerial part of *Murdannia loriformis* was acquired from EES Biotech Sdn Bhd, Penang, then dried and ground into a fine powder. The powder was then added to 200 mL of deionized water in a 250 mL beaker and heated at 70 °C for 1 hour. Using Whatman No. 1 filter paper, the extracts were filtered and stored at 4 °C for future use. This solution was considered as 100% *Murdannia loriformis* extract (MLE). The *Escherichia coli* ATCC 25922 PK/5 and *Staphylococcus aureus* subsp. aureus ATCC 29213 PK/5 were purchased from Oxoid. The chemicals were used without further purification.

Identification of phytoconstituent in MLE

The phytochemical screening test was conducted using standard procedures Sofowora, 1993; Trease and Evans, 1989; Harborne, 1973 to identify the chemical compounds in the MLE [15]. Table 1 summarizes the experimental for the selected screening test for this study. Carbohydrates content was determined using the calculation method suggested by Guide to Nutrition Labelling and Claims (2010) [16]. The protein content was determined using the Kjeldahl method, protein content was determined as $N \times 6.25$. The average nitrogen (N) content of proteins was found to be about 16 percent, which led to the use of the calculation N x 6.25 (1/0.16 = 6.25) to convert nitrogen content into protein content. The functional group in compounds was determined using a Nicolet FTIR spectrophotometer (Thermoscientific Nicolet 6700, USA). A small amount of powdered *Murdannia loriformis* was respectively placed directly on the germanium piece of the infrared spectrometer with constant pressure applied, and data of infrared absorbance, collected over the wave number ranged from 500 to 4000 cm^{-1} and computerized for analyses by using the Omnic software (version 5.2). The reference spectra were acquired from the cleaned blank crystal prior to the presentation of each sample replicate.

Synthesis of AgNPs: Effect of Variable Parameters

The preparation of AgNPs was observed by the appearance of the characteristic of surface plasmon resonance (SPR) due to the combined vibration of free electrons of AgNPs in resonance with the light wave. The optimization studies were carried out for the formation AgNPs in order to find the optimized condition using MLE as a reducing agent and $AgNO_3$ as the metal precursor. As to ensure the results of the experiments were reproducible, the experiments were run in triplicates. The formation of AgNPs at different pH, MLE concentrations, $AgNO_3$ concentration, temperature, and reaction time were analyzed using a

UV-Vis spectrophotometer.

Table 1. Screening test for identification of phytochemicals in MLE

Test	Experimental	Explanation
Tannin	About 0.5 g of the dried powdered samples were boiled in 20 ml of water in a test tube and then filtered. A few drops of 0.1% ferric chloride were added.	Brownish green or a blue-black colouration indicates the presence of tannins.
Flavonoids	NaOH (2 mL, 10%) was added to MLE, and the solution turned to yellowish colour. Dilute HCl was added to the mixture.	The yellowish colour will turn colourless if flavonoids are present.
Saponins	A small portion of the crude sample was dissolved in 1 mL of ethanol and then diluted with distilled water. The mixture was placed in a shaker for 15 minutes.	A layer of foam (around 1 cm) is formed if saponins are present in the mixture.
Sterols	Chloroform solution of the extract when shaken with concentrated sulphuric acid.	The red colour of the solution indicates the presence of sterols.
Terpenoids	This test is known as the Salkowski test. Chloroform (2 mL) was added to 5 mL of MLE. Then, 3 mL of concentrated H_2SO_4 was added carefully into the mixture.	A reddish-brown layer formed on the surface of the mixture indicates the presence of terpenoids.

Effect of pH

The effect of pH on the synthesis of AgNPs was studied. At this stage, 1 mL of 2 mM of $AgNO_3$ as the metal precursor and 9 mL of 100% MLE as reductant were kept constant. The pH of the solution was adjusted to pH 2, 4, 6, 8, and 10 using 0.1 M of NaOH and H_2SO_4, respectively.

Effect of $AgNO_3$ as metal precursor

The effect of metal precursor concentration on the synthesis of AgNPs was examined using 1 mL of varied $AgNO_3$ concentrations from 1 mM to 15 mM. In this part, 9 mL of 100% MLE was used as a reductant at constant pH 8 and room temperature.

Effect of contact time

The effect of contact time on the synthesis of AgNPs was set at different time intervals, which were 20, 40, and 60 min. In this experiment, 1 mL of 2 mM of $AgNO_3$ as a metal precursor, 9 mL of 100% MLE as a reductant, and pH 8 were kept constant.

Effect of MLE concentration as reductant

In order to optimize the amount of extract as a reductant for the synthesis of AgNPs, 100% MLE concentration (10 g in 200 mL solution) was prepared, and the solution was diluted to 25, 50, and 75%, respectively. In this experiment, 1 mL of 2 mM of $AgNO_3$ as a metal precursor and 9 mL of reductant was kept constant at pH 8.

Characterization of AgNPs

Characterization of AgNPs was carried out using various characterization techniques. Information about optical properties, surface, morphology, particle size, shape, crystal structure, and chemical composition related to the sample was unveiled.

The optical characteristics of the samples were determined using Lambda 35 Perkin Elmer UV-vis spectroscopy with a 10 mm quartz sample cuvette optical path length. The synthesized AgNPs were placed in a sample cuvette and then scanned in a sample chamber. The range of the scan was 400 to 800 nm. The increase in the relative intensity of the SPR peaks

indicates a growing concentration of AgNPs in the system. The shape, size, and average size distribution were determined utilizing Phillips CM12 TEM with Docu version 3.2 image processing, High-Resolution Transmission Electron Microscope (HRTEM) 200 kV with Field Emission TECNAI G20S-TWIN, FEI, and Malvern Zetasizer, respectively. By enabling a high-energy electron to pass through the sample during the TEM measurement, an image with atomic resolution is produced. In the meantime, HRTEM gives crystallographic information about samples by measuring the interplanar spacing (d-spacing) and grain boundaries with atomic resolution.

The X-ray diffraction (XRD) investigation was carried out using a Philips FW1710 and Cu K radiation. The development of diffraction patterns is analysed and identified by comparing the diffracted beams to the reference database stored in the International Centre for Diffraction Data (ICDD) library. The diffracted patterns reveal whether the sample materials are pure or contaminated. Thermo Scientific (Nicolet 6700) FTIR spectrometer was used to analyse functional groups that exist in AgNPs in the range of 500-4000 cm^{-1}. FTIR spectroscopy is used to determine whether biomolecules in MLE are involved in AgNP production.

The criteria of stability of AgNPs are measured when the values of zeta potential range from higher than +30 mV to lower than -30 mV. Surface zeta potentials were measured using the laser zeta meter (Zeta Sizer- Nano Zs). Colloidal AgNPs (5 mL) was diluted with double distilled water (50 mL) using NaCl as suspending electrolyte solution (2 $x10^{-2}$ M NaCl). The pH was then adjusted to the required value. The samples were shaken for 30 minutes. After shaking, the equilibrium pH was recorded, and the zeta potential of the AgNPs was measured. A zeta potential was used to determine the surface potential of the AgNPs. The chemical composition of the samples has been obtained with EDX using a Hitachi S3700N SEM instrument equipped with a Bruker Quantax EDX system**.**

The preparation of AgNPs was observed by the appearance of the characteristic of surface plasmon resonance (SPR) due to the combined vibration of free electrons of AgNPs in resonance with the light wave. The formation of AgNPs at different $AgNO_3$ concentrations from 1 mM to 15 mM was analyzed using a UV-Vis spectrophotometer. To study the stability of synthesized AgNPs, the formation of AgNPs was further investigated using 2, 5, and 10 mM of initial concentration of metal precursor at longer reaction time (1 week and 1 month) and characterized using UV-vis, TEM, and Zeta potential.

Antibacterial test

The production of fresh germs is required for antimicrobial experimentation. Fresh culture is used to cultivate microorganisms that were present 24 hours prior. The linear culture was employed to create a new culture. A single colony was extracted from the cultures and dissolved in the culture's nutrient broth after the loop had been sterilized by heat and cooled. After the culture medium containing the bacteria had been transferred, the tubes holding the normal saline were thoroughly mixed with a vortex for 24 hours until the suspension turbidity was equal to 0.5 McFarland. This opacity is equal to 1.5 x 10^8 CFU/mL. Two bacterial species, namely *E. coli* (ATCC No. 25922) (EC) and *S. aureus* (ATCC No. 29213) (SA), were procured from Next Gene Scientific Sdn. Bhd as Culti-loops. Each bacterial strain was activated on Mueller Hilton Agar, constant at 37 °C for 18 hours. Then 30 µL of the broth was transferred to nutrient agar and incubated at 37 °C for another 24 hours; cell concentration was 10^8 cfu/mL. The effects of antibacterial were studied using the disc diffusion technique. The microbiological suspension of single-colonies of bacteria was generated in accordance with the standard at 0.5 McFarland's to study the antibacterial impact of the disc diffusion technique. On agar nutrition, several bacteria were cultivated independently. 10 mL of different concentrations of AgNPs (2, 5, and 10 mM) and negative controls (MLE) were put onto the disc using the sampler. The plates were then incubated in an oven set to 37°C. Additionally, there was no microbial cloud formation after 24 hours.

Results and Discussion

Three approaches were used to identify phytoconstituents in MLE: phytochemical screening

and carbohydrate and protein content testing. To identify the chemical components found in the MLE, a phytochemical screening test was performed. Table 2 displays the phytochemical screening results, which revealed the presence of flavonoids and sterols but no alkaloids, terpenoids, or saponins.

Table 2. Phytochemical compounds from the screening test

Chemical Compound	Presence	Description
Alkaloids	--	Alkaloids are absent
Terpenoids	--	Terpenoids are absent
Flavonoids	++	Flavonoids are present
Saponins	--	Saponins are absent
Sterols	++	Sterols are present

Carbohydrates content was determined using the calculation method suggested by Guide to Nutrition Labelling and Claims (2010) [16]. The protein content was determined using the Kjeldahl method. The total carbohydrates and protein content in the MLE were found to be 67.20% and 8.90%, respectively. FTIR spectroscopic analysis was then applied to characterize MLE and the synthesized MLE-mediated AgNPs (Figure 2). The FTIR spectrum of AgNPs showed a strong peak at 3257-3371 cm^{-1}, which is a characteristic of the -OH stretching modes in the hydroxyl functional groups. Distinct peaks at 1632-1638 cm^{-1} were observed, in which the second peak is related to the hydroxyl functional groups of alcohols and phenolic compounds that might exist in MLE.

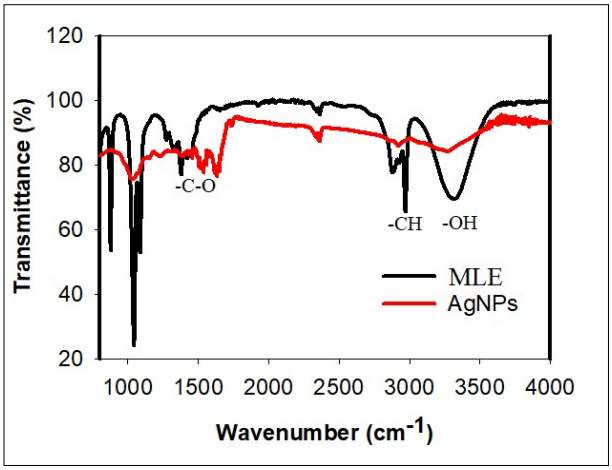


Figure2. FTIR spectra for MLE and MLE-mediated AgNPs

The distinct band within 1632-1645 cm^{-1} could be linked to the aromatic compounds of carbon and carbon double bonds. The sharp band at 1032-1051 cm^{-1} indicates the presence of the -C-O group, and the absorption bands at 1714-1732 and 1635-1655 cm^{-1} correspond to the presence of the carbonyl group within the extract. The observed peaks in the range of 1075-1079 cm^{-1} can be related to the combination of alcohols and phenols. The band at 2923 - 2913 cm^{-1} indicates -CH stretching vibrations. Most of the absorption bands that appeared in the IR spectrum of the aqueous MLE could also be observed in the IR spectra of synthesized AgNPs. This shows that the phytoconstituents biomolecules protect the AgNPs from aggregation. The synthesis of AgNPs by MLE as source of biomolecules was done by some metabolite's functional groups such as alcohols. Similar findings have also been reported in other studies [17].

Synthesis of AgNPs: Optimization studies

AgNPs were formed as a result of the reduction of Ag^+ by MLE. The presence of a band indicative of Surface Plasmon Resonance (SPR) around 410-455 nm validated the development of AgNPs. The AgNPs have free electrons, which cause the SPR absorption band to form as a result of the coupled vibration of AgNPs' free electrons in resonance with light waves. Reaction time, pH, precursor concentration, MLE concentration, and temperature were among the synthesis parameters studied. The findings are organized under the following headings.

Effect of pH

The influence of pH on the formation of AgNPs has been investigated using a pH range of 2-10 and was plotted in Figure 3(a). From Figure 3(b), it can be seen that the intensity of the SPR peak increases when it increases pH from pH 2 to pH 10. In view of the results obtained, the formation of AgNPs is favourable under basic conditions. The addition of NaOH does not bring negative consequences on the formation of AgNPs. Alas, the SPR peak of synthesized AgNPs is higher than in acidic form. However, with the addition of acid solution, the SPR peaks show lower and broader absorbance compared to pH 8 and 10. It can be observed that the SPR peaks for acidic conditions (pH 2) appear at a relatively short wavelength of around 401 nm, while the SPR peaks are shifted towards a longer wavelength (red shift) at 423 nm in the case of the basic medium as shown in Figure 3 (c). The red shift in a basic medium indicates relatively large AgNPs sizes compared with the cases of neutral and very acidic conditions (pH 2).

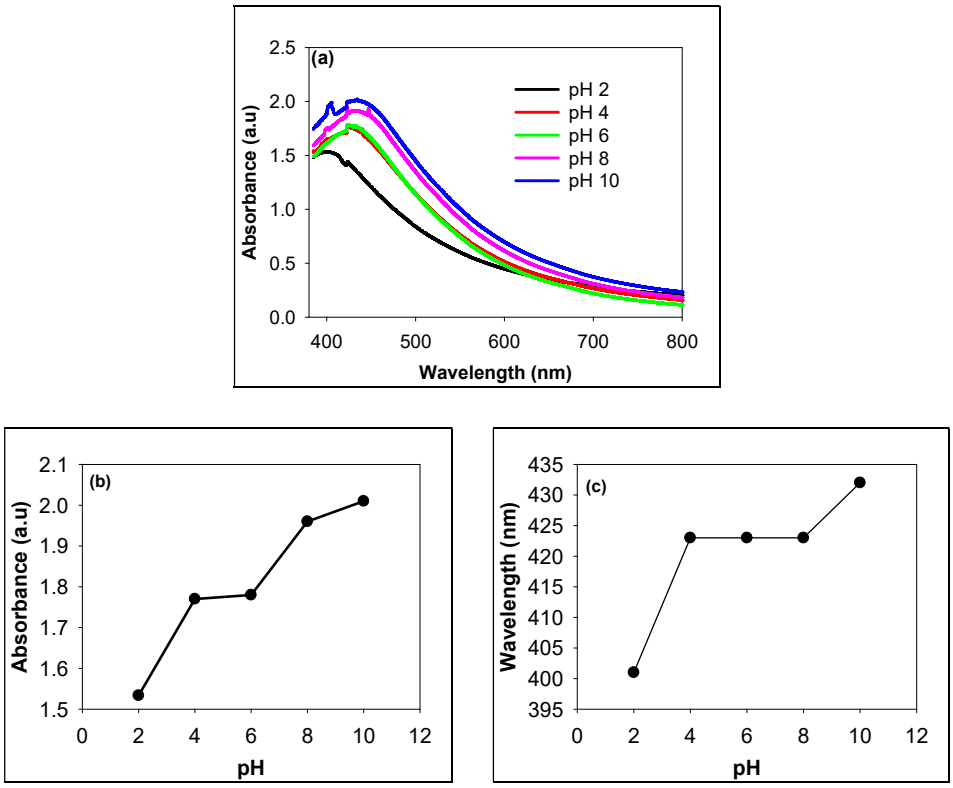


Figure 3. Effect of pH on SPR peak of synthesized AgNPs

Effect of concentration of MLE

Figure 4(a) shows the SPR peak for the effect of MLE concentration as a reducing agent in the formation of synthesized AgNPs. As seen in Figure 4(b), the intensity of SPR peak at 423 nm increases when the initial concentration of MLE increases from 25% to 100%. The

increases in SPR peak with increasing concentrations of MLE can be explained by the increase in the amount of active ingredient in a higher concentration of MLE. At low concentrations of MLE (25% and 50%), the synthesized AgNPs do not have enough reducing agents for synthesizing AgNPs and fail to stabilize the high surface energy of AgNPs. Similar findings have also been reported in other studies [10].

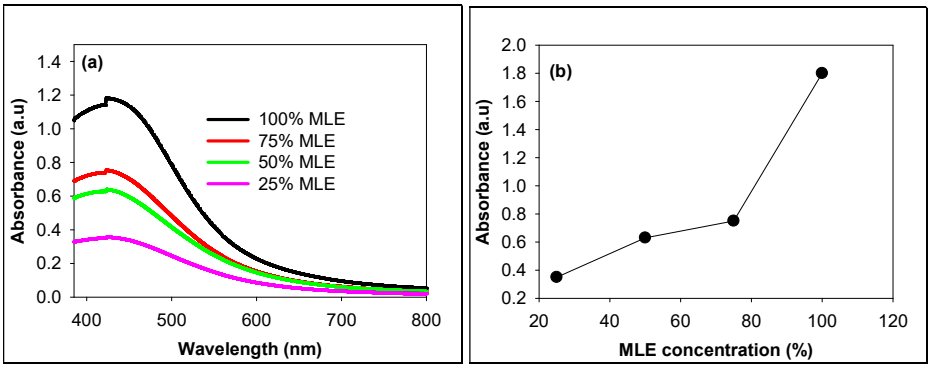


Figure 4. Effect of MLE concentration on SPR peak of synthesized AgNPs

Effect of reaction time

The effect of reaction time on the SPR peak of synthesized AgNPs is shown in Figure 5(a). The intensity of the SPR peak increases with increasing the reaction time from 20 mins to 60 mins, as shown in Figure 5(b). It was noted that with an increase in contact time, the SPR peak becomes sharper. Formation of AgNPs started within 20 mins and increased up to 60 mins. For the stability study, the SPR peak was evaluated for 24-hour, 1-week, and 1-month contact time, as shown in the same spectra in Figure 5(a). However, the SPR peaks in Figure 5 (b) show higher and sharper absorbance compared to the initial reaction time (20-60 mins). It can be observed that the SPR peaks are shifted towards a longer wavelength (red shift) at 479 nm - 482 nm, as shown in Figure 5(c). The redshift at longer contact times indicates relatively larger size AgNPs were obtained. This is due to unstable AgNPs produced and cause agglomeration after a longer contact time.

Effect of concentration silver nitrate

Figure 6 (a) shows the SPR peak for the effect of different concentrations of silver nitrate as a metal precursor from 1 to 15 mM at 1 h reaction time. It can be seen that the intensity of the SPR peak of synthesized AgNPs appears to increase with increasing silver nitrate concentration until it reaches a maximum SPR peak at 430 nm for 5 mM, as shown in Figure 6 (b) – (c). However, the after the SPR peak decreased for higher concentration. No significant SPR peak for 1, 2, and 4 mM of silver nitrate, indicating that low concentrations of Ag^{+} are not enough to induce the formation of AgNPs. For 10 mM and 15 mM silver nitrate concentration, the SPR peaks decreased with increasing silver nitrate concentration due to the agglomeration of AgNPs at high concentrations of the metal precursor.

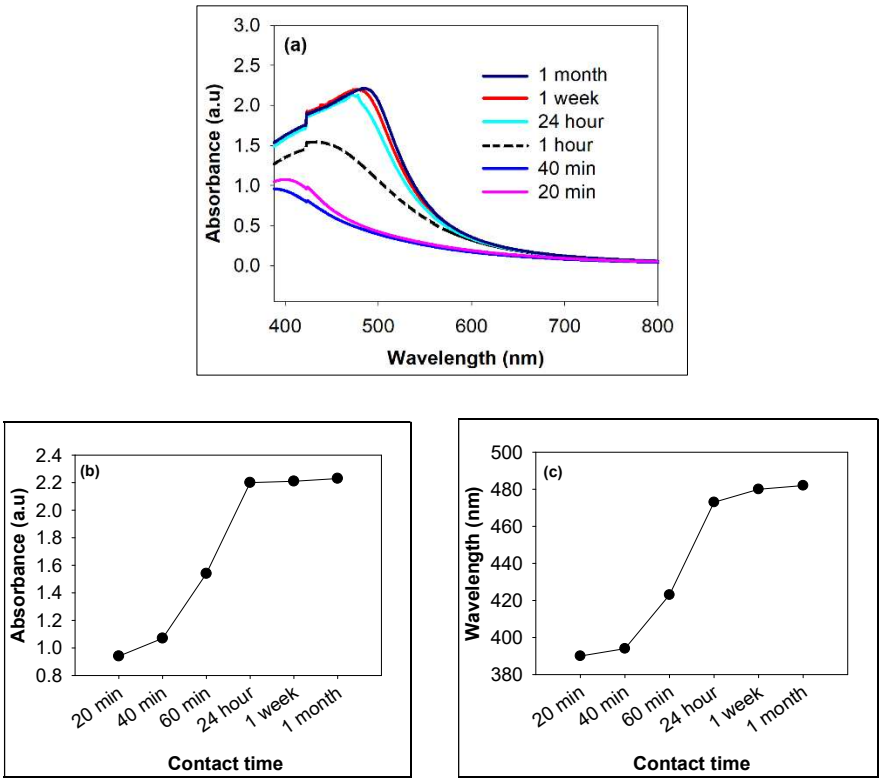


Figure 5. Effect of contact time

Characterization of AgNPs

AgNPs were synthesized at selected parameters, and the optimum condition was further characterized to evaluate their features, such as size, shape, crystallinity, morphology, form, elemental composition, and surface chemistry.

Transmission electron microscopic (TEM) analysis

Figure 7(a-c) show the TEM, HRTEM, and size distribution (histogram) of synthesized AgNPs, respectively. From Figure 7(a), the shape of the colloidal AgNPs was quasi-spherical, and the particles were observed to be evenly distributed. Figure 7(b) shows the HRTEM image of a single AgNP; from the HRTEM, it can also be seen that AgNPs are capped with the phytoconstituents, which is likely to be MLE as a reducing as well as capping agent. The lattice spacing of 0.23 nm was calculated for the HRTEM of a single AgNP, which is associated with (111) plane of AgNPs and with a diameter of 16.16 nm. This indicates the success in the use of MLE not only as a reductant, as it was intended but also as a capping agent to avoid agglomeration of the particles. From Figure 7 (c), the range of particle size of the AgNPs, as calculated from the histogram, was between 8.25 and 19.34 nm with an average particle size of 12.60 nm ± 2.83 nm. Similar findings have also been reported in other studies about the plant extract capped the AgNPs [17, 18].

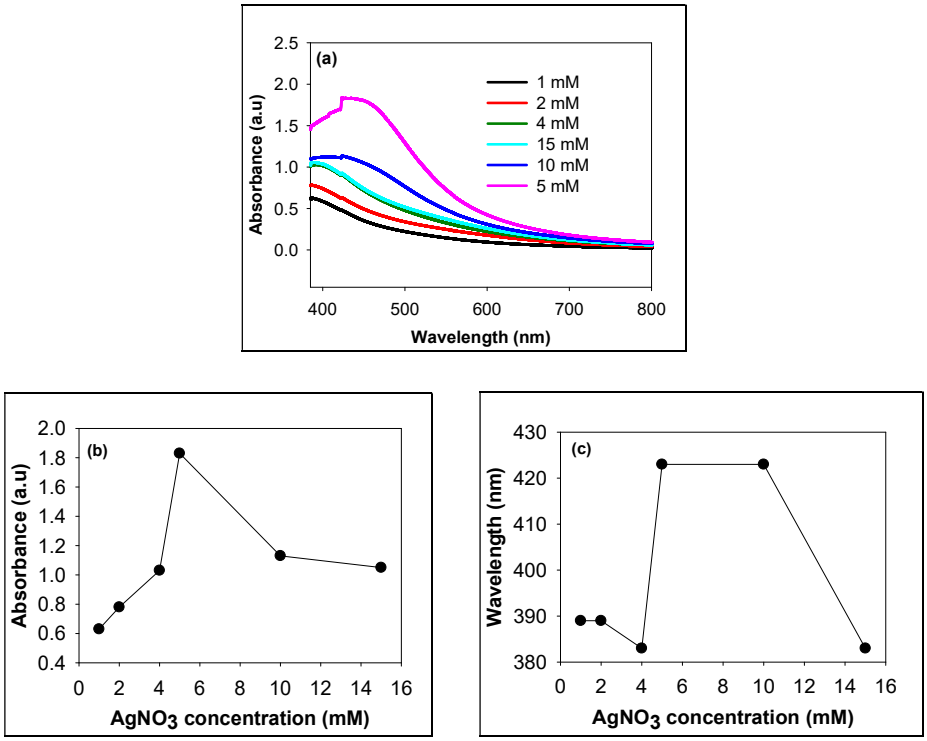


Figure 6. Effect of concentration of metal precursor

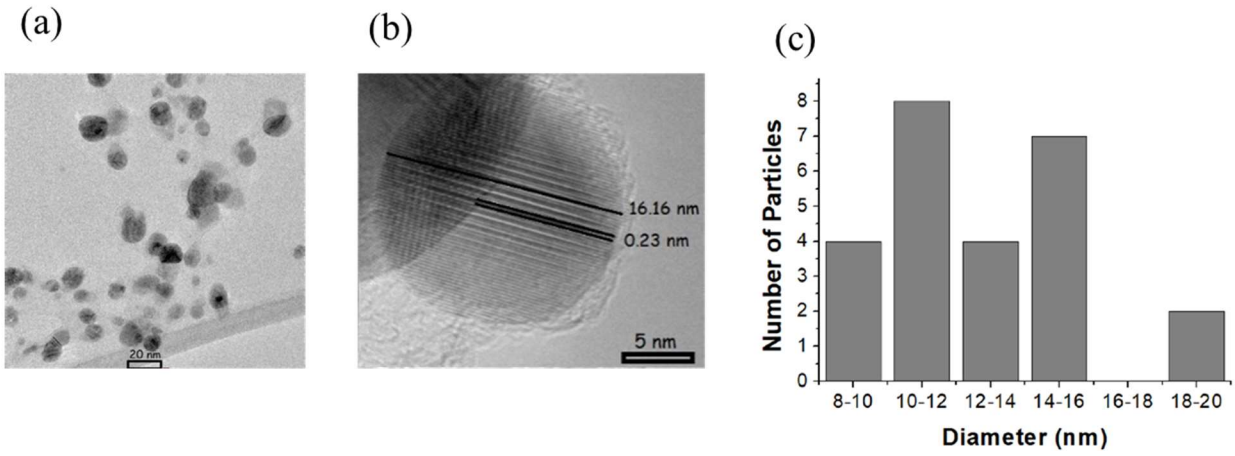


Figure 7. (a) TEM image, (b) HRTEM, and (c) histogram for the size distribution of 2 mM MLE-mediated AgNPs

The crystallinity of Synthesized AgNPs

Figure 8 shows the XRD pattern that proved the crystallinity of the synthesized AgNPs. The freeze-dried MLE-mediated AgNPs' XRD peaks matched the FCC structure of silver at 2 of 38.08°, 44.16°, 64.40°, and 76.85°, corresponding to the (111), (200), (220), and (311) planes, respectively. The (111) plane is found to be more intense than other planes, indicating that growth is concentrated along the (111) plane. The same pattern was also reported in other studies [19, 20].

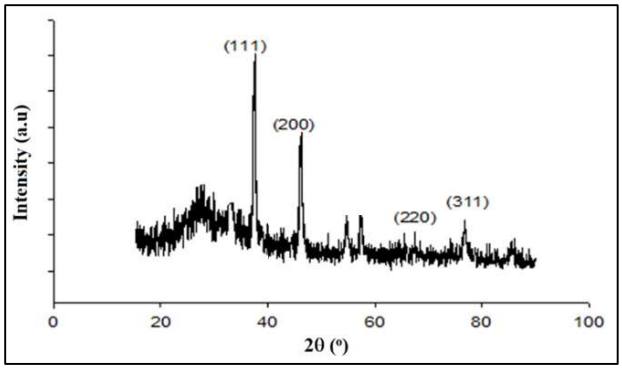


Figure 8. XRD pattern for MLE-mediated AgNPs

Particle size distribution and zeta potential

The Malvern Zetasizer was used to determine the particle size distribution and the zeta potential. Figure 9(a) depicts the hydrodynamic diameter size for synthesized AgNPs prepared using a different initial concentration of metal precursor of 1, 2, 5, and 10 mM. From

Figure 9(a), it can be seen that the smallest hydrodynamic diameter size of 55.25 nm for synthesized AgNPs prepared at 5 mM and the biggest size of 86.09 nm at 2 mM of initial metal precursor concentration. The increases in the hydrodynamic size of synthesized AgNPs at 2 mM initial concentration might be explained by the optimum amount of the active ingredient in MLE reacted with metal precursor at 2 mM. However, with the increasing initial concentration of metal precursor to 5 mM and 10 mM, the amount of active ingredient is not enough to reduce and stabilize the synthesized AgNPs at high concentrations.

The results obtained were supported by the zeta potential value of synthesized AgNPs at a different initial concentration, as shown in

Figure 9(b). The results showed that synthesized AgNPs prepared using 2 mM have the highest zeta potential value of 23.61 mV. The high potential value could be attributed to the capping action of MLE phytoconstituents, resulting in well-dispersed synthesized AgNPs at 2 mM concentration. The zeta potential for 5 mM and 10 mM of synthesized AgNPs was decreased to 15.80 and 9.75 mV, respectively. It is known that colloids with high zeta potential (negative or positive) are electrically stable, while colloids with low zeta potential tend to coagulate or flocculate [11].

The PDI of the synthesized AgNPs (Figure 9(c)) was in the range between 0.27 and 0.40, showing that the synthesized AgNPs are monodispersed (for monodispersed systems, the PDI should be 0.01 - 0.7 [14]. Colloids with a high zeta potential (negative or positive) are electrically stable, whereas colloids with a low zeta potential coagulate or flocculate [21]. The difference in size between HRTEM and particle sizer measurements could be attributed to the particle sizer assessing the hydrodynamic size of the AgNPs (size of the dispersed AgNPs solvated along with the phytoconstituents of MLE as capping and stabilizing agents).

Figure (d) shows the particle size analysis for synthesized AgNPs prepared at an optimum concentration of 2 mM of initial metal precursor concentration. The particle size analyzer detected two particle size ranges (1-10 nm and 10 - >100 nm). This finding implies that the AgNPs produced are polydispersed particles. Smaller particles (1-10 nm) have a lower peak intensity, whereas larger particles (10 -100) have a greater intensity with a Z-average of 86.09 nm. Small particles may arise in the proximity of larger ones. According to Yin et al., small particles surrounding large particles are most likely generated via second-round nucleation. The larger AgNPs were produced by accelerated crystal development, but their varied sizes of AgNPs may occur due to their formation at different times [22].

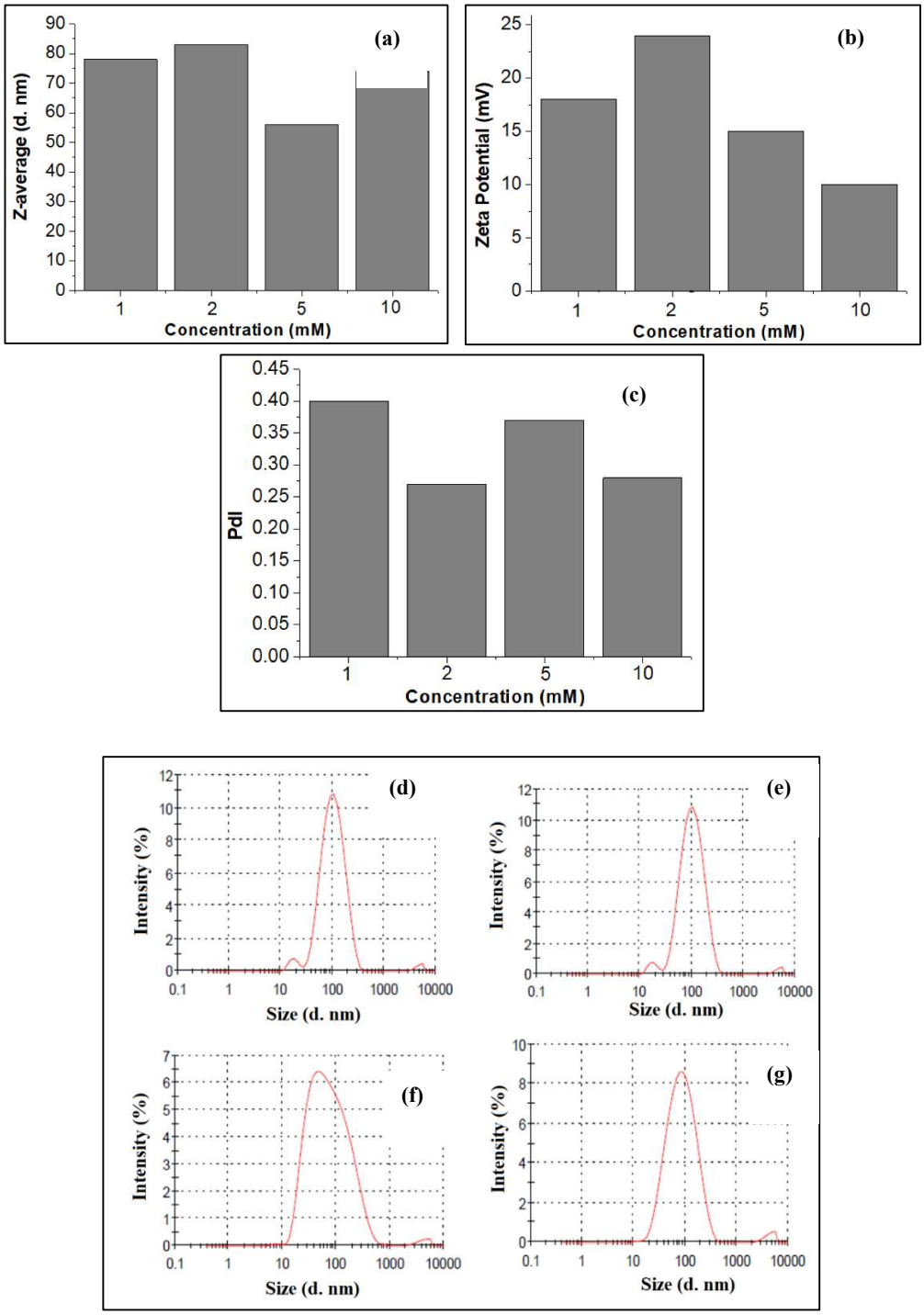
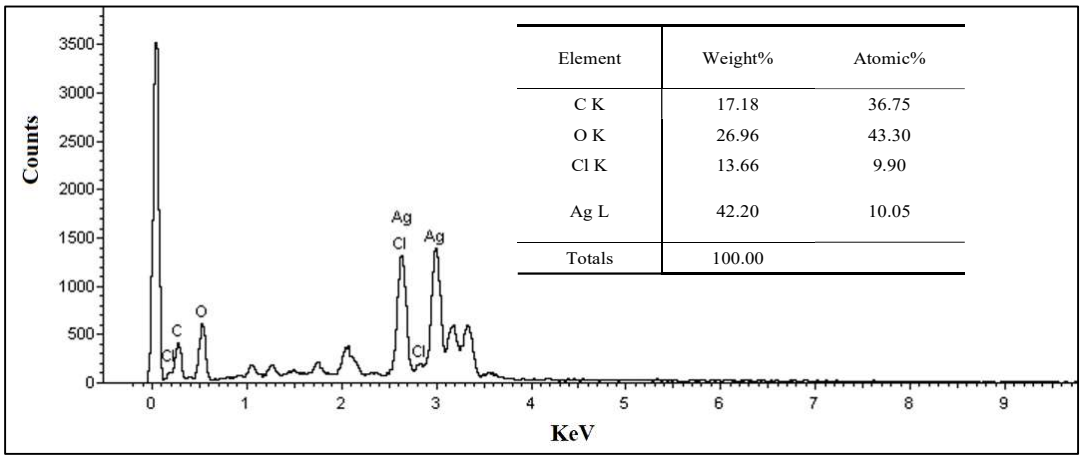


Figure 9. (a) Hydrodynamic size of synthesized AgNPs (b) Zeta potential of synthesized AgNPs (c) Polydispersity index of synthesized AgNPs. Particle size analysis of synthesized AgNPs at (d) 1 mM, (e) 2 mM, (f) 5 mM, and (g) 10 mM initial concentration

Chemical composition analysis

The chemical composition of the synthesized AgNPs was determined by energy-dispersive X-ray spectroscopy (EDX), as shown in Figure 10. It can be seen that the EDX spectrum consisted of Ag, C, O, and Cl. The EDX data of synthesized AgNPs shows a peak at around 2.6 keV; another intense peak appears at 3 keV for silver (42.20 wt%).



Element	Weight%	Atomic%
C K	17.18	36.75
O K	26.96	43.30
Cl K	13.66	9.90
Ag L	42.20	10.05
Totals	100.00	

Figure 10. EDX of synthesized AgNPs

Stability study of AgNPs

After 24 hours, the AgNPs' stability was checked. The synthesized AgNPs created using 2 mM $AgNO_3$ as the metal precursor was shown to be as stable as when they were originally formed. This is seen in Figure 11(a). Even after a 24 h reaction period, the colour of the colloidal AgNPs solution changed from pale yellow to dark brown without any sedimentation. It was thought that the phytoconstituents in the MLE were effective in giving the MLE-mediated AgNPs stability. AgNPs are coated by the phytoconstituents in MLE, which prevents aggregation and provides stability for a while. MLE have large concentrations of protein and carbohydrates, which may be what prevents AgNPs that are mediated by MLE from agglomerating.

However, when the concentration of metal precursor increased to 5 mM and 10 mM, the stability of AgNPs decreased significantly, as shown in Figure 11 (b-c). The color of the solution was dark brown, but after 24 h, the precipitation of AgNPs occurred due to the instability of the MLE-mediated AgNPs. Agglomeration of AgNPs shows the larger size of nanoparticles.

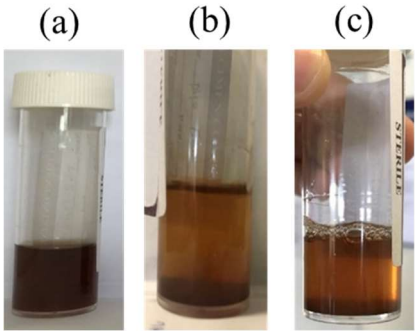


Figure 11. Colour changes of MLE-mediated AgNPs at different concentrations of silver nitrate as metal precursor; (a) 2 mM, (b) 5 mM, and (c) 10 mM

The TEM images were displayed in Figure 12(a) through (c) at various concentrations. Using 5 and 10 mM of $AgNO_3$ as the metal precursor, the synthesized AgNPs are clearly shown from the TEM pictures that the particles of AgNPs are agglomerated and form larger particles at high concentrations.

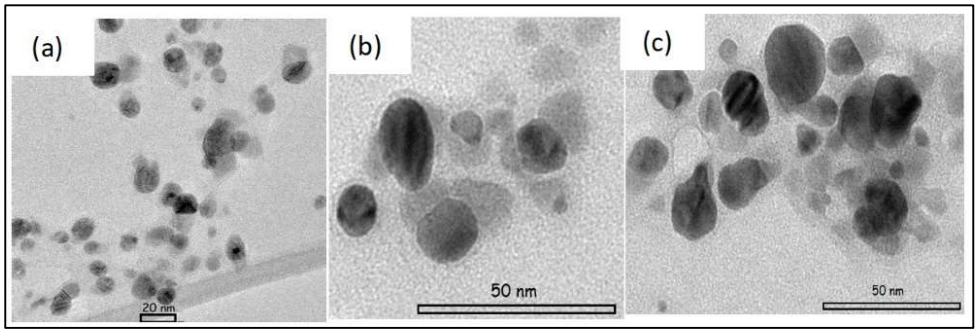


Figure 12. TEM images of MLE-mediated AgNPs at different concentrations; (a) 2 mM, (b) 5 mM, and (c) 10 mM

Figure 13 shows the SPR peak for different concentrations of silver nitrate as a metal precursor (2 mM, 5 mM, and 10 mM) after 24 h reaction time. It can be seen that the intensity of the SPR peak of AgNPs using 2 mM of $AgNO_3$ is higher than SPR for 5 mM and 10 mM concentrations. It also clearly showed the red shift in peak values from 439 nm to 434 nm and 396 nm for 5 mM and 10 mM, respectively. The red shift of the SPR peak indicated the formation of larger AgNPs.

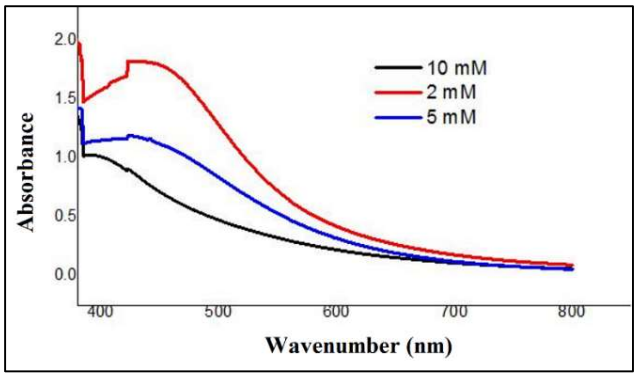


Figure 13. SPR peak from UV-vis of AgNPs at different concentrations after 24 hours

Zeta potential is a useful tool for predicting the stability of AgNPs in solution and understanding their surface. Zeta potential measurement is a technique for determining the surface charge of NPs in a colloidal solution. Figure 14 shows the Zeta potential of AgNPs at different concentrations (2, 5, and 10 mM). From the zeta potential value, it showed that the stability of AgNPs at high concentrations suffers from stability.

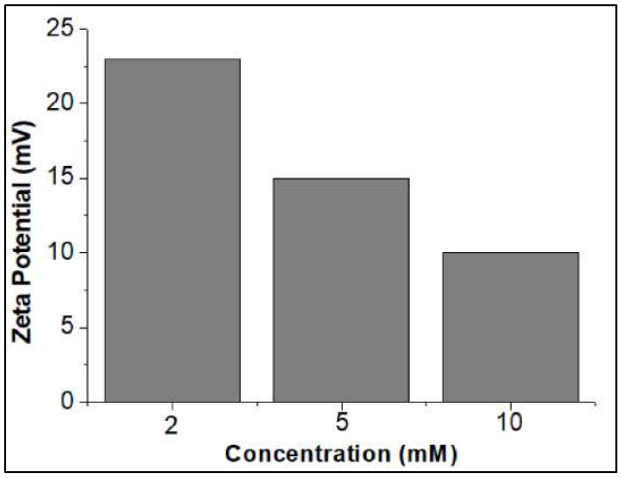


Figure 14. Zeta potential of AgNPs at different concentrations after 24 hours

This section's conclusion clearly shows that using 5 and 10 mM of $AgNO_3$ lowered the stability of synthesized AgNPs. Adopting the idea demonstrated the size distribution's heterogeneous nature [24]. Additionally, it might be because the biomolecules in the MLE were insufficiently powerful to maintain the high concentration of AgNPs. The production of precipitation for AgNPs created by increasing the concentration of metal precursor was also demonstrated in earlier research [25, 26].

According to the data above, the stability of AgNPs produced by MLE reduced as metal precursor concentration increased. AgNPs must be prepared as a homogeneous mixture with various organic, inorganic, and polymeric components for the majority of real-world applications. To study the impact of polymer on the stability and toxicity of high concentrations of AgNPs, two different polymers were evaluated as stabilizing agents for high concentrations of AgNPs (5 mM and 10 mM).

Antibacterial studies of AgNPs

The antibacterial efficacy of synthesized AgNPs was tested against Gram-positive (*Staphylococcus aureus*) and Gram-negative (*Escherichia coli*) pathogens. Each pathogen strain was purchased from Next Gene Scientific Sdn Bhd. Antimicrobial tests were then conducted according to the American Society for Testing and Materials (ASTM) standard method E2783-11. Biosynthesized AgNPs showed significant antimicrobial activity against both the pathogenic bacteria, i.e., *E. coli* and *S. aureus*. The mean diameter of the inhibitory zone (mm) around each well was measured and tabulated in Table 3 result shows *Murdannia loriformis* extract didn't exhibit any significant antibacterial activity against test pathogens even at high concentrations, which might be due to the active constituents responsible for the antibacterial activity is not present in aqueous leaf extract, or the concentrations are very low. *E. coli* (Gram-negative bacteria) and *S. aureus* (Gram-positive bacteria) were sensitive to synthesized AgNPs. The most sensitive is *E. coli,* around 18.27-22.09 mm, while *S. aureus,* around 9.95-10.99 mm in diameter, is related to concentration bacteria 30 µL. It was also observed that the maximum zone of inhibition increases with increasing concentration of AgNPs, where *E. coli* (Gram-negative) exhibited a higher zone of inhibition as compared to *S. aureus* (Gram-positive) (Figure 15). From the observation, different concentrations of MLE-mediated AgNPs did not bring much difference in antibacterial properties against both bacteria.

This might be due to the rigid peptidoglycan layer on the Gram-positive bacterial cell wall compared to Gram-negative bacteria preventing the AgNPs from penetrating, resulting lower zone of inhibition. The exact mechanism behind the antibacterial activity of AgNPs is not very clear, but many proposals have been

put forward for the same. The most accepted hypothesis are i) the formation of pits on the outer membrane progressively release the lipopolysaccharides and membrane proteins, ii) cells treated with AgNPs lead to increase conductivity resulting in leakage of the intracellular molecules, and iii) AgNPs interrupts the ATP metabolism and DNA replication preferentially by targeting the sulfur and phosphorous rich macromolecules resulting programmed cell death.

Table 3 Antibacterial activity of synthesized AgNPs against test bacterial pathogens.

Test	**Zone of Inhibition (mm)**				
Concentration (mM)/ Bacteria	MLE	1	2	5	10
E.coli	0	18.27± 1.37	19.55± 1.81	21.78± 1.51	22.09± 0.44
S.aureus	0	10.99± 0.42	9.11±0.28	9.18±0.18	9.95± 0.26

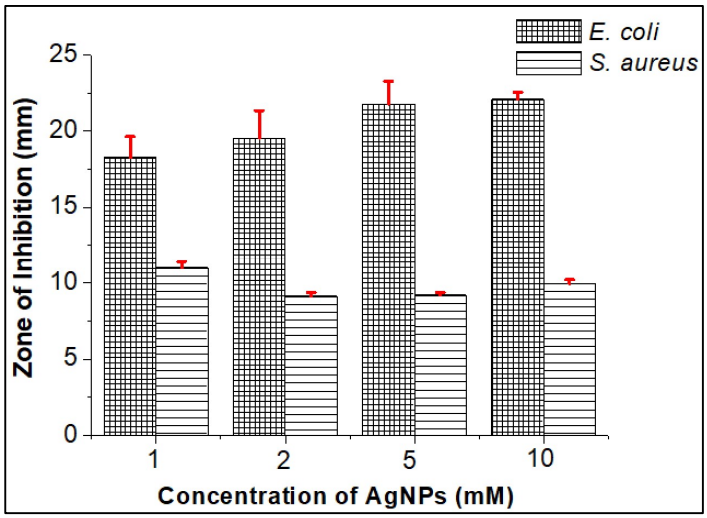


Figure 15. Antibacterial activity means the zone of inhibition (mm) of synthesized AgNPs against pathogenic bacterial strains

Conclusion

AgNPs were successfully synthesized via biological method using MLE as a reducing agent and silver nitrate as the metal precursor. Phytochemical identification revealed that the MLE showed a high concentration of protein and carbohydrate as primary metabolites and the presence of flavonoids and sterols as secondary metabolites, which displayed dual performance of reducing agents, as well as capping agent/stabilizers. TEM images verified the formation of the well-dispersed and quasi-spherical shape of AgNPs with a size range between 8.25 nm and 19.34 nm with an average size of 12.60 nm ± 2.83 nm at the optimized condition of 0.05 g/L (devoted as 100%) concentration of MLE, 2 mM of metal concentration, pH of 10 and 24 hr reaction time at room temperature. At optimized conditions, the AgNPs were highly crystalline in nature with FCC geometry, identified with XRD analysis. The stability of AgNPs synthesized at optimized conditions was confirmed by UV-vis spectral and zeta potential analysis. The synthesized AgNPs were seen to be as stable as when they were first made based on SPR peak in UV-Vis plot as well as did not show any precipitation or colour change in the colloidal AgNPs solution. The stability of synthesized AgNPs can be obtained by phytoconstituents in MLE coat these AgNPs or form an

organic matrix to embed them, thus preventing their aggregation and providing stability for a prolonged period of time. The zeta potential value of 23.61 mV also supports this conclusion. However, the stability of AgNPs decreased when the concentration of metal precursor increased. From the TEM image, the AgNPs were agglomerated when the concentration of $AgNO_3$ increased from 2 mM to 5 mM and 10 mM. Moreover, the Zeta potential values were decreased from 23.63 mV to 15.80 mV, and 9.75 mV as the stability of AgNPs decreased when 5 mM and 10 mM of initial concentration of metal precursors were used. The antibacterial study shows that the maximum zone of inhibition increases with increasing concentration of AgNPs where *E. coli* (Gram-negative) exhibited a higher zone of inhibition as compared to *S. aureus* (Gram-positive) with the value of maximum zone of inhibition around 18.27-22.09 mm for E. coli while S. aureus around 9.95-10.99 mm in diameter related to concentration bacteria of 30 µL. More extensive analysis is required for appropriate synthesis parameters and adequate concentration selection for use in biomedical applications and antibacterial control systems.

Acknowledgement

The authors acknowledge the materials, facilities, and financial support provided by University Teknologi MARA, Cawangan Pulau Pinang. This research was supported by the Malaysia Ministry of Higher Education – Fundamental Research Grant Scheme (FRGS/1/2019/STG01/UiTM/ 02/1) and (FRGS/1/2021/STG05/UiTM/02/ 9).

References

1. Royle, M., Bot, I., Mts, H. and Rafinesque, S. (2000). 8. Murdannia Royle, Ill. Bot. Himal. Mts. 1: 403. 1840, *nom. cons.* 5–12. *Flora of China*, 24: 25-31.
2. Soraya, I., Sulaiman, C., Mohamad, A. and Ahmed, O. H. (2021). *Murdannia loriformis* : A review of ethnomedicinal uses, phytochemistry, pharmacology, contemporary application, and toxicology. *Evidence-Based Complementary and Alternative Medicine* (*eCAM*), 2021: 9976202.
3. Poonthananiwatkul, B., Lim, R. H. M., Howard, R. L., Pibanpaknitee, P. and Williamson, E. M. (2015). Traditional medicine use by cancer patients in Thailand. *Journal of Ethnopharmacology*, 168: 100-107.
4. Jiratchariyakul, W. and Kummalue, T. (2011). Experimental therapeutics in breast cancer cells. *Breast Cancer-Current and Alternative Therapeutic Modalities,* 2011: 243-269.
5. Kunnaja, P., Wongpalee, S. P., & Panthong, A. (2014). Evaluation of anti-inflammatory, analgesic, and antipyretic activities of the ethanol extract from *Murdannia loriformis* (Hassk.) Rolla Rao et Kammathy. *BioImpacts, 4*(4): 183-189.
6. Mohamad, N. N., Basir, M. R., Mahmood, A., Bakhari, N. A., Mydin, M. M., Arshad, N. M., Hamid, H. A., and Isa, N. (2022). Synthesis of silver nanoparticles using beijing grass extract as reducing agent and the comparative study of AgNPs toxicity. *International Journal Electroactive Materials*, 10: 1-11.
7. Mohamad, N. N., Mahmood, A., Bakhari, N. A., Mydin, M. M., Arshad, N. M. and Isa, N. (2021). Studies on surface plasmon resonance of *Murdannia loriformis* silver nanoparticles. *Journal of Physics: Conference Series*, 2129(1): 12084.
8. Azhar, A. S., Kamis, W. Z. W., Hamid, H. A., Kassim, N. F. A. and Isa, N. (2021). Removal of tartrazine dye using *Kyllinga Brevifolia* Extract and silver nanoparticles as catalysts. *Journal of Physics: Conference Series*, 2129(1): 12033.
9. Isa, N., Kian, T. W., Kawamura, G., Matsuda, A. and Lockman, Z. (2018). Synthesis of TiO_2 nanotubes decorated with ag nanoparticles (TNTs/AgNPs) for visible light degradation of methylene blue. *Journal of Physics: Conference Series*, 1082(1): 12105.
10. Abdul Aziz, N. S., Isa, N., Osman, M. S., Wan Kamis, W. Z., So'aib, M. S. and Mohd Ariff, M. A. (2022). A mini review on the effects of synthesis conditions of bimetallic Ag/Si nanoparticles on their physicochemical properties. *International Journal of Nanoscience and Nanotechnology*, 18(4): 219-232.

11. Isa, N., Osman, M. S., Abdul Hamid, H., Inderan, V. and Lockman, Z. (2022). Studies of surface plasmon resonance of silver nanoparticles reduced by aqueous extract of shortleaf spikesedge and their catalytic activity. *International Journal of Phytoremediation*, 20:1-12.
12. Srikar, S. K., Giri, D. D., Pal, D. B., Mishra, P. K. and Upadhyay, S. N. (2016). Green synthesis of silver nanoparticles: a review. *Green and Sustainable Chemistry*, 6(1): 34-56.
13. Jamkhande, P. G., Ghule, N. W., Bamer, A. H. and Kalaskar, M. G. (2019). Metal nanoparticles synthesis: An overview on methods of preparation, advantages and disadvantages, and applications. *Journal of Drug Delivery Science and Technology*, 53: 101174.
14. Isa, N., Wan Kamis, W. Z., Inderan, V., Husin, N. I., Ahmad, F. N., Bashirom, N. H. and Lockman, Z. (2019). Shape, size and dispersion of plant-driven silver nanoparticles for removal of methylene blue dyes. *Journal of Physics: Conference Series*, *1349*(1): 012115.
15. Usman, H., Abdulrahman, F. I. and Usman, A. (2009). Qualitative phytochemical screening and in vitro antimicrobial effects of methanol stem bark extract of *Ficus thonningii* (Moraceae). *African Journal of Traditional, Complementary and Alternative Medicines*, *6*(3): 289-295.
16. Ministry of Health Malaysia. (2010). Guide to Nutrition Labelling and Claims (2010). Food Safety and Quality Division, Ministry of Health Malaysia, Putrajaya.
17. Isa, N., Sarijo, S. H., Aziz, A. and Lockman, Z. (2017). Synthesis colloidal *Kyllinga brevifolia*-mediated silver nanoparticles at different temperature for methylene blue removal. In *AIP Conference Proceedings*, 1877(1): 070001.
18. Muniandy, S. S., Sasidharan, S. and Lee, H. L. (2019). Green synthesis of Ag nanoparticles and their performance towards antimicrobial properties. *Sains Malaysiana*, 48(4): 851-860.
19. Isa, N. and Lockman, Z. (2019). Methylene blue dye removal on silver nanoparticles reduced by *Kyllinga brevifolia. Environmental Science and Pollution Research*, *26*(11): 11482-11495.
20. Das, M. P., Livingstone, J. R., Veluswamy, P. and Das, J. (2018). Exploration of *Wedelia chinensis* leaf-assisted silver nanoparticles for antioxidant, antibacterial and in vitro cytotoxic applications. *Journal of Food and Drug Analysis*, 26(2): 917-925.
21. Abdelghaffar, F., Mahmoud, M. G., Asker, M. S. and Mohamed, S. S. (2021). Facile green silver nanoparticles synthesis to promote the antibacterial activity of cellulosic fabric. *Journal of Industrial and Engineering Chemistry*, 99: 224-234.
22. Mata, R., Nakkala, J. R. and Sadras, S. R. (2015). Biogenic silver nanoparticles from *Abutilon indicum*: their antioxidant, antibacterial and cytotoxic effects in vitro. *Colloids and Surfaces B: Biointerfaces*, 128: 276-286.
23. Yin, Y., Li, Z.-Y., Zhong, Z., Gates, B., Xia, Y. and Venkateswaran, S. (2002). Synthesis and characterization of stable aqueous dispersions of silver nanoparticles through the Tollens process. *Journal of Materials Chemistry*, 12(3): 522-527.
24. Stebounova, L. V, Guio, E. and Grassian, V. H. (2011). Silver nanoparticles in simulated biological media: a study of aggregation, sedimentation, and dissolution. *Journal of Nanoparticle Research*, 13(1): 233-244.
25. Sosa, Y. D., Rabelero, M., Treviño, M. E., Saade, H. and López, R. G. (2010). High-yield synthesis of silver nanoparticles by precipitation in a high-aqueous phase content reverse microemulsion. *Journal of Nanomaterials*, 2010: 392572.
26. Perugu, S., Nagati, V. and Bhanoori, M. (2016). Green synthesis of silver nanoparticles using leaf extract of medicinally potent plant Saraca indica: a novel study. *Applied Nanoscience*, 6(5): 747-753.

Malaysian Journal of Analytical Sciences (MJAS)
Published by Malaysian Analytical Sciences Society

MULTI-TRACE METALS DETERMINATION OF PENINSULAR MALAYSIA STINGLESS BEE HONEYS FROM DIFFERENT REGIONS AND SEASONS USING INDUCTIVELY COUPLED PLASMA-OPTICAL EMISSION SPECTROMETRY AND CHEMOMETRIC TECHNIQUES

(Penentuan Logam Pelbagai Surih Madu Lebah Tanpa Sengatan dari Pelbagai Rantau dan Musim Berbeza Menggunakan Plasma Gandingan Teraruh-Spektrometri Pancaran Optik dan Teknik Kemometrik)

Syazwani Dzolin[1], Wan Aini Wan Ibrahim[1*], Naji Arafat Mahat[1,2*], Dzulkiflee Ismail[3] and Aidil Fahmi Shadan[4]

[1]Department of Chemistry,
Faculty of Science,
Universiti Teknologi Malaysia,
81310 UTM, Johor Bahru, Johor, Malaysia
[2]Centre for Sustainable Nanomaterials,
Ibnu Sina Institute for Scientific and Industrial Research,
Universiti Teknologi Malaysia,
81310 UTM, Johor Bahru, Johor, Malaysia
[3]School of Health Sciences,
Universiti Sains Malaysia,
16150 Kubang Kerian, Kelantan, Malaysia
[4]Department of Chemistry Malaysia,
Jalan Sultan, 46661 Petaling Jaya, Selangor, Malaysia

[*]Corresponding author: waini@utm.my, wawi4476@gmail.com

Received: 21 September 2022; Accepted: 30 January 2023; Published: 22 February 2023

Abstract

Demand for authenticating and distinguishing the provenance of bee honey among consumers is continuously rising. Considering vast variations in prices attributable to different geographical origins, suitable indication on labeling of honey products is important for consumer protection. Since concentrations of trace metals can be closely related to geographical origin, the use of spectroscopy and chemometric techniques for ascertaining the validity of such claim may prove relevant. In this study, multi-trace metals in stingless bee honey of *Heterotrigona itama* species, from different regions and seasons (rainy and dry) in Peninsular Malaysia (Kedah, Johor, Selangor and Pahang) were determined *via* inductively coupled plasma-optical emission spectrometry (ICP-OES). Principal component analysis (PCA) was then applied to recognize the distribution patterns. Subsequently, linear discriminant analysis (LDA) was applied to perform further classification. With the use of LDA, cross-validation was found as 95.8% and 89.6% during rainy and dry seasons, respectively. Combination of ICP-OES data with PCA and LDA techniques has provided accurate classification of the Malaysian stingless bee honey samples according to their respective origins. This study provided some elemental information on distribution of stingless bee honey samples at spatial and temporal levels, and could be used as a reference for their provenance establishment and authenticity.

Keywords: honey, stingless bee, provenance, authenticity, spectroscopy, chemometric

Abstrak

Permintaan untuk mengesahkan dan membezakan asal usul madu lebah di kalangan pengguna terus meningkat. Mengambil kira variasi besar harga byang disebabkan oleh asal geografi yang berbeza, petunjuk yang sesuai pada pelabelan produk madu adalah penting untuk perlindungan pengguna. Oleh kerana kepekatan logam surih berkait rapat dengan asal geografi, penggunaan teknik spektroskopi dan kemometrik untuk menentukan kesahihan tuntutan tersebut mungkin terbukti relevan. Dalam kajian ini, logam pelbagai surih dalam madu lebah tanpa sengatan dari spesies *Heterotrigona itama*, dari pelbagai rantau dan musim (hujan dan kering) di Semenanjung Malaysia (Kedah, Johor, Selangor dan Pahang) ditentukan melalui plasma gandingan teraruh-spektrometri pancaran optik (ICP-OES). Analisis komponen utama (PCA) kemudian digunakan untuk mengenal corak taburan. Seterusnya, analisis diskriminan linear (LDA) telah digunakan untuk melaksanakan klasifikasi lanjutan. Dengan penggunaan LDA, pengesahan silang masing-masing adalah 95.8% dan 89.6% pada musim hujan dan kering. Gabungan data ICP-OES dengan teknik PCA dan LDA telah memberikan klasifikasi tepat sampel madu lebah tanpa sengatan Malaysia mengikut asal usul masing-masing. Kajian ini memberikan beberapa maklumat unsur mengenai taburan sampel madu lebah tanpa sengatan pada tahap spasial dan temporal, dan dapat digunakan sebagai rujukan untuk asal usul dan keasliannya.

Kata kunci: madu, lebah tanpa sengatan, asal usul, ketulenan, spektroskopi, kemometrik

Introduction

Honey is the oldest natural sweetening agent with various nutritional and therapeutic values [1]. Being a natural product, composition of honey is diverse, ranging from sugars, flavor compounds, amino acids, enzymes, flavonoids, gluconic acid, lactone, nitrogenous compounds, proteins, vitamins (vitamin B6, thiamine, niacin, riboflavin and pantothenic acid) [2 - 5] phenols, pigments as well as multi-trace metals [2, 6, 7]. Modern researchers have reported several honey biological activities such as antioxidant activity [8], decreases factors of cardiovascular risk [9] and improve resistance against pathogenic organisms [10].

To date, consumer demands for genuine honey of high qualities are continuously increasing. Since the beginning of honey trade, negative perceptions concerning processed honey products (adulteration) are also growing. Honey adulteration is the major problem influencing the overall perception of honey in terms of quality, price and human health (potential genotoxic, cytotoxic and carcinogenic effects of hydroxymethylfurfural) [11]. According to [1], two major factors related to honey authenticity; (i) origin of the honey (geographical and botanical origins) and (ii) mode of honey production (harvesting and processing techniques). Since years ago, internationally, the Codex Alimentarius have developed the authenticity standard of honey by providing the essentials of identity and quality of honey requirements for human consumption. This standard can be applied to all types of honey produced by bees and it covers all types of honey conditions [12].

Recently in Malaysia, Department of Standards Malaysia have developed a standard for *Kelulut* (Stingless bee) honey (MS 2683:2017) in 2017 [13]. In this Malaysian standard, it covered the quality requirements, sampling methods, sample preparation, hygiene, packaging as well as labeling of stingless bee honey for direct human consumption. Besides being great pollinators in ecosystem, stingless bees able to modify floral nectars into distinctive aroma and flavor of honey [14] that is favorable by local consumers.

Honey produced by stingless bee species especially by Meliponinae is appreciated by consumers worldwide [14] including Malaysia. Meliponinae was reported to have distinct characteristics compared to other bee species such as absence of sting, short foraging distance and build hives in horizontal position to store nectar and pollen [15, 16]. Due to the insufficient knowledge of Malaysian stingless bee honey composition, there is a shortage of identity of its geographical origin especially related to the present of multi-trace metals signature. As reported by [2], multi-trace metals content is important as it much dependent on the soil and the environment of plants where the stingless bees collect nectar in the production of honey. In addition, anthropogenic activities such as agricultural practices and industrial can also influence the presence of multi-trace metals in honey [17]. Atanassova et al. [18] reported that during different vegetation season, honeys could exhibit different multi-trace metals concentrations even though it comes from same geographical region, same beehive and same locality.

The assessment of multi-trace metals concentrations can be useful in discriminating honey based on their geographical origin [19]. Few authors have begun to apply analytical approaches such as flame atomic absorption spectroscopy (FAAS) [20, 21], graphite furnace atomic absorption spectrometry (GFAAS) [22], inductively coupled plasma-mass spectrometry (ICP-MS) and inductively coupled plasma-atomic emission spectrometry (ICP-AES) [23] and inductively coupled plasma-optical emission spectrometry (ICP-OES) [24, 25] to determine the

presence of multi-trace metals in honey samples.

In Malaysia, studies on multi-trace metals analysis have been performed by Moniruzzaman et al. [22] and Chua et al. in 2012 [23] on various type of Malaysian bee honey but none of the studies reported on the honey provenance establishment of stingless bee species. Shadan et al. [24] reported for the first time on the provenance establishment of stingless bee honey from five districts of Johor region (Segamat, Muar, Batu Pahat, Kota Tinggi and Johor Bahru). Their study focuses on the provenance establishment of the honeys using chemometric techniques namely principal component analysis (PCA) and linear discriminant analysis (LDA). The multi-trace metals profile detected the present of Ag, Al, As, B, Ba, Be, Cd, Co, Cr, Cu, Fe, Mg, Mn, Mo, Ni, Pb, Sb, Se, Sn and Zn. Despite its natural occurrence in most regions of Malaysia, there is still a shortage of studies on the geographical origin of stingless bee honey. The identity and quality standards of the honey are difficult to ascertain.

The incorporation of chemometric techniques into spectroscopy methods is an effective method for identifying minor and major compounds in honey that can serve as unique signatures for its botanical or geographical origin [26]. Therefore, the aims of our study were: (i) to determine eighteen multi-trace metals in stingless bee (*Heterotrigona itama*) honey samples collected from four regions of Peninsular Malaysia, namely Kedah, Johor, Selangor, and Pahang during two different seasons (rainy and dry); and (ii) to classify stingless bee honey samples by regions of each season based on their multi-trace metal concentrations using ICP-OES in combination with PCA and LDA techniques.

Materials and Methods

Instrument and apparatus

The analysis was performed using ICP-OES, Perkin Elmer (PE 4300 DV) model (Shelton, USA), located at the Department of Chemistry, Petaling Jaya, Selangor. The operating conditions for determining multi-trace metals in stingless bee honey samples were as follows: radio frequency power (0.7-1.5 kW; 1.2-1.3 kW for axial), Ar plasma gas flow (radial: 10.5-15 L/min; axial: 15 L/min), Ar auxiliary gas flow rate (1.5 L/min) and viewing height (5-12 mm).

Reagents

Analytical grade HNO_3 (65% v/v) was purchased from Merck KGaA, (Darmstadt, Germany). Ultra-pure water (resistivity, 18.2 MΩ cm^{-1}) was produced from a Milli-Q water purification system (Millipore, Bedford, MA, USA) and was used throughout the preparation of solutions. Multi-element standard solution was obtained from Agilent Technologies (Santa Clara, USA).

Sample collection, preparation and analysis

Honey samples from stingless bees (*Heterotrigona itama*) were harvested in November 2016 and February 2017, respectively, during rainy and less rainy seasons. At the beginning of this study, we decided to collect stingless bee honey samples throughout Peninsular Malaysia, but because of the limited number of beekeepers registered with the Malaysian Agricultural Research and Development Institute (MARDI), we are focusing only on the registered beekeepers from selected districts in this study. A total of thirty-two stingless bee honey samples were collected from the northern (Kedah: Padang Terap, Kulim, Yan and Baling), southern (Johor: Segamat, Johor Bahru, Pontian and Mersing), western (Selangor: Sabak Bernam, Klang, Kuala Selangor and Hulu Selangor) and eastern (Pahang: Jerantut, Rompin, Temerloh and Kuantan) regions of Peninsular Malaysia.

The honey samples were harvested directly from beekeepers during rainy and less rainy seasons, with the mean maximum temperature being 27.9℃ and 35.6℃, respectively. All the stingless bee honey samples were harvested without any treatment and kept in separate amber glass bottles at 12℃. To minimize the final acidity of honey samples after preparation, the acid mineralization method was performed, as suggested by Chua et al. [23] with a few modifications. Approximately 1 g of each honey sample was digested and mineralized using 65% concentrated HNO_3 (10 mL) by heating the mixture till near to dryness. The mixture was then made up to a volume of 50 mL with deionized water (DI), filtered and kept in a glass bottle at 12℃ prior to analysis. Using the same sample preparation procedure, a blank control sample that contained 10 mL of HNO_3 (65% v/v) was used in the preparation of calibration and quality control samples. The varying concentrations of working solutions and quality control samples were freshly prepared *via* serial dilution from a stock solution containing 100 mg/L of multi-elements in HNO_3.

Chemometric approach dataset

The data set consisted of thirty-two stingless bee honey samples separated by geographical origins and eighteen multi-trace metals. The samples which came from the sixteen districts of the four regions were divided as follows:

1. Northern region: Padang Terap (PT), Kulim (KM), Yan (YN) and Baling (BG)
2. Southern region: Segamat (ST), Johor Bahru (JB), Pontian (PN) and Mersing (MG)

3. Western region: Sabak Bernam (SB), Klang (KL), Kuala Selangor (KS) and Hulu Selangor (HS)
4. Eastern region: Jerantut (JT), Rompin (RN), Temerloh (TH) and Kuantan (KN)

Upon completion of data entry in Microsoft Excel® spreadsheet (Microsoft Corporation, Washington, USA) and IBM® SPSS statistics 20.0 software, the data were exported into Minitab® 17 software (Minitab Inc., State College, PA).

Principal component analysis (PCA) and linear discriminant analysis (LDA)

For studying the organization of the overall dataset, PCA was utilized following the steps proposed by Shlens [27] viz. standardization of dataset, calculation of covariance matrix, obtaining the principal components (PCs) and data translation into components. Being the supervised statistical method, LDA categorically clusters objects into user-defined groups/clusters by calculating linear discriminant function to create a model that would enable correct classification of objects within a given dataset. For validating the developed model for a given dataset, the "leave-one-out" technique cross-validation approach was utilized.

Results and Discussion

Analytical parameters and method accuracy

Thirty-two stingless bee honey samples were analyzed using ICP-OES to determine their multi-trace metal concentrations (3 replicates). The limits of detection (LOD) and limit of quantitation (LOQ) for ICP-OES were estimated from blank analysis (7 replicates). The LOD and LOQ were calculated as 3SDblank/slope and 10SDblank/slope, respectively. The proposed method with matrix matching calibration used in this study is shown in Table 1.

Table 1. Wavelength, R^2, regression equation, LODs, LOQs and % RSD for multi-trace metals determination in stingless bee honey using ICP-OES

Metals	Wavelength (nm)	Coefficient of Determination (R^2)	Equation	Limit of Detection (mg/L)	Limit of Quantitation (mg/L)	Relative Standard Deviation (%)
Ag	328.068	0.9999	y = 1.0445x + 0.004	0.048	0.159	3.6
Al	396.153	0.9992	y = 1.0255x +0.0045	0.069	0.230	5.3
As	193.696	0.9999	y = 0.9681x + 0.008	0.024	0.103	1.8
Ba	455.403	0.9998	y = 1.0301x - 0.0008	0.063	0.212	4.9
Be	313.107	0.9991	y = 1.0175x - 0.0033	0.056	0.186	4.3
Cd	226.502	0.9998	y = 1.0132x - 0.0024	0.043	0.145	3.4
Co	228.616	0.9998	y = 1.0294x - 0.003	0.048	0.159	3.7
Cr	267.716	0.9997	y = 1.03x - 0.0027	0.049	0.164	3.8
Cu	327.393	0.9999	y = 1.0369x - 0.0002	0.040	0.135	3.1
Mn	257.61	0.9993	y = 1.0398x - 0.0023	0.066	0.220	5.1
Ni	231.604	0.9999	y = 1.0247x - 0.0034	0.046	0.154	3.6
Pb	220.353	0.9999	y = 1.0019x + 0.0019	0.021	0.071	1.6
Se	196.026	0.9998	y = 0.98x + 0.0049	0.028	0.094	2.1
Tl	190.801	0.9999	y = 0.9923x + 0.0012	0.025	0.085	2.0
Th	283.73	0.9997	y = 1.015x + 0.0011	0.044	0.148	3.4
U	385.958	0.9983	y = 0.94x - 0.021	0.060	0.199	4.8
V	292.402	0.9999	y = 1.0184x - 0.0034	0.050	0.165	3.8
Zn	213.857	0.9997	y = 1.0072x + 0.0011	0.044	0.148	3.4

Note: Silver (Ag), aluminum (Al), arsenic (As), barium (Ba), beryllium (Be), cadmium (Cd), cobalt (Co), chromium (Cr), copper (Cu), manganese (Mn), nickel (Ni), lead (Pb), selenium (Se), thallium (Th), thorium (Th), uranium (U), vanadium (V) and zinc (Zn).

Multi-trace metals concentrations in stingless bee honey samples

The preliminary findings for multi-trace metals analysis presented in this study demonstrated the potential for provenance establishment of Malaysian stingless bee honey samples. Concurrently, a total of eighteen multi-trace metals were determined after digestion process using ICP-OES. For these metals, some trace metals cannot be detected in some types of honey samples and some exhibited low or high concentration based on certain areas and regions. It may be because of the differences in soil composition, floral type, floral density, nectar or pollen [28 - 30]. Study by Pohl [31] suggested another factor which may contribute to the diversified trace metals content such as beekeeping practices, environmental pollution and honey processing. In an industrial area, toxic trace metals have been reported to be presented high concentrations in honeys [32]. According to Fatima et al. [33], the composition of Malaysian stingless bee honey from Trigona species varies according to geographical or botanical origin, as well as fruit or flower season. Therefore, these trace metals may give useful information in order to validate the geographical origin (provenance) of stingless bee honey samples.

Table 2 shows the most abundant metals (Al and Zn) obtained in stingless bee honey from four regions of Peninsular Malaysia. Bees are exposed to Al from various sources of their foraging activities for nectar as this element is reported to be abundant in Earth's crust [34]. In this study, the highest concentration of Al in stingless bee honey samples of rainy and dry seasons were 0.666 and 0.477 mg/L, respectively. The Al values obtained in this study was slightly similar to the study by Chua et al. [23] as they reported the range of Al concentration was between 0.708 to 1.872 mg/L in various type of honey from Malaysia. Previous research by Altun et al. [35] on honey samples from South and East regions of Turkey using ICP-MS found the highest concentration was 0.96 mg/L. In addition, Di Bella et al. [36] reported the highest concentration of Al was 5.67 mg/L in all honeys from Sicily and Calabria, Italy whereas Czipa et al. [37] found 4.39 mg/L of Al in Hungary honeys. According to Oroian et al. [38], due to neurological and cancer effects, Al is not essential to be consumed in high dosage.

The recommended daily consumption of Zn was 7.5 mg/kg and 13.5 mg/kg for children and adults, respectively [39]. In this study, the lowest and the highest Zn concentrations were less than 1 mg/L in all honeys. Since the highest concentration of Zn in this study was 0.549 mg/L, it showed Zn level was within the acceptable limits. Honeys from Hatay, Turkey also showed lower Zn concentration (0.237 mg/L) [35]. Conversely, other studies obtained high Zn concentration values in Anatolia honey (1.1-12.7 mg/L) [21] and Eastern Solvakia honey (1.3 mg/L) [17]. Chua et al. [23] reported Zn concentration of forest Malaysian honeys between 2.353 to 18.112 mg/L which is higher compared to our study.

Table 3 shows the low concentrations metals present in stingless bee honey. The content of Cr and Ni in this study (<1 mg/L) attributed to the uncontaminated environment as the main sources of livelihood is agriculture and not heavily industrialized. The Cr concentrations of our honey samples are similar to the Cr concentrations of Turkey honey (0.0024-0.0379 mg/L) [21], Eastern Solvakia honey (0.0268-0.0433 mg/L) [17] and Hatay honey (0.1-0.54 mg/L) [40]. In contrast, various type of honey samples from Malaysia possessed high Cr concentration of the range 1.8-3.8 mg/L as discussed by Chua et al. [23]. In this study, the highest concentration of Ni during rainy and dry seasons was 2.939 and 0.0406 mg/L, respectively whereas Chua et al. [23] obtained 0.084 mg/L of Ni from Malaysian forest honey sample. The mean Ni concentration of Argentine honey was 0.03 mg/L [41].

Copper (Cu) is an important element in eukaryotes aerobic respiration [42] and vital in formation of haemoglobin as well as in production of melanin for skin, hair and eyes pigmentation [38]. The mean range concentration of Cu in this study (0.015-0.128 mg/L) was slightly similar to the mean range (0.046-0.236 mg/L) of various honey samples as reported by Chua et al. [23]. The maximum and minimum concentration values for Mn exhibited 0.031 and 0.795 mg/L, respectively. These results showed lower values compared to results from Chua et al. [23]. However, our study was higher than Irish honey samples (0.004 mg/L) [43].

Selenium (Se) is a nutritious element for humans and it plays an important role in reproduction process, DNA synthesis and protection against infection [35]. In this study, the highest Se concentration determined in stingless bee honeys was 0.023 mg/L which was lower than Se concentration of Malaysian Tualang honey produced by sting bees (17.202 mg/L) [23]. However, our result exhibited slightly higher compared to Argentine honeys [41] and honeys from North East of Romania [38].

Table 2. Most abundant trace metals in stingless bee honey samples from four regions of Peninsular Malaysia

Season	Region	Al (mg/L)	Zn (mg/L)
Rainy	**Pahang (East)**		
	Mean ± SD	0.561 ± 0.0965	0.3483 ± 0.1817
	Range (min-max)	0.425 - 0.666	0.127 - 0.549
	Kedah (North)		
	Mean ± SD	0.3778 ± 0.0592	0.0839 ± 0.019
	Range (min-max)	0.278 - 0.42	0.057 - 0.104
	Selangor (West)		
	Mean ± SD	0.3614 ± 0.0207	0.1322 ± 0.0267
	Range (min-max)	0.331 - 0.388	0.093 - 0.16
	Johor (South)		
	Mean ± SD	0.3792 ± 0.017	0.0858 ± 0.0444
	Range (min-max)	0.36 - 0.405	0.052 - 0.159
Dry	**Pahang (East)**		
	Mean ± SD	0.1763 ± 0.0748	0.0381 ± 0.0104
	Range (min-max)	0.119 - 0.316	0.029 - 0.057
	Kedah (North)		
	Mean ± SD	0.2806 ± 0.1468	0.1064 ± 0.0433
	Range (min-max)	0.1068 - 0.447	0.068 - 0.1808
	Selangor (West)		
	Mean ± SD	0.1225 ± 0.0457	0.0633 ± 0.0181
	Range (min-max)	0.091 - 0.203	0.0397 - 0.0885
	Johor (South)		
	Mean ± SD	0.2318 ± 0.1683	0.0575 ± 0.0035
	Range (min-max)	0.063 - 0.477	0.052 - 0.0615

SD = standard deviation (n = 12). One-way ANOVA with Tukey's HSD post hoc test with significant value of 0.05 was used for determining the mean differences in the concentrations of multi-trace metals in stingless bee honey samples among the different regions. *The mean difference is significant at the 0.05 level.

Table 4 shows heavy metals concentrations obtained from Malaysian stingless bee honey samples. Excess heavy metals such as As, Cd, Co and Pb cause an excessive production of reactive oxygen species (ROS) causing oxidative stress [44]. According to Bogdanov et al. [45], Cd and Pb are considered as bio-indicators for contamination of honey. Pollutants from industries might contaminate soil and air. Cd is an element that passed from soil to plants and nectar whereas Pb contamination correlates with air pollution [17]. The lowest and the highest concentrations of As, Cd, Co and Pb were <1 mg/L in all stingless bee honey samples. The honey samples of this study are harvested directly from beekeepers that are located mostly far from the main road and the factories area. Moreover, our data for As, Cd, and Pb concentrations were within the recommended limits as stated in Malaysia Food Act 1983 (Regulation 38) and Food and Agriculture Organization (FAO) and World Health Organization (WHO) [46].

Table 3. Low concentrations metals in stingless bee honey samples from four regions of Peninsular Malaysia

Season	Region	Ba (mg/L)	Cr (mg/L)	Cu (mg/L)	Mn (mg/L)	Ni (mg/L)	Se (mg/L)
Rainy	**Pahang (East)**						
	Mean ± SD	0.0926 ± 0.0073	0.0604 ± 0.0018	0.0360 ± 0.0083	0.064 ± 0.0037	2.1903 ± 0.5129	0.0196 ± 0.0028
	Range (min-max)	0.081 - 0.1	0.058 - 0.063	0.028 - 0.047	0.043 - 0.121	1.542 - 2.939	0.013 - 0.023
	Kedah (North)						
	Mean ± SD	0.0869 ± 0.0076	0.0592 ± 0.0017	0.03375 ± 0.0128	0.0614 ± 0.0254	0.0355 ± 0.0052	0.0176 ± 0.0042
	Range (min-max)	0.074 - 0.094	0.056 - 0.061	0.023 - 0.055	0.034 - 0.093	0.031 - 0.043	0.011 - 0.022
	Selangor (West)						
	Mean ± SD	0.0768 ± 0.0078	0.0589 ± 0.0024	0.0373 ± 0.0077	0.0563 ± 0.0269	0.1468 ± 0.0074	0.0203 ± 0.0027
	Range (min-max)	0.064 - 0.084	0.055 - 0.062	0.026 - 0.046	0.032 - 0.097	0.133 - 0.153	0.016 - 0.025
	Johor (South)						
	Mean ± SD	0.0703 ± 0.0109	0.0565 ± 0.0031	0.0522 ± 0.0447	0.0715 ± 0.0614	0.0348 ± 0.0069	0.0114 ± 0.0029
	Range (min-max)	0.053 - 0.082	0.053 - 0.062	0.024 - 0.128	0.031 - 0.175	0.029 - 0.046	0.005 - 0.016
Dry	**Pahang (East)**						
	Mean ± SD	0.08 ± 0.0203	0.0626 ± 0.003	0.0454 ± 0.0278	0.2428 ± 0.3086	0.0322 ± 0.0009	0.0036 ± 0.0014
	Range (min-max)	0.066 - 0.117	0.059 - 0.068	0.018 - 0.093	0.059 - 0.795	0.031 - 0.034	0.002 - 0.007
	Kedah (North)						
	Mean ± SD	0.065 ± 0.0106	0.0982 ± 0.0582	0.0258 ± 0.0022	0.086 ± 0.0446	0.0339 ± 0.0025	0.0143 ± 0.0028
	Range (min-max)	0.057 - 0.0843	0.056 - 0.2001	0.023 - 0.0292	0.046 - 0.1615	0.03 - 0.0372	0.01 - 0.0189
	Selangor (West)						
	Mean ± SD	0.0709 ± 0.0058	0.0653 ± 0.0033	0.0416 ± 0.0152	0.0553 ± 0.0185	0.035 ± 0.0039	0.0097 ± 0.0060
	Range (min-max)	0.0646 - 0.081	0.061 - 0.071	0.0226 - 0.058	0.034 - 0.0818	0.031 - 0.0406	0.003 - 0.0212
	Johor (South)						
	Mean ± SD	0.0712 ± 0.0095	0.0581 ± 0.0044	0.0239 ± 0.0086	0.0551 ± 0.0124	0.0314 ± 0.0017	0.0087 ± 0.0065
	Range (min-max)	0.058 - 0.0842	0.0505 - 0.061	0.015 - 0.037	0.037 - 0.0664	0.0293 - 0.034	0.001 - 0.0189
[a]Trigona Type 1	Lenggong, Perak			ND			
[a]Trigona Type 2	Lenggong, Perak			ND			
[a]Trigona Type 3	Serdang, Selangor			2.4 ± 0.06			
[a]Trigona Type 4	Serdang, Selangor			2.93 ± 0.36			

SD = standard deviation (n = 12); ND = not detected. One-way ANOVA with Tukey's HSD post hoc test with significant value of 0.05 was used for determining the mean differences in the concentrations of multi-trace metals in stingless bee honey samples among the different regions. *The mean difference is significant at the 0.05 level. [a]Results are expressed in mg/kg [22].

Table 4. Heavy metals in stingless bee honey samples from four regions of Peninsular Malaysia

Season	Region	As (mg/L)	Cd (mg/L)	Co (mg/L)	Pb (mg/L)
Rainy	**Pahang (East)**				
	Mean ± SD	0.0092 ± 0.0037	0.003 ± 0	0.0128 ± 0.0014	0.008 ± 0.0041
	Range (min-max)	0.004 - 0.014	0.003	0.011 - 0.014	0.004 - 0.014
	Kedah (North)				
	Mean ± SD	0.0068 ± 0.0021	0.004 ± 0	0.004 ± 0	0.0048 ± 0.0019
	Range (min-max)	0.004 - 0.01	0.004	0.004	0.002 - 0.008
	Selangor (West)				
	Mean ± SD	0.0019 ± 0.0033	0.004 ± 0	0.005 ± 0	0.0067 ± 0.0036
	Range (min-max)	0.002 - 0.009	0.004	0.005	0.003 - 0.011
	Johor (South)				
	Mean ± SD	0.0052 ± 0.0054	0.004 ± 0	0.0042 ± 0.0004	0.0075 ± 0.0061
	Range (min-max)	0.001 - 0.016	0.004	0.004 - 0.005	0.002 - 0.018
Dry	**Pahang (East)**				
	Mean ± SD	0.0123 ± 0.0019	0.0089 ± 0.008	0.004 ± 0	0.0012 ± 0.0011
	Range (min-max)	0.01 - 0.016	0.004 - 0.023	0.004	0.001 - 0.003
	Kedah (North)				
	Mean ± SD	0.0139 ± 0.0034	0.0268 ± 0.0371	0.0052 ± 0.0007	0.0043 ± 0.0015
	Range (min-max)	0.008 - 0.0185	0.004 - 0.0913	0.004 - 0.0059	0.001 - 0.006
	Selangor (West)				
	Mean ± SD	0.0144 ± 0.0028	0.0046 ± 0.0007	0.0049 ± 0.0009	0.0035 ± 0.002
	Range (min-max)	0.0096 - 0.018	0.004 - 0.0058	0.004 - 0.0059	0.002 - 0.0065
	Johor (South)				
	Mean ± SD	0.0150 ± 0.0059	0.0042 ± 0.0004	0.0045 ± 0.0007	0.0036 ± 0.0016
	Range (min-max)	0.006 - 0.0024	0.004 - 0.0049	0.004 - 0.0056	0.001 - 0.006
[a]Trigona Type 1	Lenggong, Perak	0.043 ± 0.002	1.03 ± 0.25	ND	ND
[a]Trigona Type 2	Lenggong, Perak	0.027 ± 0.001	0.78 ± 0.04	ND	0.691 ± 0.002
[a]Trigona Type 3	Serdang, Selangor	0.043 ± 0.001	0.51 ± 0.01	ND	0.043 ± 0.001
[a]Trigona Type 4	Serdang, Selangor	0.052 ± 0.002	0.33 ± 0.04	ND	0.052 ± 0.002
[b]Food Act 1983 (Regulation 38)	General limit for honey	1	1		2
[c]FAO and WHO	General limit for food		1		2

SD = standard deviation (n = 12); ND = not detected. One-way ANOVA with Tukey HSD post hoc test with significant value of 0.05 was used for determining the mean differences in the concentrations of multi-trace metals in stingless bee honey samples among the different regions. *The mean difference is significant at the 0.05 level. [a,b,c] Results are expressed in mg/kg [22, 46].

Trace metals concentrations of stingless bee honey samples from four regions of Peninsular Malaysia were shown in Table 5. In this study, the concentrations obtained for Ag and U were lower to those found by Chua et al. [23]. Additionally, Be and V metals have been determined in stingless bee honey samples but absent in various honey samples from Malaysia [23]. The presence of rare earth elements (REE), such as Ce, Dy, Er, La, Ho, Sm and Th are associated with the used of fertilizers to increase plants productivity [47]. From the results obtained, both rainy and dry seasons possessed low concentration of Th metal.

Table 5. Trace metals in stingless bee honey samples from four regions of Peninsular Malaysia

Season	Region	Ag (mg/L)	Be (mg/L)	Tl (mg/L)	Th (mg/L)	U (mg/L)	V (mg/L)
Rainy	**Pahang (East)**						
	Mean ± SD	0.0066 ± 0.0005	0.002 ± 0	ND	0.0132 ± 0.0018	ND	0.0034 ± 0.0005
	Range (min-max)	0.006 - 0.007	0.002	ND	0.011 - 0.016	ND	0.003 - 0.004
	Kedah (North)						
	Mean ± SD	0.0055 ± 0.0009	0.002 ± 0	ND	0.0118 ± 0.0015	ND	0.003 ± 0
	Range (min-max)	0.005 - 0.007	0.002	ND	0.009 - 0.014	ND	0.003
	Selangor (West)						
	Mean ± SD	0.0062 ± 0.0004	0.002 ± 0	ND	0.0105 ± 0.0012	0.0007 ± 0.0018	0.003 ± 0
	Range (min-max)	0.006 - 0.007	0.002	ND	0.009 - 0.012	0.002 - 0.006	0.003
	Johor (South)						
	Mean ± SD	0.005 ± 0	0.002 ± 0	ND	0.0098 ± 0.0011	ND	0.0033 ± 0.0005
	Range (min-max)	0.005	0.002	ND	0.008 - 0.011	ND	0.003 - 0.004
Dry	**Pahang (East)**						
	Mean ± SD	0.0052 ± 0.0004	0.002 ± 0	0.0002 ± 0.0004	0.0127 ± 0.0007	ND	0.003 ± 0
	Range (min-max)	0.005 - 0.006	0.002	0.001	0.011 - 0.014	ND	0.003
	Kedah (North)						
	Mean ± SD	0.0065 ± 0.0008	0.0037 ± 0.001	0.0002 ± 0.0004	0.0102 ± 0.0013	0.0103 ± 0.0066	0.0045 ± 0.0009
	Range (min-max)	0.005 - 0.0073	0.002 - 0.0043	0.0012	0.0083 - 0.013	0.0078 - 0.0173	0.003 - 0.0053
	Selangor (West)						
	Mean ± SD	0.006 ± 0.0011	0.0031 ± 0.0012	0.0002 ± 0.0004	0.0113 ± 0.0024	0.0064 ± 0.0107	0.0041 ± 0.0011
	Range (min-max)	0.005 - 0.0074	0.002 - 0.0043	0.0001 - 0.0013	0.0081 - 0.015	0.0002 - 0.0034	0.003 - 0.0053
	Johor (South)						
	Mean ± SD	0.0056 ± 0.001	0.0026 ± 0.001	ND	0.011 ± 0.0019	0.0042 ± 0.0076	0.0036 ± 0.001
	Range (min-max)	0.005 - 0.0073	0.002 -0.0043	ND	0.0082 - 0.013	0.0157 - 0.0175	0.003 - 0.0054

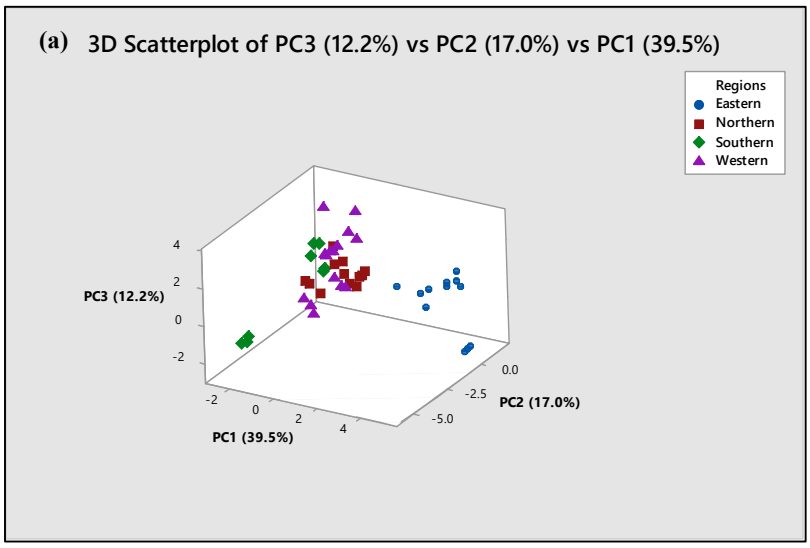
SD = standard deviation (n = 12); ND = not detected. One-way ANOVA with Tukey's HSD post hoc test with significant value of 0.05 was used for determining the mean differences in the concentrations of multi-trace metals in stingless bee honey samples among the different regions. * The mean difference is significant at the 0.05 level.

The data from multi-trace metal concentrations suggested that stingless bee honey samples from four regions of Peninsular Malaysia indicate the honey good quality. Different geographical regions are probably related to the variations in the multi-trace metal concentrations. Increases in anthropogenic activities such as agricultural practice, industries, traffic, coal mining and burning contribute to the accumulation of hazardous multi-trace metals in the ecosystem and become part of the regional environmental compartments [17, 24, 48, 49]. Atanassova et al. [18] reported that during different vegetation seasons, honey could exhibit different multi-trace metal concentrations even though it comes from the same geographical region, same beehive, and same locality.

Principal component analysis (PCA)

For better illustration, PCA was performed on eighteen multi-trace metals to study the overall organization of data for all stingless bee honey samples from the different geographical origins. In this study, it is possible to separate honey samples by their multi-trace metals distribution. The starting part of PCA calculations was the matrix of data with dimensions ($n \times p$), where n is the number of cases (rows) and p is the number of variables (columns). In the matrix, rows represented the honey samples geographical origins and the column represented the multi-trace metals in stingless bee honey samples. As a result of PCA analysis, thirteen and fourteen new variables were obtained, which were represented by eigenvalues for rainy and dry seasons, respectively.

The significance of a factor is explained by its eigenvalue. The factor with the highest eigenvalue is considered the most important. As a result, eigenvalues of 1 or greater are considered significant [50]. The results for the rainy season, as demonstrated in Figure 1(a), showed the first three principal components (PC1-3), with eigenvalues > 1, had 68.7% of the total variability among the thirteen variables in the original data, where in PC1, PC2 and PC3 contributed to 39.5%, 17.0% and 12.2%, respectively. Based on the eigenvalue criterion, PCs with eigenvalues of greater than 1 are considered important [51]. The first PC was principally correlated (loading > 0.30) with five trace metals (Al, Cd, Co, Ni and Zn) that were detected at low concentrations in stingless bee honey samples. While copper, manganese and lead metals were the dominant contents in PC2 and metal content of As, Th, U and V loaded highly in PC3.



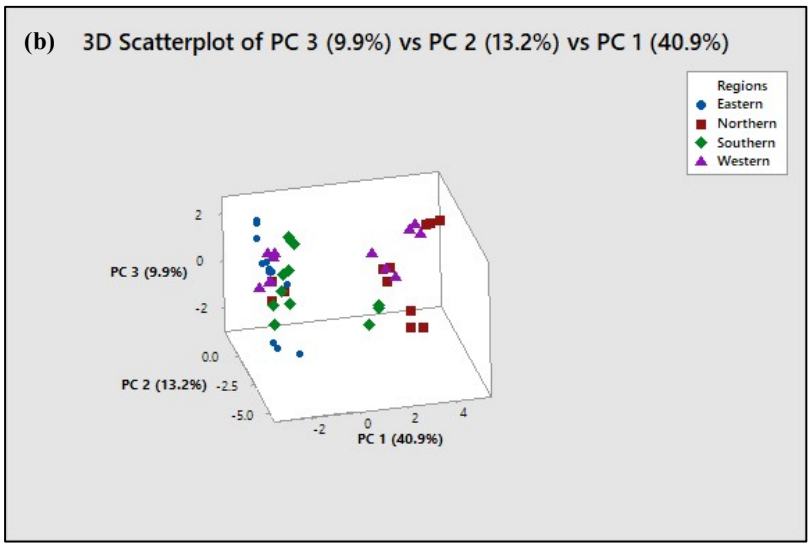


Figure 1. A three-dimensional PCA plot (PC1, PC2 and PC3) for the concentration of eighteen multi-trace metals during (a) rainy and (b) dry seasons

As shown in Figure 1(b), during the dry season, the first three principal components (PC1-3), with eigenvalues greater than one, had 64% of the total variability, where PC1, PC2 and PC3 accounted for 40.9%, 13.2% and 9.9%, respectively. The results showed that a three-factor model could explain 64% of the total variance. The first three PCs (loading plot > 0.3) showed that the Be, Co, Se, Th, U, and V metals have high weights in PC1; Ba, Cd, Mn, and Tl metals loaded high in PC2; and the dominating content in PC3 were Al, As, Cu, and Ni metals. The variability of these multi-trace metal concentrations could be a result of geographical variation. The distribution of stingless bee honey varies between rainy and dry seasons. During the rainy season, as shown in Figure 1(a), the northern, southern, and western regions are close to each other, indicating similarity in multi-trace metal compositions. The eastern region, on the other hand, is separated from the other three regions. As shown in Figure 1(b), the distribution pattern was different during the dry season. This study discovered a relationship between multi-trace metal compositions and the seasons.

As studied by Biluca et al. [52] and Pucholobek et al. [53], Mn metal exhibited the highest concentration in stingless bee honey produced in Brazil through PCA, indicating that geographical origin may influence the concentration of metals in honey. In this study too, Mn is evidently present in high concentrations in the stingless bee honey samples in Peninsular Malaysia during both the rainy and dry seasons. The fact that specific studies focusing on the distributions of Mn across the different locations in Peninsular Malaysia remain unreported, suitable attempt to elucidate such a matter proves necessary.

Linear discriminant analysis (LDA)

LDA simplifies the observation and interpretation of information on graphical representations [51]. The classification results obtained using LDA technique is shown in Figure 2(a) and (b). An accuracy of 95.8% (rainy season) and 89.6% (dry season) success rate in honey samples regions classifications were achieved by the cross-validation (leave-one-out) LDA technique, in order to evaluate the performance of developed classification models. A neat and no neat separation between regions can be observed during rainy and dry seasons, respectively. Although no neat separation was obtained during dry season, however, all the stingless bee honey sample was confirmed to be harvested from the beekeepers of selected districts of four regions.

A study by Nomikos and MacGregor [54], explained that, with highly correlated variables, only few PCs are needed to explain the significant in the data set. Additionally, by using cross-validation technique, the number of PCs to retain can also be determined. The power of PCA technique can be observed by plotting the scores of PCs, in which the objects will exhibit measurement similarities to form clusters and moreover, an isolated object (outlier) can be seen clearly. As shown in Figure 1(a) and (b), an exploratory PCA was run on the entire data set to get a sense of the data distribution for each region.

During both rainy and less rainy seasons, overlapping regions for stingless bee honey were observed, with a minor clustering for their geographical origins. Therefore, in this study, by considering three PCs, rainy and less rainy seasons represented 68.7% and 64.0% of the variations, respectively. Further classification by the LDA technique exhibited an improvement in percent of classification to 95.8% (rainy) and 89.6% (less rainy). The selection techniques allowed a reduction from eighteen trace metal concentrations to only ten. The presence of Al, As, Cd, Co, Cu, Mn, Ni, Th, U, and V in both rainy and less rainy seasons appears to provide suitable chemical signatures of the Malaysian stingless bee hone's geographical origins. This percentage can be considered satisfactory as the number of stingless bee honey samples was small. A previous study by Shadan et al. [24] reported 70.2% of variations using the first three PCs and improved to 96.2% using the LDA technique. Their study was similar to our study, but they only examined five districts in the southern region (Johor) of Peninsular Malaysia during the less rainy season in February to July 2016. The composition of stingless bee honey varies according to geographical or botanical origin, as well as fruit or flower season [33].

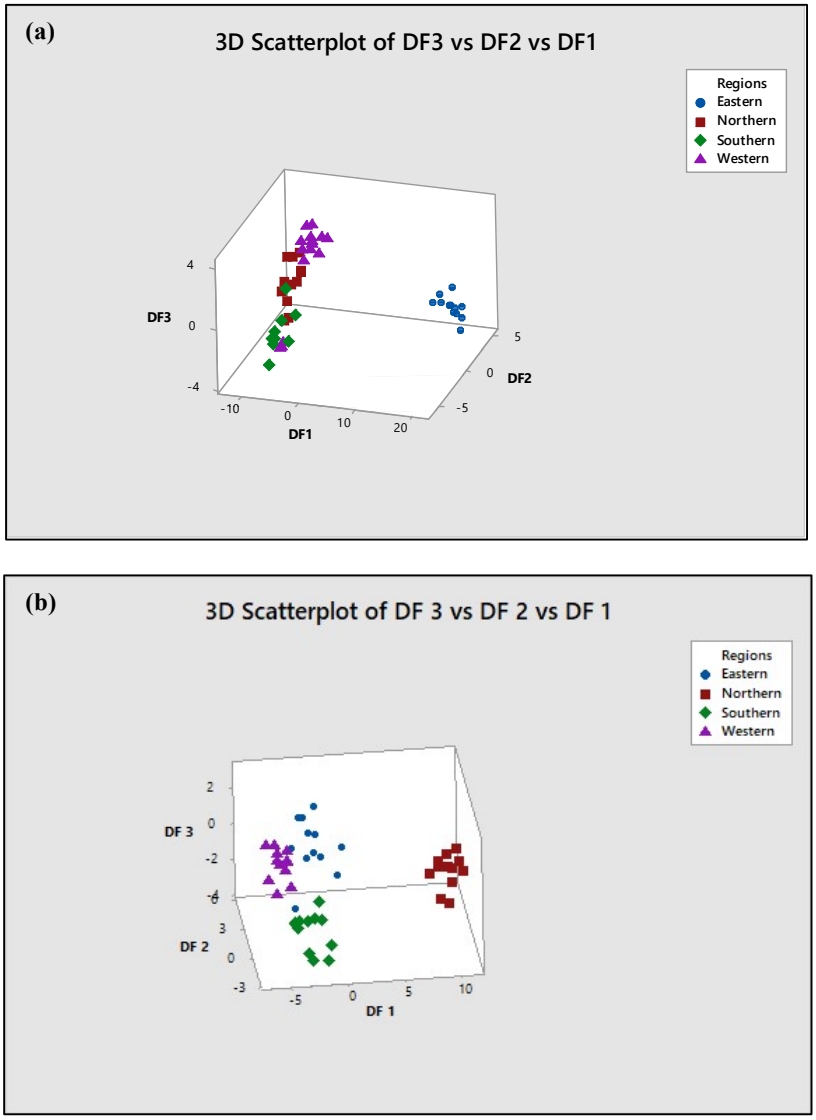


Figure 2. A three-dimensional LDA plot (DF1, DF2 and DF3) after removal of outliers and (b) dry season

Conclusion

This study filled some information gaps on multi-trace metals in *Heterotrigona itama* stingless bee honey from four regions of Peninsular Malaysia, namely Kedah, Johor, Selangor, and Pahang. For the first time, discussion on eighteen multi-trace metals (Ag, Al, As, Ba, Be, Cd, Co, Cr, Cu, Mn, Ni, Pb, Se, Th, Tl, U, V and Zn) concentrations of stingless bee honey sample collected from Padang Terap, Kulim, Yan and Baling (Kedah), Pontian and Mersing (Johor), Sabak Bernam, Klang, Kuala Selangor and Hulu Selangor (Selangor) as well as Jerantut, Rompin, Temerloh and Kuantan (Pahang) were made. Cross-validation results were excellent during the rainy and less rainy seasons, with 95.8% and 89.6%, respectively. It could be attributed to regional differences in the composition of multi-trace metals. This study supported the possibility of assigning a relationship between multi-trace metal compositions and their geographical origins, following the integration of such data with chemometric techniques like PCA and LDA. Further research should concentrate on bioavailability studies to estimate the degree of intake that is suitable for the human digestive system as metals show varied absorption interactions.

Acknowledgement

We are grateful for the financial support of the work by the Ministry of Higher Education Malaysia (MOHE) and Universiti Teknologi Malaysia (UTM) *via* Fundamental Research Grant Scheme (FRGS) (vote number R.J130000.7854.5F268), and UTM Fundamental Research Grant (UTMFR) funding (vote number Q.J130000.2554.21H56).

Conflict of Interest Statement

The authors declare no conflict of interest regarding the publication of this paper.

References

1. Siddiqui, A. J., Musharraf, S. G. and Choudhary, M. I. (2017). Application of analytical methods in authentication and adulteration of honey. *Food Chemistry,* 217: 687-698.
2. Alqarni, A. S., Oways, A. A. and Mahmoud, A. A. (2016). Physicochemical characteristics, total phenols and pigments of national and international honeys in Saudi Arabia. *Arabian Journal of Chemistry,* 9(1): 114-120.
3. Bertoncelj, J., Doberšek, U., Korošec, M. and Golob, T.. (2007). Evaluation of the phenolic content, antioxidant activity and colour of Slovenian honey. *Food Chemistry,* 105(2): 822-828.
4. Turkmen, N., Sari, F., Poyrazoglu, E. S. and Velioglu, Y. S. (2006). Effects of prolonged heating on antioxidant activity and colour of honey. *Food Chemistry,* 95(4): 653-657.
5. Wang, X. H., Gheldof, N. and Engeseth, N. J. (2004). Effect of processing and storage on antioxidant capacity of honey. *Journal of Food Science,* 69(2): 96-101.
6. Ajibola, A., Idowu, G. O., Amballi, A. A., Oyefuga, O. H. and Iquot, I. S. (2007). Improvement of some haematological parameters in albino rats with pure natural honey. *Journal of Biological Science Research,* 2(1): 67-69.
7. Bogdanov, S., Jurendic, T., Sieber, R. and Gallmann, P. (2008). Honey for nutrition and health: a review. *Journal of the American College of Nutrition,* 27(6): 677-689.
8. Jamróz, M. K., Paradowska, K., Zawada, K., Makarova, K., Kaźmierski, S. and Wawer, I. (2014). 1H and 13C NMR-based sugar profiling with chemometric analysis and antioxidant activity of herbhoneys and honeys. *Journal of the Science of Food and Agriculture,* 94(2): 246-255.
9. Yaghoobi, N., Al-Waili, N., Ghayour-Mobarhan, M., Parizadeh, S. M. R., Abasalti, Z., Yaghoobi, Z., Yaghoobi, F., Esmaeili, H., Kazemi-Bajestani, S. M. R., Aghasizadeh, R., Saloom, K. Y. and Ferns, G. A. A. (2008). Natural honey and cardiovascular risk factors; effects on blood glucose, cholesterol, triacylglycerole, CRP, and body weight compared with sucrose. *The Scientific World Journal,* 8: 463-469.
10. Sajid, M. and Azim, M. K. (2012). Characterization of the nematicidal activity of natural honey. *Journal of Agricultural and Food Chemistry,* 60(30): 7428-7434.
11. Zábrodská, B. and Vorlová, L. (2015). Adulteration of honey and available methods for detection–a review. *Acta Veterinaria Brno,* 83(10): 85-102.
12. Codex Alimentarius Committee on Sugars (2001). Codex Standard 12, revised Codex Standard for Honey. *Standards and Standard Methods*, 11: 1-7.
13. Department of Standards Malaysia. (2017). Kelulut (Stingless Bee) Honey-Specification: MS 2683: 2017. In Malaysian Standard; Department of Standards Malaysia: Shah Alam, Malaysia, pp. 1-33.
14. da Silva, I. A. A., da Silva, T. M. S., Camara, C. A., Queiroz, N., Magnani, M., de Novais, J..S., Soledade, L.E. B., Lima, E. O, de Souza, A. L., and de Souza, A. G. (2013). Phenolic profile, antioxidant activity and palynological analysis of stingless bee honey from Amazonas,

Northern Brazil. *Food Chemistry,* 141(4): 3552-3558.
15. Michener, C. D. (2013). The meliponini. In: Vit, P., Pedro, S. R. M., Roubik, D., (Eds). 2013. Pot-honey A legacy of stingless bees. Springer, New York, pp. 3-17.
16. Vit, P., Pedro, S. R., M. and Roubik, D. (2013). Pot-honey A legacy of stingless bees. Springer, New York.
17. Kováčik, J., Grúz, J., Biba, O. and Hedbavny, J. (2016). Content of metals and metabolites in honey originated from the vicinity of industrial town Košice (eastern Slovakia). *Environmental Science and Pollution Research,* 23: 4531-4540.
18. Atanassova, J., Pavlova, D., Lazarova, M. and Yurukova, L. (2016). Characteristics of honey from serpentine area in the Eastern Rhodopes Mt., Bulgaria. *Biological Trace Element Research,* 173: 247-258.
19. Alvarez-Suarez, J. M., Tulipani, S., Díaz, D., Estevez, Y., Romandini, S., Giampieri, F., Damiani, E., Astolfi, P., Bompadre, S. and Battino, M. (2010). Antioxidant and antimicrobial capacity of several monofloral Cuban honeys and their correlation with color, polyphenol content and other chemical compounds. *Food and Chemical Toxicology,* 48(8-9): 2490-2499.
20. Mbiri, A., Onditi, A., Oyaro, N. and Murago, E. (2011). Determination of essential and heavy metals in Kenyan honey by atomic absorption and emission spectroscopy. *Journal of Agriculture, Science and Technology,* 13(1): 107-115.
21. Tuzen, M., Silici, S., Mendil, D. and Soylak, M. (2007). Trace element levels in honeys from different regions of Turkey. *Food Chemistry,* 103(2), 325-330.
22. Moniruzzaman, M., Chowdhury, M. A. Z., Rahman, M. A., Sulaiman, S. A. and Gan, S.H. (2014). Determination of mineral, trace element, and pesticide levels in honey samples originating from different regions of Malaysia compared to Manuka honey. *BioMed Research International,* 2014: 359890.
23. Chua, L.S., Abdul-Rahaman, N., Sarmidi M. R., and Aziz, R. (2012). Multi-elemental composition and physical properties of honey samples from Malaysia. *Food Chemistry,* 135(3): 880-887.
24. Shadan, A. F., Mahat, N. A., Wan Ibrahim, W. A., Ariffin, Z. and Ismail, D. (2018). Provenance establishment of stingless bee honey using multi-element analysis in combination with chemometrics techniques. *Journal of Forensic Sciences,* 63(1): 80-85.
25. Ruschioni, S., Riolo, P., Minuz, R. L., Stefano, M., Cannella, M., Porrini, C., and Isidoro, N. (2013). Biomonitoring with honeybees of heavy metals and pesticides in nature reserves of the Marche Region (Italy). *Biological Trace Element Research,* 154: 226-233.
26. Dzolin, S., Wan Ibrahim, W. A., Mahat, N. A., Abdul Keyon A. S. and Ismail., Z (2019). Unique signatures of honey as a means to establish provenance. *Malaysian Journal of Analytical Sciences,* 23(1): 1-13.
27. Shlens, J. (2014). A tutorial on principal component analysis. https://arxiv.org/abs/1404.1100, Access on 20 December 2016.
28. dos Santos, J. S., dos Santos, N. S., dos Santos, M. L. P., dos Santos, S. N. and Lacerda, J. J. J. (2008). Honey classification from semi-arid, Atlantic and transitional forest zones in Bahia, Brazil. *Journal of the Brazilian Chemical Society,* 19: 502-508.
29. Fernández-Torres, R., Perez-Bernal, J. L., Bello-Lopez, M. A., Callejon-Mochon, M., Jimenez-Sanchez, J. C. and Guiraúm-Pérez, A. (2005). Mineral content and botanical origin of Spanish honeys. *Talanta,* 65(3): 686-691.
30. Yarsan, E., Karacal, F., Ibrahim, I. G., Dikmen, B., Koksal, A. and Das, Y. K. (2007). Contents of some metals in honeys from different regions in Turkey. *Bulletin of Environmental Contamination and Toxicology,* 79: 255-258.
31. Pohl, P. (2009). Determination of metal content in honey by atomic absorption and emission spectrometries. *TrAC Trends in Analytical Chemistry,* 28(1): 117-128.
32. Bratu, I. and Georgescu, C. (2005). Chemical contamination of bee honey–identifying sensor of the environment pollution. *Journal of Central European Agriculture,* 6(1): 95-98.
33. Fatima, I. J., Mohd Hilmi, A. B., Salwani, I. and Lavaniya, M. (2018). Physicochemical characteristics of Malaysian stingless bee honey from trigona species. *IIUM Medical Journal Malaysia,* 17(1): 187-191.
34. Exley, C. (2013). Human exposure to aluminium. *Environmental Science: Processes & Impacts,* 15(10): 1807-1816.
35. Altun, S. K., Dinç, H., Paksoy, N., Temamoğulları, F. K., and Savrunlu, M. (2017). Analyses of mineral content and heavy metal of honey samples from south and east region of Turkey by using ICP-MS. *International Journal of Analytical Chemistry,* 2017: 6391454 .
36. Di Bella, G., Turco, V. L., Potortì, A. G., Bua, G. D., Fede, M. R., and Dugo, G. (2015). Geographical discrimination of Italian honey by multi-element analysis with a chemometric approach. *Journal of Food Composition and Analysis,* 44: 25-35.
37. Czipa, N., Andrási, D. and Kovács, B. (2015).

Determination of essential and toxic elements in Hungarian honeys. *Food Chemistry,* 175: 536-542.

38. Oroian, M., Amariei, S., Leahu, A., and Gutt, G. (2015). Multi-element composition of honey as a suitable tool for its authenticity analysis. *Polish Journal of Food and Nutrition Sciences,* 65(2): 93-100.
39. Sandstead, H., Dintzis, F. R., Bogyo, T. P., Milne, D. A., Jacob, R. A., and Klevay, L. M. (1990). Dietary factors that can impair calcium and zinc nutriture of the elderly. *Progress in Clinical and Biological Research,* 326: 241-262.
40. Yücel, Y. and Sultanoğlu, P. (2013). Characterization of Hatay honeys according to their multi-element analysis using ICP-OES combined with chemometrics. *Food Chemistry,* 140(1-2): 231-237.
41. Conti, M. E., Finoia, M. G., Fontana, L. Mele, G., Botrè, F., and Iavicoli, I. (2014). Characterization of Argentine honeys on the basis of their mineral content and some typical quality parameters. *Chemistry Central Journal,* 8: 1-10.
42. Rubino, J. T and Franz, K. (2012). Coordination chemistry of copper proteins: how nature handles a toxic cargo for essential function. *Journal of Inorganic Biochemistry,* 107(1): 129-143.
43. Downey, G., Hussey, K., Kelly, J. D., Walshe, T. F and Martin, P. G. (2005). Preliminary contribution to the characterisation of artisanal honey produced on the island of Ireland by palynological and physico-chemical data. *Food Chemistry,* 91(2): 347-354.
44. Erdei, S. (2002). Heavy metal induced physiological changes in the antioxidative response system. *Acta Biologica Szegediensis,* 46(3-4): 89-90.
45. Bogdanov, S., Haldimann, M., Luginbühl W., and Gallmann, P. (2007). Minerals in honey: environmental, geographical and botanical aspects. *Journal of Apicultural Research,* 46(4): 269-275.
46. Legal Research Board. Laws of Malaysia. (2016). Food Act 1983 (Act 281) and Regulations. International Law Book Services. pp 261.
47. Batista, B. L., Da Silva, L. R. S., Rocha, B.A., Rodrigues, J. L., Berretta-Silva, A. A., Bonates, T. O., Gomes, V. S. D., Barbosa R. M. and Barbosa. F. (2012). Multi-element determination in Brazilian honey samples by inductively coupled plasma mass spectrometry and estimation of geographic origin with data mining techniques. *Food Research International,* 49(1): 209-215.
48. He, Z. L., Yang, X. E. and Stoffella, P. J. (2005). Trace elements in agroecosystems and impacts on the environment. *Journal of Trace Elements in Medicine and Biology,* 19(2-3): 125-140.
49. Kreitals, N. M. and Watling. J. R. (2014). Multi-element analysis using inductively coupled plasma mass spectrometry and inductively coupled plasma atomic emission spectroscopy for provenancing of animals at the continental scale. *Forensic Science International,* 244C: 116-121.
50. Hayton, J. C., Allen, D. and Scarpello, V. (2004). Factor retention decisions in exploratory factor analysis: A tutorial on parallel analysis. *Organizational Research Methods,* 7(2): 191-205.
51. Pellerano, R. G., Uñates, M. A., Cantarelli, M. A., Camiña J. and Marchevsky, E. J. (2012). Analysis of trace elements in multifloral Argentine honeys and their classification according to provenance. *Food Chemistry,* 134(1): 578-582.
52. Biluca, F. C., de Gois, J. S., Schulz, M., Braghini, F., Gonzaga, L. V., Maltez, H. F., Rodrigues, E., Vitali, L., Micke, G. A., Borges, D. L.G., Costa, A. C. O., and Fett. R. (2017). Phenolic compounds, antioxidant capacity and bioaccessibility of minerals of stingless bee honey (Meliponinae). *Journal of Food Composition and Analysis,* 63: 89-97.
53. Pucholobek, G., de Andrade, C. K., Rigobello, E. S., Wielewski, P., de Toledo, V. A. A. and Quináia, S. P. (2022). Determination of the Ca, Mn, Mg and Fe in honey from multiple species of stingless bee produced in Brazil. *Food Chemistry,* 367: 130652 .
54. Nomikos, P. and MacGregor, J. F. (1994). Monitoring batch processes using multiway principal component analysis. *American Institute of Chemical Engineers Journal,* 40(8): 1361-1375.

Malaysian Journal of Analytical Sciences Vol 27 No 2 2023

Page

Analytical Method

1. INFLUENCE OF DEEP EUTECTIC SOLVENT (DES) ON CLEAVAGE SPECIFICITY OF LIGNIN-DERIVED OIL PALM BIOMASS 231
Siti Khadijah Amran, Afiqah Liana Sazali, Khairul Faizal Paee, Mohd Razealy Anuar, and Tau-Len Kelly Yong

Environmental Analysis

2. RADIOLOGICAL RISKS RELATED TO NATURAL RADIONUCLIDE IN SELECTED FISH FROM EAST COAST OF PENINSULAR, MALAYSIA 242
Muhammad Nur Rashidi Rosli, Madihah Jafar Sidik, Wahmisari Priharti, and Nurashikin Abd Azis

Nano or Advanced Materials Analysis

3. PHYSICAL AND CHEMICAL PROPERTIES ON REDUCTION BEHAVIOUR OF CHROMIUM DOPED TO MOLYBDENUM OXIDE IN CARBON MONOXIDE ENVIRONMENT 251
Nur Syakirah Abdul Rahim, Alinda Samsuri, Mohd Nor Latif, Maratun Najiha Abu Tahari, Fairous Salleh, Tengku Shafazila Tengku Saharuddin, Norliza Dzakaria, and Muhammad Rahimi Yusop

Nano or Advanced Materials Analysis

4. HYDROLYSIS OF CELLULOSE TO GLUCOSE CATALYZED BY NOBLE METAL PALLADIUM (Pd) SUPPORTED ON SILICA-ALUMINA 261
Puteri Nurain Syahirah Megat Muhammad Kamal, Muhammad Danial Hafiy Mohamad Zabidi, and Amin Safwan Alikasturi

Analytical Method

5. DETERMINING NEREISTOXIN RESIDUE IN PALM OIL MATRIX-AN EXTENSION TO THE METHOD FOR THIOSULTAP DISODIUM RESIDUE DETERMINATION 271
Chee Beng Yeoh, Farah Khuwailah Ahmad Bustamam, Najwa Sulaiman, Mei Huey Saw, and Nik Sasha Khatrina Khairuddin

Organic or Inorganic Analysis

6. SYNTHESIS, CRYSTAL STRUCTURE, SPECTROSCOPIC CHARACTERISATION, AND PHOTOPHYSICAL PROPERTIES OF IRIDIUM(III) COMPLEX WITH PYRIDINE-FORMIMIDAMIDE ANCILLARY LIGAND 280
Nurul Husna As Saedah Bain, Noorshida Mohd Ali, Yusnita Juahir, Suzaliza Mustafar, Mohammad Kassim, Saifful Kamaluddin Muzakir@Lokman, Bohari Mohd Yamin, and Jean-Claude Daran

Analytical Method

7. A REVIEW ON EXTRACTION OF LIPID FROM MICROALGAE USING MICROWAVE-ASSISTED EXTRACTION 292
Tan Yeong Hwang, Chai Mee Kin, Wong Ling Shing, and Geetha Subramaniam

Nano or Advanced Materials Analysis

8. SYNTHESIS, CHARACTERIZATION AND PHOTOCATALYTIC ACTIVITIES OF Mg-DOPED ZnO FOR DEGRADATION OF METHYLENE BLUE DYE UNDER UV LIGHT IRRADIATION 304
Hartini Ahmad Rafaie, Zul Adlan Mohd Hir, Nurul Infaza Talalah Ramli, and Muhd Firdaus Kasim

Organic and Inorganic Analysis

9. A REVIEW OF THE SYNTHESIS AND MODIFICATION OF PVA-ALGINATE AS BINDER OF METAL ATOM 314
Norul Azilah Abdul Rahman, Mazni Musa, Karimah Kassim, and Nur Rahimah Said

Analytical Method

10. APPLICATION OF RESPONSE SURFACE METHODOLOGY ON THE EXTRACTION OF CAFFEINE IN TEA AND COFFEE USING HIGH PERFORMANCE LIQUID CHROMATOGRAPHY TECHNIQUE 329
Ibrahim Ali Al-Seade, Fouad Fadhil Al-Qaim, Zainab Haider Mussa, Lubna Raad Al-Ameer, and Nurfaizah Abu Tahrim

Organic or Inorganic Analysis

11. MICROWAVE-ASSISTED AND CONVENTIONAL SYNTHESIS OF HALOGENATED COUMARIN-AZO DERIVATIVES AND STRUCTURAL-ACTIVITY RELATIONSHIP STUDY FOR ANTIMICROBIAL POTENTIAL 342
Nur Arif Mortadza and Zainab Ngaini

Analytical Method

12. MOLECULARLY IMPRINTED POLYMERS FOR DOMOIC ACID DETECTION IN SELECTED SHELLFISH TISSUE 353
Fatin Nabilah Muhamad, Hafiza Mohamed Zuki, Marinah Ariffin, and Azrilawani Ahmad

Nano or Advanced Materials Analysis

13. RECOVERY OF PHOSPHATE FROM ARTIFICIAL HUMAN URINE USING MAGNESIUM-MODIFIED BIOCHAR FOR IMMOBILIZATION OF LEAD IN SOIL 368
Soon Kong Yong, Nurul Fariha binti Mohd Idrus, Nur Qursyna Boll Kassim, Mohamad Azwani Shah Mat Lazim, and Robert Thomas Bachmann

Analytical Method

14. OPTIMISATION OF THE LIQUID CHROMATOGRAPHY MASS SPECTROMETRY TRIPLE-QUADRUPOLE AND LOW-COST MICROEXTRACTION ANALYSIS FOR CARBAMAZEPINE 386
Siti Sabrina Kasri, Hannis Fadzillah Mohsin, Wan Nurhayati Wan Hanafi, Wardah Tahir, and Chia Chay Tay

Nano or Advanced Materials Analysis

15. INFLUENCE OF MONOMERS ON THE PROPERTIES OF EPITOPE IMPRINTED SOL-GEL ON SILICA SURFACE FOR HEPARIN ADSORPTION 396
Nur Farhanah Samrat, Lee Jia Yee, Azalina Mohamed Nasir, and Noorhidayah Ishak

Organic or Inorganic Analysis

16. RECOVERED PALLADIUM COMPLEXES AS A POTENTIAL HOMOGENEOUS CATALYST FOR C-H FUNCTIONALIZATION AND ANTIBACTERIAL AGENT 407
Nur Anis Nabilah Mohd Fuzi, Siti Khadijah Rahmat, Muhammad Hazim Abdul Aziz, Mohammad Noor Jalil, Shamsul Bahrin Gulam Ali, and Khairil Anuar Jantan

Analytical Method

17. NOVEL ALGINATE-CHITOSAN AMINE-FUNCTIONALIZED SILICA COATED MAGNETIC COMPOSITE FOR HEAVY METALS REMOVAL IN WATER 422
Gimba Joshua Dagil, Ng Nyuk-Ting, Aemi Syazwani Abdul Keyon, Wan Aini Wan Ibrahim, and Sheela Chandren

Polymer Analysis

18. MICROSCOPIC, SPECTROSCOPIC AND THERMOANALYTICAL CHARACTERIZATION OF MODIFIED OF PALM OIL AND RICE BRAN OIL INTO BIOPOLYMERS 440
Hui Ying Wong, Radiah Ali, and Sabiqah Tuan Anuar

Malaysian Journal of Analytical Sciences (MJAS)
Published by Malaysian Analytical Sciences Society

INFLUENCE OF DEEP EUTECTIC SOLVENT (DES) ON CLEAVAGE SPECIFICITY OF LIGNIN-DERIVED OIL PALM BIOMASS

(Pengaruh Pelarut Eutektik Dalam Terhadap Kespesifikan Lignin Terbitan Biojisim Kelapa Sawit)

Siti Khadijah Amran, Afiqah Liana Sazali, Khairul Faizal Pa'ee, Mohd Razealy Anuar, and Tau-Len Kelly Yong*

Universiti Kuala Lumpur,
Branch Campus Malaysian Institute of Chemical and Engineering Technology,
Lot 1988 Kawasan Perindustrian Bandar Vendor, Taboh Naning,
78000 Alor Gajah, Melaka, Malaysia.

Corresponding author: kytlen@unikl.edu.my

Received: 28 September 2022; Accepted: 25 January 2023; Published: 19 April 2023

Abstract

Carbon fibre is widely used in industry, but its high cost limits its use. Interestingly, lignin has the potential to serve as a carbon fibre precursor with properties similar to those of polyacrylonitrile (PAN) and pitch-based precursors. Oil palm frond (OPF), lignocellulosic biomass composed of cellulose, hemicellulose and lignin, is an attractive source of biomass for lignin extraction. This study proposes lignin extraction from OPF using a deep eutectic solvent (DES). DESs are eutectic mixtures of hydrogen bond acceptors (HBAs) and donors (HBDs) with much lower melting points than their constituents. This study used choline chloride (ChCl) and glycerol as HBA and HBD because they are easy to prepare, have low toxicity and are biodegradable and ecologically benign. Lignin extraction from OPF was conducted in a batch reactor at different reaction temperatures (130 °C–170 °C) and reaction times (3–6 h) using a 1:3 molar ratio of ChCl:Glycerol. The results show that DES can extract lignin with low particulate matter content (4.53%) at a higher reaction temperature (170 °C) and longer reaction time (6 h). However, extracted lignin with low ash and volatile matter contents was obtained at a lower reaction temperature (130 °C) and shorter reaction time (3 h). The carbon content of the extracted lignin was significantly influenced by the reaction temperature and reaction time, with a lower reaction temperature and moderate reaction time capable of producing lignin with a carbon content of >50%

Keywords: carbon fibre, lignin, deep eutectic solvent, oil palm biomass

Abstrak

Gentian karbon digunakan secara meluas dalam industri, walaupun penggunaannya dihadkan oleh kos prekursor yang mahal. Lignin mempunyai potensi sebagai prekursor untuk gentian karbon dengan sifat yang setanding dengan poliakrilonitril dan prekursor berasaskan pitch. Pelepah kelapa sawit, sejenis biojisim lignoselulosa yang mengandungi selulosa, hemiselulosa, dan lignin merupakan sumber biojisim yang menarik untuk pengekstrakan lignin. Penyelidikan ini mencadangkan pengekstrakan lignin daripada pelepah kelapa sawit menggunakan pelarut eutektik dalam (DES). DES ialah campuran eutektik yang terdiri daripada penerima ikatan hidrogen (HBA) dan penderma ikatan hidrogen (HBD) dan mempunyai takat lebur yang jauh lebih rendah daripada

juzuk masing-masing. Kajian ini menggunakan kolin klorida dan gliserol sebagai HBA dan HBD kerana ia mudah disediakan, mempunyai ketoksikan yang rendah, boleh terbiodegradasi, dan tidak berbahaya dari segi ekologi. Pengekstrakan lignin daripada pelepah kelapa sawit dijalankan dengan menggunakan reaktor kelompok pada suhu tindak balas (130 °C–170 °C) dan masa tindak balas (3–6 jam) yang berbeza bersama dengan kolin klorida dan gliserol pada nisbah molar 1:3. Kajian ini membuktikan bahawa DES mampu mengekstrak lignin dengan bahan zarah yang rendah (4.53%) pada suhu tindak balas yang lebih tinggi (170 °C) dan masa tindak balas yang lebih lama (6 jam). Walaubagaimanapun, lignin dengan kandungan abu dan bahan meruap yang rendah diperolehi pada suhu tindak balas yang rendah (130 °C) dan masa tindak balas yang singkat (3 jam). Kandungan karbon di dalam lignin yang diekstrak dipengaruhi oleh suhu tindak balas dan masa tindak balas, dengan suhu tindak balas yang lebih rendah dan masa tindak balas sederhana mampu menghasilkan lignin dengan kandungan karbon lebih daripada 50%.

Kata kunci: gentian carbon, lignin, pelarut eutektik dalam, biojisim kelapa sawit

Introduction

The exceptional mechanical, electrical and thermal properties of carbon fibre have led to its widespread use in various fields, including military and aerospace engineering, construction and medicine [1]. The global market for carbon fibre is predicted to quadruple in a decade, reaching over $3 billion and exceeding 100,000 tonnes [2]. However, the rapid growth of industrial applications of carbon fibre hinges on the material's affordability without compromising its physical properties. The high cost of carbon fibre is directly proportional to the cost and yield of the precursor from which it is derived. A large proportion of carbon fibre is manufactured using wet and solution-spun PAN, an expensive precursor that accounts for 51% of the price of carbon fibre. Significant research is being conducted on the synthesis of low-cost carbon fibre because of the growing demand for the commercialisation of carbon fibre in various sectors.

Lignin, an aromatic polymer found in nature, has recently attracted considerable attention because of its low price, high carbon content and bio-renewability. Lignin is a promising replacement for petroleum-based PAN for producing carbon fibres because of its high carbon content (60%–65%) [3]. In addition to cellulose and hemicellulose, lignin is a key component of lignocellulosic biomasses. Lignin is a by-product of the paper industry that cannot be recycled; its decomposition produces furans and dioxins, which deplete atmospheric oxygen [4]. Lignin's aromatic compounds, availability of phenolic and aliphatic hydroxyl groups, high carbon content, thermal stability and abundance make it a superior choice for synthesising carbon fibres compared with cellulose and other renewable carbon sources.

According to Chen et al. [5], lignin valorisation necessitates the effective extraction of lignin with properties amenable to further processing. Condensed lignin and/or pseudo-lignin resulting from traditional pretreatment methods, such as dilute acid and steam explosion, are unusable for further processing. Research into lignin valorisation has led to the development of pretreatment technologies that utilise ionic liquids and organic solvents derived from biomass. DESs are ionic solvents composed of HBA and HBD, which combine to form a eutectic with a significantly lower melting point than its constituents [6]. Most DESs are produced by reacting ChCl (as HBA) with HBDs, such as amines, carboxylic acids and polyols. DES has been suggested as a promising solvent for processing lignocellulosic biomass, especially for lignin valorisation [7–9].

Currently, lignocellulosic treatments are used to produce high-quality cellulose. Nonetheless, the separation of lignin from a native structure has received less attention, making it difficult to obtain homogeneous lignin with the requisite structure and molecular weight [10]. Recent studies have shown that ChCl and acid-based DES effectively extract lignin from lignocellulosic biomass. Lignin extracted from biomass using DES has distinct structural characteristics, such as a lack of ether linkages and a low molecular weight distribution [8, 11]. Hydrogen bonds in DES molecules are crucial for lignin extraction. Di Marino et al. [12] hypothesised that increasing the amount of water in the biomass could improve the solubilisation ability of DES for biomass by increasing the formation of hydrogen bonds between the DES and components of the biomass.

Lignin is extracted from various natural sources using several methods, each yielding lignin with its unique structure and physicochemical properties. Therefore, one of the most challenging and critical processes in biological refining is lignin extraction from lignocellulosic materials. Currently, the most common lignin are sulphate lignin, soda lignin, and kraft lignin [13]. However, the high sulphur and ash content of sulphate lignin render it unsuitable for further processing and usage. Although lignin-derived alkali pulping does not contain sulphur, the extraction method has many disadvantages, including a low-extraction yield, excessive alkali consumption and environmental contamination [14, 15]. Furthermore, reaction parameters, such as reaction time, temperature, solvent concentration and biomass/solvent ratio, substantially affect the extraction yield and structural characteristics of lignin produced by organic solvent-based extraction.

Lignin extracted using DES treatments was discovered to have a high yield, high purity and low molecular weight, which would be advantageous for biomass valorisation [9]. It is known to have unique structural properties; however, these properties have not been studied or addressed. Therefore, the fundamental properties of lignin must be examined to establish its potential as a carbon precursor. The Oak Ridge National Laboratory (ORNL) established a set of criteria to assess the viability of lignin as a carbon fibre precursor, as shown in Table 1 [16].

Table 1. Lignin specification as carbon fibre precursor [13]

Criteria	Value (wt.%)
Lignin Purity	99%
Ash Content	<0.1
Volatile Matter	<5.0
Particulate Matter	100% removal for matter >1μm in diameter

Materials and Methods

Synthesis of DES

The DESs were prepared by mixing ChCl and glycerol in a 1:3 molar ratio and heating to 100 °C with constant stirring. In our previous study, DES with a molar ratio of 1:3 produced the highest lignin yield from OPF. Heating and stirring were repeated until a clear, homogeneous and stable liquid were obtained. The DESs were then cooled and stored at room temperature for 24 h. DES synthesis was successful if the solution was colourless and remained liquid after 24 h.

Preparation of OPF

The biomass was dried overnight at 45 °C before being cooled to room temperature. 500g of the samples were ground and sieved to sizes between 250–500 μm. Solid-liquid extraction with 3L ethanol was used to remove extractives from the samples. The extracted samples were collected after 6 h and washed with ethanol before being oven-dried overnight at 45 °C.

Experimental works

The OPF was mixed with DESs at a solid loading ratio of 1:10 and subjected to various reaction times and temperatures in a 100-mL batch reactor. The reaction parameters used in these experiments are listed in Table 2. The mixture was immediately immersed in an ice bath after completion of the reaction to quench the reaction. The solution fraction (SF) and solid residue (SR) fractions were separated by centrifugation at 4000 rpm for 15 min. SR was washed with 95% ethanol until the liquid was clear. Subsequently, the SF was combined with an ethanol-washing liquid to form SF1. Deionised water was added to SF1 in a 1:2 volume ratio of ethanol to water to precipitate lignin. After 15-min centrifugation at 4000 rpm, the precipitated lignin was successfully separated from the SF1. The lignin precipitate was washed twice with deionised water to remove solvent impurities and obtain extracted lignin. Lignin was then dried for 24 h at 40 °C.

Table 2. Reaction parameter for experimental work

Abbreviation	Reaction Time (hours)	Reaction Temperature (°C)
DESL-01	3	130
DESL-02		150
DESL-03		170
DESL-04	4	130
DESL-05		150
DESL-06		170
DESL-07	5	130
DESL-08		150
DESL-09		170
DESL-10	6	130
DESL-11		150
DESL-12		170

Particulate matter content analysis

The particulate matter content was determined using the method described by Luo [17]. Approximately 0.25 g of DES-L was dissolved in 100 mL of a 5% NaOH solution. The flask was then immersed in a water bath at 100 °C for 60 min. The sample was filtered to separate insoluble particles. The percentage of insoluble matter was calculated using Equation 1 based on the residual solid mass and mass of the original sample.

$$\text{Particulate Matter} = \left(\frac{m_2}{M_1}\right) \times 100\% \quad (1)$$

where m_2 is the mass of residual solid (g) and M_1 is the mass of the lignin sample (g).

Ash content analysis

The ash content was determined using TAPPI Standard Test Method T 413 om-93. Approximately 0.05 g of DES-L was combusted at 900 °C in a muffle furnace. As shown in Equation 2, the ash content was calculated by dividing the weight fraction of residual ash by the initial weight of the sample.

$$\text{Ash Content} = \left(\frac{m_2}{M_1}\right) \times 100\% \quad (2)$$

where m_2 is the mass of residual ash (g) and M_1 is the mass of the lignin sample (g).

Volatile matter content analysis

The volatile matter content of the DES-L was determined according to the method outlined by Luo [17]. Approximately 0.25 g of DES-L was heated for 6 h at 250 °C in a muffle furnace. The volatile matter content was calculated based on the weight loss of the DES-L relative to the weight of the initial sample (Equation 3).

$$\text{Ash Content} = \left(\frac{M_1 - m_2}{M_1}\right) \times 100\% \quad (3)$$

where m_2 is the mass of the residual lignin sample (g) and M_1 is the mass of the lignin sample (g).

Carbon content analysis

The carbon content of the DES-L was determined using a CHNS/O analyser.

Results and Discussion

Carbon content

The carbon content of the precursor is essential. The low carbon content in the precursor indicated a high content of non-carbon elements in the sample, which resulted in higher weight losses during carbonisation and higher production costs [18]. High-quality carbon fibre requires a carbon content of at least 92 wt% after carbonisations.

The carbon content of lignin extracted at different temperatures (130 °C–170 °C) and reaction times (3–6 h) are shown in Figure 1. The highest carbon content

was 54.1% at 150 °C for 3 h. In contrast, the lowest carbon content attained was 31.5% at 130 °C for 3 h. The carbon content varies with reaction temperature and time, with no discernible trend. The ORNL does not specify the carbon content requirements for lignin as a carbon fibre precursor. However, it is widely accepted that the carbon content of the extracted lignin must be >50% to produce significant carbon fibre yields [19]. As a result, it was concluded that the reaction time and temperature affect the carbon content of the extracted lignin.

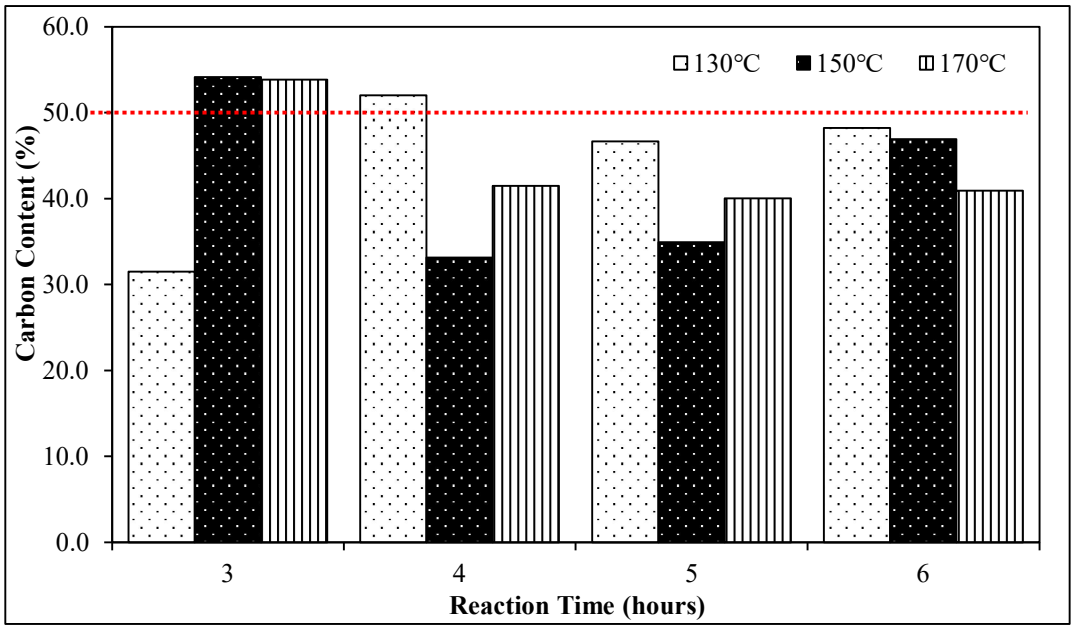


Figure 1. Carbon content (%) at different temperatures (130 °C–170 °C) and reaction times (3–6 h) and a solid loading ratio of 1:10

In this study, only the DESL-02 (150 °C and 3 h), DESL-03 (170 °C and 3 h), and DES-L04 (130 °C and 4 h) samples yielded lignin with a carbon content of >50%. The obtained lignin had a lower carbon content than the previously reported lignin at various reaction temperatures and times. For example, coniferyl alcohol, a common precursor of lignin in softwood, contains approximately 72% carbon.

While sinapyl alcohol, a common lignin monomer found in hardwood, contains 63% carbon, PAN, the most important precursor material used in the industrial production of carbon fibre, contains 68% carbon [17]. The required carbon content differed according to different studies. Previous studies showed that the required carbon content varies. For example, Souto et al. [19] suggested that the carbon content must be >50%, whereas Bengtsson et al. [3] concluded that the carbon content of extracted lignin must be >60% to produce carbon fibres with a high yield after conversion. According to Nunes and Pardini [20], the carbon content of lignin varies depending on the type of biomass, with kraft and sugarcane lignin containing 62% and 58% carbon, respectively.

Alvarez-Vasco et al. [9] demonstrated that lignin extraction with DES results from breaking ether bonds in the lignin carbohydrate complex (LCC), thereby improving lignin solubility in DES. It has been proposed that the breakage of ether bonds and the solvent properties of DES significantly influence the depolymerisation of lignin, facilitating its separation from lignocellulosic biomass. Lignin is more soluble in DES because of the increased cleavage of β-O-4 linkages.

The glycerol-based DES used in this study has a moderate acid-base catalysis mechanism that is advantageous for cleaving labile ether bonds, thus improving lignin solubility in DES. The effectiveness of acid-based DES for lignin extraction has been investigated, and the enhanced hydrogen bond interaction between acidic DES and LCC has been shown to facilitate lignin extraction [21]. However, the increased lignin solubility in DES results in more carbon loss to the liquid fraction and a faster depolymerisation rate at higher temperatures [22]. The carbon content of the recovered lignin decreased as the temperature increased because of the increase in the lignin carbon loss to the liquid fraction.

Nevertheless, recognising that the reaction time significantly affects the carbon content of the extracted lignin is critical. The reaction temperature determined the effect of reaction time on the carbon content. In this study, a shorter reaction time of 3 h and a moderate reaction temperature of 150 °C were optimal for extracting lignin from OPF with higher carbon content. According to Zhang et al. [23], the higher the carbon content of lignin, the more aromatic the structures in the lignin monomers. However, the structure of lignin is extremely complex, with heterogeneous molecular weights, numerous functional groups and varying amounts of monolignols (p-coumaryl alcohol, coniferyl alcohol and sinapyl alcohol) linked by various interunit chemical bonds. As a result, the reduced aromatic structure of the extracted lignin accounts for the lower carbon content observed in this study.

Our previous study found that the presence of phenolic compounds in extracted lignin was lower (0.07–0.15 g/mmol) than previously reported in the literature. Consequently, the extracted lignin had less aromatic compounds and reactivity. Lignin is extracted using DES by ether connection cleavage, specifically β-O-4 bonds, which are the weakest links in the lignin unit. However, in this study, DES treatment produced lignin with reduced aromatic structures, resulting in a carbon content of 31.5%–54.1% at different reaction temperatures and times.

Ash content

Ash is the residue left over by high-temperature combustion at 900 °C. Lignin must have low inorganic content as a carbon fibre precursor. The ash content should be <0.1 wt% to ensure that the carbon fibre has minimal defects and imperfections. The lignin source and extraction method heavily influenced the ash content of the extracted lignin. Figure 2 illustrates the effect of temperature (130 °C–170 °C) and reaction time (3–6 h) on ash content.

In this study, the lignin ash content was 9.1%–15.7% with increased reaction times (3–6 h) and temperatures (130 °C–170°C), producing higher lignin ash content. As a result, lignin with low ash content can be produced at a lower reaction temperature (130 °C) and in a shorter reaction time (3 h). The increased condensation of ash caused the high ash content with other by-products as the reaction time and temperature increased.

The ash content determined in this study did not meet the ORNL standard of <0.1%, which makes it a suitable precursor for carbon fibre production [16]. The ash content must be low to avoid a negative impact on the tensile qualities of the manufactured carbon fibre, which is detrimental to the mechanical properties of the carbon fibre produced [3].

The biomass source and extraction method determine the ash content of the extracted lignin. Herbaceous biomass contains significantly more ash than wood, typically containing <1% ash. Calcium, potassium and magnesium are the most abundant elements in wood ash, whereas sodium and silicon are in smaller quantities. However, the source and quantity of minerals in the extracted lignin were significantly more dependent on the extraction method than on plant species. Alkaline pulping processes, such as kraft, produce lignin with high ash content (43.6%), whereas autohydrolysis (1.2%) and organosolv (0.1%) produce lignin with low ash content [24].

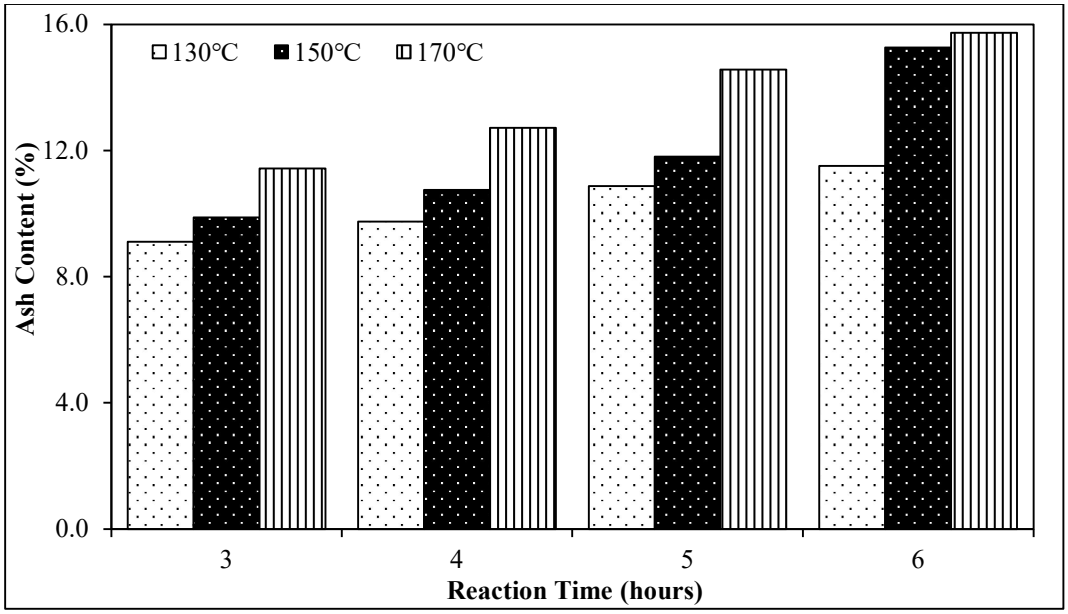


Figure 2. Ash content (%) at different temperatures (130–170 °C), reaction times (3–6 h) and a solid loading ratio of 1:10

Volatile matter content

Volatile matter refers to the portion of a sample that can readily volatilise at high temperatures under typical conditions. This volatile substance typically consists of combustible and non-combustible gases. The volatile matter content of the extracted lignin must be evaluated because it can alter the carbon fibre structures through evaporation, especially during carbonisation at high heating rates. Carbonisation significantly modifies the surface and porosity of carbon fibres by releasing volatile components, resulting in surface flaws and defects. Therefore, low volatile matter content is desired to reduce the flaws in manufactured carbon fibre [25].

As demonstrated in Table 1, the volatile matter content must be <5% for a precursor to be viable for carbon fibre production. Figure 3 depicts the volatile matter content of lignin extracted at various reaction temperatures (130 °C–170 °C) and reaction times (3–6 h). The volatile matter content of lignin ranged was 3.4%–9.4%.

The volatile matter content increased with reaction time (3–6 h) at all temperatures. For example, at 130 °C, the volatile matter content increased linearly from 3.4% to 4.7% between 3 h and 6 h. Additionally, at 150 °C, the volatile matter content varied between 5.3% and 8.8%. Higher reaction temperatures produce lignin with larger amounts of volatile compounds. The increase in volatile matter content with increasing temperature is attributable to the decreased bond strength of lignin at higher temperatures, which produces volatile macromolecules [26]. Low temperatures and shorter reaction times made lignin more thermally resistant to volatilisation, as evidenced by its lower volatile matter content at 130 °C and 3 h.

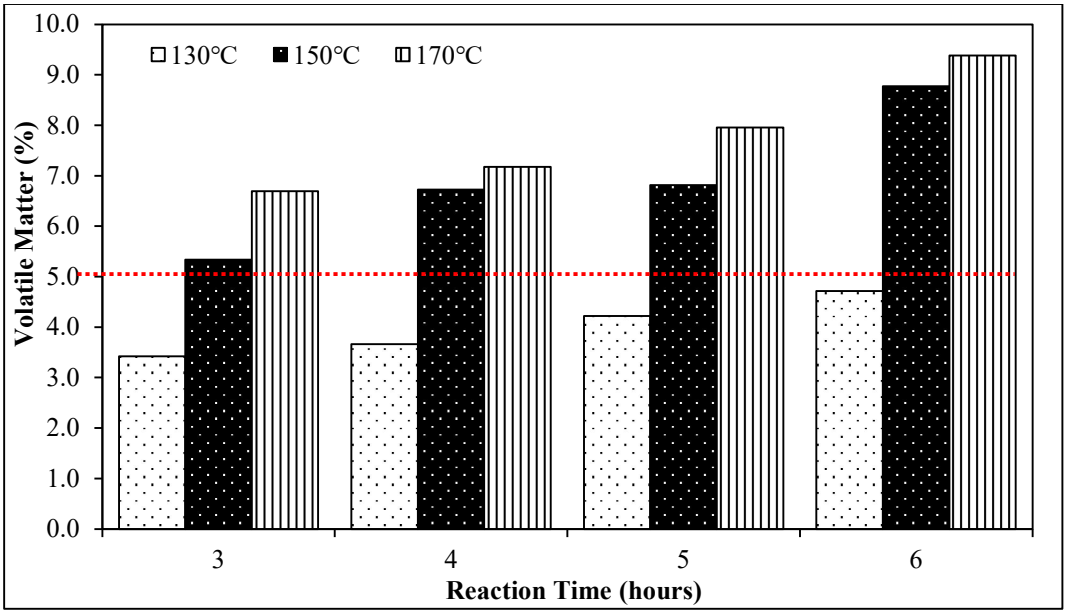


Figure 3. Volatile matter content (%) at different temperatures (130–170 °C), reaction times (3–6 h) and a solid loading ratio of 1:10

In addition, the volatile matter content of lignin extracted at 130 °C for all reaction times (3–6 h) met the ORNL requirement that it should contain <5% volatile matter to be suitable as a carbon fibre precursor. Higher temperatures (150 °C–170 °C) produce lignin with a volatile matter content of >5% [16]. Thus, we can conclude that temperature is important in determining the amount of volatile matter in lignin extracted using DES.

Furthermore, the volatile matter content reported in this study was significantly lower than those reported in previous studies [24,27]. The extraction conditions, solvent type and biomass source, affected the volatile matter content of lignin. According to Omar et al. [25] and Atnaw et al. [28], OPF has high volatile matter contents of 82.4% and 85.1%, respectively. The high volatile matter content of the OPF is attributable to the higher volatile matter content of the lignin recovered in this study.

It is possible that the high inorganic content of lignin, as reflected by its high ash content, could have influenced the volatile matter content. As a result of their catalytic effect on lignin decomposition, the inorganic matter may promote the formation of volatile matter [29]. As depicted in Figure 2, the volatile matter and ash contents exhibited a similar trend, which explains the results obtained for the volatile matter content.

Particulate matter content

As a precursor to carbon fibre, lignin must be devoid of solid particles of >1 µm in size. Particulate matter is the amount of solid particles entrapped in lignin. Natural particles, such as sand, clay and cellulose, are the most prevalent causes of structural defects in carbon fibre. The mechanical properties of carbon fibres, such as modulus and tensile strength, are reduced by high particulate matter content, increasing the breaking point of the fibre [16]. Figure 4 shows the effect of temperature (130 °C–170 °C) and reaction time (3–6 h) on the particulate matter content of DES-L.

Particulate matter content decreased with increasing temperature and reaction time. The highest particulate matter content of 15.5% was obtained after 3 h at 130 °C, whereas the lowest particulate matter content (4.5%) was obtained at 6 h and 170 °C. These findings exceed the ORNL's requirement of 100% removal of particulate matter of >1 µm in diameter.

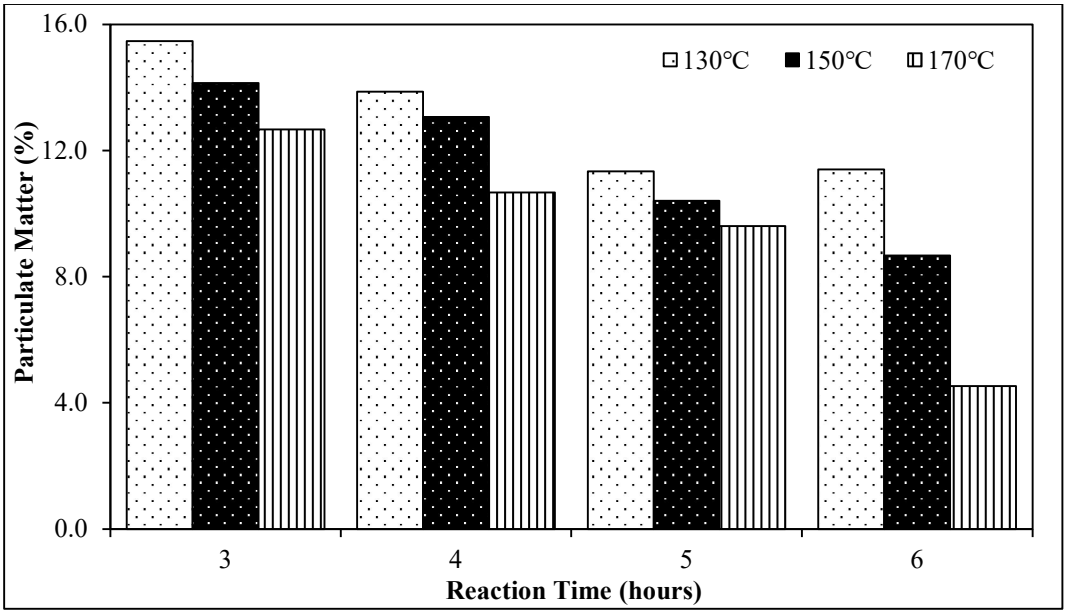


Figure 4. Particulate matter content (%) at different temperatures (130–170 °C), reaction times (3–6 h) and a solid loading ratio of 1:10

The incomplete breakdown of cellulose increases the number of high-molecular-weight compounds in the SR, which explains why lignin extracted using the DES system has a high particulate matter content. Furthermore, owing to the partial breakdown of cellulose, particles and pollutants increased the amount of particulate matter in the lignin. The incomplete removal of extractives during OPF solid-liquid extraction may also contribute to the high particle matter content. The results show that low particulate matter lignin can be obtained at higher temperatures and longer reaction times.

Conclusion

Investigating the fundamental properties of lignin extracted from OPF using DES is critical to assess its viability as a carbon fibre precursor. This study found that reaction temperature and time affect the properties of lignin. The particulate matter content was low at high temperatures (170 °C) and long reaction times (6 h). However, a lower temperature and shorter reaction time are appropriate for lignin extraction with a low ash and volatile matter content. The highest carbon content (54.1%) was obtained at 150 °C for 3 h. The low carbon content of lignin obtained in this study was attributable to the enhanced cleavage of ether linkages by glycerol-based DES, which improved lignin solubility in the solvent and, thus, increased carbon loss into the liquid fraction. Thus, this study establishes the viability of using DES as solvents for effective lignin cleavage and efficient lignin separation from LCC linkages. The viability of the extracted lignin as a carbon fibre precursor should also be examined further by determining other fundamental properties, such as purity, molecular weight and glass transition temperature.

Acknowledgement

The Malaysian Ministry of Higher Education sponsored this study via the Fundamental Research Grant Scheme (FRGS) FRGS/1/2020/STG05/UNIKL/02/1.

References

1. Lim, T. H., Kim M. S., Yeo, S. Y. and Jeong, E. (2018). Preparation and evaluation of isotropic and mesophase pitch-based carbon fibers using the pelletizing and continuous spinning process. *Journal of Industrial Textiles,* 48(7): 1242-1253.

2. Holmes, M. (2017). Lowering the cost of carbon fiber. *Reinforced Plastics* 61(5): 279-283.
3. Bengtsson, A., Bengtsson, J., Sedin, M. and Sjöholm, E. (2019). Carbon fibers from lignin-cellulose precursors: Effect of stabilization conditions. *ACS Sustainable Chemistry and Engineering* 7(9): 8440-8448.
4. Culebras, M., Sanchis, M. J., Beaucamp, A., Carsi, M. and Kandola, B. K. (2018). Understanding the thermal and dielectric response of organosolv and modified kraft lignin as a carbon fibre precursor. *Green Chemistry* 20(19): 4461-4472.
5. Chen, Z., Ragauskas, A. and Wan, C. (2020). Lignin extraction and upgrading using deep eutectic solvents. *Industrial Crops and Products,* 147: 1-32.
6. Abbott, A. P., Boothby, D., Capper, G., Davies, D. and Rasheed, R. K. (2004). Deep eutectic solvents formed between choline chloride and carboxylic acids: versatile alternatives to ionic liquids. *Journal of the American Chemical Society,* 126(29): 9142-9147.
7. Kim, K. H., Dutta, T., Sun, J. and Simmons, B. (2018). Biomass pretreatment using deep eutectic solvents from lignin derived phenols. *Green Chemistry,* 20(4): 809-815.
8. Xia, Q., Liu, Y., Meng, J., Cheng, W. and Chen, W. (2018). Multiple hydrogen bond coordination in three-constituent deep eutectic solvents enhances lignin fractionation from biomass. *Green Chemistry,* 20(12): 2711-2721.
9. Alvarez-Vasco, C., Ma, R., Quintero, M., Gua, M. and Geleynse, S. (2016). Unique low-molecular-weight lignin with high purity extracted from wood by deep eutectic solvents (DES): A source of lignin for valorization. *Green Chemistry,* 18(19): 5133-5141.
10. Wang, S., Bai, J., Innocent, M. T., Wang, Q., Xiang, H. and Tang, J. (2021). Lignin-based carbon fibers: Formation, modification and potential applications. *Green Energy and Environment,* 7(4): 578-605.
11. Jablonsky, M., Skulcova, A. B. and Vrska, M. (2015). Deep Eutectic Solvents: Fractionation of wheat straw. *BioResources,* 10(4): 8039-8047.
12. Di-Marino, D., Stockmann, D., Kriescher, S. and Stiefel, S. (2016). Electrochemical depolymerisation of lignin in a deep eutectic solvent. *Green Chemistry,* 18(22): 6021-6028.
13. Huang, D., Li, R., Xu, P., Tao, L. and Rui, D. (2020). The cornerstone of realizing lignin value-addition: Exploiting the native structure and properties of lignin by extraction methods. *Chemical Engineering Journal,* 402: 126237.
14. Xu, L., Zhang, S., Zhong, C., Li, B. Z. and Yuan, Y. J. (2020). Alkali-based pretreatment-facilitated lignin valorization: A review. *Industrial and Engineering Chemistry Research,* 59(39): 16923-16938.
15. Evdokimov, A., Kurzin, A., Fedorova, O. and Lukanin, P. (2018). Desulfurization of kraft lignin. *Wood Science and Technology,* 52(4): 1165-1174.
16. Baker, D. A. and Rials, T. G. (2013). Recent advances in low-cost carbon fiber manufacture from lignin. *Journal of Applied Polymer Science,* 130(2): 713-728.
17. Luo, J. (2010). Lignin-Based Carbon Fiber. Thesis from University of Maine.
18. Kadla, J. F., Kubo, S., Venditti, R., Gilbert, R. D. and Compere, A. L. (2002). Lignin-based carbon fibers for composite fiber applications. *Carbon,* 40(15): 2913–20.
19. Souto, F., Calado, V. and Pereira, N. (2018). Lignin-based carbon fiber: A current overview. *Materials Research Express,* 5(7): 072001.
20. Nunes, K. D. and Pardini, L. C. (2019). Purification and characterization methods for lignin biomass as a potential precursor for carbon materials. *Cellulose Chemistry and Technology,* 53(3-4): 227-242.
21. Hong, S., Sun, X., Lian, H., Pojman, J. A. and Mota-Morales, J. D. (2016). Zinc-based deep eutectic solvent-mediated hydroxylation and demethoxylation of lignin for the production of wood adhesive. *RSC Advances,* 6(92): 8959989608.
22. Asawaworarit, P., Daorattanachai, W., Laosiripojana, W. and Sakdaronnarong, C. (2019). Catalytic depolymerization of organosolv lignin from bagasse by carbonaceous solid acids derived from hydrothermal of lignocellulosic compounds. *Chemical Engineering Journal,* 356: 461-471.

23. Zhang, R., Du, Q., Wang, L., Zheng, Z. and Guo, L. (2019). Unlocking the response of lignin structure for improved carbon fiber production and mechanical strength. *Green Chemistry,* 21(18): 4981-4987.
24. Sameni, J., krigstiin, S., Rosa, D. and Leao, A. (2014). Thermal characteristics of lignin residue from industrial processes. *BioResources,* 9(1): 725-737.
25. Omar, N. N., Abdullah, N., Mustafa, I. S. and Sulaiman, F. (2018). Characterisation of oil palm frond for bio-oil production. *ASM Science Journal,* 11(1): 9-22.
26. Khalid, K. A., Karunakaran, V., Ahmad, A. A., Pa'ee, K. F., Abd-Talib, N. and Yong, T. L. (2020). Lignin from oil palm frond under subcritical phenol conditions as a precursor for carbon fiber production. *Malaysian Journal of Analytical Sciences,* 24(4): 484-494.
27. Karunakaran, V, Abd-Talib, N. and Yong, T. L. (2020). Lignin from oil palm empty fruit bunches (EFB) under subcritical phenol conditions as a precursor for carbon fiber production. *Materials Today: Proceedings,* 31(February): 100-105.
28. Atnaw, S. M., Sulaiman, S. A. and Yusup, S. (2013). Syngas production from downdraft gasification of oil palm fronds. *Energy,* 61: 491-501.
29. Qu, W., Liu, J., Xue. Y., Wang, X. and Bai, X. (2018). Potential of producing carbon fiber from biorefinery corn stover lignin with high ash content. *Journal of Applied Polymer Science,* 135(4): 1–11.

Malaysian Journal of Analytical Sciences (MJAS)
Published by Malaysian Analytical Sciences Society

RADIOLOGICAL RISKS RELATED TO NATURAL RADIONUCLIDE IN SELECTED FISH FROM EAST COAST OF PENINSULAR, MALAYSIA

(Risiko Radiologi Berkaitan Radionuklid Tabii Dalam Ikan Terpilih Dari Pantai Timur Semenanjung, Malaysia)

Muhammad Nur Rashidi Rosli[1*], Madihah Jafar Sidik[2], Wahmisari Priharti[3], and Nurashikin Abd Azis[4]

[1]Preparatory Centre for Science and Technology,
Universiti Malaysia Sabah, 88400 Kota Kinabalu, Sabah, Malaysia
[2]Borneo Marine Research Institute,
Universiti Malaysia Sabah, 88400 Kota Kinabalu, Sabah, Malaysia
[3]Telkom University, J1. Telekomunikasi No.1, Dayeuhkolot, Kab. Bandung, Indonesia
[4]Faculty of Security and Governance,
North Borneo University College, 88450 Kota Kinabalu, Sabah

**Corresponding author: mnrashidirosli@ums.edu.my*

Received: 12 July 2022; Accepted: 27 February 2023; Published: 19 April 2023

Abstract

Systematic investigations are essential in establishing the current water quality because numerous industrial and anthropogenic sources are responsible for polluting the ecosystem along Peninsular Malaysia's east coast. Since aquatic stocks play a significant role in the daily diets of the surrounding populations, the present study used the ICP-MS technique to measure the levels of three natural radionuclides ^{232}Th, ^{238}U and ^{40}K in three fish species collected from three locations along the east coast of Peninsular Malaysia. The activity concentration ranges from 23.13 ± 1.70 to 43.31 ± 2.10 Bq kg^{-1}for ^{40}K, 0.06 ± 0.01 to 0.33 ± 0.05 Bq kg^{-1} for ^{232}Th and 0.11 ± 0.08 to 0.48 ± 0.10 Bq kg^{-1} for ^{238}U. The determined activity concentration of radionuclides was used to estimate the annual effective dose and cancer risk. The findings showed that the predicted yearly effective doses (μSv year^{-1}) for ^{232}Th, ^{238}U and ^{40}K were 1.67, 0.70, and 11.92 correspondingly, which were much lower than the UNSCEAR recommendation and considered to be safe. Based on the estimated annual effective dose and a life expectancy of 70 years, the cancer risk factor for adults is predicted to be 3.00×10^{-5}. Compared to the UNSCEAR cancer risk factor of 8.4×10^{-3} and ICRP cancer risk factor of 3.5×10^{-3}, this value is much lower. According to the current study, the dose that locals consume from eating fish is safe for human consumption, relatively minimal, and does not impair human health.

Keywords: Bioaccumulation, natural radionuclide. activity concentration, ingestion dose, cancer risk

Abstrak

Penyiasatan sistematik adalah penting dalam menentukan kualiti air semasa kerana banyak sumber perindustrian dan antropogenik bertanggungjawab dalam mencemarkan ekosistem di sepanjang pantai timur Semenanjung Malaysia. Memandangkan stok akuatik memainkan peranan penting dalam diet harian populasi sekitar, kajian ini menggunakan teknik ICP-MS untuk mengukur tahap tiga radionuklid semula jadi ^{232}Th, ^{238}U dan ^{40}K dalam tiga spesies ikan yang dikumpulkan dari tiga lokasi di sepanjang pantai

timur Semenanjung Malaysia. Kepekatan aktiviti berkisar antara 23.13 ± 1.70 hingga 43.31 ± 2.10 Bq kg^{-1}untuk ^{40}K, 0.06 ± 0.01 hingga 0.33 ± 0.05 Bq kg^{-1} untuk ^{232}Th dan 0.11 ± 0.08 hingga 0.48 ± 0.10 Bq kg^{-1} bagi ^{238}U. Kepekatan aktiviti radionuklid yang ditentukan telah digunakan untuk menganggarkan dos berkesan tahunan dan risiko kanser. Penemuan menunjukkan bahawa dos berkesan tahunan yang diramalkan (μSv $tahun^{-1}$) untuk ^{232}Th, ^{238}U dan ^{40}K adalah masing-masing 1.67, 0.70, dan 11.92, yang jauh lebih rendah daripada pengesyoran UNSCEAR. Berdasarkan anggaran dos berkesan tahunan dan jangka hayat 70 tahun, faktor risiko kanser untuk orang dewasa diramalkan ialah 3.00×10^{-5}. Berbanding dengan faktor risiko kanser UNSCEAR sebanyak 8.4×10^{-3} dan faktor risiko kanser ICRP sebanyak 3.5×10^{-3}, nilai ini jauh lebih rendah dan selamat. Menurut kajian semasa, dos yang diambil oleh penduduk tempatan daripada memakan ikan adalah selamat untuk dimakan manusia, agak minimum, dan tidak menjejaskan kesihatan manusia.

Kata kunci: Bioakumulasi, radionuklid semula jadi. kepekatan aktiviti, dos pengambilan, risiko kanser

Introduction

Radionuclides in the water may contribute to internal exposure more frequently by ingestion, despite the fact that people are constantly exposed to external radiation from cosmic and terrestrial sources. ^{232}Th and ^{238}U are two prominent examples of radioactive elements that spontaneously decay and release energy, subatomic particles, and the remainder, or smaller offspring nuclei than the original [1]. The majority of the radioactive decay in the natural decay ^{232}Th and ^{238}U are gamma emitters, which are a significant source of external exposures [2]. However, some of their decay products, such as ^{222}Rn, are alpha emitters, while others, such as ^{214}Bi are beta emitters, with ^{40}K potentially producing more internal exposure routes from environmental sources. These levels can be increased by anthropogenic activities, which are subsequently enhanced by artificial radioactive sources released into the environment [2–4].

By nature of undersea earthquakes, underwater volcanic activity, weathering and mineral recycling of terrestrial rocks, and movement of the seabed, seawater naturally includes radioactivity [5]. The ^{226}Ra (^{238}U), ^{228}Ra (^{232}Th) decay series radionuclides are consequently transferred to water through leaching action as a result of extensive contact with a variety of minerals and geological materials, such as igneous rocks and ores, which frequently contain high concentrations of natural radionuclides [6]. It is known that human activities, such as the burning of fossil fuels in coal-fired power plants, the extraction of natural gas and oil, the mining and processing of ores, and the manufacturing of these fuels, enhance naturally occurring radioactivity in aquatic ecosystems. The reprocessing of spent nuclear fuel, underwater nuclear device testing, nuclear power plant leak accidents, and the post-nuclear disposal of hazardous and radioactive material are further anthropogenic contributors [1, 7-9].

Because uranium and thorium radionuclides enter the human body predominantly through food intake and only to a much lesser extent through respiration, the breakdown sequence of these radionuclides is crucial [10]. In the meantime, ^{40}K is significant since it is a marine environment radionuclide with a long half-life (1.25 × 109 years) [11]. Even though radionuclides in the ocean exhibit complex behaviours (for example, uranium is quite soluble in sea water while thorium is almost completely insoluble, radium and radon are soluble in water), they can spread throughout the marine ecosystem in a number of ways, including by becoming dissolved in the seawater, attached to plankton suspended in the seawater, attached to sediment on the seabed, and through contaminated marine organisms, such as fish, shellfish, and other seafood [12]. Therefore, a deeper understanding of the concentration of radionuclide activity in various reference organisms is crucial to estimating radiological risk to the environment [13].

Due to their high toxicity and the cumulative behaviour of these creatures, the dissolution of radionuclides into seawater adversely affects the biological balance of the environment and the activity of aquatic organisms [14]. For evaluating radiological effects on human health and marine environment, radionuclide concentrations in seawater and marine life are crucial inputs [15]. It is common knowledge that marine creatures naturally accumulate radionuclides, and that they can offer valuable data for radio-ecological and radiological

research [16, 17]. Fish and seafood are significant sources of protein for many developing nations and are significant dietary sources in many regions of the world [18]. In terms of total consumption and protein content per capita, Malaysia is regarded as one of Southeast Asia's top seafood eaters [19].

The distribution of radioactivity in seafood varies depending on feeding habits and origin areas [3, 5, 22]. Since the consumption of marine fish is among the highest in the world, it is relevant to note that the information on the radionuclide balance in sea fish is of correspondingly larger value [20, 22]. Human uptake is obviously influenced by food habits. The literature that is currently accessible still lacks information on the bioaccumulation and distribution of natural radionuclides in sea fish and sea water. Given the importance of this information, the current study's objectives are to assess the activity concentrations of ^{232}Th, ^{238}U and ^{40}K in edible marine life caught along Peninsular Malaysia's east coast, as well as the ingestion dose, and the risk of cancer for the local population. This information could be used to inform public health policies and recommendations related to seafood consumption and environmental protection in the region.

Materials and Methods

Samples and sampling location

The east coasts of Peninsular Malaysia were chosen to gather fresh samples of three different species of fish: *Rastrelliger, Megalaspis cordyla*, and *Decapterus maraudsi*. Nine samples total, ranging in mass from 125 to 260 g, were collected for each location, three samples from each species. These study locations were selected because of their biodiversity and fish farming methods, which serve as important sources of seafood for Peninsular Malaysia. The samples were taken between March 2016 and February 2017, from coastal locations of Tanjung Lumpur (3.759865° N, 103.315066° E) in Pahang, Kerteh (4.5079° N, 103.4430° E) in Terengganu, and Chendering (5.2666° N, 103.1656° E) in Terengganu, all of which are bordered by several fishing communities. In each situation, there are multiple gas-fired power plants close by, including the 324 MW Petronas power plant in Pahang, the 1136 MW Sultan Ismail power plant in Terengganu, and the 808 MW Paka power station in Terengganu. These are also well known for a few offshore sectors such as petrochemical and metal refining sectors.

Sample treatment

To separate the head, stomach contents, gills, and tissues of the fish flesh, the fish samples were first rinsed in distilled water. Fish samples of known weight were cleaned with distilled water and dried in an oven at 80 °C to stabilise the weight. This dry sample was ground into fine granules of about 500 m. The following step involved combining 0.1 g of sample with 4.0 mL of nitric acid and 6.0 mL of hydrochloric acid. A clear solution was created by digesting the mixture in a microwave for 55 minutes. Following filtering, distilled water was added until the volume of the sample solution reached 100 mL, at which point its radionuclide concentration was evaluated using ICP-MS technique. To prevent potential contamination from digestion processes, 5 standards and 1 blank solution were run using the same reagents in each case. Control sample were used in this study and treated in the same way as the fish samples from the East Coast of Peninsular Malaysia, except that they not come from the study area and therefore serve as a comparison group.

Sample analysis

An Induced Coupling Mass-Plasma Spectrometer (ICP-MS) that was calibrated using the SRM standard MA-A-2 (TM) Fish Flesh Homogenate was used to analyse samples that had been produced in solution form [21, 22]. ICP-MS is the combination of a mass spectrometer and an ICP (Induced Coupled Plasma) high temperature source. The atoms of the elements in the sample are changed into ions by the ICP source. A mass spectrometer is then used to separate and find these ions [23]. As shown in Table 2, ICP-MS generated radionuclide weights (w), which were used to calculate the concentration of radionuclide activity (A).

Determination of radionuclide activity concentration, annual effective dose and cancer risk

The concentration of radionuclide activity, A (Bq kg^{-1}) was determined using Equation (1) below

$$A = \frac{\lambda \theta N_A}{M} \times \frac{w}{W} \quad (1)$$

Where λ is the decay constant of the radionuclide, θ is the abundance of radionuclides in the universe, N_A (mol^{-1}) is the Avogadro constant, M (g mol^{-1}) is the molecular weight of the radionuclide. W (g) is the sample weight and w (mg kg^{-1}) are the natural radionuclide content in the sample obtained from ICP-MS [21, 22]. The values of w dan A for the three radionuclides are shown in Table 2.

From ^{232}Th, ^{238}U dan ^{40}K activities, the annual effective dose, D (µSv year^{-1}) is calculated using Equation 2 below

$$D = I \times A \times E \quad (2)$$

Where I (kg tahun^{-1}) is the annual fish intake rate of 57.3 kg year^{-1} [24], A (Bq kg^{-1}) is the concentration of radionuclide activity and E (µSv Bq^{-1}) is the factor conversion of radionuclide activity to dose for adults (> 17 years) [25]. Assuming that an individual's life expectancy is 70 years, R is estimated from Equation 3 below

$$R = D \times 70 \times (5 \times 10^{-8}) \quad (3)$$

Where, 5×10^{-8} (µSv^{-1}) is a cancer risk factor for low doses [26]. This research focused on the population for the age category> 17 (adults) because adults are the main consumers of Malaysian fish [22, 24]. The annual effective dose of D (µSv year^{-1}) and cancer risk R, are as in Table 3.

Results and Discussion

Activity concentrations of ^{232}Th, ^{238}U and ^{40}K

ICP-MS showed average natural radionuclide content of ^{232}Th (^{228}Ra), ^{238}U (^{226}Ra) and ^{40}K in the samples. From these, calculations were performed using Equation (1) to estimate the concentration of radionuclide activity. ^{232}Th (^{228}Ra) concentrations in marine environment is substantially lower than that of ^{238}U (^{226}Ra) when it comes to natural radionuclides. The findings are consistent with uranium's solubility in water and thorium's low solubility [4, 27], which are somewhat counterbalanced by thorium's higher abundance in the earth's crust. The dry weight basis activity concentrations of the examined radionuclides in fish, along with their uncertainties, are reported in Table 1. In turn, it may be anticipated that the accumulation of thorium in marine fish will be somewhat lower than that of the uranium chain nuclides.

For all three study sites, the current analysis reveals higher quantities of ^{238}U than ^{232}Th in the fish. Between the three research locations, there is also a significant difference ($p < 0.05$) in the concentrations of ^{238}U and ^{232}Th in the fish samples, according to statistical analysis (ANOVA). In addition, the spread of ^{232}Th, ^{238}U and ^{40}K in aquatic ecosystems can occur through solid suspension which in turn involves other aquatic components such as plankton and coral reefs. The chemical nature of the water, the physiology of the fish including the feeding behaviour and digestion of food by the fish can also affect the number of radionuclides accumulated in the body of the fish [2 - 4, 23]. *Megalaspis cordyla* had the lowest mean activity of ^{238}U among fin fishes, at 0.11 ± 0.08 Bq kg^{-1}, and the highest was 0.48 ± 0.10 Bq kg^{-1} (*Rastrelliger*). The small differences in ^{238}U uptake by the studied fishes may be explained by biological factors unique to each fish, including feeding habits, particulate ingestion with food (in the case of *Rastrelliger*, which has a varied diet regardless of the prey species, such as macroplankton and fish larvae), physiological behaviour, and the radionuclide distribution within the marine compartments [28].

When levels in other places are compared, Table 2 demonstrates that the current values of ^{238}U accord with those that have been previously reported from the same sites [5] and from the Indian coastal seas [29], but less so than the data from the Aleutian Islands [28] and Nigeria [30]. The outcomes in each of these situations are far worse than what is now observed. In contrast, Rosli et al. 2018 [22] reported average activity ranges for ^{232}Th and ^{238}U in the soft tissue of fish collected from the Terengganu coast in Malaysia of 0.30 to 0.51 Bq kg^{-1} and 1.07 to 1.15 Bq kg^{-1}, respectively. Compared to ^{238}U in fish, the mean activity of ^{232}Th in fishes ranging from 0.06 ± 0.01 Bq kg^{-1} (*Megalaspis cordyla*) to 0.33 ± 0.05 Bq kg^{-1} (*Decapterus maraudsi*). This finding

confirms that thorium is insoluble in water and that uranium is soluble in it [4]. The outcomes are comparable to those of a prior study done on various fish species in the same study settings [3]. However, no significant differences were found for the ^{232}Th activity in the literature (Table 2), with the exception of the Ondo area of Nigeria [30], regardless of fish species or study sites.

According to Table 1, the average activity concentration of ^{40}K was often higher than that of ^{232}Th and ^{238}U activities. This is to be expected as this radionuclide is widely distributed in marine environments and is involved in the metabolism of species living there [31]. The fin fishes measured at this time have similar mean ^{40}K activity, ranging from 23.13 ± 1.70 Bq kg^{-1} 1 (*Megalaspis cordyla*) to 43.31 ± 2.10 Bq kg^{-1} (*Megalaspis cordyla*). The significantly higher findings for ^{40}K are consistent with expectations given that the potassium-rich fish bones make up a significant portion of the weight of each sample. Due to its great natural abundance, the discovery of 40K in every sample was anticipated [32]. The current ^{40}K results are consistent with previous fish investigations conducted at the same site (Tanjung Lumpur, Pahang), with values ranging from of 31.55 ± 2.20 Bq kg^{-1} to 32.10 ± 1.90 Bq kg^{-1} [5]. A quick review of the literature reveals a heterogeneous distribution of ^{40}K in various areas. For example, fish collected from the water near Vizag, India [33] had a relatively lower mean activity of ^{40}K, while fish from the coastal waters near oil producing regions in Nigeria [30], India [29], and the North Atlantic Ocean [11] had significantly higher concentrations.

Furthermore, it was discovered that the areas surrounding Tanjung Lumpur, Pahang, had the highest quantities of all detected radionuclides in fish samples. The diverse range of activity (such as housing, tourism, power plants, petroleum, chemical industries, etc.) in the Tanjung Lumpur area, as well as industrial and urbanisation effluents, may be contributing to an increase in radionuclide concentrations in the marine environment. These are just a few of the many potential causes. The range of results reported by earlier studies overlaps with the concentration of radioactive activity recorded in this investigation. This shows that the findings of this study are consistent with those of earlier research, as seen in Table 2.

Table 1. Arithmetic mean + SD of ^{226}Ra, ^{228}Ra and ^{40}K activity concentration (Bq kg^{-1}) and annual effective dose (μSv y^{-1}) due to the ingestion of collected fishes (d.w.)

Sample Code	Radionuclides	Mean Activity Concentration, *A* (Bq kg^{-1})			Grand Mean Activity Concentrations *A* (Bq kg^{-1})	Annual Effective Dose, *D* (μSv y^{-1})
		Tanjung Lumpur (Pahang)	Kerteh (Terengganu)	Chendering (Terengganu)		
FS	^{232}Th	0.33 ± 0.05	0.12 ± 0.02	0.08 ± 0.01	0.18 ± 0.03	2.37
	^{238}U	0.36 ± 0.08	0.19 ± 0.05	0.12 ± 0.07	0.22 ± 0.06	0.57
	^{40}K	31.55 ± 2.20	39.01 ± 2.80	24.03 ± 1.80	31.53 ± 8.65	11.12
FC	^{232}Th	0.09 ± 0.03	0.07 ± 0.01	0.06 ± 0.01	0.07 ± 0.02	0.92
	^{238}U	0.26 ± 0.10	0.11 ± 0.08	0.11 ± 0.02	0.16 ± 0.06	0.41
	^{40}K	43.31 ± 2.10	41.27 ± 3.20	23.13 ± 1.70	35.91 ± 12.83	12.76
FK	^{232}Th	0.19 ± 0.07	0.12 ± 0.05	0.09 ± 0.01	0.13 ± 0.04	1.71
	^{238}U	0.48 ± 0.10	0.43 ± 0.08	0.39 ± 0.12	0.43 ± 0.10	1.11
	^{40}K	32.10 ± 1.90	37.66 ± 2.20	30.63 ± 2.00	33.47 ± 4.28	11.89

Table 2. Comparisons of radionuclide activity concentration, A (Bq Kg^{-1}) with previous study

Sample Name	Mean Activity Concentrations A (Bq kg^{-1})			Location	References
	^{232}Th	^{238}U	^{40}K		
Decapterus maraudsi	0.08 – 0.33	0.12 – 0.36	24.03 – 39.01	Malaysia	Present study
Megalaspis cordyla	0.06 – 0.09	0.11 – 0.26	23.13 – 43.31	Malaysia	Present study
Rastrelliger	0.09 – 0.19	0.39 – 0.48	30.63 – 37.66	Malaysia	Present study
Not specified	0.19 – 0.74	0.63 – 2.19	22.10 – 100.20	Malaysia	Khandaker et al. [5]
	-	0.118 – 0.468	56.0 – 70.7	USA	Hong et al. [28]
	ND – 1.50	ND – 1.00	48 -230	Malaysia	Amin et al. [3]
	0.47 – 1.35	0.50 – 1.67	31.2 – 42.6	Malaysia	Khandaker et al. [5]
	0.28 – 1.02	0.50 – 0.95	31.8 – 58.30	Malaysia	Khandaker et al. [5]
	35.9 – 62.9	24.5 – 70.0	586 - 836	Nigeria	Ademola and Eheidu [30]
	0.58	0.105	64.3 ± 0.5	India	Narayana [29]
	0.30 – 0.51	0.10 – 1.00	36.70 – 82.38	Malaysia	Rosli et al. [22]
	0.25 – 0.31	1.07 – 1.15	470 - 486	Irish and North Sea	IAEA 2013 [35]
	-	2.0 – 30.2	32 - 149	Portugal	Carvalho [11]

Annual effective dose

Humans are exposed to radiation from natural sources on average at a rate of 2.4 mSv per $year^{-1}$ [2]. The average annual absorption dose for the radioactive series of uranium and thorium was 0.12 mSv $year^{-1}$ and 0.17 mSv $year^{-1}$, respectively, totalling 0.29 mSv $year^{-1}$ [2, 32]. Human exposure levels, however, differ based on geology, geography, and climate [2]. The presence of heavy metals and natural radioactivity has an impact on this level as well [34]. The effective dosage to humans is further increased by the anthropogenic radioactive content of fish and the absorption of radionuclides through diet [11].

The daily intake of ^{40}K was discovered to be significantly higher ($p < 0.001$) than that of the other radionuclides by ANOVA analysis. Intakes of ^{238}U (1.7%) and ^{232}Th (1.1%) are insignificant when compared to the radionuclide ^{40}K. (96.7 %). According to Table 3, ^{40}K was responsible for the greatest annual effective dosage of 11.92 Sv $year^{-1}$. However, the ^{40}K content in the body is tightly homeostatically regulated, meaning that it is not impacted by changes in radionuclide levels in the environment. Instead, the actively maintained amount is managed by the body to reach the typical range needed for system operation [33, 36, 37]. Adult males have roughly 3700 Bq of ^{40}K, which means that the amount of ^{40}K in the body is constant. This isotope administers a dose to soft tissue of 0.18 mSv $year^{-1}$ and to bone of 0.14 mSv $year^{-1}$ [34, 38].

Between the study locations, there are significant differences ($p < 0.05$) in the annual effective dose of ^{238}U and ^{232}Th. While ^{232}Th provided 1.67 µSv $year^{-1}$ and ^{238}U contributed 0.70 µSv $year^{-1}$ of the annual effective dosage, respectively. When compared to earlier studies [11, 13], the annual effective dosage brought on by the

ingestion of ^{232}Th and ^{238}U radionuclides is incredibly low. The findings of this study also demonstrated that the yearly effective dose average was lower than that stated by UNSCEAR (2.4 mSv year^{-1}) and ICRP (1.0 mSv year^{-1}) for annual effective doses originating from natural sources [2, 34]. According to the United Nations Scientific Committee on the Effects of Atomic Radiation (UNSCEAR) [2], the average global effective dose from ingesting uranium and thorium series nuclides is 120 µSv year^{-1}, while for ^{40}K it is 170 µSv year^{-1}, ignoring any substantial radiological concerns.

Table 3 shows that the risk of cancer, *R* for adults is based on the total dose of exposure. It is significantly lower than the UNSCEAR cancer risk factor of 8.4×10^{-3} (estimated from UNSCEAR total natural radiation dose of 2.4 mSv year^{-1}) and the cancer risk factor by ICRP of 3.5×10^{-3} (estimated from the recommended level of intake dose 1.0 mSv year^{-1}). Based on Table 3, the average population in one million adults eating sample fish in this study, only about 30 people are estimated to have a risk of death from cancer compared to 3500 people, as predicted by ICRP (1990) and $8^{40}0$ people, as predicted by UNSCEAR (2000) [2, 34, 38].

Cancer risk factor

Table 3. Annual effective dose, *D* and cancer risk factor, *R* due to the consumption of natural radionuclide from the marine fish

Sample	*D* (µSv year^{-1})				*R* ($\times 10^{-5}$)			
	^{232}Th	^{238}U	^{40}K	Total	^{232}Th	^{238}U	^{40}K	Total
FS	2.37	0.57	11.12	14.06	0.83	0.20	3.89	4.92
FC	0.92	0.41	12.76	14.09	0.32	0.14	4.47	4.93
FK	1.71	1.11	11.89	14.71	0.60	0.39	4.16	5.15
Average	1.67	0.70	11.92	14.29	0.59	0.25	4.17	3.00
World average	120	120	170	290	-	-	-	-

Conclusion

Present study shows the concentration of naturally occurring radioactive materials in the widely consumed fish collected from the coastal waters around Peninsular Malaysia. Activity concentrations of 0.06 – 0.33 Bq kg^{-1} for ^{232}Th, 0.11 – 0.48 Bq kg^{-1} for ^{238}U and 23.13 – 43.31 Bq kg^{-1} for ^{40}K in various fish samples agreed with the values previously reported by other researchers and UNSCEAR. The total annual effective dose obtained was in the range of 14.06 – 14.71 µSv year^{-1} and the average value of 14.29 µSv year^{-1}. The estimated cancer risk for adults from the annual effective dose is 3.00×10^{-5}. This value is significantly lower than the UNSCEAR cancer risk factor of 8.4×10^{-3} and the ICRP cancer risk factor of 3.5×10^{-3}. Therefore, it can be concluded that the fish in this study are radiologically safe for the use of nearby residents.

Acknowledgement

Author expresses their sincere gratitude to the Universiti Malaysia Sabah for the financial support (Skim Penyelidikan Lantikan Baharu (SPLB) SLB2203, Universiti Kebangsaan Malaysia and Malaysian Fisheries Development Board (LKIM) for providing infrastructure facilities.

References

1. Broecker, W. S. (1981). Geochemical tracers and ocean circulation in evolution of physical oceanography, B. A. Warren and C. Wunsch, eds. Cambridge, MA: MIT Press.
2. UNSCEAR (United Nations Scientific Committee on the effects of Atomic Radiation). (2008). Sources and effects of Ionizing radiation. Exposures of the public and workers from various sources of radiation. Report to the General Assembly with Scientific Annexes, Annex-B.
3. Amin, Y. M., Mahat, R. H., Nor, R. M., Khandaker, M. U., Takleef, G. H., and Bradley, D. A. (2013). The presence of natural radioactivity and ^{137}Cs in the South China sea bordering Peninsular Malaysia. *Radiation Protection Dosimetry*, 156: 475-480.

4. Khandaker, M. U., Norfadira, B. W., Amin, Y. M., and Bradley, D. A. (2013). Committed effective dose from naturally occurring radionuclides in shellfish. *Radiation Physics and Chemistry*, 88: 1-6.
5. Khandaker, M. U., Olatunji, M. A., Shuib, K. S. K., Hakimi, N. A., Nasir, N. L. M., Asaduzzaman, K., and Bradley, D. A. (2015). Natural radioactivity and effective dose due to the bottom sea and estuaries marine animals in the coastal waters around Peninsular Malaysia. *Radiation Protection Dosimetry*, pp. 1-5.
6. Abbasisiar, F. T., Hosseini, A., and Heravi, F. G. (2004). Determination of uranium isotopes (^{234}U, ^{238}U) and natural uranium (U-nat) in water samples by alpha spectrometry. *Iranian Journal of Radiation Research*, 2: 1-6.
7. Khan, M. F., Benjamin, J., and Godwin, S. W. (2011). Radiotoxicity via intake of marine organisms: exposure and risk assessment in South Indians. *Toxicology and Environmental Chemistry*, 93: 549-564.
8. IAEA (International Atomic Energy Agency). (1998). Inventory of radioactive waste disposals at sea (TECDOC-1105). Access from http://www-pub.iaea.org/books/iaeabooks/5786/Inventory-of-Radioactive-Waste-Disposals-at-Sea.
9. Bogatov, S., Kisselev, V., Sorokovikova, O., and Vysotsky, V. (2009). Radiation consequences of hypothetical accidents associated with transportation of spent nuclear fuel of nuclear submarines aboard floating technical base. *Radioprotection,* 44(5): 159-164.
10. UNSCEAR (United Nations Scientific Committee on the effects of Atomic Radiation). (2000). Source and effects of ionizing radiation. New York: United Nations.
11. Carvalho, F. P., Oliveira, J. M., and Malta, M. M. (2011). Radionuclides in deep-sea fish and other organisms from the North Atlantic Ocean. *ICES Journal of Marine Science*, 68: 333-340.
12. Iyengar, M. A. R. (1990). The environmental behaviour of radium. Technical Report Series, 310, International Atomic Energy Agency, Vienna; Vol. II, pp.59-128.
13. Brown, J. E., Jones, S. R., Saxen, R., Thorring, H., Vives, I., and Battle, J. (2004). Radiation doses to organisms from natural radionuclides. *Journal of Radiological Protection*, 24: A63-A77.
14. Matta, J., Milad, M., Manger, R., and Tosteson, T. (1999). Heavy metals, lipid peroxidation, and cigateratoxicity in the liver of the Caribben barracuda (*Sphyraena barracuda*). *Biological Trace Element Research*, 70: 69-79.
15. Templeton, W., Harrison, F., Knezovich, J., Fisher, N., and Layton, D. (2009). Bioconcentration of radionuclides in marine food-web organism. Battelle Pacific Northwest Laboratories, Richland, WA, 49-61.
16. Aarkrog, A., Baxter, M. S., Bettencourt, A. O., Bojanowski, R., Bologa, A., Charmasson, S., and Cunha, I. (1997). A comparison of doses from ^{137}Cs and ^{210}Po in marine food: a major international study. *Journal of Environmental Radioactivity*, 34(1): 69-90.
17. Narayana, Y., Radhakrishna, A. P., Somashekarappa, H. M., Karunakara, N., Balakrishna, K. M., and Sidappa, K. (1995). Distribution of some natural and artificial radionuclides in the environment of Coastal Karnataka of South India. *Journal of Environmental Radioactivity,* 28: 113-139.
18. Young, A. K., McCubbin, D., and Camplin, W. C. (2002). Natural radionuclides in seafood. Food Standard Agency Report, CEFAS, FSA Project 2002, R 03010.
19. Alam, L., and Mohamed, C. A. R. (2011). Natural Radionclide of ^{210}Po in the edible seafood affected by coal-fired power plant industry in Kapar coastal area of Malaysia. *Environmental Health*, 10: 43.
20. Connan, O., Germain, P., Solier, L., and Gouret, G. (2007). Variations of ^{210}Po and ^{210}Pb in various marine organisms from western English Channel: contribution of ^{210}Po to the radiation dose. *Journal of Environmental Radioactivity*, 97: 168-188.
21. Yasir, M. S., Ab. Majid, A., Ahmad Kabir, N., and Yahya, R. (2008). Kandungan logam berat dan radionuklid tabii dalam ikan, air, tumbuhan dan sedimen di bekas tapak lombong. *Malaysian Journal of Analytical Sciences,* 12(1): 172-178.

22. Rosli, M. N. R., Samat, S. B., Yasir, M. S., and Yusof, M. F. M. (2018). Determination of concentration activity natural radionuclide ^{232}Th, ^{238}U and ^{40}K in fish at the coastal area of Terengganu, Malaysia. *Sains Malaysiana,* 47(9): 2151-2156.
23. Ruth, E. W. (2005). Introduction to ICP-MS. Crustal Geophysics and Geochemistry Science Center, U.S. Geological Survey, pp. 21-52.
24. Warr, S., Rodriguez, G., and Penm, J. (2008). Changing food consumption and imports in Malaysia. Australian Government, Department of Agriculture, Fisheries and Forestry, Canberra, pp. 1-29.
25. ICRP (2012). Compendium of dose coefficients based on ICRP Publication 60: ICRP Publication 119. Oxford: Pergamon Press.
26. IAEA (2004). Radiation, people and the environment: a broad view of ionising radiation, its effects and uses as well as the measures in place to it safely. Vienna: IAEA.
27. Hyde, E. K. (1960). The Radiochemistry of Thorium. Subcommittee on Radiochemistry, National Academy of Sciences-National Research Council. Retrieved from http://www.radiochemistry.org/periodictable/pdf_books/pdf/rc000034.pdf
28. Hong, G. H., Baskaran, M., and Molaroni, S. M. (2011). Anthropogenic and natural radionuclides in caribou and muskoxen in the Western Alaskan Arctic and marine fish in the Aleutian Islands in the first half of 2000. Science of Total Environment, 409: 3638-3648.
29. Narayana, Y., Radhakrishna, A. P., Somashekarappa, H. M., Karunakara, N., Balakrishna, K. M., and Siddappa, K. (1995). Distribution of some natural and artificial radionuclides in the environment of coastal Karnataka of South India. *Journal of Environmental Radioactivity,* 28(2): 113-139.
30. Ademola, J. A. and Ehiedu, S. I. (2010). Radiological analysis of ^{40}K, ^{226}Ra and ^{232}Th in fish, crustaceans and sediment samples from fresh and marine water in oil exploration area of Ondo state, Nigeria. *African Journal of Biomedical Research*, 13: 99-106.
31. Kılıç, Ö., Belivermiş, M., Çotuk, Y., and Topçuoğlu, S. (2014). Radioactivity concentrations in mussel (*Mytilus galloprovincialis*) of Turkish Sea coast and contribution of ^{210}Po to the radiation dose. *Marine Pollution Bulletin,* 80(1-2): 325-329.
32. Samat, S. B., Green, S., and Beddoe, A. H. (1997). The ^{40}K activity of one gram of potassium. *Physics in Medicine and Biology*, 42(2): 407.
33. Patra, A. C., Mohapatra, S., Sahoo, S. K., Lenka, P., Dubey, J. S., Thakur, V. K., ... and Tripathi, R. M. (2014). Assessment of ingestion dose due to radioactivity in selected food matrices and water near Vizag, India. *Journal of Radioanalytical and Nuclear Chemistry*, 300: 903-910.
34. ICRP (1990). Recommendation of the international commission on radiological protection: ICRP Publication 60. Pergamon Press, Oxford.
35. IAEA (2013). Certified reference material for radionuclides in fish flesh sample IAEA-414 (Mixed fish from the Irish Sea and North Sea). Vienna: IAEA.
36. John, P., Margaret, M., Lynne, H., and Fred, M. (2009). Radiological and chemical fact sheets to support health risk analyses for contaminated areas. Argonne National Laboratory, Environmental Science Division: pp. 28-36.
37. Awudu, A., Faanu, A., Darko, E., Emi-Reynolds, G., Adukpo, O., Kpeglo, D., ... and Agyeman, B. (2012). Preliminary studies on ^{226}Ra, ^{228}Ra, ^{228}Th and ^{40}K concentrations in foodstuffs consumed by inhabitants of Accra metropolitan area, Ghana. *Journal of Radioanalytical and Nuclear Chemistry,* 291(3): 635-641.
38. UNSCEAR. (1993). Dose assessment methodologies. United Nations Scientific Committee on the Effects of Atomic Radiation. New York: United Nations, 121-126.

Malaysian Journal of Analytical Sciences (MJAS)
Published by Malaysian Analytical Sciences Society

PHYSICAL AND CHEMICAL PROPERTIES ON REDUCTION BEHAVIOUR OF CHROMIUM DOPED TO MOLYBDENUM OXIDE IN CARBON MONOXIDE ENVIRONMENT

(Sifat Fizikal dan Kimia terhadap Tindak Balas Penurunan Kromium yang Didopkan kepada Molibdenum Oksida di dalam Persekitaran Karbon Monoksida)

Nur Syakirah Abdul Rahim[1], Alinda Samsuri[2,3*], Mohd Nor Latif [4,5], Maratun Najiha Abu Tahari[6], Fairous Salleh[6], Tengku Shafazila Tengku Saharuddin[7], Norliza Dzakaria[8], and Muhammad Rahimi Yusop[6]

[1]*Faculty of Defence Science and Technology, Universiti Pertahanan Nasional Malaysia, Kem Perdana Sungai Besi, 57000 Kuala Lumpur, Malaysia*
[2]*Centre for Tropicalization (CENTROP), Universiti Pertahanan Nasional Malaysia, Kem Perdana Sungai Besi, 57000 Kuala Lumpur, Malaysia*
[3]*Department of Chemistry and Biology, Centre for Defence Foundation Studies, Universiti Pertahanan Nasional Malaysia, Kem Perdana Sungai Besi, 57000 Kuala Lumpur, Malaysia*
[4]*GENIUS@Pintar National Gifted Centre, Universiti Kebangsaan Malaysia, 43600 Bangi, Selangor, Malaysia*
[5]*Research Centre for Sustainable Process Technology (CESPRO), Faculty of Engineering and Built Environment, Universiti Kebangsaan Malaysia, 43600 Bangi, Selangor, Malaysia*
[6]*Department of Chemical Sciences, Faculty of Science and Technology, Universiti Kebangsaan Malaysia, 43600 Bangi, Selangor, Malaysia*
[7]*Faculty of Science and Technology, Universiti Sains Islam Malaysia, Bandar Baru Nilai, 71800 Nilai, Negeri Sembilan, Malaysia*
[8]*School of Chemistry and Environment, Faculty of Applied Sciences, Universiti Teknologi MARA, Cawangan Negeri Sembilan, Kampus Kuala Pilah, Pekan Parit Tinggi, 72000 Kuala Pilah, Negeri Sembilan, Malaysia*

[*]*Corresponding author: alinda@upnm.edu.my*

Received: 7 September 2022; Accepted: 9 December 2022; Published: 19 April 2023

Abstract

This study aimed to investigate the influence of added chromium on the physical and chemical reduction behavior of molybdenum trioxide (MoO_3) in a carbon monoxide (CO) environment. The reduction behavior of the sample was evaluated by using temperature-programmed reduction (TPR), and the phases produced by the reduced samples were analyzed using X-ray diffraction spectroscopy (XRD) and field emission scanning electron microscopy (FESEM). The TPR study was conducted using two reduction modes: non-isothermal reduction at 700°C with 20 vol. % of CO in nitrogen (N_2), followed by isothermal reduction at 700°C for an additional 60 min. The TPR profile showed that the reduction of doped and undoped MoO_3 was preceded by two reduction stages ($MoO_3 \rightarrow Mo_4O_{11} \rightarrow MoO_2$), wherein, the reduction of doped MoO_3 starting at a lower temperature (380°C-500°C) than that of undoped MoO_3 (550°C). Additionally, based on XRD analysis, it was shown that the conversion of MoO_3 to MoO_2 under CO generated an intermediate product known as Mo_4O_{11}. It is discovered that, increasing the concentration of chromium doped to MoO_3 enhanced the reducibility of oxide due to the rapid production of MoO_2 phases at T: 380ºC. Further

heating under CO atmosphere, carbide species built up in the form of Mo_2C rather than metallic Mo which might be due to excess of CO exposure to the surface layer of oxide.

Keywords: reduction, molybdenum oxide, carbon monoxide, chromium

Abstrak

Kajian ini bertujuan untuk menyiasat pengaruh penambahan kromium terhadap sifat fizikal dan kimia semasa penurunan molibdenum trioksida (MoO_3) dalam persekitaran karbon monoksida (CO). Tingkah laku penurunan sampel dinilai menggunakan teknik suhu penurunan berprogram (TPR), dan fasa yang dihasilkan oleh sampel yang diturunkan dianalisis menggunakan pembelauan sinar-X (XRD) dan pancaran medan mikroskopi elektron pengimbasan (FESEM). Kajian TPR telah dijalankan menggunakan dua mod penurunan: penurunan bukan isoterma pada 700°C dengan 20 vol. % CO dalam nitrogen (N_2), diikuti dengan pengurangan isoterma pada 700°C selama 60 minit. Keputusan TPR menunjukkan bahawa penurunan MoO_3 terdop dan tidak terdop didahului oleh dua peringkat penurunan iaitu ($MoO_3 \rightarrow Mo_4O_{11} \rightarrow MoO_2$) dengan penurunan MoO_3 terdop bermula pada suhu yang lebih rendah (380°C-500°C) berbanding MoO_3 tidak terdop (550°C). Di samping itu, telah ditentukan bahawa penurunan MoO_3 kepada MoO_2 dengan CO telah menghasilkan produk perantaraan yang dipanggil Mo_4O_{11} berdasarkan analisis sampel yang diturunkan menggunakan XRD. Telah didapati bahawa, peningkatan kepekatan kromium yang didopkan kepada MoO_3 telah meningkatkan penurunan oksida dengan pembentukan fasa MoO_2 yang lebih cepat pada T: 380ºC. Pemanasan berpanjangan di dalam persekitaran CO menyebabkan pembentukan spesies karbida dalam bentuk Mo_2C dan bukannya logam Mo yang mungkin disebabkan oleh pendedahan berlebihan CO pada lapisan permukaan oksida.

Kata kunci: Penurunan, molibdenum oksida, karbon monoksida, kromium

Introduction

Molybdenum oxide (MoO_3) has a density of 4.692 g/cm^3 and a melting point of 1068K (795°C), making it a viable source of Mo for direct alloying steel making or the manufacture of ferromolybdenum processes [1]. Because it helps quenched and tempered steels to become harder and more resilient, molybdenum is a valuable alloying agent. It also makes the steel more durable at high temperatures [2]. Electrodes for heated glass furnaces, nuclear energy applications, missile and aeroplane parts, the manufacturing of tungsten, glass to metal sealing, and colloidal form as a lubricant additive are all uses for molybdenum. As a catalyst, it can also be used in the refining of petroleum [3]. Additionally, the reduction of suitable reacting agents, such as hydrogen and carbon monoxide, is a necessary step in the synthesis of metallic molybdenum [4]. Generally, the generation of volatile molybdenum species produced at high temperatures is minimized by using the two-stage flow scheme ($MoO_3 \rightarrow MoO_2$, $MoO_2 \rightarrow$ Mo). In a single-stage conversion of the molybdenum precursor, molybdenum must also be obtained through a separate method [5].

These days, hydrogen is used as a crucial reducing agent in the chemical sector. To produce pure molybdenum metal, the reduction process that uses hydrogen as a reducing agent goes through a two-step chemical reduction procedure [6]. MoO_3 is converted to MoO_2 in the first step of this reaction, which takes place at a lower temperature (450°C-650°C) [7]. MoO_2 is further reduced to metallic molybdenum during the second reduction step. The temperature range used for this technique is 1000°C-1100°C. Additionally, a critical step in the formation of metallic molybdenum is the reduction of MoO_3 to MoO_2. According to Wang et al. [8], MoO_3 is reduced to MoO_2 by using hydrogen as a reducing agent which consisting of two reduction processes, with the production of the intermediate phase Mo_4O_{11} occurring first before MoO_2.

Carbon can be used as a reducing agent to produce pure molybdenum as a choice. This technique comprises a high-temperature (600°C-1200°C) interaction between MoO_3 and carbon [9]. Additionally, the use of carbon in reduction is efficient because the reaction between metal oxide and carbon results in a gas that can be easily separated from the solid reaction product [10]. Carbon monoxide (CO), in addition to hydrogen and carbon, has started to be utilized as a reducing agent. However, just a few studies have investigated by using CO as a reducing agent to reduce MoO_3. Additionally, the use of

chromium as an adjuvant has been extensively studied by researchers to increase the catalyst low-temperature reducibility and catalytic activity [11]. When chromium is added as a precursor, gas sensing for carbon monoxide can be improved at a relatively low temperature, according to Habib et al. [12].

In this study, the reduction behavior and degree of reduction of the molybdenum species were examined in an atmosphere with 20 vol. % of CO in N_2. The goal of this study was to identify the appropriate way to increase the reducibility of MoO_3 by adding chromium, including the best reduction temperatures. In addition, the temperature-programmed reduction (TPR) method was used to characterize the chromium-doped MoO_3 and analyze its reduction behavior in comparison to undoped species.

Materials and Methods

Materials

Commercially pure MoO_3 powder and chromium (III) nitrate, $Cr(NO_3)_3$, which were provided by BDH Chemicals Ltd. and Sigma Aldrich Chemical, respectively, served as the starting ingredients. Moreover, the impregnation procedure used ethanol, C_2H_6O (99.5%) from Systerm® as the solvent. In addition, Linde provided the gas mixture with 20 vol. % of CO in N_2.

Catalyst preparation

An aqueous solution containing chromium cation additives was used to impregnate MoO_3 powder to prepare the chromium doped with molybdenum oxide. Chromium was added in amounts of (x = 3, 9, 15) mol % of the total metal cation. Then, all prepared samples were dissolved in a mixture of distilled water and ethanol at 40°C while stirred vigorously for 4 h at room temperature (24ºC) to form a viscous mixture. The impregnated samples were first oven dried at 110°C overnight before being calcined for 4 h in air at 400°C. The doped catalyst was denoted as x Cr-MoO_3, (x = 3, 9, 15%) while for undoped catalyst was denoted as MoO_3.

Temperature-programmed reduction

Using a Micromeritic Autochem 2920 Chemisorption Analyzer apparatus, the temperature-programmed reduction (TPR) method was used to analyze the total reduction of the undoped and doped MoO_3. With a flow rate of 20 mL min^{-1}, mixed gases containing 20 vol. % of CO and 80 vol. % of N_2 were fed into the micro reactor as the reducing gas (STP). Samples of 50 mg were heated at a rate of 10°C min^{-1} to 700°C. Then, an isothermal mode of reduction was used when temperature reached at 700°C and prolong the reaction from 30 min to 60 min. All analyses were identified by a thermal conductivity detector (TCD).

Characterizations

The physicochemical properties were characterized by X-Ray Diffraction (XRD), using the Cu Kα X-ray radiation source (40 kV, 40 mA) in the XRD Bruker AXS D8 (Advance type) to record the 2θ diffraction angle from 10° to 80° at wavelength (λ = 0.154 nm). Surface area and porosity were characterized by using Brunauer-Emmett-Teller (BET) utilizing the Micromeritics ASAP 2020 equipment. The samples underwent degassing at 200°C for 4 h, before treatment under liquid N_2 at -198ºC. Following that, the surface morphology of the reduced MoO_3 was studied using a Carl Zeiss Merlin field emission scanning electron microscope (FESEM).

Results and Discussion

XRD analysis of the structural properties of doped and undoped MoO_3

The XRD patterns of undoped and doped MoO_3 with various loadings of chromium were displayed after calcined at 400°C for 4 hours (Figure 1). It shows that undoped MoO_3 patterns largely existed as MoO_3 (JCPDS 05-0508) [4]. Nevertheless, the addition of chromium to MoO_3 had little effect on their mesoporous structure, as summarised in Table 1. About the display of chromium molybdenum oxide, $Cr_2(MoO_4)_3$, just a small difference in XRD patterns was noticed (JCPDS 77-5936). Moreover, the intensity of MoO_3 peaks decreased especially for MoO_3 with higher chromium loadings. The 2θ range of MoO_3 peaks showed many new $Cr_2(MoO_4)_3$ diffraction peaks at 15 mol % of chromium loading, which demonstrated that the impregnation of chromium on the MoO_3 was truly successful at range of 2θ = 20°-40°. The interference of chromium element which altered the lattice constant of

MoO_3, was primarily responsible for the evolution of diffraction peaks. This can be attributed to the differences in atomic radius of molybdenum and chromium, which can alter the lattice parameters and spacing. It was found that the difference in atomic size, electronic interaction, and magnetic spin relations between the solute and its solvent atoms (Cr-MoO_3) which all were contributed to the lattice distortions [13].

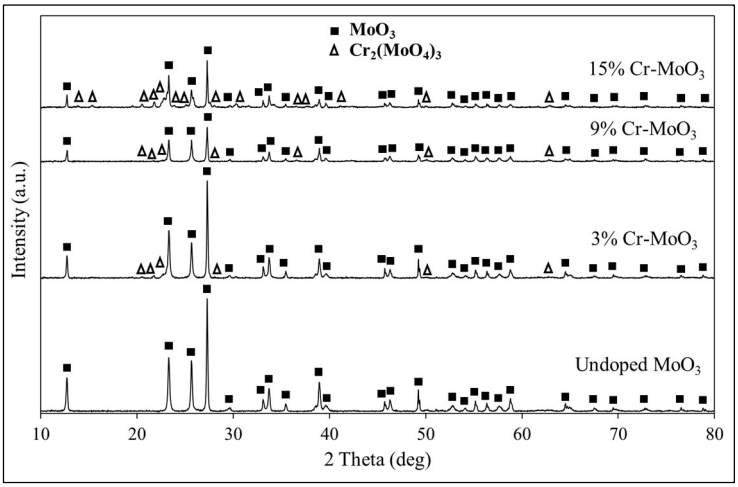


Figure 1. XRD patterns of undoped MoO_3 and chromium-doped of MoO_3 at various loadings after calcinations at 400 ºC for 4 h

BET analysis from the N_2 adsorption isotherm for structural properties

The analysis of N_2 adsorption-desorption isotherm at 77 K was used to identify the effect of the impregnation on the textural characteristics of MoO_3. Table 1 provides information about the textural properties of doped MoO_3 including BET surface area, total pore volume, and average pore size width. The surface area (BET), pore volume, and pore size of doped MoO_3 decreased as increasing the amount of chromium concentration of MoO_3 (6.85 m^2/g) > 3% Cr-MoO_3 (5.91 m^2/g) > 9% Cr-MoO_3 (3.28 m^2/g) > 15% Cr-MoO_3 (2.26 m^2/g). Decreasing of surface area of doped samples might be due to the ion-exchange that caused the low dispersion of Mo oxide after addition of chromium, which agreed with the decreasing of XRD peak intensity of MoO_3 at $2\theta = 27^o$ (Figure 1). Mesopore sizes decreased from 20.4 nm in undoped MoO_3 to 18.1 nm, 15.4 nm, and 14.3 nm with 3 mol %, 9 mol %, and 15 mol % of chromium addition, respectively. Besides, the cumulative pore volume (cm^3/g) in Table 1 demonstrated that the overall pore volume for undoped MoO_3 was 0.035 cm^3/g, and by increased the amount of chromium added had reduced the pore volume to 0.027 cm^3/g, 0.013 cm^3/g, and 0.008 cm^3/g, respectively. These demonstrated that the chromium layer present on the pore surfaces of MoO_3 had been the reason for the reduced pore size and pore volume of all doped MoO_3. Therefore, MoO_3 loaded with a higher percentage of chromium possessed smaller pore sizes and a decreased in pore volume. The decreasing of pore size and volume as increasing the addition of chromium concentration were due to the Cr salt filled in the pore of Mo oxide.

Table 1. BET analysis of chromium-doped of MoO_3 and undoped MoO_3

Catalyst	Surface Area (m^2/g)	Pore Size (nm)	Pore Volume (cm^3/g)
Undoped MoO_3	6.85	20.4	0.035
3% of Cr-MoO_3	5.91	18.1	0.027
9% of Cr-MoO_3	3.28	15.4	0.013
15% of Cr-MoO_3	2.26	14.3	0.008

TPR analysis of chemical properties

The TPR analysis was used to establish the reduction properties of each sample. The TPR profiles of prepared samples with x = 3, 9, 15 mol % of Cr-MoO_3 and undoped MoO_3 in a non-isothermal reduction under 20 vol. % of CO in N_2 and a continuation in an isothermal reduction mode at 700°C for 60 min are shown in Figure 2. Non-isothermal reduction at 700°C was added to the reduction system to prevent the production of alloy-fused mass, if the complete reduction to MoO_2 was not accomplished at a temperature below the melting point of MoO_3 (795°C) [6]. There were three reduction phases involved in the reduction of pure MoO_3 to Mo: Mo^{6+} to Mo^{5+}, Mo^{5+} to Mo^{4+}, and Mo^{4+} to Mo^0 [8]. By referring to the results obtained from the reduction of undoped and doped MoO_3 with chromium, the TPR profiles thus displayed nearly identical patterns by presenting two reduction peaks (denoted I and II), whereby the first peak owing to the reduction of MoO_3 to Mo_4O_{11} and the second peak represented the reduction of Mo_4O_{11} to MoO_2 [14].

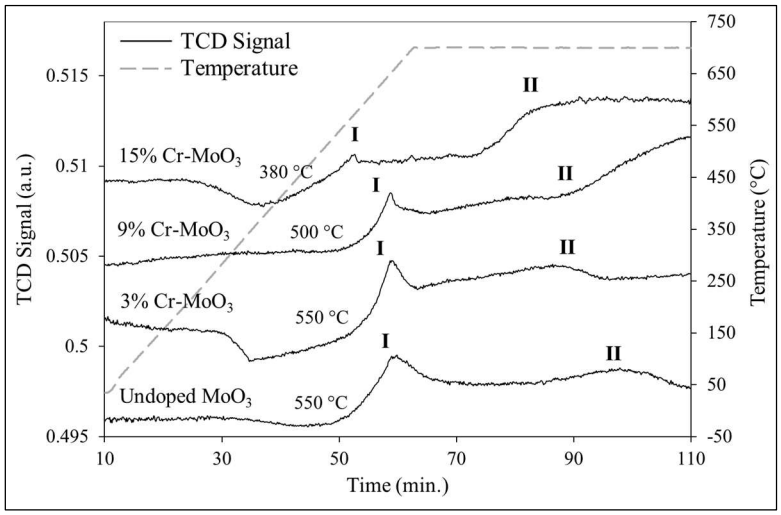


Figure 2. TPR profiles of undoped MoO_3 and chromium-doped of MoO_3

According to Dang et al. [5], the CO consumption peaks of undoped MoO_3 that began at roughly 550°C indicated that the initial phase of reduction was a Phase I as the production of Mo_4O_{11}. Due to sample modifications that took place 40 min after the isothermal reduction process began at 700°C, new peaks designated as Phase II were noticed. These peaks represented the second phase reduction of Mo_4O_{11} to MoO_2. Nonetheless, the addition of chromium to MoO_3 provided different information about the reducibility of MoO_3. The TPR results showed that the interaction between different loadings of chromium to MoO_3 decreased the reduction temperature and all peaks were shifted to a lower temperature. Besides, doping with chromium generated some amount of oxygen release and lowered the TPR reduction temperature [15].

However, TPR profile (Figure 2) also clearly shows two dominant peaks of doped MoO_3 designated as I and II. By adding 3 mol % of chromium, the reduction temperature of doped MoO_3 remained unchanged at early stage of reduction (I) as undoped MoO_3 at 550ºC. However, it was observed during the isothermal reaction, the reduction peak (II) appeared faster as compared to undoped MoO_3. Then, at 60 min and 90 min of reduction time, respectively showed the TPR profile for 9% of Cr-MoO_3 was designated as I and II. Peak I was observed at 650ºC represented the reduction of MoO_3 to Mo_4O_{11}, while peak II appeared after 20 min of isothermal reduction, which represented the complete reduction of MoO_2. At higher concentration of 15% of Cr-MoO_3, peak I and peak II shifted to a lower reduction (380°C and 10th min) as compared to undoped and lower Cr concentration. Besides, for the reduction of doped MoO_3 with 15 mol % of chromium, the TPR profile was

almost similar as it portrayed two peaks, whereby the first reduction peak was noted at about 380°C, which was lower than undoped MoO_3 (550°C), whereas the second peak began its formation at the 10th minute of isothermal reduction. As shown by the XRD analysis in Figure 4, increasing the isothermal reduction could lead to the synthesis of Mo_2C rather than metallic molybdenum [16].

It was evident that the addition of chromium to MoO_3 might have a major impact on the powder reduction by increasing the powder reducibility and oxygen storage capacity. Additionally, there were some changes in the coordination environment of molybdenum and the strength of Mo-O bonds because of the strong interaction between chromium ions and molybdenum ions in the samples [17]. In comparison to conventional Ni catalysts, Ni-Cr catalysts often exhibited substantially stronger anti-coking and anti-sintering capabilities, as well as much higher catalytic activity and stability. The smaller Ni particle size, the enhancing influence of Cr, and the increased sorption capacities for both H_2 and CO absorption are all thought to be the causes of the better catalytic performance [18] and indirectly causes the enhancement of reducibility of oxide. Next, to determine the changes in the samples, the residual obtained after TPR reduction was studied by recording the XRD pattern and examining the morphological change by using FESEM.

Crystallinity studies

The XRD profile of spent catalysts during non-isothermal reduction at 700ºC are shown in Figure 3. Major peaks of unreduced MoO_3 and the intermediary phase of Mo_4O_{11} (JCPDS 84-0687) were visible in the XRD patterns of reduced undoped MoO_3 (JCPDS 74-7383) [19]. The XRD pattern was also nearly identical to that of undoped MoO_3, with Mo_4O_{11} forming as an intermediate phase. Mo_4O_{11} was produced during the reduction of MoO_3 to MoO_2, according to Dang et al. [5]. This finding proved the formation of Mo_4O_{11} as predicted in TPR profile (Figure 2). Meanwhile, with the addition of 9 mol % of chromium, the MoO_3 phase almost disappeared and the Mo_4O_{11} phase was present as the dominant species. However, the addition of 9 mol % of chromium, showed a low intensity for the crystalline phase of Mo_4O_{11} due to the formation of $Cr_2(MoO_4)_3$ alloy (JCPDS 078-1654). Then, for the addition of 15 mol % of chromium, the patterns revealed that the reduction product was rather the same as the addition of 9 mol % of chromium with the major forms of Mo_4O_{11} and a few peaks of $Cr_2(MoO_4)_3$ alloy. However, no remaining unreduced MoO_3 peaks had been observed. Therefore, it had been discovered that adding more chromium might speed up reduction process of MoO_3.

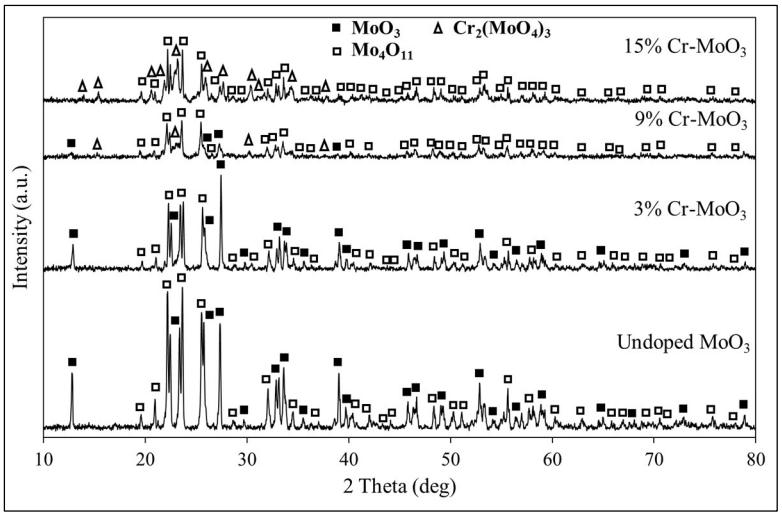


Figure 3. XRD patterns of 20 vol. % of CO in N_2 of non-isothermal reduction at 700°C

Figure 4 showed the XRD diffraction which carried out in isothermal mode for 60 min by using 20 vol. % of CO at 700°C to further reduce to MoO_2 phases. After 60 min of isothermal reduction, all samples had completely reduced to the MoO_2 phase (JCPDS 76-1807) [20]. In addition, the peaks that represented $Cr_2(MoO_4)_3$ alloy had completely disappeared in 9 mol % and 15 mol % of chromium-doped of MoO_3 samples after isothermal reduction. However, the increased addition of chromium showed that the low crystallinity of MoO_2 synthesis was affected by the formation of $Cr_2(MoO_4)_3$ alloy at range of $2\theta = 20°$-$40°$ (Figure 1) which enhanced the reduction performance of MoO_3. According to the formation of Mo_2C (JCPDS 071-0242) in 15 % of Cr-MoO_3 samples during isothermal reduction at 700°C for 60 min, carbide was formed when excessive CO was added to the MoO_2 phase. This finding was in agreement with Wang et al. [21] regarding the formation of Mo_2C.

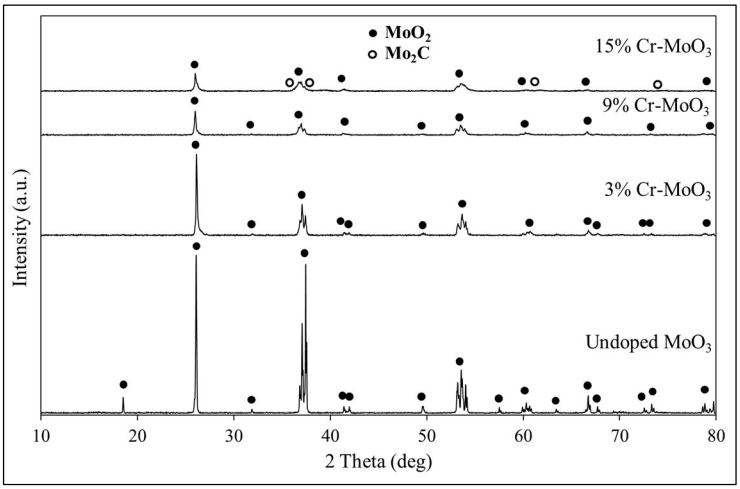


Figure 4. shows the XRD patterns of non-isothermal reduction in 20 vol. % of CO in N_2 up to 700°C and continued in isothermal mode at 700°C for 60 min

Apart from that, it can be concluded that the reduction step involved in the samples had been in the sequence of $MoO_3 \rightarrow Mo_4O_{11} \rightarrow MoO_2$ [8]. With the addition of chromium, the reducibility of MoO_3 was enhanced by changing the physiochemical properties of MoO_3, by the formation of $Cr_2(MoO_4)_3$ alloy which was confirmed by XRD analysis. As a result, it made the transition of MoO_3 to MoO_2 easier. The formation of Mo_2C instead of metallic molybdenum occurred when excessive CO was supplied to the MoO_2 phase, which was in line with the report by Alinda et al. [16] that the presence of excessive CO in the reduction process caused the formation of carbon on the external surface of Mo layer.

Morphological studies

Based on the TPR and XRD results, FESEM analysis was employed to identify new phases after the reduction process. The undoped MoO_3 morphology, according to Alinda et al. [4] is characterised by agglomerations of non-porous grains in vast numbers and with non-uniform sizes. However, as the reduction process continued, the resulting structures took on the appearance of a thin plate with an asymmetrical shape, demonstrating the rapid formation of MoO_2 phase from Mo_4O_{11} [4]. Figure 5 depicts the morphological change that occurred during the reduction of MoO_3 with various chromium loadings in 20 vol. % of CO in N_2 up to 700°C and proceeded with isothermal reduction for 60 min at 700°C.

The morphology of MoO_3 doped with 3 mol % of chromium is depicted in Figure 5(a). Figure 5(a) shows, no chromium particles had been observed on the MoO_3 surface. However, referring to BET results presented in Table 1, the surface areas eventually decreased. It revealed that the chromium added had successfully

penetrated the MoO_3 pores. After the reduction process, the MoO_2 phase with the plate-like particles and coated with small particles had been observed, as illustrated in Figure 5 (b). Other than that, as shown in Figure 5 (c) and Figure 5 (e), when the addition of chromium was increased to 9 mol % and 15 mol %, small particles had been observed on the surface of MoO_3. It seemed that the MoO_3 pores were filled with chromium and excessive chromium was attached to the surface of MoO_3, which was in agreement with the decreasing of surface area (BET) result. However, following a reduction, the MoO_2 phase developed plate-like particles with smaller particles dispersed on its surface, as depicted in Figure 5 (d) and Figure 5 (f). Another intriguing finding that can be seen in Figure 5 is the additional phase formation that occurred on the surface of the 15% of Cr-MoO_3 sample because of carbon deposition on MoO_2 surface rather than further Mo_2C production [1].

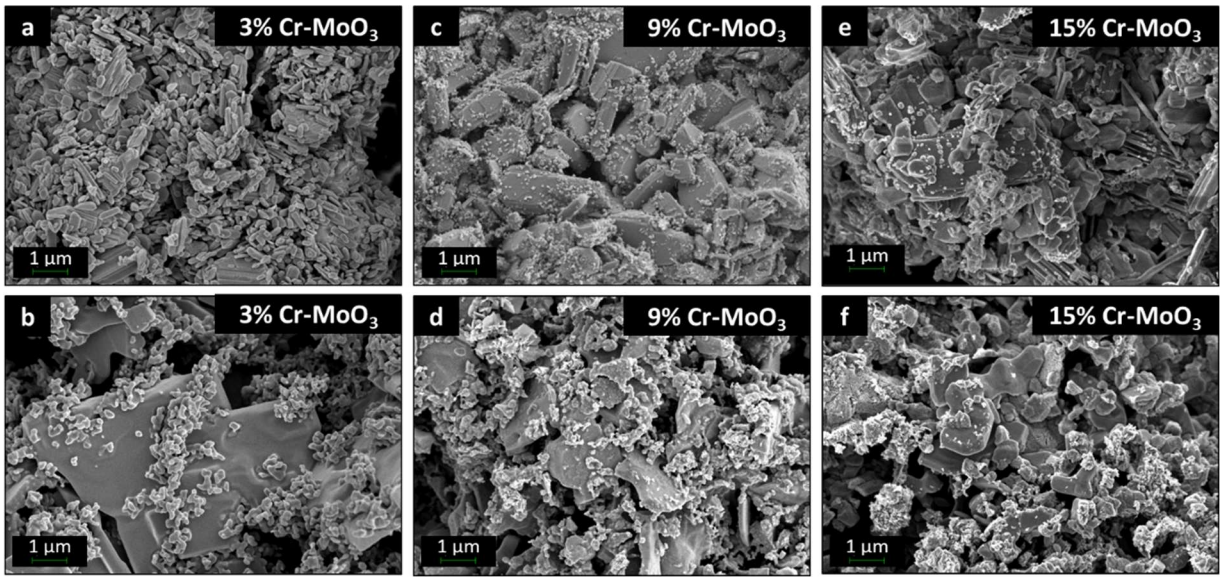


Figure 5. FESEM images before (top) and after (bottom) reduction in magnification 3,000X

Conclusion

Utilizing the TPR approach, the reduction behavior of chromium-doped and undoped MoO_3 was examined, compared, and characterized by XRD and FESEM analyses. The existence of $Cr_2(MoO_4)_3$ alloy on MoO_3 was demonstrated by the XRD data, which had the impact of accelerating the reduction process by reducing the temperature at which MoO_3 was reduced to the MoO_2 phase. As a result, adding chromium produced a two-step reduction process ($MoO_3 \rightarrow Mo_4O_{11} \rightarrow MoO_2$) that was comparable to MoO_3 that was not doped. Furthermore, better reducibility of Cr-MoO_3 was also due to the physicochemical changes on MoO_3 through the formation of successful intercalation of chromium onto the surface of MoO_3, which was further confirmed with the decreased in the surface area for chromium-doped MoO_3. However, excessive CO was added to the MoO_2 phase, Mo_2C would instead develop as opposed to metallic molybdenum.

Acknowledgement

The project was funded by research grant number RACER/1/2019/STG07/UPNM/2 from the Ministry of Higher Education (MOHE) of Malaysia, UPNM/2022/GPPP/SG/10 from Universiti Pertahanan Nasional Malaysia (UPNM), and Universiti Kebangsaan Malaysia (UKM), as well as the Centre of Research and Innovation Management (CRIM) of UKM, Malaysia for the instruments and facilities.

References

1. Wang, L., Bu, C. Y., Zhang, G. H., Wang, J. S., and Chou, K. C. (2017). Study of the reduction of industrial grade MoO_3 powders with CO or CO-CO_2 gases to prepare MoO_2. *Metallurgical and Materials Transactions B: Process Metallurgy and Materials Processing Science,* 48(4): 2047-2056.
2. Chen, X. R., Zhai, Q. J., Dong, H., Dai, B. H., and Mohrbacher, H. (2020). Molybdenum alloying in cast iron and steel. *Advances in Manufacturing*, 8(1): 3-14.
3. Jaf, Z. N., Miran, H. A., Jiang, Z. T. and Altarawneh, M. (2021). Molybdenum nitrides from structures to industrial applications. *Reviews in Chemical Engineering*, 2021:1015.
4. Samsuri, A., Latif, M. N., Shamsuddin, M. R., Salleh, F., Abu Tahari, M. N., Tengku Saharuddin, T. S., Dzakaria, N., and Yarmo, M. A. (2021). Studies on influence of hydrogen and carbon monoxide concentration on reduction progression behavior of molybdenum oxide catalyst. *International Journal of Hydrogen Energy,* 46(48): 24831-24844.
5. Dang, J., Zhang, G. H., Chou, K. C., Reddy, R. G., He, Y., and Sun, Y. (2013). Kinetics and mechanism of hydrogen reduction of MoO_3 to MoO_2. *International Journal of Refractory Metals and Hard Materials*, 41: 216-223.
6. Saghafi, M., Heshmati-Manesh, S., Ataie, A., and Khodadadi, A. A. (2012). Synthesis of nanocrystalline molybdenum by hydrogen reduction of mechanically activated MoO_3. *International Journal of Refractory Metals and Hard Materials*, 30(1): 128-132.
7. Enneti, R. K., and Wolfe, T. A. (2012). Agglomeration during reduction of MoO_3. *International Journal of Refractory Metals and Hard Materials,* 31: 47-50.
8. Wang, J., Ren, Z., Liu, W., Gao, F., and Zhou, M. (2009). Effects of RE_2O_3 doping on the reduction behavior of molybdenum oxide and properties of molybdenum powder. *International Journal of Refractory Metals and Hard Materials*, 27(1): 155-158.
9. Saghafi, M., Ataie, A., and Heshmati-Manesh, S. (2011). Effects of mechanical activation of MoO_3/C powder mixture in the processing of nano-crystalline molybdenum. *International Journal of Refractory Metals and Hard Materials*, 29(4): 419-423.
10. Wu, S., Zhou, C., Doroodchi, E., Nellore, R., and Moghtaderi, B. (2018). A review on high-temperature thermochemical energy storage based on metal oxides redox cycle. *Energy Conversion and Management*, 168: 421–453.
11. Zhang, G., Liu, J., Xu, Y., and Sun, Y. (2018). A review of CH_4–CO_2 reforming to synthesis gas over Ni-based catalysts in recent years (2010–2017). *International Journal of Hydrogen Energy*, 43(32): 15030-15054.
12. Habib, I. Y., Tajuddin, A. A., Noor, H. A., Lim, C. M., Mahadi, A. H., and Kumara, N. T. R. N. (2019). Enhanced Carbon monoxide-sensing properties of Chromium-doped ZnO nanostructures. *Scientific Reports,* 9(1): 9207.
13. Wang, T., Chen, L. Q., and Liu, Z. K. (2007). Lattice parameters and local lattice distortions in FCC-Ni solutions. *Metallurgical and Materials Transactions A: Physical Metallurgy and Materials Science,* 38(3): 562-569.
14. Samsuri, A., Tengku Saharuddin, T. S., Salleh, F., Othaman, R., Mohamed Hisham, M. W., and Yarmo, M. A. (2016). Temperature programmed reduction and x-ray diffractometry studies of MoO_3 reduction by different concentrations of carbon monoxide. *Malaysian Journal of Analytical Sciences,* 20: 382-387.
15. Saharuddin, T. S. T., Samsuri, A., Salleh, F., Othaman, R., Kassim, M. bin, Mohamed Hisham, M. W., and Yarmo, M. A. (2017). Studies on reduction of chromium doped iron oxide catalyst using hydrogen and various concentration of carbon monoxide. *International Journal of Hydrogen Energy,* 42(14): 9077-9086.
16. Samsuri, A., Tengku Saharuddin, T. S., Salleh, F., Mohamed Hisham, M. W., Othaman, R., and Yarmo, M. A. (2015). Reduction of MoO_2 to metallic molybdenum via carburization and thermal process. *Advanced Materials Research,* 1087: 64-67.
17. Sun, T., Xu, L., Wei, S., Xiao, F., Li, Z., Fan, X., and Zhou, Y. (2020). Phase evolution of

hydrothermal synthesis oxide-doped molybdenum powders. *International Journal of Refractory Metals and Hard Materials,* 86: 105085.

18. Liu, Q., Zhong, Z., Gu, F., Wang, X., Lu, X., Li, H., Xu, G., and Su, F. (2016). CO methanation on ordered mesoporous Ni-Cr-Al catalysts: Effects of the catalyst structure and Cr promoter on the catalytic properties. *Journal of Catalysis*, 337: 221-232.
19. Samsuri, A., Salleh, F., Tengku Saharuddin, T. S., Othaman, R., Mohammad Hisham, M. W., and Yarmo, M. A. (2017). Effect of noble metal silver on the reduction behaviour of molybdenum oxide using carbon monoxide. *Materials Science Forum,* 888: 377-381.
20. Latif, M. N., Samsuri, A., Mohammad Hisham, M. W., and Yarmo, M. A. (2017). Reduction of molybdenum trioxide by using hydrogen. *Materials Science Forum*, 888: 404-408.
21. Wang, L., Zhang, G. H., and Chou, K. C. (2018). Preparation of Mo_2C by reducing ultrafine spherical β-MoO_3 powders with CO or CO-CO_2 gases. *Journal of the Australian Ceramic Society*, 54(1): 97-107.

Malaysian Journal of Analytical Sciences (MJAS)
Published by Malaysian Analytical Sciences Society

HYDROLYSIS OF CELLULOSE TO GLUCOSE CATALYZED BY NOBLE METAL PALLADIUM (Pd) SUPPORTED ON SILICA-ALUMINA

(Hidrolisis Selulosa kepada Glukosa Bermangkin Logam Adi Paladium (Pd) Disokong pada Silika-Alumina)

Puteri Nurain Syahirah Megat Muhammad Kamal, Muhammad Danial Hafiy Mohamad Zabidi, and Amin Safwan Alikasturi*

Universiti Kuala Lumpur
Branch Campus Malaysian Institute of Chemical and Bioengineering Technology,
Lot 1988 Vendor City, Taboh Naning, 78000 Alor Gajah, Melaka, Malaysia

Corresponding author: aminsafwan@unikl.edu.my

Received: 22 September 2022; Accepted: 17 January 2023; Published: 19 April 2023

Abstract

Cellulose, a promising source of renewable energy, is currently receiving a lot of interest due to its potential application in the production of bioenergy. The catalytic conversion of cellulose into value-added compounds like glucose, which is subsequently fermented into bioethanol or dehydrated into platform chemicals, avoids the heavy reliance on fossil fuel economy tremendously. In this study, the catalytic conversion of cellulose to glucose was conducted using a supported noble metal catalyst. The wet impregnation method was used to synthesize 4 wt.% palladium (Pd) supported on silica-alumina (SiO_2-AlO_3), which was then calcined at 500 °C. Prior to reaction work, Fourier- transform infrared spectroscopy, thermogravimetric analysis, Brunauer-Emmett-Teller method, and particle size analysis were conducted to characterize the catalyst. To investigate the effect of the catalyst on the yield of glucose from cellulose, the catalyst loading was varied from 0.04 to 0.10 g. The results demonstrated that up to 23.6% yield of glucose was produced at 200 °C for 3 h with the catalyst and cellulose loading of 0.06 g and 0.3 g, respectively. Additionally, under these conditions, cellulose conversion was at its highest (78.7%). This study shows that the supported noble metal catalyst has the potential to enhance the hydrolysis step for the conversion of cellulose to glucose.

Keywords: glucose, heterogenous catalyst, hydrolysis of cellulose, palladium supported on silica-alumina, supported noble metal catalyst

Abstrak

Selulosa, sumber tenaga berpontesi yang boleh diperbaharui, kini menerima banyak perhatian kerana potensi aplikasinya dalam penghasilan biotenaga. Penukaran pemangkin selulosa kepada sebatian tambah nilai seperti glukosa, yang kemudiannya ditapai menjadi bioetanol atau dehidrasi menjadi bahan kimia platform, dapat membantu mengurangkan kebergantungan ekonomi kepada bahan api fosil. Di dalam kajian penyelidikan ini, penukaran pemangkin selulosa kepada glukosa telah dijalankan menggunakan mangkin logam adi yang disokong. Kaedah impregnasi basah digunakan untuk mensintesis 4 wt.% paladium (Pd) yang disokong pada silika-alumina (SiO_2-AlO_3), yang kemudiannya dikalsinasikan pada 500 °C. Sebelum memulakan kerja tindak balas, spektroskopi inframerah transformasi Fourier, analisis termogravimetri, kaedah Brunauer-Emmett-Teller, dan analisis saiz zarah

telah dijalankan untuk faktor pencirian mangkin. Untuk menyiasat kesan mangkin ke atas hasil glukosa daripada selulosa, pemuatan mangkin, berubah daripada 0.04-0.1g. Keputusan menunjukkan bahawa sehingga 23.6% glukosa dapat dihasilkan pada 200 °C selama 3 jam dengan mangkin dan pemuatan selulosa masing-masing, 0.06 g dan 0.3 g. Di samping itu, dalam keadaan ini ternyata penukaran selulosa berada pada tahap tertinggi, 78.7%. Kajian ini menunjukkan bahawa mangkin logam adi yang disokong berpotensi untuk meningkatkan langkah hidrolisis untuk penukaran selulosa kepada glukosa.

Kata kunci: glukosa, mangkin heterogen, selulosa hidrolisis, paladium disokong pada silika-alumina, mangkin logam adi disokong

Introduction

The increasing carbon footprint, greenhouse gas emissions, environmental pollution, and ecosystem imbalance are the main issues around the world today. These issues demonstrate the impending necessity for renewable energy. Biomass, or organic material derived from plants and animals, is a viable alternative for non-renewable resources as a feedstock for fuels. Biomass typically contains cellulose, lignin, and hemicellulose that can be converted into high-value chemicals and biofuels.

Cellulose, the most abundant biomass on earth, has been studied widely since its discovery in the 19th century. It is a promising source of renewable energy, and currently, it is gaining a lot of attention due to its potential use in bioenergy production [1]. However, due to high crystallinity, cellulose faces several difficulties that prohibit its extensive utilization in the production of economically competitive biofuels. According to Li et al. [2], cellulose is less susceptible to enzymatic hydrolysis, less accessible, and less reactive at a higher degree of crystallinity. Hence, it is crucial to resolve the structure of cellulose for decomposition purposes to produce platform chemicals.

Glucose, which is a cellulose monomer unit, can be a promising starting compound to produce various value-added chemicals, such as levulinic acid (LA). The production of LA from glucose requires glucose to go through several processes, including rehydration and dehydration. Up to 56.8% of LA could be produced from glucose using a solid acid catalyst at 100 °C for 6 h [3]. Many high-value-added chemicals can be synthesized from LA, such as ethyl levulinate, succinic acid, and maleic anhydride. Ethyl levulinate acts as an oxygenated additive in fuels and is one of the examples of high-value organic chemicals produced from the esterification of LA with ethanol [4,5]. Meanwhile, succinic acid and maleic anhydride are well known to be useful in the food and textile industries, respectively.

Palladium (Pd), platinum (Pt), rhenium (Re), and gold (Au) are examples of noble metals with outstanding resistance to oxidation even at high temperatures. These metals have excellent catalytic properties and are widely employed, especially in the process of hydrogenation. Pt and Pd are well known for their efficiency in the hydrogenation of carbon-carbon multiple bonds (e.g., olefinic bonds, acetylenic triple bonds, and nitro compounds) compared to other metals, such as ruthenium [6]. Increasing the amount of Pt or Pd leads to an increase in the catalytic activity for the hydrogenation process.

Pt and Pd are known for their high cost and limited availability. Hence, the internal pores of silica (SiO_2) and alumina (Al_2O_3) support can be incorporated with tiny spheres of Pt or Pd rather than using the metals in their pure form as most of their atoms are wasted as only the surface of the atoms is involved in reactions [7]. Through the incorporation on the support, almost all expensive metal atoms are available on the particle surface where they can contribute to reactions, and none are wasted.

Heterogeneous catalysts, particularly metal catalysts (i.e., noble metal) incorporated on the support, are often employed in the conversion of cellulose to sugar alcohol via hydrogenation, in which high selectivity or yield of sugar alcohols can be achieved. Sorbitol with a selectivity of 69% was produced when the reaction was catalyzed by 1.5 wt.% Pt/SBA15 (fumed silica) [8]. Meanwhile, more than 40% of sugar alcohols (i.e., hexitols, ethylene glycol, 1,2-propanediol, and glycerol) were produced when 4 wt.% Pd/CNT (carbon nanotube)

was used as a catalyst [9]. Although supported noble metal catalysts are frequently used to produce sugar alcohols from cellulose via hydrogenation, the conversion of glucose from cellulose via hydrolysis must be considered as well. According to Kobayashi et al. [10], the hydrolysis of cellulose is the rate-determining step, and the noble metal catalysts enhance both the hydrolysis and hydrogenation steps. Once glucose is produced, the conversion of cellulose to sugar alcohols would be simpler. This concept is similar to that used to produce LA from cellulose. In this case, whether LA is produced in high yield depends on the production of glucose from cellulose. A recent study by Kamal et al. [11] discovered that by employing noble metal (i.e., Pd) supported on silica-alumina (SiO_2-Al_2O_3), up to 43.3% of LA was produced with cellulose conversion up to 73.9%. This shows that highly crystalline cellulose can be hydrolyzed to yield glucose, which can then be easier converted to other products, including 5-hydroxymethylfurfural (HMF), LA, and formic acid (FA) because the process only requires dehydration and rehydration. However, it is worth noting that studies on the use of noble metals incorporated into the support for the hydrolysis of cellulose are still lacking, although studies on the decomposition of cellulose to glucose using other heterogeneous catalysts have been widely established [12,13].

For example, in the study by Boonyakarn et al. [12], up to 11% of glucose was produced from cellulose, which eventually contributed to 8% yield of LA when 0.0025 M of chromium chloride ($CrCl_3$) catalyst was employed for 5 min at 220 °C. If the reaction period is prolonged, it is anticipated that the yield of LA will be higher than 8%. Joshi et al. [13] found that employing 2 wt.% of zirconium dioxide (ZrO_2) catalyst in the system produced up to more than 5% of glucose, contributing to the highest production of LA, which is above 80%. Hence, this research focused on the study of the effect of catalyst loading on the production of glucose from cellulose using noble metal (i.e., Pd) supported on SiO_2-Al_2O_3. As a result, the most suitable catalyst loading for the conversion of highly crystalline cellulose to glucose could be determined.

Materials and Methods

Materials

The catalyst was synthesized using palladium (II) nitrate ($Pd(NO_3)_2$) with 40% w/w of Pd and SiO_2-Al_2O_3 grade 135 (100%) purchased from Sigma Aldrich. Microcrystalline cellulose (extra pure, 100%) from Acros Organics served as the experimental work's substrate. As for standard reference calibration purposes, glucose (>99.9%), HMF (>98%), LA (>98%), FA (>98%), and furfural (>99.9%) were employed. All the chemicals were of analytical grade and used without further purification (unless otherwise stated), and distilled water was used for all the experiments.

Catalyst Preparation

First, 5 g of 4 wt.% Pd/SiO_2-Al_2O_3 catalyst was prepared using the wet impregnation method following the steps described in an earlier study [11]. The catalyst support, SiO_2-Al_2O_3, was weighed for approximately 4.8 g and spread on a petri dish before diluted palladium nitrate ($Pd(NO_3)_4$) was dropped onto the support using a syringe. A spatula was used to press $Pd(NO_3)_4$ until it was thoroughly mixed with SiO_2-Al_2O_3. Prior to calcination, the prepared catalyst was dried in an oven at 110 °C for 12 h to eliminate excess moisture. The catalyst was subsequently calcined for 5 h at 500 °C. The catalyst was kept in a parafilm-sealed vial and stored in a desiccator prior to analysis and experimental work.

Catalyst characterization

The prepared catalyst was characterized by Fourier-transform infrared spectroscopy (FTIR), thermogravimetric analysis (TGA), Brunauer-Emmett-Teller (BET) method, and particle size analysis. The TGA of the prepared catalyst was performed on a Mettler Toledo STARe software. The analysis was carried out from room temperature (30 °C) to 550 °C by employing a heating rate of 10 °C/min under the flow of 20 mL/min of high-purity air. The FTIR spectrum range was recorded from 4000 to 400 cm^{-1} on a Nicolet iS10 spectrometer with a spectral resolution of 8 cm^{-1} at room temperature and an accumulation of five scans in an open-beam air background. The surface area and pore volume of the prepared catalyst were determined by the BET method using a Micromeritics 3Flex surface characteristics analyzer, where the catalyst was

degassed at 150 °C for 12 h in nitrogen (N_2) prior to analysis. A Malvern Mastersizer 3000 particle size analyzer was used to conduct the particle size analysis.

Experimental procedure

The pre-reduction of the catalyst and the experimental work for the catalytic conversion of cellulose to glucose were carried out in a 20 mL stainless steel semi-batch reactor. For the pre-reduction of the catalyst, the catalyst and distilled water were loaded accordingly into the reactor. One bar of hydrogen (H_2) was inserted into the reactor. The timer and stirrer were set for 1 h and 1300 rpm, respectively, once the desired temperature of 150 °C was achieved. After 1 h, 0.3 g of cellulose was loaded into the reactor. The air inside the reactor was purged using N_2 three times. The stirrer (1100 rpm) and timer (30 min) were set accordingly once the reaction temperature reached 200 °C. The reaction was stopped by quenching the reactor into a water bath. The samples were collected, stored in a parafilm-sealed vial, and kept in a refrigerator prior to analysis. The experimental work was repeated for 60, 120, and 180 min.

A set of data, including the weight of the filter paper before drying and the weight of the filter paper with solid residue after drying overnight, was recorded to determine the conversion of cellulose to glucose. The samples were filtered using filter paper before being dried at 60 °C overnight. The weight of the filter paper containing solid residue was recorded, and it was consistently maintained around ± 0.005 g. The final weight of cellulose and the cellulose conversion were calculated using Equations 1 and 2, respectively.

$$\text{Weight}_{\text{final cellulose (solid residue)}}\,(a) = \text{Weight}_{\text{filter paper with solid residue after drying}} - \text{Weight}_{\text{filter paper before drying}} - \text{Weight}_{\text{catalyst}} \quad (1)$$

$$\text{Cellulose conversion}\,(\%) = [(a - \text{Weight}_{\text{initial cellulose}}) / \text{Weight}_{\text{initial cellulose}}] \times 100\% \quad (2)$$

Product analysis

Glucose was quantified using a high-performance liquid chromatography system consisting of Sugar SH1011 column (SHODEX, Japan) with ion exclusion mode (column's physical size: 8.0 mm I.D. × 300 mm) and a refractive index detector as the column and detector, respectively. The mobile phase was an aqueous solution of sulfuric acid (0.05 M) flowing at a rate of 0.5 mL/min with a column temperature of 40 °C.

Results and Discussion

Catalyst characterization: TGA

Thermogravimetric analysis of the catalyst was carried out before and after calcination to validate the decomposition of nitrate precursors in the catalyst. Based on the differential thermal gravimetric analysis (TGA/DTG) pattern in Figure 1, two weight losses were observed between the temperature of 50 and 120 °C and also 200 and 300 °C for the catalyst before calcination. The first weight loss (I) can be linked to the removal of absorbed water [14,15], whereas the second weight loss (II) can be attributed to the decomposition of nitrates and the elimination of organic compounds [16]. Furthermore, at temperatures above 350 °C, no weight loss was observed, implying that no decomposition took place. Therefore, the calcination temperature was set at 500 °C to ensure the decomposition of nitrate precursors. After calcination, the catalyst only exhibited one weight loss, which occurred between 50 and 100 °C (I), according to the TGA/DTG pattern in Figure 1. However, no weight loss was recorded at temperatures higher than 100 °C, demonstrating that nitrate had completely decomposed. Hence, the optimal calcination temperature for ensuring a precursor-free catalyst is 500 °C. This finding agrees with the FTIR analysis, where no nitrate peak was found in the catalyst after calcination.

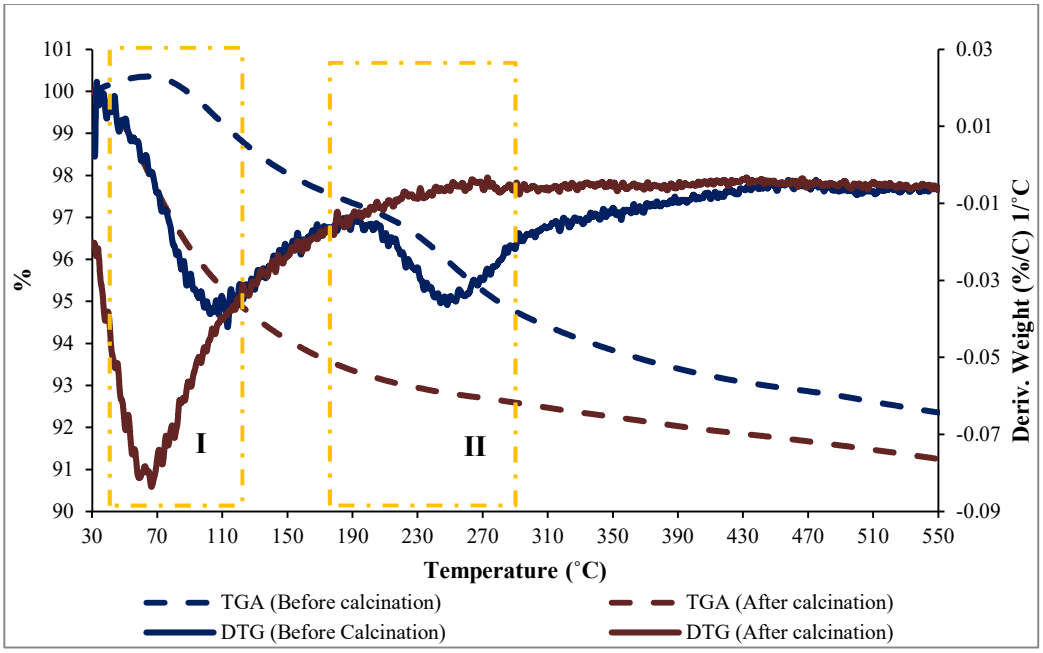


Figure 1. TGA and DTG of Pd/SiO_2-Al_2O_3 (before and after calcination)

Catalyst characterization: FTIR

The decomposition of the nitrate precursor in the synthesized catalyst was verified by FTIR. A comparison of the FTIR spectra of the catalyst before and after calcination is illustrated in Figure 2, and the functional groups present in this study are summarized in Table 1.

Table 1. Summary of the functional groups present in this study

Region	Wavelength (cm^{-1})	Peak Assignment
I	3600–3200	O-H stretching, strong, broad
II	2400–2300	C-O stretching
III	1700–1600	O-H bending
IV	1450–1300	NO_3^- (nitrate)
V	1200–1000	Si-O-Si

Based on Figure 2, the spectral range around 3600–3200 cm^{-1} (I) and 1700–1600 cm^{-1} (III) is attributed to the stretching and bending modes corresponding to water molecules by hydrogen bonding, respectively [17]. The C-O stretching band is due to the atmospheric carbon dioxide, an impurity where contamination occurred, which appeared in the spectral range of 2400-2300 cm^{-1} (II).

The spectral range around 1450–1300 cm^{-1} (IV) indicates the presence of nitrate precursor (NO_3^-) in the catalyst before calcination [18,19]. The NO_3^- bands disappeared from the catalyst after calcination, confirming the successful decomposition of nitrate under the calcination temperature of 500 °C. Hence, the optimum calcination temperature to remove nitrate precursor is 500 °C. In addition, the band assigned to Si-O-Si was observed in the spectral range of 1200–1000 cm^{-1} (V) [20]. This band proves the existence of the SiO_2 network in the catalyst.

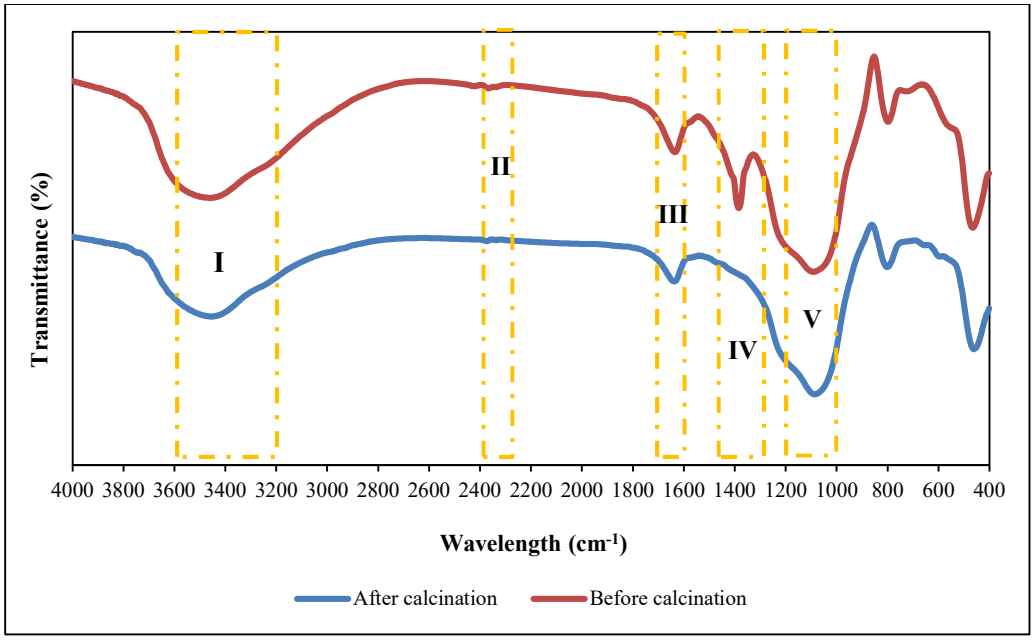


Figure 2. FTIR spectra of Pd/SiO_2-Al_2O_3 (before and after calcination)

Catalyst characterization: Surface area, pore volume, and particle size

Information on the surface area, pore size distribution, and particle size of the catalyst is essential, especially for catalytic reaction work. The BET surface area, pore volume, and particle size of the catalysts are presented in Table 2.

Table 2. BET surface area, pore volume, and particle size of the catalyst

Sample	Surface Area[a] (m^2/g)	Pore Volume[b] (cm^3/g)	Particle Size[c] (µm)
Pd/SiO_2-Al_2O_3 (before calcination)	501.9	0.2552	93.7
Pd/SiO_2-Al_2O_3 (after calcination)	485.6	0.2459	98.0

[a]: Surface area was obtained from the BET method
[b]: Pore volume was obtained from the BET method
[c]: Particle size was determined using a Malvern Mastersizer 3000 particle size analyzer

Based on Table 2, the surface area and pore volume of the catalyst decreased after the catalyst was calcined. The surface area and pore volume decreased after calcination by up to 16.2 m^2/g and 0.0093 cm^3/g, respectively. The decrease in surface area and pore volume is possibly due to the aggregation of the catalyst [21]. Even though calcination reduces the BET surface area and pore volume, it has the potential to secure the existence of a stable structure of the catalyst [22]. In addition, the catalyst has a higher surface area and pore volume than Wang et al. (329 m^2/g) [23], which are 485.6 m^2/g and 0.2459 cm^3/g, respectively.

The influence of surface area can be explained by the concept of collision theory, where the bigger the surface area, the greater the chances of the particle being exposed to each other [24]. Meanwhile, the information on pore size distribution is crucial for the catalyst's active sites [25]. According to Klinghoffer et al. [26], both properties greatly influence the catalytic activity and the reaction rate, whether they promote the reaction to be faster or otherwise.

Based on Table 2, the particle size of the catalyst increased as the surface area and the pore volume of the catalyst decreased after calcination. When the particle size of a catalyst is reduced, the surface area increases, and the shape changes, resulting in a larger number of reactive edge sites. This might be due to calcination, which results in increased crystallinity of the catalyst [27,17].

Effect of catalyst loading on the yield of glucose and conversion of cellulose

Figure 3 illustrates the effect of catalyst loading on the yield of glucose and cellulose conversion. Based on Figure 3, the highest conversion of cellulose and yield of glucose was 78.7% and 23.6%, respectively, when 0.06 g of catalyst was employed in the reaction. As catalyst loading increased from 0.04 to 0.06 g, the yield of glucose increased continuously increase. However, a further increase in catalyst loading from 0.08 to 0.10 g resulted in a decrease in the glucose yield and cellulose conversion. This finding was also observed in the study by Yan et al. [28]. This might be due to an unwanted side reaction from higher catalyst loading. Additionally, higher catalyst loading could make the reaction mixture more viscous, resulting in a slower reaction [29]. Therefore, the effect of mixing decreases and the mass transfer resistance in the mixture increases. Consequently, less cellulose is available for the reaction. Thus, no additional catalyst should be added when the amount of the catalyst has met the requirement of the reaction.

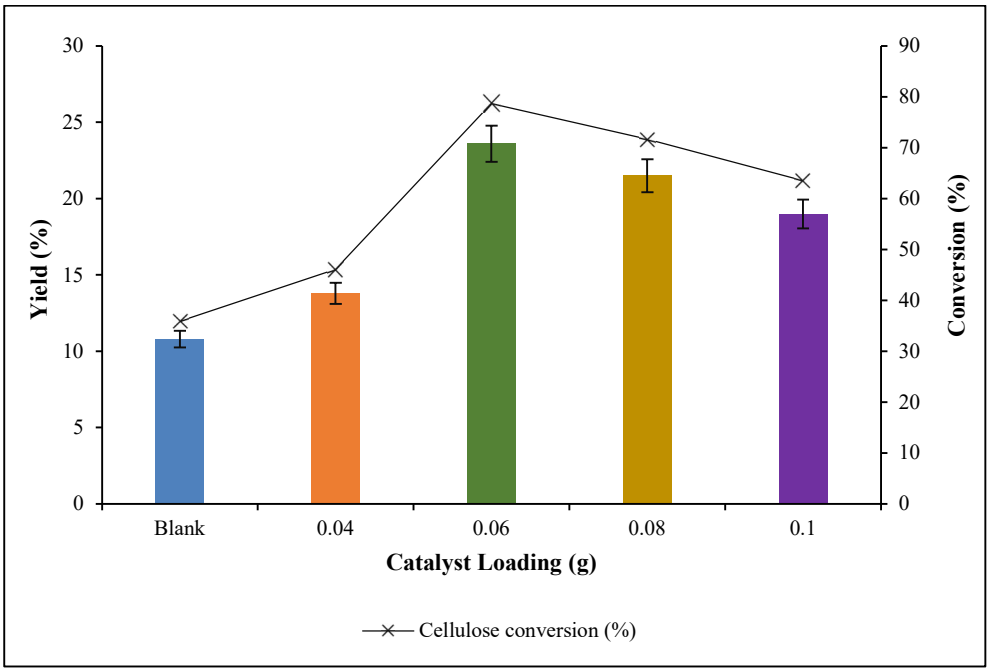


Figure 3. Effect of catalyst loading on the yield of glucose and cellulose conversion at 3 h. Note: a) Pre-reduction of catalyst conditions: 10 mL of distilled water, agitation speed of 1300 rpm, and 1 bar of H_2 for 1 h at 150 °C, b) reaction conditions: 0.3 g of cellulose, reaction temperature of 200 °C, agitation speed of 1100 rpm, and reaction time of 3 h

Besides, a reaction without the catalyst (blank) was conducted as a reference. Without the catalyst, the yield of glucose and conversion of cellulose were at their lowest levels of 10.8%, and 35.9%, respectively, as shown in Figure 3. This proves that in the presence of a catalyst, cellulose can be converted efficiently, and more glucose can be produced. The catalyst creates a distinct reaction pathway, reducing the activation energies of individual reaction stages and accelerating the process of reaching equilibrium by lowering the activation

energies of various reaction steps [30].

Conclusion

Several findings can be summarized from this study which are the TGA pattern demonstrates that the nitrate precursor in the catalyst can be decomposed at temperatures above 350 °C, the FTIR's diminishing peak at 1450–1300 cm^{-1} for the catalyst after calcination indicates that the nitrate precursor has been successfully removed at a calcination temperature of 500 °C, and the catalyst with higher surface area (485.6 m^2/g) and larger pore volume (0.2459 cm^3/g) contributed to the high yield of glucose and conversion of cellulose up to 23.6% and 78.7%, respectively. This proves that a supported noble metal catalyst with high surface area and large pore volume can provide a faster route in producing glucose from cellulose with high crystallinity.

Acknowledgment

The authors would like to express their highest gratitude for the financial support from the Ministry of Higher Education (MOHE) (under the Fundamental Research Grant Scheme, FRGS/1/2018/TK02/UNIKL/02/3), Universiti Kuala Lumpur Malaysian Institute of Chemical and Bioengineering Technology (UniKL MICET), and Majlis Amanah Rakyat Malaysia (MARA).

References

1. Robertson, G. P., Hamilton, S. K., Barham, B. L., Dale, B. E., Izaurralde, R. C., Jackson, R. D., Landis, D. A., Swinton, S. M., Thelen, K. D., and Tiedje, J. M. (2017). Cellulosic biofuel contributions to a sustainable energy future: Choices and outcomes. *Science*, 356(6345): 1-9.
2. Li, L., Zhou, W., Wu, H., Yu, Y., Liu, F., and Zhu, D. (2014). Relationship between crystallinity index and enzymatic hydrolysis performance of celluloses separated from aquatic and terrestrial plant materials. *BioResources*, 9(3): 3993-4005.
3. Kamal, P.N., Mohamad, N., Serit, M.E., Rahim, N., Jimat, N.I., and Alikasturi, A.S. (2020). Study on the effect of reaction and calcination temperature towards glucose hydrolysis using solid acid catalyst. *Materials Today: Proceedings*, 31: 282-286.
4. Pasquale, G., Vázquez, P., Romanelli, G., and Baronetti, G. (2012). Catalytic upgrading of levulinic acid to ethyl levulinate using reusable silica-included Wells-Dawson heteropolyacid as catalyst. *Catalysis Communications*, 18: 115-120.
5. Ganji, P., and Roy, S. (2020). Conversion of levulinic acid to ethyl levulinate using tin modified silicotungstic acid supported on Ta_2O_5. *Catalysis Communications*, 134: 105864.
6. Mahdaly, M. A., Zhu, J. S., Nguyen, V., and Shon, Y.-S. (2019). Colloidal palladium nanoparticles for selective hydrogenation of styrene derivatives with reactive functional groups. *ASC Omega*, 4: 20819-20828.
7. Parks, M. (2014). γ-alumina makes catalysis more accessible. Access from https://www.cpms.byu.edu/project/γ-alumina-makes-catalysis-more-accessible/. [Access online 1 September 2022].
8. Zhang, B., Li, X., Wu, Q., Zhang, C., Yu, Y., Lan, M., Wei, X., Ying, Z., Liu, T., Liang, G., and Zhao, F. (2016). Synthesis of Ni/mesoporous ZSM-5 for direct catalytic conversion of cellulose to hexitols: Modulating the pore structure and acidic sites: Via a nanocrystalline cellulose template. *Green Chemistry*, 18(11): 3315-3323.
9. Xu, S., Yan, X., Bu, Q., and Xia, H. (2017). Catalytic conversion of cellulose into polyols using carbon-nanotube-supported monometallic Pd and bimetallic Pd–Fe catalysts. *Cellulose*, 24(6): 2403-2413.
10. Kobayashi, H., Matsuhashi, H., Komanoya, T., Hara, K., and Fukuoka, A. (2011). Transfer hydrogenation of cellulose to sugar alcohols over supported ruthenium catalysts. *Chemical Communications*, 47(8): 2366-2368.
11. Kamal, P. N. S. M. M., Sapawe, N., and Alikasturi, A. S. (2022). Catalytic conversion of cellulose to levulinic acid using supported noble metal palladium catalyst. *Malaysian Journal of Analytical Sciences*, *26*(1): 119-129.

12. Boonyakarn, T., Wataniyakul, P., Boonnoun, P., Quitain, A. T., Kida, T., Sasaki, M., Laosiripojana, N., Jongsomjit, B., and Shotipruk, A. (2019). Enhanced levulinic acid production from cellulose by combined Brønsted hydrothermal carbon and Lewis's acid catalysts. *Industrial and Engineering Chemistry Research*, *58*(8): 2697-2703.
13. Joshi, S. S., Zodge, A. D., Pandare, K. V., and Kulkarni, B. D. (2014). Efficient conversion of cellulose to levulinic acid by hydrothermal treatment using zirconium dioxide as a recyclable solid acid catalyst. *Industrial and Engineering Chemistry Research,* 53(49): 18796-18805.
14. Alayat, A., Echeverria, E., Sotoudehniakarani, F., McIlroy, D. N., and McDonald, A. G. (2019). Alumina Coated Silica Nanosprings (NS) Support Based Cobalt Catalysts for Liquid Hydrocarbon Fuel Production from Syngas. *Materials*, 12(11): 1810.
15. Shaker Ardakani, L., Alimardani, V., Tamaddon, A.M., Amani, A.M., and Taghizadeh, S. (2021). Green synthesis of iron-based nanoparticles using Chlorophytum comosum leaf extract: Methyl orange dye degradation and antimicrobial properties. *Heliyon*, 7: e06159.
16. Ashok, A., Kumar, A., Bhosale, R. R., Saleh, M. A. H., and Van Den Broeke, L. J. P. (2015). Cellulose assisted combustion synthesis of porous Cu-Ni nanopowders. *RSC Advances*, 5(36): 28703-28712.
17. Mohammed, A.-H. A. K., Hussein, H. Q., and Mohammed, M. S. (2017). The effect of temperature on the synthesis of nano-gamma alumina using hydrothermal method. *Iraqi Journal of Chemical and Petroleum Engineering*, 18(1): 1-16.
18. Machingauta, C. (2013). Synthesis, characterization and application of two-dimensional layered metal hydroxides for environmental remediation purposes, Dissertation, Marquette University.
19. He, S., Zhang, L., He, S., Mo, L., Zheng, X., Wang, H., and Luo, Y. (2015). Ni/SiO_2 catalyst prepared with nickel nitrate precursor for combination of CO_2 reforming and partial oxidation of methane: Characterization and deactivation mechanism investigation. *Journal of Nanomaterials*, 2015: 48.
20. Latypova, A. R., Lebedev, M. D., Rumyantsev, E. V., Filippov, D. V., Lefedova, O. V., Bykov, A. V., and Doluda, V. Y. (2020). Amino-modified silica as effective support of the palladium catalyst for 4-nitroaniline hydrogenation. *Catalysts*, 10(4): 22-25.
21. Inmanee, T., Pinthong, P., and Jongsomjit, B. (2017). Effect of calcination temperatures and MO modification on nanocrystalline $(\gamma\text{-}\chi)\text{-}Al_2O_3$ catalysts for catalytic ethanol dehydration. *Journal of Nanomaterials*, 2017: 10.
22. Al-Fatesh, A. S. A., and Fakeeha, A. H. (2012). Effects of calcination and activation temperature on dry reforming catalysts. *Journal of Saudi Chemical Society*, 16(1): 55-61.
23. Wang, Z., Pokhrel, S., Chen, M., Hunger, M., Mädler, L., and Huang, J. (2013). Palladium-doped silica-alumina catalysts obtained from double-flame FSP for chemoselective hydrogenation of the model aromatic ketone acetophenone. *Journal of Catalysis*, 302: 10-19.
24. Sari, W. K., Supriatna, A., and Hendayana, S. (2019). Analysis of students difficulties based on respondents ability test on the topic of factors affecting reaction rate. *Journal of Physics: Conference Series*, 1157(4): 042032.
25. Xie, W., Liang, D., Li, L., Qu, S., and Tao, W. (2019). Surface chemical properties and pore structure of the activated coke and their effects on the denitrification activity of selective catalytic reduction. *International Journal of Coal Science and Technology*, 6(4): 595-602.
26. Klinghoffer, N. B., Castaldi, M. J., and Nzihou, A., (2012). Catalyst properties and catalytic performance of char from biomass gasification. *Industrial and Engineering Chemistry Research*, 51(40): 13113-13122.
27. Suttiponparnit, K., Jiang, J., Sahu, M., Suvachittanont, S., Charinpanitkul, T., and Biswas, P. (2011). Role of Surface Area, Primary Particle Size, and Crystal Phase on titanium Dioxide Nanoparticle Dispersion Properties. *Nanoscale Research Letters*, 6: 1-8.

28. Yan, S., Wang, C., Hu, H., Gu, W., Wang, Q., Jiang, L., and Zhang, Q. (2020). Mechanochemical preparation of a H_3PO_4-based solid catalyst for heterogeneous hydrolysis of cellulose. *ACS Omega*, 5(46): 29971-29977.
29. Zarin, M. A. A., Zainol, M. M., and Amin, N. A. S. (2020). Optimizing levulinic acid from cellulose catalyzed by HY-zeolite immobilized ionic liquid (HY-IL) using response surface methodology. *Malaysian Journal of Fundamental and Applied Sciences*, 16(6): 625-629.
30. Weckhuysen, B. M., and Wachs, I. E. (2001). Catalysis by supported metal oxides. In Handbook of Surfaces and Interfaces of Materials, 1: pp. 613–648.

Malaysian Journal of Analytical Sciences (MJAS)
Published by Malaysian Analytical Sciences Society

DETERMINING NEREISTOXIN RESIDUE IN PALM OIL MATRIX – AN EXTENSION TO THE METHOD FOR THIOSULTAP DISODIUM RESIDUE DETERMINATION

(Penentuan Sisabaki Nereistoxin Dalam Matriks Minyak Sawit – Penambahan Kepada Kaedah Penentuan Sisabaki Thiosultap Disodium)

Chee Beng Yeoh*, Farah Khuwailah Ahmad Bustamam, Najwa Sulaiman, Mei Huey Saw, and Nik Sasha Khatrina Khairuddin

Malaysian Palm Oil Board,
6 Persiaran Institusi, Bandar Baru Bangi, 43000 Kajang, Selangor, Malaysia

**Corresponding author: cbyeoh@mpob.gov.my*

Received: 27 July 2022; Accepted: 17 January 2023; Published: 19 April 2023

Abstract

This study aimed to incorporate the nereistoxin, a compound that is the major metabolite of all nereistoxin analogue pesticides, including thiosultap-disodium into the previously reported analytical method developed for thiosultap-disodium residue analysis in the palm oil matrix. All steps that have been developed previously for the determination of thiosultap-disodium involving liquid-liquid extraction and subsequently determination using liquid chromatograph triple quadrupole mass spectrometer (LC-MS/MS) were followed, except the omission of matrix-matched calibration curve preparation and this was substituted with the use of spiked calibration curve technique due to its better performance in overcoming the matrix effect. The performance of the analytical method was evaluated in-house and found to be satisfactory. Recoveries of the nereistoxin residue spiked at 12, 30, and 50 ng g^{-1} were at 85-95% with a relative standard deviation of below 9%. Three months of monitoring of method intermediate precision by two analysts gave a relative standard deviation value of 3.6% to 8.3% for the same spiking levels. The limit of detection (LOD) and limit of quantification (LOQ) were first estimated using the standard deviation of the calibration curve at a 95% confidence level and subsequently evaluated by actual experimental work. The values found were 5.0 ng g^{-1} and 12.0 ng g^{-1}.

Keywords: nereistoxin, palm oil, method development, dimehypo, spiked calibration

Abstrak

Kajian ini bertujuan untuk menambahkan sebatian nereistoxin, iaitu sebatian metabolit utama bagi kesemua racun perosak dari kelas analog nereistoxin termasuk thiosultap-disodium ke dalam kaedah analisa sisabaki thiosultap-disodium dalam matriks minyak sawit yang dibangunkan sebelum ini. Kesemua langkah pengolahan sampel yang telah dibangunkan sebelum ini bagi penentuan thiosultap-disodium melibatkan pengekstrakan fasa cecair-cecair lalu penentuan menggunakan kromatografi cecair spektrometri jisim caturkutub ganda tiga masih diikut, kecuali langkah persediaan keluk kalibrasi padanan-matriks telah digantikan dengan penggunaan teknik keluk kalibrasi pemakuan memandangkan prestasinya yang lebih bagus dalam mengatasi kesan dari matriks. Prestasi kaedah analitikal ini telah dinilai secara dalaman di makmal sendiri dan didapati ianya memuaskan. Nilai

perolehan semula sisabaki nereistoxin yang telah dipakukan pada 12, 30 and 50 ng g^{-1}, masing-masing adalah dalam lingkungan 85-95 % dengan nilai piawai relatif di bawah 9%. Pemantauan selama tiga bulan bagi menentukan kepersisan perantaraan kaedah oleh dua orang penganalisa berbeza memberikan nilai piawai relatif 3.6% ke 8.3% untuk kepekatan pemakuan yang sama. Had pengesanan dan had kuantitatif telah dianggarkan pada permulaan menggunakan sisihan piawai yang diperolehi daripada keluk kalibrasi pada tahap keyakinan 95% lalu pengesahan dilakukan melalui kajian secara eksperimen. Nilai yang diperolehi adalah 5.0 ng g^{-1} dan 12.0 ng g^{-1}, masing-masing.

Kata kunci: nereistoxin, minyak sawit, pembangunan kaedah, dimehypo, kalibrasi pemakuan

Introduction

Thiosultap-disodium or in its trade name dimehypo is an insecticide known for its usage in oil palm plantations for controlling foliage pests [1-3]. Hence, a study was carried out to develop a method for determining the residue of this insecticide in crude palm oil (CPO) as a proactive step in monitoring the possible pesticide residues that may be present in the local CPO [4]. The method reported was simple and effective involving an aqueous-oil liquid-liquid extraction step and omitting the need for sample clean-up, thus it is cost-effective and time-saving.

Thiosultap-disodium is a compound classified under the group of nereistoxin analogue insecticides. Compounds under this category shared the common chemical structure of their parent compound of nereistoxin (Figure 1). Upon ingestion by insects, nereistoxin analogue insecticides tend to be metabolised into nereistoxin or its uncyclized dithiol and subsequently act as the nicotinic acetylcholine receptor or ion channel complex in the central nervous system thus killing the insects [5,6]. A few other nereistoxin analogue insecticides examples are thiocyclam and Cartap (Figure 1).

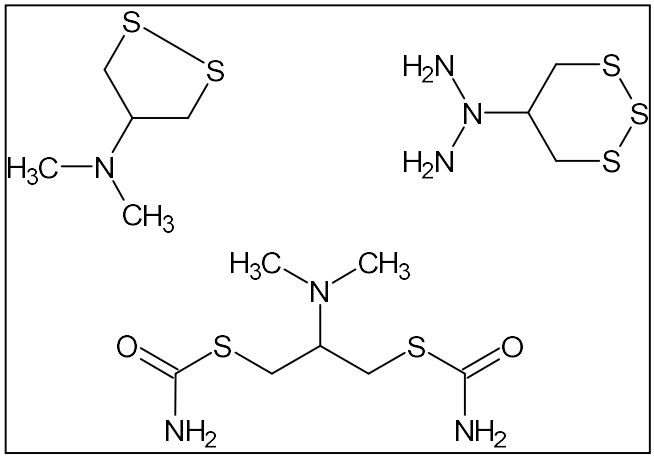


Figure 1. Chemical structure of nereistoxin (top left), thiocyclam (top right), and cartap (bottom)

Hence, it is obvious that the residue analysis method developed by Yeoh et.al. [4] in palm oil matrix for thiosultap-disodium alone is insufficient without the inclusion of determining the possible nereistoxin residue that might be present since the compound is likely to be formed as the primary metabolite in the action of the insecticide [7]. Therefore, this paper aims to re-examine the established workflow to incorporate nereistoxin as another compound of interest in order for the residue of both compounds can be determined in a single run. This article reports the performance of the analytical method to determine nereistoxin residue in palm oil matrix from the aspects of selectivity, linearity, recovery, and precision.

Materials and Methods

The performance of the previously developed analytical method for the thiosultap-disodium residue in handling the nereistoxin residue was evaluated through the analysis of control CPO samples spiked with the

nereistoxin standard. No major alteration was made to the previous method except for the inclusion of deuterated nereistoxin as an internal standard (IS).

Reagents and chemicals

All solvents used were at least of analytical reagent grade. Nereistoxin oxalate (96.1% purity) and nereistoxin oxalate D6 (99.5% purity) standard materials were obtained from Dr. Ehrenstorfer GmbH (Augsburg, Germany). Ultrapure water from Merck Millipore Direct Q® 8-UV-R water purification system (Darmstadt, Germany) was used throughout the experiments.

Blank crude palm oil (CPO) sample

CPO was obtained from a palm oil mill that processed fresh fruit bunches nearby Carey Island, Selangor, Malaysia with known records of pesticide applications. CPO obtained is considered blank upon confirmation with respective plantations in which no nereistoxin analogue insecticides have been used for at least the past 3 months before the harvesting. The CPO was filtered through anhydrous sodium sulphate (10% of blank oil weight) to ensure the sample used in method validation studies is dry and free from insoluble materials [8].

Standard solutions

Standard stock solutions of either native or isotopically labelled nereistoxin at the concentration of 100 µg mL^{-1} were prepared by dissolving 10.41 mg of nereistoxin and 10.05 mg of deuterated nereistoxin in 100 mL of methanol and stored in dark at -18°C. Working standard solutions of both compounds at 10 µg mL^{-1} were prepared by 10-fold dilution of the stock solution in methanol and stored in dark at -18°C. Prior to their use, all stocks or working standard solutions were kept for at least 1.5 h at ambient temperature.

Spiked calibration curve, linearity evaluation limit of detection (LOD) and quantification (LOQ)

Spiked calibration curves of 7 levels at 10, 20, 30, 50, 70, 90, and 100 ng g^{-1} were prepared by the addition of 5, 10, 15, 25, 35, 45, and 50 µL of nereistoxin working standard, respectively to 5 g portions of blank CPO in each level. An aliquot of 25 µL of the IS working standard was also added to each of the spiked CPO. The spiked samples obtained were then treated following the sample extraction procedures described in the later part of this section.

For linearity evaluation, it begins with the visual evaluation of the calibration curve in combination with the coefficient of determination, r^2 expression to see if a linear regression is an appropriate model for the curve. It was then followed by a residual plot that allows for graphical evaluation to observe the presence of any pattern as well as heteroscedasticity in the linear regression model.

LOD and LOQ methods were estimated from the calibration plotted curve followed by a recovery experiment that was performed at a spiking level close to LOQ for confirmation.

Recovery test samples preparation

300 g accurately weighed blank CPO was stirred in a dry and clean 500 mL beaker (tall form) with a controlled temperature at 60°C followed by the addition of 36 µl of nereistoxin stock solution (100 µg mL^{-1}). The mixture was then stirred continuously for another 40 min before the sub-sampling of spiked control samples. While stirring, 5 g of each of the control samples spiked with a nereistoxin standard at 12 ng g^{-1} of CPO were weighted. A total of 50 spiked control samples were obtained and stored in a freezer at -18°C in the dark. Samples were used in recovery and precision studies. The same procedures were repeated for the preparation of control samples spiked with nereistoxin at 30 ng g^{-1} and 50 ng g^{-1} of CPO.

Matrix effect evaluation

For matrix effect (% ME) evaluation, nereistoxin calibration curves at 6 concentration levels (10, 20, 30, 50, 70, and 100 ppb) prepared by three different techniques: neat solvent, matrix matched solution, and spiked calibration technique. The % of ME was calculated as follows:

$$\%ME = \left(1 - \frac{Slope\ of\ Calibration\ Curve\ Prepared\ in\ Solvent}{Slope\ of\ Calibration\ Curve\ Prepared\ in\ Matrix}\right) \times 100\% \quad (1)$$

Liquid chromatography triple quadrupole mass spectrometer (LC-MS/MS) analysis

LC-MS/MS analysis from Yeoh *et al.* [4] was performed on an AB Sciex QTRAP® 4500 (Foster City, CA; USA) triple quadrupole mass spectrometer coupled to an Eksigent Ekspert™ Ultra LC 100 system (Eksigent, Redwood City, CA, USA). Ionisation was in a positive mode at 5500 V and 550ºC with an electrospray probe. The Applied Biosystems Analyst 1.6 software was used to control the operation of the instrument and data acquisition or processing. Chromatography separation was achieved on a Phenomenex Kinetex® C18 100 Å 50 mm × 2.1 mm i.d., 2.6 µm particle size column, and coupled to a 2 mm × 2.1 mm i.d. Security Guard C18 column set at 40°C. The injection volume was 10 µl with a flow rate of 200 mL min^{-1}. The mobile phase is composed of methanol as the organic phase and an aqueous solution of ammonium acetate (10 mM, adjusted to pH 5.0). The following gradient elution profile was used; the initial conditions (95% aqueous phase) were maintained for 0.5 min before the organic eluent was increased to 95% in 5 min. After maintaining this high organic mobile phase for 5 min, the condition was brought back to the initial conditions in 0.5 min and kept the composition for 5 min before the next analysis, thus giving a total runtime of 16 min. The determination of nereistoxin residue was performed via multiple reaction monitoring (MRM) experiments with two precursor-daughter ion transitions. The detailed settings of the MRM experiment such as the declustering potential (DP), entrance potential (EP), collision energy (CE), and collision cell exit potentials (CXP) are summarised in Table 1. Examples of blank and nereistoxin standard chromatograms at 10 ng g^{-1} are shown in Figure 2. It can be observed that no significant interference was found within the window period of ± 30 s from the expected retention time for nereistoxin suggesting that selectivity was not a problem in this study.

Table 1. MRM parameters setting in nereistoxin and internal standard detection

Ion Transition	DP (Volt)	EP (Volt)	CE (Volt)	CXP (Volt)	Remark
150→105	20	7	22	5	Quantifying ion
150→61	20	7	31	51	Qualifying ion
156→105	39	9	18	13	Quantifying ion (IS)

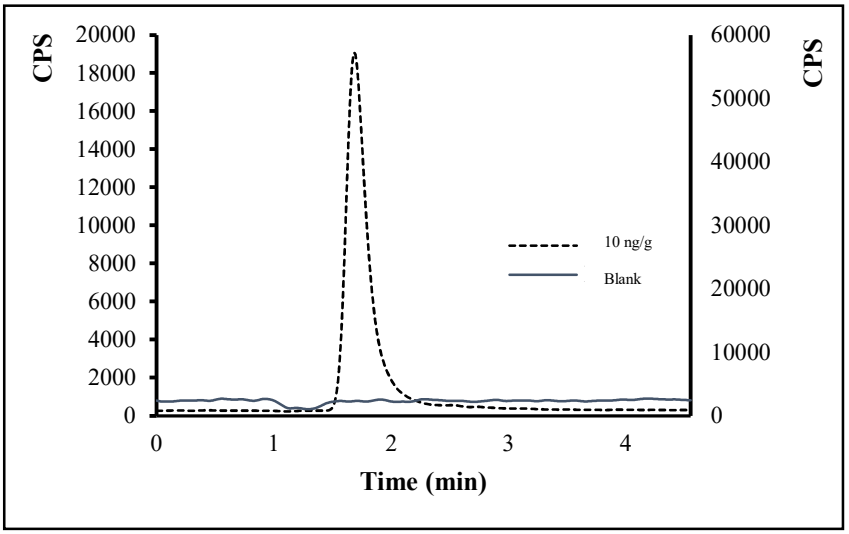


Figure 2. Overlay chromatograms of nereistoxin standard at 10 ng g-1 (dotted line and referring to right vertical axes) and blank extract (solid line and referring to left vertical axes)

Results and Discussion

Matrix effect and linearity

Figure 3 shows the calibration curves prepared using three different techniques: neat solvent, matrix matched solution, and spiked calibration technique. Results revealed that the nereistoxin signal was suffering from ~15% ion suppression due to the matrix effect. Although this was acceptable according to the SANTE guidelines [9], efforts were still made to examine the possibility of utilising other calibration techniques [10,11]. In this study, the spiked calibration technique is selected although preliminary data showed that the matrix-matched calibration technique is viable with sufficiently good linearity and recovery. Furthermore, it can be observed from Figure 3 that the spiked calibration curve is no different (%ME ~7.4%) from the calibration curve prepared in a neat solvent, thus suggesting that the spiked calibration technique is also viable for the quantification of nereistoxin residue in the palm oil matrix. Both % of ME shown by using matrix-matched and spiked calibration techniques were well within the analytical errors (± 20%) as stipulated in the SANTE guidelines [9].

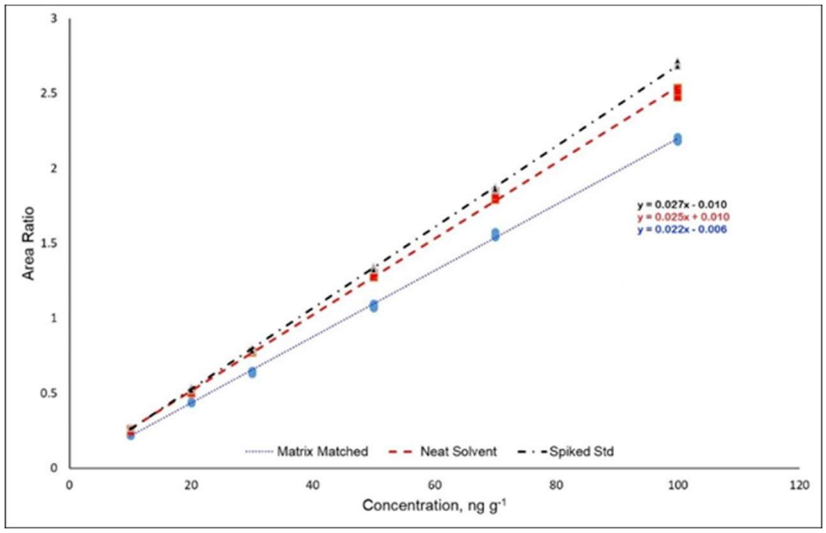


Figure 3. Comparison of calibration curves prepared in neat solvent, blank matrix extract and following spiked standard technique

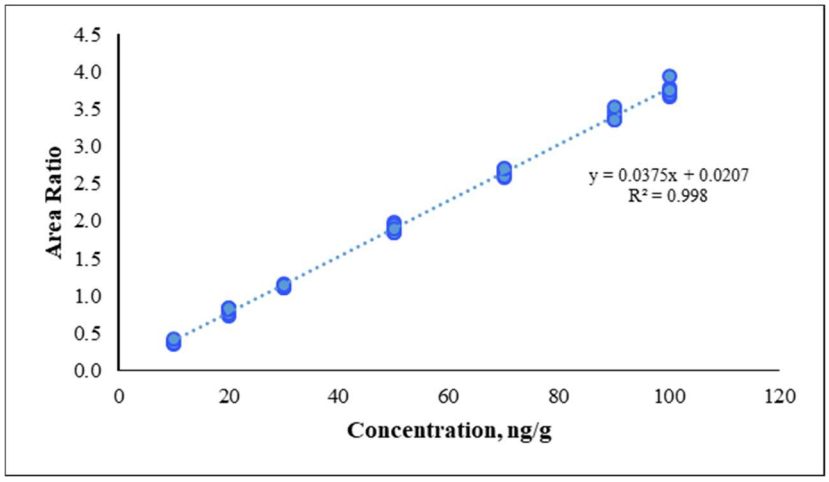


Figure 4. Nereistoxin calibration curve prepared according to the spiked standard technique

Figure 4 shows the representative spiked nereistoxin calibration curve ranging from 10 to 100 ng mL^{-1} (six injections per level) which were used for quantification in this study. It can be observed that nereistoxin responses were linear throughout the calibration range with a coefficient of determination (r^2) of 0.998. Plotting of Y residues against nereistoxin concentrations showed that the distribution of the errors was fairly randomised around the concentration axis except for some degree of increase in the standard deviation of measurements following the increase in the nereistoxin concentrations (Figure 5). This indicates the presence of heteroscedasticity in the linear regression model fitted for the calibration curve [12, 13].

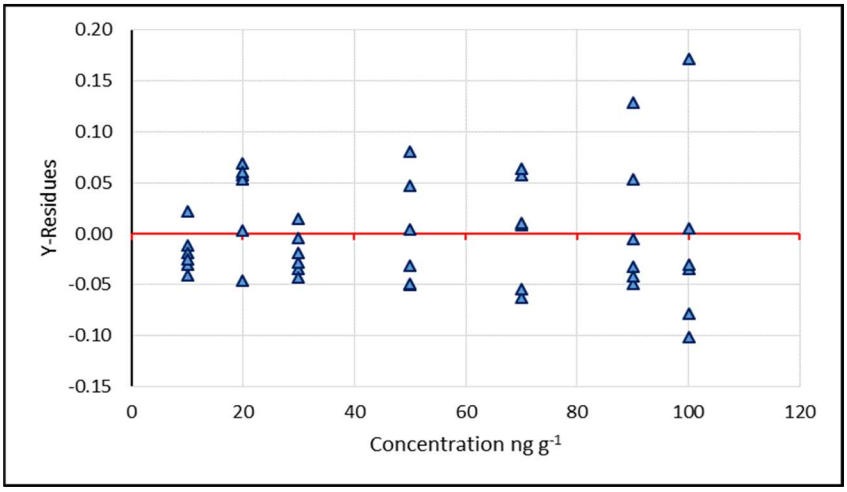


Figure 5. Residual plot for homoscedasticity evaluation

To ascertain the heteroscedasticity in the linear regression model used, the *F*-test was conducted by comparing the variances between the highest (100 ng g^{-1}) and the lowest (10 ng g^{-1}) calibration levels following Equation (2) [12-15].

$$F_{exp} = \frac{S_H^2}{S_L^2} \quad \text{and} \quad F_{tab}(f_1, f_2; 0.99) \qquad (2)$$

where F_{exp} is the experimental F value from the calibration data expressed as a ratio of the variance between the highest concentration level (S_H^2) and the lowest concentration level (S_L^2). The F_{exp} is then compared with the F_{tab} from the F-table at a 99% confidence level for $f_1 = f_2 = (n\text{-}1)$ degrees of freedom. The homoscedasticity test is passed when $F_{tab} > F_{exp}$.

Upon computation, the presence of heteroscedasticity in the calibration curve is confirmed whereby the experimental F-value (F_{exp} = 19.41) was found to be larger than the tabled F-value (F_{tab} = 10.97). Thus, a weighted linear regression model is used in this study for the quantitation of nereistoxin residue. Only a few weighting factors such as 1/X, $1/X^2$, ln X, 1/Y, $1/Y^2$, and ln Y are considered in this study depending on the built-in functions that are available in the data processing software bundled to the LC/MS/MS. The selection of a suitable weighting factor is based on the sum of absolute relative error (∑%RE) computed from each regression model for every weighting factor. A regression model that gives the lowest ∑%RE will be chosen for calibration curve construction.

Table 2 shows the regression parameters of the calibration curve generated for each weighing factor and the respective ∑%RE for the calibration data. The data show that the regression model with $1/Y^2$ as a weighting factor was chosen in this study.

Table 2. Regression parameters of the calibration curve generated for each weighing factor and the respective ∑%Re for the calibration data

Model	Weighting Factor	Slope	y-Intercept	Correlation Coefficient, r	∑%RE
1	None	0.03752	0.02073	0.99898	135.66
2	1/X	0.03763	0.01459	0.99906	131.36
3	$1/X^2$	0.03791	0.00657	0.99814	129.15
4	ln X	0.03749	0.02236	0.99880	136.80
5	1/Y	0.03764	0.01277	0.99909	129.83
6	$1/Y^2$	0.03788	0.00381	0.99830	126.85
7	ln Y	0.03763	0.01148	0.99878	128.80

Limit of detection (LOD) and limit of quantification (LOQ)

LOD and LOQ are crucial parts of method validation. In this study, LOD and LOQ were estimated from the standard deviation of the calibration curve and calculated according to Equations (3) and (4) [16-18]. The LOD and LOQ were estimated to be 5.0 ng g^{-1} and 15.0 ng g^{-1}, respectively at a 95% confidence level. The estimated LOQ was further verified through the conduct of recovery tests at 12.0 ng g^{-1}, a value close to the estimated LOQ. The results suggested that the estimated LOQ is appropriate in describing the performance of the developed method and the final LOQ was altered to 12.0 ng g^{-1} resulting from the acceptable recovery results obtained at this level of spiking.

$$LOD = 3.3 * \frac{\sigma}{s} \quad (3)$$

$$LOQ = 10 * \frac{\sigma}{s} \quad (4)$$

Where σ is the standard deviation and S is the slope of the calibration curve.

Recovery and precision

The performance of the developed method was further evaluated from the recovery study. For precision evaluation, two analysts of different analytical skills were accessed for 3 months, and the method repeatability and intermediate precision were recorded. From Table 3, it can be observed that nereistoxin recoveries throughout the assessment period were all within 80-95% with a relative standard deviation (RSD %) of < 10%. For intermediate precision evaluation, the recovery values of every measurement by both analysts across 3 months period were taken into consideration. The calculated RSD % represents the extent of error among those measurements including the factors of different analysts, different time, different reagent batches, and different spiking concentrations, of which were between 3.6% to 8.3%. Judging from the present data, the precision of the method is well accepted and far below the set value of 20% as stipulated in the SANTE guidelines [9].

Conclusions

This study demonstrates how an appropriate linear regression model (with or without weighting factor) in pesticide residue method development can be chosen based on the statistical analysis and, in brief, how the decision was made by using the incorporation of nereistoxin residue into the existing analytical method for thiosultap disodium residue in the palm oil matrix as an example. From the matrix effect evaluation, it was found that the analysis of nereistoxin residue in the palm oil matrix did not suffer much from the matrix effect and both matrix-matched, and spiked calibration curve techniques were viable and effective in quantifying the nereistoxin residue. With the introduction of the spiked calibration technique, the current method is found to be simple and effective as published in the initial method. Analysis of sodium thiosultap and nereistoxin residues in palm oil matrix can now be performed simultaneously.

Table 3. Recovery of nereistoxin residue (at different spiking levels and times of experiment by different analysts)

Spiking Level (ng g^{-1})	12 (Low)		30 (Medium)		50 (High)	
Analyst	**A**	**B**	**A**	**B**	**A**	**B**
Experiment period (Number of replicates)	**Period 1 (n= 7)**					
Average Recovery (%)	87.30	84.08	87.81	95.28	90.53	90.03
RSD (%)	6.83	8.71	8.49	7.53	4.78	4.90
Experiment period (Number of replicates)	**Period 2 (n= 7)**					
Average Recovery (%)	86.83	81.46	92.57	88.48	90.98	88.61
RSD (%)	6.05	6.83	5.35	6.62	4.86	1.92
Experiment period (Number of replicates)	**Period 3 (n= 8)**					
Average Recovery (%)	95.16	95.11	91.29	93.69	91.34	92.91
RSD (%)	3.18	4.4	1.26	2.12	1.56	2.10
	Intermediate Precision (3 Months)					
Average Recovery (%)	88.63		91.56		90.80	
RSD (%)	8.23		6.09		3.68	

Acknowledgement

The authors would like to thank the management of the Malaysian Palm Oil Board for the permission and supports to carry out this study.

References

1. Sunindyo, D., Simanjuntak, D. and Susanto, A. (2012). The effectiveness of Marathon 500SL (active ingredient:dimehypo 500 g/L) against bagworm *Metisa plana* at immature of oil palm in Afdeling III, Block 08 Q, Dolok Sinumbah Estate of PT Nusantara Plantation IV, North Sumatra Indonesia. *Proceeding of the 4th IOPRI-MPOB International Seminar: Existing and Emerging Pests and Diseases of Oil Palm, Advances in Research and Management.* Bandung, Indonesia, 13-14 December 2012. pp. 98-105.
2. Ero, M. (2016). Dimehypo (Thiosultap disodium); An alternative to methamidophos for the control of oil palm foliage pests in Papua New Guinea. Access from https://www.pngopra.org/wp-content/uploads/2018/02/OPRAtive-Word-Sci-Note-5-Dimehypo-versus-Methamidophos.pdf. [Access online 20 October 2021].
3. Wood, B. J. and Norman, K. (2019). A review of developments in integrated pest management (IPM) of bagworm (lepidoptera: psychidae) infestation in oil palms in Malaysia. *Journal of Oil Palm Research*, 31**:** 529-539.
4. Yeoh, C. B., Farah Khuwailah, A. B., Najwa, S., Nik Sasha Khatrina, K., Tay, M. G. and Saw, M. H. (2019). Development of analytical method for determination of thiosultap-disodium residue in palm oil matrix. *Journal of Oil Palm Research*, 31: 634-640.
5. Sakai, M. and Sato, Y. (1972). Metabolic conversion of the nereistoxin related compounds into nereistoxin as a factor of their insecticidal action. *In:* Tahori, A S, ed. The Second International IUPAC Congress of Pesticide Chemistry, 1971 Tel-Aviv, Israel. London, UK.: Gordon and Breach Science Publishers.
6. Copping, L. G. and Hewitt, H. G. (1998) Insecticides. *Chemistry and mode of action of crop protection agents,* pp.46-73.
7 Yang, S. H. and Choi, H. (2022). Simultaneous determination of nereistoxin insecticides in foods of animal origins by combining pH-dependent reversible partitioning with hydrophilic interaction chromatography-mass spectrometry. *Scientific Reports*, 12:10208.

8. MPOB (2005). MPOB test methods: A compendium of test on palm oil products, palm kernel products, fatty acids, food-related products and others. *MPOB test methods: a compendium of test on palm oil products, palm kernel products, fatty acids, food-related products and others.* Kuala Lumpur: Malaysian Palm Oil Board.
9. European Commission (2022). Analytical quality control and method validation procedures for pesticide residues analysis in food and feed. *Document Nº SANTE/11312/2021.*
10. Cortese, M., Gigliobianco, M. R., Magnoni, F., Censi, R. and Di Martino, P. (2020). Compensate for or minimize matrix effects? Strategies for overcoming matrix effects in liquid chromatography-mass spectrometry technique: A tutorial review. *Molecules,* 25: 3047-3078.
11. Shoeibi, S., Goudarzi, I., Rastegar, H., Janat, B., Sadeghi, N., Hajimahmoodi, M. and Amirahmadi, M. (2014). Spiked Calibration Curve: A valid method for simultaneous analysis of pesticides in melon using gas chromatography mass spectrometry (GC/MS). *Iranian Journal of Chemistry and Chemical Engineering,* 33: 21-27.
12. Almeida, A. M., Castel-Branco, M. M. and Falcão, A. C. (2002). Linear regression for calibration lines revisited: weighting schemes for bioanalytical methods. *Journal of Chromatography B,* 774**:** 215-222.
13. Astivia, O. L. O. and Zumbo, B. D. (2019). Heteroskedasticity in multiple regression analysis: What it is, how to detect it and how to solve it with applications in R and SPSS. *Practical Assessment, Research, and Evaluation*, 24(1): 1.
14. Sonawane, S. S., Chhajed, S. S., Attar, S. S. and Kshirsagar, S. J. (2019). An approach to select linear regression model in bioanalytical method validation. *Journal of Analytical Science and Technology,* 10: 7.
15. Gomes, H. D. O., Cardoso, R. D. S., Da Costa, J. G. M., Andrade Da Silva, V. P., Nobre, C. D. A., Pereira Teixeira, R. N. and Do Nascimento, R. F. (2021). Statistical evaluation of analytical curves for quantification of pesticides in bananas. *Food Chemistry,* 345: 128768.
16. ICH (2005). Validation of analytical procedures: Text and methodology. International Council for Harmonisation of Technical Requirements for Pharmaceuticals for Human Use. Q2(R1).
17. Shrivastava, A. and Gupta, V. (2011). Methods for the determination of limit of detection and limit of quantitation of the analytical methods. *Chronicles of Young Scientists,* 2: 21-25.
18. Şengül, Ü. (2016). Comparing determination methods of detection and quantification limits for aflatoxin analysis in hazelnut. *Journal Food Drug Analysis,* 24(1): 56-62.

Malaysian Journal of Analytical Sciences (MJAS)
Published by Malaysian Analytical Sciences Society

SYNTHESIS, CRYSTAL STRUCTURE, SPECTROSCOPIC CHARACTERISATION, AND PHOTOPHYSICAL PROPERTIES OF IRIDIUM(III) COMPLEX WITH PYRIDINE-FORMIMIDAMIDE ANCILLARY LIGAND

(Sintesis, Struktur Hablur, Pencirian Spekroskopi, dan Sifat Fotofizikal Kompleks Iridium(III) dengan Ligan Ansilari Piridina-Formimidamida)

Nurul Husna As Saedah Bain[1], Noorshida Mohd Ali[1,*], Yusnita Juahir[1], Suzaliza Mustafar[1], Mohammad Kassim[2], Saifful Kamaluddin Muzakir@Lokman[3], Bohari Mohd Yamin[2], and Jean-Claude Daran[4]

[1]*Chemistry Department,*
Faculty of Science and Mathematics,
Universiti Pendidikan Sultan Idris,
35900, Tanjong Malim, Perak, Malaysia
[2]*School of Chemical Sciences and Food Technology,*
Faculty of Science and Technology,
Universiti Kebangsaan Malaysia, 43600 Bangi, Selangor, Malaysia
[3]*Faculty of Industrial Sciences and Technology,*
Universiti Malaysia Pahang,
26300 Gambang, Pahang, Malaysia
[4]*CNRS, LCC (Laboratoire de Chimie de Coordination),*
Université de Toulouse,
UPS, INPT, 205, Route de Narbonne, F-31077 Toulouse, France

[*]*Corresponding author: noorshida@fsmt.upsi.edu.my*

Received: 11 November 2022; Accepted: 17 January 2023; Published: 19 April 2023

Abstract

A phosphorescent Ir(III) complex was synthesised between 2-(1*H*-1,2,4-triazol-1-yl)pyridine and Ir(III) dimer, $[Ir(2,4\text{-}F_2ppy)_2(\mu\text{-}Cl)]_2$, where ppy denotes 2-phenylpyridine by reflux method. The Ir(III) complex was fully characterised by FTIR, NMR, LC-MS, and UV-Vis absorption spectroscopic methods. The presence of a strong band at 2220 cm^{-1} due to ν(C≡N) was revealed by the IR analysis. Both pyridine and phenyl aromatic rings have C=N stretching band at 1598 cm^{-1} and C=C stretching bands at 1554 and 1400 cm^{-1}, respectively. The ^1H NMR spectrum showed signals in the aromatic range of δ 5.00–9.00 ppm corresponding to phenylpyridine protons. The ^{13}C NMR spectroscopic data were consistent with the Ir(III) complex formula, which revealed 37 carbon signals. The Ir(III) complex displayed the ESI-MS spectrum at m/z = 823. The UV-Vis spectrum displayed a weaker and broader band (374 nm) in the visible region due to the spin-forbidden ^{3}MLCT transitions. The X-ray crystallographic study revealed that the Ir(III) ion was coordinated to the pyridine-formimidamide ancillary ligand and two 2-(2,4-difluorophenyl)pyridine cyclometalating ligands in an octahedral geometry. Steady-state emission spectroscopy determined that

the Ir(III) complex emitted blue-green light in dichloromethane solution at room temperature with the vibronic structure to the peak shape (λ = 462 nm and 487 nm) due to the admixture of ^{3}LC and ^{3}MLCT character excited states.

Keywords: Ir(III) complex, formimidamide, ancillary ligand, phosphorescent, metal-to-ligand charge transfer

Abstrak

Kompleks Ir(III) berpendar fosfor disintesis antara 2-(1*H*-1,2,4-triazola-1-yl)piridina dan dimer Ir(III), [Ir(2,4-F_2ppy)$_2$(μ- Cl)]$_2$ di mana ppy mewakili 2-fenilpiridina melalui kaedah refluks. Kompleks Ir(III) dicirikan sepenuhnya melalui kaedah spektroskopi: FTIR, NMR, LC-MS, dan penyerapan UV-Vis. Kehadiran satu jalur kuat pada 2220 cm^{-1} disebabkan oleh ν(C≡N) telah dikenal pasti daripada analisis IR. Kedua-dua gelang aromatik piridina dan fenil, masing-masing mempunyai jalur regangan C=N pada 1598 cm^{-1} dan jalur regangan C=C pada 1554 dan 1400 cm^{-1}. Spektrum ^{1}H NMR menunjukkan isyarat dalam julat aromatik δ 5.00–9.00 ppm sepadan dengan proton fenilpiridina. Data spektroskopi ^{13}C NMR juga konsisten dengan formula kompleks Ir(III), yang menunjukkan 37 isyarat karbon. Kompleks Ir(III) menunjukkan spektrum ESI-MS pada m/z = 823. Spektrum UV-Vis mempamerkan jalur yang lebih lemah dan lebar (374 nm) di rantau yang boleh dilihat disebabkan oleh peralihan ^{3}MLCT spin-terlarang. Kajian kristalografi sinar-X menunjukkan ion Ir(III) dikoordinasi kepada ligan ansilari piridina-formimidamida dan dua ligan siklometalasi 2-(2,4-diflorofenil)piridina dalam geometri oktahedral. Spektroskopi pancaran keadaan-stabil menunjukkan kompleks Ir(III) memancarkan cahaya biru-hijau dalam larutan diklorometana pada suhu bilik dengan struktur vibronik kepada bentuk puncak (λ = 462 nm dan 487 nm) disebabkan oleh bauran ciri keadaan teruja ^{3}LC dan ^{3}MLCT.

Kata kunci: Kompleks Ir(III), Formimidamida, ligan ansilari, berpendar fosfor, pemindahan cas logam ke ligan

Introduction

Phosphorescent transition metal complexes have attracted increased scientific interest because they are widely used in organic light-emitting diodes (OLEDs) for next-generation lighting sources and flat-panel displays [1,2]. The spin-orbit coupling of phosphorescent transition metal complexes has been used to access the triplet excitons that fluorescent emitters previously could not reach [3,4]. Ir(III) complexes are considered to be the most promising triplet harvester because of their high phosphorescence quantum efficiencies, short phosphorescence lifetimes, and colour-tuning flexibility [5–7]. Blue OLEDs are the most severe research issues compared to red- and green-emitting materials [8,10]. In this regard, the design and synthesis of deep-blue-emitting Ir(III) complexes are challenging. Although high quantum efficiencies (QEs) exceeding 30% have been achieved for green and red OLED devices, high QEs for deep-blue OLED devices have rarely been reported because blue phosphors have faster decomposition due to their highly energetic excited states [7].

It has been found that there are numerous ways to change the emission colour of a variety of heteroleptic Ir(III) complexes with cyclometalated phenylpyridine ligands. One of the most promising techniques to produce the emission to blue is to substitute the cyclometalating ligand with an electron-withdrawing group, such as a fluorine atom that will stabilise the highest occupied molecular orbital (HOMO) orbitals that are localised on the phenyl ring and the metal atom [7,9]. Additionally, the inclusion of novel chelating ligands as ancillary ligands can lower the lowest unoccupied molecular orbital (LUMO) level [9], increasing the HOMO-LUMO energy gap. Therefore, to have stable efficiencies of blue emitters for OLEDs, Ir(III) complex must have a sufficiently large energy difference between HOMO and LUMO [7–10]. In this report, we presented the use of novel pyridine-formimidamide as the ancillary ligand for Ir(III) complex and detailed explanation of the synthesis, spectroscopic, and X-ray crystallographic analysis studies.

Materials and Methods

Materials

Unless otherwise specified, all chemicals were obtained from various sources and used exactly as obtained.

Physical measurements

Elemental analysis for carbon (C), hydrogen (H), and nitrogen (N) was performed using a CHNS-O elemental analyser model Flash EA 1112 Series. ^{1}H NMR and ^{13}C

NMR spectra using deuterated dichloromethane (CD_2Cl_2) as solvent were analysed by a nuclear magnetic resonance (NMR) spectrometer (JNM-ECX-500, JEOL). At room temperature, the IR spectrum from a Thermo Nicolet 6700 spectrometer was acquired in the 4000–500 cm^{-1} range. The mass spectrum was analysed by a liquid chromatography-mass spectrometer (LC-MS) model 6490 Triple Quadrupole, Agilent Technologies. The column used was a Phenomenex Gemini NX (C_{18}, 150 × 2.0 mm, ID 5.0 µm). The sample was prepared by dissolving 10 mg in 10 mL of acetonitrile and injected using the gradient ratio of acetonitrile and formic acid as the eluent. A Cary 60 UV-Vis spectrophotometer (Agilent Technologies) was used to analyse the UV-Vis absorption spectra in methylene chloride solution.

A photoluminescence spectrometer model FLS920 (Edinburgh Instrument) was used to obtain the steady-state emission spectrum and time-resolved fluorescence lifetime from an air-equilibrated dichloromethane solution at 298 K. Fluorescence quantum yield was measured by relative method using *tris*(2-phenylpyridine)iridium(III), $Ir(ppy)_3$ in dichloromethane solution ($\Phi = 0.4$) as the standard [11]. The equation $\Phi_s = \Phi_r(I_s/I_r)(A_r/A_s)(\eta_s^2/\eta_r^2)$ was used to calculate the quantum yield, where, Φ_s is the quantum yield of the sample, Φ_r is the quantum yield of the reference, I_s is the area of the emission fluorescence spectrum of the sample, I_r is the area of the emission fluorescence spectrum of the reference, A_s is the absorbance of the sample, A_r is the absorbance of the reference, η_s is the refractive index of the solvent for the sample, and η_r is the refractive index of the solvent for the reference.

Synthesis

Chloro-bridged iridium(III) dimer (0.0605 g, 0.1 mmol equiv.), 2-[4-(4-methyl-benzyl)-[1,2,4]triazol-1-yl]-pyridine ligand (0.0289 g, 0.25 mmol equiv.), and silver(I) oxide (0.0290 g, 0.21 mmol equiv.) in 15 mL of 1,2-dicholoroethane were refluxed in the dark and under an N_2 atmosphere for 24 h. The solution was collected by filtering through celite after it had cooled to room temperature. Then, the solution was dried over anhydrous sodium sulphate and purified with dichloromethane/methanol (90:10 v/v) solvent. The column yielded a yellowish product.

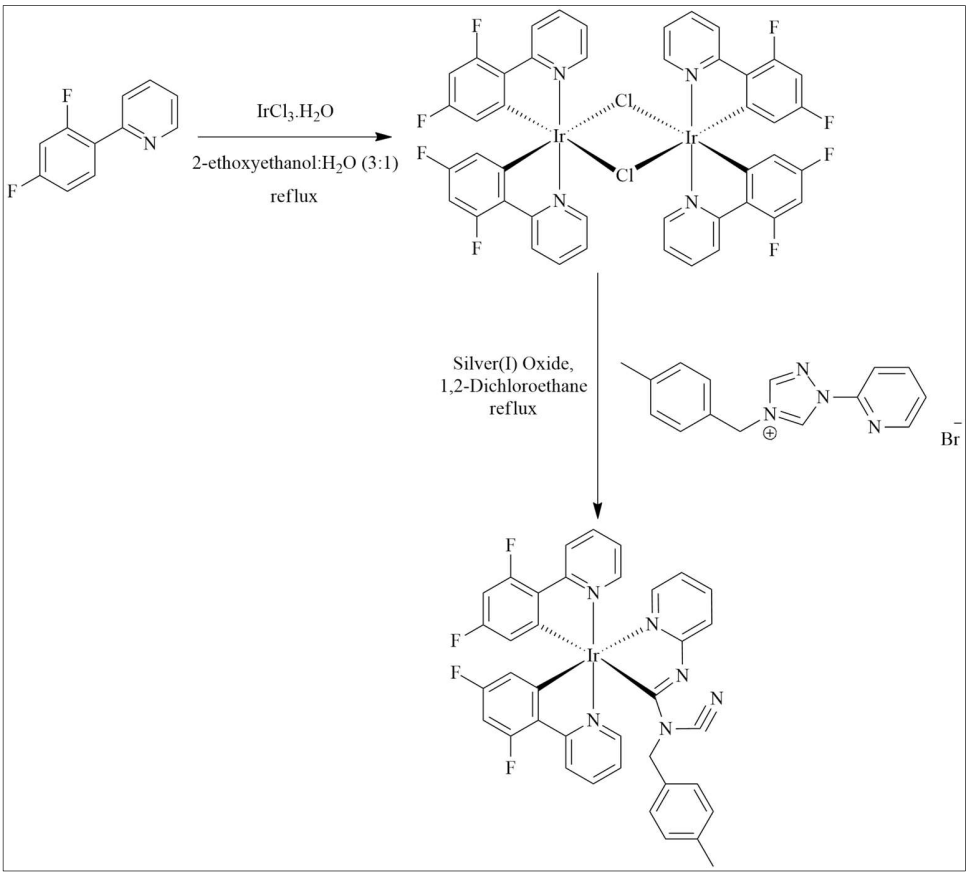
Yield: 69%. ^{1}H NMR (500 MHz, CD_2Cl_2): δ 8.21 (d, J = 8.6 Hz, 2H), 7.73 (t, J = 7.7 Hz, 1H), 7.67 (d, J = 2.3 Hz, 1H), 7.61 (t, J = 7.2 Hz, 1H), 7.49 (t, J = 8.0 Hz, 1H), 7.42 (t, J = 5.7 Hz, 1H), 7.35 (t, J = 4.0 Hz, 1H), 6.94–6.88 (m, 4H), 6.66 (t, J = 6.0 Hz, 1H), 6.46–6.42 (m, 2H), 6.28 (t, J = 11.5 Hz, 1H), 5.67 (d, J = 2.3 Hz, 1H), 5.65 (d, J = 2.3 Hz, 1H), 5.59 (t, J = 6.3 Hz, 1H), 4.88 (d, J = 14.3 Hz, 1H), 2.26 (s, 5H). ^{13}C NMR (126 MHz, CD_2Cl_2): δ 172.0, 165.3, 165.3, 165.0, 164.9, 164.5, 164.4, 162.9, 162.8, 162.5, 162.4, 160.7, 160.6, 154.5, 148.6, 147.7, 139.6, 137.8, 136.6, 133.6, 128.9, 127.7, 127.0, 123.7, 123.6, 123.4, 123.1, 123.0, 122.0, 118.2, 117.9, 112.7, 112.5, 98.4, 96.3, 20.8. FTIR (ATR, ν/cm^{-1}): 3077 (w, ν(C–$H_{aromatic}$)), 2925 (w, ν(C–H_{alkyl})), 2220 (s, ν(C≡$N_{nitrile}$)), 1600–1400 (s, ν(C=$C_{aromatic}$); s, ν(C=N_{py})), 1244 (s, ν(C–N)); 830–720 (s, δ(C–$H_{ortho/para\ out\text{-}of\text{-}plane}$); 1100–984 (s, δ(C–$H_{ortho/para\ in\text{-}plane}$). LC-MS (ESI, m/z): 823 [M+H] (calc. 822). Anal. calcd. for $C_{37}H_{25}N_6F_4Ir$: C, 54.07; H, 3.07; N, 10.23%. Found: C, 53.53; H, 3.46; N, 9.27%.

X-ray crystallographic analysis

Single crystal X-ray crystallographic study was performed using a Bruker D8 QUEST with a PHOTON III charge- integrating pixel array detector area-detector diffractometer (Bruker, AXS Inc., Madison, WI, USA) and graphite-monochromated Mo-Kα radiation (λ = 0.71073 Å). The data collected were reduced using the SAINT [12] programme, and empirical absorption correction was carried out using SADABS [12]. The structure was solved by direct methods and refined via a SHELXTL [13] software package using a full-matrix least-squares approach. The molecular graphics were created using SHELXTL software. All hydrogen atoms were assigned by assuming idealised geometries with d(C–H) = 0.93 and 0.96 Å for aromatic and aliphatic, respectively, with Uiso(H) = 1.2 Ueq(C). All non-hydrogen atoms were refined anisotropically. The PLATON programme was used for molecular structure calculation [14]. The ellipsoids of one Cl of the dichloromethane are relatively elongated, suggesting a disorder; however, any attempt to split the position of the Cl failed. Hence, it is kept as it is (Figure 3).

Results and Discussion

The chloro-bridged iridium(III) dimer, $[Ir(2,4\text{-}F_2ppy)_2(\mu\text{-}Cl)]_2$ (F_2ppy = difluorophenylpyridine), was synthesised by reacting $IrCl_3{\cdot}nH_2O$ with 2-(2,4-difluorophenyl)pyridine in a refluxed 2-ethoxylethanol/water (3:1) under an N_2 atmosphere [15] and was then used in the subsequent reaction without further purification. The previously synthesised ligand, (2-(4-methylbenzyl)-1*H*-1,2,4-triazol-1-yl)pyridine (mbpyta) [16], was refluxed with $[Ir(2,4\text{-}F_2ppy)_2(\mu\text{-}Cl)]_2$ to give $[Ir(2,4\text{-}F_2ppy)_2(mbpyf)]$ (69%). Scheme 1 depicts the schematic process leading to $[Ir(2,4\text{-}F_2ppy)_2(mbpyf)]$, including the silver carbene-complex intermediate. The difficulty and challenge of separating the pure product from the crude mixture during the purification stage prevented the yield of the synthesised Ir(III) complex from reaching 80% and above. The elemental analysis of $[Ir(2,4\text{-}F_2ppy)_2(mbpyf)]$ complex matched the suggested chemical formula. In addition, the electrospray mass spectrometry (ESMS) spectrum of the $[Ir(2,4\text{-}F_2ppy)_2(mbpyf)]$ complex was recorded to determine the molecular species in the solution (Figure S1). The observed pattern of the ESMS spectrum, which displayed a peak at m/z = 823, complemented the calculated one, suggesting that the structure of the species was $[Ir(2,4\text{-}F_2ppy)_2(mbpyf)] + H]$.



Scheme 1. Schematic reaction pathway and chemical structures of chloro-bridged iridium(III) dimer and $[Ir(2,4\text{-}F_2ppy)_2(mbpyf)]$ complex

Figure 1 depicts the IR spectrum of the $[Ir(2,4\text{-}F_2ppy)_2(mbpyf)]$ complex. A strong, significant band that can be observed at 2220 cm^{-1} is due to ν(C≡N), which resembles the predictable pattern for the nitrile group [17]. The C=N stretching band appeared at 1598 cm^{-1} [18] and C=C stretching bands appeared in two absorption bands at 1554 and 1400 cm^{-1} [19], respectively, indicating the presence of aromatic rings of

pyridine and phenyl [18]. Furthermore, a strong band was detected at 1244 cm^{-1}, representing ν(C–N). The typical weak ν(C–H) in aromatic phenyl and pyridine rings was observed at 3077 cm^{-1}, while the stretching bands for (C–H) in alkyl are shown in the spectral region of 2981–2925 cm^{-1}. Additionally, strong bending bands of (C–H) were observed in the range of 830–720 cm^{-1} for ortho/para out-of-plane and in the region of 1100–984 cm^{-1} for ortho/para in-plane substituents on the aromatic ring [17,18].

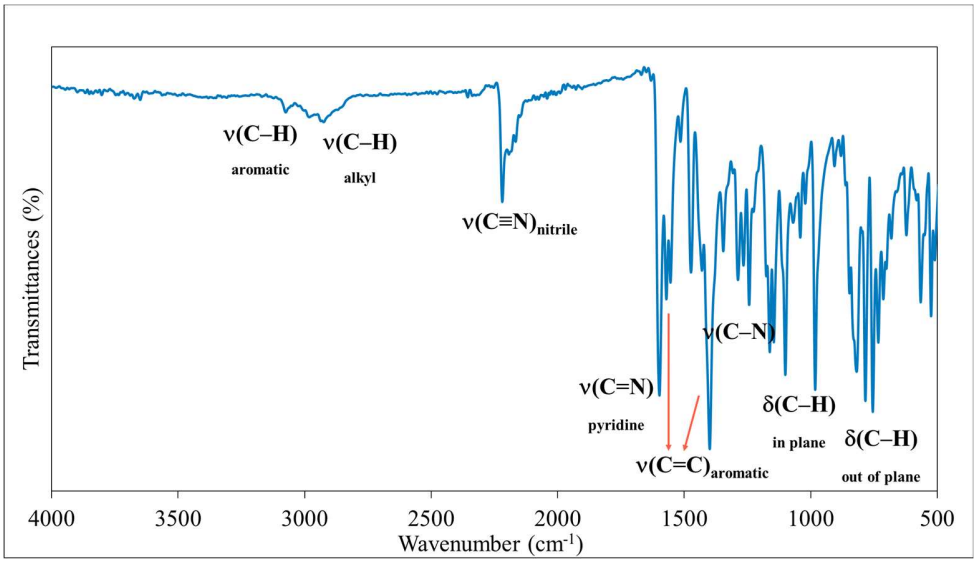


Figure 1. IR spectrum of [Ir(2,4-F_2ppy)$_2$(mbpyf)] complex

The structure of the [Ir(2,4-F_2ppy)$_2$(mbpyf)] complex was further investigated using NMR spectroscopy. The ^{1}H NMR and ^{13}C NMR spectra were recorded in deuterated dichloromethane (CD_2Cl_2) and are presented in Figures 2 and S2, respectively. Based on the HMQC spectrum, the proton resonances of the [Ir(2,4-F_2ppy)$_2$(mbpyf)] complex were assigned and compared to the ^{1}H NMR spectra of its iridium(III) dimer and ligand mbpyta in Figures S3 and S4, respectively. The aromatic signals appeared between 8.30 and 4.90 ppm, correlating to the phenylpyridine protons [6]. In addition, as expected, the signal of two singlet peaks for the mbpyta proton disappeared after deprotonation and coordination of the ancillary ligand. The multiplet signals in the aliphatic region at 2.25 ppm are caused by methylene protons at H13 and H14, together with methyl substitution groups at H19, H20, and H21 [17,18]. Hydrogen and fluorine (spin ½) have extremely strong coupling; thus, the interaction with two fluorine nuclei causes the proton signals of H5 and H5' to divide into a multiplet, while H6 and H6' split into triplets [17,18].

Furthermore, the ^{13}C NMR spectrum assisted in the structural identification of [Ir(2,4-F_2ppy)$_2$(mbpyf)]. Three distinct peaks can be ascribed to –CH_3 (20.8 ppm), –CH_2– (20.9 ppm), and C≡N (128.9 ppm) [17,18], while the other 34 significant carbon signals appeared between 96.3 and 172.0 ppm, corresponding to the number of carbon atoms in aromatic regions, consistent with the low-symmetry structure. According to Barnard and Hogan, aromatic carbon bonded to a nitrogen atom can be seen at approximately over 150 ppm, while aromatic carbon attached to a fluorine atom was found between 90 and 100 ppm [20]. Four –CF peaks appeared at 98.6, 98.4, 96.4, and 96.3 ppm, while six peaks of –C=N aromatic appeared at 162.9, 162.8, 162.5, 162.4, 160.7, and 160.6 ppm. However, a peak at 172.0 ppm ascribed to the –N–C=N bonded to the iridium atom showing a deshielded effect to the lower field of ^{13}C NMR spectrum due to the substantial electron donor effect contributed by the formimidamide ligand [21].

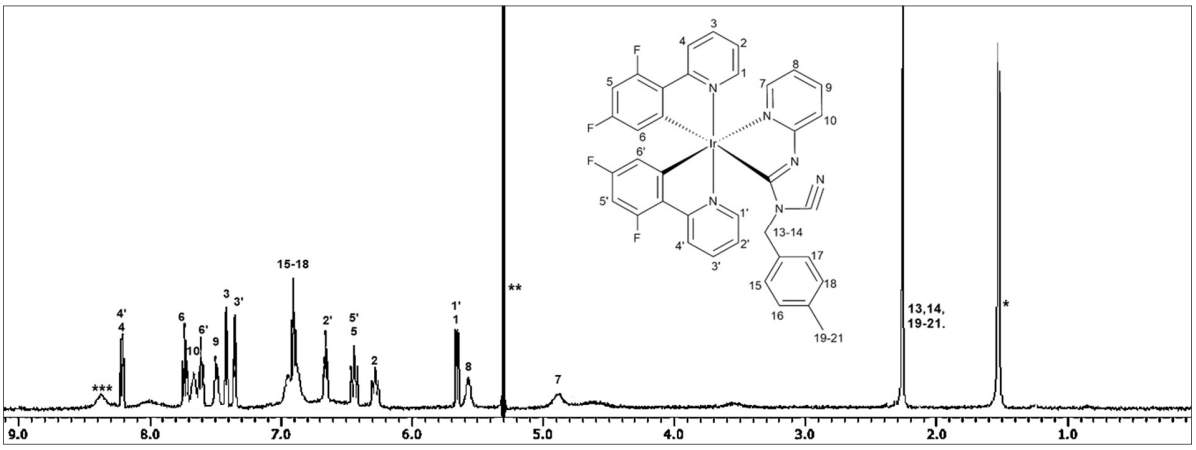


Figure 2. ^{1}H-NMR spectrum for [Ir(2,4-F_2ppy)$_2$(mbpyf)] complex in deuterated CD_2Cl_2 with its labelling scheme, H_2O is marked with *, residual solvent is marked with **, and impurity is marked with ***.

Crystal structure

Slow diffusion of hexane into a dichloromethane solution of [Ir(2,4-F_2ppy)$_2$(mbpyf)] resulted in single crystals of the compound. Despite the challenge of getting high-quality crystals, a single yellow crystal was chosen and put on a glass fibre before data collection. The [Ir(2,4-F_2ppy)$_2$(mbpyf)] complex crystallised in a monoclinic system with space group $P2_1/n$, a = 11.2164(4) Å, b = 15.5922(4) Å, c = 20.8074(7) Å, α = 90.0°, β = 91.098(2)°, γ = 90.0°, Z = 4, and V = 3638.3(2) Å^3. Table 1 presents the crystal system and refinement parameters. The ORTEP diagram of the [Ir(2,4-F_2ppy)$_2$(mbpyf)] complex with the solvated dichloromethane molecule is shown in Figure 3. Atomic coordinates and equivalent isotropic and anisotropic displacement parameters for [Ir(2,4-F_2ppy)$_2$(mbpyf)] are listed in Tables S5 and S6, respectively.

The structure of the [Ir(2,4-F_2ppy)$_2$(mbpyf)] complex is depicted in Figure 3. Two difluorophenylpyridine ligands are coordinated to the central Ir1 atom through their two pyridyl N and two phenylated C atoms, while one (2-(4-methylbenzyl)-pyridine-2-yl)formimidamide ligand is coordinated to the central Ir1 atom through its N and C atoms in a bidentate manner. The geometry of the Ir(III) complex is a distorted octahedron. The C12 and N3 atoms occupy the axial position with C12–Ir1–N3 bond angle of 176.03(12)°. The other trans atoms occupy the equatorial position with N1–Ir1–N2 and C1–Ir1–C26 bond angles of 173.08(13)° and 168.87(14)°, respectively. The steric structure of the ligands plays a significant role in the complex's distorted nature [22]. The *cis* angles about the central Ir atom are between 80.06(17)° and 96.30(13)°. The axial C12–Ir1 and N3–Ir1 are 2.017(4) Å and 2.122(4) Å, respectively. The fact that the axial N3–Ir1 bond length (2.122(4) Å) is a little bit longer than the other *trans*–oriented Ir1–N bonds (Table 2) implies that there is only weak coordination between the ancillary ligand and the central metal [23]. Other relevant bond angles and lengths are shown in Table 2. Both difluorophenylpyridine ligands are coordinated to the central Ir1 atom and give planar planes of Ir1/F1/F2/N1/(C1–C11) and Ir1/F3/F4/N2/(C12–C22) with a maximum deviation of 0.046(4) Å for C1 atom and 0.108(1) Å for Ir1 atom from the least square plane, respectively. The dihedral angle between the two planes is 79.51(7)°. The Ir1/N3/N4/N5/N6/C12/(C23–C29) fragment of the third ligand is also planar with a maximum deviation of 0.106(5) Å for the C12 atom from the least square plane. The plane makes dihedral angles of 88.96(7) ° and 89.85(8)° with the fluoropyridyl Ir1/F1/F2/N1/(C1–C11) and Ir1/F3/F4/N2/(C12–C22) planes, respectively. The cyclometallated carbon atoms C11 and C12, which are *cis* to one another, showed approximately the same distances from Ir1 (2.055(4) Å and 2.017(4) Å), which are similar to many analogous cyclometallated Ir(III) complexes [24]. The C29–N6 bond length of 1.13(9) Å indicates the presence of the nitrile triple bond functionality [6].

Table 1. Crystal data and refinement parameters for [Ir(2,4-F_2ppy)$_2$(mbpyf)] complex

Chemical formula	$IrC_{38}H_{27}Cl_2F_4IrN_6$	
Formula weight / gmol^{-1}	906.75	
Temperature / K	303(2)	
Wavelength / Å	0.71073	
Crystal system	Monoclinic	
Space group	P 2_1/n	
Unit cell dimensions / Å	a = 11.2164(4)	α = 90°
	b = 15.5922(4)	β = 91.098(2)°
	c = 20.8074(7)	γ = 90°
Volume / Å^3	3,638.3(2)	
Z	4	
Density (calculated) / Mgm^{-3}	1.655	
Absorption coefficient / mm^{-1}	3.874	
F(000)	1776	
Crystal size / mm^3	0.800 × 0.230 × 0.200	
θ range / °	2.790–28.452	
Ranges of index	$-14 \leq h \leq 15$, $-20 \leq k \leq 20$, $-27 \leq l \leq 27$	
Reflections collected	190,723	
Independent reflections	9,116 [R(int) = 0.1606]	
Completeness to theta = 25.242°	99.90%	
Method of refinement	Full-matrix least-squares on F^2	
Data / restraints / parameters	9,116 / 0 / 461	
Goodness-of-fit on F^2	1.093	
Final R indices [$I > 2\sigma(I)$]	R_1 = 0.0433, wR_2 = 0.1458	
R indices (all data)	R_1 = 0.0610, wR_2 = 0.1567	
Coefficient of extinction	n/a	
Largest diff. peak and hole / e Å^{-3}	5.519 and –1.004	

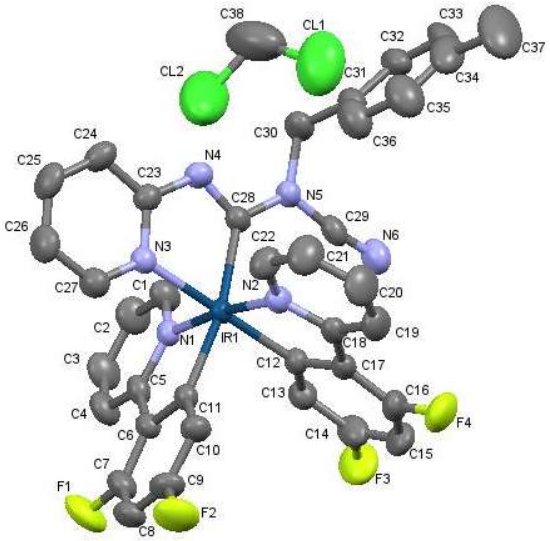


Figure 3. ORTEP diagram of the [Ir(2,4-F_2ppy)$_2$(mbpyf)] complex solvated with dichloromethane, with the numbering scheme drawn at 50% probability ellipsoid

Table 2. Selected bond lengths (Å) and angles (°) for [Ir(2,4-F_2ppy)$_2$(mbpyf)] complex

Ir1–C12	2.017 (4)	C12–Ir1–N1	93.92 (17)
Ir1–C11	2.055 (4)	C12–Ir1–N2	80.06 (17)
Ir1–N2	2.043 (4)	C12–Ir1–C11	84.83 (8)
Ir1–N1	2.043 (4)	C12–Ir1–C28	106.29 (18)
Ir1–N3	2.122 (4)	N1–Ir1–C11	79.98 (16)
Ir1–C28	2.074 (4)	N2–Ir1–C11	96.03 (16)
C28–N4	1.325(6)	N1–Ir1–C28	95.92 (16)
C28–N5	1.411(6)	N2–Ir1–C28	88.99 (16)
C29–N6	1.134(7)	N1–Ir1–N3	89.61 (14)
C28–Ir1–N3	75.25 (16)	N2–Ir1–N3	96.30 (15)
C11–Ir1–N3	94.37 (16)		

Photophysical study

Figure 4 illustrates the UV-Vis absorption spectrum of [Ir(2,4-F_2ppy)$_2$(mbpyf)] complex in a dichloromethane solution at room temperature. Most cyclometallating Ir(III) complexes have a two-part spectra absorbance pattern, with the weak intensity absorbance at the longer wavelength being associated with metal-to-ligand charge-transfer (MLCT) transitions [dπ(M)-π*(L)] near the visible region, while the shorter wavelength is attributed to spin-allowed singlet ligand-centred, ^{1}LC (π-π*) transitions of the ligands within the range of ultraviolet spectra [23–26]. The presence of phenylpyridine ligands was revealed by the intense absorption peak at 262 nm (ε = 30769.23 $M^{-1}cm^{-1}$), which is comparable to other cyclometallated Ir(III) complexes [5–9]. This peak is in the same region of the absorption spectrum as the free mbpyta ligand [16]. In addition, instead of the Gaussian form, the commonly weak, broad, and unstructured peaks due to the strong intersystem crossing by the triplet (T_1) and singlet (S_1) excited states that are driven through the central metal of an iridium atom appeared (315 nm, ε = 11031.90 $M^{-1}cm^{-1}$; 342 nm, ε = 8847.05 $M^{-1}cm^{-1}$; 374 nm, ε = 6102.56 $M^{-1}cm^{-1}$). These absorbances are related to ^{1}MLCT (ε > 10700 $M^{-1}cm^{-1}$), and ^{3}MLCT (ε ≈ 1,000–

6,000 $M^{-1}cm^{-1}$) transitions near the visible region [25–29]. Furthermore, a weak broad absorption peak at 446 nm (ε = 637.57 $M^{-1}cm^{-1}$) as a result of vibronic coupling is ascribed to the d-d transition of octahedral complexes that are forbidden due to symmetry according to the Laporte rules. However, this d-d transition band absorption is less intense than the charge transfer transition. Except for the LC transition, all these peaks are absent from the free mbpyta ligand absorption spectrum [16].

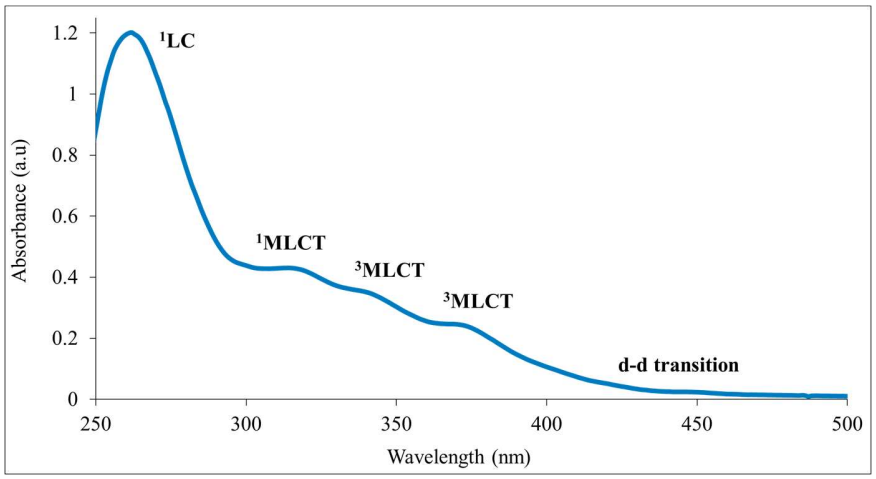


Figure 4. UV-Vis absorption spectrum of [Ir(2,4-F_2ppy)$_2$(mbpyf)] complex in a dichloromethane solution (39 μM) at 298 K labelled with the transition according to their molar absorption coefficient (ε) [30]

In Ir(III) complexes, the HOMO region is primarily metal-based and partially based on the phenyl moieties of the two phenylpyridine ligands. The photoluminescence is triggered by the excitation of an electron from the HOMO to a ligand-based π*antibonding orbital [31]. Upon excitation at λ_{ex} = 374 nm, in an air-equilibrated dichloromethane solution, the [Ir(2,4-F_2ppy)$_2$(mbpyf)] complex emits blue-green light and has a vibronic structure that reaches its peak at 298 K (Figure 5). The most visible peak is at 487 nm, while the peak at 462 nm appears as a less intense shoulder, similar to earlier Ir(III) complexes [8]. Therefore, this emission is ascribed to a transition that contains admixtures of excited states with ^{3}LC and ^{3}MLCT characters [8]. The complex's HOMO energy decreased due to the effect of the electron-withdrawing group, fluorine atoms at the 2 and 4 positions of the phenyl ring, which is *meta* with respect to the orthometallated carbon atom [30]. Furthermore, the pyridine-formimidamide auxiliary ligand is expected to increase LUMO energy, hence increasing the band gap. Thus, the emission energy of this Ir(III) complex increased and emitted blue-green light under UV light. At room temperature, the [Ir(2,4-F_2ppy)$_2$(mbpyf)] complex's emission decay time was calculated to be 29.51 ns, which is a shorter decay time compared to other cyclometallated iridium(III) complexes like FIrpic [28]. The influence of the 5d-electron densities of the iridium centre on the HOMO results in a short triplet lifetime [31]. In dichloromethane solution, the phosphorescence quantum yield (ΦP) is 0.37 compared to *fac*-Ir(ppy)$_3$ (ΦP = 0.40), and the radiative and non-radiative rate constants are 12.5 × 10^5 s^{-1} and 21.4 × 10^5 s^{-1}, respectively.

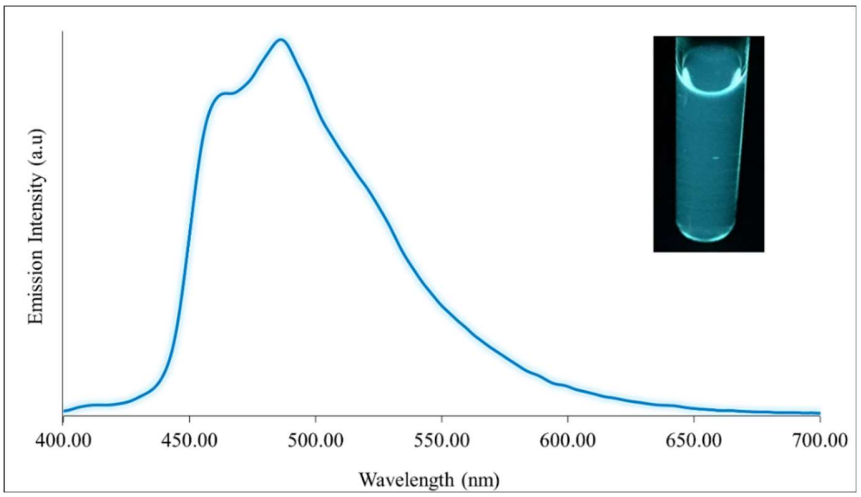


Figure 5. The emission spectrum of [Ir(2,4-F_2ppy)$_2$(mbpyf)] complex in air-equilibrated dichloromethane solution (39 μM) at 298 K. Inset: Luminescence photo of Ir(III) complex in CH_2Cl_2 under UV light

Conclusion

Ir(III) complex bearing pyridine-formimidamide ancillary ligand was successfully synthesised in good yield, characterised by spectroscopic methods, exhibited almost blue emission (λ_{em} = 464 nm) at room temperature, with phosphorescence quantum yield (Φ_p) of 0.37. The crystal structure of the Ir(III) complex was identified, and in the solid state, the Ir(III) complex approved a distorted octahedral coordination environment. This study demonstrated that substituting a pyridine-formimidamide-based ligand as an ancillary ligand could alter the electronic properties of the Ir(III) complex, paving the way for a new method for creating an innovative blue emitter of the phosphorescent complex. Therefore, time-dependent density-functional theory calculations will be conducted to investigate the relationship between triplet states and emission spectra of the synthesised Ir(III) complex.

Acknowledgement

This research was conducted under the Fundamental Research Grant Scheme (FRGS/1/2019/STG01/UPSI/02/1) awarded by the Ministry of Education Malaysia. The authors would like to extend their thankfulness to Universiti Pendidikan Sultan Idris (UPSI) for the scientific support facilities, i-CRIM Universiti Kebangsaan Malaysia (UKM) for the X-ray crystallography, luminescence, and lifetime facilities, and INFRA Laboratory Universiti Malaya (UM) for the mass spectrometer facility.

References

1. Ho, C-L., Li, H. and Wong, W-Y. (2015). Red to near-infrared organometallic phosphorescent dyes for OLED applications. *Journal of Organometallic Chemistry*, 751: 261-285.
2. Costa, R. D., Orti, E., Bolink, H. J., Monti, F., Accorsi, G., and Armaroli, N. (2012). Luminescent ionic transition-metal complexes for light-emitting electrochemical cells. *Angew. Chemie - International Edition*, 51(33): 8178-8211.
3. Barbante, G. J., Doeven, E. H., Francis, P. S., Stringer, B. D., Hogan, C. F., Kheradmand, P. R., Wilson, D. J. D., and Barnard, P. J. (2015). Iridium(III) N-heterocyclic carbene complexes: An experimental and theoretical study of structural, spectroscopic, electrochemical and electrogenerated chemiluminescence properties. *Dalton Transaction*, 44(18): 8564-8576.
4. Yang, C-H., Mauro, M., Polo, F., Watanabe, S., Muenster, I., Fröhlich, R. and De Cola, L. (2012). Deep-blue-emitting heteroleptic iridium(III) complexes suited for highly efficient phosphorescent OLEDs. *Chemistry of Materials*, 24(19): 3684-3695.

5. Yanling, S., Shuai, Z., Godefroid, G., Jinghai, Y., and Zhijian, W. (2015). Modification of the emission colour and quantum efficiency for oxazoline and thiazoline containing iridium complexes via different NiO. *The Royal Society Chemistry*, 5(24): 18464-18470.
6. Ali, N. M., Ward, M. D., Hashim, N., and Daud, N. (2017). Synthesis and photophysical properties of bis(phenylpyridine) iridium(iii) dicyanide complexes. *Materials Research Innovation*, 23(3): 135-140.
7. Lee, S., and Han, W. S. (2020). Cyclometalated Ir(III) complexes towards blue-emissive dopant for organic light-emitting diodes: Fundamentals of photophysics and designing strategies. *Inorganic Chemistry Frontier*, 7(12): 2396-2422.
8. Adeloye, A. O., Mphahlele, M. J., Adekunle, A. S., Rhyman, L., and Ramasami, P. (2017). Spectroscopic, electrochemical and DFT studies of phosphorescent homoleptic cyclometalated iridium(III) complexes based on substituted 4-fluorophenylvinyland 4-methoxyphenylvinylquinolines. *Materials*, 10(10): 1061–1082.
9. Henwood, A. F., Pal, A. K., Cordes, D. B., Slawin, A. M. Z., Rees, T. W., Momblona, C., Babaei, A., Pertegás, A., Ortí, E., Bolink, H. J., Baranoff, E. and Zysman-Colman, E. (2017). Blue-emitting cationic iridium(III) complexes featuring pyridylpyrimidine ligands and their use in sky-blue electroluminescent devices. *Journal of Materials Chemistry C*, 5(37): 9638-9650.
10. Omae, I. (2016) Application of the five-membered ring blue light-emitting iridium products of cyclometalation reactions as OLEDs. *Coordination Chemistry Reviews,* 310: 154-169.
11. Tan, G., Wang, L., Wang, S., Liu, P., Fan, H., Ho, C-L., Ma, D. and Wong, W-Y. (2019). Synthesis, photoluminescence and electroluminescence of triphenylphosphine functionalized cyclometalated iridium(III) complexes. *Dyes and Pigments*, 160: 717-725.
12. Sheldrick, G. M. SAINT V4, Software reference m anual Siemens analytical X-ray systems. Madison, WI, USA; 1996
13. Sheldrick, G. M., SADABS, Program for empirical absorption correction of area detector data. German y: University of Göttingen, Göttingen, German, 19 96
14. Sheldrick, G. M. SHELXTL V5.1, Software refere nce manual, Bruker AXS, Madison, WI, USA, 199 7
15. Sajoto, T., Djurovich, P. I., Tamayo, A., Yousufud din, M., Bau, R., Thompson, M. E., Holmes, R. J . and Forrest, S. R. (2005). Blue and near-UV pho sphorescence from iridium complexes with cyclom etalated pyrazolyl or N-heterocyclic carbene liga nds. *Inorganic Chemistry*, 44(22): 7992-8003.
16. Bain, N. H. A. S., Ali, N. M., Juahir, Y., Hashim, N ., Isa, M. I., Mohamed, A., Kamari, A. and Yamin, B.M. (2021). Synthesis and spectroscopic studies o f phenylpyridine iridium(III) complexes with deriv atives of 1*h*-1,2,4-triazole as ancillary ligands. *Indonesian Journal of Chemistry*, 21(6): 1577-1585.
17. Robert, M. S., Francis, X. W. and David, J. K. (200 5). Spectrometric identification of organic compou nds. John Wiley & Sons, Inc., New York. Seventh E dition: pp. 72-204.
18. Pavia, D. L., Lampman, G. M., Kriz, G. S. and Vyvyan, J. R. (2015). Introduction to spectroscopy. Cengage Learning 200 First Stamford Place, Stamford, USA. Fifth Edition: pp. 14-329.
19. Gokce, H., Ozturk, N., Tasąn, M., Alpaslan, Y. B., Alpaslan, G., (2016). Spectroscopic characterization and quantum chemical computations of the 5-(4-pyridyl)-1-h-1,2,4-triazole-3-thiol molecule. *Spectroscopy Letters*, 49(3): 167-179.
20. Stringer, B. D., Quan, L. M., Barnard, P. J., Wilson, D. J. D. and Hogan, C. F. (2014). Iridium complexes of n-heterocyclic carbene ligands: investigation into the energetic requirements for efficient electrogenerated chemiluminescence. *Organometallics*, 33(18): 4860-4872.
21. Huynh, H. V.; Han, Y., Jothibasu, R. and Yang, J. A. (2009). ^{13}C NMR spectroscopic determination of ligand donor strengths using n-heterocyclic carbene complexes of palladium(II). *Organometallics*, 28(18): 5395-5404.

22. Sanner, R. D., Cherepy, N. J., Paul Martinez, H., Pham, H. Q. and Young Jr, V. G. (2019). Highly efficient phosphorescence from cyclometallated iridium(III) compounds: Improved syntheses of picolinate complexes and quantum chemical studies of their electronic structures. *Inorganica Chimica Acta,* 496: 119040-119078.
23. Donato, L., Abel, P. and Zysman-Colman, E. (2013). Cationic iridium(III) complexes bearing a bis(triazole) ancillary ligand. *Dalton Transactions*, 42(23): 8402-8412.
24. Xue, J., Xin, L. J., Hou, J. Y., Duan, L., Wang, R. J., Wei, Y. and Qiao, J. (2017). Homoleptic facial Ir(III) complexes via facile synthesis for high-efficiency and low-roll-off near-infrared organic light-emitting diodes over 750 nm. *Chemistry of Materials*, 29(11): 4775-4782.
25. Bain, N. H. A. S., Ali, N. M. Juahir, Y., Hashim, N., Isa, I. M., Mohamed, A., Kamari, A., Anouar, E. H., Yamin, B. M., Tajuddin, A. M. and Baharudin, M. H. (2020). Synthesis, crystal structure, photophysical properties, DFT studies and Hirshfeld surface analysis of a phosphorescent 1,2,4-triazole-based iridium(III) complex. *Polyhedron,* 188: 114690-114701.
26. Bain, N. H. A., Ali, N. M., Juahir, Y., Hashim, N., Isa, I. M., Mohamed, A., Kamari, A., and Yamin, B. M. (2018). Synthesis of phenylpyridine iridium(III) complexes with n-heterocyclic carbene as ancillary ligand. *IOP Conference Series Materials Science Engineering,* 440: 012010-012018.
27. Monti, F., Kessler, F., Delgado, M., Frey, J., Bazzanini, F., Accorsi, G., Armaroli, N., Bolink, H. J., Ort, E., Scopelliti, R., Nazeeruddin, M. K. and Baranoff, E. (2013). Charged bis-cyclometalated iridium(III) complexes with carbene-based ancillary ligands. *Inorganic Chemistry,* 52(18): 10292-10305.
28. Baranoff, E., Curchod, B. F. E., Monti, F., Steimer, F., Accorsi, G., Tavernelli, I., Rothlisberger, U., Scopelliti, R., Grätzel, M. and Nazeeruddin, M. K. (2012). Influence of halogen atoms on a homologous series of bis-cyclometalated iridium(III) complexes. *Inorganic Chemistry,* 51(2): 799-811.
29. Ryu, C. H., Lim, J., Kim, M. B., Lee, J. H., Hwang, H., Lee, J. Y., and Lee, K. M. (2021). Tris(5-phenyl-1h-1,2,4-triazolyl)iridium(III) complex and its use in blue phosphorescent organic light-emitting diodes to provide an external quantum efficiency of up to 27.8%. *Advanced Optical Materials,* 9(7): 1-7.
30. Tom, L., Diluzio, S., Hua, C. and Connell, T. U. (2022). Understanding the role of cyclometalating ligand regiochemistry on the photophysics of charged heteroleptic iridium(III) complexes. *Journal of Coordination Chemistry,* 75(11-14): 1722-1743.
31. Schneidenbach, D., Ammermann, S., Debeaux, M., Freund, A., Zöllner, M., Daniliuc, C., Jones, P. G., Kowalsky, W. and Johannes, H-H. (2010). Efficient and long-time stable red iridium(III) complexes for organic light-emitting diodes based on quinoxaline ligands. *Inorganic Chemistry*, 49(2): 397-406.

Malaysian Journal of Analytical Sciences (MJAS)
Published by Malaysian Analytical Sciences Society

A REVIEW ON EXTRACTION OF LIPID FROM MICROALGAE USING MICROWAVE-ASSISTED EXTRACTION

(Sebuah Ulasan Terhadap Pengekstrakan Lipid Daripada Mikroalga Dengan Pengekstrakan Bantuan Gelombang Mikro)

Tan Yeong Hwang[1*], Chai Mee Kin[1], Wong Ling Shing[2], and Geetha Subramaniam[2]

[1]*Institute of Sustainable Energy,*
Universiti Tenaga Nasional, 43000 Kajang, Selangor, Malaysia
[2]*Faculty of Health and Life Science,*
INTI International University, 71800 Nilai, Negeri Sembilan, Malaysia

[*]*Corresponding author: yeonghwang113@gmail.com*

Received: 23 August 2022; Accepted: 9 December 2022; Published: 19 April 2023

Abstract

Microalgae are regarded as suitable feedstock for biofuel due to the~~ir~~ high growth rate and substantial lipid content Furthermore, the physiological functions of microalgal lipids contribute to their effectiveness as bioactive compounds with economic value particularly in pharmaceutical and health supplement industries. Extracting the stored lipid from microalgae is a major challenge for industrial applications as their tough cell wall is difficult to break down. Therefore, extraction solvents and cell disruption techniques are key procedures for high lipid extraction and recovery. Traditional methods used for cell disruption and extraction are effective but time consuming and could be detrimental to the environment. Hence, different innovative cell disruption techniques such as microwave-assisted extraction are developed to overcome these issues. This paper is a review of traditional and microwave-assisted extraction methods that are used for lipid extraction from microalgae biomass. The advantages, challenges and future trends of microwave-assisted extraction are also discussed.

Keywords: lipid extraction, microwave-assisted extraction, microalgae, traditional lipid extraction

Abstrak

Lipid yang dihasilkan oleh mikroalga dianggap sebagai bahan mentah yang sesuai untuk biofuel kerana kadar pertumbuhan dan kandungan lipid yang tinggi. Selain itu, fungsi fisiologi lipid mikroalga juga menjadikannya sebagai sebatian bioaktif yang tinggi dalam industri farmaseutikal dan suplemen kesihatan. Mengekstrakkan lipid daripada mikroalga merupakan cabaran utama untuk aplikasi perindustrian kerana dinding selnya yang kukuh dan sukar dipecahkan. Oleh hal demikian, pelarut pengekstrakan dan teknik gangguan sel adalah prosedur penting untuk pengekstrakan lipid tinggi. Kaedah tradisional yang digunakan untuk gangguan sel dan pengekstrakan adalah berkesan tetapi tidak mesra alam dan mengambil masa. Oleh hal demikian, pelbagai teknik gangguan sel inovatif seperti pengekstrakan bantuan gelombang mikro telah dibangunkan. Kertas kerja ini ialah sebuah ulasan terhadap kaedah tradisional dan pengekstrakan bantuan gelombang mikro yang telah digunakan untuk pengekstrakan lipid daripada biojisim mikroalga. Kelebihan, cabaran dan trend masa depan pengekstrakan bantuan gelombang mikro juga dibincangkan.

Kata kunci: pengekstrakan lipid, pengekstrakan bantuan gelombang mikro, mikroalga, kaedah pengekstrakan lipid tradisional

Introduction

Escalated population and economic development have led to the increase in global energy demands annually. Meanwhile, reducing consumption of fossil fuels should be mandatory considering the negative environmental impact, depleting resources and steep increase in

petroleum prices. Renewable energy is an alternative choice to fulfil energy demands with minimal environmental impact. Among the different types of existing renewable energy, liquid biofuel such as biodiesel has gained considerable attention as a future energy supply due to fact that it is biodegradable, renewable, carbon-neutral and is less flammable [1]. Biodiesel can be extracted from oil-producing, terrestrial plants, however, public conflicts relating to food security, freshwater demand and deforestation issues have been raised [2]. Hence, microalgae are currently regarded as an attractive option for biodiesel production. Compared to oil-producing terrestrial plants, microalgae have better carbon dioxide sequestration and faster growth rate [3]. Moreover, microalgae can grow in non-arable land and utilize wastewater as nutrient sources [4]. Microalgae with 30% lipid in dry biomass is estimated to produce up to 58700 litres of lipids per hectare in one year, which is considerably better than oil-producing terrestrial plants [5]. Besides that, the biodiesel that is trans-esterified from microalgal lipids has been demonstrated to meet European and United State biodiesel specifications (EN 14214 and ASTM D6751). The studies showed that microalgal biodiesel with proper blends can be used in diesel engines with low pollutant emission [6-7]. Apart from the application in biodiesel production, the physiological functions of microalgal lipid such as eicosapentaenoic acid (EPA), docosapentaenoic acid (DPA) and docosahexaenoic acid (DHA) make them high bioactive compounds with huge potential in pharmaceutical and health supplement industries [8-9].

Lipid production from microalgae involves several key processes which are cultivation, harvesting and lipid extraction. Transesterification may be included as part of the process for biodiesel production. Among these processes, lipid extraction has been found to be challenging particularly as it can affect the overall quality of the biodiesel [10-11]. During the conventional process of lipid extraction, organic solvents such as chloroform and hexane are employed, but these solvent may not be suitable enough for the complete extraction of lipids due to the hindrance of the rough cell wall contained in microalgae [12]. Some of the lipids might embedded in or cannot pass through the cell wall, and therefore cannot be extracted by the solvent [13]. Hence, it is crucial to ensure that the microalgal cell structure has been completely damaged to improve the extraction efficiency. However, selecting an ideal cell disruption technique is quite a challenging task. In lieu of considering the efficiency of the extraction process, finding a greener and more economical lipid extraction method is necessary to ensure that it will be environmentally friendly, energy efficient and suitable for upscale lipid production. Various methods are applied for extracting lipids from microalgae [14-15], out of which microwave-assisted extraction (MAE) is one of the more attractive green methods because it offers several benefits including efficient cell disruption, fast extraction and requires less consumption of solvents [16].

In this review, some basic information on microwaves and traditional methods of lipid extraction from microalgae biomass are discussed and compared. In additional, an overview of the factors, challenges and future trends of MAE are presented.

Traditional lipid extraction

Soxhlet extraction is a traditional technique used for extracting lipids from microalgae [17-18]. In the conventional Soxhlet extraction (Figure 1), the sample is placed in a porous thimble and once the distillation flask is heated, the extraction solvent evaporates and flows into the condenser where it is cooled down and condenses into liquid. This liquid then drips back into the thimble and extracts the lipids from the sample. When the thimble is almost full, a siphon aspirates the solvent from the chamber and returns it into the distillation flask. This process is repeated for several cycles until the extraction of lipids is completed. After extraction, no filtration or centrifugation is required to separate the samples and extraction solvent. Furthermore, the process is automated and no manual operation is required to rinse the sample with solvent [19]. However, several studies revealed that the lipid yield using Soxhlet extraction was very low compared to both the Folch Method and Bligh & Dyer method [20-22]. This is probably because hexane, which was commonly used in Soxhlet extraction, is nonpolar therefore is unable to effectively extract neutral lipids from microalgae [21-22]. Therefore, it was suggested that hexane be replaced by a mixture of nonpolar and polar solvents such as hexane: ethanol to extract the microalgal lipids. The studies showed that the lipid and fatty acid yield improved significantly using this combination of solvents compared to just using hexane [23-24]. Still, the time required to complete Soxhlet extraction usually lasts for several to twenty-four hours, which is extremely time-consuming compared to other lipid extraction methods, resulting in more a laborious and ineffective method for extracting high numbers of samples [23]. In the analysis of fatty acid profiles by previous research, the extraction yield of unsaturated lipids was very low compared to other extraction

methods [21, 25]. This was probably caused by the instability of unsaturated lipids due to the long-time exposure at elevated temperatures which caused the degradation of these lipids during reflux [26].

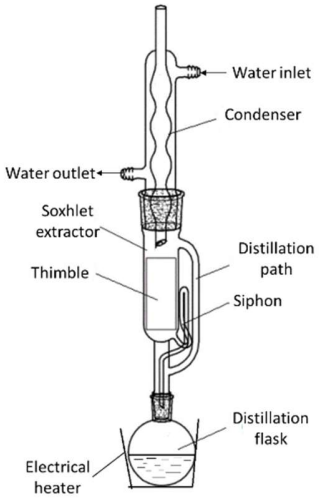


Figure 1. Soxhlet extraction

Folch Method [27] and Bligh & Dyer method [28] are common lipid extraction procedures that are frequently used for lipid extraction. In the Folch method, a mixture of organic solvents, usually chloroform and methanol at a ratio of 2:1 (v/v), is added to the microalgae biomass then vortexed for 30 seconds to several minutes. Water is then added to induce phase separation. Centrifugation is subsequently carried out in some studies to generate a clear phase separation [21, 29]. The organic phase on the top is collected and the lipids can be recovered after rotary evaporation or vacuum evaporation. The process in the Bligh and Dyer method are similar to the Folch Method whereby a mixture of chloroform, methanol and water at the ratio of 2:2:1.8 (v/v) is used as the extraction solvent [28]. The process of these two methods is easy to perform and do not require high pressure or high temperature during the extraction.

Although both the Folch and the Bligh & Dyer methods are well established for lipid extraction from solid animal tissue, the lipid extraction from microalgae could be lower [49]. In order to achieve better extraction results, the modifications of the Bligh and Dyer method has been investigated by several studies. One of the proposed modifications is the addition of sodium chloride solution instead of water [29-30] to restrict the binding of acidic lipids to denatured lipids [31]. In another study, the parameters in the Bligh and Dyer method were modified using response surface methodology [32]. The optimal extraction of 1 g dry biomass was obtained by using a solvent mixture of chloroform: methanol: water with ratio of 5.7:3:1 (v/v) under 25°C and 2-hours extraction [32].

Another reason for low extraction yield of microalgae lipids using Folch and Bligh & Dyer method is the difference between microalgal cell structure and animal tissue. Microalgae are usually covered with cell walls that isolate the intracellular compounds from the outer environment. In some cases, these cell walls are recalcitrant, complex and thick thereby hindering solvent penetration, resulting in low recovery of lipids [13, 33]. Cell disruption has been suggested to disintegrate the microalgal cell wall followed by the lipid extraction process. Many studies have shown that the yield of average lipids after cell disruption are much higher compared to lipid extraction without any cell disruption [33-37].

Microwave-assisted extraction

Microwave is an electromagnetic wave that is positioned between the X-ray and infrared rays in the electromagnetic spectrum with frequencies ranging from 300 MHz to 300 GHz. The electric and magnetic fields of the microwave are responsible for the heating effects under through the microwave dielectric heating and magnetic loss heating effects respectively. In the microwave dielectric heating, dipolar polarization and ionic conduction are two main energy transfer mechanisms that render localized and superheating of the reaction material within a very short time [38]. According to Balasubramanian et al. [25], microwaves can reach up to 80-°C or 95-°C within 100 seconds or less whereas conventional heating requires more than 1000 seconds to reach the target temperature. The slow heating rate in conventional heating is due to the heat transfer through thermal conduction and convection in which heat is transferred to the wall of the target object before reaching the internal object [38]. In this process, the energy is utilized inefficiently as it might be lost to the environment. In contrast, the molecules in the reaction material that have dipole moment absorb the microwave energy and convert it to heat through dipolar polarization and ionic conduction. In the case of MAE on microalgae, inner molecules in the microalgae cells are heated up and lead to a tremendous increase in pressure within the cells. The cell wall is then disrupted when the internal pressure exceeds the endurance limit [39]. The comparison between microwave heating and conventional thermal cell disruption is summarized in Table 1.

Table 1. Comparison between microwave heating and other conventional thermal cell disruption on microalgae.

Aspects	Microwave heating	Conventional thermal cell disruption
Heating mechanism	Dipolar polarization & ionic conduction	Conduction/convection
Time	Very fast, usually less than 1 hour	Slow, can up to several hours
Heating direction	Heat transfer from inner molecule or solvent to wall of object	Heat transfers from wall of object to the cells
Selectivity	Only polar solvent can convert microwave energy to heat	Non-selectivity
Cellular image	Microalgal cell wall is severely disrupted	Microalgal cell wall is remained intact

The cellular images under microscopy from several studies have illustrated that the microalgal cell wall was severely disrupted after microwave treatment whereas the cell wall of these microalgae remained intact after conventional heating [40-42]. Thus, target molecules such as lipid can easily spill out from the ruptured cell wall. Besides that, the volumetric heating generated by the microwave, induce the sudden rising of temperature within the cells thereby creating pressure effects on the cell wall. This phenomenon causes the diffusion of intracellular components to the exterior of the cells, eventually leading to the destruction of the cell structure and subsequent shrinking of the cell wall [42].

Different conditions of MAE can generate various lipid extraction yields and fatty acid profiles from microalgae. The parameters and lipid yields from various studies are summarized in Table 2. The effects of parameters such as solvents, extraction time, microwave power and mass of microalgae used in the lipid extraction must be studied carefully in order to achieve high extraction yield. Among these parameters, the solvent plays a determining factor on extraction yield of lipids. In some studies, the solvent in MAE acted as "pretreatment solvent" to break down the cell wall of microalgae by absorbing the microwave irradiation and increasing the temperature in the cells. The lipid was then extracted using other extraction solvents [37, 43-44]. Whereas, in other studies, the solvents not only have the function thereof, but also act as an extraction solvent to extract the lipid [41, 45-46]. To break down the cell wall effectively, polar solvents such as water, ethanol and methanol are usually chosen because of their high dielectric loss constant which is able to absorb the microwaves and convert them into heat [39-40]. On the other hand, the nonpolar solvents such as hexane and chloroform are excellent to dissolve lipids, however, they are microwave-transparent and are thereby unable to transform microwave energy into heat [46]. Lin and Lin [45] showed that the lipid extracted from *Isochrysis galbana* using nonpolar hexane was significantly lower than when polar isopropanol was used. Mansour et al. [41] also showed that the polar solvents such as methanol and ethanol, can extract higher amounts of lipid compared to nonpolar solvents. This is probably due to the strong association of lipids with proteins via hydrogen bonds which are difficult to be disrupted by nonpolar solvents. However, this association can easily be destroyed by polar solvents through the formation of hydrogen bonds [47]. Moreover, the presence of polar lipids such as phospholipid and glycolipids, are more soluble in polar solvents thereby enhance the lipid yield. Nevertheless, high amount of phospholipids might not beneficial for biodiesel production during transesterification because free fatty acids are enclosed by phospholipids which makes it difficult to be trans esterified into fatty acid methyl ester [48]. Moreover, some of the polar lipids and polar compounds that are non-saponifiable, when extracted by polar solvents may destroy the catalyst during transesterification, thereby reducing the conversion of lipids into fatty acid methyl esters [49]. In another study conducted by Dai et al. [46], however, contrasting results were obtained where nonpolar n-heptane produced better lipid extraction yields from dry microalgae powder. This contradictory result could probably be attributed to the different types of lipids present in different microalgae species.

In order to optimize lipid yield, most studies use a mixture of polar and nonpolar solvents. Several studies demonstrated that solvent mixtures can produce higher extraction yields compared to using a single solvent [15, 47, 50]. In this context, polar solvents have the capacity to absorb the microwaves and quickly induce heat production. The breakdown of cell walls and lipid-

protein linkages result in the rapid mass transfer of lipids from the interior to the exterior of the cells. The neutral lipids are then dissolved in the nonpolar solvents [50]. Besides of types of solvents, the ratio of solvents in mixture are also an important factor for extracting lipids that are suitable for biodiesel production. Iqbal et al. [49] showed that lipid extraction yields using methyl soyate with 60% ethanol was 50% higher than when methyl soyate was used with 80% ethanol. Similar results were also obtained by Saifuddin et al. [51] and Dai et al. [46] who showed that a lower proportion of polar solvents could generate higher lipid extraction.

Temperature is another crucial factor that greatly influences the extraction yield of MAE [40]. It can be controlled directly by altering the microwave setting or indirectly by adjusting the microwave power or irradiation time. Moderate power (180 – 800W) or high temperatures with long irradiation time (2- 40min) usually can generate a good lipid yield [52-55]. High temperatures with short irradiation time also can generate a good lipid yield. In the optimization study conducted by Menéndez et al. [53], the lipid and fatty acid yield extracted using MAE at 60 °C for 20 minutes was similar to the result at 90 °C for 10 minutes. Conversely, high temperature or high power with long irradiation time reduces the lipid yield and their fatty acid profiles [56-58]. At high temperatures, the amount of saturated fatty acid extracted increases while the amount of unsaturated fatty acids decreases [40, 58]. This phenomenon can be elucidated by the production of hydroxyl free radicals during MAE which have strong oxidation capacity that can cleave the double bonds of unsaturated fatty acids [44]. The reduction of unsaturated fatty acids, however, is not favorable for pharmaceutical or food production since microalgae polyunsaturated fatty acids such as DHA and EPA are bioresources with high value [8]. However, low amounts of polyunsaturated fatty acids have a positive effect on biodiesel production as high level of polyunsaturated fatty acid causes poor ignition quality and low oxidative stability [59]. Hence, temperature, power and irradiation time should be monitored carefully based on the requirement of product quality and its use.

The amount of biomass used for MAE has a considerable effect on the recovery of lipids. High amounts of biomass with either low microwave power or short irradiation time [21, 55] can result in low extraction yield. Longer irradiation time or high microwave power are required to break down the cell and improve the yield. Whereas, the lipid yield extracted from low amounts of biomass with high microwave power and long irradiation time are also suboptimal [52]. Therefore, it is essential to carefully select the optimal amount of biomass for MAE in order to maximize the lipid yield.

Advantages of MAE

Numerous studies have reported the comparison of MAE with other extraction techniques for lipid. Owing to its unique heating effect, MAE has been found to extract high amounts of lipid very quicky, usually within 40 minutes. Whereas, conventional extraction techniques such as Soxhlet extraction and water bath heating have been shown to require up to ten hours to extract similar amounts of lipids [25, 50-51]. Moreover, MAE of lipids can be operated in lower temperature environments [14]. Short reaction time and low temperature not only can reduce the change of oxidization of unsaturated lipids but also avoid degradation of proteins and bioactive compounds which can be used in bio-refinery process.

In addition, water, which is non-toxic and safe, can serve as an excellent solvent to disrupt and extract lipids using MAE [43-44]. Before extraction, dewatering and drying is usually required prior to extraction to remove water from microalgae biomass. In MAE, several studies reveal that removal of water is not necessary [60-63]. The water content in microalgae biomass or cultivation medium can be used as solvent to absorb microwaves and break down the cells [55]. Pôjo et al. [69] showed that the drying process required 89% of energy input and 70-75% total processing costs. Consequently, utilization of wet microalgae biomass can reduce the cost and energy consumption. In terms of energy consumption in different extraction techniques, MAE was observed to require lower amounts of energy (70 - 270 MJ/kg) whereas sonication, high-pressure homogenization and bead milling require more extensive energy usage (132, 529 and 504 MJ/kg respectively) [58]. In terms of cost analysis, the cost required to extract 1 kg lipid from microalgae using MAE is more than 50% lower than using Soxhlet extraction [21].

Table 2. Lipids extracted from microalgae by MAE

Microalgae Species	Dry/Wet	Solvent	Sample Weight; Solvent Volume	Microwave Setting	Lipid Extraction Yield*	Reference
Chlorella vulgaris	Wet	Chloroform-methanol (add after microwave)	1:2	100°C, 5 min	17.5%	[35]
Scenedesmus obliquus	Wet	Water	1:1	95°C, 30 min	31%	[25]
Nannochloropsis occulata	Wet	Dichloromethane	NA	140°C, 15 min	11.3%	[58]
Chlorogloeopsis fritschii				120°C, 15 min	1.4%	
Pseudochoricystis ellipsoidea				140°C, 15 min	37.5%	
Chlorella pyrenoidosa	Wet	Chloroform: methanol (1:1)	1g; 8 mL	500W, 40 s	19%	[61]
Nannochloropsis sp.	Wet	Methyl soyate: ethanol (3:2)	3.3 g; 20 mL	120 °C, 20 min	56.6%	[49]
		Chloroform: ethanol (1:2)	3.3 g; 20 mL		53.1%	
Dunaliella tertiolecta	Dry	Chloroform: methanol (2:1)	0.2g; 20 mL	490 W; 2.67 min	57.02%	[52]
Nannochloropsis sp.	Wet	Methanol: Hexane (1:2)	-	65 °C, 5 min	38.31%	[39]
Nannochloropsis sp.	Wet	Isopropanol: hexane (2:3)	15 mL; 50 mL	65 °C, 500 W; 5 min	8.19%	[62]
Tetraselmis sp.	Wet	Chloroform: methanol (2:1)	15 mL; 75 mL	65 °C, 500 W; 5 min	8.47%	
Tetraselmis sp.	Wet	NA	NA	80 - 90 °C, 5 min	20.26%	[63]
Microalgae^{+}	Wet	Chloroform: methanol (2:1)	0.5 g: 75 mL	530 W, 75s	11.6%	[60]
Nannochloropsis gaditana	Dry	Methanol	5g; 50 mL	90 °C, 10 min	40%	[53]
Scenedesmus dimorphus	Dry	Chloroform: methanol (2:1) (add after microwave)	NA	557 W, 3 min	17%	[64]
Selenastrum minutum					23%	
Chlorella					17%	

protothecoides						
Isochrysis galbana	Dry	hexane/isopropanol (2:1)	NA	NA	22.13%	[45]
Chlorococcum sp.	Dry	Distilled water	0.2 g; 100 mL	100 °C, 2 min	24.12%	[37]
Botryococcus sp. MCC31				100 °C, 6 min	48.33%	
Chlorella sorokiniana				100 °C, 6 min	24.43%	
Chlorella vulgaris	Dry	Chloroform: methanol (2:1)	1:10	100 °C, 15 min	22.68%	[65]
Nannochloropsis oculata	Wet	Ethanol (add after microwave)	1:5	443 W, 5 min	0.149 g/g	[56]
Nannochloropsis sp.	Wet	Biodiesel: ethanol (2:3)	8 g; 50mL	180 W, 15 min	0.654 g/g	[51]
Chlorella sorokiniana *Nannochloropsis salina* *Galdieria sulphuraria*	Dry	[BMIM][HSO_4] (Add After microwave)	1 g; 5g	800W, 120 °C, 60 min	0.23 g/g 0.10 g/g 0.19 g/g	[66]
Spirulina platensis	Dry	Water	1g; 10 mL	620 W, 20s	0.385 g/g	[43]
Chaetoceros calcitrans	Dry	Water	0.3 g; 20 mL	1400W, 40s	24.2%	[44]
Scenedesmus obliquus	Dry	chloroform/methanol (2:1)	NA	400W, 130°C, 30 min,	0.234 g/g	[42]
Scenesdemus quadricauda	Wet	Methanol: sulphuric acid (50:1)	500 mL; 500 Ml	473W, 8 min	41.94%	[54]
Nannochloropsis gaditana	Dry	Distilled water	NA	800W, 80 °C, 60 min	11.22%	[67]
Chlorella vulgaris	Dry	Chloroform: methanol (1:2) (Add after microwave)	NA	700W, 3 min	0.183 g/g	[68]
Chlorella pyrenoidosa	Wet	NA	NA	700W, 5 min	16.73%	[55]

* in percent dry weight

+ The name of microalgae species is not stated in original article.

Several studies also revealed the potential of microwave for direct transesterification of lipids into fatty acids, where lipid extraction and transesterification are carried out in the same process. Higher amount of fatty acid methyl ester could be attained in less time compared to transesterification after microwave-assisted extraction of lipids [61, 70-72]. Moreover, less impurities such as chlorophyll are detected in fatty acid methyl ester using microwave-assisted direct transesterification. Such processes minimize the requirement to remove impurities while simultaneously enhances the production of other high-valuable bioactive compounds [70].

Challenges and future trends

Although microwaves have been successful utilized to

disrupt the microalgae cells and extract lipids, there are several limitations in using MAE. In many studies, organic solvents especially chloroform and methanol are usually used to extract lipids during or after microwave treatment due to their excellent ability to absorb microwaves and their high solubility for different types of lipids. However, chloroform is toxic and therefore poses a health risk to the operator and may, in addition, cause environmental pollution [71]. There is a study which used ionic liquids to extract the lipids and the results showed that it could extract higher lipid yields compared to chloroform and methanol [72]. In addition to considering the extraction efficiency, safety, and being environmentally friendly, the cost of the solvent used in the MAE should not be too expensive to the point that it would hinder the development towards up-scale production. Some of the green solvents also known as deep eutectic solvents have been explored using MAE technology to recover natural products from plant material [73-75] but the application for lipid extraction from microalgae is less extensively studied.

Another challenge of MAE is identifying critical parameters from a pool of different factors for achieving high lipid extraction efficiency. There are multiple parameters in MAE that could simultaneously influence the extraction efficiency, hence, it would be better to study and optimize these parameters at the same time. In this extent, a multi-factorial approach would be superior than a one-factor-at-a-time approach because the levels of all the factors of interest can be changed simultaneously [76]. By utilizing advanced software, researchers can systematically estimate the interactions between multiple factors and decide the number of experiments required for optimizing these factors simultaneously.

In most MAE studies, once the microalgal cells have been disrupted and the lipids extracted by adding solvents, an additional separation process is needed to remove microalgae residues. Centrifugation is usually carried to achieve this. However, centrifugation consumes high energy thereby increasing production costs [77]. Herein an innovative idea is required to separate lipids from microalgae residues effectively but with low energy consumption.

Conclusion

As microalgae can accumulate high lipid content within a short period of time, it has been explored as suitable feedstock for biofuel, pharmaceutical and health supplement industries. Traditional lipid extraction such as Soxhlet extraction, Folch extraction and Bligh & Dyer extraction have been used to extract lipid from microalgae. However, the lipid extraction yield using these methods are less efficient due to the presence of microalgal cell wall. Therefore, MAE has been proposed to break down the cell wall and enhance the extraction efficiency of lipids from microalgae. It is evident that MAE has resulted in the increase in extraction efficiency and rate. These superior results can be attributed to the distinct heating mechanism of the microwave which is different from conventional heating. To optimize the extraction yield, the selected solvent should utilize the microwave to break down the cell wall prior to extracting the lipids. Most studies select a mixture of polar and nonpolar solvents as they are able to generate higher extraction yield. Other parameters including temperature, microwave power, irradiation time and amount of biomass should also be studied and optimized to achieve a higher extraction yield of lipids. Apart from high extraction efficiency and short extraction time, wet biomass can be directly used for extraction in MAE. Lipid extraction and transesterification also can be carried out in single step using microwave treatment thereby reducing the process time and necessity to remove impurities. Thus, MAE has the potential to extract microalgal lipids at the industrial level in the future. Nevertheless, it is undeniable that most of the results collected so far are from studies that still use a mixture of toxic chloroform and methanol, and centrifugation is needed to remove microalgae residues. Certainly, comprehensive research is required to explore the possibility of a greener solvent and to reduce the energy consumption in separation after extraction.

Acknowledgement

The authors would like to acknowledge Ministry of Higher Education Malaysia, MOHE: FRGS/1/2020/STG02/UNITEN/02/1 (80%) and UNITEN (UNITEN–YCU postgraduate scholarship 2021) (20%) for the financial support.

References

1. Priya, Deora, P. S., Verma, Y., Muhal, R. A., G oswami, C. and Singh, T. (2022). Biofuels: An alternative to conventional fuel and energy sour ce. *Materials Today: Proceedings*, 48: 1178-11 84.
2. Rulli, M. C., Bellomi, D., Cazzoli, A., De Carol is, G. and D'Odorico, P. (2016). The water-land -food nexus of first-generation biofuels. *Scient ific Reports*, 6: 1-10.

3. Adamczyk, M., Lasek, J. and Skawińska, A. (2016). CO_2 Biofixation and growth kinetics of *Chlorella vulgaris* and *Nannochloropsis gaditana*. *Applied Biochemistry and Biotechnology*, 179: 1248-1261.
4. Odjadjare, E.C., Mutanda, T., Chen, Y. F. and Olaniran, A. O. (2018). Evaluation of pre-chlorinated wastewater effluent for microalgal cultivation and biodiesel production. *Water (Switzerland)*, 10 (8): 1- 13.
5. Bošnjaković, M. and Sinaga, N. (2020). The perspective of large-scale production of algae biodiesel. *Applied Sciences (Switzerland),* 10 (22): 1-26.
6. Rajak, U., Nashine, P. and Verma, T. N. (2019). Assessment of diesel engine performance using *spirulina* microalgae biodiesel. *Energy*, 166: 1025-1036.
7. Tizvir, A., Shojaeefard, M. H., Zahedi, A. and Molaeimanesh, G. R. (2022). Performance and emission characteristics of biodiesel fuel from *Dunaliella tertiolecta* microalgae, *Renewable Energy*, 182: 552-561.
8. Sibi, G. (2015). Inhibition of lipase and inflammatory mediators by *Chlorella* lipid extracts for antiacne treatment. *Journal of Advanced Pharmaceutical Technology and Research*, 6 (1): 7-12.
9. Wang, S., Said, I, H., Thorstenson, C., Thomsen, C., Ullrich, M., Kuhnert, N. and Thomsen, L. (2018). Pilot-scale production of antibacterial substances by the marine diatom *Phaeodactylum tricornutum* Bohlin. *Algal Research*, 32: 113-120.
10. Byreddy, A. R., Gupta, A., Barrow, C. J. and Puri, M. (2015). Comparison of cell disruption methods for improving lipid extraction from *thraustochytrid* strains. *Marine Drugs*, 13(8): 5111-5127.
11. Xia, A., Sun, C., Fu, Q., Liao, Q., Huang, Y. and Zhu, X. (2020). Biofuel production from wet microalgae biomass: Comparison of physicochemical properties and extraction performance. *Energy*, 212: 118581.
12. Baudelet, P. H., Ricochon, G., Linder, M. and Muniglia, L. (2017). A new insight into cell walls of Chlorophyta. *Algal Research*, 25: 333-371.
13. Alhattab, M., Kermanshahi-Pour, A. and Brooks, M. S. L. (2019). Microalgae disruption techniques for product recovery: influence of cell wall composition. *Journal of Applied Phycology*, 31: 61-88.
14. Singh, R., Kumar, A. and Sharma, Y. C. (2020). evaluation of various lipid extraction techniques for microalgae and their effect on biochemical components. *Waste and Biomass Valorization*, 11(6): 2603- 2612.
15. El-Sheekh, M. M. and Hamouda, R. A. (2016). Lipids extraction from the green alga *Ankistrodesmus falcatus* using different methods. *Rendiconti Lincei*, 27(3): 589-595.
16. Moretto, J. A., de Souza, A. O., Berneira, L. M., Brigagão, L. G. G., de Pereira, C. M. P., Converti, A. and Pinto, E. (2022). *Applied Sciences (Switzerland)*, 12 (5): 1-9.
17. Guckert, J. B., Cooksey, K. E. and Jackson, L. L. (1988). Lipid solvent systems are not equivalent for analysis of lipid classes in the microeukaryotic green alga, *Chlorella*. *Journal of Microbiological Methods*, 8(3): 139-149.
18. Chen, W., Liu, Y., Song, L., Sommerfeld, M. and Hu, Q. (2020). Automated accelerated solvent extraction method for total lipid analysis of microalgae. *Algal Research*, 51: 102080.
19. Poole C. F. (2019). Liquid-Phase Extraction. Elsevier, Amsterdam: pp. 327-354.
20. de Jesus, S. S., Ferreira, G. F., Moreira, L. S. Maciel, M. R. W and Filho, M. R. (2019). Comparison of several methods for effective lipid extraction from wet microalgae using green solvents. *Renewable Energy*, 143: 130-141.
21. Zghaibi, N., Omar, R., Kamal, S. M. M., Biak, D. R. A. and Harun, R. (2019). Microwave-assisted brine extraction for enhancement of the quantity and quality of lipid production from microalgae *Nannochloropsis* sp. *Molecules*, 24(19): 1-21.
22. Castejón, N. and Señoráns, F. J. (2019). Simultaneous extraction and fractionation of omega-3 acylglycerols and glycolipids from wet microalgal biomass of *Nannochloropsis gaditana* using pressurized liquids. *Algal Research*, 37: 74-82.
23. Li, Y., Naghdi F. G., S. Garg, S., Adarme-Vega, T. C., Thurecht, K. J., Ghafor, W. A., Tannock, S. and Schenk, P. M. (2014). A comparative study: the impact of different lipid extraction methods on current microalgal lipid research. *Microbial Cell Factories*, 13(14): 1-9.
24. Escorsim, A. M., Rocha, G., Vargas, J. V. C., A. B. Mariano, Ramos, L. P., Corazza, M. L. and Cordeiro, C. S. (2018). Extraction of *Acutodesmus obliquus* lipids using a mixture of ethanol and hexane as solvent. *Biomass and Bioenergy*, 108: 470-478.

25. Balasubramanian, S., Allen, J. D., Kanitkar, A. and Boldor, Dorin. (2011). Oil extraction from *Scenedesmus obliquus* using a continuous micr owave system - design, optimization, and qualit y characterization. *Bioresource Technology*, 10 2(3): 3396-3403.
26. Muhammad, A. I., Richard, J. B., O'Hara, I., K ent, M. and Heimann, K. (2014). Effect of temp erature and moisture on high pressure lipid/oil e xtraction from microalgae. *Energy Conversion and Management*, 88: 307-316
27. Eggers, L.F., Schwudke, D. (2016). Liquid Extr action: Folch. In: Wenk, M. (eds). Encyclopedi a of Lipidomics. Springer, Dordrecht: pp. 1-6.
28. Sündermann, A., Eggers, L.F. and Schwudke, D . (2016). Liquid Extraction: Bligh and Dyer. In: Wenk, M. (eds). Encyclopedia of Lipidomics. S pringer, Dordrecht: pp. 1-4.
29. Axelsson, M. and Gentili, F. (2014). A single-st ep method for rapid extraction of total lipids fro m green microalgae. *PLoS ONE*, 9(2): 17-20.
30. Pérez, K., Ibarra, D. and Ballen-Segura, M. (20 20). Modelling biodiesel production from micro algae, using industrial wastewater as a growth m edium. *Ingeniare*, 28(4): 744-754.
31. Gorgich, M., Mata, T. M., Martins, A. A., Bran co-Vieira, M. and Caetano, N. S. (2020). Comp arison of different lipid extraction procedures a pplied to three microalgal species. *Energy Repo rts*, 6: 477-482.
32. Chatsungnoen, T. and Chisti, Y. (2016). Optimi zation of oil extraction from *Nannochloropsis s alina* biomass paste. *Algal Research*, 15: 100-1 09.
33. Park, J. Y., Lee, K., Choi, S. A., Jeong, M. J., K im, B., Lee, J. S. and Oh, Y. K. (2015). Sonicat ion-assisted homogenization system for improv ed lipid extraction from *Chlorella vulgaris*. *Ren ewable Energy*, 79(1): 3-8.
34. Garoma, T. and Janda, D. (2016). Investigation of the effects of microalgal cell concentration a nd electroporation, microwave and ultrasonicati on on lipid extraction efficiency. *Renewable En ergy*, 86: 117-223.
35. Zheng, H., Yin, J., Gao, Z. Huang H., Ji. X and Dou. C. (2011). Disruption of *Chlorella vulgari s* cells for the release of biodiesel-producing lip ids: a comparison of grinding, ultrasonication, b ead milling, enzymatic lysis, and microwaves. *A pplied Biochemistry and Biotechnology*, 164: 1 215-1224.
36. Onay, M., Sonmez, C., Oktem, H. A. and Yuce l, M. (2015). Evaluation of various extraction te chniques for efficient lipid recovery from therm o-resistant microalgae, *Hindakia*, *Scenedesmus* and *Micractinium* species. *American Journal of Analytical Chemistry*, 7: 141-150.
37. Rakesh, S., Dhar, D. W., Prasanna, R. Saxena, A. K., Saha, S., Shukla, M. and Sharma, K. (20 15). Cell disruption methods for improving lipi d extraction efficiency in unicellular microalga e. *Engineering in Life Sciences*, 15(4): 443-447 .
38. Nomanbhay, S. and Ong, M. Y. (2017). A revie w of microwave-assisted reactions for biodiesel production. *Bioengineering*, 4(2): 57-88.
39. Wahidin, S., Idris, A. and Shaleh, S. R. M. (201 4). Rapid biodiesel production using wet micro algae via microwave irradiation. *Energy Conve rsion and Management*, 84: 227-233.
40. de Moura, R. R., Etges, B. J., dos Santos, E. O., Martins, T. G., Roselet, F., Abreu, P. C. Primel, E. G. and D'Oca, Marcelo G. M. (2018). Micro wave-assisted extraction of lipids from wet mic roalgae paste: A quick and efficient method. *Eu ropean Journal of Lipid Science and Technolog y*, 120(7): 1-7.
41. Mansour, E. A., El-Enin, S. A. A., Hamouda, A . S. and Mahmoud, H. M. (2019). Efficacy of e xtraction techniques and solvent polarity on lipi d recovery from domestic wastewater microalg ae. *Environmental Nanotechnology, Monitoring and Management*, 12: 100271.
42. Zhou, X., Jin, W., Tu, R., Guo, Q., Han, S. F., C hen, C., Wang, Q., Liu, W., Jensen, P. D. and W ang, Q. (2019). Optimization of microwave assi sted lipid extraction from microalga *Scenedesm us obliquus* grown on municipal wastewater. *Jo urnal of Cleaner Production*, 221: 502-508.
43. De Sousa E Silva, A., Moreira, L. M., De Maga lhães, W. T., Farias, W. R. L., Rocha, M. V. P. and Bastos, A. K. P. (2016). Extraction of biom olecules from *Spirulina platensis* using non-con ventional processes and harmless solvents. *Jour nal of Environmental Chemical Engineering*, 5(3): 2101-2106.
44. Nogueira, D. A., da Silveira, J. M., Vidal, E. M ., Ribeiro, N. T. and Burkert, C. A. V. (2018). C ell disruption of *Chaetoceros calcitrans* by mic rowave and ultrasound in lipid extraction. *Inter national Journal of Chemical Engineering*, 201 8: 9508723.
45. Lin, C. Y and Lin, B. Y. (2015). Fatty acid char acteristics of *Isochrysis galbana* lipids extracte d using a microwave-assisted method. *Energies* , 8(2): 1154-1165.

46. Dai, Y. M., Chen, K. T. and Chen, C. C. (2014) . Study of the microwave lipid extraction from microalgae for biodiesel production. *Chemical Engineering Journal*, 250: 267-273.
47. Hidalgo, H., Ciudad, G. and Navia, R. (2016). E valuation of different solvent mixtures in esterif iable lipids extraction from microalgae *Botryoc occus braunii* for biodiesel production. *Bioreso urce Technology*, 201: 360-364.
48. Bi, Z. and He, B. B. (2016). Phospholipid trans esterification in sub-/super-critical methanol wi th the presence of free fatty acids. *Fuel*, 166: 46 1-466.
49. Iqbal, J. and Theegala, C. (2013). Microwave a ssisted lipid extraction from microalgae using b iodiesel as co-solvent. *Algal Research*, 3 (2): 34 -42.
50. Kalsum, U., Kusuma, H. S., Roesyadi, A. and M ahfud., M. (2019). Lipid Extraction from *Spirul ina platensis* using microwave for biodiesel pro duction. *Korean Chemical Engineering Resear ch*, 57(2): 301-304.
51. Saifuddin, N., Amzar, A. B. and P. Priatharsini, A. (2016). Improvement in oil extraction from microalgae/algae for biodiesel production using microwave assisted oil extraction with methyl e ster. *Research Journal of Applied Sciences, Eng ineering and Technology*, 13(4): 331-340.
52. Qv, X. Y., Zhou, Q. F. and Jiang, J. G. (2014). Ultrasound-enhanced and microwave-assisted e xtraction of lipid from *Dunaliella tertiolecta* an d fatty acid profile analysis. *Journal of Separati on Science*, 37(20): 2991-2999.
53. Menéndez, J. M. B., Arenillas, A., Menéndez D íaz, J. A., Boffa, L., Mantegna, S., Binello, A. a nd Cravotto, G. (2014). Optimization of microa lgae oil extraction under ultrasound and microw ave irradiation. *Journal of Chemical Technolog y and Biotechnology*, 89 (11): 1779-1784.
54. Onumaegbu, C., Alaswad, A., Rodriguez, C. an d Olabi, A. (2019). Modelling and optimization of wet microalgae *Scenedesmus quadricauda* li pid extraction using microwave pre-treatment m ethod and response surface methodology. *Rene wable Energy*, 132: 1323-1331.
55. Rana, M. S. and Prajapati, S. K. (2021). Micro wave-assisted pretreatment of wet microalgal b iomass for recovery of biofuel precursors. *Fuel*, 305: 121610.
56. Ali, M. and Watson, I. A. (2016). Microwave th ermolysis and lipid recovery from dried microa lgae powder for biodiesel production. *Energy T echnology*, 4 (2): 319-330.
57. Tanzi, C. D., Pingret, D., Vian, M. A. and Che mat, F. (2017). Combined microwave and simu ltaneous distillation extraction process for recov ery of lipids from fresh microalgae. *Process En gineering Journal*, 1: 1-9.
58. Biller, P., Friedman, C. and Ross, A. B. (2013). Hydrothermal microwave processing of microa lgae as a pre-treatment and extraction technique for bio-fuels and bio-products. *Bioresource Tec hnology*, 136: 188-195.
59. Bucy, H. B., Baumgardner, M. E. and Marches e, A. J. (2012). Chemical and physical propertie s of algal methyl ester biodiesel containing vary ing levels of methyl eicosapentaenoate and met hyl docosahexaenoate. *Algal Research*, 1: 57-6 9.
60. Ma, Y. A., Cheng, Y. M., Huang, J. W., Jen, J. F., Huang, Y. S. and Yu, C. C. (2014). Effects o f ultrasonic and microwave pretreatments on lip id extraction of microalgae. *Bioprocess and Bio systems Engineering*, 37 (8): 1543-1549.
61. Cheng, J., Yu, T., Li, T., Zhou, J. and Cen, K. (2013). Using wet microalgae for direct biodiese l production via microwave irradiation. *Bioreso urce Technology*, 131: 531-535.
62. Teo, C. L. and Idris, A. (2014). Enhancing the v arious solvent extraction method via microwav e irradiation for extraction of lipids from marin e microalgae in biodiesel production. *Bioresour ce Technology*, 171: 477-481.
63. Naghdi, F. G., Thomas-Hall, S. R., Durairatnam , R., Pratt, S. and Schenk, P. M. (2014). Compa rative effects of biomass pre-treatments for dire ct and indirect transesterification to enhance mi croalgal lipid recovery. *Frontiers in Energy Res earch*, 2: 1-10.
64. Axelsson, M. and Gentili, F. (2014). A single-st ep method for rapid extraction of total lipids fro m green microalgae. *PLoS One*, 9(2): 17-20.
65. Sharma, A. K. Sahoo, P. K., Singhal, S. and Jos hi, G. (2016). Exploration of upstream and dow nstream process for microwave assisted sustain able biodiesel production from microalgae *Chlo rella vulgaris. Bioresource Technology*, 216: 7 98-800.
66. Pan, J., Muppaneni, T., Sun, Y., Reddy, H. K., Fu, J., Lu, X., Deng, S. (2016). Microwave-assi sted extraction of lipids from microalgae using an ionic liquid solvent [BMIM][HSO_4]. *Fuel*, 1 78: 48-55.

67. Motlagh, S. R., Harun, R., Biak, D. R. A. and H ussain, S. A. (2019). Microwave assisted extrac tion of lipid from *Nannochloropsis gaditana* mi croalgae using [EMIM]Cl. *IOP Conference Ser ies: Materials Science and Engineering*, 778(1) : 012164.
68. Xia, A., Sun, C., Fu, Q., Liao, Q., Huang, Y., Z hu, X. and Li, Q. (2020). Biofuel production fro m wet microalgae biomass: Comparison of phy sicochemical properties and extraction perform ance. *Energy*, 212: 118581.
69. Pôjo, V., Tavares T. and Malcata F.X. (2021). P rocessing Methodologies of Wet Microalga Bio mass Toward Oil Separation: An Overview. *Mo lecules*, 26(3): 641-664.
70. Cheng, J., Huang, R., Li, T., Zhou, J. and Cen, K. (2014). Biodiesel from wet microalgae: Extr action with hexane after the microwave-assisted transesterification of lipids. *Bioresource Techn ology*, 170: 69-75.
71. Teo, C. L. and Idris, A. (2014). Evaluation of d irect transesterification of microalgae using mic rowave irradiation. *Bioresource Technology*, 17 4: 281-286.
72. Kober, M., Cohen, M., Ben-Amotz, A. and Ged anken, A. (2011). Bio-diesel production directl y from the microalgae biomass of *Nannochloro psis* by microwave and ultrasound radiation. *Bi oresource Technology*, 102: 4265-4269.
73. The National Institute for Occupational Safety a nd Health (NIOSH). (2019). Chloroform. https: //www.cdc.gov/niosh/topics/chloroform/default .html#:~:text=Chloroform%20can%20be%20to xic%20if,duration%2C%20and%20work%20b eing%20done. [Accessed online 30 July 2022]
74. Wang, J., Jing, W., Tian, H., Liu, M., Yan, H. a nd Bi, W. (2020). Investigation of deep eutectic solvent-based microwave-assisted extraction an d efficient recovery of natural products. *ACS Su stainable Chemistry Engineering*, 8 (32): 12080 -12088.
75. Doldolova, K., Bener, M., Lalikoğluc, M., Aşçı b, Y. S., Aratd, R. and Apak, R. (2021). Optimi zation and modeling of microwave-assisted extr action of curcumin and antioxidant compounds from turmeric by using natural deep eutectic so lvents. *Food Chemistry*, 353: 129337.
76. Spall, J. C. (2010). Factorial design for efficien t experimentation. *IEEE Control Systems Maga zine*, 30 (5): 38-53.
77. Najjara, Y. S. H. and Abu-Shamleh, A. (2020). Harvesting of microalgae by centrifugation for biodiesel production: A review. *Algal Research* , 51: 102046.

Malaysian Journal of Analytical Sciences (MJAS)
Published by Malaysian Analytical Sciences Society

SYNTHESIS, CHARACTERIZATION AND PHOTOCATALYTIC ACTIVITIES OF Mg-DOPED ZnO FOR DEGRADATION OF METHYLENE BLUE DYE UNDER UV LIGHT IRRADIATION

(Sintesis, Pencirian dan Aktiviti Fotokatalitik Mg di Dopkan dengan ZnO untuk Penguraian Pewarna Metilena Biru di Bawah Cahaya UV)

Hartini Ahmad Rafaie[1,3*], Zul Adlan Mohd Hir[1], Nurul Infaza Talalah Ramli[1], and Muhd Firdaus Kasim[2]

[1]Faculty of Applied Sciences,
Universiti Teknologi MARA Pahang Branch,
26400 Bandar Tun Abdul Razak Jengka, Pahang, Malaysia
[2]Center for Nanomaterials Research,
Institute of Science, Universiti Teknologi MARA,
40450 Shah Alam, Selangor, Malaysia
[3]Centre of Foundation Studies,
Universiti Teknologi MARA, Selangor Branch, Dengkil Campus,
43800 Dengkil, Selangor, Malaysia

[*]Corresponding author: hartinirafaie@uitm.edu.my

Received: 27 July 2022; Accepted: 17 January 2023; Published: 19 April 2023

Abstract

Heterogeneous photocatalysis is a viable treatment approach for removing organic dye compounds from textile wastewater, and ZnO-based photocatalysts is an appealing system to investigate. In this work, Mg-doped ZnO had been synthesized using modified sol-gel technique to evaluate the effect of different Mg molar concentrations towards the photocatalytic degradation performance of methylene blue (MB) dye. It had been characterized by X-ray diffraction (XRD), scanning electron microscope (SEM) and energy dispersive X-ray (EDS) analysis. According to XRD analysis, all samples showed a hexagonal wurtzite structure with average crystallite approximate sizes ranging between 74.82–81.64 nm. The SEM-EDS results demonstrated that the particle-like Mg-doped ZnO samples consist of elements Zn, O and Mg. The photocatalytic activity of the pure ZnO and Mg-doped ZnO was investigated through photodegradation of MB under ultraviolet radiation. The results showed that 1 mol% Mg-doped ZnO exhibited enhanced photocatalytic activity with a percentage of degradation of 89.54% and photodegradation rate constant, k of 0.0432 min^{-1}. Extended visible absorption, inhibition of photoexcited electron and hole recombination, and higher absorptivity of MB dye on the surface of Mg-doped ZnO photocatalyst might have contributed to the increased photocatalytic activity.

Keywords: magnesium, methylene blue, photocatalyst, photocatalytic, ZnO

Abstrak

Fotokatalisis heterogen adalah pendekatan rawatan yang terbaik untuk menghilangkan sebatian pewarna organik dari sisa buangan daripada industri tekstil, dan pemangkin berasaskan ZnO adalah sistem yang menarik untuk dikaji. Dalam penyelidikan ini, ZnO

yang didopkan dengan Mg telah disintesis menggunakan teknik sol-gel yang diubahsuai untuk menilai kesan kepekatan molar Mg yang berbeza terhadap prestasi penguraian pewarna metilena biru (MB) dan dicirikan dengan difraktogram (XRD), mikroskop elektron (SEM) dan sinar-X penyebaran tenaga (EDS). Dapatan dari analisis XRD, semua sampel menunjukkan struktur wurtzit heksagon dengan ukuran kristal kira-kira dalam julat 74.82-81.64 nm. Hasil SEM-EDS menunjukkan bahawa sampel ZnO yang didopkan dengan Mg terdiri daripada unsur Zn, O dan Mg. Aktiviti foto-penguraian ZnO dan Mg-doped ZnO dikaji dengan menjalankan pemerhatian penguraian larutan akues MB di bawah sinaran ultraviolet. Hasil kajian menunjukkan bahawa sampel 1 mol% ZnO yang didopkan dengan Mg menunjukkan peningkatan kecekapan fotomangkin dengan peratusan penguraian 89.54% dan kadar penguraian tetap, k 0.0432 min^{-1}. Penyerapan yang lebih meluas di kawasan cahaya nampak, penghambatan pengumpulan semula elektron dan lubang yang terangsang dengan foto, dan foto penguraian larutan akues metilena biru yang lebih tinggi pada permukaan fotokatalis ZnO yang didopkan dengan Mg mungkin menyumbang kepada peningkatan aktiviti fotokatalitik.

Kata kunci: magnesium, metilena biru, pemangkin, fotokatalitik, ZnO

Introduction

Environmental contamination has recently been recognized as one of the most serious challenges confronting modern society, with contamination of natural water supplies being the most serious, owing primarily to unmeasured population growth and increased industrial activity. The textile sector is one of the industrial processes that produces enormous amounts of wastewater. The dye effluent and colored discharge disposed into the water causes a significant impact on aquatic life and the environment due to their high stability under ambient conditions. As a result, researchers have focused on removing azo dyes from wastewater to comply with severe environmental requirements. Up to now, various treatment methods such as physical methods and chemical methods have been investigated to remove azo dyes [1]. Generally, the wastewater treatment process should be cost-effective and feasible for large-scale applications [2]. Overall, wastewater treatment might save a lot of water, and the treated water could be recycled or reused in industries like textiles and agriculture.

Recently, the utilization of oxide semiconductor nanomaterials as effective photocatalysts in wastewater treatment has become a subject of major concern [3]. Among the oxide semiconductors, zinc oxide (ZnO) is chosen as the semiconducting photocatalyst for pollution treatment in water because of its advantages such as easy to prepare, abundance, low cost, photostability, and large exciton binding energy of 60 MeV [4,5]. It also has a direct band gap energy at 3.37 eV at room temperature, making it a suitable candidate in absorbing UV-light as an excitation source [6]. Several researchers reported that ZnO has good photocatalytic activity and shows the appropriate activity in the range of solar radiation [7–9]. Unfortunately, the industrial application of ZnO in the photocatalytic field has been impeded by two significant limitations which are (i) ZnO has a high recombination ratio of photo-induced electron-hole pairs, which limits its photocatalytic effectiveness; and (ii) ZnO largely absorbs ultraviolet light (380 nm) and can only be activated by visible light, restricting its photocatalytic activity in the visible light region [10,11]. Proposing effective techniques to improve visible light absorption and reduce recombination of photo-generated electron-hole pairs to achieve high-efficiency photocatalysts is therefore critical. One of the most common methods for achieving these goals is via metal doping [12,13]. Recently, efforts have been made to improve the photocatalytic activities of ZnO nanostructures by doping various chemical elements such Al [14,15], Ni [16,17], Fe [18–20] and Ag [21,22]. Other than that, there is also a possibility that Mg-doping can also improve the photocatalytic activity of ZnO nanostructures by creating oxygen or zinc vacancies, due to the similar ionic radii of Zn^{2+} (0.060 nm) and Mg^{2+}(0.057 nm) [23–25].

In this work, Mg-doped ZnO at various concentration (1 – 10 mol%) were prepared through sol-gel method. The structural and morphological properties were characterized by XRD, and SEM equipped with EDS. Furthermore, the photocatalytic activities of pure ZnO and Mg-doped ZnO were also studied by degrading methylene blue (MB) in water.

Materials and Methods

Synthesis of photocatalyst

Commercial zinc oxide powder (denoted as pure ZnO) and magnesium nitrate ($Mg(NO_3)_2$) were purchased from Sigma-Aldrich with 99 % purity while hexamethylenetetramine (HMTA) was purchased from R&M chemicals with 99.5 % purity. For photocatalytic study {[7-(dimethylamino) phenothiazin-3-ylidene]-dimethylazanium;chloride} ($C_{16}H_{18}ClN_{13}S$) commonly known as methylene blue dye was used. The aqueous solutions were prepared with deionized water throughout the experimental process.

Mg-doped ZnO photocatalysts were synthesized using a modified sol-gel method as our previous work [26]. A mixture solution was prepared by dissolving the commercial ZnO powder and HMTA at constant molar concentration of 0.1 M in 100 ml of deionized water. For the synthesis of Mg-doped ZnO samples, magnesium nitrate ($Mg(NO_3)_2$) as a dopant source was added into the mixture solution at different mol % concentration of 1, 3, 5, 7 and 10 with respect to Zn, respectively. The mixed solution was magnetically stirred at 95 °C for 2 h to gain a homogenous mixture under vigorous stirring. The solution was aged for 24 h until a homogenous gel was formed. Next, the resulting gel was then collected and rinsed thoroughly using deionized water, followed by a drying process at 300 °C for 2 h. The pure ZnO and prepared Mg-doped ZnO photocatalysts at different doping concentration were characterized using several techniques. The crystal structures and phases of prepared nanoparticles were examined through X-ray diffraction (XRD) (PANanalytical) X'pert Pro powder diffraction equipment using Cu-Kα radiation (k = 1.54056 Å). The estimated crystallite size of pure ZnO and Mg-doped ZnO at various mol % concentration were obtained and calculated by using Scherer's as in equation (1) below [26]:

$$d = k\lambda\, \beta cos\theta \qquad (1)$$

Where k is the constant dependent on crystallite shape (0.94 nm), λ is the X-ray wavelength (1.54 Å), β is referring to the full width at the half max (FWHM) of the sample and θ is the Bragg's diffraction angle. The morphology of chosen samples was characterized by using field emission scanning electron microscopy (FE-SEM) (JEOL JSM-7600F). Subsequently, the samples were then used for photocatalytic degradation measurement.

Photodegradation evaluation

The photocatalytic activities of the pure ZnO and Mg-doped ZnO photocatalyst were evaluated by determining the degradation of methylene blue (MB) in aqueous solution on each interval at constant room temperature. The amount of catalyst used was 10 mg of pure ZnO and Mg-doped ZnO in a beaker containing 100 ml of MB solution with 5mg/L as the initial concentration. The UV-light with 365 nm wavelength with the definite power of 12 W, 230 Volts and 50 Hz frequency was used as a light source. Before switching on the lamp, the mixture was stirred in the dark for 30 min to reach adsorption-desorption equilibrium between the photocatalyst and MB. 5 ml of aliquots were extracted out at every 10 min interval and was monitored for 1 h. The schematic expression of experimental setup of photocatalytic measurement is shown in Figure 1. The photocatalytic analysis was performed using UV–Vis spectrophotometer under absorbance, (A), mode. The residual concentration of MB was measured at 664 nm using UV-vis spectrophotometer (Shidmadzu UV-1800UV). The percentage of degradation (%) was measured regarding the maximum photodegradation collected at each interval using the equation below:

$$\text{Degradation percentage (\%)} = (C_0 - C)/ C_0 \times 100 \qquad (2)$$

in which C_0 is the initial dye concentration and C being the dye concentration at time t, respectively. Photodegradation rate constant, k, was also calculated for all the samples.

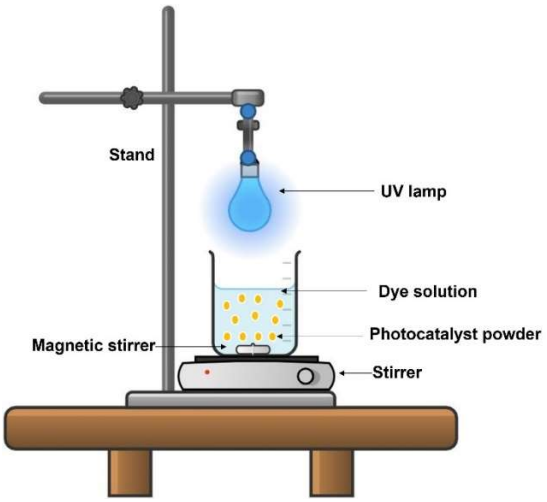


Figure 1. Schematic photodegradation measurement setup for degradation of methylene blue (MB)

Results and Discussion

Morphology of pure ZnO and Mg-doped ZnO

The morphology of pure ZnO and selected Mg-doped ZnO photocatalysts were recorded using FESEM and displayed in Figure 2. The images of pure ZnO (Figure 2(a) and (b)) were recorded at different magnification portrayed irregular rod-cubic like structures with approximately of 100- 500 nm dimensions. Image (c-d) and (e-f) represents 1 mol % Mg-doped ZnO and 10 mol % Mg-doped ZnO morphology and it was clearly seen that, similar rod-cubic like structures was formed for Mg-doped ZnO which were evenly distributed and well dispersed with the size similar to pure ZnO. Moreover, from the highly magnified image, the doping of Mg to the ZnO was not clearly shown. Besides, there are no significant changes on their size and morphology when Mg is doped to ZnO, and this might be due to the little amount of dopant that has been used during the synthesis method.

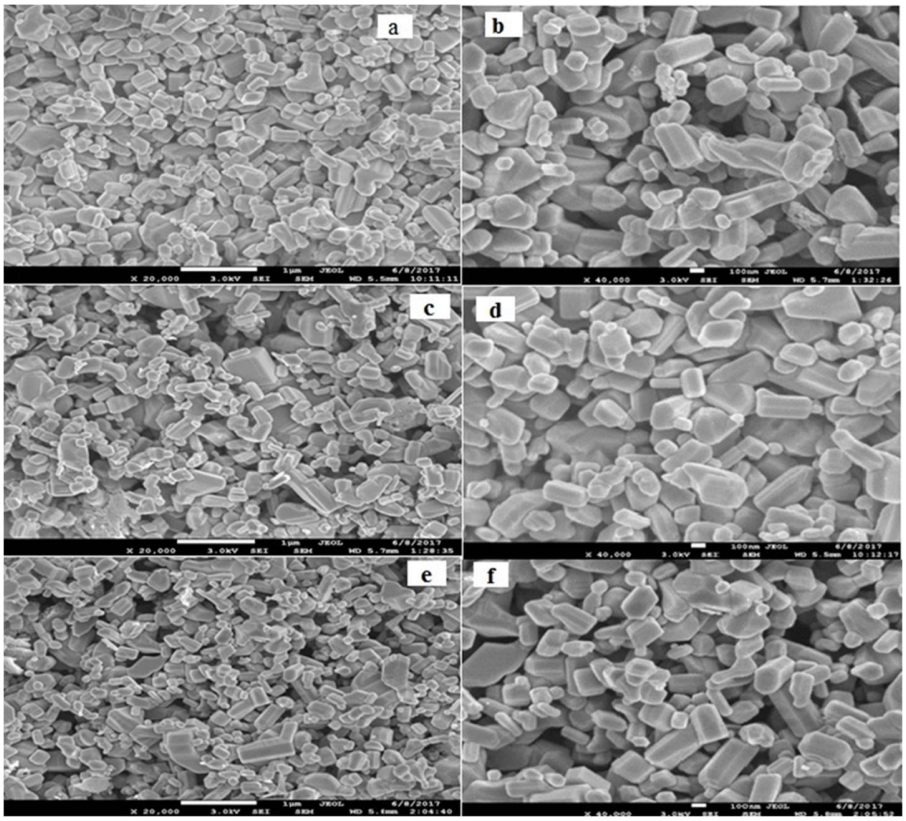


Figure 2. FESEM images of (a-b) pure ZnO, (c-d) 1 mol % Mg-doped ZnO and (d-e) 10 mol % Mg-doped ZnO at magnification 20, 000x and 40,000x

X-ray diffraction analysis

The structural properties of pure ZnO and Mg-doped ZnO photocatalysts were studied using XRD. Figure 3 represents the XRD spectra of pure ZnO and Mg-doped ZnO at different mol % of 1, 3, 5, 7 and 10, respectively. According to the XRD patterns, all the samples were highly crystalline with five major peaks that revealed the presence of hexagonal wurtzite structure of ZnO and the samples were excellent crystalline in nature. The diffraction peaks were identified at 2θ = 31.75°, 34.48°, 36.20°, 47.69°, 56.72°, 62.85°, 66.53°, 67.88° and 69.09° indexed to (100), (002), (101), (102), (110), (103), (200), (112) and (201) being in good agreement with those of JCPDS card no. (No. 05-0664) [24, 27]. Besides, there were no corresponding peak related to Mg or MgO phase due to low amount of dopant that had been used during the synthesis method, which suggested that the presence of Mg was in the form of impurity atom [28, 29]. Similar phenomenon was also reported by Moulahi et al. [30] who prepared the Mg-doped ZnO nanostructures at different concentrations via a polyol process. They observed the pure phase formation of ZnO for all the composition of Mg-doped ZnO nanostructures. Furthermore, they also found a small shift towards a higher angle with Mg concentration, suggesting the decrease of the crystallites size and which similar findings had been observed in this work.

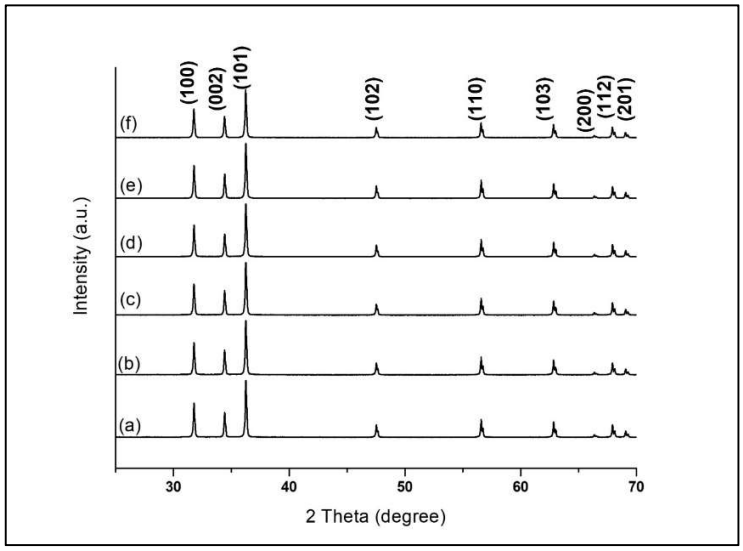


Figure 3. XRD spectra of (a) pure ZnO and Mg-doped ZnO at (b) 1, (c) 3, (d) 5, (e) 7 and (f) 10 mol % in the range of 25 – 70° prepared using modified sol-gel method

The estimated crystallite size was calculated using Scherer equation and was found to be 81.64, 80.50, 80.12, 76.65, 76.17 and 74.82 nm for pure ZnO and Mg-doped ZnO with different concentration (1, 3, 5, 7 and 10 mol %) respectively. Table 1 shows the attributed peak, FWHM and calculated value of estimated crystallite size of pure ZnO and Mg-doped ZnO at different concentration. It can be observed that the FHWM value increased as higher concentration was incorporated into the ZnO from the pure ZnO up to 10 mol % Mg-doped ZnO and the estimated crystallite sizes of the samples were found to decrease as the concentration of Mg dopant was increased. Based on Alam et al. [31] the diffraction peak shifted and wider FWHM with consistent increased in Mg doping is an indication of doping, suggesting a higher defect concentration and decreased quality of crystal with increased in Mg doping concentration. Moreover, because the ionic radii of Zn and Mg ions are similar (0.060 nm and 0.057 nm), Mg ions are expected to be replaced with Zn ions [32].

Table 1. Estimated crystallite size of pure ZnO and Mg-doped ZnO at different concentration obtained from (101) peak

Sample	Highest Peak (2θ degrees)	FWHM, β (degrees)	Estimated Crystallite Size, D (nm)
Pure ZnO	36.25	0.10693	81.64
1 mol% Mg-doped ZnO	36.25	0.10845	80.50
3 mol% Mg-doped ZnO	36.25	0.10896	80.12
5 mol% Mg-doped ZnO	36.25	0.11390	76.65
7 mol% Mg-doped ZnO	36.25	0.11461	76.17
10 mol% Mg-doped ZnO	36.23	0.11668	74.82

Photocatalytic activities analysis

Photocatalytic degradation measurements were carried out for all photocatalyst. The degradation of MB dye was measured by using pure ZnO and Mg-doped ZnO photocatalyst at different concentrations i.e., 1, 3, 5, 7 and 10 mol%, respectively under UV light irradiation for 60 minutes. Figure 4(a) shows the percentage degradation of MB under the UV light tested with the pure ZnO and Mg-doped ZnO at different concentrations. From Figure 4(a), it can be observed that the percentage of degradation of 1 mol% shows the highest percentage degradation with value of 89.54% compared to pure ZnO and other Mg-doped ZnO samples. Once 3 and 5 mol% was incorporated to the Mg-doped ZnO, the percentage of degradation showed a decrease pattern with the value of 82.99% and 84.78% and started to increase when doped with 7 (88.05%) and decreased back to 86.88% when 10 mol% Mg was applied indicating that optimization of concentration of dopant is significant to the performance of photocatalyst.

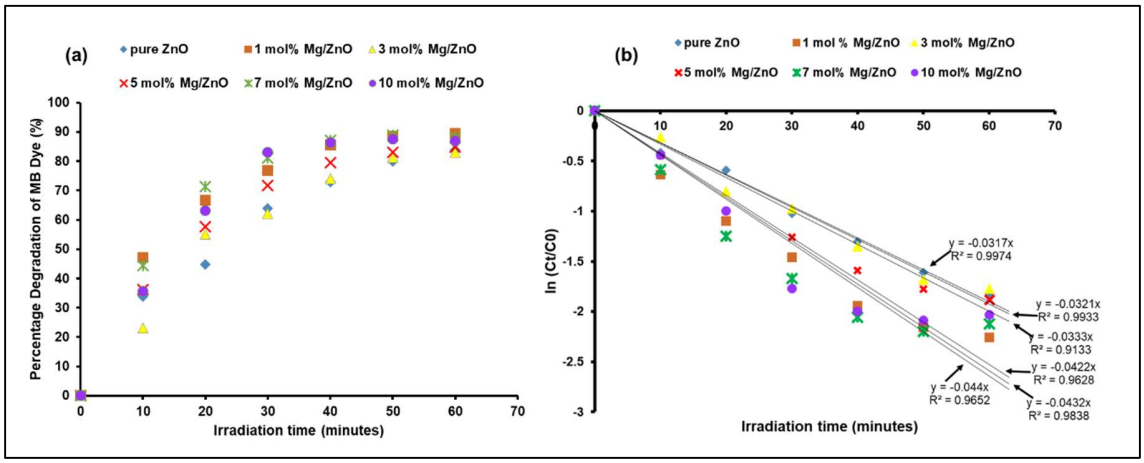


Figure 4. Plot of (a) Percentage of degradation of pure ZnO and Mg-doped ZnO and (b) ln (C/C0) vs. irradiation time for the degradation of MB using pure ZnO and Mg-doped ZnO

Vargas et al. synthesized ZnO doped with MgO in different concentrations (1, 2 and 4 mol%) using Pechini polymer precursor method and reported on the effect of MgO doped on the pollutant removal [33]. They observed that the degradation of MO dye solution was effective using MgO doped ZnO compared to ZnO samples and 2% Mg showed the most efficient in removing MO with a degradation percentage of 73% in 3 h irradiation time. Another study done by Okeke et al. worked on pure and Mg-doped ZnO prepared by one step simple process. They determined that the photodegradation performance of Mg-doped ZnO

against MB dye solution have a greater degradation percentage; more than 50% after 100 min of exposure light [32]. It is worth noting that the doped sample significantly enhanced the photocatalytic activities which is associated to the higher surface defects and smaller particle size, which consequently aid in the separation of photo-generated electron-holes pairs and slowing of their recombination rate.

The photodegradation rate constant, k of pure ZnO and Mg-doped ZnO has been assessed using the kinetic model suggested by Langmuir-Hinshelwood, which is pseudo-first kinetics model of photocatalysis [34] as stated in the Equation 3, as follows:

$$\ln(Ct/Co) = -kt \quad (3)$$

Where Ct/Co is the ratio of dye concentration at adsorption-desorption equilibrium of those at different time intervals (t) and k is the photodegradation rate constant. The results are shown in Figure 4(b) and the photodegradation rate constant value, k was obtained from the linear fitting of the plotted graph. The observed k values are listed in Table 2 together with percentage degradation of MB dye. It can be seen that, 1 mol% Mg-doped ZnO exhibited the highest photodegradation rate constant, k with value of 0.0432 min^{-1} compared to pure ZnO and other samples. Enhancement of the photocatalytic activity of 1 mol % Mg-doped ZnO compared to pure ZnO might be attributed to the increasing of surface area considering that the photocatalytic reaction occurred on the catalyst surface [35]. Moreover, as reported by Wang et al., doping of Mg^{2+} into ZnO increased the width of the band gap and therefore enhanced the photocatalytic performance as it could effectively delay the electron-hole recombination from valence band to conduction band [25]. Moreover, it can be observed that Mg-doped ZnO prepared by higher than 1 mol% Mg shows a decreasing performance which this might be due to an excessive Mg content which resulting in agglomeration of particles hence the photodegradation rate will be saturate. Samanta et al. reported that the photocatalytic performance was reduced when more Mg is loaded and concluded that there exists an optimum amount of Mg for enhancing the catalytic degradation process that influenced by band gap energy and crystallite size of the photocatalyst [36].

Table 2. Photocatalytic performance of pure ZnO and Mg-doped ZnO at different concentration

Sample	Percentage Degradation, (%) after 60 minutes	Photodegradation Rate Constant (k, min^{-1})	R^2 Value
Pure ZnO	83.86	0.0317	0.9974
1 mol% Mg-doped ZnO	89.54	0.0432	0.9838
3 mol% Mg-doped ZnO	82.99	0.0321	0.9933
5 mol% Mg-doped ZnO	84.74	0.0333	0.9133
7 mol% Mg-doped ZnO	88.05	0.4290	0.9601
10 mol% Mg-doped ZnO	86.88	0.0422	0.9628

Conclusion

Mg-doped ZnO at various concentrations were successfully prepared using sol-gel method and characterized by FESEM and XRD analysis. XRD results revealed that Mg is substituted in ZnO without altering its hexagonal wurtzite structure. FESEM analysis revealed that surface features of ZnO shows an irregular rod-cubic like structures with approximately of 100- 500 nm dimensions for all samples. For photodegradation analysis, after comparison with pure ZnO and other doped Mg-doped ZnO samples, 1 mol % Mg-doped ZnO exhibited better photocatalytic activity with degradation percentage of 89.54 % and photodegradation rate constant, k value of 0.0432 min^{-1}, respectively. These results suggest that doping play a crucial role in the efficiency of ZnO photocatalytic activities and the improved performance of Mg-doped ZnO suggests that it could be used as an alternate

photocatalyst for environmental problem.

Acknowledgement

Authors would like to thank the Ministry of Higher Education Malaysia for funding research project FRGS-RACER (600-IRMI/FRGS-RACER 5/3 (041/2019) and the Universiti Teknologi MARA Pahang Branch, as well as the Center for Nanomaterials Research, Institute of Science, Universiti Teknologi MARA Shah Alam, Selangor, Malaysia, for providing the research facilities.

References

1. Adam, R. E., Alnoor, H., Pozina, G., Liu, X., Willander, M. and Nur, O. (2020). Synthesis of Mg-doped ZnO NPs via a chemical low-temperature method and investigation of the efficient photocatalytic activity for the degradation of dyes under solar light. *Solid State Sciences*, 99: 106053.
2. Ahmad, M., Ahmed, E., Zhang, Y., Khalid, N. R., Xu, J., Ullah, M. and Hong, Z. (2013). Preparation of highly efficient Al-doped ZnO photocatalyst by combustion synthesis. *Current Applied Physics*, 13: 697-704.
3. Alam, M. S., Manzoor, U., Mujahid, M. and Bhatti, A. S. (2016). Highly responsive UV light sensors using Mg-doped ZnO nanoparticles. *Journal of Sensors,* 2016: 1-5.
4. Gaurav, K.U., Jeevitesh, K. R., Trilok, K. P., Vinod. K. and Purohit, L. P. (2019). Synthesis of ZnO:TiO_2 nanocomposites for photocatalyst application in visible light. *Vaccuum*, 160: 154-163.
5. Chen, C., Mei, W. and Yu, W. (2018). Enhanced sunlight-driven photocatalytic property of Mg-doped ZnO nanocomposites with three-dimensional graphene oxide/MoS_2 nanosheet composites. *RSC Advances,* 17399-17409.
6. Di Mauro, A., Farrugia, C., Abela, S., Ref Alo, P., Grech, M., Falqui, L., Nicotra, G., Sfuncia, G., Mio, A., Buccheri, M. A., Rappazzo, G., Brundo, M. V., Scalisi, E. M., Pecoraro, R., Iaria, C., Privitera, V. and Impellizzeri, G. (2020). Ag/ZnO/PMMA nanocomposites for efficient water reuse. *ACS Applied Bio Materials*, 3(7): 4417-4426.
7. Zhang, N. and Cu, D. (2019). Fabrication of flower-like hierarchical ZnO nanostructures with enhanced photocatalytic activity. *Surfaces and Interfaces*, 14: 251-255.
8. Ivetic, T. B., Dimitrievska, M. R. R., Fincue, N. L., Dacanin, L. R., Gúth, I. O. O., Abramovic, B. F. and Lukic-Petrovic, S. R. (2014). Effect of annealing temperature on structural and optical properties of Mg-doped ZnO nanoparticles and their photocatalytic efficiency in alprazolam degradation. *Ceramics International*, 40(1): 1545-1552.
9. Khaki, M. R. D., Shafeeyan, M. S., Raman, A. A. A. and Daud, W. M. A. W. (2017). Application of doped photocatalysts for organic pollutant degradation - A review. *Journal of Environmental Management*, 198: 78-94.
10. Li, W., Wang, G., Feng, Y. and Li, Z. (2018). Efficient photocatalytic performance enhancement in Co-doped ZnO nanowires coupled with CuS nanoparticles. *Applied Surface Science*, 428: 154-164.
11. Mardikar, S. P., Kulkarni, S. and Adhyapak, P. V. (2020). Sunlight driven highly efficient degradation of methylene blue by CuO-ZnO nanoflowers. *Journal of Environmental Chemical Engineering*, 8(2): 105065.
12. Abdolhoseinzadeh, A. and Sheibani, A. (2020). Enhanced photocatalytic performance of Cu_2O nano-photocatalyst powder modified by ball milling and ZnO. *Advanced Powder Technology*, 31: 40-50.
13. Moulahi, A. (2021). Efficient photocatalytic performance of Mg doping ZnO for the photodegradation of the rhodamine B. *Inorganic Chemistry Communications*, 133: 108906.
14. Mousavi, S. M., Mahjoub, A. R. and Abazari, R. (2017). Facile green fabrication of nanostructural Ni-doped ZnO hollow sphere as an advanced photocatalytic material for dye degradation. *Journal of Molecular Liquids*, 242: 512-519.
15. Nsib, M. F., Saafi, S., Rayes, A., Moussa, N. and Houas, A. (2016). Enhanced photocatalytic performance of Ni–ZnO/Polyaniline composite for the visible-light driven hydrogen generation. *Journal of the Energy Institute*, 89(4): 694-703.

16. Ong, C. B., Ng, L. Y. and Mohammad, A. W. (2018). A review of ZnO nanoparticles as solar photocatalysts: Synthesis, mechanisms and applications. *Renewable and Sustainable Energy Reviews*, 81: 536-551.
17. Pascariu, P., Tudose, I. V., Suchea, M., Koudoumas, E., Fifere, N. and Airinei, A. (2018). Preparation and characterization of Ni, Co doped ZnO nanoparticles for photocatalytic applications. *Applied Surface Science*, 448: 481-488.
18. Priscilla, S. J., Daniel, R., Dhakshayani, Y., Caroline, S. C. and Sivaji, K. (2021). Effect of magnesium dopant on the structural , morphological and electrical properties of ZnO nanoparticles by sol – gel method. *Materials Today: Proceedings*, 36: 793-796.
19. Raji, R., Sibi, K. S. and Gopchandran, K. G. (2018). ZnO:Ag nanorods as efficient photocatalysts: Sunlight driven photocatalytic degradation of sulforhodamine B. *Applied Surface Science*, 427: 863-875.
20. Rafaie, H. A., Aliyah, N., Nazam, A. M., Infaza, N., Ramli, T. and Mohamed, R. (2021). *S*ynthesis, characterization and photocatalytic activities of Al-doped ZnO for degradation of methyl orange dye under UV light irradiation. *Journal of the Australian Ceramic Society,* 57(2): 479-488.
21. Türkyılmaz, Ş. Ş., Güy, N. and Özacar, M. (2017). Photocatalytic efficiencies of Ni, Mn, Fe and Ag doped ZnO nanostructures synthesized by hydrothermal method: The synergistic/antagonistic effect between ZnO and metals. *Journal of Photochemistry and Photobiology A: Chemistry*, 341: 39-50.
22. Saleh, R. and Djaja, N. F. (2014). UV light photocatalytic degradation of organic dyes with Fe-doped ZnO nanoparticles. *Superlattices and Microstructures*, 74: 217-233.
23. Sengupta, J., Ahmed, A. and Labar, R. (2013). Structural and optical properties of post annealed Mg doped ZnO thin films deposited by the sol–gel method. *Materials Letters*, 109: 265-268.
24. Sharma, S., Vyas, R., Sharma, N., Singh, V., Singh, A., Kataria, V., Gupta, B. K. and Vijay, Y. K. (2013). Highly efficient green light harvesting from Mg doped ZnO nanoparticles: Structural and optical studies. *Journal of Alloys and Compounds*, 552: 208-212.
25. Riffat. S.., Momina, K, Vaneeza, A., Zohra, N.K., Unza, T. and Faiza, A. (2020). Effect of Mg doping on structural, morphological, optical and thermal properties of ZnO nanoparticles. *Optic*, 200*:* 163428.
26. Wolski, L., Whitten, J. E., Sobczak, I. and Ziolek, M. (2017). The effect of the preparation procedure on the morphology , texture and photocatalytic properties of ZnO. *Materials Research Bulletin*, 85: 35-46.
27. Tan, W. K., Abdul Razak, K., Lockman, Z., Kawamura, G., Muto, H. and Matsuda, A. (2013). Photoluminescence properties of rod-like Ce-doped ZnO nanostructured films formed by hot-water treatment of sol–gel derived coating. *Optical Materials*, 35(11): 1902-1907.
28. Wang, L., Wu, Y., Chen, F. and Yang, X. (2014). Photocatalytic enhancement of Mg-doped ZnO nanocrystals hybridized with reduced graphene oxide sheets. *Progress in Natural Science: Materials International*, 24(1): 6-12.
29. Wang, M., Xu, J., Sun, T., Tang, Y., Jiang, G. and Shi, Y. (2018). Facile photochemical synthesis of hierarchical cake-like ZnO/Ag composites with enhanced visible-light photocatalytic activities. *Materials Letters*, 219: 236-239.
30. Wang, W., Li, N., Hong, K., Guo, H., Ding, R. and Xia, Z. (2019). Z-scheme recyclable photocatalysts based on fl ower-like nickel zinc ferrite nanoparticles/ZnO nanorods: Enhanced activity under UV and visible irradiation. *Journal of Alloys and Compounds*, 777: 1108-1114.
31. Wassel, A. R., El-Naggar, M. E. and Shoueir, K. (2020). Recent advances in polymer/metal/metal oxide hybrid nanostructures for catalytic applications: A review. *Journal of Environmental Chemical Engineering*, 8(5): 104175.
32. Okeke, I.S., Agwu, A.A., Ubachukwu, I.G., Madiba, I.G, Maaza, M., Whyte, G.M. and Ezema, F.I. (2021). Impact of particle size and surface defects on antibacterial and photocatalytic activities of undoped and Mg-doped ZnO nanoparticles, biosynthesized using one-step simple process. *Vaccum*, 187: 110110.

33. M´onica , A. V., Eric, M. R., Jesús, E. D., Edgar, E. M. and Jorge, E. R. (2021). Nanoparticles of ZnO and Mg-doped ZnO: Synthesis, characterization and efficient removal of methyl orange (MO) from aqueous solution. *Ceramic international,* 47: 15668-15681.
34. Yun, S., Lee, J., Yang, J. and Lim, S. (2010). Hydrothermal synthesis of Al-doped ZnO nanorod arrays on Si substrate. *Physica B*, 405(1): 413-419.
35. Etacheri,V., Roshan, R. and V. Kumar. (2012). Mg-doped ZnO nanoparticles for efficient sunlight-driven photocatalysis. *Applied Materials Interfaces,* 4: 2717-2725.
36. Samanta, A., Goswami, M. N. and Mahapatra, P. K. (2018). Optical properties and enhanced photocatalytic activity of Mg-doped ZnO nanoparticles. *Physica E: Low-dimensional System and Nanostructures*, 104*:* 254-260.

Malaysian Journal of Analytical Sciences (MJAS)
Published by Malaysian Analytical Sciences Society

A REVIEW OF THE SYNTHESIS AND MODIFICATION OF PVA-ALGINATE AS BINDER OF METAL ATOM

(Ulasan Tentang Sintesis dan Pengubahsuaian PVA-Alginat Sebagai Pengikat Atom Logam)

Norul Azilah Abdul Rahman[1,2*], Mazni Musa[1], Karimah Kassim[3], and Nur Rahimah Said[1*]

[1]*School of Chemistry and Environment,*
Universiti Teknologi MARA, Cawangan Negeri Sembilan,
Kampus Kuala Pilah, 72000 Kuala Pilah, Negeri Sembilan, Malaysia
[2]*School of Chemistry and Environment,*
Faculty of Applied Sciences,
Universiti Teknologi MARA, 40450 Shah Alam, Selangor, Malaysia
[3]*Institute of Science (IOS),*
Level 3, Block C, Kompleks Inspirasi,
Universiti Teknologi MARA, 40450 Shah Alam, Selangor, Malaysia

[*]*Corresponding author: nurra1435@uitm.edu.my*

Received: 23 September 2022; Accepted: 17 January 2023; Published: 19 April 2023

Abstract

PVA-alginate hydrogel is formed by mixing PVA and alginate with a simple method and then dropping it into a cross-linking agent that leads to rapid gelation. The PVA-alginate hydrogel can be synthesised in water due to the high solubility of starting material. Both compounds have hydroxyl group (-OH) in their structure that helps in terms of solubility and is consequently classified as an inexpensive, safe, and environmentally friendly synthesis method. Although its starting material is soluble in water, the PVA-alginate hydrogel is lessened. This is because the formation of hydrogen bonding of -OH in the PVA-alginate structure reduces its ability. Meanwhile, the presence of carboxyl ion ($-COO^-$) in the PVA-alginate hydrogel structure acts as an active site for the metal ion to bind. Some researchers modified the PVA-alginate hydrogel to improve the binding effect to metal by increasing the active sites of metal. The PVA-alginate hydrogel can act as a metal ion binder to remove heavy metals such example from transition metal elements in wastewater that are considered harmful to the ecosystem. This review provides an overview of PVA-alginate hydrogel design and its modification to improve the binding properties, and cross-linking. Finally, the limitation of PVA-alginate and its modification were revealed with suggestions for future research in the catalytic study.

Keywords: PVA-alginate, metal binder, metal

Abstrak

Hidrogel PVA-alginat dihasilkan melalui percampuran PVA dan alginat dengan mengunakan kaedah yang mudah dan kemudian dititiskan ke dalam agen penghubung silang untuk mempercepatkan gelatin. Hidrogel PVA-alginat boleh disintesis dalam air kerana keterlarutan bahan permulaan yang tinggi. Kedua-dua sebatian mempunyai kumpulan hidroksil (-OH) dalam strukturnya yang membantu dari segi keterlarutan dan seterusnya dikelaskan sebagai kaedah sintesis yang murah, selamat dan mesra alam. Walaupun bahan permulaannya mempunyai sifat larut dalam air, PVA-algina berkurangan disebabkan pembentukan ikatan hidrogen -OH

dalam struktur hydrogel PVA-alginat mengurangkan keupayaannya. Sementara itu, kehadiran ion karboksil (-COO^-) dalam struktur PVA-alginat bertindak sebagai tapak aktif untuk pengikat ion logam. Sesetengah penyelidik mengubah suai hydrogel PVA-alginat untuk meningkatkan kesan pengikatan kepada logam dengan meningkatkan tapak aktif logam. Hidrogel PVA-alginat boleh bertindak sebagai pengikat ion logam untuk membuang logam berat contohnya daripada unsur logam peralihan dalam air sisa yang dianggap berbahaya kepada ekosistem. Kajian ini memberikan gambaran keseluruhan reka bentuk hidrogel PVA-alginat dan pengubahsuaiannya untuk meningkatkan sifat mengikat dan pautan silang. Akhirnya, batasan hidrogel PVA-alginat dan pengubahsuaiannya telah didedahkan dengan cadangan untuk penyelidikan dalam kajian pemangkin pada masa depan.

Kata kunci: PVA-alginat, pengikat logam, logam

Introduction

Heavy metals are emitted from mining, metallurgy, and manufacturing from the consumption of natural resources through the development of industry and agricultural activities. Low or trace-level concentrations of heavy metals in water are harmful to ecosystems. Industrial wastewater such as Ni, Pb, Hg, Cd, Cr, and As can interfere with the functioning of living creatures by binding with their vital cellular components. The clean-up of the contaminated water is very challenging because toxic metals are non-biodegradable [1,2]. Therefore, methods for the removal of heavy metal ions from wastewater are of great significance.

Chemical precipitation, coagulation, solvent extraction, membrane processes, electrochemical, ion exchange, and adsorption are methods for the removal of heavy metals [3]. Adsorption is the process of adsorbent as a binder that content active functional that bounded to the metal ions. Binding is a simple process, with high efficiency, and a low-cost method. Moreover, binding is an environmentally, and efficient binder used to bind heavy metals. Examples of biopolymers binder (alginate, chitosan, and cellulose hydrogels) are widely used for the removing heavy metals [4].

Alginate is widely used in research because it can be obtained in natural resources (the cell wall of brown algae) [5]. It is non-toxic and biodegradable of linear biopolymers. It has a rich carboxyl and hydroxyl functional group [4]. The presence of the carboxyl functional group has excellent form to bind with heavy metals in wastewater. The composition of alginate and cross-linking ions determines the binding strength and properties of alginate beads [5]. However, the mechanical strength, stability, and heat resistance of alginate beads are relatively low; hence their applicability is limited [1].

In research the polymer blend method is used to improve physicochemical properties of alginate. Poly(vinyl alcohol) (PVA) polymer is used to blend with alginate, it is a non-toxic, synthetic, high-strength polymer and environmentally friendly [6,7]. PVA contains a hydroxyl (-OH) group that can form hydrogen bond with -OH of alginate to form PVA-alginate (Figure 1) [8]. The produced PVA-alginate is physically stronger and more durable than alginate alone, in spite of the fact that both polymers are soluble in water [9]. Also, the chemical and physical properties of PVA-alginate can be improved by the addition of cross-link agent in the structure, such as calcium chloride ($CaCl_2$) [10-14] or the combination of $CaCl_2$ and boric acid [15-17].

PVA-alginate needs modification to improve its binding properties [18]. The aim of this review is to study the synthesis and modification of PVA-alginate to improve the binding properties. Modification of PVA-alginate is by using Polyaniline (PANI), Fe_2O_3 nanoparticles, γ-Fe_2O_3 nanoparticles, γ- Fe_2O_3-TiO_2, zeolite, zeolite-polyethylene oxide and carbon corncob- Zoogloea sp. MFQ7. The review also concentrates on suitable cross-links used to synthesis and modified PVA-alginate such as $CaCl_2$, $CaCl_2$-$B(OH)_3$ and glutaraldehyde.

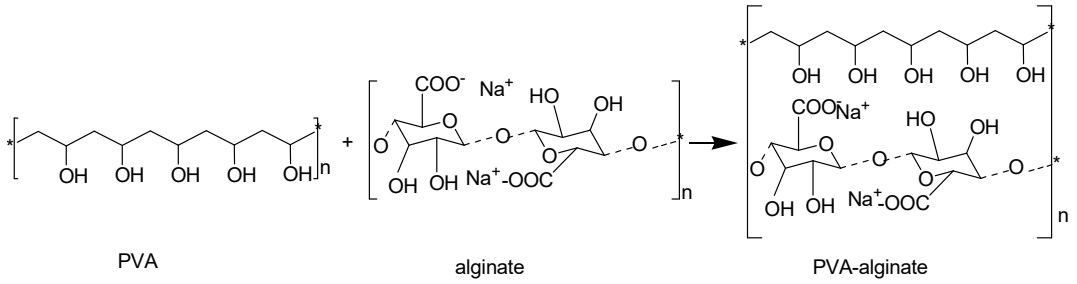


Figure 1. Chemical structure of PVA, alginate and PVA-alginate blended

Synthesis and Modification

In this paper, the PVA-alginate was synthesized by reaction between PVA and alginate. The discussion was continued with modification of PVA-alginate mixed either organic or inorganic or both compounds to take advantage of improving the binding properties. Then, capability of PVA-alginate as a binder with the transition metal was also scrutinized.

PVA has a lot of hydroxyl groups, which form hydrogen bonds with the water molecules and make it very soluble in water. The molecular weight and degree of PVA hydrolysis determine its solubility. The molecular weight is proportional to degree of hydrolysis. Meanwhile, the degree of hydrolysis is inversely correlated with its solubility. Due to the formation of intra- and inter- molecular hydrogen bonds between the hydroxyl groups amongst PVA (Figure 2), higher degree of hydrolysis was present and blunt its solubility in water. In contrast, inter- and intra- molecular hydrogen bonds are reduced due to the lower degrees of hydrolysis of steric hindrance brought on by a high concentration of hydrophobic acetate groups. Therefore, the solubility of PVA molecules in water molecules increased because the interaction of PVA and water increased [19,20].

Alginate is also soluble in water due to the presence of -COO^- and -OH functional group in the structure that can form a hydrogen bond with water. The molecular weight determines the solubility of alginate and its directly proportional to viscosity and degree of hydrolysis. The alginate has high viscosity because of the formation of a hydrogen bond due to the protonation of carboxylate groups in the backbone of alginate (Figure 3) [21]. To break the hydrogen bond between PVA and alginate during preparation by using water as a solvent is through heating [22], stirring [5], microwave [23] and distillation [22] process to form a homogenous PVA-alginate as shown in Table 1. Glycerin [7] and ferrofluids [23] are also used as solvent together with water. Preparation of PVA-alginate involves a single step (Number 10-13) or a few steps (Number 1-9). Form of PVA-alginate produced are beads [3,15], and fiber [22]. The temperature usually used is from 25 °C to 100 °C and duration to prepare PVA-alginate is 1 hours-24 hours.

Lee Te Chuan et al. [15] prepared PVA-alginate as binder of Cr^{6+}. PVA was dissolved in water and then heated with microwave for 1 minute, while alginate was also dissolved in water and stirred until dissolved. The PVA and alginate was blended until homogenous. PVA-alginate is a good binder of Cr^{6+}, where by 100% Cr^{6+} was bound to PVA-alginate. Li et al. [30] modified PVA-alginate in their study by using Polyaniline (PANI). Polyaniline (PANI) synthesized from phenylamine (PAN) was dissolved in acidified water and added with ammonium persulfate (APS). PANI obtained was added to PVA-alginate (Figure 4) because PANI contain many amine and imine functional groups, which is a good binder to metal. Amine and imine in PANI cause PANI to have three oxidation states, which are leucoemeraldine, emeraldine, and pernigraniline. During transition of PANI, electron donations occur from leucoemeraldine or emeraldine state to pernigraniline state. PVA-alginate-PANI was bound to Cr^{6+} at 95.25%.

Table 1. Preparation of PVA-alginate

No.	Step	PVA and/or Alginate	Solvent	Method	Temperature, °C	Hours	References
1	1	PVA	Water	Distillation	75-85	6	[22]
	2	Alginate	Water	Heat and stir	Not stated	Until dissolve	
	3	Mixed PVA-alginate		Stir	25	2	
2	1	PVA	Water	Microwave	100	0.017	[15]
	2	Alginate	Water	Stir	25	Dissolve	
	3	Mixed PVA-alginate		Stir		Homogenous	
3	1	PVA	Water	Heat	95	Dissolve then cools	[24]
	2						
	3	Add alginate			50	Dissolve	
4	1	PVA	Water	Stir	25	4	[23]
	2			Microwave		0.07	
	3	Alginate	Ferrofluid	Stir	25	Homogenous	
	4	Mixed PVA-alginate					
5	1	PVA	Water	Heat	80	4	[25]
	2			Microwave		0.07	
	3	Alginate	Water	-	-	-	
	4	Mixed PVA-alginate					
6	1	PVA	Water	Heat and stir Cool	80	2	[26]
	2			Stir			
	3	Alginate	Water		25	24	
	4	Mixed PVA-alginate					
7	1	PVA	Water	Heat	80	5	[18]
	2			Microwave	-	0.07	
	3	Alginate	Water	Stir	25	dissolve	
	4	Mixed PVA-alginate					
8	1	PVA-alginate	Water	Heat	90	1	[8]
	2			Stir	25	-until no burble	
9	1	Alginate	Water	Stir	25	Dissolve	[27]
	2	Add PVA		Heat and stir	80-85	3	
10	1	Alginate	Water	Stir	25	Dissolve	[5]
	2	Add PVA		Stir	25	dissolve	
11	1	PVA-alginate	Water	Heat and stir	90	dissolve	[28]
12	1	PVA-alginate	Water	Heat and stir	100	1	[6]
13	1	PVA-alginate	Water and glycerin	Heat and stir	95	Complete dissolved	[7]
14	1	PVA-alginate	Water	Heat	Not stated	Dissolve	[29]

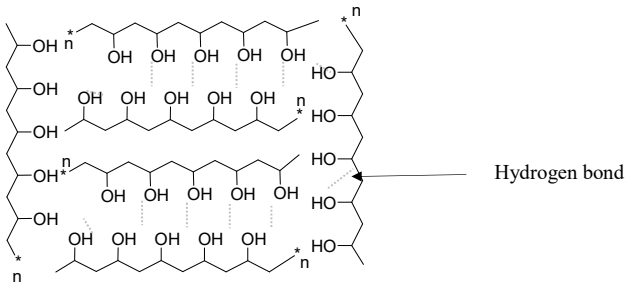


Figure 2. Hydrogen bond form between PVA

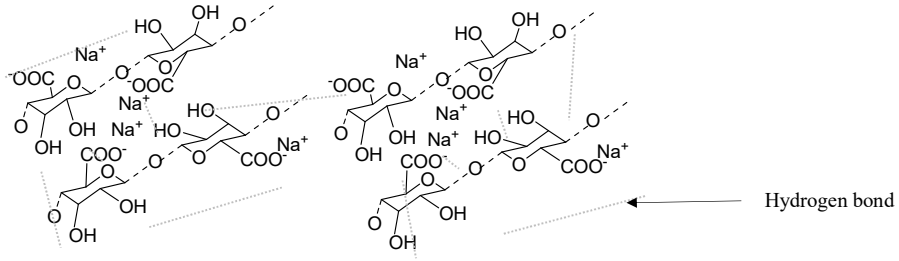


Figure 3. Hydrogen bonds formed between alginates

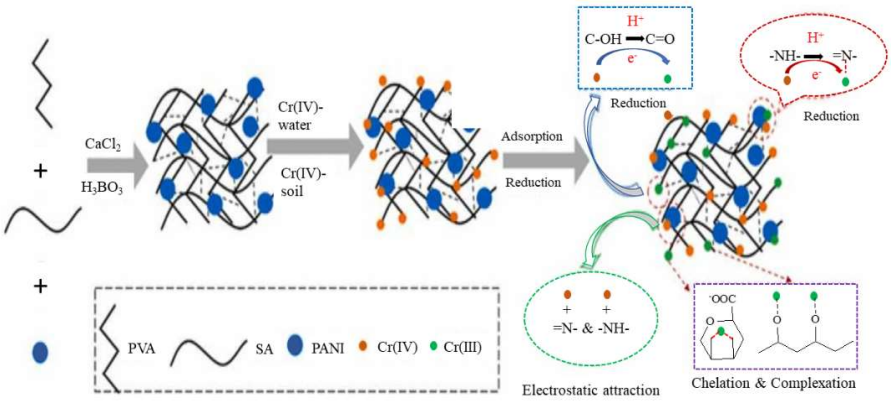


Figure 4. PVA-alginate-PANI as binder of Cr (VI) and Cr (III) [30]

Nie et al. [31] modified PVA-alginate by adding Fe_2O_3 which has surface that functionalize easily to bind with metals. Moreover, Fe_2O_3 have magnetic properties and superparamagnetic which leads to very high utilization in many fields. However, Fe_2O_3 nanoparticles are toxic causing limited usage. To reduce toxicity, they are blended with other polymers, proteins, silica or surfactant [32]. Nie synthesized Fe_2O_3 with green tea waste to reduce toxicity. Green tea was chosen because it is easy to find and many utilizations produce a lot of wastes. In addition, green tea waste contains a lot of hydroxyl groups and benzene rings known as polyphenols. Polyphenols are good as metal binders and have powerful reducibility. Fe_2O_3 was synthesized using

reflux $FeCl_2 \cdot 4H_2O$ and $FeCl_3$ dissolved in water and then added with ammonium hydroxide and heated. The Fe_2O_3 produced was added to green tea waste to obtain Fe_2O_3 nanoparticles. Fe_2O_3 was dissolve in water then added with PVA and alginate produce PVA-alginate- Fe_2O_3 nanoparticles. PVA-alginate-Fe_2O_3 nanoparticles (Figure 5) that were bound with Cr^{6+} and Cu^{2+} were 52.12 % and 59.78%, respectively. Result from three studies showed that the Cr^{6+} was excellently bound to PVA-alginate without modification.

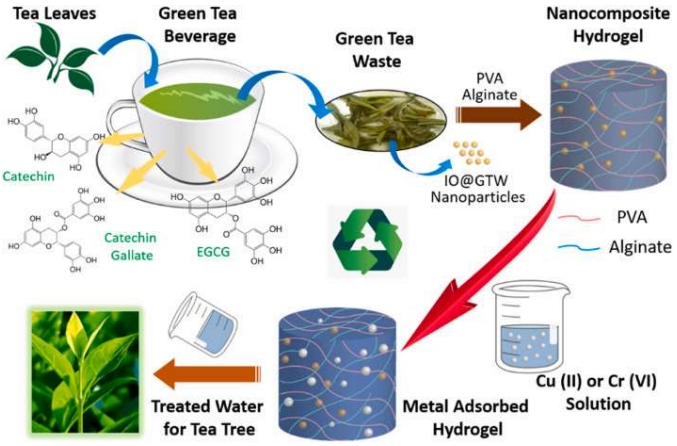


Figure 5. Synthesis of iron oxide nanoparticles by using green tea waste. Iron oxide nanoparticles were blended into PVA-alginate hydrogel to form PVA-alginate-Fe_2O_3 nanoparticles as a binder of Cu^{2+} and Cr^{6+} in an aqueous solution. The treated water was re-used for tea cultivation [31]

Zohreh Majidnia and Fulazzaky [3] also synthesized γ-Fe_2O_3 nanoparticles, magnetite (Fe_3O_4) precipitate which were acidified by using nitric acid form iron (III) nitrate nanoparticles. Then they were oxidized at 90 ºC. Then, γ-Fe_2O_3 nanoparticles were coated with trisodium citrate to remove all charges. The γ-Fe_2O_3 nanoparticles were blended with PVA-alginate to bind with Cs (I). PVA-alginate- γ-Fe_2O_3 nanoparticles that was successfully bound to Cs (I) was 91.8 %. In the study PVA-alginate also blended with titania (TiO_2) nanoparticles.

TiO_2 nanoparticles is non-toxic, have good stability, chemical and biological inert, with a larger surface area with relates to high binding properties (metal and non-metal) [33]. Zohreh Majidnia and Fulazzaky [3] prepared TiO_2 from titanium isopropoxide combined with acetyl acetone with presence of ethanol as solvent. The prepared solution was added with urea solution to deionized water via continuous stirring. The solution obtained was heated by using a furnace until yellowish white TiO_2 nanoparticles were obtained. The study found that PVA-alginate blended with TiO_2 able to bind to 90.1% Cs (I). They also prepared PVA-alginate blend with γ-Fe_2O_3 nanoparticles and TiO_2 nanoparticles. PVA-alginate- γ- Fe_2O_3-TiO_2 was successfully bound with 93.1% Cs (1). Therefore, PVA-alginate modified with Fe_2O_3 was suitable to bind more with Cs(I) that larger sized compared to Cr^{6+} small sized metal.

Ebrahimi et al. [22] synthesized PVA-alginate by reflux through distillation and stirring while alginate was heated and stirred. Then, PVA and alginate was blended until homogenous. PVA-alginate was used to bind with Cd^{2+} and it was found that 47.5% of Cd^{2+} could bind with PVA-alginate. Isawi [9] used the heating and stirring method to blend PVA and alginate. Then, zeolite was added to PVA-alginate due to its high binding properties because it is commonly used in the industry as a binder in ion-exchange separation and gas purification, molecular sieve, and soil modifier. Zeolites have a larger surface area with a small pore size. Moreover, it owes a

cage-like configuration which cause only medium size of metal ions to bind with zeolite. The larger surface area of zeolite is due to its structural form which is a three-dimensional tetrahedral framework in which each oxygen atom is shared by two tetrahedra, known as hydrated micro-porous alumino-silicate constituents [9].

Zeolite has a neutral charge caused by only Si in the structure. Substitution of Al in zeolite to replace Si causes its charge to be negative and need other metal ions (positive charge) to balance the charge, showing that it is very suitable to be a binder. Isawi [9] found PVA-alginate-zeolite (Figure 6) could bind to Pb^{2+}, Cd^{2+}, Sr^{2+}, Cu^{2+}, Zn^{2+}, Ni^{2+}, Mn^{2+}, and Li^{2+} at 99.5%, 99.2%, 98.8%, 97.2%, 95.6%, 93.1%, 92.4%, and 74.5% respectively, under pH 6. Meanwhile binding with Fe^{3+} and Al^{3+} that occurred at pH 5 were 96.5 % and 94.9 %, respectively although the binding process just allocated PVA-alginate-zeolite in solution that contained metal with shaking. Tabatabaeefar et al. [34] also used PVA-alginate-zeolite to bind with Ni^{2+} and Co^{2+} under pH 5.5 and reported that the percentages of Ni^{2+} and Co^{2+} bound were 83.7 and 84 %, respectively. A study done by Ebrahimi, et al. [22], Isawi [9] and Tabatabaeefar et al.[34] showed that larger size metals (Pb^{2+}, Cd^{2+}, Sr^{2+}, Cu^{2+}, Zn^{2+}, Ni^{2+}, Mn^{2+}, Fe^{3+} and Al^{3+}) bound excellently with PVA-alginate-zeolite. Meanwhile small size metals (Ni^{2+} and Co^{2+}) were less efficiently bound to PVA-alginate zeolite.

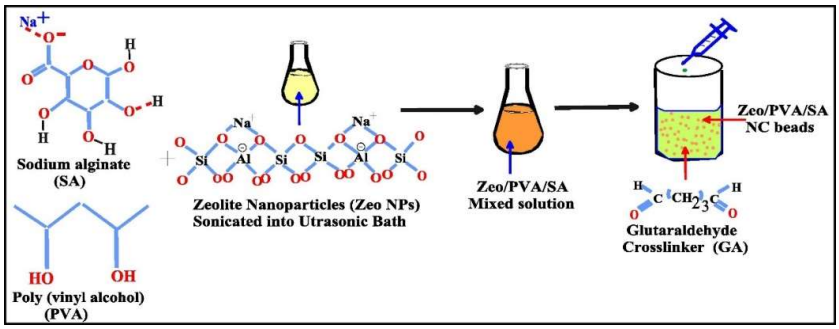


Figure 6. PVA-alginate-zeolite [9]

Although PVA-alginate-zeolite is suitable for metal binding, the large pore size on the surface of PVA-alginate-zeolite causes a barrier to the larger sized metals. Adding polyethylene oxide makes PVA-alginate-zeolite bind to the bigger sized of metals, especially metals located at the bottom of the periodic table that have a larger size. Polyethylene oxide can form cavities when added to PVA-alginate-zeolite, and thus form PVA-alginate-zeolite-polyethylene oxide (Figure 7). Fazel Zahakifar et al. [35] produced PVA-alginate-zeolite-polyethylene oxide to bind with U^{6+}. PVA and polyethylene oxide (PEO) were dissolved in a water in separate container and then heated until homogenous. Then, alginate was dissolved in water and heated until homogenous and added with zeolite. The alginate-zeolite was added to PVA-PEO. PVA-alginate-zeolite-polyethylene oxide produced was successfully bound either 81.4% of U^{6+}. Zahakifar et al. [36] also used PVA-alginate-zeolite-polyethylene oxide in their study and found 65.2 % of thorium (Th) (IV) was successfully bound with PVA-alginate-zeolite-polyethylene oxide.

Bacteria are also good in combining with PVA-alginate to bind with metal. Wang et al. [28] utilized corncob from agricultural waste. Corncob was heated by using a furnace to form carbon corncob. Carbon corncob is used for Zoogloea sp. MFQ7 bacterium to do microbial activity in anaerobic form and convert Mn^{3+} to Mn^{2+} (Figure 8). PVA and alginate were dissolved in water and heated. The cooling PVA-alginate was added with carbon corncob- Zoogloea sp. MFQ7. PVA-alginate-carbon corncob- Zoogloea sp. MFQ7 synthesized was used to bind Mn^{2+}, whereby 72.74% Mn^{2+} was successful bound.

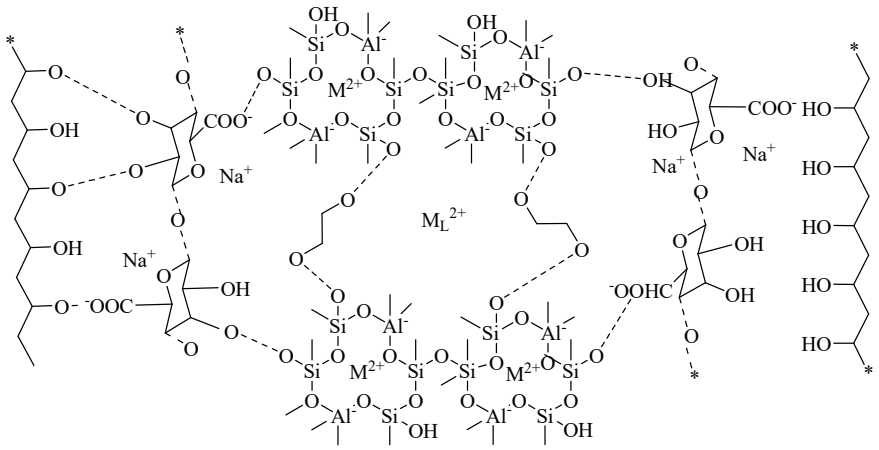


Figure 7. PVA-alginate-zeolite-polyethylene oxide (Note: M^{2+}= metal ion and M_L^{2+}= large metal ion)

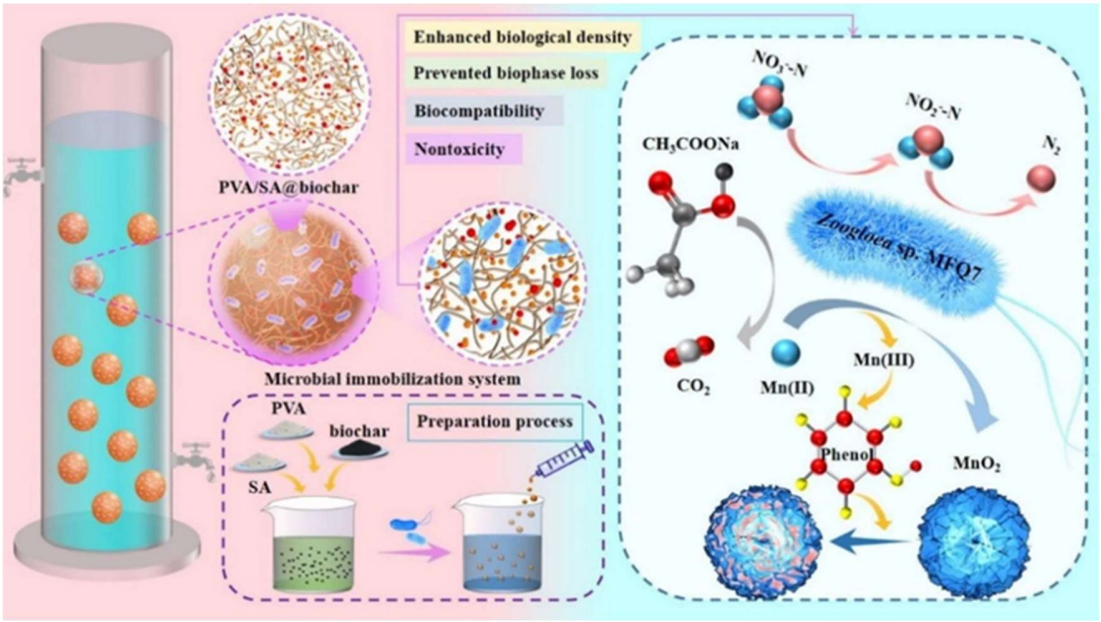


Figure 8. PVA-alginate-carbon corncob- Zoogloea sp. MFQ7 [28]

Table 2 lists modifiers to modify PVA-alginate as a binder of metals. Each modifier has criteria and is very selective to help PVA-alginate as a metal binder. PVA-alginate alone is a suitable binder for metal atoms. The surface area of PVA-alginate increases upon modification with the modifier to increase the selectivity and percentage of binding metals. The combination of PVA-alginate with modifier also increases the character of PVA-alginate as a binder towards bigger metal atoms. Usually, the best pH value condition used by researchers during the binding process is between pH 4-8 which, influence the percentage of binding PVA-alginate and modifier to metals ions.

Table 2. List of modifiers to modified PVA-alginate as a binder of metals

Modification	Metal Bind	Percentages of Binding (%)	Cross-Link	References
-	Cd^{2+} } pH5	47.5	Heat	[22]
-	Cr^{6+}	100	Boric acid, $CaCl_2$ and Na_2SO_4	[15]
Green tea waste and Iron oxide	Cr^{6+}	52.12	$CaCl_2$	[31]
	Cu^{2+} } pH 4	59.78		
Maghemite	Cs^{+} } pH 8	91.8	$CaCl_2$ H_3BO_3	[3]
Titania		90.1		
Maghemite-titania		93.1		
Polyaniline	Cr^{6+}	95.25	$CaCl_2$ H_3BO_3	[30]
zeolite nano	Pb^{2+}	99.5	Glutaraldehyde	[9]
particles	Cd^{2+}	99.2		
	Sr^{2+}	98.8		
	Cu^{2+} pH6	97.2		
	Zn^{2+}	95.6		
	Ni^{2+}	93.1		
	Mn^{2+}	92.4		
	Li^{2+}	74.5		
	Fe^{3+} } pH5	96.5		
	Al^{3+}	94.9		
Zeolite	Ni^{2+} } pH5.5	83.7	Heat	[34]
	Co^{2+}	84		
Polyethylene oxide and zeolite	U^{6+} } pH5	81.4	Heat	[35]
Polyethylene oxide and zeolite	Th^{4+} } pH5	65.2	Heat	[36]
Zoogloea sp. MFQ7 And glacial acetic acid	Mn^{2+}	72.7	$CaCl_2$	[28]

Cross-link

The combination structure of PVA and alginate are physically robust, in spite of the fact that both polymers are soluble in water [9]. To reduce the solubility and increases the physical and chemical properties of PVA-alginate by the addition of a cross-link agent in the structure. Chen et al. [37] reported that, chemical cross-linking was widely used to alter the physical properties of polymeric materials. Linking of polymer chains through chemical linkages gives a more rigid material structure and potentially a better-defined shape. The chemical cross-linking of polymers was not only limited to bulk materials, but also led to the creation of micro- or nano-sized organic particles which occurred as a covalent or ionic cross-link. List of chemical cross-links of PVA-alginate are calcium chloride ($CaCl_2$) [10-14] or the combination of $CaCl_2$ and boric acid [15-17] and glutaraldehyde [9,34]. Physical cross-link PVA-alginate is a freeze-thawing process [22,34,35].

Calcium chloride ($CaCl_2$) is the commonly used cross-linker to solidify PVA-alginate. Solidification occurs based on adsorbent via ion exchange, and chelation provides the resulting PVA-alginate gel with a significant structural strength. The ion exchange occurs when calcium ions take the place of sodium in the alginate of PVA-alginate. A polyvalent ion binding reaches the cross-linking with two carboxylic functional groups on adjacent polymer chains. Besides, this reaction can be accompanied by the chelation of calcium ions at the hydroxyl and carboxyl functional groups of sodium alginate chain [38]. Wang [39] found that the best per cent of $CaCl_2$ cross-linker used was 2 % because the function of Ca^{2+} enlarged the material suction space.

The formation eggbox model (each calcium atom is coordinated to the carboxylates and hydroxyl groups of four G monomers from two adjacent chains of alginate) was extensity studied (Figure 9) [40].

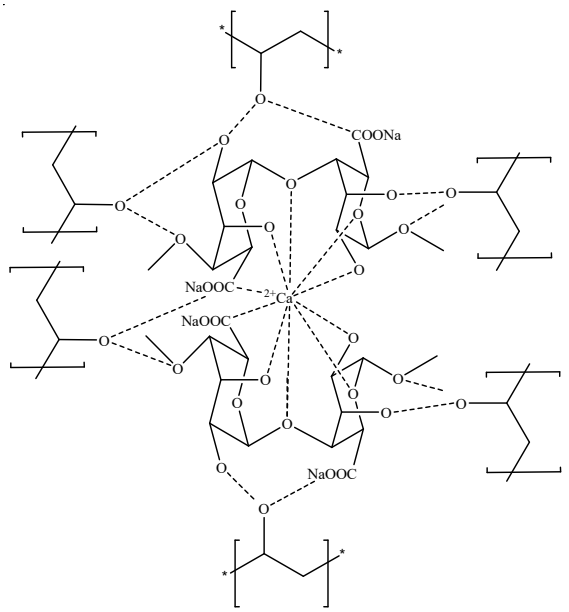


Figure 9. The reaction mechanism of $CaCl_2$ cross-linker with PVA-alginate

Mixed calcium chloride ($CaCl_2$) and boric acid ($B(OH)_3$) which were utilized as cross-linker to obtain spherical beads, prevented agglomeration during the PVA-alginate cross-linking process and improved surface properties (Figure 10). Boric acid was used to assist the cross-link between PVA polymer with tetrahydroxyborate ions ($B(OH)^{4-}$) cross-linked with the hydroxyl group (OH) on adjacent chains. The cross-link between two hydroxyls (PVA) and one borate ion is known as “di-diol” complexation. Boric acid is an electron acceptor (Lewis acid); it has an empty p orbital attracted to lone pair of the hydroxyl group of PVA. At the same time, calcium replaces the position of sodium in alginate, whereby two carboxyl’s in alginate bond to calcium. Since the crosslink process between PVA-alginate by boric is slow, it is not used as a stand-alone cross-linker as a consequence of agglomeration problem that trigged the polymer rigid to break up [41].

Glutaraldehyde is an organic compound with formula $(CH_2)_3(CHO)_2$. It consists of a five-carbon chain doubly terminated with formyl (CHO) groups. It is most widely used as a cross-link because it is inexpensive and easily available [43]. Moreover, it has good mechanical performance and stable chemical properties [44]. Glutaraldehyde has highly reactive bifunctional agent of aldehyde groups located at both ends, while able to bond to hydroxyl, imidazole group, amine, thiols and phenols [45]. The cross-linking occurs between aldehyde groups of glutaraldehyde and hydroxyl groups of alginates [9, 34] and PVA polymers [44] (Figure 11).

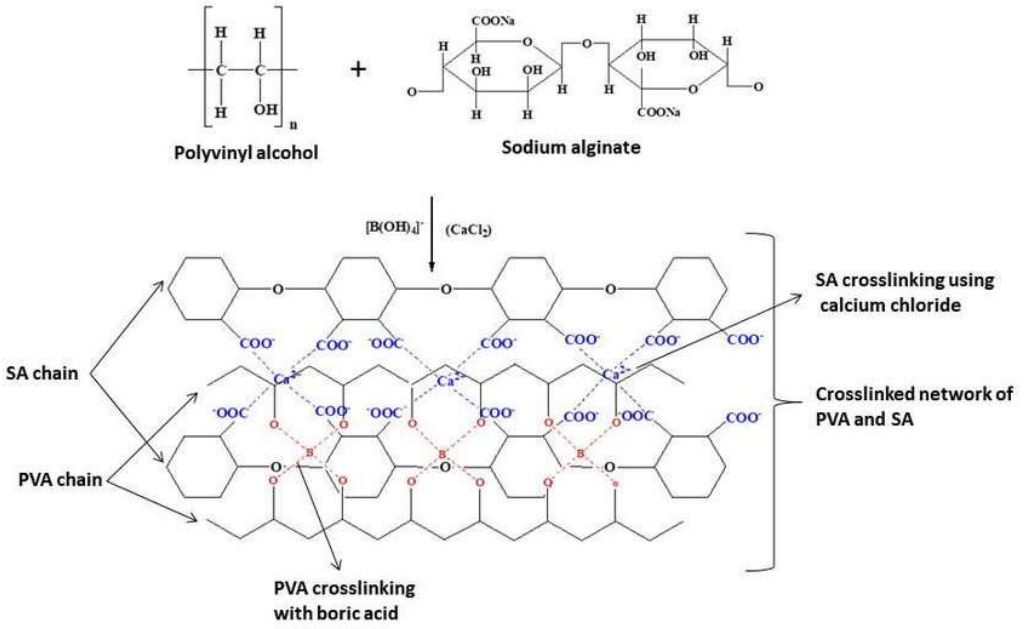


Figure 10. The reaction mechanism of $CaCl_2$ and $B(OH)_3$ cross-linker with PVA-alginate [42]

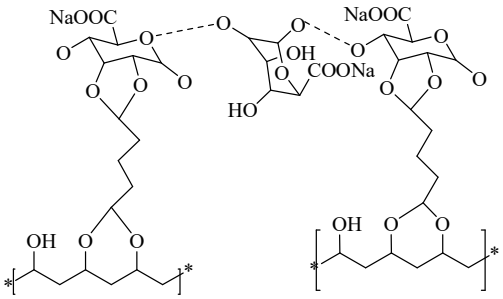


Figure 11. The reaction mechanism of Glutaraldehyde cross-linker with PVA-alginate

Freeze-thawing is a physical cross-link PVA-alginate which is widely used for pharmaceutical and biomedical applications. It is non-toxic, chemical free and biocompatibility [46]. In the freeze-thaw method, the concentration of polymer is increased due to bulk solvents or low molecule solutes freezing (crystallization). The network structure formed because chain space in the polymer was minimized and enabled the chains to align and connect to each other during the freezing process [47]. During thawing process, the polymer assembles and cross-link between the polymer due to defrosting solvent [48, 49] (Figure 12). Gel of PVA-alginate by freeze-thawing has high water uptake and is rubbery [46]. Therefore, chemical cross-link especially $CaCl_2$ as a cross-linker is preferable because it is easy to solidify and the structure strength of PVA-alginate is used as a metal binder.

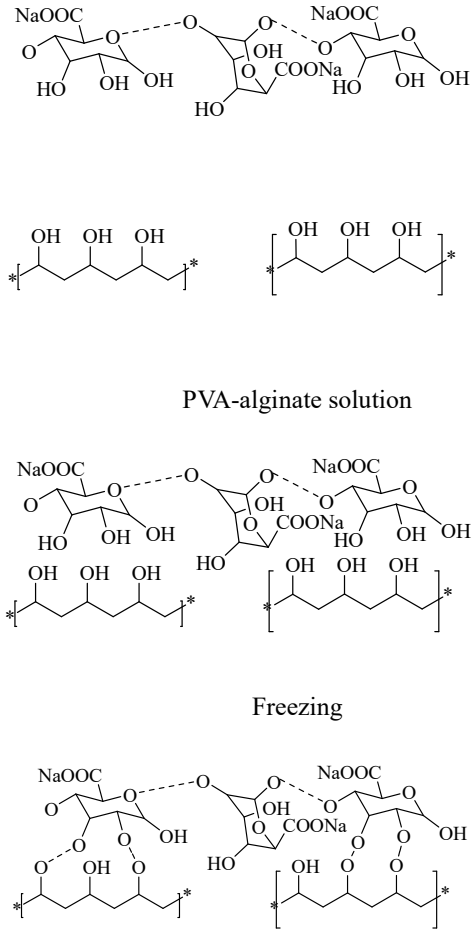


Figure 12. The reaction mechanism of freeze-thawing cross-linker with PVA-alginate

Conclusion

In this study, the synthesis and modification PVA-alginate binder were summarized. These binders have shown excellent binding performance towards metal ions. Highlights in this finding are: (i) PVA-alginate are good binder to small metal with low cost and an environmentally friendly binder, (ii) zeolites are good modifiers of PVA-alginate but only with a large sized of metal ion, (iii) PVA-alginate- zeolite- polyethylene suitable binder of larger sized of metal ion, (iv) $CaCl_2$ cross-linking agent are good to solidify PVA-alginate. Suggestions for future study are that PVA-alginate polymer is a good metal catalyst support for catalytic study of the carbon-carbon coupling reaction because it is a good metal binder and have good structural strength.

Acknowledgement

The authors would like to acknowledge the financial support from UiTM internal grant 600-RMC/GIP 5/3 (096/2022) and Faculty of Applied Sciences, Universiti Teknologi MARA (UiTM), 40450 Shah Alam, Selangor, Malaysia

References

1. Gao, X., Guo, C., Hao, J., Zhao, Z., Long, H., and Li, M. (2020). Adsorption of heavy metal ions by sodium alginate based adsorbent-a review and new perspectives. *International Journal of Biological Macromolecules*, 164: 4423-4434.
2. Mallakpour, S., and Azimi, F. (2021). Current development in poly (vinyl alcohol) nanocomposites for heavy metal ions removal. In *Handbook of Polymer Nanocomposites for Industrial Applications* (pp. 455-476). Elsevier.
3. Zohreh Majidnia, and Fulazzaky, M. A. (2017). Photocatalytic reduction of Cs(I) ions removed by combined maghemite-titania PVA-alginate beads from aqueous solution. *Journal of Environmental Management,* 191: 219-227.
4. Xiaofeng Yi, Fuliang Sun, Zhenhua Han, Fuhao Han, Jiarui He, Minrui Ou, Junjie Gu, & Xu, X. (2018). Graphene oxide encapsulated polyvinyl alcohol/sodium alginate hydrogel microspheres for Cu (II) and U (VI) removal. *Ecotoxicology and Environmental Safety,* 158: 309-218.
5. Knijnenburg, J. T., Kasemsiri, P., Amornrantanaworn, K., Suwanree, S., Iamamornphan, W., Chindaprasirt, P., and Jetsrisuparb, K. (2021). Entrapment of nano-ZnO into alginate/polyvinyl alcohol beads with different crosslinking ions for fertilizer applications. *International Journal of Biological Macromolecules*, 181: 349-356.
6. Rahman, N., and Wilfred, C. D. (2018). Removal of Mn(VII) from industrial wastewater by using alginate-poly (vinyl) alcohol as absorbent. *Journal of Physics: Conference Series,* 1123(1).
7. Du, Z., Liu, F., Xiao, C., Dan, Y., and Jiang, L. (2021). Fabrication of poly (vinyl alcohol)/sodium alginate hydrogel beads and its application in photo-Fenton degradation of tetracycline. *Journal of Materials Science*, 56(1): 913-926.
8. Liao, Q., Rong, H., Zhao, M., Luo, H., Chu, Z., and Wang, R. (2022). Strong adsorption properties and mechanism of action with regard to tetracycline adsorption of double-network polyvinyl alcohol-copper alginate gel beads. *Journal of Hazardous Materials*, 422: 126863.
9. Isawi, H. (2020). Using zeolite/polyvinyl alcohol/sodium alginate nanocomposite beads for removal of some heavy metals from wastewater. *Arabian Journal of Chemistry,* 13(6): 5691-5716.
10. Levi, S., Rac, V., Manojlovi, V., Raki, V., Bugarski, B., Flock, T., Krzyczmonik, K. E. and Nedovi, V. (2011). Limonene encapsulation in alginate/poly (vinyl alcohol). *Procedia Food Science,* 1:1816-1820.
11. Nur Habibah, Aulia Ratri Hapsari, Adhitasari Suratman, and Siswanta, D. (2020). Development of polyvinyl alcohol-sodium alginate beads as immobilization matrices of 1,5–diphenylcarbazide for the detection of Cr(VI). *Journal of Materials and Environmental Sciences*, 11(2): 176-186.
12. Eivazzadeh-Keihan, R., Farrokhi-Hajiabad, F., Aliabadi, H. A. M., Ziabari, E. Z., Geshani, S., Kashtiaray, A., ... and Mahdavi, M. (2023). A novel magnetic nanocomposite based on alginate-tannic acid hydrogel embedded with silk fibroin with biological activity and hyperthermia application. *International Journal of Biological Macromolecules,* 224:1478-1486.
13. Freitas, E. D., Freitas, V. M. S, Rosa, P. C. P, da Silva, M. G. C. and Vieira, M. G. A. (2021). Development and evaluation of naproxen-loaded sericin/alginate beads for delayed and extended drug release using different covalent crosslinking agents. *Materials Science & Engineering,* (118): 1-13.
14. Abhinandan, R., Adithya, S. P., Sidharthan, D. S., Balagangadharan, K., and Selvamurugan, N. (2021). Synthesis and characterization of magnesium diboride nanosheets in alginate/polyvinyl alcohol scaffolds for bone tissue engineering. *Colloids and Surfaces B: Biointerfaces,* 203: 111771.
15. Lee, T. C., Manap, N., Abdullah, H. Z., & Idris, M. I. (2018). Polyvinyl alcohol-alginate adsorbent beads for chromium (VI) removal. *International Journal of Engineering & Technology,* 7(3): 95-99.
16. Massana Roquero, D., Bollella, P., Katz, E., and Melman, A. (2021). Controlling porosity of calcium alginate hydrogels by interpenetrating polyvinyl alcohol–diboronate polymer network. *ACS Applied Polymer Materials,* 3(3): 1499-1507.

17. Zain, N. A. M., Suhaimi, M. S., and Idris, A. (2011). Development and modification of PVA–alginate as a suitable immobilization matrix. *Process Biochemistry,* 46(11): 2122-2129.
18. Majidnia, Z., and Fulazzaky, M. A. (2016). Photoreduction of Pb(II) ions from aqueous solution by titania polyvinylalcohol–alginate beads. *Journal of the Taiwan Institute of Chemical Engineers*, 66: 88-96.
19. Harpaz, D., Axelrod, T., Yitian, A. L., Eltzov, E., Marks, R. S., and Tok, A. I. (2019). Dissolvable polyvinyl-alcohol film, a time-barrier to modulate sample flow in a 3D-printed holder for capillary flow paper diagnostics. *Materials*, 12(3): 343.
20. Hassan, C. M., Trakampan, P., and Peppas, N. A. (2002). Water solubility characteristics of poly (vinyl alcohol) and gels prepared by freezing/thawing processes. In *Water soluble polymers* (pp. 31-40). Springer.
21. Abasalizadeh, F., Moghaddam, S. V., Alizadeh, E., Kashani, E., Fazljou, S. M. B., Torbati, M., and Akbarzadeh, A. (2020). Alginate-based hydrogels as drug delivery vehicles in cancer treatment and their applications in wound dressing and 3D bioprinting. *Journal of biological engineering*, 14(1): 1-22.
22. Ebrahimi, F., Sadeghizadeh, A., Neysan, F., and Heydari, M. (2019). Fabrication of nanofibers using sodium alginate and Poly (vinyl alcohol) for the removal of Cd^{2+} ions from aqueous solutions: Adsorption mechanism, kinetics and thermodynamics. *Heliyon*, 5(11): e02941.
23. Rahman, A. H. A., Teo, C. L., Idris, A., Misran, E., and Leong, S. A. N. (2016). Polyvinyl alcohol–alginate ferrophoto gels for mercury (II) removal. *Journal of Industrial and Engineering Chemistry*, 33: 190-196.
24. Narayanan, K. B., and Han, S. S. (2017). Dual-crosslinked poly (vinyl alcohol)/sodium alginate/silver nanocomposite beads–A promising antimicrobial material. *Food chemistry*, 234: 103-110.
25. Zohreh Majidnia, and Idris, A. (2015). Evaluation of cesium removal from radioactive waste water using maghemite PVA–alginate beads. *Chemical Engineering Journal ,* 262: 372-382.
26. Zhang, M.-K., Ling, X.-H., Zhang, X.-H., and Han, G.-Z. (2022). A novel alginate/PVA hydrogel-supported Fe_3O_4 particles for efficient heterogeneous Fenton degradation of organic dyes. *Colloids and Surfaces A: Physicochemical and Engineering Aspects*, *652*, 129830.
27. Shivakumara, L. R., and Demappa, T. (2019). Synthesis and swelling behavior of sodium alginate/poly(vinyl alcohol) hydrogels. *Turkish Journal Pharmaceutical Sciences,* 16(3): 252-260.
28. Wang, Y., Su, J., Ali, A., Chang, Q., Bai, Y., and Gao, Z. (2022). Enhanced nitrate, manganese, and phenol removal by polyvinyl alcohol/sodium alginate with biochar gel beads immobilized bioreactor: Performance, mechanism, and bacterial diversity. *Bioresource Technology*, 348: 126818.
29. Bhatti, H. N., Safa, Y., Yakout, S. M., Shair, O. H., Iqbal, M., and Nazir, A. (2020). Efficient removal of dyes using carboxymethyl cellulose/alginate/polyvinyl alcohol/rice husk composite: adsorption/desorption, kinetics and recycling studies. *International Journal of Biological Macromolecules*, 150: 861-870.
30. Li, Y., Wen, J., Xue, Z., Yin, X., Yuan, L., and Yang, C. (2022). Removal of Cr (VI) by polyaniline embedded polyvinyl alcohol/sodium alginate beads− extension from water treatment to soil remediation. *Journal of Hazardous Materials*, 426: 127809.
31. Nie, L., Chang, P., Liang, S., Hu, K., Hua, D., Liu, S., Sun, J., Sun, M., Wang, T., and Okoro, O. V. (2021). Polyphenol rich green tea waste hydrogel for removal of copper and chromium ions from aqueous solution. *Cleaner Engineering and Technology*, 4: 100167.
32. Bustamante-Torres, M., Romero-Fierro, D., Estrella-Nuñez, J., Arcentales-Vera, B., Chichande-Proaño, E., and Bucio, E. (2022). Polymeric composite of magnetite iron oxide nanoparticles and their application in biomedicine: a review. *Polymers*, 14(4): 752.
33. Kołodyńska, D., Gęca, M., Skwarek, E., and Goncharuk, O. (2018). Titania-coated silica alone and modified by sodium alginate as sorbents for heavy metal ions. *Nanoscale Research Letters*, 13(1): 1-12.

34. Tabatabaeefar, A., Keshtkar, A. R., Talebi, M., and Abolghasemi, H. (2020). Polyvinyl alcohol/alginate/zeolite nanohybrid for removal of metals. *Chemical Engineering & Technology*, 43(2): 343-354.
35. Fazel Zahakifar, Ali Reza Keshtkar, and Talebi, M. (2021). Synthesis of sodium alginate (SA)/ polyvinyl alcohol (PVA)/ polyethylene oxide (PEO)/ ZSM-5 zeolite hybrid nanostructure adsorbent by casting method for uranium (VI) adsorption from aqueous solutions. *Progress in Nuclear Energ,* 134(103642): 1-8.
36. Zahakifar, F., Keshtkar, A. R., and Talebi, M. (2021). Performance evaluation of sodium alginate/polyvinyl alcohol/polyethylene oxide/ZSM5 zeolite hybrid adsorbent for ion uptake from aqueous solutions: a case study of thorium (IV). *Journal of Radioanalytical and Nuclear Chemistry*, 327(1): 65-72.
37. Chen, J., Garcia, E. S., and Zimmerman, S. C. (2020). Intramolecularly cross-linked polymers: from structure to function with applications as artificial antibodies and artificial enzymes. *Accounts of Chemical Research*, 53(6): 1244-1256.
38. Yumin, A., Liguo, D., Yi, Y., and Yongna, J. (2022). Mechanical properties of an interpenetrating network poly (vinyl alcohol)/alginate hydrogel with hierarchical fibrous structures. *RSC Advances*, 12(19): 11632-11639.
39. Wang, X. H. (2012). Research and option in the preparation of PVA-alginate-Ca. *Applied Mechanics and Materials,* 189: 176-180.
40. Xia, M., Kang, S. M., Lee, G. W., Huh, Y. S., and Park, B. J. (2019). The recyclability of alginate hydrogel particles used as a palladium catalyst support. *Journal of Industrial and Engineering Chemistry,* 73: 306-315.
41. Nunes, M. A., Vila-Real, H., Fernandes, P. C., and Ribeiro, M. H. (2010). Immobilization of naringinase in PVA–alginate matrix using an innovative technique. *Applied Biochemistry and Biotechnology*, 160(7): 2129-2147.
42. Nataraj, D., and Reddy, N. (2020). Chemical modifications of alginate and its derivatives. *International Journal of Chemistry Research*, 2020: 1-17.
43. Pakolpakçil, A. (2022). Effect of glutaraldehyde crosslinking parameters on mechanical and wetting. *Sakarya University Journal of Science,* 26(5): 1990-1999.
44. Choi, D., Khan, M. H., and Jung, J. (2019). Crosslinking of PVA/alginate carriers by glutaraldehyde with improved mechanical strength and enhanced inhibition of deammonification sludge. *International Biodeterioration & Biodegradation*, 145: 104788.
45. Lim, D.-J. (2022). Cross-linking agents for electrospinning-based bone tissue engineering. *International Journal of Molecular Sciences*, 23(10): 5444.
46. Kamoun, E. A., Kenawy, E.-R. S., Tamer, T. M., El-Meligy, M. A., and Eldin, M. S. M. (2015). Poly (vinyl alcohol)-alginate physically crosslinked hydrogel membranes for wound dressing applications: characterization and bio-evaluation. *Arabian Journal of Chemistry*, 8(1): 38-47.
47. Zhang, H., Zhang, F., and Wu, J. (2013). Physically crosslinked hydrogels from polysaccharides prepared by freeze–thaw technique. *Reactive and Functional Polymers*, 73(7): 923-928.
48. Akter, M., Bhattacharjee, M., Dhar, A. K., Rahman, F. B. A., Haque, S., Rashid, T. U., and Kabir, S. F. (2021). Cellulose-based hydrogels for wastewater treatment: A concise review. *Gels*, 7(1): 30.
49. Tsou, Y.-H., Khoneisser, J., Huang, P.-C., and Xu, X. (2016). Hydrogel as a bioactive material to regulate stem cell fate. *Bioactive Materials*, 1(1): 39-55.

Malaysian Journal of Analytical Sciences (MJAS)
Published by Malaysian Analytical Sciences Society

APPLICATION OF RESPONSE SURFACE METHODOLOGY ON THE EXTRACTION OF CAFFEINE IN TEA AND COFFEE USING HIGH PERFORMANCE LIQUID CHROMATOGRAPHY TECHNIQUE

(Aplikasi Kaedah Gerak Balas Permukaan terhadap Analisis Kafein dalam Teh dan Kopi Menggunakan Teknik Kromatografi Cecair Berprestasi Tinggi)

Ibrahim Ali Al-Seade[1], Fouad Fadhil Al-Qaim[1], Zainab Haider Mussa[2], Lubna Raad Al-Ameer[3], and Nurfaizah Abu Tahrim[4*]

[1]Department of Chemistry,
Faculty of Science for Women, University of Babylon, PO Box 4, Hilla, Iraq
[2]College of Pharmacy,
University of Al-Ameed, Karbala PO Box 198, Iraq
[3]College of Pharmacy,
Al-Zahraa University for Women, Karbala, Iraq
[4]Department of Chemical Sciences,
Faculty of Science and Technology,
Universiti Kebangsaan Malaysia, 43600 UKM Bangi, Selangor, Malaysia

**Corresponding author: nfaizah@ukm.edu.my*

Received: 22 September 2022; Accepted: 26 December 2022; Published: 19 April 2023

Abstract

A rapid and simple extraction method was developed for the analysis of caffeine in tea and coffee using high performance liquid chromatography (HPLC). Independent factors such as extraction method, temperature and residing time were optimized using response surface methodology (RSM) followed by Box-Behnken Design (BBD). All samples were analyzed using HPLC and separated on C_{18} (150 mm × 4.6 mm, 5µm particle) column. The mobile phases were: (A) water and (B) acetonitrile at the flow rate of 1 mL min^{-1} under ultraviolet (UV) detection at 273 nm. Good linearity was obtained in the range of 1–60 mg L^{-1} (regression coefficient (R^2) > 0.995). The limit of quantification (LOQ) and limit of detection (LOD) were 1.0 and 0.4 mg L^{-1}, respectively. Relative standard deviation (RSD) at the range between 3.11 and 11.37 is deemed as highly precise and it is 92% to 98% accurate. Based on the RSM-BDD analysis, extraction of caffeine from tea was directly proportional to temperature, time and method extraction, which exhibited all independent factors of this study were significant. The most optimal condition of caffeine extraction was heat treatment at 100 °C in 16 min and free from any chemical treatment. The highest concentration of caffeine was 366 mg L^{-1} in Mahmood's green tea, while it was 334 mg L^{-1} in Mahmood's coffee. The proposed method exhibited good results and easier quantification of caffeine in different samples using HPLC, and free from possible interferents.

Keywords: caffeine, tea, coffee, Box-Behnken design, high performance liquid chromatography

Abstrak

Kaedah pengekstrakan cepat dan mudah telah dibangunkan untuk penganalisaan kafein dalam sampel teh dan kopi dengan menggunakan kromatografi cecair berprestasi tinggi (HPLC). Faktor bebas yang penting seperti kaedah pengekstrakan, suhu dan masa tinggal telah dioptimumkan menggunakan kaedah gerak balas permukaan (RSM) diikuti oleh reka bentuk Kotak-Behnken (BBD). Semua sampel telah dianalisis menggunakan HPLC dan diasingkan pada turus C_{18} (150 mm × 4.6 mm, 5µm). Fasa gerak alih yamg digunakan ialah (A) air dan (B) asetonitril pada kadar aliran 1 mL min^{-1} di bawah pengesanan ultra ungu (UV) pada 273 nm. Kelinearan yang baik diperoleh dalam julat 1–60 mg L^{-1} (pekali regresi (R^2) > 0.995). Had kuantifikasi (LOQ) dan had pengesanan (LOD) masing-masing ialah pada 1.0 dan 0.4 mg L^{-1}. Kejituan sisihan piawai relatif (RSD) pada julat antara 3.11 dan 11.37 didapati hampir tepat dan mempunyai ketepatan antara 92% hingga 98%. Berdasarkan analisis RSM-BDD, pengekstrakan kafein daripada teh adalah berkadar terus dengan suhu, masa dan kaedah pengekstrakan yang menunjukkan bahawa semua faktor bebas tersebut adalah signifikan. Keadaan pengekstrakan kafein paling optimum ialah pada suhu 100 °C selama 16 minit dan bebas daripada sebarang rawatan kimia. Kepekatan kafein tertinggi sebanyak 366 mg L^{-1} diperoleh dalam teh hijau Mahmood manakala 334 mg L^{-1} dalam kopi Mahmood. Kaedah yang dicadangkan mempamerkan keputusan yang baik dan mudah untuk mengukur kafein dalam sampel yang berbeza menggunakan HPLC.

Kata kunci: kafein, teh, kopi, reka bentuk Kotak-Behnken, kromatografi cecair berprestasi tinggi

Introduction

Caffeine is an alkaloid, which is a naturally occurring compound with a wide range of pharmacological properties [1]. Caffeine is used as stimulant drug to reduce headache and other treatment purposes. It is commonly found in popular beverages worldwide consumed during breakfast, tea and dinner. It was reported that caffeine as an antioxidant plays an important role to reduce risk of coronary heart disease [2,3].

Caffeine belongs to methylxanthine group, which is a derivative of xanthine that occurs naturally in plants with no obvious odor and slightly bitter. The empirical formula of caffeine is $C_8H_{10}N_4O_2$ and its molecular structure is shown in Figure 1. Caffeine is not easily biodegradable nor absorbed into the human system as they can be continuously present in the aquatic environment through human excretion and its bioaccumulation into the wastewater, domestic wastewater and hospital effluents [15,16,17]. Furthermore, it can further affect the marine ecosystem.

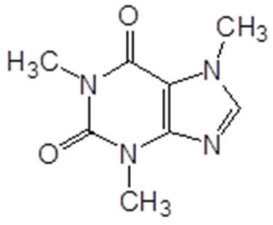


Figure 1. Structural formula of caffeine

In order to collect more information regarding the direct consumption of caffeine in consumer's daily diet, a comprehensive study of analysis of caffeine in tea and coffee samples was performed. The application of response surface methodology is vital in this study to determine the amount of consumed caffeine per cup, as there is no previous data regarding this study in Iraq. Caffeine has been analyzed in different samples such as biological fluids, foods, plants and water samples using different analytical instruments such as high-performance liquid chromatography (HPLC) [4], gas chromatography–mass spectrometry-flame ionization detection (GC–MS-FID) [5], Fourier transform-infrared spectrophotometry (FT-IR) [6], near-infrared spectroscopy (NIR) [7], Ultraviolet–Visible spectroscopy (UV-Vis) [8], FT-Raman spectrometry [9], and capillary electrophoresis (CE) [10]. Among the listed analytical techniques, HPLC offers advantages, such as simplicity and selectivity coupled with ultraviolet-visible (UV–Vis) detector, was the most preferred analysis system for the analysis of caffeine [8,11,12].

The issue of extracting caffeine from tea without using chemical reagents has led to the development of various extraction techniques. Conventional liquid–liquid extraction (LLE) and solid-phase extraction (SPE) have been used for pre-concentration and clean-up before analysis. Liquid-liquid extraction is time-consuming and hazardous to health due to the high volume of toxic solvents used [13]. Solid-phase extraction requires less

solvent, but is still time consuming, and often requires a concentration stage that presents disadvantages such as losses in the evaporation step [14]. To resolve time consumption of the proposed extraction techniques, response surface methodology has been utilized to determine the significant factors of this study.

The aims of this study are: (i) to optimize different extraction method, temperature and residing time using response surface methodology; (ii) to identify and confirm presence of caffeine in tea using LC-TOF/MS as a very accurate instrument based on mass-to-charge ratio; (iii) to determine the concentration of caffeine in real samples using HPLC-UV.

Materials and Methods

Reagents and chemicals

Caffeine (purity 99%) was purchased from Sigma-Aldrich (USA). Acetonitrile (ACN), methanol (MeOH) and ethyl acetate were HPLC-grade and provided by Sigma-Aldrich (USA). Other reagents such as hydrochloric acid and sodium carbonate were purchased from Sigma-Aldrich (USA). Double distilled water was prepared using the distillation apparatus (Manufacturer, Country of Manufacturer) in the laboratory setting.

Sample Collection

Samples are Mahmood green tea, Mahmood red tea, Al Ghazaleen red tea, Brazilian coffee and Mahmood coffee samples were collected from the local market in Babylon City, Iraq as presented in Table 1. All samples were stored at 4 ℃ refrigerator throughout the analysis to avoid further enzymatic or denaturation effect on the samples. Laboratory glassware and glass apparatuses were properly cleaned with tap water and rinsed with double distilled water.

Sample preparation

Each sample was treated with three different extraction methods (extraction method 1, extraction method 2 and extraction method 3), three different temperatures (40, 70 and 100 °C) and three different residing times (4, 10 and 16 min). Each independent factor was optimized using RSM to select the significant output.

Experimental design

Response surface methodology has been used to investigate each variable on the effectiveness of caffeine extraction through: extraction method (A), temperature (B), and residing time (C). For each of the three studied variables, high and low set points were selected to construct an orthogonal design (Table 2). Box-Behnken Design (BBD) was used to optimize the values of these three factors and reach the best response. Design included 30 treatments in three levels for three factors and consisted of six center points. The experimental design matrix and data analysis were carried out using the software package Minitab 19 statistical software. The peak area and/or concentration of caffeine was used as the HPLC response to evaluate the extraction efficiency.

Table 1. Description of tea and coffee samples

Brand Name	Origin	Expiry Date
Mahmood red tea	Produced and packed in Sri Lanka	06/2022
Mahmoud green tea	Produced and packed in Sri Lanka	02/2023
Al Ghazaleen Tea	Produced in Sri Lanka- Ceylon	04/2022
Brazilian coffee	Produced in India	09/2022
Mahmood coffee	Produced in Poland	11/2021

Table 2. The experimental range and levels of the variables in the BBD

Factor	Symbol	Range and Levels		
		Low	Centre	High
Extraction Method	A	1	2	3
Temperature (°C)	B	40	70	100
Residing time (min)	C	4	10	16

The regression equation in uncoded units was presented below:

$$CONC. = -217.7 + 55.8\,\mathbf{A} + 4.199\,\mathbf{B} + 1.89\,\mathbf{C} - 32.27\,\mathbf{A^2} - 0.04961\,\mathbf{B^2} - 1.049\,\mathbf{C^2} + 1.217\,\mathbf{AB} + 4.854\,\mathbf{AC} + 0.2958\,\mathbf{BC}$$

Three different extraction methods used in this research were:

Extraction Method 1

One gram of each tea leaves and coffee beans were soaked in 100 mL of boiled water (100 °C) separately and continuously, for 10 minutes. After cooling each extract, 5 mL aliquot was mixed with 0.1 M hydrochloric acid (2.5 mL) and saturated basic acetate solution (2 mL). The solution was centrifuged at 8000 rpm for 15 minutes. $NaHCO_3$ solution (0.1 g $NaHCO_3$ to 10 mL of water) was added to the supernatant then shaking using stir device. The solution was centrifuged again at 10000 rpm for 15 minutes, after that the extract was diluted with water into a 50 mL volumetric flask. 20 µL of final extract was filtered through a 0.45 mm membrane (Millipore) then injected into the HPLC column.

Extraction Method 2

One gram of tea and/or coffee sample has been soaked in 100 mL of hot water (100 °C) and stirring for 10 minutes. The aqueous phase was extracted with ethyl acetate using separation funnel, which is categorized as liquid-liquid extraction. Each extract was injected into the HPLC instrument.

Extraction Method 3

One gram of tea and/or coffee sample was soaked in 100 mL of hot water, separately for 10 minutes. This method does not require any treatment with reagents and/or chemicals, which is categorized as normal extraction method. After that each extract was cooled and filtered by a sterile filter (0.45 µm). Before injection into HPLC instrument, each extract was diluted in 10% double distilled water then 20 µL of extract was injected directly into the HPLC.

Preparation of stock and working solution

Caffeine stock solution of 1000 mg L^{-1} was prepared by accurately weighing 0.01 gram of standard caffeine, then dissolved in 10 mL methanol. Working standard caffeine solutions of 1, 10, 30 and 60 mg L^{-1} were prepared by serial dilution of the stock solution with double distilled water. The calibration curve of peak areas versus concentration of the standards was plotted. The caffeine content (mg L^{-1}) of the various samples was calculated by interpolation within the regression equation of the best line of fit.

Chromatographic separation

All selected samples in the present study were analyzed using high performance liquid chromatography (HPLC, Knaur Germany system) to identify and quantify caffeine compound. A binary high pressure pump and diode array detector were involved in the instrument. The separation was provided on C_{18} column (150 mm × 4.6 mm I.D., 5 µm particle size; Knuar, Germany). The mobile phase is consisted of water (A) and acetonitrile (B). The initial gradient composition (5% B) was maintained for 4 min and then linearly increased to 95% B over 9 min and maintained for 2.5 min before being decreased to 2% B over 0.1 min. Then, equilibration was performed for 2.9 min. The injection volume was 20 µL

and the flow rate was set to 0.3 mL min^{-1}. The column temperature was fixed at 35℃. All samples were subjected to 73 nm wavelength.

Mass spectrometry analysis (MS) was carried out using a time-of-flight (ToF) instrument (Bruker/Germany) equipped with a Z-spray electrospray interface. The results were obtained with the following settings: MS capillary voltages, 4000 (PI); collision energy for diclofenac, 10 eV; drying gas flow rate, 8.0 L min^{-1}; drying gas temperature, 190 °C; set capillary, 4000 V; set end plate offset, −500 V; set collision cell RF, 250 Vpp; and nebulizer pressure, 4.0 bar. The ToF results were collected between *m/z* 50 and 600. All analytes were acquired using an independent reference spray via the LockSpray interference to ensure accuracy and reproducibility; a mixture of sodium hydroxide and FA was used as the lock mass at *m/*z 90.9766–974.8132. The accurate mass was calculated using Daltonic Analysis software incorporated into the instrument.

Method validation

Analytical method was validated for linearity, limit of detection (LOD), limit of quantification (LOQ), intra day precision and accuracy. Calibration curve was performed in the range of 1 to 60 mg L^{-1}. The linearity was assessed by correlation coeficient (R^2). The LOQ and LOD values are calculated with the following equation (1):

$$\frac{S}{N} = \frac{2H}{h} \quad (1)$$

Where “S” is the signal of target peak. “N” is the noise adjacent to target peak. “H” is the height of target analyte peak so it refers to the signal “S”. “h” is the height of noise.

For repeatability measurement, samples were analyzed with three replicates in the same run. The results are represented as the percentage coefficient of variation values of the concentration of the analyte. All results were treated statistically using Microsoft Excel. Accuracy, however, was calculated after adding known amount of caffeine 1 mL of 10, 30 and 60 mg L^{-1} into 9 mL of tea sample then subtracting the peak area from the origin sample to find recovery% according to equation (2).

$$\text{Accuracy } \% = \frac{A_{spike} - A_{unspike}}{A_{standard}} \times 100\% \quad (2)$$

Where A_{spike} is adding known amount of caffeine to tea sample. $A_{unspike}$ is only tea sample. $A_{standard}$ is the standard concentration of caffeine.

Evaluation of selectivity

Selectivity was evaluated by comparing the chromatograms of three different samples: real sample, spiked real sample, and double distilled water. The results revealed that no interfering peaks visible at the same retention time of caffeine.

Results and Discussion

Method validation

The linearity of analytical method of caffeine was assessed through five concentrations of caffeine: 1, 10, 30 and 60 mg L^{-1}. All working solutions were eluted out of the column at the same retention time (10.6 min) as presented in Figure 2.

Calibration curve was obtained by plotting the peak area of caffeine against the working standard concentration. Calibration curve was fitted to the least-square linear regression. The results showed good linearity for caffeine, in which (R^2) was 0.995. It was observed that limit of quantification (LOQ) was calculated according to the injection of samples reaching up to low concentrations then calculated using equation (1), which is equivalent to 1.0 mg L^{-1}. It was observed that at 0.2 and 0.5 mg L^{-1} of caffeine, the signal was very small compared to noise signal, hence, both concentrations have signal-to-noise ratio less than 10. However, 1 mg L^{-1} of caffeine was analyzed, and it could be confirmed that the concentration has signal-to-noise ratio 10.4 means it represent LOQ.

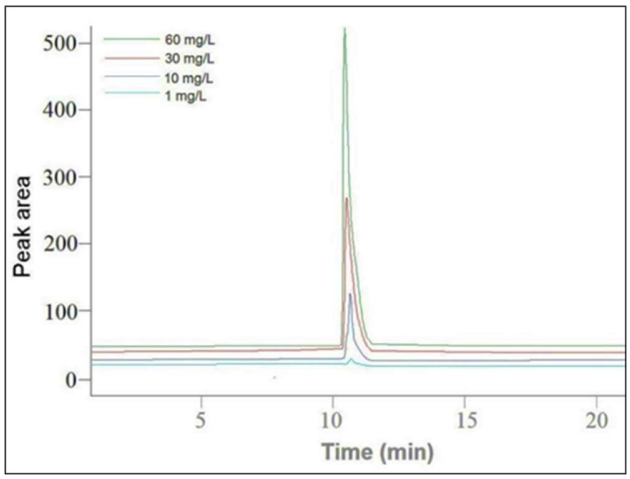


Figure 2. Chromatograms of caffeine at different concentrations (1, 10, 30 and 60 mg L^{-1})

The precision of liquid chromatography method was evaluated through analysis of three samples replicates performed within the same day (refer to Table 3). The precision was determined by analyzing three different concentrations of caffeine (10, 30, and 60 mg L^{-1}). The results were presented as RSD%, ranging from 3.11 to 11.37%, which is considered as small and precise. Accuracy was determined by adding known amounts of caffeine to the sample (10, 30 and 60 mg L^{-1}). The results are in good agreement with the acceptable values for the validation of an analytical procedure, with the accuracy ranging from 92% to 98% as presented in Table 3.

Table 3. Precision data for the analysis of caffeine

Compound	Concentration (mg L^{-1})	Accuracy %	Precision (RSD%)	LOQ (mg L^{-1})	LOD (mg L^{-1})	Regression Linear Equation
Caffeine	10	92	11.37	1.0	0.4	y = 63.96x + 83.54
	30	96	8.31			
	60	98	3.11			

Selectivity of method has been evaluated based on the comparison of standard caffeine, spiked caffeine in tea and blank sample. It was observed that no peaks interfered at the retention times of caffeine at 10.6 minute.

Box-Behnken design-based optimization

It is well known that extraction process is important to make caffeine ready for analysis, when it is present in complex samples like plants and beverages. Tea and coffee were extracted by three different methods as described previously. In comparison to second and third extraction methods, the first extraction method has produced the lowest peak area. This may be caused by the frequent sample transfers that resulted with some caffeine loss. Caffeine was dispersed between two layers in the second extraction method, which uses two immiscible solvents, but the peak area was still moderate in comparison to the third extraction method. However, the third extraction method without chemical reagents provides the most optimal caffeine recovery and less lost of caffeine compared to other extraction methods. Table 4 represents the ANOVA and regression analysis to assess the significance of independent factors, which are extraction method (A), temperature (B) and residing time (C). The model presented a high coefficient of determination (R^2 = 0.9928). This value indicated a good accordance with the experimental data and a good fitting ability for the model. Thus, the procedure demonstrated the ability of the model to work as a

predictive tool. The value of the adjusted determination coefficient (adjusted R^2 = 0.9895) is also sufficiently high to support a high significance for the model.

Box-Behnken design of response surface methodology was used for the analysis of the effect of temperature, residing time and extraction method on the extraction of caffeine and optimization of the independent variables. The linearity and quadratic effect of the independent parameters, their interaction and coefficients on the response variables were obtained by analysis of variance (ANOVA) (Table 4). The significance of the lack-of-fit, regression model and coefficient of determination (R^2) were used to judge the validity of the Box-Behnken design model. The analysis of the P-values of temperature, residing time, and extraction method, as well as the double interaction between these factors, show that those independent factors had a statistically significant effect on caffeine extraction from tea samples, with a p-value less than 0.05, which is 0.001.

Table 4. Analysis of Variance

Source	DF	Adj SS	Adj MS	F-Value	P-Value
Model	9	301901	33545	305.96	0.000
Linear	3	233097	77699	708.70	0.000
A	1	58443	58443	533.07	0.000
B	1	100806	100806	919.47	0.000
C	1	73848	73848	673.58	0.000
Square	3	28675	9558	87.18	0.000
A*A	1	7690	7690	70.15	0.000
B*B	1	14719	14719	134.26	0.000
C*C	1	10535	10535	96.09	0.000
2-Way Interaction	3	40129	13376	122.01	0.000
AB	1	10658	10658	97.21	0.000
AC	1	6786	6786	61.90	0.000
BC	1	22684	22684	206.91	0.000
Error	20	2193	110		
Lack-of-Fit	3	1295	432	8.18	0.001
Pure Error	17	897	53		
Total	29	304094			

Figure 3a represents normal distribution of the data towards the straight line (red color) in normal probability plot, means good significance of the results and no evidence of any deviation. Accumulating the datasets represented by blue dots along the straight line refers to a perfectly fitting model with no possibility of deviation. Figure 3b represents the Pareto chart, which is an indication of the individual interaction effect between the independent variables. Student's t-test was used to confirm that some factors are higher than zero point, which are significant. The vertical line (2.09) in Pareto chart refers to all factors that are statistically significant (confidence level > 95%) either individually or overlapped as they lied on the right-hand dashed line. Therefore, extraction of caffeine from tea was directly proportional to temperature, time and method of extraction. Consequently, increasing of time and temperature or development in extraction method, yield high amount of caffeine in the same sample of tea. Figure 3c shows the normal probability plot of the standardized effects with $p \leq 0.05$, to evaluate the significance of each independent factor and its interactions on extraction of caffeine from tea. Normal probability plot could be separated into two regions, right and left. Right region includes positive coefficients (from B to AC), while left region includes negative coefficients (AA to BB). It can be concluded through normal distribution of the data in normal probability plot

and perfect fitting model; Pareto chart with confidence level >95% and $p \leq 0.05$ of the combined factors such as Extraction Method with Temperature (AB), Extraction Method with Time (AC), Temperature with Time (BC), all independent factors are highly significant.

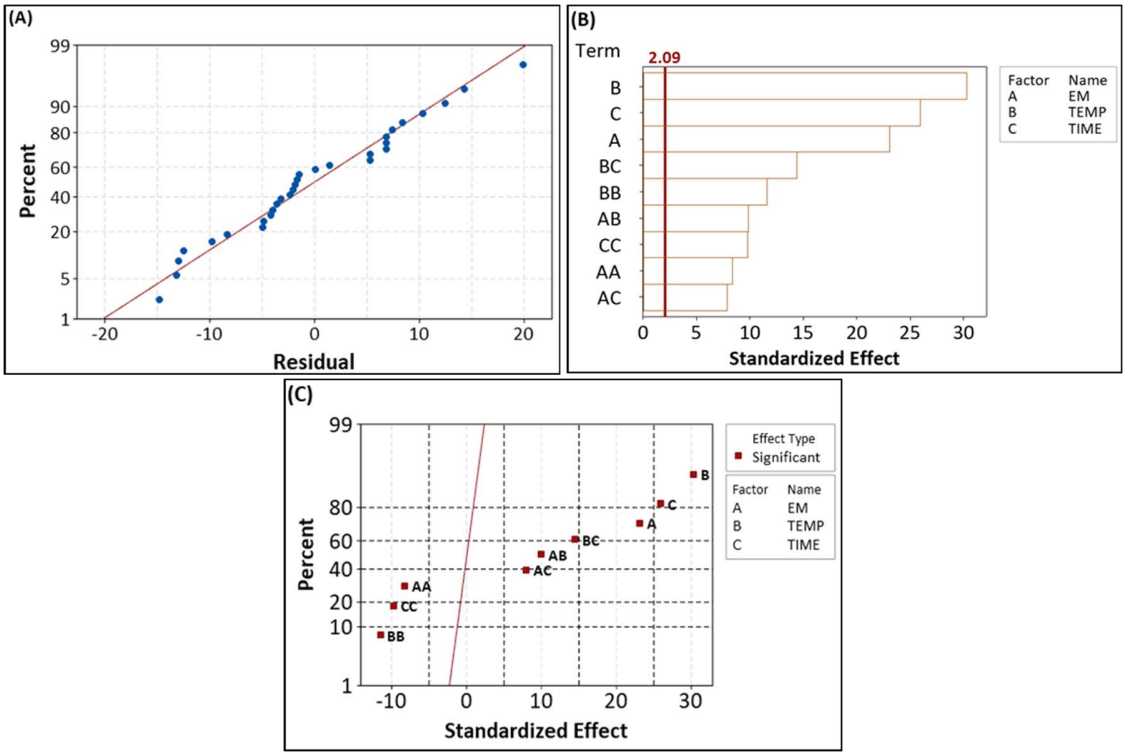


Figure 3. (a) The predicted response vs the actual response, (b) Pareto chart of standardized effects on the extraction efficiency of caffeine at $p = 0.05$, and (c) Normal probability plot of the standardized effects on the extraction efficiency of caffeine at $p = 0.05$.

The result is highly correlating that caffeine content increases considerably with heating time and specific method of extraction 3. In other words, following normal extraction without adding any chemicals is preferred. Furthermore, increasing of time reflect high positive impact on enhancement of caffeine extraction from tea leaves. These results are supported by the contour plot given in Figure 4a as can be seen, whereby tea boiled in 16 min at 100 °C resulted to caffeine concentration reaching up to 400 mg L^{-1}. Figure 4b showed the efficiency of caffeine extraction is improved with increasing time and temperature. However, it could be observed that the extraction of caffeine decreases at short time and low temperature when extraction method 3 was applied. It could be attributed to the role of heating, which accelerates the extraction of caffeine even at a shorter time as supported by the contour plot. The contour plot presented in Figure 4c, exhibited the major role of temperature regardless the type of extraction. It could be observed that all extraction methods performed in this study resulted to reasonable caffeine content. Caffeine concentration is in the range between 300-400 mg L^{-1} at 16 min and 100 °C by using extraction method 3. Similarly, extraction method 2 exhibited caffeine concentration in the range between 200 and 300 at mg L^{-1} in the same time and temperature as extraction method 3.

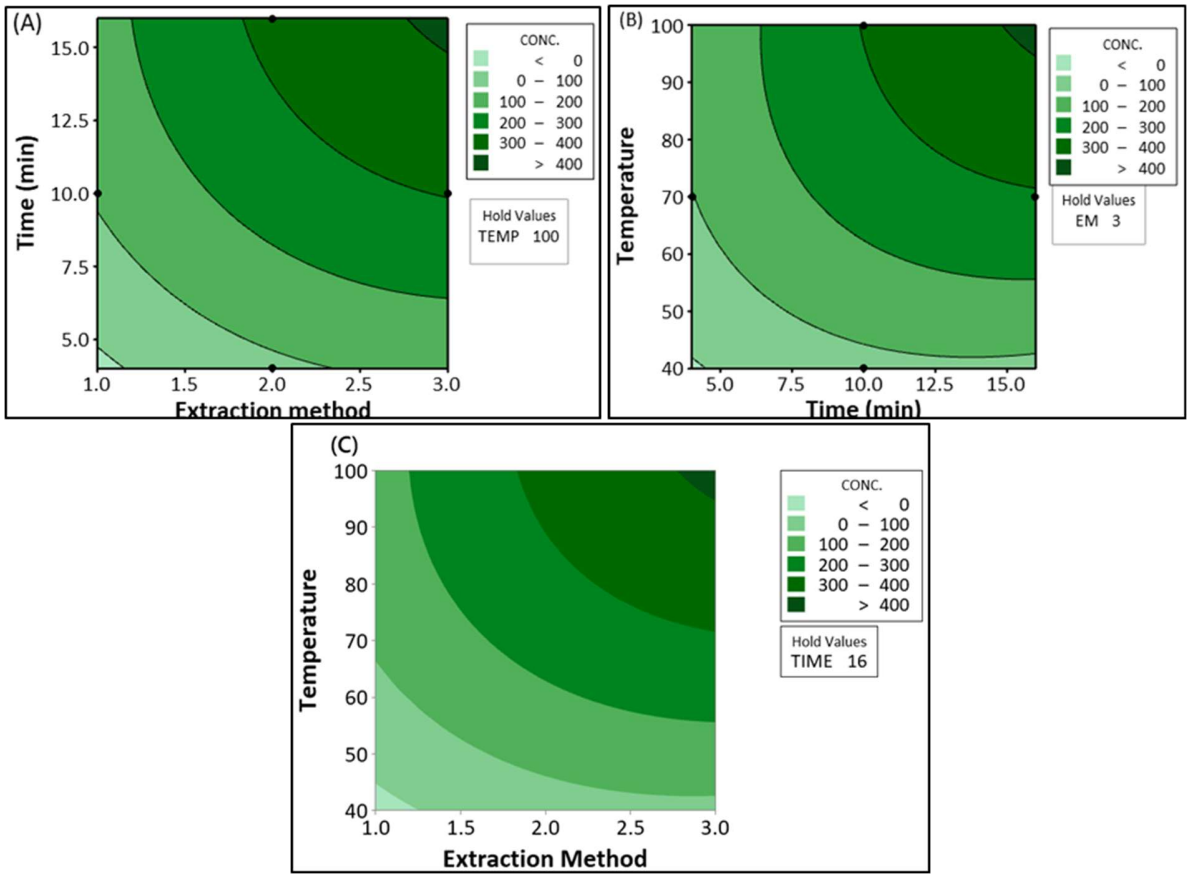


Figure 4. Response using the Box-Behnken Design obtained by contour plotting: (a) time vs. extraction method at 100°C, (b) temperature vs. time using extraction method 3, (c) temperature vs. extraction method in 16 minutes.

Analysis of caffeine in tea, and coffee

Caffeine was identified based on the mass value (*m/z*) in regards to mass spectrometry and retention times in regards to HPLC. Confirmation of presence of caffeine was carried out in the ToF/MS mode by extracting the narrow window extracted ion chromatogram (nwXIC) of the protonated molecular ion $[M+H]^+$. The nwXIC was typically extracted using a 20 mDa window. Positive identification for caffeine was based on (a) an accurate mass measurement of the base ion with an error of $\leq \pm 0.5$ ppm; and (b) LC retention time of the analyte compared with that of a standard [18]. The base peak at *m/z* 195.0884 for caffeine represented protonated molecular ion $[M+H]^+$ as shown in Figure 5. A small daughter peak at *m/z* 138.0655 appeared after the fragmentation of caffeine. This small, intense peak refers to the loss of C_2H_3NO from caffeine to form $C_6H_7N_3O$. The results agreed with previous study reported by Choi et al. [19] on the formation of metabolite of *m/z* 138.12 from caffeine after losing C_2H_3NO moiety.

For analysis of caffeine in tea and coffee samples, 100 mL of double distilled water was boiled in a glass beaker. After that heating was stopped and 1.0 gram of tea leaves or coffee beans was soaked in the boiled water. During this stage, the beaker was covered with a watch glass and stirring continued at a constant speed. Each sample was withdrawn at 1.0 mL after 10 min and filtered with 0.45 µm syringe filter. Caffeine was quantified by the developed reversed phase high pressure liquid chromatography method. All six samples

of tea leaves and coffee beans were analyzed and quantified using HPLC as shown in Table 5 and Figure 6. It was observed that caffeine has same retention time (10.6 min) in all selected samples.

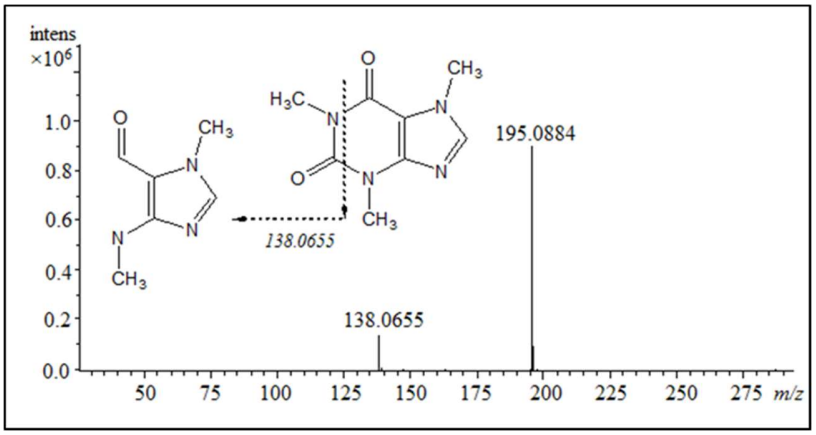


Figure 5. Mass spectrum of caffeine

Table 5. Result of caffeine content in coffee and tea samples using HPLC by extraction method without chemicals after 10% dilution

Sample Name	**Caffeine concentration (mg L^{-1}), M±SD**
Mahmood red tea	311±6.9
Mahmoud green tea	366±10.3
Al Ghazaleen Tea	290±8.1
Brazilian coffee	278±10.9
Mahmood coffee	334±5.7

Surprisingly, the highest concentration of caffeine was present in Mahmood green tea, with the concentration reaching 366 mg L^{-1} compared to Mahmood red tea, which is slightly lower at 311 mg L^{-1} . Hence, it signifies both green tea and red tea cannot be categorized as caffeine-free. Meanwhile, in coffee, the caffeine concentration was 278 and 334 mg L^{-1} in Brazilian coffee and Mahmood coffee, respectively; which is almost identical to Al Ghazaleen tea and Mahmood red tea. In comparison to other tea samples and coffee, the concentration of caffeine is high in the present study compared with that caffeine detected in BOH tea (138.3±4.5 mg/L), Milo (30.4±2.5 mg/L) and white coffee (82.7±2.9 mg/L) as presented in our previous study [18]. Similar study conducted using liquid chromatography has successfully proven that most Malaysian produced coffee and tea products are less in caffeine compared to the imported coffee and tea, which are proven to be highly concentrated with caffeine. The mean caffeine content of tea, green tea, per se, is higher than that of coffee. The fate of caffeine will remain in the body of the consumer throughout the digestion that may cause increased anxiety, increased heart rate and blood pressure, disorientation, hallucinations, acid reflux and sleep disturbance, and being excreted to the environment causing further pollution and bioaccumulation into the wastewater, aquatic and marine environment, and animals [20, 21].

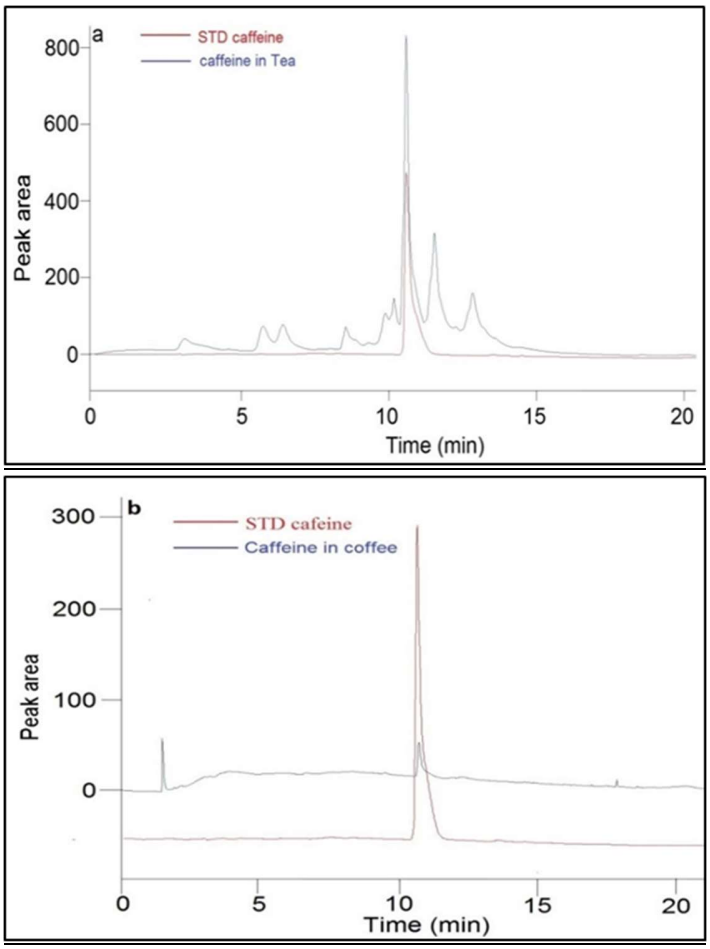


Figure 6. Chromatograms of caffeine in real samples: (a) tea leaves and (b) coffee sample

Conclusion

HPLC is a good technique and instrument to be used in identifying and quantifying caffeine in all selected samples namely tea and coffee. It was observed that HPLC reduces the labor work procedure in which requires less extensive usage of chemicals as proven by extraction method 3 with zero chemical used, but at boiling point and less than 20 minutes extraction time. Good linearity (R^2 = 0.995), a specific and sensitive detection system, low quantification limit 1 mg L^{-1} and fast analysis method are the main advantages of the proposed method. Furthermore, no interferents can be detected through this complex matrix and zero chemical compound. Highest concentration of caffeine was detected in tea sample 366 mg L^{-1} while the lowest concentration was 278 mg L^{-1} as detected in Brazilian coffee sample. This study has significantly exhibited that tea has more caffeine than coffee, which would deter the myth that tea is lighter than coffee, however, tea releases caffeine in a smaller amount but yet more long-lasting than coffee and leaves smaller carbon footprint.

Acknowledgments

This study was supported by University of Babylon, Department of Chemistry and received financial support from University of Al-Ameed.

References

1. Sierakowska, A., Jasiewicz, B. and Pospieszny, T. (2018). mass spectrometry study of new polyamine derivatives of caffeine. *Acta Chimica Slovenica*, 65(4): 795-800.
2. Ružić, I., Škerget, M. and Knez, Ž. (2010). Potential of phenolic antioxidants. *Acta Chimica Slovenica*, 57(2): 263-271.
3. Crevar, M., Ivkovic, B., Vladimirov, S., Kuntic, V. and Vujic, Z. (2008). Statistical optimization of reverse phase high performance liquid chromatography for the analysis of caffeine paracetamol and its degradation product p-aminophenol. *Acta Chimica Slovenica*, 55(3): 665-670.
4. Ali, H. S., Abdullah, A. A., Pınar, P. T., Yardım, Y. and Şentürk, Z. (2017). Simultaneous voltammetric determination of vanillin and caffeine in food products using an anodically pretreated boron-doped diamond electrode: Its comparison with HPLC-DAD. *Talanta*, 170: 384-391.
5. Rahim, A. A., Saad, B., Osman, H., Hashim, N., Yahya, S. and Talib, K. M. (2011). Simultaneous determination of diethylene glycol, diethylene glycol monoethyl ether, coumarin and caffeine in food items by gas chromatography. *Food Chemistry*, 126(3): 1412-1416.
6. Palo, M., Kogermann. K, Genina, N., Fors, D., Peltonen, J., Heinämäki, J. and Sandler, N. (2016). Quantification of caffeine and loperamide in printed formulations by infrared spectroscopy. *Journal of Drug Delivery Science and Technology*, 34: 60-70.
7. Zhang, X., Li, W., Yin, B., Chen, W., Kelly, D. P. and Wang, X. and Du, Y. (2013). Improvement of near infrared spectroscopic (NIRS) analysis of caffeine in roasted Arabica coffee by variable selection method of stability competitive adaptive reweighted sampling (SCARS). *Spectrochimica Acta A*, 114: 350 - 356.
8. Shehata, A. B., Rizk, M. S. and Rend, E. A. (2016) Certification of caffeine reference material purity by ultraviolet/visible spectrophotometry and high-performance liquid chromatography with diode-array detection as two independent analytical methods. *Journal of Food and Drug Analysis*, 24(4): 703-715.
9. Armenta., S., Garrigues, S and de la Guardia, M. (2005). Solid-phase FT-Raman determination of caffeine in energy drinks. *Analytica Chimica Acta*, 547(2): 197-203.
10. Meinhart, A. D., Bizzotto, C. S., Ballus, C. A., Prado, M. A., Bruns, R. E., Teixeira, F. J. and Godoy, H. T. (2010). Optimisation of a CE method for caffeine analysis in decaffeinated coffee. *Food Chemistry,* 120(4): 1155-1161.
11. Jeon, D. B., Hong, Y. S., Lee, G. H., Park, Y. M., Lee, C. M., Nho, E. Y. and Kim, K. S. (2017). Determination of volatile organic compounds, catechins, caffeine and theanine in Jukro tea at three growth stages by chromatographic and spectrometric methods. *Food Chemistry*, 219: 443-52.
12. Al-Qaim, F. F., Jusof, S. H., Abdullah, M. P., Mussa, Z. H., Tahrim, N. A, Khalik, W. M. A.W. M. and Othman, M. R (2017). Determination of caffeine in surface water using solid phase extraction and high-performance liquid chromatography. *Malaysian Journal of Analytical Sciences*, 21(1): 95-104.
13. Lei, Y., He, M., Chen, B. and Hu, B. (2016). Polyaniline/cyclodextrin composite coated stir bar sorptive extraction combined with high performance liquid chromatography-ultraviolet detection for the analysis of trace polychlorinated biphenyls in environmental waters. *Talanta*, 150: 310-318.
14. Zhang, H., Low, W. P. and Lee, H. K. (2012). Evaluation of sulfonated graphene sheets as sorbent for micro-solid-phase extraction combined with gas chromatography–mass spectrometry. *Journal of Chromatography A*, 1233: 16-21.
15. Feng, L., van Hullebusch, E. D., Rodrigo, M. A., Esposito, G. and Oturan, M, A. (2013). Removal of residual anti-inflammatory and analgesic pharmaceuticals from aqueous systems by electrochemical advanced oxidation processes. A review. *Chemical Engineering Journal*. 228: 944-964.
16. Nikolaou, A., Meric, S. and Fatta, D. (2007). Occurrence patterns of pharmaceuticals in water and wastewater environments. *Analytical and Bioanalytical Chemistry,* 387(4): 1225-1234.

17. Zhang, Y., Geißen, S. U. and Gal, C. (2008). Carbamazepine and diclofenac: removal in wastewater treatment plants and occurrence in water bodies. *Chemosphere*, 73(8): 1151-1161.
18. Al-Qaim, F. F., Yuzir, A. and Mussa, Z. H. (2018). Determination of theobromine and caffeine in some Malaysian beverages by liquid chromatography-time-of-flight mass spectrometry. *Tropical Journal of Pharmaceutical Research*, 17(3): 529-535.
19. Choi, E. J, Bae, S. H., Park, J. B., Kwon, M. J., Jang, S, M., Zheng, Y. F. and Bae, S. K. (2013). Simultaneous quantification of caffeine and its three primary metabolites in rat plasma by liquid chromatography–tandem mass spectrometry. *Food Chemistry*, 141(3): 2735-2742.
20. Al-Qaim, F. F., Abdullah, P., Othman, M. R., Mussa, Z. H., Zakaria, Z., Latip, J. and Afiq, W. M. (2015). Investigation of the environmental transport of human pharmaceuticals to surface water: A case study of persistence of pharmaceuticals in effluent of sewage treatment plants and hospitals in Malaysia. *Journal of the Brazilian Chemical Society*, 26: 1124-1135.
21. Al-Qaim, F. F., Abdullah, P., Othman, M. R., Latip, J. and Afiq, W. M. (2013). Development of analytical method for detection of some pharmaceuticals in surface water. *Tropical Journal of Pharmaceutical Research*, 12(4): 609-616.

Malaysian Journal of Analytical Sciences (MJAS)
Published by Malaysian Analytical Sciences Society

MICROWAVE-ASSISTED AND CONVENTIONAL SYNTHESIS OF HALOGENATED COUMARIN-AZO DERIVATIVES AND STRUCTURAL-ACTIVITY RELATIONSHIP STUDY FOR ANTIMICROBIAL POTENTIAL

(Sintesis Berbantukan Gelombang Mikro dan Konvensional Derivatif Coumarin-Azo Berhalogen dan Kajian Hubungan Struktur-Aktiviti untuk Potensi Antimikrob)

Nur Arif Mortadza and Zainab Ngaini*
Faculty of Resource Science and Technology,
Universiti Malaysia Sarawak, 94300 Kota Samarahan, Sarawak, Malaysia

**Corresponding author: nzainab@unimas.my*

Received: 21 September 2022; Accepted: 18 December 2022; Published: 19 April 2023

Abstract

Untreatable bacterial infectious diseases have become a leading cause of mortality due to the emergence of drug-resistant bacteria. The search for a new effective pharmaceutical drug can be time-consuming and expensive. Therefore, structural chemical modification of natural product-based compounds with known biological properties for potential drug candidates has gained a great interest among researchers. Microwave-assisted synthesis is quickly becoming the method of choice in modern organic synthesis for drug discovery due to benefits such as higher yield and shorter reaction time. In this study, a series of coumarin derivatives have been synthesized by incorporating halogenated azo moieties in the molecular network *via* diazo-coupling, Knoevenagel condensation, and hydrolysis reactions. Microwave-assisted organic synthesis reaction has produced overall higher yields of products (74-94 %) in 6-17 mins compared to the conventional reflux method (56-85 %) in 6-18 h. The structural activity relationship of all compounds was initially evaluated *via in silico* (molecular docking) for potential antimicrobial properties against *Escherichia coli* and *Staphylococcus aureus*. The synthesized compound gave a higher binding affinity (-6.3 to -8.9 kcal/mol) compared to ampicillin (-6.7 to -7.3 kcal/mol) and coumarin (-6.0 to -6.2 kcal/mol). *In vitro* evaluation (agar well diffusion), nevertheless, gave weak to no bacterial inhibition activity. This study is significant in searching for potential drug precursors to benefit mankind.

Keywords: diazo, docking, *In silico*, Knoevenagel, microwave

Abstrak

Penyakit berjangkit bakteria yang tidak dirawat disebabkan oleh kemunculan bakteria kerintangan ubat telah menjadi punca utama kematian. Proses pencarian ubat farmaseutikal baharu yang efektif boleh mengambil masa yang lama dan memerlukan kos yang tinggi. Oleh itu, pengubahsuaian struktur kimia sebatian yang berasaskan produk semula jadi dengan sifat biologi yang diketahui sebagai calon ubat yang berpotensi telah menarik minat dikalangan para penyelidik. Kaedah sintesis berbantukan gelombang mikro dengan cepatnya telah menjadi kaedah pilihan dalam sintesis organik moden untuk pencarian ubat berpotensi kerana kelebihannya seperti mampu menghasilkan produk yang lebih tinggi dan mengurangkan masa tindak balas. Dalam kajian ini, siri derivatif kumarin telah disintesis dengan menggabungkan moieti azo halogen dalam rangkaian molekul melalui tindak balas gandingan

diazo, pemeluwapan Knoevenagel, dan hidrolisis. Tindak balas sintesis organik berbantukan gelombang mikro telah berjaya menghasilkan produk keseluruhan yang lebih tinggi (74-94 %) dalam masa 6-17 minit berbanding kaedah refluks konvensional (56-85 %) yang memerlukan 6-18 jam. Penilaian hubungan aktiviti struktur semua sebatian untuk potensi aktiviti antimikrob terhadap Escherichia coli dan Staphylococcus aureus dinilai melalui kaedah *in silico* (dok molekul). Sebatian yang disintesis memberikan afiniti pengikatan yang tinggi (-6.3 hingga -8.9 kcal/mol) berbanding ampicillin (-6.7 hingga -7.3 kcal/mol) dan kumarin (-6.0 hingga -6.2 kcal/mol). Walaubagaimanapun, penilaian *in vitro* (penyebaran perigi agar) menunjukkan tiada aktiviti perencatan tumbuhan bakteria. Kajian ini penting dalam mencari prekursor ubat yang berpotensi untuk memberi manfaat kepada manusia.

Kata kunci: diazo, dok, *In silico*, Knoevenagel, gelombang mikro

Introduction

Untreatable infectious bacterial disease is a leading cause of mortality due to the rapid emergence of drug-resistant bacteria [1]. Antibiotics are crucial to combat many advent diseases and treat immune-compromised patients [2]. However, current antibiotics are becoming less effective against drug-resistant bacteria due to daily antibiotic consumption [3] and bacterial mutation [4]. There is an urgent need to develop new antimicrobial agents with high efficacy and effectiveness. The search for an effective pharmaceutical drug can be time-consuming and costly. Natural product-based compounds with known biological potentials have become a great source of inspiration in drug design [5]. Chemical modification of natural product-based compounds for potential drug candidates has gained significant interest among researchers [6-7]. Microwave-assisted synthesis has gained much interest in modern drug development programs due to its efficiency, shorter reaction times, and higher yields [8]. Furthermore, it is more cost-effective and environmentally friendly than the conventional approach via heating [9].

Coumarin is an example of a natural product-based compound that is naturally found in many plants [10]. Naturally occurring coumarin derivatives has many biological activities in plants especially in controlling plant growth, respiration, photosynthesis, and defense against various infections [11-12]. Coumarins' excellent biological properties have led to the development of synthetic coumarin derivatives with medical properties namely anti-bacterial, anti-cancer, anti-inflammation, anti-viral, and many others [11-14]. The biological properties of coumarin are due to its basic molecular structure, which noncovalently interact with many receptors in living organisms and resulting in a diverse range of physical activities [12&15]. Numerous ways are reported to synthesize coumarins namely Perkin reaction [16], Knoevenagel condensation [17], Pechmann condensation [18], and more [19].

In recent years, drugs which comprise two or more pharmacophore groups binding together covalently in one molecular framework have received great interest. The multi-targeted strategy has led to the development of a number of bioactive hybrid molecules with desired pharmacokinetic profiles and less tendency to drug-resistant bacteria [20]. Molecular hybridization of several pharmacophore groups acts by inhibiting two or more conventional targets at once. Structural hybridization of coumarin with other biologically active moieties is envisaged to increase their biological properties as new potential drugs [20-21]. Similar to coumarin, azo dyes are another biologically active moiety found in many natural products [22] with a wide spectrum of biological properties [23]. Azo dyes participate in various biological processes, including DNA inhibition, RNA and protein synthesis, carcinogenesis, and nitrogen fixation [24]. The incorporation of electronegative halogen substituents, on the other hand, improves the penetration of lipid membranes and increases the biological properties of molecules by making the structure more lipophilic [25-26].

This paper reports on the synthesis of coumarin incorporated with halogenated azo moiety, which is further evaluated for antibacterial properties against *E. coli* ATCC 25922 and *S. aureus* S48/81. The reaction involved a diazo-coupling reaction of halogenated azo-benzaldehyde intermediate **1a-d** followed by

Knoevenagel condensation reaction and hydrolysis (MW–assisted and conventional method) to achieve halogenated azo-coumarin derivatives **2a-d** and **3a-d**, respectively. The structure-activity relationship of the compounds for potential bacterial growth inhibition was preliminarily studied *via in silico* (molecular docking) followed by agar well diffusion (*in vitro*).

Materials and Methods

Materials and instrumentation

All purchased reactants and solvents of analytical grade were used without further purification. Microwave-assisted synthesis (MW) (was conducted using Anton Paar Monowave 300 (Austria). ^{1}H NMR and ^{13}C NMR spectra were recorded with DMSO-d6 as a solvent on a JEOL JNM-ECZ500R (Japan). Chemical shifts are given in parts per million (δ). FTIR spectra were obtained using Thermo SCIENTIFIC NICOLET iS10 (United States).

Synthesis of intermediate azo-benzaldehyde derivatives (1a-d)

A mixture of aniline derivatives (10 mmol) was dissolved in 10 mL of 25 % hydrochloric acid, HCl solution and cooled in an ice bath. Sodium nitrite, $NaNO_2$ solution (1.5 eq. mol) was added and reacted under constant stirring for 15 min. 2-Hydroxybenzaldehyde (10 mmol) dissolved in 20 mL of 1M sodium hydroxide, NaOH solution was then added to the mixture and reacted for a few minutes. The pH of the reaction was adjusted to 8-9. The reaction continued to react for 1-2 h. The reaction mixture was acidified using an HCl solution to precipitate out the crude product. The crude product was vacuum filtered, rinsed with distilled water, dried overnight, and purified *via* fast recrystallization from hot ethanol. The data analysis of **1a-d** can be obtained from supplementary file S1.

Synthesis of 3-ethylcarboxylatecoumarin-azo derivatives (2a-d)

The azo intermediate **1a-d** and diethyl malonate with a 1:1 ratio was dissolved into 20 ml of ethanol in a round bottom flask. Piperidine (0.25 eq mol) and a few drops of acetic acid were added to the reaction mixture, refluxed for 8-18 h, and confirmed *via* TLC analysis. Warm 50% ethanol (20 ml) was added to the reaction mixture and allowed to rest in ice water for 1 h. The solid product was filtered and rinsed with ethanol solution. The solid was recrystallized from ethanol to obtain a pure product. The conventional reflux heating method (I) was replaced with microwave irradiation (II) to reduce reaction time and increase product yield. The data analysis of **2a-d** can be obtained from supplementary file S2.

Synthesis of 3-ethylcarboxylatecoumarin-azo derivatives (3a-d)

Coumarin-azo **2a-d** dissolved in ethanol (15 ml) in a reaction flask followed by the addition of 1 M NaOH (15 ml). The reaction mixture was reacted for 3 h and confirmed *via* TLC analysis. The reaction mixture was then acidified with concentrated HCl and allowed to react for 15-30 min at room temperature. The solid precipitate was filtered and rinsed with hot distilled water and purified *via* hot filtration from ethanol. The conventional reflux heating method (I) was replaced with microwave irradiation (II) to reduce reaction time and increase product yield. The data analysis of **3a-d** can be obtained from supplementary file S3.

In silico study via molecular docking

Docking studies were performed using Autodock Tools and Vina. The X-ray structure of *E. coli* GyrB24 with inhibitor (PDB entry: 6yd9) and *S. aureus* GyrB ATPase domain in complex with a small molecule inhibitor (PDB entry: 3u2k) was retrieved from Protein Data Bank. The cubic grid box of 40 Å size (x, y, and z) with a spacing of 0.5 Å was centered on the active sites of the protein.

In-vitro study via agar well diffusion

In vitro screening of **1a–d**, **2a–d**, and **3a–d** was performed against *E. coli* (ATCC 25922) and *S. aureus* (ATCC 29213) *via* the agar well diffusion method. *E. coli* and *S. aureus* were cultured in Mueller-Hinton Broth (MHB) as inoculum and incubated at 37.5 ℃ with continuous shaking overnight at 180 rpm. The bacteria were spread on Mueller-Hinton Agar (MHA) plates using a bacteria suspension made with a sterilized cotton-tipped swab. A hole with a diameter of 6 to 8 mm is punched aseptically with a sterile tip and a volume of 10 µL of the synthesized compound in DMSO. The

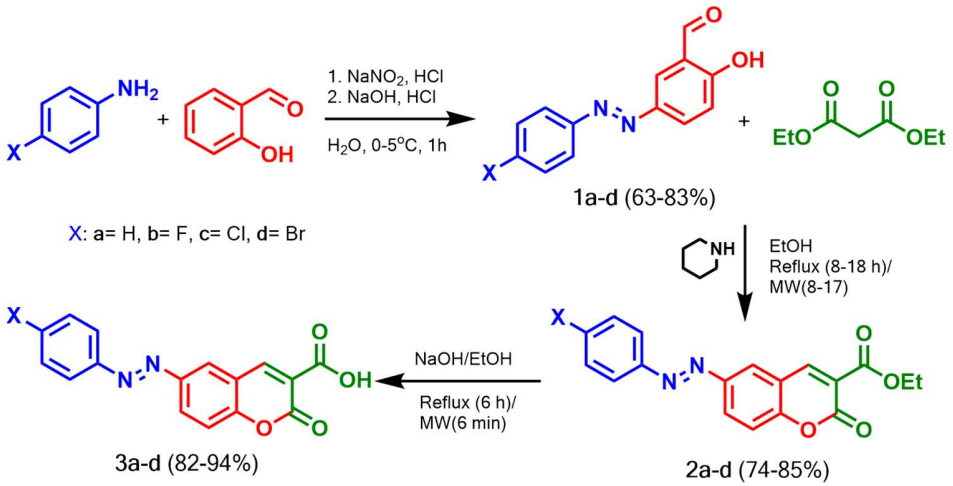
plates were incubated at 37.5 °C for 24 h. The zone of inhibition was measured in millimeters to evaluate the effectiveness of the synthesized compounds.

Results and Discussion

Chemistry

Prior to the synthesis of halogenated azo-coumarin **2a-d** and **3a-d,** an intermediate halogenated azo-benzaldehyde **1a-d** with a high yield (63-83%) was synthesized *via* diazotization of halogenated aniline in the presence of hydrochloric acid and sodium nitrite followed by coupling with 2-hydroxybenzaldehyde in basic condition. The formation of halogenated azo ethyl coumarin-3-carboxylate **2a-d** was achieved *via* Knoevenagel condensation of **1a-d** with diethyl malonate in piperidine and acetic acid as catalyst. Due to the long refluxing hour in conventional protocol employing hazardous solvent, microwave irradiation has become a great interest to introduce green and facile synthesis of one pot Knoevenagel condensation with higher yield [8]. The synthesis was comparatively performed using conventional heating and microwave irradiated (MW) synthesis. The microwave-assisted Knoevenagel condensation in MW was completed in shorter times of 8-17 min (74-85%) compared to the conventional reflux in 8-18 h (56-79%). The subsequence microwave irradiated hydrolysis of **2a-d** afforded halogenated azo coumarin-3-carboxylic **3a-d** with a higher yield and a shorter time (82-94% in 6 min) compared to the conventional procedure (76-85% and 6 h). The synthetic reactions of **1a-b**, **2a-d**, and **3a-d** are shown in Scheme 1. The yields and reaction times of conventional and microwave-assisted synthesis of **2a-d**, and **3a-d** is depicted in Table 1.

The molecular structure of all the synthesized compounds was characterized and confirmed using FTIR and NMR spectroscopy. Based on Figure 1, the formation of the N=N group of **1a-d** *via* diazo-coupling was confirmed by the strong absorption peak corresponding to the *v*(N=N) bend at 1483–1475 cm^{-1} [6&26]. The formation of **2a-d** *via* Knoevenagel reaction was indicated by the presence of *v*(C-H) stretch at 3051-3031 cm^{-1}. In addition, a strong signal at 1741–1732 cm^{-1} contributed by the *v*(C=O) lactone confirmed the formation of the coumarin lactone ring [27]. IR spectra of **3a-d** showed the presence of a strong signal in the range of 1745-1727 cm^{-1} contributed by *v*(C=O) lactone stretch and the disappearance of *v*(C-H) stretch at 3051-3031 cm^{-1} which confirmed successful hydrolysis of the ethyl group [27].



Scheme 1. Synthesis of **1a-d**, **2a-d**, and **3a-d**

Table 1. Comparison of conventional heating and MW irradiated synthesis of **2a-d** and **3a-d**

Product	Temperature (°C)		Time (min)		Yield (%)	
	Reflux	[MW]	Reflux	[MW]	Reflux	[MW]
2a	80	[140]	480	[8]	79	[85]
2b	80	[140]	600	[9]	74	[80]
2c	80	[140]	720	[11]	68	[83]
2d	80	[140]	1080	[17]	56	[74]
3a	80	[140]	360	[6]	80	[94]
3b	80	[140]	360	[6]	85	[85]
3c	80	[140]	360	[6]	77	[83]
3d	80	[140]	360	[6]	76	[82]

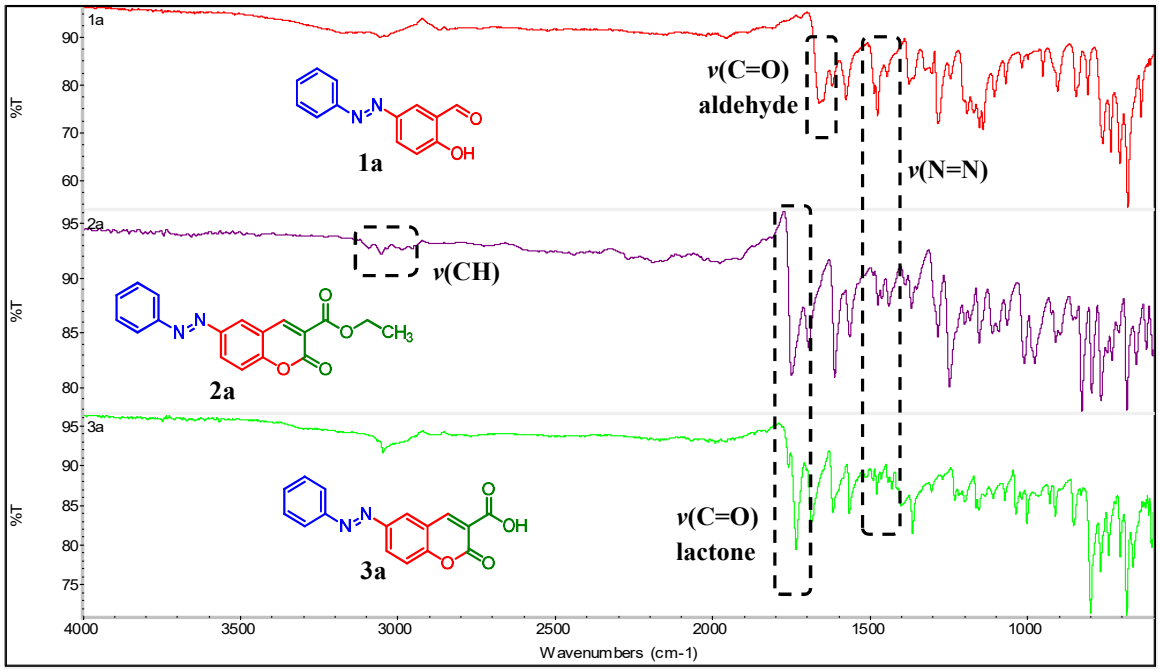


Figure 1. IR spectra of **1a**, **2a**, and **3a**

The ^{1}H NMR spectra of **1a-d**, **2a-d**, and **3a-d** showed the resonances attributed to aromatic protons at 8.93–7.20 ppm integrated with the corresponding number of aromatic protons. Figure 2 illustrated the ^{1}H spectra of **1a**, **2a**, and **3a**. The successful synthesis of -N=N- azo of **1a-d** *via* diazo coupling was confirmed by the duplet (H_a) and duplet-duplet (H_b) peaks at 8.17-8.19 ppm and 8.08-8.10 ppm, respectively. In addition, ^{1}H NMR spectra of **1a-d** showed the presence of proton for aldehyde as a singlet (H_c) at 10.37–10.36 ppm. The ^{1}H NMR spectra of **2a-d** indicated the formation of the coumarin *via* Knoevenagel condensation by the disappearance of the **1a-d** singlet aldehyde proton (H_c) peaks and the appearance of a new singlet (H_d) at 8.93 ppm. The appearance of the ethyl protons as a quartet (H_e) and triplet (H_f) at 4.34-4.55 and 1.34-1.33 ppm, respectively was also depicted by **2a-d**. The disappearance of peaks corresponded to -CH2CH3- at 4.34-1.33 ppm in the ^{1}H NMR spectra has clearly confirmed the formation of **3a-d** *via* hydrolysis.

The ^{13}C NMR spectra of **1a-d**, **2a-d,** and **3a-d** showed the resonances corresponding to aromatic carbons at 163.8–116.2 ppm. Compounds **1a-d** showed the

resonances attributed to *ν*(C=O) aldehyde at 190.6-190.4 ppm. The ^{13}C NMR spectra of **2a-d** showed the peak attributed to $–C_2H_5$ at 61.7–14.0 ppm. The resonance corresponding to *ν*(C=O) of **2a-d** and **3a-d** was observed at 163.8–156.0 ppm.

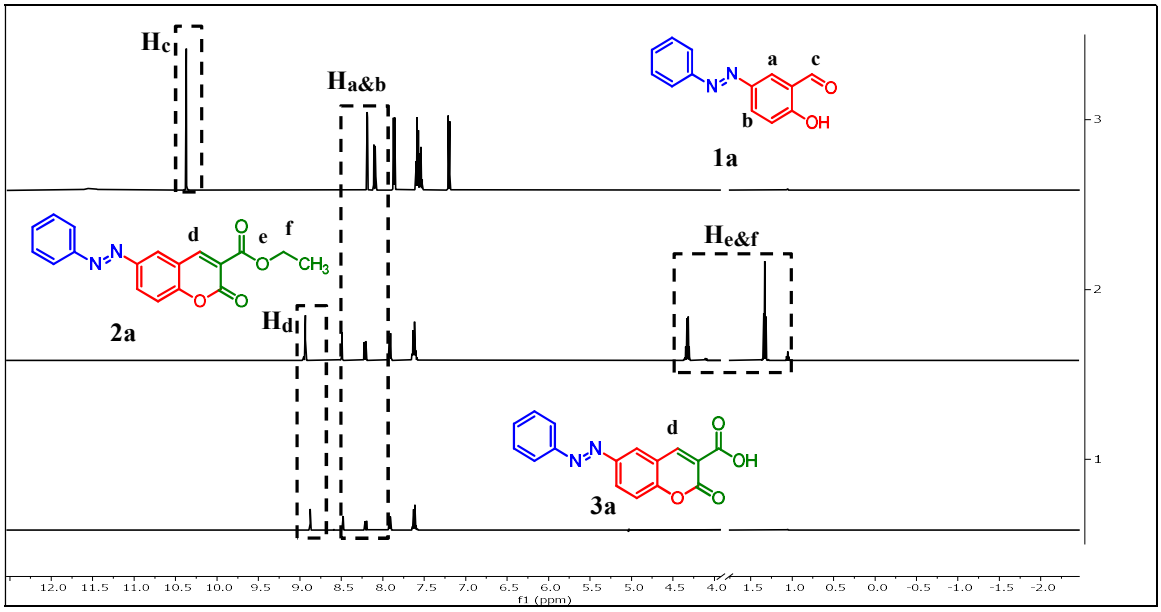


Figure 2. ^{1}H NMR spectra of **1a**, **2a**, and **3a**

Molecular docking study (*In silico*)

A preliminary study on the structural-activity relationship analysis of **1a-d**, **2a-d**, and **3a-d** as ligands was conducted to evaluate the possible binding interactions of the potential antibacterial agent. The binding affinity and interaction visualization between the ligands with DNA gyrase protein of *E. coli* GyrB24 (PDB entry: 6yd9) and *S. aureus* GyrB ATPase (PDB: 3u3k) were performed *via* Autodock Vina [28-29]. The binding affinity of **1a-d**, **2a-d**, and **3a-d** against DNA gyrase protein of *E. coli* and *S. aureus* is depicted in Table 2, where ampicillin was set as the standard drug. The drug candidates are usually chosen from the ligands that able to bind strongly to the target protein [30]. Higher binding affinity of the ligand indicates the ligand's ability to form strong binding interactions and influence the physiological function of target proteins [30].

The binding energies of **2a-d** and **3a-d** were -7.6 to -8.7 kcal/mol and -7.5 to -8.9 kcal/com, respectively for *E. coli* and *S. aureus*. The depicted binding energies of all the ligands were higher compared to the binding energy of the ampicillin (-6.7 to -7.3 kcal/mol) and coumarin (-6.0 to -6.2 kcal/mol). This indicates that coumarin azo derivatives have potential and ability to form stronger interaction, thus inhibit the bacterial enzyme activity. The intermediate **1a-d** scored the lowest (-6.3 to -6.6 kcal/mol). Among all, **3b** gave the highest binding energy -7.9 kcal/mol (*E. coli*) and -8.9 kcal/mol (*S. aureus*). Figure 3(a) depicted the interaction of **3b** to the active site of the enzyme for *E. coli*. The highly lipophilic characteristic of the compound formed hydrophobic interaction at the active site *via* π-alkyl and π-sigma bonding with the π-orbital of the alkyl group of various amino acid residues such as ILE78, PRO79, ARG76, and VAL120. An electrostatic interaction *via* the π-anion bond was also shown between the coumarin nucleus of **3b** with GLU50 residues.

The interaction of **3b** towards the active site of the *S. aureus* DNA gyrase enzyme is shown in Figure 3(b). Hydrophobic interaction *via* π-alkyl and π-sigma was observed between the benzene ring of **3b** with ILE86 and VAL131 residues. Hydrogen bond interaction was observed between the COOH of **3b** and GLU58 residue.

The presence of fluorine enables the ligand to form halogen bond interaction with GLU50 residues. In addition, van der Waals interaction between **3b** and various amino acid residues in the active site of the enzyme has also contributed to the strong ligand enzyme interaction.

Table 2. Binding affinity of **1a-d**, **2a-d**, and **3a-d** against DNA gyrase protein of *E. coli* and *S. aureus*

Compound	Binding Affinity (kcal/mol)	
	E. coli	***S. aureus***
1a	-6.5	-6.6
1b	-6.5	-6.6
1c	-6.4	-6.3
1d	-6.3	-6.3
2a	-7.8	-8.4
2b	-7.6	-8.7
2c	-7.6	-8.6
2d	-7.6	-8.6
3a	-7.9	-8.5
3b	-7.9	-8.9
3c	-7.9	-7.7
3d	-7.5	-8.7
Coumarin	-6.2	-6.0
Ampicillin	-7.3	-6.7

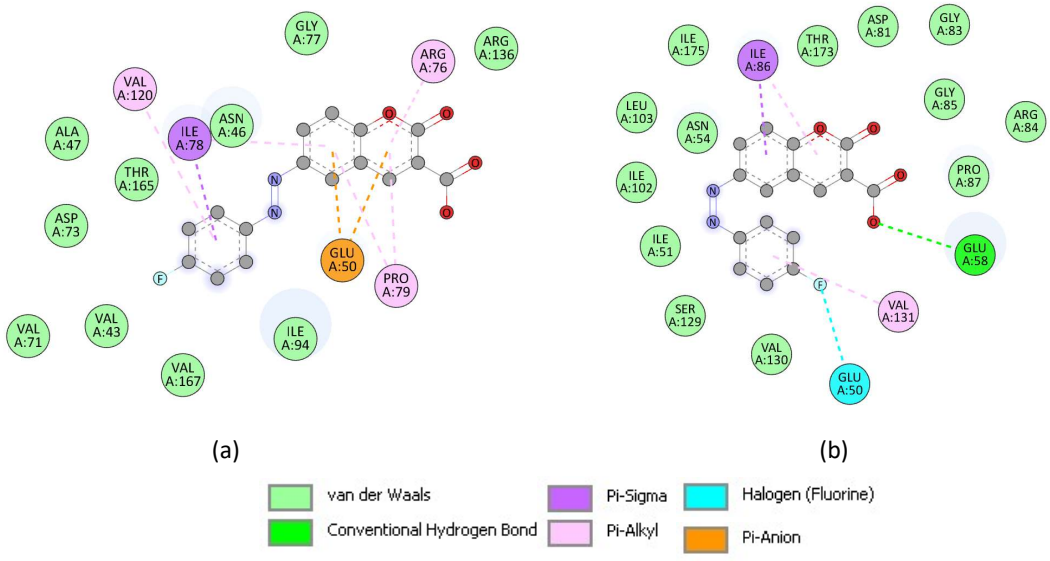


Figure 3: Interaction between **3b** and (a) *E. coli* and (b) *S. aureus*

The majority of DNA enzyme active binding sites has at least one hydrophobic pocket, and the lipophilic property makes it possible for lipophilic ligands to bind to hydrophobic protein binding sites [31].

Agar well diffusion study *(In vitro)*

Based on *in silico* strong interaction of the ligands against the DNA gyrase protein of *E. coli* and S. aureus, *in vitro* evaluations were conducted to evaluate the bacterial inhibition activity of the synthesized compounds against *E. coli* and *S. aureus via* agar well diffusion [32]. Ampicillin was used as the positive control and DMSO as the negative control. The results are depicted in Figure 4.

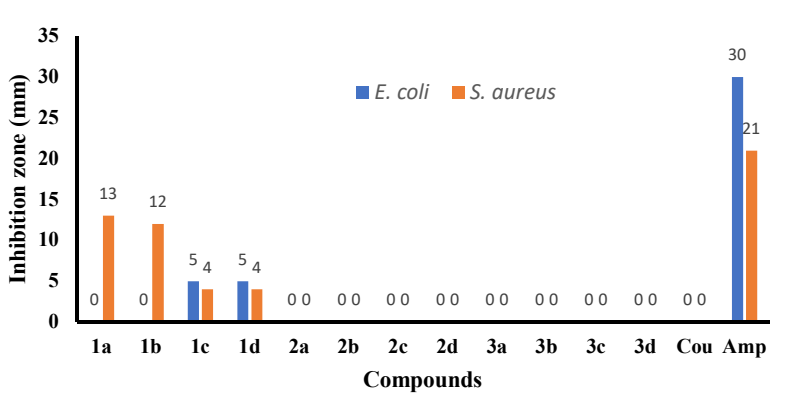


Figure 4. Inhibition activities of **1a-d**, **2a-d**, and **3a-d** against *E. coli* and *S. aureus*

Based on the results, all the synthesized azo **1a-d** showed inhibition activities against *S. aureus*. Among them **1a-b** demonstrated excellent activities on Gram positive bacteria (12-13 mm), while **1c-d** showed bacterial inhibition against both *E. coli* (5 mm) and *S. aureus* (4 mm), respectively. The bacterial inhibition activities of **1a-d** contributed to the presence of the N=N and halogens in the molecular network. The azo has the ability to protonate in acidic conditions and interact with the phosphate group on the peptidoglycan layer of bacteria, thus hindering the formation of the cell wall [6&33]. The biological activities of azo are well known for their ability to inhibit the DNA gyrase enzyme [34]. Additionally, azo can undergo tautomerization enabling it to act as both hydrogen bond acceptor and donator [24&35-36], hence increasing the biological activity. The presence of the OH group has also contributed to the inhibition activity of **1a-d** due to its ability to form hydrogen bond interaction with the biological target receptor [37-38].

The subsequence one pot cyclization of coumarin **2a-d** and **3a-d** via Knoevenagel condensation, however, reduced the inhibition activity against both bacteria strains. The compounds were inactive due to the competitive resonance and reduced electrophilicity of the lactone with the presence of azo group [9]. The formation of lactone further increases the lipophilicity of the compound, decreasing the compound permeability [39]. Poor dissolution properties of a compound could also contribute to the reduces antibacterial activity [40]. The combined interaction of hydrophilic and lipophilic characteristics in molecule structure plays a significant role in antibacterial activities [41-42].

Conclusion

The synthesis of coumarin-azo derivatives bearing halogens **2a-d** and **3a-d** has been successfully synthesized with great yield from **1a-d** *via* MW assisted Knoevenagel condensation followed by hydrolysis. Microwave-assisted synthesis promotes green chemistry by using less solvent and reaction times compared to the conventional heating method. Molecular docking evaluation of **2a-d** and **3a-d** showed higher binding affinity (-7.5 to -7.9 kcal/mol) than ampicillin (-7.2 to -7.3 kcal/mol) which indicates the potential ligands to affect enzyme activity and inhibit bacterial growth. The azo intermediate **1a–d** showed moderate inhibition activity with **1a** depicted the highest inhibition zone of 13 mm against *S. aureus*, whereas **1c-d** gave 5 mm against *E. coli* due to involvement of electron

delocalization and resonance stability. Nevertheless, the **2a-d** and **3a-d** showed no inhibition to the bacterial growth against *E. coli* and *S. aureus*. The halogenated azo intermediates exhibited a better binding tendency with target proteins as compared to the coumarin-azo derivatives. This research is essential in pharmaceutical industry for the drug development of lead chemicals.

Acknowledgment

The authors would like to thank the Ministry of Higher Education Malaysia and Universiti Malaysia Sarawak (UNIMAS) for financial support through (FRGS/1/2019/STG01/UNIMAS/01/1) and Postgraduate Research Grant through F07/PGRS/1795/2019.

References

1. Hoffman, P. S. (2020). Antibacterial discovery: 21st century challenges. *Antibiotics (Basel)*, 9(5): 213.
2. Hutchings, M., Truman, A., and Wilkinson, B. (2019). Antibiotics: past, present and future. *Current Opinion Microbiology,* 51: 72-80.
3. World Health Organization (2021). Antimicrobial resistance. https://www.who.int/news-room/fact-sheets/detail/antimicrobial-resistance [Access online 10 August 2022]
4. Revitt-Mills, S. A. and Robinson, A. (2020). Antibiotic-induced mutagenesis: Under the microscope. *Frontier Microbiology,* 11: 1-13.
5. Davison, E. K. and Brimble, M. A. (2019). Natural product derived privileged scaffolds in drug discovery. *Current Opinion Chemical Biology,* 52: 1-8.
6. Ngaini, Z. and Mortadza, N. A. (2019). Synthesis of halogenated azo-aspirin analogues from natural product derivatives as the potential antibacterial agents. *Natural Products Research,* 33(24): 3507-3514.
7. Yao, H., Liu, J., Xu, S., Zhu, Z. and Xu, J. (2017). The structural modification of natural products for novel drug discovery. *Expert Opinion Drug Discovery*, 12(2): 121-140.
8. Sharma, N., Sharma, U. K., and Van der Eycken, E. V. (2018). Microwave-assisted organic synthesis: overview of recent applications. *Green Techniques for Organic Synthesis and Medicinal Chemistry*, Second Edition, pp. 441-468.
9. Farooq, S., Ngaini, Z., Daud, A. I., and Khairul, W. M. (2021). Microwave assisted synthesis and antimicrobial activities of carboxylpyrazoline derivatives: Molecular docking and DFT influence in bioisosteric replacement. *Polycyclic Aromatatic Compound,* 42(8): 5422-5435.
10. Pereira, T. M., Franco, D. P., Vitorio, F., and Kummerle, A. E. (2018). Coumarin compounds in medicinal chemistry: some important examples from the last years. *Current Topic Medicine Chemistry,* 18(2): 124-148.
11. Annunziata, F., Pinna, C., Dallavalle, S., Tamborini, L., and Pinto, A. (2020). An overview of coumarin as a versatile and readily accessible scaffold with broad-ranging biological activities. *International Journal Molecular Sciences*, 21(13): 1-83.
12. Pereira, T. M., Franco, D. P., Vitorio, F. and Kummerle, A. E. (2018b). Coumarin compounds in medicinal chemistry: some important examples from the last years. *Current Topic Medicine Chemistry*, 18(2): 124-148.
13. Qin, H. L., Zhang, Z. W., Ravindar, L., and Rakesh, K. P. (2020). Antibacterial activities with the structure-activity relationship of coumarin derivatives. *European Journal Medicine Chemistry*, 207: 1-17.
14. Akkol, E. K., Genç, Y., Karpuz, B., Sobarzo-Sánchez, E., and Capasso, R. (2020). Coumarins and coumarin-related compounds in pharmacotherapy of cancer. *Cancers (Basel),*12(7): 1-25.
15. Detsi, A., Kontogiorgis, C., and Hadjipavlou-Litina, D. (2017). Coumarin derivatives: an updated patent review (2015-2016). *Expert Opinion Therapy Patients,* 27(11): 1201-1226.
16. Molnar, M., Lončarić, M., and Kovač, M. (2020). Green chemistry approaches to the synthesis of coumarin derivatives. *Current Organic Chemistry,* 24(1): 4-43.
17. Dinparast, L., Hemmati, S., Zengin, G., Alizadeh, A. A., Bahadori, M. B., Kafil, H. S., and Dastmalchi, S. (2019). Rapid, efficient, and green synthesis of coumarin derivatives via Knoevenagel

condensation and investigating their biological effects. *ChemistrySelect,* 4(31): 9211-9215.

18. Jadhav, N. H., Sakate, S. S., Rasal, N. K., Shinde, D. R., and Pawar, R. A. (2019). Heterogeneously catalyzed Pechmann condensation employing the tailored Zn0.925Ti0.075ONPs: Synthesis of coumarin. *ACS Omega,* 4(5): 8522-8527.
19. Lončarić, M., Gašo-Sokač, D., Jokić, S. and Molnar, M. (2020). Recent advances in the synthesis of coumarin derivatives from different starting materials. *Biomolecules,* 10(151): 1-35.
20. Ngaini, Z., Abd Halim, A. N., Rasin, F. and Wan Zullkiplee, W. S. H. (2022). Synthesis and structural-activity relationship studies of mono- and bis-thiourea derivatives featuring halogenated azo dyes with antibacterial properties. *Phosphorus, Sulfur, and Silicon and the Related Elements,* 197(9): 909-917.
21. Feng, D., Zhang, A., Yang, Y., and Yang, P. (2020). Coumarin-containing hybrids and their antibacterial activities. *Archive Pharmaceutical*, 353(6): 1-12.
22. Dembitsky, V. M., Gloriozova, T. A. and Poroikov, V. V. (2017). Pharmacological and predicted activities of natural azo compounds. *Natural Production Bioprospectives*, 7(1): 151-169.
23. Ali, Y., Hamid, S. A., and Rashid, U. (2018). Biomedical applications of aromatic azo compounds. *Mini Review Medicine Chemistry,* 18(18): 1548-1558.
24. Benkhaya, S., M'rabet, S. and el Harfi, A. (2020). Classifications, properties, recent synthesis and applications of azo dyes. *Heliyon,* 6(1): 1-26.
25. Prabhakara, C. T., Patil, S. A., Toragalmath, S. S., Kinnal, S. M. and Badami, P. S. (2016). Synthesis, characterization and biological approach of metal chelates of some first-row transition metal ions with halogenated bidentate coumarin Schiff bases containing N and O donor atoms. *Journal Photochemistry Photobiology B,* 157: 1-14.
26. Mortadza, N. A., Ngaini, Z., Arif, M. A. M. (2021). Synthesis of silver (I) coordinated of aspirinate azo ligands as potential antibacterial agents. *Defection Diffusion Forum,* 411: 17-24.
27. Madiahlagan, E., Sunil, B. N., Ngaini Z., and Hegde, G. (2019). Synthesis, liquid crystalline properties and photo switching properties of coumarin-azo bearing aliphatic chains: Application in optical storage devices. *Journal Molecular Liquids,* 292: 111328.
28. Trott, O. and Olson, A. J. (2010). AutoDock Vina: improving the speed and accuracy of docking with a new scoring function, efficient optimization and multithreading. *Journal Computational Chemistry,* 31(2): 455-461.
29. Morris, G. M., Huey, R., Lindstrom, W., Sanner, M. F., Belew, R. K., Goodsell, D. S. and Olson, A. J. (2009). AutoDock4 and AutoDockTools4: automated docking with selective receptor flexibility. *Journal of Computational Chemistry*, 30(16): 2785-2791.
30. Seo, S., Choi, J., Park, S. and Ahn, J. (2021). Binding affinity prediction for protein–ligand complex using deep attention mechanism based on intermolecular interactions. *BMC Bioinformatics,* 22(1): 542.
31. Johnson, T. W., Gallego, R. A., and Edwards, M. P. (2018). Lipophilic efficiency as an important metric in drug design. *Journal Medical Chemistry,* 61(15): 6401-6420.
32. Balouiri, M., Sadiki, M., and Ibnsouda, S. K. (2016). Methods for *in vitro* evaluating antimicrobial activity: A review. *Journal Pharmaceutical Analysis,* 6(2): 71-79.
33. Li, X., Wu, B., Chen, H., Nan, K., Jin, Y., Sun, L., and Wang, B. (2018). Recent developments in smart antibacterial surfaces to inhibit biofilm formation and bacterial infections. *Journal Materials Chemistry B,* 6(26): 4274-4292.
34. Banaszak-Leonard, E., Fayeulle, A., Franche, A., Sagadevan, S., and Billamboz, M. (2021). Antimicrobial azo molecules: A review. *Journal of the Iranian Chemical Society*, 18(11): 2829-2851.
35. Antonov, L. (2019). Tautomerism in azo and azomethyne dyes: When and if theory meets experiment. *Molecules,* 24(12): 2252.
36. Echeverría, J., Urzúa, A., Sanhueza, L., and Wilkens, M. (2017). Enhanced antibacterial activity of Ent-labdane derivatives of salvic acid (7α-hydroxy-8(17)-ent-labden-15-oic acid): effect of lipophilicity and the hydrogen bonding role in

bacterial membrane interaction. *Molecules,* 22(7): 1039.

37. Wan Zullkiplee, W. S. H., Rasin, F., Abd Halim, A. N., Mortadza, N. A., Ramli, N., Hani, N. I., and Ngaini, Z. (2021). Synthesis, biological properties and comparative molecular docking evaluation studies of 1,3 and 1,4 bis-thiourea derivatives as potential antimicrobial resistant agents. *International Journal Current Research Review,* 13(4): 22-30.
38. Qin, H. L., Zhang, Z. W., Ravindar, L., and Rakesh, K. P. (2020). Antibacterial activities with the structure-activity relationship of coumarin derivatives. *European Journal Medicine Chemistry,* 207: 112832.
39. Wang, S., Konig, G., Roth, H. J., Fouche, M., Rodde, S., and Riniker, S. (2021). Effect of flexibility, lipophilicity, and the location of polar residues on the passive membrane permeability of a series of cyclic decapeptides. *Journal Medicine Chemistry*, 64(17): 12761-12773.
40. Farooq, S., Ngaini, Z., Mortadza, N. A. (2020). Microwave-assisted synthesis and molecular docking study of heteroaromatic chalcone derivatives as potential antibacterial agents. *Bull Korean Chem Society,* 41(9): 918-924.
41. Park, K. M., Lee, S. J., Yu, H., Park, J. Y., Jung, H. S., Kim, K., Lee, C. J. and Chang, P. S. (2018). Hydrophilic and lipophilic characteristics of non-fatty acid moieties: significant factors affecting antibacterial activity of lauric acid esters. *Food Science Biotechnology,* 27(2): 401-409.
42. Johnson, T. W., Gallego, R. A. and Edwards, M. P. (2018). Lipophilic efficiency as an important metric in drug design. *Journal Medicine Chemistry,* 61(15): 6401-6420.

Malaysian Journal of Analytical Sciences (MJAS)
Published by Malaysian Analytical Sciences Society

MOLECULARLY IMPRINTED POLYMERS FOR DOMOIC ACID DETECTION IN SELECTED SHELLFISH TISSUE

(Polimer Tercetak Molekul bagi Pengesanan Domoik Asid di dalam Tisu Kerangan Terpilih)

Fatin Nabilah Muhamad, Hafiza Mohamed Zuki*, Marinah Ariffin, and Azrilawani Ahmad

Faculty of Science and Marine Environment,
Universiti Malaysia Terengganu, 21030 Kuala Terengganu, Malaysia

**Corresponding author: hafiza@umt.edu.my*

Received: 22 September 2022; Accepted: 27 February 2023; Published: 19 April 2023

Abstract

Domoic acid (DA) molecular imprinted polymers (MIP) were successfully synthesized by a bulk polymerization method using 2-hydroxyethyl methacrylate (HEMA) as a functional monomer and ethylene-glycol dimethacrylate (EGDMA) as a cross-linker. Non-imprinted polymers (NIP) were also synthesized using similar procedures, but without the addition of template molecules (DA). The presence of DA templates in MIP and the absence of DA templates in NIP was proven by Fourier-Transform Infrared (FT-IR) Spectroscopy, Brunauer, Emmett, and Teller (BET) method, and Scanning Electron Microscopy (SEM) analysis. All MIP analyses were done using a UV-Vis spectrophotometer. Binding efficiencies of MIP with domoic acid were determined using batch rebinding experiments, where the optimum mass and time obtained were 5 mg and 15 minutes, respectively. The correlation coefficients (R^2) of NIP and MIP were 0.8989 and 0.9933, respectively. The calculated limit of detection (LOD) was 1.418 ppm, and the limit of quantification (LOQ) was 4.2983 ppm. An adsorption isotherm experiment indicated that the Freundlich isotherm model yielded a better fit towards the equilibrium adsorption data. The MIP was successfully applied in the determination of DA in shellfish tissues of cockles and mussels, where the percentage recovery obtained for the spiked samples was 95.88% for cockles and 82.71% for mussels.

Keywords: molecularly imprinted polymer, domoic acid, shellfish, binding efficiency, marine neurotoxin

Abstrak

Polimer tercetak molekul (MIP) domoik asid (DA) telah berjaya disintesis melalui kaedah pempolimeran pukal menggunakan 2-hidroksietil metakrilat (HEMA) sebagai monomer berfungsi dan etilena-glikol dimetakrilat (EGDMA) sebagai penghubung silang. Polimer tidak tercetak (NIP) juga disintesis melalui kaedah yang sama tetapi tanpa penambahan templat molekul (DA). Kehadiran templat DA didalam MIP dan ketidakhadiran templat DA didalam NIP dibuktikan melalui analisis Fourier-Transform Infrared (FT-IR) Spectroskopi, kaedah Bruneaur, Emmett and Teller (BET) dan mikroskopi pengimejan elektron (SEM). Semua MIP dianalisa menggunakan UV-Vis spektrofotometer. Kecekapan pengikatan MIP dengan domoik asid ditentukan melalui ujikaji pengikatan semula secara berkelompok dimana berat dan masa optima yang diperolehi adalah 5 mg dan 15 minit masing-masing. Pekali korelasi (R^2) bagi NIP serta MIP adalah 0.8989 dan 0.9933 masing-masing. Pengiraan had pengesanan (LOD) adalah 1.4148 ppm dan had kuantiti (LOQ) adalah 4.2983 ppm. Ujikaji isoterma penjerapan menunjukkan bahawa model isoterma Freudlich menghasilkan data keseimbangan penjerapan yang lebih sesuai. MIP ini telah berjaya diaplikasikan dalam penentuan DA dalam

tisu kerangan iaitu kerang dan kupang dimana nilai peratusan pemulihan yang diperolehi bagi sampel yang dipaku adalah 95.88% bagi kerang dan 82.71% bagi kupang.

Kata kunci: molekul polimer tercetak, domoik asid, kerangan, kecekapan pengikatan, neurotoksin marin

Introduction

Domoic acid (DA) is a type of marine neurotoxin that is responsible for Amnesic Shellfish Poisoning (ASP). It was first documented in 1987, where consumers reportedly fell ill after consuming DA contaminated blue mussels harvested from eastern Prince Edward Island [1]. ASP can cause several illnesses such as diarrhea, degeneration of the nervous system in brain, and short-term memory loss [2]. In the human body, DA is known as an agonist to the glutamate receptor in the brain, where it causes disruption of the flow of mineral ions (Ca, Mg, Zn) across the cell membranes, thus affecting the hippocampus and amygdale glands in the human brain [3]. The DA toxin can be transferred to humans through the food chain via the consumption of toxic microalgae accumulated in seafood [4]. DA bio-accumulation in shellfish is aided by filtration of toxic species of red algae diatom, *pseudo-nitzschia* [5,6]. The DA molecule (shown in Figure 1), though unstable due to the oxidation of the conjugate double bond, has a strong UV chromophore, marking it as one of the most easily detected toxins [7].

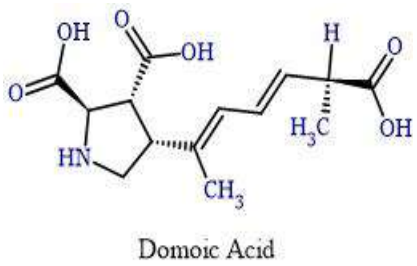


Figure 1. Chemical structure of DA

In order to protect consumers from DA poisoning, i.e., ASP, relevant permitted levels of DA concentration are established by many regulatory authorities, such as in the EU and USA, which is 20 µg of DA concentration per gram (g) shellfish meat [8, 9]. The outbreak of DA poisoning in shellfish tissue typically relates to the red tide phenomenon, which occurs during harmful algae blooms [10]. These blooms can be associated with cool and high nutrient water discharge from freshwater reservoirs [11]. Over 52 known species of *Pseudo-nitzschia* have been recorded globally, and 27 of these species are known to produce DA toxins [12]. In Malaysia, two types of DA producer algae have been recorded: *Nitzschia navis varingica*, which was discovered in peninsular Malaysia [13], and *Pseudo-nitzschia cuspidata*, which was discovered in Borneo [14].

Researchers have been using many means of analysis to detect DA in seafood. Instruments such as HPLC, GC-MS, and LC-UV are known as the established instruments used for the accurate and precise analysis of DA [15, 16]. However, these methods of analysis are time consuming and expensive. Therefore, in order to provide an alternative sensing method for DA detection, molecular recognition using imprinting polymers is being studied.

Molecularly imprinted polymers (MIPs) are specially designed sorbents that exhibit enhanced selectivity towards a specific structure [17, 18, 19]. They are able to obtain high affinity, robust and stable artificial receptors for the analyte of interest in harsh chemical and physical conditions [20, 21, 22]. The template binds with cross-linkers, monomers, and initiators to produce a set of imprinted memories for the target molecule [23]. The working mechanism of MIPs used in this study is shown in Figure 2. Template molecules (DA), monomer (HEMA), cross-linker (EGDMA), initiator (BPO), and solvent (DMSO) were used for the synthesis of MIPs.

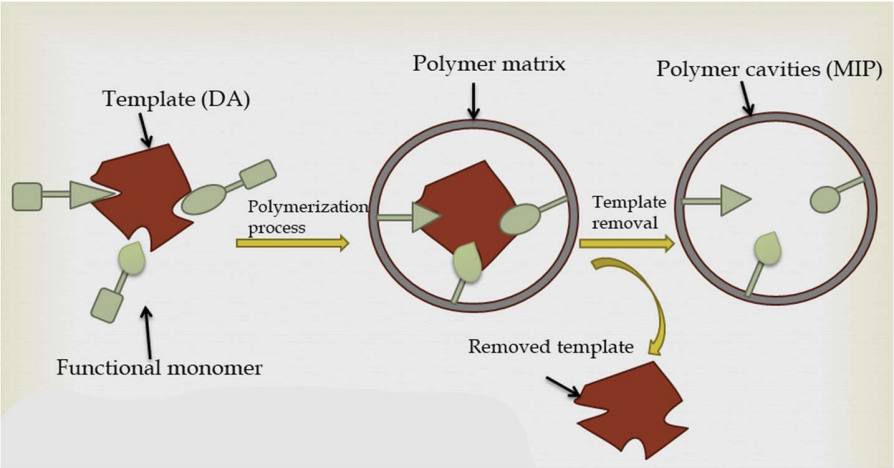


Figure 2. The schematic diagram for the working mechanism of MIP

The pre-polymerized solution was refrigerated for 1 hour in order to slow down the interaction between existing compounds in the solution with oxygen [24]. The polymerization of the MIP was conducted under low temperature conditions ranging from 40°C to 60°C. The cavities were formed by a washing method where the MIP was immersed in methanol/acetic acid (9:1, v/v) to remove the template (DA) [25]. The cavities provide a set of imprinted morphologies and memories capable of selectively binding the template. The imprinted polymer formed after template removal was used in this study to determine the adsorption capacity of MIP with DA.

Materials and Methods

Chemicals and samples

Domoic acid (DA), ethylene glycol dimethacrylate (EGDMA, 98%), hydroxyethyl methacrylate (HEMA, 98%), and benzoyl peroxide (BPO) were purchased from Merck. All other chemicals used in polymer synthesis including acetic acid, methanol, dimethyl sulfoxide (DMSO), and acetone were all analytical grade, and were purchased from Sigma Aldrich. Shellfish samples (cockle and mussel) were purchased from local fishermen and grocery stores.

Instrumentation

The characterization of MIPs and NIPs was conducted using Scanning electron microscopy (SEM), Fourier Transform Infrared (FTIR) spectrometry, and Brunauer, Emmett, and Teller (BET) Analysis. Meanwhile, the DA detection analysis was performed using Ultraviolet-Visible (UV-VIS) Spectrophotometer.

Synthesis of molecularly imprinted polymers

DA MIP was synthesized by a non-covalent bulk polymerization method. 313.3 µL DA template molecule and 520 µL of monomer (HEMA, 98%) were added into a beaker containing 4.9ml of DMSO. The solution mixture was allowed to stand for 5 minutes. Then, 3.96 mL of cross linker (EDGMA, 98%) was added into the solution, followed by 0.20g of benzoyl peroxide, to initiate the polymerization process. The solution was sonicated for 20 minutes and cooled at -20˚C for 1 hour. Then, the polymerization process of MIP was allowed to occur at 40 ˚C - 60˚C for 24 hours using a water bath. The polymers obtained were then filtered and dried for 6 hours at 50˚C in an oven. Meanwhile, NIP was synthesized with the same procedure as MIP, but without the addition of a template molecule.

Removal of DA template molecule from MIP

A template removal process was conducted to remove the imprinted DA molecule from the polymer matrix. A successive immersion technique was implemented for the removal of the template. The imprinted polymer was immersed in methanol/acetic acid (9:1, v/v) and shaken using an orbital shaker at 160 RPM for 24 hours at room temperature. The supernatant was filtered and analyzed

to confirm the removal of DA from the MIP. The template removal procedure was conducted until no DA was present in the collected supernatant. The MIP powder was then washed with methanol to remove excess acetic acid. Lastly, the polymer particles were washed with distilled water to remove the remaining solvents. The end product was dried in an oven at 50˚C for 6 hours.

Characterization of MIP and NIP

MIPs and NIPs were characterized before and after the template (DA) removal. Morphology and physical characterization studies were carried out using Scanning electron microscopy (SEM), Fourier Transform Infrared (FTIR) spectrometry, and Brunauer, Emmett, and Teller (BET) Analysis.

Batch rebinding experiment

Batch rebinding experiments were conducted to evaluate the performance of MIP binding capacity with DA. Mass and reaction time data was collected using UV-VIS spectrophotometer analysis. The data was analyzed using the Langmuir and Freudlich isotherm model in order to determine the heterogeneity and binding affinity of the MIP with DA.

Reproducibility and Reusability of MIP

Three batches of synthesized MIP were analyzed for their reproducibility by testing their responses with DA analyte for five times. The reusability of MIP was also tested by measuring several detection responses of DA analyte with the same MIP. This involved the repeated processes of reacting, re-washing, and re-reacting MIPs with DA analyte for five reusability cycles. The absorptivity of DA was measured and recorded, and the percentages of relative standard deviations (%RSD) were calculated for the reproducibility and reusability performance of MIP.

Analysis of real samples

The 20g of shellfish tissue and viscera was blended in 25 mL of distilled water and extracted by immersing 10 mL of pureed shellfish samples with 40 ml of methanol/distilled water (1:1; v/v) in a centrifuge tube. The sample mixture was shaken with a vortex and filtered using a filter paper. The remaining filtered mussel puree was removed and the supernatant collected was labeled as shellfish samples. Spiked and non-spiked samples were prepared by injecting 5ppm of DA for the spiked samples. The spiked and non-spiked shellfish samples were poured into clean vials, labeled, and refrigerated for storage at 4-5°C for further use.

Results and Discussion

Synthesis of MIP and NIP

The MIP and NIP were successfully synthesized through a non-covalent approach using the bulk polymerization method. The functional monomer, HEMA was used in the polymerization process for its neutral functionality, stability, and resistant bond strength [26]. Previous research by Ceolin et al. [27] has proven that the highest imprinting factor for MIPs can be achieved by using the molar ratio of 1:3.5:19.5 for templates, monomers, and cross-linkers. The MIP was synthesized using a 1:4:20 molar ratio of DA template to HEMA monomer to EGDMA cross-linker to provide an MIP with the highest affinity sites, higher selectivity, and adsorption capacity towards analogous compounds [28]. According to Cormack, the ratio of 1:4 of template to functional monomer is commonly used in non-covalent polymerization in favor of the template for the formation of imprinted binding sites. Large amounts of functional monomer will influence the adsorption effect and pore volume of the MIP. Additionally, the molar ratio of template to cross linker (EGDMA) used in the polymerization process is 1 to 20. The polymer to cross-linkers ratio in excess of 80% is often used in the polymerization method. The amount of EGDMA in MIP was studied by Zhao et al., proving the significant effect of cross-linkers dosage on the recognition and adsorption ability of the imprinted polymers. A low amount of EGDMA will cause poor stability and deformation of the polymer cavity, wherein, a high amount of EGDMA will affect the removal process of the template molecule. The polymerization process of MIP was initiated with the presence of BPO in DMSO. The final product obtained was in the form of white powder for both NIP and MIP [29, 30].

Characterization of MIP and NIP: Scanning electron microscopy

The structure and surface morphology of MIP and NIP were observed by using a Scanning Electron Microscope (SEM) at a magnification of 1000x. The NIP and MIP were synthesized in the form of white powder. The SEM micrographs for MIP and NIP are shown in Figure 3.

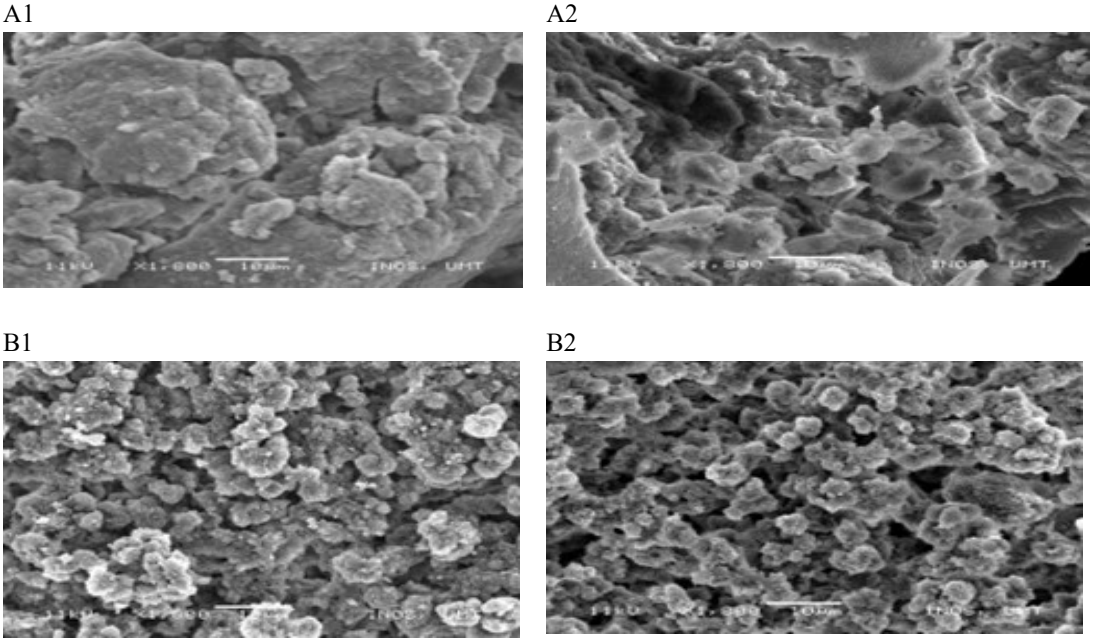


Figure 3. The morphology of MIP and NIP under SEM. A1 and A2 indicates the NIP before and after template removal. Meanwhile, B1 and B2 refer to the MIP before and after template removal

The NIPs before and after the template removal process (A1, A2) exhibit clean surface characteristics with no distinctive pores. The NIP was synthesized without the presence of a template (DA). The NIP after template removal (A2) shows a rougher surface characteristic, which was caused by the removal of unreactive substances from the polymer.

The MIP-DA complex can be seen in Figure 3 (B1 and B2). The pore diameter in B2 is clearer and more prominent when compared to B1. These pores in MIP are the cavities used for embedding the DA template molecule. After the template removal process, the MIP surface was cleaner as all the unreactive particles were flushed from the imprinted polymer, showing complex binding sites and a more distinctive shape than NIP. This difference may be caused by the stable interaction between DA and monomer, where the template was successfully imprinted onto the polymers during the pre-polymerization process. From Figure B1 and B2, it can be seen that both prepared polymer particles are non-spherical and not completely in uniform size and shape, as well as aggregation. This might be caused by the structure of monomer (HEMA) which is quite complicated and has a branched hydrocarbon tail when compared to other monomers such as methacrylic acid (MAA). Therefore, a homogenous spherical shape was unable to be maintained for both MIP and NIP. Another possible reason might due to the inconstant temperature setting (40 ˚C - 60˚C) utilized in the polymerization process. According to Mayes and Whitcombe (2005) [31], the polymerization temperature should be controlled to stabilize the interactions between template and monomer. Low polymerization temperature and low polarity solvents will favor the hydrogen bonding interactions.

Fourier transform infrared

The NIP, MIP-DA, and leached MIP were analyzed under FT-IR spectroscopy as shown in Figure 4. A wide OH stretch can be seen at 3471.68 cm^{-1}, which might indicate the presence of carboxylic acid from the ester group. The presence of imine group (-NH) can be seen at the wavenumber 3408.22 cm^{-1}, where a weak stretch in MIP-DA and MIP spectra exists. The intensity of the NH stretch in MIP is lower than MIP-DA; this might be due to the lack of DA presence in MIP after template leaching. The peak of sp^3 CH can be seen at 2954.95 cm^{-1}. The intensity of the sp3 CH stretch is almost similar for NIP and MIP-DA, while MIP shows a decrease in the peak intensity. The decrease of peak intensity in the leached MIP might indicate the successful removal of unreacted particles in polymers. At 1720.50 cm^{-1}, a peak of C=O stretching can be seen, with NIP and MIP-DA spectra exhibiting the highest intensity value, albeit MIP-DA spectra showing a slight decrease in intensity, due to the ester groups of EGDMA [32]. The decrease in intensity of C=O in MIP-DA might be due to the reaction of the cross-linker and DA in the polymer matrix. The low intensity of C=O functional group in MIP might be due to the successful removal of the template (DA). A peak of N-H bend at 1581.63 cm^{-1} can be seen in MIP-DA and MIP spectra, indicating the presence of DA in the imprinted polymer. The O-H bend of carboxylic acid was exhibited at 1444.68 cm^{-1} which can be seen present in all spectra. The presence of OH functional group denotes the esters of monomer and cross linkers in the polymer matrix. The stretching of C-O functional group was exhibited by all the spectra at 1188.15 cm^{-1} and 1139.93 cm^{-1}. The C-O peak of MIP shows a lower intensity than NIP and MIP-DA, as the unreactive particles were removed from the polymer during the leaching process. The sp2 CH bend of alkene can be seen at 991.34 cm^{-1} in the spectra of NIP, MIP-DA, and MIP.

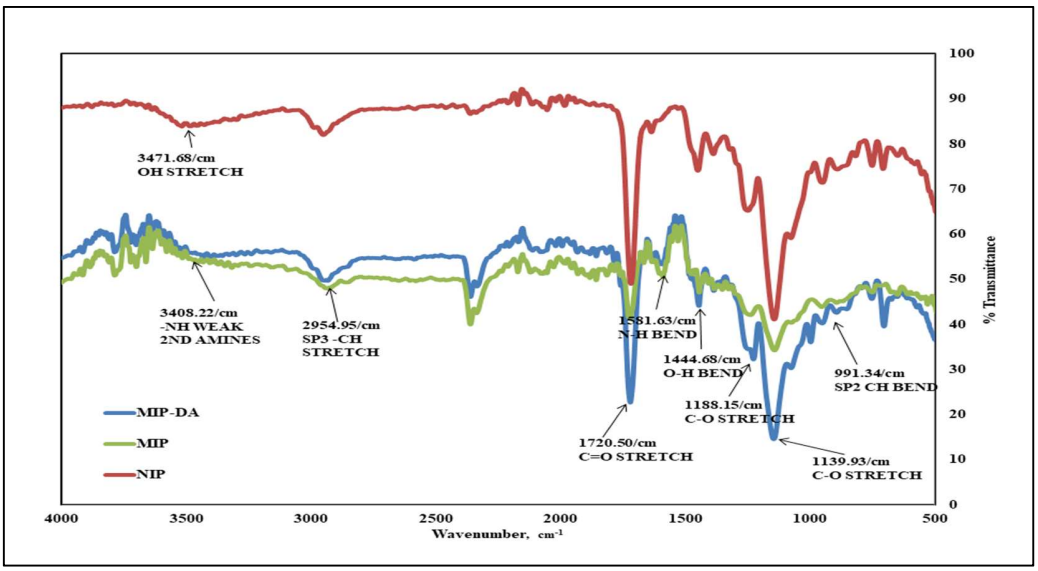


Figure 4. Infrared spectra of Non-Imprinted Polymer, NIP, Molecular Imprinted Polymer, MIP-DA, and MIP after template removal

BET porosity analysis

Figure 5 shows the adsorption-desorption isotherm analysis for NIP, MIP-DA, and MIP polymer matrix. The physisorption isotherm of all polymer matrices exhibits a type IV isotherm. Type IV isotherm is a monolayer-multilayer adsorption and capillary condensation with complete pore filling. The result indicates that the polymer matrix is mesoporous, with pores in the range of 1.5 – 100 nm. The type IV isotherm can be characterized by capillary condensation which occurs in mesoporous polymer structures that exhibit a hysteresis loop. In Figure 5 (A), the NIP exhibits H4

type, where polymer contains narrow slit pores including the pores in the micropores region, which conclude that no existing imprint is present in the NIP polymer matrix [33]. Figure 5 (B) and 5(C) prove that MIP was included in the H3 hysteresis type, indicating that the imprinted polymer structure is a non-rigid aggregate with slit shaped 'ink-bottled' pores [34]. Figure 5(C) shows a slightly wider adsorption and desorption region, which indicates an increase in the pore size of MIP after the template removal process. This can be further proven by Table 1, where the pore size of MIP before and after template removal is 11.7nm and 12.9nm respectively. The surface area and pore volume of NIP is 102 m^2/g and 0.29 cm^3/g respectively as shown in Table 1, which is smaller than MIP (a) and MIP (b). The result indicates that almost no imprint exists in NIP.

The resulting pore size of NIP might be due to swelling of non-rigid pores in the polymer matrix during the condensation process. The pore size of NIP, MIP(a), and MIP(b) is in the range of 0-100 nm, which verifies that the polymers are mesoporous.

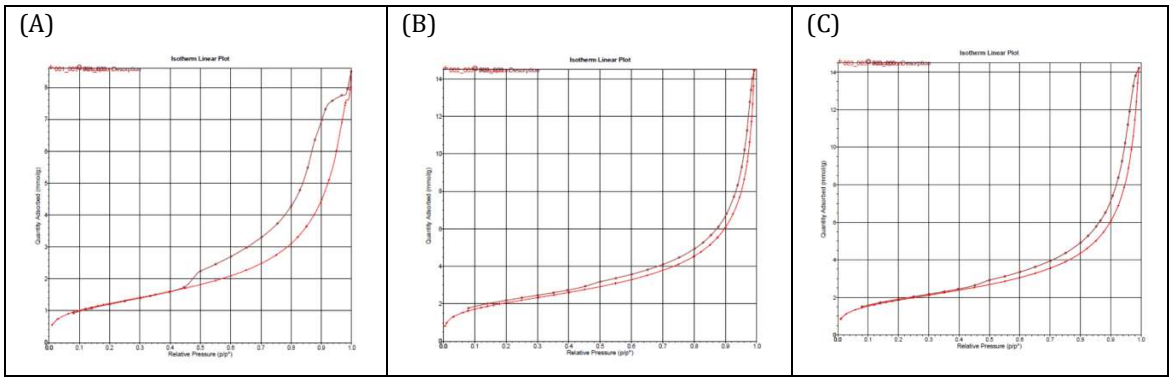


Figure 5. BET adsorption-desorption isotherm analysis of NIP (A), MIP-DA (B), and MIP after DA removal (C). Quantity adsorbed (mmol/g) versus relative pressure (p/p^o)

Table 1. Analysis of MIP and NIP porosity using BET

Sample	Surface Area (m^2/g)	Pore Volume (cm^3/g)	Pore Size (nm)
NIP	102	0.29	11.5
MIP a	170	0.50	11.7
MIP b	153	0.49	12.9

a: before template removal, b: after template removal

Validation study of DA standard solution

The standard solution of DA was validated using a UV-VIS spectrophotometer at wavelength of 242nm. The validation study was conducted for DA of various concentrations in distilled water. The absorbance value of domoic acid was used to construct a calibration plot as shown in Figure 6. The increasing absorbance value was clearly shown with increasing DA concentration. The regression correlation for the calibration curve is R^2=0.9888 with a slope value of 0.051. The limit of detection (LOD) and limit of quantification (LOQ) for DA was calculated using the formula,

$$\text{LOD} = \frac{3.3\sigma}{S} \quad (1)$$

$$\text{LOQ} = \frac{10\sigma}{S} \quad (2)$$

Where σ refers to the standard deviation of the response and S is the slope value from the calibration curve. The LOD and LOQ values calculated for DA using the formulas are 1.418 and 4.2983 ppm, respectively.

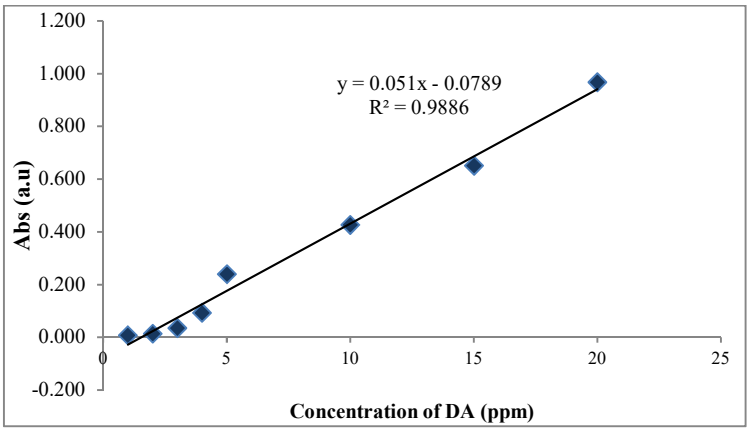


Figure 6. Calibration plot of absorbance (a.u) against concentration of DA (ppm)

Batch rebinding experiments: Adsorption capacity of DA with MIP

The effect of immersion time and mass of molecularly imprinted polymer over domoic acid adsorption capacity was investigated for optimization purposes. Figure 7 shows the graph of adsorption capacity, Q_e against immersion time of different masses of MIP with DA at fixed concentration. The binding capacity of MIP was calculated using formula 3.

$$Q_c = \frac{(C_i - C_f)V}{m} \quad (3)$$

Where Q is the adsorption capacity (mg/g), C_i and C_f indicate the initial and final concentrations of DA (ppm), V is the volume of the aqueous solution (ml), and m is the weight of the polymer (g).

The increasing trend of adsorption capacity (Q_e) values for MIP against time in different imprinted polymer weights from zero to fifteen minutes is shown. From 15 to 25 minutes of reaction time, no significant difference in Q_e values can be seen, indicating that the equilibrium concentration of DA in the system was achieved.

Meanwhile, the increasing mass of imprinted polymer shows a significant decrease in Q_e values of the MIP-DA reaction. In Figure 7, 5mg of MIP shows the highest adsorption value when compared to other masses of MIP used in the study, with a significantly large Q_e value. Low adsorption capacity shown in 10mg, 15mg, 20mg and 25mg of MIP was contributed by deep imprinted pores that cause the bleeding of excess templates in molecular imprinted polymer, resulting in the collapse of the equilibrium system [35]. The equilibrium adsorption capacity for MIP was achieved with the best reaction time and mass of MIP at 15min and 5mg, respectively. The optimum weight and reaction time obtained were 5mg and 15min, respectively.

Reaction response of DA with NIP and MIP

The study for reaction response of NIP and MIP with different concentrations of DA was conducted to determine the selectivity of the sensing system at equilibrium condition as shown in Figure 8 below. The adsorption capacity of DA from a concentration of 1 to 20 ppm shows increasing values for both MIP and NIP. The positive value of adsorption capacity for MIP shows an increasing trend from 1ppm to 20ppm. However, the Q_e value for MIP is not significantly large. The results might be due to the low imprinting effect of the MIP where weak imprinted complexes are formed due to the dominant role of the cross-linker during the pre-polymerization process [36]. The adsorption capacity of NIP during the adsorption study shows positive results

starting from 10ppm to 20ppm, which indicates the presence of non-selective binding sites on the surface of the polymer. This might be due to the swelling of polymer surface and the hydrogen bonding interaction between the COOH functional group of DA and the acidic non-specific binding sites of NIP [37].

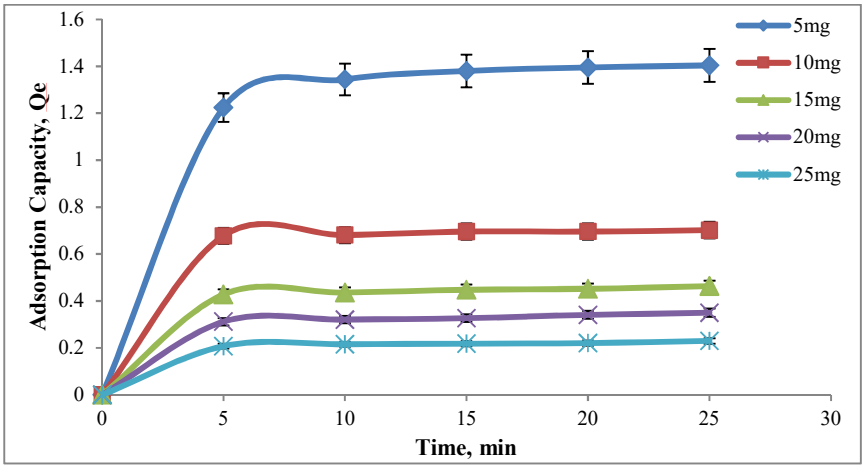


Figure 7. Optimization study of MIP with mass and time as the parameter

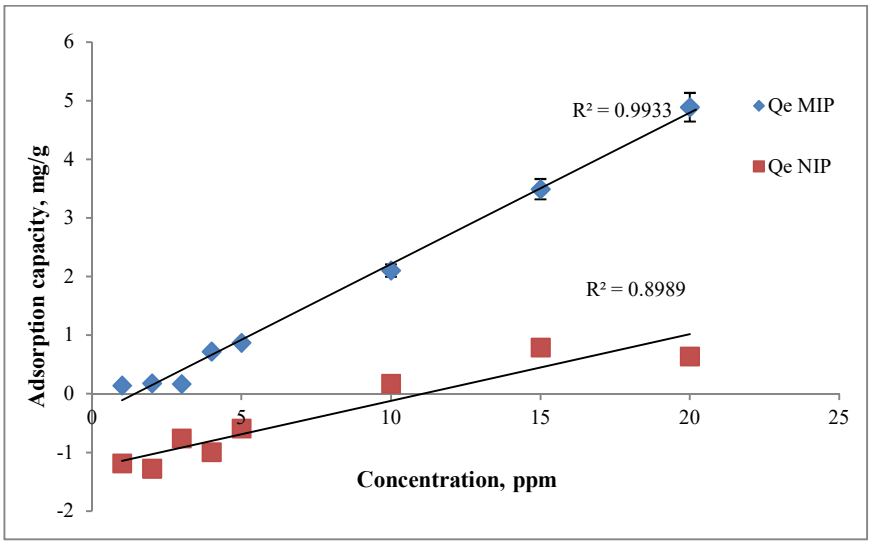


Figure 8. The adsorption capacity of NIP and MIP with various concentrations of DA in equilibrium condition

Adsorption isotherm study

Adsorption isotherm is described as the retention (release) of substances on a solid in various concentrations [38]. The Langmuir isotherm is defined as a system where homogenous adsorption of fixed, localized, identical sites project similar affinities to adsorbate, where no further reaction occurs approaching equilibrium saturation point [39]. The model can be linearized and non-linearized according to the formulas 4 and 5 shown below.

$$Qe = \frac{Q_O K_L C_e}{1+K_L C_e} \quad (4)$$

$$\frac{1}{Qe} = \left(\frac{1}{Q_O K_L}\right)\frac{1}{C_e} + \frac{1}{Q_O} \quad (5)$$

Where Q_e indicates the binding capacities at equilibrium (mg/g); Q_o denotes the maximum adsorption capacities of the adsorbate (mg/g); K_L refers to the Langmuir constant (L/mg); C_e is the concentration of domoic acid at equilibrium (ppm). The data was fitted into a Langmuir isotherm model of $1/C_e$ versus $1/Q_e$ as plotted in Figure 9(a). The separation factor, R_L of the Langmuir isotherm was calculated using formula 6.

$$R_L = \frac{1}{1+K_L C_O} \quad (6)$$

Where K_L indicates the Langmuir constant (L/mg) and C_O refers to the initial concentration of DA (ppm).

The Freundlich isotherm model is used to analyze the adsorption isotherm in order to define the surface heterogeneity and adsorption intensity of the adsorbate sites. The linear and non- linear equations of the model were indicated as shown in formula 7 and 8, respectively.

$$Q_e = K_f C_e^{\frac{1}{n}} \quad (7)$$

$$logQ_e = logK_f + \frac{1}{n} logC_e \quad (8)$$

Where K_f indicates the adsorption capacity (L/mg) and 1/n refers to the adsorption intensity. This isotherm model was fitted into a graph by plotting log C_e against log Q_e as shown in Figure 9(b).

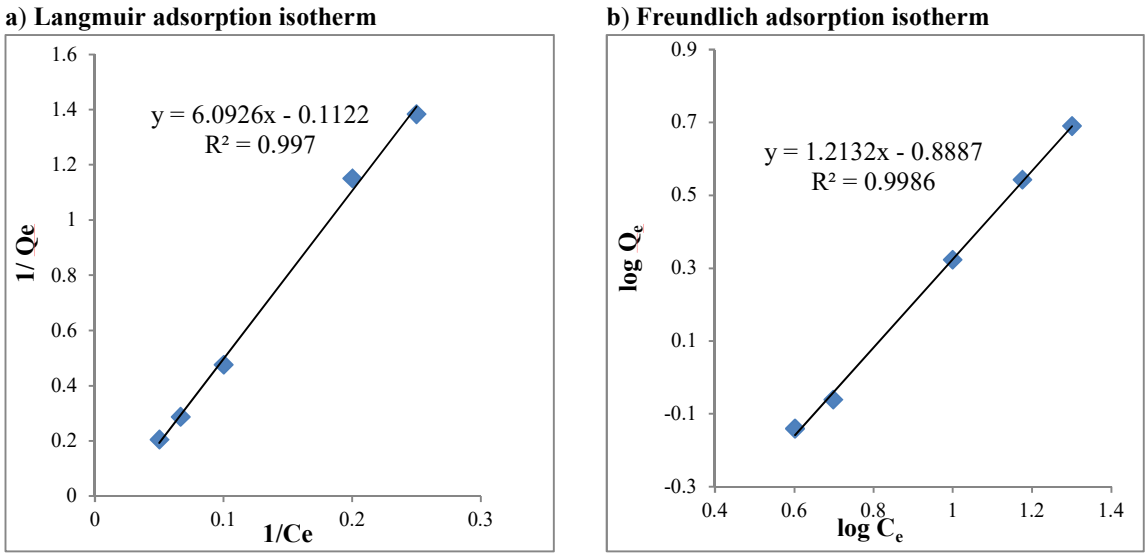


Figure 9. The graph of adsorption isotherm model study of MIP with DA where; a) Langmuir adsorption isotherm, b) Freundlich adsorption isotherm

The separation factor (R_L) value was used to conclude the favorability of adsorption. R_L values more than 1 indicate that an unfavorable adsorption occurs in the system. Linear adsorption occurs when R_L = 1, while irreversible adsorption occurs when R_L=0. However, 0 < R_L < 1 indicates favorable adsorption [40]. From table 2, the R_L values for the Langmuir isotherm were calculated, where R_L>1. It indicates unfavorable adsorption reactions occurring in the environment. The value of K_L is less than zero, which implies that a large surface area and pore volume of MIP results in a lower adsorption capacity [41].

The experimental data was fitted into the Freundlich isotherm model in order to define the surface heterogeneity and adsorption intensity of the adsorbate

sites. Meanwhile, for the Freundlich isotherm model, the value of 1/n that represents the adsorption intensity is more than 1, indicating cooperative adsorption between DA and MIP.

The R^2 of the Freundlich model is 0.9986 which is approaching 1 compared to the Langmuir model where the R^2 is 0.997. From R^2 values, the Freundlich model isotherm is better fitted for DA and MIP binding systems rather than the Langmuir isotherm model. The result suggests that multilayer chemisorption occurs for DA in MIP [42]. The calculated data for parameters representing the Langmuir and Freundlich isotherm models is tabulated in Table 2.

Table 2. Constant parameters of Langmuir and Freundlich Isotherm model for MIP

Isotherm Model	Langmuir	Freundlich
Equation	y = 6.0936x- 0.1122	y =1.2132x-0.8887
Q_o (mg/g)	-8.9126	-
K_L (L/mg)	-0.0184	-
R_L	1.1013	-
1/n	-	1.2132
n	-	0.8243
K_f (mg/g)	-	0.4112
R^2	0.997	0.9986

Reproducibility of MIP

This study was conducted to analyze the effectiveness and practicability of the preparation method and whether it can be reproduced in its entirety under changing conditions [43]. Five batches of MIP were synthesized in triplicates under optimized conditions. The data collected was analyzed, and a graph was constructed (as shown in Figure 10) to exhibit the reproducibility of the MIP sensing system. The five (5) batches of MIP showed no significant difference in absorbance values. The %RSD for the reproducibility of MIP was calculated, with the value ranging from 3.22% – 5.19% (n=5). The low values of %RSD reflect the good performances of MIP in DA determination.

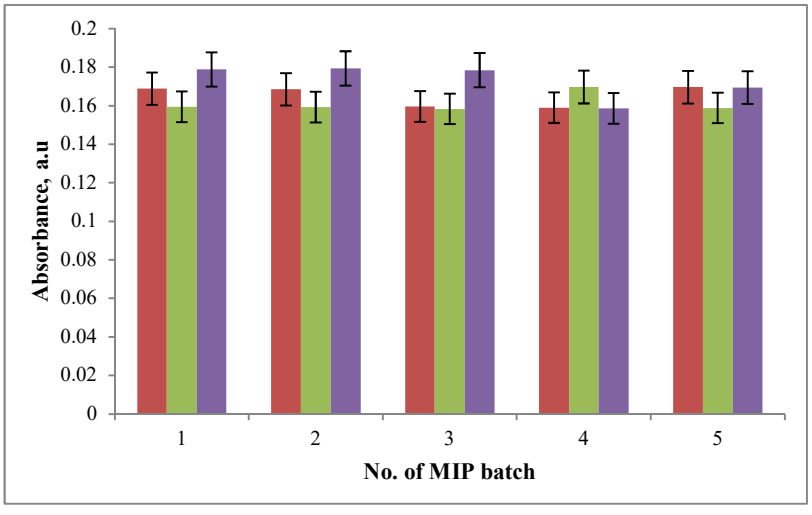


Figure 10. The reproducibility study of MIP in optimized condition

Reusability of MIP

Reusability is defined as repeat measurements made on the same subject under identical conditions. The reusability study was conducted by using one (1) set of MIP for five cycles of DA adsorption. The MIP was re-washed and re-used to reflect the reusability of the sensing system. The absorbance values for each cycle in the reusability analysis are shown in Figure 11. From Figure 11, cycles 1 to 3 show no difference in absorbance values, indicating the stability in DA detection. However, the fourth cycle shows a high value of DA present in the system. This condition might occur due to the bleeding of un-leached template molecules that are retained in the MIP from the first three cycles. The %RSD value calculated for the reusability test is 2.97% (n=5), which indicates the suitability of MIP as a disposable sensor for the detection of DA, which can be used three times.

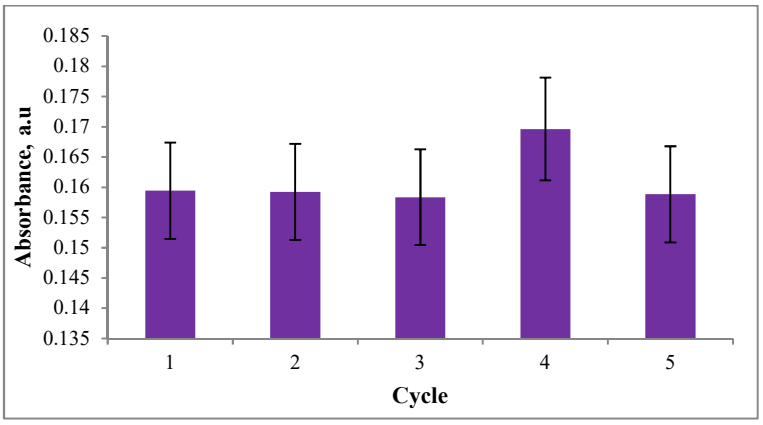


Figure 11. The reusability of MIP for adsorption of DA in 5 cycles

Application of MIP with real samples

The selected shellfish (cockle and mussel) used for this study were purchased from local fishermen and grocery stores. Table 3 shows the final concentration and percentage recovery for spiked and non-spiked cockle and mussel samples.

Table 3. Spike and recovery results of domoic acid in cockle and mussel tissue

Types of Shellfish	Non-spiked	Spiked (5 ppm)	
		Final Concentration, ppm	% Recovery
Cockle	Undetected	4.79	95.88
Mussel	Undetected	4.13	82.71

From the initial concentration (5ppm) of DA used, 4.79ppm and 4.13ppm were recovered from the spiked tissue of cockle and mussel, respectively, using the MIP sensing system. The percentage recovery for cockle and mussel was calculated to be 95.88% and 82.71%, respectively. However, no DA was presence was detected from non-spiked samples when analyzed using UV-VIS spectrophotometry.

Conclusion

In this study, a selective and sensitive MIP sensing system was successfully synthesized using non-covalent bulk polymerization techniques. The lower values of %RSD for reproducibility and reusability of MIP indicate better performances for the sensing system. From the adsorption isotherm analysis, the Freudlich isotherm model was found to be a better fit for analyzing the binding affinity of MIP with DA. The MIP sensing

system for DA was successfully applied to real samples (cockle and mussel).

Acknowledgement

The authors would like to acknowledge the Ministry of Education Malaysia through Fundamental Research Grant Scheme of FRGS/1/2015/ST04/UMT/02/1 (FRGS 59409) and Universiti Malaysia Terengganu for providing support, laboratory facilities, and instrumentation.

References

1. Maeno, Y., Kotaki. Y., Terada. R., Cho. Y., Konoki. K. and Yamashita M.Y. (2018). Six domoic acid related compounds from the red alga, chondria armata, and domoic acid biosynthesis by the diatom, Pseudo-Nitzschia Multiseries. *Scientific Reports*, 8: 356.
2. Costa, L. G., Giordano. G. and Faustman. E. M. (2010). Domoic acid as a developmental neurotoxin. *Neurotoxicology,* 31(5): 409-423.
3. Pulido, O. M. (2008). Domoic acid toxicologic pathology: A review. *Marine Drugs,* 6(2): 180-219.
4. Zaelinski, O., Busch, J. A., Cembella, A. D., Daly, K. I., Engelbrektsson, J., Hannides, A. K. and Schmidt, H. (2009). Detecting marine hazardous substances and organisms: sensors for pollutants, toxins and pathogens. *Ocean Science.* 5: 329-349.
5. Costa, P. R., Rosa, R., Duarte-Silva, A., Brotas, V. and Sampayo, M. A. M. (2005). Accumulation, transformation and tissue distribution of domoic acid, the amnesic shellfish poisoning toxin, in the common cuttlefish, sepia officinalis. *Aquatic Toxicology*, 74: 82-91.
6. Ayache, N., Fabienne. H., Veronique. M-J., Amzil. Z. and Amandine. M. N. C. (2019). Influence of sudden salinity variation on the physiology and domoic acid production by two strains of *pseudo-nitschia australis*. *Journal of Phycology*, 55(1): 186-195.
7. Kreuzer, M. P., Pravda, M., O'Sullivan, C. K. and Guilbault, G. G. (2002). Novel electrochemical immunosensors for seafood toxin analysis. *Toxicon*, 40: 1267-1274.
8. Hortigüela, M. J. and Wall, J. G. (2013). Improved detection of domoic acid using covalently immobilised antibody fragments. *Marine Drugs,* 11: 881-895.
9. Mohd Syaifudin, A. R., Jayasundera, K. P. and Mukhopadhyay, S. C. (2009). A low-cost novel sensing system for detection of dangerous marine biotoxins in seafood. *Sensors and Actuators B*, 137: 67-65.
10. Mohd Syaifudin, A. R., Jayasudera, K. P. and Mukhopadhyay, S.C. (2008). Initial investigation of using planar interdigital sensors for assessment of quality in seafood. *Journal of Sensors*, 2008: 1-9.
11. Busse, L. B., Venrick, E. L., Antrobus , R., Miller, P. E., Vigilant, V., Silver, M. W., Mengelt, C. and Mydlarz, L. and Prezelin, B. B. (2006). Domoic acid in phytoplankton and fish in San Diego, CA, USA. *Harmful Algae*, 5 (2006): 91-101.
12. Bates, S. S., Hubbard, K. A., Lundholm, N., Montresor, M. and Leaw, P. C. (2018). *Pseudo-nitzschia, Nitzschia*, and domoic acid: New research since 2011. *Harmful Algae*, 79:43.
13. Tan, S. N., Teng, S. T., Lim, H. C., Kotakid, Y., Bates, S. S., Leaw, C. P. and Lima, P. T. (2016). Diatom *Nitzschia Navis-Varingica (Bacillariophyceae)* and its domoic acid production from the mangrove environments of Malaysia. *Harmful Algae*, 60: 139-149.
14. Teng, S. T., Abdullah, N., Hanifah, A. H., Tan, S. N., Gao, C., Law, I. K., Leaw, C. P and Lim, P. T. (2021). Toxic bloom *of Pseudo-nitzschia cuspidata (Bacillariophyceae)* and domoic acid contamination of bivalve molluscs in Malaysia Borneo. *Toxicon*, 202: 132-141.
15. Mitcheli, L., Radoi, A., Guarrina, R., Massaud, R., Bala, C., Moscone, D. and Palleschi, G. (2004). Disposable immunosensor for the determination of domoic acid in shellfish. *Biosensors and Bioelectronics*. 20: 190-196.
16. Barbaro, E., Zangrando, R., Barbante, C and Gambaro, A. (2016). Fast and sensitive method for determination of domoic acid in mussel tissue. *The Scientific World Journal,* 2016: 1-6.

17. Tom, L. A., Schneck, N. A. and Walter, C. (2012). Improving the imprinting effect by optimizing template:monomer:cross-linker ratios in a molecularly imprinted polymer for sulfadimethoxine. *Journal of Chromatography B*, 909(2012):61-64
18. Haupt. K., Rangel. P. X. M. and Bui. B. T. S. (2020). Molecularly imprinted polymers: antibody mimics for bioimaging and therapy. *Chemical Reviews*, 120(17): 9554-9582.
19. Lopes, F., Pacheco, J. G., Rebelo, P. and Cristina, D. M. (2017). Molecularly imprinted electrochemical sensor prepared on a screen-printed carbon electrode for naloxone detection. *Sensors and Actuators B: Chemical*, 243 (2017): 745-752.
20. Ashley. J., Mohammad-Ali. S., Kant. K., Chidambara. V. A., Wolff. A., Bang. D. D, and Sun. Y. (2017). Molecularly imprinted polymers for sample preparation and biosensing in food analysis: progress and perspectives. *Biosensors and Bioelectronics*, 91(2017): 606-615.
21. Beltran, A., Borrull, F., Marcé, R. M. and Cormack, P. A. G. (2010). Molecularly-imprinted polymers: useful sorbents for selective extractions. *TrAC Trends in Analytical Chemistry,* 29(11): 1363-1375.
22. Zhou, W. H., Guo, X. C., Zhao, H. Q., Wua, S. X., Yang, H. H. and Wang, X. R. (2011). Molecularly imprinted polymer for selective extraction of domoic acid from seafood coupled with high-performance liquid chromatographic determination. *Talanta*, 84(3):777-782.
23. Nemoto, K., Kubo, T., Nomachi, M., Sano, T., Matsumoto, T., Hosoya, K., Hattori, T. and Kaya, K. (2007). Simple and effective 3D recognition of domoic acid using a molecularly imprinted polymer. *Journal American Chemical Society*, 129(44): 13626-13632.
24. Royani, I., Widayani., Abdullah, M. and Khairurrijal. (2014). Effect of heating time on atrazine-based MIP materials synthesized via the cooling-heating method. *Advanced Materials Research*, 896(2014): 89-94.
25. Royani, I., Widayani., Abdullah, M. and Khairurrijal. (2014). An atrazine molecularly imprinted polymer synthesized using a cooling-heating method with repeated washing: its physico-chemical characteristics and enhanced cavities. *International Journal Electrochemical Sciences*, 9: 5651-5662.
26. Kintopp, C. C. A., Furuse, A. Y., Costa, R. M., Lucena, F. S., Correr, G.M. and Gonzaga, C. C. (2020). Influence of acidic monomer concentration and application mode on the bond strength of experimental adhesives. *Brazilian Oral Research*, 2020(34):105.
27. Ceolin, G., Navarro- Villoslada F., Moreno-Bondi, MC., Horvai, G. and Horvath., V. (2009). Accelerated development procedure for molecularly imprinted polymer using membrane filterplates. *Journal of Combinatorial Chemistry*, 11(4): 645-652.
28. Hasanah, A. N., Safitri, N., Zulfa, A., Neli, N. and Rahayu. D. (2021). Factors affecting preparation of molecularly imprinted polymer and methods on finding template-monomer interaction as the key of selective properties of the materials. *Molecules,* 26: 5612.
29. Cormack, P. A. G. and Elorza, AZ. (2004). Molecularly imprinted polymers: synthesis and characterization. *Journal of Chromatography B*, 804: 174-178.
30. .Zhao, G., Liu, J., Liu, M., Xiaobin Han, X., Peng, Y., Xiatian Tian, X., Liu., J. and Zhang., S. (2020). Synthesis of molecularly imprinted polymer via emulsion polymerization for application in solanesol separation. *Applied Sciences,* 2020(10): 2868.
31. Mayes, A. G. and Whitcombe, M. J. (2005). Synthetic strategies for the generation of molecularly imprinted organic polymers. *Advanced Drug Delivery Reviews,* 57(12): 1742-1778.
32. Yang, F., Wang, R., Na, G., Yan, Q., Lin, Z. and Zhang, Z. (2018). Preparation and application of a molecularly imprinted monolith for specific recognition of domoic acid. *Analytical and Bioanalytical Chemistry* 410: 1845-1854.
33. Marinah, M. A., Yatim, N. I. and Tahir, N. M. (2015). Selective surface characteristics and extraction performance of a nitro-group explosive molecularly imprinted polymer. *Malaysian Journal of Analytical Sciences,* 19(3): 574-585.

34. Zeng, Y., Fan, C., Do, D. D. and Nicholson, D. (2014). Evaporation from an ink-bottle pore: mechanisms of adsorption and desorption. *Industrial Engineering Chemical Research,* 2014(53): 15467-15474.
35. Lorenzo, R. A. (2011). To remove or not to remove? the challenge of extracting the template to make the cavities available in molecularly imprinted polymers (MIPs). *Journal Molecular Sciences,* 12(7): 4327-4347.
36. Hasanah, A. N., Safitri, N., Zulfa, A., Neli, N. and Rahayu. D. (2021). Factors affecting preparation of molecularly imprinted polymer and methods on finding template-monomer interaction as the key of selective properties of the materials. *Molecules,* 26: 5612.
37. Anene, A., Kalfat, R., Chevalier, Y. and Hbaieb, S. (2020). Design of molecularly imprinted polymeric materials: The crucial choice of functional monomers. *HAL Open Science,* 2020(3): 769-781.
38. Limousin, G., Gaudet, J. –P., Charlet, L., Szenknect, S., Barthes, V. and Krimissa, M. (2006). Sorption isotherms: a review on physical bases, modeling and measurement. *Applied Geochemistry,* 22(2): 249-275.
39. Kundu, S. and Gupta, A. K. (2006). Arsenic adsorption onto iron oxide-coated cement (IOCC): Regression analysis of equilibrium data with several isotherm models and their optimization. *Chemical Engineering Journal*, 122(1-2): 93-106.
40. Foo, K. Y. and Hameed, B. H. (2010). Insights into the modeling of adsorption isotherm systems *Chemical Engineering Journal*, 156: 2-10.
41. Ayawei, N. (2017). Modelling and interpretation of adsorption isotherms. *Hindawi Journal of Chemistry,* 2017:1-17.
42. Hande, P. E., Samui, A. B. and Kulkarni, P.S. (2015). A molecularly imprinted polymer with flash column chromatography for the selective and continuous extraction of diphenyl amine. *RSC Advances*, 5: 73434.
43. Bartlett, J. W. and Frost, C. (2008). Reliability, repeatability and reproducibility: analysis of measurement errors in continuous variables. *Ultrasound in Obstetrics and Gynecology,* 31(4): 466-475.

Malaysian Journal of Analytical Sciences (MJAS)
Published by Malaysian Analytical Sciences Society

RECOVERY OF PHOSPHATE FROM ARTIFICIAL HUMAN URINE USING MAGNESIUM-MODIFIED BIOCHAR FOR IMMOBILIZATION OF LEAD IN SOIL

(Pemulihan Fosfat daripada Urin Manusia Tiruan Menggunakan Biochar yang diubah suai Magnesium Untuk Imobilisasi Plumbum dalam Tanah)

Soon Kong Yong [1*] Nurul Fariha Mohd Idrus[1], Nur Qursyna Boll Kassim[2], Azwan Mat Lazim[3], and Robert Thomas Bachmann[4]

[1]Soil Assessment and Remediation Research Group,
Faculty of Applied Sciences,
Universiti Teknologi MARA, 40450 Shah Alam, Selangor, Malaysia
[2]Soil Conservation and Management Research Group,
Faculty of Plantation and Agrotechnology,
Universiti Teknologi MARA , 40450 Shah Alam, Selangor, Malaysia
[3]Faculty of Science and Technology,
Universiti Kebangsaan Malaysia , 43600 Bangi, Selangor, Malaysia
[4]Green Chemistry & Sustainable Engineering Technology Cluster,
Section of Environmental and Polymer Engineering Technology,
Malaysian Institute of Chemical and Bioengineering Technology,
Universiti Kuala Lumpur, 78000 Alor Gajah, Malacca, Malaysia

[*]Corresponding author: yongsk@uitm.edu.my

Received: 22 September 2022; Accepted: 27 February 2023; Published: 19 April 2023

Abstract

Magnesium-modified biochar (MB) is used to recover phosphate (PO_4^{3-}) from urine by struvite precipitation. Pyrolysis of sawdust (SD) at 700°C and subsequent impregnation with MgO_2 produced MB. Virgin and spent MB were characterized for proximate analysis, surface morphology, elemental composition, specific surface area, and functional groups using thermogravimetric analysis (TGA), scanning electron micrography (SEM), energy dispersive X-ray (EDX) analysis, surface area analysis, and Fourier transform infrared (FTIR) spectroscopy, respectively. The batch sorption experiments were conducted on MB using artificial human urine (AHU), where residual PO_4^{3-} was quantified by colorimetry. Sorption data were analyzed using various isotherm (i.e., Langmuir and Freundlich) and kinetic models (i.e., pseudo-first and pseudo-second-order) for elucidation of sorptive potential and mechanism. Pyrolysis of SD produced porous sawdust biochar (SB) with a high surface area. However, modification with MgO_2 decreased the surface area of MB, possibly due to the loss of micropores from oxidation and deposition of struvite as confirmed by SEM-EDX analysis. FTIR analysis showed that polar functional groups such as carboxylate (1641 cm^{-1}), phenolate (1300 cm^{-1}), and amide (1674 cm^{-1}) were mainly involved in the Mg^{2+} and PO_4^{3-} adsorption. The PO_4^{3-}sorption capacity for MB was 8967 mg/g at a sorbent/solution ratio of 0.1 g/L after 120 min of contact time. Sorption of PO_4^{3-} occurred on a heterogeneous MB surface with a possible multilayer adsorption mechanism. The kinetic study suggested that the sorption of PO_4^{3-} by MB was a chemisorption process. The presence of Mg in MB aided the formation of struvite in MB and enhanced the recovery of PO_4^{3-} from

AHU. Spent MB exhibited higher ability in immobilizing soil Pb compared to ground magnesium limestone (GML) at a similar application rate (5% w/w). Spend MB can be recovered as fertilizer or immobilizing heavy metals such as lead in soil.

Keywords: oxidized biochar, magnesium peroxide, struvite, phosphate recovery, human urine

Abstrak

Biochar yang diubah suai dengan magnesium (MB) digunakan untuk memulihkan fosfat (PO_4^{3-}) daripada air kencing melalui pemendakan struvite. Pirolisis habuk papan (SD) pada 700°C dan impregnasi seterusnya dengan MgO_2 menghasilkan MB. Kedua-dua MB mentah dan terpakai dicirikan pada analisis proksimat, morfologi permukaan, komposisi unsur, luas permukaan spesifik dan kumpulan berfungsi telah dijalankan menggunakan penganalisis termogravimetrik (TGA), pengimbasan mikrografi elektron (SEM), analisis sinar-X penyebaran tenaga (EDX), penganalisis luas permukaan, dan spektroskopi Inframerah transformasi Fourier (FTIR), masing-masing. Eksperimen jerapan telah dijalankan pada MB menggunakan air kencing manusia tiruan (AHU), di mana sisa PO_4^{3-} ditentukan dengan teknik kolorimetri. Data jerapan dianalisis menggunakan pelbagai model isoterma (iaitu, Langmuir and Freundlich) dan kinetik (iaitu, pseudo-tertib-pertama and pseudo-tertib-kedua) untuk penjelasan potensi dan mekanisme jerapan. Pirolisis SD menghasilkan biochar (SB) berliang dengan luas permukaan yang tinggi. Walau bagaimanapun, pengubahsuaian dengan MgO_2 mengurangkan luas permukaan MB, mungkin disebabkan oleh kehilangan mikropori daripada pengoksidaan dan pemendapan struvite seperti yang disahkan oleh analisis SEM-EDX. Analisis FTIR menunjukkan kehadiran kumpulan berfungsi polar seperti karboksilat (1641 cm^{-1}), fenolat (1300 cm^{-1}), dan amida (1674 cm^{-1}) terlibat terutamanya dalam penjerapan Mg^{2+} dan PO_4^{3-}. Kapasiti penyerapan PO_4^{3-} untuk MB ialah 8967 mg/g pada nisbah sorben/larutan 0.1g/L selepas 120 minit masa sentuhan. Penyerapan PO_4^{3-} berkemungkinan berlaku pada permukaan MB heterogen dengan mekanisme penjerapan berbilang lapisan. Kajian kinetik menunjukan bahawa proses penjerapan PO_4^{3-} oleh MB adalah melalui proses kimia. Kehadiran Mg dalam MB membantu pemendakan struvite dalam MB, dan meningkatkan prestasi pemulihan PO_4^{3-} daripada AHU. MB terpakai lebih cekap dalam imobilisasi plumbum di dalam tanah berbanding dengan batu kapur magnesium terkisar (GML) pada kadar penggunaan yang sama (5 % w/w). MB terpakai boleh dikitar semula sebagai baja atau merawat tanah yang tercemar dengan logam berat seperti plumbum.

Kata kunci: biochar teroksida, magnesium peroksida, struvite, pengambilan semula fosfat, urin manusia

Introduction

Phosphorus is a macronutrient that occurs naturally in the orthophosphate (PO_4^{3-}) form and is essential for all living organisms [1]. According to the Malaysian Department of Environment, the permissible level of PO_4^{3-} in effluent discharge is 5 mg/L [2]. Excessive PO_4^{3-} in aquatic environments may cause eutrophication. Human urine is managed through a modern sewer system and treated biologically to effectively remove PO_4^{3-} [3]. Despite the abundance of PO_4^{3-} in human urine, its recovery is associated with the risk of pathogen infection and adverse effects of residual pharmaceutical products. Despite the challenges, human urine is a renewable source of PO_4^{3-} that can be recovered for crop production [4]. Adsorption is an energy-efficient and low-cost technique for recovering PO_4^{3-} from human urine [5]. Furthermore, the yield of PO_4^{3-} recovery can be improved by slightly increasing the pH value of human urine [6].

Biochar is a sorbent commonly used for the removal of pollutants from the environment. Pyrolysis of agricultural biomass at a high temperature (i.e., >500 °C) and anoxic conditions can produce carbon-rich and porous biochars [7]. The surface of low-temperature biochars often contains plenty of polar functional groups (i.e., phenol and hydroxyl [8]. A slightly alkaline condition allows deprotonation of the polar functional groups and may be used for adsorbing pollutants that possess a net positive charge [9]. Moreover, biochar is considered a recalcitrant organic carbon that can withstand microbial decomposition. The application of biochar allows the storage of carbon in the soil, reduces greenhouse gas emissions, and helps combat climate change [10]. The improvement of soil fertility by the addition of biochar helps the greening and reclamation of the polluted land and increases the capacity for holding cationic nutrients [11].

Residual minerals in biochar consist mainly of oxides of alkaline (i.e., K_2O) or earth alkaline metals (i.e., CaO, MgO), providing an alkaline condition that can improve

electrostatic attraction and precipitation of PO_4^{3-} ions [12]. Moreover, polar functional groups may react with Ca^{2+} or Mg^{2+} cations to acquire a positively charged surface and become a medium for binding PO_4^{3-} ion [13]. However, the CaO content in biochars may be insufficient for effectively recovering PO_4^{3-} from human urine. Various methods have been used for artificially introducing Ca and Mg into biochar. Magnesium chloride ($MgCl_2$) and oxide (MgO) were commonly used for modifying biochar [14]. An activation of biochar with MgO has successfully increased the surface functional group, porosity, surface area, and PO_4^{3-} removal [15]. The introduction of Mg is often associated with a high PO_4^{3-} removal due to the precipitation of struvite, which is formed with the addition of phosphate into a portion of ammonium and magnesium at equal ratio concentrations [16].

Even though the pyrolysis process at high temperature produces porous biochar, possible decarboxylation may cause a net loss of polar functional groups such as carboxylate and phenolate groups [17]. The presence of the negative-charged polar organic functional groups on the biochar surfaces is crucial for its function in soil fertility, including the retention of essential cations such as Mg^{2+} [18]. Oxidation can be introduced to improve the negative surface of high-temperature biochars. Recent studies have shown the great potential of combining electro-oxidation for improving the porosity and capacity of biochar to retain Mg for recovering PO_4^{3-} [19]. Alternatively, biochar can be chemically oxidized and impregnated with Mg simultaneously using magnesium peroxide (MgO_2). The oxidation and subsequent Mg-deposition can be controlled by decreasing and increasing the solution pH, respectively. The slow dissolution of MgO_2 in slightly acidic water at room temperature allows the slow release of dissolved oxygen for minimizing damage to the microporous structure of the biochar during oxidation. Upon complete dissolution of MgO_2, the adsorption and precipitation of soluble Mg^{2+} can be enhanced by slowly increasing the solution pH. In this study, sawdust is a widely available solid waste from the sawmill and was used as the precursor for the production of biochar.

Materials and Methods

Preparation of sawdust (SD) and sawdust biochar (SB)

About 10 kg of SD was collected from a furniture processing plant at Klang, Selangor. The SD was washed with tap water and oven-dried overnight at 105 °C. Then, the SD was pulverized using a mixer grinder and sieved to a particle diameter of <150 μm. About 500 g of the SD was converted into SB through slow pyrolysis at 700 °C in a furnace with nitrogen gas at a flow rate of 10 L/min. The pH value of the resulting SB was measured with a pH meter at SB/DI water mass ratio of 1:10 [20]. The SB was washed further with warm DI water until it reached a pH value of 8. The SB was then placed in the lid-covered metal crucibles and allowed to dry in a dehydrating cabinet at 60 °C for 24 h.

Modification of SB with MgO_2

The preparation of MgO_2-modified biochar (MB) followed the method described by Tan et al. [21] and is optimized at 5% w/v MgO_2 concentrations. Thirty millilitres of each MgO_2 solution were mixed with 1.0 g SB. The solution was adjusted to a pH value of 2 by adding 65% HNO_3 drop by drop using an auto titrator. The mixture was agitated for a few minutes until the effervescence ceased, and then agitated for a further 30 min. The mixture was allowed to rest overnight at room temperature (25°C). The pH of the biochar was adjusted to a pH value between 6.0 and 6.5 by adding 1.0 M NaOH using an auto titrator and then agitated for 4 h with a magnetic stirrer at room temperature. Then, MB was collected after filtration, oven-dried at 90 °C, and then pulverized to a desired particle size of 0.20–0.45 mm [21].

Chemical characterization for SD, SB, and MB

Surface morphology and elemental composition were investigated using scanning electron microscopy (SEM) with energy dispersive X-ray spectroscopy (EDX) (Hitachi TM3030plus). About 1 mg of sample was coated with a thin layer of carbon and mounted on a copper stub using double-stick carbon tape. Thermal degradation analysis was conducted on the as-receive SD (10 mg) using a thermogravimetric analyzer (TGA) (Setaram Setsys Evolution TGA-DTG/DSC High Temperature (2400) instrument at a heating rate of

10℃/min, and a peak temperature of 900 ℃ in a nitrogen atmosphere. The TGA and differential thermogravimetric (DTG) data were analyzed using AKTS Thermokinetics software. Major inorganic elements were determined using the Association of Official Analytical Chemists (AOAC) method of acid digesting the samples (1.0 g) for multi-elemental analysis by ICP-OES. The presence of functional groups on samples was studied using Fourier transform infrared (FTIR) spectroscopy. About 5 mg of sample was mixed with potassium bromide KBr at approximately 0.1% w/w and pressed into pellets. The spectra of the samples were collected using an FTIR spectrometer (Perkin Elmer) by averaging 32 scans in the range of 400 to 4000 cm^{-1}. The baseline of spectra was corrected, and the curve of spectra was smoothened. The surface area was determined with 0.5 g of SB or MB samples using N_2 sorption isotherms run on Macromeritics ASAP 2010, USA. The samples were degassed at 200 °C for 8 h prior to analysis.

Chemical characterization for soil

The soil samples were air-dried and pulverized with an agate mortar to pass a 200 μm (80 mesh) sieve. The cation exchange capacity (CEC) was determined using the sodium acetate method [22]. The pH and electrical conductivity (EC) were measured on a soil slurry with a solid/solution ratio of 1:10, using a calibrated pH meter and EC meter respectively.

Sorption of MB with artificial human urine (AHU)

For the batch sorption experiment, AHU that contains 30 g PO_4^{3-}/L was prepared according to the method described by [23] (Table 1). The pH value of AHU was adjusted to the 6.0-6.5 pH range with 1.0 N HCl and 1.0 N NaOH. Stock AHU was stored in a plastic container at 4°C. The AHU stock was warmed to room temperature before being used. Finally, 100 mg of albumin and 4.0 g of creatinine were slowly mixed into the 2.0 L of the AHU solution.

Table 1. Properties and Composition of Artificial Human Urine [23]

Property and Composition	Amount
pH	6.0 - 6.5
Specific gravity (g/mL)	1.020
Osmolality (mOsm/kg)	861
Urea (mM)	416
NaH_2PO_4 (mM)	17.60
NaCl (mM)	154.00
NH_4Cl (mM)	48.00
Na_2SO_4 (mM)	21.10

Batch adsorption experiments were conducted by studying the effect of Mg content in MB, MB dosage, contact time, and initial concentration of AHU on adsorption of PO_4^{3-} MB. Various amount of MB (i.e., 0.005, 0.01, 0.05, and 0.10 g) was weight and agitated with 30 mL of stock AHU in 50 mL centrifuge tubes using a rotator at 100 rpm at room temperature for 4 h. Blanks containing AHU without MB were also included in the same experiments. After 4 h of agitation, the residual AHU solutions were filtered with a 0.45 μm syringe filter, and the concentration of PO_4^{3-} was determined by colorimetry using a UV-VIS spectrophotometer and a combined reagent (i.e., potassium antimony tartrate solution, ammonium molybdate solution, and ascorbic acid solution). Thirteen millilitres of combined reagent were added to 1.0 mL of residual AHU solution in a 25 mL volumetric flask, topped to the mark with DI water, and shaken thoroughly. It was then allowed to stand for 30 min for colour development. The absorbance was measured at 880 nm in a 1-cm quartz cuvette. A calibration curve was prepared by plotting the absorbances of PO_4^{3-} standards with various concentrations and was then used to determine the concentration of PO_4^{3-} in AHU.

The PO_4^{3-} removal percentage and uptake were calculated using equations 1 and 2, respectively. The dosage of MB that gives the highest removal percentage

(i.e., 0.10 g) was chosen for the next sorption experiments.

$$\text{Removal percentage (\% w/w)} = \frac{\text{P}_{\text{initial}} - \text{P}_{\text{final}}}{\text{P}_{\text{initial}}} \times 100\ \% \quad (1)$$

$$\text{Uptake, } q_e \text{ (mg/g)} = \frac{(P_{initial} - P_{final})V}{M} \quad (2)$$

Where $P_{initial}$ and P_{final} (mg/L) are the initial and equilibrium concentrations of PO_4^{3-}. V is the volume of the AHU (L), and M is the mass of dry MB (g).

For the sorption isotherm experiment, 10 g of MB were agitated with 30 mL AHU at various PO_4^{3-} concentrations (i.e., 66.8, 93.1, 237, 520, 683, 734, 1636, 2472, and 3038 mg/L) in closed 50 mL centrifuge tubes using a rotator at 100 rpm and room temperature for 4 h. For sorption kinetic study, 10 g of MB was agitated at 100 rpm with 30 mL AHU (initial PO_4^{3-} concentration 374 mg/L) in a 50 mL centrifuge tube at room temperature for 4 h. All residual AHU solutions were filtered through a 0.45 µm syringe filter, and the concentration of PO_4^{3-} was determined by colorimetry. The PO_4^{3-} uptake by MB was calculated using equation 2 and studied using non-linear Langmuir (Equation 3) and Freundlich (Equation 4) isotherm models as well as non-linear pseudo-first-order (Equation 5) and pseudo-second-order (Equation 6) kinetic models.

Langmuir isotherm model:

$$q_{\text{e}} = \frac{q_{\text{max}} \cdot K_{\text{L}} \cdot C_{\text{e}}}{1 + K_{\text{L}} \cdot C_e} \quad (3)$$

Freundlich isotherm model:

$$q_{\text{e}} = K_{\text{F}} \cdot C_{\text{e}}^{1/\text{n}} \quad (4)$$

Where q_e (mg/g) is the PO_4^{3-} uptake, and C_e (mg/L) the concentration of PO_4^{3-} in residual AHU solution at equilibrium. K_L is the equilibrium constant for the Langmuir model. Lastly, K_f [(mg g^{-1})(mg L^{-1}) ^{n}] is the Freundlich constant that is related to adsorption capacity, and n is the Freundlich constant related to adsorption intensity. Graphs of q_e versus C_e were plotted to determine Langmuir and Freundlich parameters. Then the parameters were compared to determine the isotherm model that best fit the sorption data.

The pseudo-first-order model:

$$q_{\text{t}} = q_{\text{e}} \left(1 - e^{-k_1 t}\right) \quad (5)$$

The pseudo-second-order model:

$$q_{\text{t}} = \frac{k_2 \cdot q_e^2 \cdot t}{1 + K_2 \cdot q_{\text{e}} t} \quad (6)$$

Where q_e (mg/g) is the uptake of PO_4^{3-} at equilibrium and q_t (mg/g) is the amount of phosphate from AHU adsorbed at time, respectively. Next, t is the contact time in minutes, and the adsorption rate constants, k_1 (1/min) is the rate constant for the pseudo-first-order model, while k_2 (g/[mg.min]) is the rate constant of the pseudo-second-order model. Parameters for both kinetic models were determined by plotting a graph of q_t (mg/g) versus t (min).

Leaching tests

The leaching test followed the method described by [24] with several modifications. Calcium chloride solution (0.01M, pH = 7) was used to fill up the 50 mL syringe columns that were then irrigated on MB in the syringe column. Lead-contaminated soil was collected from a shooting range located in Universiti Pertahanan Nasional Malaysia (UPNM). The 50 mL syringe columns of MB were irrigated with $CaCl_2$ using a flow rate that represents the average distribution of rainfall intensity in Peninsular Malaysia (i.e., >10 mm/h) [25]. The total duration of the experiment was 36 h. The leachate produced by each column was sampled in 10 mL volume intervals. The samples were collected in acid-washed 50 mL centrifuge bottles and stored at 3.9 °C until analysis. A tip at the bottom was used to direct the outflow into sampling containers. The 50 mL syringe columns had a diameter of 3.0 cm and were filled with soil and MB to a height of 7.35 cm according to the weight ratio in Table 2. At the bottom of the 50 mL syringe columns, a 1 mm mesh-sized gauze was attached to hold the soil in place. Untreated shooting range soil and ground magnesium limestone (GML)-treated soil

were also subjected to leaching tests as the negative and positive control, respectively.

Modified selective sequential extraction (SSE)

Soil samples were incubated with GML or MB at two application rates of 1.0% w/w and 5.0% w/w (Table 2). Soil samples that were not incubated with any material were compared as control. About 1.0 g of treated soil samples were air-dried, crushed to <2 mm diameter using an agate mortar, and transferred into 50 mL polypropylene centrifuge tubes. Referring to Table 3, the extraction began from step 1 (exchangeable fraction), until step 5 (residual fraction). The supernatants were separated by centrifugation at 1,400 rpm for 10 min. Each liquid fraction was filtered through a 0.45 µm syringe filter, and the Pb content was determined in each of the five extracts of soil samples using ICP-OES [26].

Table 2. The weight (g) of shooting range soil (Soil), Mg-modified biochar (MB), and ground magnesium limestone (GML) of treated soil samples at 1.0 % (w/w) and 5.0 % (w/w) application rates for leaching test and selective sequestration extraction (SSE) experiments

Soil Amendment	**Weight (g)**	
	1.0% (w/w)	**5.0 % (w/w)**
Control	10.0 g Soil	10.0 g Soil
MB	9.9 g Soil + 0.1 g MB	9.5 g Soil + 0.5 g MB
GML	9.9 g Soil + 0.1 g GML	9.5 g Soil + 0.5 g GML

Table 3. Modified selective sequential extraction procedures

Step	**Fraction**	**Reagent**	**Conditions**
1	Exchangeable (E)	8.0 mL of 1.0 M $MgCl_2$ (pH 7)	1 h, 25°C
2	Carbonate (C)	8.0 mL of 1.0 M NaOAc (pH 5)	5 h, 25°C
3	Fe-Mn oxide (FM)	20 mL of 0.04 M $NH_2OH.HCl$ in 25% HOAc (v/v)	6 h, 96ºC
4	Organic (O)	3.0 mL of 0.02 M HNO_3 + 5.0 mL of 30% H_2O_2 (pH 2)	2 h, 85ºC
		3.0 mL of 30% H_2O_2	3 h, 85ºC
		5.0 mL of 3.2M NH_4OAC + 20% HNO_3 (v/v)	30 min, 25°C
5	Residual (R)	HNO_3-HCl digestion	

Results and Discussion

Chemical characterisation for SB, MB, and Spent MB

The elemental composition of SB, MB, and spent MB are shown in Table 4. The overall content of C in SB was relatively low possibly due to the low cellulose content in SD [27]. The pyrolysis process at high temperature (i.e., >500 °C) intensifies the degree of carbonization and increased the C content in SB to 69.03% [28]. Modification with MgO_2 introduced Mg and has slightly decreased C content in MB [29]. Soluble Mg may have been dehydrated to form MgO on the surface of MB [30]. The N content in the Spent MB content after sorption with AHU. Besides the PO_4^{3-}, urea is also present in AHU and it is naturally decomposed by microbes to form ammonium ions (NH_4^+). Possible precipitation of struvite and its attachment onto the surface of the spent MB exhibited a higher P content [31].

Figures 1 (a), (b), and (c) show the surface of SD, MB, and Spent MB, respectively. The surface of SD was originally smooth with a compact, non-porous structure. Upon pyrolysis, the surface of SB was uneven with more pores formed on its surface and with a much higher C content. A larger pore size was observed in SB compared to that for SD. Pyrolysis at a higher temperature may have allowed more removal of volatile matter from SD and developed a larger pore in SB. The quantity of micropores in SB may have increased in diverse ranges [32]. Meanwhile, The SEM images in Figure 2 show that pores were smaller, and the surface was coarser after SB was modified with MgO_2. The average pore diameter

decreased from 3 nm to 1 nm after the Mg impregnation process due to the blockage of pores in biochar by Mg compounds [33]. Figure 1 (d) shows the presence of PO_4^{3-}. Figure 2 further indicates that elemental P was associated with N, and Mg, possibly due to the formation of struvite crystals. The increasing P% in Spent MB coincides with decreasing content of Mg% and C%. The result was predictable as the low content of C% might be due to the phenolic hydroxyl and carboxylic groups on the surface of Spent MB being preoccupied with PO_4^{3-} and NH_4^+ through the ion exchange mechanism [34]. Both Na and Cl were the most obvious in Figure 2, indicating that NaCl was also co-precipitated with struvite on the surface of Spent MB. Other Mg compounds (i.e., $Mg_3(PO_4)_2$, $MgHPO_4$, or $Mg(H_2PO_4)_2$) may also be present in Spent MB but may be significant in quantity [35].

Table 4. Elemental composition of SD, SB, MB, and Spent MB

Element	Composition (wt.% d.b.)			
	SD	SB	MB	Spent MB
C	45.15	69.03	52.08	25.35
O	26.66	3.19	5.37	20.55
Mg	-	-	1.19	0.06
Si	-	-	1.50	0.06
Ca	0.00	0.00	2.36	0.22
S	0.00	0.00	1.77	1.41
N	28.19	27.78	2.27	17.35
Cl	0.00	0.00	0.00	33.89
P	0.00	0.00	0.00	1.11
Au	-	-	33.46	-

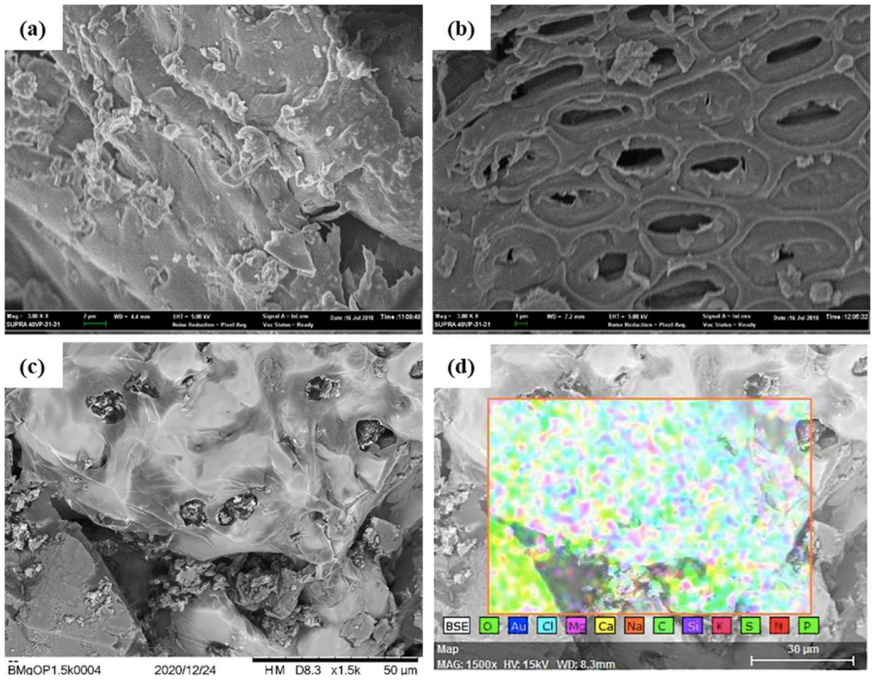


Figure 1. Scanning electron micrograph (SEM) images of (a) sawdust (SD), (b) Mg-modified biochar (MB), (c) Spent MB, and (d) combined elemental map for Spent MB

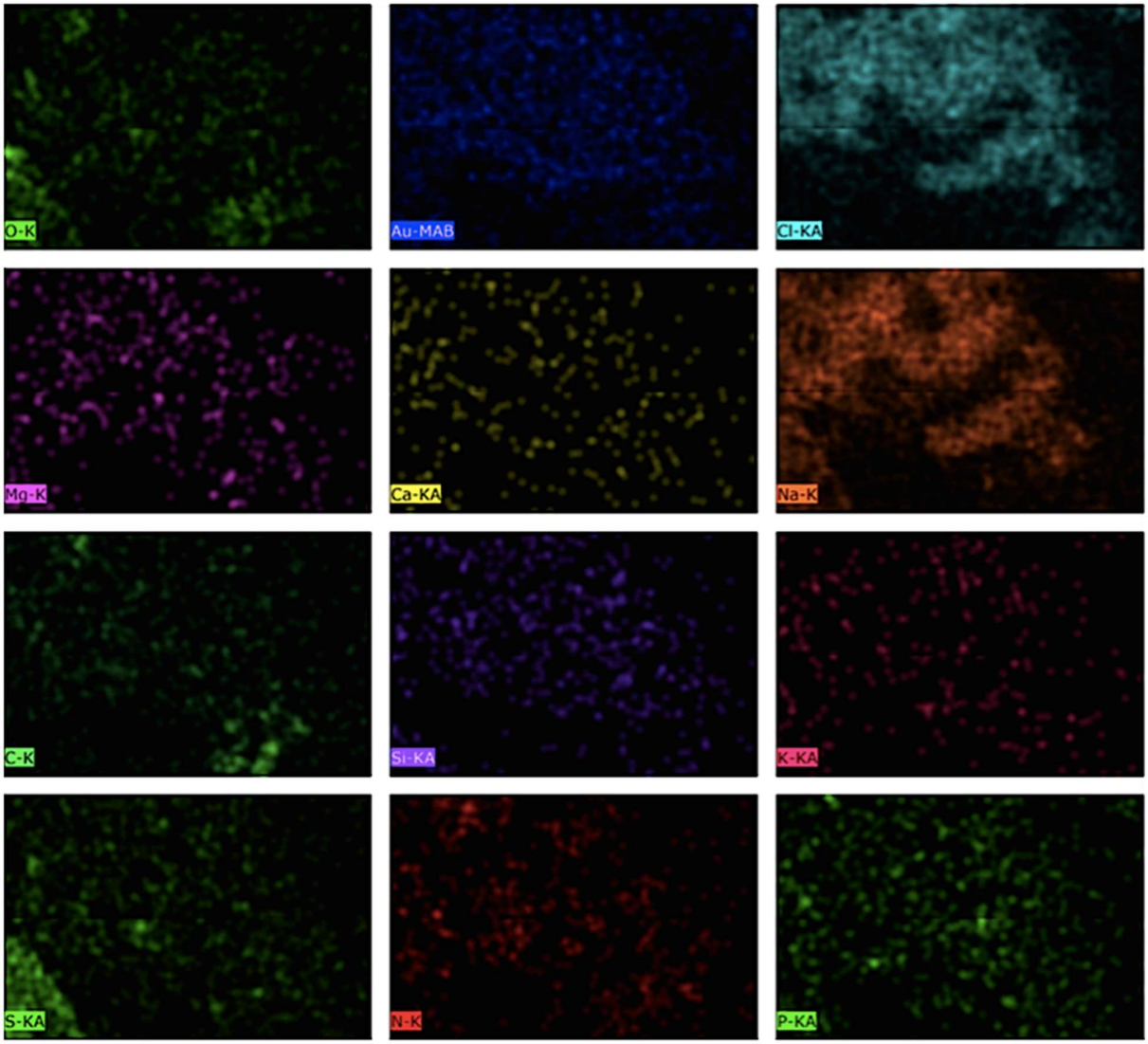


Figure 2. Elemental map of O, Au, Cl, Mg, Ca, Na, C, Si, K, S, N, and P for Spent MB

The BET surface areas and pore width of SB and MB are shown in Table 5. The high pyrolysis temperature at 700 °C allowed the formation of porous SB with a high BET surface area (145 m^2/g). This could be due to the formation of micropores when the pyrolysis temperature is greater than 500 °C [36]. Pyrolysis at a high temperature removed the volatile matter and pore-blocking tar from SD, leading to the greater formation of micropores and an increase in the BET surface area and pore volume [37]. However, the modification process with MgO_2 has also decreased the BET surface area value from 145 m^2/g to 5.05 m^2/g. This could be due to the excessive chemical oxidation by MgO_2 that converts micropore to macropore in MB [38]. The increase in average pore width (nm) in MB corroborates this hypothesis. The possible formation of Mg nanoparticle in the inner pores of MB may also cause blockage and leads to a decrease in the BET surface area [39]. During the dehydration process of MB, a higher amount of Mg concentration leads to Mg becoming hydrated thus forming an excess MgO that blocks the pores of MB [40].

Table 5. The BET surface areas (m^2/g), average pore width (nm), and CEC of sawdust biochar (SB) and Mg-modified biochar (MB), and Spent MB

Parameter	SB	MB	Spent MB
BET surface area (m^2/g)	145	5.05	-
Average pore width (4V/A) (nm)	11.62	14.88	-
CEC (cmol/kg)	0.757	1.034	1.015

The CEC values for SB, MB, and Spent MB are shown in Table 5. Modification of MB with MgO_2 marginally increased CEC values from 0.7569 cmol/kg to 1.034 cmol/kg. The CEC value for Spend MB (1.015 cmol/kg) is also similar to that of MB. The surface of MB may have been slightly oxidized by MgO_2. The insignificant increase in CEC value may also be due to a possible formation of a strong Mg-O bond that prevents deprotonation of the polar functional groups. Similarly, a potential PO_4^{3-} adsorption and precipitation of struvite did not cause further oxidation and the amount of polar functional group remains the same as that of MB. The formation of struvite may have occupied the pores and neutralized the negative charge of the polar functional groups on the surface of MB [41].

Figure 3 illustrates the vibration bands for SB, MB, and Spent MB. The hydroxyl group (-OH) is present in cellulose, hemicelluloses, and lignin which is also responsible for the binding of Mg [42]. The hydroxyl band is not observed in SB, where there was a possibility that most of the cellulose, hemicellulose and lignin degraded due to the high pyrolysis temperature. The vibration bands at 828 cm^{-1} are related to the aromatic C-H in MB, indicating that the added Mg was adsorbed [43]. The presence of the NH_4^+ band is shown at 1463 cm^{-1}-1465 cm^{-1} [44]. Furthermore, the NH_2 stretching bands for spent MB are shown at 3453 cm^{-1}. Bands at 1090-1096 cm^{-1} were due to the P-O stretching vibration of PO_4^{3-} [45]. Bands at 1641-1674 cm^{-1} are the stretching vibrations for C=O carboxylate (1641 cm^{-1}) and C=O amide (1674 cm^{-1}). The wavenumber at 1389-1467 cm^{-1} corresponds to the sp3 C-H bending vibration [46]. The presence of phenolate (1300 cm^{-1}) along with carboxylate and amide were mainly involved in the Mg and PO_4^{3-} adsorption.

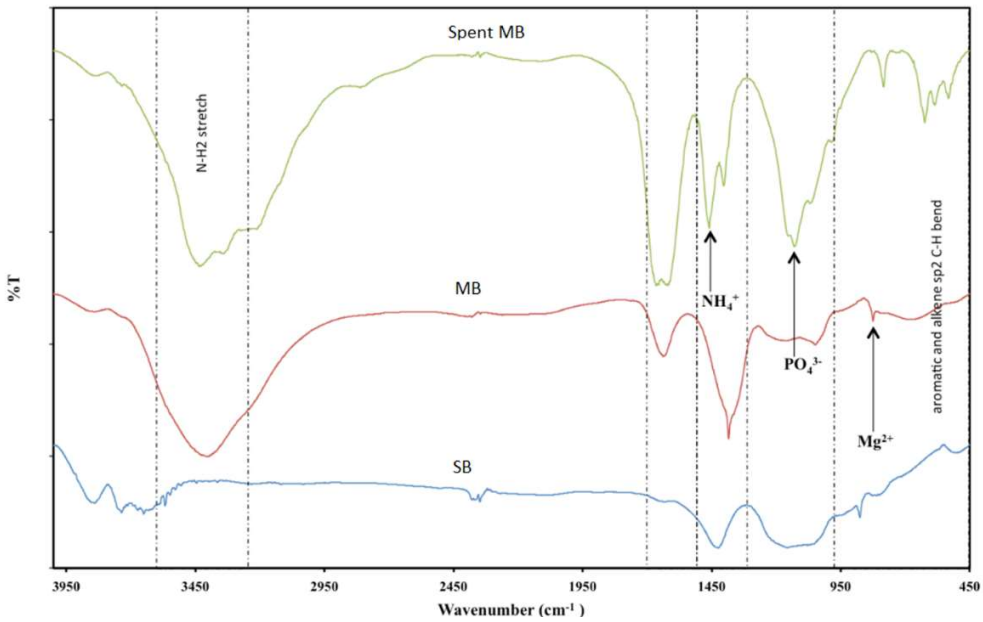


Figure 3. Stacked FTIR spectra of sawdust biochar (SB), Mg-modified biochar (MB), and Spent MB

Figure 4 shows the TG and derivative curve (DTG) thermogram of SD, MB, and Spent MB. Thermal decomposition was characterized by four different mass loss phase that has been separated by the lines for specific temperature intervals. The first decomposition stage happened to all the samples at < 300 °C. Partial decrease in total mass was observed, possibly due to the evaporation of water, and minor de-volatilization [47]. The weight loss that took place between 300 and 500 °C refers to the degradation of cellulose [48]. There were two decomposition stages between 250 °C and 350 °C at phase 2 that correspond to the sharp peak of DTG at 350 °C for MB. This indicated that the first decomposition was due to the weight loss of residual water, while the second decomposition stage could be due to the degradation of the Mg hydrates along with the third stage showing a formation of magnesium hydroxychloride (MgOHCl) [49]. Meanwhile, the second phase for Spent MB showed no peak with a flat decomposition stage starting at 250 °C. This could be due to the bonding of PO_4^{3-} from AHU. The Mg^{2+} ion forms struvite and this may lead to the absence of free $MgCl_2$ hydrates. Lastly, stage 3 and 4 thermal decompositions at 450 °C and 800 °C, respectively were attributed to the slow decomposition of residual solids that contributed to the formation of char [50].

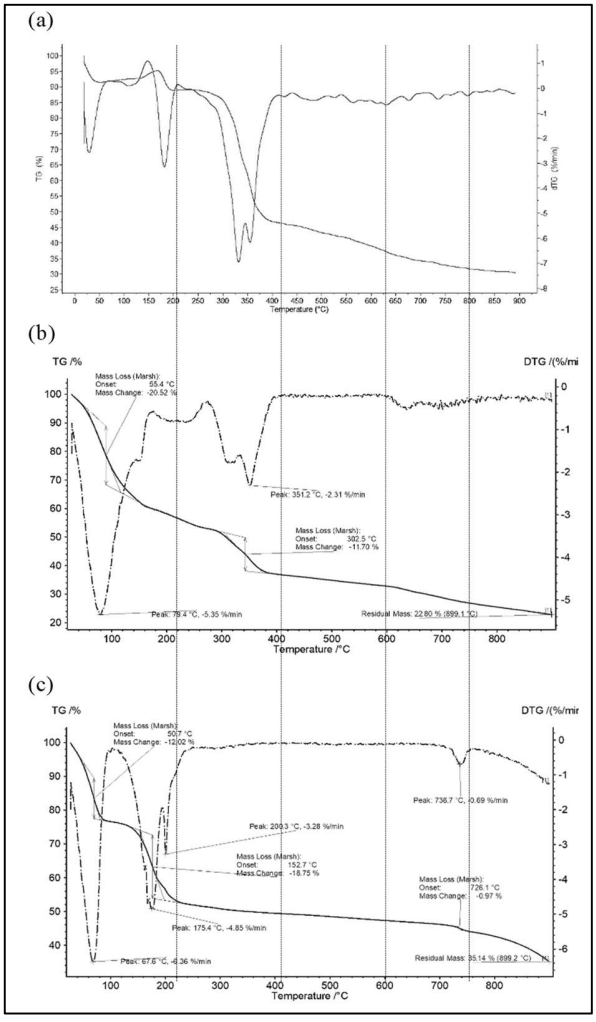


Figure 4. TGA and DTG of (a) sawdust (SD), (b) Mg-modified biochar (MB), and (c) spent MB at heating rate of 3°C/min

Batch sorption of PO_4^{3-} from AHU: Effect of initial concentration of PO_4^{3-}

The PO_4^{3-} sorption capacities of MB increased from 668 mg/g to 9554 mg/g when the initial PO_4^{3-} concentrations of AHU were increased from 6.68 mg/L to 304 mg/L. A higher concentration allows greater diffusion rates and contact of PO_4^{3-} in the aqueous phase with the surface of MB. Thus, more PO_4^{3-} can bind with polar functional groups and increase sorption capacity [51]. Adsorption isotherm parameters in Table 6 show that the PO_4^{3-} adsorption of MB fits better with the Freundlich model (i.e., R^2 = 0.827) [52]. This shows that adsorption of PO_4^{3-} occurred on heterogeneous active sites on the surface of MB. The Langmuir maximum sorption capacity for MB was 8967 mg/g.

Table 6. Parameters of isotherm (Langmuir and Freundlich) and kinetic models (pseudo-first-order and pseudo-second-order) of PO_4^{3-} sorption by MB

Isotherm Models		**Kinetic Models**	
Langmuir		**Pseudo-first-order**	
q_{max} (mg/g)	8967	k_1 (g/[mg.min])	0.053
K_L (L/mg)	0.029	q_e (mg/g)	114.5
R^2	0.773	R^2	0.850
Freundlich		**Pseudo-second-order**	
K_F	944	k_2 (g/[mg.min])	0.0762
n	2.456	q_e (mg/g)	9.937
R^2	0.827	R^2	0.903

Effect of contact time on uptake of PO_4^{3-}(mg/g)

The uptake of PO_4^{3-} by MB reached the first equilibrium in the 10th minute with PO_4^{3-} uptake of 81.1 mg/g. The second sorption equilibrium was observed in the 75th minute with a PO_4^{3-} uptake of 127 mg/g. The surface sites for binding PO_4^{3-} become limited and saturated when contact time was prolonged to two hours [53]. Removal of PO_4^{3-} from AHU may be higher if contact time is allowed to extend for a month. Precipitation and crystallization of Mg minerals may take place. Moreover, MB has an enhancement of negative-charged polar functional groups on its surface, and the main sorption sites for magnesium (i.e., phenolic and carboxyl groups) were deprotonated to allow free Mg^{2+} ions to precipitate as MgO [54]. Kinetic parameters of PO_4^{3-} sorption data analysed using non-linearised pseudo-first-order and pseudo-second-order models for MB are shown in Table 9. Adsorption of PO_4^{3-} occurred rapidly within 15 min of contact time with more than 70 mg/g of uptake. The PO_4^{3-} adsorption by MB was better described by the pseudo-second-order kinetic model with a higher correlation coefficient (i.e., 0.903) than that of the pseudo-first-order model (i.e., 0.85). This outcome suggests that the adsorption process may involve the formation of strong chemical bonds between PO_4^{3-} and the polar functional group on the surface of MB [55].

Modified selective sequential extraction

Figure 5 illustrates the percentage of Pb in the five fractions of the selective sequential extraction (SSE) for soils incubated with GML, and spent MB at 1 and 5% w/w application rate. The first fraction is the exchangeable Pb that easily reacts with the ionic content in water and becomes soluble [56]. This form of Pb is considered available and may cause adverse effects on living organisms. The percentage of exchangeable Pb (first fraction of the SSE procedure) is shown in Figure 6. Exchangeable Pb in unamended soil was the highest (0.33%). Complete immobilization of exchangeable Pb (0 %) was achieved by treating the soil with 0.5 g of spent MB (5% w/w MB). Soil treated with spent MB has a decrease of Pb in fraction 1, but an increase in fractions 2 and 3. This shows that Pb was converted to a relatively less available form that is not readily taken up by plants [34]. This could be due to the chemical reaction between soluble Pb^{2+} ions with PO_4^{3-} from spent MB, forming the insoluble Pb minerals such as $Pb_3(PO_4)_2$.

The second fraction generally refers to the Pb that is likely to bind with carbonate and is susceptible to pH alterations. Immobilization of Pb in the carbonate fraction could be due to the bonding with hydroxide ions, and the precipitation process of Pb with PO_3^{-4} or CO_2^{-3} that were abundant in spent MB [57]. According to Tessier [26], a decrease of soil pH to 5.0 in the second fraction would solubilize Pb which is particularly adsorbed in the carbonate-bound fraction. In this study, spent MB was alkaline with a pH value of 12. The alkaline nature was due to the presence of struvite and alkaline minerals in spent MB which includes hydroxides and oxides of potassium and calcium [58]. For high Pb in fraction 4 (i.e., bound to organic matter), Tessier reported that some organic matter may eventually be released into the environment as biomass may deteriorate, causing it to release the soluble Pb under certain oxidizing conditions in natural waters [26]. Fortunately, the biochar component in the spent MB is more stable than biomass and this was proven as treatment of 1 and 5% w/w of Spent MB gave the least percentage of Pb in fractions 4 of 7.3 % and 12.7 %, respectively. This may be due to the less complexation of Pb with the stable organic structure with struvite bound to MB. Most of the exchangeable Pb were probably precipitated with struvite and ash originated from SB. This shows that treatment of shooting range soil with Spent MB promoted Pb immobilization and minimizes the health risk [59].

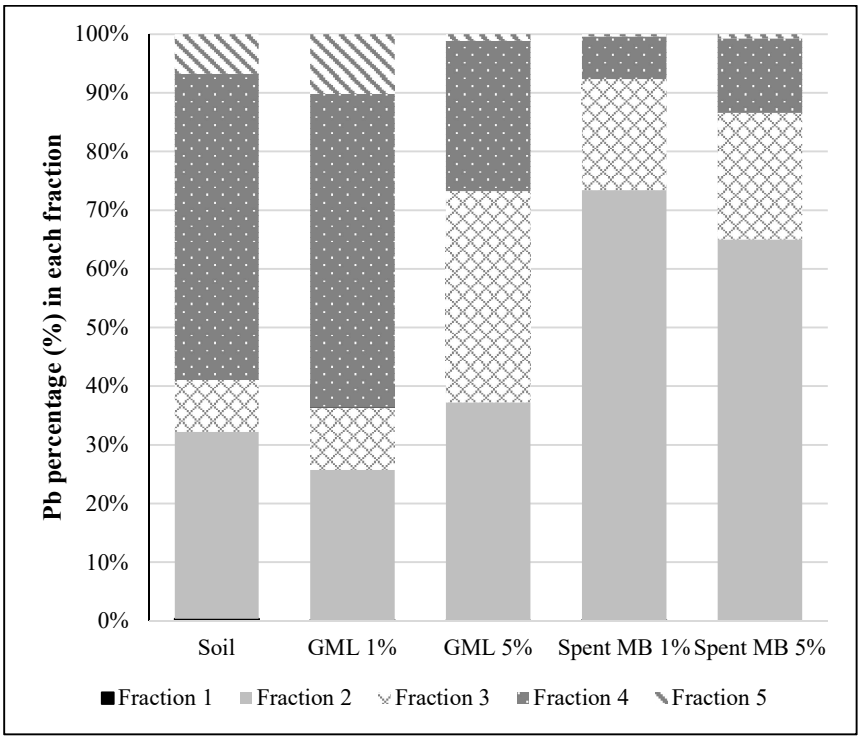


Figure 5. Percentage of lead (Pb) (% w/w) in fractions of the selective sequential extraction experiment for soil treated with GML and spent MB at 1 and 5 % w/w application rate.

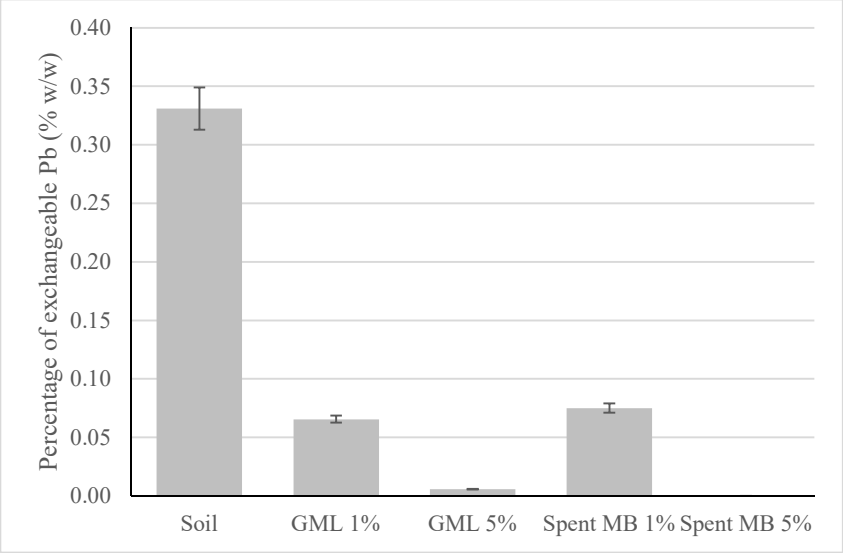


Figure 6. Percentage of exchangeable lead (Pb) (% w/w) for soil treated with ground magnesium lime (GML), and spent modified biochar (MB) at 1 and 5 % w/w application rate.

Leaching rate of Pb from soils modified with Spent MB, and Ground Magnesium Lime (GML)

Figure 7 shows the variations in the available Pb concentration of leachates from soils treated with MB and GML over the volume of 0.01M $CaCl_2$. For the untreated soil column, the concentration of Pb in leachate had increased slightly during the initial stage of the leaching process. The concentration of Pb drastically increased until it reached the maximum Pb concentration of 5.96 mg/L. Then, the Pb concentration decreased gradually to 2.40 mg/L. The overall trend for soil column leaching was gradually decreased from high concentrations of Pb compared to other samples. However, the Pb concentration in leachates coming from soil columns treated with GML and Spent MB were similar and remained constant below 1.63 mg/L. This shows that amendment with MB can mitigate Pb leaching from soil and the performance is comparable to the commercial liming agent of GML. The mechanism of Pb immobilization by struvite-modified magnesium biochar can be explained by the dissolution of PO_4^{3-} to the aqueous phase followed by the precipitation process of hydroxypyromorphite $Pb_{10}(PO_4)_6(OH)_2$ [60]. The reaction equation is represented as follows:

$$MgNH_4PO_4 \cdot 6H_2O + 2H+ \leftrightarrow Mg^{2+} + NH_4^+ + H_2PO_4 + 6H_2O + 10Pb^{2+} + 6H_2PO_4 + 2H_2O \leftrightarrow Pb_{10}(PO_4)_6(OH)_2\downarrow + 14H^+$$
$$+ Pb^{2+} + HPO_4^{2-} \leftrightarrow PbHPO_4\downarrow$$

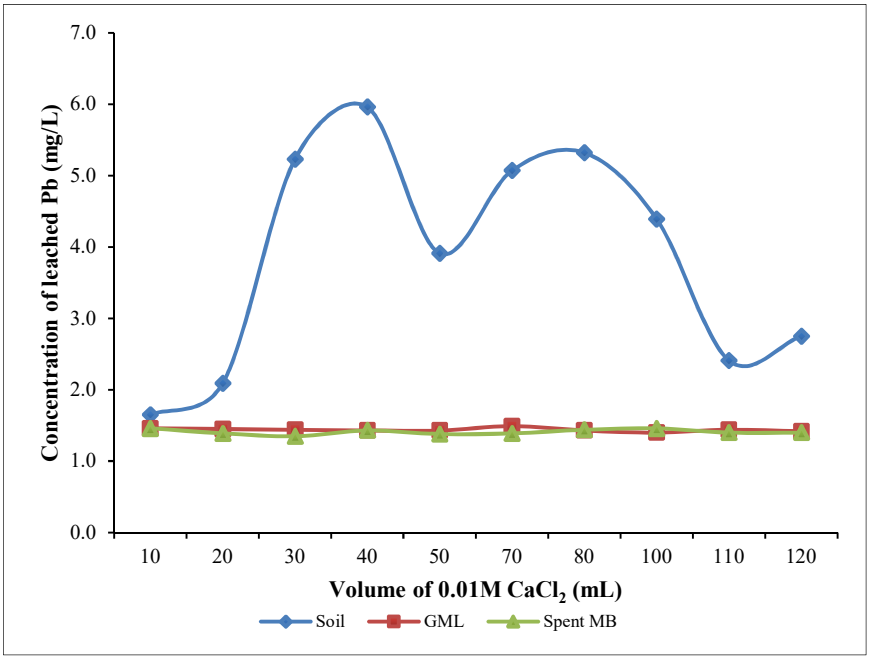


Figure 7. The concentration of Pb in leachates (mg/L) as a function of the volume of 0.01 M $CaCl_2$ solution of soil columns treated with 1 % w/w Spend MB, ground magnesium lime (GML).

Conclusion

This research exhibited the application of SB, MB, and Spent MB as adsorbents because of their features that were easily available, not harmful to the environment, its oxygenated functional groups on biochar surfaces, and the potential for higher sorption capacity. The modification process of MgO_2 seemed able to improve PO_4^{3-} uptake of SB. The SEM-EDX analysis showed that pyrolysis has helped develop macropores in SB and is still retained MB after modification with MgO_2. However, due to possible over oxidation, the microporous structure of MB was not retained. Fortunately, the modifications with MgO_2 led to additional negative-charged polar functional groups for the adsorption of Mg and the subsequent PO_4^{3-} from AHU. Although struvite crystal was successfully precipitated from AHU using MB, a significant amount of NaCl was also present in the Spent MB. Long-term application of Spent MB may introduce Na and may damage soil structure due to an increase in salinity. Even so, Spent MB has shown greater potential to immobilize Pb in soil than GML. Based on the batch adsorption study, modification of MgO_2 has produced MB with a high Langmuir maximum sorption capacity for PO_4^{3-} (i.e., 8967 mg/g), and is higher than that of biochar modified with only $MgCl_2$ (i.e., 8026 mg/g) [61]. Adsorption isotherm analysis indicated that the uptake of PO_4^{3-} by MB was best described by the Freundlich model, with an assumption that several layers of adsorption mechanism occurred on a heterogeneous surface of MB. Kinetic study results suggested that the entire adsorption process for MB was dominated by the chemisorption process via an ion-exchange mechanism. While the small amount of Mg did have some significant effect on adsorption of PO_4^{3-} onto MB. Lastly, the Pb immobilization test results for the three samples have indicated that Spent MB exhibited higher immobilization ability for Pb compared to soil with GML. Thus, amendment with the Mg-impregnated biochar can mitigate Pb leaching from soil to improve PO_4^{3-} utilization.

Acknowledgement

Authors acknowledge the Universiti Teknologi MARA for funding under the Geran Penyelidikan Khas (600-RMC 5/3/GPK (093/2020).

References

1. Mackey, K. R. M. and Paytan, A. (2009). Phosphorus cycle. Encyclopedia of Microbiology, Academic Press, Cambridge, Massachusetts, USA: pp 322-334.
2. Department of Environment Malaysia (2009). Environmental Quality (Industrial Effluent) Regulations, Ministry of Science, Technology and Environment, Kuala Lumpur.
3. Sedlak, R. (2018). Phosphorus and nitrogen removal from municipal wastewater: principles and practice. Routledge, New York, USA: pp 1-256.
4. Rittmann, B. E., Mayer, B., Westerhoff, P. and Edwards, M. (2011). Capturing the lost phosphorus. *Chemosphere*, 84(6): 846-853.
5. Sakulpaisan, S., Vongsetskul, T., Reamouppaturm, S., Luangkachao, J., Tantirungrotechai, J. and Tangboriboonrat, P. (2016). Titania-functionalized graphene oxide for an efficient adsorptive removal of phosphate ions. *Journal of Environmental Management*, 167: 99-104.
6. Yin, H., Kong, M. and Fan, C. (2013). Batch investigations on P immobilization from wastewaters and sediment using natural calcium rich sepiolite as a reactive material. *Water Research*, 47(13): 4247-4258.
7. Sohi, S. P. (2012). Carbon storage with benefits. *Science*, 338(6110): 1034-1035.
8. Ghorbani-Khosrowshahi, S. and Behnajady, M. (2016). Chromium(VI) adsorption from aqueous solution by prepared biochar from *Onopordom heteracanthom*. *International Journal of Environmental Science and Technology*, 13: 1803-1814.
9. Tan, Z., Lin, C., Ji, X. and Rainey, T. (2017). Returning biochar to fields: A review. *Applied Soil Ecology*, 116: 1-11.
10. He, Y., Zhou, X., Jiang, L., Li, M., Du, Z., Zhou, G., Shao, J., Wang, X., Xu, Z., Hosseini Bai, S., Wallace, H. and Xu, C. (2017). Effects of biochar application on soil greenhouse gas fluxes: a meta-analysis. *GCB Bioenergy*, 9(4): 743-755.
11. Ab Malek, N. A., Ibrahim, M. L. and Yong, S. K. (2020). Composite biochar derived from palm kernel shells and blood cockle shells for immobilizing lead in shooting range soil. *Malaysian Journal of Chemistry*, 22(2): 89-97.
12. Almanassra, I. W., McKay, G., Kochkodan, V., Ali Atieh, M. and Al-Ansari, T. (2021). A state of the art review on phosphate removal from water by biochars. *Chemical Engineering Journal*, 409: 128211.
13. Alling, V., Hale, S. E., Martinsen, V., Mulder, J., Smebye, A., Breedveld, G. D. and Cornelissen, G. (2014). The role of biochar in retaining nutrients in amended tropical soils. *Journal of Plant Nutrition and Soil Science*, 177(5): 671-680.
14. Qiu, M., Liu, L., Ling, Q., Cai, Y., Yu, S., Wang, S., Fu, D., Hu, B. and Wang, X. (2022). Biochar for the removal of contaminants from soil and water: a review. *Biochar*, 4(19): 1-25.
15. Xu, K., Zhang, C., Dou, X., Ma, W. and Wang, C. (2019). Optimizing the modification of wood waste biochar via metal oxides to remove and recover phosphate from human urine. *Environmental Geochemistry and Health*, 41(4): 1767-1776.
16. Shih, K. and Yan, H. (2016) Chapter 26 - The crystallization of struvite and its analog (K-Struvite) from waste streams for nutrient recycling. environmental materials and waste. Academic Press, Cambridge, Massachusetts, USA: pp. 665-686.
17. Kloss, S., Zehetner, F., Dellantonio, A., Hamid, R., Ottner, F., Liedtke, V., Schwanninger, M., Gerzabek, M. H. and Soja, G. (2012). Characterization of slow pyrolysis biochars: Effects of feedstocks and pyrolysis temperature on biochar properties. *Journal of Environmental Quality*, 41(4): 990-1000.
18. Bakshi, S., Banik, C. and Laird, D. A. (2020). Estimating the organic oxygen content of biochar. *Scientific Reports*, 10(1): 13082.
19. Jung, K. W., Hwang, M. J., Ahn, K. H. and Ok, Y. S. (2015). Kinetic study on phosphate removal from aqueous solution by biochar derived from peanut shell as renewable adsorptive media. *International Journal of Environmental Science and Technology*, 12(10): 3363-3372.

20. Fidel, R. B., Laird, D. A., Thompson, M. L. and Lawrinenko, M. (2017). Characterization and quantification of biochar alkalinity. *Chemosphere*, 167: 367-373.
21. Tan, Z., Qiu, J., Zeng, H., Liu, H. and Xiang, J. (2011). Removal of elemental mercury by bamboo charcoal impregnated with H_2O_2. *Fuel*, 90(4): 1471-1475.
22. Yong, S. K., Mohd Zin, S. N. and Mad Ariff, M. J. (2016). Effects of rain pH, soil organic matter, cation exchange capacity and total lead content in shooting range soil on the concentration of lead in leachate. *Malaysian Journal of Analytical Sciences*, 20(5): 1066-1072.
23. Chutipongtanate, S. and Thongboonkerd, V. (2010). Systematic comparisons of artificial urine formulas for in vitro cellular study. *Analytical Biochemistry*, 402(1): 110-112.
24. Iqbal, H., Garcia-Perez, M. and Flury, M. (2015). Effect of biochar on leaching of organic carbon, nitrogen, and phosphorus from compost in bioretention systems. *Science of The Total Environment*, 521-522: 37-45.
25. Varikoden, H., Samah, A. A. and Babu, C. A. (2010). Spatial and temporal characteristics of rain intensity in the peninsular Malaysia using TRMM rain rate. *Journal of Hydrology*, 387(3-4): 312-319.
26. Tessier, A., Campbell, P. G. C. and Bisson, M. (1979). Sequential extraction procedure for the speciation of particulate trace metals. *Analytical Chemistry*, 51(7): 844-851.
27. Chun, Y., Sheng, G., Chiou, C. T. and Xing, B. (2004). Compositions and sorptive properties of crop residue-derived chars. *Environmental Science & Technology*, 38(17): 4649-4655.
28. Chen, Y., Yang, H., Wang, X., Zhang, S. and Chen, H. (2012). Biomass-based pyrolytic polygeneration system on cotton stalk pyrolysis: influence of temperature. *Bioresource Technology*, 107: 411-418.
29. Li, R., Wang, J. J., Zhou, B., Ali, M. K. A. A., Zhang, Z., Gaston, L. A., Lahori, A. H., Mahar, A. (2016). Enhancing phosphate adsorption by Mg/Al layered double hydroxide functionalized biochar with different Mg/Al ratios. *Science of the Total Environment*, 559: 121-129.
30. Li, R., Wang, J. J., Zhou, B., Zhang, Z., Liu, S., Lei, S., Xiao, R. (2017). Simultaneous capture removal of phosphate, ammonium and organic substances by MgO impregnated biochar and its potential use in swine wastewater treatment. *Journal of Cleaner Production*, 147: 96-107.
31. Thant Zin, M. M. and Kim, D.-J. (2021). Simultaneous recovery of phosphorus and nitrogen from sewage sludge ash and food wastewater as struvite by Mg-biochar. *Journal of Hazardous Materials*, 403: 123704.
32. Xi, J., Li, H., Xi, J., Tan, S., Zheng, J. and Tan, Z. (2020). Preparation of high porosity biochar materials by template method: A review. *Environmental Science and Pollution Research*, 27(17): 20675-20684.
33. Chen, Q., Qin, J., Cheng, Z., Huang, L., Sun, P., Chen, L. and Shen, G. (2018). Synthesis of a stable magnesium-impregnated biochar and its reduction of phosphorus leaching from soil. *Chemosphere*, 199: 402-408.
34. Gong, Y. P., Ni, Z. Y., Xiong, Z. Z., Cheng, L. H. and Xu, X. H. (2017). Phosphate and ammonium adsorption of the modified biochar based on *Phragmites australis* after phytoremediation. *Environmental Science and Pollution Research*, 24(9): 8326-8335.
35. Cui, L., Pan, G., Li, L., Bian, R., Liu, X., Yan, J., Quan, G., Ding, C., Chen, T., Liu, Y., Liu, Y., Yin, C., Wei, C., Yang, Y. and Hussain, Q. (2016). Continuous immobilization of cadmium and lead in biochar amended contaminated paddy soil: A five-year field experiment. *Ecological Engineering*, 93: 1-8.
36. Tang, J., Zhu, W., Kookana, R. and Katayama, A. (2013). Characteristics of biochar and its application in remediation of contaminated soil. *Journal of Bioscience and Bioengineering*, 116(6): 653-659.
37. Angın, D. (2013). Effect of pyrolysis temperature and heating rate on biochar obtained from pyrolysis of safflower seed press cake. *Bioresource Technology*, 128: 593-597.

38. Yong, S. K., Bachmann, R. T. and Amin, S. (2020). Oxidised biochar from palm kernel shell for eco-friendly pollution management. *Scientific Research Journal*, 17(2): 45-60.
39. Fang, C., Zhang, T., Li, P., Feng, J., R., and Wang, C. (2014). Application of magnesium modified corn biochar for phosphorus removal and recovery from swine wastewater. *International Journal of Environmental Research and Public Health*, 11(9): 9217-9237.
40. Huang, Q., Lu, G., Wang, J. and Yu, J. (2011). Thermal decomposition mechanisms of $MgCl_2 \cdot 6H_2O$ and $MgCl_2 \cdot H_2O$. *Journal of Analytical and Applied Pyrolysis*, 91(1): 159-164.
41. Bourke, J., Manley-Harris, M., Fushimi, C., Dowaki, K., Nunoura, T., and Antal., M. J. (2007). Do all carbonized charcoals have the same chemical structure? 2. A model of the chemical structure of carbonized charcoal. *American Chemical Society*, 46(18): 5954-5967.
42. Munajad, A., Subroto, C. and Suwarno (2018). Fourier transform infrared (FTIR) spectroscopy analysis of transformer paper in mineral oil-paper composite insulation under accelerated thermal aging. *Energies*, 11(2): 364.
43. Novais, S. V., Zenero, M. D. O., Tronto, J., Conz, R. F. and Cerri, C. E. P. (2018). Poultry manure and sugarcane straw biochars modified with $MgCl_2$ for phosphorus adsorption. *Journal of Environment Management*, 214: 36-44.
44. Jing, H. P., Wang, X., Xia, P. and Zhao, J. (2019). Sustainable utilization of a recovered struvite/diatomite compound for lead immobilization in contaminated soil: Potential, mechanism, efficiency, and risk assessment. *Environtal Science Pollution Research*, 26(5): 4890-4900.
45. Chauchan, C. K., Joseph, K. C., Parekh, B. B. and Joshi, M. J. (2008). Growth and characterization of Struvite crystals. *Indian Journal of Pure and Applied Physics*, 46: 507-512.
46. Khan, S. A., Khan, S. B., Khan, L. U., Farooq, A., Akhtar, K. and Asiri, A. M. (2019). Fourier transform infrared spectroscopy: Fundamentals and application in functional groups and nanomaterials characterization. Handbook of Materials Characterization. Springer, Cham: pp. 317-344.
47. Hu, M., Chen, Z., Wang, S., Guo, D., Ma, C., Zhou, Y., Chen, J., Laghari, M., Fazal, S., Xiao, B., Zhang, B. and Ma, S. (2016). Thermogravimetric kinetics of lignocellulosic biomass slow pyrolysis using distributed activation energy model, Fraser–Suzuki deconvolution, and iso-conversional method. *Energy Conversion and Management*, 118: 1-11.
48. Zhou, C., Yang, W. and Blasiak, W. (2013). Characteristics of waste printing paper and cardboard in a reactor pyrolyzed by preheated agents. *Fuel Processing Technology*, 116: 63-71.
49. Zhang, M., Gao, B., Yao, Y., Xue, Y. and Inyang, M. (2012). Synthesis of porous MgO-biochar nanocomposites for removal of phosphate and nitrate from aqueous solutions. *Chemical Engineering Journal*, 210: 26-32.
50. Kim, J. A., Vijayaraghavan, K., Reddy, D. H. K. and Yun, Y.-S. (2018). A phosphorus-enriched biochar fertilizer from bio-fermentation waste: A potential alternative source for phosphorus fertilizers. *Journal of Cleaner Production*, 196: 163-171.
51. Haddad, K., Jellali, S., Jeguirim, M., Ben Hassen Trabelsi, A. and Limousy, L. (2018). Investigations on phosphorus recovery from aqueous solutions by biochars derived from magnesium-pretreated cypress sawdust. *Journal of Environmental Management*, 216: 305-314.
52. Vijayakumar, G., Tamilarasan, R. and Dharmendirakumar, M. (2012). Adsorption, kinetic, equilibrium and Thermodynamic studies on the removal of basic dye Rhodamine-B from aqueous solution by the use of natural adsorbent perlite. *Journal of Material Environmental Science*, 3(1): 157-170.
53. Wang, Z., Shen D., Shen F. and Li, T. (2016). Phosphate adsorption on lanthanum loaded biochar. *Chemosphere*, 150: 1-7.
54. Wang, B., Lehmann, J., Hanley, K., Hestrin, R. and Enders, A. (2016). Ammonium retention by oxidized biochars produced at different pyrolysis temperatures and residence times. *RSC Advances*, 6(48): 41907-41913.

55. Ho, Y. S. and McKay, G. (2000). The kinetics of sorption of divalent metal ions onto sphagnum moss peat. *Water Research*, 34(3): 735-742.
56. Shen, Z., Zhang, Y., Jin, F., McMillan, O. and Al-Tabbaa, A. (2017). Qualitative and quantitative characterisation of adsorption mechanisms of lead on four biochars. *Science of The Total Environment*, 609: 1401-1410.
57. Xue, Y., Gao, B., Yao, Y., Inyang, M., Zhang, M., Zimmerman, A. R. and Ro, K. S. (2012). Hydrogen peroxide modification enhances the ability of biochar (hydrochar) produced from hydrothermal carbonization of peanut hull to remove aqueous heavy metals- Batch and column tests. *Chemical Engineering Journal*, 200-202: 673-680.
58. Novak, J. M., Lima, I., Xing, B., Gaskin, J. W., Steiner, C., Das, K. C., Ahmedna, M., Rehrah, D., Watts, D. W., Busscher, W. J. and Schomberg, H. (2009). Characterization of designer biochar produced at different temperatures and their effects on a loamy sand. *Annals of Environmental Science*, 3: 195-206.
59. Wang, H., Wang, X., Li, J., Jing, H., Xia, S., Liu, F. and Zhao, J. (2018). Comparison of palygorskite and struvite supported palygorskite derived from phosphate recovery in wastewater for *in-situ* immobilization of Cu, Pb and Cd in contaminated soil. *Journal of Hazardous Material*, 346: 273-284.
60. Miretzky, P. and Fernandez-Cirelli, A. (2008). Phosphates for Pb immobilization in soils: a review. *Environmental Chemistry Letters*, 6(3): 121-133.
61. Mohd Idrus, N. F. M., Jamion, N. A., Omar, Q., Sheikh Md Ghazali, S. A. I., Abdul Majid, Z. A. and Yong, S. K. (2018). Magnesium-impregnated biochar for the removal of total phosphorous from artificial human urine. *International Journal of Engineering & Technology*, 7(11): 218-222.

Malaysian Journal of Analytical Sciences (MJAS)
Published by Malaysian Analytical Sciences Society

OPTIMISATION OF THE LIQUID CHROMATOGRAPHY MASS SPECTROMETRY TRIPLE-QUADRUPOLE AND LOW-COST MICROEXTRACTION ANALYSIS FOR CARBAMAZEPINE

(Pengoptimuman Kromatografi Cecair Spektrometer Jisim Tiga-Caturkutub dan Analisis Pengekstrakan Mikro Kos Rendah bagi Karbamazepin)

Siti Sabrina Kasri[1,2], Hannis Fadzillah Mohsin[3], Wan Nurhayati Wan Hanafi[1], Wardah Tahir[4], and Chia Chay Tay[1,5*]

[1]Faculty of Applied Sciences,
Universiti Teknologi MARA, Shah Alam, Selangor,40450, Malaysia
[2]Centre of Foundation Studies,
Universiti Teknologi MARA, Cawangan Selangor, Kampus Dengkil,
Dengkil 43800, Selangor, Malaysia
[3]Faculty of Pharmacy,
Universiti Teknologi MARA Cawangan Selangor,
Puncak Alam, 42300, Selangor, Malaysia
[4]School of Civil Engineering,
College of Engineering,
Universiti Teknologi MARA, Shah Alam, 40450, Selangor, Malaysia
[5]myBioREC, School of Civil Engineering,
College of Engineering,
Universiti Teknologi MARA, Shah Alam, 40450, Selangor, Malaysia

**Corresponding author: taychiay@uitm.edu.my*

Received: 25 September 2022; Accepted: 18 December 2022; Published: 19 April 2023

Abstract

Sensitivity and reliability have become focal points in the analysis of contaminants in wastewater. The optimisation using liquid chromatography mass spectrometry triple-quadrupole (LCMS-QQQ) and carbamazepine microextraction parameters were investigated. The optimisation of gas flow, nebuliser, fragmentor voltage, and collision energy in LCMS-QQQ were examined. Carbamazepine microextraction parameters for extraction methods, extraction tools, various solvents, and solvent volume ratios were investigated. The optimised LCMS-QQQ conditions were 11 L/min gas flow, 25 psi nebuliser, 80 V fragmentor voltage, as well as 35 eV (179.1 m/z) and 15 eV (194.1 m/z) collision energy. For microextraction analysis, liquid-liquid extraction (LLE) yielded a higher carbamazepine average recovery percentage of 96±26%–100±10% than solid phase extraction (SPE) at 4 ±0%–8±1%. The sonicator and separatory funnel similarly showed a high average recovery percentage of carbamazepine at 96±26%–100±10%, but the sonicator saves time and human resources. The average recovery percentage for carbamazepine in solvents at 100±10% was higher compared to water at 26±4%. Statistically, there was no significant difference between the various solvents used in LLE. The optimised solvent volume-ratio LLE was 1.25. This study is vital for the analysis of carbamazepine in the environment and the development of an emerging pollutants monitoring database.

Keywords: carbamazepine, liquid chromatography mass spectrometry triple-quadrupole, optimisation, microextraction

Abstrak

Sensitiviti dan kebolehpercayaan telah menjadi tumpuan dalam analisis bahan cemar dalam air sisa. Oleh itu, pengoptimuman menggunakan kromatografi cecair spektrometri jisim tiga-caturkutub (LCMS-QQQ) dan parameter pengekstrakan mikro karbamazepin telah dikaji. Pengoptimuman aliran gas, nebuliser, voltan serpihan, dan tenaga perlanggaran untuk LCMS-QQQ telah diperiksa. Parameter pengekstrakan mikro karbamazepin untuk kaedah pengekstrakan, alat pengekstrakan, pelbagai pelarut, dan nisbah isipadu pelarut telah disiasat. Keadaan optimum LCMS-QQQ ialah aliran gas 11 l/min, nebuliser 25 psi, voltan serpihan 80 V, serta tenaga perlanggaran 35 eV (179.1 m/z), dan 15 eV (194.1 m/z). Untuk analisis pengekstrakan mikro, pengekstrakan cecair-cecair (LLE) menghasilkan purata peratusan pemulihan karbamazepin yang lebih tinggi pada 96 ± 26%–100 ± 10% daripada pengekstrakan fasa pepejal pada 4 ± 0%–8 ± 1%. Sonikator dan corong pemisah menunjukkan keputusan yang sama, purata peratusan pemulihan yang tinggi bagi karbamazepin pada 96 ± 26%–100 ± 10% tetapi sonikator menjimatkan masa dan sumber manusia. Purata peratusan pemulihan untuk karbamazepin dalam pelarut pada 100 ± 10% adalah lebih tinggi berbanding dengan air pada 26 ± 4%. Pelbagai pelarut yang digunakan dalam LLE tidak menunjukkan perbezaan yang signifikan secara statistik. Nisbah isipadu pelarut LLE yang optimum ialah 1.25. Kajian ini adalah penting untuk analisis karbamazepin dalam alam sekitar dan pembangunan pangkalan data pemantauan bahan pencemar yang muncul.

Katakunci: karbamazepin, kromatografi cecair spektrometri jisim tiga-caturkutub, pengoptimuman, pengekstrakan mikro

Introduction

Carbamazepine is a pharmaceutical compound used as an anti-epileptic drug for suppressing seizures. It is a tricyclic compound that is persistent in the environment. The compound is not completely metabolised in the liver [1]. A total of 1% is excreted through urine and faeces into the sewage system and enters the wastewater treatment plants [2]. Current treatments in wastewater treatment plants are unable to remove carbamazepine because it is not designed to degrade stable contaminants, including carbamazepine [3]. Consequently, treated wastewater with carbamazepine flows into the water stream, accumulates, and causes adverse effects on human health, aquatic organisms, and the environment [4]. Long-term exposure to low concentrations of carbamazepine disrupts the human endocrine system [5]. Carbamazepine also disturbed the growth and development of zebrafish embryos and larvae [6]. In the environment, plants uptake carbamazepine, which accumulates and exposes human and aquatic organisms to risk [7]. Therefore, developing a method for isolating and analysing trace carbamazepine concentrations in wastewater is critical for improving water quality and safety for humans, aquatic organisms, and the environment.

Liquid chromatography mass spectrometry triple-quadrupole (LCMS-QQQ) has been used for the analysis of pharmaceutical compounds, industrial chemicals, and pesticides in the environment due to its high sensitivity and selectivity. Hence, it is suitable for screening and quantifying the trace concentration of carbamazepine in wastewater. Kruglova et al. [8] reported the detection of trace carbamazepine at 0.4 ± 0.1 μgL^{-1} using ultra-performance liquid chromatography/tandem mass spectrometry (UPLC-MS/MS). In the study by He et al. [9], 53.8 μgL^{-1} carbamazepine was analysed using LCMS-QQQ. Although the published methods of detection and quantitating carbamazepine can be used as a reference in the analysis of carbamazepine, optimisation of the method needs to be conducted. This is because assay performance and optimal conditions vary among different instruments and sample matrices [10].

The wastewater containing carbamazepine also has a high concentration of organic matter, microorganisms, and inorganic compounds [11]. Therefore, carbamazepine requires pre-treatment through microextraction before LCMS-QQQ analysis. The most widely used carbamazepine microextraction methods are liquid-liquid extraction (LLE) and solid-phase extraction (SPE). LLE involves the partitioning of compounds based on the solubility of the mixture in two different solvents [11]. Meanwhile, SPE uses a solid phase and a liquid phase to isolate and concentrate compounds from a solution [12]. In comparison to SPE, which requires expensive equipment and accessories,

LLE is a low-cost microextraction method suitable for research with limited funding [11, 12]. In LLE, microextraction tools, types of solvents, and solvent volume ratio are important optimisation parameters in determining the highest average recovery percentage of carbamazepine for high sensitivity and reliable results.

The objectives of this study are to optimise LCMS-QQQ through gas flow, nebuliser, fragmentor voltage, and collision energy, and to optimise microextraction methods, microextraction tools, types of solvents, and solvent volume ratio.

Materials and Methods

Chemicals and standard solutions preparation

The pharmaceutical compound carbamazepine ≥ 98% purity used was purchased from Sigma Aldrich. HPLC and LCMS grade acetonitrile, methanol, ethanol, and acetone were used in the microextraction and LCMS analysis of carbamazepine. A 500 mgL^{-1} carbamazepine stock solution was prepared by dissolving 5 mg of carbamazepine in 10 mL of methanol.

LCMS-QQQ set-up for carbamazepine analysis

A liquid chromatography system (Agilent 1200 Series, Agilent Technologies, USA) equipped with a quaternary pump, an autosampler, a column thermostat, an inline degasser, and a Zorbax Extend-C18 (100 x 2.1 mm, 1.8 µm) column was coupled to the triple quadrupole (QQQ) mass spectrometry (Agilent 6410, Agilent Technologies, USA) with an electrospray ionisation interface (ESI) MS source. The column oven and flow rate were set to 40°C and 0.2 mL/min, respectively. A 2 µL of 1 mg/L^{-1} carbamazepine was injected into the system. A binary gradient mobile phase consisting of ultrapure water (UPW) and acetonitrile (ACN) was prepared and identified as A and B solvents. Both solvents were added with 0.1% formic acid. The gradient profile was set up at initial conditions of 20%:80% (A:B, v/v) and brought to 95%:5% (A:B, v/v) for the first 2 minutes, changed to 20%:80% (A:B, v/v) for 5 minutes, and restored to 95%:5% for 7 minutes. Ionization was performed using the ESI positive mode ion polarity. During optimisation, two mass transitions for carbamazepine, 237.3 → 179.1 m/z and 237.3 → 194.1 m/z were set in multiple-reaction monitoring mode (MRM) [13]. Samples of 1 mgL^{-1} carbamazepine were prepared in triplicates. This experiment used a single factor at a time optimisation design. The optimisation parameters of carbamazepine for gas flow, nebuliser, fragmentor voltage, and collision energy were investigated according to Table 1. Identification and quantitation analysis were performed using Mass Hunter Quantitative Analysis software (Version B.03.01, Agilent Technologies, USA).

Table 1. Optimisation parameters of carbamazepine using LCMS-QQQ

Optimisation Parameters			
Gas Flow (L/min)	**Nebuliser (psi)**	**Fragmentor Voltage (V)**	**Collision Energy (eV)**
10.5	20	80	5
11.0	25	100	10
11.5	30	120	15
	35	140	20
	40		25
			30
			35
			40

The optimised parameters were used to construct the calibration curve. A series of desired carbamazepine standard solutions at 0.001 mgL^{-1} to 1 mgL^{-1} were prepared in triplicates using the 500 mgL^{-1} prepared carbamazepine stock solution. The limits of detection (LOD) and quantification (LOQ) were calculated as in Equations 1 and 2:

$$LOD = 3.3\left(\frac{SD}{S}\right) \quad (1)$$

$$LOQ = 10\ (\frac{SD}{S}) \quad (2)$$

where *SD* is the standard deviation of the response and *S* is the slope of the calibration curve.

Microextraction optimisation

The optimisation design used for microextraction optimisation was a single factor at a time, and the samples were prepared in duplicate. The microextraction methods used were LLE and SPE, followed by optimisation of the microextraction tools, and solvent versus water as in Table 2. The optimisation was further examined with various solvent combinations and solvent volume ratios as shown in Table 3. The methods were adopted from Mohamad-Nasir et al. [11]. In LLE (A), 2 mL of the 0.5 mgL^{-1} carbamazepine standard solution were added to 11 mL of methanol and 9 mL of acetonitrile. The samples were mixed for 5 minutes. For SPE (B), the cartridges were equilibrated using 2 mL of methanol. A total of 2 mL of the 0.5 mgL^{-1} carbamazepine standard solution was eluted into the cartridge, followed by 11 mL methanol and 9 mL acetonitrile. Next, samples extracted from LLE and SPE were rotavapor (IKA, Model: RV06-ML, Germany), filtered with a 0.22 µm syringe filter, and analysed using LCMS-QQQ. The LLE method was repeated under similar conditions, using the microextraction tools of a separatory funnel and sonicator for 5 minutes. Then, the experimental designs for A and B were repeated using methanol and water. After that, various solvent combinations and solvent volume ratios were examined (Table 3). The recovery percentage and average recovery percentage of carbamazepine were calculated using Equations 3 and 4, respectively.

Table 2. Optimisation of carbamazepine microextraction on microextraction methods, tools, and types of solvents

Solvents (mL)	A = LLE				B = SPE			
	A1		A2		B1		B2	
MeOH:ACN	11	9	11	9	11	9	11	9
MeOH:dH_20	11	9	11	9	11	9	11	9

Note: A1-Separatory funnel, A2-Sonicator, B1-Select HLB, B2-Envi 18, MeOH-Methanol, ACN-Acetonitrile, dH_2O-Deionised water

Table 3. Optimisation of carbamazepine microextraction using various solvent combinations and solvent volume ratios

Solvents (mL)						Solvent Volume Ratios
MeOH:ACN		MeOH:EtOH		MeOH:ACE		
8.60	11.40	8.60	11.40	8.60	11.40	0.75
9.00	11.00	9.00	11.00	9.00	11.00	0.82
10.00	10.00	10.00	10.00	10.00	10.00	1.00
11.10	8.90	11.10	8.90	11.10	8.90	1.25
12.00	8.00	12.00	8.00	12.00	8.00	1.50
13.34	6.66	13.34	6.66	13.34	6.66	2.00

Note: MeOH-Methanol, ACN-Acetonitrile, EtOH-Ethanol, ACE-Acetone

$$Recovery\ percentage, \% = \frac{Response\ reading\ of\ extracted\ samples}{Response\ reading\ of\ control}\ x\ 100\ \% \quad (3)$$

$$Average\ recovery\ percentage, \% = \frac{Total\ recovery\ percentage}{Number\ of\ replicates}\ x\ 100\ \% \quad (4)$$

Results and Discussion

LCMS-QQQ set-up for carbamazepine analysis

Table 4 shows the results of the optimisation parameters of LCMS-QQQ for carbamazepine analysis, such as gas flow, nebuliser, fragmentor voltage, and collision energy. The optimised parameters were 11 l/min for gas flow, 25 psi for the nebuliser, 80 V for fragmentor voltage, and 35 eV (179.1 m/z) and 15 eV (194.1 m/z) for collision energy. These conditions are selected because they provide the highest abundance, sharp peak shapes, and consistent retention times as shown in Figure 1. The highest abundance reflects the highest count of carbamazepine [14]. While sharp peak shapes signify the purity of carbamazepine, they reduce faulty results [15]. These outcomes lead to better sensitivity. Consistent retention time indicates the reliability of the optimisation of LCMS-QQQ.

Table 4. Optimisation parameters for carbamazepine analysis for LCMS-QQQ

Optimised Conditions	**Abundance**	
1. Gas flow (l/min)		
10.5	104922	
11.0	**125130**	
11.5	110205	
2. Nebuliser (psi)		
20	89732	
25	**97177**	
30	93617	
35	96736	
40	88544	
3. Fragmentor voltage (V)		
80	68978	
100	74817	
120	**80052**	
140	78013	
4. Collision energy (eV)	m/z 179.1	m/z 194.1
5	ND*	4356
10	ND*	12092
15	ND*	**15905**
20	ND*	15423
25	882	11660
30	1765	7472
35	**2060**	3673
40	ND*	1556

*ND: Not detected

Figure 1 shows the spectrum of counts versus acquisition time for carbamazepine concentrations. In this study, the retention time for carbamazepine was at the range of 6.01–6.20 minutes for carbamazepine at concentrations from 0.001 mgL^{-1} to 1 mgL^{-1}. From these carbamazepine concentrations, the average retention time was found to be 6.16 ± 0.0222 minutes. He et al. [9] reported an 8-minute short retention time for carbamazepine using a C_{18} column with a particle size of 2.6 µM. Generally, high particle size results in complete separation of carbamazepine in a minimum amount of time [17]. In this study, carbamazepine retention time

was shorter than He et al. [9], although they used a C18 column with a smaller particle size of 1.8 µM. This is due to the fact that optimising the LCMS-QQQ for carbamazepine analysis is vital for achieving high sensitivity, saving time, and decreasing the volume of solvents used in the LCMS-QQQ.

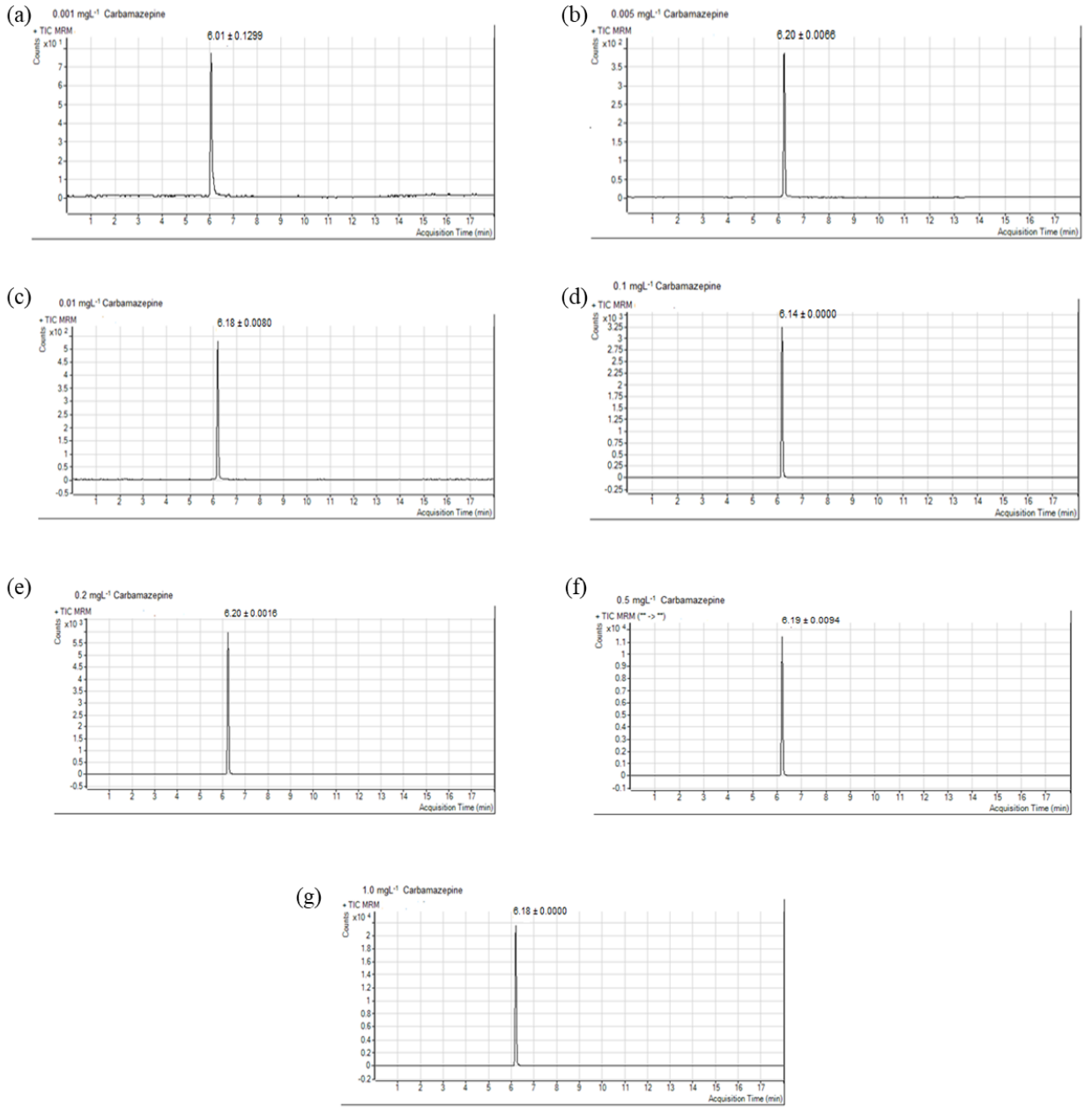


Figure 1. Carbamazepine spectrum of counts versus acquisition time for carbamazepine concentrations: (a) 0.001 mgL^{-1} carbamazepine; (b) 0.005 mgL^{-1} carbamazepine; (c) 0.01 mgL^{-1} carbamazepine; (d) 0.1 mgL^{-1} carbamazepine; (e) 0.2 mgL^{-1} carbamazepine; (f) 0.5 mgL^{-1} carbamazepine; (g) 1.0 mgL^{-1} carbamazepine

Figure 2 shows a graph of the calibration curve for carbamazepine. The equation of the graph was y = 79068x, and the value for the correlation coefficient (R^2) was 0.9940. High R^2 represents an excellent linear relationship. The linearity of the calibration curve signifies the suitability of the chromatographic method over a wide range of concentrations for the studied pharmaceutical [18]. From this study, the LOD and LOQ obtained were at 0.04 mgL^{-1} and 0.13 mgL^{-1}. These results are highly reliable, as the retention time for carbamazepine concentrations was less than 15%. Previous studies for carbamazepine analysis using LCMS-QQQ for the type of column, LOD, LOQ, and linearity are shown in Table 5. The use of column C18 with a particle size of 1.8 µm improved the efficiency of separation, resulting in better LOD, LOQ, and linearity. This confirms that the optimisation of LCMS-QQQ conducted in this study is suitable for the analysis of carbamazepine.

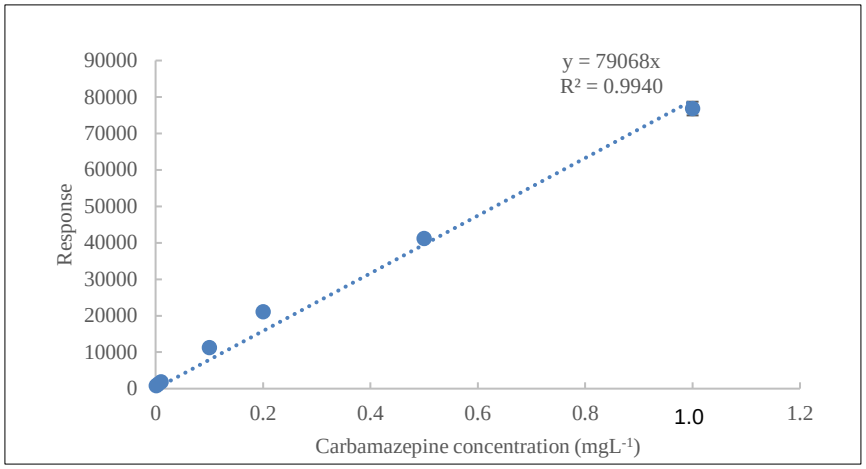


Figure 2. Calibration curve of carbamazepine

Table 5. Type of column, LOD, LOQ, and linearity of carbamazepine

Application	Type of Column and Size	LOD	LOQ	Linearity (R^2)	Reference
Quantification and screening CBZ in surface and drinking water	C_{18} 100 x 2 mm, 3 µM	0.2 ngL^{-1}	*NM	0.9900	[17]
Forensic toxicology cases	C_{18} 100 x 2.1 mm, 1.7 µM	0.12 mgL^{-1}	0.30 mgL^{-1}	0.9989	[18]
Quantification and screening CBZ in wastewater	C18 100 x 2.1 mm, 1.8 µm	0.04 mgL^{-1}	0.13 mgL^{-1}	0.9940	This study

*NM: Not mentioned

Microextraction optimisation

Figure 3 depicts a graph of the microextraction methods LLE and SPE with the average carbamazepine recovery percentage. The average recovery percentage of carbamazepine in LLE for A1 and A2 at 96 ± 26% and 100 ± 10% respectively, higher than SPE for B1 and B2 at 8 ± 1% and 4 ± 0%, respectively. Mohamad-Nasir et al. 2021 also support these results, where the 98.9% average recovery percentage of carbamazepine was higher than SPE at 16.1% [11]. The high average recovery percentage of carbamazepine in LLE was due to the direct methanol interaction with carbamazepine through mixing with the second solvent, acetonitrile [19]. Meanwhile, the low average recovery percentage of carbamazepine in SPE is associated with carbamazepine that is slightly polar, resulting in poor elution on the sorbent [21]. The use of a separatory funnel (A1) and sonicator (A2) yielded high average recovery percentages of 96 ± 26% and 100 ± 10%, respectively. Vigorous mixing increases the interaction of methanol molecules with carbamazepine. Sonicator offers the advantages of less time and human resources. For LLE (A1 and A2), solvent methanol and acetonitrile yield a higher average recovery percentage of carbamazepine at 96 ± 26%–100 ± 10% than solvent methanol and water at 36 ± 12%–26 ± 4%. In addition, Zhang et al. [20] also supported the findings that carbamazepine has low solubility in water at 0.00001 (mole fraction). The average recovery percentages of carbamazepine in SPE for solvent methanol and acetonitrile and solvent methanol and water were neglected due to their low average recovery percentages. This further confirms the effectiveness of the LLE method.

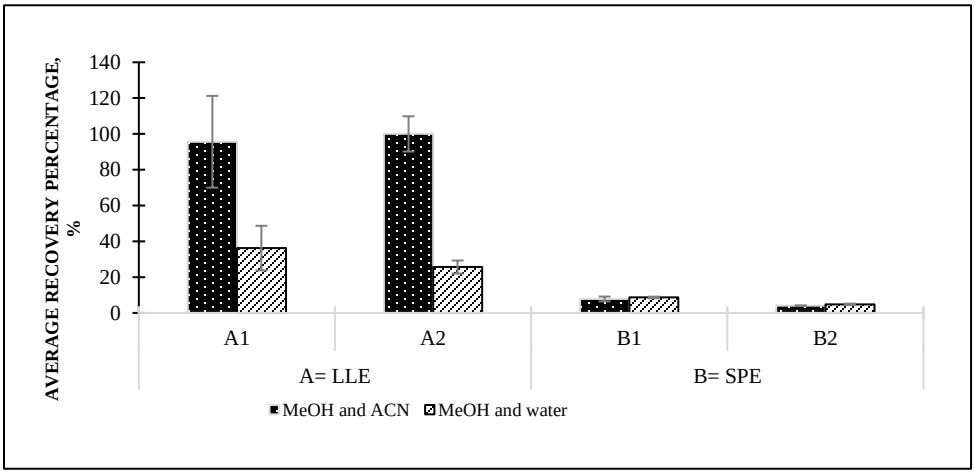


Figure 3. Average recovery percentage of carbamazepine for microextraction methods. A1: Separatory funnel; A2: Sonicator; B1: Select HLB; B2: Envi 18

Figure 4 illustrates the use of various solvents and the solvent volume ratio in LLE with the average recovery percentages of carbamazepine. The average recovery percentages of carbamazepine in methanol and acetonitrile, methanol and ethanol, and methanol and acetone were 100 ±13%, 100 ±1%, 100 ±12%, respectively. The optimum solvent volume ratios for methanol and acetonitrile, methanol and ethanol, and methanol and acetone were all at 1.25. An increase in solvent polarity resulted in an increase in carbamazepine affinity. Thus, methanol in combination with these solvents at the optimum solvent volume ratio caused maximum interaction of carbamazepine and prevented excessive use of solvents. Overall, microextraction optimisation is important in the carbamazepine analysis because it prevents contamination that damages the analytical column of LCMS-QQQ, improves accuracy, and minimises the risk of false results.

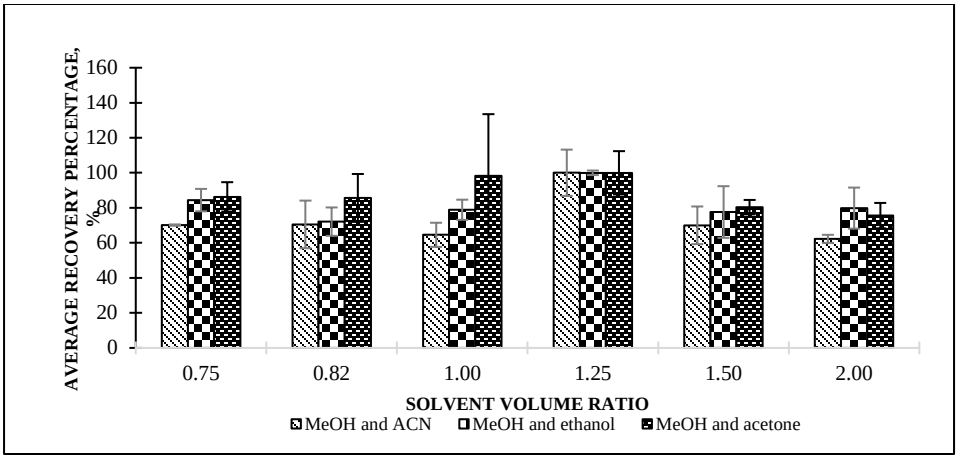


Figure 4. Average recovery percentage of carbamazepine for solvent type and solvent volume ratio

Conclusion

The optimisation parameters of LCMS-QQQ and microextraction methods for carbamazepine analysis were successfully investigated. The optimum gas flow, nebuliser, fragmentor voltage, and collision energy were at 11 l/min, 25 psi, 80 V, 35 eV (179.1 m/z), and 15 eV (194.1 m/z). For the microextraction methods, the LLE resulted in a higher average recovery percentage of carbamazepine at 96 ± 26%–100 ± 10% compared to the SPE at 4 ± 0%–8 ± 1%. The use of a sonicator and a separatory funnel yielded a high average recovery percentage at 96 ± 26% to 100 ± 10%. But, a sonicator has the advantage of saving time and human resources. The use of solvents resulted in a higher average recovery percentage of carbamazepine at 100 ± 13% compared to water at 26 ± 4%. For various solvents used in LLE, methanol and acetonitrile, methanol and ethanol, and methanol and acetone have average recovery percentages of carbamazepine of 100 ± 13%, 100 ± 1%, and 100 ± 12%, respectively. The optimal solvent volume ratio for various solvents in LLE was 1.25. The low-cost microextraction method LLE is suitable to be used in the study as it offers the advantages of simple apparatus, easy operation conditions, short time, and minimum resources used. This ensures reliable and consistent results in carbamazepine analysis for monitoring databases and policy development for emerging pollutants.

Acknowledgement

This work was supported by the University Teknologi MARA under grant 600-IRMI/FRGS 5/3 (355/2019). The authors would like to thank the UiTM Pharmacy Analytical Laboratory (UiPAL), the Faculty of Pharmacy, and the Faculty of Applied Sciences of University Teknologi MARA for providing laboratory facilities.

References

1. Zhang, Y., Geißen, S.-U. and Gal, C. (2008). Carbamazepine and diclofenac: Removal in wastewater treatment plants and occurrence in water bodies. *Chemosphere*, 73(8): 1151-1161.
2. Paltiel, O., Fedorova, G., Tadmor, G., Kleinstern, G., Maor, Y. and Chefetz, B. (2016). Human exposure to wastewater-derived pharmaceuticals in fresh produce: A randomized controlled trial focusing on carbamazepine. *Environmental Science & Technology*, 50(8), 4476-4482.
3. Rissardo, J. P. and Fornari Caprara, A. L. (2019) Carbamazepine associated urinary incontinence: a case report and literature review. *International Journal of Medical and Health Development* 24:114-117.
4. Brezina, E., Prasse, C., Meyer, J., Mückter, H. and Ternes, T. A. (2017). Investigation and risk evaluation of the occurrence of carbamazepine, oxcarbazepine, their human metabolites and transformation products in the urban water cycle. *Environmental Pollution*, 225: 261-269.

5. Street, M., Angelini, S., Bernasconi, S., Burgio, E., Cassio, A., Catellani, C.,Cirillo, F., Deodati, A., Fabbrizi, E., Fanos, V., Gargano, G., Grossi, E., Iughetti, L., Lazzeroni, P., Mantovani, A., Migliore, L., Palanza, P., Panzica, G., Papini, A.M., Parmigiani, S., Predieri, B., Sartori, C., Tridenti, G. and Amarri, S. (2018). Current knowledge on endocrine disrupting chemicals (edcs) from animal biology to humans, from pregnancy to adulthood: Highlights from a national Italian meeting. *International Journal of Molecular Sciences*, 19(6), 1647.
6. Qiang, L., Cheng, J., Yi, J., Rotchell, J. M., Zhu, X. and Zhou, J. (2016). Environmental concentration of carbamazepine accelerates fish embryonic development and disturbs larvae behaviour. *Ecotoxicology*, 25(7): 1426-1437.
7. Dordio, A. V., Belo, M., Martins Teixeira, D., Palace Carvalho, A. J., Dias, C. M. B., Picó, Y., and Pinto, A. P. (2011). Evaluation of carbamazepine uptake and metabolization by *Typha spp*., a plant with potential use in phytotreatment. Bioresource Technology, 102(17): 7827-7834.
8. Kruglova, A., Ahlgren, P., Korhonen, N., Rantanen, P., Mikola, A. and Vahala, R. (2014). Biodegradation of ibuprofen, diclofenac and carbamazepine in nitrifying activated sludge under 12°C temperature conditions. *Science of The Total Environment*, 499, 394-401.
9. He, Yonetani, T., Asada, Y., Echigo, S. and Itoh, S. (2019). Simultaneous determination of carbamazepine-n-glucuronide and carbamazepine phase I metabolites in the wastewater by liquid chromatography-tandem mass spectrometry. *Microchemical Journal*, 145: 1191-1198.
10. Stolker, A. Linda, A. M., Niesing, W., Fuchs, R., Vreeken, R. J., Niessen, W. M. A. and Brinkman, U. A. T. (2004). Liquid chromatography with triple-quadrupole and quadrupole-time-of-flight mass spectrometry for the determination of micro-constituents - A comparison. *Analytical and Bioanalytical Chemistry*, 378(7): 1754-1761.
11. Mohamad-Nasir, N., Abdul-Talib, S., Lokman, N. F., Hashim, S. N. and Tay, C. C. (2021). Efficient and low-cost extraction methods for pharmaceutical compounds of carbamazepine and caffeine. *International Transaction Journal of Engineering, Management, & Applied Sciences & Technologies*, 12(9):1-9.
12. Dugheri, S., Marrubini, G., Mucci, N., Cappelli, G., Bonari, A., Pompilio, L.T. and Arcangeli, G. (2020). A review of micro-solid phase extraction techniques and devices applied in sample pretreatment coupled with chromatographic analysis. *Acta Chromatographica*, 33(2): 99-111.
13. Daniele, G., Fieu, M., Joachim, S., Bado-Nilles, A., Beaudouin, R., Baudoin, P., James-Casas, A., Andres, S., Bonnard, M., Bonnard, I. and Vulliet, E. (2017). Determination of carbamazepine and 12 degradation products in various compartments of an outdoor aquatic mesocosm by reliable analytical methods based on liquid chromatography-tandem mass spectrometry. *Environmental Science and Pollution Research*, 24(20): 16893-16904.
14. Tuli, L., Tsai, T.-H., Varghese, R. S., Cheema, A. and Ressom, H. W. (2010). Using a spike-in experiment to evaluate analysis of LC-MS data. *2010 IEEE International Conference on Bioinformatics and Biomedicine Workshops*, 2010: 5703775.
15. Lange, V., Picotti, P., Domon, B. and Aebersold, R. (2008). Selected reaction monitoring for quantitative proteomics: A tutorial. *Molecular Systems Biology*, 4: 61.
16. Zenezini Chiozzi, R., Capriotti, A. L., Cavaliere, C., Ferraris, F., La Barbera, G., Piovesana, S. and Laganà, A. (2017). Evaluation of column length and particle size effect on the untargeted profiling of a phytochemical mixture by using UHPLC coupled to high-resolution mass spectrometry. *Journal of Separation Science*, 40(12): 2541-2557.
17. Pitt, J. J. (2009). Principles and applications of liquid chromatography-mass spectrometry in clinical biochemistry. *Clinical Biochemistry Reviews*, 30(1): 19-34.
18. Segura, P. A., MacLeod, S. L., Lemoine, P., Sauvé, S. and Gagnon, C. (2011). Quantification of carbamazepine and atrazine and screening of suspect organic contaminants in surface and drinking waters. *Chemosphere*, 84(8): 1085-1094.
19. Karinen, R., Vindenes, V., Hasvold, I., Olsen, K. M., Christophersen, A. S. and Øiestad, E. (2014). Determination of a selection of anti-epileptic drugs and two active metabolites in whole blood by reversed phase UPLC-MS/MS and some examples of application of the method in forensic toxicology cases. *Drug Testing and Analysis*, 7(7): 634-644.
20. Zhang, H., Zhu, Y., Qiao, N., Chen, Y. and Gao, L. (2017). Preparation and characterization of carbamazepine cocrystal in polymer solution. *Pharmaceutics*, 9(4): 54.
21. Al-Qaim, F., Mussa, Z., Yuzir, A., Tahrim, N., Hashim, N. and Azman, S. (2018). Transportation of different therapeutic classes of pharmaceuticals to the surface water, sewage treatment plant, and hospital samples, malaysia. *Water*, 10(7): 916.

Malaysian Journal of Analytical Sciences (MJAS)
Published by Malaysian Analytical Sciences Society

INFLUENCE OF MONOMERS ON THE PROPERTIES OF EPITOPE IMPRINTED SOL-GEL ON SILICA SURFACE FOR HEPARIN ADSORPTION

(Pengaruh Monomer terhadap Sifat-Sifat Sol-Gel Bercetak Epitop pada Permukaan Silika untuk Penyerapan Heparin)

Nur Farhanah Samrat[1], Lee Jia Yee[1], Azalina Mohamed Nasir[1*], Noorhidayah Ishak[1,2]

[1]Fakulti Teknologi Kejuruteraan Kimia,
Kompleks Pusat Pengajian Jejawi 3, Kawasan Perindustrian Jejawi,
Universiti Malaysia Perlis, 02600 Arau Perlis, Malaysia
[2] School of Chemical Engineering, Engineering Campus,
Universiti Sains Malaysia, 14300 Nibong Tebal, Penang Malaysia

[*]Corresponding author: azalina@unimap.edu.my

Received: 18 September 2022; Accepted: 22 March 2023; Published: 19 April 2023

Abstract

Heparin is a well-known anticoagulant drug commonly utilized in medical practice. Nevertheless, foreign impurities may contaminate heparin extract; thus, molecular imprinting technology is introduced to purify and separate the anticoagulant. In this study, an epitope heparin imprinted polymer was prepared using low molecular weight heparin (LMWH) as a template model in three different functional monomers: (3-aminopropyl) trimethoxysilane (APTMS), (3-mercaptopropyl) trimethoxysilane (MCPTMS), and 3-(2-aminoethylamino) propyltrimethoxysilane (AEAPTES). Meanwhile, tetrarthoxysilane (TEOS) was used as a cross-linker for the sol-gel process. The prepared epitope heparin imprinted polymer was characterized using Fourier transform infrared spectroscopy (FTIR) and scanning electron microscope (SEM). The AEAPTES-MIP demonstrated the best imprinting effect towards heparin (IF = 3.10) due to the high stability and dual functional group created strong hydrogen bonding, in comparison to APTMS-MIP (IF = 2.18) and MCPTMS-MIP (IF = 0.13). Moreover, the epitope heparin imprinted polymer exhibited higher selectivity towards macromolecule heparin than LMWH, indicating the successful identification and selection of macromolecule fragments to determine the biological activities.

Keywords: epitope imprinted, heparin, molecular imprinted polymer, sol-gel process

Abstrak

Heparin adalah ubat anti-gumpalan yang terkenal dan biasa digunakan dalam amalan perubatan. Walau bagaimanapun, ekstrak heparin berisiko tinggi bercampur dengan bahan cemar asing. Oleh itu, teknologi pencetakan molekul diperkenalkan untuk penulenan dan pengasingan heparin. Di sini, polimer bercetak epitop heparin telah dihasilkan dengan menggunakan berat heparin molekul rendah (LMWH) sebagai model templat dalam tiga monomer berfungsi berbeza yang dikaji iaitu (3-aminopropil) trimetoksisilana (APTMS), (3-merkaptopropil) trimetoksisilana (MCPTMS) dan 3-(2-aminoetillamino) propiltrimetoksisilana (AEAPTES) manakala, Tetrartoksisilana (TEOS) digunakan sebagai penyambung silang di dalam proses sol-gel. Polimer tercetak epitop heparin yang disediakan telah dianalisis menggunakan spektroskopi inframerah transformasi Fourier (FTIR) dan mikroskop

elektron pengimbasan (SEM). AEAPTES-MIP mempunyai kesan cetakan terbaik terhadap heparin dengan nilai faktor pencetakan tertinggi (IF=3.10) berbanding APTMS-MIP (IF=2.18) dan MCPTMS-MIP (IF=0.13) kerana kestabilannya yang tinggi dan kumpulan dwi berfungsi yang diwujudkan mengukuhkan ikatan hidrogen. Selain itu, polimer tercetak epitope heparin menunjukkan selektiviti tinggi terhadap makromolekul heparin berbanding LMWH. Ini membuktikan bahawa MIP berjaya digunakan sebagai pengenalpastian dan pemilihan serpihan makromolekul untuk menentukan peranan aktiviti biologinya.

Kata kunci: epitop tercetak, heparin, polimer molekul tercetak, proses sol-gel

Introduction

Heparin is a linear polysaccharide of repeating disaccharide units comprising 1,4-linkage of glucosamine and uronic acid. This drug is a popular anticoagulant for diseases such as deep vein thrombosis (DVT) and pulmonary embolism (PE), extracorporeal (hemodialysis), and surgery [1]. Heparin is derived from animal sources [2], mainly pig intestines and bovine lungs, leading to a high risk of contamination by foreign impurities [3]. Thus, an effective extraction and purification method is essential to produce pure heparin by removing impurities. Heparin extraction and purification are currently performed using capillary electrophoresis, affinity chromatography, and polyacrylamide gel electrophoresis (PAGE). Nevertheless, these techniques demonstrated multiple drawbacks, including time consuming, high maintenance, and regeneration [4, 5]. Therefore, molecular imprinting technology has been proposed as a sustainable heparin extraction and purification alternative.

Molecular imprinting is a technology that produces artificial recognition sites in polymeric matrices complementary to the template in size, shape, and chemical functionality. The functional monomer is polymerized with a template in the presence of a cross-linker. Once the template is removed, cavities are imprinted on the molecular imprinting polymer (MIP). The MIP is produced as a highly selective polymer towards a particular template [6]. Furthermore, MIP manufacturing is simple and cost-effective, with high chemical and physical robustness, and highly resistant in harsh environments, such as drastic changes in temperature, pressure, and pH [7]. Therefore, MIP is extensively applied for separation and purification. For example, MIP can separate small compounds such as enzyme lysozyme from aqueous egg white [8], Congo red dye from water [9] and purify large macromolecular compounds such as protein [11], DNA acrydite [12] and acetoside from *Cistanche tubulosa* [10].

Several methods are utilized for MIP preparation, including radical and hydro-gel processes. Nonetheless, the sol-gel method is relatively superior due to the simplicity, time efficiency, and hydrophilicity of the protein template [13]. The sol-gel process involves the condensation of a colloidal solution (sol) to form a cross-linked solid (gel) in the presence of solvent and catalyst [14]. Previously, multiple MIPs had been developed using various techniques (bulk, precipitation, and surface imprinting), but these methods share similar weaknesses, such as poor and less selective adsorption performance in recapturing large molecule structures (e.g. protein). Therefore, epitope surface imprinting techniques are introduced due to the low cost, high template utilization efficiency, and high selectivity towards the target molecule, particularly large molecules. This technique involves the imprinting of the epitope template at the material surface. The epitope template functions as a pseudo-template to replace the macromolecule and polymerizes with monomers in the presence of a cross-linker to produce MIP films. Resultantly, highly selective cavities are formed in the MIP film once the epitope template is removed, similar to the normal macromolecule MIP film. Thus, a highly selective MIP is produced to recognize and bind to the targeted macromolecule [15].

In this study, the epitope imprinted polymer for capturing large molecule heparin was developed. The low molecular weight heparin (LMWH) was used as an epitope template to capture the large heparin macromolecule, while tetraethyl orthosilicate (TEOS) acted as the cross-linker for the epitope surface imprinting in the sol-gel process. Three functional monomers, (3-aminopropyl)trimethoxysilane (APTMS), (3-mercaptopropyl)trimethoxysilane

(MCPTMS), and 3-(2-aminoethylamino) propyl]trimethoxysilane (AEAPTES), were selected to investigate the interaction of heparin adsorption in this study.

Materials and Methods

Materials

The silica-gel (230 – 400 mesh) was purchased from Merck (Germany). The heparin, 98% (for medical purposes), was purchased from AinMedicare (Malaysia). The commercial LMWH), 98%, was purchased from Easybuyer Ltd. (Shanghai, China). The three functional monomers, APTMS, MCPTMS, and AEAPTES, were purchased from Sigma-Aldrich (Germany). Meanwhile, the cross-linker, TEOS, was purchased from Acros Organics (Germany). Hydrochloric Acid (HCl), 37%, was purchased from Fisher Scientific (Germany), while ethanol, 95%, and methanol, 99.98%, were obtained from HmbG (Germany).

Activation of silica gel

The silica gel was first activated to increase the silanol group and remove metal oxide and nitrogen-containing impurities [16]. Subsequently, the silica gel was dried to remove and reduce the silica gel particle size, thus, increasing the surface area and adsorption capacity [17]. The silica gel (15 g) was then immersed in 120 mL of concentrated 6 M hydrochloric acid (HCl) and refluxed for 10 h with constant stirring. The resulting mixture was filtered, washed thoroughly with deionized water, and centrifuged at 4000 rpm for 10 min. The washing steps were repeated until the mixture became neutral (pH 7.0). Lastly, the silica gel was oven dried at 70 °C overnight.

Preparation of epitope heparin imprinted polymer by sol-gel process

A total of 0.45 g LMWH (0.05 mmol) was first dissolved in 40 mL of distilled water before adding 0.0524 of APTMS (0.1 mmol) and sonicated for 5 min. Subsequently, 0.706 g TEOS (1.8048 mmol) was added into the solution and sonicated for another 5 min. Activated silica-gel (4 g) and 0.4 mL of 0.012 M HCl were added sequentially while stirring at 100 rpm, and the suspension was later polymerized at 40 °C for 24 h. The imprinted polymer was filtered, washed with 50 mL ethanol, and neutralized with 50 mL of distilled water thrice. Similarly, the non-imprinted polymer (NIP) was prepared using the same protocol but without the template LMWH. The process was repeated using the two remaining monomers: 0.1 mmol MCPTMS and 0.1 mmol AEAPTES. Once completed, the template LMWH was extracted from the imprinted polymer via sonication for 15 min with a 50 mL mixture of methanol and hydrochloric acid (10% in water) at a ratio of 1:1. Sonication was performed for another 15 minutes with 50 mL of methanol followed by 50 mL of water. The washing steps were repeated thrice. The supernatant from every washing was tested using UV-Vis spectroscopy at 230 nm, and the washing continued until no LMWH was detected. Finally, the MIP was obtained through filtration and dried at 80 °C overnight. A similar protocol was repeated for other imprinted polymers with different monomers and NIP.

Batch rebinding experiment

The MIP and NIP (50 mg) of different monomers were placed in 15 mL centrifuge tubes, followed by adding 5 mL of 0.25 mg/mL heparin or 0.25 mg/mL LMWH solution. Subsequently, the centrifuge tubes were placed horizontally on the shaker for 4 hours at 100 rpm under room temperature. In the adsorption binding test, different concentrations of the prepared mixtures were utilized (0.0625 mg/mL to 1.0 mg/mL). Similarly, the kinetic binding analysis was performed at a constant concentration of heparin of 0.50 mg/mL, except the time measurement was evaluated from 10 min to 240 min. Once the binding has completed, the tubes were centrifuged at 4000 rpm for 10 minutes to remove the imprinted residual from the supernatant. The supernatant was then filtered from the imprinted polymers using a nylon syringe filter (0.45 μm). The LMWH and heparin concentrations in the supernatant were measured by UV–Vis spectrometer at 230 nm or 202 nm, respectively.

Characterization of the Imprinted Polymers

A scanning electron microscope (SEM) was used to study the morphology and texture of the imprinted polymers. The MIP, NIP, and silica gel were coated with platinum for 90 seconds before being observed under

high vacuum conditions at 5 kV and 3 mA current in SEM. The MIP and NIP were examined at 1000×, 5000×, and 10,000× magnifications. The MIP, NIP, and silica gel were also analyzed using the Perkin Elmer Spectrum 100 Series Fourier-transform infrared (FT-IR) spectroscopy using the KBr pellet method. The polymer (100 mg) and 200 mg of KBr powder were mixed using mortar and pestle and pressed for 2 min at 8 kPa to form transparent pellets. Finally, the pellets were placed in the FT-IR sample holder and observed at wavenumbers between 400 and 4000 cm^{-1}

Results and Discussion

FTIR Characterization of epitope heparin imprinted polymer

The FT-IR spectroscopy was used to prove the presence of amine-functional silane in the developed polymer. Figure 1 illustrates the FT-IR spectra of silica gel, APTMS-MIP, MCPTMS-MIP, AEAPTES-MIP, and APTMS-NIP. Spectra that included silica gel, MIP, and NIP exhibited similar peaks. The strong peaks at 3234.61 cm^{-1} to 3436.78 cm^{-1} corresponded to OH-group vibrations, resulting from the moisture absorbed by the imprinted polymer. Meanwhile, the peaks at 1631.92 cm^{-1} to 1671.75 cm^{-1} indicated the C-C stretching vibration of alkane. The peaks from 1022.38 cm^{-1} to 1100.75 cm^{-1} are associated with the Si-O-Si stretching. The Si–O vibration was identified at the peaks between 747.30 cm^{-1} and 806.36 cm^{-1}.

The developed polymers demonstrated unique FTIR spectra; small peaks were detected at 1410.37 cm^{-1} for APTMS-MIP, 1460.53 cm^{-1} for MCPTMS-MIP, and 1444.48 cm^{-1} for AEAPTES-MIP, representing the N-H peaks of primary amine. In addition, the N-H peaks of secondary amine were identified in AEAPTES-MIP at 1560.87 cm^{-1}. The peak of the S-H thiol group in MCTMS-MIP was observed at 2683.61 cm^{-1}, which slightly deviated from the literature (2600 cm^{-1} – 2550 cm^{-1}). These peaks indicated that the monomers had been imprinted on the silica support, hence, the successful production of epitope heparin imprinting polymer compared to silica gel.

Previously, Eskandarloo [18] synthesized (3-aminopropyl) triethoxysilane (3-APTES)-functionalized halloysite nanotubes (HNTs) by using heparin as a template to enhance the capacity of MIP binding selectivity. In contrast, the current study utilized LMWH as a template to capture large heparin, thus, known as the epitope imprinted technique. Moreover, the three types of silane groups selected for this study belonged to the trimethoxysilane group, contrary to the triethylxysilane group detected at 2900 cm^{-1} used by - Eskandarloo. The study also claimed that small peaks were detected at 1476 cm^{-1} and 2928 $cm^{-1,}$ represented by the C-N and N-H stretch, which was absent in the presence of a silane coupling agent.

SEM characterization of epitope heparin imprinted polymer

The surface morphology of silica, epitope heparin imprinted polymer, and the non-imprinted polymer was studied using SEM at 5000x magnification (see Figure 2). The silica gel [Figure 2(a)] exhibited a highly rough surface compared to other epitope imprinting and non-imprinting heparin [Figure 2 (b) - (e)], owing to the abrasive nature of silica particles. Furthermore, the imprinting polymers, APTMS-MIP [Figure 2 (b)], MCPTMS-MIP [Figure 2 (c)], and AEAPTES-MIP [Figure 2 (d)] demonstrated porous surfaces, representing the cavities resulting from the template removal. These pores can speed up the adsorption process towards the template and improve adsorption kinetic than NIP. Apart from that, this observation indicated that the epitope heparin had been imprinted on the silica gel, hence, the successful preparation of the epitope heparin polymer [19]. Conversely, the non-imprinting polymer in Figure 2 (e) manifested a clear, smooth surface without forming three-dimensional pores due to the non-template polymerization.

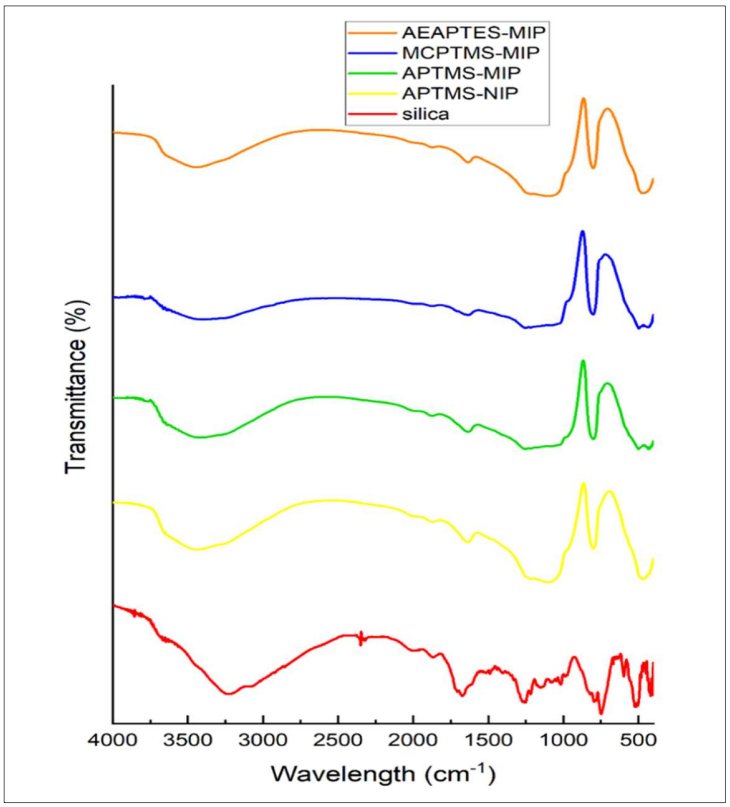


Figure 1. The FT-IR spectra of silica gel (red), APTMS-NIP (yellow), APTMS-MIP (green), MCPTMS-MIP (blue), and AEAPTES-NIP (orange)

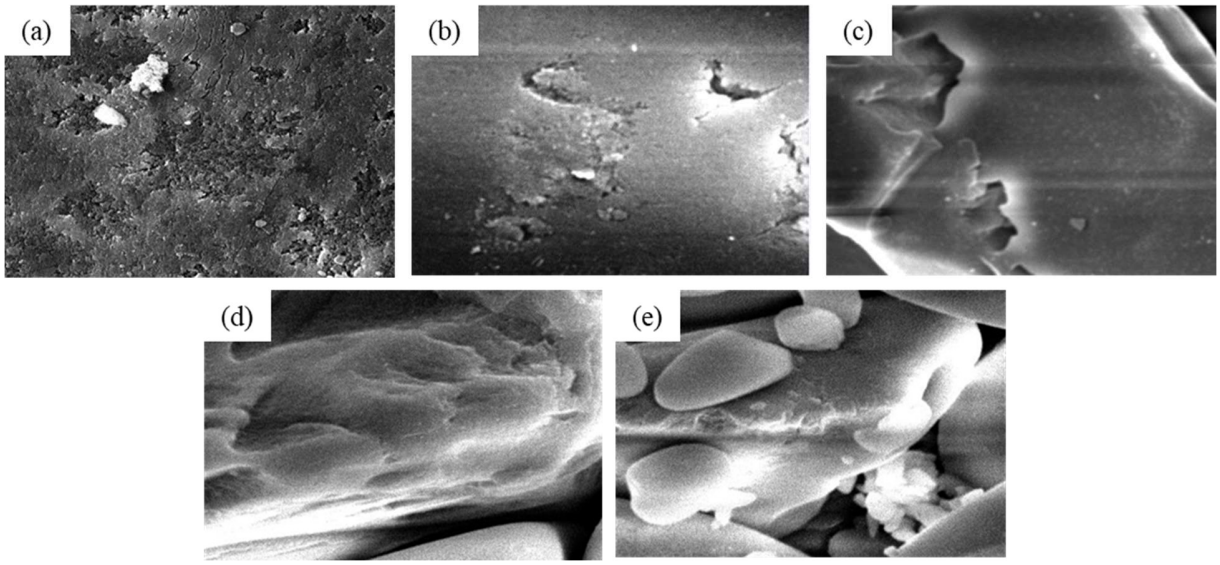


Figure 2. The SEM images of silica (a) APTMS-MIP, (b) MCPTMS-MIP, (c) AEAPTES-MIP, (d) and (e) NIP at 5000x magnification

Gossypol imprinted on silica surfaces via sol-gel surface imprinting [20] exhibited similar findings to the present study. The SEM images of gossypol-MIP illustrated rougher surfaces than gossypol-NIP and silica, indicating a successfully imprinted polymer. In addition, the silica gel surface was distinctly smoother than gossypol-MIP and gossypol-NIP.

Interactions between the functional monomer with heparin and LMWH

The present study tested three monomers, APTMS, MCPTMS, and AEAPTES, to identify the best functional monomer for the heparin imprinted polymer. The selectivity of epitope heparin imprinted polymer with different monomers was represented as an imprinting factor (IF). The comparison graphs of different monomers are plotted in Figure 3 for heparin rebinding and Figure 4 for LMWH rebinding. Generally, the monomers recorded higher IF values for heparin rebinding than LMWH rebinding, with the highest binding capacity of 23 mg/g for heparin and 9 mg/g for LMWH. The epitope MIP binding of macromolecule heparin was double that of LMWH, indicating higher adsorption towards the former than the latter. Thus, the findings supported epitope MIP utilization to capture macromolecule heparin. Similarly, Gupta et al. [21] reported that epitope-imprinted iron-binding MIP for detecting fbpA protein on *Neisseria meningitidis* bacteria demonstrated high selectivity towards the template fbpA protein (IF = 12.27 $ngmL^{-1}$). The protein epitope polymer was synthesized using the amino sequence fbpA epitope as the template. This finding suggested that the small epitope molecule could recognize macromolecules. Apart from that, Yoshimi et al. [22] used epitope surface imprinting heparin-imprinted nanoparticles for grafting on unfractionated heparin (UFH) or LMWH-immobilized glass beads, indicating that the epitope heparin imprinting polymer could capture macromolecule heparin by epitope surface imprinting.

Table 1 shows that AEAPTES recorded the highest IF values for heparin and LMWH rebinding, followed by APTMS and MCPTMS. Therefore, heparin and LMWH selectivity were the highest in AEAPTES, followed by APTMS and MCPTMS. This observation could be explained by the presence of double amine groups in AEAPTES; the primary and secondary amine established stable amine-functionalized surfaces. Resultantly, the interactions between the functional monomer and sulphate group in macromolecule heparin by hydrogen bonding increased in AEAPTES compared to APTMS with a single amine group. Meanwhile, the sulphydryl functional group (SH-group) in MCPTMS exhibited low interaction with macromolecule heparin. An earlier study by Zhu et al. [23] reported that AEAPTES had the highest thickness than other functional silanes, such as 3-aminopropyltriethoxysilane (APTES), APTMS, N-(2-aminoethyl)-3-aminopropyltrimethoxysilane (AEAPTMS), and N-(6-aminohexyl)aminomethyltriethoxysilane (AHAMTES). Moreover, AEAPTES is a more sterically hindrance of intramolecularly catalyzed hydrolysis, potentially improving the hydrolytic stability. As AEAPTES has low sensitivity to water, the polymer can generate a more reproducible silane group. Lastly, AEAPTES possess a unique structure that allows the formation of a cyclic intermediate through the coordination between the secondary amine group and the silicon atom.

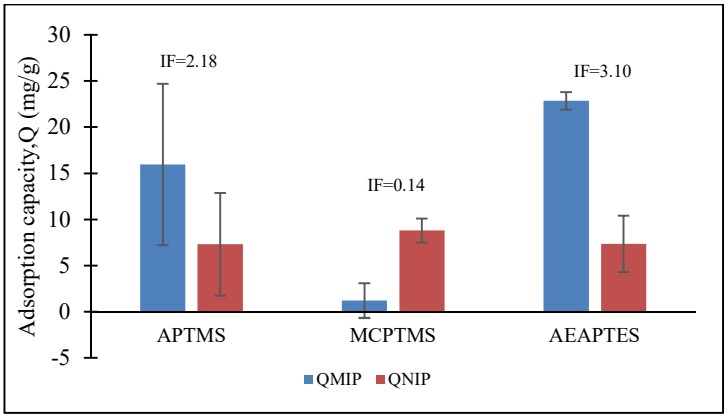


Figure 3. Heparin rebinding of different monomers

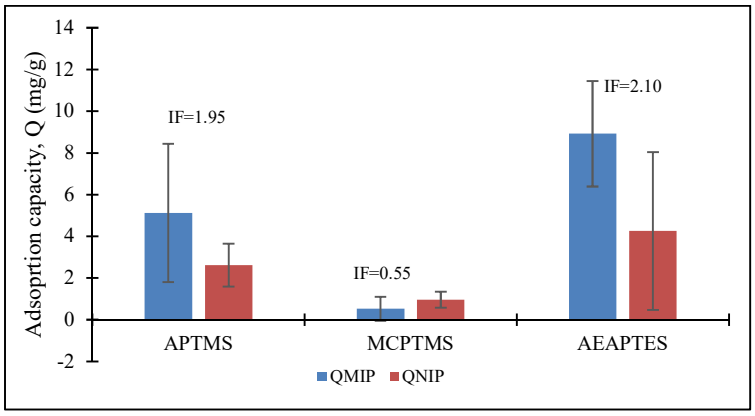


Figure 4. The LMWH rebinding of different monomers

Table 1. Heparin and LMWH rebinding performance of epitope heparin imprinted polymer with different monomers

Sample	Heparin			LMWH		
	Q_{MIP}	Q_{NIP}	IF	Q_{MIP}	Q_{NIP}	IF
APTMS	15.965	7.311	2.18	5.121	2.624	1.95
MCPTMS	1.203	8.789	0.13	0.529	0.96	0.55
AEAPTES	22.843	7.357	3.10	8.919	4.257	2.09

Q_{MIP} = MIP binding capacity, Q_{NIP} = NIP binding capacity, and IF = Imprinting factor

Adsorption and kinetic binding capacity towards heparin

Figure 5 shows the adsorption capacities of AEAPTES-MIP towards different concentrations of heparin (0.062 mg/mL - 1.0 mg/mL). There was a surge in AEAPTES-MIP and AEAPTES-NIP adsorption capacities when the heparin concentration increased from 0.0625 mg/mL to 0.5 mg/mL and remained constant thereafter. As the heparin concentration (target) increased, more heparin was available to adhere to the binding sites, increasing the heparin adsorption and binding capacities. The polymer became saturated at the equilibrium point (0.5mg/mL) as all the binding sites were occupied by heparin [24]. Based on Figure 5, AEAPTES-NIP adsorption capacity was slightly lower than AEAPTES-MIP. Meanwhile, the highest binding capacities for AEAPTES-MIP and AEAPTES-NIP were 38.19 mg/g and 35.51 mg/g, respectively. This outcome was aligned with a study by Dai et al.[22], which recorded similar adsorption capacities for the structural analogues of

AEAPTES-MIP and AEAPTES-NIP. Conversely, NIP could not produce proper binding sites that are highly complementary to the target due to the absence of a template, resulting in non-specific adsorption. Therefore, NIP adsorbed less template molecule than MIP, leading to lower adsorption capacities.

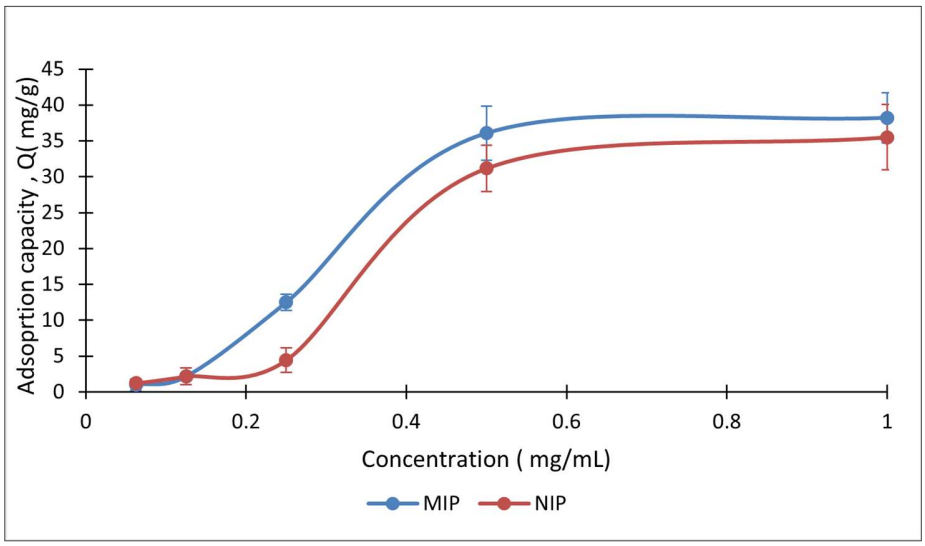


Figure 5. Batch binding test of heparin towards AEAPTES-MIP and AEAPTES-NIP

The AEAPTES-MIP and AEAPTES-NIP adsorption behaviors were determined using Langmuir and Freundlich, isotherm models. The AEAPTES-MIP is best suited to Freundlich isotherm with a linear regression coefficient (R^2) value of 0.8968. This outcome indicated that the heparin adsorption was multilayered and reversible, and the heat adsorption distribution was non-uniform on the AEAPTES-MIP heterogeneous surface. Meanwhile, AEAPTES-NIP followed the Langmuir isotherm model with an R^2 value of 0.9375. This finding suggested the reversible and energetically equivalent heparin adsorption at the homogenous site of the AEAPTES-NIP monolayer surface.

Figure 6 details the kinetic binding of heparin adsorption at 0.5mg/mL onto AEAPTES-MIP and AEAPTES-NIP between 10 to 240 minutes. The polymers adsorption capacities spiked during the first 10 to 120 minutes and decreased gradually until equilibrium was achieved. The rapid initial heparin adsorption could be explained by the abundance of polymer binding sites exposed to the target, which continued to rise with time. At 60 minutes, the binding sites became saturated, and resistance occurred between heparin and the polymer surface, making it harder to retain heparin in empty binding sites. Consequently, the adsorption rates declined and reached adsorption equilibrium [25]. The AEAPTES-NIP recorded a slightly lower adsorption capacity than AEAPTES-MIP, with the highest binding capacity of 17.1556 mg/g for the former and 18.4478 mg/g the latter.

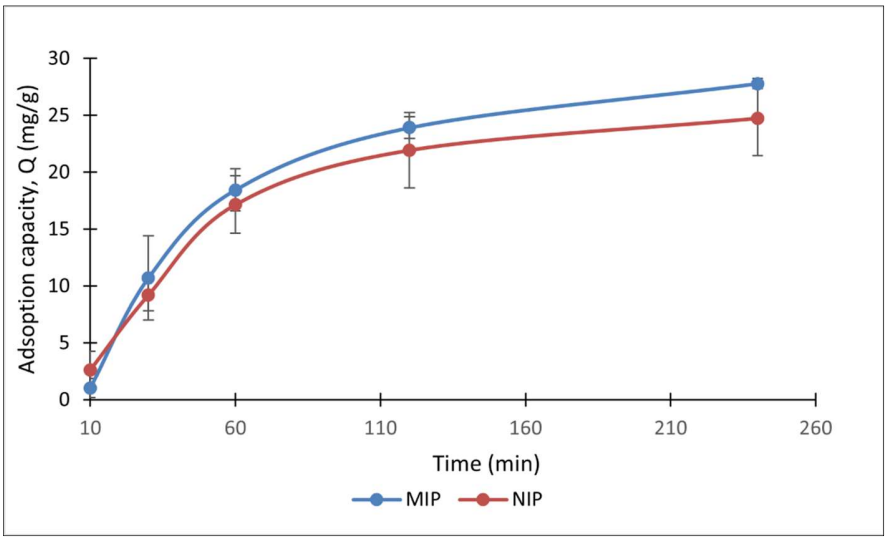


Figure 6. Kinetic binding analysis of heparin on AEAPTES-MIP and AEAPTES-NIP

The AEAPTES-NIP could not bind properly to a highly complementary target without a template, resulting in non-specific adsorption. Consequently, NIP adsorbed less template molecule than MIP, reducing adsorption capacities [26]. Furthermore, AEAPTES-MIP and AEAPTES-NIP were best suited to the pseudo-first-order with R^2 values of 0.9996 and 0.9870, respectively. These results indicated that the rate of change of heparin uptake with time is directly proportional to the difference in concentration of saturation and the amount of heparin uptake with time.

Conclusion

The prepared epitope heparin MIP samples were characterized using FT-IR and SEM in this study. The FT-IR results identified unique functional groups in the epitope heparin polymers: 1) amine group in APTMS-MIP, 2) thiol group in MCPTMS-MIP and 3) secondary amine group in AEAPTES-MIP. Meanwhile, the SEM findings indicated that all MIP exhibited rough surfaces compared to NIP, thus, confirming that the functional monomer and epitope heparin were successfully imprinted on the silica gel. Among the three selected monomers, AEAPTES-MIP demonstrated the best imprinting effect toward heparin (IF = 3.10). This functional monomer exhibited high stability and dual functional groups to create strong hydrogen bonding. Furthermore, the produced epitope heparin was proven to have high adsorption and specificity towards the macromolecule heparin template due to the higher adsorption toward heparin than LMWH. In conclusion, this study demonstrated that MIP could be synthesized using simple and fast methods, such as the proposed epitope surface imprinting and sol-gel method. These approaches can overcome the limitations of MIP and produce high selectivity heparin imprinted polymers.

Acknowledgment

The authors would like to acknowledge the support of the Ministry of Higher Education of Malaysia through the Fundamental Research Grant Scheme (FRGS/1/2020/TK0/UNIMAP/02/38) for providing the necessary fund and facilities for this research.

References

1. Haqqani, O. P., Iafrati, M. D. and Freedman, J. E. (2013). Pharmacology of antithrombotic drugs. In vascular medicine: A companion to Braunwald's heart disease: Second Edition. Elsevier Inc, Netherlands: pp.106-107
2. Bolten, S. N., Rinas, U. and Scheper, T. (2018). Heparin: role in protein purification and substitution with animal-component free material. *Applied Microbiology Biotechnology*, 102(20): 8647-8660.

3. Zhu, Y., Zhang, F. and Linhardt. R. J. (2019). Heparin contamination and issues related to raw materials and controls. Springer International Publishing, New York: pp.191-206.
4. Batra, S., Sahi, N., Mikulcik, K., Shockley, H., Turner, C., Laux, Z., Badwaik, V. D., Conte, E. and Rajalingam, D. (2011). Efficient and inexpensive method for purification of heparin binding proteins. *Journal Chromatography B Analytical Technology Biomedicine Life Sciences*, 879(24): 2437-2442.
5. Volpi, N., Maccari, F., Suwan, J. and Linhardt, R. J. (2012). Electrophoresis for the analysis of heparin purity and quality. *Electrophoresis,* 33(11): 1531-1537.
6. Ertürk, G. and Mattiasson, B. (2017). Molecular imprinting techniques used for the preparation of biosensors. *Sensors (Switzerland)*, 17(2): 1-17.
7. Vasapollo, G., Sole, R. Del, Mergola, L., Lazzoi, M. R., Scardino, A., Scorrano, S. and Mele, G. (2011). Molecularly imprinted polymers: Present and future prospective. *International Journal of Molecular Sciences,* 12(9): 5908-5945.
8. Odabaşi, M., Say, R. and Denizli, A. (2007). Molecular imprinted particles for lysozyme purification. *Materials Science and Engineering C,* 27(1): 90-99.
9. Shafqat, S. R., Bhawani, S. A., Bakhtiar, S. and Ibrahim, M. N. M. (2020). Synthesis of molecularly imprinted polymer for removal of Congo red. *BMC Chemistry,* 14(1): 1-15.
10. Zhao, X., Pei, W., Guo, R. and Li, X. (2020). Selective adsorption and purification of the acteoside in cistanche tubulosa by molecularly imprinted polymers. *Frontiers in Chemistry,* 7(January): 1-13.
11. Zhang, C., Wang, Y., Zhou, Y., Guo, J. and Liu, Y. (2014). Silica-based surface molecular imprinting for recognition and separation of lysozymes. *Analytical Methods,* 6(21): 8584-8591.
12. Dong, Z., Tan, J., Pinelo, M., Zhang, H., Wan, Y. and Luo, J. (2022). Engineering mussel-inspired coating on membranes for green enzyme immobilization and hyperstable reuse. *Industrial & Engineering Chemistry Research,* 61(15): 5042-5053.
13. Chen, L., Wang, X., Lu, W., Wu, X. and Li, J. (2016). Molecular imprinting: Perspectives and applications. *Chemistry Society Review,* 45(8): 2137-2211.
14. Esposito, S. (2019). Traditional sol-gel chemistry as a powerful tool for the preparation of supported metal and metal oxide catalysts. *Material (Basel),* 12(4): 1-25.
15. Yang, K., Li, S., Liu, L., Chen, Y., Zhou, W., Pei, J., Liang, Z., Zhang, L. and Zhang, Y. (2019). Epitope imprinting technology: Progress, applications, and perspectives toward artificial antibodies. *Advanced Materials,* 31(50): 1902048.
16. Budiman, H., Sri H. K. F. and Setiawan, A. H. (2009). Preparation of silica modified with 2-mercaptoimidazole and its sorption properties of chromium(III). *E-Journal of Chemistry,* 6(1): 141-150.
17. Shi, L., Liang, L., Wang, F., Ma, J. and Sun, J. (2014). Polycondensation of guanidine hydrochloride into a graphitic carbon nitride semiconductor with a large surface area as a visible light photocatalyst. *Catalysis Science and Technology,* 4(9): 3235-3243.
18. Eskandarloo, H., Arshadi, M., Enayati, M. and Abbaspourrad, A. (2018). Highly efficient recovery of heparin using a green and low-cost quaternary ammonium functionalized halloysite nanotube. *ACS Sustainable Chemistry and Engineering,* 6(11): 15349-15360.
19. Wang, L., Zhi, K., Zhang, Y., Liu, Y., Zhang, L., Yasin, A. and Lin, Q. (2019). Molecularly imprinted polymers for gossypol via sol-gel, bulk, and surface layer imprinting-A comparative study. *Polymers (Basel),* 11(4):1-18.
20. Zhi, K., Wang, L., Zhang, Y., Jiang, Y., Zhang, L. and Yasin, A. (2018). Influence of size and shape of silica supports on the sol-gel surface molecularly imprinted polymers for selective adsorption of gossypol. *Materials,* 11(5): 1-16.
21. Gupta, N., Singh, R. S., Shah, K., Prasad, R. and Singh, M. (2018). Epitope imprinting of iron binding protein of Neisseria meningitidis bacteria through multiple monomers imprinting approach. *Journal of Molecular Recognition,* 31(7): 1-9.

22. Yoshimi, Y., Oino, D., Ohira, H., Muguruma, H., Moczko, E. and Piletsky, S. A. (2019). Size of heparin-imprinted nanoparticles reflects the matched interactions with the target molecule. *Sensors (Switzerland),* 19(10): 1-11.
23. Zhu, M., Lerum, M. Z., & Chen, W. (2012). How to prepare reproducible, homogeneous, and hydrolytically stable aminosilane-derived layers on silica. *Langmuir,* 28(1): 416-423.
24. Baydemir, G., & Denizli, A. (2015). Heparin removal from human plasma using molecular imprinted cryogels. Artificial Cells, Nanomedicine and Biotechnology, 43(6): 403-412.
25. Öter, Ç. and Zorer, Ö. S. (2021). Molecularly imprinted polymer synthesis and selective solid phase extraction applications for the detection of ziram, a dithiocarbamate fungicide. *Chemical Engineering Journal Advances*, 7(4): 100118.
26. Dai, C., Zhang, J., Zhang, Y., Zhou, X. and Liu, S. (2013). Application of molecularly imprinted polymers to selective removal of clofibric acid from water. *PloS One,* 8(10): 78167.

Malaysian Journal of Analytical Sciences (MJAS)
Published by Malaysian Analytical Sciences Society

RECOVERED PALLADIUM COMPLEXES AS A POTENTIAL HOMOGENEOUS CATALYST FOR C-H FUNCTIONALIZATION AND ANTIBACTERIAL AGENT

(Kompleks Palladium Dipulihkan sebagai Pemangkin Homogen untuk Fungsi C-H dan Ejen Antibakteria)

Nur Anis Nabilah Mohd Fuzi[1], Siti Khadijah Rahmat[1], Muhammad Hazim Abdul Aziz[1], Mohammad Noor Jalil[1], Shamsul Bahrin Gulam Ali[2*], and Khairil Anuar Jantan[1*]

[1]*School of Chemistry and Environment,*
Faculty of Applied Sciences
Universiti Teknologi MARA,
40450 Shah Alam, Selangor, Malaysia
[2]*Faculty of Health Sciences, Bertam Campus*
Universiti Teknologi MARA,
13200 Kepala Batas, Penang, Malaysia

[*]*Corresponding author: sbahrin@uitm.edu.my & khairil0323@uitm.edu.my*

Received: 24 August 2022; Accepted: 9 December 2022; Published: 19 April 2023

Abstract

The present study describes the utilization of simple and commercially available iodine and tetraphenylphosphonium salt as leaching agents to recover palladium (Pd) from waste. This study employed a model reaction assay that utilized Pd(0) metal powder to stimulate palladium leaching from spent automotive three-way catalyst (TWC). The palladium complexes, $(Ph_4P)_2[Pd_2I_6]$, obtained were characterized with Fourier-transform infrared (FT-IR), ultraviolet-visible (UV-Vis) spectroscopy, nuclear magnetic resonances (NMR), thermogravimetric analysis (TGA), and elemental analysis. The recovered Pd complexes demonstrated excellent catalytic activity towards the methoxylation of benzo[*h*]quinoline. Furthermore, a lower to moderate product yield was recorded for the ethoxy- and isopropoxylation of benzo[*h*]quinoline. The C-H functionalization of 8-methylquinoline catalyzed by the obtained palladium complexes also documented a moderate product yield (< 65%) after 6 hours of reaction. The antibacterial activities of the $(Ph_4P)_2[Pd_2I_6]$ were evaluated through a disk diffusion test, minimum inhibitory concentration (MIC), and minimum bactericidal concentration (MBC) assays. Among the gram-positive and -negative bacteria evaluated, *Klebsiella pneumoniae* exhibited the highest sensitivity to the synthesized $(Ph_4P)_2[Pd_2I_6]$ at all concentrations. The MIC concentrations for all assessed bacteria ranged from 0.156 to 1.25 mg/mL. Moreover, bacterial growth was detected in all MBC plates, thus indicating that the $(Ph_4P)_2[Pd_2I_6]$ possessed a bacteriostatic effect and not a killing attribute.

Keywords: recovered palladium, palladium catalyst, antibacterial activity

Abstrak

Kajian ini menghuraikan mengenai penggunaan iodin dan garam tetrafenilphosphonium yang mudah dan boleh didapati secara

komersial sebagai agen larut lesap dalam proses pemulihan paladium (Pd) daripada sisa terbuang. Kajian ini melaksanakan ujian berdasarkan model tindak balas yang menggunakan serbuk logam Pd(0) untuk merangsang proses larut lesap Pd dari pemangkin tiga hala automotif (TWC) terpakai. Spesies molekul kompleks Pd dipulihkan, $(Ph_4P)_2[Pd_2I_6]$, yang diperoleh dicirikan melalui Fourier-transform inframerah (FT-IR), spektroskopi ultra ungu-nampak (UV-Vis), resonans magnet nuklear (NMR), analisis termogravimetrik (TGA) dan analisis unsur. Kompleks Pd dipulihkan yang diperoleh tersebut menunjukkan aktiviti pemangkin yang sangat baik bagi ke arah metoksilasi benzo[*h*]kuinolin. Selain itu, hasil produk yang sederhana telah direkodkan bagi etoksi dan isopropoksilasi benzo[*h*]kuinolin. Kefungsian C-H sebagai pemangkinan 8-metilquinolin oleh kompleks Pd dipulihkan juga merekodkan hasil produk yang sederhana (< 65%) selepas tindak balas selama 6 jam. Aktiviti antibakteria $(Ph_4P)_2[Pd_2I_6]$ tersebut dinilai melalui ujian resapan cakera, kepekatan perencatan minimum (MIC), dan ujian kepekatan bakteria minimum (MBC). Antara kesemua bakteria gram-positif dan -negatif yang diuji, *Klebsiella pneumoniae* menunjukkan sensitiviti tertinggi kepada $(Ph_4P)_2[Pd_2I_6]$ pada semua kepekatan. Kepekatan MIC untuk semua bakteria yang diuji direkod dalam julat 0.156 hingga 1.25 mg/ml. Tambahan pula, pertumbuhan bakteria yang dikesan dalam semua plat MBC menunjukkan bahawa $(Ph_4P)_2[Pd_2I_6]$ mempunyai kesan bakteriostatik dan tidak membunuh.

Kata kunci: paladium dipulihkan, mangkin paladium, aktiviti antibakteria

Introduction

Palladium (Pd) is a limited and significant raw material due to its scarcity and economic value [1]. Consequently, the element possesses a considerable market demand, dominated by automotive catalytic converters and electronic equipment, which account for 90% of its global production [2]. Nonetheless, Pd is primarily mined in geopolitically-unstable countries, such as Russia and South Africa, which could affect supply and pricing [3]. Furthermore, Pd mining is an energy-intensive process that employs chemical reagents [4] that are exceptionally detrimental to the environment, including published harmful effects on water and air quality, biodiversity, and housing displacement [5-7]. Consequently, a practical and realistic approach is necessary for sustainable Pd utilization.

The Pd-containing waste from three-way catalytic converters (TWC) [8] and electric and electronic equipment (EEE) [9] has accumulated worldwide. The substance is a significant but underutilized source of potentially recoverable raw material. The most common techniques for recovering Pd from waste include pyro- and hydrometallurgical methods, where both are disadvantageous. The pyrometallurgical method consumes high energy and lacks Pd selectivity [10]. The more selective hydrometallurgical techniques rely on harmful reagents, such as potent oxidizing agents, including aqua regia and cyanide to leach Pd from spent TWC and EEE under mild conditions [11].

Available energy-efficient and sustainable recovery techniques produce molecular recovery products. Serpe and colleagues [12] demonstrated an excellent method of utilizing organic compounds, such as N,N'-dimethylperhydrodiazepine-2,3-dithione diiodine adduct ($Me_2dazdt{\cdot}2I_2$), to recover Pd from model spent catalytic converter under mild conditions. Nevertheless, the recovered Pd complexes $[Pd(Me_2dazdt)_2]I_6$ require an energy-intensive step that eliminates its ligands to procure metallic Pd as the end product [12].

An intriguing application was proposed by Wilton-Ely *et al*. to utilize the recovered Pd complex directly as a homogeneous catalyst in the C-H functionalization of benzo[*h*]quinoline and 8-methylquinoline [13]. Surprisingly, the $[Pd(Me_2dazdt)_2]^{2+}$ was catalytically active toward the proposed reaction, thus outperforming the conventionally mined $Pd(OAc)_2$ [14]. Nonetheless, the relatively expensive starting materials and Lawesson's reagent employed to install sulfur groups into the ligand designs diminished the economic and environmental benefits of the recovery process. Accordingly, a simpler, cheaper, and commercially available approach was sought to address the constraint. The impressive ability of organic triiodides, tetraphenylphosphonium $[Ph_4P]^+$, in the presence of iodine in the selective dissolution of Pd from spent TWCs was demonstrated by [15] (see Scheme 1).

The present study directly utilized the recovered Pd complexes, $(Ph_4P)_2[Pd_2I_6]$, as a homogeneous catalyst in the C-H functionalization of benzo[*h*]quinoline and

8-methylquinoline in ambient air, which required nitrogen as the only directing atom. The procedures were based on the work by [13]. The Pd loading, temperature, and time were varied to optimize the catalytic reaction. The lower temperature approach was focused on enhancing the green credential of the method. The results were compared to previous findings in studies utilizing different Pd catalysts obtained from commercial or secondary sources.

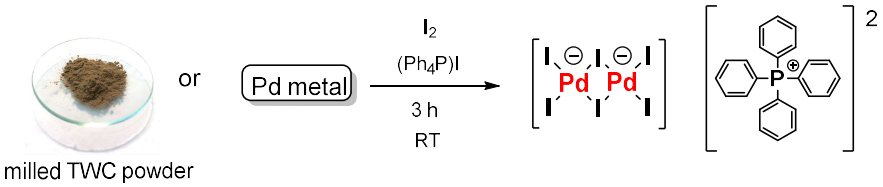
The recent emergence of antimicrobial resistance has become a critical issue worldwide [16]. Consequently, the demand to develop novel and efficient antimicrobial agents has also increased. Numerous studies have attempted to elucidate Pd compound potentials in combating human pathogens-caused illnesses [17–21]. Nonetheless, only very few studies reported the possible effects of recovered Pd against pathogenic bacteria. Thus, the present study explored the antibacterial attributes of the recovered $(Ph_4P)_2[Pd_2I_6]$ against common gram-positive and -negative bacteria.

Materials and Methods

All chemicals and solvents employed in the present study were purchased and utilized without further purification unless otherwise stated.

Synthesizing the $(Ph_4P)_2[Pd_2I_6]$ complexes

Serpe and co-workers [15] demonstrated the impressive ability of tetraphenylphosphonium $[Ph_4P]^+$ in the selective dissolution of Pd from spent TWCs (see Scheme 1). The Pd metal powder was employed as a proxy for the milled TWC mixed-metal powder to assess the Pd complex generated by the system. Tetraphenylphosphonium iodide (0.144 g, 0.31 mmol) was treated with iodine in acetone (30 mL) before adding Pd metal powder (33.1 mg, 0.31 mmol). The reaction mixture was stirred at room temperature for 3 hours until an abundant black crystalline product was precipitated. Subsequently, product re-crystallization was conducted by slowly diffusing diethyl ether into the concentrated acetone solution of the reaction mixture. The yield recorded in this study was 286 g (90%) [15].



Scheme 1. The synthesis of recovered Pd complexes [15]

Characterization of $(Ph_4P)_2[Pd_2I_6]$ complexes

The Pd complexes obtained in the current study were characterized via ^1H and ^{13}C nuclear magnetic resonance (NMR) with a JEOL JNM-ECZS 400 MHz spectrometer. A Varian Bruker AV300 spectrometer was also employed in attributing the ^1H NMR signals of the C-H functionalization catalysis reaction at 25 °C with deuterated chloroform ($CDCl_3$). Moreover, infra-red data were obtained with a Nicolet 6700 ATR spectrometer at 16 scans of 600–4000 cm^{-1} on solid samples. The specimens were also subjected to an ultraviolet-visible (UV-VIS) spectrometer (Perkin Elmer Lambda 25) to obtain the transmission and absorption spectra of the complexes within the 300–800 nm wavelength. Furthermore, elemental analyses (EA) were performed with CHNS/O Analyzer 2400 Perkin Elmer Series II, while thermogravimetric analysis (TGA) was conducted in a nitrogen atmosphere with a Mettler Toledo TGA/DSC 1LF/UMX.

The general C-H functionalization synthetic procedure

The C-H functionalization reaction in this study was performed with a Radley's Carousel 12 Reaction Station. The adaptable apparatus transforms a normal stirring hotplate into 12 parallel synthesizers capable of conducting parallel chemical reactions in an inert or ambient environment. First, individual reaction bottles (24 mm × 150 mm) were filled with alcohols, sacrificial oxidants, Pd catalysts, and substrates. The reaction

bottles were then installed on the Carousel 12 Reaction Station before the mixture was heated and stirred for 2, 4, and 6 hours. The operational temperature range of the heated base was 0–180°C at ±0.5 °C temperature precision. A single spinning magnetic field was also applied to ensure homogeneous stirring in each reaction bottle.



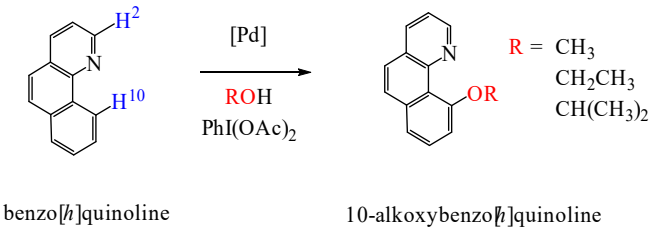
Figure 1. Radley's Carousel 12 Reaction Station

Synthesizing 10-alkoxybenzo[*h*]quinoline

Benzo[*h*]quinoline (50.0 mg, 0.28 mmol), (diacetoxyiodo)benzene (180.4 mg, 0.56 mmol), and $(Ph_4P)_2[Pd_2I_6]$ (between 1–2 mol% loads) were mixed in 2.5 mL alcohol [methanol (MeOH), ethanol (EtOH), or isopropanol and glacial acetic acid mixture] in a reaction bottle. Subsequently, individual reaction bottles were heated at 50 and 100 °C and stirred for 2, 4, and 6 hours. All solvent was then removed with a rotary evaporator, followed by the dissolution of the residue in a deuterated $CDCl_3$ for ^{1}H NMR analysis (see Scheme 2).

The ^{1}H NMR spectroscopic yield analysis was conducted by comparing the integration of the H_2 or H_{10} protons of benzo[*h*]quinoline at 9.30 and 9.05 ppm, respectively, to the peak of 10-alkoxybenzo[*h*]quinoline at 9.15 ppm. Another peak corresponding to the alkoxy group in the product was subjected to further evaluation at 4.19 (methoxy, CH_3; singlet), 1.63 and 4.45 (ethoxy, CH_2CH_3; triplet and quartet), and 1.54 and 4.76 [isopropoxy, $CH(CH_3)_2$; doublet and septet] ppm. All reactions were conducted a minimum of three times, and the yields were measured with ^{1}H NMR based on three independent experiments.

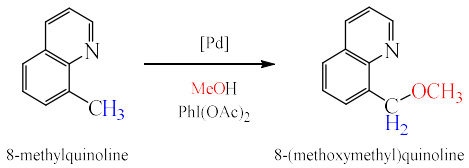
Benzo[*h*]quinoline (150.0 mg, 0.84 mmol), (diacetoxyiodo)benzene (541.2 mg, 1.68 mmol), and $(Ph_4P)_2[Pd_2I_6]$ (2 mol%) were treated in MeOH (7.5 mL) and heated at 50 °C for 2 hours for the isolated yield reaction. The products were then purified in a flash column (3:2 v/v ethyl acetate-to-n-hexane eluent) to procure 10-methoxybenzo[*h*]quinoline.



Scheme 2. The benchmark reaction for oxidative C-H functionalization

The synthesis of 8-(methoxymethyl)quinoline

A total of 42.5 mg of 8-methylquinoline (0.297 mmol), 103.3 mg of (diacetoxyiodo)benzene (0.321 mmol), and between 1–2 mol% loadings of $(Ph_4P)_2[Pd_2I_6)$ were mixed in 2.5 mL MeOH in reaction bottles. The individual reaction bottles were then heated at 50 °C and stirred for 2, 4, and 6 hours. Subsequently, the solvent was removed under reduced pressure, followed by the dissolution of the residue obtained in a deuterated $CDCl_3$ for ^{1}H NMR analysis. The product yield was determined by comparing the methyl integration (2.82 ppm) of 8-methylquinoline with the methylene (5.19 ppm) and methoxy group (3.57 ppm) in the 8-(methoxymethyl)quinoline resonances (see Scheme 3).



Scheme 3. The C-H functionalization of 8-methyl quinolone

Bacterial culture

Stock cultures of gram-negative, *Escherichia coli* (ATCC25922), *Salmonella typhimurium* (ATCC14028), *Klebsiella pneumoniae* (ATCC700603), and *Klebsiella aeruginosa* (ATCC13048), and gram-positive bacteria, *Bacillus cereus* (ATCC11778) and *Bacillus subtilis* (ATCC13124), were obtained from the Faculty of Applied Sciences, Universiti Teknologi MARA (UiTM), Shah Alam. The cultures were maintained on nutrient agar media at 37 ℃. Colony morphology observation and gram staining were performed in the present study to confirm the working strains.

Antimicrobial study: Disk diffusion method

The antibacterial activities of varying concentrations of $(Ph_4P)_2[Pd_2I_6]$ complex were screened against common gram-positive and -negative bacteria. Subsequently, the antibacterial activities of the samples were determined with the Kirby-Bauer disk diffusion method on a Muller-Hinton Agar (MHA) medium. For working cultures, 18–20 hours broth culture of each bacterium inoculum was compared with 0.5 McFarland standard (1×10^8 CFU/mL) and adjusted visually to obtain working cultures. A sterile cotton swab was dipped into the McFarland standardized inoculum, seeded and covered the MHA plate with the evenly swabbed inoculum. Next, sterile disks were placed onto each plate.

Before analysis, the $(Ph_4P)_2[Pd_2I_6]$ was dissolved in dichloromethane (DCM) into varying concentrations (1, 2, 3 and 4 mg/mL). An amount of 20 μL of each $(Ph_4P)_2[Pd_2I_6)$ concentration was pipetted onto the disks. Gentamicin (CN) (10 µg) and sterile distilled water were utilized as positive and negative controls, respectively. All of the plates were then incubated for 24 hours at 37 ℃. Following incubation, the inhibitory zone (in mm) was measured and recorded. All tests were performed in triplicate per condition.

The MIC and MBC

MIC was determined using Mueller–Hinton broth (MHB) macrodilution assays. Briefly, bacteria inoculum was prepared and adjusted to McFarland standard as before. Next, 1 mL of adjusted inoculum was transferred into 8 sterile test tubes. 1 mL of $(Ph_4P)_2[Pd_2I_6]$ complex dissolved in DCM was then added into the first tube, and 2-fold serial dilutions were performed to give the final concentrations of 10, 5, 2.5, 1.25, 0.625, 0.313, 0.156 and 0.078 mg/mL. Two additional tubes were prepared as positive growth control (MHB + bacteria) and negative control (MHB only). All tubes (in triplicate per condition) were incubated aerobically for 24 hours at 37 ℃, and MIC values were determined as the lowest concentration of the test compound that prevents microbial growth. For MBC, the MIC tubes that showed no visible apparent growth were subcultured onto the MHA plate and incubated for 24 hours at 37 ℃. No evidence of bacterial growth following incubation were confirmed as MBC values.

Statistical analysis

For antimicrobial analysis, data were statistically analyzed using GraphPrism 8.0. Results for the inhibitory zone were expressed as means ± standard error of the means (SEM). The results shown are the mean of three tested cultures plus SEM. Data were further analyzed with a two-way Analysis of Variance (ANOVA) followed by a Tukey's multiple comparison post-test. In all tests, p-values <0.05 and asterisks indicate statistically significant differences.

Results and Discussion

Transformation of recovered Pd complex from the recovery process

Scheme 1 illustrates selective Pd leaching from waste utilizing an organic triiodide salt in an organic solution

at room temperature. The peculiar features of the iodide/iodine mixture in the tetraphenylphosphonium iodide [(PPh_4)I] system could dissolve and quantitatively recover Pd from spent automotive TWC waste, generating a molecular $(Ph_4P)_2[Pd_2I_6]$ species [15]. Nonetheless, the procedure necessitates conventional thermal treatment to procure metallic Pd as the end product, thus making the technique less practical for recycling Pd. Consequently, the $(Ph_4P)_2[Pd_2I_6]$ complex obtained directly as a homogeneous catalyst for C-H activation and antibacterial agent against common pathogenic bacteria was suggested to solve the issue.

This study employed Pd metal powder as a proxy for milled TWC metal powder mix to generate the recovered Pd complex $(Ph_4P)_2[Pd_2I_6]$. Equimolar Pd powder with (PPh_4)I and iodine was dissolved in an acetone solution. The reaction mixture was stirred at room temperature for 3 hours. The resultant abundant black crystals formed were collected. The products were then re-crystallized by slowly diffusing diethyl ether (Et_2O) in a concentrated $(Ph_4P)_2[Pd_2I_6]$ acetone solution. A good yield of 90% was recorded. The infra-red and UV-Vis analysis of the $(Ph_4P)_2[Pd_2I_6]$ obtained in this study agreed well with the data reported by [15]. The complex was further characterized with NMR spectroscopy and elemental analysis to confirm the overall molecular formula.

The FT-IR analysis of the $(Ph_4P)_2[Pd_2I_6]$ chemical composition

The vibration frequencies of the $[PPh_4]^+$ counter ions remained virtually unchanged upon the Pd complex formation (see Figure 2). Furthermore, typical C-H and C-P stretching in aromatic phenyl absorptions were observed at 3049 and 1105 cm^{-1}, respectively. The aromatic C-H in-plane bending was also observed around the 1433 cm^{-1} region. The C-H bending for the monosubstituted absorption band was obscured within the 751–682 cm^{-1} band. The C=C and C-C stretching feature retentions in the infrared spectrum were observed at 1584 and 1479–1433 cm^{-1}, respectively [22]. The Pd-I stretching frequencies were not detected due to the absorption band occurring at a lower frequency region, while the other stretches agreed with a previous report [15].

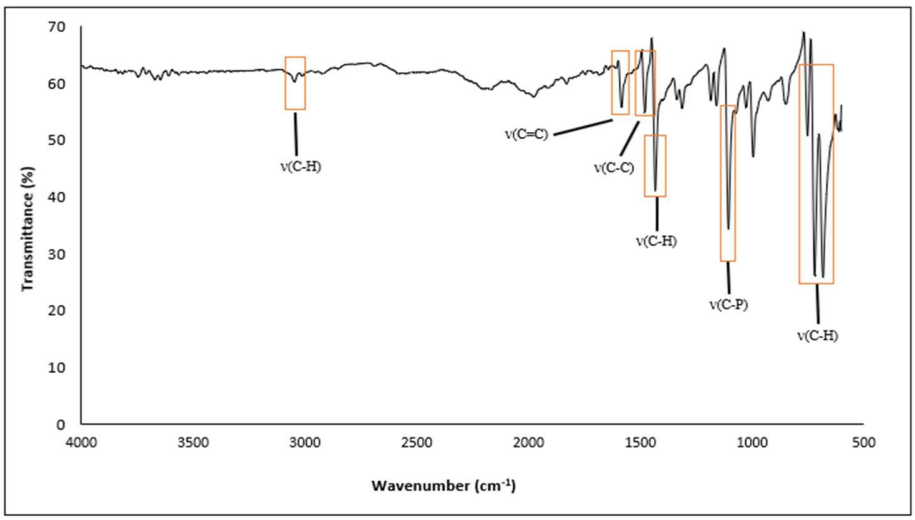


Figure 2. The FT-IR spectra of the recovered $(Ph_4P)_2[Pd_2I_6]$ complex

The $(Ph_4P)_2[Pd_2I_6]$ complexation analysis with UV-Vis spectra

Figure 3 illustrates the UV-Vis spectra of the Pd complexes procured in the current study. The presence of dimeric Pd complex, $[Pd_2I_6]^{2-}$, was confirmed by the absorption at 340 nm, while the peaks recorded at 426 and 524 nm supported the report by [15]. The absorption of PPh_4^+ was documented at approximately 260 nm, but

absorptions below 300 nm were indistinct and could not be appropriately determined [23].

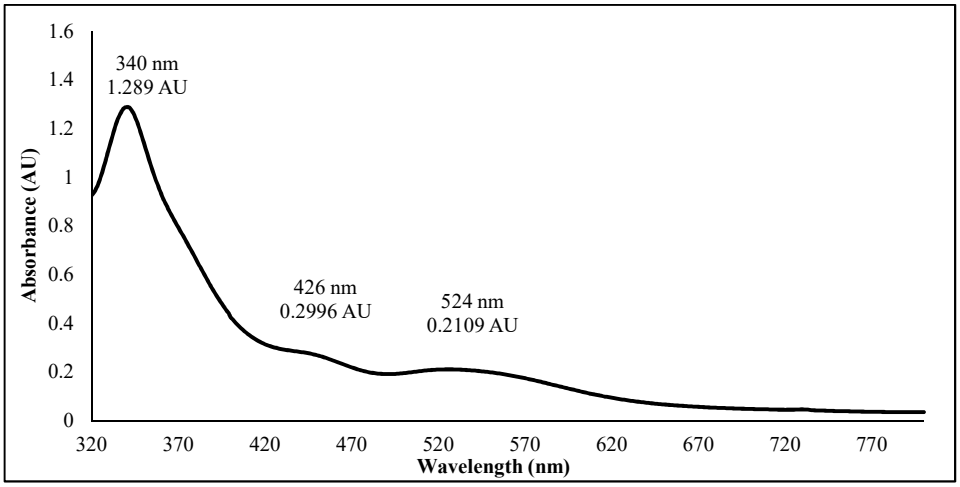


Figure 3. The UV-Vis spectra of the recovered $(Ph_4P)_2[Pd_2I_6]$ complex

The $(Ph_4P)_2[Pd_2I_6]$ molecular structure analysis via NMR spectroscopy

The NMR spectra of the $(Ph_4P)_2[Pd_2I_6]$ complex procured in this study were recorded in deuterated $CDCl_3$. The ^1H NMR analysis revealed diagnostic features of multiplet resonances at aromatic regions (7.66–7.95 ppm), which were attributed to the aromatic protons of the $[PPh_4]^+$ counter-ion phenyl groups. The carbon nuclei of $[PPh_4]^+$ counter-ions were almost unaltered compared to the precursors in the ^{13}C NMR spectrum. The ^1H NMR was set to 400 MHz, δ 7.95–7.66 ppm, while the ^{13}C NMR was at δ 117.0, 117.1, 131.0, 131.2, 134.7, 134.8, and 135.8 ppm.

The $(Ph_4P)_2[Pd_2I_6]$ organic matter composition analysis with CHNS/O analyzer

The composition of organic matter in the Pd complex [$C_{48}H_{40}I_6P_2Pd_2$ (Mw = 1653.06 g/mol)] obtained in the present study was determined with a CHNS/O analyzer. The results revealed experimental and calculated carbon and hydrogen percentages agreement, thus confirming the organic matter composition in the complex (see Table 1).

Table 1. Elemental analysis of the $(Ph_4P)_2[Pd_2I_6]$ complex

Element	Atomic Weight (g/mol)	Calculated Weight (%)	Experimental Weight (%)
C	12.011	$\frac{12.011 \times 48 \times 100}{1653.06} = 34.87$	34.9
H	1.008	$\frac{1.008 \times 40 \times 100}{1653.06} = 2.44$	2.4

Thermal stability analysis of the $(Ph_4P)_2[Pd_2I_6]$ with TGA

The thermal stability of the $(Ph_4P)_2[Pd_2I_6]$ complex from 30 to 750 °C was assessed at a 10 °C per minute heating rate (see Figure 4). The TGA isotherm exhibited slow mass declines within 30–300 °C before decreasing

significantly from 300 to 380 °C, indicating a 63% weight loss during the first stage of decomposition. The second stage of thermal decomposition was documented within 380–460 °C with a weight loss of approximately 17%. The loss in mass was relatively stable throughout the analysis. The stability of the complexes at high temperatures allowed the catalytic C-H functionalization reaction to be conducted at 100 °C.

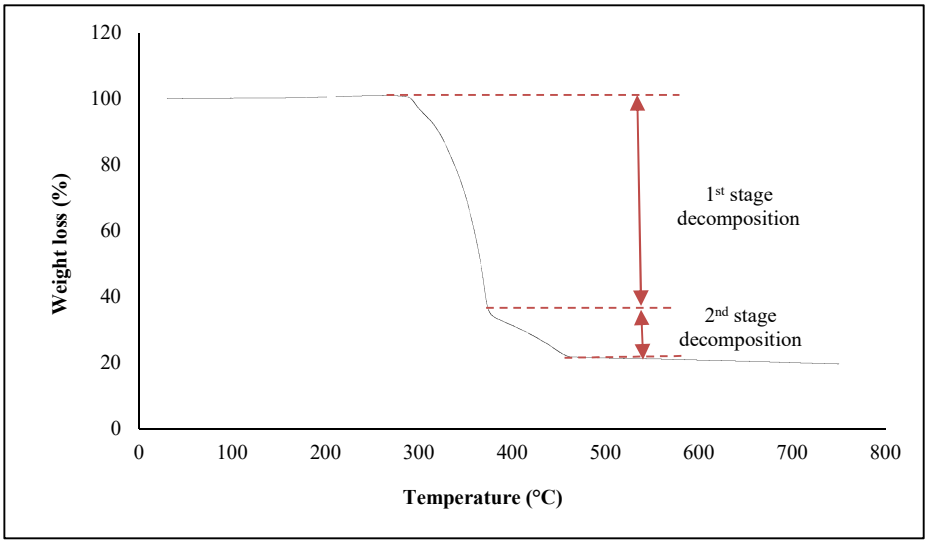


Figure 4. The TGA isotherm of the $(Ph_4P)_2[Pd_2I_6]$ complex

The catalytic activity of the $(Ph_4P)_2[Pd_2I_6]$ complex towards methoxylation of benzo[*h*]quinoline

The first comprehensive studies of Pd (II) complexes catalyzed C-H functionalization were published in the 2000s. A successful methoxylation of benzo[*h*]quinoline (see Scheme 2) in the presence of Pd acetate (1.1 mol%), the catalyst, and (diacetoxyiodo)benzene, the sacrificial oxidant, in MeOH was reported by Dick et al. [14]. Suitable high-pressure vials heated in an aluminium heating block to 100 °C were utilized in the study to yield a 95% product after 22 hours (see Table 2). In a similar manner, an 87% yield of 10-methoxybenzo[*h*]quinoline by employing recovered Pd complex, $[Pd(Me_2dazdt)_2]I_6$, (1 mol%) in 2 hours reaction time at 100°C was documented by Jantan et al. [13].

The present study slightly modified the procedure and utilized a Radley's Carousel 12 Reaction Station to investigate the catalytic activity of the recovered $(Ph_4P)_2[Pd_2I_6]$ complex towards methoxylation of benzo[*h*]quinoline (1 mol%, 2 hours, 100 °C). A quantitative product yield (90%) was obtained in 2 hours, which indicated that the reaction was more facile than the conditions documented in previous literature. The findings emphasized that the catalytic mechanism involved an oxidative addition step occured and resulted in the cyclopalladation of Pd (II) and oxidized Pd(II) to Pd(IV) before being followed by reductive elimination [14].

Table 2. Summary of catalytic activity various catalysts toward methoxylation of benzo[*h*]quinoline

Solvent	Temperature (°C)	Catalyst	Catalyst Loading (mol%)	Time (h)	NMR yield (%)
MeOH	100	$Pd(OAc)_2$	1.1	22	95
		$[Pd(Me_2dazdt)_2]I_6$	1.0	2	87
		$(Ph_4P)_2[Pd_2I_6]$	1.0	2	90

Heating MeOH (b.p. 65 °C) at 100 °C in a confined space, such as vials, could lead to potential dangers related to build-up pressure. Furthermore, energy consumption reduction from high-temperature heating is preferable. Consequently, the study decreased the reaction temperature (T) to 50 °C without changing other parameters to lower the catalytic reaction energy usage. Resultantly, a higher product yield (89%) was obtained in 2 hours of reaction time with the $(Ph_4P)_2[Pd_2I_6]$ (1 mol%) employed as a catalyst (see Figure 5). Elevating the reaction time to 6 hours also resulted in a slightly enhanced product percentage procurement (93%–96%). Moreover, an increased Pd loading by one-fold recorded a quantitative product yield of > 90%. Overall, the approach employed in this study involved milder and safer conditions and shorter reaction times.

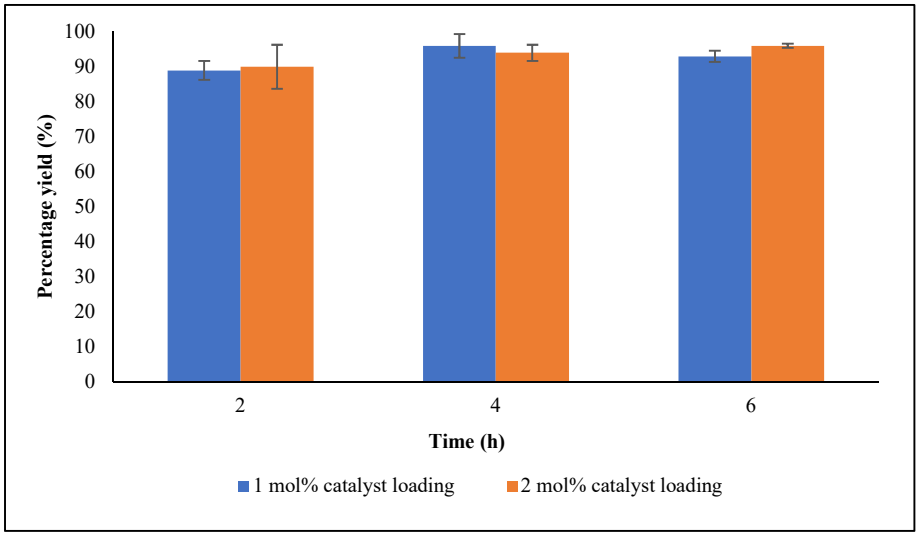


Figure 5. Methoxylation of benzo[*h*]quinoline with the $(Ph_4P)_2[Pd_2I_6]$ complex as a catalyst. Note: Solvent = MeOH, oxidant = $PhI(OAc)_2$, T = 50 °C, and t = 2, 4, and 6 hours

The successful formation of the product was further confirmed by analyzing the isolated yields of methoxylation of benzo[*h*]quinoline. The assessment was set to 2 hours of reaction time and 2 mol% of catalyst loading at 50 °C. The evaluation also validated the ^{1}H NMR integration yield. A brown oil was collected and purified in a flash column utilizing a 3:2 v/v ethyl acetate-to-hexane eluent. The pale-yellow solid isolated (154 mg, 88%) also agreed with the conversion determined in the ^{1}H NMR (90%).

Other alkoxylation of benzo[*h*]quinoline

The unexpectedly higher 10-methoxybenzo[*h*]quinoline procured at 50 °C resulted in the extension of the scope of this study into other alkoxylation of benzo[*h*]quinoline (see Scheme 2). In the assessment, the time and Pd loading were varied while the temperature was maintained at 50 °C. Furthermore, the alcohol solvent employed in the transformation was changed to ethanol and an isopropanol and acetic acid mixture, which yielded 10-ethoxybenzo[*h*]quinoline and 10-isopropoxybenzo[*h*]quinoline, respectively.

Figure 6 illustrates the experimental data of ethoxylation of benzo[*h*]quinoline at 50 °C. The 1 mol% catalyst loading produced a lower product yield (< 40%) even after 6 hours of reaction, hence implying that a temperature decrease reduces the chemical reaction rate. Nonetheless, elevating the catalyst loading to 2 mol% improved the reaction rate, which resulted in 79% yields of the desired products after 6 hours of reaction.

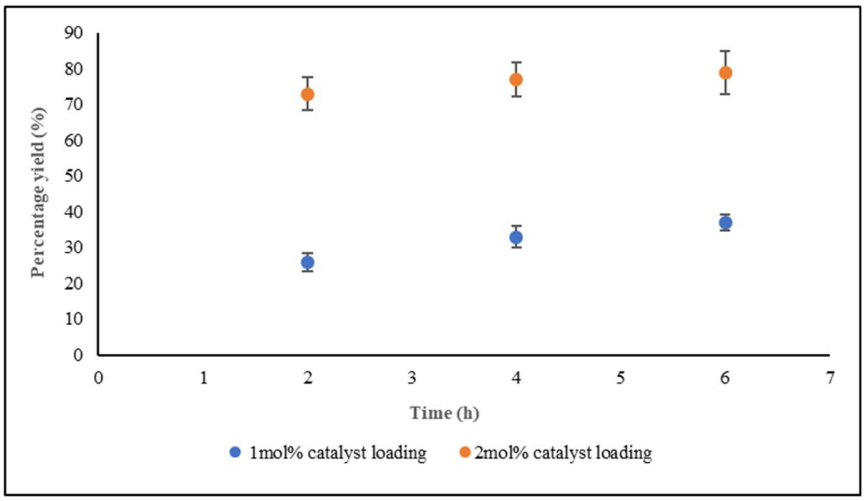


Figure 6. Ethoxylation of benzo[*h*]quinoline with the $(Ph_4P)_2[Pd_2I_6]$ complex as a catalyst. Note: Solvent = EtOH, oxidant = $PhI(OAc)_2$, T = 50 °C, and t = 2, 4, and 6 hours

A similar observation was recorded in the catalytic 10-isopropoxy benzo[*h*]quinoline reaction. Figure 7 indicates that a lower product yield (< 27%) was obtained when 1 mol% of catalyst loading was employed for reaction times between 2-6 hours at 50 °C. The results suggested that only a small proportion of benzo[*h*]quinoline molecules possess enough activation energy to react and generate a 10-isopropoxy benzo[*h*]quinoline at lower temperatures.

The increment of the catalyst loading to 2 mol% improved the reaction, which doubled the product yield. Nevertheless, a moderate 10-isopropoxybenzo[*h*]quinoline production (47%) was obtained compared to the 10-ethoxybenzo[*h*]quinoline (79%) derived after 6 hours when 2 mol% catalyst loading was employed at 50 °C. The results proved that the $(Ph_4P)_2[Pd_2I_6]$ was less catalytically active when the more sterically demanding reagent, the isopropanol and acetic acid mixture, was employed.

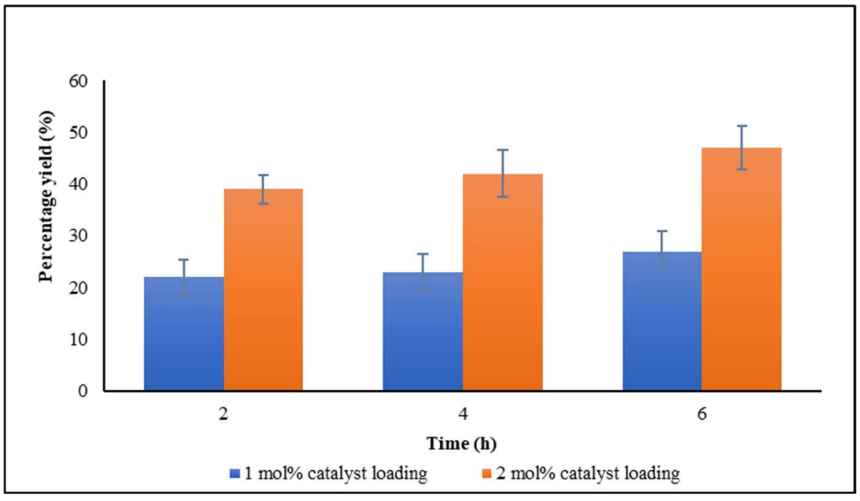


Figure 7. Isopropoxylation of benzo[*h*]quinoline utilizing the $(Ph_4P)_2[Pd_2I_6]$ complex as a catalyst. Note: Solvent = mixture of isopropanol and acetic acid, oxidant = $PhI(OAc)_2$, T = 50 °C, and t = 2, 4, and 6 hours

The C-H functionalization of 8-methylquinoline

The present study extended the catalytic alkoxylation of benzo[*h*]quinoline to synthesize 8-(methoxymethyl)quinoline (see Scheme 3). An energy-saving strategy by reducing the reaction temperature was adopted during the present study to continue building greener synthetic pathways and improve the efficiency of the required C-H functionalization. Nevertheless, the reaction of 8-methylquinoline with 1–2 mol% of the recovered $(Ph_4P)_2[Pd_2I_6]$ as the catalyst and $PhI(OAc)_2$ in methanol at 50 °C recorded a moderate yield (< 65%) after 2–6 hours of reaction time (see Figure 8). A possible explanation might be the presence of additional benzylic hydrogen atoms in the substrate, which are inert to deprotonation for directed C-H activation. Consequently, increasing the catalyst load or temperature while maintaining other reaction conditions might be required to lower the activation energy of the reaction for complete conversion.

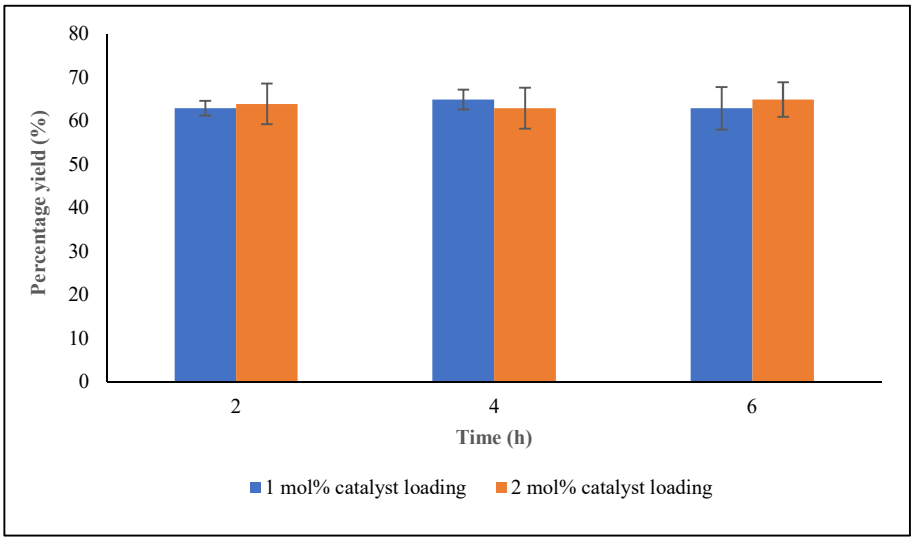


Figure 8. The C-H functionalization of 8-methylquinoline with the $(Ph_4P)_2[Pd_2I_6]$ complex as a catalyst. Note: Solvent = MeOH, oxidant = $PhI(OAc)_2$, T = 50 °C, and t = 2, 4, and 6 hours

Antibacterial activity

The antibacterial inhibition zone diameter means of the recovered $(Ph_4P)_2[Pd_2I_6]$ against six bacterial strains is demonstrated in Figure 9. The organisms evaluated in this study were sensitive towards the compound. Among the bacterial strains, *K. pneumoniae* recorded the highest inhibition zone in all $(Ph_4P)_2[Pd_2I_6]$ concentrations. *B. subtilis*, *S. typhimurium, K. pneumoniae*, and *K. aeruginosa* cultures demonstrated a significant increase in inhibition zone from the lowest to the highest $(Ph_4P)_2[Pd_2I_6]$ concentrations, while *B. cereus* and *E. coli* recorded no notable difference.

The positive control Gentamicin employed in this study exhibited an inhibition range between 21.0-24.8 mm. Previous studies have described palladium nanoparticles as useful antimicrobial agent where more inhibitory toward gram-positive bacteria (*Staphylococcus aureus)* than toward *E. coli* [25]. Palladium (II) complexes were also reported to exhibit remarkable antibacterial activity against *S. aureus* and *E.coli* [20].

Gram-negative bacteria possess lipopolysaccharide (LPS), thin peptidoglycans, and porins proteins with more lipids in their cell walls, which make them less permeable than gram-positive bacteria [26]. Nonetheless, the recovered Pd (II) complexes in this study demonstrated a more significant inhibitory toward gram-negative bacteria. The findings suggested that the complexes could compromise the membrane permeability of the gram-negative bacteria employed. A

significant inhibition improvement in at least one gram-positive bacteria, *B. subtilis*, was also recorded. A previous study supported the current results, in which Pd dichloride ligands ($PdCl_2$BLs) documented the best response against *E. coli, Pseudomonas aeruginosa, S. aureus*, and *B. subtilis* [27].

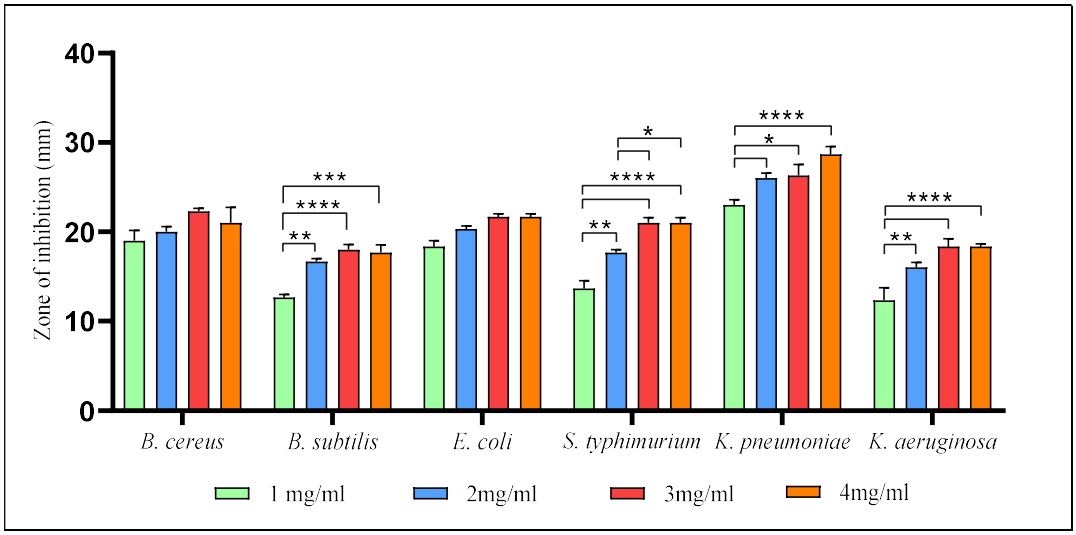


Figure 9. The inhibition zones of the recovered $(Ph_4P)_2[Pd_2I_6]$ against selected bacterial strains. The levels displayed are the mean of three tested cultures ± SEM. The asterisks indicate statistically significant differences analyzed with two-way ANOVA followed by Tukey's multiple comparison post-test

Determination of MIC and MBC

Table 3 summarises the MIC values obtained in the present study. Both *Klebsiella* species were inhibited at 0.625 mg/ml, while *E. coli* and *S. typhimurium* were at 0.156 and 0.313 mg/mL, respectively. The recovered $(Ph_4P)_2[Pd_2I_6]$ also hindered *B. cereus* growth at 0.156 mg/mL. The highest MIC value was recorded by *B. subtilis* at 1.25 mg/mL.

The study findings highlighted the potential of the $(Ph_4P)_2[Pd_2I_6]$ procured to inhibit the growth of bacteria. All MBC plates employed in the present study demonstrated bacterial growth, indicating no bactericidal activity when exposed to the $(Ph_4P)_2[Pd_2I_6]$ complex (see Table 4). Nevertheless, uncertainties remain about the killing properties of the recovered $(Ph_4P)_2[Pd_2I_6]$. Accordingly, further studies are necessary to assess the bactericidal potential of $(Ph_4P)_2[Pd_2I_6]$.

Conclusion

The present study emphasized the utilization of commercially available iodine and tetrabutylammonium iodide to recover Pd metals from TWC waste. The recovered $(Ph_4P)_2[Pd_2I_6]$ complexes were employed directly as a homogeneous catalyst in the C-H functionalization of benzo[*h*]quinoline and 8-methylquinoline. An excellent product yield of 90% was obtained in benzo[*h*]quinoline methoxylation at 100°C. A milder and safer approach adopted at a low-temperature setup (50°C) produced a similar product yield. Conversely, installing the ethoxy- and isopropoxy functional groups into the benzo[*h*]quinoline at 50°C proved challenging. A lower to moderate product yield was recorded due to the solvent stearic effect. Similarly, a reasonable procurement (65%) of 8-(methoxymethyl) quinoline was documented.

In conclusion, the novel method of employing Pd complex as a homogeneous catalyst in C-H functionalization would increase the value of the metal, especially when recovered from TWC waste. Furthermore, the burden on natural reserves as a primary source would also be reduced. This study has also

identified the bacteriostatic potential of the $(Ph_4P)_2[Pd_2I_6]$ complexes. The data provide critical preliminary insights into the role of the metal as an antibacterial agent.

Table 3. The MIC of the recovered $(Ph_4P)_2[Pd_2I_6]$ against selected bacterial strains

Bacteria	**$(Ph_4P)_2[Pd_2I_6]$ concentration (mg/mL)**								
	10	5	2.5	1.25	0.625	0.313	0.156	0.078	Positive control
E. coli	-	-	-	-	-	-	-	+	+
S. typhimurium	-	-	-	-	-	-	+	+	+
K. pneumoniae	-	-	-	-	-	+	+	+	+
K. aeruginosa	-	-	-	-	-	+	+	+	+
B. cereus	-	-	-	-	-	-	-	+	+
B. subtilis	-	-	-	-	+	+	+	+	+

Table 4. The MBC of the $(Ph_4P)_2[Pd_2I_6]$ against selected bacterial strains

Bacteria	**Minimum bactericidal concentration (mg/ml)**								
	10	5	2.5	1.25	0.625	0.313	0.156	0.078	Positive control
E. coli	+	+	+	+	+	+	+	+	+
B. cereus	+	+	+	+	+	+	+	+	+
B. subtilis	+	+	+	+	+	+	+	+	+
S. typhimurium	+	+	+	+	+	+	+	+	+
K. pneumoniae	+	+	+	+	+	+	+	+	+
K. aeruginosa	+	+	+	+	+	+	+	+	+

Note: (+) denotes bacterial growth and (-) killed bacterial growth

Acknowledgement

The authors wish to acknowledge the Ministry of Higher Education Malaysia for providing financial support through the Fundamental Research Grant Scheme (FRGS)-RACER, grant code: 600-IRMI/FRGS-RACER 5/3 (069/2019) and scholarship under the Post-Doctoral Training Scheme, grant code KPT(BS)820710105709. The authors would also like to extend their gratitude to the Faculty of Applied Sciences and Institute of Science, UiTM and Imperial College London for the support and facilities provided.

References

1. Wilburn, D. R., and Bleiwas, D. I. (2004). Platinum-group metals—world supply and demand. *US geological survey open-file report*, 1224:2004-1224.
2. McCarthy, S., Braddock, D. C., and Wilton-Ely, J. D. (2021). Strategies for sustainable palladium catalysis. *Coordination Chemistry Reviews*, 442: 213925.
3. Hagelüken, C. (2006). Markets for the catalyst metals platinum, palladium and rhodium. *Metall-Berlin,* 60(1): 31-42.
4. Hagelüken, C., and Umicore, A. G. (2012). Recycling the Platinum Group Metals: A European Perspective, Effective recycling systems for pgm-containing materials will ensure sustainable supply. *Platinum Metals Reviews*, 56(1): 29-35.
5. Sing Singh, P. K., Singh, R. S., and Singh, S. (2016). Environmental and social impacts of mining and their mitigation. In *Kolkata (India): National Seminar ESIMM-2016*.
6. Stocks, J., Blunden, J. R., and Down, C. G. (1974). Metal Mining and the Environment. *American Geological Institute: Alexandria, VA, USA*.
7. Glaister, B. J., and Mudd, G. M. (2010). The environmental costs of platinum–PGM mining and sustainability: Is the glass half-full or half-empty?. *Minerals Engineering*, 23(5):438-450.

8. Yousif, A. M. (2019). Recovery and then individual separation of platinum, palladium, and rhodium from spent car catalytic converters using hydrometallurgical technique followed by successive precipitation methods. *Journal of Chemistry*, 2019: 7.
9. Chen, M., Avarmaa, K., Klemettinen, L., O'Brien, H., Sukhomlinov, D., Shi, J., and Jokilaakso, A. (2020). Recovery of precious metals (Au, Ag, Pt, and Pd) from urban mining through copper smelting. *Metallurgical and Materials Transactions B*, 51(4): 1495-1508.
10. Benson, M., Bennett, C. R., Harry, J. E., Patel, M. K., and Cross, M. (2000). The recovery mechanism of platinum group metals from catalytic converters in spent automotive exhaust systems. *Resources, Conservation and Recycling*, 31(1): 1-7.
11. Hunt, A. J. (Ed.). (2013). *Element recovery and sustainability* (No. 22). Royal Society of Chemistry.
12. Serpe, A., Bigoli, F., Cabras, M. C., Fornasiero, P., Graziani, M., Mercuri, M. L., and Deplano, P. (2005). Pd-dissolution through a mild and effective one-step reaction and its application for Pd-recovery from spent catalytic converters. *Chemical Communications*, 8: 1040-1042.
13. Jantan, K. A., Kwok, C. Y., Chan, K. W., Marchiò, L., White, A. J., Deplano, P., and Wilton-Ely, J. D. (2017). From recovered metal waste to high-performance palladium catalysts. *Green Chemistry*, 19(24): 5846-5853.
14. Dick, A. R., Hull, K. L., and Sanford, M. S. (2004). A highly selective catalytic method for the oxidative functionalization of C− H bonds. *Journal of the American Chemical Society*, 126(8): 2300-2301.
15. Cuscusa, M., Rigoldi, A., Artizzu, F., Cammi, R., Fornasiero, P., Deplano, P., and Serpe, A. (2017). Ionic couple-driven palladium leaching by organic triiodide solutions. *ACS Sustainable Chemistry & Engineering*, 5(5): 4359-4370.
16. Arafath, M. A., Adam, F., and Hassan, M. Z. (2021). Synthesis, characterization, X-ray crystal structure and antibacterial activity of nickel, palladium and platinum complexes with Schiff base derived from N-cyclohexylhydrazinecarbothioamide and 5-(tert-butyl)-2-hydroxybenzaldehyde. *Phosphorus, Sulfur, and Silicon and the Related Elements*, 196(6): 530-537.
17. Mallikarjuna, K., Nasif, O., Ali Alharbi, S., Chinni, S. V., Reddy, L. V., Reddy, M. R. V., and Sreeramanan, S. (2021). Phytogenic synthesis of Pd-Ag/rGO nanostructures using stevia leaf extract for photocatalytic H2 production and antibacterial studies. *Biomolecules*, 11(2): 190.
18. Anju, A. R. Y. A., Gupta, K., and Chundawat, T. S. (2020). In vitro antimicrobial and antioxidant activity of biogenically synthesized palladium and platinum nanoparticles using Botryococcus braunii. *Turkish Journal of Pharmaceutical Sciences*, 17(3): 299.
19. Chlumsky, O., Purkrtova, S., Michova, H., Sykorova, H., Slepicka, P., Fajstavr, D., and Demnerova, K. (2021). Antimicrobial properties of palladium and platinum nanoparticles: A new tool for combating food-borne pathogens. *International Journal of Molecular Sciences*, 22(15): 7892.
20. Rîmbu, C., Danac, R., and Pui, A. (2014). Antibacterial activity of Pd (II) complexes with salicylaldehyde-amino acids Schiff bases ligands. *Chemical and Pharmaceutical Bulletin*, 62(1): 12-15.
21. Bandyopadhyay, N., Das, M., Samanta, A., Zhu, M., Lu, L., and Naskar, J. P. (2017). Promising antimicrobial activity of an oxime based palladium (II) complex. *ChemistrySelect*, 2(1): 230-240.
22. Haddad, B., Paolone, A., Villemin, D., Taqiyeddine, M., Belarbi, E. H., Bresson, S., and Kiefer, J. (2017). Synthesis, conductivity, and vibrational spectroscopy of tetraphenylphosphonium bis (trifluoromethanesulfonyl) imide. *Journal of Molecular Structure*, 1146:203-212.
23. Kubota, M., Ohba, S., and Saito, Y. (1991). Structure of trans-diiodobis (triphenylphosphine) palladium (II)–trichloromethane (1/1). *Acta Crystallographica Section C: Crystal Structure Communications*, 47(8): 1727-1729.
24. Dumas, A., and Couvreur, P. (2015). Palladium: a future key player in the nanomedical field?. *Chemical Science*, 6(4): 2153-2157.

25. Adams, C. P., Walker, K. A., Obare, S. O., and Docherty, K. M. (2014). Size-dependent antimicrobial effects of novel palladium nanoparticles. *PloS One*, 9(1): e85981.
26. Silhavy, T. J., Kahne, D., and Walker, S. (2010). The bacterial cell envelope. *Cold Spring Harbor Perspectives in Biology*, 2(5): a000414.
27. Sharma, N. K., Ameta, R. K., and Singh, M. (2016). From synthesis to biological impact of Pd(II) complexes: synthesis, characterization, and antimicrobial and scavenging activity. *Biochemistry Research International*, 2016: 4359375.

Malaysian Journal of Analytical Sciences (MJAS)
Published by Malaysian Analytical Sciences Society

NOVEL ALGINATE-CHITOSAN AMINE-FUNCTIONALIZED SILICA COATED MAGNETIC COMPOSITE FOR HEAVY METALS REMOVAL IN WATER

(Komposit Baharu Alginat Kitosan Difungsikan dengan Amina Bersalut Silika Bermagnet untuk Penyingkiran Logam Berat dalam Air)

Gimba Joshua Dagil[1,2], Ng Nyuk-Ting[1], Aemi Syazwani Abdul Keyon[1,3*]
Wan Aini Wan Ibrahim[1,3*], and Sheela Chandren[1,3]

[1] *Department of Chemistry, Faculty of Science, Universiti Teknologi Malaysia, 81310 UTM Johor Bahru, Johor, Malaysia*
[2] *Department of Science, Plateau State Polytechnic, Barkin Ladi, P.M.B 02023, Bukuru, Jos Nigeria*
[3] *Centre for Sustainable Nanomaterials, Ibnu Sina Institute for Scientific and Industrial Research, Universiti Teknologi Malaysia, 81310 UTM Johor Bahru, Johor, Malaysia*

**Corresponding author e-mail: aemi@utm.my; waini@utm.my*

Received: 15 August 2022; Accepted: 17 January 2023; Published: 19 April 2023

Abstract

A new effective biopolymer alginate chitosan amine-functionalized silica coated magnetic composite (alg/Cs-NH_2-SiO_2/Fe_3O_4) adsorbent was synthesized and applied for the first time to remove Pb(II), Cu(II) and Cd(II) from aqueous solution by utilizing inductive coupled plasma-optical emission spectroscopy (ICP-OES). The properties of the composite were characterized using Fourier-transform infrared spectroscopy (FTIR), Field emission scanning electron microscopy/energy-dispersive X-ray spectroscopy (FESEM/EDX), and vibrating sample magnetometry (VSM). Evaluation of alg/Cs-NH_2-SiO_2/Fe_3O_4 adsorption performance at optimum conditions revealed that the adsorbent had a maximum adsorption capacity of 41.79, 39.21, and 39.56 mg/g for Pb(II), Cu(II) and Cd(II), respectively. The adsorbent behavior was studied using Langmuir, Freundlich, Temkin, and Dubinin-Rudushkevich's isotherm models. The Langmuir isotherm and the pseudo-second-order were better fitted with the coefficient of determination (R^2) value of 0.99, indicating homogeneous surface and chemisorption processes. The thermodynamic factors indicated endothermic and spontaneous processes at 60 °C. Even after the 5th cycle adsorption-desorption experiments, the adsorbent still retained its adsorption ability above 70% metal ions removal, indicating that the adsorbent was reasonable for metal ions removal in water. Pb(II) was detected in a river near an industrial area (Taman Mewah, Kulai, Johor), which was eventually removed by the adsorbent at 86% efficiency.

Keywords: biopolymer, magnetic adsorbent, heavy metals

Abstrak

Penjerap biopolimer alginat kitosan amina bersalut silika bersalut (alg/Cs-NH_2-SiO_2/Fe_3O_4) yang berkesan telah disintesis dan digunakan buat kali pertama untuk menyingkirkan ion Pb(II), Cu(II) danCd(II) daripada air dengan menggunakan spektroskopi pelepasan atomik-plasma gandingan aruhan (ICP-OES). Ciri-ciri komposit dicirikan menggunakan spektroskopi inframerah-

transformasi Fourier (FTIR), mikroskop elektron pengimbasan pancaran medan (FESEM), spektroskopi sinar-X penyebaran tenaga (EDX), dan magnetometri getaran sample (VSM). Penilaian prestasi penjerapan alg/Cs-NH_2-SiO_2/Fe_3O4 pada keadaan optimum menunjukkan bahawa penjerap mempunyai kapasiti penjerapan maksimum 41.79, 39.21, dan 39.56 mg/g masing-masing untuk Pb(II), Cu(II) dan Cd(II). Prestasi penjerap dikaji menggunakan model isoterma Langmuir, Freundlich, Temkin, dan Dubinin-Rudushkevichs. Isoterma Langmuir dan pseudo-tertib kedua adalah lebih bertepatan dengan nilai pekali penentuan (R2) 0.99, menunjukkan permukaan homogen dan proses penjerapan secara kimia. Faktor termodinamik menunjukkan proses endotermik dan spontan pada 60 °C. Walaupun selepas lima kali eksperimen penjerapan-penyahjerapan , penjerap masih mengekalkan keupayaan penjerapannya dengan % penyingkiran ion logam melebihi 70% menunjukkan penjerap berupaya mengeluarkan ion logam daripada air. Pb(II) telah dikesan di sungai berhampiran kawasan perindustrian (Taman Mewah, Kulai, Johor), akhirnya disingkirkan pada kecekapan 86%.

Kata kunci: biopolimer, penjerap magnet, logam berat

Introduction

Clean water resources are undoubtedly a basic human need. However, population growth, industrialization and urbanization, domestic and industrial waste generation, and other anthropogenic sources of toxic pollutants have made many water resources detrimental to humans and the environment. Industries that produce large volumes of effluents include textile, breweries, mineral processing, poultry processors, paper and fiber plants, meat packers, fruit and vegetable packing operations, fertilizer plants, refiningand petrochemical operations, and many more. Wastewaters from these industries generally contain heavy metals,dyes, pesticides and, etc [1]. On top of that, they are soluble in water (i.e. dyes and pesticides), non-biodegradable with a tendency to bioaccumulate (i.e. heavy metals), and are easily transported into the food chain [2]. Having high atomic density >5 g/cm^3, heavy metals could be toxic and poisonous even at trace levels [3]. The rapid increases in contamination by heavy metals from industrial and urban wastewaters are undoubtedly worrying [4, 5, 6].

Techniques such as ion exchange, precipitation, coagulation, and floatation, have been utilized to extract and/or remove various heavy metals from water. However due to the issue of sludge/waste disposal [7], alternative methods arise. The adsorption method has been recognized as one of the promising methods since it only requires a small amount of adsorbent, thus promoting simplicity and efficiency to remove heavy metals from water [8]. It utilizes a mass transfer process through which metal ions are transported from solution onto the surface of a solid material (adsorbent) and become attached via chemical or physical interactions. Various adsorbents have been established and reported based on agricultural wastes, clay, zeolite, activated carbon, biopolymer, and others [9]. A new class of materials; organic-inorganic hybrid materials are attracting interest in creating a high-performing polymeric that shows good possibilities for removal of metal ions through modifications. These modified hybrid materials exhibit better properties than the original components [10]. Additionally, the natural materials of the hybrid, for instance, the agro-wastes products, clay, and biopolymers are environmentally friendly and are widely available to serve as alternative low-cost adsorbents to the commercially activated carbon. The need for a safe and better economical method for heavy metal removal from polluted water has challenged researcher's interest in the production of better low-cost alternatives [11]. Some low-cost agricultural by-products such as sugarcane bagasse and the neem backed, rice husks, sawdust, coconut husks, oil palm shells, etc have been described in the literature for metals removal [12]. To step up the performance of adsorbents from agricultural products, some modifications are needed to enhance their adsorption capacities as adsorbents[13, 14]. This included the utilization of magnetic aspect for nanomaterial adsorbents.

Adsorbents from magnetic nanomaterials (MNPs) usually possess a large surface area, and short diffusion route, without the tediousness of filtration and centrifuging. Easy separation of the adsorbents from water/wastewater using an external magnet makes MNPs reusable. However, the MNPs may suffer agglomeration, oxidation in the air during synthesis, not target-discriminatory towards analytes, and are incompatible

with compounds inside complicated matrices. Hence, they can be enhanced by a suitable coating modification to overcome these limitations [15]. The MNPs can be coated from being oxidized or can be dispersed under low pH conditions by surface coating with silica (SiO_2). SiO_2 is stable under the acid condition and inert to redox reactions as compared to the organic coating substances, and hence serves as an ideal shell composite to safeguard the inner magnetic core. Consequently, the SiO_2 coated layer has numerous hydroxyl groups on its surface which offer the easy possibility of the functionalization of the MNPs without damaging or changing the core of the materials. SiO_2-coating of the core-shell MNPs (Fe_3O_4@SiO_2) has been explored for many applications [15]. Features include stability, reactivity, solubility, melting points, and electronic structure relatively different from their original material to give a homogeneous size and shape as well as regulate its stability in aqueous solutions. APTES has been modified on the surface of silica-coated magnetite to form Fe_3O_4@SiO_2-NH_2 used for Zn(II) removal from contaminated effluent [16]. Mercaptamine had been used in silica coated MNPs to obtain the functionalized composite for Hg and Pb(II) removal [17]. Furthermore, As(III) removal had been achieved using encapsulated magnetite adsorbent in which the covalent bond was modified through the alginate to obtain the carboxylic functionalized adsorbent [18]. To explore the effect of the carboxylic alginate modified method, functionalization of the carboxylic group had also been done to enhance adsorption towards Pb(II) removal [19]. The application of alginate-chitosan-based amine-functionalized silica coated magnetite alg/Cs-NH_2-SiO_2/Fe_3O_4 as adsorbent for the removal of Pb(II), Cu(II), and Cd(II), in aqueous environments is still not explored and is an interesting area in adsorbent synthesis research.

This study was designed to develop a new eco-friendly adsorbent, i.e., the alginate-chitosan-based amine-functionalized silica coated magnetic (alg/Cs-NH_2-SiO_2/Fe_3O_4) adsorbents for the removal of Pb(II), Cu(II) and Cd(II) in water and wastewater. The characterization was conducted on the adsorbent, i.e., FTIR, FESEM/EDX, and VSM to ascertain the synthesis process. The optimization of the adsorption parameters such as sample pH, dosage, initial adsorbate concentration, contact time, and temperature was conducted via the batch adsorptions method. Ultimately, the adsorption, kinetic isotherm, thermodynamic, and reusability studies were done to evaluate the fundamental and economic aspects of the adsorbent. A real sample from an industrial wastewater site was applied to test the ultimate effectiveness of the adsorbent in the real application.

Materials and Methods

Chemicals, reagents, and instrumentations

Iron(III) chloride hexahydrate ($FeCl_3.6H_2O$, 99%), ethanol (99%) iron(II) chloride tetrahydrate ($FeCl_2.4H_2O$, 99%), and sodium hydroxide (NaOH), the stock solution of salts copper, lead, cadmium, alginate (alg), and chitosan (Cs) were bought from Merck (Germany). 3-aminopropyltriethoxysilane (APTES), tetraethyl orthosilicate (TEOS), concentrated NH_4OH (28%), HNO_3(65%), and HCL (37%) were purchased from Fluka Chemical. HCl (0.1M) and/or NaOH (0.1M) were used to adjust the pHs of the solutions. Analytical grade chemicals were used without further purifications. All glassware was soaked in 5% HNO_3 acid for 24 h and rinsed in deionized water to prevent metal contaminations. Several instruments were used and applied for the synthesis of magnetic alg/Cs-NH_2-SiO_2/Fe_3O_4 adsorbents. These include Avio ^{TM} parker 200 Inductive Couple Plasma-Optical Emission Spectrometry (ICP-OES) was used for the metal ions analysis. ATM 400 FTIR spectrometer from PerkinElmer (Waltham, MA, USA) was also utilized for the characterization of the synthesized adsorbents. FTIR estimations utilizing the KBr pellet procedure and transmission mode of all spectra were recorded from 400 to 4000cm^{-1}. A JSM-6701 F electron magnifying instrument from JEOL (Tokyo, Japan) was utilized for the field emission sample electron microscopy (FESEM) analysis, and the energy dispersive X-Ray examination (EDX). Vibrating sample magnetometry (VSM 7400) from Lake Shore Cryotronics (Ohio, USA) was used to evaluate the magnetic properties of the materials at a utilized greatest field of 15,000 G at room temperature.

Synthesis procedures

The synthesis of iron oxide (Fe_3O_4NPs) was by simple

co-precipitation procedure [20, 21]. This was done by mixing 8.48 g of $FeCl_3.6H_2O$ and 2.25g of $FeCl_2.4H_2O$ in a three-necked round bottom flask and stirring vigorously under argon gas at a temperature of 80 ℃ in a 100 ml volume of deionized water. Subsequently, 24 ml of ammonia (25%) was dropwise added under a constant mechanical stirring for 5 h to form black magnetic oxide (Fe_3O_4) at room temperature. The as-prepared Fe_3O_4 was washed with distilled water and methanol, separated with an external magnet, and finally oven-dried at 60 ℃ for 24 h. The final product was then kept for further experiments in an airtight container. The preparation of SiO_2/Fe_3O_4NPs was done by re-dispersing [22] 1.0 g of the Fe_3O_4NPs in deionized water (50 ml) under argon for 10 mins. After a continuous stirring of the products, TEOS (1 ml) diluted in ammonium hydroxide (2 ml) was finally added dropwise to the dispersion with more continuous mechanical stirring at room temperature for 14 h. The magnetic Fe_3O_4/SiO_2 mixture was then washed with ethanol and water and finally collected by external magnetic separation, then dried overnight in a furnace at 110 ℃.

The Cs-Fe_3O_4NPs was prepared by dissolving 2.0 g chitosan in 100 ml (2%) concentration of acetic acid to form a homogeneous solution. The content was then transferred to a three-necked flask under vigorous mechanically stirring followed by adding 20 ml of glutaraldehyde (5% wt solution) for 4 h. The Cs-Fe_3O_4 NPs formed were recovered by an external magnetic separation. The particles were allowed to settle for at least 2 min before being washed with water/ethanol about three times before finally dried in a vacuum oven at 50 ℃. The preparation of Cs-NH_2-SiO_2/Fe_3O_4 was made by dispersing 2.0 g of Cs-Fe_3O_4 in deionized water (100 ml) followed by 20 ml of APTES with vigorous mechanical stirring of the mixture at 40 ℃ for 1 h. The mixture was left overnight with vigorous stirring followed by vacuum filtration the next day and finally, oven-dried at 50 ℃ and stored for future use. Then, the preparation of the final alg/Cs-NH_2-SiO_2/Fe_3O_4 was done by dispersing 2.0 g of Cs-NH_2-SiO_2/Fe_3O_4 in deionized water (100 ml) under vigorous mechanical stirring of the mixture at 40 ℃ for 1 h. A solution containing 50 ml 0.1M $CaCl_2$ was then added dropwise by using a needle syringe to the resultant mixture in a beaker for the formation of the beads. The beads were then soaked 0.1 M $CaCl_2$ solution overnight and then washed thoroughly with distilled water, oven-dried overnight at a temperature of 50 ℃, and finally stored for further use. The proposed schematic synthesis route is presented in Figure 1.

Batch sorption experiments for metal ions adsorption

Adsorption experiments of Pb(II), Cd(II), and Cu(II) onto the newly synthesized alg/Cs-NH_2-SiO_2/Fe_3O_4 were carried out using the batch sorption method. The influence of solution pH, adsorbent dosage, contact time, temperature, and initial concentration of adsorbate was studied. 100 mL conical flasks holding 50 mL solutions of different metal ions with initial concentrations varying from 20 -100 mg/L, and fixed adsorbent dosage of 20 mg was used for the equilibrium experiments. The solution pH was set at pH 6, then shaked at an equilibrium contact time of 30 min, and temperature at 25 ℃, to establish equilibrium after which, an external magnet was used to separate the adsorbents from their respective solutions. The solutions were analyzed using an ICP-OES instrument for the residual heavy metal ions concentrations, and all experiments were conducted in triplicate. The percentage removal (%R) and the adsorption capacity (q_e) according to equations 1 and 2, respectively [24].

$$\%R = \frac{[(C_i - C_f)]}{C_i} x\ 100 \quad (1)$$

$$q_e = \frac{[(C_i - C_f)]\,V}{m} \quad (2)$$

Where, V = volume of solution (mL), qe = the adsorption capacity in (mg/g), m= quantity of adsorbent (mg), Ci = initial concentration of metal ions (mg/L), and Cf = final concentration of metal ions (mg/L).

Regeneration studies and wastewater samples treatment

The adsorption-desorption experiment for five consecutive rounds of regeneration study was conducted

until a substantial change in the performance of alg/Cs-NH_2-SiO_2/Fe_3O_4 was detected. Consequently, the adsorbed metal ions were desorbed in 5 mL HCL (0.1M), after each 5 min shaking to retrieve the adsorbent from the mixture with an external magnet, then washed with deionized water until neutral, and finally, oven-dried at 60 ºC for 24 h. ICP-OES instrument was used to investigate the residual concentration of heavy metal pollutants in the mixtures [25]. The efficiency of the alg/Cs-NH_2SiO_2/Fe_3O_4 adsorbent towards Pb(II), Cd(II), and Cu(II) from real wastewater effluents was investigated using effluents from industrial locations along the Skudai river at Taman Mewah, Kulai, Johor, Malaysia. The floating solids were eliminated through filtration. HNO_3 was utilized to digest the test samples to further eliminate matrix interferences. The metal ions residual concentrations in the samples were determined after the adsorption experiment using the synthesized adsorbent.

Results and Discussion

Synthesis route for alg/Cs-NH_2-SiO_2/Fe_3O_4 adsorbent

The alg/Cs-NH_2-SiO_2/Fe_3O_4 adsorbent was synthesized from Fe_3O_4, as a percussor coated with SiO_2, functionalized using APTES (-NH_2), blend combined with Cs, and the bound by alg to form a biopolymer composite adsorbent. The schematic synthesis route of alg/Cs-NH_2-SiO_2/Fe_3O_4 was through five steps namely, Fe_3O_4 was successfully synthesized by mixing $FeCl_3.6H_2O$ and $FeCl_2.4H_2O$). SiO_2/Fe_3O_4 was prepared from Fe_3O_4 and TEOS in diluted ammonium hydroxide. NH_2-SiO_2/Fe_3O_4 was prepared through SiO_2/Fe_3O_4 and APTES. Cs-NH_2-SiO_2/Fe_3O_4 was prepared chitosan in 100 ml (2%) concentration of acetic acid via cross-linking by glutaraldehyde. Finally, the adsorbent alg/Cs-NH_2-SiO_2/Fe_3O_4 was successfully prepared through Cs-NH_2-SiO_2/Fe_3O_4 by forming a composite with the addition of alginate. (Figure 1).

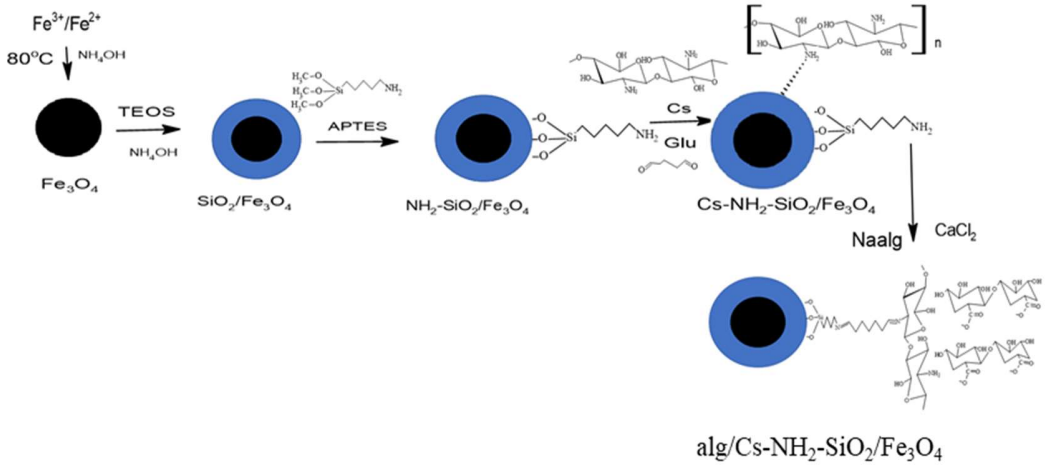


Figure 1. Schematic synthesis route of alg/Cs-NH_2-SiO_2/Fe_3O_4 adsorbent

Characterization of the synthesized alg/Cs-NH_2-SiO_2/Fe_3O_4 adsorbent

To determine the functional groups in the newly synthesized adsorbent, FTIR analysis was conducted. The FTIR spectra of the raw Cs and alg were compared to the newly synthesized material as indicated in Figure 2(a-b). The peaks for raw Cs at 3451 cm^{-1}, 2925-2885 cm^{-1}, 1652 cm^{-1}, and 1371 cm^{-1} were ascribed to the overlapping between -NH_2 and -OH stretching vibration and the intermolecular hydrogen bonding of the polysaccharide, C-H stretching vibrations of C=O saturated carbons, in acetamide group, and C-O group stretching and C-H bending vibrations. The main spectrum of raw alg (Figure 2(b)) shows 1624 cm^{-1}, 1421 cm^{-1}, and 1014 cm^{-1} which corresponds to C-H vibrational stretch and C=O vibrational stretch. The spectrum of Fe_3O_4 (Figure 2(c)) showed a peak at 574 cm^{-1} for Fe-O bond formation. The spectrum of SiO_2/Fe_3O_4 (Figure 2(d)) showed O-H

vibration, C-H stretching, C-H bending, C-O stretching peaks, Fe-O bond at 3429 cm^{-1}, 1624 cm^{-1}, 1400 cm^{-1}, 1300 cm^{-1}, and 574 cm^{-1}. Additionally, alg/Cs-NH_2-SiO_2/Fe_3O_4 showed the spectra changed with O-H vibration, C-H stretching, C-H bending, C-O stretching peaks, and Fe-O bond formation at 3149 cm^{-1}, 1542 cm^{-1}, 1053 cm^{-1}, and 596 cm^{-1}, respectively. Key findings showed that the spectra at 1658 cm^{-1}, 1025 cm^{-1}, and 623 cm^{-1} disappeared and the formation of new peaks of 1542 cm^{-1}, 1404 cm^{-1}, 1053 cm^{-1}, and 596 cm^{-1}, respectively corresponded to -NH_2,-C=O, Si-O-Si, and Fe-O, respectively, (Figure 2(f-g)), confirming new material. Consequently, the FTIR spectra of alg/Cs-NH_2-SiO_2/Fe_3O_4 presented peaks at 3400 cm^{-1} and 3200 cm^{-1} for O-H stretching and H_2O molecules, respectively, conformed to the findings of others reported in the literature [26].

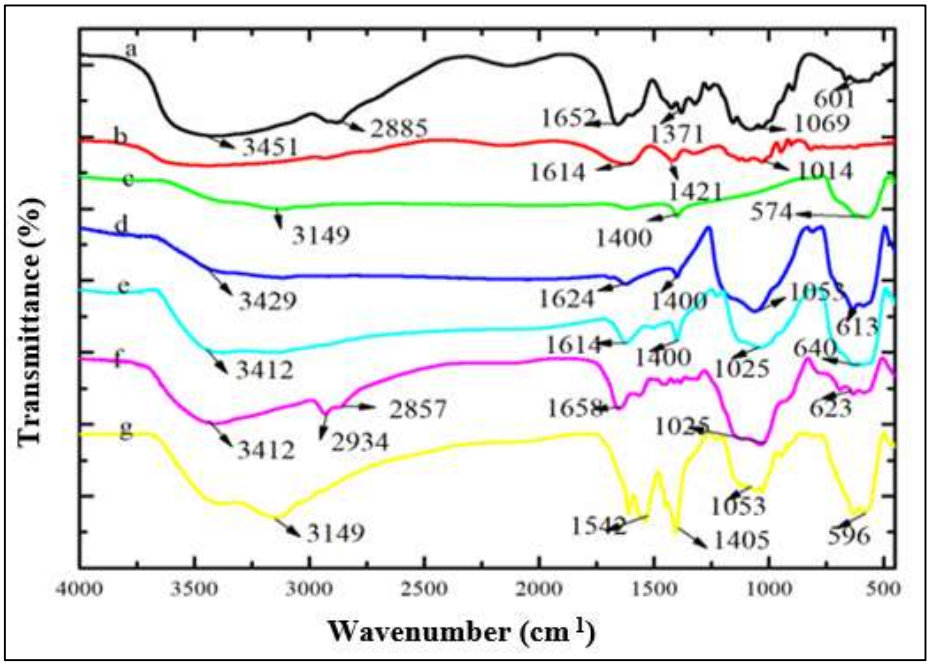
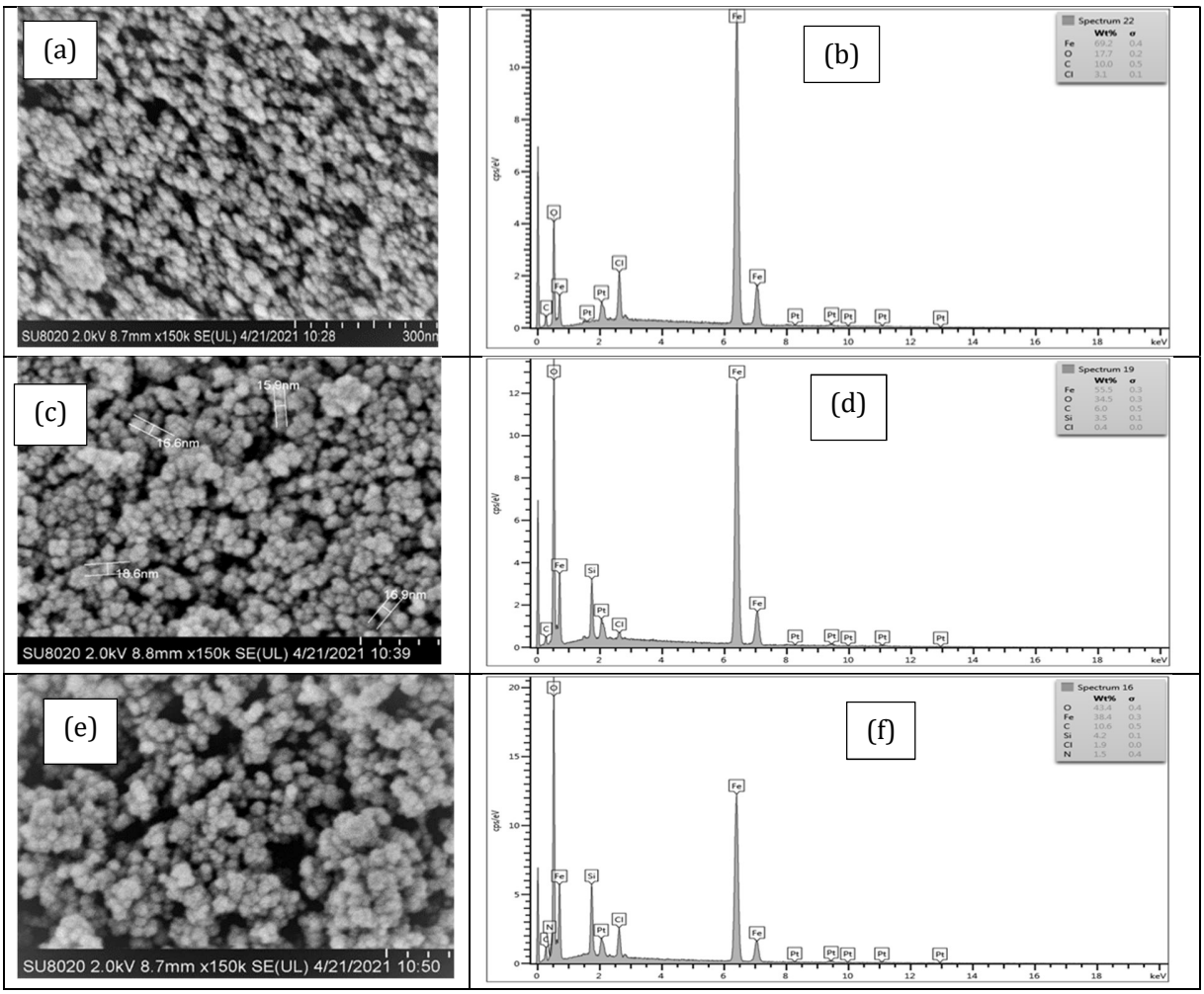


Figure 2. FTIR spectra of (a) chitosan (Cs), (b) alginate (alg) (c) Fe_3O_4, (d) SiO_2/Fe_3O_4, (e) NH_2-SiO_2/Fe_3O_4 (f) Cs-NH_2-SiO_2/Fe_3O_4 (g) alg/Cs-NH_2-SiO_2/Fe_3O_4 adsorbent

The FESEM/EDX analysis was conducted to investigate the surface morphology, particle size distributions, and the relative shape of the synthesized materials. The morphologies and the spectra of Fe_3O_4, SiO_2/Fe_3O_4, NH_2-SiO_2/Fe_3O_4, Cs-NH_2-SiO_2/Fe_3O_4, and alg/Cs-NH_2-SiO_2/Fe_3O_4 are shown in Figure 3(a-j). FESEM morphology of Fe_3O_4 (Figure 3a) showed spherical particle distribution with an average grain size range of 11-14 nm nanosized particles. The EDX spectra of Fe_3O_4 (Figure 3(b)) confirmed the element of Fe (69.20%), and O (17.70%). The FESEM morphology of SiO_2/Fe_3O_4 (Figure 3(c)) was much smoother with an increase in the nanosized average diameter of 15 - 16 nm due to the silica coatings on the surface of the magnetite, while the EDX spectra of SiO_2/Fe_3O_4 (Figure 3(d)) confirmed the element of Fe (55.50%), O (34.50%), and Si (3.5%) confirming the coating of SiO_2 on top of the magnetite during the synthesis process. The similar obs ervations were also reported by other researchers [27]. With the addition of APTES to the SiO_2 coated magnetite, the size distribution increased with changes in shape to particle diameter size range of 18-23 nm due to the -NH_2 functionalization of SiO_2/Fe_3O_4. This was well confirmed by the FTIR spectra and the EDX of NH_2-$SiO_2Fe_3O_4$ (Figure 3(f)) containing Fe (38.4%), O (43.4%), Si (4.2%), and N (1.5%) which showed the

functionalization of the SiO_2/Fe_3O_4 with APTES due to the presence of the N element. Furthermore, with the addition of Cs and alg to form alg/Cs-NH_2-SiO_2/Fe_3O_4, the FESEM morphology (Figure 3(i)) showed a more distinctive particle size distribution and shape with a denser and larger particle diameter size range of 23-50 nm and 121-148 nm, respectively. The addition of Cs and alg introduced the element of C (56.2%) (Figure 3(h) and Figure 3(j) owing to the existence of the functional groups of -NH_2 and -OH, respectively. FESEM morphology of alg/Cs-NH_2-SiO_2/Fe_3O_4 (Figure 3(i)) showed the gel formation due to the glutaraldehyde cross-linking resulting in a darker morphology with the largest diameter distribution of 114-148 nm with an oval shape liked morphology quite different from the others in conformity with other reported findings [27]. Undoubtedly, the % elemental composition of Fe, O, and Si continued to decrease with an increase in the diameter of the core-shell of the adsorbent; nevertheless, the magnetism of the final adsorbent was reasonable for removal work (Figure 4).



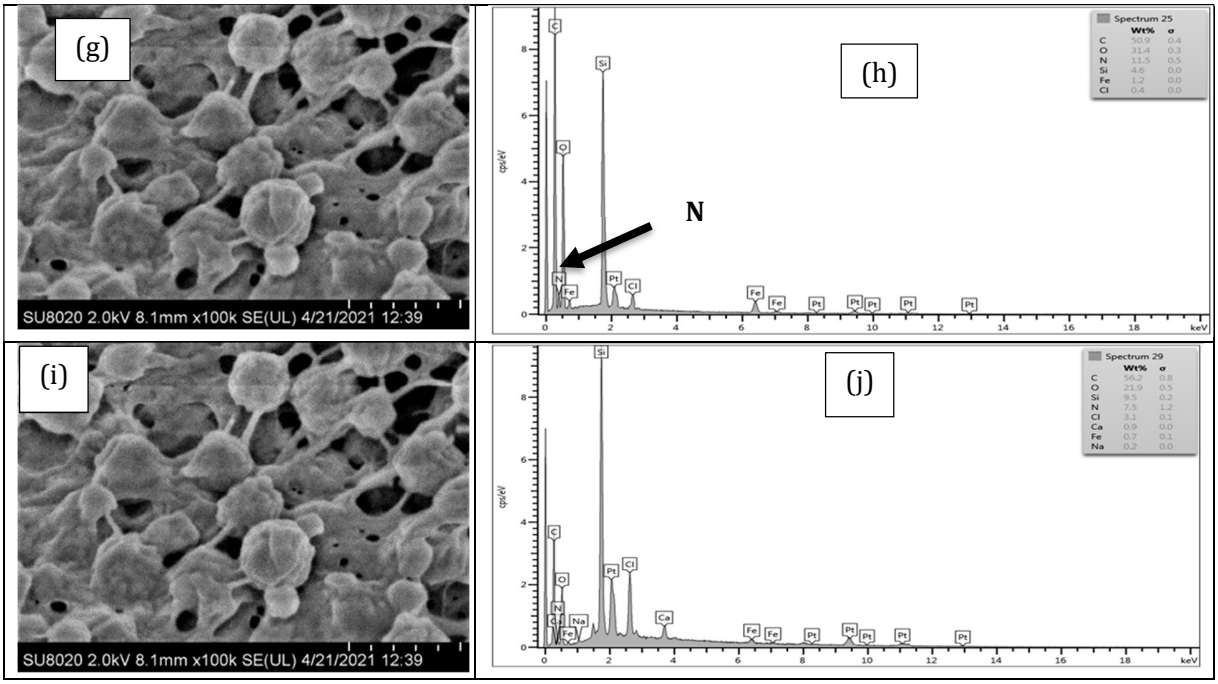


Figure 3. FESEM morphology and EDX spectra of (a-b) Fe_3O_4, (c-d) SiO_2/Fe_3O_4, (e-f)NH_2-SiO_2/Fe_3O_4, (g-h) Cs-NH_2-SiO_2/Fe_3O_4 and (i-j) alg/Cs-NH_2-SiO_2/Fe_3O_4 adsorbents Magnification. = 100K or 150K

The magnetization curves of Fe_3O_4, N H_2-SiO_2/Fe_3O_4, and alg/Cs-NH_2-SiO_2/Fe_3O_4 adsorbents were investigated via VSM polarization for before and after adsorption in the range of −15000 to 15000KOe. The magnetic hysteresis loops of Fe_3O_4, NH_2-SiO_2/Fe_3O_4, and alg/Cs-NH_2-SiO_2/Fe_3O_4 demonstrated the superparamagnetic characteristic of the materials with saturation magnetization values of 24.48, 20.10 and 14.77 emu/g, respectively (Figure 4(a-c)). The results revealed that the adsorbent alg/Cs-NH_2-SiO_2/Fe_3O_4 displayed sufficient magnetic quality to achieve magnetic separation. Hence, the VSM bends S-shape showed super-paramagnetic properties for nanocomposite well suitable for the assortment of magnetic adsorbents from aqueous solution. The decrease in the saturation magnetization values from Fe_3O_4 to alg/Cs-NH_2-SiO_2/Fe_3O_4 was due to the various modification that had taken place on top of the Fe_3O_4. Although the saturation magnetization value decreased after the immobilization process, the adsorbent responded rapidly to an external magnet and could be separated from the aqueous mixture conveniently within 45 seconds in agreement with the similar finding reported by [28].

Optimization of adsorption using the newly synthesized alg/Cs-NH_2-$SiO_2Fe_3O_4$ adsorbent

The impact of variables such as the sample pH, dosage, initial adsorbate (metals ion) concentration, contact time, and the temperature for the adsorption of selected metal ions using alg/Cs-NH_2-SiO_2/Fe_3O_4 adsorbent was analyzed and optimized utilizing the batch adsorption technique (Figure 5a-e).

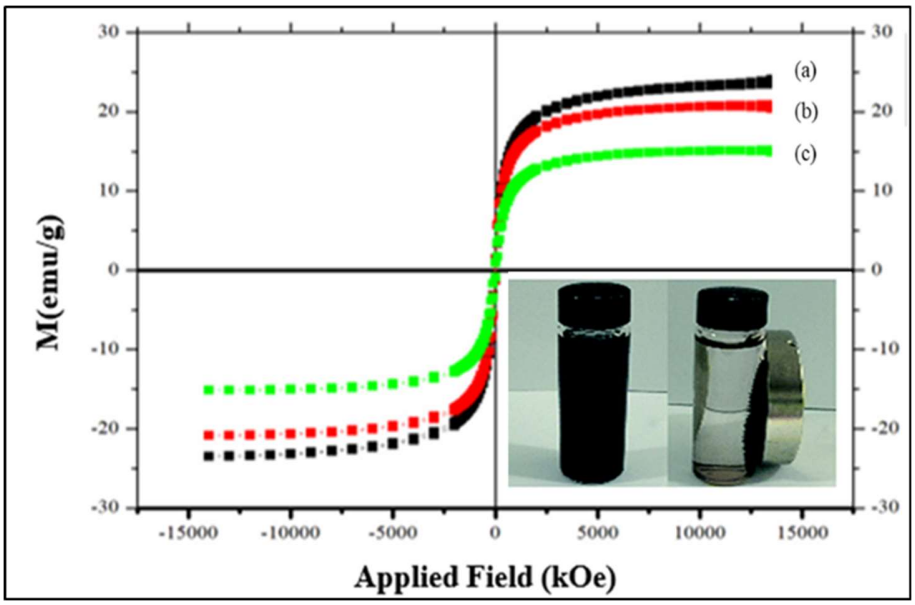


Figure 4. VSM plot for (a) Fe_3O_4 (24.48 emu/g), (b) NH_2-SiO_2/Fe_3O_4 (20.10 emu/g), (c) alg/Cs-NH_2-SiO_2/Fe_3O_4 (14.77 emu/g). The photo showed the separation of adsorbent using an external magnet.

A key to optimizing parameters in the process of metal ions adsorption onto the adsorbent was the pH of the water solution. The effect of pH was conducted by varying the pH from 2-7 and keeping other factors constant (Figure 5a). The findings revealed a maximum pH of 6 with % of metal ions removal for Pb(II), and Cd(II), except pH 7 for Cu(II) with the value of 73.74%, 68.82%, and 66.68% respectively. The adsorbent oxygenated active sites of Cs and alg were $–NH_2$, -OH, and –COOH. At lower pH, protonation occurred at the active sites of the adsorbent, and there was a competition between the protonated (H^+) active sites of the adsorbent and M^{2+} ions which induced electrostatic repulsion between the protonated sites (H^+) and M^{2+}, in turn, reduced quantity of adsorption of the metal. At greater pH values, there were the precipitations of the M^{2+} to form $M(OH)_2$, which resulted in less % metal ions adsorption with a similar pattern to other researchers [29]. Consequently, the value for optimum pH was found to be pH 6. Therefore, pH 6 was most acceptable and used in the next optimization parameter. The influence of contact time on the Pb(II), Cd(II), and Cu(II) adsorption onto alg/Cs-NH_2-SiO_2/Fe_3O_4 adsorbent was investigated. Contact time varied from 20-80 mins (Figure 5b).Time was varied while keeping other conditions constant to maximize the efficiency of the removal due to the time factor. The optimum contact time was achieved at 30 mins with % metal ions removal for Pb(II), Cd(II), and Cu(II) of 78.68, 70.66, and 70.88%, respectively. The fast % metal ions removal at the initial increased due to an abundance in the active accessible sites on the adsorbent surface for interaction with the metal ions. The adsorption accessible to active sites gradually reduced, and the interaction forces were weakened, resulting in a decrease in removal %. This observation was similar to the trends reported by some researchers that metal ions removal increased within the first few minutes of contact with the adsorbent surface [30]. Consequently, 30 mins was selected for the next optimization experiment.

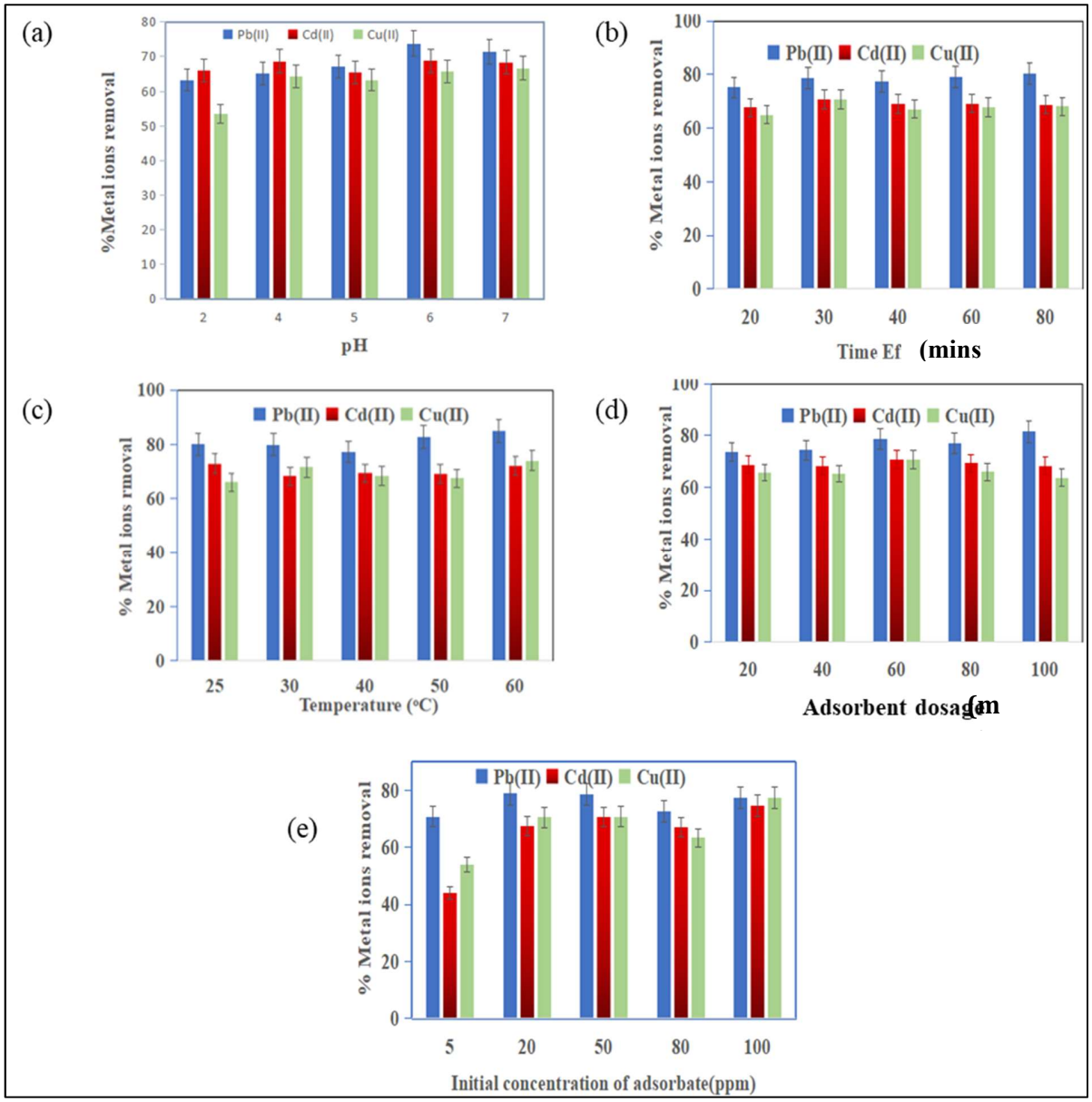


Figure 5. Effect of adsorption parameters (a) pH, (b) time effect , (c) temperature, (d) adsorbent dosage, and (e) initial concentration of adsorbate using alg/Cs-NH_2-SiO_2/Fe_3O_4 adsorbent for Pb(II), Cd(II) and Cu(II) removal in water.

The temperature effect on the removal process was a critical optimization parameter because the forces of interactions between adsorbate and adsorbent are either weakened or strengthened with changes in temperature or heat. Additionally, the mobility of metal ions increases with temperature and the affinity of the metal ions at a higher temperature also increased for most magnetic nanocomposites. A series of tests were conducted to study the effect of temperature from 20 - 60 ℃ to find the suitable temperature with the best efficiency of the removal (Figure 5c). The results showed that the optimum was achieved at 60 ℃ with % of the metal ions

of 84.76, 72.10, and 73.96 % for Pb(II), Cd(II), and Cu(II), respectively. The increasing temperature with an increase in the metal ions removal % was attributed to endothermic reactions, [31] as well as the increase in the rate of diffusion of the metal ions at greater temperatures[32]. The temperature at 60 °C was selected for the next parameter optimization. To evaluate the influence of the adsorbent dose on the removal process, the adsorbent amount varied from 20 -100 mg (Figure 5d). It was found that the optimum dosage was achieved at 60 mg, with metal ions removal % of 70.66, 78.68, and 70.88% Pb(II), Cd(II), and Cu(II), respectively. The amount of adsorbent dose was found to increase with the increase in available active sites and vice versa [33]. Consequently, 60 mg was the most appropriate dosage and was therefore adopted as the optimum dosage value for the next experiment. The effect of the initial adsorbate concentration was a crucial optimization parameter to increase the adsorbate active sides for the removal process. Concentrations from 5-100 ppm were investigated (Figure 5e). The results showed that the adsorption equilibrium was reached when the initial adsorbate concentration used was 50 ppm; the heavy metals ion % was 78.68, 70.66, and 70.88 % for Pb (II), Cd(II), and Cu(II), respectively. This agrees with the reports of others that the adsorption of metal ions increased with increasing concentrations due to the increasing availability of metal ions competing for the adsorbents active sites i.e. the more the adsorbate concentration the more the amount of the metal ions to be removed by the active sites of the adsorbent and vice versa[34]. Hence, 50 ppm was selected to be used in the next optimization temperature parameter.

Isotherm study

The equilibrium adsorption experiments of Pb(II), Cd(II), and Cu(II) onto the synthesized adsorbents alg/Cs-NH_2-SiO_2/Fe_3O_4 were studied using Freundlich, Langmuir, Temkin, and Dubinin-Radushkevich (D-R-K) isotherms models as a time function of initial concentrations at optimum conditions. Freundlich isotherm presumes multilayer and heterogeneous adsorption sites and it assumed physisorption observed adsorption mechanism [35, 36,37]. The Freundlich straight plot of the equation is given by the equation 3.

$$logq_e = logk_F + \frac{1}{n} logC_e \quad (3)$$

Where q_e and Ce are the quantity of adsorbate adsorbed per mass of the adsorbent (mg/g), and the equilibrium adsorption capacity of the metal ions pollutants (mg/L), respectively, K_F and n are the Freundlich constant suggestive of adsorbent adsorption capability (mg/g), and the heterogeneity factor, correspondingly. The isotherm findings provided the proper understanding of the kind and mechanism of the interaction behavior between the adsorbent and the adsorbate thus, additional explained the mechanism. That is the affinity of adsorbent, surface properties, and the types of the most appropriate adsorption process. The straight plots of *log* q_e against *log* C_e for Pb(II), Cd(II), and Cu(II), respectively, K_F and n for the separate metal ions were computed from intercept *(log* q_e*)* and slope *(1/n)* of the straight away lines (Table 1). The coefficient of regression (R^2) quantities were not close to unity and the KF quantities were not in harmony with the q_e experimental values. Accordingly, the Freundlich model could not sufficiently describe the adsorption processes. The extent of non-linearity between the solution concentration and adsorption was indicated by n values as shown; if $n=1$ indicated the adsorption is linear, if $n < 1$, indicated the adsorption process is through chemisorption, and if $n>1$, was for physical adsorption. Thus, $0 < n > 1$ is hereby appropriate[37]. Langmuir isotherm was established on the assumptions of monolayer and even distribution of adsorption sites on the adsorbent. Consequently, a saturation value may be achieved beyond which no extra adsorption will occur. Additionally, it was assumed that adsorption occurs through chemisorption at any given homogeneous site without interactions between the adsorbed molecules [37]. The linear Langmuir form is given by equation 4.

$$\frac{C_e}{q_e} = \frac{C_e}{q_m} + \frac{1}{q_m k_L} \quad (4)$$

Where q_m and q_e are the optimum adsorption capacity (mg/g), and the experimental adsorption capacity (mg/g), respectively, kL is the linear Langmuir constant (L/mg) and Ce is the concentration (mg/L) of residual solution. The linear plot of Ce/q_e against C_e gives a straight plot

line with an R^2 value for all the metal ions for Pb(II), Cd(II), and Cu(II) in that order. Here, values of qm and kL are computed from the linear slope ($1/qm$) and the intercept ($1/qmkL$). The findings of the adsorption procedures which fitted the Langmuir model based on the established R^2 values were close to 0.999 for Pb(II), Cd(II), except for Cu(II) < 0.999 as demonstrated in Table 2. Additionally, the experimental qe values for Pb(II) and Cd(II) were 41.8 and 39.2 mg/g, respectively, and they agreed with the calculated qm values of 39.4 and 36.6 mg/g, in that order, validating the Langmuir model's suitability to describe the adsorption processes [37,38]. The exception was Cu(II), where the experimental and calculated qe values were 39.6 and 15.6 mg/g. A separation factor constant (R_L) was introduced furthermore, to evaluate the degree of suitability of the adsorbent towards adsorbate and is described by equation 5.

$$R_L = \frac{1}{1+K_L C_o} \quad (5)$$

where K_L(L/mg) and C_o(mg/L) represent the Langmuir constant and the initial adsorbate concentration, respectively. The magnitude of R_L represents the feasibility of adsorption (Table 2). The dimension of R_L was additionally used, for the adsorption studies, if $R_L > 1$, the value indicated the adsorption is unfavorable, $R_L = 1$, indicated the adsorption is linear, and $R_L < 1$, indicated adsorption is favorable. Consequently, where $0 < R_L < 1$ confirmed R_L to be good and applicable for this study [37]. Additionally, the Temkin and the D-R-K isotherms data could not adequately explain the adsorption process of Pb(II), Cd(II), and Cu(II) onto the synthesized adsorbents alg/Cs-NH_2-SiO_2/Fe_3O_4 because of both R^2 < 0.99 (Table 1).

Table 1. Adsorption isotherm model parameters for Pb(II), Cd(II), and Cu(II) adsorption onto alg/Cs-NH_2-SiO_2/Fe_3O_4

Model	Isotherm Constant	Pb(II)	Cd(II)	Cu(II)
Freundlich	n	0.655	0.749	0.741
	k_F (mg/g)	32.0	36.5	32.0
	R^2	0.837	0.801	0.848
Langmuir	q_e (mg/g)	41.8	39.2	39.6
	R_L (mg $^{-1}$)	7.201	8.149	0.937
	R^2	0.998	0.999	0.693
	Calc qm (mg/g)	39.4	36.6	15.6
	R_L (x10^{-3})	2.760	2.440	20.640
Temkin	A	7.123	14.658	10.440
	b	169.455	203.313	202.659
	R^2	0.877	0.801	0.867
D-R-K	q_D (mg/g)	41.79	39.21	39.56
	β (mol^2/J^2)	1.21x10^7	2.58x10^7	8.36x10^6
	R^2	0.36	0.48	0.76

Kinetics study

The adsorption kinetics provides crucial information about the effective design of the time-dependent batch adsorption system [38]. To examine the adsorption kinetics of the synthesized adsorbent, the pseudo-first-order and pseudo-second-order were studied. By using a predetermined concentration of 50.0 mg/L for each of the metal ions concentrations range and a predetermined adsorbent (60.0 mg) dose, the kinetics experiments were done.

The kinetics of adsorption for Pb(II), Cd(II), and Cu(II) onto alg/Cs-NH_2-SiO_2/Fe_3O_4 was examined using Pseudo-first-order linear equation 6.

$$log(q_e - q_t) = log(q_e) - \frac{tK_1}{2.303} \quad (6)$$

Where q_e and q_t are the capacity of adsorption and the quantity of metal ions removal at equilibrium (mg/g), and the quantity of metal ions removal (mg/g) at time t (min), respectively. K_1 is the pseudo-first-order rate constant (min^{-1}) [38]. The straight plots line of *log(qe-qt)* against *t* of pseudo-first-order rate equation for Pb (II), Cd (II), and Cu (II), respectively, along with the quantities of R^2 and k_1 for the corresponding metal ions, q_e and k_1 were calculated from the slope ($-k_1/2.303$) and $ln(q_e)$ as intercepts was summarized (Table 3). Consequently, the R^2 values were < 0.999 implying that the model could not be used to adequately explained through the adsorption process.

The straight-away kinetics equation for pseudo-second-order of Pb(II), Cd(II), and Cu(II), uptake onto alg/Cs-NH_2-SiO_2/Fe_3O_4 was depicted in equation 7.

$$\frac{t}{qt} = \frac{1}{k_2 q_e^2} + \left(\frac{1}{qe}\right) t \quad (7)$$

The straight-line plot relationship of *t/qt* versus *t* straight plot for pseudo-second-order rate equation for Pb(II), Cd(II), and Cu(II), separately. Where q_e and q_t are the adsorption capacity of metal ions adsorbed at equilibrium (mg/g), and the adsorption capacity of metal ions removal (mg/g) at time *t* (min), respectively. Furthermore, k_2 is pseudo-second-order rate constant (g/mg min)[38]. The R^2 estimations for the metal ions were closer to unity, suggesting theappropriateness of the model to explain the adsorption process. Where k_2 and q_e are computed from intercept ($1/k_2 q_e^2$) and slope ($1/q_e$) correspondingly, (Table 2). Consequently, the breakthroughs discovery confirmed that the removal process was the chemisorption-regulated process in agreement with other works reported [38].

Table 2. Kinetic data parameters for Pb(II), Cd(II), and Cu(II) adsorption onto alg/Cs-NH_2-SiO_2/Fe_3O_4

Model	Parameter	Pb(II)	Cd(II)	Cu(II)
Pseudo-first- order	q_e (mg/g)	40.8	35.6	35.8
	k_L (min^{-1})	0.004	0.314	0.402
	R^2	0.39	0.24	0.59
Pseudo-second order	q_e (mg/g)	38.6	36.4	33.6
	k_2 (min^{-1})	-0.95	0.03	-0.06
	R^2	0.99	0.99	0.99

Thermodynamic study

The thermodynamic factors describe the role of temperature control on the Pb(II), Cd(II), and Cu(II) adsorption process towards the produced alg/Cs-NH_2SiO_2/Fe_3O_4, thus, establishing the practicability and workable energy requirement for the adsorption process. The thermodynamics explained the effect of the factors such as the entropy changes (ΔS), enthalpy changes (ΔH), and Gibbs free energy (ΔG), which endorse the type of the adsorption, either one of randomness or non-randomness, endothermic, or exothermic, as well as spontaneous or non-spontaneous. These factors were established using Van't Hoff equation and Gibbs free energy [39], by an operating temperature range of 313-333K at optimum conditions according to equations 8, 9, and 10.

$$lnK_C = \frac{\Delta H}{RT} + \frac{\Delta S}{R} \quad (8)$$

$$\Delta G = -RTlnK_C \quad (9)$$

$$K_C = \frac{q_e}{C_e} \quad (10)$$

Where q_e and C_e are adsorption capability in mg/g and residual analyte (mg/L) concentration after adsorption, respectively. *T* represents the temperature *(K),* and *R* stands for the general gas constant (8.3145J/mol.K = 8.314x10^{-3} kJ/mol.K), K_C is the equilibrium constant. To assess the thermodynamic parameters of the target adsorbates on the as-synthesized adsorbent, the

adsorption isotherms at various temperatures (313, 323, 333K) were conducted. The straight plot of lnK_C versus *1/T* gives a straightaway line plot with an R^2, as represented. The negative quantity of slope suggested the adsorption method is endothermic type. The quantities of ΔH, as well as ΔS, were achieved from the slope ($\Delta H/R$ = - *slope*) and intercept ($\Delta S/R$ = intercept) of the straight linear plot, correspondingly [40]. The values of ΔG (kJ/mol), ΔH (kJ/ mol), and ΔS (J/mol.k), for removal of the heavy metal's ion onto alg/Cs-NH_2-$SiO_2Fe_3O_4$ (Table 3). The positive value of ΔH for the adsorption process of metal ions suggests the endothermic nature of the adsorption process with the order Pb(II) > Cd(II) > Cu(II) at 313K. This also supported the adsorption process with temperature increasement. The positive quantities of ΔH confirmed that the interaction was endothermic and the positive quantities of ΔS provide randomness attraction [40]. The positive value of ΔS was observed for the adsorption process of the metal ions indicating an increase in randomness at the solid/solution interface during the adsorption process with the order Cd(II) > Pb(II) > Cu(II) at 313K. Negative amounts of ΔS demonstrate s the rise in the randomness of the solid/solution boundary through the adsorption process, while the negative amounts of ΔG endorse that the adsorption process is spontaneous. The negative value of ΔG indicated the spontaneity of the adsorption process with the order Pb(II) > Cd(II) > Cu(II) at 313K. Generally, the change in standard free energy is in the range of -20 to 0KJ/mol and for chemisorption varies between -80 to -400Kj/mol. The results corrosions to spontaneous physical adsorption of the metal ions which indicated the system does not gain energy. In addition, ΔH of 4.0 - 8.0 kJ/mol and 8.0 - 40.0 kJ/mol are related to Van der Waals connections and hydrogen bonding, respectively. Accordingly, ΔH for chemisorption started at 40.0 kJ/mol[35]. Consequently, adsorption is a chemisorption-regulated process (Table 3).

Table 3. Thermodynamic factors for Pb (II), Cd (II), and Cu (II) adsorption onto alg/Cs-NH_2-SiO_2/Fe_3O_4 with temperature variations

Analyte	$T(K)$	R^2	ΔG (kJ/mol)	ΔH (kJ/mol)	ΔS (kJ/mol.K)
Pb (II)	313	0.987	-1.855	+2.032	+3.990x10^3
	323		-1.883		
	333		-2.414		
Cd (II)	313	0.975	-1.787	+1.411	+8.171x10^3
	323		-1.519		
	333		-1.403		
Cu (II)	313	0.894	-0.436	+0.868	-7.569x10^3
	323		-0.594		
	333		-1.081		

Regeneration and real samples analyses

The regeneration of an adsorbent was a crucial parameter that makes it more cost-effective in the practical application to remove metal ions from water with a good recovery. In this study, the newly synthesized adsorbent was evaluated for five consecutive cycles using 5.0 ml (0.1M) HCL**.** The results of the Pb(II), Cd(II), and Cu(II)% removal by alg/Cs-NH_2-SiO_2/Fe_3O_4, adsorbent could efficiently be reused for up to 5 cycles, retaining about 70% of its potential. Consequently, the adsorbent was deemed favorable material for use in metal removal from real wastewater. Pb(II) was detected in a holding pond near an industrial area (Taman Mewah, Kulai, Johor), eventually removed by the adsorbent at 86% where by, Cd(II) and Cu(II) were not detected. The adsorbent (alg/Cs-NH_2-

SiO_2/Fe_3O_4) adsorption capacity towards Pb(II), Cd (II), and Cu(II) was compared with other adsorbents in the literature (Table 4). This adsorbent compared fairly with its contemporaries (Table 4), the *qmax* for PAN-Na-Y adsorbent has 35.39, 40.69, and 35.07 mg/g as well as Mt-Chitosan has 49.33, 28.23, and 20.60 mg/g, respectively, for the removal of Pb(II), Cd (II) and Cu(II)[37,38]. The different Pb(II), Cd (II), and Cu(II) maximum adsorption capacities depended not only on the structure and morphology of the adsorbent, and the presence of functional groups but also on adsorption variables, such as pH, adsorbent dose, metal ions concentration, and contact time. The complexity was further caused by the non-uniformity of the maximum adsorption variable used and the various procedures the adsorption capacities were measured. Finally, in the choice selecting the appropriate adsorbent, availability, reusability, and cost-effectiveness were taken into account, which this adsorbent depicted. Therefore, it is noteworthy to mention that the adsorbent alg/Cs-NH_2-SiO_2/Fe_3O_4 has a promising potential for future use for Pb(II), Cd(II), and Cu(II), removal from effluent solution (Table 4).

Table 4. Comparative study of adsorption capacity of alg/Cs-NH_2-SiO_2/Fe_3O_4 adsorbent with similar adsorbents for the removal of Pb(II), Cd(II), and Cu(II) ions from aqueous solutions

Adsorbent	Metal Ions	q_{max} (mg/g)	pH	Isotherm/Kinetics	References
alg/Cs-NH_2SiO_2/Fe_3O_4	Pb (II)	41.79	6.0	Langmuir/	This study
	Cd (II)	39.21		Pseudo 2nd order	
	Cu (II)	39.56			
PAN-Na-Y	Pb (II)	35.39	6.0	Langmuir/	[37]
	Cd (II)	40.69		Pseudo 2nd order	
	Cu (II)	35.07			
Mt-Chitosan	Pb (II)	49.33	5.0	Langmuir/Freundlich	[38]
	Cd (II)	28.23		Pseudo 2nd order	
	Cu (II	20.60			
DTPA/MGO	Pb (II)	131.40	3.0	Langmuir/	(39)
	Cd (II)	387.60		Pseudo 2nd order	
	Cu (II	286.50			
Fe_3O_4-$FeMoS_4$	Pb (II)	190.75	5.0	Langmuir	[40]
	Cd (II)	140.50		Pseudo 2nd order	
	Cu (II	110.30			

Conclusion

In this paper, the novel effective adsorbent alg/Cs-NH_2-SiO_2/Fe_3O_4 adsorbent was successfully synthesized from Fe_3O_4, as a percussor coated with SiO_2, functionalized using APTES (-NH_2), and the blend combined with chitosan bound by alginate as a binder to form the biopolymer composite adsorbent. The adsorbent was characterized for the surface morphology, using FTIR, FESEM/EDX, and VSM methods which demonstrated a successful synthesis. The adsorbent was investigated with the batch method. The evaluation of alg/Cs-NH_2-SiO_2/Fe_3O_4 adsorption performance at optimized conditions of pH, time effect, adsorbent dosage, initial adsorbate concentration, and temperature. The findings revealed that the adsorbent has a maximum adsorption capacity of 41.79, 39.21, and 39.56 mg/g for Pb(II), Cu(II), and Cd(II), respectively. In addition, the adsorbent behavior was studied for the isotherm models using Langmuir, Freundlich, Temkin, and Dubinin-Rudushkevich's isotherm model**s**. Moreover, the results demonstrated that the isotherm and kinetic studies were better fitted to Langmuir isotherm and the pseudo-second order with the coefficient of determination (R^2) close to 0.999, indicating homogeneous surface and chemisorption. The adsorption-desorption experiment for five consecutive rounds of regeneration study was

conducted until a substantial change inthe performance of alg/Cs-NH_2-SiO_2/Fe_3O_4 was detected. Consequently, the findings revealed that the adsorbent still retained its adsorption ability achieved above 70%, after the 5th recycled, which indicated the efficiency of the adsorbent. In addition, the thermodynamic factors were investigated, and the results indicated endothermic and spontaneous processes. The industrial wastewater river area of Taman Mewah, Kulai, Johor, Malaysia for the application for the real sample, and the findings revealed that only Pb(II) was detected at 86% efficiency of removal. The adsorbent (alg/Cs-NH_2-SiO_2/Fe_3O_4) adsorption capacity towards Pb(II), Cd (II), and Cu(II) were compared with other adsorbents in literature and was ranked good among its contemporaries. Therefore, it is noteworthy to mention that the adsorbent alg/Cs-NH_2-SiO_2/Fe_3O_4 has a promising potential for future use for Pb(II), Cd(II), and Cu(II), removal from effluent solution.

Acknowledgment

We are grateful for the financial support of the work by Universiti Teknologi Malaysia via Universiti Teknologi Malaysia Fundamental Research grant (UTMFR, Q.J130000.2554.20H98, reference number PY/2019/02057) and UTMShine grant (Q.J130000.2454.09G30, reference number PY/2020/03555).

References

1. Rajapaksha, P. P., Power, A., Chandra, S. and Chapman, J. (2018). Graphene, electrospun membranes, and granular activated carbon for eliminating heavy metals, pesticides, and bacteria in water and wastewater treatment processes. *Analyst Journal*, 143(23): 5629-5645.
2. Sherlala, A. I. A., Raman, A. A. A., Bello, M. M. and Asghar, A. (2018). A review of the applications of organo-functionalized magnetic graphene oxide nanocomposites for heavy metal adsorption. *Chemosphere,* 193:1004–1017.
3. Kumar, R., Kumar, S., Guglani, S., Roy, S., Kaushik, B. K., Sharma, R., et al. (2020) Temperature-aware compact modeling for resistivity in ultra-scaled cu-graphene hybrid interconnects. SPI 2020 - 24th IEEE Work Signal Power Integrity, Proceeding (January 2021): pp. 1-8.
5. Mishra, S., Bharagava, R. N., More, N., Yadav, A., Zainith, S., Mani, S., et al. (2019) Heavy metal contamination: An alarming threat to environment and human health. *Journal of Environmental and Biotechnology Sustainable Future*, 2019: 103-125.
6. Samadi, N., Hasanzadeh, R. and Rasad, M. (2015). Adsorption isotherms, kinetic, and desorption studies on removal of toxic metal ions from aqueous solutions by the polymeric adsorbent. *Journal of Applied Polymer Science*, 132(11):1-13.
7. Sadati, B. N., Rostamizadeh, K., Yaftian, M. R., Zamani, A. and Ahmadi, H. (2014). Covalently modified magnetite nanoparticles with PEG: Preparation and characterization as nano-adsorbent for removal of lead from wastewater. *Journal of Environmetal Health Sciences Engineering,* 12(1): 103.
8. Ahmad, N., Sereshti, H., Mousazadeh, M., Rashidi, N. H., Kamboh, M. A. and Mohamad, S. (2018). New magnetic silica-based hybrid organic-inorganic nanocomposite for the removal of lead(II) and nickel(II) ions from aqueous solutions. *Journal of Material Chemistry and Physics*, 226:73-81.
9. Kariuki, Z., Kiptoo, J. and Onyancha, D. (2017). Biosorption studies of lead and copper using rogers mushroom biomass 'Lepiota hystrix.' *South African Journal of Chemcal Engineering*, 23:62-70.
10. Zulfiqar, A. S., Athar, M., Salman, M. and Imran, D. M. (2017) Simultaneous removal of Pb(II), Cd(II), and Cu(II) from aqueous solutions by adsorption on Triticum aestivum - a green approach. *Journal Hydrology Current Research*, 2(4): 4-11.
11. Prasath, R. R., Muthirulan, P. and Kannan, N. (2014). Agricultural wastes as a low cost adsorbent for the removal of Acid Blue 92 dye: A comparative study with commercial activated carbon. *IOSR Journal of Agriculture and Veternary Science,* 7(2):19-32.

12. Sutirman, Z. A., Sanagi, M. M., Abd Karim, K. J., Wan, I. W. A. and Jume, B. H. (2018) Equilibrium, kinetic and mechanism studies of Cu(II) and Cd(II) ions adsorption by modified chitosan beads. *International Journal Biological Macromolecules,* 116: 255-263.
13. Noor, N. M., Othman, R., Mubarak, N. M. and Abdullah, E. C. (2017). Agricultural biomass-derived magnetic adsorbents: Preparation and application for heavy metals removal. *Journal of the Taiwan Institute of Chemical Engineers*, 78: 168-177.
14. Ng, N. T., Kamaruddin, A. F., Wan, I. W. A., Sanagi, M. M. and Abdul Keyon, A. S. (2018) Advances in organic-inorganic hybrid sorbents for the extraction of organic and inorganic pollutants in different types of food and environmental samples. *Journal of Separation Science*, 41: 195-208.
15. Wang, J., Zheng, S., Shao, Y., Liu, J., Xu, Z. and Zhu, D. (2010). Amino-functionalized Fe_3O_4@SiO_2 core-shell magnetic nanomaterial as a novel adsorbent for aqueous heavy metals removal. *Journal of Colloid Interface Science*, 349(1):293-299.
16. Jahanbakhsh, Z., Hosseinzadeh, H., Masoumi, B. (2021). Synthesis of carboxymethyl β-cyclodextrin bonded Fe_3O_4@SiO_2–NH_2 core-shell magnetic nanocomposite adsorbent for effective removal of Pb(II) from wastewater. *Journal of Sol-Gel Science and Technology*, 99(1): 230-242.
17. Lim, J. W., Kim, T. Y. and Woo, M. A. (2021) Trends in sensor development toward next-generation point-of-care testing for mercury. *Journal of Biosensors and Bioelectronics,* 183:113228.
18. Ahmad, S. Z. N., Wan, S. W. N., Ismail, A. F., Yusof, N., Mohd, Y. M. Z. and Aziz, F. (2020). Adsorptive removal of heavy metal ions using graphene-based nanomaterials: Toxicity, roles of functional groups and mechanisms. *Chemosphere Journal*, 248: 126008.
19. Yang, L., Tian, J., Meng, J., Zhao, R., Li, C., Ma, J., et al. (2018). Modification and characterization of Fe_3O_4 nanoparticles for use in adsorption of alkaloids. *Journal of Molecules*, 23(2): 562.
20. Abbaszadeh, S., Nodeh, H. R. and Alwi, S. R. W. (2018). Bio-adsorbent derived from papaya peel waste and magnetic nanoparticles fabricated for lead determination. *Journal of Pure and Applied Chemistry*. 90(1):79-92.
21. Rahimdad, N., Khalaj, A., Azarian, G. and Nematollahi, D. (2019). Electrochemical device for the synthesis of Fe_3O_4 magnetic nanoparticles. *Journal of the Electrochemical Society*, 166(2): 1-6.
22. Markus, A., Gbadamosi, A. O., Yusuff, A. S., Agi, A. and Oseh, J. (2018). Magnetite-sporopollenin/graphene oxide as new pre-concentration adsorbent for removal of polar organophosphorus pesticides in vegetables. *Journal of Environmetal Science Pollution and Research*. 25(35): 35130-35142.
23. Alizadeh. A., Khodaei, M. M., Beygzadeh, M., Kordestani, D. and Feyzi, M. (2012). Biguanide-functionalized Fe_3O_7/SiO_2 magnetic nanoparticles: An efficient heterogeneous organosuperbase catalyst for various organic transformations in aqueous media. *Bulletin of the Korean Chemical Society*, 33(8):2546-2552.
24. Li, Y., Tsend, N., Li, T. K., Liu, H., Yang, R., Gai, X., et al. (2019). Microwave-assisted hydrothermal preparation of rice straw hydrochars for adsorption of organics and heavy metals. *Journal of Bioresource and Technology*, 273(8): 136-143.
25. Haseen, U., Ali, S. G., Umar K., Ali, A., Ahmad, H. and Khan, H. M. (2021). Dimercaptosuccinic acid functionalized polystyrene column for trace concentration determination of heavy metal ions: Experimental and theoretical calculation studies. *Water (Switzerland),*13(21).
26. Hassan, A. M., Wan, I. W. A., Bakar, M. B., Sanagi, M. M., Sutirman, Z. A., Nodeh, H. R., et al. (2020) New effective 3-aminopropyltrimethoxysilane functionalized magnetic sporopollenin-based silica coated graphene oxide adsorbent for removal of Pb(II) from aqueous environment. *Journal of Environmental Management,* 253(10): 109658.

27. Ahmad, N. F., Kamboh, M. A., Nodeh, H. R., Halim, S. N. B. A. and Mohamad, S. (2017). Synthesis of piperazine functionalized magnetic sporopollenin: a new organic-inorganic hybrid material for the removal of lead(II) and arsenic(III) from aqueous solution. *Journal of Environmental Science and Pollution Research,* 24(27): 21846-21858.
28. Nasirimoghaddam, S., Zeinali, S. and Sabbaghi, S. (2015). Chitosan coated magnetic nanoparticles as nano-adsorbent for efficient removal of mercury contents from industrial aqueous and oily samples. *Journal of Industrial and Engineering Chemistry*, 27: 79-87.
29. Upadhyay, U., Sreedhar, I., Singh, S. A., Patel, C. M. and Anitha, K. L. (2021). Recent advances in heavy metal removal by chitosan-based adsorbents. *Journal of Carbohydrate Polymer,* 251(8): 117000.
30. Kloster, G. A., Mosiewicki, M. A and Marcovich, N. E. (2019). Chitosan/iron oxide nanocomposite films: Effect of the composition and preparation methods on the adsorption of congo red. *Journal of Carbohydrate Polymer,* 221(3):186-194.
31. Wang, J., Zheng, C., Ding, S., Ma, H. and Ji, Y. (2011). Behaviors and mechanisms of tannic acid adsorption on an amino-functionalized magnetic nano adsorbent. *Journal of Desalination*, 273(2–3): 285-291.
32. Li, X., Wu, X., Chen, J., Li, Y. and Yang, Y. (2019) Alginate-enfolded copper hexacyanoferrate graphene oxide granules for adsorption of low-concentration cesium ions from the aquatic environment. *Journal of Radioanalytical and Nuclear Chemistry*, 320(3): 655-63.
33. Fýl, B. A., Boncukcuoglu, R., Yilmaz, A. E. and Bayar, S. (2012) Adsorption kinetics and isotherms for the removal of zinc ions from aqueous solutions by an ion-exchange resin. *Journal of Chemical Society of Pakistan*, 34(4): 841-848.
34. Nasir, A. M., Md, N. N. A. H., Goh, P. S. and Ismail, A. F. (2018) Application of two-dimensional leaf-shaped zeolitic imidazolate framework (2D ZIF-L) as arsenite adsorbent: Kinetic, isotherm, and mechanism. *Journal of Molecular Liquids,* 250: 269-277.
35. Gubbuk, I. H. (2011). Isotherms and thermodynamics for the sorption of heavy metal ions onto functionalized sporopollenin. *Journal of Hazardous Materials*, 186(1):416-22.
36. Sutirman, Z. A., Sanagi, M. M. and Wan, A.W. I. (2021). Alginate-based adsorbents for removal of metal ions and radionuclides from aqueous solutions: A review. *International Journal Biological Macromolecules,* 174: 216-228.
37. Elwakeel, K. Z., El-Bindary, A. A., Kouta, E. Y. and Guibal, E. (2018). Functionalization of polyacrylonitrile/Na-Y-zeolite composite with amidoxime groups for the sorption of Cu(II), Cd(II) and Pb(II) metal ions. *Chemical Engineering Journal*, 332(7): 727-236.
38. Hu, C., Zhu, P., Cai, M., Hu, H. and Fu, Q. (2017). Comparative adsorption of Pb(II), Cu(II), and Cd(II) on chitosan saturated montmorillonite: Kinetic, thermodynamic and equilibrium studies. *Applied Clay Science Journal,* 143(4): 320-326.
39. Li, X., Wang, S., Liu, Y., Jiang, L., Song, B., Li, M., et al. (2017). Adsorption of Cu(II), Pb(II), and Cd(II) ions from acidic aqueous solutions by diethylenetriaminepentaacetic acid-modified magnetic graphene oxide. *Journal of Chemical Engineering Data*, 62(1): 407-416.
40. Behbahani, E. S., Dashtian, K. and Ghaedi, M. (2021). Promise magnetite LDH-based adsorbent for simultaneous removal of Pb(II), Cd(II), and Cu(II) heavy metal ions. *Journal of Hazardous Materials*, 410(11): 124560.

Malaysian Journal of Analytical Sciences (MJAS)
Published by Malaysian Analytical Sciences Society

MICROSCOPIC, SPECTROSCOPIC AND THERMOANALYTICAL CHARACTERIZATIONS OF MODIFIED PALM OIL AND RICE BRAN OIL INTO BIOPOLYMERS

(Ciri-Ciri Mikroskopi, Spekroskopi dan Termoanalitik Minyak Kelapa Sawit Dan Minyak Dedak Padi yang Diubahsuai Menjadi Biopolimer)

Hui Ying Wong[1], Radiah Ali[1], and Sabiqah Tuan Anuar[1,2]*

[1]*Faculty of Science and Marine Environment,*
Universiti Malaysia Terengganu, 21030 Kuala Nerus, Terengganu, Malaysia
[2]*Microplastic Research Interest Group (MRIG),*
Universiti Malaysia Terengganu, 21030 Kuala Nerus, Terengganu, Malaysia

[*]*Corresponding author: sabiqahanuar@umt.edu.my*

Received: 25 September 2022; Accepted: 30 March 2023; Published: xx April 2023

Abstract

This study reported an approach of producing biopolymer material from epoxidation of vegetable oils such as palm oil and rice bran oil. The epoxidation of vegetable oils converts from carbon double bonds into oxirane group and achieves by using the conventional method of *in situ* generated formic acid for 6 hours followed by further treatment with citric acid. The presence of oxirane group was proven by Spectroscopy (FTIR) analysis, and shown at the wavenumber of 773 cm^{-1}. Through direct titration, oxirane oxygen content (OOC) for epoxidized palm oil (EPO) and epoxidized rice bran oil (ERBO) were both determined as 2.89% and 3.05% respectively. Surface morphological studies were carried out for both EPO and ERBO bioplastic films by using Scanning Electron Microscopy (SEM). Further analysis with Energy Dispersive X-ray (EDX) spectroscopy showed 68.93% and 78.80% of carbon mass percentages for EPO and ERBO films, respectively. Whilst oxygen mass percentages were exhibited in EPO and ERBO as 31.07% and 21.20%. EPO film is degraded to approximate 50% at 223 °C whereas ERBO at 225 °C from thermogravimetric analysis (TGA). This green initiative of creating bioplastic film is desired to be a substitution for current plastic product which is mostly non-degradable. In long term prospect, it is also hoped to answer to the global plastic issues such as land dumping site and ocean plastic pollution that brings adverse effect to the marine organisms.

Keywords: bioplastic, Malaysian crops, edible oil, plastic pollution

Abstrak

Kajian ini melaporkan pendekatan untuk menghasilkan bahan biopolimer daripada proses pengepoksidaan minyak sayuran seperti minyak kelapa sawit dan minyak dedak padi. Pengepoksidaan minyak sayuran menukarkan daripada ikatan berganda karbon kepada kumpulan oksirana dan dicapai dengan menggunakan kaedah konvensional asid formik secara *in situ* selama 6 jam diikuti dengan rawatan lanjut dengan asid sitrik. Kehadiran kumpulan oxirane telah dibuktikan oleh Spektroskopi (FTIR) analisis, dan ditunjukkan pada nombor gelombang 773 cm^{-1}. Melalui pentitratan terus, kandungan oksigen oksiran (OOC) untuk minyak kelapa sawit terepoksida (EPO) dan minyak dedak padi terepoksida (ERBO) kedua-duanya ditentukan sebagai 2.89% dan 3.05%. Kajian

morfologi permukaan telah dijalankan untuk kedua-dua filem bioplastik EPO dan ERBO dengan menggunakan Mikroskopi Pengimbas Elektron (SEM). Analisis lanjut menggunakan spektroskopi X-ray Penyebaran Tenaga (EDX) masing-masing menunjukkan 68.93% dan 78.80% peratusan jisim karbon untuk filem EPO dan ERBO. Sementara itu, peratusan jisim oksigen dipamerkan dalam EPO dan ERBO sebagai 31.07% dan 21.20%. Filem EPO terdegradasi dianggarkan 50% pada 223 °C manakala ERBO pada 225 °C daripada analisis termogravimetrik (TGA). Inisiatif untuk mencipta filem bioplastik ini diingini untuk menjadi pengganti kepada produk plastik semasa yang kebanyakannya tidak terdegradasi. Dalam prospek jangka panjang, ia juga diharap dapat menjawab isu plastik global seperti tapak pelupusan tanah dan pencemaran plastik lautan yang membawa kesan buruk kepada organisma marin.

Kata kunci: bioplastik, tanaman Malaysia, minyak makan, pencemaran plastik

Introduction

The production of plastic globally was recorded more that 280 million tonnes in 2012, and increase to more than 335 million tones 4 years later [1]. These numbers are expected to grow exponentially over the next 20 years. Part of these plastics can be recycled; however, it was reported that only 21% is recovered over 91% plastic waste, where no less than 8 million tons of plastic as of now winds up in the sea consistently [2]. In Malaysia, the generation of plastic wastes has consistently increased 5% of every 5-years since 1995, where it was reported to produced 0.94 million tonnes in the year of 2018 [3], and projected to exceed 1 million tonnes in 2022. In environment, mismanaged plastic that underwent weathering or degradation process can broke down into smaller pieces to form secondary microplastics, which leads to many questions on the environmental, ecological and human health risks posed by them [4-5]. Therefore, the production of bio-based polymers (bioplastics) has gain interest from the world, as part of mitigation of this issue. With the price of petroleum is continually increase and the problem arise from environmental issues become the factors to utilize biodegradable products, for instance from vegetable oil. Bioplastic is considered to be a great alternative of petroleum free plastic in the industry. To maximize the value of bioplastic, its production should be done by using more environmentally friendly or greener method and resource. It could be seen that fast-growing trend on bioplastic is replacement for the petroleum in polymer industry as it is helpful in reducing a huge tons of carbon dioxide and the usage of petroleum [6].

The term of “bio” in bioplastic is defined as biological based derived plastic or polymer product such as vegetable oil, cellulose, and starch products that undergo chemical reaction to change into associated form, which later can degrade easily or able to be decomposed by microorganisms, therefore it is more sustainable and eco-friendlier [7]. For instance, vegetable oil-derived bioplastic is a type of vegetable oil-based cross-linking polymer plastics that has many repeating units. While fatty acid profiles of commodities such as soy bean and canola oils are major lipid of interest in the world in producing lipid biopolymer, local commodities Malaysia such as palm oil and rice bran oil were given consideration in this proposed study. Malaysia has ranked the top world largest exporter for palm oil production and second largest for palm oil production just a place right after Indonesia [8]. This oil can be obtained from harvesting the cluster or a bunch of palm oil fruit (*Elaeis guineensis*) at about forty to fifty kilograms. Meanwhile, rice bran oil is edible oil that is extracted from the brown husk outer layer of the rice. It has the smoke point at about 232 °C and often suitable for stir frying and deep frying in cooking. A brown husk of rice bran oil can be extracted up to 75% of the oil that is commonly wasted if there is no further research on it. Rice bran oil is obtained from the brown outer coating using hexane extraction and to get 8 to 16% of oil through the process of germ grinding, dehulling and polishing of rice [9]. Refined rice bran oil is often existed in light yellow liquid and highly stable due to the presence of tocopherols (vitamin E) of 320 mg/kg, oryzanols about 2% [9].

These oils are being utilized to produce bioplastic through feasible way of epoxidation process. Epoxidation is one of several reactions that can be carried out to utilize the fatty chain of edible oil in a reasonable cost. Various functional groups can be inserted into the double bond which acts as the reactive

site in the vegetable oils. It was widely proven that oils with high properties of saturated fatty acid and triacylglycerol's are more suitable for the application of fuel biodiesel, while polyunsaturated acids are permitted to participate in conversion of carbon-carbon double bond alkene into epoxy compound is known as epoxidation process [10] that later can be transformed to lipid biopolymer or bioplastics. Nevertheless, epoxidation of vegetable oil has become the popular research to be done by most of the scientist as it is worth at certain values. This is a solution to substitute non-renewable resources of petroleum to act as one of the plasticizers, known as epoxide. There are four major types of methods to produce epoxidation using fatty acids such as epoxidation with percarboxylic acid or acid catalyzed or enzymatic, organic or inorganic with alkaline and nitrile hydrogen peroxide, halohydrins by using hypohalous acids and salt reagent and molecular oxygen [11]. Some of the epoxides with high oxirane oxygen contents and functional epoxy group presence in the chemical structure of epoxidized vegetable oil, it is required a hardening agent to produce bio-based polymer [12]. High viscosity of vegetable oils is commonly implemented in the applications as lubricant and additives in polymer science such as resins and coatings. Our preliminary findings show that the epoxidation reaction, this can be followed by the cross-linking polymerization could be carried out on the reactive sites. Since both oils have differences in the type of fatty acids and their degree of unsaturation, this can impose conditions on their final use for the development of new products such as bio-based polymer and resins.

Materials and Methods

Materials

The following chemicals were purchased from R&M Chemicals (Malaysia): hydrogen peroxide (H_2O_2; 35%), anhydrous sodium sulphate, crystal violet indicator, HPLC grade acetonitrile, sodium chloride and glacial acetic acid. Formic acid (HCOOH; 98%), sodium bicarbonate, hydrogen bromide solution 33 wt.% in acetic acid, 2-propanol gradient grade for liquid chromatography (LiChrosolv) and acetonitrile hypergrade for LC-MS (LiChrosolv) were all purchased from Merck (KGaA, Germany). Citric acid-1-hydrate was purchased from HmbG Chemicals (Germany). Sodium hydroxide in pellets (analytical grade) was purchased from Fisher Scientific (Malaysia). Smith filter paper 101 Qualitative 90 mm was used for filtration purpose. The chemicals used in the study were of analytical grade unless stated otherwise. Palm oil and rice bran oil were purchased from the local market.

Epoxidation of palm oil (PO) and rice bran oil (RBO)

The heating process was begun from 55 °C and monitored carefully. Hydrogen peroxide (H_2O_2; 35%) of 34 mL was dropped wisely due to its exothermic effect that may cause explosion and continuously stirred with the fastest speed. The reactions were taken about six hours to complete. The epoxidized oils were washed with n-hexane, 5% wt. sodium hydroxide (NaOH) and 5% wt. sodium chloride (NaCl). Anhydrous sodium sulphate (Na_2SO_4) of 2 g was added and filtered with Buchner funnel.

Bio-polymerization using citric acid as curing agent

Concentrated citric acid was prepared by mixing 4 parts according to the weight of CA.H_2O ($C_6H_8O_7H_2O$) and one part of distilled water and heated up to 90 °C. Poured the completely dissolved solution into the glass beaker which contained 2 g of epoxidized palm oil or rice bran oil at 90 °C. Solution was stirred to form a layer of emulsion between aqueous citric acid and epoxidized oils. The viscosity would increase as the gelation formed at the same time. The solution was constantly stirred for 10 minutes at 90 °C until it gradually turned translucent and poured into the aluminium mould. The readily samples were both put into the oven (Universal Oven UF110 Memmert). Bio-polymerisation was started for 6 hours at 90 °C and 12 hours at 110 °C. Post curing at 120 °C for an hour and low drying mode at 35 °C to remove moisture for 2 hours.

Chemical analysis of oil and epoxidized oil: Liquid chromatography-mass spectrometry for fatty acid determination

An oil aliquot of 3 g (starting material) was obtained and diluted with 10 mL of ethyl acetate. It was followed by washing with 15 mL of brine (saturated sodium chloride) solution. The mixture was left for a while and later separated into two layers. Upper layer was

collected and washed with 15 mL of 1 M sodium bicarbonate ($NaHCO_3$) solution. Aqueous layer was removed and dried the upper layer with anhydrous sodium sulphate. Nitrogen evaporator (Organomation, N-EVAP 111) was used to concentrate the oils. The oils were weighted and diluted to 0.1 mg/mL in dichloromethane before LC MS/MS analysis for the analysis of fatty acid composition.

Liquid Chromatography Ion-trap Time-of-flight Mass Spectrometer (HPLC-MS-TOF, Shimadzu, Japan) is a unique combination of tandem mass spectrometer and ion trap (IT) with a time of flight (TOF) where ion trap allows MS^n capacity. A Supelco C_{18} column (250 mm x 4.6 mm i.d., particle size 5 µm) (Sigma Aldrich, ON, Canada) was used with the following linear gradient at a flow rate of 200 µL/min with an injection volume of 1 µL: Solvent A is isopropanol (IPA); Solvent B is Acetonitrile (ACN); t = 0, 20% A, hold 0.1 min; t = 25 mins 90% A. Data were acquired using ESI in the positive ion mode, with the following instrumental parameters : declustering potential (DP) at 45 V focus potential (FP) at 150 V; declustering potential 2 (DP2) at 10 V; gas (GAS 1) at 20; nebulizing gas (GAS 2) at 60; and an ion spray voltage of 5200 V [13].

Determination of oxirane oxygen content

Epoxidized oils was tested using AOCS Cd 9-57 for oxirane oxygen value. The direct titration of oils (0.5 g prepared in 10 mL glacial acetic acid) with 0.1 N 33% hydrogen bromide solution (in acetic acid) and was assisted with the use of 0.025% crystal violet indicator solution [14].

Fourier transform infrared spectroscopy (FTIR)

An amount of one-gram of each sample was used for FTIR analysis. The spectra were recorded 4 cm^{-1} resolution on IR spectrophotometer (Perkin Elmer, model FTIR Spectrum 100, Waltham, MA, USA). Data of absorbance against wavelength was generated by FTIR software (Perkin Elmer, OMNIC series suite, MA, USA). Epoxidized palm oils and epoxidized rice bran oils were recorded in transmission mode from 400 cm^{-1} to 4000 cm^{-1}.

Physicochemical analysis of of biopolymer product: Scanning electron microscopy analysis

Thin films were coated with gold using Auto Fine Coater (JFC – 1600, JEOL, Japan). The surface morphology of the bioplastic films was studied using Scanning Electron Microscopy (SEM model JSM - 6360LA, JEOL, Japan) at an accelerating voltage of 30 kV [15]. EDX analysis was done to determine the percentage of carbon and oxygen presence in the thin films.

Thermogravimetric analysis

Thermal degradation of the bioplastic films was both analysed by using thermogravimetric analyser (TGA851/LF 1100, Mettler Toledo). All samples were tested used a mass of approximately 70 mg under a nitrogen flow of 50 mL/min and heating rate of 10 °C /min within temperature range of 20 °C to 900 °C [16].

Results and Discussion

Fatty acid determination and epoxidation of edible oils

The main composition of the starting oils was determined to confirm the fatty acid profile for both starting oils and is illustrated in the Table 1. The commercial cooking oil of palm oil (olein) is made up of major of about 41.5% of C18:1 or oleic acid, followed by 40.2% of C16:0 (palmitic acid), 11.8% of C18:2 (linoleic acid), 5.3% of C18:0 (stearic acid) and 1.2% of other fatty acid constituent (e.g. lauric, myristic, palmitoleic and linolenic acids). This agreed with previous research on other commercial palm oil which usually consisting of 42-45% of palmitic acid, 40-42% of oleic acid and 9-11% of linoleic acid and very small amount of stearic and linolenic acid [17-18]. Meanwhile, rice bran oil is made up of the major composition of unsaturated fatty acids such as oleic acid (C18:1, 45.6%) and linoleic acid (C18:2, 28.3%) followed by saturated fatty acid of C16:0 (palmitic acid) at 22.1%. Previously, Purwanto (2010) and Punia et al. stated that this oil has fatty acid composition of palmitic acid (10-20%), stearic acid (1-5%), 39-43% oleic acid and 28-35% linoleic acid, depending on the method used in the oil extraction process [19-20]. The unsaturation profile of both oils was found to be suitable for further modification by epoxidation reaction.

Table 1: Major fatty acid constituent of edible oils used in the study

Fatty Acid	Composition (%)	
	Palm Olein	Rice Bran Oil
C16:0 (palmitic acid)	40.2	22.1
C18:0 (steric acid)	5.30	1.83
C18:1 (oleic acid)	41.5	45.6
C18:2 (linoleic acid)	11.8	28.3
others	1.20	2.17

Epoxidation with peracid formed *in situ* with hydrogen peroxide is a conventional method that widely used in the large-scale industry. As such, the better selection of formic acid is used in the experiment to enhance the break the unsaturated carbon double bonds into the epoxy group than acetic acid at around 60 °C [19]. There are some negative impacts of high concentration of formic acid towards the selectivity for conversion of oxirane oxygen thus reduced the final yield of epoxy group [21]. Commercialized palm oil (PO) and rice bran oil (RBO) were both underwent performic acid in situ epoxidation at 55 °C and the results shown was low epoxidation rates due to low reaction temperature, similar to the findings by Danov et al [22]. Hydrogen peroxide of 35% is dropped slowly due to its unstable reactivity and avoided adding in once the temperature exceeded higher than 85 °C. During the epoxidation process, RBO was heated to slightly viscous and turned from yellow to slight burnt brown colour in the middle of heating process. This due to the presence of phospholipid in the RBO and the antioxidant effect had caused the oil to brown darkening for several minutes during heating process. Fast stirring was continuously carried out in order to homogenize the viscous vegetable oil and but it could probably decrease the rate of epoxidation and deteriorate the formation of epoxy group [22]. Excessive epoxy ring opening reactions also would appear if the occurrence of side reactions at reaction temperature higher than 70 °C [23]. Stable oxirane rings were achieved at lower temperature and epoxidation under higher temperature was not recommended due to the exothermic effect of hydrogen peroxide that may lead to an explosion [24]. In situ generated formic acid with hydrogen peroxide was a reversible process to occur hydrolysis as it attributed by oxygen carrier from hydrogen peroxide to form peroxyformic acid. The repeatability of this method was done for several times on both PO and RBO to get the most accurate results.

A significant indication to the end of epoxidation process is the formation of light viscous liquid for both EPO and ERBO which takes about six to eight hours. This is faster than previously reported where the reaction for epoxidation process of vegetable oils could be accomplished up to 48 hours, depending on the reaction conditions and parameters [23]. Epoxidized vegetable oil (EVO) by acid generated in situ had achieved the reaction mechanism in two stages. The first step is hydrogen peroxide reacted with concentrated formic acid to form performic acid and water which is also known as hydrolysis process [24]. In the presence of water, performic acid catalysed the ring opening of unsaturated bonds of fatty acid and leading to the cleavage of oxirane rings in stage two [25]. However, a reversible process of formic acid regeneration is more likely to occur due to the unstable oxirane rings and again promote the epoxide group to undergo hydrolysis process [26].

FTIR analysis

Based on the analysis of Fourier Transform Infrared Spectroscopy (Table 1), the palm olein is converted to epoxidized palm oil. It can be seen at the C=O overtone from 3476 cm^{-1} in Figure 1(a) is changed to 3524 cm^{-1} broad stretching of OH in Figure 1(b) which resulted in ring opening of epoxy group [11, 27]. The absence of 3006 cm^{-1} at Figure 1(b) indicates the formation of epoxidation of palm oil and C=C was broken at the reaction. A missing peak of double bonds in the same figure represents that almost 100% conversion into C-O-C, epoxide group [28].

Palm oil has C=C bonds at the wavenumber of 3006 cm^{-1} at Figure 2, but the existence of epoxidation process had diminished this peak to 2927cm^{-1} CH stretching at Figure 3. In FTIR spectrum, epoxidized palm oil is shown a sharp and broader at the wavenumber of 1735 cm^{-1} C=C alkene bonding than the peak of C=O bonds at 1747 cm^{-1} in Figure 2. Stretch vibration of C-O-C ester group is noticeable at 1176 cm^{-1} [15] . Previously, it was reported that C-H rocking for epoxide band also occurred at 725 cm^{-1} in the epoxidized palm oil as proven by the wavenumber of 725 cm^{-1}. It is believed that the sensitivity of FTIR instrument lack of precision due to the disturbance of carbon dioxide because a peak of 844 cm^{-1} is not existed in the EPO, albeit small peak was observed at 831 cm^{-1}. All the functional groups of palm oil and epoxidized palm oil are tabulated in Table 2.

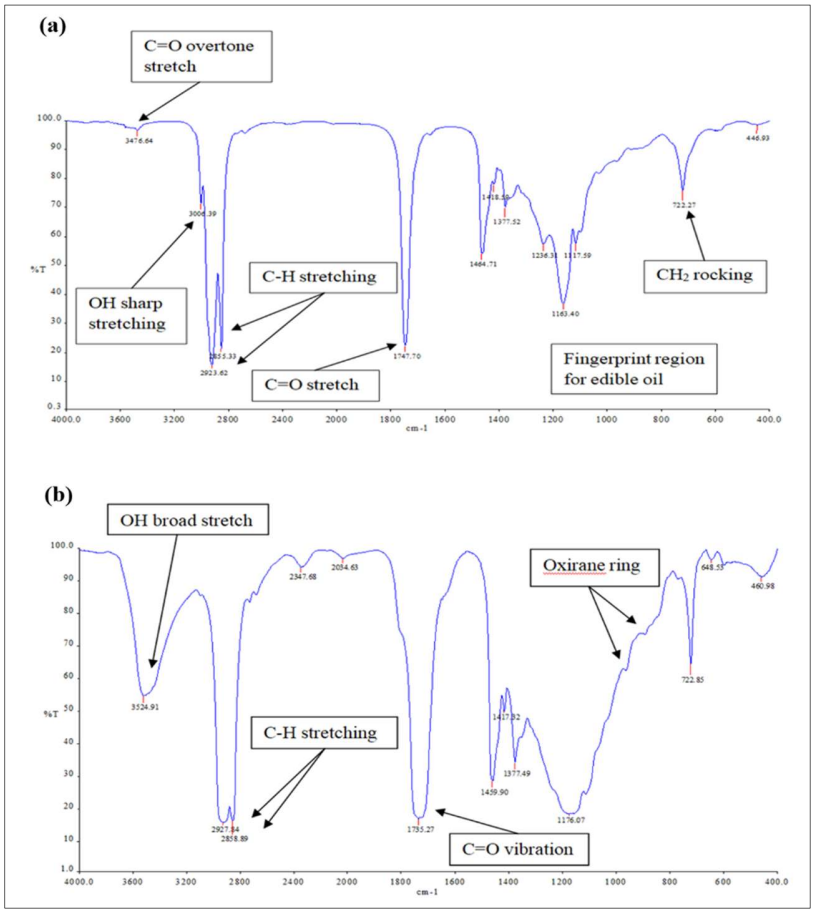


Figure 1. The FTIR spectra for (a) PO and (b) EPO

Separately, there is also an overtone of C=O at wavenumber of 3565 cm^{-1} in the RBO and a broad OH bond stretching at 3500 cm^{-1} , similarly as PO. From the IR spectrum of rice bran oil (Table 2; figure not included), it has a sharp C=O stretch at the wavenumber 1746 cm^{-1} whereas in epoxidized rice bran oil (ERBO) this peak has shifted to a lower wavelength range of 1728 cm^{-1}, similar to the infrared spectrum reported in [25]. Additionally, there is an existence of oxirane oxygen content (OOC) at the wavenumber of 773 cm^{-1} for ERBO when compares to RBO. This showed the

complete conversion of C=C double bonds into C-O bonds.

Based on the infrared frequency table, the spectrum falls under the range of wavenumber from 750 cm^{-1} to 825 cm^{-1} is a monosubstituted epoxides as a proof to RBO being epoxidized. There was a disappearance of C=C at the wavenumber of 3008 cm^{-1} of rice bran oil which is extremely approximate to the 3007 cm^{-1} reported by the author Gupta et al., [29] . From the results of rice bran oil and epoxidized rice bran oil, it could be seen that the patterns and wavenumber are almost totally matched to the experimental graph in the waste rice bran oil and epoxidized waste rice bran oil [29]. Ring opening of ERBO is indicated at 3500 cm^{-1} which has minor variation to the stated wavenumber of 3440 cm^{-1} from the same study.

Table 2. The IR frequency tables for both palm oil and rice bran oil before and after epoxidation are tabulated

		PO	RBO
	Functional Group	**Wavenumber (cm^{-1})**	**Wavenumber (cm^{-1})**
Before epoxidation	C=O (overtone)	3476	3565
	C=C (sharp stretch)	3006	3008
	C-H (stretch)	2923, 2855	2925, 2854
	C=O (stretch)	1747	1746
	CH_2 (rocking)	722	722
After epoxidation	OH (broad)	3524	3500
	C-H (stretch)	2927, 2858 c	2926, 2855
	C=O (vibration)	1735	1728
	C-O-C (vibration)	1176	1175
	C-O-C (oxirane)	831	825

Oxirane oxygen content

EPO and ERBO were later tested for the epoxy weight percentage analysis by using a direct titration method with 0.1 N hydrogen bromide (HBr) solution in 33% of acetic acid. This method was successfully measured the oxirane oxygen content (OOC) and show the epoxidation state of the reaction. An equilibrium point was achieved when the crystal violet solution had changed to blue green which represented the existence of OOC [30]. The oxirane oxygen for the EPO in the first, second and third tests (triplicate) were obtained at 2.96%, 2.80% and 2.90% respectively. Hence an average result of oxirane values was calculated for EPO as 2.89%, and this is closely approximate to the range of 2.7 to 2.9 % by author Tajulruddin et al. [31]. For ERBO that has been synthesized, the oxirane oxygen were recorded at 2.98%, 2.90% and 3.28% for triplicate analysis. The RBO was synthesized originally from waste rice husk so the ERBO has an average OOC of 3.05% which is very approximate to the 3.2% reported by Gupta et al., [29]. Hence, there was an inverse relationship between the conversions of OOC to the increasing reaction time of epoxidation. However, this would not much be affecting the final yield of the product since the difference in the percentage conversion is small. The percentage of the OOC value obtained from the current study was tabulated as below in Table 3.

Table 3. Oxirane oxygen content (OOC) of both EPO and ERBO

Sample	**1**	**2**	**3**	**Average**
EPO	2.96%	2.80%	2.90%	2.89%
ERBO	2.98%	2.90%	3.28%	3.05%

Curing of films with citric acid

A recent trend of biodegradable polymerization is usually focussed on the organic weak citric acid that made up of three carboxylic acids, COOH groups. Epoxidized oils that has good heat stabilizer are very beneficial in the production of plastics. EPO and ERBO were blended separately with 2 g of citric acid and 0.5 mL of distilled water and agitated to mix well. To promote the cross-linking of epoxidized oil and citric acid to form bio polymeric film, it was heated at 90 °C to enhance the effect. Epoxide is cyclic ethers with three membered-ring that is produced from peracids with alkenes. Vegetable oils for instance PO and RBO that are composed of oleic acid (C18:1), linoleic acid (C18:2), linolenic acid (C18:3) (Table 1) which allowed for conversion of bonds by peracids into epoxides. Asymmetric epoxides would undergo solvolysis by methanol and the ring opened by SN_2 mechanism where nucleophilic attacked at the less-substituted carbon region. In contrary, solvolysis also could be existed in acidic methanol and this reaction mechanism would be attacked at the more substituted site of carbon [32]. In the present study, citric acid acted as a curing agent and catalyst to epoxidized oils in which consisted of epoxy and triglycerides to produce polymeric films from renewable materials using vegetable oils. The reaction between epoxidized oil and citric acid was appeared in a translucent viscous gel that is known as biodegradable, non-toxic and greener biopolymer [33].

In this study, bio-polymerization process was started by mixing the epoxide oil with the curing agent at the first 6 hours (90 °C) reaction, followed by another 12 hours (110 °C) for hardening of the films in the oven. Previously, Kolanthai et al. [34] reported that the higher citric acid concentration will lead to fragility of the polymer film that might break into smaller pieces. Hence, a modified method was implemented during post-curing process. The original post-curing method by author Altuna et al. [35] was conducted at 150 °C under a monitoring period, but in the present study the temperature for post-curing was set at 120 °C for one hour to avoid the excessive burning of the samples. The biopolymer films were further dried under low oven drying mode at 35 °C for another 2 hours to remove the wettability or water content from the films. Oven dried of films were relatively carried out under a controlled environment of temperature, humidity and air circulation, thus helped to boost the water evaporation compared to the silica gel in desiccators method.

SEM-EDX analysis of bioplastic film

Scanning electron microscopy (SEM) that coupled with the function of energy dispersive X-ray (EDX) was used as a preliminary method to determine quantitative compositional data of the biopolymer film by observing the mass percentage of carbon and oxygen elements (Table 4). EPO shows that 74.72% of carbon atomic and 25.28% of oxygen atomic in the composition of its bioplastic film. While bioplastics from ERBO consists of 83.20% of carbon atomic, thus can be used to predict that the ERBO has longer chain than EPO. This is because the epoxidation will break the double bonds and increases the number of carbon single bonds as monomers repeating unit cross linked with each other in the polymerization process.

Table 4. EDX data analysis for EPO and ERBO bioplastic films produced

Sample	Element	(keV)	Mass%	Atomic%
EPO	C	0.277	68.93	74.72
	O	0.525	37.07	25.28
ERBO	C	0.277	78.80	83.20
	O	0.525	21.20	16.80

Epoxidized palm oil is suitable to cure with citric acid, as Figure 2a shows that EPO bioplastic film has a smooth and illuminating surface at 30 times of magnifications. There is a correlation to the increasing amount of citric acid blend towards the compatibility of bioplastic, similar to the previous reported findings by Ouipanich et al. [36]. Figure 2b shows the uneven surface thickness of the specimen but high miscibility due to strong hydrogen bonding interactions with epoxy, hydroxyl and carbonyl group making a smooth surface

[27]. It shows uniform vertical stripes and grid pattern under 1000 magnifications at an accelerating voltage of 10 kV. Epoxidized palm oil film is in long cross-linking shape and homogenously distributed under the boost of high temperature curing in Figure 2c. The overall of the film is concluded as very brittle due to the uneven surface thickness and fracture.

Meanwhile, epoxidized rice bran oil (ERBO) bioplastic film illustrates a clear and shiny image. It can be seen that the pattern is looked like cracked fracture dry land in Figure 3a. The crackle is short and distributed homogeneously on the entire surface of the specimen. As the numbers of crack front increasing on bioplastic film, the higher the flexibility and the ductility of the film [11]. It shows horizontal stripes at 30 times of magnification. Figure 3b is open-pores image that shows on the surface of the film and they are cross linking like bee hives, similar to the finding elsewhere [37]. The presence of voids on Figure 3b under magnification of 350 times is due to the degree of dispersion of citric acid in the polymerization of epoxidized rice bran oil. Hence, it can be explained by the increasing of natural glycerol content in vegetable oil will decrease the tendency to form void and increase the phase separation [38]. Meanwhile, in Figure 3c, a round spot is virtually observed, with the round holes shaped of the pores is noticeable at 1000 magnification of 10 kV accelerating voltage.

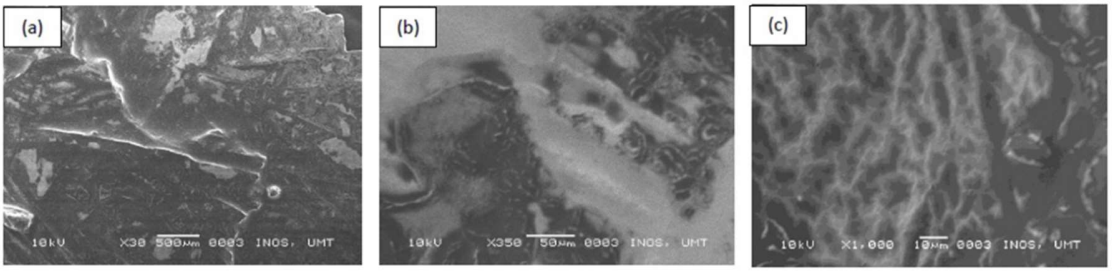


Figure 2. SEM micrograph for different magnifications of EPO bioplastic film at 10kV of (a) 30X, (b) 350X, (c) 1000X magnifications

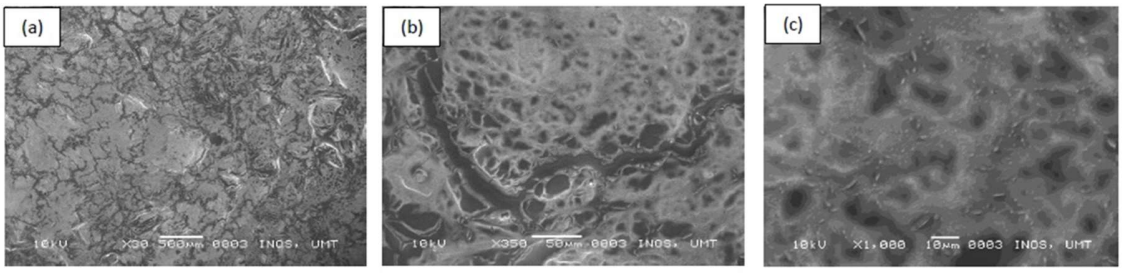


Figure 3. SEM micrograph for different magnifications of ERBO bioplastic film at 10kV of (a) 30X, (b) 350X, (c) 1000X magnifications

Thermogravimetric analysis (TGA)

Thermogravimetric is the analysis that provided information on the weight loss with the increasing of temperature in order to obtain the degradation level of biopolymeric films under an inert nitrogen environment. To observe the thermal behaviour of biopolymer films, the initial decomposition temperature, 50% degradation level and maximum decomposition rate are recorded in TGA and DTG curves. In general, the results show that the films could started degrading at higher temperature (>180 °C), thus proven that formation of biopolymers was successful. Figure 4 shows thermogravimetric

analysis of biopolymer made from EPO and ERBO is illustrated as three stages according to the percentage of degradation. While, table 5 shows the thermal degradation of biopolymer films at different temperatures.

Table 5. Thermal degradation of epoxidized oil biofilms at different temperatures

Sample	T_i(°C)	Wt.%	T_{50}(°C)	Wt.%	T_{max}(°C)	Wt.%
EPO film	29.10	70.56	223.35	36.71	895.46	8.32
ERBO film	30.28	70.54	224.90	35.29	897.65	7.30

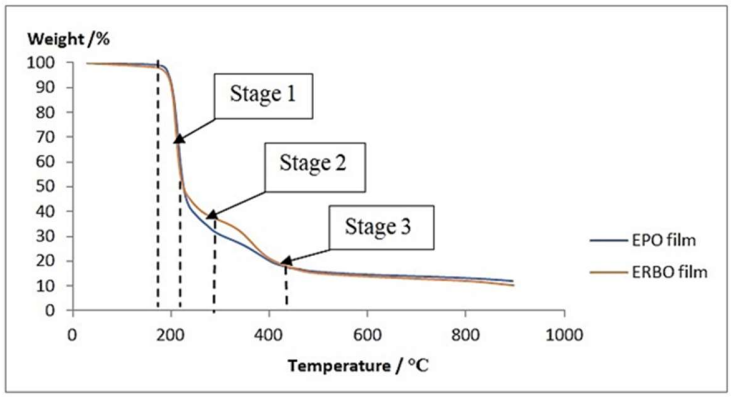


Figure 4. The thermogravimetric analysis of epoxidized palm oil (EPO) and epoxidized rice bran oil (ERBO) biopolymer films on weight percentage

From thermogravimetric analysis (TGA), the starting temperature (T_i) for biopolymer made from EPO film is 70.56 mg at 29.10 °C in Figure 5a. It is started to degrade at 182 °C and left 36.71 mg or 52% of the product at 223 °C. At 895 °C, it only contains a residue of 8.32 mg for EPO film. There is some weight loss at the initial stage of EPO biopolymer film due to the evaporation of water at the temperature between 37 °C to 176 °C, similar to the previously reported [16]. According to the first differential thermogravimetric curve (DTG), it illustrates in Figure 5b that the maximum degradation of EPO at 38% weight remained for biopolymer film at 252 °C [37].

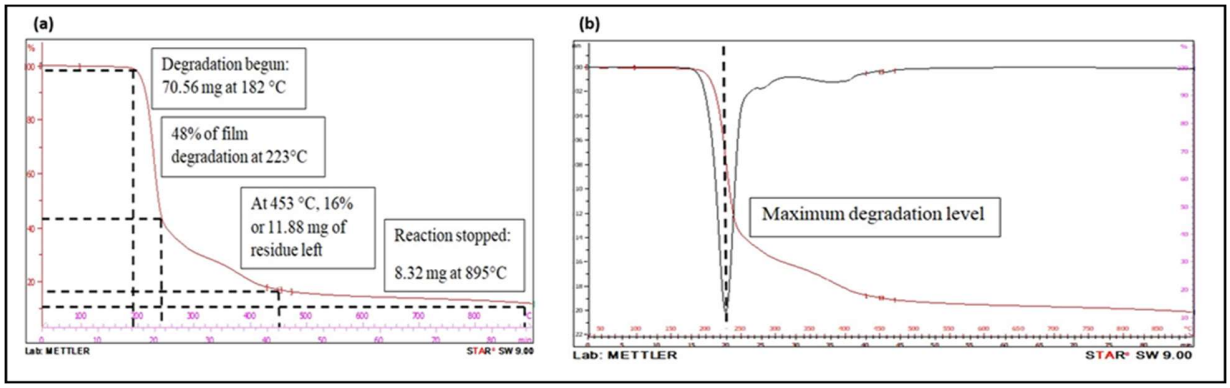


Figure 5. (a) Weight percentage of EPO from TGA curve, and (b) DTG thermograms from TGA curve of EPO

While in ERBO, it is first beginning with 70.54 mg at 30 °C in Figure 6. Then, it is started to decompose at 106 °C and remain 35.29 mg or 50% at 225 °C. At the end process of 897 °C, there is a 7.30 mg or 10% of ERBO film residue. Whilst, the differential thermogram (DTG) shows that the 257 °C is the maximum degradation level of ERBO in Figure 6 which still has 41% of the original product remained as biopolymer film. It is suggested that thermal decomposition of ERBO is well cross-linked with citric acid in order to have longer polymerization chain length, hence it is observed to degrade at slightly higher temperature compare to EPO film. This is found to be similar to the finding by an earlier study, where they reported that the contribution of network structures in enhancing the thermal stability of the biopolymer material [39].

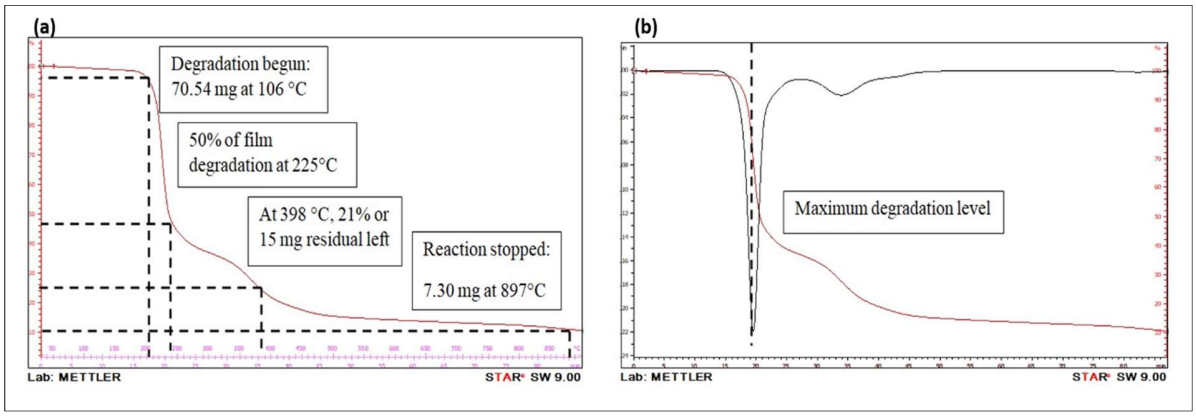


Figure 6. (a) Weight percentage of ERBO from TGA curve, and (b) DTG thermograms from TGA curve of ERBO

Conclusion

In this present study, the epoxidation process of palm oil (PO) and rice bran oil (RBO) were succesfuly converted the double bonds into epoxides that subjected for further polymerization. Oxirane oxygen content of EPO is 2.89% which is less than 3.05% of ERBO, showing that the latter has longer chain polymerization. The improvement of post-curing process shown that the cross-linking could be achieved at lower temperature while still promoting excellent polymer sturcture. From SEM analysis, bioplastic films made of EPO have smoother surface than ERBO, whilst thermogravimetric analysis (TGA) shows the degradation of both films only noticable after 180 °C, and still recorded mass residual of 10.35% (ERBO film) and 11.79% (EPO film) after 890 °C, owing to their excellent thermal stability characteristic. This shows that the PO and RBO can be used as starting material for epoxidation reaction and biopolymer transformation, and can be further explored for their degradation profile, tensile and mechanical stress as well as life-cycle assesment, thus can be used an alternative material in plastic pollution mitigation.

Acknowledgements

The authors would like to acknowledge the partial financial support (grant number TAPE55175) from the Center for Management and Innovation (CRIM), UMT and research facilities from the Faculty of Science and Marine Environment, UMT. We also thankful for the technical assistance from the MRIG members of University Malaysia Terengganu.

References

1. Plastic Europe (2017). Plastics- the facts 2017: An analysis of European plastics production, demand and waste data. *Association of Plastics Manufacturers*, Brussels, Belgium.
2. UNEP (2018). UN Environment 2018 Annual Report. Pp 1-44.

3. Chen, H. L., Nath, T. K., Chong, S., Foo, V., Gibbins, C. and Lechner, A. M. (2021). The plastic waste problem in Malaysia: management, recycling and disposal of local and global plastic waste. *SN Applied Sciences*, 3: 437.
4. Ibrahim, Y. S., Hamzah, S. R., Khalik, W. M. A. W., Yusof, K. M. K. K. and Anuar, S. T. (2021). Spatiotemporal microplastic occurrence study of Setiu Wetland, South China Sea. *Science of Total Environment,* 788: 147809.
5. Landrigan, P. J., Raps, H., Symeonides, C., Chiles, T., Cropper, M., Enck, J., Hahn, M. E., Hixson, R., Kumar, P., Mustapha, A., Park, Y., Spring, M., Stegeman, J., Thompson, R., Wan,g Z., Wolff, M., Yousuf, A. and Dunlop, S. (2022). Announcing the Minderoo – Monaco Commission on Plastics and Human Health. *Annals of Global Health*, 88(1): 73.
6. Moshood, T.D., Nawanir, G., Mahmud, F., Mohamad, F., Ahmad, M. A. and Ghani, A. A. (2021). Expanding policy for biodegradable plastic products and market dynamics of bio-based plastics: Challenges and opportunities. *Sustainability,* 13(11): 6170.
7. Narine, S. S. and Kong, X. (2005). Vegetable oils in production of polymers and plastics. In F. Shahidi (Ed.), Bailey's Industrial Oil and Fat Products 6th ed. John Wiley & Sons Ltd, United Stated: pp. 279-306.
8. Workman, D. (2018). Palm oil exports by country. Retrieved from http://www.worldstopexports.com/palm-oil-exports-by-country/
9. Thomas, A., Matthäus, B. and Fiebig, H.-J. (2015). Fats and fatty oils. In *Ullmann's Encyclopedia of Industrial Chemistry*: pp. 1-84.
10. Liu, W., Qiu, J., Fei, M., Qiu, R., Sakai, E. and Zhang, M. (2019). Balancing performance of epoxidized soybean oil (ESO)/poly(lactic acid) composites: synergistic effects of carbon nanotubes and tannic acid-induced crosslinking of ESO. *Express Polymer Letters,* 13(2): 109-122.
11. Saremi, K., Tabarsa, T., Shakeri, A. and Babanalbandi., A. (2012). Epoxidation of soybean oil. *Scholars Research Library Annals of Biological Research*, 3(9): 4254-4258.
12. Samarth, N. B. and Mahanwar, P. A. (2015). Modified vegetable oil based additives as a future polymeric material-review. *Open Journal of Organic Polymer Materials*, 5: 1-22.
13. Anuar, S. T., Zhao, Y. Y., Mugo, S. M. and Curtis, J. M. (2012). Monitoring the epoxidation of canola oil by non-aqueous reversed phase liquid chromatography/mass spectrometry for process optimization and control. *Journal of the American Oil Chemists' Society*, 89(11): 1951-1960.
14. Holser, R. A. (2008). Transesterification of epoxidized soybean oil to prepare epoxy methyl esters. *Industrial Crops and Products,* 27: 130-132.
15. Gogoi, P., Boruah, M., Sharma, S. and Dolui, S. K. (2015). Blends of epoxidized alkyd resins based on jatropha oil and the epoxidized oil cured with aqueous citric acid solution: a green technology approach. *ACS Sustainable Chemistry & Engineering*, 3(2): 261-268.
16. Almeida, C. B. de, Corradini, E., Forato, L. A., Fujihara, R. and Lopes Filho, J. F. (2018). Microstructure and thermal and functional properties of biodegradable films produced using zein. *Polímeros*, 28(1): 30-37.
17. Nainggolan, M. and Sinaga, A. G. S. (2021). Characteristics of fatty acid composition and minor constituents of red palm olein and palm kernel oil combination. *Journal of Advanced Pharmaceutical Technology and Research,* 12(1): 22-26.
18. Mancini, A., Imperlini, E., Nigro, E., Montagnese, C., Daniele, A., Orrù, S. and Buono, P. (2015). Biological and nutritional properties of palm oil and palmitic acid: Effects on health. *Molecules*, 20(9): 17339-17361.
19. Purwanto, E. (2010). The synthesis of polyol from rice bran oil (RBO) through epoxidation and hydroxylation reactions. Thesis of Master Degree, The University of Adelaide, South Australia, Australia.
20. Punia, S., Kumar, M., Siroha, A. K. and Purewal, S. S. (2021). Rice bran oil: Emerging trends in extraction, health benefit, and its industrial application. *Rice Science,* 28(3): 217-232.
21. Turco, R., Vitiello, R., Russo, V., Tesser, R., Santacesaria, E. and Di Serio, M. (2013). Selective epoxidation of soybean oil with performic acid catalyzed by acidic ionic exchange resins. *Green Processing and Synthesis*, 2(5): 427-435.

22. Danov, S. M., Kazantsev, O. A., Esipovich, A. L., Belousov, A. S., Rogozhin, A. E. and Kanakov, E. A. (2017). Recent advances in the field of selective epoxidation of vegetable oils and their derivatives: a review and perspective. *Catalysis Science & Technology,* 7(17): 3659-3675.
23. Omonov, T. S., Kharraz, E. and Curtis, J. M. (2016). The epoxidation of canola oil and its derivatives. *RSC Advances*, 6(95): 92874-92886.
24. Nihul, P. G., Mhaske, S. T. and Shertukde, V. V. (2014). Epoxidized rice bran oil (ERBO) as a plasticizer for poly(vinyl chloride) (PVC). *Iranian Polymer Journal*, 23(8): 599-608.
25. Kin Hong, L., Yusop, R. M., Salih, N. and Salimon, J. (2015). Optimization of the in situ epoxidation of linoleic acid of *Jatropha curcas* oil with performic acid. *Malaysian Journal of Analytical Sciences*, 19(1): 144-154.
26. Yunus, W. and Kuang Abdullah, D. (2009). Optimization of the epoxidation of methyl ester of palm fatty acid distillate. *Journal of Oil Palm Research*, 21: 675-682.
27. Sahoo, S. K., Khandelwal, V. and Manik, G. (2018). Development of completely bio-based epoxy networks derived from epoxidized linseed and castor oil cured with citric acid. *Polymers for Advanced Technologies*, 29(7): 2080-2090.
28. Pierucci, S., Klemeš, J. J., Piazza, L., Bakalis, S., Vianello, C., Piccolo, D. and Maschio, G. (2017). Preliminary study of epoxidation of soybean oil in stirred tank reactor: the effect of the mixing program. *Chemical Engineering Transactions*, 57: 1051-1056.
29. Gupta, N. K., Yadav, P. K. S., Eadara, R. and Singh R. P. (2016). Synthesis of Epoxy Resin from Waste Ricebran Oil. *Polymers from Renewable Resources,* 7(1): 21-32.
30. Nugrahani, R. A., Redjeki, A. S., Teresa, Y. and Hidayati, N. (2017). Synthesis of compound-containing sulphonic acid from epoxidized methyl oleic of rice bran oil and linear alkylbenzene sulphonic acid. *Journal of Chemical Technology and Metallurgy*, 52(5): 797-802.
31. Tajulruddin, W. N. W., Rahmat, A. R., Yusof, Z. A. M. and Fakhari, A. (2015). Characterization of polyol synthesized from epoxidized palm oil using Fourier transform infra-red and nuclear magnetic resonance. *Journal of Advanced Research in Applied Mechanics*, 10(1): 30-35.
32. Thakur, V. K., Thakur, M. K. and Kessler, M. R. (2017). Handbook of composites from renewable materials. Volume 6, Polymeric composites 6th ed. In: M. R. Kessler, V. K. Thakur and M. K. Thakur (Eds.), Wiley-Scrivener, Beverly, Massachusetts, USA.
33. Awale, R., Ali, F., Azmi, A., Puad, N., Anuar, H. and Hassan, A. (2018). Enhanced flexibility of biodegradable polylactic acid/starch blends using epoxidized palm oil as plasticizer. *Polymers*, 10(9): 977.
34. Kolanthai, E., Sarkar, K., Meka, S. R. K., Madras, G. and Chatterjee, K. (2015). Copolyesters from soybean oil for use as resorbable biomaterials. *ACS Sustainable Chemistry & Engineering*, 3(5): 880-891.
35. Altuna, F. I., Pettarin, V. and Williams, R. J. J. (2013). Self-healable polymer networks based on the cross-linking of epoxidised soybean oil by an aqueous citric acid solution. *Green Chemistry*, 15(12): 3360.
36. Ouipanich, S., Kaisone, T., Hanthanon, P., Wiphanurat, C., Thongjun, Y. and Nampitch, T. (2017). Effect of the citric acid as blowing agent on the compressive properties and morphology of PLA/ENR blend foams. *Applied Mechanics and Materials*, 873: 95-100.
37. Lei, B., Liang, Y., Feng, Y., He, H. and Yang, Z. (2018). Preparation and characteristics of biocomposites based on steam exploded sisal fiber modified with amphipathic epoxidized soybean oil resin. *Materials*, 11(9): 1731.
38. Samper, M. D., Ferri, J. M., Carbonell-Verdu, A., Balart, R. and Fenollar, O. (2019). Properties of biobased epoxy resins from epoxidized linseed oil (ELO) crosslinked with a mixture of cyclic anhydride and maleinized linseed oil. *Express Polymer Letters*, 13(5): 407-418.
39. Chieng, B., Ibrahim, N., Then, Y. and Loo, Y. (2014). Epoxidized vegetable oils plasticized poly(lactic acid) biocomposites: mechanical, thermal and morphology properties. *Molecules*, 19(10): 16024-16038.

Malaysian Journal of Analytical Sciences Vol 27 No 3 2023

Organic or Inorganic Analysis

1. SYNTHESIS AND CHARACTERISATIONS OF NICKEL(II)-HYDRAZONE COMPLEX AS CATALYST IN SUZUKI REACTION 453
Aisyah Ahmad Fauzi, Norul Azilah Abdul Rahman, and Nur Rahimah Said

Analytical Method

2. THE DEVELOPMENT AND QUANTITATIVE PERFORMANCE TEST OF LOW-COST VISIBLE SPECTROPHOTOMETER AND ITS COMPARISON WITH COMMERCIAL SPECTROPHOTOMETER 463
Rudi Heryanto, Dyah Iswantini, Eti Rohaeti, Mohamad Rafi, Mulyati, and Wulan Suci Pamungkas

Nano or Advanced Materials Analysis

3. POTENTIAL OF LIGNIN FROM OIL PALM BIOMASS USING DEEP EUTECTIC SOLVENT AS CARBON FIBRE PRECURSOR 471
Afiqah Liana Sazali, Siti Khadijah Amran, Khairul Faizal Paee, Mohd Razealy Anuar, and Tau-Len Kelly Yong

Computational Analysis

4. ANALYSIS OF HYPERSPECTRAL REFLECTANCE FOR DISEASE CLASSIFICATION OF SOYBEAN FROGEYE LEAF SPOT USING KNIME ANALYTICS 488
Yuhao Ang, and Helmi Zulhaidi Mohd Shafri

Organic or Inorganic Analysis

5. HIERARCHICAL ZEOLITE ZSM-5 FRAMEWORK ON THE SYNTHESIS AND CHARACTERIZATION FOR CATALYTIC CRACKING OF FLUID: A MINI REVIEW 499
Nazrizawati Ahmad Tajuddin, Nur Alyaa Kamal, Nurul Anessa Qistina Rhymme, and Salma Fawiza Sani

Organic or Inorganic Analysis

6. THE CRYSTAL STRUCTURE OF $Os_3(CO)_{11}(PPh_2(C_{10}H_7)).H_2O$: A COMBINED HIRSHFELD SURFACE ANALYSIS AND DFT CALCULATIONS 510
Husna Izzati Muhammad Nor Azharan, Enis Nadia Md Yusof, Suhana Arshad, Omar Bin Shawkataly, and Siti Syaida Sirat

Analytical Method

7. EXPLORATION OF NATURAL DEEP EUTECTIC SOLVENT AS THE ALTERNATIVE DISPERSIVE SOLVENT IN DLLME FOR THE EXTRACTION OF ANABOLIC STEROID DRUGS IN WATER 521
Azreen Asyikin Mhd Kamal, Wan Nazihah Wan Ibrahim, Mohd Sufri Mastuli, Noorfatimah Yahaya,

Sazlinda Kamaruzaman, Sheela Chandren, Nurul Auni Zainal Abidin, and Nursyamsyila Mat Hadzir

Analytical Method

8. FLUOROQUINOLONE RESIDUES IN FOOD: OCCURRENCE AND ANALYTICAL METHODS - A MINI REVIEW FROM 2000 TO 2022 533
Wen Yu Foo, Saw Hong Loh, Wan Mohd Afiq Wan Mohd Khalik, and Marinah Mohd Ariffin

Nano or Advanced Materials Analysis

9. COMPARATIVE STUDY ON THE EFFECT OF GAMMA RADIATION ON BIOPLASTICS 552
Nurul Fathihah Abu Bakar, and Siti Amira Othman

Analytical Method

10. CHROMATOGRAPHIC METHODS FOR THE DETERMINATION OF DICLOFENAC IN HUMAN BIOLOGICAL SAMPLES: A MINI REVIEW 563
Sabreenna Marsya Djuli, and Normala Abd Latip

Analytical Method

11. PLACKETT-BURMAN DESIGN OPTIMIZED DISPERSIVE LIQUID-LIQUID MICROEXTRACTION COUPLED WITH GAS CHROMATOGRAPHY-MASS SPECTROMETRY FOR DETERMINATION OF METHAMPHETAMINE FROM LABORATORY COAT MATERIALS 573
Su Chien Quah, Way Koon Teoh, Vanitha Kunalan, Noor Zuhartini Md Muslim, Warakorn Limbut,Chong Hooi Yew, Kah Haw Chang, Ahmad Fahmi Lim Abdullah

Nano and Advanced Materials Analysis

12. PHOTO-ESTERIFICATION OF WASTE COOKING OIL USING A NOVEL NANOCATALYST TIO_2 IMPREGNATED WITH EMPTY FRUIT BUNCHES ASH HETEROGENEOUS CATALYST 586
Siti Fadhilah Ibrahim, Norshahidatul Akmar Mohd Shohaimi, Mohd Lokman Ibrahim, Zul Adlan Mohd Hir, Mohd Sufri Mastuli, and Wan Nur Aini Wan Mokhtar

Analytical Method

13. IN-SYRINGE DISPERSIVE SOLID PHASE MICROEXTRACTION FOR THE DETERMINATION OF ORGANOPHOSPHORUS PESTICIDE RESIDUES IN VEGETABLES 600
Hairul Nizwan Manap, Faizah Binti Mohammad Yunus, Nur Nadhirah Mohamad Zain, Noorfatimah Yahaya, Hemavathy Surikumaran, Kumuthini Chandrasekaram, Kavirajaa Pandian Sambasevam, Muggundha Raoov

Analytical Method

14. A VALIDATED RP-HPLC METHOD FOR THE QUANTIFICATION OF LIQUID SELF-EMULSIFYING CURCUMIN: PHARMACOKINETIC APPROACH 612
Xin-Yen Chiang, Sheau-Chin Lim, Kah-Hay Yuen, Jia-Rou Khor, and Siok-Yee Chan

Nano or Advanced Materials Analysis

15. MEDIUM DENSITY FIBREBOARD (MDF) FROM OIL PALM FIBRE: A REVIEW 626
Roila Awang, Noorshamsiana Abdul Wahab, Zawawi Ibrahim, and Astimar Abdul Aziz

Natural Product Analysis

16. *Cymbopogon citratus* AND *Cymbopogon nardus* ESSENTIAL OIL COMPONENTS - FTIR, CHEMOMETRICS ASSESSMENT AND IDENTIFICATION USING GC-MS 641
Hazrulrizawati Abd Hamid

Organic and Inorganic Analysis

17. STUDY OF SOLVOTHERMAL SYNTHESIS OF MAGNESIUM-BASED METAL-ORGANIC FRAMEWORKS 653
Umar Abd Aziz, Mohamed Ibrahim Mohamed Tahir, Nurul Farhana Ahmad Aljafree, and Mohd Basyaruddin Abdul Rahman

Natural Product Analysis

18. A REVIEW ON *Piper betle* EXTRACT AND HYPOCHLOROUS ACID ON INSECTICIDAL ACTIVITY 660
Wan Zuraida Wan Mohd Zain, Muhammad Imran Hakimi Chairul, Nur'Amira Hamid, Aisha Na'illa Che Musa, Nurul Wahida Ramli, Norhazana Nor Izan, Arifin Marzuki, and Nur Diyana Zulpahmi

Malaysian Journal of Analytical Sciences (MJAS)
Published by Malaysian Analytical Sciences Society

SYNTHESIS AND CHARACTERISATIONS OF NICKEL(II)–HYDRAZONE COMPLEX AS CATALYST IN SUZUKI REACTION

(Sintesis, dan Pencirian Nikel(II)– Hidrazon Kompleks Sebagai Pemangkin dalam Tindak Balas Suzuki)

Aisyah Ahmad Fauzi[1], Norul Azilah Abdul Rahman[1,2], and Nur Rahimah Said[1*]

[1]School of Chemistry and Environment,
Faculty of Applied Sciences,
Universiti Teknologi MARA,
Cawangan Negeri Sembilan, Kampus Kuala Pilah,
72000 Kuala Pilah, Negeri Sembilan, Malaysia
[2]School of Chemistry and Environment,
Faculty of Applied Sciences Universiti Teknologi MARA,
40450 Shah Alam, Selangor, Malaysia

**Corresponding author: nurra1435@uitm.edu.my*

Received: 24 October 2022; Accepted: 18 April 2023; Published: 23 June 2023

Abstract

Dichloro-*N*'-(3-chlorobenzylidene) benzohydrazide nickel(II) complex was successfully synthesised using 4-chloro-*N*'-(4-chlorobenzylidene) benzohydrazide ligand with nickel(II) chloride. The synthesised ligand and complex were characterised by various instruments including FTIR, ^{1}HNMR, ^{13}CNMR, and UV-Vis spectroscopy. The preliminary complexation study between Ni^{2+}cation and ligand showed that 1:1 stoichiometric formation corresponded to the metal-ligand ratio. The catalytic performance of the complex was tested using a Suzuki reaction between phenylboronic acid and four different aryl bromides (1-bromo-4-nitrobenzene, 4-bromoanisole, 4-bromoacetophenone, and bromobenzene) at different solvents and bases. The per cent (%) conversion rate of reactant to the product was determined using GC-FID. The best catalytic performance was found in the reaction between phenylboronic acid and 1-bromo-4-nitrobenzene using 0.5% mmol catalyst loading, methanol as a solvent, and K_2CO_3 as a base at temperature of 65°C within 2 h reaction time, giving a conversion rate of 81.86%.

Keywords: hydrazone ligand, nickel (II)-hydrazone complex, Suzuki reaction

Abstrak

Kompleks dikloro-N'-(3-klorobenzilidena) benzohidrazida nikel(II) telah berjaya disintesis menggunakan ligan 4-kloro-*N*'-(4-klorobenzilidena) benzohidrazida dengan nikel(II) klorida. Ligan dan komplex yang disintesis dicirikan oleh pelbagai alat terdiri daripada FTIR, ^{1}HNMR, ^{13}CNMR, dan spektroskopi UV-Vis. Kajian awal pembentukan kompleks antara kation Ni^{2+} dan ligan menunjukkan stoikiometri pembentukan ialah 1:1 sepadan dengan nisbah logam-ligan. Prestasi pemangkinan komplek telah diuji menggunakan tindak balas Suzuki antara asid fenilboronik dan empat aril bromida yang berbeza (1-bromo-4-nitrobenzena, 4-bromoanisol, 4-bromoacetofinon, dan bromobenzena) pada parameter yang berbeza seperti jenis pelarut dan bes. Peratus (%) kadar

penukaran bahan tindak balas kepada produk ditentukan menggunakan GC-FID. Prestasi pemangkinan terbaik didapati dalam tindak balas antara asid fenilboronik dan 1-bromo-4-nitrobenzena dengan menggunakan pemuatan mangkin 0.5% mmol, metanol sebagai pelarut, K_2CO_3 sebagai bes pada suhu 65°C dalam masa tindak balas 2 jam memberi kadar penukaran sebanyak 81.86%.

Kata kunci: ligan hidrazon, kompleks nikel (II)-hidrazon, tindak balas Suzuki

Introduction

Suzuki reaction is one of the most used techniques for producing C-C bonds. It involves coupling an organoboron reagent with an organic halide or pseudo-halide in the presence of a palladium or nickel catalyst and a base [1]. Nickel catalyst have various advantages over palladium catalyst that are more commonly used, including the capacity to activate aliphatic electrophiles and the ability to avoid β-hydrogen elimination by alkyl-metal intermediates that help in avoiding lowering the yield [2]. In addition, nickel systems are frequently more reactive in oxidative addition or insertion reactions due to the smaller atomic radius, lower electronegativity, and greater negative redox potentials of low-valent nickel species [3]. Due to the economic aspect the selection of nickel-based catalysts is ideal for industrial-scale use more than noble metal-based catalysts due to their lower cost and high activity [4]. Many of industries use the Suzuki reaction, such as polymers, pharmaceutically active chemicals, herbicides, novel materials, liquid crystals, and chemical synthesis [5].

Improving the catalytic activity of nickel-based catalyst towards the specified reaction is important and influenced by its structure. Thus, a suitable ligand design is an essential step in the development of a catalyst that lead to higher reaction rates, improved lifetime, and stability. The ability of ligands to donate electrons is crucial in coordination chemistry because it is one of the most important factors influencing the properties and reactivities of complexes [6]. Hydrazone is a ligand that has different binding modes and lone pair electrons with the structure $R_1R_2C{=}NNH_2$. In such instances one donating element (iminic nitrogen, N), and its subgroups (acyl and aroylhydrazones) can function as bidentate (N, O) or tridentate (N, O, X=O, N, S) ligands [7, 8]. The exploration of ligands containing hydrazone is interesting because the diversity of it is seen in the coordination, a preference for higher coordination number stereochemistry, the capacity to operate as neutral or deprotonated ligands, and the ability to assume various conformations [9]. Due to its flexibility and versatility, the coordination chemistry of hydrazone-based ligands has proven to be highly relevant due to their strong complexation potential towards a wide range of metals ions and the possibility of catalytic application [5, 10].

Exploration of the capability of hydrazone as a ligand with nickel(II) catalyst, particularly is currently limited. The goal of this research is to design a novel nickel(II)-hydrazone complexes that can be used as Suzuki reaction catalysts. The optimum reaction conditions of a newly synthesised catalyst were studied and identified using several parameters.

Materials and Methods

Chemicals and instruments

All the chemicals and solvents obtained from commercial suppliers were used as received. The chemicals used were 4-chlorobenzyldehyde (Sigma), 4-chlorobenzhydrazide (Sigma), dimethyl sulfoxide (DMSO) (Merck), methanol (Merck), sodium acetate (NaOAc)(Merck), sodium carbonate (Na_2CO_3) (Sigma), potassium carbonate (K_2CO_3) (Merck), dimethylacetamide (DMA) (Merck), phenylboronic acid (Sigma), nickel(II) chloride (Merck), 1-bromo-4-nitrobenzene (Merck), 1-bromobenzene (Merck), 1-bromoacetophenone (Merck), 4-bromoanisole (Merck) and nitrogen gas. All solid products produced at the end of every synthesis were collected by high vacuum filtration or slow evaporation at room temperature.

The product was characterised using Fourier Transform Infrared (FTIR) spectroscopy, Nuclear Magnetic Resonance (NMR) and UV-Visible (UV-Vis) Spectroscopy. Meanwhile the catalytic performance was determined by using Gas Chromatography Flame Ionisation Detector (GC-FID). The FTIR spectrometer use is a Perkin Elmer Spectrum 400 where the FTIR spectra were determined as reduced total reflectance (ATR) in the range of 4000-200 cm^{-1}. The ^1H and

^{13}CNMR spectroscopy were analysed using a Bruker Advance 400 spectrometer model at 400 MHz with tetramethylsilane (TMS) as an internal standard. The UV-Visible spectroscopy use is a T80+ UV-Vis spectrometer in of 500-240 nm range. The % of conversion rate and turnover number (TON) were calculated using the below equation that use the data from GC-FID. The analysis used HP-5 capillary column (15 m x 0.25 mm x 0.25 mm) with Flame Ionization Detector. The samples were injected at 50°C, with a maximum temperature of 250°C. The temperature was raised at a rate of 15°C per minute and 1.9162 mL/min was utilised as the flow rate [7].

$$\% \text{ Conversion rate} = \frac{(A_{initial})- (A_{final})}{(A_{initial})} \times 100 \quad (1)$$

Where; $A_{initial}$ = peak area of reactant before reaction, and A_{final} = peak area of reactant after reaction

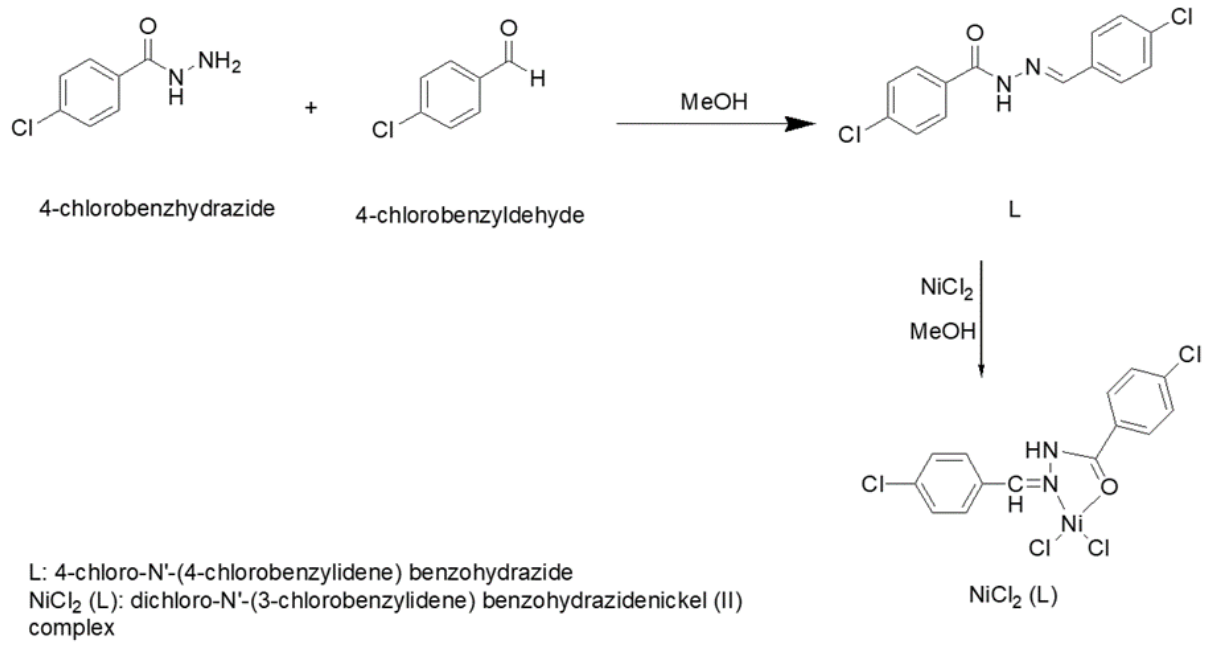
$$\text{Turnover number (TON)} = \frac{\text{Percentage of conversion rate}}{\text{Amount of catalyst loading}} \quad (2)$$

Synthesis of compounds

The outline for the preparation of nickel (II)-hydrazone complex is given in Scheme 1.

Synthesis of hydrazone ligand (L)

Hydrazone ligand prepared in the presence of nitrogen gas, an equimolar of 4-chlorobenzhydrazide (0.5 g, 2.98 mmol) and 4-chlorobenzyldehyde (0.5 g, 3.79 mmol) refluxed in 10 mL of methanol for 2 hours. The reaction mixture was then allowed to cool to room temperature before filtering using vacuum filtration to obtain a solid product. The solid was washed several times before being recrystallized from methanol forming white crystals.

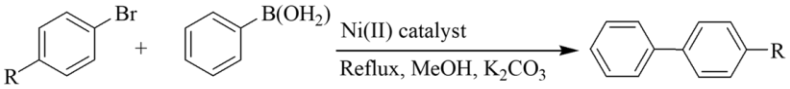


Scheme 1. Synthesis steps of nickel (II)-hydrazone complexes

Synthesis of nickel(II)-hydrazone complex ($NiCl_2(L)$)
After combining stoichiometric amounts of ligand (0.1 mmol) and nickel chloride (0.1 mmol) dissolved in methanol (15 mL), the reaction mixture was refluxed for 2 h. Filtering off the precipitates was then performed before washing the mixture with methanol and drying it in a vacuum desiccator over anhydrous $CaCl_2$.

Preliminary complexation study
A preliminary complexation study was conducted to determine the stoichiometry ratio between ligand and metal using the UV-Vis spectroscopy titration method. Solutions of hydrazone ligand and Ni^{2+} cation were prepared in DMF with concentration of 2.3×10^{-6} mmol and 1×10^{-4} mmol, respectively. The source of Ni^{2+} cation was nickel chloride. The quartz cuvette was filled with 3 mL of ligand solutions and titrated with Ni^{2+} cation solution. At each titration the solution mixture was left about 5 min before run at the UV-Vis in the 270-300 nm range [11,7].

Catalytic testing
The investigation into the catalytic activity of the complex (0.5% mmol) in the Suzuki reaction was tested by the reaction of phenylboronic acid (0.182 g, 1 mmol) with 1-bromo-4-nitrobenzene (0.20 g, 1 mmol) in 5 mL methanol under 65°C with the presence of K_2CO_3 as a base (0.276 g, 2 mmol). All chemicals were mixed in a three-neck round bottom flask and refluxed for 2 h in the presence of nitrogen gas. The mixture was then poured into a separatory funnel, followed by the addition of water (30 ml) and dichloromethane (3 x 10 ml). After allowing the mixture to settle for 30 minutes, the organic layer was collected and discarded into a beaker, and then dried over $MgSO_4$. The mixture was subsequently filtered using vacuum filtration to obtain the product. The product was evaporated using a rotary evaporator and dried in an oven. Meanwhile, the catalytic performance was analyzed using GC-FID spectroscopy. The steps were repeated with using 4-bromoacetophenone, bromobenzene and 4-bromoanisole as an aryl bromide as substituted of 1-bromo-4-nitrobenzene. Different types of solvents and bases were also tested. The reaction is shown in Scheme 2, where R is referred to as $-NO_2$, $-OCH_3$, $-COCH_3$, and H.



Scheme 2. Catalytic reaction of 1-bromo-4-nitrobenzene with phenylboronic acid

Results and Discussion

Characterization of synthesized compounds
This study successfully synthesised 4-chloro-*N*'-(4-chlorobenzylidene) benzhydrazide ligand and dichloro-*N*'-(3-chlorobenzylidene) benzohydrazide nickel(II) complex. The physical properties of the synthesised ligand and complex are listed in Table 1. According to the observations, the colour of the ligand changed because of the complexation process, from white to pale green. Meanwhile, the melting points of the complex was greater than the respective ligand due to the interaction of nickel(II) with the ligand's structures. These metal-ligand bonding in the structure of the complexes required more energy to break, which caused an increase in the melting point [7].

Table 1. Physical properties of synthesized compounds

Sample	Colour	Melting Point (°C)	Yield (%)
Ligand	White, powder	168-169	82.41
Complex	Pale green, powder	220-221	41.87

The formation of ligand and complex were confirmed using FTIR, ^{1}HNMR, ^{13}CNMR, and UV-Vis spectroscopies. The significant FTIR absorption bands a re summarised in Table 2. The successfully synthesised ligand is indicated by the presence of a strong absorption band at the range of the carbonyl group but at an unusually low value (1650 cm^{-1}), signified by the C=O amide. New medium absorption bands of C=N imine at 1600 cm^{-1} is also an important signal to confirm the formation. The C=N bond was formed by the reaction between the C=O aldehyde of 4-chlorobenzaldehyde and primary amine (-NH_2) of 4-chlorobenzhydrazide via the removal of H_2O molecules. However, the presence of a resonance effect in the structure led to the absorption band of C=N observed at a lower frequency when compared to the normal range, which is around 1650 cm^{-1}. Other absorption peaks were observed at 3218 cm^{-1} and 1090 cm^{-1}, which were attributed to the N-H and C-H stretching, respectively [7, 12]. The coordination of nickel(II) to the ligand in the FTIR spectrum could be observed by the shift of C=O and C=N stretching absorption bands to the low frequency at 1620 cm^{-1} and 1567 cm^{-1}, respectively. This observation indicated that the C=O oxygen and the C=N nitrogen were probably involved in coordinating to the central nickel (II) ion via contributing the lone pair [13].

Table 2. Significant FTIR absorption bands of synthesized compounds

Assignment	**Wavenumber (cm^{-1})**	
	Ligand	**Complex**
N-H	3218	3214
C=O amide	1650	1620
C=N imine	1600	1567
C-N	1090	1095
C-Cl	819	819

The spectra of ^{1}HNMR and ^{13}CNMR (Figure 1) were recorded for synthesised ligand, and the significant attributes are tabulated in Tables 3 and 4. A singlet appeared at 8.44 ppm and was assigned to the proton of azomethine (CH=N) proton. Another important peak at 12.00 ppm was assigned to the proton of N-H adjacent to C=O, which was observed as an enolic form [13]. The structures of the ligand were further supported by ^{13}CNMR data. The carbonyl carbon signal appeared at 162 ppm (C=O), whereas signals that appeared at 147 ppm were assigned to the carbon of the azomethine group (CH=N). The other five signals at 129-137 ppm were due to the substituted benzene ring carbon. Unfortunately, the reading of signals for the complex was unreadable due to the paramagnetic effect of nickel in the compound [14].

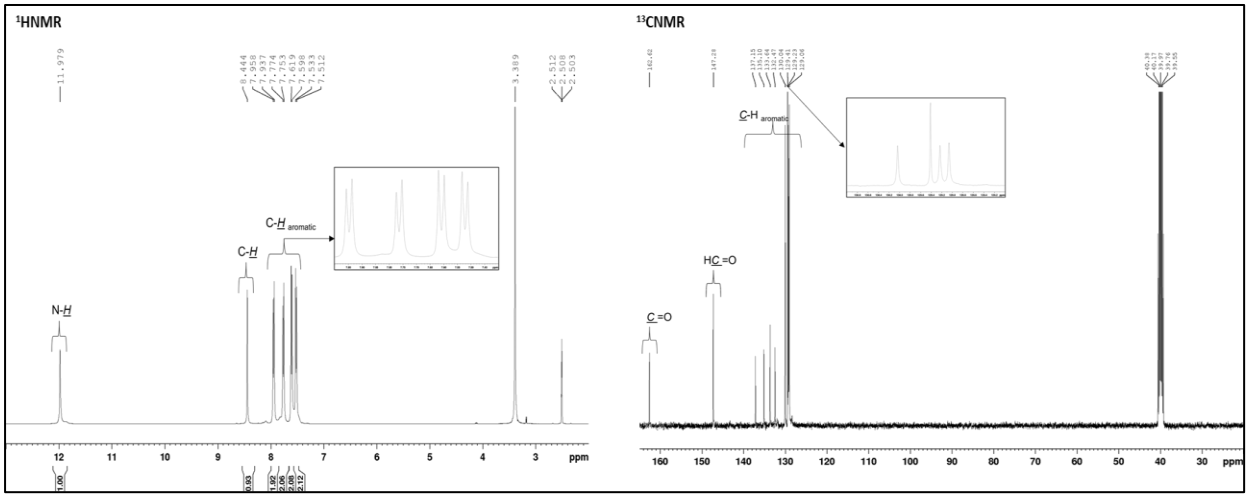


Figure 1. [1]HNMR and [13]CNMR spectra of hydrazone ligand

Table 3. Significant attributes of [1]HNMR data of ligand

Attributions	Chemical Shift, δ (ppm) Ligand
-CH aromatic	7.51 [2H]
	7.60 [2H]
	7.75 [2H]
	7.94 [2H]
-CH	8.44 [1H]
-NH	11.98 [1H]

Table 4. Significant attributes of [13]CNMR data of ligand

Attributions	Chemical Shift, δ (ppm) Ligand
C=O	162
HC=N	147
CH	129-137

Figure 2 shows the UV-Vis spectra of the ligand and complex. The ligand showed absorption bands at 257 nm and 298 nm. These wavelengths were assigned to the $\pi - \pi^*$ transition in the structure of the ligands. The spectrum of the complex also showed two absorption bands at 258 nm and 312 nm, signifying a similar pattern of the ligand in the region. These absorption bands were also presented in the spectrum of the nickel(II) complex, although they underwent red shift. The coordination of the ligand to the nickel(II) ion was supported by this shift in the spectra of the produced complex [15]. The region for nickel metal is 480 nm but it could not be observed in this study because nickel contained unpaired electrons exhibited d-d transition and paramagnetic causing weak absorption [16].

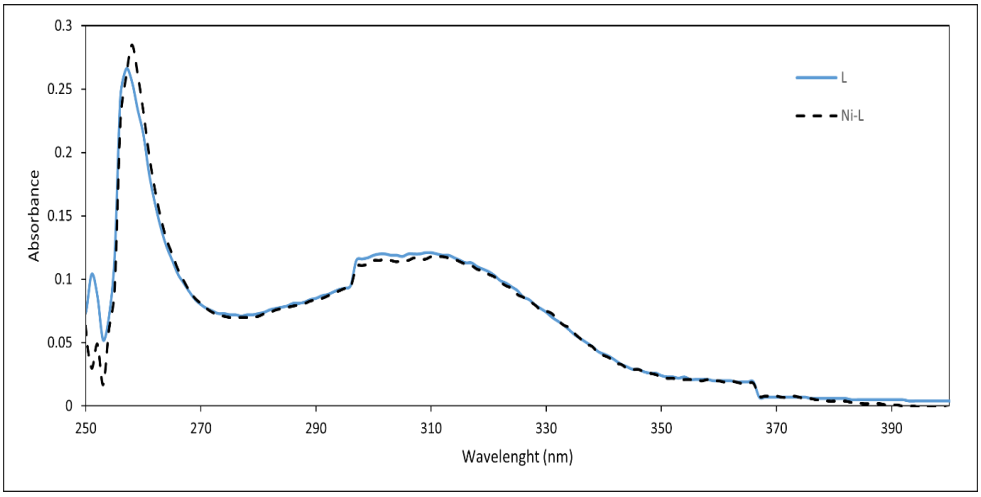


Figure 2. UV-Vis spectrum for ligand and complex

Preliminary complexation study

The preliminary complexation study using the titration method between ligand and nickel(II) was analysed via UV-Vis spectrum in the range of 270 nm to 300 nm. As seen in Figure 3, the absorption spectra of the ligand steadily increased as the mole fraction of Ni^{2+} ion increased. A graph of absorbance versus molar ratios of $[Ni^{2+}]/[L]$ was plotted. It showed that the stoichiometry was 1:1, consequently supporting the structure of the nickel complex [17].

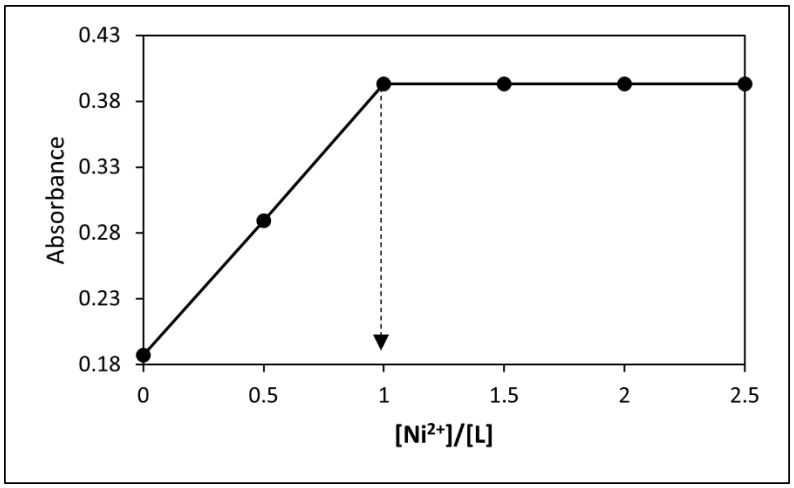


Figure 3. Graph plotted based on absorbance versus $[Ni^{2+}]/[L]$

Catalytic testing

By using 0.5% mmol of catalyst loading, the catalytic activity of Ni-L complex was investigated in a reflux system with different aryl bromides, types of solvent, and bases within a 2 h reaction time. Catalytic performance was measured using data from GC-FID spectra. The conversion rate (%) and turnover number (TON) of arylbromides were computed by using equations 1 and 2 and presented in Table 5.

Table 5. The catalytic performance of Ni-L catalyst in Suzuki Reaction

Entry	R	Solvent	Base	Conversion Rate (%)	Turnover Number (TON)
1	NO_2	MeOH	K_2CO_3	81.86	163.72
2	OCH_3	MeOH	K_2CO_3	0	0
3	$COCH_3$	MeOH	K_2CO_3	69.86	139.72
4	H	MeOH	K_2CO_3	0	0
5	NO_2	MeOH	Na_2CO_3	29.76	59.52
6	NO_2	MeOH	NaOAc	41.7	83.40
7	NO_2	DMA	K_2CO_3	37.06	74.12

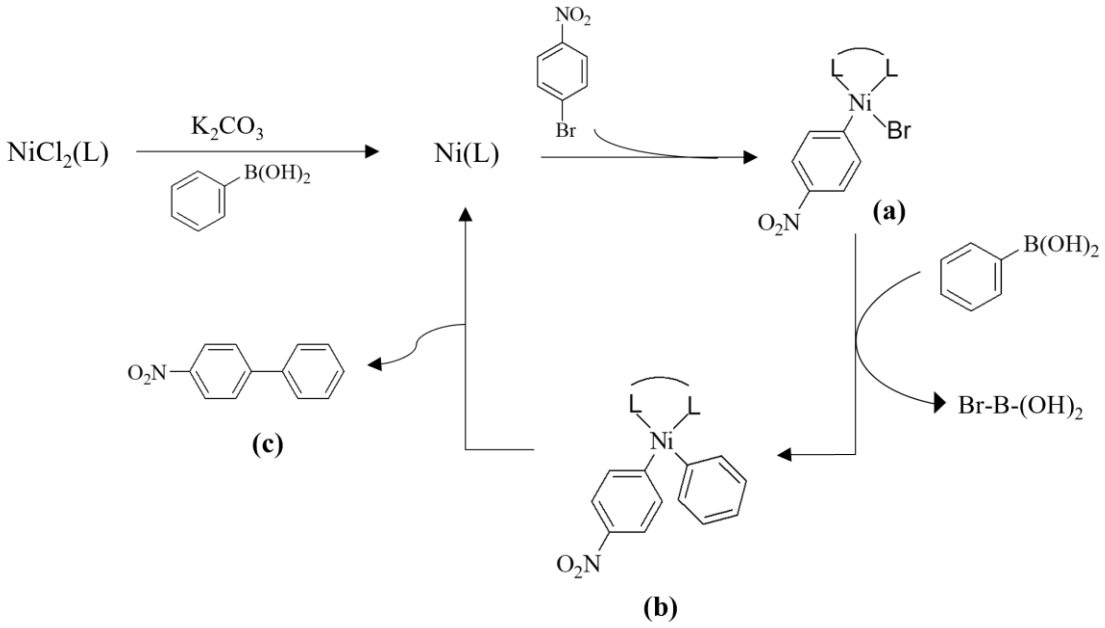
Reaction condition; Catalyst loading= 0.5 mmol%, Reaction time= 2h

In the presence of K_2CO_3 base, the complex catalytic performance of a Suzuki reaction was tested in the reaction of different types of arylbromide where R is –NO_2, -H, -OCH_3 and –$COCH_3$ (Entry 1-4) with phenylboronic acid. Based on the result in Table 5, the complex showed good catalytic activities in the reaction of 1-bromo-4-nitrobenzene (Entry 1), giving the highest conversion rate of 81.86%. The presence of NO_2 as a substituent aryl bromide caused resonance and inductive effects on electronic charge stabilisation. Meanwhile, arylbromide that contains electron donating group (EDG), such as –OCH_3, showed less reactive reaction (Entry 2). This finding is because slower rate of transmetallation occurs in EDG compared to electron-withdrawing groups (EWG) [16].

Considering the results obtained, 1-bromo-4-nitrobenzene showed relatively better catalytic activity than the other arylbromides. Therefore, 1-bromo-4-nitrobenzene was selected as the model for the study of different bases (Entries 1, 5 and 6). Three types of bases were selected, namely K_2CO_3, Na_2CO_3, and NaOAc. Meanwhile, the catalyst loading and reaction time remained constant. The reaction that used K_2CO_3 produced the highest conversion rate of 81.86% (Entry 1) as compared to other bases Na_2CO_3 and NaOAc, which showed only 29.76% (Entry 5) and 41.73% (Entry 6), respectively. K_2CO_3 is the strongest inorganic base and has a high capability of neutralising protons generated in the oxidative addition mechanism [7, 12]. On other hand, the lowest conversion rate was observed in Entry 5 by using Na_2CO_3 as a base. It has a slower rate of dissolution into a polar protic solvent that causes low yield [18].

The reaction was repeated in a different solvent, i.e., DMA (Entry 7). A similar reaction condition was used as the reaction conducted in Entry 1. The results of the catalytic reaction that used methanol as a solvent showed a higher conversion rate of 81.86% (Entry 1) compared to DMA, which only released 37.06% (Entry 7). This result concluded that the most suitable solvent for this reaction was methanol due to the solubility of starting material and K_2CO_3 in a protic solvent, which promoted rapid reaction and at the same time, pointed to hydrogen bonding as an important contribution to better coupling reactions [19].

A plausible reaction mechanism of the reaction between 1-bromo-4-nitrobenzene and phenylboronic acid is portrayed in Scheme 3. The reaction was started with the reduction of the catalyst, complex $NiCl_2$(L) to the catalytic active species Ni(L) with the presence of K_2CO_3 and phenylboronic acid, where L was the bidentate hydrazone ligand as shown in Scheme 1. The active species was Ni(0)-catalysed coupling reaction in three steps; (I) oxidative addition of 1-bromo-4-nitrobenzene to generate **(a)**, (II) transmetalation of phenylboronic acid in the formation of the complex **(b)**, and (III) reductive elimination of **(b)** to produce the product 1-nitro-4-phenylbenzene **(c)** and regeneration of active species [20].



Scheme 3. The proposed mechanism of the Suzuki reaction in the presence of a $NiCl_2(L)$ as a catalyst

Conclusion

This study successfully demonstrated the synthesis and characterisation of hydrazone ligand and nickel(II)-hydrazone complex. The synthesised nickel(II) complex can be used as a catalyst for the Suzuki reaction in MeOH as the solvent, K_2CO_3 as a base, and the reaction temperature of 65°C. The proposed complex exhibited the best catalytic performance with the highest conversion rate (%) and TON. The reaction was conducted in the presence of a small amount of catalyst loading (0.5 mmol%) at a 2h reaction time.

Acknowledgement

This research was supported by FRGS/1/2019/STG01/UITM/02/6 from Ministry of Higher Education (MOHE). The authors are grateful to the Universiti Teknologi MARA (UiTM), Cawangan Negeri Sembilan, Kampus Kuala Pilah for generously providing the research material, equipment, and instrument.

References

1. Maluenda, I., and Navarro, O. (2015). Recent developments in the Suzuki-Miyaura reaction: 2010-2014. *Molecules*, 20(5): 7528-7557.
2. Alfahd, A. Z. (2016). Synthesis of Ni(dppe)2 and Ni(I) catalysts and their ability to catalyzed cross coupling. (Doctoral dissertation).
3. Bricout, H., Carpentier, J. F., and Mortreux, A. (1998). Nickel vs. palladium catalysts for coupling reactions of allyl alcohol with soft nucleophiles: Activities and deactivation processes. *Journal of Molecular Catalysis A: Chemical*, 136(3): 243-251.
4. Bao, Z., and Yu, F. (2018). Catalytic conversion of biogas to syngas via dry reforming process. *Advances in Bioenergy,* 3: 43-76.
5. Muthumari, S., and Ramesh, R. (2016). Highly efficient palladium (II) hydrazone-based catalysts for the Suzuki coupling reaction in aqueous medium. *RSC Advances,* 6(57): 52101-52112.
6. Bhatt, V., and Ram, S. (2015). The role of ligands, polytopic ligands and metal organic ligands (Mols) in coordination chemistry. *Chemical Science Review and Letters,* 4(14): 414-428.
7. Said, N. R., Md Adib, N. N., Roszaidi, R. M., Shamsuddin, N. A. M., and Saidul Badri, N. N. H. (2020). Catalytic activity study of synthesized palladium(II)-hydrazone complexes in the heck reaction: Optimization of the amount of catalyst loading and reaction time. *Malaysian Journal of Chemistry*, 22(3): 17-24.

8. Malik, M. A., Dar, O. A., Gull, P., Wani, M. Y., and Hashmi, A. A. (2018). Heterocyclic Schiff base transition metal complexes in antimicrobial and anticancer chemotherapy. *MedChemComm,* 9(3): 409-436.
9. Dhande, V. V., Badwaik, V. B., and Aswar, A. S. (2007). Hydrazone as complexing agent: Synthesis, structural characterization, and biological studies of some complexes. *Russian Journal of Inorganic Chemistry,* 52(8): 1206-1210.
10. Adejumo, T. T., Tzouras, N. V, Zorba, L. P., Radanovi, D., Pevec, A., and Grubiši, S. (2020). Synthesis, characterization, catalytic activity, and DFT calculations of Zn(II) hydrazone complexes. *Molecules,* 25(18): 1-18.
11. Camacho-Espinoza, M., Penieres-Carrillo, J. G., Rios-Guerra, H., Lagunas-Rivera, S., and Ortega-Jiménez, F. (2019). An efficient and simple imidazole-hydrazone ligand for palladium-catalyzed Suzuki-Miyaura cross-coupling reactions in water under infrared irradiation. *Journal of Organometallic Chemistry,* 880: 386-391.
12. Shamsuddin, N. A. M., Rahman, N. A. A., Chandrasekaram, K., Alias, Y., and Said, N. R. (2021). Catalytic activity study of synthesised polystyrene-supported palladium (II)-hydrazone (CH_3) as catalyst in heck reaction. *Malaysian Journal of Analytical Sciences*, 25(6): 987-997.
13. Veeramanikandan, S., and Benita Sherine, H. (2015). Synthesis, characterization and biological applications of substituted benzohydrazide derivatives. *Der Pharma Chem, 7*: 70-84.
14. Shah, N., Sattar, A., Benanti, M., Hollander, S., and Cheuck, L. (2006). Magnetic resonance spectroscopy as an imaging tool for cancer: a review of the literature. *The Journal of the American Osteopathic Association*, 106(1): 23-27.
15. Moloney, M. G. (2008). Structure and reactivity in organic chemistry. Blackwell Publishing.
16. Golestanzadeh, M., and Naeimi, H. (2019). Palladium decorated on a new dendritic complex with nitrogen ligation grafted to graphene oxide: Fabrication, characterization, and catalytic application. *RSC Advances*, 9(47): 27560-27573.
17. Said, N. R., Rezayi, M., Narimani, L., Al-Mohammed, N. N., Manan, N. S. A., and Alias, Y. (2016). A new N-heterocyclic Carbene Ionophore in plasticizer-free Polypyrrole membrane for determining Ag^+ in tap water. *Electrochimica Acta,* 197: 10-22.
18. Forryan, C. L., Compton, R. G., Klymenko, O. V., Brennan, C. M., Taylor, C. L., and Lennon, M. (2006). Comparative solubilisation of potassium carbonate, sodium bicarbonate and sodium carbonate in hot dimethylformamide: Application of cylindrical particle surface-controlled dissolution theory. *Physical Chemistry Chemical Physics,* 8(5): 633–641.
19. Dyson, P. J., and Jessop, P. G. (2016). Solvent effects in catalysis: Rational improvements of catalysts: Via manipulation of solvent interactions. *Catalysis Science and Technology,* 6(10): 3302–3316.
20. Xiong, Y., Huang, T., Ji, X., Wu, J., and Cao, S. (2015). Nickel-catalyzed Suzuki–Miyaura type cross-coupling reactions of (2, 2-difluorovinyl) benzene derivatives with arylboronic acids. *Organic & Biomolecular Chemistry,* 13(27): 7389-7392.

Malaysian Journal of Analytical Sciences (MJAS)
Published by Malaysian Analytical Sciences Society

THE DEVELOPMENT AND QUANTITATIVE PERFORMANCE TEST OF LOW-COST VISIBLE SPECTROPHOTOMETER AND ITS COMPARISON WITH COMMERCIAL SPECTROPHOTOMETER

(Pembangunan dan Ujian Prestasi Kuantitatif dari Spektrofotometer Nampak Kos Rendah dan Perbandingannya dengan Spektrofotometer Komersil)

Rudi Heryanto[1,2], Dyah Iswantini[1,2*], Eti Rohaeti[1,2], Mohamad Rafi[1,2], Mulyati[1], and Wulan Suci Pamungkas[1]

[1] Department of Chemistry,
Faculty of Mathematics and Sciences
[2] Tropical Biopharmaca Research Center,
Institute for Research and Community Service
IPB University, Bogor 16680, Indonesia

[*]Corresponding author: dyahis@apps.ipb.ac.id

Received: 13 December 2022; Accepted: 1 April 2023; Published: 23 June 2023

Abstract

A simple, portable, visible spectrophotometer was constructed and used for analytical measurements. The spectrophotometer was built using consumer electronics components such as an LED as the light source and a web camera as the detector. Using parameters including linearity, limit of detection, quantification, and precision to analyze the methyl red and dichromate standards, the analytical performance of the webcam spectrophotometer was evaluated. Results showed that, for methyl red, the webcam spectrophotometer gave a linearity range of 2–10 ppm with a limit of detection and limit of quantification of 0.69 and 2.11 ppm, respectively, and precision as a relative standard deviation of approximately 5%. The dichromate standard gave a linearity range of 0.7–1.5 ppm with a limit of detection and limit of quantification of 0.12 and 0.41 ppm, respectively, and precision as a relative standard deviation under 5%. These analytical performances are comparable but not better than those of the two commercial spectrophotometers used as comparators. The application of a webcam spectrophotometer to quantify the rhodamine B content in a traditional food sample, *pacar cina* jelly, also gave an equivalent analytical performance, and the rhodamine B analyte quantification capability was not significantly different from that of commercial spectrophotometers.

Keywords: visible spectrophotometry, webcam spectrophotometer, analytical performance, quantitative analysis

Abstrak

Spektrofotometer nampak dan mudah alih telah dibina dan digunakan untuk pengukuran analitik. Spektrofotometer dibina menggunakan komponen elektronik pengguna seperti LED sebagai sumber cahaya dan kamera web sebagai pengesan. Menggunakan parameter termasuk kelinearan, had pengesanan, kuantifikasi dan ketepatan untuk menganalisis piawaian metil merah dan dikromat, prestasi analisis spektrofotometer kamera web telah dinilai. Keputusan menunjukkan bahawa, untuk metil merah, spektrofotometer kamera web memberikan julat lineariti 2-10 ppm dengan had pengesanan dan had kuantifikasi masing-

masing 0.69 dan 2.11 ppm, dan ketepatan sebagai sisihan piawai relatif kira-kira 5%. Piawaian dikromat memberikan julat lineariti 0.7–1.5 ppm dengan had pengesanan dan had kuantifikasi masing-masing 0.12 dan 0.41 ppm, dan ketepatan sebagai sisihan piawai relatif di bawah 5%. Prestasi analisis ini adalah setanding tetapi tidak lebih baik daripada dua spektrofotometer komersial yang digunakan sebagai pembanding. Penggunaan spektrofotometer kamera web untuk mengukur kandungan rhodamine B dalam sampel makanan tradisional, jeli *pacar cina*, juga memberikan prestasi analisis yang setara, dan keupayaan pengkuantifikasian rhodamine B tidak jauh berbeza daripada spektrofotometer komersial.

Kata kunci: spektrofotometri nampak, spektrofotometer kamera web, prestasi analisis, analisis kuantitatif

Introduction

Spectrophotometry is a qualified technical analysis method that is commonly used to provide qualitative and quantitative solutions to problems in food, agriculture, pharmacy, biology, and clinical chemistry. Spectrophotometry techniques typically used in the food sector include fluorescence, Fourier transform infrared (FTIR) spectroscopy, near infrared (NIR) spectroscopy, and ultraviolet–visible (UV–Vis) spectrophotometry. Specifically, the UV–Vis spectroscopy has been used to analyze different food matrices (such as meat, milk, coffee, wine, vegetables, fruits, drinks, and olive oil) in relation to their composition, authenticity, adulteration, and quality [1].

Concerns about food quality and safety have grown in recent years among the public, apparently due to changes in eating habits, consumer behavior, development, and improvements in food supply chain industrialization. The high quality and safety requirements of food products require high standards for quality control and processing, which in turn require appropriate analytical tools to investigate the food [2]. In line with advances in consumer electronics technology, some studies have attempted to use smartphones as food diagnostic tools, such as for food allergen determination, functional food active compound detection, and foodborne pathogen identification [3]. Other studies have attempted to develop web camera-based spectrophotometers for detecting food oils or food colorings [4]. The idea behind developing this consumer electronics-based instrument is to make it available to a wide range of users, including the possibility of citizen-based food safety control [5].

Generally, a spectrophotometer may be assembled from several components, such as a light source from a white LED, a diffraction grating using a DVD, a detector from a CCD/CMOS webcam, and an image-based data acquisition/processing software or a direct spectrum recorder [6]. As a food diagnostic tool, a low-cost multifunctional webcam spectrophotometer was developed and applied to measure molecular absorption and fluorometry. The results of the determination of the same compound are comparable with other commercial spectrophotometers [7]. Moreover, a spectrophotometer constructed with LED components as the light source and a webcam as the detector was successfully built and was capable of providing a representative spectrum from various fruits such as apples, cherries, and pears [8].

This study attempted to build a portable absorption spectrophotometer that can be used to analyze food and other related materials using consumer electronic components. The reproducibility of performance from device to device can be a major challenge when using consumer electronics in portable systems [9]. Moreover, each portable spectrophotometer must provide results with verified precision and accuracy [10]. As an initial step towards developing a portable spectrophotometer-based food analysis system, this study, in addition to presenting the constructed portable spectrophotometer configuration, also shows a performance test of the spectrophotometer using organic and inorganic standard compounds. Furthermore, a performance comparison with commercial spectrophotometers is performed. In addition, a spectrophotometer for detecting hazardous materials contained in food was successfully developed.

Materials and Methods

The main materials used in this research were purchased from Merck: methyl red, $K_2Cr_2O_7$, rhodamine B, ethanol (96%), 1,5-Diphenylcarbazide, and other reagents. A sample of *pacar cina* jelly was obtained from a local market in Bogor. The main component of the webcam

spectrophotometer is the web camera used as the detector, which is a Logitech HD c270. The commercial spectrophotometers used for comparison was the Spectronic 20D+ and Genesys 10UV (Thermo Fisher Scientific).

Webcam absorption spectroscopy development

The spectrophotometer was constructed based on the scheme shown in Figure 1(a). A white LED lamp (HPL Epistar) powered by a 9-volt battery was used as the light source. The optical layer of a DVD (GT-Pro) was used as the diffraction grating, and a webcam was used as the detector. Spectrum data acquisition was performed using Spectral Workbench, which was provided by Publiclab.org as a web instrument with a feature to capture the spectrum using a webcam and other features to visualize, manipulate, and store the spectrum from the web browser page [11]. Figure 1(b) shows the spectrophotometer built using all the components. The light source, cuvette holder, grating, and webcam were located in a black box. The grating is attached to the front of the webcam lens. The positions of the components, particularly the webcam and light source, were then determined experimentally. The webcam was placed opposite to the 45° incident light, and the distance was set to minimize the probability of saturation due to excessive light. In this spectrophotometer, the distance between the webcam used as a sensor and the light source was 25 cm (S1), and the distance between the webcam and slit was 7 cm. The slit width was set to 1 mm, and a 1 mL cuvette was placed directly behind the slit.

Calibration and mode of measurement of webcam spectrophotometer

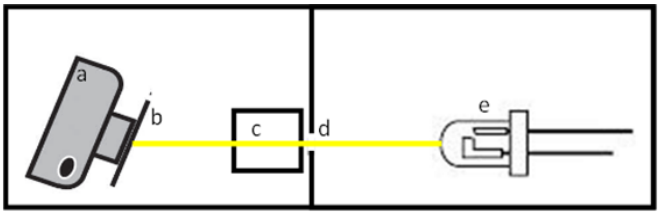
The spectrophotometer produces a sample spectrum with the aid of the tools from Spectral Workbench. Sample measurements began with a spectrophotometer connected to a computer using an I/O cable from the webcam. Using the profile that has been registered in the Spectral Workbench, the 'Capture Spectra' facility in the Spectral Workbench is used to recognize the webcam from the spectrophotometer and capture the spectra from the sample. The sample spectrum was calibrated using a CFL calibration spectrum to obtain a line spectrum with an intensity value at a certain wavelength. When the spectrophotometer was turned on (turning the white LED on), the light passed through the gap into the cuvette and towards the webcam. The grating attached in front of the webcam diffracts white light into the color components that the webcam captures, functioning as the sensor. The color spectrum of the diffraction pattern was visualized in real time on a Spectral Workbench (Figure 2). The Spectral Workbench simultaneously shows the transmission spectrum, with the y-axis representing the percentage of intensity (%I) and the x-axis representing the wavelength. To obtain the correct scale of the wavelength in the spectrum, calibration was first performed using a CFL lamp as the light source. A CFL lamp produces a well-known spectrum characterized by sharp and identifiable peaks. The Spectral Workbench performed the calibration process by adjusting the scale of the wavelength on the spectrum based on the peaks of the specified CFL emission, that is, at 436 and 546 nm.

The Spectral Workbench acquired the spectrum of the sample by transforming the color spectrum image into data. The resulting data can be exported in xls format by tabulating the wavelength and approximating the light intensity as the average values of RGB divided by 257 (interpretation of the Spectral Workbench algorithm to a single 8-bit byte pixel) (I') (S2 and S3). A percentage of approximate intensity on the y-axis of the transmission spectrum was calculated using Eq. (1):

$$\%\mathrm{I}' = \frac{\mathrm{I}'}{257} \times 100\% \,. \quad (1)$$

The webcam spectrophotometer was constructed as a single-beam spectrophotometer. To obtain the absorbance (A) of the sample, the approximate intensities of a blank and sample or standard were compared using Eq. (2):

$$\mathrm{A} = log \frac{\%I'_{blank}}{\%I'_{standard}} \,. \quad (2)$$

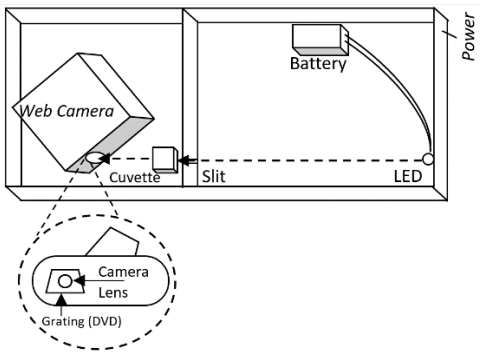


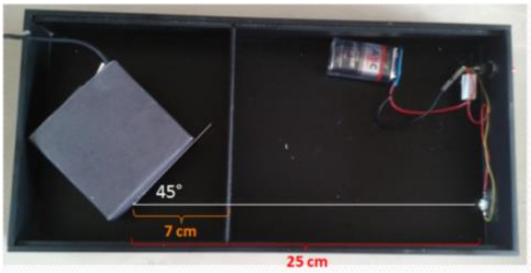
a: web camera

b: DVD grating

c: cuvette

(a)





(b)

Figure 1. Diagram illustrating general components for the webcam-based spectrophotometer (a) and scheme and view of the device from above with all of its components (ii)

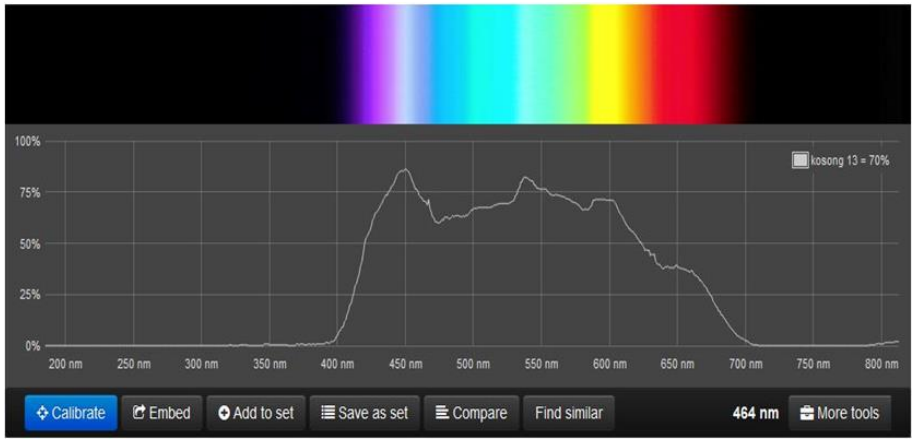


Figure 2. Example of a color spectrum and a spectrum with calibrated scale of wavelength from the webcam-based spectrophotometer

Webcam spectrophotometer performance and performance comparison with commercial spectrophotometers

The analytical performance of the webcam spectrophotometer was evaluated by determining the linearity, limit of detection, limit of quantification, and precision of methyl red and dichromate standard concentrations. The measurement results of the webcam spectrophotometer were then compared with those of the commercial spectrophotometers, Spectronic 20D+ and

Genesys 10UV (Thermo Fisher).

Linearity test

This test was performed by preparing calibration curves for five concentrations of methyl red and dichromate standard solutions. Ten milligrams of methyl red were dissolved in ethanol in a 100-mL volumetric flask. This standard solution was then diluted to yield a series of methyl red standard solutions with concentrations of 2, 4, 6, 8, and 10 ppm in a 25-mL volumetric flask. The concentrations of the methyl red standard solutions were measured directly using a spectrophotometer. Dichromate solutions were prepared using the $K_2Cr_2O_7$ standard at five different concentrations of 0.7, 0.9, 1.1, 1.3, and 1.5 ppm. The dichromate standards were measured after the first reaction with diphenylcarbazide (DPC). Each of the dichromate standard solutions (10 mL) was added to a reaction tube, followed by the addition of 0.4 mL of 0.25% DPC. After shaking the solution, 1 mL of a phosphoric acid-water mixture (1:1) was added. The solution obtained was shaken again, allowed to sit for 15 min, and finally measured with a spectrophotometer. Absorbance was measured in six replicates. Calibration curves were constructed by connecting the concentration (x-axis) and absorbance (y-axis). Linearity can be deduced from the correlation coefficient (r).

Limit of detection (LoD) and limit of quantification (LoQ)

The LoD and LoQ of the webcam spectrophotometer were determined by measuring the blank absorbance in ten replicates, and the standard deviation of the blank absorbance was calculated. The LoD and LoQ values were calculated using Eq. (3):

$$LOD = \frac{3.3 \times SD}{S}, \quad LOQ = \frac{10 \times SD}{S} \qquad (3)$$

where SD is the standard deviation of the blank absorbance, and S is the sensitivity (slope) of the calibration curve.

Precision

Precision was assessed using the relative standard deviation (RSD) of seven standard solutions with the same concentration. Methyl red was used at a concentration of 5 ppm, and dichromate was used at a concentration of 1 ppm.

Analysis of Rhodamine B in traditional food pacar cina jelly

To demonstrate the application of the spectrophotometer in sample analysis, a webcam spectrophotometer was used to determine the level of Rhodamine B in the traditional food, *pacar cina* Jelly. The results were compared to those obtained using commercial spectrophotometers. A 5 g sample of *pacar cina* jelly sample was weighed and immersed in 2% ammonia in 70% ethanol for 24 h to dissolve all the dyes. The colored solution was filtered, evaporated, and concentrated on a hot plate at 65 °C for 4 h. The concentrated solution was added to 30 mL of an aqueous solution and stirred to homogeneity. After adding the homogenous solution to a separatory funnel, 6 mL of 10% NaOH was added and shaken, followed by 30 mL of diethyl ether, which was shaken again until two layers were formed. The water layer was discarded, and the ether layer was washed with 5 mL of 5% NaOH and shaken. The ether layer was extracted three times with 10 mL of 0.1 N HCl. The HCl extracts were then collected in a 50-mL volumetric flask and diluted with 10 mL of 0.1 N HCl to the mark. The samples were then ready for measurement. The concentration of rhodamine B was measured by using a calibration curve of rhodamine B at concentration series of 1, 2, 3, 4, and 5 ppm and 0.1 mL HCl as the blank.

Results and Discussion

The analytical performance of the webcam spectrophotometer was evaluated based on the linearity, limit of detection, quantification, and precision of methyl red and dichromate standard concentrations. All measurements were performed at wavelengths of 495 and 543 nm, which are the maximum wavelengths for methyl red and dichromate, respectively. Tables 1 and 2 show the analytical performance compared with that of Spectronic 20D+ and Genesys 10UV.

Table 1. Analytical performance of spectrophotometers in determining methyl red standard concentration

Parameter	Spect. Webcam	Spectronic 20D+	Genesys10UV
Linearity(R^2)	0.9638	0.9991	0.9996
LoD (ppm)	0.7	0.1	0.1
LoQ (ppm)	2.1	0.3	0.2
Precision (%RSD)	5.2	1.6	1.7

Table 2. Analytical performance of spectrophotometers in determining dichromate standard concentration

Parameter	Spect. Webcam	Spectronic 20D+	Genesys10UV
Linearity (R^2)	0.9991	0.9983	0.9998
LoD (ppm)	0.1	$2x10^{-3}$	$4x10^{-3}$
LoQ (ppm)	0.4	$8x10^{-3}$	$1x10^{-2}$
Precision (%RSD)	2.6	0.6	0.3

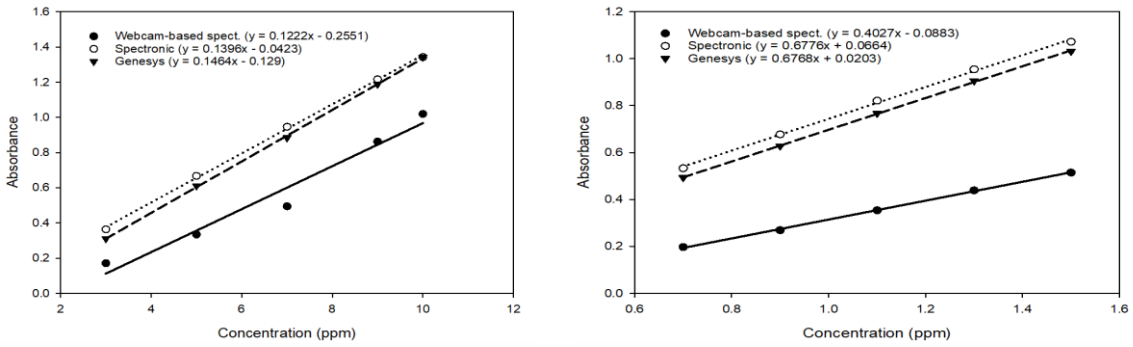
Generally, webcam spectrophotometers have not outperformed commercial spectrophotometers in terms of analytical performance. For the two standards used, the LoD, LoQ, and %RSD values of the webcam spectrophotometer were higher than those of the commercial spectrophotometers. In this study, the LoD and LoQ were calculated according to IUPAC definitions. Considering that the spectrophotometric method is used to measure standards using a simple matrix, the assumption of using blanks to determine LoD and LoQ can be fulfilled [12]. However, the linearities of commercial spectrophotometers were better than those of webcam spectrophotometers.

As shown in Figure 3, when compared to commercial instruments, the use of consumer electronics components (e.g., LED as the light source) as components of the webcam spectrophotometer results in a lower absorbance signal and a webcam as the detector results in lower calibration sensitivity. The webcam system for the detector typically undergoes signal deviation owing to the default image processing system and therefore offers limited quantitative data acquisition capability [13].

A similar phenomenon related to this analytical performance was found in another study by Danchana et al. [14], who developed a webcam-based molecular absorption spectrophotometer to measure iron levels, and in a study by Kotchabhakdi and Grudpan [15], who developed a digital camera-based atomic absorption spectrophotometer to measure metal elements in various types of food, water, and fertilizer samples. Nevertheless, the performance of this spectrophotometer was still reasonable and within the acceptable limit, as seen by the precision value that gave a lower %RSD than 2/3x CV Horwitz [16].

In this study, a webcam spectrophotometer was used to quantify the rhodamine B content in the traditional food *pacar cina* jelly. Rhodamine B is an organic chloride salt commonly used as a dye in plastics, textiles, and printing products. Rhodamine B was once used as a food additive, but its use in food is now prohibited [17]. However, some studies have found that Rhodamine B is still used illegally as a food additive, which could be harmful to consumer health [18].

Rhodamine B quantification by spectrophotometry began with a multi-stage extraction. Five samples of *pacar cina* jelly were purchased from local markets in Bogor. The samples were macerated and partitioned with various solvents to obtain rhodamine B in an HCl solution. The absorbance of the extracts was measured using a webcam spectrophotometer and subsequently compared with that of standard solutions to determine the level of rhodamine B. Measurements were performed using commercial spectrophotometers (Spectronic 20D + and Genesys 10UV). Table 3 shows the results of the rhodamine B content using the three types of spectrophotometers in conjunction with the statistical parameters of the method.



(a) (b)

Figure 3. Calibration curve for methyl red (a) and dichromate (b) standards

The webcam spectrophotometer used to quantify rhodamine B demonstrated the same pattern of analytical performance as the methyl red and dichromate determinations when compared with the two commercial spectrophotometers. The webcam spectrophotometer gave the largest relative standard deviation value compared to the two other spectrophotometers, but still maintained the precision within the acceptable limit of %RSD, which was lower than 2/3x CV Horwitz. The %CV Horwitz = $2^{1-0,5 \log C}$ acceptance limit can also be used as a starting point when the repeatability limits have not been determined through the control chart. Regarding the rhodamine B content in the samples, the three instruments yielded values that were not significantly different. Food producers used rhodamine B at a sufficiently high level, almost three times the 7.06 µg/g found in cassava chips [19]. The low F-value indicates that the model does not substantially differ in the mean of rhodamine B obtained from the three spectrophotometric methods.

Table 3. Rhodamine B content in samples and statistical parameters of method

Parameter	Spect. Webcam	Spectronic 20D+	Genesys10UV
[Rhodamin B] ($\bar{x} \pm sd$ µg/g)	21.65 ± 0.63	21.46 ± 0.34	21.83 ± 0.13
RSD (%)	2.91	1.56	0.61
2/3 CVHorwitz	6.7146	6.7236	6.7063

Note: ANOVA showed no significant difference (average of the three analyses).
($F_{calculation} = 0.9792 < F_{table}$, 0.05;2,12 = 3.8852, p = 0.4036)

Conclusion

A spectrophotometer model ("Webcam Spectrophotometer") has successfully been built utilizing consumer electronics components such as a LED as the light source and a webcam as the detector. The analytical performance was evaluated to determine the methyl red and dichromate standard solution concentrations, and the performance was compared with that of two commercial spectrophotometers. The analytical performance parameters of the webcam spectrophotometer (linearity, detection limit, quantification limit, and precision) were all within acceptable values of performance parameters and were comparable to those of commercial spectrophotometers. Further application of the spectrophotometer model to quantify the rhodamine B content in food samples demonstrated equivalent analytical performance with no significantly different analyte quantification capability compared to the other two commercial spectrophotometers. Based on the above, webcam spectrophotometers can potentially be used as an alternative instrument for food, related food materials, and product quality control.

Acknowledgement

This work was part of a research project, SP DIPA-023.04.2.189772, supported by the Ministry of Research, Technology, and Higher Education, Indonesia, and IPB University, Indonesia.

References

1. Haque, F., Bubli, S. Y., and Khan, M. S. (2021). UV–Vis spectroscopy for food analysis. *Technolgy to Measure Food Safety Quality*, 2021: 169-193.
2. Nawrocka, A., and Lamorska, J. (2013). Determination of food quality by using spectroscopic methods, in Grundas, S. and Stepniewski, A. (Eds.), IntechOpen, Rijeka, p. 14.
3. Rateni, G., Dario, P., and Cavallo, F. (2017). Smartphone-based food diagnostic technologies: A review. *Sensors*, 17(6): 1453.
4. Likith, G., Jayram, N. D., Yaswanth, B., Sreekanth, D., Deny, J., Karuthapandi, M., and Vishwa, S. V. (2021). Designing of low-cost spectrometer for sensor application, *Journal Optics*, 50(3): 489-494.
5. Nelis, J. L. D., Tsagkaris, A. S., Dillon, M. J., Hajslova, J., and Elliott, C. T. (2020). Smartphone-based optical assays in the food safety field, *TrAC Trends Analytical Chemistry*, 129: 115934.
6. Scheeline, A. (2015). Spectrometry with consumer-quality CMOS cameras, in mobile health technologies: Methods and protocols. Springer New York, pp. 259-275.
7. Silva, W. R. F., Suarez, W. T., Reis, C., dos Santos, V. B., Carvalho, F. A., Reis, E. L., and Vicentini, F. C. (2021). Multifunctional webcam spectrophotometer for performing analytical determination and measurements of emission, absorption, and fluorescence spectra. *Journal Chemical Education*, 98(4): 1442-1447.
8. Abbasi, H., Nazeri, M., and Mireei, S. A. (2016). Design and development of a LabVIEW-based LED-induced fluorescence spectroscopy system with applications in non-destructive quality assessment of agricultural products. *Journal of Physics: Conference Series,* p. 012010.
9. Das, A. (2021). Portable UV–visible spectroscopy – instrumentation, technology, and applications. *Portable Spectroscopy Spectrometry*, 2021: 179-207.
10. Scheeline, A. (2021). Smartphone technology – instrumentation and applications. *Portable Spectroscopy Spectrometry*, 2021: 209-235.
11. Balado Sánchez, C., Díaz Redondo, R. P., Fernández Vilas, A., and Sánchez Bermúdez, A. M. (2019). Spectrophotometers for labs: A cost-efficient solution based on smartphones, *Computer Application in Engineering Education*, 27(2): 371-379.
12. Kirchmer, C. J. (1987). Estimation of detection limits for environmental analytical procedures. *Detection in Analytical Chemistry,* pp. 78-93.
13. Lebourgeois, V., Bégué, A., Labbé, S., Mallavan, B., Prévot, L., and Roux, B. (2008). Can commercial digital cameras be used as multispectral sensors? A crop monitoring test. *Sensors,* 8(11): 7300-7322.
14. Danchana, K., Phansi, P., T. de Souza, C. L.C., Ferreira, S., and Cerdà, V. (2020). Spectrophotometric system based on a device created by 3D printing for the accommodation of a webcam chamber as a detection system, *Talanta*, 206: 120250.
15. Kotchabhakdi, N., and Kate Grudpan, K. (2020). A use of an everyday life camera with image processing as alternative detection for a flame photometer. *Malaysian Journal Analytical Sciences*, 24(6): 918-926.
16. Taverniers, I., De Loose, M., and Van Bockstaele, E. (2004). Trends in quality in the analytical laboratory. II. Analytical method validation and quality assurance, *TrAC Trends Analytical Chemistry*, 23(8): 535-552.
17. Cooksey, C. J. (2015). Quirks of dye nomenclature. 5. Rhodamines. *Biotechnic & Histochemistry*, 91(1): 71-76.
18. Hasanah, A. N., Musfiroh, I., Saptarini, N. M., and Rahayu, D. (2014). Identification of rhodamine B in food products and cosmetics circulated in Bandung. *Jurnal Ilmu Kefarmasian Indonesia,* 12(1): 104-109.
19. Ridjal, A. T. M. and Kasma, A. Y. (2022). Study of rhodamine B dyes content in snacks of Karuwisi Traditional Market Makassar, South Sulawesi, Indonesia. *In IOP Conference Series: Earth and Environmental Science,* 1027(1): p. 012012.

Malaysian Journal of Analytical Sciences (MJAS)
Published by Malaysian Analytical Sciences Society

POTENTIAL OF LIGNIN FROM OIL PALM BIOMASS USING DEEP EUTECTIC SOLVENT AS CARBON FIBRE PRECURSOR

(Potensi Lignin daripada Biojisim Kelapa Sawit Menggunakan Pelarut Eutektik Dalam sebagai Prekursor Gentian Karbon)

Afiqah Liana Sazali, Siti Khadijah Amran, Khairul Faizal Pa'ee, Mohd Razealy Anuar, and Tau-Len Kelly Yong

Universiti Kuala Lumpur,
Branch Campus Malaysian Institute of Chemical and Engineering Technology,
Lot 1988 Kawasan Perindustrian Bandar Vendor, Taboh Naning,
78000 Alor Gajah, Melaka, Malaysia

**Corresponding author: kytlen@unikl.edu.my*

Received: 14 September 2022; Accepted: 1 April 2023; Published: 23 June 2023

Abstract

The modern composites industry heavily relies on carbon fibre as a raw material due to its high tensile strength, fatigue resistance, and temperature resistance. Thus, researchers are investigating the use of lignin extracted from biomass as a precursor for carbon fibre to reduce costs and environmental impact. Oil palm biomass is classified as a lignocellulosic compound due to its high cellulose, hemicellulose, and lignin content. Since lignin has a complex structure with numerous linkages between its monomeric components, it can be complicated to isolate it from lignocellulosic components. Deep eutectic solvents (DESs) are a promising new class of environmentally friendly solvents owing to their low toxicity, low production cost, and high biodegradability. Lignin valorisation has received much attention due to immense ability of DES to dissolve and extract lignin without condensation. This review aimed to provide a comprehensive and comparative analysis of the physicochemical and thermal properties of DES for utilisation in lignin extraction from biomass, with a focus on its potential as a precursor for carbon fibre.

Keywords: deep eutectic solvent, carbon fibre, lignin, precursor, oil palm biomass

Abstrak

Industri komposit moden sangat bergantung pada gentian karbon sebagai bahan mentah kerana kekuatan tegangan yang tinggi, rintangan kelesuan dan rintangan suhu. Oleh itu, penyelidik sedang mengkaji penggunaan lignin daripada biojisim sebagai prekursor yang lebih mesra alam dan kos efektif untuk gentian karbon. Biojisim kelapa sawit dikategorikan sebagai lignoselulosa, kerana kandungan selulosa, hemiselulosa dan lignin yang tinggi. Walau bagaimanapun, mengasingkan lignin daripada lignoselulosa memberikan cabaran kerana strukturnya yang rumit dan mempunyai pelbagai sambungan antara komponen monomeriknya. Pelarut Eutektik Dalam (DES) ialah generasi baharu pelarut hijau yang mudah disediakan, tinggi biodegrabiliti, kos pembuatan yang rendah dan ketoksikan yang rendah. Keupayaan DES yang luar biasa untuk melarutkan dan mengekstrak lignin tanpa pemeluwapan telah mencetuskan minat yang ketara dalam valorisasi lignin. Kajian ini bertujuan untuk menganalisis secara sistematik dan perbandingan sifat fizikokimia dan terma DES untuk pengekstrakan lignin daripada biojisim, dengan

penekanan khusus pada penggunaannya sebagai prekursor untuk gentian karbon.

Kata kunci: pelarut eutektik dalam, gentian karbon, lignin, prekursor, biojisim kelapa sawit

Introduction

Advanced materials interest industrial strategists, economists, and policymakers due to their far-reaching potential and impact across various industries. Carbon fibre has a high strength-to-weight ratio and is lightweight, making it a desirable component in various high-tech and extensive applications. Bengtsson et al. [1] reported that a substantial amount (>96%) of carbon fibre is manufactured from the fossil-based polymer polyacrylonitrile (PAN), with the remainder coming from petroleum, coal-tar pitch, and rayon. The need for lightweight composites has led to the increasing popularity of carbon fibres. Hence, developing a more sustainable and cost-effective alternatives is necessary due to their high manufacturing costs and reliance on fossil-based resources.

Owing to its abundance and carbon neutrality, lignocellulosic biomass has the potential to replace fossil fuels as renewable feedstock. Lignin is a naturally occurring renewable raw material with exceptional chemical and physical properties. It is cheap and has the potential to replace feedstocks that are based on fossil fuels. Lignin extracted from palm oil biomass can be processed in several ways to yield various value-added carbon products [2]. However, physical and chemical heterogeneities of lignin render it a poor feedstock.

The hot and humid climate of Malaysia makes it ideal for growing oil palms, one of its most important crops. The palm oil milling industry produces millions of metric tonnes of waste annually. Oil palm fronds, mesocarp fibres, palm kernel shells, empty fruit bunches, and oil palm trunks are all renewable resources that make the palm oil industry a significant biomass producer [3]. Oil palm biomass is produced during milling, burned for energy recovery, or left to biodegrade in the plantation. Inefficient management practices exacerbate the production of harmful greenhouse gases. Oil palm biomass, with its high lignin content, may be able to replace PAN and pitch as carbon fibre precursors.

The environmental benefits of DESs as ‘green solvents’ have garnered widespread interest. DESs are compounds that contain at least one hydrogen bond donor (HBD) and one hydrogen bond acceptor (HBA) and form a transparent liquid eutectic mixture at temperatures ranging from 60°C to 80°C [4]. The hydrogen-bonding network formed between the components and the associated charge delocalisation causes the melting point of DES to be much lower than the melting points of the individual components [5]. Due to their low toxicity, high biodegradability, low production cost, and broad applicability, DESs have been used in various processes, such as metal extraction, bio-catalysis, CO_2 capture, and biodiesel synthesis [6].

As shown in Figure 1, several studies suggested that DESs may dissolve lignin from woody plants by disrupting the β-O-4 linkages between lignin and carbohydrates. Type III DES, which are commonly synthesised by reacting quaternary ammonium or phosphonium salts as HBAs with acids, alcohols, amines, or carbohydrates as HBDs, are the most explored for biomass treatment due to their cheap cost, non-reactivity with water, and biodegradability. However, their effectiveness depends on the specific DESs used and molar ratios. Due to their impact on biomass processing, especially the modes of action on cellulose, hemicellulose, and lignin, a complete understanding of the properties of DESs is crucial. Furthermore, lignin extracted with DES as a carbon fibre precursor has not been studied, and there have been no findings regarding its fundamental properties.

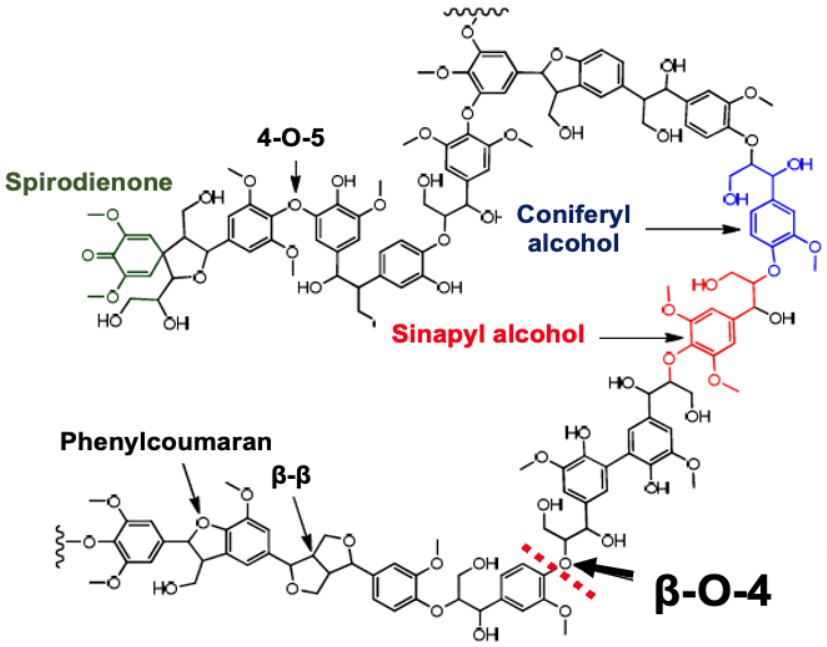


Figure 1. Selective cleavage of β-O-4 in lignin by DES

Deep eutectic solvents and its properties

DESs are eutectic mixtures of solid compounds that melt at lower temperatures than their components [7]. The hydrogen-bonding network between the components and the resulting charge delocalisation lowers the melting point. Abbott et al. [7], who discovered the dissolving power of DES mixtures, documented the first report on DESs. Understanding the HBA and HBD properties based on the functional group and mixing them in the precise molar ratios enables the synthesis of DESs to be accomplished quickly and efficiently. Finally, they have low toxicity and production costs when designed properly, particularly when produced from renewable sources.

DESs are solvents similar to ionic liquids (ILs), which are made up of a cation and an anion. ILs are widely used as solvents, although their hazardous effects on the environment and human health are well known [8]. In contrast to ILs, DES synthesis is a straightforward mixing procedure that can be scaled up to produce environmentally friendly and effective alternative solvents. Ca+X-zY is a common formula for DES, whereby Ca+ is the principal cation (typically ammonium, phosphonium, or sulfonium), and X- is a Lewis base (typically a halide anion). Figure 2 shows the interaction between the X- and z molecules of Y, where Y can be a Lewis acid or a Brønsted acid [9].

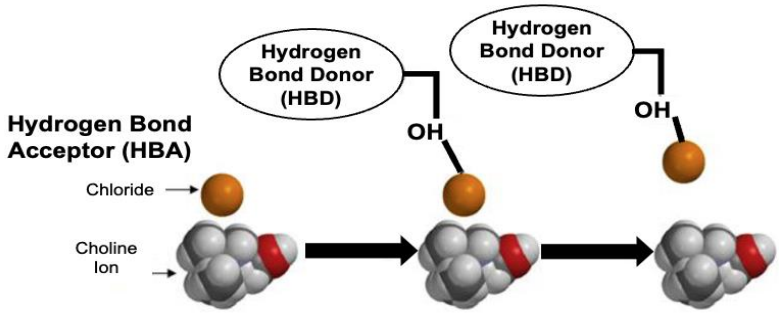


Figure 2. HBA and HBD components of DES

Table 1 shows the four distinct categories of DESs based on the chemicals used to produce them. The high melting temperatures of non-hydrated metal halides restrict the use of Type I DESs in biomass processing. On the other hand, Type II DESs are a much more cost-effective option for industrial processes because hydrated metal halides are cheaper. It is possible to tailor the physical properties of Type II DES to meet the needs of various applications by varying the HBD [8]. Type III DESs. On the other hand, Type III DESs are the most studied and investigated due to their low cost, non-reactivity with water, and biodegradability. Finally, Type IV DESs combine inorganic transition metals with urea to create eutectic mixtures, although metal salts do not typically ionise in non-aqueous media.

Table 1. Classification of DESs [8]

Type	Component	General Formula	Example
I	Metal salt organic salt	$Ca^+ X^-$ zMClx; M = Zn, Sn, Fe, Al, Ga. In	$ZnCl_2$ + ChCl
II	Metal salt hydrate + organic salt	$Ca^+ X^-$ zMClx.yH_2O; M = Cr, Co, Cu, Ni, Fe	$CoCl_2.6H_2O$ + ChCl
III	HBD + organic salt	$Ca^+ X^-$ zRZ; Z = $CONH_2$, COOH, OH	Urea + ChCl
IV	Zinc/aluminium chloride + HBD	MClx + RZ = $MCl_{x-1}{}^+$. RZ+ $MCl^-{}_{x+1}$; M = Al, Zn & Z = $CONH_2$, OH	$ZnCl_2$ + ChCl

DESs are typically formed by reacting quaternary ammonium or phosphonium salts with HBD, such as acids, alcohols, amines, or carbohydrates [10]. Quaternary ammonium salts such as choline chloride (ChCl) are common HBAs, and metal salts, urea, carboxylic acids, and polyols are examples of HBDs, as shown in Figure 3 [11]. Selecting the most appropriate HBA and HBD with the right molar ratio allows for developing DESs tailored for specific applications. For example, Francisco et al. [10] observed that lactic acid:betaine (2:1) resulted a clear liquid of DES while lactic acid:histidine (2:1) showed no evidence of melting. This demonstrates that the specific molar ratio is dependent on the type of HBA and HBD combination.

Farooq et al. [12] reported that modifying the degree of basicity of hydrogen bonds in DESs can increase their efficacy. Based on their findings, the use of acidic carboxylic acids as HBDs with higher HBD:HBA molar ratios is proposed for high extraction efficiency with biomass [12]. Although a high extraction yield is desired, the fundamental properties of the extracted compounds may vary depending on the nature of the raw materials, particularly lignocellulosic compounds, which include various constituents. Information on the physiochemical and thermal properties of DES is required owing to the growing interest in this compound. The freezing point and decomposition temperature of DESs and physicochemical properties (viscosity, density, refractive index, and pH) vary with HBA and HBD combinations and molar ratios. The review on the physicochemical and thermal properties of DES is important because these properties are related to a potential lignin valorisation pathway, particularly as a carbon fibre precursor.

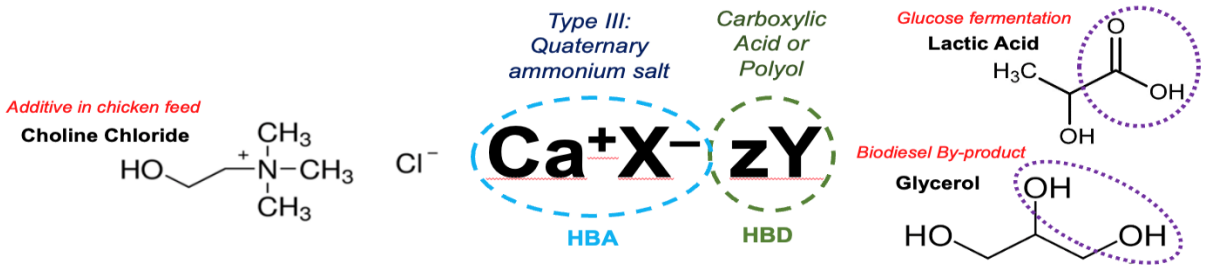


Figure 3. HBAs of quaternary ammonium salts (ChCl) and HBDs of carboxylic acids (lactic acid) and polyols (glycerol)

Viscosity

The viscosity of a fluid indicates the extent to which it resists its movement. The higher viscosity of DESs as compared to organic solvents makes handling, stirring, and filtration more challenging. The type of HBD, molar ratio, and temperature play a role in the viscosity of binary eutectic mixtures owing to hydrogen-bonding, Van der Waals, and electrostatic interactions [13]. Yusof et al. [14] reported that an increased number of hydroxyl groups produced higher viscosity due to the increased adhesive force between molecules provided by the increased number of hydrogen bonds. For example, citric acid, which has three carboxyl groups, forms stronger hydrogen bonds with ChCl owing to its larger molecular size. Therefore, the molecules in the ChCl:citric acid system are less mobile than those in the ChCl:malic acid system. Meanwhile, the hydrogen bond interaction between ChCl and lactic acid is weaker owing to its smaller molecular size [15].

Due to the sparse network between the different groups in DES, decreasing the salt molar ratio can decrease viscosity [16]. For instance, as the molar ratio of ChCl increased, the viscosity of ChCl:glycerol decreased, most likely due to the dissolution of intermolecular hydrogen bonds, resulting in molecular disruption [17]. Therefore, the frictional forces were diminished, and the molecular motion became less restricted. On the other hand, the viscosity of the DES increased as the molar ratio of HBD increased. For example, increasing the molar ratio of HBD causes the viscosity of ChCl:fructose to increase from 28.31 cP to 72.42 cP. This may be due to the increased hydrogen bond strength between the chloride ion and hydrogen atom due to the higher fructose concentration [15]. In addition, the viscosity significantly varies with temperature. Increasing the temperature caused the viscosity of the DES to decrease. Shear impact and thermal expansion can weaken the internal structure of DESs, leading to low viscosity [18]. Francisco et al. [19] stated that higher temperatures could increase the kinetic energy and reduce viscosity by weakening the attractive forces between molecules.

Density

The density influences the diffusion rate of the solvent and its ability to mix with other liquids. Density can be affected by various factors such as temperature, pressure, intermolecular interactions, and molecular weight. The density differences could be attributed to the different arrangements or packing of DES molecules [13]. Designing a DES without establishing a correlation between HBD and density is impossible. The density of DES is affected by the number of hydrogen bonds present in the solution [14, 20].

Fuad et al. [15] reported that DESs containing high-molecular-weight compounds have a greater density in the eutectic mixture than DES containing low-molecular-weight compounds. Since lactic acid had a relatively low-molecular-weight (90.08 g/mol), the ChCl:lactic acid mixture had a low-density of 1134 kg/m^3. On the other hand, ChCl:maltose density is 1431 kg/m^3 high molecular weight (342.3 g/mol) of maltose [15]. The density of a DES is also affected by the organic salt-to-HBD molar ratio. For instance, increasing the molar ratio of ChCl:glycerol from 1:1 to 1:4 resulted in an increase in density from 1160 kg/m^3 to 1210 kg/m^3

[21]. As the salt concentration relative to the HBD increased, the liquid became more structured, and the free volume decreased. When the free volume decreases, the molecular mobility decreases and the viscosity gradually increases [19].

Yadav and Pandey [22] stated that the DES density can be altered by the presence of water, making it less dense. For example, the density decreased from 1219.4 kg/m^3 to 1111.3 kg/m^3 when 50 vol% of water was added to the DES solution [23]. In addition, increasing the temperature reduced the DES density. Shahbaz et al. [24] reported that the rapid motion of DES particles increases the number of voids within the molecule as the temperature increases, making the DES less dense.

pH

The pH of a solution can affects chemical reactions in several ways, making it a crucial physical property. The applications of DESs in catalysis, biological activities, and metal treatment depend on the pH. Donor and acceptor acidity and basicity are responsible for the pH of DESs [25]. Hydrogen bonding and other molecular interactions between these ions and other species in the solvent affect the pH. For example, the ChCl:glycerol solution has a higher pH than the ChCl:malic acid solution (4.9 vs 2.4) [25]. This study demonstrated that DES acidity increased when acidic compounds were added to HBD.

Hayyan et al. [26] investigated numerous molar ratios of ChCl and fructose-based DES. They found that when the HBD content was reduced, the pH decreased as well. In addition, the pH value declined with increasing temperatures. For instance, at a molar ratio of 1:1, the pH of ChCl:fructose declined from 6.1 to 4.4 as the temperature increased from 25°C to 85°C [26]. Hypothetically, the slightly acidic pH of the DES aids lignin extraction. Although the acidity of the DES is important, it is not the most crucial factor for isolating lignin from lignocellulosic biomass. However, the extraction of lignin can be affected by factors such as the swelling of the material, the amount of carbohydrates bound to lignin, and the proportion of syringyl to guaiacyl units in the lignin structure [27].

Refractive index

The refractive index is important for understanding molecular interactions and free volumes, which heavily depend on the optical properties of the medium [28]. Salmaliyan et al. [29] found a positive correlation between the refractive index and density. Therefore, a DES with a higher refractive index is typically denser. Changes in the molar ratio, temperature, and chemical structure affect the refractive index of the DES. Chen et al. [30] observed that the refractive index of ChCl:lactic acid was 1.4590 at a molar ratio of 1:2 but declined to 1.4399 at a molar ratio of 1:4. Hence, it can be concluded that the higher the lactic acid concentration, the lower the refractive index of the DESs. A reduced concentration reduces the number of light-striking molecules, resulting in a lower refractive index ([31].

In contrast, DESs have a refractive index that decreases with temperature. For example, the refractive index of ChCl:ethylene glycol decreased from 1.468 to 1.4610 when the temperature increased from 298.15 K to 328.15 K [30]. At higher temperatures, the refractive index of the DES was reduced due to changes in its physical properties and the motion of its molecules [30]. In addition, the density and refractive indices of ChCl:ethylene glycol and ChCl:glycerol, as well as their aqueous mixes, were investigated at standard atmospheric pressure and temperatures between 298.15 K and 333.30 K [32]. A linear decrease in the density and refractive index with increasing temperature and an increase with increasing DES molar ratios were observed for pure and aqueous solutions. Furthermore, at constant molar ratios, DES with glycerol had a higher refractive index than DES with ethylene glycol.

Freezing temperature

Freezing temperature is also an important factor when assessing the liquidability of DES. All of the reported DESs have freezing points below 150°C, which are lower than their individual freezing points [13]. Donors such as carboxylic acids and sugar-derived polyols lower the freezing point of acceptor salts. The strength of hydrogen bonds is also affected by the composition of the salt owing to the charged shield [13]. In addition, the strength of the intermolecular interactions in the structure significantly affects the freezing point [33].

The freezing point of the DES mixture is typically lower than that of the individual HBAs and HBDs formed. For example, Abbott et al. [7] hypothesised that a ChCl:urea mixture with a molar ratio of 1:2 would have a freezing point of 12°C, which is lower than those of ChCl (303°C) and urea (133°C). DESs with freezing points lower than 50°C are preferable as solvents or liquids in various applications owing to their wide liquid range. Freezing point depression is proportional to the HBA and HBD interaction strength, which depends on their structures and molar ratios. Smith et al. [8] postulated that charge delocalisation due to hydrogen-bonding between the HBD and halide ion is responsible for the sharp decrease in the freezing point of DESs. Moreover, the freezing point of DES is affected by entropy change during liquid formation and the internal energy of DES molecules. Glycerol is one of the few HBDs that can yield a liquid DES at room temperature when combined with ChCl. This is possible due to the low eutectic melting point of −40°C at molar ratios of 1:2–1:4. Carboxylic acids, including levulinic acid, malonic acid, and phenylpropionic acid, have been shown to form liquid DES at room temperature [13].

For ChCl-based DES, the choice of the HBDs is decisive in producing a eutectic combination with a low melting temperature. Polyols such as glycerol or ethylene glycol HBD typically have lower freezing temperatures and may remain liquid below room temperature. This indicates that ChCl-based DESs using polyols as HBDs are viable alternatives to conventional solvents [34]. Qin et al. [35] suggested that the freezing points of DES are significantly affected by the molar ratio of HBA to HBD and that HBD compounds determine the lowest freezing point. It is theorised that freezing point depression is proportional to the molecular weight of the organic acids, with a larger effect for those with lower molecular weights.

Decomposition temperature

The decomposition temperature is the temperature range wherein the DESs are stable in the liquid phase. It is affected by various variables, including temperature, pressure, molar ratio, and heating rate. In addition, the constituent proportions and molar ratios influence DES stability and thermal behaviour [36]. However, analysis of thermal stability is relatively scarce. The robust hydrogen-bond networks of DESs may contribute to their thermal degradation characteristics. Hydrogen bonds hinder molecular escape, complicating DES decomposition. The maximum degradation temperature increased because the DESs required more energy to break bonds. Since the hydrogen bond interactions weaken with increasing temperature, DES separates into HBDs and HBAs. HBDs with lower thermal stability and boiling points then volatilise/decompose first, whereas HBAs volatilise/decompose at higher temperatures [37].

Florindo et al. [38] evaluated the decomposition temperature of various DESs. The decomposition temperature of DES was measured between 126.85°C and 226.85°C. The highest temperature at which ChCl:glutaric acid decomposed was 239.05°C, while the lowest was 124.68°C for ChCl:malic acid. In addition, Chemat et al. [39] found that the decomposition temperature of ChCl:urea+L-arginine increased from 215.38°C to 230.07°C as the molar ratio of L-arginine increased. A higher decomposition temperature resulted in a greater thermal stability. The Intermolecular interactions and coordination nature of the ions in the mixture may account for the enhanced thermal stability of ChCl:urea+L-arginine [39].

Delgado-Mellado et al. [40] found that ChCl:glycerol eutectic mixtures were stable due to the increased thermal stability of glycerol. These findings indicated that the thermal decomposition of ChCl and the vaporisation of glycerol simultaneously occurred in ChCl:glycerol, resulting in a single mass loss step due to the decomposition temperature of ChCl (250°C), which was close to the glycerol boiling point (290°C) [40]. Therefore, the higher decomposition temperature of DES may be attributed to the high thermal stability of glycerol, which ensures that the eutectic mixture never solidifies. As a result, HBD with low volatility and high thermal stability should be used to produce DES with high stability.

Lignin extraction from biomass by using DESs

Several obstacles must be overcome to extract lignin from biomass successfully. Pure lignin is difficult to

extract from lignocellulosic biomass due to the highly linked structures of lignin and carbohydrates [41]. The condensation and oxidation of lignin also occur during isolation, thereby increasing the complexity of the process. In biomass, lignin and carbohydrate compounds form lignin-carbohydrate complexes (LCCs) with strong bonding strengths, which may affect their extraction [42]. There are eight types of lignin-carbohydrate bonds: benzyl ether, benzyl ester, glycosidic or phenyl glycosidic, hemiacetal or acetal linkages, and ferulate or diferulate esters. Tarasov et al. [43] found that LCCs facilitate bond cleavage and increase the accessibility of enzymes to biomass.

A thorough understanding of the LCC structure may help devise the best methods for breaking bonds to separate lignocelluloses efficiently and selectively. In recent years, there has been a surge in research and development of greener solvents for lignin isolation. DES can dissolve lignin from woody plants by rupturing lignin-carbohydrate bonds, thus liberating lignocellulose components [44]. The combination of HBA and HBD facilitates the breakdown of the ether bond between the phenyl propane units, resulting in low-molecular-weight lignin [45]. Evidence suggested that DES can improve the efficiency of biomass enzymatic saccharification despite its low polysaccharide solubility [46]. The rate of lignin extraction is affected by the structure of lignocellulosic biomass, which varies between species. The high solubility of lignin in DESs makes it an ideal solvent for isolating lignin from biomass. Therefore, the use of DESs to extract lignin holds great promise. Achieving biorefinery goals heavily relies on the efficient fractionation of biomass components. Several studies have demonstrated that different DES can be used to extract lignin from biomasses successfully (Table 2).

Understanding the relationship between the various types of functional groups in HBD is crucial to developing a DES capable of extracting lignin with specific properties. Although carboxylic acids and polyols are commonly used as HBAs, ChCl is more commonly used as a HBD. Alvarez-Vasco et al. [45] compared the effectiveness of DESs in extracting lignin from hardwood and softwood species. Four HBDs (glycerol, levulinic acid, lactic acid, and acetic acid) and ChCl were used in this study. DESs extracted 79% of lignin from hardwood poplar but only 58% from softwood Douglas fir (softwood). These results indicated that DESs can successfully extract lignin from plants with a purity of 95%. Chen et al. [44] investigated lignin extraction from poplar wood. A ChCl:lactic acid molar ratio of 1:9 was the optimal molar ratio for dissolving 95% of lignin from poplar wood at 120°C for 6 h, with a lignin purity of 98.1%. Tan et al. [47] reported that the extraction efficiency of DES is significantly affected by the functional groups present in the acid component. The HBD with a carboxylic acid double bond improved lignin extraction due to its short alkyl chain and OH group.

In the past, studies on DES have shown that they have the potential to be the most effective method for high-yield lignin extraction. The amount of lignin extracted depends on many variables, such as reaction time, temperature, and molar ratio. Increasing the reaction temperature is necessary to improve lignin extraction, thus decreasing the viscosity and improving DES diffusion into the lignocellulosic matrix [56]. Increasing the temperature enhances the molecular polarity and ionic properties of the DES. Therefore, it promotes the breakdown of the intermolecular hydrogen bond network to increase the solubility of lignin [10]. A higher acid concentration in the DESs promotes lignin extraction and leads to lower residue recovery [48]. This was corroborated by Tan et al. [47], who found that increasing the molar ratio of HBD to HBA in DES may have a synergistic effect, effectively increasing its ability to extract more lignin. The physicochemical and thermal properties of DESs, such as freezing point, density, surface tension, and viscosity, are also noteworthy because they can affect the isolation of lignin. In addition, the selectivity of HBD and HBA largely depends on their low cost and biocompatibility [57].

Table 2. Previous studies on lignin yield (%) with various reaction conditions

DESs	Molar Ratio	Feedstock	Reaction Temperature (°C)	Reaction Time (hr)	Lignin Yield (%)	References
ChCl: LA	1:2	Poplar	145	6	78.5	[45]
	1:2	Corncob	90	24	64.7	[48]
	1:5	Corncob	90	24	77.9	[48]
	1:10	Corncob	90	24	86.1	[48]
	1:15	Corncob	90	24	93.1	[48]
	1:5	Rice straw	60	12	60	[49]
	1:9	Poplar	120	6	95	[44]
	1:10	Willow	120	12	91.8	[50]
	1:5	Sugarcane bagasse	80	12	50.6	[51]
	1:10	Eucalyptus	110	6	80	[52]
ChCl:Glycerol	1:2	Corncob	150	15	59.0	[53]
	1:2	Switchgrass	110	1	76.6	[37]
ChCl:Ethylene Glycol	1:2	Corncob	90	24	87.6	[48]
ChCl:Oxalic Acid	1:2	Rice straw	120	1	75.9	[54]
	1:1	Corncob	90	24	98.5	[48]
ChCl: Urea	1:2	Corncob	80	15	27.1	[53]
	1:2	Rice straw	130	8	44.7	[55]

Lignin extraction from wheat straw increased from 48.76% after 2 h to 73.75% after 12 h [58]. On the other hand, the amount of lignin extracted increased from 90°C to 145°C but declined when the temperature was increased to 180°C. Lignin is most efficiently extracted from poplar and Douglas fir at 145°C with ChCl:lactic acid [45]. Moreover, lignin extraction was affected by the molar ratio of ChCl to carboxylic acid. The lactic acid:ChCl molar ratio increased the lignin extraction rate from 64.7% to 93.1% [48]. In addition, when the ChCl:lactic acid ratio increased from 1:1 to 1:15, the percentage of lignin extracted increased from 33% to 61%. [47].

The hydrophilic amorphous fractions of cellulose and hemicellulose facilitate extensive interactions between the fibres and solvents. Owing to their relatively high chloride ion concentration and activity, DESs are anticipated to play a crucial role in dissolving lignin. As shown in Figure 4, DES can break down LCC linkages due to the hydrogen-bonding interactions between the HBA anion and the hydroxyl group in the LCCs [9]. Several studies have found that DESs affect cellulose solubility, which is likely the cause of the observed interactions [59-61]. To dissolve cellulose, the hydrogen bonds between cellulose molecules and their intramolecular bonds must be broken. In addition, the inherent charge of the fibre may need to be considered [60]. During lignin extraction, the chemical bonds between cellulose, lignin, and hemicellulose are broken, leading to the formation of cellulose pulp. Thus, lignin degradation products are soluble in DES.

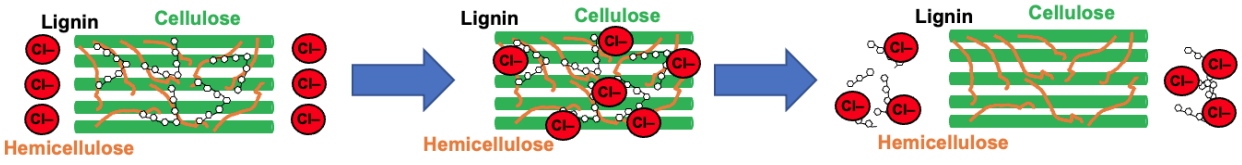


Figure 4. Isolation of lignin from the LCCs

Lignin extraction from oil palm biomass

Lignin from oil palm biomass can be extracted by using DESs. These studies have been performed to remove lignin from cellulose and hemicellulose [62-64]. However, it should be noted that these studies explored the possibility of removing lignin from LCCs. However, since lignin was not the primary focus of these studies, there are few studies on the fundamental properties, structures, or functional groups of the isolated lignin.

New et al. [23] obtained oil palm fronds delignification rate of 16.31% with a ChCl:urea molar ratio of 1:2 at 120°C for 4 h. Tan et al. [65] focused on the delignification of empty fruit bunches by using ChCl as the HBA and various types of HBD, including carboxylic acid and polyol. The study discovered that acids could extract a significant amount of lignin from empty fruit bunch (EFB), with ChCl:lactic acid yielding 88%. However, the near-neutral pH of the eutectic system is thought to be responsible for the 22% lower yield observed in lignin extraction using ChCl:glycerol [65]. Lignin can be extracted more efficiently with DES at an acidic pH than with DES at a neutral pH. Cl- in DES form's hydrogen bonds with hydroxyl groups in lignocellulose, cleaving LCC and releasing the constituent lignin and hemicellulose [66].

Tan et al. [47] examined the effects of different acidic hydroxyl groups, including lactic, malic, citric, formic, and acetic acids, on lignin extraction from EFB under the same conditions (120°C and 8 h). The lignin yield from ChCl:lactic acid was 33.5% at a molar ratio of 1:1, which increased to 61% at a molar ratio of 1:15. Lignin is more readily obtained using ChCl:lactic acid (monocarboxylic acids) than using ChCl:citric acid (dicarboxylic acid) or other HBD types. This was consistent with the findings of Hou et al. [54], who discovered that the delignification efficiency of dicarboxylic acids for rice straw pre-treatment was lower than that of monocarboxylic acids. ChCl:malic acid and ChCl:citric acid was significantly more viscous than ChCl:lactic acid. Lower extraction efficiencies could have resulted from a lack of solvent interactions with lignin due to low molecular mobility [47].

Lignin extraction from empty fruit bunches by using ChCl:lactic acid and ChCl:glycerol is efficient, with a lignin yield of 74.61% [67]. They found that a high HBD molar ratio and prolonged reaction time facilitated the lignin extraction. They concluded that DES could reveal biomass recalcitrance and increase the surface area for more efficient lignin extraction. However, ChCl:lactic acid was more effective than ChCl:glycerol in disrupting aromatic-dominated lignin linkages and cellulose crystallinity associated with β-(1,4)-glycosidic linear bonds. Despite having multiple HBD sites (-OH), the longer hydrocarbon site chain in glycerol molecules resulted in a lower hydrogen-bonding capacity and solubilising ability [67, 68].

The chemical structure and composition of lignin significantly differ depending on its origin, type, and extraction method. Lignin in oil palm biomass must be characterised for this reason. The chemical structure of lignin has been investigated by using various analytical methods. Thus, the most beneficial lignin modification can be identified and evaluated via structural elucidation. Fourier transform infrared spectroscopy (FTIR) was used to determine the chemical composition and functional properties of the extracted lignin. The primary functional groups in lignin include hydroxyl, methoxy, and carbonyl groups [69]. The FTIR spectra of lignin extracted from oil palm biomass using various DES have been reported by Tan et al. [47]. The FTIR analysis showed that all spectra contained guaiacyl lignin units, G (1269 cm^{-1} and 850 cm^{-1}), and syringyl, S (1328 cm^{-1} and 1118 cm^{-1}). The peaks at 1421 cm^{-1}, 1508 cm^{-1}, and 1593 cm^{-1} belong to aromatic skeleton vibrations (C-C). The peak between 850 cm^{-1} and 650 cm^{-1} was characteristic of aromatic C-H bending. Peaks at 3371 cm^{-1} and 1365 cm^{-1} were also identified as phenolic and aliphatic OH in lignin, respectively. Unconjugated C=O was detected at 1700 cm^{-1}. The number of lignin functional groups is affected by the HBD type. The potential of lignin as an aromatic feedstock is related to its aromatic structure and hydroxyl and carbonyl groups. This suggested that DES-extracted lignin, which retains all necessary structures and high intensities, may be particularly suitable for manufacturing aromatic chemicals.

The phenolic hydroxyl group (PhOH) content indicates

the reactivity of lignin for further modification because PhOH is the most reactive functional group in lignin [70]. The solubility and derivatisation potential of lignin are significantly affected by the presence of PhOH groups. The PhOH content in lignin from EFB was found to be the highest when using ChCl:lactic acid, as opposed to ChCl:malic acid, ChCl:formic acid, or ChCl:citric acid [47]. However, the PhOH content declined from 3.72 mmol/g to 3.33 mmol/g when the molar ratio of ChCl:lactic acid was increased to 1:15. Increasing the acidity of the solvent caused lignin condensation, which reduced PhOH content [47].

Lignin as carbon fibre precursor

Carbon fibres have high tensile strength, fatigue resistance, and heat tolerance despite their lightweight. Carbon fibre is an important and promising raw material for fibre-reinforced composites, particularly for high-performance applications. Nonetheless, the precursor materials significantly affected the final carbon fibre properties. Approximately 90% of the raw material for carbon fibres is PAN, making it the most widely used precursor. The remaining 10% were rayon or petroleum pitches. PAN-based carbon fibre-reinforced composites have been singled out by the US Department of Energy as a material with immense potential for use in lightweight vehicles with a 60% weight reduction [71]. While conventional carbon fibre-reinforced composites are inexpensive, PAN-based carbon fibres can be up to ten times more expensive. In addition, the time and energy spent on the thermal treatment necessary to convert PAN into carbon fibre considerably increases the cost of the process.

The high cost of fossil-based PAN precursors accounts for a significant portion of the cost of producing carbon fibre, making it necessary to develop cost-effective precursors, preferably from renewable sources. The prominence of lignin arises from its potential as a cheap carbon fibre precursor and its abundance and sustainability [72]. In addition, lignin is the most appealing renewable precursor for carbonaceous materials due to its aromatic properties and high carbon content (> 60%) [2]. Because lignin has a low decomposition temperature, partially oxidised properties, and high carbon content, it can be melt-spun and stabilised at a higher heating rate [73]. They are non-petroleum-based and, therefore, more environmentally friendly resources.

Compared to alternative materials, the production cost of carbon fibre made from lignin is lower. However, impurities in isolated lignin and complex structures may compromise the mechanical properties and carbon fibre construction. A study was conducted to identify differences between unmodified and modified lignin carbon fibres. Untreated lignin was found to have a tensile strength of 0.38 GPa and a yield of 31%, while treated lignin carbon fibre achieved tensile strengths of 0.710 GPa and yields of 41% [71].

Highly pure lignin with precisely controlled properties is essential for producing high-performance carbon fibres. Highly pure lignin is required to produce carbon fibres with exceptional characteristics and minimal impurities (ash, volatile, and particulate matter). High carbon content, narrow molecular weight distribution, and sufficiently high glass transition temperature all play important roles in the conversion of lignin into carbon fibre through spinning, thermal stabilisation, and carbonisation [2]. Oak Ridge National Laboratory developed a set of specifications to evaluate the potential of lignin as a precursor to carbon fibre [74]. Table 3 presents the specifications.

Table 3. Lignin as carbon fibre precursor

Criteria	Value (wt.%)
Lignin Purity	99
Ash Content	< 0.1
Volatile Matter	< 0.5
Particulate Matter	100% removal of matter >1 μm in diameter
Carbon content	> 60

A lignin purity greater than 99% is required as a carbon fibre precursor. Carbon fibre relies on its high purity to maintain its mechanical properties. Nonetheless, the extraction and use of lignin are complicated by its structural complexity and heterogeneity, primarily linked by aryl ether bonds and C-C bonds. The ability of DES to break β-O-4 aryl ethers and specific lignin-carbohydrate covalent bonds has been reported to increase lignin solubilisation significantly compared to conventional pre-treatment methods [75]. Many studies have successfully used DES to extract high purity lignin from biomass as shown in Table 2. In their study of lignin extraction from poplar using various DESs, Chen et al. [44] found that increasing the reaction temperature from 100°C to 130°C resulted in a higher purity of lignin (98%) due to the breakdown of hemicellulose. Furthermore, lignin purity of 95% from willow was achieved by using ChCl:lactic acid at a molar ratio of 1:10 [76]. These results confirmed the viability of ChCl:lactic acid for efficient isolation and extraction of high purity lignin. Li et al. [50] extracted lignin with high purity (94.46%) using a ChCl:lactic acid eutectic mixture with a molar ratio of 1:10 for 12 h at 120°C.

Ash is the residue remaining after the high-temperature (900°C) combustion. Most ash is composed of minerals found in biomass, such as calcium, magnesium, and potassium. The amount of inorganic matter in the recovered lignin must be kept to a minimum because it affects the mechanical properties of the carbon fibre. Therefore, it should be less than 0.1 wt.%. The stability of a polymer is determined by its volatility. The volatile matter content was determined by comparing the mass of the samples before and after 6 h of heating at 250°C. The volatile matter content of lignin must be less than 5 wt.% for no volatiles to be released during carbonisation. Carbonisation changes porosity [2]. As a result, the high volatile content of lignin could lead to a flaw on the surface of the carbon fibre.

Carbon fibre extracted from lignin was superior due to its low solid particle content. Lignin extraction removes solid particles larger than 1 μm in diameter [77]. Particles, such as sand or clay, are the main cause of impurity precipitation during the extraction process [78]. These impurities must be eliminated because they alter the mechanical properties of the carbon fibre, especially its fibre breakage point, by decreasing its modular and tensile strengths [74].

The extracted lignin should have a carbon content of at least 60 wt.%. The carbon content of commercial lignin is typically 59% to 61% [79]. Since lignin loses mass during carbonisation, the precursor must have a high carbon content and a low amount of non-carbon elements. High-quality carbon fibre requires a carbon content of at least 92 wt.% after the carbonisation of the precursor. A study has shown that ChCl:lactic acid at a molar ratio of 1:10 produced lignin with a high carbon content of 60.08% and negligible nitrogen (0.41%), hydrogen (5.50%), and oxygen (33.50%) content [76].

Furthermore, a uniform structure in carbon fibre is formed after carbonisation only if its molecular weight distribution is narrow [71]. Therefore, it is essential to determine the average molecular weight of lignin and its glass-transition temperature. The average molecular weight is essential for analysing the heterogeneity of long-chain lignin [80]. There is a correlation between the average molecular weight and glass transition temperature, the temperature at which lignin becomes brittle when cooled and soft when heated. However, the melt-spinning process requires a high glass transition temperature to prevent decomposition during the fibre-spinning process. Alvarez-Vasco et al. [45] reported that lignin extracted using ChCl:lactic acid has a low and narrow molecular weight range of 490 g/mol to 2600 g/mol, with an average molecular weight of approximately 890 g/mol. Results showed that DES depolymerises native lignin by selectively cleaving ether linkages without condensation. Lyu et al. [76] investigated the characteristics of lignin extracted from willow using ChCl:lactic acid at a 1:10 molar ratio. They observed that the average molecular weight decreased from 1806.7 to 1042.5 g/mol with a longer reaction time. The rate of lignin macromolecule degradation increases over time owing to the absence of intermolecular lignin bonds [81].

Conclusion

This mini review showed that DESs have the potential to be used as solvents in biomass processing. Organic

acid-based DESs have shown promise for biomass processing due to their ability to extract lignin in a simple, single-stage process while maintaining high purity. Many industrial processes would benefit from the use of DESs owing to their low density, low viscosity, and high thermal stability. Selecting appreciate HBD functional groups and molar ratio is important as it affects the physicochemical and thermal properties of the compounds through intermolecular interactions. On the other hand, the composites and polymer industries have recognised the value of carbon fibre, prompting researchers to explore lignin from biomass for its potential as a low cost, more environmentally friendly and economically viable precursor. More studies are needed to investigate the application of DES with varied functional groups of HBA to HBD for lignin extraction from oil palm biomass, with a particular focus on the effect of varying molar ratios and other operating conditions such as temperature and reaction time. Furthermore, to assess its feasibility as a carbon fibre precursor, the fundamental properties of lignin-derived oil palm biomass must be established, which are critical in establishing whether the isolated lignin is viable as a carbon fibre precursor.

Acknowledgement

This work was supported by the Ministry of Education, Malaysia, under the Fundamental Research Grant Scheme (FRGS) (FRGS/1/2020/STG05/UNIKL/02/1).

References

1. Bengtsson, A., Hecht, P., Sommertune, J., Ek, M., Sedin, M. and Sjöholm, E. (2020). Carbon fibers from lignin–cellulose precursors: effect of carbonization conditions. *ACS Sustainable Chemistry & Engineering*, 8(17): 6826-6833.
2. Chatterjee, S. and Saito, T. (2015). Lignin-derived advanced carbon materials. *ChemSusChem*, 8(23): 3941-3958.
3. Loh, S. K. (2017). The potential of the Malaysian oil palm biomass as a renewable energy source. *Energy Conversion and Management*, 141: 285-298.
4. Loow, Y. L., New, E. K., Yang, G. H., Ang, L. Y., Foo, L. Y. W. and Wu, T. Y. (2017). Potential use of deep eutectic solvents to facilitate lignocellulosic biomass utilization and conversion. *Cellulose*, 24(9): 3591-3618.
5. Soltanmohammadi, F., Jouyban, A. and Shayanfar, A. (2021). New aspects of deep eutectic solvents: Extraction, pharmaceutical applications, as catalyst and gas capture. *Chemical Papers*, 75(2): 439-453.
6. Liu, Y., Xue, J., Zhou, X., Cui, Y. and Yin, J. (2021). Deep desulfurization performance of thiophene with deep eutectic solvents loaded carbon nanotube composites. *Royal Society Open Science*, 8(4): 201736.
7. Abbott, A. P., Capper, G., Davies, D. L., Rasheed, R. K. and Tambyrajah, V. (2003). Novel solvent properties of choline chloride/urea mixtures. *Chemical Communications*, (1): 70-71.
8. Smith, E. L., Abbott, A. P. and Ryder, K. S. (2014). Deep eutectic solvents (DESs) and their applications. *Chemical Reviews*, 114(21): 11060-11082.
9. Smink, D., Juan, A., Schuur, B. and Kersten, S. R. (2019). Understanding the role of choline chloride in deep eutectic solvents used for biomass delignification. *Industrial & Engineering Chemistry Research*, 58(36): 16348-16357.
10. Francisco, M., van den Bruinhorst, A. and Kroon, M. C. (2012). New natural and renewable low transition temperature mixtures (LTTMS): Screening as solvents for lignocellulosic biomass processing. *Green Chemistry*, 14(8): 2153-2157.
11. Tang, X., Zuo, M., Li, Z., Liu, H., Xiong, C. and Zeng, X. (2017). Green processing of lignocellulosic biomass and its derivatives in deep eutectic solvents. *ChemSusChem*, 10(13): 2696-2706.
12. Farooq, M. Q., Odugbesi, G. A., Abbasi, N. M. and Anderson, J. L. (2020). Elucidating the role of hydrogen bond donor and acceptor on solvation in deep eutectic solvents formed by ammonium/phosphonium salts and carboxylic acids. *ACS Sustainable Chemistry & Engineering*, 8(49): 18286-18296.
13. Zhang, Q., Vigier, K. D. O., Royer, S. and Jerome, F. (2012). Deep eutectic solvents: Syntheses, properties and applications. *Chemical Society Reviews*, 41(21): 7108-146.

14. Yusof, R., Abdulmalek, E., Sirat, K. and Rahman, M. B. A. (2014). Tetrabutylammonium bromide (TBABr)-based deep eutectic solvents (DESs) and their physical properties. *Molecules*, 19(6): 8011-8026.
15. Fuad, F. M., Nadzir, M. M. and Harun, A. (2021). Hydrophilic natural deep eutectic solvent: A review on physicochemical properties and extractability of bioactive compounds. *Journal of Molecular Liquids*, 339: 116923.
16. Yue, D., Jing, Y., Ma, J., Yao, Y. and Jia, Y. (2012). Physicochemical properties of ionic liquid analogue containing magnesium chloride as temperature and composition dependence. *Journal of Thermal Analysis and Calorimetry*, 110(2): 773-780.
17. Zhang, H., Lang, J., Lan, P., Yang, H., Lu, J. and Wang, Z. (2020). Study on the dissolution mechanism of cellulose by ChCl-based deep eutectic solvents. *Materials*, 13(2): 278.
18. Ghaedi, H., Ayoub, M., Sufian, S., Shariff, A. M. and Lal, B. (2017). The study on temperature dependence of viscosity and surface tension of several phosphonium-based deep eutectic solvents. *Journal of Molecular Liquids*, 241: 500-510.
19. Francisco, M., van den Bruinhorst, A. and Kroon, M. C. (2013). Low-transition-temperature mixtures (LTTMs): A new generation of designer solvents. *Angewandte Chemie International Edition*, 52(11): 3074-3085.
20. Abbott, A. P., Barron, J. C., Ryder, K. S. and Wilson, D. (2007). Eutectic-based ionic liquids with metal‐containing anions and cations. *Chemistry–A European Journal*, 13(22): 6495-6501.
21. D'Agostino, C., Harris, R. C., Abbott, A. P., Gladden, L. F. and Mantle, M. D. (2011). Molecular motion and ion diffusion in choline chloride based deep eutectic solvents studied by 1H pulsed field gradient NMR spectroscopy. *Physical Chemistry Chemical Physics*, 13(48): 21383–21391
22. Yadav, A. and Pandey, S. (2014). Densities and viscosities of (choline chloride urea) deep eutectic solvent and its aqueous mixtures in the temperature range 293.15 K to 363.15 K. *Journal of Chemical & Engineering Data*, 59(7): 2221–2229.
23. New, E. K., Wu, T. Y., Lee, C. B. T. L., Poon, Z. Y., Loow, Y. L., Foo, L. Y. W. and Mohammad, A. W. (2019). Potential use of pure and diluted choline chloride-based deep eutectic solvent in delignification of oil palm fronds. *Process Safety and Environmental Protection*, 123: 190-198.
24. Shahbaz, K., Mjalli, F. S., Hashim, M. A. and AlNashef, I. M. (2011). Prediction of deep eutectic solvents densities at different temperatures. *Thermochimica Acta*, 515(1-2): 67-72.
25. Skulcova, A., Russ, A., Jablonsky, M. and Sima, J. (2018). The pH behavior of seventeen deep eutectic solvents. *BioResources*, 13(3): 5042-5051.
26. Hayyan, A., Mjalli, F. S., AlNashef, I. M., Al-Wahaibi, T., Al-Wahaibi, Y. M. and Hashim, M. A. (2012). Fruit sugar-based deep eutectic solvents and their physical properties. *Thermochimica Acta*, 541: 70-75.
27. Torres, P., Balcells, M., Cequier, E. and Canela-Garayoa, R. (2020). Effect of four novel bio-based DES (deep eutectic solvents) on hardwood fractionation. *Molecules*, 25(9), 2157.
28. Zhu, J., Yu, K., Zhu, Y., Zhu, R., Ye, F., Song, N. and Xu, Y. (2017). Physicochemical properties of deep eutectic solvents formed by choline chloride and phenolic compounds at T= (293.15 to 333.15) K: The influence of electronic effect of substitution group. *Journal of Molecular Liquids*, 232: 182-187.
29. Salmaliyan, M., Malek Ghaeni, F. and Ebrahimnia, M. (2017). Effect of electro spark deposition process parameters on WC-Co coating on H13 steel. *Surface and Coatings Technology*, 321: 81-89.
30. Chen, Y., Peng, X., Bi, Z., Yu, D., Zhang, Y., Guo, Y. and Mu, T. (2021). Factors affecting the refractive index of amino acid-based deep eutectic solvents. *Chemical Thermodynamics and Thermal Analysis*, 3: 100016.
31. Chemat, F., You, H. J., Muthukumar, K. and Murugesan, T. (2015). Effect of L-arginine on the physical properties of choline chloride and glycerol based deep eutectic solvents. *Journal of Molecular Liquids*, 212: 605-611.
32. Leron, R. B., Soriano, A. N. and Li, M. H. (2012). Densities and refractive indices of the deep eutectic solvents (choline chloride + ethylene glycol or glycerol) and their aqueous mixtures at the temperature ranging from 298.15 To 333.15K.

Journal of the Taiwan Institute of Chemical Engineers, 43(4): 551-557.

33. Paveglio, G. C., Milani, F. A., Sauer, A. C., Roman, D., Meyer, A. R. and Pizzuti, L. (2021). Structure-physical properties relationship of eutectic solvents prepared from benzyltriethylammonium chloride and carboxylic acids. *Journal of the Brazilian Chemical Society*, 32: 542-551.
34. Wang, Y., Ma, C., Liu, C., Lu, X., Feng, X. and Ji, X. (2020). Thermodynamic study of choline chloride-based deep eutectic solvents with water and methanol. *Journal of Chemical and Engineering Data*, 65(5): 2446–2457.
35. Qin, H., Hu, X., Wang, J., Cheng, H., Chen, L. and Qi, Z. (2020). Overview of acidic deep eutectic solvents on synthesis, properties and applications. *Green Energy and Environment*, 5(1): 8-21.
36. Kalhor, P. and Ghandi, K. (2019). Deep eutectic solvents for pretreatment, extraction, and catalysis of biomass and food waste. *Molecules*, 24(22): 4012.
37. Chen, W., Xue, Z., Wang, J., Jiang, J., Zhao, X. and Mu, T. (2018). Investigation on the thermal stability of deep eutectic solvents. *Acta Physico-Chimica Sinica*, 34(8): 904-911.
38. Florindo, C., Oliveira, F. S., Rebelo, L. P. N., Fernandes, A. M. and Marrucho, I. M. (2014). Insights into the synthesis and properties of deep eutectic solvents based on cholinium chloride and carboxylic acids. *ACS Sustainable Chemistry & Engineering*, 2(10): 2416-2425.
39. Chemat, F., Anjum, H., Shariff, A. M., Kumar, P. and Murugesan, T. (2016). Thermal and physical properties of (choline chloride+ urea+ l-arginine) deep eutectic solvents. *Journal of Molecular Liquids*, 218: 301-308.
40. Delgado-Mellado, N., Larriba, M., Navarro, P., Rigual, V., Ayuso, M., García, J. and Rodríguez, F. (2018). Thermal stability of choline chloride deep eutectic solvents by TGA/FTIR-ATR analysis. *Journal of Molecular Liquids*, 260(2017): 37-43.
41. Acciardo, E., Tabasso, S., Cravotto, G. and Bensaid, S. (2022). Process intensification strategies for lignin valorization. *Chemical Engineering and Processing-Process Intensification*, 171: 108732.
42. Kim, J. S., Lee, Y. Y. and Kim, T. H. (2016). A review on alkaline pre-treatment technology for bioconversion of lignocellulosic biomass. *Bioresource Technology*, 199: 42-48
43. Tarasov, D., Leitch, M. and Fatehi, P. (2018). Lignin–carbohydrate complexes: properties, applications, analyses, and methods of extraction: A review. *Biotechnology for Biofuels*, 11(1): 1-28.
44. Chen, Y., Zhang, L., Yu, J., Lu, Y., Jiang, B., Fan, Y. and Wang, Z. (2019). High-purity lignin isolated from poplar wood meal through dissolving treatment with deep eutectic solvents. *Royal Society Open Science*, 6(1): 181757.
45. Alvarez-Vasco, C., Ma, R., Quintero, M., Guo, M., Geleynse, S., Ramasamy, K. K. and Zhang, X. (2016). Unique low-molecular-weight lignin with high purity extracted from wood by deep eutectic solvents (DESs): A source of lignin for valorization. *Green Chemistry*, 18(19): 5133-5141.
46. Gunny, A. A. N., Arbain, D., Nashef, E. M. and Jamal, P. (2015). Applicability evaluation of deep eutectic solvents–cellulase system for lignocellulose hydrolysis. *Bioresource Technology*, 181: 297-302.
47. Tan, Y. T., Ngoh, G. C. and Chua, A. S. M. (2019). Effect of functional groups in acid constituent of deep eutectic solvent for extraction of reactive lignin. *Bioresource Technology*, 281: 359-366.
48. Zhang, C. W., Xia, S. Q. and Ma, P. S. (2016). Facile pretreatment of lignocellulosic biomass using deep eutectic solvents. *Bioresource Technology*, 219: 1-5.
49. Kumar, A. K., Parikh, B. S. and Pravakar, M. (2016). Natural deep eutectic solvent mediated pretreatment of rice straw: bioanalytical characterization of lignin extract and enzymatic hydrolysis of pretreated biomass residue. *Environmental Science and Pollution Research*, 23(10): 9265-9275.
50. Li, T., Lyu, G., Liu, Y., Lou, R., Lucia, L. A., Yang, G. and Saeed, H. A. (2017). Deep eutectic solvents (DESs) for the isolation of willow lignin (*Salix matsudana* cv. Zhuliu). *International Journal of Molecular Sciences*, 18(11): 2266.

51. Satlewal, A., Agrawal, R., Das, P., Bhagia, S., Pu, Y., Puri, S. K. and Ragauskas, A. J. (2019). Assessing the facile pretreatments of bagasse for efficient enzymatic conversion and their impacts on structural and chemical properties. *ACS Sustainable Chemistry & Engineering*, 7(1): 1095-1104.
52. Shen, X. J., Wen, J. L., Mei, Q. Q., Chen, X., Sun, D., Yuan, T. Q. and Sun, R. C. (2019). Facile fractionation of lignocelluloses by biomass-derived deep eutectic solvent (DES) pretreatment for cellulose enzymatic hydrolysis and lignin valorization. *Green Chemistry*, 21(2): 275-283.
53. Procentese, A., Johnson, E., Orr, V., Campanile, A. G., Wood, J. A., Marzocchella, A. and Rehmann, L. (2015). Deep eutectic solvent pretreatment and subsequent saccharification of corncob. *Bioresource Technology*, 192: 31-36.
54. Hou, X. D., Li, A. L., Lin, K. P., Wang, Y. Y., Kuang, Z. Y. and Cao, S. L. (2018). Insight into the structure-function relationships of deep eutectic solvents during rice straw pretreatment. *Bioresource Technology*, 249: 261-267.
55. Pan, M., Zhao, G., Ding, C., Wu, B., Lian, Z. and Lian, H. (2017). Physicochemical transformation of rice straw after pretreatment with a deep eutectic solvent of choline chloride/urea. *Carbohydrate Polymers*, 176: 307–314.
56. Bubalo, M. C., Ćurko, N., Tomašević, M., Ganić, K. K. and Redovniković, I. R. (2016). Green extraction of grape skin phenolics by using deep eutectic solvents. *Food Chemistry*, 200: 159-166.
57. Atilhan, M., Altamash, T. and Aparicio, S. (2019). Quantum chemistry insight into the interactions between deep eutectic solvents and SO_2. *Molecules*, 24(16): 2963.
58. Liu, C., Fang, H., Qiao, Y., Zhao, J. and Rao, Z. (2019). Properties and heat transfer mechanistic study of glycerol/choline chloride deep eutectic solvents based nanofluids. *International Journal of Heat and Mass Transfer*, 138: 690-698.
59. Anderson, J. L., Ding, J., Welton, T. and Armstrong, D. W. (2002). Characterizing ionic liquids on the basis of multiple solvation interactions. *Journal of the American Chemical Society*, 124(47): 14247-14254.
60. Rahman, M. B. A., Ishak, Z. I., Abdullah, D. K., Aziz, A. A., Basri, M. and Salleh, A. B. (2012). Swelling and dissolution of oil palm biomass in ionic liquids. *Journal of Oil Palm Research*, 24: 1267-1276.
61. Swatloski, R. P., Spear, S. K., Holbrey, J. D. and Rogers, R. D. (2002). Dissolution of cellulose with ionic liquids. *Journal of the American Chemical Society*, 124(18): 4974-4975.
62. Nor, N. A. M., Mustapha, W. A. W. and Hassan, O. (2016). Deep eutectic solvent (DES) as a pretreatment for oil palm empty fruit bunch (OPEFB) in sugar production. *Procedia Chemistry*, 18: 147-154.
63. Tajuddin, N. A., Harun, S., Sajab, M. S., Zubairi, S. I., Jahim, J. M., Markom, M. and Hashim, N. (2019). Influence of deep eutectic solvent (DES) pretreatment on various chemical composition of empty fruit bunch (EFB*). International Journal of Engineering and Technology*, 8(12): 266-274.
64. Zulkefli, S., Abdulmalek, E. and Rahman, M. B. A. (2017). Pretreatment of oil palm trunk in deep eutectic solvent and optimization of enzymatic hydrolysis of pretreated oil palm trunk. *Renewable Energy*, 107: 36-41.
65. Tan, Y. T., Ngoh, G. C. and Chua, A. S. M. (2018). Evaluation of fractionation and delignification efficiencies of deep eutectic solvents on oil palm empty fruit bunch. *Industrial Crops and Products*, 123: 271-277.
66. Liu, Y., Chen, W., Xia, Q., Guo, B., Wang, Q., Liu, S., Liu, Y., Li, J. and Yu, H. (2017). Efficient cleavage of lignin–carbohydrate complexes and ultrafast extraction of lignin oligomers from wood biomass by microwave-assisted treatment with deep eutectic solvent. *ChemSusChem*, 10(8): 1692-1700.
67. Teh, S. S., Loh, S. K. and Mah, S. H. (2019). Development of choline-based deep eutectic solvents for efficient concentrating of hemicelluloses in oil palm empty fruit bunches. *Korean Journal of Chemical Engineering*, 36(10): 1619-1625.
68. Teles, A. R. R., Capela, E. V., Carmo, R. S., Coutinho, J. A., Silvestre, A. J. and Freire, M. G. (2017). Solvatochromic parameters of deep eutectic solvents formed by ammonium-based salts and

carboxylic acids. *Fluid Phase Equilibria*, 448: 15-21.

69. Lu, Y., Lu, Y. C., Hu, H. Q., Xie, F. J., Wei, X. Y. and Fan, X. (2017). Structural characterization of lignin and its degradation products with spectroscopic methods. *Journal of Spectroscopy*, 2017: 8951658.
70. Haz, A., Strizincova, P., Majova, V., Sskulcova, A., Surina, I. and Jablonsky, M. (2016). Content of phenolic hydroxyl groups in lignin: Characterisation of 23 isolated non-wood lignin with various acids. *International Journal of Recent Scientific Research*, 7: 11547-11551.
71. Baker, D. A., and Rials T.G (2013). Recent advances in low-cost carbon fiber manufacture from lignin. *Journal Applied Polymer Science,* 130(2): 713-728.
72. Bengtsson, A., Bengtsson, J., Sedin, M. and Sjöholm, E. (2019). Carbon fibers from lignin-cellulose precursors: effect of stabilization conditions. *ACS Sustainable Chemistry & Engineering*, 7(9): 8440-8448.
73. Fang, W., Yang, S., Wang, X. L., Yuan, T. Q. and Sun, R. C. (2017). Manufacture and application of lignin-based carbon fibers (LCFs) and lignin-based carbon nanofibers (LCNFs). *Green Chemistry*, 19(8): 1794-1827
74. Baker, F. S., Griffith, W. L. and Compere, A. L. (2005). A low-cost carbon fiber from renewable resources. Report US Department of Energy, Energy Efficient and Renewable Energy, pp. 1-28.
75. Tan, Y. T., Chua, A. S. M. and Ngoh, G. C. (2020). Deep eutectic solvent for lignocellulosic biomass fractionation and the subsequent conversion to bio-based products–a review. *Bioresource Technology*, 297: 122522.
76. Lyu, G., Li, T., Ji, X., Yang, G., Liu, Y., Lucia, L. A. and Chen, J. (2018). Characterization of lignin extracted from willow by deep eutectic solvent treatments. *Polymers*, 10(8): 869.
77. Khalid, K. A., Karunakaran, V., Ahmad, A. A., Pa'ee, K. F., Abd-Talib, N. and Yong, T. L. K. (2020). Lignin from oil palm frond under subcritical phenol conditions as a precursor for carbon fiber production. *Malaysian Journal of Analytical Sciences*, 24(4): 484-494.
78. Compere, A. L., Griffith, W. L., Leitten Jr, C. F. and Petrovan, S. (2004). Improving the fundamental properties of lignin-based carbon fiber for transportation applications. In *Proceedings of the 36th International SAMPE Technical Conference*, pp. 2246-2254.
79. Kadla, J. F., Kubo, S., Venditti, R. A., Gilbert, R. D., Compere, A. L. and Griffith, W. (2002). Lignin-based carbon fibers for composite fiber applications. *Carbon*, 40(15): 2913-2920.
80. Tolbert, A., Akinosho, H., Khunsupat, R., Naskar, A. K. and Ragauskas, A. J. (2014). Characterization and analysis of the molecular weight of lignin for biorefining studies. *Biofuels, Bioproducts and Biorefining*, 8(6): 836-856.
81. Prado, R., Brandt, A., Erdocia, X., Hallet, J., Welton, T. and Labidi, J. (2016). Lignin oxidation and depolymerisation in ionic liquids. *Green Chemistry*, 18(3): 834-841.

Malaysian Journal of Analytical Sciences (MJAS)
Published by Malaysian Analytical Sciences Society

ANALYSIS OF HYPERSPECTRAL REFLECTANCE FOR DISEASE CLASSIFICATION OF SOYBEAN FROGEYE LEAF SPOT USING KNIME ANALYTICS

(Analisis Refleksi Hiperspektra untuk Klasifikasi Penyakit Bintik Daun Frogeye Kacang Soya Menggunakan Analisis KNIME)

Yuhao Ang, and Helmi Zulhaidi Mohd Shafri

Department of Civil Engineering and Geospatial Information Science Research Centre (GISRC), Faculty of Engineering,
Universiti Putra Malaysia (UPM), 43400 Serdang, Selangor, Malaysia

**Corresponding author: helmi@upm.edu.my*

Received: 10 October 2022; Accepted: 13 April 2023; Published: 23 June 2023

Abstract

The feasibility of classifying soybean frogeye leaf spot (FLS) has been investigated with the advance of hyperspectral technology. Hyperspectral reflectance data of healthy and FLS disease soybeans were used. The first step was to smooth out the data by using a filtering technique namely Savitzky-Golay to eliminate the noise of the spectrum. In order to select the most significant wavelengths, genetic algorithm (GA) was used as a forward feature selection technique. This analysis involved the implementation of machine learning (ML) algorithms, including decision trees, random forests, and stacking, to classify soybean FLS severity levels. Preprocessing ML steps including converting class numbers to strings, identifying and removing missing values, partitioning and normalizing data were implemented prior to the development of the model. Overall accuracy and the receiver operating characteristic curve measure were used to assess the performance of this analysis. All of these steps were carried out through KNIME analytical platform. Based on the results of the analysis, GA-stacking and random forest algorithms achieved the best overall accuracy of 85.9% and 84.3%, respectively. In terms of reproducibility, data flow control, data exploration, analysis and visualization, KNIME Analytics Platform provided great convenience in connecting tools graphically and ensuring the same results on different operating systems. The rapid implementation of workflow in KNIME Analytics Platform provided the opportunity to process hyperspectral reflectance data to classify crop diseases.

Keywords: hyperspectral reflectance, forward feature selection, genetic algorithms, machine learning, KNIME analytics platform

Abstrak

Kebolehlaksanaan mengklasifikasikan bintik daun frogeye kacang soya (FLS) telah disiasat dengan kemajuan teknologi hiperspektral. Data reflektan hiperspektral kacang soya yang sihat dan penyakit FLS telah digunakan. Langkah pertama ialah melicinkan data dengan menggunakan teknik penapisan iaitu Savitzky-Golay untuk menghapuskan hingar spektrum. Untuk memilih panjang gelombang yang paling ketara, algoritma genetik (GA) digunakan sebagai teknik pemilihan ciri ke hadapan. Analisis ini melibatkan pelaksanaan algoritma pembelajaran mesin (ML), termasuk pohon keputusan, hutan rawak, dan pemadatan, untuk mengklasifikasikan tahap keparahan FLS kacang kedelai. Langkah-langkah pra pemprosesan ML termasuk menukar nombor

kelas kepada rentetan, mengenal pasti dan mengeluarkan nilai yang hilang, mempartisi dan menormalisasi data telah dilaksanakan sebelum pembangunan model. Ketepatan keseluruhan dan ukuran lengkung ciri operasi penerima digunakan untuk menilai prestasi analisis ini. Kesemua langkah ini telah dijalankan melalui platform analisis KNIME. Berdasarkan keputusan analisis, algoritma GA-stacking dan random forest masing-masing mencapai ketepatan keseluruhan terbaik iaitu 85.9% dan 84.3%. Dari segi kebolehulangan, kawalan aliran data, penerokaan data, analisis dan visualisasi, Platform Analisis KNIME memberikan kemudahan besar dalam menyambungkan alatan secara grafik dan memastikan hasil yang sama pada sistem pengendalian yang berbeza. Pelaksanaan pantas aliran kerja dalam Platform Analisis KNIME memberi peluang untuk memproses data reflektan hiperspektral dalam klasifikasi penyakit tanaman.

Kata kunci: reflektan hiperspektral, pemilihan ciri ke hadapan, algoritma genetik, pembelajaran mesin, platform analisis KNIME

Introduction

As a legume, soybean is an essential source of proteins and fatty acids, the major feed sources of proteins, and the second primary producer of editable oils. The total production for soybean around the world was 367.76 million tons in 2021 and it is estimated that there will be a decrease of 17.04 million tons or 4.63% in the soybean production across the globe [1]. Apparently, the use as a primary source in pig feed increases the consumption of soybean worldwide. However, several diseases have severely harmed the quality and the seed of soybean. For example, frogeye leaf spot (FLS) is a soybean foliar disease caused by the fungus *Cercospora sojina* Hara (CSH) leads to yield losses, seed damage, and economic losses. FLS infections may result in yield losses of up to 60% [2, 3]. FLS is a polycyclic illness which its infection, symptom development, and reproduction may occur several times within the span of a single season [4]. It is crucial to assess and to detect the expanse of disease so that its economic losses can be estimated and proper management can be implemented.

The present method for determining the severity of foliar disease is mostly dependent on visual assessment. Experts physically evaluate the size of lesion area, the leaf color patterns, the distribution and the shape of leaves, the number of stems and branches, and also the density of soybean [5]. However, the visual assessment method is bias and can be altered by the experimental observations of experts. Another assessment method is molecular procedures such as enzyme-linked immunosorbent assay (ELISA) and polymerase chain reaction (PCR), which are very sensitive and capable of detecting disease. The drawback of this approach is time-consuming and destructive [6]. Thus, non-destructive highly efficient methods such as remote sensing tool remains warranted to assess the severity of soybean diseases.

Hyperspectral reflectance has attracted much focus in identifying and estimating the severity level of soybean disease. The hyperspectral technique consists of a narrow bandwidth and more than ten different channels that are capable of identifying subtle changes in an object of interest. Hyperspectral technique is frequently used to determine biophysical properties of certain crops, such as chlorophyll content, moisture content, trace element content, crop cell structure and nutrient contents [7-9]. Several studies have demonstrated the effectiveness and the potential of hyperspectral reflectance in identifying disease severity, such as rice false smut disease [10], citrus disease [11], oil palm *Ganoderma* disease [12], and soybean stem rot disease [13].

Rapid development of an automation system for classifying disease of the infected crops is an emerging area in precision agriculture. Machine learning (ML) method has been adopted to develop classification models using hyperspectral reflectance data for crop disease detection such as support vector machine, random forest (RF) and artificial neural network [14]. [15] has successfully developed random forest algorithms to classify wheat and rye leaves rust based on pure spectra. The result showed that the RF model based on the selected spectral wavelength achieved promising accuracy with the accuracy of 96.6%. In addition, hyperspectral data contain extra, redundant and highly correlated information across a large number of wavelengths, which can increase the complexity of analysis. Therefore, data dimensionality reduction, which cut down and optimize the whole wavelength, is

required. Several methods have been used effectively to reduce the dimensionality of hyperspectral data, including generic algorithms [16], principal component analysis (PCA) [17], and successive projection algorithm 18], and others [19-21]. To detect Huanglongbing disease in citrus, [11] used PCA to reduce the number of spectral features, and the selected PC scores were used in the classification algorithms such as quadratic discriminant analysis (QDA) and k-nearest neighbor (KNN). The results showed that the selected features achieved an overall average classification accuracy of 86% and 93% using KNN-based and QDA-based algorithms, respectively. In another similar study, [22] applied feature selection technique based on successive projection algorithm (SPA) to detect vineyard disease. The result demonstrated that SPA technique performed better than common VIs with the overall classification accuracy of about more than 96% for both DA and SVM. Nevertheless, implementing data dimensionality reduction in analyzing hyperspectral reflectance data can sometimes be computationally demanding.

The KNIME analytics platform is an open-source software that aims to solve these problems by creating a platform that can easily be extended with new tool integrations, which features a strongly typed data system, and permits creators to record in detail each step of the workflow [23]. One of the KNIME's benefits is its multimode of nodes for performing a sequence of ML process with its offerings of various advanced ML algorithms. In this study, the hyperspectral analysis was conducted to classify the FLS disease on codeless platform. This is the first study to use such platform to perform the hyperspectral processing including the feature selection and the classification approaches in KNIME analytics platform. Therefore, the main objectives of this study are to estimate FLS disease class using hyperspectral reflectance, to evaluate the performance of proposed feature selection by comparing with full dataset and to determine the feasibility of classifying FLS through the proposed ML method.

Materials and Methods

Data acquisition

Leaf hyperspectral reflectance data were collected using a FieldSpec® HandHeld 2 spectrometer (Analytical Spectral Devices, Inc., Colorado, USA). The hyperspectral region ranged from 325 to 1075 nm, with a resolution of 3 nm. The number of hyperspectral channels is 512. Each diseased or healthy leaf was considered as one sample. A total of 440 samples, comprising 340 diseased and 100 healthy leaves, were collected and evaluated. Four severity classes such 0%–1% (class 1), 1%–3% (class 2), 3%–6% (class 3), 6%–20% (class 4), and lastly the healthy leaves were regarded as class 0. The data was obtained from [24], which has been appropriately cited.

Preprocessing

The wavelengths were cut to remove the excitation wavelength and keep the useful wavelength that represent the reflectance of the disease. Only useful wavelength interval from 450 nm to 1000nm was remained. Then, the preprocessing technique such as Savitzky-Golay filter was used. The purpose of Savitzky-Golay filter is to smooth the original data while also eliminating noise from the spectrum [25]. The length of the filtering window and the order of the polynomial interpolation were set to 11 and 3, respectively. In addition, the first and second derivatives orders were generated over the course of the investigation. The preprocessing workflow was implemented using the installed KNIME interactive R statistics integration to use the R package and to execute them in KNIME analytic platform, as shown in Figure 1.

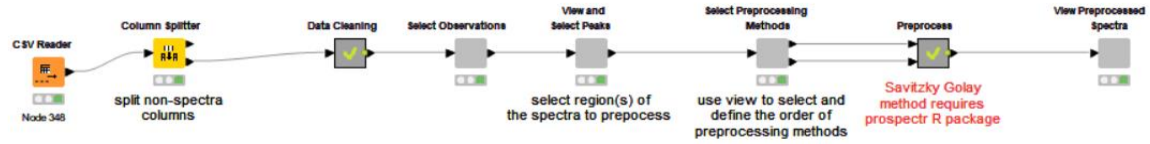


Figure 1. The workflow of preprocessing

Processing

Forward feature selection method such as genetic algorithm was applied to select the useful wavelengths and to eliminate the redundant wavelengths. The genetic algorithm is a chaotic approach for optimizing functions that is based on evolution and genetics. In genetic algorithm, an optimal set is determined based on evolution. The first step in selecting the features is to generate a population based on the subsets of possible features. The subsets from this population are then evaluated using a predictive model to obtain the weights of each individual on the populations. By that, N individuals are chosen, where N is the size of the population, given that previously calculated weights, and two new individuals are generated from each pair of individuals. In this way, each generation have the same number of individuals as the previous one which can bring it forwards when the algorithms run in many iterations. The next step is reproduction, which entails this numbers will be used to randomly split the parents' genes into pieces of varying sizes. The first new person will have the first piece from parent A and the second chunk from parent B. The second new person will be made out of the first and the second halves of parent B. Lastly, mutation mitigates the risk of the search falling into a local optimum and getting stuck. At each generation, in addition to the crossover, a random mutation is added. The reproduction and the mutation processes are then repeated once the new population has been produced, with the weights of each individual being recalculated. A workflow illustrating the forward feature selection process is shown in Figure 2. Using the KNIME workflow, raw data was recorded using the 'CSV Reader' node, and then combined with the 'Number to String' node to represent the disease severity classes into a string, and finally a metanode that comprised of several nodes was created to execute genetic algorithms via a sequence of forward feature selections.

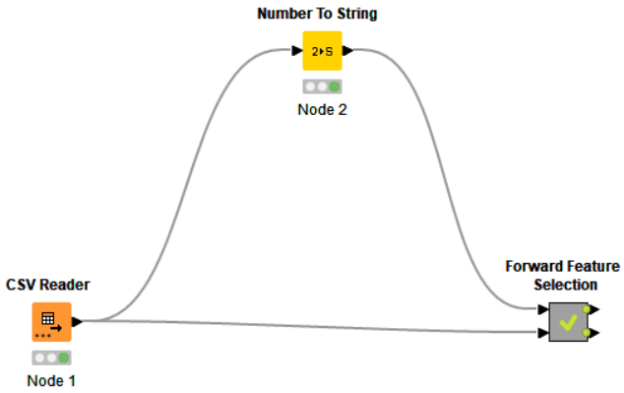


Figure 2. The workflow of feature selection

Modelling methods

Several ML algorithms were used to classify the severity level of FLS disease in soybean. Decision tree, random forest and stacking were used as the ML algorithms in this study. Each of the ML algorithms were implemented in the KNIME workflow. In general, raw data was recorded using a CSV Reader node, then the preprocessing ML steps such as converting the class numbers to strings, and identifying and removing missing values were carried out, followed by data partitioning (X-partitioner and X-aggregator) and normalization (normalizer and apply normalizer). Next, ML algorithms namely random forest, decision tree, and stacking were implemented and evaluated using a scorer and receiver operating characteristic (ROC) curve. The mechanisms of each ML algorithms are stated as followed.

Random forest: Random forests combine multiple trees and assemble decision trees through 'bagging' to create a final model. In this method, bootstrapping is used to select 'k' samples from the original dataset at random. The output is finalized by aggregating the predictions of each decision trees. These samples are used to build decision trees and create output depending on its predictions. The model parameters are adjusted accordingly through trial and error. The split criterion is assigned as information gain. The tree depth and the minimum node size were tuned accordingly and set to 5 and 2, respectively. The workflow of random forest is shown in Figure 3.

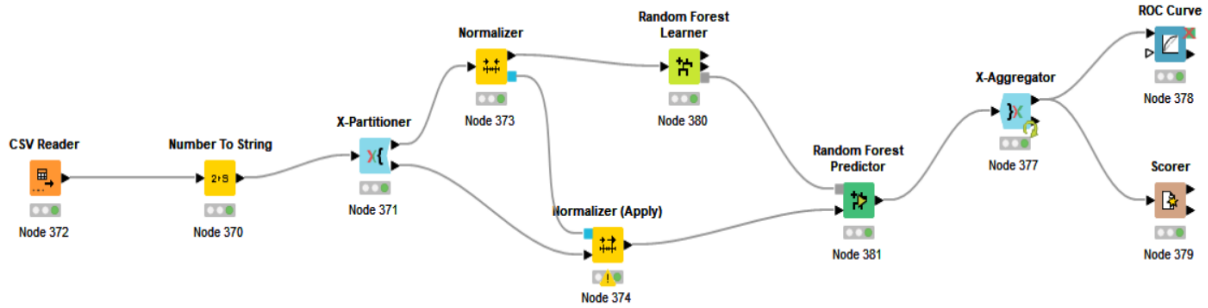


Figure 3. The workflow of random forest algorithm

Stacking: In stacking, heterogeneous base learners consisting different ML models are applied and trained in parallel. Then, heterogeneous base-learners are combined in aggregating the output of each single base-leaners by training a meta-learner to create a prediction based on different base learner's predictions. The purpose of the meta-learner is to determine how to combine the input predictions made by the base-learners with the output made by the training dataset to achieve better predictions [26]. Stacking algorithm was implemented by utilizing KNIME Weka Data Mining Integration, which provide Knime plugins that include the Weka data mining framework's functionality [27]. In this study, Naïve Bayes, J48 and Kstar algorithms were selected as base learners, and logistic regression was used as meta-learner. The workflow of stacking algorithm is shown in Figure 4.

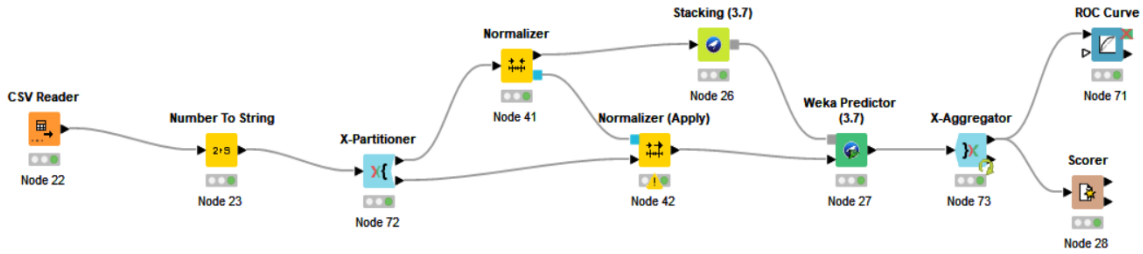


Figure 4. The workflow of stacking algorithm

Decision trees: A decision tree is a tree-representation classifier in which each leaf node corresponds to a class label and each inside node represents a feature. Branches represent conjunctions of features that lead to those class labels. Pruning is applied as it is the important part in decision trees, used to decrease the size of the decision tree. Several parameters were set such as quality measures (Gini index), minimum number records per node (8) and pruning method (Minimum Description Length). The workflow of decision tree is shown in Figure 5.

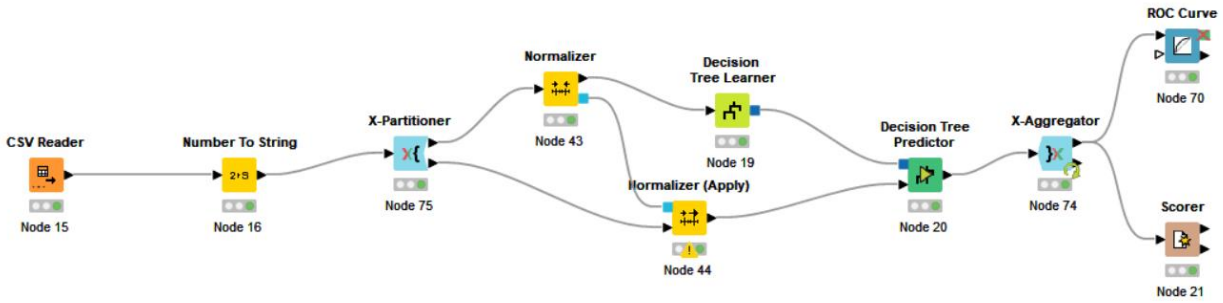


Figure 5. The workflow of decision tree algorithm

Performance evaluation

Cross-validation was used as a resampling strategy in the evaluation process to assess the ML models. The number of groups into which a particular data sample to be divided is denoted by K-fold, which is used to separate each observation from the original dataset into an equal probability of occurring in the training and the test sets. In this investigation, K was set to 10, training the (K-1) folds and testing the model with the Kth fold remaining. The procedure is repeated K times until the final average score is determined. Cross-validation is applied for the evaluation metrics in the accuracy assessment. In order to analyze the efficacy of the ML algorithms, accuracy assessment is important in the classification of FLS diseases. The accuracy of each ML algorithms was evaluated using ground truth data for the five severity classes of soybean FLS. The confusion matrix approach was used to assess the performance of a classification model by comparing the actual classes to the predictions of the ML model. The overall accuracy was computed by summing the number of correctly classified classes and dividing it by the total number of classes. This overall accuracy is the outcome of ML algorithms classifying the severity levels of soybean FLS using leaf hyperspectral data. The ROC measure is also used to quantify the prediction accuracy of a predictive model. It is based on the trade-off between the true positive rate and the false positive rate when probability threshold is used.

Results and Discussion

Spectral reflectance for raw, first and second derivatives of FLS disease

Spectral reflectance profile taken from sample spectra is shown graphically for each severity stages of soybean FLS (class 0, 1, 2, 3 and 4) in Figure 6. Basically, the spectral profile showed a low reflectance in the visible region with small peak in the green region indicating a sudden increase beginning at 690 nm reaching a peak in the NIR region. These are regular for green plant reflectance spectra. A comparison of profile showed larger difference in the reflectance between each severity classes of soybean FLS at some wavelengths compared to other wavelengths.

In the visible spectrum (607– 690 nm), soybean FLS with different severity stages were very similar and many overlapped each other, while in the infrared region (702 – 966 nm), the spectra of soybean FLS with different severity classes separated from each other. Healthy soybean had the highest NIR reflectance compared to others in 774 nm till 806 nm (Figure 6). The second highest were soybeans with class 1 and 2. Soybean FLS with class 4 had the lowest reflectance.

The first derivative of spectral reflectance is shown in Figure 7(a). Overall, the first derivative of spectral reflectance of FLS soybean disease exhibited a tiny reflectance peak about 515 nm and a substantial first derivative reflectance peak in the red-edge area (679 – 714 nm). Healthy soybean with class 0 indicates the highest peak at 717.87nm in the red edge region, which is more prone to shifting to the right as compared to FLS soybean disease. The second derivative of spectral reflectance of FLS soybean disease is shown in Figure 7(b). Second derivative reflectance spectra with FLS soybean disease showed distinct peaks at 685 nm and 732 nm.

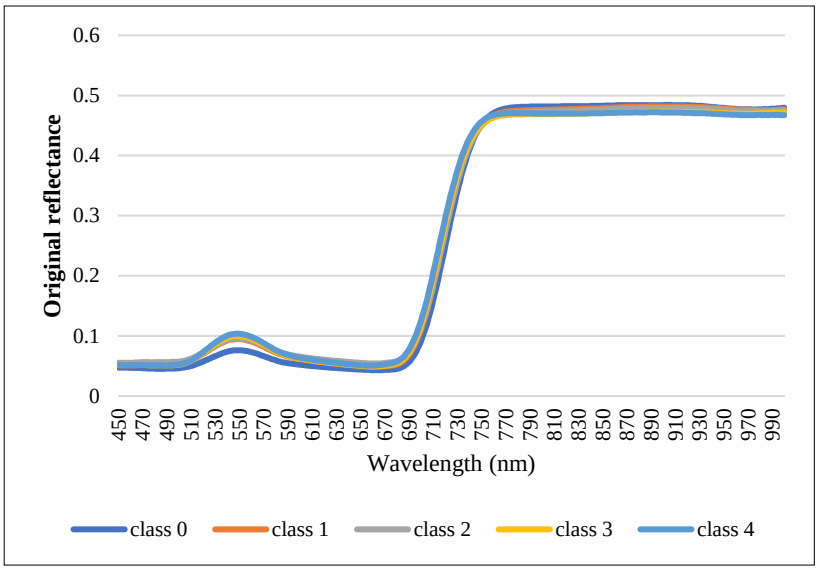


Figure 6. Original spectral reflectance of FLS disease

The first derivative equation is crucial in plant disease detection with space of the lesion density function at a fixed position [28]. The spectrum will become complicated and complex as the number of disease symptoms increases. Different stages of disease severity attributed to the collected spectrum variation when plants in the particular area facing disease spreads. Therefore, the first derivative can remove both additive and multiplicative effects in spectrum [29]. Lu et al. [30] showed that the first derivative between 500 – 1000 nm was better in discriminating leaf curl on tomatoes than the original reflectance spectrum. In general, the first and the second derivatives indicated the potential for estimating crop disease because of their insensitivity to the soil background [31, 32].

Classification of soybean FLS disease using ML models

Table 1 shows the overall accuracy of ML algorithms used in the classification of soybean FLS disease. Random forest and stacking achieved the best overall accuracy using the selected first and second derivatives of spectral reflectance. Random forests achieved an overall accuracy of 84.3% and 77.7% for both selected first and second derivatives of spectral reflectance, respectively. The stacking algorithms have improved to 85.9% and 79.1% from 70% and 56.1% on both selected first and second derivatives of spectral reflectance, respectively.

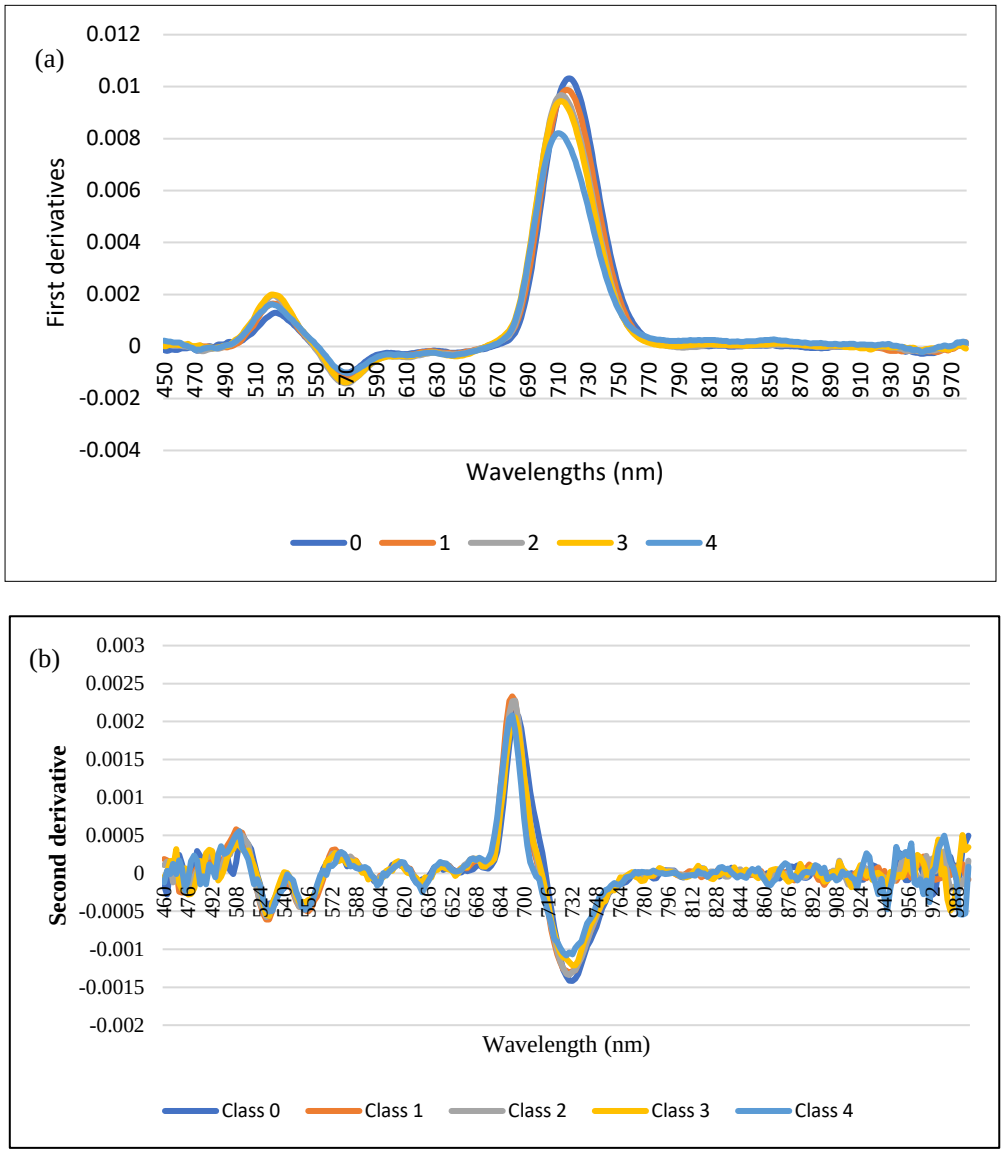


Figure 7. (a) First derivative of spectral reflectance of FLS disease and (b) Second derivative of spectral reflectance of FLS disease

Table 1. Overall accuracy of ML models

Data	Raw	First derivative (full)	Second derivative (full)	First derivative+ Savitzky-Golay+feature selection (genetic algorithms)	Second derivative+ Savitzky-Golay+feature selection (genetic algorithms)
Decision tree	55.4	64.7	55.9	65.0	62.7
Random forest	68.4	75.9	69.5	84.3	77.7
Stacking	69.7	70.0	56.1	85.9	79.1

Decision tree had the lowest and the poorest accuracy performance even after the feature selection algorithm was implemented. For example, only small increases with 0.2% for implementing the feature selection using the first derivative data. Noticeably, there was not much difference between the accuracy of decision tree algorithms using raw data and second derivative.

Based on the above results, incorporating genetic algorithms (GA) as feature selections has improved the overall accuracy for most of the ML algorithms since GA can effectively screen the useful characteristic bands for soybean FLS disease detection, thereby reducing the number of variables in the model, and thus producing high classification accuracy. Our result agrees with the studies of Chen et al. [33], who proved that genetic algorithms and following support vector machine is the best performance model with overall accuracy of 90.7% for leaves and 92.6% for stems.

Adding to performance analysis, Figure 8 illustrates the ROC curve for stacking algorithm, which is the best among the other algorithms. This analysis contributes an insight into how well the model classify the different severity classes (classes 0, 1, 2, 3 and 4) of soybean FLS. Overall, the curve reached a high value for the metric area under curve, in this case, 95% area of the graph was under the curve, showing the model is good in separating the soybean FLS classes.

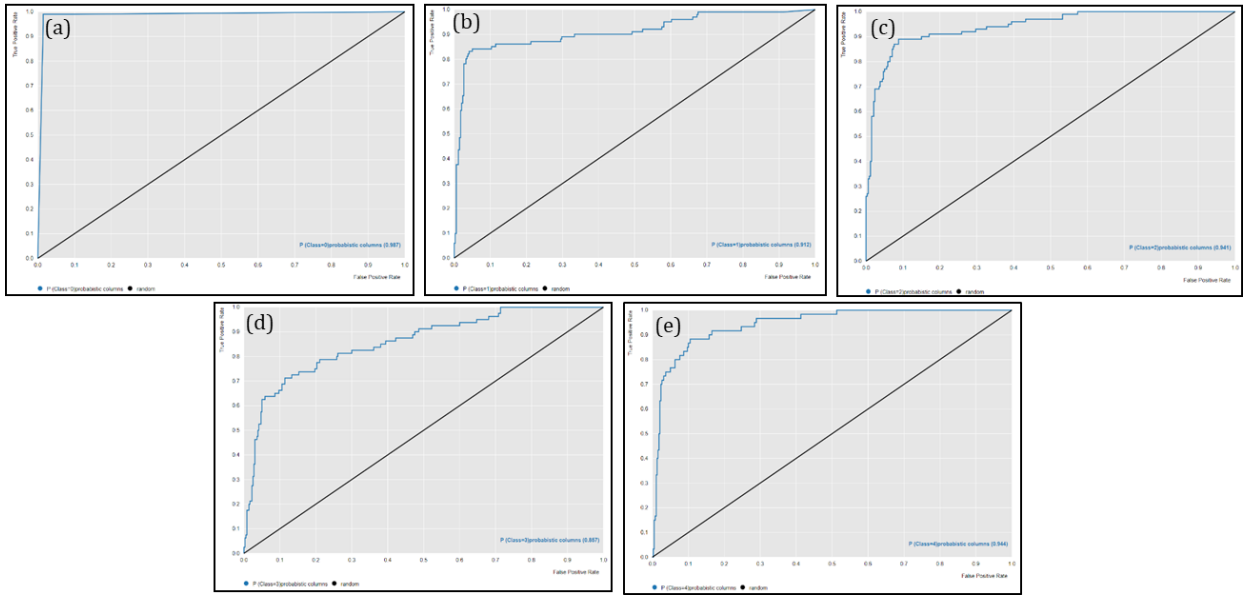


Figure 8. Stacking model ROC curve for class 0-4: (a) Class 0, (b) Class 1, (c) Class 2, (d) Class 3 and (e) Class 4

Conclusions

Based on the results, it was concluded that stacking algorithm achieved the highest accuracy after genetic algorithm implementation. Future studies will assess different feature selection techniques to analyze hyperspectral reflectance in the classification of crop disease. Different preprocessing techniques will also be adopted to ensure the proper removal of noise in spectrum. Besides, several ML algorithms will be proposed and applied on the analysis of hyperspectral reflectance. KNIME integrations provide additional functionality such as processing of complex hyperspectral preprocessing (e.g. Savitzky-Golay), as well as the use of advanced ML algorithms. Therefore, the functionality of KNIME as a codeless tool for analyzing hyperspectral reflectance should be further investigated in order to confirm its practicality and usefulness. The results obtained make it possible to

provide fast implementation of workflow, including model development for evaluating the degree of crop disease using hyperspectral reflectance data. Future studies will utilize other advanced machine learning algorithms to improve the accuracy of the model.

Acknowledgement

We would like to acknowledge the Malaysian Ministry of Higher Education (MOHE) for supporting us through the Malaysian Research University Network (MRUN) Long-Term Research Grant Scheme (LRGS). It is supported under Grant no: 203.PKOMP.6770007 with UPM vote no: 6300268-10801. A credit is also given to [24] for the permission to use their data in this study.

References

1. USDA Foreign Agricultural Service (2022). World Agricultural Production. Access from https://www.fas.usda.gov/data/world-agricultural-production.
2. Dashiell, K. E. and Akem, C. N. (1991). Yield losses in soybeans from frogeye leaf spot caused by *Cercospora sojina*. *Crop Protection*, 10(6): 465-468.
3. Mwase, W. F. and Kapooria, R. G. (2001). Incidence and severity of frogeye leaf spot and associated yield losses in soybeans in agroecological zone II of Zambia. *Mycopathologia*, 149(2): 73-78.
4. Mian, M. A. R., Missaoui, A. M., Walker, D. R., Phillips, D. V. and Boerma, H. R. (2008). Frogeye leaf spot of soybean: A review and proposed race designations for isolates of *Cercospora sojina* Hara. *Crop Science*, 48(1): 14-24.
5. George, A. P., Broadley, R. H., Nissen, R. J. and Ward, G. (2002). Effects of new rest-breaking chemicals on flowering, shoot production and yield of subtropical tree crops. *Acta Horticulturae*, 575(4): 835-840.
6. Bukhari, K. A. I. M., Nithya, K., Valluvaparidasan, V., Paranidharan, V. and Velazhahan, R. (2012). Detection of *Colletotrichum falcatum* causing red rot of sugarcane by enzyme-linked immunosorbent assay. *Archives of Phytopathology and Plant Protection*, 45(7): 823-830.
7. Clevers, J. G. P. W., Kooistra, L. and Schaepman, M. E. (2010). Estimating canopy water content using hyperspectral remote sensing data. *International Journal of Applied Earth Observation and Geoinformation*, 12(2): 119-125.
8. Peng, Y., Zhang, M., Xu, Z., Yang, T., Su, Y., Zhou, T., Wang, H., Wang, Y. and Lin, Y., 2020. Estimation of leaf nutrition status in degraded vegetation based on field survey and hyperspectral data. *Scientific Reports*, 10(1): 1-12.
9. Sonobe, R., Yamashita, H., Nofrizal, A. Y., Seki, H., Morita, A. and Ikka, T. (2021). Use of spectral reflectance from a compact spectrometer to assess chlorophyll content in *Zizania latifolia*. *Geocarto International*, 2021: 1-13.
10. Liu, Z. Y., Shi, J. J., Zhang, L. W. and Huang, J. F. (2010). Discrimination of rice panicles by hyperspectral reflectance data based on principal component analysis and support vector classification. *Journal of Zhejiang University: Science B*, 11(1): 71-78.
11. Sankaran, S. and Ehsani, R. (2010). Spectral evaluations for developing optical methods of Huanglongbing (HLB) detection in citrus orchards. *Biosystems*, 2021: 121-123.
12. Izzuddin, M. A., Seman Idris, A., Nisfariza, M. N., Nordiana, A. A., Shafri, H. Z. M. and Ezzati, B. (2017). The development of spectral indices for early detection of Ganoderma disease in oil palm seedlings. *International Journal of Remote Sensing*, 38(23): 6505-6527.
13. Vigier, B. J., Pattey, E. and Strachan, I. B. (2004). Narrowband vegetation indexes and detection of disease damage in soybeans. *IEEE Geoscience and Remote Sensing Letters*, 1(4): 255-259.
14. Zhang, N., Yang, G., Pan, Y., Yang, X., Chen, L. and Zhao, C. (2020). A review of advanced technologies and development for hyperspectral-based plant disease detection in the past three decades. *Remote Sensing*, 12(19): 1-34.
15. Wójtowicz, A., Piekarczyk, J., Czernecki, B. and Ratajkiewicz, H. (2021). A random forest model for the classification of wheat and rye leaf rust symptoms based on pure spectra at leaf scale. *Journal of Photochemistry and Photobiology B: Biology*, 223: 112278.

16. Chen, X., Dong, Z., Liu, J., Wang, H., Zhang, Y., Chen, T., Du, Y., Shao, L. and Xie, J. (2020). Hyperspectral characteristics and quantitative analysis of leaf chlorophyll by reflectance spectroscopy based on a genetic algorithm in combination with partial least squares regression. *Spectrochimica Acta - Part A: Molecular and Biomolecular Spectroscopy*, 243: 118786.
17. Liu, Z. Y., Wu, H. F. and Huang, J. F. (2010). Application of neural networks to discriminate fungal infection levels in rice panicles using hyperspectral reflectance and principal components analysis. *Computers and Electronics in Agriculture*, 72(2): 99-106.
18. Zhu, H., Chu, B., Zhang, C., Liu, F., Jiang, L. and He, Y. (2017). Hyperspectral imaging for presymptomatic detection of tobacco disease with successive projections algorithm and machine-learning classifiers. *Scientific Reports*, 7(1): 1-12.
19. Wei, X., Johnson, M. A., Langston, D. B., Mehl, H. L. and Li, S. (2021). Identifying optimal wavelengths as disease signatures using hyperspectral sensor and machine learning. *Remote Sensing*, 13(14): 1314283.
20. Tian, L., Xue, B., Wang, Z., Li, D., Yao, X., Cao, Q., Zhu, Y., Cao, W. and Cheng, T. (2021). Spectroscopic detection of rice leaf blast infection from asymptomatic to mild stages with integrated machine learning and feature selection. *Remote Sensing of Environment*, 257(8): 112350.
21. Zhang, J., Cheng, T., Guo, W., Xu, X., Qiao, H., Xie, Y. and Ma, X. (2021). Leaf area index estimation model for UAV image hyperspectral data based on wavelength variable selection and machine learning methods. *Plant Methods*, 17(1): 1-14.
22. Al-Saddik, H., Simon, J. C. and Cointault, F. (2019). Assessment of the optimal spectral bands for designing a sensor for vineyard disease detection: The case of 'Flavescence dorée.' *Precision Agriculture*, 20(2): 398-422.
23. Fillbrunn, A., Dietz, C., Pfeuffer, J., Rahn, R., Landrum, G. A. and Berthold, M. R. (2017). KNIME for reproducible cross-domain analysis of life science data. *Journal of Biotechnology*, 261(July): 149-156.
24. Liu, S., Yu, H., Sui, Y., Zhou, H., Zhang, J., Kong, L., Dang, J. and Zhang, L. (2021). Classification of soybean frogeye leaf spot disease using leaf hyperspectral reflectance. *PLoS ONE*, 16(9): 1-23.
25. Ruffin, C. and King, R. L. (1999). The analysis of hyperspectral data using Savitzky-Golay filtering-theoretical basis (part 1). In *IGARSS'99 Proceedings: Remote Sensing of the System Earth—A Challenge for the 21st Century: IEEE 1999 International Geoscience and Remote Sensing Symposium, 28 June–2 July 1999, Congress Centrum Hamburg*: pp. 756-758.
26. Džeroski, S. and Ženko, B. (2004). Is combining classifiers with stacking better than selecting the best one? *Machine Learning*, 54(3): 255-273.
27. Hall, M., Frank, E., Holmes, G., Pfahringer, B., Reutemann, P. and Witten, I. H. (2009). The WEKA data mining software: An update. *ACM SIGKDD Explorations Newsletter*, 11(1): 10-18.
28. Gregory, P. H. (1968). Interpreting plant disease dispersal gradients. *Annual review of Phytopathology*, 6(1): 189-212.
29. Tsai, F. and Philpot, W. (1998). Derivative analysis of hyperspectral data. *Remote Sensing of Environment*, 66(1): 41-51.
30. Lu, J., Zhou, M., Gao, Y. and Jiang, H. (2018). Using hyperspectral imaging to discriminate yellow leaf curl disease in tomato leaves. *Precision Agriculture*, 19(3): 379-394.
31. Li, Y., Demetriades-Shah, T. H., Kanemasu, E. T., Shultis, J. K. and Kirkham, M. B. (1993). Use of second derivatives of canopy reflectance for monitoring prairie vegetation over different soil backgrounds. *Remote Sensing of Environment*, 44(1): 81-87.
32. Muhammed, H. H. (2005). Hyperspectral crop reflectance data for characterising and estimating fungal disease severity in wheat. *Biosystems Engineering*, 91(1): 9-20.
33. Cen, Y., Huang, Y., Hu, S., Zhang, L. and Zhang, J. (2022). Early detection of bacterial wilt in tomato with portable. *Remote Sensing*, 14(12): 2882.

Malaysian Journal of Analytical Sciences (MJAS)
Published by Malaysian Analytical Sciences Society

HIERARCHICAL ZEOLITE ZSM-5 FRAMEWORK ON THE SYNTHESIS AND CHARACTERIZATION FOR CATALYTIC CRACKING OF FLUID: A MINI REVIEW

(Kerangka Hierarki Zeolit ZSM-5 Terhadap Sintesis san Pencirian untuk Pemecahan Pemangkin Cecair: Sebuah Ulasan Ringkas)

Nazrizawati Ahmad Tajuddin*, Nur Alyaa Kamal, Nurul Anessa Qistina Rhymme, and Salma Fawiza Sani

School of Chemistry and Environment,
Faculty of Applied Sciences,
Universiti Teknologi MARA,
40450 Shah Alam, Selangor, Malaysia

**Corresponding author: nazriza@uitm.edu.my*

Received: 13 December 2022; Accepted: 18 April 2023; Published: xx June 2023

Abstract

This review discusses the modified hierarchical framework of zeolite ZSM-5 through top-down and bottom-up techniques, which progressed via a soft template through a combination of dealumination and desilication. Several experiments have been reviewed to increase the catalytic cracking performance of Z SM-5 zeolite, including fluid catalytic cracking (FCC) activity. Template-assisted or post-treatment procedures may be used to create hierarchical zeolites, with mesopores or macropores boosting the accessibility of acid sites in micropores and the hierarchical pore structure. The physiochemical characterization investigation revealed that the hierarchical catalysts had a substantial surface area and pore characteristi cs compared to the parent samples, making them an attractive alternative to be used in the FCC catalyst. It is important to develop a low-cost and effective process for manufacturing hierarchical zeolite.

Keywords: Zeolite Socony mobile five, modification of hierarchical framework, fluid catalytic cracking, catalytic activity

Abstrak

Ulasan ini membincangkan kerangka hierarki zeolite ZSM-5 yang diubah melalui teknik atas ke bawah dan bawah ke atas, yang berkembang melalui templat lembut melalui gabungan dealuminasi dan desilikasi. Beberapa eksperimen telah dikaji untuk meningkatkan prestasi pemecahan pemangkin zeolite ZSM-5, termasuk aktiviti pemecahan pemangkin cecair (FCC). Prosedur yang dibantu templat atau pasca rawatan boleh digunakan untuk menghasilkan zeolite hierarki, dengan mesopori atau makropora meningkatkan capaian asid di mikropori dan struktur pori hierarki. Penyelidikan pencirian fisiokimia menunjukkan bahawa pemangkin hierarki mempunyai ciri luas permukaan dan liang yang besar jika dibandingkan dengan sampel induk, menjadikannya alternatif yang menarik untuk digunakan dalam pemangkin FCC. Dalam penghasilan hierarki zeolite,proses kos yang rendah dan berkesan adalah menjadi keutamaan.

Kata kunci: Zeolite Socony Mobile five, modifikasi hierarki rangka-kerja, pemecahan pemangkin cecair, aktiviti katalitik

Introduction

Zeolites are microporous aluminosilicate minerals that serve as heterogeneous catalysts in a variety of applications including petroleum refining, oil refineries, fluid catalytic cracking (FCC), oligomerization, esterification, alkylation, and acylation [1]. Zeolite is a crystalline inorganic polymer that is mostly composed of tetrahedral [SiO_4] and [AlO_4] ions and water molecules [2]. Recently, scientists have paid close attention to Zeolite Socony Mobil 5 (ZSM-5) because of its outstanding chemical conversion in several industrial sectors [3]. A prior study confirmed that the ZSM-5 zeolite has been expanding zeolite application as a catalyst and adsorbent in many areas due to its molecular sieving properties, great surface acidity, strong hydrothermal stability, large Si/Al proportions (from tens to hundreds), and environmentally friendly synthesis [4, 5].

Nowadays, research on zeolite is focusing on customizing its acidity and porosity beyond mesoporous capability [6]. In fact, its high acid centre and structure selectivity make it as an interesting catalyst in organic synthesis, primarily for cracking reactions. Another research also stated that zeolite ZSM-5 has been applied as a catalyst in a wide variety of chemical activities such as cracking, isomerization, and alkylation [7]. Meanwhile, a study done by Widayat et al. [8] discovered that cracking is a process that is widely applied in research and industrial applications, primarily in fields especially involved hydrocarbons. Regrettably, the hydrocracking process is typically forced to involve relatively high temperatures, which can be hazardous to the environment. Thereby, transition metals, silica, zeolite-modified zeolite, mesoporous mixed oxide catalyst, and metal organic frameworks have been used in catalytic cracking. As it is an effective catalyst for oil cracking due to its high temperature stability, microcrystalline shape, and propensity to precipitate reactants trapped in pores, ZSM-5 zeolite is thus particularly important for the catalytic cracking process [8]. Thus, this review is intentionally to gather all information and related data to ZSM-5 in catalytic cracking. Zeolites are extremely useful as catalysts for several important reactions involving organic molecules. The most important are cracking, isomerisation and hydrocarbon synthesis. Zeolites can promote a diverse range of catalytic reactions including acid-base and metal induced reactions.

Hierarchical ZSM-5 is a type of zeolite catalyst that has been modified to contain both micro- and mesopores, which increases its surface area and enhances its catalytic activity. This modification is achieved by a post-synthesis treatment, which involves the removal of some of the material that fills the micropores of the zeolite. While hierarchical ZSM-5 has shown promising results in various catalytic reactions, including the conversion of biomass to fuels and chemicals, there are some concerns about the reproducibility and scalability of the synthesis method. Some studies have reported variations in the performance of hierarchical ZSM-5 catalysts depending on the synthesis conditions, which may limit their practical application. Furthermore, the precise mechanisms by which the hierarchical structure enhances the catalytic activity of ZSM-5 are not yet fully understood. This makes it challenging to design and optimize hierarchical ZSM-5 catalysts for specific catalytic reactions. Therefore, a review of the hierarchical ZSM-5 synthesis method is needed to evaluate the reproducibility and scalability of the method and to provide insights into the mechanisms underlying the enhanced catalytic activity of hierarchical ZSM-5. Such a review can help to identify areas for further research and development, ultimately leading to more effective and practical catalysts for various industrial applications.

Development of hierarchical zeolite ZSM-5 (HR-ZSM-5)

A research revealed that the conventional microporous ZSM-5 has limited pores and diffusion channels, hence limiting its use [9]. According to Jia et al. [10], the typical crystal size of standard ZSM-5 zeolites is in micrometre or submicrometer, which lengthens the retention time of macromolecular intermediates and products in the inter channel. Consequently, the small pores of such zeolites are susceptible to be clogged rapidly due to coke deposition, accelerating the deactivation process of zeolite catalysts. Nonetheless, Speight's study discovered that catalytic cracking of gas oil can result in the production of coke because it is a

heat-absorbing process, indicating that heat is absorbed by the process and the temperature of the reaction mixture decreases as the reaction progresses, necessitating the need for a heat source [11]. This heat is generated by the burning of coke produced throughout the operation. Coke is a significant, yet unfavourable, by product of cracking because it occurs on the surface and in the pores of the catalyst throughout the cracking process, blocking active sites and disabling them. In the meantime, diffusion issues come up within the zeolite crystals when large reactants or products are applied, causing in pore clogging in both conventional and non-traditional chemical reactions. Widayat et al. [8] concurred that the function of zeolite as a catalyst is confined by its minute pores, which impede the diffusion of bigger particles during the mass transfer process. Hence, ZSM-5 zeolite will be modified to maximize the surface porosity. Several strategies have been investigated to enhance the structure of ZSM-5 zeolite. According to a new finding by Talebian-Kiakalaieh and Tarighi [1] found that modified zeolites encompass mesoporous materials, large-cavity, nanosized zeolites, hierarchical zeolites, and ultra large-pore zeolites. Nanosized zeolite crystals have low product yields, and zeolites generated with only a mesoporous framework are pricy, hence their applicability are confined. They suggested that the zeolite ZSM-5 framework will be developed to include hierarchical zeolites with microporous and mesoporous structures, which will have a high economic value. Přech et al. [12] also agreed that micropores and mesopores coexist in hierarchical zeolites, helping reactants and products to diffuse more efficiently. This triggered to development of hierarchical zeolite ZSM-5 as mentioned below.

The development of hierarchical ZSM-5 zeolite can be done in a variety of ways. Again, Jia et al. [10] postulated that hierarchical zeolite ZSM-5 can be produced using both bottom-up and top-down methods. These methods include desilication (base leaching) and dealumination (acid leaching). According to Talebian-Kiakalaieh and Tarighi [1], it is ideal to add a post-synthesis treatment that includes desilication and dealumination, coupled with soft tessellation with surfactant and steaming, in order to produce a stable zeolite ZSM-5. Furthermore, Peron et al. [13] emphasized that combining desilication with dealumination may be the optimum way for generating hierarchical zeolites with the appropriate balance of mesoporosity, crystallinity, and acidity. On the other hand, soft templating seems to be more versatile owing to the ease with which it can be implemented and, more importantly, due to the fact that it can alter mesoporosity from inside the zeolite framework [1].

In order to effectively synthesize hierarchical ZSM-5 zeolites with high mesoporous and hierarchy factors, a new soft template was developed and employed as a mesoporogen [14]. During the high-temperature hydrothermal crystallization process, the covalent link of Si-O-Si between the as-produced soft template and the mordenite framework inverted (MFI) frameworks maintains a constant connection. The structure of this soft-connection template's mode efficiently prevents the production of amorphous materials, and it may introduce several mesopores while using few micropores. The particles of as-synthesized hierarchical ZSM-5 zeolites about 1 µm in size and made of nanocrystals of 60-150 nm. These hierarchical samples exhibit excellent tolerance for hydrothermal treatment due to the nature of zeolite and it possesses a considerable microporosity. Additionally, the hierarchical structure exhibits excellent catalytic performance in the reactions of alkylation between benzene and benzyl alcohol, cracking of 1,3,5-tri-isopropylbenzenenzene, and thermal cracking of low-density polyethylene (LDPE), respectively, due to the intra-crystalline mesopores, large external surface areas, and abundantly accessible acid sites.

Acidity may be modified or rectified by the metal ion-exchange process and pre-treatment or post-synthesis treatment can be used to improve other structural properties. As an example, it can state unequivocally that alkali treatment is an efficient and straightforward way for creating mesoporous medium, which reduces channel length and corrects the diffusion restriction. As a result of this change, access to active sites has increased. Moreover, several attempts have been undertaken to optimize the Si/Al ratio or the synthesis

working parameters, such as temperature and stirring duration [15].

By adding ZSM-5 zeolite with 65:1 SiO_2/Al_2O_3 ratio, HR-ZSM-5 zeolite was successfully created [1]. The mesoporous structure of the synthesized ZSM-5 zeolite was induced in the second step using the desilication, dealumination, and soft tessellation techniques. This method produces desilicated ZSM-5 by heating synthesized ZSM-5 for an hour at 80 °C with 50 wt.% NaOH solution in deionized water. Before being dried overnight, the mixture was properly cleaned and filtered. They dealuminized the ZSM-5 zeolite in their experiment by soft-templating with surfactant after three hours of acid leaching with H_2SO_4 solution at 80 °C cetrimonium bromide (CTAB). Each 20 g of desilicated or dealuminated ZSM-5 was dissolved in a 0.3 M NH_4OH solution containing CTAB, and then subjected to a hydrothermal procedure at 150 °C. They claimed that the final HR-ZSM-5 has undergone three successive phases of ion exchange with 1 M NH_4OH solution (80 °C, 2 h), and the powder has then been calcined at 550 °C for five hours before being applied to the fluid catalytic cracking (FCC) catalyst.

Effect of HR-ZSM-5 on the physiochemical properties

Due to their exceptional physical and chemical characteristics, zeolites such as ZSM-5 and ZSM-11 are frequently explored for catalytic cracking of big molecules. Distribution, strength of active sites, and acidity of zeolites are the most crucial elements for improving the catalytic performance of a process [16, 17]. In addition, the pore size and shape of zeolites are critical in influencing the selectivity and yield of the desired products. Consequently, it is vital to comprehend the structure-activity connection of zeolites in order to build effective catalysts for a variety of industrial processes.

Initially, the ICP-OES was used to determine the chemical composition of the parent and hierarchical zeolites that were produced (Table 1) [1]. The hierarchical HR-ZSM-5 (86.34) and parent ZSM-5 (65.55) SiO_2/Al_2O_3 ratios demonstrated that the hierarchical sample had a higher SiO_2/Al_2O_3 ratio than the parent ZSM-5. The increasing of SiO_2/Al_2O_3 ratio was due to the acid leaching by H_2SO_4 after base leaching with NaOH. Research done by Talebian-Kiakalaieh and Tarighi [1] reported that the specific surface area (S_{BET}) (Table 1) of parent ZSM-5 zeolite was 399 m^2/g which then increased to 462 m^2/g. In fact, the pore volume (V_p) showed an improvement in value from 0.20 to 0.59 cm^3. The average pore diameter (D_p) of parent formed when compared to hierarchical samples, showed a significant rise from 2.01 to 5.07 nm [1]. Large pores which might be attributed to the big holes in HR-ZSM-5 via framework dealumination/desilication processes and broad pores which could be generated from the transition of micropores to mesopores initiated by using surfactant for alteration. In their experiment, the mesoporous pore showed significant development when the parent ZSM-5 increased from 0.06 to 0.47 cm^3/g of HR-ZSM-5. These findings revealed that acid/base treatments of ZSM-5 zeolites, as well as the soft templating process, resulting in the development of outstanding hierarchical zeolites. Meanwhile, Wang et al. [15] experiment postulated that the N_2 adsorption–desorption isotherm of ZSM-5 zeolite sample obtained, has features of both type I and type IV(a) profiles with two steep uptake steps, one at $P/P_0 < 0.02$ and the other at $0.45 < P/P_0 < 0.90$, which corresponded to micropore filling and mesopore capillary condensation, respectively. Unnikrishnan and Sabarish [18] agreed that the unaltered sample has the type I isotherm, which was the characteristic isotherm for microporous materials. The changed sample, on the other hand, has type IV isotherm. They added that BJH model was used to analyse the pore size distributions of the samples. Unmodified and adjusted sample pore diameters are predicted to be 2 and 10–20 nm, respectively. As a result, the increased mesoporosity in ZSM-5 zeolite was formed in their study. The porosity of ZSM-5 zeolite influences molecular adsorption, separation, and diffusion and among the dominating factors affecting its catalytic activity[19].

The PXRD patterns of parent ZSM-5, base/acid leached ZSM-5, and hierarchical HR-ZSM-5 samples, as shown in Figure 1a, were all identical to the standard ZSM-5 peaks, with no extra unexplained peaks, demonstrating

that all of the synthesised samples were true MFI-type material [13]. There were no significant changes in the intensity, breadth, or location of the XRD peaks after dealumination and desilication of the ZSM-5 catalyst. Moreover, no specific peaks associated with the amorphous phase have been discovered. According to Ghrib et al. [20], the growth of ZSM-5 crystallizations were more difficult to detect owing to their tiny size. Earlier study found that both the parent ZSM-5 zeolite and the hierarchical sample had a decrease in reflection intensity [1]. The insertion of mesopores into parent zeolite results in a decrease in crystallinity and a broadening of peak width, confirming the scission of Al-O bonds and the formation of hydroxyl nests (cavities), which caused the unit cell sizes to expand with the desilication treatment because of selective silicon extraction, resulting in larger unit cell sizes. Yang et al [6] discovered a dense pore opening on the surface crystallite of the hierarchical zeolite. FESEM and HRTEM images (Figure 1b) further confirmed mesopores structures have been observed throughout the zeolite matrix.

Meanwhile, Jia et al. [21] shown in their experiment that the asymmetric stretching of SiO_4 and AlO_4 tetrahedra in the zeolite framework is believed to be due to vibrational modes around 547 and 1222 cm^{-1}, respectively. Another research discovered the distinctive bands in the FTIR spectra of parent ZSM-5 and hierarchical HR-ZSM-5 samples corresponded to internal and exterior symmetric and asymmetric stretching, double ring vibrations, and T-O bending, as shown in Figure 1c, demonstrating that the pure ZSM-5 phase was found in both samples [1]. In Sabarish and Unnikrishnan's work [18], NH_3-TPD analysis was used to investigate the acidity of the synthesized parent and hierarchical ZSM-5 zeolite. They claimed that the hierarchical sample had a 16.5% lower total acidity than the parent sample. When the framework Al atom was removed, the overall acidity of the hierarchical zeolite was reduced. Figure 1d shows the acidity profiles of synthesized ZSM-5 and HR-ZSM-5, with two peaks in the weak and medium regions. According to them, the strength of medium acidity fell dramatically following the base/acid washing and soft templating processes. The low-temperature peak indicated NH_3 molecule desorption from weak acid sites, while the high-temperature peak represented NH_3 molecule desorption from strong acid sites [18]. The formation of a mesoporous framework resulted in a little decrease in the intensity of the surfactant-modified sample.

As mentioned earlier, the acidity plays a major role in the fluid cracking process. In this type of reaction, the existence of a strong acid sites can significantly alter the catalyst's performance. Based on NH_3-TPD analysis done by Emori et al. [22], the standard zeolite had acid sites capable of adsorbing ammonia on its surface. Their result showed low Si/Al ratio which explained the elevated acidity (large amount of acid sites). High acidity prevails when the aluminium acid sites, one of the acidity sources on zeolitic materials, are separated in this structure. These aluminium atoms were more acidic than those closer together in the zeolite structure. Again, Talebian-Kiakalaieh and Tarighi [1] also postulated that the HR-ZSM-5 sample demonstrated a 36% drop in overall acidity when compared to the parent ZSM-5 which due to the removal of Si or Al atoms from the zeolite framework [1]. Desilication resulted in a decline in Brönsted acidity, as well as a minor rise in Lewis acid sites, which had similar consequences.

Table 1. ICP-OES analysis and result of N_2 adsorption-desorption for the ZSM-5 and HR-ZSM-5[1]

Sample	**SiO_2**	**Al_2O_3**	**SiO_2/Al_2O_3**	**S_{BET} (m^2/g)**
ZSM-5	72.11	1.10	65.55	399
HR-ZSM-5	87.20	1.00	87.20	462

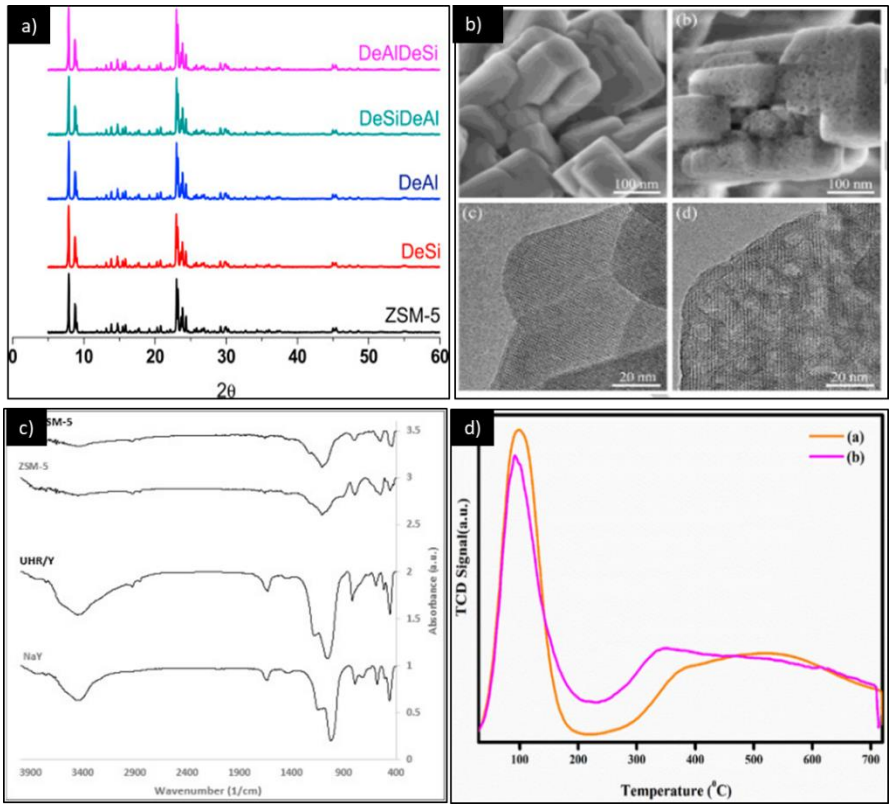


Figure 1. a) PXRD pattern for ZSM-5 [13], b) FESEM and HRTEM images of hierarchical zeolites [6], c) FTIR spectra for ZSM-5 and HR-ZSM-5 [1] and d) NH_3-TPD analysis of a) ZSM-5 b) HR-ZSM-5 [18]

According to Kantarelis et al. [23], the hydrothermal stability of the zeolite was critical for cleaning up coked catalysts. Moreover, they noted that post-treatment procedures increased the thermal stability of hierarchical samples by transforming the original zeolites' microporosity to a structure containing mesopores. Figure 2a depicted the impact of desilication on zeolite thermal stability, which they indicated had no influence on thermal stability as tested [23]. This is shown by the comparability of the mass and DSC curves following heating in an oxidative atmosphere. The observed differences in the two samples' actual thermal deterioration were linked to physiosorbed water, which happened when the samples were exposed to the atmosphere before being tested. Another study proposed that the synthesized parent and hierarchical zeolites in Figure 2b exhibited a single small weight loss in the 80-200 ℃ range, corresponding to physically adsorbed water and demonstrating the strong heat thermal of the catalysts [1]. Additionally, no weight loss was observed at temperatures beyond 200 °C, indicating that the catalysts were thermally stable. The high crystallinity explains the remarkable thermal stability of HR-ZSM-5. In contrast to the first assertion, Widayat and Annisa [8] proposed that the morphology of synthesized ZSM-5 was amorphous (Figure 2c-2d). The surface structure of the catalyst clustered together, while commercial ZSM-5 exhibited a separated structure owing to its very high crystallinity. However, as shown in Figure 2e-f, SEM pictures corroborated the hexagonal shape of ZSM-5 crystals with a size of that generated larger agglomerates [1].

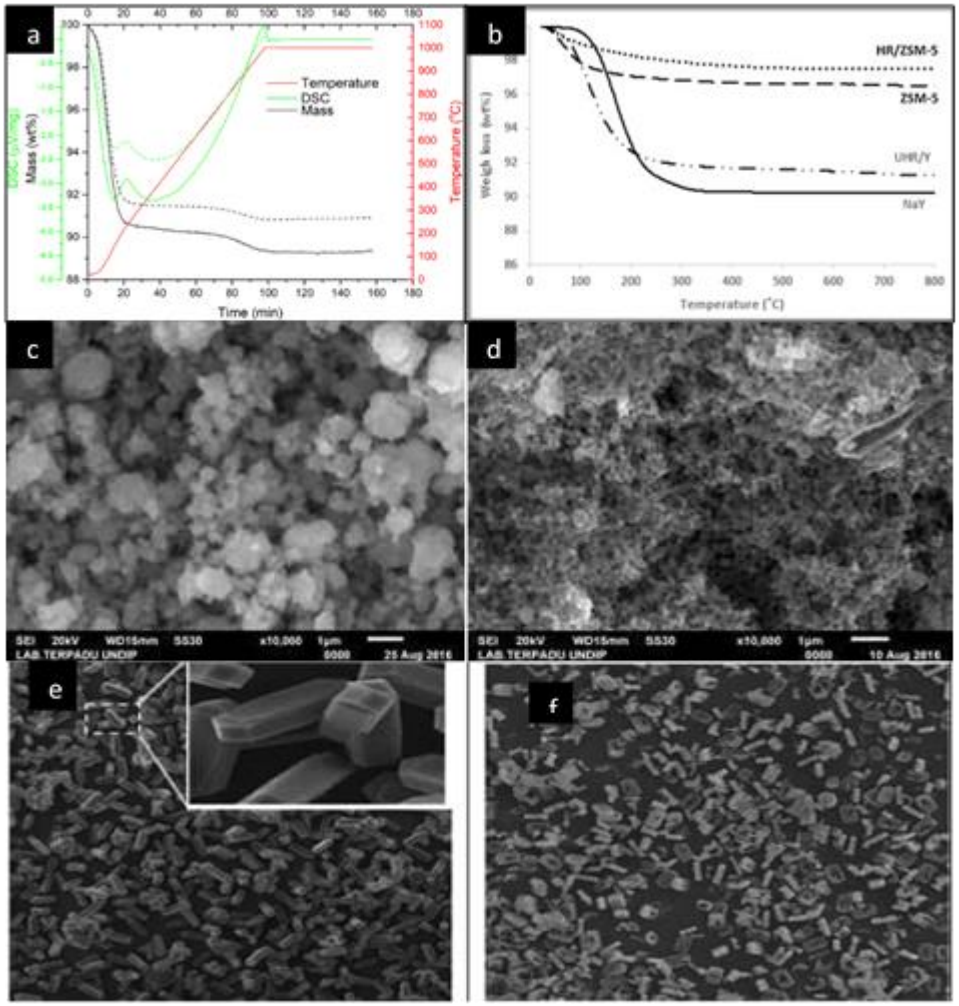


Figure 2. a) The effect of desilication on zeolite thermal stability [23], b) The result of TG-DTA plots for parent ZSM-5 and HR-ZSM-5 [1], c) SEM images of a HR-ZSM-5 and d) SEM images of ZSM-5 [8], e) SEM image of ZSM-5 and f) SEM image of HR-ZSM-5 from different source [1]

Fluid catalytic cracking of gas oil

Fluid catalytic cracking (FCC) has emerged as the primary force behind oil refining performance improvement since its inception in 1942 [16, 24]. It has been discovered over time that FCC is a flexible process that can transform feeds of various origins, including vacuum oils, residual oils, crude oil, scrap tires, pyrolysis oil, polyethylene plastic waste, and biomass derived oils, into high value transportation fuels and light olefin feeds for the petrochemical industry [25, 26]. The feedstock quality has the greatest influence on the performance of the FCC unit (FCCU) across all independent factors [27]. The processing of secondary gas oils (from cokers, visbreakers, and residual hydrocrackers) is more difficult than the processing of straight run vacuum gas oils (SRVGOs) in the FCCU [16]. Secondary gas oils do in fact have larger levels of refractory condensed aromatic compounds and basic nitrogen [28]. Hence, the quantity and quality of the secondary gas oil fraction present in the FCC feed mix are directly associated to the performance of the FCCU [29, 30].

It has been reported that Microactivity Test (MAT) apparatus was used to catalyze the catalytic cracking of gas oil [12]. The catalyst activity test was conducted in the MAT unit (ASTM-D3907), which was a plug flow reactor (PFR) for cracking vacuum gas oil (VGO). The principal constituents of the cracking products, were hydrocarbons, oxygenated chemicals (mostly water, CO, and CO_2), and coke [12]. The gaseous hydrocarbon component was divided into dry gas (hydrogen, methane, ethane, and ethene) and liquefied petroleum gas fractions (LPG; propane, propene, butenes, and butanes). There are three different liquid hydrocarbons; C_{5+} gasoline (212 °C), light cycle oil (LCO; 221-360 °C), and heavy cycle oil (HCO; >360 °C), and these cracking products were examined using specific analytical tools including the MAT unit. The formula for the typical MAT conversion is (Y_{HCO} + Y_{LCO}) = 100%. The selectivity of propene has been calculated as a proportion of all C_3 hydrocarbons (C_3 olefinicity). The selectivity of butenes in total C_4 hydrocarbons is expressed as a percentage (C_4 olefinicity).

Meanwhile, according to Ibarra et al. [13], the catalytic cracking of the VGO was carried out in riser simulator. The product stream was collected from the reaction chamber using a fast-triggered vacuum pump attached to an auxiliary chamber (30 cm^3), and then evaluated online using gas chromatography (GC). They stated that the mass loss after burning of spent catalysts in a TGA-Q 5000 TA Instruments thermobalance, from 300°C to 550°C at a 3°C min^{-1} heating rate, was used to determine the amount of coke. Meanwhile, in literature experiment, they highlighted that VGO has been injected into the catalyst bed at a rate of 55 ml/h using a syringe pump in the presence of N_2 as the inert carrier gas (5–10 ml/min) at the correct temperature [1].

Equation. (1) and (2) have been used to determine the reaction conversion product yields:

$$Conversion(\%) = \frac{W_f - \frac{R \times W_i}{100} - W_Q}{W_f} \times 100 \quad (1)$$

$$Yield(\%) = \frac{W_i - X_i}{W_F} \times 100 \quad (2)$$

W_f is injected feed weight (g), W_L is liquid product weight (g), R is weight percentage (wt%) linked to the product evaporated up to 216℃, W_Q is liquid held up at reactor outflow (g) and W_i is each product's mass fraction [1].

Effect of HR-ZSM-5 mesoporous on the FCC activity

This section explored the effect of mesoporosity of synthesised hierarchical zeolites (HR-ZSM-5) on FCC catalyst activity and stability for the transformation of VGO to value-added chemicals such as gasoline, propylene, and olefins. It has been reported that zeolites with a mesoporous structure were able to boost the interaction between catalyst active sites and bulky molecules of feedstock (VGO) and ultimately increase the production of value-added chemicals such as gasoline, propylene, and olefins [1]. The reaction conversion (99.2%) and propylene yield (16.41 wt.%) obtained in their study were the highest than those obtained in the previous studies as shown in Figure 3, indicating that the synthesized FCC-4 catalyst had significant activity. Besides, García et al. [31] agreed that large molecules can be cracked more easily with hierarchical zeolites, which also provided selectivity for bulky intermediates. Furthermore, it was obvious that coke was formed at a faster rate for hierarchical catalysts but due to the presence of more saturated hydrocarbon molecules that resist in a hierarchical catalyst, coke that forms in a mesoporous structure would be easier to burn in the regenerator.

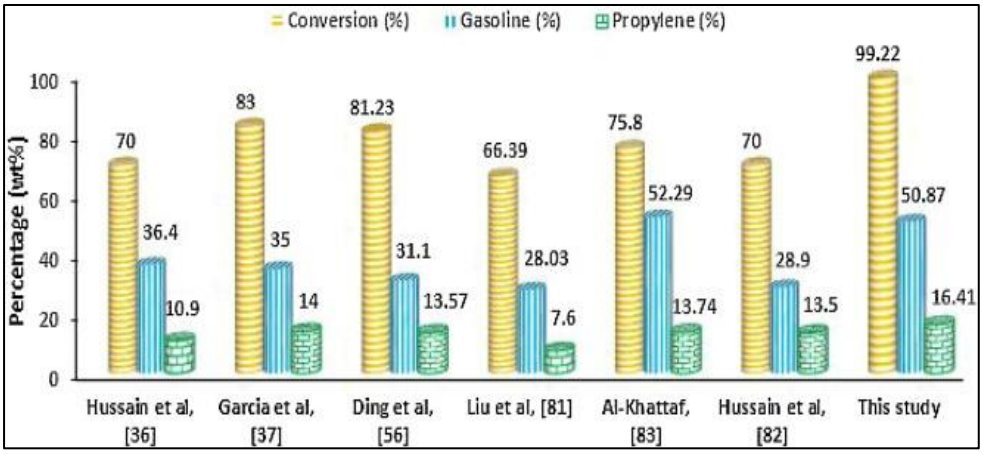


Figure 3. The analysis efficiency of FCC catalysts to other publications. The conversion, gasoline, and propylene yields were shown in comparison [1].

A recent study has discovered four different forms of fluid catalytic cracking (FCC) using HR-ZSM-5 zeolite, that was created by mixing the basic components, which include P_2O_5@ZSM-5, kaolin, Al_2O_3, $Ce(NO_3)_3.7H_2O$, and a binder [1]. Cerium has been used to control zeolite acidity while increasing catalyst acidity in the FCC catalyst framework. The FCC catalyst in a specific form was generated by placing the slurries in a spray dryer with an initial temperature of 210 °C and a mixing speed of 300 rpm. The catalyst was calcined for 4 hours at 650 °C. In another work, diammonium phosphate ($H_9N_2O_4P$) was immersed in distilled water to infuse with P_2O_5, then HR-ZSM-5 zeolite was added and refluxed for 2 hours [1]. The mixture was then dried for 12 hours at 70 °C before being calcined for 3 hours at 500 °C. Three distinct binders were employed in the manufacturing of FCC catalysts: alumina sol, a colloidal silica dispersion with an alkaline 40% aqueous dispersion (LUDOX-40), and alumina silica sol. It has been reported that the alumina sol binder was created by preparing 10 mL $Al(NO_3)_3.9H_2O$ solution (1 M), and 2.3 mL NH_4OH (25 wt.%) one drop at a time, and eventually adjusting the pH up to 4. Additionally, 1 g of aluminium sulphate was dissolved in 50 mL of water and the pH was adjusted to 2.5 by adding 20% H_2SO_4 dropwise. The physical and chemical characteristics of the FCC catalysts varied according to the use of various binders, with the alumina sol binder yielding the maximum activity and selectivity. The researchers also discovered that the calcination temperature had a substantial influence on catalyst performance, with higher temperatures leading to a lower activity and selectivity. This agglomeration in a meso and macroporous matrix results in the development of a hierarchical porous structure in the catalyst particle, which allows for sequential reactant dispersion and partial cracking of larger feedstock molecules, followed by cracking of the resulting chains within the catalyst's micropore structure.

Conclusion

Ultimately, the modified hierarchical framework of zeolite ZSM-5 through top-down and bottom-up techniques, which progressed via soft template through a combination of dealumination and desilication, has been comprehensively explained. Several experiments have been undertaken to increase the catalytic cracking performance of ZSM-5 zeolite, including catalytic cracking activity. Factors influencing ZSM-5 zeolite catalytic performance were reviewed from the viewpoints of ZSM-5 zeolite with particular shape, hierarchical ZSM-5 zeolite, and acid characteristics. By incorporating ZSM-5 zeolite with hierarchical structure, the diffusion length of a molecule may be lowered and the diffusion efficiency of a molecule can be raised. Template-assisted or post-treatment procedures may be used to create hierarchical ZSM-5 zeolites. The inclusion of mesopores or macropores boosted the

accessibility of acid sites in micropores, resulting in ZSM-5 zeolite with a hierarchical pore structure, which is particularly advantageous for post-treatment procedures that improve catalytic cracking efficiency. Characterization investigation revealed that the hierarchical catalysts had a substantial surface area and pore characteristics compared to parent samples. Moreover, the hierarchical zeolites demonstrated exceptional hydrothermal stability, making them an attractive alternativeto be used in FCC catalyst. Above all, options to increase catalytic cracking performance are still being evaluated in the laboratory, and it is critical to develop a low-cost and effective process for manufacturing hierarchical ZSM-5 zeolite. Hence, the catalytic cracking performance may be increased by inserting hierarchical ZSM-5 zeolite.

Acknowledgements

The authors would like to thank the RMC, Universiti Teknologi MARA, Shah Alam for the project opportunity under Grant Penyelidikan Khas (600-RMC/GPK 5/3 (117/2020).

References

1. Talebian-Kiakalaieh A., and Tarighi S. (2020). Synthesis of hierarchical Y and ZSM-5 zeolites using post-treatment approach to maximize catalytic cracking performance. *Journal of Industrial and Engineering Chemistry*, 2020: 88167-177.
2. Król, M. (2020). Natural vs. synthetic zeolites. *Crystals*, 10(7): 622.
3. Hartmann M., Thommes M., and Schwieger W. (2021). Hierarchically-ordered zeolites: A critical assessment. *Advanced Materials Interfaces*, 8(4): 2001841.
4. Hamidzadeh M., Saeidi M., and Komeili S. (2020). Modified seeding method to produce hierarchical nanocrystalline ZSM-5 zeolite. *Materials Today Communications*, 25: 101308
5. Feliczak-Guzik, A. (2018). Hierarchical zeolites: Synthesis and catalytic properties. *Microporous and Mesoporous Materials*, 25933-25945.
6. Yang S., Yu C., Yu L., Miao S., Zou M., Jin C., Zhang D., Xu L. and Huang S. (2017). Bridging dealumination and desilication for the synthesis of hierarchical MFI zeolites. *Angewandte Chemie*, 129(41): 12727-12730.
7. Kadja, G. T. M., Suprianti, T. R., Ilmi, M. M., Khalil, M., Mukti, R. R. and Subagjo. (2020). Sequential mechanochemical and recrystallization methods for synthesizing hierarchically porous ZSM-5 zeolites. *Microporous and Mesoporous Materials*, 2020: 308110550.
8. Widayat W., Annisa A. N. and Soedarto J. (2017). Synthesis and characterization of ZSM-5 catalyst at different temperatures. 214: 012032.
9. Gu Y., Wang X., Qin Z., Mintova S. and Liu X. (2020). Intra-crystalline mesoporous ZSM-5 zeolite by grinding synthesis method. *Microporous and Mesoporous Materials*, 306: 110437.
10. Jia, X., Khan, W., Wu, Z., Choi J. and Yip, A. C. K. (2019). Modern synthesis strategies for hierarchical zeolites: Bottom-up versus top-down strategies. *Advanced Powder Technology*, 30(3): 467-484.
11. Speight J. G. (2020). Feedstock types and properties. *The Refinery of the Future*: pp. 1-42.
12. Přech, J., Pizarro, P., Serrano, D. P. and Áejka J. (2018). From 3D to 2D zeolite catalytic materials. *Chemical Society Reviews*, 47(22):8263-8306.
13. Peron, D. V., Zholobenko, V. L., de Melo, J. H. S., Capron, M., Nuns, N., de Souza, M. O., Feris, L. A., Marcilio, N. R., Ordomsky, V. V. and Khodakov A.Y. (2019). External surface phenomena in dealumination and desilication of large single crystals of ZSM-5 zeolite synthesized from a sustainable source. *Microporous and Mesoporous Materials*, 28657-28664.
14. Song, G., Chen, W., Dang, P., Yang, S., Zhang, Y., Wang, Y., ... and Li, F. (2018). Synthesis and characterization of hierarchical ZSM-5 zeolites with outstanding mesoporosity and excellent catalytic properties. *Nanoscale Research Letters*, 13(1): 1-13.
15. Wang, Y., Song, J., Baxter, N. C., Kuo, G. T. and Wang, S. (2017). Synthesis of hierarchical ZSM-5 zeolites by solid-state crystallization and their catalytic properties. *Journal of Catalysis*, 349: 53-65.

16. Stratiev, D., Shishkova, I., Ivanov, M., Dinkov, R., Georgiev, B., Argirov, G., ... and Sotirova, E. (2021). Role of catalyst in optimizing fluid catalytic cracking performance during cracking of h-oil-derived gas oils. *ACS Omega*, 6(11): 7626-7637.
17. Shu, Q., Tang, G., Lesmana, H., Zou, L. and Xiong, D. (2018). Preparation, characterization and application of a novel solid Brönsted acid catalyst $SO_4^{2-}/La^{3+}/C$ for biodiesel production via esterification of oleic acid and methanol. *Renewable Energy*, 119: 253-261.
18. Sabarish, R. and Unnikrishnan G. (2020). A novel anionic surfactant as template for the development of hierarchical ZSM-5 zeolite and its catalytic performance. *Journal of Porous Materials*, 27(3):691-700.
19. Liu, X. and Sun, Y. (2020). Effect of ethanol on the morphology and textual properties of ZSM-5 zeolite. *Catalysts*,10(2):198.
20. Ghrib, Y., Frini-Srasra, N., Srasra, E., Martínez-Triguero, J. and Corma A. (2018). Synthesis of cocrystallized USY/ZSM-5 zeolites from kaolin and its use as fluid catalytic cracking catalysts. *Catalysis Science & Technology*, 8(3): 716-725.
21. Jia, Y., Shi, Q., Wang, J., Ding, C. and Zhang K. (2020). Synthesis, characterization, and catalytic application of hierarchical nano-ZSM-5 zeolite. *RSC Advances*, 10(50): 29618-29626.
22. Emori, E. Y., Hirashima, F. H., Zandonai, C. H., Ortiz-Bravo, C. A., Fernandes-Machado, N. R. C. and Olsen-Scaliante, M. H. N. (2017). Catalytic cracking of soybean oil using ZSM5 zeolite. *Catalysis Today*, 2017: 279168-279176.
23. Kantarelis, E., Javed, R., Stefanidis, S., Psarras, A., Iliopoulou E. and Lappas A. (2019). Engineering the catalytic properties of HZSM5 by cobalt modification and post-synthetic hierarchical porosity development. *Topics in Catalysis*, 62(7-11):773-785.
24. Bai, P., Etim, U. J., Yan, Z., Mintova, S., Zhang, Z., Zhong, Z. and Gao, X. (2019). Fluid catalytic cracking technology: current status and recent discoveries on catalyst contamination. *Catalysis Reviews*, 61(3): 333-405.
25. Al-Khattaf, S., Saeed, M. R., Aitani A., and Klein M. T. (2018). Catalytic cracking of light crude oil to light olefins and naphtha over e-cat and MFI: Microactivity test versus advanced cracking evaluation and the effect of high reaction temperature. *Energy and Fuels*, 32(5): 6189-6199.
26. Tian, Y., Che, Y., Chen, M., Feng, W., Zhang, J. and Qiao, Y. (2019). Catalytic upgrading of vacuum residue-derived cracking gas-oil for maximum light olefin production in a combination of a fluidized bed and fixed bed reactor. *Energy & Fuels*, 33(8): 7297-7304.
27. Oloruntoba, A., Zhang, Y. and Hsu, C. S. (2022). State-of-the-art review of fluid catalytic cracking (FCC) catalyst regeneration intensification technologies. *Energies*, 15(6):2061.
28. Mikhaylova, P., de Oliveira, L.P., Merdrignac, I., Berlioz-Barbier, A., Nemri, M., Giusti, P. and Pirngruber, G. D. (2022). Molecular analysis of nitrogen-containing compounds in vacuum gas oils hydrodenitrogenation by (ESI+/-)-FTICR-MS. *Fuel*, 2022: 323.
29. Stratiev, D., Shishkova, I., Ivanov, M., Dinkov, R., Georgiev, B., Argirov, G., ... and Nenov, S. (2021). Catalytic cracking of diverse vacuum residue hydrocracking gas oils. *Chemical Engineering & Technology*, 44(6): 997-1008.
30. Stratiev, D., Shishkova, I., Ivanov, M., Chavdarov, I. and Yordanov, D. (2020). Dependence of fluid catalytic cracking unit performance on H-oil severity, catalyst activity, and coke selectivity. *Chemical Engineering & Technology*, 43(11): 2266-2276.
31. García, J. R., Falco, M. and Sedran, U. (2017). Intracrystalline mesoporosity over Y zeolites. Processing of VGO and resid-VGO mixtures in FCC. *Catalysis Today*, 2017: 296247-296253.

Malaysian Journal of Analytical Sciences (MJAS)
Published by Malaysian Analytical Sciences Society

THE CRYSTAL STRUCTURE OF $Os_3(CO)_{11}(PPh_2(C_{10}H_7)).H_2O$: A COMBINED HIRSHFELD SURFACE ANALYSIS AND DFT CALCULATIONS

(Struktur Hablur $Os_3(CO)_{11}(PPh_2(C_{10}H_7)).H_2O$: Gabungan Analisis Permukaan Hirshfeld dan Pengiraan DFT)

Husna Izzati Muhammad Nor Azharan[1], Enis Nadia Md Yusof[2], Suhana Arshad[3], Omar Bin Shawkataly[4], and Siti Syaida Sirat[1,5*]

[1]*Faculty of Applied Sciences, Universiti Teknologi MARA, Cawangan Negeri Sembilan, Kampus Kuala Pilah, 72000 Kuala Pilah, Negeri Sembilan, Malaysia*
[2]*Chemistry Section, School of Distance Education, Universiti Sains Malaysia, 11800, Minden, Penang, Malaysia*
[3]*X-ray Crystallography Unit, School of Physics, Universiti Sains Malaysia, USM, Penang, 11800, Malaysia*
[4]*Academy of Sciences Malaysia, Level 20, West Wing, MATRADE Tower, Jalan Sultan Haji Ahmad Shah, off Jalan Tuanku Abdul Halim, 50480 Kuala Lumpur, Malaysia*
[5]*Atta-ur-Rahman Institute for Natural Product Discovery (AuRIns), Universiti Teknologi MARA, Kampus Puncak Alam, 42300 Bandar Puncak Alam, Selangor, Malaysia*

[*]*Corresponding author: sitisyaida@uitm.edu.my*

Received: 25 January 2023; Accepted: 8 May 2023; Published: 23 June 2023

Abstract

The molecular structure of $Os_3(CO)_{11}(PPh_2(C_{10}H_7)).H_2O$ was investigated by a single crystal X-ray diffraction. The compound crystallizes in the triclinic, *P-1* space group with unit cell parameters a = 12.4377(14), b = 12.4413(13), c = 12.4718(13) Å, α = 87.3030(19), β = 63.7889(17) and γ =79.3982(19)°. The asymmetric unit of this structure consists of one-triangulo-triosmium complex molecule and one water molecules. The crystal packing of the title compound is stabilized by O–H···O and C–H···O hydrogen bonds as well as C–H···π interaction. The intermolecular interactions were investigated by Hirshfeld surfaces analysis, showing high contribution of O···H/H···O contacts. The molecular electrostatic potential and frontier molecular orbitals of the title compound were further investigated using Density Functional Theory (DFT), revealing that the nucleophilic regions are located at the carbonyl group. There is a large energy gap (6.095 eV) between HOMO and LUMO.

Keywords: triosmium, phosphine ligand, Hirschfeld surface analysis, crystal structure

Abstrak

Struktur molekul $Os_3(CO)_{11}(PPh_2(C_{10}H_7)).H_2O$ telah disiasat melalui pembelauan sinar-X hablur tunggal. Sebatian itu menghablur dalam kumpulan ruang triklinik, *P-1* dengan parameter sel unit a = 12.4377(14), b = 12.4413(13), c = 12.4718(13) Å, α = 87.3030(19), β = 63.7889(17) dan γ =79.3982(19)°. Unit asimetri struktur ini terdiri daripada satu molekul komplek *triangulo-triosmium* dan satu molekul air. Pembungkusan hablur sebatian distabilkan oleh ikatan hidrogen O–H···O dan C–H···O serta interaksi C–H···π. Interaksi antara molekul telah disiasat oleh analisis permukaan Hirshfeld, menunjukkan O···H/H···O adalah penyumbang utama interaksi. Potensi elektrostatik molekul dan orbital molekul sempadan bagi sebatian ini telah disiasat

selanjutnya menggunakan Teori Fungsian Ketumpatan (DFT), mendedahkan bahawa kawasan nukleofilik terletak pada kumpulan karbonil. Terdapat jurang tenaga yang besar (6.095 eV) antara HOMO dan LUMO.

Kata kunci: triosmium, ligan fosfina, analisis permukaan Hirshfeld, struktur hablur

Introduction

The chemistry of triosmium metal clusters with simple substituted tertiary phosphine has been thoroughly studied [1, 2, 3]. Several triosmium metal clusters were reported to exhibit a wide range of catalytic activity [4]. The geometric structure of the metal clusters significantly impact important catalytic activity in which certain geometric structures may interact with the intermediates in the catalytic process. Besides, metal clusters may give an insight to reaction mechanism that have limitations in mononuclear chemistry [5]. Due to their potential application in the catalysis, exploring new triosmium cluster with monodentate phosphine ligands is our research interest. In this study, the $PPh_2(C_{10}H_7)$ (diphenylphosphinonapthalene) ligand has been selected for substitution with $Os_3(CO)_{11}(CH_3CN)$ due to its versatility as a chiral ligand in some catalytic reaction [6, 7]. The reaction produced $Os_3(CO)_{11}(PPh_2(C_{10}H_7)).H_2O$ (**1**) in moderate yield and was successfully determined by a single-crystal X-ray diffraction. The crystal structure of this triosmium cluster was previously obtained from the reaction between $Os_3(CO)_{12}$ and 1,8-bis(diphenylphosphino)naphthalene (dppn) in the presence of trimethylamine oxide [8]. However, the previously reported crystal structure is slightly different from the title compound. The reported structure contains a dichloromethane whereas the title compound contains a water molecule. The title compound was synthesized using a different synthesis method. The present paper describes the X-ray crystallographic structure analysis, Hirshfeld surface analysis, and Density Functional Theory (DFT) calculations.

Materials and Methods

General techniques

All synthesis work was carried out under an oxygen-free-nitrogen (OFN) atmosphere using standard Schlenk techniques. Chemicals were purchased from Sigma-Aldrich and used as received. $Os_3(CO)_{11}(CH_3CN)$ and (diphenylphosphinonapthalene) ($PPh_2(C_{10}H_7)$) were prepared by the published procedure [6, 9]. The IR spectrum was recorded with a solid sample on an Attenuated Total Reflectance Fourier Transform Infrared (ATR-FTIR), Perkin Elmer 2000 FT-IR spectrometer. NMR spectra were recorded using a Bruker Ascend 500 MHz Spectrometer operating at 500 MHz (^{1}H) and at 202 MHz (^{31}P). Chemical shifts are given in ppm relative to TMS (^{1}H) and 85% H_3PO_4 (^{31}P). Product separation was performed on glass plates (20 X 20 cm) coated with 0.5 mm Silica Gel (Merck, $60GF_{254}$).

Synthesis and crystallization of 1

A solution of $Os_3(CO)_{11}(CH_3CN)$ (80 mg, 0.087 mmol) and $PPh_2(C_{10}H_7)$ (26 mg, 0.087 mmol) in dichloromethane (CH_2Cl_2) (25 mL) was stirred at room temperature for 60 min. The solution was dried in-*vacuo* and the residue chromatographed by preparative thin layer chromatography on silica gel with C_6H_{14}/CH_2Cl_2 (3:2) as the eluent. The desired product was isolated as the second (yellow) band in 50% yield and recrystallized from CH_2Cl_2/CH_3OH. IR (ATR): ν(CO) 2105m, 2050sh, 2011s, 2001s, 1984s, 1950s cm^{-1}. ^{1}H NMR ($CDCl_3$): δ 7.98-7.41 (m, 17H, Ph, $C_{10}H_7$). ^{31}P NMR ($CDCl_3$): δ -2.34 ppm ($PPh_2(C_{10}H_7)$).

Single crystal X-ray diffraction

The single crystal X-ray diffraction study were grown from solvent-solvent diffusion of CH_2Cl_2/CH_3OH and collected on a Bruker SMART APEXII-DUO CCD area-detector diffractometer with graphite monochromatic Mo Kα radiation (λ = 0.71073 Å). The collected three-dimensional intensity data was performed using the APEX2 software [10], where the cell refinement and data reduction were performed using the SAINT program [10]. The structure was solved by direct method using the program SHELXLTL [11] and refined by full-matrix least-squares technique on F^2. The absorption correction was applied to the final crystal data using the SADABS software [10]. All the geometrical calculations were carried out using the program PLATON [12]. The anisotropic displacement parameters were refined for all non-hydrogen atoms. The molecular graphic and packing diagrams were drawn using

Mercury program [13].

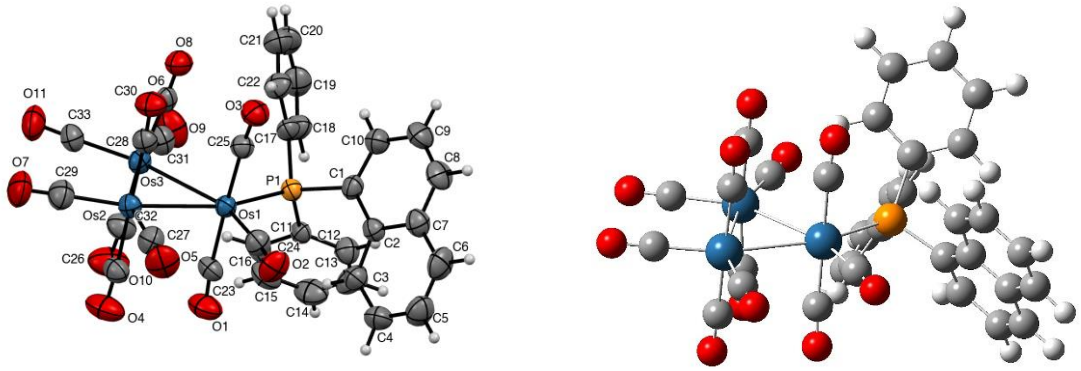
Density functional theory (DFT) calculation

All DFT calculations were performed using the Gaussian09 [14] and the Gaussview5 software [15]. The initial molecular structure and geometry of **1** was obtained from the X-ray crystallographic data. The optimization of the geometry structure was achieved using M06-2X exchange correlation functional [16, 17] with LanL2DZ pseudopotential on Os and 6-31(d, p) Pople basis set for all other atoms [18, 19, 20]. The harmonic frequency calculations were performed at the same level of theory and the stationary points were verified to have no imaginary frequencies.

Results and Discussion

Single crystal X-ray diffraction

The molecular structure of the title compound consists a triangular arrangement of three Os atoms. The $PPh_2(C_{10}H_7)$ occupies the equatorial site with an assigned numbering scheme, as can be seen from Figure 1(a). Figure 1(b) is an optimize structure obtained by Density Functional Theory (DFT) calculation. The crystal structure of **1** is crystallized in a triclinic *P-1* space group and successfully refined with unit cell parameters, a= 12.4377(14) Å, b= 12.4413(13) Å, c= 12.4718(13) Å, α= 87.3030(19)°, β= 63.7889(17)°, γ = 79.3982(19)° and Z= 2. The crystal data and refinement details are presented in Table 1. The crystal of **1** differs to the previously reported structure by virtue of containing a water solvate. Selected bond length and bond angles are listed in Table 2. The bond length and bond angles from the X-ray diffraction are comparable to DFT calculation. The longest Os–Os bond (Os1–Os3) in **1** is Os–Os *cis* to $PPh_2(C_{10}H_7)$. This has been observed in many other $Os_3(CO)_9(PR_3)$ [where PR_3 = Group 15 monodentate ligand]. The elongation of this bond length has been ascribed to the effect of substituting a CO ligand with a PR_3 ligand [1, 21]. PR_3 ligand is a good σ-donor that promotes a higher electron density in the Os framework which is relieved by expansion [21]. The $PPh_2(C_{10}H_7)$ occupy equatorial position on Os1 with the value of Os–P bond length is 2.378 (2) Å and comparable to those in $Os_3(CO)_{11}PPh_3$ [2.370(2) Å] [1], $Os_3(CO)_{11}P(p\text{-}C_6H_4Me)_3$ [2.374(3) Å] [2], $Os_3(CO)_{11}(\eta^1\text{-}^tBu_2PC_2H_4CN)$ [2.394(5) Å] [6]. The Os–C(CO) bond lengths are in the range 1.880(8) - 1.963(10) Å, average 1,933 Å and in a good agreement with expected values [1, 2]. The Os–C–O bond angles (at equatorial) are essentially linear in the range from 176.97-179.65° whereas the Os–C–O bond angles (at axial) are 174.68-176.01°. In the crystal packing, the molecular structure of **1** is linked by O–H···O and C–H···O hydrogen bonds as shown in Figure 2. The presence of C–H···π interactions (Table 3) further stabilized the crystal structure.



(a) (b)

Figure 1. (a) Molecular structure of **1** by X-ray diffraction and (b) the optimized structure performed in DFT at M06 -2X/LanL2DZ/6-31(d,p) level of theory. (H_2O molecule is omitted for clarity)

Table 1. Crystal data of **1**

CCDC No	2219979
Chemical formula	$C_{33}H_{19}O_{12}Os_3P$
Formula weight	1209.05
T(K)	297(2)
λ (Å)	0.71073
Crystal system	triclinic
Space group	*P-1*
Unit cell dimensions	
a (Å)	12.4377(14)
b (Å)	12.4413(13)
c (Å)	12.4718(13)
α (°)	87.3030(19)
β (°)	63.7889(17)
γ (°)	79.3982(19)
V ($Å^3$)	1700.6(3)
Z	2
Density (calculated) (g/cm^3)	2.361
F (0 0 0)	1112
Absorption coefficient (mm^{-1})	11.289
Crystal size (mm)	0.10 x 0.24 x 0.39
θ Range (°)	1.9-35
Reflections collected/unique	23334/8876
R_{int}	0.049
Data/restrains/parameter	8876/0/442
$R[F^2 > 2\sigma(F^2)]$, $wR(F^2)$, S	0.0477, 0.1464, 1.02
Largest difference in peak and hole (e $Å^{-3}$)	4.00 and -2.48

Table 2. Selected bond lengths and bond angles of **1**

Bond	**Bond Length (Å) (X-ray Diffraction)**	**Bond Length (Å) M06-2X/LanL2DZ/6-31(d,p)**
Os1–Os2	2.8881 (5)	2.86587
Os1–Os3	2.9077(5)	2.91398
Os2–Os3	2.8838 (4)	2.89236
Os1–P1	2.378 (2)	2.37501
$Os1–C23_{ax}$	1.950 (8)	1.94612
$Os1–C24_{eq}$	1.880 (8)	1.88889
$Os1–C25_{ax}$	1.930 (8)	1.94024
$Os2-C26_{ax}$	1.948 (10)	1.95390
$Os2–C27_{eq}$	1.932 (9)	1.91539
$Os2–C28_{ax}$	1.956 (9)	1.95452
$Os2–C29_{eq}$	1.903 (10)	1.91407
$Os3–C30_{ax}$	1.963 (10)	1.94649
$Os3–C31_{eq}$	1.917 (9)	1.91198
$Os3–C32_{ax}$	1.958 (10)	1.94641
$Os3–C33_{eq}$	1.924 (9)	1.91676

P1–C1	1.841 (7)	1.84103
O10–C32	1.131 (12)	1.14625
O11–C33	1.113 (11)	1.14550
Bond	**Bond Angle (°) (X-ray Diffraction)**	**Bond Angle (°) M06-2X/LanL2DZ/6-31(d,p)**
Os2–Os1–Os3	59.677(10)	60.049
P1–Os1–Os3	103.11(5)	100.466
P1–Os1–Os2	162.52(5)	160.514
Os1–$C23_{ax}$–O1	173.6(9)	174.678
Os1–$C24_{eq}$–O2	174.8(8)	176.972
Os1–$C25_{ax}$–O3	174.8(7)	175.161
Os2–$C26_{ax}$–O4	173.2(9)	175.906
Os2–$C27_{eq}$–O5	177.6(10)	179.502
Os2–$C28_{ax}$–O6	174.9(8)	176.009
Os2–$C29_{eq}$–O7	178.6(10)	179.604
Os3–$C30_{ax}$–O8	175.4(7)	175.830
Os3–$C31_{eq}$–O9	176.6(9)	178.289
Os3–$C32_{ax}$–O10	174.1(9)	175.737
Os3–$C33_{eq}$–O11	178.3(9)	179.653

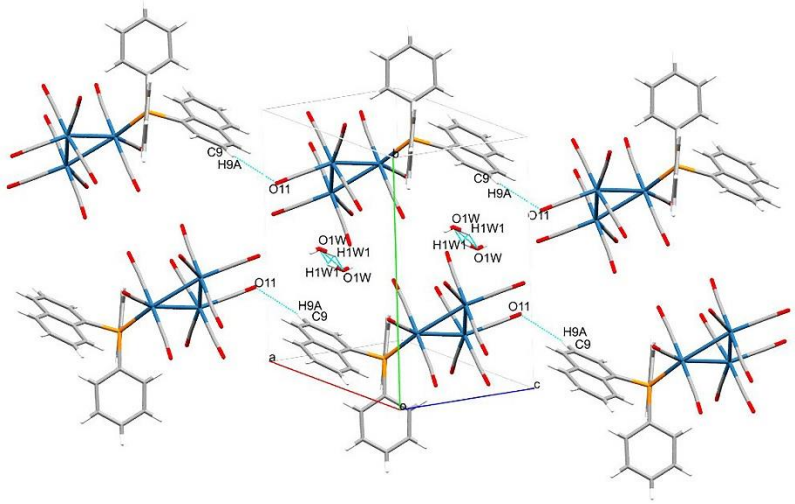


Figure 2**.** Packing diagram of **1** showing O–H···O and C–H···O interactions

Table 3. Hydrogen bond geometries of **1** (Å, °)

D–H···A	**D–H**	**H···A**	**D···A**	**D–H···A**	**Symmetry Code**
O1W–H1W1···O1W^{i}	0.85	2.28	2.837 (17)	124	(i) 1-x,-1-y,-z
C9–H9A···O11^{ii}	0.93	2.60	3.370 (14)	141	(ii) -1+x, y, 1+z.
C18–H18A···*Cg*3^{i}	2.86	143	3.649 (12)	22	(i) x,y,z
C19–H19A···*Cg*1^{ii}	2.83	132	3.528 (12)	62	(ii) 1-x,-y,-z
C19–H19A···*Cg*5^{ii}	2.78	143	3.568 (12)	63	(ii) 1-x,-y,-z

*Cg*3, *Cg*1, *Cg*5 are the centroid of C11–C16, C1–C2–C7–C8–C9–C10, C1–C10, respectively.

Frontier molecular orbitals

The highest occupied molecular orbitals (HOMO) and the lowest unoccupied molecular orbitals (LUMO) are called as frontier molecular orbitals which principally determine the kinetic stability and reactivity of molecules [22]. The HOMO orbitals are mainly located at triangular Os atoms, CO groups and partially on the two phenyl rings. In contrast, the distribution of the LUMO orbitals are prominently accumulated at the naphthalene ring. The distribution of HOMO and LUMO are shown in Figure 3. The HOMO and LUMO orbitals are lying at -6.974 eV and -0.879 eV, respectively. Therefore, the energy gap is 6.095 eV. Generally, a larger energy gap implies a high kinetic stability and low chemical reactivity [23,24].

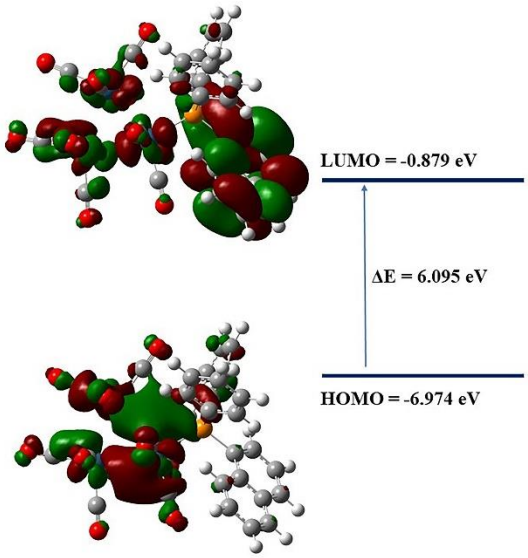


Figure 3. The HOMO-LUMO diagram of **1**

Molecular electrostatic potential

The molecular electrostatic potential (MEP) surfaces are regions around the molecule that provides a relevant guide about the net electrostatic effect at a point by the total charge distribution around the molecule. It also correlates with dipole moments, electronegativity, partial charges, and chemical reactivity of the molecule [25]. The MEP surface is computed using DFT at the 0.0004 a.u. isodensity surface, illustrated in Figure 4. As shown in the surface of **1**, the color code of the map gives the range values between -3.025×10^{-2} a.u (red) towards -3.025×10^{-2} a.u (blue). The regions of the respective colors indicating the most negative electrostatic potential (red) and the most positive electrostatic potential (blue) while zero electrostatic potential (green). The MEP surface showed the most negative regions (red) around the carbonyl groups which can be considered as possible nucleophilic sites. In contrast, the blue region indicates the positive regions suggesting electrophilic sites which are observed at the phenyl and naphthalene ring.

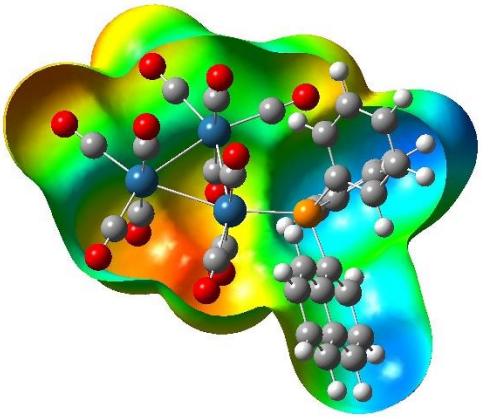


Figure 4. Molecular electrostatic potential diagram of **1**

Hirshfeld surface analysis

Hirshfeld surfaces and the associated 2D fingerprint were calculated using the CrystalExplorer 17.5 [26]. The Hirshfeld surface analysis was used to validate the contributions of the various intermolecular interactions in the crystal structure [27]. The 3D d_{norm} surface of the title compound is shown in Figure 5. The bright-red spot on the d_{norm} surface indicating the presence of strong hydrogen bond which connects the adjacent molecules *via* O1W–H1W1···O1W interaction. The 2D fingerprint plots of a Hirshfeld surfaces were successfully elucidated and delineated into O···H/H···O, H···H, C···H/H···C, O···O, O···C/C···O and C···C contacts are shown in Figure 6. The most dominant contributor on the Hirshfeld surface corresponding to the O···H/H···O contacts with the percentage of 42.8% correspond to C–H···O and O–H···O interactions. H··H (17.6%) contacts are the second largest contributor out of the overall Hirshfeld surface. The C···H/H···C (15.4%) contacts represented by the two wings of spike in the region (d_e~1.6 Å, d_i~ 1.0 Å). The other contacts which are O···O, and O···C/C···O, show the percentage contributions of 11.6% and 11.2%, respectively. The fingerprint of O···C/C···O shows a pair of spikes at (d_e~ 1.7 Å, d_i~ 1.5 Å). The least significant contributions come from the C···C contacts (1.3%) with respect to the total Hirshfeld surface area. On the other hand, the participation of C–H···π interactions can be further visualized under the shape-index surface mapping as illustrated in Figure 7. The presence of the orange spot indicates the existence of C–H···π interactions in the aromatic rings. These intermolecular interactions help to further stabilize the crystal structure of **1** [28].

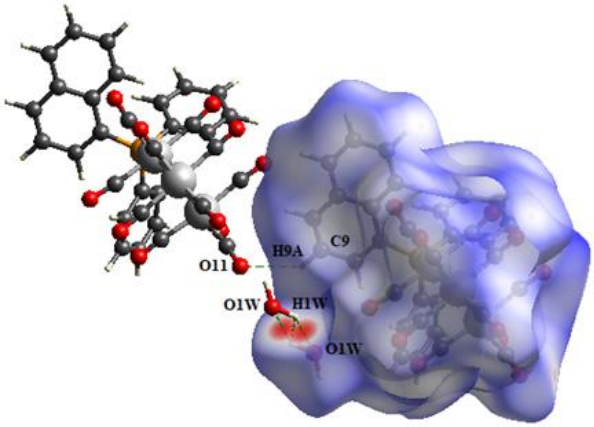


Figure 5. The 3D d_{norm} surface of **1**

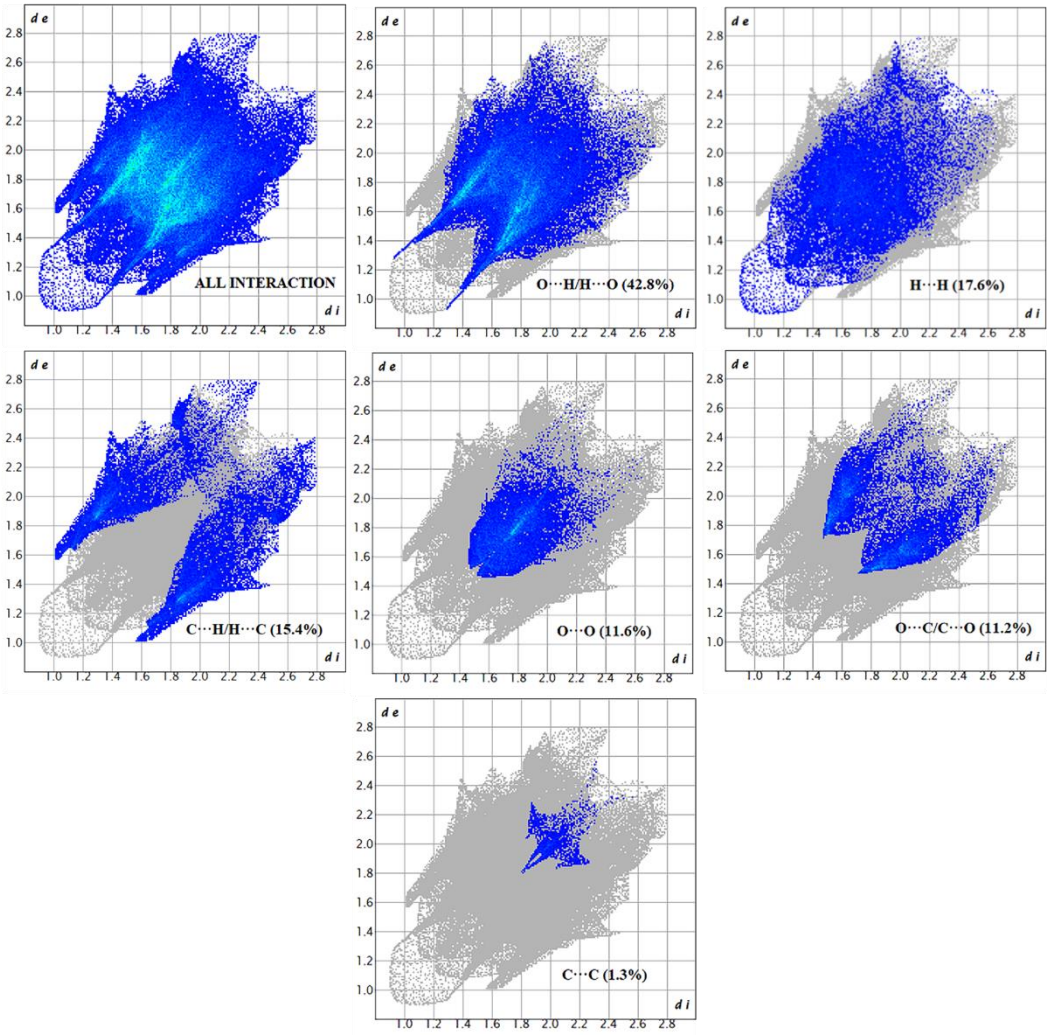


Figure 6. The 2D fingerprint plots of **1** with their respective percentage contribution

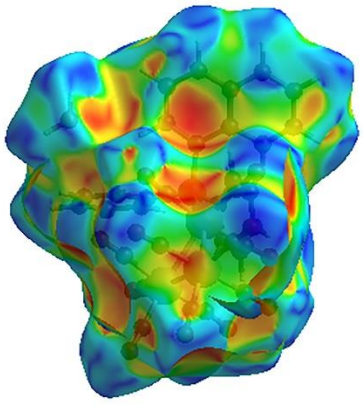


Figure 7. Surface property mapped under shape index of **1**

Conclusion

A new structure of **1** was synthesized and confirmed by spectroscopy characterization and single crystal X-ray diffraction. The molecular structure optimized by DFT is consistent with the crystal X-ray diffraction data. Based on the comparison between the geometry parameters such as bond distances and bond angles, the values of the X-ray diffraction data fall within the expected range of the theoretical data by DFT. The Hirshfeld surface analysis reveal that the intermolecular interactions are dominated by O···H/H···O contacts with 42.8% contribution of total Hirshfeld surfaces, which stabilize the crystalline structure. In addition, the analysis on the frontier molecular orbital showed the title compound possess large energy gap (6.095 eV) which could be attributed to high kinetic stability.

Supplementary material

CCDC-2219979 contains the supplementary crystallographic data for this paper. These data can be obtained free of charge at www.ccdc.cam.ac.uk/consts/retrieving.html (or from the Cambridge Crystallographic data centre (CCDC), 12, Union Road, Cambridge CB2 IE2, UK, Fax: C44 (0)1223- 336033; email-deposit@ccdc.cam.ac.uk).

Acknowledgement

The authors are grateful to Dr. Imthyaz Ahmed Khan for the guidance in the synthesis of the title compound. SSS acknowledged Ministry of Higher Education, Malaysia under the Fundamental Research Grant Scheme (FRGS) (Project Number: FRGS/1/2021/STG04/UITM/02/4) for financial support.

References

1. Biradha, K., Hansen, V. M., Leong, W. K., Pomeroy, R. K. and Zaworotko, M. J. (2000). Steric and electronic influences in $Os_3(CO)_{11}(PR_3)$ structures. *Journal of Cluster Science,* 11(2): 285-306.
2. Mikeska, E. R., Powell, C. B., and Powell, G. L. (2021). Triosmium carbonyl clusters containing a mixture of dppm and dppe ligands. *Journal of Chemical Crystallography*, 51(4): 457-464.
3. Sarker, J. C., Rahman, S., Ghosh, S., Hogarth, G. and Kabir, S. E. (2020). Reactions of the lightly-stabilized triosmium cluster $Os_3(CO)_8\{\mu_3\text{-}Ph_2PCH(Me)P(Ph)C_6H_4\}(\mu\text{-}H)$ with two-electron donor ligands. *Polyhedron,* 186: 114608.
4. Malosh, T. J. and Shapley, J. R. (2010). Fluorous triosmium clusters. Preparation, properties, and reactivity of $Os_3(CO)_{11}\{P(CH_2CH_2(CF_2)_5CF_3)_3\}$ and $Os_3(CO)_{10}\{P(CH_2CH_2(CF_2)_5CF_3)_3\}_2$. Crystal structure of $Os_3(CO)_9(PPh_3)_2\{P(CH_2CH_2(CF_2)_5CF_3)_3\}$. Ring opening metathesis polymerization of norbornene by. *Journal of Organometallic Chemistry,* 695(14): 1776-1786.
5. Otero, Y., Peña, D., De Sanctis, Y., Arce, A., Ocando-Mavarez, E., Machado, R. and Gonzalez, T. (2014). Reactivity of triosmium clusters with 3,4-dimethyl-1-phenylphosphole and cyanoethyldi-tert-butylphosphine ligands: X-ray crystal structures of $[Os_3(CO)_9(\mu\text{-}OH)(\mu\text{-}H)(\eta^1\text{-}PhPC_4H_2Me_2)]$ and $[Os_3(CO)_{11}(\eta^1\text{-}{}^tBu_2PC_2H_4CN)]$. *Transition Metal Chemistry,* 39(2): 239-246.
6. Elard, M., Denis, J., Ferreira, M., Bricout, H., Landy, D., Tilloy, S. and Monflier, E. (2015). Rhodium catalyzed hydroformylation assisted by cyclodextrins in biphasic medium: Can sulfonated naphthylphosphanes lead to active, selective and recyclable catalytic species? *Catalysis Today,* 247: 47-54.
7. Ager, D. J., East, M. B., Eisenstadt, A. and Laneman, S. A. (1997). Convenient and direct preparation of tertiary phosphines via nickel-catalysed cross-coupling. *Chemical Communications,* 1997(24): 2359-2360.
8. Bruce, M. I., Humphrey, P. A., Schmutzler, R., Skelton, B. W. and White, A. H. (2004). Reactions of 1,8-bis(diphenylphosphino)naphthalene with $Os_3(CO)_{12}$: C-H and C-P bond cleavage reactions. *Journal of Organometallic Chemistry,* 689(14): 2415-2420.
9. Nicholls, J. N., Vargas, M. D., Deeming, A. J. and Kabir, S. E. (1989). Some useful derivatives of dodecacarbonyltriosmium. *Inorganic Synthesis,* 26: 289-293.
10. Bruker, SAINT, and SADABS. (2009). Bruker AXS Inc, Madison, Wisconsin, USA.

11. Sheldrick, G. M. (2008). A short history of SHELX. *Acta Crystallographica. Section A, Foundations of Crystallography,* 64(1): 112-122.
12. Spek, A. L. (2009). Structure validation in chemical crystallography. *Acta Crystallographica Section D: Biological Crystallography,* 65(2): 148-155.
13. MacRae, C. F., Sovago, I., Cottrell, S. J., Galek, P. T. A., McCabe, P., Pidcock, E., Platings, M., Shields, G. P., Stevens, J. S., Towler, M. and Wood, P, A. (2020). Mercury 4.0: From visualization to analysis, design and prediction. *Journal of Applied Crystallography*, 53(1): 226-235.
14. Frisch, M. J., Trucks, G. W., Schlegel, H. B., Scuseria, G. E., Robb, M. A., Cheeseman, J. R., Scalmani, G., Barone, V., Mennucci, B., Petersson, G. A., Nakatsuji, H., Caricato, M., Li, X., Hratchian, H. P., Izmaylov, A. F., Bloino, J., Zheng, G., Sonnenberg, J. L., Hada, M., Ehara, M., Toyota, K., Fukuda, R., Hasegawa, J., Ishida, M., Nakajima, T., Honda, Y., Kitao, O., Nakai, H., Vreven, T., Montgomery, J. A., Jr., Peralta, J. E., Ogliaro, F., Bearpark, M., Heyd, J. J., Brothers, E., Kudin, K. N., Staroverov, V. N., Kobayashi, R., Normand, J., Raghavachari, K., Rendell, A., Burant, J. C., Iyengar, S. S., Tomasi, J., Cossi, M., Rega, N., Millam, J. M., Klene, M., Knox, J. E., Cross, J. B., Bakken, V., Adamo, C., Jaramillo, J., Gomperts, R., Stratmann, R. E., Yazyev, O., Austin, A. J., Cammi, R., Pomelli, C., Ochterski, J. W., Martin, R. L., Morokuma, K., Zakrzewski, V. G., Voth, G. A., Salvador, P., Dannenberg, J. J., Dapprich, S., Daniels, A. D., Farkas, Ö., Foresman, J. B., Ortiz, J. V., Cioslowski, J. and Fox, D. J. (2016). *Gaussian 09*, Revision E.01, (Gaussian, Inc., Wallingford CT).
15. Nielsen, A. and Holder, A. J. (2009). GaussView5, Gaussian Inc, Pittsburgh. *Journal of Chemical Information and Modeling,* 53(9): 1689-1699.
16. Zhao, Y., and Truhlar, D. G. (2008). The M06 suite of density functionals for main group thermochemistry, thermochemical kinetics, noncovalent interactions, excited states, and transition elements: Two new functionals and systematic testing of four M06-class functionals and 12 other function. *Theoretical Chemistry Accounts,* 120(1-3): 215-241.
17. Jacquemin, D., Perpète, E. A., Ciofini, I., Adamo, C., Valero, R., Zhao, Y., and Truhlar, D. G. (2010). On the performances of the M06 family of density functionals for electronic excitation energies. *Journal of Chemical Theory and Computation,* 6(7): 2071-2085.
18. Wadt, W. R. and Hay, P. J. (1985). Ab initio effective core potentials for molecular calculations. Potentials for main group elements Na to Bi. *The Journal of Chemical Physics,* 82(1): 284-298.
19. Hay, P. J. and Wadt, W. R. (1985a). Ab initio effective core potentials for molecular calculations. Potentials for K to Au including the outermost core orbitale. *The Journal of Chemical Physics,* 82(1): 299-310.
20. Hay, P. J. and Wadt, W. R. (1985b). Ab initio effective core potentials for molecular calculations. Potentials for the transition metal atoms Sc to Hg. *The Journal of Chemical Physics,* 82(1): 270-283.
21. Bruce, M. I., Liddell, M. J., Shawkataly, O. B., Bytheway, I., Skelton, B. W., and White, A. H. (1989). Cluster Chemistry. LIX. Stereochemistry of group 15 ligand-substituted derivatives of $M_3(CO)_{12}$ (M = Ru, Os). D. Synthesis and characterisation of some tetra-substituted ruthenium complexes: X-ray structures of $Ru_3(CO)_8(L)_4$ (L = PMe_2Ph and $P(OR)_3$, R = Me, Et, and Ph). *Journal of Organometallic Chemistry,* 369(2): 217-244.
22. Armaković, S. J., Mary, Y. S., Mary, Y. S., Pelemiš, S. and Armaković, S. (2021). Optoelectronic properties of the newly designed 1,3,5-triazine derivatives with isatin, chalcone and acridone moieties. *Computational and Theoretical Chemistry,* 1197: 113160.
23. Ding, L. P., Zhang, F. H., Zhu, Y. S., Lu, C., Kuang, X. Y., Lv, J. and Shao, P. (2015). Understanding the structural transformation, stability of medium-sized neutral and charged silicon clusters. *Scientific Reports,* 5(1): 15951.
24. Aihara, J. I. (1995). Kinetic stability of fullerenes with four-membered rings. *Journal of the Chemical Society, Faraday Transactions,* 91(24): 4349-4353.

25. Kenouche, S., Sandoval-Yañez, C. and Martínez-Araya, J. I. (2022). The antioxidant capacity of myricetin. A molecular electrostatic potential analysis based on DFT calculations. *Chemical Physics Letters,* 801: 139708.
26. Spackman, P. R., Turner, M. J., McKinnon, J. J., Wolff, S. K., Grimwood, D. J., Jayatilaka, D. and Spackman, M. A. (2021). CrystalExplorer: A program for Hirshfeld surface analysis, visualization and quantitative analysis of molecular crystals. *Journal of Applied Crystallography,* 54(3): 1006-1011.
27. Spackman, M. A. and Jayatilaka, D. (2009). Hirshfeld surface analysis. *CrystEngComm,* 11(1): 19-32.
28. Kumar, A., Singh, P., Kumar, R., Yadav, P., Jaiswal, A. and Tewari, A. K. (2023). An experimental and theoretical study of the conformational stability of triazinone fleximers: Quantitative analysis for intermolecular interactions. *ChemistrySelect*, 8(5): e202203862.

Malaysian Journal of Analytical Sciences (MJAS)
Published by Malaysian Analytical Sciences Society

EXPLORATION OF NATURAL DEEP EUTECTIC SOLVENT AS THE ALTERNATIVE DISPERSIVE SOLVENT IN DLLME FOR THE EXTRACTION OF ANABOLIC STEROID DRUGS IN WATER

(Penerokaan Pelarut Eutektik Semulajadi Sebagai Alternatif Pelarut Serakan dalam DLLME untuk Pengekstrakan Ubat Steroid Anabolik dalam Air)

Azreen Asyikin Mhd Kamal[1*], Wan Nazihah Wan Ibrahim[1], Mohd Sufri Mastuli[1], Noorfatimah Yahaya[2], Sazlinda Kamaruzaman[3], Sheela Chandren[4], Nurul Auni Zainal Abidin[5], and Nursyamsyila Mat Hadzir[1]

[1]*Faculty of Applied Sciences, Universiti Teknologi MARA, 40450 Shah Alam, Selangor, Malaysia*
[2]*Integrative Medicine Cluster, Advanced Medical and Dental Institute, Universiti Sains Malaysia, 13200 Kepala Batas, Penang, Malaysia*
[3]*Department of Chemistry, Faculty of Science, Universiti Putra Malaysia, Serdang, Selangor, Malaysia*
[4]*Department of Chemistry, Faculty of Science, Universiti Teknologi Malaysia, 81310 UTM Johor Bahru, Johor, Malaysia*
[5]*Faculty of Applied Sciences, Universiti Teknologi MARA, Negeri Sembilan Branch,72000 Kuala Pilah, Negeri Sembilan, Malaysia*

*****Corresponding author: wannazihah@uitm.edu.my*

Received: 13 February 2023; Accepted: 18 April 2023; Published: 23 June 2023

Abstract

By combining hydrogen bond donors such as D-sorbitol, glucose, and sucrose with hydrogen bond acceptors like L-proline and lactic acid, a successful preparation of six new types of eco-friendly solvent known as natural deep eutectic solvents (NADES) was achieved. Their capability as dispersive solvent substituting hazardous and non-biodegradability organic solvents was explored in vortex-assisted dispersive liquid-liquid microextraction (VADLLME) method for determination of anabolic steroid drugs in aqueous samples. Optimization combination of hydrogen bond donor-hydrogen bond acceptor and their molar ratio were investigated, and the result showed high viscosity of lactic acid: sorbitol at a molar ratio of 2:1, whereby recorded the highest extraction efficiency towards the determination of nandrolone and testosterone. This optimum NADES combination was then performed in three significant VADLLME procedures, including the volume of NADES as the dispersive solvent, type, and volume of extraction solvent. The VADLLME optimal conditions are as follows: NADES dispersive solvent volume of 500 µL, chloroform as an extraction solvent and extraction solvent volume at 200 µL. Under the optimum conditions, good linearity was achieved (0.5 - 10 mg/L) with the coefficient of determination (R^2) of 0.9990 and 0.9996 for the nandrolone and testosterone, respectively. The LOD values were recorded in the range of 0.0020 - 0.0117 mg/L, while LOQ values were recorded in the range of 0.0067 - 0.0392 mg/L, respectively. The developed NADES-VADLLME method was applied for the determination of nandrolone and testosterone in tap water samples, with relative recovery values ranging from 88.63 - 97.23%. Based on the results obtained, the developed method demonstrated excellent sensitivity for the extraction of nandrolone and testosterone in water samples. The prepared NADES showed great potential as an alternative green dispersive solvent for the extraction of anabolic steroids active contaminants in the aquatic system.

Keywords: natural deep eutectic solvents, dispersive liquid-liquid microextraction, anabolic steroid drugs, dispersive solvent, green analytical chemistry

Abstrak

Dengan menggabungkan penderma ikatan hidrogen seperti D-sorbitol, glukosa, dan sukrosa dengan penerima ikatan hidrogen seperti L-prolin dan asid laktik, penyediaan enam jenis pelarut mesra alam baharu dikenali sebagai pelarut eutektik dalam semulajadi (NADES) telah berjaya disediakan. Keupayaan mereka sebagai pelarut serakan menggantikan pelarut organik berbahaya dan tidak boleh terbiodegradasi telah diterokai dalam kaedah pengekstrakan mikro cecair-cecair serakan dibantu vorteks (VADLLME) untuk penentuan ubat steroid anabolik di dalam sampel akueus. Pengoptimuman gabungan penderma ikatan hidrogen dan nisbah molarnya telah disiasat dan hasilnya menunjukkan kelikatan asid latik:sorbitol yang tinggi pada nisbah molar 2:1 menunjukkan kecekapan pengkestrakan tertinggi terhadap penentuan nandrolon dan testosteron. Gabungan optimum NADES ini kemudiannya dilakukan dalam tiga prosedur utama VADLLME termasuk isipadu NADES sebagai pelarut serakan, jenis dan isipadu pelarut pengekstrakan. Keadaan optimum VADLLME seperti berikut: isipadu pelarut dispersif NADES 500 µL, kloroform sebagai pelarut pengekstrakan dan isipadu pelarut pengekstrakan pada 200 µL. Pada keadaan optimum, kelinearan yang baik telah dicapai (0.5 - 10 mg/L) dengan pekali penentuan (R^2) masing-masing 0.9990 dan 0.9996 untuk nandrolon dan testosteron. Nilai LOD direkodkan dalam julat 0.0020 - 0.0117 mg/L manakala nilai LOQ masing-masing direkodkan dalam julat 0.0067 - 0.0392 mg/L. Kaedah NADES-VADLLME yang dibangunkan telah digunakan untuk penentuan nandrolon dan testosteron di dalam sampel air paip, dengan nilai pemulihan antara 88.63 - 97.23%. Berdasarkan keputusan yang diperoleh, kaedah yang dibangunkan menunjukkan sensitiviti yang sangat baik untuk pengestrakan nandrolon dan testosteron dalam sampel air. NADES yang disediakan menunjukkan potensi besar sebagai pelarut dispersif hijau alternatif untuk pengestrakan bahan cemar aktif steroid anabolik dalam sistem akuatik.

Kata kunci: pelarut eutektik dalam semulajadi, pengekstrakan mikro cecair-cecair serakan, ubat steroid anabolik, pelarut serakan, kimia analitikal hijau

Introduction

The misuse of anabolic drugs has been a crisis way before the pandemic, especially during international sports events. This drug is controlled and typically used to treat problems of hormone in males and Autoimmune Deficiency Syndrome (AIDS) patients that causes muscle loss [1]. Anabolic steroids, including testosterone, nandrolone, methandrostenolone, and others, were strictly used by professional bodybuilders for several decades. However, in recent times, recreational power athletes have regularly started using these drugs due to their impact on muscle growth and performance enhancement in sports [2-3]. The drug test was performed as a qualitative measurement in which it is a presumptive test that detects the drugs qualitatively, which includes opiates, methamphetamine, cocaine, amphetamines, marijuana, ecstasy, oxycodone, methadone, benzodiazepines, a tricyclic antidepressant, and PCP [4]. This urine test may provide a false-positive result that shows the presence of drugs even though a person has not used it, and this has raised some issues due to inaccurate results of the test, especially in forensic chemistry [5]. In order to identify the number of drugs present, the sample must be sent to the laboratory for further analysis and undergoes several steps prior to analysis. Nonetheless, drug testing has been improved in recent years, whereby the ability to identify long-term steroid metabolites, as well as more technologies, have enhanced that ability to detect metabolites at lower thresholds [6]. Nevertheless, these drugs are regularly being improvised to become accessible, which puts one step ahead of athletes to cheat. Each steroid tested in laboratories should store the baseline standards for reference in future testing and thus reducing the likelihood of a person to be tested positive only because the individual has higher levels of testosterone naturally compared to the general population. However, the laboratory test is time-consuming due to the multiple steps of analysis as well as the high labor and cost. Sample preparation takes up to 80% of the total analysis time and is critical in preparing the sample for analysis since it has a significant effect on analyte detection and quantification. These may include extraction, pre-concentration, clean-up, and derivatization steps before the analysis [7]. Therefore, the common conventional extraction methods such as liquid-liquid extraction (LLE) have been evolving into green extraction liquid-liquid microextraction (LLME) to determine drugs in

biological samples by miniaturizing the volume of the solvent and reducing the laborious steps.

Deep eutectic solvents (DESs) are a new class of green and inexpensive solvents. NADES has a variety of physiochemical properties, which gain its recognition as an alternative to ionic liquids and conventional organic solvents with biodegradability, non-flammability, and the potential as customizable for particular purposes [8]. Deep eutectic solvents (DES) consist of two non-toxic components that are mixed and form a new composition of solvent with a low melting point, low vapor pressure, low or negligible toxicity and biodegradable. The incredibly low melting point characteristic of this solvent is due to the formation of intramolecular hydrogen bonds within their molecular structure [9]. The hydrogen bonding between NADES effect varies in chemical properties such as polarity, viscosity, and hydrophilicity or hydrophobicity. In recent studies, DES has been applied as an extractant to substitute hazardous, costly, and non-environmentally friendly organic solvents in the extraction of organic pollutants [10]. For instance, Santana-Mayor et *al*. have successfully utilized DES as an extractant of phthalates and adipate from environmental water samples, with recoveries ranging from 70% to 127% [11]. Apart from that, Khezeli et al. employed DES as an extraction solvent of phenolic acids based on an ultrasonicated-assisted liquid-liquid microextraction method with high recoveries ranging from 94.7% to 104.6% in various vegetable oils samples [12]. Another type of deep eutectic solvent that is made up of primary metabolites components in living cells such as urea, amino acids, sugars, choline, and organic acids is called natural deep eutectic solvent (NADES) [13]. NADES is an alternative to DES due to continued safety concerns regarding DES. As a result, researchers have turned to natural sources and ingredients. A biodegradability in wastewater using microorganisms with closed bottle test, phytotoxicity test on wheat, and vitro toxicity test using fish and human cell lines were evaluated on choline chloride-based with glycerol, oxalic acid, and glucose and found that low toxicity in all tests, making them a great potential of green solvents in the applications of cosmetics, pharmaceutical, and food industry [14].

In this research, the utilization of NADES as a dispersive solvent is studied to substitute the toxic organic solvent in the DLLME method assisted by vortex agitation, abiding by the green chemistry principles. A dispersive solvent must be soluble in both organic solvent and aqueous phase [15]. NADES act as a disperser to assist the interaction of analytes in sample and extractant as well as favor the separation of two phases of sample solution and extraction solvent by allowing the formation of the cloudy solution containing tiny droplets, which speeds up the mass transfer process due to large contact surface area. The most common disperser solvents applied in DLLME are methanol, acetonitrile, and acetone [16]. Therefore, this study will focus on the vortex-assisted dispersive liquid-liquid microextraction (VADLLME) technique with the aid of DES as a dispersive solvent. The goal of this study was to develop a simple, rapid, inexpensive, and efficient sample preparation strategy for the measurement of testosterone and nandrolone in water samples prior to HPLC-DAD analysis. The technique is much simpler and eliminates the need for converting derivatization into a volatile phase during sample preparation. Additionally, it has the capability to simultaneously analyze multiple target analytes within a single run [17, 18]. Besides, this technique is trustworthy, particularly in clinical application fields such as toxicological diagnostic, therapeutic drug monitoring, and newborn screening. Various composition of NADES was studied from different hydrogen bond donor (D-sorbitol, glucose and sucrose) and hydrogen bond acceptor (proline and lactic acid), and molar ratio optimization was evaluated to obtain selective extraction on targeted analytes. The optimum NADES combination was then performed in three significant VADLLME procedures, including the volume of NADES as the dispersive solvent, type, and volume of extraction solvent.

Materials and Methods

Materials

Testosterone ($C_{19}H_{28}O_2$, ≥98%), nandrolone ($C_{18}H_{26}O_2$, ≥98%), lactic acid ($C_3H_6O_3$, 85%) solution ACS reagent, L-proline ($C_5H_9NO_2$, 99.5%) reagent standard, glucose ($C_6H_{12}O_6$, 99.5%) reagent standard, sucrose ($C_{12}H_{22}O_{12}$, 99.5%) reagent standard, D-sorbitol ($C_6H_{14}O_6$, 98%) reagent standard. Chloroform ($CHCl_3$, 98%), ethanol

(C_2H_6, 99.9%), acetonitrile (C_2H_3N, 99.9%) HPLC grade, 1-dodecanol ($C_{12}H_{26}O$, 98%), ethyl acetate ($C_4H_8O_2$, 98%), and dichloromethane (CH_2Cl_2, ≥ 99.8%) were all purchased from Sigma Aldrich.

HPLC instrumentation

The HPLC separations were carried out on a Dionex Bonded Silica C_{18} column (4.6 x 150 mm, 5 µm) (Acclaim™ Polar Advantage II) equipped with the ultraviolet detector and a 20 µL sample loop. The chromatographic condition was optimized by varying the mobile phase composition with acetonitrile-water, and the flow rate was set at 1.0 mL min^{-1} as well as the detection wavelength at 242 - 254 nm for all the analytes and recorded using Chromeleon software [19].

FTIR analysis

Attenuated Total Reflectance (ATR) Fourier Transform Infrared (FTIR) Spectroscopy (PerkinElmer, USA) was applied in this study to determine the functional groups and possible interactions between the NADES. The type of crystal used as zinc selenide. All the samples were scanned in the range of 650 to 4000 cm^{-1} for 16 times.

Preparation and optimization of NADES

NADES was prepared by varying a few parameters, such as the type of NADES and the molar ratio of NADES. Firstly, the optimization of different groups of hydrogen bond acceptor (HBA) (organic acid – lactic acid and amino acids – L-proline) with sugars (monosaccharide – glucose, disaccharide – sucrose, and alcohol sugar – D-sorbitol) as hydrogen bond donor (HBD) by mixing and heating the components at 80°C in sonicator until a homogenous solution is formed [20]. These selected NADES were proved to act as good dispersers in DLLME due to their properties of being highly soluble and denser than water which led the targeted analyte easily diffuse in extractant solvent and increased their recovery from environmental water samples [21]. The combinations of NADES studied were as follows: Proline: Sorbitol (Pro: Sor), Proline: Glucose (Pro: Glu), Proline: Lactic Acid (Pro: LA), Lactic Acid: Glucose (LA: Glu), Lactic Acid: Sucrose (LA: Suc), and Lactic Acid: Sorbitol (LA: Sor) followed by identifying the optimum HBA: HBD mixture as disperser solvent by using the different molar ratio as follow: HBA: HBD, 1:1, 1:2, 1:3, 2:1, 3:1. Figure 1 presenting the molecular structure of HBA components together with HBD components.

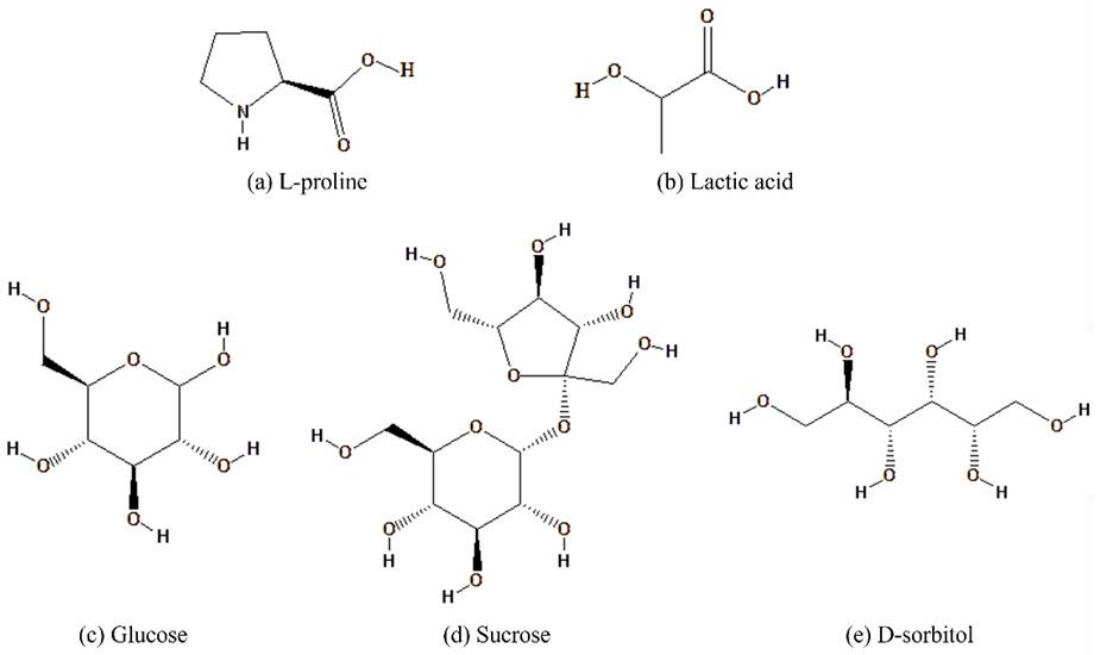


Figure 1. Molecular structure of HBA components: (a)-(b) and HBD components: (c)-(e)

Vortex-assisted dispersive liquid-liquid microextraction (VADLLME) procedure

The procedure began by adding extraction (chloroform) and dispersive (NADES) solvent into 5 mL of distilled water spiked with 1 mg/L of target analytes. The mixture was vortexed for 15 s until the formation of a cloudy solution and centrifuged for 10 min at 4000 rpm to form the two aqueous layers of phase. The bottom layer (organic phase containing analytes) was taken out and blown with nitrogen gas until dried. The dried organic phase was reconstituted in 50 µL of methanol and 50 µL of ultrapure water since chloroform cannot be directly injected into the instrument [19]. Then, the solution was injected into the HPLC system. Figure 1 shows the schematic diagram of VADLLME.

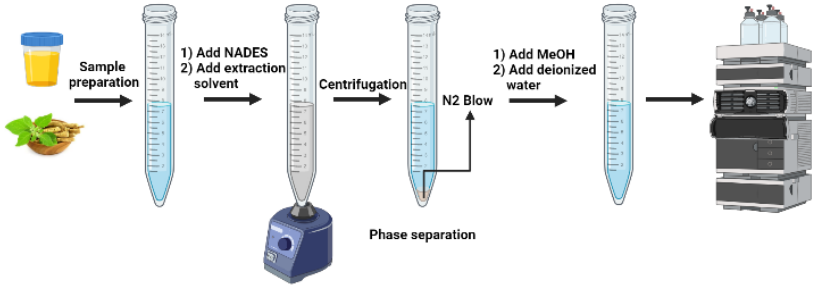


Figure 2. VADLLME process

Results and Discussion

FTIR analysis

FTIR analysis is commonly used to characterize a sample by determining the functional groups of the bonds and atoms within the molecules [22]. Thus, the hydrogen bonding formed in developed NADES was studied, including their functional groups. The wavenumbers for all synthesized NADES are recorded in Table 1. From the table, all the synthesized NADES showed a broad band at 3200 - 3600 cm^{-1}, indicating the formation of hydrogen bonds between the two components of HBA and HBD, as portrayed in Figure 3 (i). Apart from that, only Pro: Sor, Pro: Glu, and Pro: LA provided N-H bending at the range of 1609.3 - 1612.0 $cm^{-1,}$ which came from the functional group of L-proline and all synthesized NADES portrayed C-H stretching at the range of 2929.6 - 2992.1 cm^{-1}. The functional groups of all NADES except Pro: Sor and Pro: Glu displayed C=O of the carboxyl group between 1712.8 - 1723.7 cm^{-1}. Other medium-intense bands were observed at 1027.7 - 1222.9 cm^{-1} in which, indicating the C-O stretching of alcohol in their structure, as shown in Table 1. Besides, the C=O bond at 1719.8 cm^{-1} of lactic acid was shifted to the higher wavelength at 1721.7 cm^{-1} LA: Sor (1:1), as displayed in Figure 3 (ii), implying the formation of a hydrogen bond [23]. These prove that all the NADES were prepared successfully.

Table 1. Wavenumbers of IR for synthesized NADES

Type of NADES and Molar Ratio	Wavenumber (cm^{-1})				
	O-H Stretching	C-H Stretching	C=O Stretching	N-H Bending	C-O Stretching
Pro: Sor (1:1)	3288.2	2943.6	-	1612.0	1039.5
Pro: Glu (1:1)	3255.8	2929.6	-	1611.9	1027.7
Pro: LA (1:1)	3366.3	2992.1	1712.8	1609.3	1128.0
LA: Glu (1:1)	3335.9	2930.5	1721.2	-	1029.6
LA: Suc (1:1)	3320.5	2933.9	1723.7	-	1032.7
LA: Sor (1:1)	3336.2	2940.7	1721.7	-	1222.9
LA: Sor (2:1)	3352.2	2940.6	1721.5	-	1221.3

Figure 3 (ii) shows the correlation between lactic acid, sorbitol and LA: Sor mixture at molar ratios (1:1) and (2:1). In comparison between the molar ratio of LA: Sor (1:1 to 2:1), a few bands that significantly differed in intensity from each other was observed on Figure 3 (ii). In spectra for LA: Sor at molar ratio 1:1, the absorption band of OH at 3336.2 cm^{-1} was shifted to a higher wavenumber at 3352.2 cm^{-1} (molar ratio 2:1), proving the increasing number of hydrogen bonds formed in the NADES when the lactic acid molecule was increased as recorded in Table 1 [24-25]. Apart from that, the intensity at 1721.5 cm^{-1} and 1221.3 cm^{-1} of LA: Sor (2:1) were greater due to the greater number of the carboxyl group and C-O band, correspondingly because of the increasing number of the molecule of lactic acid [26]. Other than that, both spectra for LA: Sor molar ratio show identical absorption bands as parent lactic acid and sorbitol.

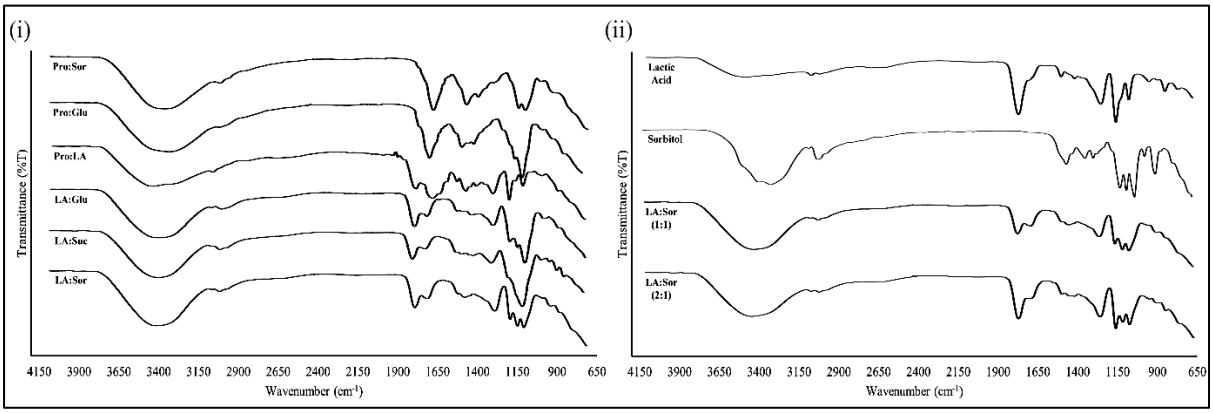


Figure 3. FTIR spectra of (i) synthesized NADES and (ii) lactic acid, sorbitol and optimized NADES (LA: Sor) at two different molar ratios (1:1 and 2:1)

Effect type of NADES (Different mixture of HBA: HBD) and it is the molar ratio

Disperser in DLLME is responsible for assisting the interaction of analyte towards extraction solvent. A tiny droplet of disperser properties contributes to the large surface area that enhances the mass transfer between two phases [27]. In order to determine the most appropriate NADES as the dispersive solvent, proline and lactic acid as HBA were prepared with various types of sugars (glucose, sucrose, and D-sorbitol) as HBD at the molar ratio of (1:1). The analytical results in Figure 4(i) showed the combination of NADES increasing as follows: (Pro: Sor < Pro: Glu < Pro: LA < LA: Glu < LA: Suc < LA: Sor). This indicates that the combination of organic acids with sugar alcohol as NADES prone to enhance the extraction efficiency of testosterone and nandrolone. Compared to all sugar in this study, sorbitol is a sugar alcohol which has a hydroxyl group with a straight chain structure compared to glucose and sucrose, which has a cyclic structure. This improves the solubility and viscosity of the sorbitol, which enhances the efficiency of lactic acid: sorbitol is a dispersive solvent [9, 28]. Therefore, LA: Sor NADES was selected for subsequent optimization of the molar ratio of NADES.

Herein, the most optimal molar ratio of HBA to HBD was determined to allow the appropriate number of hydrogen bonding formed in order to obtain higher extraction efficiency. It is explained that the more the hydrogen bonding, the more viscous the NADES resulting in a low capability to disperse in the sample solution [28]. Nonetheless, less hydrogen bonding formed means less viscous, and it could not provide the maximum efficiency as a disperser. Therefore, pertinent viscosity from the hydrogen bonding should be optimized from the molar ratio of the HBA and HBD. In this study, NADES with different molar ratios (1:1, 1:2, 2:1, 1:3, and 3:1) of lactic acid (HBA): sorbitol (HBD) were prepared accordingly, and their capability affecting the extraction of steroid drugs were determined. As demonstrated in Figure 4 (ii), the extraction efficiency has improved with an increasing number of moles up to two moles of lactic acid. This is explained by how the

structure of lactic acid consists of two HBA groups and by occupying those groups with one mole of sorbitol that might be existed as a stable compound [29]. When the molar ratio is 1:3 (LA: Sor) and 3:1, the analytical response declined slightly subsequently due to the high viscosity of sorbitol and lactic acid, respectively [30]. Hence, the desired molar ratio of lactic acid to sorbitol was chosen to be 2:1.

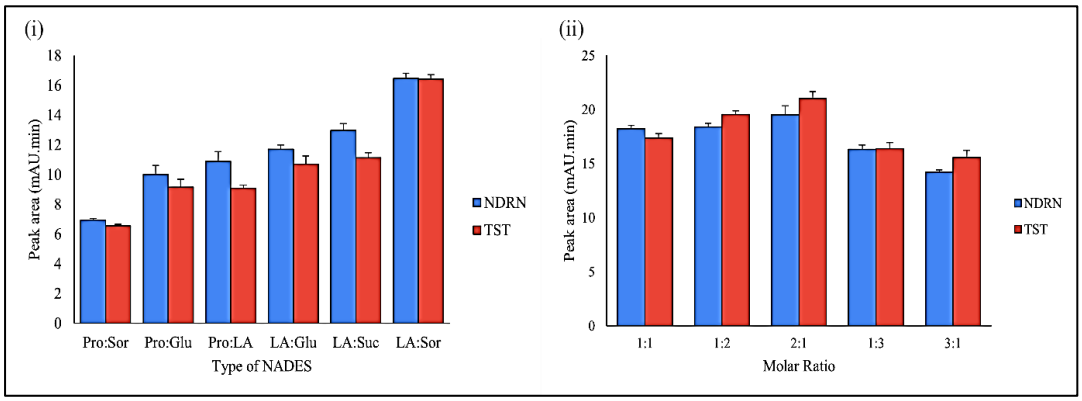


Figure 4. (i) Optimization of NADES combination and the (ii) molar ratio of optimized NADES (LA: Sor)

Effect volume of NADES

The volume of the disperser solvent causes changes in the sedimented phase volume (extraction solvent) and thus affects the extraction efficiency. Therefore, it is crucial to vary the disperser solvent volume and the extraction solvent volume simultaneously to achieve a constant volume of the sedimented phase containing analytes [16]. In the meantime, the ratio between the extraction solvent volume and the disperser solvent volume is also important, and it should be adjusted accordingly to form a cloudy solution. Hence, the impact of the volume of dispersion solvent on the extraction efficiency was investigated in the range of 200 - 600 µL. The volume of NADES that is lower than 200 µL was not evaluated as the volume of NADES must be the same or larger than the extractant to assist the partition coefficient of the analytes onto the extractant. During this optimization, one factor at a time approach was applied in the study, and thus, the extraction solvent was fixed at 200 µL. As depicted in Figure 5, the peak areas were gradually increased until 500 µL and declined slightly afterwards due to the dissolution of target analytes in the aqueous sample [31]. Therefore, the volume of NADES at 500 µL was optimized for further optimization.

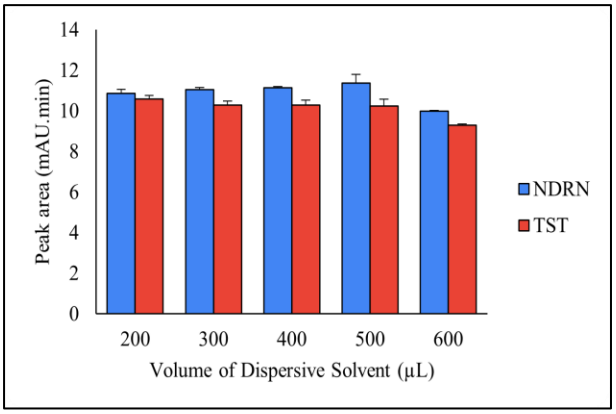


Figure 5. Optimization volume of dispersive solvent

Effect type and volume of extraction solvent

Choosing an appropriate organic solvent is significant to establish a successful microextraction method because its physicochemical properties should be suitable with the analytes for the extraction to occur. Various factors should be taken into consideration when selecting the appropriate extractant. For instance, the extraction solvent should be insoluble in water while having decent solubility of the target analytes, having a higher or lower density than the aqueous solution with high affinity for the analyte of interest and excellent chromatographic resolution. Furthermore, the extractant also must be soluble in the NADES prepared. For the extraction of steroid drugs, the selected solvent was investigated based on a previous study by [19, 32], including 1-dodecanol, ethyl acetate, hexane, dichloromethane and chloroform was experimented with as the potential extractant. However, only dichloromethane and chloroform formed a clear separation phase with an aqueous solution, while the other organic solvents did not form a clear separation phase at all or a very ambiguous phase separation formed. Based on the results tabulated in Figure 6 (i), chloroform provided the highest peak area for all the studied steroid drugs because chloroform is more non-polar and has high density than dichloromethane. This non-polar nature of chloroform significantly facilitates the isolation of non-polar anabolic steroid drugs resulting in good analytical response [29]. Thus, chloroform which provides high extraction capability for steroids, was selected as the extraction solvent for further optimization.

The volume of extraction solvent is key in extraction techniques. The amount of extraction solvent is required to be as minimal as possible for the purpose of environmental protection and to obtain an excellent analytical signal. Nonetheless, the amount should be large enough to ensure a sufficient amount of organic phase prior to chromatographic analysis and maximize the isolation of target compounds in the extractant [33]. Therefore, the impact of the volume of extractant on the extraction efficiency was studied in the range of 100 - 500 µL. The volume of chloroform that is lower than 100 µL was not evaluated as the amount of the extraction solvent left after extraction is insufficient, hindering the collection process. As outlined in Figure 6 (ii), 200 µL was observed to have a higher peak area, and there was an achievement in the equilibrium state of the extraction. At higher volume, the peaks of the analyte started to split and consequently, 200 µL of chloroform was employed in this study despite the volume of the sedimented phase [34].

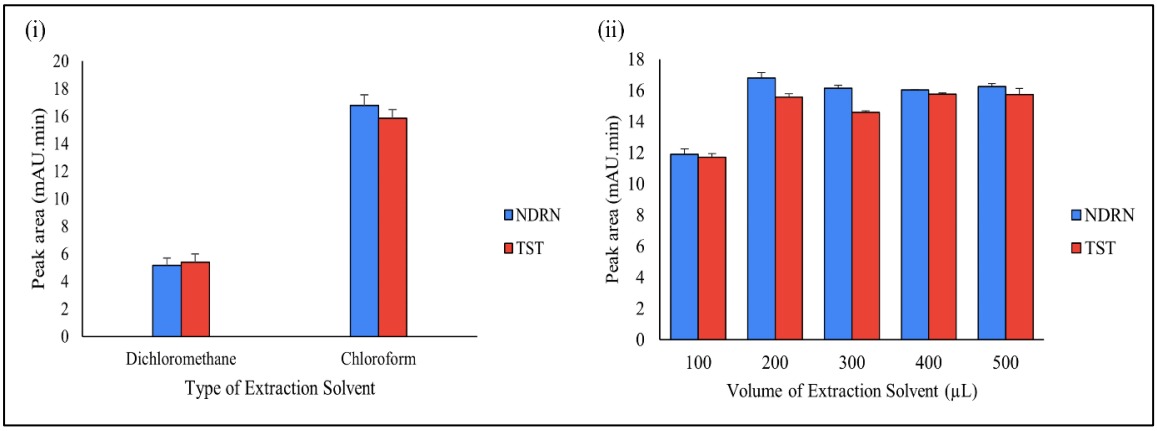


Figure 6. (i) Optimization type and (ii) volume of extraction solvent

Method validation

The capability of NADES (LA: Sor) as a disperser solvent was studied in a real sample solution to investigate the matrix effect on the extraction of anabolic steroids. Tap water samples were sonicated and filtered before being spiked with standard analyte concentrations ranging from 0.5 - 10 mg/L to construct a calibration curve. The analytical characteristics of the target steroid under optimized parameters are presented in Table 2. Both nandrolone and testosterone provide

dynamic linearity with an outstanding coefficient (R^2), 0.9996 and 0.9990, respectively. The value of LOD and LOQ was determined by using blank determination with the formula LOD = 3 *s/m,* while LOQ = 10 *s/m* is the standard deviation of blank signals, while *m* is the slope of the calibration curve. The values of LODs and LOQs showed to be in the range of 0.0020 - 0.0117 mg/L and 0.0067 - 0.0392 mg/L, respectively. The relative recoveries (RR) of both analytes have been found at 97% for nandrolone and 89% for testosterone at a spiking level of 1 mg/L with relative standard deviation (RSD), 0.79% and 0.42%, respectively. The precision of the method was determined in terms of intra-day and inter-day by spiking two analytes concentration (1 and 3 mg/L) into sample solution as listed in Table 3. Three replicates were employed to measure the intra-day on the same day and inter-day throughout 3 consecutive days. As shown in Table 3, the relative recovery of inter-precision for testosterone is considerably low, which can be explained by the degradation of the stock solution due to the nature of testosterone that is affected by light while conducting the experiment [35]. It is advised to keep the standard and stock solution short and out of light. The RSD values representing the precision of intra-day and inter-day appeared to be in the range of 0.05 - 0.20% and 0.07 - 0.35%, respectively. Figure 7 illustrates HPLC-DAD chromatograms of (i) unspiked, (ii) spiked with 1 mg/L and (iii) 3 mg/L of anabolic drugs of real samples. All peaks in spiked water sample extracts were finely separated with good resolution in less than 6 mins. Thus, the overall results suggest that this method could be satisfactorily applied for anabolic drug analysis and monitoring.

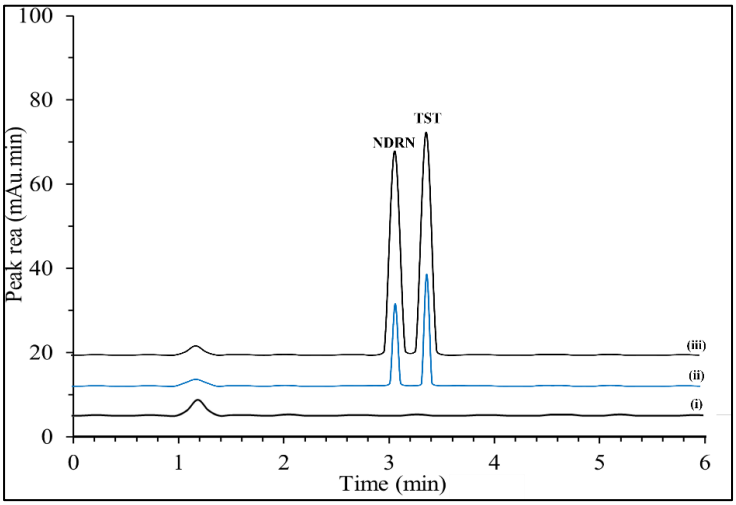


Figure 7. Chromatograms of HPLC-DAD of (i) unspiked, (ii) spiked with 1 mg/L and (iii) 3 mg/L of anabolic drugs in tap water under optimal conditions

Conclusion

The newly proposed NADES as a dispersive solvent in the DLLME technique provided remarkable linearity, acceptable LOD and LOQ, as well as outstanding precision values and satisfactory relative recoveries for the two target analytes under optimized conditions in which 97.23% for nandrolone and 88.63% for testosterone. The DLLME method in this research was employed successfully when extraction solvent was highly dispersed in the sample solution with the assistance of NADES as disperser by utilizing vigorous agitation of the vortex. Moreover, the newly prepared natural source of amino acid and organic acid-based NADES exhibited no toxicity to normal cell lines, affirming that the NADES used in this study is safe and green for the environment. Briefly, the proposed NADES in DLLME approach is environmentally favorable and practical for the extraction of drugs. NADES, in this study, is also expected to display great potential for the analysis of various organic contaminants, heavy metals, and other types of drugs.

Table 2. Analytical characteristics of the proposed procedure and recoveries of nandrolone and testosterone in tap water

Analyte	LOD (mg/L)	LOQ (mg/L)	Linear Range (mg/L)	R^2	RR (%)	RSD (%)
Nandrolone	0.0117	0.0392	0.5 - 10	0.9996	97.23	0.79
Testosterone	0.0020	0.0067	0.5 - 10	0.9990	88.63	0.42

Table 3. Precision (intra-day and inter-day) of the proposed method

Analyte	Concentration (mg/L)	Intra-Precision (n=3)		Inter-Precision (n=3)	
		RR (%)	RSD (%)	RR (%)	RSD (%)
Nandrolone	1	109.37	0.07	77.95	0.35
	3	94.12	0.05	93.59	0.07
Testosterone	1	116.41	0.20	61.09	0.25
	3	89.95	0.06	40.88	0.09

Acknowledgement

The authors would like to convey their sincere appreciation to the GIP Grant, Reference code: 600-RMC/GIP 5/3 (063/2022), for their financial support for this research. The authors also acknowledge the Faculty of Applied Science of Universiti Teknologi MARA for the facilities provided to carry out this project.

References

1. Kernas, H. (2019). Use steroids with caution. Retrieved from New Straits Times: https://www.nst.com.my/lifestyle/heal/2019/12/551192/use-steroids-caution. [Access online 15 Mac 2022].
2. Ghazali, A. (2014). Steroid. Retrieved from MyHealth Kementerian Kesihatan Malaysia: http://www.myhealth.gov.my/en/steroid/. [Access online 15 March 2022].
3. El Osta, R., Almont, T., Diligent, C., Hubert, N., Eschwège, P. and Hubert, J. (2016). Anabolic steroids abuse and male infertility. *Basic and Clinical Andrology*, 26(1): 2.
4. U.S. Food and Drug Administration (FDA) (2018). Drugs of abuse home use test. Retrieved from https://www.fda.gov/medical-devices/drugs-abuse-tests/drugs-abuse-home-use-test. [Access online 16 March 2022].
5. Sissons, B. (2018). What to know about urine drug screening. Retrieved from Medical News Today: https://www.medicalnewstoday.com/articles/323378. [Access online 20 March 2022].
6. National Institute on Drug Abuse. (2018). Steroids and other appearance and performance enhancing drugs (APEDs). National Institute on Drug Abuse (NIDA): pp. 1-35.
7. Buszewski, B. and Szultka, M. (2012). Past, present, and future of solid phase extraction: A review. *Critical Reviews in Analytical Chemistry*, 42(3): 198-213.
8. Miličević, N., Panić, M., Valinger, D., Cvjetko Bubalo, M., Benković, M., Jurina, T., Gajdoš Kljusurić, J., Radojčić Redovniković, I. and Jurinjak Tušek, A. (2020). Development of continuously operated aqueous two-phase microextraction process using natural deep eutectic solvents. *Separation and Purification Technology*, 244: 116746.
9. Cunha, S. C. and Fernandes, J. O. (2018). Extraction techniques with deep eutectic solvents. In *TrAC Trends in Analytical Chemistry*, (105): 225-239.

10. Craveiro, R., Aroso, I., Flammia, V., Carvalho, T., Viciosa, M. T., Dionísio, M., Barreiros, S., Reis, R. L., Duarte, A. R. C. and Paiva, A. (2016). Properties and thermal behavior of natural deep eutectic solvents. *Journal of Molecular Liquids*, 215: 534-540.
11. Santana-Mayor, Á., Socas-Rodríguez, B., Rodríguez-Ramos, R., Herrera-Herrera, A. V. and Rodríguez-Delgado, M. Á. (2021). Quality assessment of environmental water by a simple and fast non-ionic hydrophobic natural deep eutectic solvent-based extraction procedure combined with liquid chromatography tandem mass spectrometry for the determination of plastic migrants. *Analytical and Bioanalytical Chemistry*, 413(7): 1967-1981.
12. Khezeli, T., Daneshfar, A. and Sahraei, R. (2016). A green ultrasonic-assisted liquid-liquid microextraction based on deep eutectic solvent for the HPLC-UV determination of ferulic, caffeic and cinnamic acid from olive, almond, sesame and cinnamon oil. *Talanta*, 150: 577-585.
13. Liu, W., Zong, B., Wang, X., Cai, J. and Yu, J. (2019). A highly efficient vortex-assisted liquid-liquid microextraction based on natural deep eutectic solvent for the determination of Sudan I in food samples. *RSC Advances*, 9(30): 17432-17439.
14. Vanda, H., Dai, Y., Wilson, E. G., Verpoorte, R. and Choi, Y. H. (2018). Green solvents from ionic liquids and deep eutectic solvents to natural deep eutectic solvents. *Comptes Rendus Chimie*, 21(6): 628-638.
15. Leong, M. I., Fuh, M. R. and Huang, S. Da. (2014). Beyond dispersive liquid-liquid microextraction. *Journal of Chromatography A*, 1335: 2-14.
16. Saraji, M. and Boroujeni, M. K. (2014). Recent developments in dispersive liquid-liquid microextraction microextraction techniques. *Analytical and Bioanalytical Chemistry*, 406: 2027-2066.
17. Taylor, A. E., Keevil, B. and Huhtaniemi, I. T. (2015). Mass spectrometry and immunoassay: How to measure steroid hormones today and tomorrow. *European Journal of Endocrinology*, 173(2): D1-D12.
18. Koal, T., Schmiederer, D., Pham-Tuan, H., Röhring, C. and Rauh, M. (2012). Standardized LC-MS/MS based steroid hormone profile-analysis. *Journal of Steroid Biochemistry and Molecular Biology*, 129(3-5): 129-138.
19. Dmitrieva, E., Temerdashev, A., Azaryan, A. and Gashimova, E. (2020). Quantification of steroid hormones in human urine by DLLME and UHPLC-HRMS detection. *Journal of Chromatography B*, 1159: 122390.
20. Elik, A., Demirbas, A. and Altunay, N. (2019). Developing a new and simple natural deep eutectic solvent based ultrasonic-assisted microextraction procedure for determination and preconcentration of As and Se from rice samples. *Analytical Methods*, 11(27): 3429-3438.
21. Carbonell-Rozas, L., Canales, R., Lara, F. J., García-Campaña, A. M. and Silva, M. F. (2021). A natural deep eutectic solvent as a novel dispersive solvent in dispersive liquid-liquid microextraction based on solidification of floating organic droplet for the determination of pesticide residues. *Analytical and Bioanalytical Chemistry*, 413(25): 6413-6424.
22. Shafie, M. H., Yusof, R. and Gan, C. Y. (2019). Synthesis of citric acid monohydrate-choline chloride based deep eutectic solvents (DES) and characterization of their physicochemical properties. *Journal of Molecular Liquids*, 288: 111081.
23. Ortega-Zamora, C., González-Sálamo, J., Hernández-Sánchez, C. and Hernández-Borges, J. (2020). Menthol-based deep eutectic solvent dispersive liquid–liquid microextraction: a simple and quick approach for the analysis of phthalic acid esters from water and beverage samples. *ACS Sustainable Chemistry & Engineering*, 8(23): 8783-8794.
24. Mogaddam, M. R. A., Nemati, M., Farajzadeh, M. A., Lotfipour, F., Nabil, A. A. A., Mohebbi, A. and Ghorbanpour, H. (2022). Application of natural deep eutectic solvents-based in-syringe dispersive liquid-liquid microextraction for the extraction of five acaricides in egg samples. *International Journal of Environmental Analytical Chemistry*, 102(16): 3806-3821.

25. Santana-Mayor, A., Herrera-Herrera, A. V., Rodriguez-Ramos, R., Socas-Rodriguez, B. and Rodriguez-Delgado, M. A. (2021). Development of a green alternative vortex-assisted dispersive liquid–liquid microextraction based on natural hydrophobic deep eutectic solvents for the analysis of phthalate esters in soft drinks. *ACS Sustainable Chemistry & Engineering*, 9(5): 2161-2170.
26. Liu, X., (2021). IR spectrum and characteristics absorption bands. Retrieved from Kwantlen Polytechnic University: https://kpu.pressbooks.pub/organicchemistry/chapter/6-3-ir-spectrum-and-characteristic-absorption-bands/. [Access online 08 February 2023].
27. Grau, J., Azorín, C., Benedé, J. L., Chisvert, A. and Salvador, A. (2022). Use of green alternative solvents in dispersive liquid-liquid microextraction: A review. *Journal of Separation Science*, 45(1): 210-222.
28. Santana, A. P. R., Mora-Vargas, J. A., Guimarães, T. G. S., Amaral, C. D. B., Oliveira, A. and Gonzalez, M. H. (2019). Sustainable synthesis of natural deep eutectic solvents (NADES) by different methods. *Journal of Molecular Liquids*, 293: 111452.
29. Elencovan, V., Yahaya, N., Raoov, M., Nadhirah, N. and Zain, M. (2022). Exploring a novel silicone surfactant-based deep eutectic solvent functionalized magnetic iron particles for the extraction of organophosphorus pesticides in vegetable samples. *Food Chemistry*, 396: 133670.
30. Matong, J., Mpupa, A. and Nomngongo, P. N. (2018). Ultrasound assisted-homogeneous liquid-liquid phase microextraction based on deep eutectic solvents and ethyl acetate for preconcentration of selected organochlorine pesticides in water samples. *Eurasian Journal of Analytical Chemistry*, 13(5): 59.
31. Barfi, B., Asghari, A., Rajabi, M., Goochani Moghadam, A., Mirkhani, N. and Ahmadi, F. (2015). Comparison of ultrasound-enhanced air-assisted liquid-liquid microextraction and low-density solvent-based dispersive liquid-liquid microextraction methods for determination of nonsteroidal anti-inflammatory drugs in human urine samples. *Journal of Pharmaceutical and Biomedical Analysis*, 111: 297-305.
32. Kintz, P., Gheddar, L. and Raul, J. S. (2021). Simultaneous testing for anabolic steroids in human hair specimens collected from various anatomic locations has several advantages when compared with the standard head hair analysis. *Drug Testing and Analysis*, 13(7): 1445-1451.
33. Elencovan, V., Joseph, J., Yahaya, N., Abdul Samad, N., Raoov, M., Lim, V. and Zain, N. N. M. (2022). Exploring a novel deep eutectic solvents combined with vortex assisted dispersive liquid–liquid microextraction and its toxicity for organophosphorus pesticides analysis from honey and fruit samples. *Food Chemistry*, 368: 130835.
34. Chang, C. C. and Huang, S. Da. (2010). Determination of the steroid hormone levels in water samples by dispersive liquid-liquid microextraction with solidification of a floating organic drop followed by high-performance liquid chromatography. *Analytica Chimica Acta*, 662(1): 39-43.
35. American Society of Health-System Pharmacists (2019). Testosterone injection. Retrieved from https://tinyurl.com/5ycvs3py. [Access online 27 March 2023].

Malaysian Journal of Analytical Sciences (MJAS)
Published by Malaysian Analytical Sciences Society

FLUOROQUINOLONE RESIDUES IN FOOD: OCCURRENCE AND ANALYTICAL METHODS - A MINI REVIEW FROM 2000 TO 2022

(Sisa Fluorokuinolon di dalam Makanan: Kemunculan dan Kaedah Analisis – Satu Ulasan Mini Tempoh 2000 hingga 2022)

Wen Yu Foo, Saw Hong Loh, Wan Mohd Afiq Wan Mohd Khalik, and Marinah Mohd Ariffin*

Faculty of Science and Marine Environment,
Universiti Malaysia Terengganu, 21030 Kuala Nerus, Terengganu, Malaysia

Corresponding author: erin@umt.edu.my

Received: 13 March 2023; Accepted: 10 May 2023; Published: 23 June 2023

Abstract

Fluoroquinolones are used to treat and prevent serious bacterial infections. They are widely applied in the husbandry and veterinary areas as well as in the human medication scope. There is an emerging concern about the residues of fluoroquinolones in the environment. Once in the environment, especially in the water bodies, they will be taken up and accumulated in our livestock, which subsequently enters our body through our food resources. Therefore, the residues of fluoroquinolones in animal-based food are required to be monitored and assessed. The development of existing methods is crucial to provide accurate data on the fluoroquinolone residues in different food samples. This review presents an overview of the proposed methods from 2000 to 2022 for the analysis of fluoroquinolones in food samples. The extraction techniques were mostly combined with liquid chromatography and fluorescent detection. These methods allow for low detection limits and high recovery values. The ideal detection limit is less than 10 μg L^{-1}. The main drawback of the screening test is low sensitivity and it may provide false positive results. A quantitative analytical method is important in giving the most accurate result from the determination of fluoroquinolones residues in different food matrices. One of the important factors to allow a low detection limit is the extraction method used. The solid phase extraction methods are the most widely used method for sample preparation. In addition, the physical and chemical properties, classification, toxicology, side effect of fluoroquinolones and occurrence of these residues in food samples were discussed in this paper.

Keywords: antibiotics, fluoroquinolones, food, extraction

Abstrak

Fluorokuinolon digunakan untuk merawat dan mencegah jangkitan bakteria yang serius. Ia digunakan secara meluas dalam bidang penternakan dan veterinar serta dalam skop perubatan manusia. Terdapat kebimbangan yang timbul tentang sisa fluorokuinolon di alam sekitar. Apabila berada di alam sekitar, terutamanya di dalam air, ia akan diambil dan terkumpul dalam ternakan kita, dan seterusnya memasuki badan kita melalui sumber makanan kita. Oleh itu, sisa fluorokuinolon dalam makanan berasaskan haiwan perlu dipantau dan dinilai. Pembangunan kaedah sedia ada adalah penting untuk menyediakan data yang tepat tentang sisa fluorokuinolon dalam sampel makanan yang berbeza. Kajian ini membentangkan gambaran keseluruhan kaedah yang dicadangkan terutamanya dari 2000 hingga 2022 untuk analisis fluorokuinolon dalam sampel makanan. Kaedah pengekstrakan yang paling

banyak bergabungan dengan kromatografi cecair dan pengesanan pendarfluor. Kaedah ini membenarkan had pengesanan rendah dan nilai pemulihan yang tinggi. Had pengesanan yang ideal adalah kurang daripada 10 μg L^{-1}. Kelemahan utama ujian saringan ialah kepekaan yang rendah dan ia mungkin memberikan keputusan positif palsu. Kaedah analisis kuantitatif adalah penting dalam memberikan hasil yang paling tepat daripada penentuan sisa fluorokuinolon dalam matriks makanan yang berbeza. Salah satu faktor penting untuk membenarkan had pengesanan yang rendah ialah kaedah pengekstrakan yang digunakan. Kaedah pengekstrakan fasa pepejal ialah kaedah yang paling banyak digunakan untuk penyediaan sampel. Di samping itu, sifat fizikal dan kimia, klasifikasi, toksikologi, kesan sampingan fluorokuinolon dan kejadian sisa ini dalam sampel makanan turut dibincangkan dalam kertas ini.

Kata kunci: antibiotik, fluorokuinolon, makanan, pengekstrakan

Introduction

Antibiotics have been used since old times. The first modern antibiotic, namely penicillin was discovered by Alexander Fleming in the 20th century. Penicillin has been widely applied in wartime mainly because no significant medicine is available to treat infections such as pneumonia, gonorrhoea or rheumatic fever [1]. The introduction of antibiotics has been recognised as one of the greatest inventions due to its effectiveness in treating various diseases in the form of microbial. Since penicillin was recognised in World War II, it has been manufactured in massive-scale production, making it a life-saving substance from the limited supply into a widely available medicine.

Antibiotics are antimicrobial substances that fight against bacteria. It is one of the most efficacious medicines that fight against bacteria and infection. However, virus-form diseases such as flu cannot be treated by antibiotics. Generally, the immune system in our bodies produces natural killer cells to function as bacterial killers. However, when the rapid propagation of bacteria occurs in our bodies, our immune system fails to cope with the infection. Therefore, antibiotics are needed to assist in curing infections. Antibiotics can be classified into several groups based on the type of action, sources to make antibiotics, the spectrum of activity, chemical structure and function of the antibiotics [2]. In the early stage, antibiotics are introduced from the natural plant extract while in the latter day, it has been produced chemically either in the form of fully synthetic or semi-synthetic. To date, the application of antibiotics has been widespread and extended to prevent and treat bacterial infection in the veterinary, aquaculture and domestic fields. In the United States, antibiotics are employed in livestock to speed up growth and increase the size of animals bred for food [3]. In aquaculture enterprises, antibiotics are frequently applied to those aquafarming organisms with impairing immune systems. Some household cleaning products are fortified with synthetic antibacterial, antiseptic and antimicrobial substances especially triclosan against bacteria on the household surface [4].

The issue of antibacterial resistance detected in humans has become the biggest concern nowadays with the widespread application and improper use of antibiotics. In consequence, the bacteria may mutate and emerge into the immortal stage, making resistant bacteria survive antibiotic treatment. This will then threaten our lives, causing antibiotics to be ineffective in treating diseases. Fluoroquinolones are one of the frequently applied antibacterial in food animals. Fluoroquinolones are used to treat enteric infections and respiratory diseases. This antibiotic possesses low toxicity and it can fight a broad spectrum of pathogenic bacteria towards farmed animals [5]. Therefore, the food animals sold may retain the trace residue of fluoroquinolones and the transmission from food to humans may be biomagnified.

Physical and chemical properties of fluoroquinolones

Fluoroquinolones are a group of broad-spectrum antimicrobial drugs from the class of quinolones with the attachment of the fluorine group in the ring. It is active against Gram-negative and Gram-positive bacteria [6]. As shown in Figure 1, the position of R_1 increases the potency of the molecules where the alkyl substituent is usually attached to it. R_2 and X improve the activities of both Gram-negative and Gram-positive. F refers to the fluorine atom that increases the Gram-

negative activity and the position of R_3 increases only the Gram-positive activity [7]. Different classes of fluoroquinolones have different substituent rings attached to them and thus affect the physical and chemical properties in terms of solubility in different parts of the membrane in the body. Fluoroquinolones are effective in the inhibition of bacterial chromosome replication and long-established in treating respiratory diseases and bacterial infections in food animals [8]. Fluoroquinolones are synthetic antibacterial agents which are not derived from living organisms [9]. Recently, there is a report on quinolone resistance due to bacteria mutation as a result of improper overuse of this antibiotic [10].

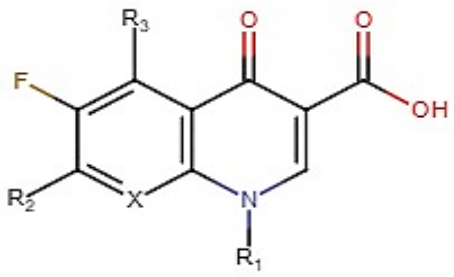


Figure 1. Molecular structure of fluoroquinolones. Ciprofloxacin denotes as X=C-H, R_1=cyclo propyl, R_2=piperazinyl, and R_3=H. Gatifloxacin denotes as X=C-OMe, R_1=cyclo propyl, R_2=piperazinyl, and R_3=H. Ofloxacin denote as X and R_1=benzoxazine, R_2=piperazinyl, and R_3=H

Generally, fluoroquinolones can be absorbed well in gastrointestinal and endocrine organs, as well as penetrate through the bones and cerebrospinal fluid. The partitioning coefficient (log K_{ow}) and bioconcentration factor (BCF) values of fluoroquinolone are considered low [11]. Fluoroquinolones are slightly water soluble over a pH range from 6 to 8 which is known as amphoteric character, acting as base and acid. They can be absorbed via oral administration [12] as well as injection. For instance, ciprofloxacin is a light-yellow crystalline substance with a melting point of 255-257°C and the water solubility is 86 mg L^{-1} at 25°C [13]. Flumequine is a white powder which is insoluble in water but soluble in organic solvents [14]. Thus, the flumequine is absorbed in the lipid membrane and it possesses strong stability. The melting point is 253-255°C.

Fluoroquinolone antibiotics

Fluoroquinolones are used to treat serious bacterial infections, especially infections in the skin, bone, joint, urinary tract and respiratory tract. It is also widely applied in husbandry and veterinary fields to prevent the action. Fluoroquinolone is a strong antibiotic where it can easily penetrate the body cells and destruct the DNA in the cell. However, it cannot treat serious contagious infections such as colds and flu [15].

Classification of fluoroquinolones

More and more fluoroquinolones are being invented and it is hard to prescribe antibiotics. The most common synthetic fluoroquinolone antimicrobial is ciprofloxacin which is the cheapest and most frequently employed in treating animals [16]. The position of fluorine atoms substituted in each molecule seems to enhance the phototoxicity and their origin modification [17]. This enhancement provides more effective microbial activities and broadens the spectrum of activities. However, this modification also increases bacteria resistance. Table 1 shows the classification of fluoroquinolones according to their antimicrobial spectrum.

Table 1. The classification of fluoroquinolones [18]

Classification	Examples of Agents	Antimicrobial Spectrum	Indication
First generation	Nalidixic acid, Cinoxacin	Gram-negative organisms except for Pseudomonas species.	Uncomplicated urinary tract infections.
Second generation	Norfloxacin, Lomefloxacin, Enoxacin, Ofloxacin, Ciprofloxacin	All gram-negative organisms but some gram-positive organisms.	Uncomplicated and complicated urinary tract infections, pyelonephritis, sexually transmitted diseases, prostatitis, and skin infection.
Third generation	Lexofloxacin, Sparfloxacin, Gatifloxacin, Moxifloxacin	Expanded spectrum in gram-positive coverage, atypical pathogens.	Acute exacerbations of chronic bronchitis, and pneumonia.
Fourth generation	Trovafloxacin	Broader coverage than the third generation.	Abdominal infections, nosocomial, pneumonia, pelvic infections.

Transmission route of fluoroquinolones into human

Fluoroquinolone's main administration is via oral but some fluoroquinolones are taken intravenously [19]. The fluoroquinolones are manufactured in tablet or capsule forms. The fluoroquinolones enhance their function by inhibiting the bacteria from building the cell wall and altering the ability to the reproduction of the bacteria. When fluoroquinolones are consumed, they penetrate the membrane and are stored in the gastrointestinal tract, which is then absorbed as nutrients. After a while, they circulate in the blood and reach the target bacteria [20].

Fluoroquinolones can be transferred through the maternal plasma into breast milk. The rate of transmission depends on the maternal factor, physiochemical properties and infant factor [21]. The composition of particular breast milk and the pH affect the number of antibiotics transferred. However, fluoroquinolones are most likely to concentrate in the plasma compared to breast milk because fluoroquinolones are weak acidic drugs [22]. Hence, the antibiotic has a lower chance to transmit to the infant. Indeed, fluoroquinolones are not recommended for breastfeeding mothers although ciprofloxacin is proven with no harm to both the breastfeeding mother and the infant [23-24].

Some of the transmission of fluoroquinolones is from food-producing animals such as livestock and poultry [25]. The by-products especially meat, dairy products and eggs may contain the residue of fluoroquinolones and thus food chain is also one of the transmission sources.

Transmission route of fluoroquinolones into animal

The fluoroquinolones used in livestock, poultry and veterinary are not only for the treatment of the illness of animals but also for illness prevention. This practice has been a part of the modern food-animal production industries. The utilization of the antibiotic as a therapy for preventing bacteria and promoting growth [26]. In general, antibiotics are added to feed for growth promotion [27]. The dosage applied for growth promo-

tion might be low, but it is a long-term application. Their accumulation of the antimicrobial is then causing drug resistance in the tissues of these animals. Fluoroquinolones are prescribed to treat gastrointestinal infections and microbiota modification in the intestine, as well as enhance the immune system [28]. The fluoroquinolones are given in form of oral, by injection, by drinking water, intra-mammary and mostly by feeding [25]. For example, enrofloxacin is injected into cattle for the treatment of bovine respiratory disease [29].

Effects of fluoroquinolones towards living organisms

Fluoroquinolone residues have brought a lot of negative effects on humans and animals. The maximum residue limits of some fluoroquinolones from liver, muscle and kidney tissues, such as enrofloxacin, and ciprofloxacin have been established as no more than 200, 100, and 300 μg kg^{-1}, respectively by European Union [30], as summarized in Table 2.

Table 2. Maximum residue limits of fluoroquinolones by the European Union [30]

Fluoroquinolone Active Substances	Marker Residue	Animal Species	MRL (μg/kg)	Target Tissues
Enrofloxacin	Sum of enrofloxacin and ciprofloxacin	Bovine, ovine, caprine	100	Muscle
			100	Fat
			300	Liver
			200	Kidney
			100	Milk
		Porcine, rabbit	100	Muscle
			100	Fat
			200	Liver
			300	Kidney
		Poultry	100	Muscle
			100	Skin and fat
			200	Liver
			300	Kidney
		All other food producing species	100	Muscle
			100	Fat
			200	Liver
			200	Kidney

Side effects on human

The most general side effects of fluoroquinolones are diarrhoea, vomiting, nausea and dyspepsia which belong to indigestion problems. One of the serious adverse side effects is the central nervous system (CNS) effect which will lead to headaches, dizziness, convulsion and confusion. Dairy products which consist of fluoroquinolones, especially the ciprofloxacin will cause accumulation in the cartilage of bones and arthropathy which then lead to joint's disease, as well as foetal impairment [31]. According to the United States Food and Drug Administration (USFDA) (2018), fluoroquinolones increase the risk of mental health including disturbances in attention, nervousness, disorientation, as well as memory impairment [32]. Some people get serious blood sugar disturbances such as hypoglycaemia, which is suffering from low blood sugar.

Side effects on animals

Fluoroquinolones are evenly applied in veterinary medicine, cattle management and aquaculture. The application of fluoroquinolones has resulted in diffuse retinal degeneration which then leads to blindness in animals [33]. However, it depends on the accumulation of drugs and the duration of the treatment. Some of the

side effects that occur in animals from the drug administration are similar to humans.

Antibiotics resistance of fluoroquinolones

The residues are risky to public health as the stimulation of bacterial resistance is getting worse and the bacteria may be mutated in the tissues [34]. Fluoroquinolones are broad-spectrum antibiotics which accelerate the spread and development of the multi-drug resistant strain. Overuse of antibiotics leads to the change and elimination of their effectiveness which then causes difficulty in curing the serious infection. For instance, medical advance treatments like organ transplantation, cancer chemotherapy and some major surgery need antibiotics for the prevention of infection [35]. The bacterial resistance may jeopardise these treatments. According to Institute for Medical Research (IMR), gram-negative bacilli such as E. coli have shown resistance to one of the fluoroquinolones, ciprofloxacin. The rise of fluoroquinolone resistance infections in Malaysia is mainly due to medical control practices and animal husbandry [36].

Restriction of fluoroquinolones in food products

To address the bacterial resistance issues, the Food and Drug Administration (FDA) has warned about the effect of overusing fluoroquinolones, that these antibiotics are only applied when there are no alternative treatment options [32]. Several restrictions have been applied to the use of fluoroquinolones by the FDA. Some of the classes of the fluoroquinolones such as Marbofloxacin which is generally applied in veterinary medicine and cattle management have been banned due to their high absorptivity and penetration into the tissue [33]. According to European Medicines Agency (EMA's) Pharmacovigilance Risk Assessment Committee (PRAC), fluoroquinolones are not recommended in treating mild infection and lower urinary infections [37]. According to the European Union (EU), fluoroquinolones as growth promoters have been banned in food processing animals because they are considered a non-essential antibiotic [36].

Poultry is the most important food industry in Malaysia as poultry including beef, chicken and pork are the main protein sources for Malaysian [38]. According to Lai (2020), 49.4 kg of poultry meat is consumed per person in 2020. The consumption of poultry has increased by 40% from 2006 to 2019 and it is estimated to exceed 50 kg in 2025 [39]. In poultry farming, fluoroquinolones are often used for therapeutic. The most common fluoroquinolone used in poultry production is enrofloxacin (ENRO). The application of other groups of fluoroquinolones such as flumequine (FLU), danofloxacin (DANO), difloxacin (DIFLO), oxolinic acid (OXO) and sarafloxacin (SARA) has been licensed in the European Union (EU) and these medicines are only allowed for veterinary medicinal treatment but not for growth promoter [40]. The use of ENRO for the treatment of bacterial infections in poultry has been banned in 2005 according to USFDA. This was due to the presence of Campylobacter resistance species in chickens cured with this antimicrobial. Fluoroquinolones no longer inhibit the growth of Campylobacter in poultry as the fluoroquinolones-resistance Campylobacters have been detected in poultry faeces [41]. This indicated that the antibiotics have accumulated in the animal body and contaminated the agricultural production indirectly as the excrement may be the organic fertilizers to the fruits and vegetables [42]. It caused antibiotic pollution in the soil and affected the nutrition intake of the crops. Apart from being released to the land, the antibiotics may be accumulated and they may either leach into groundwater or be transported to the surface waters [43]. Since poultry has been improved from a small food production unit to a large-scale supply chain over these years, the spread of antimicrobials is increasing dramatically. The use of antimicrobials in food-producing animals has to be controlled and restricted under Maximum Residue Limits (MRLs).

As mentioned earlier, the antibiotics that are not fully absorbed in the animals will be excreted in faeces and this will contaminate the soil system [44]. Soil manure which consists of animal faeces, compost and green manure is great in providing fertility to the soil. It contains the main nutrients required for vegetable growth. However, the repeated fertilisation in the agriculture farming system with the soil manure has led to the accumulation of antibiotics in the soil, and in turn,

to food such as vegetables and fruits [45]. There is lacking research on the accumulation of antibiotics in ripened plants, although the antibiotics uptakes are mainly via leaves and roots [46]. The presence of antibiotics has affected plant growth and the seed germination process indirectly. Although the detection of fluoroquinolones was only 0.2 mg kg^{-1} in soil manure, the biotransformation of antibiotics from the soil to the plants could occur, leading to the promotion of antibiotic resistance to humans, animals and the environment [47]. Although the residues of antibiotics in soil (8.4%) are more than in crops (5.6%), the accumulation can be increased with large-scale production of crops and the rise of crop consumption by humans [48].

Some of the antibiotic contamination in the environment is caused by antibiotic manufacture. According to Fick et al. the concentration of quinolones was found 14 mg L^{-1} in the wastewater effluent. It may be caused by the illegal dumping of antibiotic residues and this affected the surrounding environment including the groundwater and the soil [49]. Thus, the runoff of surface water or leaching of groundwater will affect the crop indirectly, affecting the consumers' health. Moreover, the transport of the residues in the waterway may influence the aquatic organisms [50].

Antibiotic residues can be detected in other food, especially honey and baby food. Honey is a natural by-product that is mainly used for nutritional and medicinal purposes. It contains hydrogen peroxide which was used to be an antibacterial treatment in old times. The unusual antibiotic residue found in honey was mainly caused by the environment and inappropriate beekeeping practices [51]. The sugar syrup solution which is mixed with the antibiotics is introduced into bee hives and consumed by bees [52]. This leads to antibiotic contamination in honey. Research revealed that the honey consisted of antibiotics residues namely oxytetracycline and chloramphenicol that exceeded regulatory values [53]. Although the European Community regulations did not set up the MRL for antibiotics in honey, the use of antibiotics in bee farming has been banned by some countries [54].

Some the fluoroquinolones such as ciprofloxacin, levofloxacin and moxifloxacin are used to treat infection of the urinary tract, pneumonia and mycobacterium tuberculosis in paediatrics. However, fluoroquinolones are banned for paediatrics in Korea because the study showed that fluoroquinolones have lost their function gradually in treating multidrug-resistant infections [55]. Some of the meat containing baby food such as beef and chicken might contain antibiotics residue too. There are lacking regulations and legislation concerning the tolerance value of fluoroquinolones in processed food [56]. Apart from meat and vegetables, the egg is an important protein source for children. When the animals are injected with veterinary drugs, the residues remain in various tissues in the body, carrying the residues to the eggs laid directly. Moreover, antibiotics are also used in farmed fish to treat diseases by treating the water or aquaculture. This results in the spread of the residues among humans and the environment [57].

Sample preparation for the extraction of fluoroquinolones in food

Several studies are reporting the detection of fluoroquinolones in animal-based food such as milk, honey, chicken, egg, beef and yoghurt. Therefore, it is important to determine the antibiotic residues in food to guarantee food safety and ensure the consumer health policy.

Screening assay testing

Screening assay testing is commonly applied as a semi-quantitative method to identify the presence of the analytes in the sample. Screening is one of the easiest, most rapid and low-cost assay methods that provides high reproducibility and reliable results.

The presence of ciprofloxacin can be detected by β-gal colorimetric assay. This assay is commonly used in inspecting cultured cells and recognising the recombinant fusion genes. It provides a linear correlation between the bacteria inside the fluoroquinolones and β-gal activity. Ortho-nitrophenyl-β-galactoside (ONPG) increases the sensitivity of β-gal activity detection in ciprofloxacin [58]. The interaction between bacteria strains with antimicrobial detection in milk has proven its specificity without giving false

positive results. One of the greatest benefits of using the screening method is less amount of additional reagent is required. The screening method usually examines the optical density (OD) and the growth curve of the bacterial strain [59]. Although screening testing is simple and able to give a rapid response, it only detects the presence of fluoroquinolones without sufficient sensitivity [60].

Chromatographic techniques

From 2000 to 2022, liquid chromatography is still the most frequently employed quantitation instrument for the determination of fluoroquinolones. It is always coupled to sample preparation such as solid phase extraction, micro-solid phase extraction, and dispersive liquid-liquid microextraction to eliminate matrix effects and improve sensitivity.

Solid phase extraction

Solid phase extraction (SPE) is a sample extraction technique that concentrates and purifies analytes from complex sample matrix by sorption onto sorbents loaded in a cartridge device. The SPE isolates a species from a sample or cleans up a sample before analysis using an instrument. The general steps in performing SPE are washing, conditioning, loading and eluting. Compared to liquid-liquid extraction which separates analytes from the sample via partitioning between two immiscible solvents, SPE does not require large amounts of organic solvents. SPE provides a more complete extraction of the analytes and a more efficient separation of the interferences from analytes because there is a variety of sorbents and elution solvents that differ in polarity.

SPE of fluoroquinolones is an effective way for both extraction and clean-up especially after the samples undergo deproteination with an acid such as trichloroacetic acid (TCA) and trifluoroacetic acid (TFA) [61]. The use of SPE offers clean extract to reduce instrument maintenance. According to Herrera-Herrera (2009), the use of SPE with pre-treatment using acids (TCA, TFA) resulted in high recovery that was more than 75% and ultra-trace LOD that was in the range of 0.5-6.8 μg L^{-1} [61].

The fluoroquinolones namely norfloxacin, ofloxacin, ciprofloxacin, pefloxacin, lomefloxacin, danofloxacin, enrofloxacin, sarafloxacin, difloxacin, oxolinic acid, and flumequine were separated with a reversed-phase HPLC coupled with fluorescence detection. The clean-up of the milk samples was succeeded by SPE with LODs ranging from 1-9 μg L^{-1} except for enrofloxacin which was 23 μg L^{-1}. The residues were not exceeding MRL established by Professional Regulation Commission (PRC) and European Union Legislation.

The combination of molecularly imprinted polymers (MIPs) with the SPE cartridge demonstrated high recovery of the ciprofloxacin, enrofloxacin, norfloxacin, lomefloxacin and sarafloxacin from milk samples that were more than 96%. The LODs were ranging 10 and 20 ng mL^{-1}, indicating that MIP-based SPE offered superior purification and sensitivity to the normal SPE [62]. MIP is a synthetic polymer for targeted molecules or selectively given analyte or a group of compounds [63]. MIP is capable to withstand various conditions such as extreme sample pH values, high temperature, and high pressure and it can be reused multiple times [64]. MIP allows better sample clean-up and enhances the detection sensitivity of the analytes. There were several studies reveal that MIP-based SPE was successful as a sample clean-up tool for the isolation of tetracycline antibiotics in lobster, duck, honey and egg. The recovery was above 95% and the LODs were in the range of 0.1-0.3 μg kg^{-1} [65]. The determination of tetracycline in milk and honey with the molecularly imprinted monolith SPE achieved the recoveries of 73.3% - 90.6% from the milk samples and 62.6-82.3% from the honey samples [66]. The MIP monolithic column was polymerised directly and saved lots of procedures like grinding and sieving. However, some studies were reporting the limitation of using MIP such as template leaching problems, low loading capacity, high consumption of organic solvents in conditioning, low affinity binding and the application being limited to polar compounds [42, 56].

The development of magnetic graphene dispersive SPE provides higher stability, larger surface area for adsorption and resistance to acid and alkali. Most of the studies have proven that magnetic graphene is efficient

in extracting pesticides, oxytetracycline in water samples and sulfonamides in milk samples [67-69]. The determination of fluoroquinolones in bovine milk, chicken muscle and egg using magnetic graphene dispersive SPE shows that the recoveries, LOQs and LODs ranged 82.4-108.5%, 0.2-0.8 ng g^{-1}, and 0.05-0.3 ng $g^{-1,}$ respectively. The development of ionic liquid-modified Fe_3O_4 as the adsorbent in magnetic SPE for the determination of fluoroquinolones in milk and pork offered good sensitivity with LODs ranged 0.33-0.78 ng mL^{-1} and LOQs ranged 1.09-2.60 ng mL^{-1}, where the analytes responses were enriched for 29.1-43.9 folds, succeeding the ultra-trace detection of fluoroquinolones in complicated food samples. The recovery of fluoroquinolones from milk and pork samples gained insignificant matrices ranging from 85.4-105.9% and 85.2-103.7%, respectively [70].

The detection of five fluoroquinolones namely norfloxacin, ciprofloxacin, enrofloxacin, danofloxacin and sarafloxacin in fish using ultra-performance liquid chromatography (UPLC) with a fluorescence detector (FD) demonstrated fast analysis and high-resolution selectivity. The fish samples underwent microwave-assisted extraction and clean-up with SPE. The combination of both techniques resulted in a clean extract with recoveries ranged 90-107%. The microwave-assisted extraction utilized a shorter extraction time and minimal solvent. Nevertheless, the sample required further SPE clean-up to eliminate the matrix effect from fish [71].

The development of another sample preparation technique known as QuEChERS is quick, easy, cheap, effective, rugged and safe. This method is rapid and easy to use to separate the sample matrix. Generally, this method is widely applied in the clean-up of food samples with high water content such as fruits and vegetables, especially for the determination of pesticide residues. However, this method is lacking attention to determining the residues of the antibiotics in the food samples. According to Aguilera-Luiz et al. the clean-up step is straightforward with QuEChERS by the addition of EDTA in the extractant solution. It acts as a buffer to QuEChERS and increases the recoveries of the analytes. The recovery study was performed using a spiked milk sample and acceptable recoveries were attained in the range of 70.6-111.3%. However, the intra-day repeatability was recorded as 20% which was considered high as compared to inter-day repeatability [72]. The coupling of QuEChERS clean-up and the UPLC-MS/MS was applied for the determination of veterinary drugs in fish and shrimp samples. Enrofloxacin which is not permitted for use was found in freshwater and marine seafood as high as 7% [73]. In conclusion, the QuEChERS technique is simple, eco-friendly, low cost and fast. There is no filtration and condensation step as well as lesser solvent is consumed. It can be applied to a wide range of complex matrices especially those with high moisture content. Nevertheless, this method could be further modified and improved for better precision.

Apart from clean-up, sample pre-treatment is also required attention to remove interferences with larger particle sizes. For instance, the combination of methanol and trichloroacetic acid (TCA) can easily clear unwanted precipitation and reduce the interaction of lipids and proteins [74]. The combination of methanol with base has shown ineffective sensitivity. Ultra-filtration is needed to increase the detectability of fluoroquinolones without any other protein and lipids component [75].

Liquid-liquid extraction

Liquid-liquid extraction (LLE) is an extraction method that separates compounds according to their solubility in two different immiscible solvents. It is commonly used in the petroleum industry because of its versatility and effectiveness in reducing complex samples [76]. However, there is lacking studies on the extraction of fluoroquinolones in food samples by LLE probably due to the efficiency in extracting organic compounds from complicated matrices.

18 types of veterinary drugs including tylosin, oxolinic acid, flumequine and sulphadimidine were extracted from baby food by LLE. Acidified acetonitrile was added as sample pre-treatment steps to denature the precipitation of proteins and enzymes in the sample. The interferences were reduced before the UPLC tandem mass spectrometer analysis. The results revealed that

this sample pre-treatment step successfully offered a cleaner extract and recovered 120% of one of the fluoroquinolones, flumequine from the samples [77]. Although LLE provides high recovery, the drawbacks of this method include high solvent consumption and waste generation as compared to SPE. It also results in poorer selectivity, emulsion formation and high labour costs [78]. Hence, the SPE is far better than LLE. SPE can extract diverse organic analytes from different samples with superior selectivity compared to LLE [79].

Micro-solid phase extraction

Micro-solid phase extraction (μ-SPE) is developed for rapid sample preparation procedures with minimal solvent. It is known as a miniature SPE. According to Vakh (2018), the fluoroquinolones were extracted by automated magnetic dispersive μ-SPE where the sample solution was injected into a fluidized reactor followed by online separation based on fluidized beds using magnetic nanoparticles, Zr-Fe-C that acted as adsorbents. The LODs and LOQs were in the range of 1.5 to 3.0 μg L^{-1} and 5 to 10 μg L^{-1}. High recovery was obtained for all of the analytes [80]. A core-shell magnetic porous organic polymer has been utilized to extract fluoroquinolone antibiotics in honey samples. The technique was integrated with HPLC-FD and achieved superior sensitivity with LODs in the range of 1.5 to 5.4 ng L^{-1} and enrichment of 84.4-91.7 for ofloxacin, ciprofloxacin and lomefloxacin, and enrofloxacin [81]. The magnetic nanoparticles offered a large ratio of surface area to sample solution volume, a safer technique with low toxic levels and cost-effectiveness [80]. Although μ-SPE applies minute amounts of solvent and indirectly enhances the sensitivity, the major drawbacks are the relative recovery is slightly lower and the insignificant reproducibility problem [42]. Apart from these, μ-SPE is also lacking commercially available stationary phases [82].

Dispersive liquid-liquid microextraction

Dispersive liquid-liquid microextraction (DLLME) was introduced by Assadi et al. to isolate polyaromatic hydrocarbons (PAHs) from water samples [83]. The main advantage of DLLME is its simple, rapid and inexpensive operation [84]. The criteria for an extraction solvent in DLLME is it must have low solubility in the aqueous phase, whereas the dispersive solvent must be miscible with both the extraction solvent and aqueous sample [85]. The DLLME only involves two steps, where both the extraction solvent and disperser solvent are injected rapidly into the sample solution with a syringe. The formation of a cloudy solution containing fine droplets of extraction will be fully dispersed and removed by centrifugation to separate the solutions based on their densities [86].

Yu demonstrated DLLME by employing the deep eutectic solvent (DES) as the extraction solvent. The technique provided fast kinetics to enhance mass transfer because of the large surface area with fine droplets [87]. This method produced good reproducibility which was less than 7.6%. The enrichment factor was in the range of 531-838 folds. DES used in this method is non-toxic and environmentally friendly. Except for milk samples, the DLLME offered good linearity ranged 0.02 to 3.2 μg mL^{-1} and 0.03 to 4.8 μg mL^{-1} with LOD less than 0.01 μg mL^{-1} in determining fluoroquinolones in the honey and water samples [87].

The development of DLLME with the use of switchable polarity dispersive solvent (DLLME-SPDS) has overcome the drawback of conventional DLLME. The centrifugation step was eliminated to simplify the procedure. The determination of ofloxacin in chicken meat samples has applied acrylic acid as the solvent and sodium hydroxide as the alkaline agent in this method. The recoveries obtained were satisfactory in the range of 90.4-102.1% for the spiked chicken meat samples [88]. Despite the various advantages, DLLME is lacking selectivity for complicated matrices [42].

Accelerated solvent extraction

Accelerated solvent extraction (ASE) works at elevated temperatures and high pressure to keep the solvent in a liquid state. The high pressure and increased temperature increase the extraction yield and shorten the extraction time [89]. This method had been applied for the extraction of 15 types of fluoroquinolones in swine, bovine and chicken. The ASE extract required further clean-up by SPE before HPLC-UV analysis. The

recoveries obtained ranged from 70.7-111.1%. The ASE coupled with SPE provided high recoveries and the ASE system was fully automated to ease the operation. The combination of these techniques can separate efficiently, characterise and quantify multiple residues in the food samples [90]. The ASE combined with magnetic SPE was also applied for the extraction of 10 fluoroquinolones in aquatic products. The recoveries obtained were satisfactory in the range of 81.6-105.8% [70]. Overall, the ASE increases the extraction yield, enhances the quality of the extracts, and it is rapid and fully automated. The main drawbacks are the preparation of the extraction cell is time-consuming and a clean-up process is needed. This extraction method is considered limited due to the high operation cost. The high pressure has to be maintained and the temperature is kept elevated along the process. Table 3 summarizes the previously reported techniques for the determination of fluoroquinolones in food.

Conclusion

The lack of analysis of fluoroquinolones in our food samples has to be a concern to maintain a healthy life. The development of a more efficient and effective quantitative analysis is important to obtain reliable residue data. Even though some of the techniques allow for low detection limits and high recovery values, many come with challenging extraction methods to gain better results for ultra-trace levels in food analysis. Most of the studies applied SPE as sample preparation. However, the modified SPE such as magnetic SPE and MIP-SPE are proven to be better than the conventional cartridge-based SPE especially in sensitivity attained. µ-SPE provides a greener technique but the extraction capacity is limited, leading to lower recovery and selectivity as compared to SPE. SPE can extract diverse analytes from different samples and this approach is simple compared to the other techniques. However, it is time-consuming and labour-intensive. Thus, more studies are needed regarding the advanced modification of SPE in sample preparation of food samples as SPE is the most widely used method from 2000 till 2022. In view of that, synthesis of selective adsorbent and liquid extractant for the recognition and extraction of fluoroquinolones is the way forward to enhance the clean-up procedure to offer clean extracts and ultra-trace detection from food samples. On top of that, consolidating automation into sample preparation could further simplify the routine analysis and increase the sample throughput to overcome the shortcoming of microextraction techniques.

Table 3. Summary of previously reported techniques for the determination of fluoroquinolones in food

Food	Analytes	Extraction	Recovery (%)	LOD and LOQ (µg L^{-1})	Instrumentation	References
Milk	Enrofloxacin, Ciprofloxacin, Sarafloxacin, Difloxacin	Acidified ethanol, isolation & retention on cation exchange solid phase extraction, elution with basic ethanol	70-90	0.3-1.2 5.0	HPLC-FD	[91]
Bovine Milk	Fleroxacin, Ciprofloxacin, Lomefloxacin, Danofloxacin, Enrofloxacin, Sarafloxacin, Difloxacin	Deproteinization with TCA, solid phase extraction	73-113	0.5-6.8 1.7-22.2	HPLC-FD	[61]
Milk	Norfloxacin, Ofloxacin, Ciprofloxacin, Pefloxacin,	Solid phase extraction	69-88	1-9 except for enrofloxacin which is 23	HPLC-FD	[92]

	Lomefloxacin, Danofloxacin, Enrofloxacin, Sarafloxacin, Difloxacin, Oxolinic acid, Flumequine					
Milk	Ciprofloxacin, Norfloxacin, Enrofloxacin, Lomefloxacin	MIP-SPE	96	10-20 20-50	HPLC	[62]
Baby Food	Fleroxacin, Norfloxacin, Ofloxacin	Automated magnetic dispersive (SPME)	86-122	1.5-3 5-10	HPLC-FD	[80]
Honey, Milk, Water.	Enrofloxacin, Ciprofloxacin, Lomefloxacin, Gatifloxacin, Sparfloxacin	SO-DLLME-DES-BE	90-110 95-104 87-114	<10 <30	MECC	[87]
Baby Food	18 types of veterinary drugs	LLE with acidified acetonitrile	120	1.0 3.3	UPLC-MS/MS	[77]
Milk	18 types of veterinary drugs	QuEChERS, addition of EDTA as buffer	70.6-111.3	1-4 3-10	UPLC-MS/MS	[72]
Lobster, Duck, Honey, Egg	Tetracycline	MIP-SPE		0.1-0.3	HPLC-MS/MS	[65]
Milk, Honey	Tetracycline	MIP-SPE	73.3-90.6; and 62.6-82.3	10.2-18.8	HPLC-DAD	[66]
Chicken Meat	Ofloxacin	DLLME with switchable polarity dispersive solvent. (DLLME-SPDS)	90.4-92.6 for 5μg/kg 98.7-102.1 for 50 μg/kg	0.071-0.214	HPLC-FD	[88]
Fish	Norfloxacin, Ciprofloxacin, Enrofloxacin, Danofloxacin, Sarafloxacin	Microwave-assisted extraction-SPE	90-107	0.1-1.2 0.2-20.2	UPLC-FD	[71]
Goat Milk	Enrofloxacin, Ciprofloxacin	SPE	84-88	15 20	HPLC-DAD	[93]
Milk, Pork	Norfloxacin, Ciprofloxacin, Lomefloxacin, Enrofloxacin	Magnetic solid phase extraction, Fe_3O_4 as sorbent	85.4-105.9 85.2-103.7	0.33-0.78 1.09-2.60	HPLC-DAD	[94]

Water, Meat	Ofloxacin, Norfloxacin, Ciprofloxacin, Enrofloxacin, Difloxacin, Sarafloxacin, Pefloxacin, Danofloxacin	Magnetic solid phase extraction, Fe_3O_4 as sorbent	82.5-112.5 75.3-104.7	0.0007-0.006 0.0025-0.02	HPLC-MS	[95]
Milk	Fleroxacin, Enoxacin, Pefloxacin, Norfloxacin, Ciprofloxacin, Lomefloxacin, Enrofloxacin, Gatifloxacin, Sparfloxacin, Levofloxacin	MIP-SPE	84.1-104.7	1.34 7.35	HPLC-DAD	[96]
Fish, Shrimp	Flumeuquine, Ciprofloxacin, Enrofloxacin, Ofloxacin	QuEChERS	72-114	0.01-0.3	UPLC-MS/MS	[73]
Swine, Bovine, Chicken	15 types of fluroquinolones	Accelerated solvent extraction, clean up with solid phase extraction	70.7-111.1	3 10	HPLC-UV	[90]
Aquatic Products	Sarafloxacin, Ofloxacin, Enrofloxacin, Danofloxacin, Lomefloxacin, Pefloxacin, Ciprofloxacin, Enoxacin, Norfloxacin, Difloxacin	Accelerated solvent extraction and magnetic solid-phase extraction.	81.6-105.8	0.02-0.29	HPLC-MS	[70]

Acknowledgement

The authors would like to acknowledge the University of Malaysia Terengganu (UMT), especially the Faculty of Science and Marine Environment (FSSM) for their support in conducting this study.

References

1. Gaynes, R. (2017). The discovery of penicillin-new insights after more than 75 years of clinical use. *Emerging Infectious Disease,* 23(5): 849-853.
2. Ullah, H. and Ali, S. (2017). Classification of anti‐bacterial agents and their functions, in: antibacterial agents. IntechOpen, United Kingdom: pp. 138.
3. Meek, R.W., Vyas, H. and Piddock, L. J. V. (2015). Nonmedical uses of antibiotics: Time to restrict their use? *PLOS Biology,* 13(10): e1002266.
4. Aiello, A. E., Marshall, B., Levy, S. B., Della-Latta, P., Lin, S. X. and Larson, E. (2005). Antibacterial cleaning products and drug resistance. *Emerging Infectious Disease,* 11(10):1565-1570.
5. Grobbel, M., Lübke-Becker, A., Wieler, L. H., Froyman, R., Friederichs, S. and Filios, S. (2007). Comparative quantification of the in vitro activity of veterinary fluoroquinolones. *Veterinary Microbiology,* 124(1-2):73-81.

6. Xu, J., Li, X., Li, C., Chen, J. and Xiao, Y. (2018). Hexafluoroisopropanol-induced salt-free catanionic surfactant coacervate extraction method for determination of fluoroquinolones in milk samples. *Food Chemistry*, 242: 122-130.
7. Pham, T. D. M., Ziora, Z. M. and Blaskovich, M. A. T. (2019). Quinolone antibiotics. *Medicinal Chemistry Communication*, 10: 1719-1739.
8. Herrera-Herrera, A.V., Hernández-Borges, J., Rodríguez-Delgado, M.A., Herrero, M. and Cifuentes, A. (2011). Determination of quinolone residues in infant and young children powdered milk combining solid-phase extraction and ultra-performance liquid chromatography-tandem mass spectrometry. *Journal of Chromatography A*, 1218(42): 7608-1764.
9. Schenck, F. J. and Callery, P. S. (1998). Chromatographic methods of analysis of antibiotics in milk. *Journal of Chromatography A*, 812: 99-109.
10. Lindgren, P. K., Karlsson, Å. and Hughes, D. (2003). Mutation rate and evolution of fluoroquinolone resistance in *escherichia coli* isolates from patients with urinary tract infections. *Antimicrob Agents Chemotheraphy*, 47(10): 3222-3232.
11. Peixoto, P. S., Tóth, I. V., Segundo, M. A. and Lima, J. L. F. C. (2016). Fluoroquinolones and sulfonamides: Features of their determination in water. A review. *International Journal of Environmental Analytical Chemistry*, 96(2): 1-18.
12. Brouwers, J. R. B. J. (1987). Pharmacokinetics of the newer fluoroquinolones. *Pharmaceutish Weekblad*, 9: S16-22.
13. United States Food and Drug Administration. (2009). CIPRO® Tablets CIPRO® Oral Suspension. https://www.accessdata.fda.gov/drugsatfda_docs/label/2009/019537s073,020780s030lbl.pdf. [Access online 27 April 2023].
14. National Library of Medicine. Flumequine. https://pubchem.ncbi.nlm.nih.gov/compound/Flumequine. [Access online 27 April 2023].
15. Almalki, Z. S., Yue, X., Xia, Y., Wigle, P. R. and Guo, J. J. (2017). Utilization, spending, and price trends for quinolones in the US medicaid programs: 25 years' experience 1991-2015. *PharmacoEconomics-Open*, 1(2):123-131.
16. Mohammed, H., Abdou, A., Eid, A. and Zakaria, A. (2016). Rapid tests for detection of ciprofloxacin residues in liquid milk. *Benha Veterinary Medical Journal*, 30(1): 246-253.
17. Domagala, J.M. (1994). Structure-activity and structure-side-effect relationships for the quinolone antibacterials. *Journal of Antimicrobial Chemotherapy*, 33: 685-706.
18. King, D. E., Malone, R. and Lilley, S. H. (2000). New classification and update on the quinolone antibiotics. *American Family Physician*, 61(9): 2741-2748.
19. Pitman, S. K., Hoang, U. T. P. Wi, C. H., Alsheikh, A. Hiner, D. A. and Percival, K. M. (2019). Revisiting oral fluoroquinolone and multivalent cation drug-drug interactions: Are they still relevant? *Antibiotics (Basel)*, 8(3): 108-115.
20. Drusano, G., Labro, M. T., Cars, O., Mendes, P., Shah, P., Sörgel, F. and Webel, W. (1998). Pharmacokinetics and pharmacodynamics of fluoroquinolones. *Clinical Microbiology and Infection*, 4(2): S27-S41.
21. Mathew, J. L. (2004). Effect of maternal antibiotics on breastfeeding infants. *Postgraduate Medical Journal*, 80: 196-200.
22. Bourget, P., Quinquis-Desmaris, V. and Fernandez, H. (1993). Ceftriaxone distribution and protein binding between maternal blood and milk postpartum. *The Annals of Pharmacotherapy*, 27(3): 94-97.
23. Ward, R. M., Bates, B. A., Benitz, W. E., Burchfield, D. J., Ring, J. C. and Walls, R. P. (2001). The transfer of drugs and other chemicals into human milk. *Pediatrics*, 108: 776-789.
24. Gardner, D. K., Gabbe, S. G. and Harter, C. (1992). Simultaneous concentrations of ciprofloxacin in breast milk and in serum in mother and breast-fed infant. *Clinical Pharmacy*, 11(4): 352-354.
25. Mehdi, Y., Létourneau-Montminy, M.P., Gaucher, M. L., Chorfi, Y., Suresh, G., Rouissi, T., Brar, S.K., Côté, C. Ramirez, A. A. and Godbouat, S. (2018). Use of antibiotics in broiler production: Global impacts and alternatives. *Animal Nutrition*, 4: 170-178.

26. Wegener, H.C. (2012). Antibiotic resistance-linking human and animal health, in: Improving food safety through a one health approach: workshop summary. National Academy of Sciences, United States. Access from https://www.ncbi.nlm.nih.gov/books/NBK114485/?report=printable. [Access online 30 April 2023].
27. Hughes, P. and Heritage, J. (2004). Antibiotic growth-promoters in food animals. Access from https://www.fao.org/3/y5159e/y5159e08.htm. [Access online 30 April 2023].
28. Torok, V. A., Allison, G. E., Percy, N. J., Ophel-Keller, K. and Hughes, R. J. (2011). Influence of antimicrobial feed additives on broiler commensal post hatch gut microbiota development and performance. *Applied and Environmental Microbiology*, 77(10): 3380-3390.
29. Abutarbush, S. M., Schunicht, O. C., Wildman, B. K., Hannon, S. J., Jim, G. K., Ward, T. I. and Booker, C.W. (2012). Comparison of enrofloxacin and ceftiofur sodium for the treatment of relapse of undifferentiated fever/bovine respiratory disease in feedlot cattle. *The Canadian Veterinary Journal*, 53(1): 57-62.
30. European Union (2009). Commission Regulation (EU) No 37/2010 of 22 December 2009 on pharmacologically active substances and their classification regarding maximum residue limits in foodstuffs of animal origin. Access from https://eur-lex.europa.eu/legal-content/EN/TXT/PDF/?uri=CELEX:32010R0037. [Access online 28 April 2023].
31. Filip, C., Ceană, D. E. and Tero Vescan, A. (2014). Clinical aspects HPLC method with fluorescence detection for the identification and quantitative determination of fluoroquinolones in milk. *Acta Medica Transilvanica*, 11(1): 151-153.
32. Food and Drug Administrative. (2018). FDA updates warnings for fluoroquinolone antibiotics on risks of mental health and low blood sugar adverse reactions. Access from https://www.fda.gov/news-events/press-announcements/fda-updates-warnings-fluoroquinolone-antibiotics-risks-mental-health-and-low-blood-su gar -adverse. [Access online 28 April 2023].
33. Pallo-Zimmerman, L. M., Byron, J. K. and Graves, T. K. (2010). Fluoroquinolones: Then and now. *Compendium*, 32(7): 1-9.
34. Fàbrega, A., Sánchez-Céspedes, J., Soto, S. and Vila, J. (2008). Quinolone resistance in the food chain. *International Journal of Antimicrobial Agents*, 31: 307-315.
35. Prestinaci, F., Pezzotti, P. and Pantosti, A. (2015). Antimicrobial resistance: A global multifaceted phenomenon. *Pathogens and Global Health*, 109: 309-318.
36. Azmi, M., Hassali, A., Rhu, H., Ashutosh, Y., Verma, K., Hussain, R. and Sivaraman, S. (2018). Antibiotic use in food animals. Universiti Sains Malaysia, Malaysia. Access from https://www.reactgroup.org/wp-content/uploads/2018/11/Antibiotic_Use_in_Food_Animals_Malaysia_Overview_2018web.pdf. [Access online 30 April 2023].
37. European Medicines Agency (2018). Fluoroquinolone and quinolone antibiotics: PRAC recommends restrictions on use new restrictions follow a review of disabling and potentially long-lasting side effects. Access from https://www.ema.europa.eu/en/news/fluoroquinolone-quinolone-antibiotics-prac-recommends-new-restrictions-use-following-review. [Access online 30 April 2023].
38. Ferlito, C. (2020). The poultry industry and its supply chain in Malaysia: Challenges from the Covid-19 Emergency. [Access online 30 April 2023].
39. Lai, Y. (2020). Poultry firms count on nuggets and sausages to feed sales growth. The edge markets, Malaysia. Access from https://www.theedgemarkets.com/article/poultry-firms-count-nuggets-and-sausages-feed-sales-growth. [Access online 30 April 2023].
40. Urraca, J. L., Castellari, M., Barrios, C. A. and Moreno-Bondi, M. C. (2014). Multiresidue analysis of fluoroquinolone antimicrobials in chicken meat by molecularly imprinted solid-phase extraction and high performance liquid chromatography. *Journal of Chromatography A*, 1343: 1-9.

41. Sproston, E. L., Wimalarathna, H. M. L. and Sheppard, S. K. (2018). Trends in fluoroquinolone resistance in *Campylobacter*. *Microbial Genomics*, 4(8): e000198.
42. Zhang, C., Deng, Y., Zheng, J., Zhang, Y., Yang, L., Liao, C., Su, L,, Zhou, Y., Gong, D., Chen, L. and Luo, A. (2019). Application of the QuEChERS methodology in the determination of antibiotics in food: A review. *TrAC Trends in Analytical Chemistry*, 118: 517-537.
43. Boxall, A. B. A., Blackwell, P., Cavallo, R., Kay, P. and Tolls, J. (2002). The sorption and transport of a sulphonamide antibiotic in soil systems. *Toxicology Letters*, 131: 19-28.
44. Pan, X., Qiang, Z., Ben, W. and Chen, M. (2011). Residual veterinary antibiotics in swine manure from concentrated animal feeding operations in Shandong Province, China. *Chemosphere*, 84(5): 695-700.
45. Karci, A. and Balcioğlu, I. A. (2009). Investigation of the tetracycline, sulfonamide, and fluoroquinolone antimicrobial compounds in animal manure and agricultural soils in Turkey. *Science of Total Environment*, 407(16): 4652-4664.
46. Ahmed, B. M., Rajapaksha, A. U., Lim, J. E., Vu, N. T., Kim, I. S., Kang, H. M., Lee, S. S. and Ok, Y. S. (2014). Distribution and accumulative pattern of tetracyclines and sulfonamides in edible vegetables of cucumber, tomato, and lettuce. *Journal of Agricultural and Food Chemistry*, 63(2): 395-405.
47. Tadić, Đ., Bleda Hernandez, M. J., Cerqueira, F., Matamoros, V., Piña, B. and Bayona, J. M. (2021). Occurrence and human health risk assessment of antibiotics and their metabolites in vegetables grown in field-scale agricultural systems. *Journal of Hazardous Materials*, 401: 123424.
48. Zhao, F., Yang, L., Chen, L., Li, S. and Sun, L. (2019). Bioaccumulation of antibiotics in crops under long-term manure application: Occurrence, biomass response and human exposure. *Chemosphere*, 219: 882-895.
49. Fick, J., Söderström, H., Lindberg, R. H., Phan, C., Tysklind, M. and Larsson, D. G. J. (2009). Contamination of surface, ground, and drinking water from pharmaceutical production. *Environmental Toxicology and Chemistry*, 28(12): 2522-2527.
50. Pan, M., and Chu, L.M. (2017). The fate of antibiotics in soil and their uptake by edible crops. *Science of the Total Environment.* 599-600: 500-512.
51. Al-Waili, N., Salom, K., Al-Ghamdi, A. and Ansari, M. J. (2012). Antibiotic, pesticide, and microbial contaminants of honey: Human health hazards. *The Scientific World Journal*, 2012: 930849.
52. Randox Food Diagnostics (2019). Antibiotics in honey – treatment against bee diseases. Access from https://www.randoxfood.com/antibiotics-in-honey-treatment-against-bee-diseases/. [Access online 30 April 2023].
53. Ortelli, D., Edder, P. and Corvi, C. (2004). Analysis of chloramphenicol residues in honey by liquid chromatography-tandem mass spectrometry. *Chromatographia*, 59(1-2): 61-64.
54. Forsgren, E. (2010). European foulbrood in honey bees. *Journal of Invertebrate Pathology*, 103: S5-S9.
55. Choi, S. H., Kim, E.Y. and Kim, Y. J. (2013). Systemic use of fluoroquinolone in children. *Korean Journal of Pediatrics*, 56: 196-201.
56. Rodriguez, E., Moreno-Bondi, M. C. and Marazuela, M. D. (2011). Multiresidue determination of fluoroquinolone antimicrobials in baby foods by liquid chromatography. *Food Chemistry*, 127(3):1354-1360.
57. World Health Organization (2006). Antimicrobial use in aquaculture and antimicrobial resistance. Access from https://agsci.oregonstate.edu/sites/agscid7/files/snic/antimicrobial-use-in-aquaculture-and-antimicrobial -resistance.pdf. [Access online 30 April 2023].
58. Kalunke, R.M., Grasso, G., D'Ovidio, R., Dragone, R. and Frazzoli, C. (2018). Detection of ciprofloxacin residues in cow milk: A novel and rapid optical β-galactosidase-based screening assay. *Microchemical Journal*, 136: 128-132.

59. Appicciafuoco, B., Dragone, R., Frazzoli, C., Bolzoni, G., Mantovani, A. and Ferrini, A. M. (2015). Microbial screening for quinolones residues in cow milk by bio-optical method. *Journal of Pharmaceutical and Biomedical Analysis,* 106: 179-185.
60. Pikkemaat, M. G. (2009). Microbial screening methods for detection of antibiotic residues in slaughter animals. *Analytical and Bioanalytical Chemistry*, 395: 893-905.
61. Herrera-Herrera, A. V., Hernández-Borges, J. and Rodríguez-Delgado, M. Á. (2009). Fluoroquinolone antibiotic determination in bovine, ovine and caprine milk using solid-phase extraction and high-performance liquid chromatography-fluorescence detection with ionic liquids as mobile phase additives. *Journal of Chromatography A,* 1216(43): 7281-7287.
62. Wang, G. N., Yang, K., Liu, H. Z., Feng, M. X. and Wang, J. P. (2016). Molecularly imprinted polymer-based solid phase extraction combined high performance liquid chromatography for determination of fluoroquinolones in milk. *Analytical Methods,* 8(27): 5511-5518.
63. Poole, C. F. (2020). Solid-phase extraction. Elsevier, United States: pp. 215-233.
64. Sarafraz-Yazdi, A. and Razavi, N. (2015). Application of molecularly-imprinted polymers in solid-phase microextraction techniques. *TrAC Trends in Analytical Chemistry,* 73: 81-90.
65. Jing, T., Gao, X. D., Wang, P., Wang, Y., Lin, Y. F., Hu, X. Z., Hao, Q. L., Zhou, Y. K. and Mei, S. R. (2009). Determination of trace tetracycline antibiotics in foodstuffs by liquid chromatography-tandem mass spectrometry coupled with selective molecular-imprinted solid-phase extraction. *Analytical and Bioanalytical Chemistry,* 393(8): 2009-2018.
66. Sun, X., He, X., Zhang, Y. and Chen, L. (2009). Determination of tetracyclines in food samples by molecularly imprinted monolithic column coupling with high performance liquid chromatography. *Talanta*, 79(3): 926-934.
67. Sun, Y., Tian, J., Wang, L., Yan, H., Qiao, F. and Qiao, X. (2015). One pot synthesis of magnetic graphene/carbon nanotube composites as magnetic dispersive solid-phase extraction adsorbent for rapid determination of oxytetracycline in sewage water. *Journal of Chromatography A,* 1422: 53-59.
68. Li, Y., Wu, X., Li, Z., Zhong, S., Wang, W., Wang, A. and Chen, J. R. (2015). Fabrication of $CoFe_2O_4$-graphene nanocomposite and its application in the magnetic solid phase extraction of sulfonamides from milk samples. *Talanta,* 144: 1279-1286.
69. Bai, S. S., Li, Z., Zang, X. H., Wang, C. and Wang, Z. (2013). Graphene-based magnetic solid phase extraction-dispersive liquid-liquid microextraction combined with gas chromatographic method for determination of five acetanilide herbicides in water and green tea samples. *Chinese Journal of Analytical Chemistry,* 41(8): 1177-1182.
70. Dan, W., Ming, G. and Ju, Z. (2020). Determination of 10 fluoroquinolones residues in aquatic products by accelerated solvent extraction, magnetic solid-phase extraction, and high-performance liquid chromatography-tandem mass spectrometry. *Chinese Journal of Chromatography,* 38(12): 1413-1422.
71. Aufartová, J., Brabcová, I., Torres-Padrón, M. E., Solich, P., Sosa-Ferrera, Z. and Santana-Rodríguez, J. J. (2017). Determination of fluoroquinolones in fishes using microwave-assisted extraction combined with ultra-high performance liquid chromatography and fluorescence detection. *Journal of Food Composition and Analysis,* 56: 140-146.
72. Aguilera-Luiz, M. M., Vidal, J. L. M., Romero-González, R. and Frenich, A. G. (2008). Multi-residue determination of veterinary drugs in milk by ultra-high-pressure liquid chromatography-tandem mass spectrometry. *Journal of Chromatography A,* 1205(1-2):10-16.
73. Dinh, Q. T., Munoz, G., Vo Duy, S., Tien Do, D., Bayen, S. and Sauvé, S. (2020). Analysis of sulfonamides, fluoroquinolones, tetracyclines, triphenylmethane dyes and other veterinary drug residues in cultured and wild seafood sold in Montreal, Canada. *Journal of Food Composition and Analysis,* 94: 103630.

74. Rodriguez, E., Moreno-Bondi, M. C. and Marazuela, M. D. (2008). Development and validation of a solid-phase extraction method coupled to liquid chromatography with fluorescence detection for the determination of fluoroquinolone residues in powdered infant formulae. application to the analysis of samples from the spanish and latin american market. *Journal of Chromatography A*, 1209(1-2): 136-144.
75. Idowu, O. R. and Peggins, J. O. (2004). Simple, rapid determination of enrofloxacin and ciprofloxacin in bovine milk and plasma by high-performance liquid chromatography with fluorescence detection. *Journal of Pharmaceutical and Biomedical Analysis*, 35(1): 143-153.
76. Klemz, A. C., Weschenfelder, S. E., de Carvalho Neto, S. L., Pascoal Damas, M. S., Toledo Viviani, J. C., Mazur, L. P., Marinho, B. A., dos Santos Pereira, L., da Silva, A., Borges Valle, J. A., de Souza, A. A. U., and de Souza, S. M. A. G. U. (2021). Oilfield produced water treatment by liquid-liquid extraction: A review. *Journal of Petroleum Science and Engineering*, 199: 108282.
77. Aguilera-Luiz, M. M., Martínez Vidal, J. L., Romero-González, R. and Garrido Frenich, A. (2012). Multiclass method for fast determination of veterinary drug residues in baby food by ultra-high-performance liquid chromatography-tandem mass spectrometry. *Food Chemistry*, 132(4): 2171-2180.
78. Campíns-Falcó, P., Sevillano-Cabeza, A., Herráez-Hernández, R., Molins-Legua, C., Moliner-Martínez, Y. and Verdú-Andrés, J. (2022). Solid-phase extraction and clean-up procedures in pharmaceutical analysis, in: *Encyclopedia of Analytical Chemistry*. John Wiley & Sons, United Kingdom: pp. 1-22.
79. Andrade-Eiroa, A., Canle, M., Leroy-Cancellieri, V. and Cerdà, V. (2016). Solid-phase extraction of organic compounds: A critical review. *TrAC Trends in Analytical Chemistry*, 80: 655-667.
80. Vakh, C., Alaboud, M., Lebedinets, S., Korolev, D., Postnov, V., Moskvin, L., Osmolovskaya, O. and Bulatox, A. (2018). An automated magnetic dispersive micro-solid phase extraction in a fluidized reactor for the determination of fluoroquinolones in baby food samples. *Analytica Chimica Acta*, 1001: 59-69.
81. Tian, C., Ren, X., He, M., Chen, B. and Hu, B. (2021). Core-shell magnetic porous organic polymer for magnetic solid-phase extraction of fluoroquinolone antibiotics in honey samples followed by high-performance liquid chromatography with fluorescence detection. *Journal of Separation Science*, 45(4): 874-882.
82. van Hout, M. W. J., Niederländer, H. A. G., de Zeeuw, R. A. and de Jong, G. J. (2003). New developments in integrated sample preparation for bioanalysis, In: *Handbook of Analytical Separations*. Elsevier, United States: pp. 1-44.
83. Xu, H., Ding, Z., Lv, L., Song, D. and Feng, Y. Q. (2009). A novel dispersive liquid-liquid microextraction based on solidification of floating organic droplet method for determination of polycyclic aromatic hydrocarbons in aqueous samples. *Analytica Chimica Acta*, 636(1): 28-33.
84. Rezaee, M., Assadi, Y., Milani Hosseini, M. R., Aghaee, E., Ahmadi, F. and Berijani, S. (2006). Determination of organic compounds in water using dispersive liquid-liquid microextraction. *Journal of Chromatography A*, 1116(1-2): 1-9.
85. Li, Y., Zhang, W., Wang, R. G., Wang, P. L. and Su, X. O. (2015). Development of an efficient and sensitive dispersive liquid-liquid microextraction technique for extraction and preconcentration of 10 β2-agonists in animal urine. *PLoS ONE*, 10(9): e0137194.
86. Zgoła-Grześkowiak, A. and Grześkowiak, T. (2011). Dispersive liquid-liquid microextraction. *TrAC Trends in Analytical Chemistry*, 30: 1382-1399.
87. Yu, K., Yue, M. E., Xu, J. and Jiang, T. F. (2020). Determination of fluoroquinolones in milk, honey and water samples by salting out-assisted dispersive liquid-liquid microextraction based on deep eutectic solvent combined with MECC. *Food Chemistry*, 332: 127371.
88. Timofeeva, I., Timofeev, S., Moskvin, L. and Bulatov, A. (2017). A dispersive liquid-liquid microextraction using a switchable polarity dispersive solvent. Automated HPLC-FLD determination of ofloxacin in chicken meat. *Analytica Chimica Acta*, 949: 35-42.

89. Giergielewicz-Mozajska, H., Dabrowski, L. and Namieśnik, J. (2001). Accelerated solvent extraction (ASE) in the analysis of environmental solid samples - some aspects of theory and practice. *Critical Reviews in Analytical Chemistry*, 31(3): 149-165.
90. Yu, H., Tao, Y., Chen, D., Pan, Y., Liu, Z., Wang, Y., Huang, L., Dai, M., Peng, D., Wang, X. and Yuan, Z. (2012). Simultaneous determination of fluoroquinolones in foods of animal origin by a high performance liquid chromatography and a liquid chromatography tandem mass spectrometry with accelerated solvent extraction. *Journal of Chromatography B, Analytical Technologies in the Biomedical and Life Sciences*, 885-886: 150-159.
91. Roybal, J. E., Pfenning, A. P., Turnipseed, S. B., Walker, C. C. and Hurlbut, J. A. (1997). Determination of four fluoroquinolones in milk by lquid chromatography. *Journal of AOAC International*, 80(5): 982-987.
92. Yang, G., Lin, B., Zeng, Z., Chen, Z. and Huang, X. (2005). Multiresidue determination of eleven quinolones in milk by liquid chromatography with fluorescence detection. *Journal of AOAC International*, 88(6):1688-1694.
93. Cinquina, A.L., Roberti, P., Giannetti, L., Longo, F., Draisci, R., Fagiolo, A. and Brizioli, N. R. (2003). Determination of enrofloxacin and its metabolite ciprofloxacin in goat milk by high-performance liquid chromatography with diode-array detection: Optimization and validation. *Journal of Chromatography A*, 987(1-2): 221-226.
94. Zhang, M., Chen, J., Zhao, F. and Zeng, B. (2020). Determination of fluoroquinolones in foods using ionic liquid modified Fe_3O_4/MWCNTs as the adsorbent for magnetic solid phase extraction coupled with HPLC. *Analytical Methods*, 12(36): 4457-4465.
95. Yu, H., Jia, Y., Wu, R., Chen, X. and Chan T. W. D. (2019). Determination of fluoroquinolones in food samples by magnetic solid-phase extraction based on a magnetic molecular sieve nanocomposite prior to high-performance liquid chromatography and tandem mass spectrometry. *Analytical and Bioanalytical Chemistry*, 411(13): 2817-2826.
96. Liu, P.Y., Shen, J., Gao, L., Liu, L., Li, R. and Li, Q. (2010). Determination of fluoroquinolones in milk by high-performance liquid chromatography using mixed-templates imprinted polymer extraction. *Asian Journal of Chemistry*, 22(8): 6275-6288.

Malaysian Journal of Analytical Sciences (MJAS)
Published by Malaysian Analytical Sciences Society

COMPARATIVE STUDY ON THE EFFECT OF GAMMA RADIATION ON BIOPLASTICS

(Kajian Perbandingan Tentang Kesan Sinaran Gamma Terhadap Bioplastik)

Nurul Fathihah Abu Bakar, and Siti Amira Othman*

Faculty of Applied Sciences and Technology,
Universiti Tun Hussein Onn Malaysia, 84600, Pagoh, Johor, Malaysia

Corresponding author: sitiamira@uthm.edu.my

Received: 20 January 2023; Accepted: 9 May 2023; Published: 23 June 2023

Abstract

Conventional plastic is made from petrochemical substances. Its non-biodegradable properties negatively impact the environment, causing landfill pollution and affecting wildlife and aquatic life. It uses non-renewable sources that will be depleted in a few years if there is no solution to this situation. This study was carried out to produce bio-plastic made from renewable sources: 10 g of corn starch, 5 ml of glycerol and vinegar, and 60 ml of distilled water. The produced bio-plastic was exposed to gamma radiation to observe the difference between irradiated and non-irradiated bio-plastics. Surface morphology and chemical properties like absorption spectra, functional group and chemical bonding were characterized using Opto Digital Microscope, Ultra-Violate Visible (UV-Vis) Spectrophotometer and Fourier Transform Infrared Spectroscopy (FTIR). The results indicate that exposure to gamma radiation causes the bio-plastic surface to be darker with some degradation. Irradiated bio-plastic degrades faster than the ones not irradiated. The samples were characterized using UV-Vis, prepared in different glycerol concentrations to determine which concentration gave the best absorption peak. The absorption peaked at 270 nm wavelength in the highest glycerol concentration. Functional groups like alcohols, carbonyl and ester were also found in the sample's solution. All functional groups that contribute to the bio-plastic properties could be stretched and bent to enhance their performances as a packaging application. Overall, exposure to gamma radiation improves the bio-plastic quality as a packaging application that can be used in the food and pharmaceutical industries.

Keywords: Effect of gamma radiation, bioplastics, radiation, ionizing

Abstrak

Plastik konvensional diperbuat daripada bahan petrokimia. Sifat tidak terbiodegradasinya memberi kesan negatif kepada alam sekitar, menyebabkan pencemaran tapak pelupusan dan menjejaskan hidupan liar dan akuatik. Ia menggunakan sumber tidak boleh diperbaharui yang akan habis dalam beberapa tahun jika tiada penyelesaian kepada keadaan ini. Kajian ini dijalankan untuk menghasilkan bio-plastik yang diperbuat daripada sumber boleh diperbaharui: 10 g kanji jagung, 5 ml gliserol dan cuka, dan 60 ml air suling. Bio-plastik yang dihasilkan telah didedahkan kepada sinaran gamma untuk melihat perbezaan antara bio-plastik yang disinari dan tidak disinari. Morfologi permukaan dan sifat kimia seperti spektrum serapan, kumpulan berfungsi dan ikatan kimia telah dicirikan menggunakan Mikroskop Opto Digital, Spektrofotometer Cahaya Nampak-Ultraungu (UV-Vis) dan Inframerah Transformasi Fourier (FTIR). Keputusan menunjukkan bahawa pendedahan kepada sinaran gamma menyebabkan permukaan bio-plastik menjadi lebih gelap dengan sedikit degradasi. Bio-plastik yang disinari merosot lebih cepat daripada yang tidak disinari. Sampel telah dicirikan menggunakan UV-Vis, disediakan dalam kepekatan gliserol yang berbeza untuk menentukan kepekatan

yang memberikan puncak penyerapan terbaik. Penyerapan memuncak pada panjang gelombang 270 nm dalam kepekatan gliserol tertinggi. Kumpulan berfungsi seperti alkohol, karbonil dan ester juga ditemui dalam larutan sampel. Semua kumpulan berfungsi yang menyumbang kepada sifat bio-plastik boleh diregangkan dan dibengkokkan untuk meningkatkan prestasi mereka sebagai aplikasi pembungkusan. Secara keseluruhan, pendedahan kepada sinaran gamma meningkatkan kualiti bio-plastik sebagai aplikasi pembungkusan yang boleh digunakan dalam industri makanan dan farmaseutikal.

Kata kunci: Kesan sinaran gama, bioplastik, sinaran, pengionan

Introduction

Radiation processing is used for packaging applications, especially for medical products and in the food industry [1]. Presently, packaging materials are mostly made from synthetic plastic, making it crucial to see the effect of irradiation on these materials. Apart from radiation treatment, a few other methods can be applied for packaging applications, such as UV-ray, ionizing ray, and light pulse. There was an attempt to use UV-ray for surface sterilization. It depends on the intensity rate applied for the packaging applications. However, the UV ray's penetration ability is limited [2]. Hence, it is only suitable for packaging materials with very low contamination.

Using an ionizing ray is another method for packaging applications. It uses Cobalt-60 as a source that emits gamma radiation. It is very convenient for killing bacteria [2]. Ionizing radiation is commonly used for bulk packaging of acidic foods such as aseptic bag-in-box. This method applies a radiation dose of 25 kGy equivalent to 2.5 mrad. However, the effects of gamma radiation on food have been a huge concern in the manufacturing process because it needs heavy shielding to prevent radiation leakage. It also requires careful process design, high maintenance, and expensive equipment.

Radiation treatment is chosen to radiate packaging materials because it does not leave any residue on the treated surface nor affect the immediate environment, making it the perfect solution for packaging materials. Packaging materials are any material used to protect something. Many sources have been used in packaging materials, including glass, metals, papers and plastics. However, a special variety of plastics have been introduced in the manufacturing industry for packaging. These plastics are made from petroleum and other chemicals with unhealthy side effects for the product and its surrounding, leading to the invention of bio-plastic, a more convenient and safer packaging material.

Plastics have been widely used for packaging applications for 70 years [3, 4]. Its versatility and durability give it an advantage over other materials. It is inexpensive, lightweight, heat-sealable and has good flexibility for fabrication into various shapes [5]. However, petroleum-based plastics are detrimental to the environment. Conventional plastics are made from petroleum, making them non-biodegradable and non-renewable [6, 7]. This disadvantage leads to huge environmental problems and municipal waste. The solution to this problem is to produce a new type of plastic made from bio-based materials. Unfortunately, recent studies found that no bio-based plastics could combine all the features and functionalities of conventional plastics [8]. Hence, there is ongoing research on producing bio-based plastics that achieve all the required properties of conventional plastics.

Another definition of bio-plastic can be explained from two perspectives. The first one is its functionality. Bio-plastic is biodegradable plastic from organic waste, while the second one is by its source materials. It uses renewable or biomass materials that are processed into plastic. Bio-plastics are a type of biological material that is degradable and eco-friendly in its chemical nature. They are produced using a few methods, such as microorganisms cultured under different nutrients and environmental conditions [9]. Bio-based plastics are man-made or man-processed, derived from biological resources. Bio-plastics are classified into two types: photodegradable and semi-biodegradable [10]. The history of bio-based plastics is much earlier than our conventional plastics. The first bio-based plastics, called thermoplastics, were made from celluloid in the 1860s [11]. Unfortunately, the numerous inventions of bio-based plastics stayed in the laboratory and was not

commercially exploited because, in the 1950s, the petrochemical industry had developed cheap and synthetic polymers made up from crude oils.

What we have now are synthetic plastics that are usually made from petroleum. 4% of the world's petroleum sources are reserved for manufacturing plastics [12]. More than 200 billion pounds of plastics are produced yearly [13], indicating how crucial plastic is worldwide. Within a few years, sources will deplete if nothing is done about it. These synthetic plastics contribute to environmental pollution because they are not eco-friendly. The chemicals used to make synthetic plastics are non-biodegradable, taking a long time to decay. Some plastics take up to 1000 years to decay [14]. On top of that, plastics also affect wildlife, destroying habitats, especially the marine ecosystem. Aquatic life often mistakes plastics for food, causing them to suffocate or entangled by the plastics [15].

Conventional plastics are compounded with several additives to improve their product performance and tensile strength. These factors lead to health hazards for humans. In addition, a very cautious handling process is needed during the plastic manufacturing, which may cause industrial accidents [16]. Our study is important for several reasons. Firstly, inventing a bio-plastic requires a study of its properties and functions to ensure it is similar to or better than conventional plastic for use as packaging. Hopefully, over time, bio-plastic will replace conventional plastic. Secondly, bio-plastic can help lessen global environmental pollution because it uses natural sources as its base. Therefore, bio-plastics are eco-friendly (bio-degradable) and take less time to decay. Thus, overcoming conventional plastic adverse effects on the marine ecosystem.

Thirdly, although producing bio-plastics may require a higher capital, it should not be a problem due to ample bio-based sources. Currently, there is a high demand for bio-plastic from the industry. Moreover, petroleum price is expected to increase due to its depletion and high demand. Finally, bio-plastic is irradiated using gamma radiation by emitting a high photon energy that can penetrate the material, ensuring the entire packaging has been radiated. It is a non-polluting radiation, making it safer for the products inside the packaging [9]. Furthermore, the properties of the packaging application were studied so that they could be customized for use in different applications, making it particularly beneficial to the food processing industry.

The objectives of this research are including produce biodegradable plastic using corn starch, analyze the chemical properties of irradiated bio-plastic by using ultraviolet-visible spectrophotometer (UV-Vis) and Fourier transform infrared spectroscopy (FTIR), and study the bio-plastic surface morphology using Opto Digital Microscope.

Materials and Methods

This study employed 10 g of corn starch, 60 mL of distilled water, 5 mL of glycerol, and vinegar. The sample was prepared by adding 60 ml of distilled water and corn starch. The mixture was stirred until it formed a uniform and homogenous suspension. Following that, glycerol was added to the mixture and stirred well. Then, vinegar was added to the mixture. After thoroughly combining all materials, the heat was turned on, and the stirring procedure was resumed. During the stirring process, the temperature was raised from 30ºC to 95ºC. After a while, a thick viscous glue-like substance formed. The mixture was then poured and spread over an aluminum foil. The mixture was left to dry for a few days, as shown in Figure 1. The bio-plastic sample was cut into smaller pieces and sliced into 5 cm x 5 cm squares to facilitate the radiation procedure. They were divided into radiation and non-radiation samples. The samples were then irradiated.

The shielding blocks were arranged properly for irradiation purposes to ensure no radiation leakage while running the experiment. Cobalt-60 was chosen as the radiation source. The samples were left for a week for irradiation. Finally, all samples were sent for analysis before and after each radiation process. The radiated samples were sent for analysis to study their properties and investigate the radiation effects on the sample using Ultraviolet-Visible Spectrophotometer (UV-Vis), Opto Digital Microscope and Fourier Transformation Infrared Spectroscopy (FTIR).



(a) (b) (c)

Figure 1. (a) Corn starch, glycerol, vinegar and distilled water were measured (b) The mixture was mixed together and stirred on heating stove with medium heat until thick viscous glue-like solution formed (c) The mixture was then poured onto aluminum foil and spread out to let it dry. The drying process took several days

Results and Discussion

Ultraviolet-Visible spectrophotometer analysis

10 samples were analyzed using UV-Vis spectroscopy. The samples were divided into radiated and non-radiated samples. Five samples were radiated using Cobalt-60 and exposed to gamma radiation for a week. Then, the samples were prepared for analysis using a UV-Vis Spectrophotometer to observe the bio-plastics absorbance range under different glycerol concentrations at 200-800 nm. UV-Vis uses visible and ultraviolet lights to analyze the bio-plastics chemical structure.

Table 1. Wavelength and absorption peak of non-radiated and radiated bio-plastics

Samples Glycerol (mL)	Non-Radiated Bio-Plastic		Radiated Bio-Plastic	
	Wavelength (nm)	Absorption Peak (a.u)	Wavelength (nm)	Absorption Peak (a.u)
1.0	280	0.031	270	0.057
0.8	270	0.022	270	0.030
0.6	270	0.019	270	0.028
0.4	270	0.018	270	0.012
0.2	270	0.016	270	0.010

Table 1 shows that glycerol influenced the UV absorptivity in bio-plastics [17]. This result also indicates that glycerol concentration is directly proportional to the bio-plastics ability to absorb UV (Figure 2). The highest peak for the non-radiated bio-plastics is 0.031 a.u with 1.0 ml presence of glycerol, found at 280 nm wavelength. The glycerol is directly proportional to the level of bio-plastic transparency [18]. Studying the bio-plastic absorbance range is important because UV absorption has a significant relationship to the plastic's UV degradation. Plastics that did not absorb UV radiation are insusceptible to photo degradation [19].

This research found that bio-plastic with 1.0 ml glycerol concentration had the highest peak. We conclude that glycerol in bio-plastic resulted in better UV absorption (Figure 3). The bio-plastics ability to absorb UV is very beneficial, especially if it is used for food packaging, due to their ability to protect food products from UV radiation. It could prevent photo-oxidative degradation that might change the product's taste and smell, and induce free radicals formation. The highest peak obtained is at wavelength 270 nm with a peak 0.057 a.u. The highest peak obtained had the same glycerol concentration as non-radiated bio-plastic. This signifies

that with exposure to gamma radiation, glycerol's presence in bio-plastic plays an important role in absorbing UV radiation.

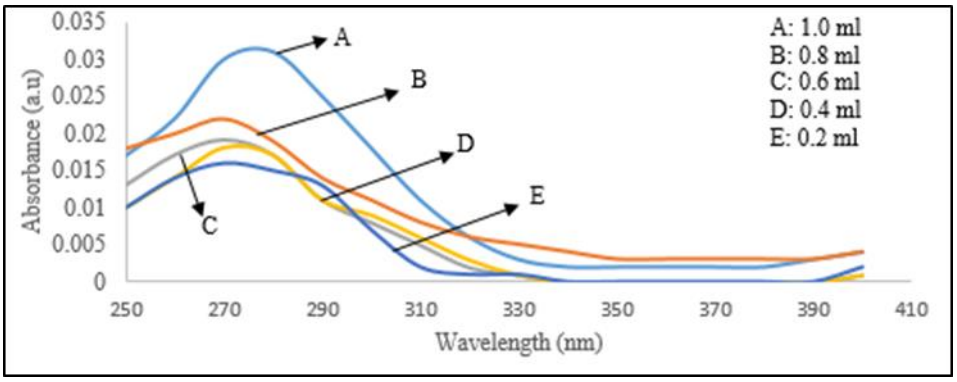


Figure 2. Concentration of different glycerol in non-radiated bio-plastics

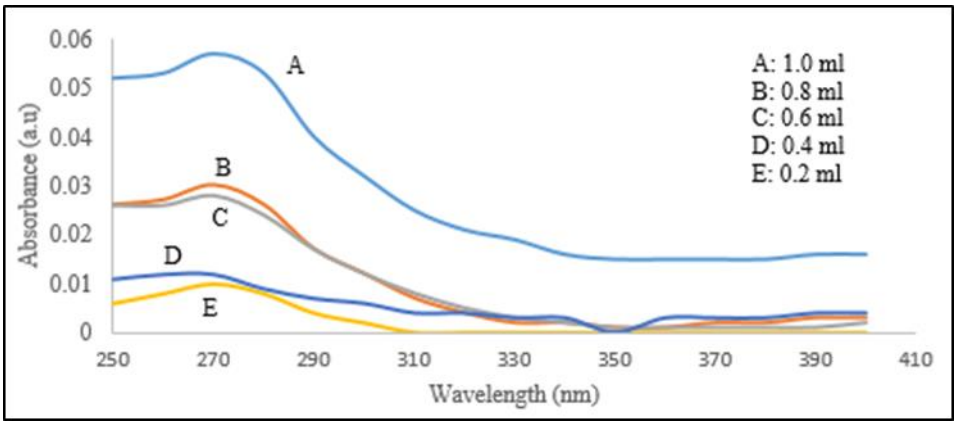


Figure 3. Concentration of different glycerol in irradiated bio-plastics

Opto-Digital Microscope DSX100

The opto-digital microscope is used to characterize the bio-plastic surface morphology. The particle distribution and deterioration effects from radiation could be seen using DSX100. The advantage of using this microscope is it magnifies and measures images in real-time. It also stores and transmits images for future viewing, making microscopy possible for beginners. The bio-plastics produced were transparent, smooth, thick and deformable, whereas conventional plastics were firm, stretchable, thin and transparent. Bio-plastic is quite soft compared to conventional plastics, making it difficult to compare the irradiation effects on both types of plastic.

The samples were analyzed for both irradiated and non-irradiated conditions. Figure 4(a) shows the surface condition of conventional plastic made of petrochemical substances. This sample was not exposed to a gamma source. Hence, the surface morphology was affected by the radiation. The surface was free of degradation effect and had a firm structure.



Figure 4. Surface morphology of (a) non-irradiated and (b) irradiated conventional plastic. While (c) non-irradiated (d) irradiated surface morphology of bio-plastic

Figure 4(b) shows the radiation effects on plastic. The plastic exposed to radiation deteriorated on its surface due to the oxygen reacting with the free radicals [6]. The free radical formation could significantly change the molecular structure [20]. Several parallel strips developed on the plastic's surface, possibly due to the radiation effects. Figure 4(c) shows the bio-plastic surface morphology in natural conditions. The surface is rigid due to using glycerol as a plasticizer agent. It shows the fracture surface of dispersed fibers without the incidence of gamma radiation [21]. The sample was brittle due to bubbles, which is problematic for the bio-plastic-making process.

The bio-plastic sample shown in Figure 4(d) has the embrittlement effect due to irradiation. Gamma rays induced chain scission and degradation effect [9], resulting in the melt viscosity and embrittlement observed in Figure 4(d). Because of radiation-induced oxidation, the surface is deepened with oxygen-containing hydrophilic groups [22], indicating that the bio-plastic surface becomes hydrophilic after irradiation. The surface of the irradiated bio-plastic also appeared darker than the non-irradiated ones because of the irradiation degradation effect. The exposure to gamma energy improved the degradation process. When exposed to radiation, the bio-plastics could be degraded by photolysis, giving the samples a lower molecular weight, thus enhancing and quickening the bio-plastics degradation process [23].

The bubbles on the surface resulted from the inadequate method when handling the samples during the drying process. The samples were left at room temperature for several days, promoting the bio-plastic surface's oxidation process. It is more convenient to dry the sample using an oven to avoid bubble formation [24]. The atmosphere in which the radiation took place modifies the effects. The differences are usually observed in the presence or absence of oxygen. However, the findings are inconsistent with some plastics degradation that was enhanced in the presence of air. This research used the natural drying process to manage the equilibrium of moisture content, which was critical to determine the ideal microbe development, material deterioration and degradation circumstances. It also aids in determining food stability at a certain moisture level in a specific environment.

Fourier transform infrared spectroscopy analysis

FTIR is chosen to describe the functional group present at the material surface before and after drying [24]. All samples were recorded in absorbance units from 4000 to 450 cm^{-1}. Four samples were analyzed which are irradiated bio-plastic and conventional plastic also non-irradiated bio-plastic and conventional plastic. Figure 5 shows the band at 3000-3600 cm^{-1} range spectra of irradiated bio-plastic indicate the O-H stretching which is broader than other absorption bands [25]. It is somehow overlaps the N-H stretching in the same region. There are four primary peaks shown in table 2 and 3 as similar to previous study [26]. The peak at 3293.22 cm^{-1} signifies the presence of alcohols group in the sample as glycerol was involved in the process of making the bio-plastic.

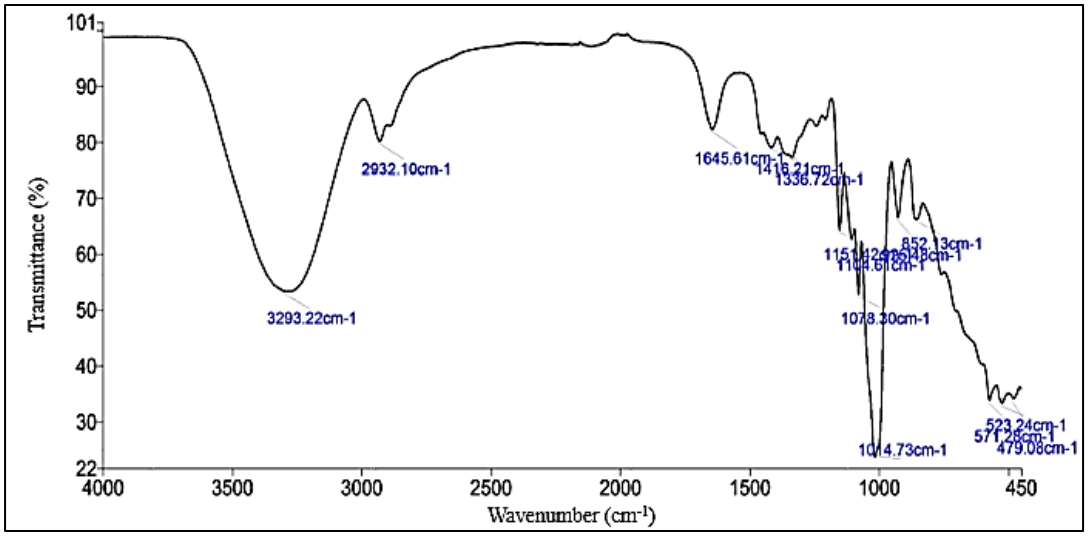


Figure 5. FTIR spectrum for irradiated bio-plastic

Another peak at 2932.10 cm^{-1} indicates the presence of the alkanes group, i.e., the C-H bond, which has medium to strong infrared absorption intensity [27]. The C=O bond at 1645.61 cm^{-1} is attributed to the stretching vibrations of strong carbonyl compounds due to the presence of ketones or aldehydes compounds produced due to thermal decomposition during the sample preparation [28, 29]. Peaks at 1014.73 cm^{-1} were due to the presence of alcohol groups C-O bond involved during the polymerization process, meaning that the starch alcohols group was involved in the hydrogen bond formation. Still, it is not as broad as the O-H bond.

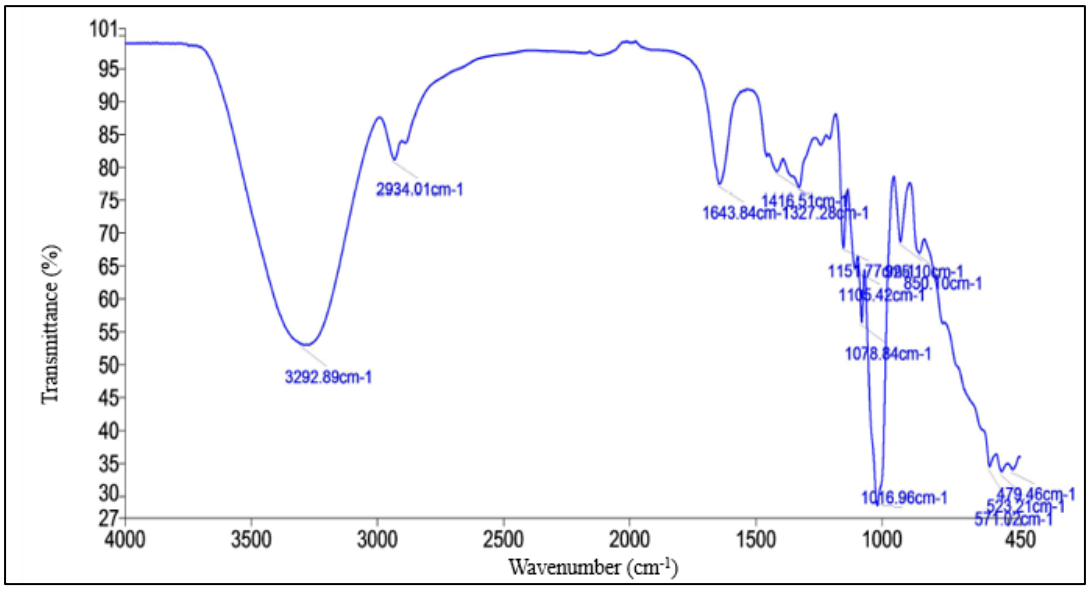


Figure 6. FTIR spectrum for non-irradiated bio-plastic

Table 2 shows the absorption spectrum for non-irradiated bio-plastic. Figure 6 shows no significant changes occurred from irradiated and non-irradiated samples except the slightly different values of wavenumber shown by the four primary peaks. However, a lower wave number indicates a stronger hydrogen bond interaction [30]. Starting from the first peak, there is a decreasing value of the alcohol group

absorption band for the non-irradiated bio-plastic and a decreasing carboxylic acids presence. Table 2 shows a radical cation, likely generated on the carbonyl function under gamma radiation. Another effect was the generation of radical cation-beta on the ester oxygen, providing an alkyl radical and an oxonium ion. The latter collapsed to release acetic acid and a carbocation. The free radical generated an oxyl radical with a carbocation in an alpha position.

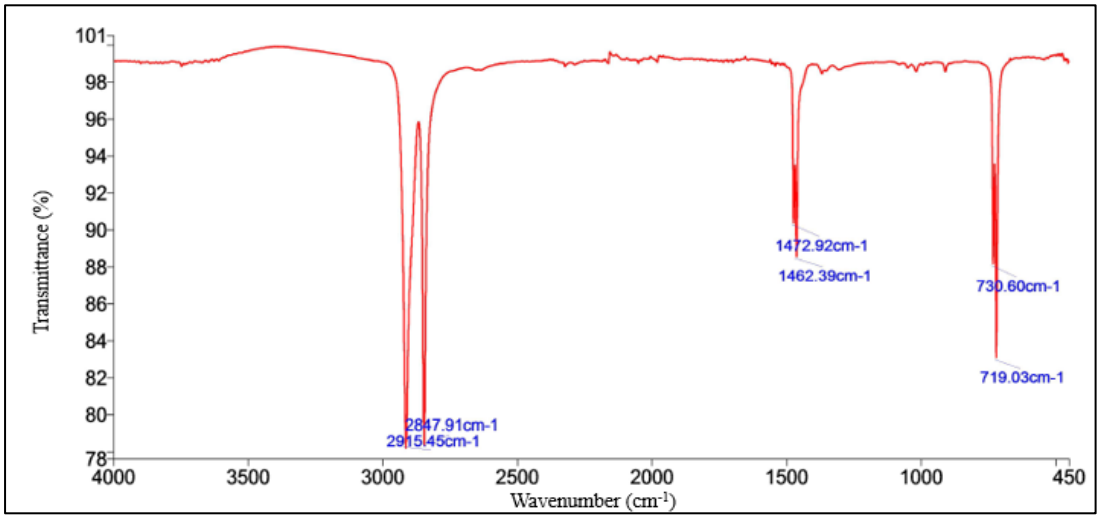


Figure 7. FTIR spectrum for irradiated conventional plastic

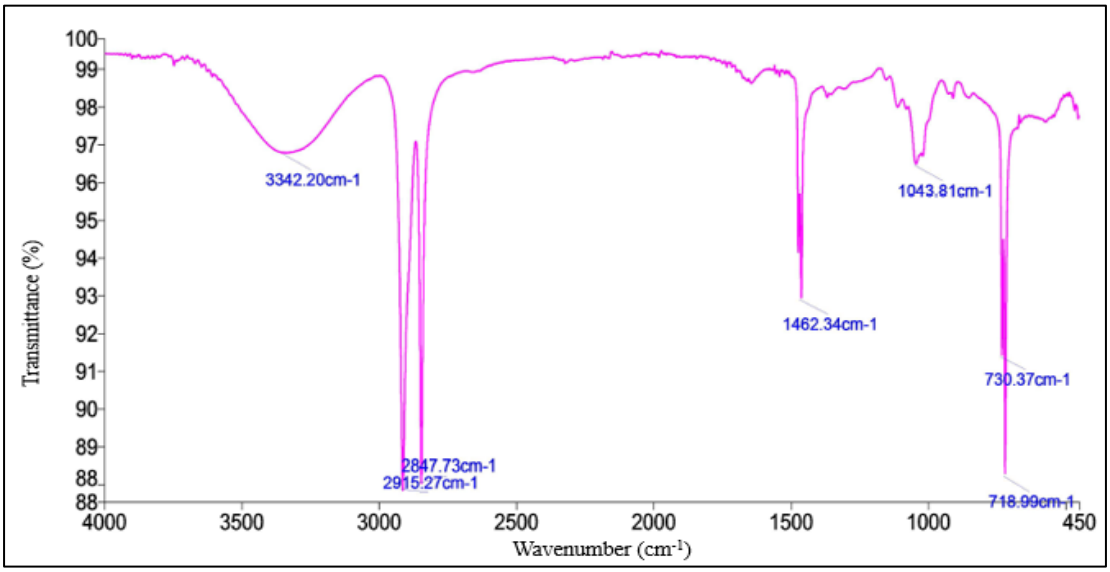


Figure 8. FTIR spectrum for non-irradiated plastic

Table 3 shows the IR spectra for both irradiated and non-irradiated plastics. No significant changes were obtained from both results except a few reduced peaks at certain wave numbers of absorption bands (Figure 7). This agrees with a previous study that there were completely unchanged peaks even after the gamma exposure [30]. The most significant difference is the reduced peak at 3342.20 cm^{-1} of non-irradiated plastic exposed to gamma radiation. The gamma exposure caused O-H scission, resulting in the formation of double bonds. The

peaks in the range of 2847-2915 cm^{-1} are similar in both plastics. These show the presence of phenolic groups O-H, which has a very broad and strong absorption bands intensity. This is due to the plastics being irradiated with gamma exposure, leading to radical oxygen formation caused by the ester linkages breaking and, possibly, forming ester radicals.

Table 2. Summary of functional groups of bio-plastics

Functional Group (Absorption Range)	Wavenumbers (cm^{-1})	
	Irradiated Bio-Plastic	Non-Irradiated Bio-Plastic
Alcohols (O-H stretch)	3293.22	3292.89
Alkanes (C-H stretch)	2932.10	2934.01
Carbonyl compounds (C=O stretch)	1645.61	1643.84
Esters (C-O stretch)	1014.73	1016.96

The oxygen radicals can easily combine with hydrogen radicals to form phenolic groups [29]. There is a shift towards a higher wavenumber from the peak at 1043.81 and 1472.92 cm^{-1} of non-irradiated and irradiated plastics, respectively (Figure 8). This shift is due to the C=O group formation. The peaks at range 718-730 cm^{-1} indicate the plastic's bending vibration bands. It has a medium intensity of alkyl halide groups. Table 2 compares the irradiated and non-irradiated bio-plastic functional groups. The wavenumber differences indicate a radiation effect on the bio-plastics. Table 3 compares the irradiated and non-irradiated conventional plastic functional groups. The most significant difference was reduced alcohol bond in the irradiated conventional plastic.

Table 3. Summary of functional groups of conventional plastics

Functional Group (Absorption Range)	Wavenumbers (cm^{-1})	
	Irradiated Plastic	Non-Irradiated Plastic
Alcohols (O-H stretch)	-	3342.20
Carboxylic acids (O-H stretch)	2915.45 & 2847.91	2915.27 & 2847.73
Alkanes (H-C-H bend)	1462.39	1462.34
Alkyl halides (C-Cl bend)	730.60 & 719.03	730.37 & 718.09

Conclusion

Results show that the irradiated bio-plastic had a higher absorption peak at wavelength 270 nm than non-irradiated bio-plastic, signifying that glycerol concentration was directly proportional to the absorption peak. Glycerol concentration was also directly proportional to the bio-plastic transparency [19], resulting in better UV absorption. Regarding surface morphology, both types of plastic showed degradation effects on their surfaces after they were irradiated. Several long gashes on the conventional plastic indicated that it absorbed the gamma radiation. Due to the gamma radiation's degradation effect, the irradiated bio-plastic surface was slightly darker than the non-irradiated bio-plastic surface. The gamma radiation caused an embrittlement effect. There were bubbles due to the problematic process of drying the bio-plastic. Irradiated bio-plastic samples displayed slightly decreased absorption spectra at 2932.10 and 1014.73 cm^{-1}. However, increased absorption peaks at 3293.22 and 1645.61 cm^{-1} indicated the presence of alcohols and carbonyl groups in the bio-plastics. For irradiated conventional plastic, there was a drastically reduced peak at 3342.20 cm^{-1}, indicating that the alcohol group was eliminated due to the plastic absorbing the gamma radiation. On the other hand, irradiation did not cause significant changes in other peaks.

Acknowledgement

The authors would like to thank the Faculty of Applied Sciences and Technology, Universiti Tun Hussien Onn Malaysia for the facilities provided that make the research possible.

References

1. Aquino, K. A. d. S. (2012). Sterilization by gamma irradiation. *Gamma Radiation,* 51(5): 978-953.
2. Ansari, I., A. and Datta, A., K. (2003). An overview of sterilization methods for packaging materials us ed in aseptic packaging systems. *Trans IChem*, 81(3): 57-65.
3. Ojumu, T. V., Yu, J. and Solomon, B. O. (2004) Pro duction of polyhydroxyalkanoates, a bacterial biod egradable polymer. *Africa Journal of Biotechnolog y*, 43(8):18-24.
4. Zinn, M, Witholtb B. and Eglia T. (2001). Occurren ce, synthesis and medical application of bacterial p olyhydroxyalkanoate. *Advance Drug Delivery*, 53(7): 5-21.
5. Marina, C.V., Salvador, C. N., Eduardo, M., N. and Elaine, A. (2017). Gamma radiation effect on sisal/ polyurethane composites without coupling agents. *Polimeros*, 27(2): 43-47.
6. Haji-Saeid, M., Sampa, M. H. O. and Chmielewski , A. G. (2007). Radiation treatment for sterilization of packaging materials. *Radiation Physics and Che mistry*, *76*(8-9): 1535-1541.
7. Boreen, A. L., Arnold, W. A. and McNeill, K. (200 3). Photodegradation of pharmaceuticals in the aqu atic environment: A review. *Aquatic Sciences.* 65(4): 320-341.
8. Riebel, M. J. (2014). Biooptical and biofunctional properties, applications and methods of polylactic acid films. *US Patent,* 01628828*,* 8(6): 996-998.
9. Silvestre, C., Duraccio, D. and Cimmino, S. (2011) . Food packaging based on polymer nanomaterials. *Progress in Polymer Science*, 36(12): 1766-1782.
10. Zhang, Q. X., Yu, Z. Z. and Xie, X. L. (2007) Prep aration and crystalline morphology of biodegradabl e starch/clay nanocomposites, *Polymer,* 48(2): 719 3-7200.
11. Madison, L. L. and Huisman, G. W. (2000). Micro bial: A review. *Journal of Industrial Engineering*, 6 3(8): 21-53.
12. Marjadi, D. and Dharaiya, N. (2012). Potential mat erials for food nanoclay. *Everyman's Science,* 57(2): 70-73.
13. Balser, K., Hoppe, L., Eicher, T., Wandel, M., Asth eimer, H., J. and Steinmeier, H. (2004). Cellulose e sters. *Ullmann's Encyclopaedia of Industrial Chem istry,* 7(24): 23-29.
14. Saraswat, Y., Patel, M., Sagar, T. and Shil, S. (2005). Bio-plastics from Starch. *Journal of Food Scienc e*, 1(73): 385-387.
15. Stevens, E. S. (2002). Green plastics: an introducti on to the new science of biodegradable plastics. Pri nceton University Press, 78(2): pp. 57-65.
16. Gáspár, M., Benko, Z., Dogossy, G., Réczey, K. an d Czigány, T. (2005). Reducing water absorption in compostable starch-based plastics. *Polymer Degra dation and Stability*, 90(3): 563-569.
17. Wellfair, S. T. (2008). Testing the degradation rates of degradable, non-degradable and bio-degradable plastics within simulated marine environments. *Jou rnal of Marine Science*, 76(2): 243-301.
18. Deanin, R. D. (1975). Additives in plastics. *Enviro nmental Health Perspectives,* 95(11): 35-39.
19. Rojas De Gante, C. and Pascat, B. (1990). Effects o f b-ionizing radiation on the properties of flexible p ackaging materials. *Packaging Technology Science ,* 3: 97-105.
20. Parparita, E., Zaharescu, T., Darie, R.N. and Vasile, C. (2015). Biomass effect on gamma-irradiation be havior of some polypropylene biocomposites. *Indu strial Engineering Chemical*, 54(12): 2404-2413.
21. Gáspár, M., Benko, Z., Dogossy, G., Réczey, K. an d Czigány, T. (2005). Reducing water absorption in compostable starch-based plastics. *Polymer Degra dation and Stability*, 90(3): 563-569.
22. Stark, N. M. and Matuana, L. M. (2007). Character ization of weathered wood e plastic composite surf aces using FTIR spectroscopy, contact angle, and X PS. *Journal of Composites,* 92(8): 1883-1890.
23. Bajer, D. and Kaczmarek, H. (2010). Study of the i nfluence of UV radiation on biodegradable blends b ased on chitosan and starch. *Journal of Advanced S cience,* 107(6): 17-24.

24. Szczepanowska H. and Wilson W. (2000). Permanancy of reprographic images on polyester film. *Journal of American Institute for Conservation,* 39(3): 234-240.
25. Ismail, N. A. (2016). Synthesis and characterization of biodegradable starch-based bioplastics. *Polymer Science*, 87(2): 77-83.
26. Lomelí-ramírez, M. G., Kestur, S. G., Manríquez-González, R., Iwakiri, S., Bolzon, G. and Muniz, D. (2014). Bio-composites of cassava starch-green coconut fiber. *Structure and properties*, 102(1): 576-583.
27. Santos, D. S., Bardi, M. A. G., Machado, L. D. B., Dias, D. B. D., Leonardo, G. A. and Kodama, K. (2009). Influence of thermoplastic starch plasticized with biodiesel glycerol on thermal properties of pp blends. *Journal of Thermal Analysis and Calorimetry,* 97(2): 565-570.
28. Wang, N., Yu, J., Chang, P. R. and Ma, X. (2009). Influence of formaide and water on properties of thermoplastic starch/poly (lactic) blends. *Carbohydrate Polymers, 75*(1): 1-8.
29. Sinha, D. (2012). Structural modifications of gamma irradiated polymers. *FTIR Study,* 3(3): 1365-1371.
30. Alp, D. and Bulantekin, Ö. (2021). The microbiological quality of various foods dried by applying different drying methods: A review. *European Food Research Technology,* 247(6): 1333-1343.

Malaysian Journal of Analytical Sciences (MJAS)
Published by Malaysian Analytical Sciences Society

CHROMATOGRAPHIC METHODS FOR THE DETERMINATION OF DICLOFENAC IN HUMAN BIOLOGICAL SAMPLES: A MINI REVIEW

(Kaedah Kromatografi Untuk Penentuan Diclofenac Dalam Cecair Tubuh Manusia: Satu Ulasan Mini)

Sabreenna Marsya Djuli[1], and Normala Abd Latip[1,2*]

[1]*Faculty of Pharmacy,*
Universiti Teknologi MARA,
42300 Bandar Puncak Alam, Selangor, Malaysia
[2]*Integrative Pharmacogenomics Institute (iPROMISE),*
Universiti Teknologi MARA,
42300 Bandar Puncak Alam, Selangor, Malaysia

[*]*Corresponding author: drnormala6351@uitm.edu.my*

Received: 2 February 2023; Accepted: 18 April 2023; Published: 23 June 2023

Abstract

Diclofenac is a non-steroidal anti-inflammatory drug (NSAID) used to treat pain and inflammatory disorders. Due to a general increase in the usage of pharmaceuticals and incomplete removal of such compounds from through treatment of wastewater, drugs such as diclofenac have been labelled as emerging contaminants of concern. This review covers the chromatographic methods that have been reported in recent literature for the determination of diclofenac in biological fluids of humans. This could be beneficial for researchers interested in the detection and quantification of diclofenac for epidemiological studies to determine the extent of contamination within human populations.

Keywords: diclofenac, chromatographic methods, human fluids

Abstrak

Diclofenac adalah sejenis ubatan anti-keradangan bukan steroid yang digunakan bagi merawat kesakitan dan gejala keradangan. Peningkatan penggunaan farmaseutikal dan kegagalan penyingkiran sepenuhnya sebatian farmaseutikal dari rawatan sisa buangan mengakibatkan diclofenac dilabel sebagai bahan pencemar baru muncul. Ulasan ini meliputi kaedah kromatografi yang telah dilaporkan dalam penerbitan terkini untuk penentuan kepekatan diclofenac dalam sampel cecair tubuh manusia. Ulasan ini diharap memberi faedah buat penyelidik yang melakukan pengesanan dan pengkuantitian diclofenac untuk kajian epidemiologi bagi penentuan kesan pencemaran ini kepada populasi manusia.

Kata kunci: diclofenac, kaedah kromatografi, sampel cecair manusia

Introduction

Diclofenac, with chemical name 2-[2-(2,6-dichloroanilino)phenyl]acetic acid (Figure 1), is a non-steroidal anti-inflammatory drug (NSAID) used to treat pain and inflammatory disorders. Its mechanism of action involves inhibiting the activity of

cyclooxygenase-1 (COX-1) and cyclooxygenase-2 (COX-2) [1]. Diclofenac is often formulated as either the sodium or potassium salt, with the difference between these two formulations being the rate of absorption and onset of action. Diclofenac potassium is more water soluble than diclofenac sodium, allowing for quicker absorption and rapid onset of pain relief [2]. Although diclofenac has useful medical applications, it has also been shown to possibly act as an endocrine-disrupting chemical (EDC). In vivo and in vitro studies have described diclofenac's potential as an EDC, with the possibility of affecting estrogen, androgen, glucocorticoid, and thyroid hormone receptors [3, 4].

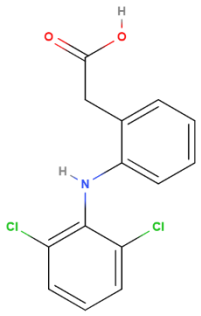


Figure 1. Chemical structure of diclofenac.

The metabolism of diclofenac in humans results in a range of metabolites, including those which are hydroxylated, methoxylated, and acyl glucuronide conjugated. The main metabolites of diclofenac are predominantly 4'-hydroxydiclofenac and 5-hydroxydiclofenac [5]. Most studies in the literature have focused on the toxic effects of diclofenac and its metabolites on avian [6, 7] and marine [8, 9] species. In humans, diclofenac shows acute toxicity. Overdose on NSAIDs such as diclofenac have been reported to result in gastrointestinal, renal, and neurological toxicity [10].

As reviewed by Sathishkumar et al. there is global occurrence of diclofenac contamination in various environmental compartments; thus, diclofenac has been labelled as a contaminant of emerging concern. Diclofenac and other pharmaceuticals can enter water environments through sources such as industrial production sites, wastewater treatment plant effluents, hospitals, and household waste. The presence of diclofenac in water environments can be attributed to a general increase in the usage of pharmaceuticals and incomplete removal of such compounds from wastewater [11]. Studies into the removal of pharmaceuticals from wastewater treatment plants have found that diclofenac and its metabolites are compounds with low removal potential and therefore high detection frequencies in wastewater [12].

Diclofenac and its metabolites have been detected in the drinking water supply of various countries. The unintended exposure of the general population to EDCs such as pharmaceuticals through drinking water supplies is of great concern. In Malaysia, a number of studies have detected diclofenac in drinking water; the maximum concentrations observed were 21.39 ng/L [13], 9.8 ng/L [14], 0.18 ng/L [15], and 0.0821 ng/L [16]. In other Asian countries, such as China, diclofenac has been detected at a maximum level of 3.7 ng/L [17]. At a Japanese drinking water purification plant, the maximum observed level of diclofenac was 16 ng/L [18]. For European countries, diclofenac was detected in surface water and groundwater intended for human consumption in France, with a maximum measured value of 56 ng/L [19]. However, another French study detected comparatively lower concentrations of diclofenac, with a maximum value of 2.5 ng/L being observed [20]. In Spain, a study found that the average concentrations of diclofenac in mineral and tap water were 25 ng/L and 18 ng/L respectively [21].

Although contamination levels of pharmaceuticals are generally lower than the typical dosages that are prescribed for medication, the long-term impacts of such exposure are still not well understood. Therefore, it is of interest to monitor the levels of pharmaceuticals, such as diclofenac, in the general population to determine whether there are long-term impacts. The aim of this review is to give a general overview on the chromatographic methods that have been reported in literature within the past decade for the determination of diclofenac in biological fluids of humans.

Determination of diclofenac in biological samples

Sample preparation

Human biological samples are complex matrices which often require preparation before analysis. The aim of

sample preparation is to obtain a sample that is free of interference and will not damage the instrument chosen for carrying out the analysis. Ideally, the sample preparation steps are minimal; and whilst 100% recovery of analytes from the sample is ideal, oftentimes reproducibility of recovery is more important [22]. In terms of determining analytes from biological samples using chromatographic methods, such as liquid chromatography-mass spectrometry (LC-MS), sample preparation is an important aspect; unwanted components that remain in the sample may interfere with the results obtained. Matrix effects are often caused by the presence of co-eluting compounds in the matrix that alter the ionization efficiency of target analytes in the sample. Matrix effects can be observed as either a loss or increase in response, ultimately affecting the accuracy, precision, and sensitivity of a method [23].

One of the most widely used methods for the extraction of analytes from biological samples is protein precipitation. It is considered as one of the fastest and simplest methods for the removal of proteins from biological samples (such as plasma or serum). However, protein precipitation often provides poor selectivity for extraction of target analytes. Another popular method for the extraction of analytes from biological samples is liquid-liquid extraction (LLE), both conventional methods and newer advances such as liquid-liquid microextraction (LLME). Conventional LLE often requires large volumes of organic solvents and is typically a time-consuming process; hence, newer advances – such as LLME – provides solutions to some the issues of LLE by consuming less solvent. Alternatively, solid-phase extraction (SPE) is another established method for the extraction of target analytes from biological samples. Advantages of SPE include high selectivity and lower organic solvent consumption compared to LLE. Additionally, SPE cartridges may also act as a filtration step, preventing suspended solids in the biological sample from clogging the analytical instrumentation. On the other hand, SPE is a time-consuming extraction process, with high running costs as cartridges are often designed for single use. Newer advances in SPE methods to provide solutions to the issue of conventional SPE include solid-phase microextraction (SPME) [24].

Gas chromatography

Gas chromatography (GC) is an analytical technique used for the separation of volatile compounds from a mixture which is in the gas phase. As a chromatographic method, GC makes use of a mobile and stationary phase; where the mobile phase is an inert gas, and the stationary phase can either be a solid or a liquid. Upon injection into the GC system, the sample is vaporized and carried through the column by the mobile phase, and compounds are separated based on their interactions with the stationary phase. Benefits of GC include relatively fast run times, good peak separation, and it works in combination with various selective detection methods. However, GC requires the compounds of interest to be thermally stable and sufficiently volatile, which can be an issue [25].

Several GC methods for the determination of diclofenac in human fluids have been developed and reported in literature within the past decade (Table 1). These include methods for serum, plasma, urine, and most recently, whole blood samples. All of the studies from Table 1 made use of capillary columns. For GC, there are two types of columns that can be used: packed columns or capillary columns. A packed column contains a fully-packed stationary phase made up of fine particles. On the other hand, a capillary column contains a stationary phase that that is coated on the inner column wall. Due to the fully-packed stationary phase, packed columns have higher internal pressures than capillary columns. Most packed columns are 2 – 6 m in length with internal diameters of 2 – 4 mm, whilst capillary columns are typically 15 – 100 m in length with internal diameters of 150 – 300 μm. In general, longer columns provide better separation as they have higher theoretical plates per meter. Owing to their internal diameters, packed columns can handle larger sample volumes than capillary columns. However, if too much sample is injected tailing may be observed, resulting in poorer separation. Therefore, capillary columns are often preferred as they provide better resolution, require smaller amounts of sample, and lower pressures compared to packed columns [31].

In terms of the stationary phase, all of the studies in Table 1 used non-polar columns based on

dimethylpolysiloxane. In general, non-polar analytes are more easily separated using a non-polar stationary phase [31]. In terms of the mobile phase, three of the studies used helium [26, 29, 30], whilst one used nitrogen [27]. Helium is often chosen as the inert gas to be used as it is more efficient than nitrogen and is safer than hydrogen. However, helium is more expensive than nitrogen, which may be a point of consideration [32].

In the studies included, the GC system is paired with either a flame ionization detector (FID) or mass spectrometer (MS) for the detection of diclofenac. The study which employed GC-tandem MS (GC-MS/MS) for the analysis diclofenac in whole blood samples reported the lowest limit of quantification (LOQ) of 0.1 µg/L [26]. In comparison, the lowest LOQ reported using GC-FID was 5.0 µg/L, for the analysis of diclofenac in urine samples [30]. Another advantage of GC-MS is its ability to provide structural information, which can be important in cases where there are co-eluting compounds; GC-FID is unable to differentiate compounds with the same retention time. This is especially significant when dealing with human biological samples, as there is often a limited sample amount. With GC-MS, the profiling of multiple EDCs from a single sample is possible even with co-eluting compounds. However, the instrumentation for GC-MS is often much more expensive than GC-FID [33].

Liquid chromatography

Liquid chromatography (LC) is an analytical method used for the separation of a mixture of compounds which are soluble in solvent. LC, like GC, makes use of a mobile and stationary phase; the difference lies in the mobile phase being a solvent or solvent mixture, and the stationary phase is a porous solid. The separation of compounds from a mixture relies on the interactions between the compounds of interest with both the mobile and stationary phases. Compounds which have higher affinity for the mobile phase will be eluted more quickly, whereas those with higher affinity for the stationary phase will remain in the column for a longer period of time [33].

Several LC methods for the determination of diclofenac in human fluids have been developed and reported in literature within the past decade (Table 2). Plasma samples have been the focus of these studies, although there are also methods for serum and urine samples reported.

Many of the studies used reversed-phase high-performance liquid chromatography (HPLC); this means that the stationary phase is hydrophobic, whilst the mobile phase is polar. The more hydrophobic the molecules being carried by the mobile phase, the more strongly adsorbed to the stationary phase they are and the longer their retention times [33]. The most common column employed by the studies in Table 2 was the octadecyl silane (ODS) column, which is often referred to as a C_{18} column. One study used an octyl silane column, also known as a C_8 column [40]. The difference between a C_{18} and C_8 column is the number of alkyl chains which are bonded to the silica. C_{18} columns are more densely packed and hydrophobic in comparison to C_8 columns; therefore, the retention times of non-polar compounds will be greater in the C_{18} column [33]. One study used a hydrophilic interaction liquid chromatography (HILIC) system, which is another mode of chromatography used for the analysis of polar and hydrophilic compounds [39]. The advantage of using HILIC over reversed-phase HPLC for the detection of polar pharmaceutical compounds, such as diclofenac, is that the analytes are better retained by the column [41].

Two of the studies used methanol/water for the solvent system [34, 35], whilst the other five studies used acetonitrile/water for the solvent system [36-40]. Historically, the most common organic solvents chosen for reversed-phase LC are methanol, acetonitrile, and tetrahydrofuran; of the three, methanol has the weakest elution strength whilst tetrahydrofuran has the strongest elution strength. However, tetrahydrofuran is rarely used nowadays due to toxicity and safety issues. The choice of acetonitrile as the organic solvent for the mobile phase is often made due to the stronger elution strength compared to methanol; furthermore, acetonitrile is less viscous than methanol resulting in improved column efficiency. Nevertheless, methanol may also be chosen as the organic solvent for the mobile phase as it is less expensive compared to acetonitrile [42].

Table 1. An overview on GC methods for the determination of diclofenac in human fluids within the past decade

Formulation	Matrix	Sample Treatment	Recovery (%)	Detector	Column	Carrier Gas	Temperature (°C)	LOQ (µg/L)	Ref.
Diclofenac sodium	Whole blood	1. LLE	92.2 – 105.9	MS/MS (m/z 277 → 242)	SH-RXI-5MS (30 m × 0.25 mm i.d., 0.25 µm film thickness)	Helium	Start at 60°C. Held for 2 min. Increased to 320°C at 15°C/min. Held for 2 min.	0.1	[26]
Diclofenac sodium	Serum, Urine	1. Derivatization (ethyl chloroformate) 2. LLE	Serum: 99 Urine: 97	FID (310 nm)	DB-1 (30 m x 0.32 mm i.d., with 0.25 µm film thickness)	Nitrogen	Start at 150°C. Held for 3 min. Increased to 280°C at 20°C/min. Held for 5 min.	1500	[27]
Diclofenac	Serum	1. LLE 2. Derivatization (N,O-Bis(trimethylsilyl)trifluoroacetamide (BSTFA) with 1% Trimethylchlorosilane (TMCS))	70.3	MS	Agilent J&W HP-5ms UI (30 m x 0.25 µm i.d., with 0.25 µm film thickness)	Not stated	Start at 120°C. Held for 1 min. Increased to 300°C at 15°C/min.	10	[28]
Diclofenac sodium	Plasma	1. Deproteination (phosphoric acid and acetone) 2. LLE 3. Derivatization (pentafluoropropionic anhydride (PFPA))	89 – 95	MS (m/z 277)	BP-1 fused silica (15 m x 0.25 µm i.d., with 0.25 µm film thickness)	Helium	Start at 150°C. Held for 4 min. Increased to 180°C at 4°C/min. Held for 0.5 min. Increased to 300°C at 60°C/min. Held for 0.5 min.	0.25	[29]
Diclofenac sodium	Urine	Ultrasound-enhanced air-assisted liquid–liquid microextraction (USE-AALLME)	74	FID	BP-20 SGE fused-silica capillary column (30 m x 0.32 mm i.d., with 0.25 µm film thickness)	Helium	Start at 100°C. Increased to 230°C at 30°C/min. Held for 10 min. Increased to 260°C at 30°C/min. Held for 7 min.	5.0	[30]

Two of the studies [39,40] made use of ammonium acetate as buffer solutions to improve peak shape [43]. The study by Klencsár et al. [38] made use of formic acid as an additive; formic acid is often used for MS studies as it provides protons for the MS analysis when carried out in positive mode [44]. It should be noted that diclofenac is a weak acid, with pKa value of 4.15 and logP value of 4.51 [45]. Three of the studies used mobile phases with pH values below 4, which means that the diclofenac is in its non-ionized form and has improved retention on the non-polar stationary phase [35, 37, 40]. Only one study used a mobile phase of pH 6.8, where the diclofenac would be in its ionized form [39]. This choice was made because the mode of chromatography used was a HILIC system, where the retention of analytes is dependent on the electrostatic interactions between the positively charged aminopropyl groups of the stationary phase and the negatively charged carboxylic acid functional groups of NSAIDs such as diclofenac.

In the studies included, the most popular LC technique is high-performance liquid chromatography (HPLC), paired with an ultraviolet (UV) detector. The main advantages of UV detectors are that they are relatively inexpensive and simple to operate [46]. However, specificity may be an issue, as there is no way to confirm that the absorption is not due to possible contaminants that also absorb across the wavelengths being observed. Another detector that can be paired with LC is an MS detector. Much like GC-MS, an advantage of liquid chromatography-mass spectrometry (LC-MS) is its ability to provide structural information, and therefore increase specificity when compared to HPLC-UV. Furthermore, MS detectors are often more sensitive than UV detectors, and lower LOQs can be obtained. However, the instrumentation for LC-MS is often much more expensive than HPLC-UV [33]. Klencsár et al. developed a novel quantification method for the detection of diclofenac using HPLC coupled to tandem inductively coupled plasma-mass spectrometry (ICP-MS), which is another type of MS that uses inductively coupled plasma to ionize the sample [38]. ICP-MS is an analytical technique for the determination of trace level elements in environmental and biological samples. Diclofenac contains chlorine (Cl) atoms, enabling the use of ICP-MS detection.

The study which employed HILIC-MS/MS reported the lowest LOQ of 0.000125 µg/L [39]. In comparison, the lowest LOQ reported using HPLC-UV was 0.0358 µg/L, for the determination of NSAIDs, including diclofenac, in human serum [35]. The lowest LOQ reported using a photodiode array (PDA) as the detector was 0.002 µg/L, for the determination of NSAIDs, including diclofenac, in human plasma and urine [37].

One of the main benefits of using LC over GC for the detection of diclofenac from human biological samples is that the samples are already in liquid form and can be injected into the LC system without the need for vaporization [33]. Furthermore, due to GC requiring volatile samples, temperatures required to run the analysis are often much higher than LC. On the other hand, the speed of elution is often much faster for GC than LC [25].

Conclusion

Several chromatographic techniques for the determination of diclofenac in human fluids have been reported in literature over the past decade such as hyphenated GC and LC techniques. Generally, the studies employing LC techniques achieved lower LOQs than those using GC. The most popular detector for the detection of diclofenac was either a UV or MS detector. Whilst UV detectors are relatively inexpensive and simple to operate, MS detectors offer improved selectivity and specificity. This is especially important as expected exposure to pharmaceuticals, such as diclofenac, through contamination of drinking water is relatively low. Therefore, the levels of diclofenac present in human biological fluids would also be expected to be at trace levels and require high sensitivity for accurate analysis.

Table 2. An overview on LC methods for the determination of diclofenac in human fluids within the past decade

Formulation	Matrix	Sample Treatment	Recovery (%)	Detector	Column	Mobile Phase	LOQ (µg/L)	Ref.
Diclofenac	Plasma, Urine	1. Protein precipitation 2. Stir bar sorptive extraction (SBSE)	69 – 74	UV (220 nm)	C_{18} (250 x 4.6 mm; 10 µm)	Methanol/0.2% acid acetic/water (70/0.2/29.8, v/v)	0.65 (Plasma), 0.45 (Urine)	[34]
Diclofenac sodium	Serum	1. Protein precipitation	98 – 99	UV (230 nm)	Shimadzu Shim-pack CLC-ODS (M) (4.6 mm i.d. x 0.25mm)	Methanol/water pH 3.5 (80:20, v/v)	0.0358	[35]
Diclofenac	Plasma, Serum, Urine	1. Protein precipitation 2. Solid-phase microextraction (SPME)	Plasma: 98 – 99 Serum: 97 – 98 Urine: 95 – 98	UV (280 nm)	Eurosphere C_{18} (250 × 4.6 mm)	Acetonitrile/water (50/50, v/v)	0.14	[36]
Diclofenac	Plasma, Urine	1. Protein precipitation 2. Magnetic solid phase extraction (MSPE)	Plasma: 99 – 101 Urine: 99 – 100	Photodiode array (275 nm)	Luna Omega C_{18} (100 mm x 2.1 mm, 1.7 µm)	Acetonitrile and potassium dihydrogen phosphate (10 mM pH 2) in water (50/50, v/v)	0.002	[37]
Diclofenac sodium	Plasma	1. Protein precipitation	93 – 96	ICP-MS/MS (m/z 35 (Cl^+) → 37 (ClH_2^+)	Pre-concentration: Waters XBridge BEH C_{18} (4.6 x 20 mm; 3.5 µm) Separation: Waters XBridge BEH C_{18} (4.6 x 150 mm; 3.5 µm)	A: 0.1% (v/v) formic acid in MQ water B: 0.1% (v/v) formic acid in acetonitrile	2	[38]
Diclofenac	Plasma	1. Protein precipitation	97 – 101	MS/MS (m/z 294 → 250)	Unison UK-Amino column (50 mm × 3 mm; 3 µm)	A: 10 mM ammonium acetate solution (pH 6.8) B: Acetonitrile	0.000125	[39]
Diclofenac potassium	Plasma	1. LLE		UV (230 nm)	Thermo BDS Hypersil C8 (250 x 4.6 mmm; 5 µm)	Acetonitrile and 0.02M ammonium acetate buffer pH 3.5 (53:47, v/v)	25	[40]

References

1. Alfaro, R. A. and Davis, D. D. (2021). Diclofenac. Access from https://www.ncbi.nlm.nih.gov/books/NBK557879/. [Access online 18 August 2021]
2. Altman, R., Bosch, B., Brune, K., Patrignani, P. and Young, C. (2015). Advances in NSAID development: Evolution of diclofenac products using pharmaceutical technology. *Drugs*, 75: 859-877.
3. Klopčič, I., Markovič, T., Mlinarič-Raščan, I., and Sollner Dolenc, M. (2018). Endocrine disrupting activities and immunomodulatory effects in lymphoblastoid cell lines of diclofenac, 4-hydroxydiclofenac and paracetamol. *Toxicology Letters*, 294: 95–104.
4. Gröner, F., Ziková, A. and Kloas, W. (2015). Effects of the pharmaceutical's diclofenac and metoprolol on gene expression levels of enzymes of biotransformation, excretion pathways and estrogenicity in primary hepatocytes of Nile tilapia (*Oreochromis niloticus*). *Comparative Biochemistry Physiology Part C: Toxicology and Pharmacology,* 167: 51-57.
5. Tang, W. (2003). The metabolism of diclofenac-enzymology and toxicology perspectives. *Current Drug Metabolism*, 4(4): 319-329.
6. Oaks, J. L., Gilbert, M., Virani, M. Z., Watson, R. T., Meteyer, C. U., Rideout, B. A., Shivaprasad, H. L., Ahmed, S., Chaudhry, M. J. I., Arshad, M., Mahmood, S., Ali, A. and Khan, A. A. (2004). Diclofenac residues as the cause of vulture population decline in Pakistan. *Nature*, 427(6975): 630-633.
7. Hussain, I., Zargham Khan, M., Khan, A., Javed, I., and Kashif Saleemi, M. (2008). Toxicological effects of diclofenac in four avian species. *Avian Pathology*, 37(3): 315-321.
8. Bonnefille, B., Gomez, E., Courant, F., Escande, A. and Fenet, H. (2018). Diclofenac in the marine environment: A review of its occurrence and effects. *Marine Pollution Bullettin*, 131: 496-506.
9. Joachim, S., Beaudouin, R., Daniele, G., Geffard, A., Bado-Nilles, A., Tebby, C., Palluel, O., Dedourge-Geffard, O., Fieu, M., Bonnard, M., Palos-Ladeiro, M., Turiès, C., Vulliet, E., David, V., Baudoin, P., James, A., Andres, S. and Porcher, J. M. (2021). Effects of diclofenac on sentinel species and aquatic communities in semi-natural conditions. *Ecotoxicology Environmental Safety*, 211: 111812.
10. Hunter, L. J., Wood, D. M. and Dargan, P. I. (2011). The patterns of toxicity and management of acute nonsteroidal anti-inflammatory drug (NSAID) overdose. *Open Access Emergency Medicine*, 3: 39-48.
11. Sathishkumar, P., Meena, R. A. A., Palanisami, T., Ashokkumar, V., Palvannan, T. and Gu, F. L. (2020). Occurrence, interactive effects and ecological risk of diclofenac in environmental compartments and biota - a review. *Science Total Environment*, 698: 134057.
12. Kołecka, K., Gajewska, M., Stepnowski, P. and Caban, M. (2019). Spatial distribution of pharmaceuticals in conventional wastewater treatment plant with Sludge Treatment Reed Beds technology. *Science Total Environment*, 647: 149-157.
13. Wee, S. Y., Haron, D. E. M., Aris, A. Z., Yusoff, F. M. and Praveena, S. M. (2020). Active pharmaceutical ingredients in Malaysian drinking water: consumption, exposure, and human health risk. *Environmental Geochemistry Health*, 42(10): 3247-3261.
14. Wee, S. Y., Ismail, N. A. H., Haron, D. E. M., Yusoff, F. M., Praveena, S. M. and Aris, A. Z. (2022). Pharmaceuticals, hormones, plasticizers, and pesticides in drinking water. *Journal Hazardous Materials*, 424: 127327.
15. Praveena, S. M., Mohd Rashid, M. Z., Mohd Nasir, F. A., Sze Yee, W. and Aris, A. Z. (2019). Occurrence and potential human health risk of pharmaceutical residues in drinking water from Putrajaya (Malaysia). *Ecotoxicology Environmental Safety*, 180: 549-556.
16. Mohd Nasir, F. A., Praveena, S. M. and Aris, A. Z. (2019). Public awareness level and occurrence of pharmaceutical residues in drinking water with potential health risk: A study from Kajang (Malaysia). *Ecotoxicology Environmental Safety*, 185: 109681.

17. Leung, H. W., Jin, L., Wei, S., Tsui, M. M. P., Zhou, B., Jiao, L., Cheung, P. C., Chun, Y. K., Murphy, M. B., and Lam, P. K. S. (2013). Pharmaceuticals in tap water: Human health risk assessment and proposed monitoring framework in China. *Environmental Health Perspective*, 121(7): 839-846.
18. Simazaki, D., Kubota, R., Suzuki, T., Akiba, M., Nishimura, T. and Kunikane, S. (2015). Occurrence of selected pharmaceuticals at drinking water purification plants in Japan and implications for human health. *Water Research*, 76: 187-200.
19. Vulliet, E. and Cren-Olivé, C. (2011). Screening of pharmaceuticals and hormones at the regional scale, in surface and groundwaters intended to human consumption. *Environmental Pollution*, 159 (10): 2929-2934.
20. Togola, A. and Budzinski, H. (2008). Multi-residue analysis of pharmaceutical compounds in aqueous samples. *Journal of Chromatography A*, 1177 (1): 150-158.
21. Carmona, E., Andreu, V. and Picó, Y. (2014). Occurrence of acidic pharmaceuticals and personal care products in Turia River Basin: From waste to drinking water. *Science Total Environment*, 484(1): 53-63.
22. Majors, R. E. (2013). Sample preparation fundamentals for chromatography. Agilent Technologies, Inc., Mississauga: pp 1-8.
23. Zhou, W., Yang, S. and Wang, P. G. (2017). Matrix effects and application of matrix effect factor. *Bioanalysis*, 9(23): 1839-1844.
24. Clark, K. D., Zhang, C. and Anderson, J. L. (2016). Sample preparation for bioanalytical and pharmaceutical analysis. *Analytical Chemistry*, 88(23): 11262-11270.
25. Al-Bukhaiti, W. Q., Noman, A., Qasim, A. S. and Al-Farga, A. (2017). Gas chromatography: Principles, advantages and applications in food analysis. *International Journal Science Innovations Discoveries*, 186: 2319-1473.
26. Szpot, P., Wachełko, O. and Zawadzki, M. (2021). Application of ultra-sensitive GC-QqQ-MS/MS (MRM) method for the determination of diclofenac in whole blood samples without derivatization. *Journal of Chromatography B: Analytical Technologies Biomedicine Life Sciences*, 1179: 122860.
27. Jalbani, N. S., Solangi, A. R., Khuhawar, M. Y., Memon, S., Junejo, R., and Memon, A. A. (2020). Gas chromatographic and spectrophotometric determination of diclofenac sodium, ibuprofen, and mefenamic acid in urine and blood samples. *Turkish Journal Pharmaceutical Sciences*, 17: 465-473.
28. Krokos, A., Tsakelidou, E., Michopoulou, E., Raikos, N., Theodoridis, G. and Gika, H. (2018). NSAIDs determination in human serum by GC-MS. *Separation,* 5(3): 37.
29. Shah, I., Barker, J., Naughton, D. P., Barton, S. J. and Ashraf, S. S. (2016). Determination of diclofenac concentrations in human plasma using a sensitive gas chromatography mass spectrometry method. *Chemistry Central Journal*, 10: 52.
30. Barfi, B., Asghari, A., Rajabi, M., Goochani Moghadam, A., Mirkhani, N. and Ahmadi, F. (2015). Comparison of ultrasound-enhanced air-assisted liquid-liquid microextraction and low-density solvent-based dispersive liquid-liquid microextraction methods for determination of nonsteroidal anti-inflammatory drugs in human urine samples. *Journal Pharmaceutical Biomedicine Analysis*, 111: 297-305.
31. Harvey, D. (2019). Gas chromatography. Access from https://chem.libretexts.org/@go/page/70719. [Access online 15 March 2023]
32. Smolková-Keulemansová, E. and Feltl, L. (1991). Comprehensive analytical chemistry. Elsevier, New York: pp. 223-462.
33. Hage, D. S. (2018). Principles and applications of clinical mass spectrometry. Elsevier, New York: pp. 1-32.
34. Jafari, Z. and Hadjmohammadi, M. R. (2020). A banana peel/silicon glue coated stir bar for extraction of aspirin, diclofenac, ibuprofen and mefenamic acid followed by high performance liquid chromatography-UV detection. *Analytical Methods*, 12: 4429-4437.
35. Ali, S. N., Akram, S., Qayoom, A., Naz, N. and Ayub, A. (2020). Liquid chromatographic method for simultaneous determination of alprazolam with NSAIDs in bulk drug, pharmaceutical formulation and human serum. *Pakistan Journal Pharmaceutical Sciences*, 33: 121-127.

36. Mirzajani, R., Kardani, F. and Ramezani, Z. (2019). Preparation and characterization of magnetic metal–organic framework nanocomposite as solid-phase microextraction fibers coupled with high-performance liquid chromatography for determination of non-steroidal anti-inflammatory drugs in biological fluids and tablet formulation samples. *Microchemical Journal*, 144: 270-284.
37. Ferrone, V., Carlucci, M., Ettorre, V., Cotellese, R., Palumbo, P., Fontana, A., Siani, G., and Carlucci, G. (2018). Dispersive magnetic solid phase extraction exploiting magnetic graphene nanocomposite coupled with UHPLC-PDA for simultaneous determination of NSAIDs in human plasma and urine. *Journal Pharmacutical Biomedicine Analysis*, 161: 280-288.
38. Klencsár, B., Balcaen, L., Cuyckens, F., Lynen, F. and Vanhaecke, F. (2017). Development and validation of a novel quantification approach for gradient elution reversed phase high-performance liquid chromatography coupled to tandem ICP-mass spectrometry (RP-HPLC-ICP-MS/MS) and its application to diclofenac and its related compounds. *Analytica Chimica Acta*, 974: 43-53.
39. Nemoto, T., Lee, X. P., Kumazawa, T., Hasegawa, C., Fujishiro, M., Marumo, A., Shouji, Y., Inagaki, K., and Sato, K. (2014). High-throughput determination of nonsteroidal anti-inflammatory drugs in human plasma by HILIC-MS/MS. *Journal Pharmaceutical Biomedicine Analysis*, 88: 71-80.
40. Dahivelkar, P. P., Bhoir, S. I., Bari, S. B., Surana, S. J. and Bhagwat, A. M. (2012). Simultaneous determination of diclofenac potassium and drotaverine hydrochloride in human plasma using reversed-phase high-performance liquid chromatography. *Journal Chromatographic Science*, 50: 694-701.
41. Alpert, A. J. (1990). Hydrophilic-interaction chromatography for the separation of peptides, nucleic acids and other polar compounds. *Journal Chromatography A.*, 499: 177-196.
42. Dong, M. and Boyes, B. E. (2018). Modern trends and best practices in mobile-phase selection in reversed-phase chromatography. *LC-GC Europe*, 31: 572-583.
43. Lim, C. K. and Peters, T. J. (1984). Ammonium acetate: A general purpose buffer for clinical applications of high-performance liquid chromatography. *Journal of Chromatography A*, 316: 397-406.
44. Núñez, O. and Lucci, P. (2014). Applications and uses of formic acid in liquid chromatography-mass spectrometry analysis. *Advances in Chemical Research*, 20: 71-86.
45. National Center for Biotechnology Information (2023). PubChem Compound Summary for CID 3033, Diclofenac. Access from https://pubchem.ncbi.nlm.nih.gov/compound/Diclofenac. [Access online 15 March 2023]
46. Wang, Q., Wang, G., Xie, S., Zhao, X. and Zhang, Y. (2019). Comparison of high-performance liquid chromatography and ultraviolet visible spectrophotometry to determine the best method to assess Levofloxacin released from mesoporous silica microspheres/nano hydroxyapatite composite scaffolds. *Experimental and Therapeutic Medicine*, 17(4): 2694-2702.

Malaysian Journal of Analytical Sciences (MJAS)
Published by Malaysian Analytical Sciences Society

PLACKETT-BURMAN DESIGN OPTIMIZED DISPERSIVE LIQUID-LIQUID MICROEXTRACTION COUPLED WITH GAS CHROMATOGRAPHY-MASS SPECTROMETRY FOR DETERMINATION OF METHAMPHETAMINE FROM LABORATORY COAT MATERIALS

(Pengekstrakan Mikro Cecair-Cecair Serakan Gandingan Kromatografi Gas-Spektrometri Jisim yang Dioptimumkan Secara Rekaan Plackett-Burman untuk Penentuan Metamfetamin Daripada Bahan Kot Makmal)

Su Chien Quah[1], Way Koon Teoh[1], Vanitha Kunalan[2], Noor Zuhartini Md Muslim[1], Warakorn Limbut[3,4,5], Chong Hooi Yew[6], Kah Haw Chang[1], Ahmad Fahmi Lim Abdullah[1*]

[1]*Forensic Science Programme, School of Health Sciences, Universiti Sains Malaysia, 16150 Kubang Kerian, Kelantan, Malaysia*
[2]*Narcotics Division, Forensic Science Analysis Centre, Department of Chemistry, Jalan Sultan, 46661 Petaling Jaya, Selangor, Malaysia*
[3]*Division of Health and Applied Sciences, Faculty of Science, Prince of Songkla University, Hat Yai, Songkhla, 90112, Thailand*
[4] *Center of Excellence for Trace Analysis and Biosensors (TAB-CoE), Prince of Songkla University, Hat Yai, Songkhla, 90112, Thailand*
[5] *Center of Excellence for Innovation in Chemistry, Faculty of Science, Prince of Songkla University, Hat Yai, Songkhla, 90112, Thailand*
[6]*Elmu Higher Education Sdn Bhd, 46200 Petaling Jaya, Selangor, Malaysia*

[*]*Corresponding author: fahmilim@usm.my*

Received: 5 February 2023; Accepted: 18 April 2023; Published: 23 June 2023

Abstract

Accumulated drug residues on contaminated clothing put the wearer at adverse health risk. Therefore, monitoring on laboratory coat contamination shall be in place to safeguard the analysts who have routine exposure in forensic laboratory environment. Using methamphetamine as surrogate drug, this study was aimed to detect the presence of methamphetamine from laboratory coat materials through a response surface methodology optimized dispersive liquid-liquid microextraction (DLLME) in couple with gas chromatography-mass spectrometry (GC-MS). In this study, a Plackett-Burman design was used to optimize the DLLME conditions, including the volumes of extraction and dispersive solvents, the duration of vortex agitation, as well as the speed and time of centrifugation. Residues collected upon DLLME procedure was priorly derivatized with trifluoroacetic acid anhydride followed by GC-MS analysis. Seven types of fabric materials which were contaminated with methamphetamine were extracted and compared. From this study, a volume of 685 µL dichloromethane as extraction solvent, 1000 µL 2-propanol as dispersive solvent, vortex agitation for 90 seconds, and centrifugation at 500 rpm for 5 minutes were determined as the optimum conditions for DLLME. Trace methamphetamine residues were successfully extracted and detected from the different types of laboratory coat materials with recovery percentage of at least 45%. The method could be proposed to laboratories for their evaluation on possible contamination to establish baseline for necessary in-house monitoring and decontamination procedures.

Keywords: Illicit drugs, methamphetamine, dispersive liquid-liquid microextraction, Plackett-Burman design, contaminated laboratory coat

Abstrak

Sisa-sisa dadah yang terkumpul pada pakaian tercemar membawa risiko mudarat kepada pemakai. Justeru, pemantauan pencemaran kot makmal harus diberi perhatian untuk melindungi penganalisis yang mempunyai pendedahan rutin dalam persekitaran makmal forensik. Dengan menggunakan metamfetamin sebagai dadah surogat, kajian ini bertujuan untuk mengesan kehadiran metamfetamin daripada bahan kot makmal melalui pengekstrakan mikro cecair-cecair serakan (DLLME) yang digandingkan dengan kromatografi gas-spektrometri jisim (GC-MS) yang telah dioptimumkan dengan kaedah gerak balas permukaan merangkumi isipadu pelarut pengekstrakan dan pelarut serakan, tempoh pengadukan pusaran, serta kelajuan dan masa pengemparan. Sisa-sisa yang dikumpulkan setelah prosedur DLLME telah diterbitkan terlebih dahulu dengan asid trifluoroasetik anhidrida diikuti dengan analisis GC-MS. Tujuh jenis bahan fabrik yang telah dicemari dengan metamfetamin telah diekstrak dan dibandingkan. Daripada kajian ini, 685 µL diklorometha sebagai pelarut pengekstrakan, 1000 µL 2-propanol sebagai pelarut serakan, pergerakan vorteks selama 90 saat, serta pengemparan pada 500 rpm selama 5 minit telah ditentukan sebagai keadaan optimum bagi DLLME. Sisa-sisa surih metamfetamin telah berjaya diekstrak dan dikesan daripada jenis bahan kot makmal yang berbeza dengan peratusan pemulihan semula sekurang-kurangnya 45%. Kaedah tersebut boleh dicadangkan kepada makmal-makmal untuk penilaian mereka terhadap pencemaran yang berkemungkinan untuk menetapkan garis dasar untuk pemantauan dalaman dan prosedur penyahcemaran yang diperlukan.

Kata kunci: Dadah haram, metamfetamin, pengekstrakan mikro cecair-cecair serakan, rekaan Plackett-Burman, kot makmal tercemar

Introduction

Handling and processing illicit drugs in a drug testing laboratory are known to have potentially contaminated various surfaces within the laboratory [1-3]. It is important to note that illicit drugs often with unknown formulation or synthesis pathway could pose serious health and safety risk to individual who had direct or even indirect contact with the constituents. Besides the cooks and operators of a clandestine drug laboratory, other vulnerable groups such as occupants residing around the clandestine laboratory, law enforcement personnel who investigate drug scene or even the laboratory analysts who perform routine analyses on illicit drugs or their associate chemical are all exposed to additional risk capable of leading to chronic health effects [4, 5]. Consensus standard for occupational exposure limits for common illicit drugs and their precursors for forensic laboratory settings are yet to be established although a study by the National Institute for Occupational Safety and Health (NIOSH) had reported that the detectable cocaine, fentanyl, heroin, and methamphetamine are present at nanogram level, respectively, in the air and on surfaces within drug testing laboratories [2].

In relation to illicit drug contamination to the public, investigations in waste waters and surface water environment to explore the health effects and the trends of drug usage in the local communities were reported [6-8]. Studies were also conducted on various daily high contact surfaces that were found to contain detectable levels of illicit drugs [9, 10], suggesting the possibility of transferring and persisting of these substances. Airborne particles of illicit drugs were also found to be persisting in the forms of residual powder or condensed aerosol [11-13]. Clandestine drug laboratories, in the stage of active or dormant, were contaminated following the activities during cooking and subsequent processing steps [4, 14], where the surface deposition of drug was reported to be as high as 860.0 µg of methamphetamine on a surface of 100 cm^2 [15]. It was also important to note that the illicit drugs and by-products during the clandestine activities could have contaminated the soil, water, and air within or proximate areas to a clandestine drug laboratory site [4, 16].

In the setting of forensic testing laboratories, there are personnel who face higher risk of drug exposure, especially individuals who handle and perform routine drug analyses [1-3]. Residual smoke pollutant could be present on the surfaces and in dust which tend to be released again into the gas phase interacting with other

contaminants and oxidants to form secondary pollutant [17, 18]. Studies have shown that the aerosolized release of illicit drug substance was evident, and drug particles could spread throughout the laboratory via touch, direct transfer, and/or suspension of particulate in the air [1-3], where the analytical balance and its surrounding area were most contaminated. Furthermore, it has been reported that the drug substance can adhere to clothing and other fabrics, even at low and sustained levels of air concentration [17, 18]. This could lead to re-exposure through contact with these contaminated materials and clothing [18].

In the United States, a study conducted by Sisco and Najarro [3] involving over 700 samples from 20 laboratories showed that the contamination levels were at the highest within the drug unit, measured with at least 10 nanograms levels in nearly all sampled areas. Cocaine and heroin were detected more frequently with the highest surface concentrations in these laboratories [3]. These two drugs were highly prevalent on the surfaces and in the air of drug testing laboratories as indicated by NIOSH [2], where 11 out 12 tested laboratories were found to contain cocaine, and heroin was found in nine laboratories. Additionally, airborne fentanyl and methamphetamine were found in four and three laboratories, respectively. All the targeted drugs i.e. cocaine, heroin, fentanyl, and methamphetamine were detected on the bench surfaces in all the twelve laboratories, except one laboratory without detectable level of methamphetamine [2]. In Australia, residues of illicit drugs were detected in police stations [16, 19], where handling of drug evidence could contribute to an elevated background level at the police stations at a level less than 50 ng. Contamination in crime scene vans and storage lockers, report preparation desks, and toxicology units were also reported [1].

Although studies have investigated on various areas within a drug testing laboratory and toxicology units for the presence of drugs, contamination level of laboratory coat worn as personal protection equipment was understudied. This study was initiated to provide some insight on drug contamination levels from a frequently overlooked perspective, specifically from the laboratory coat worn by the laboratory personnel, using methamphetamine as an indicator of the degree of contamination, since methamphetamine is among the most widely abused drug as indicated by its users followed by opiates, amphetamine-type simulant (ATS), cannabis and others [20].

Applications of DLLME in analytical chemistry included the examination of narcotics, illicit drugs, hallucinogens, and cannabinoids [21-23]. In DLLME, the mixing of extraction and dispersive solvents and addition to the aqueous sample solution led to the formation of tiny droplets dispersed throughout the aqueous phase. The creation of a large contact area allows for a fast equilibrium within short extraction time. Additionally, vortex agitation contributes to a rapid partition equilibrium while the centrifugation step facilitates the phase separation after extraction. Upon DLLME, the enriched analytes can be collected with a microsyringe from the sedimented phase and subjected to further examination [22-24].

Using dispersive liquid–liquid microextraction (DLLME) and gas chromatography-mass spectrometry (GC-MS), we reported a Plackett-Burman Design (PBD) for method optimization which was implemented for the determination of methamphetamine from the laboratory coat materials. PBD is a two-level factorial design that only requires N=4t runs (a multiple of 4 for the number of runs) to separate main effects from the interaction effects. Previous studies have also suggested its applicability and practicality in enhancing an analytical technique, particularly during the optimization step [25, 26]. It is hoped that the study would aid in proposing an analytical method to provide a quick snapshot on possible laboratory coat contamination or as a long-term monitoring program incorporated into the quality management system for appropriate laboratory clothing decontamination procedures.

Materials and Methods

Materials and chemicals

Methamphetamine hydrochloride (99.2% purity) was supplied by the Department of Chemistry Malaysia. Tetradecane standard, as the internal standard, was purchased from Dr. Ehrenstorfer GmbH (Augsburg,

Germany). Chromatography-grade acetonitrile, chloroform, dichloromethane, methanol, and 2-proponal were purchased from Merck (Whitehouse Station, NJ, USA). Trifluoroacetic acid anhydride (TFAA) (>99%) used as derivatization agent was purchased from Sigma Aldrich (St. Louis, MO, USA). All chemicals used as they are. A stock solution of methamphetamine was prepared at 50 mg/mL by dissolving 500 mg of methamphetamine standard in methanol and diluting to 10 mL in a volumetric flask. Working standard solutions were prepared by appropriately diluting the stock solution into the pre-defined concentration levels.

Laboratory coat materials

Seven types of fabric materials commonly used for making laboratory coat were obtained from local clothing retailer. These materials were then cut into squares (10 x 10 cm). Prior to the analyses, the laboratory coat materials were washed, dried, and kept in a resealable plastic bag.

Plackett-Burman design of DLLME optimization

The choice of solvents is crucial in DLLME for good extraction efficiency. A preliminary experiment on the selection of extraction (chloroform and dichloromethane) and dispersive (acetonitrile, methanol, and 2-propanol) solvents were firstly carried out. For each combination, 300 µL of each extraction solvent was used in coupled with 300 µL of dispersive solvent which was adapted from the study [21]. The combination which gave the high extraction efficiency was determined through the determination of peak area ratio, considering the peak area of methamphetamine against the peak area of internal standard. Based on the outcome, DLLME was optimized through a PBD using Minitab® 18 software (Minitab Inc., State College, PA, USA). Five factors, covering the volume of extraction solvent, volume of dispersive solvent, duration of vortex agitation, centrifugation time, and centrifugation speed were evaluated with 2 replicates and 2 center points, totaling at 26 runs as demonstrated in Table 1.

Table 1. Plackett-Burman design with five factors of variables.

Factor	Low (-1)	Medium (0)	High (+1)
Volume of extraction solvent (µL)	110	555	1000
Volume of dispersive solvent (µL)	100	550	1000
Duration of vortex agitation (s)	0	45	90
Centrifugation time (min)	5	7.5	10
Centrifugation speed (rpm)	500	1250	2000

Recovery study: Sample preparation procedure

A volume of 100 µL methamphetamine at three different concentrations, namely 5 µg/mL, 15 µg/mL, and 30 µg/mL, was separately spread over the defined area on the laboratory coat materials following the method used in surface contamination study conducted before [27]. The deposited solution was then allowed to dry for 5 mins prior to extraction, leading to the presence of defined masses of methamphetamine (0.5 µg, 1,5 µg and 3.0 µg) on each laboratory coat material. It was noted that the maximum acceptable amounts of surface methamphetamine were varied among the countries worldwide, ranging from 0.5 µg to 4.0 µg per an area of 100 cm^2 [14]. Upon drying, a 7 mL aliquot of 4% (m/v) of sodium hydroxide solution was added to culture tube with the cloth samples followed by 5 mins sonication (200 W) for basic extraction of the drug. The sonicated samples were then transferred into a 10 mL glass syringe, where the syringe plunger was depressed as much as possible to dispense the solution into a 20 cm glass culture tube. The step was repeated by transferring the laboratory coat materials from the syringe into the culture tube followed by an additional of 7 mL 4% of NaOH solution. The sample solution was again dispensed and combined. Prepared solution was then subjected to the optimized DLLME procedure. Subsequently, the extraction phase-dispersed particles found sedimented at the bottom which then were collected and evaporated to dryness under a gentle stream of purified nitrogen gas.

Sample derivatization by TFAA

The sample derivatization procedure was adapted from Abdullah and Miskelly [27]. For derivatization, the residue was added with 100 µL of dichloromethane followed by 100 µL of ethyl acetate and 50 µL of TFAA. The sample was then subjected to a 30-min incubation at 38°C in an oven. Upon incubation, the excessive solvents and TFAA were carefully evaporated using a gentle stream of nitrogen flow. The residue was then reconstituted with 1 mL of ethyl acetate containing 0.25 µL/mL of tetradecane.

GC-MS analysis

Gas chromatographic analyses were performed using a 7890B GC system equipped with a 5977-mass selective detector (MSD) and split/spitless injector (Agilent Technologies, Santa Clara, CA, USA). A HP-5MS capillary column (30 m x 0.32 mm 0.25 µm film thickness) was used for separation and purified helium gas as the carrier gas was flowed at a constant rate of 1.0 mL/min. The front inlet was set at 250°C while the oven temperature was programmed as follows: 70°C for 2 mins, increased at 20°C/min to 280°C, and then hold at 280°C for 2 mins. MassHunter Workstation Software (Version 3.1, Agilent Technologies, Santa Clara, CA, USA) was used for data acquisition and interpretation, where the results were at a rate of 1.0 sec/scan and the mass spectra was collected in scan mode from m/z 41 to m/z 500. The resulting peaks were confirmed through the comparison of retention times and determination by the National Institute of Standards and Technology (NIST) MS Search Version 2.0 along with the NIST mass spectral library (NIST17) (Gaithersburg, MD, USA).

Upon reconstitution, the sample vial was flushed with nitrogen gas, capped, and shaken well prior to GC-MS analysis. Utilizing the optimized DLLME conditions, the recovery percentages (% recovery), calculated by dividing the mass of methamphetamine determined from the standard calibration curve with the known amount of methamphetamine in percentage, and the relative standard deviations (%RSD) from the seven types of laboratory coat materials were evaluated and compared.

Results and Discussion

Selection of extraction and dispersive solvents

In a DLLME technique, extraction solvent and dispersive solvents with adequate water miscibility and higher density than water are crucial to achieve a good extraction efficiency and good GC chromatogram [28]. The extraction solvent, i.e. dichloromethane has high capability for extracting analytes with a low water solubility while being soluble in the dispersive solvent. The phase separation requires a significant density difference between the extracting solvent and water [29]. In this study, extraction efficiencies of each combination of extraction and dispersive solvents were compared and evaluated (Figure 1). It was found that a combination of dichloromethane (extraction solvent) and 2-propanol (dispersive solvent) demonstrated the highest extraction efficiency for methamphetamine at a peak area ratio of 6.127 as compared to other solvent combinations. Dichloromethane demonstrated its good extraction capability for the target analytes, and able to form an emulsion with the presence of the dispersive solvent [30,31]. On the other hand, the dispersive solvent (2-propanol) has low interfacial tension, allowing for the dissolution of both organic phase (extraction solvent) and the aqueous phase (sample solution) [32].

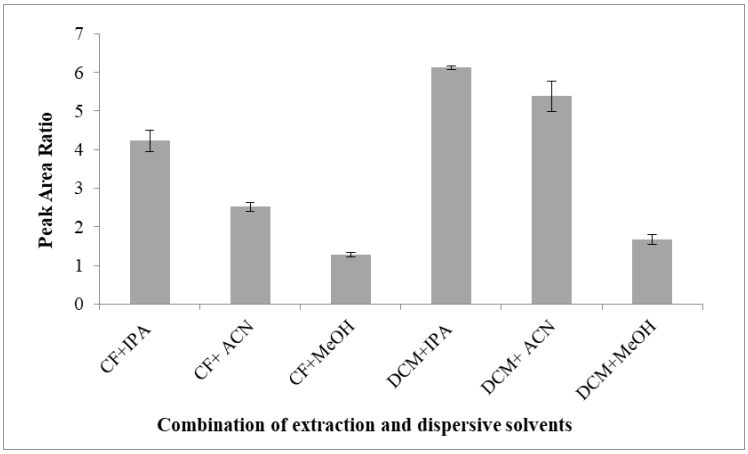


Figure 1. Extraction efficiencies with various combination of extraction and dispersive solvents at 1:1 ratio (n=7) (CF: chloroform; DCM: dichloromethane; IPA: 2-propanol; CAN: acetonitrile; MeOH: methanol)

PBD of DLLME optimization

A response surface methodology, namely the PBD was used to determine the experimental settings involving five variables for the greatest extraction efficiency of methamphetamine. The design allowed for the collection of the maximum amount of information with a minimum number of analyses [33]. The influences of each factor, including volume of the extraction solvent (x_1), volume of dispersive solvent (x_2), duration of vortex agitation (x_3), centrifugation time (x_4), and centrifugation speed (x_5), were tested. The collected experimental data were utilized to develop an estimate for a model that can adequately estimate the response variable given in the second order polynomial function as in the following equation:

Methamphetamine peak area: $$-3.202 + 0.03356x_1 + 0.002848x_2 + 0.00032x_3 + 0.3514x_4 - 0.000946x_5 - 0.00028x_1 * x_1 + 0.000002x_1 * x_2 + 0.000052x_1 * x_3 - 0.000458x_1 * x_4 + 0.000001x_1 * x_5 - 0.000002x_2 * x_3 - 0.000558x_2 * x_4$$

Analysis of variance (ANOVA) statistical test revealed that the fitted response surface model of second order was highly significant with F-value = 182.31 (p<0.001). The model explained 99.41% of the variation, with a predicted R^2 of 97.64%. The large predicted R^2 values suggested a good predictive ability of the model. Figure 2 shows the Pareto chart of the standardized effects comparing the relative magnitude and the statistical significance of main, square, and interaction effects in this study. The reference line at standardized effect of 2.16 indicated the significant effect as a significance level of 0.05. From the Pareto chart, the largest effect was contributed by the squared term for volume of extraction solvent followed by main effects of the volume of extraction volume and the time of vortex agitation.

The association between the detection of methamphetamine and each term was then determined and Table 2 demonstrates the output of the ANOVA statistical test. By considering a variable to be statistically significant at a 5% level of significance, the coefficient for the linear effect of the variables included extraction volume (p <0.001), vortex time (p <0.001) and centrifugation time (p <0.001) which were highly significant. The centrifugation speed was also statistically significant (p = 0.041), where no significant association between the volume of dispersive solvent (p = 0.375) with the recovery of methamphetamine upon DLLME procedure. The squared terms for the volume of extraction solvent were also significant at the α = 0.05 significance level (p <0.001), suggesting that the relationship between this factor and the detection of methamphetamine followed a curved line. In addition, five interaction terms were found significant in their respective coefficients which suggested their relation-

ships between the two factors. The contour plots of these interaction terms are shown in Figure 3.

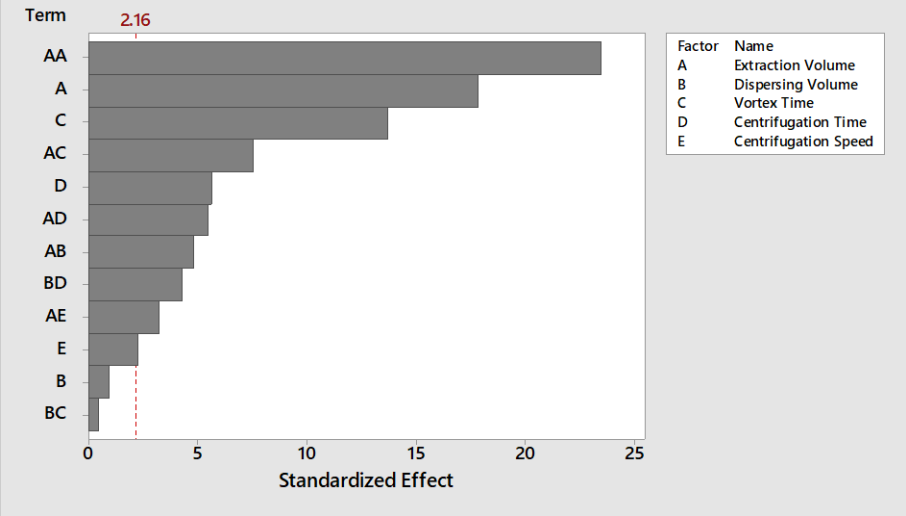


Figure 2. Pareto chart of the standardized effects

Table 2. ANOVA of the regression coefficient for the recovery of methamphetamine area

Source	DF	Adj SS	Adj MS	F-value	*p* -value
Model	12	226.054	18.8378	182.31	<0.001
Linear	5	82.938	16.5877	160.53	<0.001
x_1	1	32.975	32.9752	319.13	<0.001
x_2	1	0.087	0.0870	0.84	0.375
x_3	1	19.417	19.4174	187.92	<0.001
x_4	1	3.309	3.3085	32.02	<0.001
x_5	1	0.529	0.5289	5.12	0.041
Square	1	56.941	56.9406	551.06	<0.001
x_1*x_1	1	56.941	56.9406	551.06	<0.001
2-way interaction	6	48.088	8.0147	77.57	<0.001
x_1*x_2	1	2.426	2.4258	23.48	<0.001
x_1*x_3	1	5.885	5.8852	56.96	<0.001
x_1*x_4	1	3.119	3.1188	30.18	<0.001
x_1*x_5	1	1.099	1.0988	10.63	0.006
x_2*x_3	1	0.022	0.0223	0.22	0.650
x_2*x_4	1	1.894	1.8939	18.33	<0.001
Error	13	1.343	0.1033		
Total	25	227.397			

DF= Degree of freedom; Adj SS=Adjusted sum of squares; Adj MS=Adjusted Mean sum of squares

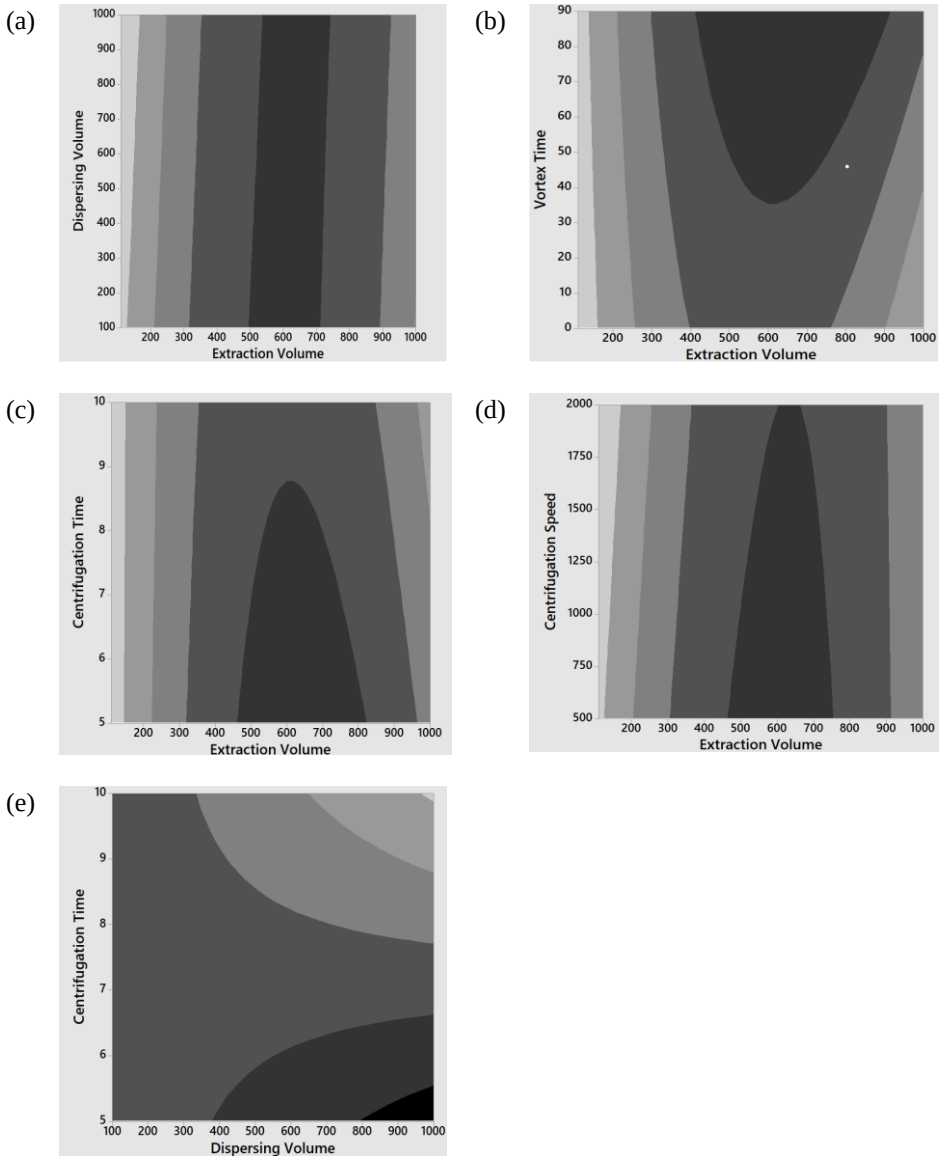


Figure 3. Contour plots showing interaction between (a) volume of extraction solvent vs volume of dispersive solvent (p<0.001); (b) volume of extraction solvent vs duration of vortex agitation (p<0.001); (c) volume of extraction solvent vs centrifugation time (p<0.001); (d) volume of extraction solvent vs centrifugation speed (p= 0.006); and (e) volume of dispersive solvent vs centrifugation time (p < 0.001)

Interaction between volume of extraction solvent and four variables (i.e. volume of dispersive solvent, duration of vortex agitation, centrifugation time, and centrifugation speed) were significant as shown in Figure 3(a)-(d). The darker regions in each figure indicated the higher extraction efficiency for methamphetamine. Based on Figure 3(a), the extraction efficiency increased with the increase of the volume of extraction solvent until certain point at approximately 700 µL and get reduced afterwards. Note also that a longer duration of vortex agitation, optimized at 90 s [Figure 3(b)], followed by a slower centrifugation time for 5 mins and shorter and centrifugation speed at 500 rpm, respectively [Figure 3(c)-(d)] were found to have

increased the extraction efficiency. The interaction between dispersive volume and centrifugation time was also highly significant [Figure 3(e)]. It was evident that with an increase in the dispersive volume up to a volume of 1000 µL and a decrease in centrifugation time to 5 mins, respectively, the efficiency of methamphetamine extraction was raised significantly.

Using the DLLME optimized conditions which shown in Table 3, a mixture containing 685 µL dichloromethane (extraction solvent) and 1000 µL 2-propanol (dispersive solvent) was injected into the sample solution. The ternary system was subjected to vortex agitation for 90 seconds, followed by centrifugation at 500 rpm for 5 mins. Note that the volume of extraction solvent was optimized to 685 µL, where this is the point indicating that when the extraction volume was too low, the extractant amount was very small and therefore unable to extract the analyte efficiently. On the contrary, the analyte would become diluted with high volume of extraction solvent, minimizing the amount of target substance to be extracted [34]. It was also observed that a longer duration of vortex agitation could aid in handling the complex matrices of the extraction, where a shorter period of centrifugation time could achieve the full separation of emulsion [35]. The equilibrium state could be immediately achieved after the addition of solvent and vortex agitation of the sample solution; therefore, a short centrifugation duration and speed were found sufficient to achieve a high extraction efficiency [36].

Table 3. Multiple response prediction for the response of methamphetamine detection.

Factor	Optimized Settings
Volume of extraction solvent	685 µL
Volume of dispersive solvent	1000 µL
Duration of vortex agitation	90 s
Centrifugation time	5 min
Centrifugation speed	500 rpm

Recovery of methamphetamine from laboratory coat materials

Laboratory coat material samples deposited with defined masses of methamphetamine (0.5 µg, 1,5 µg and 3.0 µg) were treated with proposed DLLME protocol, derivatized with TFAA, and subjected to GC-MS analysis. Figure 4 shows the mean percentages of recovery with seven type of laboratory coat materials. On average, at least 45% of methamphetamine were successfully recovered from the laboratory coat materials, depending on the concentration levels and types of fabric materials. Previously, solvent extraction [37] and liquid-liquid extraction (LLE) [38] were also used to extract methamphetamine from fabric materials followed by its detection through instrumental techniques. When compared to these conventional sample extraction methods, our DLLME procedure is less laborious while avoiding the drawbacks suffered from the conventional LLE, such as the need for excessive quantities of chemicals, reagents and sample, slow and long extraction time, and the formation of emulsions.

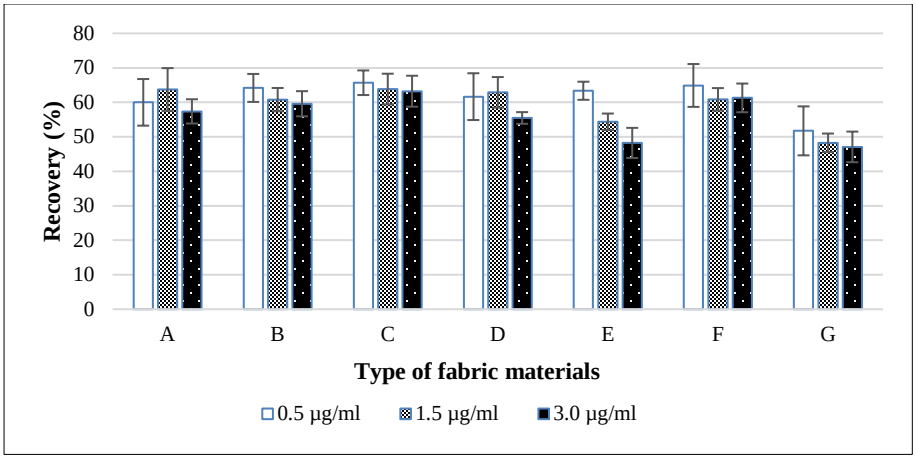


Figure 4. Mean percentages of recovery for methamphetamine from seven type of laboratory coat materials

Extraction efficiency of methamphetamine from the laboratory coat materials could be impacted by the physio-chemical interactions of solute of drugs with the surfaces and their penetration or diffusion into porous substrates [39]. It is also worth noting that the penetration is a complex phenomenon involving the interaction between solvent and porous substrates, depending on surface tension and the contact angle between each other [40]. As compared to studies which emphasized on the extraction of the drug substance from non-porous surfaces, the extraction efficiencies were also reported to be varied based on the surfaces, where only approximately 60% of the methamphetamine could be recovered from the varnished wood substrate [27].

Our study showed slightly variation in term of the amount of methamphetamine which successfully recovered from different laboratory coat materials through the application of proposed extraction protocol. In general, the %RSD reported was in an acceptable range, falling between 3.14-9.90%. Sorption of methamphetamine compounds on a fabric could have been influenced by its physical properties of the fibers, including its porosity [41]. Fabric materials with polar and slightly basic in nature, methamphetamine might also have great affinity for cotton that made up of polar cellulose, waxes, proteins, and fatty acids [42]. These factors certainly deserve further studies.

Although the DLLME procedure was found to be effective in extracting methamphetamine from the laboratory coat materials. As compared to other extraction techniques such as conventional LLE, DLLME procedure can be completed in a relatively quicker manner, consuming low volume of solvent, and requiring shorter extraction time. It is cost effective and environmentally friendly, and therefore widely applied in trace analysis [43]. DLLME also aids in minimizing the tendency of forming emulsion as frequently encountered during LLE procedure [44]. Based on our findings, it can be predicted that there is at least two-fold of drugs actually present on the laboratory coat materials than those detected by the protocol here. The laboratory monitoring program should therefore take corrective actions if recovered concentration exceeds the safe exposure level. As a future recommendation, the composition and characteristics of laboratory coat materials should be further explored to provide details insight on the influential factors that might affect the recovery of analytes.

It was noted that the proposed method was destructive in nature if the fabric material has to be cut out for extraction. Bitter [39] had proposed a wiping procedure in which a surface contaminated with methamphetamine was wiped and analyzed; however, the methamphetamine was detected at a very low amount with low recoveries, indicating the extraction might not adequately efficient to recover the target substance from porous samples. To apply the proposed method in the operational settings, similar fabric material can be

patched onto a laboratory coat and detached for extraction and analysis during routine monitoring to avoid destruction of the laboratory coats. The protocol of methamphetamine deposition used here was adapted from studies on household surfaces, and shall also be explored in future studies, especially on the contamination mechanisms and how they affect the recoveries of target substances. In general, this study has successfully demonstrated the possibility of determining methamphetamine as an indicator of clothing contamination from the fabrics, where it would benefit the screening of methamphetamine contamination on laboratory coats, and subsequently in planning the appropriate corrective or preventive actions and recommendations to address the contamination issues.

Conclusion

Determination of methamphetamine from laboratory coat materials was successfully carried out using a PBD optimized DLLME procedure coupled with GC-MS analysis. An addition of a combination of 685 µL dichloromethane (extraction solvent) and 1000 µL 2-propanol (dispersive solvent) into the sample solution followed by a 90s vortex agitation and a centrifugation at 500 rpm for 5 mins produced the highest extraction efficiency for methamphetamine. Based on the proposed procedure, at least 45% of methamphetamine could also be successfully recovered from the fabric materials. Repeatable recoveries of the drug substance were achieved from the laboratory coat materials, varied on their respective composition. As future recommendation, the properties of fabric materials that could influence the recovery of methamphetamine shall be investigated, in addition to the exploration on the contamination mechanisms of drug substances on these fabric materials.

Acknowledgement

This work was supported by the Universiti Sains Malaysia via the USM RUI grant (1001/PPSK/8012322).

References

1. Sisco, E., Najarro, M. and Burns, A. (2018). A snapshot of drug background levels on surfaces in a forensic laboratory. *Forensic Chemistry*, 11: 47-57.
2. Broadwater, K. R., Jackson, D. A. and Li, J. F. (2020). Evaluation of occupational exposures to illicit drugs at controlled substances laboratories. Health Hazard Evaluation Report 2018-0090-3366. *Department of Health and Human Services, Centers for Disease Control and Prevention, National Institute for Occupational Safety and Health*.
3. Sisco, E. and Najarro, M. (2019). Multi-laboratory investigation of drug background levels. *Forensic Chemistry*, 16: 100184.
4. Wright, J., Walker, G. S. and Ross, K. E. (2019). Contamination of homes with methamphetamine: Is wipe sampling adequate to determine risk? *International Journal Environmental Research Public Health*, 16(19): 3568.
5. United Nations Office on Drugs and Crime. (2021). Global overview: Drug demand and drug supply. World Drug Report 2021. *Vienna, Austria: United Nations*.
6. Daughton, C. G. (2010). Illicit drugs and the environment. In: Castiglioni S, Zuccato E, Fanelli R. (Editors). Illicit Drugs in the Environment, LA: John Wiley & Sons, Inc.
7. Kairigo, P., Ngumba, E., Sundberg, L. R., Gachanja, A. and Tuhkanen, T. (2020). Contamination of surface water and river sediments by antibiotic and antiretroviral drug cocktails in low and middle-income countries: Occurrence, risk and mitigation strategies. *Water*, 12(5): 1376.
8. Lin, Y. C, Hsiao, T. C. and Lin, A-YC. (2020). Urban wastewater treatment plants as a potential source of ketamine and methamphetamine emissions to air. *Water Research*, 172: 115495.
9. Jenkins, A. J. (2001). Drug contamination of US paper currency. *Forensic Science International,* 121: 189-193.
10. Smith, F. P. and McGrath, K. R. (2011). Cocaine surface contamination and the medico-legal implications of its transfer. *Egyptian Journal Forensic Sciences*, (1): 1-4.
11. Mastroianni, N., Postigo, C., López de Alda, M., Viana, M., Rodríguez, A., Alastuey, A. Querol, X. and Barceló, D. (2015). Comprehensive monitoring of the occurrence of 22 drugs of abuse and transformation products in airborne particulate

matter in the city of Barcelona. *Science of Total Environment*, 532: 344-352.

12. Nair, M. V. and Miskelly, G. M. (2019). Determination of airborne methamphetamine via capillary microextraction of volatiles (CMV) with on-sorbent derivatisation using o-pentafluorobenzyl chloroformate. *Forensic Chemistry*, 14:100161.
13. Chen, X., Wu, X., Luan, T., Jiang, R. and Ouyang, G. (2021). Sample preparation and instrumental methods for illicit drugs in environmental and biological samples: A review. *Journal of Chromatography A*, 1640: 461961.
14. Kuhn, E. J., Walker, G. S., Whiley, H., Wright, J. and Ross, K. E. (2019). Household contamination with methamphetamine: Knowledge and uncertainties. *International Journal of Environmental Research and Public Health*, 16(23): 4676.
15. Martyny, J. W., Arbuckle, S. L., McCammon, C. S., Esswein, E. J., Erb, N. and Van Dyke, M. (2007). Chemical concentrations and contamination associated with clandestine methamphetamine laboratories. *Journal of Chemical Health and Safety*, 14(4): 40-52.
16. Doran, G. S., Deans, R. M., Filippis, C. D., Kostakis, C. and Howitt, J. A. (2017). The presence of licit and illicit drugs in police stations and their implications for workplace drug testing. *Forensic Science International*, 278: 125-136.
17. Yeh, K., Li, L., Wania, F. and Abbatt, J. P. (2022). Thirdhand smoke from tobacco, e-cigarettes, cannabis, methamphetamine and cocaine: Partitioning, reactive fate, and human exposure in indoor environments. *Environment International*, 160: 107063.
18. Kerry, G. L., Ross, K. E., Wright, J. L. and Walker, G. S. (2022). A review of methods used to detect methamphetamine from indoor air and textiles in confined spaces. *Toxics*, 10(11): 710.
19. Doran, G. S., Deans, R. M., Filippis, C. D., Kostakis, C. and Howitt, J. A. (2017). Quantification of licit and illicit drugs on typical police station work surfaces using LC-MS/MS. *Analytical Methods,* 9:198-210.
20. United Nations Office on Drugs and Crime. (2020). Synthetic Drugs in East and Southeast Asia: Latest developments and challenges. *Vienna, Austria: United Nations*.
21. Teoh, W. K., Mohamed Sadiq, N. S., Saisahas, K., Phoncai, A., Kunalan, V., Md Muslim, N. Z., Limbut, W., Chang, K. H. and Abdullah, A. F. L. (2022). Vortex-assisted dispersive liquid–liquid microextraction-gas chromatography (VADLLME-GC) determination of residual ketamine, nimetazepam, and xylazine from drug-spiked beverages appearing in liquid, droplet, and dry forms. *Journal of Forensic Sciences,* 67(5): 1836-1845.
22. Lemos, V. A., Barreto, J. A., Santos, L. B., de Assis, R. dos S., Novaes, C. G. and Cassella, R. J. (2022). In-syringe dispersive liquid-liquid microextraction. *Talanta*, 238:123002.
23. Jain, R., Jain, B., Chauhan, V., Deswal, B., Kaur, S., Sharma, S. and Abourehab, M. A. (2023). Simple determination of dichlorvos in cases of fatal intoxication by gas chromatography-mass spectrometry. *Journal of Chromatography B*, 1215: 123582.
24. Meng, L., Zhang, W., Meng, P., Zhu, B. And Zheng, K. (2015). Comparison of hollow fiber liquid-phase microextraction and ultrasound-assisted low-density solvent dispersive liquid-liquid microextraction for the determination of drugs of abuse in biological samples by gas chromatography-mass spectrometry. *Journal of Chromatography B*: *Analytical Technologies in the Biomedical and Life Sciences,* 989: 46-53.
25. Manwar, J., Mahadik, K. and Paradkar, A. (2013). Plackett–Burman design: A statistical method for the optimization of fermentation process for the yeast Saccharomyces cerevisiae isolated from the flowers of *Woodfordia fruticosa. Fermentation Technology*, *2*: 109.
26. Abd El-Hamid, H. T., Al-Prol, A. E. and Hafiz, M. A. (2018). Plackett-Burman and response surface methodology for optimization of oily wastewater bioremediation by Aspergillus sp. *South Asian Journal of Research in Microbiology*, 2018: 1-9.
27. Abdullah, A. F. L. and Miskelly, G. M. (2010). Recoveries of trace pseudoephedrine and methamphetamine residues from impermeable

household surfaces: Implications for sampling methods used during remediation of clandestine methamphetamine laboratories. *Talanta.* 81(1-2): 455-461.

28. Quigley, A., Cummins, W. and Connolly, D. (2016). Dispersive liquid-liquid microextraction in the analysis of milk and dairy products: A review. *Journal of Chemistry*, 2016: 4040165.
29. Saraji, M. And Boroujeni, M. K. (2014). Recent developments in dispersive liquid–liquid microextraction. *Analytical and Bioanalytical Chemistry*, 406: 2027-2066.
30. Salim, S. A., Sukor, R., Ismail, M. N. and Selamat, J. (2021). Dispersive liquid–liquid microextraction (DLLME) and LC-MS/MS analysis for multi-mycotoxin in rice bran: method development, optimization and validation. *Toxins*, 13(4): 280.
31. Tan, Y. H., Chai, M. K. and Wong, L. S. (2018). A review on extraction solvents in the dispersive liquid-liquid microextraction. *Malaysian Journal of Analytical Sciences*, 22(2): 166-174.
32. Al-Saidi, H. M. and Emara, A. A. A. (2014). The recent developments in dispersive liquid-liquid microextraction for preconcentration and determination of inorganic analytes. *Journal of Saudi Chemical Society*, 18(6): 745-761.
33. Geiger, E. O. (2014). Statistical methods for fermentation optimization. In: Todaro CC, Vogel HC, editors. Fermentation and biochemical engineering handbook. NY: William Andrew.
34. Rahmani, M., Ghasemi, E. and Sasani, M. (2017). Application of response surface methodology for air assisted-dispersive liquid- liquid microextraction of deoxynivalenol in rice samples prior to HPLC-DAD analysis and comparison with solid phase extraction cleanup. *Talanta.* 165: 27-32.
35. Guo, L. and Lee, H. K. (2013). Vortex-assisted micro-solid-phase extraction followed by low-density solvent based dispersive liquid-liquid microextraction for the fast and efficient determination of phthalate esters in river water samples. *Journal of Chromatography A,* 1300: 24-30.
36. Sanagi, M. M., Mokhtar, S. U., Ibrahim, W. A. W. and Aboul-Enein, H. Y. (2013). Application of dispersive liquid-liquid microextraction based on solidification of floating organic droplet to the analysis of antidepressant drugs in water samples. *Sains Malaysiana,* 42(2): 1490-157.
37. Al-Dirbashi, O. Y., Ikeda, K., Takahashi, M., Kuroda, N., Ikeda, S. and Nakashima, K. (2001). Drugs of abuse in a non-conventional sample; detection of methamphetamine and its main metabolite, amphetamine in abusers' clothes by HPLC with UV and fluorescence detection. *Biomedical Chromatography*, 15: 457-463.
38. Keasey, S. J. (2011). Testing for the presence of methamphetamine residues on clothing from suspected clandestine labs. Master's Thesis, AL: University of Alabama at Birmingham.
39. Bitter, J. L. (2017). The persistence of illicit drug smoke residues and their recovery from common household surfaces. *Drug Testing and Analysis*, 9(4): 603-612.
40. Lee, S. and Obendorf, S. K. (2001). A statistical model to predict pesticide penetration through nonwoven chemical protective fabrics. *Textile Research Journal*, 71(11): 1000-1009.
41. Saini, A., Okeme, J. O., Mark Parnis, J., McQueen, R. H. and Diamond, M. L. (2017). From air to clothing: characterizing the accumulation of semi-volatile organic compounds to fabrics in indoor environments. *Indoor Air,* 27(3): 631-641.
42. Morrison, G., Shakila, N. V. and Parker, K. (2015). Accumulation of gas-phase methamphetamine on clothing, toy fabrics, and skin oil. *Indoor Air,* 25(4): 405-414.
43. Li, M. J., Zhang, H. Y., Liu, X. Z., Cui, C. Y. and Shi, Z. H. (2015). Progress of extraction solvent dispersion strategies for dispersive liquid-liquid microextraction. *Chinese Journal of Analytical Chemistry*, 43(8):1231-1240.
44. Majors, R. E. (2013). Sample preparation fundamentals to chromatography. Canada: Agilent Technologies.

Malaysian Journal of Analytical Sciences (MJAS)
Published by Malaysian Analytical Sciences Society

PHOTO-ESTERIFICATION OF WASTE COOKING OIL USING A NOVEL NANOCATALYST TIO_2 IMPREGNATED WITH EMPTY FRUIT BUNCHES ASH HETEROGENEOUS CATALYST

(Foto-Esterifikasi Sisa Minyak Masak Menggunakan Novel Nanocatalyst TiO_2 yang Diimpregnasi dengan Mangkin Heterogen Abu Tandan Buah Kelapa Sawit Kosong)

Siti Fadhilah Ibrahim[1], Norshahidatul Akmar Mohd Shohaimi[1, *], Mohd Lokman Ibrahim[2], Zul Adlan Mohd Hir[1], Mohd Sufri Mastuli[2], and Wan Nur Aini Wan Mokhtar[3]

[1]*Faculty of Applied Sciences, Universiti Teknologi MARA Pahang, 26400 Bandar Tun Abdul Razak Jengka, Pahang, Malaysia*
[2]*School of Chemistry and Environment, Faculty of Applied Sciences, Universiti Teknologi MARA, 40450, Shah Alam, Selangor, Malaysia*
[3]*Centre for Advanced Materials and Renewable Resources, Faculty of Science and Technology, Universiti Kebangsaan Malaysia, 43600 UKM Bangi, Selangor, Malaysia*

**Corresponding author: akmarshohaimi@uitm.edu.my*

Received: 29 September 2022; Accepted: 15 April 2023; Published: 23 June 2023

Abstract

Photo-esterification of Waste Cooking Oil (WCO) with TiO_2/EFBA500 photocatalyst as heterogeneous photo-catalyst has been investigated in this study. WCO is nonedible oil with high free fatty acid (FFA) content which needs esterification to reduce its FFA content followed by transesterification to produce Fatty Acid Methyl Ester (FAME). WCO was esterified with methanol through photocatalytic process with UV light irradiation as the light source. TiO_2/EFBA500 photocatalyst was synthesized using simple wet impregnation method. The samples were characterized by X-Ray Diffraction (XRD), Scanning Electron Microscope (SEM), Energy Dispersive X-ray Spectroscopy (EDX) and Ultraviolet Diffuse Reflectance Spectroscopy (UV-Vis DRS) analysis. Characterization results revealed that the bandgap energy of TiO_2/EFBA500 was successfully reduced from 3.0 eV to 2.88 eV which was suitable in UV light irradiation and needed low energy in the process. TiO_2 semiconductor composite doped with Empty Fruit Bunches Ash (EFBA) showed a very high catalytic activity for FFAs photo-esterification. Experimental results showed that the optimum condition of photo-esterification with catalyst loading to oil was 4 wt.%, 20:1 methanol to oil molar ratio and 2 h reaction time achieved the reduction of FFA content from 11.65% to 2.04% with FFA conversion of 83%. FFA content was successfully reduced indicating that photo-catalytic esterification is a viable option in order to produce FAME. Biodiesel analysis using Gas Chromatography Mass Spectrometry (GCMS) is used to calculate yield and methyl ester content according to international biodiesel standard European (EN14103).

Keywords: biodiesel, photo-esterification, transesterification, waste cooking oil, empty fruit bunches ash

Abstrak

Foto-esterifikasi sisa minyak masak (WCO) dengan foto-mangkin TiO_2/EFBA500 sebagai mangkin foto heterogen telah dikaji dalam kajian ini. WCO ialah minyak tidak boleh dimakan dengan kandungan asid lemak bebas (FFA) yang tinggi, memerlukan pengesteran untuk mengurang kandungan FFA diikuti dengan transesterifikasi untuk menghasilkan asid lemak metil ester (FAME). WCO telah diesterkan dengan metanol melalui proses fotokatalitik dan penyinaran cahaya UV sebagai sumber cahaya. Foto-pemangkin TiO_2/EFBA500 telah disintesis menggunakan kaedah impregnasi basah yang biasa. Sampel dicirikan dengan Pembelauan Sinar-X (XRD), Mikroskopi Imbasan Elektron (SEM), Serakan Tenaga Sinar (EDX) dan Spektroskopi Pemantulan Resap UV-vis (UV-Vis DRS) analisis. Keputusan perincian mendedahkan bahawa tenaga jurang jalur TiO_2/EFBA500 berjaya dikurangkan daripada 3.0 eV kepada 2.88 eV yang sesuai dalam penyinaran cahaya UV dan tenaga yang rendah diperlukan dalam proses tersebut. Komposit semikonduktor TiO_2 yang digabungkankan dengan abu tandan buah kelapa sawit kosong (EFBA) menunjukkan aktiviti pemangkinan yang sangat tinggi untuk pengesteran foto FFAs. Keputusan eksperimen menunjukkan keadaan optimum foto-esterifikasi dengan muatan mangkin nisbah kepada minyak ialah 4 wt.%, 20:1 metanol kepada nisbah molar minyak dan 2 jam masa tindak balas mencapai pengurangan kandungan FFA daripada 11.65% kepada 2.04% dengan penukaran FFA sebanyak 83%. Kandungan FFA telah berjaya dikurangkan menunjukkan bahawa pengesteran foto-mangkin adalah pilihan yang terbaik untuk menghasilkan FAME. Biodiesel dianalisis dengan Kromatografi Gas-Spektroskopi Jisim (GC-MS) analisis untuk mengira hasil dan kandungan metil ester mengikut piawaian biodiesel antarabangsa Eropah (EN14103).

Kata kunci: biodisel, foto-esterifikasi, transesterifikasi, sisa minyak masak, abu tandan buah kelapa sawit kosong

Introduction

The depletion of fossil fuels has brought about the development of a renewable and sustainable alternative energy which is environmentally friendly for the benefit of the future [1]. Fatty acid alkyl ester, also named as biodiesel, has almost the same properties as petroleum fuel which is a good replacement for conventional petroleum product especially in the transportation sector. Besides that, it produces low emission of carbon monoxide, sulfur dioxide and un-combusted hydrocarbon [2]. This alternative energy is claimed to be as clean as the biofuels produced via catalytic transesterification of triglycerides (TG) with alcohol e.g. methanol converted to fatty acid alkyl ester (biodiesel) and glycerol as by-product [3]. TG is the main component of fat and oil in vegetable oils and animal fats. Examples of vegetable oils are such as soybean oil, sunflower, cottonseed etc., [4]. Reported by Volli et al. in order to reduce the cost of biodiesel and to avoid ecological imbalance due to the use of this edible sources, non-edible sources have become a new target feedstock for the biodiesel production [5]. The examples of non-edible oil are waste cooking oil, jatropha curcas oil, greased oil and etc. [6]. The usage of non-edible oil can solve the waste management problem. It is also sustainable and is able to reduce the production cost. This type of non-edible feedstock consists of high FFA content (>1% FFA) and therefore requires a pretreatment step to reduce it [7].

Reported by Razak et al. the homogeneous catalyst has been widely used over generations [8]. However, this catalyst can harm our environment and there are many disadvantages in using this catalyst. Homogeneous catalyst cannot be reused because the reactant and the product are inseparable, and this process also triggers waste water problem during the purification process [9]. Moreover, it can reduce the yield of biodiesel production. Several types of heterogeneous catalysts have been introduced by many researchers that can solve the separation problem. The use of catalyst that can be recycled is an advantage and it will also reduce the operational cost. The example of heterogeneous catalyst includes sulfated zirconia [10], heteropoly acid [11], carbon nanotubes [12], biomass carbon based [13] and more. However, these types of thermal catalytic processes cannot outdo heterogeneous photocatalyst as it is performed at room temperature under either solar energy or artificial light sources, thus reducing the operation cost as it can save the energy [3]. As reported by Guo et al., using photocatalyst in the production of biodiesel can convert more than 90% of FFA [14]. Examples of nanomaterials are cerium oxide [15], zinc oxide [16], titanium dioxide [17], chromium (IV) [18] and metal oxide which are highly stable, very effective, and requires a low cost with high availability [19].

Photocatalyst is a light induced catalytic process that involves oxidization and/or reduction of organic molecules via redox reactions. This process generated electron-hole pair on the surface of semiconductors upon light irradiation [3]. This photocatalyst has been widely used in the applications of wastewater treatment [20], bacteria disinfection [21], hydrogen production [22] and carbon dioxide removal [23]. Photocatalyst in the photo-esterification reaction takes place when alcohol e.g., methanol reacts with positive holes (h^+), generating methanol radicals ($CH_3O^{\cdot}$) and releasing electron (e^-) which is generated under solar irradiation react with FFA formed radical of fatty acid (R-$COOH^{\cdot}$) on the surface of photocatalyst. From the intermediates of $CH_3O^{\cdot}$, R-$COOH^{\cdot}$ and H^+, then formed final products of methyl ester and water [5]. Reported by Citra Dewi & Slamet, they applied TiO_2P_{25} in the photo-esterification and successfully converted 45.2% of FFA in waste cooking oil [24]. Ghani et al., reported that they synthesized bismuth vanadate with reduced graphene oxide bismuth vanadate for photo-esterification of soap nut oil and achieved maximum conversion of FFA at 88% [6, 25]. Thus, photocatalyst is suitable and capable in the reaction process with methanol and FFA under light irradiation. Not only that, it is environmentally friendly, reusable, and produced high yield which assured the successfulness in the production for new alternative energy.

Titanium dioxide nanoparticles (TiO_2) is among high photocatalytic activity consisting of three main crystallographic phases, which are anatase, rutile and brookite [26]. It is nontoxic, easily available, superior redox ability, and photostability. It has become the main focus in bioenergy field as promising heterogeneous catalyst in the esterification process. The photocatalytic activity of TiO_2 depends on the recombination rate of the photogenerated electron hole pair (e^-/h^+). However, it is usually limited by its large bandgap (~ 3.2 eV for anatase) that increases the recombination rate [27]. In order to reduce the e^-/h^+ pair recombination rate, combining techniques with high surface area supported by materials such as zeolite [28], carbon nanotube [29], graphitic carbon nitride [30] and active carbon [31] is the best option. Besides that, it can improve reactivity and kinetic of the catalyst as they formed crystal with high specific surface area. In recent work by Corro et al. they used ZnO/SiO_2 in the photo-esterification of Jatropha Curcas Crude Oil (JCCO) which achieved 96% FFA conversion [32]. Redjeki et al. used CuO/TiO_2 by conversion FFA of Kemiri Sunan Oil around 59%. Therefore, by combining technique with other supported material can prevent the recombination rate of e^-/h^+ pair and enhanced the photocatalytic activity [33].

Recently, some researcher use ash as dopant with TiO_2 semiconductor. Ash is the industrial waste byproduct resulting from the burning of solid fuels. The constituents of ash are mostly unburned carbon, metal oxides (Si, Al, K, Fe, Ca) and other inorganic substances [34]. Reported by Suliman et al., they doped palm oil fiber ash (POFA) with TiO_2 and reduced almost 50% of chemical oxygen demand (COD) in wastewater [35]. Shi et al. also claimed that they had also doped fly ash (FA) with TiO_2 and successfully degraded 95% of phenol in aqueous solution. The concentration of metal oxide of ash materials might be an excellent opportunity when dope with TiO_2 that can enhanced the photocatalytic activity in the reaction [36]. Empty fruit bunches ash (EFBA) from palm oil mill has recently suggested as supported material in the synthesized of photocatalyst. EFBA does not only work to enhance the efficiency of the interfacial charge transfer in the photocatalytic process but also function as a major non-toxic waste sources which is low-cost adsorbent and easily available. It is safe to state that EFBA is the outcome of the thermal power generation plant. Besides that, EFBA can reduce the cost of waste management and environmental problem. In this study, the photocatalytic activity of TiO_2 alone and TiO_2 doped with EFBA is compared in removal of FFA in WCO and further utilized in transesterification for biodiesel production.

Materials and Methods

Materials

Empty fruit bunches ash (EFBA) was obtained from FTJ Bio Power Sdn. Bhd. The feedstock of waste cooking oil (WCO) was obtained from the local restaurant in Bandar Jengka Pusat, Pahang. 1.5 L of WCO is collected, filtered, and saved for analysis. Titanium Dioxide (Degussa P25), n-hexane, methanol, methyl

heptadecanoate, sodium hydroxide, potassium hydroxide, phenolphthalein is all purity > 99%, hydrochloric acid (HCl, purity >32%) were obtained from QReC. All reagent will be directly purchased with analytical grade and used without further purification.

Preparation of catalyst

EFBA was dried in the oven at 120 °C then sieved through 100 mesh screening. TiO_2-Degussa P25 (1.0 g) was mixed with EFBA (1.0 g) in 100 ml distilled water (1:1). The new nanocomposite photocatalyst was obtained from the slurry under stirring (300 rpm) for 1 h, at room temperature, on a thermoset heating plate. After filtration, the slurry was further washed with deionized water followed by drying in oven at 120 °C overnight. Finally, dried material was calcined at 500˚C for 3 h in a tube furnace with a heating rate of 5˚C/min. The sample obtained is 1.8 ± 0.3 g and denoted as TiO_2/EFBA500.

Characterization of catalyst

The catalysts were analyzed using X-Ray Diffraction (XRD) to identify the composition of samples. The diffractograms were measured in the 2θ mode, within the range of 20° to 90° at the speed of 6.0°/min. Scanning Electron Microscopy and Energy-Dispersive X-ray spectroscopy (SEM-EDX) is used to study the morphology of samples. It was done with a SEM JEOL JSM-7100F scanning electron microscope at 15.0 kV. UV-Vis Diffuse Reflectance Spectrometer (UV-Vis DRS) as to measure the bandgap of the samples.

Photocatalytic esterification of WCO

The photocatalytic esterification process was conducted in a reactor assisted by a 6 W UV lamp (λ = 365 nm) as the light source. The reaction mixture catalysed by TiO_2 and TiO_2/EFBA500 photocatalyst, stirred continuously under stirring rate of 400 rpm by using an internal magnetic stirrer which generated a strong liquid rotation leading to homogeneous irradiation of the whole reacting mixture. A 10 g of WCO was used with varies parameter of methanol to WCO molar ratio in the range of 12:1, 16:1, 20:1, 24:1, the amount of catalyst is 1 wt.%, 2 wt.%, 3 wt.%, 4 wt.%, 5 wt.%, UV irradiation time is 1 h, 2 h, 3 h, 4 h, 5 h. After esterification, the mixture was centrifuged at 5000 rpm for 15 min. The lower layer consists of unreacted triglycerides (further trans-esterification), and insoluble catalysts. The upper layer consists of unreacted methanol and water from reaction process. The catalyst was first filtered and separated, and the excess methanol was removed by drying in the oven for 15 min at 60 °C to obtain the esterified WCO for use in transesterification reaction. Acid value of the WCO was determined by titration method (in triplicates) using standard isopropanol potassium hydroxide (0.1 N) according to AOCS; Cd 3a-63. The conversion was calculated using equation 2.

Trans-esterification of WCO

Trans-esterification of WCO was performed in a 100 mL three necked flask in an oil bath equipped with magnetic stirring for temperatures up to 65 ˚C using reflux method. 1 wt.% of NaOH catalyst was added to methanol 12:1 methanol to WCO molar ratio, stirred, and addition of 5 g esterified WCO. Transesterification product was separated into two layers using separating funnel. The upper layer is Fatty Acid Methyl Ester (FAME) and the lower layer is glycerol. FAME is the main product or called biodiesel, meanwhile glycerol is the by-product in this experiment. FAME was then washed with hot water (< 90 °C). Biodiesel produced was going through yield calculation and methyl ester content by Gas Chromatography Mass Spectrometry (GCMS) analysis (GC-7860B Agilent). The temperature at injector and detector were programmed at 240 °C. The flow rate of Helium as carrier gas at 19.2 mL min^{-1} and the column temperature was set at 150 °C with ramping rate of 15 °C min^{-1}. Table 1 showed the formula to calculate biodiesel conversion, ester content and biodiesel yield according to international standard European EN14103.

Table 1. Equation to calculate the biodiesel conversion, ester content and biodiesel yield [37]

Formula	Equation
Conversion (%)	$d = \frac{A}{Mass\ of\ WCO} \times 100$
Ester content (%) from EN14103	$c = \frac{TA\ - AEI}{AEI} \times \frac{CEI\ \times VEI}{m} \times 100$
Mass of pure biodiesel from biodiesel conversion (g)	$Y\ = c\ \times A$
Pure biodiesel yield (%)	$FAME\ yield, \% = \frac{Y\ (g)}{mass\ WCO\ (g)} \times 100$

A = Mass of biodiesel collected (g), TA =Total area, AEI = Area of internal standard, CEI = Concentration (mg/mL) of methyl heptadecanoate solution, VEI = Volume of (mL) methyl heptadecanoate solution, and m = Mass of sample

Determination of acid value and FFA conversion

250 ml conical flask was prepared and 0.2 g of WCO. 10 mL toluene: isopropanol KOH (1:1) was added in the conical flask with a few drops of phenolphthalein indicator in the sample solution, titrated with 0.1 mol/L isopropanol KOH standard solution. The solution was observed from colorless to slightly red until it remained unchanged for 30 s, which meant that the titration endpoint was reached. The acid value (AV) was calculated by the following formula Eq. (1):

$$A = \frac{V\ \times C\ \times 56.11}{m} \quad (1)$$

where AV is the acid value of the sample, V is the volume of isopropanol KOH standard solution consumed to reach the titration end point, C is the concentration of KOH standard solution, 56.11 is the molecular weight of KOH, m is the weight of the test sample. The conversion rate of FFA (FFA conversion%) is considered as the fraction of the esterification reaction of FFA and methanol, and the conversion rate of FFA (FFA conversion%) was determined according to the acid value ratio using Eq. (2):

$$FFA\ conversion\ \% = \frac{A_a - A_b}{A_a} \times\ 100 \quad (2)$$

where Aa is the acid value of the WCO. Ab is the acid value of WCO after esterification.

Results and Discussion

Properties of waste cooking oil

The FFA chemical composition analysis was performed physiochemically using titration method. The results shown in Table 2 indicated that WCO has 11.65 % content of FFA with 23.30 mg KOH g^{-1} of acid value.

Table 2. The properties of waste cooking oil

Properties	Waste Cooking Oil
Acid value (mg KOH g^{-1})	23.30
Free Fatty Acid (%)	11.65
Saponification value (mg KOH g^{-1})	184
Molecular weight ($gmol^{-1}$)	915

Characterization of photo-catalyst

The diffraction pattern of raw EFBA, dry EFBA and TiO_2/EFBA500, are presented in the Figure 1. The peaks of the raw and dry EFBA showed all the cellulose materials from 2θ = 29˚ to 90˚. Dry materials that had been dried in the oven at 120 ˚C showed graphite

structure at 2θ = 27˚, 80˚ and 88˚. Also, the intensity of dry EFBA was a bit higher than raw EFBA. This was due to the drying process of EFBA at 120 ˚C which developed the crystallite size and produced the graphite structure [38]. As for TiO_2/EFBA500, it showed that dry EFBA had well embedded to the anatase and rutile phase of TiO_2. The peaks of rutile, anatase and cellulose of the EFBA were dispersed throughout the surface of the catalyst. This promoted active photocatalytic activity in the esterification. As reported by Berrones-Hernández et al. the impregnation technique promoted a deposition element of one element on another [36]. Therefore, the catalyst will have improvement in stability and efficiency in the photo esterification process due to deposition of TiO_2 on EFBA. As proven, the conversion of FFA catalyzed by TiO_2EFBA500 achieved 83% after 2 h reaction time under UV light irradiation.

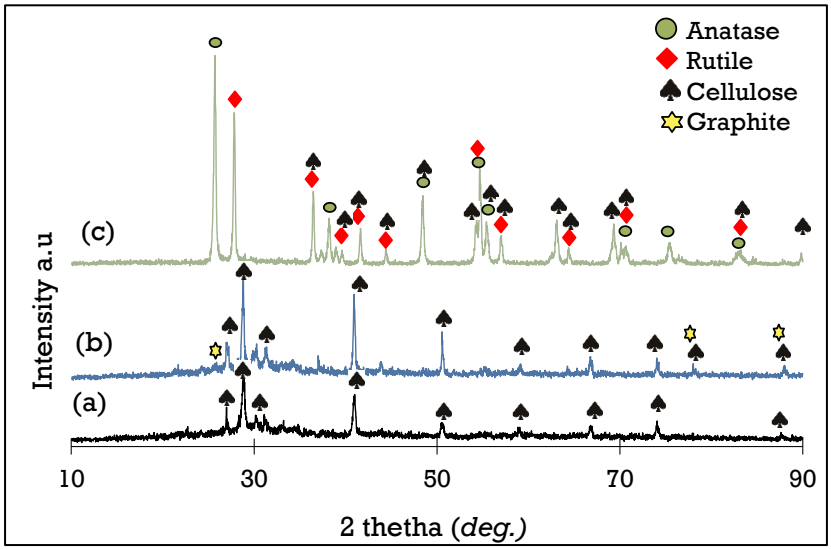


Figure 1. The XRD pattern of (a) Raw EFBA, (b) Dry EFBA and (c) TIO$_2$/EFBA500

Figure 2 showed SEM image of the dry EFBA, TiO_2, TIO$_2$/EFBA before and after being calcined at 500˚C. A micrograph showed rough appearance for all the catalyst. Raw and Dry EFBA appeared granular and spherical in shape whereas TiO_2 exhibited agglomerated nanoparticles, spherical and irregular shapes [38]. Naeem et al., reported that doping technique can prevent the agglomeration of TiO_2 nanoparticles during the reaction process [40]. From the micrograph, it showed that TiO_2 was well deposited on the surface of EFBA which successfully doped between TiO_2 and EFBA. The effect of calcination temperature at 500˚C showed ordered and homogeneous distribution of the TiO_2 nanoparticles on the EFBA composite [36]. The result from experimental data of XRD confirmed that EFBA was successfully coordinated with TiO_2 metal as TiO_2 has cubic and spherical crystal that can promote larger cluster formation on the EFBA particles [41]. The reactive species suggested favorable reduction of FFA content and active photocatalytic esterification of WCO. Furthermore, the presence of elemental composition of this catalyst was confirmed by EDX analysis in the Table 3.

Figure 3 showed the UV–vis diffuse reflectance spectra of Dry EFBA, TiO_2, TiO_2/EFBA and TiO_2/EFBA500 respectively, and the band gap energy was estimated to be about 4.0, 3.0, 2.95 and 2.88 eV, respectively using Tauc plot equation. This showed that the band gap energy of the EFBA-doped TiO_2 samples monotonically became narrower after doping and calcination at 500˚C.

Catalytic activity of the TiO_2 and TiO_2/EFBA photocatalyst

To determine the optimal conditions of FFA esterification reaction photocatalyzed by TiO_2 and TiO_2/EFBA500, we examined the effects of the reaction time under UV irradiation, methanol to WCO molar

ratio and photocatalyst/WCO mass ratio. Figure 4 and Figure 5 show the FFA content after photo esterification process using TiO_2 and TiO_2/EFBA500 respectively. There is a comparison of FFA reduction using TiO_2 and TiO_2/EFBA500 photocatalyst as TiO_2/EFBA500 photocatalyst reduced more FFA content than TiO_2 photocatalyst. As reported by Klubnuan et al. ash can modify the semiconductor material and control the bandgap energy [42]. Therefore, doping EFBA with TiO_2 can increase the crystallite size and reduce the bandgap energy from 3.0 eV to 2.88 eV confirmed by XRD and UV-Vis-DRS results which improve the photocatalytic reaction. From the results, the optimized value reduction of FFA content using TiO_2 catalyst only achieved 4.88% from 11.65% FFA content with 4 h reaction time under UV light, 20:1 methanol to WCO molar ratio and 4 wt.% TiO_2 catalyst. Same condition with different optimized parameter for TiO_2/EFBA500 photocatalyst achieved 2.04% of FFA reduction from 11.65% FFA content by 2 h reaction time, 20:1 molar ratio and 4 wt.% catalyst loading. These results suggested that TiO_2/EFBA500 photocatalyst was more active and efficient during the photo-esterification compared to TiO_2. TiO_2/EFBA500 only needed 2 h reaction time to convert 83% FFA rather than using TiO_2 that needed 4 h reaction time to convert only 58% FFA.

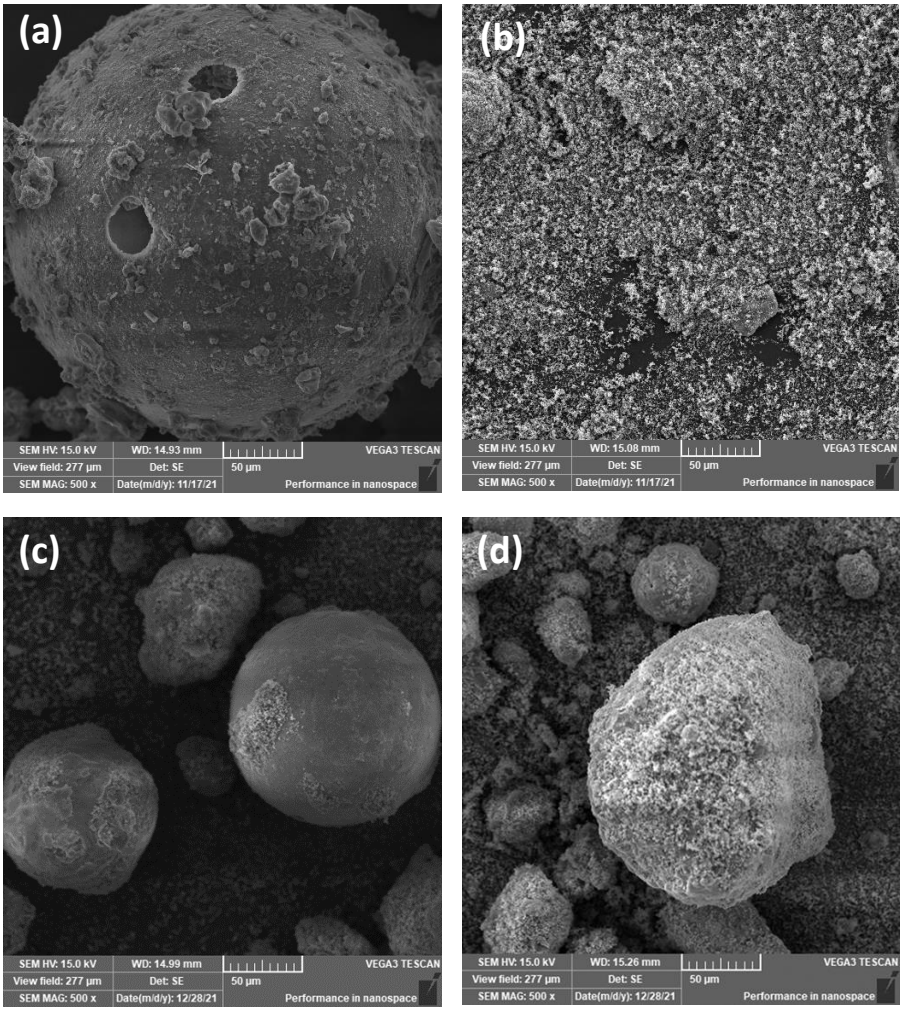


Figure 2. SEM image of the (a) Dry EFBA, (b) TiO_2, (c) TIO_2/EFBA and (d) TIO_2/EFBA500

Table 3. Elemental composition of photo-catalyst

	Elemental Composition (%)									
	C	**O**	**Ti**	**Si**	**K**	**Ca**	**Mg**	**S**	**P**	**Al**
Dry EFBA		53.86		10.85	23.80	5.39	0.71	2.50	2.45	0.16
TiO_2		48.39	51.61							
TiO_2EFBA	28.54	65.96	1.59	2.19	0.53	0.33	0.34			
TiO_2EFBA500	24.21	65.75	5.37	2.51	1.17	0.48	0.52			

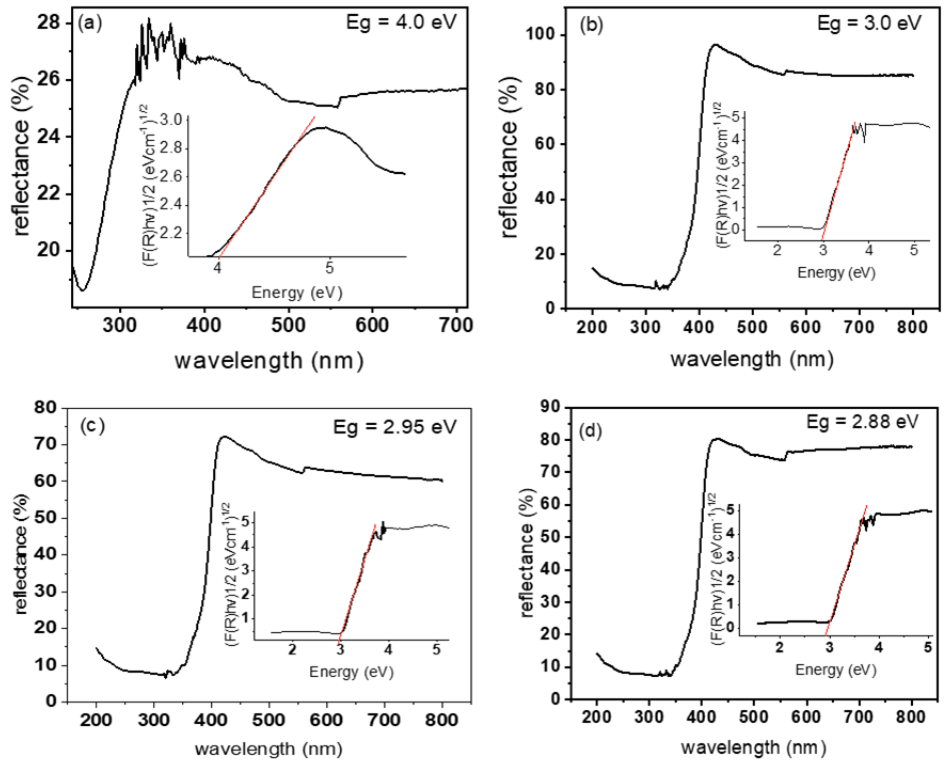


Figure 3. UV Vis DRS of (a) Dry EFBA, (b) TiO_2, (c) TiO_2/EFBA and (d) TiO_2/EFBA500

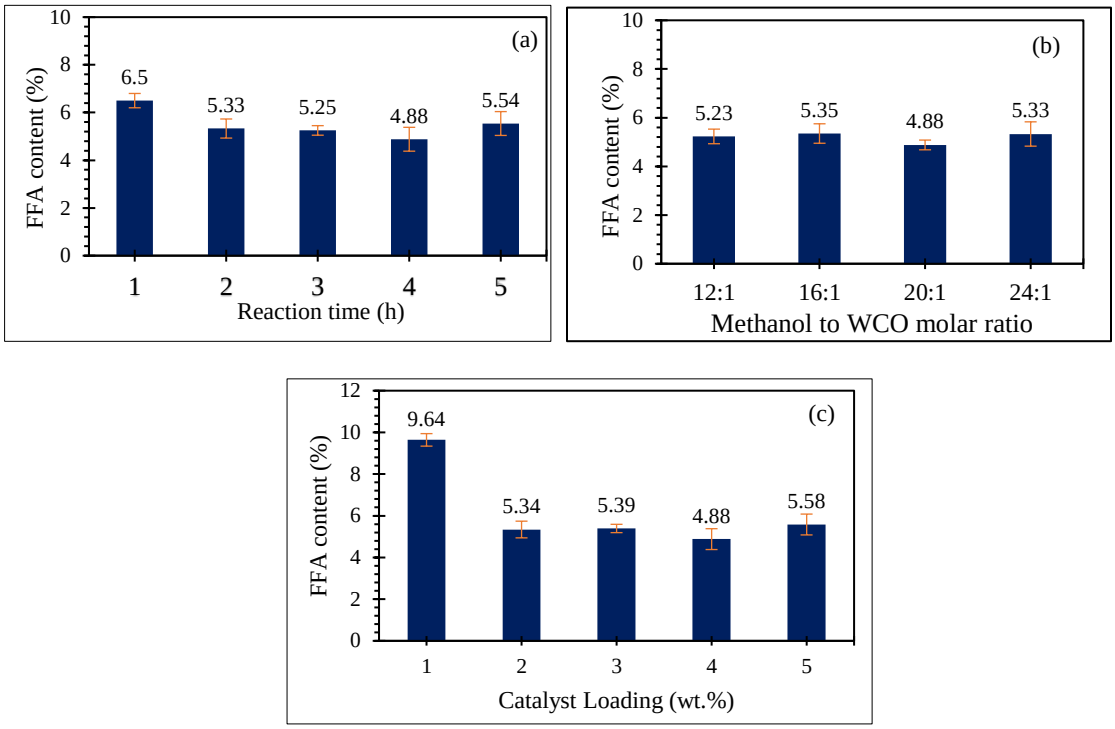


Figure 4. Photocatalytic esterification of WCO using TiO_2 photocatalyst (a) reaction time with (4 wt.% catalyst loading and 20:1 methanol to WCO ratio), (b) methanol to WCO molar ratio with (4 wt.% catalyst loading and 2 h reaction time) and (c) catalyst loading with (20:1 methanol to WCO molar ratio and 2 h reaction time).

From the FFA content results in Figure 4 and Figure 5, different parameters were studied to determine the optimized parameter for reduction of FFA content in WCO which were reaction time from 1 to 5 h, methanol to WCO molar ratio from 12:1 to 24:1 and catalyst loading from 1 wt.% until 5 wt.%. The reaction was conducted for three replications in each level. Photo-esterification of WCO contained 11.65% FFA catalyzed by TiO_2 photocatalyst showed in Figure 4 from 1 to 4 h, the FFA content decreased slowly from 6.5% until 4.88 %. Then the FFA increased again at 5 h as it faced reversible esterification reaction due to longer reaction time. Guo et al., reported that, reaction time under UV light more than 3 h will inhibit the reaction process [14]. The reason is because increasing reaction time will also increase the temperature of UV irradiation in the reactor that can cause saponification reaction. For the methanol to WCO molar ratio, the best ratio was at 20:1 as it achieved the maximum reduction of FFA content. It was the same for catalyst dosage, as the catalyst increased from 1 wt.% to 4 wt.%, the percentage of FFA content decreased from 9.64% to 4.88%. When exceeding 4 wt.%, the FFA content increased again which reduced the conversion of FFA. Adequate catalyst dosage can reduce the FFA content. However, excessive catalyst dosage can inhibit the reaction due to high viscosity in the reaction process. The maximum conversion of FFA catalyzed by TiO_2 photocatalyst reached only 58% under 4h reaction time, 20:1 methanol to WCO molar ratio and 4wt.% catalyst loading. This basis was also applied for photo-esterification in Figure 5. Photo-esterification reaction catalyzed by TiO_2EFBA500 in Figure 5 showed that the optimized parameter at 2 h reaction time, 20:1 methanol to WCO molar ratio and 4 wt.% catalyst loading reduced the FFA content from 11.65% to 2.04% in which the conversion of FFA was up to 83%.

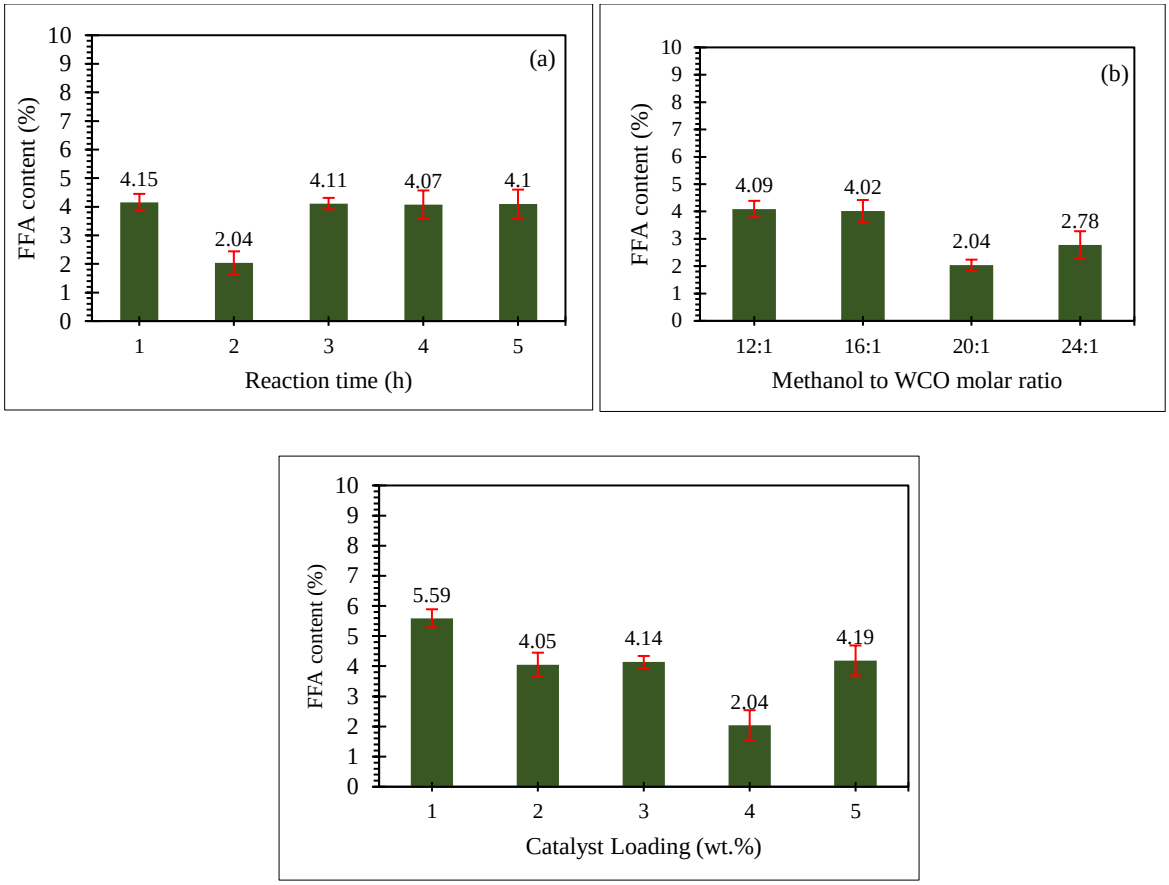


Figure 5. Photocatalytic esterification of WCO using TiO_2/EFBA500 photocatalyst (a) reaction time with (4 wt.% catalyst loading and 20:1 methanol to WCO ratio), (b) methanol to WCO molar ratio with (4 wt.% catalyst loading and 2 h reaction time) and (c) catalyst loading with (20:1 methanol to WCO molar ratio and 2 h reaction time)

After the photo-esterification process, the esterified WCO will be trans esterify for a second step reaction. The process conducted using reflux method and catalyzed by NaOH under 1 h reaction time; 12:1 methanol to oil molar ratio, 1 wt.% catalyst loading and 65 ℃. The WCO Biodiesel was analyzed using the GC-MS analysis to determine the chemical composition of the product. Each peak of the WCO Biodiesel product chromatogram was identified by comparing to published data and GC libraries. The largest peak in Figure 6 and detailed compound of fatty acid in Table 4 showed the presence of high amount of esters of oleic acid 34.84% followed by palmitic acid 29.01%, linoleic acid 9.99% along with stearic acid 4.86%, linolenic acid 1.74%, palmitoleic acid 1.42% and myristic acid 1.11% in alkali catalyzed process. As reported by Mekonnen & Sendekie, homogenous base catalyst using non-edible feedstock oil produces high yield of biodiesel that can achieve the limit set by international standard D6751 [43]. From the results, triglycerides of esterified WCO oil were successfully converted to FAME product only using a minimum range reaction parameter producing 65.5% FAME product and calculated using the equation in Table 1 [44].

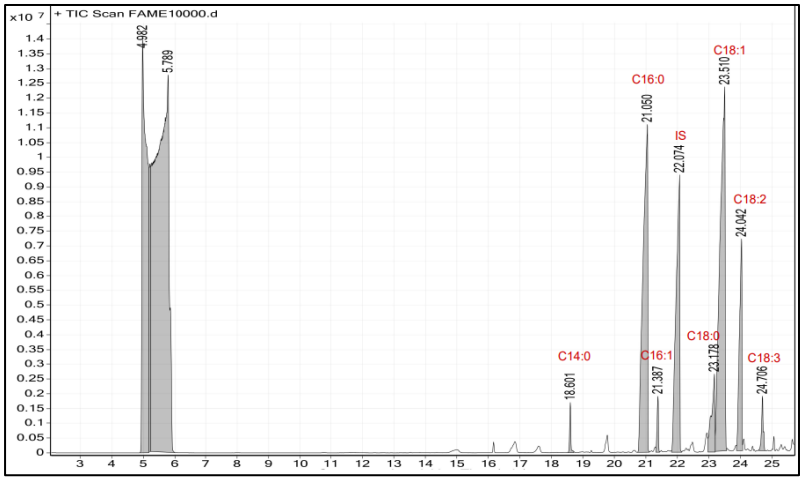


Figure 6. GCMS chromatogram of WCO Biodiesel produced by transesterification in the presence of 1 wt.% NaOH catalyst, 12:1 methanol, 65 ˚C at 1 h reaction time

Table 4. Composition of Fatty acid methyl ester in the WCO Biodiesel

Fatty Acid Compound	**Retention Time (min)**	**C N:U**	**Composition (wt.%)**
Myristic acid	18.60	C14:0	1.11
Palmitic acid	21.05	C16:0	29.01
Palmitoleic acid	21.39	C16:1	1.42
Stearic acid	23.18	C18:0	4.86
Oleic acid	23.51	C18:1	34.84
Linoleic acid	24.04	C18:2	9.99
Linolenic acid	24.71	C18:3	1.74

Conclusion

TiO_2/EFBA500 photocatalyst was prepared via simple impregnation method and used in the photo-esterification of waste cooking oil for biodiesel synthesis. Under optimum reaction conditions of 2 h reaction time with UV light irradiation, 20:1 methanol to WCO molar ratio and 4 wt.% catalyst loading achieved 83% FFA conversion and reduced from 11.65% to 2.04 FFA% content. Thus, TiO_2/EFBA500 photocatalyst is a promising catalyst for photo-esterification of waste cooking oil. TiO_2 alone can convert FFA up to 58% and doping with metal oxide compound from EFBA can enhance the effectiveness of photocatalytic activity which successfully achieved 83% FFA conversion. Therefore, photo-esterification process can increase the yield of biodiesel using high catalytic activity of semiconductor nanomaterial. It also has a low production cost as it can be carried out at room temperature and uses low quality feedstock oil. For future study, TiO_2 will be compared with other type of nanomaterials to determine the properties and mechanism of semiconductor nanomaterials doped with EFBA and also using different doping techniques.

Acknowledgment

This study was financially supported by Research Grant, FRGS with Grant No 011000 21 0002 (004/2021).

References

1. Hazmi, B., Rashid, U., Taufiq-Yap, Y. H., Ibrahim, M. L. and Nehdi, I. A. (2020). Supermagnetic nano-bifunctional catalyst from rice husk: Synthesis, characterization and application for conversion of used cooking oil to biodiesel. *Catalysts*, 10(2): 1-21.
2. Kefas, H. M., Yunus, R., Rashid, U. and Taufiq-

Yap, Y. H. (2018). Modified sulfonation method for converting carbonized glucose into solid acid catalyst for the esterification of palm fatty acid distillate. *Fuel*, 229: 68-78.

3. Oloruntoba, O. and Hamza, A. (2019). Photochemical and photocatalytic esterification of waste cooking oil under visible light irradiation using mechanochemically synthesized ZnO/silica. *Journal of Faculty of Food Engineering, University Zaria, Nigeria.*, 18(2): 89-96.
4. Singh, D., Sharma, D., Soni, S. L., Sharma, S., Sharma, P. K. and Jhalani, A. (2020). A review on feedstocks, production processes, and yield for different generations of biodiesel. *Fuel*, 262: 116553.
5. Volli, V., Purkait, K. M. and Shu, C. (2019). Preparation and characterization of animal bone powder impregnated fly ash catalyst for transesterification. *Science of the Total Environment*, 669*:* 314-321.
6. Lim, S. and Teong, L. K. (2010). Recent trends, opportunities and challenges of biodiesel in Malaysia: An overview. *Renewable and Sustainable Energy Reviews*, 14: 938-954.
7. Khalit, W. N. A. W., Asikin-mijan, N., Marliza, T. S., Gamal, M. S., Shamsuddin, M. R., Saiman, M. I., and Taufiq-Yap, Y. H. (2021). Catalytic deoxygenation of waste cooking oil utilizing nickel oxide catalysts over various supports to produce renewable diesel fuel. *Biomass and Bioenergy*, 154: 106248.
8. Razak, Z. K. A., Kamarullah, Shahida. H, Shohaimi, N. A. M., Kamalluddin, N. A. I. M. and Teh, W. N. S. W. (2020). Transesterification of palm oil for biodiesel production using Ni/Cao supported with alumina beads. *GADING Journal of Science and Technology*, 3(1): 100-106.
9. Ibrahim, S. F., Asikin-mijan, N., Ibrahim, M. L., Abdulkareem-alsultan, G., Izham, S. M. and Taufiq-Yap, Y. H. (2020). Sulfonated functionalization of carbon derived corncob residue via hydrothermal synthesis route for esterification of palm fatty acid distillate. *Energy Conversion and Management*, 210(3): 112698.
10. Zhang, Y., Wong, W.-T. and Yung, K.-F. (2014). Biodiesel production via esterification of oleic acid catalyzed by chlorosulfonic acid modified zirconia. *Applied Energy*, 116: 191-198.
11. Shin, H.-Y., An, S.-H., Sheikh, R., Park, Y. H. and Bae, S.-Y. (2012). Transesterification of used vegetable oils with a Cs-doped heteropolyacid catalyst in supercritical methanol. *Fuel*, 96: 572-578.
12. Lokman-Ibrahim, M., Khalil, N. N. A. N. A., Islam, A., Rashid, U., Fadhilah-Ibrahim, S., Mashuri, S. I. S. and Taufiq-Yap, Y. H. (2020). Preparation of Na_2O supported CNTs nanocatalyst for efficient biodiesel production from waste-oil. *Energy Conversion and Management Journal*, 205: 112445.
13. Naihi, H., Baini, R. and Yakub, I. (2021). Oil palm biomass-based activated carbons for the removal of cadmium—a review. *AIMS Materials Science*, 8(3): 453-468.
14. Guo, M., Jiang, W., Chen, C., Qu, S., Lu, J., Yi, W. and Ding, J. (2021). Process optimization of biodiesel production from waste cooking oil by esterification of free fatty acids using La^{3+}/ZnO-TiO_2 photocatalyst. *Energy Conversion and Management*, 229: 113745.
15. Mokhtar, W. N. A. W., Ramli, M. R., Jamaluddin, M. A. and Ramli, S. (2019). Rare earth metal doped CaO as catalyst for the transesterification reaction of cooking oil. *Malaysian Journal of Analytical Sciences*, 23(4): 660-666.
16. Zhu, X., Kavitha, P., and Hwang, H.-M. (2019). Green synthesis of titanium dioxide and zinc oxide nanoparticles and their usage for antimicrobial applications and environmental remediation. In *Green Synthesis, Characterization and Applications of Nanoparticles*. Elsevier Inc.
17. Manique, M. C., Silva, A. P., Alves, A. K. and Bergmann, C. P. (2016). Application of hydrothermally produced TiO_2 nanotubes in photocatalytic esterification of oleic acid. *Materials Science and Engineering B: Solid-State Materials for Advanced Technology*, 206: 17-21.
18. Corro, G., Sánchez, N., Pal, U., Cebada, S. and Fierro, J. L. G. (2017). Solar-irradiation driven biodiesel production using Cr/SiO_2 photocatalyst exploiting cooperative interaction between Cr^{6+} and Cr^{3+} moieties. *Applied Catalysis B: Environmental*,

203: 43-52.

19. Gardy, J., Hassanpour, A., Lai, X., Ahmed, M. H. and Rehan, M. (2017). Biodiesel production from used cooking oil using a novel surface functionalised TiO_2 nano-catalyst. *Applied Catalysis B: Environmental*, 207: 297-310.
20. Mashuri, S. I. S., Ibrahim, M. L., Kasim, M. F., Mastuli, M. S., Rashid, U., Abdullah, A. H., Islam, A., Asikin-Mijan, N., Tan, Y. H., Mansir, N., Kaus, N. H. M. and Hin, T. Y. Y. (2020). Photocatalysis for organic wastewater treatment: From the basis to current challenges for society. *Catalysts*, 10: 1-29.
21. Zhang, X., Sun, G., Jia, S., Xie, H., Kang, Z., Chen, W., Cui, M., Wang, B., Wang, B., Chen, X. and Yang, D. (2022). Intrinsic carbon defects induced nickel phosphate/carbon photocatalyst for high performance bacterial disinfection. *Chemical Engineering Journal*, 438: 135624.
22. Pellegrino, F., Sordello, F., Minella, M., Minero, C. and Maurino, V. (2019). The role of surface texture on the photocatalytic H_2 production on TiO_2. *Catalysts*, 9: 1-28.
23. Wang, J., Wang, Y., Yu, M., Li, G., Zhang, S. and Zhong, Q. (2022). Formation of flaky carbon nitride and beta-Indium sulfide heterojunction with efficient separation of charge carriers for enhanced photocatalytic carbon dioxide reduction. *Journal of Colloid And Interface Science*, 611: 71-81.
24. Citra Dewi, A. S. and Slamet. (2019). Novel approach of esterification process using heterogeneous catalyst in biodiesel synthesis from waste cooking oil. *IOP Conference Series: Materials Science and Engineering*, 509: 1-6.
25. Ghani, N., Iqbal, J., Sadaf, S., Nawaz Bhatti, H. and Asgher, M. (2020). comparison of photo-esterification capability of bismuth vanadate with reduced graphene oxide bismuth vanadate ($RGO/BiVO_4$) composite for biodiesel production from high free fatty acid containing non-edible oil. *Chemistry Select*, 5: 9245-9253.
26. Li, W., Liang, R., Zhou, N. Y. and Pan, Z. (2020). Carbon black-doped anatase TiO_2 nanorods for solar light-induced photocatalytic degradation of methylene blue. *ACS Omega*, 5: 10042-10051.
27. Lau, P. L. and Affam, A. C. (2019). Visible light driven photocatalyst for degradation of organophosphate pesticides: A review. *Borneo Journal of Sciences and Technology*, 1(2): 1-8.
28. Rathi, A., Barman, S., Basu, S. and Kumar, R. (2022). Post-fabrication structural changes and enhanced photodegradation activity of semiconductors@zeolite composites towards noxious contaminants. *Chemosphere*, 288: 132609.
29. Sawant, S. V, Patwardhan, A. W., Joshi, J. B. and Dasgupta, K. (2022). Boron doped carbon nanotubes: Synthesis, characterization and emerging applications – A review. *Chemical Engineering Journal*, 427: 131616.
30. Kondo, K., Murakami, N., Ye, C., Tsubota, T. and Ohno, T. (2013). Development of highly efficient sulfur-doped TiO2 photocatalysts hybridized with graphitic carbon nitride. *Applied Catalysis B: Environmental*, 142: 362-367.
31. Suliman, A., Isha, R. and Roslan, J. (2020). Effect of mass ratio of titanium dioxide and oil palm fiber ash (TiO_2 : Ash) in hybrid photocatalyst on photocatalytic seawater pretreatment. *National Conference for Postgraduate Research*: 124–132.
32. Corro, G., Pal, U. and Tellez, N. (2013). Biodiesel production from Jatropha curcas crude oil using ZnO/SiO_2 photocatalyst for free fatty acids esterification. *Applied Catalysis B: Environmental*, 129(7): 39-47.
33. Redjeki, A. S., Sukirno, S. and Slamet, S. (2021). Simultaneous photocatalytic esterification and addition reaction of fatty acids in kemiri sunan (*Reutealis trisperma* sp.) oil over CuO/TiO_2 catalyst - A novel approach. *Bulletin of Chemical Reaction Engineering* and *Catalysis*, 16(4): 816-830.
34. Alterary, S. S. and Marei, N. H. (2021). Fly ash properties, characterization, and applications: A review. *Journal of King Saud University - Science*, 33(6): 101536.
35. Shi, Z., Yao, S. and Sui, C. (2011). Application of fly ash supported titanium dioxide for phenol photodegradation in aqueous solution. *Catalysis Science and Technology*, 1: 817-822.
36. Berrones-Hernández, R., del Carmen Pérez-Luna, Y., Sánchez-Roque, Y., Pantoja-Enríquez, J., Grajales-Penagos, A. L., López-Cruz, C. F., Longoria, A., Eapen, D. and Sebastian, P. J. (2019). Heterogeneous esterification of waste cooking oil

with sulfated titanium dioxide (STi). *Bioenergy Research*, 12(3): 653-664.

37. Lokman Nolhakim, M. A. H., Shohaimi, N. A. M., Mokhtar, W. N. A. W., Ibrahim, M. L. and Abdullah, R. F. (2021). Immobilization of potassium-based heterogeneous catalyst over alumina beads and powder support in the transesterification of waste cooking oil. *Catalysts*: 11(8): 976.
38. Begum, A.,Hussain. A and Rahman, A. (2012). Effect of deposition temperature on the structural and optical properties of chemically prepared nanocrystalline lead selenide thin films. *Beilstein Journal of Nanotechnology*. 3(1): 438-443.
39. Tauanov, Z., Tsakiridis, P. E., Mikhalovsky, S. V. and Inglezakis, V. J. (2018). Synthetic coal fly ash-derived zeolites doped with silver nanoparticles for mercury (II) removal from water. *Journal of Environmental Management,*. 224: 164-171.
40. Naeem, A., Wali Khan, I., Farooq, Mahmood, T., Ud Din, I., Ali Ghazi, Z. and Saeed, T. (2021). Kinetic and optimization study of sustainable biodiesel production from waste cooking oil using novel heterogeneous solid base catalyst. *Bioresource Technology*, 328: 124831.
41. Visa, M. and Duta, A. (2013). TiO_2/fly ash novel substrate for simultaneous removal of heavy metals and surfactants. *Chemical Engineering Journal*, 223: 860-868.
42. Klubnuan, S., Suwanboon, S. and Amornpitoksuk, P. (2016). Effects of optical band gap energy, band tail energy and particle shape on photocatalytic activities of different ZnO nanostructures prepared by a hydrothermal method. *Optical Materials*, 53: 134-141.
43. Mekonnen, K. D. and Sendekie, Z. B. (2021). NaOH-catalyzed methanolysis optimization of biodiesel synthesis from desert date seed kernel oil. *ACS Omega*, 6(37): 24082-24091.
44. Efavi, J. K. Kanbogtah, D., Apalangya, V., Nyankson, E., Tiburu, E. K., Dodoo Arhin, D., Onwona-Agyeman, B. and Yaya, A. (2018). The effect of NaOH catalyst concentration and extraction time on the yield and properties of Citrullus vulgaris seed oil as a potential biodiesel feed stock. *South African Journal of Chemical Engineering*, 25: 98-102.

Malaysian Journal of Analytical Sciences (MJAS)
Published by Malaysian Analytical Sciences Society

IN-SYRINGE DISPERSIVE SOLID PHASE MICROEXTRACTION FOR THE DETERMINATION OF ORGANOPHOSPHORUS PESTICIDE RESIDUES IN VEGETABLES

(Pengestrakan Mikro Fasa Pepejal Secara Penyerakan dalam Picagari bagi Penentuan Sisa Racun Jenis Organofosforus dalam Sayur-Sayuran)

Hairul Nizwan Manap[1], Faizah Binti Mohammad Yunus[1], Nur Nadhirah Mohamad Zain[2], Noorfatimah Yahaya[2], Hemavathy Surikumaran[3], Kumuthini Chandrasekaram[4,6], Kavirajaa Pandian Sambasevam[5,7], Muggundha Raoov[1,4*]

[1]Department of Chemistry, Faculty of Science,
University of Malaya, 50603 Kuala Lumpur, Malaysia.
[2]Department of Toxicology, Advanced Medical & Dental Institute,
Universiti Sains Malaysia, 13200 Kepala Batas, Pulau Pinang, Malaysia
[3]Faculty of Bioeconomic and Health Sciences,
Universiti Geomatika Malaysia, 54200 Kuala Lumpur, Malaysia
[4]Universiti Malaya Centre for Ionic Liquids (UMCIL), Department of Chemistry,
Faculty of Science, Universiti Malaya, Kuala Lumpur, Malaysia
[5]Advanced Materials for Environmental Remediation (AMER), Faculty of Applied Sciences,
Universiti Teknologi MARA, Negeri Sembilan Branch, Kuala Pilah Campus, Kuala Pilah, Malaysia
[6]Research Services Division (BPP, Institute of Research Management & Services (IPPP),
University of Malaya, 50603 Kuala Lumpur, Malaysia
[7]Electrochemical Materi and Sensor (EMaS) Research Group,
Universiti Teknologi MARA, 40450 Shah Alam, Selangor, Malaysia

**Corresponding author: muggundha@um.edu.my*

Received: 29 December 2022; Accepted: 20 May 2023; Published: 23 June 2023

Abstract

In-syringe dispersive solid-phase microextraction with activated carbon as adsorbent was successfully developed to determine organophosphorus pesticide (OPP) residues in vegetable samples and the analytes were detected using gas chromatography-flame photometric detector (GC-FPD). Under optimized conditions (6 mg of activated carbon in 10 mL sample volume with 3 min extraction time and desorption with 300 µL of acetone), activated carbon was proven to be an effective adsorbent for the organophosphorus pesticide residues in vegetable samples with a satisfactory percentage recovery achieved from 81.46 to 108.93%. All the studied analytes showed good linearity in the range of 10 to 500 µg kg^{-1} and the correlation of determination (R^2) was from 0.9962 to 0.9985. The LODs obtained were from 0.39 to 0.84 µg kg^{-1}, and LOQs were from 1.18 to 2.56 µg kg^{-1}. This method gives precision values for both intra- and inter-day within accepted variable limits (<15 % of RSD). The in-syringe dispersive solid-phase microextraction managed to eliminate the centrifugation process, reduce chemical consumption during extraction, and additionally speed up the extraction process, making it more efficient. This developed method can be applied to real samples such as vegetables and fruit juices as well as tap, river, or ground water analysis for the determination of OPPs.

Keywords: organophosphorus pesticide, in-syringe dispersive solid phase microextraction, gas chromatography-flame photometric detector

Abstrak

Pengekstrakan mikro fasa pepejal dalam picagari dengan menggunakan karbon aktif sebagai penyerap telah berjaya dibangunkan untuk menentukan sisa racun perosak jenis organofosforus (OPP) dalam sampel sayur-sayuran dan analisis telah dikesan dengan menggunakan peralatan analisis kromatografi gas – pengesan fotometrik nyalaan (GC-FPD). Di bawah keadaan yang dioptimumkan (6 mg karbon aktif dalam isipadu sampel 10 mL dengan masa pengekstrakan selama 3 minit dan diserap dengan 300 µL aseton), karbon aktif terbukti sebagai penyerap berkesan bagi sisa racun perosak organofosforus dalam sampel sayur-sayuran berdasarkan peratusan pengesanan semula yang dicapai dari 81.5 hingga 108.9%. Semua analit yang dikaji menunjukkan garis lurus yang baik dalam julat 10 hingga 500 µg kg^{-1} dan memberikan korelasi penentuan (R^2) dari 0.9962 hingga 0.9985. Had pengesanan yang di dapati adalah dari 0.39 hingga 0.84 µg kg^{-1}, dan had pengkuantitian adalah dari 1.18 hingga 2.56 µg kg^{-1}. Kaedah ini memberi nilai ketepatan pada kedua-dua intra dan antara hari dalam sisihan piawai relatif (RSD) yang diterima (<15% daripada RSD). Pengestrakan mikro fasa pepejal secara penyerakan dalam picagari berjaya mengelakkan proses pengemparan, mengurangkan penggunaan bahan kimia dalam proses pengekstrakan dan juga proses pengekstrakan menjadi lebih pantas dan lebih cekap. Kaedah yang dibangunkan ini boleh digunakan untuk sampel sebenar seperti sayur-sayuran, jus buah-buahan dan juga sesuai untuk analisis air paip, air sungai dan air tanah untuk penentuan sisa racun perosak organofosforus.

Kata kunci: perosak jenis organofosforus, pengekstrakan mikro fasa pepejal dalam picagari, kromatografi gas – pengesan fotometrik nyalaan

Introduction

The presence of a significant amount of nutrients and minerals in fresh vegetables, fruits, and pulses makes them important healthy diet food. Unfortunately, they too can turn out to be the source of toxic substances such as pesticides [1]. Pesticides are toxic substances with mixtures of chemical or biological ingredients designed to kill, reduce, or repel insects, weeds, rodents, fungi, and other organisms that threaten public health and the economy. They have numerous beneficial effects but risks as well. Pesticides are used by farmers to protect their fruits and vegetables from diseases and pests while at the same time providing high yields [2]. More than 1100 pesticides are currently registered, according to the status list of all active pesticide chemicals on the European Union market [3]. Pesticides are also commonly utilized in agricultural activities because of their low cost and high effectiveness in controlling pests, weeds, and illnesses.

The increased manufacturing of pesticides for agricultural and non-agricultural applications has resulted in pollution of soil, air, surface, and groundwater posing a major threat to the environment and human health through direct exposure or residues in food and drinking water [4]. Table 1 lists common pesticides group based on their controlling pests. Organophosphorus pesticides (OPPs) are a class of phosphate or phosphorothioate molecules that is one of the world's ten most well-known pesticides [4]. OPPs, on the other hand, are very toxic even at low levels, and can be transmitted to humans, birds, and mammals through contaminated water, air, and food. They are usually absorbed by the lungs, mouth, or skin, and accumulate in the salivary glands, kidneys, fat, and liver [5]. Trace-level OPPs in various types of sample matrices are difficult to detect due to interference such as sugar, plant pigments, and fats.

Vegetables and fruits, which are good sources of minerals, vitamins, antioxidants, and fiber, make up 30% of a consumer's diet, according to a 2003 report by the World Health Organization (WHO). Since Cameron Highlands is one of Malaysia's major vegetable producers, it is important to examine the risk of pesticide residues in these extensively produced vegetables that are grown there for human consumption. According to studies, certain fruits, and vegetables with greater pesticide residue levels and over the maximum residue limit (MRL) may be harmful to consumers' health. Maximum Residue Limits (MRLs), which limit the concentration level of commodities, promote food safety measures as they should not exceed 0.01-0.05 mg kg^{-1}. Unfortunately, as proven by previous research, among all the vegetables, cabbage has a higher contaminant value compared to others such as spinach, tomato, and celery. While mustard show the lowest one that has been contaminated by OPPs. The observed trend in the concentration of studied OPPs was dimethoate (36.8%) > diazinon (14.3%) > parathion methyl (12.3%) >parathion ethyl (20.3%) > chlorpyriphos (14.0%) >

malathion (9.9%). The EU order of percentages of OPPs above MRLs is as; cabbage (24.8%) > cauliflower (13.6%) > broccoli (11%) 17 > cauliflower (13.6%) > lettuce (4.0%) > spinach (3.7%) > celery (1.8%) > mustard (1.8%) [6, 7].

Table 1. Common pesticide groups based on their controlling pests

Insecticides	Fungicides	Herbicides	Rodenticides	Fumigants	Insect repellents
Pyrethroids	Thiocarbamates	Bipyridyls	Warfarines	Aluminium and zinc phosphate	Diethyltoluamide
Organophosphorus	Dithiocarbamates	Chlorophenoxy	Indanodiones	Methyl bromide	
Carbamates	Cupric salts	Glyphosate		Ethylene dibromide	
Organochlorine	Tiabendazoles	Acetanilides			
Manganese compounds	Triazoles	Triazines			

The determination of OPPs in complex matrices, such as environmental, food, and biological samples, usually requires extensive sample pre-treatment [8]. Preconcentration procedures must be included in the sample preparation steps because of the high sensitivity needed for OPP testing . OPP residues persist in environmental waters, fruits, and vegetables because of inappropriate and widespread OPP application [9]. Their broad applications in agriculture or insect control in public spaces result in OPPs and their metabolites being frequently detected in vegetables, fruits, water, soil, and other environmental matrices [10]. Regular sample clean-up to pre-concentrate the OPPs uses evaporation which may cause the OPPs to degrade thus lowering the detection or recovery of OPPs.

The common extraction technique used for the analysis of pesticides is conventional liquid-liquid extraction (LLE), solid-phase extraction (SPE), and solid-phase microextraction (SPME). Lately, many researchers have modified common extraction methods such as magnetic dispersive solid phase extraction (MD-SPE), reverse micelle-supramolecular solvent micro-extraction framework with dispersive solid phase extraction (MOF-DSPE), and magnetic solvent bar-liquid phase microextraction (MSB-LPME). However, these procedures have downsides, such as using a lot of toxic and expensive organic solvents, being tedious, and taking a long time [9, 11-14]. Dispersive solid phase microextraction (DSPME) is a technique that has been recently used for the extraction, clean-up, and pre-concentration of different analytes in real samples. DSPME is an easy, fast, and cost-effective SPME procedure that can be applied to complex matrices with high extraction efficiency, high enrichment factor, and reduced usage of sample solution and chemical solvents [15].

Thus, in this study, our focus is to develop a new, simple, and rapid method for the analysis of OPPs residues in vegetables and fruits by in-syringe DSPME using activated charcoal as an adsorbent to enhance the sensitivity of the method, to eliminate the centrifugation process and to reduce the use of chemicals in the extraction.

Materials and Methods

Chemicals and reagents

The selected OPPs used in this research namely Parathion-methyl (98.5%), Fenchlorphos (99.0%), and Chlorpyrifos (99.8%) purchased from Dr. Ehrenstorfer GmbH (Germany) as shown in Figure 1. Activated charcoal was purchased from Merck (Germany). Acetonitrile and methanol were purchased from Fisher Scientific (Korea). Acetone was purchased from Friendemann Schmidt Chemical (Australia). Ultrapure

deionized water (resistivity, 18.2 MΩ cm^{-1}) was produced by a Sartorius Milli-Q system (Germany) and was used during this study for the preparation of the solution.

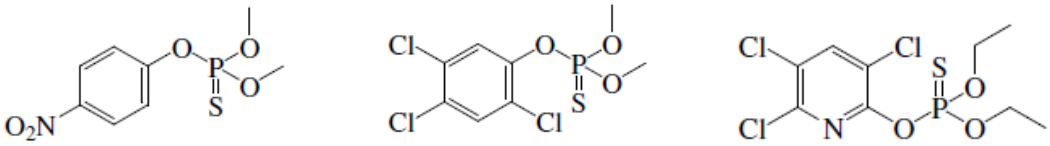


Figure 1. Structures of selected organophosphorus pesticides

GC-FPD conditions

All analysis was done using a GC-2010 Plus gas chromatography-flame photometric detector (GC-FPD) (Shimadzu, Japan) and this GC was equipped with auto-injector AOC-20i. The capillary column SGE-BP1 (30 m 0.25 mm I.D. 0.25 µm film thickness) was used to quantify OPPs. Helium gas was used as the carrier gas with a linear velocity flow mode. The pressure was 100 kPa with the total flow and column flow at 50.00 and 1.0 mL/min, respectively. The temperature of the injector and FPD detector was maintained at 260 ºC and 300 ºC, respectively. The injection was performed using splitless mode and the injection volume was set at 1 µL. The column temperature was programmed as follows: initial temperature of 100 ºC and held for 1 min, then increased to 200 ºC at the rate of 20 ºC min^{-1} and held for 8 min. The final temperature was increased to 220 ºC at the rate of 15 ºC min^{-1} and held for 2 min. The total run time for the GC analysis was 17.33 min.

In-syringe DSPME procedure

The schematic of the in-syringe DSPME procedure is shown in Figure 2. The prepared sample solution was added with 6 mg of activated charcoal and was vortexed for 3 min. Then, the mixed solution was transferred into a 10 mL syringe with a 0.45 µm syringe filter. At this time, OPPs were bonded with activated charcoal and remained inside the syringe filter. Then, the OPPs were desorbed using 300 µL acetone and the extracted OPPs were injected into GC-FPD for the quantitative analysis.

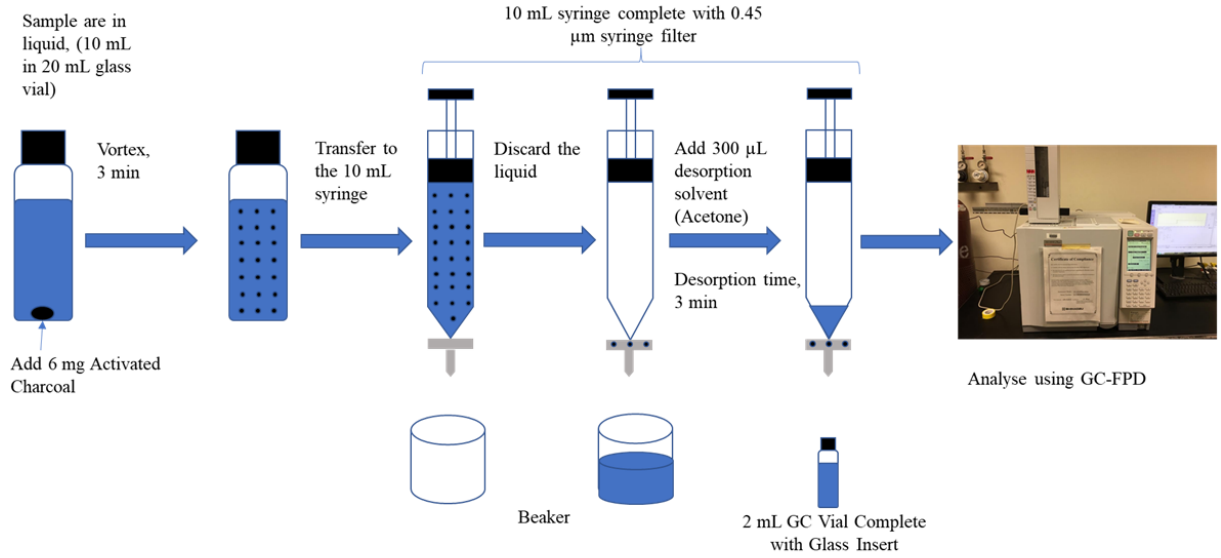


Figure 2. Schematic of in-syringe DSPME procedure

Sample collection and pre-treatment

Mustard, kale, cabbage, tomato, and strawberry were purchased from three different markets in Cameron Highland, Pahang. The representative sample (500 g) was chopped, and the sample was homogenized using the food processor. Then, sample juice was extracted using a juice extractor. The sample solution was filtered, and the suspended solid was discarded. Then, 10 mL of filtered solution was put in the 20 mL glass vial and kept in the refrigerator at 40°C till the extraction using the DSPME procedure.

Optimization of extraction conditions

To optimize the DLLME of OPPs from water samples, analytical factors that potentially affect the sample were studied. The parameters involved were tabulated in Table 2 below.

Table 2. Optimization condition

Parameters	Level
Mass of Activated carbon (mg)	2, 4, 6, 8 and 10
Extraction time (min)	1, 3, 5, 7 and 10
Desorption Solvent	Acetone, Acetonitrile and Methanol
Desorption volume (μL)	100, 300, 500, 700 and 1000
Desorption time (min)	0, 3, 5, 7 and 10
pH	5, 6, 7, 8 and 9

Method validation

Method validation (linearity, limits of detection (LOD) and quantitation (LOQ), pre-concentration factor, and recovery was performed using the proposed in-syringe DSPME method. Linearity was investigated over the range of 10 to 500 μg kg^{-1}. The LOD and LOQ values were calculated based on the standard deviation of the response of the standard blank and the slope of the calibration curve. The pre-concentration factor was calculated from the spiked peak. While recovery studies were carried out using spikes at three concentration levels (30, 50, and 100 μg kg^{-1}). All spiked samples were extracted in triplicates. All the formula is shown below;

$$\text{RSD} = \frac{\text{standard deviation}}{\text{mean}} \times 100\% \quad (1)$$

$$\text{LOD} = \frac{\text{standard deviation}}{\text{slope}} \times 3.3 \quad (2)$$

$$\text{LOQ} = \frac{\text{standard deviation}}{\text{slope}} \times 10 \quad (3)$$

$$\% \text{ Recovery} = \frac{C_{ext}}{C_{int}} \times 100 \quad (4)$$

where C_{ext} is the concentration of analyte in extractant phase; while C_{int} is the initial concentration of OPPs.

Results and Discussion

Assignment and identification of OPPs peak

The mixed OPPs standard solution (1 mg L^{-1}) was injected into GC-FPD in a splitless mode where the technical parameter such as injection volume, gas flow, and temperature gradient were optimized to get a better resolution. The peak was assigned and identified by retention time based on molecular weight and OPPs

structure as shown in Figure 3. The first peak at 12.312 min is parathion-methyl (PM), followed by fenchlorphos (FE) at 13.154 min and chlorpyrifos (CH) at 14.583 min.

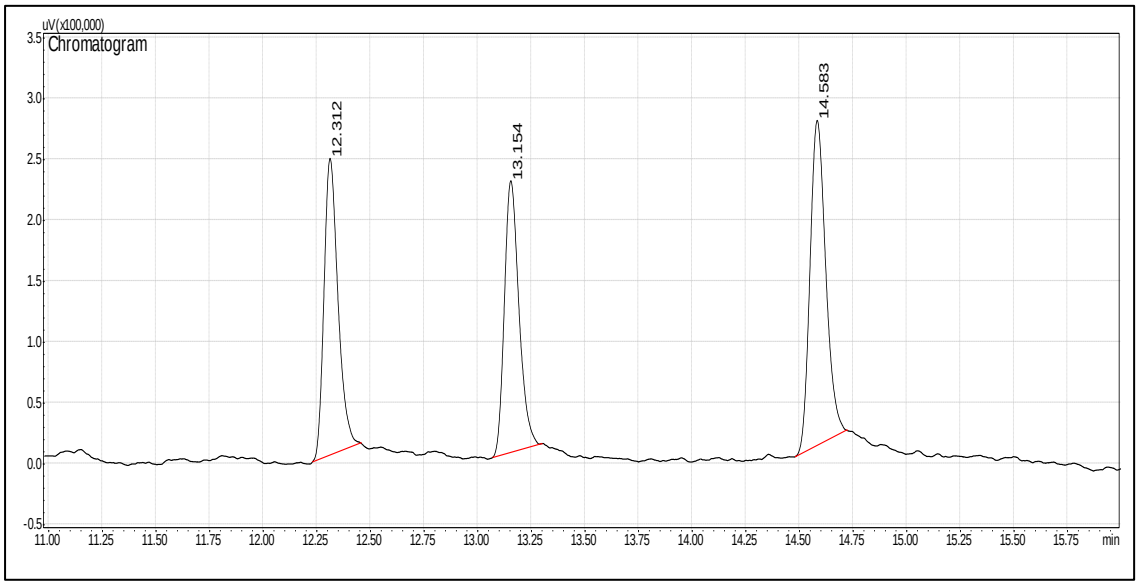


Figure 3. Chromatogram of OPPs a) parathion-methyl b) fenchlorphos c) chlorpyrifos

Optimization of extraction conditions

In this study, the effects of six critical parameters such as the mass of activated carbon, extraction times, volume, time, pH, and solvent were investigated. The optimization process is the process of changing one parameter while at the same time, keeping all other parameters of the same condition to monitor the responses. The optimization was carried out in triplicates using water as a sample matrix with a concentration of 250 µg L^{-1} each.

Effect of mass of activated carbon

The mass of adsorbent used in the extraction has a significant effect on the extraction efficiency. In this study, commercially available activated carbon was used as an adsorbent and the mass of activated carbon was studied in the range of 2-10 mg. Based on Figure 4(a), 6 mg of activated carbon gave a higher peak area as compared to below 6 mg and there is no obvious increase observed in the peak area when the mass of activated carbon is more than 6 mg. The reduced reaction could be because the saturation of active sites on the adsorbent has been exceeding. Hence, 6 mg of activated carbon was selected as the optimal adsorbent amount [9].

Effect of extraction time

Extraction time is an important factor that can influence extraction efficiency because there is a need for a short period for the binding of target compounds with the adsorbent. The effect of extraction time was studied in the range of 1-10 min. It was observed that the peak area for all OPPs increased as the extraction time increased up to 3 min and dropped thereafter when it reached more than 5 min maybe because of the desorption of analyte from the adsorbent [16]. Thus, 3 min was chosen as an optimal time for the extraction of vegetable samples as shown in Figure 4(b).

Effect of desorption solvent

Types of solvent used also play a vital role and give a significant effect on the extraction efficiency to ensure high recovery and sensitivity toward the performance [17]. Referring to Figure 4(f), acetone gave a higher peak area than methanol. To produce a very high quantity of contact area and quick migration of analytes from the aqueous sample into the extraction phase, the

extractant solvent must be disseminated into the aqueous sample as very small droplets. In comparison to the other two solvents, acetone has the lowest viscosity. The reaction decreases as the desorption solvent's viscosity rises (acetone, acetonitrile, and methanol respectively, 0.32, 0.37, and 0.55 centipoise at 20 °C). The likelihood that a reaction will occur increases with polar solvent viscosity. As a result, acetone was selected as an optimal solvent and this result was agreed with another researcher. As a result, acetone was selected as an optimal solvent and this result was agreed with another researcher [18].

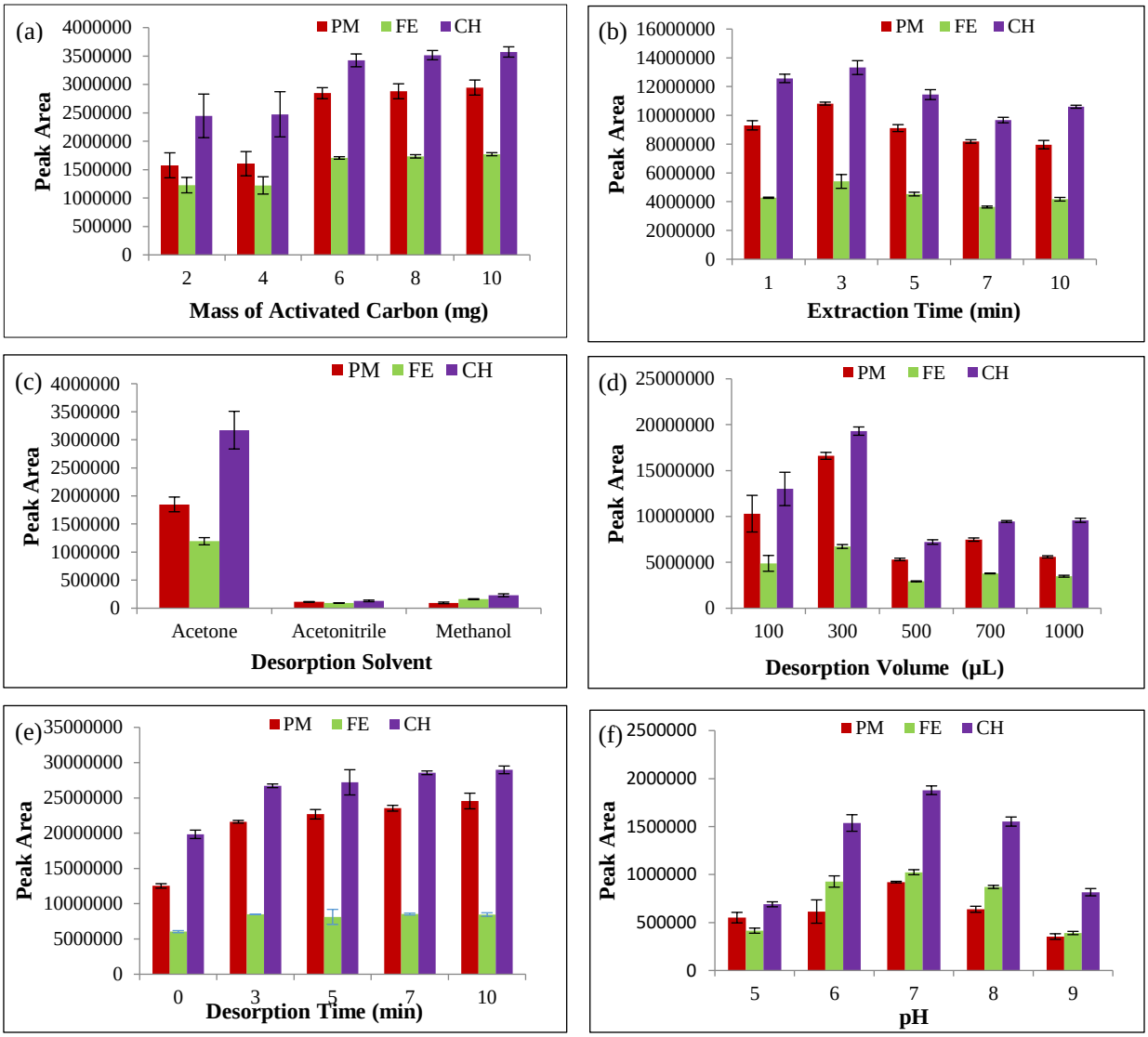


Figure 4. (a) Effect of mass of activated carbon (Extraction condition: extraction time, 5 min; desorption volume, 500 µL of acetone; desorption time, 3 min and without pH adjustment (b) Extraction time (Extraction conditions: mass activated carbon, 6 mg; desorption volume, 500 µL acetone; desorption time, 3 min); (c) Desorption volume (Extraction conditions: mass activated carbon, 6 mg; extraction time, 3 min; desorption time, 3 min); (d) Desorption time (Extraction conditions: mass activated carbon, 6 mg; extraction time, 3 min; desorption volume, 300 µL acetone); (e) pH (Extraction conditions: mass activated carbon, 6 mg; extraction time, 3 min; desorption time, 3 min; desorption volume, 300 µL acetone); (f) Desorption solvent: (Extraction conditions: mass activated carbon, 6 mg; extraction time, 5 min; desorption time, 3 min; desorption volume, 300 µL acetone) on the extraction efficiency.

Effect of desorption volume

In Figure 4(c) effect of desorption volume was studied in the range of 100 to 1000 µL. Among the studied volumes, 300 µL gives the highest peak area and this low volume fits the title micro-extraction. It was observed, that when the volume increases more than 300 µL, the peak area becomes smaller compared to those of 100 µL and 300 µL. This is probably due to the increasing dilution factor and the solubility of analytes in the aqueous phase the extraction step was increased which will lead to a decrease in the extraction efficiency. Thus, the smaller the volume is, the more concentrated the solvent becomes. Hence, an eluent volume of 300 µL was selected for further analysis as it gave the highest peak area ratio response for all four OPPs [19].

Effect of desorption time

The effect of time in the range of 0-10 min on the extraction efficiency of the targeted OPPs was investigated using acetone as the solvent. Figure 4(d) shows the peak area increases significantly between 0-3 min before decreasing when increasing the desorption time to 10 min [20]. Increase in peak area due to the response of analyte from sorbent to solution while the constant result after 5 min because of re-adsorption of analyte onto the sorbent. Hence, 3 min was selected as the optimal time in the subsequent extractions.

Effect of pH

Solution pH plays an imperative role in separation science as it controls both the degree of ionization of the materials present in the solution and the dissociation of functional groups of the analyte [21]. In this study, the pH of the sample solution was adjusted in the range of pH 5 to 9. The initial pH for the sample solution was between pH 6 to 8. Based on the graph in Figure 4(e), the optimal pH value was around pH 6-8 because of increasing in the OPPs stability between 4.5-7. When approaching pH 9 the peak area was decreasing because of OPPs start to hydrolyze as the higher the pH the faster the hydrolysis process of OPPs will be. Since the obtained pH is like the pKa value of the analyte, no pH adjustment is needed for further experiments.

Method validation

A series of spiked samples that ranged from 10 to 500 µg kg^{-1} were applied to plot the matrix match calibration curves (n=3). The method validation was done under optimized conditions (6 mg of activated carbon in 10 sample volumes with 3 min extraction time and with 300 µL of acetone). The linearity shows the correlation of determination (R^2) ranging from 0.9962 to 0.9985. The optimized method was determined by measuring the (repeatability) and inter-day (intermediate) at a spiking level of 100 µg kg^{-1} in vegetable samples. Precision was determined on the same day with five duplicates while inter-day precision was calculated with five replicates on three different days. Relative standard deviation (RSD) ranged between 0.89% to 2.17% while inter-day ranged between 1.27% to 3.13%. The assessed values on precision were found to be within the known variable limits (<15 %) [12]. Table 3 displays the linear performance, LOD, LOQ, PF, and inter-day results. In-syringe DSPME can detect and quantify the OPPs at concentrations as low as 1.18 µg kg^{-1}. The pre-concentration factor is described as enrichment factor times with theoretical volume. Based on the calculation, it was found that the pre-concentration factor for parathion-methyl, fenchlorphos, and chlorpyrifos are 5548, 1216, and 3833 respectively at the concentration of 250 µg kg^{-1}.

Table 3. Linearity, LOD, LOQ, PF, intra-day and inter-day performance for in-syringe DSPME procedure

Analyte	Linearity Range (µgL^{-1})	R^2	LOD (µgL^{-1})	LOQ (µgL^{-1})	Intra-day RSD%(n=5) at 100 (µgL^{-1})	Inter-day RSD% (n=3) at 100 (µgL^{-1})	Pre-concentration Factor at 250 (µgL^{-1})
Parathion-methyl	10-500	0.9985	0.53	1.60	2.16	0.89	5548
Fenchlorphos	10-500	0.9962	0.39	1.18	3.13	1.61	1216
Chlorpyrifos	10-500	0.9966	0.84	2.56	1.27	2.17	3833

Recovery

The recovery study was done with three different spiked levels (30, 50, and 100 µg kg^{-1}) in blank vegetable samples. Table 4 displays the relative recovery data obtained from the experiment where the recovery for parathion-methyl, fenchlorphos, and chlorpyrifos are within 81.46 to 108.85%, 97.73 to 108.93%, and 92.71 to 106.14% respectively.

Table 4. Relative Recovery for OPPs Extracted by in-syringe DSPME

Analytes	Relative Recovery (%) ± %RSD (n=3)		
	30 µg kg^{-1}	**50 µg kg^{-1}**	**100 µg kg^{-1}**
Parathion-methyl	108.85 ± 1.98	93.31 ± 3.68	81.46 ± 4.66
Fenchlorphos	108.93 ± 4.79	106.04 ± 2.21	97.73 ± 4.72
Chlorpyrifos	105.04 ± 3.59	106.14 ± 3.40	92.71 ± 2.46

Real sample analysis

The developed in-syringe DSPME method was applied to real sample analysis to determine OPPs in vegetable samples of mustard, kale, cabbage, tomato, and strawberry. All 15 vegetable samples were purchased from three different market locations in Cameron Highland, Pahang. This analysis was run in optimized in-syringe DSPME conditions. This indicates that most farmers at Cameron Highland, Pahang are following the rules and regulations set up by the Agricultural Department during farming, harvesting, and preserving the vegetables.

Conclusion

In-syringe solid phase microextraction using activated carbon as an adsorbent was successfully developed to determine the pesticide residues in vegetable samples and then were detected using GC-FPD. Under optimized conditions (6 mg of activated carbon in 10 volumes of the sample with 3 min extraction time and 300 µL of acetone), activated carbon was proven to be an effective adsorbent for pesticide residues in vegetable samples based on higher percentage recoveries achieved from 81.5 to 108.9 %. All the studied parameters showed good linearity in the range of 10 to 500 µg kg^{-1} and gives a correlation of determination (R^2) from 0.9962 to 0.9985. This method gives precision values on both and inter-day within accepted variable limits (<15 % of RSD). The in-syringe solid-phase microextraction method managed to reduce the use of chemicals in the extraction. Additionally, this method proves to be faster and more efficient than other conventional extraction methods. Table 5 shows the comparison between this project with previous studies. This developed method can be applied to real samples such as vegetables and fruit juices as well as tap, river, and groundwater analysis for the determination of OPPs.

Table 5. Comparison of current study on the analysis of pesticides

Analysis Method	Type of Sample	Linear Range (µg L^{-1})	LOD (µg L^{-1})	LOQ (µg L^{-1})	Recovery (%)	Ref.
Zinc-Base MOFs-DSPE – GC-FID	Water & fruit juice	0.1-100	0.03-0.21	0.06-0.65	92-100	[9]
QuEChERS-DLLME – GC-FID	Fruits & Vegetables	1.6-5000	0.27-0.48	0.97-1.6	84-103	[12]
SPME – GC-FPD	Vegetables	0.1-100	0.01-0.14	0.03-0.42	75-117	[16]
PDMS/MOFs-SBSE – GC-FPD	Water	0.2-100	0.043-0.085	0.06-0.22	80-115	[18]

PV in-syringe DLMPE-GC-MS	Vegetables	10-200	4.8-7.1	5.1-8.2	90.2-92.2	[20]
MWA-DLLME-GC-FID	Water	3-40000	0.65-1.3	0.77-1.92	80-99.7	[21]
SBSE-GC-FID	Vegetables and fruit juices	0.6-1000	1.7-5.6	2.0-6.4	73-104	[22]
MD-μ-SPE-GC-IMS	Water	2-1000	0.46-1.0	0.56-2.0	70-81	[23]
LLME	Water and fruit juices	0.5-400	0.1-0.35	0.18-0.66	92.2-110.5	[24]
C_{18}	Water	0.01-5.00	0.003-0.0004	0.007-0.0022	88-100	[25]
Activated carbon in-syringe DSPME	Vegetables	10-500	0.39-0.84	1.18-2.56	81.46-108.9	Current work

Acknowledgment

The authors would like to seize this opportunity to express their gratitude to the Ministry of Higher Education for the assistance and financial support under the Fundamental Research Grant Scheme (FRGS/1/2020/ STG04/UM/02/9). The authors acknowledge the Department of Chemistry, Faculty of Science, and the University of Malaya for providing the facilities. The authors also would like to acknowledge Universiti Sains Malaysia for research collaboration.

References

1. Sharma, D., Nagpal, A., Pakade, Y. B. and Katnoria, J. K. (2010). Analytical methods for estimation of organophosphorus pesticide residues in fruits and vegetables: A review. *Talanta,* 82(4): 1077-1089.
2. Samsidar, A., Siddiquee, S., & Shaarani, S. M. (2018). A review of extraction, analytical and advanced methods for determination of pesticides in environment and foodstuffs. Trends in Food Science & Technology, 71, 188-201.
3. Mukwevho, N., Fosso-Kankeu, E., Waanders, F., Kumar, N., Ray, S. S. and Yangkou Mbianda, X. (2019). Photocatalytic activity of $Gd_2O_2CO_3$·ZnO·CuO nanocomposite used for the degradation of phenanthrene. *SN Applied Sciences,* 1: 1-11.
4. Mohd, M. S., Siti, U. M., Mazidatul, A. M. and Wan, A. W. I. (2011). Determination of organophosphorus pesticides by dispersive liquid-liquid micro extraction coupled with gas chromatography-electron capture detection. *Malaysian Journal of Analytical Sciences*, 15(2): 232-239.
5. Dozein, S. V., Masrournia, M., Es' haghi, Z. and Bozorgmehr, M. R. (2021). Development of a new magnetic dispersive solid-phase microextraction coupled with GC-MS for the determination of five organophosphorus pesticides from vegetable samples. *Food Analytical Methods,* 14(4): 674-686.
6. Chambers, A. G. S. (2020). Food (Amendment) (No3) Regulations 2020.
7. Farina, Y., Abdullah, M. P., Bibi, N. and Khalik, W. M. A. W. M. (2016). Pesticides residues in agricultural soils and its health assessment for humans in Cameron Highlands, Malaysia. *Malaysian Journal of Analytical Science,* 20(6): 1346-1358.
8. Chen, J., Duan, C. and Guan, Y. (2010). Sorptive extraction techniques in sample preparation for organophosphorus pesticides in complex matrices. *Journal of Chromatography B,* 878(17-18): 1216-1225.
9. Amiri, A., Tayebee, R., Abdar, A. and Sani, F. N. (2019). Synthesis of a zinc-based metal-organic framework with histamine as an organic linker for

the dispersive solid-phase extraction of organophosphorus pesticides in water and fruit juice samples. *Journal of Chromatography A*, 1597: 39-45.

10. Wang, P., Luo, M., Liu, D., Zhan, J., Liu, X., Wang, F. and Zhou, Z. (2018). Application of a magnetic graphene nanocomposite for organophosphorus pesticide extraction in environmental water samples. *Journal of Chromatography A,* 1535: 9-16
11. Wu, L., Song, Y., Hu, M., Zhang, H., Yu, A., Yu, C., ... and Wang, Z. (2015). Application of magnetic solvent bar liquid-phase microextraction for determination of organophosphorus pesticides in fruit juice samples by gas chromatography mass spectrometry. F*ood Chemistry*, 176: 197-204.
12. Farajzadeh, M. A., Sohrabi, H. and Mohebbi, A. (2019). Combination of modified QuEChERS extraction method and dispersive liquid–liquid microextraction as an efficient sample preparation approach for extraction and preconcentration of pesticides from fruit and vegetable samples. *Food Analytical Methods*, 12: 534-543.
13. Gorji, S., Biparva, P., Bahram, M. and Nematzadeh, G. (2019). Rapid and direct microextraction of pesticide residues from rice and vegetable samples by supramolecular solvent in combination with chemometrical data processing. *Food Analytical Methods*, 12: 394-408.
14. Fernandes, V. C., Freitas, M., Pacheco, J. P., Oliveira, J. M., Domingues, V. F. and Delerue-Matos, C. (2018). Magnetic dispersive micro solid-phase extraction and gas chromatography determination of organophosphorus pesticides in strawberries. *Journal of chromatography A,* 1566: 1-12.
15. Ghorbani, M., Aghamohammadhassan, M., Chamsaz, M., Akhlaghi, H., and Pedramrad, T. (2019). Dispersive solid phase microextraction. *TrAC Trends in Analytical Chemistry*, 118: 793-809.
16. Sapahin, H. A., Makahleh, A. and Saad, B. (2019). Determination of organophosphorus pesticide residues in vegetables using solid phase micro-extraction coupled with gas chromatography–flame photometric detector. *Arabian Journal of Chemistry*, 12(8): 1934-1944.
17. Markus, A., Gbadamosi, A. O., Yusuff, A. S., Agi, A. and Oseh, J. (2018). Magnetite-sporopollenin/graphene oxide as new preconcentration adsorbent for removal of polar organophosphorus pesticides in vegetables. *Environmental Science and Pollution Research*, 25: 35130-35142.
18. Xiao, Z., He, M., Chen, B. and Hu, B. (2016). Polydimethylsiloxane/metal-organic frameworks coated stir bar sorptive extraction coupled to gas chromatography-flame photometric detection for the determination of organophosphorus pesticides in environmental water samples. *Talanta*, 156: 126-133.
19. Nodeh, H. R., Ibrahim, W. A. W., Kamboh, M. A. and Sanagi, M. M. (2017). New magnetic graphene-based inorganic–organic sol-gel hybrid nanocomposite for simultaneous analysis of polar and non-polar organophosphorus pesticides from water samples using solid-phase extraction. *Chemosphere*, 166: 21-30.
20. Amri, F., Niazi, A. and Yazdanipour, A. (2022). Three-pesticide residue analysis in tomato using a fast pressure variation in-syringe dispersive liquid-phase microextraction technique coupled with gas chromatography-mass spectrometry by assisting experimental design. *International Journal of Environmental Analytical Chemistry*, 102(3): 615-632.
21. Ayazi, Z., Jaafarzadeh, R. and Matin, A. A. (2017). Montmorillonite/polyaniline/polyamide nanocomposite as a novel stir bar coating for sorptive extraction of organophosphorous pesticides in fruit juices and vegetables applying response surface methodology. *Analytical Methods*, 9(31): 4547-4557.
22. de Souza Pinheiro, A. and de Andrade, J. B. (2009). Development, validation and application of a SDME/GC-FID methodology for the multiresidue determination of organophosphate and pyrethroid pesticides in water. *Talanta*, 79(5): 1354-1359.
23. Kermani, M., Jafari, M. T. and Saraji, M. (2019). Porous magnetized carbon sheet nanocomposites for dispersive solid-phase microextraction of organophosphorus pesticides prior to analysis by

gas chromatography-ion mobility spectrometry. *Microchimica Acta*, 186: 1-11.

24. Zohrabi, P., Shamsipur, M., Hashemi, M. and Hashemi, B. (2016). Liquid-phase microextraction of organophosphorus pesticides using supramolecular solvent as a carrier for ferrofluid. *Talanta*, 160: 340-346.
25. Hadjmohammadi, M. R., Peyrovi, M. and Biparva, P. (2010). Comparison of C_{18} silica and multi-walled carbon nanotubes as the adsorbents for the solid-phase extraction of Chlorpyrifos and Phosalone in water samples using HPLC. *Journal of Separation Science*, 33(8): 1044-1051.

Malaysian Journal of Analytical Sciences (MJAS)
Published by Malaysian Analytical Sciences Society

A VALIDATED RP-HPLC METHOD FOR THE QUANTIFICATION OF LIQUID SELF-EMULSIFYING CURCUMIN: PHARMACOKINETIC APPROACH

(Penentusahkan Kaedah FB-KCPT Untuk Kuantifikasi Kurkumin Pememulsi Diri Cecair: Pendekatan Farmakokinetik)

Xin-Yen Chiang[1], Sheau-Chin Lim[2], Kah-Hay Yuen[1], Jia-Rou Khor[1], and Siok-Yee Chan[1*]

[1]Departmental of Pharmaceutical Technology,
School of Pharmaceutical Sciences,
Universiti Sains Malaysia, 11800, Penang, Malaysia
[2]AvantSar Sdn. Bhd.,
98007, Miri, Sarawak, Malaysia

**Corresponding author: sychan@usm.my*

Received: 26 February 2023; Accepted: 15 May 2023; Published: 23 June 2023

Abstract

The current study describes a validated, reliable, simple, and sensitive high-performance liquid chromatographic method with fluorescence detection (HPLC-FL) for the determination of curcumin at the *in vitro* and *in vivo* levels in pure and Self Emulsifying Drug Delivery System (SEDDS). The mean recovery of pure curcumin was 99.1%. The calibration curves were linear over the range from 31.3 to 1000 ng/mL with correlation coefficient of $R^2 \geq 0.9999$. The lower limit of quantification (LLOQ) was 31.3 ng/mL. The validation results confirmed the linearity, accuracy, and precision of the developed method. Furthermore, the curcumin-SEDDS excipients solubility were conducted, and later curcumin loading content (LC) was determined. Moreover, pharmacokinetic parameters, mean peak plasma concentration (C_{max}), time to reach peak concentration (T_{max}), and total area under the plasma concentration-time curve from time zero to the last sampling time, i.e., 1440-minute (AUC0-1440m) were successfully measured with the values of 238.81 ng/mL, 70.83 min and 11249.60 ng.min/mL, respectively. This method is suitable to detect curcumin in pure and SEDDS formulation *in vitro* and *in vivo*.

Keywords: curcumin, plasma, self-emulsifying drug delivery system, pharmacokinetic

Abstrak

Kajian semasa menerangkan kaedah kromatografi cecair (HPLC) berprestasi tinggi yang disahkan, boleh dipercayai, mudah dan sensitif dengan pengesanan pendarfluor untuk penentuan kurkumin pada tahap *in vitro* dan *in vivo* dalam Sistem Penghantaran Ubat Pengemulsi Sendiri (SEDDS) dan tulen. Purata pemulihan kurkumin tulen ialah 99.1%. Keluk penentukuran adalah linear dalam julat dari 31.3 hingga 1000 ng/mL dengan pekali korelasi $R^2 \geq 0.9999$. Had kuantifikasi yang lebih rendah (LLOQ) ialah 31.3 ng/mL. Keputusan pengesahan mengesahkan kelinearan, ketepatan dan ketepatan kaedah yang dibangunkan. Tambahan pula, keterlarutan eksipien kurkumin-SEDDS telah dijalankan, dan kandungan pemuatan kurkumin (LC) kemudiannya ditentukan.

Selain itu, parameter farmakokinetik berjaya diukur dengan kaedah ini termasuk purata kepekatan plasma puncak (C_{max}), masa untuk mencapai kepekatan puncak (T_{max}), dan jumlah kawasan di bawah keluk masa kepekatan plasma dari masa sifar hingga masa pensampelan terakhir, iaitu, nilai 1440-minit (AUC0-1440m) masing-masing 238.81 ng/mL, 70.83 min dan 11249.60 ng.min/mL Kaedah ini sesuai untuk mengesan kurkumin dalam formula tulen dan SEDDS daripada penilaian *in vitro* kepada *in vivo*.

Kata kunci: kurkumin, plasma, sistem penyampaian ubat pengemulsi sendiri, farmakokinetik

Introduction

The dried ground rhizome of the perennial herb *Curcuma longa* Linn , or also known as turmeric, has been used in Asian medicine since the second millennium BC [1]. According to the Food and Agriculture Organization of the United Nations, turmeric has been used as food preservative, coloring and flavoring agents [2]. Turmeric is traditionally used for the treatment of wounds, inflammation and tumors [3-5]. It has been linked with antioxidant, anti-inflammatory, anti-microbial, antiproliferative, angiogenesis, anticancer, antidiabetic, antirheumatic, antiviral effects and low toxicity with promising clinical application [2, 6-9]. Recently, a study showed that curcumin minimize the effect on cognitive functions, reduce fatigue as well as improving resilience to the detrimental effects of psychological stress on mood in elderly [10].

Curcuma spp. contains turmerin (a water-soluble peptide), essential oils (such as turmerones, atlantones and zingiberene) and curcuminoids which are natural polyphenols responsible for the yellow color of turmeric. There are three types of curcuminoids, namely bis-demethoxycurcumin (BDMC), demethoxycurcumin (DMC) and curcumin **[**1,7-bis(4-Hydroxy-3-methoxyphenyl)-1,6-heptadiene-3,5-dione]. Among the three curcuminoids, curcumin which is also known as diferuloylmethane, or diferulylmethane is the most biologically active constituent.

Liu et al. reported the LLOQ of curcumin was 0.5 ng/mL through LC-MS/MS method with high sensitivity and short run time [11]. However, the curcumin extraction from rat plasma adopted by Liu et al. was complicated and time consuming [11]. May et al. used matrix-assisted laser desorption ionization time-of-flight mass spectrometry (MALDI-TOF/MS) to study curcumin and its metabolites in mouse serum and lung cell resulting in correlation coefficients of 0.94-0.99 with concentrations of 0.04-10.00 nmol curcumin [12]. Despite high sensitivity and short run time, LC-MS/MS and MALDI-TOF/MS are expensive instruments with hard overcome matrix effects [13].

High performance liquid chromatography (HPLC) also been employed in plasma curcumin quantification with limitation of long analysis run time and tedious extraction methods [14-16]. For instance, Heath et al. extracted curcumin with 95% ethyl acetate/5% methanol [14], and Pak et al. utilized a 3-step extraction which requires large plasma sample volume and uses of chloroform [15]. In another study, Schiborr and colleagues developed a sensitive HPLC-FD with an extremely short retention time at 1.2 minutes which may potentially be interfered by solvent and plasma front peaks [16]. Besides, the extraction step was repeated twice in their developed method [16].

Protein precipitation has been introduced as one of the most common and simple sample pre-treatment methods in removing the protein in plasma sample. It is a simpler method as compared to the extraction process. Ma et al. and Li et al. have developed simpler HPLC assay method using direct protein precipitation method for curcumin extraction with UV and PDA detection, respectively. The HPLC method developed in Li et al. had a relatively shorter run time of 3 minutes and lower LLOQ of 1 ng/mL as compared to Ma et al. [17, 18].

More recently, Anwar et al. modified and developed an analysis method for curcumin using Ultra Performance Liquid Chromatography (UPLC) with Quadrupole-time of flight-mass spectrometry (Q-TOF-MS/MS) [19]. This is a very sensitive chromatographic method which offered short sample retention time at 2.18 minutes; however, the extraction method used a toxic solvent, i.e., chloroform and required a large plasma sample volume of 500 µL. In addition, the technology requires expensive equipment that is not available in most

laboratories. Therefore, the aim of this study was to develop an improved method for the quantification of curcumin in plasma using simple high performance liquid chromatography (HPLC) with rapid sample pretreatment procedure. This method is also used to quantify curcumin in self-emulsifying delivery system include solubility, loading content and formulation studies.

Materials and Methods

Chemicals and reagents

Curcumin (99.8% analytical standard) was purchased from ChromaDex (Irvine, CA). Curcuma extract was purchased from Naturalin (Bio-Resources Co. Ltd, Changsha City, China). Canola oil, corn oil, soyabean oil, sunflower oil, peanut oil, and olive oil were purchased from a local store. Oleic acid, PEG-400, Tween 20®, Tween 80®, Cremophor EL®, Cremophor RH40®, and Labrasol® were sponsored by Hovid R&D, Penang, Malaysia. HPLC grade of acetonitrile (ACN) and acetic acid (100% glacial) were obtained from Merck (Darmstadt, Germany). Water for HPLC was prepared by double glass distillation and filtered through 0.45 μm nylon membrane filter (Millipore, Bedford, MA, USA). Human plasma obtained from Hospital Pulau Pinang, Malaysia.

Method development: Instrumentation and equipment

HPLC system consisted of a Waters e2695 Separations Module auto-sampler with refrigeration unit, Waters 2475 Multi-wavelengths Fluorescence Detector. Data acquisition and analyses were performed using the Empower Software 3 (2010, Waters, US).

Analytical and chromatographic conditions

Chromatographic separation was achieved on a reversed phase Waters Symmetry® C_{18} (5μm x 4.6 mm x 250 mm) column. Column and injection temperatures were both maintained at 25°C. Isocratic solvent with flow rate of 1.2 mL/min was used. The sample was injected through a fixed sample loop of 10 μL. The excitation and emission wavelengths for curcumin were set at 365 nm and 512 nm respectively. The analysis time was 6 minutes per sample.

Preparation of mobile phase

A 1% acetic acid solution was prepared by adding 4 mL of glacial acetic acid into 400 mL of distilled water. This was then eluted together with 600 mL of acetonitrile to make up a mobile phase of acetonitrile and acetic acid 60:40 (% v/v) and adjusted to pH 3.25 with acetic acid. Liquids used for the mobile phase were filtered with 0.45μm filter paper (Millipore, Merck, Germany) and kept in amber glass bottles prior to use. Fresh mobile phase was prepared daily.

Preparation of stock solutions and calibration samples

Stock solution of curcumin was prepared in ACN at a concentration of 1 mg/mL. This curcumin stock solution was diluted 50 times with ACN to a working solution of 20 μg/mL. The calibration standards were created by mixing the appropriate amount of the working standard with human control plasma to obtain a final volume of 1 mL, resulting in six calibration standards ranging - 31.3, 62.5, 125, 250, 500 and 1000 ng/mL. Standard solutions were prepared by adding volumes of 1.565, 3.125, 6.25, 12.5, 25, and 50 μL of a working solution into 998.435, 996.875, 993.75, 987.5, 975, and 950 μL of blank plasma. All solutions were protected from light and stored at 4°C. For each validation and assay run, the calibration curve of curcumin was prepared fresh from the working solution. All the plasma samples were stored at -20°C and brought to room temperature prior to use.

Sample pre-treatment procedure

Plasma samples and working solutions were thawed to room temperature before use. An aliquot (100 μL) of plasma samples were pipetted into 1.5 mL microcentrifuge tube (Eppendorf, Germany). Direct deproteinization procedure was carried out by adding 200 μL of acetonitrile. The mixture was vortex-mixed for 20 seconds and centrifuged at 12800 x g for 15 minutes. A 100 μL aliquot of the supernatant was transferred to the HPLC vials and 10 μL of the mixture was injected into the HPLC system for further analysis.

Assay validation

In order to confirm the suitability of the method for its intended use, it was validated for specificity, linearity,

precision, accuracy, limit of quantification, limit of detection and stability according to the International Conference on Harmonization guidelines [20] and Guideline on bioanalytical method validation [22].

Specificity

For a specific method, there should be no interference of impurities or other compounds in the blank plasma to the detected peak of curcumin [21]. To test specificity, 10 µL of blank plasma pre-treated according to previous section was injected for analysis. The chromatograms of spiked curcumin plasma samples were compared to the blank plasma. The specificity of the method was determined by analyzing 6 human blank plasma samples.

Linearity

Calibration standards were prepared from the curcumin stock solution at 6 concentrations ranging from 31.3 to 1000 ng/mL. Peak area of curcumin from the chromatogram was plotted against the corresponding curcumin concentrations in plasma.

Accuracy and precision

The within-day accuracy and precision of this assay were evaluated by analyzing plasma aliquots of the calibration standards in 6 replicates on the same day. The between-day accuracy and precision were determined by analyzing each calibration sample once for 6-consecutive days. According to USP [22] and FDA[21] guidelines, the acceptance criteria for within- and between-day accuracy was within ± 15% deviation (DEV) from the nominal values and precision was within 15 % relative standard deviation (RSD).

Recovery

The absolute recovery was determined at each of the calibration point. A set of drug solution was prepared at the same concentrations of curcumin and processed using the sample treatment procedure. The absolute recovery was evaluated by comparing the peak area of curcumin in the spiked plasma sample to the corresponding curcumin solution.

Stability

Due to the possibility of delayed injection or reinjection of samples in the HPLC system, the post-operative stability of treated samples in autosampler vials was assessed. In freeze-thaw stability, samples were thawed at room temperature and refrozen at -20°C over three cycles and assayed. Short-term stability was evaluated to ensure stability of curcumin in plasma to cover the sample preparation time. These samples were exposed to ambient laboratory conditions for 8 hours before curcumin assay. Whereas long-term stability of curcumin in plasma stored at -20°C was evaluated by assaying the samples at baseline, 1 month and 2 months. All stability tested samples were analyzed in 6 replicates.

Curcumin self-emulsifying formulation: Solubility study

Briefly, the solubilization capacities of various oils (Table 1) and the cosolvent, Polyethylene glycol 400, were investigated to select excipients that can solubilize the maximum amount of curcumin using the equilibrium method [23]. An excess amount of curcuma extract (2 g) was added to 10 g of the various oils, and the cosolvent separately, allowed to rotator at 10 rpm for one day at approximately 25±2°C. After that, samples were centrifuged at 12800 g for 15 min to remove the undissolved curcumin, and the supernatant was filtered through a 0.2 µm PTFE membrane filter. Later, 0.02 g of each filtrate was first dissolved in the proper volume of ACN, then further diluted with a sufficient volume of the mobile phase. Curcumin concentration in each vehicle was determined, and all measurements were in triplicate.

Evaluation of blank and loaded self-emulsifying formulation

The effectiveness of self-emulsification, also known as dispersibility assessment, is carried out based on the results of the solubility experiments, in which the selected vehicles (oil phase) were further screened with the assigned surfactants (Table 1) for their emulsification capacities by visual assessment [24]. Only formulations that were able to produce a grade A system at room temperature were chosen for curcumin-loading studies (Table 2).

Table 1. Grading system for emulsification behavior exhibited by SEDDS upon dilution

Grading	Description
Grade A	Spontaneous emulsification; demonstrating a clear appearance (60 s)
Grade B	Spontaneous emulsification; demonstrating a bluish appearance (60 s)
Grade C	Emulsion displays fine milky appearance (120 s)
Grade D	Dull, greyish white appearance with an additional oily appearance together with slow emulsification, (>120 s)
Grade E	Poor or minimal emulsification noted with large oil droplets noticed on the surface

S=Second

For the loading content (LC) evaluation; selected oil-vehicle: cosolvent with the combination of different ratios were studied. To perform the experiment, the samples were treated as per the procedure of the curcumin solubility studies, and the LC was measured via HPLC in triplicate.

Pharmacokinetic evaluation: Animals' selection

Twelve adult male Sprague-Dawley rats were selected in this study, weighing 220g to 286g. The ethical has been approved by the Animal Ethics Committee (AEC) of Universiti Sains Malaysia (USM).

Samples preparation

Similar amount of the curcumin in curcuma extracts alone, and in the loaded optimized self-emulsifying drug delivery systems (SEDDS) formulation were dissolved separately in distilled water (pH 5.6-5.8), with an administration dose of 250 mg/kg body weight of the rats through oral intubation. The formulations were well-mixed before each administration, and the dose was flushed with 2 ml of water after completion of oral administration.

***In vivo* study design**

The study was carried out according to a 2-period, 2-sequence crossover design with a one-week washout period. The rats were randomly divided into two groups with six in each. Before administration, the rats were fasted overnight for at least 12 h with free access to water. After formulation administration, the rats were fasted for 4 h, and water was withheld for 2 h. Approximately 0.3 ml blood samples were withdrawn from the tail veins of each rat on sampling intervals at 0-minute (pre-dosing), 20, 40, 60, 90, 120, 180, 240, 360, 600, 960, and 1440 min post-dosing administration [25]. The blood samples were collected into heparinized microcentrifuge tubes and then the tubes were centrifuged at 12800 g for 15 min to separate the plasma. The plasma samples were analyzed using proposed HPLC method.

Pharmacokinetic data analysis

Using C_{max}, T_{max} and AUC0-1440m as pharmacokinetic parameters, the oral bioavailability of curcumin was compared between the optimized loaded SEDDS formula and the isolated extract. The C_{max} and T_{max} were obtained directly from the plasma concentration values, whereas the $AUC_{0\text{-}1440m}$ was calculated using the trapezoidal formula.

Statistical analysis

To test the statistical significance, a one-way analysis of variance (ANOVA) with Tukey's HSD (honest significant difference) tests was used. The difference in all the analyses was considered statistically significant when $p < 0.05$. All the statistical tests were done using (Minitab® statistical software, version 17.2.1.0, Minitab Inc., USA).

Results and Discussion

Method development: HPLC-detector Condition

The excitation and emission wavelengths were set at the characteristic wavelengths of curcumin at 365nm and 512nm [26]. In this study, acetonitrile (ACN) was chosen due to its low viscosity and strong eluting power [27]. The mobile phase was optimized by manipulating the ratio of solvent and acetic acid to achieve good resolution, short run time and symmetric peak shapes. After optimization, mobile phase made up of acetonitrile and 1% acetic acid solution (60:40, v/v; pH 3.25) with a flow rate of 1.2 mL/min and a run time of 6 minutes was

used with Waters Symmetry® C_{18} column (5µm x 4.6 mm x 250 mm) in the current study.

Sample pre-treatment

A pre-treatment procedure is often needed to remove protein and potential interferences from samples prior to HPLC analysis. Various studies suggested the use of liquid-liquid/solid-liquid extraction method [15, 19] which is tedious, time-consuming and involved the use of toxic solvent. Different from liquid-liquid extraction and solid-phase extraction, protein precipitation is commonly used for fast sample clean-up and disrupting protein-drug binding [28-30]. In the current study, addition of 200 µL ACN to the plasma sample was used to deproteinize plasma protein and extract the curcumin content into solvent. This direct single deproteinization step enables us to accomplish pre-treatment step fast and easily.

Method validation

The method was validated according to the guidelines issued by the United States Pharmacopeia (USP) [22] and Food and Drug administration (FDA) [21]. The validation experiments and results obtained are described below.

Specificity

Specificity is described as the ability of a method to discriminate the analyte from all potentially interfering substances [18]. Figure 1(a) shows the sharp peak of 1000 ng/mL curcumin standard solution eluted at 4.9 minutes. Figure 1(b) shows chromatogram of blank plasma while Figure 1(c) shows plasma spiked with 1000 ng/mL curcumin standard solution, the chromatogram indicates that there is no any interference to the peak of interest. Quantitatively, the peak area of the spiked plasma and the curcumin standard solution were found to be equivalent. These results prove that the developed method is specific for curcumin analysis.

Sensitivity and linearity

In regard to the sensitivity, Signal to Noise (S/N) of the retention peak is crucial. For an acceptable detected S/N peak, the height of the corresponding peak and the difference between the largest and smallest noise values should be equal to at least five times the width at the half-height of the peak and, if possible, situated equally around the peak of interest [31]. This is also known as lower limit of detection (LLOD). In this study, the LLOD was 15.6 ng/mL.

Lower limit of quantification (LLOQ) is defined as the lowest concentration on the standard curve that can be quantified with accuracy within ±15% of nominal and precision not exceeding ±15% C.V. according to the USP [22] and FDA [21] guidelines. In the current study, even though the developed method allowed detection of as low as 15.6 ng/mL of curcumin but it was not precise as the S/N ratio is low. At concentration of 31.3 ng/mL, the accuracy and precision (C.V. %) were 95.2% and 2.1%, respectively, which met the criteria set in the guideline [21, 22]. Hence the LLOQ of the current developed method was determined to be 31.3 ng/mL.

Validation was completed by running the developed system in six independent days; hence data of all the six calibration curves was compiled for summary. Results show that all of our six calibration curves were linear in the range of 31.3-1000 ng/mL with $R^2 \geq 0.9999$.

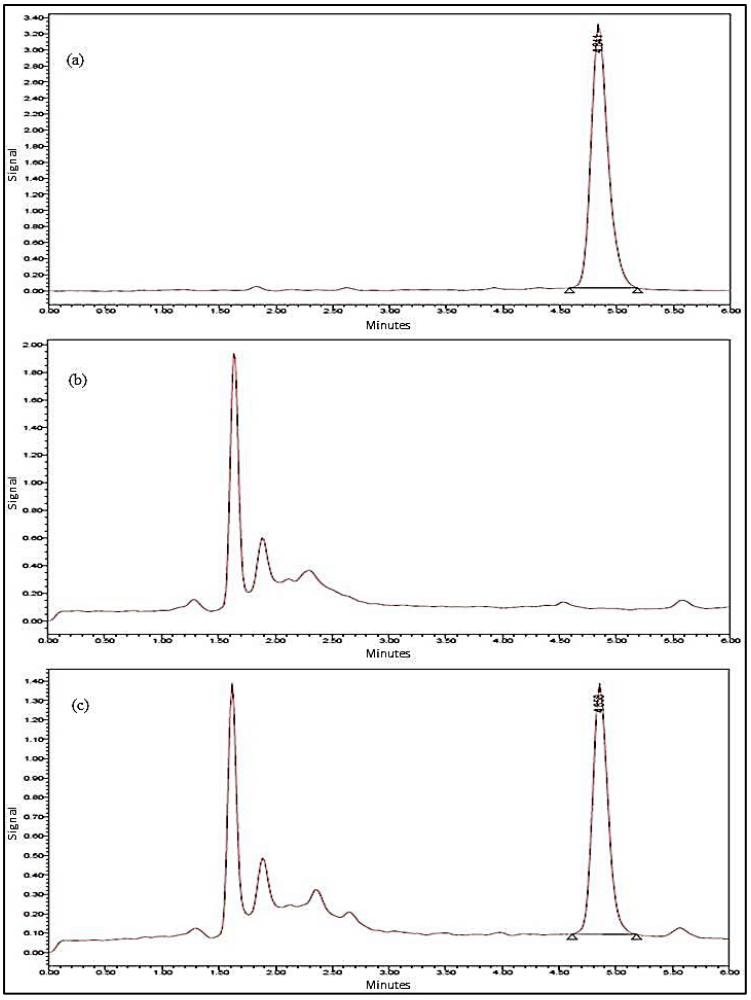


Figure 1. (a) Chromatogram of 1000 ng/mL curcumin standard solution, (b) chromatogram of blank plasma, and (c) chromatogram of plasma spiked with 1000 ng/mL curcumin standard solution. Arrow indicates curcumin retention peak.

Table 2. Regression parameters for calibration curves (n=6) of curcumin plasma assay method

Calibration Curve (Day)	**Correlation Coefficient (R^2)**	**Slope**	**Intercept**
1	0.9999	0.0086	7.2605
2	1.0000	0.0097	2.0608
3	0.9999	0.0096	-0.0870
4	1.0000	0.0096	0.2900
5	1.0000	0.0096	-2.0267
6	1.0000	0.0095	0.1690
Mean	1.0000	0.0094	1.2778
S.D.	0	0	3.2

S.D. = Standard Deviation

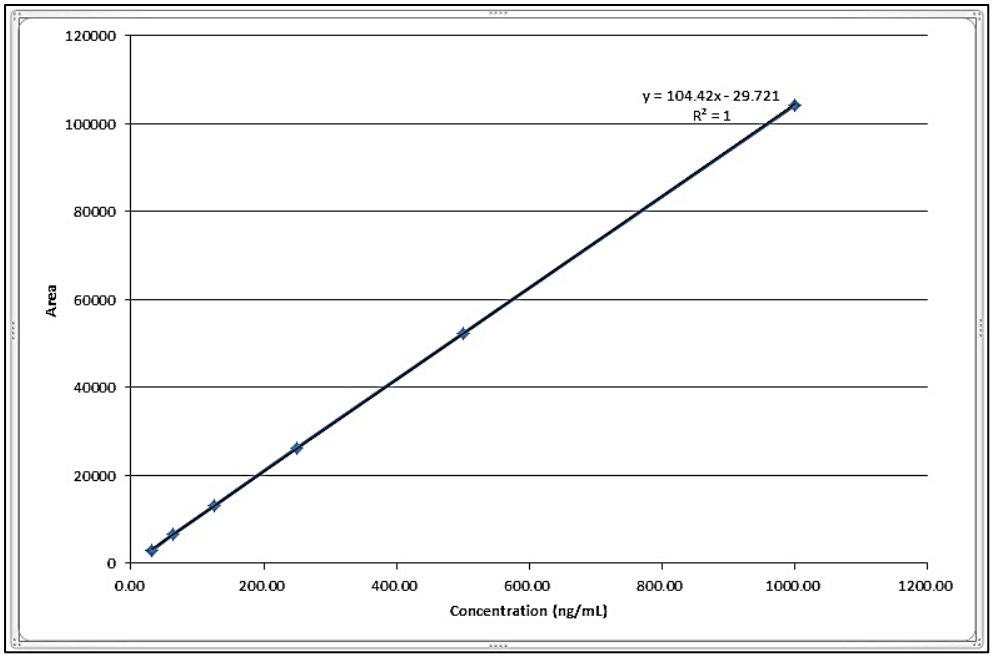


Figure 2. Example of calibration curve for curcumin plasma assay method from concentration of 31.3-1000 ng/mL

Accuracy and precision

Table 3 presents the within- and between-day accuracy and precision for each of the sample. The within-day accuracy and precision from 31.3-1000 ng/mL was in the range of 93.7-105.4 and 0.4-2.4%, respectively (Table 3 (a)). The between-day accuracy and precision from 31.3-1000 ng/mL was in the range of 96.8-100.3 and 0.4-2.3%, respectively (Table 3 (b)). In the current study, our assay successfully met the criteria for good accuracy and precision.

Recovery

A summary of the absolute recovery of curcumin was shown in Table 4. The absolute recovery of curcumin at concentrations of 31.3-1000 ng/mL was in the range of 97.9±2.1%-99.9±0.5% (Table 4). A study carried by Ma and colleagues in 2007 shown that the recovery of curcumin was 97.08% at concentration of 50 ng/mL, 95.69% at concentration of 200 ng/mL and 94.90% at concentration of 1000 ng/mL respectively [17]. Whereas the recovery of curcumin was 95.70±5.60% at concentration of 2 ng/mL, 97.70±5.80% at concentration of 20 ng/mL, 95.60±5.00% at concentration of 400 ng/mL and 96.60±8.40% at concentration of 400 ng/mL respectively in a research investigated by Li and co-workers in 2009 [18]. The absolute recovery shown in the current study was relatively high and precise as compared to the reported literature [17, 18].

Stability

Stability study is necessary in order to rule out the degradation of the investigated compound, i.e., curcumin in plasma samples. Table 5 displays the stability results of curcumin in plasma of the current study. According to Table 5, all the accuracy and precision are within 85%-115% and ≤ 15%, respectively. Post-operative stability in autosampler and short-term stability of curcumin at ambient temperature were satisfactory, with no significant degradation of curcumin being observed for up to 8 hours (Table 5(a) and (b)). Table 5(c) shows that curcumin was stable in plasma at both low and high concentration over three cycles of freeze-thaw. Although sample storage at -20°C is recommended for long term storage, the long-term stability was necessary to be evaluated at the zero-time point, 1-month and 2-months at least. Curcumin in plasma was stable for up to 2-months at -20°C (Table 5(d) and Table 5(e)). These results indicate that curcumin has an acceptable stability under all the tested conditions.

Comparison of recent method with reported method

The comparison of the recent study with the reported methods in Table 6 reveals that the optimized HPLC method developed in the recent study offers a significant advantage in terms of shorter running time. The reduced analysis time is achieved through optimized chromatographic conditions, resulting in faster elution and separation of curcumin. This not only improves the efficiency of the analysis process, but also saves valuable time in the laboratory. Despite the shorter running time, the recent method maintains comparable accuracy, and recovery in detecting curcumin levels in human plasma, making it a promising alternative for efficient and reliable curcumin analysis in clinical research and pharmaceutical applications.

Table 3. Within- and between-day accuracy and precision of curcumin plasma assay method (n=6)

QC Sample	Curcumin Concentration (ng/mL)	Mean Determined Concentration (ng/mL)	Accuracy (%)	Precision (C.V. %)
(a) Within-day	31.3	29.8	95.2	2.1
	62.5	58.6	93.7	1.7
	125	131.7	105.4	1.7
	250	247.9	99.1	2.4
	500	501.8	100.4	0.5
	1000	994.1	99.4	0.5
(b) Between-day	31.3	30.4	97.4	2.3
	62.5	60.5	96.8	1.3
	125	124.4	99.5	1.3
	250	250.1	100	1.3
	500	501.4	100.3	0.4
	1000	990.7	99.1	1

C.V. = Coefficient of Variation

Table 4. Mean recovery of curcumin in plasma (n=6)

Sample	Curcumin Concentration (ng/mL)	Absolute Recovery (%)	C.V. (%)
Curcumin	31.3	97.9	2.1
	62.5	98.9	1.7
	125	99.8	1.8
	250	98.8	2.5
	500	99.9	0.5
	1000	99	0.5

C.V. = Coefficient of Variation

Table 5. Stability of curcumin in plasma (n=6)

Sample Condition	Curcumin Concentration (ng/mL)	Mean Determined Concentration (ng/mL)	Mean Deviation (%)
(a) Short-term stability	31.3	31	-0.9
(8 hours temperature)	1000	1991.5	-0.4
(b) Post-operative stability	31.3	31.7	1.5
(8 hours in autosampler)	1000	1023.5	2.4
(c) Freeze-thaw stability	31.3	31	-0.9
(3 cycles)	1000	921.1	-7.9
(d) Long-term stability	31.3	30.9	-1.1
(1 month)	1000	952.9	-4.7
(e) Long-term stability	31.3	30.9	-1.2
(2 months)	1000	974.1	-2.6

C.V. = Coefficient of Variation

Table 6. Comparison of curcumin determination HPLC methods in human plasma

	Recent Method	Reported Method 1	Reported Method 2
Instrument	HPLC	HPLC-MS/MS	HPLC
Curcumin extraction method	Protein precipitation using acetonitrile	Liquid-liquid extraction	Protein precipitation using acetonitrile
Analysis time (min)	6	8	9
Retention time (min)	4.9	5.9	8.2
Specificity	No interference to the peak of interest	No interference to the peak of interest	No interference to the peak of interest
Sensitivity (ng/mL)	31.3	1.00	10
Linearity (R^2)	1.0000	0.998	0.999
Accuracy (Intra-Day %)	93.7-105.4	94.20-108.36	99.98-104.24
Accuracy (Inter-Day %)	96.8-100.3	94.40-108.36	100.30-102.21
Recovery (%)	≥97.9; CV=0.5-2.1	≥85.6; CV=2.44-6.86	≥101.81; CV=0.79-9.26
Stability	No significant degradation observed	No significant degradation observed	No significant degradation observed
Advantages	Short analysis time	Higher sensitivity	Higher accuracy and recovery
Reference	-	[32]	[33]

Self-emulsifying curcumin formulation: Solubility

Among the excipients studied, the solubility of curcumin in PEG-400 was significantly higher, 194.28±9.92 mg/g and the highest solubility of curcumin was observed in soyabean and corn oils at 0.71 ±4.22 mg/g and 0.71 ±5.63 mg/g ($p < 0.05$), respectively as shown in Table 7.

Table 7. Solubility study of curcumin in oil phase and co-solvent, n = 3

Potential Vehicle	Concentration of Curcumin (mg/g)	Standard Deviation
Canola oil	0.60	4.27
Corn oil	0.71	5.63
Soyabean oil	0.71	4.22
Sunflower oil	0.66	5.67
Peanut oil	0.68	2.58
Olive oil	0.61	4.67
Oleic acid	0.63	9.92
PEG-400	194.28	9.92

Evaluation of blank and loaded self-emulsifying formulation

Results revealed that the highest number of the rapidly formed (within 1 min) dispersions of "grade A" with the lowest surfactant concentrations was obtained with Cremophor EL® (50%) in soyabean oil out of the 45 formulations (from ration 1:9 to 9:1). Moreover, the curcumin loading in the curcuma extract SEDDS was the highest ($p < 0.05$) at soyabean oil: PEG-400 ratio of 3:2; thus, it was selected and combined with Cremophor EL® at a ratio of 5:5 to produce the optimized loaded SEDDS formulation (grade A).

Pre-clinical pharmacokinetic study

The concentrations of curcumin in the group of rats fed with curcuma extract loaded SEDDS formulation were significantly increased, with mean C_{max}, T_{max}, and $AUC_{0\text{-}1440m}$ values of 238.81 ng/mL, 70.83 min, and 11249.60 ng.min/mL, respectively; however, curcumin from curcuma extract alone was undetectable (below the HPLC LOQ of 31.25 ng/mL), implied that the bioavailability of this purely bioactive form was very low. Mean plasma concentrations versus time profile of curcumin are shown in Figure 3; such impact probably linked to the synergistic enhancement of curcumin absorption by PEGs and Cremophor EL® [34]. The designed SEDDS was able to offer dramatic improvements in bioavailability. Hypothetically, considering the HPLC LOQ value, the AUC was calculated for curcumin from curcuma extract alone over the time of detection for curcumin from curcuma extract loaded in SEDDS formulation. Comparing the AUC for curcumin from curcuma extract loaded in SEDDS formulation, and the hypothetical AUC for curcumin from curcuma extract alone, resulted in value of 1107.10 ng.min/mL, with 15-folds increment in the bioavailability using the developed curcuma extract-SEDD in this work. As a result, the developed curcuma extract-SEDDS formulation offered higher curcumin plasma concentration in compared to the curcumin loaded in solid lipid nanoparticles (C_{max} of 20.85 µm equal to ~7.7ng/ml) with an oral dose of 400 mg/kg [35], as well as curcumin loaded in self-micro emulsifying drug delivery system (SMEDDS) (C_{max} of 0.15 µm equal to ~0.056 ng/mL) with an oral dose of 100 mg/kg [36].

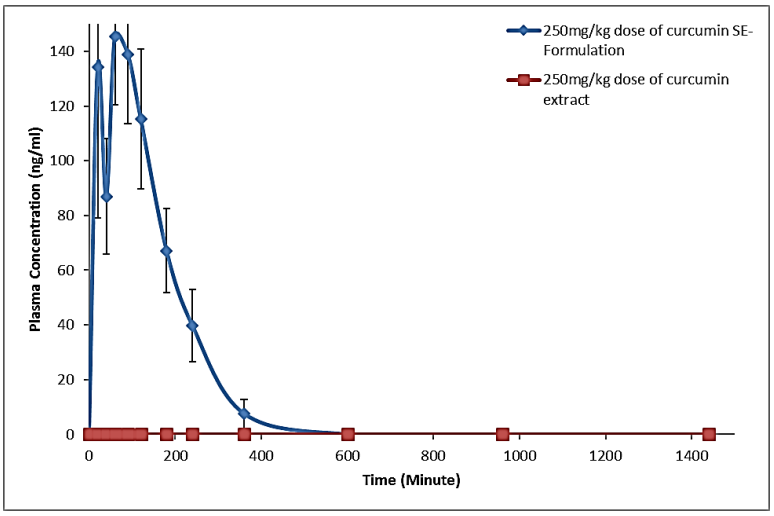


Figure 3. Mean plasma concentration-time profiles (Mean ±S.E.M., n = 6) of curcumin after oral administration of 250 mg/kg curcumin suspension and curcumin loaded in SEDDS formulation

Conclusion

A reliable, simple and sensitive high-performance liquid chromatographic (HPLC) method has been developed and validated as per the ICH guidelines for the determination of curcumin in plasma. This method offers adequate, accuracy, precision, appropriate retention time, moderate pressure and good peak shape. Curcumin remained stable for up to eight hours in the stability test, and did not degrade even after three freeze-thaw cycles. The stable long-term storage period was up to two months. The method application in quantifying the SEDDS formulation in the *in vitro* (solubility and loading content) and *in vivo* level was successfully achieved. The current method is easy and fast to perform, hence, can be applied in pharmacokinetic studies of curcumin alone, or in SEDDS formulation.

Acknowledgements

We appreciate the helpful suggestions of Mr. Goh Song Thai regarding the method development and writing assistance of Dr. Fung Wai Yee. Funding support from University Sains Malaysia 304PFARMASI 6316017 is greatly appreciated.

Conflict of interest

The authors declare there are no financial/commercial conflicts of interest.

References

1. Brouk, B. (1975). Plants consumed by man. Academic Press 2nd, New York: pp. 331-337
2. Sharma, R. A., Gescher, A. J. and Steward, W. P. (2005). Curcumin: The story so far. *European Journal of Cancer*, 41: 1955-1968.
3. Nadkarni, K. M. and Nadkarni, A. K. (1954). Dr. K.M. Nadkarni's Indian materia medica: with Ayurvedic, Unani-Tibbi, Siddha, allopathic, homeopathic, naturopathic & home remedies, appendices & indexes. Popular Prakashan Private Ltd, Bombay: pp. 45-52.
4. Bhowmik, D., Chiranjib, Kumar, K. P. S., Chandira, M. and Jayakar, B. (2009). Turmeric: a herbal and traditional medicine. *Archives of Applied Science Research*, 1(2): 86-108.
5. Sahdeo, P. and Bharat, B. (2013). Turmeric, the golden spice: from traditional medicine to modern medicine. CRC Press, Boca Raton: pp. 87-95.
6. Araujo, C. C. and Leon, L. L. (2001). Biological activities of Curcuma longa L. *Mem Inst Oswaldo Cruz*, 96(5): 723-728.
7. Maheshwari, R. K., Singh, A. K., Gaddipati, J. and Srimal, R. C. (2006). Multiple biological activities of curcumin: A short review. *Journal of Life Sciences*, 78(18): 2081-2087.
8. Hsu, C. H. and Cheng, A. L. (2007). Clinical studies with curcumin. Springer, Boston: pp. 471-480.

9. Menon, V. P. and Sudheer, A. R. (2007). Antioxidant and anti-inflammatory properties of curcumin. Springer, *Advances Experiment Medicine Biology*, 2007: 105-125.
10. Cox, K. H. M., Pipingas, A. and Scholey, A. B. (2015). Investigation of the effects of solid lipid curcumin on cognition and mood in a healthy older popu. *Journal of Psychopharmacology*, 29(5): 642-651.
11. Liu, A., Lou, H., Zhao, L. and Fan, P. (2006). Validated LC/MS/MS assay for curcumin and tetrahydrocurcumin in rat plasma and application to pharmacokinetic study of phospholipid complex of curcumin. *Journal of Pharmaceutical and Biomedical Analysis*, 40: 720-727.
12. May, L. A., Tourkina, E., Hoffman, S. R., and Dix, T. A. (2005). Detection and quantitation of curcumin in mouse lung cell cultures by matrix-assisted laser desorption ionization time of flight mass spectrometry. *Analytical Biochemistry*, 337: 62-69.
13. Chambers, E., Wagrowski-Diehl, D. M., Lu, Z. and Mazzeo, J. R. (2007). Systematic and comprehensive strategy for reducing matrix effects in LC/MS/MS analyses. *Journal of Chromatography B*, 852: 22-34.
14. Heath, D. D., Pruitt, M. A., Brenner, D. E. and Rock, C. L. (2003). Curcumin in plasma and urine: quantitation by high-performance liquid chromatography. *Journal of Chromatography B*, 783: 287-295.
15. Pak, Y., Patek, R. and Mayersohn, M. (2003). Sensitive and rapid isocratic liquid chromatography method for the quantitation of curcumin in plasma. *Journal of Chromatography B*, 796: 339-346.
16. Schiborr, C., Eckert, G.P., Rimbach, G. and Frank, J. (2010). A validated method for the quantification of curcumin in plasma and brain tissue by fast narrow-bore high-performance liquid chromatography with fluorescence detection. *Analytical and Bioanalytical Chemistry*, 397: 1917-1925.
17. Ma, Z., Shayeganpour, A., Brocks, D. R., Lavasanifar, A. and Samuel, J. (2007). High-performance liquid chromatography analysis of curcumin in rat plasma: application to pharmacokinetics of polymeric micellar formulation of curcumin. *Biomedical Chromatography*, 21: 546-552.
18. Li, J., Jiang, Y., Wen, J., Fan, G., Wu, Y. and Zhang, C. (2009). A rapid and simple HPLC method for the determination of curcumin in rat plasma: assay development, validation and application to a pharmacokinetic study of curcumin liposome. *Biomedical Chromatography*, 23: 1201-1207.
19. Anwar, M., Ahmad, I., Warsi, M. H., Mohapatra, S., Ahmad, N., Akhter, S., Ali, A. and Ahmad, F. J. (2015). Experimental investigation and oral bioavailability enhancement of nano-sized curcumin by using supercritical anti-solvent process. *European Journal of Pharmaceutics and Biopharmaceutic*, 96: 162-172.
20. The European Medicines Agency (2005). ICH guideline: Harmonised tripartite guideline, validation of analytical procedures: Test and methodology, 5-6.
21. Food and Drug Administration (1994). Reviewer guidance, validation of chromatographic methods, 1994: 4-32.
22. United States Pharmacopeial Convention (1994). U.S. Pharmacopeia, 23: 1982-1984.
23. Abou Assi, R., M. Abdulbaqi, I., Seok Ming, T., Siok Yee, C., A. Wahab, H., Asif, S. M., and Darwis, Y. (2020). Liquid and solid self-emulsifying drug delivery systems (SEDDs) as carriers for the oral delivery of azithromycin: optimization, *in vitro* characterization and stability assessment. *Pharmaceutics*, 12 (11): 1052-1060.
24. Van Staden, D., Du Plessis, J. and Viljoen, J. (2020). Development of a self-emulsifying drug delivery system for optimized topical delivery of clofazimine. *Pharmaceutics*, 12(6): 523-528.
25. Patton, T. F. and Gilford, P. (1981). Effect of various vehicles and vehicle volumes on oral absorption of triamterene in rats. *Journal of Pharmaceutical Sciences*, 70(10): 1131-1134.
26. Nascimento, T. C. F. D., Casa, D. M., Dalmolin, L. F., Mattos, A. C. D., Khalil, N. M. and Mainardes, R. M. (2012). Development and validation of an HPLC method using fluorescence detection for the quantitative determination of curcumin in PLGA

and PLGA-PEG nanoparticles. *Current Pharmaceutical Analysis*, 8: 324-333.

27. Zarzycki, P., Zarzycka, M., Ślączka, M. and Clifton, V. (2010). Acetonitrile, the polarity chameleon. *Analytical and Bioanalytical Chemistry*, 397: 905-908.
28. Blanchard, J. (1981). Evaluation of the relative efficacy of various techniques for deproteinizing plasma samples prior to high-performance liquid chromatographic analysis. *Journal of Chromatography B*, 226 (2): 455-460.
29. Polson, C., Sarkar, P., Incledon, B., Raguvaran, V. and Grant, R. (2003). Optimization of protein precipitation based upon effectiveness of protein removal and ionization effect in liquid chromatography-tandem mass spectrometry. *Journal of Chromatography B*, 785: 263-275.
30. Whittington, D., Sheffels, P. and Kharasch, E.D. (2004). Stereoselective determination of methadone and the primary metabolite EDDP in human plasma by automated on-line extraction and liquid chromatography mass spectrometry. *Journal of Chromatography B*, 809: 313-321.
31. United States Pharmacopeial Convention (2009). U.S. Pharmacopeia, 32: 1-7.
32. Wang, X.-M., Zhang, Q.-Z., Yang, J., Zhu, R.-H., Zhang, J., Cai, L.-J. and Peng, W.-X. (2012). Validated HPLC-MS/MS method for simultaneous determination of curcumin and piperine in human plasma. *Tropical Journal of Pharmaceutical Research*, 11: 621-629.
33. Gugulothu, D., Desai, P. and Patravale, V. (2013). A versatile liquid chromatographic technique for pharmacokinetic estimation of curcumin in human plasma. *Journal of Chromatographic Science*, 52(8): 872-879.
34. Zhongfa, L., Chiu, M., Wang, J., Chen, W., Yen, W., Fan-Havard, P., Yee, L. D. and Chan, K. K. (2012). Enhancement of curcumin oral absorption and pharmacokinetics of curcuminoids and curcumin metabolites in mice. *Cancer chemotherapy and pharmacology*, 69(3): 679-689.
35. Wang, W., Zhu, R., Xie, Q., Li, A., Xiao, Y., Li, K., Liu, H., Cui, D., Chen, Y. and Wang, S. (2012). Enhanced bioavailability and efficiency of curcumin for the treatment of asthma by its formulation in solid lipid nanoparticles. *International Journal of Nanomedicine*, 7: 3667-3677.
36. Grill, A.E., Koniar, B. and Panyam, J. (2014). Co-delivery of natural metabolic inhibitors in a self-microemulsifying drug delivery system for improved oral bioavailability of curcumin. *Drug Delivery and Translational Research*, 4(4): 344-352.

Malaysian Journal of Analytical Sciences (MJAS)
Published by Malaysian Analytical Sciences Society

MEDIUM DENSITY FIBREBOARD (MDF) FROM OIL PALM FIBRE: A REVIEW

(Papan Gentian Kepadatan Sederhana daripada Fibre Kelapa Sawit: Satu Ulasan)

Roila Awang*, Noorshamsiana Abdul Wahab, Zawawi Ibrahim, and Astimar Abdul Aziz

Malaysian Palm Oil Board, No.6, Persiaran Institusi, Bandar Baru Bangi, 43000 Kajang, Selangor, Malaysia

**Corresponding author: roila@mpob.gov.my*

Received: 24 October 2022; Accepted: 11 March 2023; Published: 23 June 2023

Abstract

Rubberwood was favored for the production of medium density fibreboard (MDF). However, with the increasing demand for MDF, the limited supply of rubberwood and the need for biomass conservation, fibre boards made from agricultural residue are under investigation, though their dimensional stability is a challenge. Several researchers have used various methods and techniques for the improvement of MDF mechanical and physical properties. This article reviews the current process of MDF manufacturing and performance indexes that help find the optimum criteria for board fabrication. It was discovered that oil palm fibre has its own chemical composition and thus impacts the properties of board when used as an alternative raw material for MDF production. Thus, the mechanical and physical properties of fibreboard made from oil palm-based fibre were discussed in various hybridization ratios with different types of fibre and compared with rubberwood board. Furthermore, chemical treatments, such as alkaline treatment, acetylation or soaking, and washing with boiling water or removing parenchyma cells were also studied. It was found that the dimensions of the fibre affected the mechanical properties, such as modulus of rupture (MOR), modulus of elasticity (MOE) and internal bonding (IB). The chemical changes in fibre that occur when oil palm fibre is chemically modified were also discussed and summarized.

Keywords: chemical composition, oil palm fibre, medium density fibreboard

Abstrak

Kayu getah digemari bagi pembuatan papan gentian kepadatan sederhana (MDF). Walau bagaimanapun, peningkatan permintaan bagi penghasilan MDF, bekalan kayu getah yang terhad, dan keperluan untuk pemuliharaan biojisim, papan gentian yang diperbuat daripada sisa pertanian sedang dikaji, walaupun terdapat cabaran terhadap kestabilan dimensinya. Beberapa penyelidik telah menggunakan pelbagai kaedah dan teknik bagi penambahbaikan sifat mekanikal dan fizikal MDF. Artikel ini mengkaji proses semasa dalam penghasilan MDF dan indeks prestasinya bagi membantu mengetahui kriteria optimum dalam pembuatan fabrikasi papan. Hasil kajian mendapati gentian kelapa sawit mempunyai komposisi kimianya sendiri dan seterusnya mempengaruhi sifat papan apabila digunakan sebagai bahan mentah alternatif bagi pembuatan MDF. Oleh itu, sifat mekanikal dan fizikal papan gentian yang diperbuat daripada gentian berasaskan kelapa sawit dalam pelbagai nisbah penghibridan bersama gentian yang berbeza jenis telah dibincangkan dan dibandingkan dengan papan kayu getah. Selain itu, rawatan kimia seperti rawatan alkali, asetilasi atau rendaman, dan mencuci dengan air mendidih atau mengeluarkan sel parenchyma juga turut dikaji. Kajian mendapati bahawa dimensi gentian mempengaruhi sifat mekanikal seperti modulus kepecahan (MOR), modulus kekenyalan (MOE), dan ikatan dalaman (IB). Perubahan kimia yang berlaku dalam gentian apabila gentian kelapa sawit diubah suai secara kimia turut dibincangkan dan diringkaskan.

Kata kunci: komposisi kimia, fibre kelapa sawit, papan gentian kepadatan sederhana

Introduction

Medium density fibreboard (MDF) is a composite wood product that is traditionally made by breaking down softwood into wood fibre in a defibrator. Then, it is mixed with wax and a synthetic resin binder, such as urea formaldehyde (UF) resin and forming board by using high temperature and pressure. Additives may be added during the manufacturing process to impart additional qualities. However, not all MDF are identical, such as texture, density, color and other characteristics that vary depending on the material used.

MDF has several characteristics that make it a good substitute for plywood or particle board. The material is dense, flat, sturdy, free of knots and machine-friendly. It is made up of small particles and gives dimensional stability without the presence of a noticeable grain, as wood does. MDF, unlike most plywood, has no gaps and produces sharp edges with no tear-out. Besides, MDF panels are available in a wide range of physical properties and dimensions, allowing to construct a finished product with the exact MDF features and density required. It is also an environmentally friendly product that uses renewable resources, such as kenaf, wheat straw, radiata pine, bamboo and non-wood fibres.

Rubberwood is also one of the most preferred raw materials for MDF production as compared to other renewable resources. According to Md. Rowson et al. [1], rubberwood possesses all of the necessary characteristics and its abundance makes it successful in the wood-panel industry. However, at present, rubber plantations are cultivated for the production of latex rather than wood manufacturing [1]. Therefore, rubberwood supply has recently become limited in the wood processing industry because of climatic (extended wet periods) circumstances that made rubberwood harvesting inefficient, especially on higher slopes. In addition, the resource is not available in larger, more desirable blocks, which has an impact on economies of scale. Finally, the demand outstrips supply, making rubberwood a finite (at least in short to medium term) resource.

Oil palm plantations, which are progressively replacing rubber plantations in Southeast Asia, have lately been introduced as popular fibres for new materials in MDF production. It is an under-utilized material, similar to rubber, with potential applications in a variety of industries. Oil palm fibres are now being researched for usage in various wood-based boards, pulp and paper, mushroom cultivation, and animal feed. Empty fruit bunches (EFB) are used as mulch, boiler fuel, fertilizer and for the manufacture of automobile cushions and mattresses [2]. Oil palm trunk (OPT) and oil palm frond (OPF) fibrous threads can be used to produce pulp, paper and chipboard [3]. Fruit bunch fibres can be used to make laminated isotropic fibreboard, cement board and pulp. Therefore, in addition to the research as previously mentioned, oil palm fibre also has a significant potential for converting low-value raw materials into high-quality wood panels that may be utilized as raw materials for the production of MDF.

This study aimed to review and summarize the current process of MDF production by using various agricultural biomasses. In this review, developments in MDF production from various oil palm-based fibres and factors influencing the properties of MDF will be discussed. These studies also identified the properties of MDF made from oil palm-based fibre with the greatest potential, considering their availability and the quality of boards they produce.

Medium density fibreboard raw materials

In general, the wood processing industry is undergoing significant structural changes, with a steady shift away from large-diameter trees and towards smaller-diameter second-cut trees, as well as a shift towards plantations and the estate sector. The latest developments in the MDF sector are strikingly comparable to those in the plywood industry. The main difference is that the latter arose as a result of government policies promoting domestic wood-based industries. However, MDF manufacturing plants arose as a result of raw material shortages that have become increasingly apparent in recent years, as well as the opportunity to use previously untapped resources.

Mixed tropical species, bagasse, radiant pine, rubberwood and cotton stalks, wheat straw, bamboo and rice straw are all important raw materials for MDF [4]. In Malaysia, rubberwood is the only raw material used, as opposed to particleboard or cement-bonded products, which rely on a mix of species and wood waste. Rubberwood has a light color and consistent texture; thus, making it an attractive fibre source for MDF manufacture [1].

Debarking and chipping are the first processes in the MDF manufacturing process. In a digester, cleaned chips are boiled and refined into wood fibres, which are then combined with resin and wax. Before being formed into a continuous mat, the wet fibre, resin and wax combination are dried and delivered to the mat forming. It is trimmed, sanded and cut to desired specifications in the final processing stage.

Current process for manufacturing MDF

MDF is a nonstructural fibre-based panel made out of wood fibres that have been glued together with resin under heat and pressure. Before being mixed with resin and wax, the fibres are refined in a defibrator or refiner. The surface of the fibres is coated with a bonding agent or resin. The resonant fibres are dried, then molded into mats, which are subsequently hot pressed to make a uniform board. The density ranges between 660 kg/m^3 and 850 kg/m^3 [5].

The utilization of various wood or fibrous materials in the production of MDF is shown in Table 1. Table 1 compares the mechanical and physical characteristics of various fibres with those of rubberwood. The qualities of the board were affected by both the manufacturing process and the chemical composition of the fibre. The mechanical and physical characteristics of the board are affected by the resin type, resin level, pressing time, pressing temperature, and refining parameters. Most materials use UF as a resin as compared to PF resin. In addition, it can be seen that, regardless of the type of fibre employed, higher resin content will increase MOR and MOE. However, higher pressing temperatures increase the internal bonding (IB) and lead to decrease WA and TS. Nevertheless, the mechanical (MOR and MOE) and IB of the board improve after increase refining parameters thus low WA and TS were obtained.

Figure 1 depicts the entire manufacturing process, including material preparation (chipping), fibre formation, fibre treatment, mat forming and hot pressing and board treatment. First, the wood is chipped using a chipper machine. After that, the chips are screened to separate the fibre different sizes [6]. A belt conveyor with an iron remover built over it transports the confirming chips to the chip's washer. The chips are then washed to increase their quality. After that, the chips are moved to the fibre separation section. To soften the chips, they are heated at 160°C–180°C or 6–8 bar pressure for 3 min–5 min.

To make the softened chips less prone to swelling, around 1 wt.%-2 wt.% paraffin wax is applied [7]. After that, the softened chips are transferred to the grinding chamber. The materials are mechanically decomposed in the grinding chamber with the help of water and heat. UF resin is added to pulp as it passes through the blow valve. The pulp, in the form of fibre, is placed in the dryer [8]. Moisture vaporizes in fibre and is controlled within the appropriate range. The fibre final moisture content is kept within 8%–13% (wt.). The fibre is evenly distributed into the matting conveyor belt and the preset thickness is made by using the air blow function. Hot pressing is used to get the desired thickness.

The prepress removes the air from the mat and strengthens it [18]. Fibreboard is typically categorized by density and can be produced using either the dry or wet methods. Dry method can be used on both high-density (hardboard) and medium-density (medium-density) boards (MDF). Both high-density hardboard and low-density insulation boards can be processed by using the wet method.

Table 1. Studies on the production of MDF from various wood or fibrous materials

Material	Panel Density (kg/m^3)	Resin Type	Resin Level (%)	Refining Parameter (bar, min)	Pressing Temp. (°C)	Pressing Time (min)	MOR (mpa)	MOE (mpa)	IB (mpa)	TS (%)	WA (%)	Ref.
Kenaf core	700	UF	12	7,3	175	5	28.0	3379	0.67	15.4	68	[9]
				7,5			30.3	3619	0.66	14.6	62	
Kenaf bast	700	UF	12	7,3	175	5	20.6	1921	0.24	28.8	77.9	[10]
				7,5			22.9	2113	0.17	27.1	73.9	
Bagasse	900	UF	20	NA	125	60	45.0	3532	NA	16.9	64.8	[11]
Wheat straw	750	UF	12	NA	138	7	23-14	3200-3400	0.6-0.7	10-11	NA	[5]
Canola straw	700	UF	11	NA	NA	4	21-22	2300-2400	0.53-0.55	26-29	NA	[12]
						6	20-21	2200-2300	0.52-0.54	26-29	NA	
Bamboo	734	UF	8	NA	NA	NA	26.1	2760	1.16	25	72	[13]
Rubberwood	680	UF	11	NA	170	5	30.7	2412	0.50	16.5	46.3	[14]
	751	UF	11	NA	160	6	33.7	3285	1.16	23.8	72.1	[15]
Coir	808	PF	20	NA	145	8	29.1	3143	2.1	NA	NA	[16]
Banana stem	780	UF	20	NA	170	8	50.91	3939	NA	15.70	38.5	[17]

UF: urea formaldehyde; PF: phenol formaldehyde: MOR: modulus of rupture; MOE: modulus of elasticity; IB: internal bonding; TS: thickness swelling; WA: water absorption
NA: not available

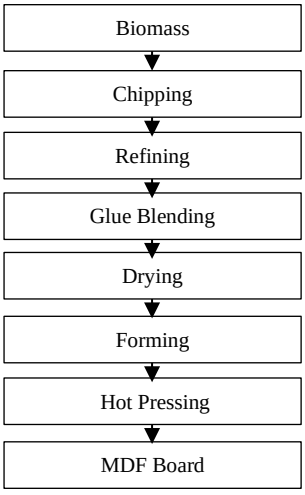


Figure 1. Flow chart for the production of MDF

Dry process fibreboard

Particleboards and dry process fibreboards are created in the same way. Resins such as UF and phenol formaldehyde (PF), as well as other additives can be sprayed on the fibres or added as the wet fibres are fed from the refiner into a blow line drier. On the other hand, some fibreboard plants add the resin to the refiner. The adhesive-coated fibres are then air-laid into a mat for pressing, similar to how particleboard mats are formed. Dry-process fibreboard pressing differs from particleboard pressing in a few ways. The fibre mat is normally pre-pressed in a band press once it is created. Next, the densified mat is trimmed with disc cutters and transferred to caul plates for hardboard pressing; in the case of MDF, the trimmed mat is directly transported to the press. All dry-formed boards are pressed in multi-opening presses at temperatures ranging from 140°C to 165°C for UF-bonded goods and 190°C for PF-bonded products [19].

Wet process hardboard

Hardboards made with a wet process differ from fibreboards made with a dry process in various ways. The fibres are first formed into a mat by using water as the distribution medium. Secondly, some wet process boards are manufactured without the use of extra binders. If there is sufficient lignin in the lignocellulosic material and it is kept after the refining process, lignin can be used as a binder. Lignin will flow and act as a thermosetting adhesive when exposed to heat and pressure, increasing the naturally occurring hydrogen bonds. In wet process hardboards, refining is a critical stage in creating strength. The refining process must also produce fibre with a high freeness or the ability to remove water from the fibrous mat easily. The soupy pulp runs quickly and easily onto a continually moving mesh screen in the wet process. Water is drained through the screen and then through a series of press rolls that wring out any remaining moisture. Wet process hardboards are pressed in steam-heated multi-opening presses. The press cycle is divided into three sections and lasts between 6 min and 15 min. The first phase, which is carried out under high pressure, eliminates the majority of the water while getting the board to the necessary thickness. The second phase major goal is to eliminate water vapor. The third phase is relatively brief and leads to the completion of the cure. The maximum pressure employed is at 5 MPa. To induce fibre-to-fibre bonding, heat is required while pressing [19].

MDF Performance Index

MDF performance index is divided into three categories: physical, mechanical and biological performance [20]. The most important physical properties are density, moisture content (MC), water absorption (WA) and thickness swelling (TS). Internal bonding (IB), modulus of elasticity (MOE), modulus of rupture (MOR) and screw holding force (face and side) are the primary mechanical characteristics, whereas the emission of formaldehyde is a major part of biological performance [20].

Physical performance

The swelling that can occur in a board is known as TS, which is inversely proportional to IB values. When the IB value is high, the TS value is usually low. This property is determined by how well the interparticle connection resists moisture absorption. The TS is affected by the MC of the mixture, pressing duration, board moisture, testing conditions and density of board. When the board is exposed to water, the amount of water absorbed into the wood substance is known as WA. It is very dependent on the structure of the wood cell [14]. However, by applying thermal treatment to the fibre, some changes are found, such as degradation of hemicellulose and reduction of hydroxyl group; thus, it reduces the TS value [15].

The drawback of MDF over plywood is that it swells more than plywood when exposed to water and a greater proportion of that expansion may not be recoverable after drying. High internal strains can be caused by in-plane movements as a result of increased or decreased moisture content in the board. These forces may be severe enough to result in buckling board, pushed-out nails and board detachment from the structure. As a result, the fibreboard must be able to swell and expand to control the destructive effect.

Heat treatment enhances the stability of wood, but it can also alter its surface features, hence its wetting properties [21]. Surface inactivation can occur when a

wood surface is exposed to a high-temperature environment [22]. When exposed to high temperatures, the wood surface undergoes a few known changes, including oxidation. Inactivation of wood surfaces, which causes poor bond quality, is a time-dependent process that can be expedited by raising the temperature [23]. Due to interference with adhesive wetting, flow and penetration, as well as the cure and resulting cohesive strength of the adhesive, an inactivated wood surface might produce adhesion issues.

Wood drying at temperatures between 160°C and 180°C causes surface composition changes, as reported by Li et al. [24]. In wood bonding, wettability is critical for good adhesion. To make close contact between wood molecules and adhesive, the adhesive must moisten, flow and penetrate the cellular structure of the wood. There is evidence that wood wettability and adhesion have a favorable relationship. Many tests have demonstrated that high drying temperatures lower the bonding strength of wood adhesives or that high temperatures reduce wood hygroscopicity and impede wettability [25]. Heat treatment causes wood fibres to become hydrophobic; thus, reduces their wetting ability [24]. Contact angle analysis can be used to determine the wettability of wood. The adhesive and coating qualities of wood and wood-based composite surfaces are vital to be determined [26]. Perfect wetting of a surface happens when the contact angle is zero.

The volume of fibre used in MDF has been shown to alter the density of the MDF produced in previous studies. Shorter fibres were well blended with longer fibres by filling the gaps between and amongst the fibres, resulting in a more uniform board with a low density. According to a study [13], the lower-density board had less swelling because it had less wood per unit volume and a low degree of hygroscopic response. Besides, to maintain homogeneous density across the length and width of the board, the fibres are required to be distributed uniformly [14].

Mechanical performance

The MOR is the maximum fibre stress computed in the upper and lower surfaces of the board. It is the material unique breaking stress, given in stress unit per unit area. MOE, on the other hand, is a measure of material stiffness that may be used to calculate the deflection of a product under stress, whereas internal bond measures the fibreboard efficiency and indicates the compatibility of resin adhesive with fibre [27]. Therefore, various factors may contribute to changes in mechanical properties, with some having better mechanical properties, as investigated by researchers. However, it was found that the main factor that affected mechanical properties of board was fibre length [28]. Fibres with a greater length and thickness provided a larger surface area for adhesive contact. According to Wan Daud & Law [29], fibre length had a bigger impact on board dimensional stability than mechanical qualities.

Oil palm biomass *vs* rubberwood

Rubberwood is an environmentally beneficial wood due to its unique characteristics and value that are not found in other materials. According to previous studies, the demand for sawn timber in furniture applications has increased yearly because consumers prefer the unique wood grain and light color of rubberwood, which is easy to work with and furnish with other materials and is durable. Rubberwood has a light-straw to light-brown color and a density of 550 kg/m^3 to 650 kg/m^3. The trunk diameter is usually between 30 cm and 35 cm, while the length is usually between 3 m and 5 m [30].

Oil palm EFB pulp fibres and rubberwood have been identified as two key sources for MDF production. Previous research has shown that oil palm EFB pulp fibres are superior to rubberwood pulp fibres because they contain fibres with higher pH values and buffering capacities. This buffering effect is caused by an acidic reaction agent that converts to a less reactive molecule and obstructs resin flow [31]. MDF made from EFB can be used instead of sawdust MDF, which is known to be less durable.

Most researchers prefer EFB to the currently available resources for manufacturing MDF as the primary raw material. As a result, the qualities of MDF will be affected by changes in the raw material. As previously stated, MDF mechanical properties and stability are greatly influenced by the technique and materials used in MDF manufacturing [32].

Properties of oil palm fibre vs rubberwood

The three main chemical components of a cellulosic fibre of wood are cellulose, hemicellulose and lignin. Cellulose is semi-crystalline polysaccharide with a large amount of hydroxyl group. This hydrophilic nature causes poor resistance to moisture absorption and poor interfacial bond. On the other hand, the physical properties of fibre used affect the mechanical properties of the board produced, such as fibre diameter, length, density, moisture gain, and cell wall. Table 2 compares chemical composition and physical properties of rubberwood and oil palm-based fibre. As listed in Table 2, the chemical composition of oil palm fibre and rubberwood vary in contents.

Generally, MDF manufactured from long fibre length, high density, thick cell wall and small lumen width produces MDF with greater MOR, MOE and IB. However, long fibre increase hydrophilicity; thus, increases their moisture absorption and board swelling. Besides, hydrophilic fibre characteristics can cause poor fibre and resin adhesion because of hydroxyl and polar group present in the component. As aforementioned, a large amount of hydroxyl group present in the fibre reduces their compatibility with resin adhesive because resin is hydrophobic. Therefore, improving adhesion between fibre and resin by reducing hydroxyl group would increase their compatibility by increase the wettability of the fibre surface [33].

EFB fibres are multicellular fibres with a central lacuna that are rigid and strong. The porous surface of EFB provides better mechanical links with resin. However, EFB fibres are coated with residual oil produced during the processing of palm oil. OPF fibre, on the other hand, consists of various sizes of vascular bundles. Vascular files are widely found in thin-walled parenchyma tissues. Each bundle consists of round gloves, vessels, fibres, phloem and parenchyma tissue. Unlike OPF, OPT is filled with relatively smooth and dense parenchyma ground tissues that comprised mainly hemicellulose and cellulose. Parenchyma ground tissues have high hydroxyl bonds which increased water uptake to retain more water as a water-transporting organ in plant trunks [34]. However, only the outer part of oil palm trunk is suitable for use because soft parenchyma tissue is high in the central region [35].

As shown in Table 2, EFB is rich in cellulose as compared to rubberwood, OPT and OPF. However, lignin and hemicellulose content of EFB is smaller if compared to rubberwood. Based on chemical composition, rubberwood is more similar to OPT except for its length, which shows rubberwood has a longest fibre than oil palm-based fibre. However, the biggest drawback of oil palm fibre is its low resistance to fungal attack because of the high carbohydrate (e.g., sugar and starch) deposited in the parenchyma.

Effect of hybridization

Many studies have been reported for enhancing the mechanical properties of MDF produced from oil palm-based fibre. This is because the properties of oil palm-based fibre affect the structural strength of the MDF produced. However, to meet the demand for environmentally friendly MDF, oil palm-based fibre is considered attractive because of their low cost, biodegradability and recyclability. Apart from these benefits, oil palm-based fibre imparts some drawbacks, including short fibre length, thin cell wall and low fibre density. Therefore, hybridization of oil palm-based fibre which is low modulus fibre with high modulus fibre like rubberwood is needed to overcome these disadvantages. This technique aims to produce MDF with better physical and mechanical properties by combining the strengths of both fibres to compensate for the weaknesses of the other. However, there are limited findings on the various blending ratios utilized and the changes of new hybrid on the properties of MDF produced. Table 3 shows the properties of MDF made from oil palm fibre (EFB, OPT and OPF), as well as rubberwood, mix tropical hardwood (MTH) and fibre mixing.

Abdul Khalil et al. [32] studied the effects of hybridization of EFB and rubberwood and discovered that MDF made from a 20:80 blend of EFB: rubberwood had better mechanical and physical qualities than MDF made from a 50:50 blend. In a separate study, Mustapha et al. [43] used EFB and kenaf fibre and found that a

50:50 EFB: kenaf resulted in lower mechanical properties as compared to 70:30 EFB:kenaf. This finding occurred because the addition of EFB fibre altered the pH value and buffering capacity; thus, affected UF resin flow which was suitable to be used with rubberwood and kenaf fibre [33]. Moreover, poor distribution of UF resin and EFB fibre resulted in the formation of lumps which released during exposure to water; thus increased the swelling thickness [33].

Table 2. Chemical composition and physical properties of oil palm fibre and rubberwood

Fibre	Density (g/cm^3)	Cellulose (%)	Lignin (%)	Hemi-cellulose (%)	Length (mm)	Diameter (µm)	Cell Wall Thickness (µm)	Lumen Width (µm)	Ref.
OPT	-	41	24.5	-	0.66	16.6	8.0	-	[36]
	-	29–37	-	12–17	-	-	-	-	[37]
	-	-	-	-	0.96	29.6	4.8	-	[29]
	0.27-0.44	-	-	-	-	-	-	-	[35]
OPF	-	49.8-56.0	20.5	-	-	-	-	-	[36]
		-	-	-	1.59	19.7	3.95	-	[29]
	-	-	-	32	-	-	-	-	[38]
EFB	0.18-1.32	50.5-62.9	17.8	-	-	19.1	3.38	-	[39]
	-	-	-	-	0.99	-	-	-	[40]
RW	0.6	44	23	-	1.34	27	6	14	[41]
	-	-	-	30.4-31.5	-	-	-	-	[42]

In another study, the capabilities of EFB fibre and its effect on mechanical qualities of MDF were demonstrated by Harmaen et al. [14]. Table 3 shows that the MDF panel made entirely of rubberwood fibres had significantly better mechanical properties (MOR, MOE, and IB) than the other ratios of rubberwood: EFB. Generally, boards having less than 50% of oil palm EFB fibre had better strength properties. Therefore, weak mechanical properties were expected, but replacing 50% rubberwood is already considerable in the industry. MDF contains 70% EFB and 30% of rubberwood surpassing the minimum requirements of MOR and MOE based on EN standards, which are 11 N/mm^2 and 1800 N/mm^2, respectively [44].

On the other hand, physical performance (TS and WA) of the panel made from rubberwood mixture decreased, indicating that lack of hydroxyl group from rubberwood fibre made it less able to absorb water. However, the density of MDF was not affected by the mixture ratio. This was because 100% rubberwood board had a higher board density. In comparison to lower density boards, Wan Daud & Law [29] mentioned that high density boards had more intimate particle contact; thus contained more wood to withstand mechanical loads.

In addition, the strength of MDF also contributed by the fibre length. As mentioned in previous study, EFB fibres are shorter than rubberwood fibres, resulting in a lower IB value. Shorter EFB fibres contributed to a higher resin-covered surface area. Based on the study, 9%-12% resin was used to cover all surfaces of rubberwood fibres; however, it was insufficient to cover the larger surface area of EFB fibres. As a result, inadequate bonding between fibres would occur throughout the board, as seen on EFB-fibreboard.

The similar trend was also recorded when blending rubberwood with OPF and MTH. However, blending OPF with rubberwood and MTH recorded a better IB value as compared to other blending ratio reported by other researchers [45]. Another study demonstrated the

use of 100% OPF at different refining parameters was performed [46], however the resin level required to achieve optimum performance much higher as compared to other reported study. As reported by Zawawi et al. [46], unlike OPT and EFB, OPF had better characteristics. OPT had higher amount of parenchyma cell, whereas EFB contained residual oil. Therefore, increment of fine fibre of nonfibrous plant material from OPT such as parenchyma tissue during refining process or fine fibre coated with residual oil from EFB reduced wettability which led to a poor bonding between fibre and resin.

MDF from 100% OPT has also been produced at different refining parameters. The pressing temperature was heated at 200°C and 10% resin level was used [47]. These MDF provided an improved IB and TS behavior. In another study reported by Zawawi et al. [48], the board from OPT offered a good surface appearance, good strength and a light color. In comparison to MDF produced from rubberwood and OPT, MDF from EFB has a darker color because of residual oil presence on the surface of EFB. Other than that, Zawawi et al. [48] also conducted research by removing parenchyma cell from OPT fibre. As expected, removing parenchyma tissue enhanced the properties of MDF by increasing the ratio of fibre; thus, facilitated mechanical interlocking with resin.

Treatment of cellulosic fibre of oil palm

The main problem of cellulosic fibre and resin is their compatibility. The hydrophilic characteristics of the cellulose fibres lead to high moisture uptake which can seriously lower the mechanical properties of board produced. In addition, pectin and waxy substance present on the fibre covers the reactive functional groups of cellulose fibre and act as barrier to interlocking with the resin. The wax in cellulosic fibre act as barrier by reducing wettability; thus, adhesion of resin into the fibre. Based on several researches, studies of the chemical treatment were conducted to enhance the properties of fibres such as improvement of wettability, surface modification, chemical groups and tensile strength of oil palm fibre, as well to improve interfacial bonding of fibre and resin [49].

Asyraf et al. [3] also reported a similar finding on chemical modification to improve mechanical properties of oil palm fibre. Their survey found that chemical modification approaches have been widely reported to overcome oil palm fibre limitation; thus, improved compatibility, hydrophobicity and interfacial bonding. This can be achieved by eliminating the fibre hydrophilic characteristics, which raise hydrophobicity and interfacial bonding between the fibre and resin, thus resulting in a greater compatibility. The reactive functional group on fibre, such as the hydroxyl group, is modified during this process by the interaction with chemical treatment. Therefore, surface impurities such as pectin, wax and hemicellulose can be removed effectively. Chemical treatment approaches that are widely used for natural fibres include alkaline, acidity, silane, acetylation and coupling agents [3, 49].

The most widely used method to treat cellulose fibre of oil palm is alkaline treatment. In this treatment, fibre is immersed in alkali solution with different temperatures for different periods and then the fibre is washed with water and oven dried. This treatment improves fibre wetting by removing of wax, hemicellulose, lignin, pectin and oil substance; thus, fibre and resin compatibility [3]. Removing this substance increased the ratio of cellulose in the material and allowed good penetration of resin into the fibre. It also reduced the fibre diameter and produced rougher surface [50]. Studies of EFB fibre by Norul Izani et al. [51] showed that the surface fibre after treatment with NaOH became smoother compared with that of untreated fibre as proven by SEM analysis. Therefore, that fibre treated with NaOH displayed improvement in mechanical and physical properties [52]. However, amongst the properties mentioned, only TS and IB value recorded the lowest and highest values from other treated fibre.

Besides, esterification of fibre also can be done to improve the fibre surface. Esterification or acetylation causing plasticization of cellulosic fibre. The reaction involves generation of acetic acid as by product. Chemical modification of acetic anhydride substitutes hydroxyl group with acetyl group; thus, allowing the fibre to become hydrophobic. A study by Zawawi et al. [53] found that acetylation processes of EFB contributed

to a reduction of TS value; thus increased the dimensional stability of MDF produce.

A comparative evaluation of MDF mechanical properties produced from EFB treated with alkaline and acetylation treatment also was reported [54]. In contrast with their earlier finding [53], the property of MDF from acetylation treatment revealed that MOR, MOE and IB values were higher as compared to alkaline treatment. Zawawi et al. [55] mentioned that alkaline treatment had successfully removed higher oil from EFB surface as compared to acetylation treatment, unfortunately, higher oil removal was not the major factor of the improvement in mechanical properties of MDF board. Similar findings were reported by Bam et al. [56] using bagasse fibre and David Chukwudi [57] using raffia fibre, whereby the acetylation treatment showed a better compatibility with UF resin than that of alkaline treatment.

As mentioned by Zhang et al. [58], adhesive penetration could be a factor to the adhesion strength of the bonded wood. Therefore, research on adhesion properties, such as wettability and pH values are necessary for a strong bond to improve mechanical properties of board. A study performed by Zawawi et al. [53] reported that adhesives used, such as UF performed a better dimensional stability at an acidic condition was because treatment using acetic acid increased resin curing times during hot pressing [54], thus reducing hydrogen bonding sites for water molecule to attach. The surface modification increased bonding strength by understanding the behavior of adhesives and fibre properties. However, reducing wettability of adhesive allowed over penetration into the fibre, resulting in small portion of adhesive remained at fibre interface. Therefore, provided inefficient mechanical property of adhesive [58].

Problems and research needs

The use of oil palm fibre (EFB/OPT/OPF) to replace rubberwood as a material for producing MDF panels has showed promise as a long-term sustainable resource for the MDF industry. However, this only applies to blending oil palm fibre with rubberwood in a ratio of less than 50%, as opposed to the existing industry technique, which allows 100% rubberwood fibre to be exposed to the MDF process and achieve good quality results. Furthermore, past research has shown that using 100% EFB induces a color shift even after the fibre has been treated. Studies to increase the strength of MDF produced, especially its mechanical properties by using 100% biomass from oil palm without increasing the resin content should also be carried out. Below are potential barriers which occur with the use of palm fibre and possible solutions.

Table 4. Potential barriers with the use of oil palm fibres and possible solutions

Barriers	Solutions
High ash and silica content	• Avoid soil contamination • Thorough separation and washing
High moisture content and bulkiness	• On site processing • Seasoning
Heterogeneity of material	• Improvement in fibre extraction technique
Short fibre length	• Optimization of pulp yield • Blending with softwood fibre
Fibre efficiency	• Process development for the mixed raw material (stems, fronds, bunches & mesocarp)
Dark colour	• Improvement in fibre washing/treatment
High resin use	• Blending with other fibre

Table 3. Mechanical and physical properties of oil palm based MDF

Ratio (%)	Panel Density (kg/m^3)	Resin Type	Resin Level (%)	Refining Parameter (bar, min)	Pressing Temp. (°C)	Pressing Time (min)	MC (%)	MOR (mpa)	MOE (mpa)	IB (mpa)	TS (%)	WA (%)	Ref.
RW:EFB (50:50)	650	UF	12	2-8	200	-	-	-	-	0.69	13.5	29.86	[35]
RW:EFB (80:20)										0.73	11.0	27.36	
RW (100)	680						6.75	30.7	2412	0.50	16.5	46.27	
RW:EFB (70:30)	678	UF	11	5	170	5-6	6.70	29.5	2264	0.53	15.6	48.98	
RW:EFB (50:50)	672						7.07	26.3	1951	0.45	14.2	54.50	[13]
RW:EFB (30:70)	667						7.18	26.2	1849	0.44	14.3	59.17	
EFB (100)	662						7.28	21.0	1313	0.45	14.8	44.42	
OPF (100)								32.4	2870	1.12	14.3		
OPF:RW,MTH (95: 5)													
OPF:RW,MTH (90:10)	-	UF	9	6, 5	200	5	-	32.9	2694	1.17	13.6	-	[41]
OPF:RW,MTH (85:15)								43.9	3515	1.05	13.5		
OPF:RW,MTH (80:20)								44.4	3862	1.26	13.8		
								45.4	3953	1.28	13.4		
OPF (100)	720	UF	12	6,5	180	5	4-5	23.7	2829	0.66	13.9		[42]
OPT (100)	720	UF	10	6, 1.7	200	5	4-5	38.3	3444	0.68	15.7	-	[43]
				6, 3.3			4-5	39.9	3538	0.72	14.6		
				6, 5.0			4-5	38.3	3597	0.73	14.6		
				6, 6.6			4-5	35.1	3421	0.73	14.4		
Parenchyma content of OPT (10)	650-750						4-5	39.6	3235	1.19	14.8		
Parenchyma content of OPT (20)	650-750	UF	8-10	6, 5	200	5	4-5	35.0	3010	1.11	15.0	-	[44]
Parenchyma content of OPT (30)	650-750						4-5	31.7	2687	0.97	15.7		

MDF: medium density fibreboard; RW: rubberwood; EFB: empty fruit bunch; OPT: oil palm trunk; OPF: oil palm frond; MTH: mix tropical hardwood; MC: moisture content; MOR: modulus of rupture; MOE: modulus of elasticity; IB: internal bonding; TS: thickness swelling; and WA: water absorption.

Conclusion

MDF produced from oil palm biomass are an important part in developing new strategies and policies that aid in reducing the dependence on rubberwood and other wood sources. Oil palm fibre has their own chemical composition and hence their properties differ from those of rubberwood. By chemically modifying oil palm-based fibre through chemical treatments, such as alkaline treatment, acetylation or soaking and washing with boil water or remove parenchyma cell, their mechanical properties such as MOR, MOE and IB could be improved. Chemically modified oil palm-based fibre exhibits better wettability, surface morphology, acidity and buffering capacity because of removed wax, lignin, pectin and oil from fibre surface. Nonetheless, identifying a MDF that has high dimensional stability would be a challenge. Poor dimensional stability of MDF can be remedied by hybridization with rubberwood or other wood source with a ratio of oil palm based less than 50%.

Acknowledgements

The authors would like to thank Director General of Malaysian Palm Oil Board (MPOB) for approval to publish this manuscript. The assistance from Nurul Hasimah is also greatly acknowledged.

References

1. Md. Rowson, A., Ummi Hani, A., Zaidon, A., Lee, S. H., Norul Hisham, H. and Siti Hasnah, K. (2022). Physical properties of hydrothermally treated rubberwood [*Hevea brasiliensis* (Willd. ex A. Juss.) Müll. Arg.] in Different Buffered Media. *Forests* 13(7): 1052.
2. Sivabalan, K., Suhaimi, H., Hamdan, Y., Kartikeyan, P. N. and Mohammad, A. (2021). The utilisation of palm oil and oil palm residues and the related challenges as a sustainable alternative in biofuel, bioenergy and transportation sector: A review. *Sustainability*, 13:3110.
3. Asyraf, M. R. M., Ishak, M. R., Agusril, S., Nurazzi, N. M., Sabaruddin, F. A., Shazleen, S. S., Norrahim, M. N. F., Rafidah, M., Ilyas, R. A., Mohamad Zakir, A. R. and Razman, M. R. (2022). Mechanical properties of oil palm fibre reinforced polymer composites: A review. *Journal of Materials Research and Technology*, 17: 33-65.
4. Pugazhenti, N. and Anand, P. (2018). A review on preparation of medium density fibreboard with different materials. *International Journal of Engineering & Technology*, 7(3.34): 962-965.
5. Philip, X. Y., James, J., Monlin, K., Womac, A. and Deland, M. (2007). Properties of medium density fibreboards made from renewable biomass. *Bioresource Technology*, 98(5): 1077-1084.
6. Anis, M., Kamarudin, H., Astimar, A. A. and Choo, Y. M. (2001) - Oil palm biomass for various wood-based products, production, processing, characterization and uses, pp. 625-652.
7. Zawawi, I, Astimar, A. A., Ridzuan, R., Wan Hasamuddin, W. H. and Zainal, N. H. (2006). Optimum parameters for the production of MDF using 100% oil palm trunks. MPOB Information Series 566, 2006.
8. Büyüksari, Ü., Hiziroglu, S., Akkılıç, H. and Ayrılmış, N. (2012). Mechanical and physical properties of medium density fibreboard panels laminated with thermally compressed veneer. *Composites Part B: Engineering*, 43(2):110–114.
9. Aisyah, H. A., Paridah, M. T., Sahri, M. H., Anwar, U. M. K. and Astimar, A. A. (2013). Properties of medium density fibreboard (MDF) from kenaf (*Hibiscus cannabinus* L.) core as function of refining conditions. *Composite Part B: Engineering*, 44(1):592–596.
10. Aisyah, H. A., Paridah, M. T., Sahri, M. H., Astimar, A. A. and Anwar, U. M. K. (2012). Influence of thermo mechanical pulping production parameters on properties of medium density fibreboard made from kenaf bast. *Journal of Applied Science*, 12(6): 575-580.
11. Das, A. K., Islam, M. A., Shams, M. I., Hannan, M. O. and Biswas, S. K. (2014). Physical and mechanical properties of UF bonded and without binding agent bagasse MDF. *Asian Journal Applied Science*, 7(1):45-50.
12. Yousefi, H. (2009). Canola straw as a bio-waste resource for medium density fibreboard (MDF) manufacture. *Waste Management*, 29(10): 2644-2648.
13. Li, X. (2004). Physical, chemical and mechanical properties of bamboo and its utilization potential for fibreboard manufacturing. Master Thesis: Louisiana State University and Agriculture and Mechanical College, USA.
14. Harmaen, A. S., Jalaluddin, H. and Paridah, M. T. (2012). Properties of medium density fibreboard panels made from rubberwood and empty fruit bunches of oil palm biomass. *Journal of Composite Materials*, 47(22): 2875-2883.
15. Ayrilmis, N., Jarusombuti, S., Fueangvivat, V. and Bauchongkol, P. (2011). Effects of thermal treatment of rubberwood fibres on physical and mechanical properties of medium density fibreboard. *Journal of Tropical Forest Science*, 23(1): 10-16.

16. Pugazhenti, N. and Anand, P. (2021). Mechanical and thermal behavior of hybrid composite medium density fibreboard reinforced with phenol formaldehyde. *Heliyon*, 7(12): e08597.
17. Rashid, M., Das, A. K., Shams, M. I. and Biswas, S. K. (2014). Physical and mechanical properties of medium density fibre board (MDF) fabricated from banana plant (*Musa Sapientum*) stem and midrib. *Journal of the Indian Academy of Wood Science,* 11: 1-4.
18. Kargarfard, A., Nourbakhsh, A. and Hosseinkhani, H. (2007). Investigation on medium density fibreboard (MDF) properties produced from horn beam wood. Pajouhesh-va-Sazandegi, 20(1): 25–31.
19. Thomas, E. (1997). Asia-Pacific Forestry Sector Outlook Study Working Paper Series. Technology Scenarios in the Asia Pacific Forestry Sector. pp. 10-46.
20. Gul, W., Khan, A. and Shakoor. A. (2017). Impact of hot-pressing temperature on medium density fibreboard (MDF) performance. *Advances in Materials Science and Engineering,* (17): 2-6.
21. Lee, S. H., Zaidon, A., Ang, A. F., Juliana, A. H., Lum, W. C., Dahali, R. and Halis, R. (2018). Effects of two-step post heat-treatment in palm oil on the properties of oil palm trunk particleboard. *Industrial Crops & Products,* 116(6): 249-258.
22. Hakimi, N. M. F., Lee, S. H., Lum, W. C., Mohamad, S. F., Osman Al Edrus, S. S., Park, B. D. and Azmi, A. (2021). Surface modified nanocellulose and its reinforcement in natural rubber matrix nanocomposites: A review. *Polymers*, 13(19): 3241.
23. Dahali, R., Lee, S. H., Ashaari, Z., Bakar, E. S., Ariffin, H., Khoo, P. S., Bawon, P. and Salleh, Q. N. (2020). Durability of superheated steam-treated light red meranti (Shorea spp.) and Kedondong (Canarium spp.) wood against white rot fungus and subterranean termite. *Sustainability*, 12(11): 4431.
24. Li, T., Cheng, D. L., Avramidis, S., Wålinder, M. E. P. and Zhou, D. G. (2017). Response of hygroscopicity to heat treatment and its relation to durability of thermally modified wood. *Construction and Building Materials*, 144(2017): 671-676.
25. Lee, S. H., Ashaari, Z., Lum, W. C., Ang, A. F., Juliana, A. H. and Halis, R. (2018). Chemical, physico-mechanical properties and biological durability of rubberwood particleboards after post heat-treatment in palm oil. *Holzforschung,* 72: 159-167.
26. Petrissans, M., Gerardin, P., Elbakali, D. and Serraj, M. (2003). Wettability of heat-treated wood. *Holzforschung,* 57: 301–307.
27. Zaidon, A., Norhairul Nizam, A. M., Mohd Nor, M. Y., Abood, F., Paridah, M. T., Nor Yuziah, M. Y. and Jalaluddin, H. (2007). Properties of particleboard made from pretreated particles of rubberwood, EFB and rubberwood-EFB blend. *Journal Applied Science,* 7(8): 1145-1151.
28. Libo, Y., Bohumil, K. and Liang, H. (2016). A review of recent research on the use of cellulosic fibres, their fibre fabric reinforced cementitious, geo-polymer and polymer composites in civil engineering. *Composites Part B: Engineering*, 92(2016): 94-132.
29. Wan Daud, W. R. and Law, N. K. (2011). Oil palm fibre as papermaking materials: Potentials & challenges. *Bioresources*, 6(1): 901-907.
30. Abdul Khalil, H. P. S., Nurul Fazita, M. R., Bhat, A. H., Jawaid, M. and Nik Fuad, N. A. (2010). Development and material properties of new hybrid plywood from oil palm biomass. *Materials and Design*, 31(1): 417-424.
31. Bhat, I. U. H., Abdullah, C. K., Abdul Khalil, H. P. S., Hakimi Ibrahim, M. and Nurul Fazita, M. R. (2010). Properties enhancement of resin impregnated agro waste: Oil palm trunk lumber. *Journal of Reinforced Plastics and Composites,* 29(22): 3301-3308.
32. Abdul Khalil, H. P. S., Firdaus, M. Y. N., Jawaid, M., Anis, M., Ridzuan, R. and Mohamed, A. R. (2010b). Development and material properties of new hybrid medium density fibreboard from empty fruit bunch and rubberwood. *Materials and Design*, 31(9): 4229-4236.
33. Paridah, M. T., Juliana, A. H. and Abdul Khalil, H. P. S. (2015). Nonwood based composites. *Current Forestry Report,* 1:221-238.
34. Abdullah, C. K., Jawaid, M., Abdul Khalil, H. P. S., Zaidon, A. and Hadiyane, A. (2012). Oil palm trunk polymer composite: Morphology, water absorption and thickness swelling behaviours. *Bioresources,* 7(3): 2948-2959.
35. Loh, Y. F., Paridah, M. T. and Hoong, Y. B. (2011). Density distribution of oil palm stem veneer and its influence on plywood mechanical properties. *Journal Applied Science,* 11(5): 824-831.
36. Abdul Khalil, H. P. S., Siti Alwani M., Ridzuan, R., Kamarudin, H. and Khairul, A. (2008). Chemical composition, morphological characteristics, and cell wall structure of

Malaysian oil palm fibres. *Polymer-Plastics Technology Engineering*, 47(3): 273-280.

37. Abdul Khalil, H. P. S., Hanida, S., Kang, C. W. and Nik Fuaad, N. A. (2007). Agro-hybrid composite: The effects on mechanical and physical properties of oil palm fibre (EFB)/glass hybrid reinforced polyester composites. *Journal of Reinforced Plastics and Composites*, 26(2):203-218.
38. Megashah, L. N., Ariffin, H., Zakaria, M. R. and Hassan, M. A. (2017). Properties of cellulose extract from different types of oil palm biomass. *IOP Conference Series: Materials Science and Engineering*, 368 (2018) 012049.
39. Asiah, A., Mohd Razi, I., Mohd Khanif, Y., Marziah, M. and Shaharuddin, M. (2004). Physical and chemical properties of coconut coir dust and oil palm empty fruit bunch and the growth of hybrid heat tolerant cauliflower plant. *Pertanika Journal Tropical Agriculture Science*, 27(2):121-133.
40. Law, K., Daud, W. and Ghazali, A. (2007). Morphological and chemical nature of fibre strands of oil palm empty-fruit-bunch (OPEFB). *Bioresource*, 2(3):351-362.
41. Saiful Azry, S. O. A. (2007). Evaluation of properties of 4-year-old rubberwood clones RRIM 2000 Series for particleboard manufacture. MSc. Thesis: Universiti Putra Malaysia, Selangor, Malaysia.
42. Jirawat, R., Thitaporn, P., Trairat, N., Suteera, W., Krissada, S., Rangsarid, K. and Chalermpol, P. (2015). Rubberwood variability in chemical and mechanical properties of pará rubber *(Hevea brasiliensis)* trees. *ScienceASia*, 251-258.
43. Mustapha, S. N. H., Norizan, C. W. C. W. N. F., Roslan, R. and Mustapha, R. (2020). Effect of kenaf/ empty fruit bunch (EFB) hybridization and weight fractions in oil palm blend polyester composite. *Journal Natural Fibres*, 2020: 1-14.
44. Chaydarreh, K. C., Lin, X., Guan, L., Yun, H., Gu, J. and Hu, C. (2021). Utilization of tea oil camellia (*Camellia oleifera* Abel.) shells as alternative raw materials for manufacturing particleboard. *Industrial Crops and Products*, 161: 113221.
45. Zawawi, I., Astimar, A. A., Ridzuan, R., Anis, M. and Ropandi, M. (2012). Production of medium density fibreboard (MDF) from oil palm fronds and its admixture. MPOB Information Series.
46. Zawawi, I., Aisyah, H. A., Ridzuan, R., Noorshamsiana, A. W., Mansur, A., Syaiful, O. and Sheng, E. L. (2021). Effects of refining parameters on the properties of oil palm frond (OPF) fibre for medium density fibreboard (MDF). *Journal of Advanced Research in Fluid Mechanical and Thermal Sciences*, 87(3): 64-77.
47. Zawawi, I., Astimar, A. A., Ridzuan, R., Anis, M. and Lee, S. J. (2013). Effect of refining parameters on medium density fibreboard (MDF) properties from oil palm trunk *(Elaeis Guineensis)*. *Journal of Composite Materials*, 3: 127-131.
48. Zawawi, I., Astimar, A. A., Ridzuan, R., Anis, M., Rosmazi, O. and Lee, S. J. (2014). Production of medium density fibreboard (MDF) from oil palm trunk (OPT). *Journal of Applied Sciences*, 14(11): 1174-1179.
49. Nurazzi, N. M., Asyraf, M. R. M., Rayung, M., Norrrahim, M. N. F., Shazleen, S. S., Rani, M. S. A., Shafi, A. R., Aisyah, H. A., Radzi, M. H. M., Sabaruddin, F. A., Ilyas, R. A., Zainudin, E. S. and Abdan, K. (2021). Thermogravimetric analysis properties of cellulosic natural fibre polymer composites: A review on influence of chemical treatments. *Polymers*, 2021: 13(16):2710.
50. Che Ibrahim, A., Ahmad Danial, A., Nor Mas Mira, A., Aziz, H., and Rosiyah, Y. (2019). Optimizing treatment of oil palm-empty fruit bunch (OP-EFB) fibre: Chemical, thermal and physical properties of alkalized fibres. *Fibres and Polymers*, 20(3):527-537.
51. Norul Izani, M. A., Paridah, U. M. K., Anwar, M. Y. and Mohd Nor, P. S. H. (2013). Effects of fibre treatment on morphology, tensile and thermogravimetric analysis of oil palm empty fruit bunches fibres. *Composites Part B: Engineering*, 45(1):1251-1257.
52. Norul Izani, M. A., Paridah, M. T., Mohd Nor, M. Y. and Anwar, U. M. K. (2013). Properties of medium density fibreboard (MDF) made from treated empty fruit bunch of oil palm. *Journal Tropical Forest Science*, 25(2): 175-186.
53. Zawawi, I., Mansur, A., Astimar, A. A., Ridzuan, R., Mohd Ariff, J., Suhaimi, M. and Aisyah Humairaa, A. (2016). Dimensional stability properties of medium density fibreboard (MDF) from treated oil palm *(Elaeis Guineensis)* empty fruit bunches (EFB) fibres. *Journal of Composite Materials*, 6: 91-99.
54. Zawawi, I., Mansur, A., Astimar, A. A., Ridzuan, R., Noorshamsiana, A. W., Aisyah, H. A., Syaiful, O. and Sheng, E. L. (2021). Oil palm empty fruit bunches (EFB): Influence of alkali and acid treatment on the mechanical properties of medium density fibreboard (MDF). *Journal of Advance Research in Fluid Mechanics and Thermal Sciences*, 79(1): 44-53.

55. Zawawi, I., Astimar, A. A., Ridzuan, R., Kamaruzaman, J., Mansur, A. and Mohd Ariff, J. (2015). Effect of treatment on the oil content and surface morphology of oil palm *(Elaeis Guineensis)* empty fruit bunches (EFB) fibres. *Wood Research*, 60(1): 157-166.
56. Bam, S. A., Gundu, D. T. and Onu, F. A. (2019). The effect of chemical treatments on the mechanical and physical properties of bagasse filler reinforced low density polyethylene composite. *American Journal Engineering Resource*, 8: 95-98.
57. David Chukwudi, A. (2015). Comparison of acetylation and alkali treatments on the physical and morphological properties of raffia palm fibre reinforced Composite. *Science Journal Chemistry*, 3: 72-77.
58. Zhang, C., Yu, L., Fatemah, F., Vijayaraghavan, S., Mesnager, J., Jollet, V. and Zhao, B. (2018). Behaviour of water/pMDI emulsion adhesive on bonding wood substrate with varied surface properties. *Industrial & Research Chemistry Research*, 57: 16318-16326.

Malaysian Journal of Analytical Sciences (MJAS)
Published by Malaysian Analytical Sciences Society

Cymbopogon citratus AND *Cymbopogon nardus* ESSENTIAL OIL COMPONENTS – FTIR, CHEMOMETRICS ASSESSMENT AND IDENTIFICATION USING GC-MS

(Komponen Minyak Pati *Cymbopogon citratus* dan *Cymbopogon nardus*- Penilaian FTIR, Kemometrik dan Penentuan Menggunakan GC-MS)

Hazrulrizawati Abd Hamid

Faculty of Industrial Sciences & Technology,
Universiti Malaysia Pahang, Lebuhraya Tun Razak, 26300 Gambang Kuantan, Pahang, Malaysia

**Corresponding author: hazrulrizawati@ump.edu.my*

Received: 24 October 2022; Accepted: 12 May 2023; Published: 23 June 2023

Abstract

Cymbopogon citratus and *Cymbopogon nardus* essential oil are high-value natural products due to their special qualities and commercial significance. In this work, the volatile compounds of the *C. citratus* and *C. nardus* natural essential oils obtained by hydro distillation and commercial sources using gas chromatography-mass spectrometry (GC-MS), Fourier transformation infrared spectroscopy (FTIR) and chemometrics methods were systematically detected and identified. The GC-MS results indicated that the main compound in the natural essential oil of *C. citratus* is citral while citronellal commercial samples of both *Cymbopogan* species are positively significant. Based on the results of GC-MS, citral was the major component in *C. citratus* while citronellal was the major component in *C. nardus*. Analyzing the FTIR data using principal component analysis (PCA), hierarchical cluster analysis (HCA), and discriminant analysis (DA) further revealed that the chemical composition of natural essential oils *C. citratus* and *C. nardus* samples were significantly different from commercial samples. This study revealed the first insight into metabolite compositional differences among *C. citratus* and *C. nardus* using quick and affordable analytical procedures.

Keywords: Fourier transformation infrared spectroscopy, chemometrics, principal component analysis, hierarchical cluster analysis, *Cymbopogon*

Abstrak

Minyak pati *Cymbopogon citratus* dan *Cymbopogon nardus* ialah produk semula jadi bernilai tinggi kerana kualitinya yang istimewa dan kepentingan komersialnya. Dalam kajian ini, sebatian meruap minyak pati semula jadi *C. citratus* dan *C. nardus* yang diperoleh melalui penyulingan hidro dan sumber komersial dikenalpasti dengan menggunakan kromatografi gas spektrometri jisim (GC-MS), spektroskopi inframerah transformasi Fourier (FTIR) dan kaedah kemometrik. Keputusan GC-MS menunjukkan bahawa sebatian utama dalam sampel komersial bagi kedua-dua spesies *Cymbopogan* secara signifikan berkorelasi positif dengan minyak pati semulajadi. Berdasarkan keputusan GC-MS, sitral adalah komponen utama dalam *C. citratus* manakala sitronelal adalah komponen utama dalam *C. nardus*. Melalui analisis data FTIR menggunakan analisis prinsip komponen (PCA) dan analisis kluster hierarki (HCA) seterusnya mendedahkan bahawa komposisi kimia minyak pati semulajadi *C. citratus* dan *C. nardus* sampel adalah berbeza dengan ketara daripada sampel komersial. Kajian ini memberikan keputusan yang jelas tentang perbezaan komposisi metabolit antara *C. citratus* dan *C. nardus* menggunakan prosedur analisis yang cepat dan berpatutan.

Kata kunci: Spektroskopi inframerah transformasi Fourier, kemometrik, analisis prinsip komponen,analisis kluster hierarki, *Cymbopogon*

Introduction

Essential oils from the *Cymbopogon* species are widely used in the perfumery, cosmetic, food and pharmaceutical industries. The most widely used species in food processing is *C. citratus*. Among aromatic species that are also important are *C. fexuosus* (East Indian *C. citratus*), *C. martini* (palmarosa), and *C. nardus* (*C. nardus* grass) [1]. Essential oils contain different volatile compounds and the most common compounds found in *Cymbopogon* essential oil are nerol, geranial, citronellol, geraniol, and piperitone [2]. Phytochemical studies of different species showed the presence of terpenoids, alkaloids, phenolic acids, tannins, and carotenoids, and the genus *Cymbopogon* was reported as a rich source of C-glycosyl flavonoids [2]. Most of the research done has focused on the species of *C. citratus*, with less emphasis on other species in the genus [3].

Numerous studies have been conducted to see the differences in chemical composition and pharmacological effects on *Cymbopogon* species. Essential oil products from the *Cymbopogon* species are also widely available in the market, but until now the validity of commercial products with natural essential oils has not been well distinguished. Difficulty discriminating between *Cymbopogon* species may also occur due to similar physical and morphological characteristics. To avoid confusion, a rapid and reliable method to discriminate *Cymbopogon* species is urgently needed. This is important for quality control, safety and effectiveness of essential oils from the *Cymbopogon* species.

The combination of spectroscopic and chemometric techniques is gaining attention because of its ability to quickly distinguish various plant species [4]. Infrared spectroscopy provides information about the vibrational of functional groups in the studied molecules and the absorption of infrared radiation by the sample [5]. The chromatographic technique is also a common method used in determining the quality of herbal medicine. Recently, the combination of chromatographic and chemometric techniques in the identification of varieties and the discovery of herbal chemical markers has increased widely [6]. Most researchers focus on establishing GC-MS fingerprints to reveal differences in the composition and chemical content of various botanical and geographical origins of plants [7]. Chemometrics tools have not been widely used in the analysis of volatile compounds for geographic origin differentiation and discrimination.

In this study, a simple and fast method for various identification and selection of chemical markers will be developed. FTIR spectroscopy and GC-MS chromatography coupled with chemometrics were used to discriminate the different botanical origins as well as the authenticity of commercial products. Furthermore, for the first time, the potential of functional groups and volatile compounds that contribute to the differences between *C. Citratus* and *C. nardus* species and commercial samples were determined through PCA and HCA models built from FTIR data.

Materials and Methods

Materials

The samples for *C. citratus* and C. *nardus* were collected from three different origins from the state of Pahang, Malaysia and the natural essential oils obtained by hydro distillation were labelled as ECC1, ECC2, ECC3 for essential oils of *C. citratus* and ECN1, ECN2, ECN3 for essential oils from *C. nardus*. Commercial essential oils purchased from three different companies and were labelled as CCC1, CCC2, CCC3 for commercial samples of *C. citratus* and CCN1, CCN2, CCN3 for commercial samples of *C. nardus*.

Sample preparation and essential oil extraction

The stalks and leaves of *C. citratus* and *C. nardus* are washed with tap water and cut into small pieces before being stored overnight in the oven (50 °C). The dried *C. citratus* and *C. nardus* are ground into small sizes. Thirty grams (30 g) of each of *C. citratus* and *C. nardus* are placed in a 2000 mL distillation flask connected directly to the Clevenger apparatus containing distillation water (1000 mL). The samples are heated at 100 °C for 2 hours. The extracted essential oils are dried

over anhydrous sodium sulphate and filtered. The volatile oils are obtained and kept for further analysis.

GC-MS analysis

A 7890A Agilent Technologies Gas Chromatography with a 5760N Mass Spectrometer equipped with an HP-5 ms (5% phenyl methyl siloxane) fused silica capillary column (30 m 0.25 mm internal diameter, film thickness 0.25 m) was used to conduct the GC-MS analysis of samples of essential oils. The temperature of the injector is fixed at 250 °C. For three minutes, the initial oven temperature of 40 °C was maintained. The temperature was then raised to 100 °C gradually at a rate of 8 °C/min. The temperature increased to 200 °C at a rate of 5 °C/min and to 250 °C at a rate of 10 °C/min. For 10 minutes, the temperature was maintained at 250 °C. At a rate of 1.0 ml/min, helium was used as the carrier gas.

FTIR analysis

The procedure begins with the crystal being wiped and cleaned with acetone to ensure precise detection. Small amounts of samples were placed onto the crystal surface in contact with the ATR at ambient temperature (25 °C). Then, after placing the essential oil on the crystal region, the pressure arm over the crystal/sample area was setup. All spectra were background corrected using an air spectrum, which was renewed after each scan. After each measurement, the ATR base was thoroughly cleaned using acetone and the surface was allowed to dry before measuring the next sample. Spectra were recorded in the range 600-4000 cm^{-1} at a resolution of 4 cm^{-1} and each spectrum consisted of 64 co-added scans. The FTIR spectrum of each sample was measured in triplicate to assess precision and ensure the reproducibility of each sample. The spectra were recorded as absorbance values.

Chemometrics

All the data obtained from the application of FTIR was subjected to chemometrics data analysis. Principal component analysis (PCA), hierarchical cluster analysis (HCA) and discriminate analysis (DA) were used to discriminate samples from different origins. XLSTAT software was used to perform chemometric analysis of FTIR and GC-MS data of *C. citratus* and *C. nardus* essential oils and commercial samples. The scattering pattern of authentic and commercial samples was displayed using two-dimensional PCA plots. HCA is a method of cluster analysis that aims to create a hierarchy of groups. The HCA dendrogram indicated significant differences and similarities. For analysis of FTIR data, the spectral ranges of 1000-3300 cm^{-1} were employed.

Results and Discussion

Identification of volatile compounds in *C. citratus* and *C. nardus*

Cymbopogon essential oils (n = 6) and commercial samples (n = 6) were analysed utilising GC-MS techniques in the current research investigation. Samples of *Cymbopogon* essential oils included a total of 111 constituents. Monoterpenes, sesquiterpenes, aldehydes, ketones, alcohol hydrocarbons, alkanes, oxygenated monoterpenes, and oxygenated sesquiterpenes comprise the volatile constituent profile of *C. citratus* essential oil Overall, the main compound identified in essential oil and commercial samples of *C. citratus* were citral and linalool (Table 1). The major volatile compound in *C. citratus* essential oil was citral, which is present almost in all the analysed samples. Prior study indicated that citral plays a crucial role in the development of the plant's taste and other food recipes [8]. Citral exhibits various important therapeutic properties like antimicrobial, antioxidant, anticancer, anti-diabetic and anti-inflammatory [9].

The frequently identified compounds of *C. nardus* samples (Table 2) were citronellal, citronellol, and D-limonene. The main constituents of the essential oil in *C. nardus*, commonly known as citronellal, and citronellol are also found in this study [10]. The absence of citronellal from Origin 3 and citronellol from Origin 1 is due to various factors related to the plant, interaction with the environment (soil type and climate, etc.), the maturity of the plant concerned, even at harvest time during the day and related to the extraction method [11]. *C. nardus* and *C. citratus* essential oils were considered important products in the food and cosmetic industry. Consumer safety greatly depends on the ability to trace the quality of *C. nardus* and *C. citratus* essential oils. The development of new analytical techniques that are robust, dependable, effective, and affordable is crucial for determining the authenticity of essential oils. There

is currently interest in chemometrics and innovative analytical techniques.

The current research uses FTIR and GC–MS techniques for the characterization of *C. nardus* and *C. citratus* essential oils. The findings demonstrate that the authenticity of *C. nardus* and *C. citratus* essential oils can be determined by FTIR and chemometrics (HCA & PCA). It takes little sample preparation to distinguish both essential oils from commercial samples. As far as we are aware, this is the first example in which the FTIR technique and chemometrics have been employed to assess the authenticity of *C. nardus* and *C. citratus* essential oils. Additionally, recent research has demonstrated the significant potential of vibrational spectroscopy in conjunction with chemometrics to deliver precise and trustworthy results for determining the authenticity of essential oils. Based on the data collected using HCA and PCA, all samples could be unambiguously identified with 100% accuracy.

Analysis of FTIR spectra of *C. citratus* and *C. nardus*

The typical FTIR spectrum of *C. citratus* and C. *nardus* essential oils obtained by hydro distillation and commercial samples are presented in Figures 1(a) and (b), respectively. In the infrared (IR) region, molecular vibrations matching a specific vibration frequency show the functional group of each sample including its molecular identification [8]. In this analysis, the differences between the samples were determined based on the wavenumber of the absorption band in the IR.

The absorption bands in Figure 1(a) at 1672 to 1612 cm^{-1} were assigned to C=C stretching vibrations of the alkenes functional group. Citral has conjugated double bonds (C=C-CHO), which are frequent in acyclic monoterpenes, as evidenced by the intense peak seen at 1672 -1612 cm^{-1} caused by vibrations of C=C (*cis* and *trans*). As can be seen in the spectrum, the intensity of the essential oil *C. citratus* peak at 1672-1612 cm^{-1} was higher than those in commercial samples. The result might be useful for faster determination of the quality of commercial products *C. citratus* essential oil. The intensity difference might due to the low content of marker compounds in *C. citratus* which was citral. The peak around 1442 to 1377 cm^{-1} could be assigned to the C-H bending vibrations of the alkanes functional group. Bands at 1194, 1154, 1153, 1120 and 1121 cm^{-1} resulted from the C-O stretching vibrations of phenolics. The peak at 1043 cm^{-1} was attributed to the stretching vibrations of C-O. The peak at 984 cm^{-1} is assigned to the C-H bending absorption of the alkenes functional group. The peak at 864, 842, 820, 747 and 748 cm^{-1} are assigned to aromatic rings =CH vibration absorption [12]

Table 1. Chemical compositions of essential oils from *Cymbopogon citratus* of different origins and commercial samples

Compounds	**Molecular Formula**	***Cymbopogon citratus***											
		Origin 1		**Origin 2**		**Origin 3**		**Company 1**		**Company 2**		**Company 3**	
		RT	**Area %**	**RT**	**Area %**	**RT**	**Area %**	**RT**	**Area %**	**RT**	**Area %**	**RT**	**Area %**
β-Myrcene	$C_{10}H_{16}$	6.619	1.09	6.604	0.93	-	-	-	-	-	-	-	-
D-Limonene	$C_{10}H_{16}$	-	-	-	-	-	-	7.388	0.71	7.366	0.92	7.377	0.23
β-(Z)-Ocimene	$C_{10}H_{16}$	7.579	0.30	8.517	0.77	-	-	-	-	-	-	-	-
Linalool	$C_{10}H_{18}O$	8.522	0.45	-	-	8.523	0.47	8.534	0.55	-	-	8.523	0.18
Citronellal	$C_{10}H_{18}O$	9.365	0.20	9.371	1.07	-	-	-	-	-	-	-	-
Nerol	$C_{10}H_{18}O$	-	-	-	-	-	-	10.533	0.64	-	-	10.522	0.36
6-Methyl-3,5-heptadiene-2-one	$C_8H_{12}O$	9.516	0.75	-	-	-	-	-	-	-	-	-	-
Cyclohexane, ethenyl-	C_8H_{14}	9.814	1.08	-	-	-	-	-	-	-	-	-	-
3-Octyne	C_8H_{14}	-	-	10.791	31.90	10.802	10.20	-	-	-	-	-	-
Cis-citral	$C_{10}H_{16}O$	-	-	-	-	-	-	10.780	4.57	-	-	10.780	1.42
Citral	$C_{10}H_{16}O$	-	-	11.246	42.37	11.274	16.32	11.207	2.74	11.235	6.92	11.212	1.28
2,3-Epoxycarane, (E)-	$C_{10}H_{16}O$	-	-	-	-	11.364	10.80	-	-	-	-	-	-
1-Propyne, 1-(methylthio)-	C_4H_6S	-	-	-	-	-	-	11.319	2.97	-	-	-	-
γ-Picoline, N-oxide	C_6H_7NO	11.381	41.32	-	-	-	-	-	-	-	-	-	-
β-Cymene	$C_{10}H_{14}$	-	-	-	-	-	-	-	-	11.414	4.52	-	-
1,4-Benzenediol, 2-(1,1-dimethylethyl)-	$C_{14}H_{22}O$	-	-	11.796	3.72	11.864	10.58	-	-	11.847	4.93	-	-
Geranic acid methyl ester	$C_{11}H_{18}O_2$	-	-	11.875	0.77	11.920	0.70	-	-	-	-	-	-
Geranyl acetate	$C_{12}H_{20}O_2$	12.622	0.66	-	-	12.627	2.66	-	-	-	-	-	-
Caryophyllene	$C_{15}H_{24}$	13.380	0.43	-	-	-	-	13.386	2.19	-	-	13.397	1.66
Butylated Hydroxytoluene	$C_{15}H_{24}O$	-	-	-	-	-	-	14.357	0.93	-	-	14.362	0.43
Caryophyllene Oxide	$C_{15}H_{24}O$	15.564	0.23	-	-	15.564	0.44	-	-	-	-	-	-
γ-Gurjunene	$C_{15}H_{24}$	16.075	3.95	-	-	16.609	0.56	-	-	-	-	-	-
α-Cadinol	$C_{15}H_{26}O$	16.412	0.87	-	-	16.407	0.52	-	-	-	-	-	-
γ-Selinene	$C_{15}H_{24}$	16.614	0.74	-	-	16.070	2.70	-	-	-	-	-	-
Juniper Camphor	$C_{15}H_{26}O$	16.990	0.39	-	-	-	-	-	-	-	-	-	-
Benzyl benzoate	$C_{14}H_{12}O_2$	-	-	-	-	-	-	17.996	1.52	17.984	0.45	-	-
Isopropyl Myristate	$C_{17}H_{34}O_2$	-	-	-	-	-	-	18.220	15.01	18.192	2.64	-	-
Versalide	$C_{18}H_{26}O$	-	-	-	-	-	-	18.928	1.77	18.911	0.48	-	-

Table 2: Chemical compositions of essential oils from *Cymbopogon nardus* of different origins and commercial samples

Compounds	**Molecular Formula**	***Cymbopogon nardus***											
		Origin 1		**Origin 2**		**Origin 3**		**Company 1**		**Company 2**		**Company 3**	
		RT	**Area %**	**RT**	**Area %**	**RT**	**Area %**	**RT**	**Area %**	**RT**	**Area %**	**RT**	**Area %**
D-Limonene	$C_{10}H_{16}$	7.394	0.52	7.383	2.57	7.355	44.04	7.355	0.19	7.388	1.20	7.388	0.31
Eucalyptol	$C_{10}H_{18}O$	-	-	-	-	-	-	7.444	0.79	7.484	3.34	7.484	1.77
Camphor	$C_{10}H_{16}O$	-	-	-	-	-	-	9.488	0.22	9.494	0.65	-	-
Linalool	$C_{10}H_{18}O$	8.534	0.34	8.523	0.34	8.528	1.10	-	-	-	-	-	-
Citronellal	$C_{10}H_{18}O$	9.477	21.95	9.393	3.59	-	-	9.376	1.02	9.387	2.73	9.404	2.33
Citronellol	$C_{10}H_{20}O$	-	-	10.533	3.33	10.583	18.31	10.516	0.41	10.516	1.03	10.533	0.85
Citral	$C_{10}H_{16}O$	10.780	0.17	11.218	0.31	10.774	0.33	-	-	-	-	11.207	0.42
2,6-Octadiene, 2,6-dimethyl	$C_{10}H_{18}$	12.206	0.48	12.201	1.61	12.201	0.34	-	-	-	-	-	-
Geranyl acetate	$C_{12}H_{20}O_2$	12.622	0.44	12.644	4.97	12.622	0.58	-	-	-	-	-	-
β-Elemene	$C_{15}H_{24}$	12.886	3.86	12.874	2.23	-	-	-	-	-	-	-	-
δ-Cadinene	$C_{15}H_{24}$	14.615	3.49	-	-	-	-	-	-	14.598	0.35	14.609	0.24
Germacrene D	$C_{15}H_{24}$	-	-	-	-	14.183	0.42	-	-	-	-	14.205	0.27
Elemol	$C_{15}H_{26}O$	-	-	-	-	15.036	1.31	-	-	-	-	15.036	0.26
γ-Eudesmole	$C_{15}H_{26}O$	14.671	2.87	16.126	0.55	-	-	-	-	-	-	-	-
Myristic acid	$C_{14}H_{28}O_2$	-	-	-	-	-	-	18.310	25.29	18.299	39.32	-	-
Isopropyl Myristate	$C_{17}H_{54}O_2$	-	-	-	-	18.181	1.71	-	-	18.074	1.15	18.389	46.39
Cis-Pinane	$C_{10}H_{18}$	18.321	0.21	-	-	18.321	0.34	-	-	-	-	-	-

The main constituents of *C. nardus* essential oil were citronellal, citronellol and geraniol [13]. The characteristic bands of citronellal and citronellol which were the major compounds in *C. nardus* dominated by the C=O stretching of the aldehyde group ascribed by the band between 1740-1700 cm^{-1}. Within the range of 2970–2850 cm^{1}, typical asymmetric and symmetric stretching vibration bands of methyl and methylene groups were found. Figure 1(b) shows low intensities of the peak at 1740-1700 cm^{-1} and 2970-2850 cm^{-1} of commercial samples compared to essential oils of *C. nardus*. Furthermore, around 1670 cm^{-1}, the olefinic unsaturation C=C stretching of conjugated double bonds emerged [14]. Sharp and medium peaks were also seen for the bending of methylene CH_2 (1450-1440 cm^{-1}) and the symmetric bending of methyl CH_3 (1377 cm^{-1}). There were also some small vibrations of functional groups (910–740 cm^{-1}) and C-O stretching (1030-1000 cm^{-1}) [9].

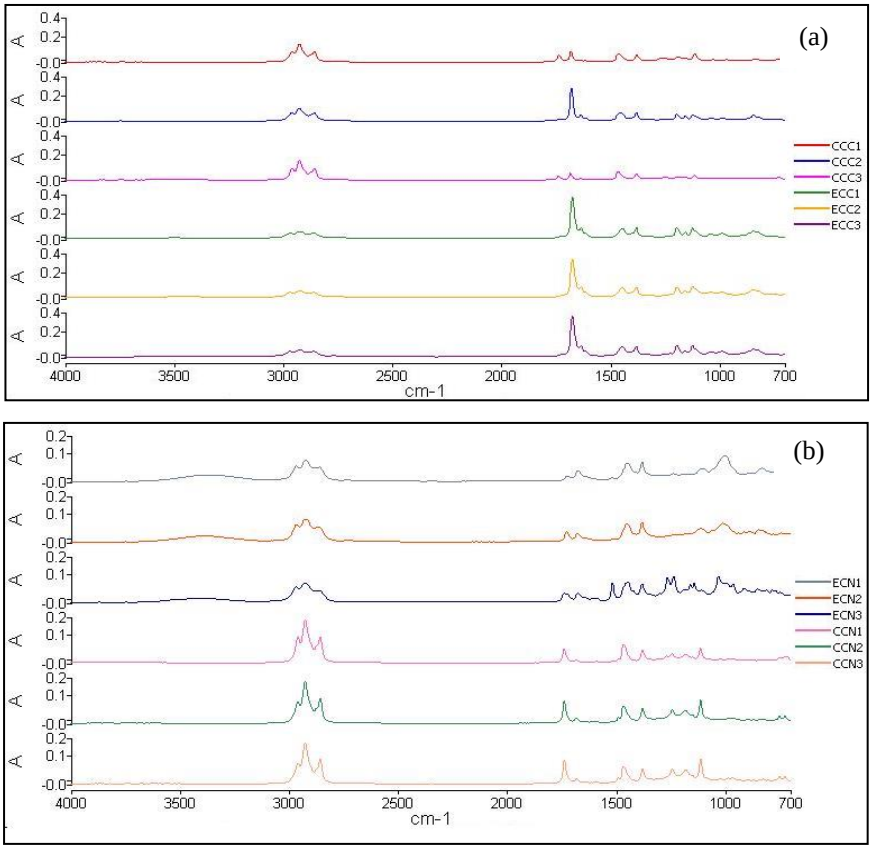


Figure 1. (a) FTIR spectra for essential oils and commercial samples of *C. citratus* (b) FTIR spectra for essential oils and commercial samples of *C. nardus*

Discrimination of samples based on FTIR data

The primary sources of variability in a dataset and the relationships between samples and variables are found using PCA analysis. The unsupervised method known as PCA provides pattern recognition data that is used to categorise and differentiate samples based on experimental data. FTIR spectroscopy is a simple, quick, and accurate method for classifying various plant species. Knowing the spectrum information rapidly could be highly important for the authentication of plant products in the market. In the present research study, FTIR data of *Cymbopogo*n essential oils (n=6) and commercial samples (n=6) were used to be distinguished by PCA analysis. The PCA showed two principal components (PCs) with 1400 variables totalling 80.37% of the total variance. PC1 encountered the most

explained variance with 61.70%. The PCA model of FTIR data showed good predictive ability as the total variance value was more than 50% [15]. The PCA analyses were performed to observe classification patterns of essential oils and commercial samples on the basis of their FTIR.

Based on the PCA plot in Figure 2(a), three clusters represented twelve samples. The cluster of ECN1, ECN2 and ECN3 appeared in the second quadrant. Meanwhile, CCN2 and CCN3 were found in the first quadrant where PC1 was negative. In addition, ECC1 and ECC2 had the largest distance from other sample clusters. Essential oils of *C. citratus* must have more distinctive functional groups compared to other samples. The findings are consistent with [16] who agreed that well-separated clusters are determined by distinctive compounds. This proved that the IR spectral characteristics of *C. citratus* essential oil samples were considerably different from those of other samples. Commercial samples of *C. citratus* clusters were located in the third quadrant. Nevertheless, it was found that commercial samples of *C. citratus* and *C. nardus* were unable to be differentiated. Therefore, it seemed quite challenging to observe the FTIR PCA score plot as FTIR can only identify the functional groups of the samples' essential oils, for which almost all samples have close similarities in terms of functional groups.

The PCA variable plot showed the discrimination of *C. citratus* and *C. nardus* essential oils attributed to a different absorbance of wave number present in the sample which was revealed by the fingerprinting FTIR spectroscopy. Based on the variables plot in Figure 2(b), the wavenumber of functional groups for samples of essential oils and commercial samples of *C. nardus* and *C. citratus* were difficult to deduce because they are overlapping each other. The loading plot unravels spectral differences responsible and have a strong impact on their clustering in the respective PC. The result of this observation indicated that the largest distance between *C. citratus* and *C. nardus* were caused by several wavenumbers representing certain functional groups listed in Table 3. Those responsible wavenumbers were determined by comparing the position of observation points in the loading plot with the PCA score plot and had variable influences on the projection (VIP) values in the range of 0.7 to 1.0. In general, variables with VIP values higher than 0.7 are considered significant for the separation of samples [17].

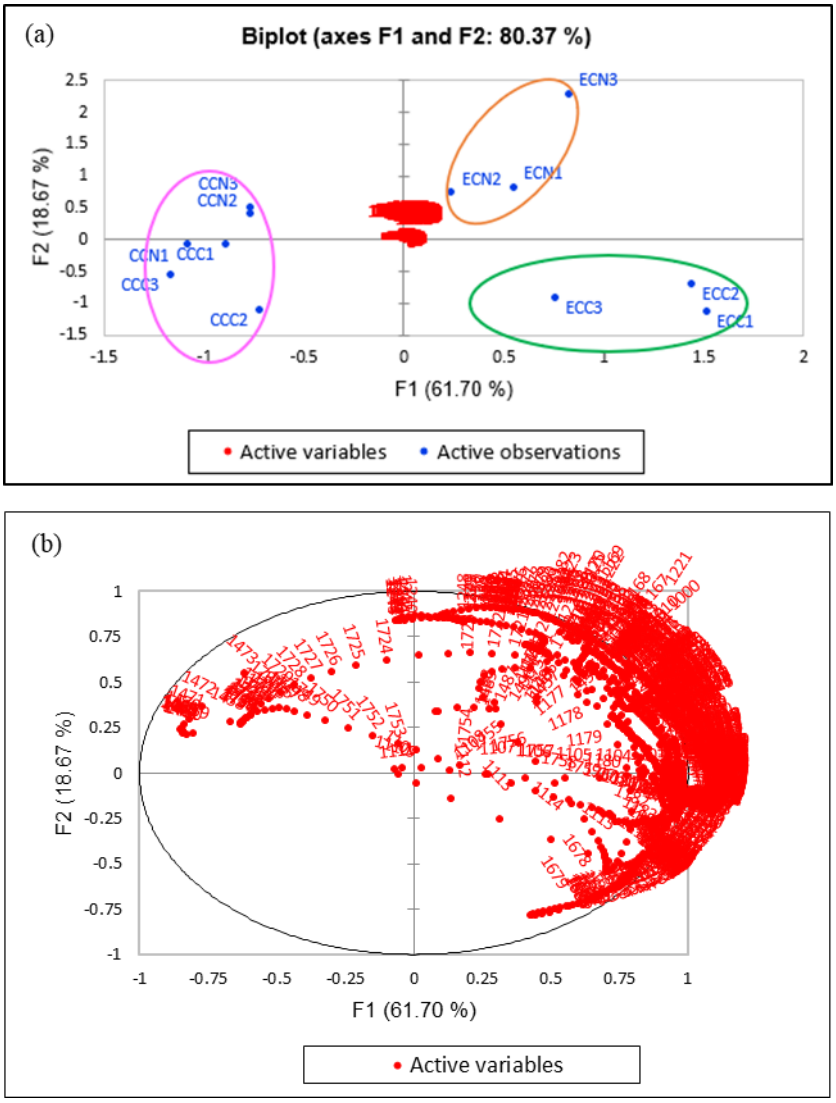
Table 3. Wavenumber responsible for the separation of *C. citratus* and *C. nardus* from PCA analysis on the loading plot

Wavenumber (cm^{-1})	**Band Assignment**	**Variable Influences on the Projection (VIP)**
1794	C=O from citronellal /citronellol	0.866
1710	C=O from citronellal /citronellol	0.941
1651	C=C from citral	0.800
1607	C=C from citral	0.812

These responsible wavenumbers are useful and could be used as a marker to discriminate *C. citratus* and *C. nardus*. In conclusion, although the distances of some clusters were very close, different sample species could still be discriminated by PCA. Overall, FTIR-PCA was able to discriminate the sample by visualizing the data on the score plot in contrast to FTIR spectra solely. This combination method could be applied as a non-destructive method for the discrimination of different species of herbs. The results revealed clear discrimination between essential oil of *C. citratus*, *C. nardus* samples and commercial samples. The result of PCA was further confirmed with HCA.

Samples of *C. citratus* and *C. nardus* essential oils and commercial samples were shown to be discriminated by the HCA dendrogram in Figure 2(c). A similar group is represented by the cluster of samples on the HCA dendrogram, as shown in the PCA plot. Commercial samples and essential oil samples were grouped into

three primary categories. On the right branch were two groups of *C. citratus* and *C. nardus* essential oil samples, and on the left branch were commercial samples. As can be observed, the commercial samples were assumed to be low-content of major chemical compounds or mixtures with other chemical substances. The clustering pattern of the examined samples was easily observed by the HCA dendrogram, and the outcomes were completely consistent with those of the PCA.



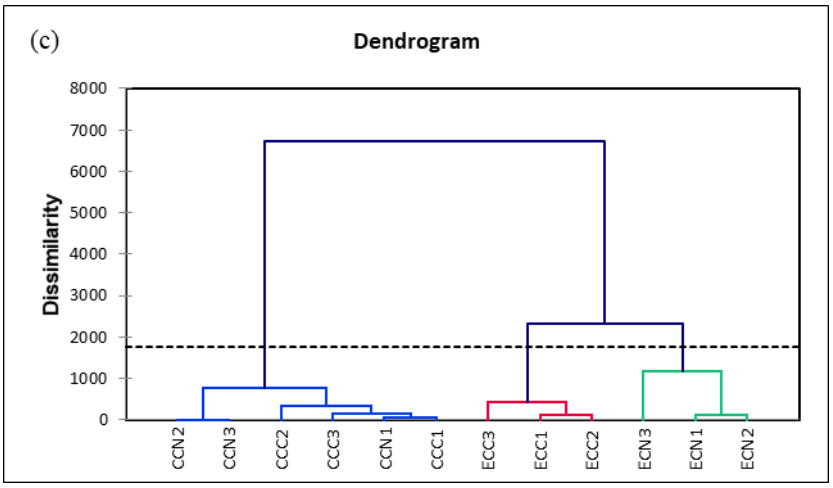


Figure 2. (a) Biplot PCA (b) variables plot and (c) HCA dendrogram of FTIR data of essential oils (n=6) and commercial samples (n=6) of *Cymbopogon* essential oils

This PCA plot was able to discriminate between *C. citratus* and *C. nardus* natural essential oils but not the commercial ones. The discriminant analysis (DA) model was built using the same pre-processed data to classify the samples based on natural essential oils and commercial samples by maximizing the covariance between the data matrix (X) (variables) and samples (Y) (origin of samples). DA is used to discriminate samples using the classification technique. Figure 3 shows the classification pattern of the samples using the DA model with variance explanation 10% and 0% of component 1 and component 2, respectively. The DA score plot showed clearer discrimination of commercial samples from *C. nardus* and *C. citratus* compared to PCA.

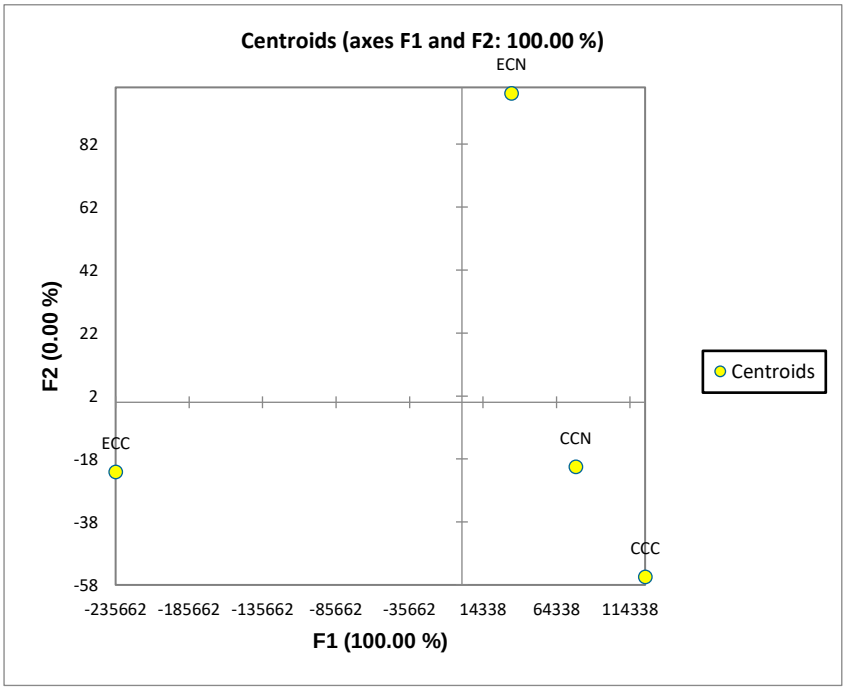


Figure 3. Discriminant analysis plot

A unidimensional test of the quality of the means of the classes identifies the significant variables in the study. Variables with p-value < 0.05 indicate significant variable that plays role in the discriminating model. The Fisher distances test at α 0.05 between the groupings is significantly different. The p-value < 0.01 indicates the natural essential oils of *C. citratus* and *C. nardus* are significantly different but there is no difference between commercial samples of *C. citratus* and *C. nardus* (Table 4). The results obtained revealed the commercial samples were either low-quality or mixtures with other chemical substances.

Table 4. The *p*-values for Fisher distances

Sample	CCC	CCN	ECC	ECN
CCC	1	0.000	< 0.0001	< 0.0001
CCN	0.000	1	< 0.0001	0.000
ECC	< 0.0001	< 0.0001	1	< 0.0001
ECN	< 0.0001	0.000	< 0.0001	1

Conclusion

C. nardus and *C. citratus* essential oils were considered important products in the food and cosmetic industry. Consumer safety greatly depends on the ability to trace the quality of *C. nardus* and *C. citratus* essential oils. The development of new analytical techniques that are robust, dependable, effective, and affordable is crucial for determining the authenticity of essential oils. There is currently interest in chemometrics and innovative analytical techniques. The current research uses FTIR techniques for the characterization of *C. nardus* and *C. citratus* essential oils. The findings demonstrate that the authenticity of *C. nardus* and *C. citratus* essential oils can be successfully determined by FTIR and chemometrics (HCA & PCA). It takes little sample preparation to distinguish both essential oils from commercial samples. As far as we are aware, this is the first example in which the FTIR technique and chemometrics have been employed to assess the authenticity of *C. nardus* and *C. citratus* essential oils.

In summary, it was successful to distinguish the essential oils of *C. citratus* and *C. nardus* from commercial samples using FTIR, and chemometrics. Through HCA and PCA analysis, the classification patterns of different samples may be readily revealed. To the best of our knowledge, this study has been the first to use chemometrics along with FTIR to assess the discrimination of *C. citratus* and *C. nardus* essential oils with commercial samples. This study has the benefit of being a thorough application of simple and easy well-known analytical methods. Nevertheless, the GCMS data obtained complements and confirms the chemical compounds in *C. citratus* and *C. nardus,* particularly the identification of citral and citronellal as major component in each species, respectively. Chemometric analysis through PCA and HCA is a fast, economic, reliable, simple and non-destructive analysis for quality control and authenticity of *C. citratus* and *C. nardus* essential oils. The findings of this study may be used to give a thorough assessment of the quality of *C. citratus* and *C. nardus* commercial products, as well as an optimal evaluation technique for medicinal herb quality management.

Acknowledgement

Financial assistance for the present study was provided by Universiti Malaysia Pahang through the research grant, RDU200303.

References

1. Verma, R. S, Singh, S., Padalia, R. C., Tandon, S., Venkatesh, K. and Chauhan A. (2019). Essential oil composition of the sub-aerial parts of eight species of Cymbopogon (Poaceae). *Industrial Crops Products,* 142: 111839.
2. Ganjewala, D. (2009). Cymbopogon essential oils: Chemical compositions and bioactivities. *International journal of Essential Oil Therapeutics,* 3:56-65.
3. Otify, A. M., Serag, A., Porzel, A., Wessjohann, L. A. and Farag, M. A. (2022). NMR metabolome-based classification of Cymbopogon species: A prospect for phyto-equivalency of its different

4. accessions using chemometric tools. *Food Analytical Methods*, 2022: 1-12.
5. Hassoun, A., Shumilina, E., Di Donato, F., Foschi, M., Simal-Gandara, J. and Biancolillo A. (2020). Emerging techniques for differentiation of fresh and frozen–thawed seafoods: Highlighting the potential of spectroscopic techniques. *Molecular Cells*, 25: 4472.
6. Ng, L. M. and Simmons, R. (1999). Infrared spectroscopy. *Analytical Chemistry* (Wash) 71:343-350.
7. Bansal, A. Chhabra, V., Rawal, R. K. and Sharma S. (2014). Chemometrics: A new scenario in herbal drug standardization. *Journal of Pharmaceutical Analysis*, 4(4): 223-233.
8. Makowicz, E., Jasicka-Misiak, I., Teper, D. and Kafarski, P. (2018). HPTLC fingerprinting—rapid method for the differentiation of honeys of different botanical origin based on the composition of the lipophilic fractions. *Molecules*, 23(7) :1811.
9. Ju, J., Xie, Y., Yu, H., Guo, Y., Cheng, Y., Zhang, R. and Yao, W. (2020). Synergistic inhibition effect of citral and eugenol against *Aspergillus niger* and their application in bread preservation. *Food Chemistry*, 310: 125974.
10. Sharma, S., Habib, S., Sahu, D. and Gupta, J. (2021). Chemical properties and therapeutic potential of citral, a monoterpene isolated from lemongrass. *Medicinal Chemistry*, 17(1): 2-12.
11. Chanthai, S., Prachakoll, S., Ruangviriyachai, C. and Luthria, D. L. (2012). Influence of extraction methodologies on the analysis of five major volatile aromatic compounds of citronella grass (*Cymbopogon nardus*) and lemongrass (*Cymbopogon citratus*) grown in Thailand. *Journal AOAC International*, 95: 763-772.
12. Dhifi, W., Bellili, S., Jazi, S., Bahloul, N. and Mnif, W. (2016). Essential oils' chemical characterization and investigation of some biological activities: A critical review. *Medicines*, 3(4): 25.
13. Mellado-Mojica E, Seeram, N. P., López, M. G. (2016). Comparative analysis of maple syrups and natural sweeteners: Carbohydrates composition and classification (differentiation) by HPAEC-PAD and FTIR spectroscopy-chemometrics. *Journal Food Composition Analysis*, 52:1-8.
14. Tankeu, S. Y., Vermaak, I., Kamatou, G. P. and Viljoen, A. M. (2014). Vibrational spectroscopy and chemometric modelling: An economical and robust quality control method for lavender oil. *Industrial Crops Products* 59: 234-240.
15. Baranska, M., Schulz, H., Walter, A., Rösch, P., Quilitzsch, R., Lösing, G. and Popp, J. (2006). Investigation of eucalyptus essential oil by using vibrational spectroscopy methods. *Vibrational Spectroscopy*, 42: 341-345.
16. Gok, S., Severcan, M., Goormaghtigh, E., Kandemir, I. and Severcan F. (2015). Differentiation of Anatolian honey samples from different botanical origins by ATR-FTIR spectroscopy using multivariate analysis. *Food Chemistry*, 170: 234-240.
17. Rottiers, H., Tzompa Sosa, D. A., Van de Vyver, L., Hinneh, M., Everaert, H., De Wever, J., ... and Dewettinck, K. (2019). Discrimination of cocoa liquors based on their odor fingerprint: A fast GC electronic nose suitability study. *Food Analytical Methods*, 12(2): 475-488.
18. Abas, F., Khatib, A., Shitan, M., Shaari, K., & Lajis, N. H. (2013). Comparison of partial least squares and artificial neural network for the prediction of antioxidant activity in extract of Pegaga (Centella) varieties from ^{1}H nuclear magnetic resonance spectroscopy. *Food Research International*, 54(1): 852-860.

Malaysian Journal of Analytical Sciences (MJAS)
Published by Malaysian Analytical Sciences Society

STUDY OF SOLVOTHERMAL SYNTHESIS OF MAGNESIUM-BASED METAL-ORGANIC FRAMEWORKS

(Kajian Sintesis Solvoterma Kerangka Logam-Organik Berasaskan Magnesium)

Umar Abd Aziz,[1] Mohamed Ibrahim Mohamed Tahir,[1,2] Nurul Farhana Ahmad Aljafree,[1,2], and Mohd Basyaruddin Abdul Rahman,[1,2*]

[1]*Foundry of Reticular Materials for Sustainability, Institute of Nanoscience and Nanotechnology,*
[2]*Department of Chemistry, Faculty of Science, Universiti Putra Malaysia, 43400 UPM Serdang, Selangor, Malaysia*

**Corresponding author: basya@upm.edu.my*

Received: 18 April 2023; Accepted: 6 June 2023; Published: 23 June 2023

Abstract

Metal-organic frameworks (MOFs) are a class of reticular materials consisting of metal ions coordinated to organic ligands. Theoretically, magnesium metal of the s-block has low electronegativity due to their large ionic radii and low ionic charges. The coordination number of magnesium immensely varies depending on the electrostatic interactions with the ligands. Therefore, designing strategic synthesis of Mg-based MOFs becomes a challenge hence its scarcity in literature. This study aims to investigate the different procedure of synthesizing Mg-MOFs using both flexible and rigid organic linkers in organic solvents at high temperature; termed solvothermal method. Magnesium nitrate hexahydrate ($Mg(NO_3)_2.6H_2O$) are used as the metal source and mixed with naturally occurring plant acids as the organic linkers; malic acid and tartaric acid. Rigidity was introduced by addition of aromatic organic ligands of benzene-1,4-dicarboxylic acid (BDC) and benzene-1,3,5-tricarboxylic acid (BTC). By varying precursor ratios and organic solvents, we hope to improve the reaction condition for the previously reported synthesis of Mg-MOFs. Single crystal X-ray diffraction (SCXRD) and powder X-ray diffraction (PXRD) analysis showed that the same quality crystals and high crystallinity powder have been produced under improved reaction conditions. The coordination of s-block metal ions has also been found to be most suited in a solvent mixture of H_2O and *N*,*N*-dimethylformamide (DMF).

Keywords: metal-organic framework, nanomaterial, solvothermal synthesis, s-block, green chemistry

Abstrak

Kerangka logam-organik (MOFs) adalah satu kelas bahan retikulasi yang terbentuk dari ion logam dikoordinasikan ke ligan organik. Secara teori, logam blok-s magnesium mempunyai nilai keelektronegatifan yang rendah kerana radius ion yang besar dan cas ion yang rendah. Nombor koordinatan antara logam magnesium berbeza-beza bergantung kepada interaksi elektrostatik dengan ligan yang berkaitan. Justeru, perancangan sintesis MOF berasaskan magnesium secara strategik adalah satu cabaran berikutan kekurangan perbincangan mengenainya dalam tinjauan literatur. Kajian ini bertujuan untuk meneliti pelbagai prosedur sintesis Mg-MOF menggunakan penghubung organik samada fleksibel mahupun tegar pada suhu yang tinggi; iaitu kaedah solvoterma. Magnesium nitrat heksahidrat ($Mg(NO_3)_2.6H_2O$) digunakan sebagai sumber logam dan dicampurkan dengan asid tumbuh-tumbuhan sebagai ligan organik semula jadi; asid malik dan asid tartarik. Ketegaran dalam kerangka dimasukkan melalui penambahan ligan aromatik organik iaitu asid benzena-1,4-dikarboksilik (BDC) dan asid benzena-1,3,5-trikarboksilik (BTC). Dengan mempelbagaikan nisbah pendahulu dan pelarut organik, kami berharap dapat menambah baik keadaan tindak balas yang

telah dilaporkan bagi sintesis Mg-MOF. Analisa pembelauan hablur tunggal sinar-X (SCXRD) dan pembelauan serbuk sinar-X (PXRD) menunjukkan bahawa hablur yang sama kualiti dan serbuk dengan kehabluran yang tinggi telah berjaya disintesis dengan penambahbaikan terhadap keadaan tindak balas. Campuran pelarut H_2O dan *N*,*N*-dimetilformamida (DMF) pula merupakan keadaan yang paling sesuai untuk pengkoordinatan logam blok-s.

Kata kunci: kerangka logam-organik, bahan nano, sintesis solvotermal, blok-s, kimia hijau

Introduction

Metal-organic frameworks (MOFs) are reticular materials composed of metal ions linked by organic ligands with specific functional groups such as carboxylate that can coordinate to the metal nodes [1]. The most dominant choices for the metals are from the p- and d-block elements due to the pronounced characteristics of transition metals such as visible light absorption, multiple oxidation states and predictable coordination geometries. On the other hand, MOFs based on s-block elements are relatively less studied. One of the main factors for the lack of interest is the unpredictable MOF structure due to having little control over the metals' coordinative behaviour. Large difference in electronegativity between s-block metal and carboxylate oxygen atom leads to a mainly ionic interaction. Thus, the coordinative nature of the metal centre throughout the network is instead determined primarily by the orientation of the functional groups, directly influenced by steric considerations [2]. Despite the setbacks, s-block MOFs can provide distinctive and intriguing properties inherited from their respective s-block elements; inexpensive and non-toxic [3]. The unpredictable coordination behaviour of the ionic metal nodes may result in interesting characteristics such as low density, flexible networks and water-soluble MOFs [4]. Therefore, s-block MOFs have the potential of a wide range of applications. Biocompatible MOFs can be designed from s-block metals such as Na^+, K^+, Mg^{2+} and Ca^{2+} which are already involved naturally in biological processes. Apart from amino acids which have been extensively studied as linkers, plant acids on the other hand have been largely under the radar and investigating their potential in biocompatible MOFs synthesis will be significant.

It is useful to study the previously reported synthesis as part of the ongoing effort to improve the methodologies of synthesizing s-block metal MOFs. While s-block metals generally have the same behaviour, ions with different properties will contribute to variations in reactivity. Mg^{2+} provides more control to the connections of metal-linker to form the framework. A larger Ca^{2+} ion compared with Mg^{2+} resulted in higher coordination number [2]. Furthermore, since s-block metals ions are hard metals, they preferably form ionic bonds with hard-heteroatom based organic ligands. Carboxylates consequently are the most used linkers. Some reports of using soft bases require modification of the heteroatom onto the organic linkers such as N-based carboxylates to yield a stable structure [5]. For the reaction condition, solvothermal synthesis has been the most widely used method with few variations on the parameters. For example, group 1 metals are best dissolved in polar solvents like ether due to the ability to coordinate to the metals [3]. Therefore, the main objective of this study is to identify the ideal method that has been used to synthesize Mg-based MOFs and make improvements on them.

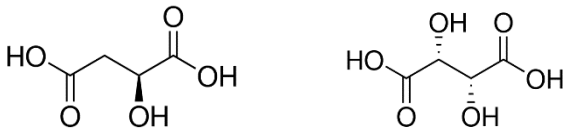


Figure 1. The organic linkers used in this study (A) L-(–)-malic acid and (B) L-(+)-tartaric acid

The solvothermal synthesis of Mg-MOF in this study are done with different combination of solvents to achieve condition than the previously reported methods. We utilize aliphatic linkers from naturally occurring plant acids for possible biocompatible applications. Previously it has been reported the pesticide encapsulation by two porous calcium L-lactate MOFs [6]. However, successful synthesis of MOFs with such properties are rare since the framework of s-block metals tend to be flexible and nonporous [2]. Therefore, we also incorporate rigid aromatic linkers that have shown the ability to form porous and more stable MOFs. Herein the s-block metal used is Mg^{2+} ion. The aliphatic linkers used are plant acids of malic acid and tartaric acid while the aromatic dicarboxylic acids are benzene-1,4-dicarboxylic acid (BDC) and benzene-1,3,5-tricarboxylic acid (BTC).

In this study, we hope to study the pattern in which s-block MOFs are synthesized and improve the established methods that has been used to synthesize Mg-MOFs. The effect of varying the synthesis parameters; solvents, temperature and time are studied. Improvements in term of less use of organic solvents, milder reaction conditions and shorter reaction time are preferred. The resulting compounds were then characterized by powder X-ray diffraction (PXRD) and, when possible, single crystal X-ray diffraction (SCXRD) [1]. Based on the findings, we outline few suggestions in approaching the synthesis of s-block MOFs using various biocompatible linkers.

Materials and Methods

Materials

All reagents and solvents were commercially purchased and used without further purification.

Synthesis of MOFs

All of the reagents were mixed in 6 ml solvents at molar ratio outlined in Table 1 & 2. A molar ratio of 1 equates to 0.4 mmol. The solvents used are *N*,*N*-dimethylformamide (DMF), deionized water (H_2O), ethanol (EtOH), dimethylacetamide (DMA) and tetrahydrofuran (THF). Unless stated, the ratio of solvents used in a mixed system are of equal parts except for triethylamine (TEA) where only 2 drops are added into the glass vial. The solutions were made to reach homogeneity by sonication, before being put into the oven at 120°C until the product is formed. The metal source used are magnesium nitrate hexahydrate ($Mg(NO_3)_2.6H_2O$). The organic ligands used as plant acids used are L-(–)-malic acid (Mal), $(CH_2CHOH)(CO_2H)_2$ and L-(+)-tartaric acid (Tar), $(CHOH)_2(CO_2H)_2$. The aromatic linkers are H_2BDC (benzene-1,4-dicarboxylic acid) and H_3BTC (benzene-1,3,5-tricarboxylic acid).

Characterization

Single crystal X-ray diffraction (SCXRD) are collected by a Gemini E Oxford Diffraction diffractometer with monochromatized Cu Kα radiation. Powder X-ray diffraction (PXRD) data are recorded at ambient temperature on a Shimadzu-600 diffractometer with Cu Kα radiation (λ=15406Å, 30kV, and 40 mA) with a scan speed of 2° min^{-1} and a step size of 0.02° in 2θ. The simulated PXRD patterns and unit cells database are obtained from the Cambridge Crystallographic Data Centre (CCDC). Both methods are used to identify the resulting solids by comparing the unit cells of the crystals with existing data and the X-ray diffraction patterns of the powders with existing spectra of their respective reagents.

Results and Discussion

The reaction conditions are chosen from methods that have been previously used to successfully synthesize MOFs across the periodic table. Polar solvents such as DMF and EtOH are some of the common solvents [7] while addition of H_2O into the mixture has been proven to yield Mg-based MOFs [2]. Where possible, SCXRD has been used to identify the resulting crystals while PXRD was used for the obtained powder.

Table 1. Parameters used for Mg-MOF reactions varying the solvent ratio

Precursors		Molar Ratio of M:L	Sample Code	Solvent Ratio			Observation
Metal	Linker			H_2O	DMF	EtOH	
Mg^{2+}	L1: Tartaric acid L2: BDC	2:1:1	1	1	-	-	No solid
			2	-	1	-	No solid
			3	-	-	1	No solid
			4	1	1	-	Crystal
			5	1	-	1	No solid
	L1: Tartaric acid L2: BTC	1:3:2	6	1	-	-	No solid
			7	-	1	-	No solid
			8	-	-	1	No solid
			9	1	1	-	Crystal
			10	1	-	1	No solid
			11	-	1	1	No solid
			12	1	1	1	No solid

Table 2. Parameters used for Mg-MOF reactions varying the molar ratio of precursors

Sample Code	Solvent	Molar Ratio of Precursors					Observation
		Mg^{2+}	BDC	BTC	Tar	Mal	
13	DMF:H_2O	2	1	-	2	-	No solid
14	DMF:H_2O	3	-	1	2	-	No solid
15	DMF:H_2O	2	1	-	-	2	No solid
16	DMF:H_2O	3	-	1	-	2	No solid
17	DMA	2	-	-	8	-	No solid
18	DMA	2	1	-	-	-	No solid
19	DMA	2	-	1	-	-	No solid
20	EtOH	2	-	-	8	-	No solid
21	EtOH	2	1	-	-	-	Powder
22	EtOH	2	-	1	-	-	Powder
23	DMF:H_2O:TEA	2	1	-	8	-	No solid
24	DMF:H_2O:THF	2	1	-	8	-	Crystal
25	DMF:H_2O:THF:TEA	2	1	-	8	-	No solid

Mg-MOF crystals

The method used for crystal **4** yields Mg(Tar)(H_2O), a rectangular MOF crystal (Figure 2A) with refcode CELJOU (Table 3). The MOF was previously synthesized by a better method in terms of solvent and reaction condition. As opposed to solvothermal synthesis with DMF:H_2O solvent at 120°C (Table 1), the original method uses only water as the medium with warming in silicone oil bath at 60°C for 5 min before being left to sit for 16 hrs. While the original method is the preferred green synthesis route, the method for crystal **4** establishes that the solvothermal synthesis with DMF as its base can act as a universal template capable to synthesize a myriad of MOF crystals. This is also observed by others whereby the decomposition of DMF to its respective formic acid and dimethylamine (base) provides the desired linker deprotonation rate capable of slowly forming high quality crystals of a lot of MOFs [7].

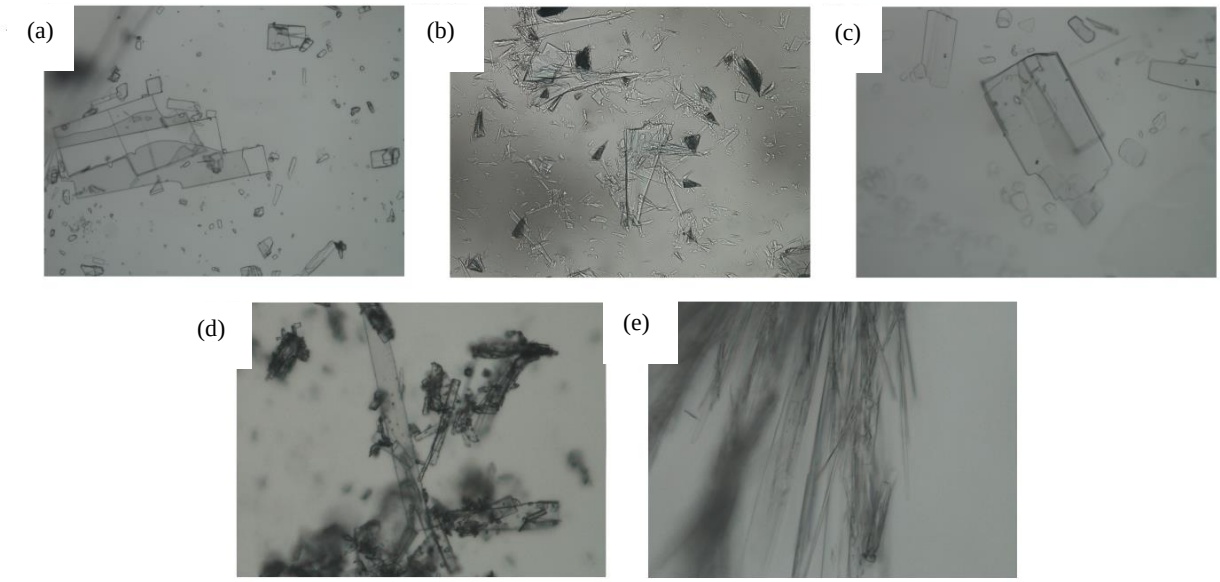


Figure 2. Microscopic view at ×20 magnification for crystals of (a) **4**; (b) **9**; (c) **24**; ×40 magnification for microcrystalline powder of (d) **21**; (e) **22**

The method used for crystal **24** synthesized Mg(Tar)(H_2O) MOF with refcode JIFXIG (Table 3) having similar morphology (Figure 2B) to crystal **4**. The original reported method uses PTFE lined autoclave at 100°C while the crystal **24** can be obtained in a normal glass vial at 120°C (Table 2). This allows for bulk synthesis to be possible since pressure resistance autoclave synthesis can only be done in small batches. Similar to the method used for crystal **4**, the use of DMF increases the control on the reaction. The deprotonation rate is highly tuneable by controlling the amount of formic acid or dimethylamine by adding them manually before the solvothermal reaction begins.

Table 3. Unit cell parameters of Mg-MOF crystals

Crystal	CCDC Refcode	Space Group	*a* / Å	*b* / Å	*c* / Å	*α* / °	*β* / °	*γ* / °	V / Å^3
4	CELJOU [8]	$P2_12_12_1$	7.904	11.119	18.213	90.0	90.0	90.0	1601
9	JIFXIG [9]	$P2_12_12_1$	7.878	11.100	18.157	90.0	90.0	90.0	1587
24	DOHDOU [10]	$R\bar{3}c$	8.148	8.148	22.788	90.0	90.0	120.0	1310

The method used for crystal **9** produces plate-like Mg($OOCH)_2$(HOOCH) MOF crystal (Figure 2C) with refcode DOHDOU (Table 3). The solvent used for crystal **9** is an equal mixture of DMF:H_2O (Table 1), while the reported previous method is DMF:EtOH:H_2O with ratio 10:0.5:0.5. This means the amount of DMF has been reduced significantly. Moreover, the previous method requires an addition of 0.1 ml of formic acid. The successful synthesis of crystal **9** shows that enough formic acid can be obtained from the disintegration of DMF at high temperature. In addition, the temperature and reaction vessel needed is also not as demanding. While the previous method is carried out in a Teflon lined autoclave at a temperature of 140°C, crystal **9** can be synthesised in a glass vial at 120°C. It is important to note that for the original method, substituting the metal precursor for other metal salts such as Mg(ClO_4)·$6H_2O$ gives the same result. Thus, it can be inferred that the same observation is true for crystal **9**.

Mg-MOF powder

There are two powder MOFs identified by their PXRD in comparison with the simulated pattern from the database. Powder **21** (Figure 2D) is the $Mg_3(BDC)_3(EtOH)_2$ MOF (Figure 3) with refcode KIFKAM [11] incorporating the BDC linker and the solvent EtOH in the framework. The reaction condition of this MOF is the same as the original reported method, except for the solvent. The use of fully EtOH instead of EtOH:H_2O mixture may be the reason for the formation of powder **21**. It has been understood that water is ineffective in synthesizing some MOFs [12], making it a suitable modulator in MOF synthesis. Thus, modulated-solvent mixture is ideal in controlling the crystallization rate [13], resulting in the preferred crystal size compared to the fast, uncontrolled synthesis of the powder. On the other hand, lowering the temperature or reducing the reaction time does not produce any crystals.

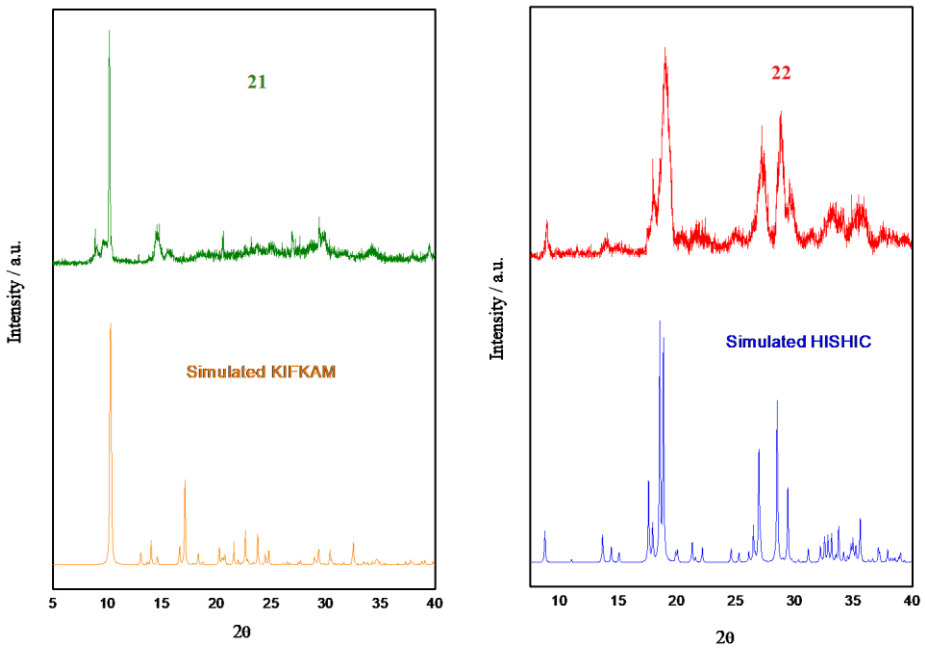


Figure 3. PXRD spectrum of powder **21** and **22** showing high crystallinity of the products. The characteristic peaks of the powder **21** and **22** match with the simulated peaks of an Mg-MOF with refcode KIFKAM and HISHAC respectively

Powder **22** (Figure 2E) is a MOF (Figure 3) with composition $Mg_3(BTC)_2(H_2O)_{12}$ with the refcode HISHIC [14]. The BTC linker and H_2O solvent are incorporated into the framework. Like powder **21**, the original method used the solvent mixture EtOH:H_2O to synthesize the crystals (Table 2). Using only the EtOH produces powder. However, the reaction condition in this case utilises a much lower temperature of 120°C compared to the original optimum temperature of 150°C for the same period of 24 hours. The lowering of the optimum temperature can be used in the bulk synthesis of powder MOF for uses in various applications, where good quality crystals are not necessarily required. For example, the encapsulation of pesticide *cis*-1,3-dichloropropene into a Ca-based MOF-1201 that has been done in its powder form [6].

Conclusion

In this study, we have explored different approaches in solvothermal synthesis of Mg-MOFs. Characterization from SCXRD and PXRD have been used to identify the synthesized compounds. Improvements have been made to certain aspects of the reaction. Lower temperature, shorter time and less use of organic solvents have been utilised. A solvent system of H_2O:DMF shows to be effective in promoting coordination of Mg^{2+} metal ions to the linkers. However, no MOF consisting of both the plant acids and rigid

linkers simultaneously were obtained. Understanding the required parameters and conditions for mixed-linker synthesis are crucial. Further studies can be done to investigate the mechanisms of incorporating mixed-linker into s-block frameworks.

Acknowledgement

The authors gratefully acknowledge the Putra Grant (UPM/700-2/1/GP-IPB/2017/9581000) from Universiti Putra Malaysia (UPM).

References

1. Yaghi, O. M. (2016). Reticular chemistry - construction, properties, and precision reactions of frameworks. *Journal of the American Chemical Society*, 138(48): 15507-15509.
2. Banerjee, D., Finkelstein, J., Smirnov, A., Forster, P. M., Borkowski, L. A., Teat, S. J., and Parise, J. B. (2011). Synthesis and structural characterization of magnesium based coordination networks in different solvents. *Crystal Growth & Design*, 11(6): 2572-2579.
3. Fromm, K. M. (2008). Coordination polymer networks with s-block metal ions. *Coordination Chemistry Reviews*, 252: 856-885.
4. Griffin, S. L. and Champness, N. R. (2020). A periodic table of metal-organic frameworks. *Coordination Chemistry Reviews*, 414: 213295.
5. Alnaqbi, M. A., Alzamly, A., Ahmad, S. H., Bakiro, M., Kagere, J. and Nguyen, H. L. (2021). Chemistry and applications of s-block metal–organic frameworks. *Journal of Materials Chemistry A*, 9(7): 3828-3854.
6. Yang, J., Trickett, C. A., Alahmadi, S. B., Alshammari, A. S. and Yaghi, O. M. (2017). Calcium $_L$-lactate frameworks as naturally degradable carriers for pesticides. *Journal of the American Chemical Society*, 139 (24): 8118-8121.
7. Rowsell J. L. C. and Yaghi, O. M. (2004). Metal–organic frameworks: A new class of porous materials. *Microporous and Mesoporous Materials*, 73(1-2): 3-14.
8. Rood, J. A., Noll, B. C. and Henderson K. W. (2010). Homochiral frameworks derived from magnesium, zinc and copper salts of $_L$-tartaric acid. *Journal of Solid State Chemistry*, 183(1): 270-276.
9. Kam, K. C., Young, K. L. M. and Cheetham, A. K. (2007). Chemical and structural diversity in chiral magnesium tartrates and their racemic and meso analogues. *Crystal Growth & Design*, 7(8): 1522-1532.
10. Rossin, A., Ienco, A, Costantino, F., Montini, T., Di Crediro, B., Caporali, M., Gonsalvi, L., Fornasiero, P. and Peruzzini, M. (2008). Phase transitions and CO_2 adsorption properties of polymeric magnesium formate. *Crystal Growth & Design*, 8(9): 3302-3308.
11. Davies, R. P., Less, R. J., Lickiss, P. D. and White, A. J. P. (2007). Framework materials assembled from magnesium carboxylate building units. *Dalton Transactions*, 24: 2528-2535.
12. Tezerjani, A. A., Halladj, R. and Askari, S. (2021). Different view of solvent effect on the synthesis methods of zeolitic imidazolate framework-8 to tuning the crystal structure and properties. *RSC Advances*, 11(32): 19914-19923.
13. Forgan, R. S. (2020). Modulated self-assembly of metal-organic frameworks. *Chemical Science*, 11(18): 4546-4562.
14. Mazaj, M., Čelič, T. B., Mali, G., Rangus, M., Kaučič, V. and Logar, N. Z. (2013). Control of the crystallization process and structure dimensionality of Mg-benzene-1,3,5-tricarboxylates by tuning solvent composition. *Crystal Growth & Design*, 13(8): 3825-3834.

Malaysian Journal of Analytical Sciences (MJAS)
Published by Malaysian Analytical Sciences Society

A REVIEW ON *Piper betle* EXTRACT AND HYPOCHLOROUS ACID ON INSECTICIDAL ACTIVITY

(Ulasan tentang Ekstrak *Piper betle* dan Asid Hipoklorus Terhadap Aktiviti Racun Serangga)

Wan Zuraida Wan Mohd Zain[1,2*], Muhammad Imran Hakimi Chairul[1], Nur'Amira Hamid[1], Aisha Na'illa Che Musa[1], Nurul Wahida Ramli[1], Norhazana Nor Izan[3], Arifin marzuki[3], and Nur Diyana Zulpahmi[1]

[1]*Faculty of Plantation and Agrotechnology, Universiti Teknologi MARA Cawangan Melaka, Kampus Jasin, Merlimau, Melaka, Malaysia*
[2]*Biocatalyst and Biobased Material Technology Research Group, School of Chemical Engineering, College of Engineering, Universiti Teknologi MARA, 40450 Shah Alam, Selangor, Malaysia*
[3]*Bubbles O² Quarters, 7-51-02, Jalan Medan Pusat Bandar 8A, 43650 Bandar Baru Bangi, Selangor, Malaysia*

[*]*Corresponding author: wanzuraida@uitm.edu.my*

Received: 20 September 2022; Accepted: 28 May 2023; Published: 23 June 2023

Abstract

Piper betle L. is a well-known medicinal plant that originates from the Asian region. This crop was used daily by the older generation as natural medicine to cure certain types of diseases. A series of phytochemical screening procedures proved that the extract of *Piper betle* contains essential phytochemicals, such as tannin, saponin, flavonoid, and alkaloid, which possess the insecticidal activity potential towards a wide range of insects. Previous studies have led to the implementation of betel extract in the agriculture sector as a pesticide or a major constituent in the production of novel insecticides. The effectiveness of betel extract as a pesticide is quite promising and it can be used as a better alternative to replace the use of harmful, chemical pesticides. Similar to betel extract, hypochlorous acid shows antimicrobial and insecticidal effects, but its true potential has not been studied thoroughly because its current usage is mainly focused on the healthcare sector as disinfectants or to aid wound healing. Both betel extract and hypochlorous acid can be beneficial to the agriculture sector, especially in pest management procedures, if its true potential is studied thoroughly to validate its mechanism or mode of action towards insects.

Keywords: *Piper betle* L., phytochemical, insecticidal activity potential, hypochlorous acid

Abstrak

Piper betle L. ialah sejenis tumbuhan ubatan yang berasal dari Asia. Generasi terdahulu telah menggunakan tumbuhan ini secara harian sebagai ubatan semula jadi untuk merawat penyakit tertentu. Beberapa siri analisis fitokimia telah membuktikan bahawa ekstrak *Piper betle* mengandungi beberapa jenis fitokimia penting termasuk tannin, saponin, flavonoid, dan alkaloid, yang memiliki ciri anti-serangga terhadap pelbagai jenis serangga. Kajian yang telah dijalankan telah membawa kepada penggunaan ekstrak sireh sebagai racun perosak atau bahan utama dalam penghasilan racun serangga yang baharu. Keberkesanan ekstrak sireh sebagai racun perosak menunjukkan hasil yang meyakinkan dan boleh digunakan sebagai alternatif yang lebih baik untuk menggantikan penggunaan racun kimia yang berbahaya. Asid hipoklorus juga menunjukkan kesan antimikrob dan anti-serangga seperti ekstrak

sireh, tetapi keupayaannya yang sebenar tidak dikaji secara mendalam kerana penggunannya lebih tertumpu dalam bidang kesihatan sebagai disinfeksi atau membantu dalam penyembuhan luka. Kedua-dua ekstrak sireh dan asid hipoklorus boleh menjadi bahan yang bermanfaat dalam sektor pertanian, terutamanya dalam kawalan makhluk perosak jika potensi sebenarnya dikaji dengan lebih mendalam bagi mengesahkan mekanisma atau cara tindakannya terhadap serangga.

Kata kunci: *Piper betle* L., fitokimia, ciri anti-serangga, asid hipoklorus

Introduction

Betel (*Piper betle* L.) from the Piperaceae family is a traditional medicinal plant that is widely used in Malaysia and Asia for various purposes [1]. It has its own common names in different regions worldwide, such as *Paan* in India and *Sireh* in Malaysia. It normally appears at the beginning originated from Malaysia, but there are also studies that have proven that this crop might have originated from Thailand since 5500 BC, Indonesia since 3000 BC, and Philippines in 2600 BC. It is estimated that around 100 varieties of betel exist worldwide and 40 of them can be found in India. Betel plants can be directly consumed through chewing or as additives to other types of plant to form a mixture. Aside from human health, betel is also used in the agricultural sector to aid in efficient plant growth.



Figure 1. Betel plant (*Piper betle* L.)

Pest management in agriculture will become more challenging due to the increasing pest resistance to chemical pesticides. The arising problems forced farmers to seek alternatives to controlling pests to avoid yield loss in the future. It is undeniable that the use of chemical pesticides was efficient initially, but it has led to undesirable side effects, such as environmental pollution. Researchers are moving forward in providing farmers with a better alternative that is more environment-friendly, effective at low cost, and able to cater to the main objective of pest control. Plants were proven to contain certain compounds that can largely ward off the insecticidal activity potential [2]. Certain regions in the country have started to use such crops in pest management.

Phytochemical screening of crops is carried out to identify the presence of a chemical or bioactive compound in a certain plant. This procedure is done in the laboratory because it involves the use of chemicals and requires specific conditions. The presence of a certain chemical compound in the plant can be clearly observed. Examples of tests conducted in the phytochemical screening are the froth test for saponin, the ferric chloride test for tannins, and test for anthraquinones. The plant extract is used as the main material for the screening procedure. Some tests require extract in powder form while others require extract in alcoholic form.

Botany of *Piper betle* L.

The Piperaceae family consists of approximately 1000 species of plants and shrubs, including *Piper betle L*. which is also known as betel vine parts. It is a well-known traditional plant due to its many medicinal benefits and can be used for many purposes. Its leaves are the most used plant parts. It has a pungent odour and requires another plant or support for the growth of its vine [3]. These plants can be classified and differentiated based on their leaves, sizes, and colour. Table 1 shows the taxonomy of *Piper betle* L. This type of medicinal plant can be widely found across the world, and most originate from Southeast Asian countries, such as Malaysia, Indonesia, Myanmar, Thailand, and the Philippines. Its name varies depending on the local community because the betel crops were named according to their local language and beliefs. India is one of the most significant countries that relate to the origin of betel. According to their beliefs, betel plant is known as Paan from the Sanskrit word “parn”, which means snake hood as the leaves resemble the shape of snakehead [3].

Table 1. Taxonomy of *Piper betle* L.

Kingdom	Plantae
Subkingdom	Viridiplantae
Infrakingdom	Stretophyta
Superdivision	Embryophyta
Division	Tracheophyta
Subdivision	Spermatophytina
Class	Magnoliopsida
Superorder	Magnolianae
Order	Piperales
Family	Piperaceae
Genus	*Piper* L.
Species	*Piper betle* L.

This crop can be planted in two types of cropping systems, i.e., open cropping system and the controlled cropping system. Under the open or natural cropping system, betels are grown attached to a supporting crop, such as *Cocos nucifera* and *Areca catechu*, which provides support to allow the betel crop to grow up to 15 meters in height.

Biological activity of *Piper betle* extract: Antibacterial Activity

Betel extracts show significant effects in terms of antibacterial properties towards various ranges of microbes that could be very useful not only in the pharmaceutical sector but also related to the agriculture sector. Generally, the antibacterial properties of a compound were studied to be implemented in the treatment of disease-causing bacteria. Some of the pathogens were also founded in food. Betel leaves have been employed as an antibacterial agent in India and other Southeast Asian countries since ancient times, and they are mentioned in various historical manuscripts dating back to the Vedic period (3,000 BC). The extracts of betel leaves, stalks, and stems, as well as the oil obtained from the plants, have all been investigated and proven to be effective against a variety of harmful bacteria [3].

The presence of several strong chemicals such as alkaloids, tannins, phenolic molecules, and glycosides might explain the considerable antibacterial action. Antibacterial properties were discovered in betel leaf extract with ethanol, ethyl acetate, and methanol as solvents, particularly in betel leaf extract [4]. Although generally the studies conducted on the antibacterial properties of betel extract were mainly focused on disease-causing bacteria in humans and animals, some of the bacterial strains were plant-associated. More research and studies should be conducted to study the antibacterial properties of betel extract against disease causing bacterial strains on plants instead of focusing on humans and animals. There are only a few studies reported that validates the effectiveness against plant pathogenic bacteria. According to Nagu [5], betel extract can be a great alternative to be treated against several phytopathogenic bacteria such as *Xanthomonas oryzae, Xanthomonas axonopodis pv. vesicatoria* and *Agrobacterium tumefaciens*. In the study, *Xanthomonas axonopodis pv. vesicatoria* was proven to be the most susceptible bacteria against all type of betel extract. The reported antibacterial properties against several bacterial species were summarized in Table 2 below.

Antilarval activity

The extract of *Piper betle* was studied and proven to contain antilarval activity against the larvae of several species. Among the studied insect species are *Chrysomya megacephala* and *Chrysomya bezziana* [3]. However, there is a significant difference in the effectiveness of different types of extract against the studied insects. Among the extracts, betel essential oil is ranked as the most effective as compared to aqueous extract and ethanol extract. In another study by [12], betel extract was also proven to have a similar effect when treated to the larvae of *Aedes aegypti*. These studies have demonstrated that betel extracts possess the antilarval activity potential that could be used as a major component in the anti-larval agent to curb the insect population.

Antifungal activity

Aside from antibacterial and antilarval properties, betel extract was also found to have antifungal properties, which were caused by several constituents in the extract, including chavicol, chavibetol, chavibetol acetate, and hydroxychavicol [3]. The tested fungi were *Aspergillus*

parasiticus, Trichophyton mentagrophyte, and *Candida albicans*. Once again, the effectiveness of each type of extract varies with chloroform extract, showing the most promising result [13].

Table 2. Bacterial strains studied against betel extract

Bacterial strain	Disease Caused by Bacteria	Isolated	Ref.
Xanthomonas oryzae	Bacterial blight	*Oryza sativa* (rice)	[6]
Xanthomonas axonopodis pv. vesicatoria	Bacterial spot	*Solanum lycopersicum* (tomato) and *Capsicum anuum* Group (pepper)	[7]
Agrobacterium tumefaciens	Crown gall disease	Soil and crown gall	[8, 9]
Xanthomonas campestris p.v. campestris	Black rot	*Brassica oleracea var. capitata* (cabbage)	[10]
Erwinia carotovorum sub sp *carotovora*	Soft rot disease	*Solanum tuberosum* (potato)	[2]
Pseudomonas syringae	Bacterial canker	*Prunus spp.*	[11]

Extraction and phytochemical screening of *Piper betle*

Betel leaf extracts that are commonly studied are aqueous, methanol, ethanol and essential oil extracts. These extracts yield different results because certain active components are only present in a certain type of extract. The percentage of each compound depends mainly on the variety of the betel and environmental factor. Essential oil (EO) extracted from betel leaves contains more than 60 active compounds, each of which has unique characteristics, that are very beneficial. Phytochemical screening is done to determine the retain extract. It is a process to detect the presence of chemical components produced by plants. The detection of phytochemicals is done mainly to determine the presence of major chemicals, such as alkaloids and saponins, but further research has proven that it could also be used to detect the presence of tannins, saponins, essential oil, and other phytochemicals produced naturally by plants [14]. *Piper betle* L. was studied for its phytochemical and was found to contain flavonoids, saponins, isoeugenol, terpenoids, alkaloids, protein, and other naturally occurring beneficial chemicals [15]. There are several methods reported for the detection of phytochemicals in an extract, including for betel extract (Table 3).

According to Mazumder [18], betel crops were one of the most highly produced crops, averaging at Rs 9000 million worth of production yearly, but it is mostly wasted or sold at a very low price [19] introduced the oil extraction method. The first oil extraction method uses the clavenger apparatus, but was unsuccessful due to the rapid formation of an emulsion. Guha introduced a series of improvements that made the extraction process more efficient. The main consideration for the oil extraction process in India is in terms of technology availability and suitable chemicals that can be easily retrieved for the extraction process to be conducted on a large scale [19]. In general, different types of extracts will yield different types of phytochemicals in the extract. In a study conducted by Saini et al. [20], ethanol extract and aqueous extract of betel crops yield the highest quantity of phytochemical that can be traced by a series of phytochemical screening procedures. It recorded a total of six phytochemicals in the extract, which are proteins, saponins, carbohydrates, alkaloids, tannins, and phenol. In contrast, in a study by [21], chloroform extract of the same species of crop yields a

high number of essential phytochemicals, including chavibetol acetate, chavicol, allylpyrocatechol, and chavibetol. It is very crucial to select a suitable extraction procedure to enable the presence of targeted phytochemicals to be studied. Phytochemicals are present in different parts, such as root, bark, stem, flower, and leaf, but their concentration varies depending on the crop variety. The Sri Lankan variety of *Piper betel* L. was studied and proven to contain safrole as the highest concentration of phytochemical with an average of 53%, followed by allylpyrocatechol acetate and eugenol with 15% and 6% concentration, respectively [22]. In contrast, the essential oil extracted from betel crops of the Malaysian variety contains a high amount of chavibetol, in approximately 70% concentration. These differences were proven to be caused by the geographical location as an environmental factor significantly affect the growth phase, as well as the physical and chemical properties of the variety.

Table 3. Series of tests conducted in phytochemical screening of betel extract

Test / Procedure	Observation (indicates presence of targeted phytochemical)	Ref.
Test for alkaloids		
Dragendraff's test	Orange-brown or reddish - brown precipitate	[16, 17]
Mayer's test	Cream precipitate	[17]
Test for glycosides		
Legal's test	Changes of color from pink to red	[17]
Keller-Killani test	Reddish-brown color	[17]
Test for saponins		
Haemolysis test	Changes of red blood cell structure observed under microscope	[17]
Foam test	Stable foam appeared	[17]
Shaking vigorously with distilled water	Lather formed	[16]
Test for flavonoids		
Shinoda test	Orange color formed	[17]
Test with concentrated sulphuric acid	Yellowish orange color formed	[16]
Test for carbohydrates		
Molisch's test	Violet color appeared	[17]
Fehling's test	Reddish-orange precipitate formed	[17]
Test for phytosterols		
Libermann-Buchard's test	Emerald green color appeared	[16, 17]
Salkowski's test	Brown color appeared	[16, 17]
Test for protein		
Biuret test	Violet color formed	[17]
Ninhydrin's test	Purple color formed	[17]
Test for phenolic compound		
Phenolic compound test	Blue color appeared	[17]
Test for tannins		
Addition of 1% gelatine and 10% sodium chloride	White precipitate formed	[17]
Test with Bramer's reagent	Brown precipitate formed	[17]
Ferric chloride test	Greenish black color appeared	[16]
Lead acetate test	White precipitate formed	[16]

Among the phytochemicals present in the betel leaf extract, the phenolic compound recorded the highest concentration compared to other groups of compounds [15]. Phenolic compounds, such as flavonoids, tannin, and carotenoids, are found in most plants. Phenolic compounds are the main compound that helps in UV protection, defence mechanism, and antioxidant properties [23]. The phenolic compounds in betel crops possess antioxidant properties. Researchers have proven and identified phenolic compounds as the most functional metabolite that can be extracted from *Piper betle* L. and it has potentials in many fields of study. These essential phytochemicals were also found in other plants that were studied for similar reasons, including antioxidant and antibacterial potential that provide better alternatives to replace harmful artificial chemicals used widely in the industry. Table 4 shows the phytochemicals present in different types of betel extracts.

Table 4. Essential phytochemicals in *Piper betle* L. extracts

Phytochemicals	Molecular Formula	Type of Extract	Ref.
Flavonoid	$C_{15}H_{10}O_5$	Ethanol extract	[20]
Alkaloids	$C_{21}H_{20}N_2O_3$	Chloroform, ethanol, and aqueous extract	[20]
Tannin	$C_{76}H_{52}O_{46}$	Aqueous and ethanol extract	[20]
Eugenol	$C_{10}H_{12}O_2$	Methanolic extract	[15]
Safrole	$C_{10}H_{10}O_2$	Methanolic extract	[15]
Chavibetol acetate	$C_{12}H_{14}O_3$	Methanolic extract	[15]
Phytosterols	$C_{29}H_{50}O$	Chloroform, ethanol, and aqueous extract	[20]
Oleic acid	$C_{18}H_{34}O_2$	Methanolic extract	[15]
Trymyristin	$C_{45}H_{86}O_6$	Methanolic extract	[15]

Figure 2 shows a molecular structure for several phytochemicals that are present in betel leaf extract. Although generally all cultivar of *Piper betle* contains similar phytochemicals, its concentration may vary due to several factors, mainly by the environmental factor at the cultivation area. Environmental factors, such as humidity, temperature, shading effect, light intensity, and nutrient availability, play a vital role in crops' growth leading to different chemical concentration for the same species that is collected from different regions and origins. Even though studies have been done to clarify the effect of aging towards the concentration of each phytochemical in the betel extract, it was concluded that the maturity stage of the crop does not largely affect the chemical constituent content of the extract.

Insecticidal activity potential of *Piper betle*

Table 5 shows the current usage of *Piper betle* extracts in pest management as an agent that significantly affects the treated pests. The studies validated the effect of the extract on different stages of insect pest. Some of the extracts acted on several stages and mechanisms, including the larvae and adult stages, affecting the egg-hatching process of insects and showing repellent properties.

Several species of the Piperaceae family, including *Piper betle* L., have been proven to contain insecticidal activity potential toward several species of pests [24]. All the *Piper* species studied were proven to contain similar essential phytochemicals that allow it to possess such potential. Traditionally, betel crops were used directly as a control agent for several insect species that could become vectors for harmful diseases. In modern agriculture, chemical components extracted from various parts of betel crops were studied and applied to produce novel insecticides [25]. Further research and advancement are in progress to produce more efficient insecticides that cause less environmental damage. The essential oil derived from plant species was proven to pose less harm to both humans and environment due to its biodegradable properties [26].

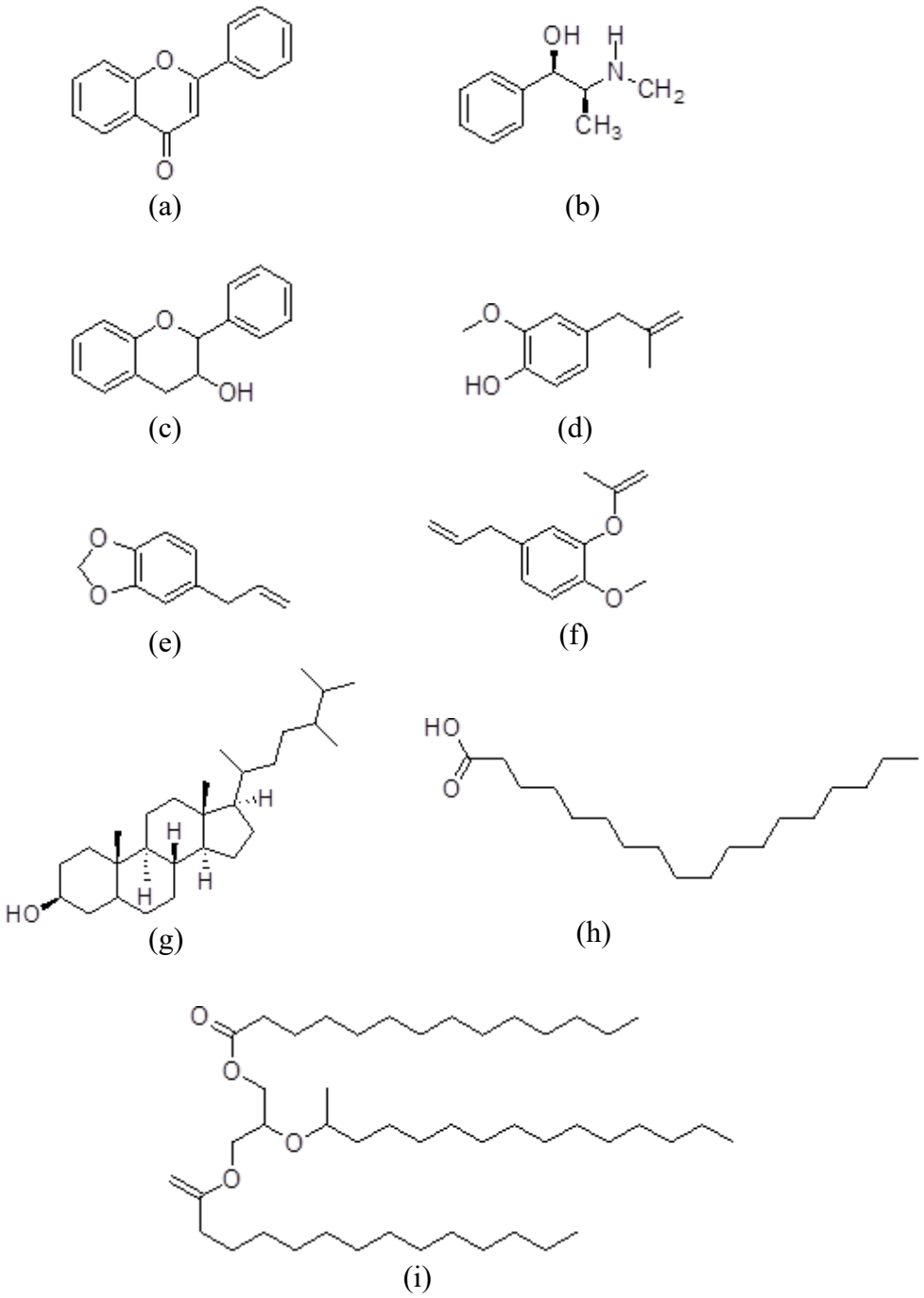


Figure 2. Molecular Structure of Some Phytochemicals Present in Betel Extract. (a) flavonoids (b) alkaloids (c) tannins (d) eugenol (e) safrole (f) chavibetol acetate (g) phytosterols (h) oleic acid (i) trymyristin

Table 5. Usage of *Piper betle* Extract as Pesticide

Insect	Test	Result / Observation	Ref.
Musca domestica	Fumigation toxicity	Provide moderate toxicity to treated insect	[27, 26, 28]
	Contact toxicity	Shows weak properties in topical application but promising result in diet exposure to larvae	
	Ovicidal effect	Shows toxicity effect but lower than eugenol	
	Oviposition repellence	Shows promising oviposition deterrence and increased with increasing concentration	
	Adulticidal bioassay	Betel essential oil with the concentration of 120 µg/cm^3 in ethanol causes 100% knock down effect	
Aedes aegypti	Larvicidal assay	Causes 100% mortality rate at the concentration of 500 ppm after 1 hour of treatment	[27, 12]
Chrysomya bezziana	Larvicidal bioassay	3% betel oil causes 100% mortality rate of 1st instar larvae after 2 hours and 74% mortality rate of 2nd instar larvae after 4 hours 4% betel oil causes 100% mortality rate of 1st instar larvae after 2 hours and 2nd instar larvae after 4 hours	[27]
Chrysomya megacephala	Larvicidal bioassay	2% betel oil causes 97% mortality rate of the larvae after 4 hours 3% and 4% betel oil causes 100% mortality rate of larvae after 3½ hours	[27]
Sitophilus oryzae	Adulticidal bioassay	1% betel oil causes 100% mortality rate of adult *Sitophilus oryzae* after 1½ hour	[27]
Cylas formicarius	Adulticidal assay	Almost all crude solvent extract provides significant effect to the adult *Cylas formicarius* with ethyl acetate recorded the highest mortality rate (100% after 48 hours), followed by crude acetone extract (70% after 48 hours) at the concentration of 20 ppm	[29]
Meloidogyne spp	Applied to tomato plant infested with *Meloidogyne spp*	The highest decrease of *Meloidogyne spp* population in the soil was recorded at 80.06% by 20% of concentration The highest decrease of *Meloidogyne spp* in the tomato root was recorded at 76.14% by 20% of concentration The highest decrease of eggs produced by *Meloidogyne spp* was recorded at 61.73% by 20% of concentration	[30, 31]
	Test on the survival of second stage juveniles (J_2s) *in vitro*	Causes higher mortality compared to control (untreated water)	
	Test on egg hatching – *in vitro*	Causes egg suppression at 100% by 80% of concentration	
Anopheles spp	Repellent test	80% of betel leaf extract shows the highest repellent percentage at 93.75% followed by 40% concentration (68.75%) and 20% concentration (50%)	[32]

Table 5 shows the insecticidal activity of betel extract for different stages of insects. Mohottalage et al. [22] conducted a study to compare the effectiveness of betel essential oil and *Ceylon citronella* oil extracted from *Cymbopogon nardus* towards adult houseflies (*Musa domestica L.*). It was found to be approximately three times more efficient than the *Ceylon citronella* oil. Adult houseflies were treated with both substances at 24 hours and 48 hours of exposure time. Another study conducted by Yushananta and Ahyanti [28] used different concentrations of betel essential oil to treat houseflies and compared the effect of concentration variation on the mortality rate. From the finding, a higher concentration of betel oil led to a higher mortality rate

for houseflies. They proved that the toxicity of betel extract was mainly caused by the presence of eugenol and safrole in high concentrations. The toxicity potential of the active compound makes it more efficient than other naturally occurring chemicals. Commercially, safrole was applied in the production of insecticide as a synergist.

The essential oil of *Piper betle* acted on the larvae and adult stages of the targeted insects with different concentrations [12]. A recent study validated that the betel oil effectively controlled the larvae of *Aedes aegypti* at the concentration of 500 ppm, higher than the concentration of widely used insecticide, known as temephos, which requires only 0.1 mg/L dose in water to control the larvae efficiently. But there is a recent report that the larvae of *Aedes aegypti* tend to become resistant towards temephos in some countries. On the other hand, there is no report of resistance when betel oil is used to control the larvae [12]. A substance that affects different stages of insects has high potential to be developed into novel insecticides as it will help increase its effectiveness towards the targeted pests. Moreover, it is better to control the pests at the early stage to curb the population of infesting pests and simultaneously reduce the total loss done by the pests. As for small-scale or large- scale production, farmers will surely use this alternative to decrease their expenditures in controlling pests and diseases for the agricultural processes. Aside from affecting adults and larvae of pests, betel EO also shows potential in terms of oviposition deterrent activity. The total number of eggs produced in the oviposition assay at the concentration of 100 ppm by using *Piper betel* L. extract yields decreased quantity by five (5) times lower than the control condition [12].

Regarding the mode of action and mechanism, each phytochemical targets and acts differently to the treated insects or pests, but it still yields the same result, causing mortality to the organisms [26] studied the insecticidal activity of betel essential oil and other chemicals, including eugenol acetate, eugenol, and β-caryophyllene, by two modes of action or treatment to the *Musa domestica*, which are contact toxicity and through fumigation. All chemicals used can be traced in the betel essential oil, but the chemicals were tested individually as a comparison to the betel essential oil. Different concentrations of each chemical were prepared by diluting it in acetone and applied to filter paper placed inside a jar. Approximately 20 starved and an anesthetized uniformly sized houseflies were placed into the jar containing the filter paper and the mortality rate was recorded after 3 hours. Another mode of action by betel oil studied by Subaharan et al. [26] is through contact toxicity, which can further be divided into two categories, namely topical application and dietary exposure to larvae.

In conclusion, the studies show promising results for the individual constituent found in betel essential oil. Almost all results for the individual chemicals were superior to the betel essential oil. It can be concluded that the substances play an important role in insecticidal activity against houseflies. Another study conducted by Yushananta and Ahyanti [28] concluded that a higher concentration of betel oil and more prolonged exposure to the betel oil causes a higher mortality rate of *Musa domestica*. The highest concentration used was 25%, which yields about eight houseflies mortalities. The highest mortality was recorded for six houseflies at an exposure time of 20 minutes.

There are several causes of death for the treated insect, either by direct contact or through fumigation that causes the chemical to enter the insect through the respiratory system. Tannins are one of the phytochemicals that is responsible for the death of insects. Tannins' mechanism targets the cell wall and digestive system of pests [28]. The nature of certain pests, e.g., houseflies tend to lick anything in its surrounding, can provide a pathway for the tannins, also known as a contact poison, to enter the inner structure of the pests. After entering the body, it inhibits significant enzyme activity and causes digestive failure, leading to death. Another example of the phytochemical mechanism in insecticidal activity is the inhibition of the respiratory system by flavonoids. This chemical constituent pathway is mainly through the airways by entering the respiratory tracts. It causes paralysis and muscle depletion by acting on the central nervous system of the affected organisms. Chavicol and eugenol, another major component in betel oil, were mainly used

as pesticide synergists due to their antiseptic properties.

Regarding the treatment at the larvae stage of certain insects, betel oil will first target the larvae's midgut epithelium, which then leads to malformed tubules that will then causes larvae mortality. Generally, different types of phytochemicals target different parts of the insect, but further research can be done to clarify which one of the phytochemicals acts, or if all phytochemicals mechanisms occur simultaneously as the mechanism was just stated individually.

Hypochlorous acid: A review

Hypochlorous acid (HOCl) is a substance that is naturally produced primarily by white blood cells, including neutrophils and eosinophils, of most mammals as a response to injury or infection [33]. This chemical is nontoxic and noncorrosive, but is effective and widely used in the pharmaceutical, health and a wide range of other sectors. For instance, this chemical can be easily found at home because it is used as an active compound in cleansers and bleaches [34]. These usages of HOCl have proven its potential, and in the future, more use of this beneficial chemical might be discovered, including in the agriculture sector, to aid the processes. There are also records showing that HOCl has already been used as one of the compounds to produce several types of pesticides. So, the implementation HOCl in the agriculture sector is not new and further development can be done to reduce the dependency on synthetic chemicals.

HOCl can be produced through several chemical processes. As stated earlier, HOCl is naturally produced by white blood cells, such as neutrophils of mammals. HOCl is produced due to oxidative burst, a condition whereby oxygen consumption rises remarkably [35]. During this process, also known as a respiratory burst, cells utilize oxygen (O_2) and, an enzyme called NADPHase, triggers the conversion of O_2 to hydrogen peroxide (H_2O_2). This enzyme is bounded to the membrane of mitochondria. The H_2O_2 then reacts with chlorine ion (Cl^-) from the cellular fluid, catalysed by a leukocyte-derived enzyme, known as myeloperoxidase, to yield HOCl. According to a study by [35], approximately 0.1 μM of HOCl can be produced from every 10^6 in vitro neutrophils that can kill *Escherichia coli* (*E. coli*) within 5 minutes. *E. coli* is a microorganism that can be found in the intestine; it is usually not harmful to health, but certain strains of *E. coli* can cause stomach pain and diarrhoea. Aside from natural production by neutrophils and eosinophils in mammals, HOCl can also be produced artificially or through the reactions of several chemicals.

There are several methods that can be used to produce HOCl. Among reactions that yield HOCl are hydrolysis of chlorine gas, electrolysis of salt solution and acidification of hypochlorite. In commercial industries, mild HOCl is produced by the acidifying of NaOCl with hydrochloric acid (HCl) [37]. Other methods to produce HOCl for industrial purposes depend on the size of the industry and available resources for the production procedures. The most widely known commercialized product containing HOCl in a low concentration as its active compound is disinfectants used in the healthcare sector. Disinfectants are used to neutralize wounds in humans due to their antimicrobial properties. The use of HOCl as the main ingredient for disinfectants is a success because it is effective against a wide range of microorganisms in a short period of time [35], and it does not interrupt the wound healing process [36]. These properties are the major factor that lead to the utilization of HOCl in the healthcare industry as suitable chemicals, especially in crucial medical processes. Each substance used was first proven to have no detrimental effects as it relates mainly to the safety of patients and the person in charge of handling the substance.

Two popular disinfectants sold in the market are Medilox® and Sterilox. The products were tested for their stability, which is a primary concern for products containing HOCl. The concentration of chlorine and the pH were proven to be in decreasing pattern over time [37]. In addition, its shelf life is short, estimated to be four days, when it is directly exposed to sunlight or UV radiation. Further research and development should improve their shelf life to produce better quality and long-lasting effects.

The potential of hypochlorous acid towards insecticidal activity

HOCl is widely known as an agent for wound healing treatment and disinfectants as it contains high potential for antimicrobial activity. This potential is also beneficial in sectors other than pharmaceutical. HOCl has the potential for an antimicrobial activity that helps to hinder and inhibit microorganism growth and population. This might lead to HOCI being used for pest control and result in a novel method to aid several processes of agricultural products for better food security. In general, not many studies have been done to verify the true potential of HOCl in controlling agricultural pests. Only a few studies have proven the benefit of using a compound containing chlorine to curb pest population, but there is evidence that household products, such as bleach, have been used as pesticides for a few varieties of pests. This method can be utilized by small-scale farmers who do not want to spend a large budget on controlling pests and diseases of their agricultural crops.

Table 6 shows the results of a study conducted by [38] to evaluate the effectiveness of commercial bleach towards the control of *Aedes aegypti*, which is the principal vector for the dengue virus. The eggs laid by the mosquitoes tend to stay dormant for a few months after it completes embryogenesis, producing an eggs bank for the mosquito species. This problem largely contributes to the rising cases of dengue fever. The mosquitoes have to be controlled as early as the egg stage. Ovicide has to be applied to kill potential eggs in an area. The main problem when using ovicide is the eggs' resistance to desiccation. The outer layer of the eggs can block the insecticide from penetrating the inner layer, and thus decreasing the effectiveness of insecticide at the larval stage of *Aedes aegypti*. In contrast, the active compound found in regular bleach was proven to be able to breakdown the outer layer, making a pathway for the insecticide to enter the eggs [39]. The active ingredient responsible for this action is sodium hypochlorite (NaOCl). The use of household bleach as an insecticide for *Aedes aegypti* is a cost-effective alternative because the bleach itself is cheap compared to insecticide, and the water applied with the bleach was proven safe for daily consumption if the concentration does not exceed four ppm.

Mackay et al. [38] conducted a study on the efficiency of commercial bleach against *Aedes aegypti.* Two types of solution were tested: bleach, and a mixture of bleach and smectite clay. The solution containing bleach and smectite clay was verified to be almost equally effective against the eggs of *Aedes aegypti* on plastic, rubber, and concrete, while the bleach solution alone was less effective against the eggs on concrete. Longer exposure time to sunlight yields fewer eggs at the end of the experiment, implying that exposure to sunlight plays a vital role in increasing the efficiency of bleach spray on eggs. In light of the discovery of the potential of bleach-containing HOCI for pest control, more studies should be conducted to uncover the true potential of HOCl in the agriculture sector. However, the use of bleach must be handled with care because household bleach is corrosive and, at a certain level of concentration, might harm the skin or cause damage to surfaces, such as plastics, some metals, paint, wood, and fabrics.

Potential pesticide formulation of hypochlorous acid and betel extract

HOCl solution and betel extract were proven to contain insecticidal activity potential towards many pests at different stages, including the egg, larval, and adult stages. Betel extract contains essential phytochemicals that provide its insecticidal activity potential, while HOCl contains antimicrobial and insecticidal activity. Improved formulations containing both HOCl and betel extract can be produced to increase their effectiveness. A pesticide formulation that can act on different mechanisms can be valuable to farmers because it can be a cost-effective alternative in pest management. The primary consideration in producing the formulation is the shelf-life of the pesticide and whether combining the compounds would produce adverse side effects. There are studies where the combination of HOCl and betel extract were tested for its effectiveness on fungi. These studies may lead to discoveries and further studies on the efficacy of formulation that combines the two essential compounds towards insecticidal activity.

Table 6. Insecticidal activity of HOCl

Insecticidal Activity Potential of HOCl	Targeted Insect Stage / Targeted Organism	Results	Ref.
Usage of HOCl in the control of Aedes aegypti	Egg stage of insect	Both solution containing bleach only and the formulation between bleach and smectite clay were proven to be effective against the egg of Aedes aegypti	[38]
Classified under the pesticide category	Adult stage of insect	Hypochlorous acid along with other disinfectants were classified under the pesticide categories by The Environmental Protection Agency (EPA)	[40]
Possess antimicrobial properties	Adult stage of insect	HOCl were proven to provide significant effect towards antimicrobial activity that was also possessed by betel extract that could lead to the production of novel insecticide	[41]; [35]
Used as germicide	Microorganism	A type of HOCl germicide known as warexin were proven to possess sporicidal and bactericidal activity potential against several bacterial strain and its effectiveness were higher compared to bleach.	[43]

Conclusion

Piper betle has considerable potential for insecticidal activity. The essential oil extracted from betel plants contains beneficial phytochemicals that can be used as a major component in novel insecticides and pesticides. Tannins, saponins, and flavonoids are examples of essential phytochemicals in betel crops. It is crucial to seek better alternatives for pest management that does not involve the use of chemicals that are harmful to the environment. Moreover, current artificial insecticides and pesticides tend to increase insect resistance up to a point that chemical insecticides are no longer effective. The formulation of betel extract and hypochlorous acid aimed to increase effectiveness as hypochlorous acid has antimicrobial activity potential. An investigation ought to be conducted for the use of betel extract against a broader range of pests. Betel extracts have been proven to be fatal against certain pest species. Future studies should focus on the extract's mechanism and the insects' taxonomy. A combination of hydroporous *Piper betle* extract and other possible solutions must be examined to increase their effectiveness. Currently, the primary use of HOCI is in the healthcare sector as disinfectant because of its antimicrobial and antifungal properties. These chemicals can be further studied to expand their usage to the agriculture sector. Household bleach that contains HOCl as its constituent has been proven to have the potential towards insecticidal activity that could largely contribute to the production of novel pesticides.

Acknowledgement

The grant 600-IRMI/FRGS 5/3 (245/2019) from the Fundamental Research grant Scheme provided funding for this study

References

1. Dasgupta, N. and De, B. (2004). Antioxidant activity of *Piper betle* L. leaf extract in vitro. *Food Chemistry*, 88(2): 219-224.
2. Rahman, S., Biswas, S. K., Kumar Biswas, S., Chandra Barman, N. and Ferdous, T. (2016). Plant extract as selective pesticide for integrated pest management biodegradation of textile dye by bacteria isolated from industrial effluent view project viral hepatitis: Current situation in Bangladesh view project plant extract as selective pesticide for integrated pest management. *Biotechnology Research Journal,* 2(1): 6-10.
3. Fazal, F., Mane, P. P., Rai, M. P., Thilakchand, K. R., Bhat, H. P., Kamble, P. S., Palatty, P. L. and Baliga, M. S. (2014). The phytochemistry, traditional uses and pharmacology of *Piper betel.* linn (Betel leaf): A pan-asiatic medicinal plant. *Chinese Journal of Integrative Medicine*, 2014:

1334.

4. Sakinah, D., Misfadhila, S. and Author, C. (2020). Review of traditional use, phytochemical and pharmacological activity of *Piper betle* L. *Galore International Journal of Health Sciences and Research,* 5(3): 59-66.
5. Jayalakshmi, B., Raveesha, K. A., Shrisha, D. L. and Amruthesh, K. N. (2013). Evaluation of *Piper betle* L. leaf extracts for biocontrol of important phytopathogenic bacteria. *International Journal of Agricultural Technology,* 9(3): 611-624.
6. Ghasemie, E., Niknejad Kazempour, M. and Padasht, F. (2008). Isolation and identification of *Xathomonas Oryzae* Pv. oryzae the causal agent of bacterial blight of rice in Iran. *Journal of Plant Protection Research,* 48(1): 53-62.
7. Mirik, M. and Aysan, Y. (2009). Detection of *Xanthomonas axonopodis* pv. vesicatoria in naturally infected pepper seeds in Turkey. *Journal of Plant Pathology*, 91(2): 433-436.
8. Ali, N., Zada, A., Ali, M. and Hussain, Z. (2016). Isolation and identification of Agrobacterium tumefaciens from the galls of peach tree. *Journal of Rural Development and Agriculture,* 1(1): 39-48.
9. Sholi, N. and Jadallah, R. (2012). Isolation and detection of Agrobacterium tumefaciens from soil. *Journal of Al Azhar University-Gaza (Natural Sciences),* 14: 77-84.
10. Vicente, J. G. and Holub, E. B. (2013). Xanthomonas campestris pv. Campestris (cause of black rot of crucifers) in the genomic era is still a worldwide threat to brassica crops. *Molecular Plant Pathology*, 14(1): 2-18.
11. Popović, T., Menković, J., Prokić, A., Zlatković, N. and Obradović, A. (2021). Isolation and characterization of *Pseudomonas syringae* isolates affecting stone fruits and almond in Montenegro. *Journal of Plant Diseases and Protection*, 128(2): 391-405.
12. Martianasari, R. and Hamid, P. H. (2019). Larvicidal, adulticidal, and oviposition- deterrent activity of *Piper betle* L. essential oil to *Aedes aegypti. Veterinary World*, 12(3): 367-371.
13. Adawiyah Umar, R., Sanusi, A., Nizam Zahary, M., Adzim Khalili Rohin, M. and Ismail, S. (2018). Chemical composition and the potential biological activities of piper betel-a review. *Malaysian Journal of Applied Sciences*, 3(1): 1-8.
14. Mojab, F., Kamalinejad, M., Ghaderi, N. and Vahidipour, H. R. (2003). Phytochemical screening of some species of Iranian plants. *Iranian Journal of Pharmaceutical Research*, 2003: 77-82.
15. Azlan, M. M. and Mohammad, M. (2018). Phytochemical compounds in the methanolic extract of *Piper betle* L. leaves. *Malaysian Applied Biology,* 47(5): 233-239.
16. Sushma, S., Pauly, S. V. and Sowmyashree, G. (2020). Phytochemical screening of inflorescence of *Piper betle. International Journal Current Pharmaceutical Research,* 12(6): 89-92.
17. Venkateswarlu, K., Devanna, N. and Prasad, N. B. L. (2014). Microscopical and preliminary phytochemical screening of '*Piper betle*'. *PharmaTutor,* 2(4): 112-118.
18. Mazumder, S., Roychowdhury, A. and Banerjee, S. (2016). An overview of betel leaf (*Piper betle* L.): A review. *Annals: Food Science & Technology*, 17(2): 367-376.
19. Guha, P. (2010). Design, development, testing and comparative evaluation of the betel leaf oil extractor. *Ama, Agricultural Mechanization in Asia, Africa & Latin America,* 41(4): 28.
20. Saini, S. A. P. N. A., Dhiman, A. N. J. U. and Nanda, S. A. N. J. U. (2016). Pharmacognostical and phytochemical studies of *Piper betle* Linn. leaf. *International Journal Pharmaceutical Sciences,* 8(5): 222-226.
21. Evans, P. H., Bowers, W. S. and Funk, E. J. (1984). Identification of fungicidal and nematocidal components in the leaves of *Piper betle* (Piperaceae). *Journal of Agricultural and Food chemistry,* 32(6): 1254-1256.
22. Mohottalage, S., Tabacchi, R. and Guerin, P. M. (2007). Components from Sri Lankan *Piper betle* L. leaf oil and their analogues showing toxicity against the housefly, *Musca domestica*. *Flavour and Fragrance Journal*, 22(2): 130-138.
23. Lin, D., Xiao, M., Zhao, J., Li, Z., Xing, B., Li, X., Kong, M., Li, L., Zhang, Q., Liu, Y., Chen, H., Qin, W., Wu, H. and Chen, S. (2016). An overview of plant phenolic compounds and their importance in human nutrition and management of type 2

diabetes. *Molecules,* 21(10): 1374.

24. Sanubol, A., Chaveerach, A., Sudmoon, R., Tanee, T., Noikotr, K. and Chuachan, C. (2014). Betel-like-scented Piper plants as diverse sources of industrial and medicinal aromatic chemicals. *Chiang Mai Journal Sciences,* 41: 1171-1181.
25. Miyakado, M., Nakayama, I., Yoshioka, H. and Nakatani, N. (1979). The piperaceae amides i: Structure of pipercide, a new insecticidal amide from *Piper nigrum* L. *Agricultural and Biological Chemistry,* 43(7): 1609-1611.
26. Subaharan, K., Senthoorraja, R., Manjunath, S., Thimmegowda, G. G., Pragadheesh, V. S., Bakthavatsalam, N., Mohan, M. G., Senthil-Nathan, S., David, K. J., Basavarajappa, S. and Ballal, C. (2021). Toxicity, behavioural and biochemical effect of *Piper betle* L. essential oil and its constituents against housefly, *Musca domestica* L. *Pesticide Biochemistry and Physiology*, 174: 104804.
27. Arambewela, L. S. R., Arawwawala, L. D. A. M., Kumaratunga, K. G., Dissanayake, D. S., Ratnasooriya, W. D. and Kumarasingha, S. P. (2011). Investigations on *Piper betle* grown in Sri Lanka. *Pharmacognosy Reviews,* 5(10): 159-163.
28. Yushananta, P. and Ahyanti, M. (2021). The effectiveness of betle leaf (*Piper betle* L.) extract as a bio-pesticide for controlled of houseflies (*Musca domestica* L.). *Open Access Macedonian Journal of Medical Sciences*, 9: 895-900.
29. Raveen, R., Kanmani, S., Lokesh, K. V., Tennyson, S., Arivoli, S. and Jayakumar, M. (2019). Efficacy of *Piper betle* leaf extracts against sweet potato weevil *Cylas formicarius* (F.). *Indian Journal of Entomology*, 81(1): 201.
30. Dammini-Premachandra, W. T. S., Mampitiyarachchi, H. and Ebssa, L. (2014). Nemato-toxic potential of betel (*Piper betle* L.) (Piperaceae) leaf. *Crop Protection*, 65: 1-5.
31. Sritamin, M., Dewa, I. and Singarsa, P. (2017). Utilization of betel leaf extract as botanical pesticides to control meloidogyne spp. and tomato plant production. *Journal of Advances in Tropical Biodiversity and Environmental Sciences,* 1(1): 15.
32. Khomsatun, K., Widyanto, A. and Susiyanti, S. (2013). Effectiveness of betel leaf extract (*Piper betle*, Linn) as Anopheles spp mosquito repellent. *Jurnal Riset Kesehatan*, 2(3): 392-396.
33. Block, M. S. and Rowan, B. G. (2020). Hypochlorous acid: A review. *Journal of Oral and Maxillofacial Surgery,* 78(9): 1461-1466.
34. Lapenna, D. and Cuccurullo, F. (1996). Hypochlorous acid and its pharmacological antagonism: An update picture. *General Pharmacology,* 27(7):1145-1147.
35. Wang, L., Bassiri, M., Najafi, R., Najafi, K., Yang, J., Khosrovi, B., ... and Robson, M. C. (2007). Hypochlorous acid as a potential wound care agent: part I. Stabilized hypochlorous acid: a component of the inorganic armamentarium of innate immunity. *Journal of Burns and Wounds*, 6: e5.
36. Robson, M. C., Payne, W. G., Ko, F., Mentis, M., Donati, G., Shafii, S. M., ... and Bassiri, M. (2007). Hypochlorous acid as a potential wound care agent: part II. Stabilized hypochlorous acid: its role in decreasing tissue bacterial bioburden and overcoming the inhibition of infection on wound healing. *Journal of Burns and Wounds,* 6: e6.
37. Eryilmaz, M. and Palabiyik, I. M. (2013). Hypochlorous acid - analytical methods and antimicrobial activity. *Tropical Journal of Pharmaceutical Research,* 12(1): 123-126.
38. Mackay, A. J., Amador, M., Felix, G., Acevedo, V. and Barrera, R. (2015). Evaluation of household bleach as an ovicide for the control of *Aedes aegypti*. *Journal of the American Mosquito Control Association*, 31(1): 77-84.
39. Trpiš, M. (1970). A new bleaching and decalcifying method for general use in zoology. *Canadian Journal of Zoology,* 48(4): 892-893.
40. Quinn, M. M., Henneberger, P. K., Braun, B., Delclos, G. L., Fagan, K., Huang, V., Knaack, J. L. S., Kusek, L., Lee, S. J., le Moual, N., Maher, K. A. E., McCrone, S. H., Mitchell, A. H., Pechter, E., Rosenman, K., Sehulster, L., Stephens, A. C., Wilburn, S. and Zock, J. P. (2015). Cleaning and disinfecting environmental surfaces in health care: Toward an integrated framework for infection and occupational illness prevention. *American Journal of Infection Control*, *43*(5): 424-434.
41. Kim, C., Her, Y., Kim, Y., Jung, C., Lim, H. and Suh, K. (2019). Evaluating the effectiveness of

HOCl application on odor reduction and earthworm population growth during vermicomposting of food waste employing *Eisenia fetida*. *PLoS One*, 14(12): e0226229.

42. Arambewela, L. S. R., Arawwawala, L. D. A. M., Kumaratunga, K. G., Dissanayake, D. S., Ratnasooriya, W. D. and Kumarasingha, S. P. (2011). Investigations on *Piper betle* grown in Sri Lanka. *Pharmacognosy Reviews,* 5(10): 159-163.
43. Velma Chandler, B. L., Pepper, R. E. and Gordon, L. E. (1925). Organic syntheses. *Journal Chem Society, Klrim., Sinteer erg. Socdincnii, Shornik,* 42(2): 6-10.

Malaysian Journal of Analytical Sciences Vol 27 No 4 2023

Page

Analytical Method

1. RECENT APPLICATIONS OF CYCLODEXTRIN-BASED ADSORBENTS IN SOLID AND LIQUID PHASE EXTRACTION FOR THE DETERMINATION OF ANTIBIOTICS: A MINI REVIEW 675
Muhammad Ariffuddin Abd Hamid, Aduloju Emmanuel Ibukun, Ilya Natasya Muaallimin, Ahmad Husaini Mohamed, Nadhiratul-Farihin Semail, Dyia Syaleyana Md Shukri, Nur Nadhirah Mohamad Zain, Sazlinda Kamaruzaman, and Noorfatimah Yahaya

Analytical Method

2. THE EFFECTS OF pH ON MICROPLASTICS REMOVAL BY ELECTROCOAGULATION PROCESS USING NICKEL ELECTRODE 693
Nor Aimi Abdul Wahab, Nor Ku Nazatul Husna Mohd Jackariya, Norain Isa, Norfaezatul Alysa Othman, Vicinisvarri Inderan, and Nur Fadzeelah Abu Kassim

Oleochemistry Analysis

3. PHYSICOCHEMICAL PROPERTIES AND BIODEGRADABILITY OF PALM OIL PRODUCTS (POP) IN MARINE ENVIRONMENT 702
Nur Azmina Roslan, Nur Aainaa Syahirah Ramli, Noorazah Zolkarnain, Siti Afida Ishak, and Razmah Ghazali

Oleochemistry Analysis

4. SYNTHESIS AND CHARACTERIZATION OF PALM OIL PENTAERYTHRITOL ESTER-BASED BIOLUBRICANT FROM MALAYSIA PALM OIL 716
Nurazira Mohd Nor, and Jumat Salimon

Nano or Advanced Materials Analysis

5. MOLYBDENUM DISULFIDE FOR PHOTOCATALYTIC DEGRADATION OF METHYLENE BLUE UNDER FLUORESCENT LIGHT 728
Siti Nor Atika Baharin, Nurul Izzah Hashim, Izyan Najwa Mohd Norsham, and Kavirajaa Pandian Sambasevam

Organic or Inorganic Analysis

6. INVESTIGATION ON CHEMICAL CONSTITUENTS IN DAMMAR RESIN EXTRACT FROM STINGLESS BEE HIVE AND ITS POTENTIAL AS CORROSION INHIBITOR 740
Mokhtar Che Ismail, Muhammad Hadi, Solhan Yahya, and Zuliahani Ahmad

Analytical Method

7. PURIFICATION OF POTENT ANGIOTENSIN CONVERTING ENZYME (ACE)-INHIBITORY PEPTIDES DERIVED FROM RED TILAPIA (*Oreochromis* Sp.) BY-PRODUCTS 754
Nur Suraya Abdul Wahab, Emmy Liza Anak Yaji, Norfahana Abd-Talib,, Mohammad Zulkeflee Sabri, Kelly Yong Tau Len, Fadzlie Wong Faizal Wong, and Khairul Faizal Paee

Organic and Inorganic Analysis

8. STABILITY OF GREEN SYNTHESIS OF SILVER NANOPARTICLES BY USING *Euphorbia milii* (EUPHORBIACEAE) LEAVES EXTRACT WITH DIFFERENT SOLVENTS AND POLARITIES 766
Nur Rasyidah Ramli, Hanis Mohd Yusoff, Maulidiani Maulidiani, Asnuzilawati Asari, and Nurul Huda Abdul Wahab

Nano or Advanced Materials Analysis

9. POTENTIALITY OF NANOSILICA-DOPED CARBON DOTS AS FLUORESCENCE DETECTOR FOR COPPER (Cu^{2+}) IONS IN SIMULATED WASTEWATER 777
Rejie C. Magnaye, Donjun C. Aguda, Kristine Rose G. Gonzales, Kyla Marie T. Plaza, and Jeoh Ysrael D. Silang

Organic and Inorganic Analysis

10. CRYSTAL STRUCTURE AND HIRSHFELD SURFACE ANALYSIS OF COMPOUND DI[2-((1E)-{2-(2-METHYLBENZYLSULFANYL) METHYLIDENE- HYDRAZIN-1-YLIDENE}METHYL)-6-METHOXY- PHENOL] 790
Enis Nadia Md Yusof, Suhana Arshad, Kwong Huey Chong, and Siti Syaida Sirat

Nano or Advanced Materials Analysis

11. REVIEW OF MOLYBDENUM DISULFIDE PREPARATION AND ITS ROLE AS A PHOTOCATALYST TO DEGRADE ORGANIC CONTAMINANTS 802
Izyan Najwa Mohd Norsham, Nur Zatulhusna Zulkifli, Kavirajaa Pandian Sambasevam, and Siti Nor Atika Baharin

Analytical Method

12. MAGNETIC NANOPARTICLE FOR REMOVING SUNSET YELLOW DYE: TAGUCHI OPTIMIZATION 816
Nurina Izzah Mohd Husani, Nur Amani Izzati Mohamad Hisham, Nor Munira Hashim, Clayrine Shima Anak Lasu, Noorfatimah Yahaya, Muggundha Raoov, and Nur Nadhirah Mohamad Zain

Analytical Method

13. VALIDATION OF HIGH-PERFORMANCE LIQUID CHROMATOGRAPHY (HPLC) METHOD FOR DELPHINIDIN-3-O-GLUCOSIDE CHLORIDE IN RAT PLASMA 840
Nur Atielah Nabila Mohd Shafawi, Ruzilawati Abu Bakar, Liza Noordin, Shafreena Shaukat Ali, and Wan Amir Nizam Wan Ahmad

Analytical Method

14. EFFECTIVE AND FAST ADSORPTIVE REMOVAL OF COOMASSIE BRILLIANT BLUE G 250 DYE FROM WATER USING Fe_3O_4 MAGNETIC NANOPARTICLES 849
Siti Khalijah Mahmad Rozi, Nur Atikah Saufi, and Nur Atiqah Nabilah Mohammad Rashidi

Natural Product Analysis

15. QUANTIFICATIONS OF LINOLEIC ACID AND β-GLUCAN IN *Lignosus rhinocerotis* EXTRACT AND ITS CYTOTOXICITY ANALYSIS IN HUMAN LUNGS EPITHELIAL BEAS-2B CELLS 865
Nurul Asma Abdullah, Siti Nurshazwani Muhamad Sayuti, Bushra Solehah Mohd Rosdan, Siew Hua Gan, Nurfadhlina Musa, and Ruzilawati Abu Bakar

Analytical Method

16. APPLICATION OF MAGNETIC BIO-POLYMER SPOROPOLLENIN AS LOW-COST ADSORBENT FOR REMEDIATION OF METHYLENE BLUE FROM AQUEOUS SOLUTION 876
Syed Fariq Fathullah Syed Yaacob, Muhamad Zulfikry Shamsudin, Arniza Khairani Mohd Jamil, Faiz Bukhari Mohd Suah, and Sharifah Mohamad

Nano or Advanced Materials Analysis

17. DEGRADATION OF AZO DYES FROM EFFLUENTS: A MINI REVIEW FOCUSING ON COMPARISON BETWEEN CURRENTLY EXISTING INDUSTRIAL METHODS AND GREEN OXIDATION CATALYSIS TREATMENT INVOLVING Fe-TAML AND H_2O_2 890
Wan Mohd Norsani Wan Nik, Nabilah Ismail, Saranraj Saravanan, Nur Khairunnisa Nazri, and Mohd Arzaimiruddin Ariffin

Natural Product Analysis

18. *Clinacanthus nutans* LEAVES DIFFERENT SOLVENT EXTRACTS EFFECTS ON PHYTOCHEMICAL SCREENING, ANTIOXIDANT ACTIVITY AND GAS CHROMATOGRAPHY-MASS SPECTROMETRY STUDY 906
Zaleha Md Toha, Nor Hasyimah Haron, Nik Nur Syazni, Melati Khairuddean, and Hasni Arsad

Malaysian Journal of Analytical Sciences (MJAS)
Published by Malaysian Analytical Sciences Society

RECENT APPLICATIONS OF CYCLODEXTRIN-BASED ADSORBENTS IN SOLID AND LIQUID PHASE EXTRACTION FOR THE DETERMINATION OF ANTIBIOTICS: A MINI REVIEW

(Aplikasi Baharu bagi Penjerap Berasaskan Siklodekstrin dalam Pengekstrakan Fasa Pepejal dan Cecair bagi Penentuan Antibiotik: Suatu Tinjauan Mini)

Muhammad Ariffuddin Abd Hamid[1], Aduloju Emmanuel Ibukun[1,2], Ilya Natasya Muaallimin[1,3], Ahmad Husaini Mohamed[4], Nadhiratul-Farihin Semail[5], Dyia Syaleyana Md Shukri[5], Nur Nadhirah Mohamad Zain[1], Sazlinda Kamaruzaman[6], Noorfatimah Yahaya[1*]

[1]*Department of Toxicology, Advanced Medical and Dental Institute (AMDI), Universiti Sains Malaysia, Bertam, 13200 Kepala Batas, Penang, Malaysia*
[2]*Department of Chemistry and Biochemistry, The Federal Polytechnic Offa. P.M.B. 420, Offa Kwara State, Nigeria*
[3]*Department of Chemical Science, Faculty of Science and Technology, Universiti Kebangsaan Malaysia, 43600 Bangi, Selangor, Malaysia*
[4]*Universiti Teknologi MARA (UiTM) Negeri Sembilan, Kampus Kuala Pilah, Pekan Parit Tinggi, 72000 Kuala Pilah, Negeri Sembilan, Malaysia*
[5]*Faculty Applied Sciences, Universiti Teknologi MARA Cawangan Perlis, Kampus Arau, 02600 Arau, Perlis.*
[6]*Department of Chemistry, Faculty of Science, Universiti Putra Malaysia, 43400 UPM Serdang, Selangor Darul Ehsan, Malaysia*

[*]*Corresponding author: noorfatimah@usm.my*

Received: 2 April 2023; Accepted: 17 June 2023; Published: 22 August 2023

Abstract

Antibiotic residues are being continuously detected in the environmental and food matrices. Though the level of antibiotic residues is typically in minute concentration, adverse effects of these antibiotics on the environment and human health have been observed. Hence, there is a demand for simple, rapid, accurate, reliable, inexpensive, and selective sample preparation with high sensitivity and throughput analysis for antibiotic compounds. Conventional extraction techniques such as liquid-liquid extraction (LLE) and solid phase extraction (SPE) are commonly used for sample preparation. However, most of the LLE and SPE techniques suffer from several major drawbacks such as consuming a large amount of toxic organic solvents, being relatively expensive, involving multi-step, time-consuming, and tedious operation. Thus, to overcome these shortcomings, a number of new-generation materials have been developed for the purification and separation of analytes. Over the past few decades, cyclodextrin-based adsorbents have drawn worldwide attention as new-generation adsorbents for sample preparation and extraction due to their extraordinary physicochemical properties. Cyclodextrin is a family of cyclic oligosaccharides built by the hydrophilic outer wall and hydrophobic cavity. These unique properties are modified with chemical functionalization to enhance their extraction capability. This review outlined the recent application of the cyclodextrin-based adsorbent in the sample preparation techniques of a variety of matrices. These methods represent fast, modern, sensitive, and efficient approaches to detecting antibiotic compounds. In this review, several new sample preparation techniques incorporated with cyclodextrin-based adsorbent developed from 2015 – 2022 is discussed in

terms of their analytical performance which includes their sensitivity and efficiency toward the extraction, preconcentration, and isolation of antibiotic compounds from various type of matrices.

Keywords: cyclodextrin adsorbent, sample preparation, antibiotics, microextraction

Abstrak

Sisa antibiotik telah dikenal pasti di matriks sekitaran dan makanan. Walaupun paras sisa antibiotik ini kebiasaannya dalam kepekatan yang sangat kecil, kesan buruk daripada antibiotik ini terhadap sekitaran dan kesihatan manusia telah dicerap. Justeru, terdapat permintaan terhadap penyediaan sampel yang ringkas, cepat, tepat, boleh diguna pakai, tidak mahal, dan selektif dengan kepekaan dan hasil yang tinggi bagi sebatian antibiotik. Setelah beberapa dekad, penjerap berasaskan siklodekstrin telah mendapat perhatian global sebagai penjerap generasi baharu bagi penyediaan sampel dan pengekstrakan disebabkan sifat fizikokimianya yang luar biasa. Tinjauan ini menggaris kasar aplikasi baharu bagi penjerap berasaskan siklodekstrin dalam teknik penyediaan sampel di dalam pelbagai jenis matriks. Teknik pengekstrakan konvensional seperti pengekstrakan larutan (LLE) dan pengekstrakan fasa pepejal (SPE) selalunya digunakan untuk penyediaan sampel. Walaubagaimanapun, kebanyakan teknik LLE dan SPE ini mempunyai beberapa kelemahan seperti menggunakan jumlah pelarut organik toksik yang banyak, agak mahal, melibatkan banyak kaedah dan mengambil masa yang panjang dan berlarutan. Justeru, bagi mengatasi kelemahan ini, beberapa jenis bahan generasi baharu telah dibangunkan bagi penulenan dan pemisahan analit. Setelah beberapa dekad yang yang lalu, bahan penjerap berasaskan siklodekstrin telah mencetuskan perhatian sebagai penjerap generasi baharu bagi penyediaan sampel dan pengekstrakan oleh kerana sifat-sifat fizikokimia yang luar biasa. Siklodekstrin adalah kumpulan bagi oligosakarida siklik terhasil dengan dinding luar yang hidrofilik dan kaviti yang hidrofobik. Sifat-sifat unik ini telah diubahsui dengan berfungsikan kimia bagi meningkatkan keupayaan pengekstrakan. Tinjauan ini menggaris kasar aplikasi baharu bagi penjerap berasaskan siklodekstrin dalam teknik penyediaan sampel di dalam pelbagai jenis matriks. Teknik-teknik ini menggunakan pendekatan yang cepat, moden, sensitif, dan efisien untuk mengesan sebatian antibiotik. Di dalam tinjauan ini, beberapa teknik penyediaan sampel baharu yang digabungkan bersama penjerap berasaskan siklodekstrin yang dibangunkan dari 2015 – 2022 dibincangkan dari segi prestasi analitikal termasuk kepekaan dan kecekapan terhadap pengekstrakan, prakepekatan, dan pengasingan bagi sebatian antibiotik daripada pelbagai jenis matriks.

Kata kunci: penjerap siklodekstrin, penyediaan sampel, antibiotik, pengekstrakan mikro

Introduction

Since their discovery, antibiotics have been widely used for the growth and function disruption of bacteria by targeting certain parts within them [1]. Antibiotics have helped to increase the average life expectancy of men because they are utilized to prevent and treat bacterial infections or as dietary supplements, bringing to heels numerous life-threatening infectious diseases [2,3]. Tetracyclines, amphenicols, macrolides, beta-lactam antibiotics, etc. are natural or semi-synthetic classes of antibiotics that are employed extensively to treat livestock against the activities of the wide variety of gram-positive and gram-negative bacteria, thus promoting healthy living and rapid growth in animal husbandry [4,5]. Antibiotics have been administered to prevent the spread of diseases, antibiotics limit or kill harmful bacteria in order to protect a flock or herd from illnesses. Their use promotes good animal health and helps with food safety, disease prevention, and the livelihood of farmers. In addition, these drugs were commonly used as non-prescription feed additives for the development and growth of farm animals [6].

However, the emergence of human antimicrobial resistance from the misuse and overuse of these antibiotics can leave residues in human and dairy products like milk, egg, and meat [3,7]. These sub-therapeutic residues in foods can lead to the occurrence of antibiotic resistance bacteria and cause liver and tissue damage, gastrointestinal and neurological disorders, teratogenesis, carcinogenesis, and allergic reactions in hypersensitive humans [3,8,9]. Hence, the existence of these minute concentrations of antibiotic residue in animal-based food products is a major risk to human health and the ecological environment, thus a public concern. Different groups of antibiotics discussed in this review are presented in Table 1.

In a bid to curtail the potential threats, and sustain food quality and safety, regulatory bodies like the US Food

and Drug Administration and European Commission have introduced and adopted the maximum residue limits (MRLs) for antibiotics and veterinary drugs in human and dairy products like milk, egg, and meat [7,10]. The MRLs are legally documented acceptable residue limits in different food matrices without toxicological effects on man. The tolerance levels adopted by China, Brazil, Canada, Codex and European Union ranged from 100 to 600 µg/kg for individual antibiotics and their combinations in dairy products (poultry, cattle, swine, fish, meat, eggs, liver, and muscle) [11–14]. MRLs for selected antibiotics in poultry and milk matrices are listed in Table 2.

Table 1. Different groups of antibiotics are discussed in this review

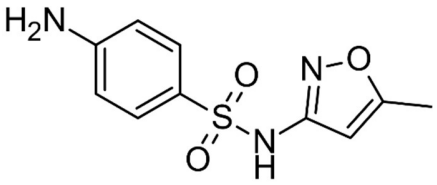
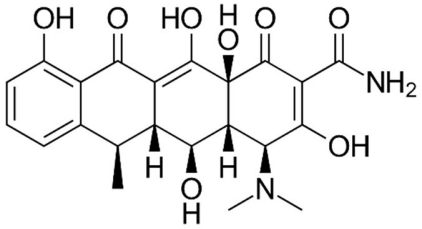
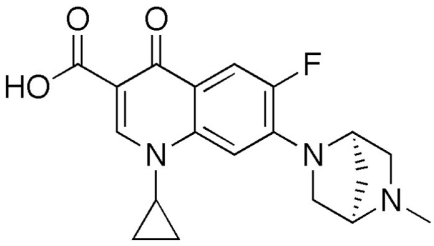
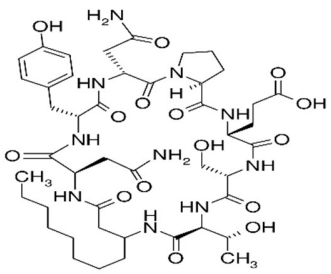
Antibiotic Groups	Name of Antibiotics	Structure
Sulfonamide	Sulfamethazine, sulfadiazine, sulfamethoxazole, sulfamerazine	
Tetracycline	Oxytetracycline, doxycycline, chlortetracycline, minocycline	
Fluoroquinolone	Danofloxacin, ciprofloxacin, ofloxacin, enrofloxacin	
Lipopeptide	Bacillomycin, daptomycin, surfactin, mycosubtilin	

Table 2. Information on MRL of antibiotics [7,10]

Analyte	MRL (µg/kg)	
	Poultry	Milk
Danofloxacin	300	30
Enrofloxacin	100	100
Ciprofloxacin	30	100
Sulfadimethoxine	100	100
Sulfamethazine	100	100
Sulfonamide	100	100
Oxytetracycline	300	100
Tetracycline	600	100
Chlortetracycline	100	100

The regulatory bodies have devised the means of regularizing the requirements for analytical methodology and result interpretations. Because of this, there is a need to develop an effective, selective, and sensitive analytical method that can detect, preconcentrate, and degrade several antibiotic residues and their derivatives at low concentrations levels from a variety of matrices. The newly developed sample pre-treatment methodology in conjunction with advanced analytical instrumentation must be able to monitor, assess, and quantify low concentrations of antibiotics in complex environmental and food matrices despite the existence of major interferences. These interfering compounds must be removed via the sample pretreatment process before analytical instrumental analysis. The methodology applied for the detection and determination of antibiotic residue falls into two categories. The first category comprises screening steps that are easy to use, cheap, and have high sample through-put, although are considered low in selectivity and sensitivity. They include surface plasmon resonance technology biosensors, magnetic immunoassays (MIAs), rapid test-kit, and enzyme-linked immunosorbent assays (ELISA). The second category includes the confirmatory methods which are specific and provide structural elucidation in conjunction with other detectors when assessing and quantifying target antibiotics [15].

Different analytical instrumentation techniques have been employed for the detection of antibiotics, including high-performance liquid chromatography (HPLC) [16], ELISA, thin-layer chromatography (TLC), gas chromatography [17], and capillary electrophoresis (CE) in conjunction with mass spectrometry, ultraviolet, fluorescence, or tandem mass spectrometry [18]. Despite the advances in technology, especially in instrument development, most analytical instruments cannot handle the samples directly due to high matrix interferences and the conditions of the complex samples. Hence, there is demand for the development of powerful and inexpensive sample preparation techniques that are simple, rapid, reliable, and accurate. Sample preparation step is required in any chemical analysis procedure. It is used to (a) convert the analyte into the instrument-compatible form, (b) eliminate major interferences and reduce matrix effects, (c) enrich the analytes and improve the sensitivity of the method, and (d) improve the precision of the methods. The ideal sample preparation requirements include exhibiting reliable analytical performance in terms of high extraction efficiency and sample clean-up, minimum toxic solvent consumption, being inexpensive, high sensitivity, reusability, high accuracy, and being environmentally friendly.

The conventional sample preparation method, solid phase extraction (SPE) is the most frequently applied method owing to its high enrichment factor, especially with the emergence and use of automated online SPE with direct injection. However, it is a time and solvent-consuming approach, with a potential loss of volatile compounds during the concentration step. Also, the clogging and plugging of the cartridges can affect

consistency in the flow of the automated SPE. These drawbacks can be ameliorated by employing different adsorbents for the preconcentration of antibiotics [19]. To overcome these shortcomings, nanomaterials were usually applied as an adsorbent in sample preparation steps. The advantages of using nanomaterials in various analytical procedures are due to their large surface areas. These can be used to improve the sensitivity and miniaturization of devices by removing interferences species and enhancing analyte concentration. Furthermore, they can be incorporated with different functional groups to improve their affinity for compounds, which makes them particularly useful in the selective extraction of target analytes from complex matrices [21].

One of the best sorption materials ever discovered is cyclodextrin (CD), a series of cyclic oligosaccharides with 6-12 d-glucopyranose units characterized by toroidal (doughnut-shaped) structure. It was first developed in 1881 by Villier from the digestion of starch with *Bacillus amylobacter*; subsequently, Schardinger established its cyclic structure in 1903 [20]. The CDs are natural, eco-friendly, non-reducing, water-soluble, macrocyclic malto-oligosaccharides comprising glucans linked together by α-(1,4) glycosidic bonding. They are produced from the degradation of starch through intramolecular transglycosylation reaction using CD glucanotransferase (CGTase enzyme). Parent CDs are of three types: α-, β- and γ- CD having six, seven, and eight α-(1,4) linked glycosyl units respectively. Moreover, the exterior surface of the CD is hydrophilic while its interior is hydrophobic; these properties entrap biological, organic, and inorganic guest compounds moderately or entirely without covalent bonding to create reversible and noncovalent inclusive complexes.

The CD-based materials has garnered a lot of attention from researchers in recent times because it is nontoxic, economical, readily available, and can be grafted on nanoparticles forming an adsorbent that creates a favorable adsorption site for small organic compounds owing to its unique hydrophobic cavities, high adsorption capacities, and fast adsorption [22]. The supramolecular host-guest interactions exist between the β-CD (host) and organic molecules (guest) which can also be reversed to allow the desorption of the organic molecules from the β-CD (Figure 1). This makes the β-CD sorption material to be reusable, recyclable, efficient, and selective [23]. Also, the outer surface of the β-CD contains hydroxide functionalities which allow metal ions to covalently bond to it; in addition, dehydration, and condensation of β-CD with carboxyl groups will yield complex structure polymers. The tunability properties of the novel β-CD adsorbents allow the efficient and simultaneous removal of different pollutants. In addition, the chemical functionalization of CDs enhances their solubility and stability towards oxygen or light, and also regulates the reactivity of guest molecules [24].

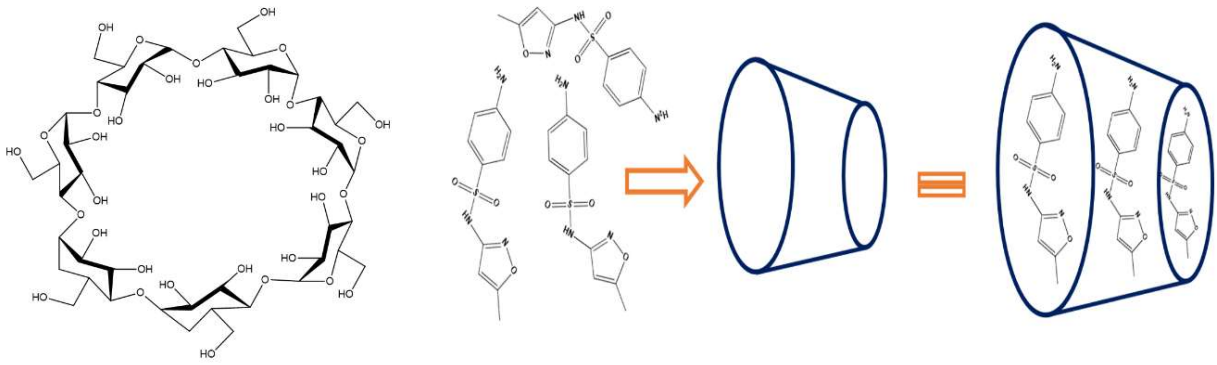


Figure 1. Structure of cyclodextrin (CD) and formation of inclusion complex with antibiotic molecules

This review paper aims to report an overview of sample preparation techniques for the determination of antibiotic compounds using CD-based adsorbents. The review highlights the analytical performances, advantages, limitations, and applications of the adsorbent in extraction techniques to extract antibiotics. Advances from 2015 to 2022 in the sample preparation of antibiotics in variety of matrices are reviewed here. Furthermore, future research of CD-based adsorbents is also elaborated. To the best of our knowledge, the application of CD-based adsorbent in sample preparation of antibiotic compounds has not been reported in an individual review.

Preparation of cyclodextrin-based adsorbents

β-cyclodextrin (β-CD) and their derivatized β-CD-based adsorbent materials have been configured with active sites using various configurations of functional groups to establish unique features which fit for adsorption and extraction performance, touted to be efficient, selective, and reusable adsorbent. As cyclic oligosaccharides makeup of the glucopyranose monomer units interconnected by α(1→4) glycosidic linkages, the presence of hydrophilic exteriors rich hydroxyl (-OH) groups and hydrophobic internal cavity in β-CD has expedited the modification or functionalization strategies with various functional groups [25]. To date, β-CD and its derivatized β-CD have been utilized as adsorbents for lipopeptide antibiotics [26], metronidazole antibiotics [27], tetracycline antibiotics [25,28–32], fluoroquinolone antibiotics [33–36], and sulfonamide antibiotics [37]. Modified CD-based adsorbents for the extraction of antibiotics can be prepared using various strategies. These include chemically modifying cyclodextrins to attach reactive groups, immobilizing them onto solid supports or nanoparticles, and employing techniques like molecular imprinting and supramolecular assembly. These strategies customize the adsorbents, allowing selective capture and extraction of antibiotics from complex samples, thereby enhancing the efficiency and reliability of the sample preparation process.

In order to achieve desired adsorbent properties and evolve as a class of multifunctional adsorbent materials, different chemical modification techniques have been employed to overcome some of the limits experienced by the β-CD, for instance strong inter/intramolecular hydrogen bonding among molecules which result in poor solubility, difficulty to separate, and maximum steric hindrance due to presence of secondary OH groups in the structure [38,39]. Yakout et al. described the formation of Cu-nanoparticles immobilized β-CD functionalized reduced graphene oxide (Cu/β-CD/rGO) via chemical reduction procedures using graphene oxide (GO) and copper nitrate trihydrate ($Cu(NO_3)_2{\cdot}3H_2O$) with sodium borohydride ($NaBH_4$) as an oxidizing agent. The Cu/β-CD/rGO nanocomposite was applied as an adsorbent for efficient extractors of tetracycline antibiotics residues. The morphological analysis revealed that the nanocomposite appeared as a random three-dimensional porous structure with uneven surfaces and the diameter determined by the dynamic light scattering (DLS) technique was found to be in the range of 17.6 to 18.8 nm. Moreover, the successful immobilization of Cu-nanoparticles and β-CD onto rGO was observed at a peak 26.3° for rGO while three peaks at 43.2°, 50.3°, and 74.0° were attributed to Cu nanoparticles which were in good agreement with standard Cu. Four types of interactions were identified which are π-π stacking interactions, cation-π-bonding, inclusion of tetracycline structure in the hydrophobic central cavity of β-CD, and cation-π bonding bridge/and cation-n bonding bridge [25]. Zhao et al. fabricated a microporous structure of monolithic polymer via radical polymerization using allyl-β-CD and methyl methacrylate as co-monomers, triallyl isocyanurate and ethylene glycol dimethacrylate as co-crosslinkers, and azobisisobutyronitrile (AIBN) as an initiator. The microporous structure in the monolithic polymer material was more than 50 nm with a specific surface area of 31.89 $m^2\ g^{-1}$. The lipopeptide antibiotics occupied molecular recognition with the allyl β-CD polymer monolithic column through multiple interactions such as hydrogen bonding, hydrophobic interaction, π-π interaction, and dipole-dipole interaction. The resulting allyl β-CD polymer monolithic column also showed good precision, excellent recovery, good repeatability, and cost-saving which provide advantages for the multi-action separation mechanisms [26].

Ying Zhang et al. reported magnetic mesoporous core-shell structured silicas containing covalently bound CDs (Fe_3O_4@SiO_2@mSiO_2-CD) using facile route by introducing β-CD-silica with core-shell structured mesoporous Fe_3O_4@SiO_2@mSiO_2 microspheres. The presented adsorbent established multiple interactions with doxycycline antibiotic such as inclusion interactions, hydrophobic interactions, electrostatic attractions, and π-π interactions. Moreover, based on the adsorption kinetic study, the maximum adsorption capacity of the adsorbent (83.33 mg g^{-1}) fitted with pseudo-second order with coefficient determination (r^2) and the adsorption process was via chemisorption procedure. The synergistic mechanism in the mesoporous structure and cavity of β-CD has provided good adsorption performance with multiple interactions with the doxycycline antibiotic, as well as the process was spontaneous and exothermic [29]. Similarly, study by Y. Li et al. (2018) found that the prepared CD metal-organic framework (CD-MOF) using γ-CDs and alkali metal cations exhibited excelled selectivity and adsorption capacity against sulfonamide antibiotics with the main force of interaction was due to the hydrogen bonding formed between the antibiotics and OH groups in the CD-MOF adsorbents. The kinetic experiments data showed that the equilibrium adsorption capacity was achieved and fitted pseudo-second-order model with $r^2 > 0.99$ and the process were facilitated by chemisorption [37].

In a study conducted by Sereshti et al., they noted that the addition of β-CD to the hydrophilic/hydrophobic deep eutectic solvent (DES) system improved the extraction efficiency for the tetracycline antibiotics as a result of selective supramolecular host-guest inclusion between the adsorbent and analytes. This was supported by the notorious feature of DES as a disperser and extraction solvent which facilitates and retains the host-guest complexation ability. Moreover, the molecular structure of β-CD which consist of hydrophobic cavity and hydrophilic external surface has made the dissolution in the DES undemanding yet at the same time retaining its ability to establish host-guest complexation [31]. Belenguer-Sapiňa et al. in their study reported that a new adsorbent based on type UMV-7 mesoporous-silica modified with γ-CD has been successfully synthesized for extraction protocol of fluoroquinolones-based veterinary antibiotics. The prepared material exhibited interparticle porosity (0.71 cm^3 g^{-1}) and intraparticle porosity (0.14 cm^3 g^{-1}) with the size of internal cavity of about 0.98 nm enabling more efficient extraction performance as well as more selective towards the targeted veterinary antibiotics [34].

Comparison of sample preparation methods

Numerous sample preparation strategies incorporated with CD-based adsorbents have been developed for the extraction and preconcentration of antibiotic molecules in a variety of matrices. The applications of CD-based adsorbents in sample preparation for the determination of antibiotics in various matrices from recent years are summarized in Table 3. Modified CD-based adsorbents offer several advantages in sample preparation for analytical purposes. They provide selectivity by specifically capturing target compounds, improving isolation from complex samples. These versatile adsorbents can be tailored to capture a wide range of analytes, making them applicable in various fields. By concentrating target analytes, the CD-based adsorbents enhance sensitivity, allowing for the detection of trace-level compounds.

Applications of cyclodextrin-based adsorbents in sample preparation

CD based adsorbents that are applied in extraction as sample treatment involved more than one interaction besides the hydrophobic guest-host inclusion complexes with the target analytes. The interior of CD is hydrophobic while the outer part is hydrophilic and it rarely occurs that the degree of the extraction capacity is much higher, indicating the synergistic interaction based on both structural components [40,41]. Owing to CD's unique structure which include reactive OH groups, it is feasible to chemically modify them to alter their solubility, increase their capacity for inclusion, or produce desirable qualities applied as adsorbent in sample treatment [35,36].

The optimization on extraction parameters in consideration of hydrophobic/hydrophilic structure of CDs as adsorbent involves improving the enrichment

factor of target analytes extracted from diverse types of samples matrices [42,43]. Different types of extraction techniques have been reported which employed CDs in quantification of antibiotics from varied type sample matrices, which include biological fluids, environmental water, and food matrices. Regardless of how simple or complex the sample matrices are, sample preparation is still essential to guarantee that the analytes are successfully isolated, cleaned up, and enriched in the final extract and are in a state that is compatible with the desired analytical technique. Natural CDs has certain solubility in aqueous solution, which limits its application in the field of adsorption due to the steric hindrance and hydrophobicity between CDs and target analytes [44,45]. So, improvement of solubility become the crucial point for CD-based adsorbent/solvent in sample preparation field to improve the target analyte (antibiotic)'s isolation and enrichment factor. The extraction from these sample matrices can be solid phase extraction (SPE) [34,37,46], solid phase microextraction (SPME) [35,47], magnetic solid phase extraction (MSPE) [37,48–51], dispersive solid phase extraction (DSPE) [36,52], and dispersive liquid-liquid microextraction (DLLME) [31,49] which are further discussed on their related CDs adsorbents as well as their application for the selective extraction/clean-up of antibiotic.

Online solid phase extraction and offline solid phase extraction

Since its inception in the early 1990s, solid phase extraction (SPE) has been a common approach for sample preparation. In comparison to the traditional liquid-liquid extraction (LLE), SPE offers simplicity, rapidity, excellent selectivity, and low cost, which have led to its widespread use especially in separation and extraction of antibiotics [53]. In addition, its use in sample preparation is beneficial for extraction, concentration, and sample cleanliness in a short amount of time due to the automation of the extraction procedure and ability to combine with different detection techniques in both on-line and off-line modes [37,53]. To date, various types of SPE adsorbents have been formulated by researchers to obtain high extraction recoveries in different complex traces. In 2018, cyclodextrin metal organic framework (CD-MOF) was developed to preconcentrate sulfonamide (SA) antibiotics and overcome prior SPE adsorbents with poor extraction performance and low hydrophobicity of SA that must be separated and preconcentrated [37]. ɣ-CD with cetyltrimethylammonium bromide (CTAB) were exploited to form a uniform cubic crystal with an average size of 200 – 500 nm and then used as SPE adsorbent for extraction of five selected SA. Elution solvent of acetonitrile/methanol (2:1, v/v) was chosen as it gave the highest recoveries of all SA about 90 – 101.2%. To validate its effectiveness in real samples, four different meats (chicken, pork, fish, and liver) with specific sample preparation were selected and good linear calibration (R^2 = more than 0.9907) were achieved with limit of detections (LODs) varied from 0.32 to 1.7 ng/mL. The prepared CD-MOF was also compared to previous SPE adsorbents [54–57] and successfully applied in SPE for SA preconcentration with high adsorption capacity in less than 10 minutes, high extraction efficiency, and satisfactory recoveries comparable with other methods.

Other than that, the man-made fluoroquinolones (FQs) antibiotic with a functional piperazine group in its structure against Gram-negative and Gram-positive bacteria were also of interest [58]. The widespread use in agricultural and veterinary sectors marked them as an emergent class of pollutant in water [59], and excessive use can cause serious safety and health problems due to their carcinogenicity and antibiotic resistance [60]. Thus, an efficient adsorbent development based on CD in SPE was invented to improve selectivity of targeted FQs. Belenguer-Sepina et al. designed the adsorbent based on porous glycidyl methacrylate (GMA) and ethylene dimethacrylate polymeric material (EDMA) with ɣ-CD as a surface modifier to extract FQs from ground water [46]. The final product of GMA-S-ɣ-CD adsorbent undergone two-step process: functionalization of CD and polymerization of GMA-co-EDMA. Raman spectrometry was used to verify the binding between functionalized CD with GMA-co-EDMA; it revealed the disappearance of thiols stretching (around 2500 cm^{-1}) indicating a good assembling between them, and presence of small peak in GMA-S-ɣ-CD indicating that the presence of small proportion -SH group did not react with modified CD.

The developed GMA-S-ɣ-CD adsorbent was then optimized and compared to previously reported β-CD polymeric material [61]. A significant improvement on recoveries was observed when ɣ-CD was used due to the similar size of targeted analytes with internal cavity of ɣ-CD. The selected optimum conditions for SPE were pH 1 of sample solution, 3 M of NaCl, 1 mL/min flow rate of sample through cartridge, 5:1 (m/v) of adsorbent with respect to sample volume, and 6 mL of methanol as elution solvent. The experimental procedure together with UPLC-MS/MS showed lower LODs between 0.2 – 0.5 µg/L with overall recoveries for five FQs more than 76%, and reusability of adsorbent was tested up to five times according to its constant recoveries. Although the enrichment and selectivity of targeted FQs were improved, the two-step process may be the limitation of this procedure.

A year later, the same group introduced a novel UVM-7 mesoporous silica modified with ɣ-CD as adsorbent for SPE for the isolation of ofloxacin, norfloxacin, and ciprofloxacin in milk samples [34]. UVM-7 material is the nanometric version of MCM-41 that has a macro and meso-pores on its structure. With the addition of CD into the structure, it will produce a truncated cone shape with hydrophilic part in the outside, and hydrophobic in the central part, making it capable to trap the host guest molecules. In this experiment, 10 mL of sample solution at pH 7 and addition of 2 M NaCl into the sample solution was used as the optimum condition for SPE. 100% of water as an efficient washing solvent was applied to remove any impurities clogging in the solid phase and 2 mL of acetonitrile as an elution solvent. Although the recoveries of extraction method were decreased between 60 – 70% due to the analytes losses during the treatment of sample, the result has a good precision to determine analyte under study in milk samples with high degree of confidence. The prepared adsorbent also showed that it is possible to reuse up to six times when dealing with real matrices.

Solid phase micro-extraction

Liu et al. 2019 successfully developed a series of β-CD with varied substituents and applied as supramolecular functional monomers for supramolecularly imprinted polymeric (SMIP) solid phase microextraction (SPME) coatings [47]. Their study showed supramolecular monomer β-CD as the promising adsorbents for the SPME of both nitrophenols and bisphenol A from water samples. The morphology of the prepared SMIP SPME coatings have been characterized by X-ray diffraction analysis (XRD), infrared analysis (IR), scanning electron microscopy (SEM), field emission SEM (FESEM), transmission electron microscopy (TEM) and atomic force microscopy (AFM) demonstrating that the ideal adsorbent has a greater number of pores (0.02 cm^3/g), enhanced intercommunity, and inclusion interaction from β-CD cavities, which boost molecular selectivity recognition. The relative accuracy for the extraction of target analyte from environmental water samples reported was from 88.2 to 90.2% with reusability of SMIP up to 100 cycles. The combination of SMIP technology with inclusion interactions contributed by β-CD cavities such as the hydrogen-bonding interactions, were the main contributions that enhance the extraction efficiency with reported LODs from 1.5 to 3 µg/L.

Another work by Celia-Ruiz et al. reported on β-CD modified nanocellulose (CD-NC) as an adsorbent material where β-CD was covalently bonded to amine-modified nanocellulose through amidation-reaction [35]. Supramolecular self-assembly of CD-modified NC by danofloxacin as guest molecule or target analyte showed excellent extraction efficiency and reusability with improved molecular recognition over its metabolite. These nanocavities with β-CD at its surface has greatly enhanced the SPME selectivity with recovery from 80 to 90% and LOD in milk samples was 2.5 µg/L. The combination of various molecular interactions, including H-bonding, dipolar interactions, and steric interactions between the hydroxyl groups of the CD and the analyte, contributes to the selective recognition of SPME packed mini column. The SPME was carried out using phosphate buffer solution with 12% acetonitrile as the eluent where all encapsulated target analyte was entirely stripped from CD-NC by electrophoretic analysis. The combination of H-bonding and dipolar interactions enabled the analyte to be further separated with higher extraction selectivity and CD-NC reusability, which has been reported to last up to 40 cycles.

Magnetic solid phase extraction and dispersive solid phase extraction

Since its first invention by Anastassiades et al. in 2003, the dispersive solid phase extraction (DSPE) technique has received tremendous attention among researchers due to its improvement on contact surfaces, enhanced adsorbent-analytes interactions, high extraction performance, low organic solvent consumption, and fast approach for extraction [62]. Native CDs such as α-, β- and γ-CD and their modified version have been notably applied in the separation analysis of various analyte compounds due to their explicit features which comprised of hydrophobic cavities and hydrophilic external surfaces as well as readily undergoing modifications. Cui et al. introduced a novel DSPE composite adsorbent prepared from ATP coupled with β-CD using glycidoxypropyltrimethoxysilane as a silane coupling agent for the quantitative determination of (fluoro)quinolones in real honey sample. The adsorption behavior is performed under acidic conditions to enable ion-exchange interactions since the quinolone antibiotic possesses cationic formation as a result of the protonation of carboxylic and amino groups in the quinolone heterocyclic ring. The recoveries of all targeted analytes improved when the ratio of ammonia in methanol increased up to 40%. Moreover, the utilization of β-CD/ATP composite-DSPE under optimum conditions achieved low LODs between the range of 0.30 to 3.95 mg L^{-1} with good recoveries between 83.6 – 88.6% and relative standard deviations (RSDs) less than 7.4%. Next, the applicability of the DSPE technique in real honey samples has successfully quantified the presence of four (fluoro)quinolones antibiotics which are ciprofloxacin, ofloxacin, gatifloxacin, and norfloxacin. The established sample preparation methodology using β-CD/ATP composite demonstrated excellent extraction efficiency due to its mesoporous feature as well as the contribution from the affinity of the hydrophobic cavity and hydrophilic external surfaces [36]. Zhang et al. synthesized porous β-CD polymer derived from CD and rigid aromatic groups tetrafluoroacetonitrile for the determination of quinolones using DSPE method. Several factors were optimized during the execution of the DSPE, including the amount of adsorbent, eluent and adsorption mount, and desorption time. The LODs of four quinolones antibiotics were obtained between 2.67 to 5.50 ng mL^{-1} with relative recoveries ranging from 96.43 to 103.3% and RSDs less than 4.5%. In addition, the robustness of the porous β-CD polymer-DSPE expressed its reliability of the method during normal usage with RSD less than 6.7%. Additionally, the established method offers low-cost extraction with good recoveries, comparable LOD with the commercialized adsorbent, and relatively wider linear range between 25 to 5000 ng mL^{-1} [52].

Magnetic solid phase extraction (MSPE) was first introduced by Šafařiková and Šafařik in 1999. It involves the use of a copper-coloured dye with an adsorbent containing a silanized iron magnetite. After the adsorbent has been absorbed, a magnetic field is then used to separate it from the sample solution. The extracted analytes are then eluted using a solvent that is suitable for the process. The eluent is then isolated from the adsorbent using a magnet. Over time, the use of the micro magnetic adsorbents that were originally developed for use with the MSPE (Figure 2) has since been replaced by more diverse nanosized adsorbents that are composed of hybrid or advanced materials [63]. Recent works showed that β-CD is usually functionalized with iron (II, III) oxide or magnetic nanoparticles with other material such as graphene oxide [49], chitosan [50], and silica [51] to enhance its selectivity in capturing those antibiotics compounds. Since MSPE has shown a great affinity towards analyte, with easy preparation steps, and be less messy and non-toxic, several works have been published to study the interaction between β-CD and antibiotics molecule. Two studies [37,48] functionalized β-CD with metal organic framework (MOF) to achieve the magnetic field capability. Both studies were on sulfonamide antibiotic using HPLC for analysis. Yang et al. [48] showed a good calibration curve ranging from 2 to 100 ng/mL with r^2 value more than 0.993. This method has a good sensitivity with LOD of 0.8 – 1.6 ng/mL. The satisfactory repeatability and reproducibility (RSD < 8%) and acceptable relative recoveries in the range of 78 – 112% were produced in chicken sample. A similar work was produced by Li et al. [37] to determine sulfonamide in meat sample. MSPE was performed on the meat sample using CD-MOF. The developed method showed a good linearity in acceptable concentration

with low detection limit of 0.32 ng/mL. The reproducibility gives a good value of RSD < 7% and acceptable recoveries (76 – 102%). Another work by Al-Afy et al. used combination of β-CD with magnetic graphene oxide coated using silica composite to extract tetracycline antibiotic from milk sample. The method showed a good LOD at 1.8 – 2.9 µg/L. This might be due to the preconcentration factor of 667. The high enrichment is from two extraction techniques applied in this work: DLLME followed by MSPE. The reproducibility and repeatability of method is within acceptable range (RSD < 8.8%) and recoveries (70.6 – 121.5%) [49]. In two previous studies [50,51], magnetic nanocomposites of CD were synthesized for the determination of fluoroquinolones in wastewater samples. Li et al. [51] determined the residue of fluoroquinolones using HPLC-MS/MS. They grafted the CD to magnetic silica composite to form Fe_3O_4@SiO_2@CD nanocomposite. Due to its core-shell sandwich structure, the analytes adsorb better on the adsorbent surface making a good detection limit at 0.0014 – 0.023 µg/L. A set of very good linearity was established ranging from 0.5 to 500 µg/L (r^2 > 09981). The method also noted a high precision (RSD < 4%) and analytes recoveries of 93.2 – 105%. Mashile et al. [50] used magnetic mesoporous carbon/β-CD-chitosan. The selective and sensitive method was based on affinity of CD enhanced by chitosan giving a low detection limit of 0.45 – 1.1 ng/L. Under optimized parameter, the used method showed a good linearity (0 – 300 µg/L, r^2 > 0.9979), robustness, accuracy, and precision (RSD < 4.4%) of fluoroquinolones in wastewater sample.

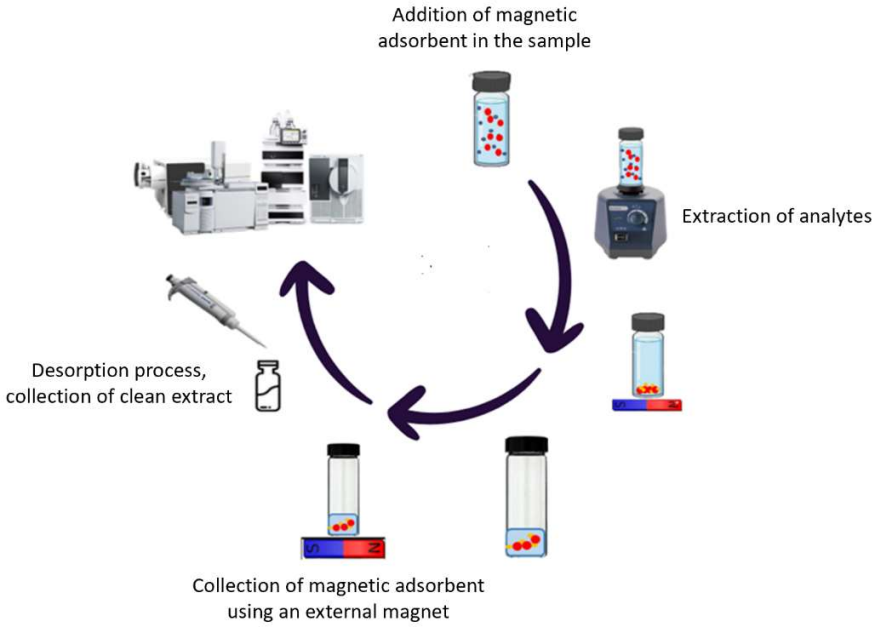


Figure 2. Schematic of MSPE process

Dispersive liquid-liquid microextraction

Dispersive liquid-liquid microextraction (DLLME) (Figure 3) is one of the liquid-based extraction techniques that involves dispersing tiny droplets of the extraction solvent throughout an aqueous sample. The exceedingly large collective surface area of the droplets allows for instant partitioning of analytes into the extraction phase. Compared to conventional liquid or solid phase extraction procedures, DLLME gives higher enrichment factors and minimal solvent consumption.

Hassan et al. developed a green method that utilizes deep eutectic solvent (DES) as a disperser/extraction co-solvent in the extraction of tetracyclines antibiotics (TCs) in water samples [31]. Hydrophobic DES octanoic acid/thymol and hydrophilic DES choline

chloride/ethylene glycol was synthesized and applied as extractant and disperser solvent respectively. The addition of β-CD in the extraction medium was to enhance its capability in higher extraction selectivity towards TCs. The dispersive effect of the extraction solvent and the stability of the murky solution were extremely higher with the addition of β-CD to DES. Furthermore, it has doubled the DLLME performance with higher recovery (74 – 113%) as compared to extraction solvent that only applied DES octanoic acid/thymol. The structure of β-CD that possesses a hydrophobic cavity and a hydrophilic external surface can interact with both hydrophobic/ hydrophilic DES. Through its hydrophobic cavity and hydrophilic surface, DES was dissolved during guest-host complexes formation and breaking into more fine droplets that maximized the contact surface of the analyte from aqueous into extraction medium. β-CD also acted as both co-extractants and co-disperser during the formation of supramolecular inclusion complexes (β-CD/TCs) and increased the selectivity during TCs migration from the sample solution. The extraction was analyzed with HPLC-DAD in environmental samples with reported LODs from 1.37 to 3.48 µg/L.

Another work by Nour Al-Afy et al. applied two types of sample preparation in combination: magnetic-SPE and DLLME in quantitation of tetracyclines (TCs) antibiotic in bovine milk samples [49]. The β-CD (Fe_3O_4@SiO_2@GO-β-CD) as the adsorbent material with the hydrophobic TC's aromatic ring can freely fit into the cavity of the β-CD and formed a strong and stable host-guest combination. The hydrophobic-hydrophobic interaction was the main factor in the inclusion complex within the inner side of the β-CD cavity instead of the amine and amide groups from TCs that was unfavorable to the formation. The hydrophilic adsorbent's structure had polar groups that made it faster to dissolve in a polar solvent, with methanol working as the best desorption solvent toward the extraction of TCs in milk samples. DLLME was utilized as the subsequent sample extraction, and it was discovered that n-hexane was the best dispersant since it was water-insoluble (low density) and offered a high enrichment factor for 667 with a cleaner baseline in the chromatogram. Fe3O4@SiO2@GO-β-CD is a favorable adsorbent due to its great ability to extract TCs from milk samples with recovery rates ranging from 70.6 to 121.5% in milk samples and from 78.5 to 109.3% in water samples. This proposed method offered high precision (RSD < 8.8%), satisfactory recovery and improved preconcentration factor with reported LODs ranged from1.8 to 2.9 µg/L.

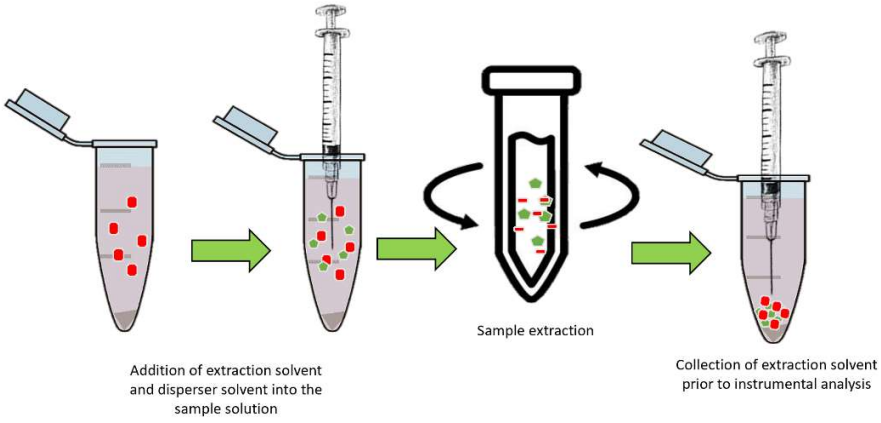


Figure 3. Schematic of DLLME process.

Table 3. The recent applications of CD-based adsorbents in sample preparation for the determination of antibiotics in various matrices.

Adsorbent	Extraction techniques	Quantitation instrument	Analytes	Sample matrix	Linearity	LOD	RSD (%)	Relative Recovery / Recovery (%)	Pre-Con factor	Reusability	Ref
β-Cyclodextrin-functionalized magnetic covalent organic framework (Fe_3O_4@COF@Au-β-CD)	MSPE	HPLC-MS/MS	Sulfonamides	Chicken	2-100 µg/kg, R^2 = 0.9936	0.8-1.6 µg/kg	2.4 – 8.6	78- 112	20	-	[48]
β-cyclodextrin functionalized silica-coated magnetic graphene oxide (Fe_3O_4@SiO_2@GO-β-CD)	MSPE	HPLC-DAD	Tetracycline	Bovine milk	10-200 µg/L, R^2 = 0.9929	1.8-2.9 µg/L	< 8.8	70.6 – 121.5	667	15	[49]
Magnetic mesoporous carbon/β-cyclodextrin–chitosan	DMSPE	HPLC-DAD	Fluoroquinolone	Wastewater	3.7-1000 ng /L, R^2 = 0.9979-0.9990	0.45-1.1 ng/L	< 4.4	93.5 – 98.8	90 – 150	-	[50]
cyclodextrin-derivatized hybrid magnetic nanocomposite (Fe3O4@SiO2@CD)	MSPE	HPLC-MS/MS	Fluoroquinolone	Water	0.5-500, µg/L, R^2 = 0.9981 - 0.9998	0.0014-0.023 µg/L	<4	93.2 – 105		5	[51]
CD-MOF	MSPE	HPLC-DAD	Sulfonamide	Meat	10-1000 ng/mL, $R^2 \geq 0.9907$	0.32-2.0 ng/mL	< 7	76 – 102	-	-	[37]
UVM-7 mesoporous silica with ɣ-cyclodextrin	SPE	LC-FLD	Fluoroquinolone	Milk	1.8-250 µg/L	30-39 ng/L	4 – 13	83 – 92 (water) 60 – 70 (milk)	-	6	[34]
ɣ- cyclodextrin (glycidyl co-ethylene dimethacrylate	SPE	UPLC-MS/MS	Fluoroquinolone	Water	0.2-500 mg/L	0.2-0.5 µg/L	-	76 – 89	-	5	[61]
β-cyclodextrin-modified nanocellulose (CD-NC)	SPME	Electrophoretic	Danofloxacin	Milk	8-800 µg/L	2.5 µg/L	-	80 – 90	-	40	[35]
Deep eutectic solvent doped β-cyclodextrin (DES-CD)	DLLME	HPLC-DAD	Tetracycline	Water	4.58-500 µg/L R^2 = 0.993-0.996	1.37-3.48 µg/L	< 4.7	74 – 113	-	-	[31]
β-CD/ATP composite	DSPE	HPLC-DAD	Fluoroquinolone	Honey	10-1500 µg/L, $R^2 > 0.9991$	0.3-3.95 µg/L	< 7.4	83.6 – 88.6	-	-	[36]
Porous β-CD polymer	DSPE	HPLC-DAD	Fluoroquinolones	Wastewater	25-5000 ng/mL, $R^2 > 0.9994$	2.67-5.50 ng/mL	< 4.5	96.43 – 103.3	-	-	[52]

**Abbreviations: MSPE – magnetic solid phase extraction, SPME – solid phase microextraction, DLLME – dispersive liquid-liquid microextraction, DSPE – dispersive solid phase extraction, SPE – solid phase extraction, HPLC-MS/MS – high performance liquid chromatography tandem mass spectrometry, HPLC-DAD – high performance liquid chromatography diode array detector, LC-FLD – liquid chromatography fluorescence detector, UPLC-MS/MS – ultra performance liquid chromatography tandem mass spectrometry*

Conclusion

The present review discussed the development of sample preparation techniques of antibiotic molecules using CD-based adsorbents. Overall, in most of the synthesis methods, the CD is attached to the adsorbent via a linker. It was noted that β-CD has been commonly used and prepared as an adsorbent in the sample preparation of antibiotic molecules, compared to other types of CDs. CD is at advantages in terms of green adsorbent as it is easy to prepare, flexible to functionalize, and improve selectivity and efficiency of extraction. Antibiotic molecules that are of the right size to enter CD cavity will exhibit higher extraction efficiency. The CD-based adsorbents offer advantages such as selectivity, versatility, efficient extraction, reduced matrix interference, compatibility with various techniques, and enhanced sensitivity. These factors make them promising adsorbents for sample preparation in the determination of targeted compounds, enabling more accurate and reliable analytical results. Future research would likely be towards the improvement of functionalities of the developed adsorbents through (a) the preparation of amphiphilic adsorbents towards variety polarity of targeted molecules, (b) use of a mixture of CDs in the preparation of adsorbents that can expand their use and efficiency, (c) production of new generation of selective CD materials with molecularly imprinted technology, and (d) combination of CD with other nanomaterials to improve their properties such as surface area, stability, and selectivity. It can be summarized that there has been a rapid development in the extraction and enrichment techniques for antibiotic molecules using CD-based materials, which were useful for monitoring antibiotics and have the potential to reduce the environmental pollution and eliminate food-chain contaminations. In the following years, an increase in the number of advanced greener sorbents and green sample preparation methods designed for monitoring antibiotics can be expected with the ultimate goal to prevent the development of antibiotic resistance phenomenon.

Acknowledgment

This study was supported by the Ministry of Higher Education Malaysia through Fundamental Research Grant Scheme (FRGS) with reference code number: FRGS/1/2021/STG04/USM/02/4 and account code number: 203.CIPPT.6711973.

References

1. Davies, J. (1996). Origins and evolution of antibiotic resistance. *Microbiología (Madrid, Spain),* 12: 9-16.
2. Karageorgou, E., Christoforidou, S., Ioannidou, M., Psomas, E., and Samouris, G. (2018). Detection of β-lactams and chloramphenicol residues in raw milk - Development and application of an HPLC-DAD method in comparison with microbial inhibition assays. *Foods* 7: 1-12.
3. Ramatla, T., Ngoma, L., Adetunji, M., and Mwanza, M. (2017). Evaluation of antibiotic residues in raw meat using different analytical methods. *Antibiotics,* 6: 1-17.
4. Karageorgou, E. G., Samanidou, V. F., and Papadoyannis, I. N. (2012). Ultrasound-assisted matrix solid phase dispersive extraction for the simultaneous analysis of β-lactams (four penicillins and eight cephalosporins) in milk by high performance liquid chromatography with photodiode array detection. *Journal of Separation Science* 35: 2599-2607.
5. Rodríguez, M. P., Pezza, H. R., and Pezza, L. (2016). Simple and clean determination of tetracyclines by flow injection analysis. *Spectrochimica Acta - Part A: Molecular and Biomolecular Spectroscopy* 153: 386-392.
6. Kasimanickam, V., Kasimanickam, M., and Kasimanickam, R. (2021). Antibiotics use in food animal production: Escalation of antimicrobial resistance: Where are we now in combating AMR? *Medical sciences (Basel, Switzerland)* 9: 14.
7. FAO, OMS, and CODEX (2015). Maximun residue limits (MRLs) and risk management recommendations (RMRs) for residues of veterinary drugs in foods CAC/MRL 2-2015. 22.
8. Abraham, E. P. (1963). The antibiotics. *Comprehensive Biochemistry,* 11: 181-224.
9. Kabir, A., Locatelli, M., and Ulusoy, H. I. (2017). Recent trends in microextraction techniques employed in analytical and bioanalytical sample preparation. *Separations,* 4: 1-15.
10. European Commission (2017). A european one

health action plan against antimicrobial resistance (AMR). *Brussels*, 24: 1-20.
11. World Health Organisation (2016). Joint FAO/WHO food standards programme codex committee on residue of veterinary drugs in foods. *Food and Agriculture Organization of the United Nations*, 1–10.
12. Smith, R. (2015). Commission Regulation (EU) No 330/2010. *Core EU Legislation*, 157-163.
13. Laura, M., Silva, D., Li, C., Bertazzi, R., Li, L., Moreira, R., and Li, C. (2015). Ultra-processed foods and the nutritional dietary profile in Brazil Alimentos ultraprocessados eperfil nutricional da dieta no Brasil. *Ultra-Processed Foods and Dietary Quality,* 49: 1-10.
14. Rabello, R. F., Bonelli, R. R., Penna, B. A., Albuquerque, J. P., Souza, R. M., & Cerqueira, A. M. F. (2020). Antimicrobial resistance in farm animals in Brazil: an update overview. *Animals*, 10(4): 552.
15. Lara, F. J., Olmo-iruela, M., Cruces-blanco, C., Quesada-molina, C., and Garcı, A. M. (2012). Advances in the determination of β -lactam antibiotics by liquid chromatography. *Trends in Analytical Chemistr,* 38: 52-66.
16. Ghasemi, R., Mirzaei, H., Afshar Mogaddam, M. R., Khandaghi, J., and Javadi, A. (2022). Application of magnetic ionic liquid-based air–assisted liquid–liquid microextraction followed by back-extraction optimized with centroid composite design for the extraction of antibiotics from milk samples prior to their determination by HPLC–DAD. *Microchemical Journal,* 181: 107764.
17. Wang, B., Wang, Y., Xie, X., Diao, Z., Xie, K., Zhang, G., Zhang, T., and Dai, G. (2020). Quantitative analysis of spectinomycin and lincomycin in poultry eggs by accelerated solvent extraction coupled with gas chromatography tandem mass spectrometry. *Foods,* 9: 1-18.
18. Chen, M., Yi, Q., Hong, J., Zhang, L., Lin, K., and Yuan, D. (2015). Simultaneous determination of 32 antibiotics and 12 pesticides in sediment using ultrasonic-assisted extraction and high performance liquid chromatography-tandem mass spectrometry. *Analytical Methods,* 7: 1896-1905.
19. Badawy, M. E. I., El, M. A. M., Kimani, P. K., Lim, L. W., and Rabea, E. I. (2022). A review of the modern principles and applications of solid - phase extraction techniques in chromatographic analysis (Springer Nature Singapore).
20. Siu, K.S., Chen, D., Zheng, X., Zhang, X., Johnston, N., Liu, Y., Yuan, K., Koropatnick, J., Gillies, E.R., and Min, W.P. (2014). Non-covalently functionalized single-walled carbon nanotube for topical siRNA delivery into melanoma. *Biomaterials,* 35: 3435-3442.
21. Tian, J., Xu, J., Zhu, F., Lu, T., Su, C., and Ouyang, G. (2013). Application of nanomaterials in sample preparation. *Journal of Chromatography A,* 1300: 2-16.
22. Basheer, A. A. (2018). New generation nano-adsorbents for the removal of emerging contaminants in water. *Journal of Molecular Liquids,* 261: 583–593.
23. Morin-Crini, N., Winterton, P., Fourmentin, S., Wilson, L. D., Fenyvesi, É., and Crini, G. (2018). Water-insoluble β-cyclodextrin–epichlorohydrin polymers for removal of pollutants from aqueous solutions by sorption processes using batch studies: A review of inclusion mechanisms. *Progress in Polymer Science,* 78: 1-23.
24. Wu, Z., Chen, C., Wang, L., Wan, H., and Guan, G. (2016). Magnetic material grafted poly(phosphotungstate-based acidic ionic liquid) as efficient and recyclable catalyst for esterification of oleic acid. *Industrial and Engineering Chemistry Research,* 55: 1833-1842.
25. Yakout, A.A., Alshitari, W., and Akhdhar, A. (2021). Synergistic effect of Cu-nanoparticles and β-cyclodextrin functionalized reduced graphene oxide nanocomposite on the adsorptive remediation of tetracycline antibiotics. *Carbohydrate Polymers,* 273:118528.
26. Zhao, Y., Si, H., Zhao, X., Li, H., Ren, J., Li, S., Wang, Q., and Zhang, J. (2021). Fabrication of an allyl-β-cyclodextrin based monolithic column with triallyl isocyanurate as co-crosslinker and its application in separation of lipopeptide antibiotics by HPLC. *Microchemical Journal,* 168: 106462.
27. Velusamy, V., Palanisamy, S., Kokulnathan, T., Chen, S. W., Yang, T. C. K., Banks, C. E., and Pramanik, S. K. (2018). Novel electrochemical

synthesis of copper oxide nanoparticles decorated graphene-β-cyclodextrin composite for trace-level detection of antibiotic drug metronidazole. *Journal of Colloid and Interface Science,* 530: 37-45.

28. Zhang, Y., Cai, X., Xiong, W., Jiang, H., Zhao, H., Yang, X., Li, C., Fu, Z., and Chen, J. (2014). Molecular insights into the pH-dependent adsorption and removal of ionizable antibiotic oxytetracycline by adsorbent cyclodextrin polymers. *PLoS ONE*, 9(1), e86228.
29. Zhang, Y., Jiang, F., Huang, D., Hou, S., Wang, H., Wang, M., Chi, Y., and Zhao, Z. (2018). A facile route to magnetic mesoporous core-shell structured silicas containing covalently bound cyclodextrins for the removal of the antibiotic doxycycline from water. *RSC Advances,* 8: 31348–31357.
30. Foroutan, R., Jamaleddin, S., Latifi, P., and Ahmadi, A. (2021). Carbon nanotubes/β-cyclodextrin/ $MnFe_2O_4$ as a magnetic nanocomposite powder for tetracycline antibiotic decontamination from different aqueous environments. *Journal of Environmental Chemical Engineering,* 9: 106344.
31. Sereshti, H., Karami, F., and Nouri, N. (2021). A green dispersive liquid-liquid microextraction based on deep eutectic solvents doped with β-cyclodextrin: Application for determination of tetracyclines in water samples. *Microchemical Journal,* 163: 105914.
32. Juengchareonpoon, K., Boonamnuayvitaya, V., and Wanichpongpan, P. (2019). Kinetics and isotherms of oxytetracycline adsorption on β-cyclodextrin/carboxymethylcellulose hydrogel films. *Aquaculture Research,* 50: 3412-3419.
33. Li, Q., Wang, D., Fang, X., Zong, B., Liu, Y., Li, Z., Mao, S., and Ostrikov, K. K. (2021). Rapid synthesis of multifunctional β-cyclodextrin nanospheres as alkali-responsive nanocarriers and selective antibiotic adsorbents. *Chemical Communications,* 57: 1161-1164.
34. Belenguer-Sapiña, C., Pellicer-Castell, E., El Haskouri, J., Simó-Alfonso, E.F., Amorós, P., and Mauri-Aucejo, A. R. (2022). A type UVM-7 mesoporous silica with γ-cyclodextrin for the isolation of three veterinary antibiotics (ofloxacin, norfloxacin, and ciprofloxacin) from different fat-rate milk samples. *Journal of Food Composition and Analysis,* 109: 104463.
35. Ruiz-Palomero, C., Soriano, M. L., and Valcárcel, M. (2015). β-Cyclodextrin decorated nanocellulose: A smart approach towards the selective fluorimetric determination of danofloxacin in milk samples. *Analyst,* 140: 3431–3438.
36. Cui, X., Zhang, P., Yang, X., Yang, M., Zhou, W., Zhang, S., Gao, H., and Lu, R. (2015). β-CD/ATP composite materials for use in dispersive solid-phase extraction to measure (fluoro)quinolone antibiotics in honey samples. *Analytica Chimica Acta,* 878: 131–139.
37. Li, Y., Zhu, N., Chen, T., Ma, Y., and Li, Q. (2018). A green cyclodextrin metal-organic framework as solid-phase extraction medium for enrichment of sulfonamides before their HPLC determination. *Microchemical Journal,* 138: 401-407.
38. Liu, Q., Zhou, Y., Lu, J., and Zhou, Y. (2020). Novel cyclodextrin-based adsorbents for removing pollutants from wastewater: A critical review. *Chemosphere,* 241: 125043.
39. Roy, A., Manna, K., Dey, S., and Pal, S. (2023). Chemical modification of β-cyclodextrin towards hydrogel formation. *Carbohydrate Polymers,* 306: 120576.
40. Szejtli, J. (2004). Past, present, and future of cyclodextrin research. *Pure and Applied Chemistry,* 76: 1825-1845.
41. Li, N., Mei, Z., and Ding, S. (2010). 2,4-Dichlorophenol sorption on cyclodextrin polymers. *Journal of Inclusion Phenomena and Macrocyclic Chemistry,* 68: 123-129.
42. Guo, Y., Guo, S., Ren, J., Zhai, Y., Dong, S., and Wang, E. (2010). Cyclodextrin functionalized graphene nanosheets with high supramolecular recognition capability: Synthesis and host-guest inclusion for enhanced electrochemical performance. *ACS Nano* 4, 5512.
43. Kashapov, R. R., Mamedov, V. A., Zhukova, N. A., Kadirov, M. K., Nizameev, I. R., Zakharova, L. Y., and Sinyashin, O.G. (2017). Controlling the binding of hydrophobic drugs with supramolecular assemblies of β-cyclodextrin. *Colloids and Surfaces A: Physicochemical and Engineering*

Aspects, 527: 55-62.

44. Peng, L.Q., Ye, L.H., Cao, J., Chang, Y. Xu, Li, Q., An, M., Tan, Z., and Xu, J. J. (2017). Cyclodextrin-based miniaturized solid phase extraction for biopesticides analysis in water and vegetable juices samples analyzed by ultra-high-performance liquid chromatography coupled with quadrupole time-of-flight mass spectrometry. *Food Chemistry,* 226: 141-148.
45. Peng, L. Q., Dong, X., Zhen, X. T., Yang, J., Chen, Y., Wang, S. L., Xie, T., and Cao, J. (2020). Simultaneous separation and concentration of neutral analytes by cyclodextrin assisted sweeping-micellar electrokinetic chromatography. *Analytica Chimica Acta,* 1105: 224-230.
46. Belenguer-Sapiña, C., Pellicer-Castell, E., Pottanam Chali, S., Ravoo, B. J., Amorós, P., Simó-Alfonso, E. F., and Mauri-Aucejo, A. R. (2021). Host-guest interactions for extracting antibiotics with a γ-cyclodextrin poly(glycidyl-co-ethylene dimethacrylate) hybrid sorbent. *Talanta,* 232: 122478.
47. Liu, Y., Liu, Y., Liu, Z., Du, F., Qin, G., Li, G., Hu, X., Xu, Z., and Cai, Z. (2019). Supramolecularly imprinted polymeric solid phase microextraction coatings for synergetic recognition nitrophenols and bisphenol A. *Journal of Hazardous Materials,* 368: 358-364.
48. Yang, Y., Li, G., Wu, D., Wen, A., Wu, Y., and Zhou, X. (2020). β-cyclodextrin-/AuNPs-functionalized covalent organic framework-based magnetic sorbent for solid phase extraction and determination of sulfonamides. *Microchimica Acta*, 187: 1-10.
49. Al-Afy, N., Sereshti, H., Hijazi, A., and Rashidi Nodeh, H. (2018). Determination of three tetracyclines in bovine milk using magnetic solid phase extraction in tandem with dispersive liquid-liquid microextraction coupled with HPLC. *Journal of Chromatography B: Analytical Technologies in the Biomedical and Life Sciences* 1092: 480-488.
50. Mashile, G. P., Mpupa, A., and Nomngongo, P. N. (2021). Magnetic Mesoporous carbon / β - cyclodextrin – chitosan nanocomposite for extraction and preconcentration of multi-class emerging contaminant residues in environmental samples. *Nanomaterials,* 11: 1-15.
51. Li, F., Wang, M., Zhou, J., Yang, M., and Wang, T. (2021). Cyclodextrin-derivatized hybrid nanocomposites as novel magnetic solid-phase extraction adsorbent for preconcentration of trace fluoroquinolones from water samples coupled with HPLC-MS/MS determination. *Microchemical Journal,* 164: 105955.
52. Zhang, J., Liu, D., Shi, Y., Sun, C., Niu, M., Wang, R., and Hu, F. (2017). Determination of quinolones in wastewater by porous β -cyclodextrin polymer based solid-phase extraction coupled with HPLC. *Journal of Chromatography B,* 1068-1069: 24-32.
53. Buszewski, B., and Szultka, M. (2012). Past, present, and future of solid phase extraction: A review. *Critical Reviews in Analytical Chemistry,* 42: 198-213.
54. Hou, X. L., Wu, Y. L., Yang, T., and Du, X. D. (2013). Multi-walled carbon nanotubes-dispersive solid-phase extraction combined with liquid chromatography-tandem mass spectrometry for the analysis of 18 sulfonamides in pork. *Journal of Chromatography B: Analytical Technologies in the Biomedical and Life Sciences,* 929: 107-115.
55. Xu, Y., Ding, J., Chen, H., Zhao, Q., Hou, J., Yan, J., Wang, H., Ding, L., and Ren, N. (2013). Fast determination of sulfonamides from egg samples using magnetic multiwalled carbon nanotubes as adsorbents followed by liquid chromatography-tandem mass spectrometry. *Food Chemistry,* 140: 83-90.
56. Luo, Y. B., Shi, Z. G., Gao, Q., and Feng, Y. Q. (2011). Magnetic retrieval of graphene: Extraction of sulfonamide antibiotics from environmental water samples. *Journal of Chromatography A,* 1218: 1353-1358.
57. Gao, Q., Luo, D., Ding, J., and Feng, Y.-Q. (2010). Rapid magnetic solid-phase extraction based on magnetite/silica/poly(methacrylic acid–co–ethylene glycol dimethacrylate) composite microspheres for the determination of sulfonamide in milk samples. *Journal of Chromatography A,* 1217: 5602-5609.
58. Lee, H-B., Peart, T. E., and Svoboda, M. L. (2007). Determination of ofloxacin, norfloxacin, and ciprofloxacin in sewage by selective solid-phase

extraction, liquid chromatography with fluorescence detection, and liquid chromatography–tandem mass spectrometry. *Journal of Chromatography A,* 1139: 45-52.

59. Barahona, F., Albero, B., Tadeo, J. L., and Martín-Esteban, A. (2019). Molecularly imprinted polymer-hollow fiber microextraction of hydrophilic fluoroquinolone antibiotics in environmental waters and urine samples. *Journal of Chromatography A,* 1587: 42-49.
60. Zhang, M., Chen, J., Zhao, F., and Zeng, B. (2020). Determination of fluoroquinolones in foods using ionic liquid modified Fe_3O_4/MWCNTs as the adsorbent for magnetic solid phase extraction coupled with HPLC. *Analytical Methods,* 12: 4457-4465.
61. Belenguer-Sapiña, C., Pellicer-Castell, E., Vila, C., Simó-Alfonso, E. F., Amorós, P., and Mauri-Aucejo, A. R. (2019). A poly(glycidyl-co-ethylene dimethacrylate) nanohybrid modified with β-cyclodextrin as a sorbent for solid-phase extraction of phenolic compounds. *Microchimica Acta,* 186: 1-11.
62. Mohamed, A. H., Noorhisham, N. A., Bakar, K., Yahaya, N., Mohamad, S., Kamaruzaman, S., and Osman, H. (2022). Synthesis of imidazolium-based poly(ionic liquids) with diverse substituents and their applications in dispersive solid-phase extraction. *Microchemical Journal,* 178: 107363.
63. Faraji, M., and Yamini, Y. (2021). Application of magnetic nanomaterials in food analysis. *Magnetic Nanomaterials in Analytical Chemistry*, 2021: 87-120.

Malaysian Journal of Analytical Sciences (MJAS)
Published by Malaysian Analytical Sciences Society

THE EFFECTS OF pH ON MICROPLASTICS REMOVAL BY ELECTROCOAGULATION PROCESS USING NICKEL ELECTRODE

(Kesan pH Terhadap Penyingkiran Mikroplastik Melalui Kaedah Elektrokoagulasi Menggunakan Elektrod Nikel)

Nor Aimi Abdul Wahab[1,3], Nor Ku Nazatul Husna Mohd Jackariya[1], Norain Isa[1,2*], Norfaezatul Alysa Othman[1], Vicinisvarri Inderan[1] , Nur Fadzeelah Abu Kassim[1]

[1]Chemical Engineering Studies, College of Engineering,
Universiti Teknologi MARA, Cawangan Pulau Pinang, Permatang Pauh Campus,
13500 Pulau Pinang, Malaysia
[2]Waste Management and Resource Recovery (WeResCue) Group,
Chemical Engineering Studies, College of Engineering,
Universiti Teknologi MARA, Cawangan Pulau Pinang, Permatang Pauh Campus,
13500 Pulau Pinang, Malaysia
[3]Department of Applied Sciences,
Universiti Teknologi MARA, Cawangan Pulau Pinang, Permatang Pauh Campus,
13500 Pulau Pinang, Malaysia

[*]Corresponding author: norain012@uitm.edu.my

Received: 25 September 2022; Accepted: 25 February 2023; Published: 22 August 2023

Abstract

pH plays an important role in microplastics (MPs) removal during the electrocoagulation (EC) process. This study investigates the influence of the initial pH on the removal of polypropylene microplastics (PPMPs) from artificial wastewater using an EC process utilizing nickel electrodes. The effect of the initial pH has been investigated by commencing several sets of continuous flow experiments at five different initial pH values (2, 4, 6, 8, and 10), keeping the concentration of PPMPs, size of PPMPs, and electrode distance constant at 250 ppm, 250 µm, and 2 cm, respectively. The results showed that the removal efficiency increased gradually from 25% at initial pH 2 and reached its maximum level at initial pH 8 with 67% removal. Then it slightly decreased as the initial pH increased to 10. The kinetic studies showed that the EC process followed a first-order kinetic model. It can be said that the most favorable supporting pH for PPMPs removal utilizing nickel electrodes in this EC treatment technique is pH 8 due to the predominant species having a high adsorption capacity for PPMPs as a pollutant. The result showed that pH plays an important role in PPMPs removal from wastewater via the EC process utilizing nickel electrodes.

Keywords: Electrocoagulation, polypropylene, microplastics, nickel electrode, pH

Abstrak

pH memainkan peranan penting dalam penyingkiran mikroplastik melalui kaedah elektrokoagulasi. Kajian ini dilaksanakan bagi melihat pengaruh pH terhadap penyingkiran mikroplastik polipropelena (PPMPs) daripada air buangan melalui kaedah

elektrokoagulasi (EC) menggunakan elektrod nikel. Pengaruh pH telah disiasat melalui beberapa set eksperimen menggunakan lima pH awal yang berbeza (2, 4, 6, 8 dan 10) dengan mengekalkan masing-masing kepekatan PPMPs, saiz PPMPs, dan jarak elektrod pada 250 ppm, 250 µm, dan 2 cm. Keputusan yang diperolehi menunjukkan bahawa kecekapan penyingkiran meningkat secara beransur-ansur daripada 25% pada pH awal 2 dan mencapai tahap maksimum pada pH awal 8 dengan penyingkiran 67%, kemudian ia sedikit menurun apabila pH awal meningkat kepada 10. Kajian kinetik menunjukkan bahawa proses EC adalah mengikut model kinetik tertib pertama. Boleh dikatakan bahawa pH sokongan yang paling sesuai untuk penyingkiran PPMPs menggunakan nikel sebagai elektrod dalam teknik rawatan EC ini ialah pH 8 disebabkan oleh, spesis utama mempunyai kapasiti penjerapan yang tinggi untuk PPMPs sebagai bahan pencemar. Keputusan menunjukkan bahawa pH memainkan peranan penting dalam penyingkiran PPMPs daripada air sisa melalui proses EC menggunakan elektrod nikel.

Kata kunci: Elektrokoagulasi, polipropelena, mikroplastik, elektrod nikel, pH

Introduction

The rapid growth of industrialization has resulted in the extensive use of plastic products in industry, agriculture, and life globally. The world's annual plastic production is expected to reach 3.3 x 10^{10} tonnes by 2050, with most of the plastic (estimation of 1.15 x 10^{6} - 2.75 x 10^{6} tonnes) will end up in the water every year [1,2]. This plastic waste breaks down into smaller plastic through photooxidation, mechanical action, and biodegradation over an extended period of time [3]. Plastic with less than 5 mm particle size is known as microplastics (MPs). Most MPs have been found in the water and generate annual economic losses to marine ecosystems [4]. The presence of MPs in natural waters is cause for concern due to their possible adverse health effects on the environment and humans [5]. MPs are hard to degrade and can exist in water for a long time. The presence of abundant chemical bonds and functional groups, a large specific area, and small size provide MPs have certain adsorption behavior toward heavy metal, organic and inorganic pollutants, thus producing complex secondary pollutants with high toxicity [6,7]. Due to their toxicity, MPs may affect animal and human health by entering the circulatory system, affecting immune response, causing neurotoxicity, and increasing human cancer risk [8]. As a result, extensive research has been conducted on MPs as a new type of emerging pollutant. Wastewater treatment plants (WWTPs) are one of the primary sources of MPs contamination [9, 10]. It was estimated that the WWTPs discharge between 50,000 and 15 million MPs daily [11]. Due to their small size (<5 mm) and low density (<1.2 g/cm^3), MPs are not completely eliminated by standard wastewater treatment techniques and are discharged to natural bodies of water together with the final effluent [3]. Hence, it is crucial to have an alternative removal method to expedite the MPs removal to overcome the limitation in the WWTPs.

Electrocoagulation (EC) method has become the focus of interest among researchers as one of the potential methods for the removal of MPs from wastewater due to its simplicity, low-cost method with environmental compatibility, energy efficiency, and sludge minimization [6,12]. EC involves the electrochemical dissolution of a metal electrode to produce metal ions [13]. These metal ions, produced at the anode, combine with hydroxide ions to form metal hydroxide coagulants. The coagulants enable the production of flocs by neutralizing the oppositely-charged colloidal particles floating in the solution and by adsorbing the dissolved pollutants. Flocs with high specific gravity will sink to the bottom of the reactor, where they will be removed through filtration, whereas lighter flocs will float to the solution's surface and be removed using skimming devices [14].

The most commonly used sacrificial anode in EC is aluminum and iron due to their low price, abundant availability, and high reactivity towards the removal of contaminants. However, these electrodes suffer the limitation of producing a high amount of sludge, corrosion, and degradation over time. Therefore, the search for new electrode material is strongly encouraged. Nickel (Ni) offers advantages as an electrode material due to increased efficiency by having higher oxidation potential, reduced corrosion, and lower sludge production. Nonetheless, the use of Ni electrodes in EC remains largely unexplored. Another critical factor that affects the EC process is the pH of the

solution, as it can impact the performance and efficiency of the EC. pH affects the stability and behavior of different hydroxide species produced in the EC process, thus influencing the formation of flocs. Hence, it is important to understand the effect of pH and relate it to the performance of the EC process.

In this work, Ni electrodes were used to investigate the effect of pH on the removal of PPMPs. A series of pH-dependent (pH 2 to pH 10) studies were examined using an EC process using a Ni electrode. The effectiveness of Ni electrodes for PPMPs removal was evaluated based on their removal efficiency (%RE). To the best of our knowledge, only a few researchers have used Ni electrodes in the EC process. Our findings suggest that turbidity monitoring for the influence of pH can provide reasonable optimization of water treatment strategies for effective MPs removal.

Materials and Methods

Materials

Commercial Ni foil (99.99%) with a thickness of 0.3 mm and a length of 4 cm x 1 cm was used as electrodes. The electrodes were cleaned with acetone, ethanol, and deionized water under sonication to remove surface grease and impurities on the electrode surfaces. This study used polypropylene microplastics (PPMPs) prepared from fully aged polypropylene storage boxes as the pollutant. The fully aged polypropylene storage boxes were cleaned and shade dried for 5 days at room temperature. After 5 days, the polypropylene was shredded into small pieces and sieved to 250 µm. The pH of the solution was adjusted using 0.1 M NaOH (99%, QReC) and HCl (37%, QReC). Turbidity measurement was conducted using a Hach 2100Q turbidity meter. The resolution of the turbidity meter was ±0.01 NTU. An air pump (Xilong) and DC power supply (PHYWE) were used in this work.

Electrocoagulation process

The PPMPs removal study was investigated using the EC method, as shown in the schematic diagram in Figure 1. The EC system consists of a reactor, a pair of Ni electrodes, a DC power source, and an air pump. The effect of pH on the removal of PPMPs was evaluated using Ni foil with a length of 4 cm x 1 cm as electrodes. The distance between the two electrodes was set at 2 cm. At this stage, the concentration of PPMPs (250 ppm), the volume of the reactor (150 mL), voltage (60 V), and reaction time (30 min) were kept constant. The pH of the solution was adjusted to pH 2, 4, 6, 8, and 10 using 0.1 M of NaOH and HCl, respectively. Air gas flow using an air pump was continuously supplied to the solution to ensure the dispersions of the PPMPs. As to ensure the results of the experiments are reproducible, the experiments were run in triplicates. After the EC process, the floc was allowed to settle for 10 min before measurements were performed. A 15 mL of the sample from the middle of reactor was taken every 5 min (up to 30 min) to study the sedimentation rate. The sample was analysed using a turbidity meter to measure its turbidity. The PPMPs removal efficiency and kinetics studies at different pH (2–10) were analyzed based on equations 1, 2, and 3. The performance at the optimized condition was obtained and used to compare their performance with other studies.

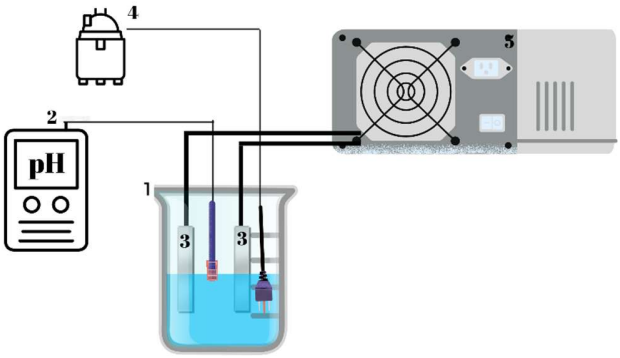


Figure 1. Schematic diagram of electrocoagulation process (1: EC cell, 2: pH meter, 3: Electrodes, 4: Air pump, 5: Power supply)

$$\text{Removal efficiency (\%)} = \frac{Turb_{\circ} - Turb_{i}}{Turb_{\circ}} \times 100\% \quad (1)$$

$$\text{Pseudo-first order kinetic} = kt + \ln\left(\frac{Turb_o}{Turb_i}\right) \quad (2)$$

$$\text{Pseudo-second order kinetic} = kt + \left(\frac{1}{Turb_i}\right) - \left(\frac{1}{Turb_o}\right) \quad (3)$$

where $Turb_o$ is the initial turbidity, $Turb_i$ is the ultimate turbidity at time t, and k is the sedimentation rate constant. For this part, the turbidity of the solution was measured at 5 mins intervals for 30 min. From the data collected during the turbidity test, the removal efficiency, reaction rate, and kinetics of PPMPs removal can be determined.

Results and Discussion

Effect of pH

The pH of the solution is one of the main factors that can affect wastewater treatment efficiency in the EC process. In this study, the effect of initial pH on the MPs removal by Ni electrodes was explored in the range of initial pH values of 2-10. Figure 2(a) shows the removal efficiencies (%) of PPMPs at different reaction times with 5 min time intervals as a function of pH with the initial pH solution range of 2 to 10, and Figure 2(b) shows the removal efficiencies (%) of PPMPs at optimum reaction time (30 min). The experimental result indicates successful removal of PPMPs with a maximum removal efficiency of 67% was observed at pH 8. At pH 8, the anodic oxidation of the metal to insoluble metal hydroxide/oxyhydroxide predominates, leading to high floc formation and high PPMPs removal efficiency [16]. The optimum removal at pH 8 shows that this method can be used to treat ordinary domestic wastewater without the need to adjust the pH, as the pH of domestic wastewater is usually between pH 6-9.2 [12].

Figure 3 displays the zeta potential value of MPs suspension after EC. The zeta potential was positive at pH < 3 and has a negative surface charge at pH values >3. The negativity of the surface charge increases with increasing pH value. The isoelectric point (point of zero charges) was determined to be approximately at pH 3.21. The lower removal efficiency was observed below pH 3 at positive zeta potential due to electrical repulsion between the particles of similar charges, which prevents aggregation [15]. At high pH, the $Ni(OH)^{-}_3$ and $Ni(OH)^{2-}_4$ may be the predominant species that cannot be adsorbed or attached to the negatively charged surface, thus reducing the MPs removal efficiency. The same experimental trend on the effect of pH has also been reported by Kartikaningsih et al. [16] for the EC of boron using Ni foam electrode, where the maximum boron removal was observed at pH 8-9. In acidic pH, the low removal efficiency was observed due to the passivation of the electrode at a potential that was more positive than the Nernst-related value and was favored over the dissolution of the nickel electrode; thus, floc formation was not conducive and had low adsorption capacity for PPMPs [17]. A downward trend was observed at pH 10 with a removal efficiency of 28% owing to the fall in the over-potential of oxyhydroxide formation at high pH.

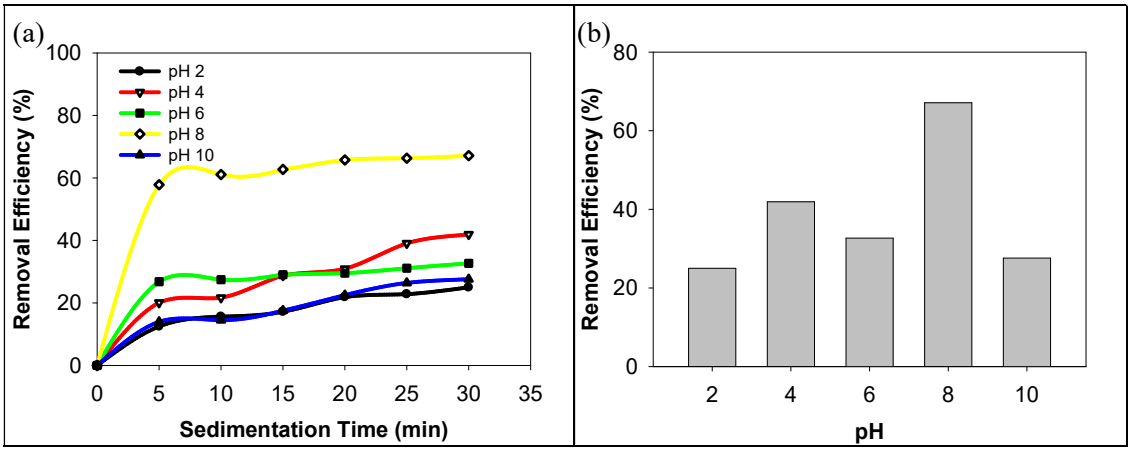


Figure 2. Effect of pH on removal efficiencies of PPMPs (a) at different reaction times and (b) at optimum reaction times

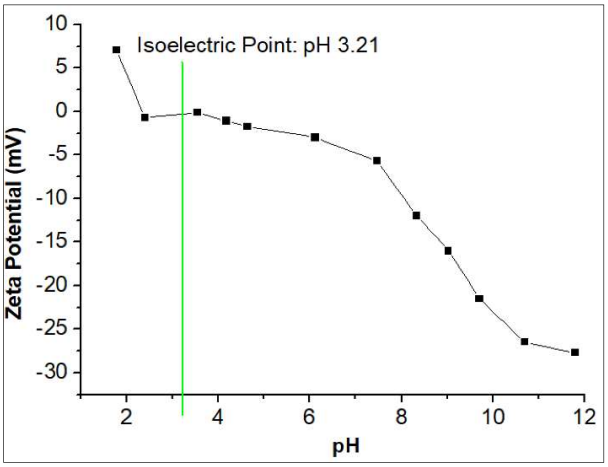


Figure 3. pH equilibrium (isoelectric measurement) for the MPs suspension after EC

As for the sedimentation behavior, it was observed that as the pH increased, the sedimentation increased, thus reducing the turbidity of the solution and resulting in higher removal efficiencies. The sedimentation was found to decrease with decreasing pH of the solution. This may be due to lesser floc formation at low pH leading to poor settling behavior. A similar effect of sedimentation for EC using Fe electrodes has been reported earlier by [18]. In the EC system, the precipitates are created by the oxidative dissolution of the metal from the anode surface's electrical double-layer structure, which is followed by the precipitation of metal hydroxides around the corrosion site [19]. The reaction is given in equations 4-6 below:

$$Ni \rightarrow Ni^{2+} + 2e^{-} \text{ (anodic dissolution)} \quad (4)$$

$$2H_2O + 2e^{-} \rightarrow 2OH^{-} + H_2 \text{ (cathodic hydrogen evolution)} \quad (5)$$

$$Ni^{2+} + 2OH^{-} \leftrightarrow Ni(OH)_2 \text{ (s) floc} \quad (6)$$

The metal undergoes anodic dissolution to produce metal ions. These metal ions then react with OH^{-} ions generated at the cathode to form different hydroxides to form flocculant. The low degree of the flocculant can remove the MPs by adsorption, while the high degree polymerization flocculant can capture and sweep MPs particles by netting because of its large surface area and many surfaces group [6].

Kinetic studies

The kinetic studies on PPMPs removal at different pH were also investigated using pseudo-first-order and pseudo-second-order kinetic models, as shown in Figures 4(a)-(e). The parameters of the pseudo-first-order and pseudo-second-order kinetic model are summarized in Table 1. For the first-order kinetic model, the straight linear line plot proves a good agreement of experimental data with R^2 of more than 0.95, which suggest that the PPMPs removal followed a pseudo-first-order kinetic model. The kinetics rate constant, *k,* was calculated from the slope of the plot and is given in Table 1. The value of *k* at the optimum pH is 0.0136 min^{-1} with the coefficient of determination (R^2) of 0.9923. However, the set of correlation coefficient (R^2) values obtained from the second-order-kinetic model was poor, suggesting that the removal of PPMPs is not a second-order-kinetic reaction.

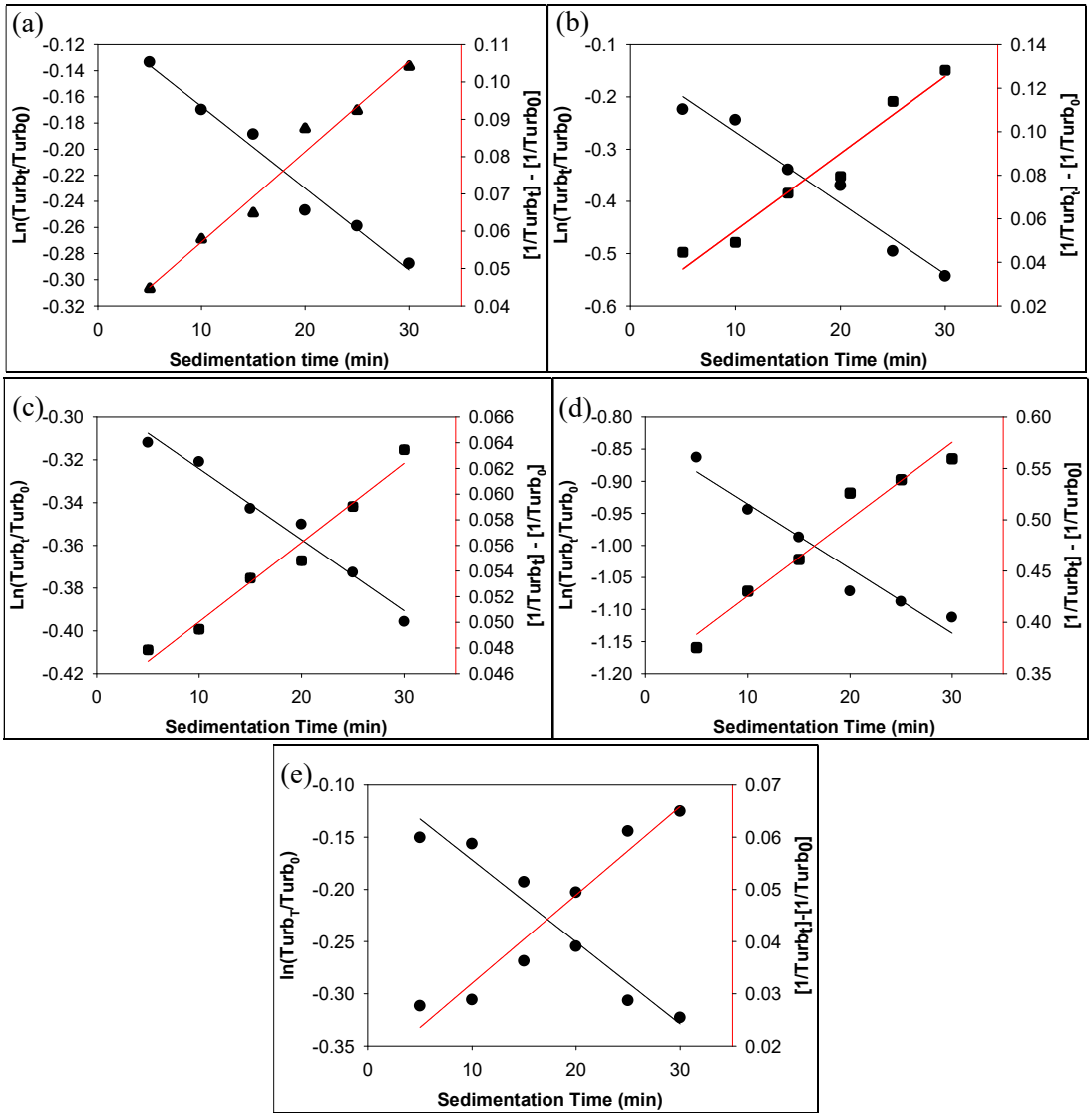


Figure 4. Pseudo-first-order (black line) and pseudo-second-order (red line) kinetics (a) pH 2 (b) pH 4 (c) pH 6 (d) pH 8 (e) pH 10

Table 1. Pseudo-first-order and pseudo-second-order rate constant

pH	Pseudo-first-order		Pseudo-second-order	
	Reaction Rate, k (min^{-1})	R^2	Reaction Rate, k (min^{-1})	R^2
2	0.0065	0.9729	0.0024	0.9220
4	0.0138	0.9639	0.0370	0.9752
6	0.0035	0.9694	0.0005	0.6857
8	0.0136	0.9923	0.0960	0.9763
10	0.0078	0.9505	0.0014	0.9398

Comparative studies on the effect of pH

Many researchers have reported on the use of EC to treat various pollutants. However, only a few studies focused on removing MPs via EC. Comparative experimental results of MPs from the literature and the result of this study are summarized in Table 2. The effect of pH on the EC process is commonly reported as one of the important parameters affecting microplastic removal efficiencies. However, most of this study focused on using conventional electrodes of Al and Fe in the EC process. Each MP is likely to respond differently to EC by the different electrodes. The results show that the EC process favors neutral pH of 7-8 for optimized MPs removal. Neutral to slightly basic pH was more conducive to the formation of floc. The floc formed gradually increased and improved the removal rate of MPs. Complete removal of PE was reported by Akarsu et al. [20] at pH 7 by utilizing an electrode combination of Al-Fe and Fe-Al. The use of different electrode combination improves the EC process and contribute to the successful removal of PE. The removal efficiencies of PPMPs in this study are lower compared to the other studies as we use the single Ni electrode without modification and shorter contact time. These are our preliminary results, and now we are focusing on improving the performance of MPs removal using Ni electrodes via the EC process by investigating the effect of other variable parameters, including the modification of the surface of Ni electrodes. The use of composite nickel electrodes may also be considered to improve the removal efficiencies of PPMPs.

Table 2. Studies on the effect of pH on microplastic removal

Electrode Material	Type of MPs	Optimum pH	Contact Time (min)	Removal Efficiency (%)	Ref
Al-Fe	PE	7.0	10	100	[20]
Al	Polyester	4.0	90	98.5	[3]
Al	PP	7.2	360	98.4	[6]
Al	PE	7.5	60	99.2	[12]
Ni	PP	8.0	30	67.0	This study

Conclusion

In this paper, the effect of pH on the removal efficiency of PPMPs via EC utilizing Ni electrodes was experimentally investigated. This is one of the early studies on this subject. A 67% removal efficiency followed a first-order- kinetic model with the kinetics rates constant (k) of 0.0136 min^{-1} with the coefficient of determination (R^2) of 0.9923 was achieved with EC using Ni electrode at 30 min reaction time which is in line with other studies. The findings suggested that EC technology is an effective method to remove MPs from simulated wastewater. However, studies should be further extended to improve the removal efficiency of PPMPs. It is suggested to modify the Ni electrode to improve its properties and optimize the EC parameter to boost its performance. Further research should focus on developing composite electrode for EC, as previous studies show that composite electrode provides excellent performance compared to a single electrode.

Acknowledgement

This research was supported by the Malaysia Ministry of Higher Education-Fundamental Research Grant Scheme (FRGS/1/2021/STG05/UiTM/02/09. The authors acknowledge the materials, facilities, and financial support provided by Universiti Teknologi MARA Cawangan Pulau Pinang.

References

1. Lebreton, L. C. M., Van Der Zwet, J., Damsteeg, J. W., Slat, B., Andrady, A., and Reisser, J. (2017). River plastic emissions to the world's oceans. *Nature Communications*, 8: 1-10.
2. Zhang, S., Shi, C., Nie, Y., Xing, B., Wen, X., and Cheng, S. (2023). Separation experiment and mechanism study on PVC microplastics removal from aqueous solutions using high-gradient magnetic filter. *Journal of Water Process Engineering*, 51: 103495.
3. Elkhatib, D., Oyanedel-Craver, V., and Carissimi, E. (2021). Electrocoagulation applied for the removal of microplastics from wastewater treatment facilities. *Separation and Purification Technology*, 276: 118877.
4. Conilie, M., Farihah, U., and Nasution, N. E. A. (2021). Utilization of plastic and fabric waste into economic valued products to minimize household waste. *IOP Conference Series: Earth and Environmental Science*, 747(1): 12107.
5. Prata, J. C., da Costa, J. P., Lopes, I., Andrady, A. L., Duarte, A. C., and Rocha-Santos, T. (2021). A one health perspective of the impacts of microplastics on animal, human and environmental health. *Science of the Total Environment*, 777: 146094.
6. Shen, M., Zhang, Y., Almatrafi, E., Hu, T., Zhou, C., Song, B., Zeng, Z. and Zeng, G. (2022). Efficient removal of microplastics from wastewater by an electrocoagulation process. *Chemical Engineering Journal*, 428: 131161.
7. Zhang, Y., Zhao, J., Liu, Z., Tian, S., Lu, J., Mu, R., and Yuan, H. (2021). Coagulation removal of microplastics from wastewater by magnetic magnesium hydroxide and PAM. *Journal of Water Process Engineering*, 43: 102250.
8. Rahman, A., Sarkar, A., Yadav, O. P., Achari, G., and Slobodnik, J. (2021). Potential human health risks due to environmental exposure to nano- and microplastics and knowledge gaps: A scoping review. *Science of the Total Environment*, 757: 143872.
9. Sun, J., Dai, X., Wang, Q., van Loosdrecht, M. C. M., and Ni, B.-J. (2019). Microplastics in wastewater treatment plants: Detection, occurrence and removal. *Water Research*, 152: 21-37.
10. Sol, D., Laca, A., Laca, A., and Díaz, M. (2020). Approaching the environmental problem of microplastics: Importance of WWTP treatments. *Science of the Total Environment*, 740: 140016.
11. Gies, E. A., LeNoble, J. L., Noël, M., Etemadifar, A., Bishay, F., Hall, E. R., and Ross, P. S. (2018). Retention of microplastics in a major secondary wastewater treatment plant in Vancouver, Canada. *Marine Pollution Bulletin*, 133: 553-561.
12. Perren, W., Wojtasik, A., and Cai, Q. (2018). Removal of microbeads from wastewater using electrocoagulation. *ACS Omega*, 3(3): 3357-3364.
13. Akarsu, C., and Deniz, F. (2021). Electrocoagulation/electroflotation process for removal of organics and microplastics in laundry wastewater. *CLEAN–Soil, Air, Water*, 49(1): 2000146.
14. Liu, Y., Zhang, X., Jiang, W. M., Wu, M. R., and Li, Z. H. (2021). Comprehensive review of floc growth and structure using electrocoagulation: Characterization, measurement, and influencing factors. *Chemical Engineering Journal*, 417(2): 129310.
15. Kiliç, M. G., Hoşten, Ç., and Demirci, Ş. (2009). A parametric comparative study of electrocoagulation and coagulation using ultrafine quartz suspensions. *Journal of Hazardous Materials*, 171(1–3): 247-252.
16. Kartikaningsih, D., Huang, Y. H., and Shih, Y. J. (2017). Electro-oxidation and characterization of nickel foam electrode for removing boron. *Chemosphere*, 166: 184-191.
17. Kartikaningsih, D., Shih, Y.-J., and Huang, Y.-H. (2016). Boron removal from boric acid wastewater by electrocoagulation using aluminum as sacrificial anode. *Sustainable Environment Research*, 26(4): 150-155.
18. Govindan, K., Oren, Y., and Noel, M. (2014). Effect of dye molecules and electrode material on the

settling behavior of flocs in an electrocoagulation induced settling tank reactor (EISTR). *Separation and Purification Technology*, 133: 396-406.

19. Widhiastuti, F., Lin, J. Y., Shih, Y. J., and Huang, Y. H. (2018). Electrocoagulation of boron by electrochemically co-precipitated spinel ferrites. *Chemical Engineering Journal*, 350(2): 893-901.
20. Akarsu, C., Kumbur, H., and Kideys, A. E. (2021). Removal of microplastics from wastewater through electrocoagulation-electroflotation and membrane filtration processes. *Water Science and Technology*, 84(7): 1648-1662.

Malaysian Journal of Analytical Sciences (MJAS)
Published by Malaysian Analytical Sciences Society

PHYSICOCHEMICAL PROPERTIES AND BIODEGRADABILITY OF PALM OIL PRODUCTS (POP) IN MARINE ENVIRONMENT

(Sifat Fizikokimia dan Kebolehbiodegradasi Produk Minyak Sawit (POP) dalam Persekitaran Marin)

Nur Azmina Roslan*, Nur Aainaa Syahirah Ramli, Noorazah Zolkarnain, Siti Afida Ishak, and Razmah Ghazali

Malaysian Palm Oil Board (MPOB),
6, Persiaran Institusi, Bandar Baru Bangi, 43000 Kajang, Selangor, Malaysia

**Corresponding author: nazmina@mpob.gov.my*

Received: 18 January 2023; Accepted: 21 June 2023; Published: 22 August 2023

Abstract

Palm oil products (POP), *i.e.*, crude palm oil (CPO), crude palm kernel oil (CPKO), refined, bleached, and deodorized (RBD) palm oil (RBDPO), and RBD palm olein (RBDPOo), are among the most highly traded POP in the world. Therefore, the quality and biodegradability of POP need to be assessed to ensure the traded POP is safe to consume and environmentally friendly. This paper investigates the physicochemical properties of POP, including moisture, slip melting point, iodine value, fatty acid content, and free fatty acid, using MPOB p2.1:2004, AOCS C c3-25, AOCS Cd 1d-92, AOCS Ce 1a-13, and MPOB p2.5:2004 test methods, respectively. Analysis showed that all the POP were within the requirements as specified by the Malaysian Standards, the Palm Oil Refiners Association of Malaysia (PORAM), the Malayan Edible Oil Manufacturers' Association (MEOMA), Codex Alimentarius, and the Malaysian Palm Oil Association (MPOA). Meanwhile, the biodegradability assessment of these POP in the marine environment was carried out according to Organization for Economic Co-operation and Development (OECD) 306, Biodegradability in Seawater test method, using the closed bottle method. The results indicated that CPO, CPKO, RBDPO, and RBDPOo can be degraded in temperate marine water at 74%, 70%, 75%, and 72%, respectively.

Keywords: biodegradation, quality, seawater, specification, standard

Abstrak

Produk minyak sawit (POP), iaitu minyak sawit mentah (CPO), minyak isirung sawit mentah (CPKO), minyak sawit ditapis, diluntur dan dinyahbau (RBDPO) dan minyak sawit olein RBD (RBDPOo), adalah antara POP yang terkenal dan diperdagangkan di dunia. Oleh itu, kualiti dan kebolehbiodegradan POP perlu dinilai untuk memastikan POP yang diperdagangkan selamat untuk dimakan dan mesra alam. Kajian ini menyiasat sifat fizikokimia POP, termasuk lembapan, takat lebur gelincir, nilai iodin, kandungan asid lemak dan asid lemak bebas menggunakan kaedah ujian MPOB p2.1:2004, AOCS C c3-25, AOCS Cd 1d-92, AOCS Ce 1a-13 and MPOB p2.5:2004. Analisis menunjukkan bahawa semua POP berada dalam perincian seperti yang ditetapkan oleh Jabatan Standard Malaysia, Persatuan Penapis Minyak Sawit Malaysia (PORAM), Persatuan Pengilang Minyak Masak Malaysia (MEOMA), Codex Alimentarius dan Persatuan Minyak Sawit Malaysia (MPOA). Sementara itu, penilaian kebolehbiodegradan POP ini dalam persekitaran marin telah dilaksanakan mengikut kaedah ujian Organisasi bagi Pembangunan

dan Kerjasama Ekonomi (OECD) 306, Biodegradasi dalam Air Laut, menggunakan kaedah botol tertutup. Keputusan menunjukkan bahawa CPO, CPKO, RBDPO and RBDPOo boleh terdegradasi dalam air marin sederhana dengan 74%, 70%, 75% and 72%, masing-masing.

Kata kunci: biodegradasi, kualiti, air laut, perincian, piawai

Introduction

Palm oil is an edible vegetable oil derived from the flesh or pulp (mesocarp) of palm fruits through the milling process and has been used for various purposes, including in food and non-food applications. Malaysia is a prominent exporter of palm oil since it represents 18.3% of the global oils and fats, thus contributing to 34.3% of the total palm oil trade in 2020 [1]. Meanwhile, in 2021, Malaysia exported 24.27 million tonnes of POP to various destinations, with more than 1.6 million tonnes exported to EU countries [2]. Further processing of crude palm oil (CPO) involves the removal of the products of hydrolysis and oxidation, color, and flavor for the production of refined products, *i.e.*, refined, bleached, and deodorized (RBD) palm oil (RBDPO) and RBD palm olein (RBDPOo), which are mainly used as cooking oil and in margarine, confectionery, non-dairy creamer, shortening, and others [3]. RBD palm kernel oil (RBDPKO) from CPKO has also been used in the same manner as CPO and in the production of oleochemical derivatives, *i.e.*, fatty acids, fatty amines, fatty alcohols, fatty methyl esters, and glycerin. These derivatives are mainly utilized as raw ingredients in the cosmetics, personal care, and household sectors for products including balms, lipsticks, soaps, detergents, and cleaning agents [3].

As product development and improvement evolve rapidly, it can be expected that there will be an increasing demand for quality improvement from consumers and their end-users. From a commercial point of view, quality is a valuable and significant attribute in edible oil commodities and their trades. Hence, it can be predicted that the trading specifications will become broader and more stringent over time. This will require reliable and accredited analysis methods to meet all statutory requirements. Failure to comply with quality specifications could affect the acceptance of the traded oils. In order to assess the quality of POP, several physicochemical analyses need to be conducted, including moisture, free fatty acid (FFA), iodine value (IV), fatty acid content (FAC), and slip melting point (SMP) [4].

Moisture is one of the most prevalent contaminants in POP. It is necessary to ensure the moisture content of POP is within the permitted limit since a high moisture content would affect hydrolytic stability [5]. In addition, some palm oil products tend to have a considerable amount of moisture and impurities due to insufficient processing, which may accelerate the microorganism's activities [6]. Besides moisture content, the amount of FFA is also a significant measure of the quality of POP since it is related to the economic value of edible oils [7]. In general, FFA is formed during oil storage through the reaction of oil and water, and a high level of FFA content implies poor POP quality [8].

The IV measures the degree of unsaturation [9] or double bonds in POP, which indicates the susceptibility of the oils to oxidation [10]. Meanwhile, the SMP is prevalently applied to analyze the melting and solidification properties of oil samples, at which the temperature of the solidified oil turns into fluid and flows into an open capillary tube [11]. The determination of SMP varies with the fatty acid chain length, trans fatty acid composition, and position of the fatty acids in the glycerol backbone, as well as unsaturation ratios [12].

Fatty acids can be classified according to their degree of saturation, *i.e.*, saturated or unsaturated fatty acids. Unsaturated fatty acids are either monounsaturated or polyunsaturated. Fatty acids play an important role in the oil and fat industry due to their health implications in the human diet and properties in industrial processes. Previous literature demonstrated the importance of the fatty acid content (FAC) of the oil in determining the biodegradation of vegetable oils [13-14]. The valuable data on the FAC of POP is also crucial since the type of fatty acids will determine the oil's nutritional status and storage stability. A previous study showed that POP was

stable up to 10 months of storage time at a low temperature of 6 ± 2 °C, indicating that these POP are suitable to be used as control samples for validation of test results [15].

Apart from the physicochemical properties, biodegradability is also considered a critical criterion for evaluating the behavior of substances or products in the environment. Assessment of the biodegradability of POP is deemed worthy since it is well known that vegetable oils, especially palm oil, are one of the most traded commodities transported *via* sea, and there is the possibility of oil spillage even though it is comparatively rare in the marine environment in comparison to mineral oil. Several incidents of accidental oil spillage caused by vessel accidents have been reported, with the most recent incidents occurring in Chinese waters, where about 9,000 tonnes of palm oil stearin were spilled. [16]. Vegetable oils are bulk liquid substances regulated as chemicals under the International Convention for the Prevention of Pollution from Ships (MARPOL) Annex II [17].

According to the GESAMP Composite List 2019 [18], most vegetable oils, including canola, sunflower, olive, and palm oils, are readily biodegradable. However, the conditions, as well as the rate of biodegradation, are yet to be revealed. Research conducted on the biodegradation of natural oils in seawater, *i.e.*, mustard, canola, and olive oil [19], revealed that canola oil could be easily degraded, followed by mustard and olive oils. The different trends in bacterial numbers were observed for the different types of oil. Most of the oil samples showed high bacterial numbers within 7 to 15 days of the biodegradation test, indicating that the oil samples are nontoxic and that the biodegradation process occurred rapidly in seawater. There was also research conducted on the microbes that possess the unique ability to bioremediate fat-containing waste. In this study, the marine strain, *Rhodococcus erythropolis* PR4, showed the potential to convert animal fats and vegetable oils into fatty acid methyl ester (FAME) derivatives in a relatively short time [20]. There was also a study on an isolated soil microbe, *Acinetobacter sp.* strain SOD-1, capable of degrading salad oil, which consists of soybean and rapeseed oil [21]. *Pseudomonas otitidis* strain was able to hydrolyze sunflower cooking oil to produce lipase [22]. Previous research on the degradation of CPO and CPKO in seawater using the modified shake flask method revealed an increase in bacterial population that peaked on days 7 and 21 before declining, indicating that palm oil is being used as a substrate for bacterial growth amidst degradation, which is aided by the lipase enzyme produced by selected bacteria [23].

The biodegradation test is crucial to assessing the biodegradation of substances in various environmental compartments. According to the OECD, Biodegradability in Seawater (OECD 306) and Marine BODIS test guidelines are frequently used to determine the biodegradability of substances in seawater, where the degradation of a substance is assessed by the measurement of dissolved oxygen over 28 days of the test period. This study aims to assess the physicochemical properties of POP under investigation, *i.e.*, moisture, FFA, IV, FAC, and SMP, using the American Oil Chemists Society (AOCS) and the Malaysian Palm Oil Board (MPOB) test methods, as well as the biodegradability of POP in the marine environment according to standard method OECD 306, Biodegradation in Seawater *via* the closed bottle method. This study can be used as a database in the event of an accidental oil spill.

Materials and Methods

The standard grade of palm oil products (POP), CPO, CPKO, RBDPO, and RBDPOo were obtained from Sime Darby Jomalina Sdn. Bhd., Selangor, Malaysia. All chemicals and solvents were utilized as received without further purification. Sodium acetate was used as a reference substance to check the validity of the test procedure and the suitability of the seawater used. A non-ionic surfactant, octylphenoxypolyethoxyethanol (IGEPAL CA-630), was used to emulsify the oil samples since they are insoluble in water.

Natural seawater was collected directly from Lowestoft, United Kingdom, and transferred into the laboratories through a pipe that extends below the sand some distance into the bay. The seawater was decanted and then filtered using Whatman 54 filters. Prior to the start

of the test, the seawater was equilibrated to the test temperature, which is 15-20 °C. Meanwhile, for the preparation of mineral stock solution A, potassium dihydrogen orthophosphate, KH_2PO_4 (8.50 g), dipotassium hydrogen orthophosphate, K_2HPO_4 (21.75 g), disodium hydrogen orthophosphate heptahydrate, $Na_2HPO_4.7H_2O$ (50.30 g), and ammonium chloride, NH_4Cl (0.50 g) were dissolved in water and made up to 1 L. Solution B was prepared by dissolving magnesium sulphate heptahydrate, $MgSO_4.7H_2O$ (22.50 g), in water and made up to 1 L. Solution C was prepared by dissolving calcium chloride dihydrate, $CaCl_2.2H_2O$ (36.40 g), in water and made up to 1 L. As for solution D, the solution needs to be freshly prepared by dissolving iron (III) chloride hexahydrate, $FeCl_3$ (0.15 g), in water and made up to 1 L. Mineral stock solutions used in the OECD 306 biodegradation test were prepared using analytical-grade reagents and deionized Ecotox Maxima-grade water. The mineral stock solutions A, B, and C were made in advance and stored at 4 ºC ± 2 ºC, while solution D was freshly made and not stored. All solutions were added at 1 mL/L to a total volume of 40 L of seawater. The prepared seawater mineral medium was aerated for 20 minutes and allowed to stand for 25 hours at 15-20 °C prior to use.

The equipment used in this study includes 300 mL Biological Oxygen Demand (BOD) bottles with glass stoppers, 4 L bottles with a liter mark, a dissolved oxygen meter (Multi 3410 WTW), an oven (ULM 500, Memmert), an analytical balance (HR 250A, A&D), a hot plate (SP 131320-33, Thermo Scientific Cimarec), gas chromatography with capillary column HP-88 (Agilent HP 6890 Series), a capillary tube for SMP with a length of 75 mm ± 0.02 mm, id 1.1 to 1.2 mm, od 1.3 to 1.4 mm, wall 0.2 mm ± 0.02 mm (Fisherbrand Microhematocrit), and a water bath (F34, Julabo).

Determination of moisture content

The moisture content of the POP was determined using the MPOB test method, MPOB p2.1:2004 [24]. This method involves heating the oil sample in an oven at 103 ± 2 °C, until all moisture and volatile substances are removed. The oil sample in a petri dish was dried and cooled in desiccators before it was weighed (approximately 10 g to the nearest 0.001 g). Then, the oil sample was heated at 103 °C for 2.5 h, left to cool to room temperature (23 to 25 °C) in a desiccator for 30 min, and further weighed. All of these stages were repeated until the weight remained constant. All analyses were conducted in duplicate, and the results were presented in the form of mean ± standard deviation. The moisture content was calculated using equation (1),

$$\text{Moisture (\%)} = \frac{\text{Mb}-\text{Md}}{\text{Mb}-\text{M}} \times 100 \quad (1)$$

Where: M = weight of the petri dish, Mb = weight of the petri dish and oil and Md = weight of the petri dish and oil after drying.

Determination of free fatty acid (FFA)

The MPOB p2.5:2004 test method [24] was used to measure the FFA in POP as a palmitic acid percentage. The oil was melted and homogenized before being weighed into a conical flask. Subsequently, neutralized isopropanol (50 mL) was poured into the flask containing the oil sample. Afterwards, a few drops of phenolphthalein were added to the mixture. The conical flask was then placed on a hot plate at 40 °C and titrated with a sodium hydroxide (NaOH) standard solution with continuous swirling before the first permanent pink color appeared. The FFA content was determined according to equation (2):

$$\text{FFA as palmitic acid (\%)} = \frac{25.6 \times \text{M} \times \text{V}}{\text{m}} \quad (2)$$

Where: M = molarity of NaOH solution, V = volume (mL) of NaOH solution, and m = weight (g) of the oil sample.

All analyses were conducted in duplicate, and the results were presented in the form of mean ± standard deviation.

Determination of iodine value (IV)

The AOCS Cd 1d-92 method was used to measure IV of the POP [25]. The oil sample was melted, homogenized, and filtered, and then the temperature was left to reduce to 68–71 °C before being weighed into a conical flask. The flask was then filled with cyclohexane: acetic acid (1:1) solution (15 mL) and Wijs solution (25 mL). The substances were thoroughly stirred before being stored for an hour in dark conditions at room temperature. Thereupon, a 10% potassium iodide (KI) solution (20 mL) was added, followed by distilled water (100 mL). The mixture was then titrated with a 0.1M sodium thiosulfate ($Na_2S_2O_3$) standard solution until the yellow color almost disappeared. The mixture was then added with a starch indicator solution (1–2 mL), followed by titration with $Na_2S_2O_3$ until the blue color diminished. These steps were repeated for the blank sample. All analyses were conducted in duplicate, and the results were presented in the form of mean ± standard deviation. The IV was expressed using equation (3):

$$\text{IV} \left(\frac{\text{g}}{\text{100g}}\text{oil}\right) = \frac{12.69 \times C \times (V1\text{-}V2)}{M} \quad (3)$$

Where: C = molarity (M) of the $Na_2S_2O_3$ solution, V1 = blank volume (mL) of $Na_2S_2O_3$ solution, V2 = test sample volume (mL) of $Na_2S_2O_3$ solution, and M = weight (g) of the oil sample.

Determination of fatty acid composition (FAC)

The AOCS Ce 2-66 and AOCS Ce 1a-13 methods were used in the preparation of fatty acid methyl esters (FAME) and quantitative analysis of FAC, respectively [25]. The preparation of FAME is important in order to enhance the volatility of the methyl ester derivatives. The FAC of the POP was determined using Agilent 6890 gas chromatography with a flame ionization detector (FID) and a capillary column HP-88 (60 m × 250 µm × 0.2 µm). The flow rate of the column was set at 0.8 mL/min. Meanwhile, the injector temperature and FID temperature were set at 250 °C. Initially, the oven temperature was programmed at 150 °C, then heated to 210 °C for 10 min with a heating rate of 3 °C/min. The injection volume was 1 µL, with a total run time of 30 min. FAME standards were used to analyze the GC chromatogram peaks. All analyses were conducted in duplicate, and the results were presented in the form of mean ± standard deviation.

Determination of slip melting point (SMP)

The SMP of POP was determined using the AOCS C c3-25 method, which applied the open capillary tube technique [25]. The palm oil samples need to be melted and homogenized first before they are filtered at 60°C in the oven and left in the oven for 10 min. Capillary tubes in triplicate were immersed in the melted oil portion until the oil ascended to a height of about 10 mm in the tube. Subsequently, the tubes with the oil sample were rapidly chilled by holding the ends of the tubes against ice until the sample hardened. These tubes were inserted into a beaker and stored in a refrigerator at 10 ± 1°C for 16 h. The tubes were taken out of the refrigerator after 16 h and affixed to a thermometer, whereby the lower ends of the tubes were even with the bottom of the thermometer's mercury bulb. The thermometer was immersed in a 400-mL beaker of distilled water, with its bottom reaching the level of the immersion mark. The water bath's initial temperature was fixed at 8–10 °C below the slip point of the oil sample. Then, the water bath was stirred with a magnetic stirrer, and the temperature was adjusted at a rate of 1 °C/min, then slowed to 0.5 °C/min as the slip point was nearly reached. The heating was carried on until the oil ascended in each tube, and the temperature was recorded. The average temperature of triplicate capillary tubes was calculated as the SMP. All analyses were conducted in duplicate, and the results were presented in the form of mean ± standard deviation.

Determination of chemical oxygen demand (COD) value

The COD test was carried out following Standard Methods for the Analysis of Water and Wastewater [26]. COD is an indicative measure of the oxygen required to oxidize soluble and particulate organic matter in water.

The sample was oxidized by refluxing in the presence of sulphuric acid/silver sulphate, and potassium dichromate. Unreduced potassium dichromate was determined by titration with a standardized iron (II) ammonium sulphate solution. The amount of dichromate reduced is proportional to the amount of oxygen required to oxidize the test substance and is expressed as mgO_2/mg. The test material was added to duplicate round bottom flasks (0.0121 g and 0.0125 g) containing deionized water, sulphuric acid/silver sulphate, mercuric sulphate, and potassium dichromate. In order to check the integrity of the test procedure, readily oxidizable reference material was tested. Blank vessels containing only reagents and deionized water were also tested. The vessels were refluxed for two hours, cooled, rinsed, and titrated with a standardized iron(II) ammonium sulphate solution (FAS) using a redox indicator.

Biodegradation tests using the OECD 306 test method

The OECD 306, Biodegradability in Seawater test method [27] is a modification of the established OECD 301D Closed Bottle and the OECD 301E Modified Screening Test [28]. The OECD 306 test evaluates the biodegradation of a substance over a set period by analyzing indirect parameters in a closed system containing seawater, the test substance, and nutrients. No additional microorganisms are added to the system. The biodegradation test was performed at Chemex Environmental International Limited, United Kingdom (UK). The natural seawater was collected from the Centre for Environment, Fisheries, and Aquaculture Science laboratories in the UK. The biodegradation test was conducted according to the OECD 306 test method at 15-20°C. The study on the effect of POP in a temperate environment is deemed necessary due to the high export of these products to EU countries.

Sodium acetate was used as a reference substance to ensure the test procedure's validity and the suitability of the inoculum used. Since the test materials are insoluble in water, a surfactant was introduced to emulsify the samples. About 0.50g of each POP was mixed with 0.25g of a non-ionic surfactant (IGEPAL CA-630). The resulting emulsion stock solution was gradually diluted by adding deionized water and then made up to volume (500 mL) to give a concentration of 1.0 g/L. The sample stock solution was then prepared by adding 1.0 g/L of the emulsion stock solution to 3.5 L of seawater mineral medium at 2.0 mL/L to give a final test concentration of 2.0 mg/L. Several replicates of BOD bottles were filled to absolute volume (300 mL) with the sample stock solution.

In order to account for any degradation of the surfactant in the test vessels, an additional 100 mL of 0.10 g of IGEPAL CA-630 stock solution was prepared and used in a series of surfactant control bottles. The surfactant control bottles were prepared by adding the surfactant stock solution to seawater mineral medium (1 ml/L) to give a final concentration of 1.0 mg/L, representing the final concentration of the surfactant used in the test sample bottles. These were used as the blank values for the calculation of the BOD for the test material. Initial dissolved oxygen (DO) concentrations were measured using a dissolved oxygen meter. The bottles were incubated in the dark at 18.7–19.2 ºC for the test period. Further measurements of DO concentration were made on bottles removed after 7, 14, 21, and 28 days. All analyses were conducted in duplicate, and the results were presented in the form of mean ± standard deviation. The BOD and percentage of degradation were calculated using equations (4) and (5), respectively.

$$\text{BOD } (mgO_2)\text{calculation } = \frac{(DOt0 - DOtt) - (DOb0 - DObt)}{\text{Concentration of test material } (\frac{mg}{L})} \times 100 \quad (4)$$

Where: DOt0 = DO of the test sample on day 0, DOtt = DO of the test sample on day t, DOb0 = DO of the blank on day 0, DObt = DO of the blank on day t*

* If materials are added using a surfactant, the DO of the surfactant control at days 0 and t are used in the place of the blank.

$$\text{Percentage of degradation (\%)} = \frac{\text{BOD} \times 100}{\text{COD}} \quad (5)$$

Results and Discussion

The physicochemical properties of the selected POP were compared with known standards for crude and refined oils such as the Malaysian Standards (MS 814:2007, Palm Oil – Specification; MS 816:2007, Palm Olein – Specification; MS 80:2011, Palm Kernel Oil – Specification), the Palm Oil Refiners Association of Malaysia (PORAM), the Malayan Edible Oil Manufacturers' Association (MEOMA), Codex Alimentarius, and the Malaysian Palm Oil Association (MPOA). The primary data were obtained from analyses conducted in the laboratory, and they were also compared with extracted data from the certificate of analysis (COA) issued by Sime Darby Jomalina Sdn. Bhd. The properties of POP from the laboratory were expressed in the form of mean value and standard deviation from three replicates, as in Tables 1–4.

Table 1. Comparison of quality characteristics of CPO

Characteristics	Specification	Primary data	COA
Moisture, %max	0.25[b]	0.17 ± 0.01	0.19
FFA, as palmitic acid, %max	5.0[a]	5.3 ± 0.00	4.1
Iodine value (Wijs)	50.1 – 54.9[a]	57.5 ± 0.17	52.6
Slip melting point	33.8 – 39.2[a]	35.4 ± 0.00	36.4

a - MS814:2007; b - PORAM/MPOA

Table 2. Comparison of quality characteristics of CPKO

Characteristics	Specification	Primary data	COA
Moisture, %max	0.5[a, b]	0.2 ± 0.02	0.1
FFA, as lauric acid, %max	5.0[a, b]	3.5 ± 0.00	2.1
Iodine value (Wijs)	19.0[a]; 16.5 – 18.75[b]	18.2 ± 0.15	18.76
Slip melting point	27.3 – 28.0[b]	27.8 ± 0.00	27.8

a - MEOMA; b - MS 80:2011

Table 3. Comparison of quality characteristics of RBDPO

Characteristics	Specification	Primary data	COA
Moisture, %max	0.1[a, b]	0.05 ± 0.01	0.02
FFA, as palmitic acid, %max	0.1[a, b]	0.20 ± 0.00	0.07
Iodine value (Wijs)	50 – 55[a]	51.7 ± 0.20	52.3
Slip melting point	33 – 39[a]	36.8 ± 0.00	36.6

a – PORAM; b – MPOA

Table 4. Comparison of quality characteristics of RBDPOo

Characteristics	Specification	Primary data	COA
Moisture, %max	0.1[b]	0.04 ± 0.01	0.040
FFA, as palmitic acid, %max	0.1[a, b]	0.2 ± 0.00	0.062
Iodine value (Wijs), min - max	56.0 – 59.1[b]	57.4 ± 0.00	58.82
Slip melting point, max	24[a]	20.4 ± 0.00	17.4
	19.2 – 23.6[b]		

a – PORAM; b - MS 816:2007

Table 5. Comparison of FAC of POP

POP	Characteristics	Specification	Primary data
CPO	C12:0	0.1 – 0.5[a]	0.2 ± 0.00
	C14:0	0.9 – 1.5[a]	1.1 ± 0.01
	C16:0	39.2 – 45.8[a]	44.8 ± 0.04
	C18:0	3.7 – 5.1[a]	4.6 ± 0.05
	C18:1	37.4 – 44.1[a]	39.0 ± 0.08
	C18:2	8.7 – 12.5[a]	9.2 ± 0.05
	C18:3	0.0 – 0.6[a]	0.2 ± 0.01
CPKO	C12:0	48[b]	47 ± 0.16
		45 – 55[c]	
	C14:0	16.7[b]	16.7 ± 0.10
		14.0 – 18.0[c]	
	C16:0	8.5[b]	8.9 ± 0.10
		6.5 – 10[c]	
	C18:0	2.1[b]	2.4 ± 0.03
		1.0 – 3.0[c]	
	C18:1	14.9[b]	16.6 ± 0.09
		12.0 – 19.0[c]	
	C18:2	2.5[b]	2.7 ± 0.02
		1.0 – 3.5[c]	
RBDPO	C12:0	0.1 – 0.5[a]	0.2 ± 0.00
	C14:0	0.9 – 1.5[a]	1.1 ± 0.00
	C16:0	39.2 – 45.8[a]	44.0 ± 0.06
	C18:0	3.7 – 5.1[a]	4.4 ± 0.00
	C18:1	37.4 – 44.1[a]	39.3 ± 0.02
	C18:2	8.7 – 12.5[a]	9.8 ± 0.03
	C18:3	0.0 – 0.6[a]	0.2 ± 0.00
RBDPOo	C12:0	0.2 – 0.4[d]	0.2 ± 0.00
	C14:0	0.9 – 1.2[d]	1.0 ± 0.02
	C16:0	38.2 – 42.9[d]	38.5 ± 0.04
	C18:0	3.7 – 4.8[d]	4.2 ± 0.07
	C18:1	39.8 – 43.9[d]	43.7 ± 0.08
	C18:2	10.4 – 12.7[d]	11.2 ± 0.12
	C18:3	0.1 – 0.6[d]	0.2 ± 0.00

a - MS814:2007; b - MS 80:2011; c - Codex (2019); d - MS 816:2007

Moisture content

Lipids are primarily hydrophobic; however, small amounts of moisture can easily be absorbed and preserved. The presence of moisture is often unfavorable since it facilitates microbial growth and stimulates the hydrolysis of lipids, thus increasing the FFA content. In addition, it can adversely affect the oil's taste, scent, and appearance, thus reducing customer acceptance and marketability.

Tables 1–4 depict the moisture content of the POP obtained from primary and secondary sources. The maximum permissible amount of moisture is 0.25%, 0.5%, 0.1%, and 0.1% for CPO, CPKO, RBDPO, and RBDPOo, respectively [5]. It was observed that the moisture content of POP from both sources was below the permissible limit set in the specifications. It is important to ensure the moisture content is within the

limit specified by the standards since an abundance of ample moisture could facilitate microbial growth. Previous studies have shown that microorganisms species such as *Penicillium sp*. and *Aspergillus niger* can be detected in the CPO when the moisture content value is higher than 0.69% [29].

Free fatty acid (FFA)

FFA is formed by the hydrolysis of triglycerides in the oil. FFA is an undesirable component since it gives the oil an unpleasant metallic taste. High FFA content will ultimately result in rancidity, which consequently changes the sensory and nutritional quality of POP [30].

It was observed that the FFA values of CPO (Table 1), CPKO (Table 2), RBDPO (Table 3), and RBDPOo (Table 4) are still below the maximum limit stated in the specifications. However, the FFA values observed through data from the laboratory analysis were slightly higher, and this may be due to the long storage period of oils that causes hydrolysis due to the presence of moisture. In addition, CPO releases FFA naturally through the activity of enzymes in the palm fruit and by microbial lipases, which further increases the FFA value [8]. It was specified that the maximum FFA content for CPO is 5%, as stated by MPOA. Meanwhile, PORAM stipulates that the maximum FFA content for RBDPO and RBDPOo is 0.1% [31]. As for CPKO, MEOMA and MS 80:2011 standardized the FFA value not exceeding 5% [5].

Iodine value (IV)

The IV is an indicator of the relative degree of unsaturation in oil components, as calculated by the uptake of halogen. A higher IV value indicates greater unsaturation, and the oil is more prone to oxidation [32]. According to MS 814:2007, the admissible range of IV for CPO is 50.1–54.9 [33]. As for CPKO, the permissible range is 19.0 according to MEOMA [5] and 16.5–18.75 according to MS 80:2011 [34]. Meanwhile, PORAM standards stipulate that the permissible IV range for RBDPO is 50-55, and the minimum IV for RBDPOo is 56 (PORAM, 2012). According to the results obtained in Tables 1 to 4, it can be assumed that most POP possess good quality in terms of IV since the value is within the specified maximum limit. As for CPO, the IV obtained from the laboratory analysis slightly exceeds the allowable range stated in MS 814:2007. However, the IV of CPO, when tested at Sime Darby Jomalina Sdn Bhd, is still within the limit, suggesting that the CPO might have undergone some changes in its properties during storage before the procurement of oils. Significant changes in the IV of CPO after 3 months of storage at room temperature have been reported in a previous study [35]. The difference in storage duration and condition, a higher storage temperature, and the presence of sunlight can lead to a higher IV [36]. Another study suggested that high temperatures increase the oxidation rate of unsaturated fatty acids [15].

Slip melting point (SMP)

Based on the data in Tables 1 to 4, the SMP of the tested POP met the requirement specified by MS 814:2007 with a value of 33.8°C–39.2°C for CPO [33], MS 80:2011 with a value of 27.3°C–28.0°C for CPKO [34], and PORAM with a value of 33°C–39°C for RBDPO and a maximum of 24 °C for RBDPOo [31].

Fatty acid composition (FAC)

Table 5 confirmed the presence of all main components of fatty acids in oils. It was observed that the FAC of CPO, RBDPO, and RBDPOo were within the range stated by MS 814:2007 and MS 816:2007 for palm oil and palm olein, respectively [33; 37]. The specifications of the processed POP were also included in the standards mentioned. As for CPKO, the FAC value slightly exceeded the allowable range stated in MS 80:2011 but is still within the range based on the Codex standard [38].

Chemical oxygen demand (COD)

The COD value of POP obtained from the accredited laboratory that conducted the biodegradation test is shown in Table 6. It was observed that all of POP showed quite similar COD values. The COD value is essential to determining the amount of oxidizable organic material in the sample, which will reduce the dissolved oxygen (DO) levels. Low DO concentrations in water can lead to anaerobic conditions, which are unfavorable to aquatic life [39].

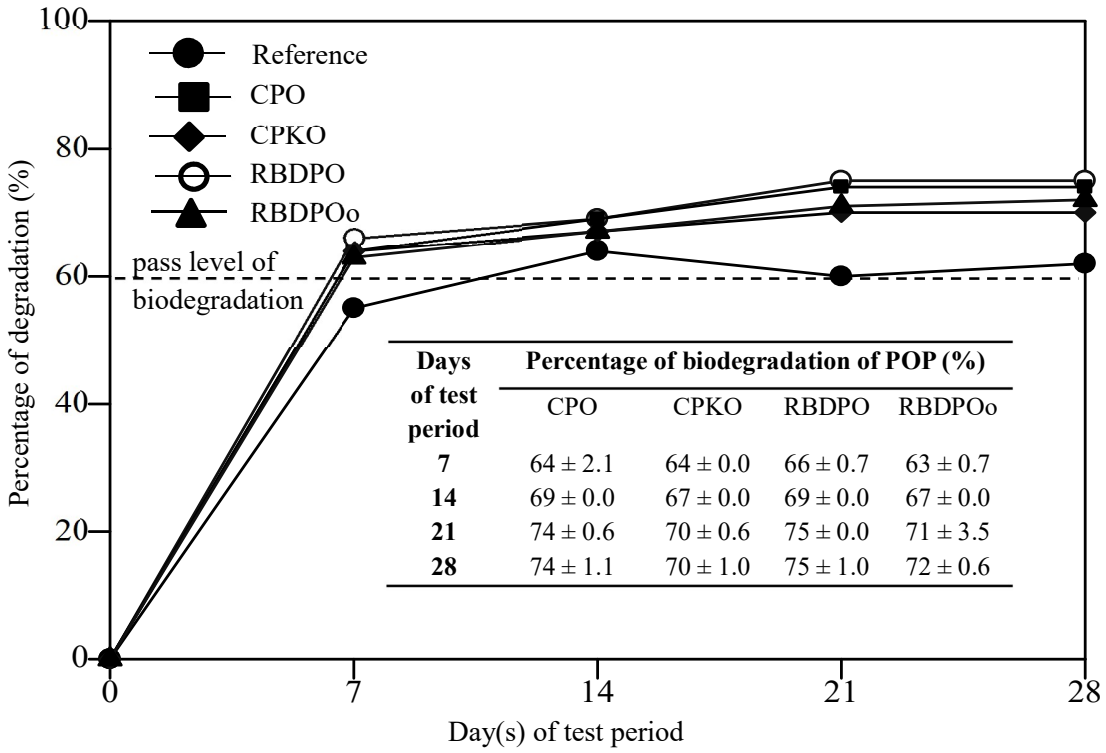
Table 6. COD value of POP

POP	ThOD/COD Value (mgO_2/g)
CPO	2456
CPKO	2489
RBDPO	2382
RBDPOo	2662

The oxygen demand value for the reference substance, sodium acetate, was calculated based on the test method (OECD, 1992), giving its theoretical oxygen demand (ThOD) value of 780 mgO_2/g.

Biodegradability assessment

All tested POP are insoluble in water; therefore, a surfactant (IGEPAL CA 630) was used to emulsify the sample. The effects of surfactant degradation were considered when calculating the degradation of the POP. It was observed that CPO, CPKO, RBDPO, and RBDPOo showed a positive result with more than 60% degradation relative to the COD value, with 60% being reached by day 7 and a maximum of 74%, 70%, 75%, and 72%, respectively, recorded on day 28 (Figure 1). A positive result of more than 60% ThOD removal within 28 days indicates that the material has the potential to biodegrade in the marine environment (OECD, 1992). This is supported by previous research on bacterial degradation of palm olein that revealed RBD palm olein was biodegradable in seawater, as indicated by the decreased DO value with increasing microbial counts over the 5 days of study. In addition, the fatty acid concentration was also found to decrease after the incubation period in seawater [40].



Days of test period	Percentage of biodegradation of POP (%)			
	CPO	CPKO	RBDPO	RBDPOo
7	64 ± 2.1	64 ± 0.0	66 ± 0.7	63 ± 0.7
14	69 ± 0.0	67 ± 0.0	69 ± 0.0	67 ± 0.0
21	74 ± 0.6	70 ± 0.6	75 ± 0.0	71 ± 3.5
28	74 ± 1.1	70 ± 1.0	75 ± 1.0	72 ± 0.6

Figure 1. Biodegradation of POP during 28-day test period

A previous study demonstrated the importance of the FAC of the oil in determining the biodegradation rate [13]. It was observed that the biodegradation process resulted in the formation of biodegradation intermediates and autoxidation products [13]. Autoxidation is a natural process of spontaneous oxidation in the presence of oxygen and can be expedited with free fatty acids, mono- and diacylglycerols, metals, e.g., iron, and thermally oxidized compounds [41]. Autoxidation of vegetable oils depends on their degree of unsaturation [42], and oils with a high unsaturated fatty acid content are more susceptible to autoxidation. The relative oxidation rates of stearic (C18:0), oleic (C18:1), linoleic (C18:2), and linolenic (C18:3) acids were reported to be 1, 100, 1200, and 2500 at 25 °C, respectively. According to Romero and Morton [43], the reaction rates of the autoxidation of oleic-linoleic acid mixtures decreased with decreasing linoleic acid molar fractions. In addition, several studies suggested the transformation of fatty acids during the degradation process [44-45]. Therefore, it can be deduced that there is a correlation between the fatty acid composition of oil and its degradation rate.

The structure of fatty acid molecules, *i.e*., characterized by the length of the carbon chain, the number of double bonds, and the exact position of these double bonds, can define and determine the biological reactivity of the fatty acid molecules [19]. Therefore, the chemical structure affects the biodegradability of a substance [46]. Table 7 shows the percentage of saturated, monounsaturated, and polyunsaturated fatty acids in POP. Based on the literature, the saturated fatty acids composition in palm oil is around 50%, with 44% palmitic acid (C16:0), and approximately 5% of stearic acid (C18:0) and remaining are the trace amounts of myristic acid (C14:0). The unsaturated fatty acids are approximately 40% of oleic acid (C18:1) and 10% consists of polyunsaturated linoleic acid (C18:2) and linolenic acid (C18:3) [47-48]. Meanwhile, for palm kernel oil, the saturated fatty acids and unsaturated fatty acids are roughly 79.1% and 20.9%, respectively [49].

Table 7. Percentage of saturated, monounsaturated and polyunsaturated fatty acids in POP

Fatty Acid Composition (%)	**POP**			
	CPO	**CPKO**	**RBDPO**	**RBDPOo**
Total saturated	50.49	74.75	49.75	43.85
Total monounsaturated	38.98	16.59	39.28	43.67
Total polyunsaturated	9.43	2.71	9.95	11.36

CPKO has the highest amount of saturated fatty acids and the lowest amount of monounsaturated and polyunsaturated fatty acids. This explained why CPKO showed a slightly low percentage of biodegradability since it is the most stable oil with the highest saturated fatty acid content compared to other POP. However, CPKO still showed the potential to be degraded in the marine environment. Meanwhile, RBDPO showed a high biodegradation percentage, mainly due to its high unsaturated fatty acid content. Unsaturated fatty acids are less stable than saturated fatty acids, making them more susceptible to oxidation [41].

In terms of microbial degradation, the initial stage for the degradation of POP would be the dissociation of ester bonds from fatty acids through the action of enzymes, including esterases and lipases. These two enzymes are synthesized by various microorganisms [50-51]. Meanwhile, the cleavage of carboxyl ester bonds is catalyzed by lipases, which are hydrophobic proteins. The carboxyl ester bonds are tri-, di-, and monoacylglycerols, the major components of animal, plant, and microbial fats and oils [52]. Both saturated and unsaturated fatty acids are biodegraded *via* a process known as β-oxidation after the initial stage of degradation.

Conclusion

The quality and biodegradability of POP are the key points in terms of their industrial use. The quality of four POP, *i.e*., CPO, CPKO, RBDPO, and RBDPOo, was determined through moisture, FFA, IV, FAC, and SMP

analyses. The properties of the POP were within the specified values as stipulated in the Malaysian Standards and also PORAM, MEOMA, Codex, and MPOA standards. Meanwhile, some of the values slightly deviated from the specified value, possibly due to the storage condition and time prior to the analysis of the sample. As for the biodegradability assessment of these POP, all samples achieved more than 60% biodegradability and, therefore, can be considered biodegradable in the marine environment. Hence, POP are not expected to cause any harm to the environment.

Acknowledgement

The authors would like to express their gratitude to the Director General of MPOB for granting permission to publish this research. The authors would also like to thank all analysts at the Analytical Testing Services Laboratory of the Advanced Oleochemical Technology Division (AOTD) for their technical assistance and services in completing this study.

References

1. Parveez, G. K. A., Tarmizi, A. H. A., Sundram, S., Loh, S. K., Ong-Abdullah, M., Palam, K. D. P., Salleh, K. M., Ishak, S. M. and Idris, Z. (2021). Oil palm economic performance in Malaysia and R&D progress in 2020. *Journal of Oil Palm Research,* 33: 181-214.
2. MPOB (2022). Monthly export of oil palm products - 2021. MPOB. Access from https://bepi.mpob.gov.my/index.php/en/export/export-2021/monthly-export-of-oil-palm-products-2021, accessed on 10 April 2022.
3. Maluin, F. N., Hussein, M. Z. and Idris, A. S. (2020). An overview of the oil palm industry: Challenges and some emerging opportunities for nanotechnology development. *Agronomy,* 10**:** 356.
4. Gupta, M. K. (2017). Chapter 1 - Requirement for successful production and delivery of the refined vegetable oils. *In:* GUPTA, M. K. (ed.) *Practical Guide to Vegetable Oil Processing (Second Edition)*. AOCS Press, p.1-5.
5. Chong, C. L. (2012). 15 - Measurement and maintenance of palm oil quality. *In:* LAI, O.-M., TAN, C.-P. & AKOH, C. C. (eds.) *Palm Oil*. AOCS Press, p.431-470.
6. Dongho, D., Gouado, I., Sameza, L. M., Mouokeu, R. S., Demasse, A. M., Schweigert, F. J. and Ngono, A. R. (2017). Some factors affecting quality of crude palm oil sold in Douala, Cameroon. *Journal of Food Research,* 6: 50-58.
7. O'brien, R. D. (2009). Fats and oils: Formulating and processing for applications, Third Edition, CRC Press.
8. Che Man, Y. B., Moh, M. H. and Van De Voort, F. R. (1999). Determination of free fatty acids in crude palm oil and refined-bleached-deodorized palm olein using fourier transform infrared spectroscopy. *Journal of the American Oil Chemists' Society,* 76: 485-490.
9. Peamaroon, N., Jakmunee, J. and Moonrungsee, N. (2021). A Simple colorimetric procedure for the determination of iodine value of vegetable oils using a smartphone camera. *Journal of Analysis and Testing,* 5**:** 379-386.
10. Tarmizi, A. H., Lin, S. W. and Kuntom, A. (2008). Palm-based standard reference materials for iodine value and slip melting point. *Analytical Chemistry Insights,* 3**:** 127-133.
11. Beare-Rogers, J. L., Dieffenbacher, A. and Holm, J. V. (2001). Lexicon of lipid nutrition (IUPAC Technical Report). *Pure and Applied Chemistry,* 73: 685-744.
12. Karabulut, I., Turan, S. and Ergin, G. (2004). Effects of chemical interesterification on solid fat content and slip melting point of fat/oil blends. *European Food Research and Technology,* 218**:** 224-229.
13. Salam, D. A., Suidan, M. T. and Venosa, A. D. (2016). Biodegradation and toxicity of vegetable oils in contaminated aquatic environments: Effect of antioxidants and oil composition. *Science of the Total Environment,* 547: 95-103.
14. Módenes, A. N., Sanderson, K., Trigueros, D. E. G., Schuelter, A. R., Espinoza-Quiñones, F. R., Neves, C. V., Zanão Junior, L. A. and Kroumov, A. D. (2018). Insights on the criteria of selection of vegetable and mineral dielectric fluids used in power transformers on the basis of their biodegradability and toxicity assessments. *Chemosphere,* 199: 312-319.

15. Ramli, N. A. S., Mohd Noor, M. A., Musa, H. and Ghazali, R. (2018). Stability evaluation of quality parameters for palm oil products at low temperature storage. *Journal of the Science of Food and Agriculture,* 98: 3351-3362.
16. Times, T. S. (2017). Beaches shut in Hong Kong after palm oil spill. Access from https://www.straitstimes.com/asia/east-asia/beaches-shut-in-hong-kong-after-palm-oil-spill. [Accessed online 17 May 2022].
17. Group of Experts on the Scientific Aspects of Marine Environmental Protection (2019). Revised GESAMP Hazard Evaluation Procedure for Chemical Substances Carried by Ships. International Maritime Organization.
18. Group of Experts on the Scientific Aspects of Marine Environmental Protection (2019). GESAMP Composite List 2019. Access from https://wwwcdn.imo.org/localresources/en/OurWork/Environment/Documents/GESAMP%20Composite%20List%20of%20hazard%20profiles-2019.pdf. [Accessed online 17 May 2022].
19. Al-Darbi, M. M., Saeed, N. O., Islam, M. R. and Lee, K. (2005). Biodegradation of natural oils in seawater. *Energy Sources,* 27: 19-34.
20. Kis, Á., Laczi, K., Zsíros, S., Rákhely, G. and Perei, K. (2015). Biodegradation of animal fats and vegetable oils by *Rhodococcus erythropolis* PR4. *International Biodeterioration & Biodegradation,* 105: 114-119.
21. Sugimori, D., Nakamura, M. and Mihara, Y. (2002). Microbial degradation of lipid by Acinetobacter sp. strain SOD-1. *Bioscience, Biotechnology, and Biochemistry,* 66: 1579-1582.
22. Ramani, K., Saranya, P., Jain, S. C. and Sekaran, G. (2013). Lipase from marine strain using cooked sunflower oil waste: production optimization and application for hydrolysis and thermodynamic studies. *Bioprocess and Biosystems Engineering,* 36: 301-315.
23. Arulasu, M. T., Ganesen, S. S. K., Lee, H. S., Tuan, A. S., Ghazali, R., Bhubalan, K. (2022). Microbial degradation of palm oil in natural seawater and identification of oil degrading bacterial consortium. *Malaysian Journal of Analytical Sciences,* 26: 976-988.
24. Kuntom, A. (2005). MPOB test methods: A compendium of test[s] on palm oil products, palm kernel products, fatty acids, food related products and others, Malaysia, Malaysian Palm Oil Board, Ministry of Plantation Industries and Commodities Malaysia.
25. Mehlenbacher, V. C. and Sallee, E. M. (2009). Official methods and recommended practices of the AOCS, American Oil Chemists Society.
26. APHA (2018). 5220 Chemical Oxygen Demand (COD); standard methods for the examination of water and wastewater. United States of America: American Public Health Association.
27. OECD (1992). Test No. 306: biodegradability in seawater, OECD Publishing.
28. Ott, A., Martin, T. J., Whale, G. F., Snape, J. R., Rowles, B., Galay-Burgos, M. and Davenport, R. J. (2019). Improving the biodegradability in seawater test (OECD 306). *Science of the Total Environment,* 666**:** 399-404.
29. Okechalu, J. N., Dashen, M. M., Lar, P. M., Okechalu, B. and Gushop, T. (2011). Microbiological quality and chemical characteristics of palm oil sold within Jos Metropolis, Plateau State, Nigeria. *Journal of Microbiology and Biotechnology Research,* 1(2): 107-112.
30. Wu, P.-F. and Nawar, W. W. (1986). A technique for monitoring the quality of used frying oils. *Journal of the American Oil Chemists' Society,* 63: 1363-1367.
31. Palm Oil Refiners Association of Malaysia (2012). *PORAM Handbook,* Malaysia, Palm Oil Refiners Association of Malaysia.
32. Sanders, T. H. (2003). Ground nut oil. *In:* Caballero, B. (ed.) Encyclopedia of food sciences and nutrition (second edition). Oxford: Academic Press, p.2967-2974.
33. Department of Standard Malaysia (2007). MS 814:2007 palm oil – specification (second revision). Malaysia: Department of Standards.
34. Department of Standard Malaysia (2011). MS 80:2011 palm oil – specification. Malaysia: Department of Standards.
35. Akusu, M. O., Achinewhu, S. C. and Mitchell, J.

(2000). Quality attributes and storage stability of locally and mechanically extracted crude palm oils in selected communities in Rivers and Bayelsa States, Nigeria. *Plant Foods for Human Nutrition,* 55**:** 119-126.

36. Akinola, S. A., Omafuvbe, B. O., Adeyemo, R. O., Ntulume, I. and Ailero, A. A. (2020). Effect of storage on the quality of processed palm oil collected from local milling points within Ile-Ife, Osun State, Nigeria. *Journal of Food Science and Technology,* 57: 858-865.
37. Department of Standard Malaysian (2007). MS 816:2007 palm oil – specification (second revision). Malaysia: Department of Standards.
38. Codex (2019). Codex standard for named vegetable oils (Codex-Stan 210-1999), Amendment 2019. Codex Alimentarius
39. Verberk, W. C. E. P., Buchwalter, D. B. and Kefford, B. J. (2020). Energetics as a lens to understanding aquatic insect's responses to changing temperature, dissolved oxygen and salinity regimes. *Current Opinion in Insect Science,* 41: 46-53.
40. Bhubalan, K., Hui-Wan, R. A. C., Renganathan, P., Tamothran, A. M., Ganesen, S. S. K., Ghazali, R. (2019). Bacterial degradation of palm olein in seawaterand identification of some cultivable strains. *Malaysian Applied Biology,* 48: 207-213.
41. Choe, E. and Min, D. B. (2006). Mechanisms and factors for edible oil oxidation. *Comprehensive Reviews in Food Science and Food Safety,* 5**:** 169-186.
42. Belitz, H., Grosch, W. and Schieberle, P. (1999). Lipids. Chapter 3. *Food Chemistry.* p.152-236.
43. Romero, A. J. R. and Morton, I. D. (1975). A kinetic study of the competitive oxidation of oleic acid-linoleic acid mixtures. *Journal of the Science of Food and Agriculture,* 26**:** 1353-1356.
44. Pereira, M. G., Mudge, S. M. and Latchford, J. (2003). Polymerisation versus degradation of sunflower oil spilled in the marine environments. *Marine Pollutution Bulletin,* 46: 1078-1081.
45. Pereira, M. G., Mudge, S. M. and Latchford, J. (2003). Vegetable oil spills on salt marsh sediments; comparison between sunflower and linseed oils. *Marine Environmental Research,* 56: 367-385.
46. Aluyor, E. O., Obahiagbon, K. O. and Ori-Jesu, M. (2009). Biodegradation of vegetable oils: A review. *Scientific Research and Essays,* 4: 543-548.
47. Prada, F., Ayala-Diaz, I. M., Delgado, W., Ruiz-Romero, R. and Romero, H. M. (2011). Effect of fruit ripening on content and chemical composition of oil from three oil palm cultivars (*Elaeis guineensis* Jacq.) grown in Colombia. *Journal of Agricultural and Food Chemistry,* 59: 10136-10142.
48. Noh, A., Rajanaidu, N., Kushairi, A., Mohd Rafii, Y., Mohd Din, A., Mohd Isa, Z. and Saleh, G. (2002). Variability in fatty acids composition, iodine value and carotene content in the MPOB oil palm germplasm collection from Angola. *Journal of Oil Palm Research,* 14: 18-23.
49. Bahadi, M., Mohamad Yusoff, M. F., Salimon, J., Ahmed Jumaah, M. and Derawi, D. (2019). Physicochemical characteristics of malaysian crude palm kernel oil. *Malaysian Journal of Chemistry,* 21: 17-27.
50. van Broekhuizen, P., Theodori, D., Le Blansch, K., and Ullmer, S. (2003). Lubrication in inland and coastal water activities. CRC Press.
51. Fingas, M. (2014). Vegetable oil spills. Handbook of oil spill science and technology. John Wiley & Sons, Inc. p.79-91.
52. Saifuddin, N. and Chua, K. (2006). Biodegradation of lipid-rich wastewater by combination of microwave irradiation and lipase immobilized on chitosan. *Biotechnology,* 5**:** 315-323.

Malaysian Journal of Analytical Sciences (MJAS)
Published by Malaysian Analytical Sciences Society

SYNTHESIS AND CHARACTERIZATION OF PALM OIL PENTAERYTHRITOL ESTER-BASED BIOLUBRICANT FROM MALAYSIA PALM OIL

(Sintesis dan Pencirian Biopelincir Berasaskan Ester Pentaeritritol Minyak Sawit daripada Minyak Sawit Malaysia)

Nurazira Mohd Nor[1,2*], and Jumat Salimon[3]

[1] *School of Chemistry and Environment, Faculty of Applied Sciences, Universiti Teknologi MARA, Cawangan Negeri Sembilan Kampus Kuala Pilah, 72000 Kuala Pilah, Negeri Sembilan, Malaysia*
[2] *Material, Inorganic and Oleochemistry (MaterOleo) Research Group, Faculty of Applied Sciences, Universiti Teknologi MARA, Cawangan Negeri Sembilan Kampus Kuala Pilah, 72000 Kuala Pilah, Negeri Sembilan, Malaysia*
[3]*Department of Chemical Sciences, Faculty of Science and Technology, Universiti Kebangsaan Malaysia, 43600 Bangi, Selangor, Malaysia*

[*]*Corresponding author: nurazira@uitm.edu.my*

Received: 24 March 2023; Accepted: 30 May 2023; Published: 22 August 2023

Abstract

Palm oil is one of the potential renewable resources in biolubricant production. However, the direct application of palm oil as biolubricant is restricted because of its low oxidative stability. It is due to the presence of oxidation active sites β- hydrogen in a glycerol backbone structure. This oxidative drawback can be overcome by molecule structural redesign through a chemical modification process such as esterification with polyhydric alcohol. The esterification of palm oil fatty acids (POFAs) with pentaerythritol (PE) was carried out in a mole ratio of 4.5:1, 1% of sulphuric acid, reaction temperature of 165 °C and reaction time of 7.2 hours. Gas Chromatography equipped with a Flame Ionization Detector (GC-FID) was used to determine the percentage of ester composition in palm oil pentaerythritol (POPE) ester. The structure of the POPE ester was confirmed by Fourier Transformation Infra-Red (FTIR) and proton and carbon Nuclear Magnetic Resonance (^{1}H-NMR and ^{13}C-NMR) spectroscopy. Results showed that POPE ester has been successfully synthesized with 85% of yield and 97.4% composition of tetraesters. The existence of the ester functional group is evidenced by FTIR at 1740 cm^{-1}, the chemical shift of ^{1}H NMR at 2.29-2.33 ppm and ^{13}C NMR at 173.24 ppm. Physicochemical properties analysis showed that POPE ester has oxidative stability at 189 °C, pour point at 17 °C, flash point at 300 °C and 147 viscosity index which makes POPE ester suitable to be used in many industrial lubrication applications.

Keywords: Esterification, oxidative stability, palm oil fatty acid, pentaerythritol

Abstrak

Minyak sawit merupakan salah satu sumber boleh diperbaharui yang berpotensi dalam penghasilan biopelincir. Walau bagaimanapun, penggunaan minyak sawit secara terus sebagai biopelincir adalah terhad kerana kestabilan oksidatifnya yang rendah. Ini disebabkan oleh kehadiran tapak aktif pengoksidaan β- hidrogen dalam struktur tulang belakang gliserol. Kelemahan

oksidatif ini boleh diatasi dengan reka bentuk semula struktur molekul melalui proses pengubahsuaian kimia seperti pengesteran dengan alkohol polihidrik. Pengesteran asid lemak minyak sawit (POFAs) dengan pentaeritritol (PE) dijalankan dalam nisbah mol 4.5:1, 1% asid sulfurik, suhu tindak balas 165 °C dan masa tindak balas 7.2 jam. Kromatografi Gas yang dilengkapi dengan Pengesan Pengionan Nyala (GC-FID) digunakan untuk menentukan peratus komposisi ester dalam ester pentaeritritol minyak sawit (POPE). Struktur ester POPE telah disahkan oleh spektroskopi transformasi Fourier infra-merah (FTIR) dan spektroskopi resonan magnetik nukleus proton dan karbon (NMR) (^{1}H-NMR dan ^{13}C-NMR). Keputusan menunjukkan bahawa ester POPE telah berjaya disintesis dengan 85% hasil dan 97.4% komposisi tetraester. Kewujudan kumpulan berfungsi ester dibuktikan melalui FTIR pada 1740 cm^{-1}, anjakan kimia ^{1}H NMR pada 2.29-2.33 ppm dan ^{13}C NMR pada 173.24 ppm. Analisis sifat fizikokimia menunjukkan bahawa ester POPE mempunyai kestabilan oksidatif pada 189 °C, takat tuang pada 17 °C, takat kilat pada 300 °C dan indeks kelikatan 147 yang menjadikan ester POPE sesuai digunakan dalam pelbagai kegunaan pelinciran industri.

Kata kunci: Pengesteran, kestabilan oksidatif, asid lemak minyak sawit, pentaeritritol

Introduction

In recent years, the development of renewable resources-based lubricants has increased due to the increasing cost of petrochemicals and rising concern for environmental pollution [1]. Rapidly depleting crude oil reserves and crude oil production also initiated high demand for industrial biolubricants. In the European region, subsidies, tax breaks and labeling programs are triggering high demand for biolubricants, especially for hydraulic fluid applications. It transmits the power to hydraulic machinery that is mostly used in the mining, industrial, agricultural and marine sectors. In this region alone the market is expected to reach US$884.6 million by 2026 [2].

The development of biodegradable and environmentally friendly biolubricants is very much needed nowadays. The world is moving rapidly towards the use of biolubricants, especially in industrial and automotive applications. More than 1700 lubricant manufacturing industries play an important role worldwide [3]. The global biolubricants market is estimated to be worth US$1.9 billion in 2020 and is expected to reach a revised size of US$2.5 billion by 2026 with a Compound Annual Growth Rate (CAGR) of 5.2%. The top market is the U.S. market at US$360.2 million in 2021, while the Chinese market is expected to reach US$230.4 million by 2026. Japan and Canada are forecast to grow at 3.7% and 4.1% CAGR respectively. In Europe, Germany is expected to grow at about 5% CAGR while the rest of the Europe market will reach US$246.8 million by the end of 2026. The driving demand for biolubricants is due to the advances in the development of engine design and operational efficiency and stringent government regulations particularly in North America and Europe, which discourage the use of synthetic and chemical-based lubricants [4].

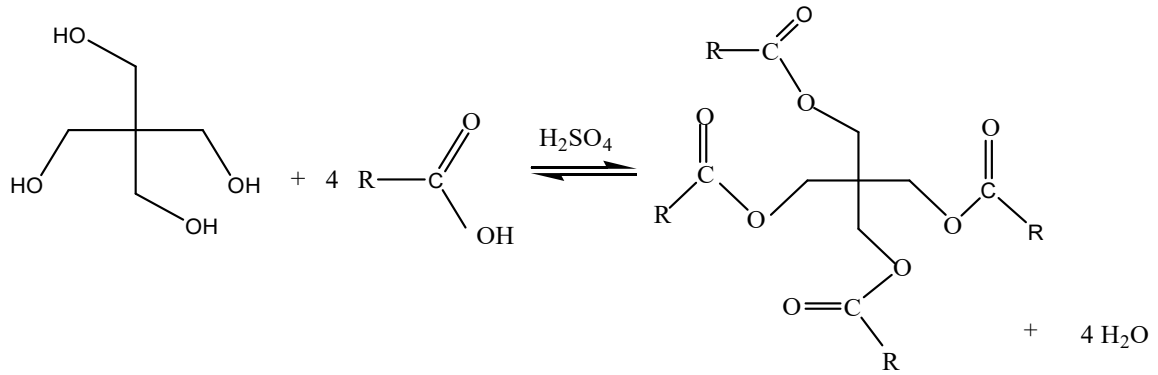
Plant oils are found to be the best alternative source to replace petrochemical because plant oils are biodegradable, non-toxic and cheaper compared to conventional sources of petrochemicals [5, 6]. Plant oils themselves exhibit good lubricity with high viscosity index [7]. However, plant oil cannot be used directly as a lubricant because of its low oxidative stability [7, 8, 9]. It is due to the presence of oxidation active sites β-hydrogen in the glycerol backbone structure, which will cause plant oil to become unstable at higher temperatures [10]. The β-hydrogen is easily removed from triacylglycerol molecules and it will form acid and olefin (unsaturated compounds). The resulting unsaturated compounds will undergo polymerization and will cause the formation of a precipitate that will increase the viscosity of plant oil [11]. The oxidative stability drawback that incurs in plant oil can be overcome by molecule structural redesign through chemical modifications.

Chemical modification processes such as transesterification and esterification are among important industrial processes due to their simplicity, viability, achievability and low-cost processes [4]. One modification that can be used is esterification with a polyhydric alcohol such as neopentylglycol (NPG) [12], trimethylolpropane (TMP) [13] and pentaerythritol (PE) [14], which will replace the glycerol backbone in plant oil structure. The advantage of using polyhydric alcohol is the absence of hydrogen in the beta position (β-

hydrogen), which enhances the thermal and oxidative stability of the lubricant at high temperatures [15,16]. The esterification of plant oil-based fatty acids with various polyhydric alcohols has been reported to successfully achieve high yields percentage and high esters selectivity [4].

Recently, palm oil which is abundantly available all over Malaysia become one of the potential plant oils that can be used as biolubricant base stock [17,18]. There are many studies reported on the production of biolubricant from palm oil and polyhydric alcohols. The production of biolubricant via transesterification of palm oil methyl ester (POME) with trimethylolpropane (TMP) was reported by Yunus et al. [19]. TMP is polyhydric alcohol that has three hydroxyl groups. The transesterification of POME and TMP that was carried out in a mole ratio of 3.9:1, a reaction temperature of 120 °C, a reaction time of 1 hour, 20 mbar of pressure, and 0.8% sodium methoxide catalyst has successfully produced 98% palm oil TMP triesters. Sulaiman et al. [20] also reported the optimization of the transesterification of POME and TMP. The optimum conditions were obtained at 3.8:1 mole ratio, a reaction temperature of 120 °C, a reaction time of 2 hours, 20 mbar of pressure and 0.9% sodium methoxide catalyst. At these optimum conditions, 86% of palm oil TMP triesters were successfully synthesized. In 2013, Salih et al. [21] reported the esterification between palm kernel oil fatty acids (PKOFAs) with TMP in a mole ratio of 4:1, reaction temperature of 150 °C, a reaction time of 5 hours and 1% sulphuric acid as catalyst. The results showed that a 68% yield of TMP ester was successfully synthesized with good lubrication properties such as a high flash point (over 300 °C), a pour point at 3 °C and a high viscosity index (157).

Other than TMP, there was also a study using pentaerythritol (PE) in the production of biolubricant. PE is polyhydric alcohol with four hydroxyl groups. In 2014, Aziz et al. [22] reported the production of biolubricant through transesterification between POME and PE in a mole ratio of 4.5:1, a reaction temperature of 158 °C, a reaction time of 1 hour and 1.19% sodium methoxide catalyst. The transesterification has produced a 40% yield of PE ester which has a flash point at 302 °C and 12.7 cSt viscosity at 100 °C. However, there is a lack of study reported on the esterification of palm oil fatty acids (POFAs) and PE. Hence, in this study, the esterification of POFAs with PE to produce palm oil pentaerythritol (POPE) ester as shown in Figure 1 is reported. Fatty acid composition of POFAs and POPE ester, as well as ester composition in POPE ester, will be analyzed by GC-FID, while the structure of POPE ester will be confirmed by FTIR and NMR spectroscopy. The physicochemical properties of POPE ester were examined by using several tests such as oxidative stability, pour point, flash point and viscosity index.



Pentaerythritol Palm Oil Fatty acid Palm Oil PE Ester Water

R= Mixed palm oil fatty acids (myristic, stearic, palmitic, oleic and linoleic acid)

Figure 1. Esterification of palm oil fatty acids (POFAs) with pentaerythritol (PE)

Materials and Methods

Materials

Palm oil was obtained from Jomalina Refinery, Teluk Panglima Garang, Selangor, Malaysia. Pentaerythritol was purchased from Sigma Aldrich. Sulphuric acid, toluene, ethyl acetate, sodium bicarbonate, sodium chloride, sodium sulphate, hydrochloric acid, n-hexane, potassium hydroxide and ethanol were purchased from Systerm.

Hydrolysis of palm oil

The hydrolysis process involves two stages which are saponification and acidification. In saponification, 50 grams of palm oil was mixed with 300 mL of alkaline ethanol in a 500 mL three-neck round bottom flask equipped with a mechanical stirrer, thermometer and reflux condenser and heated at 60 °C for 2 hours [23]. After the reaction was complete, the mixture underwent an acidification process in which 150 mL of 6N hydrochloric acid was added to neutralize the alkaline solution. The washing was continued using 200 mL of distilled water and 100 mL of hexane as solvent. The product, palm oil fatty acids (POFAs), was kept overnight by adding anhydrous sodium sulphate. The product was filtered by Whatmann No. 1 filter paper and the solvent used was isolated by a rotary evaporator at 70 °C. The product (POFAs) was analyzed using Gas Chromatography equipped with a Flame Ionization Detector (GC-FID).

Esterification of palm oil fatty acids and pentaerythritol

The esterification process was conducted by mixing palm oil fatty acids (POFAs) and pentaerythritol (PE) in a mole ratio of 4.5:1 in a 500 mL three-neck round bottom flask, equipped with a thermometer and Dean-Stark apparatus. 1% sulphuric acid and 100 mL of toluene were added to the mixture. The mixture was heated at 165 °C for 7.2 hours with continuous stirring. The product, palm oil pentaerythritol (POPE) ester, was neutralized with 150 mL of sodium hydrogen carbonate solution (5%), 150 mL of sodium chloride solution (5%) and 100 mL of ethyl acetate. The product was kept overnight by adding anhydrous sodium sulphate. The product was filtered by Whatmann No. 1 filter paper and the solvent used was isolated by a rotary evaporator at 70 °C. The POPE ester was analyzed using GC-FID, Fourier Transformation Infra-Red (FTIR) and proton and carbon Nuclear Magnetic Resonance (^{1}H-NMR and ^{13}C-NMR).

Characterization of palm oil, palm oil fatty acids (POFAs) and palm oil pentaerythritol (POPE) ester

The fatty acid composition of palm oil, POFAs and POPE ester was analyzed using GC-FID (column BPX-70). Fatty acid methyl esters (FAMEs) were prepared using two methods: base-catalyzed for palm oil and POPE ester and acid-catalyzed for POFAs. For base-catalyzed, FAME was prepared by blending 0.1 mL of oil sample with 1 mL of hexane. 1 mL of sodium methoxide solution (1.55 grams of sodium hydroxide and 50 mL of methanol) was added to the oil solution and the solution was stirred vigorously using a Vortex stirrer for 10 seconds. The solution was allowed to stand for 10 minutes to separate the clear solution of FAME from the cloudy aqueous layer. The upper FAME layer was slowly collected and injected into GC for analysis. For acid-catalyzed, 1 gram of POFAs was weighed into a 250 mL three-neck round bottom flask equipped with a mechanical stirrer, a thermometer and a reflux condenser. 3.75 mL of methanol was added with 0.75 mL of reagent mixture (5 mL of methanol and 1.25 mL of concentrated hydrochloric acid (36.5%)), followed by 0.75 mL of toluene. The mixture was heated at 65 °C for 1.5 hours. The mixture was then transferred into a separation funnel. 7.5 mL of hexane and 5 mL of distilled water were added to the mixture. The mixture was allowed to stand to separate two layers. The upper layer was slowly collected and dried using anhydrous sodium sulphate overnight. The sample was filtered and injected into GC for analysis.

The percentage of ester composition in POPE ester was determined using GC-FID (column DB-5HT). The sample was prepared by mixing 0.3 µL of POPE ester with 1mL of ethyl acetate. Subsequently, the structure of the POPE ester was confirmed using Fourier Transformation Infra-Red (FTIR) and proton and carbon Nuclear Magnetic Resonance (^{1}H-NMR and ^{13}C-NMR) spectroscopy. FTIR spectra were recorded on Perkin Elmer Infrared Spectrophotometer in the range of 500-4000cm^{-1}. ^{1}H and ^{13}C NMR were recorded on JEOL-

ECP 400 spectrometer (400 MHz ^{1}H/100.61 MHz ^{13}C) using $CDCl_3$ as a solvent.

Physicochemical properties tests of palm oil pentaerythritol (POPE) ester

The American Society for Testing Materials (ASTM) standards such as ASTM D-6186, ASTM D-5853, ASTM D-92 and ASTM D-2270 were used to measure oxidative stability, pour point, flash point and viscosity index [24]. The oxidative stability test was conducted using Differential Scanning Calorimetry (DSC). 1.5 mg of POPE ester was placed into an aluminum pan with a pinhole cover to allow interaction between the ester product and oxygen gas which acts as a reaction gas. Then, the aluminum pan was put into DSC and heated for 20 minutes up to temperatures of 250 °C by using nitrogen gas. The onset temperature was recorded to determine oxidative stability.

In the pour point test, the POPE ester was filled into a U-shaped glass tube until it reached a height of 4 cm. The thermometer was placed at one end of the U-shaped tube and both ends of the U-shaped tube were covered with parafilm. The U-shaped tube containing the POPE ester was placed in a refrigerator (minimum temperature -80 °C) for 24 hours to ensure that the POPE ester froze completely. After being left overnight, the U tube was removed and flipped upside down. The lowest temperature at which movement of the POPE ester was observed was recorded as the pour point.

For flash point testing, 2 mL of the POPE ester was placed in a crucible and heated on a heating plate. A thermometer with a maximum reading temperature of 360 °C was placed on the POPE ester to measure the temperature. The temperature was rapidly increased at first and then at a slow constant rate as the flash point approached. The lowest temperature at which the vapors above the surface of the liquid ignited was taken as the flash point.

For the viscosity index test, the Rheometer Anton Paar (Physica MCR 301 model) was used to measure the viscosity and viscosity index of the POPE ester. The diameter used for the samples was 0.051 mm. POPE ester was tested at 40 °C and 100 °C. The POPE ester's viscosity index was calculated based on the formula below:

$$\text{Viscosity index} = (L-U)/(L-H) \times 100$$

Where: U= oil's kinematic viscosity at 40 °C, L and H = values based on the oil's kinematic viscosity at 100 °C.

Results and Discussion

Palm oil (PO) is golden yellow and exists in a semi-solid form at room temperature. The liquid fraction contains unsaturated triacylglycerol (TAG) whereas the solid fraction contains more saturated TAG. TAG and fatty acid composition analyses were performed to determine their main composition in palm oil. Table 1 shows that the main TAG in palm oil is POP (39.89%), followed by POO (26.69%), PLP (7.43%), PLO (7.34%) and other TAGs. POP and POO show higher percentages because palmitic acid and oleic acid are the main fatty acid in palm oil. It is evidenced by the fatty acid composition shown in Table 2. The main fatty acid composition of palm oil is oleic acid with 44.8%, followed by palmitic acid (41.9%), linoleic acid (9.1%), stearic acid (3.6%) and myristic acid (0.6%).

The hydrolysis process was carried out to convert triacylglycerols in palm oil into palm oil fatty acids (POFAs), which will be used in the esterification process with pentaerythritol (PE). The percentage yield of POFAs after hydrolysis is 95%. Figure 2 shows a GC-FID (column BPX-70) chromatogram of fatty acid compositions in palm oil (before hydrolysis) and POFAs (after hydrolysis). The percentage composition of each fatty acid has been simplified in Table 2. POFAs also consist of five types of fatty acids. The major fatty acid composition in POFAs is oleic acid at 43.5%, followed by palmitic acid (42.5%), linoleic acid (9.5%), stearic acid (3.7%) and myristic acid (0.8%). The fatty acid composition of palm oil and POFAs is close to the value of the fatty acid composition of palm oil reported by Chowdhury et al. [25].

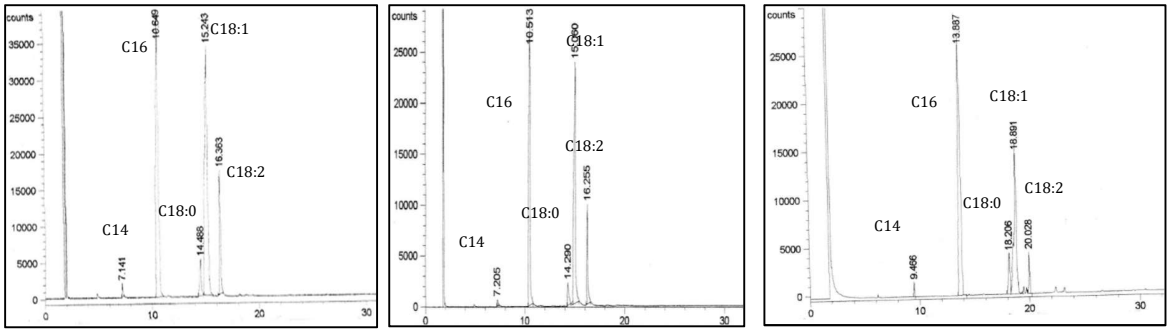
Table 1. Triacylglycerol composition (percentage) of palm oil

Triacylglycerol	Percentage (%)
Free fatty acid	7.03
Monoacylglycerol + Diacylglycerol	2.88
1-oleoyl-2,3-dilinoleoyl-glycerol (OLL)	0.04
1-palmitoyl-2,3-dilinoleoyl-glycerol (PLL)	0.68
1-miristoyl-2-linoleoyl-3-palmitoyl-glycerol (MLP)	0.07
1,3-dioleoyl-2-linoleoyl-glycerol (OLO)	0.45
1-palmitoyl-2-linoleoyl-3-oleoyl-glycerol (PLO)	7.34
1,3-dipalmitoyl-2-linoleoyl-glycerol (PLP)	7.43
1,2,3-tri-oleoyl-glycerol (OOO)	1.55
1-palmitoyl-2,3-dioleoyl-glycerol (POO)	26.69
1,3-dipalmitoyl-2-oleoyl-glycerol (POP)	39.89
1,2,3-tri-palmitoyl-glycerol (PPP)	3.11
1-sterioyl-2,3-dioleoyl-glycerol (SOO)	0.61
1-palmitoyl-2-oleoyl-3-sterioyl-glycerol (POS)	1.99
1,2-dipalmitoyl-3-sterioyl-glycerol (PPS)	0.24

Table 2. Fatty acid composition (percentage) of palm oil, POFAs and POPE ester

Fatty Acid Composition	Palm oil	POFAs	POPE Ester	Reference[25]
Myristic acid (C14)	0.6	0.8	1.0	1.2
Palmitic acid (C16)	41.9	42.5	53.5	41.8
Stearic acid (C18)	3.6	3.7	6.5	3.4
Oleic acid (C18:1)	44.8	43.5	35.1	41.9
Linoleic acid (C18:2)	9.1	9.5	3.9	11

The esterification process was carried out between POFAs and PE in the presence of sulphuric acid as a catalyst to produce POPE ester. The percentage yield of POPE ester was 85% and obtained in the semi-solid form at room temperature. Figure 2(c) shows the fatty acid compositions in POPE ester and it has been simplified in Table 2. The GC result showed that POPE ester contains 61% of saturated fatty acids and 39% unsaturated fatty acids. It means saturated fatty acids which have a straight-chain structure have a higher tendency to react with PE compared to the bent structure of unsaturated fatty acids due to less steric hindrance.



(a) (b) (c)

Figure 2. GC-FID (column BPX-70) chromatogram a) Palm oil; b) POFAs; c) POPE ester

POPE ester identification and characterization

The percentage of ester composition in POPE ester was determined by GC-FID (column DB-5HT) analysis as shown in Figure 3. Four types of esters will be produced from the esterification process, which are monoesters, diesters, triesters and tetraesters. In the esterification process, monoesters, diesters and triesters were formed as intermediate products towards the completion of the reaction producing POPE tetraesters. Figure 3 shows that 97.4% of tetraesters and 2.6% of triesters were produced in the POPE ester. Almost all hydroxyl groups in PE were successfully esterified with POFAs. This result was supported by the low hydroxyl value of POPE ester, which was 33.42 mgKOH/g compared to the hydroxyl value of PE, which was 1645 mgKOH/g. However, there were still hydroxyl groups that unsuccessfully reacted in this esterification. It can be seen by the presence of trace triester which has a hydroxyl group in its structure.

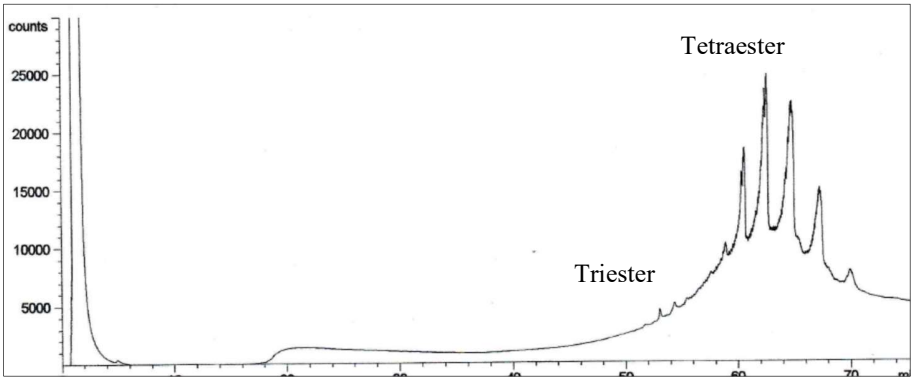


Figure 3. GC-FID (column DB-5HT) chromatogram of POPE Ester

Identification of the functional group present in the POPE ester was confirmed by FTIR analysis. The comparison between FTIR spectra of POFAs (before esterification) and POPE ester (after esterification) is shown in Figure 4. FTIR spectrum of the POPE ester shows the appearance of a C=O ester peak at 1740 cm^{-1} and the stretching of the C-O ester group exists at 1154 cm^{-1} and 1234 cm^{-1}. These values are supported by the study conducted by Nor et al. [4], which states the appearance of the stretching of the C=O ester peak is at 1738 cm^{-1} and the stretching of the C-O ester peak is at 1161 cm^{-1} and 1241 cm^{-1}. On the other hand, the FTIR spectrum of POFAs shows the stretching of the C=O group of carboxylic acid appeared at 1696 cm^{-1} and the stretching of the C-O carboxylic acid exists at 1291 cm^{-1} and 1247 cm^{-1}. According to Nor et al. [4], the stretching of the C=O group of carboxylic acid is at 1696 cm^{-1} and the stretching of C-O carboxylic acid is at 1291 cm^{-1} and 1247 cm^{-1}. The shift in wavenumbers for both spectra showed that POFAs have been successfully esterified with PE to form POPE ester.

Figure 5 shows the ^{1}H NMR spectrum of the POPE ester. In the ester structure, there are two types of protons, which are the proton of C**H**$_2$-O and the proton of C**H**$_2$-C=O. The proton of C**H**$_2$-O for the POPE ester was detected at 4.05-4.11 ppm and the proton of C**H**$_2$C=O was detected at 2.29-2.33 ppm. These values agree with the reference that exhibits a chemical shift for proton C**H**$_2$-O at 3.5- 4.8 ppm and a chemical shift for proton C**H**$_2$C=O at 2.1- 2.5 ppm [26]. POPE ester consists of a mixture of acyl groups such as myristate, palmitate, stearate, oleate and linoleate. The presence of unsaturated fatty acids was determined by the identification of the alkene group. In the alkene group, there are two types of protons, which are protons of double bond (-C=C-**H**) at chemical shift of 4.5-6.5 ppm and protons of methylene group, which are bound to double bond (-C=C-C-**H**) at chemical shift of 1.6-2.6 ppm [26]. Figure 5 shows the existence of both protons at chemical shifts of 5.33-5.39 ppm (-C=C-**H**) and 2.02-2.29 ppm (-C=C-C-**H**).

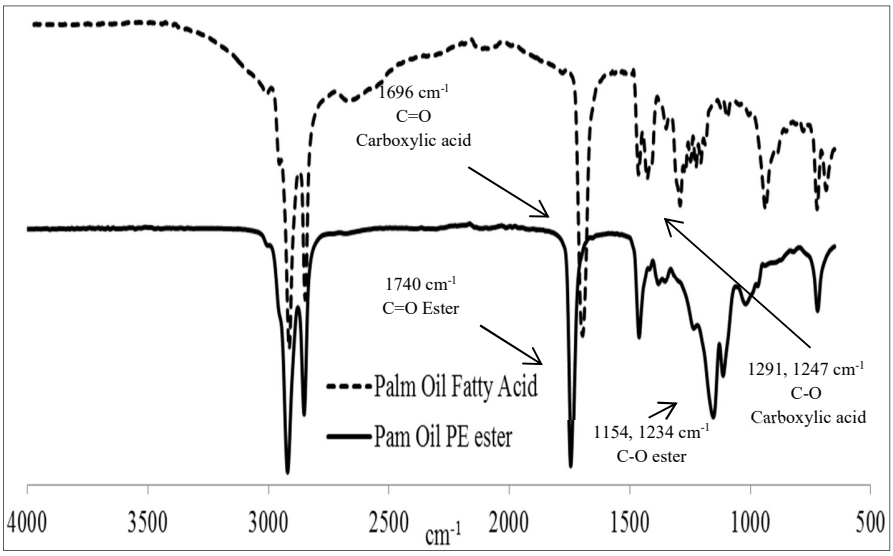


Figure 4. FTIR Spectra of POFAs and POPE ester

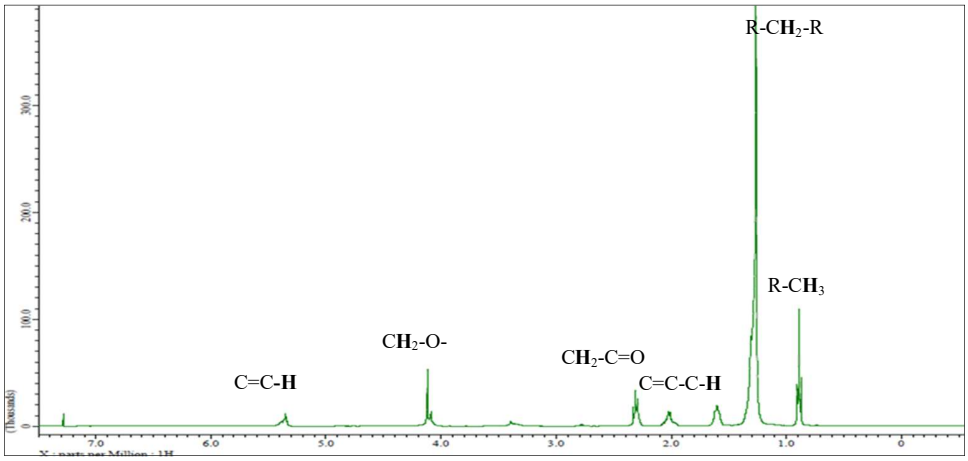


Figure 5. ^{1}H NMR Spectrum of POPE ester

Figure 6 shows the ^{13}C NMR spectrum of the POPE ester. The existence of carbon carbonyl ester (**C**=O) in the POPE ester was detected at a chemical shift of 173.24 ppm. This value is in agreement with Pavia et al. [26], who showed that the chemical shift for carbon carbonyl ester (**C**=O) was in the range of 155-185 ppm. The signal peak for carbon **C**-O, which bind fatty acid to PE was detected at chemical shift of 62.12-62.51 ppm. The presence of both carbons indicates the presence of an ester bond between POFAs and PE, which form POPE ester. The quaternary carbon for POPE ester **C**-$(CH_2OCOR)_4$ was detected at 41.78 ppm and this value is in agreement with the reference, which shows a chemical shift for quaternary carbon at 20-60 ppm [20]. The presence of unsaturated acyl groups was determined by the identification of the alkene group (**C**=C) at a chemical shift of 100-150 ppm [26]. The alkene group (**C**=C) in the POPE ester was detected at a chemical shift of 127.88-130.55 ppm.

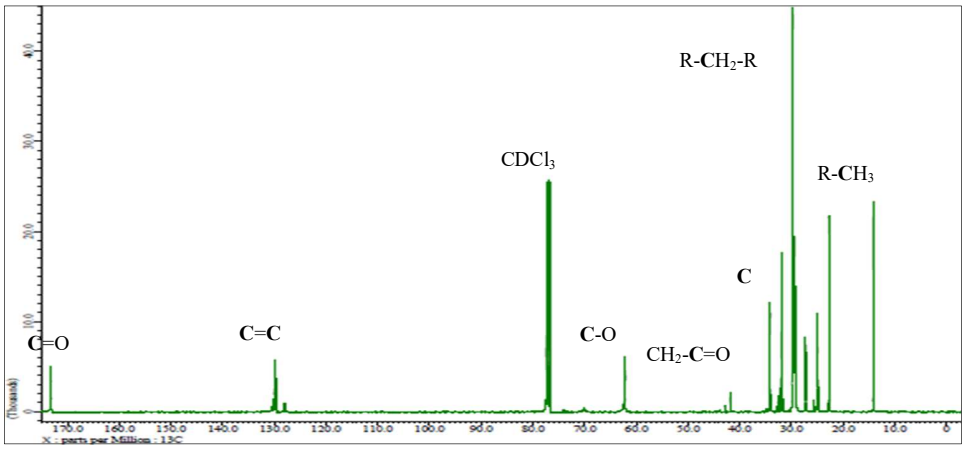


Figure 6. ^{13}C NMR Spectrum of POPE ester

Physicochemical properties of POPE Ester

POPE ester was characterized for physicochemical properties such as oxidative stability, pour point, flash point, viscosity and viscosity index. The physicochemical properties results obtained are shown in Table 3. The ability of a substance to resist oxidative degradation is an important property of biolubricant. Oxidative stability is determined by the onset temperature (OT) using Differential Scanning Calorimetry (DSC). OT is the temperature at which the occurrence of a sharp increase in the rate of oxidation of the sample. A higher onset temperature indicates that the lubricant has high oxidation stability [9]. In this study, POPE ester possesses good oxidative stability with a higher onset temperature of 189 °C compared to palm oil (181°C) due to its high percentage of saturated fatty acid (61%). Reduction of unsaturated fatty acid will reduce oxidation active site; thus, it will make POPE ester more stable at high temperatures.

The ability of a substance to remain liquid at low temperatures is an important attribute for several industrial materials, such as biolubricants, surfactants and fuels [27]. The pour point is a good indicator of its low-temperature fluidity. POPE ester has a higher pour point (17 °C) compared to palm oil (7 °C) due to the high saturated fatty acids content. High saturated fatty acids content has caused lubricant tends to form macro crystalline structures through uniform precipitation at low temperatures.

The efficiency of biolubricant in reducing friction and wear is greatly influenced by its viscosity. The least viscous biolubricant, which still forces the two moving surfaces apart is desired. If the biolubricant is too viscous, it will require a large amount of energy to move and if is too thin, the surfaces will rub and friction will be increased [9]. The viscosity of the POPE ester is in the medium range which is 60.18 cSt at 40 °C and decreased to 11.38 cS at 100 °C. It shows the viscosity of biolubricant decreases as temperature increases. The viscosity index highlights how the viscosity of biolubricant changes with variations in temperature [9]. POPE ester has a higher viscosity index which is 147 compared to palm oil (130). It shows the viscosity of the POPE ester is less affected by temperature changes and does not drastically change when the temperature varies. This is a good indicator and it is suitable for use in a large temperature range.

Flash point is often used as a descriptive characteristic of fuel oil and it is also used to describe oils that are not used as fuels such as a lubricant. The oils with a flash point that is less than 43 °C are flammable, while those having a flash point above this temperature are combustible. POPE ester showed a higher flash point at 300 °C compared to palm oil (240 °C) due to the high molecular weight of the ester and the big branched molecular structure that requires more energy to burn. A high flash point value is important to ensure that the biolubricant is not burned in the engine during its operation. Biolubricant which has a low flash point value is considered to have been contaminated by

volatile and usually requires precautions and special care when handling this biolubricant [9].

Table 3 also shows a comparison of lubrication properties between the biolubricant base stock produced (POPE ester) with commercial lubricants in the market. The selected commercial lubricants are ISO VG 100 grade lubricants, namely Denicol Compressor Oil (100A) [28] and SubsTech Hydraulic Oil (100B) [29]. Based on the comparison made, the POPE ester has a higher flash point and a higher viscosity index compared to 100A and 100B lubricants.

Table 3. Physicochemical properties of RBD palm oil and POPE ester

Physicochemical Properties	Palm Oil	POPE Ester	100A[a]	100B[b]
Oxidative stability (°C)	181	189	n/a	n/a
Pour point (°C)	7	17	-19	-27
Flash point (°C)	240	300	276	254
Kinematic viscosity at 40°C	56.97	57.47	96	96.7
Kinematic viscosity at 100°C	9.24	10.87	10.9	11
Viscosity index (VI)	130	147	97	100
ISO viscosity grade	46	46	100	100

a: 100A: Denicol Compressor Oil ISO VG 100 [22], b: SubsTech Hydraulic Oil ISO 100 [23].

Conclusion

POPE ester has been successfully synthesized from palm oil fatty acids and pentaerythritol with 85% of yield and 97.4% of tetraesters compositions. POPE ester showed good lubrication properties such as having higher oxidative stability, higher flash point and higher viscosity index compared to palm oil. The removal of β-hydrogen in palm oil and replacing pentaerythritol in POPE ester has successfully increased the lubricity properties. This makes POPE ester suitable to be used as biolubricant.

Acknowledgement

The authors would like to acknowledge Universiti Kebangsaan Malaysia for the financial support under research grants GUP-2016-012 and GUP-2016-058. The authors also thank the Ministry of Education Malaysia for providing scholarship support (MyPHD) for the author.

References

1. Hoang, T. T. K. and Kim, Il. (2015). Epoxidation and ring-opening of palm oil to produce high functionality polyols. *Australian Journal of Basic and Applied Sciences*, 9(8): 89-93.
2. Global biolubricants markets report 2022-2026: Increasing focus on biodegradable, non-toxic, and eco-friendly products (2022). Markets Report 2022-2026. https://www.globenewswire.com/en/news-release/2022/04/06/2417401/28124/en/Global-Biolubricants-Markets-Report-2022-2026-Increasing-Focus-on-Biodegradable-Non-toxic-and-Eco-Friendly-Products.html. [Accessed online 1 June 2022].
3. Kurre, S. K. and Yadav, J. (2023). A review on bio-based feedstock, synthesis, and chemical modification to enhance tribological properties of biolubricants. *Industrial Crops and Products*, 193: 116122.
4. Nor, N. M., Salih, N. and Salimon, J. (2022). Optimization and lubrication properties of Malaysia crude palm oil fatty acids based neopentyl glycol diester green biolubricant. *Renewable Energy*, 200: 942-956.
5. Cerretani, L., Bendini, A., Estrada, M. T. R., Vittadini, E. and Chiavaro, E. (2009). Microwave heating of different commercial categories of olive oil: Part I. Effect on chemical oxidative stability indices and phenolic compounds. *Food Chemistry*, 115:1381-1388.
6. Salimon, J. and Salih, N. (2009). Oleic acid diesters: Synthesis, characterization and low temperature properties. *European Journal of Scientific Research*, 32(2): 216-222.

7. Nirmal, V. P. and Dineshbabu, D. (2015). Performance and emission of *Pongamia pinnata* oil as a lubricant in diesel engine. *International Journal of Innovative Research in Science, Engineering and Technology*, 4(2): 435-441.
8. Masood, H., Yunus, R., Choong, T. S. Y., Rashid, U. and Yap, Y. H. T. (2012). Synthesis and characterization of calcium methoxide as heterogeneous catalyst for trimethylolpropane esters conversion reaction. *Applied Catalyst A: General*, 425-426:184-290.
9. Salimon, J., Salih, N. and Yousif, E. (2011). Chemically modified biolubricant basestocks from epoxidized oleic acid: improved low temperature properties and oxidative stability. *Journal of Saudi Chemical Society*, 15:195-201.
10. Resul, M. F. M. G., Ghazi, T. I. M. and Idris, A. (2012). Kinetic study of *Jatropha* biolubricant from transesterification of *Jatropha curcas* oil with trimethylolpropone: Effect of temperature. *Industrial Crops and Products*, 38: 87-92.
11. Fox, N. J. and Stachowiak, G. W. (2007). Vegetable oil-based lubricants-a review of oxidation. *Journal of Tribology International*, 40:1035-1046.
12. Arbain, N. H., Salimon, J., Salih, N. and Ahmed, W. A. (2022). Optimization of epoxidation of Malaysian *Jatropha curcas* oil-based trimethylolpropane ester biolubricant. *Applied Science and Engineering Progress*, 15 (3): 5552.
13. Salih, N. and Salimon, J. (2021). A review on eco-friendly green biolubricants from renewable and sustainable plant oil sources. *Biointerface Research in Applied Chemistry,* 11(5): 13303-13327.
14. Salih, N. and Salimon, J. (2022). A review on new trends, challenges and prospects of ecofriendly friendly green food-grade biolubricants. *Biointerface Research in Applied Chemistry*, 12(1):1185-1207.
15. Leung, D. Y. C, Wu, X. and Leung, M. K. M. (2010). A review of biodiesel production using catalyzed transesterification. *Applied Energy*, 87: 1083-1095.
16. Sripada, P. K., Sharma, R. V. and Dalai, A. K. (2013). Comparative study of tribological properties of trimethylolpropane-based biolubricant derived from methyl oleate and canola biodiesel. *Industrial Crops and Products*, 50: 95-103.
17. Nor, N. M., Derawi, D., and Salimon, J. (2017). Chemical modification of epoxidized palm oil for biolubricant application. *Malaysian Journal of Analytical Sciences*, 21(6): 1423-1431.
18. Nor, N. M., Derawi, D., and Salimon, J. (2018). The optimization of RBD palm oil epoxidation process using D-optimal design. *Sains Malaysiana*, 47(7):1359-1367.
19. Yunus, R., FakhrulRazi, T. L., OoiI, S. E., Iyuke, and Idris. A. (2003). Development of optimum synthesis method for transesterification of palm oil methyl esters and trimethylolpropane to environmentally acceptable palm oil-based lubricants. *Journal of Oil Palm Research*, 15: 35-41.
20. Sulaiman, S. Z., Chuah, A. L. and Fakhru`I-Razi, A. (2007). Batch production of trimetylolpropane ester from palm oil as lubricant base stock. *Journal of Applied Sciences*, 7: 2002-2005.
21. Salih, N., Salimon, J. and Jantan, F. N. (2013). Synthesis and characterization of palm kernel oil based trimethylolpropane ester. *Asian Journal of Chemistry*, 25(17): 9751-9754.
22. Aziz, N. A. M., Yunus, R., Rashid, U. and Syam, A. M. (2014). Application of response surface methodology (RSM) for optimizing the palm-based pentaerythritol ester synthesis. *Industrial Crops and Products*, 62: 305-312.
23. Nor, N. M., Derawi, D., and Salimon, J. (2019). Esterification and evaluation of palm oil as biolubricant base stock. *Malaysian Journal of Chemistry*, 21(2): 28-35.
24. Nadkarni, R.A. (2007). Guide to ASTM test methods for the analysis of petroleum products and lubricants. ASTM International, West Conshohocken.
25. Chowdhury, K., Banu, L. A., Khan, S. and Latif, A. (2007). Studies on the fatty acid composition of edible oil. *Bangladesh Journal of Scientific and Industrial Research*, 42(3): 311-316.
26. Pavia, D. L., Lampman, G. M. and Kriz, G. S. (2010). Introduction to spectroscopy. 4th edition. United States: Thomson Learcning, Inc.

27. Salimon, J. and Salih, N. (2010). Modification of epoxidized ricinoleic acid for biolubricant base oil with improved flash and pour points. *Asian Journal of Chemistry*, 22(7): 5468-5476.
28. Denicol Motor Oils (2020). Denicol compressor oil. https://pdf4pro.com/view/compressor-oil-iso-vg-32-46-68-100-150-denicol-5786bc.html. [Accessed online 25 December 2020].
29. SubsTech: Substances and Technologies (2012). SubsTech hydraulic oil. http://www.substech.com/dokuwiki/doku.php?id=hydraulic_oil_iso_100. [Accessed online 25 December 2020].

Malaysian Journal of Analytical Sciences (MJAS)
Published by Malaysian Analytical Sciences Society

MOLYBDENUM DISULFIDE FOR PHOTOCATALYTIC DEGRADATION OF METHYLENE BLUE UNDER FLUORESCENT LIGHT

(Molybdenum Disulfida Untuk Fotokatalitik Degradasi Metilena Biru Di Bawah Cahaya Pendarfluor

Siti Nor Atika Baharin[1, 2], Nurul Izzah Hashim[1], Izyan Najwa Mohd Norsham[1], and Kavirajaa Pandian Sambasevam[1,3*]

[1]*Advanced Material for Environmental Remediation (AMER) Research Group, Faculty of Applied Sciences, Universiti Teknologi MARA, Cawangan Negeri Sembilan, Kampus Kuala Pilah, 72000 Kuala Pilah, Negeri Sembilan, Malaysia*
[2]*Advanced Biomaterials & Carbon Development (ABCD), Universiti Teknologi MARA, 40450, Shah Alam, Selangor, Malaysia*
[3]*Electrochemical Material and Sensor (EMas) Group, Universiti Teknologi MARA, 40450 Shah Alam, Selangor, Malaysia*

[*]*Corresponding author: kavirajaa@live.com*

Received: 25 September 2022; Accepted: 20 May 2023; Published: 22 August 2023

Abstract

This work underlined the fluorescent light-driven photocatalytic degradation of methylene blue by using cauliflower-like molybdenum disulfide (MoS_2). In this study, molybdenum disulfide (MoS_2) was synthesized by using Teflon-stainless steel autoclave via the hydrothermal method. The synthesized MoS_2 were comprehensively characterized using Fourier transform infrared (FTIR), UV-visible spectroscopy, X-ray diffraction (XRD), scanning electron microscopy (SEM), and thermal gravimetry analysis (TGA). The characterization studies reveal that the composites have been successfully synthesized in which a black precipitate was obtained. Degradation of methylene blue was conducted using the synthesized MoS_2 under fluorescent light using response surface methodology (RSM) of three-factor-three-level Box-Behnken design (BBD). The parameters studied were MoS_2 weight loading, contact time under fluorescent light, and methylene blue pH value. The most effective parameter observed in the degradation of methylene blue were weight loading, followed by contact time and pH. The results showed that the optimum condition for the degradation were with the parameters of 15mg of MoS_2 weight loading, with pH 6.5 methylene blue, has the highest degradation percentage 99.93% with 120 minutes exposed time under fluorescent light for degradation.

Keywords: molybdenum disulfide, photocatalytic degradation, methylene blue, response surface methodology, Box-Behnken

Abstrak

Penyelidikan ini menggariskan degradasi fotokatalitik dipacu cahaya pendarfluor biru metilena dengan menggunakan molibdenum disulfida (MoS_2) yang berbentuk kobis bunga. Dalam kajian ini, molibdenum disulfida (MoS_2) telah disintesis dengan

menggunakan autoklaf keluli tahan karat Teflon melalui kaedah hidroterma. MoS_2 yang disintesis telah dicirikan secara komprehensif menggunakan inframerah transformasi Fourier (FTIR), spektroskopi boleh dilihat UV, pembelauan sinar-X (XRD), mikroskop elektron pengimbasan (SEM), dan analisis gravimetri terma (TGA). Kajian pencirian mendedahkan bahawa komposit telah berjaya disintesis di mana mendakan hitam diperolehi. Degradasi metilena biru telah dijalankan menggunakan MoS_2 yang disintesis di bawah cahaya pendarfluor menggunakan metodologi permukaan tindak balas (RSM) reka bentuk Box-Behnken (BBD) tiga faktor-tiga peringkat. Parameter yang dikaji ialah pemuatan berat MoS_2, masa sentuhan di bawah cahaya pendarfluor, dan nilai pH biru metilena. Parameter paling berkesan yang diperhatikan dalam degradasi metilena biru ialah pemuatan berat, diikuti dengan masa sentuhan dan pH. Keputusan menunjukkan bahawa keadaan optimum untuk degradasi adalah dengan parameter 15mg beban berat MoS2, dengan pH 6.5 metilena biru, mempunyai peratusan degradasi tertinggi 99.93% dengan 120 minit masa terdedah di bawah cahaya pendarfluor untuk degradasi.

Kata kunci: molibdenum disulfida, degradasi fotokatalitik, biru metilena, metodologi permukaan tindak balas, Box-Behnken

Introduction

With the advancements of the textile industry in recent years, an increasing number of dyes, like methylene blue have been developed. According to the World Bank analysis, textile dyeing and finishing operations accounted for over 20% of global industrial water contamination [1]. Synthetic dyes are widely utilised in a variety of industries, including food, textile, paper, rubber, plastics, cosmetics and pharmaceuticals. These manufacturers dumped massive amounts of effluent into waterways with no prior treatment. These discharges are a significant source of contamination and contributed to the deterioration of human health and environmental [2]. Dyes also have an impact on aquatic life by interfering with the photosynthesis process of aquatic plants, causing eutrophication and causing disturbance [3, 4]. Due to methylene blue (MB) properties of limited biodegradability, traditional treatment methods, such as the physical-chemical approach is ineffective [5]. The conventional water-treatments approaches applied in individual or combined systems may be applicable to treat mild polluted waste, unfortunately, all these methods do not comprehensively eliminate the pollutant and the detrimental sludge remains after the treatment. Recently, photocatalytic degradation became one of the efficient techniques to degrade pollutants [6, 7].

Photocatalytic degradation is a technique that utilize light source and forms electron-hole which produce radicals that can convert contaminant to safe and less poisonous substances. Special feature of photocatalytic degradation is that it can degrade organic pollutants that has high photochemical stability by effectively utilize light irradiation [8]-[9]. According to Poorsajadi et al., 88% of MB was degraded by using CuO/Bi_2O_3 nanocomposite as photocatalyst under UV irradiation [10]. Meanwhile, γ -Fe_3/Fe_3O_4/ SiO_2 (Ar modified) composite successfully synthesized and degraded MB in 120 min with 87.5% of degradation [11]. On the other hand, 99% of MB was removed by only 4 min by using Ternary $MoS_2/Bi_2S_3/TiO_2$ heterostructure as photocatalyst under simulated solar irradiation as the light source [12]. Molybdenum disulfide (MoS_2) can be used in degradation of organic pollutant. MoS_2 is a crystal structure that comprised S-Mo-S layers that are poorly coupled, whereby a Mo atom layer is in between two S atom layers. A spontaneously existing layered solid, namely MoS_2, seeks uses for production in either its bulk or dispersed forms. The discrete sandwiched S-Mo-S layers are fused together by poor Van der Waals interactions in hexagonally packed frameworks. These layers may shift efficiently towards each other, which enables MoS_2 as a commonly applied dry lubricant. The Van der Waals gaps between the layers are responsible for its properties like anisotropy, good catalytic property, chemical inertness, photo corrosion resistance, optical properties and biological applications [13]-[15]. Due to its distinct layered properties, cost-effectiveness, and use of solar energy, MoS_2 has been identified as a renowned metal free photocatalyst for the degradation of organic contaminants. The layered MoS_2 has effectively synthesized and reported that the metal free photocatalyst exhibited photocatalytic activity under visible light irradiation for the elimination of organic contaminants from aqueous solution [16]. MoS_2 has high photocatalytic activity and inexpensive that it has become preferable in water purification.

In this study, MoS_2 was synthesised through the hydrothermal method as fine powder to be used in the photocatalytic degradation of MB under fluorescent light via response surface methodology by using Design Expert Software of Box-Behnken design. To the best of authors' knowledge, there is no study on box Behnken optimisation design on the degradation of MB under fluorescent light by using MoS_2 as photocatalyst. Therefore, this study could pave a way for the development of facile and optimised approaches for the degradation and treatment of organic pollutants, especially dyes.

Materials and Methods

Materials

Methylene blue, 37% hydrochloric acid (HCl), distilled water, deionised water, sodium molybdate (Na_2MoO_4) and 99% Thiourea (H_2NCSNH_2) were purchased from Sigma Aldrich and all the chemicals are of analytical grade.

Instruments

Fourier transform infrared spectroscopy (FTIR) were recorded between 400 cm^{-1} and 4000 cm^{-1} (Model 100 Spectrometer, Perkin Elmer), UV-visible spectroscopy with 200 nm -800 nm of scanning wavelength (model Lambda 750, Perkin Elmer), X-ray diffractometer analysis were conducted with Panalytical model Empyrean X-ray by keeping 2θ = 10°-90° using Cu, Kα radiations (λ= 1.54059 Å). Scanning electron microscopy (model TESCAN, VEGA3) and thermal gravimetry analyser (TGA) was done by using (model NETZSCH TG 209F3) from 200 °C to 900 °C with the heating rate of 10 °C/min.

Preparation of MoS_2

Sodium molybdate dihydrate ($Na_2MoO_4.2H_2O$) of 3 g and 3.8 g of thiourea (H_2NCSNH_2) was added to 80 mL of deionised water and was stirred for 30 min. 1M HCl of 10 mL was added to the solution and then was transferred into a 100 mL of Teflon stainless steel autoclave. Next, it was heated in an oven at 120 ºC for the next 24 h. The solution was cooled at room temperature. After that, the solution was centrifuged three times and washed with deionised water. The solution was oven dried at 70 ºC for 24 h.

Characterizations of MoS_2

Sodium molybdate dihydrate ($Na_2MoO_4.2H_2O$) of 3g and 3.8g of thiourea (H_2NCSNH_2) was added to 80 mL of deionised water and was stirred for 30 min. 1M HCl of 10 mL was added to the solution and then was transferred into a 100 mL of Teflon stainless steel autoclave. Next, it was heated in an oven at 120 ºC for the next 24 h. The solution was cooled at room temperature. After that, the solution was centrifuged three times and washed with deionised water. The solution was oven dried at 70 ºC for 24 h.

Photocatalytic activity

The photocatalytic properties of MoS_2 were evaluated by employing MB as a target degradation product. To determine the MB degradation, the MoS_2 powder was first screened. Next, 0.1 g of MB contamination was added to 100 ml volumetric flask. It was then diluted to 1000 ppm followed by 100 ppm to the desired concentration of 10 ppm by using deionized water. 10 ml from 10 ppm stock solution was pipetted into the immersion tube containing the sample. Then, the sample was placed in a photoreactor for approximately 30 min in the dark to reach an equilibrium. Then, the MB containing the sample was treated under the fluorescent light for 1 h. The reacted MB was next filtered by using the syringe filter. By using UV-vis, the final products were analyzed. The MB showed a strong absorption from deep UV-region to 664 nm. A continuous screening was performed without the involvement of photocatalyst, and a control MB was left incubated without the catalyst and treatment.

$$\text{Percentage degradation efficiency (\%)} = \frac{C_0 - C}{C_0}\ x\ 100 \quad (1)$$

Where, C_o is initial concentration of MB and C is concentration of MB after the photocatalytic degradation at the specific time given [19].

Results and Discussion

Characterization of MoS_2: Fourier transform infrared spectroscopy (FTIR)

Figure 1 shows various peaks in the spectrum on MoS_2 before and after treatment with MB under fluorescent light, within range from 400 cm^{-1} to 4000 cm^{-1}. The characteristic peak of MoS_2 can be confirmed by a strong peak at 539.90 cm^{-1} indicating the presence of Mo-S in MoS_2. The presence of S-S bond at 878.73 cm^{-1}, meanwhile, absorption band at 1603.54 cm^{-1} was caused by Mo-O bonds along with OH group and their stretching vibrations. The absorption band appearred at 3376.76 cm^{-1} was due to the stretching vibration of existing OH group [20].

The FTIR spectrum of MoS_2 after the MB degradation under the fluorescent light treatment. The absorption band for the Mo-S bond at 539.9 cm^{-1}, the peak of S-S bond at 878.73 cm^{-1} and the peak of Mo-O bond at 1603.54 cm^{-1} were not as substantial as they were before the degradation. After the degradation, the absorption band of 3376.76 cm^{-1} for stretching vibration of the existing OH group was no longer visible. Several functional groups of MoS_2 were not observed after the degradation due to the leaching of the samples by repetition of drying and washing.

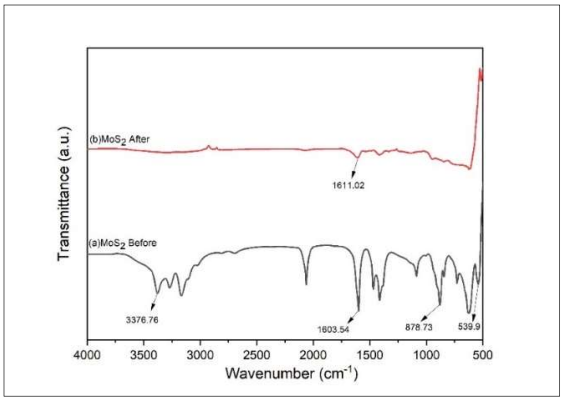


Figure 1. FTIR spectrum of MoS_2 (a) before and (b) after degradation of methylene blue under fluorescent light

UV-visible analysis

As shown in Figure 2, the synthesized MoS_2 nanoparticles showed a strong absorption in UV region with a maximum at 226 nm and a weaker broad absorption in the visible region of 400 nm, which was very similar to that of MoS_2 nanoparticles reported by [21]. Visible light covered the range of approximately 390 nm-700 nm, or 1.8-3.1 eV from the Tauc plot (in-set) the bandgap of MoS_2 was found to be 2.38 eV which revealed that it can be active in the fluorescent light region and effectively degraded the MB.

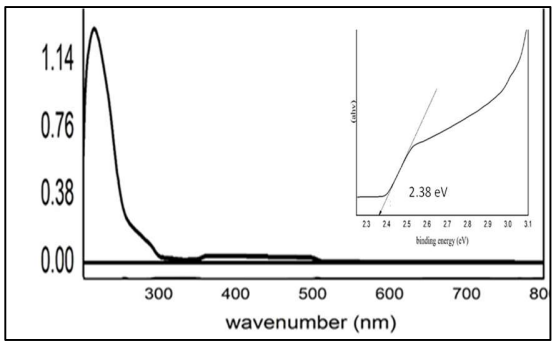


Figure 2. (a) UV-Vis spectra and in-set Tauc plot of MoS_2

X-ray diffraction analysis

Figure 3 indicates diffractogram of MoS_2 exhibited diffraction peaks at 2θ = 14.307°, 32.599°, 40.317°, and 58.235° which can be represented as indices of (002), (100), (103) and (110) of hexagonal phase for the MoS_2 structure, respectively [22]. The crystallinity size calculated was 2.6555Å with the most intense peak. The crystallinity size was calculated by using the Scherrer Equation 2.

$$D = 0.9\ \lambda / \beta \cos \theta \quad (2)$$

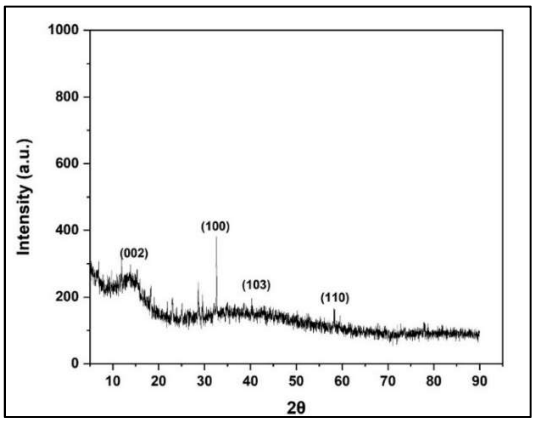


Figure 3. XRD analysis of MoS_2

Morphology analysis

SEM was utilized comprehensively to understand the morphological property of synthesized MoS_2. Figure 4 shows the surface morphology of MoS_2 in flower-like particle. the sheets of MoS_2 stacked together and displayed a 3D cauliflower-like architecture [23]-[24]. Micro-flowers of aggregated MoS_2 nano-sheets were seen in all cases, with no substantial differences. Similar hydrothermally produced materials showed the same morphology [25].

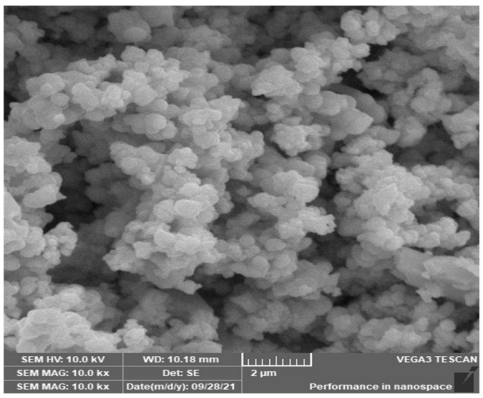


Figure 4. SEM image of MoS_2

Thermogravimetric analysis

Figure 5 illustrates product composition of MoS_2. At the temperature ranging from 200 °C to 470 °C, the TG curve can be interpreted to show three phases of decomposition. MoS_2 exhibited significant initial weight loss at about 200 °C, which could be attributed to water evaporation because of the sample not being completely dried. Furthermore, at 270 °C, MoS_2 lost weight, which could be attributed to oxidation of MoS_2 into MoO_3. The continuous weight loss in the second

phase of TG curve decomposition was caused by the thermal decomposition of the organic group. Beyond 400 °C in the final stage, this was primarily due to MoS_2 burned in the air [26].

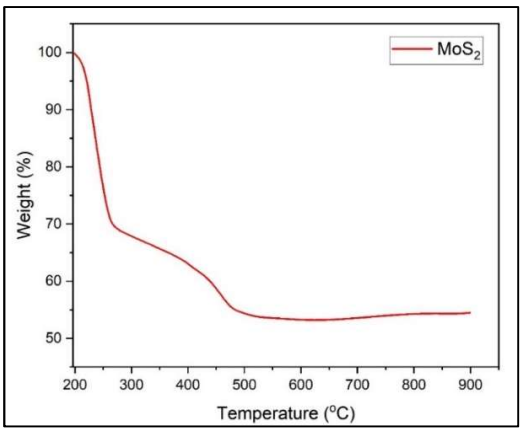


Figure 5. TGA analysis of MoS_2

Photocatalytic activity study: The photocatalytic activity of MoS_2 and methylene blue

The degradation of MB was determined by the screening study of MoS_2 powder. The degradation study of MB was then conducted by using UV-Vis spectroscopy with a maximum absorption at wavelength of 664 nm. The MB underwent treatment for 1 h after incubating for 30 min to reach an equilibrium. Figure 6 shows the UV-Vis spectra of MB before photodegradation and after photodegradation with MoS_2 under the fluorescent light in 120 min. After the photodegradation, the intensity of MB maximum peak decreased showing that MoS2 had successfully degraded MB.

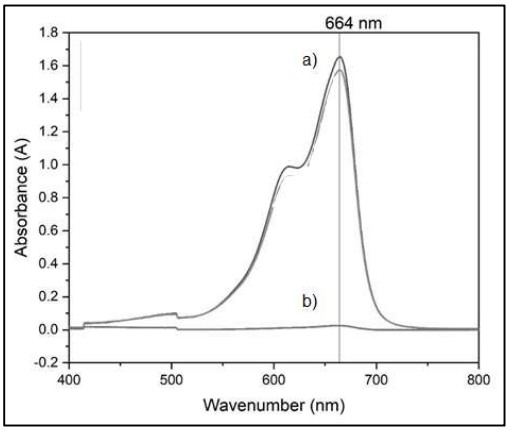


Figure 6. UV-vis spectrum of screening study of methylene blue a) before photodegradation b) after photodegradation

The response surface study

The data were analyzed and interpreted by using Design Expert Software for response surface methodology. Table 2 represents the design experiment of various variables together with experimental and predicted degradation percentage for three-factor-three-level of Box-Behnken design (BBD) response surface analysis for the degradation of MB. The effective parameters studied included A: weight loading (A: 1 mg, 8 mg and 15 mg), B: contact time (B: 5 min, 62.5 min and 120 min) and C: pH value (C: pH 4, pH 6.5 and pH 9). A total of 17 experiments were obtained at random to study

the optimized parameters and maximize the photocatalytic degradation of MB. The experimental values are tabulated in Table 2.

Table 2. Response surface analysis for design experiment of degradation of MB

Std	Weight Loading (mg)	Contact Time (min)	pH	Degradation (%)
1	1	5	6.5	24.04
2	15	5	6.5	99.00
3	1	120	6.5	52.99
4	15	120	6.5	99.93
5	1	62.5	4	37.06
6	15	62.5	4	99.23
7	1	62.5	9	47.94
8	15	62.5	9	99.08
9	8	5	4	94.03
10	8	120	4	99.57
11	8	5	9	97.44
12	8	120	9	99.00
13	8	62.5	6.5	99.43
14	8	62.5	6.5	97.87
15	8	62.5	6.5	95.73
16	8	62.5	6.5	94.59
17	8	62.5	6.5	94.24

The data pointed out in Figure 7 was compared to a straight line, indicating that the residual was normally distributed. The residual versus predicted response value, on the contrary, placed the implication of constant variance to the test. The plot should be in random scatter with a constant range of residuals within the residual range [25].

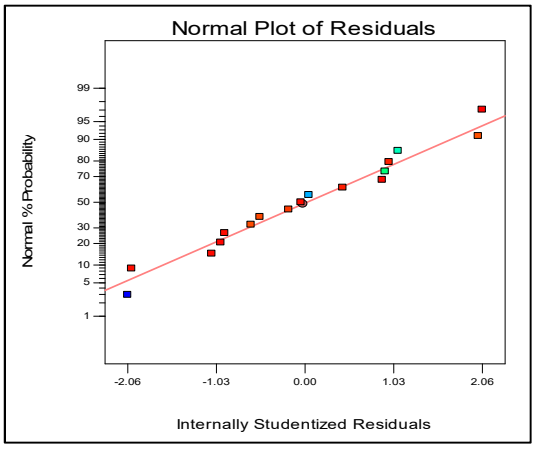


Figure 7. The normal percentage probability and internally studentized residual graph

ANOVA was used to determine the statistical significance of the BBD model. Table 3 summarizes the ANOVA results. The results showed that the acquired models can be used to successfully navigate the design space. The correlation coefficients of R^2 and adjusted R^2 were both high, with values of 0.9904 and 0.9779 demonstrating a close fit between the predicted and experimental values, respectively. The model *F*-value of 79.85 and *p*-values less than 0.0001 implied that the model was significant. Values of *"*Prob>*F"* less than 0.0500 suggested that the model terms were significant. Thus, in this case, *A*, *B*, *AB*, and A^2 were significant model terms. From the ANOVA analysis, the Lack of Fit *F*-value" was not significant. As can be seen in Table 3, the obtained *F* values for effect of weight loading, contact time and pH value were 476.46, 11.78 and 1.59, respectively, showing that the weight loading was the most significant parameter, followed by contact time and pH value. By comparing the interactive model term, *AB* had the highest *F* value of 13.52, followed by *AC* with 2.10 and BC with 0.27, indicating that the interaction of *AB* was the most significant towards photodegradation of MB.

The different MoS_2 weight loading in MB towards photocatalytic reactions are presented in Figure 8(a). It could be seen that when the weight loading of MoS_2 increases, it will increase the number of photocatalyst's active sites that were exposed to the fluorescent light. However, when weight loading exceeded 11.5 mg, the degradation decreased due to the agglomeration of the photocatalyst [27]. According to Figure 8(b), the effect of contact time of MoS_2 on the degradation efficiency of MB was studied within the range of 5 min-120 min during the photocatalytic degradation under the fluorescence light utilizing a photoreactor. It showed that the increase in contact time to 120 min elevated the efficiency of degradation. The first increase in contact time enhanced the efficiency of degradation because actives site of MoS_2 were still vacant and more photodegradation could occur rapidly. Figure 8(c) reveals that the maximum degradation took place within the pH value range of pH 6.5-pH 9 [28].

The response surface plot in three dimensional was plotted to show the interaction between the two parameters towards the photodegradation of MB. In this approach, two parameters were varied within the experimental ranges, while another one parameter was kept constant. The 3-D surface plot of photodegradation of MB as a function of weight loading and contact time is shown in Figure 9.

Table 3. Analysis of variance

Source	df	SS	MS	*F*	*p*	Remark
Model	9	10430.16	1158.91	79.85	<0.0001	significant
Weight Loading, *A*	1	6915.47	6915.47	476.46	<0.0001	
Contact Time, *B*	1	170.94	170.94	11.78	0.0110	
pH, *C*	1	23.02	23.02	1.59	0.2483	
AB	1	196.28	196.28	13.52	0.0079	
AC	1	30.42	30.42	2.10	0.1910	
BC	1	3.96	3.96	0.27	0.6175	
A^2	1	3076.81	3076.81	211.99	<0.0001	
B^2	1	0.52	0.52	0.035	0.8559	
C^2	1	9.32	9.32	0.64	0.4493	
Residual	7	101.60	14.51			
Lack of fit	3	81.87	27.29	5.53	0.0659	Not significant
Pure error	4	19.73	4.93			
Total	16	10531.76				

DF degree of freedom of different source, SS sum of square, MS mean of square, *F* degree of freedom, *P* probability.
*R^2 = 0.9904 and adj-R^2 = 0.9779

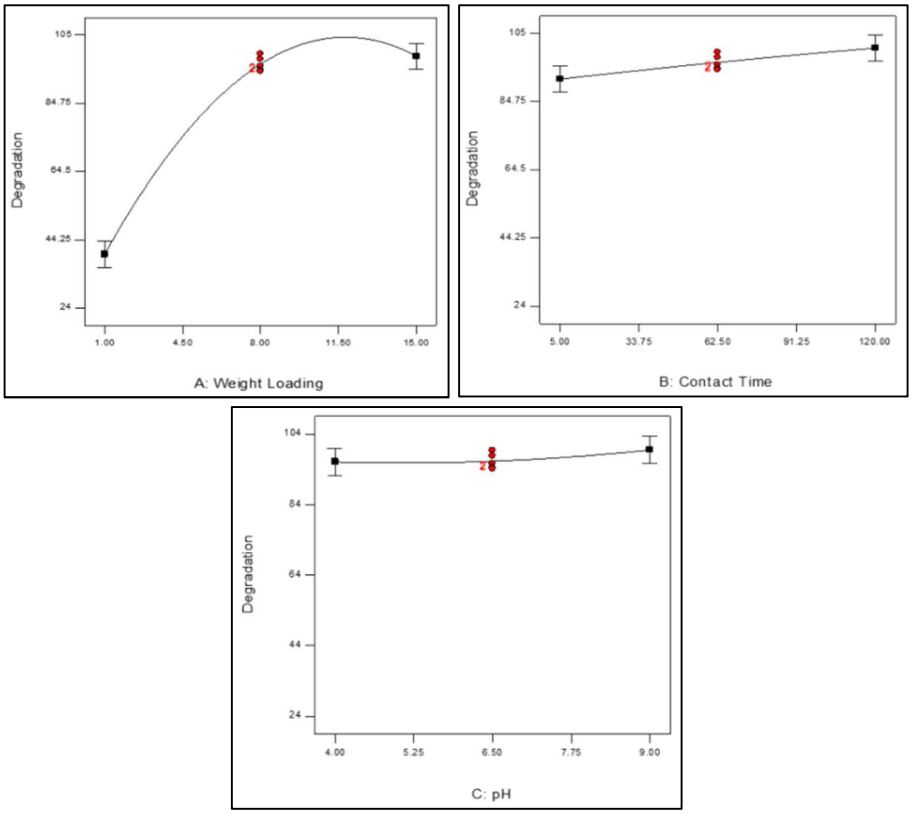


Figure 8. (a) One factor plots of degradation versus weight loading, A (b) degradation and contact time, B plotted graph (c) percentage degradation of methylene blue versus pH, C.

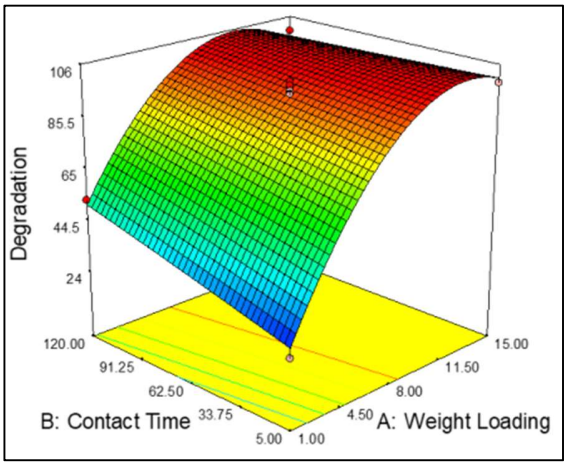


Figure 9. 3-D surface plot of two parameters toward degradation of methylene blue for weight loading and contact time

The pH value was kept constant at pH 6.5. The straight line of the contour plot indicated the interaction of weight loading and contact time. As the weight loading increased along with contact time, the percentage

degradation of MB increased. However, as the contact time increased but the weight loading decreased, the percentage degradation was low. This showed that weight loading had significantly contributed to the degradation of MB. Nevertheless, pH value did not play a significant role in the degradation of MB by using MoS_2 under the fluorescent light.

Conclusion

Based on the overall result and discussion, it can be concluded that the MoS_2 was successfully synthesised by the hydrothermal method. The synthesised MoS_2 was characterised by using FTIR, UV-vis solid, XRD, SEM and TGA analyses. The characterisation results clearly revealed that a flower-like MoS2 has been successfully synthesised. For the photocatalytic study of MB, the optimum condition for photodegradation of methylene blue by using MoS_2 were observed under pH 6.5 for MB with MoS_2 weight loading of 15 mg which ran for 120 min which had the highest percentage degradation with value 99.93% as compared to other samples under the fluorescent light. As observed, the most effective parameters in the degradation of MB were weight loading followed by the contact time and pH value.

Acknowledgement

We acknowledge School of Chemistry and Environment, Faculty of Applied Science UiTM Negeri Sembilan for the facilities that have been provided for the research. In addition, we acknowledge Fundamental Research Grant Scheme (FRGS/1/2022/STG05/UITM/02/12) from Ministry of Higher Education Malaysia and (Geran Insentif Penyeliaan [600-RMC/GIP 5/3 (103/2022) by Universiti Teknologi MARA Malaysia for financial support.

References

1. Selvam, R., Durai, N., Mubarakali, H., and Vasanthy, M. (2018). Treatment of fabric dyeing industry effluent employing low-cost material: an eco- friendly approach. *International Journal of Basic and Applied Research,* 8(9): 1298-1307.
2. Bentahar, S., Dbik, A., El Khomri, M., El Messaoudi, N., and Lacherai, A. (2018). Removal of a cationic dye from aqueous solution by natural clay. *Groundwater for Sustainable Development,* 6: 255-262.
3. Berradi, M., Hsissou, R., Khudhair, M., Assouag, M., Cherkaoui, O., El Bachiri, A., and El Harfi, A. (2019). Textile finishing dyes and their impact on aquatic environments. *Heliyon,* 5(11): e02711.
4. Krishnamoorthy, R., Choudhury, A. R., Jose, P. A., Suganya, K., Senthilkumar, M., Prabhakaran, J., Gopal, N. O., Choi, J., Kim, K., Anandham, R., and Sa, T. (2021). Long-term exposure to azo dyes from textile wastewater causes the abundance of saccharibacteria population. *Applied Sciences (Switzerland)*, 11(1):1-8.
5. Almaamary, E. A. S., Abdullah, S. R. S., Hasan, H. A., Rahim, R. A. A., and Idris, M. (2017). Rawatan metilena biru dalam air sisa menggunakan *Scirpus grossus*. *Malaysian Journal of Analytical Sciences,* 21(1): 182-187.
6. Bodzek, M., and Rajca, M. (2012). Photocatalysis in the treatment and disinfection of water. Part I. Theoretical backgrounds. *Ecology Chemical Engineering Sciences*, 19(4): 489-512.
7. Baharin, S. N. A., Rusmin, R., and Sambasevam, K. P. (2022). Basic concept and application of conducting polymers for environmental protection. *Chemistry Teacher International,* 4(2): 173-183.
8. Singh, P., Shandilya, P., Raizada, P., Sudhaik, A., Rahmani-sani, A., & Hosseini-bandegharaei, A. (2018). Review on various strategies for enhancing photocatalytic activity of graphene-based nanocomposites for water purification. *Arabian Journal of Chemistry,* 3: 1-23.
9. Zhang, L., and Jaroniec, M. (2018). Toward designing semiconductor-semiconductor heterojunctions for photocatalytic applications. *Applied Surface Science*, 430: 2-17.
10. Poorsajadi, F., Sayadi, M. H., Hajiani, M., and Rezaei, M. R. (2022). Synthesis of CuO/Bi_2O_3 nanocomposite for efficient and recycling photodegradation of methylene blue dye. *International Journal of Environmental Analytical Chemistry,* 102(18): 7165-7178.
11. Sanad, M. M., Farahat, M. M., El-Hout, S. I., and El-Sheikh, S. M. (2021). Preparation and characterization of magnetic photocatalyst from the banded iron formation for effective photodegradation of methylene blue under UV and

and visible illumination. *Journal of Environmental Chemical Engineering,* 9(2): 105127.

12. Drmosh, Q. A., Hezam, A., Hendi, A. H. Y., Qamar, M., Yamani, Z. H., and Byrappa, K. (2020). Ternary $Bi_2S_3/MoS_2/TiO_2$ with double Z-scheme configuration as high performance photocatalyst. *Applied Surface Science,* 499: 143938.
13. He, Z., & Que, W. (2016). Molybdenum disulfide nanomaterials: Structures, properties, synthesis and recent progress on hydrogen evolution reaction. *Applied Materials Today,* 3: 23-56.
14. Kumar, R., Ansari, S. A., Barakat, M. A., Aljaafari, A., and Cho, M. H. (2018). A polyaniline@MoS_2-based organic–inorganic nanohybrid for the removal of Congo red: adsorption kinetic, thermodynamic and isotherm studies. *New Journal Chemistry*, 42:18802-18809.
15. Chaudhary, N., Raj, K., Harikumar, A., Mittal, H., and Khanuja, M. (2020). Comparative study of photocatalytic activity of hydrothermally synthesized ultra-thin MoS_2 nanosheets with bulk MoS_2. *AIP Conference Proceedings*, 2276: 20030.
16. Vattikuti, S. V. P., and Shim, J. (2018). Synthesis, characterization and photocatalytic performance of chemically exfoliated MoS_2. *IOP Conference Series: Materials Science and Engineering*, 317(1): 1-5.
17. Abdulhameed, A. S., Mohammad, A. K. T., and Jawad, A. H. (2019). Application of response surface methodology for enhanced synthesis of chitosan tripolyphosphate/TiO_2 nanocomposite and adsorption of reactive orange 16 dye. *Journal of Cleaner Production,* 232: 43-56.
18. Chen, J., and Zhang, P. (2006). Photodegradation of perfluorooctanoic acid in water under irradiation of 254 nm and 185 nm light by use of persulfate. *Water Science and Technology*, 54(11-12): 317-325.
19. Ibukun, O., Evans, P. E., Dowben, P. A., and Jeong, H. K. (2019). Titanium dioxide-molybdenum disulfide for photocatalytic degradation of methylene blue. *Chemical Physics,* 525:110419.
20. Chaudhary, N., Khanuja, M., Abid, and Islam, S. S. (2018). Hydrothermal synthesis of MoS_2 nanosheets for multiple wavelength optical sensing applications. *Sensors and Actuators, A: Physical*, 277(2010): 190-198.
21. Chen, Y., Tan, L., Sun, M., Lu, C., Kou, J., and Xu, Z. (2019). Enhancement of photocatalytic performance of TaON by combining it with noble-metal-free MoS_2 cocatalysts. *Journal of Materials Science,* 54(7): 5321-5330.
22. Yang, J., Ye, M., Han, A., Zhang, Y., and Zhang, K. (2019). Preparation and electromagnetic attenuation properties of MoS_2–PANI composites: a promising broadband absorbing material. *Journal of Materials Science: Materials in Electronics,* 30(1): 292-301.
23. Peng, W., Wang, W., Han, G., Huang, Y., and Zhang, Y. (2020). Fabrication of 3D flower-like MoS2/graphene composite as high-performance electrode for capacitive deionization. Desalination, 473(August 2019), 11: 4191.
24. Ariyanta, H. A., Ivandini, T. A., and Yulizar, Y. (2021). A novel way of the synthesis of three-dimensional (3D) MoS_2 cauliflowers using allicin. *Chemical Physics Letters,* 767: 138345.
25. Koh, P. W., Yuliati, L., and Lee, S. L. (2017). Kinetics and optimization studies of photocatalytic degradation of methylene blue over Cr-doped TiO_2 using response surface methodology. *Iranian Journal of Science and Technology, Transaction A: Science,* 43(1): 95-103.
26. Bahuguna, A., Kumar, S., Sharma, V., Reddy, K. L., Bhattacharyya, K., Ravikumar, P. C., and Krishnan, V. (2017). Nanocomposite of MoS_2-RGO as facile, heterogeneous, recyclable, and highly efficient green catalyst for one-pot synthesis of indole alkaloids. *ACS Sustainable Chemistry & Engineering,* 5(10): 8551-8567.
27. Norsham, I. N. M., Sambasevam, K. P., Shahabuddin, S., Jawad, A. H., and Baharin, S. N. A. (2022). Photocatalytic degradation of perfluorooctanoic acid (PFOA) via MoS_2/rGO for water purification using indoor fluorescent irradiation. *Journal of Environmental Chemical Engineering,* 10(5): 108466.
28. Taghvaei, H., Farhadian, M., Davari, N., and Maazi, S. (2017). Preparation, characterization and photocatalytic degradation of methylene blue by Fe^{3+} doped TiO_2 supported on natural zeolite using

response surface methodology. *Advances in Environmental Technology,* 3(4): 205-216.

Malaysian Journal of Analytical Sciences (MJAS)
Published by Malaysian Analytical Sciences Society

INVESTIGATION ON CHEMICAL CONSTITUENTS IN DAMMAR RESIN EXTRACT FROM STINGLESS BEE HIVE AND ITS POTENTIAL AS CORROSION INHIBITOR

(Penyiasatan Konstituen Kimia dalam Extrak Resin Dammar daripada Sarang Lebah Tanpa Sengat dan Potensinya Sebagai Perencat Kakisan)

Mokhtar Che Ismail[1], Muhammad Hadi[1] , Solhan Yahya[2*], and Zuliahani Ahmad[2]

[1]Centre for Corrosion Research,
Department of Mechanical Engineering,
Universiti Teknologi PETRONAS,
32610 Seri Iskandar Perak, Malaysia.
[2]Faculty of Applied Science,
Universiti Teknologi MARA, Cawangan Perlis, Arau Campus,
02600 Arau, Perlis, Malaysia

**Corresponding author: solhan@uitm.edu.my*

Received: 7 April 2022; Accepted: 21 June 2023; Published: 22 August 2023

Abstract

This study aimed to determine the major compounds present in local dammar resin and its potential as an anticorrosive property. Dammar resin from a stingless bee hive was subjected to solvent extraction using an aqueous system; 70:30 v/v of ethanol: water. The yield of extraction was characterized through Fourier transform infrared (FTIR) and gas chromatography-mass spectrometry (GC-MS). A linear polarization resistance (LPR), potentiodynamic polarization, and weight loss test were performed to evaluate the corrosion rate of steel. The result shows that longipinane (18%) was the major compound present in the extract, followed by ursolic aldehyde (14%), 1H-cycloprop[e]azulene (6.85%), 3,4-dichlorophenyl thiocyanate (6%), azulene, 1,2,3,3a,4,5,6,7-octahydro-1,4-dimethyl-7-(1-methylethenyl) (4.48%), and 2,4-heptadienal (4%). The existence of aromatic structure, phenyl group, C=C, and C=O provides an active site for adsorption on the metal surface to inhibit steel corrosion. LPR and weight loss test revealed the lowest corrosion rate at the 600 ppm dammar extract and recorded about 60% and 74% inhibition efficiency respectively. Tafel analysis showed a decrease in current density from 5.8×10^{-3} to 8.0×10^{-4} after 600 ppm dammar extract was employed in the corrosive medium of 3% NaCl, eventually, giving an inhibition efficiency at 86.2%. This research signifies that the local dammar resin of stingless bee hives has great potential as a corrosion inhibitor.

Keywords: dammar resin, gas chromatography-mass spectroscopy, corrosion rate, corrosion inhibition, Tafel

Abstrak

Kajian ini bertujuan untuk menentukan sebatian utama yang terdapat dalam resin dammar tempatan dan mengenalpasti potensi sifat antikarat. Dammar daripada sarang lebah tanpa sengat telah melaui pengekstrakan pelarut menggunakan sistem akueus; 70:30 v/v etanol: air. Hasil pengekstrakan telah dicirikan melalui inframerah transfromasi Fourier (FTIR) dan kromatografi gas-

spektrometri jisim (GC-MS). Rintangan polarisasi linear (LPR), pengutuban potensiodinamik dan ujian kehilangan berat telah dilakukan untuk menilai kadar kakisan keluli. Keputusan menunjukkan bahawa longipinan (18%) merupakan sebatian utama dalam ekstrak, diikuti oleh aldehid ursolik (14%), 1H-cycloprop[e]azulene (6.85%), 3,4-diklorofenil tiosianat (6%), azulena, 1,2,3,3a,4,5,6,7-oktahidro-1,4-dimetil-7-(1-metiletenal) (4.48%) dan 2,4-heptadienal (4%). Kewujudan struktur aromatik, kumpulan fenil, C=C dan C=O menyediakan tapak aktif untuk penjerapan pada permukaan logam bagi menghalang kakisan keluli. Keputusan LPR dan ujian kehilangan berat menunjukkan kadar kakisan terendah pada ekstrak dammar 600 ppm, dan masing-masing merekodkan kira-kira 60% dan 74% kecekapan perencatan. Analisis Tafel menunjukkan penurunan ketumpatan arus dari 5.8×10^{-3} kepada 8.0×10^{-4} selepas ekstrak dammar 600 ppm digunakan dalam medium 3% NaCl, akhirnya memberikan kecekapan perencatan 86.2%. Penyelidikan ini menunjukkan resin dammar sarang lebah tanpa sengat yang diperoleh dari sumber tempatan berpotensi besar sebagai perencat kakisan logam.

Kata kunci: dammar, kromatografi gas-spektrometri jisim, kadar kakisan, perencatan kakisan, Tafel

Introduction

The strategies in managing the degradation of metal and its structure must always synchronize with the aspect of cost, energy, time, nature of the environment, and materials. Failure in handling the strategies can cause severe damage and losses, especially on a metal structure with complex designs as well as hidden structures that are hard to inspect routinely. An effort in using good substances or chemicals in controlling the corrosion attack such as corrosion inhibitors is the most practical in such conditions. The organic inhibitors adsorb on the metal surface, form a thin protective film, and give protection from the corrosive environment. Since the principle of corrosion inhibitors is to alter the corrosiveness of the environment, the technology in exploiting natural sources and organic chemicals is encouraged as well in coatings. Attempts have been made on using metals and plant-based extracts as corrosion inhibitors such as carbon, carbon black, graphene, graphite, silver, glycosides, alkaloids, amino acids, flavonoids, and many more [1-3].

However, another less researched potential source is the organic chemical originating from natural sources such as dammar resinous or propolis from beehives. This native chemical is one of the potential materials to be introduced in corrosion control strategies. It offers abundance, availability, and renewable as compared to other metallic inhibitors. Dammar resinous or propolis is a resinous substance formed by honeybees from buds, leaves, and exudates of trees and plants mixed with pollen, wax, and enzymes secreted from the bees [4, 5]. The resinous substance is generally composed of approximately 50% resin (polyphenolic fraction), 30% wax, 10% essential oils, 5% pollen, and 5% various organic and inorganic compounds. Chemicals compounds (such as flavonoid and polyphenol) in dammar and propolis or beehive extract were found to have an antioxidant property that reflects the role for inhibits an oxidation process. The use of the dammar resinous or propolis extract from bee hives as corrosion inhibitors has developed interest among researchers. Rizvi et al. reported the ethanolic extract of propolis at 250 ppm was able to inhibit steel corrosion at 70% efficiency with comprehensive adsorption [6]. While Gapsari et al. stated that 2000 ppm bee wax propolis extract was feasible to inhibit the stainless steel corrosion in sulfuric acid with up to 97% efficiency with the formation of the complex and protective film [7]. The inhibition was reported due to physisorption and temperature-dependent. The efficiency of propolis also has been discussed by Fouda et al. who explained the inhibitive action based on the adsorption of the stable complex at the carbon steel surface [8, 9].

Apart from steel, other metals also have been treated by dammar resin/bee nest/wax base [7]. A study by Hachelef et al. revealed that the efficiency of propolis extract as a corrosion inhibitor for copper alloy in NaCl gives the maximum value of the inhibitory (73.28%) at an optimum concentration of 1.25 g/L of propolis extract [8]. Varvara et al. investigated the ability of propolis against the corrosion of bronze and found that 100 ppm propolis gives up to 98% with 12h exposure to weak acid of sodium sulphate and sodium bicarbonate [9]. The inhibitory effect was reported due to the adsorption of flavonoids and phenolic compounds on the bronze surface. The anticorrosive behaviour of propolis in combating aluminium corrosion was studied by Islami et al. and it was found that the high concentration of

propolis extract may cause agglomeration thus decreasing the efficiency [10].

However, not much literature on the chemical constituents of propolis from stingless bee hives has reported the inhibition properties [4, 11]. The composition of raw propolis depends on the geographical location, nature of plants, and bee species. A study by a group of Malaysian researchers has found that the local propolis extract is composed of volatile and non-volatile compounds [12]. While Leonhardt et al. revealed the propolis from the stingless bees in Borneo comprise terpenes, alkanes, and alkenes [13]. A constituent of triterpenes and flavonoids from stingless bee hives originated from Northeast Brazil also has been explored by Freitas et al. through chemical isolation and characterization [14]. In another study, Kartal et al. reported that flavonoids, aromatic acids, diterpenic acids, and phenolic compounds were the major components accountable for the biological activities of propolis samples [15]. Since the geographical was a strong factor in the variation of bee hive constituents, hence, each of the bee hive extracts may compose of a unique constituent locally.

The extraction methods play crucial roles in determining the obtained green inhibitor's functional compounds. It includes soaking, heating reflux, enzymatic hydrolysis, Soxhlet extraction, and ultrasonic extraction methods [16]. However, in this research, the usage of the aqueous extraction technique is preferred as compared to the organic extracts as it gives polar phytochemicals that offer strong bonding with the metallic surface than the non-polar in the latter technique [2]. The preferred aqueous method using ethanol is cost-saving and commonly known as a green extractant in providing high yield efficiency [17].

Therefore, the study of potential chemical constituents extracted from local bee hives was embarked as a corrosion inhibitor focusing on properties of the main constituent present in the extract of a stingless bee hive that may contribute to the potency of anticorrosive properties against steel. This work begins with the extraction, characterization, and identification of bee hives constituents through chemical analysis, followed by a corrosion inhibitors test.

Materials and Methods

Extraction of dammar resin

Dammar resin from a stingless bee hive (Figure 1a) or locally known as *damar kelulut* was collected from a local bee farm in Merbok, Kedah, Northern Peninsular Malaysia. The dried dammar resin was crushed into a fine powder and subjected to solvent extraction in 70:30 v/v of ethanol: water. The solvent mixture was heated below 60 ºC, stirred for 24 hours, filtered, and kept at 4 ºC for 3 days before removing the ethanol using a rotary evaporator. The light brown solution obtained was dried using a freeze-dryer to remove water and moisture and kept in a closed container before characterization. Light brown powders of dammar resin extracts were obtained (Figure 1b). The powder was used to form an inhibitors solution (Figure 1c).

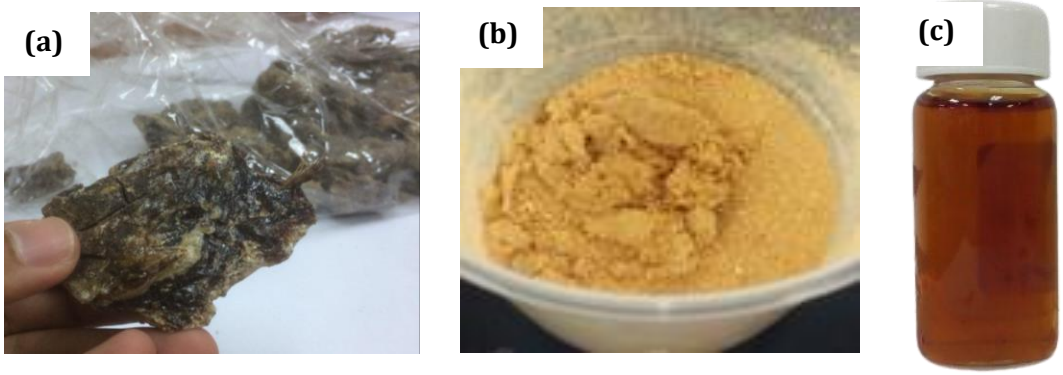


Figure 1: (a) Dammar resin; (b) Dammar resin powder after the extraction; (c) Dammar resin extract in ethanol/water system 70:30)

Characterization of dammar resin

Characterization of dammar resin extract was performed via Fourier transmission infrared (FTIR) and gas chromatography-mass spectrometry (GC-MS). FTIR analysis was carried out on a powder of dammar resin (before and after extraction) to identify the functional group present. The chromatograph and mass spectrometer calibration was performed using GC-MS Agilent 7890A gas chromatograph with a triple-axis detector. The chromatographic column used was SGE BPX-5 (30 m x 0.32mm i.d x 0.25 μm film thickness) with 5% phenyl polyphenylene-siloxane at a temperature from 50 C for 2 min, then 20 ^{o}C min^{-1} to 280 ^{o}C for 10 min, and finally 20 ^{o}C min^{-1} to 320 ^{o}C for 50 min.

Preparation of metal sample and corrosion inhibitor solution from dammar resin extract

A carbon steel S50C with a dimension of 1 cm x 1 cm x 0.6 cm was embedded in an epoxy resin with an exposed area of 1 cm^2. The specimen was polished by using different sizes of emery paper grades (from 400 to 1200), washed thoroughly with distilled water, and rinsed with ethanol [18, 19]. A solution of 3 wt.% NaCl was prepared in the 1 L flask and was used as a corrosive medium in a glass cell corrosion test. The carbon dioxide gas was purged for 1 hour to provide the glass cell containing 3 wt.% NaCl with saturated gases.

Electrochemical test

Linear polarization resistance (LPR) measurement was performed via ACM Instrument Gill 12 Weld Tester for data acquisition. A typical three-electrode glass cell was used consisting of a saturated calomel electrode AgCl (SCE) as a reference electrode and graphite as the counter electrode. The experiment was carried out at a constant temperature (within ±1° C). The potentiodynamic polarization test was performed for 24 hours. The measurement of LPR was recorded at a constant sweep rate of 0.167 mVs^{-1} and the scanning range was from -250 to +250 mV with respect to the open circuit potential (OCP). Inhibition efficiencies percentage (%IE) were determined from the corrosion current densities, I_{corr} calculated by the Tafel extrapolation method. The persistence test was carried out by immersing the metal sample in dammar extract for 1 hour to form a film. The metal samples were then dried before being exposed to a corrosive medium. The introduction of an inhibitor in 3 wt.% NaCl was carried out after a 2-hour measurement for stabilization of open circuit potential (OCP). The concentration of dammar extract as an inhibitor for this test was selected from the maximum inhibition efficiency achieved by the weight loss and LPR analysis.

Weight loss test

The weight loss test (immersion test) was carried out in a 1 L glass cell beaker containing 3 wt.% NaCl with different concentrations of dammar extract (200-1000 ppm). The immersion test was performed for 24 hours and the weight before and after immersion was recorded. The corrosion rate, CR was calculated using Eq. (1);

$$\mathrm{CR\ (mm/y)} = \frac{\mathrm{W}}{(\mathrm{D}\times\mathrm{A}\times\mathrm{T})} \times \mathrm{K} \quad (1)$$

Where, W = weight loss in grams, K = constant (87600), D = metal density in g/cm^3, A = area of the specimen (cm^2), and T = time (hour).

The inhibition efficiency was quantified using Eq. (2);

$$\mathrm{IE\%} = \frac{\mathrm{CR_0} - \mathrm{CR_i}}{\mathrm{CR_{0l}}} \times 100 \quad (2)$$

Where, CR_0 = Corrosion rate of the uninhibited system, and CR_i = Corrosion rate of the inhibited system.

Results and Discussion

Characterization of functional group in dammar extract via FTIR

Figure 2 illustrates the combination of the FTIR spectrum for dammar resin powder before extraction, after extraction and dammar extract in an aqueous solution of 70% ethanol; designated as (a), (b) and (c) respectively. The peak assignment for each spectrum was shown in Table 1.

In Figures 2 (a) and 2 (b), the spectrum shows an absorption around 3400 cm^{-1} assigned to the OH broadened band of either hydrogen bonded or hydroxyl group in the phenolic and aliphatic compounds. The absorption peaks at 2929 and 2943 cm^{-1} were due to the C-H stretch band of a methyl group. The peaks at 2868 and 2869 cm^{-1} were assigned as alkyl units of CH for a sample before extraction and ethanoic content for a sample after extraction correspondingly. The intense peak around 1693 and 1694 cm^{-1} were assigned as carboxylic acid groups (C=O). While the vibration around 1513, 1515, 1456, and 1453 cm^{-1} shows the presence of aromatic groups, C=C [7, 9]. Several peaks around 1380, 1313, 1273, 1109, 1087, and 1046 cm^{-1} for both samples exhibit the C-O stretching band of the carbonyl group and C-OH bending band. Meanwhile, a peak around 887 and 826 cm^{-1} was attributed to primary and secondary alcohol for a sample after extraction [6]. The existence of C=O, C=C, and OH in the dammar extract might contribute to the anticorrosive properties as the common criteria for a corrosion inhibitor is to have oxygen, functional groups, and aromatic rings for the best site of interaction [20, 21].

Spectra in Figure 2 (c) represent the FTIR result for dammar extract in aqueous 70% ethanol. The broad peak was observed at 3358 cm^{-1} corresponding to the OH group. Meanwhile, a peak around 2976 and 2893 cm^{-1} was assigned as ethanoic content for an extract in an aqueous solution. A peak at 1648 cm^{-1} was attributed to the C=C of the alkene and aromatic group. Several bands at 1453, 1382, 1086, and 1045 cm^{-1} were considered alcoholic functional groups of the C-O bond. Meanwhile, a band of 879 and 672 cm^{-1} is also related to the primary and secondary alcohol.

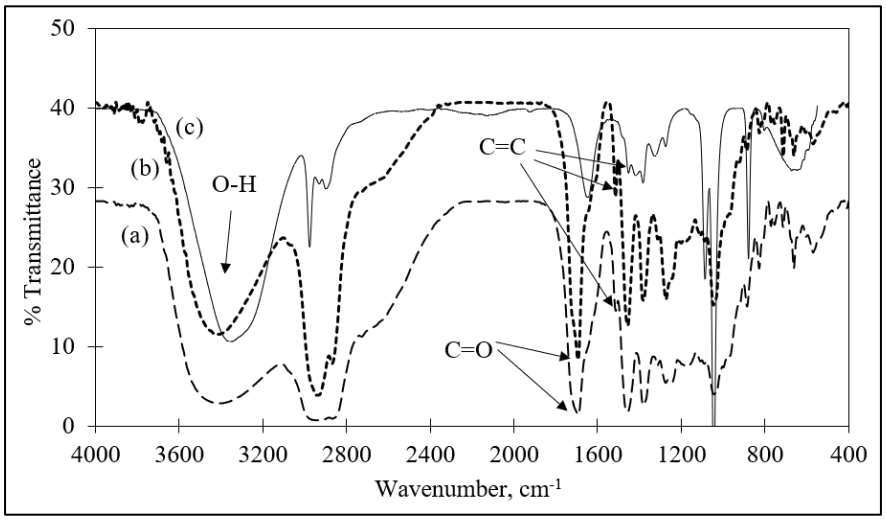


Figure 2. A powder of dammar resin (a) before extraction; (b) after the extraction; and (c) dammar extract in an aqueous solution of 70% ethanol

Table 1. Peak assignment of the FTIR spectrum for 3 samples, damar resin powder before extraction, damar extract powder after extraction and dammar extract in aqueous

Detected Wavenumber			
(a) Damar Resin Powder Before Extraction	**(b) Damar Extract Powder After Extraction**	**(c) Dammar Extract in Aqueous**	**Signal Peak Assignment**
3402	3411	3358	OH group
2929	2943	-	C-H stretch
2868	-	-	Alkyl CH
-	2869	2976, 2893	ethanoic content
1693	1694		carboxylic acid groups (C=O)
1513	1515, 1456	1648, 1453	C=C of alkene and aromatic group
1380, 1314, 1243, 1243, 1109, 1046	1380, 1273, 1109, 1047	-	alcoholic functional groups of C-O bond
		1382, 1086, 1045	C-O stretching band of carbonyl group and C-OH bending band
827, 753, 662, 570	887, 826	879, 672	primary and secondary alcohol

Identification of chemical constituents in dammar extract via GC-MS

A total of 46 constituents were finally identified via GC-MS analysis of dammar resin extract in 70% ethanol within 62.4 minutes as depicted in Table 2. The first compound, 1,3,6-Heptatriene, 2,5,6-trimethyl was detected around RT=19.5 min with an amount of 0.35%. The highest amount 18.42% was detected at RT=56.8 assigned as longipinanne. The less volatile in this extract was methyl 3 beta-hydroxyolean-18-en-28-oate since it was the last compound detected, with 3.33% amount.

Table 2. Chemical constituent of dammar extract in dammar resin (70:30 of ethanol:water) identified via GC-MS

Peak Number	**RT**	**Compound Detected**	**Total Amount (%)**
1	19.457	1,3,6-Heptatriene, 2,5,6-trimethyl	0.35
2	20.635	Copaene	1.40
3	20.85	(-)-.beta.-Bourbonene	0.62
4	20.992	Cyclohexane, 1-ethenyl-1-methyl-2, 4-bis(1-methylethenyl)-	1.39
5	21.459	1H-Cycloprop[e]azulene, 1a,2,3,4,4a,5,6,7b-octahydro-1,1,4,7-tetramethyl	6.85
6	21.62	1H-Cyclopropa[a]naphthalene, 1a,2,3,3a,4,5,6,7b-octahydro-1,1,3a,7-tetramethyl	0.80
7	21.782	Caryophyllene	3.61
8	22.037	4H-1-Benzopyran-4-one, 2-amino	0.55
9	22.385	2,4-Heptadienal	4.02
10	22.693	Humulene	1.07
11	22.803	(1R,9R,E)-4,11,11-Trimethyl-8-methylenebicyclo[7.2.0]undec-4-ene	0.78

12	23.164	.gamma.-Muurolene	0.58
13	23.334	Germacrene D	0.81
14	23.442	1-Isopropyl-4,7-dimethyl-1,2,3,4,5,6-hexahydronaphthalene	0.80
15	23.575	(3R,6R)-3-Hydroperoxy-3-methyl-6-(prop-1-en-2-yl)cyclohex-1-ene	1.39
16	23.689	(1S,2E,6E,10R)-3,7,11,11-Tetramethylbicyclo[8.1.0]undeca-2,6-diene	1.25
17	23.989	1,8-Nonadiene, 2,7-dimethyl-5-(1-methylethenyl)-	0.22
18	24.228	Naphthalene, 1,2,3,5,6,8a-hexahydro-4,7-dimethyl-1-(1-methylethyl)-,	1.00
19	25.494	Azulene, 1,2,3,3a,4,5,6,7-octahydro-1,4-dimethyl-7-(1-methylethenyl)	4.48
20	25.674	(3aS,4R,7R)-1,4,9,9-Tetramethyl-5,6,7,8-tetrahydro-4H-3a,7-methanoazulene	3.09
21	25.782	Caryophyllene oxide	1.13
22	25.89	2-Methyl-3-(3-methyl-but-2-enyl)-2	0.40
23	26.095	1,4-Methanocycloocta[d]pyridazine,1,4,4a,5,6,9,10,10a-octahydro-11,11-dimethyl	0.63
24	26.429	Cyclohexene, 4-(1,5-dimethyl-1,4-hexadienyl)-1-methyl-	0.60
25	26.741	Humulane-1,6-dien-3-ol	1.77
26	26.972	Methyl 10,12-pentacosadiynoate	0.46
27	27.164	(-)-Neoclovene-(I), dihydro	1.10
28	27.478	.alpha.-Cadinol 85709 000481-34-5 5	0.48
29	27.558	1R,4S,7S,11R-2,2,4,8-Tetramethyltricyclo[5.3.1.0(4,11)]undec-8-ene	0.39
30	29.9	Bicyclo[6.1.0]nonane, 9-bromo-9-methyl	0.17
31	31.269	2-Cyclohexen-1-one, 4-ethyl-4-meth	0.42
32	53.286	Ethyl 3-[2,2-bis(ethoxycarbonyl)ethyl]-5-methoxy-1H-pyrrolo[2,3]pyridine-2-carboxylate	0.55
33	53.521	Propanedioic acid, (triphenylphosp	0.42
34	53.673	N-(2-Chloro-1-ethoxyethyl)-N-cyano -N',N',N",N"-tetramethyl-1,3,5-triazine-2,4,6-triamine	0.49
35	54.034	2-Isopropenyl-4a,8-dimethyl-1,2,3,4,4a,5,6,7-octahydronaphthalene	0.76
36	55.739	1H-Isoindole-1,3(2H)-dione, 5,5'-oxybis[2-phenyl-	1.45
37	56.004	3-Hydroxy-4-phenyl-5-isopropyl-1,2,4-triazole	1.64
38	56.113	Cyclohexa-2,5-diene-1,4-dione, 2-methyl-5-(4-morpholinyl)-	0.68
39	56.54	Pimelic acid, 2-(2-methoxyethyl)hexyl pentyl ester	2.95
40	56.754	Longipinane	18.42
41	57.05	3-Bromo-4-methoxyphenol	2.14
42	57.482	Ursolic aldehyde TMS ether	14.13
43	57.762	9H-Fluorene-4-carboxylic acid, 9-oxo-, phenethylamide	0.62
44	58.07	3,4-Dichlorophenyl thiocyanate	6.17
45	59.319	Skatole	0.64
46	62.419	Methyl 3. beta.-hydroxyolean-18-en-28-oate	3.33

Chemical structure of major identified compounds in dammar resin extract

Figure 3 shows the chemical compounds found in dammar extract deduced from GC-MS. Out of 46 constituents in dammar extract, about 6 main compounds were identified in the range of 4 to 18%. Longipinane (18%) was the most abundant compound present followed by ursolic aldehyde (14%), 1H-cycloprop[e]azulene (6.85%), 3,4-dichlorophenyl thiocyanate (6%), azulene, 1,2,3,3a,4,5,6,7-octahydr o-1,4-dimethyl-7-(1-methylethenyl) (4.48%) and 2,4-heptadienal (4%). Most of the components present in dammar extract are classified as terpenoids.

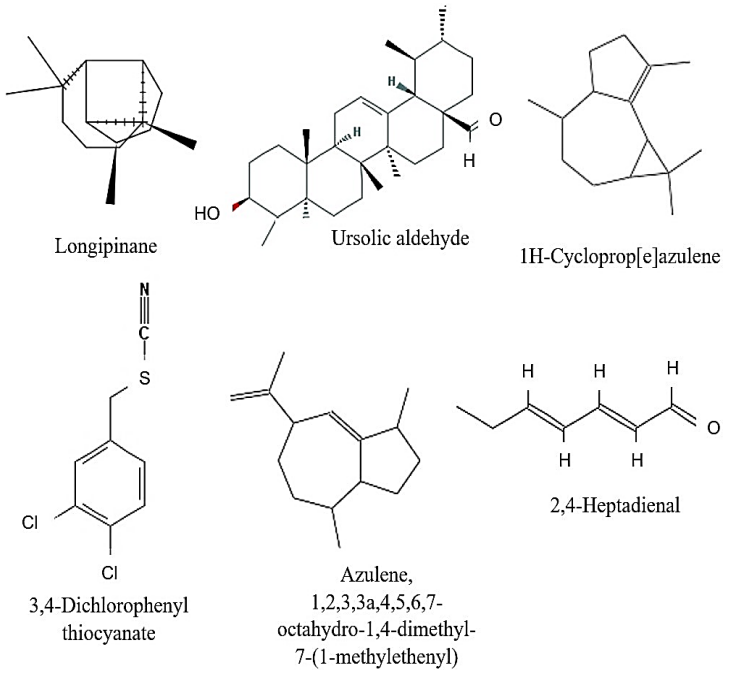


Figure 3. A main chemical compound present in dammar extract as deduced from GC-MS

Molecular structure criteria for corrosion inhibition

Table 3 summarized the main compound contains in propolis obtained from different regions. The listed propolis types have been extracted and analyzed for corrosion studies. The main compound was reported to have an anti-corrosive property.

Most of the chemical compounds in extracted dammar or propolis were built with an aromatic structure, for example, quercetin, cinnamic, and caffeic acid. Aromatic structure with delocalized electrons and functional groups provides an optimum site for interaction with metal. It is found that organic compounds containing aromatic rings and polar substituents are served as the most effective corrosion inhibitors. This agrees with studies that report each extract consists of complex phytochemicals (polar functional groups and multiple bonds) providing electron-rich sites and aiding in the adsorption of phytochemicals on a metal substrate [2, 23].

Aliphatic groups also may contribute to the interaction since their structure may occupy the limited adsorption site to retard the corrosion process. However, corrosion inhibition affected by the structure of inhibitors depends on its orientation, size, and the distribution of the electrons cloud. In agreement with a study by Varvara et al., besides aromatic structure, the presence of oxygen atoms in functional groups and various phenolic compounds are also factors for the corrosion inhibition of bronze corrosion in sodium solution [24].

Besides, the existence of methyl, CH_3 in almost all structures identified in both extracts plays an important

role in inhibition as methyl also provides a significant reaction site. The presence of particular repeating units (such as methyl and phenyl groups) of the parent chain and other substituent groups may improve the bonding strength of the group on the metal [21].

Table 3. List of main compounds in propolis discovered from different types and regions

Propolis Type	Extraction Method	Analysis	Main Compound	Ref
Bee wax propolis	Liquid-liquid extraction	FTIR and HPLC	Quercetin (2-(3,4-dihydroxyphenyl)-3,5,7- trihydroxy-4H-chromen-4-one)	[7, 9]
Propolis sample collected from Henan province (China)	Solvent extraction using ethanol	FTIR and HPLC	Pinos-trobin, trans-cinnamic acid, galangin and pinocembrin	
Ethanolic extract of propolis was provided by the Duzce University Beekeeping Research, Development and Application Centre, Yigilca, Turkey	Solvent extraction using 96% ethanol	FTIR and HPLC	3,4-dimethoxycinnamic acid, pinobanksin, caffeic acid, apigenin, isorhamnetin, curcumin, naringin, myristic acid and luteolin	[6]
Collected from Daqahlia province (delta Nile) of Egypt	Water extraction	Not included	Pinocembrin, caffeic acid, phenyl ester, quercetin and galangi	
Croatian propolis	Commercial alcoholic extract of propolis	Not included	Luteolin, 7-O- prenylpinocembrin, Cearoin, Linalool, P-methoxycinnamic acid, 3-prenyl-4-hydroxy-suberosin cinnamic acid, 3-prenylresveratro, l 6-methoxydiphyllin and Prenylated coumarin	[5, 22]
Propolis collected from the region of Bordj El Menaiel in Algeria	Ethylene glycol (30%) / water (70%)	FTIR	Not included	[8]

Linear polarization resistance (LPR)

Table 4 shows the resistance polarization value, Rp obtained from the LPR measurement. The Rp value for the blank solution without inhibitors (0 ppm) shows the lowest value with only 1225 Ohm.cm^2. Meanwhile, the highest values of Rp with 2971 Ohm.cm^2 are shown by the inhibitor's concentration at 600 ppm. It can be seen that the Rp value was increased as the concentration inhibitors increased from 200 to 600 ppm. However, the value then declined when the addition of inhibitors concentration was increased up to 800 and 1000 ppm.

The lowest value of Rp demonstrates small resistance to corrosion since no dammar extract was applied in the systems. Thus, the corrosion of steel might increase with a decrease in resistance. The greater value of Rp shown at 600 ppm was assigned that the dammar extract was capable to provide resistance to corrosion. This attributes to good inhibition which resists the chloride attack against the steel surface. The decrease in Rp values as the concentration of extract increased was due to the overdosage of inhibitor molecules that may promote the complexation. This phenomenon affects the formation of a protective film to resist corrosive ions due to repulsive interactions, thus weakening the adsorption for inhibition [25].

Table 4. Resistance polarization (Rp) value of steel corrosion by dammar extract at different concentrations

Concentration Inhibitor (ppm)	Rp (Ohm.cm^2)
0	1225
200	1413
400	2750
600	2971
800	1469
1000	1397

Corrosion rate measurement

Figure 4 shows the corrosion rate measurement employed through the weight loss method and LPR technique. The high values of corrosion rate were shown in all measured concentrations via the LPR technique compared to the weight loss method. The highest value of corrosion rate was shown by the steel sample without corrosion inhibitors (0 ppm) for both the weight loss method (0.19 mm/yr) and LPR (0.25 mm/yr). The addition of 200 to 600 ppm dammar extract reduced the corrosion rate concentration and gradually increased as the inhibitors were increased. The lowest corrosion rate was achieved via weight loss methods at 0.05 mm/yr for 600 ppm. Above the 600 ppm dammar resin, the increase in inhibitor concentration has increased the corrosion rate values up to 0.22 mm/yr. The corrosion rate values for both measurement methods showed a similar trend.

In this result, the low concentration of dammar extract provides low corrosion protection as inhibitors were unable to prevent the corrosive ion, (eg: Cl^-). Consequently, the corrosion rate was increased due to insufficient dammar extract to interact on the surface for better corrosion inhibition. Meanwhile, the overdosage of dammar extract contributes to the excess of inhibitor molecules in the solution. Eventually, various ions in the solution create the Van der Waals effect where the mutual repulsion or attraction force is triggered among the inhibitors molecules and ions in the metal/solution interface [25]. Therefore, the high corrosion rate at high inhibitor concentration is also due to the complexity of dammar extracts composition causing the desorption process [26].

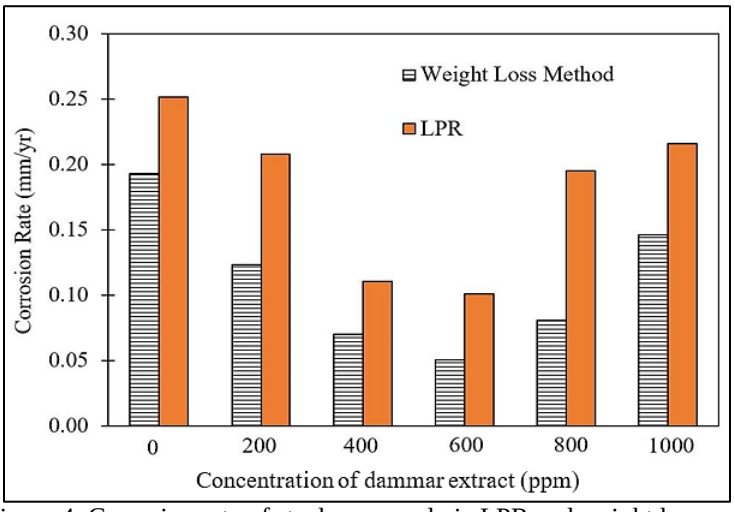


Figure 4. Corrosion rate of steel measured via LPR and weight loss method

Table 5 shows the inhibition efficiency value of steel corrosion calculated from corrosion rate values obtained via LPR and weight loss analysis in different concentrations of inhibitor. Generally, the addition of corrosion inhibitors shows enhanced corrosion inhibition. However, our results showed the inhibition efficiency was dependent on the concentration of the inhibitor.

Table 5. Inhibition efficiency of steel corrosion by dammar extract at a different concentration calculated from corrosion rate values obtained via LPR and weight loss analysis

Concentration (ppm)	**Inhibition Efficiency (IE%)**	
	LPR Analysis	**Weight Loss Analysis**
0 ppm	0	0
200 ppm	17	36
400 ppm	56	64
600 ppm	60	74
800 ppm	22	58
1000 ppm	14	24

From the tabulated data, it can be seen that the inhibition efficiency increased up to 60% and 74% as 600 ppm dammar resin was used in LPR and weight loss methods correspondingly. While the use of 1000 ppm dammar resin exhibits the lowest efficiency. The values decreased as the concentration become increased to 1000 ppm The highest efficiency was achieved at the concentration of 600 ppm of dammar resin. The maximum efficiency was shown by the 600 ppm dammar resin for both methods. It is believed that the inhibitor molecules affect the reactions and adsorbed on the mild steel plate by blocking the active sites situated on the metal surface hence inhibiting the corrosion reaction. The compounds establish a barrier associated with mass charge transfer. The hindrance against the transport of corrosive ions into the solution was contributed by the adsorption of phenolic compounds via an aromatic ring, as well as the heteroatoms of nitrogen and oxygen upon the steel plate [1].

This situation also explained the phenomenon of limiting or critical concentration and the solubility effect [27-29]. At the concentration of 600 ppm, the dammar resin molecules have covered an optimum surface coverage and inhibit the corrosion at high efficiency. As more inhibitors are added into the corrosive medium, there is a limited site for adsorption. It is observed that before and after the 600 ppm, the inhibition efficiency in both LPR and weight loss method was lesser than 60% and 74% respectively. The low efficiency shown by the highest concentration (1000 ppm) was due to the desorption process. This indicates the presence of improper surface protection on the metal substrate. The weak interaction among the inhibitor molecules and metal surfaces generated from dipole-dipole interactions has declined the adsorption capability [25]. Therefore, the adsorption and inhibition were controlled by the major structure of the chemical components in the inhibitors [27, 30] such as alkyl chain length in the inhibitor, presence of heteroatoms and heterocycles in the molecule, existence of electron donating/withdrawing functionalities, and size of rings in the inhibitors molecules as can be further investigated in Figure 3.

Figure 5 shows the Tafel plots obtained from the electrochemical measurement of steel exposed to 3% NaCl solution. The presence of 600 ppm dammar extract in 3% NaCl was measured and the electrochemical parameter was summarized in Table 6.

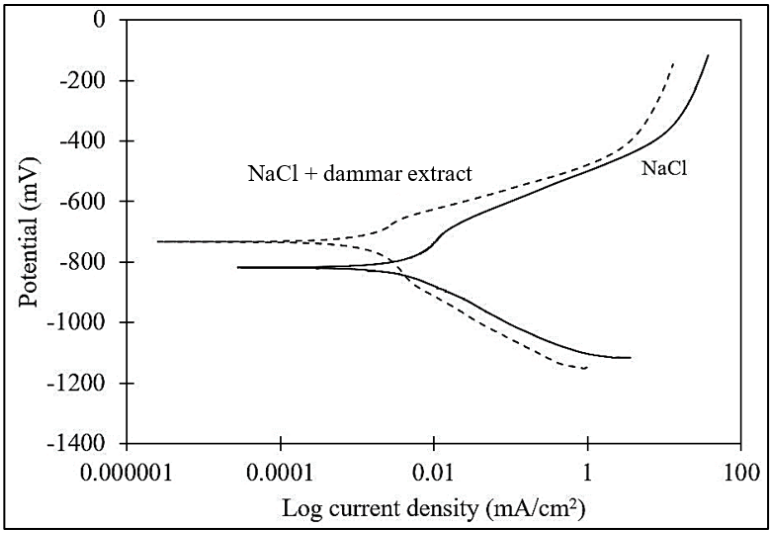


Figure 5. Potentiodynamic polarization curve of steel in NaCl and the absence and presence of 600 ppm dammar extract

Table 6. Tafel parameter obtained from potentiodynamic polarization test

Inhibitor System	**Corrosion Potential, E_{corr} (mv)**	**Current Density, I_{corr} (mA/cm^2)**	**Inhibition Efficiency (IE%)**
NaCl	-818	5.8×10^{-3}	0
NaCl + dammar extract	-725	8.0×10^{-4}	86.2

The presence of dammar extract inhibitors in 3% NaCl has shifted the E_{corr} value to a more positive potential. This signified the dammar extract inhibitors act as an anodic inhibitors type by decreasing the steel dissolution. Simultaneously, the value of current density, I_{corr} was reduced from 5.8×10^{-3} to 8×10^{-4} mA/cm^2 assigned the flow of electrons is hindered by the mass of dammar extract molecules. The changes of both E_{corr} and I_{corr} values attribute the corrosion inhibition due to the adsorption of dammar extract on the steel surface. The dammar extract molecules have hindered the corrosive ions from NaCl from further attacking the steel.

Conclusion

The overall findings from this study can be concluded as follows: The chemical constituents of dammar extract have been determined and the six major compounds were found; longipinane (18%), ursolic aldehyde (14%), 1H-cycloprop[e]azulene (6.85%), 3,4-dichlorophenyl thiocyanate (6%), azulene, 1,2,3,3a,4,5,6,7-octahydr o-1,4-dimethyl-7-(1-methylethenyl) (4.48%) and 2,4-heptadienal (4%). The existence of various functional groups such as C=C, C=O, C-OH, CH_3, phenyl group, and aromatic structure contributed to the good anticorrosive properties of the local *kelulut* dammar extract towards steel corrosion. The best concentration of dammar extract was 600 ppm with 86.2% inhibition efficiency may exhibit a practical, efficient, and excellent potential for alternative green corrosion inhibitors. Below 600 ppm, the adsorption of inhibitor on the metal surface happened at an intermediate level of inhibition. Whilst, more crowding inhibitor molecules at the metal/solution interface do not improve the corrosion inhibition. The inhibition efficiency of the dammar extract obtained from LPR and weight loss measurements were in good agreement.

Acknowledgement

The authors would like to acknowledge the Yayasan Universiti Teknologi PETRONAS, YUTP-FRG 0153AA-E41 research grant for financial support. The authors would like to thank Centralised Analytical Laboratory (CAL), UTP for the chemical analysis

services, and Sustainable Polymers Materials Research Interest Group (SuPMa) UiTM Perlis for a valuable discussion on reviewing the manuscript.

References

1. Ali Asaad, M., Bothi Raja, P., Fahim Huseien, G., Fediuk, R., Ismail, M., and Alyousef, R. (2021). Self-healing epoxy coating doped with Elaesis guineensis/silver nanoparticles: A robust corrosion inhibitor. *Construction and Building Materials*, 312: 125396.
2. Alrefaee, S. H., Rhee, K. Y., Verma, C., Quraishi, M. A., and Ebenso, E. E. (2021). Challenges and advantages of using plant extract as inhibitors in modern corrosion inhibition systems: Recent advancements. *Journal of Molecular Liquids*, 321: 114666.
3. Liu, S., Wang, X., Yin, Q., Xiang, X., Fu, X. Z., Wang, X. Z., and Luo, J. L. (2022). A facile approach to fabricating graphene/waterborne epoxy coatings with dual functionalities of barrier and corrosion inhibitor. *Journal of Materials Science and Technology*, 112: 263-276.
4. Rivero-cruz, J. F., Granados-pineda, J., Pedraza-chaverri, J., and Rivero-cruz, B. E. (2020). and Antimicrobial activities of the ethanolic extract of mexican brown propolis. *Antioxidants*, 9(70): 1-11.
5. Vrsalović, L., Gudić, S., Gracić, D., Smoljko, I., Ivanić, I., Kliškić, M., and Oguzie, E. E. (2018). Corrosion protection of copper in sodium chloride solution using propolis. *International Journal of Electrochemical Science*, 13(2), 2102-2117.
6. Rizvi, M., Gerengi, H., Yildiz, M., Kekecoglu, M., & Pehlivan, M. M. (2020). Investigation of "propolis" as a green inhibitor of SAE 1010 carbon steel corrosion in 3.5% NaCl environment. *Industrial and Engineering Chemistry Research*, 59(19): 9328-9339.
7. Gapsari, F., Soenoko, R., Suprapto, A., and Suprapto, W. (2015). Bee wax propolis extract as eco-friendly corrosion inhibitors for 304SS in sulfuric acid. *International Journal of Corrosion*, 2015: 1-10.
8. Hachelef, H., Khelifa, A., and Benmoussat, A. (2021). Propolis extract as corrosion inhibitor of iron alloy immersed in an ethylene glycol/water, 0.1 m NaCl solution. *Defect and Diffusion Forum*, 406: 265-273.
9. Varvara, S., Bostan, R., Bobis, O., Găină, L., Popa, F., Mena, V., and Souto, R. M. (2017). Propolis as a green corrosion inhibitor for bronze in weakly acidic solution. *Applied Surface Science*, 426: 1100-1112.
10. Islami, L. A., Sembodo, S., and Anawati, A. (2020). Anticorrosive behavior of propolis as a green corrosion inhibitor for aluminum. *Proceedings of the 3rd International Seminar on Metallurgy and Materials (ISMM2019): Exploring New Innovation in Metallurgy and Materials*, 2232: 020002.
11. Huang, S., Zhang, C. P., Wang, K., Li, G. Q., and Hu, F. L. (2014). Recent advances in the chemical composition of propolis. *Molecules*, 19(12): 19610-19632.
12. Ismail, T. N. N. T., Sulaiman, S. A., Ponnuraj, K. T., Man, C. N., and Hassan, N. B. (2018). Chemical constituents of Malaysian apis mellifera propolis. *Sains Malaysiana*, 47(1): 117-122.
13. Leonhardt, S. D., Blüthgen, N., and Schmitt, T. (2011). Chemical profiles of body surfaces and nests from six Bornean stingless bee species. *Journal of Chemical Ecology*, 37(1): 98-104.
14. Freitas, M. O., Ponte, F. A. F., Lima, M. A. S., and Silveira, E. R. (2008). Flavonoids and triterpenes from the nest of the stingless bee Trigona spinipes. *Journal of the Brazilian Chemical Society*, 19(3): 532-535.
15. Kartal, M., Kaya, S., and Kurucu, S. (2002). GC-MS analysis of propolis samples from two different regions of Turkey. *Zeitschrift Fur Naturforschung - Section C Journal of Biosciences*, 57(9-10): 905-909.
16. Shang, Z., and Zhu, J. (2021). Overview on plant extracts as green corrosion inhibitors in the oil and gas fields. *Journal of Materials Research and Technology*, 15: 5078-5094.
17. Popov, S. A., Sheremet, O. P., Kornaukhova, L. M., Grazhdannikov, A. E., and Shults, E. E. (2017). An approach to effective green extraction of triterpenoids from outer birch bark using ethyl acetate with extractant recycle. *Industrial Crops and Products*, 102: 122-132.
18. ASTM G 31-72. (1985). Standard practice for

laboratory immersion corrosion testing of metals. *ASTM International, Reapproved 2004*: pp.1-8.

19. ASTM G1-90. (1999). Standard practice for preparing, cleaning, and evaluation corrosion test specimens. *ASTM International, Reapproved 1999*: pp.15–21.
20. Goyal, M., Kumar, S., Bahadur, I., Verma, C., and Ebenso, E. E. (2018). Organic corrosion inhibitors for industrial cleaning of ferrous and non-ferrous metals in acidic solutions: A review. *Journal of Molecular Liquids*, 256: 565-573.
21. Popoola, L. T. (2019). Organic green corrosion inhibitors (OGCIs): A critical review. *Corrosion Reviews*, 37(2): 71-102.
22. Sayed Fouda, A. E. A. El, and Badr, A. H. (2013). Aqueous extract of propolis as corrosion inhibitor for carbon steel in aqueous solutions. *African Journal of Pure and Applied Chemistry*, 7(10): 350-359.
23. Palaniappan, N., Cole, I., Caballero-Briones, F., Manickam, S., Justin Thomas, K. R., and Santos, D. (2020). Experimental and DFT studies on the ultrasonic energy-assisted extraction of the phytochemicals of: Catharanthus roseus as green corrosion inhibitors for mild steel in NaCl medium. *RSC Advances*, 10(9): 5399–5411.
24. Varvara, S., Bostan, R., Bobis, O., Găină, L., Popa, F., Mena, V., and Souto, R. M. (2017). Propolis as a green corrosion inhibitor for bronze in weakly acidic solution. *Applied Surface Science*, 426:1100-1112.
25. Bard, and Stratmann (2003). *Encyclopedia of Electrochemistry, Corrosion and Oxide Films*. Wiley-VCH Verlag, Weinhem.
26. Adejo, S. O., Ekwenchi, M. M., Olatunde, P. O., and Agbajeola, E. F. (2014). Adsorption characteristics of ethanol root extract of *Portulaca oleracea* as eco-friendly inhibitor of corrosion of mild steel in H_2SO_4 medium. *IOSR Journal of Applied Chemistry*, 7(4): 55-60.
27. McCafferty, E. (2009). *Introduction to Corrosion Science*. Washington, DC: Springer New York Dordrecht Heidelberg London: pp.1-575.
28. Rani, B. E. A., and Basu, B. B. J. (2012). Green inhibitors for corrosion protection of metals and alloys: An overview. *International Journal of Corrosion*, 1-15.
29. Sharma, S. K. (2012). *Green Corrosion Chemistry and Engineering: Oppurtunities and Challenges*. Wiley-VCH Verlag & Co. KGaA,Weinheim Germany: pp.1-419
30. Chauhan, D. S., Ansari, K. R., Sorour, A. A., Quraishi, M. A., Lgaz, H., and Salghi, R. (2018). Thiosemicarbazide and thiocarbohydrazide functionalized chitosan as ecofriendly corrosion inhibitors for carbon steel in hydrochloric acid solution. *International Journal of Biological Macromolecules*, 107: 1747-1757.

Malaysian Journal of Analytical Sciences (MJAS)
Published by Malaysian Analytical Sciences Society

PURIFICATION OF POTENT ANGIOTENSIN CONVERTING ENZYME (ACE)-INHIBITORY PEPTIDES DERIVED FROM RED TILAPIA (*Oreochromis* Sp.) BY-PRODUCTS

(Penulenan Peptida Perencat Enzim Penukaran Angiotensin (ACE) daripada Produk Sampingan Ikan Tilapia Merah (*Oreochromis* Sp.))

Nur Suraya Abdul Wahab[1], Emmy Liza Anak Yaji[1], Norfahana Abd-Talib[1,], Mohammad Zulkeflee Sabri[2,], Kelly Yong, Tau Len[3], Fadzlie Wong Faizal Wong[4], and Khairul Faizal Pa'ee[1*]

[1]*Food Engineering Technology, Universiti Kuala Lumpur, Branch Campus Malaysian Institute of Chemical and Engineering Technology, 78000 Alor Gajah, Melaka, Malaysia*
[2]*Bioengineering Technology, Universiti Kuala Lumpur, Branch Campus Malaysian Institute of Chemical and Engineering Technology, 78000 Alor Gajah, Melaka, Malaysia.*
[3]*Process Engineering Technology, Universiti Kuala Lumpur, Branch Campus Malaysian Institute of Chemical and Engineering Technology, 78000 Alor Gajah, Melaka, Malaysia.*
[4]*Faculty of Biotechnology and Biomolecular Sciences, Universiti Putra Malaysia, 43400, UPM Serdang, Selangor, Malaysia.*

[*]*Corresponding author: khairulfaizal@unikl.edu.my*

Received: 7 October 2022; Accepted: 17 January 2023; Published: 22 August 2023

Abstract

Diet and lifestyle changes are essential alternative treatments for hypertension. Consumers are increasingly more interested in health-promoting ingredients. The use of red tilapia (*Oreochromis* sp.) by-products (RTBP) has been established as a precursor for protein hydrolysate with angiotensin I-converting (ACE)-inhibitory activity. However, the complexity of the protein hydrolysate reduces its potency. Thus, this work aimed to purify and characterise the ACE-inhibitory hydrolysate derived from red tilapia (*Oreochromis* sp.). Thermoase PC10F (EC 3.4.24.27) was used in this study to hydrolyse red tilapia by-products (*Oreochromis* sp.). Meanwhile, ultrafiltration (UF), anion-exchange principle (AEX) and hydrophobic interaction chromatogram (HIC) were applied to purify the hydrolysate. Two molecular weight cut-offs (MWCO) were used for ultrafiltration: 3 kDa and 1 kDa. The 1 kDa hydrolysate showed the highest bioactivity of 85.42% (IC_{50}=0.41 mg mL^{-}). Subsequently, the 1 kDa RTBP hydrolysate was purified based on charge using AEX. Positively charged hydrolysate demonstrated significant bioactivity of 72.32%. In the final purification steps, the hydrophobic fractions showed the highest ACE-inhibitory activity obtained through the hydrophobic interaction chromatogram. The chromatogram yielded two fractions of peaks of high ACE-inhibitory activity on the hydrophobic fraction, which were 90.44% and 95.28%, respectively. Thus, ACE-inhibitory hydrolysate of small molecular size, positive charged and hydrophobic contributed significantly to its potency.

Keywords: ACE-inhibitory activity, hydrophobicity, red tilapia by-product. protein hydrolysate, purification

Abstrak

Penukaran enzim yang dikenali sebagai Angiotensin-1 kepada Angiotensin-2 bertanggungjawab ke atas kenaikan tekanan darah yang menyebabkan hipertensi. Perubahan diet dan gaya hidup perlu diterapkan sebagai pelan rawatan alternatif. Pasaran untuk kompoun penggalak kesihatan didalam makanan semakin dicari-cari pengguna. Sejak sedekad lalu, pelbagai kajian dijalankan ke atas hasil sampingan ikan tilapia (*Oreochromis* sp.) kerana sifat biologinya terutamanya sebagai agen antihipeternsi. Kenaikkan permintaan bekalan terhadap filet ikan turut meningkatkan kadar penangkapan ikan. Maka, terdapat lebihan model pengeluaran yang dapat dieksploitasi dengan cara yang menguntungkan. Di dalam kajian ini,Thermoase PC10F menghasilkan hidrolisat penghambat ACE daripada hasil sampingan ikan tilapia merah (*Oreochromis* sp.). Manakala hidrolisat ini ditulenkan melalui ultrafiltrasi (UF), prinsip pertukaran anion (AEX) dan kromatogram interaksi hidrofobik (HIC). Dua berat molekul 3 kDa dan 1 kDa digunakan didalam proses ultrafiltrasi. Penghambatan aktiviti ACE untuk berat molekul 1 kDa lebih tinggi berbanding 3 kDa dengan jumlah 85.42%. Seterusnya, hidrolisat 1 kDa ditulenkan melalui prinsip pertukaran ion dan hidrolisat bercas positif mempunyai penghambatan aktiviti ACE yang tertinggi (72.32%) berbandingkan dengan hidrolisat bercas negatif. Akhir sekali, proses penulenan dilakukan melalui kromatogram interaksi hidrofobik dan pecahan hidrofobik mempunyai penghambatan aktiviti ACE yang tertinggi. Kromatogram menghasilkan dua bagian puncak hidrofobik yang mempunya peringkat aktiviti penghambatan ACE tertinggi sebanyak 90.44% dan 95.28%. Maka, sifat molekul yang kecil, bercas positif dan hidrofobik merupakan ciri-ciri hidrolisat penghambatan aktiviti ACE yang manjur.

Kata kunci: penghambatan aktiviti ACE, kehidrofobikan, produk sampingan ikan tilapia merah, protein hidrosilat, penulenan

Introduction

Multiple biological activities in fish protein hydrolysate, such as antioxidative, lipid homeostasis regulation, anti-inflammatory, anticancer, neuroprotective and antihypertensive, can be utilised as a functional food ingredient. [1]. ACE inhibitors comprise a novel class of medications used to treat hypertension and heart failure. In addition to their well-known role and ease of availability, synthetic medications include unwanted side effects [2-4]. Thus, the quest for alternative natural ACE-inhibitory peptides has been expanded to various food protein sources, which include aquatic protein sources.

Numerous studies on the freshwater fishes' by-product hydrolysate derived from Grass carp, Tilapia, Snakehead fish, shortfin scad fish and catfish have shown promising antihypertensive properties [4-11]. Tilapia is a freshwater fish that is widely cultured in Asian countries [4] as it multiplies and has low feed requirements [10]. With the rapid increase in fish production to cope with the fish filleting demand, more than 50% of the residuals from the total fish capture become unused as nourishment, which involves nearly 32 million tonnes of the fish by-product that can be processed into a desirable functional food [12, 13]. Tilapia is one of the most important freshwater fish species sold internationally owing to its popularity among people of various cultural, religious and economic backgrounds. Besides, red tilapia scales have between 41% and 84% protein, the highest among residues of fish farms [14, 15].

Protein complexes are among the most essential functional elements for deriving cellular biological functions [16]. Hence, the search begins for antihypertensive bioactive peptides that are inactive within the sequence of the parent protein but can be released during gastrointestinal digestion or food processing like enzymatic hydrolysis [5,13]. However, protein extracted from complex biological systems contains a complex protein combination suspended in a mixture of organic and aqueous solvents [1, 17]. The production of bioactive peptides involves several steps including the screening of enzymes, optimisation of hydrolysis conditions, as well as the purification of protein hydrolysate. Thermoase PC10F was chosen for enzymatic hydrolysis in this study, which is a commercial enzyme for thermolysin. The primary site for thermolysin cleavage specificity accommodates long hydrophobic residues. Thermolysin preferentially cleaves hydrophobic or bulky amino side chains [6,18,19]. Nevertheless, no research on the antihypertensive properties of RTBP hydrolysate using thermolysin or the commercial enzyme, Thermoase PC10F, has been conducted. In addition, purification of the protein hydrolysate-containing peptides is one of the most crucial steps in improving ACE-inhibitory

potency. The most common considerations to purify peptides are based on their specific characteristics such as molecular size (ii) charge and (iii) hydrophobicity as peptide activities are heavily influenced by the structure-determined characteristics [4-7, 9-11, 17-23].

The goal of this study was to separate and purified the hydrolysate from a red tilapia (*Oreochromis* sp.) by-products (RTBP) treated with Thermoase PC10F based on molecular size, surface charge and hydrophobicity. The core technique for protein purification was quite straightforward: all impurities were removed while preserving as much of the peptide of interest with high ACE-inhibitory activity as possible.

Materials and Methods

Protein hydrolysate preparation

Enzymatic hydrolysis was done using Thermoase PC10F enzyme. The hydrolysis of 2g of sample was mixed with Thermoase PC10F enzyme and hydrolysed with phosphate buffer, pH 7. The ratio of enzyme to sample was 1:160 was incubated at 68 °C for 6 hours in a shaking bath. The sample was immersed in boiling water for 5 minutes to stop the hydrolysis. Then, the hydrolysate (sample) was centrifuged, whereas the supernatant was collected for further analysis.

Total protein assay (Lowry assay)

Bovine serum albumin (BSA) was used as protein standard at the concentration of 50, 100, 200, 300 and 400 µg mL^{-1}. Lowry reagent solution of 1 mL was added to each sample and incubated for 20 minutes at room temperature. Then, 0.5 mL of Follin Ciocalteu's Phenol working reagent was added and mix immediately. Eppendorf tubes were incubated for 30 minutes at room temperature to allow the colour to be developed. After incubation, the values of absorbance were measured by UV-VIS spectrophotometer at 595 ηm followed by the plotting of absorbance.

Determination of ACE-inhibitory activity: Enzymatic assay with ACE

HHL of 5 mM was prepared using 0.1 M sodium phosphate buffer (pH 8.2) containing 0.3 M NaCl. The same buffer was used for solution preparation of captopril, substrate, hippuric acid, peptides and enzyme dilute. ACE (60 mU mL^{-1}) was prepared from the initial unit (2 U mL^{-1}) using the same buffer. In each assay, 10 µL of the sample and buffer (control) was pipetted into the sample Eppendorf tube. After that, 30 µL of ACE (60 mU mL^{-1}) was added to the sample and gently mixed. Next, the mixture was incubated for 10 minutes at 37 °C. 90 µL of 5 mM HHL was then added to the samples and incubated for another 60 minutes at 37 °C. Finally, 8 µL of 5M HCl was added to stop the reaction and the mixture was filtered through a 0.2 µm PVDF filter into vials.

HPLC method to determine ACE-inhibitory activity

The samples were analysed with Shimadzu LC-20AP Low Gradient System (SPD-20AV) HPLC by a C18 Thermo Scientific ODS Hypersil HPLC column. The sampler and the column temperature were kept at 4 °C and 30 °C, respectively. The injection volume with the flow rate of 20 µL and 1 mL min^{-1}, respectively, for 12 minutes was used with an isocratic solution of 0.1% trifluoroacetic acid in 12.5% acetonitrile. The absorbance was monitored with ultraviolet (UV-VIS) detection at 228 nm. Serial dilutions of HA from 0.02 to 1 mM were applied to determine the calibration curve.

Calculation of ACE-inhibitory activity

The percentage of ACE-inhibitor activity (ACEi%) was calculated based on the hippuric acid liberated using the hydrolysates sample and control (buffer) as follows (1):

$$ACEi\% = \left[\frac{(HAcontrol) - HAsample)}{HAcontrol}\right] x\ 100 \quad (1)$$

Where (ACEi%) was the percentage of angiotensin-converting enzyme inhibitory activity of hydrolysates; [$HA_{control}$] was the concentration of hippuric acid (HA) liberated using buffer instead of inhibitor in the mixture and; [HA_{sample}] was the concentration of hippuric acid liberated in the presence of inhibitors (hydrolysates).

IC_{50} determination of the hydrolysates

The IC_{50} value is defined as the concentration of hydrolysates that can inhibit half-maximal of the ACE. Sample or protein hydrolysates that yielded more than 50% ACEi% were then selected and evaluated for ACEi% in different concentrations. The IC_{50} of the hydrolysates with different enzymatic conditions were determined by the regression analysis of plotting the inverse of serially diluted hydrolysates concentration (1/1, 1/2.5, 1/5, 1/10, 1/20) as a function of the inverse of their ACEi% and expressed as mg of protein per mL. The IC_{50} of the peptides were compared with the IC_{50} of captopril as positive standards.

Determination degree of hydrolysis (DH)

The degree of hydrolysis (DH) was estimated using the o-phthaldialdehyde (OPA) method as described by Nielsen [24] and Pa'ee [25] with some modifications. The o-phthaldialdehyde (OPA) reagent was freshly prepared, comprising 0.025g of OPA (dissolved in 500 µL of pure ethanol) and 25 µL of β-Mercaptoethanol in 50 mL of 50 mM carbonate buffer pH 10.5. This OPA reagent should be protected from direct light and used within 2 hours, or it can eventually be stored under nitrogen in an ambered glass vial for 1-2 weeks at 4 °C. An aliquot of 400 µL of standard or sample was added into the 3 mL of OPA reagent and mixed for 5 seconds. The mixture was incubated at room temperature before being read at 340 nm at a spectrophotometer by UV-VIS 1800 Shimadzu. Deionised water was used as a blank and leucine dilution as a standard. The DH was calculated using the equation from the method.

Fractionation and Purification of RTBP hydrolysate: Ultrafiltration (UF)

Hydrolysates were fractionated using ultrafiltration membranes in a dead-end mode system (Amicon Model 8200 stirred ultrafiltration cell, Amicon Corp., Danvers, MA) utilising the procedures outlined by Roslan [26] with a few minor adjustments.

A stirred ultrafiltration cell has a suspended bar impeller and a stirring hot plate. Flat sheet RC membranes with 1 kDa and 3 kDa MWCO were employed. With a constant pressure at 2.5 bar and continuous stirring speed, an ultrafiltration membrane fractionated the RTBP hydrolysate. Optimal RTBP hydrolysate was separated through a 3 kDa membrane before a 1 kDa membrane. The ACE inhibitory activities and IC_{50} of 1 kDa and 3 kDa permeate were evaluated. Permeate flux was also calculated. The calculation was done as described by Roslan [26] using the following equation (2):

$$Flux = \left(\frac{Total\ quantity\ passed\ throu\ \ membrane}{Membrane\ Area}\right) L/(m^2.h) \quad (2)$$

Flux is the rate at which a membrane separation process works. It is determined by the properties of the membrane, the transmembrane strain, the system's hydrodynamics, the properties of the solvent and protein, and the amount of protein in the feed.

Adsorption equilibrium

The anionic exchanger resin (STREAMLINE DEAE) was used in this work applying a batch adsorption approach. Initially, the resin was washed twice with 10 mM potassium phosphate buffer at pH 7.0 to equilibrate the adsorption conditions. The buffer was decanted once the resin settled at the bottom of the test tube. The RTBP hydrolysate of 5 mL was added and stirred for 10 minutes to adsorb negatively charged peptides to the resin. The resin was then separated from the supernatants by centrifugation. The resin containing the adsorbed protein was eluted with potassium phosphate buffer pH 7.0 containing 1 M NaCl. The resin was regenerated using the same elution buffer. RTBP hydrolysate and supernatant were subjected to total protein assay determination. The difference in concentration between fresh feed RTBP supernatant and concentrated RTBP hydrolysate protein indicates the concentration of trapped RTBP hydrolysate protein. The percentage was calculated using the following formula:

$$Adsorption\ (\%) = \frac{RTBP\ Hydrolysate_{Feed} - Supernatant}{RTBP\ Hydrolysate_{Feed}} \times 100\% \quad (3)$$

Fractionation of hydrolysate by reverse phase-high performance liquid chromatography (RP-HPLC)

Ultrafiltered hydrolysate from subsection 2.4.3 was then subjected to RP-HPLC for hydrophobicity fractionation. Shimadzu UFLC system with column (HypersilTM BDS C18 Column, 5 µm, 250×4.6 mm, 130 Å Thermo ScientificTM) was used for the fractionation. An isocratic solution of 100% of 0.1% TFA was used to separate hydrophilic fraction, while 100% of 0.08% of TFA in Acetonitrile was used to separate the hydrophobic fraction. Hydrolysates were collected into 12 fractionations. The absorbance was monitored with ultraviolet (UV-VIS) detection at 323 nm. Each fraction was assayed for ACE-inhibitory activity.

Results and Discussion

The production of RTBP hydrolysate with ACE-inhibitory activity

A high degree of hydrolysis (DH) applying specific proteases can result in a hydrolysate with strong ACE-inhibition activity. RTBP hydrolysate with the highest DH (73.80%) was observed using Thermoase PC10F (E.C. 3.4.24.27). The hydrolysis of peptide bonds containing hydrophobic amino acids was selectively catalysed by Thermoase PC10F, producing hydrophobic peptides with known ACE-inhibitory action [25]. Ghassem [27] used thermolysin to break apart sarcoplasmic and myofibrillar muscle protein derived from *Clarias batrachus* for producing ACE-inhibitory peptide GPPP and IEKPP. GPPP has mixed inhibition mechanisms that are competitive and non-competitive, whereas IEKPP has a competitive inhibition mechanism. Hydrophobic amino acids like glycine and proline (Gly and Pro) may be key factors in ACE-inhibitory activity [25].

A series of purification steps were performed after the hydrolysis, including UF, ion-exchange chromatography and RP-HPLC to separate ACE-inhibitory peptides according to size, charge and hydrophobicity, respectively. According to Pa'ee [28], ACE activity is determined by tracking the amount of hippuric acid (HA) formed as a result of the ACE-catalysed hydrolysis of N-Hippuryl-His-Leu (HHL). As a result, ACE-inhibitory activity increases with increasing concentrations of HA catalysed by the enzyme. The ACE-inhibitory activity value of each purified technique applied to RTBP hydrolysate is shown in Table 1.

Table 1. Overall results for ACE-inhibitory activity of each purification technique

Procedure		ACE-Inhibitory Activity (%)
Crude RTBP Hydrolysate		70.67 ± 2.40
Ultrafiltration (1kDa)		85.42 ± 0.98
Ion exchange Chromatogram (IEX)		72.32 ± 1.01
Hydrophobic fraction	Peak 1	90.44 ± 4.54
	Peak 2	95.28 ± 1.63

The effect of membrane size towards permeates flux and peptide transmission

Fractionation of RTBP hydrolysate was done by a dead-end UF with two different membrane pore sizes. The cellulose membrane (RC) of MWCO of 3 and 1 kDa were used with a constant pressure of 2.5 bar and a constant stirring speed applied. Permeate flux refers to the rate at which permeate is produced during membrane separation relative to the membrane's total surface area and the amount of time involved [29]. It was shown in Figure 1 that a bigger membrane pore size, 3 kDa, has a higher permeate flux compared to 1 kDa. The line trend in Figure 1 is similar to the previous study done by Roslan [30] at different pH and stirring speeds. The MWCO describes the pore of the membrane, while the membrane represents the molecular weight of a molecule that is rejected at 90% [12, 13]. The bigger the MWCO, the more porous the membrane, whereas smaller MWCO has a smaller membrane pore [31, 32, 33]. The nature of the membrane influences the permeate flow as can be observed that the permeate flow of 3 kDa was faster compared to 1 kDa, which was 4 hours and 5 hours, respectively. The decrease in permeate flow through the membrane was attributable to

fouling, which happens due to nonpermeating solutes tending to form a gel on the surface of the membrane, thus affecting the permeate flow [34]. The formation of cake fouling was due to the perpendicular feed flow of the solutions in a dead-end UF and the concentrated suspended solid on the surface of the membrane. Nonetheless, this can be improved by applying a crossflow UF since the feed solution is tangible.

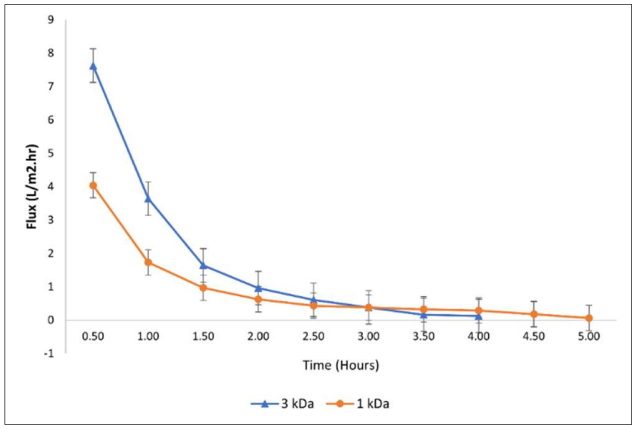


Figure 1. Effects of UF membrane pore size on permeate flux

In addition, the membrane pore size influences peptide transmission. The transmission of peptides through the membrane is highly dependent on the size and direction of membrane pores [26]. In Figure 2, the peptide transmission in 3 kDa was slightly higher compared to 1 kDa, which were 37.40% and 32.62%, respectively. Roslan [26] mentioned that transmissions of peptides through a membrane with a small pore size are lower compared to those of a larger membrane pore size, which may be due to the tendency of a larger peptides size to be retained and accumulated on the membrane surface of the smaller membrane pore size resulting a severe membrane fouling. In his study, the red tilapia by-product hydrolysate was fractionated by a single (10 and 5 kDa) and multilayer (10/5 and 5/5 kDa) membrane pore size. The highest peptide transmission was achieved at a membrane pore size of 10 kDa (87.3%), followed by 10/5 kDa (54.4%), 5 kDa (36.1%) and 5/5 kDa (20.0%). Therefore, it can be concluded that larger MWCO membranes, such as the 3 kDa membrane used in this study, produce greater permeate flux flow and higher peptide transmission.

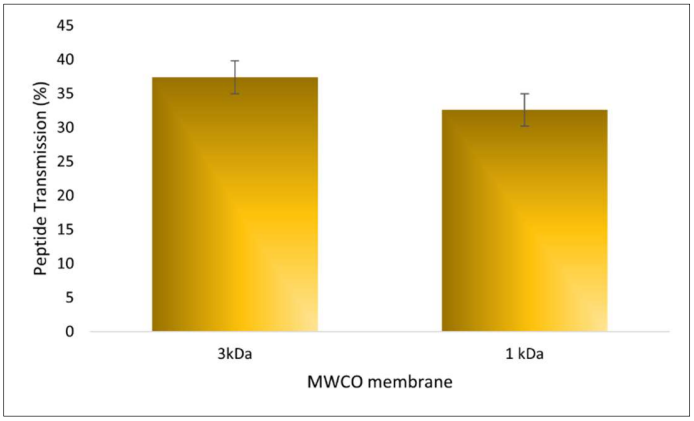


Figure 2. Effects of membrane pore size on peptide transmission

Effect of size towards potency of ACE-inhibitory activity

The 1 kDa possessed higher ACE-inhibitory activity compared to 3 kDa, which was 85.42% (Figure 3). Similar trends have been observed by Hua [4] and Ishak [35]. Hua [4] produced an antihypertensive peptide derived from tilapia collagen and the hydrolysate was separated using UF with two molecular sizes of <3 kDa and >3 kDa. The smaller fraction (<3 kDa) exhibited a higher percentage of ACE-inhibitory activity of 74.30% compared to >3 kDa, which was 58.5%. Ishak [35] studied the bioactive peptide derived from shortfin scads waste hydrolysate, (SWH), thus suggesting higher ACE-inhibitory activity of <3 kDa peptides with 81.50%. In this study, the IC_{50} value of 1 kDa RTBP hydrolysate was 0.41 mg mL^{-1}, which improved from 0.79 mg mL^{-1} (crude RTBP hydrolysate). The IC_{50} value of purified RTBP hydrolysate was comparable to the pepsin-hydrolysed tilapia frame <1 kDa protein hydrolysate [36]. The IC_{50} value was measured to assess bioactive peptide efficacy. It provides a measure of potency in pharmacological research by indicating the amount or concentration of a compound required to inhibit a biological process by 50% [37]. Therefore, the lower the IC_{50} value, the greater the potency.

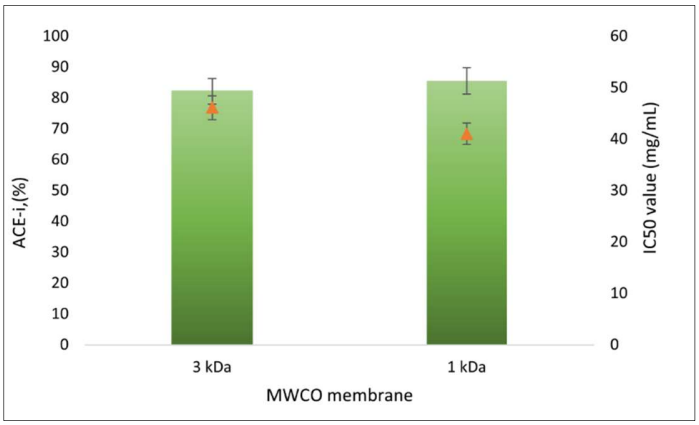


Figure 3. Effects of membrane pore size on ACE-inhibitory activity and IC_{50} value

The effect of peptides charges

In most cases, anion-exchange chromatography (AEX) can be used to separate molecules with negative charges from natural and basic molecules [38]. The peptide charged of RTBP hydrolysate was measured using Zeta potential. The electrostatic interactions between proteins and charged surfaces are also pH-dependent, as the charge of proteins depends on the pH of their surroundings [39].

Table 2. Zeta potential measurement of RTBPH

Sample	Zeta Potential (mV)
1 kDa	-8.75 ± 0.79
3 kDa	-4.82 ± 1.25

Both fractions (1 kDa and 3 kDa) were negatively charged (Table 2). Appropriate pH was used to maintain the surface charge of the RTBP hydrolysate and to avoid precipitation due to pH closer to its isoelectric point. The charges on protein molecules can change to accommodate other charged surfaces [39, 40]. The RTBP hydrolysate fraction must be negatively charged to allow the exchange of the peptides to the anionic exchange resin. The anionic exchangers could bind with the negatively charged counterions reversibly. An anion exchanger's counterion is often a weakly binding ion like Cl-, which can be changed out for stronger binding ions including negatively charged amino acids on a protein's surface. Thus, a high salt concentration buffer

was used to elute the trapped RTBP hydrolysate.

AEX of 1 kDa RTBP hydrolysate is shown in Figure 4. The absorption percentage of RTBP hydrolysate peptides to the resin was 93.99%. The non-adsorbed peptides consisted of positively charged peptides. The adsorbed peptides (negatively charged) were then eluted several times. ACE-inhibitory peptides can be observed in both the non-bound (non-absorbed) and bound (Elute 1 to 4) fractions. Meanwhile, the non-absorbed fraction (positively charged) has the highest ACE-inhibitory activity of 72.32%, whereas the elutes have the ACE-inhibitory activity from 6.07% to 52.55%. This is similar to the previous study done on Alaska pollack's frame hydrolysate by Je [41] and catfish skin hydrolysate by Sungperm [42], which has higher ACE-inhibitory activity on positively charged fraction. Daskaya-Dikmen [44] and Manoharan [43] suggested that the presence of positively charged on the side chain coupled with other aromatic amino acids would enhance the ACE-inhibitory activity effectiveness.

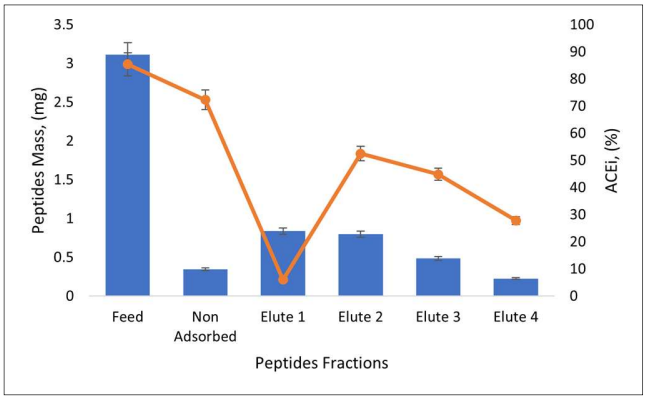


Figure 4. The peptide mass and ACE-inhibitory activity for absorption equilibrium

The effect of peptides hydrophobicity

Specific amino acids play a vital role in determining the type of bioactivity (Acquah, et al., 2018). ACE-inhibitory activity is inhibited more effectively by antihypertensive peptides, which typically have aromatic amino acid residues at the C-terminus and hydrophobic amino acid residues at the N-terminus [4], [23], [43–46]. The hydrophobic interaction chromatogram (HIC) was separated using RP-HPLC. The positively charged peptides fraction was further purified, and the fraction of chromatogram's peaks and its ACE-inhibitory activity is shown in Figure 5.

Both hydrophilic and hydrophobic chromatograms produced peaks at 0-5 minutes (Fraction 1) and 5-10 minutes (Fraction 2). The ACE-inhibitory activity of Fraction 1 and Fraction 2 from the hydrophobic fraction showed the highest bioactivity of 90.44% and 95.28%, respectively. However, hydrophilic peptides demonstrated inferior ACE-inhibitory activity in Fraction 1 (47.80%) and Fraction 2 (11.59%) (Figure 5). Ishak [35] observed similar ACE-inhibitory activity (87.99%) from a purified peptide fraction derived from shortfin scad applying RP-HPLC. Pa'ee [25] suggested that hydrophobic peptides tend to possess more ACE-inhibitory activity. In addition, the abundance of the hydrophobic fragment in the RTBP hydrolysate may be due to the enzymatic hydrolysis of Thermoase PC10F. The hydrophobicity of a peptide chain depends on several factors, including the extent to which it is hydrolysed, the processing conditions used, the type of protease employed, the average hydrophobicity value of the protein precursors and the sequence of hydrophobic amino acid residues in the peptide chain [47]. According to several studies, aliphatic amino acids at the N-terminus, positively charged amino acids in the central position, as well as proline, tyrosine, phenylalanine and tryptophan are the main structural components in the C-terminal of ACE inhibitory peptides with high ACE inhibitory action. Additionally, the amino ends of proteins tend to contain hydrophobic amino acids with

aliphatic side chains such as glycine, isoleucine, leucine and valine [4, 23, 40, 41, 44]. An ACE-inhibitory peptide that has proline residue at C-terminal tends to have competitive inhibition as mentioned above on *Clarias batrachus* [27], VAP derived from Grass crap [12] and LYPPP and YSMYPP, both of which were derived from snakehead fish [7].

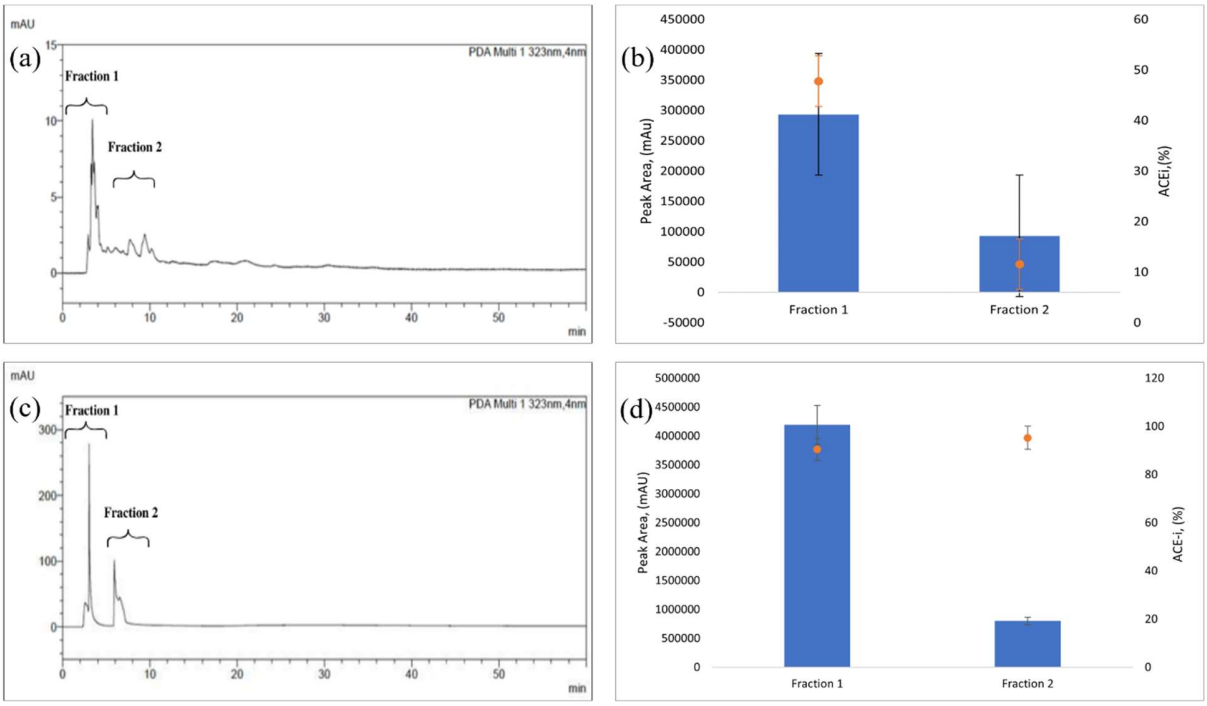


Figure 5. Chromatograms and the ACE-inhibitory activity of purified RTBP hydrolysate (a) Chromatogram fraction of hydrophilic peak (b) Hydrophilic fraction and its ACE-inhibitory activity (c) Chromatogram fraction of hydrophobic peak (d) Hydrophobic fraction and its ACE-inhibitory activity.

Conclusion

RTBP hydrolysate applying Thermoase PC10F liberated potent ACE-inhibiting peptides. Thermoase PC10F displayed high DH and ACE-inhibitory activity at 73.80% and 70.67%, respectively. 1 kDa RTBP hydrolysate has a stronger ACE-inhibitory activity of 85.42 %. The non-absorbed fraction yielded the highest ACE-inhibitory activity of 72.32%, indicating that it has positively charged characteristics. The purified RTBP hydrolysate yielded two fractions of high ACE-inhibitory activity (more than 90%) on the hydrophobic fraction. The reaction specificity of the Thermoase PC10F allowed the release of hydrophobic peptides. Furthermore, the determination of peptide sequence is crucial to decern its structure-activity relationship, molecular docking and dynamic studies, and other *in silico* studies.

Acknowledgement

This work was supported by the Ministry of Education (MOE) under the Fundamental Research Grant Scheme (FRGS), FRGS/1/2018/STG05/UNIKL/02/8 and Short-Term Research Grant (STR15074) awarded by Universiti Kuala Lumpur.

References

1. Gao, R., Yu, Q., Shen, Y., Chu, Q., Chen, G., Fen, S., Yang, M., Yuan, L., McClements, D. J. and Sun, Q. (2021). Production, bioactive properties, and potential applications of fish protein hydrolysates: Developments and challenges. *Trends in Food Science & Technology*, 110: 687-699.
2. Memarpoor-Yazdi, M., Zare-Zardini, H., Mogharrab, N. and Navapour, L. (2020).

Purification, characterization and mechanistic evaluation of angiotensin converting enzyme inhibitory peptides derived from Zizyphus jujuba fruit. *Scientific Reports*, 10(1): 1-10.

3. Caballero, J. (2020). Considerations for docking of selective angiotensin-converting enzyme inhibitors. *Molecules*, 25(2): 295.
4. Hua, X., Sun, L., Zhong, C., Wu, Q., Xiao, P., Yoshida, A., Liu, G. and Cao, M. (2020). Successive digestion of tilapia collagen by serine proteinase and proline specific endopeptidase to produce novel angiotensin I-converting enzyme inhibitory peptides. *Marine Life Science & Technology*, 2: 268-278.
5. Ling, Y., Liping, S. and Yongliang, Z. (2018). Preparation and identification of novel inhibitory angiotensin-I-converting enzyme peptides from tilapia skin gelatin hydrolysates: Inhibition kinetics and molecular docking. *Food & Function*, *9*(10): 5251-5259.
6. Ghassem, M., Arihara, K., Babji, A. S., Said, M. and Ibrahim, S. (2011). Purification and identification of ACE inhibitory peptides from Haruan (Channa striatus) myofibrillar protein hydrolysate using HPLC–ESI-TOF MS/MS. *Food chemistry*, 129(4): 1770-1777.
7. Ghassem, M., Babji, A. S., Said, M., Mahmoodani, F. and Arihara, K. (2014). Angiotensin I–converting enzyme inhibitory peptides from snakehead fish sarcoplasmic protein hydrolysate. *Journal of Food Biochemistry*, 38(2): 140-149.
8. Ishak, N. H. and Sarbon, N. M. (2018). A review of protein hydrolysates and bioactive peptides deriving from wastes generated by fish processing. *Food and Bioprocess Technology*, 11: 2-16.
9. Hoa, H. Q. and Duy, N. X. (2016). Ace-Inhibitory Activity Of Protein Hydrolysate From The Skin Of Striped Catfish (Pangasius hypophthalmus). *Journal Fish. Science Technology*, 3: 1-10.
10. Rincón, C. T. S. and Montoya, J. E. Z. Effects of enzymatic hydrolysis conditions on the antioxidant activity of red tilapia (*Oreochromis* spp.) viscera hydrolysates. *Current Pharmaceutical Biotechnology*, 21:1-13.
11. Pędziwiatr, P., Zawadzki, D. and Michalska, K. (2017). Aquaculture waste management. *Acta Innovation*, 22(22): 20-29.
12. Chen, J., Wang, Y., Zhong, Q., Wu, Y. and Xia, W. (2012). Purification and characterization of a novel angiotensin-I converting enzyme (ACE) inhibitory peptide derived from enzymatic hydrolysate of grass carp protein. *Peptides*, 33(1): 52-58.
13. Chen, J., Chen, Y., Xia, W., Xiong, Y. L., Ye, R. and Wang, H. (2016). Grass carp peptides hydrolysed by the combination of Alcalase and Neutrase: Angiotensin-I converting enzyme (ACE) inhibitory activity, antioxidant activities and physicochemical profiles. *International Journal of Food Science & Technology*, 51(2): 499-508.
14. Roslan, J., Yunos, K. F. M., Abdullah, N. and Kamal, S. M. M. (2014). Characterization of fish protein hydrolysate from tilapia (*Oreochromis niloticus*) by-product. *Agriculture and Agricultural Science Procedia*, 2: 312-319.
15. Sierra-Lopera, L. M. and Zapata-Montoya, J. E. (2021). Optimization of enzymatic hydrolysis of red tilapia scales (*Oreochromis sp*.) to obtain bioactive peptides. *Biotechnology Reports* 30:1-10.
16. Zahiri, J., Emamjomeh, A., Bagheri, S., Ivazeh, A., Mahdevar, G., Tehrani, H. S., Mirzaie, M., Fakgheri, B. A. and Mohammad-Noori, M. (2020). Protein complex prediction: a survey. *Genomics*, 112(1): 174-183.
17. Dycka, F., Bobal, P., Mazanec, K. and Bobalova, J. (2012). Rapid and efficient protein enzymatic digestion: an experimental comparison. *Electrophoresis*, 33(2): 288-295.
18. Adekoya, O. A. and Sylte, I. (2009). The thermolysin family (M4) of enzymes: therapeutic and biotechnological potential. *Chemical Biology & Drug Design*, 73(1): 7-16.
19. MacLeod-Carey, D., Solis-Céspedes, E., Lamazares, E. and Mena-Ulecia, K. (2020). Evaluation of new antihypertensive drugs designed in silico using Thermolysin as a target. *Saudi Pharmaceutical Journal*, 28(5): 582-592.
20. Mahmoodani, F., Ghassem, M., Babji, A. S., Yusop, S. M. and Khosrokhavar, R. (2014). ACE inhibitory activity of pangasius catfish (Pangasius sutchi) skin and bone gelatin hydrolysate. *Journal*

of Food Science and Technology, 51(9): 1847-1856.
21. Ke, M., Shen, H., Wang, L., Luo, S., Lin, L. and Yang, J. (2016). Modern proteomics-sample preparation, analysis and practical applications. Springer International. Switzerland: pp. 345-382.
22. Baynes, J. W. and Dominiczak, M. H. (2019). Medical Biochemistry. Elsevier. China.
23. Acquah, C., Wei, Y. Sharadwata, C. and Dominic P. (2018). Structure - informed separation of bioactive peptides. *Journal Food Biochemistry*, 43(1): 1-10.
24. Nielsen, P. M., Petersen, D. and Dambmann, C. J. (2001). Improved method for determining food protein degree of hydrolysis. *Journal of Food Science*, 66(5): 642-646.
25. Pa'ee, K. F., Razali, N., Sarbini, S. R., Ramonaran Nair, S. N., Yong Tau Len, K. and Abd-Talib, N. (2021). The production of collagen type I hydrolyzate derived from tilapia (*Oreochromis* sp.) skin using thermoase PC10F and its in silico analysis. *Food Biotechnology*, 35(1): 1-21.
26. Roslan, J., Kamal, S. M. M., Yunos, K. F. M. and Abdullah, N. (2017). Assessment on multilayer ultrafiltration membrane for fractionation of tilapia by-product protein hydrolysate with angiotensin I-converting enzyme (ACE) inhibitory activity. *Separation and Purification Technology*, 173: 250-257.
27. Ghassem, M., Arihara, K. and Babji, A.S. (2012). Isolation, purification and characterisation of angiotensin I-converting enzyme-inhibitory peptides derived from catfish (Clarias batrachus) muscle protein thermolysin hydrolysates. *International Journal of Food Science Technology*, 47(11): 2444–2451.
28. Pa'ee, K. F., Gibson, T., Marakilova, B. and Jauregi, P. (2015). Production of acid whey hydrolysates applying an integrative process: Effect of calcium on process performance. *Process Biochemistry*, 50(2): 302-310.
29. Alonso, G., del Valle, E. and Ramirez, J. R. (2020). Desalination in nuclear power plants. *Woodhead Publishing, Elsevier*, pp: 31–42.
30. Roslan, J., Kamal, S. M. M., Yunos, K. F. M. and Abdullah, N. (2019). Assessment on flux reduction and protein rejection behavior in fractionating tilapia by-product protein hydrolysate by ultrafiltration membrane. *Pertanika Journal of Science and Technology*, 27(S1): 67-80.
31. Ali, N. A., Hassan, F. and Hamzah, S. (2012). Preparation and characterization of asymmetric ultrafiltration membrane for effective recovery of proteases from surimi wash water. *Frontiers of Chemical Science and Engineering*, 6(2): 184-191.
32. Singh, R. (2005). Introduction to membrane technology. *Hybrid Membrane System of Water Purification*: pp. 1-56.
33. Sofiah, H., Nora'aini, A., Asmadi, A. and Abdul Wahab, M. (2014). Preparation and characterization of asymmetric ultrafiltration membrane for lysozyme separation: Effect of polymer concentration. *ARPN Journal of Engineering and Applied Science*, 9(12): 2543-2550.
34. Zain, M. M., Mohammad, A. W. and Hairom, N. H. H. (2017). Flux and permeation behaviour of ultrafiltration in sugaring out cellulose hydrolysate solution: A membrane screening. *Journal of Physical Science*, 28(1): 25-38.
35. Ishak, N. H., Shaik, M. I., Yellapu, N. K., Howell, N. K. and Sarbon, N. M. (2021). Purification, characterization and molecular docking study of angiotensin-I converting enzyme (ACE) inhibitory peptide from shortfin scad (*Decapterus macrosoma*) protein hydrolysate. *Journal of Food Science Technology*, 58(12): 4567-4577.
36. Lin, H. C., Alashi, A. M., Aluko, R. E., Sun Pan, B. and Chang, Y. W. (2017). Antihypertensive properties of tilapia (*Oreochromis* spp.) frame and skin enzymatic protein hydrolysates. *Food & Nutrition Research*, 61(1): 1-12.
37. Aykul, S. and Martinez-Hackert, E. (2016). Determination of half-maximal inhibitory concentration using biosensor-based protein interaction analysis. *Analytical biochemistry*, 508: 97-103.
38. Liu, C., Fang, L., Min, W., Liu, J. and Li, H. (2018). Exploration of the molecular interactions between angiotensin-I-converting enzyme (ACE) and the inhibitory peptides derived from hazelnut (*Corylus heterophylla* Fisch.). *Food Chemistry*, 245(2888): 471-480.

39. de Vos, W. M. and Lindhoud, S. (2019). Overcharging and charge inversion: Finding the correct explanation(s). *Advance Colloid Interface Science*, 274(3): 1-8.
40. Fekete, S., Beck, A., Veuthey, J. L. and Guillarme, D. (2015). Ion-exchange chromatography for the characterization of biopharmaceuticals. *Journal of Pharmaceutical and Biomedical Analysis*, 113: 43-55.
41. Je, J. Y., Park, P. J., Kwon, J. Y. and Kim, S. K. (2004). A novel angiotensin I converting enzyme inhibitory peptide from Alaska pollack (*Theragra chalcogramma*) frame protein hydrolysate. *Journal of Agricultural and Food Chemistry*, 52(26): 7842-7845.
42. Sungperm, P., Khongla, C. and Yongsawatdigul, J. (2020). Physicochemical properties and angiotensin I converting enzyme inhibitory peptides of freshwater fish skin collagens. *Journal of Aquatic Food Product Technology*, 29(7): 650-660.
43. Manoharan, S., Shuib, A. S. and Abdullah, N. (2020). Structural characteristics and antihypertensive effects of angiotensin-I-converting enzyme inhibitory peptides in the renin-angiotensin and kallikrein kinin systems. *African Journal of Traditional Complement Alternative Medicines,* 14(2): 383-406.
44. Daskaya-Dikmen, C., Yucetepe, A., Karbancioglu-Guler, F., Daskaya, H. and Ozcelik, B. (2017). Angiotensin-I-converting enzyme (ACE)-inhibitory peptides from plants. *Nutrients*, *9*(4): 1-19.
45. De Leo, F., Panarese, S., Gallerani, R. and Ceci, L. R. (2009). Angiotensin converting enzyme (ACE) inhibitory peptides: Production and implementation of functional food. *Current Pharmaceutical Design*, 15(31): 3622-3643.
46. Ko, A. J., Kang, N., Kim, J. L. J., Park, W. K. S. and Jeona, Y. K. Y. (2016). Angiotensin I-converting enzyme inhibitory peptides from an enzymatic hydrolysate of flounder fish (*Paralichthys olivaceus*) muscle as a potent anti-hypertensive agent. *Process Biochemistry,* 51(4): 535-541.
47. Acquah, C., Di Stefano, E. and Udenigwe, C. C. (2018). Role of hydrophobicity in food peptide functionality and bioactivity. *Journal of Food Bioactives*, 4: 88-98.

Malaysian Journal of Analytical Sciences (MJAS)
Published by Malaysian Analytical Sciences Society

STABILITY OF GREEN SYNTHESIS OF SILVER NANOPARTICLES BY USING *Euphorbia milii* (EUPHORBIACEAE) LEAVES EXTRACT WITH DIFFERENT SOLVENTS AND POLARITIES

(Kestabilan Sintesis Hijau Nanopartikel Perak dari Ekstrak Daun *Euphorbia milii* (Euphorbiaceae) menggunakan Pelarut dan Kekutuban yang Berbeza)

Nur Rasyidah Ramli[1], Hanis Mohd Yusoff[1,2], Maulidiani Maulidiani[1], Asnuzilawati Asari[1,2], and Nurul Huda Abdul Wahab[1,2*]

[1]*Faculty of Science and Marine Environment, Universiti Malaysia Terengganu, 21030 Kuala Nerus, Terengganu, Malaysia*
[2]*Advanced Nano Materials (ANoMa) Research Group,Faculty of Science and Marine Environment, Universiti Malaysia Terengganu, 21030 Kuala Nerus, Terengganu, Malaysia*

**Corresponding author: nhuda@umt.edu.my*

Received: 15 January 2023; Accepted: 2 July 2023; Published: 22 August 2023

Abstract

Silver nanoparticle (AgNP) synthesis can be produced by chemical, physical, and green synthesis methods. In this study, green synthesis of AgNPs was conducted by using *Euphorbia milii (E. milii)* leaf extract as the reducing agent. *E. milii*, also called crown-of-thorn or in Malay *'Mahkota duri'* was used as the targeted plant in this study due to its rich phytochemical contents. The leaves were extracted into six different solvents (hexane, chloroform, ethyl acetate, acetone, methanol and distilled water) by increasing polarities to extract different varieties of compounds that were applied as reducing agents in the synthesis of AgNPs. The crude extract was added to 1 mM $AgNO_3$ solution and kept in the dark at room temperature for 24 hours. The process was repeated for all crude extracts with different solvent polarities. The AgNPs solution obtained was analysed by using a UV-Vis spectrophotometer, Fourier-transform infrared spectroscopy (FTIR), and scanning electron microscope (SEM). The stability of the AgNPs was observed and compared between different extracts from different polarities. The wavelength of UV-Vis obtained for the 6 sets was between 415 nm and 485.5 nm. The formation of AgNPs based on the surface plasmon resonance band is proved by the peak that appeared around λ = ~450 nm. The FTIR spectroscopy of the various extracts indicated the presence of OH, C-H stretching, C=O stretching, C=C stretching and C-O stretching, respectively, as compared with the FTIR spectrum for AgNPs for the synthesis and stabilization of the AgNPs. SEM images showed the different sizes of AgNPs for different extracts, with a range of about 67 to 843 nm.

Keywords: green synthesis, reducing agent, green AgNPs, euphorbiaceae, *Euphorbia milii*

Abstrak

Sintesis nanopartikel perak (AgNPs) boleh dihasilkan melalui kaedah sintesis kimia, fizikal dan hijau. Dalam kajian ini, sintesis hijau AgNPs telah dijalankan menggunakan ekstrak daun *Euphorbia milii* (*E. milii*) yang bertindak sebagai agen penurunan. *E. milii* atau juga dipanggil mahkota duri atau dalam bahasa Melayunya 'Mahkota duri' telah digunakan sebagai tumbuhan sasaran

dalam kajian ini kerana kandungan fitokimia yang kaya. Daun diekstrak ke dalam enam pelarut berbeza (heksana, kloroform, etil asetat, aseton, metanol, dan air suling) dengan meningkatkan kekutuban untuk mengekstrak pelbagai sebatian yang berbeza yang digunakan sebagai agen pengurangan dalam sintesis AgNPs. Ekstrak mentah telah ditambah ke dalam larutan 1 mM $AgNO_3$ dan disimpan dalam gelap pada suhu bilik selama 24 jam. Proses ini diulang untuk semua ekstrak mentah dengan kekutuban pelarut yang berbeza. Penyelesaian AgNP yang diperolehi dianalisis dengan menggunakan spektrofotometer UV-Vis, spektroskopi inframerah transformasi Fourier (FTIR), dan mikroskop elektron pengimbasan (SEM). Kestabilan AgNP diperhatikan dan dibandingkan dari ekstrak yang berbeza kekutubannya. Panjang gelombang UV-Vis yang diperoleh untuk 6 set adalah antara julat 415-485.5 nm. Pembentukan AgNP berdasarkan jalur resonans plasmon permukaan dibuktikan oleh puncak yang muncul sekitar λ = ~450 nm. Spektroskopi FTIR bagi pelbagai ekstrak menunjukkan kehadiran OH, regangan CH, regangan C=O, regangan C=C dan regangan CO, masing-masing berbanding dengan spektrum FTIR untuk AgNP untuk sintesis dan penstabilan AgNPs. Imej SEM menunjukkan saiz AgNP yang berbeza untuk ekstrak berbeza dengan julat kira-kira 67 hingga 843 nm.

Kata kunci: sintesis hijau, agen penurun, AgNPs hijau, euphorbiaceae, *Euphorbia milii*

Introduction

Silver nanoparticles (AgNPs) are useful in various applications that have attracted much interest among researchers [1]. The production of AgNPs can involve chemical, physical, biological, and photochemical methods [2]. For the production of AgNPs, chemical and physical methods are usually used at the industrial level [3]. However, this method was a concern in biomedical applications because of the toxicity of reducing and capping agents, high temperature, and pressure in the protocol [4]. Capping agents such as alkylamines and alkanethiols had the function to stabilise the AgNPs from aggregation. The use of this capping agent and the reduction from this method can result in hazardous by-product formation that can affect the use of AgNPs in biomedical fields and chemical applications. To overcome this problem, green synthesis methods are used as a substitute for chemical and physical procedures [3] by using biological extracts such as plants, bacteria, or other potential natural reducing agents [5].

Plants provide a better platform for nanoparticle synthesis as they are free from toxic chemicals and natural capping agents [6]. In this study, *Euphorbia milii* (*E. milii*) was chosen as a targeted plant because it is rich in bioactive compounds and has high total flavonoid content [7]. Euphorbia is the largest genus, widely distributed primarily in tropical countries that acts as medicinal plants. *E. milii* is a flowering plant commonly known as the “Christ plant” or “Christ thrown” [8] and is widely used in folk medicine for the treatment of warts (South Brazil), cancer, and hepatitis (China). A previous study on *E. milii* was carried out on polar crude extract to isolate the active chemical components [7]. *E. milii* leaves act as reducing biological agents and bind together with silver metal ion solutions to form AgNPs. The reducing agents are widely distributed in the biological system [4]. The study presented here describes the effect of different polarities in the crude extract on the stability of the AgNPs.

Materials and Methods

Materials and instrumentation

Silver nitrate ($AgNO_3$) was purchased from Sigma Aldrich. The absorption spectra of synthesized AgNPs were recorded by using UV-visible spectroscopy from 300-800 nm (Shimadzu UV-1800). The Fourier Transform Infrared (FTIR) extracts and AgNPs were taken by Perkin Elmer Spectrum 100 by using the ATR method and recorded between 4000 and 400 cm^{-1}. The Scanning Electron Microscope (SEM) images were taken by JEOL 6360 LA with working distance and accelerating voltage, 15 mm and 15 kV, respectively. The sample for SEM was sonicated 3 times (15 minutes each) before it was mounted on an Indium tin oxide (ITO) substrate. Then, the sample was coated with metal gold.

Collection of the plant sample

The sample of *Euphorbia milii* leaves was collected from Kota Sarang Semut, Kedah (November 2020). The botanical identity of the plant specimen of *E. milii* leaves was confirmed by the Biological Laboratory, Universiti Malaysia Terengganu.

Preparation and extraction of *E. milii* leaves

E. milii leaves (70 g) were cleaned under running tap

water and dried at room temperature for seven days before grounded into powder form by using a grinder. Then, the powders were soaked with the first non-polar solvent, which is hexane and filtered to collect the hexane extract. The residue from hexane was repeated with different solvents by increasing the polarity (chloroform<ethyl acetate<acetone<methanol <distilled water) using the same method continuously at room temperature for 72 hours. Each extract was concentrated by using a rotary evaporator (Büchi Rotavap R-200 CH-9230, Switzerland) under reduced pressure (337-218 mbar) at 35-40 °C for 15-30 min. The six crude extracts obtained were weighed and stored in a chiller (4 °C) for further analysis.

Green synthesis of AgNPs

The green synthesis followed the method developed by Alsalhi, et al. with some modifications. To prepare AgNPs, 10 mg crude extract was added to 10 ml Mili-Q water. Then, it was filtered by using a syringe filter (0.2 µm). The mixture (5 ml) was added to 1 mM AgNPs solution (50 mL) [9]. The mixture was kept in the dark at room temperature for one day (until the color changed from colorless to brown). The process was repeated with different crude extracts, as shown in Figure 1.

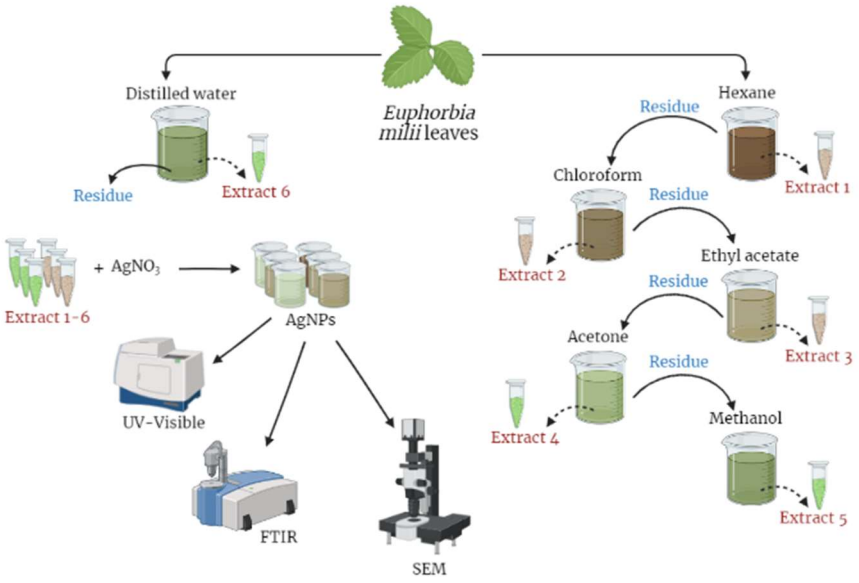


Figure 1. Overall experimental process

Results and Discussion

Green synthesis of AgNPs

The present study explored green synthesis of AgNPs was by using *E. milii* leaf extracts as a reducing agent. The reaction mixture turned from colorless to yellowish brown, which is the preliminary indication of the synthesis of AgNPs. Six conjugated AgNPs were made from $AgNO_3$ with different crude extracts. These conjugates were characterised as AgNPs-hexane extract (SH), AgNPs-chloroform extract (SC), AgNPs-ethyl acetate extract (SE), AgNPs-acetone extract (SA), AgNPs-methanol extract (SM) and AgNPs-distilled water extract (SDW-reference). AgNPs synthesis was confirmed with SEM analysis and discussed in a later section.

Characterization of AgNPs: Fourier-transform infrared spectroscopy (FTIR)

Fourier-Transform Infrared Spectroscopy (FTIR) analysis of the obtained crude extracts (Figure 2) revealed different characteristic peak values with various functional compounds. Table 1 shows the peak assignment for six extracts. The major bands at 3341 cm^{-1}, 3248 cm^{-1}, and 3333 cm^{-1} represented the O-H group of carboxylic acid. The absorption band observed at ~2926 cm^{-1} corresponded to the stretching vibration of

the C-H bond in the aliphatic hydrocarbon chains. The band at ~1636 cm^{-1} was attributed to C=C stretching vibrations of phenolic compounds such as polyphenols and flavonoids [10]. The C-H aliphatic band at approximately 1358-1396 cm^{-1} showed the presence of alkyl halides. The C-N bands at 1211 cm^{-1}, 1219 cm^{-1}, 1242 cm^{-1}, and 1258 cm^{-1} showed the presence of aliphatic amines. Lastly, the C-O bands at 1026 cm^{-1}, 1042 cm^{-1} and 1072 cm^{-1} showed the presence of alcohol, carboxylic acids, esters and ethers. The carboxyl and hydroxyl ions in the molecules develop a protective layer on the surface of AgNPs [9].

The FTIR spectra were carried out to recognize the existence of different functional groups. As shown in Figure 3, all conjugated samples compared to reference samples showed the formation of the O-H group (3333 cm^{-1}), C=C carbonyl-carbonyl group (1636 cm^{-1}), and C-H oop aromatic band (664 cm^{-1}).

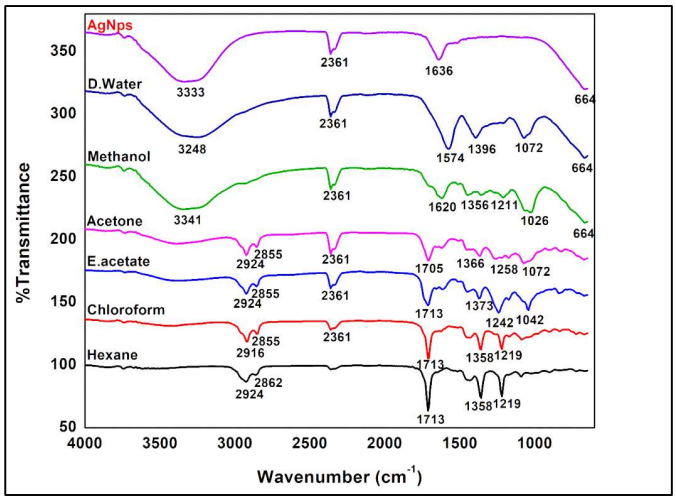


Figure 2. FTIR analysis for crude extracts

Table 1. Peak assignment for crude extracts

Peak Assignment	**Wavenumber (cm^{-1})**						
	Hexane	Chloroform	Ethyl Acetate	Acetone	Methanol	D. Water	AgNPs
O-H stretching	-	-	-	-	3341	3248	3333
C-H stretching	2926	2916	2924	2924	-	-	-
C=O stretching	1713	1713	1713	1705	-	-	-
C=C stretching	-	-	-	-	1620	1574	1636
C-H aliphatic	1358	1358	1373	1366	1356	1396	-
C-N	1219	1219	1242	1258	1211	-	-
C-O	-	-	1042	1072	1026	1072	-
C-H oop aromatic band	-	-	-	-	664	664	664

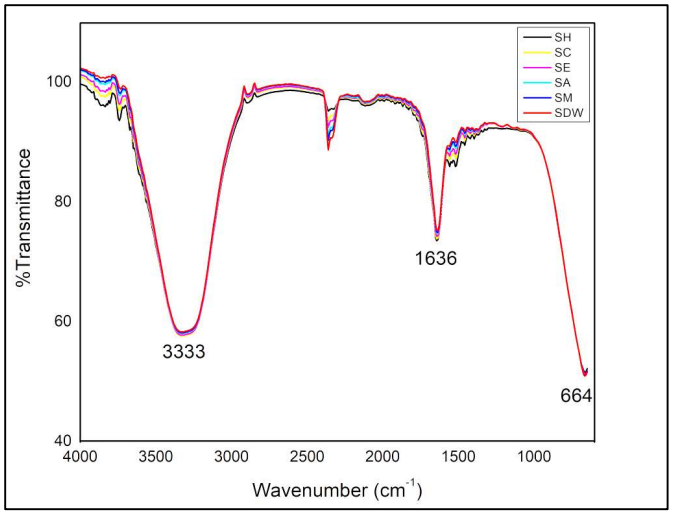


Figure 3. FTIR analysis for conjugated AgNPs

Ultraviolet-visible spectroscopy

The common phenomenon of surface plasmon resonance (SPR) in AgNPs has been studied in metal nanoparticles where electrons are excited by photons of incident light [2]. When excited by light, the induced charges characteristic of surface plasmons can propagate as an electromagnetic wave parallel to the metal surface. The most important factor in determining the frequency and intensity of plasmon resonance is their surface polarization. This is because it provides the main restoring force for electron oscillation [11]. All six conjugates were characterised by using UV-Vis spectroscopy to confirm the formation of the AgNPs. Based on all solvent systems, SH was the most unstable because the peak occurred only in 3 days. There was also no color change after the synthesis. While SC, SE, SA, SM, and SDW were more stable than SH because their peak occurred in 7, 42, 63, 63, and 64 days respectively (Figure 4 - Figure 8). As can be seen in UV-Vis spectra, the range of wavelength is from 401 to 456 nm. Table 2 shows the wavelength of AgNPs for each extract. The surface plasmon resonance band for spherical AgNPs was usually in the range of 390-450 nm [2] and 410-455 [12]. The optical properties of spherical AgNPs were highly dependent on the nanoparticle diameter. Smaller nanospheres primarily absorbed light and had peaks near 400 nm, while larger spheres had peaks that broadened and shifted towards longer wavelengths (known as red-shifting) [13]. Table 3 shows the references from other studies.

Table 2. Maximum peak for each AgNP

Conjugated AgNPs	Wavelength (nm)	Stability (Day)
AgNPs-hexane extract (SH)	427	3
AgNPs-chloroform extract (SC)	416	63
AgNPs-ethyl acetate extract (SE)	436	63
AgNPs-acetone extract (SA)	415	7
AgNPs-methanol extract (SM)	In-plane dipole: 401 In-plane quadrupole: 485	64
AgNPs-distilled water extract (SDW)	456	42

Table 3. References for the maximum peak from other studies

Plant	Solvent Extract	Wavelength (nm)	Stability (Day)	Reference
Ipomoea carnea Jacq.	Methanol	300-550	1	[14]
Terminalia catappa	n-Hexane	419	1	[15]
Terminalia catappa	Chloroform	418	7	[15]
Terminalia catappa	Ethyl acetate	264	1	[15]

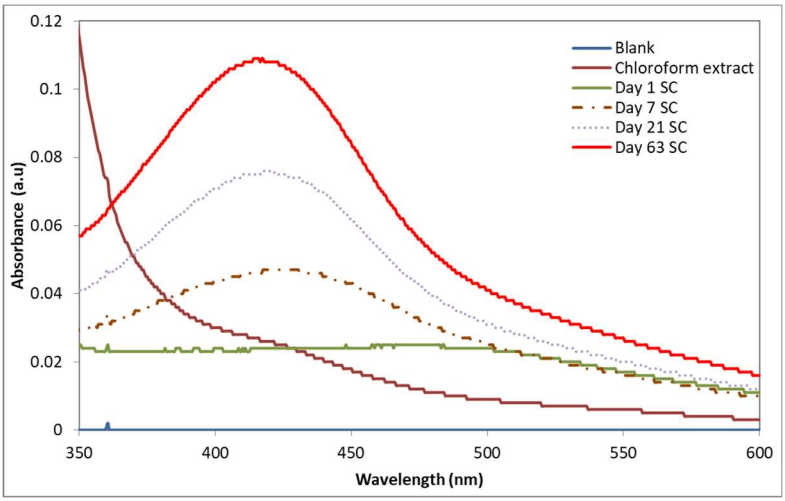


Figure 4. UV-Visible of SC

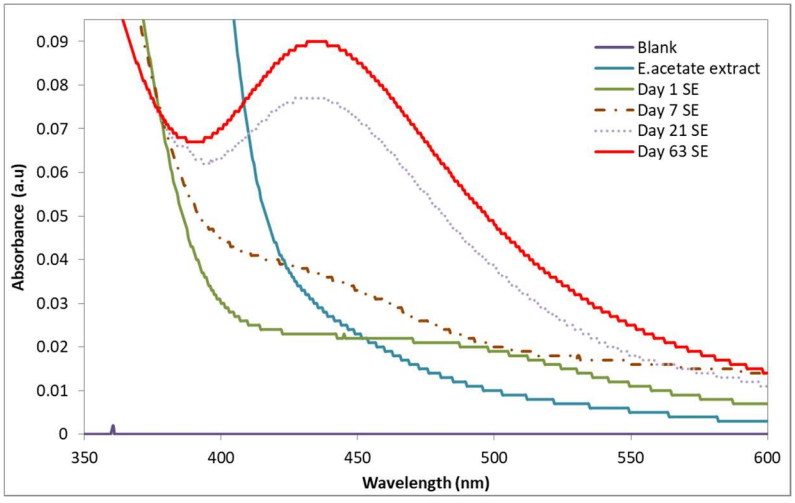


Figure 5. UV-Visible of SE

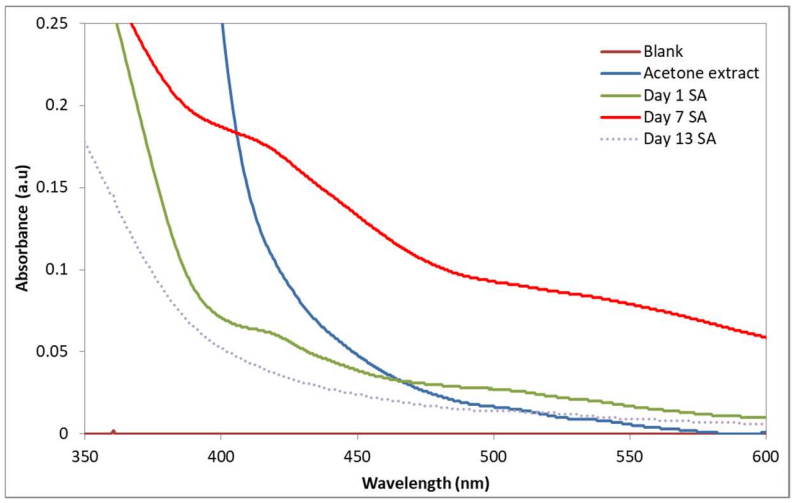


Figure 6. UV-Visible SA

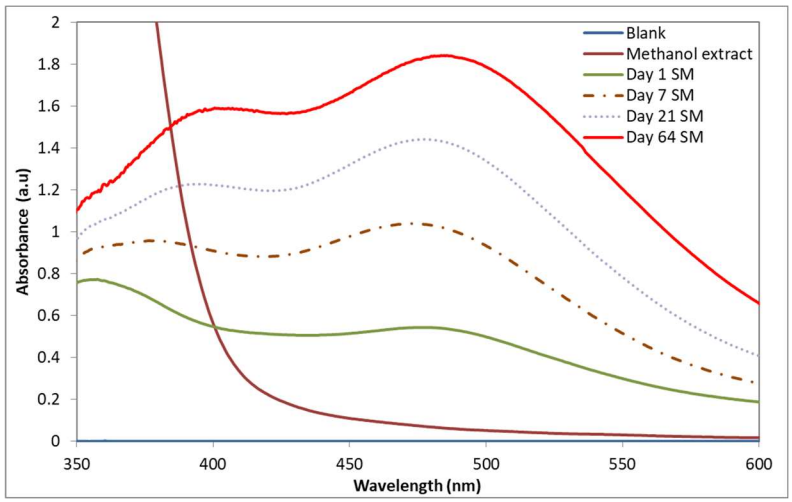


Figure 7. UV-Visible of SM

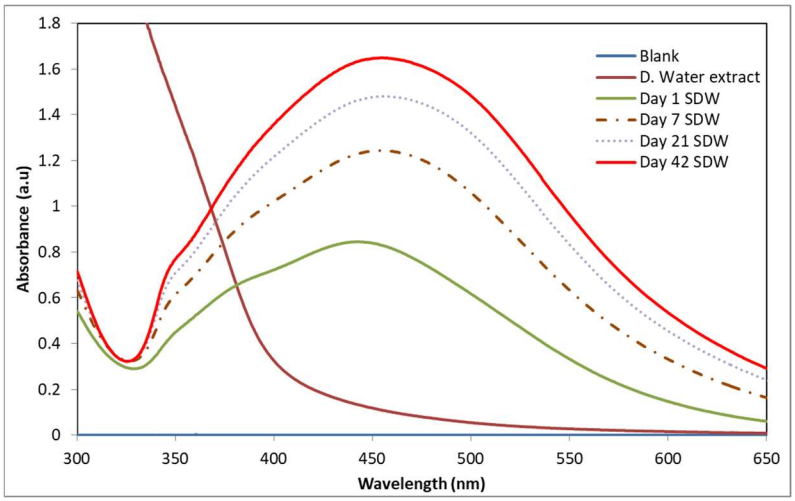


Figure 8. UV-Visible of SDW

Scanning electron microscope (SEM)

SEM technique was employed to visualise the size and shape of AgNPs. The SEM images of the AgNPs for each crude are shown in Figure 9. The smallest was from SE, which is 67-441 nm and the largest was from SH which is 771-843 nm (Table 4). The shape of all crude was mostly spherical. Compared to other studies using aqueous extract, *Euphorbia serpens* leaf had a spherical shape with particle sizes from 30 to80 nm [16], the spherical shape of *Euphorbia hirta* had a range of sizes between 50 and 80 nm [17], range sizes of *Boerhavia procumbens* was 20-80 nm with spherical shape [18], and Shireen, et al. stated that *A. americana, M. spicata, and M. indica* had mostly spherical and few triangular, rods and cubic shape [19].

Table 4. Range of size for AgNPs from various crude extract

AgNPs from Various Crude Extract	Size Range (nm)	Shape	References
(a) AgNps-hexane extract (SH)	771-843	Spherical	-
(b) AgNPs-chloroform extract (SC)	100-186	Spherical	-
(c) AgNPs-ethyl acetate extract (SE)	67-441	Spherical	-
(d) AgNPs-acetone extract (SA)	86-174	Spherical	-
(e) AgNPs-methanol extract (SM)	92-107	Spherical	-
(f) AgNPs-distilled water extract (SDW)	356	Spherical	-
Aqueous extract of *Euphorbia serpens* leaf	30-80	Spherical	[16]
Aqueous extract of *Euphorbia hirta* leaf	50-80	Spherical	[17]
Aqueous extract of *Boerhavia procumbens*	20-80	Spherical	[18]
Aqueous extract of *A. americana, M. spicata, and M. indica*	30-100	Mostly spherical Few triangular, rods and cubic	[19]

Conclusion

Six crude extracts of *E. milii* leaves were successfully utilized as capping and reducing agents for AgNP synthesis. The reaction conditions were optimized for approximate uniform dispersion of green synthesized AgNPs. The FTIR analysis suggested the presence of carboxylic acid, polyphenols, flavonoids, alkyl halides, aliphatic amines, alcohol, esters and ethers, responsible for the capping and stabilizing of AgNPs. UV-Vis spectroscopy confirmed the formation of AgNPs in all crude extracts by exhibiting the SPR band between 401 and 456 nm. SH was the most unstable AgNPs compared to other conjugated AgNPs. The shape for all conjugated AgNPs was spherical, with the sizes SH >SDW >SC >SM >SA >SE. Therefore, these studies concluded that six leaf extracts could be utilised for the green synthesis of AgNPs.

Acknowledgements

The authors would like to express appreciation to the Faculty of Science and Marine Environment, Universiti Malaysia Terengganu for providing laboratory facilities and Ministry of Higher Education (MOHE) for research grant Fundamental Research Grant Scheme FRGS/1/2020/STG04/UMT/03/1 for financial support.

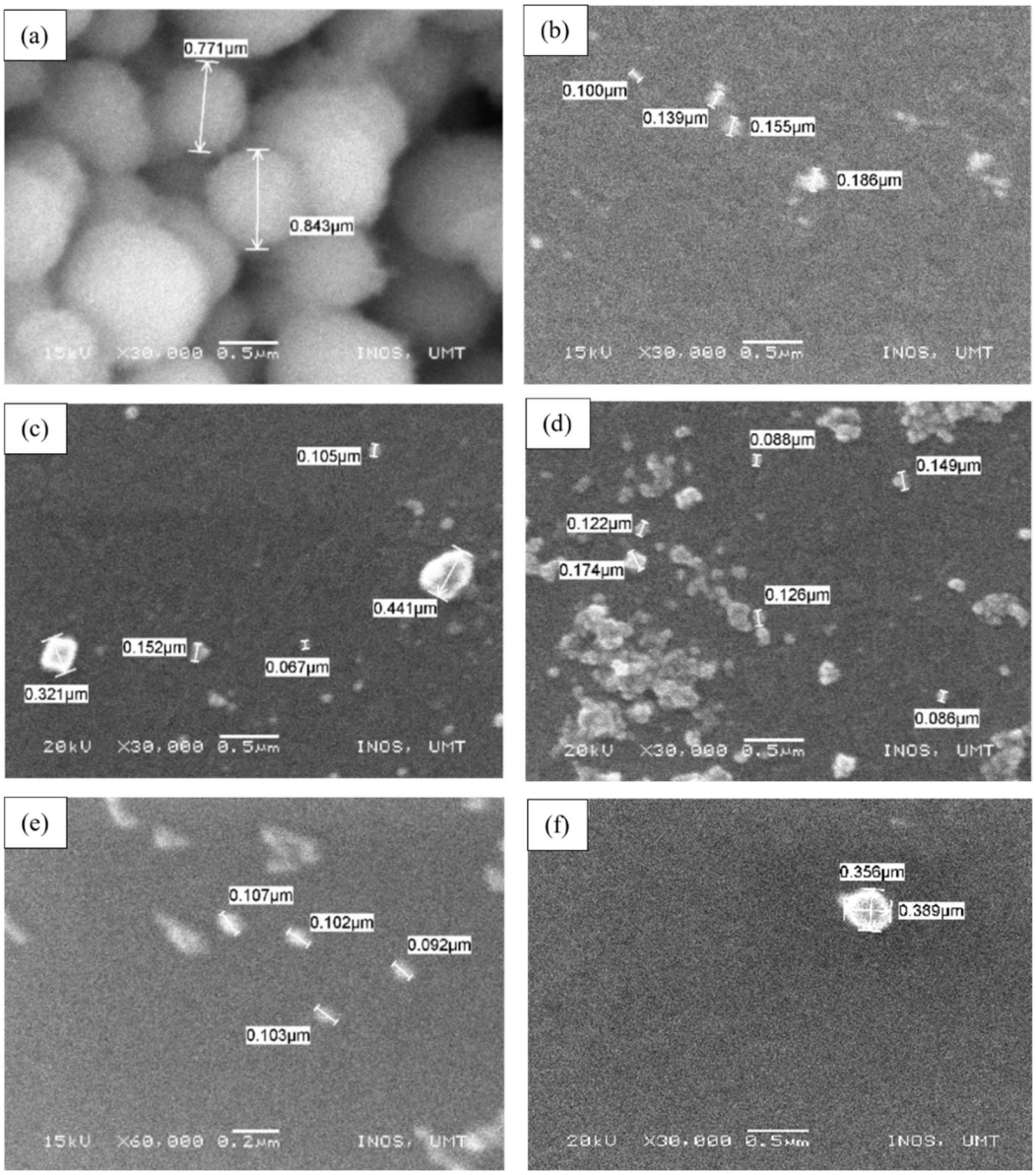


Figure 9. SEM result for AgNPs mediated with a) SH b) SC c) SE d) SA e) SM and f) SDW

References

1. Xu, L., Wang, Y. Y., Huang, J., Chen, C. Y., Wang, Z. X., and Xie, H. (2020). Silver nanoparticles: Synthesis, medical applications and biosafety. *Theranostics*, 10(20): 8996-9031.
2. Saidi, M. N. S., Yusoff, H. M., Irsyad, U. H. B., Apaalasamy, S., Hassim, A. D. M., Yusoff, F., Asari, A., and Wahab, N. H. A. (2020). Stability and antibacterial properties of green synthesis silver nanoparticles using *Nephelium lappaceum* peel extract. *Malaysian Journal of Analytical Sciences,* 24(6): 940-953.
3. Lekha, N. K., Khaga, R. S., Hari, P., Kshama, P., Bipeen, D., Ganga, D. C., Yuba, R. P., & Surya, K. K. (2022). Green synthesis of silver nanoparticles from root extracts of *rubus ellipticus* sm. And comparison of antioxidant and antibacterial activity. *Journal of Nanomaterials,* 11: 1832587.
4. Borase, H. P., Patil, C. D., Salunkhe, R. B., Narkhede, C. P., Salunke, B. K., and Patil, S. V. (2013). Phyto-synthesized silver nanoparticles: a potent mosquito biolarvicidal agent. *Journal of*

Nanomedicine and Biotherapeutic Discovery, 3(1): 1-7.

5. Gaurav, P., Priya, R., and Anjana, P. (2019). Green synthesis of nanoparticles: A greener approach for a cleaner future. *Micro and Nano Technologies,* 1-26.
6. Krithiga, N., Rajalakshmi, A., and Jayachitra, A. (2015). Green synthesis of silver nanoparticles using leaf extracts of *Clitoria ternatea* and S*olanum nigrum* and study of its antibacterial effect against common nosocomial pathogens. *Journal of Nanoscience,* 2015: 1-8.
7. Abd Mutalib, N. S. A., Yusuf, N., Asari, A., Aziz, A. N., and Wahab, N. H. A. (2020). Qualitative and quantitative of phytochemical analysis of Malaysian *Euphorbia milii* (Euphorbiaceae) and its antioxidant activities. *Malaysian Applied Biology,* 46(4): 233-239.
8. Kamurthy, H., Dontha, S., and Rajani, K. (2015). Phytochemical screening on *euphorbia milii* red flowers- isolation of terpenoids, flavone and phenol. *American Journal of Ethnomedicine*, 2(6): 322-332.
9. AlSalhi, M. S., Elangovan, K., Ranjitsigh, A. J. A., Murali, P., and Devanesan, S. (2019). Synthesis of silver nanoparticles using plant derived 4-N-methyl benzoic acid and evaluation of antimicrobial, antioxidant and antitumor activity. *Saudi Journal of Biological Sciences,* 26: 970-978.
10. Lubis, F. A., Malek, N. A. N. N., Sani, N. S., and Jemon, K. (2022). Biogenic synthesis of silver nanoparticles using *Persicaria odorata* leaf extract: Antibacterial, cytocompatibility, and in vitro wound healing evaluation. *Particuology,* 70: 10-19.
11. Wiley, B. J., Sang, H. I., Zhi-Yuan, L., McLellan, J., Siekkinen, A., and Xia, Y. (2006). Manuevering the surface plasmon resonance of silver nanostructures through shape-conrolled synthesis. *Journal of Physical Chemistry B,* 110: 15666-15675.
12. Isa, N., Osman, M. S., Abdul Hamid, H., Inderan, V., and Lockman, Z. (2023). Studies of surface plasmon resonance of silver nanoparticles reduced by aqueous extract of shortleaf spikes edge and their catalytic activity. *International Journal of Phytoremediation*, 25(5): 658-669.
13. Paramelle, D., Sadovoy, A., Gorelik, S., Free, P., Hobley, J., and Fernig, D. G. (2014). A rapid method to estimate the concentration of citrate capped silver nanoparticles from UV-visible light spectra. *Analyst,* 139(19): 4855-4861.
14. Singh, R., and Navneet. (2021). Green synthesis of silver nanoparticles using methanol extract of ipomoea carnea Jacq. To combat multidrug resistance bacterial pathogens. *Current Research in Green and Sustainable Chemistry,* 4: 100152.
15. Payapo, I. A., Zakir, M., and Soekamto, N. H. (2017). Synthesis of silver nanoparticles using bioreductor of ketapang leaf extract (*Terminalia catappa*) and its potential as sunscreen. *Indonesia Chimica Acta,* 10(1): 1-19.
16. Ahmad, N., Fozia, Jabeen, M., Haq, Z. U., Ahmad, I., Wahab, A., Islam, Z. U., Ullah, R., Bari, A., Abdel-Daim, M. M., El-Demerdash, F. M., and Khan, M. Y. (2022). Green fabrication of silver nanoparticles using euphorbia serpens kunth aqueous extract, their characterization, and investigation of its in vitro antioxidative, antimicrobial, insecticidal, and cytotoxic activities. *BioMed Research International,* 2022: 5562849.
17. Bennet Rohan, D., Raji, P., Divya Kumar, M., Gandham, R. G., Kripu Sharma, V., Keerthana, D., Karishma, S., Antony, V. S., Iyappan, P., Thirumurugan, R., Sajna, K. P., Paulraj, P., Jenifer Selvarani, A., and Prakash, P. (2020). Green synthesis and antibacterial activity studies of silver nanoparticles from the aqueous extracts of euphorbia hirta. *Journal of Pure and Applied Microbiology,* 14(1): 301-306.
18. Rizwan, M., Amin, S., Malikovna, B. K., Rauf, A., Siddique, M., Ullah, K., Bawazeer, S., Farooq, U., Mabkhot, Y. N., and Ramadan, M. F. (2020). Green synthesis and antimicrobial potential of silver nanoparticles with *boerhavia procumbens* extracts. *Journal of Pure an Applied Microbiology,* 14(2): 1437-1451
19. Shireen, F., Bashir, A., Ahmad, L., Khan, S., Rauf, A., Khalil, A. A., Zia, A., Mabkhot, Y., Almarhoon, Z., Hassanien, M., and Sharifi-Rad, J. (2022). Anti-neoplastic and cytotoxic evaluation of green AgNPs and crude extracts from *Agave americana*, *Mentha*

spicata, and *Mangifera indica* leaves. *Journal of Nanomaterials*, 2022: 9723074.

Malaysian Journal of Analytical Sciences (MJAS)
Published by Malaysian Analytical Sciences Society

POTENTIALITY OF NANOSILICA-DOPED CARBON DOTS AS FLUORESCENCE DETECTOR FOR COPPER (Cu^{2+}) IONS IN SIMULATED WASTEWATER

(Potensi Nanosilica-Didop Titik Carbon Sebagai Pengesan Pendaflour untuk Ion Kuprum (Cu^{2+}) dalam Simulasi Air Sisa)

Rejie C. Magnaye*, Donjun C. Aguda, Kristine Rose G. Gonzales, Kyla Marie T. Plaza, and Jeoh Ysrael D. Silang

Department of Chemical Engineering,
College of Engineering,
Batangas State University – The National Engineering University,
Golden Country Homes Subdivision, Alangilan, Batangas City, Philippines

**Corresponding Author: rejie.magnaye@g.batstate-u.edu.ph*

Received: 6 February 2023; Accepted: 30 May 2023; Published: 22 August 2023

Abstract

Industrialization has a major impact on the ecosystem and the natural water composition particularly in places close to cities and manufacturing areas. Copper (Cu^{2+}) ion is one of the heavy metals present in the industrial effluent and is considered to be a toxic heavy-metal contaminant accounting to its extreme persistence and bioaccumulation. Current techniques for determining Cu^{2+} ions in water include atomic absorption spectrometry (AAS), X-ray fluorescence spectrometry (XRF) and electrochemical methods, which provide high precision but have high maintenance costs and complicated preparation. Thus, an inexpensive, nontoxic and rapid sensing system for copper detection is needed. Herein, a simple and effective route for designing a fluorescence detector for Cu^{2+} ions tracing was developed through a microwave-assisted rapid synthesis of carbon dots and nanosilica from Taal volcanic as its dopant. The parameters affecting the performance of the Taal Volcanic Ash Nanosilica-doped Carbon Dots (TVA/SiO_2-Cdots), such as silica dosage, agitation speed and contact time were investigated and optimized. Under optimized conditions, the TVA/SiO_2-Cdots showed the detection of Cu^{2+} ions in simulated wastewater. The optical properties of the synthesized TVA/SiO_2-Cdots were determined using Fourier transform infrared spectroscopy (FTIR) and UV-Visible spectrophotometer which explained the quenching of TVA/SiO_2-Cdots photoluminescence upon addition of Cu^{2+} ions. It has functional groups of Amine, C=C and C-O bonds. The mathematical correlation between photoluminescence (PL) intensity ratio of SiO_2-Cdots and Cu^{2+} ion concentration in simulated wastewater was found to be a Gaussian equation. The result showed that the model has no significant difference with the detected concentrations using ultraviolet spectrophotometric screening method.

Keywords: carbon dots, copper ions, mathematical modelling, nanosilica, photoluminescence intensity

Abstrak

Pembangunan industri memberi impak besar terhadap ekosistem dan komposisi air semulajadi terutamanya di kawasan-kawasan

berdekatan dengan bandar dan kawasan pembuatan. Ion kuprum (Cu^{2+}) adalah salah satu daripada logam berat yang terdapat dalam air sisa industri dan dianggap sebagai pencemar logam berat toksik kerana ketekalan dan bioakumulasi yang tinggi. Teknik semasa untuk menentukan ion Cu^{2+} dalam air termasuk spektrometri serapan atom (AAS), spektrometri sinar-X pendaflour (XRF) dan kaedah elektrokimia, yang memberikan ketepatan yang tinggi tetapi memerlukan kos penyelenggaraan yang tinggi dan persediaan yang rumit. Oleh itu, sistem pengesanan untuk penentuan kuprum yang murah, tidak toksik dan cepat diperlukan. Di sini, satu laluan yang mudah dan berkesan untuk reka bentuk pengesan pendaflour untuk pengesan ion Cu^{2+} telah dibangunkan melalui sintesis cepat bantuan gelombang mikro titik karbon dan nanosilika dari abu gunung berapi Taal sebagai bahan tambahannya. Parameter-parameter yang mempengaruhi prestasi abu gunung berapi Taal nanosilika-didop titik karbon (TVA/SiO2-Cdots), seperti dos silika, kelajuan pengadunan, dan masa sentuhan telah dikaji dan dioptimumkan. Di bawah keadaan yang dioptimumkan, TVA/SiO_2-Cdots menunjukkan pengesanan ion Cu^{2+} dalam simulasi air sisa. Sifat optik TVA/SiO_2-Cdots yang disintesis ditentukan menggunakan spektroskopi inframerah transformasi Fourier (FTIR) dan spektrofotometer UV-Cahaya Nampak yang menjelaskan pemelindapan fotoluminesens TVA/SiO_2-Cdots dengan penambahan ion Cu^{2+}. Ia mempunyai kumpulan berfungsi amina, C=C, dan C-O. Korelasi matematik antara nisbah intensiti fotoluminesen (PL) SiO_2-Cdots dan kepekatan ion Cu^{2+} dalam simulasi air sisa didapati sebagai persamaan Gauss. Keputusan menunjukkan bahawa model ini tidak mempunyai perbezaan yang signifikan dengan kepekatan yang dikesan menggunakan kaedah saringan spektrofotometri ultraungu.

Kata kunci: titik karbon, ion kuprum, pemodelan matematik, nanosilika, intensiti fotoluminesens

Introduction

Heavy metal contamination is one of the prevailing issues detrimental to human health and environment. As a result of continuous industrialization, the heavy metals found in nature seep through municipal water supplies. Concentrations of copper, lead, cadmium, chromium, mercury and arsenic are the most concerning, mainly because of their relatively high concentrations in industrial wastewater. Copper exposure can have serious consequences for human health. At great amounts of exposure, copper attacks the internal organs and builds up in the brain to cause nausea, vomiting, coma, and even death. People who survive contact with high exposures of copper may be left with pruritic dermatitis, anemia, and muscular convulsions. Due to these complications, the regulation and detection of the amount of copper in municipal wastewaters is needed [1].

High performance liquid chromatography (HPLC) combined with electrochemical- or UV-Vis-detectors and atomic absorption spectroscopy (AAS) are the most used methods for the detection of heavy metal ions. Despite the high levels of sensitivity and precision achieved by these techniques, the majority of them need expensive, complicated equipment that must be operated by skilled personnel, making them challenging to employ in on-site measurements for portable detection [2]. This leads to the discovery of photometry, fluorescence analysis, electrochemical methods, phosphorescence analysis, and chemiluminescence. These methods are operationally simple, fast, and low cost. Therefore, the developments of simple, sensitive, and reliable spectral analytical methods are still greatly significant.

Due to their multiple intriguing features, carbon dots (CDs) have recently become a distinct class of fluorescent nanomaterials. They are thought to be superior to traditional fluorescent materials like semiconductor quantum dots and organic dyes due to their exceptional features like high aqueous solubility, low toxicity, great biocompatibility, functionalizability, and photostability [3]. Moreover, studies show that silica doping in carbon dots improves its efficiency and luminosity. These silicas are extracted either from wastes such as bricks, concrete, and other construction waste materials, or in nature including sand, gravel, clay, and volcanic ash. In bulk volcanic ash, the chemical composition is mainly determined by the magma from which it is generated. The mineral composition of volcanic ash consists of about 45–75 wt.% of silica [4].

Many studies prove how detrimental the emission of volcanic ash is for both human health and the surroundings. This ash is also a potential source of silica, which could be synthesized to nanosilica, and doped into metal detecting carbon dots. Previous studies proved that doping carbon dots had led to an improved quantum yield. Moreover, heteroatom dope escalates as a more

effective and general strategy to construct the optic and electron transfer properties of CDs. Hence, in this study, the researchers assessed the potentiality of utilizing nanosilica from Taal volcanic ash as a doping agent to carbon dots for Cu^{2+} ions tracing. The researchers also concentrated on the goal of developing a mathematical model that could be utilized to assess its applicability in determining copper ion pollutants with reasonable sensitivity and validity.

The nanosilica-doped dots were used for the detection of Copper (Cu^{2+}) ions in wastewater. Taal volcanic ash (TVA) underwent a series of processes to produce silica, and afterward was subjected for characterization. Taal volcanic ash silica-doped carbon dots (TVA/SiO_2-Cdots) served as a fluorescence detector that is limited to Cu^{2+} ions tracing only. In this study, its reactivity with other metals was no longer investigated. The effects of silica dosage, agitation and contact time in the PL intensity ratio of TVA/SiO_2-Cdots with Copper (Cu^{2+}) ions in simulated wastewater were determined in this study. Included also is the characterization of physicochemical properties of both carbon dots and TVA/SiO_2-Cdots. Moreover, the determination of the effects of PL intensity ratio of TVA/SiO_2-Cdots in simulated wastewater with an increasing amount of Cu^{2+} ions was conducted. The simulated wastewater was prepared for a practical application of Cu^{2+} tracing.

Materials and Methods

Production of nanosilica

Volcanic ash samples collected were subject to sieving to separate it according to particle size. A 40g sample of volcanic ash was prepared. This undergoes acid leaching particularly, 3M HCl solution to remove impurities. The sample was allowed to be soaked in the acid for three hours. Then washed until neutral (with pH ranging from 6.5 to 7.5) and dried in an oven at 100 °C for 6 hours. After drying, the sample went through reflux with 4M NaOH solution at 1:8 (w/v ratio) for four hours at 90-100 °C. The sample was left undisturbed overnight. Then, filtered using silica crucible and washed with warm water. After that, the HCl was added via burette. Note that there is a continuous addition of HCl until there is the formation of white gel, which is the Silica, and until the solution is acidic. Then, subjected it to further washing to be neutralized (with pH ranging from 6.5 to 7.5) and then dried in the oven for 6 hours at 120 °C.

To turn this silica into nanosilica, the dried sample was refluxed at 90-100 °C with 200 mL of 6M HCl solution for 5 hours. After 5 hours of reflux, HCl was decanted and added 160 mL 4M NaOH solution. This solution was subjected to constant stirring for about 4 hours before the addition of H_2SO_4. Note that there is a continuous addition of sulfuric acid until the formation of white precipitates and until the solution is acidic. The precipitates that will be formed is filtered and washed until neutral (with pH ranging from 6.5 to 7.5) and then, dried in the oven for 30 hours at 70 °C. The mass of the completely dried solid was recorded, which is the Nanosilica and the sample was prepared for the next stage of the study.

Preparation of carbon dots

The carbon dots were prepared by microwave-assisted rapid production. Under agitation, 0.57g of L-cysteine was dissolved in 10 mL of deionized water, and 1.5g of citric acid was then added. The resulting solution was heated in a microwave for 4 minutes after being subjected to ultrasonication for 10 minutes. After the reaction, the product was allowed to cool naturally to room temperature before being dissolved with agitation in 10 mL of deionized water to produce a brown solution. In order to eliminate the contaminant, it was centrifuged for 10 minutes at 4000 rpm before being filtered. The obtained solution was extracted by ethyl acetate and then kept in a refrigerator under 4 °C for later use [5].

Preparation of nanosilica-doped carbon dots

An amount 5 mL of carbon dots was mixed with various concentrations of silica (0.1, 0.3 and 0.5 g). It was then added to 25 mL of ethanol separately, and was stirred for 30 minutes at room temperature. After that, the reaction mixture was centrifuged at 3000-5000 rpm for 15-45 mins and the supernatant was discarded. The remaining pellets of silica-doped carbon dots were collected and washed three times with ethanol, and finally resuspended in ethanol with a concentration of 10 mg/mL.

Photoluminescence intensity metering of best TVA/SiO_2-Cdots

The prepared TVA/SiO_2-Cdots with varying parameters were mixed with copper-containing and non-copper-containing simulated wastewater. The simulated wastewater in this study was made using a standard preparation by Official Methods of Analysis of AOAC International. Simulated wastewater was prepared by dissolving 1.9645 g $CuSO_4 \cdot 5H_2O$ in H_2O and diluting it to 500 mL (1 mL = 1 mg Cu). After mixing thoroughly, the fluorescence spectra were recorded after 10 minutes at room temperature. Photos of the carbon dots were taken using an iPhone 11 Pro to collect light frequency, and the photographs were converted to luminous intensity using Image J Batch Software [6]. The fluorescence intensity ratio is measured at the excitation wavelength (λ_{ex}) of 365 nm using UV light [7].



Figure 1. Luminous intensity metering set up

The difference in the photoluminescence ratio of TVA/SiO_2-Cdots in simulated wastewater and copper-containing-simulated water was used to determine the reactivity of TVA/SiO_2-Cdots with Copper ions. Thus, the parameters having the highest photoluminescence intensity difference were considered to be the best parameters.

Preparation of simulated wastewater at increasing Cu^{2+} ions concentration

For Cu^{2+} detection, copper sulfate pentahydrate ($CuSO_4 \cdot 5H_2O$) was utilized as the source for Cu^{2+} ions. 20 mL of prepared TVA/SiO_2-Cdots was dissolved in 100 mL of simulated wastewater. 5 mL TVA/SiO_2-Cdots aqueous solution was added to a beaker and the $CuSO_4 \cdot 5H_2O$ solution was subsequently added along with increasing concentrations. The concentrations of Cu^{2+} ions are 0,1, 2, 3, 4, 5, 6, 7, 8, 9 and 10 ppm. Magnetic stirrer rotating at 3000 rpm facilitates uniform concentration at 20 °C.



Figure 2. Schematic Roadmap of Research Methodology

Characterization of nanosilica-doped carbon dots: Fourier transform infrared spectroscopy (FTIR)

Fourier transform infrared (FT-IR) spectrum was conducted to recognize the surface functional groups and conjugations existing on the TVA/SiO_2-Cdots' surface. Specific functional group of the molecule is read by its band association which gives the identification of the functional groups that constitute the material.

Dynamic light scattering (DLS)

To determine the particle size and particle size distribution of the sample, DLS was used. It determines the particle size distribution by measuring the random changes in the intensity of light scattered from a suspension or solution.

Formulation of mathematical model

In order to formulate a mathematical model that will describe the relationship between the photoluminescence intensity ratio of SiO_2-Cdots and Cu^{2+} ion concentration in simulated wastewater, Matlab R2011-A was used in calculating the desired parameters for the mathematical model. After analysis of different models, the Gaussian method of modeling was selected as the best fit to represent the effects of increasing heavy metal concentration in simulated wastewater to photoluminescence intensity of TVA/SiO_2-Cdots. This method was selected over the other five methods namely exponential of 2nd power, Fourier of 2nd power, linear model of 3rd power and rational. For all generated equations, P(C) is the photoluminescence intensity (RLU) as a function of heavy metal concentration, C in parts per million.

Validation of generated model using ultraviolet spectrophotometric screening method

To validate the degree of acceptability of the generated models, various concentrations of Cu^{2+} in simulated wastewater were prepared prior to ultraviolet spectrophotometric screening. A Shimadzu UV/VIS spectrophotometer, UV-2700 was used for measuring the absorbance and recording the spectra. Wavelength range for copper examination using UV-Vis spectrophotometry is 185-500 nm [8]. The results were used to plot a calibration graph which was used to determine the concentration of Cu^{2+} in produced water.

A 20 mL of prepared TVA/SiO_2-Cdots was dissolved in 100 mL of simulated wastewater. 5 mL TVA/SiO_2-Cdots aqueous solution was added to a 10 mL volumetric flask and the 5 mL of $CuSO_4 \cdot 5H_2O$ solution was subsequently added along with concentrations of 1 ppm to 10 ppm. The solutions were left to stand for 30 minutes and then analyzed using the UV-Vis spectrometer at a wavelength of 206 nm and the absorbance was taken.

Statistical treatment

For the determination of the effect of given parameters to the photoluminescence intensity of synthesized TVA/SiO_2-Cdots, Minitab and analysis of variance was used. The Taguchi orthogonal array design was utilized to determine the effect of TVA/SiO_2-Cdots with copper ions (Cu^{2+}) in photoluminescence (PL) intensity in terms of three factors including silica dosage, agitation rate, and contact time.

For the simulated wastewater with Cu^{2+}, empirical models and data curves relating the photoluminescence intensity and the increasing concentration Cu^{2+} ions were constructed using MATLAB R2011-A. One-way ANOVA was used to determine the effect PL Intensity of TVA/SiO_2-Cdots upon increasing Cu^{2+} Ion concentration in simulated wastewater. Two paired t-tests were employed to determine the degree of comparability between the concentrations obtained from the generated model from that of detected concentration using ultraviolet spectrophotometric screening method.

Results and Discussion

Parameters that affect the PL intensity of TVA/SiO_2-Cdots with copper (Cu^{2+}) ions in simulated wastewater

Using Image J batch software, the PL intensity of the synthesized carbon dots was recorded at 17.692. This intensity is low and suggests that doping carbon dots with other material is a must in order to increase its PL intensity. In this study, the effect of varying parameters including silica dosage, agitation rate and contact time to the photoluminescence (PL) intensity of TVA/SiO_2-Cdots copper ions (Cu^{2+}) in simulated wastewater was

evaluated using the 3^3 Taguchi design which has 3 levels and 3 factors. The difference in the PL intensity of TVA/SiO_2-Cdots in simulated wastewater and copper-containing water determined the reactivity of TVA/SiO_2-Cdots with copper ions.

Table 1. PL Intensities of TVA/SiO_2-Cdots with and without copper

Silica Dosage	Agitation Rate	Contact Time	PL Intensity (Without Cu^{2+})	PL Intensity (With Cu^{2+})
0.1	3000	15	41.509	49.276
0.1	4000	30	43.059	51.139
0.1	5000	45	45.198	52.808
0.3	3000	30	44.110	52.79
0.3	4000	45	46.694	55.445
0.3	5000	15	43.956	53.159
0.5	3000	45	51.529	64.677
0.5	4000	15	45.268	55.092
0.5	5000	30	45.682	55.498

Based on the experimental results, the highest PL intensity recorded from both with and without copper ions were under the operational conditions 0.5 g, 3000 rpm and 45 minutes.

Table 2. Response table for signal to noise ratios

	Level	Silica Dosage (g)	Agitation Rate (rpm)	Contact Time (min)
Without Copper	1	32.72	33.16	32.78
	2	33.05	33.06	32.92
	3	33.52	33.05	33.58
	Delta	0.80	0.11	0.80
	Rank	1	3	2
With Copper	1	34.16	34.84	34.39
	2	34.61	34.62	34.50
	3	35.31	34.62	35.18
	Delta	1.15	0.22	0.79
	Rank	1	3	2

According to the values of S/N ratios for with and without copper ions, level 3 is considered best for silica dosage, level 1 for agitation rate and level 3 for contact time. These findings relate to the optimized value for each parameter such as 0.5 grams silica dosage, 3000 rpm agitation rate and 45 minutes contact time. From the table, it was shown that the most significant factor in PL intensity for with and without copper ions is the silica dosage which has the highest S/N ratio followed by the contact time and lastly is the agitation rate.

The results obtained are likewise comparable to those observed in the S/N ratios. According to the data, level 3 had the highest value in silica dosage, level 1 is best for agitation rate, and level 3 for contact time both for with and without copper ions. These results are also related to the optimal value for each parameter, such as 0.5 grams silica dosage, 3000 rpm agitation rate and 45 minutes contact time. According to the table, the silica dosage is the most important parameter in PL intensity followed by the contact time and lastly is the agitation rate with respect to means.

Table 3. Response table for means

	Level	Silica Dosage (g)	Agitation Rate (rpm)	Contact Time (min)
Without Copper	1	43.26	45.72	43.58
	2	44.92	45.01	44.28
	3	47.49	44.95	47.81
	Delta	4.24	0.77	4.23
	Rank	1	3	2
With Copper	1	51.07	55.58	52.51
	2	53.79	53.89	53.14
	3	58.42	53.82	57.64
	Delta	7.35	1.76	5.14
	Rank	1	3	2

Analysis of Variance (ANOVA) is used to determine and evaluate the overall effect of the different parameters on the experiment response, which is the PL intensity of the TVA/SiO_2-Cdots. The *p*-values of silica dosage, agitation rate and contact time without copper ions are both 0.011, 0.048, and 0.011, respectively. With copper ions, the *p*-values of silica dosage and contact time are 0.011 and 0.042, respectively while the agitation rate is 0.393. The values of the parameters are all less than the significance level of 0.05, therefore it indicates that there is a significant effect between the response (PL intensity) and factors (silica dosage, agitation rate and contact time).

The *F*-value is the test statistic that also determines the association of the response variable to the factors. The large *F*-value of silica dosage from with and without Copper ions compared to other parameters implies that it is statistically significant. The value of sum of squares (SS) is crucial as it influences the effectiveness of the response. The greater the SS value, the more effective it is. The SS values of each parameter are 26.9367 for silica dosage, 0.8909 for agitation rate and 26.8309 for contact time without copper ions and 80.990, 4.660, and 39.593 respectively for copper ions. The percentage contribution of silica dosage, agitation rate, and contact time are 42.44%, 1.41% and 42.28%, respectively without copper ions. On the other hand, the percent contribution for the TVA/SiO_2 with copper ions are 53.29% for silica dosage, 3.07 for agitation rate and 26.04% for contact time. The silica dosage for both the TVA/SiO_2 with and without copper ions has the highest SS value and % contribution which indicates that the silica dosage heavily impacted the absorption process. On the other hand, the agitation rate had the lowest % contribution. As can be observed, the results of ANOVA analysis for PL intensity of TVA/SiO_2-Cdots is similar to those of the results from S/N ratios.

In addition, using *t*-test, the *p*-value of TVA/SiO_2-Cdots with and without the addition of copper ions is 6.86E-0.5, it is found out that there is a significant difference in PL intensity ratio of TVA/SiO_2-Cdots upon the addition of Cu^{2+} ions in simulated wastewater.

Characterization of the best TVA/SiO_2-Cdots particle size and particle size distribution

The synthesized Cdots presented an average particle size diameter of 6.37 nm. After doping with nanosilica particles, the average diameter of the obtained TVA/SiO_2-Cdots increased to about 17.46 nm, suggesting the successful doping of nanosilica on the surface of carbon dots.

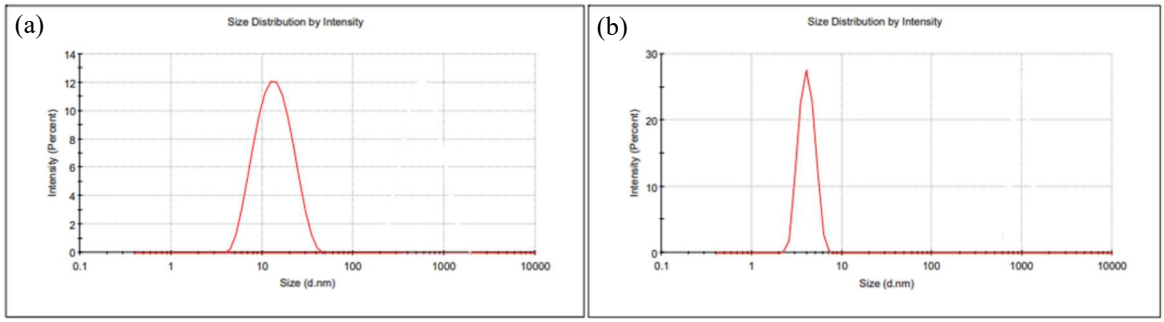


Figure 3. Particle size distribution of (a) Cdots and (b) TVA/SiO_2-Cdots

Table 4. Particle Size Distribution of Cdots and TVA/SiO_2 – Cdots

Sample	Z – Average (d.nm)	Peak	Size	Intensity	St. Dev. (d.nm)
Cdots	6.37 nm	Peak 1	7.63	100.0	2.797
TVA/SiO_2 – Cdots	17.46 nm	Peak 1	14.92	100.0	19.62

Particle size distribution is determined through dynamic light scattering (DLS) by measuring the random changes in the intensity of light scattered from a suspension or solution. The synthesized Cdots presented an average particle size diameter of 6.37 nm. A stable nanometric solution must have a size diameter of 1 to 100 nm. This confirms that the Cdots are nanometric. Particle size distribution of Cdots were shown in Figure 3 and Table 4. After doping with nanosilica particles, the average diameter of the obtained TVA/SiO_2-Cdots increased to about 17.46 nm, suggesting the successful doping of nanosilica on the surface of carbon dots.

Functional group and its conjugation

The distinct absorption peaks that defined the optical properties of Cdots were 3319.79, 1732.54, 1625.16, 1398.57, 1243.27 and 1013.58 cm^{-1}. The functional groups determined were N-H group, C=O group, C=C bond having an olefinic conjugated diene [9], C-H group, C-O group respectively. Typical conjugations with other double bond structures such as the C=C, C=O or aromatic rings will reduce the intensity frequency with strong or intense absorption bands [2].

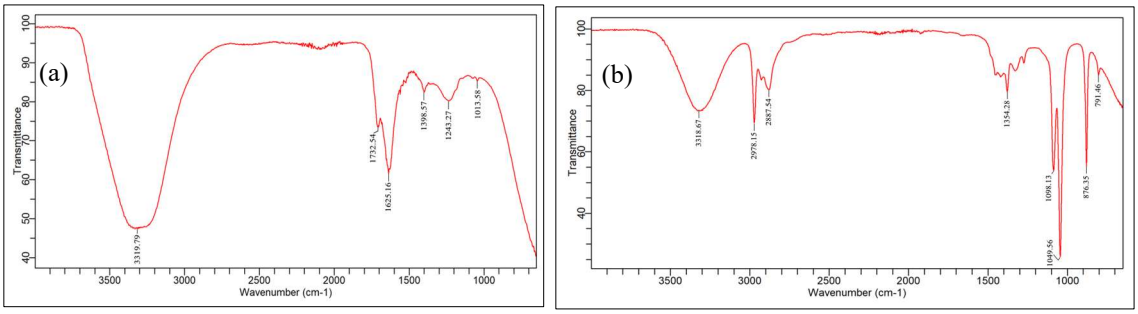


Figure 4. FTIR spectra of Cdots (a); TVA/SiO_2Cdots (b)

As for synthesized TVA/SiO_2-Cdots, the distinct peaks that determined their optical properties were observed at 3318.67, 2978.15, 1354.28, 1098.13, 1049.56, 876.35 and 791.46 cm^{-1}. The functional groups determined were N-H group, O-H group, sulfoxide group, C-O bond, strong Si-O-C bond, and strong C-Cl bond, respectively. The participation of the carbon dots in the synthesis of TVA/SiO_2-Cdots is determined because all the bands

were shifted. The broad bands at 2978.15-2887.54 and 3318.67 cm^{-1} in the synthesized TVA/SiO_2-Cdots which are assigned to the O-H and N-H functional groups accounts to the solubility and stability of the synthesized TVA/SiO_2-Cdots [9]. The presence of the said functional also plays a major factor in the color tuning of the synthesized TVA/SiO_2-Cdots. The blue shift in the emission wavelength of the TVA/SiO_2-CDots can be attributed to an amine state, which can emit shorter wavelengths under UV excitation [2]. The presence of functional groups such as hydroxyl group containing medium emission, and sulfoxide and C-Cl bond which both contain strong emission proves the higher strength of emission of TVA/SiO_2-Cdots compared to the synthesized carbon dots. In addition, the greater number of chemical bonds present in the TVA/SiO_2-Cdots indicates its high reactivity to heavy metals [10].

Determination of PL Intensity TVA/SiO_2-Cdots upon increasing Cu^{2+} ion concentration in simulated wastewater

The detection of Cu^{2+} ions using TVA/SiO_2-Cdots was conducted at different concentrations between a range of 0 to 10 ppm. The results revealed that there was a drastic reduction in the PL intensity at 365 nm as the Cu^{2+} concentration increased, demonstrating excellent sensing of the metal ion in the system. The PL intensity is significantly reduced and the emission wavelength of the fluorescent material along with a quencher do not change. As the concentration of Cu^{2+} increases from 0 ppm to 10 ppm, the PL intensity of TVA/SiO_2-Cdots decreases from 245.9760 to 58.7867. Thus, the PL intensity of synthesized TVA/SiO_2-Cdots is Cu^{2+} metal-ion-concentration-dependent.

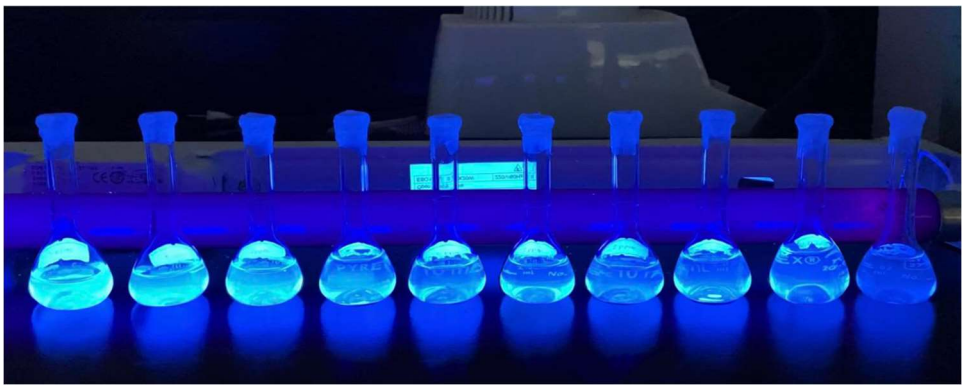


Figure 5. PL intensity of TVA/SiO_2-Cdots with the increasing Cu^{2+} ion concentration in simulated wastewater

Table 6. PL Intensities of TVA/SiO_2-Cdots with the increasing Cu^{2+} ion concentration in simulated wastewater

$CuSO_4 \cdot 5H_2O$ Concentration (ppm)	**Photoluminescence Intensity (Simulated Wastewater)**
0	245.9760
1	162.4328
2	134.9339
3	128.6127
4	125.5015
5	119.3487
6	108.4712
7	98.4624
8	86.7122
9	72.5457
10	58.7867

The fluorescence-quenching mechanism of normal CDs can be attributed to several factors such as inner filter effects, non-radiative recombination pathways, electron transfer and ion-binding interaction [11]. The fluorescence-quenching mechanism of TVA/SiO_2-Cdots was assessed using the UV–visible spectroscopy. The broad absorption band of TVA/SiO_2-Cdots around 185 and 400 nm showed definite reduction upon increasing Cu^{2+} metal ion concentrations, therefore indicating the formation of complexations between the functional groups of TVA/SiO_2-Cdots and Cu^{2+} ions.

On the basis of this observation, the researchers propose that the formation of complexation between TVA/SiO_2-Cdots and Cu^{2+} results in electron transfer between Cu^{2+} ions and TVA/SiO_2-Cdots (nonradiative energy), which plays a major role in quenching the PL intensity of TVA/SiO_2-Cdots. The figure below shows the fluorescence-quenching mechanism of TVA/SiO_2-Cdots by Cu^{2+} metal ions. In fact, the main reason for the decrease of PL intensity of such quantum dots is the defects that existed in their structures that led to trap electrons and hence decrease the PL intensity. By surface modification of the quantum dots, the defects centers were significantly decreased and therefore the PL intensity is increased. Due to the high PL intensity of the synthesized carbon quantum dots, we used them to the detection of Cu^{2+} ions. The results showed Cu^{2+} can quench PL intensity of carbon dots due to the bonding between of N functional groups of CQD and Cu^{2+}.

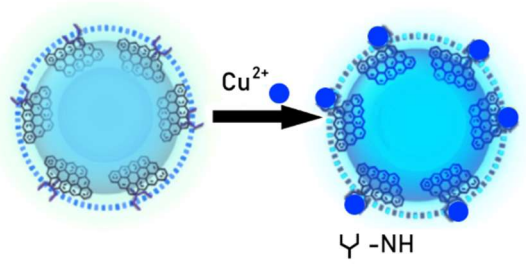


Figure 6. Quenching mechanism of carbon dots

A one-way ANOVA was performed to compare the effect of increasing Cu^{2+} ion concentration in simulated wastewater and TVA/SiO_2-Cdots PL intensity. Since the data obtained had a p-value of 2.34E-07, which is less than 0.05, it meant that increasing Cu^{2+} ion concentration in simulated wastewater has a high effect on the PL intensity of TVA/SiO_2-Cdots. The obtained F-stat value (58.41) is greater than the *F*-critical value (4.35) which is equivalent to a *p*-value less than alpha. Both of these mean that the PL intensity of TVA/SiO_2-Cdots was significantly affected by an increase in Cu^{2+} ion concentration in simulated wastewater.

Table 7. Statistical result for the effect in PL intensity of TVA/SiO_2-Cdots upon increasing Cu^{2+} ion concentration in simulated wastewater

Medium	Mean Square	Sum of Squares	*F*-Stat	*p* - value	*F*-critical
Simulated Wastewater	1288.45	25769.08	58.41	2.34E-07	4.35

Mathematical model on the effect of Cu^{2+} ion concentrations on the PL intensity of TVA/SiO_2-Cdots in simulated wastewater

After analysis of different models, the Gaussian method of modeling was selected as the best fit to represent the effects of increasing heavy metal concentration in simulated wastewater to photoluminescence intensity of TVA/SiO_2-Cdots. This method was selected over the other five methods namely exponential of 2nd power, Fourier of 2nd power, linear model of 3rd, power and rational.

Table 8. Generated model curves describing the effect of Cu^{2+} ion concentrations to PL intensity of TVA/SiO_2-Cdots in simulated wastewater

Types of Models Fit	Method	Equations Generated	SSE	R^2	Adjusted R^2	RMSE
Exponential (2nd Power)	Non-linear Squares	$P(C)= 73.73e^{-3.105C} + 172.3e^{-0.08933C}$	489.32	0.9811	0.9730	8.361
Fourier (2nd Power)	Non-linear Squares	$P(C)= 1.791x10^{14} - 2.387x10^{14}\cos(0.0002733*C) - 3.831x10^{11}\sin(0.0002733*C) + 5.969x10^{13}\cos(5.466x10^{-4}*C) + 1.915x10^{11}\sin(5.466x10^{-4}*C)$	127.86	0.9951	0.9901	5.0569
Gaussian (2 terms)	**Non-linear Squares**	$\boldsymbol{P(C)= 501.7e^{(\frac{-2.658-C}{2.308})^2} + 127.5e^{(\frac{2.839-C}{2.099})^2}}$	**12.908**	**0.9995**	**0.9990**	**1.1067**
Linear Model (Poly 3)	Linear Squares	$P(C)= -0.5801C^3 + 9.983C^2 - 59.85C + 230.9$	1268.2	0.9676	0.9230	13.46
Power	Non-linear Squares	$P(C)= -7.128C^{1.1239} + 160$	1007.4	0.9798	0.9771	7.9349
Rational	Linear Squares	$P(C)= \frac{-56.35C^3 - 7.285C^2 + 277C + 28}{C^2 + 2.889C + 2.382}$	22.598	0.9991	0.9983	2.126

In selecting the best mathematical model from the generated equation shown above, the equation's fitness must be measured in terms of SSE, adjusted, and root mean squared error. Similarly, the model with the lowest SSE and RMSE is the best fit because these assess the errors from the data points. The model that is closest to one in terms of R^2 is the most suitable [12]. Based on the generated models, the Gaussian equation has the lowest SSE and RMSE and it also has the closest value of 1 in terms of the R^2 and adjusted R^2 values.

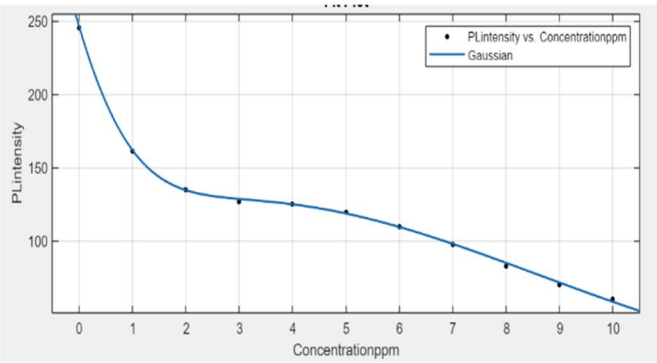


Figure 7. Curve fit of Gaussian method for Cu^{2+}

This model is best described by the equation for Cu^{2+}:

$$P(C) = 501.7\, e^{-(\frac{C+2.658}{2.308})^2} + 127.5\, e^{(\frac{2.839-C}{2.099})^2} \quad (1)$$

where P(C) is the PL intensity in RLU as the function of heavy metal concentration, C in ppm.

Comparison of the Cu^{2+} ion concentration calculated from the generated model with the detected concentrations using ultraviolet spectrophotometric screening method

In the table above, the amount of calculated concentration from the selected model is shown. The photoluminescence intensity of TVA/SiO_2-Cdots decreases along with increasing formulated concentration of Cu^{2+} ions. The calculated concentration using the model provides values that are approximately the same as the detected concentration using the ultraviolet spectrophotometric screening method, with a maximum deviation (by virtue of difference) of 0.2587 and minimum deviation of 0.0013. Furthermore, the model fits more effectively at low to moderate concentrations.

Table 8. Concentration of Cu^{2+} ion based on calculated and detected values

Formulated $CuSO_4 \cdot 5H_2O$ Concentration (ppm)	Photoluminescence Intensity	Calculated Concentration using the Model (ppm)	Detected Concentration
1	162.4328	0.9869	0.9974
2	134.9339	1.9787	1.9653
3	128.6127	3.0212	2.9876
4	125.5015	3.8967	4.0259
5	119.3487	4.9221	4.9208
6	108.4712	6.0951	5.8364
7	98.4624	6.9563	7.0113
8	86.7122	7.8677	7.9274
9	72.5457	8.9208	9.0692
10	58.7867	9.9652	9.9865

Table 9. Statistical result for the comparison of calculated and detected concentration of Cu^{2+} ion in simulated wastewater

Mean Difference	Standard Deviation	Standard Error Mean	*t* -Value	*p* - value	*t*-Critical Value
0.01171	-	-	-0.331	7.48E-01	2.262

Note. p – value depicts a value greater than α = 0.05 has no significant effect

The p-value calculated is greater than 0.05 which denotes the acceptance of the null hypothesis. Thus, there is no significant difference between Cu^{2+} concentrations calculated from the generated mathematical model with that detected from the UV-Vis screening method.

Conclusion

The following conclusions were based on the mathematical analysis of the data using the appropriate computer software and the in-depth interpretation of the results and findings. Varying parameters such as silica dosage, agitation rate, and contact time play significant roles in copper detection. There is the presence of amine N-H, carbonyl C=O, C=C, C-H, and C-O groups in the Cdots, whereas the presence of N-H, O-H, and sulfoxide groups as well as C-O, strong C=C, and strong C-Cl bonds in TVA/SiO_2-Cdots, which are responsible for their color emission, stability, and reactivity. Moreover, the results of dynamic light scattering measurements indicated that upon silica doping, the average diameter of CDs in ethanol had increased, indicating a success in the doping process. The photoluminescence intensity at 365 nm decreased significantly along with the increasing Cu^{2+} ion concentration in the range of 0 to 10 ppm in simulated wastewater, which indicated that the photoluminescence intensity of TVA/SiO_2-Cdots was quenched by Cu^{2+} ions. The generated mathematical model in equation 1, can be used to determine Cu^{2+} concentrations at specific ranges having no significant

difference with the ultraviolet spectrophotometric screening method.

Acknowledgements

The researchers would like to express their gratitude and appreciation to Batangas State University Alangilan and Analytical Research Center (ARC) – Pablo Borbon Campus for allowing them to maximize its full potential as an experimental laboratory workplace and to all the people who interceded for the success of this research.

References

1. Min, K. J. (2018). Synthesis and characterization of dried leaves derived carbon quantum dots for metal ions sensing and photocatalytic application. Doctoral dissertation, UTAR, Malaysia: pp. 1-74.
2. Nandiyanto, A. B. D., Oktiani, R. and Ragadhita R. (2019). How to read and interpret FTIR spectroscope of organic material. *Journal of Science & Technology*, 4(1): 97.
3. Nanowerk (2017). What are quantum dots? Access from https://www.nanowerk.com/what_are_quantum_dots.php
4. Langmann, B. (2013). Volcanic ash versus mineral dust: Atmospheric processing and environmental and climate impacts. *ISRN Atmospheric Sciences,* 2013: 1-17.
5. Lin, H., Huang, J. and Ding, L. (2019). Preparation of carbon dots with high-fluorescence quantum yield and their application in dopamine fluorescence probe and cellular imaging. *Journal of Nanomaterials*, 2019: 1-9.
6. Canson, M., Cantos, J. and de Guzman, M. (2016). Modelling the effect of varying Cr^{+6} and Cu^{+2} concentration on the luminous intensity of *Photobacterium phosphoreum* in simulated seawater. Dissertation Batangas State University, Philippine.
7. Bagheri, Z., Ehtesabi, H., Rahmandoust, M., Ahadian, M. M., Hallaji, Z., Eskandari, F. and Jokar, E. (2017). New insight into the concept of carbonization degree in synthesis of carbon dots to achieve facile smartphone based sensing platform. *Scientific Reports,* 7(1): 11013.
8. American Public Health Association (2002). Standard methods for the examination of water and wastewater.
9. Wang, R., Lu, K. Q., Tang, Z. R., and Xu, Y. J. (2017). Recent progress in carbon quantum dots: synthesis, properties and applications in photocatalysis. *Journal of Materials Chemistry A*, 5(8): 3717-3734.
10. Stepanidenko, E. A, Skurlov, I. D., Khavlyuk, P. D., Onishchuk, D. A., Koroleva, A.V., Zhizhin, E.V., Arefina, I. A., Kurdyukov, D. A., Eurov, D. A. and Golubev, V. G. (2022). Carbon dots with an emission in the near infrared produced from organic dyes in porous silica microsphere templates. *Nanomaterials,* 12: 543.
11. Ding, Z-Z., Zheng, G-S., Lou, Q., Han, J-F., Wu, M-Y., Shen, C-L., Zang, J-H, Liu, K-K., Dong, L. and Shan, C-X. (2021). A confined carbon dot-based self-calibrated fluorescence probe for visible and highly sensitive moisture readouts. *Journal Physics D: Applied Physics,* 55: 154001.
12. Liu, J., Li, R., and Yang, B. (2020). Carbon dots: A new type of carbon-based nanomaterial with wide applications. *ACS Central Science*, 6(12): 2179-2195.

Malaysian Journal of Analytical Sciences (MJAS)
Published by Malaysian Analytical Sciences Society

CRYSTAL STRUCTURE AND HIRSHFELD SURFACE ANALYSIS OF COMPOUND DI[2-((1E)-{2-(2-METHYLBENZYLSULFANYL) METHYLIDENE- HYDRAZIN-1-YLIDENE}METHYL)-6-METHOXY- PHENOL]

(Struktur Hablur dan Analisis Permukaan Hirshfeld bagi sebatian Di[2-((1E)-{2-(2-Metilbenzilsulfanil)Metiliden-Hidrazin-1-Iliden}Metil)-6-Metoksi-Fenol])

Enis Nadia Md Yusof[1*], Suhana Arshad[2], Kwong Huey Chong[3], and Siti Syaida Sirat[4,5]

[1]*Chemical Sciences Programme, School of Distance Education, Universiti Sains Malaysia, 11800 Minden, Penang, Malaysia*
[2]*X-ray Crystallography Unit, School of Physics, Universiti Sains Malaysia, Penang 11800, Malaysia*
[3]*Department of Chemistry, Faculty of Science, Universiti Putra Malaysia, 43400 UPM Serdang, Selangor Darul Ehsan, Malaysia*
[4]*School of Chemistry and Environment, Faculty of Applied Sciences, Universiti Teknologi MARA, Cawangan Negeri Sembilan, Kampus Kuala Pilah, 72000 Kuala Pilah, Negeri Sembilan, Malaysia*
[5]*Atta-ur-Rahman Institute for Natural Product Discovery (AuRIns), Universiti Teknologi MARA, Kampus Puncak Alam, 42300 Bandar Puncak Alam, Selangor, Malaysia*

[*]*Corresponding author: enisnadia@usm.my*

Received: 19 June 2023; Accepted: 23 July 2023; Published: 22 August 2023

Abstract

In this work we report crystal structure and Hirshfeld surface analysis of compound di[2-((1*E*)-{2-(2-methylbenzylsulfanyl)methylidene- hydrazin-1-ylidene}methyl)-6-methoxy- phenol] (**HL**), which has a dimeric dithiocarbazate backbone. **HL** has a non-planar structure due to strong intra-bonds that create two S(6) graph-set motifs, preventing free rotation by locking its atoms in a nearly planar arrangement. The crystal packing involves intermolecular C—H···S and C—H···π interactions that form a two-dimensional sheet parallel to the *ac*-plane which extends into a three-dimensional network arrangement via π···π interactions involving the centroid of the phenyl ring. Hirshfeld surface analysis describes that the major contribution to the overall crystal packing is from H···H contacts, followed by H···C/C···H contacts, which signify the presence of C—H···π interactions. The presence of intermolecular C—H···S interactions can be confirmed through the involvement of S···H/H···S contacts.

Keywords: dithiocarbazate, dimeric, crystal structure, Hirshfeld surface analysis

Abstrak

Dalam kajian ini, kami melaporkan struktur hablur dan analisis permukaan Hirshfeld bagi sebatian di[2-((1E)-{2-(2-metilbenzilsulfanil)metilidena-hidrazin-1-ilidena}metil)-6-metoksi-fenol] (**HL**), yang mempunyai rangkaian dithiocarbazat berbentuk dimerik. **HL** mempunyai struktur tidak rata disebabkan oleh ikatan dalaman yang kuat yang membentuk dua motif set-

graf S(6), menghalang putaran bebas dan mengunci atom-atomnya dalam susunan hampir rata. Penempatan hablur melibatkan interaksi intermolekul antara C—H···S dan C—H···π yang membentuk satu lapisan dua dimensi sejajar dengan satah *ac* dan meluas ke susunan rangkaian tiga dimensi melalui interaksi π···π yang melibatkan pusat gelang fenil. Analisis permukaan Hirshfeld menjelaskan bahawa sumbangan utama kepada penempatan kristal secara keseluruhan adalah daripada sentuhan H···H, diikuti oleh sentuhan H···C/C···H, yang menunjukkan kewujudan interaksi C—H···π. Kewujudan interaksi intermolekul antara C—H···S dapat disahkan melalui keterlibatan sentuhan S···H/H···S.

Kata kunci: dithiocarbazat, dimerik, struktur hablur, analisis permukaan Hirshfeld

Introduction

Dithiocarbazate Schiff bases have gained significant attention due to their diverse range of biological and pharmacological activities [1–5]. These compounds consist of a dithiocarbazate moiety (depicted in Figure 1), which is formed by condensing a primary amine with carbon disulfide and subsequently reacting it with an aldehyde or ketone to create the Schiff base. These ligands bear structural similarities to thiosemicarbazone and hydrazone ligands. Even minor modifications in the molecular structure of dithiocarbazate derivatives can result in intriguing biological properties [2, 6]. Moreover, these ligands possess both soft sulfur and hard nitrogen donor atoms, enabling them to coordinate with various metal ions to form metal complexes that exhibit fascinating physicochemical and enhanced biological characteristics. In this study, our focus lies on synthesizing di[2-((1E)-{2-(2-methylbenzylsulfanyl)methylidene- hydrazin-1-ylidene}methyl)-6-methoxy- phenol] (**HL**) and performing a single crystal X-ray diffraction (XRD) analysis to determine the crystal characteristics of **HL**. In addition, the significant intermolecular interactions have been studied using Hirshfeld surface analysis.

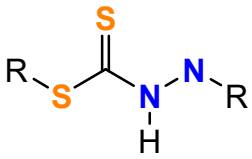


Figure 1. Dithiocarbazate backbone (R = alkyl/aryl/H)

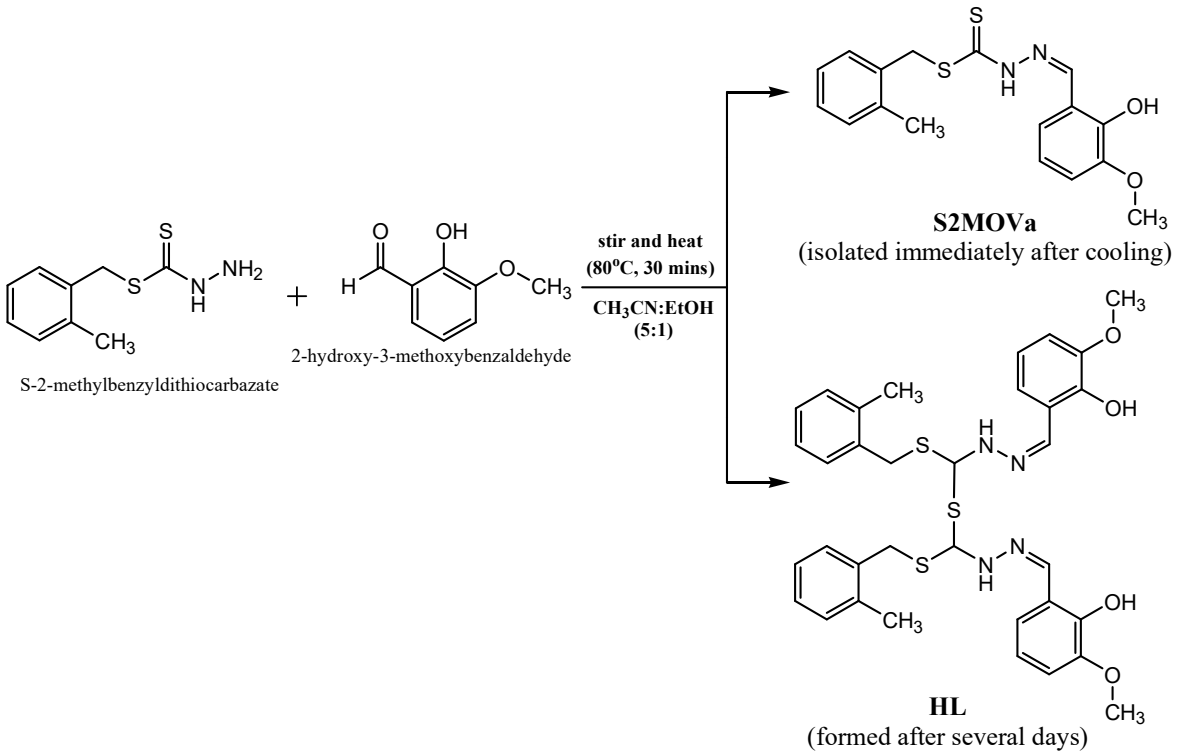
Materials and Methods

Materials

Analytical reagent grade solvents and reagents were utilized without additional purification. The following chemicals were employed: Hydrazine hydrate (Fluka), 2-methylbenzyl chloride (ACROS), potassium hydroxide (HmbG), carbon disulfide (BDH), and 2-hydroxy-3-methoxybenzaldehyde (Merck). The solvents used were acetonitrile (Baker) and absolute ethanol with a purity of 99.8% (Scharlau).

Synthesis and crystallization of di[2-((1E)-{2-(2-methylbenzylsulfanyl)methylidene- hydrazin-1-ylidene} methyl)-6-methoxy- phenol] (HL)

The formation of the **HL** was synthesized using established literature procedures [4,7]. To initiate the synthesis, S-2-methylbenzyldithiocarbazate (2.12 g, 10 mmol) was dissolved in 100 mL of hot acetonitrile. This solution was then combined with an equimolar amount of 2-hydroxy-3-methoxybenzaldehyde (1.52 g, 10 mmol) dissolved in 20 mL of absolute ethanol. The resulting mixture was stirred at 80 °C for 30 minutes and allowed to sit at room temperature overnight. The completion of the reaction was checked using thin layer chromatography (TLC) plate. Following this, light yellow crystalline solid, 2-((1E)-{2-(2-methylbenzyl sulfanyl)methylidene-hydrazin-1-ylidene}methyl)-6-methoxy-phenol was obtained. The yellow crystalline solid was then recrystallized from a mixture of CH_3CN and EtOH in a 1:1 ratio. After several days of allowing the recrystallization solution to sit at room temperature, yellow plate-shaped crystals of the compound were formed. The single crystal X-ray diffraction analysis confirmed the unexpected product of di[2-((1E)-{2-(2-methylbenzylsulfanyl)methylidene- hydrazin-1-ylidene}methyl)-6-methoxy- phenol] (**HL**). The synthetic scheme for the formation of **HL** is shown in Scheme 1.



Scheme 1. Synthetic pathway for the formation of **HL**

X-ray crystallography refinement

X-ray analysis was conducted on a single crystal suitable for analysis using a CCD area-detector. CuKα radiation with a wavelength of 1.54178 Å was used. A high-quality crystal, clear and light yellow in color, measuring 0.58 × 0.31 × 0.15 mm, was carefully extracted and observed under a microscope for data collection. The APEX2 software was utilized for data collection, while cell refinement and data reduction were carried out using the SAINT software [8]. The crystal structure was solved using the Direct Method in the SHELXTL program and refined using its' full-matrix least squares technique on F^2 with anisotropic displacement parameters. Absorption correction was applied to the final crystal data using the SADABS software [8]. All geometric calculations were performed using the PLATON program [9]. Molecular graphics were generated using SHELXTL [10]. The non-hydrogen atoms were refined anisotropically, while the hydrogen atoms were positioned geometrically [C—H = 0.93, 0.96 or 0.97 Å] and refined using a riding model with isotropic displacement parameters set to 1.2 (for C) or 1.5 (for C_{methyl}) times the equivalent isotropic U values of the parent carbon atoms. The methyl groups were modelled using a rotating groups model. Additionally, hydrogen atoms bonded to oxygen atoms were located and distinguished through the differences observed through overlapping Fourier maps and freely refined [O-H = 0.76(4) and 0.81(4) Å]. In the final refinement, three outliers (991, 913, and 912) were omitted for clarity. Table 1 provides a summary of the crystal data and relevant refinement parameters for the **HL**.

Hirshfeld surface analysis

Hirshfeld surface and 2D-fingerprint plots calculations were carried out using CrystalExplorer 17.5 [11] on crystal structure imported from CIF file. The Hirshfeld Surfaces for **HL** were mapped with normalized contact distances (d_{norm}), shape index and curvedness functions.

Table 1. Crystallographic refinement parameters of **HL**

Parameters	
CCDC deposition numbers	2072116
Molecular formula	$C_{34}H_{34}N_4O_4S_4$
Molecular weight	690.89
Crystal system	Triclinic
Space group	*P*-1
a/Å	9.5955 (6)
b/Å	11.5562 (14)
c/Å	16.3622 (12)
α/°	71.797 (8),
β/°	88.527 (6),
γ/°	84.712 (7)
V/ Å^3	1716.2 (3)
Z	2
D_{calc} (Mg m^{-3})	1.337
μ (mm^{-1})	2.90
Radiation λ (Å)	1.54178
F(000)	724
Reflections measured	27271
Ranges/indices (*h*, *k*, *l*)	*h* = −11→11 *k* = −14→13 *l* = −20→20
θ limit (°)	4.0-71.7
Unique reflections	6608
Observed reflections ($I > 2\sigma(I)$)	5939
Parameters	427
R_1 [a], wR_2 [b] [$I \geq 2\sigma(I)$]	0.056/0.177
Goodness of fit [c] on F^2	1.10
R_{int}	0.049
Largest diff. peak and hole, e/Å^{-3}	0.66 and −0.35

w = $1/[\sigma^2(F_o^2) + (0.1009P)^2+1.0249P]$, where $P = (F_o^2 + 2F_c^2)/3$; [a] $R = \Sigma||F_o| - |F_c||/\Sigma|F_o|$, [b] $wR = \{w\Sigma(|F_o| - |F_c|)^2/\Sigma w|F_o|^2\}\}^{1/2}$, [c] $GOF = \{\Sigma w(|F_o| - |F_c|)^2/(n-p)\}^{1/2}$, where *n* is the number of reflections and *p* the total number of parameters refined

Results and Discussion

Molecular structure and crystal packing of HL

The molecular structure of the compound **HL** with assigned atom-numbering scheme are presented in Figure 2. The molecular structure of **HL** is crystallized in Triclinic crystal system with *P*-1 space group. All selected bond lengths and angles listed in Table 2 are found within the normal ranges. **HL** consist of dimeric dithiocarbazate backbone with two terminal toluene and 2-methoxyphenol moieties. Intramolecular O1—H1O1···N2 and O3—H1O3···N4 hydrogen bonds are observed with the non-bonding distances (O···N) and the angles (O—H···N) of the intramolecular hydrogen bond of 2.642(3 Å) Å, 159(5)° and 2.679(3) Å, 151(5)°, respectively. Subsequently, these bonds create two *S*(6) graph-set motif, preventing any free rotation of atom, hence locking them (O1/N2/C9-C11 and O3/N4/ C24-C26) in a nearly planar arrangement. Both sulphur and nitrogen bond lengths are found within the normal range where S1—S3 bond length is 2.0411 (9) Å and the N1—N2 as well as N3—N4 bond lengths are 1.406 (3) Å and 1.408 (3) Å, respectively. Figure 2 shows the non-planar

structure of **HL** where the terminal methyl substituted benzene rings are twisted at C1—S2—C2—C3 and C16—S4—C17—C18 torsion angles of −151.6 (2)° and −159.8 (2)°, respectively. Moreover, the terminal 2-methyl phenol rings are likewise observed to be twisted at C1—N1—N2—C9 torsion angle of −156.7 (2)° whereas on the other side of the molecule, the ring is observed to be slightly twisted with C16—N3—N4—C24 torsion angle of −173.9 (2)°. Additionally, the dihedral angles between the phenyl rings (Table 3) are also compared whereby the angles are in the range of 20°-72°, which further confirms the non-planar structure of **HL**.

In the arrangement of the crystal structure as shown in Figure 3 and Table 4, the molecules of **HL** are connected in a one-dimensional chain along the *a*-axis through intermolecular C7—H7···S3 hydrogen bonding. These intermolecular C—H···S interactions are further reinforced by intermolecular C—H···π interactions, specifically C19—H19···*Cg*2 (as indicated in Table 4), where *Cg*2 represents the centroid of the C25-C30 phenyl rings. These interactions result in the formation of a two-dimensional sheet parallel to the *ac*-plane. Furthermore, the crystal structure is strengthened by π···π interactions involving the centroid of the phenyl ring, *Cg*2 (C10-C15),where the centroid to centroid distance is 3.6423(16) Å. These π···π interactions results into extending the two-dimensional *ac*-sheets into a three-dimensional network arrangement.

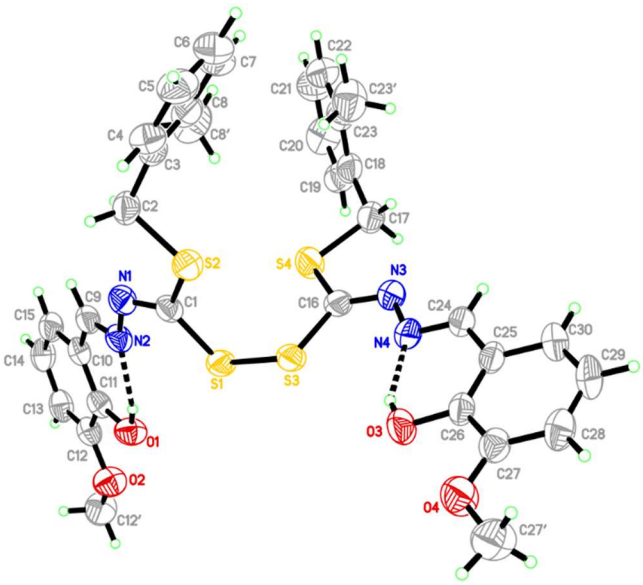


Figure 2. The molecular structure of **HL** with 50% ellipsoids probability with atomic numbering scheme. The dashed lines represent the intramolecular O—H···N hydrogen bonds.

Table 2. Selected bond lengths (Å), bond angle and torsion Angles (°) of **HL**

Bond Length (Å)		**Bond Angle (°)**		**Torsion Angle (°)**	
S1—C1	1.794 (3)	C1—S1—S3	104.56 (9)	C1—N1—N2—C9	−156.7 (2)
S1—S3	2.0411 (9)	C1—S2—C2	101.34 (13)	C16—N3—N4—C24	−173.9 (2)
S2—C1	1.744 (3)	C16—S3—S1	104.80 (9)	N2—N1—C1—S2	179.86 (18)
S2—C2	1.833 (3)	C16—S4—C17	100.72 (14)	N2—N1—C1—S1	2.6 (3)
S3—C16	1.789 (3)	C12—O2—C12′	117.0 (3)	C2—S2—C1—N1	−5.2 (3)
S4—C16	1.744 (3)	C27—O4—C27′	117.0 (3)	C2—S2—C1—S1	172.15 (16)
S4—C17	1.830 (3)	C1—N1—N2	112.1 (2)	S3—S1—C1—N1	177.5 (2)
O1—C11	1.360 (3)	C9—N2—N1	113.4 (2)	S3—S1—C1—S2	0.04 (17)
O2—C12′	1.431 (4)	C16—N3—N4	113.0 (2)	C1—S2—C2—C3	−151.6 (2)
O3—C26	1.352 (3)	C24—N4—N3	112.6 (2)	S2—C2—C3—C4	−89.6 (3)
O4—C27	1.361 (4)	N1—C1—S2	122.3 (2)	N1—N2—C9—C10	−179.3 (2)
O4—C27′	1.428 (4)	N1—C1—S1	120.4 (2)	N2—C9—C10—C11	4.3 (4)
N1—C1	1.273 (3)	S2—C1—S1	117.30 (14)	N4—N3—C16—S4	179.39 (19)
N1—N2	1.406 (3)	C3—C2—S2	105.05 (18)	N4—N3—C16—S3	1.4 (3)
N2—C9	1.285 (4)	C3—C8—C8′	122.1 (3)	C17—S4—C16—N3	0.7 (3)
N3—C16	1.280 (4)	N2—C9—C10	121.8 (3)	C17—S4—C16—S3	178.70 (18)
N3—N4	1.408 (3)	N3—C16—S4	121.7 (2)	S1—S3—C16—N3	−170.1 (2)
N4—C24	1.278 (4)	N3—C16—S3	119.8 (2)	S1—S3—C16—S4	11.91 (18)
C2—C3	1.498 (4)	S4—C16—S3	118.51 (15)	C16—S4—C17—C18	−159.8 (2)
C17—C18	1.502 (4)	C18—C17—S4	108.5 (2)	N3—N4—C24—C25	−179.0 (2)
C9—C10	1.455 (4)	C18—C23—C23′	122.0 (3)	N4—C24—C25—C30	177.0 (3)
C24—C25	1.449 (4)	N4—C24—C25	122.9 (3)	O3—C26—C27—O4	−1.5 (4)
C8—C8′	1.506 (5)	O3—C26—C27	118.0 (3)		
C23—C23′	1.492 (5)				

Table 3. The dihedral angles between the phenyl rings

Ring-Ring	**Dihedral Angle (°)**
A-B	64.47 (15)
A-C	51.44 (17)
A-D	49.63 (16)
B-C	20.75 (16)
B-D	65.86 (15)
C-D	71.47 (17)
A-B	64.47 (15)

Ring A, B, C & D are C3-C8, C10-C15, C18-C23 and C25-C30, respectively

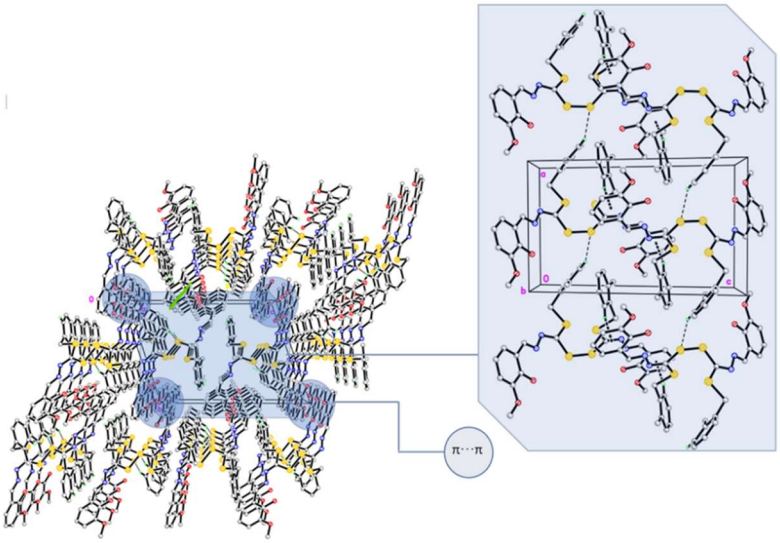


Figure 3. The crystal packing of **HL** showing a three-dimensional network molecular arrangement *via* intermolecular C—H···S, C—H···π and π···π interactions.

Table 4. Intra- and intermolecular hydrogen bonds and π···π interaction geometries (Å, °)

Bond	Bond Length, (Å)			Angle
D—H···A	D—H	H···A	D···A	D—H···A, (°)
O1—H1O1···N2	0.76(4)	1.92(4)	2.642(3)	159(5)
O3—H1O3···N4	0.81(4)	1.94(4)	2.679(3)	151(5)
C7—H7···S3^{i}	0.93	2.83	3.694(4)	155
C19—H19···*Cg*2^{ii}	0.93	2.78	3.607(4)	149
*Cg*1···*Cg*1^{iii}	-	-	3.6423(16)	-

(i) -1+*x*,*y*,*z*; (ii) 1-*x*,1-*y*,1-*z*; (iii) 1-*x*,-*y*,2-*z*. *Cg*1 and *Cg*2 is the centroid of C10-C15 and C25-C30, respectively

Hirshfeld surface analysis

Hirshfeld surface analysis was employed to conduct a thorough investigation of the intermolecular interactions within compound **HL**. This technique is highly valuable for visualizing and quantifying the diverse intermolecular interactions within the crystal structure. In Figure 4, the Hirshfeld surface is plotted using d_{norm}, enabling the visualization of intermolecular interactions through color codes (red, white, and blue). The red color signifies the closest or strongest contacts, indicating the sum of d_i (distance from a point on the surface to the nearest nucleus internal to the surface) and d_e (distance from a point on the surface to the nearest nucleus external to the surface), with de being shorter than the sum of the relevant Van der Waals radii. Conversely, weak intermolecular interactions are represented by white and blue color codes [12]. Notably, the dark red region surrounding each molecule corresponds to significant C—H···S interactions within the crystal packing. Additionally, the mapping of shape index and its curvature helps visualize π···π and C—H···π interactions involving phenyl rings. In Figure 5(a), the red concave regions exhibiting 'bow-tie' patterns on the shape index surface indicate the presence of aromatic stacking (π···π) interactions involving *Cg*1···*Cg*1, as well as the occurrence of C—H···π (C19—H19···*Cg*2) interactions. Figure 5(b) displays the Hirshfeld surface mapped over curvedness, highlighting flat surface patches characteristic of planar stacking involving *Cg*1···*Cg*1.

Furthermore, two-dimensional (2D) fingerprint plots are generated to provide quantitative information related to the type of intermolecular contacts present within the crystal [12,13]. The 2D fingerprint plots of Hirshfeld surfaces were successfully outlined into H···H, H···C/C···H, S···H/H···S, O···H/ H···O, H···N/N···H, C···C, N···C/C···N, O···C/C···O, S···N/N···S, N···N, S···C/C···S, and O···O contacts. The 2D fingerprint plots of the intermolecular contacts with their respective percentage contribution are presented in Figure 6. The H···H contacts contribute to the overall crystal packing at 42.6%. These dominant contacts may have attributed to the large hydrogen content of the molecule as observed through the exhibition of the two tips at $d_e + d_i$ = 2.3 Å. A pair of characteristic wings of H···C/C···H (22.3%) contacts at $d_e + d_i$ = 2.7 Å signifies the presence of C—H···π interactions in the compound. The existence of intermolecular C—H···S interactions can be confirmed through the involvement of 12.5% of S···H/H···S contacts as characterized by a pair of sharp peaks with spikes at $d_e + d_i$ = 2.7 Å. The H···N/N···H contacts contributing to about 3.7% in the Hirshfeld surface analysis is represented by a pair of diffuse spikes at $d_e + d_i$ = 2.8 Å. However, the weak C···C, N···C/C···N, O···C/C···O, S···N/N···S, N···N, S ···C/C···S, and O···O contacts minorly contributes in the **HL** compound with 2.7%, 1.7%, 0.9%, 0.6%, 0.4%, 0.3%, and 0.1%, respectively. All these intermolecular interactions aids in the stabilization of the **HL** molecular assembly [14].

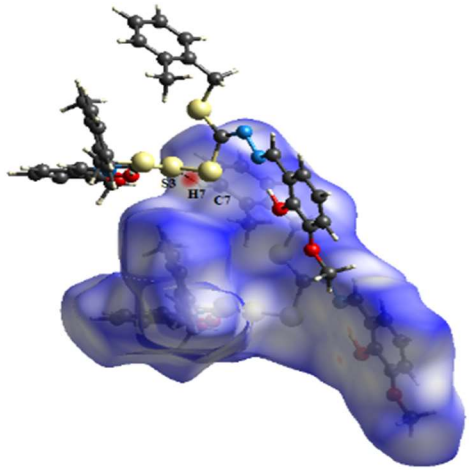


Figure 4. Hirshfeld surface mapped over d_{norm} showing hydrogen-bonding interaction with their neighbouring molecules

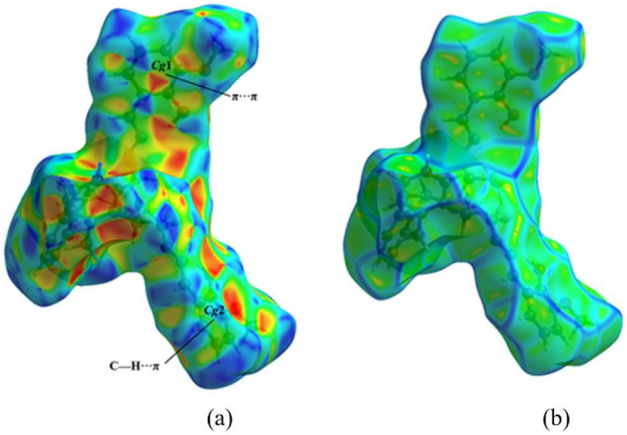


Figure 5. Hirshfeld surface mapped over (a) shape index and (b) curvedness

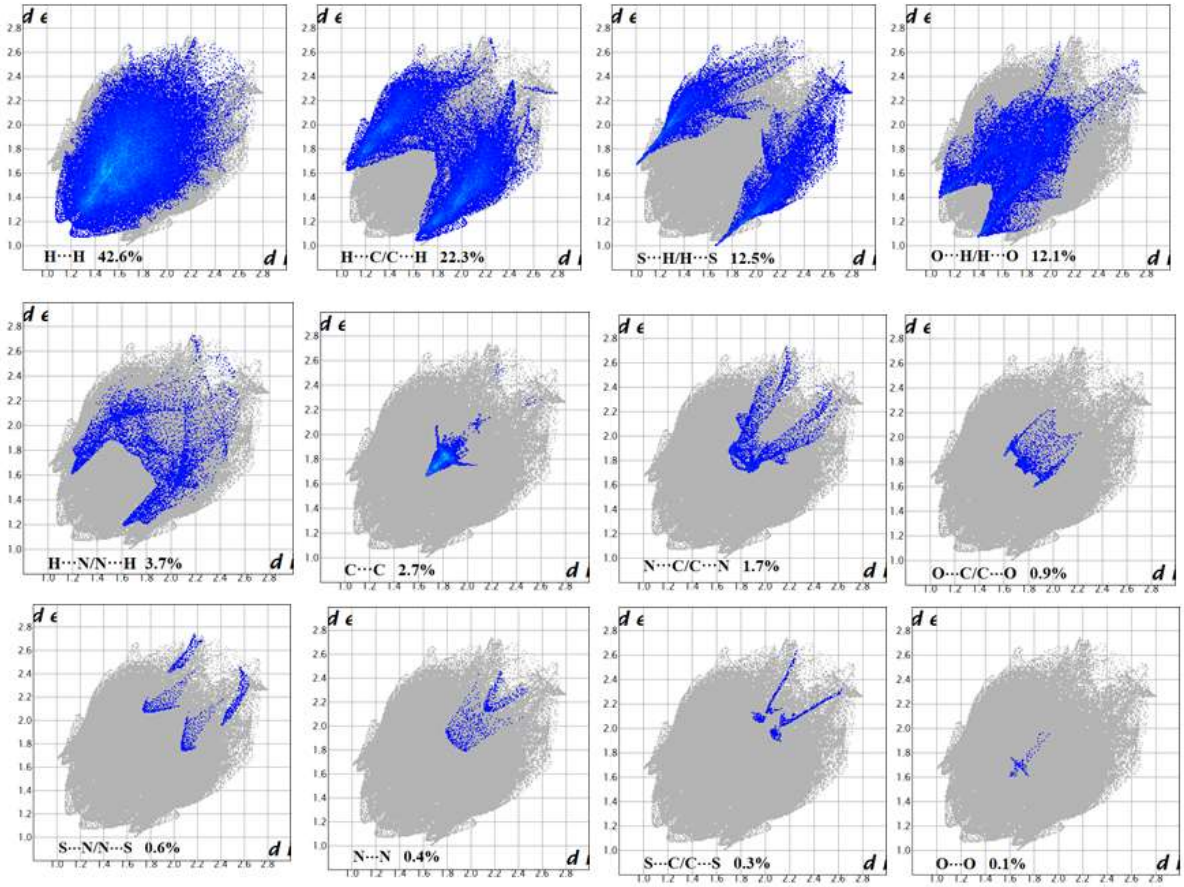


Figure 6. The 2D fingerprint plots of the intermolecular contacts with their respective percentage contribution

Database survey

There are three similar crystallographic literatures when compared to **HL** in the database, and the details are compiled in Table 5. Among them, Derivative (I) closely resembles **HL**, with the only difference being the S-bound R group. In Derivative (I), the S-bound R group is a S-methylbenzyl ester with a methyl group in the para position, and it has a 2-hydroxylbenzene ring bound to the imine-C. Figure 7 illustrates the close similarity between (I) and (II), where the only distinction lies in the S-bound R group, with R = *p*-methylbenzyl (GUPDAZ [15]) and R = H (LUGLUD [16]). Both (I) and (III) exhibit complete molecules generated by crystallographically imposed twofold symmetry, similar to **HL**. The S—S bond length of **HL** falls within the experimental range of 2.0373 (4) Å in (II) and 2.0504 (7) Å in (III). Similarly, the C—S—S—C torsion angle of **HL** exhibits the lowest angle compared to 90.70 (8) (I), (91.54 (6) (II), and 96.2 (1) (III). By comparing all the data, all four molecules mentioned in Table 5 adopt a similar conformation.

Table 5. Comparison of key geometric parameters (Å, °) in structures related to **HL**

Compound	Symmetry	S-S	C-S-S-C	Refcode	Reference
HL	2	2.0411 (9)	89.2(1)	-	This work
(I)	2	2.0439 (8)	90.70 (8)	GUPDAZ	[15]
(II)	-	2.0373 (4)	91.54 (6)	LUGLUD	[16]
(III)	2	2.0504 (7)	96.2 (1)	CUHHET	[17]

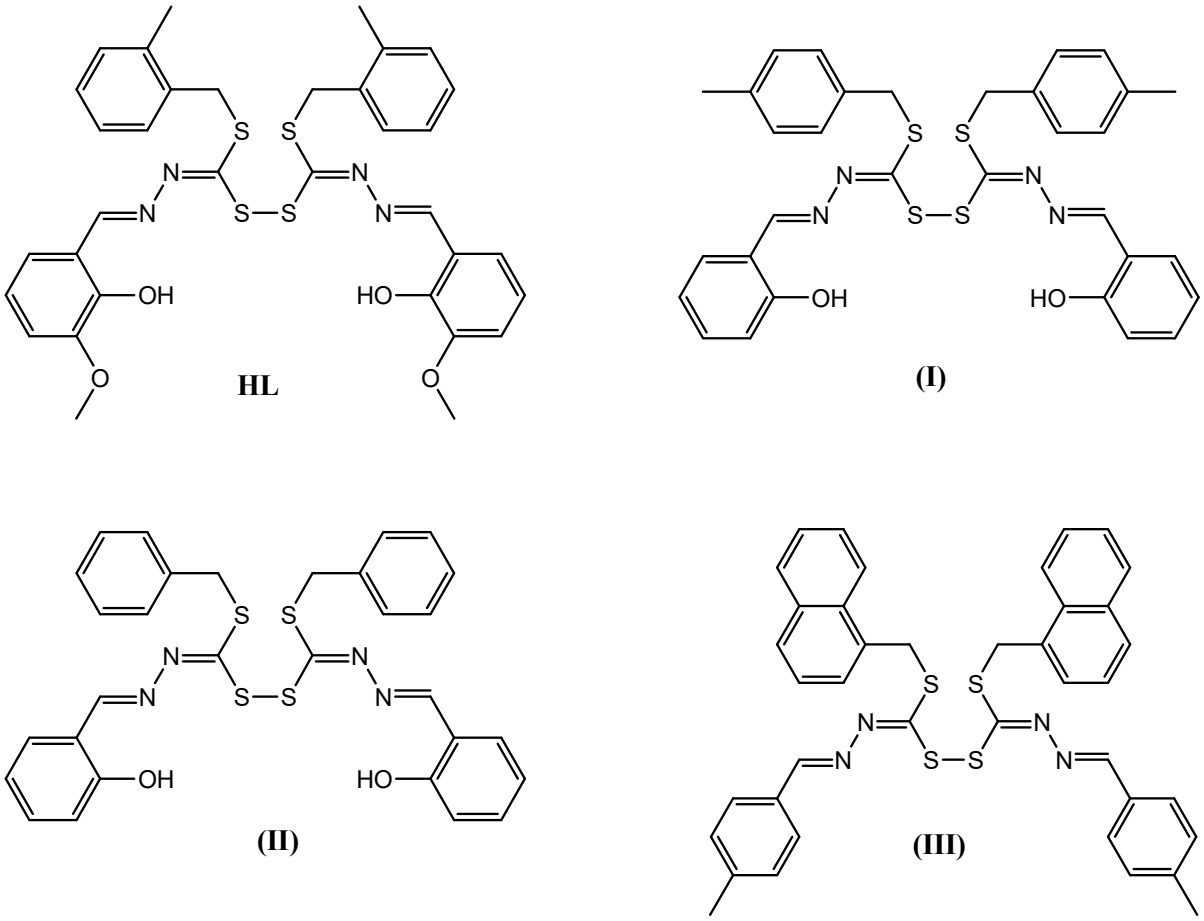


Figure 7. Molecular structures of **HL**, (I), (II), and (III)

Conclusions

A new structure of **HL** was synthesized and confirmed by single crystal X-ray diffraction analysis. The crystal system of the molecule was found to be triclinic, with the space group *P*-1. Furthermore, the Hirshfeld surface analysis revealed the existence of intriguing C—H···S intermolecular interactions within the crystal structure. Notably, the two-dimensional fingerprint plots emphasized the significance of H–H contacts, which accounted for the majority (42.6%) of the total Hirshfeld surface area. These findings shed light on the unique molecular arrangement and bonding patterns of **HL**, paving the way for further investigations into its properties and potential applications.

Appendix A. Supplementary data

CCDC No: 2072116 contains the supplementary crystallographic data of the synthesized compound. These data can be obtained free of cost via http://www.ccdc.cam.ac.uk/conts/retrieving.html, or from the Cambridge Crystallographic Data Centre, 12 Union Road, Cambridge CB2 1EZ, UK; fax: (+44) 1223–336–033; or e-mail: deposit@ccdc.cam.ac.uk.

Acknowledgements

The research described in this study was supported by the Short-Term Grant Scheme (304/PJJAUH/6315525) from Universiti Sains Malaysia. We express our gratitude to the School of Distance Education and School of Chemical Sciences at Universiti Sains Malaysia, as well as the Department of Chemistry at the Faculty of Science, Universiti Putra Malaysia (UPM), for providing the necessary facilities for this research. Additionally, we would like to acknowledge the valuable assistance of Dr. Thahira Begum, a former

associate professor at the Department of Chemistry, Faculty of Science, UPM, during this research project.

References

1. Li, M. X., Zhang, L. Z., Chen, C. L., Niu, J. Y., and Ji, B. S. (2012) Synthesis, crystal structures, and biological evaluation of Cu(II) and Zn(II) complexes of 2-benzoylpyridine Schiff bases derived from S-methyl- and S-phenyldithiocarbazates. *Journal of Inorganic Biochemistry,* 106: 117-125.
2. Bhat, R. A., Kumar, D., Alam, A., Mir, B. A., Srivastava, A., Malla, M. A., and Mir, M. A. (2018). Synthesis, characterization, thermal and DFT studies of S-methyl-β-N-(3-(2-nitrophenyl)allylidene)dithiocarbazate as anti-bacterial agent. *Journal of Molecular Structure*, 1173:72-80.
3. Santra, A., Brandao, P., Mondal, G., Bera, P., Jana, A., Bhattacharyya, I., Pramanik, C., and Bera, P. (2020). The role of methyl and benzyl substituted dithiocarbazate of 2-acetyl pyridine for the formation of bridged dimeric and unbridged monomeric copper(II) complexes and catecholase mimetic activity of the complexes. *Polyhedron*, 176:114277.
4. Yusof, E. N. M., Ravoof, T. B. S. A., Tiekink, E. R. T., Veerakumarasivam, A., Crouse, K. A., Tahir, M. I. M., and Ahmad, H. (2015). Synthesis, characterization and biological evaluation of transition metal complexes derived from N, S bidentate ligands, *International Journal of Molecular Sciences,* 16: 11034-11054.
5. Yusof, E. N. M., Latif, M. A. M., Tahir, M. I. M., Sakoff, J. A., Simone, M. I., Page, A. J., Veerakumarasivam A., Tiekink, E. R. T., and Ravoof, T. B. S. A. (2019). o-Vanillin derived Schiff bases and their organotin(IV) compounds: synthesis, structural characterisation, in-silico studies and cytotoxicity, *International Journal of Molecular Sciences,* 20: 854.
6. Zahan, R., Rahi, M. S., Sheikh, M. C., Miyatake, R., Zangrando, E., Naz, T., Islam, M. A. A. A. A., and Reza, M. A. (2019). Design, synthesis and X-ray structural studies of novel [acetonitrile-benzyl-3-N-(2, 4 dihydroxyphenylmethylene) hydrazine carbodithioato-κ3-N′, S, O] nickel(ll) complex that potently inhibit cell proliferation through regulation of apoptosis related genes, *Applied Organometallic Chemistry*, 33: 1-16.
7. Yusof, E. N. M., Ravoof, T. B. S. A., Jamsari, J., Tiekink, E. R. T., Veerakumarasivam, A., Crouse, K.A., Tahir, M. I. M., and Ahmad, H. (2015). Synthesis, characterization and biological studies of S-4-methylbenzyl-β-N-(2-furylmethylene)dithiocarbazate (S4MFuH) its Zn^{2+}, Cu^{2+}, Cd^{2+} and Ni^{2+} complexes, *Inorganica Chimica Acta.* 438: 85-93.
8. Blessing, R. H. (1995). An empirical correction for absorption anisotropy, *Acta Crystallographica Section A*, A51: 33-38.
9. Sheldrick, G. M. (2008) A short history of SHELX, *Acta Crystallographica Section A Foundations of Crystallography*, A64: 112-122.
10. Spek, A. L. (2009). Structure validation in chemical crystallography, *Acta Crystallographica Section D Biological Crystallography*, D65:148-155.
11. Spackman, P. R., Turner, M. J., McKinnon, J. J., Wolff, S. K., Grimwood, D. J., Jayatilaka, D. and Spackman, M. A. (2021). CrystalExplorer: A program for Hirshfeld surface analysis, visualization and quantitative analysis of molecular crystals. *Journal of Applied Crystallography*, 54(3): 1006-1011.
12. Spackman, M. A. and Jayatilaka, D. (2009). Hirshfeld surface analysis. *CrystEngComm*, 11(1): 19-32.
13. Melvin, M. K., Skelton, B. W., Eggers, P. K., and Raston, C. L. (2022). Synthesis, crystallization and Hirshfeld surface analysis of transition metal carboxylate pentapyridines, *CrystEngComm*, 24: 57-69.
14. Seth, S. K., Sarkar, D., Roy, A., and Kar, T. (2011). Insight into supramolecular self-assembly directed by weak interactions in acetophenone derivatives: Crystal structures and Hirshfeld surface analyses, *CrystEngComm*, 13: 6728-6741.
15. Paulus, G., Kwong, H. C, Crouse, K. A., and Tiekink, E. R. T. (2020). 2-[(1E)-[(Z)-2-({[(1Z)-[(E)-2-[(2-Hydroxyphenyl)methylidene]hydrazin-1-ylidene]({[(4-methylphenyl)methyl]sulfanyl})methyl] disulfanyl

}({[(4-methylphenyl)methyl]sulfanyl})methylidene)hydrazin-1-ylidene]methyl]phenol: Crystal structure, Hirshfeld surface anaanalysis and computational study. *Acta Crystallographica Section E: Crystallographic Communications*, 76:1245-1250.

16. Islam, M. A. A. A. A., Sheikh, M. C., Islam, M. H., Miyatake, R., and Zangrando, E. (2016). Crystal structure of 1,2-bis((benzylsulfanyl){2-[1-(2-hydroxyphenyl)ethylidene]hydrazin-1-ylidene}methyl) disulfane, *Acta Crystallographica Section E: Crystallographic Communications*, 72: 337-339.
17. How, F. N. F., Crouse, K. A., Tahir, M. I. M., and Watkin, D. J. (2009). Synthesis and structure determination of *S*,*S*'-(Naphthalen-2-ylmethyl sulfanyl (1-p-tolyl-ethylidene) hydrazine. *Journal of Chemical Crystallography*, 39: 894-897.

Malaysian Journal of Analytical Sciences (MJAS)
Published by Malaysian Analytical Sciences Society

REVIEW OF MOLYBDENUM DISULFIDE PREPARATION AND ITS ROLE AS A PHOTOCATALYST TO DEGRADE ORGANIC CONTAMINANTS

(Ulasan Penyediaan Molibdenum Disulfida dan Peranannya Sebagai Pemangkin Fotodegradasi Pencemaran Organik)

Izyan Najwa Mohd Norsham [1], Nur Zatulhusna Zulkifli[1], Kavirajaa Pandian Sambasevam[1,2]
Siti Nor Atika Baharin[1,3*]

[1]*Advanced Material for Environmental Remediation (AMER) Research Group, Faculty of Applied Sciences, Universiti Teknologi MARA, Cawangan Negeri Sembilan, Kampus Kuala Pilah, 72000 Kuala Pilah, Negeri Sembilan, Malaysia.*
[2]*Electrochemical Material and Sensor (EMas) Group, Universiti Teknologi MARA, 40450 Shah Alam Selangor, Malaysia*
[3]*Advanced Biomaterials & Carbon Development (ABCD), Universiti Teknologi MARA, 40450 Shah Alam, Selangor, Malaysia*

[*]*Corresponding author: atikabaharin@uitm.edu.my*

Received: 22 September 2022; Accepted: 23 July 2023; Published: 22 August 2023

Abstract

Photocatalytic degradation appeared as a future alternative for the removal of many organic contaminants with high efficiency and energy-saving technology. As a photocatalyst, molybdenum disulphide (MoS_2) exhibits good photocatalytic properties due to great potential for organic contaminant degradation. It is ascribed that various approaches for MoS_2 preparation serve a diverse number of exposed active sites that facilitate MoS_2 efficiency for photocatalytic reaction. Several methods have been extensively applied to improve MoS_2 photocatalytic efficiency, including synthesized different surface morphology and heterojunction formation with other semiconductors. Therefore, it will increase the photocatalytic activities of the composites by combining MoS_2 with other semiconductor photocatalyst materials. Integration of MoS_2 as a binary or ternary photocatalyst will produce a synergic effect that hinders the recombination process and enhancement of the surface areas. On the other hand, it improved on conductivity of the nanosheets, whereby it is believed to be able to deal with photocatalytic material challenges and provide efficient solutions to deal with degradation of organic contaminants.

Keywords: conducting polymer, metal disulphide, organic pollutants, photocatalytic degradation, sustainable water management

Abstrak

Degradasi fotokatalitik muncul sebagai alternatif masa depan untuk penyingkiran banyak bahan cemar organik dengan kecekapan tinggi dan teknologi penjimatan tenaga. Molibdenum disulfida (MoS_2) sebagai fotomangkin mempamerkan sifat fotokatalitik yang baik kerana potensi besar untuk degradasi bahan cemar organik. Disifatkan bahawa pelbagai pendekatan penyediaan MoS_2 menyediakan bilangan tapak aktif terdedah yang berbeza yang memudahkan kecekapan MoS_2 untuk tindak balas fotokatalitik. Beberapa kaedah telah digunakan secara meluas untuk meningkatkan kecekapan fotokatalitik MoS_2, termasuk morfologi permukaan yang berbeza yang disintesis dan pembentukan heterojunction dengan semikonduktor lain. Oleh itu, dengan menggabungkan MoS_2 dengan bahan semikonduktor fotomangkin lain, ia akan meningkatkan aktiviti fotomangkin komposit. Penyepaduan MoS_2 sebagai fotomangkin binari atau ternari akan menghasilkan kesan sinergik yang menghalang proses

penggabungan semula dan peningkatan kawasan permukaan. Sebaliknya, ia bertambah baik dalam kekonduksian helaian nano di mana ia dipercayai mampu menangani cabaran bahan fotokatalitik dan menyediakan penyelesaian yang cekap untuk menangani degradasi bahan cemar organik

Kata kunci: pengalir polimer, logam disulfida, bahan pencemar organik, degradasi fotokatalitik, pengurusan air yang mampan

Introduction

Photocatalytic from semiconductors are more desirable and simpler to be used for environmental remediation, whereby it emphasizes on green energy technology. The semiconductor materials performance depends on the photocatalysts potential to absorb split and transport photogenerated electrons and holes for the absorption of light energy in the available region. Molybdenum disulphide (MoS_2) shows considerable absorption in the solar spectrum visible region or sunlight, which is the renewable source with a lower bandgap [1]. MoS_2 consists of sulfur with *p* and molybdenum with *d* atomic orbitals. The presence of *d* electrons in the conduction and valance bands indicated an interaction with the *p* orbital in the sulfur. As a *d*-block element, molybdenum acts as a catalyst due to its ability to modify oxidation or to absorb and activate other substances on its surface in the case of metals. Besides, the molybdenum experienced a strong spin-orbital coupling at 4*d* electrons that reduced the degenerated energy level [2].

However, various methods have been used to develop the photocatalytic ability of MoS_2 that include photocatalyst combination, surface morphology modification, heterojunction integration with other semiconductors and doping process [3]. The mechanical and chemical approaches allow to obtain a single layer of MoS_2. The thin layered MoS_2 is prepared using different synthesis techniques, such as hydrothermal, exfoliation, solvothermal and chemical vapor deposition techniques.

Single and bulk layer of MoS_2 as photocatalyst in the photodegradation approach is widely used to degrade organic pollutants. Furthermore, MoS_2 as a semiconductor photocatalyst demonstrates active surface sites and small band gaps, which are efficient in the aqueous solution for reactive species generation. Despite its distinct chemical, electrical and physical characteristics, MoS_2 inherits semiconductors characteristics for water purification due to its excellent potential in light response. MoS_2 monolayer sites are considerably more resistant to photocatalytic degradation. Furthermore, Saha et al. (2019) stated that the integration of MoS_2 with conducting polymer as a binary photocatalyst would improve the photocatalytic activity [4]. For instance, MoS_2 with polyaniline will be able to solve the problems of current photocatalytic structures. Moreover, it provides an ideal solution for the separation of contaminants from wastewater for water purification, as polyaniline generates a highly charged carrier to assist the photocatalytic degradation processes. Recently, Feng et al. showed $MoS_2/TiO_2/ZnS/CdS$-Mn as the ternary photocatalyst with high photocatalytic efficiency and degradation for azo dye under sunlight irradiation at a removal rate of 98% in 100 min [5].

The development of photocatalytic method with the aid of MoS_2 is important to assist valued industries in ensuring organic contaminants can be removed from the environment. Additionally, MoS_2 can conduct the semiconductors characteristics for water purification due to its excellent light response capability. Therefore, by identifying the best approach for preparation of MoS_2, its excellent physical, chemical and electrical properties at maximum level can be sustained for high-performance photocatalytic reactions. Moreover, integrating MoS_2 with other photocatalysts will solve the problems of current photocatalytic structures and provide an ideal solution for separation of organic contaminants. Consequently, the most excellent interaction, either as a single, binary, or ternary photocatalyst can be pointed out to assist in photocatalytic activities. The execution using MoS_2 with other photocatalysts will come up with a great deal in the improvement of energy efficiency.

.

Fundamental of photocatalytic degradation

A substantial amount of studies was performed in recent years with advanced oxidation processes (AOPs) and as a result, different types of AOPs were discovered. AOPs

tend to be a potential research area that has been shown to be efficient for the removal of water and soil soluble organic pollutants that cause almost complete degradation. Several AOPs include photolysis, ozonolysis and photocatalysis. Amongst the AOPs, photocatalytic activity was proven to be a viable tool for the degradation of organic compounds. Besides, the approach is more effective than other AOPs, since it can easily neutralize different organic pollutants [6].

Photocatalytic degradation is a chemical response under the action of light and photocatalyst. Additionally, photocatalytic activity is a molecular degradation caused by photon absorption that has an identical light absorption range with the wavelengths in sunlight. It is the best method for water treatment since it relies on the range of light intensity and wavelengths [7]. It is often used in organic pollutant degradation due to its effectiveness, flexibility, reproducibility and simplicity. Photocatalysts are the foundation of the photocatalytic method. A photocatalyst is a compound triggered by adsorbing a photon and can activate a reaction without being utilized. Therefore, semiconductor photocatalyst is globally used in photocatalytic approaches [8].

Mechanism of action for photocatalytic degradation

Photocatalytic degradation mechanism has been frequently used to remove organic contaminants due to environmental operating pressure and temperature, total mineralization and intermediate products without secondary emission and low operating expenses. The mechanism of the photocatalytic reaction is complex and has many intermediate steps [9]. The theory of photocatalytic is to transform the light energy under light irradiation into chemical energy and to create a corresponding free group of radicals with a redox capability. In a previous study by Mirza Hedayat et al., photocatalytic was observed as an effective approach for removal of organic pollutants in wastewater purification [10]. However, a study conducted by Ajmal et al. stated that heterogeneous AOPs, involving photocatalytic dye degradation with semiconductor nanoparticles were assumed to be an effective treatment for dye contamination [11]. The indirect heterogeneous method of the photocatalytic oxidation using semiconductive compounds could be summed up, as shown in Figure 1.

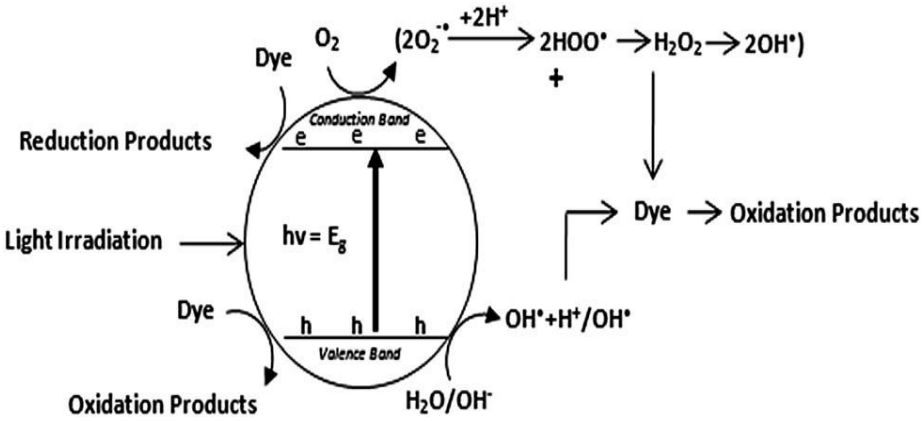


Figure 1. Pictorial illustrated the direct dye removal process [11]

The photocatalytic reaction was caused by the recruitment of a photoelectron of a photocatalytic semiconductor from the occupied valence band. From the result of irradiation, the metal oxides filled the empty conduction band. The absorbed photon had energy (*hv*) equal to or higher than the bandgap of the photocatalyst. The excitation phase in the valence band left behind a hole and produced the electron and hole pair. Then, the photogenerated holes reacted with water in the valence band to create OH radical by ionization of water. Next, as the photogenerated hole binds with OH to produce radical hydroxyl, the oxygen induced electron was used to produce anionic radical superoxides. The superoxide ions prevented electron-hole recombination. Lastly, the

superoxide created the radical hydroperoxyl and dissociated H_2O_2 into highly reactive hydroxyl radicals. The oxidation and reduction processes happened frequently on the surface of the photoexcited semiconductor photocatalyst.

Preparation of molybdenum disulfide

MoS_2 is a layered transition metal dichalcogenide formed by loading the slightly interacted 2D S-Mo-S layer like graphite that demonstrates many useful applications. This includes hydrogen generation, solid-state lubricants and as a photocatalyst for pollutant degradation or hydrogen production. It has excellent anti-friction efficiency and resistance to abrasion process. Various morphologies of MoS_2 (Figure 2) were successfully prepared, including nanowires, nanotubes, nanorods, inorganic fullerene structures, nanospheres, hollow spheres and nanoflowers [12]. However, there were concerns in the limited reproducibility, low production efficiency and photocatalytic performance of the molybdenum disulphide. Therefore, a robust synthetic method was developed to overcome the issues [13].

Hydrothermal process

The hydrothermal procedure requires crystallizing the substance in aqueous solution at high pressure and The hydrothermal procedure requires crystallising the substance in aqueous solution at high pressure and temperature in a sealed vessel known as an autoclave, which can sustain a high temperature of 600°C to 700°C [14]. Moreover, it is an affordable and standardised process for MoS_2 synthesising. Hydrothermal synthesis is a promising way to develop nanostructures composites, especially for MoS_2 with various morphologies. Additionally, more MoS_2 layers that were exposed to the environment with higher chemical activities could be produced [15]. A study by Li et al. examined the morphology, structure and photocatalytic properties of MoS_2, which were prepared by hydrothermal process [16]. MoS_2 samples with four different morphologies, hollow MoS_2 (H-MoS_2), flowerlike MoS_2 (F-MoS_2), spherical MoS_2 (S-Mo-S_2) and coil MoS_2 (C-MoS_2) were analysed through the scanning electron microscope (SEM). Figure 2(a) reveals H-MoS_2 morphology with small holes on the surfaces of primary nanoparticles and microspheres. The size and number of primary particles were impacted directly by the hydrothermal reaction temperature. Figure 2(b) shows F-MoS_2 at approximately 600 nm in diameter. The MoS_2 surface consisted of a small-sized 2D-curl MoS_2 layer and the structure was uniform. Figure 2(c) shows S-MoS_2 that consisted mainly of nanoparticles of about 120 nm in diameter and with significantly lower wrinkles and a smoother surface. Figure 2(d) displays C-MoS_2 with a uniform diameter of 280 nm. F-MoS_2, with the smallest surface area, had the highest degradation rate, while H-MoS_2, with the greatest surface area, had the lowest degradation rate of MB.

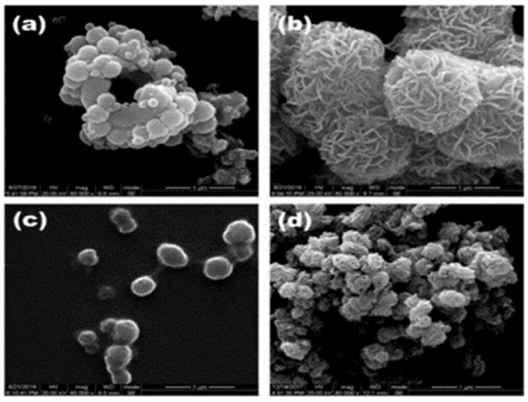


Figure 2. SEM images of (a) H-MoS_2; (b) F-MoS_2; (c) S-MoS_2; (d) C-MoS_2 [16]

Solvothermal method

Solvothermal process is a method of producing single crystals at high temperature and pressure from a non-aqueous solution in an autoclave. It was developed using the hydrothermal process and the major difference between solvothermal method and the latter is the organic solvent rather than water used for preparation [1]. A study by Vattikuti et al. analysed the X-ray diffraction (XRD) patterns, as shown in Figure 3. Both samples, the nanosheets and nanospheres, exhibited crystallite nature of MoS_2 materials with a XRD pattern indexed at 14˚, 32˚, 39.5˚ and 58˚, corresponding to (002), (100), (103) and (110) crystal planes of the MoS_2 structure [3]. The research stated that solvothermal synthesised MoS_2 nanocomposites could be modelled into nanorods using different sulphur sources, such as sodium sulphide and hydrogen sulphide (H_2S) in acidic media with different conditions and concentrations of citric acid to enhance specific textural and structural morphologies.

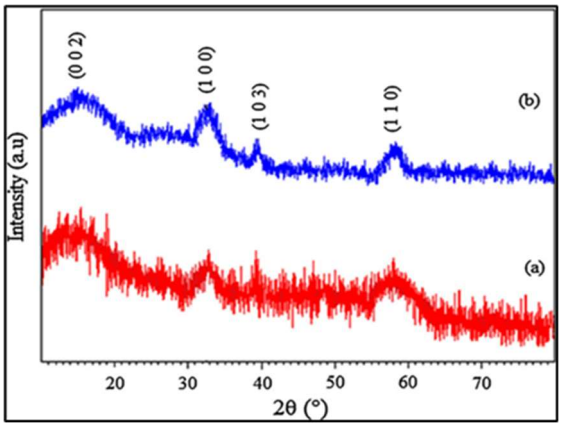


Figure 3. XRD patterns of MoS_2 a) nanospheres and b) nanosheets [3]

Another research by Sun et al. disclosed the formation influence of F-MoS_2 , with the effects of various reaction time. The samples were collected in solvothermal conditions at 190°C for 6 hr, 12 hr, 18 hr and 24 hr. Then, the samples were annealed for 5 hr at 500°C in a nitrogen atmosphere. However, after 6 hr, 12 hr and 18 hr, the products showed diffraction peaks due to MoO_2 as an impurity. It was also observed that the diffraction peak intensity, due to MoS_2, continued to rise and the diffraction peak intensity of MoO_2 dropped significantly (Figure 4). The diffraction peaks of MoO_2 faded when the reaction time was 24 hr and some diffraction peaks at 2θ = 13.9°, 34.5° and 60.4° were indexed using 2H-MoS_2. Therefore, it was suggested that hydroxylamine hydrochloride, which served as a reducing agent, reacted with a portion of sodium molybdate at an early stage of the reaction, giving MoO_2. This MoO_2 then reacted with S^{2-} that was obtained from the thiourea reaction that transformed MoO_2 into MoS_2 and was later applied for photocatalytic degradation [17].

Exfoliation method

The process of exfoliation involves electrochemical, chemical and liquid-phase exfoliations [18]. A study by Bai et al. reported that exfoliation approach could be used to extract monolayer and MoS_2 nanosheets in layered structures [19]. Alternatively, 1T metallic MoS_2, also known as metallic octahedral type could be obtained by ion intercalation. The most common method of intercalating alkali metal ions is particularly by lithium-ion intercalation [20]. MoS_2 exfoliation is a possible large-scale route for the production of semiconductor material with a controllable band gap that is capable of absorbing photons in the visible range [21]. In the same vein, Khan et al. concluded that the prepared composites of MoS_2/TiO_2 by in situ addition of exfoliated MoS_2 demonstrated higher output of photogenerated electron-hole pairs and accelerated charging transfer, as more active edges were available in MoS_2 that resulted in increased photocatalytic activity [22]. Figure 5 proved that the loading of exfoliated MoS_2 resulted in enhanced photodegradation activity due to

greater separation of the load carrier from the visible light. The absorption bands showed a red change when loaded with MoS_2. This was linked to the nanosized MoS_2 sheets, which provided more active surface area and optimal energy levels to increase the chemical activity. Therefore, in the presence of sunlight, the photocatalytic reaction significantly increased.

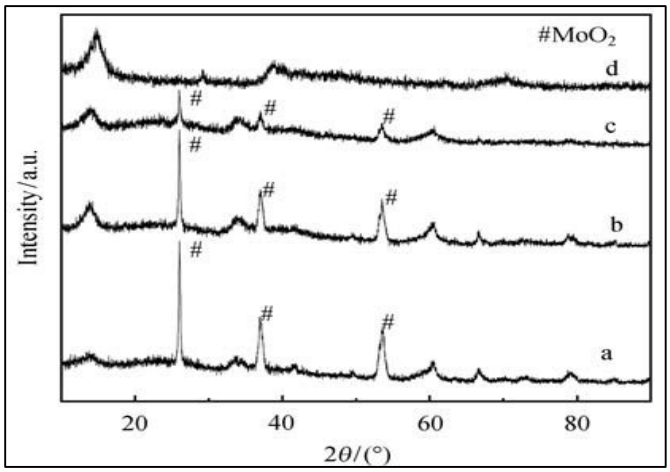


Figure 4. XRD patterns of MoS_2 prepared under different reaction time. (a) 6 hours; (b) 12 hours; (c)18 hours; (d) 24 hours [17]

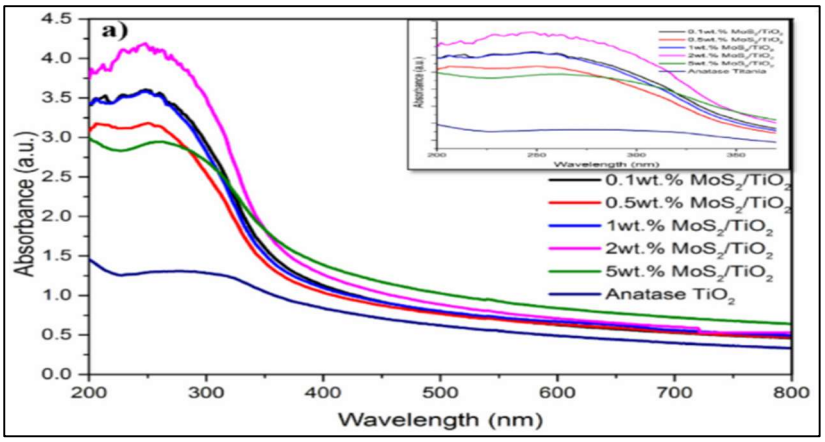


Figure 5. UV-Vis absorption spectrum of pure anatase TiO_2 and prepared photocatalysts [22]

Chemical vapor deposition method

Chemical vapour deposition (CVD) is a mechanism that produces great-quality MoS_2 layers. It has controllable size and uniform morphology by the chemical reaction at a specific temperature and gas flow between molybdenum and sulphur sources. CVD is an effective method for the synthesis of large single-layer MoS_2 film and can be categorised roughly into two types; the one-step and two-step procedures. One-step CVD generates MoS_2 by evaporating the sources of molybdenum and sulphur. Through sputtering procedure, molybdenum is dispersed onto a substrate in the two-step method. Then, it is placed in a sulphur atmosphere and reduced to graphite-like MoS_2 at a higher temperature [23]. The X-ray photoelectron spectroscopy (XPS) measurements were performed to investigate the stoichiometry ratio of the free thin films, which was prepared by CVD method using MoS_2. The peaks at 232.2 eV, 229.0 eV, 226.2 eV, 162.9 eV and 161.7 eV corresponded to Mo^{4+} $3d_{3/2}$, Mo^{4+} $3d_{5/2}$, S 2S, S $2p_{1/2}$ and S $2p_{3/2}$, respectively. Furthermore, the $3d_{5/2}$ peak of Mo and $2p_{3/2}$ peak of S were placed at binding energies that corresponded to the

Mo-S crystal. The peaks referred to a synthesised 2H structure of MoS_2. The Mo and S atomic ratios were 1:2.2, 1:2.35, 1:2.31 and 1:2.44, respectively, for concentrations of 0.0500 M, 0.0250 M, 0.0125 M and 0.007 M. All peaks were aligned without significant deviation. MoS_2 was synthesised and characterised successfully and the result showed that the CVD process was effective [24]. On the contrary, Najmaei et al. (2013) stated that other procedures to synthesise MoS_2 were by direct sulphurisation of films that contained molybdenum with CVD method [25]. Conversely, by this synthetic route, the inefficient consistency happened, which was caused by their low carrier mobility at 0.004 $cm^2 V^{-1} s^{-1}$ to 0.04 $cm^2 V^{-1} s^{-1}$. This process carries a considerable degree of difficulty in the preparation of precursors and in achieving adequate efficiency, which has limited effectiveness. Table 1 shows a summary of the synthesis method for MoS_2 composite.

Table 1. Summary of synthesis of MoS_2

Method of Synthesis	Type of Catalyst	Organic Pollutant	Type of Light	% Degradation	Ref.
Hydrothermal	MoS_2/PANI	4-chlorophenol (4-CP)	UV	75	[4]
	TiO_2-MoS_2	Rhodamine (RB)	Visible	90	[26]
Solvothermal	MoS_2/Cds	Methylene Orange (MO)	Visible	85	[27]
	BiOI/MoS_2	Mercury	Visible	58	[28]
Exfoliation	$BiOIO_3$/g-C_3N_4/MoS_2	Mercury	Visible	70	[28]
	WS_2/MoS_2	RhB	Xe lamp	85	[29]
Chemical vapor	MoS_2/ZnO	MB	UV-Vis	81	[30]

MoS_2 as photocatalyst in photodegradation of organic contaminants

MoS_2 has become one of the most effective photocatalysts with the introduction of two-dimensional functional materials based on a high photocatalytic ability, good adsorption, low cost and non-toxicity. Furthermore, MoS_2-based composites are known as potential photocatalysts for the removal of environmental pollutant, as it accelerates photo-induced electron transportation and reduces levels of electron recombination. Various photocatalysts took advantage of semiconductor properties of MoS_2 constructing composite catalysts and showed favourable photocatalytic performance over organic compounds. Table 2 shows MoS_2 as a photocatalyst in the degradation of organic contaminants. The photodegradation efficiency (E%) was calculated using the following equation [31].

$$E\% = (C_0\text{-}Ct)/C_0 \times 100\% \quad (1)$$

Where C_0 is the whole amount of organic pollutants in the solution before illumination; Ct is the concentration of organic pollutants in solution at time t. There are two ways to determine residual concentrations after pollutants have been degraded. One method is to measure the linear relationship between the precise concentration of contaminants and the absorbance by an ultraviolet-visible (UV-Vis) spectrophotometer. Another option is to use high-performance liquid chromatography to quantify pollutants in aqueous solutions (HPLC).

MoS_2 as a single photocatalyst

A single photocatalyst consists of only one component in a composite. For example, metal oxides or metal sulphides, such as ZnO and MoS_2. Single photocatalyst operates based on its own unique and distinctive properties [32]. Vattikuti et al. highlighted that shape and size control was crucial during the production of single MoS_2 for obtaining well-defined structures with distinct features. MoS_2 morphology and scale are pivotal in sensors and catalysis [33]. Besides, the photocatalytic

activity can be tuned and enhanced by using appropriate doping. Moreover, MoS_2 has a benefit over other semiconductor photocatalyst materials, such as SnO_2, TiO_2 and ZnO for photocatalytic degradation due to its lower bandgap of ~1.9 eV. Therefore, MoS_2 is able to absorb both UV and visible solar spectrum [34]. It is reported that the single layer of MoS_2 with p-type doping has an acceptable band structure, high thermal conductivity and electrostatic integrity, which can be used as an effective single layer for self-consistent photocatalyst. The dielectric constant measures the material ability to absorb light. The peaks are mainly within 350 nm to 700 nm, which is in visible light range. Consequently, MoS_2 exhibited great sunlight absorption and optimal to be used as photocatalysts, which originated from the electronic structure of the MoS_2 single layer [35].

MoS_2 based composites of semiconductor as binary photocatalyst

Saha et al. traced the drawbacks of MoS_2, such as agglomeration between the composites and low electronic conductivity. It could be overcome by inserting 2D MoS_2 layers with 1D conducting polymer [4]. Therefore, photocatalytic response could be boosted by the integration of a single photocatalyst into composites. A binary photocatalyst is the hybridisation between two photocatalysts with different bands and electronic structures, which can resolve photocatalyst limitations. According to Norsham et al., the reaction of MoS_2/rGO resulted in synergic effects that hindered the recombination process and enhancement of the surface areas [36]. A research by Kasim et al. proved that MoS_2/PPy nanocomposite as a binary photocatalyst produced better visible light absorption compared to polypyrrole and pure MoS_2 under the same condition. The introduction of small quantities of polypyrrole coated with MoS_2 boosted the photodegradation of 2-chlorophenol because molybdenum had a narrow bandgap and produced reaction species in an aqueous solution, as confirmed in Figure 6. Moreover, polypyrrole could absorb visible light, whereby photogenerated electrons were efficiently transferred from the excited state into the conductive band of MoS_2 particles [37].

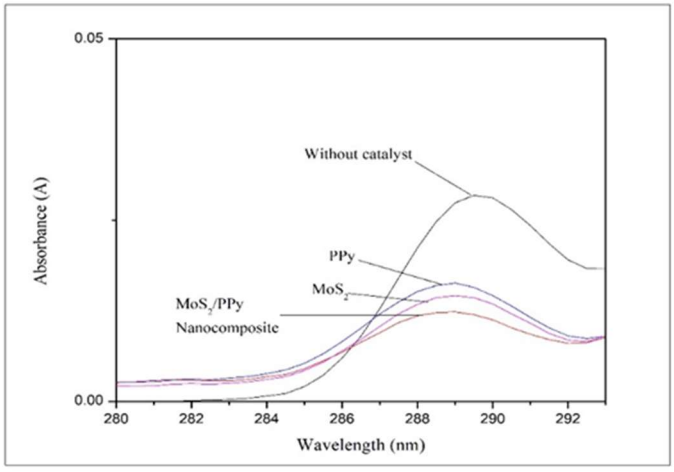


Figure 6. Different absorbance for different catalysts (condition: 0.01 g nanocomposite, 5mL of 50 mg/L of 2-chlorophenol at pH 5 and exposed to the sunlight for 3 hours) [37]

Ren et al. synthesized a novel 3D heterojunction composed of flowerlike nanosheets of MoS_2 stacked with $CoFe_2O_4$ nanorods. Particularly, as a binary photocatalyst, MoS_2/$CoFe_2O_4$ exhibited higher photocatalytic reactions under visible light irradiation to degrade organic dyes. The lower efficiency of pure $CoFe_2O_4$ nanorods for photodegradation signified that F-MoS_2 could be classified as the dominant active component for removing Congo red (CR) particles. The photodegradation efficiency of MoS_2/$CoFe_2O_4$

heterojunctions increased gradually as the MoS_2 content rose [38].

MoS_2 based composites and semiconductor as ternary photocatalyst

A previous study reported that ternary photocatalyst would assist to improve separation and photocatalytic stability of charge carriers. This was extensively used in the development of photocatalysts to optimise the performance. Ternary photocatalyst is the integration of three photocatalysts in a composite. Zhang et al. stated that hybrid photocatalysts had attracted intense attention by combining a set of conjugated polymers with an inorganic semiconductor [39]. Conjugated polymers could improve light production and promote separation of photogenerated carriers, leading to improvement for photocatalytic composites. Furthermore, loading noble metals to the composites as the ternary photocatalyst provided another useful inhibiting solution recombination of electron-hole pairs. A novel ternary photocatalyst, g-C_3N_4/Ag/MoS_2 was synthesised by attaching Ag nanoparticles on MoS_2 microsphere and g-C_3N_4, which provided high photocatalytic efficiency for respective single and binary photocatalysts, such as MoS_2, g-C_3N_4 and Ag/MoS_2. The pure g-C_3N_4 (Figure 7) showed two major peaks at about 27.3° and 13.1°, respectively, indexed as (002) and (100) reflections. Besides, g-C_3N_4/MoS_2, Ag/MoS_2 and g-C_3N_4/Ag/MoS_2 showed identical XRD structures, suggesting that the formation of g-C_3N_4 or Ag nanoparticles did not change their crystalline structure. The primary cause for this was the low concentration of Ag nanoparticles in the composite and overlap of the g-C_3N_4 (100) with the main (113) MoS_2 diffraction peak [40]. Recently, Zhang et al. proved that the ternary composite of MoS_2/Au/TiO_2 with optimal composition had degraded over 89.73% of methylene blue solution within 100 min under visible light [41]. The composite band alignment had strictly limited the formation of electron-hole pairs under visible light irradiation. Therefore, the integration of MoS_2 with Au and TiO_2 would increase the degradation of methylene blue percentage and significantly improve its catalytic activity by creating efficient use of their unique properties (Figure 8). The ternary composites exhibited a faster degradation rate attributed to the presence of synergistic effect of the materials. The results from a study by Pant et al. stated that the ternary composite of MoS_2/CdS/TiO_2 increased visible light activity in the composite compared to pure TiO_2 nanofibres [42]. This data illustrated the importance of carbon nanofibre absorption capacity together with the interaction of MoS_2 and CdS. The lower bandgap of CdS compared to TiO_2 was beneficial to absorb visible light at a wavelength of <510 nm. The photogenerated electrons in the CdS activated TiO_2 photocatalyst to transfer from CdS to TiO_2, leaving the photogenerated holes in CdS behind. However, this charge carrier separation restrained the rapid charge formation, resulting in the increment of the photocatalytic activity of TiO_2. Therefore, by loading the MoS_2 into the composite, it enhanced the separation of electron-hole pairs and promoted the separation and transfer of photogenerated electrons. Photocatalysts are the foundation of the photocatalytic method. A photocatalyst is a compound that is triggered by adsorbing a photon and can activate a reaction without being utilised [47]. Nevertheless, some research has proven that there are some limitations in semiconductor photocatalysts, whereby the electrons and holes are readily recombined, leading to a drop in quantum elimination of the processes. Next, small photocatalyst surface area leading to a low organic pollutant degradation level and weak visible light absorption limits its application. Multiple approaches have been developed to maximise the concentration of charge carriers and to inhibit recombination of the electron-hole photocatalysts in semiconductors [48].

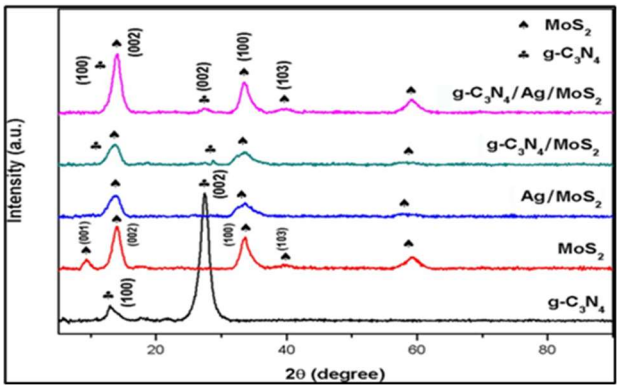


Figure 7. XRD patterns of the g-C_3N_4, MoS_2, Ag/MoS_2, g-C_3N_4/ MoS_2, and g-C_3N_4/Ag/MoS_2 samples

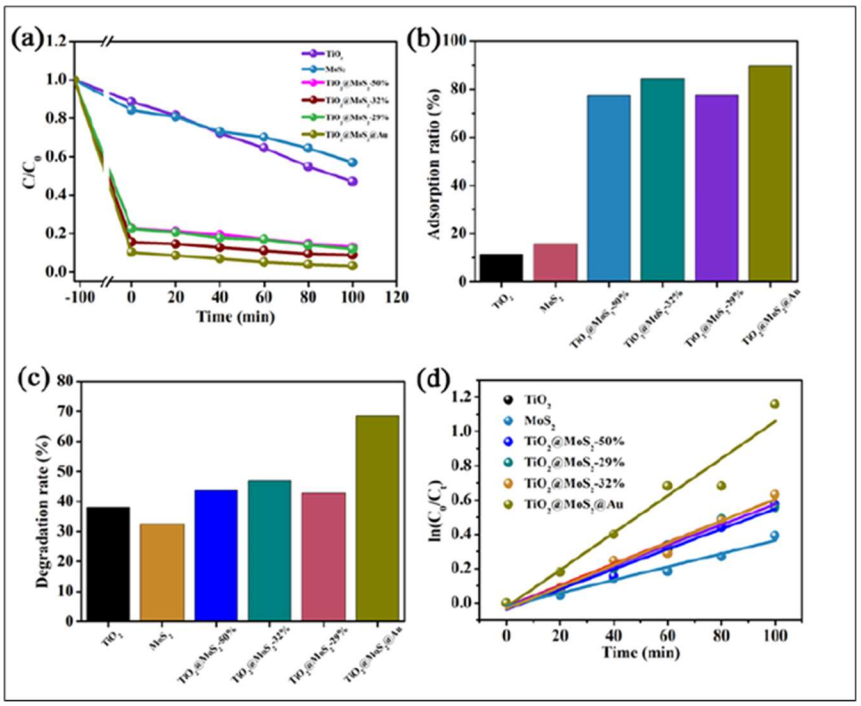


Figure 8. (a) Adsorption performance (b) methylene blue adsorption rate after stirring (dark condition), (c, d) photocatalytic degradation of methylene blue under visible light irradiation [41]

The obtained results from a study by Pant et al. stated that the ternary composite of MoS_2/CdS/TiO_2 increased the visible light activity in the composite compared to pure TiO_2 nanofibers [42]. This data illustrated the important carbon nanofiber absorption capacity together with the interaction of MoS_2 and CdS. The lower bandgap of CdS compared to TiO_2 is beneficial to absorb visible light at a wavelength of <510 nm. The photogenerated electrons in the CdS activated TiO_2 photocatalyst to transfer from CdS to TiO_2, leaving the photogenerated holes in CdS behind. However, this charge carrier separation restrains the rapid charge formation, resulting in the increment of the photocatalytic activity of TiO_2. Thus, by loading the MoS_2 into the composite, it enhanced the separation of the electron-hole pairs and promoted the separation and transfer of photogenerated electrons.

Table 2 Summarize MoS_2 composites or semiconductor as photocatalyst

Type of Catalyst	Example	Organic Pollutant	Light Source	% Degradation	Ref
Single Photocatalyst	MoS_2	Thiobencarb (TBC)	Visible light	95	[43]
Binary Photocatalyst	MoS_2/ZnO	Methylene blue (MB)	UV–vis light	85	[30]
	MoS_2-PPY	2-Chlorophenol	Visible light	79.59	[37]
	MoS_2/RGO	MB	UV–Vis	98	[44]
Tertiary Photocatalyst	n-BiVO4@p-MoS_2 with core-shell structure	Chromium	Visible light	85	[31]
	BiOBr/MoS_2/graphene oxide	Tetracycline antibiotics	Visible light	98	[45]
	MoS_2/ graphitic-C_3N_4@TiO_2	MB	visible light	97.5	[46]

Photocatalysts are the foundation of the photocatalytic method. A photocatalyst is known as a compound that is triggered by adsorbing a photon and can activate a reaction without being utilized [47]. Nevertheless, some research has proved that there are some limitations in semiconductor photocatalysts in which the electrons and holes are readily recombine leading to a drop in quantum elimination of the processes. Next, small photocatalyst surface area leading to a low organic pollutant degradation level and weak visible light absorption limits its application. Multiple approaches have been developed to maximize the concentration of charge carriers and to inhibit the recombination of the electron-hole photocatalysts in semiconductors [48].

Conclusion

Based on the literature data, it can be concluded that different MoS_2 composites with different morphology and photocatalyst combination undergo different mechanisms of preparation based on their suitability and condition. Besides, the photocatalytic performance of a single semiconductor is limited due to the recombination of charge carriers. Therefore, heterojunction is an effective method to improve charging carriers separation. The ternary semiconductor composites could be expected to provide a great opportunity for multiphoton excitation of photoactive materials with lower energy photons.

References

1. Wu, M. Hong, Li, L., Liu, N., Wang, D. Jin, Xue, Y. Cheng, and Tang, L. (2018). Molybdenum disulfide (MoS_2) as a co-catalyst for photocatalytic degradation of organic contaminants: A review. *Process Safety and Environmental Protection*, 118: 40-58.
2. Wang, Z. M. (Ed.). (2013). MoS_2: Materials, physics, and devices (Vol. 21). *Springer Science and Business Media.*
3. Vattikuti, S. V. P., and Byon, C. (2017). Molybdenum disulfide-based photocatalysis: bulk-to-single layer structure and related photomechansim for environmental applications. *Nanoscaled Films and Layers*, 2: 239.
4. Saha, S., Chaudhary, N., Mittal, H., Gupta, G., and Khanuja, M. (2019). Inorganic–organic nanohybrid of MoS_2-PANI for advanced photocatalytic application. *International Nano Letters*, 9(2):127-139.
5. Feng, H., Zhou, W., Zhang, X., Zhang, S., Liu, B., and Zhen, D. (2019). Synthesis of Z-scheme Mn-CdS/MoS_2/TiO_2 ternary photocatalysts for high-efficiency sunlight-driven photocatalysis. *Advanced Composites Letters*, 28: 1-10.
6. Rauf, M. A., and Ashraf, S. S. (2009). Fundamental principles and application of heterogeneous photocatalytic degradation of dyes in solution. *Chemical Engineering Journal*, 151(1-3): 10-18.

7. Rajamanickam, D., Dhatshanamurthi, P., and Shanthi, M. (2015). Preparation and characterization of SeO_2/TiO_2 composite photocatalyst with excellent performance for sunset yellow azo dye degradation under natural sunlight illumination. *Spectrochimica Acta - Part A: Molecular and Biomolecular Spectroscopy*, 138: 489-498.
8. Li, T., Hu, X., Liu, C., Tang, C., Wang, X., and Luo, S. (2016). Efficient photocatalytic degradation of organic dyes and reaction mechanism with $Ag_2CO_3/Bi_2O_2CO_3$ photocatalyst under visible light irradiation. *Journal of Molecular Catalysis A: Chemical*, 425:124-135.
9. Aliaga, J., Cifuentes, N., González, G., Sotomayor-Torres, C., and Benavente, E. (2018). Enhancement of photocatalytic activity of the heterojunction of two-dimensional hybrid semiconductors ZnO/V_2O_5. *Catalysts*, 8(9):374-377.
10. Mirza Hedayat, B., Noorisepehr, M., Dehghanifard, E., Esrafili, A., and Norozi, R. (2018). Evaluation of photocatalytic degradation of 2, 4-dinitrophenol from synthetic wastewater using Fe_3O_4, SiO_2, TiO_2/rGO magnetic nanoparticles. *Journal of Molecular Liquids*, 264: 571-578.
11. Ajmal, A., Majeed, I., Malik, R. N., Idriss, H., and Nadeem, M. A. (2014). Principles and mechanisms of photocatalytic dye degradation on TiO_2 based photocatalysts: comparative overview. *RSC Advances*, 4(70): 37003-37026.
12. Chang, L., Yang, H., Fu, W., Zhang, J., Yu, Q., Zhu, H., and Zou, G. (2008). Simple synthesis of MoS_2 inorganic fullerene-like nanomaterials from MoS_2 amorphous nanoparticles. *Materials Research Bulletin,* 43(8-9): 2427-2433.
13. Hou, S. X., Wu, C., and Huo, Y. J. (2017). Controllable preparation of nano molybdenum disulfide by hydrothermal method. *Ceramics-Silikaty*, 61:158-162.
14. Kaur, K., Badru, R., Singh, P. P., and Kaushal, S. (2020). Photodegradation of organic pollutants using heterojunctions: A review. *Journal of Environmental Chemical Engineering*, 8(2):103666.
15. Zhang, X., Ma, G., and Wang, J. (2019). Hydrothermal synthesis of two-dimensional MoS_2 and its applications. *Tungsten,* 1(1):59-79.
16. Li, Y., Xiang, F., Lou, W., and Zhang, X. (2019). MoS_2 with structure tuned photocatalytic ability for degradation of methylene blue. In *IOP Conference Series: Earth and Environmental Science*, 300(5): 0502021.
17. Sun, Y., Wang, S., and Wang, Q. (2009). Flowerlike MoS_2 nanoparticles: solvothermal synthesis and characterization. *Frontiers of Chemistry in China,* 4(2)*:*173-176.
18. Gupta, A., Arunachalam, V., and Vasudevan, S. (2016). Liquid-phase exfoliation of MoS_2 nanosheets: The critical role of trace water. *Journal Physic Chemistry Letters,* 7: 4884-4890.
19. Bai, S., Wang, L., Chen, X., Du, J., and Xiong, Y. (2014). Chemically exfoliated metallic MoS_2 nanosheets: A promising supporting co-catalyst for enhancing the photocatalytic performance of TiO_2 nanocrystals. *Nano Research,* 8:175-183
20. Chang, K., Hai, X., Pang, H., Zhang, H., Shi, L., Liu, G., Liu, H., Zhao, G., Li, M., and Ye, J., (2016). Targeted synthesis of 2H- and 1T-phase MoS_2 monolayers for catalytic hydrogen evolution. *Advance Materials,* 28:10033-10041.
21. Quinn, M. D. J., Ho, N. H., and Notley, S. M. (2013). Aqueous dispersions of exfoliated molybdenum disulfide for use in visible-light photocatalysis. *ACS Applied Materials and Interfaces*, 5(23):12751-12756.
22. Khan, R., Riaz, A., Javed, S., Jan, R., Akram, M. A., and Mujahid, M. (2018). Synthesis and characterization of MoS_2/TiO_2 nanocomposites for enhanced photocatalytic degradation of methylene blue under sunlight irradiation. *In Key Engineering Materials,* 778: 137-143.
23. Yue, J., Jian, J., Dong, P., Luo, L., and Chang, F. (2019). Growth of single-layer MoS_2 by chemical vapor deposition on sapphire substrate. In *IOP Conference Series: Materials Science and Engineering* 592(1): 012044.
24. Kwack, Y. J., and Choi, W. S. (2019). Chemical vapor deposition-free solution-processed synthesis method for two-dimensional MoS_2 atomic layer films. *Nanotechnology*, 30(38): 385201.
25. Najmaei, S., Liu, Z., Zhou, W., Zou, X., Shi, G., Lei, S., and Lou, J. (2013). Vapour phase growth

and grain boundary structure of molybdenum disulphide atomic layers. *Nature Materials*, 12(8): 754-759.

26. Liu, H., Ting, Lv, Chunkui, Z., Xing, S., and Zhenfeng, Z. (2015). Efficient synthesis of MoS_2 nanoparticles modified TiO_2 nanobelts with enhanced visible-light-driven photocatalytic activity. *Journal of Molecular Catalysis A: Chemical* 396: 136-142.
27. Alomar, M., Yueli, L., Wen, C., and Hussain, F. (2019). Controlling the growth of ultrathin MoS_2 nanosheets/CdS nanoparticles by two-step solvothermal synthesis for enhancing photocatalytic activities under visible light. *Applied Surface Science,* 480: 1078-1088.
28. Guan, Y., Wu, J., Liu, Q., Gu, M., Lin, Y., Qi, Y., ... and Li, Q. (2019). Fabrication of BiOI/MoS_2 heterojunction photocatalyst with different treatment methods for enhancing photocatalytic performance under visible-light. *Materials Research Bulletin,* 120: 110579.
29. Luo, S., Dong, S., Lu, C., Yu, C., Ou, Y., Luo, L., ... and Sun, J. (2018). Rational and green synthesis of novel two-dimensional WS_2/MoS_2 heterojunction via direct exfoliation in ethanol-water targeting advanced visible-light-responsive photocatalytic performance. *Journal of Colloid and Interface Science,* 513: 389-399.
30. Krishnan, U., Kaur, M., Kaur, G., Singh, K., Dogra, A. R., Kumar, M., and Kumar, A. (2019). MoS_2/ZnO nanocomposites for efficient photocatalytic degradation of industrial pollutants. *Materials Research Bulletin,* 111: 212-221.
31. Zhao, W., Liu, Y., Wei, Z., Yang, S., He, H., and Sun, C. (2016). Fabrication of a novel P–N heterojunction photocatalyst n-BiVO4@p-MoS_2 with core–shell structure and its excellent visible-light photocatalytic reduction and oxidation activities. *Applied Catalysis B: Environmental,* 185: 242-252.
32. Khan, M. M., Adil, S. F., and Al-Mayouf, A. (2015). Metal oxides as photocatalysts. *Journal of Saudi Chemical Society*, 19(5): 462-464.
33. Vattikuti, S. V., Prabhakar, and Byon, C. (2017). Hydrothermally synthesized ternary heterostructured MoS_2/Al_2O_3/g-C_3N_4 photocatalyst. *Materials Research Bulletin*, 96: 233-245.
34. Vattikuti, S. P., Byon, C., Reddy, C. V., Venkatesh, B., and Shim, J. (2015). Synthesis and structural characterization of MoS_2 nanospheres and nanosheets using solvothermal method. *Journal of Materials Science,* 50(14): 5024-5038.
35. Li, Y., Li, Y. L., Araujo, C. M., Luo, W., and Ahuja, R. (2013). Single-layer MoS_2 as an efficient photocatalyst. *Catalysis Science and Technology*, 3(9): 2214-2220.
36. Norsham, I. N. M., Sambasevam, K. P., Shahabuddin, S., Jawad, A. H., and Baharin, S. N. A. (2022). Photocatalytic degradation of perfluoroctanoic acid (PFOA) via MoS_2/rGO for water purification using indoor fluorescent irradiation. *Journal of Environmental Chemical Engineering*, 10(5): 108466.
37. Kasim, M. S., S. N. A. Baharin, F. Yunus, S. Shahabuddin, and N. R. A. M. Noor. (2022) Molybdenum disulphide/polypyrrole hybrid composite for photocatalytic degradation of 2-chlorophenol from aqueous solution. *Akademi Sains Malaysia* 136(6) (2020): 66-72.
38. Ren, B., Shen, W., Li, L., Wu, S., and Wang, W. (2018). 3D $CoFe_2O_4$ nanorod/flower-like MoS_2 nanosheet heterojunctions as recyclable visible light-driven photocatalysts for the degradation of organic dyes. *Applied Surface Science*, 447: 711-723.
39. Zhang, J., Huang, Y., Dan, Y., and Jiang, L. (2019). P_3HT/Ag/TiO_2 ternary photocatalyst with significantly enhanced activity under both visible light and ultraviolet irradiation. *Applied Surface Science*, 488: 228-236.
40. Lu, D., Wang, H., Zhao, X., Kondamareddy, K. K., Ding, J., Li, C., and Fang, P. (2017). Highly efficient visible-light-induced photoactivity of Z-scheme g-C_3N_4/Ag/MoS_2 ternary photocatalysts for organic pollutant degradation and production of hydrogen. *ACS Sustainable Chemistry and Engineering*, 5(2): 1436-1445.
41. Zhang, Y., He, S., He, Z., Zhang, Y., Feng, Y., Wang, Y., and Zhang, M. (2022). Preparation of MoS_2 and MoO_3 modified TiO_2 composites with enhanced visible-light photocatalytic activity for

dye degradation. *International Journal of Electrochemical Science,* 17(2): 220210.

42. Pant, B., Park, M., & Park, S. J. (2019). $MoS_2/CdS/TiO_2$ ternary composite incorporated into carbon nanofibers for the removal of organic pollutants from water. *Inorganic Chemistry Communications,* 102: 113-119.
43. Huang, S., Chen, C., Tsai, H., Shaya, J., and Lu, C. (2018). Photocatalytic degradation of thiobencarb by a visible light-driven MoS_2 photocatalyst. *Separation and Purification Technology,* 197: 147-155.
44. Zou, L., Qu, R., Gao, H., Guan, X., Qi, X., Liu, C., ... and Lei, X. (2019). MoS_2/RGO hybrids prepared by a hydrothermal route as a highly efficient catalytic for sonocatalytic degradation of methylene blue. *Results in Physics,* 14, 102458.
45. Li, Y., Lai, Z., Huang, Z., Wang, H., Zhao, C., Ruan, G., and Du, F. (2021). Fabrication of BiOBr/MoS_2/graphene oxide composites for efficient adsorption and photocatalytic removal of tetracycline antibiotics. *Applied Surface Science,* 550: 149342.
46. Karpuraranjith, M., Chen, Y., Rajaboopathi, S., Ramadoss, M., Srinivas, K., Yang, D., and Wang, B. (2022). Three-dimensional porous MoS_2 nanobox embedded g-C3N4@TiO_2 architecture for highly efficient photocatalytic degradation of organic pollutant. *Journal of Colloid and Interface Science,* 605: 613-623.
47. Baharin, S. N. A., Rusmin, R., and Sambasevam, K. P. (2022). Basic concept and application of conducting polymers for environmental protection. *Chemistry Teacher International,* 4(2): 173-183.
48. Zhu, X. (2015). Exfoliation of two-dimensional materials. Doctoral dissertation, University of Akron: pp. 16-17.

Malaysian Journal of Analytical Sciences (MJAS)
Published by Malaysian Analytical Sciences Society

MAGNETIC NANOPARTICLE FOR REMOVING SUNSET YELLOW DYE: TAGUCHI OPTIMIZATION

(Zarah Nano Magnetit untuk Penyingkiran Pewarna Kuning Matahari Terbenam: Pengoptimuman Taguchi)

Nurina Izzah Mohd Husani[1], Nur Amani Izzati Mohamad Hisham[2], Nor Munira Hashim[1], Clayrine Shima Anak Lasu[1], Noorfatimah Yahaya[1], Muggundha Raoov[3], and Nur Nadhirah Mohamad Zain[1]*

[1]*Department of Toxicology, Advanced Medical And Dental Institute, Universiti Sains Malaysia, 13200 Kepala Batas, Penang, Malaysia*
[2]*Faculty of Science and Technology, Universiti Sains Islam Malaysia, Bandar Baru Nilai, 71800, Nilai, Negeri Sembilan, Malaysia*
[3]*Department of Chemistry, Faculty of Sciences, Universiti Malaya, 50603 Kuala Lumpur, Malaysia*

**Corresponding author: nurnadhirah@usm.my*

Received: 9 March 2022; Accepted: 30 May 2023; Published: 22 August 2023

Abstract

This study describes the role of magnetite nanoparticle (MNP) or Fe_3O_4, which are magnetic nanomaterials (MNMs), as adsorbents for the removal of a synthetic azo dye called sunset yellow FCF (SY) from aqueous samples. Improper release of the SY dye into water can have significant adverse effects on the environmental, including disruption of photosynthesis, obstructs sunlight penetration, and risks to aquatic life and human health. Therefore, it is crucial to develop effective methods for removing the SY dye from water sources. This research aims to investigate the potential of Fe_3O_4 magnetic nanoparticles in removing the SY dye from water samples. By analyzing the effects of Fe_3O_4 nanoparticles, this study aims to provide insights into their efficiency and effectiveness as a potential solution for the removal of the SY dye, contributing to the development of sustainable water treatment strategies. The adsorbents was prepared using co-precipitation method, and their characteristics were analyzed using various instruments. Furthermore, the study investigated the adsorption conditions, including the optimization of pH, adsorbent dosage, and contact time using the Taguchi optimization method. The optimization for the effect of temperature and initial concentration of dye was conducted separately. The results of this study showed that the interaction between the homogenous surface of the adsorbents and the adsorbates or analytes molecules involved chemisorption and monolayer adsorption. The adsorption was found to be feasible, spontaneous, increased randomness, and endothermic. Additionally, the prepared adsorbents were validated by applying to remove the SY dye from three actual wastewater samples. The removal percentage ranged approximately from 30% to 85% with a low relative standard deviation (RSD% < 9.2%). This demonstrated that the adsorbents remained reliable for removing the dye from real samples were spiked with a high concentration of analytes. Overall, this study presents a promising approach for removing the SY dye from wastewater samples. It shows that even the bare form of MNMs base can be extensively developed for analyte removal from real aqueous samples.

Keywords: magnetic nanoparticles, sunset yellow dye FCF, Taguchi optimization, adsorption, wastewater

Abstrak

Artikel ini menerangkan peranan zarah nano magnetit (MNP) atau Fe_3O_4, yang merupakan bahan nano magnetik (MNMs), sebagai bahan jerap untuk menyingkirkan pewarna azo sintetik yang dipanggil kuning matahari terbenam FCF (SY) daripada sampel berakua. Pembebasan pewarna SY yang tidak betul ke dalam air boleh memberi kesan buruk yang ketara kepada alam sekitar, termasuk gangguan fotosintesis, menghalang penembusan cahaya matahari, dan risiko kepada hidupan akuatik serta kesihatan manusia. Oleh itu, adalah penting untuk membangunkan kaedah yang berkesan untuk mengeluarkan pewarna SY daripada sumber air. Penyelidikan ini bertujuan untuk menyiasat potensi nanopartikel magnet Fe_3O_4 dalam menyingkirkan pewarna SY daripada sampel air. Dengan menganalisis kesan nanopartikel Fe_3O_4, kajian ini bertujuan untuk memberikan pandangan tentang kecekapan dan keberkesanannya sebagai penyelesaian yang berpotensi untuk penyingkiran pewarna SY, menyumbang kepada pembangunan strategi rawatan air yang mampan. Bahan jerap telah disediakan menggunakan kaedah pemendakan bersama, dan ciri-cirinya dianalisis dengan menggunakan pelbagai instrumen. Tambahan pula, kajian ini menyiasat keadaan penjerapan, termasuk pengoptimuman pH, dos penjerap, dan masa sentuhan menggunakan kaedah pengoptimuman Taguchi. Pengoptimuman untuk kesan suhu dan kepekatan awal pewarna dijalankan secara berasingan. Hasil kajian ini menunjukkan bahawa interaksi antara permukaan homogen bahan jerap dan bahan dijerap atau molekul analit melibatkan penjerapan kimia dan monolapisan. Penjerapan didapati tersaur, spontan, peningkatan kerawakan, dan endoterma. Tambahan pula, bahan jerap yang disediakan telah disahkan potensinya dengan menggunakannya untuk menyingkirkan pewarna SY daripada tiga sampel air buangan sebenar. Peratusan penyingkiran berjulat kira-kira dari 30% hingga 85% dengan sisihan piawai relatif rendah (RSD% < 9.2%). Ini menunjukkan bahawa bahan jerap kekal boleh dipercayai untuk menyingkirkan pewarna daripada sampel sebenar yang telah dicemari dengan kepekatan analit yang tinggi. Secara keseluruhan, kajian ini membentangkan pendekatan yang menjanjikan dalam mengeluarkan pewarna SY daripada sampel air buangan. Ia menunjukkan bahawa walaupun bentuk yang asas MNMs dapat dibangunkan secara meluas untuk penyingkiran analit daripada sampel berakua sebenar.

Kata kunci: zarah nano magnetit, pewarna kuning matahari terbenam FCF, pengoptimuman Taguchi, penjerapan, air kumbahan

Introduction

In this modern world, rapid industrialization has led to a gradual increase in environmental pollution [1]. Among the various types of pollution, water pollution is particularly concerning. Water is not only essential for human body, it is also crucial for human daily activities such as agriculture, industrial production, and drinking water [2, 3, 4]. Unfortunately, the scarcity of clean water caused by pollution erodes all these benefits. Water pollution occurs mainly due to the discharge of emerging contaminants (EC) from various industries, such as heavy metals, pesticides, polyaromatic hydrocarbons, and dyes, as highlighted Belachew et al. [5]. This problem needs to be addressed urgently to ensure that the water sources can be preserved and the maintained for healthy environment. Through the implementation of stringent regulations and effective strategies, water pollution can be prevented and its quality can be restored.

Dyes, as one type of EC, are colorants that can be transferred from a liquid onto numerous substrates and are usually used in industries such as printing, textile, plastics, rubbers, and foodstuffs [6, 7]. They are also popular as food colorants in the food industry to enhance taste and to improve the appearance of food. Food colorants are broadly classified into two categories which are natural colorants and synthetic colorants. Due to their excellent stability, effectiveness, and low-cost production, synthetic colorants are extensively used in the industry [8]. Natural dyes are produced from various sources, such as animal, plant, and mineral deposits. The commonly used natural dyes include brown (caramel), yellow (turmeric), and red (beet juice). On the other hand, the synthetic dyes, which are produced through chemical processes, offer a wider variety of colors. Some of these dyes include Sunset Yellow, Allura Red, Brilliant Blue, and Tartrazine[9].

One specific synthetic azo dye, Sunset Yellow FCF (SY), known as CI Food Yellow 3, INS No.110 and Orange Yellow S, has the chemical name disodium 2-hydroxy-1-(4-sulphonatophenylazo)naphtha-lene-6-sulphonate [8]. SY in the form of powder present as orange-red colour and is soluble in water. It used in pharmaceuticals, cosmetics, and food products [10]. In the food industry, SY is commonly used to produce apricot jam, lemon curd, sweets, beverage mixes, custard powders, and instant noodles [11]. Apparently,

this type of synthetic dye is beneficial in many fields, especially in the food industry.

However, despite its usefulness in various fields, it still has limitations, especially when released abundantly into water without pre-treatment. This can affect the water ecosystem and human beings, as they are interconnected through the food chain and food web. Nwuzor et al. mentioned that some dyes are lost in streams during the industrial colouring process, and these dyes are toxic and can disrupt the water's nature state by hindering sunlight penetration, disrupting photosynthesis, and causing aesthetic issues. Furthermore, they can cause allergies and affect neurobehavioral and reproductive parameters, leading to symptoms such as diarrhea and allergies [11]. Therefore, the presence of dyes like SY as water effluents without proper treatment could have a negative impact on aquatic organisms and human health.

Therefore, remedies should be outlined to curb this issue. According to a previous study by Villar Blanco et al., three forms of techniques can be implemented including physicochemical, physical, and biological. Several actions such as oxidation, ion exchange, flocculation, filtration, ozonation, membrane separation, precipitation, and adsorption have been employed to treat the issue. However, most of these processes encountered some limiting factors, such as high operating costs, difficulties in timing and implementation, and the generation of toxic by-products and sludges [14, 15]. As a result, many of them cannot be efficiently utilized. However, Jeeva et al. stated that adsorption is the most efficient method to treat effluents due to its simplicity, cost-effectiveness, and directness. It is extensively applied to remove pollutants from wastewater as it exhibits high removal efficiency [16].

Adsorption is a process that involves the accumulation of molecules on the surface or at the interface between two phases [17]. It is also known as a separation process in which molecules tend to accumulate on the surface of the adsorbent due to the presence of attractive forces, such as the Van der Waals force. This accumulation creates an adsorbate film on the adsorbent's surface [18]. Thus, it is evident that the adsorbate and adsorbent are essential elements in an adsorption process, highlighting the importance of choosing a suitable adsorbent to ensure the effective adsorption of the targeted analyte (adsorbate) [19].

Recently, magnetic nanoparticles, such as iron oxide (Fe_3O_4), have been recognized as effective adsorbents for pollutants' removal in recent years. Previous studies have validated the use of Fe_3O_4 in developing a simple, inexpensive, and efficient adsorption method [20]. Fe_3O_4, also known as magnetite or magnetic nanoparticles (MNPs), is derived from nanomaterials (NMs). NMs are generally small-sized materials ranging from 1 to 100 nm [21]. These characteristics contributed to their larger surface area and unique properties, making them ideal sorbents.

Furthermore, the use of MNPs derived from NMs is favored due to their susceptibility to external magnetic fields. This property eliminates the need for cumbersome processes like centrifugation and filtration, as the sorbents can be easily and quickly separated from the liquid reaction system using a magnet [22]. As a result, the adsorption or removal of analytes (such as dyes) from water samples becomes more straightforward and accessible. Importantly, the aforementioned benefits highlight that Fe_3O_4 can be implemented to enhance the adsorption process of various analytes, including dyes.

Based on the preceding discussion, the main objective of this study was to investigate the performance of Fe_3O_4 in removing a synthetic azo dye, sunset yellow FCF (SY), from water samples. The study involved optimizing several parameters that influenced the removal performance of SY, such as pH, contact period, temperature, adsorbent dosage, and initial concentration of SY. The application of the Taguchi method in designing the optimization study was also examined. Furthermore, the study explored the kinetics reaction and isotherm adsorption of Fe_3O_4 in removing SY from an aqueous solution to understand the adsorption mechanism. Additionally, a thermodynamics study was conducted to assess the viability and spontaneity of the process. Finally, the optimized values were applied to

real water to validate the performance of the proposed method for practical sample analysis.

Materials and Methods

Chemicals and reagents

Ferrous chloride tetrahydrate ($FeCl_2.4H_2O$) and ferric chloride hexahydrate ($FeCl_3.6H_2O$) from R&M Chemicals (Edmonton, Canada) were used to synthesize the MNPs, Fe_3O_4. Methanol was supplied by HmbG Chemicals (Cologne, Germany), and a 25% ammonia solution (NH_3) utilized was from Merck, Darmstadt, Germany. The Sunset Yellow FCF powder was purchased from R&M Marketing (Essex, U.K.). All reagents and chemicals were used without further purification.

Instrumentation

The experiments were conducted using deionized water obtained from the Sartorius Stedim deionized water dispenser, Milli–Q® system (Arium 611 DI). A pH meter (BP3001 Trans Instruments) was utilized for measuring and adjusting the pH value. A UV-vis spectrophotometer (Perkin Elmer Lambda25) was employed to determine residual concentrations of the Sunset Yellow FCF at λ_{max} = 480.9 nm. An incubator shaker (IKA, KS4000 control) was used to shake the sample solution at 300 rpm with adjustable temperature and time, while mechanical shaker (Orbitron) was used to shake the solution at a similar speed and at room temperature with adjustable time.

Synthesis of Fe_3O_4

In this study, Fe_3O_4 was prepared using a conventional co-precipitation method with slight modification [23]. Firstly, $FeCl_2.4H_2O$ and $FeCl_3.6H_2O$ were mixed and dissolved in 50 mL of deionized water. Then, the mixture was stirred under nitrogen gas at 50°C for 30 min. Subsequently, ammonia solution (25%) was added into the mixture solution to allow the magnetization process, and the mixture was agitated for an hour at 90°C under nitrogen gas before the final products were collected by an external magnet, followed by washing step using 50 mL methanol and 50 mL deionized water alternately for several times. Afterward, the products were dried in an oven overnight. Finally, the dried products were crushed and ground using a pestle and mortar, before stored for further use.

Characterization of the synthesized Fe_3O_4

For the characterization process, several instruments were employed to examine the physical characteristics of the synthesized Fe_3O_4. A vibrating sample magnetometer (VSM, model Lake Shore/7404, McCourkle Boulevard, WO, USA) was used to investigate the magnetic properties of the adsorbent. Fourier transform-infrared spectroscopy (FT-IR) with the KBr technique from model Thermo Nicolet model in Waltham, USA, and thermogravimetric analysis (TGA, model Perkin Elmer) was utilized to identify the functional groups and the thermal stability of Fe_3O_4, respectively. The morphology of the synthesized Fe_3O_4 was examined using a transmission electron microscope (TEM, Phillips CM12 Version 3.2 model, Hillsboro, USA) and a scanning electron microscope (SEM, QUANTA FEG650 model, Hillsboro, Oregon, USA). X-ray diffractometer (XRD) from Siemens D5000 model (Frimley, UK) was applied for the phase identification of adsorbent crystallinity and unit cell dimension. Additionally, Brunauer-Emmet-Teller (BET) analysis was conducted using Quantachrome model (Boynton Beach, FL, USA) to measure the surface area of the adsorbent and determine the physical adsorption of gas particles on a solid surface. Prior to BET analysis, the prepared adsorbent was degassed at 80°C for 2 h to remove moisture.

Adsorption experiments

All the adsorption experiments were conducted using a 20 mL glass vial containing a specific amount of Fe_3O_4 adsorbent mixed with 10 mL of a sample solution containing a predetermined concentration of SY dye as the analyte. The vials were then placed on an incubator or a mechanical shaker at designated temperature for a specific duration at a consistent speed of 300 rpm. The adsorption experiments were carried out by varying different parameters, including pH (2.0, 3.0, 4.0, and 5.0), contact period (10, 20, 30, and 40 min), adsorbent dosage (5, 10, 15, and 20 mg), temperature (298, 313, and 333 K) and initial concentration of SY dye (5, 10, 20, 40, and 60 ppm).

During the experiment, the pH of the solution was

adjusted by adding hydrochloric acid, HCl (0.1 M), or sodium hydroxide, NaOH (0.1 M). After adsorption, Fe_3O_4 adsorbents were separated using an external magnet, and the remaining solutions were analyzed using a UV-vis spectrophotometer at λ_{max}= 480.9 nm. All the experiments were conducted in triplicate. Finally, the percentage removal (R%) of each run was calculated by using equation (1):

$$R\ (\%) = \frac{Co-Ce}{Co} \times 100\% \quad (1)$$

where C_o refers to the initial concentration of the dye and C_e refers to the equilibrium concentration of the SY FCF dye (ppm).

Optimization for adsorption experiments

In this study, two methods were employed to conduct the optimization. The optimization for the effects of pH, contact period, and adsorbent dosage was performed using the Taguchi Orthogonal Array design. Several values were selected for each factor (pH, contact period, and adsorbent dosage), and the experiments were conducted based on the pre-designed data. Additionally, the values for the initial concentration of SY and temperature were predetermined and kept constant for the Taguchi experiment.

Subsequently, separate procedures were conducted at various initial concentrations of SY and different temperatures to optimize the effect of initial concentration and temperature. During these runs, the pH value, adsorbent dosage, and contact period were maintained constant at pH 3, 10 mg, and 10 min, respectively. These values were then optimized based on the outcomes of the Taguchi experiment.

Taguchi method for optimization

The Taguchi method is an effective strategy for designing an experiment to obtain the optimum process results, which was proposed by Dr. Genichi Taguchi [24]. It is a method that combines multiple factors at various levels while ensuring equal consideration of all levels of each factor, thereby reducing the number of experimental runs. To conduct the Taguchi method, several procedures were adopted during the process. According to Nandhini et al. (2014), the three main procedures adopted in designing parameters using the Taguchi method are as follows: (1) experimental planning, which involves the selection of factors (*P),* their values (levels, *L*) and the appropriate Taguchi orthogonal array design, (2) implementation of the experimental design based on the designed table, and (3) analysis of results using Analysis of Variance (ANOVA), main effect plot of signal-to-noise (S/N) ratio, and means to determine the optimum value for the control factors [25].

In this study, the three main procedures were adopted. The Taguchi method was conducted at varying ranges of controllable factors, namely pH (2.0, 3.0, 4.0, and 5.0), contact period (10, 20, 30, and 40 min), and adsorbent dosage (5, 10, 15, and 20 mg). Simultaneously, the initial concentration and temperature were fixed at 10 ppm (10 mL) and room temperature, respectively. Since there were three factors (*P)* with four testing conditions values (*L*) for each factor, the Taguchi experiment was conducted by implementing Taguchi design: L_{16} (*P*= 3, *L*= 4). Table 1 below shows the selected parameters for this study. Meanwhile, Table 2 shows the experimental plan based on L_{16} (*P*= 3, *L*= 4) design, and Table 3 depicts the experimental runs with the actual values of testing conditions for each run. Signal to noise ratio and the implementation of ANOVA were also observed to determine the optimum conditions and assess the contribution of each factor sequentially.

Table 1. Selected experimental factors and their corresponding values at different levels

Symbol	Factors	Units	Levels			
			1	2	3	4
A	pH	-	2	3	4	5
B	Contact period	min	10	20	30	40
C	Adsorbent dosage	mg	5	10	15	20

Table 2. 16 runs based on Taguchi design L16 (P= 3, L= 4)

No. of Run	Factors and Their Levels		
	pH	Contact Period	Adsorbent Dosage
1	1	1	1
2	1	2	2
3	1	3	3
4	1	4	4
5	2	1	2
6	2	2	1
7	2	3	4
8	2	4	3
9	3	1	3
10	3	2	4
11	3	3	1
12	3	4	2
13	4	1	4
14	4	2	3
15	4	3	2
16	4	4	1

Table 3. 16 runs of Taguchi optimization experiment and their respective testing conditions values

No. of Run	pH	Contact Period	Adsorbent Dosage
1	2	10	5
2	2	20	10
3	2	30	15
4	2	40	20
5	3	10	10
6	3	20	5
7	3	30	20
8	3	40	15
9	4	10	15
10	4	20	20
11	4	30	5
12	4	40	10
13	5	10	20
14	5	20	15
15	5	30	10
16	5	40	5

Optimization for the effect of temperature and initial concentration

This study was conducted using various initial concentrations of SY (5, 10, 20, 40, and 60 ppm) in 10 mL of sample solution at different temperatures of 298, 313, and 333 K, separately. Meanwhile, other factors such as pH value, contact period, and adsorbent dosage were fixed at their optimized values obtained from the Taguchi experiment: pH 3, 10 min, and 10 mg, respectively.

Adsorption isotherm, kinetic, and thermodynamic study

To further investigate the reaction mechanism and adsorbent behaviour toward the analyte, detailed evaluation of kinetic, isotherm, and adsorption thermodynamics were conducted. The behaviour of Fe_3O_4 toward SY dye was studied using several well-known models. The thermodynamic study was then investigated using entropy (ΔS°), enthalpy (ΔH°), and free Gibbs energy (ΔG°).

Adsorption kinetics study

The use of kinetic model in a study can evaluate the sorption mechanism and potential rate-determining steps [23, 26]. In this study, two models were utilized to investigate the kinetic behavior of Fe_3O_4 toward SY dye: the pseudo-first order and pseudo-second order. The pseudo-first order model is a kinetic model that was proposed Lagergren in 1898, and it is the most commonly employed kinetic model for liquid-solid adsorption systems [15, 27]. To pursue this study on SY adsorption onto Fe_3O_4 adsorbent, the pseudo-first order model was described based on pseudo-first order linear equation, equation (2):

$$\log (q_e - q_t) = \log q_e - \frac{k1}{2.303} t \quad (2)$$

The pseudo-second order model is another well-known kinetic model. This model has been implemented in several sorption systems to successfully examine chemisorption interactions, which includes the exchange of electrons and valance sharing between the adsorbent and analyte [23, 28]. For this study, the determination of kinetic behavior using the pseudo-second order model was expressed by the following linear equation, equation (3):

$$\frac{t}{q_t} = \frac{1}{k_2 q_e^2} + \frac{t}{q_e} \quad (3)$$

where q_e and q_t (mg/g) represent the amount of SY FCF dye adsorbed at equilibrium and at time t (min), respectively. k_1 (min^{-1}) is the rate constant for the first order adsorption, and k_2 (g/mg.min) is rate constant for the second order adsorption.

Furthermore, the suitability of the model to determine adsorption kinetics was also assessed by calculating the normalized standard deviation Δq (%) and relative error (%) based on equations (4) and (5), respectively:

$$\Delta q\ (\%) = \sqrt{\frac{((q_{exp} - q_{cal})/ q_{exp})^2}{N-1}} \times 100 \quad (4)$$

$$\text{Relative error } (\%) = \left(\frac{q_{exp} - q_{cal}}{q_{exp}}\right) \quad (5)$$

where N represents the number of data points, while q_{exp} and q_{cal} represent the experimental and calculated adsorption capacities, respectively.

Adsorption isotherms study

Adsorption isotherm models are crucial for predicting and comparing the performance of an adsorption process [29]. In this study, five isotherm models were implemented to investigate the adsorption of SY dye onto Fe_3O_4. The models used were Langmuir, Freundlich, Dubinin-Radusckich, Halsey, and Temkin isotherm models.

$$\frac{C_e}{q_e} = \frac{1}{q_m}.C_e + \frac{1}{b.q_m} \quad (6)$$

$$\log q_e = \frac{1}{n} \log C_e + \log K_F \quad (7)$$

C_e ($mg.L^{-1}$) represents the initial concentration of the adsorbate according to the Langmuir model and the concentration at equilibrium according to the Freundlich model. q_e ($mg.g^{-1}$) represents the amount of adsorbate adsorbed at equilibrium. The Langmuir model is characterized by the parameters q_m ($mg.g^{-1}$) and b ($L.mg^{-1}$), which represent the maximum adsorption capacity and the rate of adsorption, respectively. The Freundlich model is characterized by the parameters K_F ($mg.g^{-1}$) and n, which represent the adsorption capacity and intensity, respectively.

The Dubinin-Radusckich model is generally used to express the adsorption mechanism with Gaussian energy

$$\ln q_e = \ln q_m - \beta E^2 \quad (8)$$

$$E = RT \ln \left[1 + \frac{1}{C_e}\right] \quad (9)$$

$$\ln q_e = \left[\frac{1}{n} \ln K_H\right] - \frac{1}{n} \ln C_e \quad (10)$$

$$q_e = \beta \ln K_T + \beta \ln C_e \quad (11)$$

The adsorption energy constant, denoted by β, can be calculated using the Dubinin-Radusckich equation. Additionally, β is equal to RT/b_τ at a given temperature (T in Kelvin), which corresponds to the Temkin equation. The universal gas constant, represented by R, is measured in units of $kJ.mol^{-1}$. The Halsey isotherm constants, denoted as K_H and n, are obtained from the slope and intercept of the ln q_e against ln C_e, respectively. The Temkin constant, KT, is related to the equilibrium binding energy, and b_τ is associated with the heat of adsorption.

The Langmuir model is an empirical model that assumes a homogenous surface of the adsorbent and involves monolayer adsorption, with the adsorbed layer having a thickness of one molecule [23, 29], while the Freundlich isotherm model is an empirical model which generally used to illustrate heterogeneous adsorbents data. In this study, the Langmuir and Freundlich model parameters were described through their linear equations (6) and (7), respectively.

onto heterogeneous surfaces [30], while the Halsey model is suitable for multilayer adsorption and illustrates the heterosporous nature of a material [31]. Additionally, the Temkin is an empirical isotherm model that considers the interactions between adsorbent and adsorbate while neglecting the concentration values, which are extremely high or low [30].

This study determined the parameters of the Dubinin-Radusckich, Halsey, and Temkin isotherm models using linear equations. Equations (8) and (9) corresponded to the Dubinin-Radusckich isotherm model, while equations (10) and (11) are for the Halsey and Temkin isotherm models, respectively.

Adsorption thermodynamic

Thermodynamics must be considered in adsorption

experiments to demonstrate the viability and spontaneity of the process [23]. Thermodynamic parameters can be determined in an adsorption process as they are temperature-dependent [32]. In this research, the effects of temperature on the thermodynamic parameters such as ΔH°, ΔS°, and ΔG° were investigated at three different temperatures (298, 313, and 333 K). Subsequently, the Van Hoff plot was obtained by plotting ln k_d against 1/T based on equation (12). The slope of the curve was used to calculate ΔH°, while ΔS° was determined the y-intercept.

$$\ln k_d = -\frac{\Delta H^\circ}{RT} + \frac{\Delta S^\circ}{R} \quad (12)$$

The equilibrium constant, which represents the ratio of the forward and reverse reaction rates at equilibrium, is denoted by k_d.

Pre-treatment of real samples

Wastewater samples were randomly collected from various industrial areas around the Kepala Batas area (5.5172° N, 100.4315° E). All samples were filtered using a nylon filter and stored in appropriate containers before use.

Method validation and real sample analysis

To validate the proposed method, linearity, and repeatability (intra-day and inter-day) were evaluated under optimized conditions. The linearity of SY in water samples was assessed by constructing a calibration curve ranging from 2 to 80 ppm. The coefficient of determination (R^2) value was obtained from a linear plot of absorbance (A) versus analyte concentration (ppm).

Accuracy (removal) and precision (relative standard deviation, RSD%) were assessed by analyzing effluent wastewater samples with a spiked standard solution at three different concentration levels (5, 20, and 60 ppm). Equation (1) was used to calculate accuracy, while equations (13) and (14) were employed to calculate the precision.

$$SD = \sqrt{\frac{\sum(\bar{x}-x)^2}{n-1}} \quad (13)$$

$$RSD = \frac{SD}{\bar{x}} \times 100 \quad (14)$$

In a set of measurements with a sample size of n, where $\bar{x}$ represents the mean and x represents the result of each individual run, the standard deviation (SD) is a measure of the spread or variability of the data.

To assess the reliability of the proposed method, three real samples were spiked with three different analyte concentrations and analyzed using a UV-vis spectrophotometer. The analysis aimed to investigate the matrix effect on the removal of SY by Fe_3O_4.

Results and Discussion

Characterization of the adsorbent

FTIR analysis was conducted to identify the vibration of functional groups present on the surface of the prepared Fe_3O_4. The FTIR spectrum of Fe_3O_4 is shown in Figure 1, and the data are presented in Table 4. Based on the figure, two prominent peaks were in the spectrum of Fe_3O_4. A strong and broad peak was identified at 3417.6 cm^{-1}, corresponding to O-H stretching due to the presence of the O-H bond in the structure. Additionally, a strong peak related to Fe-O stretching was observed at a wavenumber of approximately 587.0 cm^{-1} in the FTIR spectrum. This peak indicates the successfully synthesized of Fe_3O_4.

Then, the thermal stability of the adsorbents was assessed using TGA analysis, and the results are shown in Figure 2. Based on the TGA curve, significant weight loss was observed in the temperature range of 31-120℃, gradually increasing from 120-390℃, due to the evaporation and loss of water content from Fe_3O_4

structure. This observation is consistent with the findings reported by Mokadem et al. [33]. Furthermore, the results indicated that no significant weight loss occurred at higher temperature (>390°C). Similar trends were reported by Cao et al., where no significant changes were observed in the TGA results near 400°C [34]. Therefore, it can be concluded that Fe_3O_4 exhibits excellent stability, as only 7% of the weight was decomposed at elevated temperatures[35].

Moreover, VSM was used to investigate the magnetic behavior of the synthesized Fe_3O_4. The hysteresis loop of the adsorbents is shown in Figure 3. The Fe_3O_4 particles exhibited a maximum saturation (Ms) of 135.26 emu/g, indicating a high magnetic strength that falls within the acceptable range for the adsorption process. Additionally, the adsorbents exhibited a superparamagnetic characteristic [20] as evidenced by the S-shaped curved in the hysteresis loop.

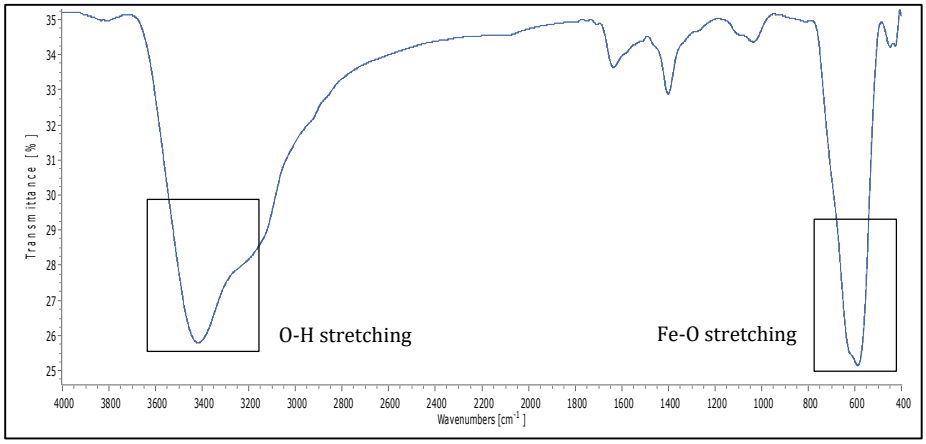


Figure 1. FTIR spectrum of Fe_3O_4

Table 4. FTIR frequencies of adsorbents

Characteristics	**Fe_3O_4**
Assignments	**Wavenumbers (cm^{-1})**
Fe-O stretch	587.0
O-H stretch	3417.6

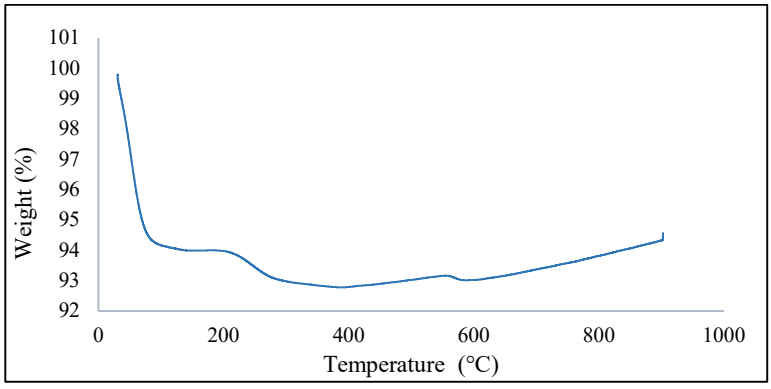


Figure 2. TGA curve of Fe_3O_4

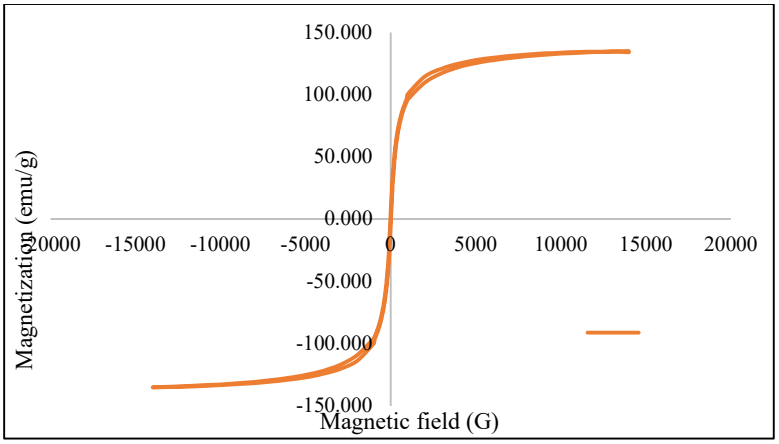


Figure 3. VSM analysis of Fe_3O_4

Microscopic morphological analysis of the prepared adsorbents was conducted using TEM and SEM techniques to examine their surface features. TEM images, shown in Figure 4 (a-i), revealed that the particles had an average diameter of approximately 10.42 nm. The Fe_3O_4 particles were observed to be spherical and uniform in size [36] when captured at various scales ranging from 50 to 500 nm. The images also displayed the aggregation of these small spherical particles into larger aggregates. On the other hand, the SEM image of Fe_3O_4, depicted in Figure 5, exbibited a beaded, rough, and agglomerated surface structure.

Crystallinity identification was performed using XRD, and the results are plotted in Figure 6. The diffraction peaks of the Fe_3O_4 exhibited good crystallinity [37]. The solid samples showed diffraction peaks at the 2θ values of 30.50, 35.73, 43.51, 54.30, 57.30, and 63.04, corresponding to the (220), (311), (400), (422), (511) and (440) cubic spinel planes of Fe_3O_4 particles, respectively. These values correspond to the joint committee on powder diffraction standard card number (88-0866 and 19-0629) [36, 37].

The BET surface area of Fe_3O_4 was found to be 44.6795 m^2/g. The nitrogen adsorption-desorption isotherm, depicted in Figure 7, indicated that the samples followed a type IV isotherm and exhibited a H3 hysteresis loop. This finding confirmed the mesoporosity of the adsorbents, with pores in the range of 1.5-100 nm [36, 38]. Furthermore, the pore diameters for Fe_3O_4, calculated to be approximately 14.44 nm using the Barret–Joyner–Halenda model (BJH), further supported the existence of the adsorbents as mesoporous materials. Mesoporous materials have pore sizes between microporous (< 2 nm) and macroporous (> 50 nm) materials. They offer numerous advantages, such as high surface area, stability, and pore volume. Therefore, Fe_3O_4, being in the mesoporous region, exhibited its mesoporosity characteristics, which are beneficial for adsorbate adsorption.

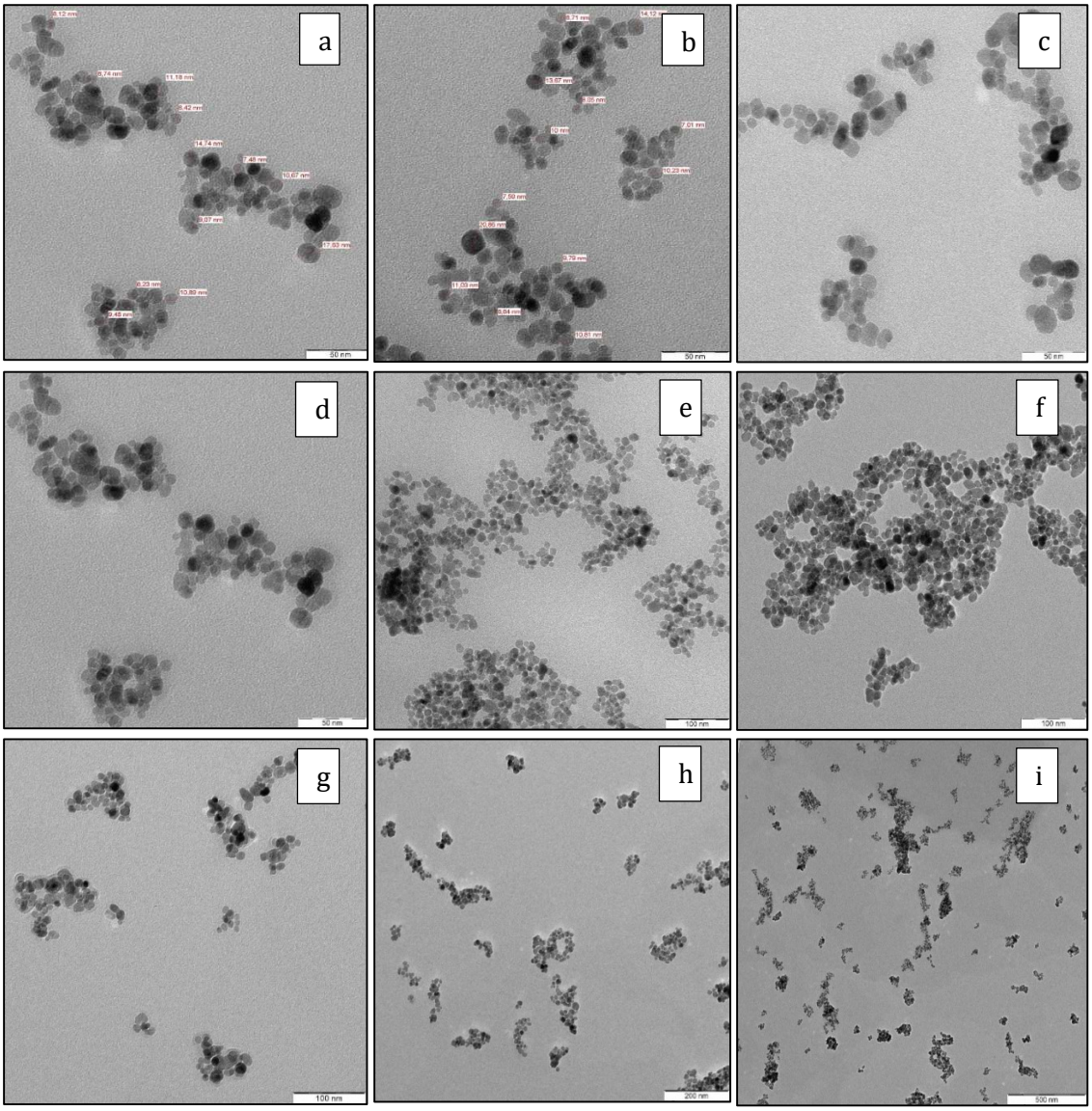


Figure 4. TEM images of Fe_3O_4. The scale bar at = 50 nm (a-d) 100 nm (e-g) 200 nm (h) 500 (i)

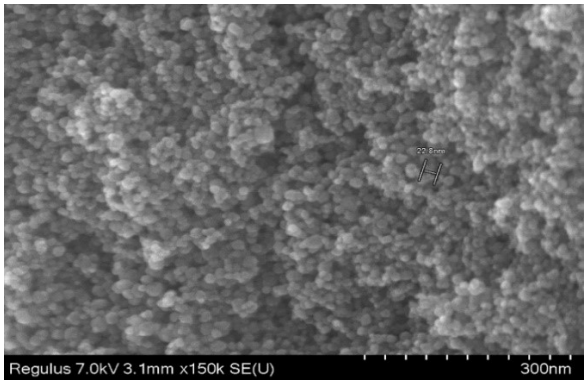


Figure 5. SEM image of Fe_3O_4

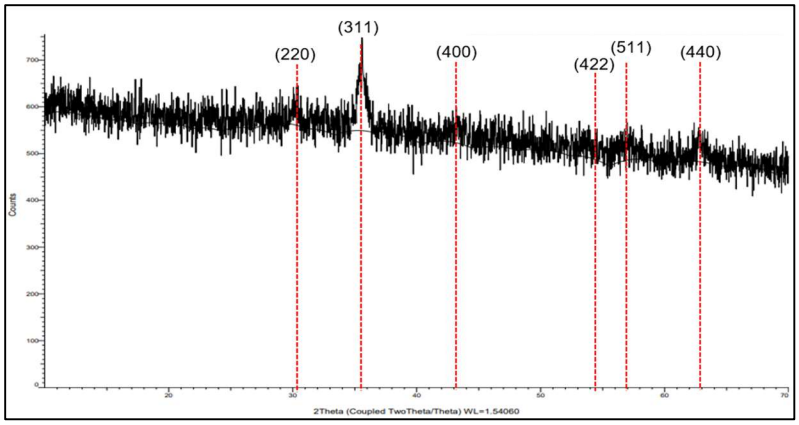


Figure 6. XRD patterns of Fe_3O_4

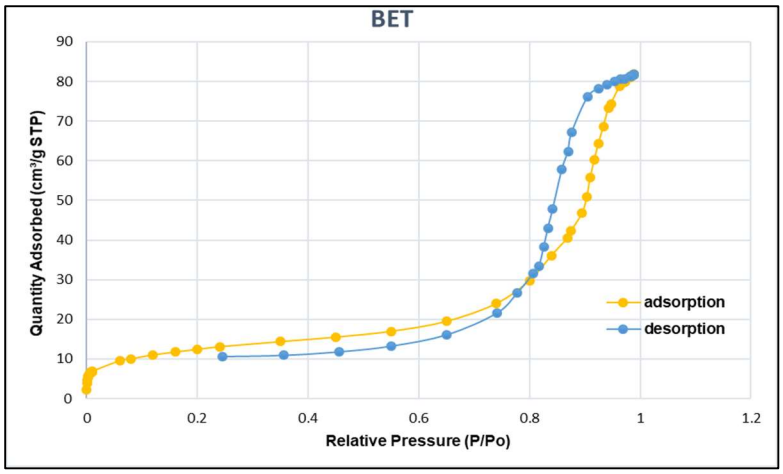


Figure 7. Nitrogen adsorption-desorption isotherm of Fe_3O_4

Optimization for adsorption experiment: Taguchi optimization, the main effect plot for the S/N ratio, and implementation of ANOVA

As mentioned earlier, the Taguchi method was used to optimize three controllable factors: pH, contact period, and adsorbent dosages, with four levels for each factor (testing conditions). Table 5 shows the L_{16} orthogonal array design used in this study and the results obtained after each run. The significance order of the controllable factors was determined and is presented in Table 6. The significance order was determined by analyzing the rank of S/N ratio and considering the delta values, which represent the relative magnitude of effects by comparing the highest and lowest average characteristics for each controllable factor [26, 39].

The results show that the average removal percentage of SY dye (Table 5) ranged from 62.1% to 91.9%, depending on the combination of controllable factors. Additionally, it was observed (Table 6) that the contact period had the most significant variation in the S/N ratio, followed by the adsorbent dosage, and pH. In other words, the contact period had the most significant influence on the adsorption process, while the pH value had the least significant contribution. The optimal conditions for each factor in the adsorption process are also indicated in Table 6.

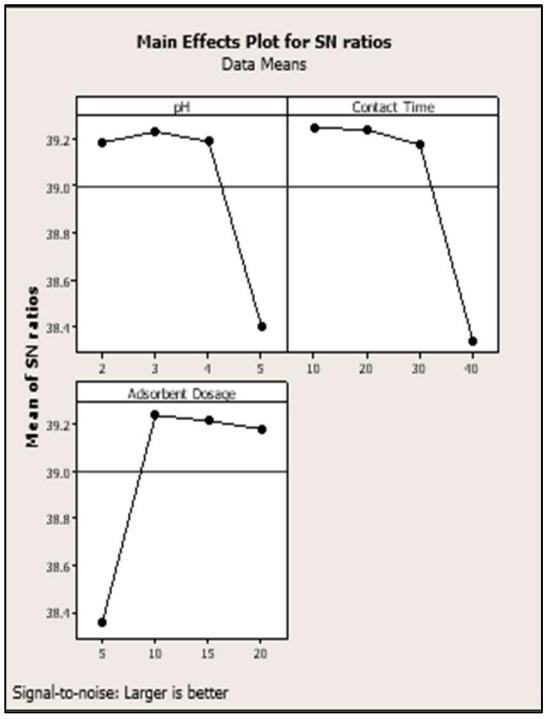


Figure 8. The response curves for the individual effects of SY dye adsorption parameters on S/N ratio

Moreover, the comparative response curves for the independent effects (main effect plot) of the adsorption parameters on the SY removal efficiency can be referred to in Figure 8. Based on the figure, it can be observed that the removal of SY dye increased as the pH increased from 2 to 3. However, the removal trend decreased when the pH value was further increased to 5. The decrease in dye removal can be attributed to the negative charge on adsorbent surface at higher pH [40], which reduces the electrostatic interaction between the dye and the adsorbent surface.

This decrease in removal efficiency is a result of the presence of SY dye as anionic ions ($D\text{-}SO_3^-$) in an aqueous solution, where the sulfonate groups ($D\text{-}SO_3Na$) of the dye dissociate upon dissolution [41]. Under basic conditions at higher pH value, the adsorbent surface becomes deprotonated and acquires a negative charge. As a result, electrostatic repulsion occurs between the analyte and the adsorbent, leading to a lower removal percentage [20].

A similar study conducted by Rajabi et al. (2015) revealed that the optimal pH for removing SY is 3 because the surface of APTES-modified MNPs has a positive charge in acidic media, which facilitates easier adsorption compared to alkaline pH [42]. This occurs because the surface of modified MNPs tends to attract negatively charged anionic dye molecules. Another study by Bagheri et al. found that the optimal pH for removing SY is 4. The accumulation of SY onto the surface of Fe3O4-MNPs loaded on activated carbon (Fe3O4-MNPs-AC) at a mild pH level can be enhanced by the combination of hydrogen and electrostatic attraction. However, at higher pH levels, the negative and repulsive forces between the anionic dye and the negatively charged adsorbent can hinder the further accumulation of SY on the adsorbent [43]. The trend observed in both studies is similar to the trend observed in our study, where removal of SY is favored at lower pH levels.

Furthermore, a higher pH value resulting from the presence of OH^- ions from NaOH would also lead to competition with the anionic dye for the active sites of the adsorbent. As a result, the electrostatic interaction between the dye and the adsorbent is reduced due to this competition. In contrast, a lower pH value generates H^+

ions on the external sites of the adsorbent. This increased the electrostatic interaction between the dye and the nano adsorbents [40], such as Fe_3O_4, because the negatively charged dye is attracted to the protonated (positively charged) surface of the adsorbent. Consequently, this enhances their interaction and facilitates the removal process.

However, a slight decrease in dye adsorption was observed below pH 3, which may be attributed to the dissolution of the metal oxide structure. Metal oxides are typically stable over a wide range of pH value, but in extremely acidic solutions, some metal oxides dissolution may occur [2]. This explains the trend line observed in Figure 8, indicating that pH 3 was determined to be the optimal pH condition.

Furthermore, the adsorbent dosage plot exhibited a similar trend line to the pH plot. A significant increase in removal capability was observed when the adsorbent dosage increased from 5 to 10 mg. However, the removal percentage decreased consistently as the adsorbent dosage increased to 20 mg. The initial increase in removal percentage was attributed to the accessibility of active sites, but it eventually became saturated, leading to reduced removal. At higher dosage, the overlapping particles blocked the binding sites, contributing to the decrease in removal ability [40]. Therefore, the trend line observed in Figure 8 indicated that the optimum dosage should be 10 mg. This trend is consistent with studies conducted by Chukwuemeka-Okorie et al. and Sartape et al. for the removal of sunset yellow and malachite green, respectively [45, 44].

The contact time trend was also crucial in determining the removal of SY by Fe_3O_4. Based on Figure 8, it can be observed that the removal of SY dye decreased as the contact time increased from 10 to 40 min. This result indicates that the shorter shaking times resulted in more efficient removal due to saturation of the binding sites on Fe_3O_4, rendering them unavailable for further adsorption of SY and ultimately reducing the removal rate of the dye. A similar trend was reported in a study by Aziz et el., where the percentage recovery of the analyte decreased with increasing contact time [46].

Moreover, the aqueous suspensions of Fe_3O_4 are generally unstable and can quickly aggregate, limiting their effectiveness [22, 47]. Therefore, the decrease in removal rate with increasing contact time can also attributed to the instability of Fe_3O_4 in the aqueous solution and the subsequently agglomeration of the adsorbent. This hinders the effective of SY dye. Consequently, the trendline would decrease, and in this study, and a contact time 10 min was considered the optimal value, which is adequate for the adsorption process.

Next, ANOVA analysis was conducted to evaluate the contribution of each factor to the efficiency of SY dye removal and to gain a better understanding of the obtained findings and their acceptability within the controllable factors [26, 48]. The ANOVA results are tabulated in Table 7. Based on the results, it can be concluded that the experiments were performed under controlled conditions, as the error value is below 50% contribution [26]. Additionally, the contribution percentage in Table 7 indicate that the contact period had the most significant effect, with the highest contribution percentage, while pH had the least significant effect on SY dye removal by Fe_3O_4.

Effect of temperature and initial concentration of SY dye

Moving on the effect of temperature and initial concentration on SY removal by Fe_3O_4, Figure 9 illustrates the binding. In can be observed that the removal percentage increased from 5 ppm to 20 ppm and then decreased as the initial concentration increased to 60 ppm, for all temperatures (298, 313, and 333 K). The initial increase in SY can be attributed to the availability of adsorption sites on the adsorbent and fewer collision between SY molecules, allowing for greater adsorption of analytes at low concentration [49, 50]. However, at higher initial concentrations, the surface area and available adsorption sites available on Fe_3O_4 became limited compared to the number of dye molecules present [20]. A similar finding was obtained by Aziz et al. for the adsorption of copper (II) onto palm oil boiler mill fly ash (POFA) at different initial concentration [46]. In this study, an initial concentration of 20 ppm was chosen as the optimum concentration for SY dye.

Table 5. Removal of SY dye for each run and S/N ratios

Run	pH	Contact Time (min)	Adsorbent Dosage (mg)	Removal (%)			Average Removal (%)	S/N Ratio
				R1	R2	R3		
1	2	10	5	91.8768	91.8349	91.8554	91.8557	39.2621
2	2	20	10	91.5772	91.6026	91.4493	91.5430	39.2325
3	2	30	15	90.9665	90.9170	90.6991	90.8609	39.1675
4	2	40	20	90.1886	89.5809	89.3903	89.7199	39.0576
5	3	10	10	91.6790	91.6889	91.6355	91.6678	39.2443
6	3	20	5	91.6385	91.5604	91.5673	91.5887	39.2368
7	3	30	20	91.3041	91.7280	90.8469	91.2930	39.2085
8	3	40	15	91.4412	91.4764	91.2512	91.3896	39.2179
9	4	10	15	91.5512	91.4914	91.4267	91.4898	39.2274
10	4	20	20	91.4919	91.2922	91.3568	91.3803	39.2170
11	4	30	5	89.0153	89.5729	90.6890	89.7591	39.0608
12	4	40	10	91.5900	91.5293	91.5631	91.5608	39.2342
13	5	10	20	91.6389	91.6059	91.5816	91.6088	39.2387
14	5	20	15	91.7294	91.7031	91.7489	91.7271	39.2500
15	5	30	10	91.7673	91.5475	91.7440	91.6863	39.2461
16	5	40	5	63.8219	60.6472	61.8655	62.1115	35.8577

Table 6. S/N ratios response

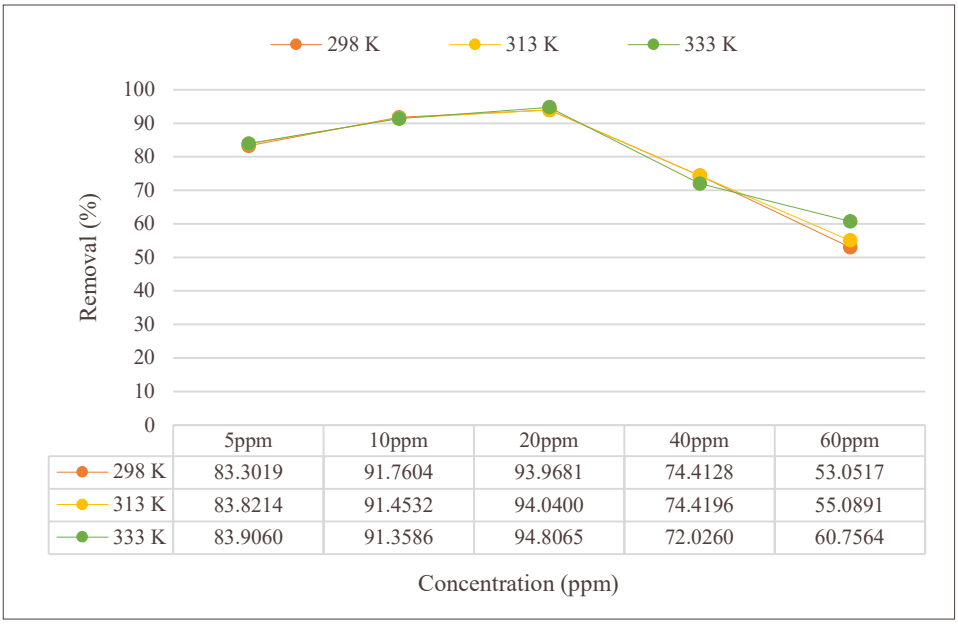
Level	pH	Contact Period	Adsorbent Dosage
1	39.18	39.24*	38.36
2	39.23*	39.23	39.24*
3	39.18	39.17	39.22
4	38.40	38.34	39.18
Delta	0.83	0.90	0.88
Rank	3	1	2

*The maximum S/N ratio, which indicates the optimum conditions

Table 7. Analysis of Variance

Variance Source	DF	SS	MS	F-ratio	P-value	% Contribution
pH	3	1.921	0.6404	0.89	0.475	18.17
Contact Period	3	2.305	0.7683	1.12	0.381	21.80
Adsorbent Dosage	3	2.213	0.7376	1.06	0.403	20.93
Error	6	4.133	0.6888			39.10
Total	15	10.572				100.00

Regarding the effect of temperature, it was observed that all three temperatures showed nearly identical removal ability. The removal percentage at 298 K, 313 K, and 333 K, as shown in Figure 9, were consistent for each SY concentration. However, at the highest concentration of 60 ppm, the removal percentage at 333 K was slightly higher than the other two temperatures. This result is consistent with thermodynamics considerations, indicating that the adsorption process is endothermic. Therefore, a temperature 298 K, corresponding to room temperature, was selected as the optimum temperature.



	5ppm	10ppm	20ppm	40ppm	60ppm
298 K	83.3019	91.7604	93.9681	74.4128	53.0517
313 K	83.8214	91.4532	94.0400	74.4196	55.0891
333 K	83.9060	91.3586	94.8065	72.0260	60.7564

Figure 9. Removal percentage based on initial concentration of SY dye and temperature. Condition: 10 mg of Fe_3O_4; contact period: 10 min; pH: 3

Adsorption kinetic study

The kinetic study was conducted, and the obtained data was used to plot the y against x curves based on the linear equations of the pseudo-first order (Equation 2) and pseudo-second order (Equation 3). It was observed that the data for the pseudo-second order exhibited the highest R^2 value, approaching one (R^2= 0.9812). Based on this result, it can be concluded that the adsorption behavior of SY dye onto Fe_3O_4 followed the pseudo-second order kinetic model. The pseudo-second order curve, along with the linear equation and the R^2 value, can be seen in Figure 10. Additionally, the kinetic parameters associated with this kinetic model are presented in Table 8.

Furthermore, the validity of the result was confirmed by the close agreement between the calculated q_e (7.905 mg/g) and the experimental q_e (9.732 mg/g). The low values of standard deviation and relative error (%) also indicate a better fit of this model to the data. Moreover, the data fitting well with the pseudo-second order suggests that the rate-limiting step involve chemisorption [26], which occurs between the dye and the adsorbent.

Table 8. Pseudo-second order model parameters

Kinetic model	Parameters	Value
	q_e exp (mg/ g)	**9.732**
Pseudo-second order	q_e cal (mg/g)	7.905
	K_2 (g/mg min)	0.041
	h (mg/g min)	2.587
	$t^{0.5}$(min)	0.005
	R^2	0.9812
	Δq(%)	10.839
	Relative error (%)	18.773

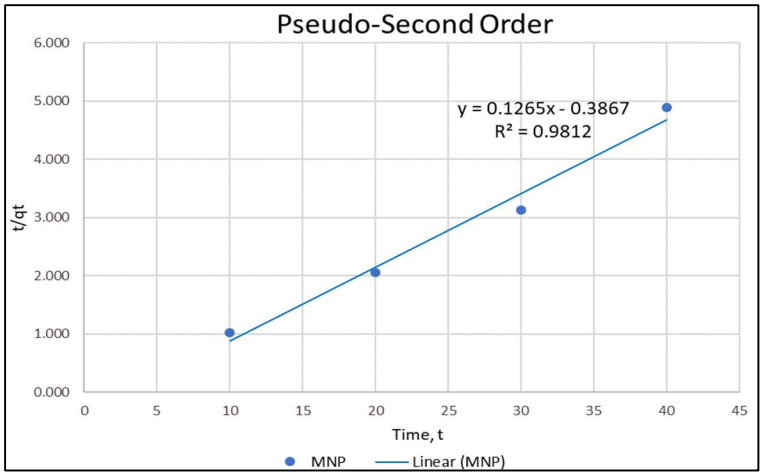


Figure 10. Adsorption kinetic of Sunset Yellow FCF based on pseudo-second order model

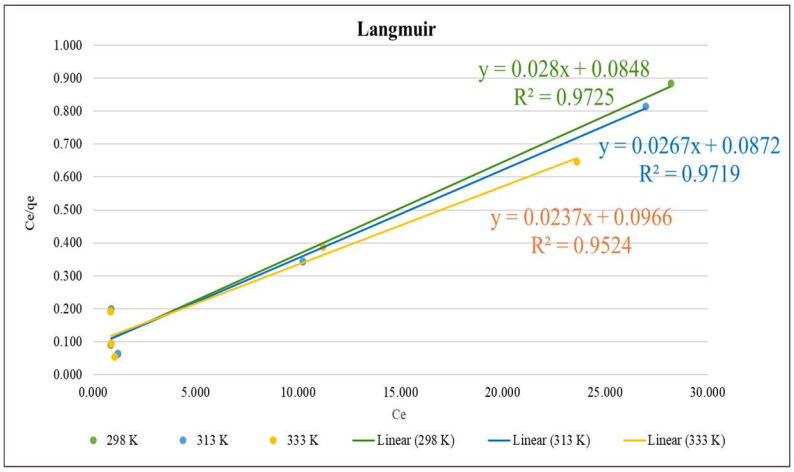


Figure 11. Adsorption isotherm of Sunset Yellow FCF based on Langmuir model

Adsorption isotherm study

Furthermore, the isotherm experiment was conducted using several models, and the data obtained was used to plot linear curves based on Equations (6), (7), (8), (10), and (11) for Langmuir, Freundlich, Dubinin-Radusckich, Halsey and Temkin models, respectively. Based on the obtained curved, the Langmuir model exhibited the highest R^2 value, approaching 1. Therefore, it could be concluded that the Langmuir model best fits the data from this study. The curve of this model, along with the calculated parameters, is shown in Figure 11 and Table 9, respectively.

Based on the observed results indicating adherence to the Langmuir model, it suggests that monolayer adsorption occurred, forming a single molecule thickness of adsorbates. Additionally, it validates the homogeneity of the Fe_3O_4 adsorbent used in this study. Furthermore, the calculated R_L values in Table 9, obtained using equation (15), indicate that the isotherm adsorption was favorable as all the calculated values between 0 and 1. Thus, it confirmed that Fe_3O_4 is suitable for the adsorption of SY dye under the conditions employed in this study.

$$R_L = \frac{1}{1 + bC_0} \quad (15)$$

Where b = Langmuir constant, and C_0 = initial concentration of sunset yellow (ppm)

Table 9. Langmuir isotherm model parameters

Isotherm Model	Parameters	Temperature		
		298 K	313 K	333 K
Langmuir	q_m (mg/g)	35.7140	37.4530	42.1940
	b (L/mg)	0.3300	0.3060	0.2450
	R^2	0.9725	0.9719	0.9524
	R_L	0.0481	0.0517	0.0636

Adsorption thermodynamic

Table 10 presents the thermodynamic parameters for the removal of SY dye by Fe_3O_4. Based on the results, the calculated ΔG° (J/mol) values in this study were negative. This indicates the spontaneous nature and thermodynamic feasibility [19, 40] of the process at all temperatures. Additionally, the positive value of enthalpy, ΔH° (J/mol), suggest that the adsorption process is endothermic. In contrast, the positive entropy value, ΔS° (J/Kmol), indicates an increase in randomness at the solid/liquid interface during the adsorption process [40, 51]. Furthermore, it suggests a favorable affinity between the adsorbent and the dye [39].

Table 10. Thermodynamic parameters of SY adsorption onto Fe_3O_4

Temperature (K)	ΔG° (J/mol)	ΔH° (J/mol)	ΔS° (J/Kmol)
298	-302.759		
313	-531.646	9.988	42.628
333	-1210.139		

Method validation and real sample

To validate the proposed method, the calibration curve of A versus analyte concentration (ranging from 2 to 80 ppm) yielded an R^2 value of 0.9933. The removal percentage and RSD% for inter-day (n=5) and intra-day (n=7) are presented in Table 11. The removal (%) for inter- and intra-day ranged from 34.02% to 82.87% and 33.67% to 82.92%, respectively, while the RSD% for inter-day and intra-day ranged from 2.45% to 6.91% and 2.49% to 6.70%, respectively.

Furthermore, when three real wastewater samples from different locations were spiked with analyte initial concentrations of 5, 20, and 60 ppm, and analyzed using UV–Vis spectrophotometer, the sample removal (%) ranged from 30.10% to 84.43%, with RSD% ranging from 1.18% to 9.12%, as shown in Table 12. The results indicated that these real wastewater samples had a slightly complicated matrix, as the removal performance was somewhat affected and reduced compared to deionized water, especially at high initial concentrations of the analyte. However, the majority of removal performances achieved high removal percentage, indicating that the Fe_3O_4 adsorbent was still capable of removing the SY dye from real water samples despite the matrix effect. This suggests that the adsorbent is practical for the removal of sunset yellow dye from wastewater samples. The method can be further developed in the future to improve analyte removal performance.

Table 11. Linearity, repeatability, and precision of the SY dye removal method

Calibration Equation	R^2	Spiked Concentration (ppm)	Inter-day (n=5)		Intra-day (n=7)	
			Removal (%)	RSD (%)	Removal (%)	RSD (%)
y = 0.04466x + 0.02	0.9933	5	82.8634	2.4592	82.9134	2.4943
		20	56.8058	6.9072	56.8189	6.6933
		60	34.0207	3.3867	33.6763	2.9314

Table 12. Three real sample analysis results (Removal% and RSD%)

Calibration equation	R^2	Spiked Concentration (ppm)	Wastewater A		Wastewater B		Wastewater C	
			Removal (%)	RSD (%)	Removal (%)	RSD (%)	Removal (%)	RSD (%)
y = 0.04466 x + 0.02	0.9933	5	82.8634	2.4592	84.4256	2.8177	80.8072	3.0819
		20	56.8058	6.9072	72.1046	2.7646	53.6209	9.1147
		60	34.0207	3.3867	38.9779	4.3579	30.1158	1.1881

Conclusion

In this study, magnetite or magnetic nanoparticles (MNPs) with the chemical formula Fe_3O_4, a basic form of magnetic nanomaterials (MNMs), were successfully synthesized using co-precipitation method. These MNPs were employed as an adsorbent for the removal of sunset yellow FCF dye from aqueous samples. Various instruments such as VSM, TGA, FTIR, SEM, TEM, XRD, and BET were utilized to investigate the physical characteristics of the prepared adsorbents, including their properties, structures, surface areas, and functional groups.

To determine the optimized conditions for the removal of SY dye by Fe_3O_4, an adsorption study was conducted. The Taguchi method was employed for the optimization experiments, and the optimal testing conditions were found to be pH 3, 10 mg adsorbent dose, and 10 min contact time. Additionally, when the optimization for the effect of temperature and initial concentration of the dye was carried out separately, the optimum initial concentration of the dye was observed to be 20 ppm. Furthermore, room temperature was chosen as the optimum temperature, as consistent results were obtained across the all-tested temperatures. The application of these optimized conditions in further adsorption studies revealed that the kinetics behavior of the adsorbents towards SY dye followed the pseudo-second order model, while the isotherm study showed good fit with the Langmuir model. This indicates a chemical interaction or chemisorption between the adsorbents and adsorbate molecules, forming a monolayer adsorption. Moreover, the adsorption study demonstrated feasibility, endothermic nature, and spontaneous occurrence with increasing randomness.

Subsequently, the real wastewater samples from three different areas were used for method validation and real sample analysis. These samples were spiked with three different concentrations of analytes. The removal percentage ranged from 30% to 85%, with a low range of RSD% (1.8% to 9.2%). This suggests that the proposed adsorbent could effectively remove SY dye from real wastewater samples, albeit with slight influence from the matrix effect. Therefore, this study provides valuable insights into the nature of Fe3O4 and confirms the validity and practicality of the proposed method for removing SY dye from real wastewater samples. Further comprehensive studies can be conducted to enhance the removal performance.

Acknowledgements

The authors would like to express their gratitude to the Ministry of Higher Education, Malaysia for providing funding for this project through the Fundamental Research Grant Scheme (FRGS) with reference code FRGS/1/2021/STG04/USM/02/8 and account code 203.CIPPT.6711974. The authors are also thankful to the Advanced Medical and Dental Institute, Universiti Sains Malaysia, for providing the necessary resources to complete this project.

References

1. Jeeva, M., Lakkaboya, S. K., and Wan Zuhairi, W. Y. (2019). The adsorption of direct brown 1 dye using kaolinite and surfactant modified kaolinite. *Bulletin of the Geological Society of Malaysia*, 2019(67): 35-45.
2. Xiao, W., Jiang, X., Liu, X., Zhou, W., Garba, Z. N., Lawan, I., Wang, L., and Yuan, Z. (2021). Adsorption of organic dyes from wastewater by metal-doped porous carbon materials. *Journal of Cleaner Production*, 284: 124773.
3. Lu, Y., Song, S., Wang, R., Liu, Z., Meng, J., Sweetman, A. J., Jenkins, A., Ferrier, R. C., Li, H., Luo, W., and Wang, T. (2015). Impacts of soil and

water pollution on food safety and health risks in China. *Environment International*, *77*: 5-15.

4. Ma, X., Liu, Y., Li, X., Xu, J., Gu, G., and Xia, C. (2015). Water: The most effective solvent for liquid-phase hydrodechlorination of chlorophenols over Raney Ni catalyst. *Applied Catalysis B: Environmental*, 165: 351-359.
5. Belachew, N., and Hinsene, H. (2020). Preparation of cationic surfactant-modified kaolin for enhanced adsorption of hexavalent chromium from aqueous solution. *Applied Water Science*, 10(1): 38.
6. Foroughirad, S., Haddadi-Asl, V., Khosravi, A., and Salami-Kalajahi, M. (2020f). Synthesis of magnetic nanoparticles-decorated halloysite nanotubes/poly([2-(acryloyloxy)ethyl]trimethylammonium chloride) hybrid nanoparticles for removal of Sunset Yellow from water. *Journal of Polymer Research*, 27(10): 320.
7. Mosayebian, M. B. and Reza Moradi, K. M. (2021). Modelling the degradation of sunset yellow FCF azo dye by Fe_2O_3/Bentonite catalyst using artificial neural networks. *Journal of Nanoanalysis*, 8(3): 209-220.
8. Rovina, K., Acung, L. A., Siddiquee, S., Akanda, J. H., and Shaarani, S. M. (2017h). Extraction and analytical methods for determination of sunset yellow (E110)—a review. *Food Analytical Methods*, 10: 773-787.
9. Gholami, Z., Marhamatizadeh, M. H., Yousefinejad, S., Rashedinia, M., and Mazloomi, S. M. (2021). Vortex-assisted dispersive liquid-liquid microextraction based on hydrophobic deep eutectic solvent for the simultaneous identification of eight synthetic dyes in jellies and drinks using HPLC-PDA. *Microchemical Journal*, 170: 106671.
10. El-Borm, H., Badawy, G., Hassab El-Nabi, S., El-Sherif, W., and Atallah, M. (2020). Toxicity of sunset yellow FCF and tartrazine dyes on DNA and cell cycle of liver and kidneys of the chick embryo: the alleviative effects of curcumin. *Egyptian Journal of Zoology*, 74(74): 43-55.
11. Rovina, K., Siddiquee, S., and Shaarani, S. M. (2016k). Highly sensitive determination of sunset yellow FCF (E110) in food products based on chitosan/nanoparticles/MWCNTs with modified gold electrode. *IOP Conference Series: Earth and Environmental Science*, 36(1): 012023.
12. Nwuzor, I. C., Chukwuneke, J. L., Nwanoneyi, S. C., Obasi, H. C., and Ihekweme, G. O. (2018). Modification and Physiochemical Characterization of Kaolin Clay for Adsorption of Pollutants from Industrial Paint Effluent. *European Journal of Advances in Engineering and Technology*, 5(8): 609-620.
13. Villar Blanco, L., González Sas, O., Sánchez, P. B., Domínguez Santiago, Á., and González de Prado, B. (2022). Congo red recovery from water using green extraction solvents. *Water Resources and Industry*, 27: 100170.
14. El Mouhri, G., Merzouki, M., Belhassan, H., Miyah, Y., Amakdouf, H., Elmountassir, R., and Lahrichi, A. (2020). Continuous adsorption modelling and fixed bed column studies: Adsorption of tannery wastewater pollutants using beach sand. *Journal of Chemistry*, 2020: 7613484.
15. Benjelloun, M., Miyah, Y., Akdemir Evrendilek, G., Zerrouq, F., and Lairini, S. (2021). Recent advances in adsorption kinetic models: Their application to dye types. *Arabian Journal of Chemistry*, 14(4): 103031.
16. Lawal, I. A., Lawal, M. M., Azeez, M. A., and Ndungu, P. (2019). Theoretical and experimental adsorption studies of phenol and crystal violet dye on carbon nanotube functionalized with deep eutectic solvent. *Journal of Molecular Liquids*, 288: 110895.
17. Panda, S. K., Aggarwal, I., Kumar, H., Prasad, L., Kumar, A., Sharma, A., Vo, D. V. N., Van Thuan, D., and Mishra, V. (2021). Magnetite nanoparticles as sorbents for dye removal: A review. *Environmental Chemistry Letters*, 19(3): 2487-2525.
18. Soliman, N. K., and Moustafa, A. F. (2020). Industrial solid waste for heavy metals adsorption features and challenges: A review. *Journal of Materials Research and Technology*, 9(5): 10235-10253.
19. Husin, N. A., Muhamad, M., Yahaya, N., Miskam, M., Syazni Nik Mohamed Kamal, N. N., Asman, S., Raoov, M., and Mohamad Zain, N. N. (2021). Application of a new choline-imidazole based deep

eutectic solvents in hybrid magnetic molecularly imprinted polymer for efficient and selective removal of naproxen from aqueous samples. *Materials Chemistry and Physics*, 261: 124228.

20. Husin, N. A., Hashim, N. M., Yahaya, N., Miskam, M., Raoov, M., and Zain, N. N. M. (2021). Exploring magnetic particle surface embedded with imidazole-based deep eutectic solvent for diclofenac removal from pharmaceutical wastewater samples. *Journal of Molecular Liquids*, 332: 115809.
21. Rodríguez-Ramos, R., Santana-Mayor, Á., Socas-Rodríguez, B., and Rodríguez-Delgado, M. Á. (2021). Recent applications of deep eutectic solvents in environmental analysis. *Applied Sciences (Switzerland)*, 11(11): 11114779.
22. Wei, X., Wang, Y., Chen, J., Xu, P., Xu, W., Ni, R., Meng, J., and Zhou, Y. (2019). Poly(deep eutectic solvent)-functionalized magnetic metal-organic framework composites coupled with solid-phase extraction for the selective separation of cationic dyes. *Analytica Chimica Acta*, 1056: 47-61.
23. Badu Latip, N. M., Gopal, K., Suwaibatu, M., Hashim, N. M., Rahim, N. Y., Raoov, M., Yahaya, N., and Mohamad Zain, N. N. (2021). Removal of 2,4-dichlorophenol from wastewater by an efficient adsorbent of magnetic activated carbon. *Separation Science and Technology (Philadelphia)*, 56(2): 252-265.
24. Rezaei, H., Haghshenasfard, M., and Moheb, A. (2017). Optimization of dye adsorption using Fe_3O_4 nanoparticles encapsulated with alginate beads by Taguchi method. *Adsorption Science and Technology*, 35(1–2): 55-71.
25. Nandhini, M., Suchithra, B., Saravanathamizhan, R., and Prakash, D. G. (2014). Optimization of parameters for dye removal by electro-oxidation using Taguchi design. *Journal of Electrochemical Science and Engineering*, 4(4): 227-234.
26. Korake, S. R., and Jadhao, P. D. (2021). Investigation of Taguchi optimization, equilibrium isotherms, and kinetic modeling for cadmium adsorption onto deposited silt. *Heliyon*, *7*(1): e05755.
27. Wang, J., and Guo, X. (2020). Adsorption kinetic models: Physical meanings, applications, and solving methods. *Journal of Hazardous Materials*, 390: 122156.
28. Ebelegi, A. N., Ayawei, N., and Wankasi, D. (2020ab). Interpretation of adsorption thermodynamics and kinetics. *Open Journal of Physical Chemistry*, 10(03): 166-182.
29. Chen, X. (2015). Modelling of experimental adsorption isotherm data. *Information (Switzerland)*, 6(1): 14-22.
30. Al-Ghouti, M. A., and Da'ana, D. A. (2020). Guidelines for the use and interpretation of adsorption isotherm models: A review. *Journal of Hazardous Materials*, 393: 122383.
31. Al-Khateeb, L. A., Hakami, W., and Salam, M. A. (2017). Removal of non-steroidal anti-inflammatory drugs from water using high surface area nanographene: Kinetic and thermodynamic studies. *Journal of Molecular Liquids*, 241: 733-741.
32. Thaligari, S. K., Srivastava, V. C., and Prasad, B. (2016). Adsorptive desulfurization by zinc-impregnated activated carbon: characterization, kinetics, isotherms, and thermodynamic modelling. *Clean Technologies and Environmental Policy*, 18(4): 1021-1030.
33. Mokadem, Z., Mekki, S., Saïdi-Besbes, S., Agusti, G., Elaissari, A., and Derdour, A. (2017). Triazole containing magnetic core-silica shell nanoparticles for Pb^{2+}, Cu^{2+} and Zn^{2+} removal. *Arabian Journal of Chemistry*, 10(8): 1039-1051.
34. Cao, H., He, J., Deng, L., and Gao, X. (2009). Fabrication of cyclodextrin-functionalized superparamagnetic Fe_3O_4 /amino-silane core-shell nanoparticles via layer-by-layer method. *Applied Surface Science*, 255(18): 7974-7980.
35. Hashim, N. M., Mohamad, M., Kamal, N. N. S. N. M., Aziz, M. Y., Mohamad, S., Yahaya, N., and Zain, N. N. M. (2023). Revolutionizing drug removal: Green magnetic nanoparticles functionalized with hydrophobic deep eutectic solvents for anti-inflammatory drug adsorption. *Journal of Molecular Liquids*, 383: 122082.
36. Mamman, S., Suah, F. B. M., Raaov, M., Mehamod, F. S., Asman, S., and Zain, N. N. M. (2021). Removal of bisphenol A from aqueous media using a highly selective adsorbent of hybridization

cyclodextrin with magnetic molecularly imprinted polymer. *Royal Society Open Science*, 8(3): 201604

37. Shahriman, M. S., Mohamad Zain, N. N., Mohamad, S., Abdul Manan, N. S., Yaman, S. M., Asman, S., and Raoov, M. (2018). Polyaniline modified magnetic nanoparticles coated with dicationic ionic liquid for effective removal of rhodamine B (RB) from aqueous solution. *RSC Advances*, 8(58): 33180–33192.
38. Meftah Elgubbi, H., Salhah Othman, S., and Wahida Harun, F. (2020). Modification of kaolinite clay using benzyltriethylammonium chloride as a surfactant: Preparation and characterization. *International Journal of Engineering & Technology*, 9(4): 31088.
39. Mosoarca, G., Popa, S., Vancea, C., and Boran, S. (2021). Optimization, equilibrium and kinetic modeling of methylene blue removal from aqueous solutions using dry bean pods husks powder. *Materials*, 14(19): 14195673.
40. Noreen, S., Mustafa, G., Ibrahim, S. M., Naz, S., Iqbal, M., Yaseen, M., Javed, T., and Nisar, J. (2020). Iron oxide (Fe_2O_3) prepared via green route and adsorption efficiency evaluation for an anionic dye: Kinetics, isotherms and thermodynamics studies. *Journal of Materials Research and Technology*, 9(3): 4206-4217.
41. De Sá, F. P., Cunha, B. N., and Nunes, L. M. (2013). Effect of pH on the adsorption of sunset yellow FCF food dye into a layered double hydroxide (CaAl-LDH-NO_3). *Chemical Engineering Journal*, 215–216: 122-127.
42. Rajabi, H. R., Arjmand, H., Hoseini, S. J., and Nasrabadi, H. (2015). Surface modified magnetic nanoparticles as efficient and green sorbents: Synthesis, characterization, and application for the removal of anionic dye. *Journal of Magnetism and Magnetic Materials*, 394: 7-13.
43. Bagheri, A. R., Ghaedi, M., Asfaram, A., Bazrafshan, A. A., and Jannesar, R. (2017). Comparative study on ultrasonic assisted adsorption of dyes from single system onto Fe3O4 magnetite nanoparticles loaded on activated carbon: Experimental design methodology. *Ultrasonics Sonochemistry*, 34: 294-304.
44. Chukwuemeka-Okorie, H. O., Ekuma, F. K., Akpomie, K. G., Nnaji, J. C., and Okereafor, A. G. (2021). Adsorption of tartrazine and sunset yellow anionic dyes onto activated carbon derived from cassava sievate biomass. *Applied Water Science*, 11(2): 27.
45. Sartape, A. S., Mandhare, A. M., Jadhav, V. V., Raut, P. D., Anuse, M. A., and Kolekar, S. S. (2017). Removal of malachite green dye from aqueous solution with adsorption technique using *Limonia acidissima* (wood apple) shell as low-cost adsorbent. *Arabian Journal of Chemistry*, 10: 3229-3238.
46. Aziz, A. S. A., Manaf, L. A., Man, H. C., and Kumar, N. S. (2014). kinetic modeling and isotherm studies for copper(II) adsorption onto palm oil boiler mill fly ash (POFA) as a natural low-cost adsorbents. *BioResources*, 9(1): 336-356.
47. Marć, M., Drzewiński, A., Wolak, W. W., Najder-Kozdrowska, L., and Dudek, M. R. (2021). Filtration of nanoparticle agglomerates in aqueous colloidal suspensions exposed to an external radio-frequency magnetic field. *Nanomaterials*, 11(7):1737
48. Madan, S. S., and Wasewar, K. L. (2017). Optimization for benzeneacetic acid removal from aqueous solution using CaO_2 nanoparticles based on Taguchi method. *Journal of Applied Research and Technology*, *15*(4): 332-339.
49. Oetjik, W., and Aida Ibrahim, S. (2021). A review: The effect of initial dye concentration and contact time on the process of dye adsorption using agricultural wastes adsorbent. *Progress in Engineering Application and Technology*, *2*(2): 2773-5303.
50. Panda, H., Tiadi, N., Mohanty, M., and Mohanty, C. R. (2017). Studies on adsorption behavior of an industrial waste for removal of chromium from aqueous solution. *South African Journal of Chemical Engineering*, *23*: 132-138.
51. Javadian, H., Koutenaei, B. B., Shekarian, E., Sorkhrodi, F. Z., Khatti, R., and Toosi, M. (2017). Application of functionalized nano HMS type mesoporous silica with N-(2-aminoethyl)-3-aminopropyl methyldimethoxysilane as a suitable adsorbent for removal of Pb(II) from aqueous

media and industrial wastewater. *Journal of Saudi Chemical Society*, 21: 219-230

Malaysian Journal of Analytical Sciences (MJAS)
Published by Malaysian Analytical Sciences Society

VALIDATION OF HIGH-PERFORMANCE LIQUID CHROMATOGRAPHY (HPLC) METHOD FOR DELPHINIDIN-3-O-GLUCOSIDE CHLORIDE IN RAT PLASMA

(Pengesahan Kaedah Kromatografi Cecair Berprestasi Tinggi (KCPT) bagi Delfinidin-3-O-Glukosida Klorida dalam Plasma Tikus)

Nur Atielah Nabila Mohd Shafawi[1], Ruzilawati Abu Bakar[2], Liza Noordin[3], Shafreena Shaukat Ali[1], and Wan Amir Nizam Wan Ahmad[1]

[1]*School of Health Sciences, Health Campus, Universiti Sains Malaysia Kubang Kerian, 16150 Kota Bharu, Kelantan, Malaysia*
[2]*Department of Phamacology, School of Medical Sciences, Health Campus, Universiti Sains Malaysia Kubang Kerian, 16150 Kota Bharu, Kelantan, Malaysia*
[3]*Department of Physiology, School of Medical Sciences, Health Campus, Universiti Sains Malaysia Kubang Kerian, 16150 Kota Bharu, Kelantan, Malaysia*

[*]*Corresponding author: wanamir@usm.my*

Received: 7 April 2023; Accepted: 23 July 2023; Published: 22 August 2023

Abstract

This study involved the development and validation of a high-performance liquid chromatography (HPLC) assay for the determination of delphinidin-3-O-glucoside chloride, specifically to be applied in future pharmacokinetic and bioavailability studies in rats supplemented with roselle extract. The HPLC method was validated following solid-phase extraction, with six validation parameters (linearity, recovery, precision, accuracy, limit of detection (LOD), and limit of quantification (LOQ) assessed according to Food and Drug Administration guidelines. Chromatographic separations were performed using Agilent Reverse Phase EC-C18 (4.6×150 mm; 2.7 µm particle size) and mobile phase acetonitrile with 0.1% trifluoracetic acid in an aqueous solution (81:19, v/v). The calibration curve of delphinidin-3-O-glucoside chloride had a coefficient determination (R^2) of ≥95.0% and recovery percentage of 80.37%. It also showed good precision and accuracy, and its method detection and quantification limits were 47 ng/mL and 213 ng/mL, respectively. In conclusion, the validated HPLC method in this study can be used to determine the pharmacokinetic of delphinidin-3-O-glucoside chloride or other type of anthocyanins in the future.

Keywords: delphinidin-3-o-glucoside chloride, rat plasma, high-performance liquid chromatography, method validation

Abstrak

Kajian ini melibatkan pembangunan dan pengesahan kaedah kromatografi cecair berprestasi tinggi (KCPT) bagi pengesanan sejenis antosianin, iaitu delfinidin-3-O-glukosida klorida, khususnya bertujuan untuk digunakan dalam kajian lanjutan untuk farmakokinetik dan bioavailibiliti antosianin di dalam tikus yang disuplementasi dengan ekstrak rosel. Kaedah KCPT ini disahkan menggunakan kaedah pengekstrakan fasa pepejal dan enam parameter pengesahan dinilai mengikut garis panduan Pentadbiran Makanan dan Dadah iaitu kelinearan, pemulihan, ketepatan, kejituan, had pengesanan, dan had kuantifikasi. Pengasingan kromatografik dilakukan menggunakan Agilent Fasa Berbalik EC-C18 (4.6×150 mm; 2.7µm saiz partikel) manakala fasa gerak

adalah asetonitril bersama 0.1% trifluoroasetik asid di dalam air (81:19, v/v). Lengkung penentukuran delfinidin-3-0-glukosida klorida mempunyai penentuan pekali (R^2) ≥95.0% dan peratusan pemulihan delfinidin-3-0-glukosida klorida adalah 80.37%. Delfinidin-3-0-glukosida klorida juga menunjukkan ketepatan dan kejituan yang baik dan had pengesanan dan kuantifikasi kaedah untuk delfinidin-3-0-glukosida klorida masing-masing adalah 47 ng/mL dan 213 ng/mL. Kesimpulannya, kaedah HPLC yang disahkan dalam kajian ini boleh digunakan untuk menentukan tahap antosianin dalam kajian farmakokinetik pada masa depan.

Kata kunci: delfinidin-3-o-glukosida klorida, plasma tikus, kromatografi cecair berprestasi tinggi, pengesahan kaedah

Introduction

In recent years, anthocyanins have come into the interest of researchers from various fields due to their health-promoting properties. One major health benefit associated with anthocyanin intake is a reduced risk of coronary heart disease [1]. Anthocyanins are naturally occurring, water-soluble pigments found in the vacuoles of vascular plants that serve multiple functions, such as aiding in pollinating plants by luring insects and animals with their color and potent UV absorbance [2]. Anthocyanins give out red, purple, and blue pigments, resulting from the conjugated bonds in flowers, tubers, and fruits. They are classified under the flavonoid class and phenolic photochemical subclass [3]. While water-soluble, their stability varies according to pH, temperature, light, and structure [4]. As a result, anthocyanins appear red in acidic environments and blue in alkaline environments. Accordingly, they are commonly found in plants and the most prevalent anthocyanins in nature are cyanidin, delphinidin, and pelargonidin, which are present in 50% of flowers, 69% of fruits, and 80% of colored leaves [5]. However, in current study, we choose to focus on delphinidin since it is one of the most abundant types of anthocyanin found in roselle calyx extract, which is the interest of our research team.

To date, several analytical methods, especially liquid chromatography, are available for the detection of anthocyanins in biological fluid and tissue [6-10]. Liquid chromatography, including high-performance liquid chromatography (HPLC), allows the effective separation and identification of compounds in various biological samples, suitable for both qualitative and quantitative analysis. However, variability in experimental condition factors, such as extraction method, quantification, and parameter analysis, hinders the reproducibility of this method for obtaining the most efficient recovery of anthocyanins. Additionally, large sample volumes are required for the detection of anthocyanins, as shown in past studies [7, 11]. Although these protocols have been demonstrated to be efficient, none specifically focus on the anthocyanin delphinidin-3-O-glucoside chloride.

Despite these shortcomings, prior validation of HPLC provides documented evidence of a reliable analytical method for the sensitive quantification of compounds present in samples, thus providing valuable data. Therefore, the development and validation of a new HPLC protocol for the determination of anthocyanin, specifically delphinidin-3-O-glucoside chloride, is much needed as a potential reference protocol to be applied in future pharmacokinetic and bioavailability studies in rats supplemented with roselle extract. By employing six validation parameters according to FDA guidelines (linearity, recovery, precision, accuracy, limit of detection (LOD), and limit of quantification (LOQ), this study describes a rapid, sensitive, and specific HPLC protocol for the detection of delphinidin-3-O-glucoside chloride in small volumes of rat plasma.

Materials and Methods

Chemicals and reagent

Delphinidin-3-O-glucoside chloride (catalog no. CFN92038) and its internal standard, cyanidin-3-5-0-diglucoside chloride (catalog no. CFN92138) were purchased from ChemFaces (Wuhan China) (Figure 1). Acetonitrile (ACN), and methanol were of HPLC grade from Merck (Darmstadt, Germany) while sulfosalicyclic acid, trifluoroacetic acid (TFA) and formic acid (FA) were of analytical grade from Sigma-Aldrich (St Louis, USA). Water used was deionized and distilled using the Water Prodigy System (Labconco, MO, USA).

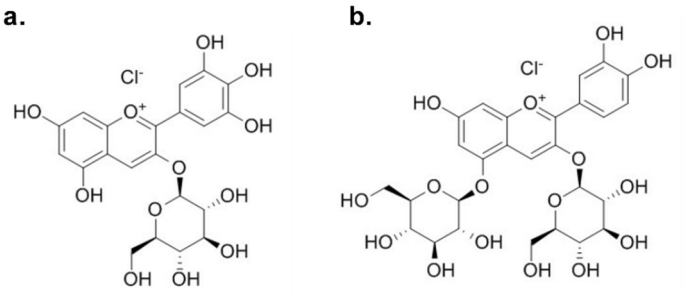


Figure 1 . Chemical structure for a. delphinidin-3-O-glucoside chloride with molecular formula of $C_{21}H_{21}ClO_{12}$, and b. cyanidin-3-5-O-diglucoside chloride with the molecular formula of $C_{27}H_{31}O_{16}C_l$

Chromatographic condition

The HPLC system consisted of a pump (Gilson 307), a column heater, an autosampler (Gilson GX-271) and detector (UV/VIS-155) from Gilson (Wisconsin, USA). Gilson Trilution® LC software was used for data acquisition. Chromatographic separations were performed on Agilent Reverse Phase EC-C18 (4.6 × 150 mm I.D, particle size 2.7 µm) (Agilent Technologies, California, USA) with flow rate of 0.5 mL/min, injection volume of 10 µL and detected at 525 nm. The mobile phase is composed of ACN with 0.1% of TFA in aqueous solution (81:19, v/v) and degassed in an ultrasonic bath (FB15063) from Fisher Scientific (USA). All solutions were filtered through a 0.45 µm membrane (Sartorious, Germany) prior to use.

Preparation of stock, standard working solutions and plasma samples

Standard stock solutions of delphinidin-3-O-glucoside chloride (100 µg/mL) and its internal standard (100 µg/mL) were prepared by dissolving 1 mg of each in 10 mL methanol, respectively. A working solution of the internal standard was prepared by diluting the stock solution of cyanidin-3-5-0-diglucoside chloride with mobile phase to give a final concentration of 500 ng/mL. Five selected delphinidin-3-0-glucoside chloride concentrations of 250, 500, 1000, and 2000, 3000 ng/mL in buffer were prepared by further dilution of the stock solution with appropriate volumes of mobile phase accordingly.

Blank plasma was obtained from untreated rats and 500 µL of plasma spiked with delphinidin-3-O-glucoside chloride to achieve five concentrations of 250, 500, 1000, and 2000, 3000 ng/mL for calibration curve. Quality control (QC) samples of low, medium, and high concentration (350, 1500, 2500 ng/mL) were prepared similarly to the standard calibration. All stock solutions were stored at 4 °C and all working solutions were freshly prepared daily.

Solid phase extraction

The plasma samples spiked with delphinidin-3-O-glucoside chloride and its internal standard were subjected to solid phase extraction to remove unwanted analytes or impurities using Water Sep-Pak tC18 cartridge (Massachusetts, USA). Protein precipitation of plasma sample was done by adding 500 µL of 0.1 % TFA aqueous solution and 100 µL of 20 % sulfosalicylic acid aqueous solution in 500 µL of plasma, vortex mixed and centrifuged at 4000 × *g* for 20 mins at 4˚C and supernatant was kept for further separation. Following that, the cartridge was first pre-conditioned with 2 mL of methanol followed by 2 mL of 0.1% TFA in aqueous solution. The supernatant plasma sample was then loaded into the cartridge and then eluted with 1 mL of methanol. Eluted sample was then centrifuged at 5000 rpm for 10 minutes using an Ultrafree®-MC centrifugal filter (Merck, Germany) and the supernatant was evaporated to dryness using nitrogen gas. Dried residue then was reconstituted with 100 µL of mobile phase and then injected into HPLC for analysis.

Method validation

Plasma calibration curves were prepared and analyzed in triplicate for intra-day and inter-day to assess the linearity, precision, accuracy, recovery, LOD, LOQ, selectivity, sensitivity, and stability according to the

CDER [12].

Results and Discussion

Chromatographic condition

Based on our team's previous optimization study [13], for this study, we chose a composition of ACN with 0.1% TFA in an aqueous solution (81:19, v/v) as a mobile phase. Although in prior research rapid resolution liquid chromatography analysis was conducted for the identification of another type of anthocyanin (cyanidin-3-O-glucoside), this protocol still produced a good peak of delphinidin-3-0-glucoside chloride content and effectively separated it from its internal standard (cyanidin-3-5-0-glucoside chloride).

Solid-phase extraction

Several parameters, such as percentage of recoveries, chromatographic peak shape obtained, and peak tailing, were some of the factors that needed to be considered when choosing a suitable extraction method. In this experiment, we thus chose solid-phase extraction rather than liquid-liquid extraction based on our team's previous optimization study [13]. Furthermore, as Sep-Pak tC18 cartridges are widely employed to purify anthocyanin due to their simplicity and efficiency [14-17], we incorporated Sep-Pak tC18 cartridges into our SPE extraction method.

Recovery

In this study, we obtained delphinidin-3-O-glucoside chloride recoveries using two different methods: area ratio and slope ratio. We quantified recovery by finding the ratio of the slopes of the calibration curve for the extracted (in plasma) to non-extracted (in buffer) samples. The recovery of delphinidin-3-O-glucoside chloride revealed the mean recovery percentage to be 80.377%, while the slope ratio was 71.43%. Generally, recovery need not be 100% when 80–90% recovery is considered optimal. Tables 1 and 2 summarize the percentage recoveries and their standard deviations (SD) at different extract concentrations.

The assay sample was calculated from the following equation 1:

$$\text{Recovery (\%)} = (\text{mean area ratio extracted} / \text{mean area ratio non-extracted}) \times 100 \quad (1)$$

Table 1. Recovery of delphinidin-3-O-glucoside chloride by area ratio

Concentration (ng/mL)	Mean Area Ratio (Non-Extracted)	SD	Mean Area Ratio (Extracted)	SD	Percentage Recovery (%)
3000	2.068	0.246	1.514	0.161	73.199
2000	1.387	0.275	1.035	0.258	74.662
1000	0.776	0.050	0.507	0.259	65.365
500	0.294	0.065	0.277	0.175	94.350
250	0.203	0.052	0.191	0.046	94.311
Mean					80.377 ±11.823

Table 2. Recovery of delphinidin-3-O-glucoside chloride by ratio of slopes

	Combined Standard Curve (Non-Extracted)	Combined Standard Curve (Extracted)
Intercept, a	-0.0097	0.0437
Slope, b	0.0007	0.0005
R^2	0.9648	0.9653
Recovery by the ratio of slope	0.0005/0.0007 = 71.43 %	

Calibration curve, precision, accuracy, and linearity

The concentration of a drug in an unknown sample can be determined using calibration curves to compare the unknown concentration to a set of standard samples with known concentrations [18]. The calibration curve of delphinidin-3-O-glucoside chloride was linear in the concentration range (250 ng/mL, 500 ng/mL, 1000 ng/mL, 2000 ng/mL, and 3000 ng/mL) in rat plasma. Five concentrations were selected to produce a calibration curve for delphinidin-3-O-glucoside on intraday (Figure 2) and inter-days (Figure 3). Five to eight points should make up the calibration curve to cover the expected analyte concentration range in the test samples [19-20].

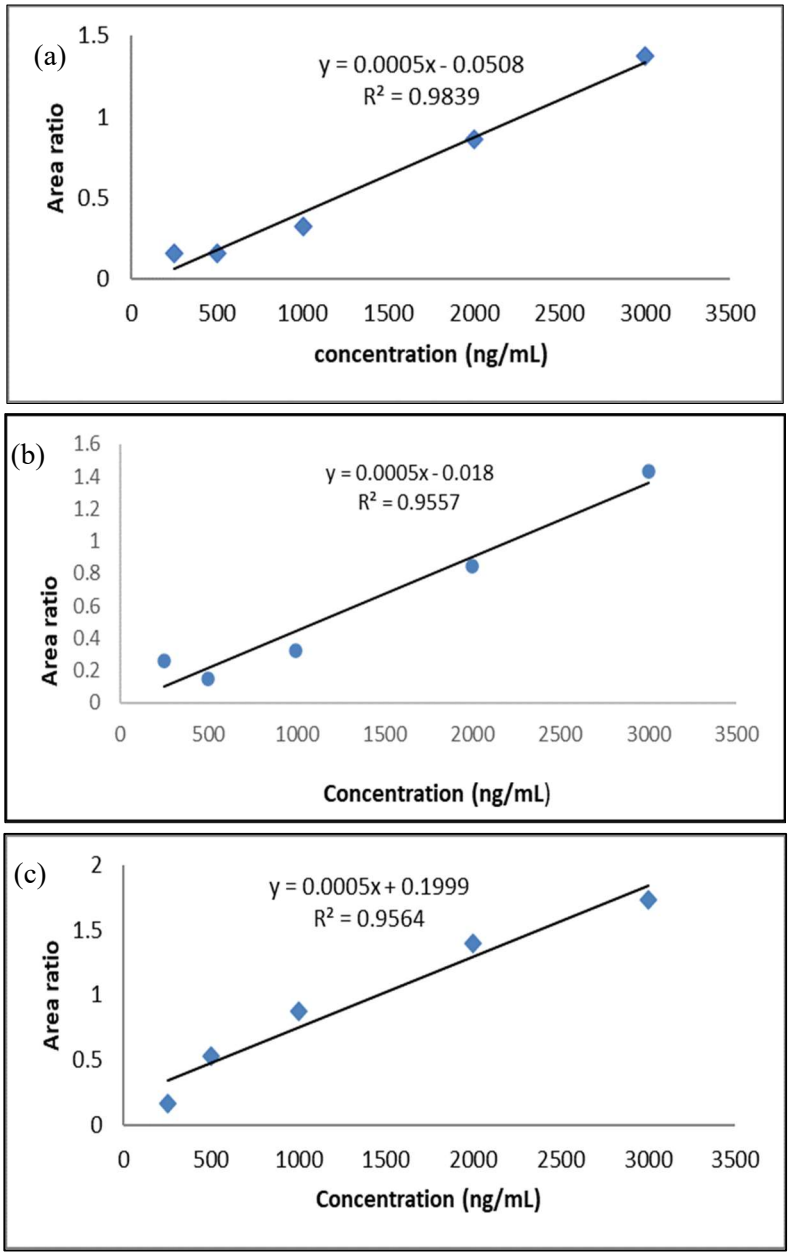


Figure 2. Intra-day validation: calibration curves of the area ratio of delphinidin-3-O-glucoside chloride to cyanidin-3-5-0-glucoside chloride versus delphinidin-3-O-glucoside chloride's concentrations a) validation 1, b) validation 2, and c) validation 3.

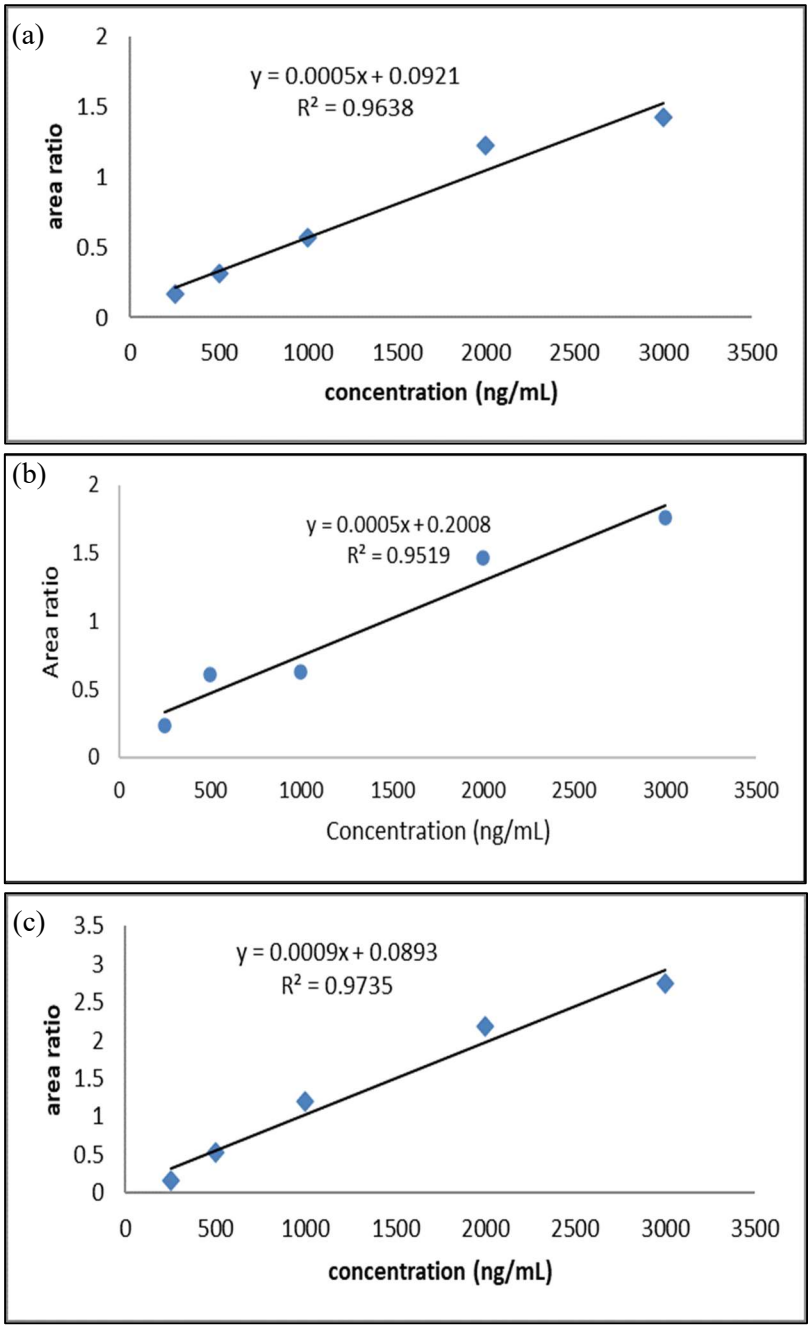


Figure 3. Inter-day validation: calibration curves of the area ratio of delphinidin-3-O-glucoside chloride to cyanidin-3-5-0-glucoside chloride versus delphinidin-3-O-glucoside chloride's concentrations a) validation day, 1 b) validation day 2, and c) validation day 3

The precision and accuracy of the assay were determined from the low (350 ng/mL), medium (1500 ng/mL), and high (2500 ng/mL) QC plasma samples. Intra- and inter-day were determined for each QC rat plasma sample, with each sample in triplicates for each day, and expressed as a percentage of the coefficient of variation (CV). The assay's mean analyte recovery rate served as the accuracy definition. The precision determined at each concentration should not exceed 15% CV, except for LOQ, which should not exceed 20%

CV, according to the CDER (2018). It also strongly advises against using accuracy and precision data independently, especially when it comes to drugs. The precision and accuracy results determined for the HPLC method's intra- and inter-day values are shown in Table 3.

Table 3. Precision and accuracy of delphinidin-3-O-glucoside chloride in intraday

Concentration (ng/mL)	Mean (ng/mL)	SD	Precision (CV)	Accuracy (%)	Percentage Difference
Delphinidin-3-O-glucoside chloride intraday (within batch) (*n*=3)					
2500	2495	0.03	2.72	99.8	- 0.2
1500	1305	0.05	8.12	87.0	- 13.0
350	389	0.005	3.36	87.1	12.86
Delphinidin-3-O-glucoside chloride intraday (between batch) (*n*=9)					
2500	2315	0.12	9.84	92.6	- 7.4
1500	1616	0.07	7.63	92.3	7.73
350	341	0.01	4.89	97.4	- 2.57

The lowest analyte concentration in a sample that may be quantitated is known as LOD, although it is not always possible to determine it under certain experimental conditions. In contrast, the LOQ in the calibration curve can be consistently measured with relative standard deviation (RSD; 20%) and precision (80-120%). In this study, LOD and LOQ were 47 ng/mL and 213 ng/mL, respectively. However, some research findings on delphinidin's LOD and LOQ are far different from these values. For instance, a recent study on the determination of delphinidin-3-O-glucoside in plasma using ultra-high performance liquid chromatography–tandem mass spectrometry (UHPLC-MS) found LOD to be 2.3 ng/mL and LOQ to be 8.1 ng/mL [21]. Another study proposing the determination of anthocyanin and non-anthocyanin in Jussara extracts via UPLC-MS showed that the LOD and LOQ of delphinidin-3-O-glucoside were 5.60 µg/L and 18.50 µg/L, respectively [22]. A third study found the LOD to be 0.14 mg/kg and LOQ to be 0.42 mg/kg for delphinidin-3-O-glucoside in grape extract [23].

Conclusion

In conclusion, this developed and validated HPLC method coupled with SPE for sample preparation is rapid and convenient for the quantification of delphinidin-3-O-glucoside chloride in rat plasma samples. The calibration curve of delphinidin-3-O-glucoside chloride was linear in the concentration range. Intra- and inter-day validation showed a good coefficient of determination above 0.95. The mean recovery was 80.377%, while the slope ratio was 71.43%. This study therefore showed good precision and accuracy data for delphinidin-3-O-glucoside chloride in rat plasma. Except for LOQ, which should not exceed 20% of the CV, CDER [15] states that the precision determined at each concentration should not be greater than 15% of the CV. The LOD and LOQ were 47 ng/mL and 213 ng/mL, respectively. To conclude, the validations in this study indicate that these findings, as determined via HPLC, are achievable, reproducible, and reliable for further studies of anthocyanin pharmacokinetics and bioavailability in rat plasma.

Acknowledgement

This research is fully supported by the Ministry of Agriculture's Herbal Research Grant Scheme (HRGS) (304.PPSK.6150169.K123).The authors fully acknowledged Ministry of Higher Education (MOHE) and Universiti Sains Malaysia for the approved fund which makes this important research viable and effective.

References

1. Shan, X., Lv, ZY., Yin, M. J., Chen, J., Wang, J, and Wu, Q. N. (2021). The protective effect of cyanidin-3-glucoside on myocardial ischemia-reperfusion injury through ferroptosis. *Oxidative Medicine and Cellular Longevity*, 6(2021): 1-5.
2. Wang, M., Zhang, Z., Sun, H., He, S., Liu, S.,

Zhang, T., Wang, L. and Ma, G. (2022). Research progress of anthocyanin prebiotic activity: A review. *Phytomedicine*, 20(102): 154145.

3. Khoo, H. E., Azlan, A., Tang, S. T. and Lim, S. M. (2017). Anthocyanidins and anthocyanins: Colored pigments as food, pharmaceutical ingredients, and the potential health benefits. *Food & Nutrition Research*, 61(1): 1361779.
4. Rosales, T. K. O. and Fabi, J. P. (2022). Nanoencapsulated anthocyanin as a functional ingredient: Technological application and future perspectives. *Colloids and Surfaces B: Biointerfaces*, 2022: 112707.
5. Liu, Y., Tikunov, Y., Schouten, R. E., Marcelis, L. F., Visser, R. G. and Bovy, A. (2018). Anthocyanin biosynthesis and degradation mechanisms in solanaceous vegetables: A Review. *Frontiers in chemistry*, 6: 52.
6. Chen, Y., Chen, H., Zhang, W., Ding, Y., Zhao, T., Zhang, M., Mao, G., Feng, W., Wu, X. and Yang, L. (2019). Bioaccessibility and biotransformation of anthocyanin monomers following *in vitro* simulated gastric-intestinal digestion and *in vivo* metabolism in rats. *Food & Function*, 10(9): 6052-6061.
7. Harada, K., Kano, M., Takayanagi, T., Yamakawa, O. and Ishikawa, F. (2004). Absorption of acylated anthocyanins in rats and humans after ingesting an extract of *Ipomoea batatas* purple sweet potato tuber. *Bioscience, Biotechnology, and Biochemistry*, 68(7): 1500-1507.
8. Jokioja, J., Percival, J., Philo, M., Yang, B., Kroon, P. A. and Linderborg, K. M. (2021). Phenolic metabolites in the urine and plasma of healthy men after acute intake of purple potato extract rich in methoxysubstituted monoacylated anthocyanins. *Molecular Nutrition & Food Research*, 65(9): 2000898.
9. Lang, Y., Tian, J., Meng, X., Si, X., Tan, H., Wang, Y., Shu, C., Chen, Y., Zang, Z., Zhang, Y, and Wang, J. (2021). Effects of α-casein on the absorption of blueberry anthocyanins and metabolites in rat plasma based on pharmacokinetic analysis. *Journal of Agricultural and Food Chemistry.* 28(69) :6200-6213.
10. Stuppner, S., Mayr, S., Beganovic, A., Beć, K., Grabska, J., Aufschnaiter, U., Groeneveld, M., Rainer, M., Jakschitz, T., Bonn, G. K. and Huck, C. W. (2020). Near-infrared spectroscopy as a rapid screening method for the determination of total anthocyanin content in *Sambucus fructus*. *Sensors*. 2(17): 4983.
11. Frank, T., Janßen, M., Netzel, M., Straß, G., Kler, A., Kriesl, E. and Bitsch, I. (2005). Pharmacokinetics of anthocyanidin‐3‐glycosides following consumption of *Hibiscus sabdariffa* L. extract. *The Journal of Clinical Pharmacology*. 45(2): 203-210.
12. Centre for Drug Evaluation and Research (2018). Bioanalytical Method Validation Guidance for Industry. Access from https://www.fda.gov/files/drugs/published/Bioanalytical-Method-Validation-Guidance-for-Industry.pdf
13. Sauji, N. A., Wan-Ahmad, W. A. N., Nordin, L. and Bakar, R. A. (2022) Development and optimization of a rapid resolution liquid chromatography method for cyanidin-3-o-glucoside in rat plasma. *Malaysian Journal of Analytical Sciences.* 26(2): 360-369.
14. Ahmadiani, N., Sigurdson, G. T., Robbins, R. J., Collins, T. M. and Giusti, M. M. (2019). Solid phase fractionation techniques for segregation of red cabbage anthocyanins with different colorimetric and stability properties. *Food Research International*, 120: 688-696.
15. Da-Costa, C. T., Horton, D. and Margolis, S. A. (2000). Analysis of anthocyanins in foods by liquid chromatography, liquid chromatography-mass spectrometry and capillary electrophoresis. *Journal of Chromatography*, 881(1-2): 403-410.
16. Diaconeasa, Z., Rugină, D. and Socaciu, C. (2016). High-purity anthocyanins isolation using solid phase extraction tehniques. *Food Science and Technology*, 73(1): 1-6.
17. Xu, Y., Hu, D., Bao, T., Xie, J. and Chen, W. (2017). A simple and rapid method for the preparation of pure delphinidin-3-o-sambubioside from roselle and its antioxidant and hypoglycemic activity. *Journal of Functional Foods*, 39: 9-17.
18. Agyei, E. and Edward, M. (2019). Calibration curve. Undergraduate scholarly showcase. Access from https://journals.uc.edu/index.php/Undergradshowc

ase/article/view/1111

19. Betz, J. M., Brown, P. N. and Roman, M. C. (2011). Accuracy, precision, and reliability of chemical measurements in natural products research. *Fitoterapia*, 82(1): 44-52.
20. McMillan, J. (2013). Principles of Analytical Validation. In P. Ciborowski and J. Silberring (Eds.), Proteomic profiling and analytical chemistry. Elsevier, Amsterdam: pp. 205-215.
21. Kaiser, M., Müller-Ehl, L., Passon, M. and Schieber, A. (2020). Development and validation of methods for the determination of anthocyanins in physiological fluids via UHPLC-MS. *Molecules*, 25(3): 518.
22. Vieira, G. S., Marques, A. S. F., Machado, M. T. C., Silva, V. M. and Hubinger, M. D. (2017). Determination of anthocyanins and non-anthocyanin polyphenols by ultra performance liquid chromatography/electrospray ionization mass spectrometry (UPLC/ESI–MS) in Jussara (*Euterpe edulis*) extracts. *Journal of Food Science and Technology,* 54(7): 2135-2144.
23. Shim, Y. S., Kim, S., Seo, D., Park, H. J. and Ha, J. (2014). Rapid method for determination of anthocyanin glucosides and free delphinidin in grapes using UHPLC. *Journal of Chromatographic Science*, 52(7): 629-635.

Malaysian Journal of Analytical Sciences (MJAS)
Published by Malaysian Analytical Sciences Society

EFFECTIVE AND FAST ADSORPTIVE REMOVAL OF COOMASSIE BRILLIANT BLUE G 250 DYE FROM WATER USING Fe_3O_4 MAGNETIC NANOPARTICLES

(Penjerapan Penyingkiran Pewarna Coomassie Brilliant Biru G 250 Secara Berkesan dan Pantas Menggunakan Fe_3O_4 Magnetik Nanopartikel)

Siti Khalijah Mahmad Rozi[1,2*], Nur Atikah Saufi[1], and Nur Atiqah Nabilah Mohammad Rashidi[1]

[1]*Faculty of Chemical Engineering & Technology, Universiti Malaysia Perlis, Kompleks Pusat Pengajian Jejawi 3, 02600 Arau,Perlis, Malaysia*
[2]*Centre of Excellence for Biomass Utilization, Universiti Malaysia Perlis, 02600 Arau, Perlis, Malaysia*

**Correspondence: khalijahrozi@unimap.edu.my*

Received: 29 March 2023; Accepted: 23 July 2023; Published: 22 August 2023

Abstract

Coomassie Brilliant Blue G 250 (CBB G 250) is mainly generated from industrial textile effluent. Due to its non-degradable nature, it is not only environmentally hazardous, but also affect human health, causing irritations of the eye, respiratory or gastrointestinal tract. Therefore, a strategy for treating this colorant is necessary. This research highlights the synthesis of Fe_3O_4 Magnetic nanoparticles (Fe_3O_4 MNPs) as a low-cost adsorbent for removal of CBB G 250 dye from aqueous solutions. Fe_3O_4 MNPs were synthesized using chemical coprecipitation method. Characterization results revealed that the peaks at 537, 3400 and 1604 cm^{-1} in the Fourier Transform Infrared Spectroscopy spectrum represented the Fe-O band, O-H stretching and bending on the Fe_3O4 MNPs surface, respectively. Crystal phase analysis indicated that Fe_3O_4 MNPs has a cubic spinel structure. Morphological analysis showed Fe_3O_4 MNPs are in nano-sized, spherical in shape, and have uniformly distributed particle size. The result from magnetic and surface area analyses demonstrated that Fe_3O_4 MNPs have 63.30 emu g^{-1} saturation magnetization and 123.5 m^2 g^{-1} surface area. Thermal stability analysis showed that adsorbed water and hydroxyl group (6.25%) were lost at temperature below 100 °C. At temperature between 260 °C and 540 °C, approximately 2.09% weight loss were recorded due to change from magnetite (Fe_3O_4) to maghemite (Ɣ- Fe_2O_3) in crystal phase. Elemental analysis revealed that the Fe_3O_4 MNPs showed 24.50 % of Fe and 75.50 % of O. Following the confirmation of Fe_3O_4 MNPs structure, the impact of various parameters such as adsorbent dosage (0.02-0.14 g), contact time (5-20 minutes), initial concentration (25-100 ppm) and pH (3-10) on the adsorption of CBB G 250 dyes were investigated. Experimental results showed that Fe_3O_4 MNPs achieved 95% removal of CBB G 250 at optimum conditions of 0.12 g dosage, 15 minutes contact time, 50 ppm initial dye concentration and at pH value of 8. Adsorption isotherms and kinetics revealed that the adsorption process using Fe_3O_4 MNPs in this study obeys both Langmuir and Freundlich isotherm and pseudo-second-order kinetic. The results obtained from this study confirmed that Fe_3O_4 MNPs can be used as an adsorbent material for the removal of dye from effluent.

Keywords: Fe_3O_4 magnetic nanoparticles, adsorbents, Coomassie Brilliant Blue G 250, dye removal

Abstrak

Coomassie Brilliant Blue G 250 (CBB G 250) ialah efluen tekstil perindustrian yang kebanyakannya dihasilkan daripada efluen tekstil. Disebabkan sifatnya yang tidak terdegradasi, ia berbahaya kepada alam sekitar dan kesihatan manusia dan membawa

kepada kerengsaan mata, saluran pernafasan atau gastrousus. Oleh itu, strategi untuk merawat pewarna ini adalah perlu. Oleh itu, penyelidikan ini mengetengahkan sintesis Magnetik nanopartikel Fe_3O_4 (Fe_3O_4 MNPs) sebagai penjerap kos rendah untuk penyingkiran pewarna CBB G 250 daripada larutan akueus. MNP Fe_3O_4 telah disintesis dengan menggunakan kaedah kopresipitasi kimia. Keputusan pencirian mendedahkan bahawa puncak pada 537, 3400 dan 1604 cm^{-1} dalam spektrum Spektroskopi Inframerah Transformasi Fourier masing-masing mewakili jalur Fe-O, regangan O-H dan lenturan pada permukaan Fe_3O_4 MNPs. Analisis fasa kristal menunjukkan bahawa Fe_3O_4 MNPs mempunyai struktur spinel padu. Analisis morfologi menunjukkan Fe_3O_4 MNPs dalam saiz nano, dalam bentuk sfera, dan mempunyai saiz zarah teragih seragam. Hasil daripada analisis magnet dan kawasan permukaan menunjukkan bahawa Fe_3O_4 MNPs mempunyai 63.30 emu g^{-1} kemagnetan tepu dan 123.5 m^2 g^{-1}, masing-masing. Analisis kestabilan terma menunjukkan bahawa air terjerap dan kumpulan hidroksil (6.25 %) hilang pada suhu di bawah 100 °C. Pada suhu 260 hingga 540 °C, penurunan berat lebih kurang 2.09 % direkodkan hasil daripada perubahan daripada magnetit (Fe_3O_4) kepada maghemit (ɣ- Fe_2O_3) seperti dalam fasa kristal. Analisis unsur mendedahkan bahawa Fe_3O_4 MNPs masing-masing menunjukkan 24.50% dan 75.50% Fe dan O. Selepas struktur Fe_3O_4 MNPs disahkan, pelbagai parameter seperti kesan dos penjerap (0.02-0.14 g), masa sentuhan (5-20 minit), awal kepekatan (25-100 ppm) dan pH (3-10) pada penjerapan pewarna CBB G 250 telah disiasat. Keputusan eksperimen menunjukkan bahawa Fe_3O_4 MNPs mencapai 95% pada keadaan optimum pada 0.12 g dos, 15 minit masa sentuhan, 50 ppm kepekatan awal dan nilai pH 8. Isoterma dan kinetik penjerapan mendedahkan bahawa proses penjerapan menggunakan Fe_3O_4 MNPs pada kajian ini mematuhi kedua-dua Langmuir dan Freundlich isoterm dan kinetik pseudo-second order, masing-masing. Keputusan yang diperolehi daripada kajian ini mengesahkan bahawa Fe_3O_4 MNPs boleh digunakan sebagai bahan penjerap untuk penyingkiran bahan pewarna daripada efluen.

Kata kunci: magnetik nanopartikel Fe_3O_4, penjerap, Coomassie Brilliant Blue G 250, penyingkiran pewarna

Introduction

One of the biggest and most urgent problem in the modern world is environmental pollution. Textile industries are one of the major polluters not only due to high amounts of water used in manufacturing, but the industry also generate high liquid effluent pollutants. In the textile industry, the largest amount of coloured aqueous waste is disposed through dyeing processes, and not only does it has strong persistent color, but also high biological demand for oxygen (BDO) [1].The presence of these dyes in water causes cancer, toxicity, birth defect and teratogenicity, reducing light penetration into the water and consequently preventing photosynthesis of aquatic plants [2]. Coomassie Brilliant Blue G 250 (CBB G 250) is one of the triphenylmethane dyes used widely in the textile industry. These dyes are hazardous to both the environment and human health because of its non-degradable nature, and causes eye irritations as well as respiratory and gastrointestinal tract irritations. Therefore, it is important to treat these types of dyes [3].

Various techniques are currently being used in order to remove dye effluents that are released into open waters, and this includes coagulation [4], precipitation [5], oxidation-ozonation [6], adsorption [7], ion exchange [8], and biological methods. Adsorption method is considered one of the most promising method due to its flexibility, ease of operation, simple design and high efficiency [8]. It has therefore been used extensively in recent years to treat colours. Common adsorbents such as activated carbon, biochar and graphene oxide have been used previously for the removal of dyeing from wastewater. However, these sorbents have several drawbacks, one of which occur during the separation process, a common issue as these sorbents require centrifugation, a procedure which prolongs analysis time especially when dealing with large sample volume [9]. Thus, it cannot be used extensively for the removal of organic dyes from aqueous environment. Therefore, it is necessary to develop a reliable, easy and rapid adsorbent for efficient treatment of dyeing effluents.

One of the potential adsorbent is magnetic nanoparticle (MNPs). Among the various types of MNPs, iron oxides such as magnetite (Fe_3O_4), maghemite (γ-Fe_2O_3) and hematite (α-Fe_2O_3) are common and attractive options due to their biocompatibility, great saturation magnetization and magnetic susceptibility. The advantages of Magnetite (Fe_3O_4) include the best magnetization among the iron oxides, low price, low toxicity and a high specific surface area. Fe_3O_4 magnetic

nanoparticle (Fe_3O_4 MNPs) can also be an adsorbent for remediation of organic dye such as CBB G 250 due to its unique features [10]. Since the use of Fe_3O_4 MNPs is seldom documented for decontamination of CBB G 250 from water environment, it is a good idea to study efficiency of Fe_3O_4 MNPs as an adsorbent for treatment of organic dyes from aqueous environment.

The purpose of this study is to develop Fe_3O_4 magnetic nanoparticles (Fe_3O_4 MNPs) for adsorption of CBB G 250 from aqueous solution. The structure of Fe_3O_4 MNPs was characterized using Fourier Transform Infrared Spectroscopy (FTIR), X-ray Diffraction (XRD), Field Emission Scanning Electron Microscopy (FESEM), Energy Dispersive X-ray Spectroscopy (EDX), Thermogravimetric analysis (TGA), Vibrating Sample Magnetometer (VSM) and Brunauer-Emmett-Teller (BET). After the structures of Fe_3O_4 MNPs were confirmed, it was then used as an adsorbent for treatment of CBB G 250 from aqueous environment. During the application part, the screening of several parameters such as dosage of adsorbent, contact time, initial dye concentration, pH of the solution were performed in order to determine characteristcis that influence the efficiency of Fe_3O_4 MNPs to adsorb CBB G 250. Widely-used models were described and analyzed to evaluate the best theoretical adsorption capacity such as adsorption kinetic (pseudo-first, second order and intraparticle diffusion) as well as some isotherm models (Langmuir and Freundlich). The regeneration performance of the Fe_3O_4 MNPs was also examined in six consecutive cycles.

Materials and methods

Chemicals

Iron (III) chloride hexahydrate, iron (II) chloride tetrahydrate and aqueous ammonia were purchased from Fluka Analytical (Germany). The standard for Coomassie Brilliant Blue G 250 (CBB G 250) was obtained from Supelco (Belleffonte, USA). The stock solutions of CBB G 250 dye were prepared in distilled water at 100 ppm. All stock solutions were kept at 4 ºC.

Instrumentation

The functional groups of the synthesized nanoparticles were first characterized using a FTIR spectrometer (Spectrum 400 PerkinElmer) with a diamond ATR accessory, absorption mode with 4 scans at a resolution of ±4 cm^{-1}, and a wavenumber range of 4000 to 450 cm^{-1}. FESEM images and EDX analysis of the prepared Fe_3O_4 MNPs were performed using scanning electronic microscopy (SEM HITACHI SU8220, OXFORD Instruments) that was equipped with an energy dispersive X-ray spectrometry. The crystal phase of the prepared nanoparticles was determined using a PANanalytical EMPYREAN X-ray powder diffraction (XRD) diffractometer (CuK, radiation, $\lambda = 1.541874$ nm), at a scanning speed of 0.07 / min from 15 to 75 (2θ). The surface area and pore size were measured using Brunauer-Emment-Teller (BET) by nitrogen adsorption isotherm at 77.350 K in Micromeritics (ASAP2020, Georgia, and USA). The magnetic properties were analysed using vibrating sample magnetometer (VSM LakeShore 7400 series, Tokyo, Japan). A thermogravimetric analyzer (Perkin Elmer, TGA 4000, Waltham, MA, USA) was used to study the thermal behavior of the prepared adsorbents at temperatures ranging from 30 ºC to 900 ºC with a heating rate of 20 ºC min^{-1} under nitrogen flow. Adsorption studies of CBB G 250 dye were performed using UV spectrophotometer (Shimmadzu, Kyoto, Japan) at a wavelength of 590 nm.

Synthesis of Fe_3O_4 MNPs

The preparation of Fe_3O_4 MNPs were adapted from work published by Zarei et al. [11]. Briefly, 3.1736 g of $FeCl_2.4H_2O$ and 7.5709 g of $FeCl_3.6H_2O$ were dissolved in 320 mL deionized water. The solution was agitated for 1 hour at 80 ºC. 40 mL of aqueous ammonia was then added slowly into the reaction mixture and was further agitated for another 1 hour before allowed to cool to room temperature. The obtained Fe_3O_4 MNPs were magnetically collected and rinsed five times with hot water until the filtrate turned neutral. Figure 1 depicts the schematic synthesis of Fe_3O_4 MNPs.

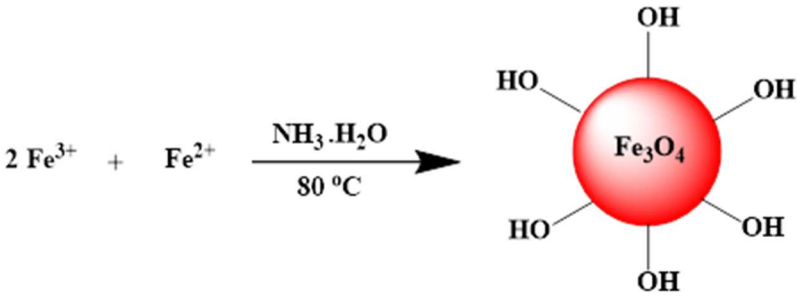


Figure 1. Schematic illustration of synthesis Fe_3O_4 MNPs

Batch adsorption studies

The batch adsorption of CBB G 250 dye from water using Fe_3O_4 MNPs is illustrated in Figure 2. İn this experiment, a quantity of Fe_3O_4 MNPs was added to 10 mL of 50 ppm CBB G 250 dye solution in 50 mL centrifuge tube at room temperature. 0.1 M NaOH and 0.1 M HCl were used to alter the pH of the solution. The solutions were shaken and stirred in an incubator shaker. An external magnet was used to isolate the Fe_3O_4 MNPs from the sample solution. In this experiment, several parameters were studied, such as: 1] adsorbent dosage (0.02–0.14 g), 2] contact time (5-20 min), 3] initial concentrations of CBB G 250 dye (25-100 ppm), and 4] pH of the solutions (3-9) [3]. The concentration of the treated dye in the clear filtrate was determined using an UV spectrophotometer at a wavelength of 590 nm. The removal percentage, (%R) and adsorption capacity (qe) were defined using Equation 1 and Equation 2, respectively [12].

$$R(\%) = \frac{Ci-Ce}{Ci} \times 100\% \quad (1)$$

The equation shown above indicates initial concentration (C_i) and final concentrations (C_e) in ppm of dye ion. Meanwhile,

$$q_e(mg/g) = \frac{C_o-C_e}{m} \times v \quad (2)$$

İn this second equation, q_e denotes adsorption capacity; C_o denotes the initial concentration (ppm); C_e is the final concentration (ppm); m is the adsorbent dosage (g) and v is the volume of working solution.

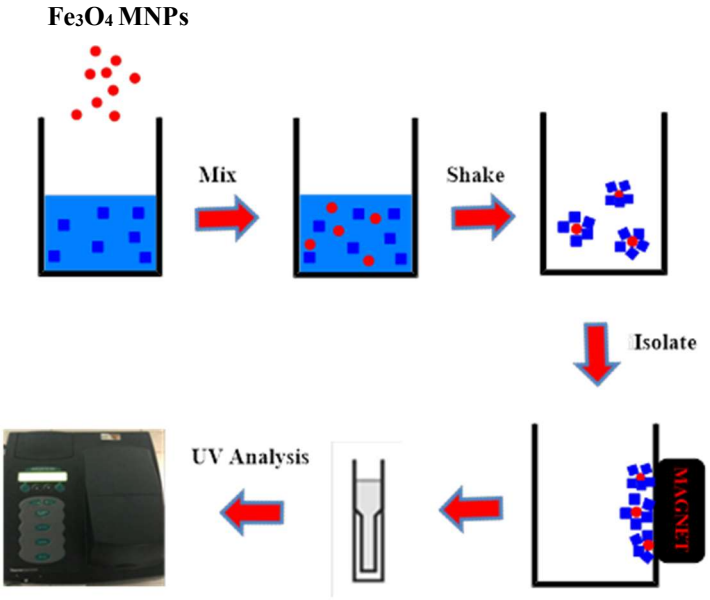


Figure 2. The removal process of CBB G 250 dye using Fe_3O_4 MNPs

Results and Discussion

Characterization

The investigation of FTIRs in the produced Fe3O4 MNPs was performed to examine the functional groups. and the result is illustrated in Figure 3(a). The peak at 537 cm^{-1} in the FTIR spectrum represents the Fe-O band vibration. The two peaks at 3400 and 1604 cm^{-1} adsorption are equivalent to O-H stretching and bending respectively, on the Fe_3O_4 MNPs surface [13]. XRD were used to determine the crystal phases of the prepared Fe_3O_4 MNPs (Figure 3(b)). The spectrum of Fe3O4 MNPs showed the presence of diffraction peaks at 2θ=30.42°, 35.59°, 43.42°, 53.63°, 57.35°, and 63.02° and are respectively assigned to the (220), (311), (400), (422), (511), and (440) planes of Fe_3O_4 (JCPDS 88-O4 0866). These peaks indicate that Fe_3O_4 MNPs has a cubic spinel structure [14].

The magnetic behavior of the Fe_3O_4MNPs was investigated using vibration sample magnetometry (VSM) at room temperature. As observed in Figure 3(c), the superparamagnetic behavior of Fe_3O_4 MNPs indicates a remanence characteristic and a coercivity near to zero. The result of the VSM demonstrates that Fe_3O_4 MNPs have a 63.30 emu g-1 saturation magnetization. The result suggests that manufactured Fe_3O_4 MNPs can be easily collected with an external magnet in water solution (see photo inset of Figure 3(c)). Following this, an analysis was done to study the surface area of Fe_3O_4 MNPs in nitrogen adsorption/desorption (Figure 3(d)). The result shows the specific surface area of Fe_3O_4 MNPs is 123.5 m^2 g^{-1}. It depicts that Fe_3O_4 MNPs have high surface area, suggesting this adsorbent as a good adsorbing agent of organic dyes, particularly CBB G 250 [15].

In order to identify thermal stability of Fe_3O_4 MNPs, thermogravimetric analysis (TGA) was carried out. Thermogram of Fe_3O_4MNPs is presented in Figure 3(e). The finding shows that adsorbed water and hydroxyl group (6.25 %) were lost at temperature below 100 ℃. At temperature between 260 and 540 ℃, the weight loss of approximately 2.09 % was recorded as a result of change from magnetite (Fe_3O_4) to maghemite (ϒ-Fe_2O_3) in crystal phase [16].

FESEM analysis was used to investigate the morphology of prepared Fe_3O_4 MNPs. The FESEM images of synthesized Fe_3O_4 MNPs is shown in Figure 4 ((A)-(B)). Fe_3O_4 MNPs were observed in nano-sized, spherical in shape, and have a uniformly distributed particle size [17]. The elemental analysis was performed to confirm the composition of the Fe_3O_4 MNPs and the EDX spectrum of Fe_3O_4 MNPs is shown in Figure 4(C). The EDX results revealed 24.50% Fe and 75.50% of O [18], thus confirming the successful synthesis of the Fe_3O_4 MNPs.

The optimization of the parameter for CBB G dye removal: Effect of adsorbent dosage

The amount of adsorbent is crucial to achieve the maximum removal of CBB G 250 dye. Seven different amounts of Fe_3O_4 MNPs (0.02-0.14g) were used for the adsorption of CBB G 250 dye. Figure 5(a) displays the influence of the adsorbent mass on the removal of target CBB G 250 dye. As seen from the result, as the mass of Fe_3O_4 MNPs increases, so did its adsorption efficiency due to initial availability of the large number of active sites on Fe_3O_4 MNPs [19]. The maximum percentage removal of targeted dye was found at 0.12g of Fe_3O_4 MNPs. Beyond the 0.12g dosage, the adsorption efficiency of Fe_3O_4 MNPs reached equilibrium. This indicates that the active site of the Fe_3O_4 MNPs had become saturated [20]. Consequently, 0.12g was selected for the subsequent experiments.

Effect of contact time

The maximal adsorption of CBB G 250 requires sufficient contact time. The time profile for adsorption was explored by varying the time between 5 and 20 minutes of adsorption. The adsorption recoveries of CBB G 250 increased for up to 15 minutes, after which it plateaued (Figure 5(b)), thus no longer actively absorbing. This is because initially, there are many accessible sites for interaction of CBB G 250 dye which readily allows adsorption. However, as time progresses, more active sites are occupied, which leads to the saturation of the active site on the Fe_3O_4 MNPs becoming saturated after 15 minutes. Hence, 15 minutes of contact time was chosen for future experiments.

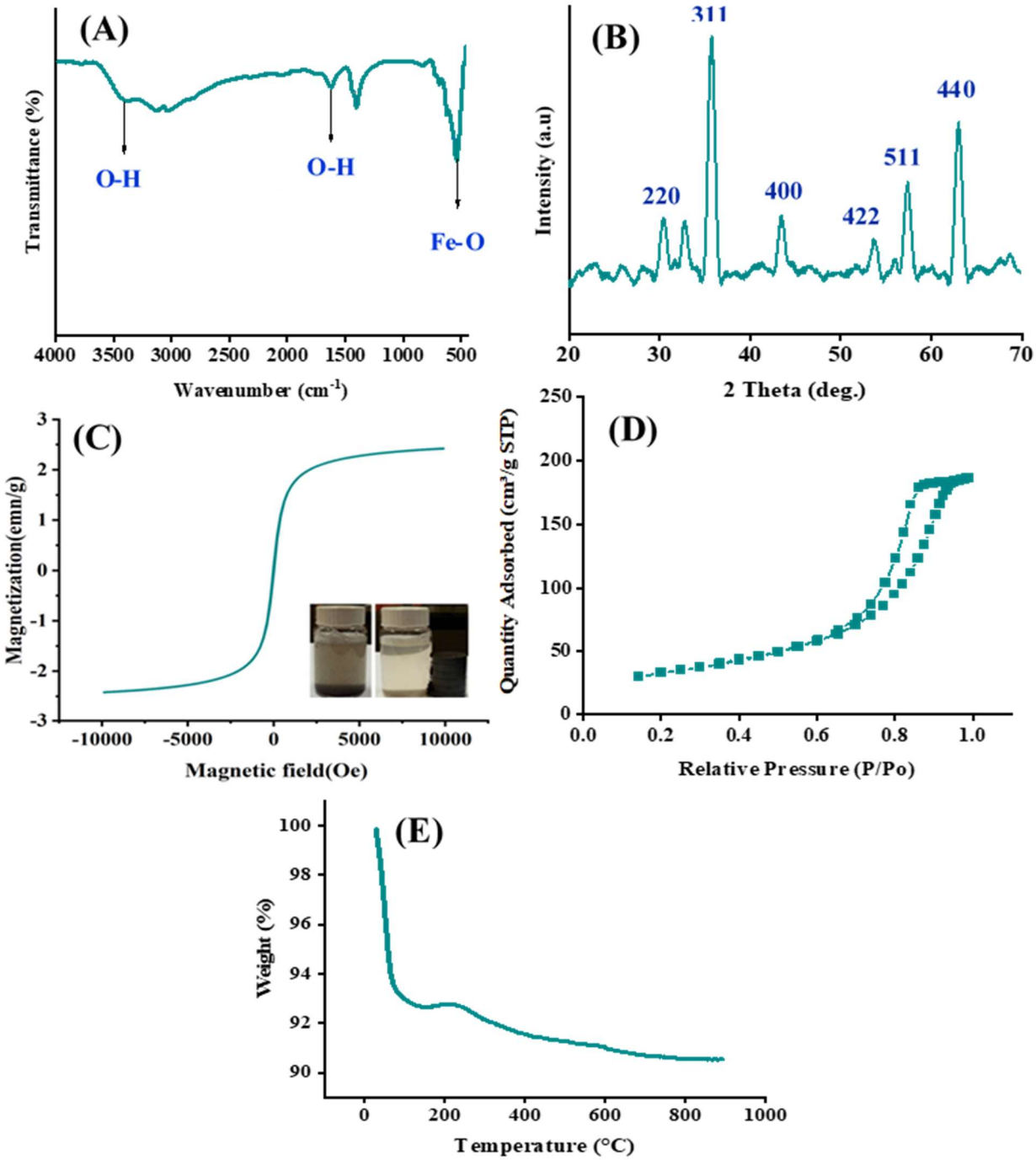


Figure 3. (a) FTIR, (b) XRD, (c) VSM, (d) BET and (e) TGA analyses of Fe_3O_4 MNPs

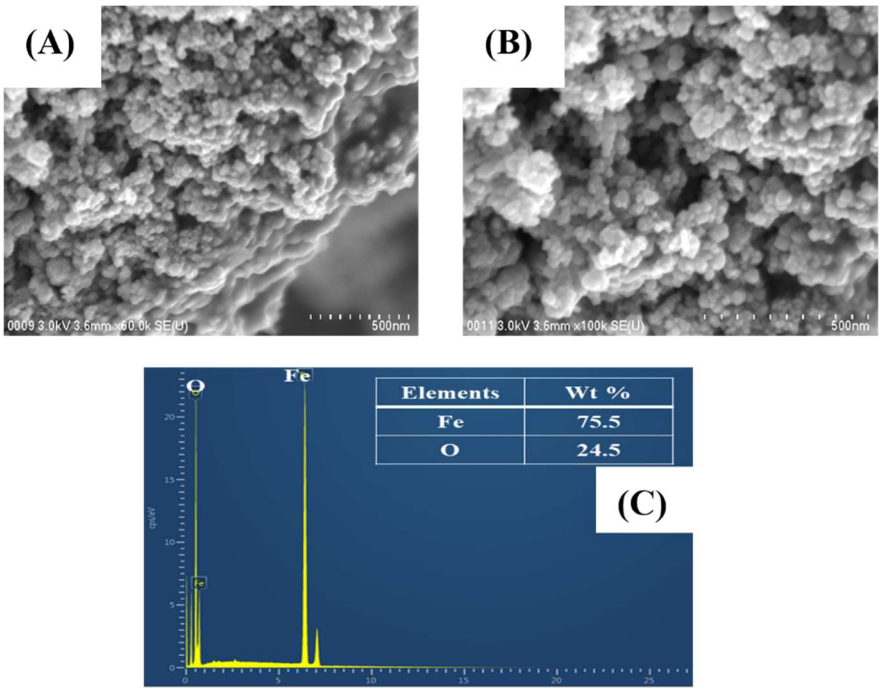


Figure 4. (a-b) Morphological image and (c) EDX spectrum of Fe_3O_4 MNPs

Effect of initial concentration

A suitable concentration of CBB G250 dye is important to achieve a better adsorption efficacy of targeted dye on Fe_3O_4 MNPs. The initial concentrations of CBB G 250 dye ranged from 25 to 100 ppm. Figure 5(c) shows an increasing trend up until 50 ppm of initial dye concentration, suggesting that there are unoccupied active sites on the Fe_3O_4 MNPs adsorbent surface at this stage. The maximum adsorption removal (92%) of targeted dye using Fe_3O_4 MNPs was found at 50 ppm of initial concentration. Beyond this point, the adsorption efficiency of CBB G 250 using Fe_3O_4 MNPs decreases due to the saturation of adsorption sites on the adsorbent surface. This finding agrees with the research conducted by Pandey et al. [21], who reported that the percentage adsorption of Brilliant Green (BG) dye removal decreases with the rise in BG dye concentration. Pandey and coworkers also reported that with the rise in BG dye concentration, the surface area and active sites of the adsorbent became saturated, which then reduces the percentage adsorption of BG. Hence, 50 ppm of initial CBB G 250 concentration was selected for subsequent studies.

Effect of pH

The adsorbent's efficacy is significantly influenced the surface load of the adsorbent material, its ionizing nature of target analytes and the ionization/dissociation of the adsorbed molecules functional groups. Based on Figure 5(d), the high removal of CBB G 250 more than 80% was obtained from pH 3 until pH 10. This phenomenon can be explained based on the structure of CBB G 250 dye and Fe_3O_4 MNPs. Betancur Jiang et al. [22] revealed that Fe_3O_4 MNPs is electropositive for pH < 6 and electronegative for pH > 6.5 which meant that the isoelectric point of Fe_3O_4 MNPs falls between pH 6 and 6.5. Therefore, under acidic conditions, the electropositive Fe_3O_4 MNPs interacted well with the negative charges of the SO_3^- CBB G 250 dye via electrostatic attraction (Figure 6(a)). Meanwhile, under neutral conditions, Fe_3O_4 MNPs adsorbed CBB G 250 dye through hydrogen bonding (Figure 6(b)). Under alkaline conditions, the electronegative Fe_3O_4 MNPs interacted with the positive charges of the N^+ CBB G 250 dye via electrostatic attraction (Figure 6(c)), indicating the good removal of CBB G 250 dye using Fe_3O_4 MNPs at this condition . In this case, pH 8, the natural pH of the sample, is selected as the best pH to use.

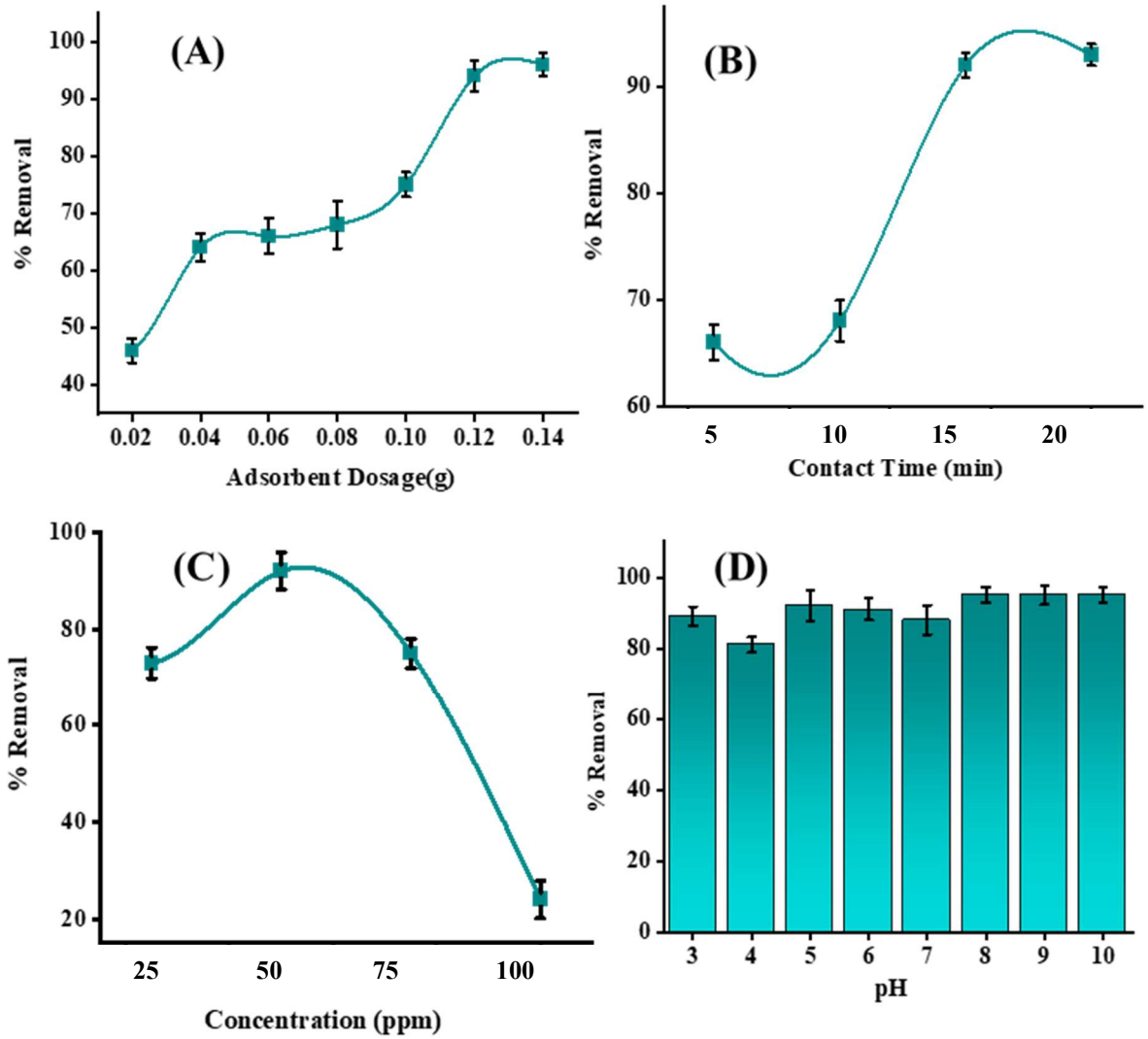


Figure 5. Effect of (a) adsorbent dosage, (b) contact time, and (c) initial concentration; and pH on removal of CBB G 250

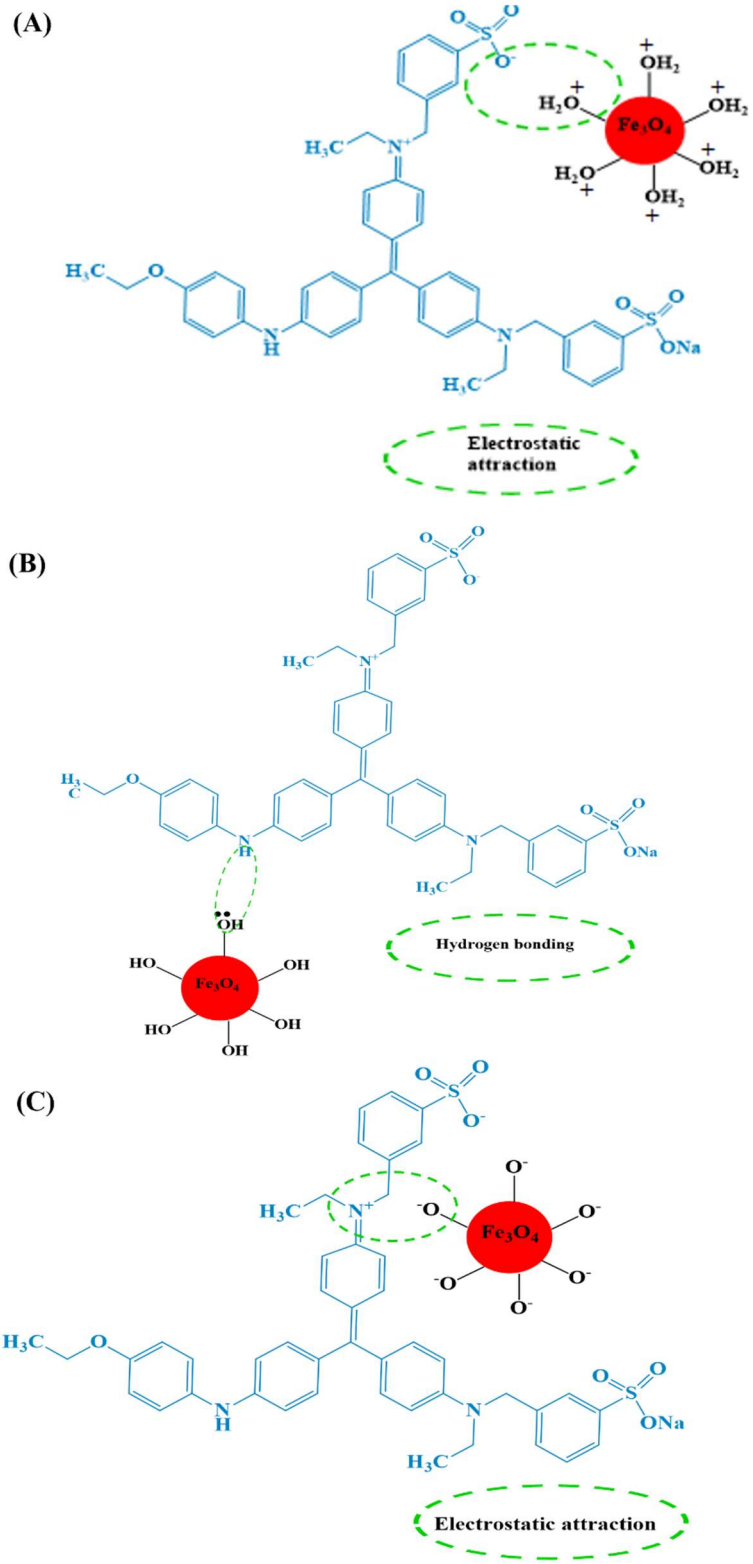


Figure 6. Schematic illustration of adsorption CBB G 250 on Fe_3O_4 MNPs in (a) acidic, (b) neutral and (c) alkaline media

Adsorption kinetic models

The kinetic model delivers a relationship between the rate of adsorption as well as the type of reaction mechanism engaged. To better understand the adsorption mechanism of CBB G 250 dye molecules onto Fe_3O_4 MNPs, the pseudo first-order (Figure 7(a)), pseudo second-order (Figure 7(b)) and intraparticle diffusion (Figure 7 (c)) were used in this study. The kinetic parameters of different models are shown in Table 1. According to this table, the pseudo second-order models fit the experimental data better than that of the pseudo-first-order and the intraparticle diffusion kinetic models, obtaining a correlation coefficient of 0.9507. This indicated that most of the CBB G 250 molecules were adsorbed onto the surface of Fe_3O_4 MNPs by chemisorption mechanism, which involves valence forces via the sharing or exchanging of electrons. Additionally, the adsorption mechanism might depend on both the adsorbate and the adsorbent. The result obtained in this work is similar with the results reported in other published works by Dhananasekaran et al. [23] and Kadeche et al. [24].

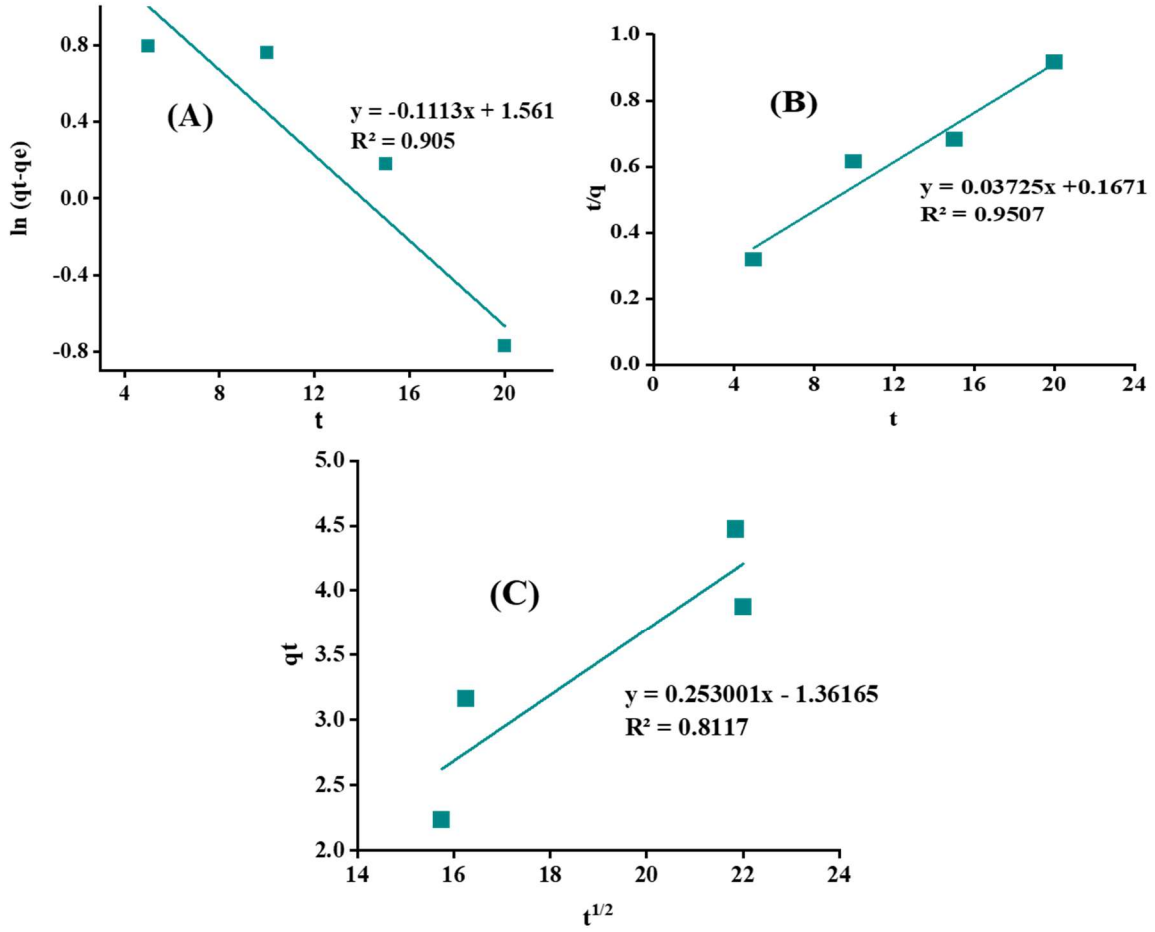


Figure 7. (a) Pseudo-first-order, (b) Pseudo-second-order and (c) Intraparticle Diffusion of removal CBB G 250 by Fe_3O_4 MNPs

Table 1. Kinetic modeling constants and coefficient of determination for adsorption of CBB G 250

Model	Equation /Value
Pseudo-first-order kinetics	$\ln(q_e - q_t) = \ln q_e - k_1 t$
q_e(mg g^{-1})	6.262
R_1^2	0.905
k_1 (min^{-1})	-0.111
Pseudo-second-order kinetics	$\frac{t}{q_1} = \frac{1}{k_2 q_e^2} + \frac{t}{q_e}$
q_e (mg g^{-1})	5.43
R_2^2	0.951
k_2 (g $mg^{-1}min^{-1}$)	0.037
Intraparticle Diffusion	$q_t = k_{id} t^{1/2} + C_i$
R^2	0.957
k_{id} (mg g^{-1} min^{-1})	0.253
Ci (mg g^{-1})	7.939

Adsorption isotherm models

In order to describe further the interaction between the adsorbent and adsorbates, adsorption isotherm models such as Langmuir (Figure 8(a)) and Freundlich (Figure 8(b)) models were studied to fit the equilibrium data. Table 2 shows the adsorption of isotherm constant for CBB G 250 on Fe_3O_4 MNPs. From the table, the high correlation coefficient values for Langmuir (R^2 = 0.998) and Freundlich (R^2 = 0.999) models strongly imply that the Fe_3O_4 MNPs adsorption of CBB G 250 dye closely follows both Langmuir and Freundlich models of adsorption under the present experimental conditions. This finding is similar to previous study by Kulal & Badalamoole [25] who also found that adsorption of Rhodamine 6G (R6G) dye by Magnetite nanoparticle embedded Pectin-graft-poly (N-hydroxyethylacryl amide) hydrogel followed both Langmuir and Freundlich equations. Othman et al. [26] also stated that the analysis of adsorption of methylene blue using graphene oxide-magnetic iron oxide nanoparticles revealed that the data is well fitted with Langmuir and Freundlich adsorption isotherm model ($R^2 > 0.97$), indicating the multilayer adsorption of dye on the surface of adsorbent.

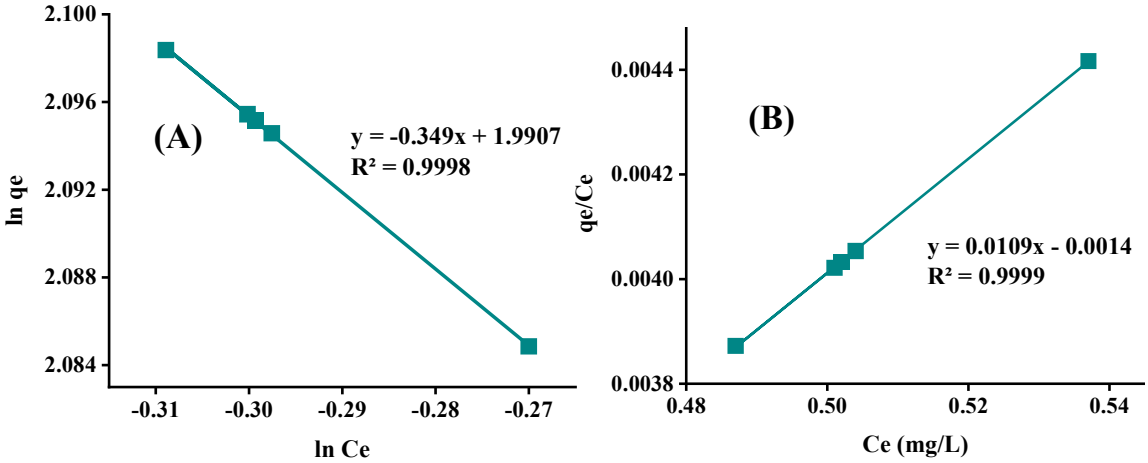


Figure 8. (A) Freundlich adsorption isotherm (B) Langmuir adsorption isotherm of removal CBB G 250 dye by Fe_3O_4 MNPs

Table 2. Isotherm modeling constants and coefficient of determination for adsorption of commassie brilliant blue G 250

Model / Isotherm constant	Equation /Value
Freundlich adsorption isotherm	$\ln q_e = \ln K_F + \frac{1}{n} \ln C_e$
q_e(mg g^{-1})	124.33
R_1^2	0.998
k_F	7.3207
$\frac{1}{n}$	-0.349
Langmuir adsorption isotherm	$\frac{q_e}{C_e} = \frac{C_e}{q_m} + \frac{1}{q_m b}$
q_m (mg g^{-1})	91.743
R_2^2	0.9999

Analysis of CBB G 250 Dye Loaded Fe_3O_4 MNPs

The FTIR spectra of the synthesized Fe_3O_4 MNPs, raw CBB G 250 and CBB G 250 loaded Fe_3O_4 MNPs are shown in Figure 9. From the spectrum of CBB G 250 loaded Fe_3O_4 MNPs, the broad peak at 3439 cm^{-1} is attributed to the overlapping of OH band from Fe_3O_4 MNPs and NH stretching from CBB G 250. Additionally, the peaks at 3179 cm^{-1}, 2052 cm^{-1} and 1063 cm^{-1} suggest the presence of CH stretching and CN stretching, respectively, of CBB G 250. Furthermore, the peak found at 1588 cm^{-1} indicated C=C stretching of CBB G 250. This result proved that CBB G 250 was adsorbed on the surface of Fe_3O_4 MNPs.

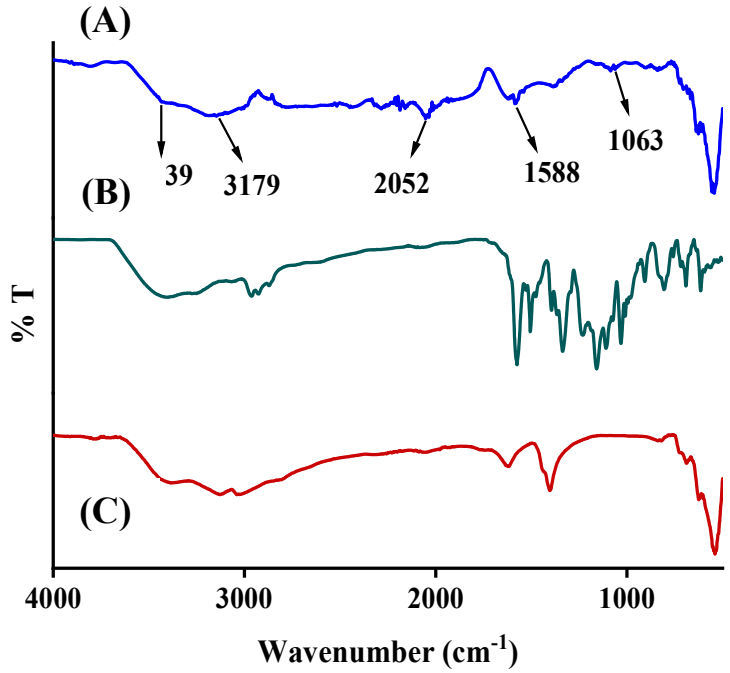


Figure 9. FTIR spectrum of (a) CBB G 250 loaded Fe_3O_4 MNPs (b) CBB G 250 dye (c) Fe_3O_4 MNPs

Recyclability of Fe_3O_4 MNPs

When estimating the efficacy of Fe_3O_4 MNPs in absorbing CBB G 250 in the environment, reusability is a crucial element to take into consideration. Fe_3O_4 MNPs were washed and dried multiple times with ethanol, before being utilized in a second adsorption, to estimate the reusability or adsorption of Fe_3O_4 MNPs. As shown in Figure 10, Fe_3O_4 MNPs can be reused at least six times without any apparent decrease of its efficiency in CBB G 250 removal, suggesting the regeneration efficacy and stability of the prepared adsorbent.

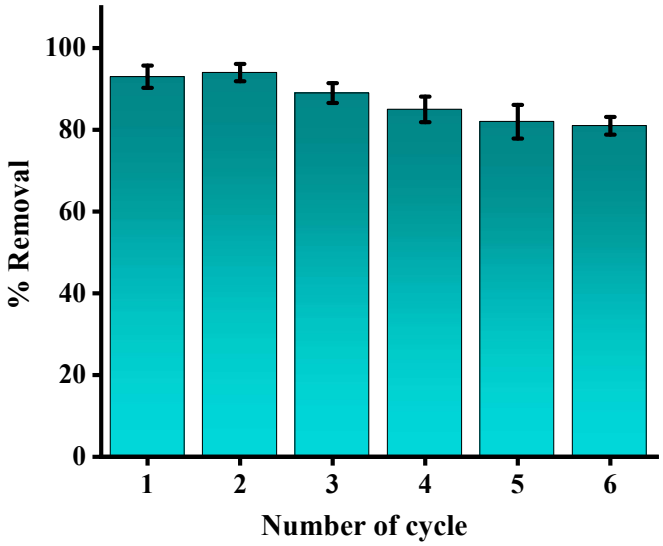


Figure 10. Reusability of Fe_3O_4 MNPs for adsorption efficiency of CBB G 250

Comparison of Fe_3O_4 MNPs with other reported adsorbents for removal of CBB G 250 dye

In Table 3, the present adsorbent, Fe_3O_4 MNPs, was evaluated with previously reported adsorbents for the adsorption of CBB G 250 dye from aqueous environment in terms of amount of adsorbent, contact time, percentage removal, adsorption capacity, kinetic study and isotherm study. The results revealed that proposed Fe_3O_4 MNPs is rapid, reliable, and a highly efficient adsorbent for the treatment of CBB G 250 from water sample. Fe_3O_4 MNPs has the highest adsorption capacity and good percentage removal of CBB G 250 with comparable amount of dosage and contact time as compared to other reported adsorbents.

Conclusion

This present study shows that the synthesized Fe_3O_4 MNPs can be potentially used for the removal of organic dyes from aqueous environment. FESEM, FTIR, and EDX, as well as XRD, TGA, and BET analyses confirmed the successful synthesis of Fe_3O_4 MNPs. Experimental results show that Fe_3O_4 MNPs achieved 95% adsorption at optimum conditions of; 1) 0.12 g dosage, 2) 15 minutes contact time, 3) 50 ppm initial dye concentration, and 4) pH value of 8. The Fe_3O_4 MNPs can also be reused up to six times without losing efficiency. FTIR analysis proved that CBB G 250 dye was adsorbed by Fe_3O_4 MNPs, as evidenced by the intense peaks attributed to the CBB G 250 in the FTIR spectrum. This study demonstrated that Fe_3O_4 MNPs are appropriate for decontamination and treatment of organic contaminants from aqueous environments because they provide excellent magnetic separation, aqueous sample stabilization, high recoveries, and rapid separation.

Table 3. Comparison of the developed adsorbent with other published adsorbents for adsorption of Coomassie brilliant blue dye

Material	Dye	Amount of Adsorbent (g)	Contact Time (min)	Percentage Removal (%)	Adsorption Capacity (mg/g)	Kinetic Study	Isotherm Study	References
Chitin	CBB	0.1	30	65	8.550	Pseudo-second order kinetics	Langmuir isotherm model	[23]
Snail shell powder	CBB	0.02	30	86.3	-	-	Freundlich isotherm model	[2]
Starch/poly(alginicacid-cl-acrylamide) nanohydro- gel (ST/PL(AA-cl-AAm) NHG)	CBB	0.1	150	78.56	31.24	Pseudo-second-order kinetics	Langmuir isotherm model	[27]
α-chitin nanoparticles (CNP)	CBB	0.1	30	98.6	8.550	Pseudo second order kinetics	Langmuir isotherm model	[23]
Activated Carbon from Apricot Stone (ASAC)	CBB	0.1	55		10.09	Pseudo-second order kinetics	Freundlich model	[28]
Sodium bentonite (Bent-Na)	CBB	-	15	85.62	6.848	Pseudo-second order kinetics	Langmuir isotherm model	[24]
Iron-pillared bentonite (PILC-Fe)	CBB	-	15	97.58	9.125	Pseudo-second order kinetics	Langmuir isotherm model	[24]
o-ECNFs	CBB	5.0	300	-	107.80	Elovich model	Redlich-Peterson	[29]
m-ECNFs	CBB	5.0	300	-	46.90	Elovich model	Redlich-Peterson	[29]
Fe_3O_4 MNPs	CBB G 250	0.12	15	95	124.33	Pseudo-second-order model	Langmuir isotherm & Freundlich model	This study

References

1. Verma, R. K., Sankhla, M. S., Rathod, N. V., Sonone, S. S., Parihar, K., and Singh, G. K. (2021). Eradication of fatal textile industrial dyes by wastewater treatment. *Biointerface Research Applied Chemistry*, 12: 567-587.

2. Ibrahim, Hanadi K., Muneer A. Amy, and Eman T. K. (2019). Decolorization of Coomassie brilliant blue G-250 dye using snail shell powder by action of adsorption processes. *Research Journal of Pharmacy and Technology,* 12: 4921-4925.

3. Ezzat, A. O., Tawfeek, A. M., Rajabathar, J. R., and Al-Lohedan, H. A. (2022). Synthesis of new hybrid structured magnetite crosslinked poly ionic liquid for efficient removal of Coomassie brilliant blue R-250 dye in aqueous medium. *Molecules*, 27(2): 441.
4. Nahiun, K. M., Sarker, B., Keya, K. N., Mahir, F. I., Shahida, S., and Khan, R. A. (2021). A review on the methods of industrial wastewater treatment. *Scientific Review*, 7(3): 20-31.
5. Saya, L., Malik, V., Gautam, D., Gambhir, G., Singh, W. R., and Hooda, S. (2022). A comprehensive review on recent advances toward sequestration of levofloxacin antibiotic from wastewater. *Science of The Total Environment*, 813: 152529.
6. Kumar, M., Sridharan, S., Sawarkar, A. D., Shakeel, A., Anerao, P., Mannina, G., ... and Pandey, A. (2022). Current research trends on emerging contaminants pharmaceutical and personal care products (PPCPs): A comprehensive review. *Science of The Total Environment*, 2022: 160031.
7. Jing, G., Meng, X., Sun, W., Kowalczuk, P., and Gao, Z. (2023). Recent advances in treatment and recycling of mineral processing wastewater. *Environmental Science: Water Research & Technology*, 9: 1290-1304.
8. Chai, W. S., Cheun, J. Y., Kumar, P. S., Mubashir, M., Majeed, Z., Banat, F., ... and Show, P. L. (2021). A review on conventional and novel materials towards heavy metal adsorption in wastewater treatment application. *Journal of Cleaner Production*, 296: 126589.
9. Ariffin, M. M., Azmi, A. H. M., Saleh, N. M., Mohamad, S., and Rozi, S. K. M. (2019). Surfactant functionalisation of magnetic nanoparticles: A greener method for parabens determination in water samples by using magnetic solid phase extraction. *Microchemical Journal*, 147(1): 930-940.
10. Ajinkya, N., Yu, X., Kaithal, P., Luo, H., Somani, P., and Ramakrishna, S. (2020). Magnetic iron oxide nanoparticle (IONP) synthesis to applications: present and future. *Materials*, 13(20): 4644.
11. Zarei, A. R., Nedaei, M., and Ghorbanian, S. A. (2018). Ferrofluid of magnetic clay and menthol based deep eutectic solvent: Application in directly suspended droplet microextraction for enrichment of some emerging contaminant explosives in water and soil samples. *Journal of Chromatography A*, 1553: 32-42.
12. Shokry, H., Elkady, M., and Hamad, H. (2019). Nano activated carbon from industrial mine coal as adsorbents for removal of dye from simulated textile wastewater: Operational parameters and mechanism study. *Journal of Materials Research and Technology*, 8(5): 4477-4488.
13. Rozi, S. K. M., Berhanundin, K. M., Ishak, A. R., Mohd, F. L., Rasdi, N. C. D., Rahim, N. Y., ... and Abdullah, A. M. (2023). Novel magnetic eggshell membrane functionalized with waste palm fatty acid for selective adsorption of oil from aqueous solution. *Malaysian Journal of Analytical Sciences*, 27(1): 74-86.
14. Shahriman, M. S., Zain, N. N. M., Mohamad, S., Manan, N. S. A., Yaman, S. M., Asman, S., and Raoov, M. (2018). Polyaniline modified magnetic nanoparticles coated with dicationic ionic liquid for effective removal of rhodamine B (RB) from aqueous solution. *RSC Advances*, 8(58): 33180-33192.
15. Shahriman, M. S., Ramachandran, M. R., Zain, N. N. M., Mohamad, S., Manan, N. S. A., and Yaman, S. M. (2018). Polyaniline-dicationic ionic liquid coated with magnetic nanoparticles composite for magnetic solid phase extraction of polycyclic aromatic hydrocarbons in environmental samples. *Talanta*, 178: 211-221.
16. Bakhshaei, S., Kamboh, M. A., Nodeh, H. R., Zain, S. M., Rozi, S. K. M., Mohamad, S., and Mohialdeen, I. A. M. (2016). Magnetic solid phase extraction of polycyclic aromatic hydrocarbons and chlorophenols based on cyano-ionic liquid functionalized magnetic nanoparticles and their determination by HPLC-DAD. *RSC Advances*, 6(80): 77047-77058.
17. Ahmad, N., Sereshti, H., Mousazadeh, M., Nodeh, H. R., Kamboh, M. A., and Mohamad, S. (2019). New magnetic silica-based hybrid organic-inorganic nanocomposite for the removal of lead(II) and nickel(II) ions from aqueous solutions. *Materials Chemistry and Physics*, 226: 73-81.

18. Yaacob, S. F. F. S., Abd Razak, N. S., Aun, T. T., Rozi, S. K. M., Jamil, A. K. M., and Mohamad, S. (2018). Synthesis and characterizations of magnetic bio-material sporopollenin for the removal of oil from aqueous environment. *Industrial Crops and Products*, 124: 442-448.
19. Yusoff, M. M., Raoov, M., Yahaya, N., and Salleh, N. M. (2017). An ionic liquid loaded magnetically confined polymeric mesoporous adsorbent for extraction of parabens from environmental and cosmetic samples. *RSC Advances*, 7(57): 35832-35844.
20. Yusoff, M. M., Yahaya, N., Saleh, N. M., and Raoov, M. (2018). A study on the removal of propyl, butyl, and benzyl parabens via newly synthesised ionic liquid loaded magnetically confined polymeric mesoporous adsorbent. *RSC Advances*, 8(45): 25617-25635.
21. Pandey, S., Do, J. Y., Kim, J., and Kang, M. (2020). Fast and highly efficient removal of dye from aqueous solution using natural locust bean gum-based hydrogels as adsorbent. *International Journal of Biological Macromolecules*, 143: 60-75.
22. Betancur, J. C., Montoya, P. M., and Calderón, J. A. (2019). Gold recovery from ammonia-thiosulfate leaching solution assisted by PEI-functionalized magnetite nanoparticles. *Hydrometallurgy*, 189: 105128.
23. Dhananasekaran, S., and Palanivel, R. (2015). Adsorption of methylene blue, bromophenol blue and coomassie brilliant adsorption of methylene blue, bromophenol blue and Coomassie brilliant blue by a -chitin nanoparticles. *Journal of Advanced Research*, 7: 113-124.
24. Kadeche, A., Ramdani, A., Adjdir, M., Guendouzi, A., Taleb, S., Kaid, M., and Deratani, A. (2020). Preparation, characterization and application of Fe-pillared bentonite to the removal of Coomassie blue dye from aqueous solutions. *Research on Chemical Intermediates*, 46: 4985-5008.
25. Kulal, P., and Badalamoole, V. (2020). Magnetite nanoparticle embedded Pectin-graft-poly (N-hydroxyethylacrylamide) hydrogel: Evaluation as adsorbent for dyes and heavy metal ions from wastewater. *International Journal of biological macromolecules*, 156: 1408-1417.
26. Othman, N. H., Alias, N. H., Shahruddin, M. Z., Bakar, N. F. A., Him, N. R. N., and Lau, W. J. (2018). Adsorption kinetics of methylene blue dyes onto magnetic graphene oxide. *Journal of Environmental Chemical Engineering*, 6(2): 2803-2811.
27. Sharma, G., Naushad, M., Kumar, A., Rana, S., Sharma, S., Bhatnagar, A., J. Stadler, F., Ghfar, A. A., and Khan, M. R. (2017). Efficient removal of Coomassie brilliant blue R-250 dye using starch/poly (alginic acid-cl-acrylamide) nanohydrogel. *Process Safety and Environmental Protection*, 109: 301-310.
28. Cherfi Abdelhamid, A. M. (2014). Kinetic and equilibrium studies of Coomassie Blue G-250 adsorption on apricot stone activated carbon. *Journal of Environmental & Analytical Toxicology*, 05(2): 1000264.
29. Thamer, B. M., Aldalbahi, A., Moydeen A, M., El-Hamshary, H., Al-Enizi, A. M., and El-Newehy, M. H. (2019). Effective adsorption of Coomassie brilliant blue dye using poly (phenylene diamine) grafted electrospun carbon nanofibers as a novel adsorbent. *Materials Chemistry and Physics*, 234(1): 133-145.

Malaysian Journal of Analytical Sciences (MJAS)
Published by Malaysian Analytical Sciences Society

QUANTIFICATIONS OF LINOLEIC ACID AND β-GLUCAN IN *Lignosus rhinocerotis* EXTRACT AND ITS CYTOTOXICITY ANALYSIS IN HUMAN LUNGS EPITHELIAL BEAS-2B CELLS

(Kuantifikasi Asid Linoleik dan β-Glukan dalam Ekstrak *Lignosus rhinocerotis* dan Analisis Kesitotoksikan dalam Sel Epitelium Bronkus Manusia BEAS-2B)

Nurul Asma Abdullah[1*], Siti Nurshazwani Muhamad Sayuti[2], Bushra Solehah Mohd Rosdan [1], Siew Hua Gan[3], Nurfadhlina Musa[4], and Ruzilawati Abu Bakar[5]

[1]*School of Health Sciences, Universiti Sains Malaysia, 16150 Kubang Kerian, Kelantan, Malaysia*
[2]*Universiti Sains Malaysia Institutional Animal Care and Use Committee (USM IACUC), Universiti Sains Malaysia, 16150 Kubang Kerian, Kelantan, Malaysia.*
[3]*School of Pharmacy, Monash Universiti Malaysia, Bandar Sunway, Selangor, Malaysia.*
[4]*Human Genome Centre, School of Medical Sciences, Universiti Sains Malaysia, 16150 Kubang Kerian, Kelantan Malaysia.*
[5]*Department of Pharmacology, School of Medical Sciences, Universiti Sains Malaysia, 16150 Kubang Kerian, Kelantan Malaysia.*

[*]*Corresponding author: nurulasma@usm.my*

Received: 26 February 2023; Accepted: 23 July 2023; Published: 22 August 2023

Abstract

Lignosus rhinocerotis, a polypore found in the tropical forests of Malaysia is traditionally used by the locals to treat various diseases. The objectives of the study were to quantify linoleic acid and β-glucan, characterize polysaccharide structure as well as to evaluate the cytotoxicity effects of *L. rhinocerotis* extracts. The linoleic acid and β-glucan concentrations in six different extracts of *L. rhinocerotis* were quantified using HPLC and β-glucan assay kit, respectively and the polysaccharide structure were analyzed using FTIR and XRD. The proliferation rate of human bronchial epithelial BEAS-2B cells treated with the *L. rhinocerotis* extracts were also analyzed. The highest linolic acid content and β-glucan composition were found in petroleum ether extract and hexane residue, respectively. Cold water and petroleum ether extracts showed cytotoxic effect with 30% reduction of cell viability at 72 hours at the concentration of 62.5-250 µg/mL while the other extracts are not cytotoxic. Quantification of linoleic acid and β-glucan as well as characterization of polysaccharide structure in *L. rhinocerotis* extracts have been successfully determined. The observed effects on BEAS-2B cells are likely attributable to the immunomodulatory properties exhibited by the active compounds of linoleic acid and β-glucan.

Keywords: *Lignosus rhinocerotis*, linoleic acid, beta-glucan, high performance liquid chromatography, cytotoxicity

Abstrak

Lignosus rhinocerotis merupakan polipor yang terdapat di hutan tropika Malaysia telah digunakan secara tradisi oleh penduduk tempatan untuk merawat pelbagai penyakit. Kajian ini bertujuan untuk mengukur tahap asid linoleik dan β-glukan, mencirikan struktur polisakarida serta menilai kesan sitotoksisiti ekstrak *L. rhinocerotis*. Tahap asid linoleik dan β-glukan di dalam enam ekstrak *L. rhinocerotis* yang berlainan masing-masing diukur dengan kaedah HPLC dan kit ujian mezayme yis dan cendawan β-glukan. Struktur polisakarida juga dianalisa menggunakankan kaedah FTIR dan XRD. Titisan sel epitelium bronkus manusia

BEAS-2B dikultur dan dirawat dengan ekstrak *L. rhinocerotis* dan ujian kesitotoksikan telah dijalankan. Petroleum eter menghasilkan jumlah asid linoleik yang paling tinggi, manakala ekstrak residu heksana menghasilkan komposisi β-glukan tertinggi. Ekstrak air sejuk dan petroleum eter menunjukkan kesan sitotoksik ringan pada kepekatan 62.5-250.0 µg/mL dengan penurunan kadar kebolehhidupan sel adalah tidak melebihi 30% manakala kebanyakan ekstrak lain tidak sitotoksik. Tahap asid linoleik dan β-glukan serta pencirian struktur polisakarida di dalam ekstrak *L. rhinocerotis* telah berjaya ditentukan. Kesan ekstrak ini terhadap titisan sel epitelium bronkus manusia BEAS-2B juga telah berjaya dikaji dan berkemungkinan disebabkan oleh sifat imunomodulator yang ditunjukkan oleh sebatian aktif, iaitu asid linoleik dan β-glukan.

Kata kunci: *Lignosus rhinocerotis*, asid linoleic, β-glukan, kromatografi cecair berprestasi tinggi, kesitotoksikan

Introduction

Lignosus rhinocerotis (*L. rhinocerotis*) or domestically known as tiger milk mushroom by the local community in Malaysia, is a polypore found in the tropical rainforests in Malaysia. *L. rhinocerotis* is traditionally used to reduce body temperature, as a postpartum medicine for women after childbirth, as a contraceptive and in the treatment of breast and cervical cancers [1], asthma, cough, joint pain, food poisoning, liver-related illnesses as well as a general tonic [2].

Besides, *L. rhinocerotis* is believed to possess anti-inflammatory activities against inflammatory mediators during inflammation. This action may be contributed by the high amounts of active compounds found in this fungus, primarily the polysaccharide of β-glucans and the polyunsaturated fatty acid of linoleic acid. β-glucans are mostly derived from the fruiting bodies of mushrooms, and it is believed to be an immune system booster where it has demonstrated to effectively stimulate the host immune response against microbial infections [3]. Additionally, β-glucan is also used as an adjuvant to enhance the effectiveness of modern medicine [4]. Meanwhile, linoleic acid which is an omega-6 polyunsaturated fatty acid; a precursor for arachidonic acid which is often associated with inflammation [5]. The low levels of pro-inflammatory cytokines such as TNF-α and IL-6 and the high levels of anti-inflammatory cytokines including IL-10 was reported in corresponding to the presence of polyunsaturated fatty acid in the plasma, suggesting its effect in inflammation [6]. In our previous study, the volatile compositions of *L. rhinocerotis* in hot water extract showed that linoleic was the one with the most abundant polyunsaturated fatty acids when analyzed through gas chromatography-mass spectrometry (21.35%) [7].

Numerous studies have reported on the cytotoxicity of L. *rhinocerotis* extracts. According to Fauzi et al. [8], *L. rhinocerotis* is reported to induce apoptosis in HCT 116 colon cancer cells. *L. rhinocerotis* was also found to induce apoptosis that led to cell death in the human breast carcinoma cell line, MCF-7 and the human lung carcinoma cell line, A549 [9]. In this study, human lungs epithelial BEAS-2B cells was chosen because of its role in conserving the normal airway function by acting as defensive barrier and secreting the inflammatory mediator in response to the inflammation. BEAS-2B is widely used as a pulmonary epithelium model in many types of in vitro studies including toxicology testing [10], respiratory injury and remodeling [11].

Thus, the objectives of the study were to quantify linoleic acid and β-glucan as well as to characterize polysaccharide and crystalline structure in *L. rhinocerotis* extracts. The cytotoxicity of the extracts in human lungs epithelial BEAS-2B cells was also evaluated.

Materials and Methods

Sample preparations

The samples were prepared by dissolving *L. rhinocerotis* powder in methanol. Water-based extract such as hot water, cold water, hexane residue and petroleum ether residue extracts were prepared at 8 mg/mL while the concentration for solvent-based extracts such as hexane and petroleum ether extracts were at 100 µg/mL. Table 1 shows three different extraction methods used for the extraction of *L. rhinocerotis*.

HPLC analysis for linoleic acid

A reversed phase high performance liquid chromatography (HPLC) was performed on an Agilent

1260 Infinity System (Agilent Technologies, Santa Clara, USA). Instrument control and data collection were carried out using an Agilent OpenLab ChemStation Edition C.01.05 software. The column used was COSMOSIL 5C18-MS-II (250 X 4.6 mm I.D: 5 µm) (Nacalai Tesque, Inc, Japan) coupled with a guard column (10 X 4.6 mm I.D: 5 µm) (Nacalai Tesque, Inc, Japan) with similar packing material. The detection was done by an ultraviolet detector at 208 nm. The mobile phase used was a combination of acetonitrile, methanol, and hexane in the ratio of 90:8:2 with the addition of 0.2% acetic acid at a flow rate of 1.0 mL/min. Indomethacin was used as internal standard. The total analytical time was approximately 10 minutes. HPLC method validation were performed according to FDA guideline [11] to evaluate calibration curves, linearity, precision, accuracy, and recovery.

Quantification of β-glucan

Quantification of β-glucan in *L. rhinocerotis* extracts was conducted using mushroom and yeast Beta-Glucan Assay Kits (Megazyme, Bray, Ireland) where both total and alpha glucans were measured. Concentrations of β-glucan were determined by subtracting the concentrations of alpha glucan from the total values.

Table 1. Different extraction methods for the extraction of *L. rhinocerotis*

Extraction Method	Soxhlet	Maceration	Ultrasound-Assisted Extraction
Step by step procedures	1. TMM powder (50 mg) was transferred into an extraction thimble. 2. Distilled water (500 ml) was put into a round bottom flask. Soxhlet extraction set was set up. 3. The extract was then concentrated using a rotating evaporator. 4. The concentrated extract was dried, weighed, and stored in a tightly capped container for further use.	1. TMM powder (50 g) was macerated in 500 ml of water for 24 hours in cold room (4 °C) with agitation. 2. After 24 hours, the extract was centrifuged at 2500 g for 10 min. 3. The supernatant was collected and dried using freeze dryer.	1. TMM powder (50 mg) was dissolved in 500 ml of solvents and transferred into a water bath sonicator for 30 min at 40 °C. 2. The solution was centrifuged at 2500 g for 10 min. Then, the supernatant was concentrated, dried and stored. 3. The pellet was resuspended in 500 ml of water before being subjected to ultrasound in a water bath sonicator for another 30 min prior to centrifugation at 2500 g for 10 min. 4. The supernatant was collected, concentrated, dried, weighed and stored.
Product	Hot water extract	Cold water extract	Step 1-2: hexane and petroleum ether extract. Step 3-4: hexane residue and petroleum ether residue extract.

Determination of polysaccharide structural analysis

Fourier-transform infrared spectroscopy (FTIR) was used to determine polysaccharide structural analysis in *L. rhinocerotis* extracts. Infrared radiation (IR) spectra of *L. rhinocerotis* crude extract was performed using KBr-disk method where the sample was ground with KBr powder and pressed into 1 mm pallet. The pallet was analyzed using FTIR spectrometer (Tensor 27, Bruker, Germany) spectrometer in the range 4000-400 cm^{-1}.

Determination of crystalline structure

The X-ray diffraction (XRD) of *L. rhinocerotis* crude extract was analyzed using diffractometer (D2 Phaser, Bruker, Germany). Copper lamp radiation (Cu Kα) was applied to the sample at 10mA and 30 kV with rotation speed of 15.0 s. The diffraction angle was shifted from 10º to 90º to identify the crystalline structure.

BEAS-2B cell culture

BEAS-2B was purchased from American Type Culture Collection (Manassas, USA) (resource number: ATCC® CRL 9609™). The cells were cultured in a complete Dulbecco Modified Eagle's Medium (DMEM) at 37oC and 5% carbon dioxide humidified atmosphere. Complete DMEM was prepared by adding 1% penicillin-streptomycin and 10% fetal bovine serum. Cells from passage 6 to 8 were used in all experiment.

Proliferation assay

BEAS-2B cells were seeded at 2 x 103 cells per well. After 24 hours, the cells were treated with six different extracts: hot water, cold water, hexane, petroleum ether, hexane residue and petroleum ether residue extract at various concentrations (250, 125, 62.5, 31.25 and 15.625 µg/mL, respectively) for 24, 48 and 72 hours. An untreated negative control was included in the study. Proliferation assay was carried out using MTS assay kit (Promega, USA) following the manufacturer's instruction.

Statistical analysis

Statistical analyses were performed using the Statistical Package of Social Science software, version 21.0. A one-way ANOVA was used to analyze the findings. All statistical analyses were performed at significance level of $p < 0.05$.

Results and Discussion

Chromatography

A typical chromatogram of the analysis of linoleic acid in *L. rhinocerotis* extracts obtained on COSMOSIL 5C18-MS-II column, is shown in Figure 1. The calibration curve for linoleic acid was linear in the concentration range of 5 to 200 µg/mL. The inter- and intra-day calibration curves showed consistent linearity, as seen in consistency of intercept, slope and coefficient of correlation. A typical concentration curve for linoleic acid had a slope of 0.0053, an intercept of 0.0005 and r^2 = 0.9978 (Figure 2).

The precision of the test was evaluated by determining the relative standard deviation (RSD) of the measured peak area ratios for different drug concentrations. RSD was calculated as follows: $\bar{x}$ = mean of peak area ratio and s = standard deviation of peak area ratio. Based on the FDA guideline [12], the acceptable precision for each concentration is RSD < 15% except for the limit of detection concentration which is at 20%. Accuracy was expressed as the mean percentage of analyte recovered in the assay with a targeted acceptable range within 80-120%. Our data indicated that the method is both precise (relative standard deviation less than 15%) and accurate (mean percentage recovery of between 80-120%).

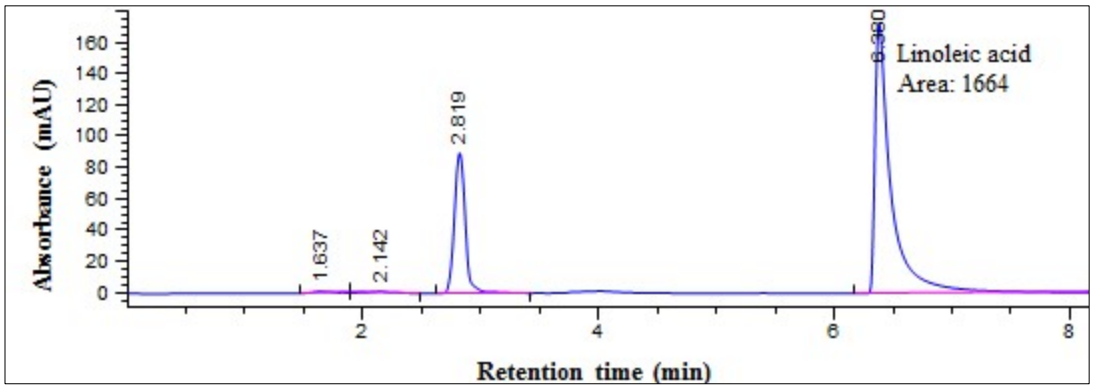


Figure 1. Chromatogram of linoleic acid (6.680 min) and internal standard, indomethacin (2.819 min) when using combinations of acetonitrile, methanol and hexane for mobile phase in the ratio of 90:8:2 with the addition of 0.2% acetic acid at a flow rate of 1.0 mL/min. The detection was done by an ultraviolet detector at 208 nm.

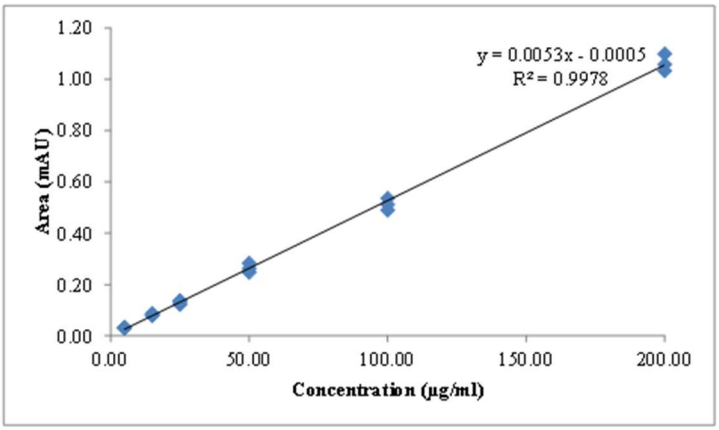


Figure 2. A typical concentration curve for linoleic acid

Measurement of linoleic acid in *L. rhinocerotis* extracts

Table 2 shows the amount of linoleic acid in 100g of the extracts. Based on the results, water-based extracts such as hot water, cold water, hexane residue and petroleum ether residue extracts recorded a low amount of linoleic acid which is approximately 0.05g in 100g of extract. The non-polar extracts such as hexane and petroleum ether yielded significantly higher amounts of linoleic acid which are 16.79 and 17.55g in 100g of extract, respectively.

Table 2. Measurement of linoleic acid in *L. rhinocerotis* extracts

Extract	Mean Linoleic Acid Content in Extract (g) ± Standard Deviation
Hot water	0.049 ± 0.277
Cold water	0.049 ± 0.115
Hexane	16.790 ± 0.629*
Petroleum ether	17.550 ± 0.221*
Hexane residue	0.046 ± 0.113
Petroleum ether residue	0.048 ± 0.133

*p <0.05

Analysis of β-glucan in *L. rhinocerotis* extracts

Analysis of β-glucan composition in water-based *L. rhinocerotis* extracts indicated that it is present at 29.0, 33.6, 39.8 and 32.1g in 100g extracts of hot water, cold water, hexane residue and petroleum ether residue extracts, respectively. On the other hand, the amount of β-glucan in non-polar extracts such as hexane and petroleum ether extracts were 31.5 and 24.1g, respectively. Hexane residue is the best extract for β-glucan (Table 3).

Table 2. Measurement of β-glucan in *L. rhinocerotis* extracts

Extract	Mean β-Glucan Content in Extract (g) ± Standard Deviation
Hot water	29.0 ± 0.001*
Cold water	33.6 ± 0.006*
Hexane	31.5 ± 0.001*
Petroleum ether	24.1 ± 0.001*
Hexane residue	39.8 ± 0.002*
Petroleum ether residue	32.1 ± 0.004*

*p <0.05

Analysis of the FTIR spectrum

The FTIR spectrum of *L. rhinocerotis* crude extract was shown in Figure 3a. A broad band observed at 3423 cm^{-1} is attributed to –OH group stretching vibration in the polysaccharide or moisture of sample [13]. The band 2931 cm^{-1} is attributed to the C-H stretching vibration which include CH, CH_2 and CH_3 stretching, which are the characteristic absorptions of polysaccharides. The band between 1000 and 1200 cm^{-1} region indicated the presence of C-O stretching vibration of C-O-H and C-O-C glycosidic bonds are also characteristic of polysaccharides. An intense band in the region 1639 cm^{-1} is associated to the C=O stretching vibration of amide I group [14].

X-ray diffraction (XRD)

The crystallinity of the *L. rhinocerotis* crude extract was evaluated and the diffractogram pattern is shown in the Figure 3B. The sample shows diffraction peak at 13.8, 20.5º, 21.2, 25.7 and 33.9º 2θ (Degrees) of the crystallinity. The computed crystallinity is at 19.5% and amorphous is at 80.5% within 10 to 90º 2θ.

The effect of extract on cell viability

Analysis of cell proliferative activity was conducted by MTS in BEAS-2B treated with various concentrations (250, 125, 62.5, 31.25 and 15.625 µg/mL) of *L. rhinocerotis* extracts after 24, 48 and 72 hours of incubation is shown in Figure 4. The viability of cell treated with hot water extract, hexane residue extract and petroleum ether residue extract did not show any significant different after 3-day treatment. However, petroleum ether extract at the concentration of ⩾ 31.25 µg/mL showed significant reduction throughout the 3-day treatment. Cell treated with cold water extract at the concentration of 125 and 250 µg/mL also significantly reduced, starting from the second day of the treatment. Reduction in cell viability could also be seen in cell treated with hexane extract (125 and 250 µg/mL) on day 3.

Mushrooms are rich in polyunsaturated fatty acids especially linoleic acids. Our results indicated that linoleic acid concentration was significantly lower in water-based extracts than in solvent-based extracts which extracted a higher number of compounds. Hexane and petroleum ether which are non-polar, can pull out non-polar compounds [15] in extraction of fatty acids from flaxseed oil. The reason is that the organic solvents used for the extraction process were specific for the extraction of fatty acids. It is plausible that the non-polar solvents such as hexane and petroleum ether attract the long hydrocarbon alkane chain present in fatty acids. The effect was similarly shown in another study on the extraction of fatty acids from flaxseed oil where non-polar solvents such as hexane and petroleum ether fatty acids were found to be better at extracting fatty acids as compared to polar solvents [15].

Linoleic acid is the most abundant polyunsaturated fatty

acid in *L. rhinocerotis* and represents about 21.35% of total volatile compounds [7]. A study on fatty acid analysis from nine wild edible mushrooms (*Aleurodiscus vitellinus, Cortinarius magellanicus, Hydropus dusenii, Cyttaria hariotii, Fistulina antarctica, F. endoxantha, Grifola gargal, Lepista nuda and Ramaria patagonica*) from Argentina indicated that linoleic acid was the predominant fatty acid found in the investigated mushroom species [16]. Another study on the phytochemical analysis of the *Rhizopogon luteolus* showed that eight fatty acids were detected in *R. luteolus* with linoleic acid, making up 45.8% of the total fatty acids present [17]. Twenty-eight fatty acids were detected in 16 strains of *Pleurotus ostreatus* mushroom lipids where the linoleic acid was predominant in all samples (56.8–80.5%) [18], indicating that it is an important constituent to be analyzed in mushroom samples.

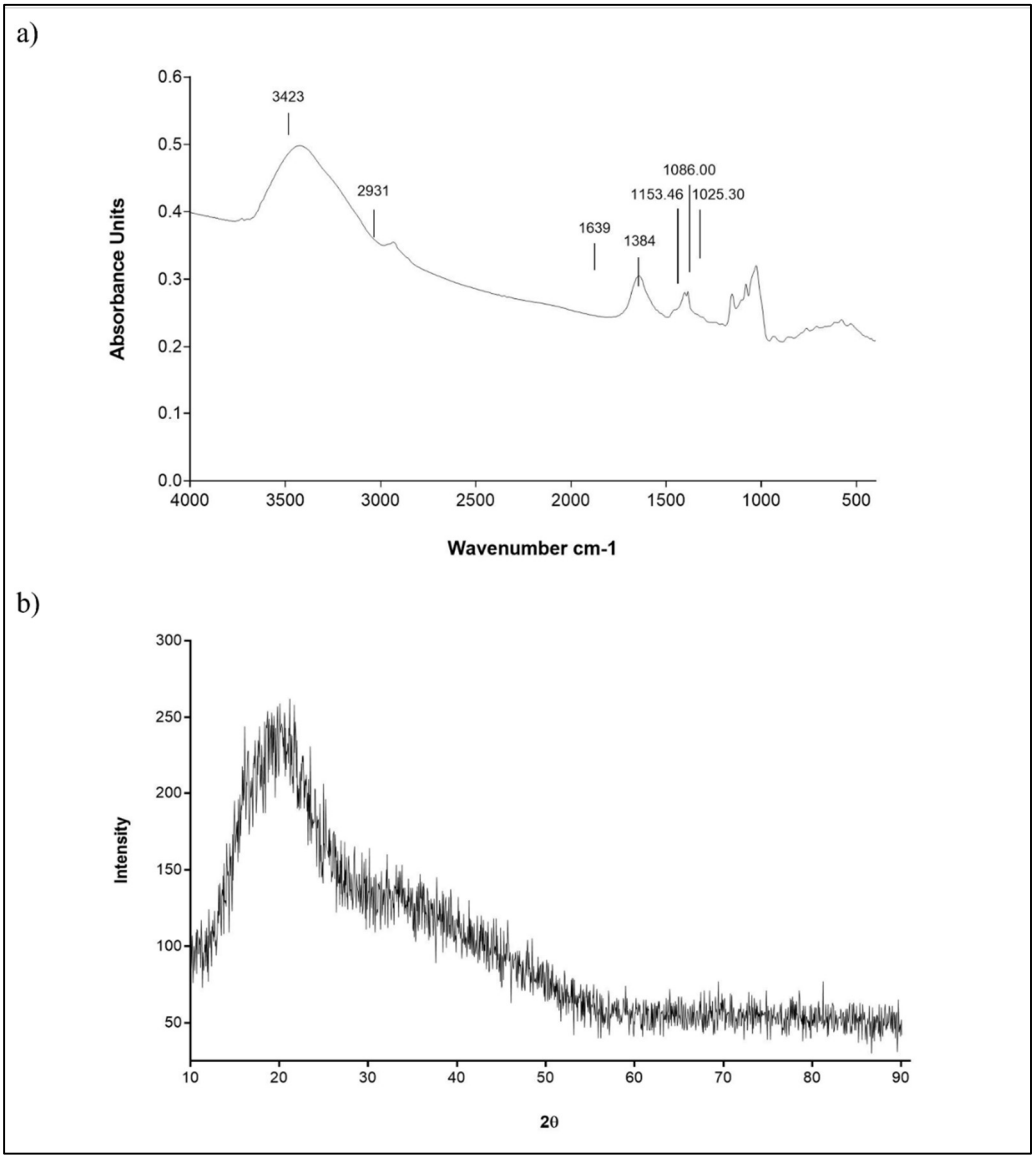


Figure 3. Analyses of (a) FTIR spectra and (b) XRD of *L. rhinocerotis* crude extract

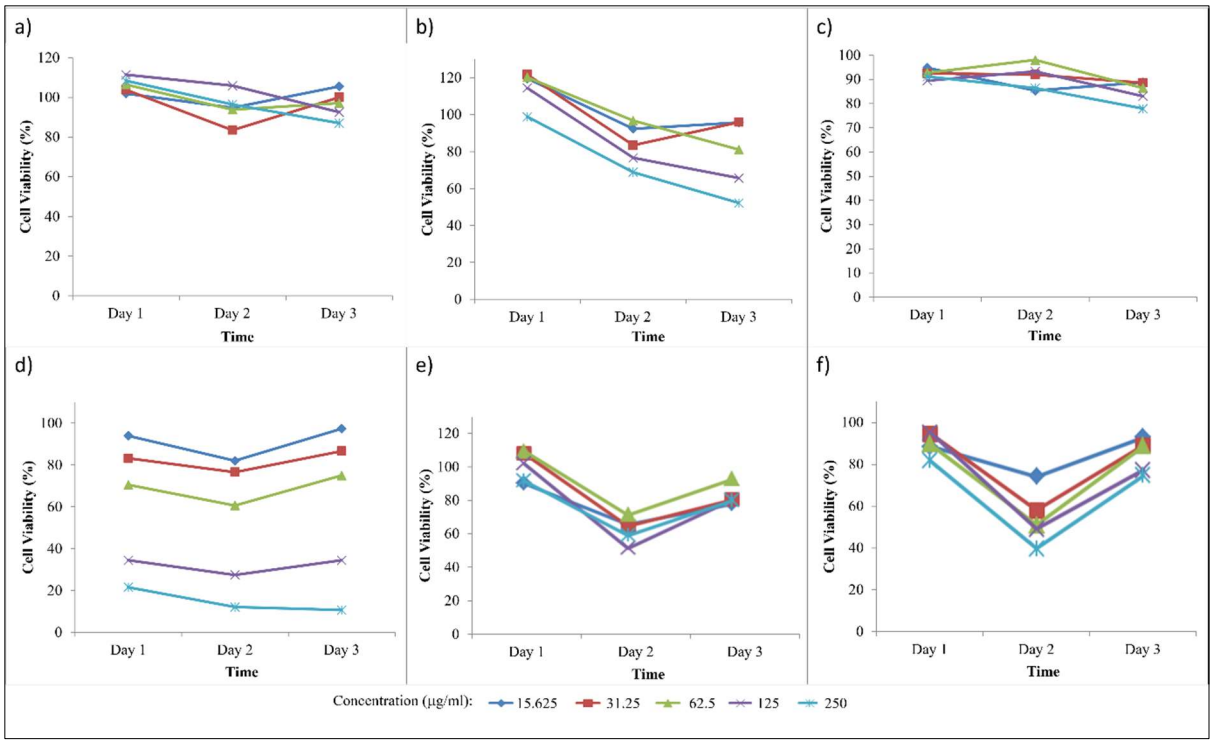


Figure 4. The effects of various concentrations of a) hot water, b) cold water, c) hexane, d) petroleum ether, e) hexane residue and f) petroleum ether residue extracts on viability of BEAS-2B cell line. Untreated cells were used as a control. The differences between concentrations of each extract were tested statistically using Kruskal-Wallis. Data are presented as mean ± standard deviation for three independent experiments. *$p < 0.05$ vs control.

There are several studies reported on the β-glucan composition in *L. rhinocerotis* with conflicting data. Jamil et al. [19] reported that β-glucan constituted more than 50% of glucan content in *L. rhinocerotis* while another study Lau et. al. [1] reported that β-glucan constituted the majority of glucan, ranging from 82 to 93% (w/w). However, another study on the β-glucans content stated that β-glucan constituted only 9% of total glucan compositions [20]. Meanwhile, the data obtained from this study shows that β-glucans make up more than 20% of total glucan in all extracts. Nevertheless, the difference in β-glucan content may be attributed to the different extraction method used in each study.

The peak characteristic of FTIR spectrum suggested the presence of both polysaccharide and protein. The absorption bands of O-H, C-H and C-O groups represent the typical polysaccharide characteristic in FTIR [21]. The amide group is characterized by the peptide bond of secondary structure of protein [22]. The absorption bands of O-H, C-H and C-O groups represent the typical polysaccharide characteristic in FTIR [21]. Previous studies reported the presence of polysaccharides as the major constituents in *L. rhinocerotis* extracts [23]. The XRD result confirms the existence of both broad peak amorphous behavior and a small crystalline structure region in *L. rhinocerotis* crude extract which is very common in nature. The profile suggested the sample is composed of monodisperse particle. Several studies also reported the similar profile pattern [9,24,25].

In this study, cold water and petroleum ether extracts between 62.5 and 250.0 µg/ml show cytotoxic effect since the reduction of cell viability at 72 hours is more than 30%. Other extracts did not show cytotoxic effect against BEAS-2B cell line. The data is consistent with a previous study on the anti-proliferative effect of the cold sclerotia of *L. rhinocerotis* [9]. Lee et al. [9]

hypothesized that the cytotoxic effect of the cold-water extract was due to the presence of thermolabile compounds in cold water extract which were absent in hot water extract. The study reported that cytotoxic cold-water extracts contained more proteins than non-cytotoxic hot water extract, suggesting that the cytotoxic activity might be attributed to the additional proteins in the cold-water extract. In the case of cytotoxic effect shown by petroleum ether extract, it might be attributed to the presence of alkaloids and terpenoids that might be present in the extract since petroleum ether has the ability to extract these compounds [26]. In fact, many plants that are reported to have toxic properties usually contain certain terpenoid and alkaloids [27]. Interestingly, *L. rhinocerotis* extracts did not confer any apoptotic effect on normal lungs epithelial cell line, BEAS-2B. It is plausible that the *L. rhinocerotis* extracts used in the study do not cause harmful effect to the normal cell line.

Conclusion

In conclusion, quantification of linoleic acid in hot water, cold water, hexane, petroleum ether, hexane residue and petroleum ether residue extract of *L. rhinocerotis* has been successfully determined using HPLC. In addition, the amount of β-glucan in *L. rhinocerotis* extract has also been successfully quantified using the optimized method. The characterization of polysaccharide and crystalline structure in *L. rhinocerotis* extracts have been also successfully determined. All extracts (especially at high concentration, 125 and 250 µg/mL) showed reduced proliferative activities as compared to control at 72 hours; although the majority of the extracts were not cytotoxic to BEAS-2B cell line. The observed effects are likely due to the high content of immunomodulatory active compounds, such as linoleic acid and β-glucan, present in the extract.

Acknowledgement

This study was supported by the Universiti Sains Malaysia Research University Grant (Grant No: 1001/PPSK/8012344).

References

1. Lau, B. F., Noorlidah A., Norhaniza A., Hong B. L., and Pei J. T. (2015). Ethnomedicinal uses, pharmacological activities, and cultivation of Lignosus Spp. (Tiger′s milk mushrooms) in Malaysia – A review. *Journal of Ethnopharmacology*, 169: 441-458.
2. Lee, S. S., Chang, Y. S. and Noraswati, M. N. R. (2 009). Utilization of macrofungi by some indigenou s communities for food and medicine in Peninsular Malaysia. *Forest Ecology and Management,* 257(1 0): 2062-2065.
3. Zhu, F., Bin D., Zhaoxiang B., and Baojun Xu. (20 15). Beta-glucans from edible and medicinal mushr ooms: characteristics, physicochemical and biologi cal activities. *Journal of Food Composition and An alysis,* 41:165-173.
4. Chen, S-N., Ching-Sheng C., Ming-Hsin H., Sherwin C., William W., Cheng-Jeng T., and Chung-Lun L. (2014). The effect of mushroom beta-glucans from solid culture of *Ganoderma lucidum* on inhibition of the primary tumor metastasis. *Evidence-Based Complementary and Alternative Medicine*, 2014: 1-7.
5. Choque, B., Daniel C., Vincent R., and Philippe L. (2014). Linoleic acid: Between doubts and certainties. *Biochimie,* 96: 14-21.\
6. Ferrucci, L., Cherubini, A., Bandinelli, S., Bartali, B., Corsi, A., Lauretani, F., ... and Guralnik, J. M. (2006). Relationship of plasma polyunsaturated fatty acids to circulating inflammatory markers. *The Journal of Clinical Endocrinology & Metabolism,* 91(2): 439-446.
7. Johnathan, M., Gan, S. H., Ezumi, M. F., Faezahtul, A. H., and Nurul, A. A. (2016). Phytochemical profiles and inhibitory effects of Tiger Milk mushroom (*Lignosus rhinocerus*) extract on ovalbumin-induced airway inflammation in a rodent model of asthma. *BMC Complementary and Alternative Medicine*, 16(1), 1-13.
8. Fauzi, S. Z.C., Nor-Fadilah R., Lek, M. L., Kok, L. P., Norfazlina, M. N., Nurshahirah, N., Florinsiah, L., and Farida, Z. M. Y. (2015). Anti-proliferative effect of *Lignosus rhinocerus* extract on colorectal cancer cells via apoptosis and cell cycle arrest. *International Journal of Pharmaceutical Sciences Review and Research,* 33(1): 13-17.
9. Lee, M. L., Tan, N. H., Fung, S. Y., Tan, C. S., and

Ng. S. T. (2012). The antiproliferative activity of sclerotia of *Lignosus rhinocerus* (Tiger Milk Mushroom). *Evidence-Based Complementary and Alternative Medicine*, 2012: 1-5.

10. Anthérieu, S., Anne, G., Nicolas, B., Mélissa, S., Delphine, A., Guillaume, G., and Jean-Marc L-G. (2017). Comparison of cellular and transcriptomic effects between electronic cigarette vapor and cigarette smoke in human bronchial epithelial cells. *Toxicology In Vitro*, 45: 417-425.
11. Britt, R., Michael, T., Christina, P., and Prakash, S.Y. (2017). C108 getting inflamed: Markers of lung injury and remodeling: brain-derived neurotrophic factor promotes remodeling mechanisms in human airway epithelial cells. *American Journal of Respiratory and Critical Care Medicine*, 195: 15.
12. U.S. Department of Health and Human Services, Food and Drug Administration. (2018). Bioanalytical method validation guidance for industry."U.S. Department of Health and Human Services, Food and Drug Administration, no. May: 1–41. Access from https://www.fda.gov/files/drugs/published/Bioanalytical-Method-Validation-Guidance-for-Industry.pdf.
13. Dore, C., Monique, A., Maria, S., Leonardo de S., Iuri, B., and Edda L. (2014). Antioxidant and anti-inflammatory properties of an extract rich in polysaccharides of the mushroom *Polyporus dermoporus*. *Antioxidants,* 3(4): 730-744.
14. Riaz, T., Rabia, Z., Faiza, Z., Kanwal, I., Nawshad, M., Sher, Z. S., Abdur, R., Syed A. A. R., and Ihtesham, U. R. (2018). FTIR analysis of natural and synthetic collagen. *Applied Spectroscopy Reviews,* 53(9): 703-746.
15. Gutte, K. B., Akshaya, K. S., and Rahul, C. R. (2015). Effect of ultrasonic treatment on extraction and fatty acid profile of flaxseed oil. *Oilseeds and Fats, Crops and Lipids,* 22(6): D606.
16. Toledo, C., Carolina, B., Ângela, F., Lillian, B., and Isabel, F. (2016). Chemical and antioxidant properties of wild edible mushrooms from native Nothofagus Spp. forest, Argentina. *Molecules,* 21(9): 1201.
17. Tel-Çayan, G., Akhtar, M., Mehmet, E. D., Mehmet, Ö., Achyut, A., and Aziz, T. (2016). A new fatty acid ester from an edible mushroom *Rhizopogon luteolus*. *Natural Product Research,* 30(20): 2258-2264.
18. Koutrotsios, G., Nick, K., Pantelis, S., Andriana, C. K., and Georgios, I. Z. (2017). Bioactive compounds and antioxidant activity exhibit high intraspecific variability in *Pleurotus ostreatus* mushrooms and correlate well with cultivation performance parameters. *World Journal of Microbiology and Biotechnology,* 33(5): 98.
19. Jamil M., Nor-Azreen, Norasfaliza R., Noraswati M. N. R., Mohd-Hafis-Yuswan, M. Y., Nur Syahidah S., and Norihan M. S. (2013). LCMS-QTOF determination of lentinan-like β-D-glucan content isolated by hot water and alkaline solution from Tiger's milk mushroom, termite mushroom, and selected local market mushrooms. *Journal of Mycology,* 2013: 1-8.
20. Kong, B-H., Nget-Hong T., Shin-Yee F., Jayalakshmi, P., Chon-Seng T., and Szu-Ting, N. (2016). Nutritional composition, antioxidant properties, and toxicology evaluation of the sclerotium of Tiger milk mushroom *Lignosus Tigris* cultivar E. *Nutrition Research,* 36(2): 174-183.
21. Chen, Y, Hui, Z., Yuanxing, W., Shaoping, N, Chang, L., and Mingyong, X. (2015). Sulfated modification of the polysaccharides from *Ganoderma atrum* and their antioxidant and immunomodulating activities. *Food Chemistry,* 186: 231-238.
22. Zheng, H-G., Chen, J-C., Weng M-J, Ahmad I., and Zhou, C-Q. (2020). Structural characterization and bioactivities of a polysaccharide from the stalk residue of *Pleurotus Eryngii*. *Food Science and Technology*, 40: 235-241.
23. Choong, Y-K, Kavithambigai, E., Xiang-Dong, C., and Shaiful Azuar, M. (2019). Extraction and fractionation of polysaccharides from a selected mushroom species, *Ganoderma lucidum*: A critical review. In Fractionation. IntechOpen: pp. 78047.
24. Barbosa, J. R., Maurício, M. S. F., Luã, C. O., Luiza, H. S. M., Andryo, O. A-V., Rafael, M O, Julio, C. P., Davi do Socorro B. B., and Raul, N. C. J. (2020). Obtaining extracts rich in antioxidant polysaccharides from the edible mushroom

pleurotus ostreatus using binary system with hot water and supercritical CO_2. *Food Chemistry,* 330: 127173.

25. Savi, A., Gabrielle, C. C., Vidiany, A. Q. S., Edimir, A. P., and Sirlei, D. T. (2020). Chemical characterization and antioxidant of polysaccharide extracted from *Dioscorea bulbifera*. *Journal of King Saud University – Science*, 32(1): 636-642.
26. Prashant, T., Kumar, B., Kaur, M., Kaur, G., and Kaur, H. (2011). Phytochemical screening and extraction: A review. *Internationale Pharmaceutica Sciencia,* 1(1): 98-106.
27. Wink, M. (2015). Modes of action of herbal medicines and plant secondary metabolites. *Medicines,* 2(3): 251-286.

Malaysian Journal of Analytical Sciences (MJAS)
Published by Malaysian Analytical Sciences Society

APPLICATION OF MAGNETIC BIO-POLYMER SPOROPOLLENIN AS LOW-COST ADSORBENT FOR REMEDIATION OF METHYLENE BLUE FROM AQUEOUS SOLUTION

(Aplikasi Magnetik Bio-Polimer Sporopollenin Sebagai Penjerap Kos-Rendah untuk Pemulihan Metilena Biru daripada Larutan Akueus)

Syed Fariq Fathullah Syed Yaacob[1,3*], Muhamad Zulfikry Shamsudin[1], Arniza Khairani Mohd Jamil[1], Faiz Bukhari Mohd Suah[3], and Sharifah Mohamad[1,2*]

[1]*Department of Chemistry, Faculty of Science, Universiti Malaya, 50603 Kuala Lumpur, Malaysia*
[2]*University Malaya Centre for Ionic Liquids (UMCiL), University of Malaya, 50603 Kuala Lumpur, Malaysia*
[3]*School of Chemical Sciences, Universiti Sains Malaysia, Pulau Pinang 11800, Malaysia*

[*]*Corresponding author: syedfariq@usm.my; sharifahm@um.edu.my*

Received: 28 September 2022; Accepted: 21 June 2023; Published: 22 August 2023

Abstract

Adsorption processes using low-cost sorbents such as bio-polymer adsorbents are an attractive option for removing methylene blue from wastewater. This study involved magnetic sporopollenin (MSp) synthesis and its application for removing methylene blue (MB) from an aqueous solution via adsorption process. The synthesized MSp was characterized by FT-IR and FESEM analyses. The effects of pH 2 - pH 8, sorbent dosage (10 mg - 50 mg), and contact time (0 - 60 min) were studied in batch mode and optimized. Adsorption isotherms models, Langmuir and Freundlich were used to simulate the equilibrium data. The Freundlich isotherm model is best fitted with the experimental data compared to the Langmuir model. A maximum absorption capacity (q_m) of 6.357 mg/g was obtained for MB. In addition, pseudo-first-order and pseudo-second-order were used to study the kinetics of MB adsorption onto MSp. The dye adsorption process obeyed the pseudo-second-order kinetic expression as proven by the high correlation coefficient (R^2 = 0.999). Overall, these findings confirmed the potential of MSp as an alternative and efficient sorbent for the removal of MB dye, offering promising prospects for wastewater treatment applications.

Keywords: magnetic nanoparticles, sporopollenin, methylene blue, isotherm, kinetics

Abstrak

Proses penjerapan menggunakan penjerap kos rendah seperti penjerap bio-polimer merupakan pilihan yang menarik untuk penyingkiran metilena biru daripada air sisa. Kajian ini melibatkan sintesis sporopollenin magnetik (MSp) dan aplikasinya untuk penyingkiran metilena biru (MB) daripada larutan akueus melalui proses penjerapan. MSp yang disintesis dicirikan oleh analisis FT-IR dan FESEM. Kesan pH 2 - pH 8, dos sorben (10 mg - 50 mg), dan masa dikaji (0 - 60 min) dalam mod kelompok dan dioptimumkan. Model isoterma penjerapan, Langmuir dan Freundlich digunakan untuk mensimulasikan data keseimbangan. Model isoterma Freundlich paling sesuai dengan data eksperimen berbanding dengan model Langmuir. Kapasiti penyerapan maksimum (q_m) sebanyak 6.357 mg/g diperolehi untuk MB. Di samping itu, pseudo-tertib pertama dan pseudo-tertib-kedua digunakan untuk mengkaji kinetik penjerapan MB ke MSp. Proses penjerapan pewarna mematuhi ekspresi kinetik pseudo-tertib-

kedua seperti yang dibuktikan oleh pekali korelasi tinggi (R^2 = 0.999). Secara keseluruhan, penemuan ini mengesahkan potensi MSp sebagai sorben alternatif dan cekap untuk penyingkiran pewarna MB, menawarkan prospek yang menjanjikan untuk aplikasi rawatan air sisa.

Kata kunci: magnetik nanopartikel, sporopollenin, metilena biru, isoterma, kinetik

Introduction

Recently, the abundance of pollutants in water has become a severe environmental issue. Amongst the industrial activities, dyeing industries are aggressively moving forward because of the extensive use of dyes in manufacturing industries, such as food, textile, paper, and plastic. Until now, more than 100,000 synthetic dyes have been produced, creating significant problems for the environment and human beings due to their toxicity and mutagenic effects [1]. The removal of synthetic dyes is an important concern as the incomplete degradation of dyes causes the production of carcinogenic and harmful amines [2]. Furthermore, the presence of color substances in the water may decrease light transmission and photosynthesis activity, leading to bacteria growth and hence inhibiting the growth of the plant and aquatic ecosystem in the water [3].

Methylene blue (MB) dye is a cationic dye commonly used in the industry's coloring processes. It also has broader applications, including usage as a temporary hair colorant, a colorant for cotton and wools, and a coating for paper stock. MB has been classified as a non-biodegradable dye and needs to be treated before being discharged into the environment [1]. MB can cause harmful side effects to humans, such as vomiting, shock, increased heart rate, and jaundice in newborn babies.

Many treatment techniques have been applied to different types of water and wastewater contaminated with dyes. These treatment techniques, include physical or chemical treatment processes. Treatment processes, include chemical coagulation [4], ozonation [5], oxidation [6], photodegradation [7], ion exchange [8], irradiation [9], nanofiltration [10], and adsorption [11]. Unfortunately, several of these techniques are costly, require various tools, and have limitations. Based on the literature [12], low-cost sorbent has been developed as an alternative for dye removal. Several low-cost adsorbents have been investigated for dye removal such as wood waste activated carbon [13], olive oil activated carbon [14], apricot stone activated carbon [15], weeds activated biochar [16], and ZnO-nano rods-activated carbon [17].

With the prevalence of adsorption as an essential technique for purifying dye-contaminated wastewater, the development of magnetic nanoparticles (MNPs) sorbent materials such as magnetite (Fe_3O_4) has gained notable recognition in water purification [18]. It is based on the advantages of having a simple manipulation process, high separation efficiency under an external magnetic field, and easy functional modifications for specificity and operation conditions [19]. Moreover, the high surface area-to-volume ratio properties possessed by MNPs ensure a better adsorption capacity and high recovery compared to other sorbents [20]. Nevertheless, adsorption also has a certain limitation that needs to be countered. For example, separation and recovery processes. After adsorption, separating the adsorbent from the solution can be challenging, especially when dealing with fine particles or colloidal materials. Thus, this process often requires additional filtration or centrifugation steps. Next, limitation is the environmental impact which some traditional adsorbents may have environmental implications due to their non-biodegradability or potential release of toxic substances during the adsorption process. Hence, these issues need to be countered properly.

Sporopollenin is a natural bio-polymer obtained from *Lycopodium clavatum*, which is highly resistant to chemical reactions, has a stable chemical structure and occurs naturally as a component of spore walls [21]. Furthermore, sporopollenin exhibits significant stability even after prolonged exposure to mineral acids and alkaline. Due to its efficiency and biocompatibility, sporopollenin is a well-known potential biomaterial used to remove various types of dye from the aqueous solutions. Sunset yellow [22], methyl orange [23], crystal violet [24] and Rhodamine B [25] have been successfully absorbed from an aqueous solution by

sporopollenin and its derivatives. Moreover, biopolymer sporopollenin is typically biodegradable, minimizing the environmental impact associated with the disposal of used adsorbents.

Sporopollenin loaded with magnetic functionality increases the total efficiency of the adsorption process and helps facilitate fast recovery. By incorporating magnetic nanoparticles or attaching magnetic moieties to the bio-polymer sporopollenin, it becomes responsive to external magnetic fields. This enables easy separation and recovery of the adsorbent from the solution by using a magnetic field, simplifying the overall process. Hence, a composite made from magnetic material is a suitable sorbent and thus a potential candidate for the removal of MB. A simple method for loading sporopollenin microcapsules with nanoparticles and insoluble salts is through a chemical reaction or a precipitation process that generates the encapsulated compounds inside the sporopollenin shell. This method produced magnetic sporopollenin loaded with magnetite nanoparticles and low solubility of organic salts [26].

Magnetic sporopollenin (MSp) was prepared as adsorbents in this study to remove MB dyes (Figure 1) from an aqueous solution. Two models, Langmuir and Freundlich, were used to describe the sorption process of MB adsorption onto the magnetic sporopollenin. Furthermore, the kinetics of MB adsorption onto the magnetic sporopollenin was investigated by using a pseudo-first-order and a pseudo-second-order models.

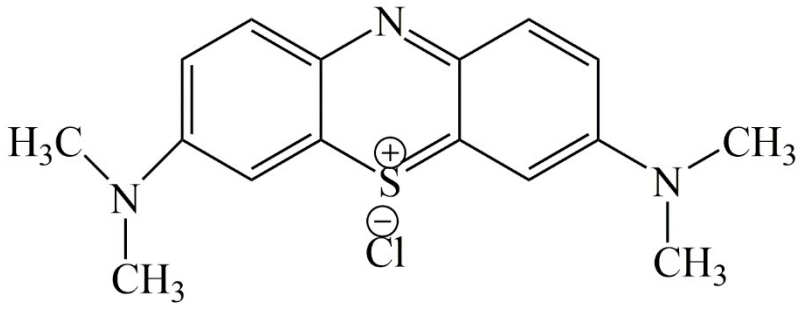


Figure 1. Structure of methylene blue (MB)

Materials and Methods

Materials

Analytical grade ammonia, ethanol, hydrochloric acid and sodium hydroxide pellet were purchased from Merck (Darmstadt, Germany) and used without further purification. Ferrous chloride tetrahydrate (CAS no. 13478-10-9) and ferric chloride hexahydrate (CAS no. 10025-77-1) were obtained from Sigma-Aldrich (Steinheim, Germany). All commercial grade solvents were stored over molecular sieves (4 Å, 8–12 mesh) from Aldrich (Steinheim, Germany). *Lycopodium clavatum* with a particle size of 25 µm was purchased from Aldrich (Steinheim, Germany). Methylene blue was obtained from Merck (Steinheim, Germany). The pH of the solution was adjusted by mixing an appropriate amount of HCl and/or NaOH (0.1 M). Deionized water that passed through a Milli-Q system (Lake End, UK) was used to prepare the solutions.

Instrumentation

Fourier transform infrared (FTIR) spectrometry (Spectrum 400 Perkin Elmer, Waltham, MA, USA) utilizing the ATR technique. Field emission scanning electron microscopy (FESEM) analysis was performed by using scanning electronic microscopy (HITACHI SU8220), OXFORD Instrument (Oxfordshire, UK). Ultraviolet-Visible (UV-Vis) spectrophotometer (Shimadzu, Tokyo, Japan) equipped with 1 cm quartz cells.

Preparation of magnetic sporopollenin (MSp)

MSp was prepared as follows: 13.32 g $FeCl_3.6H_2O$, 19.88 g $FeCl_2.4H_2O$, 5 mL of 5M HCl, 40 mL deionized water and 5 mL of ethanol were mixed in a 100 mL flask. The solution was stirred at room temperature until a complete dissolution of the salts. Then, 1.0 g of the

freshly prepared sporopollenin was redispersed in 30 mL of this solution and stirred for 2 h at room temperature. The sporopollenin suspension was filtered, and the filtrate was quickly washed with deionized water and immediately transferred to a 1.0 M ammonia solution. After 2 h stirring at room temperature, the MSp (with a core of magnetic nanoparticles) were collected by neodymium magnet, washed thoroughly with deionized water, and dried under vacuum. Figure 2 shows the preparation of MSp sorbent.

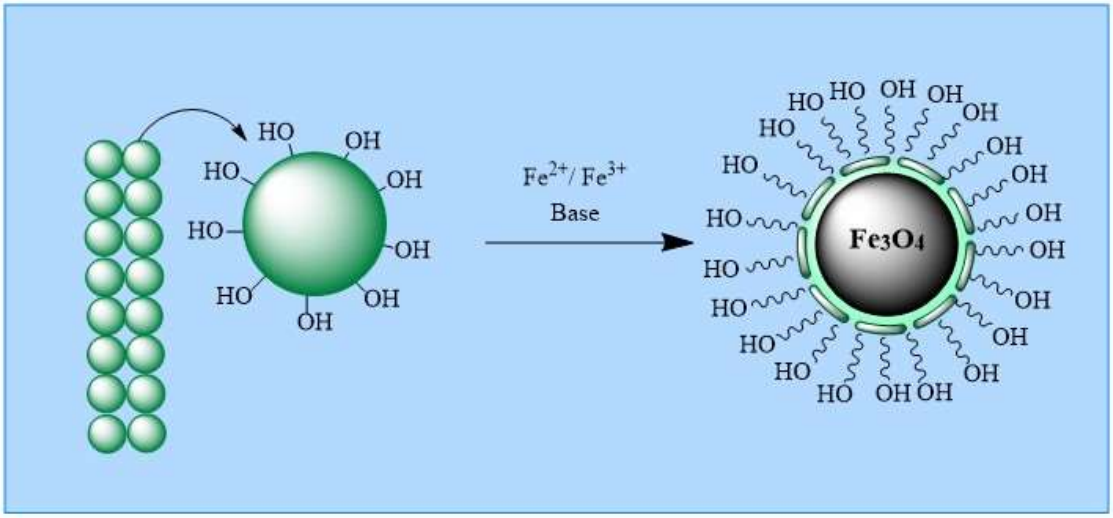


Figure 2. Synthesis of magnetic sporopollenin (MSp)

Sorption study

The batch sorption study was carried out to evaluate the MB removal efficiency of MSp sorbent. Different parameters, such as sorbent dosage (10 mg - 50 mg), pH (pH 2 - pH 8), and contact time (0 - 60 min) were optimized to achieve the optimum sorption results. The experiments were conducted in 25 mL Erlenmeyer flasks with glass caps containing the amount of the sorbent and concentration of sorbate solution, i.e., 5 ppm aqueous solution of MB. The Erlenmeyer flasks were stirred on a horizontal shaker operating at a constant speed (100 rpm) at room temperature for 10 min to obtain sorption equilibrium. Then, the sorbent was removed before measurement by using an external magnet. The MB concentration before the treatment and the residual concentration of MB in the aqueous phase after the treatment was analysed through UV-Vis spectrophotometer at 664 nm. The percentage removal and adsorption capacity of MB utilizing the synthesized MSp were calculated using Eq.1 and Eq.2, respectively. The percentage removal and q_e of MB were calculated through Eq. (1) as follows:

$$\frac{C_i - C_f}{C_i} \times 100\ \% \quad (1)$$

Where, C_i (mol L^{-1}) is initial concentration of MB before sorption, and C_f (mol L^{-1}) is final concentration of MB after adsorption.

$$q_e = \frac{V\,(C_0 - C_e)}{W} \quad (2)$$

Where, q_e is adsorption capacity (mg g^{-1}), V is aqueous volume (L), W is adsorption dosage (mg), and C_e (mol L^{-1}) and C_o (mol L^{-1}) are residual and initial concentrations of MB.

Results and Discussion

Characterization of adsorbent

The FTIR spectra provided information about the presence of functional groups. The FT-IR spectra for the synthesized MSp and sporopollenin were similar except for the characteristic peaks near 570 cm^{-1}, corresponding to (–Fe-O) bond stretching in Fe_3O_4. This characteristic peak showed that the sporopollenin was successfully magnetized with Fe_3O_4 [27]. The remaining peaks with their corresponding assignment were as follow: 3289 cm^{-1} (–OH), 1646 cm^{-1} (–C=O), 1546 cm^{-1} (–C=C), 1442 cm^{-1} (–C-C), 1260 cm^{-1} and 1113 cm^{-1} (–C-O) as shown in Figure 3.

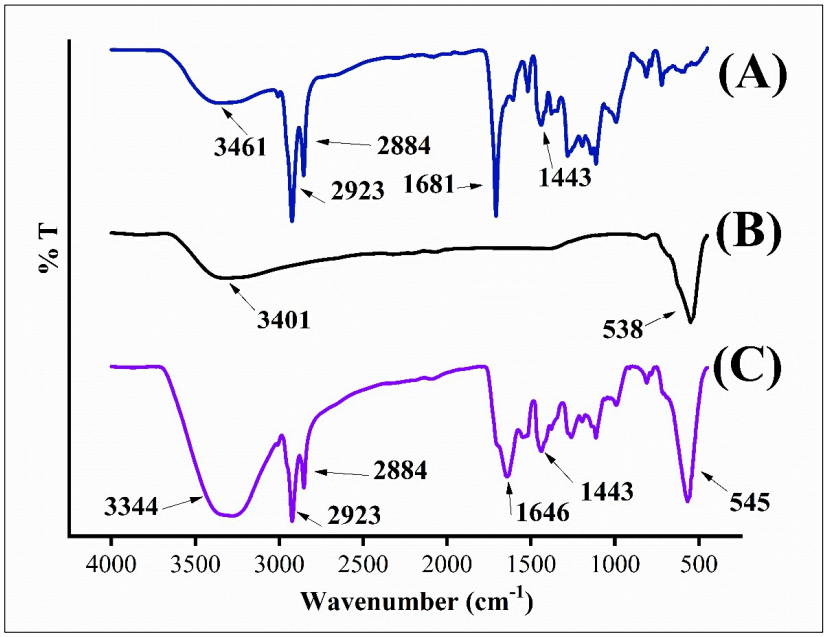


Figure 3. FTIR spectra of (a) raw Sp, (b) MNP, and (c) MSp

Field emission scanning electron microscopy (FESEM) is widely used to observe synthesized materials morphology and size distribution. FESEM images in Figure 4(a) show an open uniform pores structure and smooth surface morphology of sporopollenin. Meanwhile, Figure 4(b) shows a surface loaded with magnetic nanoparticles, which caused the change of porous structure to become limpid. This scenario confirmed that sporopollenin's surface has been successfully magnetized and was predominantly localized with magnetic nanoparticles [28].

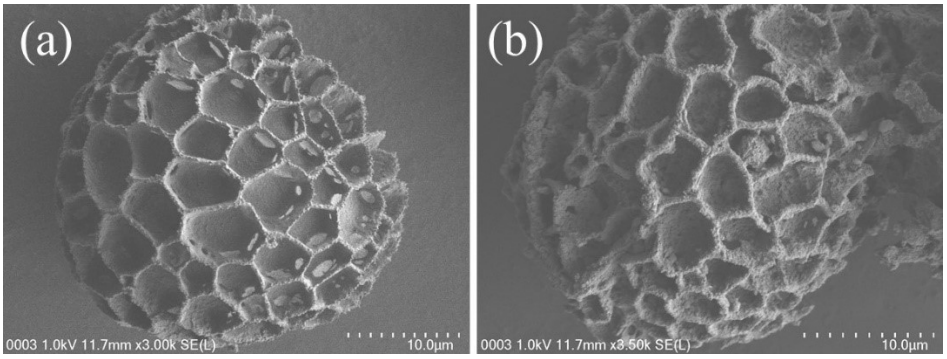


Figure 4. FESEM images of (a) sporopollenin and (b) MSp

Optimization of effective parameters on the removal of MB: Effect of sorbent dosage

Figure 4(a) shows the sorbent dosage's effect on MB adsorption. From the results, the percentage of MB removal increased rapidly from 61% to 90%, with increasing sorbent mass from 10 mg to 50 mg. The removal of MB was greater with the increase of sorbent dosage due to more available sites for adsorption. The amount of sorbent for further adsorption experiments was selected as 30 mg because beyond this point; there was no signification increase in adsorption of the MB. Therefore, all experiments were carried out with a fixed amount of 30 mg sorbent.

Effect of solution pH

This study investigated the effect of solution pH on the removal of MB (Figure 5b) at different pH ranges. The removal of MB increased with the pH of the solution from pH 2 to pH 8. Above pH 8, the removal of MB reached an equilibrium. This was due to the cation exchange between the sorbent and dye solution. The reported pH_{zpc} for MNP was pH 6.5 [29]. Beyond the pH_{zpc} point, the sorbent surface was in its protonated form, resulting in electrostatic repulsion between the positively charged MB and the sorbent surface. The higher amount of hydrogen ions in the solution prevented the negative charge formation on the MSp surface; thus, reducing the dye uptake. Above the pH_{zpc} point, the sorbent surface deprotonated the hydroxyl groups on the surface of MSp and provided more negative sites for electrostatic attraction between the cationic form of the dye molecules and the sorbent surface. Percentage removal was higher at this point; thus, the optimum pH for the maximum adsorption capacity of MB was determined to be pH 8.

Effect of contact time

Figure 5(c) shows that the amount of MB adsorbed (mg/g) increased with the contact time as predicted. During the first 5 min of the adsorption process, the percentage removal rapidly increased. As the contact time increased to 10 min, the adsorption of MB dye reached a maximum level and achieved an equilibrium. By further increment from 10 min to 60 min, the percentage of removal showed no significant changes that could be due to saturated binding sites on surface of MSp. Thus, 10 min was sufficient for removing MB and selected as the optimum contact time for further analysis.

Sorption isotherm

Adsorption isotherms described how analytes interact with sorbent materials in optimizing adsorbents. Therefore, the relationship between the removal ability of the material and the concentration of the contaminant solution can be illustrated by adsorption isotherms. It is crucial to establish the most appropriate correlation for the equilibrium curve to optimize the design of an adsorption system to remove dye from the solutions [30]. The investigation of the adsorption process was employed by Langmuir and Freundlich isotherm models. Furthermore, linearized forms of their equations have been used to describe the isotherm curves. The relative parameters of each equation were obtained by using the linear regressive analysis. In this study, the adsorption isotherm of MB by MSp was measured by shaking it for 10 min at different initial concentrations at pH 8 at room temperature.

The Langmuir isotherm suggested that sorption occurred on a homogeneous surface to obtain maximum adsorption capacity. No further adsorption process will occur if a solute occupies the site [31-32]. Langmuir isotherm models assumed the sorbate's monolayer coverage on a sorbent surface at a constant temperature. The linear fit of Langmuir for the adsorption of MB onto MSp is shown in Figure 6(a). The following equation represents the Langmuir isotherm:

$$\frac{C_e}{q_e} = \frac{C_e}{q_m} + \frac{1}{q_m b} \quad (3)$$

Where q_e is amount of solute sorbed on the surface of the sorbent, C_e is equilibrium ion concentration in the solution, q_m is maximum surface density at monolayer coverage, and b is Langmuir adsorption constant. The plot of $\frac{C_e}{q_e}$ vs. C_e for the sorption gives a straight line of slope $\frac{1}{q_o}$ (Figure 6a).

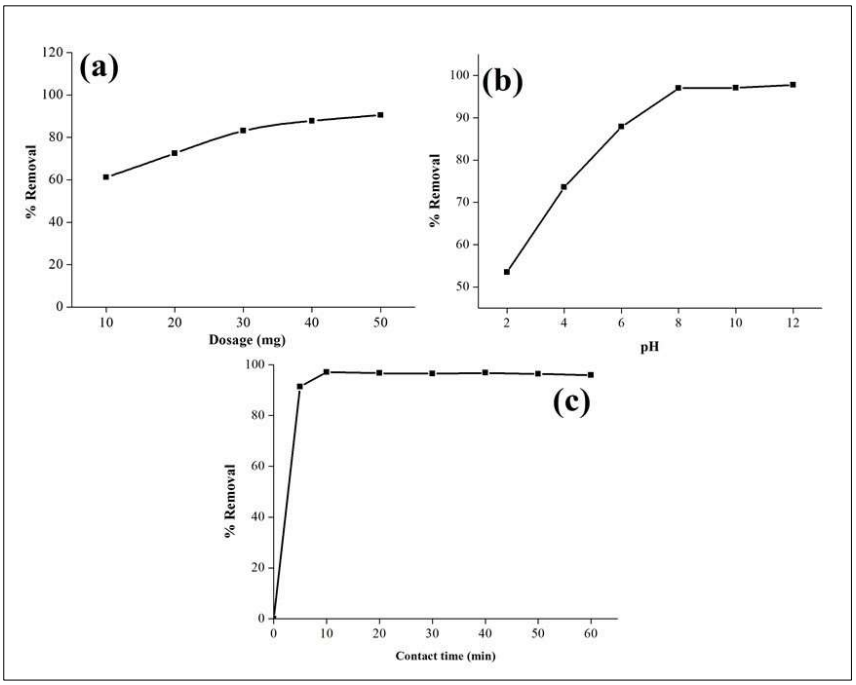


Figure 5. The effect of (a) dosage, (b) pH, and (c) contact time on the sorption of MB

The value of q_m, b and R^2 are presented in Table 1. The results indicated that the linear form of the Langmuir model showed a minimal deviation from the fitted equation as indicated by the R^2 value of 0.9637. This result suggested that the Langmuir model could not describe the relationship between the adsorbed amount of MB and its equilibrium concentration in the solution. Hence, the adsorption data would not follow the Langmuir model as compared to the Freundlich model.

Freundlich isotherm model suggested the sorbent surface heterogeneity with different energy of active sites and reversible adsorption which is restricted to multilayer formation. The Freundlich isotherm equation is shown as below:

$$\log q_e = \log K_F + \frac{1}{n}\log C_e \quad (4)$$

Where K_F and n are Freundlich constants related to the adsorption capacity and adsorption intensity, respectively. q_e is equilibrium solute concentration on sorbent, and C_e is equilibrium concentration of the solute.

The linear plot of $logq_e$ versus $logC_e$ for the Freundlich isotherm is shown in Figure 6(b). The constants of K_F and $1/n$ can be evaluated from the intercept and slope of the linear plot of experimental data are shown in Table 1. A larger value of K_F indicates the greater adsorption capacity while n values indicate the favourability of the adsorption process. If n is above unity, then the adsorption process is favourable.

The Freundlich isotherm plot was found to be linear over the studied concentration range, and the correlation coefficient (R^2 = 0.9988) obtained was higher than the Langmuir isotherm model. In addition, the Freundlich constant, K_F was 82.38 L/mg. In the present study, the value of n (indicative of favorability) is 1.476, which is above unity, indicating the favourability of the adsorption process. This showed that the interaction force between the MB dye and MSp sorbent was strong. Therefore, the Freundlich model is a good model to describe the adsorption data. The applicability of the

Freundlich adsorption model proposed the multilayer coverage of MB dye on the surface of MSp. Hence, the Freundlich model's experimental data indicated that the MSp surface's nature is heterogeneous with different adsorption sites.

Similarly, Boukhemkhem and Rida [33] reported a good adsorption potential (n = 4.17) for MB uptake modified Tamazert kaolin. The Freundlich model best fits to describe the adsorption of MB onto Tamazert kaolin relative to the Langmuir isotherm models implying multilayer adsorption onto a heterogeneous surface. In contrast, Mosleh and co-workers [34] reported magnetic sporopollenin supported polyaniline (MSP-PANI) for removal of lead ion (Pb^{2+}) was suitable for Langmuir isotherm with the maximum adsorption capacity of 163 mg/g and followed the monolayer pattern. Similarly, for magnetic sporopollenin supported magnesium nanocomposite (MSP@MgO) for removal of tetracycline (TCP) reported by Algethami and co-workers [35]. The adsorption models were investigated, and the process was fitted with the Langmuir model with adsorption capacities of 110 mg/g. Overall, the isotherm mechanism depended on the nature of the interactions between the adsorbent and the adsorbate.

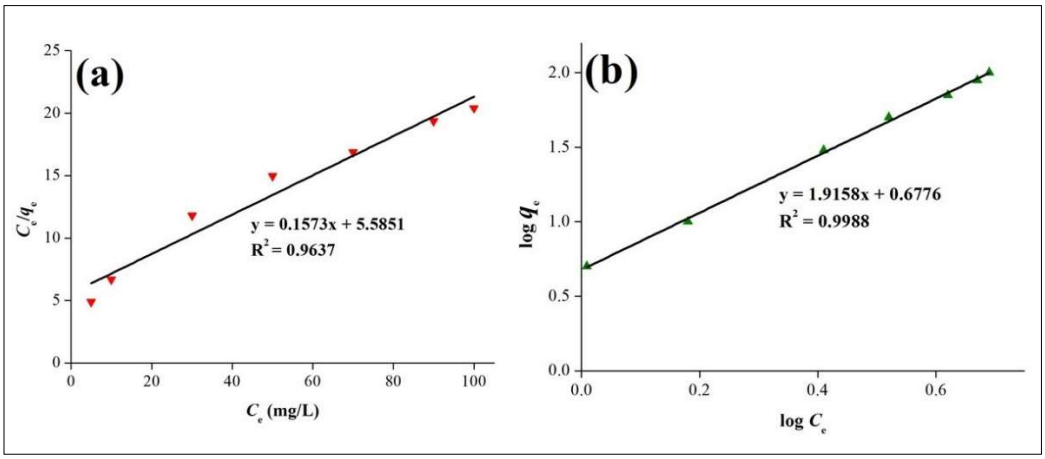


Figure 6. (a) Langmuir isotherms; (b) Freundlich isotherms for removal of MB by MSp

Table 1. Isotherm constants and regression data for adsorption of MB onto MSp at room temperature

Langmuir Constant			Freundlich Constant		
q_m (mg/g)	b (L/mg)	R^2	K_F (L/mg)	n	R^2
6.357	0.027	0.9637	82.38	1.476	0.9988

Sorption kinetics

Adsorption kinetics can describe a relationship between the amount of MB dye adsorbed to MSp in the aqueous solution. The analysis of the kinetic data is essential to generate an equation that accurately represents the results and could be used for design purposes [36]. The adsorption of MB dye onto MSp was further studied in terms of the kinetic model via pseudo-first-order and pseudo-second-order equations. The boundary layer resistance will be affected by the rate of adsorption with an increase in the contact time, which will increase the mobility of the adsorbate during adsorption. Since the uptake of adsorbates at the active sites of MSp is a rapid process, the adsorption rate is governed mainly by either the liquid phase mass transfer or the rate of intraparticle mass transfer.

Pseudo-first-order model

The pseudo-first-order model rate is based on the sorption capacity of the sorbent. The first-order model is

extensively applied for the adsorption of any solute from solution by the standard exchange procedure, which is fast and is mainly controlled by diffusion [37]. The plots of log ($q_e - q_t$) versus *t* are shown in Figure 7. The pseudo-first-order equation is expressed as:

$$log\ (q_e - q_t) = log\ q_e - K_1 t \quad (5)$$

Where, q_e and q_t are amounts of MB (mg g^{-1}) absorbed at equilibrium and at the time, *t,* respectively and K_1 is first order rate constant (min^{-1}). The values of q_e and K_1 are obtained from the linearity of pseudo-first-order rate by plotting $log\ (q_e - q_t)$ versus time, *t*.

The rate constant, K_1 and q_e are tabulated in Table 2. From Table 2, the value of R^2 = 0.7465 was low. Also, the calculated equilibrium adsorption capacities ($q_{e\ cal}$) by MSp was 0.276 mg/g, which is not consistent with the experimental data (q_e = 4.855 mg/g); hence this value is not in good agreement. This showed that the adsorption of MB onto MSp is not based on first-order kinetics.

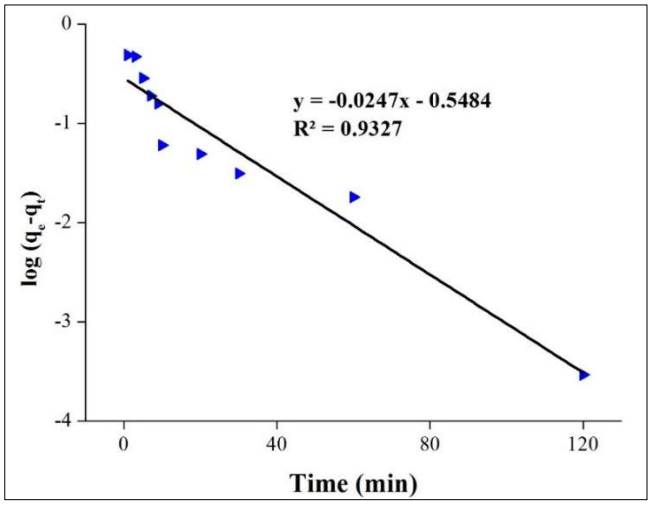


Figure 7. Pseudo-first order kinetic of MB.

Pseudo-second-order model

On the other hand, the pseudo-second-order model proposes that chemisorption is the rate-limiting step and that adsorption occurs on localized sites where no interactions between adsorbates arise [36]. Figure 8 shows the linear plots for the initial concentration studied.

The pseudo-second-order kinetic model applied for analyzing chemisorption kinetics from liquid solutions can be represented by Eq. (6) as follows.

$$\frac{t}{q_t} = \frac{1}{K_2 q_e^2} + \frac{t}{q_e} \quad (6)$$

Where K_2 is rate constant of pseudo-second-order adsorption (g/mg min). The value of K_2 and q_e can be described from the slope and the intercept of the graph $\frac{t}{q_t}$ versus t, respectively.

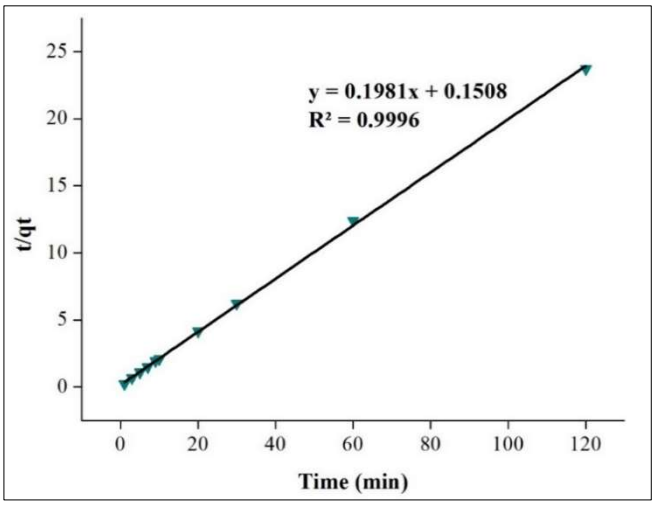


Figure 8. Pseudo-second order kinetic of MB

From Table. 2, the correlation coefficient (R^2) for the pseudo-second-order model is better (0.9996) than the pseudo-first-order model. The calculated equilibrium adsorption capacities ($q_{e\,cal}$) by MSp was found to be 4.684 mg/g, which is consistent with the experimental data ($q_{e\,exp}$ = 4.855 mg/g). A comparison between the calculated ($q_{e\,cal}$) and experimental ($q_{e\,exp}$) adsorption capacities revealed the pseudo-second-order model high applicability to describe the sorption process. Hence, the adsorption of MB onto MSp indicated that the adsorption kinetic is better represented by the pseudo-second-order model. Because of these results, it can be said that the pseudo-second-order kinetic model provided a good correlation for the adsorption of MB onto MSp in contrast to the pseudo-first-order model. This trend showed that the electron sharing between adsorbate and adsorbent is suited to uptake MB from aqueous media with high efficiency [38]. Numerous authors have reported similar pseudo-second-order kinetics, for adsorption of MB on different adsorbents, such as polyvinyl alcohol/carboxymethyl cellulose isolated from pineapple peel (PVA/CMC/GO/bentonite) [39], carboxymethyl cellulose-acrylamide-graphene oxide (CMC/AAm-GO) [40], and chitosan-g-poly(acrylic acid) modified cellulose nanowhiskers (Chitosan-g-PAA/CNW) [41].

Table 2. Kinetic parameters for adsorption of MB onto MSp

C_0	$q_{e\,exp}$ (mg/g)	Pseudo-First-Order Model			Pseudo-Second-Order Model		
		q_e (mg/g)	K_1 (1/min)	R^2	q_e (mg/g)	K_2	R^2
30	4.855	0.276	0.055	0.7465	4.684	0.855	0.9996

Comparison of sorption capacities of MSp with other adsorbents for MB removal

A comparison between MSp and other reported adsorbents in the literature is listed in Table 3. The performances were evaluated regarding the adsorption capacities. The data showed that the sorption capacity of MSp is relatively high as compared to other common sorbents except for several adsorbents such as spent rice biomass.

Table 3. The sorption capacities of the proposed MSp compared to other common adsorbents for the removal of MB

Adsorbent	Type of Analyte	Sorption Capacities (mg/g)	Ref
Glass wool	MB	2.20	[42]
Cashew nutshell	MB	5.31	[43]
Pyrolyzed petrified sediment	MB	2.39	[44]
Spent rice biomass	MB	8.30	[45]
Coir pith carbon	MB	5.87	[46]
Mansonia wood sawdust	MB	15.32	[47]
Padina sanctae-crucis	Methyl violet	10.02	[48]
Calcined lotus leaf	Methyl violet	26.32	[49]
Walnut shells	MB & methyl violet	6.5	[50]
Magnetic sporopollenin (MSp)	MB	6.4	This study

Conclusion

This study offered a unique method for removing methylene blue (MB) from aqueous solutions by implementing the economical adsorbent magnetic bio-polymer sporopollenin (MSp). The successful synthesis of MSp is confirmed by characterization by using FESEM analysis and FTIR spectroscopy. The optimum adsorption capacity of MB was achieved, and investigation of adsorption mechanisms sorption isotherms and isotherm kinetics revealed the Freundlich model and pseudo-second-order providing the best fit with the multilayer sorption on a heterogeneous surface. Some future prospects can be considered, including incorporating sporopollenin into polymer-based matrices, such as hydrogels or composite materials, to create hybrid adsorbents. The porous nature and flexibility of polymer matrices can enhance the adsorption capacity and stability of sporopollenin, making it suitable for various applications. Additional isotherm models, such as the Temkin model, Hasley model and Dubinin-Radushkevich isotherms model can be done to provide further insights into the adsorption behavior of methylene blue. These models can help characterize the energetic heterogeneity of the adsorbent surface, assess the feasibility of adsorption processes, and improve the understanding of the adsorption mechanisms. Lastly, in terms of regeneration and reusability to investigate the regeneration potential of MSp after MB adsorption. This is to ensure the restoration of the adsorption capacity of MSp, allowing for its repeated use and reducing overall operational costs.

Acknowledgement

Authors would like to acknowledge the valuable support from the University of Malaya Research Grants (Project No RP020A-16SUS), (Project No RG381-17AFR), (Project No. PG046-2015A), and the Ministry of Higher Education for scholarship (MyBrain15) provided.

References

1. Mazzeo, L., Marzi, D., Bavasso, I., Bracciale, M. P., Piemonte, V., and Di Palma, L. (2022). Characterization of waste roots from the as hyperaccumulator *Pteris vittata* as low-cost adsorbent for methylene blue removal. *Chemical Engineering Research and Design,* 186: 13-21.
2. Lade, H., Kadam, A., Paul, D., and Govindwar, S. (2015). Biodegradation and detoxification of textile azo dyes by bacterial consortium under sequential microaerophilic/aerobic processes. *EXCLI Journal,* 14: 158-174.
3. Durrani, W. Z., Nasrullah, A., Khan, A. S., Fagieh, T. M., Bakhsh, E. M., Akhtar, K., Khan, S. B., Din, I. U., Khan, M. A., and Bokhari, A. (2022). Adsorption efficiency of date palm based activated carbon-alginate membrane for methylene blue. *Chemosphere,* 302: 134793.
4. Sadri Moghaddam, S., Alavi Moghaddam, M. R., and Arami, M. (2010). Coagulation/flocculation process for dye removal using sludge from water treatment plant: Optimization through response surface methodology. *Journal of Hazardous Materials,* 175(1): 651-657.

5. Sripiboon, S., and Suwannahong, K. (2018). Color removal by ozonation process in biological wastewater treatment from the breweries. *IOP Conference Series: Earth and Environmental Science,* 167: 012010.
6. Khalaf, R. M., Kariem, N. O., and Khudhair, A. A. M. (2018). Removal of textile dye from aqueous media using an advanced oxidation process with UV/H_2O_2. *IOP Conference Series: Materials Science and Engineering,* 433: 012039.
7. Soltani, N., Saion, E., Hussein, M.Z., Erfani, M., Abedini, A., Bahmanrokh, G., Navasery, M., and Vaziri, P. (2012). Visible light-induced degradation of methylene blue in the presence of photocatalytic ZnS and CdS nanoparticles. *International Journal of Molecular Sciences,* 13(10): 12242-12258.
8. Huang, R., Zhang, Q., Yao, H., Lu, X., Zhou, Q., and Yan, D. (2021). Ion-exchange resins for efficient removal of colorants in bis(hydroxyethyl) terephthalate. *ACS Omega,* 6(18): 12351-12360.
9. Son, G., and Lee, H. (2016). Methylene blue removal by submerged plasma irradiation system in the presence of persulfate. *Environmental Science and Pollution Research,* 23(15): 15651-15656.
10. Cheng, S., Oatley, D. L., Williams, P. M., and Wright, C. J. (2012). Characterization and application of a novel positively charged nanofiltration membrane for the treatment of textile industry wastewaters. *Water Research,* 46(1): 33-42.
11. Tharaneedhar, V., Senthil Kumar, P., Saravanan, A., Ravikumar, C., and Jaikumar, V. (2017). Prediction and interpretation of adsorption parameters for the sequestration of methylene blue dye from aqueous solution using microwave assisted corncob activated carbon. *Sustainable Materials and Technologies,* 11: 1-11.
12. Ighalo, J. O., Omoarukhe, F. O., Ojukwu, V. E., Iwuozor, K. O., and Igwegbe, C. A. (2022). Cost of adsorbent preparation and usage in wastewater treatment: A review. *Cleaner Chemical Engineering,* 3: 100042.
13. Kaith, B. S., Dhiman, J., and Kaur Bhatia, J. (2015). Preparation and application of grafted Holarrhena antidycentrica fiber as cation exchanger for adsorption of dye from aqueous solution. *Journal of Environmental Chemical Engineering,* 3(2): 1038-1046.
14. Hazzaa, R., and Hussein, M. (2015). Adsorption of cationic dye from aqueous solution onto activated carbon prepared from olive stones. *Environmental Technology & Innovation,* 4: 36-51.
15. Djilani, C., Zaghdoudi, R., Djazi, F., Bouchekima, B., Lallam, A., Modarressi, A., and Rogalski, M. (2015). Adsorption of dyes on activated carbon prepared from apricot stones and commercial activated carbon. *Journal of the Taiwan Institute of Chemical Engineers,* 53: 112-121.
16. Güzel, F., Sayğılı, H., Akkaya Sayğılı, G., Koyuncu, F., and Yılmaz, C. (2017). Optimal oxidation with nitric acid of biochar derived from pyrolysis of weeds and its application in removal of hazardous dye methylene blue from aqueous solution. *Journal of Cleaner Production,* 144: 260-265.
17. Dil, E. A., Ghaedi, M., Ghaedi, A. M., Asfaram, A., Goudarzi, A., Hajati, S., Soylak, M., Agarwal, S., and Gupta, V. K. (2016). Modeling of quaternary dyes adsorption onto ZnO–NR–AC artificial neural network: Analysis by derivative spectrophotometry. *Journal of Industrial and Engineering Chemistry,* 34: 186-197.
18. Nodehi, R., Shayesteh, H., and Rahbar-Kelishami, A. (2022). Fe_3O_4@NiO core–shell magnetic nanoparticle for highly efficient removal of Alizarin red S anionic dye. *International Journal of Environmental Science and Technology,* 19(4): 2899-2912.
19. Yaacob, S. F. F. S., Jamil, A. K. M., Kamboh, M. A., Ibrahim, W. A. W., and Mohamad, S. (2018). Fabrication of calixarene-grafted bio-polymeric magnetic composites for magnetic solid phase extraction of non-steroidal anti-inflammatory drugs in water samples. *PeerJ, 6*: e5108.
20. Yaacob, S. F. F. S., Abd Razak, N. S., Aun, T. T., Rozi, S. K. M., Jamil, A. K. M., and Mohamad, S. (2018). Synthesis and characterizations of magnetic bio-material sporopollenin for the removal of oil from aqueous environment. *Industrial Crops and Products,* 124: 442-448.
21. Yaacob, S. F. F. S., Jamil, R. Z. R., and Suah, F. B. M. (2022). Sporopollenin based materials as a

versatile choice for the detoxification of environmental pollutants—A review. *International Journal of Biological Macromolecules*, 207: 900-1004.

22. Bişgin, A. T., Nalvuran, Z., and Gezici, O. (2021). Simultaneous preconcentration and spectrophotometric determination of two colorants (E110 and E133) in some foodstuffs using a new mussel-inspired adsorbent. *Journal of AOAC International,* 104(1): 137-147.
23. Ayar, A., Gezici, O., and Küçükosmanoğlu, M. (2007). Adsorptive removal of methylene blue and methyl orange from aqueous media by carboxylated diaminoethane sporopollenin: On the usability of an aminocarboxilic acid functionality-bearing solid-stationary phase in column techniques. *Journal of Hazardous Materials,* 146(1): 186-193.
24. Gezici, O., Küçükosmanoğlu, M., and Ayar, A. (2006). The adsorption behavior of crystal violet in functionalized sporopollenin-mediated column arrangements. *Journal of Colloid and Interface Science,* 304(2): 307-316.
25. Ecer, Ü., Şahan, T., Zengin, A., and Gubbuk, İ. H. (2022). Decolorization of Rhodamine B by silver nanoparticle–loaded magnetic sporopollenin: characterization and process optimization. *Environmental Science and Pollution Research*, 29(52): 79375-79387.
26. Ahmad, N. F., Kamboh, M. A., Nodeh, H. R., Halim, S. N. B. A., and Mohamad, S. (2017). Synthesis of piperazine functionalized magnetic sporopollenin: a new organic-inorganic hybrid material for the removal of lead(II) and arsenic(III) from aqueous solution. *Environmental Science and Pollution Research,* 24(27): 21846-21858.
27. Kamboh, M. A., and Yilmaz, M. (2013). Synthesis of N-methylglucamine functionalized calix [4] arene based magnetic sporopollenin for the removal of boron from aqueous environment. *Desalination,* 310: 67-74.
28. Yilmaz, E. (2012). Enantioselective enzymatic hydrolysis of racemic drugs by encapsulation in sol–gel magnetic sporopollenin. *Bioprocess and Biosystems Engineering,* 35(4): 493-502.
29. Khoeini Sharifabadi, M., Saber-Tehrani, M., Waqif Husain, S., Mehdinia, A., and Aberoomand-Azar, P. (2014). Determination of residual nonsteroidal anti-inflammatory drugs in aqueous sample using magnetic nanoparticles modified with cetyltrimethylammonium bromide by high performance liquid chromatography. *The Scientific World Journal,* 2014: 127835.
30. Dąbrowski, A. (2001). Adsorption—from theory to practice. *Advances in Colloid and Interface Science,* 93(1-3): 135-224.
31. Mehmood, T., Khan, A. U., Raj Dandamudi, K. P., Deng, S., Helal, M. H., Ali, H. M., and Ahmad, Z. (2022). Oil tea shell synthesized biochar adsorptive utilization for the nitrate removal from aqueous media. *Chemosphere,* 307: 136045.
32. Gao, Z., Wang, J., Muhammad, Y., Hu, P., Hu, Y., Chu, Z., Zhao, Z., and Zhao, Z. (2022). Hydrophobic shell structured NH2-MIL(Ti)-125@mesoporous carbon composite via confined growth strategy for ultra-high selective adsorption of toluene under highly humid environment. *Chemical Engineering Journal,* 432: 134340.
33. Boukhemkhem, A., and Rida, K. (2017). Improvement adsorption capacity of methylene blue onto modified Tamazert kaolin. *Adsorption Science & Technology*, 35(9-10): 753-773.
34. Mosleh, N., Najmi, M., Parandi, E., Nodeh, H. R., Vasseghian, Y., and Rezania, S. (2022). Magnetic sporopollenin supported polyaniline developed for removal of lead ions from wastewater: Kinetic, isotherm and thermodynamic studies. *Chemosphere*, 300: 134461.
35. Algethami, J. S., Yadav, K. K., Gacem, A., Ali, I. H., Rezania, S., Alhar, M. S. O., Mezni, A., Jeon, B. H., and Chaiprapat, S. (2023). Magnetic sporopollenin supported magnesium nanoparticles for removal of tetracycline as an emerging contaminant from water. *Environmental Science and Pollution Research*, 2023: 1-12.
36. Ho, Y. S., and McKay, G. (1999). Pseudo-second order model for sorption processes. *Process Biochemistry,* 34(5): 451-465.
37. Reçber, Z. B., Burhan, H., Bayat, R., Nas, M. S., Calimli, M. H., Demirbas, Ö., Şen, F., and Hassan, K.-M. (2022). Fabrication of activated carbon supported modified with bimetallic-platin ruthenium nano sorbent for removal of azo dye

from aqueous media using enhanced ultrasonic wave. *Environmental Pollution,* 302: 119033.

38. Lyu, F., Niu, S., Wang, L., Liu, R., Sun, W., and He, D. (2021). Efficient removal of Pb(II) ions from aqueous solution by modified red mud. *Journal of Hazardous Materials*, 406: 124678.
39. Dai, H., Huang, Y., and Huang, H. (2018). Eco-friendly polyvinyl alcohol/carboxymethyl cellulose hydrogels reinforced with graphene oxide and bentonite for enhanced adsorption of methylene blue. *Carbohydrate Polymers*, 185: 1-11.
40. Varaprasad, K., Jayaramudu, T., and Sadiku, E. R. (2017). Removal of dye by carboxymethyl cellulose, acrylamide and graphene oxide via a free radical polymerization process. *Carbohydrate Polymers*, 164: 186-194.
41. Melo, B. C., Paulino, F. A., Cardoso, V. A., Pereira, A. G., Fajardo, A. R., and Rodrigues, F. H. (2018). Cellulose nanowhiskers improve the methylene blue adsorption capacity of chitosan-g-poly (acrylic acid) hydrogel. *Carbohydrate Polymers*, 181: 358-367.
42. Chakrabarti, S., and Dutta, B. K. (2005). On the adsorption and diffusion of methylene blue in glass fibers. *Journal of Colloid and Interface Science,* 286(2): 807-811.
43. Senthil Kumar, P., Abhinaya, R.V., Gayathri Lashmi, K., Arthi, V., Pavithra, R., Sathyaselvabala, V., Dinesh Kirupha, S., and Sivanesan, S. (2011). Adsorption of methylene blue dye from aqueous solution by agricultural waste: Equilibrium, thermodynamics, kinetics, mechanism and process design. *Colloid Journal,* 73(5): 651.
44. Aroguz, A. Z., Gulen, J., and Evers, R. H. (2008). Adsorption of methylene blue from aqueous solution on pyrolyzed petrified sediment. *Bioresource Technology,* 99(6): 1503-1508.
45. Rehman, M. S. U., Kim, I., and Han, J.-I. (2012). Adsorption of methylene blue dye from aqueous solution by sugar extracted spent rice biomass. *Carbohydrate Polymers,* 90(3): 1314-1322.
46. Kavitha, D., and Namasivayam, C. (2007). Experimental and kinetic studies on methylene blue adsorption by coir pith carbon. *Bioresource Technology,* 98(1): 14-21.
47. Ofomaja, A. E. (2008). Kinetic study and sorption mechanism of methylene blue and methyl violet onto mansonia (*Mansonia altissima*) wood sawdust. *Chemical Engineering Journal,* 143(1): 85-95.
48. Mahini, R., Esmaeili, H., and Foroutan, R. (2018). Adsorption of methyl violet from aqueous solution using brown algae *Padina sanctae*-crucis. *Turkish Journal of Biochemistry,* 43(6): 623-631.
49. Sharafzad, A., Tamjidi, S., and Esmaeili, H. (2021). Calcined lotus leaf as a low-cost and highly efficient biosorbent for removal of methyl violet dye from aqueous media. *International Journal of Environmental Analytical Chemistry,* 101(15): 2761-2784.
50. Halysh, V., Sevastyanova, O., Riazanova, A. V., Pasalskiy, B., Budnyak, T., Lindström, M. E., and Kartel, M. (2018). Walnut shells as a potential low-cost lignocellulosic sorbent for dyes and metal ions. *Cellulose,* 25(8): 4729-4742.

Malaysian Journal of Analytical Sciences (MJAS)
Published by Malaysian Analytical Sciences Society

DEGRADATION OF AZO DYES FROM EFFLUENTS: A MINI REVIEW FOCUSING ON COMPARISON BETWEEN CURRENTLY EXISTING INDUSTRIAL METHODS AND GREEN OXIDATION CATALYSIS TREATMENT INVOLVING Fe-TAML AND H_2O_2

(Degradasi Pewarna Azo daripada Efluen: Sebuah Mini Ulasan yang Memfokuskan Perbandingan Antara Teknik Industri yang Kini Wujud dan Rawatan Pemangkinan Pengoksidaan Hijau Melibatkan Fe-TAML dan H_2O_2)

Wan Mohd Norsani Wan Nik[1], Nabilah Ismail[2*], Saranraj Saravanan[2], Nur Khairunnisa Nazri[2], and Mohd Arzaimiruddin Ariffin[3]

[1]*Faculty of Ocean Engineering Technology and Informatics,Universiti Malaysia Terengganu, 21030 Kuala Nerus, Terengganu, Malaysia*
[2]*Faculty of Science and Marine Environment,Universiti Malaysia Terengganu, 21030 Kuala Nerus, Terengganu, Malaysia*
[3]*Faculty of Mechanical Engineering, Universiti Teknologi MARA Cawangan Terengganu, Kampus Bukit Besi 23200, Jln Kuala Berang, Terengganu, Malaysia.*

[*]*Corresponding author: nabilah.i@umt.edu.my*

Received: 7 March 2023; Accepted: 3 June 2023; Published: 22 August 2023

Abstract

Dyes are widely used as coloring agents globally in the industrial field, especially in the textile industry. As proof, 10,000 types of dyes have been introduced and are continuously used, reaching a usage viability of 700,000 tons. The widespread use of synthetic dyes is caused by their economic factors, ready availability, superior strength, and ability to cover a wide range of shades. However, the discharge of commercial dyes is increasing at a swift rate as industrialization continues to grow, leading to severe hazards to living organisms due to their toxic and harmful impacts. The discharge of dyes into water reservoirs is a concern because of their high toxicity and bioaccumulation in living organisms. One of the most used commercial dyes, azo dyes, possesses a benzidine function that needs to be treated soon due to its side effects. Dyes contain toxicity and have a strong tendency toward eutrophication. The major globally concerned issues are water and soil pollution. The massive use of these dyes in industrial sectors is the main reason behind these environmental issues. Even at concentrations lower than one ppm, around 10% of the untreated discharged dyes impart an intense color, making the water highly detrimental. As an unwanted consequence, this exhibits an immense environmental hazard to the surroundings. Thorough studies on dye metabolites and their constituents have been developed to reduce the acute diverse effects of dyes. However, a few outdated techniques such as ozonation and chlorination are still being utilized to break down untreated dye discharge for various reasons, including economic factors. In this review, the ability of the green oxidation catalysis method of degradation to degrade dye is reviewed owing to its eco-friendliness and safety.

Keywords: azo dyes, green oxidation, catalysis, degradation of dyes, toxicity

Abstrak

Pewarna telah digunakan secara meluas sebagai agen pewarna di dalam bidang industri global, terutamanya di dalam bidang tekstil. Buktinya, terdapat 10,000 jenis pewarna telah diperkenalkan dan digunakan secara berterusan sehingga mencapai tahap penggunaan 700,000 tan. Penggunaan pewarna sintetik yang secara meluas adalah disebabkan faktor ekonominya yang sedia ada, kekuatan yang unggul, dan kebolehan untuk meliputi julat warna. Pembuangan pewarna komersil telah meningkat secara pantas selari dengan kadar pertumbuhan perindustrian, menyebabkan risiko yang serius kepada hidupan bernyawa telah dikenal pasti kerana impak pewarna yang toksik dan berbahaya. Pembuangan pewarna di dalam takungan air diberi perhatian kerana kesan toksik yang tinggi dan bioakumulasi dalam hidupan bernyawa. Pewarna komersil yang sangat biasa digunakan, pewarna azo memiliki fungsi benzidine yang perlu dirawat dengan segera kerana kesan sampingannya. Pewarna mempunyai toksik yang tinggi dan mempunyai kecenderungan yang kuat terhadap eutrofikasi. Isu utama yang menjadi perhatian secara global adalah pencemaran air dan tanah. Penggunaan perwarna secara berleluasa dalam sektor industri adalah punca utama isu pencemaran ini berlaku. Walaupun pada kepekatan bawah daripada 1 ppm, sekitar 10% pewarna yang dibuang dan tidak dirawat menghasilkan warna yang terang yang menyebabkan kandungan air menjadi sangat berbahaya. Sebagai kesan yang tidak diingini, bahan ini menunjukkan bahaya kepada alam sekitar dan sekelilingnya. Satu kajian yang mendalam mengenai metabolit pewarna dan unsur-unsur ini telah dibangunkan untuk mengurangkan pelbagai kesan pewarna yang berbahaya. Walau bagaimanapun, beberapa teknik yang lama seperti pengozonan dan pengklorinan masih digunakan untuk merawat pewarna yang dibuang dan tidak dirawat atas beberapa faktor termasuk faktor ekonomi. Dalam ulasan ini, kebolehan cara pemangkinan pengoksidaan hijau untuk degradasi pewarna diulaskan kerana ianya mesra alam dan selamat.

Kata kunci: pewarna azo, pengoksidaan hijau, pemangkinan, degradasi pewarna, ketoksikan

Introduction

The critical part of natural dye removal is using the appropriate method without creating environmental problems. As it is known, textile dyes discharge uncountable effluents that extant significant ecological issues. These effluents are mostly from dye manufacturing and textile wet processing industries. About 7 x 107 tons of synthetic dyes are produced annually worldwide, with over 10 000 tons of dyes being used by textile industries [1]. The discharge of dye is likely to rise phenomenally due to the growth in fiber consumption worldwide, such as wool, silk, and leather, which are included in the usage of clothes and bags, among others. Almost all modern dyes are degradation resistant and chemically stable by bleach, sunlight, water, and perspiration in a brief time or even a lifetime [2]. Since its structure contains an aromatic and -N=N- group, it harms the environment by being highly toxic, carcinogenic, and teratogenic [3]. The degradation of the dye-effluent-containing wastewater is quite tricky due to its resistance. Azo dyes are synthetic and organic chemical compounds applied in many industries, such as fabrics, medicine, food, and cosmetics. In addition, azo dyes contain combinations of the azo group chemically represented as (R-N = N-R'), with (-N=N-). Examples of azo dyes are orange (II), tartrazine, Congo red, eriochrome black T, methylene blue, and brilliant green [4]. Dyes in wastewater, especially azo dyes like Orange (II), create aesthetic problem [2] that limits the usage of the water and lessens the effectiveness of wastewater treatment using microbiological method due to its toxicity to the environment and harm to organisms [5].

There are physical, chemical, and biological methods to degrade dyes. One of the commonly used physical methods is adsorption, which is performed by removing organic compounds in water involving separating substances from one phase to the surface of another. Adsorption using activated carbon is an efficient process for organic micro-pollutant removals such as pesticides, fertilizers, cosmetics, pharmaceuticals, and personal care products, which are deployed by porous materials [6]. However, the cost of production, as well as the regeneration of activated carbon, is expensive. Various chemical methods have been employed by breaking the chemical bond, such as the azo bond, for degradation and decolorization of the dyes. Examples of chemical methods include ozonation, the Fenton reagent method, and photocatalytic reactions. The drawbacks of chemical methods are their less efficiency, limited versatility, high cost, and utilize a significant amount of energy. Abundant studies and research have taken severe actions, especially in attempting new methods for

wastewater purifying treatment with less chemical impact on nature in terms of economically controlled [7]. An escalating number of contaminants continuously flow into the water supply annually, ranging from common contaminants like heavy metals to emerging micro-pollutants such as nitrosamines and endocrine disruptor compounds [7].

The possible method that can be conducted to overcome this kind of drawback is the application of green chemistry with the use of green oxidation catalyst technique through the Fe (III)–TAML-H_2O_2 system. Green oxidation technique is a technique that uses an oxidizing agent, which is safer towards the environment since it consumes less energy, low cost, and is environmentally friendly. The oxidizing agent usually oxidizes dye and eventually degrades its color. With current concerns regarding the treatment of dye effluents, there is an urgent need for a much greener degradation of pollutants. Besides being the greener method, it is also efficient, as proven by research that dye and other contaminants including 17α-ethynyl estradiol can be 100% degraded using this method [8]. In conclusion, it can be proved that Fe (III)-TAML-H_2O_2 systems have substantial potential in providing a greener technology.

Common azo dyes

Orange (II)

Orange (II) dye with IUPAC name [*p*-(2-hydroxy-1-naphthylazo) benzenesulfonic acid sodium salt]$^+$ as shown in Figure 1 with a molecular formula of $C_{16}H_{11}N_2NaO_4S$ is a most common anionic dye that is water soluble. (Usage) It is commonly used in industry for a range of raw materials such as nylon, aluminum, cosmetics, wool, silk, and detergents [9]. (Harmful effect) The orange (II) dye causes severe health issues in humans. The toxicity of orange (II) dye can cause upper respiratory tract, mucous membrane, eye, and skin irritation after ingestion. It can also lead to anemia, which can cause severe nausea, headaches, and water-borne diseases such as bone marrow loss [9]. Chronic toxicity is developed from the electron-withdrawing character of the azo group, which causes electron deficiency and reduces to carcinogenic amino compounds [10]. However, it is proven that azo dyes are able to permeate.

Organisms affect their metabolic processes by reacting with reducible chemicals produced. Production of 1-amino-2-naphthol from reduced Orange (II) dye can stimulate tumors in the bladder. In addition, Orange (II) dye can undergo enzymatic breakdown effortlessly and produce aromatic amines that can cause methemoglobinemia [11] and tend to oxidize the hem iron of hemoglobin from Fe(II) to Fe(III) and block oxygen-binding activity [12]. Besides, ingestion of Orange (II) dye is considered genotoxic [9]. Therefore, the dye needs to be removed, especially from the environment, to prevent the toxicity of the dye. The toxicity and carcinogenic nature are shown by removing Orange (II) dye by biodegradation and photosensitization on TiO_2 particles. The biodegradation of Orange (II) dye is carcinogenic towards the metabolic intermediates [2]. The generation of toxic intermediates during the process is possible and most likely to occur from the high solubility of the dye in water. There are some works of orange (II) dye removal reported. However, most of them revealed some side effects and need to be more environmentally friendly. Several degradation methods used in the degradation of Orange (II) dye include Fenton's reagent, photocatalyst, and heterogeneous [13].

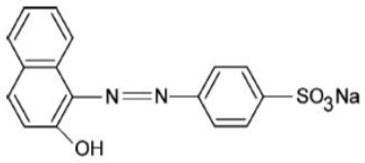


Figure 1. Structure of Orange (II) [p-(2-hydroxy-1-naphtlyazo) benzene sulfonic acid sodium salt]

Tartrazine

Tartrazine (Yellow Dye No.5), as shown in Figure 2, is an anionic azo dye widely used in the food industry as a coloring agent. Tartrazine originates from coal tar, which has been identified to have high toxicity and the ability to cause mutations in living things due to its high solubility in water. The high solubility in water makes the tartrazine interact with the body and form allergic reactions when in contact with the cellular processes in the body. Tartrazine is potentially phototoxic [14] and

proved as a possible cause of angioedema, urticaria, and asthma [15]. Since food azo dyes are not eco-friendly [16] as it is non-biodegradable, the conventional biological treatment processes are inefficient for degrading these dyes in wastewater. Hence, physio-chemical processes are typically used for azo dyes wastewater treatment. However, the removal processes produce a lump of sludge that requires good treatment. This dye has been degraded by the benzoic acid/TiO_2 system with 99.08% removal within 90 minutes [17]. The optimum H_2O_2 concentration for T degradation is 2 mM. Under experimental conditions, 95% of the T can be degraded by a novel Fe-composite (NZ-A-Fe) containing iron in a natural zeolite [18].

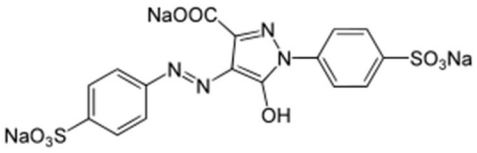


Figure 2. Chemical structure of tartrazine

Congo red

Figure 3 shows the structure of Congo red dye or knowns as sodium salt of 3,3′-([1,1′-biphenyl]-4,4′-diyl) bis (4-aminonaphthalene-1-sulfonic acid). Congo red is water soluble and yields a red colloidal solution. It is a well-known dye belonging to an anionic group commonly used in most industries, including the textile and paper industry. As an additional usage, it plays a vital role in diagnosing amyloidosis for amyloid as a pH indicator [19]. In addition, it also helps to detect free hydrochloric acid in gastric contents. Congo red adversely affects the human body, leading to diseases such as platelet aggregation, thrombocytopenia, and disseminated micro-embolism by lowering blood protein content [20]. Regarding this severe problem, several methods have been studied for successfully degrading Congo red using different nanomaterials [21] such as TiO_2 nanoparticles and bimetallic Fe–Zn nanoparticles [22].

The commonly used metallic nanoparticles such as Ru act as electron donors in azo bond conversion using a reducing agent through electron transfer. As desired results, the degradation rate of Congo red has increased by 200% [23]. Extract from Chinese spinach leaf, *Amaranthus gangeticus Linn,* has been used to synthesize silver nanoparticles with good catalytic efficiency by 50% within 15 minutes [24] for degrading Congo red dye. In addition, the biogenic silver nanoparticles with Senna leaf demonstrated 89.6% degradation of Congo red, onion silver nanoparticles, and acacia catechu with 96% and 97% degradation, respectively [25].

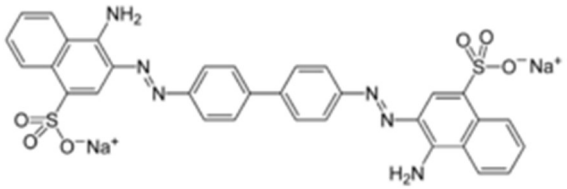


Figure 3. Chemical structure of Congo Red dye

Eriochrome Black T

Eriochrome Black T or Sodium 1-[1-Hydroxynaphthylazo]-6-nitro-2-naphthol-4-sulfonate structure is shown in Figure 4. It is commonly utilized in silk, wool, and nylon dyeing. It is also widely used in today's laboratories to determine the pre-accurate estimation of Zn^{2+}, Ca^{2+}, and Mg^{2+} ions [26]. Carcinogenic azo dye is one of the trademarks of Eriochrome Black T with its intermediate product called Naphthoquinone, which is toxic and not a desired product [27]. A severe problem has arisen worldwide for successfully treating Eriochrome Black T-containing effluent since it can potentially be harmful if not well treated [28]. Nevertheless, the breakdown of Eriochrome Black T has been carried out by numerous researches as a future need basis using different nanomaterials.

It was successfully found that the photocatalytic degradation of Eriochrome Black T has been enhanced to 88% with crystalline anatase TiO_2 under basic conditions around pH 11.0, which occurred from the higher concentration of hydroxyl radicals [29]. Generally, TiO_2 nanostructures of different shapes with Fe^{3+} and Pt^{4+} impregnation [30] successfully photodegraded Eriochrome Black T by about 82% within 90 mins under UV irradiation.

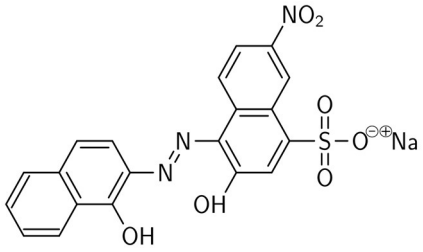


Figure 4. Chemical structure of Eriochrome Black T

Methylene blue

Methylthioninium chloride, commonly called Methylene blue, is a common thiazine dye used as a chemotherapeutic agent and anti-malarial in aquaculture [31]. The structure of methylene blue is shown in Figure 5 below. This dye gives side effects such as headache, shortness of breath, vomiting, high blood pressure, and allergic reaction [32]. Thiazine dye can effectively undergo degradation by a variety of nanomaterials, including copper-supported clay nanocomposite [33], ZnSe/Graphene nanocomposites, and titanium dioxide [34]. The implementation of Cu-supported organo-treated clay can result in the complete removal of the dye. However, 99.6% degradation efficiency has been obtained [35] using ZnSe/Graphene nanocomposites.

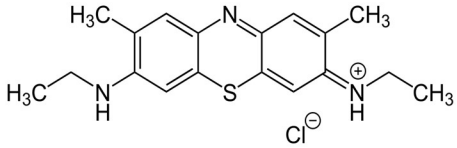


Figure 5. Chemical structure of methylene blue dye

Brilliant green

Brilliant green (zelyonka or zelenka), as shown in Figure 6, is a universally known cationic dye used as a biological stain and an antiseptic [36]. This dye displays an explicitly tremendous effect on gram-positive bacteria. This Brilliant green is highly carcinogenic to target organs and lungs after ingestion [37]. About 92% of the dye has been adsorbed by nano ferrites effectively under optimized conditions [38]. TiO_2 nanoparticles and Graphene oxide are usually doped with alkaline earth metal ions such as Sr^{2+}. Graphene oxide nanoparticles showed a degradation value of 93% in 10 min [39], while 96% of degradation efficiency was obtained when doped with TiO_2 nanoparticles within 1 hour [40].

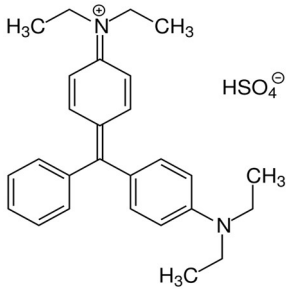


Figure 6. Chemical structure of the brilliant green dye

Current approach used in dye wastewater treatment place for dye degradation

Since dyes started being used in the textile industry, comprehensive treatment methods have yet to be introduced for dye wastewater treatment. As there are few techniques introduced since then, oxidation, anaerobic treatment, adsorption, and coagulation are majorly used methods in physical and chemical treatments for effluents containing various dyes. Therefore, there are some current approaches used in dye wastewater treatment places for dye degradation, which are direct chemical oxidation, oxidative processes with H_2O_2, ozonation, oxidation processes with sodium hypochlorite, photochemical oxidation process, electrochemical oxidation process, and combination of advanced chemical and biological processes.

Direct chemical oxidation

Direct chemical oxidation is an old conventional method for degrading water-soluble dyes in textile wastewater. Nonetheless, water-insoluble disperse dyes have chlorine decolorization resistance, making decolorization of reactive dyes require extended time for treatment. Moreover, dye chromophores with an amino or substituted amino group are susceptible to rapid chlorine decolorization. The chlorine treatment produces toxic chlorinated organics including halogenated hydrocarbons that harm humans and the environment [41]. The general advantages of chemical oxidation are rapid reaction rates, mineralization of organics, and removal of soluble and insoluble dyes, with the overall disadvantage of not being suitable for dispersed dyes. They release toxic compounds such as

aromatic amines and involve complex chemistry [42].

Oxidative processes with hydrogen peroxide

The oxidative process with hydrogen peroxide (H_2O_2) is an alternative wastewater treatment that has been done using two systems: a homogenous system and a heterogenous system [43]. A homogenous system uses UV light, chemical activators, and soluble catalysts (Fenton reagents). The Fenton reagent utilizes hydrogen peroxide, which is then activated by iron salts and Fe^{2+} salts. This is done without UV producing hydroxyl radicals (OH). These radicals are strong oxidants than H_2O_2 and ozone but are harmful to environments when released into thin air. At the same time, the heterogenous system uses semiconductors like TiO_2 and modified zeolites with Fe and Al, such as FeY11.5 and FeY5.

The homogenous catalytic oxidation demonstrated color removal of 56.20% at a pH of 4 for Remazol Rose RB and Remazol Arancio 3R dye-containing effluents [44] with a minimal 0.18 M of H_2O_2 and 1.45 mM of Fe^{2+}. Meanwhile, heterogenous catalytic oxidation led to color removal of 53% - 83% at pH 3-5 for Procion Marine H-pEXL dye-containing effluents [45] with H_2O_2 and FeY11.5 within 10 mins. As for H_2O_2 and FeY5 at pH= 5 using the same textile effluent in the treatment, 95% color removal was achieved within 10 min of oxidation and 97% for 60 min of oxidation [46].

Ozonation process

Ozonation is the most straightforward process, which depends on oxidizing agents and ozone. The ozone efficiently decomposes organic pollutants from industrial effluents and cleaves aromatic rings in textile dyes. Ozone with conjugated double bonds decomposes organic dyes and produces carcinogenic compounds. This process has most probably been used with a physical method to reduce its toxicity with extra costs required. Based on several studies, it was proven that ozone can react with dye molecules either directly or indirectly [47]. Since the ozone molecule is an electron acceptor, the hydroxide ions catalyze the ozone decomposition into hydroxyl radicals (·OH) in effluents through the direct pathway. However, due to its complicated process, the indirect path is not recommended for industrial dye degradation.

The main advantages of ozonation are that ozone does not affect wastewater in terms of volume and minimizes the production of extra sludge apart from its application in a gaseous state. The disadvantages of ozonation include its destabilization by the temperature, the short half-life of around 20 min, and the installation of an ozonation plant that requires additional cost. The combination with irradiation [48] improves the performance of ozonation. In a study, the treatment of wastewater containing dye effluent indicated color removal of 62% with ozone [49], followed by chemical coagulation using $Ca(OH)_2$.

Oxidation process with sodium hypochlorite

The oxidation process with sodium hypochlorite starts when the Cl^- ion attacks the amino group in the dye molecule, followed by initiation and azo-bond cleavage acceleration. This dye removal and decolorization process can be favored by increasing the chlorine concentration and decreasing pH [50]. The dye-containing amino or substituted amino groups on the naphthalene ring, such as naphtylamino-sulphonic acid and amino-naphthol, are most vulnerable to the decolorization of chlorine. Thus, this process is unsuitable for dispersing dye. The negative effect of this treatment is that it is prone to release aromatic amines and toxic molecules into water, making it a less desired treatment. Furthermore, pigments used worldwide contain chlorine of approximately 40% [51], while this method uses less than 0.02% of the total chlorine production.

Photochemical oxidation process

The presence of H_2O_2 is most necessary for the photochemical process. This process decomposes dye molecules into low-weight organic molecules such as water, carbon dioxide, hydrides, and inorganic oxides. The additional by-products produced are organic and inorganic acids, organic aldehydes, and halides, which vary depending on the initial materials used in decolorization treatment. The generation of hydroperoxide radicals is shown in Equation 1, while hydroxyl radicals as shown in Equation 2 will initiate the dye decomposition.

$$H_2O_2 + HO\cdot \rightarrow HO_2\cdot + H_2O \quad (1)$$

$$H_2O_2 + h\upsilon \rightarrow 2HO\cdot \quad (2)$$

The treatment is set up in a batch or continuous column unit and mainly depends on the dye structure, pH, and intensity of the UV radiation. This photo-oxidation treatment displayed color removal around 81% - 94% after 1 hour with 88 mM H_2O_2 with minimal pH at 4 [52] for Acid Red G dye-containing effluent.

Electrochemical oxidation process

The electrochemical treatment is a unique treatment that presents high removal efficiencies and pollution control for dispersed and metal complex dyes known as acid dyes. The oxidizing agent in the electrochemical process is hypochlorous acid or hypochlorite ion produced from naturally occurring chloride ions [53]. The by-products are commonly less hazardous than any other oxidation process discharged into the water without health precautions or environmental risks.

Some advantages of this treatment include the requirement of no additional chemicals, simplified operation, prevention of the production of unwanted by-products, and minimization of all emissions such as the emission of solid waste, liquid effluent, and gases [54]. Electrochemical oxidation is believed to be an economical and efficient treatment for recycling textile wastewater. However, since the metallic electrode in the cell generates metallic hydroxide, this process has usage limits.

The color removal for the effluent containing blue-26 anthraquinone dye demonstrated the highest percentage within 220 min of electrolysis, a higher rate at neutral pH of 7 using NaCl, and a current density of 4.5 A/dm^2 [55]. The color removal obtained was 95.2% for the same dye-containing effluent in a flow reactor working at a rate of 5 mL/min and a current density of 29.9 mA/cm^2.

Combination of advanced chemical and biological processes

Photodegradation and biodegradation are the most appropriate methods for degrading the harmful compounds in wastewater. Aromatic hydrocarbons and phenols use photodegradation to degrade effluents containing dye. Generally, the pollutants are eliminated using biodegradation by microbes. Implementation of chemical oxidation together with biological processes proves the enhancement of efficiency and lowers operating costs [56].

The process begins when H_2O_2 and Fe (II) are operated in optimum requirements in the combined process. At 25 °C, the biological reactor was operated for 10 cycles for 12 hours per cycle. After adjusting to neutral pH in the first cycle, the biological reactor was supplemented with 2.5 L of wastewater. Adding 2.5 L of activated sludge made the final volume 5 L. The reactor was supplemented with 2.5 L of effluent to compensate for the quantity of treated effluent released. Chemical Oxygen Demand (COD) and Dissolved Organic Carbon (DOC) were examined at the end of each cycle. Automatic unit control and data acquisition were attained using Lab View 5.0 software [57]. The advantages of this method are enhanced efficiency and lower operating costs. This system significantly achieved 99% of color removal, COD removal of 88%–98%, and 91%–98% of DOC removal. Furthermore, this combined system reduced operating costs by 24–39%. The by-products include DCIP reductase, veratryl alcohol oxidase, riboflavin reductase, azo reductase, and laccase. However, this method involves complicated processes with high maintenance costs.

Proposed approach in degradation of Orange (II) dye in wastewater

This part explains the oxidation of the Fe-TAMLs/ H_2O_2 System (Oxidative Catalysis), the general procedure for degradation of Orange II by Fe(III)TAML-H_2O_2, and toxicity measurements of Orange (II) dye. This method can potentially reduce cost as the reagent requirement can be decreased as oxidation efficiency.

Oxidation of Fe-TAMLs/ H_2O_2 system (oxidative catalysis)

Collins and Lenoir developed a landmark example based on a Fe (III) metal center coordinated to a tetra-amido macrocycle that coordinates the metal with four anionic amide groups (Fe-TAML). The activation of H_2O_2 acts as a terminal oxidant owing to its highly active characteristics toward the complete degradation of

different species in aqueous solutions such as resistant chlorinated phenol derivatives, water effluents, and dyes from paper industries [58]. This green oxidation method is a notable application involving the total degradation of organophosphorus pesticides such as Parathion and Fenitrothion with a prevalent agricultural use [59].

Iron (III)-Tetra Amidato Macrocyclic Ligand (TAML) is a unique catalyst suitable for commercialized industrial uses in wastewater treatment. The development of this catalyst started over 20 years, which revealed its unique properties. Common biochemical elements form this catalyst with little or no toxicity properties impacting its biodegradable functionalities. It has high stability in various ranges of pH and is also water-soluble. Besides, it is effective at minute concentrations from 0.1 to 4 ppm.

Fe-TAML catalysts that exhibit oxidation catalysis act as among the finest green catalysts [60]. The use of hydrogen peroxide as an essential source of oxidizing equivalent can be done flawlessly by TAML oxidant activators [61]. The oxidation mechanism of catalysis by Fe (III)-TAML is crucial for industrial and academic purposes. The synthetic oxidation catalyst process displays unprecedented selectivity and high reactivity water while utilizing environmentally friendly oxidants. This research could be a milestone in the further development of green chemistry in the future [61]. Green oxidation catalysis is a frontier at risk elimination for further development. Green procedures that decrease risk detoxify effluent streams and serve as substitutes for polluting processes have been used in several circumstances. Further improvement of TAML systems is potentially suitable for various new green applications from the intermediate, which allows the process.

The dye is reduced by TAML activators when compared with incumbent technologies. The TAML risk reduction theory is supported by mechanistic understanding developed by previous studies proposed in Fenton chemistry, which served as a foundation for developing efficient catalysts [62]. The Fe (II) salts activate the oxidation process in the presence of H_2O_2 known as Fenton chemistry. This chemistry induces the generation of radical species in solution and a wide range of organic substrates with poor selectivity [63].

The tendency to decompose the oxidant, which implies the need for over-stoichiometric amounts of H_2O_2, is one of the main drawbacks of this system [64]. It also requires help controlling the coordination of the oxidation state of the metal and geometry, which undoubtedly leads to the coexistence of some analogous oxidation processes. Nevertheless, it appears to be fine and produces toxic by-products like other wastewater treatment methods, whereas only produces organic compounds in excess amounts. Catalytic oxidation processes can be found in applications including environmental clean-up using soluble iron complexes. Compared to the electrochemical method, this system is cost-effective and relies on readily available and inexpensive reagents such as hydrogen peroxide and ferrous ions. Besides, it is simple to set up and operate and can be applied to a wide range of wastewater samples or dye formulations. It is easy to control the reaction conditions such as pH, temperature, and dosage of H_2O_2, in addition to its high degradation efficiency.

General procedure for degradation of Orange II by Fe(III)TAML-H_2O_2

Under isothermal conditions, Orange (II) was added along with buffered solution stirring at a precision temperature of ± 0.5 °C. Then, the final concentration of H_2O_2 of 0.01 M was achieved after a diverse amount of 30% H_2O_2 was added. The absorption band for Orange (II) at the maximum was then examined. More precisely, it was only done once using a UV-Vis spectrophotometer. Lastly, quenching of the mixture was carried out by an appropriate method for the analysis, which involved adding a quenching agent to neutralize the oxidizing species and stop the reaction. A sodium bisulfite solution was prepared by dissolving a proper amount of sodium bisulfite powder in deionized water. The concentration of sodium bisulfite should be sufficient to react with the excess hydrogen peroxide and oxidizing species present in the mixture. Once the desired reaction time has elapsed, the sodium bisulfite solution was carefully added to the reaction mixture. The amount of sodium bisulfite required depends on the specific reaction conditions and the concentration of the oxidizing agents. It was typically added in excess to

ensure complete quenching. After that, the reaction mixture was thoroughly mixed to ensure proper contact between the quenching agent and the reactive species. The mixture was allowed to stand briefly to provide a complete reaction and neutralization of the oxidizing agents.

Toxicity measurements of Orange (II) Dye

The toxicity of the dye and degradation products was analyzed using *Daphnia magna* of one day born at different concentrations of *Daphnia magna* (0.8, 1.3, 2.2, 3.6, 6.0, and 10.0 mg/L). Laboratory-grown daphniids were fed with *Scenedesmus subspicatus chodat,* cultured microbes. Doubly distilled water was used to prepare all the solutions at 20 °C under room temperature. Then, each test beaker was filled with 10 daphniids and 50 mL of final volume to identify the toxicity levels by immobilization test method for 24 hours of exposure. Results were evaluated based on the immobilization percentage obtained by dividing the number of immobilized organisms by the total organisms. The toxicity of wastewater samples is considered toxic when the immobilization percentage is higher than 50% [65].

Main findings for degradation of Orange II by Fe(III)TAML-H_2O_2

In optimizing the degradation of Orange (II) dye, the parameters involved were the concentration of Fe-TAML, H_2O_2, and pH. Initially, the Fe-TAML catalyst (0.5 µM) and H_2O_2 (16 mM) showed the color removal of 41% from wastewater in the Fe-TAML-H_2O_2 system after 30 minutes at 50 °C in the first trial [66] as shown in Figure 7(a). Moreover, the reduction of color differed from 9% to 42%, which led to the final color of 495 ± 68 CPU over seven repetitions without any mixings. The final color of 348 ± 8 CPU while mixing was used. The production of hydroxyl radicals occurred with the reaction between aqueous Fe^{2+} salts and H_2O_2 solutions. The color evaluation was performed by ultraviolet-visible spectroscopy (UV-Vis).

The maximum color removal of 44% was obtained under the most favorable conditions of the catalyst at 1 µM and H_2O_2 at 16 µM, which suggests its ability to reduce cost and time significantly, as claimed by Pinzon-Espinosa [67]. Maximum color removal of about 55% as shown in Figure 7(b) was reached within approximately four hours. Based on Fe-TAML catalyst degradation characteristics that can speed up the rate of reaction and lower the activation energy, color removal will reach its maximum within one hour with conditions of catalyst at 3 µM and H_2O_2 at 20µM.

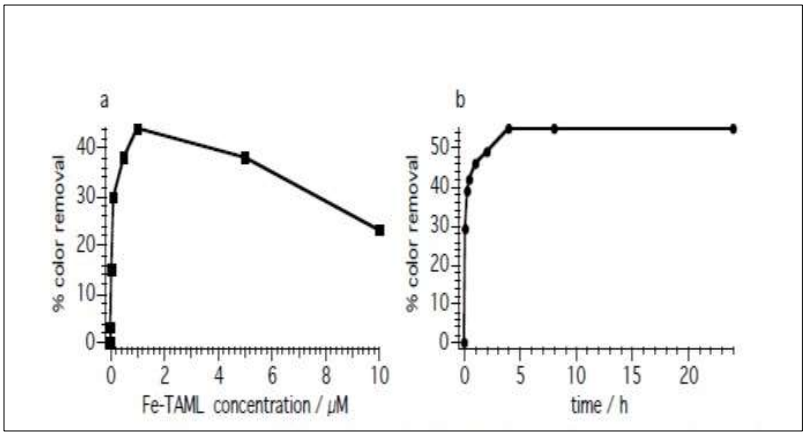


Figure 7. Effects of color removal dependence on Fe-TAML concentration (30 min)

Color removal probability was tested using Fe-TAML-H_2O_2, which might be caused by the reaction with catalyst breakdown derivatives, which are free Fe^{2+}/Fe^{3+}. The reactions were examined when the Fe-TAML catalyst was replaced by $FeCl_3$ [51]. The concentration of Fe^{3+} was similar to the catalyst concentration of Fe-TAML, which was about 1µM. There was no effect observed following the addition of

Fe^{3+}. Hence, the Fe-TAML-H_2O_2 combination is responsible for the degradation of the color. The H_2O_2 concentrations and reaction time, along with the optimization of the catalyst (by investigating the concentration, reaction time, and pH of the solution), were examined. The system's efficiency was demonstrated by a significant surge in color removal within a slight array of catalyst concentrations of 0.05 to 0.1 μM. Since Fe-TAML catalyzed H_2O_2 disproportionation at catalyst concentration larger than 5 μM, less color was removed [68].

The oxidation of Orange (II) was monitored by electronic spectroscopy. The dye has an intense absorption band with a maximum of 485 nm in water. Hydrogen peroxide oxidized Orange (II) very slowly, while Fe (III)-TAML activators immensely increased the rate. The spectral changes observed during catalyzed oxidation of Orange (II) dye are presented in Figure 8 below:

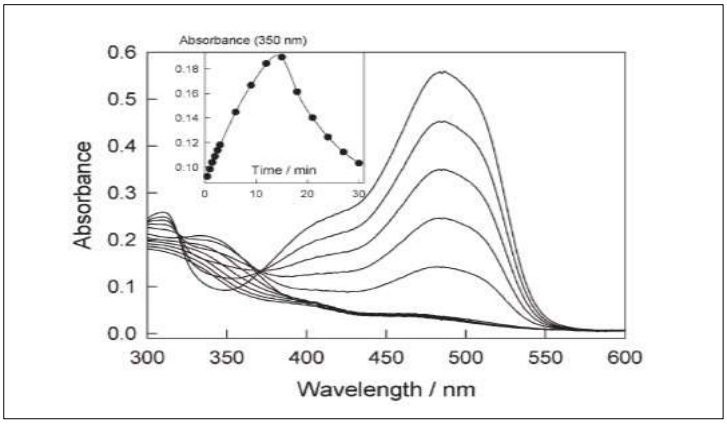


Figure 2. Spectral changes of Orange (II) catalytic oxidation

During treatment with the Fe-TAML-H_2O_2 system, the complex nature of the effluent brings difficulty in determining a high degree of certainty. The complexity of the effluent can arise from various factors, such as the presence of multiple contaminants, varying concentrations of pollutants, and diverse chemical compositions. These complexities make it difficult to precisely predict the treatment process's outcome and determine the certainty level in achieving desired results, thus may require a combination of scientific understanding, practical experience, and ongoing refinement of the treatment approaches. Still, several chemical analyses and spectroscopic methods can provide certain conceptions, including UV-Vis spectroscopy [66]. Firstly, the difference in ionization spectra revealing phenolic α-carbonyl and phenolic group structures in the sample of effluent fragment ions can provide evidence of the presence of phenolic alpha carbonyl groups in the sample. Phenolic alpha carbonyl groups typically refer to a carbonyl (C=O) group adjacent to a phenolic (OH) group. These groups can exhibit specific characteristic peaks in ionization spectra. The fragment ions can provide evidence regarding the presence of phenolic alpha carbonyl groups in the sample. Phenolic groups, referring to compounds containing a hydroxyl (OH) group attached to an aromatic ring, also exhibit characteristic features in ionization spectra. In mass spectrometry, phenolic compounds can produce a molecular ion peak (M+) corresponding to the intact molecule with the hydroxyl group.

The second treatment step involved exposing the Fe-TAML-H_2O_2 effluent to sodium periodate as oxidants using an oxidative procedure to maintain the facile, one-pot conversion approach [69]. Thirdly, the removal of aliphatic double bonds like stilbenes or alkenes from the treated material was demonstrated by controlled hydrogenation and effluents treated with Fe-TAML-H_2O_2. Lastly, groups of carbonyls like quinones and α-carbonyls were reduced using sodium borohydride indicating two types of structures that were eliminated

from the treated samples. However, Fe-TAML-H_2O_2 treatment removed the mentioned structure efficiently. Some methods could ensure the structure is eliminated from the effluent, which include UV-Vis spectroscopy, high-performance liquid chromatography (HPLC), mass spectroscopy, and total organic carbon (TOC) instrument. Apart from that, some studies revealed that lowering the concentration of starting color is possible with Fe-TAML catalyst, even in the absence of H_2O_2. Non-aqueous chemistry describes that Fe-TAML catalyst can rapidly activate O_2. Direct reaction of the Fe-TAML catalyst with O_2 reduces the Fe-TAML catalyst. The catalyst then reacts with oxygen to oxidize other chromophores. [70]. As seen in Figure 9, the Fe-TAML catalyst is pH dependent. Meanwhile, pH 11 shows a higher initial rate compared to pH 9.

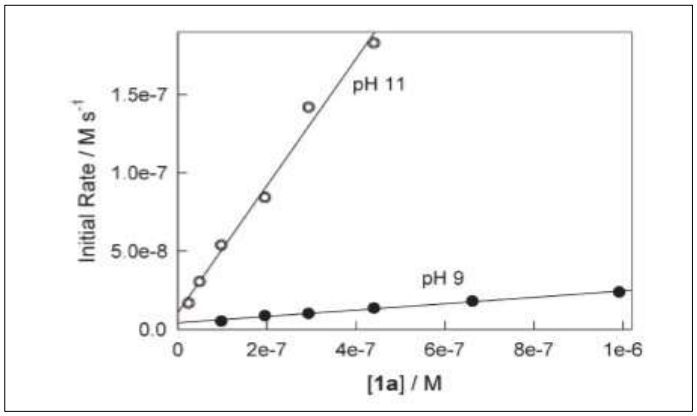


Figure 3. Initial rates of catalyzed bleaching of Orange (II) dye by H_2O_2 as a function at pH 9 and 11. Conditions:[Orange (II)] 4.5 x 10^{-5} M, [H_2O_2] 3.3 x 10^{-4} M, 25 ℃

The evaluation of toxicity was done before and after the degradation. The non-toxic compounds, such as more minor aromatic compounds, carboxylic acid, and inorganic ions, were produced as degradation products. The initial toxicity of Orange (II) decreased after the treatment. The test sample's value measured toxicity using one-day-old *Daphnia magna* exposed to different dye concentrations. The percentage of immobilized or decreased *Daphnia magna* was calculated by plotting a dose-response curve representing the dye concentration versus the response (mortality or immobilization) of Daphnia magna. Later, the median lethal concentration (LC50) was determined, which is the concentration at which 50% of the Daphnia Magna are immobilized or deceased. This value indicates the toxicity of the Orange (II) dye to the test organism. The larger the number of values, the smaller the toxicity level. Figure 10 illustrates the effects of orange (II) and the degradation on the immobilization of D. Magna, showing maximum toxicity of 20% observed in both experiments. Daphnia *magna* in the control tubes showed zero mortality. This result demonstrates that the Fe (III)–TAML catalyzed degradation of Orange (II) by H_2O_2 is safe and free from the formation of toxic oxidation products [71].

Conclusion

Green oxidation catalysis treatment involving Fe (III)–TAML-H_2O_2 system has been proven to significantly impact the degradation of azo dye compared to other existing industrial methods. Based on this study, the system significantly degraded Orange (II) dye into non-toxic organic and biodegradable products. Meanwhile, the other method harms the environment and consumes more energy and cost. Extensive mineralization can be observed in its green chemistry principles, such as synthesized biofuels and green ZnO [72]. Oxidation has the potential to occur quickly compared to other chemical systems formerly conducted. The ecotoxicological examination suggests that the described method is much more environmentally harmless than metal catalysts including ruthenium (Ru) or osmium (Os). Thus, the application of green chemistry in the oxidation catalysis treatment

involving the Fe (III)TAML-H_2O_2 system is greatly needed to treat dye effluents. In summary, Fe (III)TAML-H_2O_2 system has been significantly proven to carry substantial potential in providing a greener technology.

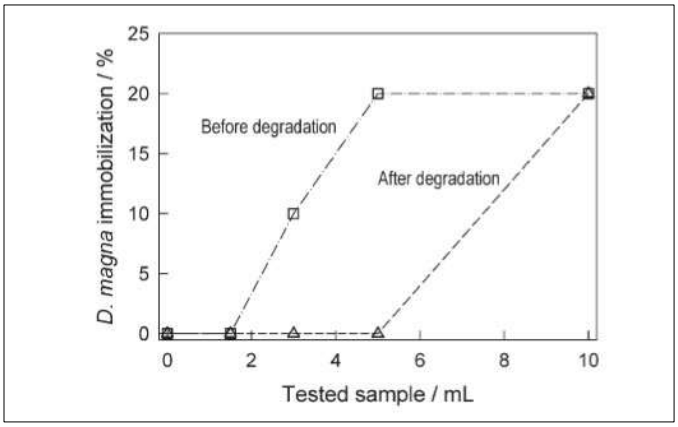


Figure 4. Effects of Orange (II) and its degradation products on immobilization of *Daphnia magna*. Conditions: [Orange II] 1 x 10^{-4} M, [H_2O_2] 1 x10^{-2} M, 25°C, pH 10 (0.02 M carbonate)

Acknowledgment

The authors would like to acknowledge the Ministry of Education Malaysia for the Fundamental Research Grant Scheme FRGS 59474 (FRGS/1/2017/ STG01/UMT/ 03/1) and the Faculty of Science and Marine Environment, University Malaysia Terengganu for facilities and support.

References

1. Chandanshive, V., Kadam, S., Rane, N., Jeon, B. H., Jadhav, J., and Govindwar, S. (2020). In situ, textile wastewater treatment in high rate transpiration system furrows planted with aquatic macrophytes and floating phytobeds. *Chemosphere*, 252: 126513.
2. Tkaczyk, A., Mitrowska, K., and Posyniak, A. (2020). A review of synthetic organic dyes as contaminants of the aquatic environment and their implications for ecosystems. *Science of the Total Environment*, 717: 137222.
3. Haque, M. M., Haque, M. A., Mosharaf, M. K., and Marcus, P. K. (2021). Decolorization, degradation, and detoxification of carcinogenic sulfonated azo dye methyl orange by newly developed biofilm consortia. *Saudi Journal of Biological Sciences*, 28(1): 793-804.
4. Pinheiro, L. R. S., Gradíssimo, D. G., Xavier, L. P., and Santos, A. V. (2022). Degradation of azo dyes: bacterial potential for bioremediation. *Sustainability*, 14(3): 1510.
5. Mittal, J. (2020). Permissible synthetic food dyes in India. *Resonance*, 25(4): 567-577.
6. Jiang, N., Shang, R., Heijman, S. G., and Rietveld, L. C. (2018). High-silica zeolites for adsorption of organic micro-pollutants in water treatment: A review. *Water Research*, 144: 145-161.
7. Stackelberg, P. E., Furlong, E. T., Meyer, M. T., Zaugg, S. D., Henderson, A. K., and Reissman, D. B. (2004). Pharmaceutical compounds and other organic wastewater contaminants exist in a conventional drinking-water-treatment plant. *Science of the Total Environment*, 329(1-3): 99-113.
8. Pan, Z., Stemmler, E. A., Cho, H. J., Fan, W., LeBlanc, L. A., Patterson, H. H., and Amirbahman, A. (2014). Photocatalytic degradation of 17α-ethinylestradiol (EE2) in the presence of TiO_2-doped zeolite. *Journal of Hazardous Materials,* 279: 17-25.
9. Gupta, V. K., Mittal, A., Gajbe, V., and Mittal, J. (2006). Removal and recovery of the hazardous azo dye acid orange 7 through adsorption over bottom ash and de-oiled soya waste materials. *Industrial & Engineering Chemistry Research*, 45(4): 1446-

1453.

10. Smaranda, C., Comanita, E. D., Apostol, L. C., and Gavrilescu, M. (2016). Kinetic studies on the biosorption of Acid orange 7 onto Phaseolus vulgaris L. *Series of Physics and Chemistry Science*, 1(1): 68-97.
11. Greluk, M., and Hubicki, Z. (2011). Efficient removal of Acid Orange 7 dye from water using the strongly basic anion exchange resin Amberlite IRA-958. *Desalination*, 278(1-3): 219-226.
12. Abbott, L. C., Batchelor, S. N., Smith, J. R. L., and Moore, J. N. (2009). Reductive reaction mechanisms of the azo dye orange II in aqueous solution and in cellulose: from radical intermediates to products. *The Journal of Physical Chemistry A*, 113(21): 6091-6103.
13. Wei, J., Zheng, Z., Huang, L., Qiu, Z., Xia, Q., Zhou, S., ... and Zeng, D. (2023). Effective removal of Orange II dye by porous Fe-base amorphous/Cu bimetallic composite. *Colloids and Surfaces A: Physicochemical and Engineering Aspects*, 656: 130388.
14. Iervolino, G., Vaiano, V., Sannino, D., Rizzo, L., Sarno, G., Ciambelli, P., and Isupova, L. A. (2015). Influence of operating conditions in the photo-Fenton removal of tartrazine on structured catalysts. *Chemical Engineering Transactions*, 43: 979-984.
15. Modirshahla, N., Behnajady, M. A., and Kooshaiian, S. (2007). Investigation of the effect of different electrode connections on the removal efficiency of Tartrazine from aqueous solutions by electrocoagulation. *Dyes and Pigments*, 74(2): 249-257.
16. Mafra, M. R., Igarashi-Mafra, L., Zuim, D. R., Vasques, E. C., and Ferreira, M. A. (2013). Adsorption of remazol brilliant blue on an orange peel adsorbent. *Brazilian Journal of Chemical Engineering*, 30: 657-665.
17. Zhou, Y., Qin, Y., Dai, W., and Luo, X. (2019). Highly efficient degradation of tartrazine with a benzoic acid/TiO2 system. *ACS omega*, 4(1): 546-554
18. Russo, A. V., Merlo, B. G., and Jacobo, S. E. (2021). Adsorption and catalytic degradation of tartrazine in aqueous medium by a Fe-modified zeolite. *Cleaner Engineering and Technology*, 4:100211.
19. Shu, J., Wang, Z., Huang, Y., Huang, N., Ren, C., and Zhang, W. (2015). Adsorption removal of Congo red from aqueous solution by polyhedral Cu_2O nanoparticles: kinetics, isotherms, thermodynamics, and mechanism analysis. *Journal of Alloys and Compounds*, 633: 338-346.
20. D'Souza, E., Fulke, A. B., Mulani, N., Ram, A., Asodekar, M., Narkhede, N., and Gajbhiye, S. N. (2017). Decolorization of Congo red mediated by marine Alcaligenes species isolated from Indian West coast sediments. *Environmental Earth Sciences*, 76(20): 721.
21. Guo, H. X., Lin, K. L., Zheng, Z. S., Xiao, F. B., and Li, S. X. (2012). Sulfanilic acid-modified P25 TiO_2 nanoparticles with improved photocatalytic degradation on Congo red under visible light. *Dyes and Pigments*, 92(3): 1278-1284.
22. Gautam, R. K., Rawat, V., Banerjee, S., Sanroman, M. A., Soni, S., Singh, S. K., and Chattopadhyaya, M. C. (2015). Synthesis of bimetallic Fe–Zn nanoparticles and its application towards adsorptive removal of carcinogenic dye malachite green and Congo red in water. *Journal of Molecular Liquids*, 212: 227-236.
23. Gupta, S., Giordano, C., Gradzielski, M., and Mehta, S. K. (2013). Microwave-assisted synthesis of small Ru nanoparticles and their role in degradation of Congo red. *Journal of Colloid and Interface Science*, 411: 173-181.
24. Kolya, H., Maiti, P., Pandey, A., and Tripathy, T. (2015). Green synthesis of silver nanoparticles with antimicrobial and azo dye (Congo red) degradation properties using *Amaranthus gangeticus* Linn leaf extract. *Journal of Analytical Science and Technology*, 6: 1-7.
25. Althaaly, A. F. M., Al-Thabaiti, S. A., and Khan, Z. (2022). Biogenic silver nanoparticles: synthesis, characterization, and degradation of Congo red. *Journal of Materials Science: Materials in Electronics*, *33*(7): 4450-4466.
26. Jo, K. D., and Dasgupta, P. K. (2003). Continuous on-line feedback-based flow titrations. Complexometric titrations of calcium and magnesium. *Talanta*, 60(1): 131-137.

27. San, N. O., Celebioglu, A., Tümtaş, Y., Uyar, T., and Tekinay, T. (2014). Reusable bacteria immobilized electrospun nanofibrous webs for decolorization of methylene blue dye in wastewater treatment. *RSC Advances*, *4*(61): 32249-32255.
28. Ejhieh, A. N., and Khorsandi, M. (2010). Photodecolorization of Eriochrome Black T using NiS–P zeolite as a heterogeneous catalyst. *Journal of Hazardous Materials*, 176(1-3), 629-637.
29. Kazeminezhad, I., and Sadollahkhani, A. (2014). Photocatalytic degradation of Eriochrome black-T dye using ZnO nanoparticles. *Materials Letters*, 120: 267-270.
30. Kansal, S. K., Sood, S., Umar, A., and Mehta, S. K. (2013). Photocatalytic degradation of Eriochrome Black T dye using well-crystalline anatase TiO_2 nanoparticles. *Journal of Alloys and Compounds*, 581: 392-397.
31. Burhenne, J., Riedel, K. D., Rengelshausen, J., Meissner, P., Müller, O., Mikus, G., ... and Walter-Sack, I. (2008). Quantification of cationic anti-malaria agent methylene blue in different human biological matrices using cation exchange chromatography coupled to tandem mass spectrometry. *Journal of Chromatography B*, 863(2): 273-282.
32. Methylene Blue (2017). The American Society of Health-System Pharmacists. Access from https://www.ashp.org/drug-shortages/current-shortages/drug-shortage-detail.aspx?id=47&loginreturnUrl=SSOCheckOnly
33. Mekewi, M. A., Darwish, A. S., Amin, M. S., Eshaq, G., and Bourazan, H. A. (2016). Copper nanoparticles supported onto montmorillonite clays as efficient catalyst for methylene blue dye degradation. *Egyptian Journal of Petroleum*, 25(2): 269-279.
34. Pandey, A., Kalal, S., Ameta, C., Ameta, R., Kumar, S., and Punjabi, P. B. (2015). Synthesis, characterization and application of naïve and nano-sized titanium dioxide as a photocatalyst for degradation of methylene blue. *Journal of Saudi Chemical Society*, 19(5): 528-536.
35. Hsieh, S. H., Chen, W. J., and Yeh, T. H. (2015). Degradation of methylene blue using ZnSe–graphene nanocomposites under visible-light irradiation. *Ceramics International*, 41(10): 13759-13766.
36. Garg, A., and Kumar, N. (2011). Formulation, characterization and application on nanoparticle: a review. *Der Pharmacia Sinica*, 2(2): 17-26.
37. Sathasivam, M., Aparna, R. S. L., Prasad, R. G. S. V., and Cheok, K. Y. (2013). Photocatalytic effect of titanium dioxide nanoparticles and effect of copper as a dopant in degradation of dibutyl pthalate and butylhydroxyanisole. *Journal of Bionanoscience*, *7*(5): 568-574.
38. Hashemian, S., Dehghanpor, A., and Moghahed, M. (2015). $Cu0.5Mn0.5Fe_2O_4$ nano spinels as potential sorbent for adsorption of brilliant green. *Journal of Industrial and Engineering Chemistry*, 24: 308-314.
39. Ghaedi, M., Zeinali, N., Ghaedi, A. M., Teimuori, M., and Tashkhourian, J. (2014). Artificial neural network-genetic algorithm based optimization for the adsorption of methylene blue and brilliant green from aqueous solution by graphite oxide nanoparticle. *Spectrochimica Acta Part A: Molecular and Biomolecular Spectroscopy*, 125: 264-277.
40. Sood, S., Umar, A., Mehta, S. K., Sinha, A. S. K. and Kansal, S. K. (2015). Efficient photocatalytic degradation of brilliant green using Sr-doped TiO_2 nanoparticles. *Ceramics International*, 41(3): 3533-3540.
41. Xu, H., Chen, R., Liang, S., Lei, Z., Zheng, W., Yan, Z., ... and Feng, C. (2022). Minimizing toxic chlorinated byproducts during electrochemical oxidation of Ni-EDTA: Importance of active chlorine-triggered Fe(II) transition to Fe (IV). *Water Research*, 219: 118548.
42. Li, C., He, L., Yao, X., and Yao, Z. (2022). Recent advances in the chemical oxidation of gaseous volatile organic compounds (VOCs) in liquid phase. *Chemosphere*, 2022: 133868.
43. Pan, H., Gao, Y., Li, N., Zhou, Y., Lin, Q., and Jiang, J. (2021). Recent advances in bicarbonate-activated hydrogen peroxide system for water treatment. *Chemical Engineering Journal*, 408: 127332.
44. Zaharia, C., Suteu, D., Muresan, A., Muresan, R.,

and Popescu, A. (2009). Textile wastewater treatment by homogenous oxidation with hydrogen peroxide. *Environmental Engineering and Management Journal*, 8(6): 1359-1369.

45. Neamţu, M., Zaharia, C., Catrinescu, C., Yediler, A., Macoveanu, M., and Kettrup, A. (2004). Fe-exchanged Y zeolite as catalyst for wet peroxide oxidation of reactive azo dye Procion Marine H-EXL. *Applied Catalysis B: Environmental*, 48(4): 287-294.
46. Zaharia, C., Diaconescu, R., and Surpăţeanu, M. (2007). Study of flocculation with Ponilit GT-2 anionic polyelectrolyte applied into a chemical wastewater treatment. *Open Chemistry*, 5(1): 239-256.
47. Adams, C. D. and Gorg, S. (2002). Effect of pH and gas-phase ozone concentration on the decolorization of common textile dyes. *Journal of Environmental Engineering*, 128(3): 293-298.
48. Zaharia, C., Suteu, D., Muresan, A., Muresan, R., and Popescu, A. (2009). Textile wastewater treatment by homogenous oxidation with hydrogen peroxide. *Environmental Engineering and Management Journal*, 8(6): 1359-1369.
49. Sarasa, J., Roche, M. P., Ormad, M. P., Gimeno, E., Puig, A., and Ovelleiro, J. L. (1998). Treatment of a wastewater resulting from dyes manufacturing with ozone and chemical coagulation. *Water Research*, 32(9): 2721-2727.
50. Omura, T. (1994). Design of chlorine-fast reactive dyes: Part 4: degradation of amino-containing azo dyes by sodium hypochlorite. *Dyes and pigments*, 26(1): 33-50.
51. Slokar, Y. M., and Le Marechal, A. M. (1998). Methods of decoloration of textile wastewaters. *Dyes and pigments*, 37(4): 335-356.
52. Surpăţeanu, M., and Zaharia, C. (2004). Advanced oxidation processes for decolorization of aqueous solution containing Acid Red G azo dye. *Central European Journal of Chemistry*, 2: 573-588.
53. Anjaneyulu, Y., Sreedhara Chary, N., and Samuel Suman Raj, D. (2005). Decolourization of industrial effluents–available methods and emerging technologies–a review. *Reviews in Environmental Science and Bio/Technology*, 4: 245-273.
54. Babu, B. R., Parande, A. K., Raghu, S., and Kumar, T. P. (2007). Cotton textile processing: waste generation and effluent treatment. *Journal of Cotton Science*, 11(3): 142-153.
55. Vlyssides, A. G., Papaioannou, D., Loizidoy, M., Karlis, P. K., and Zorpas, A. A. (2000). Testing an electrochemical method for treatment of textile dye wastewater. *Waste Management*, 20(7): 569-574.
56. Oller, I., Malato, S., and Sánchez-Pérez, J. (2011). Combination of advanced oxidation processes and biological treatments for wastewater decontamination—a review. *Science of the Total Environment*, 409(20): 4141-4166.
57. Donkadokula, N. Y., Kola, A. K., Naz, I., and Saroj, D. (2020). A review on advanced physico-chemical and biological textile dye wastewater treatment techniques. *Reviews in Environmental Science and Biotechnology*, 19: 543-560.
58. Chahbane, N., Popescu, D. L., Mitchell, D. A., Chanda, A., Lenoir, D., Ryabov, A. D., Schramm, K.W. and Collins, T. J. (2007). Fe–TAML-catalyzed green oxidative degradation of the azo dye Orange II by H_2O_2 and organic peroxides: products, toxicity, kinetics, and mechanisms. *Green Chemistry*, 9(1): 49-57.
59. Chanda, A., Khetan, S. K., Banerjee, D., Ghosh, A., and Collins, T. J. (2006). Total degradation of fenitrothion and other organophosphorus pesticides by catalytic oxidation employing Fe-TAML peroxide activators. *Journal of the American Chemical Society*, 128(37): 12058-12059.
60. Collins, T. J., Khetan, S. K., and Ryabov, A. D. (2010). Chemistry and applications of iron–TAML catalysts in green oxidation processes based on hydrogen peroxide. *Handbook of Green Chemistry: Online*: pp. 39-77.
61. Anastas, P. T. (Ed.). (2013). *Handbook of green chemistry*. Wiley-VCH: pp. 1-59.
62. Strukul, G., and Scarso, A. (2013). Environmentally benign oxidants. *Liquid Phase Oxidation via Heterogeneous Catalysis: Organic Synthesis and Industrial Applications*: pp. 1-20.
63. Kuo, W. G. (1992) Decolorizing dye wastewater with Fenton's reagent. *Water Research,* 26: 881-886.
64. Collins, T. J., Khetan, S. K., and Ryabov, A. D. (2009). Chemistry and applications of iron-TAML

catalysts in green oxidation processes based on hydrogen peroxide. *Handbook of Green Chemistry*, 1: 39-77.

65. ISO 6341 (1982). Water quality-determination of the inhibition of the mobility of *Daphnia magna* Straus (Cladocera, Crustacea). Technical Committee: ISO/TC 147/SC 5 Biological methods.
66. Horwitz, C. P., Collins, T. J., Spatz, J., Smith, H. J., Wright, L. J., Stuthridge, T. R., Wingate, K.G and McGrouther, K. (2006). Iron-TAML® catalysts in the pulp and paper industry. *ACS Symposium Series,* 921:156-169.
67. Pinzón-Espinosa, A., Collins, T. J., and Kanda, R. (2021). Detoxification of oil refining effluents by oxidation of naphthenic acids using TAML catalysts. *Science of the Total Environment*, 784: 147148.
68. Beach, E. S., Malecky, R. T., Gil, R. R., Horwitz, C. P., and Collins, T. J. (2011). Fe-TAML/hydrogen peroxide degradation of concentrated solutions of the commercial azo dye tartrazine. *Catalysis Science & Technology*, 1(3): 437-443.
69. Spannring, P., Yazerski, V., Bruijnincx, P. C., Weckhuysen, B. M., and Klein Gebbink, R. J. (2013). Fe-catalyzed one-pot oxidative cleavage of unsaturated fatty acids into aldehydes with hydrogen peroxide and sodium periodate. *Chemistry–a European Journal*, 19(44): 15012-15018.
70. Xie, J., Xie, J., Miller, C. J., and Waite, T. D. (2023). Enhanced direct electron transfer mediated contaminant degradation by Fe(IV) using a carbon black-supported Fe(III)-TAML suspension electrode system. *Environmental Science & Technology*, 57(6): 2557-2565.
71. Bae, J. S., and Freeman, H. S. (2007). Aquatic toxicity evaluation of new direct dyes to the *Daphnia magna*. *Dyes and Pigments*, 73(1): 81-85.
72. Batra, V., Kaur, I., Pathania, D., and Chaudhary, V. (2022). Efficient dye degradation strategies using green synthesized ZnO-based nanoplatforms: A review. *Applied Surface Science Advances*, 11: 100314.

Malaysian Journal of Analytical Sciences (MJAS)
Published by Malaysian Analytical Sciences Society

Clinacanthus nutans LEAVES DIFFERENT SOLVENT EXTRACTS EFFECTS ON PHYTOCHEMICAL SCREENING, ANTIOXIDANT ACTIVITY AND GAS CHROMATOGRAPHY-MASS SPECTROMETRY STUDY

(Kesan Pelbagai Ekstrak Pelarut Bagi Daun *Clinacanthus nutans* ke atas Pemeriksaan Fitokimia, Antioksidan dan Kajian Kromatografi Gas-Spektrometri Jisim)

Zaleha Md Toha[1], Nor Hasyimah Haron[1], Nik Nur Syazni[1], Melati Khairuddean[2], and Hasni Arsad[1,*]

[1]*Advanced Medical and Dental Institute,*
Universiti Sains Malaysia, Bertam,
13200 Kepala Batas, Penang, Malaysia
[2]*School of Chemistry,*
Universiti Sains Malaysia,
11800 Minden, Penang, Malaysia

**Corresponding author: hasniarsad@usm.my*

Received: 13 April 2023; Accepted: 3 July 2023; Published: 22 August 2023

Abstract

Clinacanthus nutans (CN) is widely grown in Southeast Asia, especially in Malaysia. People belief that consuming the leaves can treat various diseases it has many medicinal properties. The aim of this study is to investigate the potential of different solvent systems of CN leaves as a source of natural antioxidant by screening its phytochemical constituents and presence of major active compounds with potential biological activities. CN leaves were extracted using different solvent followed by its polarity (methanol, hexane, dichloromethane and aqueous residue). Phytochemical's determination involved total flavonoid content (TFC) and phenolics (TPC) assay. Antioxidant activity was measured using 2, 2-diphenyl-1-picrylhydrazyl (DPPH) scavenging assay and ferric reducing antioxidant powder (FRAP). The chemical constituents of all extracts were identified using gas chromatography-mass spectrometry (GCMS). The percentage of extract yield has more on aqueous fraction (82.84%) and the lower very lower amount of methanol extracts (3.63%). The TFC and TPC were a result of higher and lower phytochemicals content, which were aqueous residue and dichloromethane fractions, respectively. The percentage of scavenging ability of DPPH was higher in aqueous residue (80.994%) and followed by crude methanol extracts (51.829%), dichloromethane fraction (32.426%) and hexane fraction (11.038%). Ferric reducing antioxidant (FRAP), to confirm the existence of antioxidant constituents was found to be higher and a lower activity is shown by aqueous residue and dichloromethane fractions. GCMS was identified as bioactive compounds in all different solvent extracts that indicated various medicinal properties. Thus, aqueous residue and crude methanol extracts CN leaves extracts may be explored as new sources of antioxidants in medicinal plant research. However, dichloromethane indicated a variety of bioactive compounds and medicinal properties.

Keyword: *Clinacanthus nutans*, phytochemical, antioxidant, gas chromatography-mass spectrometry, solvent

Abstrak

Clincanthus nutans (CN) banyak ditanam di Asia Tenggara khususnya di Malaysia. Orang ramai percaya bahawa dengan memakan daunnya boleh merawat pelbagai jenis penyakit kerana mempunyai banyak khasiat perubatan. Objektif kajian ini adalah untuk mengkaji potensi pelbagai ekstrak pelarut bagi daun CN yang menjadi sumber antioksidan semulajadi dengan membuat penyaringan konstitiuen fitokimia dan mengesan kehadiran sebatian aktif utama yang berpotensi dalam aktiviti biologi. Pelbagai jenis pelarut digunakan untuk mengekstrak daun CN mengikut tahap polarity yang berbeza (metanol, heksana, diklorometana dan sisa akueus). Penentuan fitokimia melibatkan pengiraan jumlah kandungan flavonoid (TFC) dan ujian fenolik (TPC). Aktiviti antioksidan diukur menggunakan bahan ujian memerangkap 2, 2-difenil-1-pikrilhidrazil (DPPH) dan serbuk antioksidan penurun ferik (FRAP). Juzuk kimia semua ekstrak yang dikenalpasti telah menggunakan kromatografi gas-spektrometri jisim (GCMS). Keputusan menunjukkan peratusan hasil ekstrak mempunyai lebih banyak pada pecahan akueus (82.84%) dan jumlah peratusan ekstrak yang sangat rendah dalam ekstrak metanol (3.63%). Keputusan TFC dan TPC adalah hasil daripada kandungan fitokimia yang lebih tinggi dan lebih rendah, yang masing-masing merupakan sisa akueus dan pecahan diklorometana. Peratusan keupayaan penghapusan DPPH adalah lebih tinggi dalam sisa akueus (80.994%) dan diikuti oleh ekstrak metanol mentah (51.829%), pecahan diklorometana (32.426%) dan pecahan heksana (11.038%). Ujian FRAP untuk mengesahkan kewujudan juzuk antioksidan didapati lebih tinggi dan aktiviti yang lebih rendah ditunjukkan oleh sisa akueus dan pecahan diklorometana. GC-MS digunakan bagi mengenalpasti kehadiran sebatian bioaktif dalam semua ekstrak ini yang mempunyai nilai perubatan. Oleh itu, sisa akueus dan ekstrak methanol mentah daun CN boleh diterokai sebagai sumber antioksidan baru dalam penyelidikan tumbuhan ubatan. Walaubagaimanapun, diklorometana menunjukkan pelbagai sebatian bioaktif dan mempunyai nilai perubatan.

Kata kunci: *Clinacanthus nutans*, fitokimia, antioksidan, kromatografi gas-spektrometri jisim, pelarut

Introduction

Medicinal plant is one of the biodiversity that can be abundantly found in Malaysia. The excellent source of medicinal plants contains medicinal derivatives and phytochemicals that are beneficial for human health [1]. Medicinal plant plays a vital role in the identification of new beneficial medicinal components and their phytochemical constituents such as antioxidant, anticancer, antihypertension, antidiabetics, antihyperglycemics, antiaging and others. The applications of phytochemicals are widely used in agriculture and cosmetic that has minimal side effects as compared to the use of used synthetic products or drugs [2].

In ancient time, traditional people have been using medicinal herb for the prevention and treatment of disease. Currently medicinal plants are developed as plant derived drug. Various communities use the leaves of CN in Malaysia, Thailand and Indonesia for medicinal purposes such as antiviral, anticancer and anti-inflammatory activities and also to treat fever and diabetes. History of traditional medicine and ethnopharmacological reports of CN are partly established and therefore scientific investigations are required to justify its therapeutic potential [3]. CN is from Acanthaceae family and is known as 'Belalai gajah' in Malaysia. This small plant with full green leaves has a lot of potential phytochemicals such as vitexin, clinamide group, clinacoside group and others [4]. CN also reported to have a lot of antioxidant and benefits of phytochemical compounds. Previous study exhibited CN to have potential flavonoid group such as anticancer agents like quercitine, catechin and luteolin [5, 6]. The pharmacological effects of CN serve as antibacterial, antioxidant, antiproliferative, anti-inflammatory and antiherpes [7]. Traditionally CN in Thailand is used for inflammation, rashes, diabetes, hypertension and diuretic [5, 8].

Plant extraction investigation is important in medicinal plant research for therapeutic purpose to avoid damage to the biomolecules in the plants. The extraction method provides active plant metabolites such as alkaloids, glycoside, phenolics, terpenoids and flavonoids that have natural potential of biological activity. Medicinal plants contain antioxidants that prevent oxidative damage caused by free radicals in the human body [9]. Thus, this study aims to investigate the effects of different solvent extraction of CN leaves on phytochemical, antioxidant and potential of chemical compounds by gas chromatography-mass spectrometry.

Materials and Methods

Plant collections and botanical species identification

The plants of CN were collected and harvested from a farm located at Pongsu Seribu (HERBagus), 13200 Kepala Batas, Seberang Perai Utara, Pulau Pinang. The complete specimen, including roots, flowers, leaves and all parts of plant, was collected (Figure 1). These complete samplings were then sent to Unit Herbarium, School of Biology, and Universiti Sains Malaysia (USM) for voucher specimen preparation of the herbarium. The last step involved herbarium and plant identification by an expert taxonomist from USM. The complete herbarium was deposited with reference number of voucher specimen 111536.

Preparations of plant solvent extractions using partition coefficient

Crude methanol extract and fraction (hexane, dichloromethane and aqueous residue) were prepared using fresh CN cleaned leaves. The process of extraction started with blending the leaves into small pieces and soaking them in a mixture of solvent consisting of 80% methanol and distilled water for 24 h at room temperature. Then, it is filtered and continuously soaked for 2 times to ensure exhaustive extraction. The yield in the form of methanol crude extracts was kept at -20 ^{o}C until it was used. The filtrate was concentrated in a vacuum rotary evaporator at 40°C until about 1/10 of the original volume was left. Then, the leftover filtrate was freeze-dried to obtain the 80% methanol crude extract. The crude was used for successive solvent and partitioning extractions with different solvents of increasing polarity, starting with hexane, dichloromethane and aqueous residue by liquid-liquid extractions. The extracts of partitioning were concentrated to dryness by using a rotary evaporator. The dried powdered extracts were then stored in screw-capped glass bottles and kept in a refrigerator at 4 ^{o}C until further use.

Phytochemical analysis: Total flavonoid content

Total Flavonoid Content (TFC) was determined using aluminium chloride method with some modifications following the method of Kim et al. [10]. The extracts, standard and aluminium chloride ($AlCl_3$) solution were prepared by diluting with distilled water. Then the mixture in the wells was incubated for 10 min in the dark at room temperature. The absorbance was measured at 415nm using microplate reader. All samples were assays in triplicate. The quercitine was used as positive control and standard. The content of total flavonoid compounds was calculated as mean ± SD (n=3) from standard curve quercitine and expressed as milligrams of quercitine (QUE) in 1g of the extract and dried powder.

Total phenolic content

Total phenolic content (TPC) or Folin Ciocalteu assay were determined with modifications of colorimetric method from Sahu and Saxena [11]. Sodium carbonate ($NaHCO_3$) (7.5%) and Folin Ciocalteu reagent (2.5%) were diluted in deionized water. The extracts and gallic acid then were mixed with Folin Ciocalteu and incubated for 5 min. Then sodium carbonate was added into mixture of extracts and Folin Ciocalteu in the well plates. The mixture was incubated about 1h in the dark and measured at 765 nm using microplate reader. Gallic acid was used as standard. The total phenolic content was expressed as mean ± SD (n=3) from standard curve gallic acid and as milligrams gallic acid equivalent (GAE) in 1g of the extract and dried powder.

Antioxidant assay: 2, 2-diphenyl-1-picrylhydrazyl

Free radical scavenging effect of the 2, 2-diphenyl-1-picrylhydrazyl (DPPH) was used to evaluate the antioxidants activity of different solvents extracts of CN leaves as described in the method of Sigma protocol (1898-66-4) (D9132) ($C_{18}H_{12}N_5O_6$) (Mw: 394.33). Trolox was used as a reference compound. In brief, each extract concentration (50 µL) was mixed with 200 µL of DPPH solution (0.2 mM DPPH in 100 mL of methanol). The mixture was incubated in the dark for 30 min at 30 ^{o}C. The absorbance was measured at 517 nm against a blank methanol without the DPPH solution using microplate reader (Biotek, Model ELx808, Agilent Technologies, and Wilmington, DE, USA). The percentage of inhibition free radicals by each extract was calculated using the equation given below:

$$\% \text{ scavenging of DPPH} = (\text{Abs control} - \text{Abs sample}/\text{Abs control}) \times 100 \quad (1)$$

where Abs control is the absorbance of the DPPH solution without extracts. The capacity of the extracts to reduce DPPH was obtained from the standard curve, and the results are expressed as percentage inhibition against extract concentration.

FRAP assay

Ferric reducing antioxidant powder (FRAP) was used to determine the total antioxidant activity of different solvent extracts of CN leaves following methods described by Shui and Leong [12] with some modifications. $FeSO_{4\ was}$ diluted in deionized water. Then warmed FRAP as working solution was added in all sample extracts. After that, it was incubated in the dark for 1hr and the absorbance at 593 nm. Gallic acid was used as a positive control. The total antioxidant ability was expressed as the concentration of $FeSO_4$ standard solution.

Chemical profiling (GC-MS analysis)

GC-MS analysis was performed based on the methods described by Abdul Rahim [13]. The samples were analyzed by using an Agilent 7890A Gas Chromatograph (Agilent Technologies, Wilmington, DE, USA). Briefly, a 1 mg aliquot of an extract was weighed and added into a GC vial. The powder was then mixed with 1 mL of methanol. Next, the 10 µL mixture was injected into the GC-MS system via splitless mode. The GC-MS system was connected to an MS/MS triple quad detector. The HP-5MS GC column with an inner column and film thickness diameter of 0.25 mm x 30 m x 0.25 µm was used for the GC-MS analysis. The initial oven temperature was set at 100 ºC for 2 min before it was increased gradually to the final temperature of 280 ºC within 17 min at a rate of 10 ºC/min. Helium was used as the carrier gas with a rate of 1 mL/min. All samples were analyzed in three replicates. The spectra of the chromatogram peaks were compared against the National Institute of Standards and Technology (NIST) database library to identify the retention time (R_t) index of common primary and secondary metabolites.

Statistic

All the experiments were conducted in triplicates. The values are expressed as the mean ± standard deviation (SD). The statistical analyses were done using SPSS 25.0 windows statistical package software (SPSS Inc., Chicago, IL). Significant difference between extracts were analysed using one way analysis (ANOVA) followed by Tukey's multiple comparison test.

Results and Discussion

Traditionally CN plant was used as alternative medicinal for various cancer diseases. Many previous studies on CN used parts of leaves because they are green (Figure 1) and have high medicinal properties. In this study CN leaves extracts were prepared using solvents based on their increasing order of polarity (methanol, hexane, dichloromethane and aqueous residue). Currently many research were justified by scientific evidence that CN leaf extracts in chloroform, methanol, and water have the potentials to be used for antiproliferative and anticancer activities against various cancer cell lines [14]. Medicinal plant with anticancer properties is based on phytochemical, antioxidant and analysis of active compounds derivatives present in plant extracts [15]. In this experiment, 80% methanol and fractionation based on polarity was used. This method is effectiveness for plant extract because the different solvents and polarities give significance effects on the chemical contents of the extracts that are important to identify the optimal solvents for the extraction of antioxidant compounds from medicinal plants [16]. The crude methanol was mixed with distilled water because water was employed for the extraction and its universal solubility of polar compounds, while methanol was chosen due its ability to extract lower molecular weight polyphenols and its tendency to yield relevant antioxidant and cytotoxic compounds from CN [17]. Whereas the crude methanol extract was fractionated using different solvents to concentrate and enhance the purity of active compounds and remove unwanted interferences [18].

Extraction of yield of CN leaves was carried out using four different solvents. The yields obtained were extracted from a total dry weight of 500g CN leaves. Among the extract, the highest and the lowest yields were obtained by aqueous residue and hexane extracts, respectively (Table 1). The total percentage of all extracts obtained is 89.67% from the dry weight CN. The high yield in aqueous residue was probably due to the high solubility of phytochemical compounds such as

flavonoids and phenolic contents. Phytochemical is important in developing drug and curing health problems. Various types of solvents used in extraction can recover higher extract yield and some bioactive in plant [19]. This study revealed the significant difference in the extract yield obtained by different solvents.



Figure 1. Whole plant of *Clinacanthus nutans*

Table 1. Percentage yield of methanol extracts and fractions of *Clinacanthus nutans* leaves

No.	Solvent Extracts	Dry Weight (g)	Extract Yield (g)	Percentage of Yield (%)
1.	Methanol	500	18.9167	3.6334
2.	Hexane	15	0.1527	1.018
3.	Dichloromethane	15	0.3276	2.184
4.	Aqueous	15	12.426	82.84

Each value is expressed as mean (n=3)

Phenolics and flavonoids are secondary metabolites and are widely distributed in various plants [20, 21, 22]. Secondary metabolites from medicinal plant were extracted using different solvents. Solvents widely used for extractions are water, ethanol, methanol, acetone and solvent mixtures of different ratios with water, with or without acid. Phenolic constituents and secondary metabolites of plant extraction are based on solvents and its polarity. Phenolic plays a role as primary antioxidant and free radical inhibitors. Whereas flavonoids are polyphenolic compound from numerous phenolics and widely spread in the plant kingdom. Previous studies reported the function of flavonoids such as UV protection, disease resistance, pigmentation and nitrogen fixation simulation in the nodules [23]. This study on phytochemical analysis focuses on the content of flavonoids (TFC) and phenolics (TPC) content (Table 2). The result found that the highest contents of TFC and TPC were in aqueous residue and lower content of TFC and TPC were found in is dichloromethane fractions. Nevertheless, it is reported that the biological properties depend not only on the total extract yield but also on its phytochemical composition [19].

Table 2. Total flavonoids and phenolic content of *Clinacanthus nutans* leaves different solvent extracts and fractions. Mean±SD. (n=3)

Solvents Extracts	Total Flavonoid Content (mgQUE/g)	Total Phenolic Content (mgGAE/g)
Methanol	14.229±0.055	562.784±0.012
Hexane	33.735±0.337	327.548±0.049
Dichloromethane	9.663±0.072	97.191±0.059
Aqueous	27.503±0.089	628.959±0.026

QE-quercitine equivalents; GAE-gallic acid equivalents. Data represented as means ± standard deviation (SD) of replicates (n=3)

Antioxidant molecules were reported in several medicinal plants beneficial in the treatment of several human disease [19] and has the ability to prevent oxidative stress. In the human body, the cell damage caused increasing level of free radical which correlates with and causes various diseases. The free radical was neutralized through antioxidant function [24, 25]. The antioxidant activity of CN could explain its wide-ranging reported bioactivities such as antidiabetic, anticancer, anti-inflammatory and wound healing activities [26]. In this study the antioxidant effects were determined by DPPH and FRAP assays. Both assays involved concentration from 0.031 to 1.0 mg/mL and the significance difference ($p<0.05$) between all the concentrations was observed. The evaluation of DPPH radical scavenging activity inhibition was higher in the crude methanol extract and the lowest was hexane factions (Figure 2). While the FRAP assay resulted clearly in the same result whereby crude methanol extract was higher and the hexane fractions were lower (Figure 3) and this may be due to various kinds of antioxidants present in the samples which react differently with the radical used. Every method has its own advantages and limitations in terms of cost, availability of chemicals, tediousness, preparation time, reproducibility and others [27]. The 1 mg/mL of CN showed the highest percentage of DPPH scavenging activity of crude methanol extract, 51.83±0.010 % followed by dichloromethane fraction (32.43±0.58%), aqueous residue (21.03±0.23%) and hexane fractions (17.38±0.23%).

The result obtained in the previous study by Ismail et al. [28], showed higher hexane fractions percentage of DPPH scavenging values (1530±3.74%) followed by dichloromethane (1039±0.87%), aqueous residue (744.30±8.45%) and lower was crude methanol (560.50±2.45%). It showed different result because the antioxidant activity can be associated with a deficient amount of nitrogen level of the soil level of moisture at different location [29]. The second most commonly used method in the determination of antioxidant is ferric reducing antioxidant power (FRAP) assay [30]. FRAP is an indicator of their potential to confirm antioxidant activity based on the reaction which measures reduction of ferric to ferrous and increase in the absorbance of the reaction mixture that indicates an increase in the reduction power [31]. Standard control of DPPH and FRAP assay were used trolox and gallic, respectively. Thus, the comparison of DPPH and FRAP activity was difficult due to different control standard was used gallic acid and trolox [31, 32, 33]. The solvent effect is an important parameter for the chemical behaviour of antioxidant compounds [30].

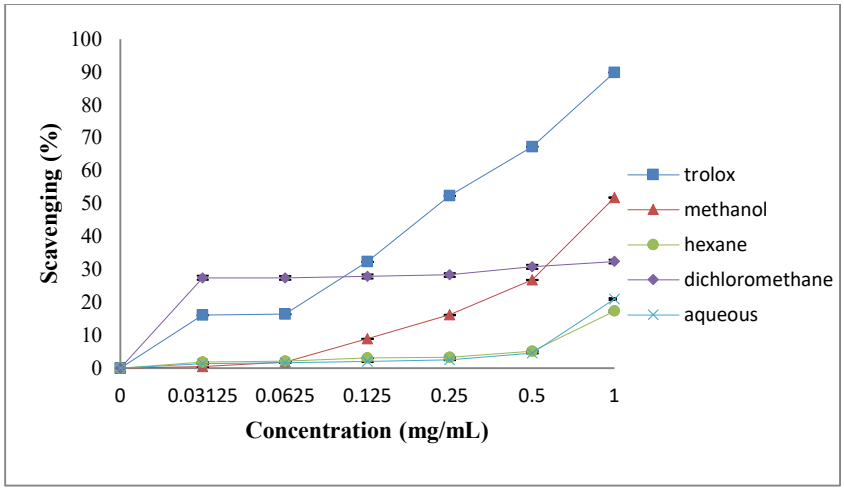


Figure 2. DPPH free radical scavenging activities of various solvent extracts of *Clinacanthus nutans* leaves and trolox

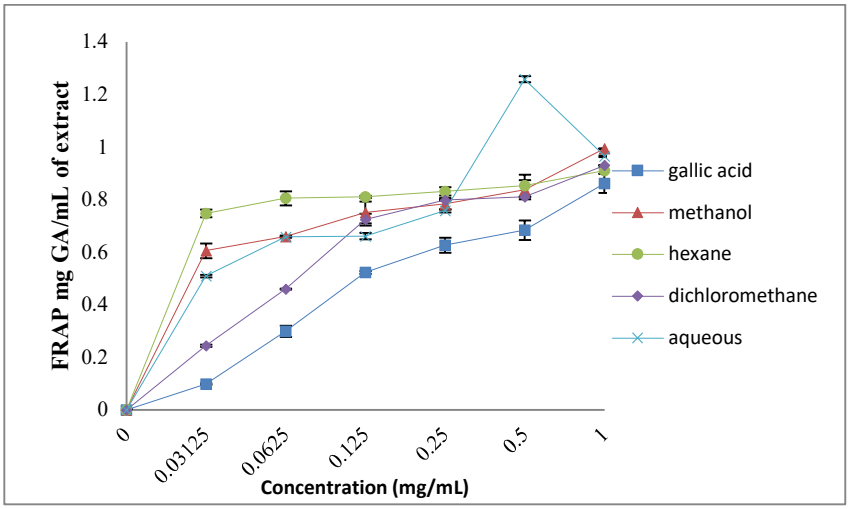


Figure 3. Ferric Reducing Antioxidant Power (FRAP) of the extracts

The phytochemical screening using GCMS found 43compounds presence with various biological activities in different solvent extracts (Table 3). The highest compounds found in hexane fractions were 23 followed by dichloromethane (16), methanol (5) and aqueous fractions (3). From this investigation most of these major compounds are known to exhibit various pharmacological activities. From the investigations methanol extracts contain sugar group such as methylgalactoside and galactoside and also contains fatty acid ester from lineloic acid group and organosulfur. The hexane fractions have the highest phytochemicals, 23 compounds from fatty acid ester (linoleic ester, palmitic acid, methyl ester), terpenoids (diterpene) and alkene. In dichloromethane fractions through the GC-MS analysis the presence of fatty acid ester (linoleic acid, methyl ester), organosulfur, phytosterols/steroid, terpenoids, triterpene and amide were found. In aqueous fractions the phytochemical compounds are present only alkene and diamine group. From these results the variety of phytochemical compounds group is highly present in dichloromethane fractions. The compounds of α and β-Amyrin from triterpene group present in dichloromethane fractions in this experiment are known to possess antidiabetic, anti-inflammatory, antiarthritic and anticancer activities [19, 34]. Amyrins can be found in various plants and plant material such as leaves, bark, wood and resins [35].

Table 3. Phytochemical compounds identified and biological activities of different solvents and fractions of *Clinacanthus nutans* leaves by GC-MS

Retention Time (minutes)	Compound Name	Peak Area (%)[a]				Compound Nature	Biological Activities
		Methanol	Hexane	Dichloromethane	Aqueous		
14.058	Methyl.beta-d-galactopyranoside	29.17	ND	ND	ND	Sugar	Antioxidant, antibacterial
14.058	.alpha-D-Galactopyranoside, methyl	29.17	ND	ND	ND	Sugar	Antimicrobial, antinociceptive cytotoxicity
14.058	.beta.-D-glucopyranoside, methyl	29.17	ND	ND	ND	Sugar	Antimicrobial and antibacterial
18.894	1,2-Benzenedicarboxylic acid, bis(2-methylpropyl) ester	ND	0.39	ND	ND	Fatty acid ester	Antimicrobial activity and hypoglycemic effect
18.894	Phthalic acid, butyl isohexyl ester	ND	0.39	ND	ND	Fatty acid ester	Antifungal
20.024	Hexadecanoic acid, methyl ester	0.93	21.03	3.40	ND	Fatty acid ester	Antioxidant, flavour, hypocholesterolemic, nematicide, antiandrogenic, cancer preventive
20.024	Pentadecanoic acid, 14-ethyl-, methyl ester	ND	21.03	3.40	ND	Fatty acid ester	Antibacterial
20.277	Diphenyl sulfone	0.70	ND	0.36	ND	Organosulfur	Antimicrobial, Antibacterial and antifungal
20.53	Benzenepropanoic acid, 3,5-bis(dimethylethyl)-4-hydroxy-, methyl	ND	0.11	ND	ND	Fatty acid	Antifungal , antioxidant
21.593	n-Hexadecanoic acid	ND	0.10	ND	ND	Palmitic acid (fatty acid)	Antifugal, antioxidant, hypocholesterolemic, nematicide, anti-androgenic flavour, haemolytic, 5-Alpha reductase inhibitor, potent antimicrobial agent, antimalarial and antifungal
22.555	Hexadecanoic acid, 15-methyl-, methyl ester	ND	0.48	ND	ND	Fatty acid ester	Antioxidant, nematicide, pesticide, flavour and antiandrogenic
22.555	Heptadecanoic acid, methyl ester	ND	0.48	ND	ND	Fatty acid ester	Antioxidant

24.849	9,12-Octadecadienoic acid, methyl ester	ND	ND	0.96	ND	Fatty acid ester	Antiinflammatory, hypocholesterolemic, cancer preventive, nematicide, hepatoprotective, insectifuge, antihistaminic, antieczemic, antiacne, antiandrogenic, antiarthritic, anticoronary
24.849	9,12-Octadecadienoic acid (Z,Z)-, methyl ester	ND	ND	0.96	ND	Fatty acid ester	Antimicrobial activity, antiinflammatory, hypercholesterolemic, cancer preventive
24.849	9,15-Octadecadienoic acid, methyl ester,(Z,Z)-	ND	ND	0.96	ND	Fatty acid ester	Antimicrobial and anticancer
25.001	9,12-Octadecadienoic acid, methyl ester	ND	10.45	ND	ND	Fatty acid ester	Antiinflammatory, hypocholesterolemic, cancer preventive,nematicide, hepatoprotective, insectifuge, antihistaminic, antieczemic, antiacne, antiandrogenic, anthiarthritic, anticoronary
25.001	9,12-Octadecadienoic acid (Z,Z)-methyl ester	ND	10.45	ND	ND	Fatty acid ester	Anti-inflammatory, hypocholesterolemic, cancer preventive, hepatoprotective, nematicide, insectifuge, antihistaminic, antieczemic, antiacne, 5-alpha reductase inhibitor antiandrogenic, antiarthritic, anticoronary
25.001	10,13-Octadecadienoic acid, methyl ester	ND	10.45	ND	ND	Fatty acid ester	Anticancer activity, antitumor, in vitro cytotoxicity, antioxidant
25.119	9,12,15-Octadecatrienoic acid, methyl ester	ND	ND	3.58	ND	Fatty acid ester	Antiinflammatory, hypocholesterolemic and antiarthritic, antioxidant and antimicrobial
25.119	9,12,15-Octadecatrien-1-ol,(Z,Z,Z)-	ND	ND	3.58	ND	Fatty acid ester	Antioxidant and antibacterial properties
25.119	9,12,15-Octadecatrienoic acid, methyl ester, (Z,Z,Z)	ND	ND	3.58	ND	Fatty acid ester	Antiinflammatory, hypocholesterolemic and antiarthritic cancer-preventive, hepatoprotective, antioxidant and hypocholesterolemic
25.439	9,12,15-Octadecatrienoic acid, methyl ester, (Z,Z,Z)-	ND	41.89	ND	ND	Fatty acid ester	Antiinflammatory, hypocholesterolemic and antiarthritic cancer-preventive, hepatoprotective, antioxidant, antimicrobial ,hypocholesterolemic
25.439	9,12,15-Octadecatrienoic acid, methyl ester, (Z,Z,Z)-cis,cis,cis-7,10,13-Hexadecatriena	ND	41.89	ND	ND	Fatty acid ester	Antiadrogenic
25.692	Phytol	ND	3.36	ND	ND	Terpenoid (diterpene)	Antifungal, stimulant ,antimalarial

26.249	Octadecanoic acid, methyl ester	ND	9.01	1.25	ND	Fatty acid methyl ester	Antiinflammatory, hypocholesterolemic and antiarthritic, antimicrobial and anticancer
27.059	9,12,15-Octadecatrienoic acid,(Z,Z,Z)-	ND	4.88	ND	ND	Fatty acid	Anticancer, antibacterial, antioxidant, antipyretic, cardioprotective, neural function, antiandrogenic and antiarthritic
27.059	9,12,15-Octadecatrienoic acid, ethyl ester,(Z,Z,Z)-	ND	4.88	ND	ND	Fatty acid ester	Antimicrobial, antioxidant and anticancer
27.059	9,12,15-Octadecatrienal	ND	4.88	ND	ND	Alkene	Antibacterial and antioxidant
39.188	.gamma.-Sitosterol	ND	ND	14.21	ND	Steroid	Antidiabetic, antioxidant , antibacterial and prophylactic activities
39.188	Stigmasterol, 22,23-dihydro-	ND	ND	14.21	ND	Terpenoid	Anticancer, antioxidant, hypoglycemic, hypocholesterolemic, antiviral
39.188	.beta.-Sitosterol	ND	ND	14.21	ND	Steroids	Antioxidant, antimicrobial, angiogenic, immunomodulator, antidiabetic, antiinflammatory, anticancer and antinociceptive
39.593	Bicyclo[10.1.0]tridec-1-ene	ND	0.16	ND	ND	Fatty acid (Linoleic acid)	Antioxidant
42.275	.beta.-Amyrin	ND	ND	7.36	ND	Triterpene	Analgesic, antiinflammatory, anticonvulsant, antidepressive, gastroprotective, hepatoprotective, antipancreatic, anticholytic, antihyperglycemic and hypolipidemic effects
42.275	.alpha.-Amyrin	ND	ND	7.36	ND	Triterpene	Analgesic, antiinflammatory, anticonvulsant, antidepressive, gastroprotective, hepatoprotective, antipancreatic, anticholytic, antihyperglycemic and hypolipidemic effects
42.663	Docosanoic acid, methyl ester	ND	0.18	ND	ND	Fatty acid ester	Antimicrobial and antifungal
42.663	Octadecanoic acid, 11-methyl-, methyl ester	ND	0.18	ND	ND	Fatty acid ester	Anticancer
42.933	1,2-Benzenedicarboxylic acid, mono (2-ethylhexyl) ester	ND	0.65	ND	ND	Fatty acid ester	Antimicrobial, antiinflammatory, antioxidant, hypoglycemic effect and anticancer
44.738	9,12-Octadecadienoic acid (Z,Z)-2,3-dihydroxypropyl ester	ND	0.31	ND	ND	Fatty acid ester	Antiatherosclerotic, antiinflammatrory, analgesic, anthirheumatic and antioxidant

44.738	9,12-Octadecadienoic acid (Z,Z)-2-hydroxy-1-(hydroxymethyl)ethyl ester	ND	0.31	ND	ND	Fatty acid ester	Hypcholesterolemic, nematicide, anthiarthritic, hepatoprotective , antiandrogenic, hypcholesterolemic 5-alpha reductase inhibitor, antihistaminic, anticoronory, insectifuge, antieczema and antiacne
45.683	9- Octadecenamide, (Z)-	ND	ND	1.79	ND	Amide	Antifungal and antibacterial
45.936	Cyclotrisiloxane, hexamethyl-	ND	ND	ND	100	Alkane	Antimicrobial, antioxidant and antibacterial
45.936	Tetrasiloxane, decamethyl	ND	ND	ND	100	Alkane	Antibacterial and antifungal
45.936	1,2-Propanediamine	ND	ND	ND	100	Diamine	Antimicrobial

*ND= not detected

CN has been reported to have various phenolic, terpenoids and some other bioactive compounds such as benzenoids, cerbrosides, glycoglycerides, fatty acids, chlorophyll derivatives, phytosterols and sulphur containing glucosides that contribute to its diverse bioactivities [36]. Phytol that is present in hexane fractions, is an important terpenoid or diterpene that possesses antimicrobial, antioxidant and anticancer activities [19, 37, 38, 39]. Terpenoids and alkaloids compound have also been reported to have potent activity against gastric ulcers and relax cardiovascular muscle [40]. The terpenoids are widely distributed in nature and are found in higher plants. They represent the second largest class of secondary metabolites with more active constituents. It is now known that terpenes with a pleasant aroma are extracted from the vegetable or plants containing them and some are precursors of vitamins and insecticides [35, 41]. The various phenolic and fatty acid compounds were found in ethanol and ethyl acetate leaf extract of CN [26, 42]. Phenolics compounds esters, alkanes, aldehydes, alkenes and ketones are the other major volatile compounds which have antiulcer, anti-inflammatory, antiarthritic, antidiabetic, hypolipidemic and cytotoxic activities [40, 43]. Plant phenolics are one of the most abundant vital group of phytochemicals and are widely known for their antioxidant and radical scavenging activity with potential impacts on human health. The phenolics are natural antioxidants which can control oxidative stress related degenerative disease. The adverse effects of oxidative stress have been found to be controlled by the antioxidant activities of this group of bioactive compounds. [6]. The compounds have attracted great attention recently due to their potential to neutralize reactive oxygen species and other free radicals. Phenolic and flavonoid compounds display antitumor, antiadhesive, antimicrobial and anti-inflammatory properties and protection against chronic disease by the reduction of oxidative stress solely or synergistically with other phenolic containing amalgams [25]. In this study the various phenolics group was found in all the solvent and different extracts tested on CN extracts. Thus, it is shown that all the solvent extractions important roles as antioxidant are widely distributed in plants and possess ultraviolet protection, pigmentation and disease resistance [9].

Ester is a major compounds and origin from phenolics groups which shown presence in this all solvent extraction through GCMS analysis. Fatty acid is one of the groups of esters. Previous study on ethanol and ethyl acetate extract of CN indicated the presence of ester group compounds such as palmitic acid, myristic acid, linoleic acid or omega 3 fatty acid, stearic acid and oleic acid [26]. In this study the presence of ester group of linoleic acid in hexane fractions and dichloromethane fractions was shown while palmitic acid found in hexane fractions. Fatty acid methyl ester was found in hexane and dichloromethane fraction at a retention time of 26.249 minutes with percentage peak area for hexane and dichloromethane 9.01% and 1.25%, respectively. The methyl ester, stearic acid or stearate is a saturated 19-carbon-chained compound also known as octadecanoic acid methyl ester was reported to have antimicrobial, antiviral, potential anticancer properties [44], anti-inflammatory, hypocholesterolaemia, antiarthritic and antimicrobial [44, 45, 46]. In addition, phytochemical compounds found from GC-MS were not only phenolic and flavonoid contents but also consist of many other compounds such as diterpene, aromatic methyl esters, fatty acid, ester, fatty acid, vitamin and so on which were compared by NIST mass spectra l library [29]. Previous study of CN extract leaf oven and air-dried leaves demonstrated that the CN exhibited better antioxidant with the presence of phenolics, terpenoids and sulphur containing glucosidase compounds [26, 47]. Glucosidase is one of the sugar group that present in this study such as methygalactosidase and galactosidase that are present in methanol crude extract which has potential biological activity such as antioxidant and antibacterial [48, 49, 50]. Organosulfur is also present in dichloromethane fractions for antimicrobial, antibacterial and antifungal potential [51].

In this study the method of extraction involved the proses of fractionated on the crude extracts of CN leaves. The fractionated crude extracts used polar and nonpolar solvents that obtain phytoconstituent which rich of biological active standardize fractions [6]. Previous study indicated the effect of phytochemical compounds present in leaves CN is caused by first step method involved the crude extraction with macerating

the leaves with methanol to water (4:1) at room temperature. This method involved lower temperature in order to avoid degradation of compounds to produce polyphenols which produce many biological compounds functions [29, 51]. This extraction method has ability to produce biological activities profiling.

Conclusion

The greenly leaves of CN aqueous fractions and crude methanol extracts from different solvent extracts exhibited higher yield percentage of extracts and high values phytochemicals of flavonoid and phenolic contents. In addition, antioxidant study of DPPH radical scavenging and FRAP activity indicated the highest result was methanol crude extract and dichloromethane fractions may be explored as new sources of antioxidants in medicinal plant research. However, from the GCMS analysis, it is found that the dichloromethane fractions indicated a variety of bioactive compounds and medicinal properties. Furthermore, cytotoxicity study of the antioxidant and phytochemicals rich fractions is necessary to verify their suitability for future pharmaceutical applications.

Acknowledgement

This work was supported and funded by a FRGS grant (203/CIPPT/6711340) from the Ministry of Higher Education, Government of Malaysia and a USM Bridging Grant (304/CIPPT/6316239) to Hasni Arsad.

References

1. Azwanida, N. N. (2015). A review on the extraction methods use in medicinal plants, principle, strength and limitation. *Medicinal Aroma Plants*, 4: 196.
2. Kamala, A., Middha, S. K., Gopinath, C., Sindhura, H. S., and Karigar, C. S. (2018). In vitro antioxidant potentials of Cyperus rotundus L. rhizome extracts and their phytochemical analysis. *Pharmacognosy Magazine*, 14(54): 261.
3. Kamarudin, M. N. A., Sarker, M. M. R., Kadir, H. A., and Ming, L. C. (2017). Ethnopharmacological uses, phytochemistry, biological activities, and therapeutic applications of *Clinacanthus nutans* (Burm. f.) Lindau: A comprehensive review. *Journal of ethnopharmacology*, 206: 245-266.
4. Ghasemzadeh, A., Hawa, Z. E., Jaafar, H., Rahmat, R. and Devarajan T. (2014). Evaluation of bioactive compounds, pharmaceutical quality and anticancer activity of curry leaf (*Muraya koenigii* L.). *Evidence Based Complementary Alternative Medicine*, 2014: 873803.
5. Phua, Q. Y., Subramaniam, S., Lim, V., and Chew, B. L. (2018). The establishment of cell suspension culture of sabah snake grass (*Clinacanthus nutans* (Burm. F.) Lindau). *In Vitro Cellular & Developmental Biology-Plant*, 54: 413-422.
6. Alam, M. A., Zaidul, I. S. M., Ghafoor, K., Sahena, F., Hakim, M. A., Rafii, M. Y., ... and Khatib, A. (2017). In vitro antioxidant and, α-glucosidase inhibitory activities and comprehensive metabolite profiling of methanol extract and its fractions from *Clinacanthus nutans*. *BMC Complementary and Alternative Medicine,* 17(1): 1-10.
7. Wanikiat, P., Panthong, A., Sujayanon, P., Yoosook, C., Rossi, A. G., and Reutrakul, V. (2008). The anti-inflammatory effects and the inhibition of neutrophil responsiveness by *Barleria lupulina* and *Clinacanthus nutans* extracts. *Journal of Ethnopharmacology*, 116(2): 234-244.
8. Vachirayonstien, T., Promkhatkaew, D., Bunjob, M., Chueyprom, A., Chavalittumrong, P., and Sawanpanyalert, P. (2010). Molecular evaluation of extracellular activity of medicinal herb *Clinacanthus nutans* against herpes simplex virus type-2. *Natural Product Research*, 24(3): 236-245.
9. Sulaiman, I. C., Basri, M., Chan, K. W., Ashari, S. E., Masoumi, H. R. F., and Ismail, M. (2015). In vitro antioxidant, cytotoxic and phytochemical studies of *Clinacanthus nutans* Lindau leaf extracts. *African Journal of Pharmacy and Pharmacology*, 9(34): 861-874.
10. Kim, D. O., Jeong, S. W., and Lee, C. Y. (2003). Antioxidant capacity of phenolic phytochemicals from various cultivars of plums. *Food Chemistry*, 81(3): 321-326.
11. Sahu, R. and Saxena, J. (2013). Screening of total phenolic and flavonoid content in conventional and non conventional species of curcumin. *Journal of Pharmacognosy and Phytochemistry*, 2:1.
12. Shui, G. and Leong, L. P. (2006). Residue from star fruit as valuable source for functional food ingredients and antioxidant nutraceuticals. *Food Chemistry*, 97: 2.
13. Abdul Rahim, M. H., Zakaria, Z. A., Mohd Sani, M. H., Omar, M. H., Yakob, Y., Cheema, M. S., ... and Abdul Kadir, A. (2016). Methanolic extract of *Clinacanthus nutans* exerts antinociceptive activity via the opioid/nitric oxide-mediated, but cGMP-independent, pathways. *Evidence-Based Complementary and Alternative Medicine*, 2016: 1494981.

14. Yong, Y. K., Tan, J. J., Teh, S. S., Mah, S. H., Ee, G. C. L., Chiong, H. S., and Ahmad, Z. (2013). *Clinacanthus nutans* extracts are antioxidant with antiproliferative effect on cultured human cancer cell lines. *Evidence-Based Complementary and Alternative Medicine*, 2013: 462751.
15. Tanih, N. F., and Roland, N. N. (2013). The acetone extract of *Sclerocarya birrea* (Anarcardiaceae) posses antiproliferative and apoptotic potential against human breast cancer cell lines (MCF-7). *Scientific World Journal*, 2013: 956206.
16. Majeed, M., Hussain, A. I., Chatha, S. A., Khosa, M. K., Kamal, G. M., Kamal, M. A., ... and Liu, M. (2016). Optimization protocol for the extraction of antioxidant components from *Origanum vulgare* leaves using response surface methodology. *Saudi Journal of Biological Sciences*, 23(3): 389-396.
17. Haron N. H, Abas R., Md Toha Z., Hamdam M. R., Azman N., Samian M. R., and Arsad H. (2016). Effect of different solvent extracts on phenolic, flavonoid and antioxidant content and antiproliferative activity of Clinacanthus nutans leaves extract. In proceedings of the 41th Annual *Conference of the Malaysian Society for Biochemistry and Molecular Biology, Pullman Kuala Lumpur, Malaysia*, 18 August 2016.
18. Dai, J., and Mumper, R. J. (2010). Plant phenolics: extraction, analysis and their antioxidant and anticancer properties. *Molecules*, 15: 7313-7352.
19. Swamy, M. K., Arumugam, G., Kaur, R., Ghasemzadeh, A., Yusoff, M. M., and Sinniah, U. R. (2017). GC-MS based metabolite profiling, antioxidant and antimicrobial properties of different solvent extracts of Malaysian *Plectranthus amboinicus* leaves. *Evidence-Based Complementary and Alternative Medicine,* 2017: 1517683.
20. Bonoli, M., Marconi, E., and Caboni, M. F. (2004). Free and bound phenolic compounds in barley (*Hordeum vulgare* L.) flours: Evaluation of the extraction capability of different solvent mixtures and pressurized liquid methods by micellar electrokinetic chromatography and spectrophotometry. *Journal of Chromatography A*, 1057(1-2): 1-12.
21. Kaisoon, O., Siriamornpun, S., Weerapreeyakul, N., and Meeso, N. (2011). Phenolic compounds and antioxidant activities of edible flowers from Thailand. *Journal of Functional Foods*, 3(2): 88-99.
22. Tungmunnithum, D., Thongboonyou, A., Pholboon, A., and Yangsabai, A. (2018). Flavonoids and other phenolic compounds from medicinal plants for pharmaceutical and medical aspects: An overview. *Medicines*, 5(3): 93.
23. Kamala, A., Middha, S. K., Gopinath, C., Sindhura, H. S., and Karigar, C. S. (2018). In vitro antioxidant potentials of *Cyperus rotundus* L. rhizome extracts and their phytochemical analysis. *Pharmacognosy Magazine*, 14(54): 261.
24. Anju, T. and Sarita, S. (2010). Suitability of Foxtail millet (*Setaria italica*) and Barnyard millet (*Echinocloa frumentoceae*) for development of low glycemic index biscuits. *Malaysian Journal Nutrition*, 16: 361-368.
25. Shah, M. D., Seelan, J. S. S., and Iqbal, M. (2020). Phytochemical investigation and antioxidant activities of methanol extract, methanol fractions and essential oil of *Dillenia suffruticosa* levels. *Arabian Journal of Chemistry*, 13: 7170-7182.
26. Kamarudin, M. N. A., Sarker, M. M. R., Kadir, H. A., and Ming, L. C. (2017). Ethnopharmacological uses, phytochemistry, biological activities, and therapeutic applications of *Clinacanthus nutans* (Burm. f.) Lindau: A comprehensive review. *Journal of Ethnopharmacology*, 206: 245-266.
27. Shah, P., and Modi, H. A. (2015). Comparative study of DPPH, ABTS and FRAP assays for determination of antioxidant activity. *International Journal for Research in Applied Science and Engineering Technology*, 3(6): 636-641.
28. Ismail, N. Z., Md Toha, Z., Muhamad, M., Nik Mohamed Kamal, N. N. S., Mohamad Zain, N. N., and Arsad, H. (2020). Antioxidant effects, antiproliferative effects, and molecular docking of *Clinacanthus nutans* leaf extracts. *Molecules*, 25(9): 2067.
29. Ismail, N. Z., Arsad, H., Samian, M. R., and Hamdan, M. R. (2017). Determination of phenolic and flavonoid contents, antioxidant activities and GC-MS analysis of *Clinacanthus nutans* (Acanthaceae) in different locations. *AGRIVITA, Journal of Agricultural Science*, 39(3): 335-344.
30. Arulkumar, A., Rosemary, T., Paramasivam, S., and Rajendran, R. B. (2018). Phytochemical composition, in vitro antioxidant, antibacterial potential and GC-MS analysis of red seaweeds (*Gracilaria corticata* and *Gracilaria edulis*) from Palk Bay, India. *Biocatalysis and Agricultural Biotechnology*, 15: 63-71.
31. Hamid, H. A, and Yahaya, I. H. (2016). Cytotoxicity of *Clinacanthus nutans* extracts on human hepatoma (HepG2) cell line. *International Journal of Pharmacy and Pharmaceutical Sciences*, 8(10): 8-10.

32. Pannangpetch, P., Laupattarakasem, P., Kukongviriyapan, V., Kukongviriyapan, U., Kongyingyoes, B., & Aromdee, C. (2007). Antioxidant activity and protective effect against oxidative hemolysis of *Clinacanthus nutans* (Burm. f) Lindau. *Songklanakarin Journal Science Technology,* 29: 1-9.
33. Haida, Z., and Hakiman, M. (2019). A review of therapeutic potentials of *Clinacanthus nutans* as source for alternative medicine. *Sains Malaysiana*, 48: 12.
34. Ghosh, G., Panda, P., Rath, M., Pal, A., Sharma, T., and Das, D. (2015). GC-MS analysis of bioactive compounds in the methanol extract of Clerodendrum viscosum leaves. *Pharmacognosy Research*, 7(1): 110.
35. Nogueira, A. O., Oliveira, Y. I. S., Adjafre, B. L., de Moraes, M. E. A., and Aragao, G. F. (2019). Pharmacological effects of the isomeric mixture of alpha and beta amyrin from *Protium heptaphyllum*: a literature review. *Fundamental & Clinical Pharmacology*, 33(1): 4-12.
36. Aslam, M. S., Ahmad, M. S., and Mamat, A. S. (2015). A review on phytochemical constituents and pharmacological activities of *Clinacanthus nutans*. *World,* 2: 4.
37. Swamy, M. K., and Sinniah, U. R. (2015). A comprehensive review on the phytochemical constituents and pharmacological activities of *Pogostemon cablin* Benth.: An aromatic medicinal plant of industrial importance. *Molecules,* 20(5), 8521-8547.
38. Wei, L. S., Wee, W., Siong, J. Y. F., and Syamsumir, D. F. (2011). Characterization of anticancer, antimicrobial, antioxidant properties and chemical composition of *Peperomia pellucida* leaf extract. *Acta Medica Iranica*, 49(10): 670-674.
39. Song, Y., and Cho, S. K. (2015). Phytol induces apoptosis and ROS mediated protective autophagy in human gastric adenocarcinoma AGS cells. *Biochemistry and analytical Biochemistry*, 4: 211.
40. Olivia, N. U., Goodness, U. C., and Obinna, O. M. (2021). Phytochemical profiling and GC-MS analysis of aqueous methanol fraction of Hibiscus asper leaves. *Future Journal of Pharmaceutical Sciences*, 7: 1-5.
41. Newman, D. J., Cragg, G. M, and Snader K.M. (2000). The influence of natural products upon drug discovery. *Natural Products Reports*, 17: 215-234.
42. Sulaiman, I. C., Basri, M., Chan, K. W., Ashari, S. E., Masoumi, H. R. F., and Ismail, M. (2015). In vitro antioxidant, cytotoxic and phytochemical studies of *Clinacanthus nutans* Lindau leaf extracts. *African Journal of Pharmacy and Pharmacology*, 9(34): 861-874.
43. Kumar, P. P., Kumaravel, S., and Lalitha, C. (2010). Screening of antioxidant activity, total phenolics and GC-MS study of Vitex negundo. *African Journal of Biochemistry Research*, 4(7): 191-195.
44. Ragupathi, V., Stephen, A., and Kumaresan S. (2018). Pass-assisted prediction of biological activity spectra of methanolic extract of *Gymnopilus junonius*, a wild mushroom from southern western Ghats, India. *European Journal of Pharmaceutical and Medical Research*, 5(4): 340-437.
45. Chandrasekaran, M., Senthilkumar, A., and Venkatesalu, V. (2011). Antibacterial and antifungal efficacy of fatty acid methyl esters from the leaves of Sesivium portulacastrum L. *European Review Medicine Pharmacology Sciences*, 15(7):775-780.
46. Yu, F. R., Lian, X. Z., Guo, H. Y., McGuire, P. M., Li, R. D., Wang, R., and Yu, F. H. (2005). Isolation and characterization of methyl esters and derivatives from *Euphorbia kansui* (Euphorbiaceae) and their inhibitory effects on the human SGC-7901 cells. *Journal Pharmacy and Pharmaceutical Sciences*, 8(3): 528-35.
47. Khoo, L.W., Mediani, A., Zolkeflee, N. K. Z., Leong, S. W., Ismail, I. S., Khatib, A., Shaari K., and Abas F. (2015). Phytochemical diversity of *Clinacanthus nutans* extracts and their bioactivity correlations elucidated by NMR based metabololomics. *Phytochemicals Letter*, 14:123-133.
48. Sharma, A. and Rai, P. K. (2018). Assessment of bioactive compounds in *Brassica juncea* using chromatographic techniques. *Journal of Pharmacognosy and Phytochemistry*, 7(3):1274-1277.
49. Swargiary, A. and Daimari, M. (2021). GC-MS analysis of phytocompounds and antihyperglycemic property of *Hydrocotyle sibthorpioides* Lam. *SN Applied Sciences*, 3: 36.
50. Shaheed, K. A., Alsirraj, M. A., Allaith, S. A., Noori, N. A., Obaid, M. H., and Mouhsan, Z. M. (2018). The biological activities of seeds extracts for fenugreek and black cumin and its inhibitory influences towards some pathogens. *Iraq Medical Journal*, 2(2): 46-50.
51. Gobis, K., Foks, H., Bojanowski, K., Augustynowicz-Kopeć, E., and Napiórkowska, A. (2012). Synthesis of novel 3-cyclohexylpropanoic acid-derived nitrogen heterocyclic compounds and their evaluation for tuberculostatic activity.

Bioorganic & Medicinal Chemistry, 20(1): 137-144.

52. Blicharski, T., and Oniszczuk, A. (2017). Extraction methods for the isolation of isoflavonoids from plant material. *Open Chemistry*, 15(1): 34-45.

Malaysian Journal of Analytical Sciences Vol 27 No 5 2023

		Page
	Natural Product Analysis	922
1.	METABOLITE PROFILING AND BIOLOGICAL ACTIVITIES OF EXTRACTS FROM ENDOPHYTIC FUNGI ISOLATED FROM MANGROVE PLANT *Avicennia lanata* *Nurul Izzati Rosdi and Noor Wini Mazlan*	
	Analytical Method	
2.	DEVELOPMENT OF A HOME-BUILT UV-VISIBLE SPECTROPHOTOMETER EMPLOYING ARDUINO MICROCONTROLLER SYSTEM FOR CHEMICAL ANALYSIS *Anis Nur Shasha Abdul Halim, Tam Yi Qian, Aemi Syazwani Abdul Keyon, and Nur Safwati Mohd Nor*	935
	Nano or Advanced Materials Analysis	
3.	PHOTOCATALYTIC PERFORMANCE OF MOLYBDENUM DISULPHIDE-GRAPHENE OXIDE IN PERFLUOROOCTANOIC ACID (PFOA) DEGRADATION UNDER INDOOR LIGHT EMITTING DIODE (LED) IRRADIATION *Zulhatiqah Zolekafeli, Kavirajaa Pandian Sambasevam, and Siti Nor Atika Baharin*	946
	Analytical Method	
4.	EXPERIMENTAL AND THEORETICAL OPTIMIZATION OF EMULSIFICATION LIQUID-LIQUID MICROEXTRACTION FOR DETERMINATION OF HERBICIDES USING FATTY ACID DEEP EUTECTIC SOLVENTS *Nur Hidayah Sazali, Nur Amanina Ajman, Wan Nazwanie Wan Abdullah, and Nurul Yani Rahim*	956
	Environmental Analysis	
5.	ASSESSMENT OF IONIC SPECIES IN RAINWATER TOWARD pH VARIABILITY BETWEEN HIGHLANDS AND LOWLAND IN MALAYSIA *Puteri Marlini Zaini, Ku Mohd Kalkausar Ku Yusof, and Siti Kamilah Che Soh, and Samsuri Abdullah*	971
	Nano or Advanced Materials Analysis	
6.	THE INFLUENCE OF H_3PO_4 CONCENTRATION ON THE YIELD, POROUS STRUCTURE, AND SURFACE CHEMICALS OF SARAWAK WILD BAMBOO ACTIVATED CARBON *Mahanim Sarif, Hashim Bojet, Tumirah Khadiran, Rafidah Jalil, Puad Elham, Nicholas Andrew Lissem, Johari Zainudin, Wan Ching Ching, and Rickey Anak Dayus*	980

Analytical Method

7. A NEW GOLD NANOPARTICLES MODIFIED SCREEN PRINTED PAPER CARD BASED MICROFLUIDIC DEVICE 993
Salamatu Hayatu, AbduRahman Abdul Audu, Magaji Ladan, and Nor Azah Yusof

Organic and Inorganic Analysis

8. BENZIMIDAZOLE DERIVATIVES AS POTENTIAL NEURAMINIDASE INHIBITORS: CONVENTIONAL AND MICROWAVE SYNTHESIS, *In Vitro* AND MOLECULAR DOCKING ANALYSIS 1003
Nurasyikin Hamzah, Shafida Abd Hamid, Aisyah Saad Abdul Rahim, and Habibah Abdul Wahab

Nano or Advanced Materials Analysis

9. SYNTHESIS AND CHARACTERIZATION OF MAGNESIUM OXIDE NANOPARTICLES BY USING BANANA PEEL (*Musa acuminata* CAVENDISH) EXTRACT 1017
Nor Syazwanie Mohd Saidi, Kooh Jhi Ying, Hanis Mohd Yusoff, and Nurhanna Badar

Organic and Inorganic Analysis

10. CURRENT PROGRESS IN DYE-SENSITISED SOLAR CELLS (DSSCs) FEATURING DONOR-Π-ACCEPTOR SYSTEM OF MIXED MOIETIES:A REVIEW 1035
Wan M. Khairul, and Muhammad Aidil Zailani

Oleochemistry Analysis

11. OPTIMIZATION OF SUNFLOWER OIL HYDROLYSIS USING THE D- OPTIMAL DESIGN 1062
Muhammad Muizzuddin Khairuddin, Asiah Abdullah, Nur Nadia Dzulkifli, and Nurazira Mohd Nor

Natural Product Analysis

12. THE LATENT CYTOTOXICITY EFFICIENCY OF THE CHEMICAL CONSTITUENTS OF *Morus rubra* LINN. BARK ON CANCER CELL LINES 1079
Maria Carmen Tan, Jasmine Ting, and Glenn Oyong

Natural Product Analysis

13. PHYTOCHEMICAL ANALYSIS OF COMMERCIAL *Ziziphus mauritiana* LEAF TEAS BY LIQUID CHROMATOGRAPHY COUPLED WITH ION TRAP/TIME-OF-FLIGHT MASS SPECTROMETRY 1089
Siti Umairah Mokhtar, Nurul Fadilah Suardi, Ulia Maisarah Musni, Fathul Aiman Fahmi,Muhammad Syahmi Faiz Shamsuddin

Nano or Advanced Materials Analysis

14. GRATED COCONUT RESIDUE MODIFIED BY A CATIONIC SURFACTANT FOR REMOVAL OF REACTIVE ORANGE 16 DYE 1100
Nur Zara Syazana Zali, Shariff Ibrahim, Megat Ahmad Kamal Megat Hanafiah, and Sabiha Hanim Saleh

Analytical Method

15. DETECTION AND IDENTIFICATION OF ILLICIT DRUGS IN VAPE LIQUID SAMPLES USING THE ENZYME MULTIPLIED IMMUNOASSAY TECHNIQUE, THIN LAYER CHROMATOGRAPHY AND GAS CHROMATOGRAPHY-MASS SPECTROMETRY 1111
Low Jen Hou, Wan Nur Syuhaila Mat Desa, Halijah Miran, Wan Nazirah Wan Yusuf and Ruzilawati Abu Bakar

Analytical Method

16. GLYCIDYL ESTERS: AN UPDATED MINI-REVIEW OF ANALYTICAL METHODS (2015-2022) 1126
Nor Syuhada Mat Shukri, Nur Syafiqah Subri, Siti Munirah Ishak, Nur Nadhirah Mohamad Zain, Mazidatulakmam Miskam, Wan Nazwanie Wan Abdullah, Sazlinda Kamaruzaman, Nor Suhaila Mohamad Hanapi, Wan Nazihah Wan Ibrahim, Muggundha Raoov, and Noorfatimah Yahaya

Food Analysis

17. CHARACTERIZATION OF *Artocarpus altilis* POWDER AS A POTENTIAL HEALTH SUPPLEMENT INGREDIENT 1147
Noorazwani Zainol, Harith Syahmie Zulfikree, Nor Farahiyah Aman Nor, Harisun Yaakob, and Dayang Norulfairuz Abang Zaidel

Analytical Method

18. ENHANCING PRE-CONCENTRATION OF Pb(II) THROUGH SYNTHESIS OF TANNIN ACID-CHITOSAN (TAC) AS SOLID PHASE EXTRACTION ADSORBENT 1160
Dewi Fortuna, Dwi Siswanta, and Nurul Hidayat Aprilita

Malaysian Journal of Analytical Sciences (MJAS)
Published by Malaysian Analytical Sciences Society

METABOLITE PROFILING AND BIOLOGICAL ACTIVITIES OF EXTRACTS FROM ENDOPHYTIC FUNGI ISOLATED FROM MANGROVE PLANT *Avicennia lanata*

(Profil Metabolit dan Aktiviti Biologi Ekstrak daripada Kulat Endofitik Dipencilkan daripada Tumbuhan Bakau *Avicennia lanata*)

Nurul Izzati Rosdi[1] and Noor Wini Mazlan[1,2*]

[1]*Faculty of Science and Marine Environment,*
Universiti Malaysia Terengganu, 21030, Kuala Nerus, Terengganu, Malaysia.
[2]*Institute of Marine Biotechnology,*
Universiti Malaysia Terengganu, 21030, Kuala Nerus, Terengganu, Malaysia.

[*]*Corresponding author: noorwini@umt.edu.my*

Received: 4 April 2023; Accepted: 17 August 2023; Published: 30 October 2023

Abstract

Endophytic fungi are important in drug discovery for their unique secondary metabolites, besides the extract obtained are sustainable, reproducible and culturable under laboratory conditions as compared to their host plants. However, the use of single culture leads to the production of known compounds with similar bioactivities. Therefore, single culture and co-culture between *Fusarium* sp. and *Curvularia* sp. which have been isolated from mangrove plant *Avicennia lanata* were cultured on malt agar and rice media on 7, 15 and 30 days to trigger the production of metabolites that may absent in their single cultures. In this study, dereplication study was applied to speed up the identification of secondary metabolites in the extracts. Then, the data was processed utilising MZmine 2.40.1 and SIMCA P+ 15.0 software coupled with macro analysis and Dictionary of Natural Product (DNP) database for dereplication studies. The antioxidant activity of the extracts were evaluated by using DPPH scavenging assay. Amongst the extract obtained from malt agar medium, the extract of co-culture on day 7 (MAFC7) showed the most potent activity with IC_{50} value of 0.6 mg/mL. For the rice medium, the extract from single culture *Curvularia* sp. on day 15 showed the most significant activity with IC_{50} value of 1.1 mg/mL. While, the agar disk-diffusion method was used to evaluate the antibacterial activity of the extracts and the results indicated that the extracts exhibited activity against Gram-positive bacteria, specifically *Micrococcus* sp., *Staphylococcus aureus*, and *Bacillus cereus*. The antibacterial activity of the co-culture extracts were the most active with minimum inhibition concentration (MIC) values of 0.256 mg/mL – 5.0 mg/mL. In conclusion, the extracts obtained from co-culture showed potent antioxidant and antibacterial activities that could be further scaled-up and investigated for future pharmacological properties.

Keywords: *Fusarium* sp., *Curvularia* sp., co-culture, antioxidant, antibacterial

Abstrak

Kulat endofit adalah penting dalam penemuan ubat untuk metabolit sekunder yang unik, selain itu ekstrak yang diperolehi adalah mampan, boleh dihasilkan semula dan dikultur di bawah keadaan makmal berbanding dengan tumbuhan perumah. Walau

bagaimanapun, penggunaan kultur tunggal kebiasaannya membawa kepada penghasilan sebatian yang diketahui dengan bioaktiviti yang sama. Oleh itu, kultur tunggal dan kultur bersama antara *Fusarium* sp. dan *Curvularia* sp. yang telah dipencilkan daripada tumbuhan bakau *Avicennia lanata* telah dikulturkan pada agar malt dan media beras pada hari ke-7, 15 dan 30 hari untuk mencetuskan penghasilan metabolit yang berbeza yang mungkin tidak hadir dalam kultur tunggal mereka. Dalam kajian ini, kajian dereplikasi telah digunakan untuk mempercepatkan pengenalpastian metabolit sekunder dalam ekstrak. Kemudian, data telah dianalisis menggunakan perisian MZmine 2.40.1 dan SIMCA P+ 15.0 beserta analisis makro dan pengkalan data Kamus Bahan Semulajadi (DNP) bagi kajian dereplikasi. Aktiviti antioksidan bagi ekstrak telah dinilai menggunakan asai skaveng DPPH. Antara ekstrak yang diperolehi daripada medium agar malt, ekstrak kultur bersama pada hari ke-7 (MAFC7) menunjukkan aktiviti yang berpotensi dengan nilai IC_{50} sebanyak 0.6 mg/mL. Bagi medium beras, ekstrak daripada kultur tunggal *Curvularia* sp. pada hari ke-15 menunjukkan aktiviti yang paling ketara dengan nilai IC_{50} sebanyak 1.1 mg/mL. Sementara itu, kaedah penyerapan cakera agar telah digunakan untuk menilai aktiviti antibakteria ekstrak dan keputusan menunjukkan bahawa ekstrak menunjukkan aktiviti melawan bakteria Gram-positif termasuk *Micrococcus* sp., *Staphylococcus aureus* dan *Bacillus cereus*. Aktiviti antibakteria bagi ekstrak kultur bersama adalah yang paling aktif dengan nilai kepekatan rencat minima (MIC) pada 0.256 mg/mL– 5.0 mg/mL. Kesimpulannya, ekstrak yang diperolehi daripada kultur bersama menunjukkan aktiviti antioksidan dan antibakteria yang bagus yang boleh dilanjutkan untuk skala besar dan disiasat untuk sifat farmakologi masa hadapan.

Kata kunci: *Fusarium* sp., *Curvularia* sp., kultur bersama, antioksidan, antibakteria

Introduction

Natural products are molecules derived from plants, microorganisms or animals that naturally produce primary and secondary metabolites which continuing provide varities bioactive metabolites. Overall, more than 70% of antibacterial and anticancer compounds are natural products origin [1]. Endophytic fungi are the organism live commonly within most plant species' tissues. The endophyte occupies host tissues without causing any diseases and found mostly in terrestrial plants [2]. Endophytic fungi play an important role in plant habitat adaptation, enhancing plant production and defending plant against biotic and abiotic stress [3]. In the past few years, the metabolites isolated from the endophytic fungi including steroids, alkaloids, anthraquinones, terpenes, flavonoids and cyclic peptides that are known for their biological activities, such as antibacterial, antitumour, antiviral, antifungal and anti-inflammatory [4]. In this study, endophytic fungi *Fusarium* sp. and *Curvularia* sp. have been isolated from the mangrove plant *Avicennia lanata*. *Fusarium* genus is recognised as one of the major sources of secondary metabolites with a variety of biological activities, including antioxidant activity [5]. *Fusarium* sp. has produced a variety of secondary metabolites, including peptides, alkaloids, terpenoids, amides, pyranones, and quinones with pharmacological potential [6]. Meanwhile, *Curvularia* sp. is known as pathogen associated with humans and plants. Some of *Curvularia* species are economically important pathogens worldwide, while other species are found in combination with different hosts as pathogens or epiphytes [7]. Many biologically active secondary metabolites were previously reported from *Curvularia*, for example, 11-α-methoxycurvularin, curvularin, cytochalasin B, dehydrocurvularin, radicinol and radicinin [8]. Endophytic fungi *Curvularia* sp. also produce a variety of bioactive secondary metabolites including polyketides and steroids [9]. However, the single fungi reproduce the same compounds and similar biological activities. Therefore, co-culture has been a useful research method which effectively triggers the new metabolites that are silent in single culture.

A co-cultivation is a method to challenge two or more microorganisms by imitating the actual natural microbial community competition that is carried out in a laboratory scale, becomes a successful strategy to produce novel bioactive natural products [10]. The co-culture between endophytic fungi may trigger the production of new secondary metabolites that are silent under normal condition. Production of bioactive secondary metabolites during co-culture may be related to various mechanisms, including competition for space and nutrients in which the parameter is the most important for microbial growth and survival in a competitive environment [11, 12]. Marine-derived microorganisms such as bacteria and fungi proved to be prolific sources of novel bioactive compounds which are not only considerable interest as a new drug for the

treatment of cancer, but also for other malignancies such as chronic pain [13]. Conventional method only focused on major compounds due to diversity of metabolites, thus it is challenging especially in data interpretation. Therefore, modern technologies and techniques have been developed in natural product discovery to produce a great outcome in research.

Metabolomics study is considered as a modern technique that is developed for systematic procedures to explore various mechanism as well as detecting metabolites changes in specific organism [14]. The presence of metabolites in microbes can easily be measured and compared via metabolomics. Metabolomics is used to fast track the identification of metabolites in a mixture of extract prior to isolation work to avoid repetitive works. The metabolomic study uses multivariate analysis to classify mass data collection and groups by monitoring their distribution accordingly with subjected parameter. Therefore, a clear overview of metabolites in the extract can be detected by liquid chromatography-mass spectrometry (LC-MS) coupled with multivariate analysis such as principal component analysis (PCA) and orthogonal partial least square discriminant analysis (OPLS-DA) [15]. In this study, the extracts from a co-culture between *Fusarium* sp. and *Curvularia* sp. was carried out to provide a better understanding on the metabolites as compared to the metabolites in their independent cultures.

Materials and Methods

Preparation of fungal strain

Stock cultures of endophytic fungi *Fusarium* sp. and *Curvularia* sp. isolated from the root of *Avicennia lanata* were obtained from Fungus Laboratory, Centre of Research and Field Service, Universiti Malaysia Terengganu (UMT). The single colony of both endophytic fungi were inoculated on malt agar plate independently and incubated in an incubator at 28 ± 1 ºC for 7 – 15 days for further work.

Inoculation of fungal on malt agar and rice media

Malt agar medium consists of 10.0 g of agar (Oxoid, Malaysia) and 7.5 g of malt extract (Oxoid, Malaysia) and were transferred into 500 mL of Schott Duran bottle. 500 mL of milli-Q water was added into the bottle and autoclaved. A 25 mL of warm agar medium was poured into labelled agar plates, left to cool and stored inverted at 4 °C. The fresh malt agar containing actively growing culture of *Fusarium* sp. and *Curvularia* sp. were cut into 5 x 5 mm cubes, placed on malt agar plates for single and co-culture and incubated at 28 ± 1 °C for 7, 15 and 30 days. The growth of mycelia of *Fusarium* sp. and *Curvularia* sp. in single and co-culture agar plates were monitored daily based on the shape and colour. Once the incubation period was completed, the agar plates containing the actively growing mycelia of single and co-culture *Fusarium* sp. and *Curvularia* sp. were cut and transferred into conical flasks, then 50 mL of ethyl acetate (Fisher Scientific, Malaysia) was added, sonicated for 1 h and filtered into round bottom flasks by using cotton wool (50 mL/extraction, three times). The organic phase was concentrated under vacuum by using a rotary evaporator (Buchi, Switzerland) to give an extract. The extracts were kept at 4 ºC prior to further analysis.

Meanwhile, cultivation of single and co-culture between the fungi in sterile rice medium was also carried out for up-scaling. 15 g of rice and 15 mL of milli-Q water were added into 250 mL of conical flasks. The conical flasks were covered with cotton wool and aluminium foil and kept overnight before autoclaved. The flasks were left to cool. A fresh malt agar plate containing actively growing culture of *Fusarium* sp. and *Curvularia* sp. were cut and placed on the rice medium for single and co-culture and incubated at room temperature for 7, 15 and 30 days. Once the incubation period was completed, 100 mL of ethyl acetate (Fisher Scientific, Malaysia) was added into each flask, sonicated for 1 h and filtered into round bottom flasks by using cotton wool (100 mL/extraction, three times). The organic phase was concentrated under vacuum by using a rotary evaporator (Buchi, Switzerland). The extracts were kept at 4 ºC prior to further analysis [16].

Antioxidant activity

The antioxidant activity of extracts from single and co-cultures were evaluated by using 2,2-diphenyl-1-picrylhydrazyl (DPPH) (Sigma-Aldrich, Malaysia) *in vitro* assay. The free radical scavenging activity of each sample was determined by measuring the changes of

absorbance colour from violet of DPPH into yellow by using microplate spectrophotometer (Thermo, United States) at 520 nm [18]. 50% of inhibition concentration (IC_{50}) value was defined as the concentration of the sample that scavenged 50% of DPPH radical.

5 mg/mL of extracts obtained from malt agar culture and 10 mg/mL of extract from rice culture were dissolved in dimethyl sulfoxide (DMSO) with 2-fold serial dilution method to give eight concentration values of 0 mg/mL to 5 mg/mL and 0 mg/mL to 10 mg/mL, respectively. Quercetin was used as a positive control and DMSO was used as the negative control. 4.73 mg of DPPH powder was dissolved in 200 mL of methanol (Merck, Germany), transferred into 500 mL of Schott Duran bottle and covered with aluminium foil. 20 µL of each concentration was pipetted into respective wells of the 96-well plate. 200 µL of DPPH solution was then added to each well containing extract and incubated for 30 min in dark at room temperature. The absorbance was measured by using a microplate spectrophotometer (Thermo, United States) at 520 nm. All determinations were performed in triplicate to obtain a mean value and the radical scavenging activity was calculated by using the following formula:

$$\text{DPPH scavenging effect (\%)} = ((A_0 - A_1) / A_0) \times 100 \quad (1)$$

Where as A_0 = the absorbance of the control, and A_1 = the absorbance of the extract mixed by DPPH

The half percentage of inhibition samples concentration (IC_{50}) was determined from the linear regression curve.

Antibacterial activity

The antibacterial activity of extracts from single and co-cultures used the disk-diffusion method [19]. Three Gram-positive strains – *Micrococcus* sp., *Staphylococcus aureus*, and *Bacillus cereus*, and three Gram-negative bacteria – *Salmonella* sp., *Escherichia coli* and *Vibrio parahaemolyticus* were obtained from Institute of Marine Biotechnology, UMT. 28 g of nutrient agar (Oxoid, Malaysia) /1 L, 55.1 g of marine agar (Difco, Malaysia) /1 L and 35 g of Mueller-Hinton agar (Merck, Germany) /1 L of milli-Q, stirred until homogenised and autoclaved. Each extract was prepared with 2-fold dilution to give eight concentration values of 0 mg/mL to 10 mg/mL in DMSO. Then, 20 µL of extract was loaded onto Whatman paper AA disks (Whatman, China).

Each bacterium strain was streaked on nutrient and marine agar plates, incubated at 37 °C for 24 h. After 24 h, 2 mL of sterile milli-Q water was transferred into McFarland tube and bacteria strains were added. Optical density (OD) (BioMērieux, France) was adjusted at 0.5 MFU (McFarland Unit) and 100 µL of bacterial inoculum was uniformLy spread by using sterile cotton swab onto Mueller-Hinton agar plates. The Whatman paper AA disks (Whatman, China) containing samples were placed inverted onto agar plates (3 replicates) and incubated at 37 °C for 24 h. 30 µg oxytetracycline, 10 µg ampicillin, 10 unit penicillin and 10 µg gentamycin antibiotic disks (Oxoid, United State) were used as positive control, and DMSO as negative control. For initial screening, 10 mg/mL of extract was tested on the Gram-positive and Gram-negative bacteria strains in order to observe the presence of inhibition growth zone between the extracts and bacteria.

After 24 h of incubation, inhibition zone diameter (IZD) around the Whatman paper AA disks (Whatman, China) containing extract was observed. The IZD was measured and expressed in millimetre (mm), and minimum inhibitory concentration (MIC) was taken as the lowest concentration of the extracts that inhibited the visible growth of bacteria after overnight incubation.

HRESI-LCMS analysis and data processing

1 mg of each extract was dissolved in 1 mL of methanol prior to analysis by using Accela high performance liquid chromatography (HPLC) (Thermo Scientific, UK) coupled with a 280 nm and 360 nm UV detector and an Exactive-Orbitrap high-resolution mass spectrometer (Thermo Scientific, UK) including a methanol blank. The column size used was HiCrom, ACE (Berkshire, UK) C_{18}, of 75 mm x 3.0 mm, 5 µm.

The mobile phase used was micropore water (A) and acetonitrile (B) with 0.1% formic acid at a flow rate of 300 µL/min was applied linearly. The gradient program started at 10% B and linearly increased to 100% B within 30 min and remained isocratic for 5 min before linearly decreasing back to 10% B in 1 min. The column was then reequilibrate with 10% B for 9 min before the next injection. The total analysis time was 45 min for each sample. The injection volume was 10 µL with tray temperature maintained at 12 ºC. High-resolution mass spectroscopy was carried in both positive and negative ESI ionisation switch modes with a spray voltage of 4.5 kV. The capillary temperature was set at 320 ºC with mass range from *m/z* 150 – *m/z* 1500 for ESI-MS range. HRESI-LCMS was used to conduct the dereplication study on the extracts, then data processed with MZmine 2.40.1 software, an in-house macro coupled with the Dictionary of Natural Product (DNP) 2015 and SIMCA P+ 15.0 (Umetrics AB, Umeå, Sweden). The mass spectral data was processed by using the procedure by MacIntyre et al., which was established in the Natural Products Metabolomics Group Laboratory at Strathclyde Institute of Pharmacy and Biomedical Sciences (SIPBS) as described here [16, 17]. The LC-MS chromatograms and spectra were viewed by using MZmine 2.40.1. Raw data were initially sliced into negative and positive data sets utilising the MassConvert software package from ProteoWizard (pwiz).

Results and Discussions

Extract yields of *Fusarium* sp. and *Curvularia* sp.

Daily monitoring of *Curvularia* sp. resulted in black colour of mycelia and grew all over the plate by day 9. Meanwhile, *Fusarium* sp. had yellow and slightly pink colour and occupied the whole plate by day 8. In a co-culture, *Fusarium* sp. ramified faster than *Curvularia* sp. as shown in Figure 1. Previous study reported that the fungi contained a variety of bioactive compounds with unique structures including benzopyranones, alkaloids, flavonoids, chinones, quinones, phenolic acids, terpenoids, steroids, xanthones, tetralones, and others. The bioactive metabolites are commonly used as antibiotics, agrochemicals, antiparasitics, immunosuppressants, anticancer and antioxidants agents [3]. The extract from single culture of *Fusarium* sp. 30 days (F30) from rice medium gave the highest extract yield with 204.76±12.6 mg (Table 1). Meanwhile, the extract yield from co-culture also increased from day 7 (FC7 = 151.23±17.4 mg) to 189 mg for day 15 and day 30 (FC15 & FC30 extracts). The use of sterile rice as an alternative substrate promoted a better amount of fungus mycelial that led to the production of higher yield of extract that could be used in pharmacological purposes and other applications as compared to inoculation on agar plates.

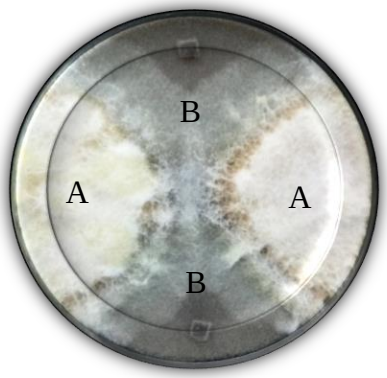


Figure 1. The co-culture between *Fusarium* sp. (A) and *Curvularia* sp. (B) on malt agar plate after 21 incubation days

Antioxidant activity

The scavenging activity of the extracts that were obtained from both media showed a significant activiy (Table 1). Extracts from malt agar plates showed a potent activity with IC_{50} values of 0.6 mg/mL – 2.4 mg/mL. While, the activity of extracts from single culture day 7 of *Fusarium* sp. and *Curvularia* sp. was also observed; MAF7 (IC_{50} = 1.7 mg/mL) and MAC7 (IC_{50} = 0.85 mg/mL), respectively. However, the extracts from agar culture that were incubated between day 15 and day 30 decreased in activity. Interestingly, the activity of extracts from co-culture grown on agar plates increased as compared to their single culture's extract. The co-culture between two or more fungi in a confined vessel promoted the competition of nutrients and space, thus triggering the production of metabolites that may responsible in increased activity. Therefore, a co-culture between *Fusarium* sp. and *Curvularia* sp. in a larger volume was introduced in this study. The use of rice as an alternative substrate gave essential nutrient for

the growth of fungi, besides it is more economic to produce better amount of extract that may have the same metabolites with similar biological activities to the extract that obtained from malt agar culture. Amongst the co-culture extracts, culture of FC15 grown on day 15 possessed in enhanced scavenging activity with IC_{50} value of 2.8 mg/mL as compared to FC7 (IC_{50} = 4.1 mg/mL) and FC30 (IC_{50} = 4.8 mg/mL). The endophytic fungi were reported possessing bioactive compounds including phenols, in which the hydroxyl groups have a potent antioxidant activity. The phenolic group is very active agent in DPPH solution because the bond dissociation energy in O-H is lower, thus it is easier to lose H atom [34]. A study on *Curvularia* sp. reported that various functional groups such as aromatic, carboxylic acid [35], phenol, ester and ketone were identified [36].

Table 1. Yield and antioxidant activity of extract at 50% of inhibition concentration value (mg/mL)

Substrate	Extracts	Extract yield (mg)	IC_{50} (mg/mL)
Malt agar medium	***Fusarium* sp.**		
	MAF7	4.08±0.4	1.7
	MAF15	11.19±1.1	2.4
	MAF30	13.53±1.2	2.4
	***Curvularia* sp.**		
	MAC7	6.63±0.2	0.85
	MAC15	7.06±0.5	0.9
	MAC30	8.4±0.3	1.0
	Co-culture		
	MAFC7	6.4±0.2	0.6
	MAFC15	4.03±0.2	0.8
	MAFC30	7.00±0.2	0.9
Rice medium	***Fusarium* sp.**	**Extract yield (mg)**	**IC_{50} (mg/mL)**
	F7	143.2±4.7	9.2
	F15	201.8±43.8	4.6
	F30	204.76±12.6	8.2
	***Curvularia* sp.**		
	C7	98.03±12.9	3.0
	C15	134.50±9.1	3.0
	C30	170.13±9.6	1.1
	Co-culture		
	FC7	151.23±17.4	4.1
	FC15	189.16±9.1	2.8
	FC30	189.45±14.5	4.8
Quercetin			0.3

*Legend: MA = malt agar; F7 = extract from single culture *Fusarium* sp. day 7; F15 = extract from single culture *Fusarium* sp. 15 days; F30 = extract from single culture *Fusarium* sp. 30 days; C7 = extract from single culture *Curvularia* sp. day 7; C15 = extract from single culture *Curvularia* sp. 15 days; C30 = extract from single culture *Curvularia* sp. 30 days; FC7 = extract from co-culture between *Fusarium* sp. and *Curvularia* sp. day 7; FC15 = extract from co-culture between *Fusarium* sp. and *Curvularia* sp. 15 days (FC15); FC30 = extract from co-culture between *Fusarium* sp. and *Curvularia* sp. 30 days. The data were expressed as mean ±SD (n=3).

Antibacterial activity

The antibacterial activity of the extracts showed more selectivity towards the Gram-positive bacteria with MIC values of 0.156 mg/mL – 10 mg/mL (Table 2), however, no activity was observed against the Gram-negative bacteria, except on *Salmonella* sp. Amongst the extracts, extracts from agar plate showed a potent activity as compared to the extracts from rice medium, except extracts from single culture of *Curvularia* sp. day 7 (C7) and day 15 (C15) also inhibited the growth of *Salmonella* sp. with MIC values of 5.0 mg/mL. The antibacterial results showed there was a significant loss of biaoactivity in the extracts grown in rice medium as compared to extracts from rice culture. Althought, the ability of the extracts to inhibit more specific activity on the bacteria used in this study, cultivation of the fungi on agar plate also can be optimised in rice medium for their mass production purposes by monitoring the diversity of chemical profiles in the extracts.

Dereplication study on extracts

Amongst the the extracts, extracts from a co-culture between *Fusarium* sp. and *Curvularia* sp. day 15 (FC15) in rice as a substrate was the optimum condition for mass production of their bioactive metabolites in these two fungi. The other parameters that have to be considered were shorter period and yield of the extract in order to have an adequate starting material for further isolation work. Dereplication studies on HRESI-LCMS data coupled with multivariate analysis on the extracts were evaluated that correlated with their bioactivities. Further investigation on FC15 extract was carried out by observing the occurrence of the metabolites in total ion chromatogram (Figure 2A). Distribution of the known and unknown compounds (highlighted rows) in the FC15 extract (Table 3) was dereplicated and putatively identified by using Dictionary of Natural Product (DNP) database. The FC15 extract possessed microlides, cyclic peptides and polyketides compounds that were putatively identified as 24-demethyl bafilomycin C1, cyclosporine C and monocerin, respectively, earlier were isolated from *Streptomyces* sp. and fungi [20].

A PCA model (Figure 2B) was also used to examine the variation and the diversity of the various extracts. However, the PCA model gave a low predictability score with Q^2 = 0.276. No significant variation can differentiate the extracts. Thus, the differences between the extracts were visualised by a supervised model. The supervised OPLS-DA (Figure 2C) scores scatter plot showed the difference between the most antioxidant active extract (colored violet) of *Fusarium* sp. (FC15), and other extracts (colored blue) that have moderate activity (FC7, FC30, C7, C15, and C30). Meanwhile, from the S-loadings (Figure 2D) scatter plot, metabolites can be predicted to be responsible for the most active group and be targeted for mass production prior to isolation work. From FC15 extract, the metabolite at *m/z* 276.159 $[M+H]^+$ was putatively identified as annotine that previously has been isolated from *Lycopodium annotinum* [24]. While, the ion peak at *m/z* 367.124 $[M+H]^+$ matched with 3-O-α-L-rhamnopyranosyl-D-galactose; 2-ac earlier reported from bacterial cell wall polysaccharides, and the ion peak at *m/z* 515.3331 $[M+H]^+$ was putatively identified as serratamolide A, that previously were isolated from bacteria *Serratia marcescens* [25]. The ion peak at *m/z* $[M+H]^+$ 309.132 was putatively identified as monocerin, that has been isolated from *Helminthosporium monoceras*, *Fusarium larvarum* and *Exserohilum rostratum* [26]. Other metabolites were also observed at *m/z* 213.112 $[M+H]^+$ and $[M-H]^-$ 257.045 that were putatively identified as canadensolide; 1',3β-Dihydro and simonyellin; 5-Deoxy, respectively, earlier were isolated from *Penicillium* sp. [27]. The ion peaks at *m/z* 243.050 $[M+H]^+$ and 301.075 $[M-H]^-$ were putatively identified as 3,4,5-trihydroxy-1,2-benzenedicarboxylic acid; 3,5-di-me ether and 1-deoxyxylitol; D-form, 2,4-methylene, 5-tosyl, respectively. While, the *m/z* $[M+H]^+$ 226.071, 241.143, 276.195 and $[M-H]^-$ 265.111, 595.359 were putatively identified as serine; (R)-form, N-(2-hydroxybenzoyl), armillariol C, 6-[2-(1-Hydroxybutyl)-4-methylphenyl]-5-hexenamide; (E)-form, vasconine and thiomarinol H, respectively. These metabolties have been isolated from *Actinomadura madurae* IFM 0745, *Armillaria* sp. strain 488, *Streptomyces* X537 [21], *Narcissus vasconicus* [28] and *Pseudoalteromonas* sp. SANK73390 [29], respectively. Other ion peaks in the FC15 extract have been dereplicated as presented in Table 3. Five discriminationg metabolites were also observed at *m/z* $[M+H]^+$ 369.131, 309.110 and *m/z* [M-

H]$^-$ 307.113, 593.343, 181.094, which did not find any match from the database.

Table 2. Antibacterial activity of extracts at minimum inhibition concentration (MIC) values (mg/mL)

		Gram positive bacteria			**Gram negative bacteria**		
Substrate	**Extracts**	***Micrococcus* sp.**	***S. aureus***	***B. cereus***	***Salmonella* sp.**	***E. coli***	***V. parahaemolyticus***
Malt agar medium	***Fusarium* sp.**	**Minimum Inhibitory Concentration (MIC) (mg/mL)**					
	MAF7	n.d	n.d	n.d	n.d	n.d	n.d
	MAF15	0.156	n.d	5.0	n.d	n.d	n.d
	MAF30	n.d	n.d	5.0	n.d	n.d	n.d
	***Curvularia* sp.**						
	MAC7	2.5	5.0	5.0	n.d	n.d	n.d
	MAC15	5.0	5.0	5.0	n.d	n.d	n.d
	MAC30	5.0	2.5	10.0	5.0	n.d	n.d
	Co-culture						
	MAFC7	5.0	2.5	5.0	5.0	n.d	n.d
	MAFC15	5.0	5.0	n.d	5.0	n.d	n.d
	MAFC30	5.0	2.5	5.0	5.0	n.d	n.d
Rice medium	***Fusarium* sp.**	**Minimum Inhibitory Concentration (MIC) (mg/mL)**					
	F7	n.d	n.d	n.d	n.d	n.d	n.d
	F15	n.d	n.d	n.d	n.d	n.d	n.d
	F30	n.d	n.d	n.d	n.d	n.d	n.d
	***Curvularia* sp.**						
	C7	n.d	n.d	5.0	n.d	n.d	n.d
	C15	n.d	n.d	5.0	n.d	n.d	n.d
	C30	n.d	n.d	n.d	n.d	n.d	n.d
	Co-culture						
	FC7	n.d	n.d	n.d	n.d	n.d	n.d
	FC15	n.d	n.d	n.d	n.d	n.d	n.d
	FC30	n.d	n.d	n.d	n.d	n.d	n.d

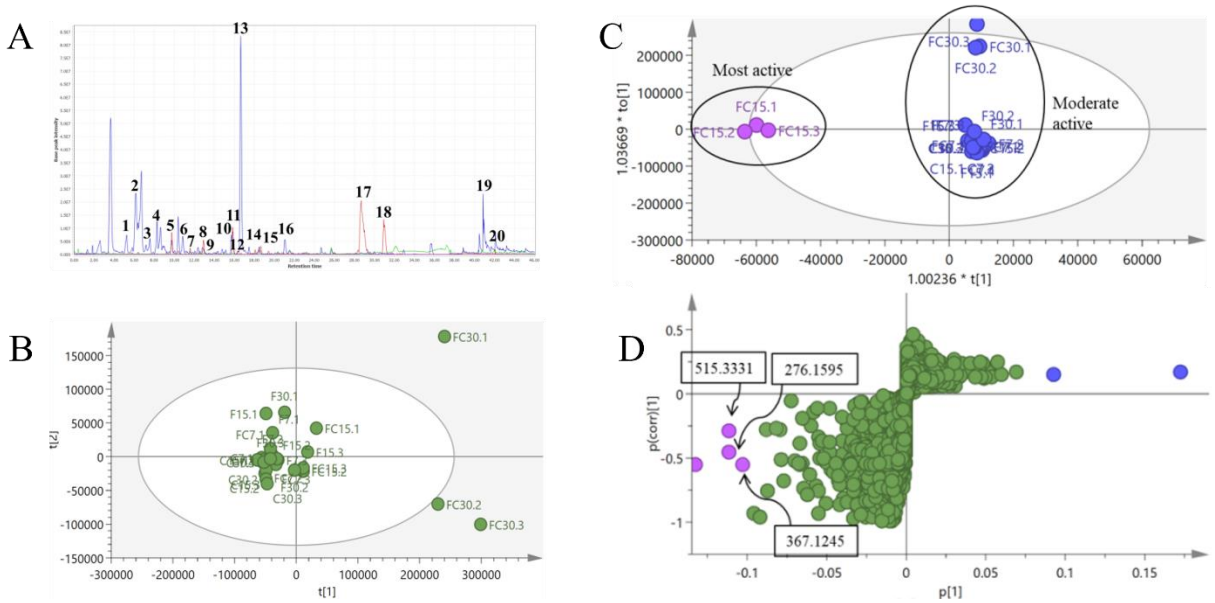


Figure 2. (A) Total ion chromatogram of co-culture extract between *Fusarium* sp. and *Curvularia* sp. FC15 (blue and red represent positive and negative ionisation modes, respectively; green and pink represent positive and negative ionisation modes of blank methanol, respectively). Dereplication of numbered peaks is shown on Table 3. (B) PCA scores scatter plot of single and co-culture extracts *($R^2(Y) = 0.72$; $Q^2 = 0.276$)* (C) OPLS-DA scores scatter plot *($R^2 = 0.951$; $Q^2 = 0.620$; Q^2(Y intercept))* from permutation test = −0.623) and (D) S-loadings plot . Legend: set F7.1-F7.3 = single culture *Fusarium* sp. incubation day 7; set F15.1-F15.3 = single culture *Fusarium* sp. incubation 15 days; set F30.1-F30.3 = single culture *Fusarium* sp. incubation 30 days; set C7.1-C7.3 = single culture *Curvularia* sp. incubation day 7; set C15.1-C15.3 = single culture *Curvularia* sp. incubation 15 days; set C30.1-C30.3 = single culture *Curvularia* sp. incubation 30 days; set FC7.1-FC7.3 = co-culture between *Fusarium* sp. and *Curvularia* sp. incubation day 7; set FC15.1-FC15.3 = co-culture between *Fusarium* sp. and *Curvularia* sp. incubation 15 days; set FC30.1-FC30.3 = co-culture between *Fusarium* sp. and *Curvularia* sp. incubation 30 days, n=3.

Table 3. List of compounds indicated on the total ion chromatogram for the extract of co-culture between *Fusarium* sp. and *Curvularia* sp. (FC15) that were putatively identified using the Dictionary of Natural Product database. Highlighted rows represent the unknown compounds as indicated with their MZmine IDs

Peak ID	ESI Modes/ MZmine ID	Rt (min)	MS (*m/z*)	Molecular Weight (g/mol)	Chemical Formula	Chemical Name	Tolerance (ppm)	Sources	Peak Area
1	P_7286	5.67	243.0500	242.0427	$C_{10}H_{10}O_7$	3,4,5-trihydroxy-1,2-benzenedicarboxylic acid; 3,5-di-me ether	0.3258		1.19E+03
2	P_8297	7.52	226.0711	225.0638	$C_{10}H_{11}NO_5$	serine; (R)-form, N-(2-hydroxybenzoyl)	0.3462	*Actinomadura madurae* IFM 0745	5.89E+04
3	P_7603	7.60	276.1595	275.1522	$C_{16}H_{21}NO_3$	annotine	0.1932	*Lycopodium annotinum*	1.25E+08
4	P_16421	8.94	213.1122	212.1048	$C_{11}H_{16}O_4$	canadensolide; 1',3β-dihydro	0.1758	*Penicillium canadense* *Aspergillus indicus*	2.07E+06
5	N_4	9.76	301.0758	302.0831	$C_{13}H_{18}O_6S$	1-deoxyxylitol; D-form, 2,4-methylene, 5-tosyl	2.3556		8.11E+02
6	P_15803	11.06	241.1435	240.1363	$C_{13}H_{20}O_4$	armillariol C	0.3857	*Armillaria* sp. strain 488	2.00E+04
7	N_808	11.10	307.1131	308.1204	$C_7H_{26}N_4OP_4$	No hits			2.86E+04
8	N_7080	12.51	265.1116	266.1189	$C_{17}H_{16}NO_2$	vasconine	2.8423	*Narcissus vasconicus*	2.67E+06
9	P_559	13.33	707.3983	706.3911	$C_{38}H_{58}O_{12}$	bafilomycin C1; 24-demethyl	-2.4354	*Streptomyces* sp. CS	5.19E+04
10	P_20981	15.03	369.1319	368.1246	$C_{18}H_{12}N_{10}$	No hits			1.57E+05
11	N_14832	15.74	367.1245	368.1318	$C_{14}H_{24}O_{11}$	3-O-α-L-rhamnopyranosyl-D-galactose; 2-ac	-0.1576	Bacterial cell-wall polysaccharides	9.21E+07
12	P_558	16.34	515.3331	514.3258	$C_{26}H_{46}N_2O_8$	Serratamolide A	0.7494	*Serratia marcescens*	2.25E+04
13	P_21898	14.94	309.1102	308.1029	$C_8H_{12}N_{12}S$	No hits			1.08E+03
14	N_8	18.79	257.0459	258.0532	$C_{14}H_{10}O_5$	simonyellin; 5-deoxy	1.5973	*Penicillium allii*	6.84E+04
15	P_60	18.75	1218.8435	1217.8362	$C_{62}H_{111}N_{11}O_{13}$	cyclosporin C	-0.0526	*Acremonium luzulae* *Fusarium solani*	4.02E+04
16	P_42112	22.90	276.1958	275.1886	$C_{17}H_{25}NO_2$	6-[2-(1-hydroxybutyl)-4-methylphenyl]-5-hexenamide; (E)-form	0.164	*Streptomyces* X537	7.05E+04
17	N_14830	28.67	593.3433	594.3506	$C_{34}H_{57}PS_3$	No hits			5.10E+08
18	N_14831	30.94	595.3591	596.3663	$C_{31}H_{52}N_2O_9$	thiomarinol H	-1.5705	*Pseudoalteromonas* sp. SANK73390	1.93E+08
19	P_7605	42.15	309.1329	308.1256	$C_{16}H_{20}O_6$	monocerin	-1.1412	*Helminthosporium monoceras* *Fusarium larvarum* *Exserohilum rostratum*	2.06E+08
20	N_14889	40.86	181.0946	182.1019	$C_5H_8N_8$	No hits			8.10E+05

Previous studies reported that serratamolide A possessing antimicrobial activity on the Gram-positive bacterium methicillin-resistant *Staphylococcus aureus* (MRSA) [30], while, bafilomycin C1; 24-Demethyl inhibited *Penicillium avellaneum* UC-4376 with minimal inhibitory amount at 10 µg/disc and possessed cytotoxic activity against tumour (P388) and lung cancer (A-549) cells at concentration 10^{-4} M with cell line inhibitory rate at 97.9% and 96.9%, respectively [21]. Meanwhile, compound cyclosporine C possessed a strong antifungal activity on fungi *Alternaria* sp. (MIC = 0.1 µg/mL – 0.5 µg/mL) and *Penicillium* sp. (MIC = 2.0 µg/mL - 5.0 µg/mL) [23]. Monocerin from *Fusarium* sp. possessed antioxidant activity at more than 324 µM [31] and antibacterial activity on *S. aureus* (MIC = 62.5 µg/mL) and *E. coli* (MIC = 15.62 µg/mL), while thiomarinol H also inhibited *S. aureus* [32, 33].

Conclusion

The extracts from co-culture on malt agar plate possessed a stronger antioxidant activity as compared to their independent extracts. Meanwhile, the antibacterial activity of the extracts demonstrated more selective inhibition on the Gram positive bacteria. Optimisation of the co-culture between *Fusarium* sp. and *Curvularia* sp. in sterile rice medium for up-scaling, increased the antioxidant activity in the co-culture FC15 extract as compared to other extracts. The supervised OPLS-DA scores scatter plot showed the difference in diversity of various metabolites between the most active antioxidant FC15 extract as compared to others. Therefore, the co-culture between two fungi triggers the silent gene to produce difference metabolites that absent in their independent extracts that can be further explored for pharmaceutical purposes.

Acknowledgement

We would like to thank Universiti Malaysia Terengganu for providing funding support for this project (UMT/TAPE-RG/2018/55148), Institute of Marine Biotechnology and Centre of Research and Field Service, UMT.

References

1. Cruz, J. S., da Silva, C. A., and Hamerski, L. (2020). Natural products from endophytic fungi associated with *Rubiaceae* species. *Journal of Fungi*, 6(3): 128.
2. Farhat, H., Urooj, F., Tariq, A., Sultana, V., Ansari, M., Ahmad, V. U., and Ehteshamul-Haque, S. (2019). Evaluation of antimicrobial potential of endophytic fungi associated with healthy plants and characterization of compounds produced by endophytic *Cephalosporium* and *Fusarium solani*. *Biocatalysis and Agricultural Biotechnology*, 18: 101043.
3. Basheer, M., Mekawey, A., Kafrawy, S., and Abouzeid, M. (2018). Antimicrobial activities of endophytic fungi of red sea aquatic plant *Avicennia marina*. *Egyptian Journal of Microbiology*, 53(1): 231-240..
4. Zheng, R., Li, S., Zhang, X., and Zhao, C. (2021). Biological activities of some new secondary metabolites isolated from endophytic fungi: A review study. *International Journal of Molecular Sciences*, 22: 959.
5. Tadpetch, K., Chukong, C., Jeanmard, L., Thiraporn, A., Rukachaisirikul, V., Phongpaichit, S., and Sakayaroj, J. (2015). Cytotoxic naphthoquinone and a new succinate ester from the soil fungus *Fusarium solani* PSU-RSPG227. *Phytochemistry Letters*, 11: 106-110.
6. Li, M., Yu, R., Bai, X., Wang, H., and Zhang, H. (2020). *Fusarium* : A treasure trove of bioactive secondary metabolites. *Natural Product Reports*, 37: 905-923.
7. Khiralla, A., Spina, R., Saliba, S., and Laurain-Mattar, D. (2019). Diversity of natural products of the genera *Curvularia* and *Bipolaris*. *Fungal Biology Reviews*, 33(2): 101-122.
8. Srivastava, A. K., Singh Kapkoti, D., Gupta, M., Rout, P. K., Singh Bhakuni, R., and Samad, A. (2021). Enhanced production of phytotoxic polyketides isolated from *Curvularia lunata* by applying chemical stresses. *Industrial Crops and Products*, 160: 113156.
9. Kaaniche, F., Hamed, A., Abdel-Razek, A., Wibberg, D., Abdissa, N., Zendah el Euch, I., and Sewald, N. (2019). Bioactive secondary metabolites from new endophytic fungus *Curvularia* sp. isolated from *Rauwolfia macrophylla*. *PLoS ONE*, 14(6): e0217627.

10. Wakefield, J., Hassan, H. M., Jaspars, M., Ebel, R., and Rateb, M. E. (2017). Dual induction of new microbial secondary metabolites by fungal bacterial co-cultivation. *Frontiers in Microbiology*, 8: 1284.
11. Vinale, F., Nicoletti, R., Borrelli, F., Mangoni, A., Parisi, O. A., Marra, R., Lombardi, N., Lacatena, F., Grauso, L., Finizio, S., Lorito, M., and Woo, S. L. (2017). Co-culture of plant beneficial microbes as source of bioactive metabolites. *Scientifc Reports*, 7(1): 14330.
12. Caudal, F., Tapissier-Bontemps, N., and Edrada-Ebel, R. (2022). Impact of co-culture on the metabolism of marine microorganisms. *Marine Drugs*, 20: 153.
13. Chagas, F. O., and Pupo, M. T. (2018). Chemical interaction of endophytic fungi and actinobacteria from *Lychnophora ericoides* in co-cultures. *Microbiology Research*, 212-213: 10-16.
14. Li, X., Zhang, X., Ye, L., Kang, Z., Jia, D., Yang, L., and Zhang, B. (2019). LC-MS-Based metabolomic approach revealed the significantly different metabolic profiles of five commercial truffle species. *Frontier Microbiology*, 10: 2227.
15. Nagarajan, K., Ibrahim, B., Ahmad Bawadikji, A., Lim, J. W., Tong, W. Y., Leong, C. R., Khaw, K. Y., and Tan, W. N. (2021). Recent developments in metabolomics studies of endophytic fungi. *Journal Fungi (Basel)*, 8(1): 28.
16. Mazlan, N. W., R. Tate, Y. M. Yusoff, , C. Clements and R. Edrada-Ebel (2019). Metabolomics-guided isolation of anti-trypanosomal compounds from endophytic fungi of the mangrove plant *Avicennia Lanata*. *Current Medicinal Chemistry*, 27(11): 1815-1835.
17. Macintyre, L., Zhang, T., Viegelmann, C., Juarez Martinez, I., Cheng, C., Dowdells, C., Abde mohsen, U. R., Gernert, C., Hentschel, U., and Edrada-Ebel, R. (2014). Metabolomic tools for secondary metabolite discovery from marine microbial symbionts. *Marine Drugs*, 12(6), 3416-3448.
18. Wright, G. D. (2019). Unlocking the potential of natural products in drug discovery. *Microbiology Biotechnology*, 12(1): 55-57.
19. Marcellano, J., Collanto, A., and Fuentes, R. (2017). Antibacterial activity of endophytic fungi isolated from the bark of *Cinnamomum mercadoi*. *Pharmacognosy Journal*, 9: 405-409.
20. Li, J., Lu, C., and Shen, Y. (2010). Macrolides of the bafilomycin family produced by *Streptomyces* sp. CS. *The Journal of Antibiotics*, 63(10): 595-599.
21. Lu, C., and Shen, Y. (2004). Two new macrolides produced by *Streptomyces* sp. CS. *Journal of Antibiotics (Tokyo)*, 57(9): 597-600.
22. Sugiura, Y., Sugita-Konishi, Y., Kumagai, S., and Reiss, E. (2003). Experimental murine hyalohyphomycosis with soil-derived isolates of *Fusarium solani*. *Medical mycology: Official publication of the International Society for Human and Animal Mycology*, 41: 241-247.
23. Moussaïf, M., Jacques, P., Schaarwächter, P., Budzikiewicz, H., and Thonart, P. (1997). Cyclosporin C is the main antifungal compound produced by *Acremonium luzulae*. *Applied and Environmental Microbiology*, 63: 1739-1743.
24. Halldórsdóttir, E., Jaroszewski, J., and Olafsdottir, E. (2009). Acetylcholinesterase inhibitory activity of lycopodane-type alkaloids from the icelandic *Lycopodium annotinum* spp. *alpestre*. *Phytochemistry*, 71: 149-157.
25. Zhu, L., Pang, C., Chen, L., and Zhu, X. (2018). Antibacterial activity of a novel depsipeptide and prodigiosine of *Serratia marcescans* S823. *Natural Products Chemistry & Research*, 6(2): 312.
26. Savi, D., Noriler, S., Ponomareva, L., Thorson, J., Rohr, J., Glienke, C., and Shaaban, K. (2019). Dihydroisocoumarins produced by *Diaporthe cf. heveae* LGMF1631 inhibiting citrus pathogens. *Folia Microbiologica*, 65: 381-392.
27. Chen, M.-J., Narkunan, K., and Liu, R.-S. (1999). Total synthesis of natural bicyclic lactones (+)-dihydrocanadensolide, (±)-avenociolide, and (±)-isoavenociolide via tungsten−π-allyl complexes. *The Journal of Organic Chemistry*, 64(22): 8311-8318.
28. Bastida, J., Codina, C., Francesc, V., Rubiralta, M., Quirion, J.-C., and Weniger, B. (1992). *Narcissus* alkaloids, XIV. (+)-8-O-acetylhomolycorine and vasconine, two novel alkaloids from *Narcissus vasconicus*. *Journal of Natural Products*, 55: 122-125.

29. Li, B., Wever, W., Walsh, C., and Bowers, A. (2014). Dithiolopyrrolones: Biosynthesis, synthesis, and activity of a unique class of disulfide-containing antibiotics. *Natural Product Reports*, 31(7): 905-923.
30. Clements, T., Ndlovu, T., and Khan, W. (2019). Broad-spectrum antimicrobial activity of secondary metabolites produced by *Serratia marcescens* strains. *Microbiological Research*, 229: 126329.
31. Tianpanich, K., Prachya, S., Wiyakrutta, S., Mahidol, C., Ruchirawat, S., and Kittakoop, P. (2010). Radical scavenging and antioxidant activities of isocoumarins and a phthalide from the endophytic fungus *Colletotrichum* sp. *Journal of Natural Products*, 74: 79-81.
32. Marion, O., Gao, X., Marcus, S., and Hall, D. (2008). Synthesis and preliminary antibacterial evaluation of simplified thiomarinol analogs. *Bioorganic & medicinal chemistry*, 17: 1006-1017.
33. Pinheiro, E., Pina, J., Feitosa, A., Carvalho, J., Borges, F., Marinho, P., and Marinho, A. (2017). Bioprospecting of antimicrobial activity of extracts of endophytic fungi from *Bauhinia guianensis*. *Revista Argentina de Microbiología*, 49(1): 3-6.
34. Quiroga, J., Romo, P. E., Ortiz, A., Isaza, J. H., Insuasty, B., Abonia, R., and Cobo, J. (2016). Synthesis, structures, electrochemical studies and antioxidant activity of 5-aryl-4-oxo-3,4,5,8-tetrahydropyrido[2,3-d]pyrimidine-7-carboxylic acids. *Journal of Molecular Structure*, 1120: 294-301.
35. Kannan, K. P., Govindasamy, R., Rajendran, R., Manoharan, S., and Dhakshinamoorthy, M. (2016). Hydrocarbons from *Curvularia lunata*-a novel promising endophytic fungi isolated from *Solanum trilobatum* linn. *International Journal of Chemistry, Pharmacy & Technology*, 1: 10-17.
36. Varma, G. B., Fatope, M. O., Marwah, R. G., Deadman, M. E., and Al-Rawahi, F. K. (2006). Production of phenylacetic acid derivatives and 4-epiradicinol in culture by *Curvularia lunata*. *Phytochemistry*, 67(17): 1925-1930.

Malaysian Journal of Analytical Sciences (MJAS)
Published by Malaysian Analytical Sciences Society

DEVELOPMENT OF A HOME-BUILT UV-VISIBLE SPECTROPHOTOMETER EMPLOYING ARDUINO MICROCONTROLLER SYSTEM FOR CHEMICAL ANALYSIS

(Pembangunan Spektrofotometer Ultraungu-Nampak Binaan Sendiri Menggunakan Sistem Pengawal Mikro Arduino untuk Analisis Bahan Kimia)

Anis Nur Shasha Abdul Halim[1], Tam Yi Qian[1], Aemi Syazwani Abdul Keyon [1,2*], and Nur Safwati Mohd Nor [3]

[1]Department of Chemistry, Faculty of Science, Universiti Teknologi Malaysia, 81310, Johor Bahru, Johor, Malaysia
[2]Centre for Sustainable Nanomaterials, Ibnu Sina Institute for Scientific and Industrial Research, Universiti Teknologi Malaysia, 81310, Johor Bahru, Johor, Malaysia
[3]Department of Applied Mechanics and Design, Faculty of Mechanical Engineering, Universiti Teknologi Malaysia, 81310 UTM, Johor Bahru, Johor, Malaysia.

[*]Corresponding author: aemi@utm.my

Received: 13 March 2023; Accepted: 22 August 2023; Published: 30 October 2023

Abstract

This work demonstrated the development and the application of a home-built spectrophotometer device employing Arduino microcontroller. Arduino UNO microcontroller was utilized as a data acquisition system. Arrangement of the system's hardware was based on the working principle of a commercially available benchtop instrument. For the first time in the scope of Arduino-based spectrophotometer, the developed device consisted of double light sources and innovative monochromator design to cater the requirement of ultraviolet (UV) and visible ranges. A visible white LED and UV LED emitting between 190 and 600 nm spectrum were employed. Light dependent resistor (LDR) and GUVA-S12SD UV sensor were utilized as light detectors. Innovative monochromator system was incorporated with combination of stepper motor and DVD disc as a diffraction grating for wavelength selection. The effectiveness of the UV range in the device was tested using bisphenol A (BPA) and triclosan, while Reactive Orange 16 and Reactive Red 120 dyes for visible range. The device could detect BPA from 10 to 50 ppm concentration (obtained through external linear graph producing R^2 = 0.9970), while triclosan from 1 to 5 ppm (R^2 = 0.9971). The limit of detection (LOD) and the limit of quantitation (LOQ) for BPA were 7.01 ppm and 23.38 ppm, respectively. The LOD and LOQ for triclosan were 0.60 ppm and 1.99 ppm, respectively. The results obtained from the device on all analytes were validated with a commercially available benchtop UV-vis spectrophotometer. The linearity of BPA from 10 to 50 ppm obtained a correlation of R^2 = 0.9941. Triclosan showed R^2 = 0.9965 for linearity from 1 to 5 ppm. The LOD and LOQ were 8.58 ppm and 28.61 ppm, respectively. The LOD and LOQ for triclosan were 0.66 ppm and 2.19 ppm respectively. As for visible range, the benchtop spectrophotometer could detect Reactive Orange 16 from 10 to 50 ppm concentration (R^2 = 0.9967) while Reactive Red 120 (R^2 = 0.9958). The LOD and LOQ for Reactive Orange 16 were 6.76 ppm and 22.52 ppm, respectively. The LOD and LOQ for Reactive Red 120 were 6.94 ppm and 23.13 ppm, respectively. Nearly identical R^2, LOD and LOQ were obtained for both home-built Arduino device and the benchtop UV-visible spectrophotometer. These data indicated positive outcomes with accuracy percentage 95% and 97.2% for BPA and triclosan, 98.6% and 93.5% for Reactive Orange 16 and Reactive Red 120 dye of the home-built Arduino spectrophotometer.

Keywords: arduino, home-built, UV-visible spectrophotometer, dye analysis, pollutant analysis

Abstrak

Kajian ini menunjukkan pembangunan dan aplikasi peranti spektrofotometer binaan sendiri yang menggunakan mikropengawal Arduino. Pengawal mikro Arduino UNO telah digunakan sebagai sistem pemerolehan data. Susunan perkakasan sistem adalah berdasarkan prinsip kerja instrumen komersil. Buat pertama kali dalam skop spektrofotometer berasaskan Arduino, peranti yang dibangunkan terdiri daripada sumber cahaya berganda dan reka bentuk monokromator yang inovatif untuk memenuhi keperluan julat ultraungu (UV) dan boleh dilihat. LED putih yang kelihatan dan LED UV yang memancarkan antara spektrum 190 dan 600 nm telah digunakan. Perintang bergantung cahaya (LDR) dan sensor UV GUVA-S12SD digunakan sebagai pengesan cahaya. Sistem monokromator yang inovatif telah digabungkan dengan gabungan motor pelangkah dan cakera DVD sebagai parut difraksi untuk pemilihan panjang gelombang. Keberkesanan julat UV dalam peranti telah diuji menggunakan bisphenol A (BPA) dan triclosan, manakala pewarna Reactive Orange 16 dan Reactive Red 120 untuk julat yang boleh dilihat. Peranti boleh mengesan BPA dari 10 hingga 50 ppm kepekatan (diperolehi melalui graf linear luaran yang menghasilkan R2 = 0.9970), manakala triclosan dari 1 hingga 5 ppm (R^2 = 0.9971). Had pengesanan (LOD) dan had kuantiti (LOQ) untuk BPA ialah 7.01 ppm dan 23.38 ppm, masing-masing. LOD dan LOQ untuk triclosan ialah 0.60 ppm dan 1.99 ppm, masing-masing. Keputusan yang diperoleh daripada peranti pada semua analit telah disahkan dengan spektrofotometer UV-vis komersil. Kelinearan BPA dari 10 hingga 50 ppm memperoleh korelasi R^2 = 0.9941. Triclosan menunjukkan R^2 = 0.9965 untuk lineariti dari 1 hingga 5 ppm. LOD dan LOQ masing-masing ialah 8.58 ppm dan 28.61 ppm. LOD dan LOQ pula untuk triclosan masing-masing adalah 0.66 ppm dan 2.19 ppm. Bagi julat yang boleh dilihat, spektrofotometer komersil boleh mengesan Jingga Reaktif 16 daripada kepekatan 10 hingga 50 ppm (R^2 = 0.9967) manakala Merah Reaktif 120 (R^2 = 0.9958). LOD dan LOQ untuk Oren Reaktif 16 masing-masing ialah 6.76 ppm dan 22.52 ppm. LOD dan LOQ untuk Reactive Red 120 ialah 6.94 ppm dan 23.13 ppm, masing-masing. R^2, LOD dan LOQ yang hampir sama diperolehi untuk kedua-dua peranti Arduino yang dibina sendiri dan spektrofotometer komersil. Data ini menunjukkan hasil positif dengan peratusan ketepatan 95% dan 97.2% untuk BPA dan triclosan, 98.6% dan 93.5% untuk Reactive Orange 16 dan Reactive Red 120 bagi pewarna spektrofotometer Arduino yang dibina sendiri.

Kata kunci: arduino, binaan sendiri, spektrofotometer UV-cahaya nampak, analisis pewarna, analisis bahan pencemar

Introduction

Water-soluble dye residues in particular from the chemically intensive textile industry's waste fluids have the potential to be a major source of environmental contamination because they can infiltrate several environmental compartments through soil, air, and water [1]. Several studies have shown that a sizeable portion (about 20%) of the dyes used in the textile industry each year, such as Rhodamine B, Victoria blue, Rose Bengal, Indigo Red, Caramine, Red 120, Eriochrome, Methylene Blue (MB), Black-T (EBT), and Thymol blue, are lost during the synthesis and processing processes and end up in wastewater [2]. Azo dyes are a common chemical pollutant found in environmental and water contamination. These dye-polluted effluents include colourful pigments that are toxic, non-biodegradable, and dangerous to living things [2; 3]. Thus, it is crucial to remove dyes from effluent due to being able to cause serious health related problems as well as disruption towards the ecosystems [4]. Azo dyes are typically used in a number of products, including textiles, paper, food or leather. One of the major classes of hazardous organic compounds, according to researchers, is made up of textile and industrial colourants. According to the World Bank, the textile finishing and dyeing sectors account for a significant portion of the 17–20% water pollution [2]. Owing to their toxicity and carcinogenicity, these compounds and their degradation products can be harmful [5]. Furthermore, several forms of dyes can have adverse effects on various organisms, including humans, and certain bacterial and mammalian assays that can be genotoxic [6].

A synthetic molecule known as bisphenol A (BPA) is often employed as a monomer, especially in the creation of epoxy resins and polycarbonate. Polycarbonates are used in a variety of products, including water bottles, baby feeding bottles, toys, cutlery, thermal paper, and medical equipment due to its ability to withstand high temperatures (up to 145 °C) [7]. There is growing evidence that certain chemicals, known as endocrine disrupting chemicals (EDCs), such as estradiol, nonylphenol, medicines, and some pesticides, can interact with endocrine systems if they are present in drinking water at a very low concentration [8]. One of the EDCs is BPA that may give potential threats to human beings, leading to hormonal complications, cancers, hypospadias, miscarriages, endometriosis, and infertility [9]. BPA can increase cellular response by interacting with

oestrogen receptors since its structure is similar to that of oestradiol and diethylstilbestrol. Moreover, research on lab animals demonstrated negative impacts on health even at low BPA dosages [7]. The quality and safety of marine products were negatively impacted by the pollutants found in the seawater and sediment columns, which would feed benthic and pelagic animals and enter the food chain. Due to its probable link to harmful health impacts like obesity, neurobehavioral issues, and reproductive and neurobehavioral issues like prostate cancer, bisphenol-A has drawn a lot of attention [10].

The broad-spectrum of the antibacterial agent triclosan is frequently found in pharmaceutical and personal care products (PPCPs). Many bacteria and fungi are fungicidal to TCS [11]. Triclosan is one of the most widely used biocides and it is frequently found in aquatic habitats. To protect against bacteria [11], Triclosan is frequently utilized in pharmaceutical and personal care products, hand soap, and wet wipes [12]. Direct contact with personal care items as well as other sources, such as food, water, and dust, can expose individuals to triclosan [13]. People can be exposed to triclosan as a result of its presence in aquatic and terrestrial areas which has occurred either directly through the use of PPCPs or indirectly through bioaccumulation [14]. Triclosan was discovered in bodily fluids such blood, breast milk, urine, and these substances affect the endocrine system and can cause hormonal abnormalities [14]. Triclosan may hinder the development of species in both terrestrial and aquatic habitats and potentially endanger the health of people who are exposed to these conditions. Broad-spectrum antibacterial activity is a property of triclosan. Triclosan has a negative impact on wastewater because activated sludge microbes are directly exposed to it, which inhibits bacterial growth, reduces bacterial diversity and abundance, and alters the composition of bacterial communities[15].

A device used for analysis called an Ultraviolet-visible (UV-Vis) light spectrophotometer examines the analyte absorbances of light, at specific wavelengths where different materials absorb and reflect these wavelengths differently [16]. For the analysis of pollutants, UV-Vis, atomic absorption spectroscopy (AAS), and tabletop devices with chromatographic bases are frequently utilized. In addition to these benchtop devices, on-site chemical analysis may save overall analysis costs because the result from on-site testing just needs to be validated by a simpler conclusive analysis. Thus, bringing heavy, complex instruments for on-site investigation is also impractical. There is a rising need for straightforward methods for on-site pollutants analysis in industrial wastes, leachates, landfills, and other sources of pollution due to ecological issues. Furthermore, a prospective complimentary element to a chemical analysis is the availability of an affordable and portable instrument to do the pollutant analysis on-site. For instance, applications for civil lawsuits and environmental monitoring both need quick decision-making. Low-cost, effective microcontrollers are employed as control-processing units in a variety of portable and handheld instruments. Amongst the most extensively used open-source microcontrollers is the Arduino. Arduino can be programmed with the measurement algorithms, calibration function, and drift corrections required for the entire instrument activity by using the numerical final result shown on a computer as input [17]. Prior to the previous 20 years, their increased application in industrial machines, cars, and domestic appliances made microcontrollers the top-selling products in the market for electronic chips despite their niche [18].

Portable devices based on the Arduino microcontroller are touted to have low manufacturing costs, simple operations, quick manufacture, and low power consumption [19]. To measure wavelengths for educational purposes, Widiatmoko and a colleague [20] constructed a spectrophotometer out of cardboard, a digital camera for the hardware, a photodiode sensor, and a microcontroller. They used image processing to acquire optical wavelengths with a theoretical resolution of up to 0.2 nm. However, Zhang et al. [21] developed a portable spectrophotometer for measuring the quality of water utilizing LEDs as the light source and photodiode sensors to detect specific wavelength peaks at 420 nm, 455 nm, 515 nm, 560 nm, 605 nm, and 630 nm. The created spectrophotometer was able to differentiate between ammonia and nitrite nitrogen contamination in lab-made water. In truth, the chemical structures of the contaminants in our environment vary greatly. This indicates that they must be detected in the UV band as

well, which is a feature that the majority of the portable photometers/spectrophotometers made at home lack.

This paper presents the development of a home-built spectrophotometer employing Arduino microcontroller for selected chemicals screening purpose. This brings to specific objectives which are to develop a home-built spectrophotometer equipped with Arduino platform as a microcontroller for automation. Next, to test the effectiveness and validate the UV detection of the home-built spectrophotometer device using BPA and triclosan. Lastly, to test the effectiveness and validate the visible detection of the home-built spectrophotometer device using Reactive orange 16 and Reactive Red 120. This study aims to develop a home-built spectrophotometer device based on spectroscopy principle. Different from other methods, the present device consisted of visible white LED and UV LED emitting between 190 and 600 nm spectrum. The developed device consisted of double light sources and innovative monochromator design to cater to the requirement of ultraviolet (UV) and visible ranges. A visible white LED and UV LED emitting between 190 and 600 nm spectrum were employed. Light dependent resistor (LDR) and GUVA-S12SD UV sensors were utilized as light detectors. An innovative monochromator system was incorporated with combination of stepper motor and DVD disc as a diffraction grating for wavelength selection. The effectiveness of the UV range in the device was tested using bisphenol A (BPA) and triclosan, while Reactive Orange 16 and Reactive Red 120 dyes were used for visible range. The wavelength will be detected by TSL1401CL from the sample, and it will give an output which will be displayed in a serial monitor. Afterwards, the results on all analytes from the device will be validated using commercially available benchtop UV-vis spectrophotometer.

Materials and Methods

Components and specifications

The arrangement of the hardware in the home-built spectrophotometer was based on the working principle of the benchtop instrument Shimadzu UV-1800 UV-Vis Spectrophotometer. There were two light sources used in this research namely white light LED with 8500K color temperature and UV LED with range from 190 to 380nm. Next, the "entrance slit" for the photometer was made with a piece of cardboard. The dispersion device or monochromator was made by assembling a cut up DVD with a 28byj-48 stepper motor which allows movement of the diffracted light. There was also an Edmund Optics achromatic lens that corrected chromatic distortion. Two pieces of slits with the same length were placed side by side. Furthermore, the sample holder (also known as cuvette) filled with sample solution followed by the detection using Light Dependent Resistor (LDR) sensor and GUVA-S12SD UV detector. These detectors were chosen due to their suitability of wavelength range for UV and visible analytes. Some of the detectors that were considered before were BPW34, ML8511 UV sensor, TSL1401 and TCS3200 color sensor. All of the detectors have different wavelength ranges for UV and visible but do not meet the criteria for developing the simple home-built spectrophotometer. An innovative monochromator system was incorporated with combination of step motor and disc as a diffraction grating for wavelength selection to complete the system. The schematic of a home-built spectrophotometer is shown in Figure 1 while the real device photograph is shown in Figure 2. The calibration on the distance between detector and sample cuvette was made and showed that 16cm gives the best reading of the detector. As the photoresistor detector converted the absorbed light into electrical current, the data can be transferred to the monitor via Arduino. The wavelengths were chosen by rotating the motor, and one specific visible wavelength band was chosen to pass through a handcrafted slit. The slit permits a restricted spectral bandwidth to exit the monochromator. This incident beamed on the sample held in the sample holder which was the source of this outgoing spectrum. The detectors will then read the absorbance of the samples and display the data on the serial monitor in the Arduino IDE software. Then, it will then be connected to Excel worksheet for further wavelength calculations. The wavelengths were calculated using Eq. 1:

$$n\lambda = d \sin\theta \quad (1)$$

where λ is the wavelength of a specific color; n = 1 (grating order); d = 740 (distance between slits in a DVD); and θ = diffraction angle.

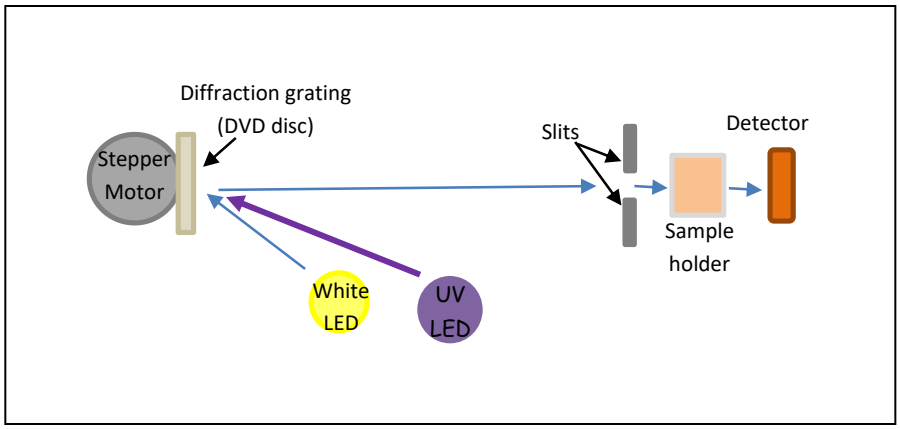


Figure 1. The schematic diagram of a portable spectrophotometer

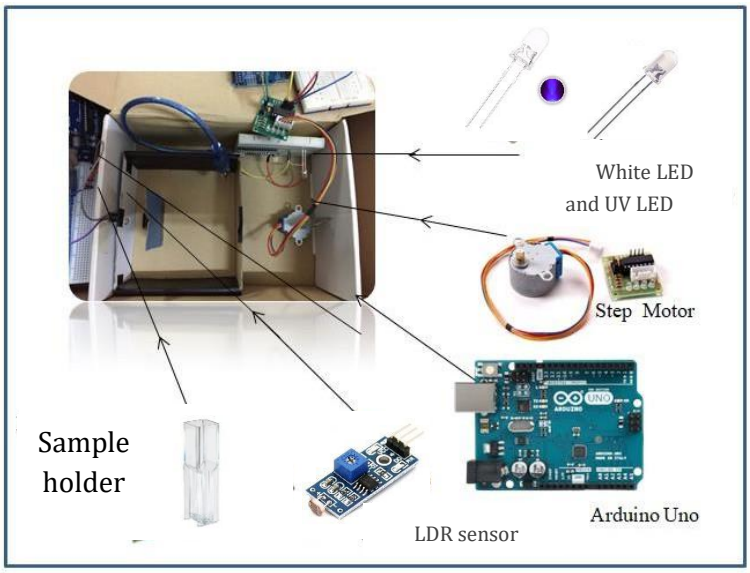


Figure 2. Portable spectrophotometer hardware arrangement

The concentration value of a chemical substance was approximately proportional to the quantity of light it absorbs when introduced to monochromatic radiation, according to Beer Lambert's law. Once the voltage readings for the light collected in the detector for the comparison and the substance being examined were gathered, the absorbance value was calculated using the following calculation in Eq.2:

$$A = \log_{10} \frac{P}{Po} = -\log_{10}(T) \qquad (2)$$

where A is absorbance; P is magnitude of transmitted light through the sample; Po is magnitude of transmitted light through the reference; and P/Po = T, which is transmittance.

Comparable to most industrial benchtop spectrophotometers, this newly built home-built Arduino spectrophotometer was small and lightweight. The home-built Arduino spectrophotometer was also very compatible with current common laboratory usage because, unlike many other home-built spectrophotometers, it can measure both UV-Vis spectrums while remaining compatible with current generic cuvettes.

Arduino programming

Arduino Uno and Arduino Nano were programmed with the system operating logic flow using the Arduino IDE 1.8.13 software as shown in Figure 3. The data of the analog transmittance signals from the UV and visible

photodetectors will transform into digital signals and can be monitored through the Arduino serial monitor.



Figure 3. Arduino sketchpad in Arduino IDE software

Experimental setup

The user can select wavelengths for the UV and visible range between 190 nm and 600 nm depending on the desired analysis. For each sample's individual spectrophotometric analysis, quartz cuvettes were employed. The cuvette was filled with a minimum of 1.5 mL of the sample solution, with the optically transparent surfaces towards the light source and detector. BPA, triclosan, Reactive orange 16 and Reactive Red 120 absorb UV and visible wavelength, peaking at 226 nm, 282 nm, 493 nm and 534 nm respectively.

Preparation for BPA sample follows the steps accordingly. Firstly, the stock solution was prepared by weighing BPA powder for 100 mg and placed in 100 mL volumetric flask. Then 5mL of 30% ethanol solution was added to dissolve the powder and filled up until it reached the mark. Then 1, 2-, 3-, 4-, and 5-mL solutions were taken into another 100 mL volumetric flask, and they were filled with 30% ethanol until the mark was reached. Thus, the concentration will be for 10, 20, 30, 40 and 50 ppm. While for triclosan sample preparation, 500 mg L^{-1} of stock solution was prepared by weighing the triclosan for 0.025 g. The triclosan was dissolved in ethanol/acetone (1:1) solution for each 10 mL. Then, it was diluted into a 50 mL volumetric flask with distilled water until it reached the mark. The stock solution was kept at -20 °C. Next, 0.02 mL of solution was taken using micropipette into a 10 mL volumetric flask. The volumetric flask was filled with distilled water until it reached the mark and labelled as 1 ppm. This step was repeated for 0.04 mL, 0.06 mL, 0.08 mL and 0.1 mL of solution respectively and the volumetric flask was labelled for 2 ppm, 3 ppm, 4 ppm and 5 ppm.

For the sample preparation of the Reactive Orange 16, a stock solution was prepared by mixing 100 mg of dry analyte in 100 mL of volumetric flask to make 1000 ppm solution. Standard working solutions which have 1, 2, 3, 4 and 5 mL accordingly of Reactive Orange 16 were made by diluting of appropriate serial dilution of the stock solution to 100 mL with distilled water. Thus, making the concentration for 10, 20, 30, 40 and 50 ppm of sample. Sample preparation for Reactive Red 120, a. stock solution was prepared by mixing 100 mg of dry analyte in 100 mL of volumetric flask to make 1000 ppm solution. Standard working solutions which have 1, 2, 3, 4 and 5 mL accordingly of Reactive Orange 16 were

made by diluting the appropriate serial dilution of the stock solution to 100 mL with distilled water. Thus, this made the concentration for 10, 20, 30, 40 and 50 ppm of sample. Measurements were taken accordingly, of all the samples data using the benchtop instrument which was the UV-Vis spectrophotometer with wavelength range from 190 nm to 600 nm. After that, the measurements of the samples were taken using the developed portable spectrophotometer device. The samples were poured in a cuvette and placed in the sample holder to record the absorbance. Table 1 included a list of the components as well as their local market prices. This spectrophotometer is estimated to cost around RM348.30 to build.

Table 1. List of components for home-built spectrophotometer

Components	**Quantity**	**Unit Price (RM)**	**Total (RM)**
Arduino Uno	1	31.90	31.90
Stepper motor and driver	1	9.50	9.50
Breadboard	1	6.80	6.80
Resistor	2	0.05	0.10
Jumper wire	1	2.50	2.50
Light Dependent Resistor	1	1.10	1.10
GUVA-S12SD UV detector	1	24.40	24.40
Push button	1	0.60	0.60
White LED	1	0.10	0.10
UV LED	1	0.30	0.30
DVD	1	1.00	1.00
Achromatic lens	1	270.00	270.00
Total cost (RM)			348.30

Results and Discussion

A home-built spectrophotometer was successfully built by equipping it with two light sources, UV and visible light detectors, and a monochromator which consisted of achromatic lens, DVD disc, and slit. The measuring method, calibration operations, and drift correction needed for the entire instrument functioning were written into the Arduino microcontroller, with the numeric result presented on screen. The data acquisition algorithm was successfully uploaded to the hardware setup of home-built spectrophotometer via the USB port. The detectors were chosen due to their suitability of wavelength range for UV and visible analytes. Some of the detectors that were considered before but not suitable due to the analyte's wavelength range were BPW34, ML8511 UV sensors and TSL1401 and TCS3200 color sensors. Calibration of the sensors were also conducted to allow the optimum detection of the sensors towards the light source, which resulted in 16 cm apart between light source and sensors to achieve the right spectrum and data reading. The difference in absorption between both devices and benchtop instruments were likely attributed to the use of different light sources, detectors and internal algorithms in the device employing Arduino microcontroller with UV-vis spectrophotometer. The Arduino microcontroller with UV-vis spectrophotometer uses were more sensitive and advanced detectors. In the device, the light source was calibrated as well as the sensors. The most accurate data obtained by the sensors was when the light source and sensors were 16 cm apart. This was demonstrated by the sensor calibration findings at various distances from the light source, which ranged from 2 cm to 22 cm with intervals of 2 cm (Figure 4). The highest reading of LDR was 16 cm, which gave the brightest spectrum detection in the home-built spectrophotometer.

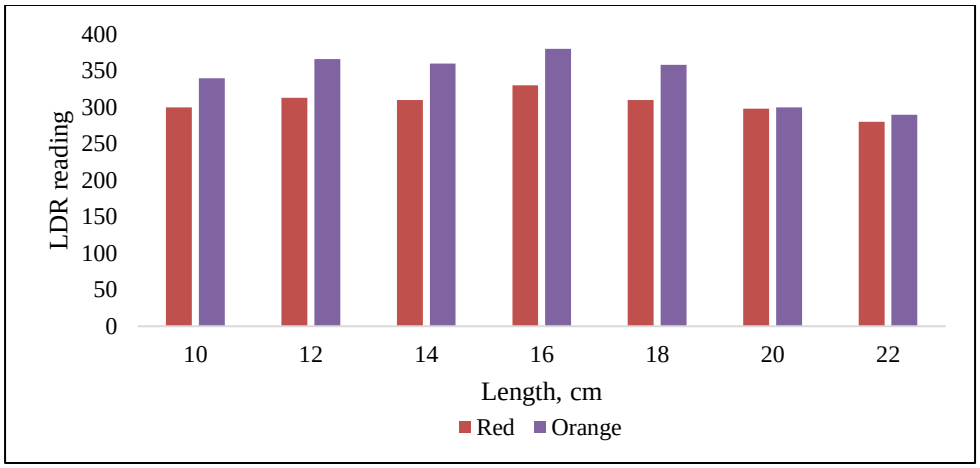


Figure 4. Calibration of different lengths between light source and sensors

To investigate whether the developed Arduino-based spectrophotometer device was functioning well, the device was applied to analyse BPA, triclosan, Reactive Orange 16 and Reactive Red 120 similar with that in benchtop UV-Visible spectrophotometer. The device could detect BPA from 10 to 50 ppm concentration (obtained through external linear graph producing R^2 = 0.9970) as shown in Figure 5a, while triclosan from 1 to 5 ppm (R^2 = 0.9971) as shown in Figure 5b. The limit of detection (LOD) and the limit of quantitation (LOQ) for BPA were 7.01 ppm and 23.38 ppm, respectively. The LOD and LOQ for triclosan were 0.60 ppm and 1.99 ppm, respectively. The results obtained from the device on all analytes were validated with a commercially available benchtop UV-vis spectrophotometer. In Figure 5c the linearity of BPA from 10 to 50 ppm obtained a correlation of R^2 = 0.9941. Triclosan showed R^2 = 0.9965 for linearity from 1 to 5 ppm as shown in Figure 5d. The LOD and LOQ were 8.58 ppm and 28.61 ppm, respectively. The LOD and LOQ for triclosan were 0.66 ppm and 2.19 ppm respectively. Different from BPA, this UV analyte triclosan, has concentration ranges 1 – 5 ppm lower than BPA due to its low concentration detection in wastewater. However, with the components used in the home-built spectrophotometer, it can only detect low concentrations starting from 1 ppm onwards.

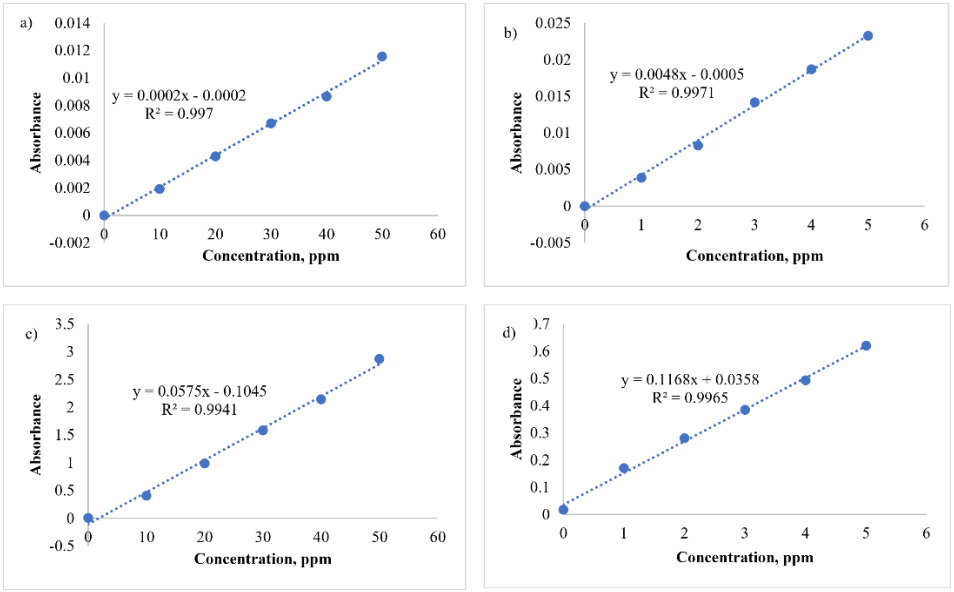


Figure 5. a) Calibration graph of BPA using the home-built spectrophotometer device b) Calibration graph of triclosan using the home-built spectrophotometer device c) Calibration graph of BPA using benchtop UV-Vis spectrophotometer d) Calibration graph of triclosan using benchtop UV-Vis spectrophotometer

As for visible range, the home-built spectrophotometer could detect Reactive Orange 16 from 10 to 50 ppm concentration (R^2 = 0.9958) as shown in Figure 6a while Reactive Red 120 (R^2 = 0.9967) in Figure 6b. The LOD and LOQ for Reactive Orange 16 were 6.76 ppm and 22.52 ppm, respectively. The LOD and LOQ for Reactive Red 120 were 6.94 ppm and 23.13 ppm, respectively. The analytes were validated with a commercially available benchtop UV-vis spectrophotometer. In Figure 6c, the linearity of Reactive Orange 16 from 10 to 50 ppm obtained a correlation of R^2 = 0.9984. Reactive Red 120 showed R^2 = 0.9974 for linearity from 10 to 50 ppm as shown in Figure 6d. The LOD and LOQ for Reactive Orange 16 were 4.43 ppm and 14.77 ppm, respectively. The LOD and LOQ for Reactive Red 120 were 3.60 ppm and 12.02 ppm respectively. As compared to the benchtop UV-Vis spectrophotometer, the home-built spectrophotometer showed lower absorbance measurement due to some factor when handling the experiment using home-built spectrophotometer. It was slightly a different spectrum color from the diffraction grating that affects the measurement.

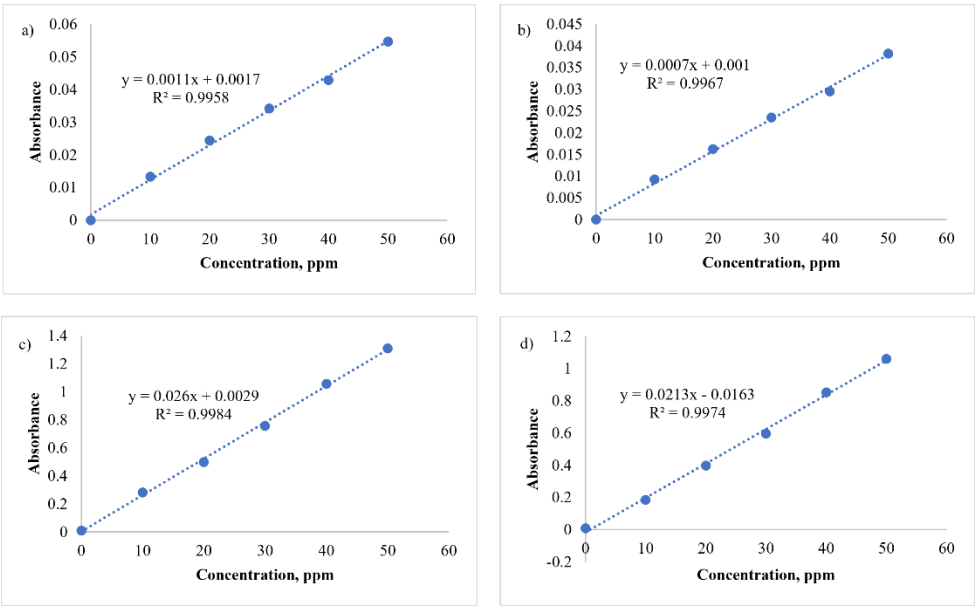


Figure 6. a) Calibration graph of Reactive Orange 16 using the home-built spectrophotometer device b) Calibration graph of Reactive Red 120 using the home-built spectrophotometer device c) Calibration graph of Reactive Orange 16 using benchtop UV-Vis spectrophotometer d) Calibration graph of Reactive Red 120 using benchtop UV-Vis spectrophotometer.

Another result that can be observed was the accuracy between the benchtop instrument and the portable Arduino device. The accuracy value was calculated using the following calculation in Eq 3:

$$y = mx + c \quad (3)$$

Nearly identical R^2, LOD and LOQ were obtained for both home-built Arduino device and the benchtop UV-visible spectrophotometer. These data indicated positive outcomes with accuracy percentage 95% and 97.2% for BPA and triclosan, 98.6% and 93.5% for Reactive Orange 16 and Reactive Red 120 dye of the home-built Arduino spectrophotometer. Comparison of the results between the benchtop instrument and home-built spectrophotometer devices showed a little difference in the accuracy percentage.

Conclusion

An automated Arduino-based semi-quantitative spectrophotometer device equipped with double light sources and innovative monochromator design for chemical analysis was developed to cater the requirement of UV and visible ranges required by a spectrophotometer for various chemical compounds. This home-built spectrophotometer device can be

further made as on-site analytical tool for dye contaminants in environment, quality control device as well as other functions in future studies. As a result, this system is reasonably priced, easy to maintain due to its small size, microcontroller-based, and amenable to further expansion for data acquisition automation via microcontroller. Other than that, this home-built spectrophotometer device development also encourages more inventions of Arduino based instrumentation for various other analytes and samples.

Acknowledgement

Aemi Syazwani Abdul Keyon is grateful for the financial support of the work by the Universiti Teknologi Malaysia via the UTMShine grant (reference number PY/2020/03555, cost centre number Q.J130000.2454.09G30). Nur Safwati Mohd Nor thanked Universiti Teknologi Malaysia via UTM Encouragement Research grant for financial support grant (cost centre number Q.J130000.3851.18J86).

References

1. Copaciu, F., Opriş, O., Coman, V., Ristoiu, D., Niinemets, Ü., and Copolovici, L. (2013). Diffuse water pollution by anthraquinone and azo dyes in environment importantly alters foliage volatiles, carotenoids and physiology in wheat *(Triticum aestivum*). *Water, Air, & Soil Pollution,* 224(3): 1-11.
2. Rafiq, A., Ikram, M., Ali, S., Niaz, F., Khan, M., Khan, Q., and Maqbool, M. (2021). Photocatalytic degradation of dyes using semiconductor photocatalysts to clean industrial water pollution. *Journal of Industrial and Engineering Chemistry,* 97: 111-128.
3. Chen, S., Zhang, J., Zhang, C., Yue, Q., Li, Y., and Li, C. (2010). Equilibrium and kinetic studies of methyl orange and methyl violet adsorption on activated carbon derived from *Phragmites australis*. *Desalination, 252*(1-3): 149-156.
4. Ray, S. C., and Jana, N. R. (2017). Application of carbon-based nanomaterials for removal of biologically toxic materials. In *Carbon Nanomaterials for Biological and Medical Applications* (pp. 43-86).
5. Perez-Urquiza, M., Ferrer, R., and Beltran, J. L. (2000). Determination of sulfonated azo dyes in river water samples by capillary zone electrophoresis. *Journal of Chromatography A,* 883: 277-283.
6. Carneiro, P. A., Umbuzeiro, G. A., Oliveira, D. P., and Zanoni, M. V. (2010). Assessment of water contamination caused by a mutagenic textile effluent/dyehouse effluent bearing disperse dyes. *Journal Hazardous Materials,* 174(1-3): 694-699.
7. Rajabnejad, S.-H., Badibostan, H., Verdian, A., Karimi, G. R., Fooladi, E., and Feizy, J. (2020). Aptasensors as promising new tools in bisphenol A detection - An invisible pollution in food and environment. *Microchemical Journal,* 155: 104722.
8. Zhang, Y., Causserand, C., Aimar, P., and Cravedi, J. P. (2006). Removal of bisphenol A by a nanofiltration membrane in view of drinking water production. *Water Research,* 40(20), 3793-3799.
9. Boas, M., Feldt-Rasmussen, U., and Main, K. M. (2012). Thyroid effects of endocrine disrupting chemicals. *Molecular Cellular Endocrinology,* 355(2): 240-248.
10. Oketola, A. A., and Fagbemigun, T. K. (2013). Determination of nonylphenol, octylphenol and bisphenol-a in water and sediments of two major rivers in Lagos, Nigeria. *Journal of Environmental Protection,* 4: 38- 45.
11. Zheng, G., Yu, B., Wang, Y., Ma, C., and Chen, T. (2020). Removal of triclosan during wastewater treatment process and sewage sludge composting-A case study in the middle reaches of the Yellow River. *Environmental International,* 134: 105300.
12. Kamińska, G., Marszałek, A., Kudlek, E., Adamczak, M., and Puszczało, E. (2022). Innovative treatment of wastewater containing of triclosan – SBR followed by ultrafiltration/adsorption/advanced oxidation processes. *Journal of Water Process Engineering,* 50: 103282.
13. Han, M., Wang, Y., Tang, C., Fang, H., Yang, D., Wu, J., and Jiang, Q. (2021). Association of triclosan and triclocarban in urine with obesity risk in Chinese school children. *Environmental International,* 157: 106846.
14. Nandikes, G., Pathak, P., Razak, A. S., Narayanamurthy, V., and Singh, L. (2022). Occurrence, environmental risks and biological remediation mechanisms of Triclosan in wastewaters: Challenges and perspectives. *Journal of Water Process Engineering, 49*: 103078.
15. Dong, X., He, Y., Peng, X., and Jia, X. (2021). Triclosan in contact with activated sludge and its

impact on phosphate removal and microbial community. *Bioresource Technology,* 319: 124134.

16. Poh, J.-J., Wu, W.-L., Goh, N. W.-J., Tan, S. M.-X., and Gan, S. K.-E. (2021). Spectrophotometer on-the-go: The development of a 2-in-1 UV–vis portable arduino-based spectrophotometer. *Sensors and Actuators A: Physical,* 325: 112698.
17. Morais, C. d. L. M. d., Carvalho, J. C., Sant'Anna, C., Eugênio, M., Gasparotto, L. H. S., and Lima, K. M. G. (2015). A low-cost microcontrolled photometer with one color recognition sensor for selective detection of Pb2+ using gold nanoparticles. *Analytical Methods,* 7(18): 7917-7922.
18. Mabbott, G. A. (2014). Teaching electronics and laboratory automation using microcontroller boards. *Journal of Chemical Education,* 91(9): 1458-1463.
19. Singh, H., Singh, G., Mahajan, D. K., Kaur, N., and Singh, N. (2020). A low-cost device for rapid 'color to concentration' quantification of cyanide in real samples using paper-based sensing chip. *Sensors and Actuators B: Chemical,* 322: 128622.
20. Widiatmoko, E., Budiman, M., and Abdullah, M. (2011). A simple spectrophotometer using common materials and a digital camera. *Physics Education,* 46(3): 332.
21. Zhang, X., Fang, Y., and Zhao, Y. (2013). A portable spectrophotometer for water quality analysis. *Sensors & Transducers,* 148(1): 47.

Malaysian Journal of Analytical Sciences (MJAS)
Published by Malaysian Analytical Sciences Society

PHOTOCATALYTIC PERFORMANCE OF MOLYBDENUM DISULPHIDE-GRAPHENE OXIDE IN PERFLUOROOCTANOIC ACID (PFOA) DEGRADATION UNDER INDOOR LIGHT EMITTING DIODE (LED) IRRADIATION

(Prestasi Fotokatalitik Molibdenum Disulfida-Grafena Oksida dalam Degradasi Asid Perfluorooktanoik (PFOA) di bawah Penyinaran Diod Pemancar Cahaya Dalaman (LED))

Zulhatiqah Zolekafeli[1], Kavirajaa Pandian Sambasevam[1,2,3], Siti Nor Atika Baharin[1,3*]

[1]Advanced Materials for Environmental Remediation (AMER), Faculty of Applied Sciences, Universiti Teknologi MARA Cawangan Negeri Sembilan Kampus Kuala Pilah, 72000 Kuala Pilah, Negeri Sembilan, Malaysia
[2]Electrochemical Material and Sensor (EMas) Group, Universiti Teknologi MARA, 40450 Shah Alam, Selangor, Malaysia
[3]Advanced Biomaterials & Carbon Development (ABCD), Universiti Teknologi MARA, 40450 Shah Alam, Selangor, Malaysia

[*]Corresponding author: atikabaharin@uitm.edu.my

Received: 30 May 2023; Accepted: 7 September 2023; Published: 30 October 2023

Abstract

In this research, molybdenum disulphide-graphene oxide (MoS_2-GO) was used as photocatalyst for the degradation of perfluorooctanoic acid (PFOA) under 12-watt light emitting diode (LED) irradiation. The photocatalyst performance was evaluated by a series of experiment; effect of contact time, trapping experiments and recyclability studies. Effect of contact time revealed MoS_2-GO degraded PFOA with 80.77% at 120 equilibrium time. Langmuir-Hinshelwood (L-H) kinetic model was applied to study the kinetic model with (R^2) of 0.8726 at half-life ($t_{1/2}$) 2.31 h under LED light irradiation. The trapping experiment shows that photocatalytic process was dominant by $\bullet O_2^-$, where $\bullet O_2^-$, supported by proton ion (h^+), is the major active species whereas •OH only played a minor part in the entire photocatalytic process. The recyclability study revealed the MoS_2-GO can be reused for up to six cycles. The employed photocatalyst in the sixth cycle was analyzed using FTIR and the FTIR spectrum shows that the peak diminishes its intensity after reusability at peaks of 1300 cm^{-1} to 1800 cm^{-1} for carbonyl (C=O), epoxy, the C=C stretching mode and carbonyl (>C=O), 750 cm^{-1} to 1250 cm^{-1} indicates the S-S bond, and at 3038 cm^{-1} that is attributed to the O-H stretching vibrations. Thus, this research proposed a performance evaluation of MoS_2-GO as photocatalyst for photocatalytic degradation of PFOA under indoor LED light irradiation.

Keywords: molybdenum disulphide, photodegradation, perfluorooctanoic acid, light emitting diode

Abstrak

Dalam penyelidikan ini, molibdenum disulfida-grafena oksida (MoS_2-GO) digunakan sebagai pemangkin foto untuk degradasi asid perfluorooktanoik (PFOA) di bawah penyinaran diod pemancar cahaya (LED) 12 watt. Prestasi pemangkin foto telah dinilai oleh satu siri eksperimen; kesan masa sentuhan, eksperimen perangkap dan kajian kitar semula. Kesan masa sentuhan mendedahkan MoS_2-GO merendahkan PFOA dengan 80.77% pada 120 masa keseimbangan. Model kinetik Langmuir-

Hinshelwood (L-H) telah digunakan untuk mengkaji model kinetik dengan (R^2) sebanyak 0.8726 pada separuh hayat ($t_{1/2}$) 2.31 h di bawah penyinaran cahaya LED. Eksperimen perangkap menunjukkan bahawa proses fotokatalitik didominasi oleh $\bullet O_2^-$, di mana $\bullet O_2^-$, disokong oleh ion proton (h^+), adalah spesies aktif utama manakala •OH hanya memainkan peranan kecil dalam keseluruhan proses fotokatalitik. Kajian kebolehkitaran semula mendedahkan MoS_2-GO boleh digunakan semula sehingga enam kitaran. Pemangkin foto yang digunakan dalam kitaran keenam telah dianalisis menggunakan FTIR dan spektrum FTIR menunjukkan bahawa puncak mengurangkan keamatannya selepas kebolehgunaan semula pada titik 1300 cm^{-1} hingga 1800 cm^{-1} untuk karbonil (C=O), epoksi, mod renggangan C=C dan karbonil (>C=O), 750 cm^{-1} hingga 1250 cm^{-1} mewakili ikatan S-S, dan di titik 3038 cm^{-1} yang mewakili ikatan renggangan O-H. Oleh itu, penyelidikan ini mencadangkan penilaian prestasi MoS_2-GO sebagai pemangkin foto untuk degradasi fotokatalitik PFOA di bawah penyinaran cahaya LED dalaman.

Kata kunci: molibdenum disulfida, fotodegradasi, asid perfluorooktanoik, diod pemancar cahaya

Introduction

Earth's surface is about 71% covered with water and over 96.5% of the Earth's water is held by oceans. In addition to these places, water may be found in air as water vapour, in water bodies such as rivers and lakes, icecaps and glaciers, Earth's soil moisture and aquifers. When harmful chemicals or microbes are released into water resources directly from industrial, commercial, or residential sources, water pollution occurs. Additionally, polluted soils can leak pollutants into streams and lead to environmental problems [2]. Therefore, non-conventional chemical emissions into water supply, surface water and drainage have resulted in significant distress.

Perfluorinated compounds (PFCs) have sparked alarm for the environment and human health because of their persistence and tendency to accumulate heavy metals. PFCs also affect hormones and induce immunotoxicity, neurotoxicity as well as developmental issues [13]. A member of PFC family, called perfluorooctanoic acid (PFOA) has raised controversy amongst the nation due to its necessity in the manufacture of Teflon, high temperature lubricants, protective coatings and surfactants [8]. Likewise, PFOA provides advantages, including improvement of stain, grease and in waterproofing. According to the US Environmental Protection Agency these pollutants are frequently found in industrial, consumer and food products. But, unlike other persistent pollutants, PFOA is easily soluble in water and readily migrated into aquifers [19]. As a result, it can bioaccumulate in the bloodstream and liver instead of fatty tissues [17].

In addition, owing to its carbon-fluorine (C-F) bond, PFOA is a remarkably stable and lasting compound which does not naturally break down. For this reason, the environment or anybody exposed to PFOA might possibly be harmed. Considering the harmful consequences that it has on the environment and to protect as well as nurture the environment for all living organisms, an innovation that can properly break down PFOA is required. The photocatalytic breakdown of PFOAs by photo-oxidative and photo-reductive degradation appears to be more suitable than the other ways outlined above. Additionally, photocatalysis oxidation has become a very promising technology due to its wide range of uses in photocatalytic process, powerful oxidising capacity, and absence of secondary pollutants. Additionally, it has advanced significantly in theory and application [7, 9, 22]. Previously, studies by Hao et al. with $BiPO_4$ photocatalyst and Sahu et al. with Ag-TiO_2 photocatalyst degraded PFOA by 72% and 57.7% when exposed to fluorescent lamp radiation for two hours and seven hours respectively. Meanwhile, Trojanowicz et al. used TiO_2 as a photocatalyst to degrade PFOA with 55.9% efficiency over the course of two hours [3, 13, 15].

Heterogeneous photocatalytic oxidation of PFOA appears as a potent, economical alternative strategy due to the ease of generating active oxygen-containing species under UV-visible irradiation, ease of photocatalyst separation and ability to recycle the catalyst. Heterostructure photocatalysts with semiconductor are employed in various fields, including electronics, catalysts, solar panels, and supercapacitor materials. According to Li et al., integrating a semiconductor with another semiconductor can enhance

light absorption and reduce photo-generated electron hole recombination [7]. Two-dimensional (2D) nanostructures have drawn attention as substitutes to photocatalytic materials in the pursuit for highly efficient photocatalytic materials due to their photocatalytic performance being driven by visible light [16]. This is because the outstanding optical and electrical features of the 2D materials demonstrate the capacity to confine electrons in their ultrathin layer. Moreover, due to their high electrochemical nature on the basal planes and edges of 2D materials in energy conversion (e.g., TMDs), well-balanced hydrogen binding Gibbs free energy on the basal sites (e.g., 1T′ MoS_2) high specific surface area, abundance of surface-active sites as well as their superior external performance, the 2D materials of MoS_2 have great structural advantages in photocatalysis [11]. Additionally, the large specific surface area of the 2D design makes surface reactions possible.

A good charge carrier for semiconductors may be found in the molecularly thick, 2D nanomaterials known as graphene, which are composed of sp2 carbon atoms that are arranged in a honeycomb structure [12]. Graphene is employed as a remarkable electron-acceptor or transport material in photocatalysis because of its capacity to decrease photogenerated electron hole recombination and increase light adsorption [6]. In addition, it has been shown that the enormous specific surface area of graphene and effective electron transport properties has made it into a fantastic co-catalyst for photocatalytic activity. [5].

While PFOA is chemically stable, photodegradation is observed to be effective when exposed to UV light. The limitations of light sources like halogen or xenon bulbs are high cost, short lifespan, poor light penetration, and low luminous efficiency. Therefore, the advantages of light emitting diode (LED) sources include the requirement for a separate water-cooling facility removal to maintain a constant temperature, flexibility of LED source placement within the designed reaction system and addition of a co-catalyst; hence, securing the enhancement of photocatalytic activity under the visible-light region. Consequently, in this work, MoS2-GO was used as a photocatalyst material to break down PFOA by using indoor LED light. As per of our knowledge, there is no attempt had been made utilizing indoor LED light as the source of light for photodegradation of PFOA.

Materials and Methods

Materials

The MoS_2-GO composites were synthesised via hydrothermal method under acidic conditions using the sodium molybdate (Na_2MoO_4) and thiourea as starting materials and successfully characterised in prior studies as outlined in literature [9].

Analytical method

The amount of PFOA in the aqueous phase was determined by using the High-Performance Liquid Chromatography (HPLC) instrument. The manual sample injector (injection volume: 20 µL), degasser, pump, and column oven (40ºC) comprised the HPLC system (Agilent 1100 series HPLC). The separating column was served by C18. The samples were isocratically eluted with acetonitrile (ACN) and aqueous NaH_2PO_4 (5 mMol, adjusted to pH 7.0) (50:50, v/v) as the eluents at a flow rate of 1.0 mL min^{-1} and 210 nm, respectively.

Contact time and kinetic study

In this work, the kinetic research of MoS_2-GO composites on the PFOA degradation was studied by using the Langmuir-Hinshelwood (L-H) kinetic model. By breaking down PFOA while being exposed to a 12-watt LED lamp's light, the MoS_2-GO photocatalytic activity was assessed. By oxidising PFOA while being illuminated by a 12-watt LED light, the MoS_2-GO photocatalytic activity was assessed. A photoreactor with several quartz tube reactors served as setting for the photocatalytic testing. In this photocatalytic experiment, 0.002 g of MoS_2-GO composite was placed in a beaker along with 20 mL of a 50 mg/L PFOA stock solution. Then, to guarantee that adsorption/desorption equilibrium was reached, the solution was stirred continuously for 30 min. At this time (t = 0), 20 mL of each solution that contained 50 mg/L (C_o) was introduced to the UV photoreactor. The mixture was subsequently centrifuged and filtered to get rid of the composite. HPLC-UV detection was used to measure

the amount of PFOA present during the photocatalytic degradation process. The C/C_o ratio was calculated by using PFOA absorption measurements for each sample, whereby C_o was the PFOA concentration at t = 0 min and C was the PFOA concentration at a specified time.

Trapping experiment

The trapping experiment was to examine the reactive species (such as h^+, •OH, e^-, and $•O_2^-$) which could be formed during photocatalysis and interact with PFOA. Trapping tests were carried out under identical experimental circumstances as those in the photodegradation experiments, with the exception that certain scavengers were introduced to the suspensions before being exposed to LED irradiation. The hydroxyl radical (•OH) scavenger was isopropanol (IPA, 1 mmol/L) [7], while the superoxide radical ($•O_2^-$) scavenger was p-benzoquinone (BQ, 0.1 mmol/L) [20].

Recyclability of the photocatalyst

Prospect of recycling and renewing the photocatalyst was examined over six cycles. After cleaning with methanol and water and drying for 12 h in a vacuum at 70˚ C, the photocatalyst was recycled. FTIR analysis was applied to check for any chemical modifications in the regenerated photocatalyst.

Results and Discussion

Photodegradation experiment: Contact time and kinetic study

To further study the impact of contact duration on the kinetic behaviour of the photodegradation process, the materials were evaluated with LED irradiation from 0 min to 120 min and in the dark for 30 min to further study the impact of contact duration on the kinetic behaviour of the photodegradation process. Figure 1 shows little deterioration in the dark area with the changing trend shown when the adsorption/desorption equilibrium was established. Between 0 and 30 minutes, there was a noticeable rapid decrease; between 60 min and 120 min, there was a gradual decline and continual stagnation. As the active sites of photocatalyst were initially unoccupied, the increase happened quickly at first. Thereafter, PFOA was instantly degraded by the photocatalysts. Most active sites were interacting, slowing the rate at which PFOA degraded since there were less opportunities for holes and electrons to join. Many research studies on heterogeneous photocatalysts in photodegradation demonstrated a finding that was consistent with the Langmuir-Hinshelwood (L-H) kinetic model for organic pollutants. (Equation 1) [9].

$$ro = -\frac{dC}{dt} = \frac{kKc}{1+Kc} \quad (1)$$

Where, *ro* is the reactant degradation rate, *k* is reaction rate constant, *K* is adsorption equilibrium constant, and *C* is reactant concentration. $Kc << 1$ in the L-H equilibrium can be simplified to a pseudo-first-order kinetic model by considering the low concentration of PFOA utilised in the experiment (Equation 2).

$$-\frac{dC}{dt} = kKc = k_{obs}C \quad (2)$$

Further set the limit of C = Go at t=0, the Equation 2 can be integrated, which resulted in Equation 3.

$$-Ln\frac{C}{C_o} = k_{obs}t \quad (3)$$

According to a plot of Ln C/Co vs irradiation time presented in Figure 1, the kinetic constants for the observed variables pseudo-first-order rate constant k, coefficient of determination R^2, and half-life $t_{1/2}$ were respectively, 0.005 min^{-1}, 0.8726, and 138.6 min. Table 1 displays the kinetic characteristics (pseudo-first order) of various photocatalyst types in the PFOA degradation. Most degrading techniques utilise the use of fluorescent, UV, visible or simulated solar radiation. By using indoor LED lighting as a source of light in the PFOA degradation process, inadequate information was found. The data revealed that PFOA was rapidly degraded under visible light without having Sb_2O_3 as the photocatalyst since Sb_2O_3/TiO_2 had a bigger k constant (0.0126 min^{-1}) and a shorter t half-life (6.612 h) than TiO_2. Further, $NaIO_4$ was shown to have better kinetic performance than Ag-TiO_2 with 0.0096 min^{-1} k constant than 0.00217 min^{-1}. While Ag-PFOA TiO_2 content was reduced by 72% under fluorescent light, $BiPO_4$ was discovered to have good degrading efficiency. Notably, kinetic results from this study showed that MoS_2-GO could break down PFOA when exposed to indoor LED light, with a 2.31-hour reduction in half of PFOA

concentration from its original concentration [1, 6, 13, 20].

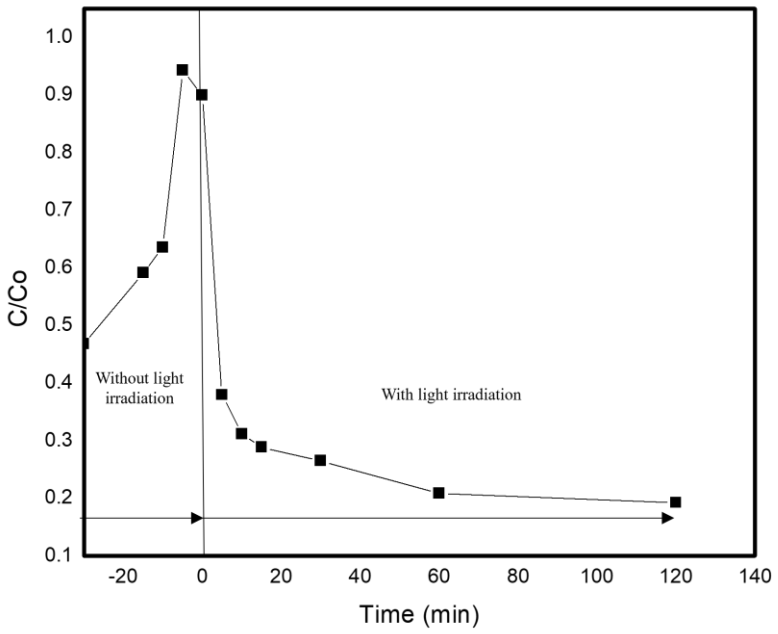


Figure 1. Effect of contact time for photocatalytic degradation of PFOA (50 mg/L PFOA, 12-watt LED light, 2 mg/L of catalyst loading)

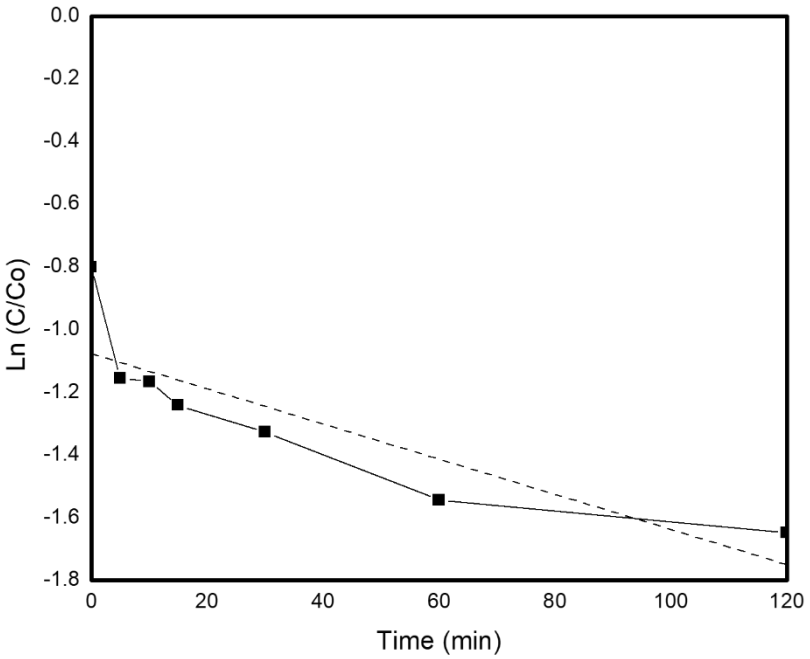


Figure 2. Kinetic plot of *Ln* (C/C_o) versus irradiation time for photocatalytic degradation of PFOA

Table 1. Kinetic parameters (pseudo-first order) of different types of photocatalyst in degrading PFOA

Type of Photocatalyst	Light Source	Contact Time (h)	Initial Concentration (mg/L)	R^2	k (min^{-1})	$t_{1/2}$ (h)	Degradation (%)	Ref.
Ag-TiO_2	Fluorescent lamp	7	60	0.7267	0.00217	Not mention	57.7	[13]
$NaIO_4$	UV	Not mention	0.004	Not mention	0.0096	Not mention	70	[16]
TiO_2	UV	2	5	Not mention	0.0063	18.78	55.9	[15]
Sb_2O_3/TiO_2	UV	2	5	Not mention	0.0126	6.612	81.7	[15]
$BiPO_4$	Fluorescent lamp	2	0.05	Not mention	0.00667	Not mention	72	[3]
MoS_2-rGO-15	Indoor fluorescent	3	50	0.972	0.0758	1.524	98	[9]
MoS_2-GO	LED irradiation	2	50	0.8726	0.005	2.31	80.77	This study

Trapping experiment

Many reactive species, including proton ion (h^+), •OH, e^-, and $•O_2^-$ may be generated during photocatalysis and may react with PFOA. Trapping investigations into the active species during the photocatalytic PFOA degradation were conducted to better understand the photocatalysis process. According to Figure 3, there was no discernible difference in the photocatalytic PFOA degradation with isopropanol (IPA, 1 mmol/L, a scavenger of •OH) as compared to without a scavenger. This suggested that •OH was not the main active component. The photodegradation was completely quenched when p-benzoquinone (BQ, 0.1 mmol/L, quencher of $•O_2^-$) was added, indicating that $•O_2^-$ was the main active species and crucial to the photocatalytic activity. It was clear from this that the important oxidative species was $•O_2^-$ produced by the interaction of photogenerated electrons and O_2, while the photogenerated h^+ also supported the absolute term for PFOA degradation in the nanohybrid composite photocatalyst system. It might be presumed that $•O_2^-$ played a significant part in the photocatalytic process based on the trapping analysis (Figure 3). These findings implied that $•O_2^-$, supported by h^+, was the major active species and the fundamental mechanism for the powerful photocatalytic activity, whereas •OH only played a minor part in the entire photocatalytic process [3, 10, 18].

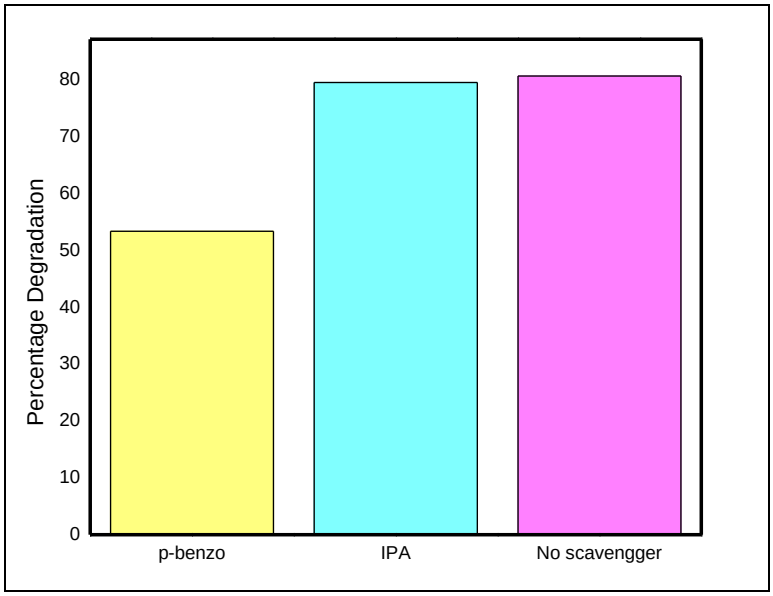


Figure 3. Trapping experiment of the active species during photocatalytic degradation of PFOA over nanocomposite alone and with the addition of BQ (quencher of $\bullet O_2^-$) and IPA (quencher of •OH) under indoor LED light irradiation

Recyclability of study

The most noteworthy aspect of photocatalytic degradation studies is a reusable, sustainable photocatalyst. After a few cycles of use, a promising photocatalyst must be able to maintain good degrading performance. The photocatalyst was cleaned with ethanol and water prior to the experiment and then dried in a vacuum for 2 h at 70 °C. Figure 4 shows that after six further experiments, the deterioration efficiency was reduced by about 30%. As a result, it was determined that the MoS_2-GO might be reused and renewed for up to six cycles. The six cycles of photocatalyst were examined by using FTIR to demonstrate the causes of MoS_2-GO's reduced degradation efficiency. According to Figure 5, the FTIR spectrum demonstrated that the peak intensity decreased after reusability due to lesser affinity as most active sites interact, reducing the production of free radicals and, consequently, the degradation process. They might be seen in the missing peaks at 1300 cm^{-1} to 1800 cm^{-1} for carbonyl (C=O), epoxy, the C=C stretching mode and carbonyl (>C=O), 750 cm^{-1} to 1250 cm^{-1} indicates the S-S bond, and at 3038 cm^{-1} is attributed to the O-H stretching vibrations that resulted from the repeated washing recyclability of the composites [14,15,21]. The recyclability of study may be extended up to seven cycles or more however, the increasing of missing peaks which indicated the availability of MoS_2-GO nanocomposites showed that the degradation process was performed by absorption of light source since the LED irradiation range was applied in a broad wavelength of 275nm to 950nm.

Conclusion

Under the 12-watt indoor LED light irradiation, GO, MoS_2, and MoS_2-GO composites were successfully fabricated, characterised and used as a catalyst for PFOA photodegradation. With increasing loading and contact duration, MoS_2-GO demonstrated the greatest PFOA degradation. The Langmuir-Hinshelwood model employed a pseudo-first order rate law to define the kinetics of PFOA photodegradation. According to the stability and reusability studies, MoS_2-GO may be used up to six times without losing its properties. The greatest degrading effectiveness of photocatalysts in PFOA had proved that MoS_2-GO was successfully used as a photocatalyst. Moreover, by adding the p-benzoquinone scavenger to MoS_2-GO composites it accelerated the breakdown of PFOA, whereby $\bullet O_2^-$ was the main active species and an important player in the photocatalytic reaction. Overall, the research findings showed that MoS_2-GO as a versatile photocatalysts that can degrade

the organic wastes by using low cost and safe indoor LED light.

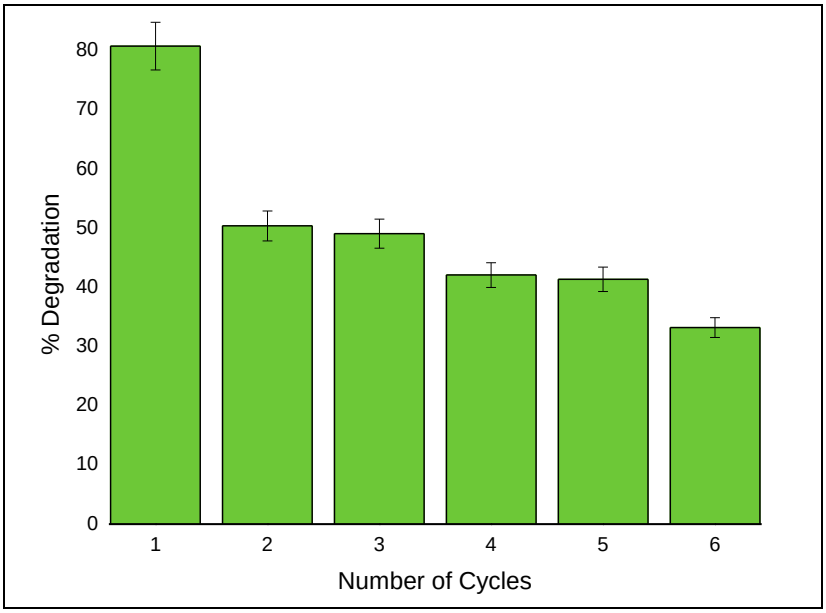


Figure 4: The recyclability study of degradation of PFOA

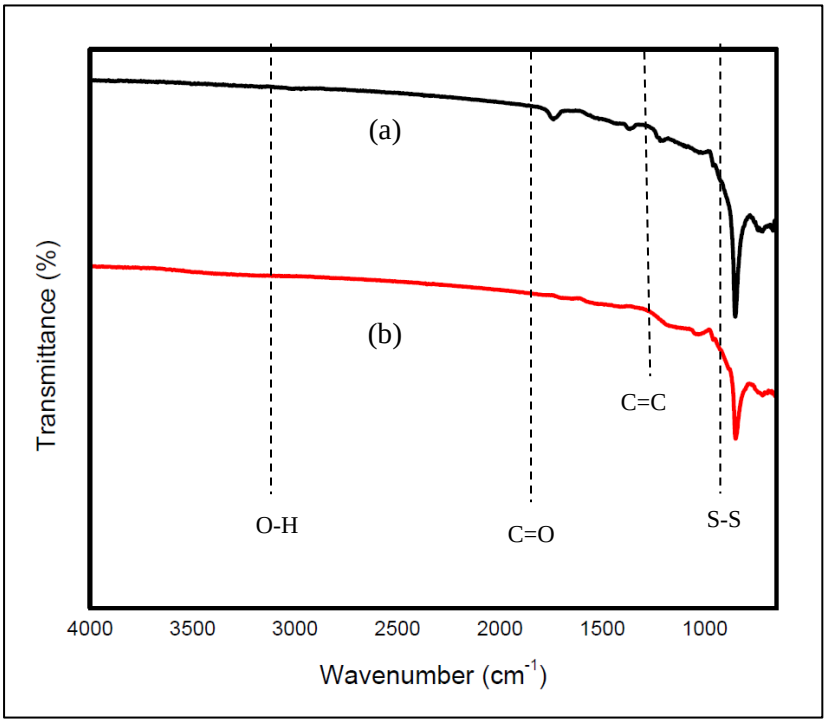


Figure 5. FTIR spectrum of (a) MoS_2-GO before and (b) MoS_2-GO after recyclability study

Acknowledgement

We acknowledge the School of Chemistry and Environment, Faculty of Applied Science UiTM Negeri Sembilan, Kuala Pilah Campus for the facilities that were provided for the research. This project was supported by financial grants such as the Fundamental Research Grant Scheme [FRGS/1/2022/STG05/UITM/02/12] by Ministry of the Higher Education Malaysia.

References

1. Cao, M. H., Wang, B. B., Yu, H. S., Wang, L. L., Yuan, S. H., and Chen, J. (2010). Photochemical decomposition of perfluorooctanoic acid in aqueous periodate with VUV and UV light irradiation. *Journal of Hazardous Materials*, 179(1-3), 1143-1146.
2. EFSA Panel on Contaminants in the Food Chain (EFSA CONTAM Panel), Schrenk, D., Bignami, M., Bodin, L., Chipman, J. K., del Mazo, J., ... and Schwerdtle, T. (2020). Risk to human health related to the presence of perfluoroalkyl substances in food. *EFSA Journal*, 18(9): e06223.
3. Hao, S., Zhao, X., Cheng, Q., Xing, Y., Ma, W., Wang, X., ... and Xu, X. (2020). A mini review of the preparation and photocatalytic properties of two-dimensional materials. *Frontiers in Chemistry*, 8: 582146.
4. Huang, Y., Kong, M., Westerman, D., Xu, E. G., Coffin, S., Cochran, K. H., ... and Dionysiou, D. D. (2018). Effects of HCO_3–on degradation of toxic contaminants of emerging concern by UV/NO_3^-. *Environmental Science & Technology*, 52(21): 12697-12707.
5. Khan, M., Assal, M. E., Tahir, M. N., Khan, M., Ashraf, M., Hatshan, M. R., ... and Adil, S. F. (2022). Graphene/inorganic nanocomposites: Evolving photocatalysts for solar energy conversion for environmental remediation. *Journal of Saudi Chemical Society*, 26(6): 101544.
6. Li, M., Yu, Z., Liu, Q., Sun, L., and Huang, W. (2016). Photocatalytic decomposition of perfluorooctanoic acid by noble metallic nanoparticles modified TiO_2. *Chemical Engineering Journal*, 286: 232-238.
7. Li, Y., Xiang, F., Lou, W., and Zhang, X. (2019). MoS_2 with structure tuned photocatalytic ability for degradation of methylene blue. In *IOP Conference Series: Earth and Environmental Science* (Vol. 300, No. 5, p. 052021). IOP Publishing.
8. Lohmann, R., Cousins, I. T., DeWitt, J. C., Gluge, J., Goldenman, G., Herzke, D., ... and Wang, Z. (2020). Are fluoropolymers really of low concern for human and environmental health and separate from other PFAS?. *Environmental Science & Technology*, 54(20): 12820-12828.
9. Norsham, I. N. M., Sambasevam, K. P., Shahabuddin, S., Jawad, A. H., and Baharin, S. N. A. (2022). Photocatalytic degradation of perfluorooctanoic acid (PFOA) via MoS_2/rGO for water purification using indoor fluorescent irradiation. *Journal of Environmental Chemical Engineering*, 10(5): 108466.
10. Olatunde, O. C., Kuvarega, A. T., and Onwudiwe, D. C. (2020). Photo enhanced degradation of polyfluoroalkyl and perfluoroalkyl substances. *Heliyon*, *6*(12): e05614.
11. Patterson, C. L., & Haught, R. C. (2021). Regulatory considerations to ensure clean and safe drinking water. In *Handbook of water purity and quality* (pp. 93-135). Academic Press.
12. Rafiei-Sarmazdeh, Z., Zahedi-Dizaji, S. M., and Kang, A. K. (2019). Two-dimensional nanomaterials. London, UK: IntechOpen.
13. Sahu, S. P., Qanbarzadeh, M., Ateia, M., Torkzadeh, H., Maroli, A. S., and Cates, E. L. (2018). Rapid degradation and mineralization of perfluorooctanoic acid by a new petitjeanite $Bi_3O(OH)(PO_4)_2$ microparticle ultraviolet photocatalyst. *Environmental Science & Technology Letters*, 5(8): 533-538.
14. Santoso, S. P., Angkawijaya, A. E., Bundjaja, V., Hsieh, C. W., Go, A. W., Yuliana, M., ... and Ismadji, S. (2021). TiO_2/guar gum hydrogel composite for adsorption and photodegradation of methylene blue. *International Journal of Biological Macromolecules*, 193: 721-733.
15. Trojanowicz, M., Bartosiewicz, I., Bojanowska-Czajka, A., Kulisa, K., Szreder, T., Bobrowski, K., ... and Kisała, J. (2019). Application of ionizing radiation in decomposition of perfluorooctanoate (PFOA) in waters. *Chemical Engineering*

Journal, 357: 698-714.

16. Wang, H., Liu, X., Niu, P., Wang, S., Shi, J., and Li, L. (2020). Porous two-dimensional materials for photocatalytic and electrocatalytic applications. *Matter*, 2(6): 1377-1413.
17. Wang, P., Liu, D., Yan, S., Cui, J., Liang, Y., and Ren, S. (2022). Adverse effects of perfluorooctane sulfonate on the liver and relevant mechanisms. *Toxics*, 10(5): 265.
18. Wen, Y., Rentería-Gómez, A., Day, G. S., Smith, M. F., Yan, T. H., Ozdemir, R. O. K., ... and Zhou, H. C. (2022). Integrated photocatalytic reduction and oxidation of perfluorooctanoic acid by metal–organic frameworks: key insights into the degradation mechanisms. *Journal of the American Chemical Society*, 144(26): 11840-11850.
19. Xu, B., Liu, S., Zhou, J. L., Zheng, C., Weifeng, J., Chen, B., ... and Qiu, W. (2021). PFAS and their substitutes in groundwater: Occurrence, transformation and remediation. *Journal of Hazardous Materials*, 412: 125159.
20. Yao, X., Zuo, J., Wang, Y. J., Song, N. N., Li, H. H., and Qiu, K. (2021). Enhanced photocatalytic degradation of perfluorooctanoic acid by mesoporous Sb_2O_3/TiO_2 heterojunctions. *Frontiers in Chemistry*, 9: 690520.
21. Ye, L., Liu, J., Jiang, Z., Peng, T., and Zan, L. (2013). Facets coupling of BiOBr-g-C_3N_4 composite photocatalyst for enhanced visible-light-driven photocatalytic activity. *Applied Catalysis B: Environmental*, 142: 1-7.
22. Zhang, F., Wang, X., Liu, H., Liu, C., Wan, Y., Long, Y., and Cai, Z. (2019). Recent advances and applications of semiconductor photocatalytic technology. *Applied Sciences*, *9*(12): 2489.

Malaysian Journal of Analytical Sciences (MJAS)
Published by Malaysian Analytical Sciences Society

EXPERIMENTAL AND THEORETICAL OPTIMIZATION OF EMULSIFICATION LIQUID-LIQUID MICROEXTRACTION FOR DETERMINATION OF HERBICIDES USING FATTY ACID DEEP EUTECTIC SOLVENTS

(Pengoptimuman Secara Eksperimen dan Teori bagi Pengemulsi Mikroekstraksi Cecair-Cecair untuk Penentuan Racun Perosak Menggunakan Pelarut Eutektik Terdalam Asid Lemak)

Nur Hidayah Sazali, Nur Amanina Ajman, Wan Nazwanie Wan Abdullah, and Nurul Yani Rahim*

School of Chemical Sciences, Universiti Sains Malaysia, 11800 USM Pulau Pinang, Malaysia

**Corresponding author: nurulyanirahim@usm.my*

Received: 20 July 2023; Accepted: 7 September 2023; Published: 30 October 2023

Abstract

Fatty acid deep eutectic solvents (DES) became known as a promising alternative to traditional organic solvents for various extraction processes. In this study, a hydrophobic DES comprising a mixture of lauric acid (C_{12}) and pelargonic acid (C_9) at a molar ratio of 1:3, was utilized to extract 2,4-D and MCPA herbicides from aqueous solutions. FTIR and TGA were utilized in order to characterize the synthesized DES. Emulsification liquid-liquid microextraction (ELLME) technique is employed to enhance the efficiency of extraction. Furthermore, response surface methodology (RSM) was applied to optimize the extraction process of these herbicides while considering parameters such as volume of DES and emulsifying agent and pH. RSM method has various advantages, including its simplicity, fast, low cost, and great extraction efficiency. It also helps in selecting the optimum condition method to analyze the relationship between the variable, where pH 2, 265 µL volume of DES and 200 µL volume of tetrahydrofuran (THF) were the optimal conditions obtained in this study. Under these conditions, the coefficients of determination (R^2) were obtained between 65% and 79%. In addition, the results obtained from the experiment are comparable to or closely aligned with RSM, hence there was a good fit between the two methods. These results revealed that the fatty acid-based DES demonstrated remarkable efficiency in extracting 2,4-D and MCPA herbicides as well as contributing to the development of environmentally friendly extraction techniques.

Keywords: response surface methodology, 2,4-Dichlorophenoxyacetic acid, 2-methyl-4-chlorophenoxyacetic acid, hydrophobic DES, emulsification liquid-liquid microextraction, pesticides

Abstrak

Pelarut eutektik terdalam asid lemak (DES) dikenali sebagai alternatif kepada pelarut organik tradisional untuk digunakan dalam pelbagai proses pengekstrakan. Dalam kajian ini, DES hidrofobik yang terdiri daripada campuran asid laurik (C_{12}) dan asid pelargonik (C_9) pada nisbah molar 1:3, telah digunakan untuk mengekstrak racun herba 2,4-D dan MCPA daripada larutan akueus. FTIR dan TGA telah digunakan untuk mengenalpasti DES yang disintesis. Teknik pengekstrakan mikro cecair-cecair pengemulsi

(ELLME) digunakan untuk meningkatkan kecekapan pengekstrakan. Tambahan pula, metodologi permukaan tindak balas (RSM) digunakan bertujuan untuk mengoptimumkan proses pengekstrakan racun herba ini dan mempertimbangkan parameter seperti isipadu DES dan agen pengemulsi dan pH. Kaedah RSM ini mempunyai pelbagai kelebihan, termasuk kesederhanaan, pantas, kos rendah, dan kecekapan pengekstrakan yang hebat. RSM juga membantu dalam memilih keadaan kaedah yang optimum untuk menganalisis hubungan antara pembolehubah, di mana pH 2, 265 µL isipadu DES dan 200 µL isipadu tetrahydrofuran (THF) adalah keadaan optimum yang diperolehi dalam kajian ini. Dengan keadaan ini, pekali penentuan (R^2) diperoleh antara 65% dan 79%. Di samping itu, keputusan yang diperoleh daripada data eksperimen adalah setanding atau sejajar rapat dengan data RSM, oleh itu terdapat kesesuaian yang baik antara kedua-dua kaedah. Keputusan ini mendedahkan bahawa DES berasaskan asid lemak menunjukkan kecekapan yang luar biasa dalam mengekstrak racun herba 2,4-D dan MCPA serta menyumbang kepada pembangunan teknik pengekstrakan mesra alam.

Kata kunci: metodologi permukaan tindak balas, 2,4-Dichlorophenoxyacetic acid, 2-methyl-4-chlorophenoxyacetic acid, DES hidrofobik, pengekstrakan mikro cecair-cecair pengemulsi, racun herba

Introduction

Providing a safe and healthy environment for everyone while concurrently reducing the hazardousness effects of current pollutants is one of the major challenges encountered by modern industry. Pesticides account for 9 of the top 12 most harmful and persistent pollutants identified by the Stockholm Convention on Persistent Organic Pollutants [1]. Herbicides, insecticides, fungicides, and other pesticides are used extensively in agriculture, and as a result, these compounds are dispersed in the environment in large quantities [2]. Therefore, the presence of pesticide residues in water, soil, and agricultural products has the potential to surpass the permitted thresholds, resulting in significant environmental contamination [2] and even human health problems [3]. Phenoxy acid herbicides are extensively employed in agricultural practices for the purpose of managing the proliferation of undesirable weeds [4]. These compounds' cost-effectiveness and high efficacy at low concentrations are widely acknowledged, albeit accompanied by potential hazards to human health [5]. Following application, these herbicides have the potential to readily infiltrate water systems as a result of their high-water solubility. They are known to have mutagenic, teratogenic, and carcinogenic properties that can lead to cytotoxicity and DNA damage after extended exposure. Detecting these substances in food and environmental samples raises significant concerns regarding their potential impact on human and animal consumption [6]. Hence, it is imperative to closely monitor the presence of these herbicides in both food and environmental samples to ensure adherence to established environmental quality standards.

Concerned with the safety of the environment and people's health, experts have been working hard to find sensitive and careful ways to test for pesticides. In order to determine these pesticides, a sample pre-treatment plays an important role during the analytical procedure. The techniques used for sample pre-treatment revolve mainly around extracting analytes from the sample matrix into a suitable solvent for the sample to be pre-concentrated and cleaned. Conventional sample pre-treatments such as liquid-liquid and solid phase extraction are commonly employed for pre-concentration of phenoxy acid herbicides [4, 6]. The use of these procedures is commonly hindered by labour and cost intensiveness, as well as the substantial consumption of toxic solvents, hence rendering these techniques incongruent with sustainable development objectives.

Microextraction techniques have emerged as a recent approach for the analysis of pesticides in environmental and food samples. These techniques have been chosen for their miniaturization, simple operation, low cost, and minimal sample and solvent consumption [3]. Solid phase micro-extraction (SPME), magnetic solid phase extraction (MSPE), emulsification liquid-liquid microextraction (ELLME), and dispersive solid phase extraction (DSPE) are the most frequently used pre-treatment methods for analysing pesticides in food samples and environmental water [7]. Out of these techniques, ELLME stands out as a widely utilized pre-treatment method for pesticide residues [7] due to its simplicity, ease of operation, rapidity, and high extraction efficiency [8]. In ELLME, sample solutions are treated with extraction solvents of high solubility

and emulsifier solvents to extract the target analytes. Among the plethora of microextraction techniques, ELLME offers several advantages, such as small amount of organic solvent consumption, time savings, and greater extraction efficiency [9].

For the development of ELLME conditions, organic solvents must be used in the determination of various types of pesticides. However, a massive number of organic solvents contribute to negative impacts on human health and the environment. The advent of green chemistry has led to the proposal of deep eutectic solvents (DES), a novel group of environmentally friendly solvents, as a potential substitute for traditional solvents, due to their green features [10]. Usually, DES is made from economical materials using simple preparation steps. It is ideal for microextraction methods due to its great thermal stability and biodegradability features. In its typical form, DES is produced by combining two substances, a hydrogen bond donor (HBD) and a hydrogen bond acceptor (HBA), which are then hydrogen-bonded to one another to produce a molecule with a low melting point [11].

Recently, researchers have proposed the utilization of hydrophobic deep eutectic solvents (DES) to extract analytes from water samples. Hydrophobic DES are formed by combining one or two hydrophobic components, resulting in DES with hydrophobic nature. Consequently, researchers have directed their attention towards the potential of hydrophobic deep eutectic solvents (DES) derived from fatty acids. Previous studies have demonstrated the efficacy of hydrophobic deep eutectic solvents (DES) as extraction media for a diverse range of analytes. Florida et al. initially reported the utilization of hydrophobic DES synthesis by combining two fatty acids, HBA and HBD, to remove bisphenol A [12]. Subsequently, DES derived from fatty acids was used for harmful industrial dye removal [13] in addition to the recognition of benzophenone and salicylate UV filters [14].

Additionally, it is crucial to optimize the extraction process in analytical methods to minimize the utilization of materials, decrease process costs, and streamline time-consuming steps. In this context, optimization studies involving chemometric modelling hold significance. Response surface methodology (RSM) is a computational approach to optimizing intricate processes [15]. The statistical technique employed in this study aims to optimize the values of a dependent variable by considering multiple independent factors. Its purpose is to facilitate a comparison between theoretical predictions and empirical observations [16]. The RSM method enables the efficient testing of all variables associated with consumer evaluation within a condensed timeframe during the optimization process. This enhances the efficiency of the laboratory testing procedure. Consequently, this leads to a decrease in expenses, utilization of resources, and the requisite number of experimental trials [11], [16]. In addition to these, using quantitative data in the context of Response Surface Methodology (RSM) enables the evaluation of relationships and interactions among multiple parameters. This facilitates the identification of the most favorable conditions in an experiment. Additionally, mitigating matrix impact and enhancing analyte extraction efficiency are supplementary benefits [11].

In light of the explanations mentioned above, this study aimed to synthesize a deep eutectic solvent composed of fatty acids, specifically lauric acid and pelargonic acid. Additionally, the fatty acids DES was analysed characterized by using thermogravimetric analysis (TGA) and Fourier transform infrared spectroscopy (FTIR). Moreover, two types of herbicides, 2,4-D and MCPA were extracted by using this DES. To achieve the best extraction effect, the application of response surface methodology (RSM) was employed to determine the optimum conditions by considering a few important variables (volume of DES, volume of emulsifier solvent, and pH).

Materials and Methods

Materials

All the pesticides used namely MCPA and 2,4-D (purity, ≥ 98.0%) were purchased from Sigma-Aldrich (St Louis, MO, USA). Lauric acid (purity ≥ 98.0%) and pelargonic acid (purity, ≥97.0%) were also supplied by Sigma-Aldrich (St Louis, MO, USA). Hydrochloric acid (37%) and acetonitrile were obtained from QRec (Auckland, New Zealand). Tetrahydrofuran (analytical

grade) was purchased from Merck (Darmstadt, Germany). The herbicide stock solutions were prepared in acetonitrile at a concentration of 1000 μg mL^{-1}. The stock solutions of each herbicide were serially diluted in acetonitrile to create working solution combinations of 10 μg mL^{-1}.

Instrumentations

The FTIR spectra were recorded using Perkin Elmer 2000 FTIR instrument (Waltham, MA, USA) to verify functional groups present in the synthesized DES. The spectra were obtained during 16 scans within the range of 400–4000 cm^{-1}. Thermogravimetric analysis (TGA) was performed using Perkin Elmer STA 6000 (Waltham, MA, USA) under 5 mL min^{-1} nitrogen flow, at temperature ranging from 30 to 600 °C and heating rate of 10 °C min^{-1}. UV-2600 Spectrophotometer (Shimadzu, Japan) was used to determine concentration of herbicides in sample by using standard quartz cells with a path length of 1 cm. The pH value was measured with a HANNA HI 5221-02 Laboratory Research Grade Benchtop pH/mV Meter with 0.001 pH resolution.

Preparation of DES

The DES was synthesized in the same way as in the previous study by Florindo et al. [12] by combining two distinct fatty acids in a sealed glass vial and it was heated in a water bath at 40°C for 30 minutes. After synthesis, a homogeneous and clear solution was observed. The DES used in this work was prepared with the following ratio: Lauric acid: Pelargonic acid (1:3).

Emulsification liquid-liquid microextraction

In this work, 10 mL of aqueous solution containing targeted analytes (1.0 μg mL^{-1}) adjusted to pH 4 to 6 using 0.1 M hydrochloric acid or 0.1 M sodium hydroxide solutions was placed in 15 mL centrifuge tube. To extract the targeted analytes, DES and tetrahydrofuran were added to the aqueous solution with a micropipette. A cloudy solution was observed after the addition of emulsifier solvent (THF) into the extraction mixture which initiates the process of the aggregation and emulsification of DES. Subsequently, the extraction process was conducted using ultrasound in an ultrasonic bath for a duration of 15 minutes. The targeted analytes were removed to the DES phase as the aggregated DES dispersed into small droplets. After 10 minutes of centrifugation at 4000 rpm, two-phase separation was observed. The upper aqueous phase was extracted using a syringe, while the bottom layer was collected. The measurements for MCPA and 2,4-D were made at 290nm and 230nm, respectively using UV-Vis Spectrophotometer.

Response surface methodology

Response surface methodology (RSM) is a method employed to optimize chemical reactions to achieve the desired outcome. The experimental design was a Box-Behnken design (BBD) for three independent factors. The volume of DES, volume of THF, and pH of solution are three independent factors influenced the microextraction. Initially, physical experiments were conducted by systematically manipulating the experimental parameters to obtain the corresponding response values. Subsequently, the relationship between the input parameters and responses was established using a second-order polynomial or exponential function. Lastly, through the examination of surface graphs and the utilization of ANOVA, the optimal points were identified. Minitab Statistical Software, version 21 (Minitab Inc., United States) was employed to perform the BBD design and statistical analysis.

Results and Discussion

Characterization of DES: FTIR analysis

The synthesis of hydrophobic DES involved the combination of two fatty acids, namely lauric acid and pelargonic acid, in a molecular ratio of 1:3. As shown in Figure 1, The confirmation of the existence of functional groups in the synthesized DES was achieved by the utilization of FTIR analysis. The spectral data for each sample was obtained via 16 scans at a resolution of 4 cm^{-1}. Data was collected at wavenumbers from 500 to 4000 cm^{-1}.

The peaks were found in the range of 2850 to 2855 cm^{-1} and 2911 to 2925 cm^{-1} which attributed to the CH_2 and CH_3 groups, respectively, represented the fatty acids. Other significant peaks were observed at 1688 and 1705 cm^{-1}, which correspond to the stretching mode of the C = O group. Then, a broad absorption band was identified as the hydroxyl group (O-H) of the fatty acids, as

detected within the range of 3000 cm^{-1} and 3500 cm^{-1}. This phenomenon occurs when the O-H stretching absorption of these dimers exhibits significant intensity and broadness, primarily due to the influence of hydrogen bonding. The O-H bond demonstrates a propensity to oscillate at different frequencies and positions, resulting in enhanced band elongation [17]. The presence of O-H stretch was also detected between 1410 cm^{-1} and 1426cm^{-1} and 926 cm^{-1} and 940 cm^{-1}. The possible DES structure from the combination of lauric acid and pelargonic acid with molar ratio of 1:3 can be predicted as in Figure 2. In this DES structure, pelargonic acid acts hydrogen bonding donor, while lauric acid acts as hydrogen bonding acceptor. Therefore, the presence of these notable peaks proves that DES was successfully synthesized.

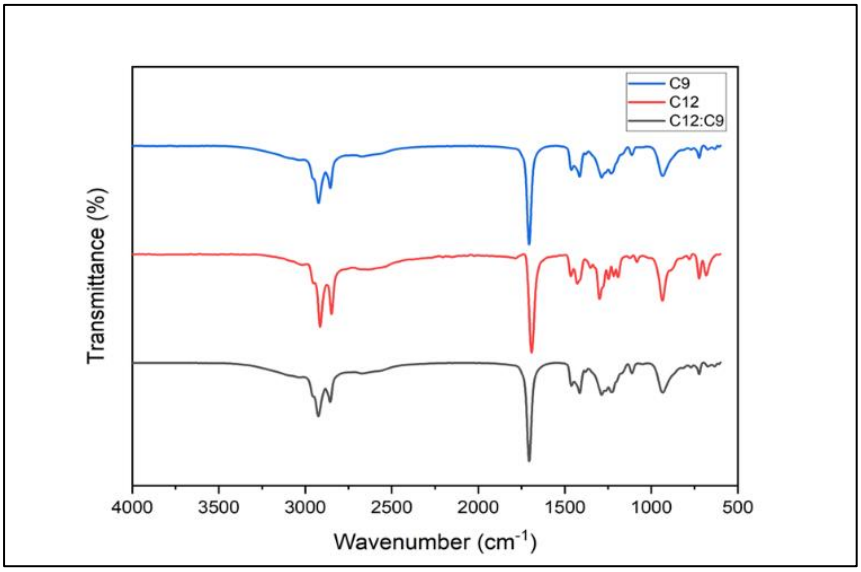


Figure 1. FT-IR spectra of the DES (C_{12}: C_9) and its individual components: C_{12} (lauric acid) and C_9 (pelargonic acid).

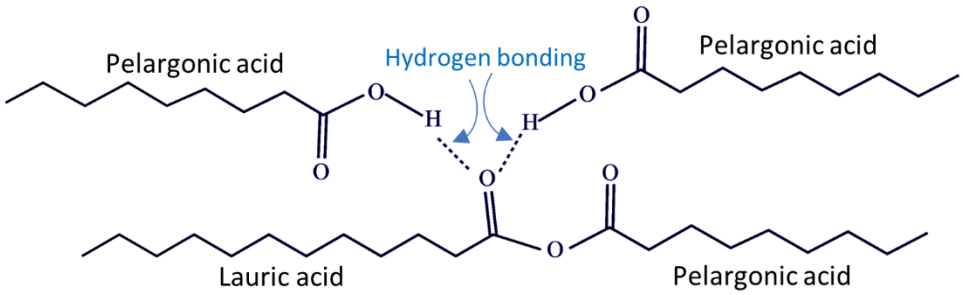


Figure 2. The possible structure of synthesized DES (combination of lauric acid and pelargonic acid with molar ratio (1:3))

Thermogravimetric analysis

As shown in Figure 3, thermogravimetric analysis (TGA) was utilized to examine the thermal properties of the synthesized DES. The TGA curve illustrates a single thermal decomposition (Td) temperature for each sample. Lauric acid, C_{12} exhibited a weight loss at 190.03 °C while pelargonic acid, C_9 showed at 166.58 °C. The weight loss for DES began at 189.97 °C. The thermal decomposition (Td) temperature determines the maximum temperature at which DES can remain liquid without decomposing. The observation of a high Td temperature indicates that a substantial amount of

energy is required to disrupts the intermolecular hydrogen bonding among the fatty acids present within the DES. Therefore, this temperature range significantly influences the applicability of DES as a solvent [18, 19]. After 200°C, the DES, and its starting materials, decomposed rapidly. There was no further degradation detected at temperatures above 200°C. This study demonstrates that DES containing lauric acid and pelargonic acid is considered thermally stable by having a high Td temperature.

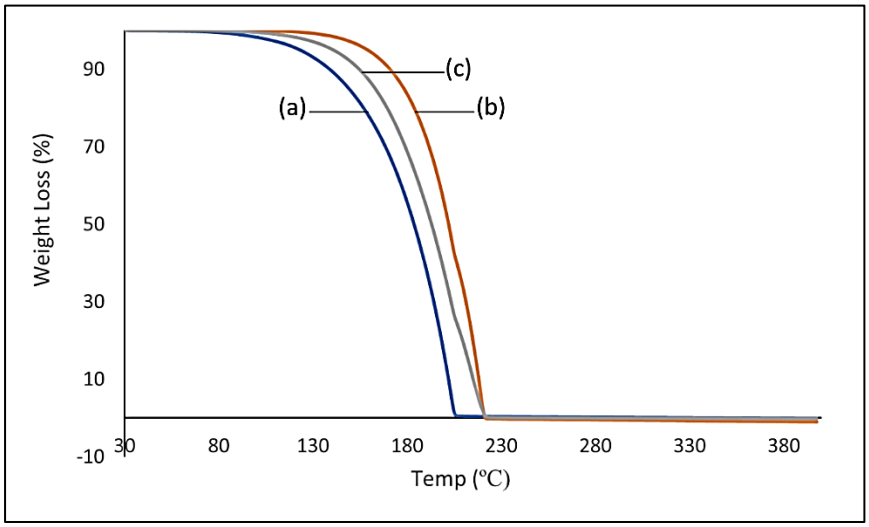


Figure 3. Thermal decomposition of the synthesized DES (C_{12}: C_9) and its raw material. (a) pelargonic acid, (b) lauric acid, (c) DES (C_{12}: C_9)

Experimental optimisation of ELLME: Effect of volume of DES

The first consideration in determining the amount of the extraction solvent should be to achieve a high level of selectivity to facilitate the effective extraction of the desired analytes. Additionally, it is crucial to ensure that the solvent has minimum solubility in water [20, 21]. The DES in this work utilized a combination of lauric acid and pelargonic acid with ratio of 1:3 as described by Sazali et al. [22]. From the previous study, DES (C_{12}:C_9) exhibited highest extraction for MCPA and 2,4-D compared to other DES. The extraction capacity of this DES is influenced by the ability of fatty acids in DES to form hydrogen bonding interaction with the analytes. This phenomenon is attributed to the DES's low viscosity and high diffusivity properties. The main interaction occurred between the analytes and DES are primarily governed by intermolecular hydrogen bonding and hydrophobic interaction, which can be attributed to the hydrophobic nature of DES [12]. For optimal results in emulsification microextraction, an appropriate volume of extraction solvent must be used during the process [22]. Figure 4 showed the optimal volume of DES for MCPA was observed to be 500 µL. In contrast, for 2,4-D the optimal extraction volume is determined to be 30 µL of DES. However, it was observed that an increase in volume resulted in a decrease in the extraction efficiency of 2,4-D. The decrease in solubility of analytes within the DES phase can be ascribed to the dilution effect, which occurs when the volume of DES is increased. As a result, the loss in solubility ultimately results in a corresponding decrease in extraction efficiency [22, 24]. Contrarily, the situation differs for MCPA, as it requires a higher volume of DES. This is because the fatty acid DES used may have a high affinity for these analytes, enabling their efficient extraction [24]. Therefore, a higher volume of DES, up to a maximum of 500 µL, may be necessary to accommodate the MCPA herbicides effectively. Therefore, 500 µL and 30 µL volume of DES were chosen for MCPA and 2,4-D, respectively, for further experiments.

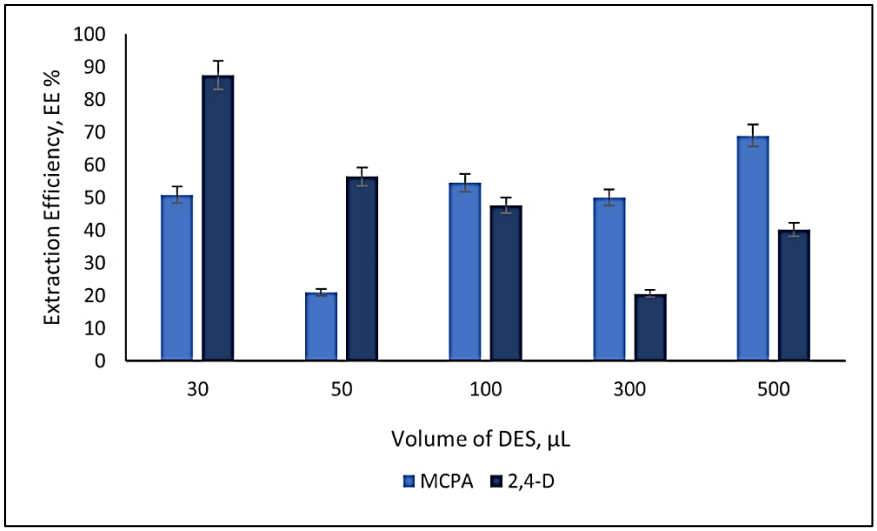


Figure 4. Effect of volume of DES. Condition: volume of THF: 500 µL; pH 4

Effect of volume of THF

The ELLME-DES approach involves the addition of an aprotic solvent as an emulsifier, resulting in the self-aggregation and subsequent separation of the DES molecules in the aqueous phase. Indeed, the emulsifier solvent tends to exhibit favourable interactions with water molecules than the DES. As a result, the DES exhibits self-aggregation, forming minute droplets that significantly enhance the contact surface area. This process facilitates the efficient mass transfer of the analytes from the aqueous phase to the DES phase [26, 27].

In this part, the impact of emulsifier solvent volume was studied by adjusting THF volume from 200 to 900 µL. Figure 5 shows the optimum value of THF was determined to be 500 µL and 200 µL for MCPA and 2,4-D, respectively. A potential reason for the observed low THF volume was achieved for 2,4-D could attributed to the high solubility of 2,4 D in aqueous phase. However, increasing the volume of THF leads to a decrease in extraction efficiency. The occurrence can be attributed to the high concentration of emulsifier, which significantly increases the solubility of both the extractant and analytes in the aqueous phase. Consequently, their distribution into the organic phase diminishes during extraction [9]. Furthermore, phenoxy acid herbicides, such as 2,4-D and MCPA, possess notable polarity and exhibit good solubility in water, thereby occasionally posing challenges in their precise extraction [28, 29]. To optimize the extraction process, it is important to control the volume of THF to maintain a sufficient concentration of the target analytes in the organic phase while minimizing their solubility in the aqueous phase. Thus, the optimal volume of emulsifier solvent was found to be 500 µL for MCPA and 200 µL for 2,4-D for further analysis.

Effect of pH solution

The pH of the sample solution is a crucial parameter as it influences the degree of ionization as well as the species of the analytes. Ionized forms of the target analytes may significantly affect the extraction efficiency [29]. In this study, the extractions were conducted at varying pH levels, from 2 to 10 adjusting using hydrochloric acid or sodium hydroxide solutions at 0.1 M. Herbicide extraction efficiency appears promising in an acidic environment (pH 2–6), as seen in Figure 6. The presence of herbicides such as MCPA and 2,4-D in their neutral form is primarily attributed to their inherent characteristics observed under acidic conditions. The effectiveness of partitioning into the hydrophobic DES is facilitated by their acidic nature [30]. The electronegative atoms of 2,4-D and MCPA form hydrogen bonds with the hydrogen bond donors (HBD) in their neutral state, thereby enhancing the solubility of the analytes in the deep eutectic solvent (DES) phase. The pH of the sample solutions was

adjusted to an acidic level for the subsequent investigations, as previous research has indicated that acidic conditions are optimal for the efficient extraction of most herbicides.

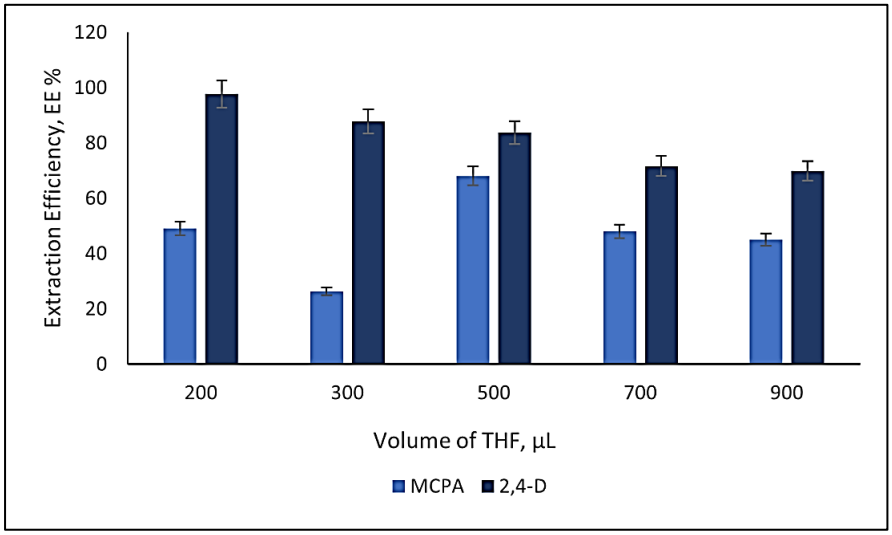


Figure 5. Effect of Volume of THF. Condition: volume of DES: 30 µL (2,4-D), 500 µL (MCPA); pH 4

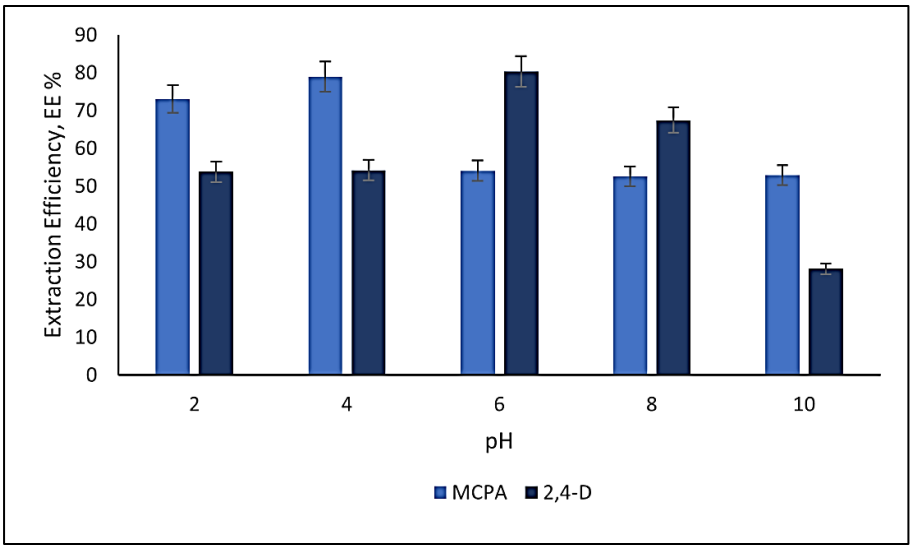


Figure 6. Effect of pH. Condition: volume of DES: 30 µL (2,4-D), 500 µL (MCPA); volume of THF: 200 µL (2,4-D), 500 µL (MCPA)

Theoretical optimization of ELLME using response surface methodology (RSM)

Response surface methodology (RSM) is a prominent statistical and mathematical technique that often aids in the systematic design of experiments [31]. Box-Behnken design (BBD) was utilized to determine the optimal combination of selected variables to conduct RSM analysis. This technique extensively analyses selected parameters and their interconnections [32]. The level of factors used in BBD are listed in Table 1. The design is based on three independent variables: volume of DES, volume of THF, and pH.

Table 1. Level of factors used in BBD.

Parameters	Unit	Lowest Value	Highest Value
Volume of DES	µL	30	500
Volume of THF	µL	200	900
pH		2	10

BBD serves as a valuable tool in minimizing the number of experiments, particularly during the initial stages. It facilitates the identification of influential factors in the response [33]. By conducting BBD (Box-Behnken Design), it is possible to identify crucial operational variables that can optimize the extraction efficiency of MCPA and 2,4-D herbicides. The variables were optimized using the two-level factorial design (low and high), as shown in Table 1. The effects of all variables on the extraction were determined through a series of 13 separate experiments. The present study utilized a statistical analysis technique known as analysis of variance (ANOVA) to investigate the impact of independent factors on microextraction efficiency. The results of ANOVA were determined by calculating the F and P-values, as shown in Table 2.

The determination of the significant association between the variables influencing the extraction efficiency, namely the volume of DES, volume of THF, and pH, and the response, represented by the peak area, was accomplished through the analysis of p-values and F-values. Models that exhibit greater F-values and lower p-values are suggestive of statistical significance. For a model term to be considered statistically significant, its p-value must be less than 0.05. Table 2 shows the F-values and p-values corresponding to the developed model, precisely 0.63 and 0.742 for MCPA, and 1.19 and 0.494 for 2,4-D herbicides, respectively. As shown, the main factors possess negligible effects, as indicated by their high p-values (> 0.05). A significant in lack of fit ($p<0.000$) was observed in both models, showing that the models inadequately specify the relationship between the variables and the response. In addition, the goodness of fit of the model was assessed by examining the coefficient of determination (R^2), which were 0.6527 and 0.7814 for MCPA and 2,4-D, respectively. These data indicated that 65.27% and 78.14% of the variability in MCPA and 2,4-D, respectively. According to the R^2 value of the model, it is possible that the connection between the variables and the response is not entirely represented. This implies that additional optimization or an alternative method may be required to attain a more accurate fit with the data. A possible explanation for this phenomenon is the presence of a weak correlation between the variables, which may hinder the model's ability to forecast the accurate relationships among the variables [34]. Besides, this can be explained by the high p-value ($p>0.05$), which suggests that none of the variables have statistical significance. Consequently, all the factors under consideration are independent, as they exhibit no mutual influence and do not significantly impact the interaction between one another. One of the variables can be changed independently without significantly impacting the response of the experiment. The following regression equation (1) and (2) represents the relationship between the variables studied (volume of DES, volume of THF, and pH) for MCPA and 2,4-D, respectively:

$$Y= 0.146+ 0.000148X_1 - 0.000090X_2 - 0.0077X_3 - 0.000001X_1^2 - 0.000000X_2^2 - 0.00024\,X_3^2 + 0.000000\,X_1\,X_2 + 0.000001\,X_1\,X_3 + 0.000011X_2\,X_3 \quad (1)$$

$$Y= 0.340 + 0.000748X_1 - 0.000800X_2 - 0.0235X_3 - 0.000001X_1^2 + 0.000001X_2^2 + 0.00055\,X_3^2 - 0.000000X_1\,X_2 + 0.000007X_1\,X_3 + 0.000022X_2\,X_3 \quad (2)$$

Where Y is absorbance, and X_1 , X_2 , X_3 are variables terms of volume of DES, volume of THF, and pH, respectively.

An interaction plot provides a visual representation of the relationship between a continuous response variable and the influence of a specific variable on another. This interaction plot shows the influence of two or more variables on the response [35]. Figure 7 and Figure 8 illustrate the interaction effect of variables on the extraction of 2,4-D and MCPA extractions.

Table 2. Analysis of Variance (ANOVA) of MCPA and 2,4-D

Analyte: MCPA					
Source	**DF**	**Adj SS**	**Adj MS**	**F-Value**	**P-Value**
Model	9	0.007886	0.000876	0.63	0.742
Linear	3	0.004335	0.001445	1.03	0.490
vol of DES	1	0.001081	0.001081	0.77	0.444
vol of THF	1	0.000759	0.000759	0.54	0.515
pH	1	0.002496	0.002496	1.78	0.274
Square	3	0.002141	0.000714	0.51	0.703
vol of DES*vol of DES	1	0.001855	0.001855	1.33	0.333
vol of THF*vol of THF	1	0.000043	0.000043	0.03	0.873
pH*pH	1	0.000033	0.000033	0.02	0.887
2-Way Interaction	3	0.001410	0.000470	0.34	0.803
vol of DES*vol of THF	1	0.000475	0.000475	0.34	0.601
vol of DES*pH	1	0.000001	0.000001	0.00	0.980
vol of THF*pH	1	0.000933	0.000933	0.67	0.474
Error	3	0.004197	0.001399		
Total	12	0.012083			

Analyte: 2,4-D					
Source	**DF**	**Adj SS**	**Adj MS**	**F-Value**	**P-Value**
Model	9	0.064872	0.007208	1.19	0.494
Linear	3	0.029353	0.009784	1.62	0.351
Vol of DES	1	0.017391	0.017391	2.88	0.189
Vol of THF	1	0.011101	0.011101	1.84	0.268
pH	1	0.000861	0.000861	0.14	0.731
Square	3	0.026184	0.008728	1.44	0.385
Vol of DES*Vol of DES	1	0.003066	0.003066	0.51	0.528
Vol of THF*Vol of THF	1	0.012900	0.012900	2.13	0.240
pH*pH	1	0.000180	0.000180	0.03	0.874
2-Way Interaction	3	0.009335	0.003112	0.51	0.701
Vol of DES*Vol of THF	1	0.005184	0.005184	0.86	0.423
Vol of DES*pH	1	0.000182	0.000182	0.03	0.873
Vol of THF*pH	1	0.003969	0.003969	0.66	0.477
Error	3	0.018144	0.006048		
Total	12	0.083016			

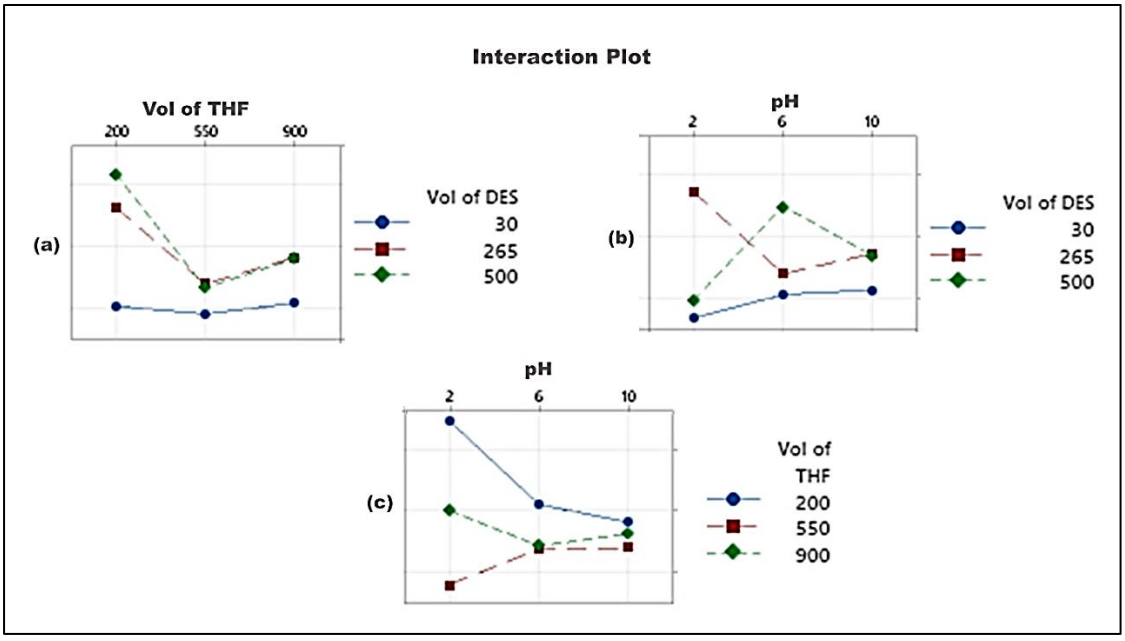


Figure 7. The interaction plot of 2,4-D sample, (a) volume of DES-volume of THF, (b) volume of DES-pH, (c) volume of THF-pH

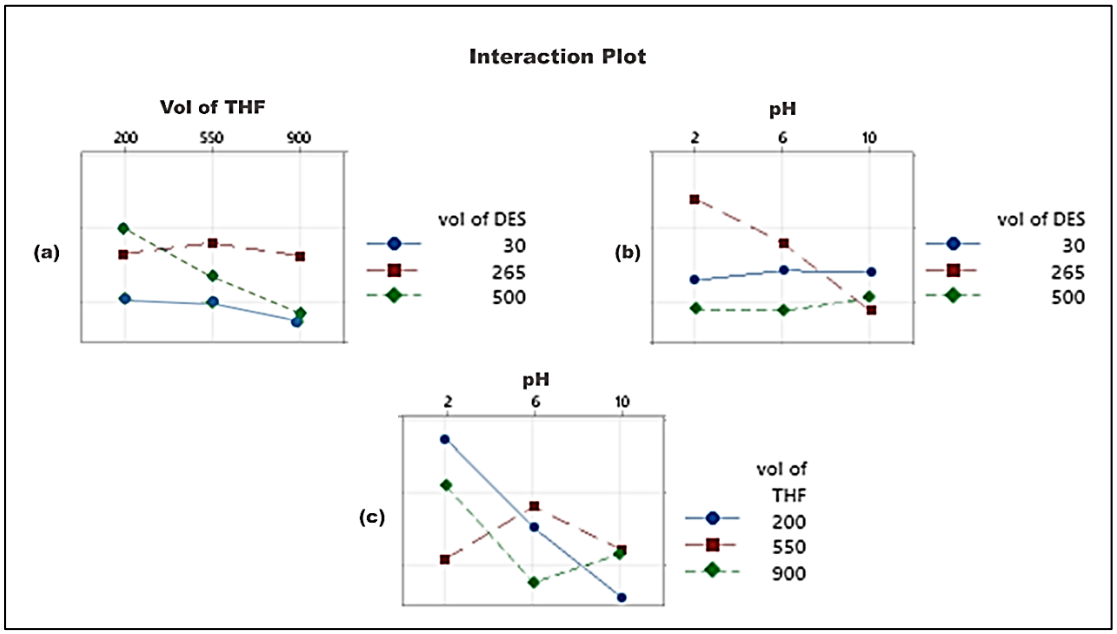


Figure 8. The interaction plot of MCPA sample, (a) volume of DES-volume of THF, (b) volume of DES-pH, (c) volume of THF-pH

As shown in Figure 7(a) and Figure 8(a), the absorbance exhibited a positive correlation with the increase in the DES volume and a decrease in the THF volume, specifically at a volume of 200 µL. The enhancement of mass transfer of 2,4-D and MCPA from aqueous phase into DES phase was observed when 500 µL of DES was utilized. This improvement can be attributed to the establishment of sufficient hydrogen bonding and

hydrophobic interactions between the analytes and DES. The effective dispersion of DES in the aqueous phase requires the addition of an appropriate volume of THF, owing to the miscibility of DES in the aqueous phase. However, an increase in THF volume caused noticeable declines in response for both analytes. This can be attributed by the challenges encountered during emulsification of DES, which subsequently enhanced the solubility of the analytes in the aqueous phase. Consequently, this leads to a decrease in the extraction efficiency [26, 37].

Furthermore, it was observed that both 2,4-D (Figure 7(b) and 7(c)) and MCPA (Figure 8(b) and 8 (c)) exhibited good responses at acidic conditions with pH 2. The acidic condition enhances the efficacy of analyte extraction. This observation is consistent with the anticipated behavior of these herbicides, as they often possess acidic properties that aid in their solubility inside the hydrophobic DES [37]. However, with an increase in pH, there was a noticeable decline in extraction efficiency. This decline in extraction efficiency can be attributed primarily to the ionization of the herbicides during the reaction [9]. The ionization results in an increase in the herbicides' water solubility, posing a difficult in mass transfer into the hydrophobic DES phase. Consequently, the extraction efficiency diminishes as the herbicides' solubility in the aqueous phase increases. This study's findings indicate that the extraction level in acidic circumstances is similar to the outcomes observed in the experimental results (Figure 6). Thus, this observation further emphasizes the importance of considering the pH of the extraction system when designing and optimizing extraction methods for analytes in achieving high extraction efficiency.

Referring to the experimental result obtained above, there are some noticeable discrepancies between the experimental data and the predicted data from BBD, specifically volume of DES and THF for both analytes. These discrepancies between the experimental data and BBD suggested the potential existence of unaccounted factors or variables that could impact the effectiveness of the extraction process. This phenomenon arises from conducting experimental investigations by systematically varying one variable at a time, whereas the other independent variables remained constant at their original levels. Consequently, the accuracy of this experiment may be compromised due to the challenge of ascertaining the relationship among all the variables [38]. This finding contradicts the BBD, which provided a simultaneous dual effect among the two variables. This feature helps the researchers in identifying the variables that make the most significant contribution to the model [39]. In order to improve the extraction, BBD suggested that high extraction efficiency can be achieved by utilizing a volume of 500 µL and 200 µL for DES and THF, respectively, for extraction of 2,4-D and MCPA.

The optimal condition determined through BBD involved 265 µL and 200 µL volume of DES and THF with pH 2 for both 2,4-D and MCPA. The optimal volume for DES was 265 µL, rather than the previously mentioned value of 500 µL. The rationale behind this decision was based on the potential diluting impact caused by an increase in DES volume, which subsequently reduces extraction efficiency. Furthermore, it has been proposed that the volume of THF should be similar to the volume of DES [9, 22]. Therefore, utilization of an equal amount of THF and DES results in better interaction and improved mass transfer of analytes to the DES phase from the aqueous solution [9].

The findings of this study demonstrate the advantages of utilizing BBD as a methodology for identifying the most favorable situations. Utilizing a BBD allows for a more complete and reliable extraction procedure by considering the combined impacts of various variables. This approach facilitates a comprehensive analysis of the relationships between variables and assists in determining the optimal circumstances for attaining a significant degree of extraction efficiency. Identifying ideal conditions provides valuable insights for future studies and can serve as a guiding principle to achieve high efficiency in similar extraction procedures.

Conclusion

In this study, a fatty acid deep eutectic solvent was successfully synthesized using lauric acid and pelargonic acid. The confirmation of DES was achieved

through FTIR spectra analysis, which enabled the identification of significant peaks associated with DES in the extraction process. The optimization of the variables influencing the ELLME method was carried out experimentally and theoretically. Furthermore, response surface methodology (RSM) based on Box Behnken design was utilized to optimize the overall extraction method, considering various factors and their interrelationships with each parameter. The findings of this study highlighted the significance of BBD as a suitable method for understanding and optimizing the complex relationship between multiple variables involved in the extraction process. The optimal conditions proposed through BBD for extraction of 2,4-D and MCPA can be achieved by applying 265 µL and 200 µL volume of DES and THF at pH 2. Thus, hydrophobic DES from a combination of lauric acid and pelargonic acid can functionally be used as an extraction solvent in the extraction process, especially for determination of pesticides. Studying BBD method provides valuable insights for future development in extraction method to be used on real sample since the extraction parameters were systematically evaluated, leading to improved extraction efficiency and accuracy.

Acknowledgement

The authors gratefully acknowledge the financial support from School of Chemical Sciences, Universiti Sains Malaysia.

References

1. Florindo, C., Branco, L. C., and Marrucho, I. M. (2017). Development of hydrophobic deep eutectic solvents for extraction of pesticides from aqueous environments. *Fluid Phase Equilibria*, 448: 135-142.
2. Musarurwa, H., and Tavengwa, N. T. (2021b). Sustainable extraction of pesticides in food and environmental samples using emerging green adsorbents. *Sustainable Chemistry and Pharmacy*, 24: 100545.
3. Jouyban, A., Farajzadeh, M. A., and Mogaddam, M. R. A. (2020). In matrix formation of deep eutectic solvent used in liquid phase extraction coupled with solidification of organic droplets dispersive liquid-liquid microextraction; application in determination of some pesticides in milk samples. *Talanta*, 206: 120169.
4. Quintana, J. B., Rodil, R., Muniategui-Lorenzo, S., López-Mahía, P., and Prada-Rodríguez, D. (2007). Multiresidue analysis of acidic and polar organic contaminants in water samples by stir-bar sorptive extraction-liquid desorption-gas chromatography-mass spectrometry. *Journal of Chromatography A*, 1174(1-2): 27-39.
5. Araujo, L., Prieto, A., Troconis, M., Urribarri, G., Sandrea, W., and Mercado, J. (2011). Determination of acidic herbicides in water samples by in situ derivatization, single drop microextraction and gas chromatography-mass spectrometry. *Journal of the Brazilian Chemical Society*, 22(12): 2350-2354.
6. Hou, X., Tang, S., Guo, X., Wang, L., Liu, X., Lu, X., and Guo, Y. (2018). Preparation and application of guanidyl-functionalized graphene oxide-grafted silica for efficient extraction of acidic herbicides by Box-Behnken design. *Journal of Chromatography A*, 1571: 65-75.
7. Musarurwa, H., and Tavengwa, N. T. (2021a). Deep eutectic solvent-based dispersive liquid-liquid micro-extraction of pesticides in food samples. *Food Chemistry*, 342:127943.
8. Klamtet, J. (2016). Ultrasound-assisted emulsification dispersive liquid-liquid microextraction for preconcentration and determination of cadmium in natural water samples by spectrophotometric technique. *NU. International Journal of Science*, 13(2): 38-48.
9. Mohamad Yusoff, N. A. N., Rahim, N. Y., Mohammad, R. E. A., Yahaya, N., and Miskam, M. (2021). Deep eutectic solvent-based emulsification liquid-liquid microextraction for the analysis of phenoxy acid herbicides in paddy field water samples. *Royal Society Open Science*, 8(3): 1-12.
10. Cannavacciuolo, C., Pagliari, S., Frigerio, J., Giustra, C. M., Labra, M., and Campone, L. (2023). Natural deep eutectic solvents (NADESs) combined with sustainable extraction techniques: a review of the green chemistry approach in food analysis. *Foods*, 12(1): 56.

    Altunay, N., Ünal, Y., and Elik, A. (2020). Towards green analysis of curcumin from tea, honey and

spices: Extraction by deep eutectic solvent assisted emulsification liquid-liquid microextraction method based on response surface design. *Food Additives & Contaminants: Part A*, 37(6): 869-881.

11. Florindo, Catarina, Romero, L., Rintoul, I., Branco, L. C., and Marrucho, I. M. (2018). From phase change materials to green solvents: Hydrophobic low viscous fatty acid-based deep eutectic solvents. *ACS Sustainable Chemistry and Engineering*, 6(3): 3888-3895.
12. Arcon, D. P., and Franco, F. C. (2020). All-fatty acid hydrophobic deep eutectic solvents towards a simple and efficient microextraction method of toxic industrial dyes. *Journal of Molecular Liquids*, 318: 114220.
13. Zhang, K., Li, S., Wang, Y., Fan, J., and Zhu, G. (2020). Air-assisted liquid-liquid microextraction based on solidification of floating deep eutectic solvent for the analysis of ultraviolet filters in water samples by high performance liquid chromatography with the aid of response surface methodology. *Journal of Chromatography A*, 1618: 460876.
14. Mohamad Said, K. A., and Mohamed Amin, M. A. (2016). Overview on the response surface methodology (RSM) in extraction processes. *Journal of Applied Science & Process Engineering*, 2(1): 8-17.
15. Moria, K., Khurshid, H., Mustafa, M. I., Alhothali, A., and Bamasag, O. (2022). Application of the response surface methodology (RSM) in the optimization of acenaphthene (ACN) removal from wastewater by activated carbon. *Sustainability*, 14(14): 8581.
16. Shishov, A., Boczkaj, G., Bulatov, A., and Andruch, V. (2022). Deep eutectic solvents or eutectic mixtures? characterization of tetrabutylammonium bromide and nonanoic acid mixtures. *The Journal of Physical Chemistry B*, 126(21): 3889-3896.
17. Ribeiro, B. D., Florindo, C., Iff, L. C., Coelho, M. A. Z., and Marrucho, I. M. (2015). Menthol-based eutectic mixtures: Hydrophobic low viscosity solvents. *ACS Sustainable Chemistry and Engineering*, 3(10): 2469-2477.
18. Delgado-Mellado, N., Larriba, M., Navarro, P., Rigual, V., Ayuso, M., García, J., and Rodríguez, F. (2018). Thermal stability of choline chloride deep eutectic solvents by TGA/FTIR-ATR analysis. *Journal of Molecular Liquids*, 260(2017): 37-43.
19. Dadfarnia, S., and Haji-Shabani, A. M. (2014). Choice of solvent in liquid-phase microextraction. *Miniaturization in Sample Preparation, Barwick 1997*: 253-275.
20. Nedaei, M., Zarei, A. R., and Ghorbanian, S. A. (2018). Development of a new emulsification microextraction method based on solidification of settled organic drop: Application of a novel ultra-hydrophobic tailor-made deep eutectic solvent. *New Journal of Chemistry*, 42(15): 12520-12529.
21. Sazali, N. H., Miskam, M., Suah, F. B. M., and Rahim, N. Y. (2022). Analysis of herbicide mixtures in environmental samples with emulsification liquid-liquid microextraction using fatty acids deep eutectic solvents. *International Journal of Environmental Analytical Chemistry*, 00(00): 1-20.
22. Liu, L., and Zhu, T. (2017). Emulsification liquid–liquid microextraction based on deep eutectic solvents: an extraction method for the determination of sulfonamides in water samples. *Analytical Methods*, 9(32): 4747-4753.
23. Rodríguez-Ramos, R., Santana-Mayor, Á., Socas-Rodríguez, B., and Rodríguez-Delgado, M. Á. (2021). Recent applications of deep eutectic solvents in environmental analysis. *Applied Sciences (Switzerland)*, 11(11): 4779.
24. Khezeli, T., Daneshfar, A., and Sahraei, R. (2015). Emulsification liquid–liquid microextraction based on deep eutectic solvent: An extraction method for the determination of benzene, toluene, ethylbenzene and seven polycyclic aromatic hydrocarbons from water samples. *Journal of Chromatography A*, 1425: 25-33.
25. Behbahani, M., Najafi, F., Bagheri, S., Bojdi, M. K., and Hassanlou, P. G., Bagheri, A. (2014). Coupling of solvent-based de-emulsification dispersive liquid–liquid microextraction with high performance liquid chromatography for simultaneous simple and rapid trace monitoring of 2,4-dichlorophenoxyacetic acid and 2-methyl-4-chlorophenoxyacetic acid. *Environmental*

Monitoring and Assessment, 186(4): 2609-2618.

26. Qurratu, A., and Reehan, A. (2016). A review of 2, 4-Dichlorophenoxyacetic acid (2, 4- D) derivatives: 2, 4-D dimethylamine salt and 2, 4-D butyl ester. *International Journal of Applied Engineering Research*, 11(19): 9946-9955.
27. Li, N., Chen, J., and Shi, Y. (2017). Magnetic polyethyleneimine functionalized reduced graphene oxide as a novel magnetic solid-phase extraction adsorbent for the determination of polar acidic herbicides in rice. *Analytica Chimica Acta*, 949: 23-34.
28. Van Scoy, A. R., and Tjeerdema, R. S. (2014). Environmental fate and toxicology of chlorothalonil. *Reviews of Environmental Contamination and Toxicology*, 232: 89-105.
29. Ji, Y., Meng, Z., Zhao, J., Zhao, H., and Zhao, L. (2020). Eco-friendly ultrasonic assisted liquid–liquid microextraction method based on hydrophobic deep eutectic solvent for the determination of sulfonamides in fruit juices. *Journal of Chromatography A,* 1609: 460520.
30. Tangsiri, R., and Nezamzadeh-Ejhieh, A. (2020). Cadmium sulfide nanoparticles: Synthesis, brief characterization and experimental design by response surface methodology (RSM) in the photodegradation of ranitidine hydrochloride. *Chemical Physics Letters*, 758: 137919.
31. Deb, A., Debnath, A., and Saha, B. (2021). Sono-assisted enhanced adsorption of eriochrome Black-T dye onto a novel polymeric nanocomposite: kinetic, isotherm, and response surface methodology optimization. *Journal of Dispersion Science and Technology*, 42(11):1579-1592.
32. Shanmugam, B. K., Vardhan, H., Raj, M. G., Kaza, M., Sah, R., and Hanumanthappa, H. (2021). Application of fractional factorial design for evaluating the separation performance of the screening machine. *International Journal of Coal Preparation and Utilization*, 42(11): 3369-3379.
33. Cheng, C. L., Shalabh, and Garg, G. (2014). Coefficient of determination for multiple measurement error models. *Journal of Multivariate Analysis*, 126: 137-152.
34. Kumari, P. P., and Lavanya, M. (2021). Optimization of inhibition efficiency of a schiff base on mild steel in acid medium: Electrochemical and RSM approach. *Journal of Bio- and Tribo-Corrosion*, 7(3): 110.
35. Moghadam, A. G., Rajabi, M., and Asghari, A. (2018). Efficient and relatively safe emulsification microextraction using a deep eutectic solvent for influential enrichment of trace main anti-depressant drugs from complicated samples. In *Journal of Chromatography B: Analytical Technologies in the Biomedical and Life Sciences*, 1072: 50-59.
36. Florindo, C., Lima, F., Branco, L. C., and Marrucho, I. M. (2019). Hydrophobic deep eutectic solvents: A circular approach to purify water contaminated with ciprofloxacin. *ACS Sustainable Chemistry & Engineering*, 7(17): 14739-14746.
37. Bezerra, M. A., Santelli, R. E., Oliveira, E. P., Villar, L. S., and Escaleira, L. A. (2008). Response surface methodology (RSM) as a tool for optimization in analytical chemistry. *Talanta*, 76(5): 965-977.
38. Siewe, F. B., Kudre, T. G., and Narayan, B. (2021). Optimisation of ultrasound-assisted enzymatic extraction conditions of umami compounds from fish by-products using the combination of fractional factorial design and central composite design. *Food Chemistry*, 334: 127498.

Malaysian Journal of Analytical Sciences (MJAS)
Published by Malaysian Analytical Sciences Society

ASSESSMENT OF IONIC SPECIES IN RAINWATER TOWARD pH VARIABILITY BETWEEN HIGHLANDS AND LOWLAND IN MALAYSIA

(Penilaian Spesis Ionik Dalam Air Hujan Terhadap Kepelbagaian pH di Antara Tanah Tinggi dan Tanah Rendah di Malaysia)

Puteri Marlini Zaini[1], Ku Mohd Kalkausar Ku Yusof[1*,] and Siti Kamilah Che Soh[1], and Samsuri Abdullah[2]

[1]*Faculty of Science and Marine Environment, Universiti Malaysia Terengganu, 21030 Kuala Nerus, Terengganu, Malaysia*
[2]*Faculty of Ocean Engineering Technology and Informatics, Universiti Malaysia Terengganu, 21030 Kuala Nerus, Terengganu, Malaysia*

**Corresponding author: kukausar@umt.edu.my*

Received: 23 June 2023; Accepted: 9 August 2023; Published: 30 October 2023

Abstract

This study investigated the variability of ionic species and pH in rainwater chemistry during wet fallout events in Highlands (Cameron Highlands, CH) and lowlands (Petaling Jaya, PJ) in 2019. A total of 1,040 datasets were obtained from the Malaysia Meteorological Department. Descriptive analysis, Mann-Whitney U test, Spearman correlation test, and discriminant analysis were employed. The selected variables included pH, H^+, Na^+, K^+, Ca^{2+}, Mn^{2+}, Zn^{2+}, Cl^-, NO^{3-}, and SO_4^{2-}. Mn^{2+} exhibited a significant difference (p <0.05) between CH and PJ. Rainfall at PJ was more acidic due to higher concentrations of Cl^-, SO_4^{2-}, and NO^{3-}. pH in CH showed a strong positive correlation with Na^+, K^+, and Ca^{2+} as compared to PJ, attributed to atmospheric neutralizing reactions between acids (HNO_3 and H_2SO_4) and alkaline compounds ($CaCO_3$, NaCl, and KNO_3) present in suspended fine particles during wet fallout. Discriminant analysis, by using the confusion matrix, demonstrated significant differences in the overall performances of anions, cations, and pH in rainwater chemistry between CH and PJ, achieving 94.32% classification accuracy. This study highlighted the variability of ionic species and pH in rainwater chemistry between highlands and lowland areas. The findings contributed to understanding atmospheric heterogeneous reactions and factors that influenced rainwater chemistry at different geographic locations.

Keywords: wet fall-out, ionic species, statistical analysis, Petaling Jaya, Cameron Highlands

Abstrak

Kajian ini mengkaji kebolehubahan spesies ionik dan pH dalam kimia air hujan semasa berlakunya hujan di tanah tinggi (Cameron Highlands, CH) dan tanah rendah (Petaling Jaya, PJ) pada tahun 2019. Sebanyak 1,040 set data diperoleh daripada Jabatan Meteorologi Malaysia. Analisis deskriptif, ujian Mann-Whitney U, ujian korelasi Spearman, dan analisis diskriminasi telah digunakan. Pemboleh ubah yang terpilih termasuk pH, H^+, Na^+, K^+, Ca^{2+}, Mn^{2+}, Zn^{2+}, Cl^-, NO^{3-}, dan SO_4^{2-}. Mn^{2+} menunjukkan perbezaan yang signifikan (p <0.05) antara CH dengan PJ. Hujan di PJ lebih berasid sebab disumbangkan oleh kepekatan Cl^-,

SO_4^{2-}, dan NO_3^- yang lebih tinggi. pH di CH menunjukkan korelasi positif yang kuat dengan Na^+, K^+, dan Ca^{2+} berbanding dengan PJ, disebabkan oleh tindak balas peneutralan atmosfera antara asid (HNO_3 dan H_2SO_4) dengan sebatian alkali ($CaCO_3$, NaCl, dan KNO_3) yang terdapat dalam zarah halus yang terampai semasa hujan. Analisis diskriminasi, menggunakan matriks kekeliruan, menunjukkan perbezaan ketara dalam prestasi keseluruhan anion, kation, dan pH dalam kimia air hujan antara CH dengan PJ, mencapai ketepatan pengelasan 94.32%. Kesimpulannya, kajian ini mengetengahkan kebolehubahan spesies ion dan pH dalam kimia air hujan antara kawasan tanah tinggi ddengan tanah rendah. Penemuan ini menyumbang kepada pemahaman tindak balas heterogen atmosfera dan faktor yang mempengaruhi kimia air hujan di lokasi geografi yang berbeza.

Kata kunci: hujan, spesies ionik, analisis statistik, Petaling Jaya, Cameron Highlands

Introduction

Rainwater chemistry is a heterogenous atmospheric reaction, whereby the conversion from gas to particle occurs. The gaseous and aerosol released can originate from natural (marine spray, haze, resuspension) or anthropogenic activities (industrial process, transportation, agricultural pesticide spray that can be transported by winds from elsewhere [1]. The repetitive process from dry to wet deposition in the atmosphere is important with the nutrient cycle cleansing the pollutant in our ambient air [2]. The continuity of these processes occurs through day and night, regardless of the geolocation or even the altitude, including highland or lowland. According to Li et al. [3], the chemical composition of highlands would provide us with regional information regarding atmospheric pollution as compared to what the lowland offers as the local condition. Do et al. [4] reported that industrial development has resulted in an increase of SO2 and NOx emissions that finally led to significant disruption in atmospheric conditions, and thus affected the pH value in rainwater.

In Malaysia, a lot of highland areas were spotted, but a few were explored in the tourism sector such as Cameron Highlands, Pahang, and Kundasang, in Sabah. The Highlands and lowlands are both crucial for natural ecosystems. With reference to Razali et al., areas located at more than 1,000 m above sea level are categorized as mountains and classified as reserved forests or catchment forests, which serve as major sources of hydroelectric production for lowlands [5]. Lowland areas are experiencing higher population growth than high plateau areas, as they offer greater opportunities to stimulate the economy. In this study, rainwater samples were acquired from the Malaysian Meteorological Department (MMD) from two different sites, namely Cameron Highlands (CH) and Petaling Jaya (PJ) in the year 2019. The aims of this study are: (1) to assess the difference of pH, cation, and anion in rainwater between CH and PJ, representing highlands and lowland, respectively; (2) to investigate the relationship between the contribution of chemical composition (anion and cation) toward the fluctuation of pH value throughout 2019.

Materials and Methods

The chemical composition dataset

This study selected CH as the highland area and PJ as the lowland area. The 2019 rainwater data for the two sites were acquired from the Malaysian Meteorological Department (MMD) on a weekly basis which accounted from January to December. Since this study focused on the differences between highland and lowland areas, the total days of rainfall between these sites most likely differed. PJ recorded a total of 50 weeks available for the rainwater volume, while CH only provided 44 weeks out of 52 weeks in 2019. Therefore, the total data extracted at PJ and CH were 750 (50 weeks × 15 variables) and 440 (44 weeks × 10 variables), respectively. For CH, the variables involved in this study were H^+, Na^+, Ca^{2+}, Mn^{2+}, Zn^{2+}, Cl^-, NO_3^-, SO_4^{2-}, and pH. However, PJ recorded a higher number of variables, which included H^+, Na^+, Ca^{2+}, NH_4^+, Mg^{2+}, Ca^{2+}, Cu^{2+}, Mn^{2+}, Pb^{2+}, Zn^{2+}, Fl^-, Cl^-, NO_3^- SO_4^{2-}, and pH. Only the variables available in the two domains were selected and analyzed for a better understanding of statistical analysis. From the enumerated variables, only pH, H^+, Na^+, K^+, Ca^{2+}, Mn^{2+}, Zn^{2+}, Cl^-, NO_3^-, and SO_4^{2-} were selected for additional univariate and multivariate statistical analysis for both zones.

Study area

Ghosh et al. [6] described CH as the location of the borderline between a humid rainforest climate and a subtropical upland climate. CH (4° 29’ 3’’N, 101° 22 17’’E) is situated at 912m – 1,960m above sea level with a temperature range between 16°C and 22˚C, and total average rainfall fluctuated between 1800 and 3000 mm, a perfect setting for an agricultural area [7]. The local community's commitment mainly depends on tea estate farmlands such as strawberry farms, and vegetable farms as well as flower gardens like lavender gardens and rose gardens [5]. The major drawback in air quality and rainwater chemistry was probably contributed by the uncontrolled routine application of chemical pesticides in CH. The farms and estates had the possibility of excessive consumption of pesticides, herbicides, and fertilizers that may influence the concentration of ionic species in rainwater, resulting in unstable pH readings in the rainwater.

Petaling Jaya (3° 06’ 07’’N, 101° 38; 42’’E) with location at 556m above sea level is one of the busiest cities in Klang valley, which is encircled by Kuala Lumpur, Sungai Buloh, Shah Alam, and Puchong. According to Morissey et al. [8], PJ with a size of 97.2 km^2 recorded a temperature between 31°C and 33°C, making June and July being recorded as the driest month. In rainfall volume, PJ received heavy annual rainfall which accumulated up to 3300 mm. Shabanda et al. [9] emphasized that Petaling Jaya is an urban area involved in various industries, high traffic, and commercial and residential areas. Petaling Jaya industries include manufacturing, electrical and electronics, machinery, food and beverage, plastics, and chemical industries. Unlike CH, the variability in chemical composition in PJ rainwater might differ due to higher contributions from fossil fuel combustion, municipal waste, and industrial activities, which are exacerbated by the meteorological conditions [2]. Figure 1 illustrates the variation of land use activities in CH and PJ.

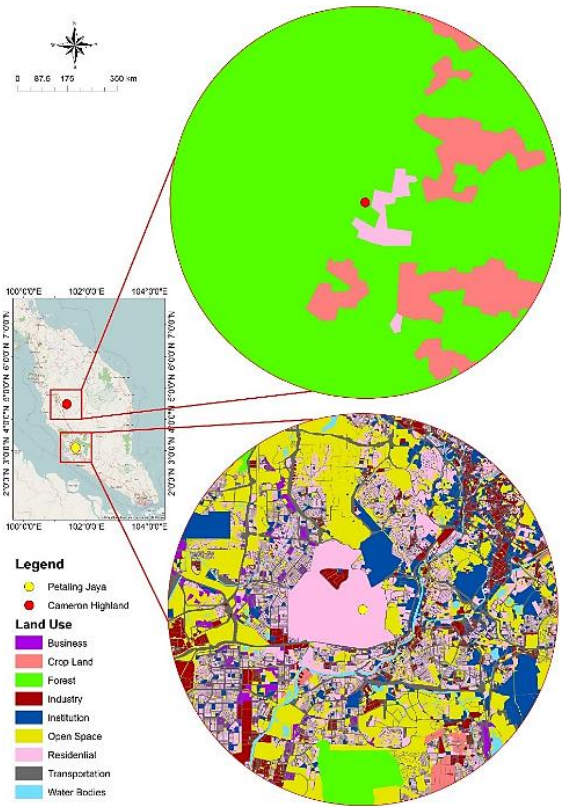


Figure 1. The illustration of land use activities in Petaling Jaya and Cameron Highlands

Statistical analysis: Pre-treatment dataset

Any missing data in this study were identified and removed from the datasets to increase data accuracy and uniformity. The data were mostly indicated as "Not Available" because an inadequate sample was recorded within that particular week. Not only that, but any variable was also recorded lower than the detection limit (LDL), and any results that showed no variation between weeks in 2019 were removed. The raw data received from MMD contained redundant and inconsistent data that had to be reduced to improve data coherence and reduce data corruption and database size. In this study, data transformation is a process of changing the format or structure of data. In this study, standardization methods were used to change the scale of data across a range. To proceed with multivariate statistical analysis like discriminant analysis, the datasets had to be standardized first. The transformation dataset process benefited this study in two ways; firstly, it canceled the unit with different variables and secondly, it reduced the range limit between variables. Data with a substantial gap such as between H^+ (e.g., 0.000005 µmol/L) and NO_3^- (100 µmol/L) could make H^+ seemed less important, yet both ions played an important role in determining the acidity in rainwater. Therefore, having a transformation dataset range (e.g., -1,1 or 0 -1) helps to reduce issues in this study [12]. Therefore, this study employed the standardization techniques, and the formula is written as below:

$$Z = \frac{x-\mu}{\sigma} \quad (1)$$

Where, x = individual data, μ = mean (average), and σ = standard deviation

Descriptive analysis

The data visualization in this study was performed by using R Studio (R development, 4.2.2). Martins et al. [10] substantiated the role of descriptive analysis in assessing activities that influence the characteristics of a given source. It entails employing techniques such as the box-whisker plot (boxplot) to draw informed conclusions. In the context of the standard boxplot, an issue arises when dealing with data that exhibit asymmetry or heavy-tailedness, resulting in an inflated identification of values as atypical. Notably, Cable and Deng [11] previously conducted a comprehensive study, quantifying the concentration of ionic species and pH in the Detroit Metropolitan area. The boxplots depicted the upper and lower limits, corresponding to 1.5 times the interquartile range (IQR) away from the box, while the median was represented by a vertical line within the box. This insightful methodology facilitated a thorough understanding of data distribution, identification of outliers, and exploration of the relations between ion concentrations and pH in CH and PJ.

Normality test, comparative, and correlation analysis

The normality test employed in this study utilized the Shapiro-Wilk test, with a sample size of less than 500 ($n < 500$), implemented by using XLSTAT (ver. 2019, USA). To visualize the Spearman Rank correlation analysis, the corrplot library function within R Studio (R development, 4.2.2) was utilized. Prabhaker et al. [12] conducted a statistical analysis and reported a *p*-value of greater than 0.05, indicating acceptance of the null hypothesis (H_0), and thus suggested a normal distribution. Conversely, for the alternative hypothesis (H_a), a *p*-value of below 0.05 was observed. In this study, the Shapiro-Wilk test rejected the null hypothesis ($p > 0.05$) for all variables, indicating that non-parametric analysis was necessary due to the non-normal nature of data. Consequently, given the non-parametric nature of the data, this study employed appropriate non-normal data analysis techniques. To compare independent datasets, the Mann-Whitney U test was employed, which utilized medians as the basis for comparison of each individual variable between the CH and PJ groups.

Spearman correlation analysis was conducted to explore the relation between pH, cation, and anion in the CH and PJ groups, with a significance level at 0.05. The strength of the correlation was classified as strong ($r > 0.70$), moderate ($0.30 \leq r \leq 0.69$), or weak ($r < 0.30$), as per the classification proposed by Ibrahim et al. [13]. The Spearman correlogram provided a visual representation of the correlations observed in the data. Positive correlations were depicted by blueish cubic representations, while inversible correlations were indicated by reddish cubic representations. Blank

(white) cell areas indicated correlations that were statistically insignificant with a 95% confidence interval (p >0.05).

Results and Discussion

Variation of pH, cations, and anions in rainwater

Figure 2 illustrates the pH fluctuated between 4.18 and 5.92 in both areas during 2019. From the times series analysis, the overall mean pH measurement for CH and PJ were 4.87 ± 0.27 and 4.59 ± 0.76, respectively. For the record, pH in CH ranged 4.27-5.58 while CH showed a greater variance of 4.18-5.92, with the lowest value being recorded in Week 8 (February). In comparison, there were only two noticeable circumstances in that CH showed a greater pH value as compared to PJ: Week 11 – Week 18 and Week 36 – Week 44. The study conducted by Park et al. [14] provided evidence which supported the significant role of precipitation quantity in influencing rainwater acidity and pH. This influence was attributed to the dilution effect on ion concentrations during precipitation events. Regions with higher rainfall, such as high plateaus of Cameron Highlands, underwent more pronounced dilution of ionic species as compared to areas with lower rainfall, like Petaling Jaya, resulting in lower total mean concentrations of ionic species in the Cameron Highlands relative to Jaya Petaling. In contrast, Payus et al. [15] postulated the occurrence of neutralizing reactions between cations and anions within rainwater, leading to an equilibrium of ionic species concentrations. Furthermore, the study highlighted the substantial impact of atmospheric scavenging, a process involving the removal of airborne particles and gases from the atmosphere through precipitation, on the concentration of ionic species in rainwater and consequent modulation of rainwater pH levels.

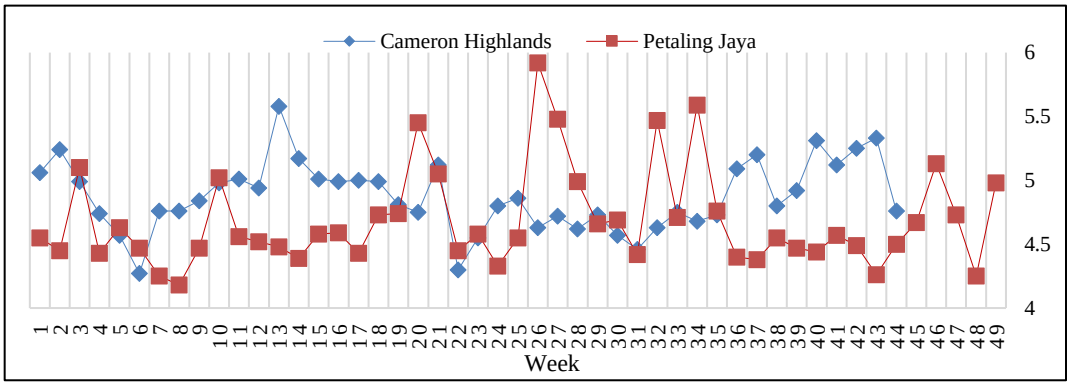


Figure 2. Time series analysis on pH variation in Cameron Highlands and Petaling Jaya during 2019.

Additionally, a higher temperature in the cloud led to an increased concentration of Cl^-, resulting in a decreased pH level of rainwater. This phenomenon was attributed to the heightened availability of gaseous molecules and high solubility of HCl in water. While the study placed considerable emphasis on pH, it was essential to direct attention toward the diverse array of cations and anions requiring investigation [14]. In the comparison of all variables, H^+ was determined to be the lowest concentration in both areas, with individual means that ranged from 0.000016 µmol/L - 0.00002628 µmol/L. The presence of H^+ ions in rainwater inflicted the rainwater acidity level. The higher the H^+ concentration present in rainwater, the lower the pH value in rainwater it gets. However, it will also depend on the influence of the external factor, including the type of anthropogenic activities and meteorological conditions, exacerbated by uncontrolled on vehicle possession in Malaysia especially in urban areas [16]. In this study, Na^+, NH_4^+, Ca^{2+}, Cl^-, NO_3^-, and SO_4^{2-} were among the abundance of species discovered in rainwater. Table 1 tabulates the rudimentary descriptive analysis which showed the min, max, mean, and standard deviation of individual species found in CH and PJ.

Together, the Mann – Whitney U test was integrated into the table to verify the differences in each individual -

species at different lowlands and highlands. NO_3-, NH_4^+, SO_4^{2-}, Cl^-, Na^+, and Ca^{2+} were the concentrated ions as compared to others, with PJ showing a higher concentration than CH. Despite having differences in terrain structure, agricultural activities, as well as industrial and urbanization effects, Khan et al. [2] confirmed that the only explanation that PJ had concentrated ions was due to fractional acidity (FA). The divergence in FA between developed and less developed areas suggested a significant variation in the neutralization of alkaline ions in rainwater, primarily due to the considerable influence of NO_3- and SO_4^{2-} on rainwater acidification. For instance, the average NO_3- found in PJ was approximately 69.7% lower as compared to what was recorded in PJ. This pattern was similar with SO_4^{2-}, Cl^-, Na^+, Ca^{2+} were all 66.7%, 53.4%, 51.9%, and 49.7% lower, respectively. Not only on the average value for individual species, but also the observation from the max values also proved that the differences between types of anthropogenic activities operated in both areas proved the hypothesis constructed in this study.

Table 1. Statistic description of rainwater anion, cation (μmol/L) and pH in Petaling Jaya and Cameron Highlands

	Petaling Jaya				**Cameron Highlands**				**Mann – Whitney U test (*p*-value)**
Variable	**Mean**	**Min**	**Max**	**Std. Dev**	**Mean**	**Min**	**Max**	**Std. Dev**	
NO_3^-	41.50	5.95	127.57	21.73	12.56	0.02	43.79	9.71	<0.0001
NH_4^+	36.79	0.10	140.67	27.11	*	*	*	*	NA
SO_4^{2-}	19.73	2.97	51.36	10.78	6.58	0.15	25.08	5.67	<0.0001
Cl^-	14.54	3.65	39.68	8.99	6.78	0.08	25.79	5.69	<0.0001
Na^+	9.45	1.66	27.01	6.11	4.55	0.55	26.19	4.73	<0.0001
Ca^{2+}	7.37	0.90	23.14	4.64	3.71	0.43	18.1	3.42	<0.0001
K^+	2.69	0.40	13.52	2.22	1.93	0.37	8.02	1.53	0.033
Mg^{2+}	1.07	0.20	2.62	0.70	*	*	*	*	NA
Fl^-	0.80	0.05	1.70	0.40	*	*	*	*	NA
Zn^{2+}	0.63	0.01	9.21	1.37	0.16	0.01	0.51	0.11	<0.0001
Mn^{2+}	0.17	0.00	1.06	0.17	0.21	0.00	1.31	0.29	**0.4690**
Cu^{2+}	0.13	0.01	4.34	0.61	*	*	*	*	NA
Pb^{2+}	0.02	0.00	0.59	0.08	*	*	*	*	NA
H^+	0.00	0.00	0.00	0.00	0.00	0.00	0.00	0.00	0.0000
pH	4.59	0.00	5.92	0.76	4.87	4.27	5.58	0.27	0.0000

Asterisk (*): the individual datasets was recorded below the detection limit.
NA: The analysis can't perform due to incompatibility comparison between CH & PJ
Bolded result: The result is not significantly differed between CH and PH with 95% confidence interval.

From the result, NO_3^- and NH_4^+ were the only variables which showed a huge gap in the range. The NO_3^- in CH ranged between 0.02 μmol/L - 43.77 μmol/L, whereas PJ recorded 5.95 μmol/L - 127.57 μmol/L and 0.10 μmol/L - 140.67 μmol/L for both ions, respectively. The possible reasons that caused acid rain in urban areas were rapid industrialization, urbanization and rapid increase in automobiles, fossil fuel combustion, and the emission of SO_2 and NO_x from vehicles into the atmosphere [17]. A higher concentration of SO_2 and NO_x in the atmosphere could lower the pH of rainwater during wet falls because these were acidic species. Higher levels of Cl^- observed at Petaling Jaya may be associated with the formation of HCl in the atmosphere. Since the data showed non - parametric type, the comparison analysis was performed by using Mann – Whitney U Test. The independent comparison test between these two locations proved that there was a significant difference (p <0.05) for all variables, except for Mn^{2+}. In other words, the existence of manganese

ions in both rainwaters was found comparable even though there was fluctuation in overall concentration throughout 2019. The finding revealed in Mann – Whitney result was supported by the Discriminant Analysis (DA), whereby the classification between CH and PJ unquestionably differed with a total of 94.32% dissimilarities.

The influence of cations and anions on the pH variability

In this study, the second objective of the study was achieved as the statistical evaluation between the pH and the group of cations and anions was performed by Spearman's rank correlation analysis. It helped to characterize the effect of these ionic species concentrations in rainwater with the pH as it discovered the strength of correlation. Among all, there were a few that had a significant correlation toward pH. H^+ was the only variable that had a significant correlation (p <0.05) in both areas, with Cameron Highlands having an inverse strong correlation with CH than Petaling Jaya, with r = -1.00 and -0.88, respectively. pH and H^+ had an inversely strong proportional relationship, the higher the concentration of H^+, the lower the concentration of pH [18]. This relationship could be described in the equation of pH = -log [H^+]. Other than H^+, other variables such as Zn^{2+}, NO_3^-, and SO_4^{2-} were the ions that demonstrated a significant correlation toward pH, and these were only found in CH. Despite H^+, other variables did not possess a significant correlation in PJ.

For the record, SO_4^{2-} was the only ion which showed the highest correlation indication with r (SO_4^{2-}/pH) = -0.75, followed by r (NO_3^-/pH) = -0.53, and r (Zn^{2+}/pH) = -0.40. The observation derived from this investigation aligned closely with the research conducted by Zeng and Han, wherein the ratio of SO_4^{2-} to NO_3^- exceeded the value of 1. This noteworthy observation suggested the influence of stationary sources of pollutant emissions, such as the transportation and dispersion of pollutants emitted during coal combustion activities. An inverse–strong correlation was observed, which might probably be due to the availability of H_2SO_4 in the atmosphere, forming acidic precipitation in CH [19]. For both locations, there was a strong correlation of r (Na^+/K^+) = 0.73 – 0.82, whereby CH had a higher correlation as compared to PJ. Zeng and Han, and Zeng et al. explained that a stronger correlation of Na^+ with K^+ and Ca^{2+} was due to atmospheric neutralizing reactions between the acids (HNO_3 and H_2SO_4) with alkaline compounds ($CaCO_3$, NaCl, and KNO_3) that existed in suspended fine particles [20,21]. The strength and direction of correlation between different ions indicated the effects of ions concentration on pH concentration, which resulted in the acidity or alkalinity of the rainwater of the particular area [22]. Figure 3 illustrates the overall correlation analysis between chemical composition toward pH variability in rainwater for CH and PJ, representing highland and lowland as hypothesized in this study.

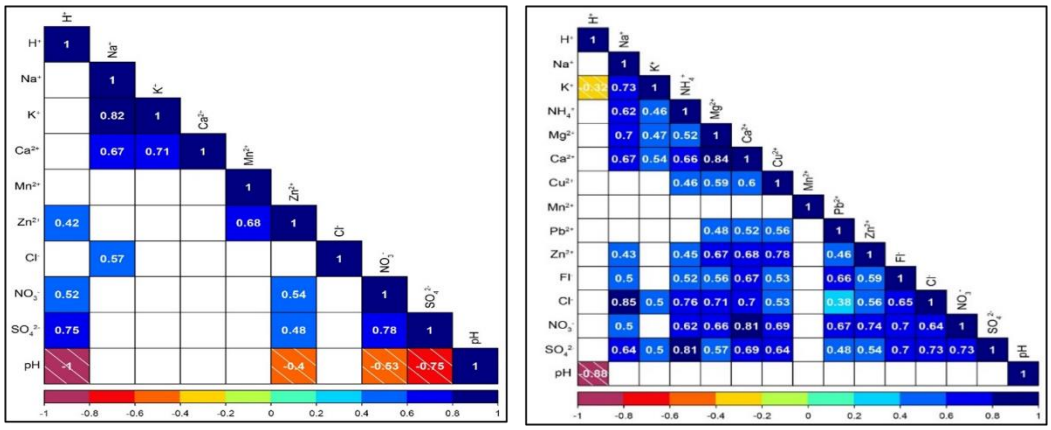


Figure 3. Spearman's correlation coefficient between pH and ionic species at Cameron Highlands (left) and Petaling Jaya (right). The colored cells denoted with a significance level of p <0.05, while white cells denote statistically non – significant correlation (p >0.05)

Conclusion

In brief, the study revealed that rainwater in both highland (CH) and lowland (PJ) regions could be classified as acidic, with the pH threshold for acid rain established at 5.6. Comparatively, the average pH value in PJ (4.59) was lower than in CH (4.87). The lowest pH values were observed in February 2019 during the Northeast Monsoon (NEM) period, characterized by increased precipitation on the Peninsula's east coast, although the study focused on the west coast, which might have been influenced by the nearby Titiwangsa mountain range. Statistical analysis demonstrated that various ions, including Na^+, NH_4^+, Ca^{2+}, Cl^-, NO_3^-, and SO_4^{2-}, significantly influenced the H^+ concentration and pH value. The Mann-Whitney U Test revealed significant differences among all variables, except for Mn^{2+}. Discriminant Analysis indicated substantial dissimilarity (94.32%) in overall performance between CH and PJ. Spearman's rank correlation analysis highlighted significant correlations between pH and ionic species, with three ionic species that affected pH value in CH, while none were significant in PJ. The fluctuation in pH variability throughout 2019 was attributed to interactions between ions such as NO_3^- and SO_4^{2-} and alkaline compounds ($CaCO_3$, NaCl, and KNO_3) during the dry deposition process. To advance research and practical applications, future studies should adopt a holistic approach, encompassing factors like climate change, trans boundary haze pollution, and monsoon patterns, conducting spatial and temporal surveys in Malaysia, considering variations in altitude, rainfall volume, population density, traffic levels, and land use types. Regular monitoring on a weekly, monthly, or annual basis would offer valuable insights.

Acknowledgements

The authors gratefully acknowledge the support of this research by Universiti Malaysia Terengganu by giving us the precious opportunity through Talent and Publication Enhancement Research Grant (TAPE-RG) (Vot No.: 55348). The authors want to thank Faculty of Science and Marine Environment for providing all technical supports throughout this study. Lastly, the authors are also thankful to the Malaysian Meteorological Department (MMD) for their full support and assistance in providing the dataset.

References

1. Jain, C.D., Madhavan, B.L. and Ratnam, M.V. (2019). Source apportionment of rainwater chemical composition to investigate the transport of lower atmospheric pollutants to the UTLS region. *Environmental Pollution*, 248: 166-174.
2. Khan, M.F., Maulud, K.N.A., Latif, M.T., Chung, J.X., Amil, N., Alias, A., Nadzir, M.S.M., Sahani, M., Mohammad, M., Jahaya, M.F., Hassan, H., Jeba, F., Tahir, N.M., and Abdullah, S.M.S. (2018). Physicochemical factors and their potential sources inferred from long-term rainfall measurements at an urban and remote rural site in tropical areas. *Science of Total Environment*, 613-614: 1401-1416.
3. Li, J., Wu, H., Jiang, P., and Fu, C. (2022). Rainwater chemistry in a subtropical high – altitude mountain site, South China: Seasonality, source apportionment and potential factors. *Atmospheric Environment*, 268: 118786.
4. Do, L.T.T., Griffith, S.M., Tseng, W-T., and Lin, N-H. (2021). Long-term trend of wintertime precipitation chemistry at a remote islet site influenced by anthropogenic emissions from continental East Asia. *Atmospheric Environment*, 262: 118626.
5. Razali, A., Syed, Ismail, S. N., Awang, S., Mangala, S. P., and Zainal Abidin, E. (2018). Land use change in highland area and its impact on river water quality a review case studies in Malaysia. *Ecology Process*, 7: 19.
6. Ghosh, R. S. (2014). Retrieved from Communities Struggle for Sustainable Rural Development In The Cameron Highlands. Access https://propernet.ias.unu.edu/activities/lp/2014lp/2014lp_cameron
7. Mohammadi, A., Shahabi, H., and Ahmad, B. (2019). Land-cover change detection in a part of Cameron Highlands, Malaysia using ETM+ Satellite imagery and support vector machine (SVM) algorithm. *Environment Asia*, 12(2):145-154.
8. Morrissey, K., Chung, I., Morse, A., Parthasaranth, S., Roebuck, M.M., Tan, M.P., Wood, A., Wong, P-F., and Frostic, S.P. (2021). The effects of air quality on hospital admissions for chronic

respiratory diseases in Petaling Jaya, Malaysia, 2013-2015. *Atmosphere*, 12(8): 1060.

9. Shabanda, I. S., Koki, I. B., Low, K. H., Md Zain, S., Khor, S. M., and Abu Bakar, N. K. (2019). Daily exposure to toxic metals through urban road dust from industrial, commercial, heavy traffic, and residential areas in Petaling Jaya, Malaysia: a health risk assessment. *Environmental Science Pollution*, 26: 37193-37211.
10. Martins, E. H., Nogarotto, D. C., Mortatti, J., and Pozza, S. A. (2019). Chemical composition of rainwater in an urban area of the southeast of Brazil. *Atmospheric Pollution Research*, 10(20): 520-530.
11. Cable, E. and Deng, Y. (2018). Trace elements in atmospheric wet precipitation in Detroit metropolitan area: Levels and possible sources. *Chemosphere,* 210: 1091-1098.
12. Mishra, P., Pandey, C. M., Singh, U., Gupta, A., Sahu, C., and Keshri, A. (2019). Descriptive statistics and normality tests for statistical data. *Annals of Cardiac Anaesthesia*, 22(1): 67.
13. Ibrahim, Y.S., Hamzah, S.R., Khalik, W.M.A.W.M., Yusof, K.M.K.K., and Anuar, S.T. (2021). Spatiotemporal microplastic occurrence study of Setiu Wetland, South China Sea. *Science of Total Environment*, 788: 147809.
14. Park, S. M., Seo, B. K., Lee, G., and Kahng, S. H. (2015). Chemical composition of water-soluble inorganic species in precipitation at Shihwa basin, Korea. *Atmosphere*, 6: 732-750.
15. Payus, C. M., Jiklim, C., and Sentian, J. (2020). Rainwater chemistry of acid precipitation occurrences due to long-range transboundary haze pollution and prolonged drought events during southwest monsoon season: climate change driven. *Heliyon,* 6: e04997.
16. Zhou, S., Xu, Z., Liu, W., Wu, Y., Zhao, T., Jiang, H., Zhang, J., Zhou, L., and Wang, Y. (2019). Chemical composition of precipitation in Shenzhen, a coastal mega-city in South China: Influence of urbanization and anthropogenic activities on acidity and ionic composition. *Science of the Total Environment,* 662: 218-226.
17. Shivashankara, G. P., and Sharmila, G. V. (2012). pH and chemical composition of bulk precipitation Karnataka, India. *International Conference on Biotechnology and Environment Management,* 42: 1-10.
18. Yue, F. J., Waldron, S., Li, S. L., Wang, Z. J., Xu, S., Zhang, Z. C., and Oliver, D. M. (2019). Land use interacts with changes in catchment hydrology to generate chronic nitrate pollution in karst waters and strong seasonality in excess nitrate export. *Science of the Total Environment,* 696: 134062.
19. Zeng, H., and Han, G. (2021). Rainwater chemistry observation in a karst city: variations, influence factors, sources and potential environmental effects. *Peer J Life & Environment*, 2021: e11167.
20. Zeng, H., Han, G., Wu, Q., and Tang, Y. (2020). Effects agricultural alkaline substances on reducing the rainwater acidification: Insight from chemical composition and calcium isotopes in a karst forest area. *Agriculture, Ecosystems and Environment*, 290: 115166.
21. Zeng, J., Yue, F. Y., Li, S. L., Wang, Z. J., Wu, Q., Qin, C. Q., and Yan, Z. L. (2019). Quantifying depression trapping effect on rainwater chemical composition during rainy season in karst agricultural area, southwestern China. *Atmospheric Environment,* 218: 116998.
22. Ubuoh, E. A., Nwogu, F. U., and Osuagwu, E. C. (2021). Wet deposition chemistry and neutralization potential in oil producing region of southern Nigeria. *Journal of Environmental Management,* 289: 112431.

Malaysian Journal of Analytical Sciences (MJAS)
Published by Malaysian Analytical Sciences Society

THE INFLUENCE OF H_3PO_4 CONCENTRATION ON THE YIELD, POROUS STRUCTURE, AND SURFACE CHEMICALS OF SARAWAK WILD BAMBOO ACTIVATED CARBON

(Pengaruh Kepekatan H_3PO_4 Terhadap Hasil, Struktur Berliang dan Bahan Kimia Permukaan Karbon Teraktif Buluh Liar Sarawak)

Mahanim Sarif[1,*], Hashim Bojet[2], Tumirah Khadiran[1], Rafidah Jalil[1], Puad Elham[1], Nicholas Andrew Lissem[2], Johari Zainudin[2], Wan Ching Ching[2] and Rickey Anak Dayus[2]

[1]*Wood Chemistry and Non Wood Utilization Programme, Forest Products Division, Forest Research Institute Malaysia, 52109 Kepong, Selangor, Malaysia*
[2]*Sarawak Timber Industry Development Corporation (STIDC), Jalan Stadium, Petra Jaya, 93050 Kuching, Sarawak*

[*]*Corresponding author: mahanim@frim.gov.my*

Received: 19 April 2023; Accepted: 11 August 2023; Published: 30 October 2023

Abstract

Activated carbon (AC) is a versatile porous material with numerous applications in various industries. In this study, ACs with both specific surface area and mesoporous developed structure were prepared using Sarawak wild bamboos, i.e., *Gigantochloa levis* (beting) and *Bambusa vulgaris* (aur), as a carbon precursor. The bamboos were chemically activated with phosphoric acid (H_3PO_4) at various concentrations, and then carbonized using a tubular furnace at 500 °C for 3 hr under an inert nitrogen gas flow. The proximate and ultimate analyses of AC were measured. The chemical and porous structure of AC were characterized using Brunauer, Emmett, and Teller (BET), Fourier transform infrared spectroscopy (FTIR), and field emission scanning electron microscopy (FESEM). The results show that by increasing the H_3PO_4 concentration, the surface area of bamboo AC was increased. The AC yield between 58% and 62% was obtained at 1%–9% v/v H_3PO_4 impregnations. The highest surface area of 1319 and 1285 m^2/g were obtained at 9% v/v H_3PO_4 impregnation of beting and aur bamboos, respectively. Therefore, ACs can be prepared using low H_3PO_4 impregnation concentration, but high quality ACs comparable to other ACs from different biomass with good yield and textural characteristics are also producible. This could lower the production cost of ACs from bamboo due to the use of cheap and novel raw materials from different species of bamboo by using only the minimum concentration of activating agent in the production.

Keywords: activated carbon, bamboo, chemical activation, surface area

Abstrak

Karbon teraktif (AC) ialah bahan berliang serba boleh dengan pelbagai aplikasi dalam pelbagai industri. Dalam kajian ini, AC dengan kedua-dua kawasan permukaan tertentu dan struktur liang meso telah disediakan menggunakan buluh liar Sarawak; *Gigantochloa levis* (beting) dan *Bambusa vulgaris* (aur) sebagai prekursor karbon. Buluh tersebut diaktifkan secara kimia dengan asid fosforik (H_3PO_4) pada pelbagai kepekatan, dan kemudian dikarbonisasi menggunakan relau tiub pada suhu 500 °C selama 3 jam dengan aliran gas nitrogen. Analisis proksimat dan unsur karbon, hidrogen, nitrogen, sulphur ke atas AC telah diukur. Struktur

kimia dan keliangan AC dicirikan menggunakan, Brunauer, Emmett, dan Teller (BET), spektroskopi inframerah transformasi Fourier (FTIR) dan Mikroskopi elektron pengimbasan pelepasan medan (FESEM). Keputusan menunjukkan bahawa dengan meningkatkan kepekatan H_3PO_4, luas permukaan AC buluh meningkat. Hasil AC dalam julat antara 58% hingga 62% diperolehi pada impregnasi 1% - 9% v/v impregnasi H_3PO_4. Luas permukaan tertinggi 1319 m^2/g dan 1285 m^2/g diperolehi pada 9% v/v H_3PO_4 impregnasi buluh beting dan aur. Oleh itu, AC boleh disediakan menggunakan kepekatan impregnasi H_3PO_4 yang rendah, tetapi AC berkualiti tinggi setanding dengan AC lain daripada biojisim berbeza dengan hasil yang baik dan ciri tekstur juga boleh dihasilkan. Ini boleh mengurangkan kos pengeluaran AC daripada buluh kerana penggunaan bahan mentah yang murah dan baru daripada spesies buluh yang berbeza dengan hanya menggunakan kepekatan minimum agen pengaktif dalam pengeluaran.

Kata kunci: karbon teraktif, buluh, pengaktifan kimia, luas permukaan

Introduction

Activated carbon (AC) is a unique and multifunctional substance due to its high porosity and large surface area, which leads to high adsorption capability. AC pores exhibit strong van der Waals forces, which are linked to its adsorption capabilities. ACs are widely utilized in various applications, including water purification, gas storage, water treatment, as a catalyst, and as a material for double layer capacitors [1-3], environmental remediation, air purification, food processing, medicinal uses, and recovery of metals in hydrometallurgy [4]. The demand for AC will continue to rise as its applications expand.

Commercial AC is often produced from coal, which is a non-renewable resource with limited availability. Biomass has emerged as an alternate raw material for the manufacturing of AC to circumvent this constraint. Approximately 80%~85% of the total AC production is derived and explored from non-renewable coal-based resources with the remaining from renewable sources such as agricultural residues, wood [4], palm, coconut shell [4], coffee endocarp, fine cone biomass [1], hazelnut shells, olive, peach, apricot and cherry stones, grape seeds, and eucalyptus leaves [3]. Bamboo is another biomass material that has a good potential to be used as a carbon precursor to produce AC [5-8]. Bamboo is a fast-growing plant, rich with lignin (32%–33%) and alpha cellulose (45%–46%), which makes it suited to be used as a carbon precursor to produce AC. The porous structure (micropores, mesoporous, and macropores) of AC from biomass is made up of cellulose and lignin. The chemical composition of the raw material and the parameters of the manufacturing process determine the characteristics of AC [1]. In other words, the structural properties of AC, i.e., porous structure (pore size and surface area) and surface chemistry depend on the carbon precursors and the manufacturing processes.

There are two manufacturing processes of AC known as physical activation and chemical activation methods. Physical activation is recognized as a two-step method because it involves carbonization followed by activation. Chemical activation is a single-step method in the presence of chemical activator, whereby carbonization and activation take place simultaneously. Nevertheless, chemical activation has shown more advantages over physical activation because it produces ACs with higher yield and higher surface area even at moderate temperatures with only one step activation [4, 9]. Basically, carbonization is the conversion of raw materials into charcoal and the formation of initial porosity through thermal decomposition resulting in a higher carbon content without non-carbon components in the substance. Meanwhile, activation is a process to create advanced porosity by opening previously inaccessible initial holes, forming new pores, and enlarging existing pores [10].

The most common chemical activators used in chemical activation method to produce AC are H_3PO_4, alkali metal compounds such as sodium hydroxide (NaOH), potassium hydroxide (KOH), sodium carbonate (Na_2CO_3), and potassium carbonate (K_2CO_3), and zinc chloride ($ZnCl_2$) [2, 11-12]. Among the alkali metal compounds, KOH is often carried out at high temperatures of 700~900 °C with a high impregnation ratio (IR = KOH: biomass precursor) of 5:1 and very effective in creating micropores, small mesopores, and very high specific BET surface area of above 2000 m^2g^{-1} [3]. However, chemical activation using KOH activation has low carbon yield and has detrimental impacts on

human health and environment. On the other hand, H_3PO_4 can be operated at low temperatures of 400~600 °C with a low IR (weight ratio of H_3PO_4 to biomass precursor) of 3:1, results in BET surface area of approximately 1000~1500 m^2g^{-1} consisting of mainly mesopores. As a dehydrating catalyst, H_3PO_4 does not only promote bond cleavage reactions but also facilitate crosslinking via cyclization, condensation, and forming a layer of linkage such as phosphate and polyphosphate esters, which could protect the internal pore structure, and thus prevent excessive burn-off in carbon activation. With the considerations of environmental impacts, energy cost, and carbon yield, H_3PO_4 is highly attractive and has been in demand for large-scale AC production in recent decades [4].

In this paper, AC was prepared using two different Sarawak wild bamboo species, i.e., *Gigantochloa levis* (Beting) and *Bambusa vulgaris* (Aur) through the H_3PO_4 chemical activation. They can easily be found in almost all Sarawak regencies. To the best of our knowledge, there are no previous reports on the preparation of AC from Beting) and Aur bamboos using low concentration H_3PO_4 chemical activation. There is a shortage of data, particularly regarding the properties of AC. Therefore, the effects of H_3PO_4 concentration on the AC yield, porous structure, and surface chemicals of beting and aur bamboos were examined in this study.

Materials and Methods

Materials

Two different species of Sarawak wild bamboo, i.e., *Gigantochloa levis* (beting) and *Bambusa vulgaris* (aur), approximately aged 4 years old were supplied by Sarawak Timber Industry Development Corporation (STIDC). Both bamboos were originated from Kota Samarahan, Sarawak, Malaysia. Mixed portion of bamboos (top, middle, bottom) were used as the carbon precursor throughout the study. The bamboo internodes were cut and chipped into small size and oven-dried at 103±2 °C for 48 hr to remove water content. The dried bamboos were ground and sieved through a 1.0-mm sieve. The ground bamboo was known as dried bamboo particle. The analytical grade of H_3PO_4 was used as a chemical activator. The chemicals and reagents used in this study were purchased from Sigma-Aldrich.

Preparation of bamboo activated carbon

The method used to prepare the bamboo AC was adopted from Tumirah et al. [12]. Approximately 5g of dried bamboo particle was impregnated with 50 mL of different concentrations (1%, 3%, 6%, and 9% v/v) of H_3PO_4. The samples were shaken overnight using an orbital shaker at 100 rpm at 70±3 °C. Then, the samples were heated using sand bath until all the excess water was evaporated. The chemical activation of bamboo was carried out using a tubular furnace at 500 °C for 3 hr under an inert nitrogen gas flow. The resulting bamboo ACs were obtained after washing with hot water and oven-dried at 103±2 °C for 24 hr. The experimental set up for chemical activation is shown in Figure 1.

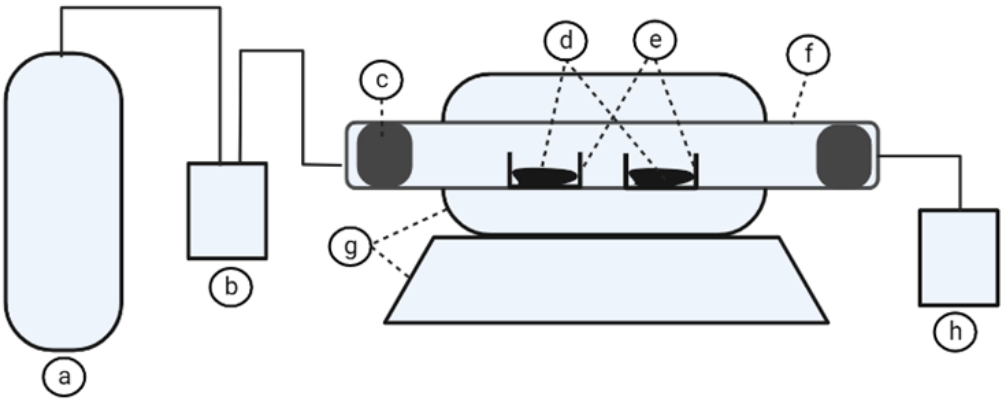


Figure 1. Experimental set up for chemical activation. Notes: (a) N_2 gas tank (b) Flow meter (c) Glass Block (d) Activated Sample (e) Sampling boat (f) Glass tube (g) Furnace (h) Water bottle (N_2 flow indicator)

.

Characterization of bamboo activated carbon: Chemical composition

The internodes of bamboos were ground into 250 µm size and used for the chemical analysis. The resulting material was placed in a sealed plastic container and labelled for the chemical analysis which comprises holocellulose, alpha cellulose, and lignin analysis using the test method of Wise et al. [13], TAPPI 203 om-93 [14], and TAPPI T222 om-02 [15], respectively. Additionally, holocellulose is a necessary preparatory stage to determine the alpha-cellulose content.

Proximate and ultimate analysis

The proximate analysis was carried out to determine the proximate amount of moisture content, volatile matter content, and ash content using the British Standard BS EN 14774-2:2009, British Standard EN 15148:2009, and British Standard EN 14775:2009, respectively.

The ultimate analysis was performed using CHNS Analyzer, LECO Instrument Model 628 at Global Testing and Consultancy for Rubber (G-TACR), Malaysian Rubber Board (MRB). The analysis was carried out to determine carbon (C), hydrogen (H), nitrogen (N), and sulphur (S) content in the bamboo samples.

Fourier transform infrared spectroscopy (FTIR)

The sample was ground and sieved with a 150-µM mesh. Exactly 2 mg of each sample was mixed with 100 mg of potassium bromide (KBr) powder, and the mixture was further ground and pressed into a 13-mm diameter disc. The IR spectra were recorded on a Spectrum 100 FTIR spectrometer (Perkin Elmer, CA, USA), equipped with a mid-infrared deuterated triglycine sulphate (DTGS) detector. The spectra were obtained in the frequency range of 4000–450 cm^{-1} with a resolution of 4 cm^{-1} and with a total accumulation of 16 scans.

Percentage of yield

The yield of bamboo AC is defined as a ratio of weight of the resultant bamboo AC to that of the bamboo raw. The yield of bamboo AC is measured using Equation 1 as follows [16]:

$$\text{Yield of bamboo AC (\%)} = (W_1 / W_0) \times 100 \quad (1)$$

where, W_0 is the mass of bamboo raw and W_1 is the mass of carbonized bamboo after washing with hot water and oven-drying.

Surface area and porous structure characterization

The surface area and porous structure of bamboo AC were characterized using the nitrogen adsorption-desorption technique at 77 K of accelerated surface area and porosimeter analyser (Micromeritic, ASAP 2020). The porous structure of bamboo AC is referring to pore size, pore size distribution, pore volume, and surface area. The surface area of bamboo AC was analysed using the BET equation, while porous structure was calculated using the desorption Barret–Joyner–Halenda (BJH) equation. Both equations are as in the instrument software package.

Surface morphology characterization

The bamboo AC samples used for FESEM analysis were prepared by placing the dried samples onto the specimen stub. The sample surface was sputter coated with a thin film of platinum before any observation was made. The morphology structure of AC was observed under the Model: Nova NanoSEM 230, THERMO SCIENTIFIC formerly known as FEI at a magnification of 5000× at a scanning voltage of 10 kV.

Results and Discussion

Characteristics of raw material: Chemical composition

In general, biomass contains three main cellulosic components (hemicelluloses, cellulose, and lignin) and closely associated in a complex structure. Previous study reported that the range of cellulose and hemicelluloses content for various types of bamboo is from 37% to 47% and 15% to 30%, respectively [17]. The characteristics of beting and aur bamboos were evaluated and compared with other literatures. The

chemical contents of bamboos for this study were (44%–46 % cellulose, 25%–33% hemicellulose, and 32%–33% lignin. This result is close to the chemical composition of other bamboo species as depicted in Table 1. During the carbonization of biomass, the hemicelluloses and cellulose decompose mostly into volatile products, while the lignin content is more difficult to decompose and contributes to the formation of a solid residue called char. Meanwhile, the fixed carbon and ash content decreased with the increase in the volatile content [16]. The chemical composition of bamboo is almost similar to that of the woody biomass materials [18, 19]. High phenolic content in lignin compound of biomass makes it important in the AC preparation because it leads to higher carbon yields than those obtained from the other two main macromolecular compounds of biomass: cellulose and hemicellulose [20]. Thus, Beting and Aur bamboos have great potential as a precursor to produce high quality AC because the result is within the range of chemical content. The formation of micropores and macropores of AC are strongly influenced by cellulose and lignin content of raw material. Table 1 also presents that the density and thickness of beting and aur bamboos was around 706–785 kg/m^3 and 8.16–10.51 mm, respectively.

Table 1. Chemical and physical analyses of different bamboo species

Analysis	**Unit**	***Gigantochloa levis* (beting) (This study)**	***Bambusa vulgaris* (aur) (This study)**	***Gigantochloa nigrociliata* (Tabah)[17]**	***Schizostachyum brachycladum* (Tamblang)[17]**
Chemical					
Alpha cellulose	%	46.39	44.97	44.94	42.52
Hemicellulose	%	25.73	33.17	16.99	16.73
Lignin	%	32.25	33.33	22.91	21.23
Physical					
Thickness	mm	10.51	8.16	-	-
Density	kg/m^3	785	706	-	-

Proximate and ultimate analysis

The proximate analysis of raw bamboo is very important to determine the quality of AC produced and the distribution of its contents. Four important parameters that need to be measured comprises moisture content, volatile matter content, ash content, and fixed carbon content. The moisture content present in the sample can also be considered as water vapor when it is heated to high temperatures. Hence, the volatile matter content and moisture content tend to leave the sample when heated. In view of the proximate analysis data, beting and aur bamboos show high moisture content (32%–41%) and high percentage of volatile matter (83%–90%), while the ash content and fixed carbon content of the bamboo sample was 1.4%–3.84% and 8.58%–12.88%, respectively. This gives an overview about the properties and components of bamboo [20]. The high volatile matter and low ash content of biomass resources enable them suitable to be used as starting materials to produce ACs [21]. High volatile matter content usually reduces the solid yield in the carbonization stage, while low inorganic content is vital due to their abilities to produce low ash and high fixed carbon content [22]. Apart from ash content, fixed carbon content is very important to determine the quality of AC produced from raw bamboo. The content of fixed carbon will be increased after converting it to AC. Due to its relatively high volatile matter content and low ash content, bamboo has the potential as a suitable precursor for conversion to AC. The low ash content indicates that inorganic impurities would have little impact on pore growth during the activation process. Since minerals including silica, alumina, iron, magnesium, and calcium make up majority of ash's composition, ash is an unwanted contaminant that presents in AC [5].

The ultimate analysis shows that raw bamboo and AC has 40%–43% and 69.85% of carbon, while 1.40%–3.84% and 7.22% of ash, respectively. It was predicted that compared to the raw material, AC has higher amount of carbon and ash. Past study investigated the carbonization of Pawlonia wood with phosphoric acid and discovered another pattern that is also comparable [21]. Besides the experimental conditions of the carbonization and activation steps, the porous structure of AC is also influenced by the original nature and structure of the starting material. The results of proximate and ultimate analyses from different biomass of wood and non-wood are shown in Table 2.

Table 2. Proximate and ultimate analyses of biomass and its activated carbon

Analysis	Bamboo (This study)	Bamboo [17]	Paulownia Wood [21]	Bamboo Activated carbon [5]	Pawlonia Activated carbon [21]
Proximate (%)					
Moisture Content	31.60-40.92	7.67-9.27	3.50	5.27	2.30
Volatile matter	83.29-90.02	83.48-84.56	76.54	10.64	17.80
Ash content	1.40-3.84	2.92-4.26	1.05	7.22	2.63
Fixed carbon	8.58-12.88	3.222-4.61	18.91	76.86	77.27
Ultimate (%)					
Carbon	40.39-42.85	41.26-42.47	45.83	69.85	70.83
Hydrogen	2.14-3.14	6.09-6.10	0.29	-	3.41
Oxygen	54.77-56.13	-	47.48	-	25.76
Nitrogen	0.24-0.25	0.95-1.03	0.40	0.23	-
Sulphur	0.08-0.09	-	-	1.71	-

Characteristics of activated carbons produced: Yield of activated carbon

In general, the bamboo-based ACs exhibit various physiochemical properties at various H_3PO_4 concentrations, including the product yield. Yield of bamboo AC is defined as the weight of carbonized bamboo after washing using hot water to remove H_3PO_4 residue or contaminants and oven dried. With the increase of H_3PO_4 concentration, the yield of beting and aur ACs were increased from 58.0% to 62.0% and 58.1% to 60.1%, respectively (Figure 2). According to Ismail et al. [23], H_3PO_4 impregnation acts as a reactant to create crosslinks and as an acid catalyst to enhance the bond breaking of the carbon precursors during the activation. Phosphate and polyphosphate species are created because of the crosslinking of the H_3PO_4 and organic components in the biomass sample, and they may persist on the AC structure even after washing. Hence, more H_3PO_4 usage led to a larger AC yield and increment of leftover solid biomass by reducing tar formation and the emission of volatile compounds during the carbonization reaction [23]. The yield of both bamboo ACs obtained was higher than that of the ACs reported from other biomasses, such as bamboo (36.8%–40.2%), coconut shell (50.84%), and durian shell (45.5%) [23-25]. This shows that bamboo is one of the potential carbon precursors to produce AC.

Surface characteristics of porous activated carbon

One of the methods to determine the surface functionalities of a material and performing qualitative analysis is FTIR spectroscopy. Therefore, by employing the FTIR spectral analysis at the mid-infrared range (4000–450 cm^{-1}), the functional groups that are present in raw bamboo and manufactured ACs can be determined. Figure 3(a) and (b) shows the results of spectrum for raw bamboo and ACs, respectively. Figure 3(a) shows that the bamboo precursor created more bands than the manufactured ACs. Beting and aur raw bamboos show a broad absorption band at 3340 to 3348 cm^{-1} due to the O–H stretching and H-bonded bond structure of the main functional groups of phenols, alcohols, and waters. The C–H stretching and O–H stretching bond structure, which contains a functional

group of alkanes (cellulose and lignin) and carboxylic acids, was attributed to a small peak at 2881 and 2889 cm^{-1}. The minor peak in the C–H stretching bond structure can also comprise methyl (CH_3), methylene (CH_2), and aliphatic saturated functional groups (CH) [20]. The C=C stretching bond structure from the functional group of alkenes (lignin) is best described by the small peak at 1605 cm^{-1}, whereas the peak at 1463 cm^{-1} defined the C–H bending bond from the functional group of alkanes (cellulose, hemicellulose, and lignin). The peak marked at 1050 cm^{-1} indicates the C–O stretching bond structure from the functional group of alcohol (cellulose, hemicellulose, and lignin), carboxylic acids, and esters. The C–O stretching bond structure of the functional group of glycosides linkage is likewise recognized by the peaks band around 1100 to 1000 cm^{-1} [26].

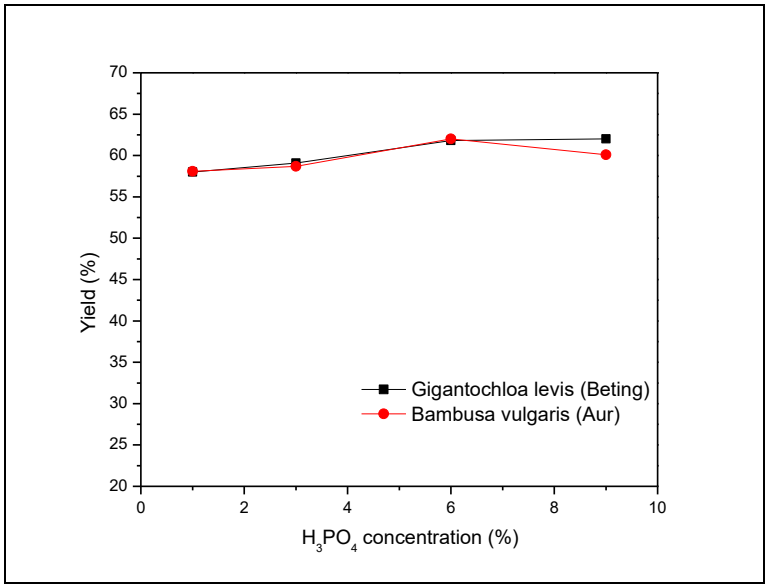


Figure 2. Effect of H_3PO_4 concentration on the yield of bamboo AC

The AC has less absorption peaks than the raw bamboo depending on the H_3PO_4 concentration used. It suggests that H_3PO_4 concentrations had less impact on the surface functionalities, while majority of the organic matter from raw bamboo was removed during the activation process [23]. Figure 3(b) reflects the results where the band at 3700 cm^{-1} is responsible for hydroxyl bonding group O–H with H-bonded vibration. The absorption band at 3340 to 3348 cm^{-1} disappeared due to the formation of polyphosphate and inorganic species in the AC [27]. Meanwhile, the stretching of C=O bands were attributed to the aromatic structures around 1540 cm^{-1}. The peak at 1210 cm^{-1} might be attributed to P=OOH, O–C stretching vibrations in the P–O–C linkage, and hydrogen-bonded P=O stretching mode. The peak at 1000 cm^{-1} can be caused by the stretching vibrations in P–O–P polyphosphate chains, and P^+–C^- in acid phosphate esters. Aromatic structures are responsible for the weaker bonds around 560 cm^{-1}. These results are in a good agreement with the study by Yorgun et al. [21]. Basically, during the H_3PO_4 chemical activation process, four main reactions will occur which are dehydration, depolymerization, the formation of aromatic ring, and the elimination of phosphate group [28]. H_3PO_4 acts as a dehydrating catalyst during acid hydrolysis to promote decomposition and depolymerization of the biopolymers (cellulose, hemicellulose, lignin). The increasing concentration of H_3PO_4 will enhance its ability as the dehydrating catalyst that removes excess water and converts the methyl group in the bamboo to AC with rich-pore structure [12, 29].

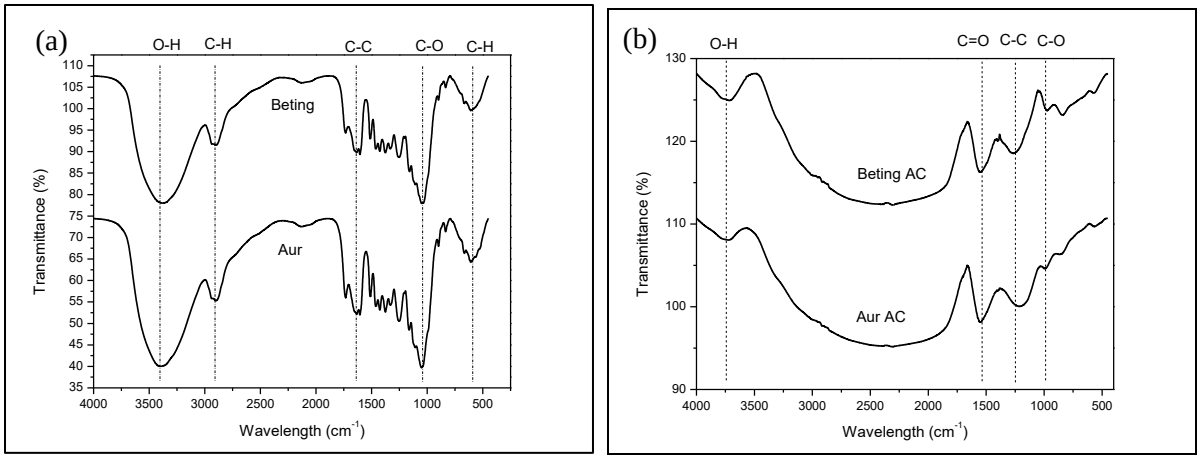


Figure 3. FTIR spectra of bamboo (a) raw precursor (b) porous activated carbon

Surface area and porous structure

Surface area and porous structure (pore size and pore volume) of bamboo AC is important to note to determine its end application. The effect of H_3PO_4 on the surface area and porous structure of bamboo AC was investigated using N_2 adsorption-desorption spectroscopy at 77 K. The effects of carbon precursor (bamboo species) on the surface area and porous structure of bamboo AC were also studied. Figure 4(a) and (b) summarizes the surface area and porous structure of ACs. The figure shows that the porous structure (pore size and pore volume) of bamboo AC increased with increasing H_3PO_4 concentration. These results indicate that high concentration H_3PO_4 impregnation benefitted the formation of pores [4, 30].

Furthermore, the surface area of bamboo AC increased with the increasing of H_3PO_4 concentration. The effect of an increased H_3PO_4 concentration on the BET surface area and pore volume was stronger at 9% v/v H_3PO_4. At this concentration, the maximum surface area of 1319 and 1285 m^2/g, total pore volume of 0.68 and 0.73 cm^3/g, and pore size of 3.6 nm were obtained in beting and aur ACs, respectively, which are comparable with that of the commercial AC (500–1500 m^2/g) [31]. The lowest H_3PO_4 concentration (1% v/v) shows the lower surface area and total pore volume of 368–381 m^2/g and 0.17 cm^3/g, respectively. The surface area and total pore volume can also be compared with the raw material of bamboo. There is no formation or presence of pores and also any increment of pore volume in the raw bamboo. The surface area and pore volume were only 0.437 m^2/g and 0.000826 cm^3/g, respectively. The effect of H_3PO_4 concentration on the surface area and total pore volume of the AC is shown in Figure 4(a) and (b). The process of thermal degradation and volatilization accelerates further when carbonization is applied to an impregnated bamboo, resulting pores forming and surface area increasing [21]. It is believed that the porosity of AC was mainly caused by the H_3PO_4 remaining in the impregnated material. The H_3PO_4 introduced into the interior of the bamboo particle during impregnation can inhibit the contraction of the structure during carbonization, thus producing a porous structure when it is extracted by washing after carbonization. The H_3PO_4 can accelerate the hydrolysis of lignocellulosic material, thus it promotes the formation bond cleavage in the biopolymer structure of bamboo. This can weaken the bonding within the structure and favouring the swelling of the biomaterial, which promotes the formation of pores and the increment of pore volume. As the H_3PO_4 dosage increases, it is reasonable to expect more potential sites could be penetrated and occupied by H_3PO_4, which enhances the pore-opening and widening processes. Besides that, during the carbonization at 500 °C using the tubular furnace, H_3PO_4 exhibits the formation of volatile cellulose products which causes the bamboo biopolymer structure begins to dilate and cross-link between the biopolymer chains through the ester linkages formation in the H_3PO_4 and OH groups. The similar findings were also reported by Feng et al. [4], Tumirah et al. [12], and Jagtoyen & Derbyshire [29].

The production of ACs with high surface areas from a low cost and renewable material is indeed of importance from the viewpoint of economic and environmental aspects. High surface area of bamboo AC is believed to provide large space to trap chemical contaminants if it is used as an absorbance. Table 4 summarizes the surface area and porous structure of bamboo ACs prepared using the H_3PO_4 chemical activation method.

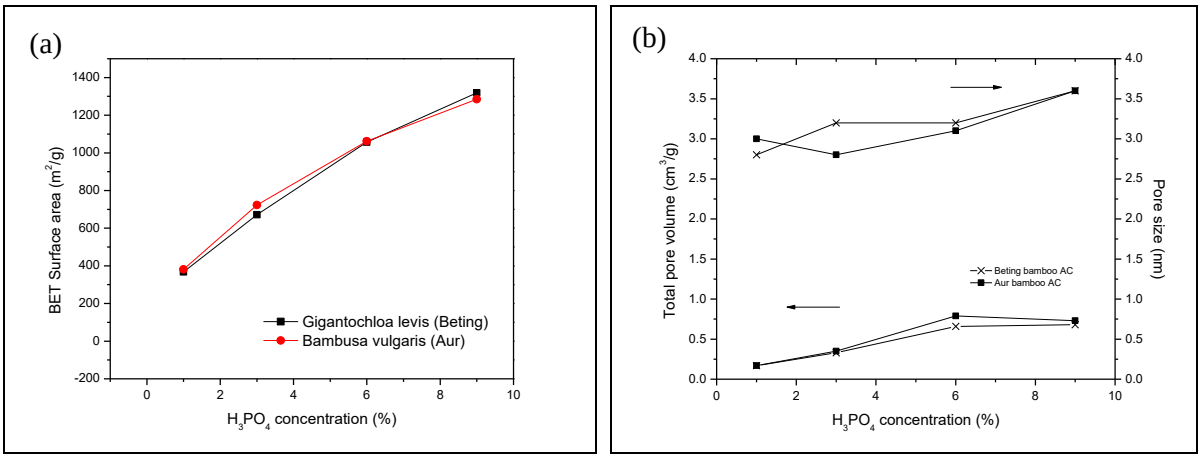


Figure 4. Effect of H_3PO_4 concentration on (a) the BET surface areas, (b) the total pore volume and pore size of activated carbons

Surface morphology of bamboo raw material and activated carbon

The FESEM analysis at the magnification scale of 5000× were carried out to confirm the textural properties and differences in the surface morphology of bamboo raw material and ACs (Figure 5). According to Figure 5(a) and (c), the micrographs of bamboo show no evidence of pore presence on the surface. The surface textures were rough, uneven, and undulating, due to the condensable volatile compounds that have gathered on the carbon surface. During activation and carbonization, most volatile matter was released thus showing surface changes of pores opening in bamboo ACs as shown in Figure 5(b) and (d). The AC's surface also generated well-developed pores because of the H_3PO_4 concentration [2]. The differences between these two carbonaceous materials' exterior morphologies can be related to the activation of H_3PO_4, which primarily involves the production of volatile chemicals and the interaction between the activating agent and the carbon precursor. The reaction between the carbon and the activating agent causes pore volume to increase as well as the formation of new pores during the chemical activation process. Similar trend was also found by Ismail and Yorgun et al [21,23]. Therefore, H_3PO_4 is a successful activation agent for producing ACs with large surface area.

Potential application of bamboo activated carbon

The performance of AC is largely depending on its surface area, porous structure, and chemical surface characteristics [32-34]. AC was used as an absorbance material because it has a massive surface area and well-developed pore structure (Table 3). These properties enable AC to have an excellent adsorption ability. Therefore, AC is widely used as a component in the water filtration system to remove contaminants. However, the adsorption effectiveness of AC is depending on the pores and pore size distribution relative to the size of adsorbent (organic matter) [35]. For example, the natural organic matter adsorption occurs in micropores and mesopores of AC [36]. However, AC with macropores is needed to filter bacteria [37]. Wang et al. [38] reported that the most suitable pore size range of AC for microbial attachment is between 2 and 5 μm. Therefore, the surface area and porous structure of bamboo AC obtained in this study indicates that it has the potential to be used as an absorbance material.

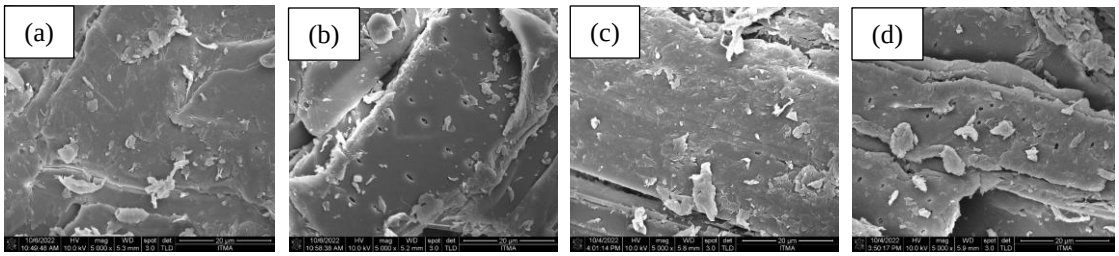


Figure 5. FESEM micrograph of (a) beting bamboo raw (b) beting bamboo activated carbon at 9% v/v H_3PO_4 impregnation (c) aur bamboo raw (d) aur bamboo activated carbon at 9% v/v H_3PO_4 impregnation

Table 3. Application of activated carbon prepared using phosphoric acid chemical activation method of varies carbon precursor as an absorbance material

Carbon Precursor	**BET Surface Area (m^2/g)**	**Pore Size**	**Adsorbents**	**Findings**	**References**
Mango kernel	490.43	38.9 μm	Cr (VI)	The maximum adsorption capacity of Cr (IV) was 7.8 mg/g at pH 2, T: 35 ^oC	[39]
Tea waste	824	<50 nm	Oxytetracycline	The maximum adsorption capacity of oxytetracycline was 175 mg/g at T: 20 ^oC	[40]
Coconut shell	2648	1-7 nm	benzene	Excellence benzene adsorption performance	[41]
Coconut front	483	29.72 Å	Carbofuran insecticide	Adsorption capacity was found to be 198.4 mg/g at T: 30 ^oC	[42]
Banana tree pseudo-stem fiber	1975	-	Methylene blue dye	Adsorption capacity of 728 mg/g at T: 30 ^oC	[43]
Typha orientalis leaves	1238	-	Pb(II)	The maximum adsorption capacity was found to be 7.95 mg/g	[44]
Bamboo	2237	Micropores	Ciprofloxacin	Adsorption amounts reach 613 mg/g	[45]
Coconut shell	89.09	-	Methylene blue	Adsorption amount 14.35-16.92 mg/g	[46]

Conclusion

In this work, the Sarawak wild bamboo, *Gigantochloa levis* (beting) and *Bambusa vulgaris* (aur) was used as a carbon precursor to produce ACs through the H_3PO_4 chemical activation method. The effect of H_3PO_4 concentration on the surface area, porous structure, and yield of AC was studied. The concentration of H_3PO_4 greatly influences the surface area, porous structure, and yield of AC. The maximum surface area of 1319 and 1285 m^2/g were obtained at 9% v/v H_3PO_4 impregnation

of beting and aur bamboos, respectively. Furthermore, the maximum AC yield of 62% was obtained at 9% H_3PO_4 impregnation of beting bamboo and 6% H_3PO_4 impregnation of aur bamboo. The results show that bamboo is proven to be an effective precursor and has the potential to be a promising precursor to produce ACs. The large surface area AC that was produced can be used as an extremely promising adsorbent for various environmental applications. Low cost ACs could be produced by using cheap raw materials and an appropriate production technique. Cost is the key factor in determining the potential of an adsorbent in the industry. To produce low-cost ACs, it is necessary to look at novel source materials. To our knowledge, no research has been done on using bamboo as a raw material to prepare ACs using the low concentration of H_3PO_4 chemical activation. This is to supplement the information on the properties of AC which is particularly lacking.

Acknowledgement

This work was jointly carried out by Forest Research Institute Malaysia (FRIM) and Sarawak Timber Industry Development Corporation (STIDC). Authors would like to acknowledge all staff members of Bioenergy Laboratory and Wood Preservative Analysis Laboratory for their helpful and kindness, cooperative and supports.

References

1. Negara, D. N. K. P., Nindhia, T. G. T., Surata, I. W., Sucipta, M. and Hidajat, F. (2019). Activated carbon characteristics of tabah bamboo that physically activated under different activation time. *IOP Conference Series: Materials Science and Engineering,* 539(1): 012011.
2. Mohd Iqbaldin, M. N., Khudzir, I., Mohd Azlan M. I., Zaidi, A.G., Surani, B. and Zubri, Z. (2013). Properties of coconut shell activated carbon. *Journal of Tropical Forest Science,* 25(4): 497-503.
3. Bagheri, N. and Abedi, J. (2009). Preparation of high surface area activated carbon from corn by chemical activation using potassium hydroxide. *Chemical Engineering Research and Design*, 87(8): 1059-1064.
4. Feng, J., Zhu, H., Xu, Y., Jiang, J. and Pan, H. (2021). Preparation and characterization of high-performance activated carbon from papermaking black-liquor at low temperature. *Journal of Analytical and Applied Pyrolysis*, 159: 105292.
5. Mahanim, S. M. A., Wan Asma, I., Rafidah, J., Puad, E. and Shaharuddin, H. (2011). Production of activated carbon from industrial bamboo wastes. *Journal of Tropical Forest Science,* 23 (4): 417-424.
6. Huang, Y. P., Hou, C. H., His, H. C. and Wu, J. W. (2015). Optimization of highly microporous activated carbon preparation from Moso bamboo using central composite design approach. *Journal of Taiwan Institute of Chemical Engineers,* 50: 266-275.
7. Huang, G. Wang, Y., Zhang, T., Wu, X. and Cai, J. (2019). High-performance hierarchical N-doped porous carbons from hydrothermally carbonized bamboo shoot shells for symmetric supercapacitors. *Journal of Taiwan Institute of Chemical Engineers,* 96: 672-680.
8. Negara, D. N. K. P., Nindhia, T. G. T., Surata, I. W., Hidajat, F. and Sucipta, M. (2020). Textural characteristics of activated carbons derived from Tabah bamboo manufactured by using H_3PO_4 chemical activation. *Materials Today: Proceedings,* 22: 148-155.
9. Tay, T., Ucar, S. and Karagöz, S. (2009). Preparation and characterization of activated carbon from waste biomass. *Journal of Hazardous Materials,* 165(1): 481-485.
10. Li, W., Yang, K., Peng, J., Zhang, L., Guo, S. and Xia, H. (2008). Effects of carbonization temperatures on characteristics of porosity in coconut shell chars and activated carbons derived from carbonized coconut shell chars. *Industrial crops and products*, 28(2):190-198.
11. Supriya, S., Palanisamy, P. N. and Shanthi, P. (2014). Preparation and characterization of activated carbon from casuarina for the removal of dyes from textile wastewater. *International Journal of ChemTech Research,* 6 (7): 3635-3641.
12. Tumirah, K., Mohd Zobir, H., Zulkarnain, Z. and Rafaedah, R. (2015). Textural and chemical properties of activated prepared from tropical peat soil by chemical activation method. *BioResources,* 10 (1): 986-1007.

13. Wise, L. E., Murphy, M. and D' Addieco, A.A. (1946). Chlorite holocellulose: Its fractiontion and bearing on summative wood analysis and on studies on the hemicelluloses. *Paper Trade Journal* 122 (2): 35-43.
14. TAPPI. 203 om-93. Alpha, Beta and Gamma Cellulose in Pulp. (2009). Technical Association of the pulp and industry, Atlanta.
15. TAPPI. T222 om-02Acid-Insoluble Lignin in Wood and Pulp. (2002). Technical Association of the pulp and industry, Atlanta.
16. Liu, Q-S., Zheng, T., Wang, P. and Guo, L. (2010). Preparation and characterization of activated carbon from bamboo by microwave-induced phosphoric acid activation. *Industrial Crops and Products,* 31(2): 233-238.
17. Negara, D.P., Nindhia, T.T., Surata, I.W. and Sucipta, M. (2017). Chemical, strength and microstructure characterization of Balinese bamboos as activated carbon source for adsorbed natural gas application. *IOP Conference Series: Materials Science and Engineering.* 201(1): 012033.
18. Kasim, J. Ahmad, A. J., Mohamod A. L. and Khoo, K. C. (1994). A note on the proximate chemical composition and fibre morphology of bambusa vulgaris. *Journal of Tropical Forest Science,* 6 (3): 356-358.
19. Azeez, M. A. and Orege, J. I. (2018). Chapter 3: Bamboo, its chemical modification, and products. In H. P. S. Abdul Khalil (Ed.), *Bamboo*. IntechOpen. http://dx.doi.org/10.5772/intechopen.76359: 25-48.
20. AssefaAragaw, T. (2016). Proximate analysis of cane bagasse and synthesizing activated carbon: Emphasis on material balance. *Journal of Environmental Treatment Techniques,* 4(4): 102-110.
21. Yorgun, S. and Yıldız, D. (2015). Preparation and characterization of activated carbons from Paulownia wood by chemical activation with H_3PO_4. *Journal of the Taiwan Institute of Chemical Engineers*, 53: 122-131.
22. Shamsuddin, M. S., Yusoff, N. R. N. and Sulaiman M. A. (2016). Synthesis and characterization of activated carbon produced from kenaf core fiber using H_3PO_4 activation. *Procedia Chemistry,* 19: 558-565.
23. Ismail, I.S., Rashidi, N.A. and Yusup, S. (2022). Production and characterization of bamboo-based activated carbon through single-step H_3PO_4 activation for CO_2 capture. *Environmental Science and Pollution Research*, 29(9): 12434-12440.
24. Chandra, T. C., Mirna, M. M., Sunarso, J., Sudaryanto, Y. and Ismadji, S. (2009). Activated carbon from durian shell: Preparation and characterization. *Journal of the Taiwan Institute of Chemical Engineers,* 40(4): 457-462.
25. Liang, Q., Liu, Y., Chen, M., Ma, L., Yang, B., Li, L. and Liu, Q. (2020). Optimized preparation of activated carbon from coconut shell and municipal sludge. *Materials Chemistry and Physics,* 241: 122327.
26. Bakri, M. K. and Jayamani, E. (2016). Comparative study of functional groups in natural fibers: Fourier transform infrared analysis (FTIR). *Futuristic Trends in Engineering, Science, Humanities, and Technology,* 1: 167-174.
27. Hesas, R. H., Wan Daud, W. M. A., Sahu, J. N. and Arami-Niya, A. (2013). The effects of a microwave heating method on the production of activated carbon from agricultural waste: A review. *Journal of Analytical and Applied Pyrolysis,* 100: 1-11.
28. Suárez-García, F., Martínez-Alonso, A. and Tascón, J. M. D. (2004). Activated carbon fibers from Nomex by chemical activation with phosphoric acid. *Carbon,* 42(8-9): 1419-1426.
29. Jagtoyen, M. and Derbyshire, F. (1993). Some considerations of the origins of porosity in carbons from chemically activated wood. *Carbon,* 31(7): 1185-1192.
30. Wang, Y. X., Ngo, H. H. and Guo, W. S. (2015). Preparation of a specific bamboo based activated carbon and its application for ciprofloxacin removal. *Science of The Total Environment,* 533: 32-39.
31. Nachenius, R. W., Ronsse, F., Venderbosch, R. H., and Prins, W. (2013). Chapter two - biomass pyrolysis. In D. Y. Murzin (Ed.), *Advances in Chemical Engineering*, (Vol. 42, pp. 75–139). Academic Press Inc.
32. Karanfil, T., Kitis, M., Kilduff, J. E. and Wigton, A.

(1999). Role of granular activated carbon surface chemistry on the adsorption of organic compounds. 2. Natural organic matter. *Environmental Science Technology,* 33(18): 3225-3233.

33. Moore, B. C., Cannon, F. S., Westrick, J. A., Metz, D. H., Shrive, C. A., DeMarco, J. and Hartman, D. J. (2001). Changes in GAC pore structure during full-scale water treatment at Cincinnati: A comparison between virgin and thermally reactivated GAC. *Carbon,* 39(6): 789-807.
34. Lu, Z., Sun, W., Li, C., Cao, W. Jing, Z., Li, S., Ao, X., Chen, C. and Liu, S. (2020). Effect of granular activated carbon pore-size distribution on biological activated carbon filter performance. *Water Research,* 177: 115768.
35. Nowotny, N., Epp, B., von Sonntag, C. and Fahlenkamp, H. (2007). Quantification and modeling of the elimination behavior of ecologically problematic wastewater micropollutants by adsorption on powdered and granulated activated carbon. *Environmental Science & Technology,* 41(6): 2050-2055.
36. Hsieh, C-T. and Teng, H. (2000). Influence of mesopore volume and adsorbate size on adsorption capacities of activated carbons in aqueous solutions. *Carbon,* 38(6): 863-869.
37. Walker, G. M. and Weatherley, L. R. (1998). Bacterial regeneration in biological activated carbon systems. *Process Safety and Environmental Protection,* 76(2): 177-182.
38. Wang, J. Z., Summers, R. S. and Miltner, R. J. (1995). Biofiltration performance: Part 1, relationship to biomass. *Journal American Water Works Association, 87*: 55-63.
39. Rai, M.K., Shahi, G., Meena, V., Meena, R., Chakraborty, S., Singh, R.S. and Rai, B.N. (2016). Removal of hexavalent chromium Cr(VI) using activated carbon prepared from mango kernel activated with H_3PO_4. *Resource-efficient technologies*, 2: S63-S70.
40. Kan, Y., Yue, Q., Li, D., Wu, Y. and Gao, B. (2017). Preparation and characterization of activated carbons from waste tea by H_3PO_4 activation in different atmospheres for oxytetracycline removal. *Journal of the Taiwan Institute of Chemical Engineers*, 71: 494-500.
41. Zhang, Z., Lei, Y., Li, D., Zhao, J., Wang, Y., Zhou, G., Yan, C. and He, Q. (2020). Sudden heating of H_3PO_4-loaded coconut shell in CO_2 flow to produce super activated carbon and its application for benzene adsorption. *Renewable Energy*, 153: 1091-1099.
42. Njoku, V.O., Islam, M.A., Asif, M. and Hameed, B.H. (2014). Preparation of mesoporous activated carbon from coconut frond for the adsorption of carbofuran insecticide. *Journal of Analytical and Applied Pyrolysis*, 110: 172-180.
43. Silva, M. C., Spessato, L., Silva, T. L., Lopes, G. K., Zanella, H. G., Yokoyama, J. T., Cazetta, A. L. and Almeida, V. C. (2021). H_3PO_4–activated carbon fibers of high surface area from banana tree pseudo-stem fibers: adsorption studies of methylene blue dye in batch and fixed bed systems. *Journal of Molecular Liquids*, 324: 114771.
44. Anisuzzaman, S. M., Joseph, C.G., Daud, W. M. A. B. W., Krishnaiah, D. and Yee, H. S. (2015). Preparation and characterization of activated carbon from *Typha orientalis* leaves. *International Journal of Industrial Chemistry*, 6: 9-21.
45. Wang, Y. X., Ngo, H. H. and Guo, W. S. (2015). Preparation of a specific bamboo based activated carbon and its application for ciprofloxacin removal. *Science of the Total Environment*, 533: 32-39.
46. Lee, C. L., Chin, K. L., H'ng, P. S., Rashid, U., Maminski, M. and Khoo, P. S. (2021). Effect of pretreatment conditions on the chemical–structural characteristics of coconut and palm kernel shell: A potentially valuable precursor for eco-efficient activated carbon production. *Environmental Technology & Innovation*, 21: 101309.

Malaysian Journal of Analytical Sciences (MJAS)
Published by Malaysian Analytical Sciences Society

A NEW GOLD NANOPARTICLES MODIFIED SCREEN PRINTED PAPER CARD BASED MICROFLUIDIC DEVICE

(Nanopartikel Emas Baru Diubahsuai Skrin Dicetak Kad Kertas Berasaskan Peranti Mikrobendalir)

Salamatu Hayatu[1,2,3], AbduRahman Abdul Audu[2], Magaji Ladan[2], and Nor Azah Yusof[3,4]

[1]*Department of Pure and Applied Chemistry,*
Faculty of Science, Kaduna State University, Kaduna P.M.B 2339, Nigeria
[2]*Department of Pure and Industrial Chemistry,*
Faculty of Science, Bayero University, Kano P.M.B 3011, Nigeria
[3]*Department of Chemistry,*
Faculty of Science, Universiti Putra Malaysia, 43400 UPM, Serdang, Selangor, Malaysia
[4]*Institute of Nanoscience and Nanotechnology,*
Universiti Putra Malaysia, Serdang, Selangor, Malaysia.

Corresponding author: salamatu.hayat@kasu.edu.ng

Received: 9 January 2023; Accepted: 23 July 2023; Published: 30 October 2023

Abstract

This work offers a novel platform for the straightforward and low-cost manufacture of paper microfluidic devices known as gold nanoparticles modified screen printed paper electrode AuNPs/SPPE. The component can function as an electrochemical cell as well as a microfluidic device. Different paper cards were evaluated for hydrophobicity, and metallic gold card was selected due to its superior hydrophobic properties. Thus, waxing and other pretreatment steps are eliminated. The AuNPs/SPPE was created by screen printing on metallic gold card using commercial silver ink. Working electrode was modified using synthesized gold nanoparticles (AuNPs). The presence and widespread distribution of Au particles are shown by SEM and EDX study. The conductivity and resistivity study shows good conductance. The device was applied in tramadol detection, tramadol was studied electrochemically using cyclic voltammetry technique, where it was oxidized at 0.1 to 0.3 volts. Positive results obtained from electrochemical investigation suggest good and promising future applications.

Keywords: microfluidic, screen printing, paper device

Abstrak

Kerja ini menawarkan platform baru untuk pembuatan peranti mikrofluidik kertas yang mudah dan kos rendah yang dikenali sebagai nanopartikel emas yang diubah suai skrin dicetak kertas elektrod AuNPs/SPPE. Komponen ini boleh berfungsi sebagai sel elektrokimia serta peranti mikrofluidik. Kad kertas yang berbeza dinilai untuk hidrofobisiti, dan kad emas logam dipilih kerana sifat hidrofobik yang unggul. Oleh itu, waxing dan langkah-langkah pretreatment lain dihapuskan. AuNPs/SPPE dicipta melalui percetakan skrin pada kad emas logam menggunakan dakwat perak komersial. Elektrod kerja diubah suai menggunakan nanopartikel emas yang disintesis (AuNPs). Kehadiran dan pengedaran zarah Au yang meluas ditunjukkan oleh kajian SEM dan

EDX. Kajian kekonduksian dan rintangan menunjukkan kelakuan yang baik. Peranti ini digunakan dalam pengesanan tramadol, tramadol dikaji secara elektrokimia menggunakan teknik voltammetrik kitaran, di mana ia teroksida pada 0.1 hingga 0.3 volt. Hasil positif yang diperolehi daripada penyiasatan elektrokimia menunjukkan aplikasi masa depan yang baik dan menjanjikan.

Kata kunci: mikrobendalir, percetakan skrin, peranti kertas

Introduction

Microfluidic is a portable device that requires a small volume of sample and can easily be integrated into a point of care diagnostics equipment, that can be used in remote settings, with poor infrastructure [1-2]. Because of its intriguing benefits and cutting-edge platform that is still being researched, microfluidics has garnered a lot of attention. The development of fabrication techniques, novel substrates, and detection techniques is ongoing. As a result, low-cost materials and low-cost fabrication and detection designs are emerging [1-6] in response to the growing demand for low-cost devices that will greatly simplify lives all over the world. Paper substrates are now included in microfluidic systems [5-10], which is a novel development that researchers are exploring since it is portable, inexpensive, and requires a small amount of sample [7-9]. Hydrophobic and hydrophilic patterns are typically formed on the paper to create microfluidic paper devices. The hydrophilic region is produced by screen printing the ink onto the patterned paper, and the hydrophobic portion is produced by melting photoresist or wax onto the paper [1,5]. Dungchai et al. used photoresist to form the hydrophobic barrier on a filter paper [5]. The wax technique is the most popular. The wax has been applied in a variety of ways, according to reports. A fabrication technique utilizing chromatographic paper was created by Songjaroen et al. [3]. The paper was dipped into melted wax, and the wax penetrating the area not covered by the iron template created the hydrophobic region. While, Zhang and Zha employed filter paper with a paraffin copper sheet attached. When heated, the paraffin melted through the filter paper and formed the hydrophobic barriers [4].

The increasing demand for point of care testing has prompt fabrication of rapid and quantitative microfluidic paper devices [1,8-13,16] for hard drugs detection [11-13]. Rapid and quantitative microfluidic paper devices [1,8-13,16] for the detection of hard drugs [11–13] have been made as a result of the rising need for point-of-care testing. The availability of microfluidic devices can reduce the short- and long-term negative impacts of hard drugs, such as overdose, addiction, fatalities, and consumption, as the victim can be quickly identified in the general population [12-13]. Screen printing was employed due to its miniaturization ability, low cost, versatility, and ease of mass production [11,14]. This technique has been employed in the production of electrodes used in commercial electrochemical test strips [11,15-16]. The distribution of wax on the surface of the material might not be uniform depending on the application method. Thus, complete hydrophobicity of the paper cannot be assured. In order to address this problem, many paper cards were examined. And we report a novel substrate metallic gold card that has a hydrophobic nature. The fabrication is greatly facilitated by the removal of a key wax application step. Without any additional card pretreatment, the gold card can be screen-printed with Ag ink (silver ink) directly. When used as an ion selective electrode, silver ink exhibits greater sensitivity to various ions [17].

Gold nanoparticles (AuNPs) are considered to be highly stable metal nanoparticles that display a number of exceptional qualities, such as facial synthesis and surface modification, excellent biocompatibility, and strong Surface Plasmon Resonance (SPR) in the visible region of the spectrum, which make them the ideal candidate for detection of analytes with the naked eye [18]. Additionally, they have special optical and electrochemical properties that make them useful for sensing various analytes [19]. Due to the special characteristics of gold nanoparticles, which include their ability to withstand surface oxidation and chemical inertness, modification of electrode with gold nanoparticles is garnering considerable interest [20]. The sensitivity of the sensing platform can be improved by modifying the working electrode with AuNPs. In this study, a microfluidic paper device was created for tramadol detection by screen printing silver ink onto a

card and modifying the working electrode with AuNPs. Tramadol can bind to the surface of these particles through the amino group by electrostatic contact, because oxygen-containing rings of hybrid aromatics display noticeably better binding to AuNPs [18]. By coordinating interactions with the electron-deficient surfaces of metal nanoparticles, hydroxyl groups containing electron-rich oxygen atoms are more likely to be bonded to the surface of metal nanoparticles [19]. This newly fabricated microfluidic device may function as both a microfluidic system and an electrochemical sensor.

Materials and Methods

All chemicals used were of analytical grade. Chloro auric acid ($HAuCl_4$), silver acetate, carbon conducting ink and silver conductive ink from Sigma Aldrich (USA), sodium citrate dihydrate, sodium acetate, ammonia, ethylamine, acetic acid and formic acid from Kermel chemicals (China), hydroxyl ethyl cellulose (HEC) from Koch-Light laboratories (England), potassium ferricyanide, potassium chloride from Harris reagent (England).

Synthesis of silver ink

In a glass vial, 2.0 g of silver acetate and 5 mL of ethylamine were combined, and 5 mL of ammonia was then added to the mixture to create a transparent solution. Followed by dropwise addition of 0.4 mL formic acid to the clear solution, which caused it to turn from light brown to black to gray. Lastly, 0.2 g of HEC was added to the solution while being continuously stirred [21].

Synthesis of AuNPs (gold nanoparticles)

In 200 mL of deionized water, 7.0 mg of $HAuCl_4$ was dissolved to create a pale-yellow solution. 50 mL of the solution were heated to a boil while being vigorously stirred, and 5 mL of 40 mM sodium citrate were added dropwise. Till a steady deep red color was obtained after 15 minutes of continuous heating and stirring [22]. The solution was kept at or below 7 ^oC.

Fabrication of device

Two distinct patterns were created in Corel Draw. The first pattern, which is made up of circles with 1.6 cm in diameter, was printed using a printer on the card. The second pattern, the electrode layout, was printed on an A4 laser sheet using an HP laser jet 5100M. The electrode layout consists of the working electrode (WE), reference electrode (RE), and counter electrode (CE). The design on the laser sheet was exposed to a mesh, and the mesh was used to screen print silver ink onto the card as displayed in figure 1 [15]. The card was cured for 30 minutes at 120°C. Individual electrochemical cells or sensor strips were cut off. The working electrode was modified using gold nanoparticles. Gold nanoparticles modified screen printed paper electrode was prepared by drop coating the working electrode with 10 µL of AuNPs and the solution was allowed to dry at room temperature. For microfluidic system, 10 µL of AuNPs was drop coated onto the working electrode, with subsequent addition of 10 µL of 1 µM tramadol onto the AuNPs solution.

Characterization

Scanning electron microscopy (SEM) was used to examine the morphology of the AuNPs and Ag ink, and energy dispersive X-ray spectroscopy was used to examine the elemental spectra (EDX). Using a digital multimeter (DT9205A), the resistance of the manufactured devices was measured, and resistivity was computed using the formula.

$$\rho = RA/l \quad (1)$$

Where, ρ is Resistivity, R is the resistance, A is the cross-sectional area and L is the length, while conductivity was calculated using the formula

$$\sigma = 1/\rho \quad (2)$$

Where σ is the conductivity, and ρ is the resistivity [23].

Electroanalytical measurement

DropSens potentiostat (United Kingdom) coupled to a computer and the sensor strip, which has three electrodes: a working electrode, counter electrode, and reference electrode, were used to perform electrochemical measurements.

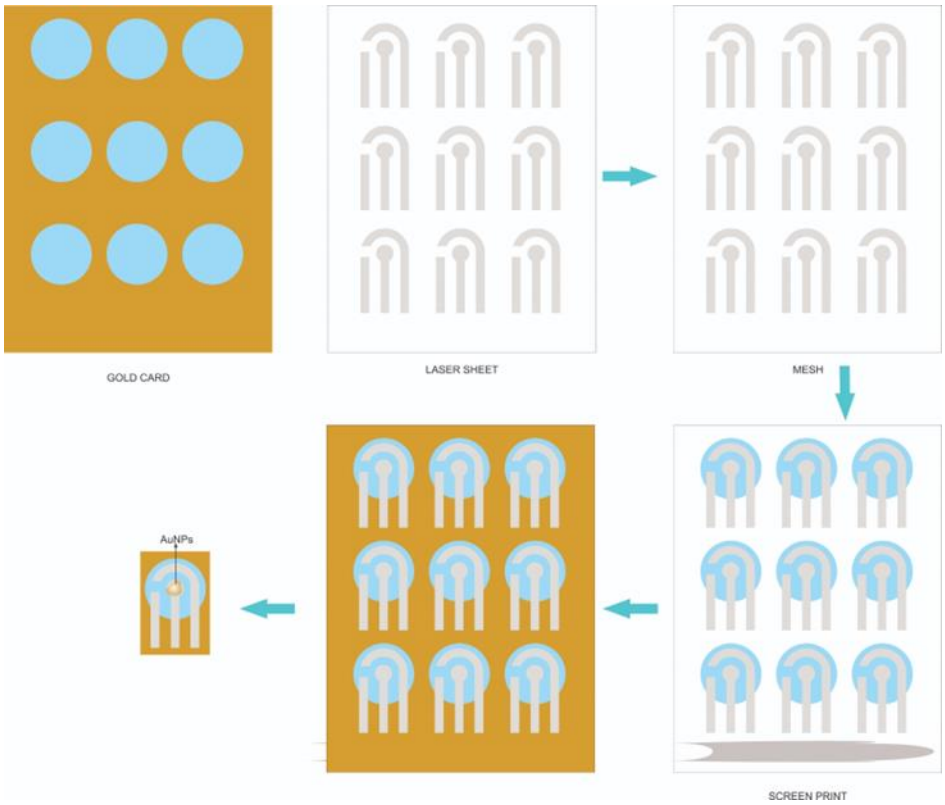


Figure 1. Schematic illustration of the fabrication steps

Results and Discussion

Scanning electron microscope

SEM Phenom Prox was used to capture the SEM imaging at 500x magnification, 100 µm interval, and 15 kV. The sample holder was created using aluminum foil as the blank. The images in Figure 2a have no particles at all dispersed across the surface. Figure 2b, on the other hand, shows an image of Ag ink with a white deposit covering the surface. Figure 2c displays image of surface without any particles at all. Figure 2d shows an image of gold nanoparticles, which are depicted as dazzling white deposits covering the surface. It has a highly distinct distribution of AuNPs dispersed widely throughout the surface.

Energy dispersive X-ray spectroscopy

The elemental spectra and value of Ag ink are shown in Figure 3a. Using the SEM image, several spectrums were captured at various distributions (Figure 2b). There is one prominent peak and several smaller peaks of silver in the spectral image, which indicates the presence of silver and the value confirms that silver is widely spread. The other elements were impurities discovered on the aluminum blank before the addition of silver, according to the elemental values obtained. The elemental spectra and value of AuNPs are shown in Figure 3b. Using the SEM image, several spectrums were captured at various distributions (Figure 2d). One sharp peak and several smaller peaks of AuNPs can be seen in the spectral image, which indicates the presence of AuNPs and the value confirms that AuNPs are widely spread. Due to the small quantity of contaminants present, the finding further supports the suitability of the process employed to create AuNPs and their purity. The aluminum blank included every element that has been seen with Ag ink and AuNPs. These are therefore impurities that are present on the blank.

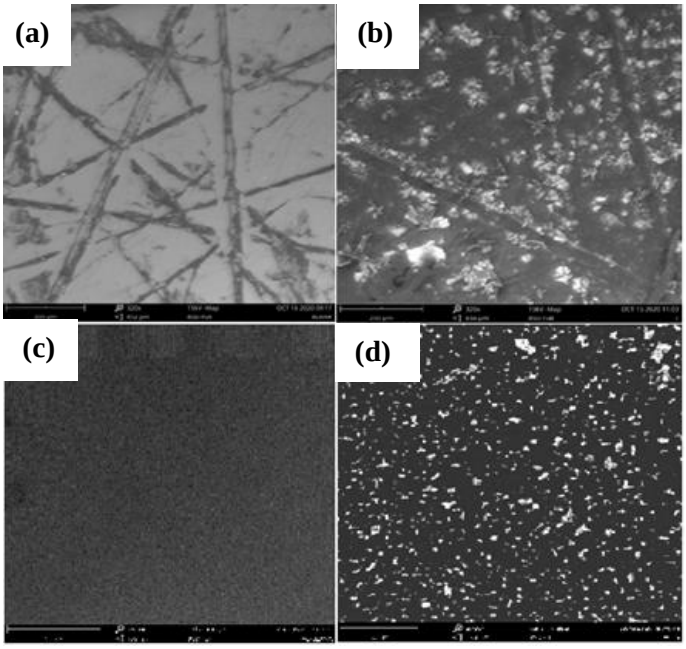
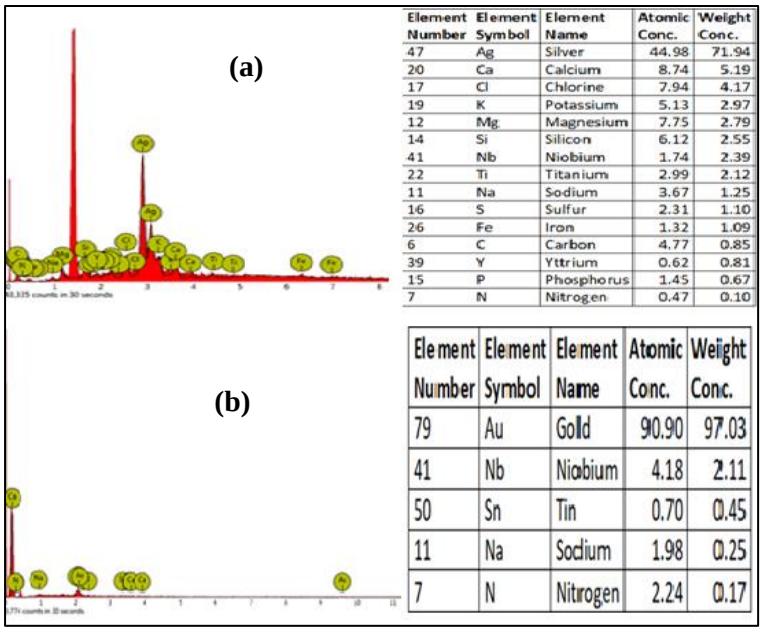


Figure 2. SEM image of (a) blank, (b) prepared Ag ink, (c) blank, and (d) AuNPs



Element Number	Element Symbol	Element Name	Atomic Conc.	Weight Conc.
47	Ag	Silver	44.98	71.94
20	Ca	Calcium	8.74	5.19
17	Cl	Chlorine	7.94	4.17
19	K	Potassium	5.13	2.97
12	Mg	Magnesium	7.75	2.79
14	Si	Silicon	6.12	2.55
41	Nb	Niobium	1.74	2.39
22	Ti	Titanium	2.99	2.12
11	Na	Sodium	3.67	1.25
16	S	Sulfur	2.31	1.10
26	Fe	Iron	1.32	1.09
6	C	Carbon	4.77	0.85
39	Y	Yttrium	0.62	0.81
15	P	Phosphorus	1.45	0.67
7	N	Nitrogen	0.47	0.10

Element Number	Element Symbol	Element Name	Atomic Conc.	Weight Conc.
79	Au	Gold	90.90	97.03
41	Nb	Niobium	4.18	2.11
50	Sn	Tin	0.70	0.45
11	Na	Sodium	1.98	0.25
7	N	Nitrogen	2.24	0.17

Figure 3. EDX image (a) spectral image of Ag ink with elemental values (b) spectral image of AuNPs with elemental values

Microfluidic paper device

The typical substrate for paper-based printed electronics is a paper with a hydrophobic resin coating on the surface. Hydrophilic and evenly absorbent characteristics, thus, are incompatible with the needs of printed electronics [24]. A variety of paper cards were examined to find the one with the highest hydrophobicity. When a drug sample was dropped, art card figure 4A gave a good print, but it absorbed and flowed. Figure 4B Teslin card, which is typically used to

create I.D. cards, could not produce a nice print right away. Moreover, the laser sheet figure 4C did not print well. Metallic silver and gold card figure 4D and E offered a nice print, did not absorb, and could be bent without harming the conducting part. Metallic silver and gold card were selected as the best substrates for additional examination. The image of the single sensor strip printed with commercial silver ink is shown in Figure 4F.

Conductivity and resistivity

Ag ink that had been synthesized had a conductivity of 23.1 mS. (millisiemens). The resistivity of the printed ink was calculated using the formula in equation 1. After printing with carbon ink, synthesized silver ink, and commercial silver ink on a paper card, the resistance of each ink was measured using a multimeter. The depiction of data recorded is shown in Table 1; commercial silver ink had a lower resistance. Hence, for more investigation, commercial silver ink was chosen. A lack of information from the synthesis process prevented the successful synthesis of Ag ink.

Gold and silver card printed with commercial silver ink were heated at 60 ºc. As can be seen in table 2, the resistance measurement decreased after 30 minutes, but not after an hour. As a result, 30 minutes was determined to be the ideal heating time. Resistance values obtained in table 2 were utilized in calculating the resistivity with the above resistivity formula. Gold card had a higher conductivity than silver card because it has a lower resistance than silver card. Due to the high conductivity that metal-coated papers typically display, they can perform in a variety of ways [25]

.

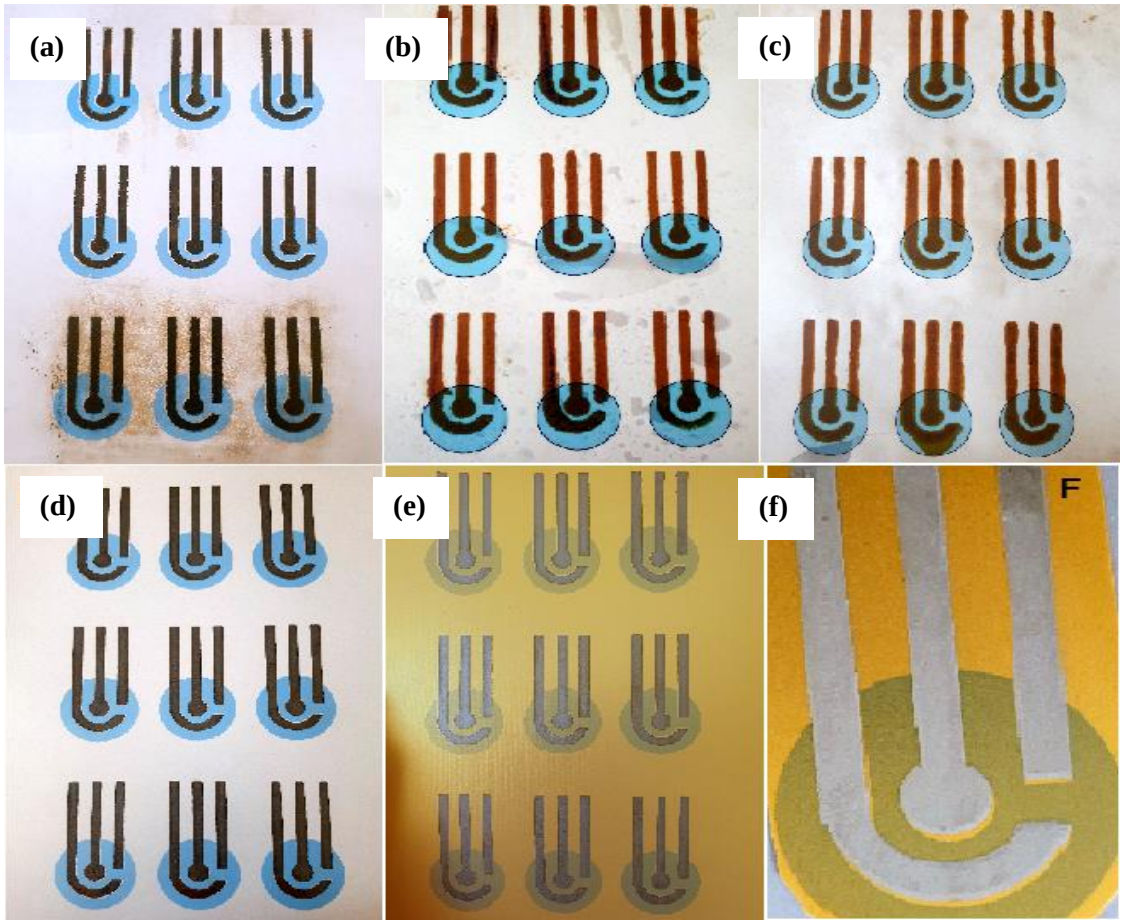


Figure 4. (a) Art card, (b) Teslin card, (c) laser sheet, (d) silver card, (e) gold card, (f) and single sensor strip

Electrochemical analysis

The electrochemical analysis employed the cyclic voltammetric approach, which provides data on the investigation of a reversible redox reaction. With the three-electrode sensor attached to a potentiostat, cyclic voltammetry was performed. The freshly created AuNPs/SPPE were studied using the cyclic voltammetric technique to determine their oxidation and reduction peak currents, which also shows an electron transfer reaction has taken place. Thus, indicating the feasible application of the sensor. With gold card AuNPs/SPPE in 2 mM $K_3Fe(CN)_6$ with 0.1 M KCl, a broad oxidation peak was seen at around 0.4 V to 0.55 V, whereas a minor reduction peak was seen at 0.15 V to 0.3 V in figure 5A. With the silver card AuNPs/SPPE, a broad oxidation peak was also seen between 0.3 and 0.45 V, whereas the reduction peak was shown between 0.2 and 0.45 V in figure 5B. When ferricyanide is subjected to cyclic voltammetry, ferricyanide is reduced to ferrocyanide and vice versa, demonstrating that the reaction is reversible and that a one electron transfer diffusion reaction has occurred [26]. These findings reveal that the oxidation peaks, which signify the formation of oxide, exhibit a greater current for gold card AuNPs/SPPE than for silver card AuNPs/SPPE, further demonstrating the superior conductivity of gold card.

The gold card AuNPs/SPPE was selected for further analysis. Figure 6 shows the results of the AuNPs/SPPE study in acetate buffer and tramadol. The cyclic voltammogram showed no oxidation peak but a small reduction peak in acetate buffer, while an oxidation peak current was obtained at around 0.1V to 0.3V and a reduction peak current at around 0.00V to -0.15V for acetate buffer with tramadol. As a result, AuNPs enhance detection capabilities and provide evidence of an oxidation reaction between AuNPs and tramadol.

Table 1. Resistance Measurement of different inks printed on gold and silver cards

Gold Card Electrodes	Working Electrode	Reference Electrode	Counter Electrode
Carbon ink	516	465	785
Prepared Silver ink	42.5	70.5	135.6
Commercial Silver ink	3.1	2.6	4.1
Silver card Electrodes			
Carbon ink	292	263	414
Prepared Silver ink	43.1	24.1	51.6
Commercial Silver ink	4.3	3.6	6.6

Table 2. Resistance measurement, resistivity and conductivity of gold and silver card with commercial silver ink after heating

Electrode	W.E	R.E	C.E
Gold card/Resistance	1.9	1.7	2.4
Resistivity (Ω cm)	3.4×10^{-5}	3.5×10^{-5}	2.5×10^{-5}
Conductivity (mS)	29367.54	28487.43	39479.54
Silver card/Resistance	2.43	2.2	2.9
Resistivity (Ω cm)	4.35×10^{-5}	4.5×10^{-5}	3.06×10^{-5}
Conductivity (mS)	22962.27	22013.05	32673.012

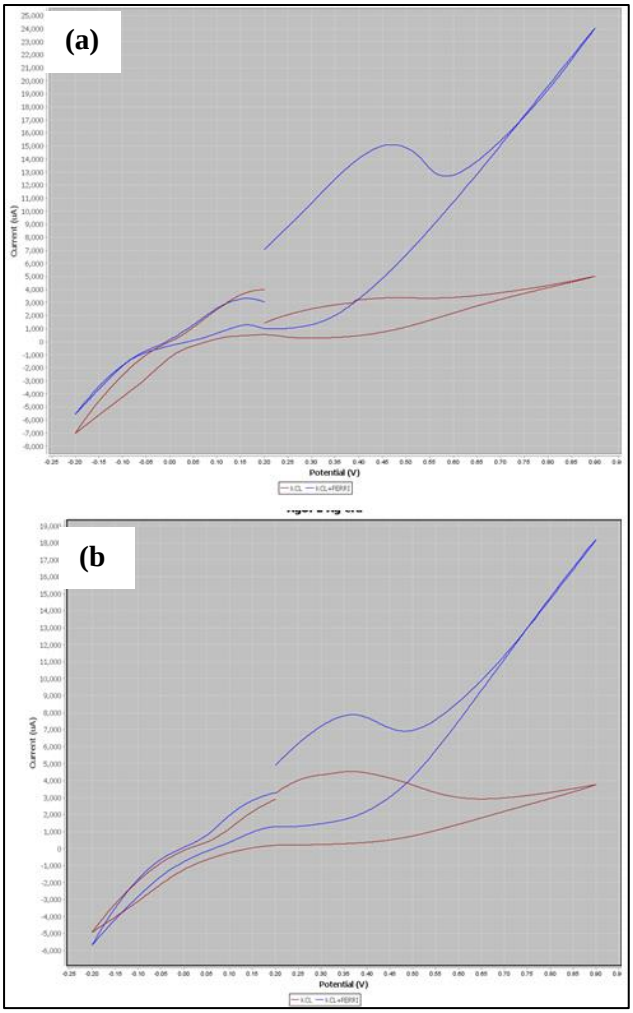


Figure 5. Cyclic voltammogram (a) Au card AuNPs/SPPE in 2 mM ferricyanide and 0.1 M KCl (blue line) 0.1 M KCl (red line) and (b) Ag card AuNPs/SPPE in 2 mM ferricyanide and 0.1 M KCl (blue line) 0.1 M KCl (red line)

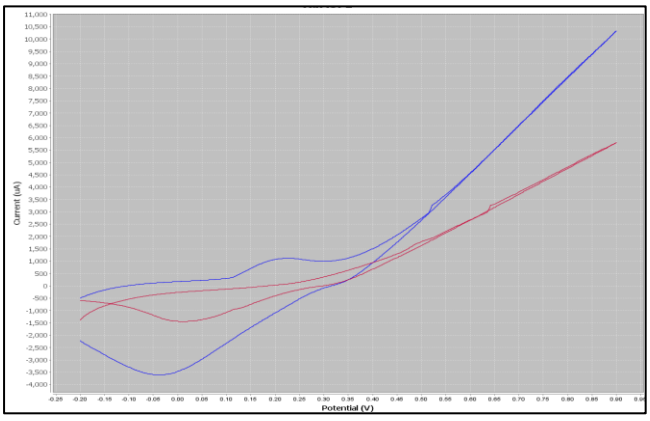


Figure 6. Cyclic Voltammograms of 0.1M Acetate Buffer (Red line), 1µM Tramadol (Blue line) for AuNPs/SPPE

Conclusion

Paper electrodes with gold nanoparticle modifications were successfully created using the screen-printing technique. The intriguing aspect of this research is that the metallic gold card we used as a substrate, which is also inexpensive, allowed us to forgo the wax phase. According to the conductivity value, the card exhibits very high conductance and produced a good print with the inks. Since the current was larger for the gold card, the electrochemical experiment further establishes the high conductivity of the manufactured sensor strip. Using cyclic voltammetry, the electrochemical method of detecting tramadol proved successful. We are certain that the manufactured sensor strip can be used in electrochemical detection based on this initial electrochemical measurement.

Acknowledgement

The research was financially supported by the grants under TETFUND Institution Based Research (IBR) and National Research Fund; TETFund/DR&D/CE/NRF/CC/15/Vol1.

References

1. Coltro, T., Cheng, C., Carrilho, E., and Jesus, D. P. De. (2014). Recent advances in low-cost microflui dic, *Electrophoresis*, 2014: 1-16.
2. Dutse, S. W., and Yusof. N. A. (2011). Microfluidi cs-based lab-on-chip systems in DNA-based biosen sing: an overview. *Sensors*, 11, 5754-5768.
3. Songjaroen, T., Dungchai, W., Chailapakul, O., an d Laiwattanapaisal, W. (2011). Novel, simple and l ow-cost alternative method for fabrication of paper -based microfluidics by wax dipping. *Talanta* 85(5): 2587-2593.
4. Zhang, A. L., and Zha, Y. (2012). Fabrication of pa per-based microfluidic device using printed circuit technology. *AIP Advances*, 2(2): 4733346.
5. Dungchai, W., Chailapakul, O., and Henry, C. S. (2 009). Electrochemical detection for paper-based mi crofluidics, *Analytical Chemistry*, 81(14): 5821-58 26.
6. Kong, X., Chong, X., Squire, K., and Wang, A. X. (2018). Microfluidic diatomite analytical devices f or illicit drug sensing with ppb-Level sensitivity. *S ensors & Actuators: B. Chemical*, 259: 587-595.
7. Ansari, N., Lodha, A., Pandya, A., and Menon, S. K. (2017). Determination of cause of death using p aper-based microfluidic device as a colorimetric pr obe. *Analytical Methods*, 9(38): 5632-5639.
8. Martinez, A. W., Phillips, S. T., Carrilho, E., Iii, S. W. T., Sindi, H., and Whitesides, G. M. (2008). Si mple telemedicine for developing regions: Camera phones and paper-based microfluidic devices for re al-time, off-site diagnosis. *Analytical Chemistry*, 8 0(10): 3699-3707.
9. Musile, G., Wang, L., Bottoms, J., Tagliaro, F., and McCord, B. (2015). The development of paper mic rofluidic devices for presumptive drug detection. *A nalytical Methods*, 7(19): 8025-8033.
10. Sharma, N., Barstis, T., and Giri, B. (2018). Advan ces in paper-analytical methods for pharmaceutical analysis. *European Journal of Pharmaceutical Scie nces*, 111: 46-56.
11. De Araujo, W. R., Cardoso, T. M. G., da Rocha, R. G., Santana, M. H. P., Muñoz, R. A. A., Richter, E. M., and Coltro, W. K. T. (2018). Portable analytica l platforms for forensic chemistry: A review. *Analy tica Chimica Acta*, 1034: 1-21.
12. Oliveira, X. G., Munoz, R. A. A., Henry, C. S., and Coltro, W. K. T. (2018). Detection of analgesics an d sedation drugs in whiskey using electrochemical paper-based analytical devices. *Electroanalysis*, 30 8: 1-9.
13. Harper, L., Powell, J., and Pijl, E. M. (2017). An o verview of forensic drug testing methods and their suitability for harm reduction point-of-care service s. *Harm Reduction Journal*, 14: 52.
14. Zhang, D., and Liu, Q. (2016). Biosensors and bioe lectronics on smartphone for portable biochemical detection. *Biosensors and Bioelectronic*, 75: 273-2 84.
15. De Araujo, W. R., and Paixão, W. R. (2014). Fabri cation of disposable electrochemical devices using silver ink and office paper. *Analyst*, 139(11): 2742-2747.
16. Adkins, J., Boehle, K., and Henry, C. (2015). Elect rochemical paper-based microfluidic devices. *Elect rophoresis*, 36(16): 1811-1824.
17. Tayyab, S., Naqvi, R., Rasheed, T., Naeem, M., Na jam, M., Majeed, S., … and Shafi, S. (2020). Fabri cation of iron modified screen-printed carbon elect

rode for sensing of amino acids. *Polyhedron,* 180: 1 14426.

18. Mohseni, N., Bahram, M., and Baheri, T. (2017). C hemical nose for discrimination of opioids based o n unmodified gold nanoparticles. *Sensors and Actu ators, B: Chemical,* 250: 509-517.
19. Lodha, A., Pandya, A., Sutariya, P. G., and Menon, S. K. (2014). A smart and rapid colorimetric metho d for the detection of codeine sulphate, using unmo dified gold nanoprobe. *RSC Advances,* 4(92): 5044 3-50448.
20. Johan, M. R., Chong, L. C., and Hamizi, N. A. (20 12). Preparation and stabilization of monodispersed colloidal gold by reduction with monosodium gluta mate and poly (methyl methacrylate). *International Journal of Electrochemical Science,* 7: 4567-4573.
21. Mou, Y., Zhang, Y., Cheng, H., Peng, Y., and Che n, M. (2018). Fabrication of highly conductive and flexible printed electronics by low temperature sint ering reactive silver ink. *Applied Surface Science,* 4 59(7): 249-256.
22. Tukur, S. A., Yusof, N. A., & Hajian, R. (2014). G old nanoparticles-modified screen-printed electrod e for determination of Pb (II) ion using linear swee p anodic stripping voltammetry. *IEEE Sensors Jou rnal,* 15(5): 2780-2784.
23. Ghosale, A., Shankar, R., Ganesan, V., and Shrivas , K. (2016). Direct-writing of paper based conducti ve track using silver nano-ink for electroanalytical application. *Electrochimica Acta,* 209: 511-520.
24. Joubert, T., Bezuidenhout, P. H., Chen, H., Smith, S., and Land, K. J. (2015). Inkjet-printed silver trac ks on different paper substrates. *Materials Today: P roceedings,* 2(7): 3891-3900.
25. Liu, H., Qing, H., Li, Z., Long, Y., Lin, M., Yang, H., and Li, A. (2017). Paper: A promising material for human-friendly functional wearable electronics . *Materials Science & Engineering Research*, 112: 1-22.
26. Muhammad, S., Zahra, U. B., Ahmad, A., Shah, L. A., and Muhammad, A. (2020). Understanding the basics of electron transfer and cyclic voltammetry o f potassium ferricyanide - An outer sphere heteroge neous electrode reaction. *Journal of the Chemical S ociety of Pakistan,* 42(6): 813-817.

Malaysian Journal of Analytical Sciences (MJAS)
Published by Malaysian Analytical Sciences Society

BENZIMIDAZOLE DERIVATIVES AS POTENTIAL NEURAMINIDASE INHIBITORS: CONVENTIONAL AND MICROWAVE SYNTHESIS, *In Vitro* AND MOLECULAR DOCKING ANALYSIS

(Terbitan Benzimidazola yang Berpotensi sebagai Perencat Neuraminidase: Sintesis secara Konvensional dan Gelombang Mikro, Analisis *In Vitro* dan Pengedokan Molekul)

Nurasyikin Hamzah[1], Shafida Abd Hamid[1,4]*, Aisyah Saad Abdul Rahim[2], and Habibah Abdul Wahab[3]

[1]*Department of Chemistry, Kulliyyah of Science, International Islamic University Malaysia, Bandar Indera Mahkota, 25200 Kuantan, Pahang, Malaysia*
[2]*Faculty of Pharmacy, UiTM Puncak Alam Campus, 42300 Bandar Puncak Alam, Selangor, Malaysia*
[3]*School of Pharmaceutical Sciences, Universiti Sains Malaysia, 11800, Penang, Malaysia*
[4]*SYNTOF, Kulliyyah of Science, International Islamic University Malaysia, Bandar Indera Mahkota, 25200 Kuantan, Pahang, Malaysia*

[*]*Corresponding author: shafida@iium.edu.my*

Received: 27 March 2023; Accepted: 23 July 2023; Published: 30 October 2023

Abstract

As a continuous effort to discover potential neuraminidase (NA) inhibitors, two series of benzimidazole derivatives consisting of esters, **5(a–g)** and carboxylic acid moieties, **6(a–g)** were synthesised under conventional and microwave conditions. The efficiency of both methods was compared, and their ability to inhibit the action of NA enzyme was examined *in silico* and *in vitro*. The microwave synthesis of the target compounds was more efficient and convenient than the conventional method as the former accelerated the reaction from hours to minutes, giving comparable yields. All compounds obtained were confirmed by the ^{1}H, ^{13}C NMR, and mass spectroscopic data. Out of six compounds tested in the carboxylic acid series, only **6f** showed inhibitory action towards NA with 15.2%. The binding interactions of **6(a–g)** were investigated further by molecular docking on the NA active site (PDB ID: 3TI6). **6f** was found to interact in the 430-loop cavity mainly by hydrophobic interactions. **6f** interacted at different active sites compared to DANA and oseltamivir. Although the compounds showed low inhibitory action, with strategic structural improvements, the benzimidazoles have the potential to be developed as NA inhibitors.

Keywords: benzimidazole, MAOS, Neuraminidase inhibitor, Molecular docking, MUNANA

Abstrak

Sebagai usaha berterusan untuk menemukan perencat neuraminidase (NA) yang berpotensi, dua siri terbitan benzimidazola yang terdiri daripada ester, **5(a–g)** dan moieti asid karboksilik, **6(a–g)** telah disintesis dalam keadaan konvensional dan gelombang mikro. Kecekapan kedua-dua kaedah telah dibandingkan dan keupayaan mereka untuk merencat enzim NA telah diselidik secara *in silico* dan *in vitro*. Sintesis sebatian sasaran melalui gelombang mikro adalah lebih cekap dan mudah berbanding kaedah konvensional kerana proses tindak balas dipercepat dari beberapa jam ke minit, memberikan hasil yang setanding. Semua sebatian yang diperoleh adalah bertepatan dengan data ^{1}H, ^{13}C NMR, dan spektroskopi jisim. Daripada enam sebatian yang diuji dalam siri

asid karboksilik, hanya **6f** menunjukkan tindakan perencatan terhadap NA sebanyak 15.2%. Interaksi pengikatan **6(a–g)** telah dikaji dengan lebih lanjut melalui pengedokan molekul terhadap tapak aktif NA (PDB ID: 3TI6). **6f** didapati berinteraksi dalam rongga 430 gelung terutamanya oleh interaksi hidrofobik. **6f** berinteraksi di tapak aktif yang berbeza berbanding DANA dan oseltamivir. Walaupun sebatian menunjukkan tindakan perencatan yang rendah, dengan penambahbaikan struktur strategik, benzimidazola mempunyai potensi untuk dibangunkan sebagai perencat NA.

Kata kunci: Benzimidazola, MAOS, Perencat neuraminidase, Pengedokan molekul, MUNANA

Introduction

Three main types of human influenza virus (A, B, and C) were reported with both types A and B virulent to humans [1]. The H1N1 influenza attack in 2009, derived from a triple-reassortant influenza virus comprising genes from avian, swine, and human origin, had caused the first pandemic outbreak of this century, raising the influenza pandemic alert level to phase 6 [2-4] until August 2010, after which the World Health Organization declared the end of the H1N1 pandemic. Vaccination is one of the most effective ways of protecting the body against viral infection. However, several drawbacks appeared in applying vaccines, such as the requirements of a new vaccine based on predicted strains that are circulating during flu season [5] and the lack of time to produce a mass number of vaccines, especially when the outbreak strikes [6]. Therefore, an anti-influenza drug is preferably applied as a forefront target in the early treatment of influenza attack.

The M2 ion protein channel and neuraminidase (NA) are two primary targets in the development of antiviral agents for influenza infection treatment or prevention [7, 8]. The M2 ion channel inhibitors (e.g., amantadine and rimantadine (adamantanes)) act by preventing the viral to uncover inside the cell. Unfortunately, these drugs are only useful for influenza virus having the M2 protein, such as type A, but ineffective for those without, such as influenza B [9]. In addition, the drugs are also associated with several adverse effects [10] and demonstrated resistance in most strains, making them less effective for treating the disease [11, 12].

On the other hand, NA works by cleaving the terminal sialic acid from the virion progeny and the host-cell surface. In doing so, it then assists the virus's movement through the respiratory tract [13, 14]. The NA active sites are surrounded by the conserved residues of amino acids of both influenza A and B strains. Thus, these sites become the ideal target for the design of NA inhibitors. Along with the advanced development in structure-based drug design and the availability of NA crystal structure, several NA inhibitors, such as zanamivir, oseltamivir, peramivir, and laninamivir, were developed to treat influenza [15]. Zanamivir (Relenza®) is a polar compound that needs to be administered by inhalation, which makes it inconvenient especially for children and elderly people. Oseltamivir carboxylate (Tamilflu®), while available in the form of tablets, can cause nausea and vomiting. Peramivir (Rapiacta®, Peramiflu®) received a fast-track designation from the US Food and Drug Administration to be used as a drug and was approved later for intravenous administration in December 2014. However, the reported side effects of this drug include gastrointestinal problems and abnormal neutrophil counts [16]. Laninamivir, recently authorised in Japan, was found to effectively inhibit H5N1 influenza virus and oseltamivir resistance mutants by single inhalation. It was also recently reported to be as efficient as zanamivir towards children affected with the influenza virus [17], although laninamivir is much more convenient as it only requires single inhalation for the treatment [4].

Benzimidazole is a heteroaromatic compound possessing diverse therapeutic and biological properties. Its derivatives were found to act as proton pump inhibitors (e.g., omeprazole), anthelmintics (e.g., mebendazole), and inodilators (e.g., pimobendan) [17]. Compounds possessing benzimidazole scaffold were also reported to exhibit antimicrobial and antifungal activities towards *S. aureus*, *E. coli, Xanthomonas sp*., and *Salmonella sp*., [18-21], antihistamine [22-25], anticancer [24, 26], and antifungal activities [26, 27]. These interesting properties warrant benzimidazole to be considered a privileged structure as the structure can be manipulated or modified to suit many different biological targets [28, 29].

Gedye et al. [30] were the first to introduce the application of microwave in organic transformation and Giguere et al. [31] then opened up a new perspective on microwave reaction. Since then, many chemical syntheses utilising either domestic or single-mode microwave reactors have been reported [32-34]. Apart from shortening the reaction time and improving reproducibility, the percentage yield can be increased with low by-products formed [35, 36]. In contrast to the normal conventional method, the microwave method involves a conduction heating mechanism, where energy is transferred from the vessel wall to the adjacent solvent before it moves within the bulk solvent containing the reaction mixture. This process results in slow heating and thus requires a lot of energy to heat the glassware compared to the reaction mixture itself, making the temperature inside the target mixture often cooler than the outside [37].

The design of NA inhibitors mainly involves sialic acid, benzoic acid, and cyclopentane scaffolds. Only recently, benzimidazoles have also been investigated as NA inhibitors [37, 38]. Owing to benzimidazole's interesting structure and various therapeutic applications, we were interested to discover the potential of benzimidazole derivatives as NA inhibitors. In this work, the designed compounds were synthesised via microwave and conventional approaches. Both methods were compared, and the isolated compounds were evaluated by molecular docking and NA inhibition assay.

Materials and Methods

A single-mode microwave reactor (CEM™ Discover Labmate) was used for microwave experiments. ^{1}H, ^{13}C, and ^{19}F nuclear magnetic resonance (NMR) experiments were performed using an NMR spectrometer (Bruker AVANCE III 500 MHz). The chemical shifts are expressed in parts per million (ppm), and the splitting of signals are assigned as singlet (s), doublet (d), triplet (t), doublet of doublet (dd), and multiplet (m). Mass spectroscopic (MS) analyses were performed by an Agilent 1100 Series spectrometer. All chemicals purchased from suppliers were used without further purification.

Synthesis: Ethyl 4-fluoro-3-nitrobenzoate, 2

Conventional condition:

To a solution of 4-fluoro-3-nitro benzoic acid, **1** (2.00 g, 10.40 mmol) in ethanol (25 mL), 2.5 mL concentrated H_2SO_4 was added and refluxed at ~78 °C for 4–6 h. The progress of the reaction was monitored every hour by thin-layer chromatography (TLC). Upon completion, the solvent was removed under pressure. The mixture was dissolved in ethyl acetate (25 mL) and extracted with water containing 10% $NaHCO_3$. The organic layer was washed with water and dried in anhydrous Na_2SO_4. Filtered and concentrated crude product *in vacuo* was later purified using preparative thin-layer chromatography (PTLC) with ethyl acetate (EtOAc)/hexane (Hex) of 1:4 to give the ester product. The product obtained after concentrated *in vacuo* was 1.96 g (85%) of yellow solid.

Microwave condition:

Compound **2** was obtained after irradiation of a mixture containing 4-fluoro-3-nitrobenzoic acid, **1** (0.25 g, 1.35 mmol), 4% H_2SO_4 equiv. to the starting material, and 1.0 mL of ethanol. Similar work-up was carried out as in conventional procedure. The yellow solid obtained after concentrated *in vacuo* gave 0.21 g (74%).

R_f = 0.69 (EtOAc/Hex, 1:4). ^{1}H NMR (500 MHz, $CDCl_3$): δ 1.43 (t, J = 5.0 Hz, $OCH_2C\underline{H_3}$), 4.44 (q, J = 5.0, 10.0 Hz, $OC\underline{H_2}CH_3$), 7.39 (t, J = 10.0 Hz, benzene-$\underline{H_5}$), 8.31–8.35 (m, benzene-$\underline{H_6}$), 8.74 (dd, J = 5.0, 7.0 Hz, benzene-$\underline{H_2}$); ^{13}C NMR (125 MHz, $CDCl_3$): δ 14.26, 62.13, 118.74, 127.61, 127.79, 136.49, 136.57, 158.03, 163.64; ^{19}F NMR (500 MHz, $CDCl_3$): -110.75; ESI-MS m/z calcd. for $[C_9H_8FNO_4]^+$ 213.2; found $[M + Na]^+$ 236.0.

Ethyl 4-(2-hydroxy-ethylamino)-3-nitro-benzoate, 3

Microwave condition:

4-fluoro-3-nitrobenzoic acid ethyl ester, **2** (0.25 g, 1.17 mmol) in 1 mL CH_2Cl_2 was mixed with N,N-diisopropylethylamine (DIPEA) (0.38 mL, 1.76 mmol), and ethanolamine (0.085 mL, 1.4 mmol) was added dropwise to the solution. The mixture was then irradiated in a CEM™ microwave at a temperature of 120 °C for 2 min (hold time). Upon completion, the mixture was filtered by suction and washed with hexane

to afford a yellow solid. The product was dried in a desiccator without further purification to give **3** (0.30 g, 94%).

Conventional condition:
4-fluoro-3-nitrobenzoic acid ethyl ester, **2** (1.00 g, 4.69 mmol) in 25 mL CH_2Cl_2 was mixed with DIPEA (1.51 mL, 7.0 mmol), and ethanolamine (0.33 mL, 5.63 mmol) was added dropwise to the solution. With the drying tube filled with anhydrous $CaCl_2$ attached to the round bottom flask, the mixture was stirred overnight at room temperature until a yellow precipitate formed. The precipitate was filtered by suction, washed with hexane, and dried in a desiccator without further purification to give **3** (1.18 g, 99%).

R_f = 0.60 (EtOAc/Hex, 4:1). ^{1}H NMR (500 MHz, $CDCl_3$): δ 1.40 (t, 3H, *J* = 5.0, 10.0 Hz, $OCH_2C\underline{H_3}$), 3.57 (q, *J* = 5.0, 10.0 Hz, $C\underline{H_2}CH_2OH$), 3.99 (q, *J* = 5.0, 10.0 Hz, $CH_2C\underline{H_2}OH$), 4.37 (q, *J* = 5.0, 10.0 Hz, $OC\underline{H_2}CH_3$), 6.92 (d, *J* = 10 Hz, benzene-$\underline{H_5}$), 8.31–8.34 (m, benzene-$\underline{H_6}$, 8.89 (d, *J* = 0.0 Hz, benzene-$\underline{H_2}$); ^{13}C NMR (125 MHz, $CDCl_3$): 14.39, 44.98, 60.72, 61.09, 113.48, 117.84, 129.47, 131.58, 136.43, 147.75, 165.16; ESI-MS m/z calcd. for $[C_{11}H_{14}N_2O_5]^+$ 254.2; found $[M + H]^+$ 255.1.

Ethyl 3-amino-4-(2-hydroxy ethylamino) benzoate, 4
Microwave condition:
A mixture of 4-(2-hydroxy-ethylamino)-3-nitrobenzoic acid ethyl ester, **3** (0.60 g, 2.63 mmol), NH_4HCO_2 (0.52 g, 8.25 mmol), and 10% Pd/C (0.30 g) in 2 mL of ethanol was irradiated in a microwave at 100 °C for 2 min (hold time). The pressure profile was monitored using the Synergy^{TM} programme so that the pressure did not exceed 20 atm. Upon completion, the catalyst was filtered through Celite and washed with ethanol, while the filtrate was concentrated *in vacuo* to afford a brown solid. The product **4** (0.50 g, 94%) was used for subsequent reaction without further purification.

Conventional condition:
A mixture of 4-(2-hydroxy-ethylamino)-3-nitrobenzoic acid ethyl ester, **3** (0.35 g, 1.38 mmol), NH_4HCO_2 (0.30 g, 4.82 mmol), and 10 % Pd/C (0.18 g) in 5 mL of ethanol was refluxed at 79–80 °C for 1–2 h until all reactants were consumed, as monitored by TLC. Upon completion, the catalyst was filtered through Celite by suction and washed with ethanol, while the filtrate was concentrated *in vacuo* to afford a brown solid **4** (0.31 g, 99%). The compound was used for the subsequent reaction without further purification.

R_f = 0.69 (EtOAc/Hex, 1:4). ^{1}H NMR (500 MHz, $CDCl_3$): δ 1.43 (t, *J* = 5.0 Hz, $OCH_2C\underline{H_3}$), 4.44 (q, *J* = 5.0, 10.0 Hz, $OC\underline{H_2}CH_3$), 7.39 (t, *J* = 10.0 Hz, benzene-$\underline{H_5}$), 8.31–8.35 (m, benzene-$\underline{H_6}$), 8.74 (dd, *J* = 5.0, 7.0 Hz, benzene-$\underline{H_2}$); ^{13}C NMR (125 MHz, $CDCl_3$): δ 14.26, 62.13, 118.74, 127.61, 127.79, 136.49, 136.57, 158.03, 163.64; ^{19}F NMR (500 MHz, $CDCl_3$): -110.75; ESI-MS m/z calcd. for $[C_9H_8FNO_4]^+$ 213.2; found $[M + Na]^+$ 236.0.

General procedure for the preparation of compounds 5(a–g)
Microwave method:
A solution of 3-amino-4-(2-hydroxy-ethanolamine)-benzoic acid ethyl ester (**4**) (1 equiv.) in CH_3CN (1 mL) was mixed with K10-montmorillonite (0.02–0.26 g) and the corresponding aldehyde (2.1 equiv. with respect to the starting material). The mixture was irradiated in the CEM^{TM} microwave at 80 °C, 150 W, 5 bar, and held for 5 min. Then, another aliquot of aldehyde (2.1 equiv.) was added, and the reaction mixture was irradiated again at the same condition as before. The reaction was monitored by TLC and was left for a few days before doing the work-up. K10-montmorillonite was removed by filtration, washed with DCM, and evaporated *in vacuo* to afford a brown precipitate. The crude product was later purified using PTLC (EtOAc/Hex, 4:1).

Conventional method:
A solution of 3-amino-4-(2-hydroxy-ethanolamine)-benzoic acid ethyl ester (**4**) (1 equiv.) in CH_3CN (5–10 mL) was mixed with K10-montmorillonite (0.30–0.50 g) and the corresponding aldehyde (2.1 equiv. with respect to the starting material). The reaction was refluxed at 78–80 °C for 4–5 h, and the progress was monitored by TLC every hour. Upon completion, K10-montmorillonite and CH_3CN were removed by filtration and under pressure, respectively, before the crude product was purified using PTLC (EtOAc/Hex, 4:1).

The product obtained in the conventional method was compared with the product obtained from microwave synthesis based on the R_f value.

5a

^{1}H NMR (500 MHz, $CDCl_3$): δ 1.31 (t, *J* = 10.0, 15.0 Hz, $CH_2C\underline{H_3}$), 1.44 (t, *J* = 10.0, 15.0 Hz, $OCH_2C\underline{H_3}$), 1.76 (br, s, $\underline{H_2}O$), 2.89 (q, *J* = 10.0, 15.0 Hz, $C\underline{H_2}CH_3$), 4.09 (t, *J* = 5.0, 10.0 Hz, $C\underline{H_2}CH_2OH$), 4.24 (t, *J* = 5.0, 10.0 Hz, $CH_2C\underline{H_2}OH$), 4.39 (q, *J* = 10.0, 15.0 Hz, $OC\underline{H_2}CH_3$), 5.09 (br, s, OH), 7.21 (d, *J* = 15.0 Hz, benzene-$\underline{H_7}$), 7.77 (d, *J* = 15.0 Hz, benzene-$\underline{H_6}$), 7.87 (s, benzene-$\underline{H_4}$); ^{13}C NMR (125 MHz, $CDCl_3$): δ 11.64, 14.43, 20.95, 46.53, 60.43, 60.74, 108.70, 120.71, 123.65, 124.31, 137.77, 141.22, 158.68, 166.86; ESI-MS m/z calcd. For $[C_{11}H_{16}N_2O_3]^+$ 262.3; found $[M + H]^+$ 263.1.

5b

^{1}H NMR (500 MHz, $CDCl_3$): δ 1.34 (d, *J* = 10.0 Hz, $H(C\underline{H_3})_2$), 1.40 (t, *J* = 10.0, 15.0 Hz, $OCH_2C\underline{H_3}$), 3.28 (septet, *J* = 10.0, 15.0 Hz, $\underline{H}(CH_3)_2$), 3.75 (br, s, $O\underline{H}$), 3.99 (t, *J* = 10.0 Hz, $C\underline{H_2}CH_2OH$), 4.31 (t, *J* = 10.0 Hz, $CH_2C\underline{H_2}OH$), 4.36 (q, *J* = 10.0, 15.0 Hz, $OC\underline{H_2}CH_3$), 7.30 (d, *J* = 15.0 Hz, benzene-$\underline{H_7}$), 7.86 (d, *J* = 15.0 Hz, benzene-$\underline{H_6}$), 8.35 (sharp, s, benzene-$\underline{H_4}$); ^{13}C NMR (125 MHz, $CDCl_3$): δ 14.36, 21.51, 26.34, 45.87, 60.75, 60.82, 109.14, 121.22, 123.73, 124.38, 138.18, 141.90, 162.42, 167.29; ESI-MS m/z calcd. for $[C_{15}H_{20}N_2O_3]^+$ 276.3; found $[M + H]^+$ 277.1.

5c

^{1}H NMR (500 MHz, $CDCl_3$): δ 0.98 (t, *J* = 10.0 Hz, $CH_2CH_2C\underline{H_3}$), 1.44 (t, *J* = 10.0, 15.0 Hz, $OCH_2C\underline{H_3}$), 1.74 (sextet, *J* = 10.0, 15.0 Hz, $CH_2C\underline{H_2}CH_3$), 2.85 (t, *J* = 10.0, 15.0 Hz, $C\underline{H_2}CH_2CH_3$), 4.09 (t, *J* = 5.0, 10.0 Hz, $C\underline{H_2}CH_2OH$), 4.25 (t, *J* = 5.0, 10.0 Hz, $CH_2C\underline{H_2}OH$), 4.39 (q, *J* = 10.0, 15.0 Hz , $OC\underline{H_2}CH_3$), 5.07 (br, s, $O\underline{H}$), 7.22 (d, *J* = 15.0 Hz, benzene-$\underline{H_7}$), 7.78 (dd, *J* = 0.0, 15.0 Hz, benzene-$\underline{H_6}$), 7.85 (s, benzene-$\underline{H_4}$); ^{13}C NMR (125 MHz, $CDCl_3$): δ 13.89, 14.43, 21.00, 29.47, 46.59, 60.47, 60.73, 108.72, 120.72, 123.61, 124.34, 137.65, 141.26, 157.59, 166.83; ESI-MS m/z calcd. for $[C_{15}H_{20}N_2O_3]^+$ 276.3; found $[M + H]^+$ 277.1.

5d

^{1}H NMR (500 MHz, $CDCl_3$): δ 0.93 (t, *J* = 10.0 Hz, $CH_2CH_2CH_2C\underline{H_3}$), 1.39 (septet, *J* = 10.0, 15.0 Hz, $CH_2CH_2C\underline{H_2}CH_3$), 1.43 (t, *J* = 7.5Hz, $OCH_2C\underline{H_3}$), 1.71 (quintet, *J* = 8.0 Hz, $CH_2C\underline{H_2}CH_2CH_3$), 2.86 (t, *J* = 8.0 Hz, $C\underline{H_2}CH_2CH_2CH_3$), 4.09 (t, *J* = 5.0 Hz, $C\underline{H_2}CH_2OH$), 4.25 (t, *J* = 5.0 Hz, $CH_2C\underline{H_2}OH$), 4.40 (q, *J* = 7.5 Hz, $OC\underline{H_2}CH_3$), 5.11 (br, s, OH), 7.21 (d, *J* = 8.5 Hz, benzene-$\underline{H_7}$), 7.77 (dd, *J* = 1.5, 8.5 Hz, benzene-$\underline{H_6}$), 7.85 (s, benzene-$\underline{H_4}$); ^{13}C NMR (125 MHz, $CDCl_3$): δ 13.74, 14.43, 22.45, 27.28, 29.67, 46.65, 60.41, 60.73, 108.69, 120.63, 123.58 124.29, 137.60, 141.16, 157.79, 166.80; ESI-MS m/z calcd. for $[C_{16}H_{22}N_2O_3]^+$ 290.4; found $[M + H]^+$ 291.1.

5e

^{1}H NMR (500 MHz, $CDCl_3$): δ 0.82 (t, *J* = 10.0, 15.0 Hz, $CH(CH_3)CH_2C\underline{H_3}$), 1.28 (d, *J* = 10.0 Hz, $CH(C\underline{H_3})CH_2CH_3$), 1.38 (t, *J* = 10.0 Hz, $OCH_2C\underline{H_3}$), 1.56–1.91 (m, $CH(CH_3)C\underline{H_2}CH_3$), 3.03 (sextet, *J* = 10.0, 15.0 Hz, $C\underline{H}(CH_3)CH_2CH_3$), 3.95 (t, *J* = 10.0 Hz, $C\underline{H_2}CH_2OH$), 4.30–4.38 (m, $OC\underline{H_2}CH_3$ and $CH_2C\underline{H_2}OH$), 7.33 (d, *J* = 15.0 Hz, benzene-$\underline{H_7}$), 7.87 (dd, *J* = 5.0, 12.5 Hz, benzene-$\underline{H_6}$), 8.37 (s, benzene-$\underline{H_4}$); ^{13}C NMR (125 MHz, $CDCl_3$): δ 12.04, 14.36, 19.58, 29.13, 33.28, 45.66, 60.79, 61.10, 109.05, 121.45, 123.69, 124.47, 138.12, 142.23, 161.72, 167.26; ESI-MS m/z calcd. for $[C_{16}H_{22}N_2O_3]^+$ 290.2; found $[M + H]^+$ 291.1.

5f

^{1}H NMR (500 MHz, $CDCl_3$): δ 0.80 (t, *J* = 10.0, 15.0 Hz, $CH(CH_2C\underline{H_3})_2$), 1.38 (t, *J* = 10.0, 15.0 Hz, $OCH_2C\underline{H_3}$), 1.67–1.90 (m, $CH(C\underline{H_2}CH_3)_2$), 2.86 (quintet, *J* = 5.0, 10.0 Hz, $C\underline{H}(CH_2CH_3)_2$), 3.97 (t, *J* = 10.0 Hz, $C\underline{H_2}CH_2OH$), 4.32–4.39 (m, $OC\underline{H_2}CH_3$ and $CH_2C\underline{H_2}OH$), 7.37 (d, *J* = 15.0 Hz, benzene-$\underline{H_7}$), 7.90 (dd, *J* = 0.0, 15.0 Hz, benzene-$\underline{H_6}$), 8.42 (s, benzene-$\underline{H_4}$); ^{13}C NMR (125 MHz, $CDCl_3$): δ 11.96, 14.35, 27.45, 40.46, 45.72, 52.09, 60.73, 60.85, 109.35, 121.07, 123.62, 124.40, 138.14, 142.05, 160.84, 167.35; ESI-MS m/z calcd. for $[C_{17}H_{24}N_2O_3]^+$ 304.4; found $[M + H]^+$ 305.2.

5g

^{1}H NMR (500 MHz, $CDCl_3$): δ 1.43 (t, *J* = 10.0, 15.0 Hz, $OCH_2C\underline{H_3}$), 1.74 (br, s, H_2O), 2.11 (s, $SC\underline{H_3}$), 2.92

(t, J = 10.0, 15.0 Hz, $CH_2C\underline{H_2}SCH_3$), 3.17 (t, J = 10.0, 15.0 Hz, $C\underline{H_2}CH_2SCH_3$), 4.07 (t, J = 5.0, 10.0 Hz, $C\underline{H_2}CH_2OH$), 4.29 (t, J = 5.0, 10.0 Hz, $CH_2C\underline{H_2}OH$), 4.39 (q, J = 10.0, 15.0 Hz, $OC\underline{H_2}CH_3$), 4.57 (br, s, OH), 7.27 (d, J = 10.0 Hz, benzene-$\underline{H_7}$), 7.82 (dd, J = 5.0, 12.5 Hz, benzene-$\underline{H_6}$), 7.97 (d, J = 5.0 Hz, benzene-$\underline{H_4}$); ^{13}C NMR (125 MHz, $CDCl_3$): δ 14.41, 15.82, 27.80, 31.90, 46.76, 60.20, 60.82, 108.97, 120.66, 123.82, 124.48, 137.47, 141.00, 155.87, 166.73; ESI-MS m/z calcd. for $[C_{15}H_{20}N_2O_3S]^+$ 309.1; found $[M + H]^+$ 309.1.

General procedure for the preparation of compounds 6(a–g)

Microwave condition:

The obtained ester product **5(a–g)** in THF:H_2O (2:1) was mixed with 4 N NaOH (0.5 mL). The mixture was irradiated in the microwave at 120 °C for 2–5 min. Upon completion, THF was removed under pressure, and the product was acidified using 2 M HCl to maintain the pH at 6–7. Removing excess water *in vacuo* gave a white precipitate, which later was dissolved in butanol to separate the carboxylic acid and salt. The filtrate was again evaporated under vacuum to obtain the crude product. Purification was later carried out using PTLC (EtOAc/Hex, 4:1) by dissolving the crude product with methanol.

Conventional condition:

The obtained ester product **5(a–g)** either in THF (2 mL) or in a ratio of THF:H_2O (2:1) was added with 4 N NaOH (1–5 mL). The mixture was refluxed for 2–18 h at 66–68 °C until all reactants were fully converted to the desired acid, as observed in the TLC. Upon completion, THF was removed under pressure and acidified using 2 M HCl to maintain the pH at 6–7. Removing excess water *in vacuo* gave a white precipitate, which later was dissolved in butanol to separate the carboxylic acid and salt. The filtrate was again evaporated under vacuum to obtain the crude product. Purification was done using PTLC (EtOAc/Hex, 4:1) by dissolving the crude product with methanol.

6a

R_f = 0.70 ($MeOH/CHCl_3$, 4:1). ^{1}H NMR (500 MHz, D_2O): δ 1.43 (t, J = 5.0, 10.0 Hz, $CH_2C\underline{H_3}$), 3.13 (q, J = 5.0, 10.0 Hz, $C\underline{H_2}CH_3$), 3.96 (t, J = 5.0 Hz, $C\underline{H_2}CH_2OH$), 4.45 (t, J = 5.0 Hz, $CH_2C\underline{H_2}OH$), 7.64 (d, J = 10.0 Hz, benzene-$\underline{H_7}$), 7.93 (d, J = 10.0 Hz, benzene-$\underline{H_6}$), 8.07 (s, benzene-$\underline{H_4}$); ^{13}C NMR (125 MHz, D_2O): δ 9.88, 19.40, 46.68, 59.17, 111.32, 115.43, 125.67, 132.57, 133.25, 134.31, 157.68, 174.02; ESI-MS m/z calcd. for $[C_{12}H_{14}N_2O_3]^+$ 234.3; found $[M + H]^+$ 235.1.

6b

^{1}H NMR (500 MHz, D_2O): δ 1.36 (d, J = 5.0 Hz, $H(C\underline{H_3})_2$), 3.39 (septet, J = 5.0, 10.0 Hz, $\underline{H}(CH_3)_2$), 3.94 (t, J = 5.0, 10.0 Hz, $C\underline{H_2}CH_2OH$), 4.41 (t, J = 5.0, 10.0 Hz, $CH_2C\underline{H_2}OH$), 7.53 (d, J = 10.0 Hz, benzene-$\underline{H_7}$), 7.84 (dd, J = 0.0, 5.0, 10.0 Hz, benzene-$\underline{H_6}$), 8.10 (d, J = 5.0 Hz, benzene-$\underline{H_4}$); ^{13}C NMR (125 MHz, D_2O): δ 20.74, 25.89, 45.52, 59.88, 109.99, 118.52, 123.69, 130.81, 136.73, 140.68, 163.71, 175.84; ESI-MS m/z calcd. for $[C_{13}H_{16}N_2O_3]^+$ 248.1; found $[M + H]^+$ 249.1.

6c

^{1}H NMR (500 MHz, D_2O): δ 1.03 (t, J = 5.0, 10.0 Hz, $CH_2CH_2C\underline{H_3}$), 1.91 (sextet, J = 5.0, 10.0 Hz, $CH_2C\underline{H_2}CH_3$), 3.20 (t, J = 5.0, 10.0 Hz, $C\underline{H_2}CH_2CH_3$), 3.99 (t, J = 5.0 Hz, $C\underline{H_2}CH_2OH$), 4.57 (t, J = 5.0 Hz, $CH_2C\underline{H_2}OH$), 7.81 (d, J = 10.0 Hz, benzene-$\underline{H_7}$), 8.08 (d, J = 10.0 Hz, benzene-$\underline{H_6}$), 8.25 (s, benzene-$\underline{H_4}$); ^{13}C NMR (125 MHz, D_2O): δ 12.69, 19.62, 27.02, 47.32, 59.04, 112.78, 115.87, 126.89, 127.87, 129.74, 134.94, 156.90, 169.12; ESI-MS m/z calcd. for $[C_{13}H_{16}N_2O_3]^+$ 248.1; found $[M + H]^+$ 249.1.

6d

^{1}H NMR (500 MHz, D_2O): δ 0.97 (t, J = 5.0, 10.0 Hz, $CH_2CH_2CH_2C\underline{H_3}$), 1.46 (sextet, J = 5.0, 10.0 Hz, $CH_2CH_2C\underline{H_2}CH_3$), 1.85 (quintet, J = 5.0, 10.0 Hz, $CH_2C\underline{H_2}CH_2CH_3$), 2.99 (t, J = 5.0, 10.0 Hz, $C\underline{H_2}CH_2CH_2CH_3$), 3.98 (t, J = 5.0 Hz, $C\underline{H_2}CH_2OH$), 4.42 (t, J = 5.0 Hz, $CH_2C\underline{H_2}OH$), 7.57 (d, J = 10.0 Hz, benzene-$\underline{H_7}$), 7.88 (d, J = 10.0 Hz, benzene-$\underline{H_6}$), 8.14 (s, benzene-$\underline{H_4}$); ^{13}C NMR (125 MHz, D_2O): δ 13.04, 21.83, 26.31, 28.98, 45.71, 59.92, 109.87, 123.65, 130.73, 140.70, 159.06, 175.84; ESI-MS m/z calcd. for $[C_{14}H_{18}N_2O_3]^+$ 262.3; found $[M + H]^+$ 263.1.

6e

^{1}H NMR (500 MHz, D_2O): δ 0.92 (t, J = 5.0 Hz,

$CH(CH_3)CH_2C\underline{H_3}$), 1.47 (d, J = 5.0 Hz, $CH(C\underline{H_3})CH_2CH_3$), 1.84–1.96 (m, $CH(CH_3)C\underline{H_2}CH_3$), 3.52 (sextet, J = 5.0, 10.0 Hz, $C\underline{H}(CH_3)CH_2CH_3$), 4.01 (t, J = 5.0 Hz, $CH_2C\underline{H_2}OH$), 4.63 (t, $CH_2C\underline{H_2}OH$), 7.80 (d, J = 5.0 Hz, benzene-$\underline{H_7}$), 8.04 (dd, J = 10.0 Hz, benzene-$\underline{H_6}$), 8.17 (s, benzene-$\underline{H_4}$); ^{13}C NMR (125 MHz, D_2O): δ 10.64, 17.72, 28.07, 32.39, 47.09, 59.02, 112.18, 114.81, 126.38, 130.71, 133.63, 133.78, 159.91, 173.48; ESI-MS m/z calcd. for $[C_{14}H_{18}N_2O_3]^+$ 262.3; found $[M + H]^+$ 263.1.

6f

^{1}H NMR (500 MHz, D_2O): δ 0.77 (t, J = 5.0, 10.0 Hz, $CH(CH_2C\underline{H_3})_2$), 1.71–1.84 (m, $CH(C\underline{H_2}CH_3)_2$), 3.03 (m, $C\underline{H}(CH_2CH_3)_2$), 3.92 (t, J = 5.0 Hz, $C\underline{H_2}CH_2OH$), 4.42 (t, J = 5.0 Hz, $CH_2C\underline{H_2}OH$), 7.54 (d, J = 10.0 Hz, benzene-$\underline{H_7}$), 7.82 (d, J = 10.0 Hz, benzene-$\underline{H_6}$), 8.09 (s, benzene-$\underline{H_4}$); ^{13}C NMR (125 MHz, D_2O): δ 11.11, 27.37, 39.93, 45.50, 60.12, 110.08, 118.37, 123.58, 130.81, 136.72, 140.64, 161.89, 175.84; ESI-MS m/z calcd. for $[C_{15}H_{20}N_2O_3]^+$ 276.3; found $[M + H]^+$ 277.1.

6g

^{1}H NMR (500 MHz, D_2O): δ 2.10 (s, $SC\underline{H_3}$), 2.97 (t, J = 5.0, 10.0 Hz, $CH_2C\underline{H_2}SCH_3$), 3.13 (t, J = 5.0, 10.0 Hz, $C\underline{H_2}CH_2SCH_3$), 3.86 (t, J = 5.0 Hz, $C\underline{H_2}CH_2OH$), 4.21 (t, J = 5.0 Hz, $CH_2C\underline{H_2}OH$), 7.38 (d, J = 10.0 Hz, benzene-$\underline{H_7}$), 7.79 (dd, J = 10.0 Hz, benzene-$\underline{H_6}$), 8.07(s, benzene-$\underline{H_4}$); ^{13}C NMR (125 MHz, D_2O): δ 14.35, 26.60, 30.69, 45.70, 59.81, 109.81, 118.76, 123.80, 130.77, 136.66, 140.58, 156.24, 175.60; ESI-MS m/z calcd. for $[C_{13}H_{16}N_2O_3S]^+$ 280.3; found $[M + H]^+$ 281.1.

Molecular docking analysis

The structures were drawn and optimised into three-dimensional structures using Avogadro software [39]. Then, AutoDockTools (https://ccsb.scripps.edu/mgltools/) was employed to add non-polar hydrogens and merge them, define the atom types, and compute the Gasteiger charges. For the target protein, the NA protein structure (PDB ID: 3TI6) was retrieved from www.rcsb.org/pdb. Ligand, water, and ions were removed. Using AutoDockTools, polar hydrogen and Kollman charges were added before the file was saved in .pdbqt format. The size of grid points was set to 26, 30, and 40 with the grid centre to be 28.750, 14.639, and 19.556, for x-, y-, and z-coordinates, respectively. The spacing between points was set as default. Finally, Maestro 13.3 (Maestro, Schrödinger, LLC, New York, NY, 2021.) and PyMOL (PyMOL Molecular Graphics System, Version 2.0 Schodinger, LLC) were used to visualise the conformation of the best docking compounds.

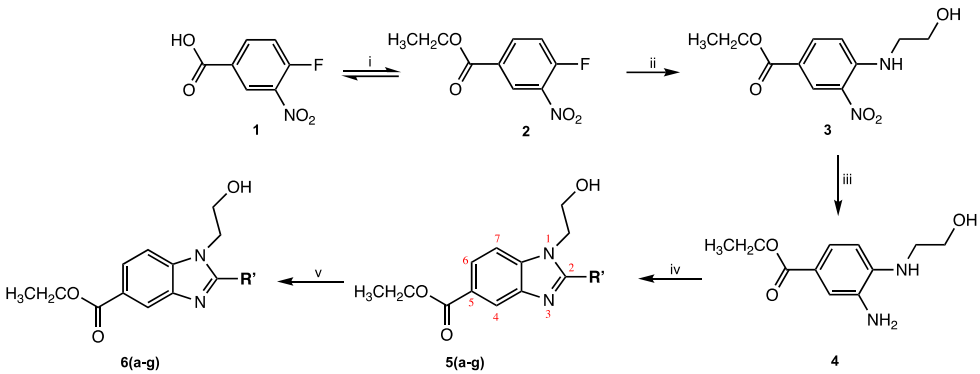
Enzyme inhibition study

The NA inhibition assay protocol was taken from Potier et al. [40] and Blick et al. [41]. The assay was performed in triplicate in a 96-well microplate. Firstly, 2-(*N*-morpholino)ethanesulfonic acid (MES) buffer (25 µL) was added to well 2–12. Then, the benzimidazole derivative (50 µL) was placed in the first well, and serial dilution was performed by taking 25 µL of the drug from the first well. To the plate, NA H1N1 (25 µL) virus was mixed with the dissolved benzimidazole in each well, sealed with aluminium foil, and then incubated at 37 °C for 30 min. 2'-(4-methylumbelliferyl)-alpha-D-N-acetylneuraminic acid (MUNANA) working solution was prepared 5 min before the end of the incubation period. After 30 min, MUNANA (50 µL) was added to each well, and two positive controls were prepared by adding (25 µL NA + 50 µL MUNANA) and (50 µL NA + 50 µL MUNANA), and a blank with 50 µL MES buffer into each well separately before they were incubated again at 37 °C for another 1 h. A stop solution (100 µL) was added to each well to terminate the reaction, and the microplate was immediately inserted into the microplate reader to measure the fluorescence of absorbance. The wavelengths set for the fluorescence detection were 355 nm and 460 nm for excitation and emission, respectively.

Results and Discussion

Chemistry

The multi-step reactions to prepare alkyl benzimidazoles **5(a–g)** in conventional and microwave approaches are outlined in Scheme 1. The spectroscopic data for this series confirmed the synthesised structures with the appearance of the aliphatic substituent signals in ^{1}H NMR and the presence of quaternary carbon in ^{13}C NMR that correlates with cyclisation occurring at C-2 around 159 ppm.



Label	R'
a	-CH_2CH_3
b	-$CH(CH_3)_2$
c	-$(CH_2)_2CH_3$
d	-$(CH_2)_3CH_3$
e	-$CH(CH_3)CH_2CH_3$
f	-$CH(CH_2CH_3)_2$
g	-$(CH_2)_2SCH_3$

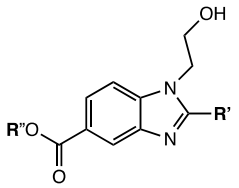
Scheme 1. Reagents and conditions: Conventional: (i) CH_3CH_2OH, H_2SO_4, 4–6 h, ~78 °C, 85%; (ii) $NH_2(CH_2)_2OH$, DIPEA, DCM, overnight, rt, 99%; (iii) Pd/C, NH_4HCO_2, ethanol, 1–2 h, 79–80 °C, 99%; (iv) K10-montmorillonite, MeCN, **R**'CHO, 4–5 h, 78–80 °C, 52–89%; (v) 4 N NaOH, THF, 2 M HCl, 4–6 h, 66–68 °C, 45–95%; Microwave: (i) CH_3CH_2OH, H_2SO_4, 15 min, 130 °C, 1–98%; (ii) $NH_2(CH_2)_2OH$, DIPEA, DCM, 2 min, 120 °C, 94%; (iii) Pd/C, NH_4HCO_2, ethanol, 2 min, 100 °C, 94%; (iv) K10-montmorillonite, MeCN, **R**'CHO, 5 min, 80 °C, 150 W, 5 bar, 29–66%; (v) 4 N NaOH, THF, 2 M HCl, 2–5 min, 120 °C, 59–90%. The numbering of the benzimidazoles is as indicated in **5(a–g)**

Due to the low solubility of the ester moieties in the buffer solution, the compounds were hydrolysed to carboxylic acids **6(a–g)** to increase their polarity. The disappearance of ester group signals in both ^1H and ^{13}C NMR spectra confirmed the formation of the products. Single crystals of **5c**, **5g**, and **6f** characterised by X-ray crystallography further confirmed their molecular structures [42-44]. The yield and duration for the preparation of the compounds from both conventional and microwave experiments are summarised in Table 1. Both techniques exhibited good to excellent conversions during esterification, S_NAr, reduction, and hydrolysis reactions, ranging from 59% to 94% for microwave and 45% to 99% for the conventional method. In contrast, during the cyclisation step, most of the compounds obtained gave low to moderate yields (23–69%), except **5f** (89%). However, there was a marked difference in terms of the duration needed to complete the reaction. In general, the reactions need 5–10 min under the microwave condition, although in some cases, the reactions can be performed in 2 min for the target compounds to yield almost similar results as under conventional conditions.

Neuraminidase inhibition assay

Benzimidazole carboxylic acid series **6(a–g)** were selected for bioassay analysis as the compounds showed good solubility in MES buffer. The NA inhibition assay was performed following the established protocols [39, 45]. One of the most potent NA inhibitors, 2,3-didehydro-2-deoxy-*N*-acetylneuraminic acid (DANA), was used as a control for comparison. Once cleaved by the NA, MUNANA substrate will release the fluorescent methylumbelliferone and will be detected by the fluorometric method. The intensity of fluorescence relates directly to the amount of NA activity. The NA inhibition results for **6(a–g)** series tested at a single concentration of 250 µg/mL are shown in Figure 1. Compound **6f** gave the best inhibition at 15.2%, while the remaining compounds were shown to give inhibition of less than 10%. The data demonstrated that branched alkyl moieties at the C-2 position, such as in **6f** and **6b**, are slightly more tolerable for the inhibitory activity. In contrast, different alkyl chain substituents (up to four carbons) at the C-2 position are not favourable even with the presence of sulphur, as observed in compounds **6a**, **6c**, **6d**, and **6g**. Compound **6e**, although also possesses branched alkyl substituent at the C-2 position, showed lower inhibition results than **6f** and **6b**. Unfortunately, we cannot provide a detailed explanation for this observation other than the unsymmetrical branched alkyl that may affect the inhibition towards the enzyme.

Table 1. Reaction time and yield of products of benzimidazole derivatives under microwave and conventional conditions



5 & **6**

Compound			Time		[a]Yield (%)	
	R'	R"	Microwave (min)	Conventional (h)	Microwave	Conventional
2	-	-	15	2	74	85
3	-	-	2	24	94	99
4	-	-	2	1-2	94	99
5a		$-CH_2CH_3$	10	5	55	53
5b		$-CH_2CH_3$	10	4	51	69
5c		$-CH_2CH_3$	10	5	30	52
5d		$-CH_2CH_3$	10	5	40	23
5e		$-CH_2CH_3$	10	5	48	64
5f		$-CH_2CH_3$	10	5	66	89
5g		$-CH_2CH_3$	10	5	35	47
6a		H	5	3	76	45
6b		H	5	2	70	79
6c		H	5	3	83	77
6d		H	5	5	84	75
6e		H	5	18	59	95
6f		H	5	2	90	81
6g		H	5	8	86	74

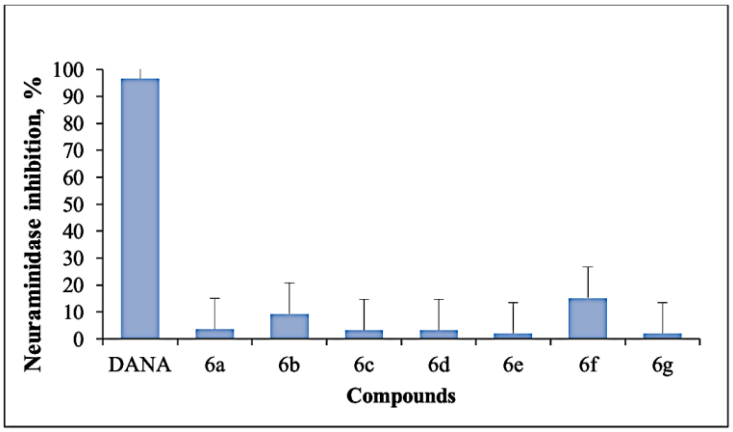


Figure 1. Percentage inhibition of **6(a–g)** analogues with DANA as a control at 250 µg/mL

Molecular docking

A molecular docking study was performed to gain a better understanding of how **6f** interacts in NA active sites at the molecular level. The NA crystal structure of 2009 H1N1 (PDB ID: 3TI6) with DANA as a reference was used in the study. The co-crystallised oseltamivir in the protein was removed and re-docked again into the NA active sites. Comparison between the co-crystallised and re-docked oseltamivir docking poses shows that the re-dock oseltamivir bound at the same location with the original ligand with slightly different conformation to give RMSD of 1.566 Å, suggesting the reliability of the docking algorithm in AutoDock VINA as the value is below the cut-off point 2.0 Å.

The NA active site of the 2009 pandemic H1N1 is unique from other N1-NA subtypes as it only consists of a sialic acid cavity and a 430-loop cavity with the absence of a 150-loop [39, 45]. In this study, DANA, which was used as a reference in the NA assay and docking study, gave the best docking energy of -6.1 kJ/mol, a slightly lower value than **6f** (-6.5 kJ/mol). Interestingly, the best docking pose of **6f** was found to bind at the 430-loop region, in contrast to DANA, which was found to bind at the sialic acid active site (Figure 2a). Further analysis on the 2D-ligand interaction between **6f** and DANA with 3TI6 was evaluated using Maestro (Schrödinger Release 2022-3, 2021).

Figure 2b(i) shows that there are nine amino acid residues take place in the binding interactions of **6f** in the 430-cavity with one hydrogen bond interaction between the carboxylic acid moiety and SER404. The remaining interactions are mostly hydrophobic interactions with ASN347, ARG371, ASN 372, ILE427, TRP403, LYS432, PRO431, ILE149, and ARG118 residues. The 3-pentanyl moiety of **6f** was found to interact with the ILE149 residues, suggesting that this type of branch alkyl group forms favourable hydrophobic interactions compared to other substituents in the carboxylic acid series. Meanwhile, DANA, which prefers to sit in the sialic acid cavity, also has one hydrogen bond interaction with THR225, while the remaining residues mainly form hydrophobic interactions. Although hydrophobic interaction is not as strong as hydrogen bonds, it can affect the docking free energy between ligand and enzyme. However, the presence of carboxylic acid group, especially for NA inhibitors, is crucial as it forms a strong hydrogen bond between the polar and charged residues of arginine with the oxygen atoms, which could give partial stability to the overall binding [46].

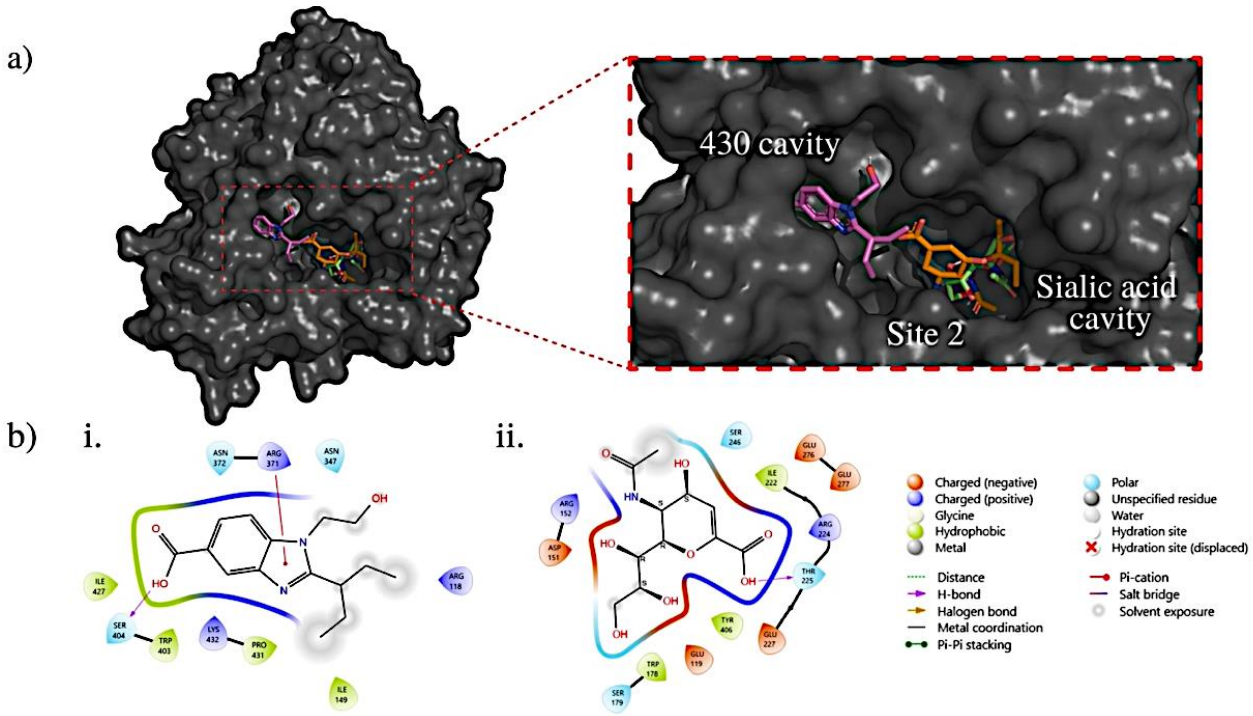


Figure 2. a) Best score docking poses of **6f** (yellow) in the 430-cavity in relation to the original ligand in the crystal structure (oseltamivir-orange) at site 2 and DANA (green) in the sialic acid region and b) the 2D-ligand interaction of i) **6f** and ii) DANA calculated in 4 Å distances from H1N1-NA (PDB ID: 3TI6) residue

Conclusion

In the present study, two series of benzimidazole analogues **5(a–g)** and **6(a–f)** were synthesised with good to excellent yields using both microwave and conventional methods. Microwave reaction was more effective than the conventional method as it can speed up the reaction time, although the yields obtained were generally slightly lower than those obtained by the conventional method. Compound **6f** was found to give the highest NA inhibition activity with 15.2% at 250 µg/mL, while others gave less than 10% inhibition. It is interesting to note that the molecular docking analysis revealed **6f** to bind at the 430-cavity of the NA active site, in contrast to DANA, which is at the sialic acid site, and oseltamivir at site 2. Despite the low inhibition data, the results show that benzimidazoles have the potential to be developed as NA inhibitors. Subsequent structural improvements of the benzimidazole scaffold could be designed towards more effective NA inhibitors.

Acknowledgement

The authors gratefully acknowledge the Ministry of Higher Education (MOHE) for the FRGS Grant (FRGS0510-119) and MOSTI for the grant (304/PFARMASI/650544/I121) and (CLB10-01) to fund the research work. NH is grateful to IIUM for the Academic Staff Trainee Scheme (ASTS) for the scholarship.

References

1. Bouvier, N. M, and Palese, P. (2008). The biology of influenza viruses. *Vaccine*, 26 (suppl. 4): D49-D53.
2. Shinde, V., Bridges, C. B., Uyeki, T. M., Bo, S., Balish, A., Xu, X., Lindstrom, S., Gubareva, L.V., Deyde, V., Garten, R.J., Harris, M., Gerber, S., Vagasky, S., Smith, F., Pascoe, N., Martin, K., Dufficy, D., Ritger, K., Conover, C., Quinlisk, P., Klimov, A., Bresee, J.S., and Finelli, L. (2009). Triple-reassortant swine influenza A (H1) in humans in the United States, 2005-2009. *The New England Journal of Medicine*, 360: 2616-2625.
3. Sinha, A. K., Roy, A., Das, B., Das, S., and Basak, S. (2009). Evolutionary complexities of swine flu

H1N1 gene sequences of 2009. *Biochemical and Biophysical Research Communications*, 390: 349-351.

4. Bassetti, M., Castaldo, N., and Carnelutti, A. (2019). Neuraminidase inhibitors as a strategy for influenza treatment: pros, cons and future perspectives, *Expert Opinion on Pharmacotherapy*, 20: 1711-1718.
5. Kayser, V. and Ramzan, I. (2021). Vaccines and vaccination: history and emerging issues. *Human Vaccines & Immunotherapeutics*, 17: 5255-5268.
6. Carvalho, S. B., Peixoto, C., Manuel, M. J., and Ricardo, R. J. (2021). Downstream processing for influenza vaccines and candidates: An update. *Biotechnology and Bioengineering*, 118: 2845-2869.
7. Farrukee, R., and Hurt, A. C. (2017). Antiviral drugs for the treatment and prevention of influenza. *Current Treatment Options in Infectious Diseases*, 9: 318-332.
8. Balgi, A. D., Wang, J., Cheng, D. Y., Ma, C., Pfeifer, T. A., Shimizu, Y., Anderson, H. J., Pinto, L. H., Lamb, R. A., DeGrado, W. F., and Roberge, M. (2013). Inhibitors of the influenza A virus M2 proton channel discovered using a high-throughput yeast growth restoration assay. *PLoS One*, 8(2): e55271.
9. Wang, T., and Wade, R. C. (2001). Comparative binding energy (COMBINE) analysis of influenza neuraminidase-inhibitor complexes. *Journal of Medicinal Chemistry*, 44: 961-971.
10. Jefferson, T., Demicheli, V., Rivetti, D., Jones, M., Di Pietrantonj, C., and Rivetti, A. (2006). Antivirals for influenza in healthy adults: Systematic review. *Lancet*, 367: 303-313.
11. Bright, R. A., Shay, D. K., Shu, B., Cox, N. J., and Klimov, A. I. (2006) Adamantane resistance among influenza a virus isolated early during the 2005-2006 influenza season in the United States. *JAMA*, 295: 891-894.
12. Vorobjev, Y. N. (2021) An effective molecular blocker of ion channel of M2 protein as anti-influenza a drug. *Journal of Biomolecular Structure and Dynamics*, 39: 2352-2363.
13. McAuley, J. L., Gilbertson, B. P., Trifkovic, S., Brown, L. E., and McKimm-Breschkin, J. L. (2019) Influenza virus neuraminidase structure and functions. *Frontiers in Microbiology*, 10: 39.
14. Chand, P., Babu, Y.S., Bhantia, S., Rowland, S., Deghani, A., Kotian, P.L., Hutchison, T.L., Ali, S., Brouillette, W., El-Kattan, Y., and Lin, T. H. (2004). Syntheses and neuraminidase inhibitory activity of multisubstituted cyclopentane amide derivatives *Journal of Medicinal Chemistry*, 47: 1919-1929.
15. Sarukhanyan, E., Shanmugam, T. A., and Dandekar, T. (2022). In silico studies reveal peramivir and zanamivir as an optimal drug treatment even If H7N9 avian type influenza virus acquires further resistance. *Molecules*, 27: 5920.
16. Alame, M. M., Massaad, E., and Zaraket, H. (2016). Peramivir: A novel intravenous neuraminidase inhibitor for treatment of acute influenza infections. *Frontiers in Microbiology*, 7: 450.
17. Alamgir, M., Black, D. St. C., and Kumar, N. (2007). Synthesis, reactivity and biological activity of benzimidazoles. In Khan MTH (ed) Topics in Heterocyclic Chemistry, Springer, Berlin, Germany, 9, pp. 87-118.
18. de Oliveira, H. C., and Rodrigues, M. L. (2021). Repurposing benzimidazoles to fight Cryptococcus. *Fungal Biology Reviews*, 37: 27-40.
19. Garudachari, B., Satyanarayana, M. N., Thippeswamy, B., Shivakumar, C. K., Shivananda, K. N., Hegde, G., and Isloor, A. M. (2012). Synthesis, characterization and antimicrobial studies of some new quinoline incorporated benzimidazole derivatives. *European Journal of Medicinal Chemistry*, 54: 900-906.
20. Liu, H-B., Gao, W-W., Tangadanchu, V. K. R., Zhou, C-H., and Geng, R-X. (2018 Novel aminopyrimidinyl benzimidazoles as potentially antimicrobial agents: Design, synthesis and biological evaluation. *European Journal of Medicinal Chemistry,* 143: 66-84.
21. Marinescu, M., Tudorache, D. G., Marton, G. I., Zalaru, C-M., Popa, M., Chifiriuc, M-C., Stavarache, C-E., Constantinescu, C., Marinescu, M., Tudorache, D.G., Marton, G.I., Zalaru, C-M., Popa, M., Chifiriuc, M-C., Stavarache, C-E., and Constantinescu, C. (2017) Density functional theory molecular modeling, chemical synthesis, and

antimicrobial behaviour of selected benzimidazole derivatives. *Journal of Molecular Structure*, 1130: 463-471.

22. Wang, X. J., Xi, M. Y., Fu, J. H., Zhang, F. R., Cheng, G. F., Yin, D. L., and You, Q. D. (2012). Synthesis, biological evaluation and SAR studies of benzimidazole derivatives as H1-antihistamine agents. *Chinese Chemical Letters*, 23: 707-710.
23. Zhou, S., and Huang, G. (2020). Synthesis of anti-allergic drugs. (2020). *RSC Advances*, 10: 5874-5885.
24. Bistrović, A., Krstulović, L., Harej, A., Grbčić, P., Sedić, M., Koštrun, S., Pavelić, S.K., Bajić, M., and Raić-Malić, S. (2018). Design, synthesis and biological evaluation of novel benzimidazole amidines as potent multi-target inhibitors for the treatment of non-small cell lung cancer. *European Journal of Medicinal Chemistry*, 143: 1616-1634.
25. Ren, Y., Wang, Y., Li, G., Zhang, Z., Ma, L., Cheng, B., and Chen, J. (2021). Discovery of novel benzimidazole and indazole analogues as tubulin polymerization inhibitors with potent anticancer activities. *Journal of Medicinal Chemistry*, 64: 4498-4515.
26. Burger-Kentischer, A., Finkelmeier, D., Keller, P., Bauer, J., Eickhoff, H., Kleymann, G., Abu Rayyan, W., Singh, A., Schröppel, K., Lemuth, K., Wiesmüller, K. H., and Rupp, S. (2011). A screening assay based on host-pathogen interaction models identifies a set of novel antifungal benzimidazole derivatives. *Antimicrobial Agents and Chemotherapy*, 55: 4789-4801.
27. Kankate, R. S., Gide, P. S., Belsare, D. P. (2019). Design, synthesis and antifungal evaluation of novel benzimidazole tertiary amine type of fluconazole analogues. *Arabian Journal of Chemistry*, 12: 2224-2235.
28. Guo, Y., Hou, X., Fang, H. (2020). Recent applications of benzimidazole as a privileged scaffold in drug discovery. *Mini-Reviews in Medicinal Chemistry*, 21: 1367-1379.
29. Mermer, A., Keles, T., and Sirin, Y. (2021). Recent studies of nitrogen containing heterocyclic compounds as novel antiviral agents: A review, *Bioorganic Chemistry*, 114: 105076.
30. Gedye, R., Smith, F., Westaway, K., Ali, H., Baldisera, L., Laberge, L., and Rousell, L. (1986). The use of microwave ovens for rapid organic synthesis. *Tetrahedron Letters*, 27: 279-282.
31. Giguere, R. J., Bray, T. L., Duncan, S. M., and Majetich, G. (1986). Application of commercial microwave ovens to organic synthesis. *Tetrahedron Letters*, 27: 4945-4958.
32. Martina, K., Cravotto, G., and Varma, R. S. (2021). Impact of microwaves on organic synthesis and strategies toward flow processes and scaling up. *Journal of Organic Chemistry*, 86: 13857-13872.
33. Nain, S., Singh, R., and Ravichandran, S. (2019). Importance of microwave heating in organic synthesis. *Advanced Journal of Chemistry-Section A*, 2: 94-104.
34. Soni, J. P., Joshi, S. V., Chemitikanti, K.S., Shankaraiah, N. The riveting chemistry of poly-aza-heterocycles employing microwave technique: A decade review. *European Journal of Organic Chemistry*, 2021: 1476-1490.
35. Sharma, N., Sharma, U. K., and Van der Eycken, E. V. (2018). Microwave-assisted organic synthesis: Overview of recent applications. In Zhang W, Cue BW (eds) Green techniques for organic synthesis and medicinal chemistry, 2nd edition, John Wiley & Sons Ltd., New Jersey: pp. 441-468.
36. Kuhnert, N. (2002). Microwave-assisted reactions in organic synthesis-are there any nonthermal microwave effects?. *Angewandte Chemie International Edition,* 41: 1863-1866.
37. Zarubaev, V. V., Vasilieva, S. V., Esaulkova, Y. L., Garshinina, A. V., Veprintseva, V. M., Galochkina, A. V., Protsak, Y. S., Teselkin, I. V., Morkovnik, A. S., Divaeva, L. N., and Lavrentieva, I. N. (2018). Protective activity of novel benzimidazole derivatives at experimental influenza infection. *Russian Journal of Infection and Immunity*, 8: 195-200.
38. Kutkat, O., Kandeil, A., Moatasim, Y., Elshaier, Y. A. M. M., El-Sayed, W. A., Gaballah, S. T., El Taweel, A., Kamel, M. N., El Sayes, M., Ramadan, M. A., El-Shesheny, R., Abdel-Megeid, F. M. E., Webby, R., Kayali, G., and Ali, M. A. (2022). *In Vitro* and *In Vivo* antiviral studies of new heteroannulated 1,2,3-triazole glycosides targeting the neuraminidase of influenza A viruses.

Pharmaceuticals, 15: 351.

39. Malbari, K. D., Chintakrindi, A. S., Ganji, L. R., Gohil, D. J., Kothari, S. T., Joshi, M. V., and Kanyalkar, M. A. (2019). Structure-aided drug development of potential neuraminidase inhibitors against pandemic H1N1 exploring alternate binding mechanism. *Molecular Diversity*, 23: 927-951.
40. Potier, M., Mameli, L., Bélisle, M., Dallaire, L., Melanxon, S. B. (1979). Fluorometric assay of Neuraminidase with a sodium (4-methylumbelliferyl-α-D-N-acetylneuraminate) substrate. *Analytical Biochemistry*, 94: 287-296.
41. Blick, T. J., Tiong, T., Sahasrabudhe, A., Varghese, J. N., Colman, P. M., Hart, G. J., Bethell, R. C., and McKimm-Breschkin, J. L. (1995). Generation and characterization of an influenza virus Neuraminidase variant with decreased sensitivity to the Neuraminidase-specific inhibitor 4-guanidino-Neu5Ac2en. *Virology*, 214: 475-484.
42. Hamzah, N., Ngah, N., Hamid, S. A., and Abdul Rahim, A. S. (2011). Ethyl 1-(2-hydroxyethyl)-2-[2-(methylsulfanyl) ethyl]-1H-benzimidazole-5-carboxylate. *Acta Crystallographica Section E*, E68: o197-o198.
43. Hamzah, N., Ngah, N., Hamid, S. A., and Abdul Rahim, A. S. (2011). Ethyl 1-(2-hydroxyethyl)-2-propyl-1H-benzimidazole-5-carboxylate. *Acta Crystallographica Section E*, E67: o2704.
44. Hamzah, N., Ngah, N., Hamid, S. A., and Abdul Rahim, A. S. (2012). 2-sec-Butyl-1-(2-hydroxyethyl)-1H- benzimidazole-5-carboxylic acid. *Acta Crystallographica Section E*, E68: o1995.
45. Li, Q., Qi, J., Zhang, W., Vavricka, C. J., Shi, Y., Wei, J., Feng, E., Shen, J., Chen, J., Liu, D., He, J., Yan, J., Liu, H., Jiang, H., Teng, M., Li, X., and Gao, G. F. (2010). The 2009 pandemic H1N1 neuraminidase N1 lacks the 150-cavity in its active site. *Nature Structural & Molecular Biology*, 17: 1266-1268.
46. Taylor, N. R., and von Itzstein, M. (1994). Molecular modelling studies on ligand binding to sialidase from influenza virus and the mechanism of catalysis. *Journal of Medicinal Chemistry*, 37: 616-624.

Malaysian Journal of Analytical Sciences (MJAS)
Published by Malaysian Analytical Sciences Society

SYNTHESIS AND CHARACTERIZATION OF MAGNESIUM OXIDE NANOPARTICLES BY USING BANANA PEEL (*Musa acuminata* CAVENDISH) EXTRACT

(Sintesis Hijau dan Pencirian Nanopartikel Magnesium Oksida Menggunakan Ekstrak Kulit Pisang (*Musa acuminata* Cavendish)

Nor Syazwanie Mohd Saidi[1], Kooh Jhi Ying[1], Hanis Mohd Yusoff[1,2*] and Nurhanna Badar[1,2]

[1]*Faculty of Science and Marine Environment, Universiti Malaysia Terengganu, 21030 Kuala Nerus, Terengganu, Malaysia*
[2]*Advance Nano-Materials (ANoMa) Research Group, Faculty of Science and Marine Environment, Universiti Malaysia Terengganu, 21030 Kuala Nerus, Terengganu, Malaysia*

[*]*Corresponding author: hanismy@umt.edu.my*

Received: 18 May 2023; Accepted: 9 August 2023; Published: 30 October 2023

Abstract

The synthesis of metal oxide nanoparticles with the use of plant extract is a promising alternative to chemical synthesis methods. In the study, magnesium oxide nanoparticles (MgO-NPs) were synthesized by using *Musa acuminata* Cavendish banana peel extract solution. The precursor materials used were $Mg(NO_3)_2.6H_2O$ and dried Cavendish banana peel extract solution. Different concentration of $Mg(NO_3)_2.6H_2O$, different volume of extract solution, and different calcination temperature were used to conduct this study. The green synthesized MgO-NPs were characterized by thermogravimetric analysis (TGA), Fourier transform infrared (FTIR) spectroscopy, ultraviolet-visible (UV-Vis) spectroscopy, scanning electron microscopy (SEM) and x-ray diffraction (XRD). The FTIR spectra showed O-H stretch at 3,340 cm^{-1} (peel extract solution), 3,308 cm^{-1}/3,348 cm^{-1} (pre-calcine sample), and 3,086.11 cm^{-1}/3,194.12 cm^{-1} (calcined at 600 °C). The spectra also showed Mg-O stretching at 655.80 cm^{-1} and 594.08 cm^{-1} for pre-calcine and calcined samples, respectively. The wavelength of UV-Vis obtained for 4 sets of green synthesis was around 265 nm due to the surface plasmon resonance band. Thus, confirmed the formation of MgO-NPs. SEM images of MgO-NPs samples showed a mixture of non-uniform sizes and shapes that were agglomerated with average size range of about 90 nm to 320 nm. XRD diffraction analyses displayed the MgO-NPs as a cubic structure.

Keywords: green synthesis, magnesium oxide nanoparticles, *Musa acuminata*, sustainable materials

Abstrak

Sintesis nanopartikel logam oksida dengan menggunakan ekstrak tumbuhan dapat menjanjikan kaedah alternatif kepada sintesis kimia. Dalam kajian ini, nanopartikel magnesium oksida (MgO-NPs) telah disintesis menggunakan larutan ekstrak kulit pisang *Musa acuminata* Cavendish. Bahan prekursor yang digunakan ialah magnesium nitrat heksahidrat ($Mg(NO_3)_2.6H_2O$) dan larutan ekstrak kulit pisang Cavendish yang kering. Kepekatan $Mg(NO_3)_2.6H_2O$, isipadu larutan ekstrak, dan suhu pengkalsinan yang berbeza telah digunakan untuk menjalankan kajian ini. MgO-NPs yang disintesis hijau dicirikan oleh Analisis Termogravimetrik (TGA), Spektroskopi Infra Merah Transformasi Fourier (FTIR), Spektroskopi Ultraviolet-Visible (UV-Vis), Mikroskop Imbasan

Elektron (SEM) dan Pembelauan Sinar-X (XRD). Spektra FTIR telah menunjukkan kewujudan regangan O-H pada 3,340 cm^{-1} (larutan ekstrak), 3,308 cm^{-1}/ 3,348 cm^{-1} (sampel sebelum proses kalsin) dan 3,086.11 cm^{-1}/3,194.12 cm^{-1} (MgO-NPs dikalsinkan pada 600 °C). Spektra FTIR juga menunjukkan regangan Mg-O pada 655.80 cm^{-1} dan 594.08 cm^{-1} untuk sampel sebelum dan selepas proses pengkalsinan. Panjang gelombang UV-Vis bagi keempat-empat set adalah pada 265 nm adalah disebabkan oleh jalur resonans plasmon permukaan yang membuktikan pembentukan MgO-NPs. Imej SEM menunjukkan campuran bentuk dan saiz tidak sekata yang teraglomerat dengan anggaran purata saiz sekitar 90 nm hingga 320 nm. Analisis XRD memperlihatkan MgO-NPs sebagai struktur kubik.

Kata kunci: sintesis hijau, nanopartikel magnesium oksida, *Musa acuminata*, bahan lestari

Introduction

Green chemistry has first been introduced in the America's Pollution Prevention Act of 1990 aiming to reducing pollution at its sources and producing less costly chemical products [1]. According to Murcia et al., there are 12 principles of green chemistry which are waste prevention, atom economy, less hazardous chemical synthesis, designing safer chemicals, safer solvents and auxiliaries, use of renewable feedstocks, reduce derivatives, catalysis, design for degradation, real time pollution prevention, design for energy efficiency and safer chemistry for accident prevention [2]. In synthetic chemistry, green synthesis of nanoparticles, a single-step pollution-free synthesis method [3,4] has been reported to fulfil at least five principles of green chemistry, such as waste prevention, reduce derivatives, safer solvent and auxiliaries, renewable feedstocks and less hazardous chemical synthesis [5]. This production approach is not only environmentally friendly but they are also cost-efficient as well as less toxic [6]. Green synthesis of nanoparticles which employs extracts, such as microorganisms and plant parts like leaves, fruits, and seeds [7] as a reducing and capping agent is a great alternative to the expensive physicochemical methods which poses environmental and biological threat due to the usage of toxic organic solvent and hazardous reagents [8]. Farani et al. has remarked that these natural resources contain biomolecules, polysaccharides, phenolics, vitamins and amino acids which give reducing agent properties to them [9]. Phytochemicals such as terpenoids, aldehyde, carboxylic acids and amides also contribute in the reduction and stabilization [5].

The green synthesis method is broadly used as an alternative to the chemical synthesis method in synthesizing nanoparticles [10]. In the synthesis of magnesium oxide nanoparticle (MgO-NPs), plants extract such as *Embilica officinalis* [11], Neem plant [12], Aloe vera [13] and *Trachyspermum ammi* [14] have been used in the green synthesis as this route replaces the usual conventional physicochemical techniques, such as the sol-gel method, chemical precipitation, and hydrothermal [15]. Fruit waste extract *Nepehelium lappaceum* L peels [16] *Persimmon* peels and *Citrus aurantium* peels have also been used to synthesize MgO-NPs [17, 18]. Although green synthesis of metal oxide nanoparticles by using fruit waste extracts has been extensively studied, the study on biological synthesis specifically for MgO-NPs has not been done widely [19]. The exploration of resources of potential reducing agent is necessary to ensure the efficiency of green synthesis [5].

Magnesium oxide nanoparticles (MgO-NPs) are known to exhibit the ability to withstand extreme conditions and high biocompatibility [20]. MgO-NPs have received a lot of interests for their variety kind of applications [21]. It has been found that MgO-NPs has higher surface to volume ratio and higher surface energy as compared to bulk MgO due to its small particles size [22]. They are evidenced to be great refractory and superconducting materials as they possess good optical and magnetic properties [22]. In biomedicine, MgO-NPs are applied for bone regeneration, relief of heartburns as well as antitumor [23]. They are also known as nontoxic antibacterial agents that is relatively easy to be obtained among all the metal oxide nanoparticles [24]. The properties of the nanoparticles are depending on the size and geometrical structure of the nanoparticles [25]. Therefore, the optimization of reaction conditions, such as volume of extract use, pH value, temperature of reaction, temperature of calcination and volume of starting materials is crucial as these conditions affect the

size, shape, form and stability of the nanoparticles produced [26], tailoring the properties of nanoparticles to suit different desired applications.

In this study, *Musa acuminata* or cavendish banana peel extract was used as reducing and capping agent. Phytochemical tests conducted in previous research showed the presence of secondary metabolite compounds, including alkaloids, flavonoids, saponins, and polyphenols in banana peel extract [27] making it suitable as reducing and capping agent. Previous studies have reported the usage of banana peel extract as a capping agent in the production of metal nanoparticles [28]. Banana peel utilization in the synthesis of ZnO-NPs have also been reported [27,29,30,31,32]. Abdullah et al. [30] in their comparative study of green and chemical synthesis by using cavendish banana peel in the synthesis of zinc oxide nanoparticles (ZnO-NPs) have noted that green synthesized ZnO-NPs exhibited higher crystallinity and smaller particle size. The green synthesized nanoparticles also showed high photocatalytic activity comparable to their chemically synthesized counterpart. On this note, green approach is proven compatible to that of chemical approach [30]. The optimization of metal oxide synthesis by using cavendish banana peel has been done as well [29].

While the usage of this peel in metal oxide synthesis has been explored, especially through ZnO-NPs production, the research using banana peel extract are still very limited for MgO-NPs, especially the optimization of synthesis conditions. The study using banana peel extract as reducing agent in the synthesis of MgO-NPs will further explore its potential in metal oxide nanoparticles synthesis. The optimization of conditions by using two different methods with different volume of extracts, different volume of starting materials and different concentration of starting materials were done in this study. MgO-NPs were also produced by calcination with two different temperatures. The study utilizing these parameters is important as they have major impact on the morphology and the biological applications of the nanoparticles produced. Different volume of extracts, mainly determines the yield of nanoparticles [26]. This approach differed from previous study, whereby each parameter was studied while the others were kept constant [33]. Instead of focusing on the effect of one parameter at a time on the nanoparticles, this study focused on the effect of four parameters concurrently on the nanoparticles. The produced MgO-NPs were characterized by using thermogravimetric analysis (TGA), Fourier transform infrared (FTIR) spectroscopy, ultraviolet-visible (UV-Vis) spectroscopy, scanning electron microscopy (SEM) and X-ray Diffraction (XRD) to further understand the effects of parameters on the size, surface morphology and crystallite structure of MgO-NPs.

Other than that, the utilization of the peel which contributes to a major agriculture waste [34] allows the researchers to harness renewable feedstocks as well as preventing waste and derivatives that align with the principles of green chemistry. By using banana peel as reducing agent, the researchers manage to provide safer chemicals and solvents which is better to the people and environment. In the synthesis methods, low temperature and short reaction time were operated allowing efficient energy consumption and high feasibility. Hence, the usage of banana peels extract is considered environmentally, socially and economically sustainable, making it a ‘green’ approach.

Materials and Methods

Materials

Magnesium nitrate hexahydrate ($Mg(NO_3)_2$) were purchased from Sigma Aldrich and used without further purification. *Musa acuminata* Cavendish bananas were brought from local supermarket in Petaling Jaya, Selangor. Distilled water was used to prepare all the solutions and Whatman No. 1 filter paper was used to filter MgO-NPs solution.

Synthesis of magnesium oxide nanoparticles (MgO-NPs): Preparation of banana peel extract

The *Musa acuminata* Cavendish banana peels were rinsed thoroughly with distilled water and cut into smaller pieces. The peels were oven dried at 150 ºC for 4 h and ground into powder. A total of 20 g powdered banana peel was added in a beaker with 200 mL of distilled water. The mixture was heated at 70 ºC–80 ºC for 1 h and filtered with filter paper. Excess extract solution was kept in the refrigerator (maximum 24 h).

Phytochemical tests of banana peel extract

To investigate the compounds presence in the banana peel extract, several phytochemical tests were carried out. This included saponin test, alkaloid test, tannin test, phenol test, flavonoid test, terpenoid test, and glycoside test. Table 1 shows a list of methods for each test. Each test was performed at least three times and only tests which appeared positive in two or more tests were considered to confirm the presence of the active compounds in banana peel extract.

Table 1. Phytochemical tests methods.

Tests	Methods
Saponin Test	1 mL of peel extract solution was added with 2 mL of distilled water in a test tube. The solution was shaken vigorously and was observed for a stable persistent froth for 10 min.
Wagner's Test	0.5 mL of peel extract solution were treated with a few drops of Wagner's reagent (iodine in potassium iodide). The colour changes were observed, and a brown precipitate formed to indicates the presence of alkaloid.
Mayer's Test	0.5 mL of peel extract solution was treated with a few drops of Mayer's reagent (potassium mercuric iodide). A yellow cream precipitate formed to indicates the presence of alkaloid.
Tannin Test	0.5 mL of peel extract solution was added with 1 to 2 drops of 10% iron (III) chloride solution. A dark green or blue-green coloration indicates the presence of tannins.
Phenol Test	0.5 mL of peel extract solution was put into test tube was added followed with 2 to 3 drops of 10% iron (III) chloride solution. The presence of green or blue colour indicates the presence of phenolic compound.
Flavonoid Test	0.5 mL of peel extract solution was treated with few drops of concentrated sulphuric acid. The colour changes were observed, and a formation of orange colour indicates the presence of flavonoid.
Salkowski Test	0.5 mL of peel extract solution was added with 2 mL of chloroform followed by 3 mL concentrated H_2SO_4 carefully to form a layer. Terpenoids are present if a reddish-brown colouration is observed.
Liebermann's Test	3 mL of peel extract solution was added with 2 mL of $CHCl_3$ and 2 mL of CH_3COOH. A blue colour solution changes into green colour indicated the presence of glycosides.

Green synthesis of magnesium oxide nanoparticles (MgO-NPs)

MgO-NPs were synthesized with two different set of conditions, (A) 30 mL peel extract with 150 mL $Mg(NO_3)_2$ (0.05 M) aqueous solution; (B) 25 mL peel extract with 200 mL $Mg(NO_3)_2$ (0.10 M) aqueous solution. An amount 30 mL of banana peel extract was added to 150 mL of $Mg(NO_3)_2$ (0.05 M) aqueous solution. The reaction mixture was stirred at a constant temperature of 80 °C by using a magnetic stirrer hot plate for 2 h. Color changes were noted for the reaction mixture as it indicates the formation of precipitate.

After the 2 h of constant stirring and heating, the mixture was cooled down to room temperature. The cooled mixture was centrifuged at 8,000 rpm for 20 min. The mixture was filtered and oven dried at 80 °C overnight. The fully dried precipitate was ground with mortar and pestle.

Thermogravimetric analysis (TGA) was conducted prior to calcination to determine the suitable calcination temperature. To obtain the final product, MgO-NPs, the ground samples from previous step were calcined in the furnace at the suitable temperatures for 5 h. The procedure was repeated with Condition B.

Characterization of magnesium oxide nanoparticles (MgO-NPs): Thermogravimetric analysis (TGA)

Perkin Elmer Pyris 6 TGA thermogravimetric analyzer was used to quantitatively monitor the weight change in the sample as a function of temperature. About 5 mg of pre-calcine MgO-NPs were weighed and used on each analysis to avoid any influence of sample quantity in the analysis. The analyses were performed in the presence of nitrogen gas with a constant flow rate of 20 mL min^{-1} throughout the process. The analyses were conducted within temperature range of 30 °C to 900 °C at a ramping rate of 10 °C min^{-1}. The TGA graph were obtained after the analyses.

Fourier transformation infrared (FTIR) spectroscopy

The FTIR analyses were performed by using Shimadzu model IRTracer-100 spectrophotometer in the range of 400 cm^{-1} to 4,000 cm^{-1} with the attenuated total reflectance (ATR) technique. The diamond on the sample platform was cleaned with acetone by using lens paper. A background scan without any sample on the diamond was done. A small amount (about 5 mg) of pre-calcine MgO-NPs were placed on the diamond until it was fully covered for each analysis. The pressure arm was placed into position and locked over the diamond filled with sample. Force was applied on the sample, pushing it onto the diamond surface. Finally, the sample was analyzed with the software and the FTIR spectra were obtained.

Ultraviolet-Visible (UV-Vis) spectroscopy

Shimadzu UV–Visible spectrophotometer model UV-1800 was utilized for the characterization of MgO-NPs. The baseline was set with the blank. The reference cuvette and measurement cuvette were filled with distilled water. The cuvettes were placed and aligned properly in the spectrometer. After setting the baseline, the measurement cuvette was removed and rinsed twice before filling with sample. The cuvette was ensured that it was clear from fingerprints and placed into the spectrometer for analysis. The wavelength range of the analyses were set to be within 200 nm to 800 nm with a resolution of 1 nm. The absorbance spectra were collected after the analyses.

Scanning electron microscopy (SEM)

The morphology of MgO-NPs samples was analyzed from the images generated from the TESCAN VEGA scanning electron microscope. To prepare the samples, double-sided carbon adhesives were applied onto the SEM stubs and the protective films were removed.

Then, the MgO-NPs samples were placed on the adhesives and coated them with gold (Au) by using the gold sputtering machine. The coated samples (on the stubs) were loaded onto the sample stage in the SEM chamber. Then, suitable spots for desired structure or morphology of MgO-NPs were located and the SEM images were captured at 4 magnifications, 5kx, 10kx, 15kx, 20kx.

X-ray diffraction (XRD)

To identify phases and patterns of MgO-NPs, XRD analyses were conducted by using Rigaku Miniflex II diffractometer (30 kV, 15 mA) with Cu K-α radiation (1.5418 Å) with a Bragg's angles, 2θ range of 20° to 80° with a scan rate of 2°/min.

The MgO-NPs samples were ground by using agate mortar and pestle to produce a uniform fine powder. The samples were placed onto a glass sample holder with a square hollow-ground side. The excess samples were cleared by sliding across the sample holder with a glass plate. Then, the surface of the samples was smoothed with the back of the glass plate. Any excess samples on the glass sample holder (around hollow-ground side) were wiped off. The sample holder was carefully

inserted onto the sample holder slot, ensuring no sample spills for the XRD analyses.

Results and Discussion

Several phytochemical tests were conducted on the Cavendish banana peel extract solution to confirm the bioactive compounds and the functional groups responsible for the reduction and capping of MgO-NPs. Table 2 shows that alkaloid, tannin, phenol, flavonoid, and terpenoid were present in banana peel extract solution.

The phytochemical tests were carried out in triplicate and labelled as 1, 2, and 3 for each compound to confirm the consistency and accuracy of the results. The presence of the compound of interest in the peel extract solution will only be considered if two or more positive results were obtained from the tests. The findings were mostly similar to previous studies [27, 35], however with a slight difference. In their studies, saponin and glycoside were present in banana peel extract solution while it was not present in this study. The different outcomes could be due to the drying condition of the banana peels [36].

Table 2. Phytochemical test results of Cavendish banana peel extract solution

	Tests	1	2	3
Saponin	Foam Test	-	-	-
Alkaloid	Mayer's Test	+	+	+
	Wagner's Test	+	+	+
Tannin	Ferric Chloride Test	+	+	+
Phenol	Ferric Chloride Test	+	+	+
Flavonoid	Flavonoid Test	+	+	+
Terpenoid	Salkowski's Test	+	+	+
Glycoside	Liebermann's Test	-	-	-

Note: (+): detected, (-): not detected

Thermogravimetric analysis (TGA)

Thermogravimetric analyses were carried out to determine the suitable temperature for calcination of the green synthesized MgO-NPs [37]. Figure 1 shows the thermogravimetric graph of two pre-calcined samples with two different sets of volume and concentration of starting materials. Based on Figure 1, the initial stage of weight loss below 100 °C was due to the evaporation of moisture and other volatile compounds [38], whereas the weight loss started at below 550 °C was due to the decomposition of the phytochemical compounds in peel extract and other organic compounds [37,39].

TGA curve for the MgO samples showed that weight loss of almost 87% from 30 °C had occurred continuously up to 600 °C as the graph showed almost a plateau thereafter. This indicated that MgO-NPs synthesized by using Method A and Method B were thermally almost stable starting at 600 °C and continuing up to the maximum temperature of 900 °C [39]. From this information, the green synthesized pre-calcine samples were subjected to calcination at 600 °C and 800 °C. It can be concluded that the formation of MgO synthesized with both Condition A and Condition B took place with heating at more than 600 °C.

Fourier transformation infrared (FTIR) spectroscopy

FTIR results were obtained for MgO-NPs synthesized with Condition A are shown in Figure 2, the broad peak centered at (a) 3340.71 cm^{-1}, (b) 3308.85 cm^{-1}, and (c) 3086.11 cm^{-1} were due to the stretching vibration of O-H group [38,39]. The presence of O-H groups is supported by the absorption peak at (a) 1635.64 cm^{-1} and (b) 1620.21 cm^{-1}, which corresponded to the bending mode of O-H bond [18].

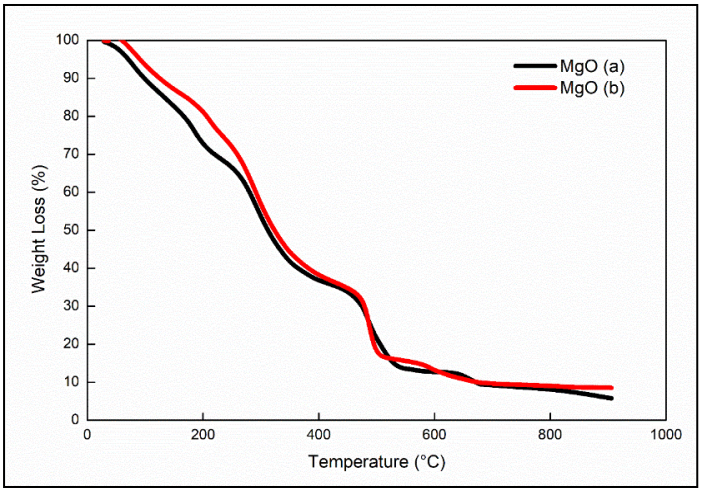


Figure 1. TGA graph of pre-calcine sample synthesised with (a) condition a (b) condition b before calcination.

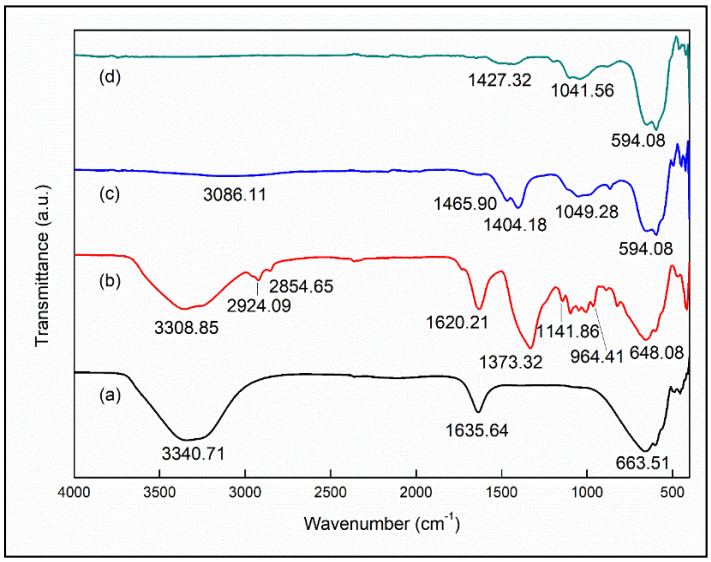


Figure 2. FTIR Spectra of MgO (Condition A): (a) banana peel extract solution (b) before calcine; (c) calcined at 600 °C; (d) calcined at 800 °C

The O-H groups located around 1630 cm^{-1} could be from the hydroxyl groups of the phytochemical compounds in the peel extract that were involved in the capping reaction [39]. Overall based on Figure 2 (b), Figure 2 (c) and Figure 2 (d), both O-H peaks became narrower and eventually disappeared with increasing calcination temperature as elimination of water molecules in the samples increased [40].

Other than O-H stretching, the broad peak centered at (a) 3340.71 cm^{-1} could also be the stretching vibration of N-H groups, which is a feature of phenolic compounds, such as glycosides, tannins, and flavonoids [41]. This finding agreed with the phytochemical test result conducted. Moreover, the two small absorption peaks at 2924.09 cm^{-1} and 2854.65 cm^{-1} shown in Figure 2 (b) represented the C-H stretching vibration in CH_2 groups which could be due to the phytochemical compounds [42]. The peaks slowly became indistinguishable as the calcination temperature increased. This meant that the capping reaction with phytochemical compounds had occurred [43].

The absorption peak at (b) 1373.32 cm^{-1} represented the C-H bending vibration. Whereas the peaks at (c)1404.18 cm^{-1} to 1465.90 cm^{-1} and (d) 1427.32 cm^{-1} were assigned to Mg-H which indicated the formation of hydride ion [44]. Besides, absorption peaks located between (b) 964.41 cm^{-1}, and 1141.86 cm^{-1} were most likely attributed to C-O and C-O-C diagnostic bonds [42]. The peaks at 2924.09 cm^{-1} and 1141.86 cm^{-1} in Figure 2 (b) proved the presence of polysaccharides, polyphenols and proteins [38] as the peaks corresponded to the functional groups contained in those phytochemicals in the pre-calcined MgO-NPs. The peaks became narrower when the samples were calcined, indicating that possibly the phytochemicals had undergone capping reaction.

The appearance of extra peaks at 3086.11 cm^{-1}, 1465.90 cm^{-1}, 1404.18 cm^{-1}, 1049.28 cm^{-1} and (d) 1427.32 cm^{-1}, 1041.56 cm^{-1} might be due to: (1) formation of crystalline inorganic compounds present in the peel extract during the calcination process; and (2) strong bonds that stabilized the formation of MgO-NPs after the decomposition of phytochemicals which remained over the surface of MgO-NPs [41]. The broad absorption peaks at (b) 648.08 cm^{-1} and (c, d) 594.08 cm^{-1} from all FTIR spectra obtained for green synthesized MgO-NPs with Condition A, indicated the stretching vibration mode for the Mg-O compound group [39]. The summary band assignment is shown in Table 3.

Table 3. Band assignment of peel extract and MgO-NPs (Condition A)

Band Assignment	**Wavenumber (cm^{-1})**			
	Banana Peel Extract	**Before Calcine**	**Calcined (600 °C)**	**Calcined (800 °C)**
O-H stretch	3340.71	3308.85	3086.11	-
N-H stretch	3340.71	-	-	-
C-H stretch	-	2924.09 & 2854.65	-	-
O-H bend	1635.64	1620.21	-	-
C-H bend	-	1373.32	-	-
Mg-H	-	-	1404.18 & 1465.90	1427.32
C-O	-	1141.86	-	-
C-O-C	-	964.41	-	-
Mg-O	-	648.08	594.08	594.08

Similar FTIR results were obtained for MgO-NPs synthesized with Condition B, as shown in Figure 3. The broad peak centered at (a) 3340.71 cm^{-1}, (b) 3348.42 cm^{-1}, and (c) ,194.12 cm^{-1} were due to the O-H stretch [18]. Also, the absorption peaks at (a) 1635.64 cm^{-1} and (b) 1,627.92 cm^{-1}, which corresponded to the bending mode of O-H bonds which came from the hydroxyl groups of the phytochemicals of peel extract solution that were involved in the capping reaction [18,39].

Similarly, based on Figure 3 (b), Figure 3 (c) and Figure 3 (d), both O-H peaks became narrower and eventually disappeared with increasing calcination temperature when more water molecules were evaporated [40]. As mentioned, the broad peak centered at (a) 3340.71 cm^{-1} could also be the stretching vibration of N-H groups other than O-H groups. N-H groups are a feature of phenolic compounds, such as glycosides, tannins, and flavonoids [41] which agrees with the phytochemical test results of the extract.

Furthermore, the two small absorption peaks observed in Figure 3 (b) at 2924.09 cm^{-1} and 2851.49 cm^{-1} represented the C-H stretching vibration in CH_2 groups. This could be attributed to the phytochemical compounds [42]. As the calcination temperature increased, the peaks became increasingly indistinguishable. This indicated that the phytochemical compound capping reaction had taken place.

The C-H bending vibration is represented by the absorption peak at (b) 1334.74 cm^{-1}. The peaks at (c)

1411.89 cm^{-1} – 1473.62 cm^{-1} were attributed to Mg-H indicating the presence of hydride ion [44]. Besides, C-O and C-O-C diagnostic bonds were most likely responsible for absorption peaks between (b) 964.41 cm^{-1}, and 1141.86 cm^{-1} [42]. When the samples were calcined, the peaks narrowed, indicating that the phytochemicals had undergone a capping reaction.

The extra peaks that appeared at 3194.12 cm^{-1}, 1473.62 cm^{-1}, 1411.80 cm^{-1}, 1056.99 cm^{-1} and (d) 1049.28 cm^{-1} could be because of: (1) the formation of crystalline inorganic compounds present in the extract solution during the calcination process; and (2) strong bonds that stabilized the formation of MgO-NPs after the degradation of phytochemicals which remained over the surface of MgO-NPs [41].

Based on all the FTIR spectra obtained for green synthesized MgO-NPs with Condition B, the broad absorption peaks at (b) 655.80 cm^{-1} and (c, d) 594.08 cm^{-1} indicated the stretching vibration mode for the Mg-O compound group [39] which confirmed the production of MgO. The summary band assignment is shown in Table 4.

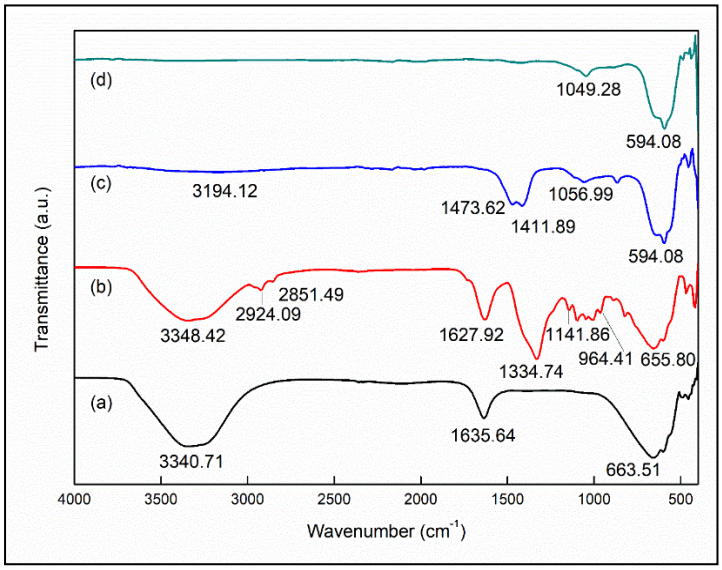


Figure 3. FTIR Spectra of MgO (Condition B): (a) banana peel extract solution (b) before calcine; (c) calcined at 600 °C; (d) calcined at 800 °C

Table 4. Band assignment of peel extract and MgO-NPs (Condition B)

Band Assignment	**Wavenumber (cm^{-1})**			
	Banana Peel Extract	**Before Calcine**	**Calcined (600 °C)**	**Calcined (800 °C)**
O-H stretch	3340.71	3348.42	3194.12	-
N-H stretch	3340.71	-	-	-
C-H stretch	-	2924.09 & 2851.49	-	-
O-H bend	1635.64	1627.92	-	-
C-H bend	-	1334.74	-	-
Mg-H	-	-	1411.89 & 1473.62	-
C-O	-	1141.86	-	-
C-O-C	-	964.41	-	-
Mg-O	-	655.80	594.08	594.08

Ultraviolet-Visible (UV-Vis) Spectroscopy

The synthesis of MgO-NPs was confirmed by the appearance of a maximum surface plasmon resonance (SPR) detected by UV-Vis spectroscopy. SPR located at different wavelengths can affect the shape, size and well distribution of green synthesized NPs [45].

The size of MgO-NPs produced through green synthesis tended to be small when the SPR band is located at wavelength lesser than 300 nm. However, the absorption peak shifted to larger wavelength (red-shift) with increasing particle size [46]. As shown in Figure 4, the absorption of the MgO-NPs synthesized with Condition A, calcined at 600 °C and 800 °C showed wavelengths at 264.50 nm and 265.50 nm, respectively. On the other hand, the absorption band of MgO-NPs formed with Condition B (Figure 5) was located at wavelength 264 nm for both calcination temperatures (600 °C and 800 °C).

According to previous studies, the absorption of UV-Vis spectrum of MgO-NPs was reported between 260 nm–300 nm [18, 39, 42, 47, 48]. Therefore, the absorption peak of MgO-NPs obtained with both conditions were within the accepted wavelength range. This meant that, the change in concentration of $Mg(NO_3)_2.6H_2O$ and volume of extract solution did not have a significant effect on the formation of MgO-NPs. However, MgO-NPs calcined at 800 ℃ showed a higher absorbance value indicating more yield of MgO-NPs [33]. This was due to the faster rate of crystal growth at higher temperature as thermal energy increased [49].

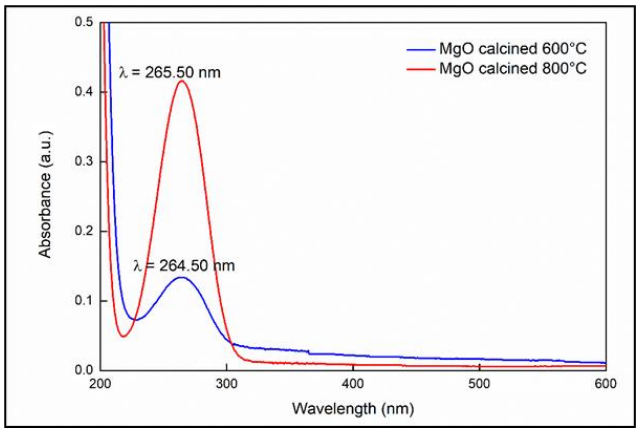


Figure 4. UV-Vis spectra of MgO-NPs (Condition A) calcined at 600 and 800 °C

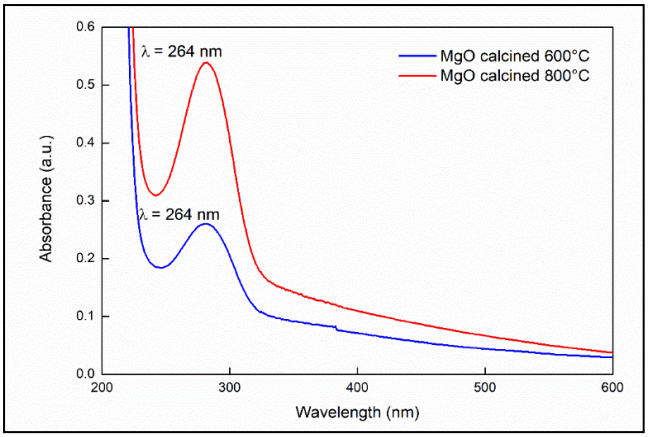


Figure 5. UV-Vis spectra of MgO-NPs (Condition B) calcined at 600 and 800 °C

Scanning electron microscope (SEM)

The morphology of the MgO-NPs is presented in Figure 6, Figure 7, Figure 8, and Figure 9. In general, the average particle size for MgO-NPs synthesized with Condition A and Condition B with different calcination temperatures varies.The products of green synthesis with Condition A, calcined at 600 °C and 800 °C, as well as products formed with Condition B, calcined at 600 °C were not within the nanoparticles size range. Whereas, the MgO-NPs produced with Condition B and calcined at 800 °C was within the nanoparticle size range of 1 nm – 100 nm [50]. The bigger particle size for MgO-NPs calcined was due to secondary phase, $Mg(OH)_2$, present in the MgO lattice causing it to be less crystalline [49]. This finding contradicts other study which stated that higher calcination temperature increases the particle size. However, the study only studied the effect of calcination temperature while other conditions were kept constant [51].

Based on previous studies, the concentration and amount of extract used, reaction temperature, and pH value could affect the variable parameters, such as size, shape, and agglomeration [52, 53]. Figure 6 shows the SEM images of MgO-NPs synthesized with Condition A with calcination temperature of 600 °C. The particles had non uniform shape with an average size of 316.78 nm, the smallest particle was about 107 nm while the largest particle was about 550 nm with some degree of agglomeration.

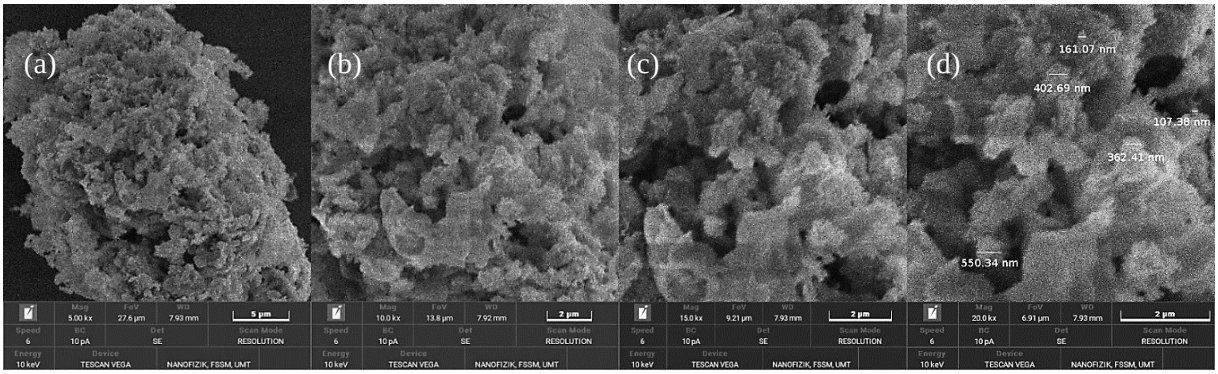


Figure 6. SEM images of MgO-NPs (Condition A) calcined at 600°C; at (a) 5,000x, (b) 10,000x, (c) 15,000x, and (d) 20,000x magnification

As shown in Figure 7, the particles synthesized with Condition A and calcined at 800 °C also had a non-uniform shape with an average size of 140.52 nm. The smallest particle was about 62 nm while the largest particle was about 255 nm with some degree of agglomeration as well.

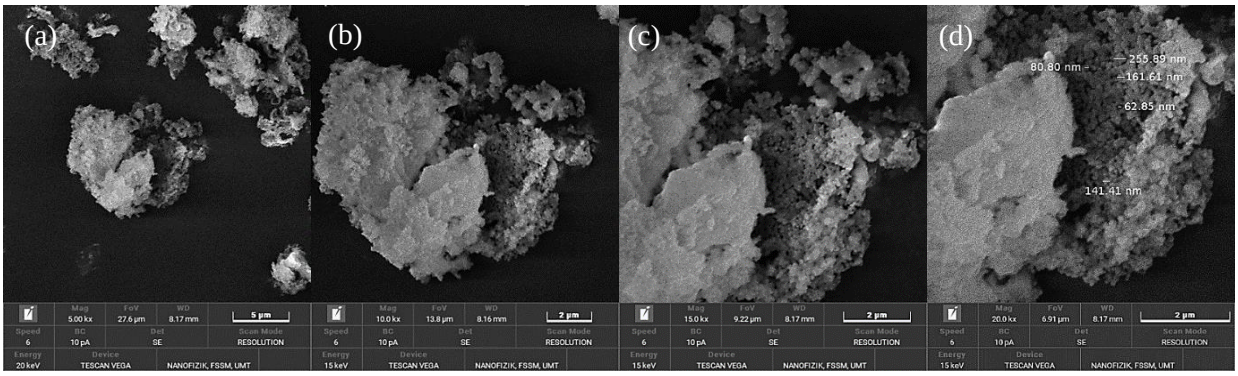


Figure 7. SEM images of MgO-NPs (Condition A) calcined at 800 °C; at (a) 5,000x, (b) 10,000x, (c) 15,000x, and (d) 20,000x magnification

Furthermore, Figure 8 shows the SEM images of synthesized MgO-NPs with Condition B and calcined at 600 °C. Most of the particles had irregular shapes with a mean particle size of 208.31 nm. The smallest particle was around 148 nm, and the biggest particle was about 255 nm. Some degree of agglomeration was observed.

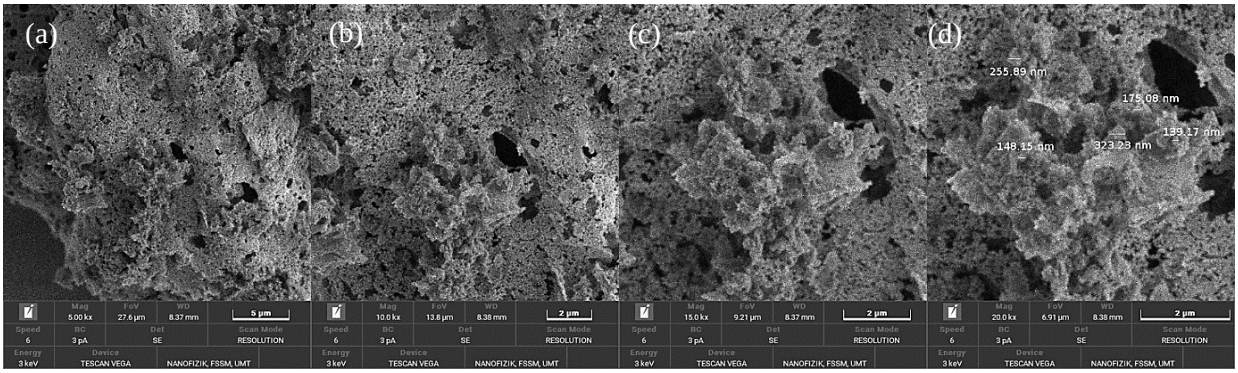


Figure 8. SEM images of MgO-NPs (Condition B) calcined at 600°C; at (a) 5,000x, (b) 10,000x, (c) 15,000x, and (d) 20,000x magnification

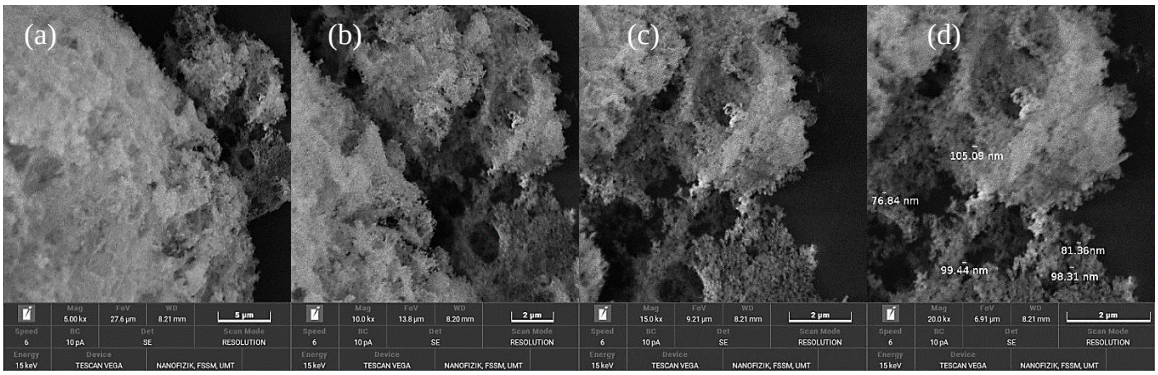


Figure 9. SEM images of MgO-NPs (Condition B) calcined at 800°C; at (a) 5,000x, (b) 10,000x, (c) 15,000x, and (d) 20,000x magnification

Lastly, Figure 9 shows the SEM images of MgO-NPs synthesized with Condition B and calcined at 800 °C. Most of the particles had non-uniform size and shapes with smaller crystallite as compared to other samples. The average particle size was 92.20 nm, with smallest particle of about 80 nm and largest particle of about 105 nm. Overall, all samples were highly agglomerated.

X-ray diffraction (XRD)

The synthesized MgO-NPs were subjected to x-ray diffraction analyses to confirm the presence and size of the NPs, obtain the crystallinity or amorphic nature, and detect possible impurities [41]. Figure 10 and Figure 11 show the x-ray diffraction pattern for MgO-NPs synthesized with Condition A and Condition B, respectively. Based on the PDF reference card No.9000493, the MgO-NPs obtained were in cubic structure with space group Fm-3m (225). Similar results were obtained for MgO-NPs synthesized with Condition A and Condition B. All the peaks observed for the MgO-NPs as listed in Table 5 and Table 6 were also in agreement with the PDF reference card No.9000493 and previous studies [45,49,51].

The presence of MgO-NPs was confirmed as all the samples (calcined at 600 °C and 800 °C) showed the presence of peaks corresponding to (111), (200), (220), (311) and (222) planes. Other than that, the sharp characteristic peaks in the diffractogram indicated the highly crystalline structure of MgO-NPs [49]. The MgO

peaks became sharper as the calcination temperature increased as evidenced in the Figures and Tables.

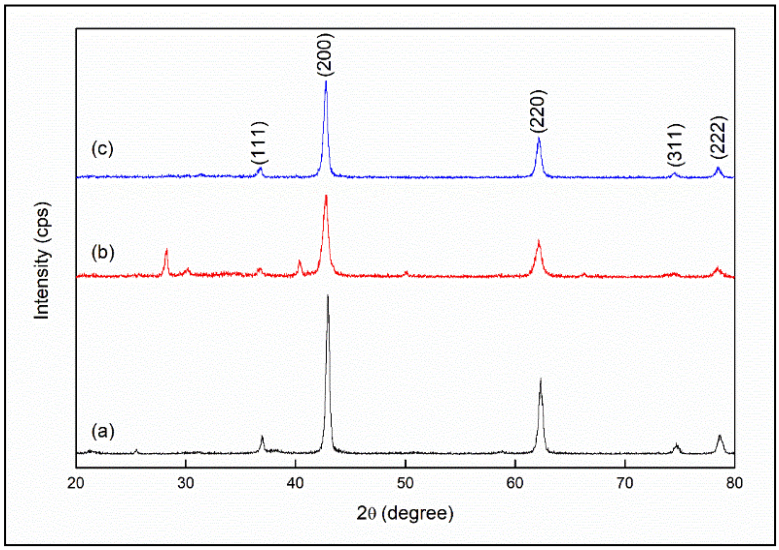


Figure 10. XRD of MgO-NPs (Condition A) (a) commercial and calcined at (b) 600 °C, and (c) 800 °C

Table 5. Crystallinity parameter of MgO-NPs synthesised with Condition A

(a) Calcined at 600 °C

2θ (°)	β (°)	Intensity (cps)	Lattice Plane	Mean Particle size (nm)
28.280	0.301	50	-	-
30.17	0.48	12	-	-
36.72	0.45	13	111	19.44
40.40	0.33	30	-	-
42.757	0.544	164	200	16.39
49.991	0.19	13	-	-
62.17	0.61	70	220	15.89
66.30	0.41	6	-	-
74.51	1.17	5	311	8.91
78.34	0.78	15	222	13.73

(b) Calcined at 800 °C

2θ (°)	β (°)	Intensity (cps)	Lattice Plane	Mean Particle Size (nm)
36.80	0.48	25	111	18.23
42.736	0.414	290	200	21.53
62.10	0.449	126	220	21.58
74.45	0.41	16	311	25.43
78.49	0.43	32	222	24.93

However, several peaks corresponded to impurities were detected for the MgO-NPs calcined at 600 °C. The extra impurities peaks detected were caused by stable crystalline inorganic compounds formed during the calcination of pre-calcine samples containing $Mg(OH)_2$ and strong bonds that remained over the surface of MgO-NPs [41]. On the other hand, no peaks other than the characteristic peaks of MgO were detected for the

MgO-NPs calcined at 800 °C, indicating that pure MgO-NPs were synthesized.

The average crystallite size of the MgO-NPs was estimated by using the Debye Scherrer's formula. When calcined at 600 °C, MgO-NPs synthesized with Condition A were approximately 9 nm–20 nm, but when calcined at 800 °C, they were roughly 18 nm–25 nm. Besides, MgO-NPs synthesized by using Condition B had a diameter of 9 nm–20 nm when calcined at 600 °C and was 17 nm–23 nm when calcined at 800 °C.

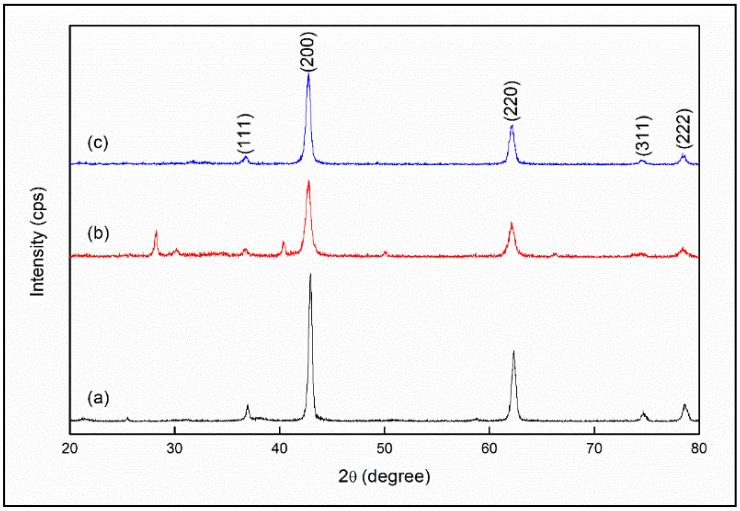


Figure 11. XRD of MgO (Condition B) (a) commercial and calcined at (b) 600 °C, and (c) 800 °C

Table 6. Crystallinity parameter of MgO nanoparticles synthesised with Condition B

(a) Calcined at 600 °C

2θ (°)	β (°)	Intensity (cps)	Lattice Plane	Mean Particle Size (nm)
28.280	0.301	50	-	-
30.17	0.48	12	-	-
36.72	0.45	13	111	19.44
40.40	0.33	30	-	-
42.757	0.544	164	200	16.39
49.991	0.19	13	-	-
62.17	0.61	70	220	15.89
66.30	0.41	6	-	-
74.51	1.17	5	311	8.91
78.34	0.78	15	222	13.73

(b) Calcined at 800 °C

2θ (°)	β (°)	Intensity (cps)	Lattice Plane	Mean Particle Size (nm)
36.84	0.50	23	111	17.50
42.744	0.465	301	200	19.17
62.10	0.529	129	220	18.32
74.46	0.45	16	311	23.17
78.44	0.54	31	222	19.85

Conclusion

In summary, MgO-NPs have been successfully synthesized by using cavendish banana peel extract as reducing and capping agent, proving the concept of waste-to-wealth. The synthesis of MgO-NPs by using this banana peels with two methods of study which employed different volume of extracts and starting materials as well as different volume of starting materials were both reproducible as they both showed similar thermal stability. FTIR has shown that the mechanism of synthesis in this study were reduction and capping as the peaks of functional groups for biomolecules in the plants appeared in the pre-calcined samples for both methods. However, the peaks disappeared after calcination showing the occurrence of a full reduction and capping of the produced nanoparticles. Morphology and shapes of nanoparticles are dependent of the concentration and volume of starting materials, volume of extracts and calcination temperatures. As shown in SEM images, method A produced spherical shaped nanoparticles while method B produced irregular shaped nanoparticles. In the future, further research on the relationship between morphology of MgO-NPs and the properties of MgO-NPs can be studied in order to customizing the applications of MgO-NPs in the biological, physical and all nanotechnology-related fields. Overall, the best results obtained were from Condition B (25 mL extract with 0.1 M concentration of starting materials), thus sustainable and optimized synthesis methods have been successfully developed for future exploration of MgO-NPs. More waste products can be explored in the future providing more sustainable resources of reducing agent for the synthesis of MgO-NPs.

Acknowledgement

Authors would like to thank Universiti Malaysia Terengganu for providing funding support for this project (UMT/TAPE-RG/2021/55338) and Faculty of Science and Marine Environment for providing the logistical support including the laboratory and needed instruments in completing this study.

References

1. United States Environmental Protection Agency (2023). Basics of green chemistry. https://www.epa.gov/greenchemistry/basics-green-chemistry [Accessed on 17 July 2023].
2. Murcia, J. E., Martinez, S., Martins V., Herrera, D., Buitrago, C., Velasquez, A., Ruiz, F. and Torres, M. (2023). Risk assessment and green chemistry applied to waste generated in university laboratories. *Heliyon*, 9(5): e15900.
3. Khandel, P., Yadaw, R. K., Soni, D. K., Kanwar, L. and Shahi, S. K. (2018). Biogenesis of metal nanoparticles and their pharmacological applications: present status and application prospects. *Journal of Nanostructure in Chemistry,* 8(3): 217-254.
4. Kumar, P. P., Bhatlu, M. L. D., Sukanya, K., Karthikeyan, S, and Jayan, N. (2020). Synthesis of magnesium oxide nanoparticle by eco-friendly method (green synthesis)–A review. *Materials Today: Proceedings*, 37: 3028-3030.
5. Singh, J., Dutta, T., Kim, KH., Rawat, M., Samdar, P. and Kumar, P. (2018). 'Green' synthesis of metals and their oxide nanoparticles: applications for environmental remediation. *Journal of Nanobiotechnology*, 16(1): 84.
6. Narendhran, S., Manikandan, M. and Shakila, P. B. (2019). Antibacterial, antioxidant properties of *Solanum trilobatum* and sodium hydroxide-mediated magnesium oxide nanoparticles: a green chemistry approach. *Bulletin of Materials Science*, 42(3): 1-8.
7. Ganapathi Rao, K., Ashok, C. H., Venkateswara Rao, K., Shilpa Chakra, C. H. and Akshaykranth, A. (2015). Eco-friendly synthesis of MgO nanoparticles from orange fruit waste. *International Journal Advance Research Physical Science*, 2: 1-6.
8. Vishwasrao, C., Momin, B. and Ananthanarayan, L. (2019). Green synthesis of silver nanoparticles using sapota fruit waste and evaluation of their antimicrobial activity. *Waste and Biomass Valorization*, 10(8): 2353-2363.
9. Farani R. M., Farsadrooh, M., Zare, I., Gholami, A. and Akhavan, O. (2023). Green synthesis of magnesium oxide nanoparticles and nanocomposites for photocatalytic antimicrobial, antibiofilm and antifungal applications. *Catalysts*, 13(4): 642.

10. Chaudhary, J., Tailor, G., Yadav, M., and Mehta, C. (2023). Green route synthesis of metallic nanoparticles using various herbal extracts: A review. *Biocatalysis and Agricultural Biotechnology*, 50: 102692.
11. Ramanujam, K., and Sundrarajan, M. (2014). Antibacterial effects of biosynthesized MgO nanoparticles using ethanolic fruit extract of *Emblica officinalis*. *Journal of Photochemistry and Photobiology B: Biology*, 141: 296-300.
12. Moorthy, S. K., Ashok, C. H., Rao, K. V., and Viswanathan, C. (2015). Synthesis and characterization of MgO nanoparticles by neem leaves through green method. *Materials Today: Proceedings*, 2(9): 4360-4368.
13. Umaralikhan, L., and Jamal Mohamed Jaffar, M. (2018). Green synthesis of MgO nanoparticles and its antibacterial activity. *Iranian Journal of Science and Technology, Transaction A: Science*, 42(2): 477-485.
14. Dabhane, H., Ghotekar, S., Zate, M., Kute, S., Jadhav, G. and Medhane, V. (2022). Green synthesis of MgO nanoparticles using aqueous leaf extract of Ajwain (*Trachyspermum ammi*) and evaluation of their catalytic and biological activities. *Inorganic Chemistry Communications*, 138: 109270.
15. Duong, T. H. Y., Nguyen, T. N., Oanh, H. T., Dang Thi, T. A., Giang, L. N. T., Phuong, H. T., Anh, N. T., Nguyen, B. M., Quang, V. T., Le, G. T. and Nguyen, T. van. (2019). Synthesis of magnesium oxide nanoplates and their application in nitrogen dioxide and sulfur dioxide adsorption. *Journal of Chemistry*, 2019: 4376429.
16. Suresh, J., Yuvakkumar, R., Sundrarajan, M., and Hong, S. I. (2014). Green synthesis of magnesium oxide nanoparticles. *Advanced Materials Research*, 952: 141-144.
17. Ali, R., Shanan, Z. J., Saleh, G. M., and Abass, Q. (2020). Green synthesis and the study of some physical properties of MgO nanoparticles and their antibacterial activity. *Iraqi Journal of Science*, 61(2): 266-276.
18. Vijayakumar, S., Punitha, V. N., and Parameswari, N. (2021). Phytonanosynthesis of MgO nanoparticles: Green synthesis, characterization and antimicrobial evaluation. *Arabian Journal for Science and Engineering*, 2021: 1-6.
19. Prasanth, R., Kumar, S. D., Jayalakshmi, A., Singaravelu, G., Govindaraju, K. and Kumar, V. G. (2019). Green synthesis of magnesium oxide nanoparticles and their antibacterial activity. *Indian Journal of Geo Marine Sciences,* 48(8): 1210-1215.
20. Amina, M., al Musayeib, N. M., Alarfaj, N. A., El-Tohamy, M. F., Oraby, H. F., Al Hamoud, G. A., Bukhari, S. I., and Moubayed, N. M. S. (2020). Biogenic green synthesis of MgO nanoparticles using *Saussurea costus* biomasses for a comprehensive detection of their antimicrobial, cytotoxicity against MCF-7 breast cancer cells and photocatalysis potentials. *PLoS ONE*, 15: 0237567.
21. Balakrishnan, G., Velavan, R., Mujasam Batoo, K., and Raslan, E. H. (2020). Microstructure, optical and photocatalytic properties of MgO nanoparticles. *Results in Physics*, 16: 103013.
22. Ammulu, M. A., Vinay Viswanath, K., Giduturi, A. K., Vemuri, P. K., Mangamuri, U. and Poda, S. (2021). Phytoassisted synthesis of magnesium oxide nanoparticles from *Pterocarpus marsupium* rox.b heartwood extract and its biomedical applications. *Journal of Genetic Engineering and Biotechnology*, 19: 21.
23. Pugazhendhi, A., Prabhu, R., Muruganantham, K., Shanmuganathan, R. and Natarajan, S. (2019). Anticancer, antimicrobial and photocatalytic activities of green synthesized magnesium oxide nanoparticles (MgONPs) using aqueous extract of Sargassum wightii. *Journal of Photochemistry and Photobiology B: Biology*, 190: 86-97.
24. Cai, L., Chen, J., Liu, Z., Wang, H., Yang, H. and Ding, W. (2018). Magnesium oxide nanoparticles: Effective agricultural antibacterial agent against *Ralstonia solanacearum*. *Frontiers in Microbiology*, 9: 790.
25. Chandrasekar, M., Subash, M., Perumal, V., Panimalar, S., Aravindan, S., Uthrakumar, R., Inmozhi, C., Isaev, A. B., Muniyasamy, S., Raja, A. and Kaviyarasu, K. (2022). Specific charge separation of Sn doped MgO nanoparticles for photocatalytic activity under UV light irradiation. *Separation and Purification Technology*, 2021: 294.
26. Pandit, C., Roy, A., Ghotekar, S., Khusro, A., Islam, M. N., Emran, T. bin, Lam, S. E., Khandaker, M. U.

and Bradley, D. A. (2022). Biological agents for synthesis of nanoparticles and their applications. *Journal of King Saud University - Science*, 34(3): 101869.

27. Marfu'ah, S., Rohma, S. M., Fanani, F., Hidayati, E. N., Nitasari, D. W., Primadi, T. R., Ciptawati, E., Sumari, S., and Fajaroh, F. (2020, May). Green synthesis of ZnO nanoparticles by using banana peel extract as capping agent and its bacterial activity. *2nd International Conference on Chemistry and Material Science (IC2MS)*, 833: 1-7.
28. Naganathan, S. and Thirunavukkarasu, S. (2017). Green way genesis of silver nanoparticles using multiple fruit peels waste and its antimicrobial, antioxidant, and anti-tumor cell line studies. *2nd International Conference on Mining, Material and Metallurgical Engineering,* 191: 1-7.
29. Abdullah, F. H., Abu Bakar, N. H. H. and Abu Bakar, M. (2020). Low temperature biosynthesis of crystalline zinc oxide nanoparticles from Musa acuminata peel extract for visible-light degradation of methylene blue. *Optik*, 206: 164279.
30. Abdullah, F. H., Abu Bakar, N. H. H. and Abu Bakar, M. (2021). Comparative study of chemically synthesized and low temperature bio-inspired Musa acuminata peel extract mediated zinc oxide nanoparticles for enhanced visible-photocatalytic degradation of organic contaminants in wastewater treatment. *Journal of Hazardous Materials*, 406: 164279.
31. Hussien, N. A. (2023). Antimicrobial potential of biosynthesized zinc oxide nanoparticles using banana peel and date seeds extracts. *Sustainability (Switzerland)*, 15(11): 9048.
32. Hussien, N. A., al Malki, J. S., al Harthy, F. A. R., Mazi, A. W. and Al Shadadi, J. A. A. (2023). Sustainable eco-friendly synthesis of zinc oxide nanoparticles using banana peel and date seed extracts, characterization, and cytotoxicity evaluation. *Sustainability*, 15(13): 9864.
33. Shittu, H. O., Igiehon, E., Eremwanarue, A. O., Oijagbe, R. E., Momoh, M. O. and Agbontian, M. A. (2021). Optimization of phytosynthesis of magnesium oxide and magnesium chloride nanoparticles. *Nigerian Journal of Biotechnology*, 37(2): 74-83.
34. Vu, H. T., Scarlett, C. J. and Vuong, Q. V. (2018). Phenolic compounds within banana peel and their potential uses: A review. *Journal of Functional Foods*, 40: 238-248.
35. Gillani, S. F., Ali, S., Tahir, H. M., Shakir, H. A. and Hassan, A. (2020). Phytochemical analysis, antibacterial and antibiogram activities of fruits peels against human pathogenic bacteria. *International Food Research Journal*, 27(5): 963-970.
36. Nguyen, V. T., and Le, M. D. (2018). Influence of various drying conditions on phytochemical compounds and antioxidant activity of carrot peel. *Beverages,* 4(4): 80.
37. Saikumari, N., Dev, S. M., and Dev, S. A. (2021). Effect of calcination temperature on the properties and applications of bio extract mediated titania nano particles. *Scientific Reports*, 11(1): 1-17.
38. Kumar, S. A., Jarvin, M., Inbanathan, S. S. R., Umar, A., Lalla, N. P., Dzade, N. Y., Algadi, H., Rahman, Q. I. and Baskoutas, S. (2022). Facile green synthesis of magnesium oxide nanoparticles using tea (*Camellia sinensis*) extract for efficient photocatalytic degradation of methylene blue dye. *Environmental Technology and Innovation*, 28: 102746.
39. Essien, E. R., Atasie, V. N., Oyebanji, T. O. and Nwude, D. O. (2020). Biomimetic synthesis of magnesium oxide nanoparticles using *Chromolaena odorata* (L.) leaf extract. *Chemical Papers*, 1-9.
40. Yusoff, H. M., Idris, N.H., Hipul, N. F., Yusoff, N. F. M., Izham, N. Z. M. and Bhat, I. U. H. (2020). Green synthesis of zinc oxide nanoparticles using black tea extract and its potential as anode material in sodium-ion batteries. *Malaysian Journal of Chemistry,* 22(2): 43-51.
41. Hii, Y. S., Jeevanandam, J. and Chan, Y. S. (2019). Plant mediated green synthesis and nanoencapsulation of MgO nanoparticle from *Calotropis gigantea*: Characterisation and kinetic release studies. *Inorganic and Nano-Metal Chemistry*, 48(12): 620-631.
42. Essien, E. R., Atasie, V. N., Okeafor, A. O. and Nwude, D. O. (2020). Biogenic synthesis of magnesium oxide nanoparticles using *Manihot*

esculenta (Crantz) leaf extract. *International Nano Letters*, 10(1): 43-48.

43. Latha, C. K., Raghasudha, M., Aparna, Y., Ramchander, M., Ravinder, D., Jaipal, K., Veerasomaiah, P. and Shridhar, D. (2017). Effect of capping agent on the morphology, size and optical properties of In_2O_3 nanoparticles. *Materials Research*, 20(1): 256-263.
44. Yusoff, H. M., Hazwani, N. U., Hassan, N. and Izwani, F. (2015). Comparison of sol gel and dehydration magnesium oxide (MgO) as a catalyst in Michael addition reaction. *International Journal of Integrated Engineering*, 7(3): 43-50.
45. Hassan, S. E. D., Fouda, A., Saied, E., Farag, M., Eid, A. M., Barghoth, M. G. and Awad, M. F. (2021). Rhizopus Oryzae-mediated green synthesis of magnesium oxide nanoparticles (MgO-NPs): A promising tool for antimicrobial, mosquitocidal action, and tanning effluent treatment. *Journal of Fungi, 7*(5): 372.
46. Osuntokun, J., Onwudiwe, D. C. and Ebenso, E. E. (2019). Green synthesis of ZnO nanoparticles using aqueous *Brassica oleracea* L. var. italica and the photocatalytic activity. *Green Chemistry Letters and Reviews*, 12(4): 444-457.
47. Dobrucka, R. (2018). Synthesis of MgO nanoparticles using Artemisia abrotanum herba extract and their antioxidant and photocatalytic properties. *Iranian Journal of Science and Technology, Transactions A: Science*, 42(2): 547-555.
48. Vidhya, E., Vijayakumar, S., Nilavukkarasi, M., Punitha, V. N., Snega, S., and Praseetha, P. K. (2021). Green fabricated MgO nanoparticles as antimicrobial agent: Characterization and evaluation. *Materials Today: Proceedings*, 45: 5579-5583.
49. Farizan, A. F., Yusoff, H. M., Badar, N., Bhat, I. U. H., Anwar, S. J., Wai, C. P., Asari, A., Kasim, M. F., and Elong, K. (2023). Green synthesis of magnesium oxide nanoparticles using Mariposa *Christia vespertilionis* leaves extract and its antimicrobial study toward *S. aureus* and *E. coli*. *Arabian Journal for Science and Engineering*, 48(6): 7373-7386.
50. Adamo, G., Campora, S. and Ghersi, G. (2017). Nanostructures for novel therapy: synthesis, characterization and applications. Elsevier, Amsterdam: pp. 57-80.
51. Venkatachalam, A., Jesuraj, J. P., and Sivaperuman, K. (2021). *Moringa oleifera* leaf extract-mediated green synthesis of nanostructured alkaline earth oxide (MgO) and its physicochemical properties. *Journal of Chemistry*, 2021: 4301504.
52. Rahmani-Nezhad, S., Dianat, S., Saeedi, M., and Hadjiakhoondi, A. (2017). Synthesis, characterization and catalytic activity of plant mediated MgO nanoparticles using *Mucuna pruriens* L. seed extract and their biological evaluation. *Journal of Nanoanalysis*, 4(4): 290-298.
53. Zhang, D., Ma, X. L., Gu, Y., Huang, H., and Zhang, G. W. (2020). Green synthesis of metallic nanoparticles and their potential applications to treat cancer. *Frontiers in Chemistry,* 8(799): 1-18.

Malaysian Journal of Analytical Sciences (MJAS)
Published by Malaysian Analytical Sciences Society

CURRENT PROGRESS IN DYE-SENSITISED SOLAR CELLS (DSSCs) FEATURING DONOR-π-ACCEPTOR SYSTEM OF MIXED MOIETIES: A REVIEW

(Kemajuan Terkini Sel Suria Peka Cahaya (DSSCs) Menampilkan Sistem Moiti Campuran Penderma-π-Penerima: Satu Ulasan)

Wan M. Khairul[*]*, and Muhammad Aidil Zailani*

Faculty of Science and Marine Environment,
Universiti Malaysia Terengganu, 21030 Kuala Nerus, Terengganu, Malaysia

[*]*Corresponding author: wmkhairul@umt.edu.my*

Received: 27 July 2023; Accepted: 13 September 2023; Published: 30 October 2023

Abstract

In recent years, the quest to propose an ideal molecular system acting as dye-sensitised solar cells (DSSCs) bearing single molecular system have attracted great interest. This is due to their promising potential to convert solar energy into electrical energy at low cost. The alteration of molecular framework is essential to propose a rigid rod donor-π-acceptor system in enhancing its electronic properties to be applied as active layer in this type of solar cells. In recent years, mixed moieties molecules are actively being proposed as this combination proven to provide better performance of efficiency. However, the molecules bearing different moieties with different atomic features are rather scarce. The extended conjugation and the push-pull phenomenon within the molecular backbones may provide efficient electronic properties with alteration from different substituents. The development of DSSCs featuring conjugated mixed moieties are relatively new and scarce. Thus, this review article provides an insight general idea on the fundamental aspects of DSSCs as its progresses in term of its essentials features and compositions which focusing on the utilisation of these moieties. It is hope that this contribution may equip one's understanding in venturing similar work on this type of molecular system.

Keywords: DSSCs, conjugation, donor-π-acceptor, acetylene, azomethine

Abstrak

Sejak kebelakangan ini, pencarian untuk mencadangkan sistem molekul unggul yang bertindak sebagai sel suria peka cahaya (DSSC) menampilkan system molekul tunggal telah menarik perhatian yang tinggi. Ini adalah disebabkan kerana ia menjanjikan potensi untuk menukar tenaga suria kepada tenaga elektrik pada kos yang rendah. Pengubahsuaian kerangka molekul adalah penting bagi mencadangkan sistem penderma-π-penerima rod tegar dalam meningkatkan sifat elektroniknya untuk diaplikasikan sebagai lapisan aktif dalam sel suria ini. Sejak beberapa tahun lalu, molekul-molekul tercampur moiti secara aktifnya banyak dicadangkan kerana penggabungan ini telah membuktikan prestasi keberkesanan yang baik. Walau bagaimanapun, molekul-molekul yang menampilkan moiti berbeza dengan tampilan atom berlainan adalah amat jarang. Pemanjangan konjugasi dan fenomena tolak-tarik di dalam kerangka molekul mampu menyediakan sifat elektronik berkesan melalui pengubahsuian daripada pelbagai kumpulan pengganti. Pembangunan DSSC yang menonjolkan campuran moiti terkonjugat ialah agak baharu dan jarang dilaporkan. Oleh yang demikian, artikel ulasan ini menyediakan hala tuju idea secara umum terhadap aspek-aspek asas DSSC dan

kemajuannya befokuskan ciri-ciri penting dan komposisinya yang memfokuskan penggunaan moiti-moiti ini. Diharapkan agar sumbangan ini dapat menlengkapkan pemahaman seseorang dalam penglibatan kerja yang sama terhadapa sistem molekul jenis ini.

Kata kunci: DSSC, konjugasi, penderma-π-penerima, asetilina, azometina

Introduction

The sun is the single most vital energy provider for life on Earth. It provides energy to plants and planktons for photosynthesis process. In turn, the planktons and plants are then consumed by animals, providing energy for them. Almost all of the electricity that we use nowadays is also provided by the sun, albeit not in a straightforward way. Examples are wind energy caused by movement of air due to heat from the sun, hydropower energy that derived energy from water that fell as rain after being evaporated by the sun, and also fossil fuels, which are formed from the biomass of animals and plants [1]. Through the use of photovoltaic cells or solar cells, energy in sunlight can also be directly harvested to obtain electricity.

Sunlight is a form of electromagnetic radiation, consisting of 56% infrared, 36% visible and 7% ultraviolet radiation, with the remainder consisting of other electromagnetic radiations [1]. Earth received around 1.8 x 10^{14} kW of energy from sunlight. When sunlight hits the earth's atmosphere, around 40% of the sunlight is reflected back into space or absorbed by the atmosphere, so around 60 % or 1.08 x 10^{14} kW reaches the earth's surface [2]. The absorption of sunlight is due to molecules in the atmosphere such as water, carbon dioxide, ozone and oxygen. Water and carbon dioxide absorb the infrared radiation while ozone and oxygen absorb the ultraviolet radiation, thus changing the composition of the sunlight reaching the earth's surface to comprise of around 50% visible radiation and 47% infrared. The sunlight reaching earth's surface exists in two forms, direct radiation and diffuse radiation, with the latter resulted from the many scattering and absorption processes occurring when the sunlight travels through the atmosphere [1].

The total amount of energy from the sun reaching the earth's surface is around 3.4 x 10^{6} EJ [1], which is several thousand times the global energy consumption in 2019, which is 173,340 TWh [3], or around 624 EJ. Thus, there is tremendous potential in directly harnessing solar energy through photovoltaic cells for our future energy needs.

Development of dye-sensitised solar cells (DSSCs)

History of solar cells

Solar cells generate power via photovoltaic effect in which sunlight is converted into electrical current. Photovoltaic effect was first observed by Alexandre Edmond Becquerel in 1839. His cell was a wet cell, with either silver chloride or silver bromide coated electrodes immersed in acidic solution and contained within a black container. He observed that the voltage of the cell increased when its silver electrodes were exposed to sunlight [4]. In 1883, Charles Fritts as can be observed in Figure 1 created the first solar cell using selenium coated with a thin layer of gold, but its efficiency was only around 1% [5].

In 1946, Russel Ohl patented the first p-n junction silicon solar cell. He noticed that a silicon sample with a crack had current flowing in it when exposed to light. The crack formed at the boundary between the positively and negatively-doped part of the silicon, and when connected to a circuit, the photon in light imparts energy to the electron building up on the negatively-doped part to flow to the positively-doped part, thus generating electrical current. But the solar cell's efficiency was only 1% [6]. The first practical solar cell was developed by Daryl Chapin, Calvin Fuller and Gerald Pearson from Bell Labs in 1954. They first discovered that silicon with lithium and gallium impurities became very sensitive to light. They experimented with different impurities to further improve their silicon solar cells, and resulted in the use of boron and arsenic as the doping materials for their silicon solar cells, with efficiency of 6% [6].

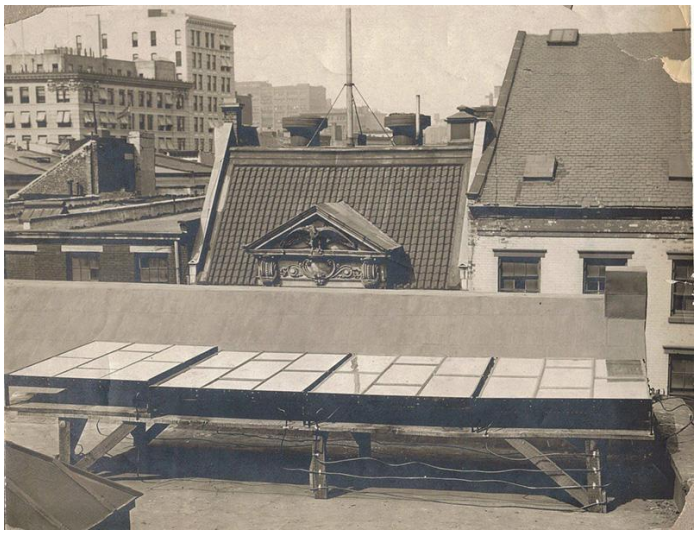


Figure 1. First solar panels installed by Charles Fritts in New York City, 1884

Solar cells were first put to practical use in 1958 when solar cells fabricated by Hoffman Electronics were used as power source for Vanguard satellite of the United States space programme [5], and solar cells were widely used in satellites afterwards. Since then, the use of solar cells has expended greatly, with it being the third most important renewable energy source after hydropower and wind power in the early 2010s and potential to overtake wind power in terms of installed power generation capacity [1].

Types of solar cells

Other than silicon solar cells, other types of solar cells have been developed. The different types of solar cells are usually grouped into three categories: first generation, second generation and third generation solar cells [7]. Silicon solar cells, or more specifically crystalline silicon wafer solar cells, are grouped in the first-generation solar cells. It is the oldest solar cells technology and currently the most widely used solar cells with around 95% market share in 2017 [8], due to silicon being cheap and abundant [7], and also due to efficient supply chain, standardisation and strongly reduced profit margins, which help to reduce the price of the solar cells [8]. There are two types of crystalline silicon wafer used in solar cells: monocrystalline silicon and polycrystalline silicon. Monocrystalline silicon wafer solar cells are fabricated through Czochralski process, which is an expensive and complicated process to produce single silicon crystal without any crystal grains. The more widely used ones are the polycrystalline silicon wafer solar cells due to their ease of fabrication and lower cost, but with the trade-off of lower efficiency [9].

The second-generation solar cells consist of thin film solar cells designed to be an alternative to crystalline silicon solar cells and achieving acceptable efficiencies with lowered costs. Some early examples are amorphous silicon (a-Si) solar cells, first prepared in 1972 by David Carlson and Christopher Wronski from RCA Laboratories with 1.1% efficiency, and the development of copper sulphide and cadmium sulphide thin film solar cells with efficiency over 10% by researchers at University of Delaware in 1980 [4].

Amorphous (a-Si) solar cells are attractive because it can be produced using low processing temperature and lower amount of energy, with possibilities of using low-cost polymer and other flexible substrates. Therefore, a-Si solar cell is comparatively cheaper than the crystalline silicon solar cells, but with caveat of lower efficiency at around 4-8 % [9]. Other promising materials used in second-generation solar cells are copper-indium-gallium diselenide (CIGS) thin film, which can reach efficiency of 20 % [9], and cadmium-telluride (CdTe) thin film. But second-generation solar cells are not as used as widely as the first-generation

solar cells due to technological problems and module stability [10].

The third generation of solar cells consists of diverse cell types such as dye-sensitised solar cells (DSSCs), organic solar cells, perovskite cells and quantum dot cells [7]. Quantum dot cells are developed with aim for the nanocrystals semiconductor material to replace bulk state semiconductor material such as Si, CdTe or CIGS [9]. Organic solar cells are solar cells with organic polymers as semiconductor materials. Thin layers of polymers consist of mixture of amorphous and crystalline regions, which can have major role in the carrier transport in the bulk material [7]. Perovskite cells are solar cells consisting of perovskite material with formula of ABX_3, where A represents a protonated amino group, B stands for Pb or Sn, and X stands for halides [11]. They have low bulk-trap density, ambipolar charge transport, wide band absorption and long charge carrier diffusion lengths, making them a highly promising candidate for solar cells as proposed by Akinoglu and team [7] with highest efficiency of 22% have been achieved, but with major drawback such as stability and reproducibility issues that prevents them from being commercialised widely [11]. DSSC was first successfully developed by Brian O'Regan and Michael Grätzel [12], with efficiency of around 7% under direct sunlight by utilising a nanoporous titanium dioxide (TiO_2) as thin layer semiconductor material with dye molecules adsorbed on its surface to absorb photons and converting it into electricity.

O'Regan and Grätzel's DSSC

The successful development of efficient DSSC by was spearheaded by Michael Grätzel and Brian O'Regan from 1988 until 1991 [12]. Although there were multiple attempts for creating DSSC previously, but all of it were of very low efficiency [13]. Previous attempts only achieved low absorption of incident monochromatic light via a layer of sensitiser on smooth surface, and using several layers of sensitiser to overcome the problem was unsuccessful.

There were also attempts to increase the dye molecules that could be adsorbed on the semiconductor surface via increasing the roughness of the semiconductor, but the conversion efficiency of the cells remains under 1%. Furthermore, the dye previously used were lacking in stability. Gratzel and O'Regan's device consisted of TiO_2 nanoparticles with average size of 15 nm deposited on a conducting glass surface to form a thin film with thickness of 10 μm as the photoanode, while the dye they used was a trimeric ruthenium complex, with iodide/triiodide redox mediator. The absorption spectrum of the thin film sensitised with the dye was redshifted and it achieved almost 100 % absorption of light in the visible spectrum under 550 nm. The conversion efficiency of the cells at one tenth and full sunlight were at 7.9 % and 7.12 % respectively, with the performance increasing to 12 % under diffuse sunlight. The cell performance was also considerably more stable compared with previous cells, with less than 10 % change in photocurrent produced by the cell after two months of testing [13]. The DSSC as invented by O'Regan and Grätzel was a significant development in DSSC history, and their device is still being studied and continuously improved by other researchers to this day.

Advantages of DSSCs

DSSCs have been gaining interest from researchers because they offer several advantages compared to the conventional silicon crystalline solar cells that are widely used today. Among the advantages of DSSCs is their capability to perform well under low light condition, as showcased by O'Regan and Grätzel in 1991 [12] when they obtained DSSC efficiency of 12% under diffuse sunlight compared to DSSC efficiency of 7.1-7.9% under direct sunlight. Unlike the silicon wafer solar cells, the performance of DSSCs is less affected by light intensity and the angle of incident, which makes DSSCs suitable for light harvesting under indoor lighting and low-level outdoor lighting [14]. Thus, DSSCs have potential for widespread application in portable electronics capable of self-powering without the need for power source from batteries, which is crucial as the Internet of Things (IOT) becoming more popular [15].

Another advantage is that DSSCs can possibly be offered with various design options, such as varying their transparency and colours. They also can be flexible and lightweight [16], which makes them

suitable for applications in small, portable electronics for indoor use, and also for application through integration in buildings and automobiles, thus helping to reduce their energy use carbon footprint. Furthermore, DSSCs are simpler and less energy intensive to produce compared to the conventional silicon wafer solar cell, which makes them possibly more practical and cost-efficient for large scale production [17]. With low energy use for DSSCs production, the energy payback time for DSSCs can be achieved in less than a year [16], which is much shorter than energy payback time for silicon solar cells [18]. Through molecular engineering of the dyes used in DSSCs, the optical properties of DSSCs can be transformed.

Challenges for widespread adoption of DSSCs

There are still several challenges that need to be overcome or mitigated before the DSSCs can be applied in large scale like the silicon crystalline solar cell. One of them is the relatively low efficiency of DSSCs. The highest cell performance achieved with DSSC is 14.3% [19]. Meanwhile, the efficiency of conventional crystalline silicon solar cells used are usually around 14-18% [10]. Other challenge is the price-competitiveness of DSSCs. At the time the first efficient DSSC was invented by Gratzel and O'Regan in 1991, the price of silicon crystalline solar cells was still high. But now, as of 2022, their price has dropped tremendously [7]. In fact, the cost effectiveness of using silicon solar cells for electrical generation have become higher than producing electricity at power plants using coal, oil or natural gas, which could possibly reduce interest for research in to improve efficiency of alternative solar cells such as DSSCs.

Commercialisation of DSSC

As for 2020, there has been penetration of DSSCs in the solar cell market, but the global solar cell market is still dominated with silicon wafer solar cell, with around 95 % market share [20]. The applications for DSSCs are as shown in Figure 2 below:

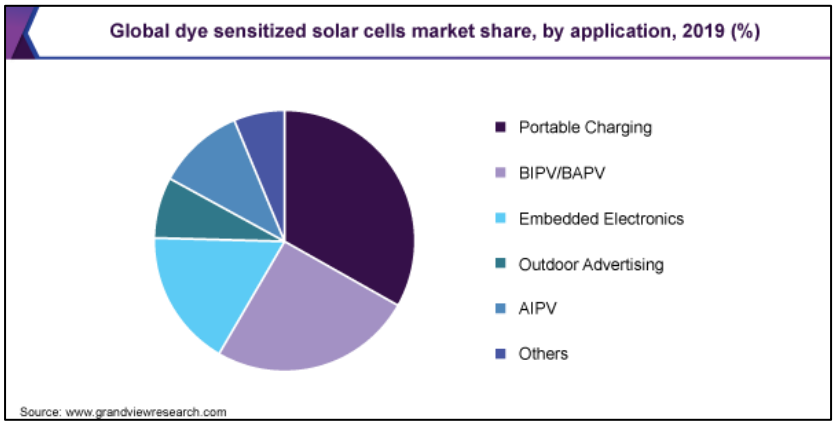


Figure 2. Global market share of DSSCs by application as for 2020

The value of the global DSSCs market is at USD 90.5 million in 2019 [21]. It was forecasted to continue growing in the future, due to the increased concerns about energy sustainability and impacts of the energy generation from non-renewable resources on the environment. DSSCs are mainly used in portable charging, building integrated photovoltaics/building applied photovoltaics (BIPV/BAPV), embedded electronics, outdoor advertising and automobile integrated photovoltaics (AIPV). Although DSSCs can have hard time to compete against the dominance of silicon based solar cells in large scale, outdoor application, but it has significant potential for indoor use [22] due to its excellent performance under low-light condition, variable design in their colour and transparency, lightweight and flexible material.

There are a number of companies involved in the DSSCs market. One of the notable companies is G24 Power, previously known as G24i. It was the first company to

produce DSSC for commercial application, with their products being used in backpacks and bags [23]. Their DSSC products are marketed under the brand name GCell (gcell.com). The next company is 3GSolar. Their products are advertised to eliminate the need for constant battery changing and charging in wireless electronic devices for the lifetime of the devices (3gsolar.com). Another player in the DSSC market is Solaronix. The company is deeply involved in the market because it not only offers DSSC kits, but it also offers the materials needed for making DSSC, such as the electrolytes, dyes, and TiO_2 paste for photoanode [24].

Main components of DSSC

A typical DSSC consists of four main components:

a) Electrolyte/redox mediator
b) Counter electrode
c) Photoanode/working electrode
d) Metal oxide nanoparticles (commonly TiO_2) with dyes molecules adsorbed on its surface

A diagram of typical DSSC as coined by Nazeeruddin [17] is depicted in Figure 3 below.

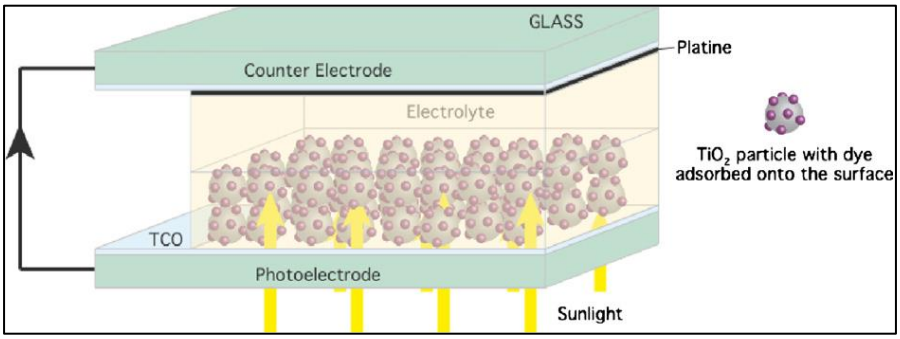


Figure 3. Schematic diagram of a DSSC

Electrolyte/redox mediator

The function of electrolyte is providing medium for the flow of electrons from the counter electrode (cathode) to the dye molecules adsorbed on the semiconductor layer (usually TiO_2) surface at the photoanode. There are several types of electrolytes used in DSSC, which are:

a) Liquid electrolyte, example is I^-/I_3^- electrolyte
b) Solid state electrolyte, example is spiro-OMeTAD
c) Quasi solid state electrolyte, example is I^-/I_3^- absorbed in PET matrix

The most commonly used type of electrolyte in DSSC is liquid electrolyte. A good liquid electrolyte needs to be chemically stable, has low viscosity to enhance electron transport capability, capable of good dissolution of the redox couple but does not significantly dissolve the dye and the semiconductor layer [16]. Among the liquid electrolytes, I^-/I_3^- electrolyte is commonly used because it demonstrated favourable kinetics. The I_3^- reacted slower with the electrons in TiO_2 than the time needed for electron injection from the dye into TiO_2 conduction band, while I^- reacts more favourably with the oxidised dye molecules than the injected electrons in TiO_2 [25]. Thus, recombination reaction could be slowed, and high efficiency can be achieved.

Other liquid electrolytes have been used in DSSC, such as Br^-/Br_3^-, $SCN^-/(SCN)_2$, $SeCN^-/(SeCN)_3^-$, $Fe(CN)_6^{3-}$ /$Fe(CN)_6^{4-}$ and Co(II)/Co(III) complex. Another type of liquid electrolyte that has been developed is ionic liquid electrolyte. It is basically a room temperature molten salt, unlike earlier liquid electrolytes in which the redox couples are dissolved in an organic solvent. But, ionic liquid electrolytes can and still have some additional solvent in it, albeit in lower amount. The salts used consists of organic cationic parts, such as alkylimidazolium, trialkylsulfonium, phosphonium and tetraalkylammonium, while for the anionic parts, halides such as iodide, and other types of anions such as PF_6^-, BF_4^- and CF_3COO^- were used [26]. Ionic liquid

electrolytes' advantage compared to the earlier liquid electrolytes is their low volatility, which ensure the electrolyte possess higher stability, but in turn, they usually have low viscosity, and thus low ion mobility [27].

The main drawback with most liquid electrolyte is their long-term stability, due to the volatility of the solvent used and prone to leakage. Thus, solid state electrolyte has been developed to overcome the issues. Solid state electrolyte consists of hole transporting materials (HTM) that function via the movement of positive charge between neighbouring molecules, as opposed to liquid electrolyte where charge transport is due to movement of redox mediators [16]. The most successful solid-state electrolyte that has been developed was the organic molecule spiro-OMeTAD. It is capable of achieving incident photon to electron conversion efficiency (IPCE) of 33%, originally yielding efficiency of 0.74 % [28]. However, the efficiency of solid-state electrolytes is still lacking compared to liquid electrolytes, mainly due to the very fast recombination between electrons in TiO_2 with holes in the HTM [29], and also the poor contact between the dye and electrolytes [12].

Another alternative electrolyte that has been developed is quasi solid-state electrolyte that can show the properties of liquid and solid simultaneously. The advantages of quasi solid-state electrolyte are their stability from leakage and vaporization of the electrolyte, close interfacial contact with the TiO_2, and relatively good ambient ionic conductivity [25]. An example of quasi solid-state electrolyte is from the work of Sun and co-workers [30], where they used polyethylene terephthalate to act as matrix for the iodide/triiodide liquid electrolyte by absorbing the liquid electrolyte to become quasi solid-state electrolyte.

Counter electrode

Counter electrode accepts electrons from the external circuit and utilise it to catalyse redox reactions in the electrolyte. A counter electrode consists of a conductive substrate (usually glass) that is coated with a thin layer of catalytic material. Among the properties for a good counter electrode are high catalytic activity, good conductivity, high reflectivity, large and porous surface area, suitable thickness of the coated catalytic layer, good stability against degradation, compatible energy level with the potential of the redox couple electrolyte, and good adhesion of the catalytic layer with conducting substrate [31].

The conductive substrate is coated with catalytic materials to reduce the charge transfer overpotential by increasing the speed of the reaction. Charge transfer overpotential originates from the electrolyte/counter electrode interface, and high charge transfer overpotential causes the output voltage of the DSSC to be significantly reduced. The magnitude of the charge transfer overpotential is dependent upon the electrocatalytic properties of the counter electrode surface towards mediator reduction [32], and coating the surface of the conducting substrate with catalytic material helps to increase conductivity and improve electrocatalytic activity of the counter electrode [33].

As for the catalytic layer, the most commonly used material is platinum. It was used in the pioneering work of O'Regan and Grätzel DSSC in 1991. It is widely used because of its ideal properties such as high catalytic activity, high electrical conductivity, good stability and high reflectivity [33]. In the DSSC fabricated by O'Regan and Grätzel, the conducting substrate used was the FTO coated glass, but it has high charge transfer resistance in iodide/triiodide electrolyte, and its surface is also very unconducive for the reduction of triiodide to iodide. Due to the ideal properties of platinum, it was chosen as the catalytic layer for the counter electrode of DSSC, and it has been popular since 1991 [33].

The platinum layer's thickness on the DSSC may significantly affect its performance. Nearly two decades ago Fang and team found out that the different layer thickness ranged from 25 nm to 415 nm did not prominently affect the charge transfer resistance at the electrolyte-counter electrode interface. They also discovered that increasing the thickness from 2 nm to 415 nm decreases the sheet resistance of the counter electrode, but no significant difference was observed in the DSSC performance. Thus, 2 nm of platinum layer

was sufficient for the DSSC to obtain good efficiency [34].

Other factors, such as the size and shape of the platinum particles also affect the performance of the DSSC. Platinum nanoparticles perform better than bulk platinum in DSSC due to their large surface area, high electrical conductivity, low charge transport resistance, good resistance against corrosion, and high transmittance [35]. Platinum nanoparticles with variety of shapes have been developed to increase their surface area and improve their properties in counter electrode.

One example is platinum nanocup developed by Jeong and co-workers [36]. In their work, they synthesised two platinum nanocup in different sizes and compared their performance with planar platinum for the counter electrode. The platinum nanocups have larger surface area than the planar platinum, so more sites are available for catalytic process on the platinum nanocup surface. Thus, it enables more electrochemical reduction by reducing the charge-transfer resistance at the counter electrode/electrolyte interface. The lowering of internal resistances of RCT helps in increasing the fill factor and short circuit current of the DSSC. The DSSC with the platinum nanocup array with a diameter of 300 nm at a 400 nm pitch size showed a power conversion efficiency of 9.75%, which is 24% higher than the 7.87% power conversion efficiency of DSSC with the planar platinum.

Although platinum has ideal properties for counter electrode, it also has several disadvantages, such as its high price, low abundance, and weak corrosion resistance against the commonly used iodide/triiodide electrolytes, so many researchers have been developing alternatives material for platinum in counter electrode. One of the alternative materials is carbon. It possesses suitable properties for counter electrode material, such as good catalytic activity, high conductivity, large and porous surface area, and chemical resistance against electrolyte and dye solution. More importantly, it is also available abundantly on earth and also cheaper to obtain than platinum, so it is a promising material [31]. There are different types of carbon materials used for counter electrode materials, examples are graphene, carbon nanotubes, carbon nanofibers, activated carbon, graphite, and carbon black [33].

Photoanode/working electrode

Photoanode, also called as working electrode, receives electrons from the excited dye molecules, which then would flow to the counter electrode through external circuit. A photoanode consists of transparent conducting substrate deposited with a layer of metal oxide semiconductor material. The conducting substrate must be high transparency for the dye molecule to be able to absorb light, and low electrical resistivity to minimise energy losses and facilitate electron transport process. The transparent conducting substrate is usually made of glass substrate for physical support, with a layer of transparent conducting oxide (TCO) on it. Examples of TCO materials are fluorine doped tin oxide (FTO), indium doped tin oxide (ITO), aluminium doped zinc oxide (AZO) and antimony doped tin oxide (ATO).

Among them, FTO is the most widely used TCO because of their suitable properties such as good light transmittance, good electrical conductivity, good adhesion with the glass substrate, high Mohs hardness, good resistance against corrosion, chemically stable, and can resist heat up to 600 °C [33]. The high heat resistance is important because the catalytic layer deposited on the conductive glass substrate needs to be solidified by calcination at high temperature. Other than glass, polymers and metals also have been used for the physical support, with polymers such as polyethylene terephthalate and polyethylene naphthalate, and metals such as stainless steel, titanium and tungsten.

For the semiconductor metal oxide layer, it should have several properties to make it an ideal material [37]:

a) Large surface area so more dye can be adsorbed on it
b) Facilitates fast electron transport from the excited dye to the external circuit
c) Optimum pore size for good diffusion of dye and electrolyte on it
d) High resistance against photo-corrosion
e) Capable of absorbing and scattering light to facilitate the dye functioning efficiently

f) Good electron acceptor
g) Good interfacial contact with the dye molecules and also the TCO layer on the substrate

The semiconductor material also must have band-gap of more than 3 eV [30]. The higher the band-gap, the UV light absorbed from the sun would be lower, thus reducing reactive holes formed in the semiconductor when it is excited by the sunlight. The reactive holes are undesirable because they can disturb and damage the organic compounds in DSSC, such as the dye molecules, via oxidation reaction [28]. Examples of materials that have been used for photoanode are titanium dioxide (TiO_2), zinc oxide (ZnO), tin oxide (SnO_2) and zinc stannate (Zn_2SnO_4). Their band-gaps are as depicted in Figure 2.4 below as proposed by team of Gong in 2012 [25].

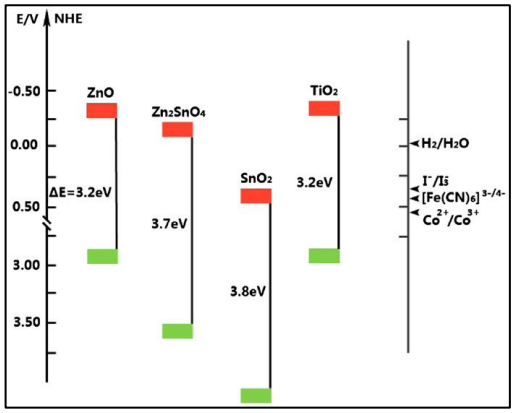


Figure 4. Band-gaps of materials for photoanode

The most widely used material for photoanode is TiO_2. In their 1991 work, O'Regan and Grätzel pioneered the use of it in DSSC, and to this day, it is still popular due to its low cost, easy availability and non-toxic [12]. It usually exists in three crystalline forms, which are rutile, anatase and brookite, with band-gaps of 3.05 eV, 3.20 eV and 3.28 eV, respectively [31]. Among the three, anatase-form TiO_2 is the most preferred form for use in DSSC. In comparison to the anatase-form TiO_2, rutile-form has smaller band-gap. DSSC using the rutile-form TiO_2 has lower photocurrent due to the lower amount of dye molecules adsorbed on the TiO_2 film surface, which is because of their smaller surface area than anatase-form TiO_2. In addition, electron transport is also slower in the rutile form than in the anatase form due to differences in the extent of inter-particle connectivity associated with the particle packing density [38]. As for the brookite-form TiO_2, although it has wider band-gap than anatase-form TiO_2, the brookite-form has lower dye loading due smaller surface area for the dye on the brookite surface compared to anatase surface. The conduction band edge in brookite-form is similar or below that of the anatase-form photoanode. Undesirable recombination side reaction is lower in brookite cell, thus enabling it to obtain higher open circuit voltage than anatase cell. But, the electron transport is significantly slower in brookite cell compared to the anatase cell due to its lower electrical conductivity, thus tremendously reducing its electron collection efficiency compared to anatase cell [39].

Other than TiO_2, other photoanode materials that have been frequently used are ZnO. In fact, ZnO has been studied for semiconductor use in DSSC since 1972, way earlier than TiO_2 [40]. Although it has been overtaken by TiO_2, ZnO can still be considered as a suitable alternative to anatase-form TiO_2, due to their nearly similar conduction band edge and same band-gap, and higher electron mobility in ZnO than TiO_2 [25], which facilities electron transportation by decreasing the recombination loss [40]. It is also relatively easy to synthesise highly crystalline ZnO (wurtzite-form) with different morphologies, such as nanoparticles, nanowires, nanorods, nanotubes, tetrapods, nanoflowers, nanosheets, and branched nanostructures [16]. However, ZnO have several disadvantages such as low carrier concentration, low fill factor, poor stability in acidic dyes and slow electron injection kinetics [41]. The highest DSSC efficiency achieved using ZnO photoanode is 8.03% [42], which is still low compared to the highest DSSC efficiency achieved with TiO_2 photoanode at 14.3% [19]. Even with many other metal oxide alternatives, TiO_2 is still the superior material of choice for photoanode.

The performance of TiO_2 and any other photoanode material is mainly affected by three factors, which are the size/surface area of the particles, the morphology/shape of the particles, and the

composition/purity of the photoanode material [31]. Nanoparticle-sized material is better than bulk size material, due to the higher surface area provided by the nanoparticles, which enable it to adsorb more dye molecules on it. O'Regan and Grätzel achieved high efficiency DSSC by using TiO_2 nanoparticles with average size of 15 nm. But smaller particle size does not guarantee better performance, [43]. They compared the performance of several TiO_2 nanoparticles films, and they observed that the films with larger particle size achieved higher short-circuit current density and better conversion efficiency. They concluded that even though the surface area of the smaller particles is larger than of the bigger particles, the bigger particles may have better dye adsorption properties by providing easier access for the dyes to its surface, resulting in a higher number of electrons and holes produced. The size distribution range of the nanoparticles also plays a role. In a study by Dhungel and Park [44], TiO_2 film with smaller size distribution range have poor interconnection between the nanoparticles, so its porosity is increased, which in turn increased the area available for the adsorption of dye after sintering. So, the size of the nanoparticles, their size distribution and surface area need to be optimised to ensure higher dye adsorption on the surface.

The next main factor is morphology or shape of the particles. There have been numerous studies on tuning the morphology of the TiO_2 nanoparticles to improve their performance. A study by Wang et al. [45] compared the performance between monolayer, double layer and multilayer TiO_2 photoanode. Small nanoparticles have large surface area, thus capable of adsorbing more dyes than large particles, but they have poorer light scattering ability than large particles. Poor light scattering ability leads to weaker absorbance of longer wavelength red light.

To overcome that, Wang and co-workers [45] have developed a multilayer photoanode structure incorporating nanoparticles layer (23 nm), followed by nanoparticles-scattering particles (50 nm) mixture layer and nanoparticles-scattering particles (100 nm) mixture layer, and lastly with scattering particles (100 nm) layer, with purpose to balance the surface area for dye adsorption with light scattering ability. Their multilayer cells achieved higher light harvesting efficiency (10.2%) than the monolayer and double layer cells. However, the mesoporous nanostructure still suffers from low electrical conductivity and the pores facilitate recombination reactions to occur. Thus, many researchers have been focused on developing new nanostructured photoanode material to obtain high conductivity and also high dye loading. Examples are nanowires, nanotubes and hollow spheres [37].

The last main factor is composition/purity of the photoanode material. Electronic band structure of semiconductors can be altered by substitutional doping, which is done by substituting some of the semiconductor atoms with different atoms of similar atomic radius [46]. TiO_2 photoanode has been doped with several materials, such as copper [47], sulfur [48], and calcium [49], and all of them successfully obtained higher cell efficiency compared to the undoped TiO_2 photoanode. Other than doping, semiconductor material has been used as composite within combination with other component, in which the mixture can be in the form of core-shell or layered frameworks [46]. Examples of TiO_2 composites are TiO_2-ZnO composite [50], TiO_2-SnO_2 composite [51], and TiO_2 nanorod-nanoparticle composite [52].

Dye/photosensitiser

Dye, also called as photosensitiser, absorbs light, resulting in excited electron which is then injected into the conduction band of the metal oxide semiconductor layer (usually TiO_2) in photoanode. The oxidised dye would then be reduced to its normal state by receiving electron from the electrolyte. The dyes used can be either metal based dyes, most commonly using ruthenium (Ru) metal, or metal-free organic dyes, which are either synthetic dyes or natural dyes extracted from plants. A good dye is vital to achieve DSSC with high conversion efficiency. Characteristics of a good dye are as follows [16]:

a) The dye should strongly absorb wavelength ranging from the visible region to the near-infrared region
b) The dye should have anchoring groups such as carboxylic acid (COOH), phosphonic acid

(H_2PO_3) or sulfonic acid (SO_3H) groups for it to be able to bind onto the semiconductor surface

c) The excited state level of the dye should be higher in energy than the conduction band edge of n-type semiconductor, so that an efficient electron transfer process between the excited dye and conduction band (CB) of the semiconductor can take place

d) For dye regeneration, the oxidized state level of the dye must be more positive than the redox potential of electrolyte

e) Unfavourable dye aggregation on the semiconductor surface should be avoided through optimization of the molecular structure of the dye or by addition of co-adsorbers that prevent aggregation

f) The dye should be stable against degradation by light, in addition to possessing electrochemical and thermal stability

By having a wide and intense absorption spectrum both the visible and the near-IR, the dye can absorb lighter, which in turn can lead to more photocurrents being produced [53]. Approximately 46% of total energy from sunlight is in the infrared region [1], which is only weakly absorbed by the commonly used crystalline silicon solar cell. The weak absorbance is compensated by using relatively thick silicon layer (~100 μm), but this led to increased material cost and some losses in power conversion efficiency due to recombination reaction [54]. Thus, DSSC has an advantage over crystalline silicon solar cell due to its cheaper material, much thinner structure (~20 μm), and higher potential capability to absorb light in the near-infrared region. And by utilising strong light absorbing dye (i.e., high molar absorption coefficient), the semiconductor layer can be made thinner, thus reducing the material used and also minimising the unwanted recombination reactions from occurring [55].

Anchoring groups bind the dye molecules to the semiconductor metal oxide surface, with carboxylic acid, cyanoacrylic acid and phosphonic acid being among the most frequently used anchoring groups [56-57]. They bind to the metal oxide by reacting with the hydroxyl group on it to form ester linkage. Anchoring groups can profoundly affect the operating parameters of DSSC, such as light absorption, molecular orbital distribution, frontier orbital energy levels, band structures of the photoanode, electron transport between the dye and photoanode, charge recombination, and overall solar-to-electron conversion efficiencies of the DSSC [57].

In order to ensure efficient charge injection, the energy level of lowest unoccupied molecular orbital (LUMO) of the dye molecule should be slightly above (i.e. more negative) the conduction band (CB) edge of the semiconductor metal oxide, while the energy level of highest occupied molecular orbital (HOMO) should be lower (i.e. more positive) than the redox potential of redox mediator. The difference between E_{LUMO} and E_{CB} acts as an enthalpic driving force for electron injection from the excited dye to the semiconductor by ensuring the injection process is kinetically favourable. And by having the dye's highest occupied molecular orbital (HOMO) to be below the electrolyte redox potential, this induces the process of electron transfer to the excited dye, which regenerates the dye in its ground state. This separates the charges and is the major mechanism for charge separation in the DSSC [58].

Dye aggregation on semiconductor surface is generally unwanted because it can cause low conversion efficiency of the DSSC via reduction of electron injection yield from the dyes to the CB of semiconductor due to intermolecular energy transfer [59]. The common structure is that the dyes would form a homogenous monolayer on the semiconductor surface with relatively uniform spacing between the dye molecules. There are several ways in which the dye molecules could aggregate either laterally or longitudinally on the semiconductor surface as depicted in Figure 2.5. Longitudinally, the dye molecules could clump together haphazardly, resulting in unequal spacing between them. Another way is the dye molecules also could cluster too close to each other, thus forming an aggregate layer. While for lateral aggregation, instead of being adsorbed on the semiconductor surface, a dye molecule could interact with the tip of another dye molecule that is adsorbed on the semiconductor surface [57] (Figure 5).

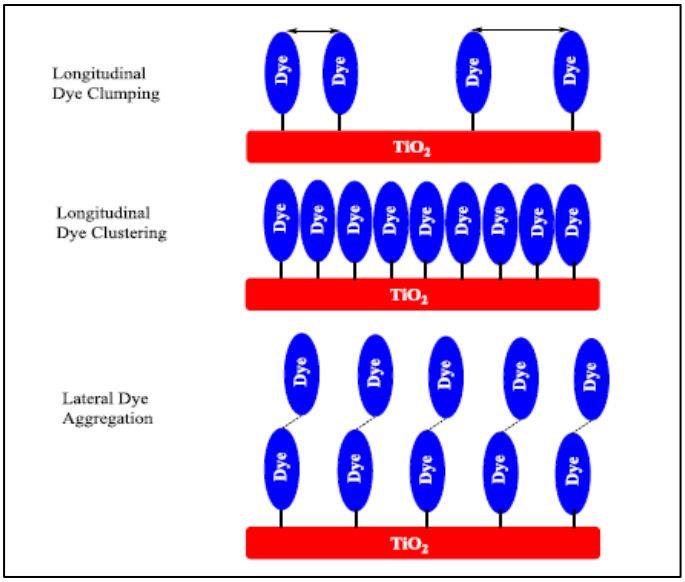


Figure 5. The possible dye molecules' arrangement on TiO_2 surface

The methods that have been used to prevent dye aggregation were tuning the molecular design of the dye molecule, using co-adsorbent in tandem with the dye, or using a different dye compound as co-sensitizer. The dye can become degraded due to seepage of moisture or oxygen in DSSC, and exposure to UV light in sunlight, which could directly excite the semiconductor and may lead to irreversible oxidation of the dye [60]. Under illumination, degradation can occur during the excited state dye or the oxidised state dye. The electron injection from excited dye state to the CB is extremely fast, so light induced degradation is thought to mostly happen at the oxidised state dye. For widespread DSSC utilisation to be become viable, other than improving the power conversion efficiency, it is vital to also increase the stability of DSSC. One way to achieve that is by using a dye possessing good light, electrochemical, and thermal stability, so the dye is capable of operating consistently without significant degradation and performance loss for at least for 20 years [55].

As mentioned previously, the three dye types that have been used in DSSC are either metal based dyes, most commonly using ruthenium (Ru) metal, metal-free synthetic organic dyes, or natural dyes extracted from plants. Metal based dyes have been frequently studied for DSSC application because of their broad absorption spectra and favourable photovoltaic properties. The structure of metal-based dye generally consists of complex with a central metal ion and auxiliary ligands with one or more anchoring group. The metal complex is able to absorb light in the visible spectrum of sunlight due to metal to ligand charge transfer (MLCT) process. Substituents such as alkyl, aryl or heterocyclic alkyl can be used to modify the photophysical and electrochemical properties of the ligands, and thus helps to improve the DSSC performance via tuning the energy levels of the MLCT states, optimisation of electron injection process and improvement of dye regeneration kinetics [16].

Among the metal-based dyes, Ru based dyes have the best performance record, with their broad absorption spectrum, optimum excited and ground state energy levels, relatively long excited-state lifetime, and good electrochemical stability [16]. The first DSSC with high efficiency developed by O'Brian and Grätzel in 1991. They used ruthenium complex dye. In 1993, Nazeeruddin et al. managed to fabricate DSSC with conversion efficiency of 10% by using cis-RuL_2-$(NCS)_2$ dye that incorporates 2,2'-bipyridyl-4,4'-dicarboxylic acid as ligands, with codename N3 dye. It was the first time a DSSC device managed to achieve conversion efficiency of 10 % and above [16].

N3 dye possess superb qualities, such as broad visible light absorption spectrum with threshold up to 800 nm, relatively long excited state lifetime, and excellent adsorption to the TiO_2 semiconductor surface via four carboxylates anchoring groups that are linked to the two bipyridyl moieties. The four carboxylates anchoring groups also facilitates improved electronic coupling between the charge-transfer excited state and the conduction band wave function manifold of the semiconductor [61]. Later on, the team studied the effects of protonation on the several Ru complex dyes also with 2,2‘-bipyridyl-4,4‘-dicarboxylic acid as ligands. One of the synthesised dyes, the doubly protonated $(Bu_4N)_2[Ru(dcbpyH)_2(NCS)_2]$ with codename N719, exhibited a higher power conversion efficiency than the other dyes [62]. Since then, the N3 and N719 dyes are considered as reference dyes for DSSC, and are also used by other researchers as template for designing other Ru based dyes by modifying its ligand moieties [16].

Other than Ru, other metals such as osmium (Os), copper (Cu), and platinum (Pt) have been investigated for their potential application in metal complex dye. Os complex dyes have been studied because it exhibited excellent photosensitisation, with better MCLT than that of Ru complex dyes [63]. The synthesis of several Os polypyridyl complexes for comparison with Ru polypyridyl complexes, and they discovered that the Os polypyridyl complexes exhibited broadening of the light absorption and extended the spectral response of nanocrystalline TiO_2 photoelectrodes to higher wavelength values while still maintaining the same performance as Ru polypyridyl complexes [64]. However, Os based dyes suffers from poor reduction of adsorbed dyes by the iodide/triiodide redox couple due to the process being kinetically unfavourable in comparison with the charge recombination process, thus limiting its photocurrent efficiency [65-66]. Among the earliest Pt complex dyes used in DSSC were square-planar platinum(II) diamine dithiolate dyes [67], and they managed to achieve efficiency of 2.6%. Other examples of Pt complex dyes are phenothiazine-based platinum(II)–acetylide dyes developed by Siu et al. [68] and platinum(II) bis(aryleneethynylene) dyes [69]. They managed to achieve highest efficiency of 5.78% and 1.57%, respectively. Still, there are much more studies need to be done for improving the performance of non-Ru complex dyes to become comparable to Ru complex dyes.

Although Ru based dyes have excellent properties, there are several drawbacks associated with it, such as the high cost of Ru metal, non-abundant supply, and the sophisticated synthesis and purification steps [25]. Recently, metal-free organic dyes have been subject to numerous studies in hope of developing promising alternatives comparable or superior in performance to Ru based dyes. Organic dyes have several advantages over Ru and also other metal-based dyes, such as easier to synthesise and purify, lower material cost, low concern of supply limitations, higher molar absorption coefficients, and wider variety of structural design modification of the organic dyes are possible to tune their properties [59].

The usually high molar absorption coefficients of organic dyes in comparison to the metal-based dyes allows the use much thinner semiconductor layer, thereby facilitating the charge transport in the photoanode and minimising energy loss, and also improving the pore filling properties for quasi-solid-state or solid-state electrolyte in porous dye-sensitized TiO_2 films [70]. Usually, organic dyes are designed with the template of donor-π bridge-acceptor (D-π-A) structure, as shown in Figure 6 below which in this particular work carried out by Shalini et al. [55] involved D-π-A structure adsorbed on TiO_2. By adjusting the design template, it is possible to broaden the absorption spectra, shift the HOMO and LUMO energy levels, and improve the intramolecular charge separation of the organic dye [16]. When a dye absorbs light, electron is transported from the donor part through the π-bridge to the acceptor part, which is then injected into the CB of semiconductor. D-π-A structure ensures that the majority of electron transport occurs in one direction.

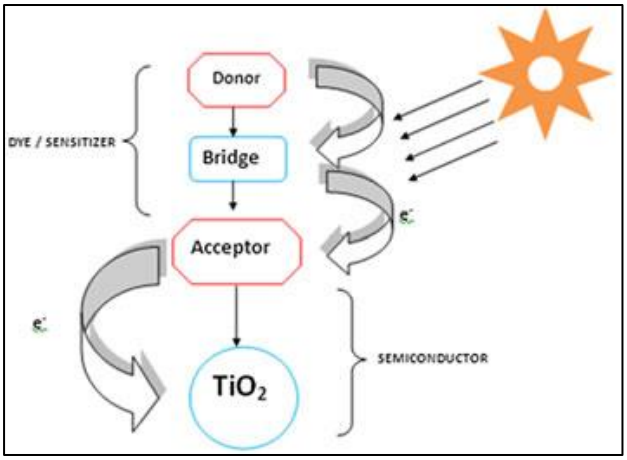


Figure 6. Schematic diagram of dye with D-π-A structure adsorbed on TiO_2

Working mechanism of DSSC

When a dye (S) is exposed to sunlight, it absorbs a photon to become photoexcited state (S*), in which an electron becomes excited and moved from HOMO to LUMO of the dye (Eq. 1). The photoexcited dye then injects an electron from its LUMO into the CB of photoanode (i.e. TiO_2), thus becoming oxidised dye (S^+) in the process (Eq. 2). The oxidised dye is then reduced to its normal state (S) by accepting electron from the redox mediator, i.e. I^- in I^-/I_3^- redox couple, thus regenerating the dye (Eq. 3). Meanwhile, the electron injected into the CB of TiO_2 travels through the interconnected TiO_2 nanoparticles and arrived at the TCO coated glass (i.e. FTO glass), and then it enters the external circuit and transported to the counter electrode (i.e. Pt-coated FTO glass), in which it reduced the I_3^- ion to regenerate I^- ion (Eq. 4) and thus completing the circuit. However, there are also other unwanted reactions that can interfere with the electron transport process, which are recombination reaction of the injected electron in the CB of semiconductor with the oxidised dye (Eq. 5), reaction of the injected electron with the electrolyte at the semiconductor/electrolyte interface, referred as dark current (Eq. 6), and also relaxation of the photoexcited dye (Eq. 7). The unwanted reactions can reduce the performance of DSSC if not mitigated or overcome. The electron cycle process is pictured in Figure 7 below as proposed by Ooyama & Harima [59].

.

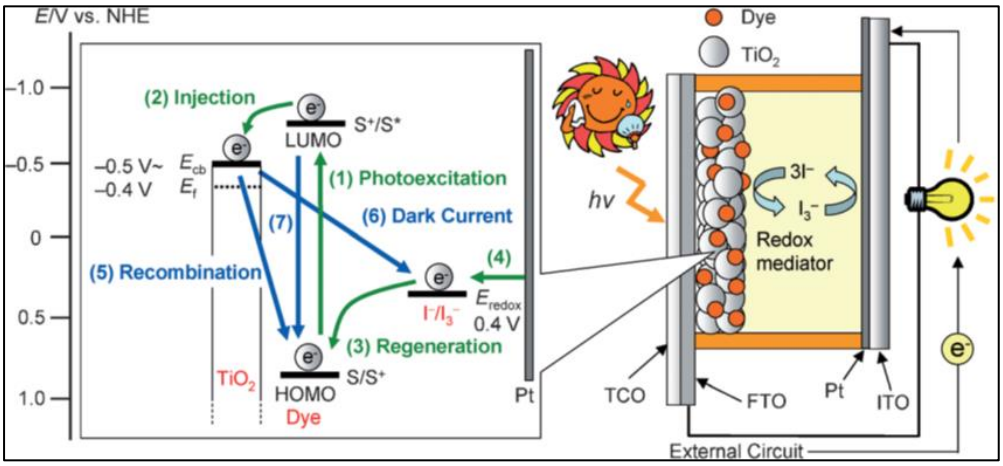


Figure 7. Electron cycle process in DSSC. The green arrows represent the processes required for the generation of photocurrents. The blue arrows represent recombination processes (electron-loss processes)

$S + photon \rightarrow S^*$ (1)

$S^* \rightarrow S^+ + e^-$ (2)

$2\ S^+ + 3\ I^- \rightarrow 2\ S + I_3^-$ (3)

$I_3^- + 2\ e^- \rightarrow 3\ I^-$ (4)

$S^+ + e^- \rightarrow S$ (5)

$I_3^- + 2\ e^- \rightarrow 3\ I^-$ (6)

$S^* \rightarrow S$ (7)

Parameters of DSSC performance

The performance of DSSC is evaluated via several parameters: incident photon to current conversion efficiency (IPCE), photocurrent/voltage curves (J/V curves), open-circuit photovoltage (V_{oc}), short circuit photocurrent density (J_{sc}), fill factor (ff), and solar energy conversion efficiency (η) [59].

IPCE, also referred as external quantum efficiency, is defined as the photocurrent density produced by the electrons flowing in the external circuit under monochromatic illumination of the cell divided by the photon flux hitting the DSSC [16]. The equation to calculate IPCE is as shown in Eq. 8:

$$\%\ \text{IPCE} = 1240\ (\text{eV nm})\frac{J_{ph}(\text{mA cm}^{-2})}{\lambda\ (\text{nm})\times I\ (\text{mW cm}^{-2})} \quad (8)$$

Where J_{ph} is the short-circuit photocurrent, density generated by monochromatic light, and λ is the wavelength while I is the intensity of the monochromatic light. IPCE provides information the monochromatic quantum efficiency of the DSSC [16].

J/V curves for DSSC is usually measured under standard AM 1.5 simulated sunlight (100 mW cm^{-2}). From the J/V curves, four values can be obtained directly: J_{sc}, V_{oc}, J_{mp} and V_{mp}, where J_{mp} and V_{mp} are the photocurrent and photovoltage at maximum power, respectively. A typical J/V curves is depicted in Figure 8 below [64].

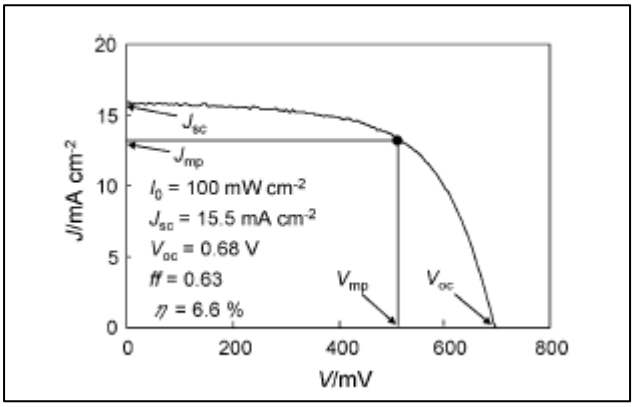


Figure 8. Typical J/V curves of a DSSC

V_{oc} is the difference in potentials between the two terminals of the cell when the circuit is being illuminated and in open state (J=0) [71]. V_{oc} can be derived from Eq. 9 shown below.

$$V_{oc} = \frac{E_{cb}}{e} + \frac{k_B T}{e}\ln\left(\frac{n}{N_{cb}}\right) - E_{redox} \quad (9)$$

Where E_{cb} is the energy level of the CB of the semiconductor, E_{redox} is the redox potential of the redox mediator, n is the number of electrons in the semiconductor, and N_{cb} is the effective density of states [59]. The maximum V_{oc} value can be defined as the difference between the E_{cb} of the semiconductor and the redox potential of redox mediator. However, the actual V_{oc} is usually lower than theoretical due to the inefficiency in electron cycle process causing losses of electrons through reactions such as recombination and dark current. The V_{oc} value could be enhanced via increasing the E_{cb} of semiconductor or lowering the E_{redox} of the redox couple [72].

J_{sc} is the photocurrent density measured when the DSSC is short-circuited, i.e. no opposing voltage that inhibits electron flow [71]. Its value is dependent upon absorption coefficient of the dye, in addition to the interaction between photoanode and the dye. To obtain

high J_{sc} value, the dyes should be capable of intense light-absorption over broad wavelength of sunlight, the electron injection process from the excited dye to the photoanode should be highly efficient, and the oxidised dye should be effectively reduced by the redox mediator [59].

Fill factor (ff) is defined as the ratio where product of current and voltage at maximum power is divided by the V_{oc} and J_{sc} as shown in Eq. 10.

$$\mathrm{ff} = \frac{J_{mp} \times V_{mp}}{J_{sc} \times V_{oc}} \quad (10)$$

The ff is determined from the J/V curve. It is essentially a comparison of how much the rectangular area defined by J_{sc} and V_{oc} is filled by rectangular area as defined by J_{mp} and V_{mp}. Thus, if the J_{mp} and V_{mp} rectangle completely fill the J_{sc} and V_{oc} rectangle, the ff value becomes unity [59]. However, the ff value is usually around 0.6 – 0.8 due to charge recombination and electron loss [71]. Electron loss are caused by the combination of series resistance in the DSSC, such as sheet resistances of the substrate and counter electrode, electron transport resistance through the photoanode, ion transport resistance, and the charge-transfer resistance at the counter electrode.

Energy conversion efficiency (η) is calculated by dividing the maximum electrical output of the DSSC divided by incident power from the sunlight as defined in Eq. 11.

$$\eta = \frac{J_{sc} \times V_{oc} \times \mathrm{ff}}{P_{in}} \quad (11)$$

Where η is the power conversion efficiency, J_{sc} is the short circuit photocurrent density, V_{oc} is the open circuit photovoltage, ff is the fill factor, and P_{in} is the incident light intensity. The incident power is usually set to the irradiance of the AM 1.5 spectrum with value of 100 mW/cm^2. From the energy conversion efficiency, it provides information about the generated power of DSSC and the light conversion into electricity and photovoltaic parameters. To improve the energy conversion efficiency, all of the components of DSSC must be optimised, with the dye as the most important component to be optimised. Numerous scientists have conducted studies to adjust their photophysical and electrochemical properties of the dyes by molecular design to improve their properties [59]. External factors, such as overall light intensity, spectral intensity distribution and temperature also affect the performance of DSSC [71].

Organic dyes as photosensitiser

There has been intense interest in research and development of organic dyes for application in DSSC due to their potential advantages against ruthenium and other metal complex dyes, such as higher molar extinction coefficient, flexibility in designing the molecules, lower material costs, and being relatively easy to prepare [59, 73]. But organic dyes also have several drawbacks compared to ruthenium complex dyes, such as narrow absorption in the visible spectrum, dye molecules aggregation, short electron lifetime in the excited state, and low stability in the long term. These drawbacks need to be overcome for organic dyes to become more efficient as photosensitisers in DSSC. The structural design of an organic dye is commonly based on the donor-pi-acceptor (D-π-A) structure as shown in Figure 9. According to Ooyama and Harima [59], an organic dye should fulfil several requirements:

a) The organic dye must have at least one anchoring group for adsorption onto the TiO_2 surface, for example –COOH group. A carboxyl group can form an ester linkage, a chelating linkage, and a bidentate bridging linkage with the TiO_2 surface to provide a strongly bound dye and good electron communication between the dye and the surface

b) For efficient electron injection from the excited dye to the CB of TiO_2, the energy level of the LUMO of the dye must be higher (more negative) than that of the CB of the TiO_2 electrode, while for efficient regeneration of the oxidized state by electron transfer from the I^3-/I^- redox couple in the electrolyte, the energy level of the HOMO of the dye must be lower (more positive) than that of the I^3-/I^- redox potential

c) Have high molar absorption coefficients over the wide range of sunlight for high light harvesting efficiency

d) The flow of electrons in the excited state of a dye should be highly unidirectional with path from the donor part to the acceptor part to provide efficient electron injection from the excited dye to TiO_2 through good electronic coupling between the LUMO of the dye and the CB of TiO_2.

e) Possess chemical stability in its photoexcited state and in the redox reactions throughout the reaction cycle so the DSSC can last longer

f) The dyes should not excessively aggregate on the TiO_2 surface because it could cause low conversion efficiency of the DSSC. Aggregated dyes reduce the electron-injection yield from the dyes to the CB of TiO_2 owing to intermolecular energy transfer between the dyes through the stacked π-bridge, especially dyes with long conjugation

g) Recombination of injected electrons with dye cations and I^{3-} ions in the electrolyte should be suppressed. Wide spatial separation between the moieties of positive charge density on the exited dye and the TiO_2 surface facilitates efficient charge separation, thus inhibiting the recombination process. Hydrophobic substituents on the dye skeleton act as barriers to prevent hydrophilic I^{3-} ions from approaching the TiO_2 surface, thereby retarding charge recombination.

D-π-A dyes consisting of electron-donating and electron–accepting groups linked through π-conjugated bridges featuring broad and intense absorption spectrum are expected to be one of the most promising classes of organic sensitizers that meet the above requirements, because D-π-A structure offers flexible designs that make it possible to obtain desirable dye properties with molecular engineering for various designated function of interests.

D-π-A dye design

As mentioned previously, the D-π-A structure consists of three parts, which are the donor part (D), π-bridge, and acceptor part (A), with donor part conjugated with the acceptor part though the π-bridge. Requirements a) to c) can be fulfilled by adjusting the photophysical and electrochemical properties of the dyes via the inclusion of electron-donating and electron-accepting groups onto the chromophore skeleton and extending the length of π-conjugation, which causes shift in the energy levels of the HOMOs and LUMOs [59]. By increasing the electron-donating ability of the donor part and electron-accepting ability of the acceptor part, the energy gaps between the HOMO and LUMO are reduced, thus resulting in redshifting of the absorption peaks. So, the dyes can absorb more sunlight in the visible region. Redshifting is vital because compared with metal complex dyes, organic dyes exhibited sharp and narrow absorption bands in the visible region, which impairs light-harvesting capabilities [75].

For requirements d)–f), they should be fulfilled through the introduction of sterically hindered substituents, such as hydrophobic long alkyl chains and aromatic units, onto the chromophore skeleton [59]. One of the main drawbacks of these D-π-A dyes is the formation of strong π-stacked aggregates between dye molecules on TiO_2 surfaces, which tends to reduce electron-injection yields from the dyes to the CB of TiO_2, due to intermolecular energy transfer between dyes. The sterically hindered substituents (bulky groups) help to prevent the aggregation of dye molecules on TiO_2 surfaces by inhibiting the π-π stacking between the dyes, and also prevent the ions in electrolyte from approaching the TiO_2 surface, thus reducing the electron recombination between the electrolyte ions and electrons in TiO_2 [76].

Utilisation of mixed moieties of D-π-A system as dyes for DSSC

In this section, several selected prior studies involving application of different selected mixed moieties featuring numerous substructures of D-π-A system in DSSCs have been focused, reviewed and discussed in relation to the scope of mixed moieties system. Thorough discussion on their characteristics and

molecular build-up are presented in respect to the unique highlights on their functionalities and performances.

Acetylene

The moiety of acetylene has been known over the years as active materials in numerous applications, synthesised in recent decades via Sonogashira cross coupling reaction [77-78]. Over a decade ago, Song et al. [79] had synthesised four dyes with triphenylamine as donor part, cyanoacrylic or carboxylic acid as acceptor part, with phenylacetylene moiety as linker. They varied the structure of the phenylacetylene linker part and the acceptor part while keeping the donor part unchanged (Figure 9).

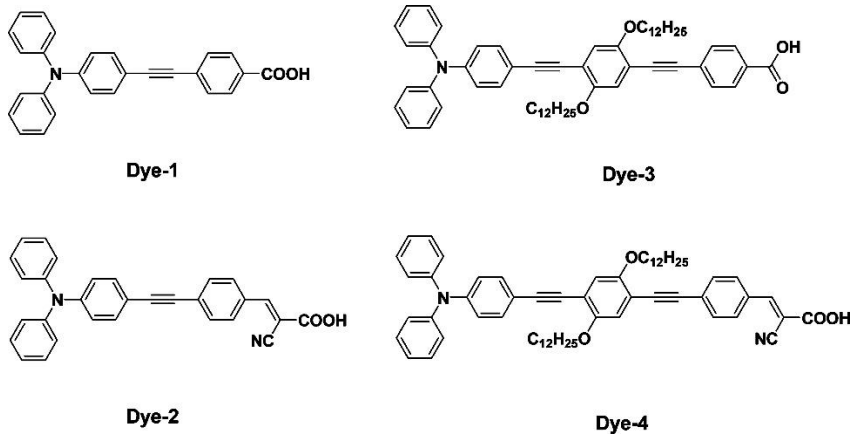


Figure 9. Structures of dyes bearing four dyes with triphenylamine as donor part, cyanoacrylic or carboxylic acid as acceptor part, with phenylacetylene moiety as linker

In recent years some alternatives have been proposed involving rather similar motifs and expected to behave fairly equal as acetylenes involving thiourea [80] and chalcone [81] derivatives with the focus in optoelectronics interests. The properties of the dyes and their DSSC performance were compared with that of the reference Ru complex N719 dye. In general, Dye-3 and Dye-4 with longer conjugation length of the double phenylacetylene moiety exhibited red-shifting in their absorption spectrum compared to the Dye-1 and Dye-2 with only one phenylacetylene moiety. It is also almost the same with their emission spectrum, except that Dye-2 and Dye-4 with cyanoacrylic acid moiety as donor part, in which the trend is reversed. The molar absorption coefficient of Dye-3 and Dye-4 are also higher than that of Dye-1 and Dye-2, but all of the values are still overwhelmingly higher than that of the reference dye N719 (1400 dm^3 mol^{-1} cm^{-1}). The performance of the dyes in DSSC is tabulated in Table 1 below as synthesised by Song et al. [79].

Table 1. Performance of DSSCs using dyes

Dye	V_{oc} (V)	J_{sc} (mA/cm^2)	ff	η (%)
N719	0.66	14.82	0.47	4.54
Dye-1	0.70	4.62	0.62	2.00
Dye-2	0.71	8.56	0.47	2.89
Dye-3	0.79	6.64	0.59	3.06
Dye-4	0.73	9.30	0.49	3.61

The V_{oc} of all the organic dyes are higher than N719 dye, which is theorised to occur due to inhibition of the charge recombination at the photoanode/dye/redox electrolyte interface and the semirigid phenylacetylene spacers. Dye-3 and Dye-4 with longer conjugation length achieved higher energy conversion efficiency than Dye-1 and Dye-2. The investigation on the effects of acetylene moiety as π-spacer on their properties and

DSSC performance also have been investigated prior [82]. They designed and synthesised four organic dyes containing acetylene moiety for comparison with five dyes without acetylene moiety (Figure 10). The dyes incorporating acetylene moiety exhibited red-shifting in their absorption spectrum due to the increased conjugation length, but the degree of re-shift in dyes with acetylene moiety is quite weaker compared to dyes with ethylene (double bond) moiety. Introduction of acetylene moiety only barely influenced the HOMO level of the dyes, but the dyes with ethylene moiety experienced negative shifting of its HOMO level.

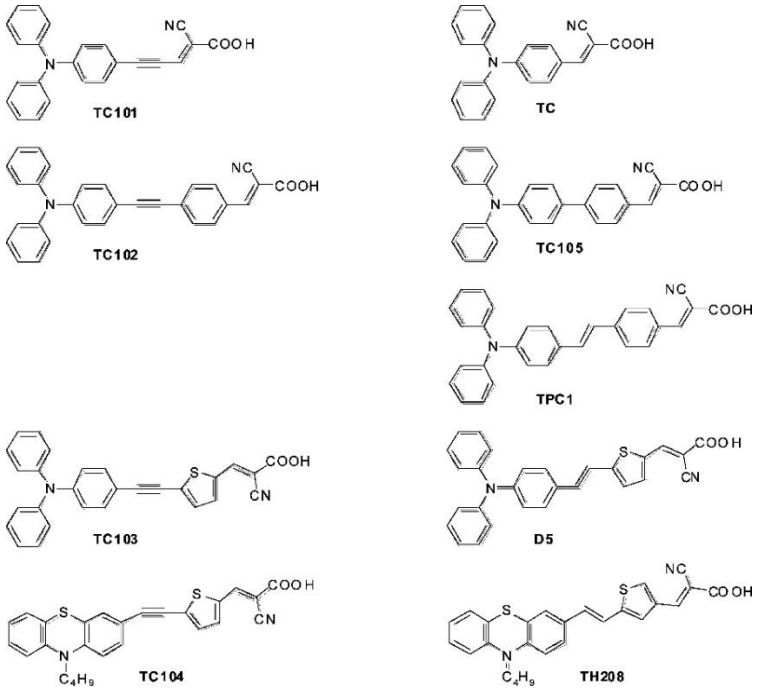


Figure 10. Dyes synthesised by Teng et al. [82] investigated the effects of acetylene moiety as π-spacer on their properties and DSSC performance.

Their designated DSSC performance of the dyes is tabulated in Table 2 below. Dyes with acetylene moiety only showed slight improvement in their energy conversion efficiency, compared to ethylene moiety which significantly improved the energy conversion efficiency, which is due to the lower J_{sc} of dyes containing acetylene moiety than dyes with ethylene moiety. But, DSSC using acetylene-based dyes showed improvement in their IPCE, due to the enhanced electron transfer yield of DSSC with introduction of triple bond.

Based on the selected studies, incorporation of acetylene moiety in dyes can induce red-shifting in their absorption spectrum via extension of conjugation length, which is important for the dye because more sunlight can be absorbed. Acetylene moiety also helped to improve the energy conversion efficiency of DSSC, but ethylene moiety showed much higher improvement in energy conversion efficiency. An advantage of acetylene moiety over ethylene moiety is their faster electron transfer yield, which enhance the IPCE of acetylene-based dye compared to ethylene-based dye. So, acetylene moiety can improve the properties of dyes and their DSSC performance, but more work needs to be done on the molecular design of dyes with acetylene moiety as linker in organic dyes, because ethylene moiety generally possesses better characteristics.

Table 2. Performance of synthesised dyes in DSSC

Dye	J_{sc} (mA·cm^{-2})	V_{oc} (V)	ff	η (%)
TC101	6.35	623	0.742	2.94
TC102	7.72	694	0.803	4.30
TC103	9.60	671	0.776	5.00
TC104	8.84	610	0.742	4.00
TC	5.26	636	0.776	2.60
TC105	7.58	693	0.773	4.06
TPC1	10.39	702	0.785	5.73
D5	12.41	663	0.760	6.25
TH208	11.99	643	0.743	5.73

Azomethine/Schiff base

Lokhande et al. [83] have come up with four new organic Schiff bases employing N-hexyl/N-phenyl carbazole moiety as a donor, 1-chlorobuta-1,3-diene as a π-bridge and 4-amino salicylic acid as acceptor for application as photosensitisers in DSSC (Figure 11). Incorporation of chlorine group along with additional π-bond worked effectively to improve the overall performance of dyes. Introduction of two acceptor units in 3b resulted in the decrement of HOMO-LUMO band gap with a bathochromic shift in absorption wavelength and broadening of the absorption spectrum. Introduction of hexyl unit in dyes exhibited better DSSC performance than the dyes with phenyl unit due to reduced aggregation of dye molecules on the TiO_2 surface [78].



Figure 11. Four those dyes designed and synthesised by Lokhande et al. in 2019 acting as photosensitisers in DSSC

In recent years, incorporation of theoretical studies on the physico-chemical and performance of these motifs are actively being performed. Particularly on the theoretical studies on the inclusion of azomethine moiety as linker in dye molecules. They investigated 10 dyes, of which three have already been reported experimentally and theoretically and of which seven are new structures inspired by the former. The effect of the pi-bridge was evaluated by combining azomethine, thiophene, and benzene derivatives using two and three units. In all cases, the inclusion of azomethine improved the electronic properties such as UV-Vis absorption, charge transfer from the donator part to acceptor part and the electron injection according to HOMO and LUMO levels, and chemical reactivity [84]. The incorporation of triphenylamine-thiopene based dyes with azomethine moieties as π-bridge, and their results showed that the dye with azomethine moieties were

capable of absorbing significant portion of light in the visible spectrum, suggesting its suitability for potential photovoltaic applications with further modification to its overall structure [85].

Heterocyclic

Heterocyclic is any cyclic organic compounds that contain at least one carbon atom with at least one other element such as nitrogen, oxygen and sulfur. In recent years, these compounds have been investigated greatly as spacer or linker in dyes for DSSCs applications. One of the derivatives of this heterocyclic moieties which has great potential to be utilized is known as isoindigo (Figure 12). It has been attracting great interest as an ideal building block for the electroactive materials for optoelectronics interest particularly in DSSCs. This is due to the fact that, it can afford high yields and turnovers [86]. Like other typical building block for organic electronics applications, it can be further developed into numerous molecular and polymeric materials with extended photophysical properties.

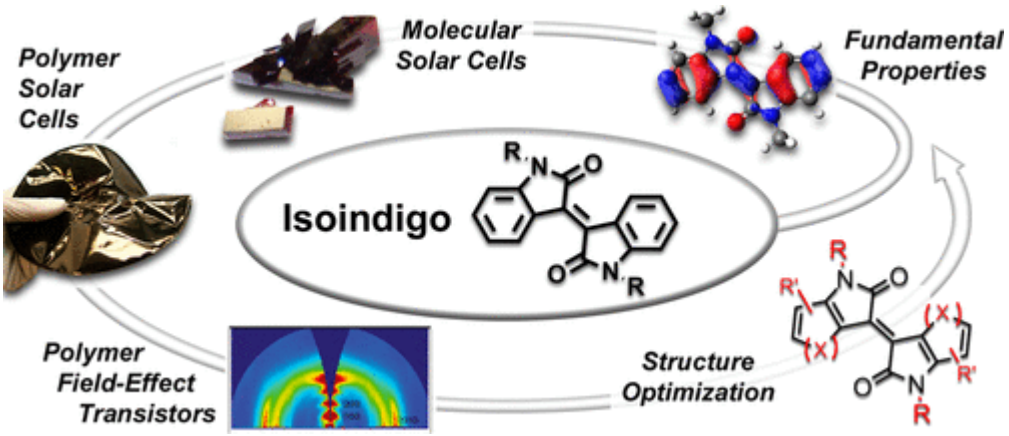


Figure 12. Numerous potential applications of isoindigo as building block in optoelectronics including in solar cells interests [86]

Isoindigo derivatives also have become a major focus recently in DSSCs acting as dyes. Synergistic studies involving computational approach of density functional theory (DFT) and the conventional experimental have become major interests among chemists and physicists in recent years. Hadsadee et al. [87] has utilized metal-free dyes based on isoindigo by performing DFT in order to improve efficiency in DSSCs. They have proposed triphenylamine as donor, thiophene as the π'-linker between the donor and auxiliary acceptor, and a phenyl or thiophene ring as the π-linker between the auxiliary acceptor and acceptor. The outcomes proven to exhibit good charge transfer properties and proven that the π-linker on photovoltaic would influence the performance in organic dyes.

By also incorporating DFT studies, a series of push−pull heterocyclic dyes of N, N diphenylhydrazones were prepared to study the effect of structural modifications with different π-spacers and electron withdrawing groups were studied further for their optical and non-linear properties. These derivatives were investigated for their potential as photosensitizers for nanocrystalline TiO_2-based DSSCs [88].

In designing and proposing well-performed DSSCs, the dyes should be highly efficient which the roles and influences of the donor (D) and acceptor (A) as well as ideal spacer or likers should be considered and chosen carefully. Due to its unique nature, heterocyclics containing sulfur and nitrogen like benzothiadiazole [89] were also explored and afforded great outcomes by altering the molecular backbones of the dyes. Similar computational method also can be utilised in other quite similar heterocyclic derivatives such as phenothiazine which in this study, the modification towards the bridging cores on their various properties such as structural, photovoltaic, electronic, and optical

properties were investigated further [90]. In 2020, a series of novel organic dyes containing bearing D-π-A system of phenothiazine were designed, synthesized and studied on their photophysical properties also pairing with DFT studies. It shows that, with the alteration on the substituents, the fundamental and thorough intramolecular charge transfers in these dyes can be understood further. [91]

Optical and redox properties of dyes are also essential features in photovoltaic studies. Incorporation of pyrrole and thiophenes in the molecular framework proven to that this sensitizer for DSSCs the best conversion efficiency up to 2.21%. This is mostly due to the contribution of the higher molar extinction coefficient, long π-conjugation of the heterocyclic system, higher oxidation potential and strong electron donating capacity of the ethoxyl group compared to the pirrolyl moiety [92].

With all the latest work and findings involving mixed moieties of D-πA system as dyes for DSSC and the greater impact these systems can contribute in solar cells studies, more exploration and in depth understanding on their fundamental features should be carried out. In recent years, typical experimental work paired with computational theoretical studies have shown that, a thorough details on the functionalities and performances of these developed DSSCs can be understood further. These two distinctive approaches are compatible to each other in supporting the development of an ideal usable DSSCs as an alternative green energy sources.

Conclusion and Future Outlook

There has been a thorough discussion on the fundamental aspects of DSSCs and other related elements featured in the build-up. The aim now is to explore various mixed moieties system that beneficial in term of extending the conjugation within the molecular framework of D-π-Acceptor system. The contribution of various substituents to the core of the molecules are also essential and may play a major role in giving the desired outcomes of the cells' efficiency and performances. In this contribution, a concise initial development of DSSC, its components and the overall working mechanism of the DSSC have been explored. Furthermore, the requirements for ideal organic dyes in DSSCs and the previous studies related to the application of acetylene and azomethine in dyes for DSSCs have been reviewed. Based on the reviewed works, dyes with acetylene, azomethine and heterocyclic mixed moieties have shown promising results for DSSC application and can be improved with further molecular tuning of the dyes. The ventures on the combination between these hybrid moieties as potential candidates as π-bridge in a dye molecule for DSSC should be taken into consideration Interestingly, focusing on the use of both acetylene and azomethine and taking highly elongated conjugation of these two can offer, there is no known research yet involving these moieties in individual molecular frameworks to date. Thus, the potentials are endless.

Acknowledgement

The authors would like to express gratitude to the Organisation for the Prohibition of Chemical Weapons (OPCW) (Grant numbers: 53309 (UMT's referral code), OPCW's Project Account No: L/ICA/ICB/217568/18) for research grant support, and Universiti Malaysia Terengganu for facilities and research aids.

References

1. Breeze, P. (2019). Power Generation Technologies (3rd ed.), Oxford: Elsevier: pp. 293-321.
2. World Energy Council (2013). World Energy Resources: Solar. https://www.worldenergy.org/assets/images/imported/2013/10/WER_2013_8_Solar_revised.pdf. [Access online 20 June 2023].
3. Ritchie, H. and Roser, M. (2020). Energy Production and Consumption. OurWorldInData. https://ourworldindata.org/energy-production-consumption. [Access online 20 June 2023].
4. Kumavat, P. P., Sonar, P. and Dalal, S. D. (2017). An overview on basics of organic and dye sensitized solar cells, their mechanism and recent improvements. *Renewable and Sustainable Energy Reviews*, 78: 1262- 1287.
5. Rhodes, C. J. (2010). Solar energy: Principles and possibilities. *Science Progress*, 93(1): 37-112.
6. American Physical Society (2009). This month in physics history - April 25, 1954: Bell Labs

demonstrates the first practical silicon solar cell. https://www.aps.org/publications/apsnews/200904/physicshistory.cfm. [Access online 4 May 2023].

7. Akinoglu, B. G., Tuncel, B. and Badescu, V. (2021). Beyond 3rd generation solar cells and the full spectrum project. Recent advances and new emerging solar cells. *Sustainable Energy Technologies and Assessments*. 46: 101287-101308.
8. Simke, W.C. (2019). Development of photovoltaic technologies for global impact. *Renewable Energy.* 138: 911-914.
9. Sharma, S., Jain, K. K. and Sharma, A. (2015). Solar cells: In research and applications—a review. *Materials Sciences and Applications,* 6(12): 1145-1155.
10. Badawy, W. A. (2015). A review on solar cells from Si-single crystals to porous materials and quantum dots. *Journal of Advanced Researchl,* 6(2): 123-132.
11. Tonui, P., Oseni, S. O., Sharma, G., Yan, Q. and Mola, G. T. (2018). Perovskites photovoltaic solar cells: An overview of current status. *Renewable and Sustainable Energy Reviews,* 91: 1025-1044.
12. Sharma, K., Sharma, V. and Sharma, S. S. (2018). Dye-sensitized solar cells: Fundamentals and current status. *Nanoscale Research Letters,* 13(381):1-46.
13. O'Regan, B. and Grätzel, M. (1991). A low cost, high-efficiency solar cell based on dye-sensitized colloidal TiO_2 films. *Nature.* 353: 737-740.
14. Lee, C.-P., Lin, C.-A., Wei, T.-C., Tsai, M.-L., Meng, Y., Li, C.-T., Ho, K.-C., Wu, C.-I, Lau, S.-P. and He, J.-H. (2015). Economical low-light photovoltaics by using the Pt-free dye-sensitized solar cell with graphene dot/PEDOT:PSS counter electrodes. *Nano Energy*, 18: 109-117.
15. Juang, S.S.-Y., Lin, P.-Y., Lin, Y.-C., Chen, Y.-S., Shen, P.-S., Guo, Y.-L., Wu, Y.-C. and Chen, P. (2019). Energy harvesting under dim-light condition with dye-sensitized and perovskite solar cells. *Frontiers in Chemistry*, 7(209):1-9.
16. Hagfeldt, A., Boschloo, G., Sun, L., Kloo, L. and Petterson, H. (2010). Dye-sensitized solar cells. *Chemical Reviews,* 110(11): 6595-6663.
17. Nazeeruddin, M. K. (2011). Dye-sensitized solar cells: A brief overview. *Solar Energy.* 85(6): 1172-1178.
18. Selvaraj, P., Baig, H., Mallick, T. K., Siviter, S., Montecucco, A., Li, W., Paul, M., Sweet, T., Gao, M., Knox, A. R. and Sundaram, S. (2018). Enhancing the efficiency of transparent dye-sensitized solar cells using concentrated light. *Solar Energy Materials and Solar Cells,* 175: 29-34.
19. Kakiage, K., Aoyama, Y., Yano, T., Oya, K., Fujisawa, J., and Hanaya, M. (2015). Highly-efficient dye-sensitized solar cells with collaborative sensitization by silyl-anchor and carboxy-anchor dyes. *Chemical Communications.* 51: 15894-15897.
20. Fraunhofer Institute for Solar Energy Systems ISE (2021). *Photovoltaics Report*. https://www.ise.fraunhofer.de/en/publications/studies/photovoltaics-report.html. [Access online 20 April 2023].
21. Grand View Research (2020). Dye sensitized solar cell market size, share & trends analysis report by application (portable charging, BIPV/BAPV, embedded electronics, outdoor advertising, automotive (AIPV)), and segment forecasts, 2020 – 2027. https://www.grandviewresearch.com/industry-analysis/dye-sensitized-solar-cell-market. [Access online 15 May 2023].
22. Belessiotis, G.V., Ibrahim, I., Karagianni, C. S. and Falaras, P. (2021). DSSCs for indoor environments: from lab scale experiments to real life applications. *SVOA Materials Science & Technology.* 3(1): 1-5.
23. Salton, J. (2009). World's first commercial application of DSSC solar technology is in the bag. New Atlas. https://newatlas.com/first-commercial-application-dssc-solar-technology/13100/. [Access online 20 June 2023].
24. Solaronix.com (2022). Solaronix - innovative solutions for solar professionals. https://solaronix.com. [Access online 20 June 2023].
25. Gong, J., Liang, J. and Sumathy, K. (2012). Review on dye sensitized solar cells (DSSCs): Fundamental concepts and novel materials. *Renewable and Sustainable Energy Reviews,* 16(8): 5848-5860.

26. Gorlov, M. and Kloo, L. (2008). Ionic liquid electrolytes for dye-sensitized solar cells. *Dalton Transactions.* 20: 2655-2666.
27. Yu, Z., Vlachopoulos, N., Gorlov, M. and Kloo, L. (2011). Liquid electrolytes for dye-sensitized solar cells. *Dalton Transactions.* 40: 10289-10303.
28. Bach, U., Lupo, D., Comte, P., Moser, J.E., Weissörtel, F., Salbeck, J., Spreitzer, H. and Grätzel, M. (1998). Solid-state dye-sensitized mesoporous TiO_2 solar cells with high photon-to-electron conversion efficiencies. *Nature.* 395: 583-585.
29. Boschloo, G. (2019). Improving the performance of dye-sensitized solar cells. *Frontiers in Chemistry*. 7(77):1-9.
30. Sun, K. C., Sahito, I. A., Noh, J. W., Yeo, S. Y., Im, J. N., Yi, S. C., Kim, Y. S. and Jeong, H. S. (2016). Highly efficient and durable dye-sensitized solar cells based on a wet-laid PET membrane electrolyte. *Journals of Materials Chemistry A*, 4(2): 458-465.
31. Karim, N. A., Mehmood, U., Zahid, H. F. and Asif, T. (2019). Nanostructured photoanode and counter electrode materials for efficient dye-sensitized solar cells (DSSCs). *Solar Energy*. 185: 165-188.
32. Papageorgiou, N. (2004). Counter-electrode function in nanocrystalline photoelectrochemical cell configurations. *Coordination Chemistry Reviews.* 248: 1421-1446.
33. Wu, J., Lan, Z., Lin, J., Huang, M., Huang, Y., Fan, L., Luo, G., Lin, Y., Xie, Y. and Wei, Y. (2017). Counter electrodes in dye-sensitized solar cells. *Chemical Society Reviews*. 46: 5975-6023.
34. Fang, X., Ma, T., Guan, G., Akiyama, M., Tetsuya, K. and Abe, E. (2004). Effect of the thickness of the Pt film coated on a counter electrode on the performance of a dye-sensitized solar cell. *Journal of Electroanalytical Chemistry*, 570(2): 257-263.
35. Thomas, S., Deepak, T. G., Anjusree, G. S., Arun, T. A., Nair, S. V. and Nair, A. S. (2014). A review on counter electrode materials in dye-sensitized solar cells. *Journal of Materials Chemistry A.* 2: 4474-4490.
36. Jeong, H., Pak, Y., Hwang, Y., Song, H., Lee, K. H., Ko, H.C. and Jung, G. Y. (2012). Enhancing the charge transfer of the counter electrode in dye-sensitized solar cells using periodically aligned platinum nanocups. *Small*, 8(24): 3757-3761.
37. Ahmad, M. S., Pandey, A. K. and Rahim, N. A. (2017). Advancements in the development of TiO_2 photoanodes and its fabrication methods for dye sensitized solar cell (DSSC) applications. A review. *Renewable and Sustainable Energy Reviews.* 77: 89-108.
38. Park, N.-G., van de Lagemaat, J. and Frank, A.J. (2000). Comparison of dye-sensitized rutile- and anatase-based TiO_2 solar cells. *The Journal of Physical Chemistry B*, 104(38): 8989-8994.
39. Kusumawati, Y., Hosni, M., Martoprawiro, M. A., Cassaignon, S. and Pauporté, T. (2014). Charge transport and recombination in TiO_2 brookite-based photoelectrodes. *The Journal of Physical Chemistry C*, 118(41): 23459-23467.
40. Mohammadian-Sarcheshmeh, H., Arazi, R. and Mazloum-Ardakani, M. (2020). Application of bifunctional photoanode materials in DSSCs: A review. *Renewable and Sustainable Energy Reviews.* 134: 110249-110250.
41. Raj, C.C. and Prasanth, R. (2016). A critical review of recent developments in nanomaterials for photoelectrodes in dye sensitized solar cells. *Journal of Power Sources.* 317: 120-132.
42. He, Y., Hu, J. and Xie, Y. (2015). High-efficiency dye-sensitized solar cells of up to 8.03% by air plasma treatment of ZnO nanostructures. *Chemical Communications*, 51(90): 16229-16232.
43. Chou, T.P., Zhang, Q., Russo, B., Fryxell, G.E. and Cao, G. (2007). Titania particle size effect on the overall performance of dye-sensitized solar cells. *The Journal of Physical Chemistry C*, 111(17): 6296-6302.
44. Dhungel, S. K. and Park, C. W. (2013). Impact of size distribution of nanoparticles in TiO_2 paste for its application in dye sensitized solar cells. *The Himalayan Physics*, 4(4): 27-31.
45. Wang, Z. S., Kawauchi, H., Kashima, T. and Arakawa, H. (2004). Significant influence of TiO_2 photoelectrode morphology on the energy conversion efficiency of N719 dye-sensitized solar cell. *Coordination Chemistry Reviews*, 248(13): 1381-1389.

46. Devadiga, D., Selvakumar, M., Shetty, P. and Santosh, M. S. (2021). Recent progress in dye sensitized solar cell materials and photo-supercapacitors: A review. *Journal of Power Sources,* 493: 229698-229755.
47. Dahlan, D., Saad, S. K. M., Berli, A. U., Bajili, A. and Umar, A. A. (2017). Synthesis of two-dimensional nanowall of Cu-doped TiO_2 and its application as photoanode in DSSCs. *Physica E,* 91: 185-189.
48. Mahmoud, M. S., Akhtar, M. S., Mohamed, I. M. A., Hamdan, R., Dakka, Y. A. and Barakat, N. A. M. (2018). Demonstrated photons to electron activity of S-doped TiO_2 nanofibers as photoanode in the DSSC. *Materials Letters,* 225: 77-81.
49. Prabavathy, N., Balasundaraprabhu, R., Balaji, G., Malikaramage, A. U., Prasanna, S., Sivakumaran, K., Kumara, G. R. A., Rajapakse, R. M. G. and Velauthapillai, D. (2019). Investigations on the photo catalytic activity of calcium doped TiO_2 photo electrode for enhanced efficiency of anthocyanins-based dye sensitized solar cells. *Journal of Photochemistry & Photobiology A: Chemistry*, 377: 43-57.
50. Chen, X., Du, Q., Yang, W., Liu, W., Miao. Z. and Yang, P. (2017). A double-layered photoanode made of ZnO/TiO_2 composite nanoflowers and TiO_2 nanorods for high efficiency dye-sensitized solar cells. *Journal of Solid State Electrochemistry*, 22: 685-691.
51. Bakr, Z. H., Wali, Q., Ismail, J., Elumalai, N. K., Uddin, A. and Jose, R. (2018). Synergistic combination of electronic and electrical properties of SnO_2 and TiO_2 in a single SnO_2-TiO_2 composite nanofiber for dye-sensitized solar cells. *Electrochimica Acta,* 263: 524-532.
52. Chatterjee, S., Webre, W. A., Patra, S., Rout, B., Glass, G. A., D'Souza, F. and Chatterjee, S. (2020). Achievement of superior efficiency of TiO_2 nanorod-nanoparticle composite photoanode in dye sensitized solar cell. *Journal of Alloys and Compounds.* 826: 154188-154196.
53. Zhang, S., Yang, X., Numata, Y. and Han, L. (2013). Highly efficient dye-sensitized solar cells: Progress and future challenges. *Energy & Environmental Science,* 6: 1443-1464.
54. Bhattacharya, S. and John, S. (2019). Beyond 30% conversion efficiency in silicon solar cells: A numerical demonstration. *Scientific Reports.* 9: 12482-12497.
55. Shalini, S., Balasundaraprabhu, R., Kumar, T. S., Prabavathy, N., Senthilarasu, S. and Prasanna, S. (2016). Status and outlook of sensitizers/dyes used in dye sensitized solar cells (DSSC): A review. *International Journal of Energy Research,* 40(10): 1303-1320.
56. Galoppini, E. (2004). Linkers for anchoring sensitizers to semiconductor nanoparticles. *Coordination Chemistry Reviews,* 248: 1283-1297.
57. Zhang, L. and Cole, J. M. (2015). Anchoring groups for dye-sensitized solar cells. *ACS Applied Materials & Interfaces*, 7(6): 3427-3455.
58. Cahen, D., Hodes, G., Grätzel, M., Guillemoles, J. F. and Riess, I. (2000). Nature of photovoltaic action in dye-sensitized solar cells. *The Journal of Physical Chemistry B,* 104(9): 2053-2059.
59. Ooyama, Y. and Harima, Y. (2012). Photophysical and electrochemical properties, and molecular structures of organic dyes for dye-sensitized solar cells. *ChemPhysChem,* 13(18): 4032-4080.
60. Asghar, M. I., Miettunen, K., Halme, J., Vahermaa, P., Toivola, M., Aitola, K. and Lund, P. (2010) Review of stability for advanced dye solar cells. *Energy & Environmental Science,* 3(4): 418-426.
61. Nazeeruddin, M. K., Kay, A., Rodicio, I., Humphry-Baker, R., Müller, E., Liska, P., Vlachopoulos, N. and Grätzel, M. (1993). Conversion of light to electricity by *cis*-X_2Bis(2,2'-bipyridyl-4,4'-dicarboxylate)ruthenium(II) charge-transfer sensitizers (X = Cl^-, Br^-, I^-, CN^-, and SCN^-) on nanocrystalline TiO_2 electrodes. *Journal of the American Chemical Society,* 115(14): 6382-6390.
62. Nazeeruddin, M. K., Zakeeruddin, S. M., Humphry-Baker, R., Jirousek, M., Liska, P., Vlachopoulos, N., Shklover, V., Fischer, C.-H. and Grätzel, M. (1999). Acid-base equilibria of (2,2-bipyridyl-4,4-dicarboxylic acid)ruthenium(II) complexes and the effect of protonation on charge-transfer sensitization of nanocrystalline titania. *Inorganic Chemistry,* 38(26): 6298-6305.
63. Swetha, T., Reddy, K. R. and Singh, S. P. (2015). Osmium polypyridyl complexes and their

applications to dye-sensitized solar cells. *The Chemical Records*, 15(2): 457-474.

64. Sauvé, G., Cass, M. E., Coia, G., Doig, S. J., Lauermann, I., Pomykal, K. E. and Lewis, N. S. (2000). Dye sensitization of nanocrystalline titanium dioxide with osmium and ruthenium polypyridyl complexes. *The Journal of Physical Chemistry B*, 104(29): 6821-6836.
65. Alebbi, M., Bignozzi, C. A., Heimer, T. A., Hasselmann, G. M. and Meyer, G. J. (1998). The limiting role of iodide oxidation in cis-$Os(dcb)_2(CN)_2/TiO_2$ photoelectrochemical cells. *The Journal of Physical Chemistry B*, 102(39): 7577-7581.
66. Kuciauskas, D., Freund, M. S., Gray, H. B., Winkler, J. R. and Lewis, N. S. (2001). Electron transfer dynamics in nanocrystalline titanium dioxide solar cells sensitized with ruthenium or osmium polypyridyl complexes. *The Journal of Physical Chemistry B*, 105(2): 392-403.
67. Islam, A., Sugihara, H., Hara, K., Singh, L. P., Katoh, R., Yanagida, M., Takahashi, Y., Murata, S. and Arakawa, H. (2000). New platinum(II) polypyridyl photosensitizers for TiO_2 solar cells. *New Journal of Chemistry*. 24(6): 343-345.
68. Siu, C.-H., Lee, L.T.L., Yiu, S.-C., Ho, P.-Y., Zhou, P., Ho, C.-L., Chen, T., Liu, J., Han, K. and Wong, W.-Y. (2015). Synthesis and characterization of phenothiazine-based platinum(II)–acetylide photosensitizers for efficient dye-sensitized solar cells. *Chemistry: A European Journal*. 22: 3750-3757.
69. Dai, F.-R., Chen, Y.-C., Lai, L.-F., Wu, W.-J., Cui, C.-H., Tan, G.-P., Wang, X.-Z., Lin, J.-T., Tian, H. and Wong, W.-Y. (2012). Unsymmetric platinum(II) bis(aryleneethynylene) complexes as photosensitizers for dye-sensitized solar cells. *Chemistry: An Asian Journal*, 7(6): 1426-1434.
70. Lee, C.-P., Li, C.-T. and Ho, K.-C. (2017). Use of organic materials in dye-sensitized solar cells. *Materials Today*, 20(5): 267-283.
71. Yahya, M., Bouziani, A., Ocak, C., Seferoğlu, Z. and Sillanpää, M. (2021). Organic/metal-organic photosensitizers for dye-sensitized solar cells (DSSC): Recent developments, new trends, and future perceptions. *Dyes and Pigments*, 192: 109227-109265.
72. Ning, Z., Fu, Y. and Tian, H. (2010). Improvement of dye-sensitized solar cells: what we know and what we need to know. *Energy & Environmental Science*, 3(9): 1170-1181.
73. Kim, B.-G., Chung, K. and Kim, J. (2013). Molecular design principle of all-organic dyes for dye-sensitized solar cells. *Chemistry - A European Journal*, 19(17): 5220-523.
74. Ndaleh, D. N. D., Nugegoda, D., Watson, J., Cheema, H. and Delcamp, J. H. (2021). Donor group influence on dye-sensitized solar cell device performances: balancing dye loading and donor size. *Dyes and Pigments*, 187: 109074-109082.\
75. Mahmood, A., Khan, S.U.-D., Rana, U.A. and Tahir, M.H. (2019). Red shifting of absorption maxima of phenothiazine based dyes by incorporating electron-deficient thiadiazole derivatives as p-spacer. *Arabian Journal of Chemistry*, 12(7): 1447-1453.
76. Yu, Q.-Y., Liao, J.-Y., Zhou, S.-M., Shen, Y., Liu, J.-M., Kuang, D.-B. and Su, C.-Y. (2011). Effect of hydrocarbon chain length of disubstituted triphenyl-amine-based organic dyes on dye-sensitized solar cells. *The Journal of Physical Chemistry C*, 115(44): 22002-22008.
77. Khairul, W. M., Wahab, F. F. A., Che Soh, S. K., Shamsuddin, M. and Daud, A. I., (2020). Palladium(II)-pivaloyl thiourea complexes: synthesis, characterisation and their catalytic activity in mild Sonogashira cross-coupling reaction. *Chemical Physics Letters*, 756: 137842-137850.
78. Zaini, M. F., Khairul, W. M., Arshad, S., Abdullah, M., Zainuri, D. A., Rahamathullah, R., Rosli, M. I., Aziz, M. S. A. and Razak, I. A. (2020). The structure-property studies and mechanism of optical limiting action of methyl 4-((4-aminophenyl)ethynyl)benzoate crystal under continuous wave laser excitation. *Optical Materials*, 107: 110087-110105.
79. Song, J., Zhang, F., Li, C., Liu, W., Li, B., Huang, Y. and Bo, Z. (2009). Phenylethyne-bridged dyes for dye-sensitized solar cells. *The Journal of Physical Chemistry C*, 113(30): 13391-13397.

80. Jasman, S. M., Khairul, W.M., Tagg, T., Kubulat, K., Rahamathullah R., Arshad, S., Razak, I. A. and Tahir, M. I. M. (2015). Synthesis, crystal structure, and electrical studies of naphthoyl-thiourea as potential organic light emitting diode, *Journal of Chemical Crystallography*, 45: 338-349.
81. Lee, S. T., Khairul, W. M., Lee, O. J., Rahamathullah, R., Daud, A. I., Ku Bulat, K. H., Sapari, S., Razak, F. A. I and Krishnan, G. (2021). Electronic, reactivity and third order nonlinear optical properties of thermally-stable push-pull chalcones for optoelectronic interest: experimental and DFT assessments. *Journal of Physics and Chemistry of Solids*, 159: 110276-110290.
82. Teng, C., Yang, X., Yang, C., Tian, H., Li, S., Wang, X., Hagfeldt, A. and Sun, L. (2010). Influence of triple bonds as π-spacer units in metal-free organic dyes for dye-sensitized solar cells. *The Journal of Physical Chemistry C*, 114(25): 11305-11313.
83. Lokhande, P.K.M., Sonigara, K.K., Jadhav, M.M., Patil, D.S., Soni, S.S. and Sekar, N. (2019). Multi-dentate carbazole based schiff base dyes with chlorovinylene group in spacer for dye-sensitized solar cells: A combined theoretical and experimental study. *Chemistry Select*, 4(14): 4044-4056.
84. Delgado-Montiel, T., Soto-Rojo, R., Baldenebro-López, J. and Glossman-Mitnik, D. (2019). Theoretical study of the effect of different π bridges including an azomethine group in triphenylamine-based dye for dye-sensitized solar cells. *Molecules*, 24(21): 3897-3913.
85. Sarswat, P. K., Sathyapalan, A., Zhu, Y. and Free, M. L. (2013). Design, synthesis, and characterization of TPA-thiophene-based amide or imine functionalized molecule for potential optoelectronic devices. *Journal of Theoretical and Applied Physics*, 7(4):1-9.
86. Stalder, R., Mei, J., Graham, K. R., Estrada, L. A. and Reynolds, J. R. (2014). Isoindigo, a versatile electron-deficient unit for high-performance organic electronics. *Chemistry of Materials*, 26(1): 664-678.
87. Hadsadee, S., Promarak, V., Sudyoadsuk, T., Keawin, T., Kungwan, N. and Jungsuttiwong, S. (2020). Theoretical study on factors influencing the efficiency of *d–π′–a′–π–a* isoindigo-based sensitizer for dye-sensitized solar cells. *Journal of Electronic Materials*, 49: 318-332.
88. Fernandes, S. S. M., Belsley, M., Pereira, A. I., Ivanou, D., Mendes, A., Justino, L. L. G., Burrows, H. D. and Raposo, M. M. M. (2018). Push−pull n,n-diphenylhydrazones bearing bithiophene or thienothiophene spacers as nonlinear optical second harmonic generators and as photosensitizers for nanocrystalline TiO_2 dye sensitized solar cells. *ACS Omega*, 3: 12893-12904.
89. Mustafa, F. M., Abdel-Latif, M. K., Abdel-Khalek, A. A. and Kühn, O. (2023). Efficient D-π-π-A-type dye sensitizer based on a benzothiadiazole moiety: A computational study. *Molecules*, 28(13): 5185-5197.
90. Kacimi, R., Raftani, M., Abram, T., Azaid, A., Ziyat, H., Bejjit, L., Bennani, M. N., and Bouachrine, M. (2021). Theoretical design of D-π-A system new dyes candidate for DSSC application. *Heliyon*, 7: e07171-e707181.
91. Mantur, S., Patil, M. K., Nadaf, A. A., Najare, M. S., Yaseen, M., Inamdar, S. R. and Khazi, I. A. (2020). Synthesis, characterization and photophysical properties of π-conjugated novel phenothiazine substituted acrylonitrile D–A derivatives: Orange to red emission. *Chemical Data Collections*, 30: 100543-100556.
92. Fernandes, S. S. M., Castro, M. C. R., Ivanou, D., Mendes, A. and Raposo, M. M. M. (2022). Push-pull heterocyclic dyes based on pyrrole and thiophene: Synthesis and evaluation of their optical, redox and photovoltaic properties. *Coatings*, 12: 34-46.

Malaysian Journal of Analytical Sciences (MJAS)
Published by Malaysian Analytical Sciences Society

OPTIMIZATION OF SUNFLOWER OIL HYDROLYSIS USING THE D-OPTIMAL DESIGN

(Pengoptimuman Hidrolisis Minyak Bunga Matahari Menggunakan Reka Bentuk D-Optimal)

Muhammad Muizzuddin Khairuddin[1], Asiah Abdullah[1,2], Nur Nadia Dzulkifli[1,2], and Nurazira Mohd Nor[1,2*]

[1]School of Chemistry and Environment,
Faculty of Applied Sciences,
Universiti Teknologi MARA, Cawangan Negeri Sembilan, Kampus Kuala Pilah,
72000 Kuala Pilah, Negeri Sembilan, Malaysia
[2]Material, Inorganic and Oleochemistry (MaterOleo) Research Group,
Faculty of Applied Sciences,
Universiti Teknologi MARA, Cawangan Negeri Sembilan Kampus Kuala Pilah,
72000 Kuala Pilah, Negeri Sembilan, Malaysia

[*]Corresponding author: nurazira@uitm.edu.my

Received: 24 May 2023; Accepted: 7 September 2023; Published: xx October 2023

Abstract

The hydrolysis process of sunflower oil (SFO) was carried out to produce sunflower oil fatty acids (SFOFAs). The optimization of reaction parameters was performed using response surface methodology (RSM) via D-optimal design. The optimization parameters were varied from 1.0 to 2.5 M molarity of ethanolic KOH, 50 to 70°C of reaction temperature and 0.5 to 2.5 hours of reaction time. The highest percentage of SFOFAs yield was 96.68% with a free fatty acid (FFA) of 103.23%, which was achieved at optimal conditions: 2.3 M ethanolic KOH concentration, reaction temperature of 50.14°C and 0.97 hours of reaction time. The structure of SFO and SFOFAs were confirmed using Fourier Transform Infrared Spectroscopy (FTIR) and Nuclear Magnetic Resonance (NMR). SFOFAs was monitored by the absence of C=O (ester) at 1746.33 cm^{-1} and the existence of C=O (carboxylic acid) at 1710.23 cm^{-1} with OH stretching at 2400-3400 cm^{-1} in SFOFAs FTIR spectrum. Under the NMR spectrum of SFOFAs, the absence peak of ester (C=O) at 172.79 to 173.21 ppm (^{13}C NMR), the emergence peak of OH at 10.61 ppm (^{1}H NMR) and the peak of carbon for carboxylic acid (C=O) (^{13}C NMR) at 180.45 ppm showed that the fatty acid was successfully obtained.

Keywords: D-optimal design, hydrolysis, response surface methodology, saponification, sunflower oil

Abstrak

Proses hidrolisis minyak bunga matahari (SFO) telah dijalankan untuk menghasilkan asid lemak minyak bunga matahari (SFOFA). Pengoptimuman parameter tindak balas dilakukan menggunakan kaedah permukaan tindak balas (RSM) melalui reka bentuk D-optimal. Parameter pengoptimuman telah diubah daripada 1.0 hingga 2.5 M kemolaran etanol KOH, 50 hingga 70 °C suhu tindak balas dan 0.5 hingga 2.5 jam masa tindak balas. Peratusan tertinggi hasil SFOFAs ialah 96.68% dengan asid lemak bebas (FFA) sebanyak 103.23%, yang dicapai pada keadaan optimum: kepekatan KOH etanol 2.3 M, suhu tindak balas 50.14 °C dan 0.97 jam masa tindak balas. Struktur SFO dan SFOFAs telah disahkan menggunakan spektroskopi infra-merah transformasi Fourier (FTIR) dan resonans magnetik nuklear (NMR). SFOFAs dilihat dengan ketiadaan C=O (ester) pada 1746.33 cm^{-1} dan kewujudan C=O

(asid karboksilik) pada 1710.23 cm^{-1} dengan regangan OH pada 2400-3400 cm^{-1} dalam spektrum FTIR SFOFAs. Di bawah spektrum NMR SFOFAs, kehilangan puncak ester (C=O) pada 172.79 hingga 173.21 ppm (^{13}C NMR), kemunculan puncak OH pada 10.61 ppm (^{1}H NMR) dan puncak karbon untuk asid karboksilik (C=O) (^{13}C NMR) pada 180.45 ppm menunjukkan bahawa asid lemak berjaya diperolehi.

Kata kunci: reka bentuk D-optimal, hidrolisis, kaedah permukaan tindak balas, penyabunan, minyak bunga matahari

Introduction

Nowadays, the increase in the use of petrochemical products in daily life has caused various environmental problems [1]. The petrochemicals are used in many industries like plastics, soaps and detergents, solvents, drugs, fertilizer and pesticides [2]. The use of petrochemical products is an international issue because they contribute to environmental problem, global warming and climate change due to the disadvantages of petrochemical product such as low biodegradability (20-30%), toxic to the environment, cause an increase of the greenhouse gases that affect global warming and the material come from non-renewable sources [2-6]. The use of petrochemical products needs to be changed to other alternatives that do not have a negative impact on the environment. A suitable alternative is to replace petrochemical products with biobased products such as plant oil.

Fatty acid and glycerol are essential raw materials in the oleochemical industry [4]. It is widely used as a raw material in the food, cosmetic and pharmaceutical industries. Fatty acid can be obtained from the hydrolysis of plant oil and fats via saponification as shown in Figure 1 [7, 8]. Fatty acid can also be used as a starting material in the production of biolubricant (polyol ester) [9, 10]. There are several plant oils used in the production of fatty acids, including sunflower oil. There are various type of fatty acids in sunflower oil (SFO) such as palmitic (5.2%), stearic (2.7%), oleic (37.2%), linoleic (53.8%) and linolenic (1.0%) [11], which make the ingredients suitable for hydrolysis process. The hydrolysis reaction can be catalyzed using acid, base or enzyme (lipase) [4]. Nowadays, researchers focus more on potassium hydroxide catalyzed (base catalyze) hydrolysis in order to reduce energy consumption [12].

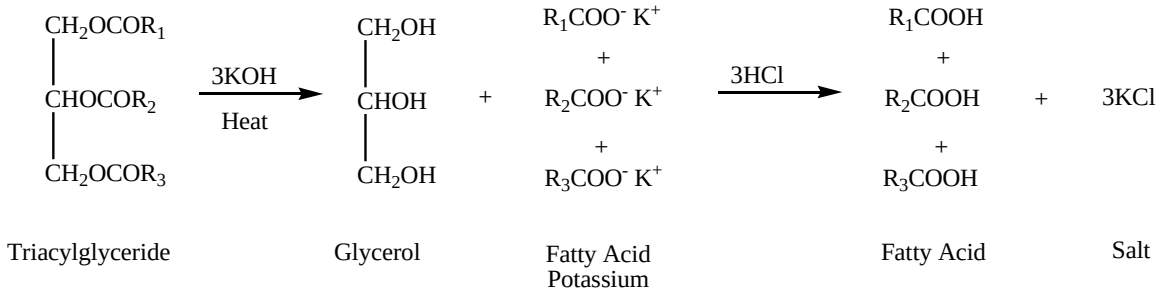


Figure 1. Hydrolysis process of triacylglycerol in plant oil

Based on the previous studies, there are several researchers who have carried out the hydrolysis process of plant oil in such as Bahadi et al. [4], who used different ethanolic KOH concentration, time and temperature for the optimization of the hydrolysis of crude palm kernel oil. The results of the study found that the free fatty acid (FFA) and yield obtained were 98% and 84.7% respectively with the optimum condition being 2.16 hours, 1.77 M ethanolic KOH at a temperature of 70 °C. Nor et al. [13] carried out hydrolysis of RBD palm oil using base catalyst. The conditions used were 1.5 M ethanolic KOH, 2.0 hours at a temperature of 60 °C and the yield produced was 95%. Ferreira et al. [14] also conducted the hydrolysis process of cottonseed, olive and palm kernel oil by using lipase enzyme from *Geotrichum candidum* (GCL-1) as catalyst. The result showed that GCL-1 gave the highest activity of hydrolysis only for plant oil that contained high amount of unsaturated fatty acids (cottonseed and olive oil) with optimum condition at 46.8% m/m oil, 6.6

U/g of reaction mixture at 40°C. In another study, Salimon et al. [8] carried out hydrolysis for preparing fatty acids from *Jatropha curcas* seed oil. The result of the study showed that the maximum recovery of FFA was 102.2% and the optimum condition were 1.75 M ethanolic KOH, 2.0 hours at a temperature of 65°C.

This research focus on using D-optimal design from response surface methodology for optimization process for hydrolysis of sunflower oil. Previous studies on the hydrolysis of sunflower oil focus more on using enzyme as catalyst [15, 16] and the used of base catalyze (potassium hydroxide) is limited. Most of the optimization process is done using conventional methods. There is no study done using the statistical method for hydrolysis of sunflower oil via D-optimal design.

Response Surface Methodology (RSM) is a practical method that uses mathematical and statistical analysis to fit empirical models to experimentally collect data [17]. The RSM can be used to optimize the reaction process since, in comparison to conventional method, it minimizes the overall number of experimental trials, operational costs, and time [10]. Typically, the prediction of responses in optimization process are specifically based on linear and quadratic models as shown in equation (1). As a result, an optimization study can be carried out to evaluate the experimental condition.

$$Y = \beta_0 + \Sigma\beta_i x_i + \Sigma\beta_{ii} x_i^2 + \Sigma\Sigma\beta_{ij} x_{ixj} \quad (1)$$

Where Y for response, β_0 for constant, β_i for linear, βii for square regression coefficient and β_{ij} for interaction regression coefficient and x_i and x_{ixj} are assigned as independent variables [18, 19]. D-optimal design is a useful tool to determine the factors that are significant to the experimental condition to achieve the best performance. The concept of D-optimal design exhibits remarkable flexibility and efficiency by accommodating a wide range of factors, both in terms of quantity and characteristics, as well as diverse levels of factor configurations and model specifications. It uniquely maximizes the determinant of the information matrix associated with the model, thereby systematically selecting the most informative experimental runs from a given set of candidates. This paper offers details on practical use for D-optimal design to optimize the hydrolysis of sunflower oil to obtain sunflower oil fatty acids (SFOFAs). D-optimal design was applied by using percentage yield and free fatty acids as responses to determine the optimal conditions for the hydrolysis.

Materials and Methods

Sunflower oil was obtained from IKO company, Negeri Sembilan, Malaysia. Potassium hydroxide (KOH), hydrochloric acid 37% (HCl), n-hexane 99%, ethanol 95% and anhydrous sodium sulphate (Na_2SO_4) were purchased from Systerm chemical Co, Malaysia. All chemicals utilized were analytical reagent grade and used without the need for additional purification steps.

Hydrolysis of sunflower oil

The hydrolysis of sunflower oil (SFO) involves two stages which are saponification and acidification. The hydrolysis was carried out using sunflower oil (SFO) with alkaline ethanol to produce sunflower oil fatty acids (SFOFAs). At saponification stage, 12.5 grams of SFO was mixed with 75 mL of alkaline ethanol into 250 mL two neck round bottom flask equipped with a reflux condenser, thermometer and mechanical stirrer. The mixture was heated and continuously stirred at 300 rpm using magnetic stirrer. After that, the mixture undergoes acidification process where 25 mL of hydrochloric acid was added to neutralize the alkaline solution. The washing continues by adding 50 mL of distilled water and 25 mL of n-hexane. After washing, anhydrous sodium sulphate was added to the product (SFOFAs) for overnight and the product was filtered using Whatman No 1 filter paper and the solvent was removed by using rotary evaporator [20]. At the next stage, the percentage free fatty acid (FFA) of SFOFAs was determined.

Optimization of hydrolysis

Software from Design Expert version 13 was employed for this optimization. There are three parameters used in the optimization of hydrolysis, namely the molarity of catalyst used (ethanolic KOH) (A), reaction temperature (B) and reaction time (C). The range used for the molarity of ethanolic KOH was 1.0 M to 2.5 M, the range for reaction temperature was 50 to 70 °C and the

range for reaction time was 0.5 to 2.5 h as shown in Table 1. The implementation of hydrolysis reaction based on D-optimal design in response surface methodology has generated 20 runs randomly for the hydrolysis of sunflower oil (SFO). Each experiment was carried out according to the parameter conditions set by the design model to obtain the responses, which were percentage yield and percentage FFA of SFOFAs. A regression coefficient R^2 was used to evaluate the model's adequacy and best fit [21].

Table 1. Parameter and level for D-optimal design of hydrolysis

Parameter	Unit	Symbol	Variable Level		
			-1	0	+1
Molarity ethanolic KOH	M	A	1.0	1.75	2.5
Temperature	°C	B	50	60	70
Time	h	C	0.5	1.5	2.5

Determination of percentage free fatty acids

Percentage of free fatty acids (FFA) were determined based on the study by Japir et al. [22]. 0.5 gram of oil sample was weighted, and 50 mL of neutralized isopropyl alcohol was added into the conical flask. The mixture was heated up to 40 °C until it fully dissolved. Then, 1 mL of indicator (phenolphthalein) was added to the mixture. Next, the mixture was titrated with 0.1N NaOH until light pink color appeared. The percentage FFAs as oleic acid was calculated using equation (2) below:

$$\%\ FFA\ as\ Oleic\ Acid = \frac{28.2\ x\ N\ x\ V}{W} \quad (2)$$

Where N is normality of NaOH (Eq/L); V is volume of NaOH solution used (mL); and W is weight of oil sample (g).

Verification of the model

The fitness of the constructed model was evaluated by comparing the actual values of the SFOFAs yield and SFOFAs FFA at optimum conditions with the predicted values. The model was validated using the value of Residual Standard Error (RSE), where the value cannot exceed more than 5% [17]. The percentage of RSE was calculated using equation (3).

$$\%\ RSE = \frac{(actual\ value - predicted\ value)}{predicted\ value}\ x\ 100 \quad (3)$$

Structure analysis of sunflower oil and sunflower oil fatty acids

Fourier Transform infrared spectroscopy (FTIR) and Nuclear Magnetic Resonance (NMR) were used to determine the functional groups and identify the structure of SFO and SFOFAs, respectively. Perkin Elmer Infrared spectrometer was used for FTIR in the range of 650 to 4000 cm^{-1}. NMR analysis was carried out using a JOEL-ECP 400 spectrometer at 400 MHz (^{1}H NMR) and 100.61 MHz (^{13}C NMR) and deuterated chloroform ($CDCl_3$) was used as a solvent.

Results and Discussion

Hydrolysis of sunflower oil

The hydrolysis of SFO with ethanolic KOH produced SFOFAs. The aim of this optimization is to produce a high percentage yield and high percentage FFA of SFOFAs. Table 2 shows the tabulated 20 experimental runs with results for both actual and predicted responses, namely the percentage yield of SFOFAs annotated as Y_1 and the percentage of FFA of SFOFAs annotated as Y_2 based on the conditions that have been generated from D-optimal design. The actual response values are almost equal to the predicted response values.

Table 2. Experimental runs, factors and responses of SFOFAs from D-optimal design

Run	Factors			Responses			
	Molarity Ethanolic KOH (M)	Reaction Temp. (°C)	Reaction Time (h)	Yield, Y_1 (%)		FFA, Y_2 (%)	
				Actual	Predicted	Actual	Predicted
1	1.7	50	1.60	95.81	95.08	100.03	100.28
2	1.0	57	2.50	82.70	82.36	88.93	88.58
3	2.4	60	0.59	89.91	91.07	96.16	98.01
4	1.7	61	1.91	91.02	91.79	96.39	98.18
5	1.7	61	0.53	90.53	91.51	97.60	97.72
6	2.5	70	0.50	86.01	85.95	92.59	92.28
7	1.0	50	0.50	84.38	85.64	91.08	92.85
8	1.7	61	0.53	94.48	91.51	99.98	97.72
9	2.5	50	2.50	88.14	88.68	96.03	96.56
10	1.7	50	1.60	95.73	95.08	101.54	100.28
11	1.0	57	1.39	88.31	87.44	96.70	94.79
12	2.0	70	2.50	88.00	87.35	95.75	94.64
13	2.5	61	1.60	90.76	90.04	99.39	98.33
14	1.0	70	2.50	86.19	86.67	93.44	94.49
15	2.0	70	2.50	88.03	87.35	95.44	94.64
16	1.0	70	1.25	90.79	90.24	99.12	98.51
17	2.5	61	1.60	90.32	90.04	97.79	98.33
18	1.8	70	1.20	91.70	93.04	97.79	99.32
19	1.7	61	1.91	89.64	91.79	97.12	98.18
20	2.5	50	0.50	96.37	96.18	104.1	103.26

Model selection is made based on the highest polynomial order in which all terms are significant, and the model is not an alias. Table 3 and Table 4 show sequential model sum of squares of percentage yield and percentage FFA. By examining the sum of squares of the model for both response variables indicates that the quadratic model stands out. This is evident from the highest F-values observed, which are 18.61 for Y_1 and 9.89 for Y_2, as well as the lowest p-values recorded, specifically 0.0002 for Y_1 and 0.0024 for Y_2. The model's F-value indicates the superior explanatory capability of the research model for both response variables.

Table 3. Sequential model sum of squares of percentage yield response

Source	Sum of Squares	dF	Mean Square	*F*-value	*p*-value model	
Mean vs Total	1.618E+05	1	1.618E+05			
Linear vs Mean	62.63	3	20.88	1.67	0.2128	
2FI vs Linear	42.48	3	14.16	1.17	0.3586	
Quadratic vs 2FI	**133.33**	**3**	**44.44**	**18.61**	**0.0002**	**Suggested**
Cubic vs Quadratic	15.03	5	3.01	1.70	0.2877	Aliased
Residual	8.85	5	1.77			
Total	1.620E+05	20	8102.50			

Table 4 . Sequential model of sum square of percentage FFA response

Source	Sum of Squares	dF	Mean Square	*F*-value	*p*-value model	
Mean vs Total	1.876E+05	1	1.876E+05			
Linear vs Mean	53.34	3	17.78	1.53	0.2442	
2FI vs Linear	68.04	3	22.68	2.51	0.1044	
Quadratic vs 2FI	**87.86**	**3**	**29.29**	**9.89**	**0.0024**	**Suggested**
Cubic vs Quadratic	24.04	5	4.81	4.32	0.0671	Aliased
Residual	5.57	5	1.11			
Total	1.878E+05	20	9391.57			

Model selection is also made based on the non-significant lack of fit value. Table 5 and Table 6 show lack of fit tests for percentage yield and percentage FFA. The value for lack of fit analysis is opposite to the value of the sequential analysis of the sum of squares where the lack of fit analysis gives the smallest F-value and the largest p-value or is not significant (>0.05) Based on the analysis of lack of fit, it shows that the quadratic model is the suitable model for the both responses based on the non-significant p-values.

Table 5. Lack of Fit Tests for percentage yield

Source	Sum of Squares	dF	Mean Square	F-value	p-value model	
Linear	190.85	11	17.35	9.80	0.0104	
2FI	148.37	8	18.55	10.47	0.0096	
Quadratic	**15.03**	**5**	**3.01**	**1.70**	**0.2877**	**Suggested**
Cubic	0.0000	0				Aliased
Pure error	8.85	5	1.77			

Table 6. Lack of Fit Tests for percentage FFA

Source	Sum of Squares	dF	Mean Square	*F*-value	*p*-value model	
Linear	179.94	11	16.36	14.69	0.0041	
2FI	111.90	8	13.99	12.56	0.0064	
Quadratic	**24.04**	**5**	**4.81**	**4.32**	**0.0671**	**Suggested**
Cubic	0.0000	0				Aliased
Pure error	5.57	5	1.11			

Figure 2 shows the actual and predicted value of percentage yield (a) and percentage FFA (b) of SFOFAs. It shows that the plot is scattered along the straight regression line. The normal probability plot proves the accuracy of the individual experimental done.

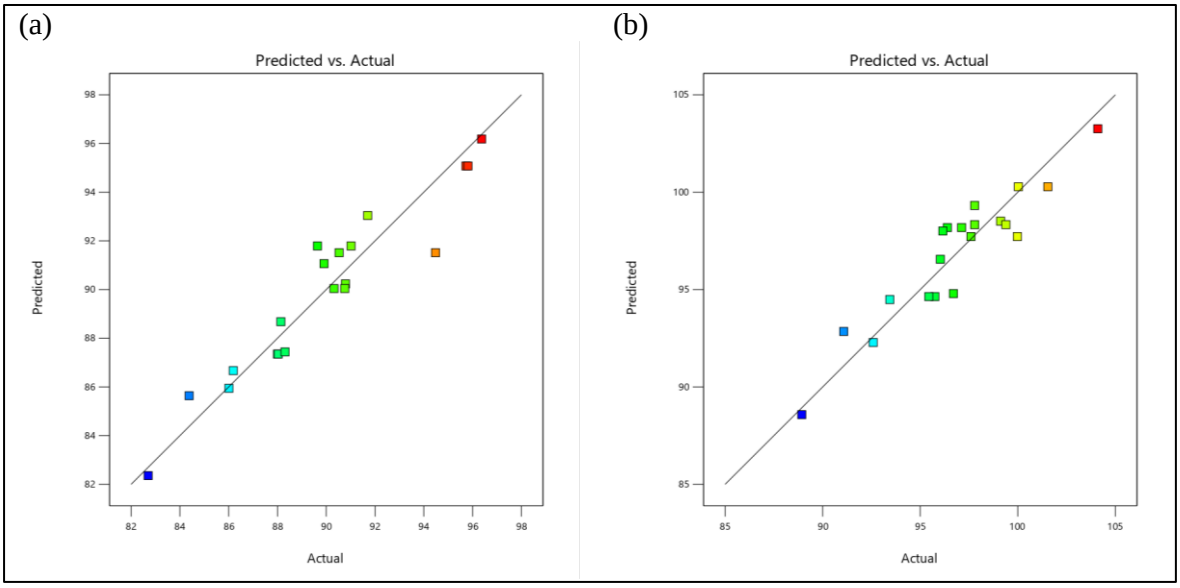


Figure 2. Actual and predicted value for a) SFOFAs yield and b) SFOFAs FFA

D-optimal design fitting

The ANOVA data analysis for percentage yield and percentage FFA of SFOFAs are shown in Table 7. The SFOFAs yield (Y_1) and SFOFAs FFA (Y_2) with p-values of 0.0004 (Y_1) and 0.0017 (Y_2), which are less than 0.05, indicate that the model for both responses are significant. The model F-values of 11.09 (Y_1) and 7.85 (Y_2) imply the model is also significant. Based on the F-values, there are only a 0.04% (Y_1) and 0.17% (Y_2) chances that an F-value this large could occur due to noise. The R^2 value for Y_1 is 0.91 and for Y_2 is 0.88. The model shows an adequate precision ratio of 12.6511 for Y_1 and 12.0673 for Y_2. Both adequate precision for Y_1 and Y_2 are desirable, which imply an adequate signal due to the value are greater than 4. Furthermore, the lack of fit for both Y_1 (0.2877) and Y_2 (0.0671) are not significant with p-value more than 0.05 which indicates that the model is satisfactorily fitting. The equation for regression line that are suggested by the model design for percentage yield of SFOFAs (Y_1) and percentage FFA of SFOFAs (Y_2) are shown in equation (4) and (5).

$$\text{Yield } (Y_1) = 93.35 + 1.52A - 1.28B - 1.96C - 2.90AB - 4.11A^2 - 3.58C^2 \quad (4)$$

$$\text{FFA } (Y_2) = 99.70 + 1.81A - 1.89C - 3.37AB - 2.56A^2 - 3.72C^2 \quad (5)$$

ANOVA analysis from the Table 7 shows for the Y_1, the linear relationship between three variable parameters which are the molarity ethanolic KOH (A) and the reaction temperature (B) are significant (p-value < 0.05) and the reaction time (C) is highly significant (p-value < 0.01). The interaction between the three parameters (AB, AC, BC) has been seen to be highly significant for AB (p-value < 0.01) but the interaction between AC and BC are not significant (p-value > 0.05). For Y_2, the linear relationship between parameters A, B and C shows that A and C are highly significant (p-value < 0.01) while B is not significant (p-value > 0.05). The interaction between AB, AC and BC shows that only AB is highly significant while AC and BC are not significant. For both Y_1 and Y_2, only the interaction between molarity ethanolic KOH (A) and reaction temperature (B) gives an effect in this optimization of hydrolysis.

Response surface analysis

The interaction effect between the reaction variables (A, B and C) on the percentage yield and percentage FFA of SFOFAs can be illustrated by using 3D response

surfaces and contour graphs. Figure 3 shows the interaction effect between ethanolic KOH molarity and reaction temperature (AB) on SFOFAs yield and SFOFAs FFA. Figure 3(a) shows that as the molarity of ethanolic KOH increases from 1 to 1.7 M, the percentage yield increases, but the percentage yield decreases as the molarity of ethanolic KOH increases from 1.7 to 2.5 M. As the temperature increases from 50 to 70°C, the percentage yield decreases. Increasing the molarity of ethanolic KOH and temperature cause the percentage yield to decrease. High temperatures can cause the breaking down of molecules (thermal degradation) and using high concentration of ethanolic KOH can lead to additional unwanted reactions, like excessive saponification. Figure 3(b) shows that the higher the molarity of ethanolic KOH and the reaction temperature, the lower the percentage of FFA. The 3-D surface contour has illustrated the maximum for both SFOFAs yield (Y_1) and SFOFAs FFA (Y_2) can be reached at a lower level of 50°C reaction temperature, and at the upper level of 2.3 M for molarity of ethanolic KOH.

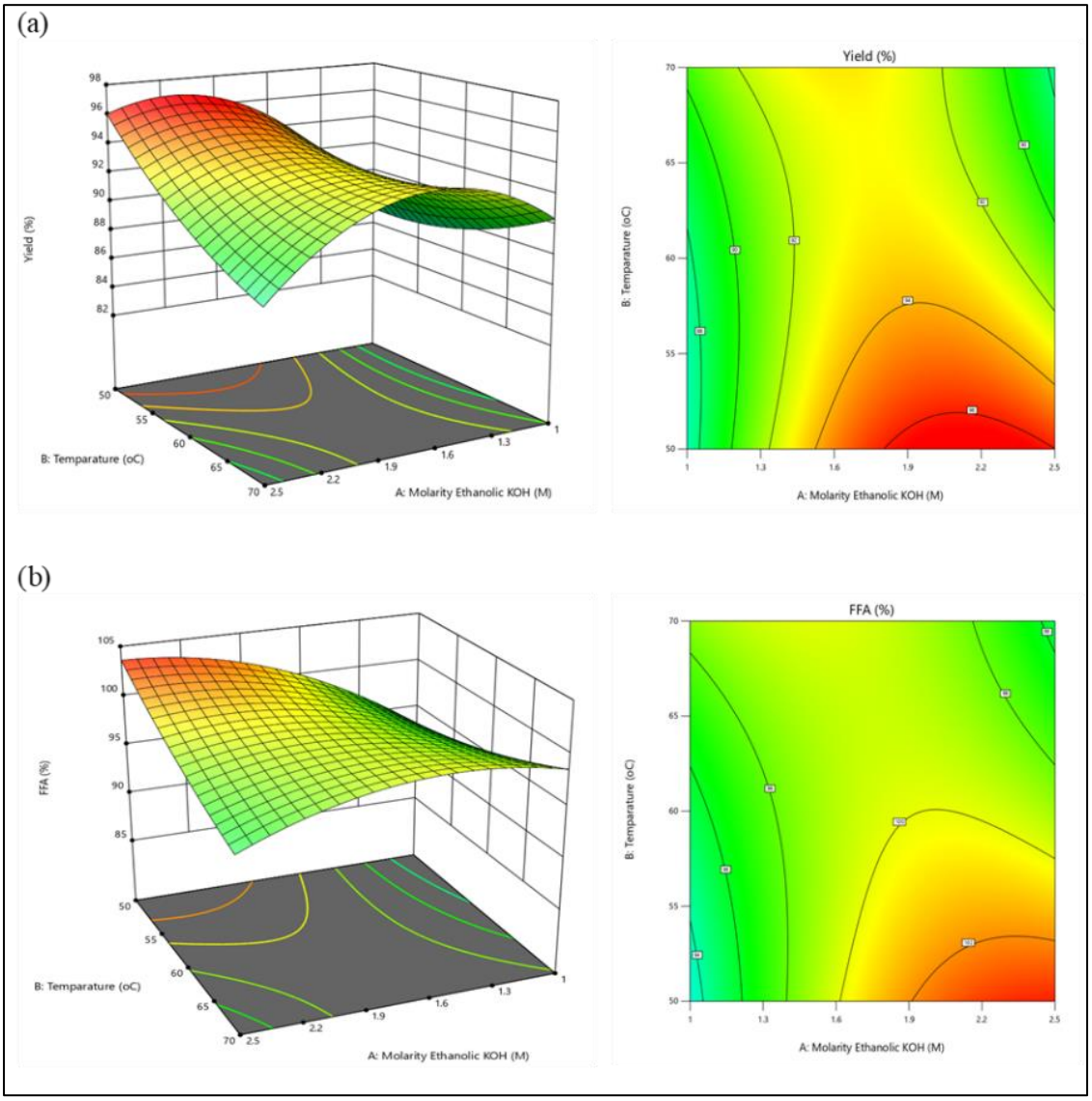


Figure 3. 3D surface and contour plot of molarity ethanolic KOH vs reaction time (AB) for a) percentage yield and b) percentage FFA

D-optimal design model verification

The numerical optimization was carried out to determine the optimum condition for hydrolysis of sunflower oil. The parameters A, B and C have been set in range to obtain the maximum percentage yield and percentage FFA of SFOFAs. The higher the desirability of the functions, the more accurate the model. Table 8 summarizes the limitation applied to obtain the optimum condition setting for higher percentage yield and higher percentage FFA of SFOFAs. The parameters A, B and C were set in a range while the responses were set at the maximum value. The desirability of the predicted model is equal to 1.00, which indicates that the model gives the ideal value. Figure 4 shows the estimated prediction from the numerical optimization model for hydrolysis of SFO.

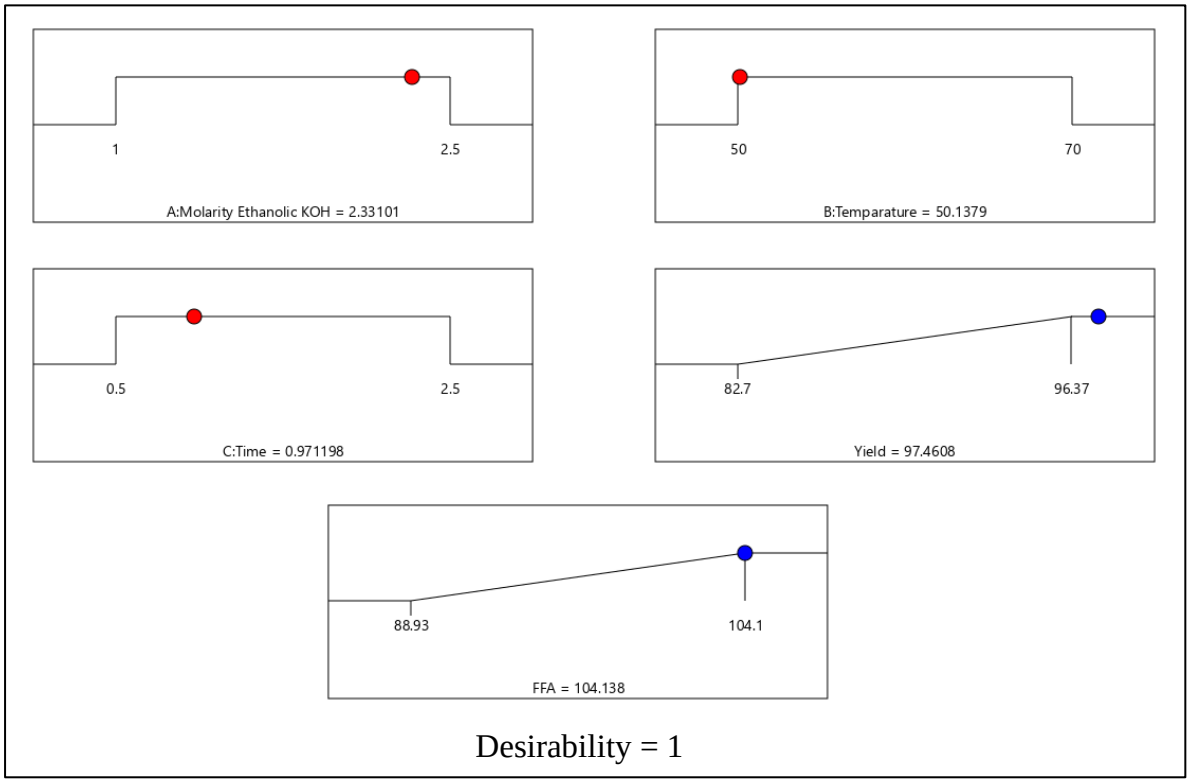


Figure 4. D-optimal predicted model at optimum condition for the hydrolysis of SFO

The suitability of the model generated from D-optimal design has been proven and verified by carrying out the hydrolysis process from three sets of reaction conditions that were chosen randomly. The actual and predicted value was compared by calculating the Residual Standard Error (RSE) value for each experiment and was only accepted if the value did not exceed 5%. The result from the Table 9 shows that all RSE values are less than 5%, indicating that this model is acceptable.

The predicted optimum condition from D-optimal design for hydrolysis of SFO was successfully acquired at 2.3 M of molarity ethanolic KOH, reaction temperature of 50.14 °C for 0.97 hour. Under this reaction condition, 96.68% SFOFAs yield with 103.23% of SFOFAs FFA were obtained. Table 10 shows the actual and predicted data for optimum condition. The validation of the optimum condition has been done with the RSE calculated, showing that the value was less than 5% where 0.80% for SFOFAs yield and 0.87% for SFOFAs FFA.

Table 7. ANOVA analysis data and regression model for hydrolysis of SFO

Responses	ANOVA Value	Model	Factor and Their Interaction									Lack of Fit
			A	B	C	AB	AC	BC	A^2	B^2	C^2	
Yield	Sum of Squares	238.44	23.20	16.19	37.05	46.96	4.09	5.28	67.68	4.76	43.86	15.03
	df	9	1	1	1	1	1	1	1	1	1	5
	Mean Square	26.49	23.20	16.19	37.05	46.96	4.09	5.28	67.68	4.76	43.86	3.01
	F-value	11.09	9.71	6.78	15.51	19.66	1.71	2.21	28.33	1.99	18.36	1.70
	p-value	0.0004	0.0109	0.0263	0.0028	0.0013	0.2198	0.1679	0.0003	0.1885	0.0016	0.2877
	Status	***	**	**	***	***			***		***	
	R^2 = 0.9089, Adequate Precision = 12.6511											
FFA	Sum of Squares	209.25	32.78	4.68	34.56	63.43	0.0047	12.21	26.15	1.57	47.16	24.04
	df	9	1	1	1	1	1	1	1	1	1	5
	Mean Square	23.25	32.78	4.68	34.56	63.43	0.0047	12.21	26.15	1.57	47.16	4.81
	F-value	7.85	11.07	1.58	11.67	21.43	0.0016	4.12	8.84	0.5311	15.93	4.32
	p-value	0.0017	0.0076	0.2370	0.0066	0.0009	0.9689	0.0697	0.0140	0.4828	0.0026	0.0671
	Status	***	***		***	***			**		***	
	R^2 = 0.8761, Adequate Precision = 12.0673											

Note: A = Molarity ethanolic KOH; B = Reaction temperature; C = Reaction time; *** = Highly significant ($p<0.01\%$); ** = Significant ($p<0.05\%$)

Table 8. Restraints for optimization of hydrolysis of SFO parameter and responses for RSM

Parameter and Responses	Goal	Lower Limit	Upper Limit	Weight	Importance
A: Molarity ethanolic KOH	in range	1.0	2.5	1	3
B: Reaction temperature	in range	50.0	70.0	1	3
C: Reaction time	in range	0.5	2.5	1	3
Yield of SFOFAs	maximize	82.7	96.37	1	3
FFA of SFOFAs	maximize	88.93	104.1	1	3

Table 9. Actual and predicted data for verification model

Molarity Ethanolic KOH (M)	Reaction Temp. (°C)	Reaction Time (h)	Yield of SFOFAs (%)			FFA of SFOFAs (%)		
			Actual	Predicted	RSE	Actual	Predicted	RSE
2.2	55.0	1.5	92.35	94.5618	2.34	100.73	110.371	0.63
2.1	65.0	2.0	89.72	90.28	0.62	98.11	97.4848	0.64
1.9	69.0	2.1	90.67	97.63	0.04	97.27	97.5302	0.27

Table 10. Actual and predicted data for optimum condition

Molarity Ethanolic KOH (M)	Reaction Temp. (°C)	Reaction Time (h)	Yield of SFOFAs (%)			FFA of SFOFAs (%)		
			Actual	Predicted	RSE	Actual	Predicted	RSE
2.3	50.14	0.97	96.68	97.461	0.80	103.23	104.138	0.87

Comparison between current work and existing literature

Increasing temperature leads to a general acceleration of the hydrolysis rate due to heightened kinetic energy in molecules. Elevated temperatures facilitate more robust collisions between oil and hydroxide (OH) molecules, thereby promoting the cleavage of ester bonds within the oil [23]. Similarly, extending the reaction time also results in a higher yield of hydrolysis. The molarity of the catalyst plays a pivotal role in enhancing the hydrolysis yield. Elevating the catalyst's molarity increases the yield of hydrolysis by providing an alternative reaction pathway with lower activation energy. The outcomes of the experiment revealed a percentage yield of 96.68% for SFOFAs, accompanied by a 103.23% of free fatty acids (FFA) from SFOFAs, achieved under optimal conditions. These optimal conditions encompassed a molarity of 2.3 M for molarity of ethanolic KOH, a reaction temperature of 50.14°C, and a reaction duration of 0.97 hours. By comparison, the study contrasted with previous findings, **by** Bahadi et al. [4] wherein the yield of palm kernel oil was 84.7%, accompanied by a 98% percentage of free fatty acids, realized under optimal conditions of 2.16 hours, a temperature of 70°C, and a molarity of 1.77 M ethanolic KOH. Notably, the temperature and reaction duration in the present experiment were observed to be lower than those of the referenced study. This discrepancy can be attributed to the utilization of a higher molarity of ethanolic KOH in the current study compared to the study conducted by [4]. This distinction underscores the influence of elevated ethanolic KOH molarity in effecting a reduction in both reaction temperature and duration for the hydrolysis process.

FTIR analysis of SFO and SFOFAs

FTIR spectroscopy was used to determine the functional groups in SFO and SFOFAs before and after hydrolysis. Figure 5 shows the FTIR spectra of SFO and SFOFAs and Table 7 shows the functional group and wavenumber of SFO and SFOFAs FTIR spectra. Before hydrolysis (SFO), a sharp peak appeared at 1746.33 cm^{-1} indicating stretching vibration for C=O (ester carbonyl). After hydrolysis (SFOFAs), the peak for C=O (ester carbonyl) has disappeared, and a new sharp peak appeared at 1710.23 cm^{-1} indicating stretching vibration for C=O (carboxylic acid) and broad OH peak for COOH appeared at range 2400 to 3400 cm^{-1} which showed hydrolysis has successfully converted the ester to carboxylic acid.

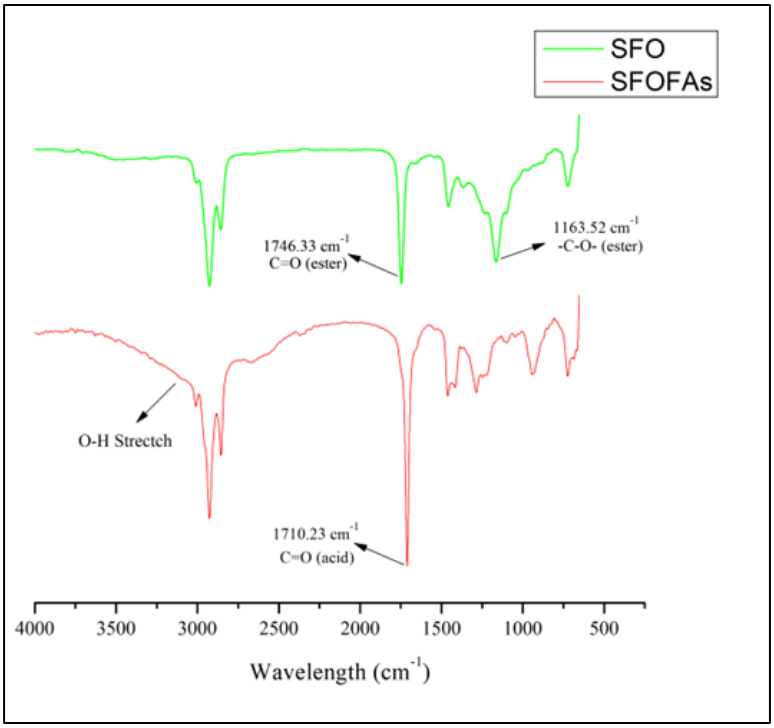


Figure 5. FTIR spectra of SFO and SFOFAs

Table 11. Functional group and wavenumber of FTIR spectra of SFO and SFOFAs

Functional Group	Wavenumber (cm^{-1})	
	SFO	SFOFAs
OH stretching (carboxylic acid)	-	2400-3400
C=C bending vibration (aliphatic)	3007.93	3007.93
C-H stretching vibration (aliphatic)	2926.56, 2857.78	2926.93, 2856.16
C=O stretching vibration (ester)	1746.33	-
C=O stretching vibration (carboxylic acid)	-	1710.23
-C-O stretching vibration (ester)	1232.81, 1163.52	-
-C-O stretching vibration (carboxylic acid)	-	1292.04, 1249.00

NMR analysis of SFO and SFOFAs

NMR has been used to elucidate the structure of SFO and SFOFAs. Figure 6 shows the ^{1}H NMR spectra of SFO and SFOFAs and ^{1}H NMR chemical shift of SFO and SFOFAs represented in Table 8. There are three peaks that have been focused on to determine whether the ester is successfully converted to fatty acid. From the ^{1}H NMR spectrum of SFO, two important peaks appeared at the range of 4.14-4.18 ppm and 4.29-4.33 ppm that signified the presence of -CH_2-COOR- and -CH-COOR- respectively. These two peaks represented proton from glycerol backbone in SFO and these two peaks diminished in ^{1}H NMR spectrum of SFOFAs indicating the hydrolysis process was successfully carried out. New peak appeared at downfield region around 10.61 ppm in ^{1}H NMR spectrum of SFOFAs, which confirmed the formation of fatty acid (-COOH) in SFOFAs. Since both SFO and SFOFAs dissolved in deuterated chloroform ($CDCl_3$), the solvent peak appeared at 7.28 ppm. Another type of proton has been tabulated in Table 8.

^{13}C NMR spectra and chemical shift of SFO and

SFOFAs were shown in Figure 7 and Table 9, respectively. There are several prominent peaks at 62.09 ppm (-CH_2-O), 68.90 ppm (-CH-O) and 172.79-173.21 ppm (O=C-OR) from SFO spectrum and peak at 180.45 (O=C-OH) from SFOFAs spectrum. Carbon for -CH_2-O- and -CH-O comes from the glycerol backbone in SFO. These two peaks disappeared at SFOFAs spectrum showing that the glycerol backbone had been removed. Peak at 172.79-173.21 ppm corresponding to O=C-OR ester had shifted to downfield region at peak 180.45 ppm corresponding to carboxylic acid in SFOFAs spectrum showing ester had been converted to fatty acid. Solvent peak ($CDCl_3$) was determined at 76.71-77.36 ppm. Table 7 shows another type of carbon present in SFO and SFOFAs. Chemical shift for peaks obtained for ^{1}H NMR and ^{13}C NMR are in a good agreement with the theoretical values.

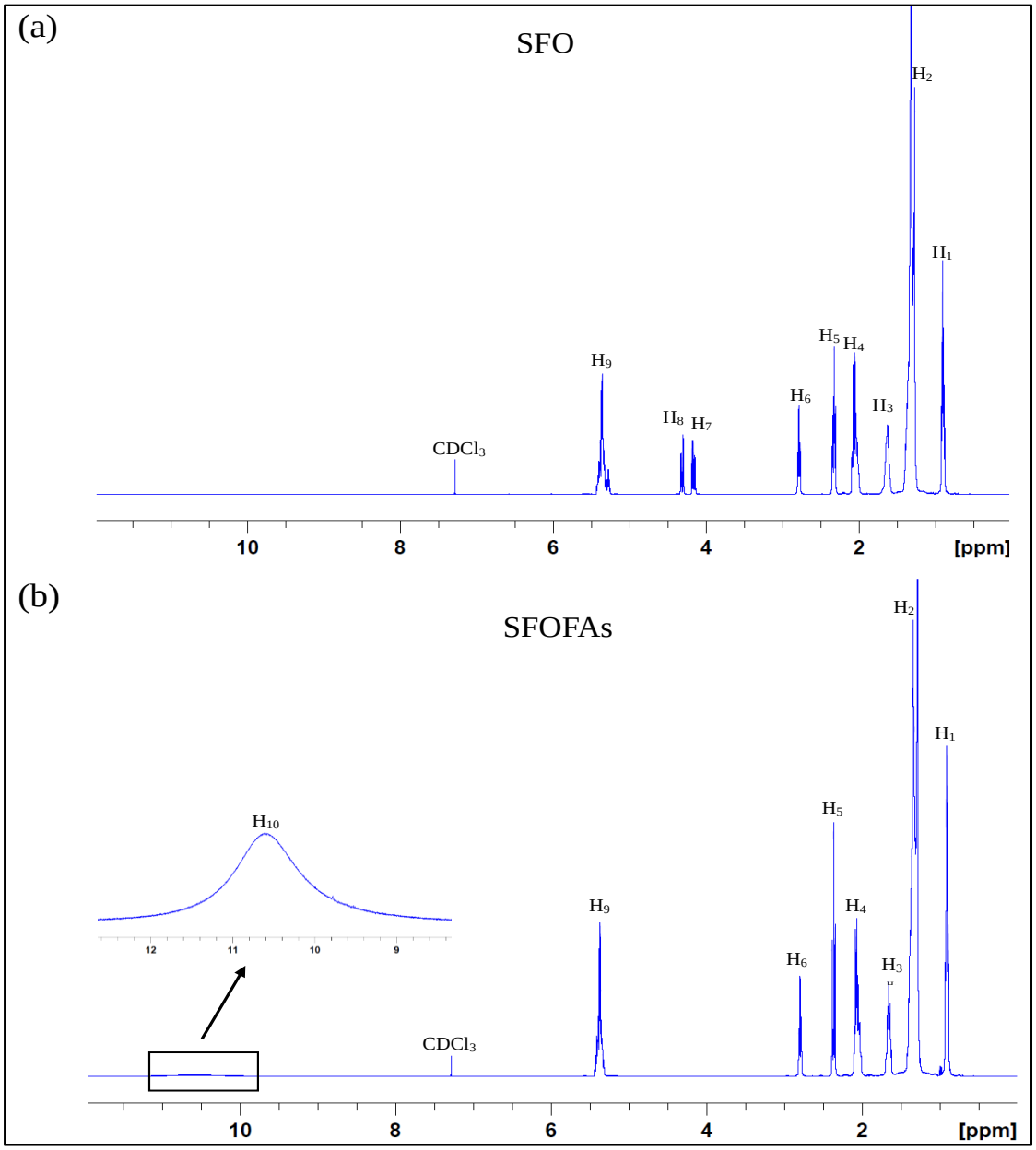


Figure 6. ^{1}H NMR spectra for a) SFO and b) SFOFAs

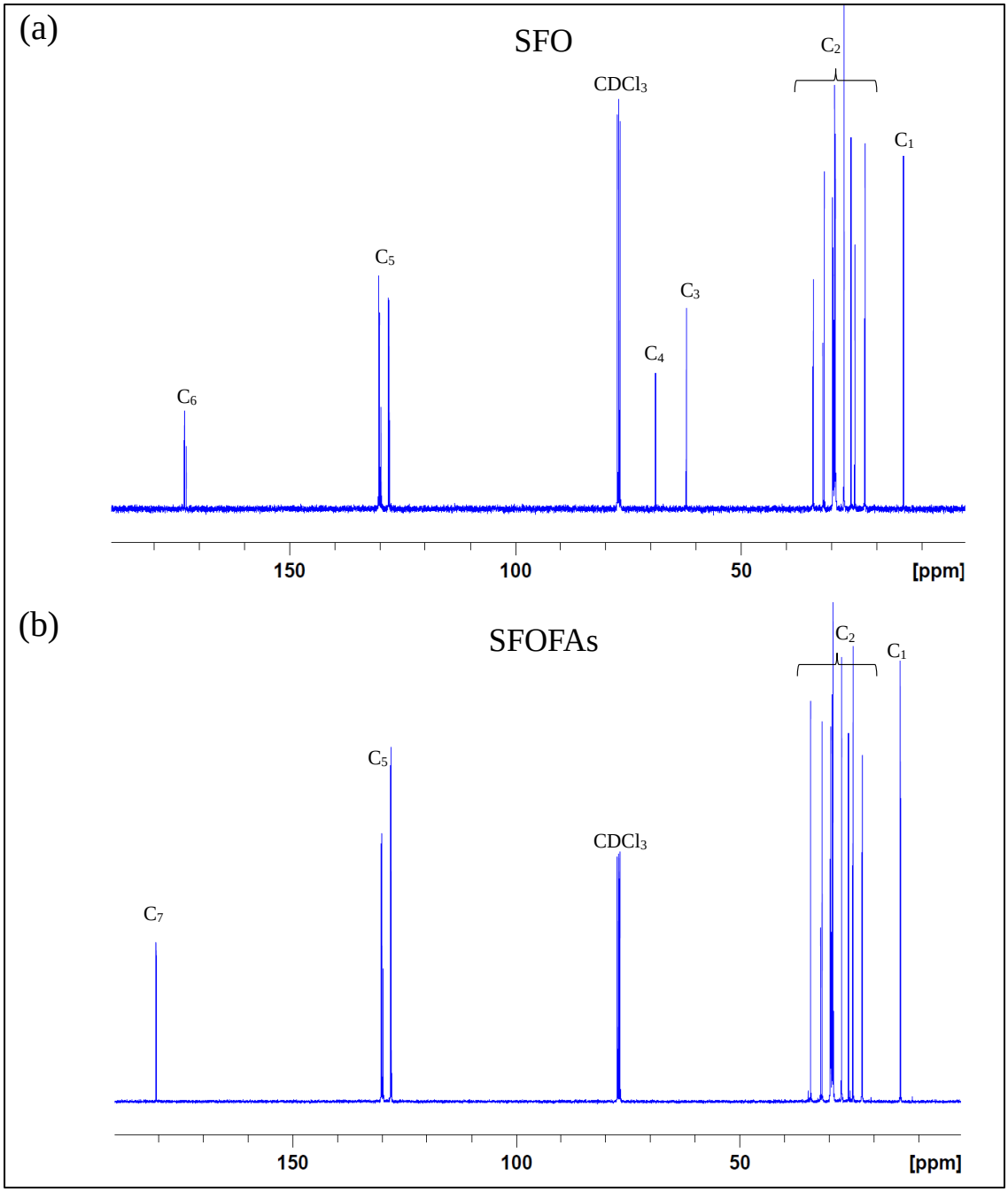


Figure 7. ^{13}C NMR spectra for a) SFO and b) SFOFAs

Table 12. Chemical shift of ^{1}H NMR spectra of SFO and SFOFAs

	Type of Proton	Chemical Shift (ppm)		
		SFO	SFOFAs	Theoretical*
H_1	-C**H**$_3$	0.88-0.92	0.89-0.93	0.70-1.3
H_2	-C**H**$_2$-	1.29-1.41	1.29-1.40	1.2-1.4
H_3	O=C-CH$_2$-C**H**$_2$-	1.61-1.63	1.64-1.68	1.5-2.0
H_4	-CH=CH-C**H**$_2$-	2.00-2.09	2.03-2.10	1.6-2.6
H_5	O=C-C**H**$_2$-	2.30-2.35	2.35-2.38	2.1-2.5
H_6	=CH-C**H**$_2$-CH=	2.77-2.80	2.78-2.81	2.5-3.0
H_7	-C**H**$_2$-COOR- (glycerol)	4.14-4.18	-	4.0-4.5
H_8	-C**H**-COOR- (glycerol)	4.29-4.33	-	4.0-4.5
H_9	-C**H**=CH-	5.28-5.41	5.34	4.5-6.5
H_{10}	COO**H**	-	10.61	10-12

*[24, 25]

Table 13. Chemical shift of ^{13}C NMR spectra of SFO and SFOFAs

	Type of Carbon	Chemical Shift (ppm)		
		SFO	SFOFAs	Theoretical*
C_1	-**C**H$_3$	14.05-14.09	14.02	8-30
C_2	-**C**H$_2$-	22.56-34.18	22.65-34.10	15-55
C_3	-**C**H$_2$-O (glycerol)	62.09	-	40-80
C_4	-**C**H-O (glycerol)	68.90	-	40-80
C_5	-**C**=C-	127.90-130.20	127.90-130.17	65-90
C_6	O=**C**-OR (ester)	172.79-173.21	-	155-185
C_7	O=**C**-OH (carboxylic acid)	-	180.45	155-185

*[24]

Conclusion

The hydrolysis process of sunflower oil with ethanolic KOH was successfully carried out to produce the sunflower oil fatty acids. The process responses of SFOFAs yield and SFOFA FFA were improved during the optimization process using D-optimal design from response surface methodology. The optimum condition for hydrolysis of SFO was successfully acquired at 2.3 M of molarity ethanolic KOH, reaction temperature of 50.14 °C for 0.97 hour and produced 96.68% yield with 103.23% of FFA. The RSE value of less than 5% indicates that the model design produced was suitable.

Acknowledgement

The authors would like to express their gratitude to the Universiti Teknologi MARA (UiTM) for the project funding under research grant MyRA Lepasan PhD (LPhD) (600-RMC/GPM LPHD 5/3 (177/2021)).

References

1. Fernandes, K. V., Papadaki, A., da Silva, J. A. C., Fernandez-Lafuente, R., Koutinas, A. A., and Freire, D. M. G. (2018). Enzymatic esterification of palm fatty-acid distillate for the production of polyol esters with biolubricant properties. *Industrial Crops and Products,* 116(2): 90-96.
2. Sharma, A., Sharma, P., Sharma, A., Tyagi, R., and Dixit, A. (2017). Hazardous Effects of petrochemical industries: A review. *Recent Advances in Petrochemical Science,* 3(2): 25-27.
3. Katopodis, T., and Sfetsos, A. (2019). A review of climate change impacts to oil sector critical services and suggested recommendations for industry uptake. *Infrastructures,* 4(4): 74.
4. Bahadi, M., Yusoff, M. F., Salimon, J., and Derawi, D. (2020). Optimization of response surface methodology by d-optimal design for alkaline hydrolysis of crude palm kernel oil. *Sains Malaysiana,* 49(1): 29-41.

5. Hasanuddin, N. I., Dzulkifli, N. N., Sarijo, S. H., and Ghazali, S. A. I. S. M. (2020). Physicochemical characterization and controlled release formulation on intercalated 2-methyl-4-chlorophenoxy acetic acid-graphite oxide (MCPA-GO) nanocomposite. *Indonesian Journal of Chemistry,* 20(2): 299-306.
6. Pawar, R. V., Hulwan, D. B., and Mandale, M. B. (2022). Recent advancements in synthesis, rheological characterization, and tribological performance of vegetable oil-based lubricants enhanced with nanoparticles for sustainable lubrication. *Journal of Cleaner Production,* 378(9): 134454.
7. Hermansyah, H., Kubo, M., Shibasaki-kitakawa, N., and Yonemoto, T. (2006). Mathematical model for stepwise hydrolysis of triolein using *Candida rugosa* lipase in biphasic oil – water system. *Biochemical Engineering Journal,* 31: 125-132.
8. Salimon, J., Abdullah, B. M., and Salih, N. (2011). Hydrolysis optimization and characterization study of preparing fatty acids from Jatropha curcas seed oil. *Chemistry Central Journal,* 5(67): 1-9.
9. Samidin, S., Salih, N., and Salimon, J. (2021). Synthesis and characterization of trimethylolpropane based esters as green biolubricant basestock. *Biointerface Research in Applied Chemistry,* 11(5): 13638-13651.
10. Nor, N. M., Salih, N., and Salimon, J. (2022). Optimization and lubrication properties of Malaysian crude palm oil fatty acids based neopentyl glycol diester green biolubricant. *Renewable Energy,* 200(8): 942-956.
11. Wai, P. T., and Jiang, P. (2019). Catalytic developments in the epoxidation of vegetable oils and the analysis methods of epoxidized products. *RSC Advances,* 9(65): 38119-38136.
12. Salimon, J., Abdullah, B. M., and Salih, N. (2012). D-optimal design optimization of *Jatropha curcas* L. seed oil hydrolysis via alkali-catalyzed reactions. *Sains Malaysiana,* 41(6): 731-738.
13. Nor, N. M., Derawi, D., and Salimon, J. (2019). Esterification and evaluation of palm oil as biolubricant base stock. *Malaysian Journal of Chemistry,* 21(2): 28-35.
14. Ferreira, M. M., de Oliveira, G. F., Basso, R. C., Mendes, A. A., and Hirata, D. B. (2019). Optimization of free fatty acid production by enzymatic hydrolysis of vegetable oils using a non-commercial lipase from *Geotrichum candidum*. *Bioprocess and Biosystems Engineering,* 42(10): 1647-1659.
15. Anand, A., and Weatherley, L. R. (2018). The performance of microbial lipase immobilized onto polyolefin supports for hydrolysis of high oleate sunflower oil. *Process Biochemistry,* 68: 100-107.
16. Primožič, M., Habulin, M., and Knez, Ž. (2003). Parameter optimization for the enzymatic hydrolysis of sunflower oil in high-pressure reactors. *Journal of the American Oil Chemists' Society,* 80(7): 643-646.
17. Zakaria, F., Tan, J. K., Mohd Faudzi, S. M., Abdul Rahman, M. B., and Ashari, S. E. (2021). Ultrasound-assisted extraction conditions optimisation using response surface methodology from *Mitragyna speciosa* (Korth.) Havil leaves. *Ultrasonics Sonochemistry,* 81: 105851.
18. Salimon, J., Abdullah, B. M., and Salih, N. (2016). Optimization of the oxirane ring opening reaction in biolubricant base oil production. *Arabian Journal of Chemistry,* 9: S1053-S1058.
19. Nor, N. M., Derawi, D., and Salimon, J. (2018). The optimization of RBD palm oil epoxidation process using D-optimal design. *Sains Malaysiana,* 47(7): 1359-1367.
20. Japir, A. A. W., Salimon, J., Derawi, D., Yahaya, B. H., Bahadi, M., Al-Shuja'A, S., and Yusop, M. R. (2018). A highly efficient separation and physicochemical characteristics of saturated fatty acids from crude palm oil fatty acids mixture using methanol crystallisation method. *OCL - Oilseeds and Fats, Crops and Lipids, 25*(2): 203.
21. Borugadda, V. B., and Goud, V. V. (2015). Response surface methodology for optimization of bio-lubricant basestock synthesis from high free fatty acids castor oil. *Energy Science and Engineering,* 3(4): 371-383.
22. Japir, A. A. W., Salimon, J., Derawi, D., Bahadi, M., Al-Shuja'A, S., and Yusop, M. R. (2017). Physicochemical characteristics of high free fatty acid crude palm oil. *OCL - Oilseeds and Fats, Crops and Lipids,* 24(5): 506.
23. Shah, S. A. A., Ahammad, N. A., Din, E. M. T. E.,

Gamaoun, F., Awan, A. U., & Ali, B. (2022). Bio-convection effects on prandtl hybrid nanofluid flow with chemical reaction and motile microorganism over a stretching sheet. *Nanomaterials,* 12(13): 2174.

24. Pavia, D. L., Lampman, G. M., Kriz, G. S., and Vyvyan, J. R. (2015). Introduction to spectroscopy (5th edition). Cengage Learning.
25. Chiplunkar, P. P., and Pratap, A. P. (2016). Utilization of sunflower acid oil for synthesis of alkyd resin. *Progress in Organic Coatings,* 934): 61-67.

Malaysian Journal of Analytical Sciences (MJAS)
Published by Malaysian Analytical Sciences Society

THE LATENT CYTOTOXICITY EFFICIENCY OF THE CHEMICAL CONSTITUENTS OF *Morus Rubra* LINN. BARK ON CANCER CELL LINES

(Keberkesanan Kesitotoksian Laten Bahan Kimia daripada Jujukan Kulit *Morus rubra* Linn. ke atas Titisan Sel Kanser)

Maria Carmen Tan[1*], Jasmine Ting[1], and Glenn Oyong[2]

[1]*Chemistry Department,*
De La Salle University, 2401 Taft Avenue, Manila 1004, Philippines
[2]*Molecular Science Unit Laboratory Center for Natural Sciences and Environmental Research,*
De la Salle University, 2401 Taft Avenue, Manila 1004, Philippines

**Corresponding author: maria.carmen.tan@dlsu.edu.ph*

Received: 18 April 2023; Accepted: 7 September 2023; Published: 30 October 2023

Abstract

Owing to the intricate nature of cancer treatment, traditional herbal medicines are being regarded as potential anticancer agents, primarily due to their reported low toxicity in normal cells. With this in mind, this study's primary objective was to identify the constituents present in the semi-purified 15% ethyl acetate fraction of *Morus rubra* bark (**M1**) and to investigate its antiproliferative property on immortalized cell lines (HT- 29, HepG2, BxPC-3, MCF-7, HeLa, and THP-1) by an *in vitro* cell viability assay with Zeocin and dimethylsulfoxide (DMSO) as the positive and negative controls. The chemical constituents present in **M1** were identified using gas chromatography-mass spectrometry (GC-EI-MS). The NIST library v 2.0 was used to putatively identify the thirteen (13) compounds observed in the GC-EI-MS chromatogram which were primarily tocopherols (27.58%) and phytosterols (44.06%). **M1** exhibited high cytotoxicity in HepG2 cell lines (IC_{50} = 7.09 µg/mL) and was followed by MCF-7 (IC_{50} = 7.12 µg/mL), HT-29 (IC_{50} = 7.98 µg/mL), HeLa (IC_{50} = 16.63 µg/mL), BxPC-3 (IC_{50} = 16.89 µg/mL) and THP-1(IC_{50} = 17.43 µg/mL). **M1** did not exhibit cytotoxicity on normal HDFn while Zeocin on normal cells were exceedingly disruptive. The data generated from this work suggests that **M1** could be an effective chemotherapeutic agent due to the presence of phytosterols and tocopherols.

Keywords: Moraceae, *Morus rubra*, gas chromatography-electron ionization-mass spectrometry, retention index, cell viability assays

Introduction

Mulberry, which is under the botanical order Rosales, family Moraceae, and genus *Morus*, is found in many areas of the world specifically in the sub-tropic regions of Asia such as Japan, India, China, and Korea as well as other regions, for instance North America and Africa [1]. The practice of mulberry cultivation using diverse morphological cultivars is estimated to have started around 400-500 years ago [2]. Several studies have documented the aqueous, methanolic, and ethanolic extracts of *Morus* species. The phytochemicals obtained were characterized to demonstrate several bioactivities

such as anti-oxidative, anti-diabetic, anti-stress, nephroprotective, antimicrobial, anti-mutagenic, anticancer, anxiolytic, hepatoprotective, anthelmintic, antimicrobial, immune-modulatory and cholesterol lowering effects [1].

Organic acids, sugars, flavonoids, alkaloids, steroids, some vitamins, and minerals such as Na, K, Fe, P, Mg, S were found in the extract of the *Morus* genus [2, 3]. It was also indicated that genetic, cultural, and ecological factors can influence the percentage composition of the compounds isolated from extracts of the Morus genus. Among the species under the genus, *M. nigra* (black mulberry), *M. rubra* (red mulberry), and *M. alba* (white mulberry) are the most recognized cultivated species of mulberry due to its availability and use in traditional medicines for diseases such as rheumatoid arthritis and the common cold [1].

The fruit of the mulberry species specifically *M. rubra* (purple), *M. nigra* (black) and *M. alba* (white), were found to contain higher vitamin C content for lighter colored species compared to the darkly colored species. The darkly colored berries demonstrated a higher total antioxidant capacity (TEAC) compared to the lighter colored berries due to the presence of anthocyanins. Previous reports have shown that anthocyanin pigments are medically beneficial due to their antioxidant capacity which can prevent or reduce free radical induced damage and inflammation [4-7]. Flavonoids such as rubraflavones A, B, C, and D were likewise isolated from *M. rubra*. These compounds are known to be antihyperglycemic phytochemicals which induce insulinogenic action [8, 9]. Further, the presence of phenolic acids in the fruit, such as cinnamic acid, were found to contribute to the antioxidant property of the plant and to neutralize carcinogenic substances such as nitrosamine. Among the three species, *M. nigra* exhibited the highest phenolic acid content [5, 7].

Glucopyranosides isolated from an ethanolic extract from the leaves of *M. alba* inhibited HL60 cell line proliferation and initiated an immune response which caused the differentiation in the expression of the CD66b and CD 14 antigens [7]. The rich quercetin content in the leaf of *M. alba* prevented P-glycoprotein (P-gp) production in the tumor's ATP-dependent pump which was construed to be responsible for exporting xenobiotic compounds out of the cell which may be the cause of multidrug resistance (MDR) of some aggressive malignant tumors [7].

M. rubra leaf extract's anticancer property was correlated with its ability to cause the accumulation of cells at the G1 phase via inhibitory action or through down-regulation of cyclins and kinases (CDKs)10. As a result, the said extract attenuated cell population at the S phase where DNA synthesis occurs. Additionally, *M. rubra* leaf extracts induced apoptosis by matrix metalloproteinase (MMP) depolarization in a dose-dependent manner as well as the inhibition of human telomerase reverse transcriptase (hTERT) expression, which caused the cessation of the proliferation of cancer cells [10]. *M. rubra* extract presented modest discriminating cytotoxicity on WiDr cells assessed along with foreskin fibroblast cells [11]. In fact, the aforementioned *M. rubra* extracts at 600 mg/mL dilution considerably amplified cell numbers at the G0/G1phase [11].

A study by Abbas et al. [12] reported a new stilbene, 2',3',4',5',5'-pentahydroxy-cis-stilbene isolated from the ethanol fraction which was obtained from the methanol extract of *M. nigra* stem bark. The new stilbene exhibited an effective antioxidant activity with an IC_{50} of 4.6 μM. The isolation of prenylated flavonoids from the stem bark of *M. nigra* extract from several distinct fractions (n-hexane, dichloromethane, and ethanol) was also reported. To the best of our knowledge, this is the first study aimed to provide the characterization and the investigation of the cytotoxicity on selected immortalized cell lines from a semi-purified extract prepared from the dried bark of the red mulberry species.

Materials and Methods

Plant material

M. rubra bark (Figure 1) was gathered from Abucay, Bataan, Philippines (14.7128° N, 120.4934° E) on well-cultivated arable land. The plant identity was established and validated by the Bureau of Plant Industry in Malate, Manila, Philippines.



Figure 1. Images of *Morus rubra* Linn

GC-EI-MS analysis

Dried *M. rubra* bark (3 g) was ground and extracted with methanol. The mixture was filtered using filter paper (Whatman 91) and then desolvated under nitrogen for one hour. The crude extract was reconstituted in 5% ethyl acetate in petroleum ether (PE). The resultant solution underwent separation using 5% increments of 5% ethyl acetate in PE as an eluent through column chromatography. The semi-purified fraction collected from 15% ethyl acetate in PE (2.9 mg) was then reconstituted and filtered through a syringe with a 0.45 μm nylon membrane and labeled as **M1**.

M1 was explored using an Agilent gas chromatograph-mass spectrometer (GC-MS) 7890B, by an HP-5ms (5% phenyl methyl siloxane) Ultra Inert column (30 m x 250 mm x 0.25 mm) and ultra-pure helium gas as the carrier gas to examine the vaporizable components. Helium gas constraints were stipulated using the following parameters: flow rate of helium gas was at 1 mL/min, the pressure kept at 8.2 psi, with an average velocity of 36.62 cm/sec and a holdup time of 1.37 min. The splitless inlet was conserved at 250 °C at 8.2 psi, with a total flow of 24 mL/min, and a septum purge flow speed of 3 mL/min. The injector temperature was maintained at 250 °C. The temperature gradient was initially at 70 °C with an automated linear ramp of 2 °C / min until 135 °C and was continued at this temperature for 10 minutes. Additional temperature changes were attained at 4 °C / min until 220 °C and were retained for 10 minutes. The temperature was then augmented to 270 °C at a 3.5 °C / min rate and was continuous for 37 minutes [13].

NIST library, v. 2.0 was used to identify the compounds, and the average percentage of the peak area was managed from the subsequent total ion chromatograms. The consequent data was established by assessing the analytes according to their elution succession on a non-polar stationary phase. A homologous series of *n*-alkanes was used to calculate the retention indices for each compound's entirety observed in the spectrum. The experiments were undertaken in three replicates.

Cell viability assay

The **M1** fraction obtained through the extraction technique previously described in the GCMS experiments was used for the PrestoBlue-based cytotoxicity assays on the preceding human cancer cell lines (ATCC, Manassas, Virginia, U.S.A.): colon adenocarcinoma (HT-29), hepatocarcinoma (HepG2), pancreatic adenocarcinoma (BxPC-3), breast adenocarcinoma (MCF-7), cervical adenocarcinoma (HeLa), and acute monocytic leukemia (THP-1). The primary culture of normal human dermal fibroblast neonatal (HDFn) (ThermoFisher Scientific, Gibco®, USA) was utilized as normal cell control. The cells were maintained and provided by the Cell and Tissue Culture Laboratory, Molecular Science Unit, Center for Natural Sciences and Environmental Research, De La Salle University. Cells were cultured in complete DMEM

(Dulbecco's Modified Eagle Medium with 10% fetal bovine serum and 1X antibiotic-antimycotic) (Thermo Fisher, Invitrogen, USA) and were incubated at 37°C with 5% CO_2 in a humidified chamber. The *in vitro* assays' constraints were described in our formerly published work [12] and stringently followed the protocols described therein. Zeocin (Thermo-Fisher, Invitrogen, USA), a cytotoxic intercalating agent, was used as positive control while DMSO was applied as negative vehicle control. All tests were performed in three replicates. Optical density ($O.D._{570\ nm}$) readings were utilized to determine cytotoxicity indexes, which were plotted against log concentrations from which the half-maximal inhibitory concentrations (IC_{50}) were derived. GraphPad Prism version 8.02 (GraphPad Software, Inc., USA) was applied to plot the non-linear regressions and was also employed for statistical analysis using ANOVA with Tukey's post-hoc assessment in an alpha of 0.05 level of significance.

Results and Discussion

GC-EI-MS characterization of M1 fraction

GC-EI-MS was used to identify the chemical constituents present in the 15% ethyl acetate in PE of **M1** fraction**.** As observed in the GC chromatogram, thirteen volatile components were identified and verified through the NIST library for spectral library matching and comparison of retention indices (RI) [14] (Figure 2). Identified compounds (Table 1) were listed according to their elution succession through a HP-5ms column. The **M1** fraction comprised the following constituents: tocopherols: [2R-[2R*(4R*,8R*)]]-2H-1-benzopyran-6-ol,3,4-dihydro-2,8-dimethyl-2-(4,8,12 trimethyl tetradecyl) or δ-tocopherol (3.36%), γ-tocopherol (7.40%), vitamin E (20.18%); diterpene: phytol (16.42%); diterpene acetate: phytol acetate (2.04%); and triterpenes: squalene (3.87%), γ-sitosterol (11.61%), β-amyrin (1.36%), lanosterol (3.87%), Lupeol (6.14%) and 3 β-D:B-friedo-B':A'-neogammacer-5-en-3-ol (6.81%); triterpene acetate:3β-lanosta- -8-24-dien- 3-ol acetate (9.50%) and 3 β -lup-20(29)-en-3-ol acetate (6.81%).

Major classes of compounds that were detected from the **M1** fraction included triterpenes and tocopherols, which are known to have several biochemical properties. The constituents identified from the extract are also known to exhibit cholesterol-lowering, anti-inflammatory, antibacterial, anti-ulcerative, and antiproliferative effects.

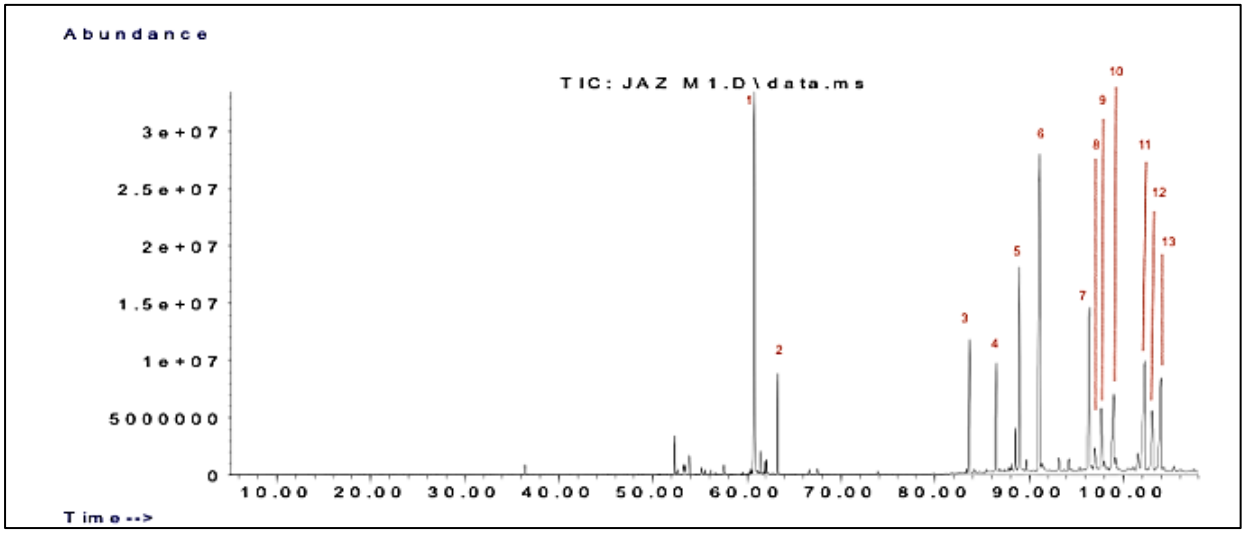


Figure 2. Total ion GCMS chromatogram of **M1**

Table 1. Constituents of **M1** fraction (15% ethyl acetate in PE)

	Compound	RT (min.)	RI[a]	% Peak Area	Functionality
1	Phytol	60.81	2117±0.25	16.42	Diterpene
2	Phytol Acetate	63.29	2119±0.00	2.04	Diterpene acetate
3	Squalene	83.62	2824±0.13	3.87	Triterpene
4	[2R-[2R*(4R*,8R*)]]-2H-1-Benzopyran-6-ol,3,4-dihydro-2,8-dimethyl-2-(4,8,12-trimethyltridecyl)/ δ-tocopherol	86.46	2837±0.26	3.36	Tocopherol
5	γ-tocopherol	88.96	2843±0.23	7.40	Tocopherol
6	Vitamin E	91.15	3429±0.51	20.18	Tocopherol
7	γ-Sitosterol	96.40	3492±0.18	11.61	Triterpene
8	β-Amyrin	97.010	3408±0.07	1.36	Triterpene
9	Lanosterol	97.69	3423±0.15	3.87	Triterpene
10	Lupeol	98.98	3453±0.20	6.14	Triterpene
11	3 β-Lanosta-8-24-dien-3-ol acetate	102.30	3425±0.23	9.50	Triterpene acetate
12	3 β-D:B-Friedo-B':A'-neogammacer-5-en-3-ol	103.08	3439±0.11	4.77	Triterpene
13	3 β -Lup-20(29)-en-3-ol acetate	103.99	3456±0.16	6.81	Triterpene acetate

[a]Retention Index (HP-5ms column)

Cytotoxicity assessment of M1:

The examination of the antiproliferative capacity of **M1** on normal HDFn cells ensued no observable cytotoxicity, which afforded an IC_{50} value exceeding 100 µg/mL. Figures 3 and 4 show graphical representations of the percent cell viability as a function of the logarithm (log_{10}) of the concentrations. The characteristic inhibitory dose-response sigmoidal curve or distribution was exhibited in the majority of the plots. Charts reflecting the inhibitors' cytotoxic action on the specific cell lines' viability are displayed in Figure 4. The half-maximal inhibitory concentrations (IC_{50}) of the agents used are presented in Table 3.

One-way ANOVA on HT-29 trials showed that the paired treatments of **M1** versus Zeocin were similar ($p > 0.05$) and **M1** versus DMSO were dissimilar ($p < 0.05$). Statistical evidence also pointed out that there was similarity in the mean of **M1** (M = 7.98, SE = 1.15) and the mean of Zeocin (M = 11.60, SE = 1.08) but was different for DMSO trials (M > 100, SE = 37.93). The outcome revealed that the cytotoxicity of the inhibitors **M1** and Zeocin was analogous.

HepG2 tests presented that **M1** cytotoxic action was akin to Zeocin activity and found no significant differences ($p > 0.05$) as seen in post hoc data. Conclusions for the nonlinear fitting of the log (inhibitor) vs. normalized response using variable slope analyses illustrated that **M1** (M = 7.09, SE = 1.13) and the mean of Zeocin (M = 1.05, SE = 1.05) were similar in action but was markedly unlike DMSO trials (M > 100, SE = 5.85).

The cytotoxic action of **M1** on BxPC-3 experiments was typical of Zeocin activity ($p > 0.05$) as established in multiple comparisons. The means and standard error of the **M1** trials in BxPC-3 cells using the negative control DMSO (M > 100, SE = 2.33) were seen to be non-cytotoxic to these cells, whereas **M1** (M = 16.89, SE = 1.07) and the mean of Zeocin (M = 11.83, SE = 1.05) were comparable and were significantly distinct to DMSO tests.

Data generated using the inhibitor **M1** on MCF-7 cell lines indicated a half-maximal inhibitory concentration

of 7.09 µg/mL with a standard error of 1.07. Tukey's post hoc multiple comparison conveyed that there were considerable differences (p <0.05) in the means of the inhibitors **M1** and Zeocin (M = 8.85, SE = 1.06) to the negative control DMSO (M = >100, SE = 43.15). MCF-7 treated with **M1** and Zeocin were construed to be statistically alike (p >0.05).

One-way ANOVA analyses of the potential inhibitors on HeLa cells showed that the paired trials of **M1** vs. Zeocin were analogous (p > .05), and **M1** vs. DMSO were unrelated (p <0.05). Similarity the means of **M1** (M = 16.63, SE = 1.08) and Zeocin (M = 13.71, SE = 1.07) were noticeably different for DMSO trials (M > 100, SE = 1.96). The cytotoxic capacity of the inhibitors **M1** and Zeocin corresponded to each other. THP-1 presented the following IC_{50} data on the inhibitors: **M1** (M = 17.43, SE = 1.05); Zeocin (M = 8.15, SE = 1.05); and DMSO (M = >100, SE = 1.57). Multiple comparisons or Tukey's post hoc analyses expressed considerable differences (p <0.05) in M1 vs. DMSO and Zeocin vs. DMSO trials. The antiproliferative activity of **M1** and Zeocin on acute monocytic leukemia cells were found to be similar.

M1 was not cytotoxic to normal HDFn, with an IC_{50} value greater than 100 µg/mL. Post hoc comparisons of **M1** and human cell lines trials established that there were substantial variances, and that the null hypothesis (one curve for all data sets) was excluded (log IC_{50} the equivalent for all data sets). This was confirmed by the extra sum-of-squares F-test of the best-fit-parameter (IC_{50} concentration) between individual cell line experiments, F (6, 49) = 1.978, P = 0.0869, and to the observations in the dose-response curve fits F (12, 154) = 121.4, p <0.0001. Zeocin trials with each cancer cell line were observed to be similar (p >0.05). Zeocin a recognized cytotoxic proponent furnished IC_{50} values of 4.40, 11.60, 6.10, 11.83, 8.85, 13.71 and 8.15 µg/mL for HDFn, HT-29, HepG2, BxPC-3, MCF-7, HeLa, and THP-1, respectively and one-way ANOVA data disclosed similarity in the trials (p >0.05). Post hoc comparison of the half-maximal inhibitory concentration for the cancer cell line treatments also verified the results' congruency.

M1 presented the highest effectiveness towards HepG2 with a half-maximal inhibitory concentration of 7.09 µg/mL which was followed by MCF-7, HT-29, HeLa, and BxPC-3, which gave IC_{50} values of 7.12, 7.98, 16.63, 16.89 µg/mL, correspondingly. Substantial variances, as obtained in Tukey's post hoc multiple comparisons, were established in HT-29 vs. HDFn, HepG2 vs. HDFn, and MCF-7 vs. HDFn (p <0.05). The other paired treatments were deduced to be statistically similar (p>0.05). The figures of the subgroups of all the human cell lines and Zeocin demonstrated that the subcategories were comparable (p >0.05). It was found that HepG2, MCF-7, and HT-29 cancer cell lines were positively affected by **M1** and exhibited minimal half-maximal inhibitory concentrations (< 8 µg/mL), which were acquired for all of the trials. HeLa, BxPC-3, and THP-1 were moderately responsive to **M1**. Normal HDFn trials treated with **M1** were substantiated to be non-cytotoxic and presented half-maximal inhibitory concentrations of more than 100 µg/mL; while Zeocin on normal cells were exceedingly damaging as manifested in the IC_{50} = 4.40 µg/mL.

Results obtained from the cell viability assay of **M1** can be explained by the bioactivities reported from previous studies suggesting that phytosterols and tocopherols present in the extract can affect the signal transduction pathway in cancer cells. Targeted analyses have shown that phytosterols and tocopherols can prevent angiogenesis and induce apoptosis in tumor cells by an up-/down-regulating expression such as NF-κB [15] or by cell cycle arrest [16]. As observed in published studies, phytosterols are cytotoxic to common cancer cell lines such as breast (MCF-7) and colon (HT-29) which deemed phytosterols to be promising compounds against cancer. This is further confirmed by the ability of phytosterols to affect the following: inhibit angiogenesis; induce apoptosis (by controlling the cell proliferation process by cell cycle arrest); increase ceramide activities, protein phosphatase 2A (PP2A), and pro-apoptotic MAP kinase; and limiting the supply of nutrients to cancer cells [17, 18]. γ-Sitosterol was found to induce cell arrest in the G_2/M phase and cause apoptosis for MCF-7 and A549 cell lines by reducing the c-Myc expression [19]. The ability of phytosterols, such as those found in the isomers of sitosterol, to induce cell

arrest in the G_0/G_1 phase was believed to manifest the cytotoxic effect on the HT-29 cell line [20]. Another common phytosterol present in plants, lupeol, is known to have multiple-targeting capabilities that have the following properties: anti-inflammatory capability through different mechanisms; anti-diabetic effect by inhibiting the alpha-amylase; and anti-carcinogenic action as linked to the arrest of the cell cycle of cancer cells in G_2-M-phase. Lupeol was also established to induce apoptosis on different cancer cell lines through the following signal transduction pathways: Ras-induced protein kinase C-alpha/ornithine decarboxylase; p13K/AKt, MAPKs; and NF-κB signaling. Furthermore, lupeol activated an extrinsic apoptotic pathway by increasing the Fas receptor on prostate cancer. Lupeol has been heralded as a probable chemo preventive and anti-inflammatory agent by inhibiting hepatocellular carcinoma receptor 3 (DR 3) expression and reducing the production of IL-4 through T-helper type 2 cells, respectively [16].

The mechanisms linked to β-amyrin as an anti-inflammatory agent was found to be involved in the inhibition of NF-κB, activation of CREB, reduction of neutrophil filtration, curtailment of oxidative stress, and the depletion of the production of proinflammatory cytokine TNF-α for acute periodontal inflammation. Furthermore, β-amyrin induced a cytotoxic effect against human bladder cancer cells (NTUB1) when treated with cisplatin after 24 hrs. β-amyrin, which was isolated and purified from plants, hampered collagen-induced platelet aggregation with an IC_{50} value of 4.5ug/mL, which was comparable to the effects of aspirin (11 µg/mL) [21]. A polyunsaturated hydrocarbon triterpene, squalene, found to be present in the bark extract has been known to be an essential precursor for synthesizing phytosterols in plants specifically growth hormones, terpenoids, sterol, steroids, pigments, essential oils, and other defense compounds in the body. While the acyclic structure of squalene is responsible for connecting the lipid layers to the biological membrane's intermembrane, the structure of the molecule can scavenge free radicals by either donating or receiving electrons thereby preventing bio membrane damage [22, 23].

In addition to triterpenes, diterpenes have also been reported to exhibit antitumor effects. Phytol and its derivatives have often been reported as notable constituents of essential oils present in plants. Aside from being one of the components used in the formulation of fragrances, phytol is known to have multiple therapeutic functions such as anti-inflammatory, immune-modulating, antimicrobial, and cytotoxic as well as apoptosis-inducing effects in cancer cells. Since PPARs and NF-κB are known to be important regulators of inflammatory, immune response, and antiproliferative agents of cancer, phytol is perceived to be a modulator in the treatment of degenerative diseases [15].

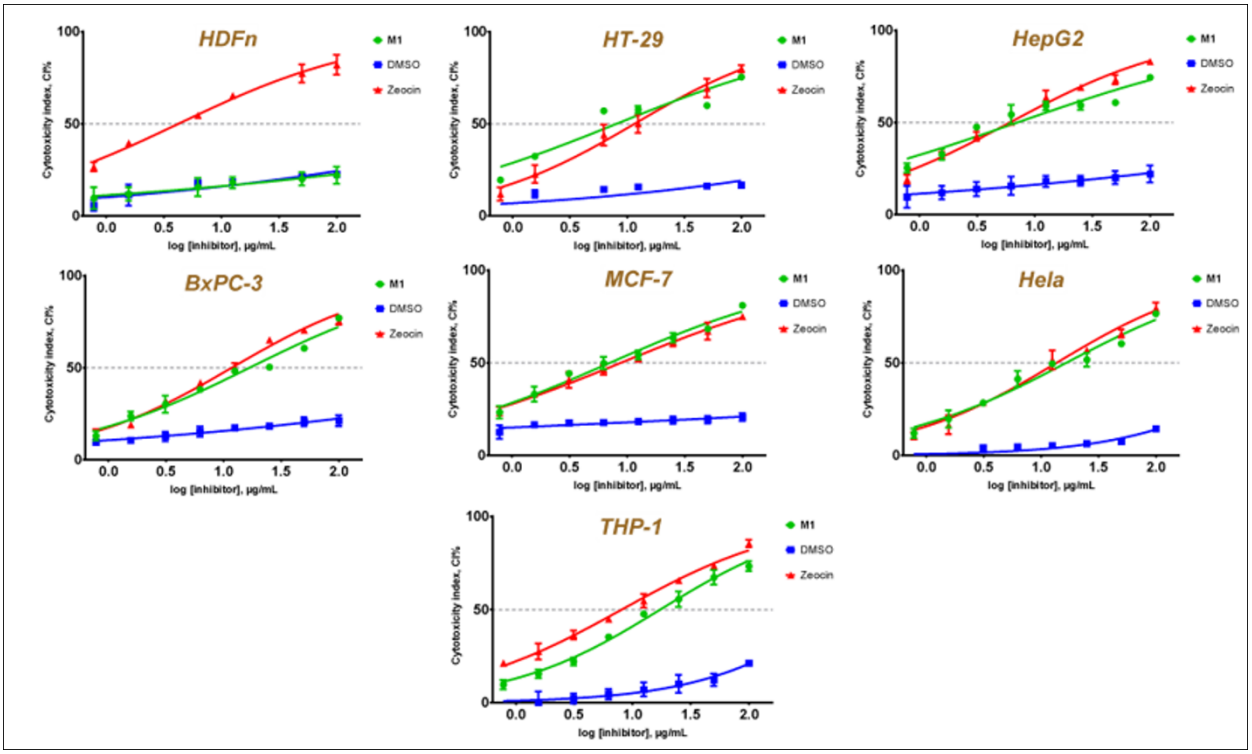
Tocopherols have been communicated to affect human mastocytoma (HMC-1), MCF-7, U937 myeloid leukemia, and HT-29 cell lines. Vitamin E inhibits the proliferation of U937 by inhibiting the formation of oxLDL-induced macrophage foam cells by affecting the two expressions, NF-κB pathway and P-selection [24]. Among all tocopherols, delta-tocopherol induced apoptosis to HMC-1 cells at high concentrations. The proinflammatory response of reactive oxygen species (ROS) and stress-activated expressions, Nrf2 and NF-κB, are enhanced by delta-tocopherol. Delta-tocopherol also prevented lipid accumulation and antiangiogenic effects. Some studies imparted evidence that vitamin E could inhibit the proliferation of vascular smooth muscle cells by preventing PKC phosphorylation and stimulating platelet-derived growth factors. In contrast, vitamin E with tocopherol associated proteins (TAP) and albumin, have molecular functions such as modulating gene expression by acting as a transporter of ligands to enzymes and regulating enzymes ligand transfer. These functions are usually observed for antioxidants [24]. In a separate study, vitamin E was found to function as a free radical scavenger which prevents the reduction of DNA oxidative damage as verified by the decline of urinary excretion of 8-oxodeoxyguanosine (a product of DNA oxidation) [24,25] The accompaniment of chronic inflammation with oxidative stress was hypothesized to provide a suitable environment for cancer development. By addressing the reduction of biochemical markers affiliated to cancer development, the selection of M1 in its potential herbal and pharmaceutical effects proves

promising [2,26].

Table 2. Cytotoxic Activities (IC_{50}) of Inhibitors Against HDFN, HT-29, HEPG2, BXPC-3, MCF-7, HELA and THP-1

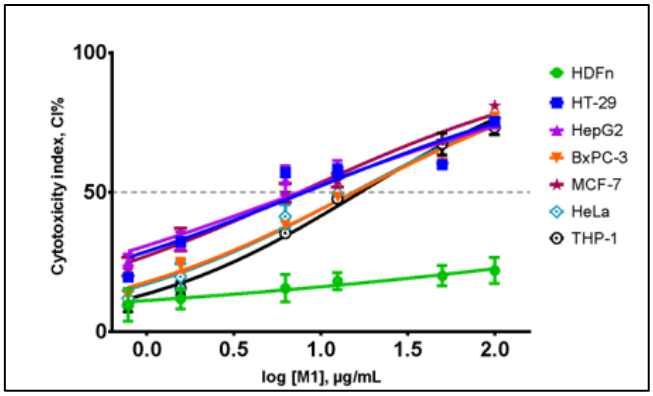
Cell Line	IC_{50}* (µg/mL)		
	M1	DMSO	Zeocin
HDFn	>100	>100	4.40
HT-29	7.98	>100	11.60
HepG2	7.09	>100	6.11
BxPC-3	16.89	>100	11.83
MCF-7	7.12	>100	8.85
HeLa	16.63	>100	13.71
THP-1	17.43	>100	8.15

*IC_{50} values were extrapolated from dose-response curves calculated from nonlinear regression analysis using GraphPad Prism 8.02. One-way ANOVA was the treatment employed for each cell line to evaluate the significant variances among the data groups. The statistical analyses are as follows: HDFn, F (2, 21) = 32.06, $P < 0.0001$; HT-29, F (2, 21) = 11.65, $P = 0.0004$; HepG2, F (2, 21) = 14.23, $P = 0.0001$; BxPC-3, F (2, 21) = 6.586 $P = 0.0060$; MCF-7, F (2, 21) = 13.28, $P = 0.0002$, HeLa, F (2, 21) = 11.17, $P = 0.0005$, THP-1, F (2, 21) = 11.20, $P = 0.0005$.



Data are shown as mean ± SEM. GraphPad Prism 8.02 was used to perform extra sum-of-squares F-test to (A) evaluate the significance of the best-fit-parameter (half-maximal inhibitory concentration) among different treatments, and to (B) determine the differences among the dose-response curve fits. HDFn F(Dfn, DFd) = (A) F (2, 21) = 9.964, $P = 0.0009$ and (B) F (4, 66) = 616.9, $p < 0.0001$; HT-29 (A) F (2, 21) = 3.436, $P = 0.0512$ and (B) F (4, 66) = 149.6, $p < 0.0001$; HepG2 (A) F (2, 21) = 5.731, $P = 0.0103$ and (B) F (4, 63) = 370.9, $p < 0.0001$; BxPC-3 (A) F (2, 21) = 6.638, $P = 0.0058$ and (B) F (4,66) = 480.9, $p < 0.0001$; MCF-7 (A) F (2, 21) = 6.602, $p = 0.0060$ and (B) F (4, 66) = 640.8, $p < 0.0001$; HeLa (A) F (2, 21) = 5.135, $P = 0.0153$ and (B) F (4, 66) = 468.8, $p < 0.0001$; THP-1 (A) F (2, 21) = 6.140, $P = 0.0080$ and (B) F (4, 66) = 699.3, $p < 0.0001$.

Figure 3. Dose-response curves showing the cytotoxic a of M1, DMSO, and Zeocin on the cell viability of HDFn, HT-29, HepG2, BxPC-3, MCF-7, HeLa, and THP-1. Each plot displays the effect of **M1** and controls against each cell line



Each plot displays the effect of **M1** against each cell line. Data are shown as mean ± SEM. GraphPad Prism version 8.02 was used to perform extra sum-of-squares F-test to (A) evaluate the significance of the best-fit-parameter (half maximal inhibitory concentration) among different treatments, and to (B) determine the differences among the dose-response curve fits. The results are: **M1**, (A) F (6, 49) = 1.978, P = 0.0869 (B) F (12, 154) = 121.4, p <0.0001.

Figure 4. Dose-response curves showed the cytotoxic activities of M1 on the cell viability of HDFn, HT-29, HepG2, BxPC-3, MCF-7, HeLa, and THP-1

Conclusion

M1 was found to be rich in phytosterols and tocopherols, which have been reported to be anticancer agents. This thereby presents *M. rubra* bark as a potential raw material for such applications. The most responsive cancer cells to M1 were HepG2, MCF-7, and HT-29. Hela, BxPC-3, and THP-1 were moderately responsive to **M1**. Normal HDFn trials treated with **M1** were not affected by the inhibitor, whereas Zeocin was highly cytotoxic to wild type HDFn cells. Due to the low toxicity of **M1** to normal human dermal fibroblasts, we the researchers recommend that further bioassays be performed to reveal the signaling pathways that could be modulated in aberrant cells and that *in vivo* assays also be done to substantiate *Morus rubra* as a possible anticancer agent.

Acknowledgement:

A research grant, P/N 21FU1TAY19-1TAY20, from De La Salle University Science Foundation, through the University Research Coordination Office, is gratefully acknowledged.

References

1. Hussain, F., Rana, Z., Shafique, H., Malik, A., and Hussain, Z. (2017). Phytopharmacological potential of different species of *Morus alba* and their bioactive phytochemical: A review. *Asian Pacific Journal of Tropical Biomedicine*, 7(10): 950-956.
2. Ercisli, S., and Orhan, E. (2001). Chemical composition of white (*Morus alba*), red (*Morus rubra*) and black (*Morus nigra*) mulberry fruits. *Food Chemistry*.103(4):1380-1384.
3. Ercisli, S., Tosun, M., Duralija, B., Voća, S., Sengul, M., and Turan, M. (2008). Phytochemical content of some black (*Morus nigra* L.) and purple (*Morus rubra* L.) mulberry genotypes. *Food Technology and Biotechnology*, 48(1):102-106.
4. Koca, I., Ustun, N. S., Koca, A. F., and Karadeniz, B. (2008). Chemical composition, antioxidant activity and anthocyanin profiles of purple mulberry (*Morus rubra*) fruits. *Journal of Food Agriculture and Environment*, 6(2): 39.
5. Gundogdu, M., Muradoglu, F., Sensoy, R.G., and Yilmaz, H. (2011). Determination of fruit chemical properties of *Morus nigra* L., *Morus alba* L. and *Morus rubra* L. by HPLC. *Scientia Horticulturae*, 132: 37-41.
6. Xiao, N. S., Guan, G. Y., and Jiang, Y. (2012). Advances in studies on pharmacological effects of plants in *Morus* L. *Yao Xue Xue Bao,* 27(1): 70-74.
7. Yang, S., Wang, B. L., and Li, Y. (2014). Advances in the pharmacological study of *Morus alba* L. *Acta Pharmaceutica Sinica*, 49(6): 824-831.
8. Sharma, S. B., Gupta, S., Ac, R., and Singh, U. R., Rajpoot, R., and Shukla, S. K. (2010).

Antidiabetogenic action of *Morus rubra* L. leaf extract in streptozotocin‐induced diabetic rats. *Journal of Pharmacy and Pharmacology*, 62(2): 247-55.

9. Reuter, S., Gupta, S. C., Chaturvedi, M. M., and Aggarwal, B. B. (2010). Oxidative stress, inflammation, and cancer: how are they linked?. *Free Radical Biology and Medicine*, 49(11): 1603-1616.
10. Demir, S., Turan, I., Aliyazicioglu, Y., Kilinc, K., Yaman, S. O., Ayazoglu, Demir, E., Arslan, A., Mentese, A., and Deger, O. (2017). *Morus rubra* extract induces cell cycle arrest and apoptosis in human colon cancer cells through endoplasmic reticulum stress and telomerase. *Nutrition and Cancer*, 69(1):74-83.
11. Demir, S., Turan, I., Aliyazicioglu, Y., Kilinc, K., Yaman, S. O., Ayazoglu Demir, E., ... and Deger, O. (2017). *Morus rubra* extract induces cell cycle arrest and apoptosis in human colon cancer cells through endoplasmic reticulum stress and telomerase. *Nutrition and Cancer,* 69(1): 74-83.
12. Abbas, G. M., Abdel, Bar, F. M., Baraka, H. N., Gohar, A. A., and Lahloub, M. F. (2014). A new antioxidant stilbene and other constituents from the stem bark of *Morus nigra* L. *Natural product research*, 28(13): 952-959.
13. Tan, M. C., Carranza, M. S., Linis, V. C., Malabed, R. S., and Oyong, G. G. (2019). Antioxidant, cytotoxicity, and antiophidian potential of *Alstonia macrophylla* bark. *ACS omega*, 4(5): 9488-9496.
14. The Pherobase: Database of pheromones and semiochemicals. c2021. Available from http://www.pherobase.com. Access date [2021 Sept 13].
15. Islam, M. T., Ali, E. S., Uddin, S .J., Shaw, S., Islam, M. A., Ahmed, M. I., Shill, M. C., Karmakar, U. K., Yarla, N. S., Khan, I. N., and Billah, M. M. (2018). Phytol: A review of biomedical activities. *Food and Chemical Toxicology*, 121: 82-94.
16. Saleem, M. (2009). Lupeol, a novel anti-inflammatory and anti-cancer dietary triterpene. *Cancer Letters*, 285(2):109-115.
17. Ferdosh, M. S. U., Haque, S., Akanda, M. J., Ghafoor, K., Ah, R., Ali, M. E., Kamaruzzaman, B. Y. M. B. F., Shaarani, S., and Islam Sarker, M. Z. (2018). Techniques for the extraction of phytosterols and their benefits in human health: a review. *Separation Science and Technology*, 53(14): 2206-2223.
18. Shahzad, N., Khan, W., Shadab, M. D., Ali, A., Saluja, S. S., Sharma, S., Al-Allaf, F. A., Abduljaleel, Z., Ibrahim, I. A., Abdel-Wahab, A. F., and Afify, M. A. (2017). Phytosterols as a natural anticancer agent: Current status and future perspective. *Biomedicine & Pharmacotherapy*, 88: 786-794.
19. Sundarraj, S,, Thangam, R,, Sreevani, V,, Kaveri, K,, Gunasekaran, P,, Achiraman, S., and Kannan, S. (2012). γ-sitosterol from *Acacia nilotica* L. induces G2/M cell cycle arrest and apoptosis through c-Myc suppression in MCF-7 and A549 cells. *Journal of Ethnopharmacology*, 141(3): 803-809.
20. Roy, M. K., Kobori, M., Takenaka, M., Nakahara, K., Shinmoto, H., and Tsushida, T. (2006). Inhibition of colon cancer (HT-29) cell proliferation by a triterpenoid isolated from *Azadirachta indica* is accompanied by cell cycle arrest and up-regulation of p21. *Planta medica*, 72(10): 917-923.
21. Vázquez, L. H., Palazon, J., and Navarro-Ocaña, A. (2012). The pentacyclic triterpenes α,β-amyrins: A review of sources and biological activities. *Phytochemicals-A Global Perspective of Their Role in Nutrition And Health*. *IntechOpen:* pp: 487-502.
22. Ronco, A. L., and De Stéfani, E. (2013). Squalene: a multi-task link in the crossroads of cancer and aging. *Functional Foods in Health and Disease*, 3(12): 462-476.
23. Lim, W. M., and Teo, S. S. (2019). Identification of antioxidant properties of *Morus rubra*. *International Journal of Complementary & Alternative Medicine*, 12(1): 31-34.
24. Zingg, J. M. (2019). Vitamin E: Regulatory role on signal transduction. *IUBMB Life*, 71(4): 456-478.
25. Azzi, A. (2019). Many tocopherols, one vitamin E. *Molecular Aspects of Medicine*, 61: 92-103.
26. Singh, N., Baby, D., Rajguru, J. P., Patil, P. B., Thakkannavar, S. S., and Pujari, V. B. (2019). Inflammation and cancer. *Annals of African Medicine*, 18(3): 121.

Malaysian Journal of Analytical Sciences (MJAS)
Published by Malaysian Analytical Sciences Society

PHYTOCHEMICAL ANALYSIS OF COMMERCIAL *Ziziphus mauritiana* LEAF TEAS BY LIQUID CHROMATOGRAPHY COUPLED WITH ION TRAP/TIME-OF-FLIGHT MASS SPECTROMETRY

(Analisis Fitokimia Teh Daun *Ziziphus mauritiana* Komersial oleh Kromatografi Cecair Bergabung dengan Perangkap Ion/Spektrometri Jisim Masa Penerbangan)

Siti Umairah Mokhtar*, Nurul Fadilah Suardi, Ulia Maisarah Musni, Fathul Aiman Fahmi, Muhammad Syahmi Faiz Shamsuddin

Faculty of Industrial Science and Technology, University Malaysia Pahang Al-Sultan Abdullah, Lebuhraya Persiaran Tun Khalil Yaakob, 26300 Gambang, Pahang, Malaysia

**Corresponding author: umairah@umpsa.edu.my*

Received: 22 June 2023; Accepted: 22 August 2023; Published: 30 October 2023

Abstract

Ziziphus mauritiana (Z. mauritiana) tea is a medicinal herbal tea that is widely sold and consumed especially in Malaysia due to the belief of this herbal tea's beneficial health effects. However, there are limited comprehensive studies on the phytochemicals profiling of this herbal tea that have been published to date. Therefore, this study investigates the effects of different infusion times and volumes of water on the phytochemical's profiles of *Z. mauritiana* tea infusions. Phytochemical screening was conducted to identify the presence of saponin and flavonoid while the total phenolic content (TPC) of the herbal tea was quantified using the Folin-Ciocalteu assay method. The gallic acid standard calibration curve showed good correlation coefficient, R^2, at 0.9987. From the TPC study, it was indicated that 10 minutes of infusion time of Z. *mauritiana* infused tea with 200 mL water resulted in higher TPC (32.01 mg GAE/g) compared to other infusion times (15 and 20 minutes) and volume of water (50 and 150 mL). For chemical profiling of phytochemical compounds in tea infusion, the advanced chromatographic method of Liquid Chromatography Mass Spectrometry-ion-trap-time of flight (LCMS-IT-TOF) was applied to provide highly accurate analysis for phytochemical analysis and revealed the identification of 14–23 compounds, including phenolic, saponin, terpenoid, glycosides and alkaloid compounds in the *Z. mauritiana* infused tea sample.

Keywords: *Ziziphus mauritiana*, herbal tea, phytochemical, LCMS-IT-TOF, phenolic

Abstrak

Teh *Ziziphus mauritiana* (*Z. mauritiana*) ialah teh herba perubatan yang banyak dijual dan digunakan terutamanya di Malaysia kerana wujudnya kepercayaan bahawa teh herba ini mempunyai kesan kesihatan yang baik. Namun, sedikit sahaja kajian komprehensif yang telah diterbitkan setakat ini mengenai pemprofilan fitokimia teh herbanya. Oleh itu, kajian ini menyiasat kesan masa infusi dan isi padu air yang berbeza terhadap profil fitokimia infusi teh *Z. mauritiana*. Saringan fitokimia telah dijalankan untuk mengenal pasti kehadiran saponin dan flavonoid serta jumlah kandungan fenolik (TPC) teh herba yang dikuantifikasikan dengan menggunakan metode asai Folin-Ciocalteu. Keluk penentukuran piawai asid galik menunjukkan pekali korelasi yang baik, R^2, dengan nilai R^2 pada 0.9987. Daripada kajian TPC tersebut, ditunjukkan bahawa infusi selama 10 minit di dalam teh *Z.*

mauritiana dengan 200 mL air menghasilkan TPC yang lebih tinggi (32.01 mg GAE/g) berbanding dengan tempoh infusi (15 dan 20 minit) dan isi padu air (50 dan 150 mL) yang lain. Untuk pemprofilan kimia sebatian fitokimia di dalam infusi teh, kaedah kromatografi lanjutan iaitu Kromatografi Cecair Spektrometri Jisim-ion-perangkap-masa penerbangan (LCMS-IT-TOF) telah digunakan untuk menyediakan analisis yang sangat tepat untuk analisis fitokimia dan mendedahkan pengesanan 14 –23 sebatian termasuk sebatian fenolik, saponin, terpenoid, glikosida, dan alkaloid di dalam sampel teh *Z. mauritiana*.

Kata kunci: *Ziziphus mauritiana*, teh herba, fitokimia, LCMS-IT-TOF, fenolik

Introduction

The use of herbs or medicinal plants to develop products for medicines and supplements has increased rapidly over the past few decades due to the various medicinal benefits of those plants. Herb plants consist of unpurified plant extracts that consist of various constituents to cure certain types of diseases and enhance general health and well-being [1]. According to the World Health Organization (WHO), medicinal plants is a natural plant material that has been used in both developed and developing countries for many years because of their natural composition contained in the plant cause the least complications and more than 80% of the population in the world depend more on traditional drugs derived from traditional herb plants [2].

Ziziphus mauritiana plant is commonly referred to as Bidara by Malaysians and belongs to the Rhamnaceae family. This tree is native to Southeastern Asia's warm climate region [3]. It can withstand adverse conditions such as salinity, drought, and waterlogging, making it adaptable to a variety of soil types [3]. Bidara leaves, fruit, seed, and other plant parts have been used in traditional medicine and rituals to treat a variety of diseases. Malay people believed that cleansing a deceased body with Bidara leaves softens the body, strengthens the skin, and slows the decaying process [3].

In addition, fresh or dried flowers, fruits, leaves, seeds, and roots can all be used to make herbal teas by pouring boiling water over them and soaking it for a few minutes. After that, the herbal tea is strained, sweetened, and served. Many companies sell herbal teas due to their major source of dietary antioxidants, and scientists have been studying polyphenolic compounds, as well as vitamins and carotenoids, for decades [4]. However, the suitability and health effects of drinking this herbal tea still lacking to date and the bioactive compounds contained in this infused herbal tea remain unclear. The safety and quality of unregistered herbal tea for human health is a major concern. Contaminants from natural and anthropogenic sources frequently reduce the quality of medicinal herbs and herbal remedies, causing side effects and even fatal death. Indeed, many herbal products lack sufficient information on their acute and chronic toxicity, standardization, stability, and quality. Therefore, if the plant material is intended for human consumption, it is very crucial to ensure the chemical profile as well as metallic and nonmetallic elements in the herbal extract or herbal tea.

A study on the identification of phytochemical compounds in *Ziziphus* jujube leaf tea has been conducted previously by using HPLC-DAD-ESI-TOFMS. Based on the study, reported that the infusion tea does not contain caffeine and theophylline but is rich in flavonoids with possible sedative activity. It revealed that this infusion has good radical scavenging ability and can be a healthy beverage for the public [5]. Based on the study, the application of advanced mass spectrometry provides higher sensitivity and accuracy in the identification of both targeted and non-targeted compounds [6].

Therefore, this study aims to explore the effects of different infusion parameters towards the phytochemical content as well as to investigate the chemical profile of *Z. Mauritiana* tea infusion by identifying the primary phytochemical compounds qualitatively. A hybrid technology LC-IT-TOF/MS was implemented to explore the phytochemical compounds in infused tea which can offer high speed and high accuracy determination.

Materials and Methods

Reagents and materials

Methanol, gallic acid, Folin-Ciocalteu reagent, sodium carbonate anhydrous powder and 2N sodium hydroxide

were obtained from Sigma Aldrich (St. Louis, USA). All of the chemicals and solvents were of high analytical grade. Three brands of herbal tea samples were purchased from online local shops namely brands A, B and C, respectively.

Infusion method of herbal tea

1 g of tea samples was mixed with 50, 100, 150, and 200 mL of hot distilled water (95 °C) to make the tea infusion. After 5 minutes of infusion, the solution was cooled to around 50 °C. After that, the infused teas were filtered using a Whatman paper filter No. 1 before analysis. This study was adjusted by varying the volume of water (50, 100, 150 and 200 mL) and infusion time (10, 15 and 20 minutes). To find the ideal conditions for infusing *Z. mauritiana* tea at different volumes and times, the infusion process was optimized using a constant mass, which was 1 g of *Z. Mauritiana* tea. Each sample was prepared in triplicate.

Qualitative test for saponin and flavonoid

Qualitative phytochemical analysis of saponin and flavonoid compounds in tea samples was conducted using standard methods [7]. For the saponin test, 2 mL of *Z. Mauritiana* herbal tea was mixed with 6 mL of water in a graduated cylinder. The mixture was vigorously shaken, and the presence of saponins was determined by the formation of persistent 2 cm foam. As for the flavonoid test, 2 mL of *Z. Mauritiana* herbal tea was mixed with 1 mL 2N sodium hydroxide. The presence of flavonoids is indicated by the presence of yellow color.

Total phenolic content

The total phenolic content was determined using the Folin-Ciocalteu colorimetric method with gallic acid as a control. A gallic acid standard solution with concentration ranges of 0.05 to 0.4 mg/mL was prepared for the standard calibration curve. In this method, 1 mL *Z. Mauritiana* herbal tea and 2.5 mL Folin-Ciocalteu (0.2 N) reagent were mixed. Then, 2 mL of sodium carbonate (37.7 g/L) was added and thoroughly mixed. Then, 7.5 mL of distilled water was added to dilute it. The mixture was covered with parafilm foil and incubated in a dark place for 2 hours at 30°C. The absorbance was then measured in a UV-Vis spectrophotometer (Shimadzu) at 760 nm. The obtained result was calculated and expressed as mg of gallic acid equivalents (mg GAE)/mL of tea infusion as stated in Equation 1.

$$Total\ Phenolic\ Content = \frac{\mathrm{CV}}{m} \quad (1)$$

Where C is the concentration of *Z. Mauritiana* leaves herbal tea (mg/mL), V is the volume of *Z. Mauritiana* herbal tea (mL) and m is the weight of *Z. Mauritiana* herbal tea (g).

Analysis by LCMS-IT-TOF

For the phytochemical screening of *Z. Mauritiana* herbal tea sample, LC-MS analysis was performed using the Shimadzu Prominence Series LC coupled to the LCMS-IT-TOF (Shimadzu, Kyoto, Japan). Prominence Series components included two LC-20AD pumps, SIL-20A Autosampler, and a CBM-20A System Controller. The column used for reversed-phase LC analysis was a Shimadzu Shimpack VP-ODS packed with 4.6 µm particles (4.6 x 150 mm). The instrument was controlled through an LCMS solution, and data analysis was performed using the same software. The mobile phases consisted of eluent A (0.1% formic acid in water, v/v) and eluent B (0.1% formic acid in acetonitrile, v/v) with a flow rate of 0.5 mL/min. The injection volume was 10 µL with a gradient elution at the flow rate of 0.5 mL/min: 1% B (0 ~ 1 min), and was linearly increased to 35% (1 ~ 16 min), 35-100% (16 ~ 18 min) and 100% (18 ~ 20 min). Re-equilibration duration was five minutes between individual runs.

Data analysis

All data acquired were processed by Shimadzu LC-solution software (Kyoto, Japan), Version 3.0. The experimental results were performed in triplicate. The processed data was compiled in the Microsoft Excel software and further Mean, SD, relative standard deviation (%RSD), and Percentage Relative Error (%RE) values were calculated.

Results and Discussion

Effect of different parameters to the infused herbal tea

Observation of color was conducted to view the effect

of different water volumes on the color intensity of tea infusion. All brands of tea revealed that the intensity of the color decreased as water volume increased as can be seen in Figure 1. It can be seen that 50 mL has darker color compared to 100 mL, 150 mL and 200 mL. This is due to the increased volume of water used for infusion resulting in the dilution of the chemical compounds.

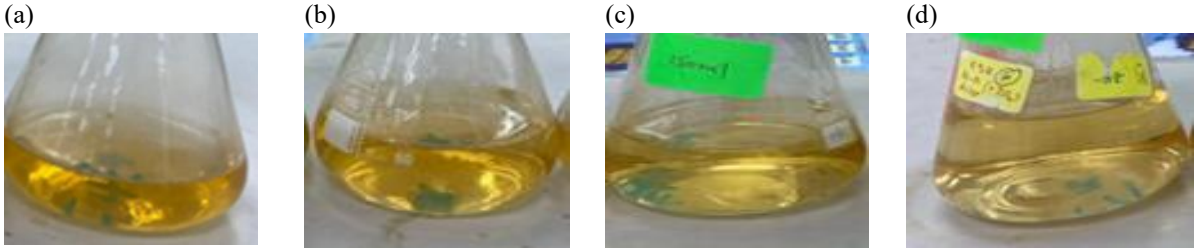


Figure 1. Color of infused *Z. mauritiana* tea at (a) 50 mL, (b) 100 mL, (c) 150 mL and (d) 200 mL

Furthermore, infusion tea with different infusion times (5, 10, 15 and 20 minutes) indicated that the intensity of the yellowish color of the infused tea decreased as infusion time increased. It revealed that 10 minutes of infusion time give darker color followed by 15 and 20 minutes of infusion time, respectively. According to previous studies, the flavor, color, and taste of tea beverages are said to be affected by a long infusion time. The infusion's turbidity increases as the infusion time increases due to the increase in protein and pectic structures, which are expressed at the same time [3]. Observing the turbidity through a UV spectrophotometer, the water-soluble compounds in the tea were found to pass quickly to the water, and the number of water-soluble compounds in the infusion increased slowly even as the infusion time increased [4]. Moreover, the brightness of the infusions decreased as infusion time increased. It can be stated that as the infusion time increases, undesirable compounds pass into the infusion, the emergence of some decomposed and degraded components, and increased turbidity cause a decrease in the brightness of the infusion. The number of compounds in the infusion increases with infusion time and these compounds affect the color of the tea, the change in color of the infusion is to be expected [5].

Qualitative test for saponin

A qualitative test of saponin was conducted to identify the presence of saponin in *Z. mauritiana* tea with infused parameter of 50 mL water and 10 mins. Saponins are amphipathic glycosides distinguished phenomenologically by the soap-like foam produced when shaken in aqueous solutions and structurally by the presence of one or more hydrophilic glycoside moieties combined with a lipophilic triterpene derivative. From this study, Brand A and C proved the presence of saponin after the mixture was shaken vigorously while Brand B does not record the presence as shown in Figure 2.

Based on previous studies on different tea plants, saponin content may vary but the processing of tea did not significantly affect them. Saponin can be found in many medicinal plants such as *alstonia scholaris, curcuma longa, jasmin sambac, phyllantus acidus* as well as *ziziphus mauritiana* [8]. This compound is beneficial as it has several pharmacological properties namely antimicrobial, antifungal, anti-inflammatory and antioxidant.

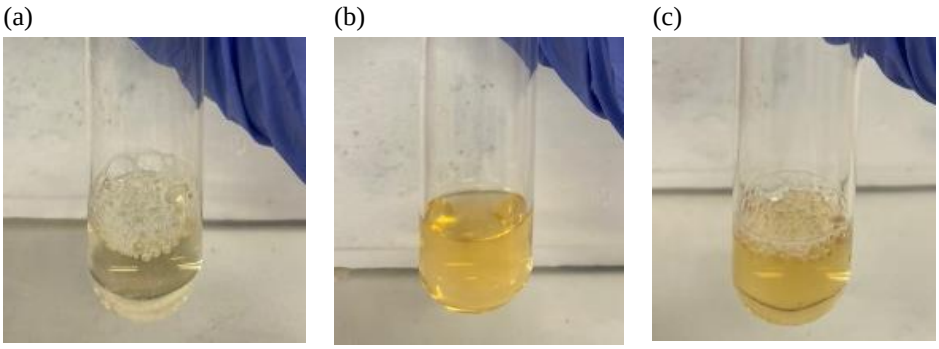


Figure 2. Saponin test in infused herbal tea at volume 50 mL and 10 min infusion time (a) Brand A (b) Brand B and (c) Brand C

Qualitative Test for Flavonoid

This test was conducted at infusion parameters; 50 mL water and 10 mins infusion time. The presence of flavonoids is indicated by the presence of an intense yellow color in the mixture as compared to blank infused tea [9]. Figure 3 shows that all brands contain flavonoids in herbal teas based on qualitative tests of flavonoids. Brand B shows the highest content of flavonoids due to the brownish-yellow color of the herbal tea of which is darker than Brand A, Brand C as well as the control (blank infused *Z. mauritiana* tea). Flavonoids and flavonols are typically yellow or ivory-colored pigments. Notably, the anthoxanthins content will impact the yellow colors [10]. Tea is particularly rich in three flavonoid classes: flavan-3-ols (or catechins), ooligomeric flavonoids (including thearubigins and theaflavins generated during fermentation), and flavonols (e.g. quercetin). These flavonoid oligomers in tea have very complex chemical structures that have yet to be fully characterized. The most common flavonol found in tea is quercetin [11, 12].

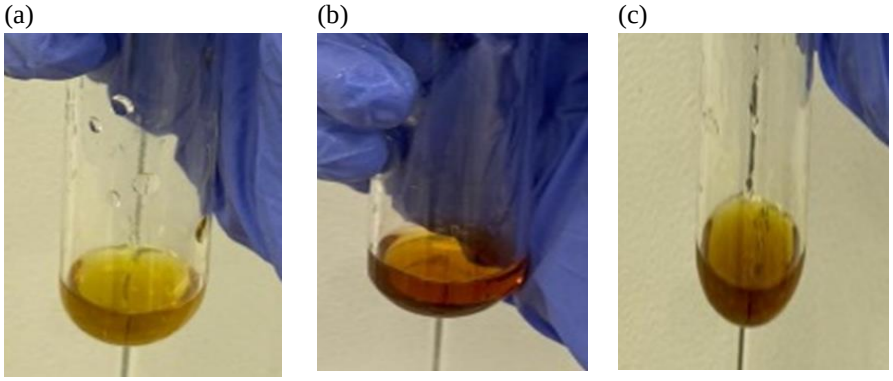


Figure 3. Flavonoid test in infused herbal tea at 10 mins infusion time and 50 mL of water volume (a) Brand A (b) Brand B and (c) Brand C

Effect of different water volumes on the TPC value of infused tea

Gallic acid was used as the standard calibration curve in TPC analysis and was measured using a UV-Vis Spectrophotometer at a wavelength of 765 nm. The correlation coefficient, R-value, obtained from the experiment showed a value of 0.9987 indicating excellent linearity of absorbance versus concentration.

Based on Figure 4, brand A had the most phenolic compounds, followed by brand B and brand C. Unlike the previous study, the amount of TPC increased by the increment of water volume for Brand A tea. More TPC values resulting from the increment of water volume in

Brand A might be due to better solvation of TPC in the sample as a result of interactions (hydrogen bonds) between the polar sites of the TPC molecule and the water [13]. Meanwhile, TPC for Brand B and C decreased as the volume increased to 200 mL. The phenolic compounds were expected to be reduced by the increment of water volume [6]. These results might be due to the other factors that potentially affect the phenolic content such as the drying process, topographical location of the planting and cultivation, season, climate and the storage conditions of the tea sample. This phenolic compound also contributes to antioxidant activity as well as contributes to the quality in terms of modifying color, taste, aroma and flavor [14].

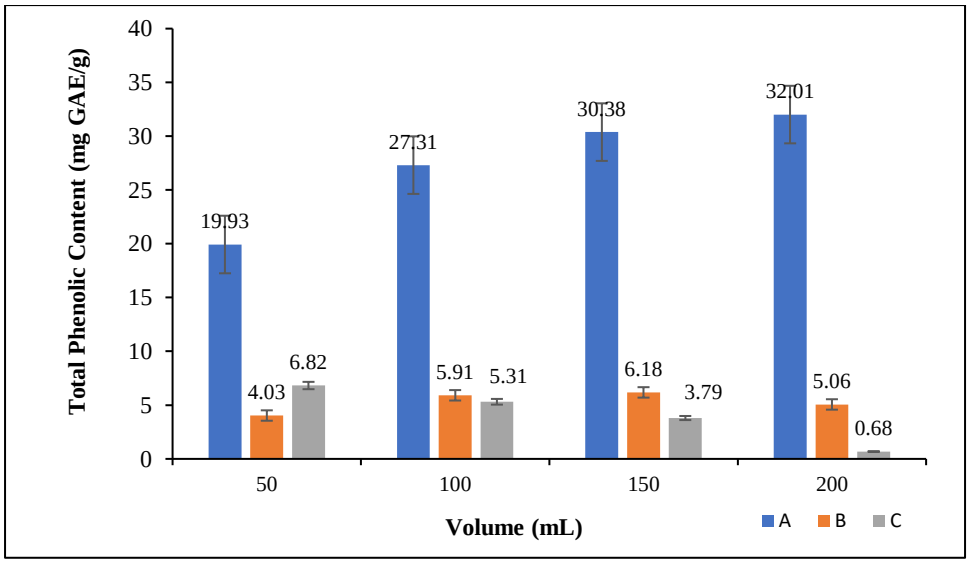


Figure 4. Total phenolic content for all types of brands with different volumes in mg GAE/g

Effect of different infusion time to TPC value of infused tea

Based on Figure 5, the amount of TPC in Brand A and B decreased by the increment of infusion time from 10 until 20 minutes. According to a previous study, increment of infusion time increases the chances of oxidation of phenolics due to their long exposure to unfavorable environmental factors such as temperature and oxygen [14]. However, TPC in Brand C increased at 15 minutes before being reduced at 20 minutes infusion time. As stated by a previous study, 10 minutes of infusion time for loosely packed teas is enough to infuse all the phenolic content into the water [15]. From this result, it concluded that *Z. mauritiana* Brand A significantly demonstrated the highest TPC values at different parameters as compared to Brands B and C. Brands B and C do not give much significant difference in the TPC value at different infusion times and water volumes.

LCMS-IT-TOF Analysis for *Z. Mauritiana* herbal teas

From the qualitative test and TPC test, it was shown that Brand A gave the highest amount of compounds compared to Brand B and C, thus, Brand A then continued for the analysis using advanced LCMS-IT-TOF. The identification and analysis of compounds detected were based on precursor ions and accurate mass measurement of either $[M+H]^+$, $[M+K]^+$, $[M+NH4]^+$ and $[M+Na]^+$. Table 1 indicated the identification of the active components in *Z. Mauritiana* herbal teas.

Based on Table 1, LCMS-IT-TOF analysis successfully detected 14 compounds based on their accurate mass categorized as amine, fatty acids, phenolic glycosides, phenolic and alkaloid. As can be seen in Figure 6, it revealed that *m/z* 304.2968 gave the highest intensity of the mass compared to others. Based on the accurate mass, it revealed that nitrosoxacin A was identified. This compound belongs to the class of organic compounds

known as trialkylamines. The other four main measured masses in Figure 6(a) were *m/z* 288.2696, 332.3311, 367.1376 and 381.1430 identified as amine, phenolic and indole compounds, respectively. Abietylamine is tricyclic abietane diterpenoids which mainly found in plants and exhibits pharmacological activity such as antimalaria properties [16].

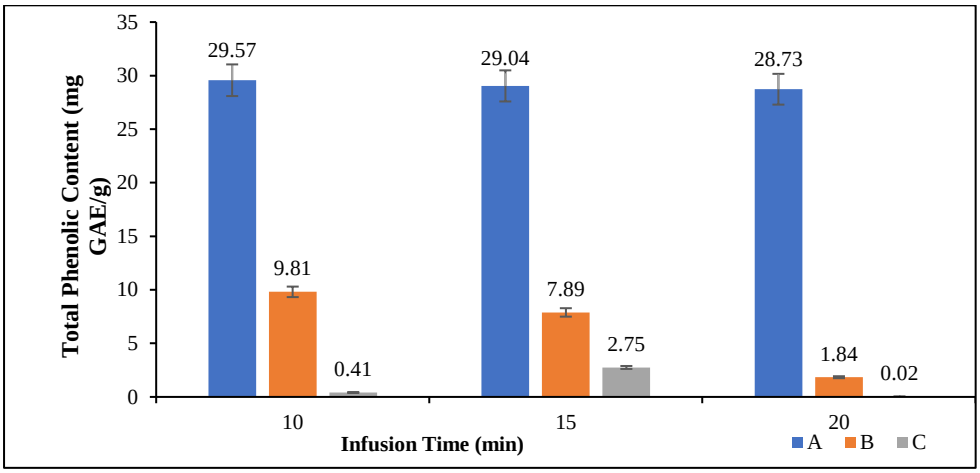


Figure 5. Total phenolic content for all types of brands with different infusion times in mg GAE/g

Meanwhile, dihydroconiferin belongs to the class of organic compounds known as phenolic glycosides, a plant metabolite that was quantitatively identified in a plant called *Lactuca orientalis* [17]. Varespladib (*m/z* 381.1430) is an anti-inflammatory agent which disrupts the first step of the arachidonic acid pathway of inflammation. All detected compounds in this sample were different compared to the previous study using the same herbal tea. There are three unknown compounds were identified to be further investigated for structure elucidation. The fragment ions can be used to study the elucidation of the proposed structures of the unknown compounds.

Based on Table 2, amount 23 compounds were identified using advanced LCMS-IT-TOF and categorized into four groups: saponin, terpenoids, glycosides, and phenols. As compared to Table 1, *Z. mauritiana* infused tea with different volumes of water affected the number of compounds detected. In 150 mL volume of water, it revealed that more compounds can infuse from the tea. Only nitrosoxacin A and camphor azine were detected in both infused samples at masses of *m/z* 304.2975 and *m/z* 318.2879. Camphor and its derivatives are considered among the most significant natural product, which has considerable pharmacological effects including antibacterial, antifungal, antiviral, anticancer and antidiabetic activity [18]. Based on previous studies, nitrosoxacin A and camphor azine were not detected in other infused herbal teas and no study has discovered these compounds in tea leaves. A further investigation on the potential and properties of nitrosoxacin A and camphor azine in *Z. mauritiana* tea can be conducted. Additionally, based on Figure 6, there are two possible molecular formulas detected at *m/z* 332 which showed a higher response, either $C_{23}H_{41}N$ and $C_{19}N_{41}NO_3$ at the volume of 200 mL (Figure 6a) and 150 mL (Figure 6b), respectively. Both molecular formulas indicated isomer compounds were identified and the possible compounds are amine and fatty acid.

In this study, it is noticed that changes in infusion parameters (volume and time) affected the number of compounds detected by LCMS-IT-TOF. Optimum infusion parameters play an important role in the infusion method to diffuse more compounds in the sample and thus be able to be detected by the chromatography method. From this, it can be concluded that the extractability of bioactive compounds from tea leaves depends on the infusion parameters.

Table 1. Number of compounds and its possible name detected in *Z. Mauritiana* herbal tea infused at the volume of 200 mL (10 minutes infusion time) by LCMS-IT-TOF.

No	Formula	Possible Detected Compounds	Ion	Measured *m/z*	Group of Compounds
1	$C_{20}H_{33}N$	Abietylamine	$[M+H]^+$	288.2696	Amine
2	$C_{16}H_{34}N_2O_2$	Nitrosoxacin A	$[M+NH_4]^+$	304.2968	Amine
3	$C_{20}H_{32}N_2$	Camphor Azine	$[M+NH_4]^+$	318.2893	Ketone
4	$C_{23}H_{41}N$	Benzylamine, N,N-dioctyl-	$[M+H]^+$	332.3311	Amine
5	$C_{17}H_{26}N_2O_4$	Bestatin Methyl Ester	$[M+Na]^+$	345.1777	Organic carbonic acids
6	$C_{19}H_{34}O_6$	Dodecanoic acid	$[M+H]^+$	359.2428	Fatty acids
7	$C_{16}H_{27}NO_8$	1-Aminoadamantane citrate monohydrate	$[M+H]^+$	362.1802	Amine
8	$C_{16}H_{24}O_8$	Dihydroconiferin	$[M+Na]^+$	367.1376	Phenolic glycosides
9	$C_{21}H_{20}N_2O_5$	Varespladib	$[M+H]^+$	381.1430	Indoles
10	$C_{30}H_{54}O_3$	2,3-Didodecoxyphenol	$[M+K]^+$	501.3701	Phenolic
11	$C_{26}H_{54}N_2O_7$	Glucoalkaloid	$[M+K]^+$	545.3584	Alkaloid
12	$C_{27}H_{57}NO_{10}$	Unknown	$[M+Na]^+$	578.3871	Unknown
13	$C_{29}H_{62}N_2O_7$	Unknown	$[M+K]^+$	589.4198	Unknown
14	$C_{30}H_{62}N_2O_{10}$	Unknown	$[M+Na]^+$	633.4245	Unknown

It also noted that even though TPC values showed the highest value in Brand A, the number of phenolic compounds detected by LC analysis is not much as expected. It can be due to the phenolic compounds being evaporated prior to LC analysis. Most phenolic compounds are volatile compounds which give the aroma to the herbal tea [19]. Sample preparation prior to LC analysis and the limited mass library could also be the reasons for only several phenolics being identified in this study. Hence, further studies are needed to comprehensively identify individual active compounds present in the infused *Z. mauritiana* tea prepared using different water volumes, infusion times as well as infusion temperatures, which might provide more details.

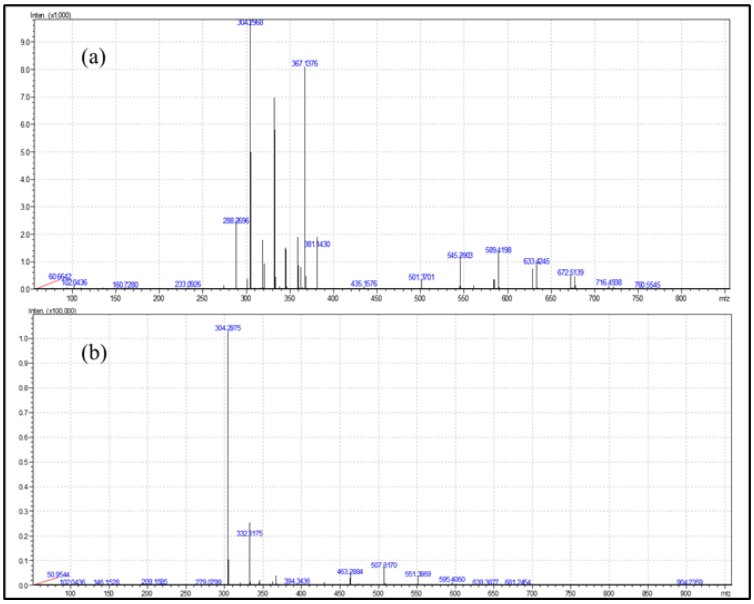


Figure 6. Mass spectra for *Z. mauritiana* infused tea (Sample A) (a) infused with 200 mL volume of water and (b) infused with 150 mL volume water

Table 2. Number of compounds and their possible name detected in *Z. Mauritiana* herbal tea infused at the volume of 150 mL (10 minutes infusion time) by LCMS-IT-TOF

No	Formula	Possible Detected Compound	Ion	Measured m/z	Group of Compounds
1	$C_{16}H_{34}N_2O_2$	Nitrosoxacin A	$[M+NH_4]^+$	304.2975	Amine
2	$C_{21}H_{36}O$	3-Pentadecylphenol	$[M+H]^+$	305.2851	Phenol
3	$C_{20}H_{32}N_2$	Camphor azine	$[M+NH4]^+$	318.2879	Ketone
4	$C_{19}H_{30}N_2O$	5-(Nonyloxy)tryptamine	$[M+NH4]^+$	320.2675	Amine
5	$C_{19}H_{41}NO_3$	2-hydroxypropylazanium Hexadecanoate	$[M+H]^+$	332.3175	Fatty acid
6	$C_{20}H_{44}O_3$	Unknown	$[M+H]^+$	333.3362	Unknown
7	$C_{23}H_{18}N_2$	Unknown	$[M+Na]^+$	345.1360	Unknown
8	$C_{16}H_{36}N_2O_5$	Unknown	$[M+Na]^+$	359.2500	Unknown
9	$C_{24}H_{14}N_2O$	5,6-Diphenyl-2-diazoacenaphthene-1-one	$[M+NH4]^+$	364.1434	Acenaphthene
10	$C_{11}H_{24}N_2O_{10}$	2,2'-Bipyridinate Octahydrate	$[M+Na]^+$	367.1340	Pyridine
11	$C_{19}H_{24}O_8$	Aigialomycin B,	$[M+H]^+$	381.1532	Glucoside
12	$C_{20}H_{46}N_2O_3$	Unknown	$[M+Na]^+$	385.3378	Unknown
13	$C_{28}H_{43}N$	Bis(4-Octylphenyl)Amine,	$[M+H]^+$	394.3436	Amine
14	$C_{28}H_{38}N_{20}$	N,N-dihexyl-2-(2-phenyl-1H-indol-3-yl)acetamide	$[M+H]^+$	419.3052	Phenolic
15	$C_{22}H_{40}N_2O_6$	Unknown	$[M+H]^+$	429.2957	Unknown
16	$C_{28}H_{51}NO_2$	N-(2-Decyltetradecyl)-Maleimide	$[M+H]^+$	434.4018	Unknown
17	$C_{27}H_{48}O_3$	Trihydroxycoprostane	$[M+Na]^+$	443.3488	Saponin
18	$C_{21}H_{48}N_2O_7$	Unknown	$[M+Na]^{bc}$	Q1	Unknown
19	$C_{29}H_{44}O_5$	Triterpenoids	$[M+H]^+$	473.3277	Terpenoids
20	$C_{30}H_{50}O_6$	Protoaescigenin	$[M+H]^+$	507.3675	Saponin
21	$C_{27}H_{42}N_2O_6$	Hydrocortisone-21-lysinate	$[M+NH4]^+$	508.3360	Ester
22	$C_{27}H_{48}N_2O_8$	Serratamolide D	$[M+Na]^+$	551.3293	Unknown
23	$C_{29}H_{46}N_2O_7$	Kalimantacin C	$[M+NH4]^+$	552.3616	Fatty acid

Conclusion

In this study, infusion parameters such as volume of water and infusion time were successfully demonstrated to give different visual appearances and affect the total phenolic content (TPC) of infused *Z. Mauritiana* tea. This infused herbal tea from Brand A, B and C were compared qualitatively and quantitatively. Based on phytochemical screening, it proved the presence of flavonoid and saponin in all samples however saponin was absent in brand B. In TPC analysis, infused tea from brand A at different volumes (50, 150, 200 mL) and different infusion times (10, 15, 20 min) showed the highest TPC value compared to others. In this study, an efficient LCMS-IT-TOF method was successfully performed to identify and compare the phytochemical compounds in infused *Z. mauritiana* tea by using 150 mL and 200 mL water, respectively. It proved that less amount of water used to infuse resulted in a higher number of phytochemical compounds. Results showed that most of the compounds detected were categorized as amine, fatty acids, phenolic glycosides, phenolic, alkaloid, saponin, terpenoids and glycosides. Moreover, only nitrosoxacin A and camphor azine were detected in both infused samples. It is concluded that the different infusion parameters gave a significant effect on TPC value as well as the phytochemical compounds in the infused tea which can be led to different biological activities. Hence, further studies could be planned to focus on the novel compounds extracted from *Z. mauritiana* tea that might benefit human health as compared to other herbal tea.

Acknowledgement

The author would like to express our gratitude to

University Malaysia Pahang Al-Sultan Abdullah (UMPSA) for supporting this research through grant no. RDU200310.

References

1. Yadav, R., and Agarwala, M. (2011). Phytochemical analysis of some medicinal plants. *Journal of Phytology,* 3(12): 10-14.
2. Jamshidi-Kia, F., Lorigooini, Z., and Amini-Khoei, H. (2018). Medicinal plants: Past history and future perspective. *Journal of HerbMed Pharmacology,* 7(1): 1-7.
3. Orwa, C., Mutua, A., and Simons, A. (2009). *Ziziphus mauritiana.* Agroforestry database: A tree reference and selection guide: pp.1-6.
4. Zeng, L., Ma, M., Li, C. and Luo L. (2017) Stability of tea polyphenols solution with different pH at different temperatures. *International Journal of Food Properties,* 20(1): 1-18.
5. Zhang, R., Chen, J., Shi, Q., Li, Z., Peng, Z., Zheng, L., and Wang, X. (2014). Phytochemical analysis of chinese commercial Ziziphus jujube leaf tea using high performance liquid chromatography-electrospray ionization-time of flight mass spectrometry. *Food Research International,* 56: 47-54.
6. Guo, S., Duan, J. ao, Tang, Y., Qian, Y., Zhao, J., Qian, D., Su, S., and Shang, E. (2011). Simultaneous qualitative and quantitative analysis of triterpenic acids, saponins and flavonoids in the leaves of two Ziziphus species by HPLC-PDA-MS/ELSD. *Journal of Pharmaceutical and Biomedical Analysis,* 56(2): 264-270.
7. Sofowora A. (1993). Medicinal plants and traditional medicines in Africa. Chichester John Willey & Sons New York: pp. 256.
8. Abuga, I., Sulaiman, S. F., Abdul Wahab, R., Ooi, K. L., and Abdull Rasad, M. S. B. (2022). Phytochemical constituents and antibacterial activities of 45 Malay traditional medicinal plants. *Journal of Herbal Medicine,* 32: 100496.
9. PushaRani, V., Deepak Kumar, K., Parimalam, M., Delphine Jaya Mary, J. and Meena Kumari, G. (2017) Screening of medicinal plant *Justicia gendarussa* Burm. F for its antibacterial and antioxidant activity from differen localities. *International Journal of Current Research,* 9(4): 49063-49066.
10. Cheng, G., Bai, Y. J., Zhao, Y. Y., Tao, J., Liu, Y., Tu, G. Z., Ma, L., Liao, N., and Xu, X. (2000) Flavonoids from *Ziziphus jujuba* Mill var. spinosa. *Tetrahedron,* 56: 8915-8920.
11. Abdullah, S. S. S., and Mazlan, A. N. (2020). Quantification of polyphenols and antioxidant activity in several herbal and green tea products in Malaysia. *Materials Today: Proceedings,* 31: A106-A113.
12. Pereira, V. P., Knor, F. J., Vellosa, J. C. R., and Beltrame, F. L. (2014). Determination of phenolic compounds and antioxidant activity of green, black and white teas of *Camellia sinensis* (L.) Kuntze, Theaceae. *Revista Brasileira de Plantas Medicinais,* 16(3): 490-498.
13. Ho, L-H., Ramli, N. F., Tan, T-C., Muhamad, N., and Haron, M. N. (2018) Effect of extraction solvents and drying conditions on total phenolic content and antioxidant properties of watermelon rind powder. *Sains Malaysiana,* 47(1): 99-107.
14. Castiglioni S, Damiani E, Astolfi P, Carloni P. (2015) Influence of steeping conditions (time, temperature, and particle size) on antioxidant properties and sensory attributes of some white and green teas. *International Journal of Food Science and Nutrition,* 66(5): 491-497.
15. Nikniaz, Z., Mahdavi, R., Ghaemmaghami, S. J., Yagin, N. L., Nikniaz, L. (2016) Effect of different brewing times on antioxidant activity and polyphenol content of loosely packed and bagged black teas (*Camellia sinensis* L.). *Avicenna Journal of Phytomedicine*, 6(3): 313-321.
16. Sadashiva, M. P., Gowda, R., Wu, X., Inamdar, G. S., Kuzu, O. F., Rangappa, K. S., Robertson, G. P., and Gowda, D. C. (2015). A non-cytotoxic N-dehydroabietylamine derivative with potent antimalarial activity. *Experimental Parasitology,* 155: 68-73.
17. Stojakowska, A., Michalska, K., Kleczek, N., Malarz, J., and Beharav, A. (2018) Phenolic and terpenoids from a wild edible plant *Lactuca orientalis* (Boiss.) Boiss.: A preliminary study. *Journal of Food Composition and Analysis,* 69: 20-24.

18. Mahdy, A. H. S., Zayed, S. E., Abo-Bakr, A. M., and Hassan, E. A. (2022) Camphor: Synthesis, reactions and uses as a potential moiety in the development of complexes and organocatalysts. *Tetrahedron,* 121: 132913.
19. Schieber, A., and Wust, M. (2020) Volatile phenols – Important contributors to the aroma of plant-derived foods. *Molecules,* 25: 4529-4540.

Malaysian Journal of Analytical Sciences (MJAS)
Published by Malaysian Analytical Sciences Society

GRATED COCONUT RESIDUE MODIFIED BY A CATIONIC SURFACTANT FOR REMOVAL OF REACTIVE ORANGE 16 DYE

(Sisa Kelapa Parut Diubahsuai oleh Surfaktan Kationik untuk Menyingkirkan Pewarna Reaktif Oren 16)

Nur Zara Syazana Zali[1], Shariff Ibrahim[2*], Megat Ahmad Kamal Megat Hanafiah[3], and Sabiha Hanim Saleh[2]

[1]Top Glove Worldwide Sdn. Bhd, 41050 Klang, Selangor, Malaysia
[2]School of Chemistry and Environment, Faculty of Applied Sciences, Universiti Teknologi MARA, 40450 Shah Alam, Selangor, Malaysia
[3]Faculty of Applied Sciences, Universiti Teknologi MARA, 264000 Jengka, Pahang, Malaysia

**corresponding author: sha88@uitm.edu.my*

Received: 13 June 2023; Accepted: 17 September 2023; Published: 30 October 2023

Abstract

Hexadecylpyridinium chloride monohydrate, a cationic surfactant, was employed to chemically modify coconut-grated residue to adsorb reactive orange 16 (RO16). The pH point of zero charge (pHPZC) and surface area were used to characterise the raw coconut grated residue (RGC) and the surfactant-modified grated coconut residue (SMGC). The pHPZC was 5.5, and the Brunauer-Emmett-Teller surface area was 1.86 m^2 g^{-1}. The dye solution pH and dose effects on RO16 adsorption were tested in a batch adsorption system. Maximum sorption was seen at an SGMC concentration of 10 g L^{-1}, while optimal adsorption was observed at a low pH. When dye-loaded SGMC was exposed to a basic solution, the desorption percentage increased to almost 70%, whereas low desorption was observed under acidic conditions. Furthermore, the isotherm study discovered that the Freundlich model explained RO16 adsorption of SMGC better than the Langmuir model. The Langmuir isotherm recorded a maximum adsorption capacity of 9.72 mg g^{-1}.

Keywords: cationic surfactant, coconut, reactive dye, adsorption

Abstract

Heksadekilpiridinium klorida monohidrat, sejenis surfaktan kationik, telah digunakan untuk memodifikasi kimia sisa parut kelapa untuk menjerap reaktif oren 16 (RO16). pH titik cas sifar (pHPZC) dan luas permukaan digunakan untuk pencirian sisa parut kelapa mentah (RGC) dan sisa parut kelapa yang dimodifikasi dengan surfaktan (SMGC). Nilai pHPZC adalah 5.5, dan luas permukaan Brunauer-Emmett-Teller adalah 1.86 m^2 g^{-1}. Kesan pH larutan pewarna dan dos terhadap penjerapan RO16 telah diuji dalam sistem penjerapan kelompok. Penjerapan maksimum dilihat pada kepekatan SGMC 10 g L^{-1}, manakala penjerapan optimum diperhatikan pada pH rendah. Apabila SGMC yang memuatkan pewarna terdedah kepada larutan alkali, peratus penjerapan semula meningkat hampir ke 70%, manakala penjerapan rendah diperhatikan dalam keadaan berasid. Selain itu, kajian isoterm menemui bahawa model Freundlich menjelaskan penjerapan RO16 pada SMGC dengan lebih baik daripada model Langmuir. Isoterma Langmuir mencatatkan kapasiti penjerapan maksimum sebanyak 9.72 mg g^{-1}.

Kata kunci: surfaktan kationik, kelapa, pewarna reaktif, penjerapan

Introduction

Many dye effluents are harmful to the environment and wildlife [1]. Global production of dye chemicals for commercial and industrial use totals approximately 700,000 tons annually, representing over 100,000 different colours [2]. Reactive dyes are among the popular choices for dyeing cotton and other cellulose fabrics due to their bright colour shades [3] and are readily water-soluble and easy to apply [4]. According to Allègre et al. [5], over 80,000 tons of reactive chemicals are produced annually, enabling pollution estimates given their extensive application, and after dyeing processes, treatment baths are discharged, including an initial dye bath with extremely high salt concentration and dark hue from substantial organic material resulting from additives used to facilitate dye uptake during fabric treatment. This causes environmental concerns as only 30% of reactive dye typically binds with fabric, meaning that the remaining unfixed dye gives colour to their effluent [6].

Dyes have been removed from effluent using various methods [7]. However, adsorption remains one of the best methods for removing various colour substances [8]. Due to some limitations associated with using activated carbon as an adsorbent, such as processes for regeneration and reactivation [9], alternative adsorbents sourced from plants have been actively explored. Many works have found the potential of plant-based adsorbents to remediate various water and wastewater pollutants [10].

Agricultural waste applied to treat wastewater has several advantages, including chemical stability, an abundant source, low cost, and environmental friendliness [11]. Many have reported that modifying raw agricultural waste improves sorption capacity [12]. Meanwhile, the successful modification of biomass with cationic surfactant in removing reactive dye has been extensively reviewed [13]. According to Kosaiyakanon and Kungsanant [14], cationic surfactants increased the adsorption affinity of negative dyes and introduced a positive charge to adsorbent surfaces. This enables the biosorbent surface and negatively charged anionic dye to attract electrostatically [15], as illustrated in Figure 1.

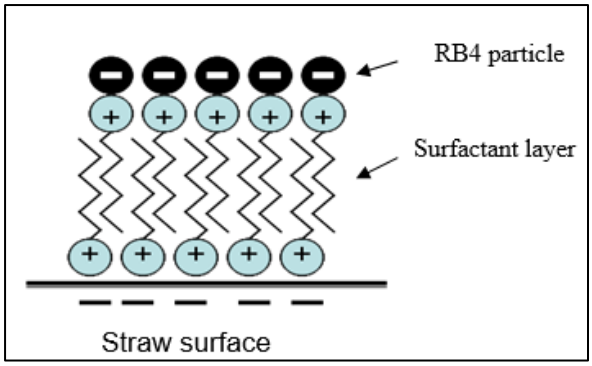


Figure 1. Schematic diagram showing reactive dye attracted to opposite charges on modified straw [15]

This study investigated the effectiveness of the cationic surfactant hexadecylpyridinium chloride monohydrate (CPC, $C_{21}H_{38}NCl$) in removing the anionic dye reactive orange 16 (RO16) from an aqueous solution. According to earlier studies, CPC cations on the adsorbent surface would modify surface characteristics and improve anionic contaminant adsorption [15,16]. Coconut flesh residue has been extensively studied to remove heavy metals like Cd (II) ion [17], Pb(II) ion [18], Ni(II) ion [19] and removal of dyes [20].

Materials and Methods

Materials

Reactive orange 16 (Figure 2) and CPC (98% purity) were purchased from Aldrich. Meanwhile, hexane was obtained from R&M Chemicals (UK). Distilled water was used throughout the adsorption experiments.

Preparation of surfactant-modified grated coconut residue

The preparation of surfactant-modified grated coconut residue (SMGC) has been reported before [21]. In summary, SMGC was prepared by shaking 1 L (2.50 mmol/L) CPC with a specific amount of dried, hexane-pretreated raw grated coconut residue (RGC). The treated grated coconut residue was separated from the liquid, washed with distilled water, and dried overnight in an oven at 60 °C. An anionic dye solution was made by dissolving the RO16 dye in distilled water.

Characterisation of surfactant-modified grated coconut residue

For characterisation, the pH point of zero charge (pHPZC) was measured using the salt addition method [22]. Briefly, NaCl solutions were prepared with volumes of 50 mL and a concentration of 0.01 M, covering pH values from 4 to 12. Each solution was supplemented with 0.15 g of SMGC and mixed for 48 hours at 150 rpm. The initial and final pH values were measured to determine the pHZPC, indicating the point of zero charge where ΔpH equals zero, signifying no surface charge.The surface area was measured using the Brunauer-Emmett-Teller (BET) method through N_2 adsorption, employing the Micromeritics 2010 instrument from Instrument Corporation, USA. Surface morphology testing was carried out using a field emission scanning electron microscope (FESEM-Zeiss Supra 40V) at 5000x magnification.

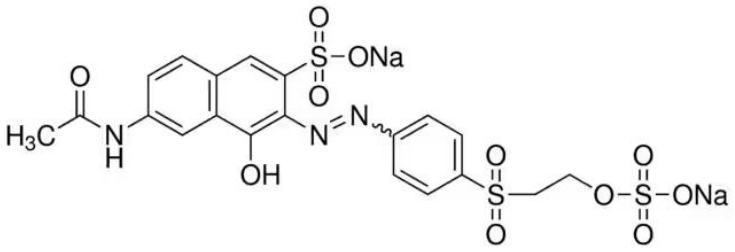


Figure 2. Chemical structure of RO16

Adsorption studies

The dynamic study involved agitating different concentrations of SMGC (10 and 20 g L^{-1}) with RO16 at a concentration of 100 mg L^{-1}. The solution was then sampled at specific time intervals for analysis. In the batch isotherm experiment, SMGC and RO16 were mixed and agitated for 60 minutes. While many parameters can influence the adsorption performance of the reactive dye on the biosorbent, this study focused on two important parameters: the pH of the dye and the dosage of the adsorbent. The SMGC dosage ranged from 5 to 50 g L^{-1} to examine the impact of different doses, while the pH of RO16 was adjusted from 3 to 9 to assess the pH effect. Throughout the study, samples were shaken using an Innova 2100 platform shaker. The pH of the solution was measured with a Mettler Toledo S20 pH meter, and the concentration of dye samples was determined using a HACH DR2800 portable spectrophotometer (UK) at a maximum absorbance wavelength of 493 nm. The initial pH of the dye solution was 5.5 at a concentration of 100 mg L^{-1}, and the agitation speed, adsorbent size, and dosage were set at 200 rpm, 0.12–0.25 mm, and 10 g L^{-1}, respectively, unless specified otherwise.

Desorption of dye-loaded adsorbent

RO16 desorption from dye-loaded SMGC was achieved by dispersing it at 10 g L^{-1} in deionised water at various pHs for 3 h. The mixtures were filtered and analysed at 493 nm using a HACH DR2800 portable spectrophotometer. Equation 1 calculates the desorption percentage:

$$\text{Percentage of desorption (\%)} = \frac{q_{e(des)}}{q_{e(ads)}} \text{ x } 100 \quad (1)$$

Where $q_{e(des)}$ is the desorption of RO16 (mg g^{-1}) and $q_{e(ads)}$ is the amount of RO16 adsorbed (mg g^{-1}).

Best fitting model estimation

The fit of the equation to the experimental data was established by regression correlation coefficients (R^2) and error estimation. The R^2 nearest to unity is assumed to fit best, whereas a lower Marquardt's percentage standard deviation (MPSD) (Equation 2) is better for error estimation:

$$\mathrm{MPSD} = 100\left(\sqrt{\frac{1}{p-n}\sum_{i=1}^{p}\left[\frac{(q_{e,meas}-q_{e,calc})}{q_{e,meas}}\right]_i^2}\right) \quad (2)$$

Where p represents the number of experimental data, and n is the model equation's parameters. The experimental data are $q_{e,meas}$ and the model equation data are $q_{e,calc,}$

Results and Discussion

Adsorbent characterisation

The pHPZC of the adsorbents was used to determine the ideal pH for anion adsorption and the nature of the interaction [23]. The calculated pHPZC of the SMGC was 5.50. When the pH is less than the pHPZC, the adsorbent positive surface charge favours anion adsorption [24]. The removal of Remazol Brilliant Blue in industrial waste sludge exhibited an identical behaviour, with a notable increase in removal as the pH decreased [23]. Given the above, physisorption would be expected as the adsorption mechanism due to the anionic dyes' electrostatic interaction with the active centres of the adsorbents, as suggested by Karaman et al. [16] in their research of cationic surfactant-modified carbon for removing Congo Red dye.

The textural analysis showed that the SMGC had a relatively low BET surface area of 1.86 $m^2\ g^{-1}$ and pore volume of 2.04×10^{-3} $cm^3\ g^{-1}$. These findings suggest that textural properties may not play a significant role in adsorption compared to other factors. For comparison, the reported BET surface area for acid-washed coconut grated in a separate study by Khalid and Hanafiah [20] was 23.673 $m^2\ g^{-1}$, significantly higher than SMGC as acid washing exposes more internal surface area by removing compounds and expanding pores. In contrast, Namasivayam and Sureshkumar [25] reported that surfactant modification coats and constricts pore networks of biomass, limiting accessible surface for nitrogen adsorption analysis.

The scanning electron microscopy (SEM) images (Figure 3), captured at 5,000x magnification, revealed that the SMGC exhibited a slightly more uniform surface than the untreated RGC. This coating effect resulted in a smoother morphology, as observed through the SEM analysis of SMGC. These findings are consistent with a study conducted by Chen et al. [26], in which they observed that untreated silkworm exuviae displayed a compact, uneven, and folded surface, while modified silkworm exuviae treated with hexadecyltrimethylammonium bromide, exhibited a porous and flexible surface.

In our previous work [21], we conducted an analysis to confirm the successful attachment of the cationic surfactant CPC to the surface of RGC. This was achieved through functional group analysis using Fourier transform infrared (FTIR) spectroscopy. The FTIR analysis revealed the presence of two distinct new peaks at wavenumbers 2921 and 2853 cm^{-1} in the spectrum of SMGC, which were attributed to the asymmetric and symmetric C-H stretching vibrations of the cationic surfactant CPC, respectively. The emergence of these characteristic peaks provided strong evidence in support of the effective binding of the cationic surfactant to the RGC surface, which was consistent with other reported surfactant-modified biomass studies [27].

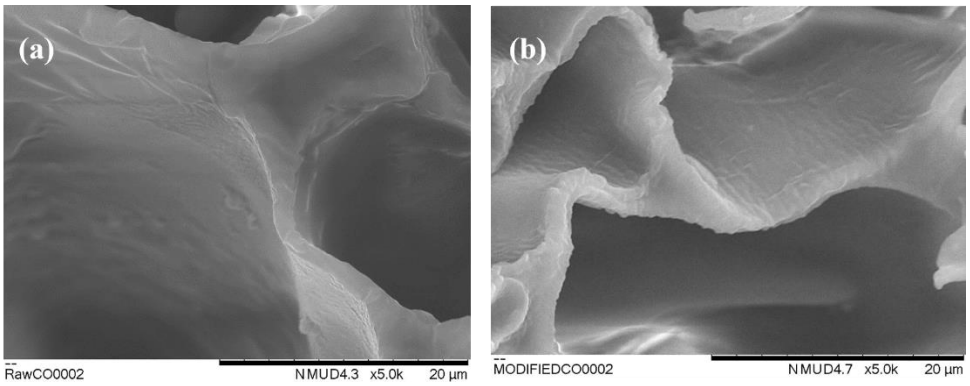


Figure 3. SEM micrographs of (a) RGC and (b) SMGC at 5000x magnification

Dynamic adsorption studies

A rapid initial phase and slow continuation are the characteristics of the adsorption reaction before it reaches equilibrium. For the SMGC dosage of 10 and 20 g L^{-1}, the equilibrium time was 30 min. Two widely used models, pseudo-first-order and pseudo-second-order, were used to investigate the dynamics of RO16 sorption onto SMGC, as given by Equations 3 and 4, respectively:

$$q_t = q_e\left(1 - e^{-k_1 t}\right) \quad (3)$$

$$q_t = \frac{q_e^2 k_2 t}{(1+q_e k_2 t)} \quad (4)$$

Adsorption capacities at time t and equilibrium are denoted by q_t and q_e, respectively, while the first-order and second-order rate constants are denoted by k_1 and k_2, respectively. Equations 3 and 4 are non-linear equations that were fitted using Polymath software. The results of the fitting are shown in Fig. 4 and Table 1. For both dosages (10 and 20 g L^{-1}), the R^2 for the pseudo-second-order model (>0.98) was slightly higher than that for the pseudo-first-order model (>0.94). The MPSD error value was also lower for the pseudo-second-order model (<6.64) than the pseudo-first-order model (<10.76). Furthermore, the pseudo-second-order model's calculated adsorption capacities ($q_{e,cal}$) and experimental adsorption capacities ($q_{e,exp}$) were nearly identical, indicating a better fit of this model to the experimental data. This finding is consistent with other surfactant-modified adsorbent for dye removal [28].

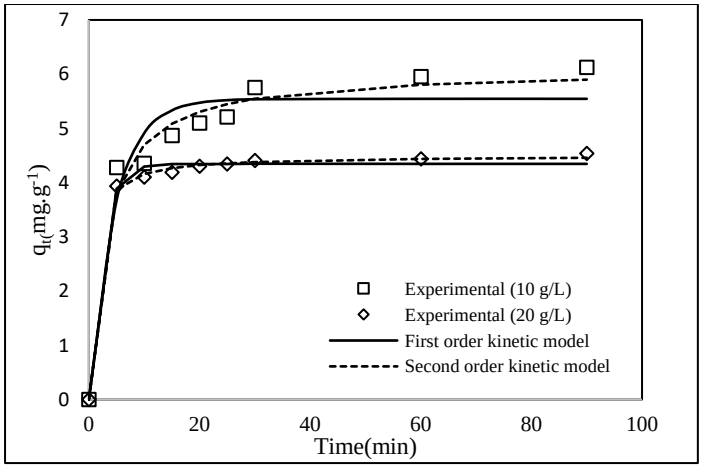


Figure 4. Adsorption dynamic by the nonlinear method for the adsorption of RO16 onto SMGC

Table. 1. Pseudo-first-order and pseudo-second-order rate constants and error analysis.

		Kinetic Model Constants				Error Analysis			
Experimental		Pseudo First Order		Pseudo Second Order		Pseudo First Order		Pseudo Second Order	
Dosage ($g\ L^{-1}$)	Exp. q_e ($mg\ g^{-1}$)	k_1 (min^{-1})	q_e ($mg\ g^{-1}$)	k_2 (min^{-1})	q_e ($mg\ g^{-1}$)	R^2	MPSD	R^2	MPSD
10	5.75	0.22	5.54	0.05	6.09	0.94	10.76	0.98	6.64
20	4.41	0.45	4.35	0.27	4.50	0.98	3.23	0.99	1.42

Isotherm adsorption studies

Establishing the best equilibrium data correlations will help the adsorption system design [29]. Two well-known models are the Langmuir and Freundlich isotherms, which explain how adsorbate molecules are distributed in solid phases at adsorption equilibrium. Equation 5 is the Langmuir isotherm model [30] for monolayer adsorption on a physically homogeneous surface without molecule interaction:

$$q = \frac{Q_{max}}{1+bc_e} \quad (5)$$

Where Q_{max} is the maximum adsorption capacity, b is an adsorption energy constant, and C_e represents dye solution equilibrium.

The empirical Freundlich isotherm model (Equation 6) [31] describes interactions between adsorbed molecules on heterogeneous surfaces with multilayer adsorption:

$$q = K_F c_e^{\ 1/n} \quad (6)$$

Where K_F is the adsorption capacity and n is a heterogeneity-dependent empirical formula. Fig. 5 shows Polymath's trial-and-error fitting of Equations 5 and 6. With its higher regression coefficients and lower MPSD error value, the Freundlich isotherm more closely represents the experimental data (Table 2). The Langmuir model demonstrated the Q_{max} of 9.72 mg g^{-1}.

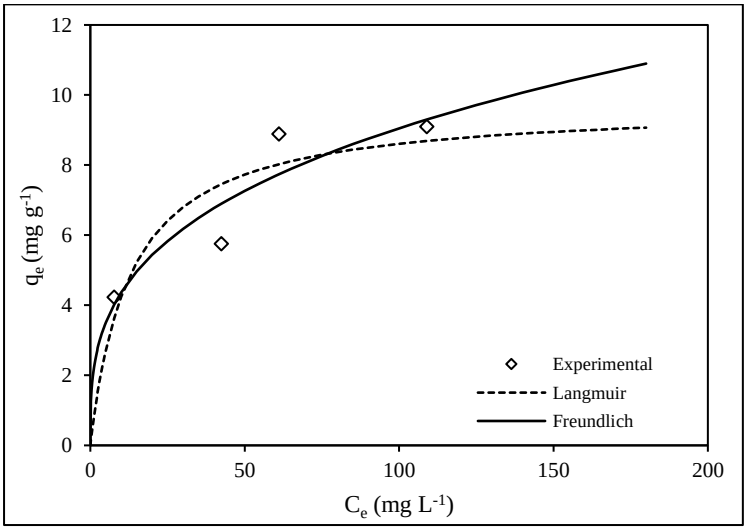


Figure 5. Adsorption isotherms by the nonlinear method for the adsorption of RO16 onto SMGC

Table 2. Freundlich and Langmuir isotherm constants and error analysis for RO16 adsorption

Isotherm Models Constant				Error Analysis			
Langmuir		Freundlich		Langmuir		Freundlich	
Q_{max} (mg.g^{-1})	b (L.mg^{-1})	K_F	n	R^2	MPSD	R^2	MPSD
9.72	0.08	2.11	3.16	0.92	24.40	0.95	17.25

Influence of pH

This study investigated the effect of pH on RO16 adsorption by varying the initial pH of the RO16 solution from 3 to 9. It was discovered that pH significantly impacts RO16 adsorption onto SGMC (Figure 6). The amount of RO16 removed decreased as the initial pH of the solution increased. At initial pH levels of 3, 5, 7, and 9, RO16 adsorption was 3.33, 3.25, 3.13, and 2.86 mg g^{-1}, equivalent to 100%, 97.63%, 93.84%, and 85.91% removal, respectively. Due to the negatively charged RO16 molecules' electrostatic repulsion with the adsorbent surface, RO16 removal was lower at pH 7 and 9. This was consistent with our data on pHPZC, which demonstrated that the SMGC became negatively charged when the pH of the dye solution exceeded 5.50, making it unfavourable for anionic contaminants such as RO16.

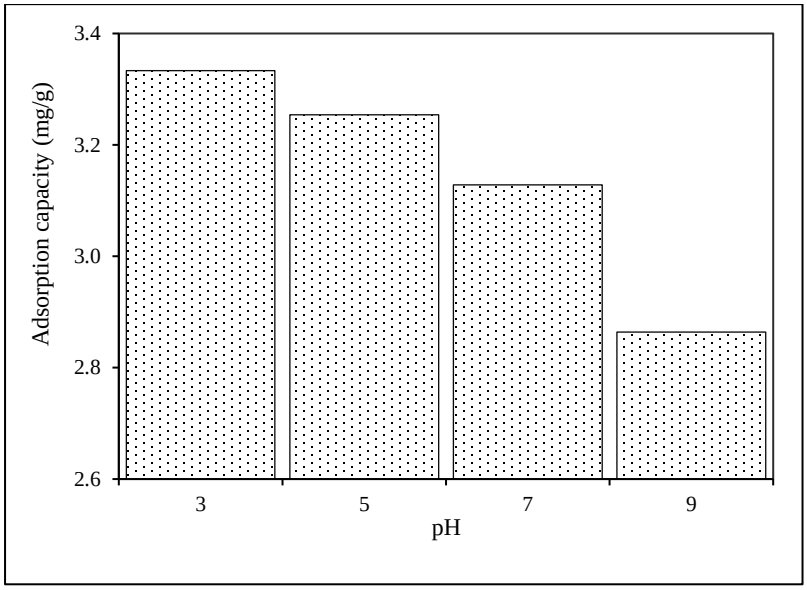


Figure 6. Effect of pH on the adsorption of RO16 onto SGMC

Influence of adsorbent dosage

As shown in Figure 7, as the amount of adsorbent used increased from 5 to 10.0 g L^{-1}, the RO16 dye adsorption capacity increased from 2.63 to 5.75 mg g^{-1}, equivalent to 13.17%-57.54% removal at equilibrium. The adsorption capacity for SGMC declined above 10.0 g L^{-1} to 1.99 mg g^{-1}, although at this point, the maximum removal of 100% was observed. The declining adsorption capacity at adsorbent dosages greater than 10 g L^{-1} is mainly due to the unsaturation of adsorption sites through adsorption. This is in line with the findings reported by Suhaimi et al. [32] in their study, which asserted that the overcrowding of the adsorbent sites was responsible for the decreasing removal capacity of methylene blue using bamboo-derived biochar.

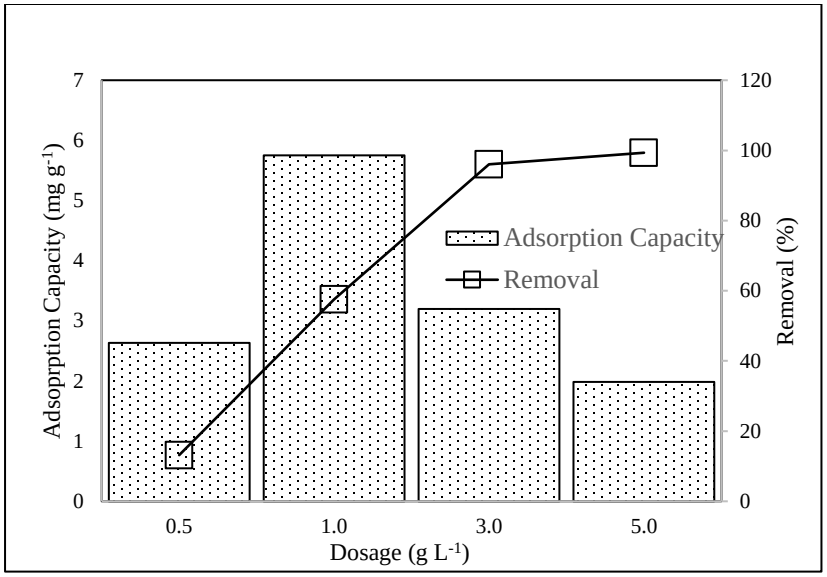


Figure 7. Effect of dosage on the adsorption of RO16 onto SGMC

Dye desorption

Figure 8 shows RO16 dye desorption from SMGC-loaded dye at different pH levels. As the pH increased, more dyes were desorbed. RO16 desorbed was 0%, 0.14%, 29.24%, and 68.38% at pH 3, 5, 8, and 11, respectively. As solution pH rises, the adsorbent surface net positive charge decreases. The electrostatic attraction of negatively charged dye particles to the more negatively charged SGMC surface indirectly aided desorption. This observation is consistent with research on reactive dye desorption using cationic polymer/bentonite by Li et al. [33].

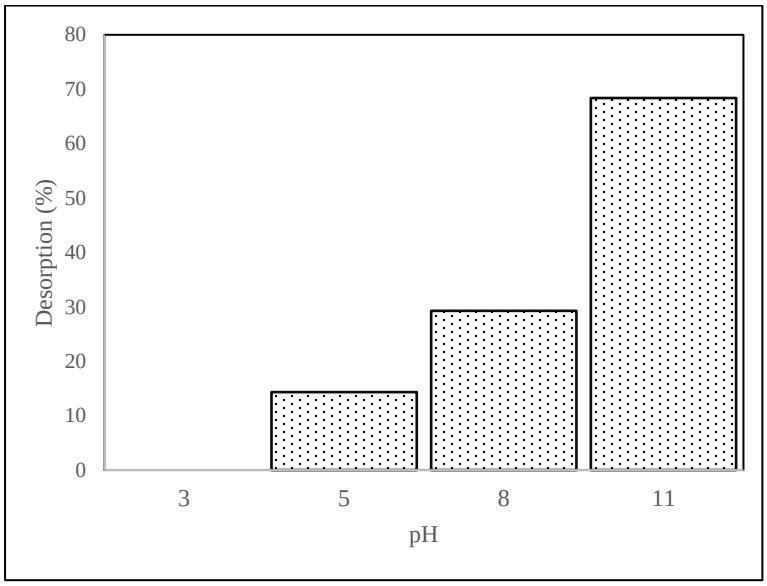


Figure 8. Desorption of RO16 from the dye-loaded SGMC

Conclusion

The results indicate that modifying the surface of grated coconut with a surfactant produced a promising reactive dye adsorbent for aqueous solutions. The pHPZC studies revealed that the SGMC had a net zero surface charge at a solution pH of 5.5, whereas the surface area

was relatively small at 1.86 m^2 g^{-1}. In the batch study, adsorption depended on the pH of the dye solution and the amount of adsorbent. The percentage of dye removed was greater in acidic conditions, with pH 3 showing the highest removal, whereas the adsorbent dosage of 10 g L^{-1} provided the highest adsorption capacity. With a maximum adsorption capacity of 9.72 mg g^{-1}, the Langmuir isotherm correlated best with the equilibrium adsorption data. The desorption of dye-loaded SMGC increased with increasing water pH and vice versa. Due to its abundance, ease of modification, and low cost, the application of SMGC proved to be an effective substitute treatment method for dye wastewater.

Acknowledgement

The authors would like to express their gratitude to the Faculty of Applied Sciences, Universiti Teknologi MARA, Shah Alam, for their generous support in providing the laboratory facilities necessary for conducting this research.

References

1. Katheresan, V., Kansedo, J., and Lau, S. Y. (2018). Efficiency of various recent wastewater dye removal methods: A review. *Journal of Environmental Chemical Engineering*, 6(4): 4676-4697.
2. Abdi, J., Vossoughi, M., Mahmoodi, N. M., and Alemzadeh, I. (2017). Synthesis of metal-organic framework hybrid nanocomposites based on GO and CNT with high adsorption capacity for dye removal. *Chemical Engineering Journal*, 326: 1145-1158.
3. Sreelatha, G., Ageetha, V., Parmar, J., and Padmaja, P. (2011). Equilibrium and kinetic studies on reactive dye adsorption using palm shell powder (an agrowaste) and chitosan. *Journal of Chemical & Engineering Data*, 56(1): 35-42.
4. Aksu, Z. and Dönmez, G. (2003). A comparative study on the biosorption characteristics of some yeasts for Remazol Blue reactive dye. *Chemosphere*, 50: 1075-1083.
5. Allègre, C., Moulin, P., Maisseu, M., and Charbit, F. (2006). Treatment and reuse of reactive dyeing effluents. *Journal of Membrane Science*, 269(1-2): 15-34.
6. Chollom, M. N., Rathilal, S., Alfa, D., and Pillay, V. L. (2015). The applicability of nanofiltration for the treatment and reuse of textile reactive dye effluent. *Water SA*, 41(3): 398-405.
7. Shindhal, T., Rakholiya, P., Varjani, S., Pandey, A., Ngo, H. H., Guo, W., ... and Taherzadeh, M. J. (2021). A critical review on advances in the practices and perspectives for the treatment of dye industry wastewater. *Bioengineered*, 12(1): 70-87.
8. Bhatnagar, A., Jain, A. K., Gupta, V. K., Jain, S., and Suhas, S. (2003). A comparative assessment of adsorbents prepared from industrial wastes for the removal of cationic dye. *Journal of the Indian Chemical Society*, 80: 267-270.
9. Demirbas, A. (2009). Agricultural based activated carbons for the removal of dyes from aqueous solutions: a review. *Journal of Hazardous Materials*, 167(1-3): 1-9.
10. Dai, Y., Sun, Q., Wang, W., Lu, L., Liu, M., Li, J., ...and Zhang, Y. (2018). Utilizations of agricultural waste as adsorbent for the removal of contaminants: A review. *Chemosphere*, 211: 235-253.
11. Anastopoulos, I., Bhatnagar, A., Hameed, B. H., Ok, Y. S., and Omirou, M. (2017). A review on waste-derived adsorbents from sugar industry for pollutant removal in water and wastewater. *Journal of Molecular Liquids*, 240, 179-188.
12. Liu, G., Dai, Z., Liu, X., Dahlgren, R. A., and Xu, J. (2022). Modification of agricultural wastes to improve sorption capacities for pollutant removal from water–a review. *Carbon Research*, 1(1): 24.
13. Rasheed, T., Shafi, S., Bilal, M., Hussain, T., Sher, F., and Rizwan, K. (2020). Surfactants-based remediation as an effective approach for removal of environmental pollutants—A review. *Journal of Molecular Liquids*, 318: 113960.
14. Kosaiyakanon, C., and Kungsanant, S. (2020). Adsorption of reactive dyes from wastewater using cationic surfactant-modified coffee husk biochar. *Environment and Natural Resources Journal*, 18(1): 21-32.

15. Ibrahim, S., Shuy, W. Z., Ang, H. M., and Wang, S. (2010). Preparation of bioadsorbents for effective adsorption of a reactive dye in aqueous solution. *Asia-Pacific Journal of Chemical Engineering,* 5(4): 563-569.
16. Karaman, C., Karaman, O., Show, P. L., Karimi-Maleh, H., and Zare, N. (2022). Congo red dye removal from aqueous environment by cationic surfactant modified-biomass derived carbon: equilibrium, kinetic, and thermodynamic modeling, and forecasting via artificial neural network approach. *Chemosphere,* 290: 133346.
17. Ofomaja, A. E., & Ho, Y. S. (2007). Effect of pH on cadmium biosorption by coconut copra meal. *Journal of Hazardous Materials,* 139(2): 356-362.
18. Rahim, A. R. A., Rabat, N. E., Johari, K., Saman, N., and Mat, H. (2019). Removal of lead (II) ions from aqueous solution using desiccated coconut waste as low-cost adsorbent. *CET Journal-Chemical Engineering Transactions,* 72.
19. Saleem, M., Wongsrisujarit, N., and Boonyarattanakalin, S. (2016). Removal of nickel (II) ion by adsorption on coconut copra meal biosorbent. *Desalination and Water Treatment,* 57(12): 5623-5635.
20. Khalid, K., and Hanafiah, M. A. K. M. (2014). Kinetic and isotherm adsorption studies of methylene blue on sulfuric acid treated spent grated coconut (*Cocos nucifera*). *Advanced Materials Research,* 970: 192-197.
21. Saidin, N. S., Hanafiah, M. A. K. M., Fatimah, I, Shaharudin, S. F., and Ibrahim, S. (2022). Utilisation of cationic surfactant modified grated coconut residue for the removal of reactive orange 16 dye from aqueous solutions: A fixed-bed column study. *Malaysian Journal of Chemistry,* 24: 150-157.
22. Kooh, M. R. R., Dahri, M. K., and Lim, L. B. (2017). Removal of the methyl violet 2B dye from aqueous solution using sustainable adsorbent Artocarpus odoratissimus stem axis. *Applied Water Science,* 7: 3573-3581.
23. Santos, S. C., Vilar, V. J., and Boaventura, R. A. (2008). Waste metal hydroxide sludge as adsorbent for a reactive dye. *Journal of Hazardous Materials,* 153(3): 999-1008.
24. Navya, A., Nandhini, S., Sivamani, S., Vasu, G., Sivarajasekar, N., and Hosseini-Bandegharaei, A. (2020). Preparation and characterization of cassava stem biochar for mixed reactive dyes removal from simulated effluent. *Desalination and Water Treatment,* 189: 440-451.
25. Namasivayam, C., and Sureshkumar, M. V. (2008). Removal of chromium (VI) from water and wastewater using surfactant modified coconut coir pith as a biosorbent. *Bioresource Technology,* 99(7): 2218-2225.
26. Chen, H., Zhao, J., Wu, J., and Dai, G. (2011). Isotherm, thermodynamic, kinetics and adsorption mechanism studies of methyl orange by surfactant modified silkworm exuviae. *Journal of Hazardous Materials,* 192(1): 246-254.
27. Abdelwahab, N. A., Shukry, N., and El-Kalyoubi, S. F. (2021). Separation of emulsified oil from wastewater using polystyrene and surfactant modified sugarcane bagasse wastes blend. *Clean Technologies and Environmental Policy,* 23: 235-249.
28. Khatibi, A. D., Yilmaz, M., Mahvi, A. H., Balarak, D., and Salehi, S. (2022). Evaluation of surfactant-modified bentonite for Acid Red 88 dye adsorption in batch mode: kinetic, equilibrium, and thermodynamic studies. *Desalination and Water Treatment,* 271: 48-57.
29. Yagub, M. T., Sen, T. K., Afroze, S., and Ang, H. M. (2014). Dye and its removal from aqueous solution by adsorption: a review. *Advances in Colloid and Interface Science,* 209: 172-184.
30. Langmuir, I. (1916). The constitution and fundamental properties of solids and liquids. Part I. Solids. *Journal of the American Chemical Society,* 38: 2221-2295.
31. Freundlich, H. M. F. (1906). Over the adsorption in solution. The *Journal of Physical Chemistry,* 57: 385-471.
32. Suhaimi, N., Kooh, M. R. R., Lim, C. M., Chou Chao, C. T., Chou Chau, Y. F., Mahadi, A. H., ... and Thotagamuge, R. (2022). The use of gigantochloa bamboo-derived biochar for the removal of methylene blue from aqueous solution. *Adsorption Science & Technology,* 202: 1-12.

33. Li, Q., Yue, Q. Y., Su, Y., Gao, B. Y., and Li, J. (2009). Two-step kinetic study on the adsorption and desorption of reactive dyes at cationic polymer/bentonite. *Journal of Hazardous Materials*, 165(1-3): 1170-1178.

Malaysian Journal of Analytical Sciences (MJAS)
Published by Malaysian Analytical Sciences Society

DETECTION AND IDENTIFICATION OF ILLICIT DRUGS IN VAPE LIQUID SAMPLES USING THE ENZYME MULTIPLIED IMMUNOASSAY TECHNIQUE, THIN LAYER CHROMATOGRAPHY AND GAS CHROMATOGRAPHY-MASS SPECTROMETRY

(Pengesanan dan Pengenalpastian Dadah Terlarang dalam Sampel Cecair Vape Menggunakan Kaedah Imunoasai Berganda Enzim, Kromatografi Lapisan Nipis dan Kromatografi Gas Spektrometri Jisim)

Low Jen Hou[1,2], Wan Nur Syuhaila Mat Desa[3] , Halijah Miran[1,2], Wan Nazirah Wan Yusuf[1,2] and Ruzilawati Abu Bakar[1,*]

[1]*Department of Pharmacology, School of Medical Sciences, Universiti Sains Malaysia Health Campus, 16150 Kubang Kerian, Kelantan, Malaysia.*
[2]*Hospital Universiti Sains Malaysia, 16150 Kubang Kerian, Kelantan, Malaysia.*
[3]*Forensic Science Programme, School of Health Sciences, Universiti Sains Malaysia Health Campus, 16150 Kubang Kerian, Kelantan, Malaysia*

[*]*Corresponding author: ruzila@usm.my*

Received: 22 June 2023; Accepted: 4 October 2023; Published: 30 October 2023

Abstract

Vaping is a common phenomenon in the world including in Malaysia, and one that involves all strata of society. Recently, vaping has become an unintended mode of delivery for various illicit drugs of abuse. The objective of this study is to detect and identify the presence of illicit substances including opiates, tetrahydrocannabinol (THC), amphetamine-type stimulants (ATS), benzodiazepines (BZD), barbiturates, phencyclidine, ketamine and mitragynine in three vape liquid samples provided by the National Anti-Drugs Agency (NADA), Kelantan, Malaysia. Some of these drugs have been linked to fainting episodes after vaping. The samples were analysed using enzyme multiplied immunoassay technique (EMIT), thin layer chromatography (TLC) and gas chromatography-mass spectrometry (GC-MS). One of the samples was found to contain ketamine (the band was seen on the TLC plate and the result was further confirmed using GC-MS, with 99% match) with an estimated concentration of at least 25000 ng/mL by linear extrapolation of the calibration curve. Two other samples were noted to contain nicotine (bands were seen on TLC plate and also confirmed by GC-MS). Ketamine abuse is not widely reported because the vast majority of drug-screening setups do not offer testing for ketamine. Ultimately, vape liquid samples in this study were found to contain illicit drugs such as ketamine and nicotine. This suggest that tighter regulation would help curb this health bane on society.

Keywords: vape, illicit drugs, enzyme multiplied immunoassay technique, thin layer chromatography, gas chromatography mass spectrometry

Abstrak

Vape atau rokok elektronik merupakan fenomena yang lazim di dunia termasuklah di Malaysia melibatkan semua lapisan masyarakat. Kebelakangan ini vape telah menjadi salah satu cara penggunaan dadah terlarang. Objektif kajian ini untuk mengesan

dan mengenalpasti dadah terlarang termasuk opiat, tetrahidrokanabinol (THC), amphetamine-type stimulant (ATS), benzodiazepin (BZD), barbiturat, phencyclidine, ketamin and mitragynine yang terdapat di dalam 3 sampel vape daripada pihak Agensi Anti Dadah Kebangsaan (AADK), Kelantan, Malaysia yang mana telah dikaitkan dengan keadaan tidak sedarkan diri pengguna vape tersebut. Sampel-sampel tersebut telah dianalisa dengan menggunakan kaedah imunoasai berganda enzim, kromatografi lapisan nipis dan kromatografi gas spektrometri jisim. Salah satu sampel didapati mengandungi ketamin (Jalur yg berkenaan kelihatan pada plat TLC dan disahkan oleh GC-MS dengan 99% kepastian) dengan kepekatan yang dianggarkan sekurang-kurangnya 25000 ng/mL daripada unjuran lengkung kalibrasi. Dua sampel yang lain didapati mengandungi nikotin (jalur yang berkenaan kelihatan pada plat TLC dan disahkan melalui GC-MS). Penyalahgunaan ketamin kurang dilaporkan kerana kebanyakan pusat saringan untuk pengesanan dadah tidak menawarkannya. Sebagai kesimpulan, sampel cecair vape dalam kajian ini didapati mengandungi dadah terlarang (ketamin) dan nikotin. Penguatkuasaan undang-undang yang lebih ketat mungkin diperlukan untuk membantu menangani kemudaratan kesihatan ini dalam masyarakat.

Kata kunci: vape, dadah terlarang, teknik imun berganda enzim, kromatografi lapisan nipis, kromatografi gas-spektrometer jisim

Introduction

Vape or electronic cigarettes (EC) are perceived by the smokers to be healthier alternatives to tobacco cigarettes [1]. These devices are used to deliver nicotine, flavourings and other chemicals via aerosolization [2, 3]. Vape liquids containing flavours, solvents and other unknown ingredients, are often heated in e-cigarettes and vape rigs, and creating an aerosol that users inhale.

Vaping is a common phenomenon globally. In Malaysia, the prevalence of EC uses increased from 0.8% in 2011 to 4.9% in 2019 [4]. Alarmingly, a cross-sectional study conducted in 2018 showed 73% of the students from a secondary school in Kuala Lumpur were EC users [5]. Unlike tobacco cigarette, ECs and vapes have been not regulated in Malaysia to date: there is no regulation; neither towards the group of users, the electronic device used (safety or design) nor the liquid contents. Therefore, the sale of these devices and related products to users including underage children or youth is possible which could lead to health risk problems and also criminal abuse of the vape liquid.

Daily vaping has been reported to increase the risk of developing myocardial infarction and E-cigarette or Vaping Use-Associated Lung Injury (EVALI). These problems may arise through various mechanisms, including oxidative stress and inflammation, DNA damage, altered haemodynamic and platelet activity [6-8]. Vape liquid's flavour has been reported to contain illegal psychoactive drugs which was adulterated in addition to the four primary components of vape liquids (propylene glycol, glycerol, various flavourings, nicotine). Previous literatures have reported the detection of amphetamine-type stimulants (ATS) [9], tetrahydrocannabinol (THC) [10, 11] and even various new psychoactive substances (NPS) [12] in vape liquids. These substances may cause significant health and development effects, especially among young users due to the are exposure to drugs of abuse via vaping itself and other side effects of vaping.

The presence of illicit drugs in vape liquids is factual. These have also been reported in other studies [13,14]. Analysis of drug of abuse in vape liquid was not implemented due to the absence of regulation and enforcement on vape liquid ingredients. To date, there is no standard procedure for the analysis of vape liquid, or suspected adulterated vape liquids when those samples are submitted for analysis to government laboratories. Therefore, this study reports on in-house exploratory screening and confirmatory analysis method of illicit substances in vape liquid. Three vape liquid samples were collected from National Anti-Drugs Agency (NADA), Kelantan, Malaysia and were tested for the presence of illicit drugs including opiates, THC, ATS, BZD, barbiturates, phencyclidine, ketamine and mitragynine. The samples were assessed following Pharmacology Laboratory, Hospital USM procedures and forensic narcotic screening protocols.

Materials and Methods

Chemicals and reagents

Methamphetamine (MA) hydrochloride, methyl enedioxymethamphetamine (MDMA) hydrochloride, nitrazepam, nimetazepam, diazepam, flunitrazepam and

mitragynine drug standards were purchased from Lipomed (via Labchem, Malaysia). Amphetamine sulphate, alprazolam, ketamine hydrochloride and nicotine were purchased from Sigma Aldrich, (USA). Morphine, codeine, oxazepam and midazolam were purchased from Cerilliant (Texas, USA).

Thin layer chromatography (TLC) reagents used in liquid-liquid extraction and as mobile phase components, ethyl acetate, methanol, ammonia 28%, chloroform, iso-propanol and petroleum benzine, were acquired from Merck, USA. The visualization reagents, ninhydrin, hexachloroplatinic acid, potassium iodide, sulphuric acid, naphthyl ethylenediamine, glacial acetic acid and bismuth nitrate were purchased from Merck, USA. Fast Black K, dimethylaminobenzaldehyde were acquired from Sigma Aldrich (USA). Sodium nitrite and ammonium sulphamate were bought from Acros Organic (New Jersey, USA).

Sample preparation: Drug standard

The drug standards methamphetamine (MA) hydrochloride, methylenedioxymethamphetamine (MDMA) hydrochloride, nitrazepam, nimetazepam, diazepam, flunitrazepam, mitragynine amphetamine sulphate, alprazolam, ketamine hydrochloride, nicotine, morphine, codeine, oxazepam and midazolam were prepared at 100 ng/mL concentration.

EMIT

For immunoassay analysis, vape liquid samples (sample 1, sample 2 and sample 3) were subjected to analysis without further sample preparation.

TLC

For TLC, the samples were subjected to liquid-liquid extraction (LLE). For benzodiazepine analysis, neutral extraction was performed by adding 0.6ml petroleum benzine to 0.3 ml of vape liquid sample and was centrifuged at 1000 rpm for 5 min. The top layer of the mixture that was the organic layer was removed. The sample was dried at 50 ^{o}C.

For ATS, mitragynine and for the analysis of other slightly alkaline substances such as ketamine and nicotine, the samples were first alkalinized to about pH 10 by adding dilute NaOH to 0.3 mL of vape liquid sample each. Basic extraction was then performed by adding 1ml of chloroform to the flask as the extraction solvent.

Extraction procedure

1 mL of vape liquid sample and 2 mL of chloroform were added to the tubes. The tubes were shaken on a rotator for 10 min. This was followed by centrifugation at 3000 rpm for 30 min. After centrifugation, the chloroform phase was transferred into V-tubes and evaporated to dryness under a stream of nitrogen at 45 °C. The dried extract was reconstituted with 70 µL of methanol, vortex-mixed and injected into the GC-MS system.

EMIT screening

The vape liquid samples were screened by a Viva-E drug analyser (Siemens, Germany) for the presence of opiates, tetrahydrocannabinol (THC), amphetamine-type stimulants (ATS), benzodiazepines (BZD), barbiturates and phencyclidine which uses Enzyme Multiplied Immunoassay Technique (EMIT).

Thin layer chromatography

Thin layer chromatography was performed for analytes that had significant readings on EMIT screening, as part of confirmation. 20µL of extracted vape liquid samples were spotted onto TLC silica plates, alongside drug standards to determine presence of substance of abuse using a TLC spotter.

For ATS TLC plate, the bottom of the spotted plate was placed in ethyl acetate/methanol/ammonia (8.5: 1.0: 0.5) for development and sprayed with visualization reagent (10% ninhydrin and Fast Black K). The spot retention factor (R_{fs}) values were compared against ATS standards including methamphetamine, amphetamine and 3,4-methylenedioxy-methamphetamine (MDMA). While this plate was specifically optimized for the ATS detection, it also can detect other amines, such as ketamine and mitragynine.

For BZD TLC plate, acetone/hexane mixtures (1:3) were used as developing solvent system. Both

unhydrolyzed and hydrolysed vape samples were spotted onto the TLC plates. The spot Rfs were compared against benzodiazepine standards including oxazepam, nitrazepam, nimetazepam, flunitrazepam, midazolam. Dragendorff's reagent and Bratton-Marshall's reagent were used as visualization reagents for unhydrolyzed and hydrolysed samples respectively.

For mitragynine plate, ethyl acetate/hexane (7:3) was used as a mobile phase. Spot R_{fs} were compared against mitragynine standard. Ehrlich's reagent (5% dimethylaminobenzaldehyde in 95% ethanol) was used as the visualization reagent.

Gas chromatography mass spectrometry

Drug standard mixtures and all the vape liquid samples (diluted and extracted) were analysed using GC-MS method to confirm the presence of the substances found during TLC. Narcotic scan program parameters were able to resolve all drug standards of interest. An Agilent 7890B Gas Chromatography System and 7683 Autosampler Agilent (USA) paired with Agilent 5977B Mass Spectrometry detector was used. Enhanced Chemstation software (Version F.01.03.2357) Agilent Technologies Inc. (USA) was used for instrument control and data acquisition. Spectral library comparisons for compound identification are referred to National Institute of Standards and Technology, NIST 14 Mass Spectral Library and Search Software (Version 2014).

Separation was carried out using HP5 MS capillary column (30 m x 250 m x 0.25 m) with helium carrier gas at a constant flow of 1.0 mL/min and injection in split mode ratio of 50 mL/min. The injector was heated to 27 °C and the transfer line is heated to 280 °C. Initial oven temperature is 80 °C then ramped at 20 °C/min to 150 °C and hold for 2 minutes. Second ramp is at 20 °C/min to 300 °C and hold for 14 minutes. The mass spectra were collected after 3 minutes solvent delay time. The ionisation voltage was 70 eV and the mass range were 40-500 m/z.

Results and Discussion

EMIT

EMIT screens were negative for opiates, THC, barbiturates and phencyclidine in all three examined vape liquid samples. Conversely, EMIT recorded readings for ATS in sample 1 and sample 2 whilst trace readings for BZD compounds were detected in all three samples.

TLC

None of the samples contains ATS. However, one band with higher Rf was noted on the ATS plate (Table 1).

ATS TLC plates revealed that none of the sample contains ATS compounds. In sample 1, the R_f values of the two bands were not comparable to the ATS standards. Interestingly, in vape liquid sample 2, bands for methamphetamine, amphetamines or MDMA were detected on ATS plate despite EMIT screening for ATS recorded detection of 6323.5 ng/mL. Nonetheless, a brownish band at R_f 0.75 and a large violet coloured band at R_f 0.93 were observed on the ATS plate. Although for the screening for MDMA revealed a violet band, the violet band in sample 2 may not be the same compound as MDMA since the R_f was different (R_f 0.93) compared to the Rf for MDMA was 0.57.

For BZD TLC plate there was a band that was compatible with flunitrazepam in sample 1, while there was one vague band compatible with diazepam is in sample 2 and 3. The presence of these unknown bands on both plates required further analytical evaluation to determine the compound. TLC for mitragynine was also performed to sample 1, however the results was negative. The amounts in sample 2 and 3 were insufficient for testing, thus was not performed.

Table 1. Summary of TLC analysis of ATS and BZD plate

Standards and Samples	ATS Plate			BZD Plate		
	Number of Band	Colour of Band	R_f Value	Number of Band	Colour of Band	R_f Value
Methamphetamine standard	1	Grey	0.56			
MDMA standard	1	Violet	0.57			
Amphetamine standard	1	Light Yellow	0.61			
Nimatezepam standard				1	Yellow	0.18
Nitrazepam standard				1	Yellow	0.12
Flunitrazepam standard				1	Yellow	0.15
Diazepam standard				1	Yellow	0.26
Sample 1	2	Pink Violet	0.44 0.75	1	Yellow	0.15
Sample 2	2	Brownish Violet	0.75 0.93	1	Pale yellow	0.26
Sample 3	0	Not available	Not available	1	Pale yellow	0.26

GC-MS

The chromatogram of the mixed drug standards showed that ATS standards eluted earlier than the BZD substances (Figure 1). All drugs were well separated and adequately resolved, despite there being similar chemical properties among the ATS group. Similarly, all four BZD standards separated adequately within analysis run time.

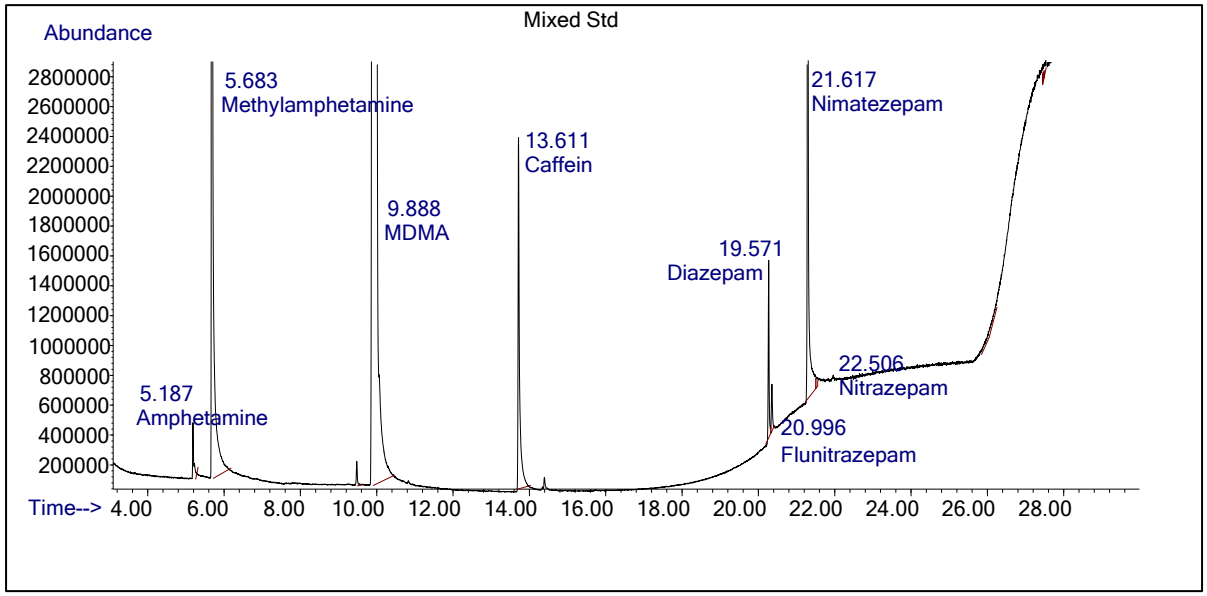


Figure 1. GC-MS total ion chromatogram (TIC) of mixed ATS and benzodiazepine (BZD) drug standards for cross reference with neat and extracted vape liquid samples

A large peak with retention time (R_t) ranging from R_t 3.553 to R_t 5.643 in mixtures of glycerine, L-arabinatol and ethyl acetate was noted in GC-MS total ion chromatogram (TIC) of diluted vape liquid samples (Figure 2). These compounds could be carriers for the vape liquid active compounds.

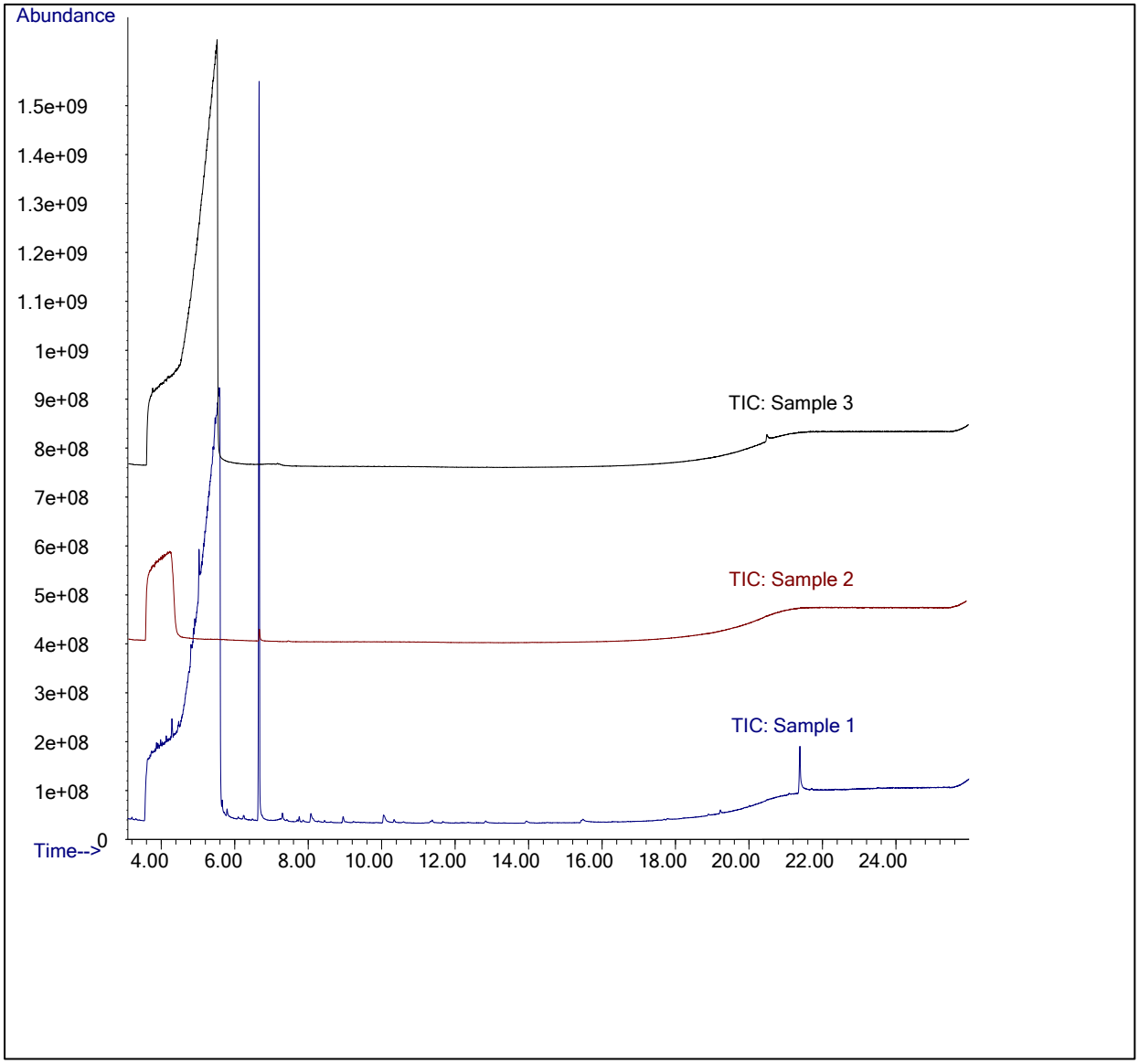


Figure 2. GC-MS total ion chromatogram (TIC) of neat vape liquid samples (2% vol/vol methanol).

Since amphetamine and methamphetamine compounds appeared at R_t 5.185 and R_t 5.679 respectively as shown in Figure 1, the presence of carrier peaks (shown in Figure 2) could have obscured the peaks of ATS compounds. Therefore, extraction was further performed on the samples in order to eliminate the effect of carrier. As a result, better TIC profiles were observed in the extracted vape liquid sample 1, 2 and 3.

Sample 1

GC-MS analysis was unable to detect the presence of the ATS compounds in sample 1. However, two prominent compounds were present at high levels peaks of R_t 6.674

and R_t 21.591 as shown in Figure 3. A mass spectral library search tentatively identified the peaks as 2-Heptenoic acid, heptadecyl ester (25% Qual) and 2,3-Diphenylbenzo-1,4-dioxin (27% Qual) respectively. Because the elution time of Sample 1 peak at R_t 21.591 is very close to the retention time of nimatezepam standard, there was a possibility of the GC chromatographic shift. The shift was checked out by comparing the mass spectrum of the compound and it was confirmed that neither nimatezepam nor lunitrazepam were present in sample 1 (Figure 4).

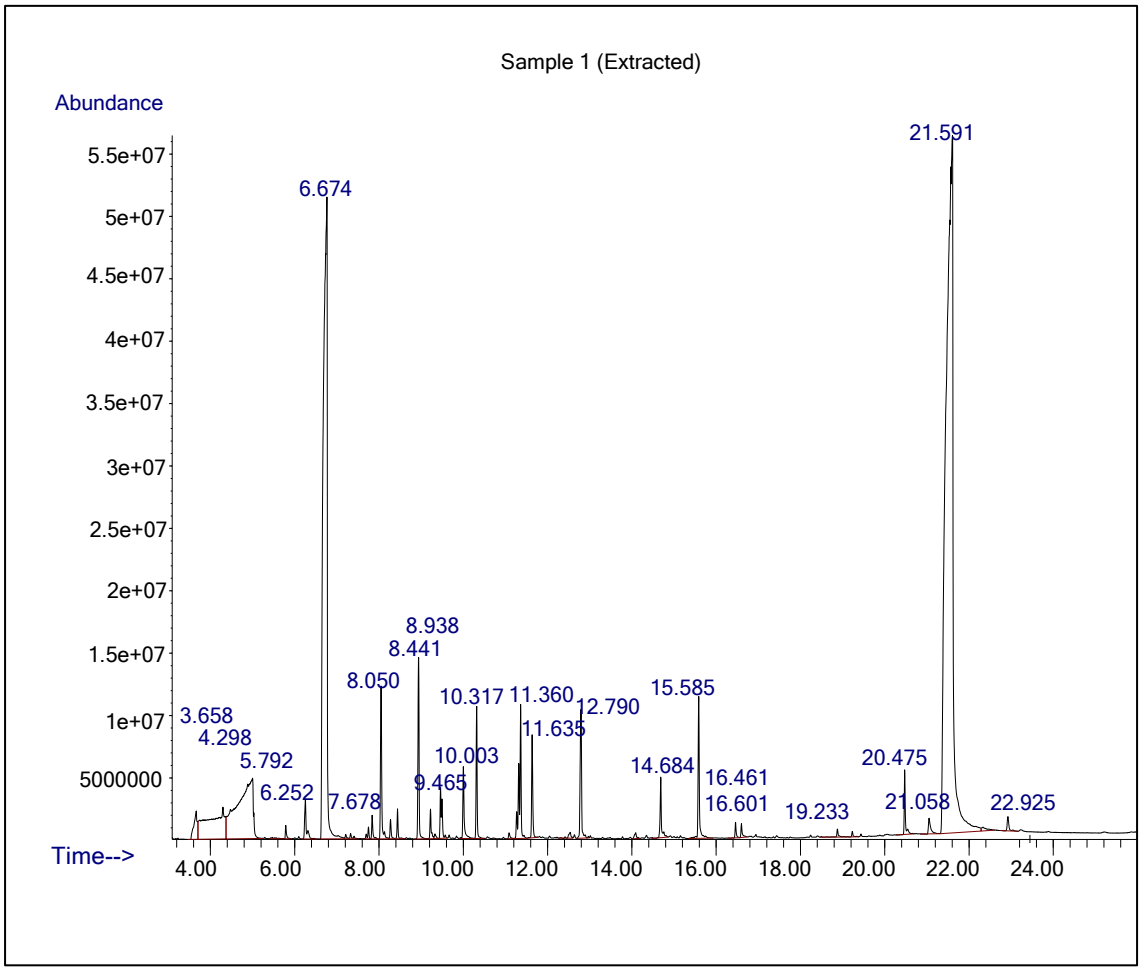


Figure 3. GC-MS total ion chromatogram (TIC) of extracted vape liquid sample 1

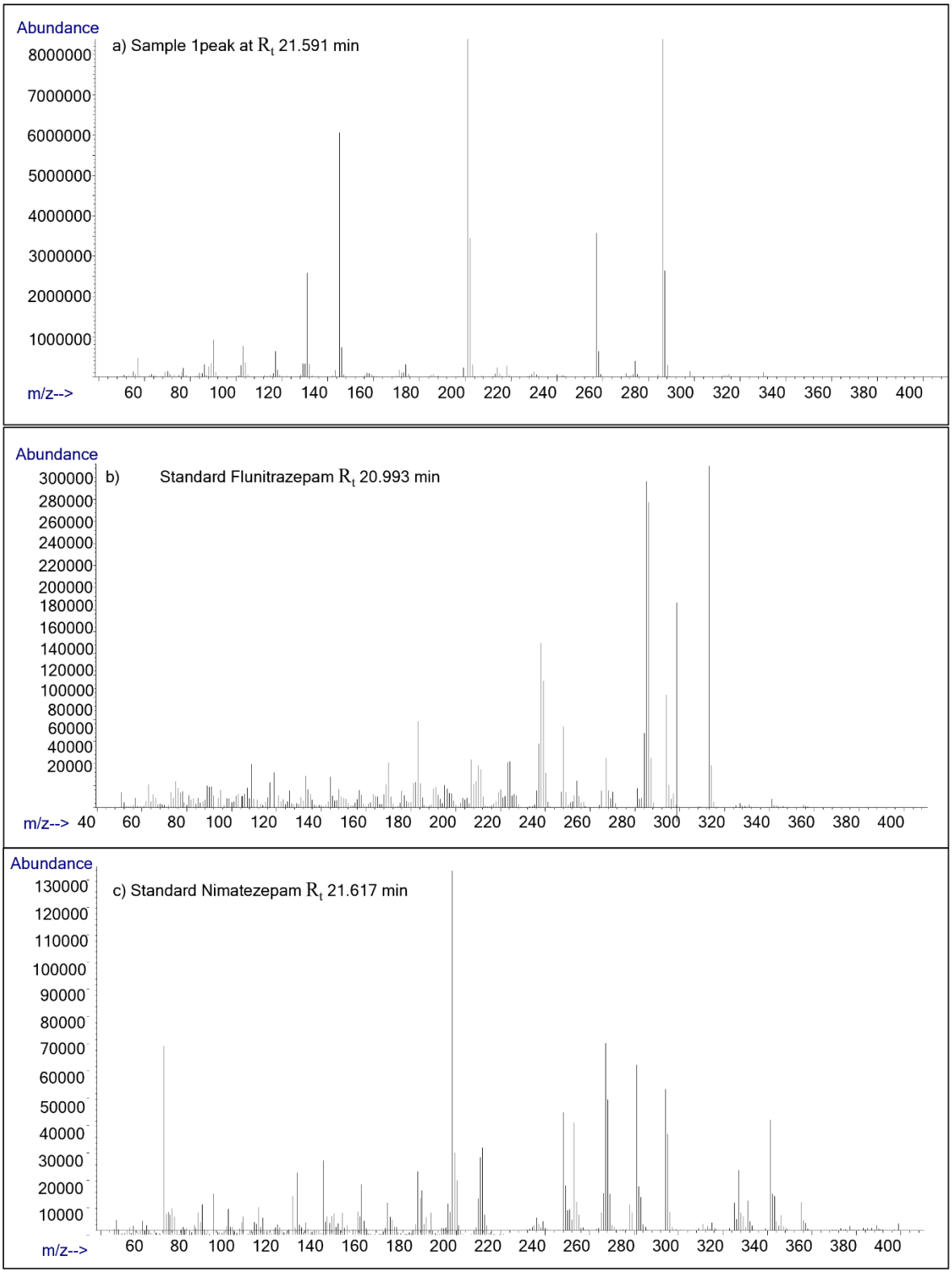


Figure 4. Mass spectrum of benzodiazepines in comparison to sample 1 peak R_t 21.591

Sample 2

The analysis of sample 2 using GC-MS identified peaks for nicotine and ketamine from the extracted sample (95-99% certainty according to NIST14 database), eluted at Rt 7.6 and Rt 13.9 respectively (Figure 5). Nicotine was identified with major fragments at 84 and 133 m/z as seen in Figure 6. The molecular ion, M+, appears at m/z = 162 and M-1 peak (m/z = 161,) was characteristic for cyclic amines [15]. Ketamine was identified at 179 and 220 m/z as shown in Figure 7.

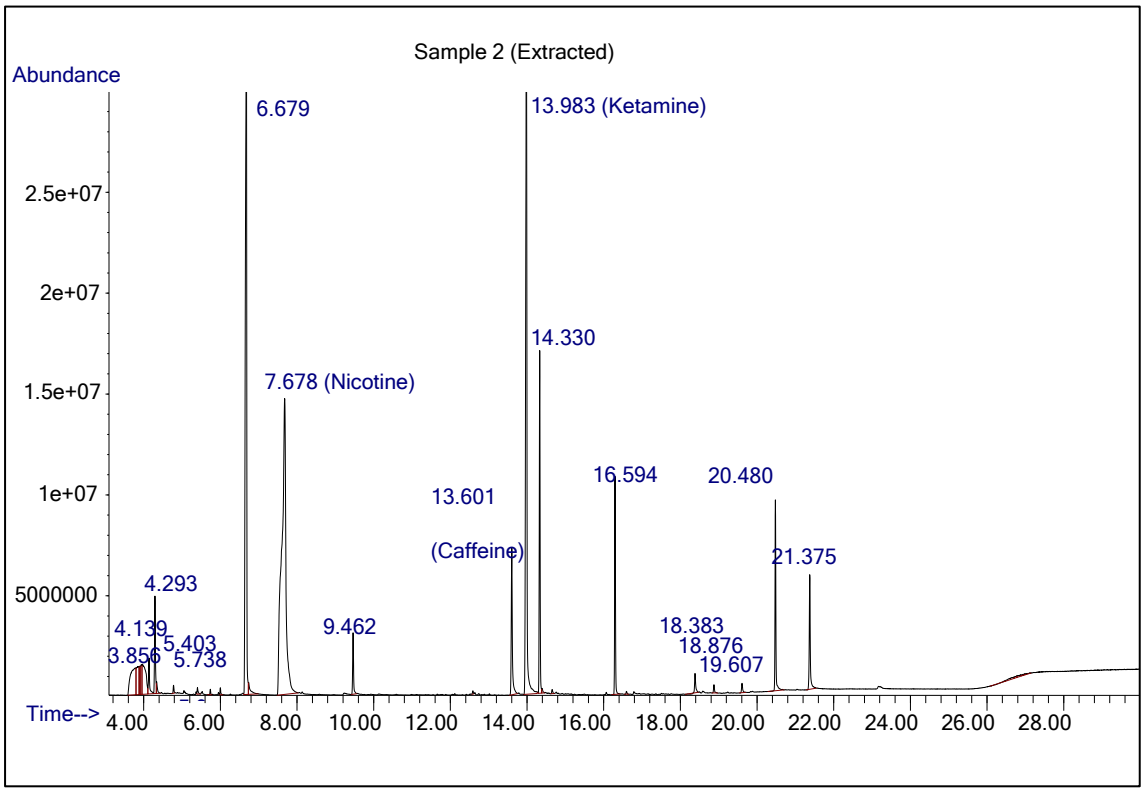


Figure 5. GC-MS total ion chromatogram (TIC) of extracted vape liquid sample 2

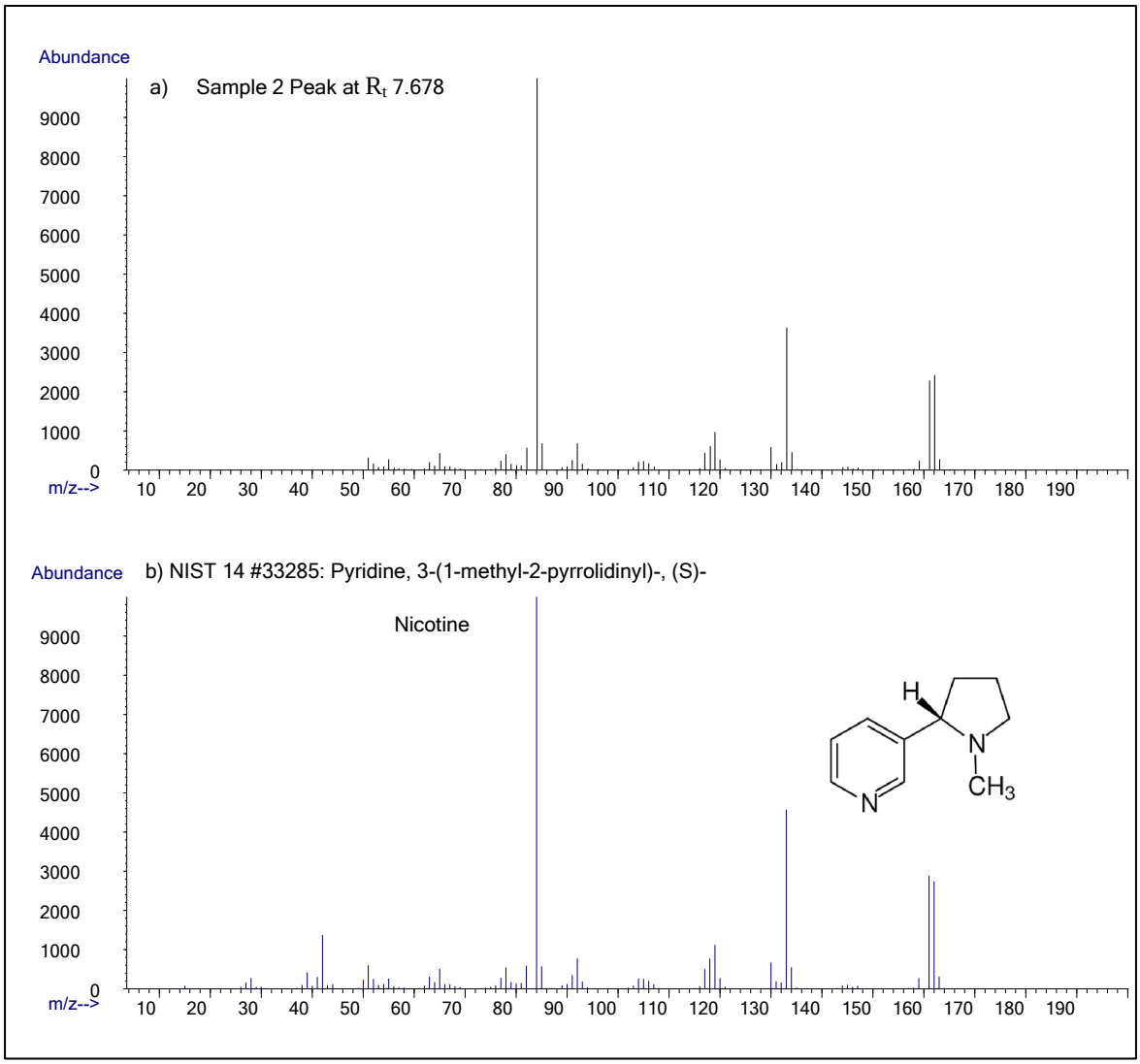


Figure 6. Mass spectrum of peak RT 7.675 identified as Pyridine, 3-(1-methyl-2-pyrrolidinyl)-, (S)-, generally known as nicotine.

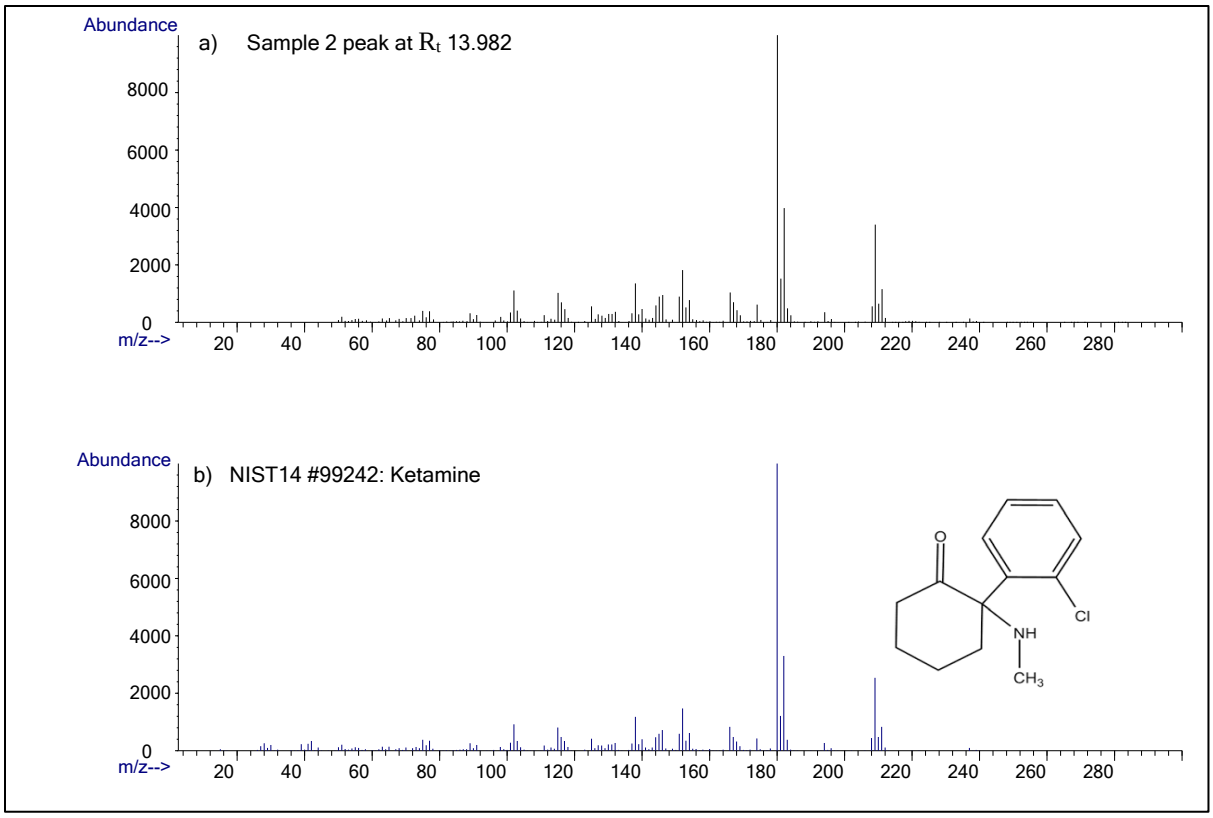


Figure 7. Mass spectrum of peak RT 13.983 identified as ketamine

Sample 3

TIC confirms the absence of ATS compounds in sample 3 in GC-MS analysis (Figure 8). In comparison to the other two samples, nicotine and ketamine were not detected. To confirm the BZD plate which obtained a band consistent to the diazepam standard, the mass spectrum of sample at RT 19.615 compared to diazepam peak RT 19.575 as presented in Figure 9.

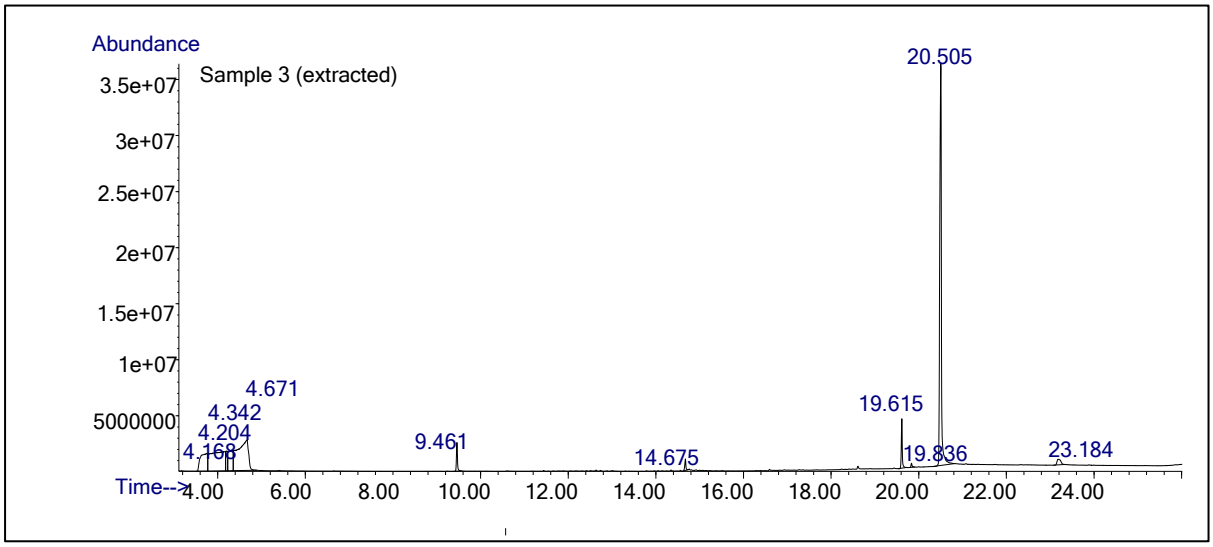


Figure 8. GC-MS total ion chromatogram (TIC) of extracted vape liquid samples sample 3

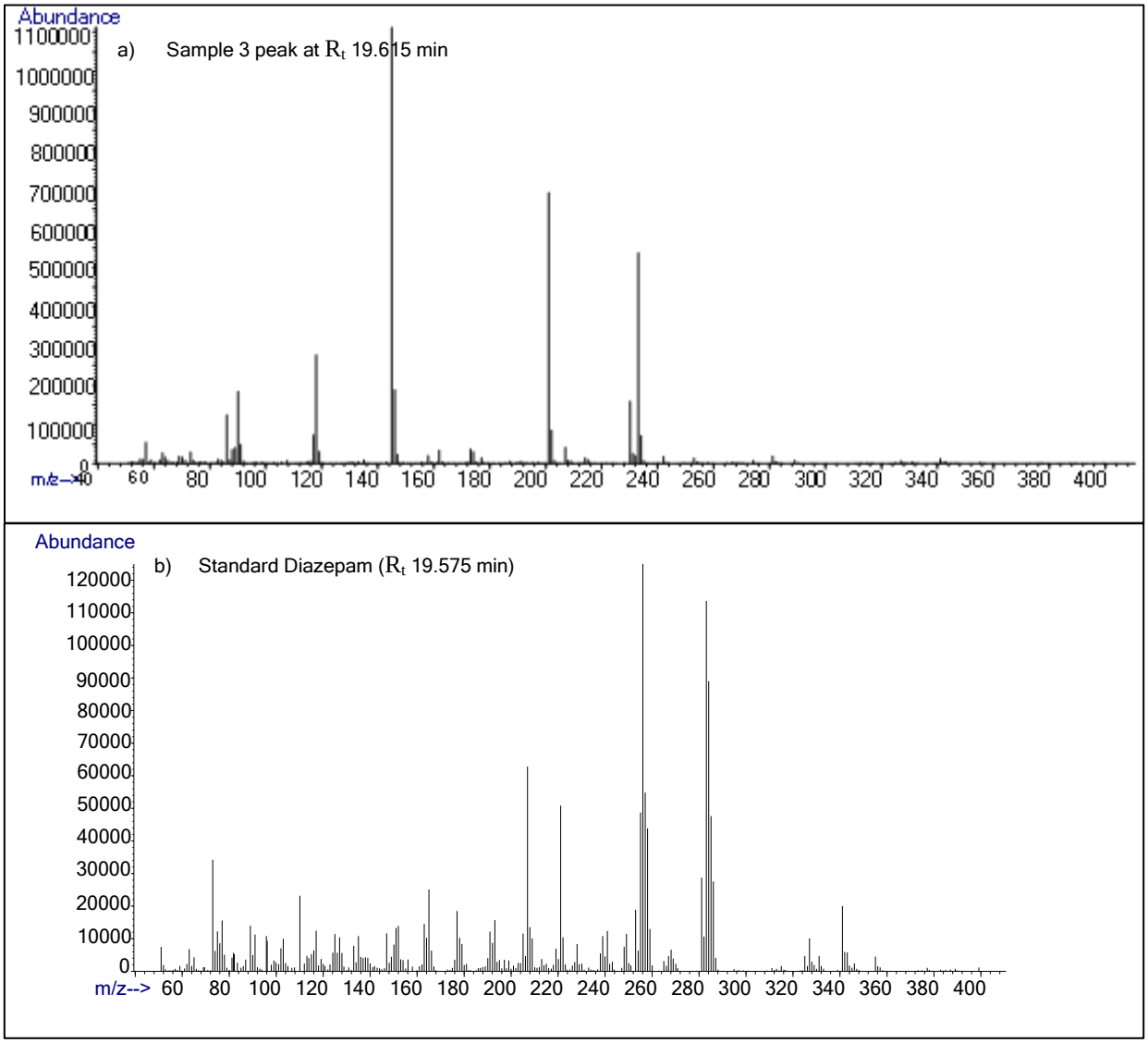


Figure 9. Mass spectrum of sample 3 peak R_t 19.615 in comparison to diazepam standard R_t 19.575

Vaping was originally intended to be a substitute to smoking, primarily serving as a nicotine delivery tool and reducing the number of harmful substances and carcinogens found in regular cigarettes. However, it has become an emerging system of illicit drug delivery [16] for various drugs of abuse, exacerbated by poor regulation from the authority. Ketamine has been discovered in recent raids in Malaysia [17] and also been reported in vape in previous surveys [12], but is relatively uncommon, most likely due to gross under detection since ketamine was not a drug that is routinely screened.

Abuse of methamphetamine dominates current cases in Kelantan [18], alongside benzodiazepines (nimetazepam, nitrazepam) and to a lesser extent opiates and THC. Ketamine on the other hand is infrequently reported, as it is not officially part of drug screening in district hospitals, or even in most tertiary referral centres in Kelantan. No exact history was available from subjects who used these vape samples. However, on further questioning, NADA did reveal general phenomena of light-headedness and fainting after using

this vape. The symptoms could be either due to ketamine or high levels of nicotine in the vape liquid.

Ketamine is a dissociative hallucinogen used clinically for the induction and maintenance of anaesthesia, acting via NMDA receptor blockade which explained the effects of light-headedness and fainting experienced by those using this vape liquid. Ketamine was not detected during screening since EMIT screening for ketamine was not available. The sample volume provided was also inadequate for a ketamine dipstick. While the ATS TLC plate revealed suspicious bands, we could not definitively confirm the presence of ketamine until GC-MS analysis was performed.

Even at lower doses, ketamine can cause changes in sensory perception, including visual or auditory hallucinations and a sensation of feeling detached from oneself and one's surroundings, hence its categorization as a dissociative. Other adverse effects include disorientation, confusion, or loss of motor coordination, dizziness, nausea, or vomiting. Increased blood pressure, heart rate, breathing, or body temperature are commonly seen. At high doses, ketamine induces loss of consciousness and unresponsiveness with respiratory depression (shallow or irregular breathing). The lethal dose for ketamine for a 70 kg adult is estimated to be about 4200 mg. LD_{50} in rats are established at 447 mg/kg. Typical doses used for anaesthesia range around 450-750mg and recreational use (via snorting) ranges around 75-125 mg.

Nicotine was detected in two of the vape samples. This result is alarming since nicotine use may result in dependence and abuse. With greater delivery, faster rate of absorption and higher nicotine concentration, the risk of dependence may be higher. Furthermore, the pharmacological effects of nicotine in the brain are influenced by the mode of administration and dose [19]. Since vaping has the potential of high and rapid nicotine delivery, vaping can cause or maintain nicotine dependence – this is why vaping as a method for smoking cessation is controversial [20]. It has been reported that a cigarette contains between 6.17-28.86 mg of nicotine, varying between cigarette brands [21]. Nicotine concentration in vape liquid varies considerably, ranging from 0-87.2 mg/mL [22]. The amount of nicotine delivered and the way in which it is delivered influence the addictiveness of a tobacco product [23]. As the vapers under the impression that vaping is safer than cigarette smoking, they may not control the amount of vape used. In addition, the heating process for vapes may lead to the generation of hazardous compounds [24]. Drugs may be abused freely in future through vaping since it is not obvious that the person took drugs using vape compared to "chasing the dragon", one of the current modes of administration using aluminium foils adopted by the drug users.

Conclusion

We detected ketamine in 1 of the 3 vape samples and nicotine in 2 samples collected from NADA. The presence of psychoactive substances in vape is a concerning issue as these products are sold to school going children. Here, we would like to ask for a reassessment of the risks and dangers of vaping and potentially the enactment of stricter laws and regulations to cover its use (essentially to ensure it does not contain dangerous psychoactive substances) and trade (limiting its availability to underaged children).

Acknowledgements

The authors would like to thank Muhamad C Ismail of AADK Kota Bharu for supplying the vape samples. The authors would also like to thank Mr Mohd Lukman Muhamad from Pharmacology Laboratory, Hospital Universiti Sains Malaysia for technical assistance in vape extraction and thin layer chromatography.

References

1. Choi, K., Fabian, L., Mottey, N., Corbett, A. and Forster, J. (2012). Young adults' favorable perceptions of snus, dissolvable tobacco products, and electronic cigarettes: Findings from a focus group study. *American Journal of Public Health*, 102(11): 2088-2093.
2. Brown, C. J. and Cheng, J. M. (2014). Electronic cigarettes: Product characterization and design considerations. *Tobacco Control*, 23(Suppl. 2): 4-10.
3. Centers for Disease Control and Prevention (2020). E-cigarette, or vaping, products visual dictionary. Access from https://www.cdc.gov/tobacco

/basic_information/e-cigarettes/pdfs/ecigarette-or-vaping-products-visual-dictionary-508.pdf.

4. Driezen, P., Nordin, A. S. A., Hairi, F. M., Yee, A., Tajuddin, N. A. A., Hasan, S. I., Danaee, M., Kamaludin, I. S., Kaai, S. C., Yan, M., Grey, M., Quah, A. C. K., Thompson, M. E. and Fong, G. T. (2022). E-cigarette prevalence among Malaysian adults and types and flavors of e-cigarette products used by cigarette smokers who vape: Findings from the 2020 ITC Malaysia Survey. *Tobacco Induced Diseases*, 20:1-7.
5. Nur Atikah, A. H., Wee, L. H., Nur Zakiah, M. S., Chan, C. M. H., Mohamed Haniki, N. M., Swinderjit, J. S. and Siau, C. S. (2019). Factors associated with different smoking statuses among Malaysian adolescent smokers: A cross-sectional study. *BMC Public Health*, 19(Suppl 4): 1-8.
6. Alzahrani, T., Pena, I., Temesgen, N. and Glantz, S. A. (2018). Association between electronic cigarette use and myocardial infarction. *American Journal of Preventive Medicine*, 55(4): 455-461.
7. Buchanan, N. D., Grimmer, J. A., Tanwar, V., Schwieterman, N., Mohler, P. J. and Wold, L. E. (2020). Cardiovascular risk of electronic cigarettes: A review of preclinical and clinical studies. *Cardiovascular Research*, 116(1): 40-50.
8. Rebuli, M. E., Rose, J. J., Noël, A., Croft, D. P., Benowitz, N. L., Cohen, A. H., Goniewicz, M. L., Larsen, B. T., Leigh, N., McGraw, M. D., Melzer, A. C., Penn, A. L., Rahman, I., Upson, D., Crotty Alexander, L. E., Ewart, G., Jaspers, I., Jordt, S. E., Kligerman, S., Loughlin, C. E., McConnell, R., Neptune, E. R., Nguyen, T. B., Pinkerton, K. E. and Witek, T. J. (2023). The e-cigarette or vaping product use-associated lung injury epidemic: pathogenesis, management, and future directions: An official american thoracic society workshop report. *Annals of the American Thoracic Society*, 20(1): 1-17.
9. Krakowiak, R. I., Poklis, J. L. and Peace, M. R. (2019). The analysis of aerosolized methamphetamine from e-cigarettes using high resolution mass spectrometry and gas chromatography mass spectrometry. *Journal of Analytical Toxicology*, 43(8): 592-599.
10. Chadi, N., Minato, C. and Stanwick, R. (2020). Cannabis vaping: Understanding the health risks of a rapidly emerging trend. *Paediatrics and Child Health*, 25: S16-S20.
11. Tai, H., Swartz, M. D., Marsden, D. and Perry, C. L. (2020). The future of substance abuse now: Relationships among adolescent use of vaping devices, marijuana, and synthetic cannabinoids. *Substance Use and Misuse*, 56(2): 192-204.
12. Blundell, M., Dargan, P. and Wood, D. (2018). A cloud on the horizon–a survey into the use of electronic vaping devices for recreational drug and new psychoactive substance (NPS) administration. *QJM: An International Journal of Medicine*, 111(1): 9-14.
13. Duffy, B., Li, L., Lu, S., Durocher, L., Dittmar, M., Delaney-Baldwin, E., Panawennage, D., LeMaster, D., Navarette, K. and Spink, D. (2020). Analysis of cannabinoid-containing fluids in illicit vaping cartridges recovered from pulmonary injury patients: identification of vitamin e acetate as a major diluent. *Toxics*, 8(1): 8.
14. Almazrouei, E. S., Bintamim, A. A., Khalil, S. E. A., Alremeithi, R. and Gewily S. (2022). The identification of drugs of abuse in E-cigarette samples seized in Dubai between 2016 and 2020. *Forensic Science International*, 333: 111233.
15. Zaharia, M., Borhan, A., Gherca, D., Pui, A., Gradinaru, R., Zbancioc, G. and Drochioiu, G. (2014). Study on the mechanism of ferrite-induced dinitrophenol photodegradation. *European Journal of Mass Spectrometry*, 20(2):193-197.
16. Breitbarth, A. K., Morgan, J. and Jones, A. L. (2018). E-cigarettes - An unintended illicit drug delivery system. *Drug and Alcohol Dependence*, 192: 98-111.
17. The Star. (2022). Syndicate supplying vape liquid drug busted. Access from https://www.thestar.com.my/news/nation/2022/10/16/syndicate-supplying-vape-liquid-drug-busted.
18. Zainudin, A. M., Ibrahim, N. N. I. N., Hou, L. J., Rasool, A. H. G., Ramli, N., Miran, H. and Yusuf, W. N. W. (2022). Urine drugs of abuse testing at Hospital Universiti Sains Malaysia: A review of trends from 2009 - 2019. *Malaysian Journal of Medicine and Health Sciences*, 18(2): 58-63.
19. Hukkanen, J., Jacob, P. and Benowitz, N. L. (2005).

Metabolism and disposition kinetics of nicotine. *Pharmacological Reviews*, 57(1): 79-115.

20. Marques, P., Piqueras, L. and Sanz, M. J. (2021). An updated overview of e-cigarette impact on human health. *Respiratory Research*, 22(1): 1-14.
21. Taghavi, S., Khashyarmanesh, Z., Moalemzadeh-Haghighi, H., Nassirli, H., Eshraghi, P., Jalali, N. and Hassanzadeh-Khayyat, M. (2012). Nicotine content of domestic cigarettes, imported cigarettes and pipe tobacco in iran. *Addiction & Health*, 4(1-2): 28-35.
22. St Helen, G. and Eaton, D.L. (2018). Public health consequences of e-cigarette use. *JAMA Internal Medicine*, 178(7): 984-986.
23. U.S. Department of Health and Human Services (2014). The health consequenses of smoking: 50 years of progress. A report of the Surgeon General. U.S. Department of Health and Human Services, Centers for Disease Control and Prevention, National Center for Chronic Disease Pervention and Health Promotion, Office on Smoking and Health.
24. Hutzler, C., Paschke, M., Kruschinski, S., Henkler, F., Hahn, J. and Luch, A. (2014). Chemical hazards present in liquids and vapors of electronic cigarettes. *Archives of Toxicology*, 88(7):1295-1308.

Malaysian Journal of Analytical Sciences (MJAS)
Published by Malaysian Analytical Sciences Society

GLYCIDYL ESTERS: AN UPDATED MINI-REVIEW OF ANALYTICAL METHODS (2015-2022)

(Glisidil Ester: Suatu Tinjauan Terkini Ulasan Mini bagi Kaedah Analisis (2015-2022))

Nor Syuhada Mat Shukri[1], Nur Syafiqah Subri[1], Siti Munirah Ishak[2], Nur Nadhirah Mohamad Zain[2], Mazidatulakmam Miskam[3], Wan Nazwanie Wan Abdullah[3], Sazlinda Kamaruzaman[4], Nor Suhaila Mohamad Hanapi[5], Wan Nazihah Wan Ibrahim[5], Muggundha Raoov[6], and Noorfatimah Yahaya[2*]

[1]Faculty of Industrial Science & Technology, Universiti Malaysia Pahang, Lebuhraya Tun Razak, 26300 Gambang, Kuantan, Pahang, Malaysia
[2]Department of Toxicology, Advanced Medical and Dental Institute (AMDI), Universiti Sains Malaysia, 13200 Bertam Kepala Batas, Penang, Malaysia
[3]School of Chemical Sciences, Universiti Sains Malaysia, 11800, USM Pulau Pinang, Malaysia
[4]Department of Chemistry, Faculty of Science, Universiti Putra Malaysia, 43400 UPM Serdang, Selangor Darul Ehsan, Malaysia
[5]Faculty of Applied Sciences, Universiti Teknologi MARA, 40450, Shah Alam, Selangor, Malaysia
[6]Department of Chemistry,Faculty of Science, Universiti Malaya, Kuala Lumpur 50603, Malaysia

[*]Corresponding author: noorfatimah@usm.my

Received: 2 September 2022; Accepted: 21 August 2023; Published: 30 October 2023

Abstract

Recent issues on the presence of glycidyl ester (GE), a potentially carcinogenic compound, in food have sparked consumer worry. Fatty acid esters of glycidol pose potential food safety concerns and have been classified by IARC as a "likely human carcinogen". They are generated during the high-temperature deodorization step. Vegetable oils consist primarily of five fatty acids, palmitic acid, linolenic acid, linoleic acid, oleic acid, and stearic acid. Palm kernel and coconut oil also contain significant quantities of lauric acid and myristic acid. These fatty acids of edible oil undergo various reactions, producing different GE. Researchers have developed a GE quantitation method called "indirect" methodology, but this method uses hydrolysis to release glycidol from GE instead of directly targeting the intact fatty acid esters. It also requires a derivatization step before gas chromatography-mass spectrometry (GC–MS) analysis. While the early methods developed to target these contaminants exclusively utilized the 'indirect' approach, they were critical in bringing attention to the presence of GE in oils. The factors that are highly related to GE formations include process temperature, process duration, and the presence of precursors. This paper reviews previous studies on various methods and instruments that focused on detecting GE in different matrices from 2015 to 2022.

Keywords: glycidyl ester, deodorization, hydrolysis

Abstrak

Isu terkini mengenai kehadiran ester glisidil (GE), sebatian berpotensi karsinogenik, di dalam makanan telah mencetuskan kebimbangan dalam kalangan pengguna. Ester asid lemak glisidol menimbulkan potensi keselamatan makanan dan telah

diklasifikasikan oleh IARC sebagai "kemungkinan karsinogen manusia". Ia dihasilkan semasa proses penyahbauan pada suhu tinggi. Minyak sayuran yang utama terdiri daripada lima asid lemak, asid palmitik, asid linolenat, asid linoleat, asid oleik, dan asid stearat. Biji kelapa sawit dan minyak kelapa juga mengandungi asid laurik dan asid miristik dalam jumlah yang banyak. Asid-asid lemak dalam minyak yang boleh dimakan tersebut melalui pelbagai tindak balas, menghasilkan GE yang berbeza. Para penyelidik telah membangunkan kaedah kuantitasi GE yang disebut metodologi "tidak langsung", tetapi kaedah ini menggunakan hidrolisis untuk membebaskan glisidol dari GE dan bukannya menyasarkan secara terus ester asid lemak yang utuh. Kaedah ini juga memerlukan langkah derivatisasi sebelum analisis kromatografi gas-spektrometri jisim (GC–MS). Meskipun kaedah-kaedah awal yang dibangunkan untuk mengesan bahan cemar ini menggunakan pendekatan tidak langsung secara eksklusif, kaedah-kaedah tersebut sangat penting dalam mengarah perhatian kepada kehadiran GE di dalam minyak. Antara factor-faktor yang berkait rapat dengan penghasilan GE termasuklah suhu proses, masa proses dan kehadiran pelopor. Makalah ini membentangkan resensi kajian-kajian terdahulu mengenai pelbagai kaedah dan instrumen yang tertumpu kepada pengesanan GE dalam pelbagai matriks dari tahun 2015 hingga 2022.

Kata kunci: glisidil ester, penyahbauan, hidrolisis

Introduction

Glycidyl fatty acid esters or glycidol (GE) are contaminants commonly found in most refined fats and oils, including edible oil such as palm oil and vegetable oil or any food made from these oils like margarine and fried products. Palm oil, corn oil, and coconut oil have been recorded with the highest presence of GE. The food industry uses palm oil because of its stability to high temperatures and long shelf life [1]. In some research, GE has been found in infant formula due to the use of vegetable oils [2]. It was also reported that the most abundant GE of fatty acids were esters of the palmitic and oleic acids [3]. Hence, the presence of GE has raised the concern of many people as GE is a carcinogenic compound. In general, a process called oil deodorization at a temperature within 230 ℃ to 270 ℃ could lead to the formation of GE as byproducts [4]. Specifically, this compound is formed from diacylglycerol (DAG) or monoacylglycerol (MAG) at high temperatures. The release of glycidol happens after GE is broken down during the digestion process. According to a report in European Food Safety Authority (EFSA) Journal in 2016, of all the available refined vegetable oils, palm-based fat and oils contain the highest amount of monochloropropanediol (MCPD) in the form of ester. Figure 1 and Figure 2 depict the general structure of GE and the chemical structures of several GE, respectively.

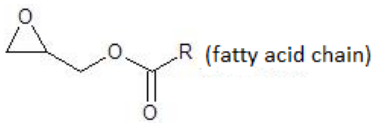


Figure 1. General structure of GE

Since gut lipases rapidly digest GE to free glycidol, GE intake should be considered a source of glycidol. Therefore, International Agency for Research on Cancer (IARC) suggested the application of the ALARA (As Low As Reasonably Achievable) principle on this genotoxic carcinogenic compound [3]. In 1990, the U.S. National Toxicology Program declared the multisite carcinogenicity of glycidol towards rodents. Later in 2010, an estimation of 1.3 mg/kg/day of glycidol was recorded for human cancer potency by the California Environmental Protection Agency [5].

As mentioned above, the presence of GE is due to the process of oil deodorization at high temperatures. The synergistic interaction between stripping stream rate and temperature is significant to the formation of GE. In the refining process of conventional edible oils, deodorization is the last procedure performed. The main purpose of this step is to remove undesirable substances. This is done to achieve the standard of oil production in taste, odor, color, and oxidative stability [6]. According to Stadler (2015), MCPD and GE's formation pathways in oil are different. Unlike MCPD, GE cannot be generated from triacylglycerols (TAG), but it is generated through intramolecular conversion and a free fatty acid chain loss. GE can also be generated via hydrolysis of MAG [4]. Arisseto et al. [8] proposed the formation of GE via either the internal nucleophilic attack of DAG or the nucleophilic attack of acyloxonium ion generated from the displacement of hydroxide group [7]. Even though GE could be formed

in all edible oil during the deodorization process, they tend to occur at the highest concentration in palm oil [8].

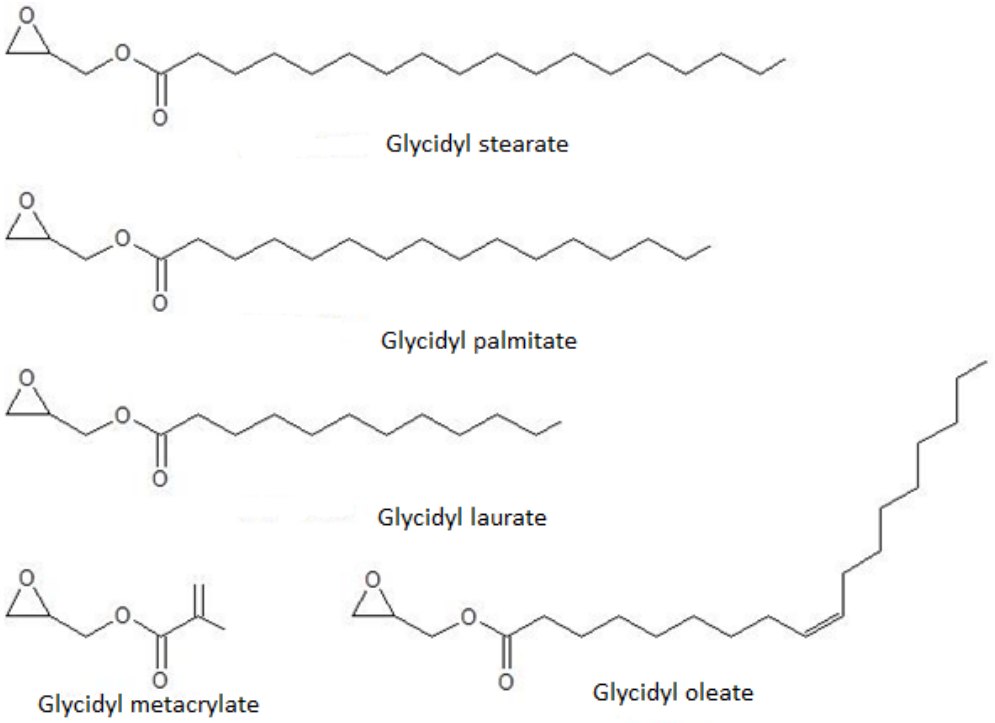


Figure 2. Chemical structures of several GE

Responding to such concern, much research is currently focusing on determining the presence of GE in edible oil. Edible oil such as palm oil was typically chosen as it provides the primary source of GE. Zelinkova et al. [10] studied the direct analysis of glycidyl ester laurate, myristate, palmitate, stearate, oleate, linoleate, and linolenate, and this method was successfully applied for the quantitation of GE in edible oils. Some research focused on determining the effect of frying temperature on GE formation since frying is one of the most convenient and common food preparation processes. According to Aniolowska et al. [3], by subjecting fat to high temperatures in the presence of the water and air during the deep-frying process, high number of new compounds that may be formed during the various hydrolytic, thermal, and oxidative reactions could be detected. In the frying process, the product of oil degradation, DAG, would react at high temperatures to form GE. GE also increased in concentration with increasing frying duration, frying temperature, and NaCl concentration [9]. Heating meat at high temperatures using an open fire charcoal grill can also generate a significant level of GE [10]. In 2017, the European Commission recommended compiling analytical data on the occurrence of GE in a broader range of food than only for oils, fats, and margarine [11]. At around the same time, the American Oil Chemists' Society (AOCS) publicized three methods suitable for analyzing GE, namely Cd 29a-13, Cd 29b-13, and Cd 29c-13 [4].

Due to the major advancement in analytical detection technologies, it is possible to analytically detect processing-derived food contaminants like GE at the level of parts per billion (ppb) [12] by using either direct or indirect approaches [7]. The direct methods allow the use of instruments like liquid chromatography-mass spectrometry (LC-MS) for quantitative and qualitative analysis of MCPD esters and GE, exactly as they are found in food. On the other hand, the indirect determination is based on the conversion of GE to glycidol. Glycidol will then be separated, derivatized, chromatographically isolated, and quantified. Several

analytical methods have been customized to accommodate the indirect method for measuring GE and MCPD ester in oils and fats [11]. Solid-phase extraction (SPE) or gel permeation chromatography clean-up is adequate to achieve acceptable separation of GE and MCPD from the oil matrix [11]. Wang et al. reported the involvement of cation-mediated and free radical-mediated intermediates in the formation mechanisms of GE [13]. Elimination of fatty acid radical or hydroxyl radical would form a free radical intermediate with five or six-membered cyclic acyloxionium structure. The presence and reactivity of chlorine compounds play vital roles in the formation of MCPD esters and, to a certain degree, GE.

In recent years, the amount of GE found in processed food and edible oils has significantly increased. Their presence is concerning to public health due to their ability to release potentially toxic glycidol via hydrolysis in the digestive tract [14]. The high level of chlorinated metabolites, the use of fertilizers that contain chloride salt, and the use of HCl-activated clays during the bleaching step of the refining process of palm oil contributed to its high GE concentration compared to other edible oils. Owing to the potential health risks and the levels of these contaminants in edible oils and foodstuff, the European regulatory has set limits of 1 mg/kg and 0.5 mg/kg of bound glycidol in processed food and infant formulas, respectively. One of the main strategies to contain the formation of GE is by removing the chlorinated precursor before deodorization [14], other than blending oils, refining methods improvement and acid and enzymatic degumming.

To produce refined oil of high quality in terms of organoleptic quality, stability, and nutritional quality, undesirable compounds are removed for safe human consumption [15]. The amount of GE contents in refined palm oil (RPO) range from 0.30 to 18.00 mg/kg, much higher than the level of GE in other oils like maize oil, olive oil, etc., which is in the range of 15 to 650 μg/kg. As shown in Figure 1 and Figure 2, GE contain an epoxide group and an ester group in addition to the long chain of fatty acid compositions. Both GE and its free form after hydrolysis in gastrointestinal tract, glycidol, are carcinogenic due to the presence of epoxide group that can react with DNA to form DNA adducts. Glycidol is known as genotoxic non-threshold carcinogen with evidences of toxicity in animal even at a very small dose [15], suggesting neurotoxicity, mutagenicity, and reproductive toxicity [16]. Detection of GE using indirect quantification based on gas chromatography-mass spectrometry (GC-MS) requires extensive sample preparation including transesterification, neutralization and derivatization steps and thus, more time-consuming. Albeit needing a high number of internal standards to detect a wide range of GE, direct methods based on LC-MS are much simpler and more commonly applied for the analysis of GE present in oily matrices due to their high sensitivity and specificity [17].

In this review, analytical method development including the sample preparation and detection of different types of GE are summarized in Table 1. The present article will address the development of sample preparation methods and analytical detection system of GE in various matrices, from the year 2015 to 2022.

Analytical Determination of GE

AOCS has published three indirect methods, namely Cd 29a-13, Cd 29b-13 and Cd 29c-13 to determine the amount of MCPD esters and glycidol in edible oils such as palm oil, canola oil and sunflower oil [4]. In these methods, the sum of MCPD esters and GE from various sources were expressed as free 3-MCPD and free glycidol. For instance, in the AOCS Official Method Cd 29c-13, the addition of dilute sodium hydroxide solution or sodium methoxide in methanol frees up glycidol and 3-MCPD via base catalysis, while the addition of excess acidic chloride-containing salt solution stops the reaction [18]. The free glycidol reacts with inorganic chloride to generate additional 3-MCPD and 2-MCPD. Then phenylboronic acid (PBA) is used for derivatization process, followed by the determination by GC-MS [4]. On the other hand, having the reaction stopped with an acidic chloride-free salt solution in excess does not generate additional 3-MCPD from free glycidol. As a result, this method allows for the indirect detection of GE (bound glycidol) under the assumption that no other compounds present are reactive towards inorganic chloride at ambient temperature to produce 3-MCPD [18].

In 2015, there were research developed to study the effect of the type of oil and degree of degradation on GE content during the frying process of French Fries. The study with the main purpose to determine the content of GE in oil that used for frying French fries were developed by Anilowska et al. By using LC-MS the presence of GE can be determined and the sample were analyzed for the acid and anisidine values, colors, refractive index (RI), composition of fatty acid and also content and composition of the polar fraction [19]. As in this study it was observed that the higher of time frying the content of GE were decreased. It is recorded with losses from 47% in the rapeseed oil and 78% in palm oil. This data was recorded after the frying process finished.

As the fat were extracted from the French fries, the GE analysis were conducted on the frying oil samples [19]. This lab work developed a double SPE procedure, chloroform and acetone were used as the medium for the oil to be dissolved. Spike extract was applied for the simultaneous determination of GE, it was used as the internal standard. The percent of recovery for each of 5 standard spiked GE which is 500 ng g^{-1},1000 ng g^{-1}, 2500 ng g^{-1} and 12, 500 ng g^{-1} were 99.5-103%, 98.5-1025%, 98.0-101.5% and 89-97.5% respectively. In the fresh oil that ranged from 0.80 to 25.34 kg^{-1} the total amount of GE can be detected. The GE content for all of the samples decreased during the frying process that was carried out. In within 24 hours (1 day), GE content in palm oil and palm olein recorded about 44% and 38% losses respectively. Within 40 hours after the frying process the losses for both of these oils, which is palm oil and olein were 78% and 67% respectively. From this observation it was stated that the main parameter of the losses of GE was dependent on the type of oil used. The time range was considered as the minor effect to the losses of GE in this oil. The GE degradation was stated to undergo fast degradation in the palm oil compared to the rapeseed oil.

The data obtained from the result showed that GE tend to undergo the stabilization while in the frying condition [19]. There was thing that can influence the content of GE in the ready product, it was the composition of the oil used for the pre-frying process. This phenomenon arises due to the fat exchange that occurs between the frying medium and the products being fried during the frying process [19]. The initial absorption of fat quality during the frying process can impact the subsequent increase in GE content within the fat. The duration of frying also plays a role in the reduction of GE levels within the extracted fat from fried French fries, potentially influencing the conversion and composition of GEs in this context. Moreover, the GE content can be significantly related to the aid and refractive index value. From this study, the GE content with the highest amount can be found in the fresh oil which is in palm olein (25 mg/kg) and the lowest content of GE was found in the rapeseed oil (0.8 mg/kg) [19].

Becalski et al. [5] published data on the presence of 2 and 3-MCPD ester and glycidol ester (MCPD and GE) in over 100 edible fats, oils, and products comprising fats and oils. In this study, GE and MCPD esters were determined using stable isotope dilution analysis with a glycidol-d5 labelled standard by LC-MS/MS in the mode atmospheric pressure chemical ionization (APCI), and GC-MS in the mode SIM after derivatization. All of the food samples were purchased in the local market in Ottawa, Canada. The sample was homogenized first before proceeding with the next step. LC-MS/MS was used for the determination of target glycidol fatty ester. The target of GE which was lauric and mystric revealed the recovery from the spiked cookies was 102% and 109% respectively. Meanwhile, the recovery of glycidyl laurate 103% and myristate 101% from the spiked of virgin olive oil. From the observation, the unprocessed oil does not contain any detectable levels of GE or MCPD ESTERS except for palm oil that recorded 100-550 ng/g for MCPD ESTERS. The GE and MCPD ESTERS concentration in processed oil or fats were found to be high, at 10.6 and 17.1 g/g, respectively.

Table 1. Extraction and determination of glycidyl esters (2015–2022)

Analytes	Extraction Techniques	Quantitation Instruments	Sample Matrices	Linearity (mg/kg)	LOD (mg/kg)	Precision, RSD%	Relative Recovery/ Recovery, %	Concentration Found (mg/kg)	References
2-MCPD 3-MCPD GE	SPE	LC-MS/MS	Edible oil	N/A	N/A		101 - 109	N/A	[5]
2-MCPD 3-MCPD GE	Pressurized liquid extraction: Oven temperature: 40 ◦C, pressure: 103 bar, pre-heating time 1 min, static extraction time 5 min, heat	GC-MS Column: DB5-MS Temperature was programmed as follows: 60 ◦C for 1.0 min, from 60 ◦C to 150 ◦C at 6 ◦C min^{-1}, 2.0 min at 150 ◦C and from 150 ◦C to 300 ◦C at 10 ◦C min^{-1}	Food matrices	20-1850	7-17	<17	82-114	The highest levels of both 3-MCPDEs and GEs were found in margarines followed by a potato crisps sample from sliced potatoes and fine bakery wares such as cookies, fatty cake products and puff pastries	[23]
3-MCPD GE	Petroleum ether extraction	GC-MS Column: Restek Rxi-5 ms Temperature was programmed as follows: 60 °C for 1 min, 6 °C min^{-1} to 190 °C, 30 °C min^{-1} to 280 °C, isothermal 10 min Sample volume:1 µL with pulse pressure of 25 psi	Sunflower oil	N/A	N/A	N/A	98.8-102.0 98.7-100.2	N/A	[21]
2-MCPD 3-MCPD GE	Accelerated solvent extraction (ASE) Extraction solvent: A mixture of isohexane and acetone (80/20, v/v)	GC-MS Column: DB5-MS GC oven temperature programme was 60°C (held for 1 min), ramped at 6°C min−1 to 180°C, followed by 30°C min−1 to 300°C (held for 10 min)	Infant formula	0.5-2.0	0.04-0.05	<12	94.7-109	0.011-0.070	[24]

	ASE conditions: pressure, 1500 psi; temperature, 100°C; heating period 6 min; extraction (static) time 5 min, with three static cycles per sample. flush volume 100%; and purge time, 60 s								
Glycidol	Double SPE Extraction solvent: chloroform diluted with acetone to the mark	LC-MS consists of ternary pump and autosampler equipped with APCI interface. Column: Luna 3 µm PFP(2) 100 Å column equipped with precolumn. Separation temperature: 25°C. Flow rate: 0.2 mL min−1, sample injection volume: 10 µL	Palm oil	N/A	N/A	N/A	N/A	5.04-38.95	[3]
GE	SPE	LC-MS equipped with APCI interface (positive mode)	Refined oil	5-1000 ng/mL^{-1}	27.7-45 $ng\ g^{-1}$	<5.4	89 - 103	0.33-12.7	[22]

	Extraction solvent: chloroform that is diluted with acetone to the mark. Reverse phase: Cartridge conditioned with methanol, eluted with SPE manifold under gravity (1 drop per 2-3 seconds), solvent evaporated (at 40 °C in a nitrogen stream) Normal phase: Cartridge conditioned with n-hexane/ethyl acetate (95:5 v/v)	APCI parameters applied: corona discharge current, 2 μA; shield voltage, 600 V; capillary voltage, 59 V; vaporizing gas temperature, 500 °C, drying gas temperature, 250°C; dwell time, 200 ms each Column: Luna 3 μm PFP(2) 100 Å column equipped with a precolumn Separation temperature: 25 °C. Flow rate: 0.2 mL min−1, sample injection volume: 10 μL							
Glycidol 3-MCPDE	LLE Extraction solvent: mixture of solvent consists of hexane: MTBE (1:2)	GC-MS by SIM Injection temperature: 180 °C. Column: capillary column VF-1ms Flow rate: 1.2 mL/min. The following temperature program was used in the oven: 60°C (held for 1 min), 6°C/min to 190°C, 20°C/min to 280°C (held for 30 min)	Infant formula	0-5.97 0-2.60	0.10 E: 0.08	<15	82-97 93-108	Not detected (ND) to 0.75	[2]
G-laurate G-palmitate G-Stearate G-oleate G-linoleate G-Linolenate G-palmitate	LLE Extraction solvent: 20% Na_2SO_4 (w/v); 2 × 2 mL n-heptane SPE Extraction solvent: 500 mL n-hexane: ethyl acetate (85:15, v/v). Cartridge conditioned with elution solvent (n-	GC-MS with SIM mode. Column: J&W DB-5 MS GC Injection (pulse pressure 200 kPa for 0.30 min) at a Temperature of 250°C Flow rate: 1.2 mL/min. The transfer line temperature was set to 300 °C. The oven temperature program was as follows: initial temperature 60°C held for 1 min, 6°C/min till	Food matrices	N/A	N/A		92.3-103.3	N/A	[11]

	hexane: ethyl acetate, 85:15, v/v)	150°C (held for 2 min), 30°C/min till 300°C held for 10 min HPLC-MS Mobile phase A: (methanol:H2O, 92:8,v/v) and mobile phase B (2-propanol) were programmed as follows: isocratic elution 100% mobile phase A till 18.0 min, linear gradient 100% B till 18.1 min, isocratic elution 100% B till 25.0 min, linear gradient 100% A till 25.1 min, isocratic elution 100% A till 35.0 min. The flow rate was 1 mL/min, Column temperature: 40°C APCI at gas pressure of 30 psi, vaporization temperature of 500 °C							
2-MCPD 3-MCPD GE	Microwave extraction The septa used was 22 mm EPA Septa Silicone/PTFE, 3.2mm thick. Extraction solvent: Ethyl acetate Time: 10 min	GC-MS Column: HP 5 MS capillary column Injector temperature: 250°C Flow rate: constant of 1.7 mL/min, the transfer line was at 250°C, the ion source at 230°C and the quadrupole at 150°C. The GC column oven was programmed from an initial temperature of 80°C held for 1 min, increased at a rate of 10°C/min up to 200°C, and then ramped up again at 15°C/min up to 250°C, which was held for 15 min	Food matrices	0-5 0-5 0-10	0.0008-0.03	N/A	N/A	N/A	[25]

3-MCPD GE	LLE Extraction solvent: ethyl acetate and LC/MS grade water. Incubation temperature: 35°C and 500 rpm for 1.5 hours. Centrifuged for 20 minutes.	LC-MS/MS equipped with ESI source Column: Pursuit XRs C18 column Column temperature: constant at 30°C Initial flow rate: 200 µL/min , 100% mobile phase A (2 mM ammonium formate/0.05% formic acid, 92:8 MeOH/H2O) for 2 min Injection volume: 5 µL	Infant formula	N/A	N/A	1.0-9.5	88.7-107.5	0.090 -5.92 µg/g 0.89 -8.19 µg/g	[26]
GE	Solvent extraction Extracting solvent: n-hexane Steamed over boiling water for 5 min.	GC-MS Capillary column: Agilent TG-5MS Constant flow rate of 1.18 mL/min GC oven temperature program followed by: 80°C with an increase 171 of 5°C/min to obtain 155°C, followed by increase by 60°C/min to obtain 300°C that 172 was held for 5 min	Edible oil	N/A	0.01	N/A	N/A	N/A	[27]
3-MCPD GE	SPE Extraction solvent: diethyl ether	GC-MS/MS Column: two HP-5MS Injector Temperature: 250°C Injection volume: 2 µL Flow rate: constant 1 mL min^{-1} Transfer line Temperature: 280°C Backflush time: 5 min Backflush pressure: 50 psi	Fish oil	N/A	0.05 0.02	0.2-6.1 4.6-14.4	93.4 98.9	0.37	[28]
2-MCPD 3-MCPD Glycidol	SPE Extraction solvent: Ethyl acetate	GC-MS	Food matrices	N/A	N/A	N/A	82-109	N/A	[8]

3-MCPD GE	**N/A**	**GC-MS LC-MS/MS**	**Food and Oil**	**N/A**	**0.05**	**N/A**	**N/A**	**N/A**	**[7]**
3-MCPD Glycidyl ester	Extraction with methyl tert-butyl ether and diethyl ether	GC-MS Column: Rxi-17Sil Ms Temperature program: 85°C(hold 0.5 min) to 150 °C at 6°C/min to 180°C at 12°C/min to 280°C at 25°C/min (hold 7 min)	Edible oil	N/A	0.13-0.14	N/A	N/A	N/A	[31]
Glycidyl palmitate Glycidyl palmitate D5	FTIR wavelength range between 4000 and 600cm^{-1} with 40 interferograms at a resolution of 4 cm^{-1} NMR Frequency of 499.887 MHz followed by parameters: temperature of the machine set at 26 °C, number of scans was 64, pulse width (90° pulse angle) was 8.6 ms, and relaxation delay time was 2.0 s to complete the total acquisition time of 3.53 min. The spectral width adjusted from − 1 to 14 ppm	GC-MS Mode: SIM	Palm based cooking oil	>0.997	0.24	N/A	N/A	0.6-21.3	[30]
3-Chloro-1,2-propanediol and 2-Chloro-1,3-propanediol, glycidyl stearate, rac 1,2-Bis-palmitoyl-3-chloropropanediol, 1,3-Dipalmitoyl-2-chloropropanediol	Agilent Intuvo 9000 GC system coupled to triple Quadrupole mass spectrometer Working in splitless mode in MMI conditions (initial conditions 60°C	Gas chromatography tandem mass spectrometry (GC–MS/MS) Column: DB-17-MS Flow of 1.2 ml/min	Extra virgin olive oil	N/A	0.01	>11	81-115	25 µg/mL	[32]

	Rate 300°C/min to 280°C, hold time 10 min). Oven temperature: 60°C hold time 1 min, rate 20°C/min to 160°C; rate 10°C/min to 220 °C; rate 25°C/min to 320°C hold time 4 min, post run 325°C, total run time 20 min								
3-MCPD esters 2-MCPD esters Glycidyl esters	HS–SPME Derivation temperature: 100°C Extraction time: 80 min	GC-MS Column: HP-5 Oven temperature: initial temperature 50°C hold 1 min, increase of 2°C/min to 90°C then by 40°C/min to 325°C hold 4 min and post-run at 325°C for 5 min	100–500 mg of oil sample or 100 µL of PP-MCPD ESTERSs (500 µg/mL)	N/A	3.9 µg/L	0.51-5.04	91.1-102.1	N/A	[29]
3-MCPD esters Glycidyl esters	Reax 2 rotatory shaker from Heidolph Centrifuged at 5000 rpm for 10 min	Ultra-high performance liquid chromatography tandem mass spectrometry with triple quadrupole analyzer (UHPLC-MS/MS-QqQ) Mobile phase: Solvent A methanol:H2O (90:10, v/v) with 2 mM ammonium formate and 0.05% (v/v) of formic acid Solvent B isopropanol:H2O (98:2, v/v) with 2 mM ammonium formate and 0.05% (v/v) of formic acid at flow rate of 0.2 mL min^{-1} Injection volume: 5 µL Column temperature: kept at 25 °C	Oil samples	0.9932-0.9995	1.72	< 20	N/A	10 mg/L	[17]
3-MCPD esters 2-MCPD esters Glycidyl esters	A capillary column HP-5MS (30 m, id 0.25 mm, film thickness 0.25 µm, 5%-Phenyl methylpolysiloxane	GC-MS Column: HP5-MS	Frying oils	0.06-5 0.03-3 0.06-2	0.0015 0.0019 0.013	1.5 5.17 2.79	94.90 95.15 91.03	N/A	[9]

2-MCPD esters 3-MCPD esters Glycidyl esters	A high-speed vertical shaker Extracted at 1500 rpm for 5 min , added 10 g of sodium sulfate anhydrous, extracted at 1500 rpm for 3 min , centrifuged at 4800 rpm	GC-MS/MS 70 °C for 0.02 min increased to 280 °C at a rate of 8.5 °C/s for 8 min then increased to 330 °C at a rate of 10 °C/s for 14.5 min	60 samples from different manufacturers	N/A	0.0003-0.0032	< 15	75 - 110	0.0023-0.0011	[10]

Wenzl et al. [20] in 2015, has reported that the EFSA and Joint Research Centre (JRC) were cooperate in order to obtain the data regarding the analysis of 3-monochloropropane-1,2-diol (3MCPD) and 2-monochloropropane-1,3-diol (2MCPD) and glycidyl ester (GE). They had developed a suitable method for analysis of these compounds. The tests were run under the different types of food such as meat products, potato based-snacks, cereal-based snack and margarines. In this study, the method developed will determine the ester-bound analytes, and the other analysis will determine the free 2-MCPD and 3-MCPD. The GE will be converted to the monobromopropandeiol ester and well known as MBPD. Both MCPD and MBPD will undergo the process transesterification before the derivatization process takes place. During the derivatization process the analytes will be treated with phenylboronic acid (PBA) in organic solvent. Gas chromatography mass spectrometry (GC-MS) was used to measure the PBA derivatives. The quantifications used the stable isotope labelled analogues. The sample extraction used was pressurized liquid extraction (PLE) with presence of tert-Butyl methyl ether 100% solvent and with temperature of 40 ℃. The fat from the food matrices were extracted and were determined by gravimetry. Both MCPD esters and GEs showed limits of quantification (LOQs) of 100 μg/kg or lower. In this study, the MCPD ester will be expressed as free MCPD meanwhile GEs will be expressed as glycidol. The estimated amount of LOD and LOQs for GEs were 17 μg/kg and 31 μg/kg respectively. For all of the targeted analyte, the gas chromatography mass spectrometry (GC-MS) with the presence of electron ionization with the selected ion monitoring mode.

In 2015, Dingel et al. [21] has reported the study on the non-formation of the 3-MCPD ESTERS and GE during the deep frying of the potatoes crisps in the large scale. In this study, high oleic-sunflower oils (HOSO) were used for deep frying. GC-MS was used to analyze the sample of potato crisps. There were 9 samples that were used for this analysis. All of the samples were collected directly from the German production line. The potato crisps sample weighed approximately 35 g. The sample preparation process began with the use of a typical laboratory mill for finely ground samples. The petroleum ether was then used to extract the compounds. The HOSO frying oils were utilized immediately for the analysis without any pre-treatment needed. The sample aliquots were dissolved in tert-butyl methyl ether before being spiked with the internal standard 3-MCPD-1, 2-bs-palmitoylester-d5. In this experiment, ester cleavage occurs, and it will halt once the acidified sodium chloride or sodium bromide solution is introduced to both aliquots. Each sample was extracted using a diethyl or ethyl acetate combination. Before the assays were evaporated, phenylboronic acid (PBA) was employed to mix the organic extracts of each experiment. As a result, GE's recovery was estimated to be between 98.7% and 100.2%. MCPD ESTERS and GE were both varied in terms of measurement uncertainty as a result of the experiment. Furthermore, it did not show any increases when compared to the oil utilized at the start of this investigation. The MCPD ESTERS and GE levels in this study were also low, ranging between 0.10 and 0.85mg/kg fat and 0.09 (LOQ) and 0.91 mg/kg, respectively. From the result obtained there were no significant changes in level of MCPD ESTERS and Ge while frying process occurred.

Research study regarding the monitoring of the glycidyl ester (GE) in the refined vegetables oils by using liquid chromatography-single-quadrapole mass spectrometry (LC-MS) was performed by Aniolowska et al. in 2015. Basically, refined vegetable oils from the retail outlet in Poland was used in order to analyze the GE [22]. For the analysis, 12 rapeseed oil samples, 4 sunflower oil samples, and 4 palm oil samples were employed. This study's analyses were carried out in duplicate. The high-performance liquid chromatography (HPLC) was used to extract GE-rich extracts from oils. Except for water, all of the solvents utilized in the LC-MS study were under HPLC grade. The extraction method used was double solid phase extraction (SPE). Methanol was used to condition the reverse phase of the SPE cartridge, whereas n-hexane or ethyl acetate was used to condition the normal phase of the SPE cartridge. In this study, the composition of the fatty acid can be determined by using gas chromatography (GC). From the result obtained, different analytes possess different concentrations, and the concentration of the analytes were range within 0.17 and 44.33 mg/kg. The LODs were determined within the

range 1.1 to 1.8 ng/mL while the LOQs were in range of 3.8 to 6 ng/mL. From the calibration curves the correlation was good with R^2 within 0.9981 and 0.9990. The percentage of recovery values were recorded from 89% to 103% and the standard deviation was less 5.4%. In 2016, Samaras et al. presented an indirect analytical method for simultaneous determination of 3-MCPD and GE in the various food stuff, including breads and roll, bakery wine, smoked fish products, fried and roasted meat, potato based snack, margarines and extra virgin olive oil blank sample, by using pressurized liquid extraction (PLE) and GC-MS [23]. The sample was immersed in liquid nitrogen, grinded, and then homogenized to produce a fine homogenous powder in order to increase the extraction efficiency. Based on the outcomes of literature and experimental studies, *tert*-butyl methyl ether (t-BME) was proposed as the best extractant for the determination of the MCPD esters and GE for this PLE technique. In order to overcome the overwhelming effect of fat content on the sample, for samples exceeding the 5% total fat contents (w/w), stable isotope-labelled internal standards would be added directly into 100 mg extract after PLE. After acid transesterification, the derivatization procedure was performed by using a low volume of derivatization reagent, phenylboronic acid (PBA), which provides lower background level and decreased limits of detection (LODs) compared to the AOCS methods [5]. Based on this study, the concentrations of 3-MCPD esters and GE were found to be the highest in margarines, followed by potato crisp snacks and bakery products. The targeted compounds were found only at trace levels in smoked fish, smoked meat and fried roasted meat. They were almost undetected in cereal-based products due to the products' low-fat content. This study suggested that food products prepared using palm oil are more likely to contain higher concentrations of MCPD esters and GE, implicating the threat of exposure of particularly European citizen toward these carcinogens [23].

Owing to the adverse health effects and widespread occurrence of bound MCPD and bound glycidol in foodstuff, Wohrlin et al. found it was necessary to study and monitor their concentrations in infant formula. In this study, accelerated solvent extraction (ASE) was performed to extract MCPD and GE from 14 samples of infant formula of Deutsche products [24]. After converting GE into monobromopropanediol (3-MBPD) esters, both MCPD esters and 3-MBPD esters were hydrolyzed and derivatized for detection by GC-MS. From the result, the recovery rates of the analytes can be determined by the fortification of the infant formula. It was stated that the recovery rates for 3-MCPD was between 93% to 103% while for 2-MCPD, it was between 91% to 96%. For GE it was determined that the rate of recovery values was between 92% to 109%. It was recorded that GE has the highest precision of the whole method, which is 12%. Meanwhile 3-MCP and 2-MCPD were 5% and 3% respectively [24].

Marc et al. [25] has reported the research study regarding the determination of MCPD ester and glycidyl ester (GE) by using microwave extraction in the different food stuffs in 2016. There were two types of sample preparation in this study which is sample preparation for oils and samples preparation for the infant formula. This research study used gas chromatography mass spectrometry (GC-MS) for the analysis of the sample. A new method of extraction for this study was developed which was using the microwave. Usually, the extraction method by using the microwave was used to extract the contaminants that come from non- food matrices such as soil or river water. However, this method was used by many laboratories before in order to determine the polycyclic aromatic hydrocarbons (PAH) in food matrices. In this study, the linearity of the method was studied starting from 0-10 mg/kg for the glycidol ester while the linearity for 2 and 3-MCPD ester were studied from 0-5 mg/kg. This method LOQs for both MCPD and glycidyl ester at 0.1 mg/kg, 0.02 mg/kg and 0.0025 mg/L respectively for oils, chips and crisps and infant formula. For LOD in oils was 0.03 mg/kg, 0.007 mg/kg for crisps and chips and 0.0008 mg/kg for infant formula for both MCPD and glycidyl ester.

In this study, the concern was focuses on the detection of 3-MCPD and glycidyl ester in infant formula [26].The quantitative analysis was using liquid chromatography-tandem mass spectrometry (LC-MS/MS). The method provided for extracting MCPD

and glycidyl esters from infant formula uses simple, liquid-liquid extraction processes that do not require complex instruments or expensive equipment. Ethyl acetate was used for extraction after the powdered infant formula was dissolved by using water. In this experiment all of the samples were purchased from the local market. The step of preparation of homemade infant formula for reference material were followed from the online recipe then followed by the preparation of the infant formula extracts. The infant formula extract solutions were prepared when the deuterated internal standard spiking solution of oil extract were pipetted for about 250μL of 5μg/mL into the glass centrifuge tube that contained oil extract. There were about 9 calibration curves that were used for the di-ester, monoester and glycidyl ester quantitation. The concentration prepared were 1, 2, 5, 10, 25, 50, 125, 250 and 400 ng/mL for each of the ester. The internal standard was 50 ng/mL. According to this study, infant formula was one of the food matrix components that presented a challenge due to their intricacy. It contained fats, carbs, proteins, vitamins, and minerals that had been properly homogenized and dried. During the development of this process, it was discovered that the quantity of fat extraction yields from various types of newborn formula available varied greatly from one type of infant formula to the next when the same set extraction was used. The percentage of recovery can be used to validate the method's performance. For the homemade powdered infant formula reference material, the ester recovery ranged from 84.9 percent to 109.0% on average. Meanwhile, the ester recovery rates for all concentrations and infant formulas ranged from 88.7 to 107.5 %.

The study in 2016 , Cheng et al. [27] has reported the concern to study and investigate the presence and the formation mechanism of glycidyl ester (GE) in the edible oils such as soybean oil, camellia oil and palm oil. This study focuses on the laboratory-scale preparation and refining during high temperature from 160 ℃ to 260 ℃ under nitrogen. Attenuated total reflection-Fourier transform infrared (ATR-FTIR) spectroscopy was used in this experiment in order to monitor the formation of the GE in chemical model 1,2-dipalmitin (DPG) and 1-monopalmitin (MPG). All of the sample of crude oil such as palm oil, soybean oil and camellia oil were purchased from the local market in Guangzhou China. The extraction method used in the preparation of crude oil was solvent extraction and hot pressing and cold pressing methods were also used in the preparation of crude oil. After the preparation of crude oil, the preparation of model oil was continued by using column chromatography with solvent mixture of petroleum ether and diethyl ether and about 80 g of silica gel were used. For the laboratory scale refining procedure, all of the crude oil was processed at the industry standard state. Nitrogen was used in this procedure. The main purpose of using nitrogen is to avoid oil oxidation.

The total polar components (TPC) were employed as the gravimetric method to determine the total amounts of the polar fraction after eliminating the nonpolar component using column chromatography separation. TPC was then tested for composition using thin-layer chromatography (TLC). Following that, the TPC composition was examined using high performance size exclusion chromatography (HPSEC). The GE analysis was carried out in accordance with the AOCS Official procedure. The GEs content was estimated using an indirect method based on the detection of 3-MCPD ESTERSs levels. It entailed the ester's release of 3-MCPD ESTERS and glycidol, PBA derivatization, and quantitation by gas chromatography-mass spectrometry (GC-MS). According to the main findings, no statistical differences in the GE content of the tested oils with varying refining degrees before deodorization were identified. The results also revealed that the GE level in crude oil extracted by the solvent was lower than the detection limit of 10 μg/kg. The low quantity of GE was reported in the pressing method of extracted crude oils, whereas hot-pressed oil reported the low amount of GE corresponds to cold-pressed oil. GE levels were reported to be highest in palm oil followed by camellia oil and soybean oil. The GE level was monitored by GC-MS and the linear correlation between the DPG and GE was found at R^2 =0.9607, which is relatively poor.

Rubio et al. [28] has reported the study in a novel single –step method for the simultaneous determination of 3-MCPD and GE in the sample of winterized and non-winterized fish oil by using gas chromatography

tandem-mass spectrometry (GC-MS/MS) in 2017. The process was based on the alkaline hydrolysis of ester at ambient temperature followed by a derivatization stage with phenylboronic acid (PBA) at 90 °C. The use of GC-MS/MS resulted in simpler sample treatment as well as improved limit quantification and precision of the analytical approach without the requirement for additional extract concentration. This approach verified both winterized and non-winterized fish oil by obtaining limits of quantification of 100 ng/g for 3-MCPD and 50 ng/g for glycidol. Furthermore, in order to validate the procedure, the laboratory results were compared to those obtained by an accredited reference laboratory (SGS Germany GmbH). The use of GC-MS/MS rather than GC-MS, which is often used to determine 3-MCPD and glycidyl derivatives, dramatically enhanced the signal-to-noise ratio while minimizing sample preparation and manipulation. The LOD and the LOQ for 3-MCPD were 0.05 mg/kg and 0.2 mg/kg respectively. While for glycidol, the LOD was 0.02 mg/kg and LOQ was 0.07 mg/kg. The recoveries obtained for both 3-MCPD and glycidol were almost near to 100 % which was 93.4% to 98.9% for 3-MCPD and glycidol respectively. Average value calculated were 99.8% for 3-MCPD and 99.0% for glycidol.

Previous studies on the analytical determination of the GE were fully validated only for oils, fats and margarine. This calls for a re-assessment of the critical steps in the AOCS Cd 29a-13 method, in 2017, for simultaneous determination of MCPD esters and GE in a broader range of different food, including meat, infant formula milk, fried fries, bakery product and cereal products [11]. Since overestimation of GE contents is more likely to occur with an indirect analysis of GE, the results can be confirmed by comparison of results achieved through an independent analytical method, such as the direct analysis of the GE by HPLC-MS/MS. In the direct method according to the AOCS standard method, internal standard is added to the pre-weighed fat and dissolved in cyclohexane: ethyl acetate (1:1, v/v) [11]. Before quantitative analysis, triacylglycerols (TAG) has to be removed from the extracted fats. The direct method proposed by Dubois et al. uses gel permeation chromatography (GPC) to separate the almost-similar analyte constituents. In this assay, six GE, namely glycidyl(G-) laurate, G-palmitate, G-stearate, G-oleate, G-linolate, and G-linolenate were determined, totaled up, and expressed in equimolar amounts of glycidol or glycidol equivalents for comparison of results with the indirect analysis method [11]. The results obtained from the two analysis methods were not significantly different. At 95% confidence level, only the results for three bakery products were significantly different. A linear correlation was found when plotting the difference of glycidol content measured by the direct and indirect method, against the content of MAG in the extracted fat sample. However, the results of the indirect method would be deduced as bias in the presence of higher than 1% MAG in the fat sample [11].

According to paper presented by Arisetto et al. [7], the analytical methods to determine these contaminant 3-MCPD and GE was using direct and indirect approaches. The indirect approaches were using gas chromatography coupled to mass spectrometry (GC-MS) for the analysis. This procedure necessitates the conversion of the compound into free form before the analysis can be carried out. The pros of using this approach were that it possesses a lowest number of analytical standards and was easier to comprehend the data. This method involves a few methods such as transesterification, neutralization, salting out and derivatization. Meanwhile, the direct method analysis was using high performance liquid chromatography-mass spectrometry (LC-MS/MS) for the identification and quantification of the different compounds. In direct method, a simple extraction procedure was required but it did not require transesterification and derivatization steps. In this study, samples such as fish oil, edible oil and several foodstuffs were used for the determination of 3-MCPD and GE. Generally, the LOD for both of these approaches was between 0.033 μg/kg to 50 μg/kg.

Kalkan et al. [9] evaluated the formation of 3-MCPD, 2-MCPD and GE in sunflower oil frying processes by using central composite design (CCD) methodology. Chemicals used were 3-MCPD, 3-chloro-1, 2 propanediol-d5 (3-MCPD-d5) and 2-MCPD, 2-chloro-1,3-propanediol-d5 (2-MCPD-d5), glycidyl stearate-d5 (Gly-Pd5) and glycidyl stearate (Gly-S-). Toluene,

tertbutyl methyl ether, methanol, sodium hydroxide, diethyl ether, ethyl acetate, isohexane, n-heptane, isooctane, sodium bromide, anhydrous sodium sulfate, sulfuric acid, and PBA. Sample used was frying oil that were capped into brown-stoppered flasks and stored it in refrigerator at -18 °C because to protect for deterioration until the analysis. For the determination of GE, free and bound 3-MCPD esters were converted into free 3-MCPD form by adding dilute methanolic sodium hydroxide solution. Then, free and bound 3-MCPD were analyzed in GC/MS by derivatization with PBA. The amount of GE was obtained by multiplying the difference of total 3-MCPD and free and bound 3-MCPD by conversion factor. The conversion factor was the standard addition method which GE internal standard was added into oil sample. It was calculated by using slope of calibration curve. An indicator of the acceptability of method was based on the sensitivity of an analytical method. The LOD, LOQ, recovery and relative standard deviation tests were performed. It was observed that temperature, duration and salinity were the factors that had significant effects. MCPD ester in frying was transformed into GE species with the increasing of temperature, duration and salinity. The highest 3-MCPD (0.30 mg/kg), 2-MCPD (0.09 mg/kg) and GE (0.72 mg/kg) formations were observed in the hardest conditions with 40 min., 180 °C and 300 mg NaCl/ 100 mL for oil [10].

Nguyen et al. [10] reported that a GC/MS-MS method was developed, validated and applied for the determination of MCPD ESTERSs and GEs to analyzed 60 infant formula and baby food products. Different commercial food products such as powder infant formula, liquid infant formula, cereal based and vegetables-based baby foods which include smoothies, puffs, and biscuits. All the samples were homogenized and stored at −18 °C for analysis. Fat extraction was needed to extract contaminants out of food matrices because MCPD ESTERSs and GEs was highly lipophilic. The sample was spiked with 50 µL of an internal standard mixture (5 ng/µL) and placed on high-speed vertical shaker and extracted at 1500rpm for 5min. 10g of sodium sulfate anhydrous was added to get better phase separation and salting out effect. Extracted fat were obtained by evaporation of combined upper layers to dryness under nitrogen steam at 40 °C. Food items have been reported to contain a significant amount of partial glycerides especially MAGs that can cause artifact formation of GEs during bromination of GEs. Hence, a cleanup step by aminopropyl SPE cartridge was employed to remove MAGs. The results showed low levels of MCPD ESTERSs, and GEs were observed in most vegetable oil containing products while samples with no added oil showed < LOQs levels. The degree of MCPD ESTERSs and GEs contamination was in the following order: cereal based puree liquid formula cereal-based puree powder baby puffs < powder formula < baby biscuits, with the exception for GEs where baby puffs showed the highest concentrations.

A new method was developed based on the headspace solid-phase microextraction gas chromatography–mass spectrometry (HS–SPME–GC–MS) method for the quantification of 3-MCPD ESTERSs, 2-MCPD ESTERSs and GEs in edible oils [29]. Hydrolysis method was used in this research with the addition of NaBr and NaCl to convert glycidols into 3-MBPD or 3-MCPD. The authors also stated that a critical factor for the alkaline analysis was reaction time to indicate the sensitivity. Hence, to keep higher recovery, acidic hydrolysis was employed. The method of solid phase microextraction (SPME) involved fibre coated with porous stationary phase. Since the analyte have variable partition coefficient with different fibre coatings, then type of fibres play an important role in extraction efficacy [29]. A HS–SPME–GC–MS labor-friendly method demonstrates greater precision, accuracy and adequate LOD/LOQ as compared with liquid injection of GC–MS.

The analysis traces of 3-MCPD and GE has been carried out by using ultra-high-performance liquid chromatography coupled to tandem mass spectrometry, using a triple quadrupole analyzer (UHPLC-MS/MS-QqQ) [17]. This method used a WX vortex from Velp Scientifica to homogenize the samples while a Reax 2 rotatory shaker from Heidolph extraction of the compounds. The MS conditions were optimized first then by applying full-scan MS, the characteristic ion of each compound was obtained. The target compounds were prepared at 10 mg/L in isopropanol to achieve a

proper optimization. To reduce the analysis time and obtain the best peak shapes, chromatographic parameters need to be optimized. To guarantee the reliability of the results, an internal quality control has been carried out during the analysis which consisted of blank sample, a matrix calibration line from 0.01 to 0.5 mg/L and two samples which has been already spiked and analyzed at 0.01 and 0.2 mg/kg. Each of these quality control are to check the absence of interferences, to evaluate the sensitivity and performs quantification of samples also to evaluate the efficiency of the extraction process [17]. The results showed that most detected esters in analyzed oil samples were from oleic, linoleic and linolenic acid because it was the major fatty acids that are present in oils. It is normal for extra virgin and virgin olive oil to not show high concentrations of esters since both are not submitted to any refinement process. This method has a simple and fast extraction method based on the use of solvents. By using UHPLC-MS/MS-QqQ, it takes less time to analyze the samples and by using this approach, the most significant identification and quantification of 3-MCPS and GE that are present in the samples are available.

Lastly, Goh et al. [30] had studied the detection of glycidyl ester in edible palm-based cooking oil and a total result was acquired from the market in a different oil sample. The amount of GE content from 1.338-18.362 mg/kg. The result was not surprising because all the palm oils refinery in Malaysia uses high temperature so that it has been proven for the main factor that cause formation of GE. Mixed glycerides and high portions of oleic, linoleic and linolenic acid were existing in palm-based cooking oil. In this research, GC-MS and ATR-FTIR were used for identification and quantification of GE. However, for the confirmation of the presence of GE was further by using 1H NMR spectroscopy and the results was it showed some signals that known as a characteristic of fatty acids, polyunsaturated fatty acids (PUFA) and TAG. TAG has the most abundant fatty acids that present in edible palm-based cooking oil sample [30]. NMR technique has been proven as a useful technique in order to get data verification and have a potential for alternative spectrum input in modelling process. The results showed that contamination of GE in palm-based cooking oil sample ranged from 1.338 to 18.362 mg/kg which showed a non-normal distribution.

Conclusion

The first proposed analytical method for the detection of glycidyl esters was an indirect approach which is by hydrolyzing variety of fatty acid esters, releasing free glycidol and the analysis was greatly simplified. However, this method was shown to provide inaccurate results. Hence, different methods have been developed such as by using ultra-high performance liquid chromatography tandem mass spectrometry with triple quadrupole analyzer (UHPLC- MS/MS-QqQ), GC-MS, LC-MS, GC-MS/MS and LC-MS/MS. The newly developed methods offer a superior advantage simplified clean-up procedure that only required several hours to complete that much faster than hydrolysis step and it employs several isotopically labelled internal standards that avoided the need for time consuming. Great progress has been made on the analysis of glycidyl esters in oils and other matrices over the past few years, with a number of methods producing comparable and accurate results, the analysis of complex foods is still developing. The challenges of extracting the wide variety of fat-containing foods combined with the lack of commercial reference materials slow the progress of development. However, there are a number of published methods which have recently been validated in complex foods. Moving forward, comparing their performance to one another and to standard reference materials is necessary to ensure accurate data is being produced for exposure and risk assessment purposes. In addition, further studies related to the GE formation during food processing should be extended to other thermal methods.

Acknowledgement

This study was supported by the Ministry of Higher Education Malaysia through Fundamental Research Grant Scheme (FRGS) with reference code number: FRGS/1/2021/STG04/USM/02/4 and account code number: 203.CIPPT.6711973. The authors extend their gratitude to Siti Nurfazilah Awang and Nur ‘Ain Syaheeda Azizan for their invaluable contributions to the completion of this review.

References

1. Albuquerque, T. G., Costa, H. S., Silva, M. A., and Oliveira, M. B. P. P. (2020). Are chloropropanols and glycidyl fatty acid esters a matter of concern in palm oil? *Trends in Food Science and Technology*, 105: 494-514.
2. Arisseto, A. P., Silva, W. C., Scaranelo, G. R., and Vicente, E. (2017). 3-MCPD and glycidyl esters in infant formulas from the Brazilian market: Occurrence and risk assessment. *Food Control*, 77: 76-81.
3. Aniołowska, M., and Kita, A. (2016). The effect of frying on glicydyl esters content in palm oil. *Food Chemistry*, 203: 95-103.
4. Stadler, R. H. (2015). Monochloropropane-1,2-diol esters (MCPDEs) and glycidyl esters (GEs): An update. *Current Opinion in Food Science*, 6: 12-18.
5. Becalski, A., Feng, S., Lau, B. P. Y., and Zhao, T. (2015). A pilot survey of 2- and 3-monochloropropanediol and glycidol fatty acid esters in foods on the Canadian market 2011-2013. *Journal of Food Composition and Analysis*, 37: 58-66.
6. Bognár, E., Hellner, G., Radnóti, A., Somogyi, L., and Kemény, Z. (2019). Formation of glycidyl esters during the deodorization of vegetable oils. *Hungarian Journal of Industry and Chemistry*, 46(2): 67-71.
7. Arisseto, A. P., Silva, W. C., Tivanello, R. G., Sampaio, K. A., and Vicente, E. (2018). Recent advances in toxicity and analytical methods of monochloropropanediols and glycidyl fatty acid esters in foods. *Current Opinion in Food Science*, 24: 36-42.
8. MacMahon, S. (2019). MCPD esters and glycidyl esters: A review of analytical methods. *In Encyclopedia of Food Chemistry*: pp. 569-577.
9. Kalkan, O., Topkafa, M., and Kara, H. (2021). Determination of effect of some parameters on formation of 2-monochloropropanediol, 3-monochloropropanediol and glycidyl esters in the frying process with sunflower oil, by using central composite design. *Journal of Food Composition and Analysis*, 96(7): 103681.
10. Nguyen, K. H., and Fromberg, A. (2020). Monochloropropanediol and glycidyl esters in infant formula and baby food products on the Danish market: Occurrence and preliminary risk assessment. *Food Control*, 110(11): 106980.
11. Zelinkova, Z., Giri, A., and Wenzl, T. (2017). Assessment of critical steps of a GC/MS based indirect analytical method for the determination of fatty acid esters of monochloropropanediols (MCPDEs) and of glycidol (GEs). *Food Control*, 77: 65-75.
12. Stadler, R. H., and Seefelder, W. (2016). An update on processing-derived food contaminants: acrylamide, monochloropropane-1,2-diol (MCPD) esters, and glycidyl esters. In Reference Module in Food Science. Elsevier.
13. Wang, S., Liu, G., and Cheng, W. (2021). Chloride-mediated co-formation of 3-monochloropropanediol esters and glycidyl esters in both model vegetable oils and chemical model systems. *Food Research International*, 140(381): 109879.
14. Santiago, J. K., Silva, W. C., Capristo, M. F., Ferreira, M. C., Ferrari, R. A., Vicente, E., Meirelles, A. J. A., Arisseto, A. P., and Sampaio, K. A. (2021). Organic, conventional and sustainable palm oil (RSPO): Formation of 2- and 3-MCPD esters and glycidyl esters and influence of aqueous washing on their reduction. Food Research International, 140(12): 109998.
15. Hew, K. S., Khor, Y. P., Tan, T. B., Yusoff, M. M., Lai, O. M., Asis, A. J., Alharthi, F. A., Nehdi, I. A., and Tan, C. P. (2021). Mitigation of 3-monochloropropane-1,2-diol esters and glycidyl esters in refined palm oil: A new and optimized approach. *LWT*, 139: 110612.
16. Wu, P. Y., Chen, H., Su, N. W., Chiou, T. Y., and Lee, W. J. (2021). First determination of glycidyl ester species in edible oils by reverse-phase ultra-performance liquid chromatography coupled with an evaporative light-scattering detector. *Molecules*, 26(9): 2702.
17. Hidalgo-Ruiz, J. L., Romero-González, R., Martínez Vidal, J. L., and Garrido Frenich, A. (2021). Determination of 3-monochloropropanediol esters and glycidyl esters in fatty matrices by ultra-high performance liquid chromatography-tandem mass spectrometry. *Journal of Chromatography A*, 1639: 461940.
18. FEDIOL (2015). MCPD esters and glycidyl esters. Review of mitigation measures revision 2015. 15SAF108: pp. 1-17.
19. Aniołowska, M., and Kita, A. (2015). The effect of

type of oil and degree of degradation on glycidyl es ters content during the frying of french fries. *Journ al of the American Oil Chemists' Society,* 92(11–12): 1621-1631.

20. Wenzl, T., Samaras, V., Giri, A., Buttinger, G., Ka rasek, L., and Zelinkova, Z. (2015). Development a nd validation of analytical methods for the analysis of 3- MCPD (both in free and ester form) and glyci dyl esters in various food matrices and performanc e of an ad-hoc survey on specific food groups. EFS A Supporting Publication 2015: EN-779, 12(3): 78 .
21. Dingel, A., and Matissek, R. (2015). Esters of 3-m onochloropropane-1,2-diol and glycidol: no format ion by deep frying during large-scale production of potato crisps. *European Food Research and Techn ology,* 241(5): 719-723.
22. Aniołowska, M., and Kita, A. (2016a). Monitoring of glycidyl fatty acid esters in refined vegetable oil s from retail outlets by LC–MS. *Journal of the Scie nce of Food and Agriculture,* 96(12): 4056-4061.
23. Samaras, V. G., Giri, A., Zelinkova, Z., Karasek, L ., Buttinger, G., and Wenzl, T. (2016). Analytical m ethod for the trace determination of esterified 3- an d 2-monochloropropanediol and glycidyl fatty acid esters in various food matrices. *Journal of Chroma tography A,* 1466: 136-147.
24. Wöhrlin, F., Fry, H., Lahrssen-Wiederholt, M., and Preiß-Weigert, A. (2015). Occurrence of fatty acid esters of 3-MCPD, 2-MCPD and glycidol in infant formula. *Food Additives and Contaminants - Part A Chemistry, Analysis, Control, Exposure and Risk A ssessment,* 32(11): 1810-1822.
25. Marc, C., Drouard-Pascarel, V., Retho, C., Janvion , P., and Saltron, F. (2016). Determination of MCD P esters and glycidyl esters by microwave extractio n in different foodstuffs. *Journal of Agricultural an d Food Chemistry,* 1(1): 1-15.
26. Leigh, J. K., and MacMahon, S. (2016). Extraction and liquid chromatography-tandem mass spectrom etry detection of 3-monochloropropanediol esters a nd glycidyl esters in infant formula. *Journal of Agr icultural and Food Chemistry,* 64(49): 9442-9451.
27. Cheng, W., Liu, G., and Liu, X. (2016). Formation of glycidyl fatty acid esters both in real edible oils during laboratory-scale refining and in chemical m odel during high temperature exposure. *Journal of Agricultural and Food Chemistry,* 64(29): 5919-59 27.
28. Garballo-Rubio, A., Soto-Chinchilla, J., Moreno, A ., and Zafra-Gómez, A. (2017). A novel method for the determination of glycidyl and 3-monochloropro panediol esters in fish oil by gas chromatography ta ndem mass spectrometry. *Talanta,* 165: 267-273.
29. Xu, M., Jin, Z., Yang, Z., Rao, J., and Chen, B. (20 20). Optimization and validation of in-situ derivati zation and headspace solid-phase microextraction f or gas chromatography–mass spectrometry analysi s of 3-MCPD esters, 2-MCPD esters and glycidyl e sters in edible oils via central composite design. *Fo od Chemistry,* 307(5): 125542.
30. Goh, K. M., Maulidiani, M., Rudiyanto, R., Abas, F ., Lai, O. M., Nyam, K. L., Alharthi, F. A., Nehdi, I . A., and Tan, C. P. (2021). The detection of glycid yl ester in edible palm-based cooking oil using FTI R-chemometrics and 1H NMR analysis. *Food Cont rol,* 125(1): 108018.
31. Jana, B., Hepner, R., Sellers, K., Majer, H., and Ko nschnik, J. (n.d.). Optimizing GC-MS and GC-MS/ MS analysis of 3-mcpd and glycidyl esters in edibl e oils. Technical Literature Library, *Restek Pure C hromatography*: pp 1-10.
32. Ioime, P., Piva, E., Pozzebon, M., and Pascali, J. P. (2021). Automated sample preparation and analysi s by gas chromatography tandem mass spectrometr y (GC–MS/MS) for the determination of 3- and 2-monochloropropanediol (MCPD) esters and glycid ol esters in edible oils. *Journal of Chromatography A,* 1650: 462253.

Malaysian Journal of Analytical Sciences (MJAS)
Published by Malaysian Analytical Sciences Society

CHARACTERIZATION OF *Artocarpus altilis* POWDER AS A POTENTIAL HEALTH SUPPLEMENT INGREDIENT

(Pencirian Serbuk *Artocarpus atilis* sebagai Bahan Tambahan Kesihatan Berpotensi)

Noorazwani Zainol[1*], Harith Syahmie Zulfikree[1,2], Nor Farahiyah Aman Nor[1], Harisun Yaakob[1,3], and Dayang Norulfairuz Abang Zaidel[1,4]

[1]*Food and Nutraceutical Unit, Institute of Bioproduct Development, Universiti Teknologi Malaysia, 81310 Johor Bahru, Johor, Malaysia*
[2]*Faculty of Medical Sciences, Newcastle University Medicine Malaysia, 79200 Iskandar Puteri, Johor, Malaysia*
[3]*Department of Bioprocess Engineering, Faculty of Chemical Engineering, Universiti Teknologi Malaysia, 81310 Johor Bahru, Johor, Malaysia*
[4]*Department of Chemical and Environmental Engineering, Malaysia-Japan International Institute of Technology, Universiti Teknologi Malaysia, Jalan Sultan Yahya Petra, 54100, Kuala Lumpur, Malaysia*

[*]*Corresponding author: azwani@ibd.utm.my*

Received: 5 December 2022; Accepted: 14 October 2023; Published: 30 October 2023

Abstract

Processing nutrient-dense breadfruit powder with the desired texture has gained lots of attention due to its characteristics heavily influencing its usage in food as an ingredient. This study was initiated to determine the breadfruit's characteristics in relation to its functional properties, thermal behavior, and physicochemical analysis. The native grounded breadfruit (BG) was assessed for its functional properties while its spray-dried powder (BFP and BFP+MD) was subjected to thermal behavior and physicochemical analysis. The physical properties of the breadfruit juice used for preparing BFP and BFP+MD were determined before the spray drying process. The water and oil absorption of BG were 9.08±0.20 g and 2.26±0.15 g, respectively, with the respective gelation properties observed at the concentrations of 13% and 20%. The analysis of breadfruit juice used for preparing BFP and BFP+MD revealed the following properties: pH of 6.39±0.20, TSS of 10.40% and 18.85%, and viscosity of 40 cP and 20 cP, respectively. The IC_{50} for antioxidant activity of breadfruit juice was 58.51±0.34 µg/mL, and its total phenolic content was 369.74±18.41 µg GAE/g. The analysis also revealed the following physicochemical properties of BFP and BFP+MD: moisture content (%) of 5.67±0.81 and 4.23±0.11, hygroscopicity (%) of 4.72±0.18 and 4.04±0.26, water solubility index (%) of 50.74±1.14 and 70.78±2.31, and bulk density (g/mL) of 0.55±0.02 and 0.48±0.01, respectively. BFP+MD demonstrated a lower melting point (28.29°C ± 0.20) than that of BFP (28.64°C ± 0.20). The nutritional value of BFP+MD were as follows: protein (1.7±0.10 %w/w), crude fiber (5.02±0.03 %w/w), fat (3.27±0.11 %w/w), ash (3.80±0.17 %w/w), and carbohydrate (86.84±0.18 %w/w). The evaluated characteristics enable the incorporation of breadfruit into a wide range of supplementary foods for a healthy diet.

Keywords: breadfruit powder, functional properties, thermal behavior, physicochemical analysis

Abstrak

Memproses serbuk sukun yang padat dengan nutrient serta tekstur yang diingini semakin mendapat perhatian kerana ciri-cirinya yang banyak mempengaruhi penggunaannya dalam makanan sebagai bahan ramuan. Kajian ini dilakukan untuk mengenal pasti ciri-ciri sukun dari segi sifat-sifat berfungsinya, tingkah laku terma dan analisis fizikokimia. Sifat-sifat berfungsi telah dikaji menggunakan buah sukun yang dikisar (BG), sementara tingkah laku terma dan analisis fizikokimia dijalankan ke atas sukun yang telah disembur kering (BFP dan BFP+MD). Sebelum disembur kering sifat-sifat fizikal jus sukun untuk kedua-dua BFP dan BFP+MD juga ditentukan. Keputusan BG untuk penyerapan air dan minyak masing-masing ialah 9.08±0.20 g dan 2.26±0.15, manakala sifat pembentukan gel diperhatikan pada kepekatan 13% dan 20%. Keputusan jus sukun untuk kedua-dua BFP dan BFP+MD masing-masing adalah seperti berikut: 6.39±0.20 untuk pH, 10.40% dan 18.85% untuk TSS dan 40 cP dan 20 cP untuk kelikatan,. Nilai IC_{50} aktiviti antioksidan ialah 58.51±0.34 μg/mL, dan jumlah kandungan fenolik ialah 369.74±18.41 μg GAE/g untuk jus sukun. Keputusan fizikokimia untuk BFP dan BFP+MD masing-masing ialah kandungan lembapan (%) (5.67±0.81, 4.23±0.11), higroskopisiti (%) (4.72±0.18, 4.04±0.26), indeks larut air (%) (50.74±1.14, 70.78±2.31) dan ketumpatan pukal (g/mL) (0.55±0.02, 0.48±0.01). BFP+MD menunjukkan takat lebur yang lebih rendah (28.29°C ± 0.20) daripada takat lebur BFP (28.64°C ± 0.20). Kandungan nutrisi BFP+MD yang ditentukan ialah protein (1.7±0.15 %w/w), serat kasar (5.02±0.03 %w/w), lemak (3.27±0.11 %w/w), abu (3.80±0.017 %w /w) dan karbohidrat (86.90 ±0.03 %w/w). Ciri-ciri yang diperhatikan membolehkan serbuk sukun menjadi ramuan dalam pelbagai makanan tambahan yang sihat.

Kata kunci: serbuk sukun, sifat-sifat berfungsi, tingkah laku terma, analisis fizikokimia

Introduction

As a result of the Covid-19 epidemic expanding into endemic, community well-being has taken precedence. It is critical to focus on acquiring health supplements for easy daily consumption to boost the immune system and reduce the problems associated with chronic diseases. A balanced diet should include an adequate amount of essential nutrients such as antioxidants, complex carbohydrates, low-glycemic index ingredients, and fibers that are readily accessible. Breadfruit (*Artocarpus altilis*) is one of the underutilized tropical plants recently studied for its potential health benefits to humans, either through oral consumption, e.g., food, or topical application, e.g. cosmetic ingredients. Because of its distinct qualities, such as its pale hue and bland sensory profile, it meets the requirements of the food sector, which prefers starch that is stable, white in color, and odorless [1].

Breadfruit (*A. altilis*), also known as *sukun* in Malay is a traditional crop and a reliable staple food that originates from South Pacific countries [2] Breadfruit trees are easy to grow and capable of bearing fruit in abundance. The fruits are highly nutritious and energy-rich and contain large amounts of phytochemicals which exhibit significant antioxidant properties [3, 4]. These compounds are beneficial for human health as they are associated with the prevention of cardiovascular diseases, urinary tract infections, and other chronic illnesses [5, 6]. In addition, antioxidant activity and total phenolic content are an important measure to improve food quality and prolong shelf life without imposing any undesirable effects from the addition of synthetic chemical preservatives [7, 8]. Breadfruit can also be a source of dietary fiber which aids in the regulation of blood sugar in diabetics, the reduction of unfavorable blood lipids (a risk factor for CVDs), and the management of weight. Besides providing essential minerals, breadfruit offers an alternative to gluten-free for those who are gluten intolerant, suffering from Type 2 Diabetes Mellitus, and health-conscious individuals [2-4, 6]. Breadfruit also contains highly resistant starch which has been empirically proven to offer numerous health benefits, including suppressing appetite and feeding the beneficial bacteria in the colon, boosting the number and diversity of bacteria [3]. The rheological behavior of breadfruit starch has been studied extensively in food applications. Based on rheological qualities, the stability of native and modified breadfruit starch has also been examined for its use in emulsion and baking [9]. Physical modification of starch involves the use of chemical or biological agents. Meanwhile, physical modification of starch is frequently favored in food products intended for diet [10]. By considering these properties of breadfruit, researchers can use them as intermediate ingredients or finished products to fulfill the demand of health-conscious consumers.

Apart from its potential use as an energy source, breadfruit offers a wide range of functionalities and diverse nutrients, making it great for functional food applications. Although breadfruit is healthy, it quickly deteriorates physiologically after harvesting. To reduce post-harvest losses and increase breadfruit utilization, the breadfruit can be processed into powder, which is more shelf stable. Conventional methods of oven-drying followed by grinding and spray drying in the making of breadfruit powder can help prolong its shelf life by reducing its moisture content and inhibiting microbial growth and enzymatic activity [11]. Spray drying is often used due to its rapidity and economic value. Maltodextrin is one of the drying aids that acts as a carrier or an encapsulating agent in the drying process. In addition, maltodextrin improves the properties of the powder by increasing its solubility and hygroscopicity and acting as anticaking. The production of breadfruit powder has enabled its application in a vast range of food industries. Some of the applications of breadfruit as a functional food ingredient include breadfruit flour, infant formulas, biscuits, fermented foods, extruded products, and stiff porridge [12]. Yet, the processing of breadfruit powder into a desired texture remains one of the areas that has gained a lot of attention and is under exploration.

There is a lack of research and established data supporting the eligibility of breadfruit powder for applications in food, which is largely influenced by its characteristics. Therefore, the current study focused on evaluating the functional properties, thermal behavior, and physicochemical properties of breadfruit powder. The physicochemical properties including solid and moisture content, bulk density, hygroscopicity, solubility, viscosity, antioxidant and phenolic compound, thermal behavior, and nutritional value were determined. Additionally, the functional properties such as water and oil absorption capacity, and gelation properties were used as complementary data for applications as processed food products. These findings will enhance the significance of our local sources and have a significant impact on product development for diverse age groups, which includes the application as an intermediate ingredient in health supplements for general consumption.

Materials and Methods

Material and chemicals

Matured breadfruits and corn oil were bought from a local market in Skudai, Johor, Malaysia. Maltodextrin was purchased from Agrin Chemical (M) Sdn. Bhd. Methanol, Gallic acid, Folin-Ciocalteu reagent, sodium carbonate, 1,1-diphenyl-2-picrylhydrazyl (DPPH), sodium chloride, and anticaking agent of analytical grade were purchased from SIGMA-Aldrich, US.

Preparation of breadfruit powder: Ground breadfruit powder

The matured breadfruits were washed thoroughly to remove dirt and were subsequently peeled. Next, the fruits were sliced with their core removed. Each of these samples was then dried in a hot air oven at 60 °C for six to eight hours. The dried samples were milled and ground into flour (BG) and were sieved through a 100-µm mesh to obtain fine-textured flour. Lastly, samples were packed into polyethylene bags and stored at room temperature for further use.

Spray-dried breadfruit powder

The matured breadfruits were washed thoroughly to remove dirt and were subsequently peeled. Next, the fruits were sliced with their core removed. Water was added to the sliced breadfruits at a ratio of 1:1 (breadfruit: water) and blended using a juice blender to obtain the breadfruit juice. The juice was filtered through a sieve (ASTM E11, 150-µm mesh) and transferred into a beaker. Next, 1 g of anticaking agent was added to the breadfruit juice, and the mixture was homogenized at 8000 rpm for 10 minutes. The spray dryer was set at a constant aspirator rate of 100 %, pump setting of 20%, nozzle speed of 5, and compressed air flow rate of 5 mL/min. Inlet temperatures were set at 180 °C with a constant maltodextrin concentration (30 % w/w) based on a method by Jafari et al. [13]. The process was repeated using the same parameter for breadfruit without maltodextrin. The samples prepared before the analysis were assigned as breadfruit without maltodextrin (BFP) and breadfruit powder with maltodextrin (BFP + MD).

Process yield

The weight of the dry material in the powder and juice was used to determine the spray drying yield. This factor was calculated from the following equation 1 [13]:

$$Yield\ (g) = \frac{P \times S_P}{L \times S_F} \quad (1)$$

where P is the rate of powder production (g/min), S_P is the percent of total solids of the powder, L is the feed flow rate (g/min), and S_F is the percent of total solids of the feed.

Functional properties of breadfruit samples: Water and oil absorption capacity

The water absorption capacity of the starch was studied based on the method by Pestorić et al. [14]. The methods were as follows; sample weighing 3g was dispersed in 25 mL of distilled water and placed in pre-weighed centrifuged tubes. The mixtures were stirred occasionally, held for 30 min, followed by centrifugation for 25 min at 3000 x g. The supernatant was decanted, excess moisture was removed by draining for 25 min at 50 °C, and the sample was reweighed [15]. For the determination of oil absorption, the samples weighed 0.5 g were mixed with 6 mL of corn oil in pre-weighed centrifuged tubes. The contents were stirred for 1 minute with a thin brass wire to disperse the sample in the oil. After a holding period of 30 min, the tubes were centrifuged for 25 min at 3000 x g. The separated oil was then removed with a pipette and the tubes were inverted for 25 min to drain the oil before weighing [16]. The water and oil absorption capacities were expressed as grams of water or oil bound per gram of the sample on a dry basis.

Gelation properties

Test tubes containing starch suspensions of 1%, 7%, 13%, and 20% (w/v) of material in 5 mL of distilled water were heated for 1 h in boiling water followed by rapid cooling under running water. The tubes were further cooled at 4 ℃ for 2 h. The least gelation concentration (LGC) is the concentration at which the sample does not fall or slip when the test tube is inverted [14].

Physical properties of breadfruit juice: pH

A digital pH meter was used to measure the pH of the samples. The digital pH meter was first calibrated using two buffer solutions of pH 7.0 and 4.0. The pH electrode was immersed into the beaker filled with 200 mL of samples and the readings were recorded [17].

Total soluble solids

A digital refractometer was used to measure the samples. The digital refractometer was calibrated by placing a drop of distilled water on its surface. The samples were placed on the surface of the digital refractor with a scale of 0–85 °Brix and the reading was recorded [17].

Viscosity

The viscosity of the samples was determined using a flow test at a shear rate ranging from 0.001 s^{-1} to 1000 s^{-1}, at a temperature of 25 ℃. The data obtained was generated by calculations with respect to the Herschel-Bulkley, Bingham dan Casson model [18].

Antioxidant activity of breadfruit samples

The antioxidant activity of fresh breadfruit and spray-dried breadfruit powder samples was measured by DPPH radical scavenging activity under minimal light conditions [19]. Samples of 0.4 g of breadfruit powder were weighed and dissolved in 40 mL of 80% (v/v) aqueous methanol to obtain a concentration of 10 mg/mL, followed by 20 minutes of sonication. Ascorbic acid was prepared as a standard reference at concentrations ranging from 1.25 to 200 µg/mL. Next, 0.1 mM DPPH solution was prepared by dissolving 2 mg of DPPH in 50 mL of 80% (v/v) methanol. Then, 0.5 mL of the ascorbic acid standards were added with 2 mL of DPPH solution in tubes and mixed well. After leaving the tubes in the dark for 30 minutes, the absorbance of the standards was measured using a UV-Vis spectrophotometer (DLAB SP-V1000) at 517 nm. These steps were repeated for the samples. The percentage of free radical scavenging activity at different concentrations was calculated using the formula (Eq.2):

$$DPPH\ scavenging\ activity\ (\%) = \frac{A_{517}\ control - A_{517}\ sample}{A_{517}\ control} \times 100 \quad (2)$$

A graph of free radical scavenging activity against the concentration of the standards and samples was plotted using a Microsoft Excel spreadsheet. From the graph, the linear regression ($y = ax + b$) obtained was used to determine the IC_{50} by using the formula (Eq.3):

$$IC_{50} = \frac{50-b}{a} \quad (3)$$

Total phenolic content of breadfruit samples

The total phenolic content (TPC) of fresh breadfruit and spray-dried breadfruit powder samples was measured using Folin-Ciocalteu colorimetric assay [18, 20]. Initially, 0.5g of dried breadfruit powder samples were extracted by mixing them in 10 mL of 80% (v/v) aqueous methanol solution, followed by 25 minutes of sonication. Next, 0.5 mL of the samples were introduced into the test tubes and added with 1.5 mL of Folin-Ciocalteu's reagent and 1.2 mL of 7.5% (w/v) sodium carbonate solution. The test tubes were vortexed, covered with parafilm, and allowed to settle for 90 minutes. The calibration curve was plotted by mixing 1 mL aliquots of 500, 250, 125, 62.5, and 31.25 µg/mL Gallic acid solutions with 1.5 mL of Folin-Ciocalteu's reagent and 1.2 mL of 7.5% (w/v) sodium carbonate solution. The absorbance was measured using a UV-Vis spectrophotometer at 765 nm. The absorbance was measured to determine the total phenolic content (TPC) in the samples using the formula (Eq.4):

$$TPC = C1 \times \left(\frac{V}{m}\right) \quad (4)$$

where C = total phenolic content in µg/g (in Gallic acid equivalent), $C1$ = concentration of Gallic acid established from the calibration curve (µg/ml), V = volume of extract (ml), and m = the weight of the plant extract (g).

Physicochemical properties of spray-dried breadfruit powder: Moisture content

The moisture content of the breadfruit powder samples was determined by a moisture analyzer (AND MX-50) at 80 ℃ until a constant weight was obtained [21].

Hygroscopicity

The hygroscopicity of the samples was determined by the method described by Cai and Corke (2000). Approximately 1 g of each breadfruit powder sample was weighed onto a crucible and placed in an airtight desiccator at a temperature of 25 ℃ with saturated NaCl solution (75% RH) for one week. The hygroscopicity (%) was calculated using the following formula (Eq.5):

$$Hygroscopicity\ (\%) = \frac{(W1\% + MC\%) \times 100}{(W1\% + 100)} \quad (5)$$

where,

$$W1\% = \frac{(Weight\ of\ sample\ after\ equilibrium - Weight\ of\ sample)}{Weight\ of\ sample} \times 100$$

$$MC\% = Moisture\ content\ of\ sample\ powder$$

Water solubility index

The solubility index (WSI) of the spray-dried breadfruit powder samples was determined using the method by [13, 22] with some modifications. Each powder sample weighed 2.5 g was dissolved in 30 mL of distilled water and stirred on a hotplate stirrer for 30 minutes. The mixture was centrifuged at 3000 × g for 10 minutes. The supernatant was placed in a preheated oven at 105 ℃ until a constant weight was obtained. The solubility of the breadfruit powder samples was calculated (Eq. 6) by:

$$WSI\ (\%) = \frac{Dried\ supernantant\ weight}{Initial\ sample\ weight} \times 100 \quad (6)$$

Bulk density

The bulk density of the samples was measured by pouring 2 g of each sample into a 10-mL graduated cylinder and vibrating using a vibrator. The occupied volume was observed [13, 21, 4] and the bulk density was calculated by the following equation (Eq.7):

$$Bulk\ density\ (g/mL) = \frac{m}{v} \quad (7)$$

where *m* is the mass of the breadfruit powder sample (g) and *v* is the volume (mL) occupied in the cylinder.

Differential scanning calorimeter analysis

The thermal behavior of the breadfruit powder samples was determined using the differential scanning calorimeter (DSC), (Mettler Toledo DSC1). Using standard indium and sapphire, the instrument was calibrated for heat flow and temperature. Fifteen milligrams of each sample were accurately weighed into the DSC aluminum sample and flowed using the pan and sealed with a lid while an empty pan with a lid was used as a reference. The process began by decreasing the temperature to -80 ℃ at a heating rate of 10 ℃/min, followed by a scanning from -80 ℃ to 80 ℃ at the same heating rate. Dry nitrogen gas was used as the purge gas at a flow rate of 50 mL/min [21, 23].

Nutritional value of breadfruit samples

The proximate analyses were performed to estimate the moisture, ash, fat, protein, and crude fiber contents of the breadfruit samples based on the AOAC Official Method [24]. Moisture content was determined using the oven drying method at 100 ℃ for at least five hours until a constant weight was obtained. Ash content was determined by the total mineral or inorganic residue remaining in food after either ignition or complete oxidation of organic matter following the application of the dry-ashing method. The protein content was determined based on the total nitrogen content using the Kjeldahl method. Fat content was assessed via the extraction using a non-polar solvent by the Soxhlet extraction method. The carbohydrate content in the sample was calculated by the energy difference. The calculation of the energy (kCal) of the sample was performed as follows:

$$Energy\ (in\ kCal) = 4 \times (Proteins\ and\ carbohydrates\ mass\ in\ grams) + 9 \times (mass\ of\ fat\ in\ gra \quad (8)$$

Results and Discussion

Functional properties of ground breadfruit

As depicted in Table 1, the water and oil absorption capacities of the BG sample were 9.08 ± 0.20 g/g and 2.26 ± 0.15 g/g, respectively. Oil absorption capacity is important for storage and stability especially in the development of rancidity during the storage period. In addition, a high absorption capacity allows for retaining flavor, improving mouthfeel, and increasing the soft texture in the mouth [25, 4].

Table 1. Water and oil absorption capacities of spray-dried breadfruit powder samples

Sample	Water Absorbed (g/g)	Oil Absorbed (g/g)	Gelation Capacity			
			Concentration (% w/v)			
			1	7	13	20
BG	9.08 ± 0.20	2.26 ± 0.15	-	-	+	+

Abbreviation: Grounded breadfruit (BG). Value is expressed as mean ± standard deviation (n=3). Symbol minus (-) as no gelation and (+) as has gelation capacity

Table 1 illustrates the gelation capacities of the spray-dried breadfruit powder samples. BG with 1% (-) and 7% (-) concentration showed no gelation capacity while BG with (+)13% and (+) 20% showed gelation capacity. In food industries, the gelling ability of spray-dried fruit powder is a desirable quality [25]. A higher least gelation capacity (LGC) indicates a lower ability to form a stable gel. Stable gelling formation is ideal in components with higher protein content due to the greater intermolecular contact, especially during cooking [4].

Process yields and physical properties of breadfruit juice

From the results shown in Table 2, the BFP+MD sample generated a higher yield (41.229 g) than the BFP sample (33.112 g). Noticeably, the addition of maltodextrin as a filler improved the process yield and increased the total solid content yet did not alter the pH value of the breadfruit juice. These results indicate that the addition of maltodextrin to spray-dried fruit powders does not alter their pH [17]. Moreover, the pH significantly improved the functional properties of the powder after spray drying. Thus, it is necessary to maintain a particular pH to obtain certain functionalities [26].

Table 2. Yield and physical properties of breadfruit juice

Samples	Yield (g)	pH	TSS (%)	Viscosity (cP)
BFP	33.112	6.19 ± 0.20	10.40	40
BFP+MD	41.339	6.39 ± 0.20	18.85	22

Abbreviation: Breadfruit juice without maltodextrin (BFP); Breadfruit juice with 30% maltodextrin (BFP+MD). Note that the parameters were measured for the breadfruit juice that will be spray-dried into powder.

The sample with 30% maltodextrin contained higher total solid content (18.85%) than the one without (10.40%). Solid content determines the percentage yield and quality of a product [27, 28]. Viscosity is also an important parameter to consider as it influences the emulsifying ability of powders [29]. BFP+MD exhibited a low viscosity (22 cP) compared to BFP (40 cP). This result is consistent with the findings by [30] who reported that the increase in maltodextrin concentration resulted in a reduced viscosity of spray-dried avocado powder.

Antioxidant activity and total phenolic content of breadfruit

In this study, DPPH free radical scavenging activity was used to determine the antioxidant activity and expressed in µg/mL of methanolic extract concentration required to inhibit 50% of the free radicals (IC_{50}). The capacity of the extract/sample to scavenge free radicals through hydrogen donation was assessed using the DPPH test. DPPH molecule is considered a stable free radical. DPPH appears purple/violet in a methanolic solution and will decolorize into shades of yellow in the presence of antioxidants [31]. The DPPH assay was used to measure the scavenging activity of breadfruit samples with ascorbic acid as a positive control. The free radical-scavenging antioxidants in the fruits donate hydrogen to the unpaired electron of the DPPH molecule, turning the purple-colored DPPH into its reduced form which is yellow.

Follin-Ciocalteu's colorimetric assay was performed to analyze TPC in the breadfruit samples. Follin-Ciocalteu reagent is a yellow phenol reagent containing phosphotungstate and phosphomolybdate. The reagent changes from yellow to blue when phenolic compounds are present in the sample. The changes are due to redox reactions, through which the samples turn the Follin-Ciocalteu reagent into its reduced form. Gallic acid, a type of phenolic acid was used as a standard. From the standard curve obtained, the absorbance values of the samples were used to determine the TPC which were expressed in terms of µg/mL GAE/g.

Table 3. TPC and antioxidant activity of fresh breadfruit and spray-dried breadfruit powder

Samples	TPC (µg GAE/g)	IC_{50} of DPPH (µg/mL)
BF_{fresh}	369.74 ± 18.41	58.51 ± 0.34
BFP+MD	745.26 ± 13.60	105.11 ± 3.61

Abbreviation: Freshly prepared breadfruit juice (BF_{Fresh}); Spray-dried breadfruit powder with 30% maltodextrin (BFP+MD). Value is expressed as mean ± standard deviation (n=3).

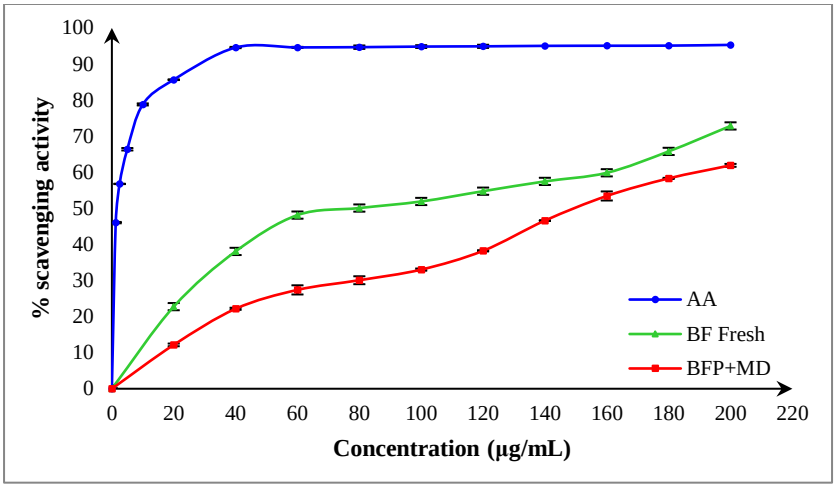


Figure 1. DPPH free radical scavenging activity of breadfruit samples. Abbreviation: Ascorbic acid (AA) as a standard, freshly prepared breadfruit juice (BF_{Fresh}) and spray-dried breadfruit powder with 30% maltodextrin (BFP+MD). Value is expressed as mean ± standard deviation (n=3)

Table 3 and Figure 1 illustrate the TPC and antioxidant activity of fresh breadfruit and spray-dried breadfruit powder with 30% maltodextrin added. Spray-dried breadfruit powder with 30% maltodextrin contained a higher total phenolic content (745.26 ± 13.60 µg GAE/g) than the fresh breadfruit (369.74 ± 18.41 µg GAE/g). Maltodextrin addition improved the phenolic contents in breadfruit during the spray drying process. In the DPPH assay, the lower the IC_{50} the better it can scavenge the radicals which are the propagators of the autoxidation of lipid molecules, and thereby break the radical-free reaction [32]. In addition, fresh juice was expected to contain higher antioxidant activity. Table 3 shows that the fresh breadfruit samples exhibited a lower IC_{50} (58.51 ± 0.34 µg/mL) than the spray-dried samples added with 30% maltodextrin (105.11 ± 3.61 µg/mL), suggesting a higher antioxidant activity in the fresh sample. Different phytochemicals with antioxidant activity have different levels of tolerance toward high temperatures and conformational changes which vary in different types of fruits [33].

Physicochemical properties of spray-dried breadfruit powder

The physicochemical properties are important in ensuring the suitability of spray-dried breadfruit powder to be utilized as food or food ingredients. Physicochemical properties such as moisture content, bulk density, hygroscopicity, and WSI are discussed in this section.

Table 4. Physicochemical properties of spray-dried breadfruit powder samples

Samples	Moisture Content (%)	Hygroscopicity (%)	WSI (%)	Bulk Density (g/mL)
BFP	10.80 ± 0.03	4.715 ± 0.18	50.74 ± 1.14	0.55 ± 0.02
BFP+MD	4.23 ± 0.11	4.035 ± 0.26	70.78 ± 2.31	0.48 ± 0.01

Abbreviation: Spray-dried breadfruit powder without maltodextrin (BFP); Spray-dried breadfruit powder with 30% maltodextrin (BFP+MD). Value is expressed as mean ± standard deviation (n=3). Water soluble index (WSI)

The spray-dried breadfruit powder samples were tested for their physicochemical and the results are summarized in Table 4. In general, the addition of 30% maltodextrin did affect the physicochemical properties of spray-dried breadfruit powder. The moisture content analysis revealed that the moisture content in spray dried-breadfruit powder with 30% maltodextrin was lower (4.23 ± 0.11%) than spray dried-breadfruit powder without 30% maltodextrin (10.80 ± 0.03%). These findings were similar to [34] which revealed that the increase in maltodextrin concentration resulted in a decrease in moisture content and water activity of spray-

dried "cempedak" powder. In industrial practice, only the powder with a moisture content below 10% is considered microbiologically safe [35] suggesting that the spray-dried breadfruit powder fulfilled this criterion. A low moisture content will also prolong the shelf life of food products by preventing microbial activity that induces food degradation [11, 36].

The sample added with 30% maltodextrin also showed lower hygroscopicity (4.035 ± 0.26%) than the one without (4.715 ± 0.18%). Hygroscopicity can be described as the tendency of a solid substance to absorb moisture from the surrounding atmosphere. Pure spray-dried fruit powders usually exhibit a high level of hygroscopic behavior. However, a spray-dried breadfruit powder with lower hygroscopicity is favored to prevent or minimize undesirable effects such as caking. Additionally, hygroscopicity determines the moisture content and behavior of adsorption isotherms at which high hygroscopic levels may lead to unwanted effects such as caking during food processing and manufacturing [37].

The addition of 30% maltodextrin increased the WSI of spray-dried breadfruit powder by 20.04 ± 0.08%. These results are consistent with [38] who reported that the addition of maltodextrin enhanced the solubility of fig powder. Producing spray-dried breadfruit powder with high WSI is desirable for producing functional food ingredients because WSI determines the powder's behavior and stability in aqueous phases [39].

The bulk density of the sample added with 30% maltodextrin exhibited a lower bulk density (0.48 ± 0.01 g/mL) than the pure sample (0.55 ± 0.02 g/mL). These findings are supported by Pui et al. [34] who described that the increase in maltodextrin resulted in a decrease in the bulk density of spray-dried "cempedak" powder. An increase in bulk density is necessary for packaging, as it enables the food product to be packed in greater quantity within a constant volume [40].

Differential scanning calorimeter analysis

DSC analysis was performed to evaluate the thermal behavior of spray-dried breadfruit powder samples. Table 5 and Figure 2 summarize the thermodynamic properties of the samples. Based on Table 5, the addition of maltodextrin in the breadfruit influences the melting temperature of both breadfruit powders, with BFP showing a higher melting temperature (28.64± 0.20 ℃) than BFP+MD (28.29± 0.20 °C) yet demonstrating a lower enthalpy (ΔH 1.99 J/g) than the BFP+MD (ΔH 2.37 J/g). This finding is similar to Nevin and Rajamohan [41] which revealed that the addition of maltodextrin with a low molecular weight requires a lower temperature but a higher enthalpy to achieve an optimum melting temperature. Furthermore, the presence of shorter glucose polymer chain lengths in maltodextrin may affect the level of stickiness and the melting temperature [23].

Table 5. The melting temperature, A1 and ΔH of spray-dried breadfruit powder samples

Samples	A1 (°C)	ΔH (J/g)
BFP	28.64 ± 0.20	1.99 ± 0.20
BFP+MD	28.29 ± 0.20	2.37 ± 0.20

Abbreviation: Spray-dried breadfruit powder without maltodextrin (BFP); Spray-dried breadfruit powder with 30% maltodextrin (BFP+MD). Value is expressed as mean ± standard deviation (n=3).

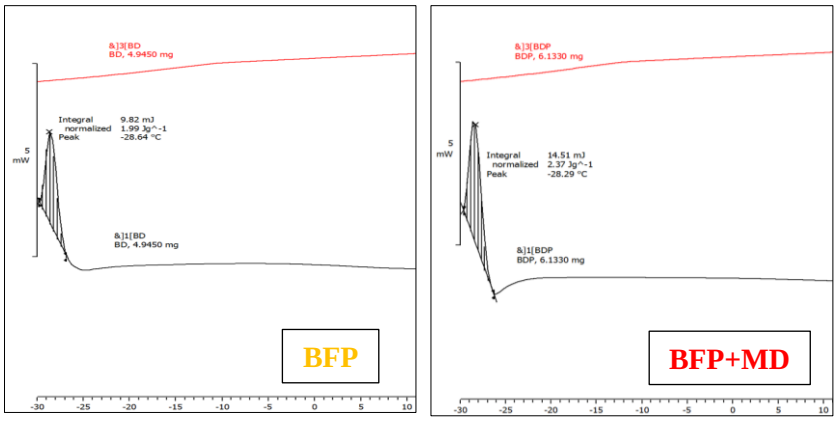


Figure 2. DSC thermogram of BFP and BFP+MD powder samples

Nutritional value of breadfruit samples

Proximate analysis is an important index to determine and classify nutritional values such as carbohydrates, protein, and fat content in a sample [42, 43]. Figure 3 and Table 6 depict the composition of nutritional values in the breadfruit samples obtained from the proximate analysis.

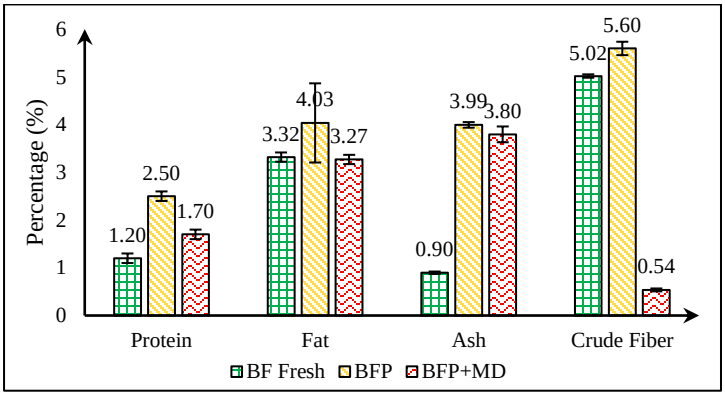


Figure 3. Nutritional value of the breadfruit samples

Table 6. Composition of carbohydrate and energy content of the breadfruit samples

Samples	Components	
	Carbohydrate (% w/w)	Energy (kCal)
BF_{Fresh}	10.42 ± 0.15	76.35 ± 0.78
BFP	73.08 ± 0.92	338.62 ± 3.79
BFP+MD	86.84 ± 0.18	383.80 ± 0.63

Abbreviation: Spray-dried breadfruit powder without maltodextrin (BFP); Spray-dried breadfruit powder with 30% maltodextrin (BFP+MD). Value is expressed as mean ± standard deviation (n=3).

Figure 3 shows that the spray-dried BFP samples generally contained the highest nutritional contents namely protein, fat, ash, and crude fiber (2.50 ± 0.10 % w/w, 4.03 ± 0.83 % w/w, 3.99 ± 0.06 % w/w, 5.60 ± 0.14 % w/w, respectively) compared to BFP + MD (1.70 ± 0.10 % w/w, 3.27 ± 0.11 % w/w, 3.80 ± 0.17 % w/w, respectively). The results demonstrate that both the BFP and BFP + MD samples of breadfruit retain their nutritional value despite the crude fiber content. Noticeably, the BFP + MD contained the lowest crude

fiber content (0.54 ± 0.03) compared to BF_{Fresh} (5.02 ± 0.04 % w/w) and BFP (5.60 0.14 % w/w). The low crude fiber content was probably due to the less soluble solid content in the breadfruit slurry before the spray dry process. Table 6 shows that BFP and BFP + MD contained high carbohydrate contents thus contributing to higher energy value.

Conclusion

Physicochemical, functional, and thermal properties determined in this research are important parameters for adding value to breadfruit processing and its utilization. These characteristics are principally responsible for the final product quality. Breadfruit as a whole is high in nutrients and a good source of energy and possesses extinguishing characteristics. Therefore, it can be potentially used in a variety of food products to offer health benefits. In addition, breadfruit powder with adequate antioxidant and total phenolic contents can be potentially incorporated into health supplementary products. Its favorable functional properties make it a suitable ingredient in the formulation of advanced food products without compromising the needs of health-conscious consumers.

Acknowledgements

This research was financially supported by Quick Win Grant, Universiti Teknologi Malaysia (UTM), Skudai. The authors would like also to thank Mr. Vijayraj Elawarasan and Puan Norasiah Sadek for their assistance with the laboratory work.

References

1. Chen, A. H. (2016). Characterization of functional properties of breadfruit flour. Thesis University of Hawaii. Access from https://scholarspace.manoa.hawaii.edu/bitstream/10125/51551/2016-12-ms-chenalfred. Pdf [Retrieved 2019].
2. Liu, Y., Brown, P. N., Ragone, D., Gibson, D. L., and Murch, S. J. (2020). Breadfruit flour is a healthy option for modern foods and food security. *PloS one*, 15(7): e0236300.
3. Ragone, D. (2018). Breadfruit — *Artocarpus altilis* (Parkinson) Fosberg. In Exotic Fruits (pp. 53-60). Academic Press.
4. Zainol, N., Noor, N. M., Zaidel, D. N. A., Taher, Z. M., Mohamed, M., and Sadek, N. (2022). Breadfruit (*Artocarpus altilis*) Studies: Rheological stability, incorporation of gluten free, and bioactive compound as an intermediate ingredient in health-related products. *ECS Transactions*, 107(1): 14455.
5. Braga, M. B., Veggi, P. C., Codolo, M. C., Giaconia, M. A., Rodrigues, C. L., and Braga, A. R. C. (2019). Evaluation of freeze-dried milk-blackberry pulp mixture: Influence of adjuvants over the physical properties of the powder, anthocyanin content and antioxidant activity. *Food Research International*, 125: 108557.
6. Singh, B., Rani, R., and Dharaiya, C. N. (2020). Application of breadfruit in food products. *Emerging Issues in Agricultural, Environmental and Applied Sciences for Sustainable Development*: pp. 58.
7. Batiha, G. E. S., Hussein, D. E., Algammal, A. M., George, T. T., Jeandet, P., Al-Snafi, A. E., and Cruz-Martins, N. (2021). Application of natural antimicrobials in food preservation: Recent views. *Food Control*, 126: 108066.
8. Ramli, A. N. M., Manap, N. W. A., Bhuyar, P., and Azelee, N. I. W. (2020). Passion fruit (*Passiflora edulis*) peel powder extract and its application towards antibacterial and antioxidant activity on the preserved meat products. *SN Applied Sciences*, *2*(10): 1-11.
9. Anwar, S. H., Rahmah, M., Safriani, N., Dian Hasni, D., Rohaya, S., and Winarti, C. (2016). Exploration of breadfruit, jicama, and rice starches as stabilizer in food emulsion. *International Journal on Advanced Science Engineering Information Technology*, 6(2): 141-145.
10. Din, Z. U., Xiong, H., and Fei, P. (2017). Physical and chemical modification of starches - a review. *Critical Reviews in Food Science and Nutrition*, 57(12): 2691-2705.
11. Phing, P. L., Abdullah, A., Sin, C. L., and Foong, S. C. Y. (2022). The effect of drying methods on the physicochemical and antioxidant properties of Bintangor orange (*Citrus nobilis*) powders. *Acta Scientiarum Polonorum Technologia Alimentaria*, 21(1): 111-122.

12. Histifarina, D. and Purnamasari,N.R. (2022). The prospect of developing breadfruit as an alternative source of food to support food diversification. *IOP Conference Series: Earth and Environmental Science*. 1012: 012023.
13. Jafari, S. M., Ghalenoei, M. G., and Dehnad, D. (2017). Influence of spray drying on water solubility index, apparent density, and anthocyanin content of pomegranate juice powder. *Powder Technology*, 311: 59-65.
14. Pestorić, M., Sakač, M., Pezo, L., Škrobot, D., Nedeljković, N., Jovanov, P., and Mandić, A. (2017). Physicochemical characteristics as the markers in predicting the self-life of gluten-free cookies. *Journal of Cereal Science*, 77: 172-179.
15. Sosulski, F. W. (1962). The centrifuge method for determining flour absorption in hard red spring wheats. *Cereal Chemistry*, 39: 344-350.
16. Lin, M. J. Y., Humbert, E. S., and Sosulski, F. W. (1974). Certain functional properties of sunflower meal products. *Journal of Food Science*, *39*(2): 368-370.
17. Chang, L. S., Tan, Y. L., and Pui, L. P. (2020). Production of spray-dried enzyme-liquefied papaya (*Carica papaya* L.) powder. *Brazilian Journal of Food Technology*, 23: 1-16.
18. Salehi, F. (2020). Physicochemical characteristics and rheological behaviour of some fruit juices and their concentrates. *Journal of Food Measurement and Characterization*, 14(5): 2472-2488.
19. Leng, L. Y., Nadzri, N., Yee, K. C., and Shaari, A. R. (2018). Antioxidant and total phenolic content of breadfruit (*Artocarpus altilis*) leaves. In *MATEC Web of Conferences*, 150: 06007.
20. Singleton, V. L., and Rossi, J. A. (1965). Colorimetry of total phenolics with phosphomolybdic-phosphotungstic acid reagents. *American journal of Enology and Viticulture*, 16(3): 144-158.
21. Roshani, S., Ghorbani-HasanSaraei, A., and Raeisi, S. N. (2021). Phytochemical content, physicochemical and microstructural properties of apple powder as affected by drying method. *Latin American Applied Research-An International Journal*, 51(1): 27-35.
22. Wang, R., Zhao, Y., Zhu, L., Fang, Z., and Shi, Q. (2020). Effect of carrier types on the physicochemical and antioxidant properties of spray-dried black mulberry juice powders. *Journal of Food Measurement and Characterization*, 14(3): 1201-1212.
23. Amin, Z. A., Koh, S. P., Hamid, N. S. A., Tan, C. P., and Long, K. (2017). New coating material for producing virgin coconut oil (VCO) microcapsules. *Food Research*, 1(1): 15-22.
24. AOAC Official Method. (2000). In Horwitz, W. (Ed). Official Method of Analytical of AOAC International. 17th edition. Washington DC: AOAC International.
25. Olu-Owolabi, B. I., Afolabi, T. A., and Adebowale, K. O. (2011). Pasting, thermal, hydration, and functional properties of annealed and heat-moisture treated starch of sword bean (*Canavalia gladiata*). *International Journal of Food Properties*, 14(1): 157-174.
26. Farhad, A., Lingyun, C., Zhenggang, W., and Zahra, E. D. (2021). Consequences of heating under alkaline pH alone or in the presence of maltodextrin on solubility, emulsifying and foaming properties of faba bean protein, *Food Hydrocolloids*, 112: 106335.
27. Henao-Ardila, A., Quintanilla-Carvajal, M. X., and Moreno, F. L. (2019). Combination of freeze concentration and spray drying for the production of feijoa (*Acca sellowiana* b.) pulp powder. *Powder Technology*, 344: 190-198.
28. Zhang, D., Xu, L., Wang, Q., Tian, X., and Li, J. (2019). The optimal local model selection for robust and fast evaluation of soluble solid content in melon with thick peel and large size by vis-NIR spectroscopy. *Food Analytical Methods*, 12(1): 136-147.
29. Ho, H., Ishii, T., Matsumiya, K., Iwasa, M., and Matsumura, Y. (2021). Utilization of dried Japanese apricot and avocado fruit powders as an emulsifying agent: The importance of the powder-dispersed phase in emulsification. *Journal of Food Engineering*, 294: 110411.

30. Dantas, D., Pasquali, M. A., Cavalcanti-Mata, M., Duarte, M. E., and Lisboa, H. M. (2018). Influence of spray drying conditions on the properties of avocado powder drink. *Food Chemistry*, 266: 284-291.
31. Rahman, M., Islam, M., Biswas, M., and Khurshid Alam, A. H. M. (2015). In vitro antioxidant and free radical scavenging activity of different parts of *Tabebuia pallida* growing in Bangladesh. *BMC Research Notes*, 8(1): 1-9.
32. Lim, Y. Y., Lim, T. T., and Tee, J. J. (2007). Antioxidant properties of several tropical fruits: A comparative study. *Food Chemistry*, 103(3): 1003-1008.
33. Saikia, S., Mahnot, N. K., and Mahanta, C. L. (2015). Effect of spray drying of four fruit juices on physicochemical, phytochemical and antioxidant properties. *Journal of Food Processing and Preservation*, 39(6): 1656-1664.
34. Pui, L. P., Karim, R., Yusof, Y. A., Wong, C. W., and Ghazali, H. M. (2020). Optimization of spray-drying parameters for the production of 'Cempedak' (*Artocarpus integer*) fruit powder. *Journal of Food Measurement and Characterization*, 14(6), 3238-3249.
35. Tze, N. L., Han, C. P., Yusof, Y. A., Ling, C. N., Talib, R. A., Taip, F. S., and Aziz, M. G. (2012). Physicochemical and nutritional properties of spray-dried pitaya fruit powder as natural colorant. *Food Science and Biotechnology*, 21(3): 675-682.
36. Tan, C. H., Hii, C. L., Borompichaichartkul, C., Phumsombat, P., Kong, I., and Pui, L. P. (2022). Valorization of fruits, vegetables, and their by-products: Drying and bio-drying. *Drying Technology*, 2022: 1-25.
37. Ribeiro, L. C., da Costa, J. M. C., and Afonso, M. R. A. (2019). Hygroscopic behaviour of acerola powder obtained by spray-drying. *Acta Scientiarum. Technology*, 41: e35382-e35382.
38. Salbi, N. M., Muhammad, N., and Abdullah, N. (2021). The effect of maltodextrin and acacia gum on encapsulation of fig powder physicochemical properties. *Journal of Advanced Research in Applied Sciences and Engineering Technology*, 22(1): 8-15.
39. Koç, G. Ç. and Dirim, S. N. (2018). Spray dried spinach juice: powder properties. *Journal of Food Measurement and Characterization*, 12(3): 1654-1668.
40. Wong, C. W. and Tan, H. H. (2017) Production of spray-dried honey jackfruit (*Artocarpus heterophyllus*) powder from enzymatic liquefied puree. *Journal of Food Scientists & Technologists*, 54(2): 564-571.
41. Nevin K. G., and Rajamohan, T. (2008). Influence of virgin coconut oil on blood coagulation factors, lipid levels and LDL oxidation in cholesterol fed Spargue-Dawley rats. *European e-journal of Clinical Nutrition and Metabolism*, 3: 1-8.
42. Kabeer, S., Govindarajan, N., Preetha, R., Ambrose, K., Essa, M. M., and Qoronfleh, M. W. (2022). Effect of different drying techniques on the nutrient and physiochemical properties of *Musa paradisiaca* (ripe Nendran banana) powder. *Journal of Food Science and Technology*, 2022: 1-10.
43. Rana, M., Sharma, P., Mahima, R. C., and Sharma, P. (2018). Proximate and phytochemical screening of the seed and pulp of *Tamarind indica. Journal of Medicinal Plants, 6*(2): 111-115.

Malaysian Journal of Analytical Sciences (MJAS)
Published by Malaysian Analytical Sciences Society

ENHANCING PRE-CONCENTRATION OF Pb(II) THROUGH SYNTHESIS OF TANNIN ACID-CHITOSAN (TAC) AS SOLID PHASE EXTRACTION ADSORBENT

(Penambahbaikkan Pra-pemekatan Pb(II) Melalui Sintesis Asid Tannin-Kitosan (TAC) Sebagai Penjerap Pengekstrakan Fasa Pepejal)

Dewi Fortuna, Dwi Siswanta[*]*, and Nurul Hidayat Aprilita*
Department of Chemistry, Faculty of Mathematics and Natural Science, Universitas Gadjah Mada, Sekip Utara, Yogyakarta, 55281, Indonesia

[*]*Corresponding author: dsiswanta@mail.ugm.ac.id*

Received: 24 May 2023; Accepted: 4 October 2023; Published: 30 October 2023

Abstract

This study was conducted to incorporate tannin acid-chitosan (TAC) in solid phase method. The synthesized material was employed as an adsorbent to examine the effectiveness of solid phase extraction for preconcentration of Pb(II) in industrial wastewater. In addition, the parameters affecting extraction optimization were investigated and TAC was performed using a mass ratio of tannin acid and chitosan of 2:1 w/w. TAC absorbent was fully characterized using FTIR to detect functional groups and SEM-EDX to assess morphology and percentage of elements. The use of the optimal parameters for preconcentration on the performance of SPE method was obtained with adsorption, desorption, and enrichment factor at pH 5, a sample flow rate of 5 mL/min, Na_2EDTA eluent flow rate of 5 mL/min, a sample volume of 10 mL, Na_2EDTA eluent volume of 5 mL, sample concentration of 6 mg L^{-1} and Na_2EDTA concentration of 0.35 M. Furthermore, preconcentration application to Pb(II) wastewater at 0.05 mg L^{-1}, 0.06 mg L^{-1}, and 0.07 mg L^{-1} were concentrated 0.28 mg L^{-1}, 0.32 mg L^{-1}, and 0.38 mg L^{-1} with a factor of 5.6, 5.35, and 5.45 times. The result showed that the proposed method was effective for SPE with TAC adsorbent and Pb(II) preconcentration.

Keywords: solid phase extraction, preconcentration, Pb(II), tannin acid-chitosan

Abstrak

Penyelidikan ini menggabungkan asid tannin-kitosan (TAC) dalam kaedah fasa pepejal. Bahan tersintesis digunakan sebagai penjerap dan bertujuan untuk mengkaji keberkesanan pengekstrakan fasa pepejal untuk pra-pemekatan Pb(II) dalam air sisa industri. Di samping itu, parameter yang mempengaruhi pengoptimuman pengekstrakan telah disiasat. Asid tannin-kitosan (TAC) dilakukan menggunakan nisbah jisim asid tanin dan kitosan 2:1 b/b. Kemudian penyerap TAC dicirikan sepenuhnya menggunakan FTIR untuk mengesan kumpulan berfungsi dan SEM-EDX untuk menilai morfologi dan peratusan unsur yang terkandung di dalamnya. Menggunakan parameter optimum untuk pra-pemekatan pada prestasi kaedah pengekstrakan fasa pepejal diperolehi, dengan penjerapan, penyahjerapan, dan instrumen pengayaan pada pH 5 dengan kadar aliran sampel 5 mL/min, kadar alir eluen Na_2EDTA 5 mL/min, a isipadu sampel 10 mL, isipadu eluen Na_2EDTA 5 mL, kepekatan sampel 6 mg L^{-1} dan kepekatan Na_2EDTA 0.35 M. Penggunaan prapekatan pada air sisa Pb(II) pada kepekatan 0.05 mg L^{-1} boleh ditumpukan kepada 0.28 mg L^{-1} dengan faktor kepekatan 5.6 kali, pada kepekatan 0.06 mg L^{-1} boleh dipekatkan kepada 0.32 mg L^{-1} dengan faktor kepekatan 5.35 kali,

dan pada kepekatan 0.07 mg L^{-1} boleh ditumpukan kepada 0.38 mg L^{-1} dengan faktor kepekatan 5.45 kali. Nilai faktor kepekatan yang diperoleh sepadan dengan teori, 6 kali, masing-masing. Keputusan menunjukkan bahawa kaedah yang dicadangkan adalah berkesan untuk pengekstrakan fasa pepejal dengan penjerap TAC dan pra-pemekatan Pb(II).

Kata kunci: pengekstrakan fasa pepejal, pra-pemekatan, Pb(II), asid tannin-kitosan

Introduction

Wastewater generated from various industries, including garbage, metal plating, and leather industries, is known to pose a significant environmental risk by releasing harmful metal ions contaminating water [1]. Among these metal ions, lead (Pb) is particularly considered due to its toxicity, even at low concentrations, and can accumulate in living organisms, leading to long-term chronic exposure [2]. Typically, the concentrations in wastewater are measured by sampling at the site and then testing in the laboratory and the process often takes several days [3]. Determination of metal levels in water is commonly performed using techniques such as atomic absorption spectroscopy (AAS) instruments [4]. The accurate analysis becomes challenging when the metal ion concentration falls significantly below the detection limit of the instrument. Therefore, preconcentration step is necessary to enhance the detection capabilities of AAS instruments and solid phase extraction (SPE) has been widely recognized as an efficient method [5].

SPE is a technique used to separate compounds in a solution based on their chemical and physical properties [6]. The process in the SPE method begins with a conditioning step in which the column is filled with an adsorbent, serving as an analyte holder, followed by a loading step passed through the column/matrix/tube. In the third step, the column/matrix/tube is washed with Aquabides recovered by passing the eluent through the column/matrix/tube to analyse the results [6, 7].

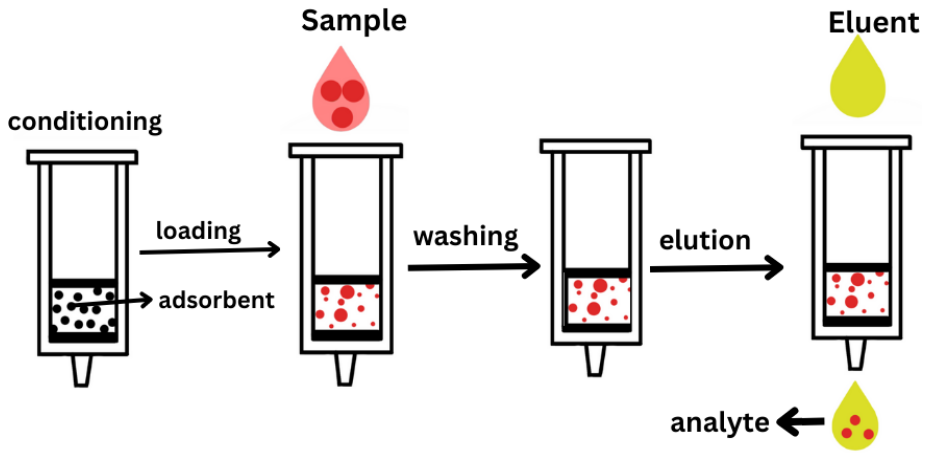


Figure 1. Main steps in solid phase extraction

Chitosan, a polymer found in crustaceans, fungal cell walls, and insect cuticles, is commonly employed as an adsorbent in SPE due to its hydroxyl and amino groups, acting as metal chelators and dye sorbents in solution [8]. Conversely, tannic acid possesses hydroxyl and carboxyl groups, making it suitable for adsorbing heavy metals. The high solubility in water necessitates immobilization with solid and porous materials, such as chitosan, to improve its applicability [9, 10]. Tannic acid and chitosan have been synthesized to obtain a new TAC adsorbent. It is more stable and effective for preconcentration/adsorption of metals riched in hydroxyl, carboxyl, and amino groups. A way to reduce metal analysis time is by combining the SPE method with TAC adsorbent.

The effectiveness of the SPE method can be evaluated based on the enrichment factor of the sample. The

enrichment factor, obtained from the performance of the SPE, reflects the increase in the absolute absorbance value, improving the validity of the concentration calculation beyond the detection limit on the linear curve [11]. In addition, optimization of parameters affecting SPE, such as solution pH, sample flow rate, eluent flow rate, sample concentration, and volume, can enhance the effectiveness of the method [12]. Previous studies also showed successful optimization of SPE parameters for preconcentrating Cd(II) and Pb(II), resulting in high concentration enrichment factors of 250 and recovery rates of 95% [13]. Similar efficiency and enrichment factor results have been achieved for Pb(II) using SPE in other studies [11, 14].

By combining the advantages of SPE with the use of TAC as an adsorbent, this study synthesizes and characterizes a novel adsorbent for preconcentration of Pb(II) from industrial wastewater. Additionally, the optimization of extraction parameters is explored to maximize the efficiency of preconcentration process. The results are expected to contribute to the development of sustainable and effective methods for preconcentration of heavy metal ions, specifically Pb(II), in industrial wastewater, facilitating the proper management and treatment of wastewater to mitigate the associated environmental and health risks.

Materials and Methods

Materials

The materials required are bi-distilled water and Merck's Pro-Analytical Quality (p.a.) chemicals, namely chitosan (%DD > 75%), tannic acid, $PbNO_3$, 25% glutaraldehyde, Na_2EDTA, filter paper, and universal pH paper.

Instrumentation

The equipment used includes laboratory glassware, stirrer, magnetic stirrer, analytical balance, oven, FTIR (Fourier Transform InfraRed, Thermo Nicolet Avatar 360), AAS (Atomic Absorption Spectrophotometer, Buck 205 Atomic Absorption Spectrophotometer), and SEM-EDX (Scanning Electron Microscope-Energy Dispersive X-ray).

Procedure: Synthesis of an adsorbent TAC

Tannic acid (up to 4g) was dissolved in 120 mL Aquabides by stirring until fully dissolved. Subsequently, 2g of chitosan was added to the solution and stirred for 6 hours using a stirrer. The stirring process was continued for 6 hours after adding 12 mL of 25% glutaraldehyde to crosslink the materials. The resulting precipitate was filtered and dried in an oven at 50 °C. The material was crushed using a mortar and pestle, followed by filtration to obtain the TAC adsorbent powder used in subsequent experiments [15].

Characterization of the TAC adsorbent

The TAC powder was subjected to characterization using an FTIR instrument (Thermo Nicolet Avatar 360) operating in the wave number range of 4000-400 cm^{-1}. This characterization aimed to identify the functional groups in the TAC powder analysed using an SEM-EDX instrument at a magnification of 1500-5000 times. The purpose of the analysis was to investigate the micro-scale properties of the material, including texture, morphology, composition, and surface characteristics.

Optimization of the SPE method

This study optimized SPE conditions by investigating different parameters. These parameters included the pH of the solution, the concentrations of the sample and eluent, the flow rates of the sample and eluent, the volumes of the sample and eluent, and the impact of eluent concentration on artificial wastewater.

Application of preconcentration to Pb(II)

The TAC adsorbent preconcentration process was applied to artificial wastewater samples containing Pb(II) ions. The experimental conditions included the pH, sample flow rate, eluent flow rate, sample volume, eluent volume, sample concentration, and optimal eluent concentration. The Pb(II) concentrations were set at 0.05, 0.06, and 0.07 mg L^{-1}, with a theoretical concentration factor of 6 times. Meanwhile, the resulting analyte concentrations were measured using an AAS instrument.

Results and Discussion

Characterization of the TAC adsorbent

The TAC adsorbent was subjected to characterization using FTIR to detect the functional groups present. The analysis results of the TAC adsorbent synthesis are presented in Figure 2, where peaks observed on the TAC adsorbent provide valuable information about the composition. Chitosan peak at 3442 cm^{-1} indicates the stretching vibrations of hydroxyl (O–H) and amino (N-H) groups. However, this peak shifts to 3434 cm^{-1} on the TAC adsorbent, suggesting the crosslinking of chitosan and glutaraldehyde [15]. Another peak shift is observed at 2932 cm^{-1} and 2955 cm^{-1}, which shifts to 2927 cm^{-1} on the TAC adsorbent, signifying the stretching vibrations of the (C–H) group [16]. Additionally, aldehyde stretching vibrations are indicated by a 2847 cm^{-1} peak on the TAC adsorbent [15]. The carboxyl group is confirmed by a peak at 1712 cm^{-1}, and the presence of the C–N group is indicated by 1341 cm^{-1} on the TAC adsorbent [16]. In chitosan, the carboxyl (C=O) stretching vibrations observed at 1642 cm^{-1} are shifted to 1627 cm^{-1}, suggesting the crosslinking of chitosan and tannic acid [15].

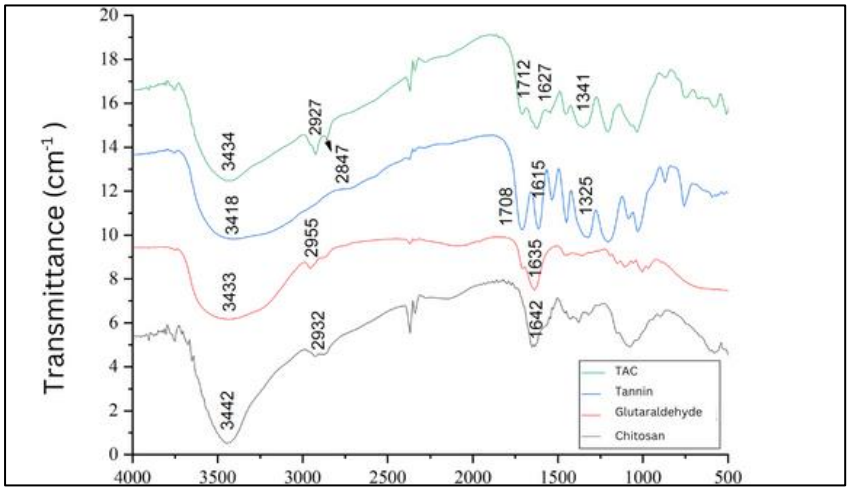


Figure 2. Spectra FTIR from tannin, acid, chitosan, glutaraldehyde, and TAC adsorbent

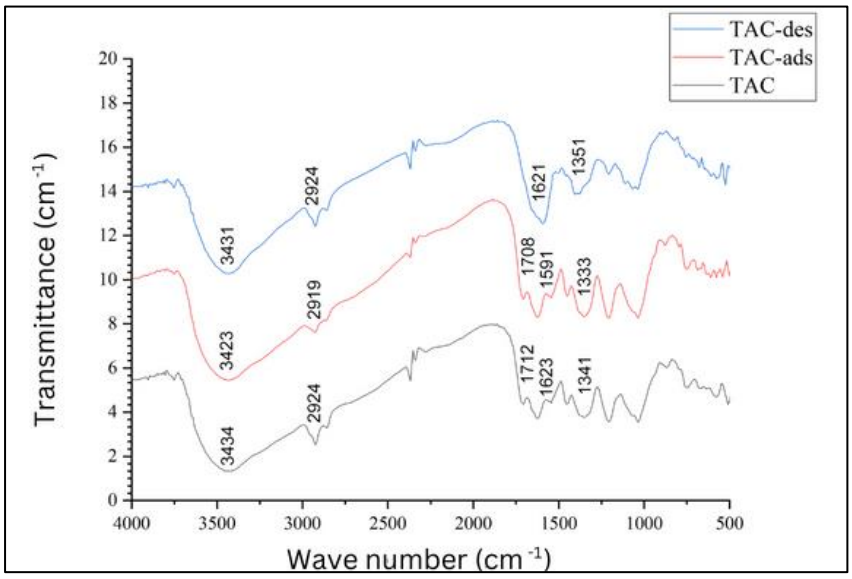


Figure 3. Spectra FTIR from TAC adsorbent, TAC-adsorption, and TAC-desorption

Characterization of the TAC adsorbent

The TAC adsorbent was analysed using Figure 3 to observe the peaks before and after adsorption and desorption. At the peak of 3434 cm^{-1}, there is a shift to 3423 cm^{-1}, indicating the narrowing of the stretching vibrations of the O–H and N–H groups. This shift suggests the interaction between the adsorbent and Pb(II) ions. In the desorbed TAC, the peak returns to 3431 cm^{-1}, indicating that Pb(II) absorbed in the adsorbent can be desorbed by the eluent. Another interaction can be observed at the 1623 cm–1 peak, which shifts to 1591 cm^{-1}, indicating C=O stretching vibration [15]. Moreover, the carboxyl and the C–N groups are visible at the peak of 1712 cm^{-1} and 1341 cm^{-1}, which shift to 1708 cm^{-1} and 1333 cm^{-1}, respectively. These shifts further confirm the interaction between the adsorbent and Pb(II) [17].

Based on the FTIR data described above, the interaction occurring in the TAC adsorbent with Pb can be estimated, as shown in Figure 4.

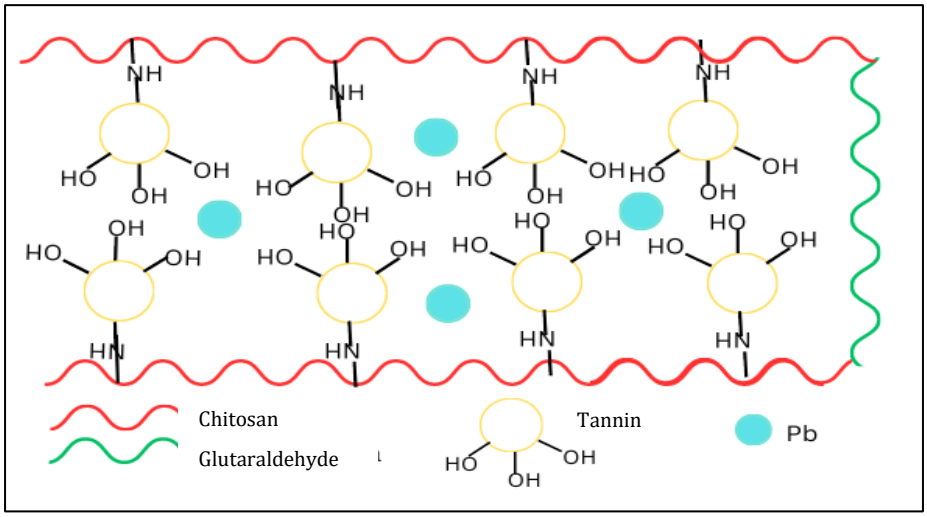


Figure 4. Estimation of the interaction between TAC adsorbent and Pb(II)

The morphology and percentage of elements present in the TAC adsorbent were assessed using SEM-EDX analysis. Figure 5 shows the morphology of the TAC adsorbent before and after adsorption and after desorption. Each sample was analysed at magnifications of 1000 and 5000 times to provide a detailed view of the surface morphology of TAC adsorbent during the different adsorption and desorption stages.

Figure 5 provides valuable insights into the structure and elemental composition of the TAC adsorbent. The adsorbent exhibits a complex and loose structure favorable for molecular diffusion and provides sufficient free space for Pb(II) molecules. In Figure 5b, the TAC adsorbent appears denser due to Pb(II) molecules filling the spaces. However, in Figure 5c, the TAC adsorbent returns to a looser structure, similar to the initial state, due to the desorption treatment. The analysis of the elements in the TAC adsorbent is presented in Table 1, displaying the mass percentage of elements in the TAC.

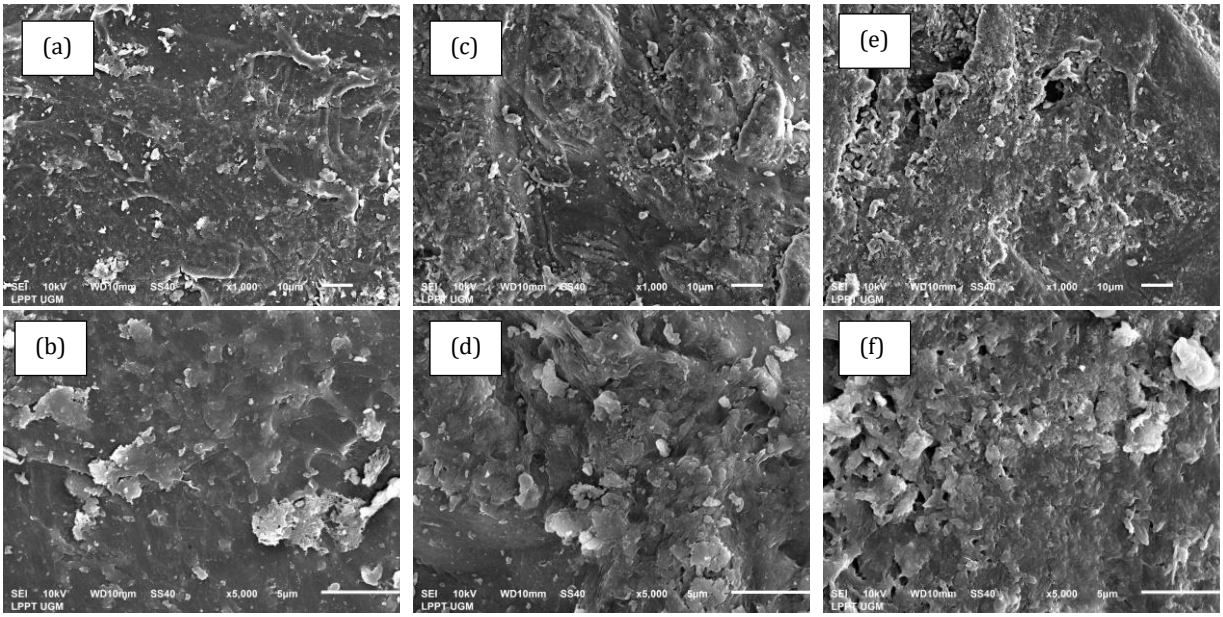


Figure 5. SEM images (a) TAC 1000x, (b) TAC 1500x, (c) TAC-adsorption 1000x, (d) TAC-adsorption 1500x, (e)TAC-desorption 1000x, and (f) TAC-desorption 1500x.

Table 1. Elemental composition in TAC before and after preconcentration

Sample	Elemental Composition (%)				
	C	N	O	Na	Pb
TAC	45.17	16.56	38.27	-	
TAC-adsorption	45.35	16.53	37.93	0.02	0.17
TAC-desorption	38.64	13.25	40.67	7.38	0.06

The TAC adsorbent contains 0.17% of the Pb element, decreasing to 0.06% after desorption. This significant decrease shows the successful desorption of Pb(II) using the Na_2EDTA eluent. The reduction in the Pb element can be attributed to the interaction between Pb(II) and the ligand of Na_2EDTA, confirming the effectiveness of the desorption process [18].

Optimization of SPE methods: pH optimization

The optimal pH of the solution plays a crucial role in the sorption of Pb(II) ions using the TAC adsorbent and the study tested pH 4, 5, 6, and 7. Figure 6(a) shows the varying percentage of Pb(II) sorption at different pH levels. The sorption capacity at low pH values (pH >4) is reduced due to the competition between hydrogen ions and Pb(II) ions for adsorption sites on the TAC adsorbent [19]. Additionally, the protonation of functional groups at lower pH values hampers the optimal adsorption of Pb(II) ions. At a higher pH (pH 5), the competition for protons decreases, leading to enhanced adsorption of Pb(II) ions on the TAC adsorbent [20]. However, at higher pH levels (pH 6-7), a decrease in adsorption is observed due to the precipitation of lead ions [19]. The optimal pH for the SPE process with Pb(II) samples is determined to be pH 5, aligning with previous results [20]. Furthermore, it is essential to consider the effect of solution pH on Pb(II) analysis and the changes in metal speciation for an effective SPE process [21].

Sample flow rate optimization

The flow rate of the sample is another influential factor in the SPE method. The study tested different sample flow rates, namely 5, 10, 15, and 20 mL/min to

determine the optimal flow rate, yielding high adsorption, desorption, and concentration factor. The results depicted in Figure 6(b) showed that the optimal sample flow rate was 5 mL/min. A low flow rate can positively affect adsorption due to selective interaction between the adsorbent and the lead metal [12]. However, at higher flow rates (10-20 mL/min), the limited contact time between the adsorbent and the metal decreases the percentage of adsorption [22]. This result aligns with previous studies, where higher flow rates result in insufficient absorption of lead metal by the adsorbent due to reduced contact time [23].

Eluent flow rate optimization

The flow rate of the eluent used for desorption significantly influences the desorption percentage and concentration factor of the SPE method. The study conducted tests with 5, 10, 15, and 20 mL/min variations for the eluent flow rate. The results in Figure 6(c), indicate that the optimal flow rate is 5 mL/min, since it provides a higher enrichment factor than other flow rates. Besides the higher enrichment factor, selecting an eluent flow rate of 5 mL/min helps avoid excessive duration [7]. This result was consistent with previous studies, where eluent flow rates in the 2-5 mL/min range were considered high for optimal SPE methods [24]. Conversely, higher flow rates (10-20 mL/min) resulted in decreased desorption and lower enrichment factors, possibly due to reduced contact between Na_2EDTA and the TAC adsorbent, which led to a decreased amount of desorbed Pb(II) analyte [25].

Sample volume optimization

The sample volume employed in the SPE method affects both the desorption percentage and the concentration factor. This study tested the optimal sample volume with 5, 10, 15, and 20 mL variations. The results in Figure 6 (d) show that the optimal sample volume is 10 mL and larger sample volumes increase the likelihood of a higher enrichment factor [26]. However, excessively large sample volumes can also reduce enrichment [12] and the obtained enrichment is low at lower volumes (5 mL) due to limited interaction between the analyte and the adsorbent [27]. In this study, the optimal results were obtained with a sample volume of 10 mL, and at higher volumes (15-20 mL), the active sites become saturated, leading to suboptimal absorption and decreased enrichment values [12]. These results are consistent with previous studies by Jiménez-Soto et al. [28] and Sanagi et al. [27], which found 10 mL to be the optimal sample volume for the SPE method.

Eluent volume optimization

The volume of eluent used for desorption affected the desorption percentage and the concentration factor in the SPE method. The study conducted tests of 5-, 10-, 15-, and 20-mL variations for the eluent volume, and the results in Figure 6(e), indicated that the optimal eluent volume was 5 mL. At higher volumes, there was a decrease in desorption due to excessive eluent volume, which had a limited effect after the analyte was sufficiently eluted. This result was consistent with the studies conducted by Sanagi et al. [27] and Maranata et al. [12], which determined the optimal eluent volume in the range of 3 to 6 mL for the SPE method.

Sample concentration optimization

The sample concentration influenced the desorption percentage and the concentration factor of the SPE method. This study tested the optimal sample concentration with 5, 6, 7, and 8 mg/L variations, and the results are shown in Figure 6(f), where the optimal result is 6 mg/L. Petrović et al. [20] stated that higher concentrations resulted in higher adsorption values as the availability of Pb(II) metal ions increased, leading to increased adsorption [29]. However, a significant decrease in adsorption occurred at higher concentrations (8 mg/L), impacting the enrichment value. This decrease was due to the saturation of active sites on the adsorbent caused by a more significant number, rendering the adsorbent suboptimal for adsorbing Pb(II) metal ions [30].

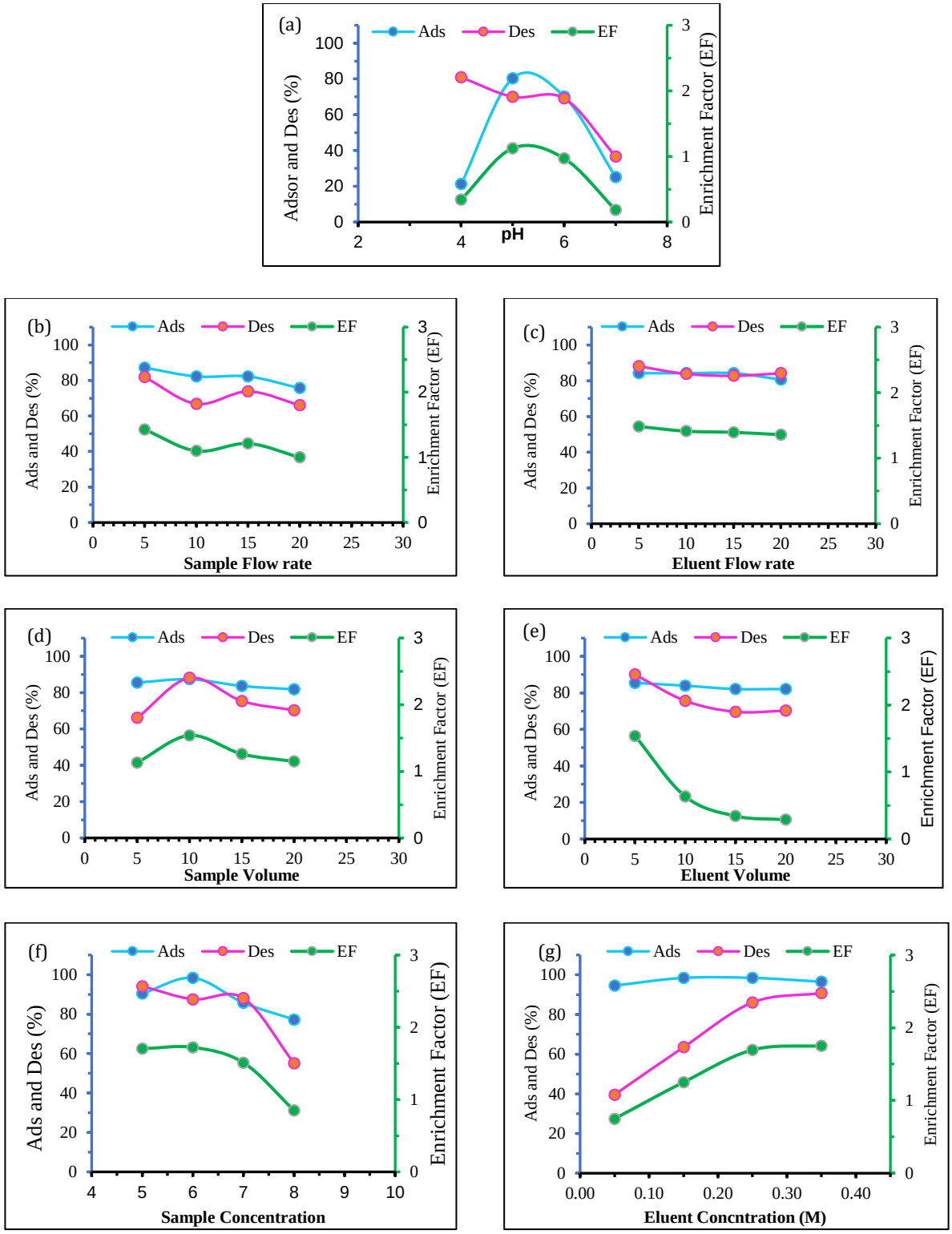


Figure 6. Effect of (a) pH (b) sample flow rate (c) eluent flow rate (d) volume sample (e) volume eluent (f) sample concentration (g) eluent concentration. (Ads is Adsorption, Des is Desorption, EF is Enrichment Factor)

Eluent concentration optimization

The eluent concentration used for desorption affected the desorption value and the factor in the SPE method. In this study, Na_2EDTA was used as the eluent because of its effectiveness compared to other solvents [31]. The optimal eluent concentration was tested with 0.05, 0.15, 0.25, and 0.35 M variations. Figure 6(g) showed that higher eluent concentrations resulted in higher desorption values and enrichment factors. The optimal eluent concentration was 0.35 M since higher concentrations fostered more interactions between the Na_2EDTA ligand and the TAC adsorbent, leading to a more effective desorption process [32]. The approximate interaction between the Na_2EDTA ligand and Pb(II) was shown in Figure 7.

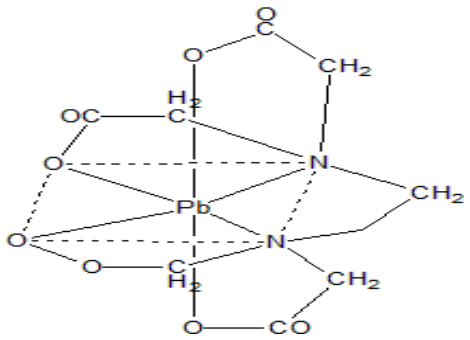


Figure 7. Approximate interaction between Na_2EDTA ligand and Pb(II)

Pre-concentration application to Pb(II)

Pre-concentration test was conducted to assess the effectiveness of SPE method with TAC adsorbent for pre-concentrating Pb(II) waste below the detection limit of the available AAS instrument (with a detection limit of 0.1 mg/L). Synthetic Pb(II) waste solutions were prepared with concentrations of 0.05 mg/L, 0.06 mg/L, and 0.07 mg/L, and were subjected to SPE using the TAC adsorbent under optimal conditions. Subsequently, desorption was performed using 5 mL of 0.035 M Na_2EDTA eluent, and the resulting samples were analysed using AAS.

Preconcentration test on Pb(II) waste showed the successful application of SPE method with TAC adsorbent. Table 2 shows the difference between the synthetic waste samples' initial and Pb(II) concentrations. The concentration was undetectable below the detection limit of the instrument but after preconcentration, Pb(II) was successfully detected. For the 0.05 mg/L, 0.06 mg/L, and 0.07 mg/L Pb(II) waste solution, the concentration was concentrated to 0.23 mg/L, 0.32 mg/L, and 0.038 mg/L with a factor of 5.6, 5.35, and 5.45, respectively. These concentration factor values obtained from the three waste variations closely approximate the theoretical factor of 6 times. Therefore, SPE method with TAC adsorbent is well-suited for preconcentration of Pb(II) metals. Preconcentration test results affirm the proposed method's efficacy and its potential for effectively concentrating Pb(II) below the detection limit of the AAS instrument.

Table 1. The result of TAC application on artificial wastewater

Wastewater Concentration (mg/L)	Wastewater Concentration (mg/L)		Enrichment Factors
	Initial	Final	
0.05	-	0.28	5.60
0.06	-	0.32	5.35
0.07	-	0.38	5.45

Conclusion

The synthesis of TAC as an adsorbent for pre-concentration using SPE method was successfully showed. The synthesized TAC adsorbent possessed active groups, including hydroxyl (–OH), amino (–NH_2), and carboxyl, which acted as effective metal chelators. By optimizing various parameters, the performance of the SPE method for pre-concentration had been significantly improved. The optimal parameters for pre-concentration using the SPE method were determined as follows pH 5, the sample flow rate of 5 mL/min, Na_2EDTA eluent flow rate of 5 mL/min, a sample volume of 10 mL, Na_2EDTA eluent volume of 5 mL, sample concentration of 6 mg/L, and Na_2EDTA concentration of 0.35 M. These parameters resulted in successful preconcentration of Pb(II) wastewater. For initial concentrations of 0.05 mg/L, 0.06 mg/L, and 0.07 mg/L, the concentrations were 0.28 mg/L, 0.32 mg/L, and 0.38 mg/L, with corresponding factors of 5.6, 5.35, and 5.45 times. Therefore, these concentration factors aligned with the theoretical value of 6 times. The results showed the effectiveness of the proposed SPE method using the TAC adsorbent for preconcentration of Pb(II). The technique offered a reliable and efficient method for preconcentration, allowing for the analysis of Pb(II) at concentrations below the detection limit of analytical instruments.

References

1. Manzoor, K., Ahmad, M., Ahmad, S., and Ikram, S. (2019). Removal of Pb(II) and Cd(II) from wastewater using arginine crosslinked chitosan-carboxymethyl cellulose beads as green adsorbent, *RSC Advances*, 9 (14): 7890-7902.
2. Taylor, P., Jinadasa, B. K. K. K., and Edirisinghe, E. M. R. K. B. (2014). Cadmium, lead and total mercury in Tilapia sp. in Sri Lankan reservoirs. *Food Additives & Contaminants : Part B : Surveillance*, 7 (1): 90-94.
3. Quinn, C. W., Cate, D. M., Miller-Lionberg, D. D., Reilly, T., Volckens, J., and Henry, C. S. (2018). Solid-phase extraction coupled to a paper-based technique for trace copper detection in drinking water. *Environmental Science Technology*, 52(6): 3567-3573.
4. Bhuyan, M. S., Bakar, M. A., Akhtar, A., Hossain, M. B., Ali, M. M., and Islam, M. S. (2017). Heavy metal contamination in surface water and sediment of the Meghna River, Bangladesh. *Environmental Nanotechnology, Monitoring Management*, 8(4): 273-279.
5. Yavuz, E., Tokalioɬlu, Ş., Şahan, H., and Patat, Ş. (2016). Nanosized spongelike Mn_3O_4 as an adsorbent for preconcentration by vortex assisted solid phase extraction of copper and lead in various food and herb samples. *Food Chemistry*, 194: 463-469.
6. Taylor, P., Aini, W., Ibrahim, W., Imad, L., Ali, A., Sulaiman, A., Sanagi, M. M., Aboul-enein, H. Y., Aini, W., Ibrahim, W., Imad, L., Ali, A., Sulaiman, A., Sanagi, M. M., and Aboul-enein, H. Y. (2014). Application of solid-phase extraction for trace elements in environmental and biological samples: A review. *Critical Reviews in Analytical Chemistry*, 44(5): 233-254.
7. Camel, V. (2003). Solid phase extraction of trace elements. *Spectrochimica Acta Part B: Atomic Spectroscopy*, 58: 1177-1233.
8. Das, D., and Pal, A. (2016). Adsolubilization phenomenon perceived in chitosan beads leading to a fast and enhanced malachite green removal. *Chemical Engineering Journal*, 290: 371-380.
9. Wang, G., Chen, Y., Xu, G., and Pei, Y. (2019). Effective removing of methylene blue from aqueous solution by tannins immobilized on cellulose microfibers. *International Journal Biology Macromolecules*, 129: 198-206.
10. Petins, M. M. C., Sarria-Villa, R. A., Benítez, R. B., and Corredor, J. A. G. (2021). Chemical modified tannins from *Pinus patula* bark for selective biosorption of gold in aqueous media. *Journal Environmental Chemical Engineering*, 9(5): 106162.
11. Su, C. K., and Lin, J. Y. (2020). 3D-printed column with porous monolithic packing for online solid-phase extraction of multiple trace metals in environmental water samples. *Analytical Chemistry*, 92(14): 9640-9648.

12. Maranata, G. J., Surya, N. O., and Hasanah, A. N. (2021). Optimising factors affecting solid phase extraction performances of molecular imprinted polymer as recent sample preparation technique. *Heliyon*, 7(1): e05934.
13. Daşbaşi, T., Saçmaci, Ş., Ülgen, A., and Kartal, Ş. (2015). A solid phase extraction procedure for the determination of Cd(II) and Pb(II) ions in food and water samples by flame atomic absorption spectrometry. *Food Chemistry*, 174: 591-596.
14. Sanmartín, R., Romero, V., Lavilla, I., and Bendicho, C. (2022). Ultrasound-assisted dispersive micro-solid phase extraction of Pb(II) in water samples with in situ synthesis of magnetic Fe_3O_4-PbS nanocomposites followed by electrothermal atomic absorption spectrometry determination. *Spectrochimica Acta - Part B Atomic Spectroscopy*, 188: 106349.
15. Zhou, Z., Liu, F., Huang, Y., Wang, Z., and Li, G. (2015). Biosorption of palladium(II) from aqueous solution by grafting chitosan on persimmon tannin extract. *International Journal Biological Macromolecular*, 77: 336-343.
16. Utami, U. B. L., Mujiyanti, D. R., and Normilawati, (2015). Kajian adsorpsi Cd(II) oleh arang apu-apu termodifikasi kitosan-glutaraldehida. *Sains dan Terapi Kimia*, 9(2): 12-22.
17. Abdulsahib, H. T., Taobi, A. H., and Hashem, S. S. (2015). A novel adsorbent based on lignin and tannin for the removal of heavy metals from wastewater. *Research Journal Pharmacognosy Phytochemistry*, 7(1): 38.
18. Zhao, Y., Ren, Y., Wang, X., Xiao, P., Tian, E., Wang, X., and Li, J., (2016). An initial study of EDTA complex based draw solutes in forward osmosis process. *Desalination*, 378: 28-36.
19. Khoramzadeh, E., Nasernejad, B., and Halladj, R. (2013). Mercury biosorption from aqueous solutions by sugarcane bagasse. *Journal Taiwan Institute Chemical Engineering*, 44(2): 266-269.
20. Petrović, M., Šoštarić, T., Stojanović, M., Milojković, J., Mihajlović, M., Stanojević, M., and Stanković, S. (2016). Removal of Pb^{2+} ions by raw corn silk (*Zea mays* L.) as a novel biosorbent. *Journal Taiwan Institute Chemical Engineering*, 58: 407-416.
21. Fei, J., Wu, X., Sun, Y., Zhao, L., Min, H., Cui, X., Chen, Y., Liu, S., Lian, H., and Li, C. (2021). Preparation of a novel amino functionalized ion-imprinted hybrid monolithic column for the selective extraction of trace copper followed by ICP-MS detection, *Analytica Chimica Acta*, 1162: 338477.
22. Sadeghi, S., and Jahani, M. (2013). Selective solid-phase extraction using molecular imprinted polymer sorbent for the analysis of Florfenicol in food samples, *Food Chemistry*, 141(2): 1242-1251.
23. Yuniar. and Yanti, H. (2021). Peningkatan limit deteksi metode pengujian logam Pb secara kolom ekstraksi fase padat menggunakan resin DOWEX 50WX2: Pengaruh pH, laju alir dan volume eluen. *Jurnal Penelitian Sains*, 21(3): 46-51.
24. Zari, N., Hassan, J., Tabar-Heydar, K., and Ahmadi, S. H. (2016). On-line green solid phase extraction of trace rare earth elements and uranium in environmental samples and ICP OES detection, *Journal Brazilian Chemical Society*, 27(10): 1881-1888.
25. Imran, K., Harinath, Y., Naik, B. R., Kumar, N. S., and Seshaiah, K. (2019). A new hybrid sorbent 2, 2'-pyridil functionalized SBA-15 (Pyl-SBA-15) synthesis and its applications in solid phase extraction of Cu (II) from water samples. *Journal of Environmental Chemical Engineering*, 7(3): 103170.
26. Liu, Q., Shi, J., Zeng, L., Wang, T., Cai, Y., and Jiang, G. (2011). Evaluation of graphene as an advantageous adsorbent for solid-phase extraction with chlorophenols as model analytes. *Journal of Chromatography A*, 1218(2): 197-204.
27. Sanagi, M. M., Salleh, S., Ibrahim, W. A. W., Naim, A. A., Hermawan, D., Miskam, M., Hussain, I., and Aboul-Enein, H. Y. (2013). Molecularly imprinted polymer solid-phase extraction for the analysis of organophosphorus pesticides in fruit samples, *Journal Food Composition Analysis*, 32(2): 155-161.
28. Jiménez-Soto, J. M., Cárdenas, S., and Valcárcel, M. (2009). Evaluation of carbon nanocones/disks as sorbent material for solid-phase extraction, *Journal of Chromatography A*, 1216(30): 5626-5633.

29. Yuvaraja, G., Pang, Y., Chen, D. Y., Kong, L. J., Mehmood, S., Subbaiah, M. V., Rao, D. S., Mouli Pavuluri, C., Wen, J. C., and Reddy, G. M. (2019). Modification of chitosan macromolecule and its mechanism for the removal of Pb(II) ions from aqueous environment. *International Journal Biology Macromolecules*, 136: 177-188.
30. Guan, Y. T., Wang, S. H., Wang, M. H., Hou, Z. X., Hu, X. D., Wang, H., Fan, H. L., and Zhang, N. (2014). Effect of initial concentration of Cu^{2+} on the adsorption performance of hydroxyapatite. *Advances Materials Research*, 989-994: 312-315.
31. Jiang, X., An, Q., Xiao, Z., Zhai, S., and Shi, Z. (2019). Versatile core/shell-like alginate @ polyethylenimine composites for efficient removal of multiple heavy metal ions (Pb^{2+},Cu^{2+}, CrO_4^{2+}): Batch and fixed-bed studies. *Materials Research Bulletin*, 118(6): 110526.
32. Chen, A., Yang, C., Chen, C., Chen, C., and Chen, C. (2009). The chemically crosslinked metal-complexed chitosans for comparative adsorptions of Cu(II), Zn(II), Ni(II) and Pb(II) ions in aqueous medium. *Journal Hazardous Materials*, 163: 1068-1075.

Malaysian Journal of Analytical Sciences Vol 27 No 6 2023

		Page
	Analytical Method	1172
1.	PRECONCENTRATION AND DETERMINATION OF NICOTINE IN TOBACCO SAMPLES BY DISPERSIVE MICRO-SOLID PHASE EXTRACTION AND GAS CHROMATOGRAPHY-MASS SPECTROMETRY *Nur Ainaa Syaza Mat Yatim, Nor Suhaila Mohamad Hanapi, Nurzaimah Zaini, Ahmad Lutfi Anis, Reena Abd Rashid, Noor Najmi Bonnia, and Wan Nazihah Wan Ibrahim*	
	Organic and Inorganic Analysis	
2.	SYNTHESIS OF 4-ARYL SUBSTITUTED CANTHIN-6-ONE WITH β-CARBOLINE SKELETON VIA PICTET-SPENGLER CONDENSATION AND CYCLIZATION REACTION *Noor Hidayah Pungot, Noor Hamizah Mohammad Tarmizi, and Siti Zafirah Zulkifli*	1183
	Nano or Advanced Materials Analysis	
3.	TRANSESTERIFICATION OF LOW-GRADE PALM COOKING OIL TO PRODUCE BIODIESEL USING SPENT BLEACHING CLAY CATALYSTS *Thivya Keasavan, Nurhannani Mohd Radzi, Wan Nazwanie Wan Abdullah, Salmiah Jamal Mat Rosid, Nurasmat Mohd Shukri, and Noorfatimah Yahaya*	1192
	Analytical Method	
4.	EVALUATING THE POTENTIAL OF CHEMOMETRICS TECHNIQUES AS RAPID SCREENING TOOLS FOR BLACK GEL INKS DISCRIMINATION *Nur Atiqah Zaharullil, Dzulkiflee Ismail, Wan Nur Syuhaila Mat Desa, and Nik Fakhuruddin Nik Hassan*	1205
	Environmental Analysis	
5.	MICROPLASTICS IN THE ENVIRONMENT: PROPERTIES, IMPACTS AND REMOVAL STRATEGIES *Iwani W. Rushdi, Rabiatul S. Rusidi, Wan M. Khairul, Sofiah Hamzah, Wan Mohd Afiq Wan Mohd Khalik, Sabiqah Tuan Anuar, Nor Salmi Abdullah, Nasehir Khan E.M. Yahya, and Alyza A. Azmi*	1216
	Analytical Method	
6.	EXTRACTION OF ESSENTIAL OIL *Citrus hystrix* BY USING ULTRASOUND -ASSISTED EXTRACTION *Ng Hui Ying, Gan Shi Min, and Saliza Asman*	1236
	Natural Product Analysis	
7.	CYTOTOXICITY STUDY, ANTIOXIDANT AND ANTIBACTERIAL ACTIVITY AGAINST PLANT PATHOGENIC BACTERIA OF METHANOL EXTRACT FROM *Coscinium fenestratum* (AKAR SEKUNYIT) *Aiza Harun, Noorshilawati Abdul Aziz, Shaari Daud, Khairil Syazwan Salim, Norlaili Abu Bakar, Siti Zaiton Mat Soad, and Norizan Ahmat*	1249

Analytical Method

8. ELECTROCHEMICAL ELIMINATION OF METHYLENE BLUE DYE USING CARBON CLOTH MATERIAL 1257
Fouad Fadhil Al-Qaim, Zainab Haider Mussa, Shaymaa Hadi Al-Rubaye, Nur Sofiah Abu Kassim, and Nurul Auni Zainal Abidin

Environmental Analysis

9. BELOWGROUND DECOMPOSITION OF SHOULDER AND RUMP FATTY FLESH IN SANDY CLAY LOAM SOIL OF RUBBER PLANTATION OF BUKIT PAYONG, MARANG 1274
Siti Sofo Ismail, Thivialosini Siva, Lee Xin Pei, and Loh Kit Yee

Organic and Inorganic Analysis

10. PREPARATION AND COMPUTATIONAL STUDY OF BIMETALLIC COBALT-IRON SUPPORTED ON ALUMINA CATALYST IN CATALYTIC OXIDATIVE DESULFURIZATION 1288
Maryam Solehah Zulkefli, Wan Nazwanie Wan Abdullah, Nor Atiq Syakila Mohd Nazmi, and Fazira Ilyana Abdul Razak

Organic and Inorganic Analysis

11. ANTIVIRAL STUDY OF SCHIFF BASE VANILLIN DERIVATIVES AGAINST NS2B-NS3 PROTEASE OF ZIKA VIRUS BASED ON PHARMACOPHORE MODELLING AND MOLECULAR DOCKING 1300
Woon Yi Law, Mohd Razip Asaruddin, and Showkat Ahmad Bhawani

Nano or Advanced Materials Analysis

12. PHOTOCATALYTIC DEGRADATION OF OFLOXACIN ANTIBIOTICBY g-C_3N_4/ZnO NANOCOMPOSITE UNDER VISIBLE LIGHT IRRADIATION 1326
Nor Fadilah Chayed, Salma Izati Sinar Mashuri, Izzati Shafiqah Zainal Abidin, Muhd Firdaus Kasim, Noor Haida Mohd Kaus, Mohd Sufri Mastuli, Umer Rashid, and Mohd Lokman Ibrahim

Organic and Inorganic Analysis

13. SYNTHESIS, CHARACTERIZATION, DENSITY FUNCTION THEORY AND CYTOTOXICITY OF ISATIN THIOCARBOHYDRAZIDE AND ITS COPPER(II) AND ZINC(II) COMPLEXES 1337
Ummi Liyana Mohamad Rodzi, Karimah Kassim, Nageswara Rao Meroshine, and Nur Azzalia Kamaruzaman

Analytical Method

14. LATENT FINGERPRINTS TECHNIQUES AND THE USE OF STARCH TO IDENTIFY THE PRINTS: A MINI-REVIEW 1349
Anis Iryani Ahmad Shukri, Norlaily Ahmad, and NorulNazilah Ablah

Environmental Analysis

15. HEAVY METAL DETERMINATION OF SHARK *Scoliodon laticaudus* IN JOHOR WATERS 1357
Ng Yenlin Erin, Adiana Ghazali, Lavannia Ravikumar, Yap Chee Kong, Noverita Dian Takarina, and Ong Meng Chuan

Nano or Advanced Materials Analysis

16. METHYLENE BLUE AND METHYL RED FROM PINEAPPLE PEEL BASED BIOSORBENT FOR MASS TRANSFER SIMULATION AND STATISTICAL APPROACH 1373
Nur Ayshah Rosli, Mohd Azmier Ahmad, and Teh Ubaidah Noh

Analytical Method

17. A COMPREHENSIVE REVIEW OF GRAPHENE NANOPLATELETS FOR REMOVAL AND DETECTION OF HEAVY METALS AND ENDOCRINE DISRUPTING COMPOUNDS 1389
Sazlinda Kamaruzaman, Najihah Mohammad Nasir, Yugarani Arivalagan, Noorfatimah Yahaya, Saw Hong Loh, Nor Suhaila Mohamad Hanapi, Wan Nazihah Wan Ibrahim, and Ili Syazana Johari

Malaysian Journal of Analytical Sciences (MJAS)
Published by Malaysian Analytical Sciences Society

PRECONCENTRATION AND DETERMINATION OF NICOTINE IN TOBACCO SAMPLES BY DISPERSIVE MICRO-SOLID PHASE EXTRACTION AND GAS CHROMATOGRAPHY-MASS SPECTROMETRY

(Pemekatan dan Penentuan Nikotin dalam Sampel Tembakau oleh Pengekstrakan Fasa Pepejal-Mikro Dispersif dan Gas Kromatografi-Spektrometri Jisim)

Nur Ainaa Syaza Mat Yatim[1], Nor Suhaila Mohamad Hanapi[1,2]*, Nurzaimah Zaini[1], Ahmad Lutfi Anis[3], Reena Abd Rashid[1], Noor Najmi Bonnia[1] and Wan Nazihah Wan Ibrahim[1,2]

[1]Faculty of Applied Sciences, Universiti Teknologi MARA, 40450 Shah Alam, Selangor, Malaysia
[2]Trace Analysis Research Group, Universiti Teknologi MARA, 40450 Shah Alam, Selangor, Malaysia
[3]Faculty of Applied Sciences, Universiti Teknologi MARA, 94300 Kota Samarahan, Sarawak, Malaysia

[*]Corresponding author: norsuhaila979@uitm.edu.my

Received: 26 July 2023; Accepted: 26 September 2023; Published: 29 December 2023

Abstract

In this study, the dispersive micro-solid phase extraction (D-µ-SPE) method was optimised and validated for preconcentration and determination of nicotine in tobacco samples, with the use of C_{18} as sorbent, coupled with gas chromatography-mass spectrometry (GC-MS). The optimisation of three extraction parameters, namely extraction time (min), mass of sorbent (mg), and desorption volume (mL), were investigated to provide better insight into its reliability as a low-consumption sorbent and rapid operation. The obtained parameters suitable for nicotine extraction were 10 min of extraction time, 50 mg of C_{18} sorbent, and 1.0 mL of desorption solvent. Nicotine was successfully extracted from tobacco samples with good linearity in the range of 0.1 – 500 mg/L, with a coefficient of determination (R^2) of 0.9997. The calculated LOD resulted in a value of 0.0983 mg/L, with the calculated LOQ being 0.2978 mg/L. The precision of the method revealed a percent relative standard deviation (% RSD) of 2.6%. In addition, good relative recovery (%) of nicotine in real samples was also achieved in the 75.5 – 96.4% range, with % RSD ranging from 3.1 - 5.7%. Hence, this study proposed an improvement to the green method towards nicotine analysis with low consumption of organic solvent, good sorbent absorptivity, and rapid and high selectivity for separation.

Keywords: Dispersive micro-solid-phase extraction, nicotine, tobacco samples, green method, C_{18} sorbent

Abstrak

Dalam kajian ini, kaedah pengekstrakan fasa pepejal-mikro dispersif (D-µ-SPE) telah dioptimumkan dan disahkan untuk pemekatan dan penentuan nikotin dalam sampel tembakau, dengan menggunakan C_{18} sebagai penjerap serta dicantumkan dengan kromatografi gas-spektrometri jisim (GC-MS). Pengoptimuman tiga parameter pengekstrakan, iaitu masa pengekstrakan (min), jisim penjerap (mg), dan isipadu penyaherapan (mL) turut dijalankan untuk memberikan gambaran yang lebih baik tentang kebolehpercayaannya sebagai penjerap yang dapat digunakan dalam kuantiti yang rendah serta operasi pengekstrakan yang pantas. Parameter yang diperoleh yang sesuai untuk pengekstrakan nikotin daripada sampel tembakau ialah 10 min masa pengekstrakan,

dengan penggunaan sebanyak 50 mg penjerap $C_{18,}$ dan isipadu penyaherapan sebanyak 1.0 mL. Nikotin berjaya diekstrak daripada sampel tembakau dengan kelinearan yang baik dalam julat 0.1 – 500 mg/L, dengan pekali penentuan (R^2) sebanyak 0.9997. Had pengesanan (LOD) yang dikira memberikan nilai 0.0983 mg/L, dengan had kuantitatif (LOQ) sebanyak 0.2978 mg/L. Ketepatan kaedah tersebut menghasilkan peratus sisihan piawai relatif (%RSD) sebanyak 2.6%. Di samping itu, pemulihan relatif (%) yang baik terhadap nikotin dalam sampel sebenar juga dicapai dalam julat 75.5 – 96.4%, dengan % RSD berjumlah dalam julat 3.1 - 5.7%. Oleh itu, kajian ini dapat mencadangkan penambahbaikan kepada kaedah hijau untuk analisis nikotin dengan penggunaan pelarut organik yang rendah, dapat memberikan penyerapan penjerap yang baik, kaedah yang pantas, dan kebolehasingan yang tinggi.

Kata kunci: Pengekstrakan fasa pepejal-mikro dispersif, nikotin, sampel tembakau, kaedah hijau, penjerap C_{18}

Introduction

Nicotine is a type of alkaloid mainly found naturally in plants from the Solanaceous family, including tobacco, tomato, potato, and green pepper [1]. Chemically known as 3-(1-methyl-2-pyrrolidinyl) pyridine, its content can reach 30-60 mg/kg, making it an immensely toxic alkaloid [2]. The human body absorbs approximately 1 mg of nicotine from smoking a cigarette, which typically contains between 8 and 20 mg [3].

The use of nicotine in tobacco products is undoubtedly a worldwide concern as it is known to cause various adverse health effects to consumers and people inhaling nicotine from second-hand smoke. It is highly addictive to its consumers, has severe systemic effects, and can also harm kidneys, lungs, reproductive systems, heart, and other vital organs [4]. Nicotine consumption also has the potential to be cancerous. It can impair the genome, interfere with cellular metabolic processes, and elevate the growth and spreading of altered cells, allowing nicotine to possess mutagenic and stimulate tumor-related activities in the body [5]. Nicotine, when acting on nicotinic cholinergic receptors, can endanger the body's systems, leading to its highly addictive nature [6]. Therefore, determining the content of nicotine in tobacco products is crucial as different brands of tobacco products, such as cigarettes, may vary in the amount of nicotine present in them [3]. Figure 1 shows the chemical structure of nicotine.

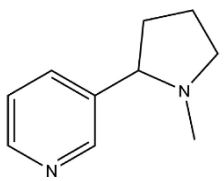


Figure 1. Chemical structure of nicotine

Sample preparation is a critical step in sample analysis. Previous studies have recorded solvent extraction as an extraction method for various samples, including nicotine in tobacco samples. A recent study utilized a solvent extraction method for the extraction of nicotine with ether, kerosene, and sulfuric acid as the extraction solvents [7]. Solvent extraction, or its other name which is liquid-liquid extraction (LLE), is an extraction technique that involves separation of compounds from two unidentical, immiscible liquids, about the liquids' respective relative solubility, typically with an organic solvent and water [8]. This extraction technique requires an extraction solvent, which is immiscible in the aqueous mixtures, to allow efficient separation of two differing liquids. In addition, the targeted analytes must be compatibly soluble and display a high partition coefficient in the extraction solvent [9]. This extraction technique involves shaking and inverting the mixture of two differing, immiscible liquids regularly for a few minutes to ensure the two liquid phases are well-mixed [9]. Expelling the solvent from the liquid phases can be done with a handheld pipette for less dense solvents than water, while denser solvents can be withdrawn from the bottom of a separatory funnel [9]. However, using organic solvents in this method may be toxic to the environment, time-consuming, and unable to separate many compounds with different polarity [8].

In recent years, dispersive micro-solid phase extraction (D-µ-SPE) has increased in recent years. D-µ-SPE is a method of extraction displayed in a miniaturized version of dispersive solid phase extraction (dSPE), extracting targeted analytes from samples rather than clean-up [11]. Sonication, stirring, vortex, or shaking are used to assist sorbent dispersion in the sample solution [11]. This is then followed by centrifugation, filtration, or

applying an external magnetic field to separate the solid sorbent [10]. The last step includes analysis of the analytes obtained in small volumes after being isolated from the sorbent [11]. D-µ-SPE absorbs fewer solvents, has a more straightforward procedure, and requires less time for operation in addition to minimizing solvent wastage, as opposed to the traditional solid phase extraction (SPE) method, which has some drawbacks involving solvent wastage, significant generation of secondary waste, apart from being lengthy and involving tedious procedures [10]. C_{18} silica, a micromaterial-type sorbent, is used for clean-up, in addition to primary-secondary amine (PSA), for the isolation of interference matrix from liquid extracts for the analysis of pesticides, specifically in vegetables [12]. As for the use of C_{18} in nicotine extraction, it has been reported in a study [13] in which nicotine was extracted from the hair of smokers and non-smokers with the use of SB-C_{18} column for SPE, assisted by molecularly imprinted polymer (MIP) as sorbent. Additionally, a study has also applied C_{18} as a sorbent through matrix solid-phase dispersion extraction method for the analysis of polyphenols in tobacco [14]. However, when it comes to the separation and preconcentration of nicotine from tobacco plants or products, there are still limited studies on the D-µ-SPE method and the use of C_{18} as a sorbent. The employment of D-µ-SPE for preconcentration of nicotine has been reported by a study [2] that applied graphene oxide as sorbent for separation and preconcentration of nicotine from environmental and biological water samples, which was then analyzed by gas chromatography with flame ionization detection (GC-FID). Other reported works did apply the D-µ-SPE method with C_{18} as a sorbent, even though it does not involve preconcentration and extraction of nicotine, such as the extraction and determination of ofloxacin and sparfloxacin from human plasma [15] and for determination of polycyclic aromatic hydrocarbon (PAHs) in water samples [16]. Considering the limitations of some sample preparation or extraction methods mentioned earlier, as well as the limited research on the efficiency of D-µ-SPE on the separation and preconcentration of nicotine in tobacco samples, it calls for an improved and alternative method to overcome these limitations.

The present study proposes an efficient technique using D-µ-SPE with C_{18} as the sorbent for preconcentration and determination of nicotine in tobacco samples, coupled with gas chromatography-mass spectrometry (GC-MS). C_{18} sorbent, commonly used in SPE [12], was studied for its potential as a quick and simple method for preconcentration and determination of nicotine in tobacco samples, utilizing D-µ-SPE. The method offers the possibility of an efficient clean-up procedure, utilizing C_{18} sorbent for a fast, easy, and cost-effective approach to preconcentration and determination of nicotine.

Materials and Methods

Chemicals and materials

Nicotine (≥ 99%), methanol (MeOH) of HPLC grade and DSC-18 (C_{18} sorbent, 50 µm particle size) were purchased from Sigma-Aldrich. Tobacco samples of different brands (labelled as 'M', 'G', and 'D') were obtained from the tobacco market available in Malaysia**.**

Preparation of standard and spiked solutions

1000 mg/L of nicotine stock solution was prepared in HPLC-grade methanol. The stock solution was stored in amber glass bottles in the refrigerator at 4 °C when not in use. A series of working standard solutions were prepared in methanol by dilution before analysis to prevent the decomposition of analytes. All spiked solutions were diluted with methanol and stored at 4 °C until further use.

Sample preparation and pre-treatment

Sample preparation was based on the methods described in the literature with some modifications [15, 17]. 2 g of tobacco samples were weighed and placed into 50 mL polyethene centrifuge tubes. 15 mL of methanol was then added to each sample and sonicated for 15 min. The resulting supernatant of each sample was then filtered through a 20-25 µm filter paper.

Optimization of parameters using one-factor-at-a-time (OFAT)

The optimization parameters used to determine the efficiency of C_{18} sorbent for the extraction of nicotine using the D-µ-SPE method were extraction time (min), mass of sorbent (mg), and desorption volume (mL). The

parameters were optimized using the One-factor-at-a-time (OFAT) approach. Each sample was spiked with 10 mg/L nicotine standard solution for the optimization study. The optimum results obtained from each parameter were used to implement subsequent parameters. The optimal conditions were then utilized for real sample analysis. For real sample analysis, the samples were spiked with 50 mg/L and 100 mg/L nicotine standard solutions. The concentration of nicotine in the filtrate and percent (%) relative recovery was calculated using the following equations:

$$\text{Concentration of nicotine} = \frac{\text{Peak area of spiked nicotine filtrate samples}}{\text{Retention factor}} \quad (1)$$

$$\%\ \text{Relative recovery} = \frac{\text{Amount recovered}}{\text{Actual amount of spiking}} \times 100 \quad (2)$$

Dispersive-micro solid phase extraction (D-µ-SPE) procedure

This part of the procedure was based on a method from the literature [15] with some modifications. 1 mL of 10 mg/L nicotine standard solution was spiked in a 50 mL centrifuge tube containing 4 mL of prepared tobacco sample filtrate and 50 mg of C_{18} sorbent. The samples were then sonicated for 10 min and centrifuged at 5000 rpm for 4 min. The sorbent was carefully collected and transferred into a microcentrifuge tube. To desorb the analytes, 1 mL of MeOH was added to the centrifuge tube containing the sorbent and vortexed for 5 min. Subsequently, to allow separation and settling of the sorbent, it was centrifuged again for another 5 min. The resulting supernatant was then filtered through a 0.22 µm nylon membrane filter before the analysis on GC-MS. Figure 2 shows the D-µ-SPE procedure by using C_{18} as a sorbent.

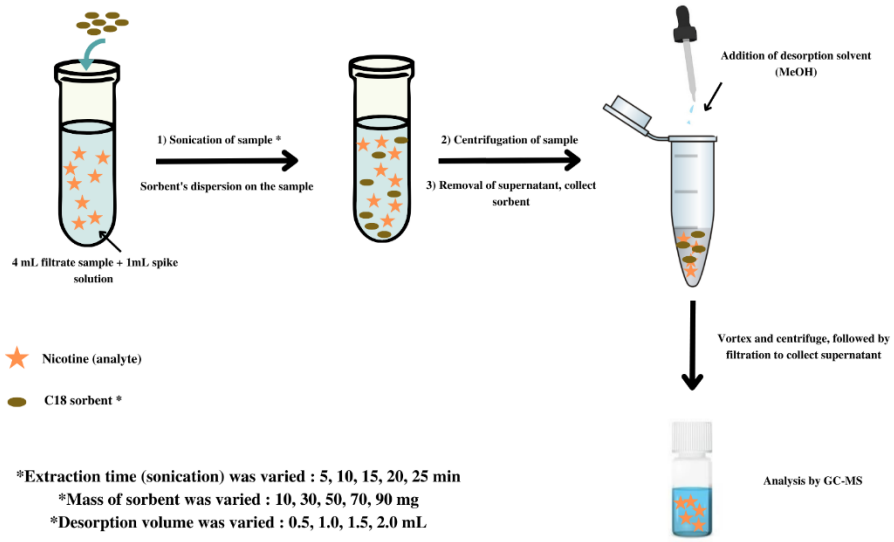


Figure 2. Dispersive micro-solid-phase extraction (D-µ-SPE) procedure by using C_{18} as sorbent

Chromatographic conditions

Chromatographic conditions were based on a method from the literature [18]. An Agilent 6890 gas chromatograph with 5973 inert mass spectrometers (USA) was used for analyzing nicotine in tobacco samples. The chromatographic separation was carried out on an InertCap 5MS/Sil column, with specifications of 0.25 mm I.D. x 30 m and df = 0.25 µm. Detection was done by MS scan (45 – 500 m/z) with an interface temperature of 280 °C. The carrier gas employed was helium, with a 36.5 cm/sec flow rate. An injection temperature of 250 °C was used. 1.0 µL of the sample

was injected into the GC-MS using splitless mode for 1 min, with a vent flow of 50 mL/min. The analysis of the samples was carried out under the following column temperature program; the initial temperature was set to 60 °C and held for 1 min, then ramped up at 10 °C/min, followed by raising the temperature to 280 °C and held for 7 min.

Validation of the analytical method

For the D-µ-SPE method, the efficiency of the analytical performance was assessed through linearity, the limit of detection (LOD), the limit of quantification (LOQ), precision, and accuracy. To assess the linearity of the analytical method, an eight-point calibration curve for nicotine was plotted by varying the concentrations of the spiked standards to achieve 0.1, 0.5, 1, 10, 50, 100, 200, and 500 mg/L in the filtrate solution (methanol obtained from the filtration of cigarette samples). Limit of detection (LOD) and limit of quantification (LOQ) were established through linear regression analysis. The precision of the method was calculated in terms of repeatability by determining the relative standard deviation (RSD). The RSD was then presented and expressed as a percentage (%RSD). The accuracy of the method was expressed in terms of percent relative recovery. Real samples were spiked with 50 mg/L and 100 mg/L nicotine standards, and the accuracy of the method was determined through percent relative recovery.

Results and Discussion

Optimization of dispersive-micro solid phase extraction (D-µ-SPE)

Optimization of D-µ-SPE parameters for the extraction of nicotine from tobacco samples was performed by varying the parameters, including extraction time, mass of sorbent, and desorption volume. These parameters were optimized based on the one-factor-at-a-time method (OFAT), where the other parameters were kept constant during the optimization of one parameter. The extraction of the samples was done in triplicates for each parameter optimized. Samples were also spiked with 50 mg/L and 100 mg/L nicotine standard solutions for real sample analysis using the optimized conditions and parameters obtained from the OFAT method.

Effect of extraction time

The effect of extraction time is vital in determining the extraction efficiency of the sample to extract the analyte selectively. For this research, the extraction efficiency was carried out by allowing the C_{18} sorbent to come into contact with nicotine (analyte) in the tobacco samples. The interaction between the sorbent and analyte in the samples was individually exposed for 5 min, 10 min, 15 min, 20 min, and 25 min. After each subsequent analysis, a graph of peak area (m/z) versus extraction time (min) was plotted to determine the optimized condition for the extraction time of nicotine. The effect of the extraction time, or the duration when the sorbent is in contact with nicotine in the samples, is shown in Figure 3.

From the results obtained for the extraction time of nicotine in tobacco samples, it was observed that the extraction efficiency of nicotine increased substantially from 5 min to 10 min. The highest extraction efficiency was acquired at the 10th minute, as shown in Figure 3(a). From 10 to 20 min, there was a gradual drop in the peak area of the analyte. The peak area remained constant from 20 min to 25 min. This implied that there was no significant improvement in the extraction efficiency of nicotine from tobacco samples, even when the extraction time was lengthened. The decline in extraction performance or efficiency in relation to its extraction time can be attributed to the back extraction of the analyte [11]. Hence, 10 min extraction time was chosen as the optimum extraction time to be used for further optimization of another parameter.

Effect of mass of sorbent

In the D-µ-SPE approach, it is necessary to consider the mass of sorbent as a crucial parameter since the amount of sorbent can significantly affect the efficiency of analyte extraction from the sample matrix through the number of adsorption sites [19]. The optimization of the mass of C_{18} sorbent involved varying the amount to 10, 30, 50, 70, and 90 mg. After each subsequent analysis, a graph of peak area (m/z) versus mass of C_{18} sorbent (mg) was plotted to determine the optimized condition for the mass of C_{18} sorbent used to adsorb nicotine from tobacco samples efficiently. The interaction mechanism between C_{18} sorbent and nicotine involves hydrophobic

interactions [13], π-π stacking, and Van der Waals forces. The hydrophobic alkyl chains of the C_{18} sorbent interact with the nonpolar regions of nicotine, while the aromatic rings in both the C_{18} sorbent and nicotine engage in π-π stacking interactions. Van der Waals forces further contribute to their attraction. The functional groups involved are the hydrophobic alkyl chains of C_{18}, the aromatic rings in both the sorbent and nicotine and the secondary amine group in nicotine. These interactions collectively facilitate nicotine's retention and separation on the C_{18} sorbent. Based on Figure 3(b), it can be observed that with an increasing mass of C_{18} sorbent up to 50 mg, the extraction efficiency of nicotine from tobacco samples increased significantly, with the highest extraction efficiency attained at 50 mg mass of C_{18} sorbent. This effect may be attributed to the increased likelihood of adsorbing analytes onto the sorbent due to the higher number of adsorption sites [19]. However, with an increasing mass of C_{18} sorbent beyond 50 mg (70 mg to 90 mg), the extraction efficiency started to decrease slowly. This condition may be due to the agglomeration of C_{18} sorbent that suppressed the action of the active sites of the sorbent, thereby lowering the extraction efficiency [15]. Furthermore, it is worth noting that samples may have trouble progressing through the system if the amount of sorbent increases [20]. Thus, to efficiently extract nicotine from tobacco samples, the mass of C_{18} sorbent of 50 mg was utilized as the second parameter for further optimization of another parameter and applied for subsequent use in real-sample analysis of tobacco samples.

Effect of desorption volume

The effect of desorption volume was also taken into consideration for efficiency studies in the extraction of nicotine in tobacco samples. This is because the efficiency of desorption capability is affected by the volume of desorption solvent used [21]. This study used methanol as the desorption solvent, and the desorption volume varied to 0.5 mL, 1.0 mL, 1.5 mL, and 2.0 mL. After each subsequent analysis, a graph of peak area (m/z) versus desorption volume (mL) was plotted to determine the optimized condition for the volume of desorption solvent used to adsorb nicotine from tobacco samples efficiently. Based on Figure 3(c), it can be observed that with an increasing desorption volume from 0.5 mL to 1.0 mL, the extraction efficiency of nicotine from tobacco samples also increased substantially. However, increasing the desorption solvent volume from 1.5 mL to 2.0 mL only lowered the extraction efficiency of nicotine from tobacco samples. This condition may be attributed to the maximum achievement of analyte enrichment when applying a lower volume of desorption solvent. Additionally, only a low volume of desorption solvent was necessary for achieving higher sensitivity of analyte extraction [22]. Hence, a desorption volume of 1.0 mL of methanol was utilized as the third parameter and applied for subsequent use in the real sample analysis of tobacco samples.

Optimum extraction conditions

The final applied C_{18}- D-μ-SPE conditions were as follows: extraction time, 10 min; mass of sorbent, 50 mg; and desorption volume, 1.0 mL. Thus, these optimum extraction conditions were applied for subsequent analysis on real samples.

Method validation and analytical performance of D-μ-SPE

Method validation was then carried out based on the optimum conditions obtained from the D-μ-SPE method. Relative recovery (%), linearity, precision, limit of detection (LOD), and limit of quantification (LOQ) were obtained for validation of this study. Good linearity in the range of 0.1 – 500 mg/L was obtained for the analyte of nicotine, with the coefficients of determination (R^2) of 0.9997. The calculated LOD was 0.0983 mg/L, while the LOQ was calculated to be 0.2978 mg/L. The precision of the method was measured through percent relative standard deviation (% RSD), which gave a value of 2.6%. Table 1 shows the validation data for D-μ-SPE of nicotine from tobacco samples using sample brand M.

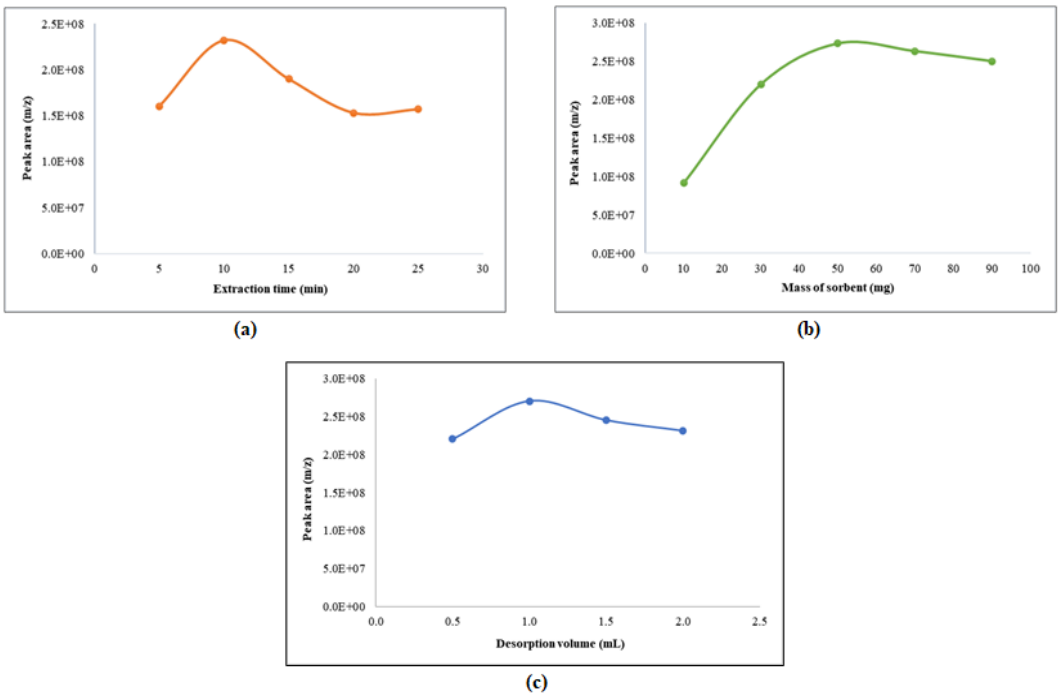


Figure 3. Optimization for the extraction performance of C_{18} using D-µ-SPE. (a) Effect of extraction time, (b) mass of sorbent and (c) desorption volume on C_{18}-D-µ-SPE of nicotine in tobacco samples.

Table 1. Quantitative results of D-µ-SPE for nicotine from tobacco samples

Sample	Analyte	Linear Range (mg/L)	Coefficient of Determination (R^2)	LOD (mg/L)	LOQ (mg/L)	RSD (%, n = 3)
Brand M	Nicotine	0.1 - 500	0.9997	0.0983	0.2978	2.6

Application of D-µ-SPE on real samples

The developed D-µ-SPE-GC-MS method was successfully applied to the extraction of nicotine from tobacco samples. The optimized parameters performed previously were used to obtain the actual concentration (mg/L) of nicotine in the tobacco samples. Relative recoveries (%) were also calculated on the real samples by spiking each real sample with 50 mg/L and 100 mg/L standard nicotine. Relative recoveries (%) of real samples showed good recoveries ranging from 75.5% to 96.4%. The analysis on real samples also displayed good repeatability with relative standard deviation (% RSD) ranging from 3.1% to 5.7%. Table 2 shows relative recoveries (%) of nicotine in tobacco real samples and % RSD (n = 3) of D-µ-SPE.

Table 2. Relative recoveries (%) of nicotine in tobacco real samples and %RSD (n = 3) of D-µ-SPE

Real samples	Spike Added (mg/L)	Actual Concentration (mg/L)	Relative Recoveries (%)	RSD (%) (n = 3)
Brand D	50	41.594	83.2	3.5
	100	84.793	84.8	4.5
Brand G	50	48.189	96.4	3.1
	100	75.489	75.5	5.7
Brand M	10	8.574	85.7	4.3

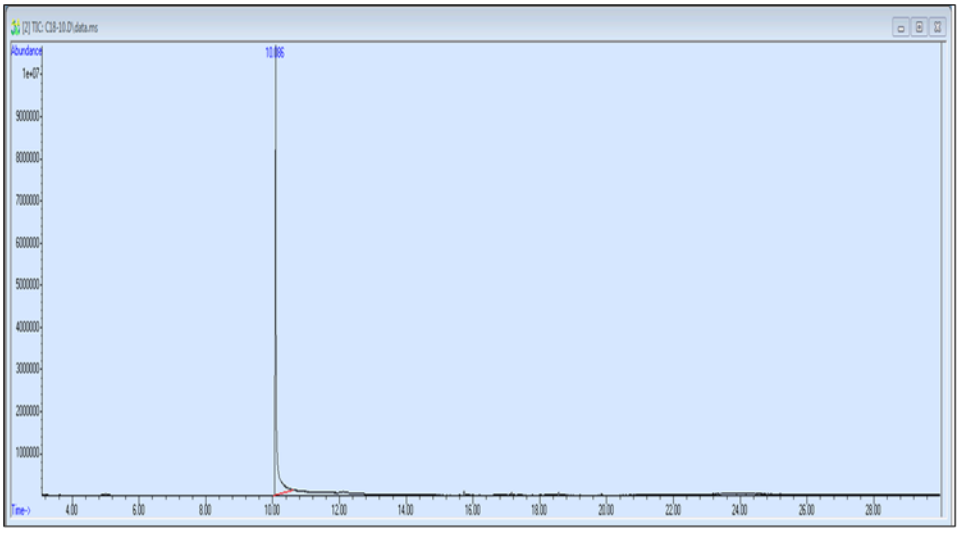


Figure 4. GC-MS chromatogram obtained for nicotine from the optimization on the effect of extraction time at 10th min

Comparison with other reported methods

Previous studies have applied various extraction methods for nicotine from different samples. A comparison study is outlined in Table 3, displaying the developed method from existing/published studies alongside the method proposed by this research for preconcentration and determination of nicotine in tobacco samples. As shown in Table 3, most of the extraction methods for nicotine from tobacco samples involve longer extraction time. For instance, a reported method [23] took 120 min to extract nicotine from waste tobacco samples using an aqueous two-phase system and solvent reverse extraction method. Extraction of nicotine by the HS-SPME method [24] and the electro-membrane extraction (EME) method [25] reported extraction time of 30 min and 20 min, respectively. In contrast, the proposed D-µ-SPE method exhibited a low extraction time of 10 min, which can significantly reduce tedious laboratory work. However, a method reported earlier using surface-enhanced Raman scattering (SERS) [26] showed the fastest extraction time, with nicotine extracted between 3 and 5 min. However, the present D-µ-SPE method demonstrated better % recovery of nicotine ranging from 75.5% to 96.4% from tobacco samples, compared to the previously developed method [26], which reported 51.47% nicotine recovery. Furthermore, the limit of detection (LOD) for the proposed D-µ-SPE method also showed a good detection limit.

Conclusion

In conclusion, the optimization and validation of the dispersive micro-solid phase extraction method using C_{18} as the sorbent have been successfully employed for the extraction and determination of nicotine in tobacco samples, coupled with gas chromatography-mass spectrometry (GC-MS) for chromatographic analysis. Three parameters were studied for optimization purposes: the effect of extraction time of the D-µ-SPE method, the effect of the mass of C_{18} sorbent, and the effect of desorption volume to extract and pre-concentrate nicotine from tobacco samples. An extraction time of 10 min, mass of C_{18} sorbent of 50 mg, and desorption volume of 1.0 mL were found to be the optimized conditions for extraction. Nicotine was successfully extracted using the above optimum conditions with the D-µ-SPE method. Good linearity in the range of 0.1 - 500 mg/L was also achieved for the analyte of nicotine, with a coefficient of determination (R^2) of 0.9997. The limit of detection (LOD) was calculated to be 0.0983 mg/L, and the limit of quantification (LOQ) was calculated to be 0.2978 mg/L. The precision of the method was measured through the percent relative standard deviation (% RSD), which gave a value of 2.6%. Additionally, good relative

recovery (%) of nicotine in real samples was achieved in the 75.5 - 96.4% range, with % RSD ranging from 3.1 - 5.7%. Hence, the D-µ-SPE method proves to be green, reducing excessive solvent consumption while being selective and rapid in preconcentration and determination of nicotine from tobacco samples. It shows promise as an alternative method for future analytical laboratory work in nicotine analysis. Compared to the previously reported methods, the D-µ-SPE method used in the present study demonstrated one of the fastest extraction times and one of the highest recoveries of nicotine from tobacco samples. A future extension to this research may be to explore more optimization conditions and study other parameters and factors that may contribute to improving the efficiency of C_{18} as a sorbent for nicotine extraction from tobacco samples using the D-µ-SPE method.

Table 3. Comparison of extraction performance between previous reports and the present work for extraction and determination of nicotine from tobacco samples.

Extraction methods	**Extraction Time (min)**	**LOD (mg/L)**	**% Recovery**	**% RSD**	**References**
Aqueous two-phase system and solvent reverse extraction	120	-	96.1	-	[23]
Headspace solid-phase micro-extraction (HS-SPME)	30	-	99.56 -99.80	3.35	[24]
Electromembrane extraction (EME)	20	0.02	81.0 – 112.8	0.2 – 7.7	[25]
Fabrication of gold nano bipyramids (Au NBPs) – AAO substrates to burn cigarettes	3 – 5	2.2	51.47	10.18	[26]
Solvent extraction	Not stated	-	0.6	-	[27]
Ultrasound-assisted extraction of nicotine-related alkaloids from tobacco samples using 1:3 CH_3OH-CH_2Cl_2	>20	1.3	95.7	1.5	[28]
Supercritical fluid CO_2 extraction	Not stated	-	47.40	-	[29]
Dispersive micro-solid phase extraction	10	0.0983	75.5 – 96.4	3.1 – 5.7	This work

Acknowledgement

The authors would like to thank Universiti Teknologi MARA for providing research facilities and the Ministry of Higher Education Malaysia for the financial support under research grant number 600-RMC/GIP 5/3 (162/2021).

References

1. Yildiz, D. (2004). Nicotine, its metabolism and an overview of its biological effects. *Toxicon*, 43(6): 619-632.
2. Mahpishanian, S. and Sereshti, H. (2014). Graphene oxide-based dispersive micro-solid phase

extraction for separation and preconcentration of nicotine from biological and environmental water samples followed by gas chromatography-flame ionization detection. *Talanta*, 130: 71-77.

3. Tayoub, G., Sulaiman, H. and Alorfi, M. (2015). Determination of nicotine levels in the leaves of some Nicotiana tabacum varieties cultivated in Syria. *Herba Polonica*, 61(4): 23-30.
4. Mishra, A., Chaturvedi, P., Datta, S., Sinukumar, S., Joshi, P. and Garg, A. (2015). Harmful effects of nicotine. *Indian Journal of Medical and Paediatric Oncology*, 36(1): 24-31.
5. Grando, S. A. (2014). Connections of nicotine to cancer. *Nature Reviews Cancer*, 14(6): 419-429.
6. Vlase, L., Filip, L., Mîndruţău, I. and Leucuţa, S. E. (2005). Determination of nicotine from tobacco by LC-MS-MS. *Studia Universitatis Babes-Bolyai Physica*, 4: 19-24.
7. Al-Dahhan, W. H., Kadhom, M., Yousif, E., Mohammed, S. A. and Alkaim, A. (2022). Extraction and determination of nicotine in tobacco from selected local cigarettes brands in Iraq. *Letters in Applied NanoBioScience*, 11(1): 3278-3290.
8. Urkude, R., Dhurvey, V. and Kochhar, S. (2019). Pesticide residues in beverages. In *Quality Control in the Beverage Industry: Volume 17: The Science of Beverages* (pp. 529–560). Elsevier.
9. Kyle, P. B. (2017). Toxicology: GCMS. In *Mass Spectrometry for the Clinical Laboratory* (pp. 131–163). Elsevier Inc.
10. Khezeli, T. and Daneshfar, A. (2017). Development of dispersive micro-solid phase extraction based on micro and nano sorbents. *TrAC - Trends in Analytical Chemistry*, 89: 99-118.
11. Sajid, M., Nazal, M. K. and Ihsanullah, I. (2021). Novel materials for dispersive (micro) solid-phase extraction of polycyclic aromatic hydrocarbons in environmental water samples: A review. *Analytica Chimica Acta*, 1141: 246-262.
12. Chisvert, A., Cárdenas, S. and Lucena, R. (2019). Dispersive micro-solid phase extraction. *TrAC - Trends in Analytical Chemistry*, 112: 226-233.
13. Yang, J., Hu, Y., Cai, J. B., Zhu, X. L., Su, Q. D., Hu, Y. Q. and Liang, F. X. (2007). Selective hair analysis of nicotine by molecular imprinted solid-phase extraction: An application for evaluating tobacco smoke exposure. *Food and Chemical Toxicology*, 45(6): 896-903.
14. Liang, F., and Zhang, Z. (2008). Determination of polyphenols in tobaccos by high performance liquid chromatography with matrix solid-phase dispersion extraction and clean-up. *Asian Journal of Chemistry*, 20(7): 4980-4986.
15. Owaid, S. J., Yahaya, N., Rahim, N. Y., Mohammad, R. A. E., Jajuli, M. N. and Miskam, M. (2020). Development of dispersive micro-solid phase extraction for the analysis of ofloxacin and sparfloxacin in human plasma. *Malaysian Journal of Analytical Sciences*, 24(6): 893-905.
16. Galán-Cano, F., Lucena, R., Cárdenas, S., and Valcárcel, M. (2011). Direct coupling of dispersive micro-solid phase extraction and thermal desorption for sensitive gas chromatographic analysis. *Analytical Methods*, 3(4): 991-995.
17. Liu, W., Zhao, R., Li, B., Wu, G. and Xue, Y. (2013). Determination of the nicotine content in solanaceae vegetables by solid-phase extraction coupled with ultra high-performance liquid chromatography-tandem mass spectrometry. *Food Analytical Methods*, 6(2): 643-647.
18. GL Sciences. (n.d.). *InertSearch for GC: Tobacco*. https://www.glsciences.com/viewfile/?p=GA143. [Accessed online 18 October 2022].
19. Mohebbi, A., Nemati, M., Afshar Mogaddam, M. R., Farajzadeh, M. A. and Lotfipour, F. (2022). Dispersive micro–solid–phase extraction of aflatoxins from commercial soy milk samples using a green vitamin–based metal–organic framework as an efficient sorbent followed by high performance liquid chromatography–tandem mass spectrometry determination. *Journal of Chromatography A*, 1673: 463099.
20. Maranata, G. J., Surya, N. O. and Hasanah, A. N. (2021). Optimising factors affecting solid phase extraction performances of molecular imprinted polymer as recent sample preparation technique. *Heliyon*, 7(1): e05934.
21. Xu, Y., Yu, X., Gui, J., Wan, Y., Chen, J., Tan, T., Liu, F. and Guo, L. (2022). Ultrasonic solvent extraction followed by dispersive solid phase extraction (d-SPE) cleanup for the simultaneous

determination of five anthraquinones in *Polygonum multiflorum* by UHPLC-PDA. *Foods*, 11(3): 386.

22. Loh, S. H., Neoh, P. E., Tai, C. T. and Kamaruzaman, S. (2018). Simple µ-Solid Phase Extraction using C_{18} film for the extraction of polycyclic aromatic hydrocarbons in coffee beverage. *Malaysian Journal of Analytical Sciences*, 22(1): 1-7.
23. Xing, J. M., Li, F. F. and Ping, J. (2009). Recovery and purification of nicotine from waste tobacco by aqueous two-phase system/reverse extraction. *Natural Product Communications*, 4(8): 1093-1094.
24. Tang, L., Yang, H., He, L., Wang, M., Zhu, B. and Liao, T. (2019). Direct analysis of free-base nicotine in tobacco leaf by headspace solid-phase micro-extraction combined with gas chromatography/mass spectrometry. *Accreditation and Quality Assurance*, 24(5): 341-349.
25. Chen, M., Qin, Y., Wang, S., Liu, S., Zhao, G., Lu, H., Cui, H., Cai, J., Wang, X., Yan, Q., Hua, C., Xie, F. and Wan, L. (2022). Electromembrane extraction of nicotine in inhaled aerosols from tobacco cigarettes, electronic cigarettes, and heated tobacco products. *Journal of Chromatography B*, 1208: 123391.
26. Lin, B., Chen, J., Zeng, Y., Li, L., Qiu, B., Lin, Z. and Guo, L. (2019). A facile approach for on-site evaluation of nicotine in tobacco and environmental tobacco smoke. *ACS Sensors*, 4(7): 1844-1850.
27. Qayyum, I., Fazal-ur-Rehman, M. and Ibrahim, M. S. (2018). Extraction of nicotine (3-(1-methyl-2-pyrrolidinyl) pyridine) from tobacco leaves separated from Gold Live Classic Brand™ cigarettes by solvent extraction approach and characterization via IR analysis. *Biosciences Biotechnology Research Asia*, 15(4): 799-804.
28. Sheng, L. Q., Ding, L., Tong, H. W., Yong, G. P., Zhou, X. Z. and Liu, S. M. (2005). Determination of nicotine-related alkaloids in tobacco and cigarette smoke by GC-FID. *Chromatographia*, 62(1-2): 63-68.
29. Ikhsanov, Y. S., Nauryzbaev, M., Musabekova, A., Alimzhanova, M. and Burashev, E. (2019). Study of *Nicotiana tabacum* L extraction, by methods of liquid and supercritical fluid extraction. *Journal of Applied Engineering Science*, 17(3): 338-353.

Malaysian Journal of Analytical Sciences (MJAS)
Published by Malaysian Analytical Sciences Society

SYNTHESIS OF 4-ARYL SUBSTITUTED CANTHIN-6-ONE WITH β-CARBOLINE SKELETON VIA PICTET-SPENGLER CONDENSATION AND CYCLIZATION REACTION

(Sintesis 4-Aril Gantian Kantin-6-One dengan Rangka β-Karbolina Melalui Kondensasi Pictet-Spengler dan Tindak Balas Kitaran)

Noor Hidayah Pungot[1,2*], Noor Hamizah Mohammad Tarmizi[1,2] and Siti Zafirah Zulkifli[1,2]

[1]*School of Chemistry and Environment, Faculty of Applied Sciences, Universiti Teknologi MARA (UiTM), 40450 Shah Alam, Selangor, Malaysia*
[2] *Organic Synthesis Laboratory, Institute of Science, Universiti Teknologi MARA, UiTM Puncak Alam Campus, 42300 Bandar Puncak Alam, Selangor, Malaysia*

[*]*Corresponding author: noorhidayah977@uitm.edu.my*

Received: 17 September 2023; Accepted: 29 October 2023; Published: 29 December 2023

Abstract

This study presents a comprehensive synthesis of 4-aryl substituted canthin-6-one through a versatile Pictet-Spengler condensation and subsequent cyclization, involving the formation of 1-aroyl substituted β-carbolines as pivotal intermediates. β-Carbolines, as indole alkaloids, serve as fundamental building blocks with diverse biological activities. In particular, canthin-6-one and its derivatives exhibit a wide range of promising biological properties, which include anti-cancer, antibacterial, anti-inflammatory, and cytotoxic effects, thus making them valuable in pharmaceutical and medicinal chemistry applications. The method outlined herein involves the utilization of readily available starting materials in a direct reaction sequence, resulting in an efficient and moderate-yield access to 4-aryl substituted canthin-6-one. Synthesizing canthine was initiated by forming the intermediates, 1-aroyl substituted β-carbolines via Pictet-Spengler condensation of different substituted aromatic glyoxals with 5-hydroxy tryptophan in the presence of trifluoroacetic acid. This synthesis route avoids the formation of tetrahydro-β-carbolines. Subsequently, the series of 1-aroyl substituted β-carboline intermediates were cyclized to yield the desired 4-aryl substituted canthin-6-one derivatives. The reaction mechanism and key intermediates are discussed, providing insights into the synthesis pathway. The structure of the synthesized compounds were confirmed by using Infrared Radiation (IR) and Nuclear Magnetic Resonance (NMR) spectroscopy. This research not only contributes to the understanding of synthetic methodologies but also paves the way for the development of novel compounds with promising pharmaceutical properties.

Keywords: β-carboline, Pictet-Spengler condensation, cyclization, canthin-6-one

Abstrak

Kajian ini membentangkan sintesis komprehensif 4-aril digantikan kantin-6-satu melalui pemeluwapan Pictet-Spengler serba boleh dan kitaran seterusnya, melibatkan pembentukan 1-aroil digantikan β-karbolin sebagai perantaraan penting. β-karbolina, sebagai alkaloid indole, berfungsi sebagai blok binaan asas dengan pelbagai aktiviti biologi. Khususnya, kantin-6-satu dan derivatifnya mempamerkan pelbagai sifat biologi yang menjanjikan, termasuk kesan anti-kanser, antibakteria, anti-radang dan sitotoksik,

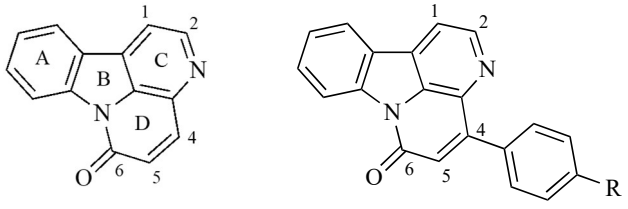
dengan itu menjadikannya berharga dalam aplikasi kimia farmaseutikal dan perubatan. Kaedah yang digariskan di sini melibatkan penggunaan bahan permulaan yang sedia ada dalam urutan tindak balas langsung, menghasilkan akses hasil yang cekap dan sederhana kepada 4-aril digantikan kantin-6-satu. Mensintesis kantin telah dimulakan dengan membentuk perantaraan, β-karbolina yang digantikan 1-aroil melalui kondensasi Pictet-Spengler bagi glioksal aromatik tersubstitusi berbeza dengan triptofan 5-hidroksi dengan kehadiran asid trifluoroasettik. Laluan sintesis ini mengelakkan pembentukan tetrahidro-β-karbolina. Selepas itu, siri perantaraan β-karbolina yang digantikan 1-aroil telah dikitar untuk menghasilkan derivatif 4-aril digantikan kantin-6-satu yang dikehendaki. Mekanisme tindak balas dan perantaraan utama dibincangkan, memberikan pandangan tentang laluan sintesis. Struktur sebatian yang disintesis telah disahkan dengan menggunakan spektroskopi sinaran inframerah (IR) dan resonans magnetik nuklear (NMR). Penyelidikan ini bukan sahaja menyumbang kepada pemahaman metodologi sintetik tetapi juga membuka jalan untuk pembangunan sebatian baru dengan sifat farmaseutikal yang menjanjikan.

Kata kunci: β-karbolina, kondensasi Picter-Spengler, kitaran, kantin-6-satu

Introduction

In field of medicinal chemistry, the search of novel compounds with therapeutic potentials never ends. Within this dynamic field, the synthesis of heterocyclic molecules has emerged as a promising pathway, offering new scaffolds for drug discovery. One such class of heterocycles, β-carbolines, has garnered increasing attention due to their diverse biological activities and potential applications in pharmaceutical research. In this work, we investigate the complex area of organic synthesis and chemical transformation to unlock the diverse potentials of β-carboline belongs to the indole alkaloid family and consists of an indole structure fused to a pyridine ring [1]. The structure of β-carboline is similar to that of tryptamine, with the ethylamine chain reconnected to the indole ring via an extra carbon atom, to produce a tricyclic ring structure [2]. Extensive studies on β-carboline have revealed exceptionally diverse biological efficacy of this natural compound.

β-Carboline has been isolated from *Peganum harmala*, a plant used as an emmenagogue and a digestive tract medicine, which is also known to evoke hallucinations. β-Carboline plays an important role in biological activities like antiparasitic, antitumor, antiviral, anti-inflammatory, and antibacterial. Although these alkaloids are highly represented in terrestrial species, large amounts of β-carboline are also isolated from marine invertebrates such as tunicates, bryozoans, soft corals, and sponges [3]. Canthine-6-one (Figure 1a) alkaloids belong to the tetracyclic subclass of β-carboline alkaloids with the addition of D ring, and have a peri-fused indolo[3,2,1-de][1,5]naphthyridine structure. They are widely found in Rutaceae and Simaroubaceae families. There are a lot of compounds that have been isolated due to their diversity in biological activities that act as anticancer, antibacterial, antifungal, anti-inflammatory, and cytotoxic agents [4]. The 4-aryl substituted canthin-6-one (Figure 1b) is one of the derivatives of β-carboline which consists of canthine as its monomer [5]. It is commonly formed by the cyclization of intermediate 1-substituted β-carboline. The derivatives of β-carboline with aroyl substitution at the C1 position were known to exhibit potent anti-inflammatory, anti-malarial, anti-cancer, anti-phospholipase, P-glycoprotein-inducer, and anti-microbial activities [6].



(a) (b)

Figure 1. (a) Canthine-6-one structure and (b) 4-Aryl substituted canthin-6-one structure

Numerous efforts have been made to synthesize not only the parent structure of β-carboline but also a variety of synthetic β-carboline derived compounds due to their notable impact in life. One of the well-known reactions that has been used to prepare β-carboline is the Pictet-Spengler reaction. To date, it has remained as one of the most powerful methods for the formation of this ring system via C-C bond formation using indole-based compound as the starting material [7]. This reaction is the most direct, and efficient synthetic method for the construction of advantaged and widely synthesized pharmacophores such as tetrahydro-isoquinolines (THIQs), tetrahydro-β-carbolines (THβCs), and polyheterocyclic frameworks [8]. The application of the Pictet-Spengler condensation reaction was the most reported method to synthesize THβCs with the aid of strong Brønsted acids to promote the ring closure of the imine [9]. Generally, Pictet-Spengler reaction can be characterized by the formation of iminium salt after an acid-catalyzed condensation of β-arylethylamine with an aldehyde or a ketone, followed by ring closure [10]. This method continues to be a prominent focus of research over the years as scientists continue to refine the methodology by applying novel reaction conditions.

However, in this study, we attempted in a more practical and convenient synthesis of the aromatic β-carbolines using 5-hydroxytryptophan and various aromatic glyoxals in the desired Pictet-Spengler reaction, followed by formation of 4-aryl substituted canthin-6-one via cyclization. This work details the efficient Pictet-Spengler condensation catalyzed by TFA, without the use of expensive metal catalysts, prolonged reaction hours or critical reaction conditions. Thus, we report herein the successful application of this versatile method for the synthesis of naturally occurring 4-aryl substituted canthin-6-one derivatives using 5-hydroxy-L-tryptophan as the starting material.

Materials and Methods

Procedure for the synthesis of intermediate 1-formyl-β-carbolines (2a-e)

To a stirred suspension of 5-hydroxy-L-tryptophan (5.69 mol, 1.3 equiv.) in 1.0 equiv. of p-toluenesulfonic acid monohydrate (TFA) (1.5 equiv.), glyoxal (4.38 mol, 1.0 equiv.) in methanol (50 ml) was added. Then, the solution was heated to 50℃ for 4 hours and the presence of phenylglyoxal was monitored by TLC analysis until it was completely consumed. The reaction mixture was poured into water and the precipitate was filtered and purified by silica gel column chromatography eluted with a gradient of acetone and petroleum ether (1:1) to afford **2a-e**.

Procedure for the synthesis of 4-aryl substituted canthin-6-ones (3a-e)

The intermediate compounds **2a-e** (2.13 mol, 1.0 equiv.) in THF (5 mL) was added into NaH solution (60% dispersion in mineral oil) and stirred at 0℃ for 15 minutes. Then, acetic anhydride (1.54 mol, 1.5 equiv.) was added into the stirred solution and heated at 70℃ for 3 hours. The reaction was monitored by using TLC analysis, and upon completion, the reaction mixture was quenched with water (50 mL), extracted with ethyl acetate (2 x 50 mL) and dried over anhydrous Na_2SO_4. The organic layer was evaporated and purified by silica gel column chromatography eluted with a gradient of n-hexane and EtOAc (8:2) to obtain **3a-e**.

Results and Discussion

(6-hydroxy-9H-pyrido[3,4-b]indol-1-yl)(phenyl)methanone (**2a**). Yield: 53%, yellow solid. IR ν cm^{-1}: 3500, 3423, 1697cm^{-1}. ^{1}H-NMR (400 MHz, METHANOL-D4) ppm: δ 7.86 (dt, J = 8.4, 1.8 Hz, 2H), 7.59-7.54 (m, 3H), 7.29-7.27 (m, 1H), 7.17-7.06 (m, 2H), 6.01 (s, 1H), 3.65-3.53 (m, 2H), 3.23-3.12 (m, 1H). ^{13}CNMR δ (100 MHz, METHANOL-D4): 191.8, 163.0, 141.8, 137.2, 137.1, 135.9, 133.6, 131.0, 130.0, 129.0, 122.0, 120.3, 118.6, 113.6, 113.1, 55.7.

(6-hydroxy-9H-pyrido[3,4-b]indol-1-yl)(4-hydroxyphenyl)methanone (**2b**). Yield: 30%, light brown solid. IR ν cm^{-1}: 3499, 3456, 1678cm^{-1}. ^{1}H-NMR (400 MHz, METHANOL-D4) ppm: δ 12.18 (br s, 1H), 9.68 (br s, 1H), 9.23 (br s, 1H), 8.68 (d, J = 4.6 Hz, 1H), 8.51 (d, J = 7.4 Hz, 1H), 8.43 (d, J = 5.5 Hz, 2H), 8.32 (d, J = 3.6 Hz, 1H), 7.87 (d, J = 6.7 Hz, 1H), 7.52 (dd, J = 8.0 Hz, 3.2 Hz, 1H), 7.12 (d, J = 3.3 Hz, 2H). ^{13}CNMR δ (100 MHz, METHANOL-D4): 170.8, 165.0, 143.9, 138.2, 136.1, 135.2, 133.2, 131.8, 130.0, 129.0, 122.0, 120.8, 118.4, 113.6, 114.5.

(6-hydroxy-9H-pyrido[3,4-b]indol-1-yl)(4-methoxyphenyl)methanone (**2c**). Yield: 42%, brown solid. IR ν cm^{-1}: 3492, 3432, 1642, 1621cm^{-1}. ^{1}H-NMR (400 MHz, METHANOL-D4) ppm: δ 8.34 (d, J = 4.4 Hz, 1H), 8.15 (m, 3H), 7.51 (d, J = 8.4 Hz, 1H), 7.49 (d, J= 8.0 Hz, 1H), 7.10 (d, J = 4.9 Hz, 1H), 7.01 (d, J = 7.4 Hz, 2H), 4.60 (s, 1H), 3.85 (s, 3H). ^{13}CNMR δ (100 MHz, METHANOL-D4): 163.5, 151.5, 136.8, 136.1, 135.9, 133.8, 136.5, 130.0, 121.2, 118.7, 117.9, 112.2, 105.5, 100.3, 54.6.

(6-hydroxy-9H-pyrido[3,4-b]indol-1-yl)(4-bromophenyl)methanone (**2d**). Yield: 57%, brown solid. IR ν cm^{-1}: 3443, 3389cm^{-1}. ^{1}H-NMR (400 MHz, METHANOL-D4) ppm: δ 12.09 (br s, 1H), 9.19 (br s, 1H), 8.51 (d, J = 5.2 Hz, 1H), 8.44 (d, J = 4.4 Hz, 1H), 8.31 (d, J = 7.0 Hz, 1H), 8.15 (d, J = 5.5 Hz, 2H), 7.82 (d, J = 8.0 Hz, 1H), 7.77 (d, J = 5.4 Hz, 2H), 7.60 (t, J = 4.1 Hz). ^{13}CNMR δ (100 MHz, METHANOL-D4): 192.8, 141.9, 137.4, 136.6, 136.0, 133.0, 131.3, 131.2, 129.2, 126.5, 122.0, 120.4, 120.2, 119.3, 113.2.

(6-hydroxy-9H-pyrido[3,4-b]indol-1-yl)(4-nitrophenyl)methanone (**2e**). Yield: 60%, brown solid. IR ν cm^{-1}: 3443, 3389cm^{-1}. ^{1}H-NMR (400 MHz, METHANOL-D4) ppm: δ 12.09 (br s, 1H), 9.19 (br s, 1H), 8.51 (d, J = 5.2 Hz, 1H), 8.44 (d, J = 4.4 Hz, 1H), 8.31 (d, J = 7.0 Hz, 1H), 8.15 (d, J = 5.5 Hz, 2H), 7.82 (d, J = 8.0 Hz, 1H), 7.77 (d, J = 5.4 Hz, 2H), 7.60 (t, J = 4.1 Hz). ^{13}CNMR δ (100 MHz, METHANOL-D4): 192.8, 141.9, 137.4, 136.6, 136.0, 133.0, 131.3, 131.2, 129.2, 126.5, 122.0, 120.4, 120.2, 119.3, 113.2.

10-hydroxy-4-phenyl-6H-indolo[3,2,1-de][1,5]naphthyridin-6-one (**3a**). Yield: 30%, light yellow solid. IR ν cm^{-1}: 3364.7, 3046.1, 1671.2, 1646.3, 1629.9, 686.6, 709.5 cm^{-1}. ^{1}H-NMR (400 MHz, METHANOL-D4) ppm: δ 8.60 (1H, d, J = 5.0 Hz, HCN), 8.31 (2H, dd, J = 8.5, 1.6 Hz, CH), 8.11 (1H, d, J = 5.5 Hz, CH), 7.91 (1H, d, J = 2.3 Hz, CH), 7.61-7.50 (5H, m, CH), 7.34-7.32 (1H, m, CH). ^{13}CNMR δ (100 MHz, METHANOL-D4): 118.8, 145.3, 132.5, 123.4, 114.5, 112.6, 128.1, 131.3, 138.1, 210.0.

10-hydroxy-4-(4-hydroxyphenyl)-6H-indolo[3,2,1-de][1,5]naphthyridin-6-one (**3b**). Yield: 16%, light brown solid. IR ν cm^{-1}: 3364.7, 3046.1, 1671.2, 1646.3, 1629.9, 686.6, 709.5 cm^{-1}. ^{1}H-NMR (400 MHz, METHANOL-D4) ppm: δ 8.60 (1H, d, J = 5.0 Hz, HCN), 8.31 (2H, dd, J = 8.5, 1.6 Hz, CH), 8.11 (1H, d, J = 5.5 Hz, CH), 7.91 (1H, d, J = 2.3 Hz, CH), 7.61-7.50 (5H, m, CH), 7.34-7.32 (1H, m, CH). ^{13}CNMR δ (100 MHz, METHANOL-D4): 118.8, 145.3, 132.5, 123.4, 114.5, 112.6, 128.1, 131.3, 138.1, 210.0.

10-hydroxy-4-(4-methoxyphenyl)-6H-indolo[3,2,1-de][1,5]naphthyridin-6-one (**3c**). Yield: 23%, brown solid. IR ν cm^{-1}: 3364.7, 3046.1, 1671.2, 1646.3, 1629.9, 686.6, 709.5 cm^{-1}. ^{1}H-NMR (400 MHz, METHANOL-D4) ppm: δ 8.60 (1H, d, J = 5.0 Hz, HCN), 8.31 (2H, dd, J = 8.5, 1.6 Hz, CH), 8.11 (1H, d, J = 5.5 Hz, CH), 7.91 (1H, d, J = 2.3 Hz, CH), 7.61-7.50 (5H, m, CH), 7.34-7.32 (1H, m, CH). ^{13}CNMR δ (100 MHz, METHANOL-D4): 118.8, 145.3, 132.5, 123.4, 114.5, 112.6, 128.1, 131.3, 138.1, 210.0.

10-hydroxy-4-(4-bromophenyl)-6H-indolo[3,2,1-de][1,5]naphthyridin-6-one (**3d**). Yield: 34%, brown solid. IR ν cm^{-1}: 3443, 3389cm^{-1}. ^{1}H-NMR (400 MHz, METHANOL-D4) ppm: δ 12.09 (br s, 1H), 9.19 (br s, 1H), 8.51 (d, J = 5.2 Hz, 1H), 8.44 (d, J = 4.4 Hz, 1H), 8.31 (d, J = 7.0 Hz, 1H), 8.15 (d, J = 5.5 Hz, 2H), 7.82 (d, J = 8.0 Hz, 1H), 7.77 (d, J = 5.4 Hz, 2H), 7.60 (t, J = 4.1 Hz). ^{13}CNMR δ (100 MHz, METHANOL-D4): 192.8, 141.9, 137.4, 136.6, 136.0, 133.0, 131.3, 131.2, 129.2, 126.5, 122.0, 120.4, 120.2, 119.3, 113.2.

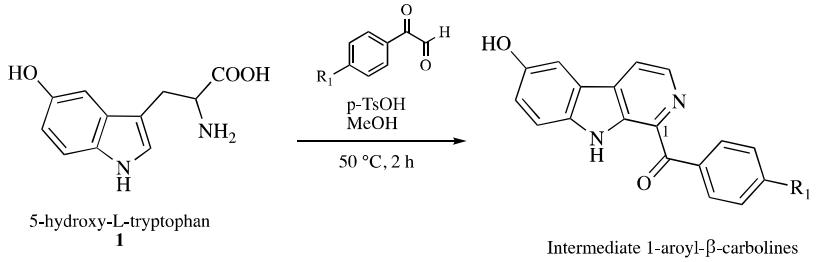
10-hydroxy-4-(4-nitrophenyl)-6H-indolo[3,2,1-de][1,5]naphthyridin-6-one (**3e**). Yield: 41%, brown solid. IR ν cm^{-1}: 3364.7, 3046.1, 1671.2, 1646.3, 1629.9, 686.6, 709.5 cm^{-1}. ^{1}H-NMR (400 MHz, METHANOL-D4) ppm: δ 8.60 (1H, d, J = 5.0 Hz, HCN), 8.31 (2H, dd, J = 8.5, 1.6 Hz, CH), 8.11 (1H, d, J = 5.5 Hz, CH), 7.91 (1H, d, J = 2.3 Hz, CH), 7.61-7.50 (5H, m, CH), 7.34-7.32 (1H, m, CH). ^{13}CNMR δ (100 MHz, METHANOL-D4): 118.8, 145.3, 132.5, 123.4, 114.5, 112.6, 128.1, 131.3, 138.1, 210.0.

The Pictet-Spengler reaction is indeed a valuable chemical transformation for the synthesis of β-carboline ring systems, and it is particularly useful when the starting materials are tryptophan or tryptophan

derivatives. This reaction involves the process of acid-catalyzed condensation of β-carboline with an aldehyde, a ketone or a glyoxal, resulting in the formation of a C-C bond and a series of analogues with a β-carboline ring system. This method has been widely used by chemists in producing new canthine derivatives. Subsequently, it continues with endo cyclization reaction between a carbon nucleophile of a sufficiently reactive aromatic moiety and an activated iminium ion resulting in formation of N-heterocyclic ring through a new C-C bond that directly forms tetrahydro-β-carboline. The tetrahydro-β-carboline (THβC) continues to undergo aromatization to form fully aromatic β-carboline [11,12]. It is important to note that the approach continues to be a prominent topic of research as chemists continue to improve the methodology by applying new reaction conditions. Several groups have been investigating the detailed mechanistic features of this reaction over the years [13].

Meanwhile, in our study, by performing the versatile route of Pictet-Spengler reaction where p-TsOH.H_2O was used as catalyst and methanol was used a medium, this simple method produces a fully aromatic β-carboline instead of the tetrahydro β-carboline. Two reactions were performed to convert intermediate 1-aroyl β-carbolines into 4-aryl substituted canthin-6-ones. In this study, a useful approach for the preparation of 1-aroyl β-carboline derivatives via acid-mediated coupling of 5-hydroxy-L-tryptophan and substituted phenylglyoxal's was described. As a result, the conversion of 5-hydroxy-L-tryptophan and phenylglyoxals directly to 1-substituted β-carboline in the presence of acid via a single step Pictet-Spengler reaction. This strategy refines the scope of Pictet-Spengler cyclization as the THβC intermediate directly oxidized to the targeted β-carboline in one-pot oxidation reaction, which also allows for product diversification at C-1 position.

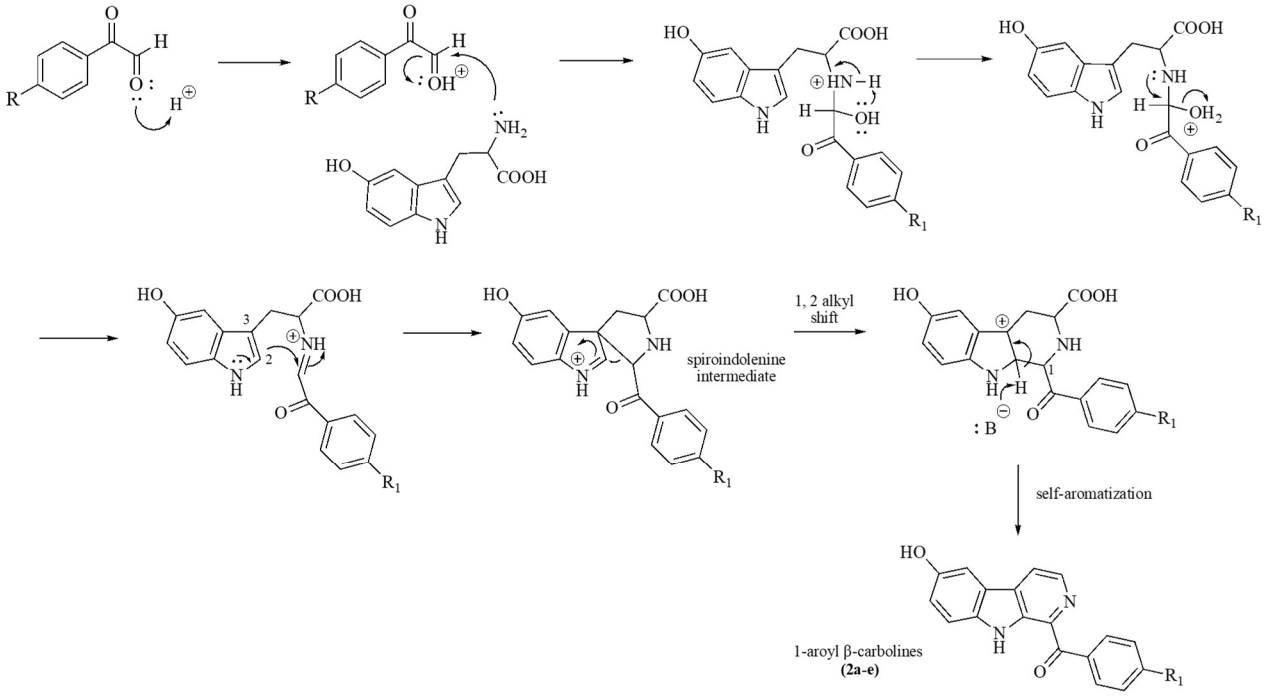
Scheme 1. The synthesis of 5-hydroxy-L-tryptophan with different substituted phenylglyoxals



Entry	R_1	Yield (%)
2a	H	53
2b	OH	30
2c	OCH_3	42
2d	Br	57
2e	NO_2	65

This approach is concise and most preferred due to its simplicity since no heat is involved to drive the reaction. Based on the results obtained, a general conclusion on the electronic effects of electron-withdrawing group (EWG) and electron-donating (EDG) could be deduced. The inductive and resonance effects cause the yields to vary correspondingly. Having EDG as substituent reduced the electrophilicity of the carbonyl carbon, resulting in a weaker reactivity with the nucleophile and hence, gave lower yield products (**2b** and **2c**) than that of using standard phenylglyoxal (**2a**). On the contrary, phenylglyoxal bearing electron-withdrawing group (**2d** and **2e**) gave higher product as anticipated. Despite being to an inductive electron-withdrawing group, halogens are activators since their ability to donate electrons to the aromatic ring via resonance is much greater.

The reaction mechanism occurs by the initial formation of iminium ion followed by electrophilic addition at the C-2 position to directly yield the six-membered ring intermediate. However, both carbon-2 and -3 of 5-hydroxy-L-tryptophan are nucleophilic. Therefore, the reaction can also proceed by the attack of carbon-3 to yield a spiroindolenine intermediate that would then undergo a 1,2-alkyl shift to form the product as depicted in Scheme 2. Both mechanisms have been proven to be true, yet the prevailing mechanism is still unknown [14].

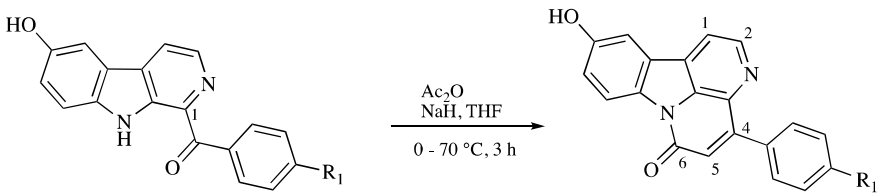


Scheme 2. Mechanism of Pictet-Spengler reaction with electrophilic addition using phenylglyoxal at carbon-3

Having the series of intermediates 1-aroyl β-carbolines (**2a-e**), the synthesis of 4-aryl substituted canthin-6-ones was performed through the cyclization in dry reaction condition for 3 hours as shown in Scheme 3. The use of sodium offers the advantage of the reaction being carried out in a nonhydrolytic solvent. It was thought that the use of sodium hydride would offer similar advantage and simultaneously would be safer and easier to handle than using the metal. The intermediate compounds (**2a-e**) were reacted with acetic anhydride in the base by using THF as the medium to get the desired target compounds in lower yields.

The synthesis of compounds (**3a-e**) was achieved by intramolecular nucleophilic substitution. The reaction mechanism begins by addition reaction whereby the nucleophilic amine of the intermediate compound attacked the acetic anhydride to form new C-C bond. Accordingly, a series of proton transfers, electron movement and intramolecular cyclization led to the formation of an Aldol intermediate via enolate ion formation. A more stable enone form of the anticipated product was eventually obtained by elimination of water.

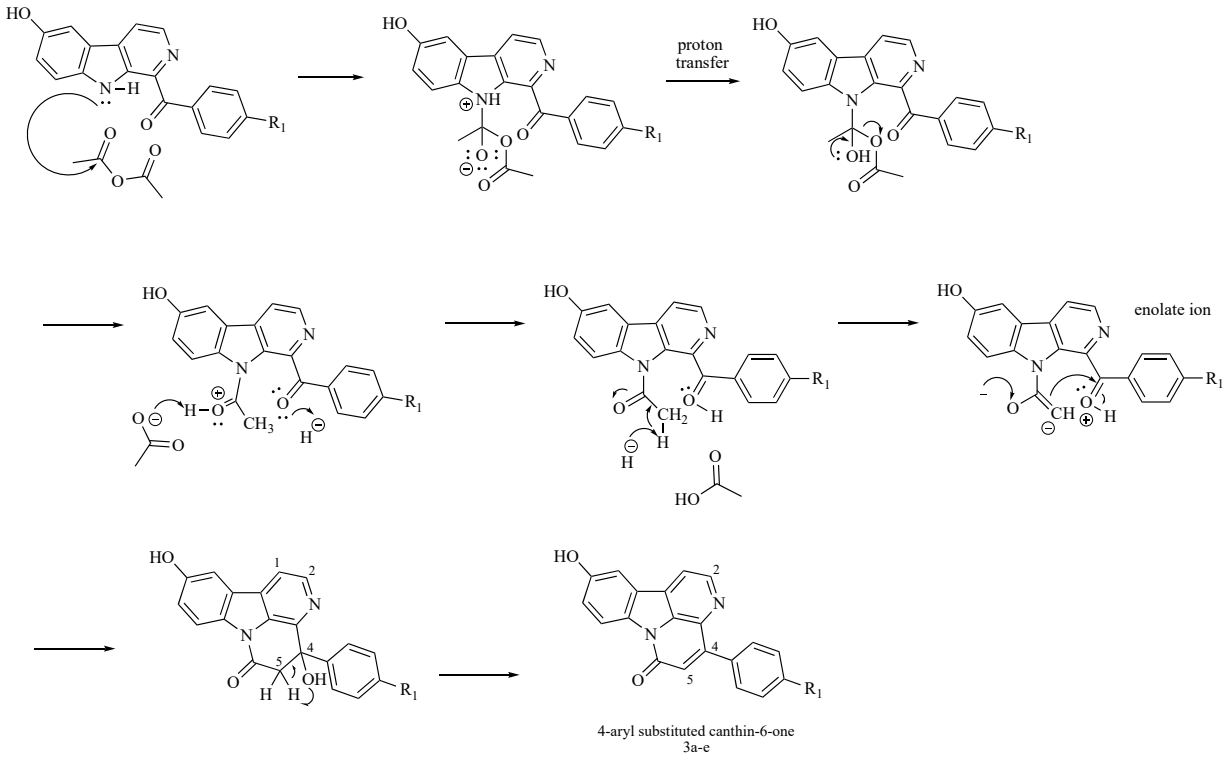
Scheme 3. Cyclization of tetrahydro-β-carboline intermediates



Intermediate 1-aroyl-β-carbolines
2a-e

4-aryl substituted canthin-6-one
3a-e

Entry	R_1	Yield (%)
3a	H	30
3b	OH	15
3c	OCH_3	23
3d	Br	34
3e	NO_2	41



Scheme 4. Mechanism of Pictet-Spengler reaction with electrophilic addition using phenylglyoxal at carbon-3

Dighe et al. [6], had successfully discovered an effective iodine-mediated oxidative Pictet-Spengler reaction in DMSO using terminal alkynes as a substitute the glyoxal to produce an intermediate of 1-aroyl-β-carboline, then it underwent cyclization to yield 4-aryl substituted canthin-6-ones. Shashikant et al. [15] their

investigations by reacting 1 with phenylacetylene in the presence of 50 mol of iodine in DMSO as the medium at 100℃ for 6 hours to yield **2a-e**. They continued their study and discovered that reacting of substituted 1-aroyl β-carbolines **2a-e** with Ac_2O in the presence of NaH as the base in THF at 70℃ for 12 hours produced the desired products in a good yield of **3a-e** in 83%. However, by employing the same procedure, we only managed to get the 4-aryl substituted canthin-6-ones in much lower yields (15-41%). This is due to the substituents on C-1 which influences the reactivity of the nucleophilic substitution in both reactions. The reaction time also affects the product yields.

Conclusion

In conclusion, we have successfully synthesized a series of 4-aryl substituted canthine-6-one derivatives through a versatile Pictet-Spengler condensation from 5-hydroxy tryptophan and subsequent cyclization using NaH, involving the formation of 1-aroyl β-carbolines as pivotal intermediates in moderate yields. This alternative is an improved Pictet-Spengler reaction in producing 1-substituted β-carboline in which tetrahydro-β-carboline. Further application of the scope and mechanism of reaction in the study towards total synthesis of novel canthine-6-one and other additional biologically active natural products are currently in progress.

Acknowledgement

The authors acknowledge the generous support of Organic Synthesis Research Laboratory, Institute of Science (IOS), Universiti Teknologi MARA, Puncak Alam Campus and Faculty of Applied Sciences, Universiti Teknologi MARA (UiTM), Shah Alam. This work was financially supported under the Fundamental Research Grant Scheme (FRGS/1/2022/STG04/UITM/02/7) funded by the Ministry of Education, Malaysia.

References

1. Banoth, K. K., Faheem, ChandraSekhar, K. V. G., Adinarayana, N. and Murugesan, S. (2020). Recent evolution on synthesis strategies and anti-leishmanial activity of β-carboline derivatives – An update. *Heliyon,* 6(9): e04916.
2. Ash'ari, N. A. N., Pungot, N. H., Shaameri, Z. and Jani, N. A. (2021). A facile synthesis of n-alkylated daibucarboline A derivative via pictet-spengler condensation of tryptamine. *Malaysian Journal of Analytical Sciences*, 25(5): 706-715.
3. Kukula-Koch, W. A., and Widelski, J. (2017). Alkaloids. *Pharmacognosy: Fundamentals, Applications and Strategy.* Academic Press: pp. 163-198.
4. Riggs, R. L., and Smith, D. M. (2008). Three heterocyclic rings fused (5-6-6). *Comprehensive Heterocyclic Chemistry III*. Elsevier: pp. 857-973.
5. Manasa, L. K., Yadav, S. S., Nagesh, N. and Alvalaa, M. (2020). Recent insights into β-carboline alkaloids with anticancer potential. *Modern Approaches in Drug Designing,* 3(1): 1-24.
6. Dighe, S. U., Samanta, S. K., Kolle, S. and Batra, S. (2017). Iodine-mediated oxidative Pictet-Spengler reaction using terminal alkyne as the 2-oxoaldehyde surrogate for the synthesis of 1-aroyl-β-carbolines and fused-nitrogen heterocycles. *Tetrahedron*, 73(17): 2455-2467.
7. Kuo, P. C., Li, Y. C., Hwang, T. L., Ma, G. H., Yang, M. L., Lee, E. J., and Wu, T. S. (2014). Synthesis and structural characterization of an anti-inflammatory principle purified from *Lindera aggregata*. *Tetrahedron Letters,* 55(1): 108-110.
8. Calcaterra, A., Mangiardi, L., Delle Monache, G., Quaglio, D., Balducci, S., Berardozzi, S., ... and Ghirga, F. (2020). The Pictet-Spengler reaction updates its habits. *Molecules,* 25(2): 414.
9. Samala, A. (2016). Therapeutic journey of synthetic β-carboline derivatives: A short review. *International Journal of Pharmacy and Analytical Research*, 5(1): 161-168.
10. Shamsujunaidi. R., Saaidin. A. S., Abdul Aziz. M. H., Mohammat. M. F. and Pungot, N. H. (2023). Studies on the synthesis of β-carboline and its derivatives as potential antimalarial drug components. *Malaysian Journal of Analytical Sciences*, 27(1): 44-53.
11. Yang, M. L., Kuo, P. C., Damu, A. G., Chang, R. J., Chiou, W. F. and Wu, T. S. (2006). A versatile route to the synthesis of 1-substituted β-carbolines by a single step Pictet-Spengler cyclization. *Tetrahedron*, 62(47): 10900-10906.

12. Duggineni, S., Sawant, D., Saha, B. and Kundu, B. (2006). Application of modified Pictet–Spengler reaction for the synthesis of thiazolo-and pyrazolo-quinolines. *Tetrahedron,* 62(14): 3228-3241.
13. Durham, S. D., Sierra, B., Gomez, M. J., Tran, J. K., Anderson, M. O., Whittington-Davis, N. A. and Eagon, S. (2017). Synthesis of β-carbolines via a silver-mediated oxidation of tetrahydro-β-carbolines. *Tetrahedron Letters,* 58(28): 2747-2750.
14. Maresh, J. J., Giddings, L. A., Friedrich, A., Loris, E. A., Panjikar, S., Trout, B. L., ... and O'Connor, S. E. (2008). Strictosidine synthase: Mechanism of a Pictet-Spengler catalyzing enzyme. *Journal of the American Chemical Society,* 130(2): 710-723.
15. Dighe, S. U., Samanta, S. K., Kolle, S. and Batra, S. (2017). Iodine-mediated oxidative Pictet-Spengler reaction using terminal alkyne as the 2-oxoaldehyde surrogate for the synthesis of 1-aroyl-β-carbolines and fused-nitrogen heterocycles. *Tetrahedron,* 73(17): 2455-2467.

Malaysian Journal of Analytical Sciences (MJAS)
Published by Malaysian Analytical Sciences Society

TRANSESTERIFICATION OF LOW-GRADE PALM COOKING OIL TO PRODUCE BIODIESEL USING SPENT BLEACHING CLAY CATALYSTS

(Transesterifikasi Minyak Masak Kelapa Sawit Gred Rendah Kepada Biodiesel Menggunakan Pemangkin Tanah Pemutih Terpakai)

Thivya Keasavan[1], Nurhannani Mohd Radzi[1], Wan Nazwanie Wan Abdullah[1*], Salmiah Jamal Mat Rosid[2], Nurasmat Mohd Shukri[3], and Noorfatimah Yahaya[4]

[1]*School of Chemical Science, Universiti Sains Malaysia, 11800 Penang, Malaysia.*
[2]*Unisza Science and Medicine Foundation Centre, Universiti Sultan Zainal Abidin, Kampus Gong Badak, 21300, Kuala Nerus, Terengganu, Malaysia.*
[3]*School of Health Sciences, Universiti Sains Malaysia, 16150 Kubang Kerian, Kelantan.*
[4]*Department of Toxicology, Advanced Medical and Dental Institute (AMDI), Universiti Sains Malaysia, 13200, Bertam Kepala Batas, Penang, Malaysia.*

[*]*Corresponding author: wanazwanie@usm.my*

Received: 15 June 2023; Accepted: 15 October 2023; Published: 29 December 2023

Abstract

In this study, spent bleaching clay doped with potassium hydroxide and sodium hydroxide (SBC/KOH and SBC/NaOH) were used as catalysts in the transesterification process of low-grade cooking oil to produce biodiesel. The physicochemical properties of the catalyst were studied using Fourier Transform Infrared Spectroscopy (FTIR), Thermogravimetric Analysis (TGA), X-ray Diffraction (XRD), Brunauer-Emmett-Teller (BET), and Field Emission Scanning Electron microscopy with Energy Dispersive X-ray Spectroscopy (FESEM-EDX). Several parameters including the types of catalyst, calcination temperature of the catalyst, catalyst dosage, ratio of oil to methanol, reaction time, and reaction temperature were used to determine the optimal conditions for the transesterification reaction. According to the experimental findings, the catalyst effectively converted free fatty acids (FFA) into fatty acid methyl esters (FAMEs). The maximum biodiesel yield of 47.66 % was obtained at optimum reaction conditions: catalyst amount 2 wt.% of SBE/KOH calcined at 500 °C (SBC/KOH 500), reaction time 2 h, reaction temperature 55 °C and oil to methanol molar ratio 1:20.

Keywords: clay, cooking oil, biodiesel, transesterification, catalyst

Abstrak

Dalam kajian ini, tanah liat peluntur bekas yang didop dengan kalium hidroksida dan natrium hidroksida (SBC/KOH dan SBC/NaOH) digunakan sebagai mangkin dalam proses transesterifikasi minyak masak gred rendah untuk menghasilkan biodiesel. Sifat fizikokimia mangkin dikaji menggunakan spektroskopi inframerah transformasi Fourier (FTIR), analisis termogravimetrik (TGA), pembelauan sinar-X (XRD), Brunauer-Emmett-Teller (BET), dan mikroskop elektron pengimbasan pancaran medan dengan serakan tenaga sinar-X (FESEM-EDX). Beberapa parameter termasuk jenis mangkin, suhu pengkalsinan mangkin, dos mangkin, nisbah minyak kepada metanol, masa tindak balas, dan suhu tindak balas telah digunakan untuk menentukan keadaan

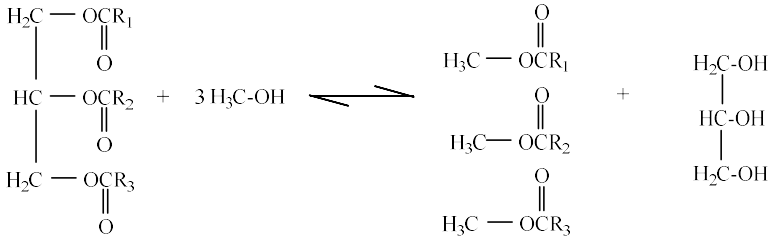
optimum bagi tindak balas transesterifikasi. Menurut penemuan eksperimen, mangkin secara berkesan menukar asid lemak bebas (FFA) kepada asid lemak metil ester (FAMEs). Hasil biodiesel maksimum sebanyak 47.66 % diperoleh pada keadaan tindak balas optimum: jumlah mangkin 2 wt.% SBE/KOH dikalsinkan pada 500 °C (SBC/KOH 500), masa tindak balas 2 jam, suhu tindak balas 55 °C dan minyak kepada metanol nisbah molar 1:20.

Kata kunci: tanah liat, minyak masak, biodiesel, transesterifikasi, mangkin

Introduction

The search for alternative fuels has gotten a lot of attention recently due to environmental concerns about the increasing uncertainty of global energy supply and production, the high price of petroleum products, and the usage of fossil fuels. Biodiesel has recently acquired appeal in both developed and developing countries' marketplaces. Biodiesel is made from vegetable oil or animal fat, which is derived from monoalkyl esters from long-chain fatty acids [1]. Biodiesel is becoming more popular as an alternative fuel due to its appealing chemical properties, such as biodegradability, non-toxicity, and carbon neutrality [2]. Biodiesel has a lot of the same qualities as petrodiesel, but it's free of harmful components like sulfur and aromatics. Diesel and biodiesel are both fuels used in internal combustion engines, but they have significant differences in terms of their origin, composition, production, and environmental impact .Biodiesel produces less NOx gases and emissions less than petrodiesel. Furthermore, biodiesel helps to reduce pollution and may reduce the effects of global warming. In comparison to petrodiesel, it is less toxic and easy to store [3]. However, there are a few disadvantages to using petrodiesel. Petrodiesel may contain a tremendous degree of pollutants and greenhouse gas (GHG) emissions, which could negatively affect individual well-being and the environment. Studies have shown that petrodiesel may emit dangerous contaminants. such as nitrogen oxide (NO), carbon monoxide (CO), sulfur dioxide (SO_2), particulate matter, and hydrocarbons [4].

Vegetable oils and animal fats must require severe transesterification to reduce oil viscosity and prevent serious damage to biodiesel. Transesterification of animal fats and vegetable oils with presence of alcohol and a catalyst produces biodiesel, a popular alternative fuel. Methanolysis, also known as transesterification, is a catalyzed reaction that produces biodiesel and glycerol. The reaction causes short-chain alcohol to replace the glycerol in the triglycerides. The process begins with three reversible processes that convert triglycerides to diglycerides, to monoglycerides, and to glycerol. From a single triglyceride molecule, each step produces an ester, giving three ester molecules [5]. The reaction is shown in scheme 1.



Triglyceride Methanol Methyl ester Glycerol

Scheme 1. Methanolysis reaction of triglyceride

In this study, heterogeneous base catalyst, potassium hydroxide (KOH), and sodium hydroxide (NaOH) were studied because it produces high biodiesel yield, high glycerol purity, low cost, and are environmentally friendly [6]. Furthermore, the heterogeneous catalyst has a larger surface area than the homogeneous catalyst. Low-grade cooking oil was selected as a feedstock due to its low viscosity and easy to obtain and spent bleaching clay (SBC) was used as a supporting catalyst.

SBC is a type of industrial waste produced by bleaching of crude palm oil in the vegetable oil refining sector [7].

SBC undergoes refining process in the palm oil industry before it is used for other purposes. SBC output is estimated to be between 1.6 and 2.0 million tonnes per year, based on oil production of 128.2 million metric tonnes in 2007 [8]. Moreover, SBC includes 20–40 % colored pigments, fat, and oil by weight, and it contains MgO, which could be used as a catalyst to speed up the production of biodiesel. Therefore, this study aims to produce biodiesel from low grade cooking oil with a highly efficient SBC nanocatalyst. Various analytical technologies were used to characterize catalysts and analyse products.

Materials and Methods

Chemicals and materials

SBC was collected from PGEO Edible Oils, Perai, Penang and low-grade cooking oil was purchased from the nearest shop. All the analytical grade chemicals (KOH, NaOH, methanol, n-hexane) were purchased from Merck.

Catalyst preparation

SBC was dried at 65 ℃ overnight in an oven before it was used for further experiments. SBC doped KOH and NaOH (SBC/KOH and SBC/NaOH) were synthesized via wet impregnation method. About 8g of calcined SBC, 8g KOH, and 120 mL deionized water were mixed and placed in a 250 mL beaker, heated at 70 ℃ for 3 hours with constant stirring. The obtained mixture was filter using filter paper and dried at 65 ℃ in an oven overnight. Next, it was ground and heated to 600 ℃ for 2 hours at a rate of 5 ℃/min in a furnace with a flow of nitrogen [9]. The same procedure was repeated with SBC/NaOH catalyst using 8g of NaOH instead of 8g of KOH during the impregnation process.

Transesterification process and identification of biodiesel products

About 0.2g of catalyst and 1:20 molar ratio of oil to methanol was added to 10g of oil. The catalyst was activated by dispersing methanol at 50 ℃ for 20 min at constant stirring. The reflux process was conducted at 55 ℃ with continuous stirring for 2 hours [10]. Once the transesterification process was completed, the product was cooled down and filtered with filter paper to separate the catalyst. The filtered liquids were placed in the separatory funnel and left overnight. After overnight, the liquids would be separated and formed into 2 layers. The lower layer was removed, and the upper layer was taken to separate the biodiesel from excess methanol and by-product. The extraction of biodiesel was conducted using Heidolph Hei-VAP rotavapor at 40 ℃ with 80 rpm. The biodiesel liquid was obtained, and by using Equation 1 below, the weight percent of FAME was calculated.

$$\text{Weight percent of FAME} = \frac{\text{Weight of transesterified liquid}}{\text{Weight of low-grade cooking oil used}} \times 100\ \% \quad (1)$$

Optimization parameters

This study was investigated with different parameters such as the effect on the type of catalyst (SBC/KOH and SBC/NaOH), calcination temperature (500 and 600 °C), catalyst dosage (1-4 wt.%), ratio of oil-to-methanol (1:12-1:20) and reaction time (1-3 hours) to predict the optimized condition for transesterification reaction. The range of each parameter was determined from previous studies [11, 12].

Characterization methods

The catalysts were characterized using several characterization methods such as Fourier-transform infrared spectrometer (FTIR), thermogravimetric analysis (TGA), X-ray diffraction (XRD), field-emission scanning electron microscopy with energy dispersive X-ray (FESEM-EDX) and Brunauer-Emmett-Teller (BET) to study the physical and chemical properties of the catalyst. The cooking oil and biodiesel were tested using Fourier-transform infrared spectrometer (FTIR) and gas chromatography with flame ion detector (GC-FID).

Results and Discussion

Characterization of catalysts

The functional groups on the surface of the catalysts were identified using FTIR spectrometer. Figure 1 shows the FTIR spectrum of pure SBC and SBC/KOH 500 catalysts. According to Cong et al. for pure SBC catalyst, there is a peak at 464 cm^{-1}

which indicates the bending vibration of Si-O-Si, while the peak at 1656 cm^{-1} refers to the stretching vibration of S=O [13]. The S=O bond was observed in SBC due to phyllosilicates group components presence in bleaching material of SBC [14]. Furthermore, the band at 3485 cm^{-1} for the SBC/KOH 500 corresponds to Si-O-H stretching vibration due to a water molecule absorbed on its surface [13]. In SBC/KOH 500 catalyst, S=O vibration can also be seen at around 1410 cm^{-1}.

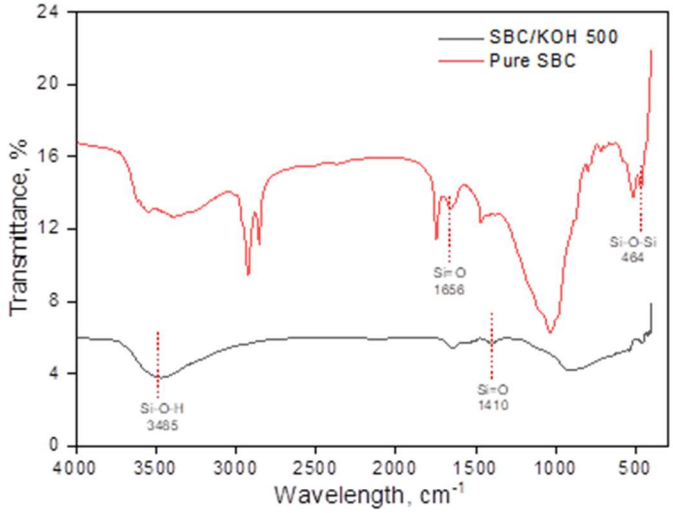


Figure 1. FTIR spectrum of pure SBC and SBC/KOH 500 catalysts

The TGA curve was obtained using thermogravimetric (TG) and derivative thermogravimetric (DTG) analysis. The weight loss curve for SBC was produced and examined using the TGA technique. The weight of SBC drops rapidly from 220 °C to 380 °C, which is due to volatile matter evaporation [13]. The second-phase weight loss indicates that the adsorbed oil on the bleaching clay contributes about 40% of the total weight. Figure 2 shows the DTG pattern in the black line suggests that peak weight loss is observed at 350 °C under an O_2 atmosphere.

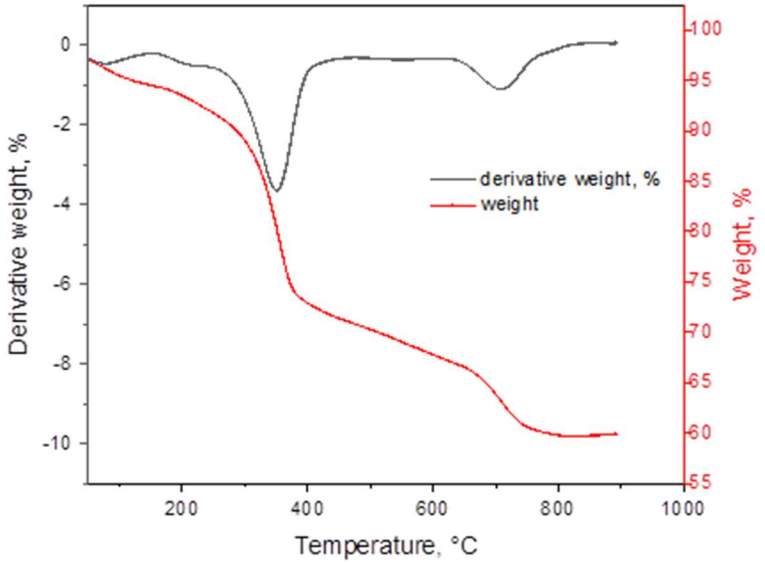


Figure 2. TGA profile of SBC as catalyst

The surface morphology and elemental compositions of the SBC/KOH 500 catalyst were identified using FESEM and EDX spectroscope. Figure 3 shows the micrograms of the SBC/KOH 500 catalyst in two different magnifications. Based on Figure 3, SBC/KOH 500 catalyst was found to have non-uniform irregular agglomerated flaky-like structures. This can be due to the calcination process, which affects the surface texture and increases the surface area for catalytic activity [11].

Next, EDX analysis was used to predict the elemental composition of the SBC/KOH 500 catalyst. The analysis result is shown in Table 1. The result proved that all elements such as K, Fe, Ca, Mg, Na, Al, and Si exist in the clay. Based on the BET analysis, SBC/KOH 500 catalyst has a higher surface area due to the higher composition of K in the catalyst (15.7 wt.%). The catalytic site for reaction increases with surface area, enhancing the productivity of the catalyst.

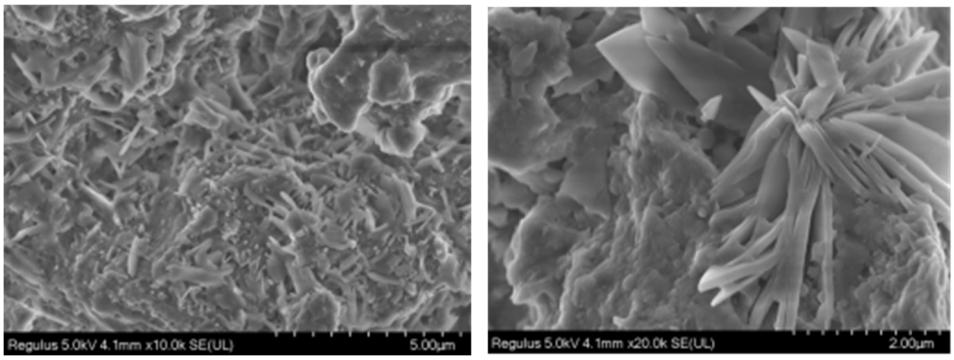


Figure 3. FESEM micrograms of SBC/KOH 500 catalyst: (i: small magnification (10k); ii: big magnification (20k))

Table 1. Elemental compositions of SBC/KOH 500 catalyst by EDX analysis

Elements	**O**	**Si**	**Al**	**Mg**	**Na**	**Fe**	**Ca**	**K**
Loading, wt.%	42.7	7.4	2.9	1.6	0.1	0.58	4.8	15.7

The XRD analysis of the SBC/KOH 500 catalyst is shown in Figure 4. The XRD pattern of SBC/KOH 500 represented the crystalline phases of quartz (SiO_2) and potassium peroxide (K_2O) [15]. The characteristic diffraction peaks for quartz (SiO_2) were found at 2θ= 20.87and 39.48° while the diffraction peaks for K_2O were observed at 2θ = 26.65, 29.46, and 36.07°. This result shows that the main component of the SBC/KOH 500 catalyst was K_2O with a small contribution from SiO_2.

The surface area, pore volume, and pore width of the catalysts were determined using BET analysis. The BET results for SBC, SBC/KOH, and SBC/NaOH catalysts were tabulated in Table 2. The surface area, pore volume, and pore width obtained for SBC/KOH catalyst were 22.62 m^2/g, 0.10 cm^3/g, and 21.05 nm, respectively. The surface area of SBC/NaOH is smaller than SBC/KOH. The higher surface area of the SBC/KOH catalyst is caused by the presence of more active sites [16]. The pore size distribution of both catalysts is represented in Figure 5.

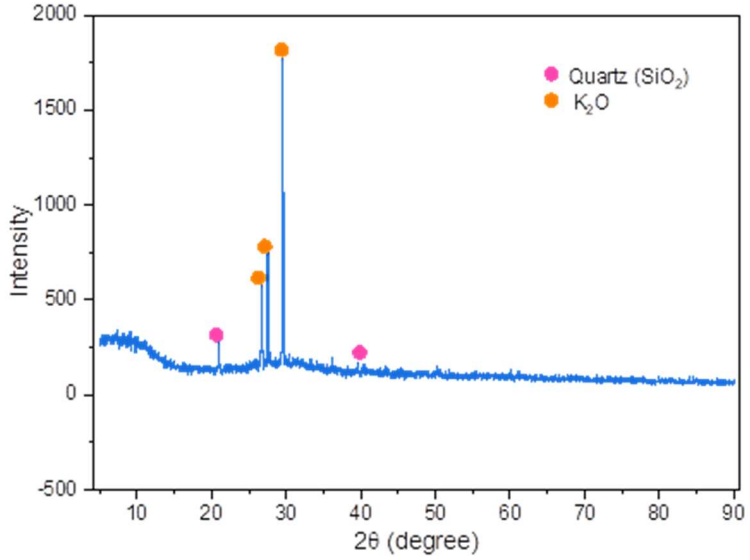


Figure 4. XRD diffractograms of SBC/KOH 500 catalyst

Table 2. Surface areas, pore volume, and pore width of the catalysts

Catalysts	BET Surface Area (m^2/g)	Pore Volume (cm^3/g)	Pore Width (nm)
SBC	3.77	0.02	21.60
SBC/KOH	22.62	0.10	21.05
SBC/NaOH	8.88	0.05	26.27

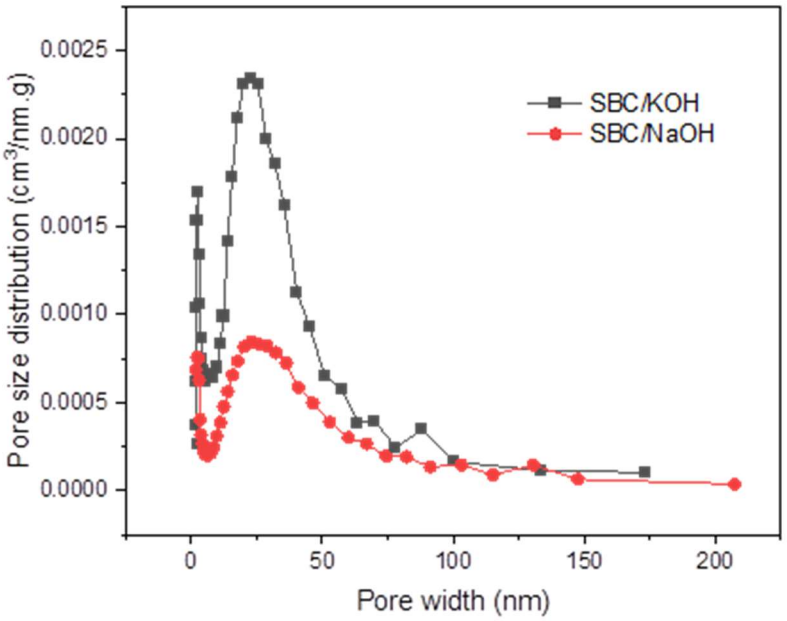


Figure 5. Pore size distribution plot of SBC/KOH and SBC/NaOH catalysts

Characterization of oil and biodiesel

Figure 6 shows the FTIR spectra of low-grade cooking oil and biodiesel produced from the SBC/KOH 500 catalyst. The stretching vibration at 1748 cm^{-1} in the FTIR spectrum indicates the presence of the C=O bond [17]. This group indicates that carbonyl functional groups are present in the oil and biodiesel. The characteristic peaks found in the region 2912 cm^{-1} and 2849 cm^{-1} indicate stretching vibrations of CH_3 and CH_2 while bending vibrations of CH_3 and CH_2 groups were found at the peak 1375 cm^{-1} and 1164 cm^{-1} respectively. The FTIR spectrum of synthesized biodiesel was found to be very similar to low-grade cooking oil due to the chemical nature similarities of the methyl esters and triglycerides. Therefore, further analysis by gas chromatography is required to support the results.

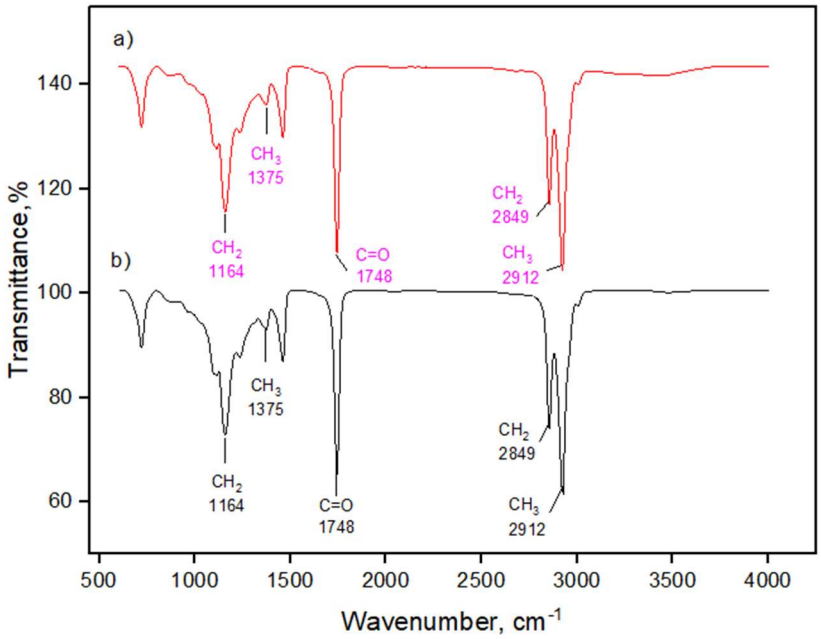


Figure 6. FT-IR spectra of low-grade cooking oil and biodiesel produced from SBC/KOH 500 catalyst

Figure 7 shows the fatty acid methyl ester (FAME) compound present in the biodiesel for SBC/KOH 500 catalyst. As described by Enguilo Gonzaga et al. low-grade cooking oil contains major fatty acids such as palmitic acid (16:0), stearic acid (18:0), oleic acid (18:1), linoleic acid (18:2), and linolenic acid (18:3) [18]. From Figure 7, the identified compounds in biodiesel were methyl myristate, methyl palmitate, methyl heptadecanoate, methyl stearate, methyl oleate and methyl linoleate. The details of the composition are tabulated in Table 3. This data was consistent with the research reported by Roschat et al. regarding the biodiesel production of Krabok seed oil through transesterification reaction using CaO as a catalyst [19]. In comparison, the biodiesel from Krabok seed oil demonstrated the major fatty acid methyl ester, namely methyl decanoate, methyl myristate, methyl palmitate, methyl heptadecanoate, methyl oleate, methyl palmitoleate, methyl stearate and methyl linoleate. The derived biodiesel using SBC/KOH 500 catalyst showed presence of similar fatty acids methyl ester. Therefore, this result shows good agreement with previous research.

Table 3. Fatty acid methyl ester (FAME) compounds present in the sample using gas chromatography with flame ion detector (GC-FID)

Sample	Tr, Retention Time (min)	ID (Peak)	FAME Compound
Biodiesel	4.376	C14:0 (8)	Methyl myristate
	5.726	C16:0 (12)	Methyl palmitate
	6.234	C17:1 (15)	Methyl heptadecanoate
	6.680	C18:0 (16)	Methyl stearate
	6.858	C18:1 (18)	Methyl oleate
	7.852	C18:3 (21)	Methyl linoleate

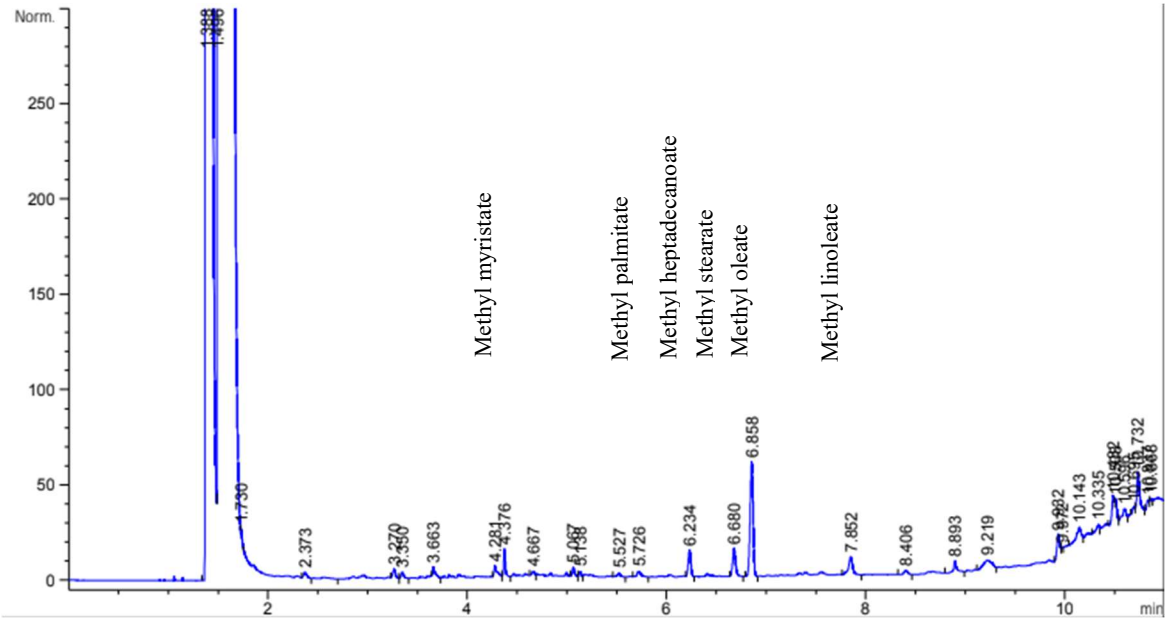


Figure 7. Characterization of biodiesel using gas chromatography using flame ion detector (GC-FID) for SBC/KOH 500 catalyst

Transesterification of low-grade cooking oil into biodiesel

Two different types of SBC catalysts were employed to study the effect of catalysts on the transesterification reaction. Figure 8 illustrates the biodiesel yield percentages obtained using SBC/KOH and SBC/NaOH. Based on the results, it is evident that the SBC/KOH catalyst outperforms the SBC/NaOH for biodiesel production, yielding a higher percentage of biodiesel (39.06%). These observations indicate that the SBC/KOH catalyst exhibits superior performance when compared to the SBC/NaOH catalyst. The high fundamental strength observed is attributed to the K^+ and OH^- pairs [18]. Besides, the higher yield can be attributed to the higher surface area of the catalyst, which provides a higher active site for the reaction. This result agrees with the findings obtained from the BET analysis. Therefore, the SBC/KOH catalyst was selected as the best catalyst for further experiments.

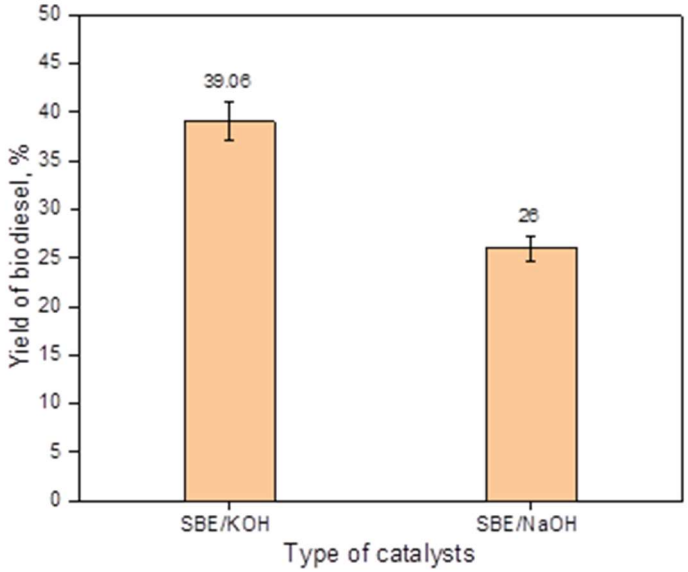


Figure 8. Effect of SBC/KOH and SBC/NaOH catalyst on biodiesel yield

The effect of calcination temperatures, specifically 500°C and 600°C, was studied using SBC/KOH. The selection of this calcination temperature was based on the findings of Cong et al., who reported it as the optimum calcination temperature for achieving high biodiesel production [13]. Hence, low calcination temperatures were chosen for energy conservation and cost reduction [20]. Figure 9 shows that the percentage biodiesel of SBC/KOH 500 and SBC/KOH 600 were found to be 47.66 and 39.06%, respectively. This finding was supported by the XRD pattern in Figure 4. The presence of SiO_2 and K_2O in XRD patterns has been found to increase the surface area of the catalyst [15]. Therefore, it can be concluded that the SBC/KOH catalyst 500 exhibits superior performance compared to the SBC/KOH 600, thereby making it the best catalyst for further experiments.

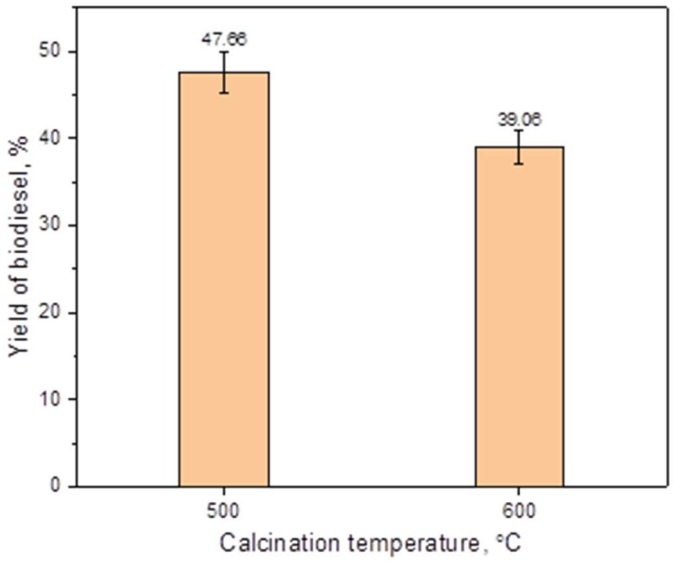


Figure 9. Effect on calcination temperature of SBC/KOH

Figure 10 displays the effect of varying the catalyst loading at 1, 2, and 4 wt.% of SBC/KOH 500. The highest biodiesel recorded was 47.66% when utilizing a catalyst consisting of 2 wt.% of SBC/KOH 500. This finding indicated that the interaction between the reactants and the solid catalyst was limited to a maximum catalyst loading of 2 wt.%, resulting in a discernible effect on the rate of the forward transesterification reaction. However, upon increasing the catalyst loading to 4 wt.%, a decrease in biodiesel production to 16.03% was observed. This is due to mixing inefficiencies resulting from the increased viscosity in the reaction vessels, which is a direct consequence of the increased catalyst concentration [21]. Since the maximum biodiesel yield was obtained when the catalyst loading was 2 wt.%, this value was chosen as the best catalyst loading for further optimization of the remaining reaction parameters.

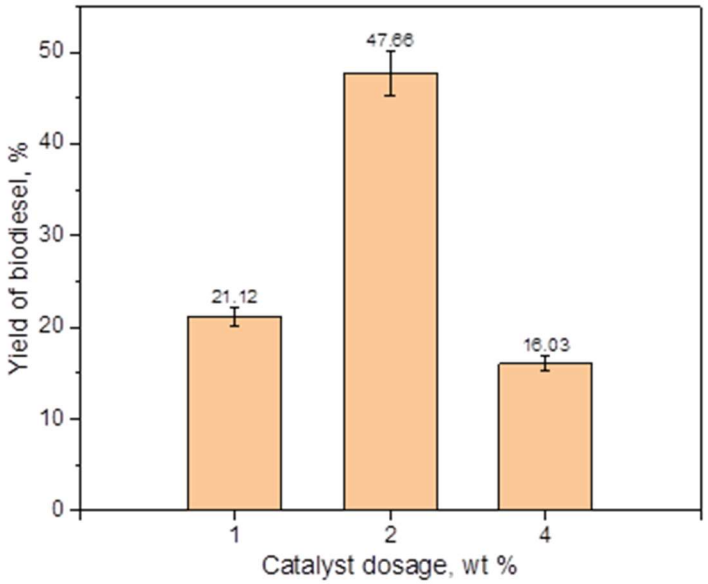


Figure 10. Effect of catalyst dosage on biodiesel yield

The effect of the ratio of oil to methanol from 1:12 to 1:20 was studied in this experiment. Based on the result in Figure 11, the percentage yield of biodiesel for the ratio of 1:12, 1:16, 1:18, and 1:20 were 30, 46.82, 47.14, and 47.66%, respectively. When the ratio of oil-to-methanol increased, the product yield also increased indicating that a large amount of methanol is required to reduce the viscosity of the reaction media and to enable the contact between the two phases [22]. Therefore, the 1:20 ratio of oil to methanol was chosen as the optimal value for the following studies.

The present study examined the effect of reaction time, with the corresponding result shown in Figure 12. The biodiesel production increased from 26.88 to 47.66% as the reaction time was increased from 1 to 2 hours. The likely reason for this observation can be attributed to the presence of the heterogeneous mass transfer system of the catalyst [18]. At 3 hours of reaction time, the biodiesel production decreased to 4.94% due to the backward reaction in the methyl ester, which produces more glycerol than methyl ester [19]. Hence, the reaction time of 2 hours was selected as the optimum time.

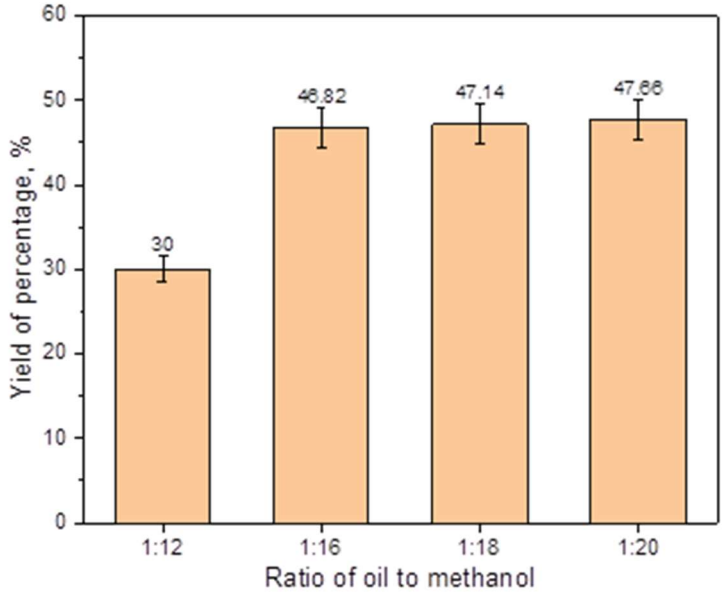


Figure 11. Effect of ratio oil to methanol in transesterification

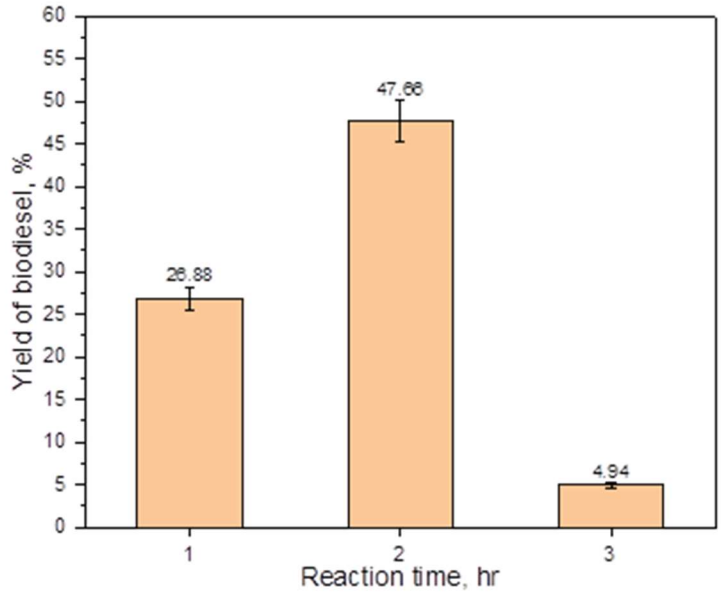


Figure 12. Effect of reaction time on the transesterification process

Conclusion

In this study, the catalytic activity of the SBC/KOH 500 catalyst for the transesterification of cooking oil to FAME was investigated. Based on the result, the SBC/KOH 500 showed the potential as a catalyst in the transesterification process and can be used as an alternative catalyst to produce biodiesel from low-grade cooking oil. The highest yield of biodiesel was 47.66% with transesterification reaction condition of 2 hours reaction time, 1:20 oil to methanol ratio, 2 wt.% catalyst loading, and temperature of 55 °C.

Acknowledgement

The authors are grateful for the financial support from the Ministry of Higher Education Malaysia for the Fundamental Research Grant Scheme (FRGS) with

Project Code: FRGS/1/2020/STG04/USM/03/2 and University Sains Malaysia, Special (Matching) Short-Term Grant with Project No: 304/PKIMIA/6315704.

References

1. Rezania, S., Oryani, B., Park, J., Hashemi, B., Yadav, K. K., Kwon, E. E., Hur, J. and Cho, J. (2019). Review on transesterification of non-edible sources for biodiesel production with a focus on economic aspects, fuel properties and by-product applications. *Energy Conversion and Management*, 201: 112155.
2. Naser, J., Avbenake, O. P., Dabai, F. N. and Jibril, B. Y. (2021). Regeneration of spent bleaching earth and conversion of recovered oil to biodiesel. *Waste Management*, 126: 258-265.
3. Chua, S. Y., Periasamy, L. A., Goh, C. M. H., Tan, Y. H., Mubarak, N. M., Kansedo, J., Khalid, M., Walvekar, R. and Abdullah, E. C. (2020). Biodiesel synthesis using natural solid catalyst derived from biomass waste — A review. *Journal of Industrial and Engineering Chemistry*, 81: 41-60.
4. Syafiuddin, A., Chong, J. H., Yuniarto, A. and Hadibarata, T. (2020). The current scenario and challenges of biodiesel production in Asian countries: A review. *Bioresource Technology Reports*, 12: 100608.
5. Miyuranga, K. V., Arachchige, U. S., Marso, T. M. M. and Samarakoon, G. (2023). Biodiesel production through the transesterification of waste cooking oil over typical heterogeneous base or acid catalysts. *Catalysts*, 13(3): 546.
6. Thangaraj, B., Solomon, P. R., Muniyandi, B., Ranganathan, S. and Lin, L. (2018). Catalysis in biodiesel production—a review. *Clean Energy*, 3(1): 2-23.
7. Naser, J., Avbenake, O. P., Dabai, F. N. and Jibril, B. Y. (2021). Regeneration of spent bleaching earth and conversion of recovered oil to biodiesel. *Waste Management*, 126: 258-265.
8. Abdelbasir, S. M., Shehab, A. I. and Khalek, M. A. A. (2023). Spent bleaching earth; recycling and utilization techniques: A review. *Resources, Conservation and Recycling Advances*, 17: 200124.
9. Yusuf, Nik N. A. N., Kamarudin, S. K. and Yaakob, Z. (2012). Overview on the production of biodiesel from Jatropha curcas L. by using heterogeneous catalysts. *Biofuels, Bioproducts & Biorefining*, 6(3): 319-334.
10. Dossin, T., Reyniers, M. and Marin, G. (2006). Kinetics of heterogeneously MgO-catalyzed transesterification. *Applied Catalysis B: Environmental*, 62 (1-2): 35-45.
11. Esan, A. O., Smith, S. M. and Ganesan, S. (2022). Dimethyl carbonate assisted catalytic esterification of palm fatty acid distillate using catalyst derived from spent bleaching clay. *Journal of Cleaner Production*, 337: 130574.
12. Hu, W., Zhou, X., Tan, J., Hou, J., Xie, Y., Wang, X., Wang, Y. and Zhang, Y. (2020). In situ transesterification of wet sewage sludge via hydrothermal process: Biodiesel production and residue utilization. *Biomass and Bioenergy*, 141: 105715.
13. Cong, W. J., Wang, Y. T., Li, H., Fang, Z., Sun, J., Liu, H. T., Liu, J. T., Tang, S. and Xu, L. (2020). Direct production of biodiesel from waste oils with a strong solid base from alkalized industrial clay ash. *Applied Energy*, 264: 114735.
14. Loh, S. K., Cheong, K. Y. and Salimon, J. (2017). Surface-active physicochemical characteristics of spent bleaching earth on soil-plant interaction and water-nutrient uptake: A review. *Applied Clay Science*, 140: 59-65.
15. Musa, M. L., Mat, R. and Tuan Abdullah, T. A. (2018). Catalytic conversion of residual palm oil in spent bleaching earth (SBE) by HZSM-5 zeolite based-catalysts. *Bulletin of Chemical Reaction Engineering and Catalysis*, 13(3): 456.
16. Rabie, A. M., Shaban, M., Abukhadra, M. R., Hosny, R., Ahmed, S. A. and Negm, N. A. (2019). Diatomite supported by CaO/MgO nanocomposite as heterogeneous catalyst for biodiesel production from waste cooking oil. *Journal of Molecular Liquids*, 279: 224-231.
17. Oyerinde, A. and Bello, E. (2016). Use of Fourier transformation infrared (FTIR) spectroscopy for analysis of functional groups in peanut oil biodiesel and its blends. *British Journal of Applied Science & Technology*, 13 (3): 1–14.
18. Enguilo Gonzaga, V., Romero, R., Gómez-Espinosa, R. M., Romero, A., Martínez, S. L. and

Natividad, R. (2021). Biodiesel Production from Waste Cooking Oil Catalyzed by a Bifunctional Catalyst. *ACS Omega*, 6(37): 24092-24105.

19. Roschat, W., Phewphong, S., Pholsupho, P., Namwongsa, K., Wongka, P., Moonsin, P., Yoosuk, B. and Promarak, V. (2022). The synthesis of a high-quality biodiesel product derived from Krabok (*Irvingia Malayana*) seed oil as a new raw material of Thailand. *Fuel*, 308: 122009.
20. Pinto, B. F., Garcia, M. A. S., Costa, J. L., De Moura, C. V. R., De Abreu, W. C. and De Moura, E. M. (2019). Effect of calcination temperature on the application of molybdenum trioxide acid catalyst: Screening of substrates for biodiesel production. *Fuel*, 239: 290-296.
21. Akbar, E., Binitha, N., Yaakob, Z., Kamarudin, S. K. and Salimon, J. (2009). Preparation of Na doped SiO_2 solid catalysts by the sol-gel method for the production of biodiesel from jatropha oil. *Green Chemistry*, 11 (11): 1862.
22. NolHakim, M. A. H. L., Shohaimi, N. A. M., Mokhtar, W. N. A. W., Lokman, I. M. and Abdullah, R. F. (2021). Immobilization of potassium-based heterogeneous catalyst over alumina beads and powder support in the transesterification of waste cooking oil. *Catalysts*, 11(8): 976.
23. Shahbazi, M. R., Khoshandam, B., Nasiri, M. and Ghazvini, M. (2012). Biodiesel production via alkali-catalyzed transesterification of Malaysian RBD palm oil – Characterization, kinetics model. *Journal of the Taiwan Institute of Chemical Engineers*, 43(4): 504-510.
24. Yaakob, Z., Mohammad, M., Alherbawi, M., Alam, Z. and Sopian, K. (2013). Overview of the production of biodiesel from Waste cooking oil. *Renewable and Sustainable Energy Reviews*, 18: 184-193.

Malaysian Journal of Analytical Sciences (MJAS)
Published by Malaysian Analytical Sciences Society

EVALUATING THE POTENTIAL OF CHEMOMETRICS TECHNIQUES AS RAPID SCREENING TOOLS FOR BLACK GEL INKS DISCRIMINATION

(Menilai Potensi Teknik Kemometrik sebagai Alat Saringan Pantas untuk Diskriminasi Dakwat Hitam Gel)

Nur Atiqah Zaharullil[1,2], Dzulkiflee Ismail[1*], Wan Nur Syuhaila Mat Desa[1], and Nik Fakhuruddin Nik Hassan[1]

[1]Forensic Science Programme, School of Health Sciences
Universiti Sains Malysia, Health Campus, 16150 Kubang Kerian, Kelantan, Malaysia
[2]Universiti Teknologi MARA Jasin Campus 77300 Melaka

[*]Corresponding author: dzulkiflee@usm.my

Received: 20 July 2023; Accepted: 15 October 2023; Published: 29 December 2023

Abstract

Examining the questioned documents can offer essential scientific proof that the documents are authentic. Examining inks and handwriting to establish authenticity, authorship, suspected counterfeiting, and/or modifications are forensic problems that require critical attention. Due to gel pens popularity and widespread usage, their emergence in criminal cases associated with questioned documents are therefore anticipated. A dissolution test by dissolving gel ink into organic solvent can sometimes be used for rapid discrimination of gel ink into either pigment-based or dye-based colourants. However, due to its extremely destructive nature, this test is unfavourable for forensic document examination purposes. The main aim of this study was to develop a model that could be used to determine the nature of colourant in black gel ink without having to perform the destructive dissolution test. To achieve this, black gel pen inks of different brands/models (n = 30) that were procured from 23 different manufacturers from Malaysia, India, and China were initially dissolved in a series of organic solvents, and the nature of their colourants was recorded. Thereafter, their infrared (IR) spectra profiles were acquired using the attenuated total reflectance - Fourier transform infrared (ATR-FTIR) spectroscopy, and then preprocessed prior to feature selection using the principal component analysis (PCA). The selected features were used for the development of a classifier using the linear discriminant analysis (LDA), whereby 98.1% of correct classification was recorded for the cross-validated samples. Furthermore, it signified the potential of this approach for rapid screening of black gel ink without having to perform the destructive dissolution test, which could be utilised by forensic document examiners.

Keywords: black gel inks, forensic science, questioned document, attenuated total reflectance infrared spectroscopy, principal component analysis

Abstrak

Meneliti dokumen yang dipertikai boleh memberikan bukti saintifik penting bahawa dokumen itu sahih. Memeriksa dakwat dan tulisan tangan untuk menentukan keaslian, kepengarangan, disyaki pemalsuan dan/atau pengubahsuaian adalah masalah forensik yang memerlukan perhatian kritikal. Disebabkan oleh populariti pen dakwat gel dan penggunaannya yang semakin meluas, kemunculan mereka dalam kes jenayah yang berkaitan dengan dokumen yang dipertikai adalah dijangkakan. Ujian pembubaran

dengan melarutkan dakwat gel ke dalam pelarut organik kadangkala boleh digunakan untuk diskriminasi pantas dakwat gel kepada sama ada berasaskan pigmen atau pewarna. Walau bagaimanapun, disebabkan sifatnya yang sangat merosakkan, ujian ini tidak sesuai untuk tujuan pemeriksaan dokumen forensik. Matlamat utama kajian ini adalah untuk membangunkan model yang boleh digunakan untuk menentukan sifat pewarna dalam dakwat gel hitam tanpa perlu melakukan ujian pelarutan yang merosakkan. Untuk mencapai matlamat ini, dakwat pen gel hitam daripada jenama/model berbeza (n = 30) yang diperoleh daripada 23 pengeluar berbeza dari Malaysia, India, dan China, pada mulanya dilarutkan dalam satu siri pelarut organik, dan sifat pewarnanya direkodkan. Berikutan itu, profil spektrum inframerah (IR) mereka diperoleh menggunakan spektroskopi jumlah pemantulan yang dilemahkan - inframerah transformasi Fourier (ATR-FTIR), dan kemudian pra-diproses sebelum pemilihan ciri menggunakan analisis komponen utama (PCA). Ciri-ciri yang dipilih telah digunakan untuk pembangunan pengelas menggunakan analisis diskriminasi linear (LDA), di mana 98.1% pengelasan yang betul telah direkodkan untuk sampel-sampel yang disahkan silang, yang menandakan potensi pendekatan ini untuk pemeriksaan pantas dakwat gel hitam tanpa perlu melakukan ujian pelarutan yang merosakkan, yang boleh digunakan oleh pemeriksa dokumen forensik.

Kata kunci: dakwat gel hitam, sains forensik, dokumen yang dipersoalkan, spektroskopi inframerah jumlah pemantulan yang dilemahkan, analisis komponen utama

Introduction

Nowadays, increase in document forgery activities and fight against these illegal activities causes serious problems and negatively affects individuals, including the private and government institutions [1]. Any documents related to criminal cases that are doubtful of authenticity and authorship, are known as questioned documents [2]. It also refers to any objects bearing handwriting, typed, and printed materials. Document examination offers a great deal of interest in the forensic document examiners' community. It includes examining of the ink written on documents, signatures and handwriting, and determining the age of the ink written on paper [3]. The commonality for forensic document examiners is to test for document alteration and defacement, distinguishing between inks with identical impressions, and determining whether the provenance of the two ink samples is either identical or otherwise [4]. All of these processes require ink analysis, which serves to discover the authenticity of documents [5]. The chemistry of ink is determined by its composition, which is different for each brand/model. Nonetheless, the existence of colours, pigments, solvents, and additives in ink recipes aids forensic document examiners in the discrimination, and classification of confiscated pens in actual cases [6].

There are several types of writing instruments used in a document, such as roller ball pens, ballpoint pens, fountain pens, and gel pens. However, gel pens are popular writing material due to their smooth and interesting writing appearance [2]. Due to this, the usage of gel pens in documents is increasing. The history of the gel pen began in 1984, whereby the Japanese Sakura Colour Products Corporation introduced the first gel pen, a type of writing instrument that used a rolling ball mechanism to transfer ink from the reservoir to paper [7]. Gel ink often contains colouring ingredients, such as dyes and pigment, a water-based solvent as a vehicle or carrier, and additional additives, such as plasticisers, surfactants, waxes, and driers to enhance its writing performance and appearance [8]. The uniqueness of each manufacturer is the type of colourant used, and the quality and quantity of additives, such as surface activators, fluorescent material, solubilisers, preservatives, and anti-corrosion agents added to the ink composition [9]. Dyes and pigments are preferred over other components since they can be seen by the naked eye, making them the most prominent aspects in the ink analysis. This feature enables the examiners to make a quick decision, and straightforward comparisons between the various inks, which is helpful for the initial assessment of an ink analysis.

The subjective judgement of forensic document examiners regarding ink analysis has somewhat diminished due to the advancement of analytical techniques. The latter technique is gaining popularity because other than being straightforward, it requires no or minimal sample preparation, and most importantly it maintains the integrity of documents [10]. Amongst the methods are the attenuated total reflectance-Fourier transform infrared (ATR-FTIR) spectroscopy [4, 11–15], and surface increase Raman scattering [10, 16–20].

Due to these, the non-destructive method is often preferred over the destructive method for document analysis.

The ATR-FTIR spectroscopy has been proven as an effective tool for ink analysis, which offers a simple tool that can provide qualitative and quantitative information for comparative analysis of ink. Additionally, these methods work in combination with the chemometrics methods, such as the principal component analysis (PCA) [5, 15], [21, 22], linear discriminant analysis (LDA) [14], and partial least square-discriminant analysis (PLS-DA) [4] for discrimination and classification of ink. Consequently, a mixture of statistical and analytical methods has been consistently applied to achieve substantial outcomes in forensic questioned document examination [4]. Despite numerous studies demonstrated a successful combination of ATR-FTIR analysis with chemometrics methods, there was a noticeable research gap that explored the practical significance of these results in effectively distinguishing between different types of inks, as the preliminary stage in ink analysis. This is significant considering that ATR-FTIR offers a non-destructive approach, and has the potential to replace traditional, destructive techniques to discriminate the ink at an early stage.

Chemometrics are mathematical and statistical approaches to chemical data that provide reliable tests for classification, discrimination, or model development for sample datasets [23]. In ink analysis, the main principle of chemometrics is to analyse and examine the data obtained from analytical methods to avoid making an unbiased decision about similarities between the ink samples. Chemometrics have a positive influence on the forensic examination of various inks. It is also a powerful tool when dealing with multi-component systems and allows for extracting maximum information from complicated datasets.

The PCA is a widely used method for pattern recognition in chemometrics. It allows for a large number of datasets, and reduces data dimension by transforming the original set of correlated variables into orthogonal variables, known as the principal components (PCs) [24]. This process is achieved by removing the noise, redundant, and highly correlated data [25]. Each PC is calculated to describe the highest proportion of variance, and most of the information is stored in the first few PCs. The number of useful PCs is less than the number of original variables [26].

The LDA is a well-known method for pattern recognition [15]. Additionally, it is a powerful classification method that applied linear classification structure that can separate a series of samples within different classes based on their spectral features. In LDA, the dimensional embeddings are reduced in a manner that effectively separates orientations of the classes projected data on any given line or space. The maximum ratio of within-class variability to between-class variability in the training set serves as the criterion for determining these vectors.

Prior to analytical analysis, the standard procedure in ink analysis commences with the dissolution test, which serves as a rapid screening technique to differentiate between unidentified ink sources and categorises ink by its colourant composition. This preliminary test was conducted by observing the degree of ink solubility that was deposited on paper after it was submerged in organic solvent. Dye-based ink readily dissolved in the solvent, causing a noticeable change in the solvent colour, whereas the pigment-based ink remained adhere to the paper substrate. A study by Mohammad Asri et al. [16] found that red gel ink dissolved in acetone compared to other organic solvents. This result was also supported by Reed [27] who claimed that acetone and hydrochloric acid were able to dissolve red and blue gel inks, respectively.

This screening test could provide rapid discrimination between unknown ink, but it is not recommended for it could obliterate the document. Therefore, this study proposed the development of a non-destructive screening test protocol based on dissolution test data. Consequently, a screening test was performed on 30 different brands of black gel ink pens to determine the colourant nature of each ink; these inks were then deposited on paper and subjected to non-destructive ATR-FTIR analysis. The ATR-FTIR data mining was

performed using PCA and LDA, and a classification model was developed. The outcome of this study would provide valuable insights of screening test using the non-destructive approach. The developed model could be utilised by forensic document examiners, as a rapid screening tool to identify the nature of colourant in black gel ink without having to perform the destructive dissolution test.

Materials and Methods

Sample collection

Thirty different brands and models of black gel inks were purchased from stationery stores and online. In this study, seven pens from each brand/model were used, totaling 210 samples of black ink. For reference, a code was assigned to each brand or model. The information and IDs used in this study are shown in Table 1.

Table 1. Details of samples

No	Brand	Model	Code ID
1	M&NISUN	606	A
2	Faber Castell	True Gel	B
3	Faber Castell	Eco Gel	C
4	Pilot	Super Gel	D
5	Pilot	Wingel	E
6	M&G	AGP02372-R3	F
7	M&G	AGP13271- Office	G
8	Pentel	BL110-Energel	H
9	NMANAN	MiWi Get	I
10	Zhi Xin	Diamond	J
11	Zhi Xin	Lovein Test Good	K
12	Zhi Xin	POS G-518	L
13	BIC	GLI X - Fine	M
14	Faster	SP-F-072	N
15	Monami	Jeller Pen 502	O
16	Monami	Jell Line	P
17	Paper Mate	Gel 300	Q
18	Unicorn	TGP-812C	R
19	CHOSCH	CS-G169	S
20	U-Fine	UC-Q8	T
21	Digno	Trinok Gel	U
22	Buncho	Fine Tech	V
23	Buncho	Jellie	W
24	TYNO	GP100	X
25	BEIFA	GA102601	Y
26	Mr DIY	Gel-067	Z
27	Zui Xua	CS801	A’
28	Test 2	GP-300	B’
29	MUJI	5110	C’
30	Stabilo	Palette	D’

Dissolution test

In questioned document examination, this test acts as a screening step to distinguish inks that are similar in colour, but with different ink colourant composition [16]. Gel ink colourants were either pigment- or dye-based. While pigment-based ink does not dissolve in organic solvents, dye-based ink does. This test aimed at identifying the colourants used in each ink sample based on their solubility in organic solvents. The results could provide an early insight to discriminate the ink samples into two groups; ink that was soluble in an organic solvent, classified as dye-based ink, whereas ink that was insoluble in organic soluble had pigment-based colourant. This test was adapted from a study by Reed [27] that used a variety of organic solvents to discriminate gel ink samples of red, blue, and black. The solvents used were polar organic solvents, such as methanol and ethanol.

Each ink was scribbled on a 4 mm x 4 mm square on a 70 gsm A4 paper until the entire square was thoroughly inked. After drying at room temperature for 10 min, the square sheet was cut and placed in a glass vial. Thereafter, 2 mL of solvents (methanol and ethanol) were drawn into the sample vial with a pipette, and subsequently stirred vigorously using a vortex mixer for 1 min. After leaving each sample at room temperature for 5 min, the solubility of ink samples in these solvents was observed and recorded. The outcomes of the dissolution test were compared with ATR-FTIR analysis and chemometrics results, which were crucial as they served as a reference point to demonstrate that ATR-FTIR analysis could provide equivalent results. Furthermore, they had the potential to substitute the dissolution test as a screening method for forensic ink analysis.

Infrared (IR) spectral acquisition

In forensic science, problems arose when the reference and unknown samples contained the same type of colourant. Therefore, discrimination of the ink by dissolution test is irrelevant. This could be resolved by using the Fourier transform infrared (FTIR) analysis to separate the ink samples, depending on the functional groups present in each sample. FTIR is preferable as it is a non-destructive analysis and requires no sample preparation. Consequently, the integrity of the document as evidence is maintained. Each absorbance spectrum was collected in the range of 4000 cm^{-1} – 600 cm^{-1} wavelengths using a LUMOS FTIR microscope (Bruker, Germany) equipped with an ATR. The ink line samples were prepared by drawing seven lines with seven gel pens from the same brand/model on a white A4 70 gsm paper. Before the spectra acquisition, all samples were stored in normal laboratory environment. The environmental conditions were maintained the same for all the samples, as they could offer an equal effect of moisture content and other environmental factors [4]. The sample was then placed on the stage under a microscope, and the seven lines drawn from each pen were measured in a low ATR pressure mode with 64 background sample scans at a resolution of 4.0 cm^{1}. In each sample measurement, the background was measured according to the aperture. All collected spectra were baseline corrected using the OPUS 7.5 software connected to the instruments.

Data preprocessing and analysis

The absorption spectrum acquired from the LUMOS FTIR microscope instrument was saved in a *.dpt format and converted into an Excel spreadsheet. The spectral range from this analysis was collected in the range of 4000 cm^{-1} – 600 cm^{-1}. However, for observation purposes and data analysis, the fingerprint region in the range of 1500 cm^{-1} – 600 cm^{-1} was selected, as this region exhibited characteristic peaks for each sample. The data from each spectrum were then preprocesses to normalised dataset. The ATR-FTIR spectra obtained from the ink samples might contain broad, low resolution, and merged peaks. Therefore, the normalised preprocessing of numerical data was necessary to minimise and refine the results [4].

Principal component analysis (PCA)

In this study, the statistical software package, Unscrambler (Version 10.4) 2016 was used to process normalised dataset. The average value from each sample spectrum was inputted to the Unscrambler to run PCA. A score plot was used to display the clustering outcome, as the samples with similar scores were placed close to each other, while those with dissimilar scores were located apart.

Linear discriminant analysis (LDA)

The classification model was built on the normalised FTIR dataset to observe whether all the IR data could be classified according to their colourant nature. The IBM Statistical Package for the Social Sciences, also known as IBM SPSS (Version 26) was used that applied the Fischer's function coefficient algorithm and leave-one-out approach, which is one of the types of cross-validation techniques.

Results and Discussion

Dissolution test

Typically, black gel pen ink contains multiple dye components, or pigments of various hues that are combined proportionally to produce black colour. To ascertain the degree of dissolution of the black gel ink samples, the colour changes in the organic solvents were observed, as the ink was introduced. In this test, 21 black gel inks failed to dissolve effectively, which suggested that they might contain pigments as colourants, whereas nine black gel inks (Codes C, D, E, H, O, U, V, W, and D') dissolved in methanol and ethanol, indicating that they contained dyes. The observation made from this test concurred with a study conducted by Reed [27]. From this test, the ink samples were able to discriminate based on the type of colourant contained in the ink.

Spectral characterization

Figure 1 and Figure 2 show the spectra from dye-based black gel ink and pigment-based black gel ink, respectively. None of the sample's spectra displayed any discriminating peaks between 4000 and 1600 cm^{-1}. The cellulose band presence in the range of 3000 cm^{-1} – 3500 cm^{-1} and 2880 cm^{-1} – 2890 cm^{-1} characterised the C-H and O-H stretching, which was from the paper composition [14]. The fingerprint region from 1500 cm^{-1} – 600 cm^{-1} exhibited the most characteristic peaks of ink [28]. Peaks in the range of 1300 cm^{-1} – 1500 cm^{-1} could be attributed to the vibration of carbon compounds, such as CH-stretching and bending vibrations in the aliphatic and aromatic compounds. Presence of peaks in the range 1550 cm^{-1} – 1610 cm^{-1} was due to nitrogen bonding in azo compounds used in ink. Primary, secondary, and tertiary alcohols appeared in the region of 1600 cm^{-1} – 1000 cm^{-1} with the presence of C-O bond peaks in stretching mode. The region below 1000 cm^{-1} was due to C-H bond in the bending mode that indicated alkenes. Lastly, the epoxy group existed in the region of 800 cm^{-1} – 900 cm^{-1}. It was suspected that this might be due to the source of additives in the gel pen ink composition. Based on the spectra observations, there were no discernible differences between the dye-based ink and pigment-based ink samples. Unfortunately, this observation was unsuccessful in distinguishing against all the black ink samples. These findings were supported by Reed [27], as visual discrimination of the spectra based on the presence or absence of peaks, and their intensities were challenging and difficult.

Principal component analysis (PCA)

The score plot of normalised dataset is reported in Figure 3, showing visual pattern recognition of normalised dataset plotted using the first two principal components, namely PC1 and PC2. The first two PCs explained 89% (PC1 75% and PC2 14%) of the total variance. A close observation of this score plot clearly showed two well-separated clusters corresponding to the dye-based groups (Group I) and pigment-based group (Group II), which were in line with the results obtained from the dissolution test. The score plot separated Group I mostly as negative value, while most of Group II as positive value at PC1. The PCA could discriminate these samples based on their colourant types. Additionally, it clearly demonstrated the link between the samples (Code D and Code E) and (Code V and Code W), which originated from the same brand located near each other under the same cluster (Group I), as they had similar ink formulation. In contrast, samples (Code F and Code G) and (Code J, Code K, and Code L) in cluster Group II were separated despite belonging to the same brand. This trend might be impacted by the presence of additive ingredients in the ink to enhance their appearance and writing performance. Code R and Code X were pigment-based ink, but their positions were distant from the cluster, suggesting that they might not be gel ink. As observed, a small number of Group II samples overlapped with each other, indicating that the samples from different brands might have varying proportions, but with similar ink compositions. Gawad et al. [29] achieved 100% discrimination power for ink

differentiation amongst 33 pens by integrating ATR-FTIR data with PCA. Qureshi et al. [6] also applied PCA with pre-treated ATR-FTIR spectral data for discrimination of local and foreign ballpoint inks. The PCA scatter plot exhibited a cumulative variance of 97% of the first two principal components. PCA with ATR-FTIR data demonstrated a significant contribution of non-destructive approaches, as useful tool for ink discrimination.

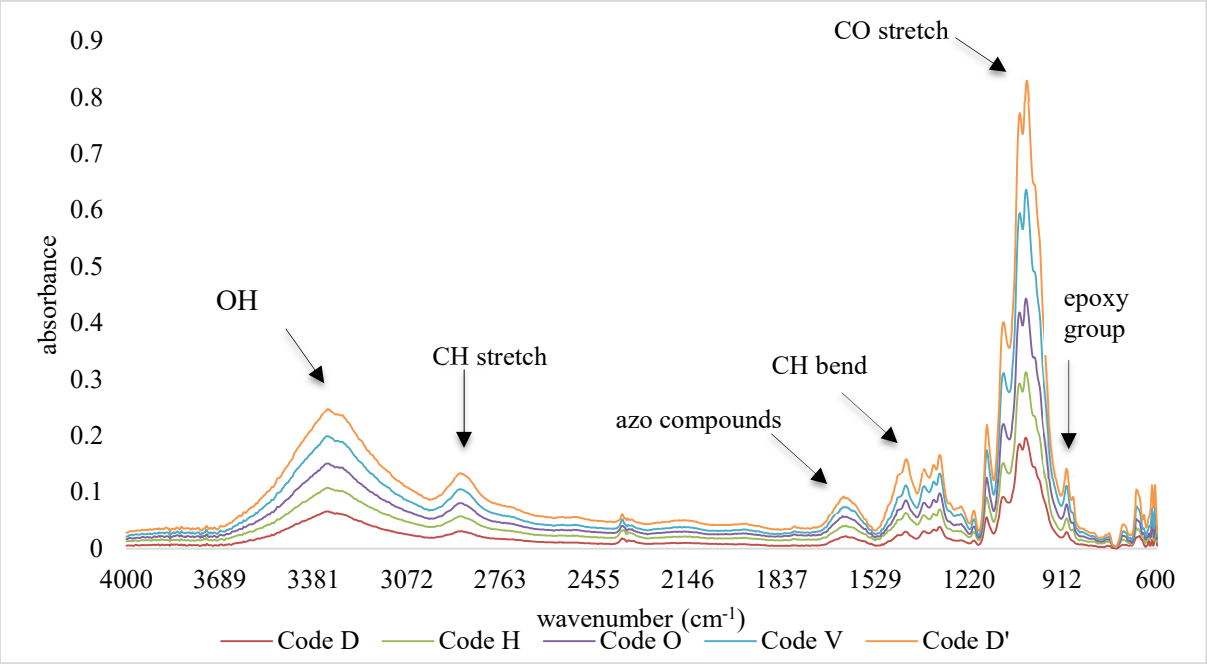


Figure 1. FTIR spectra of dyed-based black gel ink spectrum

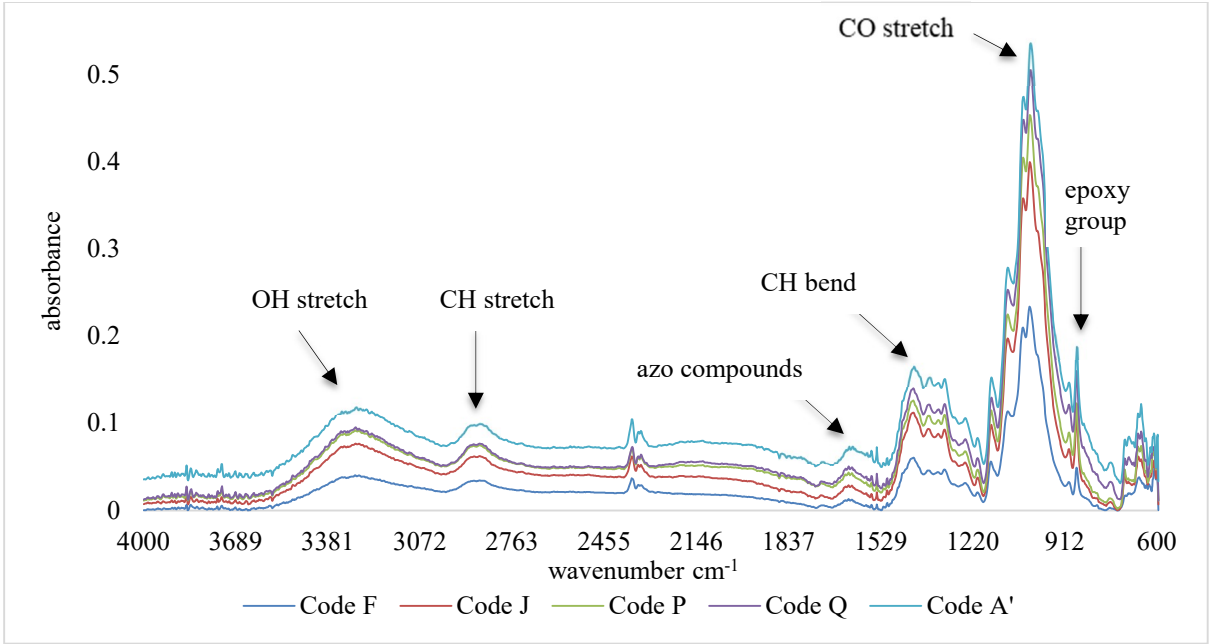


Figure 2. FTIR spectra of pigment-based black gel ink spectrum

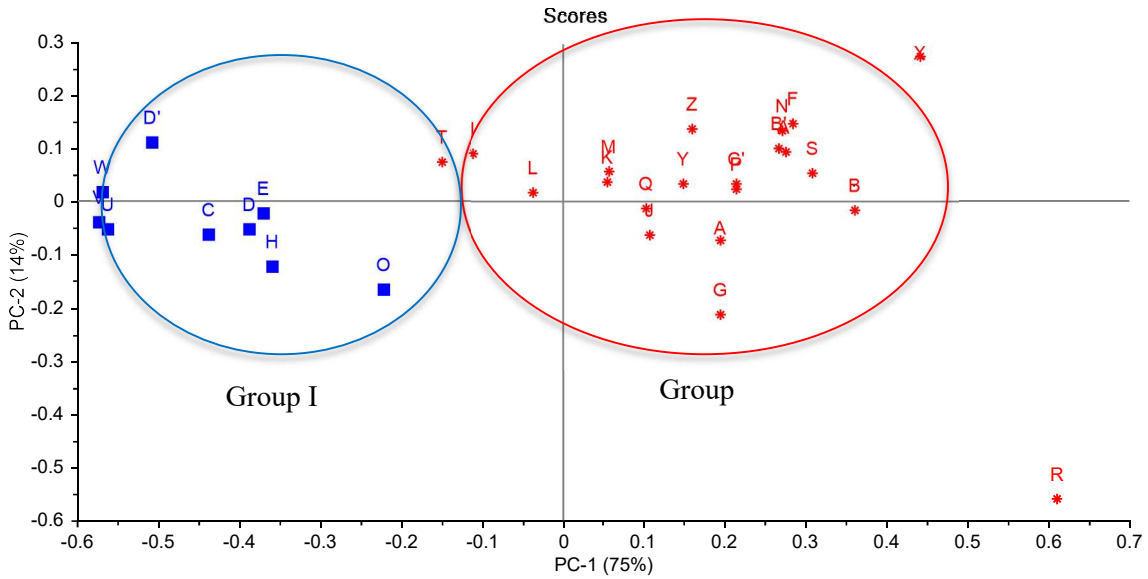


Figure 3. PCA score plot of the normalized dataset for black gel ink samples

Linear discriminant analysis (LDA)

The Wilks' Lambda measures how well each function separates cases into groups. It is equal to the proportion of the total variance in the discriminant scores that are not explained by differences amongst the groups. It shows whether these two groups (dye and pigment) differ significantly based on their means value on a set of continuous variables, which indicated the significance of the discriminant function. The value ranges from 0 to 1; the smaller the value of Wilks' Lambda indicates the greater discrimination ability of the function. Table 2 shows a high significance function (p<0.05), and provided a small Wilks' Lambda value, which was 0.254 that indicated greater discrimination ability of the function.

Table 2. Wilks' Lambda table from linear discriminant analysis

Test of Function(s)	Wilks' Lambda	Chi-square	df	Sig.
1	.254	201.661	6	.000

The classification in Table 3 reveals the results using the generated discriminant model. Of the original group used to create this model, 43 from 45 dye-based ink samples were classified correctly, and 106 from 107 pigment-based ink were classified correctly. Overall, 98% of the original group cases were classified correctly. On the other hand, the cross-validated group cases that applied leave-out-one approach, however, showed similar discriminating power (98%). Pigment colourants were perfectly classified with a good accuracy (99.1%) than dyed colourants (95.6%). The model validation for 30 unknown samples showed 100% classification. All the unknown samples were correctly assigned into its designated group according to its colourant nature. In the realm of ink analysis, previous studies have yielded promising results through the utilisation of LDA in conjunction with ATR-FTIR spectral data. Specifically, Kher et al. [30] demonstrated that 48.4% of blue ballpoint pens could be accurately classified using this approach. Furthermore, Silva et al. [14] applied LDA with ATR-FTIR data for pen classification, and reported a remarkable outcome, achieving a perfect 100% in their classification model.

These findings underscored the robustness and efficacy of LDA for ink classification.

Table 3. Classification table generated from normalized dataset of black gel ink samples

			Pigment	Dye	Total
Original	Count	Pigment	106	1	107
		Dye	2	43	45
	%	Pigment	99.1	.9	100.0
		Dye	4.4	95.6	100.0
Cross-validated	Count	Pigment	106	1	107
		Dye	2	43	45
	%	Pigment	99.1	.9	100.0
		Dye	4.4	95.6	100.0

a. 98.0% of original grouped cases correctly classified.
b. Cross validation is done only for those cases in the analysis. In cross validation, each case is classified by the functions derived from all cases other than that case.
c. 98.0% of cross-validated grouped cases correctly classified.

Conclusion

The development of classification model to discriminate the black gel ink based on its colourant nature as an alternative destructive screening test holds a significant promise. By applying this model, the screening test of the unknown ink samples could be conducted without damaging or altering the integrity of the sample. Furthermore, ATR-FTIR spectroscopy in combination with chemometrics techniques could be successfully used for the discrimination of ink when it involved large datasets. Additionally, PCA was applied resulting in good clustering of all samples based on the nature of ink colourants. The LDA classification model could quantify the predictive ability for correct classification rate of the gel ink samples by providing higher discrimination rate, which was 98% for both the original and cross-validated group cases.

Acknowledgements

The authors acknowledged the support given by the staff of the Advanced Analytical Laboratory, School of Health Sciences, USM Kubang Kerian and the study scheme awarded to Nur Atiqah Zaharullil by UiTM which has enabled this study to be conducted. The authors also acknowledged the support given by PHA Handwriting Analysis Sdn. Bhd and HFDE Services Pte. Ltd. (Singapore).

References

1. Ortiz-Herrero, L., de Almeida Assis, A. C., Bartolomé, L., Alonso, M. L., Maguregui, M. I., Alonso, R. M., and Seixas de Melo, J. S. (2020). A novel, non-invasive, multi-purpose and comprehensive method to date inks in real handwritten documents based on the monitoring of the dye ageing processes. *Chemometrics and Intelligent Laboratory Systems*, 207: 1-11.
2. Said, H. M., and Ismail, D. (2018). Study on the effect of ageing to gel pen ink on papers using attenuated reflectant mode fourier transform infrared (ATR-FTIR) spectroscopy. *The International Journal of Medicine and Sciences*, 3(1): 38-43.
3. Hoang, A. D., Tu, M. B., Ta, T. T. and Hoang, M. H. (2021). Combination of a green and a traditional method for estimating relative and absolute ink age: A case study of ballpoint pen ink dating in Vietnam. *Journal of Analytical Methods in Chemistry*, 3: 1-10.
4. Gautam, R., Chauhan, R., Kumar, R. and Sharma, V. (2021). PLS-DA and infrared spectroscopy based rapid and non-destructive discrimination of black ball and gel pen inks for forensic application. *Forensic Science International: Reports*, 3: 1-8.
5. Kumar, R. and Sharma, V. (2017). A novel combined approach of diffuse reflectance UV–Vis-NIR spectroscopy and multivariate analysis for

non-destructive examination of blue ballpoint pen inks in forensic application. *Spectrochimica Acta - Part A: Molecular and Biomolecular Spectroscopy*, 175: 67-75.

6. Qureshi, R., Wasim, M. and Ashraf, M. (2022). Forensic discrimination of blue ballpoint, gel and oil-gel pens: Application of chemometrics to ATR-FTIR Data. *International Journal of Forensic Sciences*, 7(3): 1-12.
7. Florence, D. C., Harralson, H. H. and Gbarabe, J. (2018). An introduction to gel inks: History and analysis. *Journal of Forensic Document Examination*, 28: 105-124.
8. Calcerrada, M. and García-Ruiz, C. (2015). Analysis of questioned documents: A review. *Analytica Chimica Acta*, 853(1): 143-166.
9. Narayan, V., Shalini, S. and Agrawal, N. (2015). Forensic identification and differentiation of different indian brands of gel pen inks. *International Journal for Scientific Research & Development*, 3(1): 557-561.
10. Łydżba-Kopczyńska, B., Czaja, T., Cieśla, R. and Rusek, G. (2021). Application of chemometric methods for the determination of fading and age determination of blue ballpoint inks. *Journal of Raman Spectroscopy*, 52(1): 159-169.
11. Durney, L. (2015). Using vibrational spectroscopy to analyse the effect of environmental aging on gel pen inks.Thesis of Master Degree, University of Central Lancashire.
12. Nastova, I., Grupče, O., Minčeva-Šukarova, B., Ozcatal, M. and Mojsoska, L. (2013). Spectroscopic analysis of pigments and inks in manuscripts: I. Byzantine and post-Byzantine manuscripts (10-18th century). *Vibrational Spectroscopy*, 68: 11-19.
13. Sharma, V. and Kumar, R. (2017). Dating of ballpoint pen writing inks via spectroscopic and multiplelinear regression analysis: A novel approach. *Microchemical Journal*, 134: 104-113.
14. Silva, C. S., Borba, F. de S. L., Pimentel, M. F., Pontes, M. J. C., Honorato, R. S. and Pasquini, C. (2013). Classification of blue pen ink using infrared spectroscopy and linear discriminant analysis. *Microchemical Journal*, 109: 122-127.
15. Yadav, P. K. and Sharma, R. M. (2020). Classification of fiber tip pens using attenuated total reflectance (ATR) – Fourier transform infrared (FTIR) spectroscopy in tandem with chemometrics. *Vibrational Spectroscopy*, 108: 1-17.
16. Mohamad Asri, M. N., Verma, R., Mahat, N. A., Mohd Nor, N. A., Mat Desa, W. N. S. and Ismail, D. (2022). Raman spectroscopy with self-organizing feature maps and partial least squares discriminant analysis for discrimination and source correspondence of red gel ink pens. *Microchemical Journal*, 175: 1-10.
17. Chaplin, T. and Clark, R. (2016). Raman microscopy techniques for the characterisation of pigments. *Royal Microscopical Society*, 3(3): 86-98.
18. Kunicki, M., Fabiańska, E. and Parczewski, A. (2013). Raman spectroscopy supported by optical methods of examination for the purpose of differentiating blue gel pen inks. *Problems of Forensic Sciences*, 95: 627-641.
19. Geiman, I., Leona, M. and Lombardi, J. R. (2009). Application of raman spectroscopy and surface-enhanced raman scattering to the analysis of synthetic dyes found in ballpoint pen inks. *Journal of Forensic Sciences*, 54 (4): 947-952.
20. Mazzella, W. D. and Buzzini, P. (2005). Raman spectroscopy of blue gel pen inks. *Forensic Science International*, 152 (2-3): 241-247.
21. Senior, S., Hamed, E., Masoud, M. and Shehata, E. (2012). Characterization and dating of blue ballpoint pen inks using principal component analysis of UV-Vis absorption spectra, ir spectroscopy, and HPTLC. *Journal of Forensic Sciences*, 57 (4): 1087-1093.
22. Thanasoulias, N. C., Parisis, N. A. and Evmiridis, N. P. (2003). Multivariate chemometrics for the forensic discrimination of blue ball-point peninks based on their Vis spectra. *Forensic Science International*, 138(1-3):75-84.
23. Gorziza, R., González, M., de Carvalho, C., Ortiz, R., Ferrão, M. and Limberger, R. (2022). Chemometric approaches in questioned documents. *Brazilian Journal of Analytical Chemistry*, 34: 35-51.
24. Gemperline, P. (2006). Practicle guide to chemometric. Taylor & Francis, New York: pp.1-7.

25. Axelson, D. E. (2010). Data preprocessing for chemometric and metabonomic analysis. First Choice Books:pp. 330-336.
26. Sauzier, G. Y. (2016). Applications of chemometrics to the analysis and interpretation of forensic physical evidence. Thesis of Doctor of Philosophy, Curtin University.
27. Reed, G. (2013). Multivariate profiling of gel inks. Thesis of Doctor of Philosophy, University of Strathclyde, United Kingdom.
28. Mohamad Asri, M. N. and Ismail, D. (2018). Combined principal component analysis (PCA) and hierarchical cluster analysis (HCA): An efficient chemometric approach in aged gel inks discrimination. *Australian Journal of Forensic Sciences*, 52(1): 38-59.
29. Gawad, A. A., Salama, T. M., Meshref, M., Mohamed, G. G. and Zedan, A. F. (2022). Coupling ATR-FTIR spectroscopy and chemometric analysis for rapid and non-destructive ink discrimination of forensic documents. *Egyptian Journal of Chemistry*, 65(8): 167-179.
30. Kher, A., Mulholland, M., Green, E. and Reedy, B. (2006). Forensic classification of ballpoint pen inks using high performance liquid chromatography and infrared spectroscopy with principal components analysis and linear discriminant analysis. *Vibrational Spectroscopy*, 40(2): 270-277.

Malaysian Journal of Analytical Sciences (MJAS)
Published by Malaysian Analytical Sciences Society

MICROPLASTICS IN THE ENVIRONMENT: PROPERTIES, IMPACTS AND REMOVAL STRATEGIES

(Mikroplastik dalam Alam Sekitar: Sifat, Kesan dan Strategi Penyingkiran)

Iwani W. Rushdi[1,2], Rabiatul S. Rusidi[1,2], Wan M. Khairul[2], Sofiah Hamzah[3], Wan Mohd Afiq Wan Mohd Khalik[1,2], Sabiqah Tuan Anuar[1,2], Nor Salmi Abdullah[4], Nasehir Khan E.M. Yahya[4] and Alyza A. Azmi[1,2*]

[1]Microplastic Research Interest Group (MRIG), Faculty of Science and Marine Environment, Universiti Malaysia Terengganu, 21030 Kuala Nerus, Terengganu, Malaysia.
[2]Faculty of Science and Marine Environment, Universiti Malaysia Terengganu, Universiti 21030 Kuala Nerus, Terengganu, Malaysia.
[3]Faculty of Ocean Engineering Technology and Informatics, Universiti Malaysia Terengganu, 21030 Kuala Nerus, Terengganu, Malaysia.
[4]Water Quality Laboratory, National Water Research Institute of Malaysia (NAHRIM), Lot 5377, Jalan Putra Permai, Rizab Melayu Sungai Kuyoh, 43300, Seri Kembangan, Selangor, Malaysia

**Corresponding author: alyza.azzura@umt.edu.my*

Received: 19 June 2023; Accepted: 15 October 2023: Published: 29 December 2023

Abstract

Microplastics (MPs) constitute an emerging class of pollutants that have garnered significant attention due to their omnipresence in marine and freshwater ecosystems. Particles with a diameter of less than 5 mm result from the degradation of larger plastic debris and the production of commercial plastic products. The pervasive occurrence of MPs in the environment is a primary concern due to their potential adverse effects on marine organisms and human health. MPs' high specific surface area and hydrophobicity make them effective adsorbents of other pollutants. Consequently, ingestion of MPs by organisms can lead to enhanced toxicity and bioaccumulation of these pollutants, causing significant harm to the ecosystem. This study offers a comprehensive overview of the properties of MPs, the routes of their entry into the environment, their impacts on environmental and human health, and current approaches for their removal. Physical, chemical, and biological methods for MP removal are discussed, including their benefits and drawbacks. However, there is an urgent need to develop novel, efficient, and cost-effective techniques for MP removal. The insights presented in this review aim to guide policymakers, scientists, and stakeholders in promoting sustainable management practices.

Keywords: microplastics, chemical contaminants, wastewater treatment plants, removal techniques

Abstrak

Mikroplastik (MP) merupakan kelas pencemar yang muncul dan telah mendapat perhatian utama pada masa ini kerana kehadirannya di dalam ekosistem marin dan air tawar. Zarah-zarah dengan diameter kurang daripada 5 mm ini terhasil daripada degradasi serpihan plastik yang lebih besar dan pengeluaran produk plastik komersial. Kemunculan MP yang berleluasa di alam sekitar ini telah menimbulkan kebimbangan kerana ianya berpotensi memberi kesan buruk terhadap organisma marin dan kesihatan manusia. Luas permukaan spesifik yang tinggi dan hidrofobik MP menjadikannya sebagai penjerap yang berkesan bagi bahan

pencemar lain. Oleh itu, pendedahan MP terhadap organisma boleh membawa kepada peningkatan ketoksikan dan bioakumulasi bahan pencemar ini, dan seterusnya menyebabkan kemudaratan yang ketara kepada ekosistem. Ulasan ini memberikan gambaran menyeluruh tentang sifat-sifat MP, laluan masuk ke alam sekitar, kesannya terhadap alam sekitar dan kesihatan manusia, dan pendekatan semasa untuk penyingkiran mereka. Kaedah fizikal, kimia dan biologi untuk penyingkiran MP dibincangkan, termasuk kelebihan dan kelemahannya. Walau bagaimanapun, terdapat keperluan mendesak untuk membangunkan teknik baru yang cekap dan kos yang efektif untuk penyingkiran MP. Ulasan ini memberikan pandangan yang berharga untuk penggubal dasar, saintis dan pihak berkepentingan untuk menggalakkan amalan pengurusan yang mampan dan mengurangkan percambahan MP dalam alam sekitar.

Kata kunci: mikroplastik, pencemar kimia, loji rawatan sisa air, teknik penyingkiran

Introduction

Global plastic production has grown rapidly in the past few decades. According to the United Nations, plastic production reached 359 million metric tons in 2018, a significant increase from 1.5 million metric tons in 1950 [1]. This substantial growth, amounting to over 200 times in just 68 years, can be attributed to several factors, such as population growth, urbanization, and the ascendancy of the global consumer culture. However, if the current rate of plastic production persists, experts predict that plastic waste production will triple by 2050 [2].

The increase in plastic production has led to a global surge in plastic waste generation, becoming a significant environmental concern due to the inadequate management of plastic waste. As a result, plastic debris has accumulated in various environmental matrices, such as marine and terrestrial environments. Plastic waste can persist for decades in the environment, with several harmful impacts on the environment and biota. In marine environments, the accumulation of plastic debris has been found to cause entanglement and ingestion by marine animals, leading to physical injuries, suffocation, and mortality [3]. The ingestion of plastic debris can also negatively impact the health of these organisms, such as reduced feeding efficiency, malnutrition, and reproductive impairment [4]. Additionally, plastic debris can act as a carrier for invasive species and pathogens, resulting in ecological disruptions and the spread of diseases [5,6]. In terrestrial environments, plastic debris can lead to soil and water pollution, which, in turn, can have harmful effects on soil quality, crop productivity, and human health [7, 8].

Plastic debris undergoes a process of degradation, leading to the formation of microplastics (MPs), which are defined as plastic particles smaller than 5 mm [9, 10]. MPs can be classified into two categories based on their origin: primary and secondary (Figure 1a). Primary MPs are deliberately manufactured and added to products, such as microbeads in personal care items or plastic pellets used in production processes [11, 12]. Secondary MPs are produced by the fragmentation, degradation, and weathering of larger plastic debris through natural and anthropogenic processes [13-15]. These small plastic particles enter the aquatic, terrestrial, and air environments through several activities on land and in the marine environment (Figure 1b). Table 1 summarizes the potential roots of primary and secondary MPs in the environment. Additionally, MPs are categorized according to their physical properties, including shape, size, and chemical composition. They can have either spherical or irregular shapes. They may contain various additives, such as plasticizers, stabilizers, and flame retardants, which can leach into the environment, posing potential risks to human health and ecosystems, as presented in Figure 1c [16].

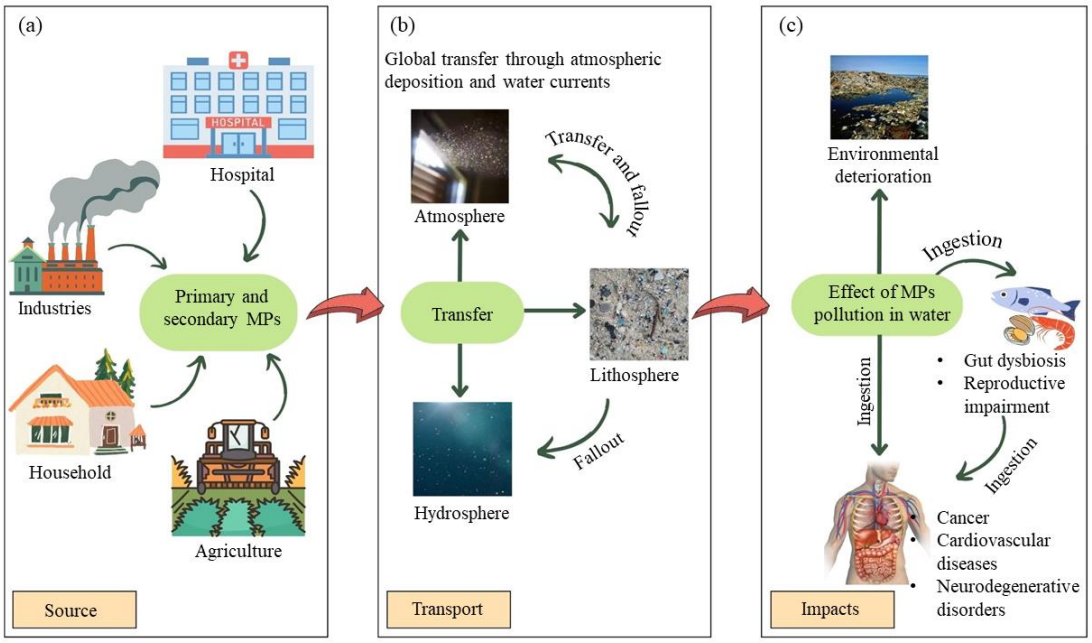


Figure 1. The schematic diagram of (a) the main sources of MPs, (b) transportation of MPs into the environment, and (c) environmental impacts and health effects on living organisms

Table 1. Summary of the potential roots of primary and secondary MPs in the environment

Primary MPs	**Secondary MPs**
Microfibres detached from synthetic textiles [17]	Degradation of larger plastics [18, 19]
Microbeads usually used in personal care, such as face scrub, body wash, toothpaste, etc. [12, 20]	Poor management of single-use plastics such as PPE [21]
Resin particles are used as industrial feedstock [22]	Aged and broken plastic debris due to environmental pressure [23, 24]
Medical applications such as dentistry products [25]	Tiny particles from the weathering of agricultural plastic film [22]
Dust from abrasions on car tires [26]	Plastic mulch film (PE) is used to improve water use efficiency and crop yield [8]
Ingredients that have been used for plastics production [2]	Plastic release during the mechanical recycling process [25]

The presence of MPs in the environment is a growing concern, and their detection has become increasingly common in various environmental compartments such as water, sediment, and soil. Among the different types of MPs, polyethylene (PE) and polypropylene (PP) are frequently detected in environmental samples, and their abundance is linked to their widespread use in products such as plastic bags, food packaging, and bottles [8, 24,

27]. Similarly, polystyrene (PS), commonly used in disposable food containers, cups, and packaging materials, is also frequently found in environmental samples, including freshwater and marine systems. Nylon (PA), utilized in textiles, fishing nets, and ropes, is another type of microplastic commonly detected in environmental samples, including water, sediment, and biota [28]. Polyethylene terephthalate (PET), used in water bottles, food packaging, and textiles, has also been found in various environmental compartments [25, 29, 30]. PET is known to resist environmental degradation, and studies have estimated its half-life to be hundreds of years under certain conditions. Table 2 summarizes the types of MPs, their applications, and estimated degradation time in the environment.

Table 2. Summary of the types, applications, and estimated degradation time of MPs

Type of Polymers	Chemical Formula	Application	Estimated Degradation Time	References
Polyvinyl chloride (PVC)	$(C_2H_3Cl)_n$	Building and construction sector	Up to 100 years	[28, 31]
Polyamide (PA) or nylon	$(C_{12}H_{22}N_2O_2)_n$	Gears, bushings, bearings, stockings, fabric, carpets, fishing line, and cable coatings	20 – 200 years	[31]
Polyethylene (PE)	$(C_2H_4)_n$	Shopping bags, cosmetic products, bottles, food packaging	Up to 1000 years	[28, 31]
Polypropylene (PP)	$(C_3H_6)_n$	Medicine bottles, bank notes, hinged caps	20-30 years	[28, 31]
Polystyrene (PS)	$(C_8H_8)_n$	Building insulation, inner line of fridge, food packaging	Up to 500 years	[28, 31]
Polyethylene terephthalate (PET)	$(C_{10}H_8O_4)_n$	Personal care products, water bottles, food packaging films	Up to 450 years	[28, 32]

Physicochemical properties of microplastic

The diverse range of MPs in the environment can be classified based on their distinctive shapes, including fibers, fragments, pellets, films, microbeads, and foams. These various shapes can result from the different types of transformations that MPs undergo, which can alter their physicochemical properties [33]. Among the various transformation processes, a previous study reported that chemical degradation induced by UV radiation is the most critical, initiating the initial degradation processes of microplastic particles [34]. The degradation of MPs can result in the formation of smaller particles, which can further contribute to the accumulation of MPs in the environment and increase the risk of exposure to humans and wildlife.

Polymers also possess unique physicochemical properties, including crystallinity, density, surface charge, surface area, surface hydrophobicity, and additives, influenced by their chemical compositions [23, 35]. The crystallinity of a polymer is a crucial characteristic that can affect the density of MPs. For instance, semi-crystalline polymers like PE and PP have low densities and tend to float in water [13, 16]. However, the crystallinity of a polymer can be altered by various environmental pressures, which can have significant implications for its other physicochemical properties [36]. Other physicochemical properties of MPs include surface charge, surface area, surface hydrophobicity, and the presence of additives, which can impact their stability, reactivity, and fate in the environment [37].

On the other hand, polymers with highly aromatic structures, such as PS, have unique physicochemical properties that make them highly adsorbent and susceptible to environmental pressures [38, 39]. In the case of PS, the strong π-electron-rich aromatic rings within the polymer structure trigger its sorption capacity and enable it to selectively adsorb certain pollutants, including aromatic organic pollutants [40]. However, environmental factors such as temperature, pH, and salinity can alter the π-electron density of the polymer, leading to changes in the sorption capacity and selectivity of the material [35]. Therefore, understanding the physicochemical properties of MPs is crucial in evaluating their fate and transport in the environment and their potential impacts on ecosystems and human health [23, 35].

Routes of entry to the environment

MPs have been identified as a pervasive and persistent form of pollution across the hydrosphere, lithosphere, and atmosphere worldwide. Figure 2 presents a schematic diagram illustrating the transportation of MPs into the environment. According to a global review by Fadare et al., MPs have been detected in various aquatic environments, including oceans, rivers, lakes, and estuaries, as well as in terrestrial environments such as soil and air [41]. A study by Zhang et al. found that MP concentrations in soils from urban areas in China ranged from 8 to 1730 particles/kg, with higher concentrations near plastic waste recycling facilities [42]. In a study on sediments from the Mekong River Delta in Vietnam, Kieu-Le et al. discovered MPs in all samples collected, with a mean concentration of 6.0 ± 2.0 particles per/g of dry sediment [43].

Similarly, microplastic concentrations ranging from 9.73 to 89.16 particles/m^{-3} were found in nine estuaries in Jakarta Bay, Indonesia [44]. MPs can be transported over long distances and accumulate in various aquatic organisms in aquatic environments, posing potential ecological and health risks. A study by Lahive et al. found widespread MP contamination in Asian freshwater ecosystems, with high concentrations detected in sediments and benthic organisms such as snails and worms. The study also revealed that MPs transferred up the food chain to fish and other aquatic organisms, potentially exposing humans through consumption [45].

Wastewater treatment plants (WWTPs) have been identified as significant contributors to MP release into the environment, releasing approximately 1,500 trillion microplastic particles annually [46]. MPs enter WWTPs through the direct discharge of microplastic-containing wastewater from domestic and industrial sources and the shedding of MPs from synthetic textiles during washing. Several studies have reported the abundance of MPs in WWTPs, highlighting their significant contribution to the overall pollution of the aquatic environment. For instance, Li et al. found that the concentration of MPs in WWTP influent ranged from 1.5 to 21.3 particles/L, with an average of 7.5 particles/L. The study also noted an increase in MP concentration in the effluent, with an average of 22.2 particles/L [47]. Mason et al. conducted a study in 17 wastewater treatment facilities in the United States, revealing an average of 0.05 MP/L in the final effluent, equating to a daily discharge into the environment of more than 4 million MPs, with microfibers identified as a dominant type of MPs in the influent and effluent of WWTPs. Regarding MP size, they also found that 57% had a size between 0.125 mm and 0.355 mm, while 43% of MPs were larger than 0.355 mm [48]. Another study by Deng et al. analyzed the influent and effluent of WWTPs in Shaoxing City, China, and found that the mean concentration of MPs in the influent was 334 particles/L, with a range of 1 to 16 particles/L from a textile dyeing WWTPs [49].

The shape and types of MPs found in WWTPs vary depending on their sources and treatment processes. For example, a study by Alvim et al. identified microbeads and fragments of larger plastic debris as the dominant types of MPs in WWTP effluent, while microfibers were more prevalent in the influent [50]. The study also found that the MPs' shape was mainly irregular, with sizes ranging from 1 to 5 mm. Another study by Viitala et al. found that fibers were the dominant shape of MPs in WWTP effluent, accounting for 77% of the total MPs, followed by fragments. Most MPs were smaller than 1 mm, with sizes ranging from 100–500 µm [51].

In the atmosphere, MPs can be transported over long distances and have been detected in remote areas such as the Arctic and Antarctic. The main sources of MPs in the atmosphere are synthetic fabrics, tire deterioration from synthetic rubber, and urban dust [52]. A study by Klein & Fischer in urban areas in Hamburg, Germany, found 2652 MPs particles in atmospheric fallout samples, with a median abundance of 275 MPs/m^2/day [53]. Sridharan et al. found that the MPs and micro rubber (MR) particles predominated in street dust samples retrieved from 15 sites in Asaluyeh, southern Iran, with average concentrations as high as 900 MPs and 250 MRs per 15g of the sample, respectively [54]. In another study by Kacprzak & Tijing, the findings demonstrate that the concentration of microfibers in the indoor environment, ranging from 1 to 60 particles/m^3, was higher compared to outdoors, with a range of 0.3 to 1.5 particles/m^3. The sizes ranged from 50 to 3250 µm indoors and 50 to 1650 µm outdoors [34]. The study also found that the concentration of microfibers in the indoor environment was higher, possibly due to friction, heating, lighting, or wear and tear of various plastic items. A previous study by Sangkhram et al. reported that airborne MPs were mostly PE, PS, PET, and other fibers, with sizes ranging from 10 to 8000 µm [55].

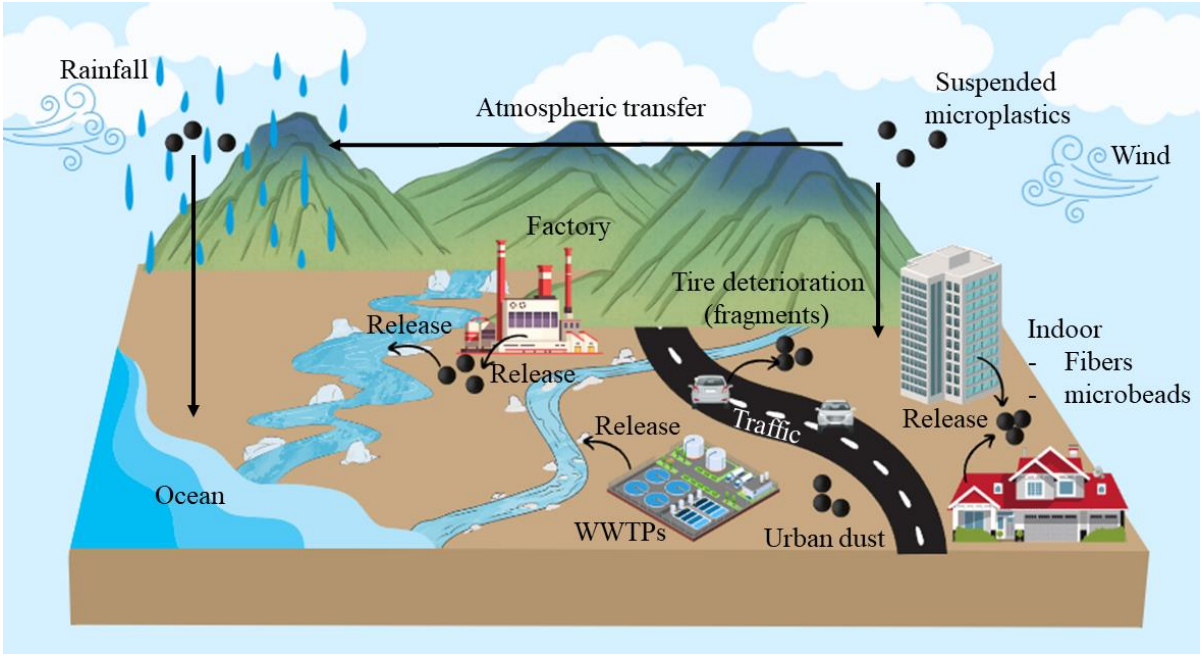


Figure 2. Schematic diagram of the transportation of MPs into the environment

Microplastics as vectors for chemical contaminants

MPs pose a significant and widespread environmental challenge. Due to their relatively high specific surface areas and hydrophobicity nature, MPs are highly effective at adsorbing various contaminants [56]. MPs are composed of various additives, such as plasticizers, fillers, and stabilizers, which complicate their composition. Moreover, when released into the environment, MPs provide surface area for the adsorption of numerous compounds from the surrounding environment. Examples of chemical pollutants that can adhere to plastics include polychlorinated biphenyls (PCBs), polycyclic aromatic hydrocarbons (PAHs), polybrominated diphenyl ethers (PBDEs), and persistent bioaccumulative and toxic substances (PBTs) [57]. When MPs absorb contaminants from the environment, their toxicity rises, potentially causing harmful effects on human health and aquatic organisms [58] [59]. The sorption of the chemical contaminants on the surface of MPs is influenced by various factors, including the type of polymers, the nature of chemical contaminants, and the

environmental conditions [60]. In this section, we explain the factors that influence the sorption behavior and mechanisms of chemical contaminants on the surface of MPs.

The functional groups of the polymers play a crucial role in the adsorption [61]. The formation of pores and oxygen-containing functional groups (including –OH, –COOH, and C–O) may increase the polarity of MP surfaces, enhancing the impact of hydrogen bonding on adsorption and decreasing their ability to adsorb weak polar organic contaminants [62, 63]. Liu et al. highlighted that their polymer types and features can influence the adsorption ability of MPs toward heavy metals. Different polymer types of MPs, including PE, PP, PS, and PVC, exhibit variations in their chemical compositions and surface properties, affecting their adsorption capacity for heavy metals. For instance, similar to the adsorption of aromatic pollutants, MPs with a higher density of oxygen-containing functional groups, such as carboxyl, hydroxyl, and amino groups, tend to exhibit enhanced adsorption capacities due to the availability of more binding sites for metal ions [64]. For example, PS, a common type of microplastic, has an aromatic compound that triggers its sorption capacity. PS tends to sorb organic aromatic pollutants at different polarities due to π-π electron interaction, making it an effective carrier of these contaminants [40]. Recent research has also demonstrated that MPs can carry hydrophilic pollutants in aqueous environments. Anastopoulos et al. have shown that PE, PVC, and polynorbornene (PN6) can transport azo dye, a model textile wastewater contaminant. PN6 demonstrated the highest sorption capability, followed by PE and PVC, due to electronegative N and O atoms in the PN6 polymeric structure, which can easily form hydrogen bonds with electropositive azo dye atoms [65]. Furthermore, biofilm formation on the surface of the MPs may affect the physical and chemical characteristics, including morphological surface and hydrophobicity, impacting the transportation, sinking, weathering, and fragmentation of MPs in the environment [66]. Cui et al. also report that the sorption of PBDEs, PCBs, α-hexabromocyclododecane (HBCDD), and organophosphate flame retardants (OPFRs) is influenced by the presence of biofilm on the surface of high-density polyethylene (HDPE) compared to virgin HDPE [36].

In the literature, it is established that the functional groups and ionic properties of chemical contaminants influence their polarity [61]. Different polymers may exhibit varying sorption capacities for hydrophobic organic contaminants [67]. The log K_{ow} is commonly used to describe the polarity of the contaminants, where organic contaminants with a higher log K_{ow} are classified as hydrophobic and are more prone to adsorption on the surface of MPs [68]. For example, a study conducted by Li et al. demonstrated that hydrophobic antibiotics with higher log K_{ow} values were more attracted to PP, PS, PE, and PVC [69]. On the other hand, the sorption behaviors of organic contaminants on the surface of MPs are significantly influenced by the molecular structure of organic pollutants. For instance, sulfanilamide antibiotics, composed of bonded carbon and hydrogen atoms, readily adhere to and bind on the surface of MPs in the environment [70].

In addition to the properties of MPs, environmental variables such as pH and salinity significantly influence the adsorption of heavy metals onto MPs. Liu et al. emphasized that the pH of the solution affects both the surface charge of MPs and the speciation of metal ions, thereby influencing their electrostatic interactions and complexation processes. Generally, MPs exhibit higher adsorption capacities for heavy metals under acidic conditions (lower pH) due to increased positive surface charge and higher concentrations of metal ions. On the other hand, the salinity of the environment can also impact heavy metal adsorption by MPs. Elevated salinity levels increase the ionic strength of the solution, leading to competition between metal ions and salt ions for adsorption sites on MPs. As a result, the adsorption of heavy metals by MPs may decrease under high salinity conditions [64]. Furthermore, the size and shape of MPs play a crucial role, with smaller MPs possessing larger surface areas and, consequently, higher adsorption capacities. Irregularly shaped MPs with rough surfaces also provide more active sites for metal binding than their spherical counterparts.

Effects of microplastics pollution in water

The presence of MPs in aquatic environments has been extensively documented in numerous studies. In a recent investigation conducted by Hu et al. [16], the influence of environmental variables on the adsorption of heavy metals onto MPs was explored. Additionally, Liu et al. emphasized that the pH of the solution affects both the surface charge of MPs and the speciation of metal ions, thereby influencing their electrostatic interactions and complexation processes. Generally, MPs exhibit higher adsorption capacities for heavy metals under acidic conditions (lower pH) due to an increased positive surface charge and higher concentrations of metal ions. On the other hand, the salinity of the environment can also impact heavy metal adsorption by MPs. Elevated salinity levels increase the ionic strength of the solution, leading to competition between metal ions and salt ions for adsorption sites on MPs. As a result, the adsorption of heavy metals by MPs may decrease under high salinity conditions [16]. This distribution of polymer types and shapes also highlights MPs' widespread contamination of freshwater ecosystems. The small size of MPs enables their easy entry into aquatic environments, where they can persist for extended periods and potentially pose significant risks to the ecosystem and human health. This section will concisely elaborate on the effects of MP pollution in water.

Effects of microplastics on the aquatic environment

MPs pose a growing concern in marine ecosystems due to their small size, making them easily mistaken for food by various marine species. The ingestion of MPs by marine organisms, such as zooplankton [71], bivalves [72] [73, 74], fishes [75], and shrimps [76], can lead to detrimental effects on their physiological functions. MPs with sharp edges can cause mechanical injuries in the digestive tract, leading to inflammation and other complications. Additionally, MPs can act as carriers of harmful chemicals, including heavy metals, organic pollutants, and plasticizers. These chemicals have the potential to pass through the gut wall and enter the circulatory system of marine organisms, leading to disruptions in reproductive and nutritional systems, as well as inducing inflammation in essential organs [4].

The vulnerability of marine organisms to the detrimental effects of MPs extends to critical stages of their life cycles. Zhang et al. highlighted the high susceptibility of sea turtle eggs to the permeation of pollutants from microplastics. MPs near sea turtle nesting areas pose a significant threat to embryonic development, diminishing hatching success and ultimately jeopardizing population sustainability. The chemicals present in MPs can interfere with embryonic development, disrupt hormonal balance, and compromise sea turtle embryos' overall health and survival [77].

Effects of microplastics on humans

The ingestion of MPs is recognized as the primary route of human exposure to these particles. Recent research has shed light on the extent of this exposure pathway and its potential implications for human health. Research indicates that the average person consumes approximately 39,000 to 52,000 synthetic plastic debris particles annually, with age and gender also having an effect [42]. Furthermore, MPs have been detected in various food items, including seafood, table salt, honey, and beverage packaging, suggesting that dietary intake is a significant contributor to human exposure [41, 78-82]. Once ingested, MPs can translocate from the gastrointestinal tract to various organs and tissues within the body. Turroni et al. emphasized that MPs can enter organs such as the liver, kidneys, and gastrointestinal tract, potentially leading to health effects [83]. The physical presence of MPs in these organs can induce mechanical damage, leading to tissue inflammation and impairing normal physiological functions [84]. Additionally, chronic exposure to MPs has been associated with impaired nutrient absorption in the gastrointestinal tract, disrupting metabolic processes and overall health [85].

Bhatt et al. [4], Golwala et al. [86], and Rahman et al. [87] highlighted the potential harm caused by the release of pollutants, including endocrine disruptors, heavy metals, and persistent organic pollutants from MPs. These pollutants accumulate in various tissues and organs, posing significant risks to human health. Chronic exposure to MPs carrying these pollutants can lead to adverse effects on tissues and systems in the

body, including inflammation, oxidative stress, and disruption of hormonal balance. MPs can potentially cause physical harm to organs by blocking the digestive tract, harming intestinal tissues, and affecting cells' filtering and phagocytic activity [88]. Moreover, in vitro studies have demonstrated that exposure to MPs and nano-plastics can trigger cytotoxic effects on cerebral and epithelial human cells through the generation of oxidative stress [89]. This type of stress arises from an imbalance between reactive oxygen species (ROS) production and the cellular ability to detoxify them, leading to the oxidation of vital cellular components such as lipids, proteins, and DNA [90]. The resulting damage can lead to various adverse health outcomes, including cell death, inflammation, and the development of chronic diseases like cancer, cardiovascular disease, and neurodegenerative disorders [91].

Microplastics removal approaches

Removing MPs in WWTPs involves implementing different physical, chemical, and biological techniques. These methods aim to effectively reduce the concentration of MPs in wastewater before its discharge into the environment. In Table 3, a summary of the existing removal techniques in WWTPs can be found, illustrating the range of approaches employed for this purpose.

Physical techniques

Filtration is a widely recognized and effective method for removing MPs from various sources. The principle behind filtration involves passing a liquid through a filter medium with pores smaller than the particle size of the target contaminants. Standard filtration tools include a funnel, filter membrane, and vacuum pump [92]. In the case of MPs, the liquid containing MPs is poured into the funnel, and the vacuum pump creates a pressure difference that drives the liquid through the filter membrane [93]. As the liquid containing MPs flows through the ultrafiltration membrane, the smaller pores of the membrane selectively block the passage of the MPs while allowing the liquid to pass through [94]. This process ensures the separation and removal of MPs, contributing to the purification of the liquid. The captured MPs remain on the surface or within the membrane, forming a retained fraction that can be subsequently collected and properly disposed of. Figure 3a clearly illustrates how membrane filtration acts as an effective barrier to the passage of MPs, highlighting its potential as a valuable method for MP removal.

Adsorption has emerged as a promising method for effectively removing MPs from aqueous solutions due to its potential for high efficiency and cost-effectiveness. In a recent study conducted by Tang et al. [59], the use of magnetic carbon nanotubes (M-CNTs) as an adsorbent material for the complete removal of three common types of MPs: polyethylene (PE), polyethylene terephthalate (PET), and polyamide (PA), was investigated. The experimental setup involved mixing 5g/L of each type of MP with 5g/L of M-CNTs and allowing them to adsorb for 300 minutes. The study revealed that the strong hydrophobic nature of the MPs played a crucial role in their adsorption onto the M-CNTs. Specifically, for PE MPs, the hydrophobicity of the particles was identified as the primary driving force behind their adsorption. The hydrophobic nature of the M-CNTs facilitated the attraction and binding of the hydrophobic MPs, leading to their effective removal from the aqueous solution. In the case of PET MPs, the adsorption mechanism involved a combination of hydrophobic interaction and π-π electron conjugation, facilitating their interaction and adsorption. Additionally, the presence of π-π electron conjugation, referring to the interaction between the aromatic rings of the MPs and the M-CNTs, further enhanced the adsorption process. Therefore, the combination of hydrophobic interaction and π-π electron conjugation contributed to the efficient removal of PET microplastics.

Similarly, for PA MPs, the adsorption mechanism was found to be more complex, attributed to multiple factors, including π-π electron interaction, complexation, electrostatic interaction, and hydrogen-bond interaction occurring on the surface of the microplastics. The π-π electron interaction involved the interaction between the aromatic rings of the PA molecules and the M-CNTs, facilitating their adsorption. Complexation, electrostatic interaction, and hydrogen-bond interaction between the functional groups present on the surface of the MPs and

the M-CNTs also contributed to the adsorption process [20].

Biochar has gained attention as a potential material for removing MPs, offering a promising alternative in addressing the growing concern of MP pollution. A recent study by Wang et al. demonstrated that biochar could remove more than 95% of MPs, making it a highly efficient solution for mitigating MP contamination. The remarkable MP removal efficiency of biochar can be attributed to several factors. The flaky-shaped particles of biochar possess unique properties that facilitate MP removal. These flaky particles can detach themselves from the main biochar structure, increasing surface area exposure and creating more binding sites for MP adsorption. This characteristic enhances the contact between biochar and microplastics, leading to a higher adsorption capacity and more effective removal. Furthermore, the van der Waals forces in the biochar structure play a significant role in MP removal. These intermolecular forces, arising from fluctuations in electron density, contribute to the attractive forces between the biochar and MPs. As a result, MPs experience reduced immobilization through mechanisms such as “Trapped” and “Entangled” (Fig. 3b), where MPs become trapped within the biochar structure or entangled with the biochar particles [96].

Chemical techniques

Coagulation and flocculation techniques have long been recognized as effective methods for removing MPs in WWTPs. The coagulation process involves the addition of coagulants, typically metal salts such as aluminum sulfate ($Al_2(SO_4)_3$) or ferric chloride ($FeCl_3$), to the wastewater. During coagulation, MPs encounter the Al^{3+} ions present in the coagulant. Figure 3c shows the illustration for the coagulation process for MPs removal. The Al^{3+} ions bind to the surfaces of the MPs through interactions with oxygen-containing functional groups, such as carboxyl, hydroxyl, or carbonyl groups. These functional groups are often present on the surface of MPs, resulting from weathering and degradation processes. The binding of Al^{3+} ions to the MPs forms complex species, such as Al-PET in the case of PET MPs, altering the surface properties of the MPs, leading to increased particle size and improved settling characteristics. Additionally, the complexation between Al^{3+} ions and MPs reduces repulsive forces between individual MP particles, promoting their aggregation and the formation of larger flocs. These larger flocs are more easily separated from the wastewater, resulting in the near-complete removal of MPs, as reported by Lu et al. [97].

The electro-coagulation technique is a recent advancement and an effective method for removing MPs from aqueous environments. The electro-coagulation process is based on the principle of electrolysis, where an electric current is applied to electrodes submerged in the wastewater. The electrodes, typically made of aluminum or iron, dissolve electrolytically, generating metal ions in the surrounding solution. The electro-coagulation process offers several mechanisms for the removal of MPs. For instance, the generated metal ions, such as Al^{3+} and Fe^{3+}, can undergo hydrolysis reactions, forming metal hydroxide species, such as $Al(OH)_3$ and $Fe(OH)_3$. These metal hydroxide species can adsorb onto the surface of MPs, promoting the accumulation and subsequent removal of the particles. In addition, the metal hydroxide species can act as coagulants, neutralizing the charge on the MPs and causing their aggregation through charge neutralization mechanisms. Various operational parameters influence the effectiveness of the electro-coagulation process for MP removal. Elkhatib et al. reported a high removal efficiency of 98.5% under specific conditions, including adjusting the initial pH to 4 and applying a current density of 2.88 mA/cm^2 to the reactor. The pH adjustment helps create favorable conditions for generating and precipitation metal hydroxide species, which aids in MP removal. The current density applied to the reactor affects the rate of metal ion generation, which, in turn, influences the coagulation and removal of MPs [98].

Photocatalytic degradation is another promising technology for efficiently removing MPs from aqueous environments. This technique harnesses the power of light to activate a catalyst, leading to the generation of electron-hole pairs that can oxidize MPs. Figure 3d demonstrates the process of photocatalytic degradation of MPs. Among the various photocatalysts investigated,

carbon and nitrogen-doped titanium dioxide (TiO_2) have shown exceptional performance in visible light absorption and the separation efficiency of electron-hole pairs, making them highly effective for photocatalytic activity. In a study by Tarazona et al., researchers examined using carbon and nitrogen-doped TiO_2 in conjunction with visible light from an LED lamp to remove MPs. The photocatalytic degradation of MPs was evaluated over 50 hours. The results indicated that the green N-TiO_2 semiconductor exhibited a reduction in the mass of high-density polyethylene (HDPE) MPs within the range of 1-6%. Furthermore, when carbon and nitrogen-doped TiO_2 were employed for a reaction time of 50 hours, the removal efficiency increased significantly to 71.77% [99]. Similarly, Nabi et al. reported a high removal efficiency of more than 95% for PS MPs using TiO_2 nanoparticle films for photocatalytic degradation [100].

Biological techniques

Microalgae have been identified as a promising bio-alternative for various wastewater treatment stages and functionalities due to their potential for removing pollutants from water bodies. While microalgae are already used for water treatment, they have been identified as a potential solution for MP removal due to their ability to interact with and aggregate with MPs, as shown in Figure 3e. Cunha et al. reported on the potential of microalgae for microplastic removal [101]. In a study conducted by Cheng and Wang, *Scenedesmus abundans* was found to effectively remove more than 85% of PS, poly(methyl methacrylate) (PMMA), and polylactide (PLA) microparticles. Hetero-aggregation was identified as the main mechanism of MP removal, wherein microalgae and MPs form aggregates through electrostatic attraction, hydrogen bonding, and van der Waals forces, leading to their separation from the water [102]. Another study by Adegoke also reported that marine seaweed, *Fucus vesiculosus*, was used to determine whether MPs could be removed by translocation in algal tissues. Small canals in the algal cells restricted the flow of MPs, causing the MP particles to become trapped. The study shows that algae removal efficiency was around 94.5% in certain regions [103]. However, MPs' removal efficiency was influenced by several factors, including microalgal density, microplastic concentration, and contact time.

.

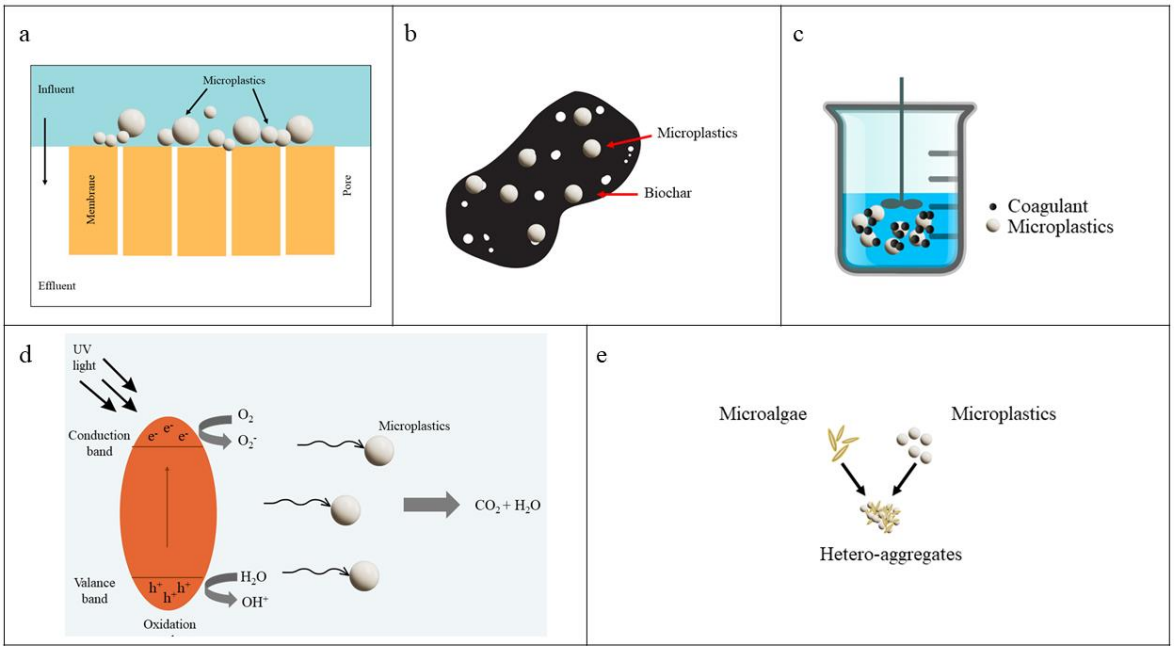


Figure 3. Schematic diagram of main MPs removal approaches (a) membrane filtration, (b) biochar adsorption, (c) coagulation treatment, (d) photocatalytic degradation, and (e) microalgae treatment.

Table 3. Summary of physical, chemical, and biological techniques for MP removal

Removal Techniques Approach	Type of MPS	Mechanisms	Efficiency	References
Filtration by biochar	PS microsphere	The van der Waals forces have resulted in less immobilization by the "Trapped" and "Entangled" mechanisms	<95%	[96]
Adsorption by magnetic carbon nanotube	PE, PET, and PA	The strong hydrophobicity of MPs caused M-CNT adsorption by PE, hydrophobic interaction and π-π electron conjugation caused MCNT adsorption by PET, and π-π electron interaction, complexation, electrostatic interaction, and hydrogen-bond interaction on the PA surface all contributed to M-CNT adsorption.	100%	[20]
Coagulation process	PET	The Al was used as a coagulant to form complexes with MPs by exchanging ligands.	Nearly 100%	[97]
Electro-coagulation	MPs from synthetic and real wastewater	Metal ions (Al^{3+}) discharged from the electrode react with the hydroxide coagulant in the water stream to generate sludge blankets for adhering MPs.	98.5%	[98]
Photocatalytic degradation by carbon and nitrogen-doped TiO_2	HDPE	Degradation of primary HDPE MPs can be accelerated and promoted by altering operational parameters such as temperature and pH during photocatalysis.	1-6% for green N-TiO_2, 71.77% for carbon and N-TiO_2	[99]
Photocatalytic degradation by TiO_2 nanoparticles film	PS	Surface hydrophilicity can facilitate the interaction between semiconductors and plastic particles, resulting in charge transfer and separation, leading to MPs' rapid breakdown.	<95%	[100]
Adsorption on microalgae	PS, PMMA, and PLA	Multiple types of MPs were removed by the microalgae *Scenedesmus abundans*, and the main mechanism of MP removal was identified as hetero-aggregation.	<85%	[102]
Adsorption on microalgae	MPs from environment	Marine seaweed, *Fucus vesiculosus*, was used to remove MPs from the environment by translocation in algal tissues.	94.5%	[103]

Limitation of different techniques and green strategies

Microplastic pollution poses a pressing environmental challenge, demanding effective management strategies. We advocate for the future emphasis on green and environmentally friendly approaches. The following outlines some research challenges and goals to reduce MPs in the environment.

Physical methods commonly used for MP removal have proven effective in eliminating high-density MPs. However, they face limitations in dealing with low-density MPs, generating secondary waste, and exhibiting varying efficacy under different environmental factors [104]. Therefore, a comprehensive approach that integrates multiple methods, such as biological treatment and chemical oxidation, becomes necessary. This integration maximizes MP removal efficacy while minimizing environmental impacts. Integrating physical methods with complementary techniques provides a more sustainable solution for microplastic removal in aquatic systems. Moreover, using environmentally friendly and biology-based materials, including starch and biochar, holds promise as adsorbents and coagulators for MP removal due to their biodegradability and environmental friendliness in aquatic environments [105].

Chemical methods, including photocatalytic oxidation and oxidation removal techniques, promise to eliminate MPs from water. However, their large-scale implementation presents challenges due to their high energy consumption, cost implications, and the potential generation of harmful by-products leading to secondary contamination. Thus, a careful evaluation of the practicality and sustainability of chemical approaches is essential to ensure their effective implementation. Additionally, selecting appropriate catalysts, optimizing operating conditions, and integrating suitable treatment technologies can further enhance the effectiveness of these methods. Regarding environmental impact assessment during sample preparation, the software tool AGREEprep may be considered in the future [106].

Biological approaches, particularly biodegradation by microorganisms, have emerged as promising and eco-friendly strategies for MP removal from aquatic systems. However, the practical implementation of this method can be impeded by the slow rate of complete degradation, leading to the release of toxic metabolites and subsequent secondary contamination [56]. Additionally, the efficacy of biological approaches is affected by multiple factors, including the type of MPs, microbial community composition, and environmental conditions like temperature, pH, and nutrient availability. Therefore, optimizing biodegradation methods, microbial communities, environmental conditions, and operational parameters is crucial to enhancing the potential of biological approaches and making them more suitable for large-scale applications.

Conclusion and Future Perspectives

The contamination of the environment with MPs, caused by anthropogenic activities, is a pervasive problem that affects all environmental matrices. MPs possess unique physicochemical properties that enable them to adsorb other pollutants and act as carriers, leading to their accumulation in the food chain and potentially causing adverse effects on human health and aquatic organisms. While biological techniques hold promise for MP remediation, their removal efficiency still lags behind physical and chemical techniques. Therefore, a multifaceted approach integrating various technologies and strategies is urgently needed. A combination of physical, chemical, and biological methods is necessary to achieve optimal removal of MPs from aquatic and terrestrial systems.

However, a careful evaluation of the limitations and potential environmental impacts of each method is crucial, and the integration of complementary methods is necessary for sustainable remediation. Moreover, effective monitoring and assessment techniques must be developed to determine the extent and sources of MP pollution, enabling the implementation of targeted management strategies to reduce and eliminate sources of contamination. Continued research is also required to identify the long-term effects of MPs on aquatic and terrestrial ecosystems and human health. Furthermore, exploring alternative materials and promoting the circular economy presents a viable solution for reducing plastic waste, significantly reducing MP pollution.

Acknowledgment

The authors gratefully acknowledge financial support from Ministry of Higher Education of Malaysia through the Fundamental Research Grant Scheme (FRGS) (FRGS/1/2020/STG05/UMT/02/1) and Universiti Malaysia Terengganu for the research facilities.

References

1. Leal Filho, W., Salvia, A. L., Bonoli, A., Saari, U. A., Voronova, V., Klõga, M., ... and Barbir, J. (2021). An assessment of attitudes towards plastics and bioplastics in Europe. *Science of the Total Environment*, 755: 142732
2. Anik, A. H., Hossain, S., Alam, M., Sultan, M. B., Hasnine, M. T. and Rahman, M. M. (2021). Microplastics pollution: A comprehensive review on the sources, fates, effects, and potential remediation. *Environmental Nanotechnology, Monitoring & Management*, 16: 100530.
3. Kumar, R., Sharma, P., Manna, C. and Jain, M. (2021). Abundance, interaction, ingestion, ecological concerns, and mitigation policies of microplastic pollution in riverine ecosystem: A review. *Science of The Total Environment*, 782: 146695.
4. Golwala, H., Zhang, X., Iskander, S. M. and Smith, A. L. (2021). Solid waste: An overlooked source of microplastics to the environment. *Science of the Total Environment*, 769: 144581.
5. Stenger, K. S., Wikmark, O. G., Bezuidenhout, C. C. and Molale-Tom, L. G. (2021). Microplastics pollution in the ocean: Potential carrier of resistant bacteria and resistance genes. *Environmental Pollution*, 291: 118130.
6. Sangkham, S., Faikhaw, O., Munkong, N., Sakunkoo, P., Arunlertaree, C., Chavali, M., ... and Tiwari, A. (2022). A review on microplastics and nanoplastics in the environment: Their occurrence, exposure routes, toxic studies, and potential effects on human health. *Marine Pollution Bulletin*, 181: 113832.
7. Huang, D., Tao, J., Cheng, M., Deng, R., Chen, S., Yin, L. and Li, R. (2021). Microplastics and nanoplastics in the environment: Macroscopic transport and effects on creatures. *Journal of Hazardous Materials*, 407: 124399.
8. Yang, C. and Gao, X. (2022). Impact of microplastics from polyethylene and biodegradable mulch films on rice (*Oryza sativa* L.). *Science of The Total Environment*, 828: 154579.
9. Kurniawan, S. B., Said, N. S. M., Imron, M. F. and Abdullah, S. R. S. (2021). Microplastic pollution in the environment: Insights into emerging sources and potential threats. *Environmental Technology & Innovation*, 23: 101790.
10. Melo-Agustín, P., Kozak, E. R., de Jesús Perea-Flores, M. and Mendoza-Pérez, J. A. (2022). Identification of microplastics and associated contaminants using ultra high resolution microscopic and spectroscopic techniques. *Science of The Total Environment*, 828: 154434.
11. Alvim, C. B., Mendoza-Roca, J. A. and Bes-Piá, A. (2020). Wastewater treatment plant as microplastics release source–Quantification and identification techniques. *Journal of Environmental Management*, *255*: 109739.
12. Katsumi, N., Kusube, T., Nagao, S. and Okochi, H. (2020). The role of coated fertilizer used in paddy fields as a source of microplastics in the marine environment. *Marine Pollution Bulletin*, 161: 111727.
13. Hanun, J. N., Hassan, F. and Jiang, J. J. (2021). Occurrence, fate, and sorption behavior of contaminants of emerging concern to microplastics: Influence of the weathering/aging process. *Journal of Environmental Chemical Engineering*, *9*(5): 106290.
14. Pan, Z., Liu, Q., Sun, X., Li, W., Zou, Q., Cai, S. and Lin, H. (2022). Widespread occurrence of microplastic pollution in open sea surface waters: Evidence from the mid-North Pacific Ocean. *Gondwana Research*, 108: 31-40.
15. Chellasamy, G., Kiriyanthan, R. M., Maharajan, T., Radha, A. and Yun, K. (2022). Remediation of microplastics using bionanomaterials: A review. *Environmental Research*, 208: 112724.
16. Hu, K., Yang, Y., Zuo, J., Tian, W., Wang, Y., Duan, X. and Wang, S. (2022). Emerging microplastics in the environment: properties, distributions, and impacts. *Chemosphere*, *297*: 134118.

17. Wang, T., Li, B., Zou, X., Wang, Y., Li, Y., Xu, Y., ... and Yu, W. (2019). Emission of primary microplastics in mainland China: invisible but not negligible. *Water Research*, 162: 214-224.
18. Lehtiniemi, M., Hartikainen, S., Näkki, P., Engström-Öst, J., Koistinen, A. and Setälä, O. (2018). Size matters more than shape: Ingestion of primary and secondary microplastics by small predators. *Food Webs*, 17: e00097.
19. Jaikumar, G., Brun, N. R., Vijver, M. G. and Bosker, T. (2019). Reproductive toxicity of primary and secondary microplastics to three cladocerans during chronic exposure. *Environmental Pollution*, 249: 638-646.
20. Tang, Y., Zhang, S., Su, Y., Wu, D., Zhao, Y. and Xie, B. (2021). Removal of microplastics from aqueous solutions by magnetic carbon nanotubes. *Chemical Engineering Journal*, 406: 126804.
21. Akhbarizadeh, R., Dobaradaran, S., Nabipour, I., Tangestani, M., Abedi, D., Javanfekr, F., ... and Zendehboodi, A. (2021). Abandoned Covid-19 personal protective equipment along the Bushehr shores, the Persian Gulf: an emerging source of secondary microplastics in coastlines. *Marine Pollution Bulletin*, 168: 112386.
22. Huang, D., Wang, X., Yin, L., Chen, S., Tao, J., Zhou, W., ... and Xiao, R. (2022). Research progress of microplastics in soil-plant system: ecological effects and potential risks. *Science of The Total Environment*, 812: 151487.
23. Ahmed, R., Hamid, A. K., Krebsbach, S. A., He, J. and Wang, D. (2022). Critical review of microplastics removal from the environment. *Chemosphere*, 293: 133557.
24. Li, J., Peng, D., Ouyang, Z., Liu, P., Fang, L. and Guo, X. (2022). Occurrence status of microplastics in main agricultural areas of Xinjiang Uygur Autonomous Region, China. *Science of The Total Environment*, 828: 154259.
25. Suzuki, G., Uchida, N., Tanaka, K., Matsukami, H., Kunisue, T., Takahashi, S., ... and Osako, M. (2022). Mechanical recycling of plastic waste as a point source of microplastic pollution. *Environmental Pollution*, 303: 119114.
26. Goßmann, I., Halbach, M., and Scholz-Böttcher, B. M. (2021). Car and truck tire wear particles in complex environmental samples–a quantitative comparison with "traditional" microplastic polymer mass loads. *Science of the Total Environment*, 773: 145667.
27. Lett, Z., Hall, A., Skidmore, S. and Alves, N. J. (2021). Environmental microplastic and nanoplastic: Exposure routes and effects on coagulation and the cardiovascular system. *Environmental Pollution*, 291: 118190.
28. Vieira, Y., Lima, E. C., Foletto, E. L., and Dotto, G. L. (2021). Microplastics physicochemical properties, specific adsorption modeling and their interaction with pharmaceuticals and other emerging contaminants. *Science of the Total Environment*, 753: 141981.
29. Maghsodian, Z., Sanati, A. M., Tahmasebi, S., Shahriari, M. H. and Ramavandi, B. (2022). Study of microplastics pollution in sediments and organisms in mangrove forests: A review. *Environmental Research*, 208: 112725.
30. Terzi, Y., Gedik, K., Eryaşar, A. R., Öztürk, R. Ç., Şahin, A. and Yılmaz, F. (2022). Microplastic contamination and characteristics spatially vary in the southern Black Sea beach sediment and sea surface water. *Marine Pollution Bulletin*, 174: 113228.
31. Hu, K., Tian, W., Yang, Y., Nie, G., Zhou, P., Wang, Y., ... and Wang, S. (2021). Microplastics remediation in aqueous systems: Strategies and technologies. *Water Research*, 198: 117144.
32. Zhang, Z., Gao, S. H., Luo, G., Kang, Y., Zhang, L., Pan, Y., ... and Wang, A. (2022). The contamination of microplastics in China's aquatic environment: Occurrence, detection and implications for ecological risk. *Environmental Pollution*, 296: 118737.
33. Vaid, M., Sarma, K. and Gupta, A. (2021). Microplastic pollution in aquatic environments with special emphasis on riverine systems: current understanding and way forward. *Journal of Environmental Management*, 293: 112860.
34. Kacprzak, S. and Tijing, L. D. (2022). Microplastics in indoor environment: Sources,

mitigation and fate. *Journal of Environmental Chemical Engineering*, 10(2): 107359.

35. Cai, L., Wu, D., Xia, J., Shi, H. and Kim, H. (2019). Influence of physicochemical surface properties on the adhesion of bacteria onto four types of plastics. *Science of the Total Environment*, 671: 1101-1107.
36. Cui, W., Hale, R. C., Huang, Y., Zhou, F., Wu, Y., Liang, X., ... and Chen, D. (2023). Sorption of representative organic contaminants on microplastics: Effects of chemical physicochemical properties, particle size, and biofilm presence. *Ecotoxicology and Environmental Safety*, 251: 114533.
37. Liu, X., Deng, Q., Zheng, Y., Wang, D. and Ni, B. J. (2022). Microplastics aging in wastewater treatment plants: Focusing on physicochemical characteristics changes and corresponding environmental risks. *Water Research*, 221: 118780.
38. Wang, X., Zhang, R., Li, Z. and Yan, B. (2022). Adsorption properties and influencing factors of Cu (II) on polystyrene and polyethylene terephthalate microplastics in seawater. *Science of the Total Environment*, 812: 152573.
39. Zhang, Y., Diehl, A., Lewandowski, A., Gopalakrishnan, K. and Baker, T. (2020). Removal efficiency of micro-and nanoplastics (180 nm–125 μm) during drinking water treatment. *Science of the Total Environment*, 720: 137383.
40. Wang, J., Liu, X., Liu, G., Zhang, Z., Wu, H., Cui, B., ... and Zhang, W. (2019). Size effect of polystyrene microplastics on sorption of phenanthrene and nitrobenzene. *Ecotoxicology and Environmental Safety*, 173: 331-338.
41. Fadare, O. O., Wan, B., Guo, L. H. and Zhao, L. (2020). Microplastics from consumer plastic food containers: are we consuming it? *Chemosphere*, 253: 126787.
42. Zhang, Y., Zhao, J., Liu, Z., Tian, S., Lu, J., Mu, R. and Yuan, H. (2021). Coagulation removal of microplastics from wastewater by magnetic magnesium hydroxide and PAM. *Journal of Water Process Engineering*, 43: 102250.
43. Kieu-Le, T. C., Thuong, Q. T., Tran, Q. V. and Strady, E. (2023). Baseline concentration of microplastics in surface water and sediment of the northern branches of the Mekong River Delta, Vietnam. *Marine Pollution Bulletin*, 187: 114605.
44. Purwiyanto, A. I. S., Prartono, T., Riani, E., Koropitan, A. F., Naulita, Y., Takarina, N. D. and Cordova, M. R. (2022). The contribution of estuaries to the abundance of microplastics in Jakarta Bay, Indonesia. *Marine Pollution Bulletin*, 184: 114117.
45. Lahive, E., Walton, A., Horton, A. A., Spurgeon, D. J. and Svendsen, C. (2019). Microplastic particles reduce reproduction in the terrestrial worm Enchytraeus crypticus in a soil exposure. *Environmental Pollution*, 255: 113174.
46. Napper, I. E. and Thompson, R. C. (2016). Release of synthetic microplastic plastic fibres from domestic washing machines: Effects of fabric type and washing conditions. *Marine pollution bulletin*, 112(1-2): 39-45.
47. Li, J., Liu, H. and Chen, J. P. (2018). Microplastics in freshwater systems: A review on occurrence, environmental effects, and methods for microplastics detection. *Water research*, 137: 362-374.
48. Mason, S. A., Garneau, D., Sutton, R., Chu, Y., Ehmann, K., Barnes, J., ... and Rogers, D. L. (2016). Microplastic pollution is widely detected in US municipal wastewater treatment plant effluent. *Environmental Pollution*, 218: 1045-1054.
49. Deng, H., Wei, R., Luo, W., Hu, L., Li, B. and Shi, H. (2020). Microplastic pollution in water and sediment in a textile industrial area. *Environmental Pollution*, 258: 113658.
50. Alvim, C. B., Mendoza-Roca, J. A. and Bes-Piá, A. (2020). Wastewater treatment plant as microplastics release source–Quantification and identification techniques. *Journal of Environmental Management*, 255: 109739.
51. Viitala, M., Steinmetz, Z., Sillanpää, M., Mänttäri, M. and Sillanpää, M. (2022). Historical and current occurrence of microplastics in water and sediment of a Finnish lake affected by WWTP effluents. *Environmental Pollution*, 314: 120298.
52. Rose, P. K., Jain, M., Kataria, N., Sahoo, P. K., Garg, V. K. and Yadav, A. (2023). Microplastics in multimedia environment: A systematic review on its fate, transport, quantification, health risk, and

remedial measures. *Groundwater for Sustainable Development*, 2023: 100889.

53. Klein, M. and Fischer, E. K. (2019). Microplastic abundance in atmospheric deposition within the Metropolitan area of Hamburg, Germany. *Science of the Total Environment*, 685: 96-103.
54. Sridharan, S., Kumar, M., Singh, L., Bolan, N. S. and Saha, M. (2021). Microplastics as an emerging source of particulate air pollution: A critical review. *Journal of Hazardous Materials*, 418: 126245.
55. Sangkham, S., Faikhaw, O., Munkong, N., Sakunkoo, P., Arunlertaree, C., Chavali, M., ... and Tiwari, A. (2022). A review on microplastics and nanoplastics in the environment: Their occurrence, exposure routes, toxic studies, and potential effects on human health. *Marine Pollution Bulletin*, 181: 113832.
56. Shi, X., Zhang, X., Gao, W., Zhang, Y. and He, D. (2022). Removal of microplastics from water by magnetic nano-Fe3O4. *Science of The Total Environment*, 802: 149838.
57. Caruso, G. (2019). Microplastics as vectors of contaminants. *Marine Pollution Bulletin*, 146: 921-924.
58. Khalid, N., Aqeel, M., Noman, A., Khan, S. M. and Akhter, N. (2021). Interactions and effects of microplastics with heavy metals in aquatic and terrestrial environments. *Environmental Pollution*, 290: 118104.
59. Tang, K. H. D. and Hadibarata, T. (2021). Microplastics removal through water treatment plants: Its feasibility, efficiency, future prospects and enhancement by proper waste management. *Environmental Challenges*, *5*: 100264.
60. Tumwesigye, E., Nnadozie, C. F., Akamagwuna, F. C., Noundou, X. S., Nyakairu, G. W. and Odume, O. N. (2023). Microplastics as vectors of chemical contaminants and biological agents in freshwater ecosystems: Current knowledge status and future perspectives. *Environmental Pollution*, 2023: 121829.
61. Torres, F. G., Dioses-Salinas, D. C., Pizarro-Ortega, C. I. and De-la-Torre, G. E. (2021). Sorption of chemical contaminants on degradable and non-degradable microplastics: Recent progress and research trends. *Science of the Total Environment*, 757: 143875.
62. Song, X., Zhuang, W., Cui, H., Liu, M., Gao, T., Li, A. and Gao, Z. (2022). Interactions of microplastics with organic, inorganic and bio-pollutants and the ecotoxicological effects on terrestrial and aquatic organisms. *Science of the Total Environment*, 838: 156068.
63. Luo, H., Tu, C., He, D., Zhang, A., Sun, J., Li, J., ... and Pan, X. (2023). Interactions between microplastics and contaminants: A review focusing on the effect of aging process. *Science of the Total Environment*, 899: 165615.
64. Liu, S., Huang, J., Zhang, W., Shi, L., Yi, K., Yu, H., ... and Li, J. (2022). Microplastics as a vehicle of heavy metals in aquatic environments: A review of adsorption factors, mechanisms, and biological effects. *Journal of Environmental Management*, 302: 113995.
65. Anastopoulos, I., Pashalidis, I., Kayan, B. and Kalderis, D. (2022). Microplastics as carriers of hydrophilic pollutants in an aqueous environment. *Journal of Molecular Liquids*, 350: 118182.
66. Tu, C., Chen, T., Zhou, Q., Liu, Y., Wei, J., Waniek, J. J. and Luo, Y. (2020). Biofilm formation and its influences on the properties of microplastics as affected by exposure time and depth in the seawater. *Science of the Total Environment*, 734: 139237.
67. He, H., Wen, H. P., Liu, J. P., Wu, C. C., Mai, L. and Zeng, E. Y. (2023). Hydrophobic organic contaminants affiliated with polymer-specific microplastics in urban river tributaries and estuaries. *Science of The Total Environment*, 899: 166415.
68. Chang, J., Fang, W., Liang, J., Zhang, P., Zhang, G., Zhang, H., ... and Wang, Q. (2022). A critical review on interaction of microplastics with organic contaminants in soil and their ecological risks on soil organisms. *Chemosphere*, 306: 135573.
69. Li, J., Zhang, K. and Zhang, H. (2018). Adsorption of antibiotics on microplastics. *Environmental Pollution*, 237: 460-467.

70. Fu, J., Li, Y., Peng, L., Gao, W. and Wang, G. (2022). Distinct chemical adsorption behaviors of sulfanilamide as a model antibiotic onto weathered microplastics in complex systems. *Colloids and Surfaces A: Physicochemical and Engineering Aspects*, 648: 129337.
71. Wang, Q., Li, J., Zhu, X., Sun, C., Teng, J., Chen, L., ... and Zhao, J. (2022). Microplastics in fish meals: An exposure route for aquaculture animals. *Science of the Total Environment*, 807: 151049.
72. González-Soto, N., Hatfield, J., Katsumiti, A., Duroudier, N., Lacave, J. M., Bilbao, E., ... and Cajaraville, M. P. (2019). Impacts of dietary exposure to different sized polystyrene microplastics alone and with sorbed benzo [a] pyrene on biomarkers and whole organism responses in mussels Mytilus galloprovincialis. *Science of the Total Environment*, 684: 548-566.
73. Teng, J., Wang, Q., Ran, W., Wu, D., Liu, Y., Sun, S., ... and Zhao, J. (2019). Microplastic in cultured oysters from different coastal areas of China. *Science of the Total Environment*, 653: 1282-1292.
74. Prata, J. C., da Costa, J. P., Lopes, I., Andrady, A. L., Duarte, A. C. and Rocha-Santos, T. (2021). A one health perspective of the impacts of microplastics on animal, human and environmental health. *Science of the Total Environment*, 777: 146094.
75. Jabeen, K., Su, L., Li, J., Yang, D., Tong, C., Mu, J. and Shi, H. (2017). Microplastics and mesoplastics in fish from coastal and fresh waters of China. *Environmental Pollution*, 221: 141-149.
76. Han, Y., Shi, W., Tang, Y., Zhou, W., Sun, H., Zhang, J., ... and Liu, G. (2022). Microplastics and bisphenol A hamper gonadal development of whiteleg shrimp (*Litopenaeus vannamei*) by interfering with metabolism and disrupting hormone regulation. *Science of the total environment*, 810: 152354.
77. Zhang, T., Lin, L., Li, D., Wu, S., Kong, L., Wang, J. and Shi, H. (2021). The microplastic pollution in beaches that served as historical nesting grounds for green turtles on Hainan Island, China. *Marine Pollution Bulletin*, 173: 113069.
78. Sridhar, A., Kannan, D., Kapoor, A. and Prabhakar, S. (2022). Extraction and detection methods of microplastics in food and marine systems: a critical review. *Chemosphere*, 286: 131653.
79. Prata, J. C., da Costa, J. P., Lopes, I., Duarte, A. C. and Rocha-Santos, T. (2020). Environmental exposure to microplastics: An overview on possible human health effects. *Science of the Total Environment*, 702: 134455.
80. Masiá, P., Ardura, A. and Garcia-Vazquez, E. (2022). Microplastics in seafood: Relative input of *Mytilus galloprovincialis* and table salt in mussel dishes. *Food Research International*, 153: 110973.
81. Alma, A. M., de Groot, G. S. and Buteler, M. (2023). Microplastics incorporated by honeybees from food are transferred to honey, wax and larvae. *Environmental Pollution*, 320: 121078.
82. Nakat, Z., Dgheim, N., Ballout, J. and Bou-Mitri, C. (2023). Occurrence and exposure to microplastics in salt for human consumption, present on the Lebanese market. *Food Control*, 145: 109414.
83. Turroni, S., Wright, S., Rampelli, S., Brigidi, P., Zinzani, P. L. and Candela, M. (2021). Microplastics shape the ecology of the human gastrointestinal intestinal tract. *Current Opinion in Toxicology*, 28: 32-37.
84. Wu, P., Lin, S., Cao, G., Wu, J., Jin, H., Wang, C., ... and Cai, Z. (2022). Absorption, distribution, metabolism, excretion and toxicity of microplastics in the human body and health implications. *Journal of Hazardous Materials*, 437: 129361.
85. Khan, A. and Jia, Z. (2023). Recent insights into up take, toxicity, and molecular targets of microplastic s and nanoplastics relevant to human health impact s. *Iscience*, 26: 106061.
86. Bhatt, P., Pathak, V. M., Bagheri, A. R. and Bilal, M. (2021). Microplastic contaminants in the aqueous environment, fate, toxicity consequences, and remediation strategies. *Environmental Research*, 200: 111762.
87. Rahman, A., Sarkar, A., Yadav, O. P., Achari, G. and Slobodnik, J. (2021). Potential human health risks due to environmental exposure to nano-and microplastics and knowledge gaps: a scoping

review. *Science of the Total Environment*, 757: 143872.

88. Guo, X. and Wang, J. (2019). The chemical behaviors of microplastics in marine environment: A review. *Marine Pollution Bulletin*, 142: 1-14.
89. Barboza, L. G. A., Vethaak, A. D., Lavorante, B. R., Lundebye, A. K. and Guilhermino, L. (2018). Marine microplastic debris: An emerging issue for food security, food safety and human health. *Marine pollution bulletin*, 133: 336-348.
90. Lee, J., Kim, J., Lee, R., Lee, E., Choi, T. G., Lee, A. S., ... and Tak, E. (2022). Therapeutic strategies for liver diseases based on redox control systems. *Biomedicine & Pharmacotherapy*, 156: 113764.
91. Mahamud, A. S. U., Anu, M. S., Baroi, A., Datta, A., Khan, M. S. U., Rahman, M., ... and Rahman, T. (2022). Microplastics in fishmeal: A threatening issue for sustainable aquaculture and human health. *Aquaculture Reports*, *25*: 101205.
92. Tirkey, A. and Upadhyay, L. S. B. (2021). Microplastics: An overview on separation, identification and characterization of microplastics. *Marine Pollution Bulletin*, 170: 112604.
93. Zhang, Y., Jiang, H., Bian, K., Wang, H. and Wang, C. (2021). A critical review of control and removal strategies for microplastics from aquatic environments. *Journal of Environmental Chemical Engineering*, 9(4): 105463.
94. Liu, W., Zhang, J., Liu, H., Guo, X., Zhang, X., Yao, X., ... and Zhang, T. (2021). A review of the removal of microplastics in global wastewater treatment plants: Characteristics and mechanisms. *Environment International*, 146: 106277.
95. Wang, Z., Lin, T. and Chen, W. (2020). Occurrence and removal of microplastics in an advanced drinking water treatment plant (ADWTP). *Science of the Total Environment*, 700: 134520.
96. Wang, Z., Sedighi, M. and Lea-Langton, A. (2020). Filtration of microplastic spheres by biochar: removal efficiency and immobilisation mechanisms. *Water Research*, 184: 116165.
97. Lu, S., Liu, L., Yang, Q., Demissie, H., Jiao, R., An, G. and Wang, D. (2021). Removal characteristics and mechanism of microplastics and tetracycline composite pollutants by coagulation process. *Science of the Total Environment*, 786: 147508.
98. Elkhatib, D., Oyanedel-Craver, V. and Carissimi, E. (2021). Electro-coagulation applied for the removal of microplastics from wastewater treatment facilities. *Separation and Purification Technology*, 276: 118877.
99. Ariza-Tarazona, M. C., Villarreal-Chiu, J. F., Hernández-López, J. M., De la Rosa, J. R., Barbieri, V., Siligardi, C. and Cedillo-González, E. I. (2020). Microplastic pollution reduction by a carbon and nitrogen-doped TiO_2: Effect of pH and temperature in the photocatalytic degradation process. *Journal of hazardous materials*, 395: 122632.
100. Nabi, I., Li, K., Cheng, H., Wang, T., Liu, Y., Ajmal, S., ... and Zhang, L. (2020). Complete photocatalytic mineralization of microplastic on TiO_2 nanoparticle film. *Iscience*, *23*(7): 101326.
101. Cunha, C., Faria, M., Nogueira, N., Ferreira, A. and Cordeiro, N. (2019). Marine vs freshwater microalgae exopolymers as biosolutions to microplastics pollution. *Environmental Pollution*, 249: 372-380.
102. Cheng, Y. R. and Wang, H. Y. (2022). Highly effective removal of microplastics by microalgae Scenedesmus abundance. *Chemical Engineering Journal*, 435: 135079.
103. Adegoke, K. A., Adu, F. A., Oyebamiji, A. K., Bamisaye, A., Adigun, R. A., Olasoji, S. O. and Ogunjinmi, O. E. (2023). Microplastics toxicity, detection, and removal from water/wastewater. *Marine Pollution Bulletin*, 187: 114546.
104. Gies, E. A., LeNoble, J. L., Noël, M., Etemadifar, A., Bishay, F., Hall, E. R. and Ross, P. S. (2018). Retention of microplastics in a major secondary wastewater treatment plant in Vancouver, Canada. *Marine Pollution Bulletin*, 133: 553-561.
105. Gao, W., Zhang, Y., Mo, A., Jiang, J., Liang, Y., Cao, X. and He, D. (2022). Removal of microplastics in water: Technology progress and green strategies. *Green Analytical Chemistry*, 3: 100042.

106. Wenzel, M., Schoettl, J., Pruin, L., Fischer, B., Wolf, C., Kube, C., ... and Tuerk, J. (2023). Determination of atmospherically deposited microplastics in moss: Method development and performance evaluation. *Green Analytical Chemistry*, 7: 100078.

Malaysian Journal of Analytical Sciences (MJAS)
Published by Malaysian Analytical Sciences Society

EXTRACTION OF ESSENTIAL OIL *Citrus hystrix* BY USING ULTRASOUND -ASSISTED EXTRACTION

(Pengestrakan Pati Minyak *Citrus hystrix* Menggunakan Pengekstrakan Bantuan Ultrasonik)

Ng Hui Ying, Gan Shi Min, and Saliza Asman*

Department of Physics and Chemistry,
Faculty of Applied Sciences and Technology, Pagoh Eucation Hub,
Universiti Tun Hussein Onn Malaysia, 84600 Pagoh, Muar, Johor, Malaysia

**Corresponding author: salizaa@uthm.edu.my*

Received: 4 August 2023; Accepted: 18 September 2023; Published: 29 December 2023

Abstract

Citrus hystrix is a famous aromatic plant that comprises biological properties such as antioxidant, antibacterial, antileukemic, and antitussive properties. Several conventional extraction methods like hydro-distillation, steam distillation and Soxhlet distillation have been used to extract essential oils (EOs), but they are time-consuming, expensive and necessitate the use of numerous solvents. Therefore, this study focused on the use of ultrasound-assisted extraction (UAE) which is a novel extraction method that has lower operating costs and shorter extraction time. UAE was performed to extract the EOs from *C.hystrix* peels by using methanol and petroleum benzine. The yield of extracted EOs were 9.43% and 2.36%, respectively. After extraction, a qualitative phytochemical analysis was carried out to detect chemical constituents in the EOs. Both EOs showed positive results in the tests of alkaloids and terpenoids. Besides, the surface morphology of fresh *C.hystrix* powder before extraction and the residual powder after extraction were compared by using a scanning electron microscope (SEM). SEM photographs of both residual powders revealed pores that appeared because of peel surfaces implosion which occurred during extraction. Functional groups at the configuration peaks were characterised by using Fourier transform infrared (FTIR) spectroscopy and chemical constituents in the EOs were analysed by using gas chromatography-mass spectrometry (GCMS). Results for both extracted EOs demonstrated the presence of OH stretching at 3625-3025 cm^{-1}, CH_3 stretching at 2939-2834 cm^{-1}, C=O stretching at 1721-1719 cm^{-1} and C=C stretching at 1624-1622 cm^{-1}. The GCMS result indicated that the main chemical compounds of both EOs were d-limonene, citronellal, and terpinen-4-ol. According to the findings, UAE extraction method was recommended due to its environmental friendliness and short extraction time.

Keywords: *C. hystrix* peel, ultrasound-assisted extraction, essential oils, phytochemical screening

Abstrak

C. hystrix merupakan tumbuhan aromatik terkenal yang terdiri daripada sifat-sifat biologi seperti sifat antioksidan, antibakteria, antileukemik dan antitusif. Beberapa kaedah pengekstrakan konvensional seperti penyulingan hidro, penyulingan wap, dan penyulingan soxhlet telah digunakan untuk mengekstrak minyak pati (EOs) namum memerlukan penggunaan banyak pelarut, memakan masa, dan mahal. Oleh itu, kajian ini tertumpu kepada penggunaan pengekstrakan bantuan ultrasonik (UAE) yang merupakan kaedah pengekstrakan novel yang mempunyai kos operasi yang lebih rendah dan masa pengekstrakan yang lebih singkat. UAE telah digunakan untuk mengekstrak EOs daripada kulit *C.hystrix* menggunakan metanol, dan petroleum benzine. Hasil kedua-dua EO yang diekstrak adalah 9.43% dan 2.36%. Selepas pengekstrakan, analisis fitokimia kualitatif telah dilakukan

untuk mengesan konstituen kimia dalam EOs. Kedua-dua EOs menunjukkan keputusan positif dalam ujian alkaloid dan terpenoid. Selain itu, morfologi permukaan serbuk *C.hystrix* segar sebelum pengekstrakan dan serbuk sisa selepas pengekstrakan telah dibandingkan dengan menggunakan pengimbas mikroskopi elektron (SEM). Gambar-gambar SEM bagi kedua-dua serbuk sisa menunjukkan liang yang hadir disebabkan oleh letupan permukaan kulit yang berlaku semasa pengekstrakan. Kumpulan-kumpulan berfungsi pada puncak konfigurasi telah dicirikan menggunakan spektroskopi inframerah transformasi Fourier (FTIR), dan juzuk-juzuk kimia dalam EOs dianalisis menggunakan kromatografi gas-spektrometri jisim (GCMS). Hasil kajian menunjukkan kehadiran regangan OH pada 3625-3025 cm^{-1}, regangan CH_3 pada 2939-2834 cm^{-1}, regangan C=O pada 1721-1719 cm^{-1}, and regangan C=C pada 1624-1622 cm^{-1} untuk kedua-dua EO yang diekstrak. Data GCMS menunjukkan komposisi kimia utama bagi kedua-dua EOs adalah D-limonene, sitronelal, dan terpinen-4-ol. Berdasarkan penemuan, kaedah pengekstrakan UAE disyorkan kerana mesra alam dan masa pengekstrakan yang singkat.

Kata kunci: kulit *C.hystrix*, pengekstrakan bantuan ultrasonik, minyak pati, penyaringan fitokimia

Introduction

In Malaysia, 17,000 tonnes of food wastes are reported per day [1]. Fruit peels are one of the wastes produced. Nowadays, fruit peels are collected and processed to extract EOs, which are applied in food and beverage industries, cosmetic industries and pharmaceutical industries. *C. hystrix*, or known as *kaffir lime*, is an aromatic plant part of the Rutaceae family with a green and bumpy peel. EOs of *C. hystrix* have bioactivities such as antioxidant, antibacterial, antileukemic and antitussive, which are functions in aromatherapy, insect repellent and additive in cosmetic products [2, 3].

Extraction methods such as hydro-distillation, steam distillation, and Soxhlet distillation [4] have been used to extract EOs from *C. hystrix* with a high yield production of EOs. However, the extraction period is quite long, and it requires a high operating cost [4]. The UAE extraction method extracts compounds from plants in a solvent by using soundwave at 20 kHz to 100 MHz frequency. Mass transfer occurs due to the ultrasound, which allows the solvent to access plant material cell components faster. Ultrasound also allows the process of erosion to occur, in which the cavitation bubbles produced by ultrasound will make the surface of plant tissues undergo implosion [5]. UAE is a beneficial method that has a short extraction time and high production yield [5]. It can provide a large yield of oil in a short extraction time by imploding cavitation bubbles caused by the ultrasound and triggering fissions at plant cell walls, whereby the percentage yield of oil obtained in 120 min of kaffir lime leaves was 1.75% and the percentage yield of oil obtained in 30 min of rapeseed oil was 21.36% [6, 7]. In this study, the peels of *kaffir lime* were employed to extract EOs with a high yield production in a short period by using UAE.

Solvent used in the extraction process is determined by the type and part of plant, bioactive chemicals of plant, compounds to be extracted from the plant, and availability of solvent [8]. Different types of solvents have different polarities. The bonds between atoms in polar solvents contain very different electronegativities while the bonds between atoms in non-polar solvents contain similar electronegativities. Quantitative and qualitative extraction of plant compounds is affected by the polarity of solvent [9]. Therefore, the yield of EOs extracted from plants by using solvents of varying polarities depends on solubility of plant compounds with the solvent. Polar solvents such as methanol and ethanol are frequently used to extract polyphenols like antioxidant compounds from a plant [7]. Non-polar solvents such as *n*-hexane and petroleum ether are used to extract alkaloids, terpenoids, coumarins and fatty acids from a plant [8]. Purity and quality of the extracted compounds might be impacted because the polarity of a polar solvent like methanol could lead to an unintended chemical reaction, decomposition or degradation of the extracted compounds [8].

Phytochemicals are compounds present in plants which give colours, aromas and flavours, such as phenolics, flavonoids, terpenoids, alkaloids, steroids, proteins and tannins. The main phytochemical contained in *C. hystrix* peel is terpenoids such as β-pinene, limonene, citronellal and sabinene [10]. Terpenoids are the largest group found in natural products, which are known as oxygen-containing terpenes. A study by Soib et al. [11] showed that the UAE method could extract the same secondary metabolites from *Carica papaya Linn* leaves like reflux and agitation methods in terms of saponins, flavonoids, glycosides, alkaloids and phenolics. According to Pandhi and Poonia [12], several phytochemical compounds, including alkaloids, phenol, tannins and flavonoids were detected in Jamum seed extracts by using the UAE method, except saponins, phytosterols, carbohydrates, glycosides and protein. Another study by Mutalib [13] discovered that the UAE approach produced the same favourable findings in photochemical screening tests of *Rosmarinus officinalis*

leaf extracts as by using the conventional methods for extraction, such as maceration, decoction, infusion, regular reflux, and Soxhlet distillation. It can be concluded that the novel UAE extraction method has great possibility of extracting secondary metabolites from plant material with its unique advantages.

In this study, the UAE technique was applied to produce a high yield in a brief amount of time with a small peel-to-solvent ratio. The findings by Kasuan et al. [3] showed that a mere 1.87% of *kaffir lime* oil was extracted from 350g of peels in 10l solvent by using an automated steam distillation process at temperature of 80 ℃ in 75 min. Comparatively, in the present study a better yield of *kaffir lime* EOs was produced by using UAE method despite only 50 min of extraction time and a lower raw material-to-solvent ratio of 1:30 g/mL. The different polarity of solvents was utilised to investigate the effectiveness of different solvents to extract the compounds. Methanol (polar solvent) and petroleum benzine (non-polar solvent) were used in the extraction of EOs from *C. hystrix* with a ratio sample (g) to solvent (ml), was 1:30. Methanol was chosen to extract EOs from C. *hystrix* peels due to its high production yield and effectiveness in extracting phenolic, flavonoid, alkaloid and terpenoids. Petroleum benzine was used to extract EOs from C. *hystrix* peels due to its low boiling point and efficacy in removing alkaloids and terpenoids [8]. Continuously, the presence of alkaloids, protein and amino acids, phenolic compounds, saponins, tannins, flavonoids and terpenoids in the EOs was demonstrated by using phytochemical screening. The morphological properties of C. *hystrix* peels before and after extraction were examined by using SEM. The presence of functional groups in the EOs was confirmed by using FTIR. The analysis of the compounds in EOs extracted was conducted by using Gas chromatography-mass spectrometry (GC-MS).

Materials and Methods

Materials

Methanol (99.9 wt.%) (LabServ) and petroleum benzine (Supelco/Germany) were used as solvents. Sodium hydroxide (98%) (Emory), copper (II) sulfate pentahydrate AR ($CuSO_4 \cdot 5H_2O$) (Emory), iron(III) chloride hexahydrate (Supelco), potassium sodium tartrate ($C_4H_4KNaO_6 \cdot 4H_2O$) Grade AR (QreC), potassium iodide (99.9%) (R&M Chemicals), iodine (PC Laboratory Reagent), sulfuric acid, chloroform, and hydrochloric acid were chemicals used in the phytochemicals screening testing.

Kaffir lime sample preparation

Fresh *kaffir lime (C. hystrix DC)* peels were purchased from a local supermarket located in Pagoh, Johor, Malaysia. The collected peels were washed several times with tap water to remove the remaining dust particles and impurities before the flesh were removed [10]. Following that, the washed peels were oven dried at 60 ℃ for 1 h to remove excess water [14]. The dried peels were blended until smooth and sieved by using an electric grinder to obtain uniform powders (Figure 1c) [15]. Then, the powders were weighed and sealed in an airtight container and stored at room temperature until ready to be used for extraction [16].

Extraction method

The extraction process was performed by using UAE method. Methanol was used as the polar solvent and petroleum benzine was used as the non-polar solvent for the extraction of *kaffir Lime* EOs. Then, 5g of powders were weighed and added into a conical flask which contained the solvents. The ratio of powder to solvent and extraction time was fixed at 1:30 g/mL and 50 mins [14, 17]. According to Liew et al. [14], the optimal raw material-to-solvent ratio for the extraction of kaffir lime peel was 1:30 g/mL. This was because when the volume of solvent increased, the contact area between solute and solvent increased, resulting in a greater mass transfer or driving force to extract bioactive compounds from the plant cells to solvent [14]. Then, the mixture sample was vortexed by using a vortex machine (Wiggens, Vortex Model 3000) at 800 rpm for 2 min as the pre-treatment of extraction. Then, the mixture was immersed into an ultrasonic bath (Wiggens Eco Series, Model UE10SFD) with ultrasonic power at 40 kHz (Figure 1e).The extracts were subsequently centrifuged at 20 ℃ with 3500 rpm for 20 min by using a centrifuge model (MPW-352R), as shown in Figure 1f. Then, the extracts were filtered to separate the solid residue from supernatant layers. The supernatant was concentrated by using a rotary evaporator (Eyela OSB-2200) equipped with a vacuum pump (Figure 1h) at 25 °C and 25 rpm by using a polar solvent [15]. Meanwhile, for the non-polar solvent extraction a reciprocal shaker water bath (Yihder, Model BT-150D) (Figure 1I) was used at 60 °C for 1 h[18]. Both extracts were concentrated by using different techniques because the boiling point of petroleum ether is lower than that of methanol; hence, it can be removed from EOs even with the water bath. To ensure that the EOs quality was consistent across all batches, the extraction process applied the same raw materials, sample preparation techniques, and UAE parameter conditions. The EOs were kept in a vial and stored at 4 ℃ until analysis [3].

Scanning electron microscope (SEM)
The surface morphology of fresh *kaffir lime* powder before extraction and residual powder after extraction were analysed by using SEM (Model EM-30N COXEM).

Fourier transform infrared spectroscopy (FTIR)
The existence of functional group in the extracted *kaffir lime* EOs was characterised by using FTIR spectrophotometer (Perkin Elmer UATR Two) under wavelength ranges between 400 cm^{-1} and 4,000 cm^{-1}.

Gas chromatography-mass spectrometry
Gas chromatography-mass spectrometry (GC-MS, GC Agilent® 7890B, MS Agilent® 5977B, Agilent Technologies, Santa Clara, CA, USA) was used to determine the chemical constituents of *kaffir lime* EOs. Firstly, the EOs were mixed with methanol in the ratio of 2:3. Head column pressures for the HP-5ms (30m x 0.25mm x 0.25µm film thickness) panel were 70kPa. GC-MS was acquired on the following conditions: Carrier gas He; flow rate 1.0 ml/min; split 1:100; injection volume 1.0 µl; injection temperature 280 °C; oven temperature progress included an initial hold at 70°C for 2 min, then increased to 7 °C/min to 320 °C for 1 min. The temperature of ion sources was maintained at 250 °C. The mass spectrum was obtained by electron ionisation at 70 eV, and the detector operated in scan mode 30 to 500 Da atomic units [18]. Chemical constituents of EOs were identified by comparing retention indices with mass spectral database libraries National Institute of Standards and Technology (NIST) [2]. Chromatograms from GC and GC-MS captured the existing sample oil constituents in terms of peak area count.

Phytochemical screening
Qualitative phytochemical analysis was performed to detect the presence of chemical constituents in extracted *kaffir lime* EOs, including alkaloids, flavonoids, terpenoids, saponins, tannins, phenols, and proteins as follows:

Test for alkaloids
10% KI was mixed with 5% iodine for the preparation of the iodine test reagent. Next, 2 to 3 drops of EOs were added to 1 mL reagent and then boiled in a water bath until the colour disappeared. The alkaloid content in the sample was indicated by the formation of a blue-black colour once the mixture cooled down [19].

Test for flavonoids
The intense yellow colour was formed when a few drops of EOs were added to 2 mL of 2% of NaOH solution. Following that, a few drops of diluted HCl resulted in the solution turning colourless. The formation and disappearance of intense yellow colour during the alkaline reagent testing indicated the presence of flavonoids in the extract [4].

Test for terpenoids
1 mL EOs was mixed with 2 mL chloroform and shaken well, followed by the addition of a few drops of concentrated H_2SO_4. Salkowski test showed a positive result when a reddish-brown colouration of the interface or golden-yellow precipitate was formed [8].

Test for saponins
1 mL of EOs was mixed with 3 mL of distilled water and the mixture was vigorously shaken for 30 s. If persistent foam or bubbles were formed for several minutes, it indicated the presence of saponins in the extract [20].

Test for tannins
A few drops of EOs were mixed with 5 mL of distilled water and then boiled in a water bath. Following that, the cooled filtrate was mixed with 5 mL of 1% w/v $FeCl_3 \cdot 6H_2O$ solution. A positive result showed a blue-green, green-black, dark blue, blue-black or dark brown formation [21].

Test for phenols
2 mL of 5% w/v aqueous $FeCl_3 \cdot 6H_2O$ solution was mixed with a few drops of EOs. The formation of a blue colour indicated a positive result [19].

Test for proteins
1.5g $CuSO_4 \cdot 5H_2O$, 6 g of $KNaC_4H_4O_6 \cdot 4H_2O$, and 2 M NaOH were mixed and then added with 1000 mL distilled water for the preparation of Biuret test reagent. Then, 2 to 3 drops of EOs were mixed with 1 mL of reagent. The formation of a purple solution indicated that the result was positive [22].

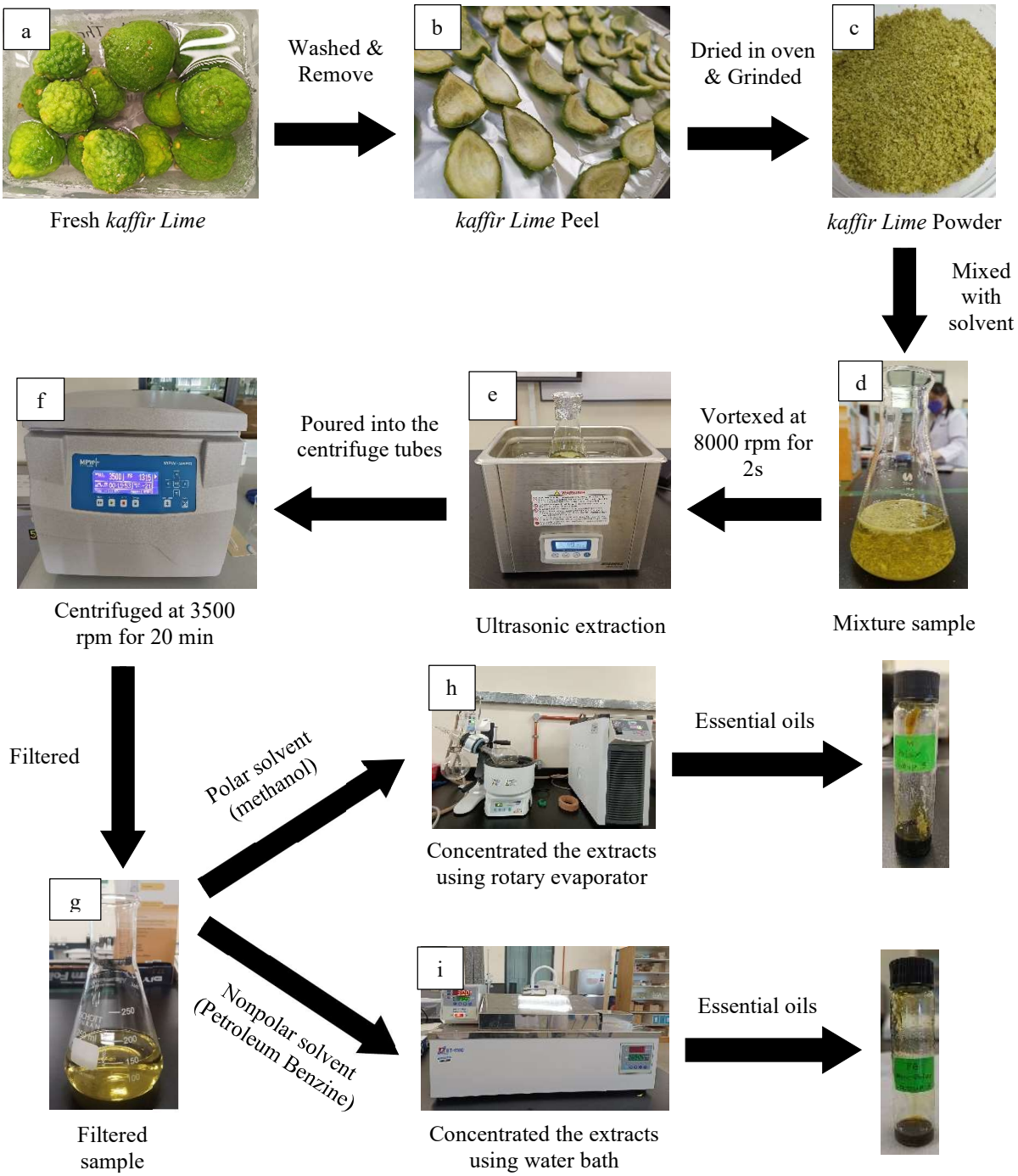


Figure 1. Schematic diagram of the extraction of the *kaffir Lime* essential oil using different polar solvents

Analytical method

The performance of the different polar solvents used in the extraction was evaluated according to the percentage yield of EOs obtained by calculated using Equation (1). The weight of extracted oil was based on fresh *kaffir lime* peels. The density of *kaffir lime* oil is in the range of 0.871g/ml [3]. From that, the weight of the obtained essential oil can be calculated by multiplying the density of the *kaffir lime* oil (0.871 g/ml) with the volume (ml) of EOs obtained.

$$\%\, Yield = \frac{Weigh\ \ of\ essential\ oil\ obtained\ (g)}{Weigh\ \ of\ fresh\ Kaffir\ Lime\ peel\ used\ (g)} \times 100\% \quad (1)$$

Results and Discussion

Percentage yield of EOs obtained

Table 1 shows the percentage yield of EOs obtained from extraction with methanol and petroleum benzine solvents. The mass and percentage yield of EO extracted by methanol (6.62 g, 9.43%) was greater than the EO extracted by petroleum benzine (1.66 g, 2.36%). This could be explained by the fact that the EOs were organic constituents, which were more likely to dissolve in organic or non-polar solvents by following the concept of like dissolving like [23]. Solutes or bioactive compounds from *kaffir lime* peels tended to dissolve more easily in the solvent close to its polarity, and thus increased the yield of EOs [24]. The dielectric constant (ε) is the important key parameter to measure the interaction between solute and solvent, which would affect the percentage yield of extracted EOs [25]. Non-polar solvents are those with dielectric constants lower than 15 [26]. Therefore, methanol is a polar protic solvent with a dielectric constant of 32.7 [27] while petroleum benzine is a non-polar solvent with a dielectric constant of 1.9 [26]. Polar protic solvents can be identified by the presence of hydrogen bonds such as the hydroxyl group (OH), whereas non-polar liquids possess similar electronegativities between atoms, such as carbon and hydrogen [28]. As a consequence, the OH group of the methanol molecule enables it to attract polar solutes and form hydrogen bonds, and thus increases the oil production. A solvent that is more likely to dissolve the solute provides a better potential to break down cell walls and extract the oil; hence, increases the amount of oil extracted [28]. According to Taesotikul et al. [29], the methanol extract yielded the most EOs with 68.86 ± 7.31% as compared to the other solvent fractions such as butanol, hexane, aqueous, and dichloromethane during the maceration technique extraction of *C. hystrix* peels oil. Furthermore, Tir et al. [25] reported that the oil yield of dichloromethane was 55.50 ± 0.56%, which was greater than the oil yield of hexane of 43.76 ± 0.81% for sesame seed oil extraction by using the Soxhlet method. This was due to the fact that opening the cell wall to allow for more complete solvent extraction of the cell contents reduced the difference in surface tensions on the phase boundary, and thus promotes phase separation [25].

Table 1. Percentage yield of EOs obtained from the extraction with solvent methanol and petroleum benzine

EOs	Methanol	Petroleum Benzine
Mass of the peels used (g)	70.20	70.20
Volume of EOs obtained (mL)	7.6	1.9
Mass of EOs (g)	6.62	1.66
Percentage yield (%)	9.43	2.36

Scanning Electron Microscope (SEM)

Figures 2a-c showed the SEM images of *kaffir lime* powder before extraction, residual powder after extraction by using methanol and residual powder after extraction by using petroleum benzine, respectively. Figure 2b and Figure 2c show a few porosities as compared to Figure 2a. The cavitation bubbles produced by ultrasound during the extraction process allowed the surface of *kaffir lime* peels to undergo implosion and caused the porosity to form [30]. Meanwhile, the changing of the surface allowed the solvents entry the cellular channels of *kaffir lime* peels to extract the compounds [31]. The implosion that occurred at the plant cell wall was related to several extraction parameter conditions in terms of types of solvent used, extraction time, extraction temperature, ultrasonic power, and liquid-to-solid ratio of extraction [22].

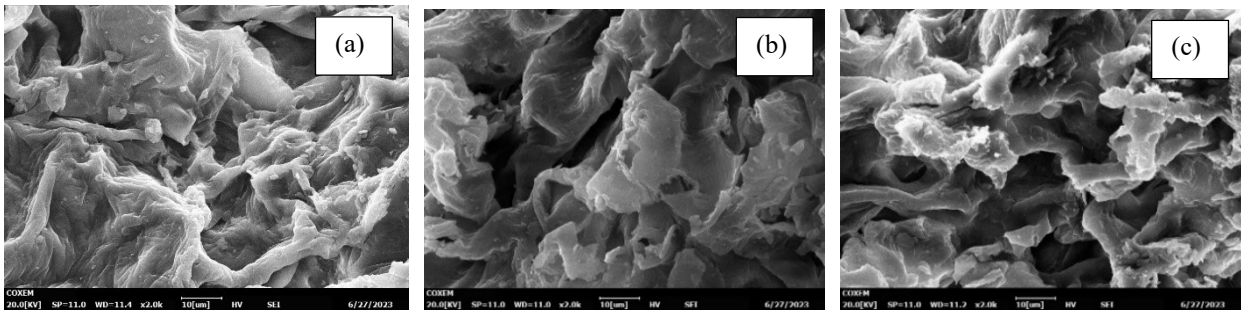


Figure 2. Photograph of SEM of (a) *kaffir lime* powder before extraction, (b) residual powder after extraction using methanol, and (c) residual powder after extraction using petroleum benzine

Phytochemical qualitative analysis

Phytochemical screening was performed to determine the secondary metabolites in the *kaffir lime* essential oils. Phytochemical qualitative analysis results are summarised in Table 2. The positive symbol (+) indicated the presence of phytochemicals while the negative symbol (-) indicated the absence of the phytochemicals in the EOs extracted by methanol and petroleum benzine. The difference in phytochemical results obtained might be due to polarity of the extraction solvent [22]. All secondary metabolites were present in the methanol extract Eos, except saponin and protein. Meanwhile, only alkaloids and terpenoids were present in the petroleum benzine extract EOs. This was because the polar solvent had a higher ability to increase cell permeability and penetrate inside the cell of a plant as compared to the non-polar solvent, and thus extract more endocellular secondary metabolites. Meanwhile, the non-polar solvent only dissolved lipophilic compounds, including terpenoids, alkaloids, alcanas, waxes, colour pigments and sterols due to the zero-polarity index; therefore, extracting fewer secondary metabolites [32].

Table 2. Result of phytochemical qualitative analysis

EOs	Result of Phytochemical Qualitative Analysis						
	Alkaloid	**Flavonoids**	**Terpenoids**	**Saponins**	**Tannins**	**Phenols**	**Proteins**
Methanol	+	+	+	-	+	+	-
Petroleum Benzine	+	-	+	-	-	-	-

Fourier transform infrared (FTIR) spectroscopy analysis

Figure 3 shows the comparison of FTIR peak configuration of EOs by using different extraction solvents: (a) methanol and (b) petroleum benzine. Similar functional groups with similar infrared absorption band intensities could be seen in both FTIR spectra. The broad peak at 3025 cm^{-1}-3625 cm^{-1} was attributable to the O-H bond stretching, indicating the existence of phenolic compounds such as terpinen-4-ol, citronellol or linalool [33]. Besides, the varied peaks at 2834 cm^{-1}-2939 cm^{-1} represented a considerable asymmetric stretching of CH_3, corresponding to an alkyl-saturated aliphatic group present in the compound [34]. The aldehyde, ester, carboxylic acid, or ketone groups were responsible for the C=O stretching at 1717 cm^{-1}-1721 cm^{-1} [34]. Furthermore, the peaks at 1622 cm^{-1}-1624 cm^{-1} contain an alkenes bond, which was a C=C stretching of aromatic rings caused by the presence of terpenes or terpenoid compounds such as D-limonene or citronellal [33]. According to Figure 3, petroleum extracts had higher intensity across all spectrum bands than methanol extracts, except O-H stretching. The solubility of a solvent might affect intensity of the peak. The polarity of functional groups in EOs can differ and the solvent of choice can have an impact on solubility and interactions of the solute and solvent. Non-polar compounds are generally more easily dissolved by non-polar solvents such as petroleum benzine [24]. It can dissolve more readily in petroleum benzine if the

functional groups in the EOs are primarily non-polar or possess low polarity, which would result in larger intensity peaks in the FTIR spectra [35]. Comparatively, polar solvents like methanol might have a poorer affinity for non-polar functional groups, which might result in reduced solubility as well as lower oil yields [24]. Table 2 shows the fact that there were greater numbers of phytochemical groups found in methanol extracts. However, some of these compounds might not have adequate IR-active functional groups to produce strong FTIR signals. A change in dipole moment in the process of vibration will affect the infrared absorption [36]. If there is little or no change in dipole moment, the radiation only interacts with vibration, with relatively little or no absorption. The intensity of absorption increases with the shift of dipole moment [36].

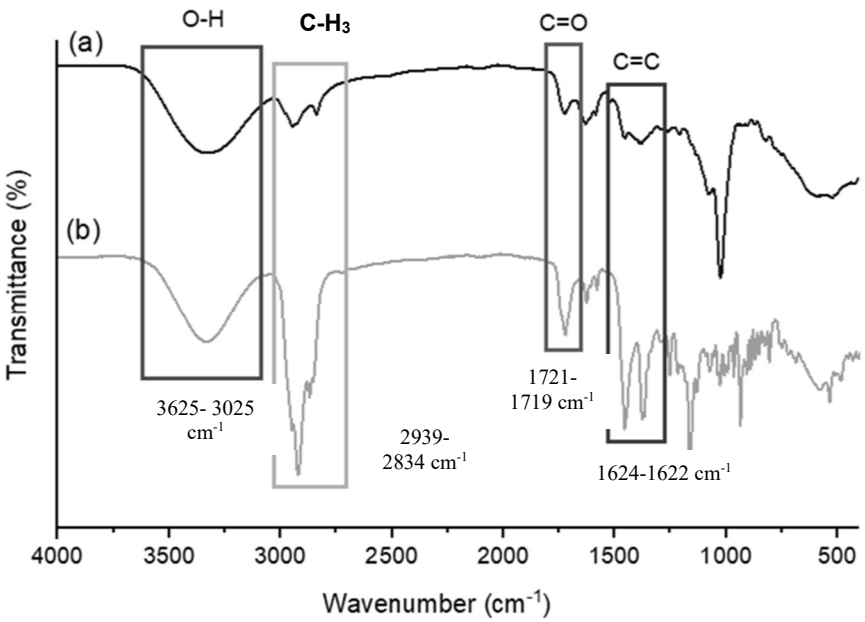
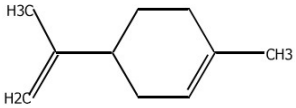
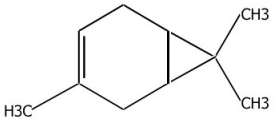
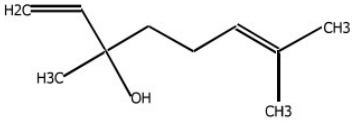
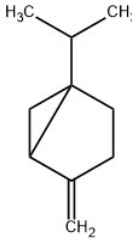
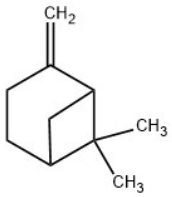
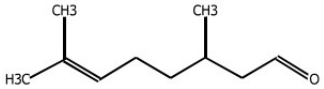
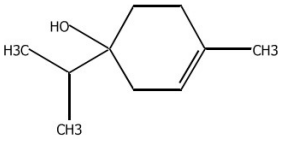
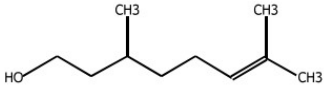
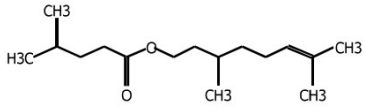


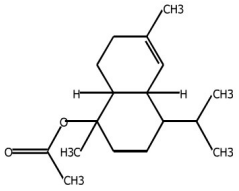
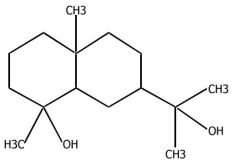
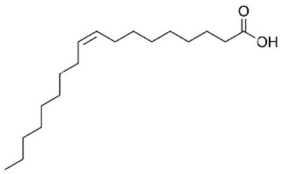
Figure 3. FTIR analysis of extraction of *kaffir Lime* essential oil using (a) methanol, and (b) petroleum benzine

Gas chromatography-mass spectrometry (GCMS) analysis

Table 3 and Figure 4 tabulate the identified chemical compounds with the different concentrations that contributed to the total EOs extracted by using methanol and petroleum benzine. Generally, the main components found from the EOs included D-limonene, β-pinene, 3-carene, linalool, citronellal, terpinen-4-ol, and citronellol. As a result, D-limonene, 3-carene, citronellol, citronellal and β-pinene were found in the EOs extracted from the *kaffir lime* peels [10]. From the result obtained, Compound 1 was a naturally occurring bicyclic monoterpene, whereas Compound 13 was a type of fatty acid. Both compounds extracted were considered non-polar compounds. However, the relative solubilities of Compound 1 and Compound 13 in both solvents might differ. Both compounds can only be solute in petroleum benzine. The terpenoid group was the majority chemical compound found in EOs. D-limonene could be considered the main component of methanol extract EOs, which provided a unique flavour, such as the smell of oranges. Previous research by [3] showed that the presence of β-pinene imparted a woody aroma to the oil, while citronellal indicated that the oil had antifungal properties and could; therefore, be used as an insect repellent.

Table 3. Chemical compounds in extracted *C. hystix* essential oil using methanol and petroleum benzine

No	Name of Compound	Structural Formula	Retention Time (min)	
			Methanol Extracts Oil	Petroleum Benzine Extracts Oil
1	Bicyclo[3.1.0]hexane, 4-methylene-1-(1-methylethyl)-		-	5.505
2	D-limonene		7.378	6.476
3	3-carene		7.690	7.005
4	Linalool		7.907	7.954
5	Sabinene		8.930	-
6	β-pinene		9.137	-
7	Citronellal		9.568	9.080
8	Terpinen-4-ol		9.879	9.646
9	Citronellol		10.548	10.595
10	Pentanoic acid, 4-methyl-,3,7-dimethyl-6-octenyl ester		12.946	12,889

11	Tau-Cadinol acetate		16.038	16.059
12	7-(2-Hydroxypropan-2-yl)-1,4a-dimethyldecahydronaphthalen-1ol		21.035	21.014
13	Oleic Acid		-	29.960

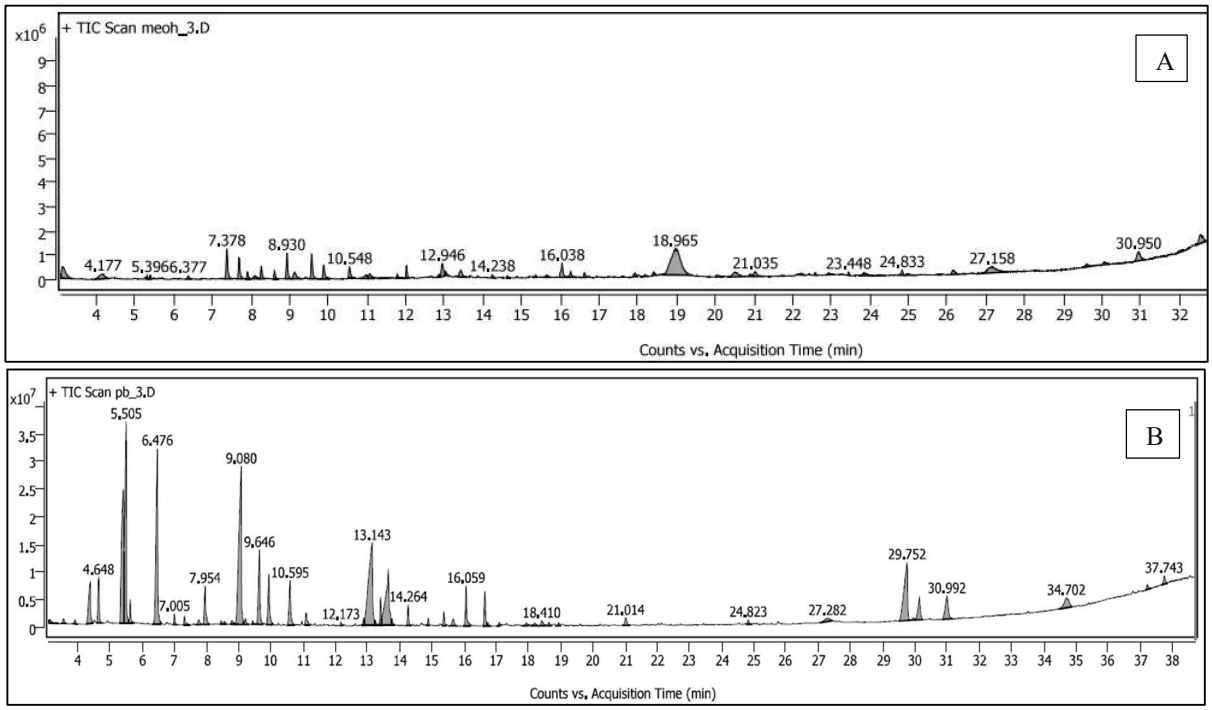


Figure 4. GCMS chromatogram of extracted *C. hystix* essential oil using (a) methanol, and (b) petroleum benzine

Conclusion

The extraction of essential Oil *C. hystrix (kaffir lime*), respectively, with methanol and petroleum benzine by using UAE was successfully studied. The percentage yield of EOs obtained for methanol extract was higher than petroleum benzine extract, which was 9.43% and 2.36%, respectively. Methanol extracted more compounds as compared to petroleum benzine due to the high polarity of solvent. Compounds that were extracted by using methanol were alkaloids, flavonoids, terpenoids, tannins and phenols while the compounds that were extracted by using petroleum benzine were only alkaloids and terpenoids. The screening phytochemical, FTIR and GCMS analyses proved that

D-limonene, β-pinene, 3-carene, linalool, citronellal, terpinen-4-ol, and citronellol were the main components found in *C. hystrix* essential oil.

Acknowledgements

This research was supported by Universiti Tun Hussein Onn Malaysia (UTHM) for the TIER 1 grant (Q513) as financial research support. The authors are also grateful to the management for providing adequate laboratory facilities in the execution of this study.

References

1. Azreen Hani and Muhd Amin Truong. (2022) Malaysia throws away 17,000 tonnes of food daily. 1st ed. News: TMR Media Sdn Bhd.
2. Husni, E., Putri, U. S. and Dachriyanus (2021). Chemical content profile of essential oil from kaffir lime (*Citrus hystrix* DC.) in Tanah Datar regency and antibacterial activity. *Advances in Health Sciences Research: 2nd International Conference on Contemporary Science and Clinical Pharmacy,* 40.
3. Kasuan, N., Muhammad, Z., Yusoff, Z., Rahiman, M. H. F., Taib, M. N., and Haiyee, Z. A. (2013). Extraction of *Citrus hystrix* D.C. (Kaffir Lime) essential oil using automated steam distillation process: Analysis of volatile compounds. *Malaysian Journal of Analytical Sciences*, 17(3): 359-369.
4. Mohideen, M., Iqbal, M., Idris, H., Abidin, Z. and Kamaruzaman, N. A. (2021). Review on extraction methods of essential oil from kaffir lime (*Citrus hystrix*) leaves. *Journal of Academia,* 9(1): 173-184.
5. Kumar K, Srivastav S and Sharanagat VS. (2021). Ultrasound assisted extraction (UAE) of bioactive compounds from fruit and vegetable processing by-products: A review. *Ultrasonics Sonochemistry*, 70: 105325.
6. Truong, D. H., Nguyen, D. H., Ta, N. T. A., Bui, A. V., Do, T. H. and Nguyen, H. C. (2019). Evaluation of the use of different solvents for phytochemical constituents, antioxidants, and in vitro anti-inflammatory activities of *Severinia buxifolia*. *Journal of Food Quality,* 2019: 8178294.
7. Mohd Sauid, S. and Aswandi, F. A. (2018). Extraction methods of essential oil from kaffir lime (*Citrus hystrix*): A review. *Malaysian Journal of Chemical Engineering and Technology*, 1: 56-64.
8. Abubakar, A. R. and Haque, M. (2020). Preparation of medicinal plants: Basic extraction and fractionation procedures for experimental purposes. *Journal of Pharmacy & Bioallied Sciences,* 12(1): 1-10.
9. Nortjie, E., Basitere, M., Moyo, D. and Nyamukamba, P. (2022). Extraction methods, quantitative and qualitative phytochemical screening of medicinal plants for antimicrobial textiles: A eeview. *Plants (Basel, Switzerland),* 11(15) : 2011.
10. Oprescu, E. E., Enascuta, C. E., Radu, E., Ciltea-Udrescu, M. and Lavric, V. (2022). Does the ultrasonic field improve the extraction productivity compared to classical methods–Maceration and reflux distillation?. *Chemical Engineering and Processing-Process Intensification,* 179: 109082.
11. Soib, H. H., Ismail, H. F., Husin, F., Abu Bakar, M. H., Yaakob, H. and Sarmidi, M. R. (2020). Bioassay-guided different extraction techniques of *Carica papaya* (Linn.) leaves on in vitro wound-healing activities. *Molecules,* 25(3): 517.
12. Pandhi, S. and Poonia, A. (2019). Phytochemical screening of Jamun seeds using different extraction methods. *The Pharma Innovation Journal,* 8(2): 226-231.
13. Mutalib, L. (2015). Comparison between conventional and modern methods for extraction of *Rosmarinus officinalis* leaves. *Zanco Journal of Medical Sciences,* 19(2): 1029-1034.
14. Liew, H. Y., Chua, B. L. and Chow, Y. H. (2020). Optimisation of ultrasonic-assisted extraction conditions of *Citrus hystrix* for the total phenolic content. *AIP Conference Proceedings*, 2233: 040003.
15. Anuar, A., Awang, M. A. and Tan, H. F. (2021). Impact of solvent selection on the extraction of total phenolic content and total flavonoid content from kaffir lime leaves: Ultrasonic assisted extraction (UAE) and microwave-assisted extraction (MAE). *AIP Conference Proceedings*, 2347: 020020.
16. Wijaya, Y. A., Widyadinata, D., Irawaty, W. and Ayucitra, A. (2017). Fractionation of phenolic compounds from kaffir lime (*Citrus hystrix*) peel

extract and evaluation of antioxidant activity. *Reaktor*, 17(3): 111.

17. Zhang, X., Gao, H., Zhang, L., Liu, D. and Ye, X. (2012). Extraction of essential oil from discarded tobacco leaves by solvent extraction and steam distillation, and identification of its chemical composition. *Industrial Crops and Products,* 39(1): 162-169.
18. Sharma, D., Rani, R., Chaturvedi, M. and Yadav, J. P. (2018). Antibacterial capacity and identification of bioactive compounds by GCMS of *Allium cepa*. *International Journal of Pharmacy and Pharmaceutical Sciences,* 10(2): 116.
19. Samraj, S. and Rajamurgugan, S. (2017). Qualitative & quantitative estimation of bioactive compounds and antioxidant activity in *Citrus hystrix*. *International Journal of Engineering Science and Computing,* 7(6): 13154-13163.
20. Herawati, D., Ekawati, E. R. and Yusmiati, S. N. H. (2020). Identification of saponins and flavonoids in lime (*Citrus aurantifolia*) peel extract. *Proceedings of the International Conference on Industrial Engineering and Operations Management,* 8: 3661-3666.
21. Suryani, N., Munawar, F. and Hajaroh, S. (2022). Phytochemical screening of active secondary metabolites and antibacterial activity kaffir lime leaf (*Citrus hystrix*) and tumeric leaf (*Curcuma longa* Linn.) against *Escherichia coli. ALKIMIA: Jurnal Ilmu Kimia Dan Terapan,* 5(2): 150-158.
22. Janairo, G., Sy, L., Leonisa, Y., Nancy, L.-L. and Robles, J. (2011). Determination of the sensitivity range of biuret test for undergraduate biology. *E-Journal of Science & Technology*, 6(5): 77-83.
23. Hasibuan, R., Sundari, R., Gultom, E., Anggraini, R. and Hidayati, J. (2021). High valued limonene in essential oil extract from lime peel waste for parfum industry. *Agrointek: Jurnal Teknologi Industri Pertanian,* 15(4): 1128-1141.
24. Syahadat, A., Yaturramadhan, H. and Diningsih, A. (2021). The effect of solvent type on oil yield on essential oil of sweet orange peel extract (*Citrus X Sinensis*). *Journal of Public Health and Pharmacy,* 3: 59-62.
25. Tir, R., Dutta, P. C. and Badjah-Hadj-Ahmed, A. Y. (2012). Effect of the extraction solvent polarity on the sesame seeds oil composition. *European Journal of Lipid Science and Technology,* 114(12): 1427-1438.
26. Lesten, E. C. C. and Kingsley, M. (2019). The influence of solvents polarity on physicochemical properties and oil yield extracted from pumpkin (*Cucurbita maxima*) seed. *Journal of Agricultural Biotechnology and Sustainable Development,* 11(3): 40-47.
27. Mohsen-Nia, M., Amiri, H. and Jazi, B. (2010). Dielectric constants of water, methanol, ethanol, butanol and acetone: Measurement and computational study. *Journal of Solution Chemistry,* 39(5): 701-708.
28. Abdullah, N., Amran, N. A. and Yasin, N. H. M. (2017). Algae oil extraction from freshwater microalgae *Chlorella vulgaris. Malaysian Journal of Analytical Sciences,* 21(3): 735-744.
29. Taesotikul, T., Kitcharoen, N., Chinpaisal, C., Phuagphong, P. and Nawanopparatsakul, S. (2023). Extraction and analyses of phytochemical compounds from *Citrus hystrix* peels for molluscicidal activities. *Thai Bulletin Pharmaceutical Sciences,* 18(1): 17-28.
30. Kurniasari, L., Djaeni, M. and Kumoro, A. C. (2023). Ultrasound-assisted extraction (UAE) of sappan wood (*Caesalpinia sappan* L.): Effect of solvent concentration and kinetic studies. *Brazilian Journal of Food Technology,* 26: 1-11.
31. Syahir, A., Sulaiman, S., Mel, M., Othman, M. and Zubaidah Sulaiman, S. (2020). An overview: Analysis of ultrasonic-assisted extraction's parameters and its process. *IOP Conference Series: Materials Science and Engineering,* 778(1): 012165.
32. Yusnawan, E. (2013). The effectiveness of polar and non-polar fractions of *Ageratum conyzoides* L. to control peanut rust disease and phytochemical screenings of secondary metabolites. *Journal of Tropical Plant Pests and Diseases*, 13(2): 159-166.
33. Malikhah, H. and Herdyastuti, N. (2023). Effect of kaffir lime (*Cytrus hystrix*) leaf extract on xanthine oxidase inhibition. *World Journal of Advanced Research and Reviews,* 17(1): 1069-1078.
34. Ramadhan, D. S., Warsito, and Iftitah, E. D. (2018). Microwave-assisted synthesis of benzimidazole

derivatives from citronellal in kaffir lime (*Citrus hystrix* DC.) oil. *IOP Conference Series: Materials Science and Engineering,* 299(1): 1-7.

35. Ahmad, I., Sabah, A., Anwar, Z., Arif, A., Arsalan, A. and Qadeer, K. (2017). Effect of solvent polarity on the extraction of components of pharmaceutical plastic containers. *Pakistan Journal of Pharmaceutical Sciences,* 30(1): 247-252.
36. El-Azazy, M., Al-Saad, K. and El-Shafie, A. S. (2023). Infrared spectroscopy-perspectives and applications. IntechOpen Publisher.

Malaysian Journal of Analytical Sciences (MJAS)
Published by Malaysian Analytical Sciences Society

CYTOTOXICITY STUDY, ANTIOXIDANT AND ANTIBACTERIAL ACTIVITY AGAINST PLANT PATHOGENIC BACTERIA OF METHANOL EXTRACT FROM *Coscinium fenestratum* (AKAR SEKUNYIT)

(Kajian Ketoksikan Sel, Aktiviti Antioksida dan Sifat Antibakteria Ekstrak Metanol dari *Coscinium Fenestratum* (Akar Sekunyit) Terhadap Bakteria Penyebab Penyakit Pokok)

Aiza Harun[1*], Noorshilawati Abdul Aziz[2], Shaari Daud[1], Khairil Syazwan Salim[1], Norlaili Abu Bakar[3], Siti Zaiton Mat So'ad[4], and Norizan Ahmat[5]

[1]*Faculty of Applied Sciences, Universiti Teknologi MARA Pahang, 26400 Bandar Jengka, Pahang, Malaysia*
[2]*Faculty of Plantation and Agrotechnology, Universiti Teknologi MARA Pahang, 26400 Bandar Jengka, Pahang, Malaysia*
[3]*Department of Chemistry, Faculty of Science and Mathematics, Universiti Pendidikan Sultan Idris, 35900 Tanjung Malim, Perak, Malaysia*
[4]*Kulliyyah of Pharmacy, International Islamic University Malaysia, 25200 Bandar Indera Mahkota, Kuantan, Pahang, Malaysia*
[5]*Faculty of Applied Sciences, Universiti Teknologi MARA Shah Alam, Selangor, Malaysia*

[*]*Corresponding author: aizaharun@uitm.edu.my*

Received: 4 June 2023; Accepted: 3 October 2023; Published: 29 December 2023

Abstract

Coscinium fenestratum (Gaertn.) Colebr. (Menispermaceae) is a large woody liana found in moist deciduous to the evergreen forest at an altitude of 350–1200m. The stem and root of this species are highly medicinal valuable, and it is believed to be an endangered species in Malaysia. This study was conducted to investigate the reaction of methanol extract from *Coscinium fenestratum* with cancer cell lines, plant pathogenic bacteria, as well as DPPH scavenging and ferric reduction antioxidant power. The antibacterial activity was evaluated from disc diffusion method and microdilution method against soft rot bacteria *Erwinia chrysanthemi* and *Erwinia carotovora*. The cytotoxicity assay was performed using MCF-7 and Caco-2 cancer cell lines. The antioxidant properties of methanol extract were assessed from DPPH radical scavenging activity and ferric reducing antioxidant power (FRAP). The cytotoxicity activity revealed the methanol extract has potential to suppress the Caco-2 cell line with the percentage cell viability at 70% compared to MCF-7 cell line. The antioxidant activity from FRAP assay recorded its value of 47.8080 µg for TE/gDW and 13.8481 µg/mL for the IC_{50} from radical scavenging activity. However, the total flavonoid content (TFC) was not detected in methanol extract of *C. fenestratum*. The antibacterial assay revealed that the extract had moderately inhibited the growth of *E. chrysanthemi* and *E. carotovora* at 400 mg/mL, with inhibition zones of 11.50 mm and 11.83 mm, respectively. Therefore, the methanol extract from *C. fenestratum* has potential to act as antioxidant and anti-soft rot agent but less potential as anti-cancer agent and anti-soft rot agent.

Keywords: antibacterial, antioxidant, cytotoxicity, *Coscinium fenestratum*, plant pathogen

Abstrak

Coscinium fenestratum (Gaertn.) Colebr. (Menispermaceae), pokok liana berkayu besar yang ditemui dalam hutan daun luruh lembap hingga ke hutan malar hijau pada ketinggian 350–1200 m. Batang dan akar spesis ini sangat bernilai dalam bidang perubatan, dan ia dipercayai spesis terancam di Malaysia. Kajian ini bertujuan untuk mengkaji tindakan ekstrak metanol daripada *Coscinium fenestratum* bertindak balas dengan garisan sel kanser, bakteria patogen tumbuhan serta penghapusan DPPH dan kuasa antioksidan penurunan ferik (FRAP). Aktiviti antibakteria dinilai daripada kaedah resapan cakera dan kaedah pencairan mikro terhadap bakteria reput lembut *Erwinia chrysanthemi* dan *Erwinia carotovora*. Ujian ketoksikan sel telah diadakan menggunakan garisan sel kanser MCF-7 dan Caco-2. Sifat antioksidan ekstrak metanol dinilai daripada aktiviti penghapusan radikal DPPH dan kuasa antioksidan penurunan ferik (FRAP). Aktiviti ketoksikan sel mendedahkan ekstrak metanol berpotensi untuk menindas garisan sel Caco-2 dengan peratusan daya maju sel pada 70% berbanding garisan sel MCF-7. Aktiviti antioksidan daripada ujian kuasa antioksidan penurunan ferik mencatatkan nilainya sebanyak 47.8080 µg TE/gDW manakala 13.8481 µg/mL untuk IC_{50} daripada aktiviti penghapusan radikal. Walau bagaimanapun, jumlah kandungan flavonoid (TFC) tidak dikesan dalam ekstrak metanol *C. fenestratum*. Ujian antibakteria mendedahkan bahawa ekstrak telah menghalang pertumbuhan *E. chrysanthemi* dan *E. carotovora* secara sederhana pada 400 mg/mL dengan zon perencatan masing-masing 11.50 mm dan 11.83 mm. Oleh itu, ekstrak metanol daripada *C. fenestratum* berpotensi bertindak sebagai agen antioksida dan anti reput lembut tetapi kurang berpotensi sebagai agen anti kanser dan anti reput buah.

Kata kunci: antibakteria, antioksidan, ketoksikan sel, *Coscinium fenestratum*, patogen tumbuhan

Introduction

The cytotoxicity evaluation of plants is a vast subject in pharmaceutical studies, especially in cancer research area [1]. Methanol and methanol-water extracts of *C. fenestratum* was reported to exhibit antiproliferative activities in a concentration-dependent manner against human HT-1080 fibrosarcoma cells among the seventy-seven Vietnamese medicinal plants. The induction of apoptosis was the reason of selective activity against lung carcinoma and/or lung metastatic cell lines, A549, LLC and B16-BL6 and characteristic morphological change and DNA fragmentation that indicated the antiproliferative activity [2]. The berberine and its derivatives revealed potent anticancer activity against human fibrosarcoma cells (HT1080) using MTT assay [3]. Thai edible plant *C. fenestratum* which was extracted with 95% ethanol and tested with cytotoxic effects using Hep2 cells showed the remarkable result with high cytotoxic activity against the Hep2 cell lines at a minimum concentration of 0.05% in ethanol extract. In addition, it demonstrated the most potent cytotoxic extract based on its lowest IC50 (5 mg/mL) [4].

Previous study of antioxidant activity indicated that the berberine isolated from stem of *C. fenestratum* has higher IC_{50} value compared to its berberine derivatives contain phenolic groups which have lower IC_{50} values [3]. Recently, it was found that combinations of two or more medicinal plants extracts can effectively increase the anticancer activity of the synergistic effect between the phytochemicals, as they are found in trace amounts, whereas the attainment of a therapeutic effect requires higher doses [5].

The high berberine content in *C. fenestratum* is the main cause of its antimicrobial properties. There is a recent report on the potent antimicrobial activity of *C. fenestratum* extracts against five human pathogenic microbes [6]. Meanwhile, the aqueous extracts of *C. fenestratum* inhibited the in vitro growth of *Clostridium tetani*. Thus, it is consistent with its traditional use as a prophylactic against tetanus. Ethanolic extract of *C. fenestratum* stem has strong inhibitory effects against *Propionibacterium acnes* and *Staphylococcus epidermidis* and this was resulted from the presence of alkaloids berberine, which could be responsible for this activity. Berberine from *C. fenestratum* also showed anti-phytopathogenic fungal activity against various fungi like *Phytophthora parasitica*, *Pythium* spp., *Colletotrichum gloeosporioides, Cercospora* spp., *Fusarium oxysporum,* and *Alternaria porri* [7].

The antibacterial activity of methanol extract of *C. fenestratum* against soft rot bacteria, such as *Erwinia* species and cytotoxicity activity against Caco-2 cell line was not well documented; this is the main reason for conducting this study.

Materials and Methods

Preparation of methanolic extract from *C. fenestratum*

The preparation of methanol extract from *C. fenestratum* (CFM) has already been mentioned in a previous work [6].

Cytotoxicity study: Cancer cell line

The MCF-7 and Caco-2 cells were cultured in complete Dulbecco's Modified Eagle Media (DMEM) containing 10% fetal bovine serum (FBS) and 1% penicillin-streptomycin. The cells were maintained at 37 °C in a humidified atmosphere with 5% CO_2 atmosphere and sub-cultured every three to four days at approximately 80% to 90% of confluence.

Cell viability assay

The cell viability assay was measured using tetrazolium salt (3-(4,5-dimethylthiazol-2-yl)-2,5-diphenyltetrazolium bromide (MTT) assay according with some modifications. A total of 1.0–2.0 × 10^5 cells/mL were seeded in a 96-well plate overnight at 37°C with 5% CO_2 atmosphere. Then, the cells were treated with serial dilution concentrations of the extracts (3.125, 6.25, 12.5, 25, 50, and 100 µg/mL) in triplicate for 24 hours at 37 °C with 5% CO_2 atmosphere. Solvent (vehicle) used to dissolve the sample was used at a final concentration of < 0.1%, which does not affect the viability of cells. After 24 hours, all media were discarded and 30 µL of MTT solution (5 mg/mL MTT in PBS) was added into each well. After four hours of incubation with MTT solution, the formazan crystals were dissolved in 100 µL DMSO and left in the dark at room temperature for an additional one hour. The absorbance measured at 570 nm and 630 nm used as reference wavelength was performed using a microplate reader (TECAN infinite M200). The wells with untreated cells were taken as the control and wells with medium with 0.1% (v/v) of DMSO were used as solvent control. Results were expressed as a percentage of the average absorbance of sample treated cells with respect to untreated ones. Percentage of cell viability (%) was calculated using the following equation 1:

$$\text{Cell viability (\%)} = \frac{(\text{Absorbance of treated cell} - \text{Absorbance blank})}{(\text{Absorbance of untreated cell} - \text{Absorbance blank})} \times 100 \quad (1)$$

Statistical analysis

Data were performed in three replicates, where Microsoft Excel was used to perform graphical representation.

Antioxidant activity: Total flavonoid content (TFC)

Total flavonoid content was determined following the method described in literature. Distilled water (100 µL) was added to each of the 96 wells, followed by 10 µL of 50 g/L $NaNO_2$ and 25 µL of sample solution. After five minutes, 15 µL of 100 g/L $AlCl_3$ was added to the mixture. Six minutes later, 50 µL of 1 mol/L NaOH and 50 µL of distilled water were added. The plate was shaken for 30 s in the plate reader prior to absorbance measurement at 510 nm. The sample was measured against a mixture of DMSO instead of the extract as blank, and the absorbance was subtracted from the absorbance of 25 µl of extract and 225 µl of water. Catechin at a final concentration ranging from 2.125–100 µg/mL was used to generate a calibration curve.

DPPH radical scavenging activity

The method of radical scavenging activity assay was adapted from previous report [8]. All the extracts and standard ascorbic acid were two-fold serially diluted from 400 ug/mL to 12.5 ug/mL. The mixture of 1 mL of each extract and 3 mL of 0.004% DPPH solution was prepared and kept in a dark place for 30 min. The absorbance of all samples was measured at 517 nm using a spectrophotometer, and the percentage of scavenging activity was calculated as follows:

$$\text{Scavenging activity (\%)} = A0 - A1/A0 \times 100 \quad (2)$$

where, A_0 represents the DPPH control absorbance, and A1 represents the extracted/standard sample absorbance.

Ferric reducing antioxidant power (FRAP)

An amount of 455.30 mg of anhydrous sodium acetate was dissolved with 50 mL of distilled water. Then, 3.97 mL of glacial acetic acid was added, and finally the

mixture was diluted to 250 mL to prepare acetic acid buffer solution at a concentration of 0.30 mol/L. TPTZ weighing 156.20 mg was taken using a chemical balance, dissolved with distilled water, and 0.17 mL of concentrated hydrochloric acid was added. The solution was diluted to 100 mL to prepare TPTZ solution at a concentration of 10 mmol/L. $FeCl_3 \cdot 6H_2O$ weighing 270.03 mg was dissolved with H_2O and diluted to 50 mL. The concentration of $FeCl_3$ solution was 20 mmol/L. Acetic acid buffer, TPTZ solution, and $FeCl_3$ solution were mixed according to the ratio (10:1:1). Then, the mixture was incubated at 37°C. The working solution must be used up within 1–2 h. Next, 180.0 µl FRAP working solution was mixed with 5-µl sample in a 96-well plate. The mixture was shaken and incubated at 37°C for 15 min in the dark. The absorbance was measured at a wavelength of 593 nm. Trolox was used as the standard, while distilled water as the blank control. Trolox concentration was selected under the condition of absorbance value ranging from 0.2 to 0.8 to generate a standard curve.

Antibacterial activity against plant pathogen: Disc diffusion method

The standardized cultured bacteria, *E. chrysanthemi* and *E. carotovora*, were prepared at an optical density (OD) of 0.1. An amount of 100 µL of standardized bacteria inoculum were swabbed on the solidified agar surface to initiate bacteria growth on the agar. Then, the sterile impregnated disc of *E. spiralis* leave extracts with concentrations of 400, 200, 100, and 50 mg/mL were aseptically placed onto the inoculated agar surface and incubated at room temperature for 24 hours. The tests were conducted in triplicate for each extract and repeated with standard disc ampicillin. The effectiveness of the extracts to act as antibacterial agent was evaluated based on the diameter of the inhibition zone (mm). The greater the inhibition zone, the higher the effectiveness of the extract towards bacteria.

Microdilution method

Minimum inhibitory concentration (MIC) and minimum bactericidal concentration (MBC) were determined by two-fold serial dilution method as described by Mogana et al. [9]. Standardized bacteria suspension were diluted with the ratio of 1:100 in nutrient broth. An amount of 180 µL of standardized inoculum was inoculated into each well of 96 well plate, followed by 20 µL of diluted extract to give a final volume of 200 µL with final concentration in each well ranging from 50 mg/mL to 0.024 mg/mL. The plates were incubated at room temperature for 24 hours. After incubation at room temperature, 20 µL of 0.5% 3-(4,5-dimethylthiazol-2-yl)-2,5-diphenyl-2H-tetrazolium bromide (MTT) was added into each well to indicate bacterial growth. The dark-blue color will indicate microbial growth, whereas yellow color will reveal the inhibition of microbial growth. The concentration at which the yellow color appeared in the well at the first place indicates the MIC value of the sample. The mixture in the MIC well was streaked on fresh agar plate to ensure the disappearance of bacterial growth. The MBC value was determined from the well next to the well of MIC value.

Results and Discussion

***In vitro* cytotoxicity assay**

Cytotoxicity is defined as the toxicity caused due to the action of chemotherapeutic agents (natural or synthetic drug) on living cells. A cytotoxic agent is a substance that kill cells including cancer cell and may stop the cell from dividing and growing abnormal and may shrink the tumor cell. The cell viability assay was performed using MTT on MCF-7 and Caco-2 cells to evaluate the cytotoxic effects of methanol extract of *C. fenestratum* (CFM). The cells were treated with serial dilution concentrations of the extracts at 3.125, 6.25, 12.5, 25, 50, and 100 µg/mL in triplicate for 24 hours. Table 1 shows the cell viability (%) value of the extract for each concentration and standard deviation. Results from Table 1 and Figure 1 indicate that all concentrations treated on MCF-7 cancer cell line was unable to reduce the cell proliferation until at highest concentration 100 ug/mL. However, according to Figure 2, the percentage of cell viability of Caco-2 cell line was slightly reduced to 70%, as the concentration of CFM increased. This salient information reveals CFM as a potent extract to inhibit Caco-2 cancer cell proliferation. The result against Caco-2 cancer cell line might be due to the abundant presence of phytochemical alkaloid in CFM [6], which is also antioxidative. A previous study also found terpenoid, phenolics, and saponin in CFM, where their presence may possibly contribute to the potent

cytotoxicity effect against Caco-2 cell line. Previous investigation by [10] reported the promising cytotoxicity effect of alkaloidal extract from *Peganum harmala* and the findings of the current study agree with their report, as the CFM is also an alkaloidal extract. Unfortunately, the combination of alkaloid, phenolic, terpenoid, and saponin in CFM to provide synergistic effect still cannot inhibit the MCF-7 cell proliferation well enough.

IC_{50} is recognized as the inhibition concentration of substance for 50% of cell growth. According to Table 2, CFM needed high concentration to inhibit 50% of cell growth for both MCF-7 and Caco-2 cell lines at 3381 µg/mL and 176.2 µg/mL, respectively. In comparison between both cell lines, CFM is considered a good inhibitor against the Caco-2 cell line.

Table 1. Cell viability (%) value of CFM extract

Concentration of sample (µg/mL)	**Percentage of Cell Viability for MCF-7 Cell (%) ± SD**	**Percentage of Cell Viability for Caco-2 Cell (%) ± SD**
0 (untreated cells)	100.00 ± 0.287	100.00 ± 0.903
3.125	171.475 ± 1.614	95.709 ± 0.0574
6.25	167.527 ± 7.371	93.830 ± 0.343
12.5	146.327 ± 1.341	90.513 ± 0.308
25	146.148 ± 2.112	87.333 ± 0.298
50	131.089 ± 0.473	85.170 ± 1.426
100	116.583 ± 3.005	70.014 ± 2.572

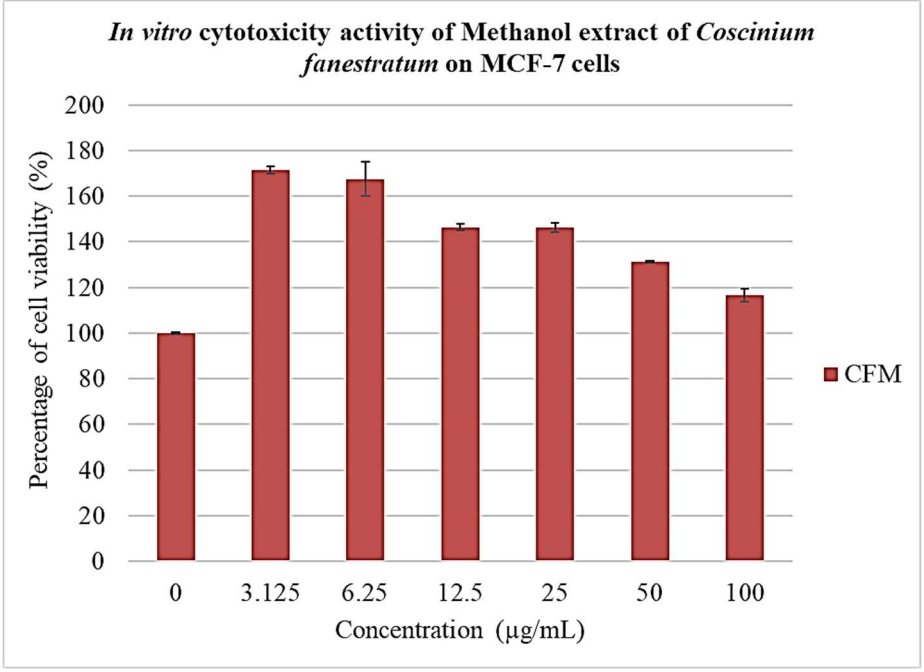


Figure 1. The percentage of cell viability of MCF-7 cells measured by MTT assay treated with CFM extract at the concentration of 3.125 to 100 µg/mL for 24 hours.

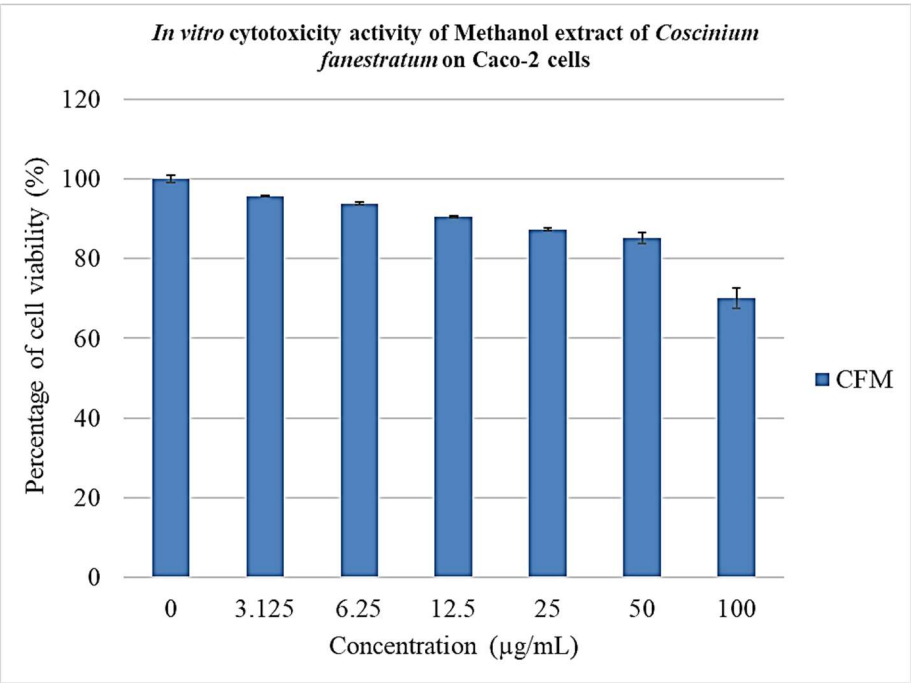


Figure 2. The percentage of cell viability of Caco-2 cell measured by MTT assay treated with CFM extract at the concentration of 3.125 to 100 µg/mL for 24 hours

Table 2. IC_{50} values of methanol crude extract of *C. fenestratum* and standard drug on MCF-7 and Caco-2 cell

Crude	IC_{50}, ug/mL (MCF-7)	IC_{50}, ug/mL (Caco-2)
CFM	338.1 ± 0	176.2 ± 0
Tamoxifen	0.4 ± 0.3	-

CFM: Methanol extract of *C. fenestratum*

Antioxidant activity

The FRAP assay is used to measure the antioxidant power based on the reduction at low pH of ferric-tripyridyltriazine (Fe^{3+}-TPTZ) to an intense blue color ferrous-tripyridyltriazine complex (Fe^{2+}-TPTZ) with an absorption maximum at wavelength 593 nm. Any changes from colorless Fe^{3+} to blue colored Fe^{2+}-tripyridyltriazine solution indicate the action of electron donating antioxidant. The FRAP value of CFM depicted in Table 3 is calculated as 47.8080 ug TE/gDW, and this value demonstrates high antioxidant power of CFM to reduce Fe^{3+} to Fe^{2+} ion. The IC_{50} value indicates the concentration of substance to scavenge 50% DPPH radical. The lower the IC_{50} value, the better the antioxidant activity is. The lower IC_{50} value of CFM at 13.8414 µg/mL revealed the remarkable potential of CFM as antioxidant agent. Moreover, this IC_{50} value is comparable with IC_{50} value of standard ascorbic acid 10.8520 µg/mL. Previous investigation [6] reported the total phenolic content (TPC) of CFM at 12.722 mg GAE/g sample, which could be one of the reasons for antioxidant properties of CFM. However, the presence of major phytochemical alkaloid and other phytochemicals, such as terpenoid and saponin [6], must not be underestimated on their contribution to antioxidant power.

Table 3. Total flavonoid content (TFC), DPPH radical scavenging activity, and ferric reduction antioxidant power (FRAP) of *Coscinium fenestratum* methanol extract

Antioxidant Activity	Methanol Extract of *C. fenestratum*	Ascorbic Acid
Total flavonoid content, (mg CE/g) (TFC)	–1.8595 ± 0.1878 (Not detected)	ND
Ferric reducing antioxidant power (ug TE/gDW)	47.8080 ± 0.4834	ND
DPPH scavenging IC50 (ug/mL)	13.8414 ± 0.1282	10.8520 ± 0.2716

Antibacterial activity

The antibacterial activity of CFM as anti-soft rot agent against two soft rot bacteria *E. chrysanthemi* and *E. carotovora* was illustrated in Table 4 and 5. This antibacterial data is the first time reported using *C. fenestratum* against *E. chrysanthemi* and *E. carotovora*. Generally, CFM extract moderately inhibited the growth of both bacteria in a concentration dependent manner (Table 4). The inhibition zone for both bacteria is not significant as the inhibition zone at 400 mg/mL is recorded as 11.5 mm and 11.83 mm. The presence of phytochemicals terpenoid and saponin [6] are believed to synergistically build the inhibitory effect on both bacteria. According to previous study [11], it was found that the growth of *E. chrysanthemi* was suppressed when using plant species, such as *E. spiralis* with inhibition zone of 16.3 mm, however the effectiveness of this plant towards *E. carotovora* was not reported. According to MIC and MBC value in Table 5, CFM is more effective to inhibit the growth of *E. carotovora* by 50% growth at MIC 15.625 µg/mL compared to *E. chrysanthemi* which is at 125 µg/mL. This means *E. carotovora* was more susceptible towards the CFM compared with *E. chrysanthemi*. The inhibitory effect was attributed with the hydroxyl group from saponin in which this group penetrated and shrunk the cell wall, and finally leading to the death of the cell [12, 13]. Previous report revealed the function of terpenoid as a plant defense to control plants from pathogen and pest and thus, prolonging the plant's lifetime [14,15].

Table 4. Antibacterial bacterial activity of methanol extract of *C. fenestratum* against *E. chrysanthemi* and *E. carotovora* from disc diffusion method

Concentration (mg/mL)	*E. chrysanthemi* inhibition zone ± SD (mm)	*E. carotovora* inhibition zone ± SD (mm)
400	11.5 ± 0.5	11.833 ± 0.29
200	6.833 ± 0.29	6.5 ± 0
100	7 ± 0	6. ± 0
50	6 ± 0	6 ± 0

Table 5. Minimum inhibitory concentration (MIC) and minimum bactericidal concentration (MBC) of methanol extract of *C. fenestratum* from microdilution method

Bacteria	MIC (µg/mL)	MBC (µg/mL)
E. chrysanthemi	62.5	125
E. carotovora	15.625	31.225

Conclusion

The methanol extract from *C. fenestratum* (*akar sekunyit*) is concluded to have good potential as an antioxidant source but less potential as an anti-cancer agent against breast cancer and colon carcinoma cell line, as well as an anti-soft rot agent. Regarding future work, it is recommended to use other types of antioxidant assays, such ORAC, ABTS, and CUPRAC, to establish its antioxidant power. Various anticancer cell lines, as well as plant pathogens, can be applied to evaluate its function in a broad spectrum of bioactivity. Isolation and identification of berberine alkaloid may also be conducted in the future.

Acknowledgment

The authors would like to express their gratitude to the science laboratory staff at Universiti Teknologi MARA (UiTM) Pahang and Assoc. Prof. Dr. Norazian Mohd Hassan from IIUM Kuantan for their assistance throughout this research.

References

1. Cuyacot, A. R., Mahilum, J.J.M. and Madamba, M.R.S.B. (2014). Cytotoxicity potentials of some medicinal plants in Mindanao, Philippines. *Pelagia Research Library*. 4(1): 81-89.
2. Ueda, J., Tezuka,Y., Banskota, A.H., Le Tran, Q., Tran, Q.K., Harimaya, Y., Saiki, I. and Kadota, S. (2002). Antiproliferative activity of Vietnamese medicinal plants. *Biological and Pharmaceutical Bulletin,* 25(6):753-60.
3. Pongkittiphan, V., Chavasiri, W. and Supabhol, R. (2023). Antioxidant effect of berberine and its phenolic derivatives against human fibrosarcoma cells. *Asian Pacific Journal Cancer Preventive*, 16(13): 5371-5376.
4. Kamkaen, N., Jenny, M., Wilkinson J.M., Cavanagh and H.M.A. (2006). Cytotoxic effect of four Thai edible plants on mammalian cell proliferation. *Thai Pharmaceutical Health Science Journal*, 1(3):189-195.
5. Moatasem, M. A., Dhifaf, J. S., Emaduldeen, H. A., Mohammed, M. T. A., Ibrahim, S. A., Dhuha, J. M., and Rana, R. K. The synergistic anticancer effect of some plant extracts in combination against human liver cancer cell line. *Asian Journal of Dairy and Food Research*, 1: 1-6.
6. Harun, A., Abdul Aziz, N. and Daud, S. (2022). The antibacterial, antifungal, antioxidant potential and total phenolic content of Malaysian endangered species *Coscinium fenestratum* from Paya Bungor Pahang. *Malaysian Journal of Analytical Sciences,* 26(4): 734-741.
7. Danapur, V., Haleshi, C. and Sringeswara A. N. (2020). Endangered medicinal plant *Cosciniumfenestratum* (Gaertn.) Colebr. - A review. *Pharmacognosy Journal,* 12(5): 1077-1085.
8. Ilias Fazna, N.F., Harun, A., Daud, S. and Abdul Aziz, N.(2023). Comparative study of antioxidant activity and total phenolic content of stem bark and leaves from *Murraya koenigii* species. *Gading Journal of Science and Technology*, 6(1): 13-24.
9. Mogana, R., Adhikari, A., Tzar, M., Ramliza, R. and Wiart, C. (2020). Antibacterial activities of the extracts, fractions and isolated compounds from *Canarium patentinervium* Miq. against bacterial clinical isolates. *BMC complementary medicine and therapies*, 20(1): 1-11.
10. Lamchouri, F., Zemzami, M., Jossang, A., Settaf, A., Israili, Z.H. and Lyoussi, B. (2013). Cytotoxicity of alkaloids isolated from *Peganum harmala* seeds. *Pakistan Journal Pharmaceutical Sciences,* 26(4):699-706.
11. Maha Yudden, N.K., Nordin, N.N., Harun, A., Rosli, N.H., Abdul Aziz, N., Daud, S. (2019). Comparative study of antioxidant activity of stem and leaves of *Entada Spiralis* and their antibacterial properties against *Erwinia Chrysanthemi*. *Science Letters*, 13(2): 37-47.
12. Soetan, K. O. (2008). Pharmacological and other beneficial effects of antinutritional factors in plants-A review, *African journal of Biotechnology*, 7(25): 4713-472.
13. Ezhilan, B. P. and Neelamegam, R. (2012). GC-MS analysis of phytocomponents in the ethanol extract of *Polygonum chinense* L. *Pharmacognosy Research,* 4(1):11-14.
14. Cheng, A., Lou, Y., Mao, Y., Lu, S., Wang, L. and Chen, X. (2007). Plant terpenoids: Biosynthesis and ecological functions. *Journal of Integrative Plant Biology*, 49(2):179-189.
15. Keawpradub, N. and Dej-adisai S. (2005). Antioxidant and cytotoxic activities of Thai medicinal plants named Khaminkhruea: *Arcangelisia flava,Coscinium blumeanum and Fibraurea tinctoria*. *Songklanakarin Journal Science Technology*, 2: 455-467.

Malaysian Journal of Analytical Sciences (MJAS)
Published by Malaysian Analytical Sciences Society

ELECTROCHEMICAL ELIMINATION OF METHYLENE BLUE DYE USING CARBON CLOTH MATERIAL

(Penghapusan Elektokimia Pewarna Biru Metilena Menggunakan Bahan Kain Karbon)

Fouad Fadhil Al-Qaim[1], Zainab Haider Mussa[2], Shaymaa Hadi Al-Rubaye[3], Nur Sofiah Abu Kassim[4], and Nurul Auni Zainal Abidin[4*]

[1]Department of Chemistry, Faculty of Science for Women, University of Babylon, PO Box 4, Hilla, Iraq
[2]College of Biotechnology, Al-Qasim Green University, Al-Qasim, Iraq
[3]Hammurabi College Medicine, University of Babylon, PO Box 4, Hilla, Iraq
[4]School of Chemistry and Environment, Faculty of Applied Sciences, Universiti Teknologi MARA (UiTM), Cawangan Negeri Sembilan, Kampus Kuala Pilah, 72000 Kuala Pilah, Negeri Sembilan, Malaysia

**Corresponding author: nurulauni@uitm.edu.my*

Received: 5 May 2023; Accepted: 24 October 2023; Published: 29 December 2023

Abstract

The effectiveness of the electrochemical technique to remove methylene blue (MB) from its aqueous solution was demonstrated in the current investigation. Various electrodes were used to explore the electrochemical process namely: aluminium (Al), copper (Cu) and carbon cloth (CC) as anode while the cathode was carbon cloth to select the highest removal%. Carbon cloth was selected as the best electrode due to its high efficiency for removal of MB dye compared to others. The effects of applied voltage, electrolysis time, and sodium chloride were investigated to identify the optimal conditions. Response surface approaches were used, however, to fully conceptualize how the factors interacted and get the best methylene blue dye elimination percentage using the electrochemical process. Rate constants ranged between 0.163 and 0.345 min^{-1}, demonstrating that high-rate constant accompanied pseudo first order kinetics, which was the dominating model throughout the investigation with high applied voltage and NaCl amount. Consumption energy was considered and measured; it was 0.104 Wh/mg at the maximum value applying 5 V referring that high consumption energy followed by high applied voltage. Utilizing response surface methodology (RSM), the electrochemical operating factor was optimized. The influence of NaCl addition rate, treatment time, and applied voltage were analysed using the optimum model derived from Box-Behnken Design (BBD), which was quadratic with MB removal (R^2 = 0.9447).

Keywords: methylene blue, electrochemical process, carbon cloth anode, energy consumption, pseudo first order kinetics

Abstrak

Keberkesanan teknik elektrokimia untuk mengeluarkan metilena biru (MB) daripada larutan akueusnya telah ditunjukkan di dalam kajian semasa. Pelbagai elektrod digunakan untuk meneroka proses elektrokimia iaitu: aluminium (Al), kuprum (Cu) dan kain karbon (CC) sebagai anod manakala katod adalah kain karbon untuk memilih penyingkiran tertinggi%. Kain karbon dipilih sebagai elektrod terbaik kerana kecekapannya yang tinggi untuk menanggalkan pewarna MB berbanding yang lain. Pemalar kadar berjulat antara 0.163 dan 0.345 min^{-1}, menunjukkan bahawa pemalar kadar tinggi mengiringi kinetik tertib pertama pseudo, yang merupakan model yang mendominasi bagi penyiasatan dengan penggunaan voltan tinggi dan jumlah NaCl. Penggunaan tenaga telah dipertimbangkan dan diukur; ia adalah 0.104 Wh/mg pada nilai maksimum menggunakan 5 V merujuk tenaga penggunaan tinggi diikuti dengan voltan gunaan tinggi. Dengan menggunakan kaedah permukaan tindak balas (RSM), faktor pengendalian elektrokimia telah dioptimumkan. Pengaruh kadar penambahan NaCl, masa rawatan, dan voltan gunaan dianalisis menggunakan model optimum yang diperolehi daripada Reka Bentuk Box-Behnken (BBD), iaitu kuadratik dengan penyingkiran MB (R^2 = 0.9447).

Kata kunci: metilena biru, proses elektrokimia, kain karbon anod, penggunaan tenaga

Introduction

It is very well known that harmful dyes are the main source of water contamination then it is considered as environmental issue concern [1]. Dyes in different names and applications are the dominant source for threaten water bodies as it is used in a variety of industries, including tanneries, paper mills, textile, leather, plastics, painting, food preserve, and pharmaceuticals [2-5]. Dyes are caused cancer and it is also participated to harm human health and animal. Their impact also extends to threaten aquatic life and environment [6-9].

The main constituent of textile industrial effluent is dyes, so it was characterised as high oxygen demand and resistant to biological treatment. Consequently, it requires extra treatment process which is tertiary treatment process [10]. One of these dyes is methylene blue which is water soluble, and it used in acid-base titrations and biological stains [11, 12, 9]. As seen in Figure 1, methylene blue is an organic chloride salt that contains 3,7-bis(dimethyamino)phenothiazine-5-ium.

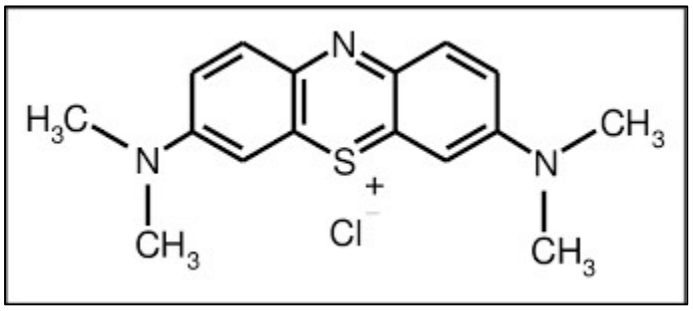


Figure 1. Chemical structure of methylene blue dye

The method most frequently employed to eliminate colour from aqueous solutions is electrochemical elimination. In contrast to other processes like photocatalysis, adsorption, membrane filtration, and reverse osmosis, the electrochemical process is simple to use, highly effective, technologically advanced, and safe. Other treatment methods like reverse osmosis, adsorption, and photocatalytic degradation were said to have certain drawbacks, such as the length of time needed for dye removal, issues with secondary pollutants, and a high cost of operation. The technologies have not shown to be particularly efficient or advantageous from an economic standpoint in eliminating colour from dye effluent [13]. However, the high prices and insufficient degradation of photocatalysis, Fenton-like processes, and ozonation processes continue to be a barrier [14]. Photocatalysis, one of the most advanced oxidation technologies, is one

of the most efficient processes because it uses an efficient semiconductor under UV/visible light irradiation and doesn't need additional chemicals or oxidants (atmospheric oxygen) to start the reaction. It is most likely among the AOPs with the highest efficiency and lowest cost [15]. The adsorption technique, on the other hand, is one of the successful methods that have been used to remove methylene blue dye due to its low cost, high efficiency, and simple operation. However, these treatment methods demand time and considerable effort to be effective [16].

The water cycle is so necessary to contaminant removal from wastewater's water system. Regarding the rigid structure of dyes, its removal from wastewater requires many steps for this purpose thus it is considered big challenge task. As we know, the main steps in wastewater treatment system are pretreatment, physical, chemical, and biological processes are reflected in the primary, secondary, and tertiary treatments, respectively according to the type of wastewater plant and target pollutants. As reported previously, conventional wastewater plants are ineffective for degradation dyes or other resistant-organic pollutants from water, resulting in other by-products more toxic than the parent compounds [17, 18]. Consequently, to avoid the issues that are linked with the conventional wastewater treatment plants, the application of advanced oxidation processes (AOPs) is the observed indication [19, 20]. These active degradation processes are able to be produced more effectively using an oxidizing agent like ozone or hydroxyl radicals to clean up the organic pollutant. After biological treatment, advanced oxidation processes can be used to get rid of the recalcitrant organic pollutants that are resistant toward the biodegradation treatment as well as to reduce the content of residual organic species.

Among the AOPs technologies such as ozonation treatment process [21], photocatalytic degradation process [22, 23], and sono-photocatalytic oxidation process [24] and electrochemical degradation process which is one of the promising technologies for its ability in remediation of organic pollutant compounds [25, 26]. Electrochemical degradation process is a promising technology due to its various benefits, which include its low cost, easy to operate, environmental compatibility and safe [20]. Anode material has interested property to assess the efficiency of electrochemical degradation method and it is considered a critical factor for this purpose [27]. However, two types of electrochemical reactions, direct and indirect electrochemical oxidation process as reported in details [28]. Electrochemical oxidation process may vary depending on the working principle. When it starts with pollutants degradation by anodic electrodes attracting the pollutants towards the anode. Following this Principle is called Direct electrochemical oxidation. On the other hand, it may be carried out by eliminating the compounds in the bulk solution concomitantly with active and strong oxidation agents like chlorine and hypochlorite [29]. Preparation of chlorine, chloride, and hypochlorite is according to the following equations:

$$2Cl^- \rightarrow Cl_2 + 2e^- \quad (1)$$

$$Cl_2 + H_2O \rightarrow H^+ + Cl^- + HOCl \quad (2)$$

$$HOCl \leftrightarrow H^+ + ClO^- \quad (3)$$

The main disadvantage in direct anode oxidation is that weaking the activity of the anode surface through fouling leading [30]. However, indirect anode oxidation is the most common for treatment of organic pollutants using boron-doped diamond (BDD) as anode [31], mixed metal oxide electrodes [32, 33] and graphite-PVC composite [34]. One of the most used electrode materials for the treatment of contaminants is BDD anode, but its high cost participates to avoid its wide application. Other materials have long-term stability issue, low degradation efficiency depending on the pollutant substrate. The most important characteristic of electrochemical oxidation process is that anodes must exhibit good evolution of oxygen to make the efficiency of electrochemical process less and the consumption of energy is high during the electrochemical process of wastewater treatment process [35].

Some process parameters were affecting electrochemical performance including electrolyte amount, applied voltage and electrolysis time. These factors were optimized conventionally by carrying a set of experiments for each factor to ensure higher

efficiency with lowest costs [36]. The literature showed that the classic optimization not effective enough to balance the optimization between the different operational factors, but treat each factor separately, but it requires a long time and effort to manually integrate between the factors [37, 38]**.** In order to facilitate the overlapping of optimal factors, a multivariable statistical technique was commonly used, which replaces the traditional methods with higher efficiency, reduces operating expenses and guarantees shorter treatment times [39]. A statistical method called response surface methodology (RSM) may be followed to study higher number of variables with lower number of experiments [40]**.** It was applied by [41] in electrocoagulation and electro-Fenton optimization for POME removal with iron and aluminium electrodes. This study aims to (i) investigate the optimum combination of electrodes (Anode – Cathode) for MB removal with electrochemical method, (ii) to optimize the most influencing factors including electrolyte amount, applied voltage and electrolysis time using response surface methodology-BBD design to achieve maximum MB dye removal efficiencies.

Materials and methods

Reagents and chemicals

Pure standards (≥98%) of methylene blue (CAS no. 61-73-4) was bought at Sigma-Aldrich (St. Louis, MO). The provider of deionized water (DIW) was EASYPure RODI (Thermo Fisher Scientific, Waltham, MA). UV-visible spectrophotometer was used for sample analysis. Copper (CAS No. 7440-50-8) sheet with 0.25 mm of thickness and 99.98% trace base metal was purchased from Merck.

Standard methylene blue dye preparation

Methylene blue stock solution (1000 mg/L) was diluted in de-ionized water and kept at 4 °C. By varying the amount of NaCl (Merck, Germany) added to MB solutions, the conductivity could be changed.

Set up of electrochemical process

A Pyrex glass vessel (100mL) was used for all analysis/A Pyrex glass electrochemical cell (reactor) was placed on top of a magnetic stirring block. Electrochemical cell setup, as shown in Figure 2.

The electrochemical cell was a glass container involved two electrodes for degradation of methylene blue at normal conditions: 1.0 atm and 20±2 ℃. The working electrode (anode) and the counter electrode (cathode) were carbon cloth in dimensions of 1cm × 1cm (1 cm^2). The gap between two electrodes was kept constant of 2 cm and both connected to the DC power supply which is working at fixed current in all electrochemical experiments. The concentration of dye was 10 mg/L in deionised water, it was prepared from the stock solution (1000 mg/L) after serial dilutions. Different concentrations of the electrolyte (NaCl) were infused into the mixture then was stirred at 500 rotation per minute under magnetic stirred device to ensure complete mixing and distribution of dye and salt in the solution. At each treated sample the corresponding current between the electrodes was recorded as well as the temperature was also monitored. The collected samples were directly analysed and the methylene blue degradation rate was measured in terms of reducing colour removal of dye at wavelength of 660 nm using UV-Visible spectrophotometry, and the range scan is between 400 to 800 nm. Three applied voltages of 2, 3 and 5 V were tested in electrochemical removing of methylene blue at fixed NaCl amount of 0.5g.

The influence of sodium chloride concentration (0.1, 0.3 and 0.5g) on the electrochemical removal of methylene blue (10 mg/L) using CC as anode at fixed 5 V was investigated. All absorbance measurements of methylene blue dye are converted into concentration using a linear calibration curve (R^2 = 0.996).

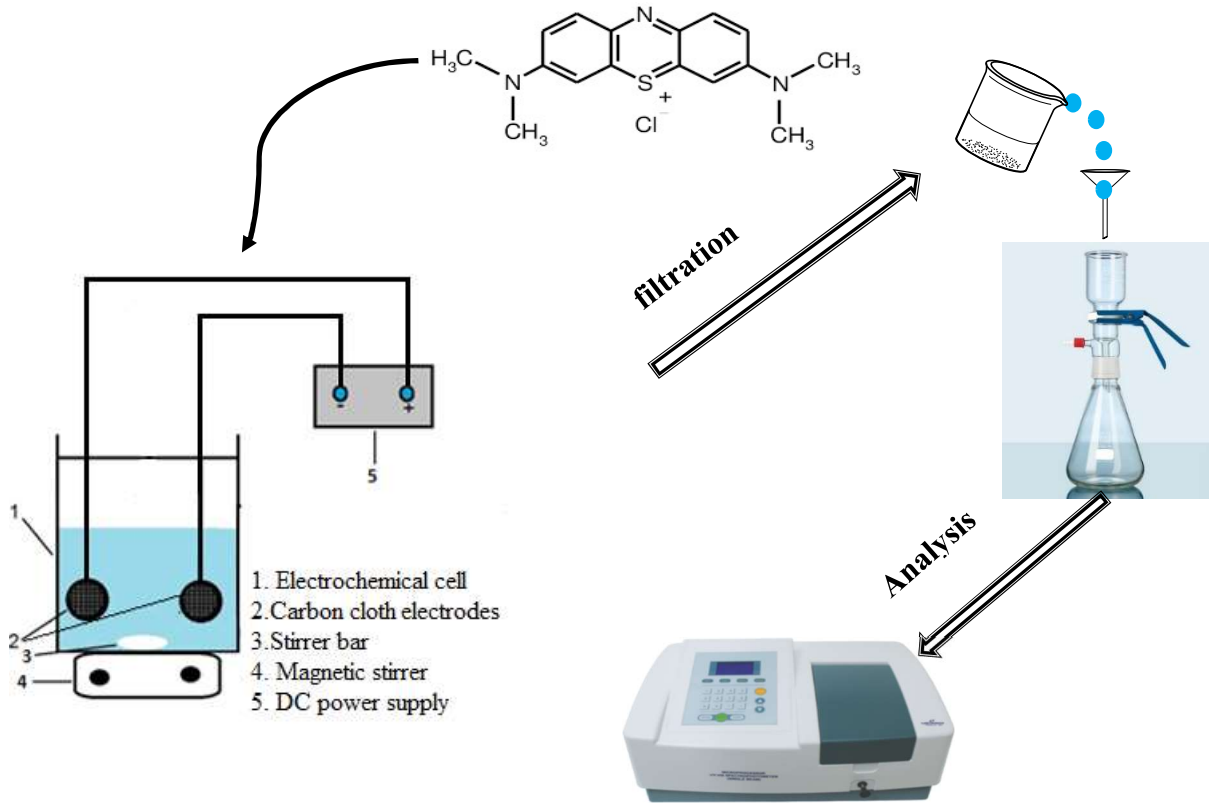


Figure 2. Electrochemical cell setup

Morphology and electrochemical characterizations of carbon cloth

The morphology and electrochemical characterizations of carbon fabric were investigated using powder X-ray diffraction (XRD, GBC MMA XRD), high-resolution transmission electron microscopy (HR-TEM, model: JEOL JEM-2011) and field emission scanning electron microscopy (FESEM, JEOL JSM-7500FA). The acceleration voltage is 15 kV and the beam current is 700 pA. All samples after treatment were analysed using U-visible spectrophotometer under maximum wavelength of 668 nm.

Box-Behnken design

Three parameters have been investigated on elimination of methylene blue dye using three-level Box-Behnken Design (BDD) namely: electrolyte amount, applied voltage and electrolysis time. Table 1 present the three parameters with their values which were processed in 45 runs and 9 centre points. The total number of experiment sets were calculated using the following equation [40]**:**

$$N = 2K(K-1) + C_0 \quad (4)$$

where C_0 is the number of a central point and K is the number of factors. The statistical studies were conducted using the Design Expert regression tool (Version MINITAB statistical software package).

Table 1. Levels and ranges of independent variables

Variable	Factors	Level		
(unit)	X	-a	0	+a
NaCl amount (g)	A	0.1	0.3	0.5
Applied voltage (V)	B	1	3	5
Electrolysis time (min)	C	4	8	12

Results and Discussion

The results presented here could introduce the efficiency of electrochemical degradation of MB via producing an active species that are strong oxidants (ClO^-). One of these active species was chloride which is presented in wastewater or added to the wastewater. Through an oxidation process at the anode electrode, these chloride ions can be converted into active chlorine (Cl_2, HOCl, and ClO). These oxidants have a long-life time to achieve the required oxidation of methylene blue dye.

Selection of electrode materials

Cu-CC, CC-CC, and Al-CC electrode material combinations were employed under the conditions of 5 volt for 20 minutes with 0.5g NaCl serving as the support electrolyte. Based on Figure 3, full elimination of MB (100%) was obtained using CC-CC electrode after 10 min; meanwhile, MB removal in terms of Cu-CC and Al-CC was 20% and 54%, respectively after 16 min. According to the statistical analysis, the electrode materials significantly affect the removal of MB (P= 0.05), according to the results. A report claims that copper anode material was an excellent option for the treatment of organic pollutants due to its antibacterial qualities, ease of ionization, high conductivity, and low toxicity [42, 43, 44].

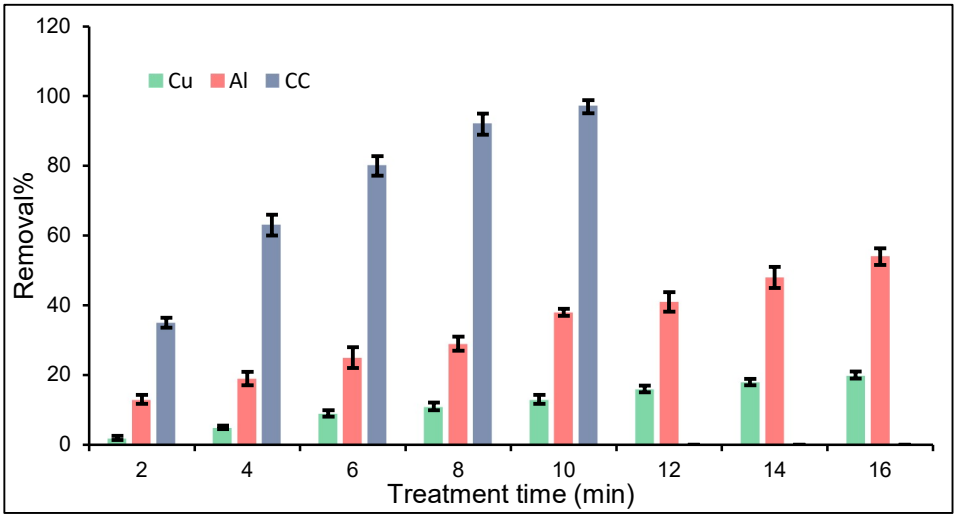


Figure 3. Selection of anode materials based on the removal% of methylene blue under these conditions: 5 V, 100 mL of solution, 5 mg/L of dye and 0.5 g NaCl

However, it was found experimentally that copper was easily corroded. In addition, the literature also showed that coper has low removal capability of MB which does not exceed (28%) [45]. As opposed to that, Al and carbon clothes were widely available with relatively low costs [46]. Furthermore, carbon clothes showed higher efficiency than Al in MB removal. The literature also supports this disadvantage of Al electrocoagulation used for POME removal with Al electrodes, the results indicated that only 42.94% of COD treated [47]. In addition, carbon clothes provide higher chemical stability, and better electrical conductivity [48]. Treatment of wastewater from poultry butcheries revealed that COD removal was 76% using graphite as anode [49]. Accordingly, the optimum electrodes combination used in this study were CC-CC based on methylene blue removal efficiency and stability of the electrolysis [50].

According to the previous report, MnO_2 based on a Pt electrode exhibited 90% removal of MB dye at the optimum conditions: pH =8, current density of 7 mA/cm^2, and supporting electrolyte of 0.05 mol/L [51]. From this point, Carbon cloth electrode exhibited a very good elimination% as shown from Figure 3.

To support the results above, characterization of carbon cloth has been investigated. The SEM image in Figure

4a, showed that the carbon cloth consists of a microstructure of embedded beam rods, this is a fictitious, two-dimensional artificial network made of organized tissue, where each fiber has a smooth surface and a constant 8.5 mm diameter. In addition, one of the characteristics of carbon cloth was that its fabric has excellent mechanical strength, flexibility, as well as high conductivity. Clear lattice fringes with 0.24 nm and 0.47 nm d-spacing, which correspond to (002) and (100) planes, are seen in Figure 4b. The pattern of electron diffraction (SAED) in the selected area, which demonstrates the crystalline nature of the porous carbon clothing, is shown in Figure 4c. However, the composition of the carbon cloth with the percentage has been included in Figure 4 d. It was observed that carbon is the major element in the sample. Consequently, the ease with which electrons and ions can approach the active surface is advantageous as it facilitates a rabid reaction producing higher power performance.

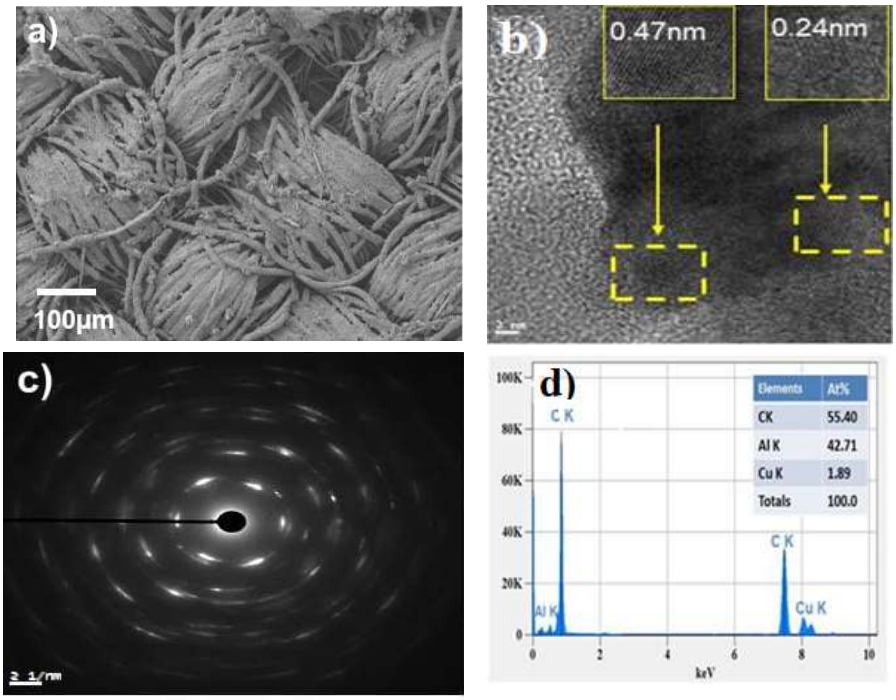


Figure 4. Characterization of carbon cloth: (a) SEM image, (b) TEM images at different magnifications of the carbon cloth (c) corresponding SAED pattern and (d) EDS analysis data for carbon cloth

The composition and phase purity of the carbon fabric were examined using the XRD pattern of the pure carbon cloth, as shown in Figure 5. The (002) and (100) planes of the carbon cloth substrate may be responsible for the acute and powerful diffraction peaks seen at 26 and 43.

Electrocoagulation modelling and optimization

Depending on the MB removal rate from the contaminated aqueous solution, the optimized operational factors of the electrochemical process were studied using three factor and three level BBD. The developed model was not much differing from the predicted values as the regression coefficient was (R^2 = 0.9447) with nine (9) center points. The experimental data for MB removal illustrated in Table 2 were then investigated and studied using analysis of variance (ANOVA). Using the values of P and F, a clear induction to the influence of an operational factor. Practical experiments have shown that using P and F values, the significance of the factors can be predicted with 95% accuracy. Higher significance obtained with a lower P (F Prob) value and a higher F value [52].

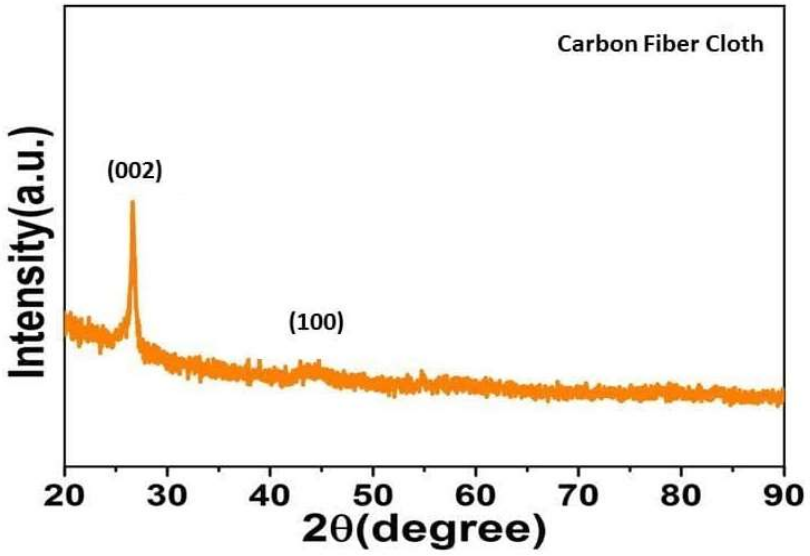


Figure 5. XRD Patterns of carbon cloth electrode

ANOVA findings showed that the F value for methylene blue dye elimination was high values, that means developed mathematical method exhibited good significance represented through preferred relationship between the response and external circumstances. Most model P values are less than 0.05, indicating that the mathematical models generated were significant. In addition, adjusted R^2 of the developed model is lower than R^2 (adjusted R^2 0.9305 < R^2 0.9447) which indicates the model has good quality. The effect of electrolyte amount (A), effect of applied voltage (B) and effect of electrolysis time (C) (p <0.05) are significant to remove MB dye.

In one reported paper, the removal of methylene blue dye was provided through a three-dimensional electrochemical process. It was observed that, through central composite design, the electrolysis time and applied voltage are the most significant factors in responses. However, initial concentration and pH factors are not significant [53].

In case of interaction factors, both interactions between (AC) and (BC) are significant meanwhile for the interaction between (AB) has no significant effect to remove MB dye. To find the relationship between each operational factor and the others, multiple regression analysis was carried out from BBD experiments. MB removal was modelled as a function of (time, electrolyte amount, and voltage) using second order polynomial equation as illustrated in (Equation 5):

$$R\% = -3.1 - 43.5\,A + 3.73\,B - 2.26\,C + 69.1A^2 + 0.108\,B^2 - 0.114\,C^2 + 6.88\,AB + 8.96 + 1.458\,BC \quad (5)$$

To evaluate the significance of each element and its relationships on treatment efficacy (%), Figure 6 shows the plot of the normal probability of the uniform effects with p = 0.05. The plot is divided into two different regions, (positive on the right side, and negative on the left side). The factors marked with red squares indicate their importance.

Table 2. The analysis of variance (ANOVA) for the second-order regression model

Source	DF	*F*-value	*P*-value	Remarks
Model	9	66.48	0.000	Significant
Linear	3	188.53	0.000	
A	1	103.51	0.000	
B	1	416.92	0.000	
C	1	45.16	0.000	
A^2	1	1.12	0.297	
B^2	1	0.03	0.870	
C^2	1	0.49	0.490	
AB	1	1.20	0.280	
AC	1	8.17	0.007	
BC	1	21.64	0.000	
Error	35			
Lack-of-fit	3	294.85	0.000	Significant
Pure error	32			
Total	44			

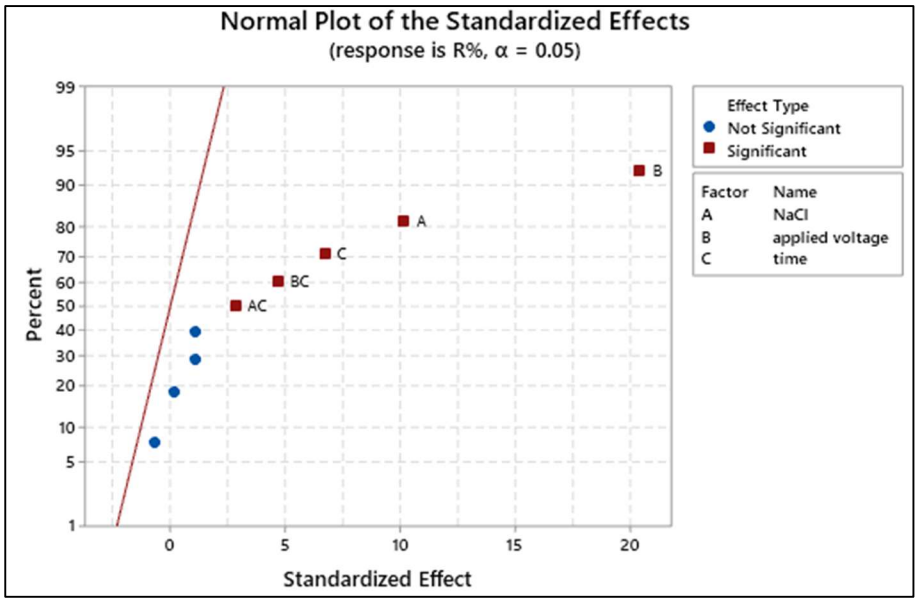


Figure 6. Plot of normalized probabilities for the impacts at p = 0.05 on removal% of MB dye

The relative importance of the individual and interaction effects was shown by the Pareto chart of the standardized effects in Figure 7. Student's t-test was used to confirm that the researched factors' impact was significantly higher than zero. The horizontal columns of a Pareto chart represented the importance of each effect. The lowest 95% confidence level statistically significant effect is shown by the vertical line (2.03) in the graph. Therefore, all values that are on the right side of the dashed line and are more than 2.03 (p = 0.05) are regarded as significant. The finding that MB removal is directly correlated with greater applied voltage, NaCl concentration, and treatment time is explained by the fact that raising these variables results in a sufficient amount of OCl^- acting as an oxidizing agent, directly assisting in the elimination of methylene blue. It is

noteworthy that the interaction between the factors (AC and BC) indicates a positive result associated with MB removal%. As a result, the effect of increasing NaCl or the applied effort relative to time leads to an increase in efficiency.

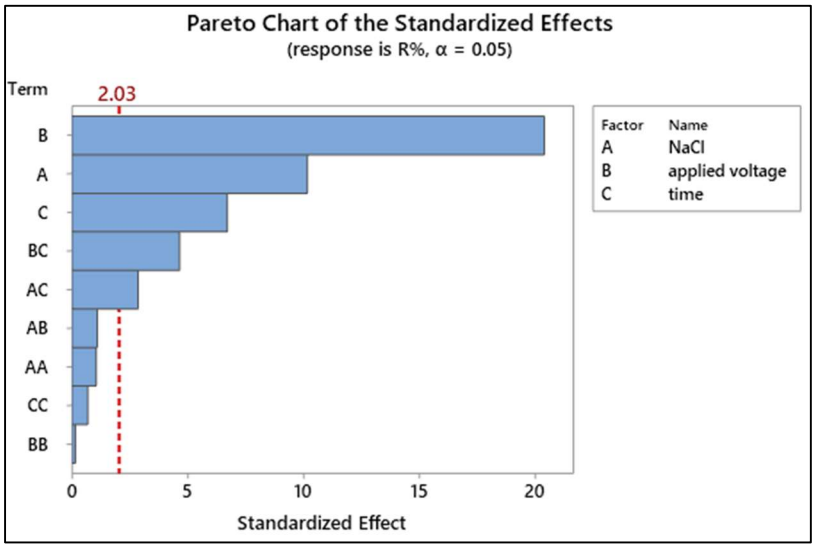


Figure 7. Chart demonstrating Pareto's standardized impacts on the percentage of removal of MB dye

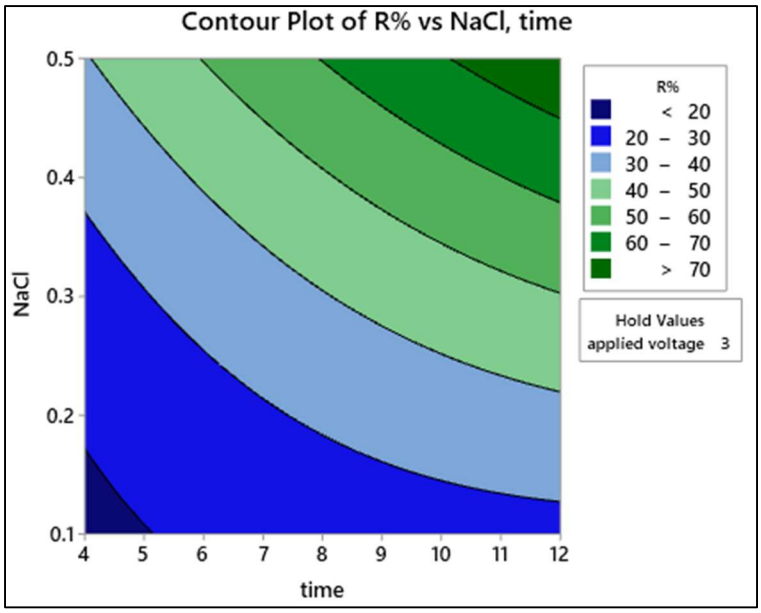


Figure 8. Contour response shows the relationship between the amount of NaCl vs electrolysis time on removal% of MB dye

It could be shown that the decolorization efficiency increases considerably with both NaCl amount and electrolysis time. In other words, increasing both NaCl amount and electrolysis time has positive impact on removal of MB dye. These results are supported by the contour plot given in Figure 8 as can be seen using 0.2-0.3g NaCl and 5-12 min of treatment time, the elimination% of MB was 20-30%. Increasing the amount of NaCl and the electrolysis time to 5 g and 10

min, respectively increases the elimination efficiency to >70%.

Figure 9 showed the efficiency of applied voltage is higher than NaCl with electrolysis time in terms of removal of MB. However, it could be noted that the elimination% raises effectively with increasing of applied voltage and time. These results are supported by the contour plot given in Figure 9 as can be seen using 3-4 V within 12 min of treatment time, the elimination% of MB was 20-40%. Increasing the applied voltage to 5 V at same period of time increases the elimination efficiency to >80%.

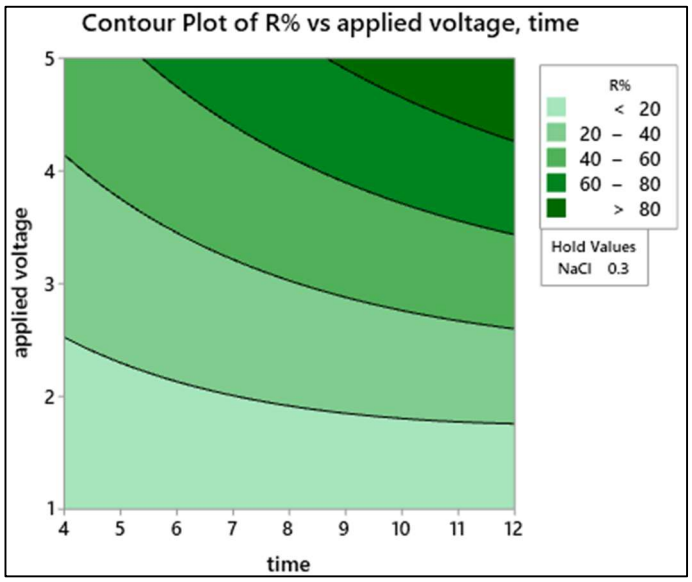


Figure 9. Contour response shows the relationship between applied voltage vs electrolysis time on removal% of MB dye

Electro-kinetics reaction

It was very well known from the results of RSM optimization that the interaction between "NaCl *vs* time" and "applied voltage *vs* time" are very significant so these two variables against time were considered in the present study. The linear time-course plot of Ln ([MB]t/[MB]0) in the elimination of MB tests in the presence of NaCl showed a pseudo-first order kinetics on the MB. The pseudo-first-order kinetic plot of MB elimination at 0.1, 0.3, and 0.5 g NaCl using 5 V is shown in an example in Figure 10. These graphs (0.988 R^2 0.99) were linear. For the experiments made possible by the applied voltage, comparable correlation coefficients were found. As a result, relative to the overall MB concentration, MB vanished at a pseudo-first-order rate for each trial. You can write the following equations:

$$-\frac{d[MB]_t}{dt} = K_{obs}[MB]_t \quad (6)$$

$$Ln\frac{[MB]_t}{[MB]_0} = -K_{obs}t \quad (7)$$

with [MB]t being the total residual concentration of MB and Kobs being the pseudo-first-order kinetic constant. Based on the slope of the linear time-course plot of Ln ([MB]t/[MB]0), Kobs was calculated for each experiment. Figure 10 displayed the profile of the methylene blue dye removal rate constant, or "Kobs," which was observed. Finding in Figure 10 showed that, under the conditions of 5 volts and 10 mg/L MB, the electrochemical elimination of MB dye followed pseudo-first order kinetics in the presence of all various NaCl concentrations. The rate range constants listed in Table 3 between 0.163 and 0.3451 min^{-1}. The rate constant that is measured at 0.3g NaCl is slightly lower than that of measured at 0.5g NaCl, the results were

0.3277 and 0.345 min^{-1}, respectively. This refers to an increase in NaCl amount would not significantly influence the MB degradation kinetics.

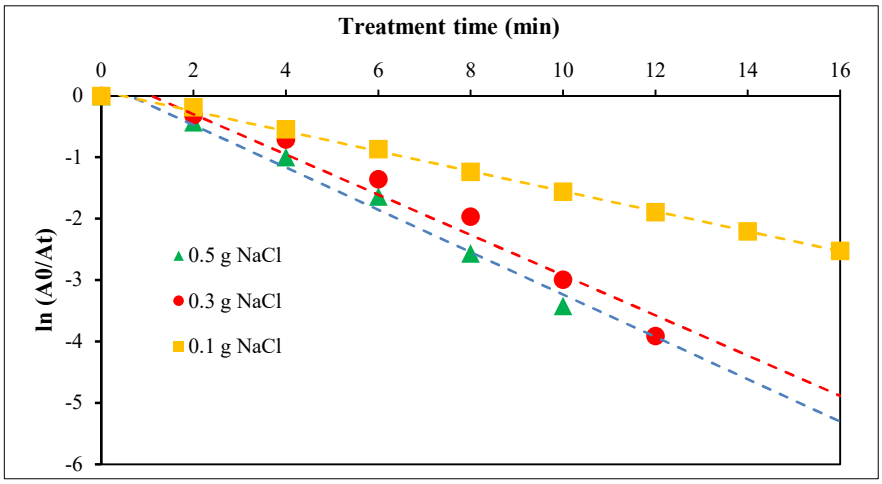


Figure 10. Impact of NaCl amount on rate constant at the following conditions: 5 volts, 10 mg/L MB, and 50 mL solution, of electrochemical degradation of MB

Table 3. Pseudo first-order rate constants for MB for various sodium chloride concentrations and voltage applications

NaCl Amount	**Effect of Sodium Chloride**		
(g)	**Equation**	**R^2**	**K_{obs} (min^{-1})**
0.1	y=0.163x+0.079	0.9981	0.163
0.3	y=-0.3277x+0.3579	0.9633	0.3277
0.5	y=-0.3451x+0.2156	0.9814	0.3451
Applied Voltage	**Effect of Applied Voltage**		
(volt)	**Equation**	**R^2**	**K_{obs} (min^{-1})**
1*	-	-	-
3	y = 0.1916 x+0.1256	0.9943	0.1916
5	y=0.3451x +0.2156	0.9814	0.3451

* There were not suitable results to be built

Kinetic study has been represented according to equations 5 and 6 so the profile plot confirmed that methylene blue dye has pseudo first-order kinetics as predominant at all applied voltage as shown in Figure 11. However, Table 4 provides a list of the reaction rate constants, K_{obs}. As we know, high applied voltage resulted quick elimination of MB dye then the rate constant could be large. On the other hand, the low applied voltage indicated that very slow removal of MB then it requires extra time to achieve the purpose. From Table 4**,** the reaction rate constants were 0.1916 and 0.3451 min^{-1} at 3 V and 5 V, respectively while it was not recorded for 1 volt as there is no significant removal.

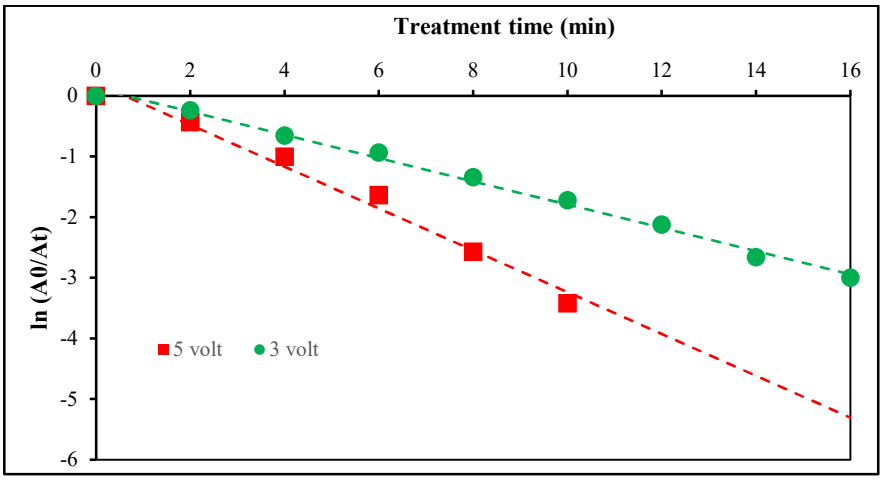


Figure 11. Impact of applied voltage on rate constant of electrochemical degradation of MB under these conditions: 0.5 g NaCl, 10 mg/L MB and 50 mL solution

Table 4. Energy consumption values of MB after electrochemical degradation process at 50 mL of 10 mg/L MB

Time	Energy consumption (Wh/mg)					
	1 V	3 V	5 V	0.1 g NaCl	0.3 g NaCl	0.5 g NaCl
2	0.0333	0.0285	0.0571	0.0392	0.0370	0.0571
4	0.0296	0.0250	0.0634	0.0317	0.0392	0.0634
6	0.0333	0.0295	0.0750	0.0344	0.0400	0.0750
8	0.0444	0.0324	0.0869	0.0375	0.0465	0.0869
10	0.0444	0.0365	0.1041	0.0421	0.0526	0.1041
12	0.0470	0.0409	-	0.0470	0.0612	-
14	0.0491	0.0451	-	0.0524	-	-
16	0.0561	0.0505	-	0.0579	-	-
18	0.06	-	-	-	-	-
20	0.0666	-	-	-	-	-
Average	0.0464	0.0360	0.0773	0.0428	0.0461	0.0773

Consumption energy

In electrochemical degradation process, when the removal% is high at short time then no consumption energy was observed. The energy consumption is calculated according to the equation 8:

$$EC = \frac{VI\Delta t}{\Delta\,[MB]} \qquad (8)$$

Where EC is the energy consumption in Wh/mg, I the current intensity (A), V the electrical potential (volt), t the treatment time (h) and [MB] the reduced mass of MB (mg).

However, the average consumption energy was 0.0428 Wh/mg in the presence of 0.1 g NaCl while it was 0.0773 Wh/mg in the presence of 0.5g NaCl even though it was similar to 0.3g NaCl as presented in Table 4. However, 0.3g NaCl exhibited results of 0.0461 Wh/mg which close to the results of 0.1g NaCl. As is well known, high applied voltage consumes high energy to achieve the electrochemical degradation of organic pollutants, so the present study was focused on this concept. Naturally, high applied voltage led to increased energy consumption. According to one previous study [53], greater applied voltages are linked to increased energy consumption and electrode corrosion. For this reason, in the current study, we concentrated on having the lowest energy consumption and best electrode

stability possible. All the consumption energy was calculated according to equation 7. The maximum average consumed energy was 0.0773 Wh/mg using 5 V while the lowest average consumption energy was 0.036 Wh/mg using 3 V as presented in Table 4. In light of this discovery, 5 volts was chosen as the ideal applied voltage for more research.

Conclusion

Electrochemical degradation process of methylene blue from its aqueous solution was carried out in this present work. Effect some independent variables such as amount of NaCl, applied voltage and electrolysis time was designed by using BDD software on removal% of MB. According to the mathematical method and BDD design plots, the most significant factors on removal% were NaCl amount (A), applied voltage (B) and electrolysis time (C). The interaction factors BC and AD, however, were equally important. On the other hand, unlike AB, the other interaction was not significant. The findings demonstrated that under the impact of sodium chloride and applied voltage, MB was removed in 10–20 minutes. Throughout the investigation, pseudo first order kinetics predominated. The rate constant, however, varied from 0.163 to 0.345 min^{-1}. In the current study, consumption energy was also considered; its range was 0.0366 to 0.104 Wh/mg.

Acknowledgements

The authors thankful the staff of the School of Chemical Science and Food Technology, Faculty of Sciences and Technology, Universiti Kebangsaan Malaysia for their support this research and other previous research.

References

1. Smith, Y.R., Bhattacharyya, D., Willhard, T. and Misra, M. (2016). Adsorption of aqueous rare earth elements using carbon black derived from recycled tires. *Chemical Engineering Journal*, 296: 102-111.
2. González, J.A., Villanueva, M.E., Piehl, L.L. and Copello, G.J. (2015). Development of a chitin/graphene oxide hybrid composite for the removal of pollutant dyes: adsorption and desorption study. *Chemical Engineering Journal*, 280: 41-48.
3. El Messaoudi, N., El Khomri, M., Dbik, A., Bentahar, S., Lacherai, A. and Bakiz, B. (2016). Biosorption of Congo red in a fixed-bed column from aqueous solution using jujube shell: Experimental and mathematical modeling. *Journal of Environmental Chemical Engineering*, 4:3848-3855.
4. Thuong, N.T., Nhi, N.T.T., Nhung, V.T.C., Bich, H.N., Quynh, B.T.P., Bach, L.G., Trinh, N.D. (2019). A fixed-bed column study for removal of organic dyes from aqueous solution by pre-treated durian peel waste. *Indonesian Journal of Chemistry*, 19: 486-494.
5. Zhou. Y., Lu, J., Zhou. Y. and Liu, Y. (2019). Recent advances for dyes removal using novel adsorbents: A review. *Environmental Pollution*, 252: 352-365.
6. Afroze, S., Sen, T. K., Ang, M. and Nishioka, H. (2016). Adsorption of methylene blue dye from aqueous solution by novel biomass Eucalyptus sheathiana bark: equilibrium, kinetics, thermodynamics and mechanism. *Desalination and Water Treatment*, 57: 5858-5878.
7. Pandian, A., Karthikeyan, C. and Rajasimman, M. (2017). Isotherm and kinetic studies on adsorption of malachite green using chemically synthesized silver nanoparticles. *Nanotechnology for Environmental Engineering*, 2: 1-17.
8. Bentahar, S., Dbik, A., El Khomri, M., El Messaoudi, N. and Lacherai, A. (2018). Removal of a cationic dye from aqueous solution by natural clay. *Groundwater for Sustainable Development*, 6: 255-262.
9. El Messaoudi, N., El Khomri, M., Goodarzvand Chegini, Z., Chlif, N., Dbik, A., Bentahar, S. and Lacherai, A. (2021). Desorption study and reusability of raw and H_2SO_4 modified jujube shells (Zizyphus lotus) for the methylene blue adsorption. *International Journal of Environmental Analytical Chemistry*, 2021: 1-17.
10. Sarasa, J., Roche, M.P., Ormad, M.P., Gimeno, E., Puig, A. and Ovelleiro, J.L. (1998). Treatment of a wastewater resulting from dyes manufacturing with ozone and chemical coagulation. *Water Research*, 32: 2721-2727.

11. Sarıcı Özdemir, Ç. (2019). Equilibrium, kinetic, diffusion and thermodynamic applications for dye adsorption with pine cone. *Separation Science and Technology*, 54: 3046-3054.
12. Adeogun, A. I. (2020). Removal of methylene blue dye from aqueous solution using activated charcoal modified manganese ferrite (AC-$MnFe_2O_4$): kinetics, isotherms, and thermodynamics studies. *Particulate Science and Technology*, 38: 756-767.
13. Ijagbemi, C.O., Chun, J.I., Han, D.H., Cho, H.Y. and Kim, D.S. (2010). Methylene blue adsorption from aqueous solution by activated carbon: Effect of acidic and alkaline solution treatments. *Journal of Environmental Science and Health, Part A*, 45(8): 958-967.
14. Modi, S., Yadav, V.K., Gacem, A., Ali, I.H., Dave, D., Khan, S.H. and Jeon, B.H. (2022). Recent and emerging trends inremediation of methylene blue dye from wastewater by using zinc oxide nanoparticles. *Water*, 14(11): 1749.
15. Kurian, M. (2021). Advanced oxidation processes and nanomaterials-a review. *Cleaner Engineering and Technology*, 2: 100090.
16. Mussa, Z.H., Al-Ameer, L.R., Al-Qaim, F.F., Deyab, I.F., Kamyab, H., Chelliapan, S. (2023). A comprehensive review on adsorption of methylene blue dye using leaf waste as a bio-sorbent: isotherm adsorption, kinetics, and thermodynamics studies. *Environmental Monitoring and Assessment*, 195(8): 940.
17. Kraft, A. (2008). Electrochemical water disinfection: a short review. *Platinum Metals Review*, 52: 177-185.
18. Oturan, M.A. (2021). Outstanding performances of the BDD film anode in electro-Fenton process: Applications and comparative performance. *Current Opinion in Solid State & Materials Science*, 25: 10092.
19. Deng, Y. and Zhao, R. (2015). Advanced oxidation processes (AOPs) in wastewater treatment. *Current Pollution Reports*, 1: 167-176.
20. Ghasemian, S. and Omanovic, S. (2017). Fabrication and characterization of photoelectrochemically-active Sb-doped Sn_x-W (100-x)%-oxide anodes: Towards the removal of organic pollutants from wastewater. *Applied Surface Science*, 416: 318-328.
21. Zhao, Q., Ge, Y., Zuo, P., Shi, D. and Jia, S. (2016). Degradation of thiamethoxam in aqueous solution by ozonation: influencing factors, intermediates, degradation mechanism and toxicity assessment. *Chemosphere*, 146: 105-112.
22. Mohamed, F.F., Allah, P.M.A., Mehdi, A. and Baseem, M. (2011). Photoremoval of malachite green (MG) using advanced oxidation process. *Research Journal of Chemistry and Environment*, 15(3): 65-70.
23. Haryadi, H., Purnama, M.R.W. and Wibowo, A. (2018). C dots derived from waste of biomass and their photocatalytic activities. *Indonesian Journal of Chemistry*, 18: 594-599.
24. Michael, I., Achilleos, A., Lambropoulou, D., Torrens, V.O., Pérez, S., Petrović, M. and Fatta-Kassinos, D. (2014). Proposed transformation pathway and evolution profile of diclofenac and ibuprofen transformation products during (sono) photocatalysis. *Applied Catalysis B: Environmental*, 147: 1015-1027.
25. Mussa, Z.H., Othman, M.R. and Abdullah, M.P. (2013). Electrocoagulation and decolorization of landfill leachate. In: *AIP Conference Proceedings. American Institute of Physics*, 2013: 829-834.
26. Zhao, W., Xing, J., Chen, D., Jin, D. and Shen, J. (2016). Electrochemical degradation of Musk ketone in aqueous solutions using a novel porous Ti/SnO_2-Sb_2O_3/PbO_2 electrodes. *Journal of Electroanalytical Chemistry*, 775: 179-188.
27. Ghasemian, S., Asadishad, B., Omanovic, S. and Tufenkji, N. (2017). Electrochemical disinfection of bacteria-laden water using antimony-doped tin-tungsten-oxide electrodes. *Water Research,* 126: 299-307.
28. Singh, S., Lo, S. L., Srivastava, V.C. and Hiwarkar, A.D. (2016). Comparative study of electrochemical oxidation for dye degradation: parametric optimization and mechanism identification. *Journal Environmental Chemical Engineering,* 4: 2911-2921.
29. Moreira, F.C., Boaventura, R.A.R., Brillas, E. and Vilar, V.J.P. (2017). Electrochemical advanced oxidation processes: a review on their application to

synthetic and real wastewaters. *Applied Catalysis B: Environmental*, 202: 217-261.

30. Feldman-Maggor, Y., Rom, A. and Tuvi-Arad, I. (2016). Integration of open educational resources in undergraduate chemistry teaching–a mapping tool and lecturers' considerations. *Chemistry Education Research and Practice*, 17: 283-295.
31. Solano, A.M.S., de Araújo, C.K.C., de Melo, J.V., Peralta-Hernandez, J.M., da Silva, D.R. and Martínez-Huitle, C.A. (2013). Decontamination of real textile industrial effluent by strong oxidant species electrogenerated on diamond electrode: viability and disadvantages of this electrochemical technology. *Applied Catalysis B: Environmental*, 130: 112-120.
32. da Silva, A.J.C., dos Santos, E.V., de Oliveira Morais, C.C., Martínez-Huitle, C.A. and Castro, S.S.L. (2013). Electrochemical treatment of fresh, brine and saline produced water generated by petrochemical industry using Ti/IrO_2–Ta_2O_5 and BDD in flow reactor. *Chemical Engineering Journal*, 233: 47-55.
33. Yahiaoui, I., Aissani-Benissad, F., Fourcade, F. and Amrane, A. (2013). Removal of tetracycline hydrochloride from water based on direct anodic oxidation (Pb/PbO_2 electrode) coupled to activated sludge culture. *Chemical Engineering Journal,* 221: 418-425.
34. Haider Mussa, Z., Fadhil Al-Qaim, F., Yuzir, A. and Shameli, K. (2020). Electrochemical degradation of metoprolol using graphite-PVC composite as anode: elucidation and characterization of new by-products using LC-TOF/MS. *Journal of the Mexican Chemical Society*, 64: 165-180.
35. Anglada, A., Urtiaga, A. and Ortiz, I. (2009). Contributions of electrochemical oxidation to waste-water treatment: fundamentals and review of applications. *Journal of Chemical Technology and Biotechnology*, 84: 1747-1755.
36. Brillas, E. (2020). A review on the photoelectro-Fenton process as efficient electrochemical advanced oxidation for wastewater remediation. Treatment with UV light, sunlight, and coupling with conventional and other photo-assisted advanced technologies. *Chemosphere*, 250: 126198.
37. Ay, F., Catalkaya, E.C. and Kargi, F. (2009). A statistical experiment design approach for advanced oxidation of direct Red azo-dye by photo-Fenton treatment. *Journal of Hazardous Materials*, 162: 230-236.
38. Roudi, A.M., Kamyab, H., Chelliapan, S., Ashokkumar, V., Kumar, A., Yadav, K.K. and Gupta, N. (2020). Application of response surface method for total organic carbon reduction in leachate treatment using Fenton process. *Environmental Technology & Innovation,* 19: 101009.
39. Ravikumar, K., Krishnan, S., Ramalingam, S. and Balu, K. (2007). Optimization of process variables by the application of response surface methodology for dye removal using a novel adsorbent. *Dye Pigment*, 72: 66-74.
40. Thirugnanasambandham, K., Sivakumar, V. and Maran, J.P. (2013). Application of chitosan as an adsorbent to treat rice mill wastewater-mechanism, modelling and optimization. *Carbohydrate Polymers*, 97: 451-457.
41. Kamyab, H., Yuzir, M.A., Al-Qaim, F.F., Purba, L.D.A. and Riyadi, F.A. (2021). Application of Box-Behnken design to mineralization and color removal of palm oil mill effluent by electrocoagulation process. *Environmental Science and Pollution Research*, 30(28): 71741-71753.
42. Barrera-Díaz, C.E., Frontana-Uribe, B.A., Roa-Morales, G. and Bilyeu, B.W. (2015). Reduction of pollutants and disinfection of industrial wastewater by an integrated system of copper electrocoagulation and electrochemically generated hydrogen peroxide. *Journal of Environmental Science and Health, Part A*, 50: 406-413.
43. Prajapati, A.K., Chaudhari, P.K., Pal, D., Chandrakar, A. and Choudhary, R. (2016). Electrocoagulation treatment of rice grain based distillery effluent using copper electrode. *Journal of Water Process Engineering*, 11: 1-7.
44. Safwat, S.M., Hamed, A. and Rozaik, E. (2019). Electrocoagulation/electroflotation of real printing wastewater using copper electrodes: a comparative

study with aluminum electrodes. *Separation Science and Technology*, 54: 183-194.

45. Niazmand, R., Jahani, M. and Kalantarian, S. (2019). Treatment of olive processing wastewater by electrocoagulation: An effectiveness and economic assessment. *Journal of Environmental Management*, 248: 109262.
46. El-Ashtoukhy, E.S.Z., Amin, N.K., Abd El-Latif, M.M., Bassyouni, D.G. and Hamad, H.A. (2017). New insights into the anodic oxidation and electrocoagulation using a self-gas stirred reactor: A comparative study for synthetic CI Reactive Violet 2 wastewater. *Journal of Cleaner Production*, 167: 432-446.
47. Nasution, A., Ng, B.L., Ali, E., Yaakob, Z. and Kamarudin, S.K. (2014). Electrocoagulation of palm oil mill effluent for treatment and hydrogen production using response surface methodology. *Polish Journal of Environmental Studies*, 23(5):1669-1677.
48. Liu, H., Cheng, S. and Logan, B.E. (2005).. Power generation in fed-batch microbial fuel cells as a function of ionic strength, temperature, and reactor configuration. *Environmental Science & Technology*, 39: 5488-5493.
49. Paulista, L.O., Presumido, P.H., Theodoro, J.D.P. and Pinheiro, A.L.N. (2018). Efficiency analysis of the electrocoagulation and electroflotation treatment of poultry slaughterhouse wastewater using aluminum and graphite anodes. *Environmental Science and Pollution Research*, 25: 19790-19800.
50. Garcia-Segura, S., Eiband, M.M.S.G., de Melo, J.V. and Martínez-Huitle, C.A. (2017). Electrocoagulation and advanced electrocoagulation processes: A general review about the fundamentals, emerging applications and its association with other technologies. *Journal of Electroanalytical Chemistry*, 801: 267-299
51. Alaoui, A., El Kacemi, K., El Ass, K., Kitane, S. and El Bouzidi, S. (2015). Activity of Pt/MnO_2 electrode in the electrochemical degradation of methylene blue in aqueous solution. *Separation and Purification Technology*, 154: 281-289.
52. Ashrafi, S.D., Safari, G.H., Sharafi, K., Kamani, H. and Jaafari, J. (2021). Adsorption of 4-nitrophenol on calcium alginate-multiwall carbon nanotube beads: Modeling, kinetics, equilibriums and reusability studies. *International Journal of Biological Macromolecules*, 185: 66-76.
53. Shokoohi, R., Nematollahi, D., Samarghandi, M.R., Azarian, G. and Latifi, Z. (2020). Optimization of three-dimensional electrochemical process for degradation of methylene blue from aqueous environments using central composite design. *Environmental Technology & Innovation*, 18: 100711.

Malaysian Journal of Analytical Sciences (MJAS)
Published by Malaysian Analytical Sciences Society

BELOWGROUND DECOMPOSITION OF SHOULDER AND RUMP FATTY FLESH IN SANDY CLAY LOAM SOIL OF RUBBER PLANTATION OF BUKIT PAYONG, MARANG

(Pereputan Bawah Tanah Bagi Daging Bahu dan Pinggul dalam Tanah Loam Berpasir Ladang Getah Bukit Payong, Marang)

Siti Sofo Ismail*, Thivialosini Siva, Lee Xin Pei, and Loh Kit Yee

Faculty of Science and Marine Environment, Universiti Malaysia Terengganu, 21030 Kuala Nerus, Terengganu, Malaysia

**Corresponding author: sofo@umt.edu.my*

Received: 17 August 2023; Accepted: 4 November 2023; Published: 29 December 2023

Abstract

Understanding the decomposition process of different body parts is crucial in estimating the postmortem interval (PMI) and/or locating a clandestine grave. Therefore, we conducted a laboratory controlled simulated burial experiment, mimicking a burial in a shallow grave under tropical climate, to comprehensively observe the changes of soil pH and the trend of decomposition rate. Fatty flesh of commercial pigs (*Sus scrofa*) from the shoulder and rump parts was buried in sandy loam soil. Firstly, a vial was firstly half-filled with the soil. The fatty flesh was placed and covered completely with the soil, then, allowed to decompose for 150 days of burial period. The associated soils were collected at 15 designated sampling points. Soil post-experimental pH was recorded, and the remaining fatty flesh was weighed. The lipids were extracted using modified Bligh-Dyer extraction method and analyzed with a gas chromatography-flame ionization detector (GC-FID). We noted differences in the trend of pH, decomposition rate, and total lipid extract concentration. The results demonstrated that generally the soil pH of both body parts changed from acidic at the early decomposition stage, to increasingly alkaline after several days of burial, and the alkalinity decreased back towards the completion of the experiment. Besides this, the soil pH of the rump increased, and the shoulder decreased at the early butyric fermentation stage. The decomposition rate of shoulder fatty flesh was higher than that of the rump at the early decomposition process with a maximum rate at the same burial interval. At the butyric fermentation stage, the total cadaveric derived lipid of the rump was higher than that of the shoulder. The findings of this study shall provide important information on the fates of different body parts and their impact on the surrounding soil pH, which can be used in forensic investigations to locate the clandestine graves and/or to estimate the PMI of the body.

Keywords: cadaveric derived lipids, rump fatty flesh, clandestine grave, postmortem interval, sandy clay loam soil

Abstrak

Pemahaman tentang proses penguraian bahagian badan yang berbeza adalah penting dalam menganggarkan selang postmortem (PMI) dan/atau untuk mencari kubur rahsia. Oleh itu, kami menjalankan eksperimen pengebumian simulasi terkawal makmal, meniru pengebumian di dalam kubur cetek di bawah iklim tropika untuk memerhati secara menyeluruh tentang perubahan pH

tanah dan trend kadar penguraian. Daging babi komersial (*Sus scrofa*) yang berlemak dari bahagian bahu dan pinggul ditanam di dalam tanah liat berpasir. Mula-mula, sebuah vial terlebih dahulu diisi separuh dengan tanah tersebut. Kemudian, daging berlemak itu diletakkan dan ditutup sepenuhnya dengan tanah, dibiarkan mereput selama 150 hari tempoh pengebumian. Tanah yang berkaitan telah dikumpulkan di 15 titik persampelan yang ditetapkan. pH tanah selepas eksperimen direkodkan dan baki daging berlemak ditimbang. Lipid telah diekstrak menggunakan Kaedah pengekstrakan Bligh-Dyer Terubahsuai dan dianalisis dengan gas kromatografi- pengesan nyalaan pengionan (GC-FID). Kami mencatatkan perbezaan dalam trend pH, kadar penguraian dan jumlah kepekatan ekstrak lipid. Keputusan menunjukkan bahawa secara amnya pH tanah kedua-dua bahagian badan berubah daripada berasid pada peringkat penguraian awal, meningkat kepada beralkali selepas beberapa hari pengebumian dan menurun kembali menghampiri selesai eksperimen. Selain itu, pH tanah bagi pinggul meningkat dan bahu menurun pada peringkat pembusukan hitam. Kadar penguraian daging lemak bahu adalah lebih tinggi daripada pinggul pada proses penguraian awal dengan kadar maksimum pada selang pengebumian yang sama. Pada peringkat penapaian butirik, jumlah lipid kadaver yang diperolehi adalah lebih tinggi daripada bahu. Penemuan ini memberikan maklumat penting tentang nasib bahagian badan yang berbeza dan kesannya terhadap pH tanah sekeliling yang boleh digunakan dalam penyiasatan forensik untuk mengesan kubur rahsia dan/atau untuk menganggarkan PMI mayat.

Kata kunci: Lipid terbitan kadaver, daging berlemak pinggul, kubur rahsia, selang masa postmortem, tanah liat berpasir

Introduction

Decomposition is defined as a process in which the tissue of dead organisms is degraded through the chemical and biological degradation of the tissue to simpler forms of matter and the physical removal of soft tissue by arthropods and scavengers [1-3]. It is a complicated process primarily dependent on a number of biotic and abiotic factors such as temperature, pH and moisture of the soil, the presence of microbial communities, burial environment and cadaver condition [3-6]. Several physical, chemical and climatic factors may delay and accelerate the decomposition process [2, 3]. Due to these factors, the decomposition rate of a buried body has been found to be much lower than that of a body on the soil surface [7, 8]. The decomposition process, which involves two principal processes of autolysis and putrefaction, can be described in a series of decay stages based on physicochemical changes [2, 7, 9, 10]. For this study, the decomposition stages were described as initial decay (0- 3 days), putrefaction (4-10 days), black putrefaction (10-20 days), butyric fermentation (20-50 days) and dry decay (> 50 days), each stage having its duration (burial interval) and characteristics [11]. The stages shall ease the documentation of physical and chemical changes that may be observed throughout the decomposition process. Furthermore, the progress of the decomposition can be measured, in particular, to evaluate the extent of tissue degradation, and subsequently, to estimate the postmortem interval (PMI).

The recovery of a clandestine grave or body and estimation of PMI are crucial in forensic investigation to give a closure to the cases. The PMI indicates the time of a person's death, potentially assisting in the identification of the deceased and reducing the number of suspects in homicide investigations [12-14]. There are a number of methods that have been used to estimate PMI, including the potassium levels of vitreous humor, analysis of body temperature or algor, livor and rigor mortis, ages of insects in immature stages that feed on a corpse, and DNA degradation [15]. However, the estimation of PMI becomes more difficult and less accurate with the longer time of death [16]. This is because at the more advanced stage of the decomposition process, the uncertainty and errors in estimating PMI will be significantly increased [15]. With this, the identification of the deceased will be more difficult, especially for a buried body, where DNA identification may not be possible as the DNA may have vanished due to the chemical reactions in the soil [17].

This paper details a simulated burial experiment in sandy clay loam soil, where the aim is to investigate the decomposition rate of different body parts, the changes in soil pH, and the concentration of cadaveric derived lipids that may be introduced into the surrounding soil. The fatty flesh of the domestic pig (*Sus scrofa*) was used to replace human tissues due to ethical issues. Pigs are known to have similar anatomical structures and functions, such as skin, body hair, cardiovascular and urinary system, and fatty acid distributions as humans

[2, 18, 19]. This simulated burial experiment was conducted with the ultimate aim to establish an alternative approach using cadaveric derived lipids to locate the clandestine graves and/or to estimate the PMI.

Lipids are one of the products that are liberated from a decomposed human body [8, 20-22]. The lipids are known to have the characteristics of chemical stability, ubiquity, diagenetic, and extreme diversity in the structures [23-24]. Hence, lipids have higher persistent characteristics and preserve longer within soil. The soil lipids have also been recognized to contain several diagnostic markers of soil environmental conditions, where the simple lipids such as fatty acids and alcohol have been considered to be good markers of origin and evolutions of lipid material in soils [25-27]. Hence, together with the unique properties of soil, the decomposition rate of different body parts, the changes in the soil pH and distribution of the extractable lipids were measured in order to investigate the extent of the decomposition process, and subsequently, elucidate the potential of cadaveric derived lipids as decomposition biomarkers. The documented lipid patterns and other decomposition information for every stage of decomposition event would yield valuable insights about the duration elapsed since death. Besides, a comparative analysis of the quantity of cadaveric lipids extracted from the soil at a particular place would prove the existence of a body in the past and, consequently, the location of a clandestine grave.

Materials and Methods

Simulated burial experiment: Sandy clay loam soil

Sandy clay loam soil was the soil of interest for this study, which is known to consist mainly of sand and silt, with a low amount of clay [28]. Sandy loam soil, with a composition of 60% sand, 30% silt, and 10% clay, was collected from a rubber plantation which is located at Bukit Payong, Marang, Terengganu (5.2248°N, 103.1075° E), to mimic the burial of one of the common body disposal sites which used to be encountered in forensic investigations.

Particle size analyzer (PSA 1190) was used to identify the mixture composition of the soil. 5-10g of oven dried soil sample was sieved to remove the small branches, and tiny stones. The sieved sample have to tumble slowly to prevent the brazil-nut-effect during the analysis. Glucagon (0.1%) was used to help the soil rich with organic matters to disperse completely to obtain the result in soil triangle graph with the composition percentage.

Experimental design

A laboratory controlled simulated burial experiment was conducted to investigate and compare the decomposition process of a different part of cadaver, i.e., shoulder and rump that was buried in sandy loam soil, under tropical climate. First, the soil was collected from approximately one meter depth, i.e., the depth of graves that are commonly encountered in forensic investigations. The soil was used to bury about 20g of pig (*Sus scrofa*) fatty flesh for each, shoulder and rump body parts in vials, mimicking a burial in a shallow grave. The accurate mass of fatty flesh at each sampling point was measured and recorded. The vials were labeled and allowed to be exposed to the ambient environment. Then, the fatty flesh was allowed to decompose for a number of designated sampling points, corresponding to the decomposition stages, with specific burial intervals. The gaps between adjacent samplings were two days for the first ten days of sampling points, representing the initial decay and putrefaction stages, and three days for the black putrefaction stage. The stages have been known as active decay stages, which was postulated to be accompanied with massive introduction of cadaveric derived materials. The soil moisture was checked consistently. At each sampling point, the remaining fatty flesh was removed from the soils and weighed. The difference of mass was used for the calculation of decomposition rate. The formula of decomposition rate is as shown below. The associated soils were stored in a freezer before being freeze-dried and subjected to further subsequent analyses. The soil was then freeze dried prior to lipid extraction.

$$Decomposition\ rate = \frac{Initial\ mass\ of\ fatty\ flesh - Final\ mass\ of\ flatty\ flesh}{Sampling\ Time\ Period} \quad (1)$$

Soil post-experimental pH

The pH of control and experimental soils was measured using a calibrated pH meter. Distilled water was added to dried soil samples in disposable culture tubes in a ratio of 1:5 of soil: water. The mixture was then mixed well and the soil was allowed to settle for at least 5 minutes. After that, the pH of the soil was measured by completely immersing the pH probe into the solution. The probe was ensured to avoid contact with the soil that had settled at the bottom of the tube. The pH reading was allowed to stabilize before recording the value. All pH measurements for every sample were repeated three times and recorded.

Total lipid extraction

Modified Bligh-Dyer extraction method was used to extract the lipids from the associated soils. Approximately 3 g of dry soil was transferred into a Pyrex culture tube. Then, 3 mL of 2:1 DCM/methanol (2:1, v/v) and 100 µL of internal standard of tetratriacontane (C-34) were added into the sample. The sample was sonicated for 15 minutes at 30°C, and this was followed by centrifuging it for 5 minutes (~3000 rpm). The supernatant was then transferred into a clean vial and the process was repeated three more times using 2 mL of DCM/methanol (2:1, v/v). After being treated with 3 mL Bligh-Dyer solvent the soil sample was sonicated for 15 minutes and centrifuged for 5 minutes (~3000 rpm). The obtained supernatant was transferred into the same vial. The Bligh Dyer solution was prepared by mixing buffered water, chloroform and methanol in a ratio of 4:5:10 [29]. The extraction was repeated three times with 2 mL Bligh-Dyer solvent. To break the organic phase, 2 mL of each buffered water and chloroform were added to the supernatant, and the mixture was centrifuged for 5 minutes. The organic layer at the bottom was transferred to a new clean vial. The process was repeated three times with 2mL chloroform. The excessive solvent was then evaporated using a mild nitrogen flow. The total lipid extract (TLE) was weighed using the following formula equation 2 and stored in the freezer prior to subsequent analyses.

$$\text{Total Lipid Extract} = \text{Final mass of vial} - \text{Initial Mass of vial} \quad (2)$$

Where, initial mass of vial = mass of empty vial, and final mass of vial = mass of vial with the extracts

Instrumental analysis

A Gas Chromatography – Flame Ionization Detector (GC-FID) (GC-6890N, Agilent) was used to analyze the samples. The GC-FID was equipped with a column of HP-5 5% phenyl methyl siloxane column, with helium as the carrier gas. After injection at 50 °C, the oven temperature was held for 2 minutes, followed by an increase in temperature to 300 °C at 10°C min^{-1}, which was held for 20 minutes. The peaks were selected by comparing the retention times with the external standard, prepared by the mixing of several lipid components, including palmitic and stearic acids, cholesterol, tetratriacontane, and triacylglycerides.

Results and Discussion

Post experimental soil pH

The breakdown of the adipose tissue in the rump and shoulder showed a similar pattern to that of previous investigations. The pH of the soil often rises in the early stages for buried corpses, then becomes more alkaline before acidifying in the later stages [30-32]. Furthermore, a similar trend in the pH changes was observed for the associated soils of the decomposing shoulder and rump fatty flesh. The post experimental soil pH increased at the early decomposition stages and decreased towards the end of the burial interval (Figure 1). The pH was acidic at the beginning of the decomposition event, then increased to become alkaline before acidifying again towards the completion of 150 days of the burial event.

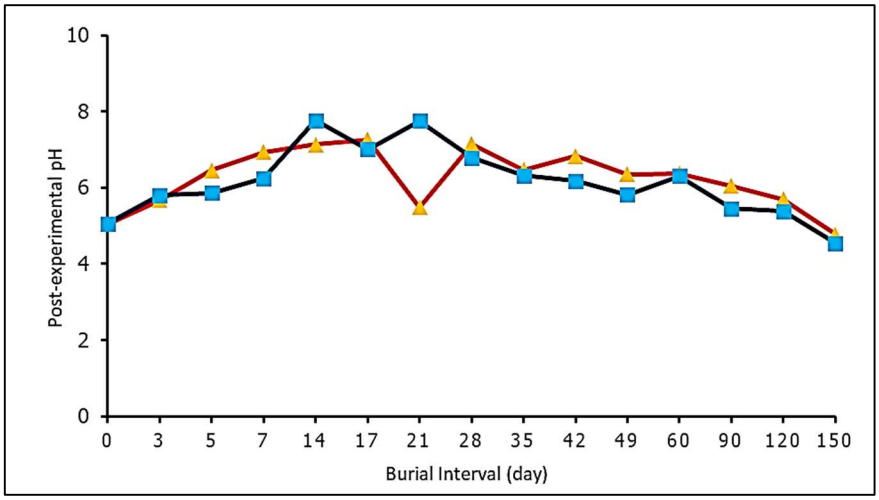


Figure 1. The changes in post experimental soil pH associated with the decomposition of pig fatty flesh of rump (blue line) and shoulder (red line) for 150 days of burial interval

The pH change was literally variable in response and slightly differed between the rump and shoulder body parts. However, the overall trend in pH changes for both body parts was similar throughout the 150 days of burial period. The pH increased between day 0 and day 14 of the burial period, corresponding to the initial and putrefaction stages of the decomposition process. The highest pH for the burial of rump and shoulder parts was observable after day 14 and day 17 of the burial period with a pH 7.77 and pH 7.26, respectively. Interestingly, on day 21 of the burial period, the soil pH of the shoulder body part increased while that of the rump fell, indicating a distinct trend in the soil pH during the early butyric fermentation stage. After 21 days of burial period, the decrease in the soil pH of decomposing rump and shoulder fatty flesh was observed, and thereafter, it continued to decline towards the completion of 150 days of burial period, with minor fluctuations. The lowest soil pH for shoulder (pH 4.78) and rump (pH 4.54) was recorded on day 150, corresponding to the dry decay stage.

The increasing in post-experimental soil pH at the first two decomposition stages, i.e., initial and putrefaction stages, may be due to the increase in the concentration of nitrogen-containing compounds, such as ammonium ions in the soil, resulting from the degradation of body macromolecules [30, 33]. After these stages, the decrease in the soil pH could be due to several reasons. Mineralization of protein and other organic nitrogen occurs via ammonification followed by nitrification of ammonia, NH_4^+, which may reduce the concentration of these nitrogen-containing compounds that are responsible for the increase in soil pH. The conversion of NH_4^+ to NO_3^- liberates protons, causing the soils to become more acidic [30, 32, 34, 35]. Besides, the continual degradation of fatty flesh may also produce non-mineralized decomposition by-products, such as acetic acid and phenolic compounds, and these may be deposited into the soil system. Organic components have been known to lower the pH and potentially inhibit subsequent decomposition events and microbial activities [34, 36]. These activities in the soil may also explain the fluctuations in the soil pH between day 17 and day 28 of the burial period for both rump and shoulder parts. These days correspond to the putrefaction and black putrefaction stages.

The decrease in the post-experimental soil pH after 21 days of burial period, continued towards the completion of the 150 days, a finding that is similar to a previous study by Haslam and Tibbett [35], which found that the soil pH became acidic when the decomposition process entered the butyric fermentation and dry decay stages. This decrease in the soil pH may also be explained by the presence of the decomposition acidic by-products as the increase in the amount of nitrate through the nitrification process has been known to result in a

decrease of soil pH [21, 35]. Moreover, the leaching of decomposition fluid which contains acidic by-products, such as volatile and long-chain fatty acids, also contributes to the decrease of soil pH (31, 38-40).

Decomposition rate

In general, the fatty flesh of both body parts demonstrated a similar trend in the decomposition rate. The decomposition rates of a cadaver for both shoulder and rump parts were high at the early stages of the process, and slowed down towards the end of the 150 days of burial interval (Figure 2). However, the trend was found to be slightly different than that commonly observed for buried cadavers [8]. Furthermore, the decomposition rate of shoulder fatty flesh was higher than that of the rump fatty flesh. This observation may indicate that the shoulder fatty flesh decomposes much faster than the rump fatty flesh.

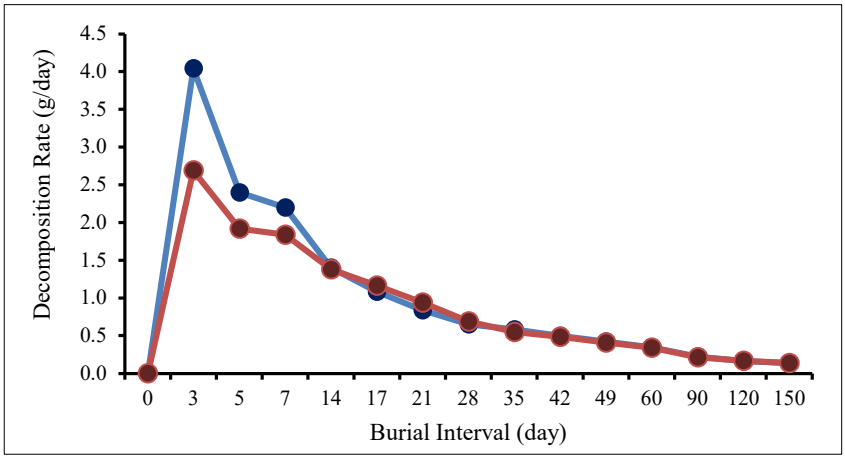


Figure 2. Graph of rate of decomposition of the burial fatty flesh of shoulder (blue line) and rump (orange line) for 150 days of burial period

The decomposition rate rapidly increased between day 0 and day 3 of the burial interval, reaching a maximum after 3 days of burial period, with magnitudes of 4.044 g/day and 2.690 g/day for the fatty flesh of shoulder and rump body parts, respectively. These days correspond to the initial decay stage. After this point, the decomposition rate decreased sharply and continued to decrease towards the end of the burial interval, reaching the lowest in the decomposition rate of shoulder and rump fatty flesh on day 150 of burial period. The lowest decomposition rates were recorded as 0.137 g/ day and 0.135 g/day for the fatty flesh of the shoulder and rump, respectively. This observation may indicate the completion of the decomposition process where most of the fatty flesh has disintegrated.

The biotic and abiotic factors of below ground are different compared to those above ground, which may reduce the activity of the decomposers [8, 34, 41]. Fiedler and Graw [42] stated that the decomposition of buried bodies depended mainly on scavenger activity, insect colonization, and temperature. Burial depth has also been identified to decrease the decomposition rate of a buried cadaver to lower the in-soil temperature, less decomposer activity, and grave moisture content [41, 43]. Considering the burial environmental factors for both rump and shoulder body parts, it has been hypothesized that the main body components of fat and muscular protein would contribute to the differences in their decomposition rates. The observation may be due to the autolysis process that took place during these days. This process has been known to involve the highest and most active degradation activity by microorganisms [4, 20, 34, 36]. The maximum decomposition rate may also be due to the higher rate of redox potential of tissues which contributed to the growth of bacteria at the end stage of autolysis during the decomposition of the fatty flesh [16, 17, 45]. Furthermore, the maximum soil microbial activity had also been observed within the first ten days of burial [44

– 46].

Total lipid extracts (TLEs)

The TLE mass recovered from the associated soils of both decomposing body parts exhibited a similar trend, i.e., increased at the beginning of the experiment, then decreased towards the completion of 150 days of the burial period. The TLE mass from both associated soils was found to slightly increase between day 0 and day 7 of the burial period, corresponding to the initial stage, and decreased towards the completion of the 150 days of the burial process. However, the mass of TLEs extracted from the associated soil of decomposing shoulder fatty flesh was lower than that of the rump fatty flesh. The mass of TLEs extracted from the soils of shoulder fatty flesh ranged from 0.0025 g to 0.0301 g/g soil dry weight, whilst, the mass of TLEs recovered from the soils of rump fatty flesh ranged between 0.0005 g/g and 0.5720 g/g soil dry weight. The lowest and the highest masses of soil TLEs of shoulder fatty flesh were recorded on day 7 (0.0025 g/g soil dry weight) and day 3 (0.0301 g/g soil dry weight), respectively. These days correspond to the initial decay (day 3) and putrefaction (day 7) stages.

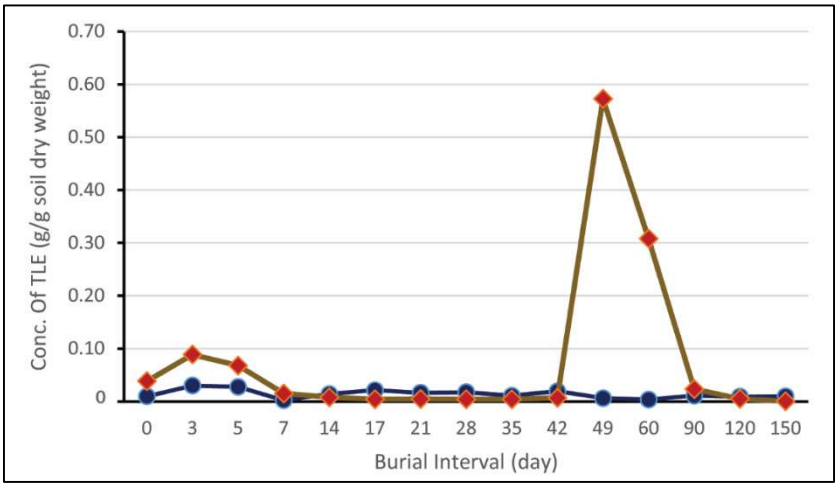


Figure 3. Total Lipid Extracts (TLEs) recovered from the soils associated with the decomposition of fatty flesh of rump (brown line) and shoulder (black line) parts for 150 days of burial interval

The trend of TLE mass of the rump fatty flesh was slightly different compared to that of the shoulder fatty flesh. Similar to that of the shoulder body part, the TLE mass increased between day 0 and day 3, corresponding to the initial decay stage. Then, the TLE mass decreased from day 5 until day 42 of the burial period, corresponding to the stages of putrefaction, black putrefaction, and butyric fermentation. After these points, the mass of TLE increased rapidly and reached the highest mass of TLE on day 49, i.e., 0.572 g/g soil dry weight. The TLE mass then decreased sharply after day 49 and this continued to the end of the burial period, reaching the lowest TLE mass on day 150, i.e. 0.0005 g/g soil dry weight.

The increase in the TLE mass that is observed at a number of burial days may potentially be the result from the leaching of cadaveric materials from the decomposing fatty flesh into the surrounding soil environment. The slight increase in the TLE mass during the initial decay and putrefaction stages agreed with the previous findings which described these first two stages as active decomposition stages [16, 47]. The decrease in the TLE mass after day 7 of burial period may explain a rapid mineralization of the introduced cadaveric materials to the simpler lipid components, such as carbon dioxide and water, as lipids are known to be vulnerable to the decomposition process when exposed to suitable conditions [48, 49]. Remarkably, the decrease in the TLE mass after this point can directly correlate with the decline in the decomposition rate of fatty flesh of both body parts.

The noticeable rapid increase in the TLE mass for rump that took place after 42 days of burial period potentially indicated a massive deposition of the cadaveric materials from the remaining fatty flesh into the surrounding soil system even though the decomposition rate started to slow down. This observation may also be a sign of slow mineralization of the cadaveric derived lipids, which may be due to the shifting in the microbial communities that were responsible for the decomposition process [45, 46, 50, 51]. The decomposition products have been suggested to impose a significant impact on the microbial communities that are responsible for the process, where they are known to either speed up or inhibit the disintegration of the fatty flesh [4, 45, 46]. It has been known that the fast-high rate of decomposition at the beginning of the experiment will be accompanied by a massive indication of the introduction of cadaveric substances into the surrounding burial soil [11, 18, 21, 31]. The mass of TLE was high at the beginning of the experiment. The potential explanation for this observation may be due to the rapid mineralization of the bigger compounds to simpler compounds. For example, the hydrolysis of triglycerides to free fatty acids and carbon dioxide. This explanation can be supported by the concentration of fatty acids detected by the GC-FID. The concentration of fatty acids was low at the beginning of the experiment, although the rate of decomposition was high.

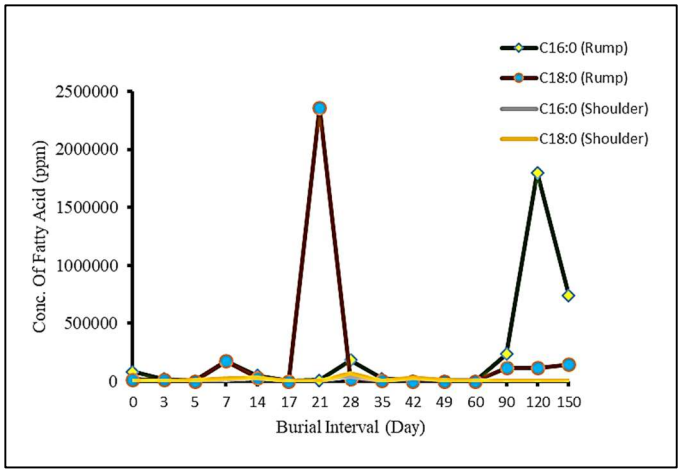


Figure 4. The concentrations of palmitic and stearic acids extracted from the soils associated with the decomposition of fatty flesh of rump and shoulder body parts

A gas chromatography–flame ionization detection (GC–FID) method was used for direct quantitative analysis of fatty acids. The analyses of cadaveric derived lipids, such as fatty acids, recovered from the associated soil was carried out to determine their potential usage for estimating the PMI. The lipid components detected were palmitic (C16:0) and stearic (C18:0) acids, together with cholesterol. Figure 4 shows the concentrations of fatty acids and cholesterol detected at different sampling points for 150 days of the burial interval. During the decomposition process, fatty acids are released from adipose tissues. The adipose tissues are made up from 60-85% lipids by weight, and 90-99% triglycerides, which would be further hydrolyzed into glycerin and free fatty acids [8]. Bull et al. [21] suggested an approximate 500-fold difference in the concentrations of palmitic (C16:0) and stearic (C18:0) acids extracted from the soils with decomposing cadaver or fatty flesh compared to that of control soils. Therefore, the presence of fatty acids in soil extracts at concentrations greater than that of the control soil can be interpreted as them having derived from anthropologically introduced organic matter such as pig adipose tissue. Furthermore, the remarkable changes in soil lipid compositions can help to confirm the prior presence of a cadaver in the suspected area. Janaway et al. [17] identified that the postmortem lipid components, such as palmitic, stearic, and oleic acids, were found as soon as 8 hours after

death, and that the most abundant lipid components in human body are oleic (C18:1), linoleic (C18:2), and palmitoleic (C16:1) acids. According to Dent et al. [8], these unsaturated fatty acids will be turned into simpler fatty acids shortly after death through hydrolysis and oxidation processes.

The majority of soil extracts showed a significant level of cholesterol along with the dominance of stearic (C18:0) and palmitic (C16:0) acids. Interestingly, the soils of both body parts had more palmitic (C16:0) acid than stearic (C18:0) acid. Furthermore, the soil of rump had greater fatty acid contents of C16:0 and C18:0 components than that of the shoulder. The total C16:0 and C18:0 concentrations of rump were determined to be 3315843.7 ppm and 2998265 ppm, respectively. The total values of C16:0 and C18:0 for the shoulder were 2108658.1 ppm and 1132487.0 ppm, respectively. There was 3840.1 ppm and 3466.9 ppm of cholesterol in the rump and shoulder, respectively.

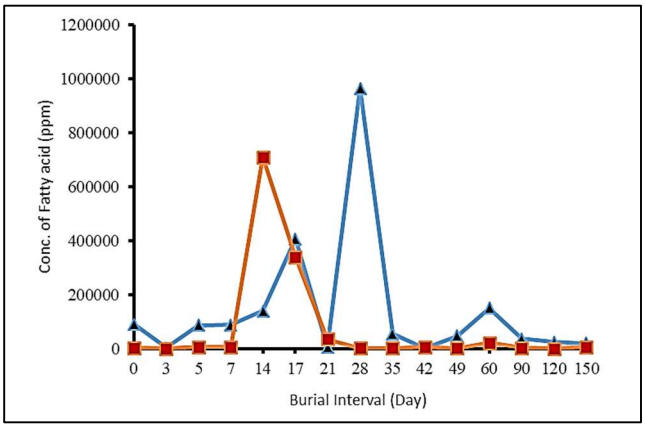


Figure 5. The concentrations of fatty acids of C16:0 and C18:0 components extracted from the soils associated with the decomposition of shoulder fatty flesh. The blue and orange lines represent the concentrations of C16:0 and C18:0 fatty acids, respectively

For the soils of the shoulder, the concentration of fatty acids generally increased between day 7 and day 21 of the burial interval, with minor fluctuations (Figure 5). These days correspond to the first three active decomposition stages of initial decay, putrefaction and black putrefaction. With a sharp increment between day 7 and day 14, the stearic acid reached maximum concentration (709127.6 ppm) on day 14, and then, the concentration of stearic (C18:0) acid decreased rapidly after this point and continued to decrease towards the completion of 150 days of the burial period. On the other hand, the palmitic acid demonstrated a first sharp increase in concentration after 17 days of the burial period, with a concentration of 138899.6 ppm, followed by a sharp decrease in the concentration of this fatty acid. The second dramatic increment in the concentration of this C16:0 component was observed after 21 days, where it reached a maximum concentration (964554.7 ppm) on day 28 of burial period. The possible explanation for this fluctuation is the introduction of different cadaveric substances during decomposition, which caused the shifting in microbial communities. Besides, there was also a slight increase in pH from day 21 to 28, which may impose an impact of the microbial community that is involved in the decomposition process. It is well known that soil microbial community has a strong correlation with soil pH [42]. The soil pH might facilitate succession of certain microbial species and induce the breakdown of lipids. The concentrations of palmitic (C16:0) and stearic (C18:0) acids decreased towards the end of the experiment. This observation was in line with the decomposition rate of the shoulder fatty flesh.

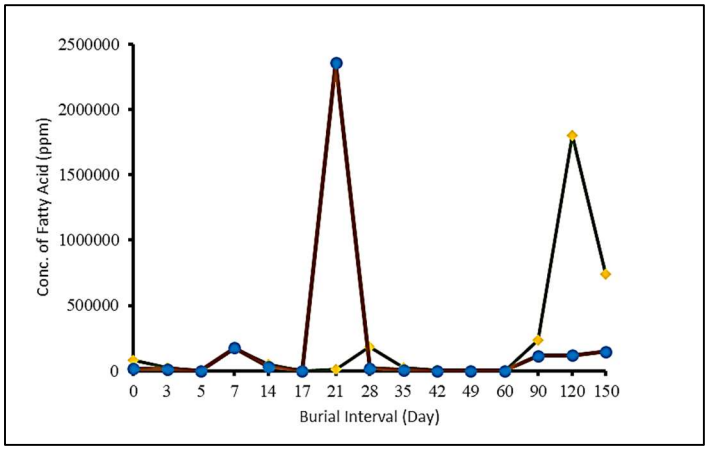


Figure 6. The concentrations of C16:0 and C18:0 extracted from the soils associated with the decomposition of rump fatty flesh. The green and brown lines represent the concentrations of C16:0 and C18:0 fatty acids, respectively.

The concentrations of palmitic and stearic acids extracted from the soils associated with the decomposition of rump fatty flesh demonstrated significantly different trends than that of the shoulder fatty flesh. Remarkably, the total concentration of C16:0 acid was higher than that of C18:0 acid. Furthermore, the concentration of palmitic acid was low at the early decomposition process before a rapid incline after 90 days of the burial event, with minor fluctuations between day 0 and day 35. The concentration of this fatty acid rapidly increased and reached a maximum (1798832.3 ppm) on day 120, corresponding to the dry decay stage. Then, the concentration of palmitic acid sharply declined after this point. The concentration of the stearic acid increased sharply after 17 days of the burial period and reached a maximum concentration (2359151 ppm) on day 21, corresponding to the black putrefaction stage. After this point, the concentration of this acid sharply declined to a much lower concentration which continued to decrease towards the completion of 150 days of the burial interval.

A higher abundance of palmitic and stearic acids extracted from the associated soils may be an indication of hydrogenation process of unsaturated acids and triacylglycerols during the decomposition of the fatty flesh of both rump and shoulder body parts. It is known that the hydrolysis of triacylglycerols is followed further by hydrogenation to form saturated components, yielding palmitic and stearic acids [8]. Moreover, the increase and decrease of the concentrations of palmitic and stearic acid may be due to the shifting of microbial communities due to the introduction of cadaveric components into the soil. The increment of fatty acid levels might be due to the initial growth and feeding stage of maggots, whereas the decrement of fatty acid might be due to the pupation period [40]. This also suggested that the activity of insects played a role in the amounts of fatty acids detected in the soil. The high concentrations of these short chain fatty acids may be explained by the observation that short-chain fatty acids had degraded faster than long-chain fatty acids [33]. This statement may also explain the low concentrations of cholesterol, and long-chain lipids extracted from the soils associated with the decomposition of both rump and shoulder body parts (Figure 7).

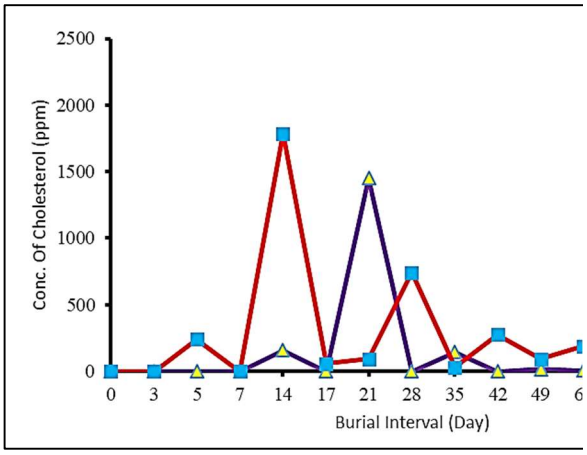


Figure 7. The concentrations of cholesterol extracted from soils associated with the decomposition of rump (purple line) and shoulder (red line).

Conclusion

This study was conducted to investigate the potential of cadaveric lipids to be developed as burial biomarkers that may aid in locating clandestine graves and/or to determine the PMI. The distribution of the cadaveric derived lipids was documented to further confirm their potential to provide useful information to aid forensic investigators as their concentrations may differ significantly, which can act as fingerprints for each of the decomposition stages. The fatty flesh of shoulder and rump demonstrated similar trends in the post experimental soil pH and decomposition rate. The post experimental soil pH was acidic at the early decomposition stages, then became alkaline, and then acidic again towards the completion of 150 days of the burial interval. The decomposition rate was found to be high at the initial stage and had reached the maximum after 3 days of the burial interval. Then, the decomposition rate then eventually decreased after this point and continuously decreased towards the completion of the process. Even though, both the body parts exhibited similar trends, the decomposition rate of fatty flesh of the shoulder was higher than that of the rump. A similar trend was also observed for their extractable derived lipids throughout the burial period. The concentrations of lipids slightly increased at beginning of experiment and decreased towards the end of experiment with minor fluctuations, which may due to the activity of the microbial community that is responsible for the decomposition process. However, the concentration of the extractable cadaveric lipids of the rump was higher than that of the shoulder. Moreover, the concentration of cadaveric lipids of the rump rapidly increased after 42 days of the burial period and decreased thereafter. The concentrations of cadaveric derived fatty acids and cholesterol extracted from the soils of both rump and shoulder were also different in their trends throughout the 150 days of the burial period. Hence, these findings may indicate that the analysis of soil cadaveric lipids can be developed as an alternative forensic tool to locate a clandestine grave and to estimate the PMI and/or to identify the victim and the criminal. It is recommended to investigate the breakdown of other body components in order to provide more evidence that different body parts break down at various rates. More information about the destiny of various body parts can therefore be obtained.

Acknowledgement

The authors would like to thank the Ministry of Higher Education Malaysia FRGS/1/2021/WAB02/UMT/03/3 for the financial aid, Faculty of Science and Marine Environment, and the Centre of Research and Field Service of Universiti Malaysia Terengganu (UMT) for providing the necessary equipment and facilities for the completion of this study.

References

1. Clark, M.A, Worrell, M.B and Pless, J.E (1997). Postmortem changes in soft tissue, in: W.D. Haglund, M.H. Sorg (Eds), Forensic taphonomy: The postmortem fate of human remains, CRC Press, Boca Raton, Florida, pp 151-160.
2. Goff, M.L. (2009). Early post-mortem changes and stages of decomposition in exposed cadavers. *Experimental and Applied Acarology*, 49: 2-36.
3. Zhou, C. and Byard, R.W. (2011). Factors and processes causing accelerated decomposition in human cadavers-An overview. *Journal of Forensic and Legal Medicine* 18(1): 6-9.
4. Vass, A.A. (2001). Beyond the grave: understanding human decomposition. *Microbial Today*, 28: 190-192.
5. Forbes, S.L, Dent, B.B. and Stuart, B.H. (2005).

The effect of soil type on adipocere formation. *Forensic Science International*, 154:35-43

6. Carter, D.O., Yellowless, D. and Tibbett, M. (2008). Temperature affects microbial decomposition of cadavers (*Rattus rattus*) in contrasting soils. *Applied Soil Ecology*, 40: 129-137.
7. VanLaerhoven, S.L. and Anderson, G.S. (1999). Insect succession on buried carrion in two biogeoclimatic zones of British Columbia. *Journal of Forensic Science*, 44(1):32-43.
8. Dent, B.B., Forbes, S.L., and Stuart, B.H. (2004). Review of human decomposition in soils. *Environmental Geology*, 45:576-585.
9. Payne, J. A. (1965). A summer carrion study of the baby pig *Sus scrofa Linnaeus. Ecology,* 46(5):592-602.
10. Eline M.J. Schotsmans, Van de Voorde, W., De Winne, J. and Andrew S.W. (2011). The impact of shallow burial on differential decomposition to the body: A temperate case study. *Forensic Science International*, 206(1-3): 43-48.
11. Ismail, S.S. and Chong, Z.Y. (2019). Decomposition of abdomen fatty flesh of cadaver buried in Nami series soil of Bukit Kor Terengganu. *Materials Today: Proceedings*, 19: 1426-1433.
12. Mann, R.W., Bass, W.M. and Meadows, L. (1990). Time since death and decomposition of the human body: variables and observation in case and experimental field studies. *Journal of Forensic Science,* 35(1): 103-111.
13. Catts, E.P. (1992). Problems in estimating the postmortem interval in death investigations. *Journal of Agricultural Entomology*, 9(4): 245-255.
14. Megyesi, M.S., Nawrocki, S.P. and Haskell, N.H. (2005). Using accumulated degree-days to estimate the postmortem interval from decomposed human remains. *Journal Forensic Science*, 50(3): 618-626.
15. Swann, L., Forbes, S. and Lewis, S. (2010). Analytical separations of mammalian decomposition products for forensic science: A review. *Analytica Chimica Acta*, 682(1-2): 9-22.
16. Teo, C.H., Hamzah, N.H., Hing, H.L. and Hamzah, S.P. (2014). Decomposition process and post mortem changes: Review. *Sains Malaysiana*, 43(12):1873-1882.
17. Janaway, R., Percival, S. and Wilson, A. (2009). Decomposition of human remains. *Microbiology and Aging*. Totowa, NJ: Humana Press, pp. 313-334.
18. Notter, S.J., Stuart, B.H., Rowe, R. and Langlois, N. (2009). The initial changes of fat deposits during the decomposition of human and pig remains. *Journal of Forensic Sciences*, 54(1): 195-201.
19. Štembírek, J., Kyllar, M., Putnová, I., Stehlík, L., and Buchtová, M. (2012). The pig as an experimental model for clinical craniofacial research. *Laboratory Animals,* 46(4): 269-279.
20. Janaway, R.C. (1987). The decay of buried remains and their associated material; in Studies in Crime: An introduction to forensic Archaeology (J. Hunter, C. Roberts, and A. Martin, Eds.). London: Routledge, 58-85.
21. Bull, I.D., Berstan, R., Vass, A. and Evershed, R.P. (2009). Identification of a disinterred grave by molecular and stable isotope analysis. *Science & Justice*, 49(2): 142-149.
22. Ioan, B.G., Manea, C., Hanganu, B., Statescu, L., Solovastru, L.G. and Manoilescu, I.R.I.N.A. (2017). The chemistry decomposition in human corpses. *Revista de Chimie*, 68(6): 1450-1454.
23. Derrien, M., Cabrera, F.A., Tavera, N.L., Manzano, C.A. and Vizcaino, S.C. (2015). Sources and distribution of organic matter along the Ring of Cenotes, Yucatan, Mexico: Sterol markers and statistical approaches. *Science of the Total Environment*, 511: 223-229.
24. Collins, S., Stuart, B. and Ueland, M. (2020). Monitoring human decomposition products collected in clothing: an infrared spectroscopy study. *Australian Journal of Forensic Sciences,* 52(4): 428-438.
25. Ambles, A., Magnoux, P., Jacquesy, R. and Fustec, E., (1989). Effects of addition of bentonite on hydrocarbon fraction of a podzol soil (A1 Horizon). *Journal of Soil Science*, 40: 485-694.
26. Jambu, P, Ambles A., Dinel H, and Seqouet B. (1991). Incorporation of natural hydrocarbons from plant residues into a hydromorphic humic podzol following afforestation and fertilization. *Journal of Soil Science*, 42: 629-636.
27. Jambu, P., Ambles, A., Jacquesy, J.C., Secouet, B., and Parlanti, E. (1993). Incorporation of natural

alcohols from plant residues into a hydromorphic forest-podzol. *Journal of Soil Science*, 44: 135-146.
28. Ritchey, E.L., McGrath, J.M. and Gehring, D. (2015). Determining Soil Texture by Feel. *Agriculture and Natural Resources Publications*. pp.139.
29. Ismail, S. S. and Daud, N. A. (2016). Lipid analysis on potential grave soil products. *Transactions on Science and Technology*, 3(3): 489-494.
30. Hopkins, D.W., Wilthire, P.E.J. and Turner B.D. (2000). Microbial characteristic of soils from graves: an investigation at the interface of soil microbiology and forensic science. *Applied Soil Ecology*, 14(3): 283-288.
31. Laura, A.B., David, O.C. and Shari, L.F. (2008). The biochemical alteration of soil beneath a decomposing carcass. *Forensic Science International*, 180(2-3): 70-75.
32. Szelecz, I., Koenig, I., Seppey, C.V., Le Bayon, R.C. and Mitchell, E. A. (2018). Soil chemistry changes beneath decomposing cadavers over a one-year period. *Forensic Science International*, 286: 155-165.
33. Comstock, J.L., Leblanc, H.N. and Forbes, S.L. (2016). Analysis of decomposition fluid collected from carcasses decomposing in the presence and absence of insects. *Soil in Criminal and Environmental Forensics Soil Forensics*, pp. 275-296.
34. David, O.C., David, Y. and Mark, T. (2007). Cadaver decomposition in terrestrial ecosystems. *Naturwissenschaften*, 94: 12-24.
35. Haslam, T.C. and Tibbett, M. (2009). Soils of contrasting pH affect the decomposition of buried mammalian (*Ovis aries*) skeletal muscle tissue. *Journal of Forensic Sciences*, 54(4): 900-904.
36. Vass, A.A., Barshick, S.A., Sega, G., Caton, J., Skeen, J.T., Love, J.C. and Synstelien, J.A. (2002). Decomposition chemistry of human remains: a new methodology for determining the postmortem interval. *Journal of Forensic Science,* 47(3): 542-553.
37. Szelecz, I., Sorge, F., Seppey, C.V., Mulot, M., Steel, H., Neilson, R., ... and Mitchell, E.A. (2016). Effects of decomposing cadavers on soil nematode communities over a one-year period. *Soil Biology and Biochemistry,* 103: 405-416.
38. Larizza, M. (2010). Physical and chemical analysis of pig carcass decomposition in fine sand (Master's thesis). Retrieved from https://ir.library.dc-uoit.ca/bitstream/10155/115/1/Larizza_Melina.pdf
39. Swann, L, Chidlow, G.E., Forbes, S.L. and Lewis, S.W. (2010). Preliminary studies into the characterization of chemical markers of decomposition for geoforensics. *Journal of Forensic Sciences*, 55(2): 308-314.
40. Swann, L., Forbes, S.L. and Lewis, S. W. (2010b). Observations of the temporal variation in chemical content of decomposition fluid: A preliminary study using pigs as a model system. *Australian Journal of Forensic Sciences*, 42(3):199-210.
41. Mann, R.W., Bass, W.M. and Meadows, L. (1990). Time since death and decomposition of the human body: variables and observations in case and experimental field studies. *Journal of Forensic Science*, 35(1): 103-111.
42. Fiedler, S. and Graw, M. (2003). Decomposition of buried corpses, with special reference to the formation of adipocere. *Naturwissenschaften*, 90: 291-300.
43. Bachmann, J. and Simmons, T. (2010). The influence of preburial insect access on the decomposition rate. *Journal of Forensic Science*, 55(4): 893-900.
44. Stokes, K.L., Forbes, S.L., Benninger, L.A., Carter, D.O. and Tibbett, M. (2009). Decomposition studies using animal models in contrasting environments: evidence from temporal changes in soil chemistry and microbial activity. Ritz, K., A. *Criminal and Environmental Soil Forensic*, pp.1-519. Porirua, New Zealand: Springer.
45. Rachel, A.P., Kerith-Rae, D., Jacqui, H., Paul, G., Natasha, B., Mark, T. and Arpad, A. V. (2009). Microbial community analysis of human decomposition on soil. *In book of Criminal and Environmental Soil Forensic*, pp 379-394.
46. DeBruyn, J.M., Hoeland, K.M., Taylor, L.S., Stevens, J.D., Moats, M.A., Bandopadhyay, S., ... and Steadman, D.W. (2021). Comparative decomposition of humans and pigs: soil biogeochemistry, microbial activity and metabolomic profiles. *Frontiers in Microbiology,*

11: 608856.

47. Sukchit, M., Deowanish, S. and Butcher, B. A. (2015). Decomposition stages and carrion insect succession on dressed hanging pig carcasses in Nan Province, Northern Thailand. *Tropical Natural History,* 15(2): 137-153.
48. Schmidt, M.W.I., Torn, M.S., Abiven, S., Dittmar, T., Guggenberger, G., Janssens, I.A., Kleber, M., Kögel-Knabner, I., Lehmann, J., Manning, D.A.C., Nannipieri, P., Rasse, D.P., Weiner, S. and Trumbore, S.E. (2011). Persistence of soil organic matter as an ecosystem property. *Nature*, 478: 49-56.
49. Jansen, B. and Wiesenberg, G.L.B. (2017). Opportunities and limitations related to the application of plant-derived lipid molecular proxies in soil science. *Soil*, 3: 211-234.
50. Janaway, R.C. (1996). The decay of buried human remains and their associated materials. In: Studies in crime: An introduction to forensic archaeology (Eds. J Hunter, C Roberts and A Martin), pp. 58-85. Batesford, London.
51. Carter, D.O. and Tibbett, M. (2006). Microbial decomposition of skeletal muscle tissue (*Ovis aries*) in a sandy loam soil at different temperatures. *Soil Biology and Biochemistry*, 38(5): 1139-1145.

Malaysian Journal of Analytical Sciences (MJAS)
Published by Malaysian Analytical Sciences Society

PREPARATION AND COMPUTATIONAL STUDY OF BIMETALLIC COBALT-IRON SUPPORTED ON ALUMINA CATALYST IN CATALYTIC OXIDATIVE DESULFURIZATION

(Penyediaan dan Kajian Pengiraan bagi Mangkin Dwilogam Kobalt-Ferum yang Disokong pada Mangkin Alumina dalam Penyahsulfuran Oksida Bermangkin)

Maryam Solehah Zulkefli[1], Wan Nazwanie Wan Abdullah[1*], Nor Atiq Syakila Mohd Nazmi[1], and Fazira Ilyana Abdul Razak[2]

[1]*School of Chemical Sciences, Universiti Sains Malaysia, 11800 Gelugor, Pulau Pinang, Malaysia*
[2]*Department of Chemistry, Faculty of Science, Universiti Teknologi Malaysia, 81310 UTM, Johor Bahru, Johor, Malaysia*

[*]*Corresponding author: wanazwanie@usm.my*

Received: 6 August 2023; Accepted: 28 November 2023; Published: 29 December 2023

Abstract

Catalytic oxidative desulfurization (Cat-ODS) is utilized to remove the sulfur content in diesel fuel. Bimetallic catalysts are introduced in the desulfurization process of model diesel fuel, which includes components like n-octane, thiophene (Th), dibenzothiophene (DBT), and 4,6-dimethyldibenzothiophene (4,6-DMDBT). The presence of dopants was confirmed by atomic absorption spectroscopy (AAS) and X-ray fluorescence (XRF). It was found that the addition dopants toward Fe/Al_2O_3 catalyst significantly increased the selectivity of catalytic performance. Using the optimized condition, 98% sulfur removal was achieved. The catalyst's reproducibility test demonstrated that it could be utilized repeatedly for up to five cycles. In addition, mechanism pathways of bimetallic catalysts, both with and without the presence of catalyst have been thoroughly optimized using density functional theory (DFT).

Keywords: desulfurization, catalyst, density functional theory, diesel model, sulfur

Abstrak

Penyahsulfuran oksida bermangkin (Cat-ODS) digunakan untuk menyingkir kandungan sulfur dalam bahan api diesel. Mangkin dwilogam diperkenalkan dalam proses penyahsulfuran bahan api diesel model, yang merangkumi komponen seperti n-oktana, thiofen (Th), dibenzothiofen (DBT), dan 4,6-dimetildibenzothiofen (4,6-DMDBT). Kehadiran dopan telah disahkan oleh spektroskopi penyerapan atom (AAS) dan analisis sinar-X pendaflour (XRF). Didapati bahawa penambahan dopan ke arah mangkin Fe/Al_2O_3 meningkatkan selektiviti prestasi mangkin dengan ketara. Menggunakan keadaan optimum, 98% penyingkiran sulfur telah dicapai. Ujian kebolehulangan mangkin menunjukkan bahawa ia boleh digunakan berulang kali sehingga lima kitaran. Di samping itu, laluan mekanisma mangkin dwilogam, dengan penggunaan mangkin dan tanpa mangkin telah dioptimumkan secara menyeluruh menggunakan teori ketumpatan fungsi (DFT).

Kata kunci: penyahsulfuran, mangkin, teori ketumpatan fungsi, model diesel, sulfur

Introduction

Acid gas combustion produced by the combustion of diesel fuel which released sulfur dioxides compounds to the atmosphere either from industries or transportation can harm the environment and endanger human health [1]. Consequently, the sulfur content in fuels has grown more restricted over the world to overcome these environmental norms and more stringent sulfur control in diesel has been implemented to lower the sulfur content up to 10 parts per million (ppm), known as ultralow-sulfur diesel, wishing to achieve soot-free Euro VI emission standards [2].

Current conventional method in the removal of sulfur, hydrodesulfurization (HDS), is less effective in the removal of aromatic sulfur compounds such as dibenzothiophene (DBT), sulfur compound that mainly exists in fuel oils, and their alkylated derivatives [3, 4]. This technology is restricted since it requires expensive process due to high operational cost, and high operational temperature in the hydrogen gas atmosphere [5]. In order to ensure that the sulfur level of diesel fuels matches the rules, many efforts have been made in searching for a prompt and efficient desulfurization system to overcome the abundance of organosulfur in diesel fuel such as extraction desulfurization (EDS), adsorptive desulfurization (ADS), and oxidative desulfurization (ODS). Among them, catalytic oxidative desulfurization (Cat-ODS) is economically feasible for large scales utilization. When compared to the traditional HDS methods, it needs less capital and has lower running expenses. ODS technology has received a lot of interest since it is useful for creating ultra-low sulfur fuels under moderate circumstances. It can operate under mild conditions due to low temperature and no need for hydrogen gas [6].

Essentially, oxidative desulfurization is divided into two major steps: the first step is the oxidation of compounds consisting of sulfur converted to sulfoxides and sulfones using a selected oxidant. Secondly is the extraction of sulfoxide and sulfone from diesel via extraction, adsorption, and distillation [7, 8]. The efficiency of ODS is greatly dependent on the proper oxidant-catalyst combination. Several oxidants, including tert-butyl hydroperoxide (TBHP), sodium hypochlorite (NaClO), and hydrogen peroxide (H_2O_2), appear to be the best competitors due to their strong oxidizing capacity [3]. Some low-cost metals features, Fe, Zn, and Mo have been discovered to be quite successful in the desulfurization of fuel oils due to their physiochemical properties [9]. According to Bakar et al. [10] pure Fe-Al_2O_3 has a modest oxidative activity and was chosen as a viable option for desulfurization as it requires minimal cost and simple recycling [11].

It has been proven that bimetallic catalysts show higher catalytic activity in the ODS process [12]. Naseri et. al. [13] synthesized bimetallic catalysts composed of molybdenum and zinc. It showed maximal removal of DBT molecules in ODS reaction using the bimetallic catalyst. The same result was observed in the study by Luna et. al. [14] where the bimetallic catalyst using tungsten and vanadium exhibited highest ODS activity. Cobalt is widely known as a catalyst in oxidation processes and hydrodesulfurization [15]. In a previous work, Sampanthar et al. [16] have shown that Mn and Co catalysts were highly active in oxidation of refractory sulfur compounds in diesel using molecular oxygen. The fabricated catalyst can improve the contact surface of the catalyst with sulfur compound. Metal doping would introduce the defects on metal oxides, which in turn plays a significant role in the desulfurization performance. Herein, low valance of Co^{2+} was substituted to the higher valance of Fe^{3+} by the lattice defects [17].

In this study, cobalt was used as a dopant to form bimetallic catalysts. The effect of dopant dosage on catalytic activity was investigated. The mechanistic pathway was postulated and verified by computational study. Co/Fe-Al_2O_3 catalyst was tested for five successive cycles under the optimized condition to ensure the accuracy of the catalytic performance. The fresh Co/Fe- Al_2O_3 catalysts were characterized by atomic absorption spectroscopy (AAS) and X-ray fluorescence (XRF).

Materials and Methods

Materials

The catalyst support used was alpha alumina Al_2O_3 beads with diameter of 3-5 mm were obtained from

Sigma-Aldrich. The dopant iron (III) nitrate nonahydrate $Fe(NO_3)_3$ and cobalt (II) nitrate $Co(NO_3)_2$ were used as dopant to synthesize bimetallic catalysts. These dopants were obtained from QRëc. Hydrogen peroxide (H_2O_2) 30% in water (QRëc) and tertbutyl hydroperoxide (TBHP) (70 wt.%) were obtained from QRëc and Across Organics. They were employed as oxidizing agent during ODS process. *N*-octane (99%) was utilized as the solvent for the model diesel fuel, which included thiophene (Th, 99%), dibenzothiophene (DBT, 97%), and 4,6-dimethyldibenzothiophene (4,6-DMDBT, 95%). *N,N*- dimethylformamide (DMF) from MERCK was used as extraction solvent to remove sulfur impurities.

Catalysts preparation

Bimetallic catalysts based with different Fe and Co metal loadings were prepared by incipient impregnation method on Al_2O_3 beads. 4g of alumina support was immersed into the 2g of $Fe(NO_3)_3$ solution until complete absorption occurred on the surface. The mixture was put onto the glass wool and dried in an oven at 100 °C for 24 hours. The furnace was set up at the temperature of 400 °C and the catalysts was heated for 5 hours to ensure all the metal counter ions and water molecule are removed. The cobalt-iron supported on alumina catalyst was prepared by doping with $Co(NO_3)_2$ after the successful impregnation with iron using the same impregnation method. A series of bimetallic catalysts with different Co salt loading was synthesized (10, 20, and 30 wt.%). The developed catalysts were designated as follows Co/Fe-Al_2O_3 (10:90), Co/Fe-Al_2O_3 (20:80), and Co/Fe-Al_2O_3 (30:70). Based on AAS analysis, it shows that there are slightly differences in active species concentration compared to theoretical calculation this might because AAS analysis fully characterized the elemental composition of the material [18]

Oxidative desulfurization and characterisation

The 500-ppm model diesel fuel was formulated with three model sulfur compounds: thiophene (Th), dibenzothiophene (DBT), and 4,6-dimethyldibenzothiophene (4,6-DMDBT) in *n*-octane solvent. Model diesel fuel (10 mL) was added to the round bottom flask, together with catalyst (0.1g) and TBHP oxidant (O/S= 3).

The ratio of S molar ratio and TBHP is (1:3) (m/v). The mixture was refluxed for 30 min with intense stirring. The resulting mixture was cooled and filtered. The oxidized diesel fuel was extracted by solvent extraction (DMF) in a 1:1 diesel-to-solvent ratio (v/v). The extraction process was rapidly agitated at room temperature for 30 minutes before the diesel and solvent phases separated. Gas chromatography (Agilent 7890A) with a flame ionisation detector (GC-FID) together with equity 5 column were used to measure the sulfur content. The synthesized catalysts were further characterised using atomic absorption spectroscopy (AAS) and X-ray fluorescence (XRF) to analyse the elements presence in the catalyst. The textural properties of the catalyst and support were analyzed by nitrogen physisorption isotherms. N_2 adsorption-desorption isotherm was performed on Micromeritics ASAP 20120 adsorption analyzer at -196 °C. The equilibrium geometries and energy of the intermediates in the hypothesised process were calculated using density functional theory (DFT). All the energy calculations in this paper were done with the Gaussian 09/Gaussian 16 programme.

Result and Discussion

Atomic absorption analysis (AAS) was performed using the direct approach to assess the total metal content in Co/Fe-Al_2O_3 catalyst. The analysis of AAS in (Table 1) confirmed the presence of Fe and Co elements for all the catalysts. The Fe and Co metal content of the bimetallic catalyst were found to be in the targeted range. The trend for Co loading is an agreement with XRF analysis.

The large quantities of weight percentages of all elements were determined using XRF analysis in comparison to the nominal weight percentage introduced to the system, and the results were illustrated in Table 2. From XRF data measurement, the actual weight percentages for the elements in Co/Fe(10:90)/Al_2O_3, which was calculated for the preparation of Co and Fe were 15.8 wt.% and 84.2 wt.%, respectively. The percentages detected were found to be lower for iron species in Co/Fe(10:90)/Al_2O_3 due to the presence of other elements in the sample matrix and affecting the accuracy of the analysis. These matrix

effects can lead to a lower measured percentage for the target [19]. Even though there was a variation in AAS and XRF measurements, the data remained compatible with results acquired with more precision [20] From the XRF data, the amount of every element calculated was approximately similar to theoretical calculation. Thus, it evidenced that all the elements were present and dispersed well on the catalyst support. From our previous publication, XRD analysis proved the presence of oxide phase of Fe_3O_4 and Co_3O_4 in the catalyst [21].

Table 1. The concentration of metal element in Co/Fe-Al_2O_3 catalyst

Catalyst	Calcination Temperature (°C)	Concentration (ppm)	
		Fe	Co
Co/Fe-Al_2O_3 (10:90)	400	0.055	0.025
Co/Fe-Al_2O_3 (20:80)	400	0.030	0.057
Co/Fe-Al_2O_3 (30:70)	400	0.026	0.061

Table 2. Composition of metal element in Co/Fe- Al_2O_3 catalyst

Catalyst	Element (wt.%)	
	Fe	Co
Co/Fe-Al_2O_3 (10:90)	84.2	15.8
Co/Fe-Al_2O_3 (20:80)	80.6	19.4
Co/Fe-Al_2O_3 (30:70)	70.0	30.0

Effect of dopant ratio

The study was carried out to investigate the removal of sulfur compounds from model diesel fuel over Co/Fe-Al_2O_3 catalyst by using different dopant ratios of Co and Fe, calcined at 400 °C in a range of 10:90, 20:80, 30:70, and the results are presented in (Figure 1). The Co/Fe ratio of 10:90 gave the highest conversion of DBT (100%), 4,6-DMDBT (79%), and thiophene (93%). The variability in reactivity of sulfur compounds is mostly due to differences in electron densities on the sulfur atom and the sulfur compound's steric hindrance. Th, DBT, and 4,6-DMDBT contain electron density on the sulfur atom of 5.696, 5.758, and 5.760, respectively [22]. The removal of 4,6-DMDBT is the lowest compared to Th and DBT, since there is a methyl group presence on 4,6-DMDBT that acts as an obstruction for sulfur atom to take an approach to the catalyst's active core. An excess of cobalt concentration may form a cluster of active species on the catalyst's surface and reduced its surface area. The high amount of cobalt also prevented the Fe active sites from being equitably distributed across the supported catalyst surface, causing the catalyst's activity to become distorted [23]. Previous research had shown that Co loading can result in variable active surface site [24], and the catalytic characteristics were shown to be reliant on the dispersion and engagement of the Co with the support [25].

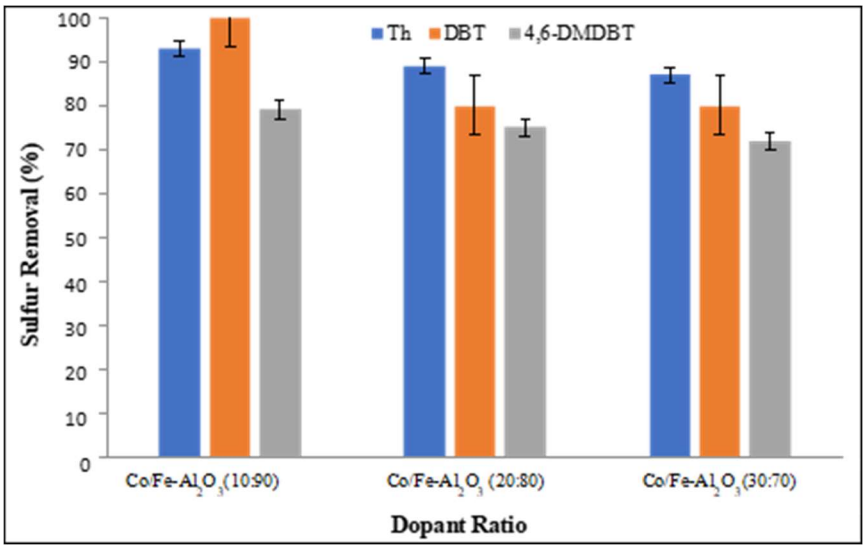


Figure 1. The impact of catalyst doses (Reaction conditions: Oxidant = TBHP, T = 50°C, time = 30 min, solvent = DMF)

Repeatability test

The repeatability investigation was performed three times to ensure accuracy. The catalytic activity of these catalysts was studied under similar preparation and experimental conditions. The outcome of three repetitions of Co/Fe(10:90)-Al_2O_3 catalyst repeatability testing as illustrated in (Figure 2). The observation showed there were not much difference in the repeatability test for the model diesel sample, indicating the accuracy of the analysis performed.

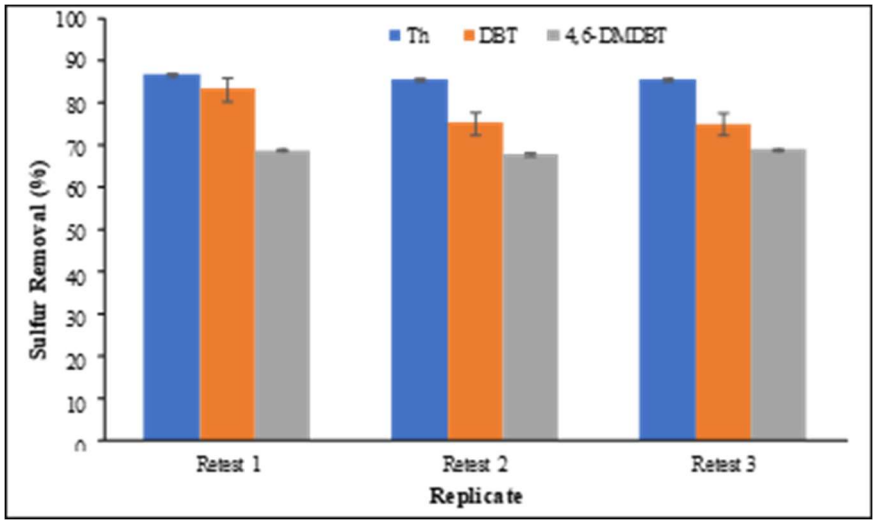


Figure 2. Repeatability test of Co/Fe- Al_2O_3 catalyst calcined at 400°C (Reaction conditions: Oxidant = TBHP, T = 50 °C, time = 30 min, solvent = DMF).

Catalyst recycling performance

The capacity of a catalyst to be recycled is crucial from an economic perspective [4]. Hence, 0.1g of Co/Fe-Al_2O_3 in the ratio of 10:90 catalyst calcined at 400 °C was tested for five consecutive cycles under similar conditions. The catalyst was retrieved, rinsed with methanol to reduce the adsorbed sulfur compound, and dried in an oven at 80 °C-100 °C for 12 hours and tested

in the next cycle. It was found that there is no significant decline in activity even after three recycling runs as shown in (Figure 3). After the fourth and fifth cycle of the reaction, a decrease in the desulfurization activity of the catalyst were observed. This may relate to the washing or activation of some active catalyst spots during the oxidation or recycling process of the catalyst. A slight decrease in sulfur removal after the fourth cycle indicates that the active site was maintained during the reaction. In addition, the surface area of the used Co/Fe-Al_2O_3 catalyst (216 m^2/g) was very close to those of the fresh one (226 m^2/g) [21]. As a result, it was discovered that the Co/Fe-Al_2O_3 catalyst had a high catalytic activity for the Cat-ODS of diesel as well as a strong resistance to sulfur.

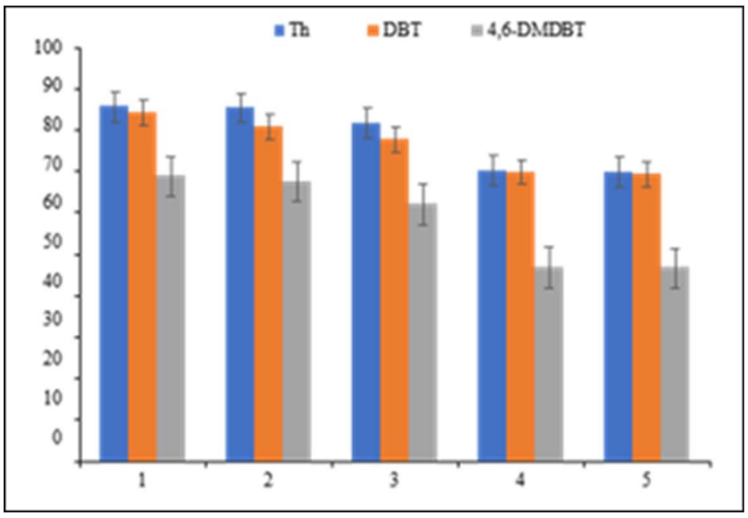


Figure 3. Catalyst cycling test of Co/Fe- Al_2O_3 catalyst calcined at 400 °C for 5 hours (Reaction conditions: Oxidant = TBHP, T = 50°C, time = 30 min, solvent = DMF)

Mechanistic study by computational

The mechanism of oxidative desulfurization with Co/Fe-Al_2O_3 catalyst in TBHP system was proposed in (Figure 4). Early research suggested that Fe^{3+}, O, and OH groups of iron oxides might engage with the thiophene ring, leading to adsorption through a variety of methodologies [26, 27]. The mechanism of the Co/Fe-Al_2O_3 catalyst include the formation of an intermediate product (1), as a consequence of the nucleophilic attack by TBHP on Co/Fe-Al_2O_3 surface when there is a reaction between TBHP and element Co or Fe. The electrophilic properties of peroxidic oxygen start to increase, made it more reactive because the electrons are extracted from the peroxyl moiety. DBT sulfoxide (3) is formed when DBT (2) is oxidised when responded to the nucleophilic attacks of sulfur in the DBT molecule (2) on the positively charged intermediate species (1). Following that, the DBT sulfoxide (3) was further oxidised to produce DBT sulfone (4) and tert-butanol (5) as by-products.

The energy level diagram for the oxidation of DBT and 4,6-DMDBT by TBHP in the presence of catalyst was displayed in (Figure 5). Several significant features were observed from the profile energy. Based on Table 3, the first oxidation of 4,6-DMDBT, -20.2 eV energy was released, higher than oxidation energy released by DBT which is -7.67 eV for the first step. Next, the second step of 4,6-DMDBT by adding oxygen to positively charge S atom demonstrated the releasing energy of about -1.65 eV. The energy required to form 4,6-DMDBT sulfoxide is 3.2 eV, which shown that is more energy required than DBT sulfoxide due to the presence of methyl group in the structure. The overall interaction energy between 4,6 DMDBT and catalyst is -23.19 eV which was less exothermic than DBT, -40.78 eV. The exothermic reactions indicate that sulfoxide and sulfone are persistent compounds. Based on the barrier heights in the reaction profile, we can see that the oxidation phase for sulfone synthesis was simpler than that of sulfoxide,

and thus the sulfone product yield is expected to be greater than sulfoxide.

The bond length for Fe-O in 4,6-DMBT is 1.81 A˚, a bit longer than the bond length in DBT (1.80 A˚). Seeing as the methyl group was qualified to donate the aromatic ring the electrons, this suggests that the methyl group would impair the S-C strength qualities. Longer bond lengths on the scission of the S-C in ODS reaction may be easier in 4,6-DMDBT [28]. However, C-S bond cleavage was difficult to occur due to the steric hindrance effect of 4,6-DMDBT. On the contrary, according to conducted experiment, the ODS response in this reaction is simpler in DBT based on total energy. This is most likely due to the fact that DBT with access to the S-atom would result in a lower barrier height than the more sterically hindered S-containing 4,6-DMDBT molecule. Prove that methyl group steric hindrance was a key factor in the ODS system's selectivity.

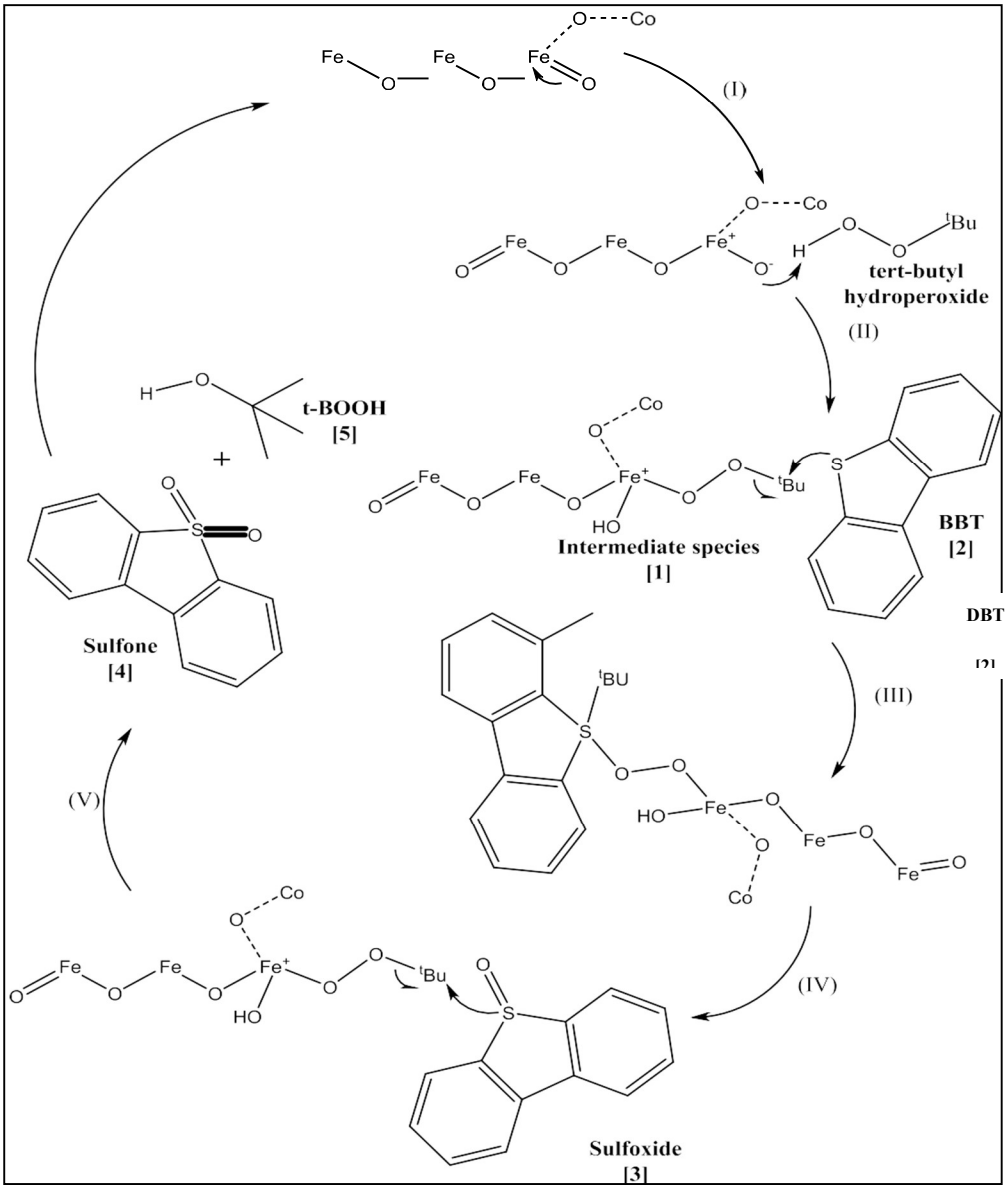


Figure 4. A proposed oxidation chemical route of dibenzothiophene by TBHP in the presence Co/Fe-Al_2O_3 catalyst

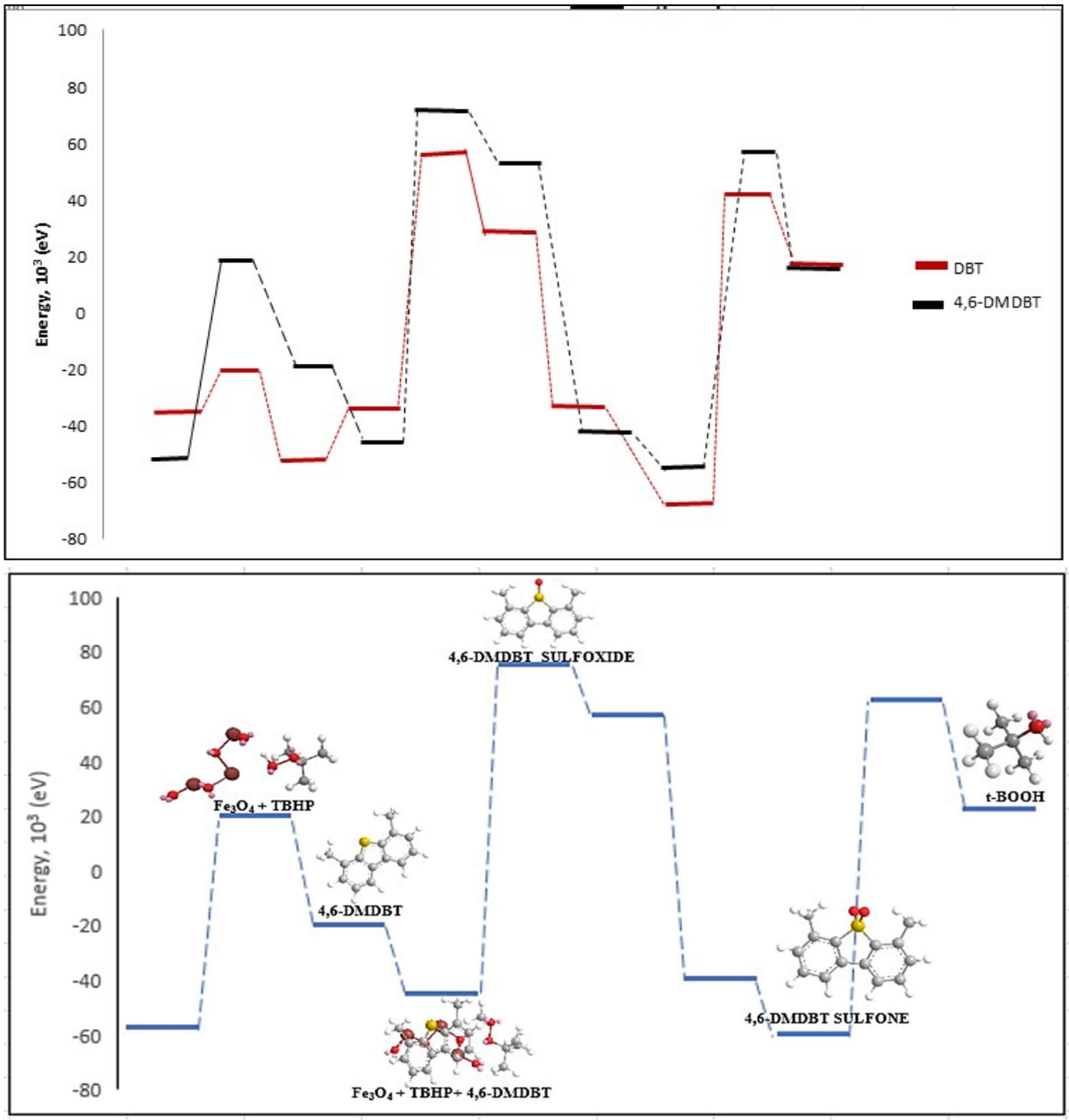


Figure 5. Energy level diagram for the oxidation of DBT and 4,6-DMDBT by TBHP in the presence of Co/Fe-Al_2O_3 catalyst

In order to determine the role of catalysts in oxidative desulfurization, an experiment was carried out in which the desulfurization process was examined without the use of a catalyst, as shown in (Figure 6). The first oxidation of DBT took place by nucleophilic attack of sulfur in DBT to oxygen in TBHP to form intermediate species. The energy required for the oxidation of DBT is 11.45 eV. This result showed that more energy was required to break the bond of reactant compared with oxidation of DBT in the presence of a catalyst. Next, the negatively charged oxygen in TBHP attacked hydrogen in intermediate to form tert-butanol and sulfoxide and the energy is released to -3.10 eV. Further reaction takes place by sulfoxide with TBHP to form sulfone and tert-

butanol. The overall activation energy of the oxidation of DBT and TBHP without the presence of a catalyst is -4.01 eV.

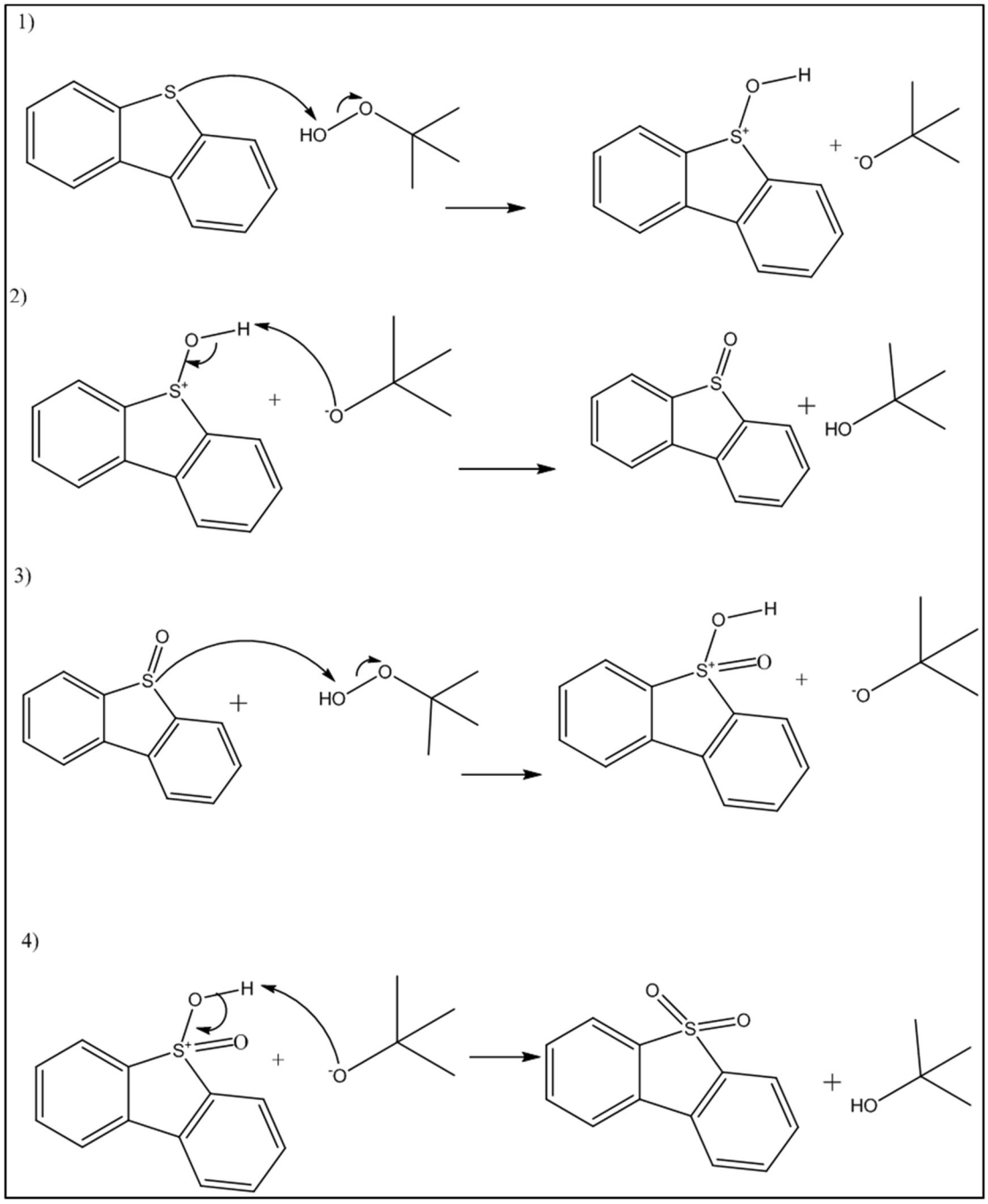


Figure 6. A proposed reaction for the oxidation of dibenzothiophene by TBHP

The activation energy in (Table 3), observed that the oxidation of DBT with catalyst released more energy than without a catalyst which is -40.78 eV and -4.01 eV. The energy profile demonstrated that all three reactions are exothermic. It shows that catalytic oxidation of DBT released more energy than uncatalyzed oxidation which

is -40.78 eV and -4.01 eV, respectively. This result revealed that catalysts can have a major influence on ODS, which is consistent with the experimental studies.

Table 3. Reaction energy for the oxidation of DBT and 4.6-DMDBT by TBHP

Steps	Ea(eV), x10^3		
	DBT		4,6-DMDBT
	Without Catalyst	With Catalyst	With Catalyst
I	11.45	-7.67	-20.2
II	-3.10	0.83	-1.65
III	-3.26	-3.83	5.69
IV	-9.10	-12.03	3.2
V		-17.81	-10.23
Overall	-4.01	-40.78	-23.19

Conclusion

Co/Fe in the ratio of 10:90 catalyst calcined at 400°C showed the highest conversion of DBT at 100%, 4,6-DMDBT (79%), and thiophene (93%). Meanwhile, Co/Fe-Al_2O_3 catalyst could retrieve its catalytic recycling performance up to five cycles. The mechanism of 4,6-DMDBT by the proposed pathway was also investigated and found that higher activation energy -23.19 eV compared to DBT, and this agreed with the catalytic activity, where DBT is easy to remove compared to 4,6-DMDBT. Furthermore, the mechanism without the catalyst of DBT released lower energy, -4.01 eV respectively. In conclusion, the presence of the catalyst can speed up the reaction in removing sulfur compounds.

Acknowledgement

The authors are grateful for the financial support from the Ministry of Higher Education Malaysia for the Fundamental Research Grant Scheme (FRGS) with Project Code: FRGS/1/2020/STG04/USM/03/2 and Universiti Sains Malaysia (USM), Special Matching Short-Term Grant with Project No :304/PKIMIA/631570.

References

1. Jha, D., Haider, M. B., Kumar, R., and Balathanigaimani, M. S. (2016). Extractive desulfurization of dibenzothiophene using phosphonium-based ionic liquid: Modeling of batch extraction experimental data and simulation of continuous extraction process. *Chemical Engineering Research and Design*, 111: 218-222.
2. Xie, Y., Posada, F., and Minjares, R. (2020). Diesel sulfur content impacts on Euro VI soot-free vehicles: Considerations for emerging markets. *Frontiers Environmental Science. Eng,* 2020: 10.
3. Betiha, M. A., Rabie, A. M., Ahmed, H. S., Abdelrahman, A. A., and El-Shahat, M. F. (2018). Oxidative desulfurization using graphene and its composites for fuel containing thiophene and its derivatives: An update review. *Egyptian Journal of Petroleum*, 27(4): 715-730.
4. Subhan, S., Rahman, A. U., Yaseen, M., Rashid, H. U., Ishaq, M., Sahibzada, M., and Tong, Z. (2019). Ultra-fast and highly efficient catalytic oxidative desulfurization of dibenzothiophene at ambient temperature over low Mn loaded Co-Mo/Al_2O_3 and Ni-Mo/Al_2O_3 catalysts using NaClO as oxidant. *Fuel*, 237: 793-805.
5. Muhammad, Y., Shoukat, A., Rahman, A. U., Rashid, H. U., and Ahmad, W. (2018). Oxidative desulfurization of dibenzothiophene over Fe promoted Co-Mo/Al_2O_3 and Ni–Mo/Al_2O_3 catalysts using hydrogen peroxide and formic acid as oxidants. *Chinese Journal of Chemical Engineering*, 26(3): 593-600.
6. Haruna, A., Merican, Z. M. A. and Musa, S. G. (2022). Recent advances in catalytic oxidative desulfurization of fuel oil–A review. J*ournal of Industrial and Engineering Chemistry*, 112: 20-36.
7. Moslemi, A., Chermahini, A. N., Sarpiri, J. N., Rezaei, S., and Barati, M. (2019). $VOHPO_4.5H_2O$/KIT-6 composites: Preparation and their application in extractive and catalytic oxidation desulfurization of benzothiophene and dibenzothiphene. *Journal of the Taiwan Institute of Chemical Engineers*, 97: 237-246.
8. Wang, L., Wu, S., Liu, S., Cui, S., Liu, J., and Zhang, S. (2018). Cobalt impregnated porous catalyst promoting ammonium sulfate recovery in

an ammonia-based desulfurization process. *Chemical Engineering Journal*, 331: 416-424.

9. Yaseen, M., Khattak, S., Ullah, S., Subhan, F., Ahmad, W., Shakir, M., and Tong, Z. (2022). Oxidative desulfurization of model and real petroleum distillates using cu or ni impregnated banana peels derived activated carbon-NaClO catalyst-oxidant system. *Chemical Engineering Research and Design*, 179: 107-118.
10. Bakar, W. A. W. A., Ali, R., Kadir, A. A. A., and Mokhtar, W. N. A. W. (2012). Effect of transition metal oxides catalysts on oxidative desulfurization of model diesel. *Fuel Processing Technology*, 101: 78-84.
11. Cristiano, D. M., Mohedano, R. D. A., Nadaleti, W. C., de Castilhos Junior, A. B., Lourenco, V. A., Goncalves, D. F., and Belli Filho, P. (2020). H_2S adsorption on nanostructured iron oxide at room temperature for biogas purification: Application of renewable energy. *Renewable Energy*, 154: 151-160.
12. Hasannia, S., Kazemeini, M., Rashidi, A. and Seif, A. (2020). The oxidative desulfurization process performed upon a model fuel utilizing modified molybdenum based nanocatalysts: Experimental and density functional theory investigations under optimally prepared and operated conditions. *Applied Surface Science*, 527: 146798.
13. Naseri, H., Mazloom, G., Akbari, A. and Banisharif, F. (2021). Investigation of Ni, Co, and Zn promoters on Mo/HY modified zeolite for developing an efficient bimetallic catalyst for oxidative desulfurization of dibenzothiophene. *Microporous and Mesoporous Materials*, 325: 111341.
14. Luna, M. L., Alvarez-Amparán, M. A. and Cedeño-Caero, L. (2019). Performance of WOx–VOx based catalysts for ODS of dibenzothiophene compounds. *Journal of the Taiwan Institute of Chemical Engineers*, 95: 175-184.
15. Cao, Y., Shen, L., Hu, X., Du, Z., and Jiang, L. (2016). Low temperature desulfurization on Co-doped α-FeOOH: Tailoring the phase composition and creating the defects. Chemical Engineering Journal, 306: 124-130.
16. Akter, N., Zhang, S., Lee, J., Kim, D. H., Boscoboinik, J. A., and Kim, T. (2020). Selective catalytic reduction of NO by ammonia and NO oxidation Over $CoOx/CeO_2$ catalysts. *Molecular Catalysis*, 482: 110664.
17. Sampanthar J. T., Xiao H., Dou J., Nah T. Y., Rong X., and Kwan W. P. (2006). A novel oxidative desulfurization process to remove refractory sulfur compounds from diesel fuel. *Applied Catalysis B: Environmental*, 63(1-2): 85-93.
18. Correa, M. A., Franco, S. A., Gómez, L. M., Aguiar, D. and Colorado, H. A. (2023). Characterization methods of ions and metals in particulate matter pollutants on $PM_{2.5}$ and PM_{10} samples from several emission sources. *Sustainability*, 15(5): 4402.
19. Lu, J., Guo, J., Wei, Q., Tang, X., Lan, T., Hou, Y. and Zhao, X. (2022). A matrix effect correction method for portable X-ray fluorescence data. *Applied Sciences*, 12(2): 568.
20. Porcaro, M., Depalmas, A., Lins, S., Bulla, C., Pischedda, M. and Brunetti, A. (2022). Nuragic working tools characterization with corrosion layer determinations. *Materials*, 15(11): 3879.
21. Nazmi, N. A. S. M., Razak, F. I. A., Mokhtar, W. N. A. W., Ibrahim, M. N. M., Adam, F., Yahaya, Rosid, S. J. M., Shukri, N. M. and Abdullah, W. N. W. (2022). Catalytic oxidative desulfurisation over $Co/Fe\text{-}\gamma Al_2O_3$ catalyst: performance, characterisation and computational study. *Environmental Science and Pollution Research*, 29: 1009-1020.
22. Otsuki, S., Nonaka, T., Takashima, N., Qian, W., Ishihara, A., Imai, T., and Kabe, T. (2000). Oxidative desulfurization of light gas oil and vacuum gas oil by oxidation and solvent extraction. *Energy & Fuels*, 14(6): 1232-1239.
23. Mokhtar, W. N. A. W., Bakar, W. A. W. A., Ali, R., and Kadir, A. A. A. (2015). Optimization of oxidative desulfurization of Malaysian Euro II diesel fuel utilizing tert-butyl hydroperoxide-dimethylformamide system. *Fuel*, 161: 26-33.
24. Mardwita, M., Yusmartini, E. S. and Wisudawati, N. (2020). Effects of cobalt and chromium loadings to the catalytic activities of supported metal catalysts in methane oxidation. *Bulletin of Chemical Reaction Engineering & Catalysis*, 15(1): 213-220.
25. Wei, S., He, H., Cheng, Y., Yang, C., Zeng, G., Kang, L. and Zhu, C. (2017). Preparation,

characterization, and catalytic performances of cobalt catalysts supported on KIT-6 silicas in oxidative desulfurization of dibenzothiophene. *Fuel*, 200: 11-21.

26. Nejad, N. F., Shams, E., and Amini, M. K. (2015). Synthesis of magnetic ordered mesoporous carbon (Fe-OMC) adsorbent and its evaluation for fuel desulfurization. *Journal of Magnetism and Magnetic Materials*, 390: 1-7.
27. Arcibar-Orozco, J. A., Acosta-Herrera, A. A. and Rangel-Mendez, J. R. (2019). Simultaneous desulfuration and denitrogenation of model diesel fuel by Fe-Mn microwave modified activated carbon: Iron crystalline habit influence on adsorption capacity. *Journal of Cleaner Production*, 218: 69-82.
28. Li, X., Qi, H., Zhou, W., Xu, W., and Sun, Y. (2019). Efficient catalytic performance of tetra-alkyl orthotitanates for the oxidative desulfurization of dibenzothiophene at room temperature. *Comptes Rendus Chimie*, 22(4): 321-326.

Malaysian Journal of Analytical Sciences (MJAS)
Published by Malaysian Analytical Sciences Society

ANTIVIRAL STUDY OF SCHIFF BASE VANILLIN DERIVATIVES AGAINST NS2B-NS3 PROTEASE OF ZIKA VIRUS BASED ON PHARMACOPHORE MODELLING AND MOLECULAR DOCKING

(Kajian Antiviral Terbitan Vanillin Bes-Schiff Terhadap NS2B-NS3 Protease Virus Zika Berdasarkan Pemodelan Farmakofor dan Dok Molekul)

Woon Yi Law*, Mohd Razip Asaruddin, and Showkat Ahmad Bhawani

Faculty of Resource Science and Technology,
Universiti Malaysia Sarawak, 94300 Kota Samarahan, Sarawak, Malaysia

**Corresponding author: mendah_wylaw@hotmail.com*

Received: 20 June 2023; Accepted: 24 October 2023; Published: 29 December 2023

Abstract

The Zika virus (ZIKV) is a mosquito-borne virus spread by the bite of *Aedes aegypti* and *Aedes albopictus* mosquitoes. The outbreak of the virus resulted in the 2015-2016 ZIKV epidemic, in which later Public Health Emergency of International Concern was declared by the World Health Organization (WHO). Despite the complications following the infection of ZIKV, clinically approved therapeutic agents and vaccines are still unavailable for the treatment of ZIKV. Schiff base vanillin derivatives, derived from vanillin and primary amines, were reported for their potential antiviral activity against a several viruses, including influenza virus and SARS coronaviruses. Therefore, they were aimed to be tested for their *in silico* antiviral activity against ZIKV NS2B-NS3 protease. In this research, ligand-based pharmacophore modelling was employed to analyse the antiviral activity of Schiff base vanillin derivatives. They were imported as test sets in the pharmacophore model generated from a list of training sets, which are reported drugs against ZIKV. Furthermore, structure-based molecular docking was also performed to analyse the docking performances of the Schiff base vanillin derivatives in the crystal structure of ZIKV NS2B-NS3 protease in a complex with a boronate inhibitor (PDB: 5LC0). The analyses were based on pharmacophore scores, binding affinities and matching interactions in comparison with the 5LC0 ligand in the active site. Based on the findings *via* ligand-based pharmacophore modelling and structure-based molecular docking, it was discovered that a number of Schiff base vanillin derivatives showed potential antiviral activity against ZIKV, thus being promising drug candidates and bringing futuristic *in vitro* and *in vivo* tests.

Keywords: Zika virus, Schiff base vanillin derivatives, pharmacophore modelling, molecular docking, computer-aided drug design

Abstrak

Virus Zika (ZIKV) adalah virus bawaan nyamuk yang disebarkan melalui gigitan nyamuk *Aedes aegypti* dan *Aedes albopictus*. Wabak virus ini menyebabkan epidemik ZIKV 2015-2016, di mana kemudian Darurat Kesihatan Awam Keprihatinan Antarabangsa telah diisytiharkan oleh Pertubuhan Kesihatan Sedunia (WHO). Walaupun komplikasi setelah jangkitan ZIKV, agen terapeutik dan vaksin yang diluluskan secara klinikal masih belum tersedia untuk rawatan ZIKV. Terbitan vanillin bes-Schiff, yang diperolehi daripada vanilin dan amina primer, telah dilaporkan aktiviti antiviral berpotensi terhadap beberapa virus, termasuk virus influenza dan koronavirus SARS. Oleh itu, mereka akan diuji untuk aktiviti antiviral secara *in silico* terhadap protease NS2B-NS3

ZIKV. Dalam penyelidikan ini, pemodelan farmakofor berasaskan ligan digunakan untuk menganalisis aktiviti antiviral terbitan vanillin bes-Schiff. Mereka diimport sebagai set ujian terhadap model farmakofor yang dihasilkan daripada senarai set latihan, iaitu ubat-ubatan dilaporkan terhadap ZIKV. Selain itu, dok molekul berasaskan struktur juga dilakukan untuk menganalisis prestasi dok terbitan vanillin bes-Schiff di dalam struktur kristal ZIKV NS2B-NS3 protease dalam kompleks dengan perencat boronat (PDB: 5LC0). Analisis dijalankan berdasarkan skor farmakofor, afiniti dok, dan interaksi yang sepadan dengan ligan 5LC0 di tapak aktif. Berdasarkan hasil pemodelan farmakofor berasaskan ligan dan dok molekul berasaskan struktur, adalah didapati bahawa beberapa terbitan vanillin bes-Schiff menunjukkan aktiviti antiviral yang berpotensi terhadap ZIKV, oleh itu menjadi calon ubat yang menjanjikan dan mampu membawa ujian *in vitro* dan *in vivo* pada masa depan.

Kata kunci: Virus Zika, terbitan vanillin bes-Schiff, pemodelan farmakofor, dok molekul, reka bentuk ubat bantuan komputer

Introduction

The Zika virus (ZIKV) is a mosquito-borne viral disease spread by the bite of *Aedes aegypti* and *Aedes albopictus* mosquitoes, which belongs to the *Flaviviridae* virus family (Figure 1). The virus belongs to the Flavivirus genus, which is the same genus as dengue, yellow fever, Japanese encephalitis, and West Nile viruses [1]. ZIKV was first discovered in 1947 in the Ziika forest of Uganda, which was identified in a Rhesus macaque monkey [2]. Infections among humans have since been detected in Africa and Asia from the 60s to 80s, which then relentlessly spread over the Western hemisphere in the past decade [2]. Major outbreaks were recorded in 2007 in Africa, which was in the Yap Islands, Micronesia [3], and later in 2013 in French Polynesia [4]. In 2015 in Brazil, ZIKV infection was detected in association with microcephaly, a condition where the size of head is smaller than the normal size [2]. Consequently, the World Health Organization (WHO) declared a Public Health Emergency of International Concern (PHEIC) from February to November 2016 [2].

ZIKV is highly infectious among pregnant women, not only it can lead to microcephaly among infants, but as well as congenital malformations, such as limb contractures, high muscle tone, eye abnormalities and hearing loss, also known as congenital Zika syndrome [2]. Other than that, other complications such as preterm birth and miscarriage might follow as well [5]. On top of that, Zika infections may also increase the risk of developing a rare autoimmune disorder, known as the Guillain–Barré syndrome [5]. The virus is not only transmitted by the bite of *Aedes aegypti* and *Aedes albopictus* mosquitoes, as well as mother-to-fetus virus transmission, sexual transmission, transfusion of blood and organ transplantation [2]. Despite numerous complications, licensed and approved drugs and vaccines are still unavailable from the treatment of Zika infections [2], which resulted in great deal of active research in different fields in search of drugs and vaccines for the medication of Zika infections.

ZIKV is a small enveloped, positive-sense single-stranded RNA virus [6]. The opening frame (ORF) encodes one polyprotein made up of 3419 amino acids, which is cleaved by the host of viral proteins into 3 structural proteins and 7 non-structural proteins [7]. The structural proteins consist of activating capsid, membrane, and envelope, while the non-structural proteins consist of NS1, NS2A, NS2B, NS3, NS4A, NS4B, and NS5 proteins [8] (Figure 2). Among all non-structural proteins, NS2B-NS3 protease serves a very crucial role in replication of virus and maturation of non-structural viral proteins, hence activating the virus [7]. NS3 protease belongs to the trypsin/chymotrypsin protease superfamily, whereby the protease domain is found at the N-terminus, and the RNA helicase domain is found at the C-terminus [9]. The NS3 helicase, which plays an imperative role in the replication and capping of RNA, is encoded by the NS3 C-terminal 440 residue region [10]. However, in order for the activation of NS3 protease, NS2B protease must be present in complex with NS3 protease [11]. Thus, the transmembrane NS2B protease combines with the N-terminal 170-residues of NS3 to form NS2B-NS3 protease, which has excellent proteolytic activity, making it an attractive and promising target for the design and development of drugs to inhibit the viral activity of NS2B-NS3 protease, which in turn to search for the medication of Zika infection [12].

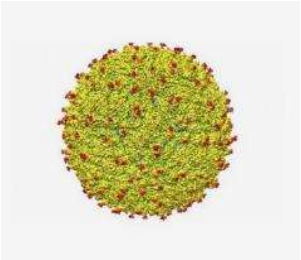


Figure 1. Representation of the surface of ZIKV [13]

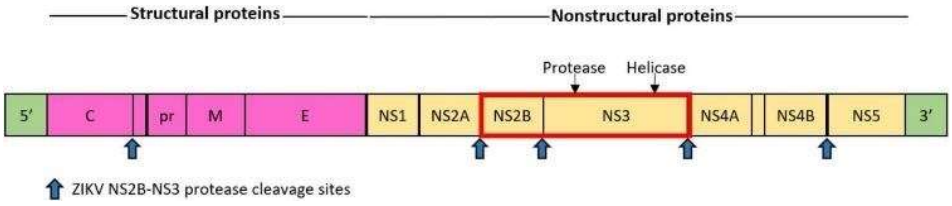


Figure 2. Representation of ZIKV genome [12]

Heretofore, clinically approved therapeutic agents and vaccines are still unavailable not only for Zika infection, but for most of the viral infections. Affected patient from ZIKV are only prescribed pain and fever reliever such as paracetamol and acetaminophen, and recommended staying hydrated, as well as getting enough rest. However, the complications as elaborated above might still follow, which describes the severity of the condition and the necessity to search for the clinically approved and licensed drugs and medications. Nevertheless, the design and discovery of drugs, medicines or novel compounds as inhibitors of viral proteases has always been a very complicated and challenging field among researchers. Not only being expensive, laborious and time-intensive, it was reported that in the past, but the process of drug discovery was also done based on serendipitous discovery from the isolation of crude extracts from different natural products, such as *Aphloia theiformis*, an edible endemic plant from Indian Ocean islands [14]. On top of that, these crude extracts and chemicals were only tested for their biological activity but not based on the biological target [15]. Fortunately, following the advance of modern technology, computer-aided drug design (CADD) allows the process of drugs discovery to be more efficient and time-saving at the cost of minimum expense. On top of that, in combination with laboratory processes, the mechanism of drug against the biological target, and the design of novel drugs or inhibitors based on the active sites of biological target can be illustrated well. Therefore, a great deal of research and efforts have been performed *via* CADD which resulted in the disclosure of numerous compounds possessing great potential as inhibitors of NS2B-NS3 protease of ZIKV (Figures 3-5).

Myriad studies shed light on the analysis of protein-ligand interaction. 2 drugs approved by Food and Drug Administration (FDA), which are asunaprevir and simeprevir, were discovered as potential NS2B-NS3 inhibitors *via* structure-based molecular docking of CADD, therefore possess potent anti-ZIKV activity [16]. Similarly, Meewan et al. reported their work in analysing 7 million compounds against the NS2B-NS3 protease through virtual screening, whereby out of all, 6 of the compounds which contain phenylquinoline and aminobenzamide groups showed positive docking result in the active site of the protease, therefore exhibiting potential antiviral activity to suppress the viral replication [12]. Furthermore, in another reported research of virtual screening of 1861 FDA approved drugs in Drug Bank against the crystal structure of NS2B-NS3 protease, antihistaminic chlorcyclizine displayed the most important interaction with the active site, thus suggesting itself for being a promising drug against ZIKV [17]. Moreover, a few clinically approved drugs showed great binding affinity in the active site of ZIKV, which includes sofosbuvir, hydroxychloroquine, azithromycin and novobiocin [9].

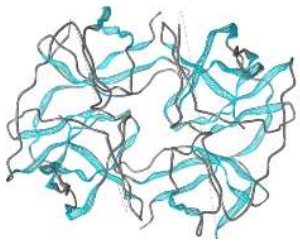


Figure 3. Crystal structure of ZIKV NS2B-NS3 Protease Shown in Structure-Based Perspective of LigandScout 4.4 [18]

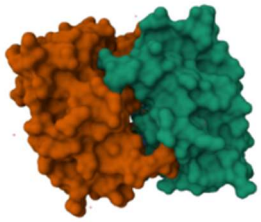


Figure 4. Crystal structure of ZIKV NS2B-NS3 Protease in Complex with Boronate Inhibitor [18]

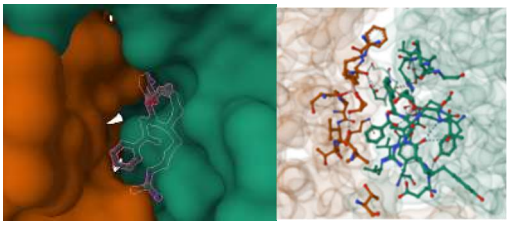


Figure 5. The boronate inhibitor in the active site of 5LC0 [18]

Among all the significant efforts of researchers, one of the class of compounds which potentially spike an interest in the Schiff base vanillin derivatives. Schiff base vanillin derivatives, which are synthesised from the Schiff base reaction between vanillin and primary amines, were reported for their potential antiviral activity against distinct types of viruses. In an earlier *in silico* research, the vanillin derivatives were reported to be able to inhibit the neuraminidase protease of influenza virus, which was later proven again by the performance of 2′-(4-Methylumbelliferyl)-*α*-*D*-*N*-acetylneuraminic acid (MUNANA) assay [19]. Similarly, the vanillin derivatives were also reported to show inhibitory activity against the main protease of severe acute respiratory syndrome coronavirus-2 (SARS-CoV 2) by the performance of both ligand-based pharmacophore modelling and structure-based molecular docking [20]. For having great interest and significant potential as antiviral compounds, but being limited in terms of the amount of research simultaneously, the present study focuses on the analysis and development of Schiff base vanillin derivatives as ZIKV NS2B-NS3 inhibitors *via in silico* methods, which are structure-based molecular docking and ligand-based pharmacophore modelling by using LigandScout 4.4.

Materials and Methods

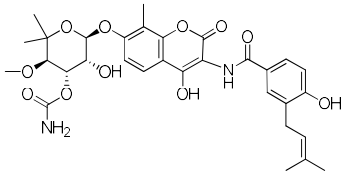
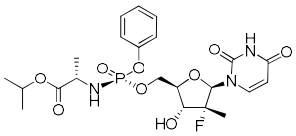
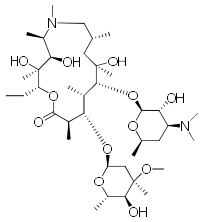
Ligand-based pharmacophore modelling was performed by using LigandScout 4.4 software. Chemical structures of training sets were downloaded from ChemSpider in the MDL-mol format, while all the chemical structures of Schiff base vanillin derivatives were drawn by using ChemDraw Ultra 12.0 and downloaded in MDL-mol format as well. Structure-based molecular docking was performed by both LigandScout 4.4 and Autodock Vina. All Schiff base vanillin derivatives were converted from the MDL-mol format to the MDL-sdf format by using

Open Babel GUI.

Ligand-based pharmacophore modelling

3 drugs which were reported in previous research for their inhibitory activity against ZIKV NS2B-NS3 protease were selected as training sets. The 3 training sets novobiocin [21], sofosbuvir [22] and azithromycin [23] were selected due to the depiction of a lot of common pharmacophore features by their molecular structures, hence being able to generate a model with as many pharmacophore features as possible. Their chemical structures are shown in Table 1 below:

Table 1. 2D and 3D chemical structures of training sets: novobiocin [21], sofosbuvir [22] and azithromycin [23]

Training Sets	2D Chemical Structure	3D Chemical Structure
Novobiocin		
Sofosbuvir		
Azithromycin		

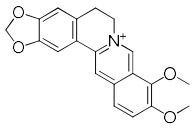
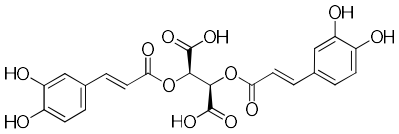
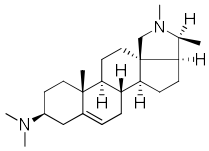
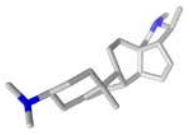
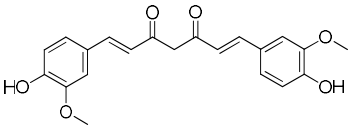
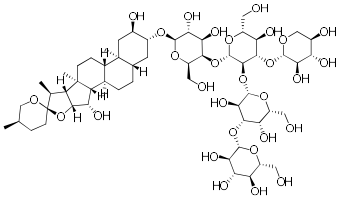
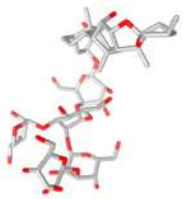
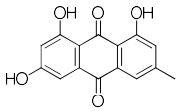
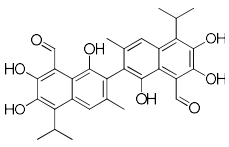
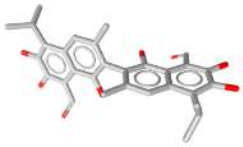
The chemical structures of the training sets were downloaded from ChemSpider in the MDF-mol format and imported into the ligand-based perspective of LigandScout 4.4 to generate the pharmacophore model based on common feature hypotheses. Test sets played imperative role in validating the reliability of the generated pharmacophore model. Hence, chemical compounds from natural products that were reported in previous literatures to possess inhibitory activity against NS2B-NS3 protease were selected as test sets to evaluate and validate the reliability of the pharmacophore model. A total of 12 chemical compounds from natural products include berberine [24], chicoric acid [25], conessine [26], curcumin [26], digitonin [26], emodin [24], gossypol [26], luteone [25], pedalitin [27], quercetin [27], reserpine [25] and rosmarinic acid [25]. These chemical compounds were downloaded from ChemSpider and imported as test sets in the ligand-based perspective of LigandScout 4.4 in the MDF-mol format (Table 2).

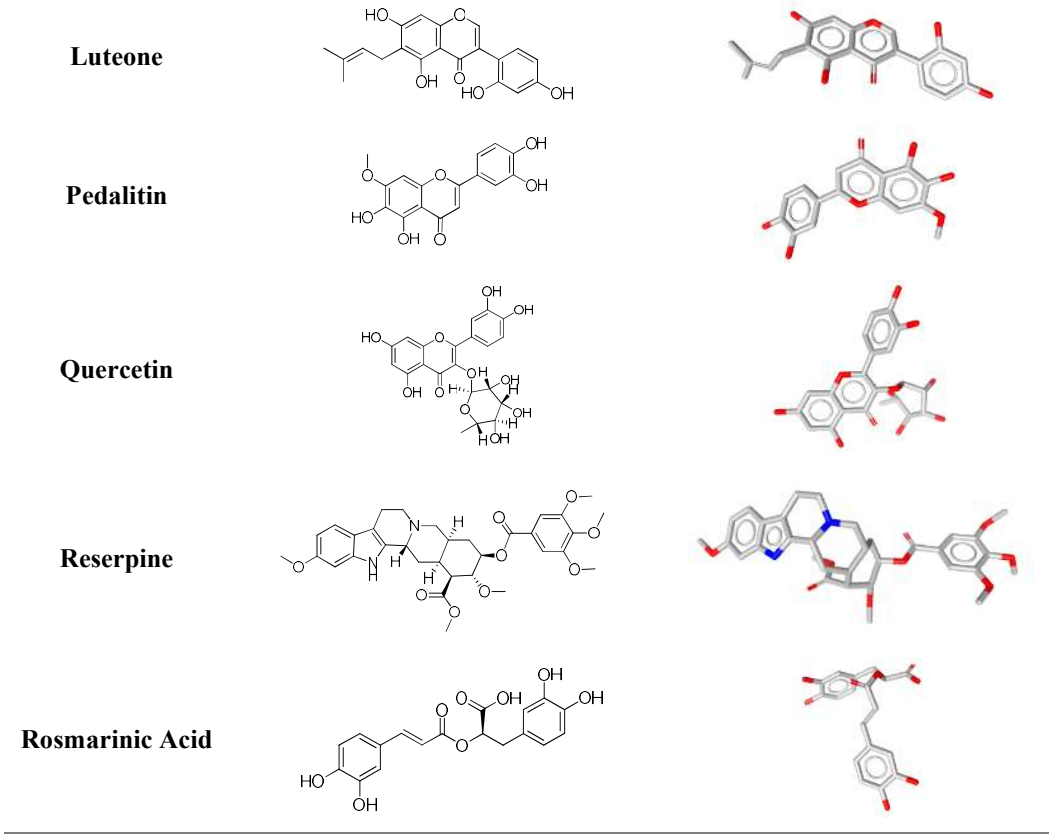
After the import of training sets and test sets, all the MMFF94 energies of the chemical structures were first minimised to ensure closest local minimum and maximum stability. Conformations of ligand sets were generated, clustered based on pharmacophore RDF-code similarity and average cluster distance calculation, and ligand-based pharmacophore modelling was performed based on pharmacophore fit. The 3 training sets generated a pharmacophore model, in which evaluations and analyses were based on the test sets' matching pharmacophore features and pharmacophore fit values in the generated pharmacophore model. The selection of test sets was based on compounds from natural products with wide difference of chemical structures and functional groups. The greater the difference in the chemical structures of the test sets, the higher the accuracy of these test sets to validate the

reliability of the pharmacophore model. If test sets were able to show pharmacophore fit values similar to or greater than the values of the training sets, as well as depicting as many matching pharmacophore features as possible, the pharmacophore model is said to be reliable for the assessment of the Schiff base vanillin derivatives as ZIKV NS2B-NS3 protease inhibitors.

The chemical structures of Schiff base vanillin derivatives were drawn and downloaded in the MDL-mol format by using ChemDraw Ultra 12.0. The Schiff base synthesis mechanism was generally as shown in Figure 6:

Table 2. 2D and 3D chemical structures of test sets from natural product

Test Sets	2D Chemical Structure	3D Chemical Structure
Berberine		
Chicoric Acid		
Conessine		
Curcumin		
Digitonin		
Emodin		
Gossypol		



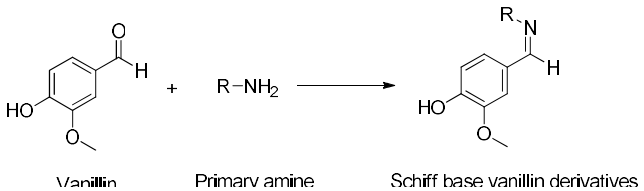


Figure 6. Schiff base synthesis mechanism

Schiff base vanillin derivatives were drawn based on the general mechanism between vanillin and primary amines, in which the list of primary amines was as follow:

(1) 1-piperidinecarboxamide
(2) 4-dinitrophenylhydrazine
(3) 2,6-dibromo-4-nitroaniline
(4) 2-amino-3-bromo-5-methylbenzoic acid
(5) 2-amino-6-bromo-4-chlorophenol
(6) 2-aminopyridine
(7) 4-bromo-3-methyl-1-phenyl-1H-pyrazol-5-ylamine
(8) 5-aminoisatoic anhydride
(9) Acetyl-L-asparagine
(10) Allylurea
(11) Anilline
(12) Benzaldehyde semicarbazone
(13) Benzohydrazide
(14) Benzotriazole-1-carboxamide
(15) Ethyl 2-aminothiazole-5-carboxylate
(16) Indole-3-acetamide
(17) Levetiracetam
(18) Methyl 2-amino-5-bromo-4-isopropylbenzoate
(19) Nicotinic hydrazide
(20) Phenylhydrazine

(21) Thiobenzamide

After all Schiff base vanillin derivatives were drawn and downloaded, they were imported as test sets into the ligand-perspective of LigandScout 4.4, together with novobiocin, sofosbuvir and azithromycin as training sets. Similarly, MMFF94 energies were minimised, conformations of all ligands were generated and clustered, and ligand-based pharmacophore modelling was run. The results were also obtained based on the vanillin derivatives' matching pharmacophore features with the features of the generated pharmacophore model, as well as their pharmacophore fit values in the model. Schiff base vanillin derivatives that displayed satisfied pharmacophore fit values and matching features were recorded and brought forward to the analyses in structure-based molecular docking.

Structure-based molecular docking

Crystal structure of Zika virus NS2B-NS3 protease in complex with a boronate inhibitor (PDB code: 5LC0) was retrieved from Protein Data Bank (PDB) and imported in the structure-based perspective of LigandScout 4.4, as shown in Figures 7 and 8.

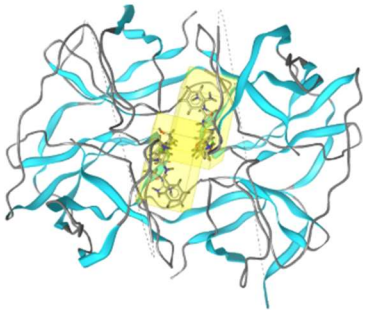


Figure 7. Crystal structure of Zika virus NS2B-NS3 protease in complex with a boronate inhibitor (PDB code: 5LC0) [18]

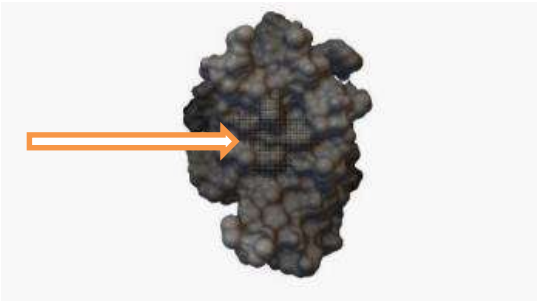


Figure 8. 3D cloud structure of Zika virus NS2B-NS3 protease in complex with a boronate inhibitor (PDB code: 5LC0) viewed by Autodock Vina

The boronate inhibitor, which is the ligand in the active site of 5LC0, shows inhibitory activity against the NS2B-NS3 protease of ZIKV (Figure 9). Therefore, evaluations and analysis were based on the alignments of the Schiff base vanillin derivatives with the pharmacophore model of the ligand to show their matched and aligned interactions with the active sites. Furthermore, the Schiff base vanillin derivatives were docked into the active sites of 5LC0 to evaluate their pharmacophore scores and binding affinities. The ligand was first selected, and the pharmacophore model of the ligand was generated. The ligand and generated pharmacophore model were then copied to the alignment perspective. The first Schiff base vanillin derivative, which is vanillin + 2-Amino-3-bromo-5-methylbenzoic acid was inserted as a single compound in the MDL-sdf format into the structure-based perspective. Again, all ligands and pharmacophore model were copied into the alignment perspective (Figure 10).

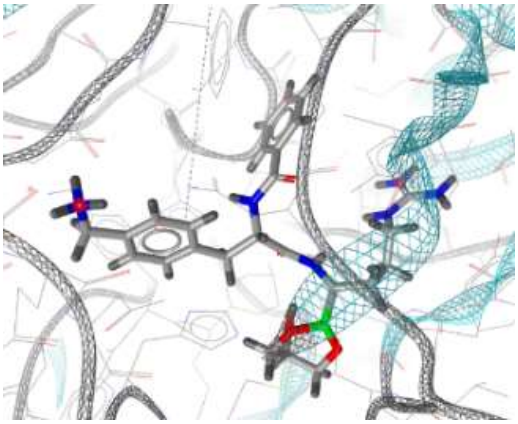


Figure 9. The boronate inhibitor in the active site of 5LC0 [18]

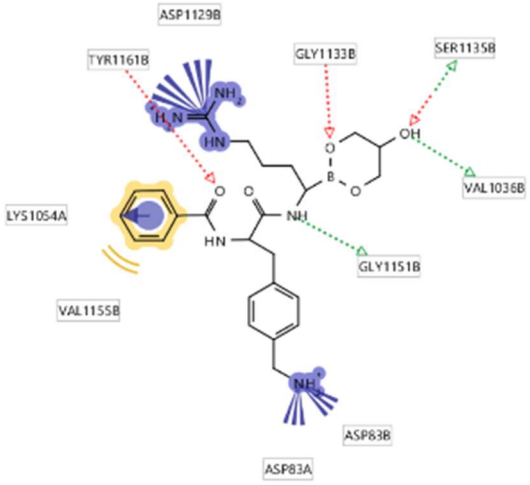


Figure 10. The protein-ligand interactions of boronate inhibitor against the NS2B-NS3 protease [18]

In the alignment perspective, the MMFF94 energy of the first Schiff base vanillin derivative was first minimized to represent minimum energy and maximum stability of the conformation. Alignment was then performed between the boronate inhibitor, and the Schiff base vanillin derivative based on common pharmacophore feature. The yellow spheres, blue features, green and red arrows were the pharmacophore features of boronate inhibitor, while the orange spots showed the common pharmacophore feature shared between the two ligands as depicted in Figure 11.

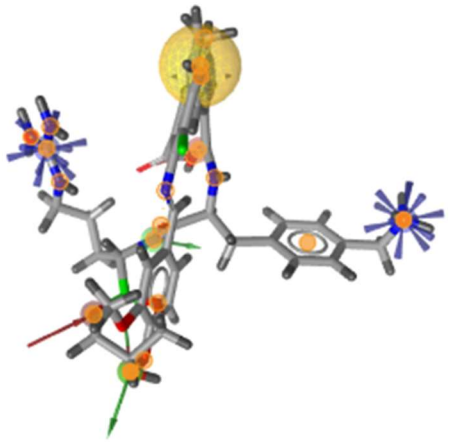


Figure 11. Alignment between pharmacophore model of boronate inhibitor and Schiff base vanillin derivative

Shared pharmacophore model was then generated, followed by merging the pharmacophores and interpolating the overlapping features. The result was as displayed in Figure 12 below.

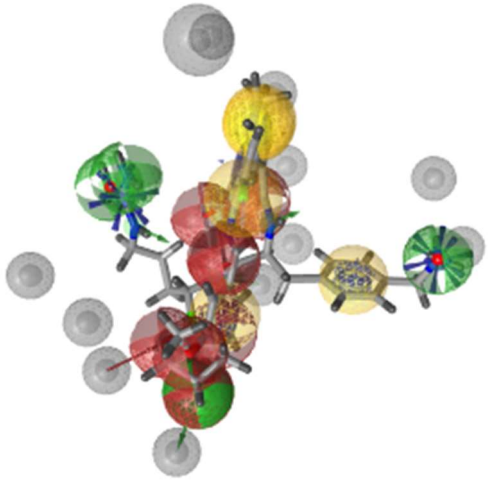


Figure 12. Shared pharmacophore featured, merged pharmacophores and interpolated overlapping features

The ligand was then injected back into the active site of 5LC0 to show the interactions of Schiff base vanillin derivatives inside the active site of NS2B-NS3 protease. From here, the interactions shown by Schiff base vanillin derivatives in compared to those depicted by boronate inhibitor in the active site of 5LC0 is analysed as portrayed in Figure 13 below.

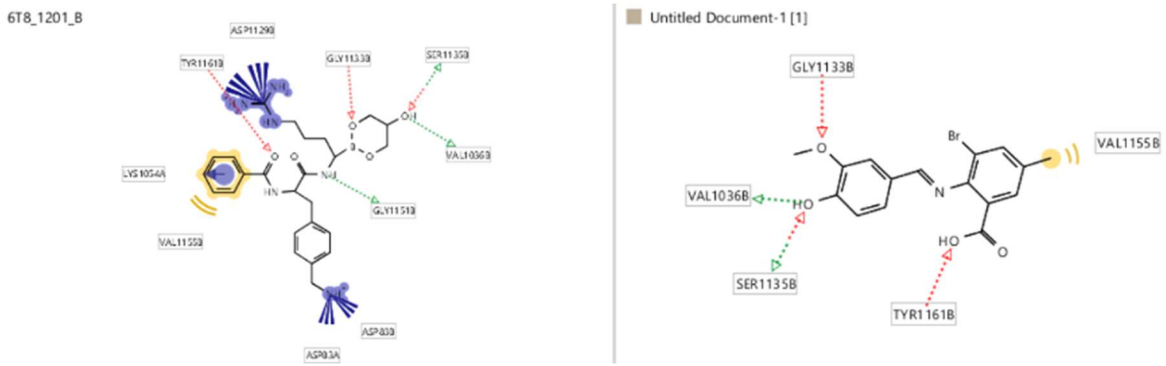


Figure 13. Protein-ligand interactions of Vanillin + 2-Amino-3-bromo-5-methylbenzoic acid, in which out of 10 interactions by boronate inhibitor, the vanillin derivative successfully matched 5 interactions

After the evaluation of interactions between the Schiff base vanillin derivative and the active sites of NS2B-NS3 protease, the vanillin derivative was then docked into the active site of the protease by using AutoDock Vina. 9 conformations of the vanillin derivatives with the best docking result obtained, and from here, the conformation with the best pharmacophore score and binding affinity was analysed. All the above steps are repeated for all drawn Schiff base vanillin derivatives, whereby the derivatives that showed the best results together with ligand-based pharmacophore modelling were recorded, evaluated and discussed.

Results and Discussion

Ligand-based pharmacophore modelling

A pharmacophore model is successfully generated from the training sets, which were novobiocin, sofosbuvir and azithromycin. The model (Figure 14) was composed of 11 pharmacophore features, which are 8 hydrogen bond acceptors (HBA), 2 hydrogen bond donors (HBD) and 1 hydrophobic interaction (HI).

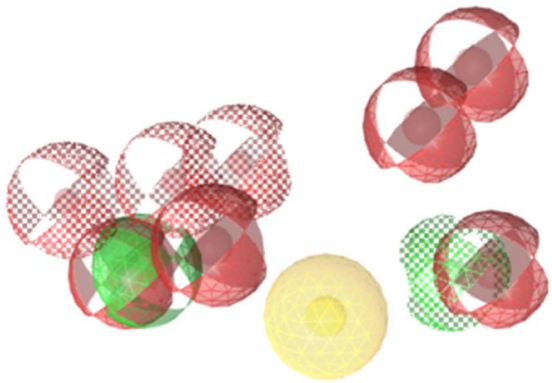


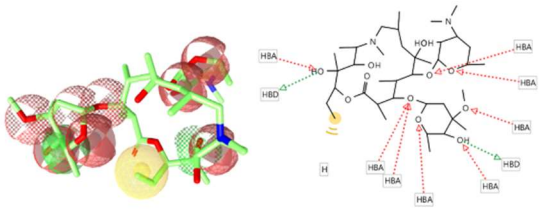
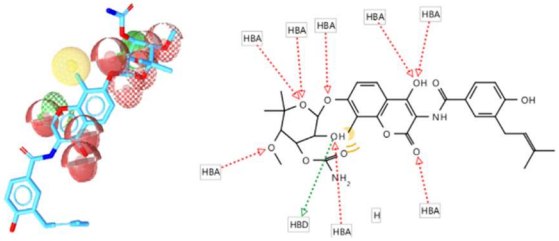
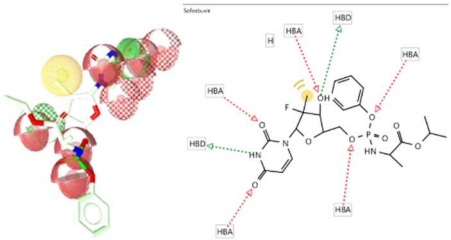
Figure 14. Generated pharmacophore model with 11 pharmacophore features

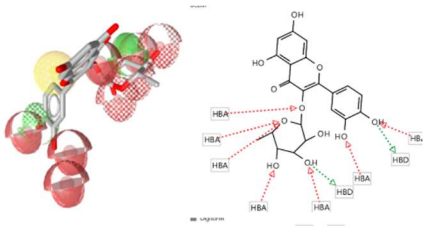
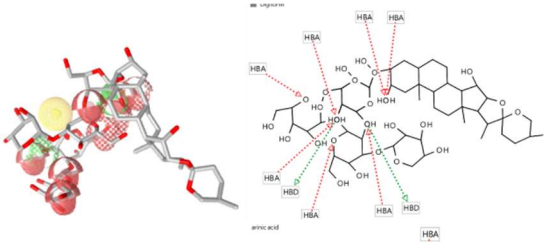
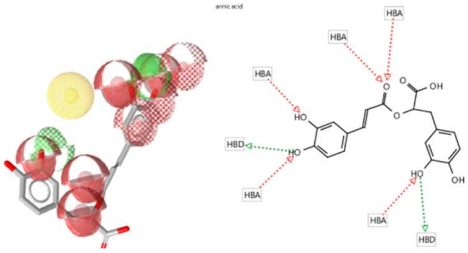
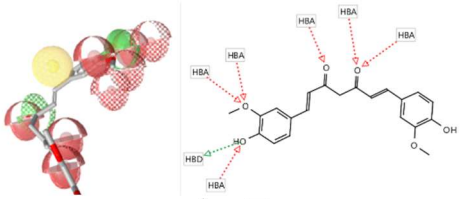
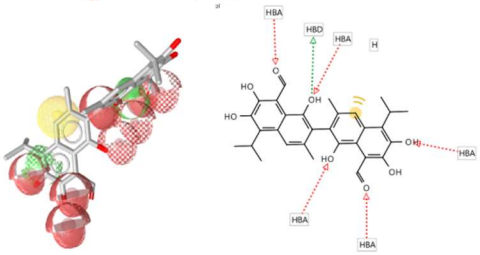
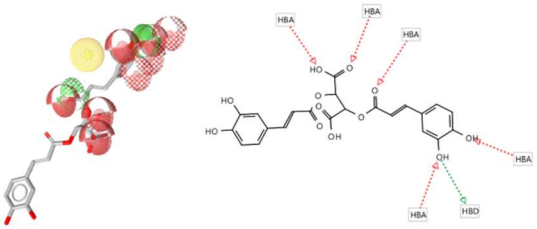
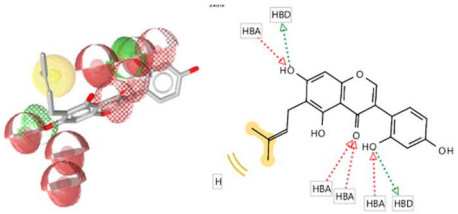
Out of 12 test sets, which were the chemical compounds from natural products for the validation of pharmacophore model, 11 test sets were able to illustrate 4 to 11 matching pharmacophore features, as well as good pharmacophore fit values. 2 test sets, which were quercetin and digitonin, showed higher fitting values than the training set. Thus, the pharmacophore model is justified for its reliability in evaluating the inhibitory activity of Schiff base vanillin derivatives against ZIKV NS2B-NS3 protease. Table 3 shows the pharmacophore fit values and matching features of test sets in the pharmacophore model, and Table 4 shows their matching features with the pharmacophore features depicted by the model.

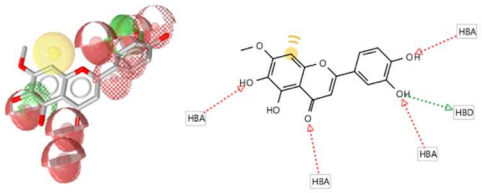
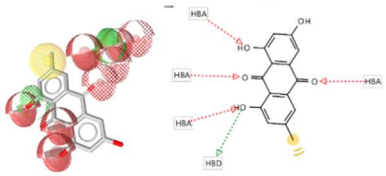
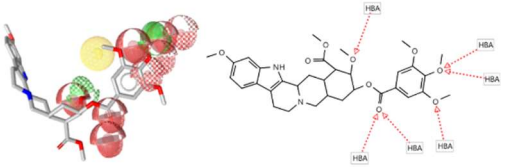
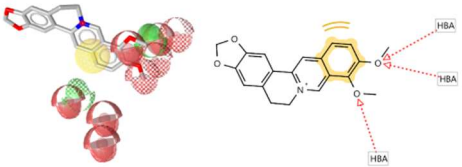
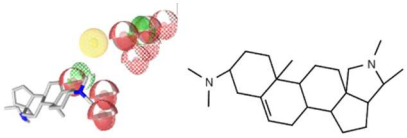
Table 3. Pharmacophore fit values and matching features of test sets in the pharmacophore model

Name of Compounds	Type	Matching Features	Pharmacophore Fit Values
Azithromycin	Training		103.19
Novobiocin	Training		95.84
Quercetin	Test		83.07
Digitonin	Test		82.53
Sofosbuvir	Training		82.21
Rosmarinic acid	Test		72.23
Curcumin	Test		72.16
Gossypol	Test		71.97
Chicoric acid	Test		66.03
Luteone	Test		65.75
Pedalitin	Test		62.69
Emodin	Test		59.30
Reserpine	Test		58.97
Berberine	Test		38.51
Conessine	Test		0.00

Table 4 Matching features of test sets with the pharmacophore features of the pharmacophore model

Name of Compounds	Matching Features	Pharmacophore Fit Values
Azithromycin		103.19
Novobiocin		95.84
Sofosbuvir		83.07

Quercetin		82.53
Digitonin		82.21
Rosmarinic acid		72.23
Curcumin		72.16
Gossypol		71.97
Chicoric acid		66.03
Luteone		65.75

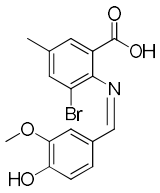
Pedalitin		**62.69**
Emodin		59.30
Reserpine		58.97
Berberine		38.51
Conessine		0.00

Schiff base vanillin derivatives were drawn by using ChemDraw Ultra 12.0 based on the Schiff base synthesis mechanism between vanillin and the listed 21 primary amines, as shown in Table 5 below.

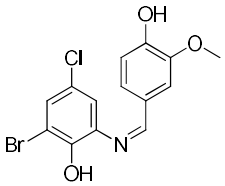
Table 5. List of Schiff base vanillin derivatives

Vanillin Associated With	Chemical Structures	Vanillin Associated With	Chemical Structures
(1) 1-piperidinecarboxamide		(12) Benzaldehyde semicarbazone	
(2) 2,4-dinitrophenylhydrazine		(13) Benzohydrazide	
(3) 2,6-dibromo-4-nitroaniline		(14) Benzotriazole-1-carboxamide	

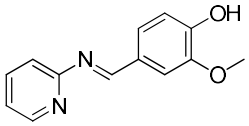
(4) 2-amino-3-bromo-5-methylbenzoic acid



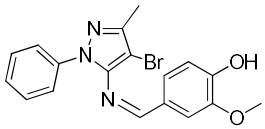
(5) 2-amino-6-bromo-4-chlorophenol



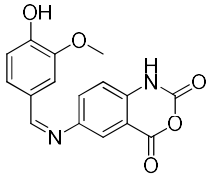
(6) 2-aminopyridine



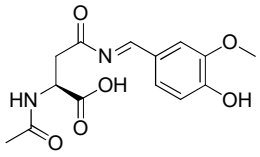
(7) 4-bromo-3-methyl-1-phenyl-1H-pyrazol-5-ylamine



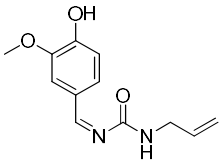
(8) 5-aminoisatoic anhydride



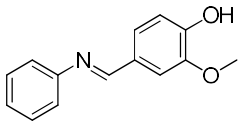
(9) Acetyl-L-asparagine



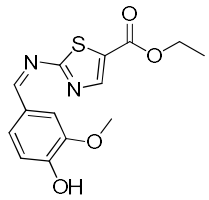
(10) Allylurea



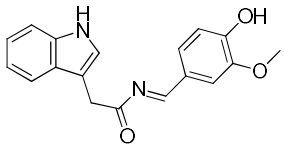
(11) Anilline



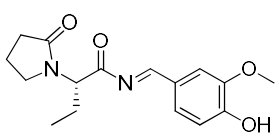
(15) Ethyl 2-aminothiazole-5-carboxylate



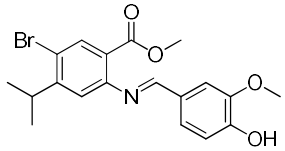
(16) Indole-3-acetamide



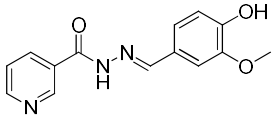
(17) Levetiracetam



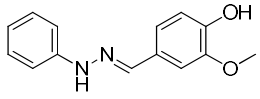
(18) Methyl 2-amino-5-bromo-4-isopropylbenzoate



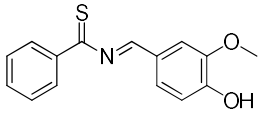
(19) Nicotinic hydrazide



(20) Phenylhydrazine



(21) Thiobenzamide



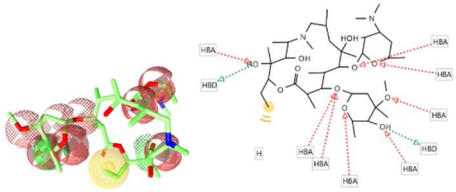
Similarly, the training sets generated a pharmacophore model with 11 features, which are 8 hydrogen bond acceptors (HBA), 2 hydrogen bond donors (HBD) and 1 hydrophobic interaction (HI). Out of 21 vanillin derivatives, a total of 19 compounds showed good pharmacophore fit values and 6 to 9 matching

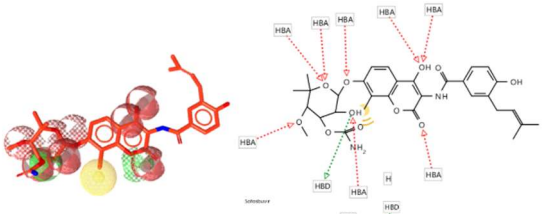
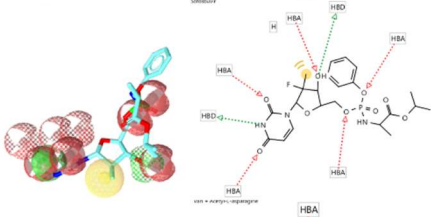
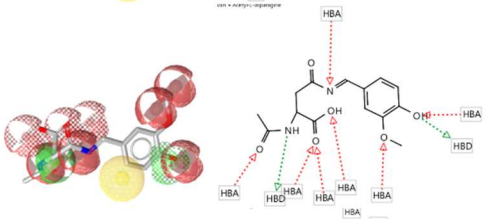
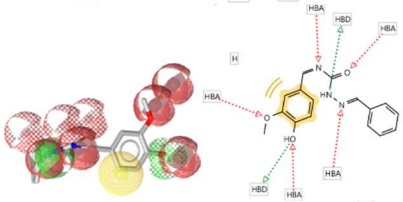
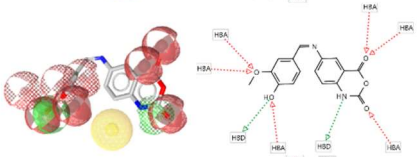
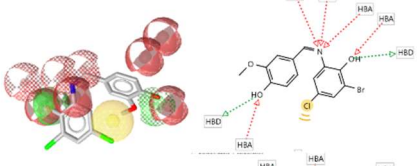
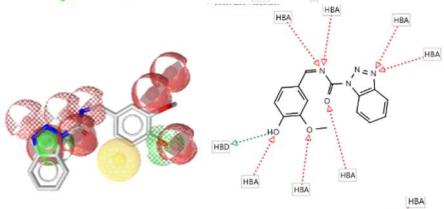
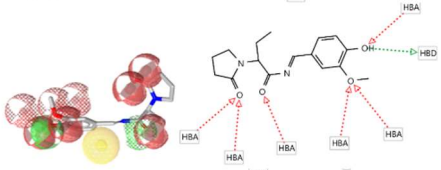
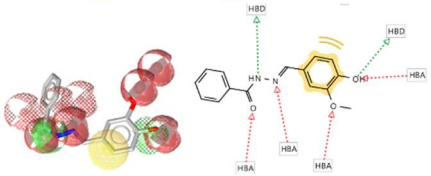
pharmacophore features out of the 11 features from the model. On top of that, compound (9) showed a fit value higher than the training set and the majority number of matching features, depicting immense potential as ZIKV NS2B-NS3 inhibitor. Nonetheless, (1) and (11) are unable to depict good matching features and pharmacophore fit values. The results of ligand-based pharmacophore modelling of Schiff base vanillin derivatives in the generated pharmacophore model were shown in Table 6, while Table 7 displayed their matching features with the pharmacophore features of the model.

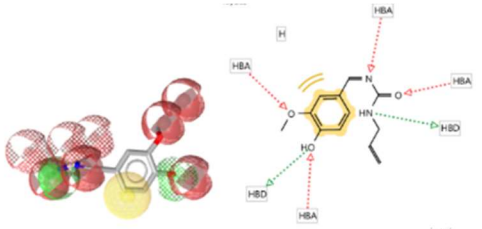
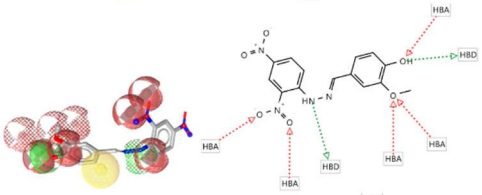
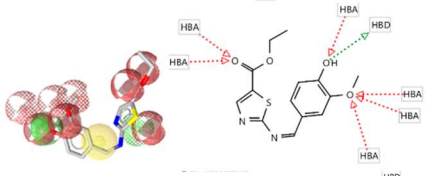
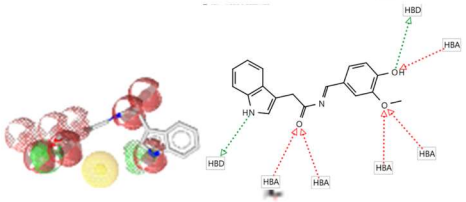
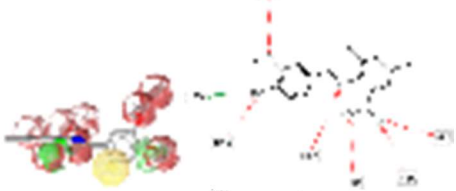
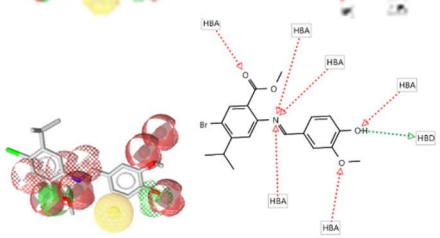
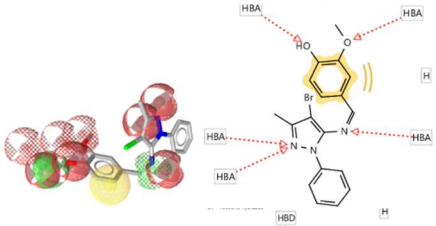
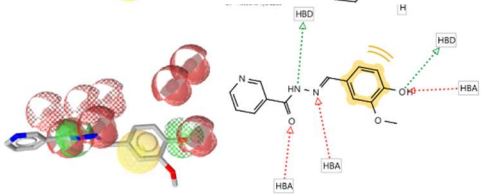
Table 6. Pharmacophore fit values and matching features of Schiff base vanillin derivatives in the pharmacophore model

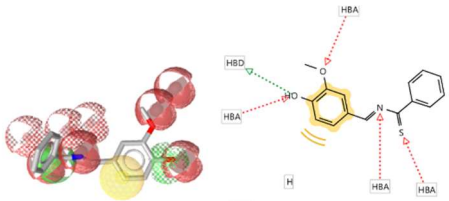
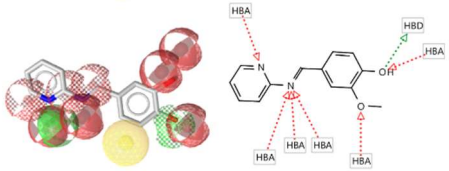
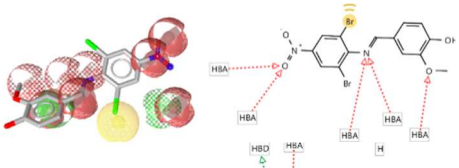
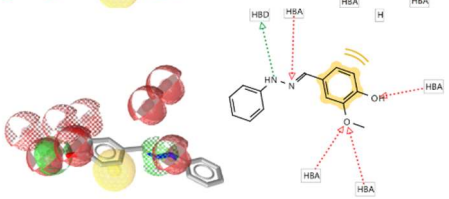
Name of Compounds	Type	Matching Features	Pharmacophore Fit Values
Azithromycin	Training		103.19
Novobiocin	Training		95.84
(9)	Test		82.40
Sofosbuvir	Training		82.21
(12)	Test		79.31
(8)	Test		79.20
(5)	Test		75.54
(14)	Test		72.38
(17)	Test		72.12
(13)	Test		71.81
(10)	Test		69.29
(2)	Test		69.17
(15)	Test		68.57
(16)	Test		68.41
(4)	Test		66.08
(18)	Test		65.32
(7)	Test		62.50
(19)	Test		62.47
(21)	Test		62.46
(6)	Test		62.15
(3)	Test		58.61
(20)	Test		55.53

Table 7. Matching features of Schiff base vanillin derivatives with the pharmacophore features of the pharmacophore model

Name of Compounds	Matching Features	Pharmacophore Fit Values
Azithromycin		103.19

Novobiocin		95.84
Sofosbuvir		82.21
(9)		82.40
(12)		79.31
(8)		79.20
(5)		75.54
(14)		72.38
(17)		72.12
(13)		71.81

(10)		69.29
(2)		69.17
(15)		68.57
(16)		68.41
(4)		66.08
(18)		65.32
(7)		62.50
(19)		62.47

(21)		**62.46**
(6)		62.15
(3)		58.61
(20)		55.53

Based on Table 8, HBA and HBD were found mostly in both hydroxyl group, OH and ether group, C-O-C of vanillin part. Similarly, HI interaction was mostly found in the benzene ring of vanillin. This depicted the importance of vanillin in showing matching interactions with the generated pharmacophore model, hence showing vanillin's potential as ZIKV NS2B-NS3 inhibitors as the training sets. On top of that, HBA and HBD were also discovered in the imine linkage, C=N of Schiff base vanillin derivatives. Hence, this explains the importance and capability of Schiff base vanillin derivatives to show similar and matching interactions with the training sets as ZIKV NS2B-NS3 inhibitors. For the primary amine part, most HBA was shown by O atom in carbonyl, C=O groups, hydroxyl, OH groups and even nitro, NO_2 group, as well as depicted by N atoms. Due to the great amount of HBA and HBD involved, the selection of primary amines in reaction with vanillin to form Schiff base vanillin derivatives should consider most of the O and N atoms. This explains why compound (9) can show exceedingly high pharmacophore fit values, even higher than one of the training sets. The primary amine of (9), which is acetyl-L-aspargine, consists of 1 OH group, 3 O of C=O and 1 N group. Therefore, in combination with the OH and C-O-C of vanillin part, (9) depicted most of the pharmacophore features by the model, as well as having suitable molecular orientation. In some of the Schiff base vanillin derivatives, HI interaction was discovered in Br and Cl atoms. Thus, due to the presence of HI interaction in the model, primary amines with group 17 atoms or aromatic rings are preferably selected. The primary amines of compound (1) and (11) lack of the required functional groups to be aligned with the pharmacophore model. 1- piperidinecarboxamide in (1) has only 1 C=O and N group, while aniline in (11) has only 1 N group and 1 benzene ring. Due to the shortage of common pharmacophore features as well as suitable alignment orientation in the pharmacophore model, (1) and (11) are unable to display good fitting results in the model. Based on the results and explanations, all 19 Schiff base vanillin derivatives possessed potential inhibitory activity against ZIKV NS2B-NS3 protease, just as the interactions shown by the training sets. Therefore, all are subjected to structure-based molecular docking for further evaluation as ZIKV NS2B-NS3 inhibitors.

Structure-based molecular docking

Based on the downloaded PDB crystal structure, the pharmacophore model and interactions of boronate inhibitor with the active sites of NS2B-NS3 protease were shown in Figure 15 below. The inhibitor showed 11 interactions, which were 3 HBA, 3 HBD, 3 positive ionisable area (PI), 1 aromatic ring (AR) and 1 HI.

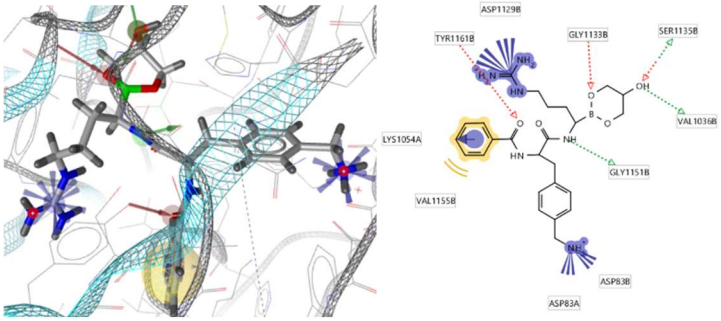


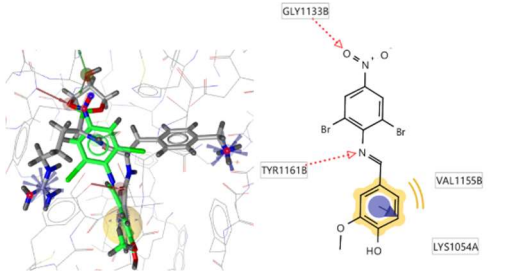
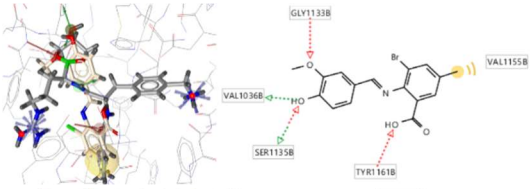
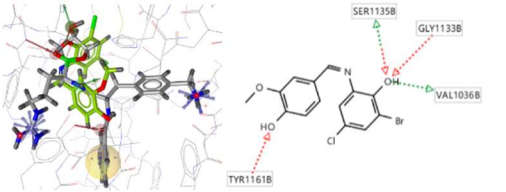
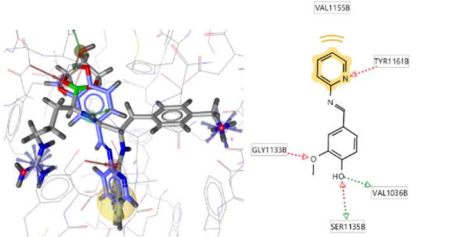
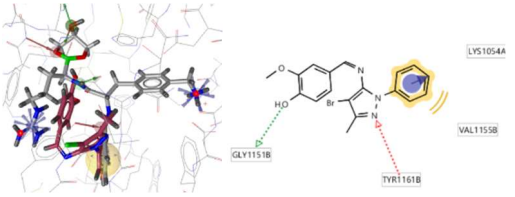
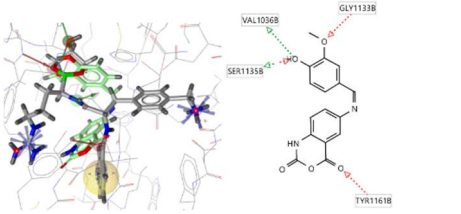
Figure 15. Pharmacophore model and interactions of boronate inhibitor with the active sites of 5LC0

Upon alignment and docking of the 19 Schiff base vanillin derivatives from ligand-based pharmacophore modelling results, 17 of them can depict 4 to 7 matching interactions with the active sites of 5LC0. On top of that, they are also able to show good pharmacophore scores and binding affinity values, hence having great inhibitory potential against NS2B-NS3 protease. Nevertheless, (1), (2), (9) and (11) were unable to show enough matching features in interaction with ZIKV NS2B-NS3 protease. This is due to the lack of enough common pharmacophore features to be aligned with the boronate inhibitor, as well as in the active site of 5LC0. Table 8 showed the pharmacophore scores and binding affinity values of the Schiff base vanillin derivatives upon docking *via* AutoDock Vina in the active site of ZIKV NS2B-NS3 protease, whereby the shaded columns, which were derivative (14), (15) and (19) showed the highest pharmacophore scores. Table 9 depicts their aligned interactions with the boronate inhibitor in the active site of ZIKV NS2B-NS3 protease.

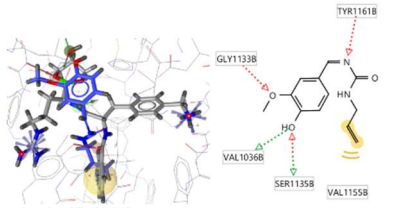
Table 8. Pharmacophore scores and binding affinity values (kcal mol^{-1}) of Schiff base vanillin derivatives upon docking by AutoDock Vina in the active site of ZIKV NS2B-NS3 protease

Schiff Base Vanillin Derivatives	Pharmacophore Scores	Binding Affinity Values (kcal mol^{-1})
(3)	46.95	-8.20
(4)	36.49	-8.60
(5)	45.23	-7.70
(6)	35.49	-7.40
(7)	37.73	-7.70
(8)	44.57	-8.10
(10)	35.93	-6.20
(12)	36.95	-8.50
(13)	37.36	-8.30
(14)	55.99	-8.90
(15)	56.30	-7.20
(16)	37.66	-8.90
(17)	35.83	-7.40
(18)	36.33	-8.50
(19)	47.07	-7.60
(20)	35.09	-7.40
(21)	46.56	-8.00

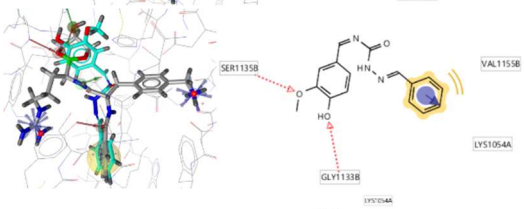
Table 9. Aligned interactions of Schiff base vanillin derivatives with boronate inhibitor in the active site of ZIKV NS2B-NS3 protease

Schiff Base Vanillin Derivatives	Aligned Interactions
(3)	
(4)	
(5)	
(6)	
(7)	
(8)	

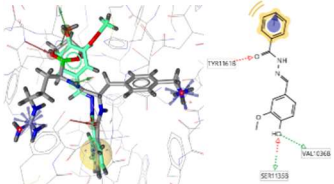
(10)



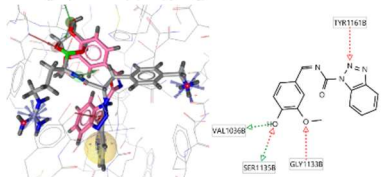
(12)



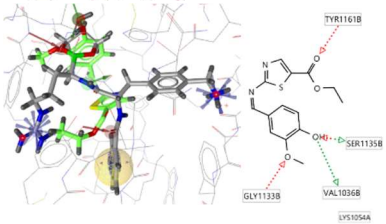
(13)



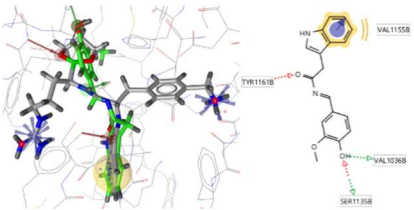
(14)



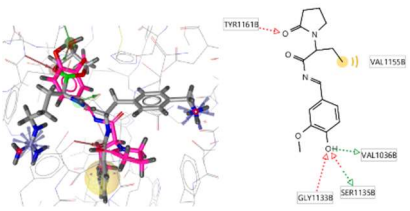
(15)



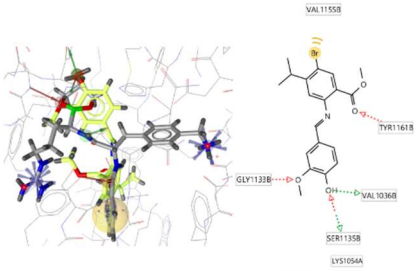
(16)



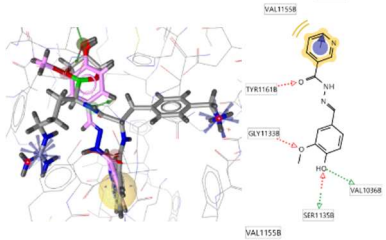
(17)



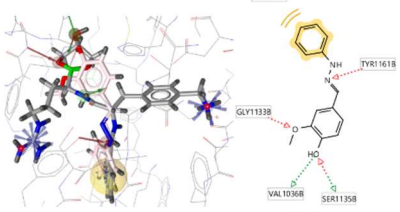
(18)



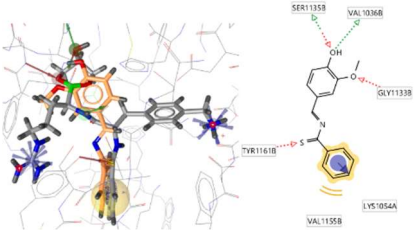
(19)



(20)



(21)



The 17 Schiff base vanillin derivatives were able to depict at least 4 matching interactions with satisfying pharmacophore scores, hence showing their potential inhibitory activity against NS2B-NS3 protease. Other than that, the molecular docking results of the Schiff base vanillin derivatives were also expressed based on their binding affinity values, which is a function of Gibbs free energy [28]. Binding affinity refers to the strength of binding interaction between a protein molecule to its ligand, which is between the 5LC0 protease with the Schiff base vanillin derivatives in this study. Being represented by the equilibrium dissociation constant, the more negative the binding affinity values, the greater the binding interaction and affinity [29]. Since binding affinity values are a function of Gibbs free energy, therefore affinity values less than -6.0 kcal mol^{-1} are considered active molecules, while affinity values greater than -6.0 kcal mol^{-1} are considered inactive molecules [29]. Based on the obtained results, the Schiff base vanillin derivatives showed binding affinity values less than -6.0 kcal mol^{-1}, ranging from -6.20 kcal mol^{-1} to -8.90 kcal mol^{-1}, indicating their property as active cluster molecules.

The interactions of the boronate inhibitor with the active sites of NS2B-NS3 protease are HBA towards TYR161B, GLY133B and SER135B, HBD towards SER135B, VAL36B and GLY151B, PI towards ASP129B, ASP83A and ASP83B, AR towards LYS54A, as well as HI towards VAL155B. The Schiff base vanillin derivatives mostly depict HBA towards TYR161B, GLY133B and SER135B, HBD towards SER135B and VAL36B, AR towards LYS54A and HI towards VAL155B. Most of the HBA and HBD were found to be depicted by the hydroxyl and ether group of the vanillin part, showing that vanillin itself plays an

imperative role in interactions with the active sites of ZIKV NS2B-NS3 protease. Moreover, the Schiff base vanillin derivatives displayed their inhibitory action against LYS54A and VAL155B, which are AR and HI through the benzene and pyridine rings of the primary amine part. This shows the potential of aromatic primary amines as NS2B-NS3 protease inhibitors, to be utilised as a starting product for the synthesis of Schiff base vanillin derivatives to inhibit NS2B-NS3 protease. This may explain the lack of potential of (9), as the primary amine of (9) is an aliphatic primary amine. Even though compound (2) shows reliable results in ligand-based pharmacophore modelling, due to the lack of enough pharmacophore features, as well as unable to depict suitable orientation in the active site of 5LC0, compound (2) is unable to align with boronate inhibitor. In another crystal structure of ZIKV NS3 protease in complex with peptidomimetic inhibitor, which is 4-guanidinomethyl-phenylacetyl-Arg-Arg-Arg-4-amidinobenzylamide, the inhibitor also showed HBA against TYR161B, GLY133B and SER135B, thus depicting the importance of interactions with these active sites [30]. Similarly, the crystal structure of ZIKV NS2B-NS3 protease with compound MI2219 (PDB code: 7VLH), and the crystal structure of Zika NS2B-NS3 protease with compound MI2220 (PDB code: 7VLI) showed HBA and HBD interaction with TYR161B, showing the imperative role of interaction with TYR161B in inhibition activity against the NS2B-NS3 protease [31], which is depicted by 16 out of 17 of the Schiff base vanillin derivatives. Compounds (1) and (11) have been shown to lack HBA and HBD interactions in ligand-based pharmacophore modelling due to the lack of required functional groups, hence they are unable to depict any interaction with these important active sites, especially TYR161B, GLY133B and SER135B. In conjunction with the results obtained from ligand-based pharmacophore modelling, all the 17 Schiff base vanillin derivatives above showed a great deal of potential as ZIKV NS2B-NS3 protease inhibitors *via in silico*, being promising drug candidates and bringing futuristic *in vitro* and *in vivo* tests to confirm the inhibitory activities.

Lipinski's rule of 5

Lipinski's rule of 5 or known as RO5 is a guideline rule which analyse and evaluate the drug likeness, and pharmacological and biological activity of chemical compounds as orally active drug for human consumption. The rule described the molecular properties crucial for a drug's pharmacokinetics in humans, known as 'ADME': absorption, distribution, metabolism, and excretion. RO5 states that for a chemical compound to be an orally active drug, the chemical compound should have:

- Not more than 5 hydrogen bond donors (HBD) (nitrogen-hydrogen and oxygen-hydrogen bonds)
- Not more than 10 hydrogen bond acceptors (HBA) (nitrogen and oxygen atoms)
- Molecular weight less than 500 g/mol
- Partition coefficient log P not greater than 5 [32]

Based on RO5, all 17 Schiff base vanillin derivatives that showed potential inhibitory activity against ZIKV NS2B-NS3 protease fulfilled all rules, having less than 5 HBD, less than 10 HBA, molecular weight less than 500 g/mol and partition coefficient log P less than 5. Therefore, they are considered to possess drug likeness as potential orally active drugs, thus supporting their role as potential NS2B-NS3 inhibitors. Table 10 summarised the RO5 results of the Schiff base vanillin derivatives.

Conclusion

From ligand-based pharmacophore modelling to structure-based molecular docking, a total of 21 Schiff base vanillin derivatives were evaluated for the ZIKV NS2B-NS3 protease inhibitory activity. Out of 21 derivatives, 17 showed potential results as NS2B-NS3 inhibitors. In ligand-based pharmacophore modelling, 19 of them showed good pharmacophore fit values, and 6 to 9 matched pharmacophore features out of 11 features depicted by pharmacophore model of training sets. In structure-based molecular docking, 17 of them showed 4 to 7 matching interactions with the 11 interactions shown by boronate inhibitor ligand in the active site of 5LC0, as well as good fit values and binding affinity values upon docking. As a result, the Schiff base vanillin derivatives that passed both ligand-based pharmacophore modelling and structure-based molecular docking are **(3), (4), (5), (6), (7), (8), (10), (12), (13), (14), (15), (16), (17), (18), (19), (20)** and **(21)**. The 17 Schiff base vanillin derivatives also fulfilled Lipinski's Rule of 5, depicting their drug likeness

properties and being potential orally active drugs. Being proven as promising drug candidates through *in silico* study, further analysis and research *in vivo* and *in vitro* becomes interesting and potential research in future to ensure the safety and lethality of these derivatives, and to bring more opportunities to more research in the study of ZIKV NS2B-NS3 inhibitors.

Table 10. Lipinski's Rule of 5 of Schiff base vanillin derivatives

Vanillin Derivatives	c log P	Hydrogen Bond Donors (HBD)	Hydrogen Bond Acceptors (HBA)	Molecular Weight (g/mol)
(3)	3.730	1	7	396.159
(4)	3.689	1	5	364.201
(5)	4.273	2	4	356.609
(6)	2.546	1	4	228.251
(7)	4.408	1	4	386.255
(8)	1.946	2	5	312.281
(10)	1.715	2	4	234.255
(12)	2.563	2	5	297.314
(13)	1.933	2	4	270.288
(14)	1.631	1	6	296.286
(15)	2.553	1	5	306.340
(16)	3.070	2	4	308.337
(17)	1.747	1	5	304.346
(18)	4.592	1	4	406.282
(19)	1.328	2	5	271.276
(20)	2.847	2	3	242.278
(21)	3.195	1	4	271.338

Acknowledgement

The study is part of postgraduate studies. Authors express gratitude to Faculty of Resource Science and Technology, Universiti Malaysia Sarawak for all the support, laboratory facilities and computational software provided.

References

1. Sikka, V., Chattu, V. K., Popli, R. K., Galwankar, S. C., Kelkar, D., Sawicki, S. G., Stawicki, S. P. and Papadimos, T. J. (2016). The emergence of Zika virus as a global health security threat: A review and a consensus statement of the INDUSEM Joint Working Group (JWG). *Journal of Global Infectious Diseases*, 8 (1): 3-15.
2. World Health Organization (2022). Zika virus. Access from https://www.who.int/news-room/fact-sheets/detail/zika-virus. [Access online 3 February 2023].
3. Lanciotti, R. S., Kosoy, O. L., Laven, J. J., Velez, J. O., Lambert, A. J., Johnson, A. J., Stanfield, S. M. and Duffy, M. R. (2008). Genetic and serologic properties of Zika virus associated with an epidemic, Yap State, Micronesia, 2007. *Emerging Infectious Diseases*, 14(8): 1232-1239.
4. Oehler, E., Watrin, L., Larre, P., Leparc-Goffart, I., Lastère, S., Valour, F., Bandouin, L., Mallet, H. P., Musso, D. and Ghawche, F. (2014). Zika virus infection complicated by Guillain-Barré syndrome – case report, French Polynesia, December 2013. *Eurosurveillance*, 19(9): 20720.
5. Pan American Health Organization (n.d.) Zika. Access from https://www.paho.org/en/topics/zika. [Access online 3 February 2023].
6. Hayes, E. B. (2009). Zika virus outside Africa. *Emerging Infectious Diseases*, 15(9): 1347-1350.
7. Rehman, H. M., Sajjad, M., Ali, M. A., Gul, R., Irfan, M., Naveed, M., Bhinder, M. A., Ghani, M. U., Hussain, N., Said, A. S. A., Al Haddad, A. H. I. and Saleem, M. (2023). Identification of NS2B-

NS3 protease inhibitors for therapeutic application in ZIKV infection: A pharmacophore-based high-throughput virtual screening and MD simulations approaches. *Vaccines*, 11(1): 131.

8. Pierson, T. C., and Diamond, M. S. (2020). The continued threat of emerging flaviviruses. *Nature Microbiology*, 5(6): 796-812.
9. Mirza, M. U., Alanko, I., Vanmeert, M., Muzzarelli, K. M., Salo-Ahen, O. M. H., Abdullah, I., Kovari, I. A., Claes, S., Jonghe, S. D., Schols, D., Schinazi, R. F., Kovari, L. C., Trant, J. F., Ahmad, S. and Froeyen, M. (2022). The discovery of Zika virus NS2B-NS3 inhibitors with antiviral activity *via* an integrated virtual screening approach. *European Journal of Pharmaceutical Sciences*, 175: 106220.
10. Li, H., Clum, S., You, S., Ebner, K. E., and Padmanabhan, R. (1999). The serine protease and RNA-stimulated nucleoside triphosphatase and rna helicase functional domains of dengue virus type 2 NS3 converge within a region of 20 amino acids. *Journal of Virology*, 73 (4): 3108-3116.
11. Shiryaev, S. A., Aleshin, A. E., Ratnikov, B. I., Smith, J. W., Liddington, R. C., and Strongin, A. Y. (2007). Expression and purification of a two-component flaviviral proteinase resistant to autocleavage at the NS2B–NS3 junction region. *Protein Expression and Purification*, 52 (2): 334-339.
12. Meewan, I., Shiryaev, S. A., Huang, C.-T., Lin, Y.-W., Chuang, C.-H., Terskikh, A. V, and Abagyan, R. (2022). Allosteric inhibitors of Zika virus NS2B-NS3 protease targeting protease in super-open conformation. *BioRxiv*.
13. National Institutes of Health (2016). Zika virus structure revealed. Access fromhttps://www.nih.gov/news-events/nih-research-matters/zika-virus-structure-revealed. [Access online 27 March 2023].
14. Clain, E., Sinigaglia, L., Koishi, A.C., Gorgette, O., Gadea, G., Viranaicken, W., Krejbich-Trotot, P., Mavingui, P., Desprès, P., dos Santos, C. N. D., Guiraud, P., Jouvenet, N. and Kalamouni, C, E. (2018).. Extract from *Aphloia theiformis*, an edible indigenous plant from Reunion Island, impairs Zika virus attachment to the host cell surface. *Scientific Reports,* 8: 10856.
15. Takenaka, T. (2008). Classical vs reverse pharmacology in drug discovery. *BJU International*, 88 (2): 7-10.
16. Pathak, N., Kuo, Y.-P., Chang, T.-Y., Huang, C.-T., Hung, H.-C., Hsu, J. T.-A., Yu, G.-Y. and Yang, J.-M. (2020). Zika virus NS3 protease pharmacophore anchor model and drug discovery. *Scientific Reports*, 10(1): 8929.
17. Santos, F. R. S., Nunes, D. A. F., Lima, W. G., Davyt, D., Santos, L. L., Taranto, A. G. and Ferreira, J. M. S. (2020). Identification of Zika virus NS2B-NS3 Protease Inhibitors by Structure-Based Virtual Screening and Drug Repurposing Approaches. *Journal of Chemical Information and Modeling*, 60 (2): 731-737.
18. Lei, J., Hansen, G., Nitsche, C., Klein, C. D., Zhang, L., and Hilgenfeld, R. (2016). Crystal structure of Zika virus NS2B-NS3 protease in complex with a boronate inhibitor. *Science*, 353 (6298): 503-505.
19. Asaruddin, M. R. (2016). Modelling and syntheses of vanillin derivatives targeting influenza virus neuraminidase. Thesis of Doctor of Philosophy, Universiti Sains Malaysia.
20. Law, W. Y., Asaruddin, M. R., Bhawani, S. A. and Mohamad, S. (2020). Pharmacophore modelling of vanillin derivatives, favipiravir, chloroquine, hydroxychloroquine, monolaurin and tetrodotoxin as M^{Pro} inhibitors of severe acute respiratory syndrome coronavirus-2 (SARS-CoV-2). *BMC Research Notes*, 13(1): 527.
21. Yuan, S., Chan, J. F.-W., den-Haan, H., Chik, K. K.-H., Zhang, A. J., Chan, C. C.-S., Poon, V. K.-M., Yip, C. C.-Y., Mak, W. W.-N., Zhu, Z., Zou, Z., Tee, K.-M., Cai, J.-P., Chan K.-H., de la Peña, J., Pérez-Sánchez, H., Cerón-Carrasco, J. P. and Yuen, K.-Y. (2017). Structure-based discovery of clinically approved drugs as Zika virus NS2B-NS3 protease inhibitors that potently inhibit Zika virus infection *in vitro* and *in vivo*. *Antiviral Research*, 145: 33-43.
22. Bullard-Feibelman, K. M., Govero, J., Zhu, Z., Salazar, V., Veselinovic, M., Diamond, M. S., and Geiss, B. J. (2017). The FDA-approved drug sofosbuvir inhibits Zika virus infection. *Antiviral Research*, 137: 134- 140.
23. Retallack, H., Lullo, E. Di, Arias, C., Knopp, K. A.,

Laurie, M. T., Sandoval-Espinosa, C., Leon, W. R. M., Krencik, R., Ullian, E. M., Spatazza, J., Pollen, A. A., Mandel-Brehm, C., Nowakowski, T. J., Kreigstein A. R. and DeRisi, J. L. (2016). Zika virus cell tropism in the developing human brain and inhibition by azithromycin. *Proceedings of the National Academy of Sciences*, 113(50): 14408-14413.

24. Batista, M. N., Braga, A. C. S., Campos, G. R. F., Souza, M. M., Matos, R. P. A. de, Lopes, T. Z., Candido, N. M., Lima, M. L. D., Machado, F. C., de Andrade, S. T. Q., Bittar, C., Nogueira, M. L., Carneiro, B. M., Mariutti R. B., Arni, R. K., Calmon, M. F. and Rahal, P. (2019). Natural Products Isolated from Oriental Medicinal Herbs Inactivate Zika Virus. *Viruses*, 11(1): 49.
25. Ahmed, S. R., Banik, A., Anni, S. M. and Chowdhury, M. M. H. (2021). Inhibitory potential of plant-derived metabolites against Zika virus: a computational-aided approach. *Phytomedicine Plus*, 1(4): 100129.
26. Gao, Y., Tai, W., Wang, N., Li, X., Jiang, S., Debnath, A. K., Du, L. and Chen, S. (2019). Identification of novel natural products as effective and broad-spectrum anti-Zika virus inhibitors. *Viruses*, 11(11): 1019.
27. Ramos, P. R. P. da S., Mottin, M., Lima, C. S., Assis, L. R., de Oliveira, K. Z., Mesquita, N. C. de M. R., Cassani, N. M., Santos, I. A., Borba, J. V. V. B., Costa, V. A. F., Neves, B. J., Guido, R. V. C., Oliva, G., Jardim, A. C. G., Regasini, L. O. and Andrade, C. H. (2022). Natural compounds as non-nucleoside inhibitors of Zika virus polymerase through integration of *in silico* and *in vitro* approaches. *Pharmaceuticals*, 15(12): 1493.
28. Schön, A., Madani, N., Smith, A. B., Lalonde, J. M., and Freire, E. (2011). Some binding-related drug properties are dependent on thermodynamic signature. *Chemical Biology & Drug Design*, 77(3): 161-165.
29. Shityakov, S., and Förster, C. (2014) *In silico* predictive model to determine vector-mediated transport properties for the blood–brain barrier choline transporter. *Advances and Applications in Bioinformatics and Chemistry*. 7: 23-36.
30. Phoo, W. W., Zhang, Z., Wirawan, M., Chew, E. J. C., Chew, A. B. L., Kouretova, J., Steinmetzer, T. and Luo, D. (2018). Structures of Zika virus NS2B-NS3 protease in complex with peptidomimetic inhibitors. *Antiviral Research*, 160: 17-24.
31. Huber, S., Braun, N. J., Schmacke, L. C., Quek, J. P., Murra, R., Bender, D., Hildt, E., Luo, D., Heine, A. and Steinmetzer, T. (2022). Structure-based optimization and characterization of macrocyclic Zika virus NS2B-NS3 protease inhibitors. *Journal of Medicinal Chemistry*, 65(9): 6555-6572.
32. Lipinski, C. A., Lombardo, F., Dominy, B. W. and Feeney, P. J. (2001). Experimental and computational approaches to estimate solubility and permeability in drug discovery and development settings1PII of original article: S0169-409X(96)00423-1. *Advanced Drug Delivery Reviews*, 46(1): 3-26.

Malaysian Journal of Analytical Sciences (MJAS)
Published by Malaysian Analytical Sciences Society

PHOTOCATALYTIC DEGRADATION OF OFLOXACIN ANTIBIOTIC BY g-C_3N_4/ZnO NANOCOMPOSITE UNDER VISIBLE LIGHT IRRADIATION

(Fotokatalitik Degradasi Ofloksasin Antibiotik oleh Nanokomposit g-C_3N_4/ZnO di Bawah Penyinaran Cahaya Tampak)

Nor Fadilah Chayed[1,2], Salma Izati Sinar Mashuri[1,2], Izzati Shafiqah Zainal Abidin[1,2], Muhd Firdaus Kasim[1,2], Noor Haida Mohd Kaus[4], Mohd Sufri Mastuli[1,2], Umer Rashid[5], and Mohd Lokman Ibrahim[1,2,3*]

[1]Centre for Functional Materials and Nanotechnology,
Institute of Science, Universiti Teknologi MARA, 40450 Shah Alam, Selangor, Malaysia
[2]School of Chemistry and Environment,
Faculty of Applied Sciences,
Universiti Teknologi MARA, 40450 Shah Alam, Selangor, Malaysia
[3]Industrial Waste Conversion Technology,
Universiti Teknologi MARA, 40450 Shah Alam, Selangor, Malaysia
[4]School of Chemical Sciences,
Universiti Sains Malaysia, 11800 Penang, Malaysia
[5]Institute of Nanoscience and Nanotechnology,
Universiti Putra Malaysia, 43400 Serdang Selangor, Malaysia

[*]Corresponding author: mohd_lokman@uitm.edu.my

Received: 15 September 2023; Accepted: 29 October 2023; Published: 29 December 2023

Abstract

A critical global environmental crisis has emerged due to the use of synthetic organic pollutants in industry, which resulted in the pollution of water. Recently, photocatalysis has attracted much attention for its potential to effectively, economically, and environmentally friendly remove organic pollutants from wastewater. ZnO is known as a potential photocatalyst for the degradation of wastewater in the UV region. However, ZnO has limited light absorption within the UV region and exhibits fast recombination of electron-hole pairs, which reduces its efficiency. To overcome this issue, a g-C_3N_4/ZnO photocatalyst for organic pollutant degradation in wastewater was developed to extend the light absorption towards the visible region. This research aims to investigate the performance of g-C_3N_4/ZnO nanocomposites in the degradation of ofloxacin (OFL). The ZnO was prepared using the sol-gel method, while the g-C_3N_4 was prepared using thermal decomposition. The composite catalyst of g-C_3N_4/ZnO was prepared by mixing g-C_3N_4 and ZnO. The prepared catalysts were characterized using X-ray diffraction (XRD), field emission scanning electron microscopy (FESEM), UV-Vis NIR spectrophotometer, high-resolution transmission electron microscopy (HRTEM), and Brunauer Emmet Teller (BET). As a result of the composite photocatalyst combining ZnO and g-C_3N_4, the band gap decreased from 3.30 eV to 2.92 eV. The degradation of OFL using g-C_3N_4/ZnO nanocomposite is 11 times higher than that of pristine ZnO and double than that of pristine g-C_3N_4.

Keywords: g-C_3N_4/ZnO, ofloxacin, degradation, photocatalysis, wastewater treatment

Abstrak

Krisis alam sekitar global yang kritikal telah muncul akibat penggunaan bahan pencemar organik sintetik di dalam industri, mengakibatkan pencemaran air. Baru-baru ini, fotokatalisis telah menarik banyak perhatian kerana potensinya untuk merawat bahan organik daripada air sisa tercemar secara berkesan, ekonomikal dan mesra alam. ZnO dikenali sebagai fotomangkin berpotensi untuk degradasi air sisa tercemar di kawasan UV. Walau bagaimanapun, ZnO mempunyai penyerapan cahaya yang terhad dalam kawasan UV hanya disebabkan oleh tenaga jurang jalur yang besar (3.37 eV) dan mempamerkan penggabungan semula pantas pasangan lubang elektron, yang mengurangkan kecekapannya. Untuk mengatasi isu ini, fotomangkin g-C_3N_4/ZnO untuk degradasi bahan organik dalam rawatan air sisa telah dihasilkan untuk meningkatkan penyerapan cahaya ke arah cahaya tampak. Matlamat penyelidikan ini adalah untuk menyiasat prestasi nanokomposit g-C_3N_4/ZnO dalam degradasi ofloksasin (OFL). ZnO disediakan menggunakan kaedah sol-gel, manakala g-C_3N_4 disediakan menggunakan penguraian terma. Mangkin komposit g-C_3N_4/ZnO disediakan dengan mencampurkan g-C_3N_4 dan ZnO. Pemangkin yang disediakan telah dicirikan menggunakan pembelauan sinar-X-(XRD), mikroskopi imbasan elektron pancaran medan (FESEM), spektrofotometer UV-Vis NIR, mikroskopi transmisi elektron resolusi tinggi (HRTEM), dan Brunauer Emmet Teller (BET). Hasil daripada fotomangkin komposit yang menggabungkan ZnO dan g-C_3N_4, jurang jalur menurun daripada 3.30 eV kepada 2.92 eV. Degradasi ofloksasin menggunakan nanokomposit g-C_3N_4/ZnO adalah 11 kali lebih tinggi daripada ZnO dan 2 kali lebih tinggi daripada g-C_3N_4 tulen.

Kata kunci: g-C_3N_4/ZnO, ofloksasin, degradasi, fotokatalisis, rawatan air tercemar

Introduction

The increasing use of pharmaceuticals in recent years has attracted researchers' attention due to their harmful impact on the environment. They have been identified as the most common organic pollutants found in wastewater from various sources, such as hospitals, households, industries, and agricultural waste. Antibiotics contribute to a large proportion of the numerous pharmaceutical products consumed due to their widespread use in veterinary and human medicine for the treatment or prevention of bacterial diseases [1, 2]. Ofloxacin (OFL) is a quinolone antibiotic known as an antibacterial agent used for the treatment of bacterial infections in body parts including the skin, kidney, soft tissue, respiratory tract, and urine tract [3]. OFL is a third-generation fluoroquinolone antibiotic and cannot be completely metabolized by the human body, in which 20-80% of the indigested agent is excreted in pharmacologically active form. It has been reported that low concentrations of OFL can accumulate in water for prolonged periods of time. The fluoroquinolones that are present in wastewater can lead to the proliferation of drug resistant bacteria through induction and selection. It can be harmful to human health and can potentially reduce the ability of human immune system to fight those bacteria strains [4–9].

OFL has been detected in water environments such as in hospital wastewater (35 µg/L), urban wastewater treatment plants (1.8 µg/L), sewage water (0.89-31.73 µg/L) and surface water (0.5-35 µg/L) [10,11]. Various methods have been extensively explored for the removal of OFL such as adsorption, biodegradation, chlorination, precipitation, coagulation etc. [6, 12-15]. However, most of the methods are unable to remove the organic pollutant completely and effectively. In recent years, photocatalysis has attracted attention for antibiotic degradation due to its high efficiency, excellent stability, and eco-friendliness compare to the conventional methods [5, 16, 17].

ZnO is a metal oxide semiconductor that has good electron transfer ability, exhibits photostability and can generate holes for strong oxidation. Despite its numerous advantages, ZnO has certain limitation of poor photocatalytic response to visible light due to having a wide band gap (3.37 eV) and fast recombination of photogenerated electron-hole pairs [18, 19]. Various approaches have been attempted to overcome this limitation, which include making suitable composites such as ZnO/CdS, ZnO/Sn_3O_4, CuO/ZnO, ZnO/TiO_2, ZnO-CoO_x-CeO_2 and etc. [20-24].

Graphitic carbon nitride (g-C_3N_4) is the most stable allotrope of carbon nitrides at ambient temperature and has received a lot of attention in recent years. The g-C_3N_4 is a metal-free n-type semiconductor polymer with a two-dimensional structure similar to graphite. In

the visible spectral range, g-C_3N_4 has a band gap of 2.7 eV, corresponding to an optical wavelength of 460 nm, making it an excellent photocatalyst. In addition to being safe and non-toxic, g-C_3N_4 is highly stable and has a strong reduction ability, as well as being light active. [25-29]. However, g-C_3N_4 also has disadvantages of photogenerated electron and holes pairs that easily recombine, which greatly reduces the performance of the photocatalyst. Since g-C_3N_4 has a large resistance, it blocks the transfer of photoexcited electrons.

The combination of g-C_3N_4/ZnO could improve the photocatalytic performance due to the complementary properties of both g-C_3N_4 and ZnO. The ability of g-C_3N_4 to absorb visible light is well known, whereas ZnO can absorb only UV light. This combination can extend the light absorption with a broader spectrum of light that can enhance the photocatalytic performance. The g-C_3N_4/ZnO composite exhibits synergistic effects, resulting in a more efficient and effective photocatalyst than either material alone. This synergy has the potential to improve electron-hole pair generation and separation which can improve the photocatalytic performance [30-33]. The formation of g-C_3N_4 and ZnO to form a heterojunction can significantly reduce the recombination rate of electron holes by modifying the charge carrier pathway at the interface. Hybrid structures can facilitate interfacial charge transfer, enabling electrons and holes to be simultaneously available for selective redox reactions [34]. In summary, heterojunction of g-C_3N_4 and ZnO provides several advantages, including improved charge separation, extended light absorption range, increased photocatalytic activity, and improved stability. Due to these characteristics, g-C_3N_4/ZnO heterojunctions are attractive for a variety of environmental and energy applications.

In the present work, g-C_3N_4/ZnO nanocomposite has been synthesized using sol-gel, thermal decomposition method followed by wet impregnation method. The photocatalytic activity was evaluated based on the degradation of OFL. It has been observed that the photocatalytic activity of the composite has improved significantly compared to the pristine.

Materials and Methods

Materials

Melamine ($C_3H_6N_6$,>99%) was used as the precursor for g-C_3N_4, Zinc acetate $Zn(CH_3COO)_2$ was used for the preparation of ZnO. The ammonium hydroxide (NH_4OH) and absolute ethanol were used as the solvent, and analytical grade of OFL (Sigma-Aldrich) was used as the organic pollutant in this study.

Preparation of the g-C_3N_4/ZnO photocatalysts

The synthesis method that was used for the preparation of ZnO catalyst is the sol-gel method. This method involves the dissolution of the starting material, $Zn(CH_3COO)_2$, in absolute ethanol. The solution was then stirred using a magnetic stirrer for an hour to make sure the solution completely dissolved and obtained a homogenous mixture. The NH_4OH, was then added to the solution to obtain pH 9. The mixture was then dried to obtain the ZnO precursor. The ZnO precursor was then annealed at 300 °C for 24 hours. The g-C_3N_4 was prepared using thermal decomposition by directly heating the melamine using a crucible and covering it with a lid at 550 °C for 3 hours. The preparation of a composite catalyst of g-C_3N_4/ZnO was done by using wet impregnation, which involved mixing g-C_3N_4 and ZnO in a 1:1 mass ratio. The solid mixture was then dissolved in deionized water and stirred for 1 hour to obtain a homogenous solution. The mixture solution was then filtered, washed with deionized water, and dried in an oven at 200 °C for 5 hours. The dry powder was then ground into a very fine powder to obtain the final products, which were ready for other characterizations.

Characterization of the g-C_3N_4/ZnO photocatalysts

The phase studies of the catalyst were performed by the XRD PANalytical X'Pert Pro MPD Diffractometer using the Bragg Brentano optical configuration under ambient conditions. The morphology and crystallite size of the photocatalysts were examined using field emission scanning electron microscopy (FESEM, JEOL JSM-7600F) equipped with energy dispersive X-ray spectroscopy (EDX) to give quantitative elemental mapping. The light absorption properties were studied using the Perkin Elmer Lambda 950 UV-Vis NIR in

reflectance mode. The surface area, pore volume, and pore diameter were determined using the N_2 adsorption-desorption isotherm by the BELJAPAN BELSORP-mini porosity analyzer.

Degradation of OFL by g-C_3N_4/ZnO

The photocatalytic activity of ZnO, g-C_3N_4, and g-C_3N_4/ZnO photocatalyst was evaluated by the determination of OFL degradation at each interval using UV-Vis NIR spectrophotometer. The photocatalytic reactor is equipped with a 150-watt LED visible lamp as the light source to carry out the photocatalytic activity (under standard temperature and pressure). The amount of 0.25 g of photocatalyst was added to 150 mL of 10 ppm OFL solution. Then, the solution was stirred for about 30 minutes in a dark condition for equilibrium adsorption, and then the light source was applied until the reaction was completed. The solution was extracted at intervals of 15 minutes. The photocatalytic analysis was performed using UV-Vis NIR spectrophotometer in absorbance mode. The photocatalytic performance of the photocatalyst was evaluated through the degradation of OFL using the following equation [1]:

$$Degradation\ (\%) = \frac{Co - Ct}{Co} \times 100\% \qquad (1)$$

where C_0 is the initial concentration of pollutant and C_t is the concentration of OFL at time (min).

Results and Discussion

Figure 1 represents the XRD patterns of pure ZnO, g-C_3N_4, and composite g-C_3N_4/ZnO. The phase structure was analyzed by the XRD Xpert Highscore Plus software. The 2θ values that correspond to the diffraction peak of the ZnO sample are 31.7°, 34.4°, 36.2°, 47.3°, 56.5°, 62.7°, 66.4°, 67.9°, and 69.0°, corresponding to (100), (002), (101), (102), (110), (103), (200), (112), (201), (004), (202), and (104) planes, which prove that the sample is pure and belongs to the hexagonal wurtzite crystalline phase of ZnO (ICDD No. 01-079-2205). The XRD pattern of g-C_3N_4 shows two peaks at 13.1° and 27.4°, which correspond to the ICDD pattern of g-C_3N_4 (ICDD No. 01-087-1526). The 13.1° peak that corresponds to the (100) plane indicates the periodic arrangement of the structural units in the layer that is graphite-like phase carbon nitride. The intensive peak at 27.4° belongs to the (002) plane and corresponds to the interlayer stacking of the conjugated carbocyclic plane [33]. The position of these two diffraction peaks is consistent with the previous report on g-C_3N_4 [35]. The XRD pattern of composite materials shows the appearance of ZnO and g-C_3N_4 peaks, which indicate the success of the composite materials.

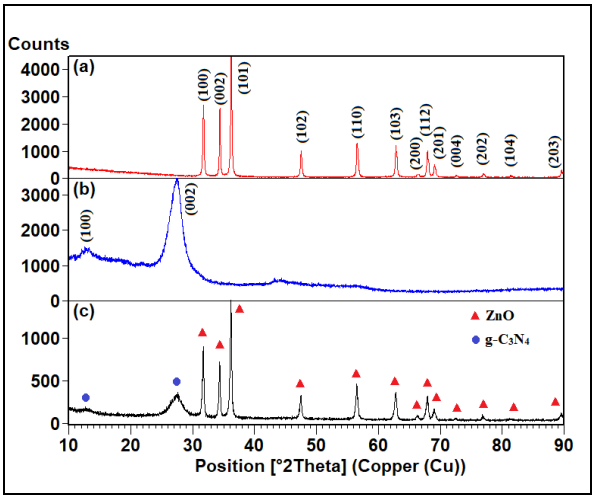


Figure 1. XRD patterns of (a) ZnO (b) g-C_3N_4 (c) g-C_3N_4/ZnO

Figure 2 represents the FESEM micrograph of pristine g-C_3N_4, pristine ZnO, and composite g-C_3N_4/ZnO at 50 k magnification. The composition of g-C_3N_4/ZnO was investigated by elemental mapping, as shown in Figure

3. (a)–(e) that confirms the uniform distribution of elements. The elements present in the material were determined using EDX analysis, as demonstrated in Figure 3 (f). The existence of Zn, O, C, and N elements can be clearly visualized in the EDX spectrum of the g-C_3N_4/ZnO, and no other elements were detected, which confirms its purity. Figure 4 (a) indicates the TEM image of g-C_3N_4/ZnO, which shows a nanospherical shape with an average crystallite size of 35 nm. The high-resolution and SAED images of g-C_3N_4/ZnO are shown in Figure 4 (b), which indicates the interplanar spacing of about 0.281 nm at the (100) plane of ZnO that is estimated from the intensity profile image.

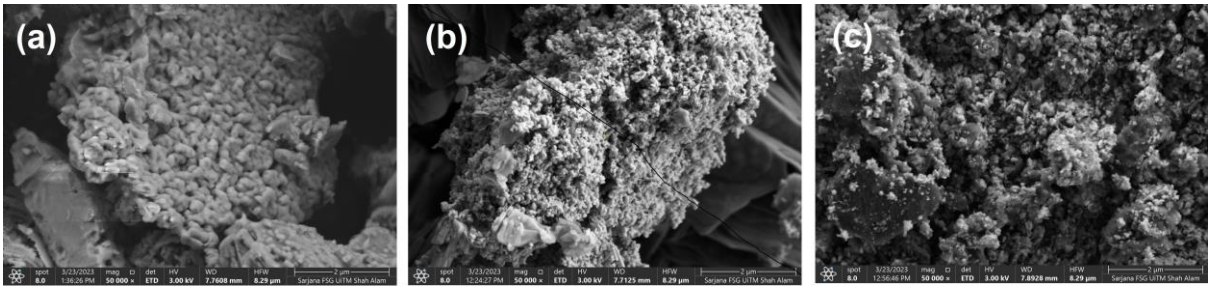


Figure 2. FESEM image of (a) g-C_3N_4 (b) ZnO (c) g-C_3N_4/ZnO at 50k magnification

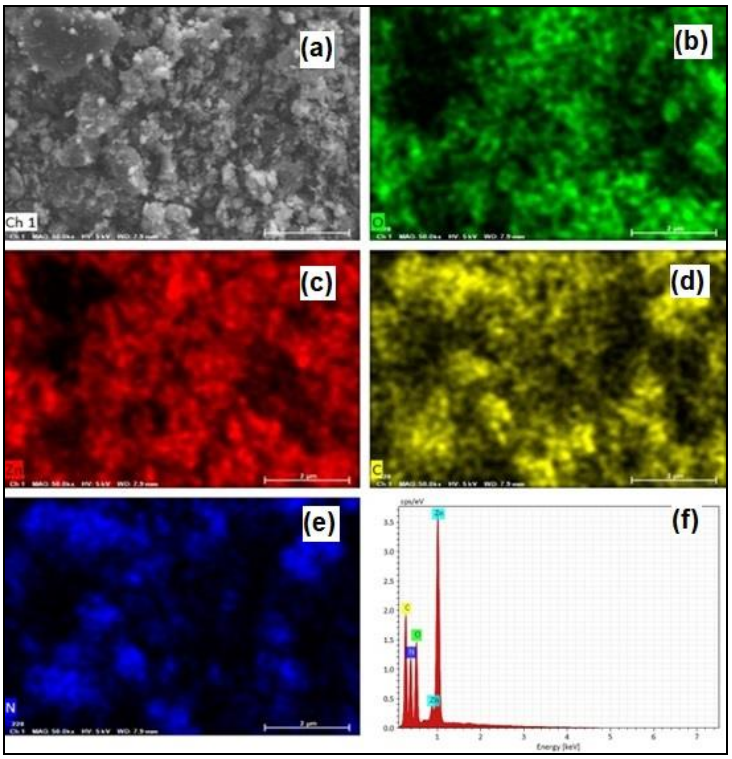


Figure 3. (a) FESEM image and elemental mapping (b) oxygen (c) zinc (d) carbon (e) nitrogen and (f) EDX spectrum of g-C_3N_4/ZnO

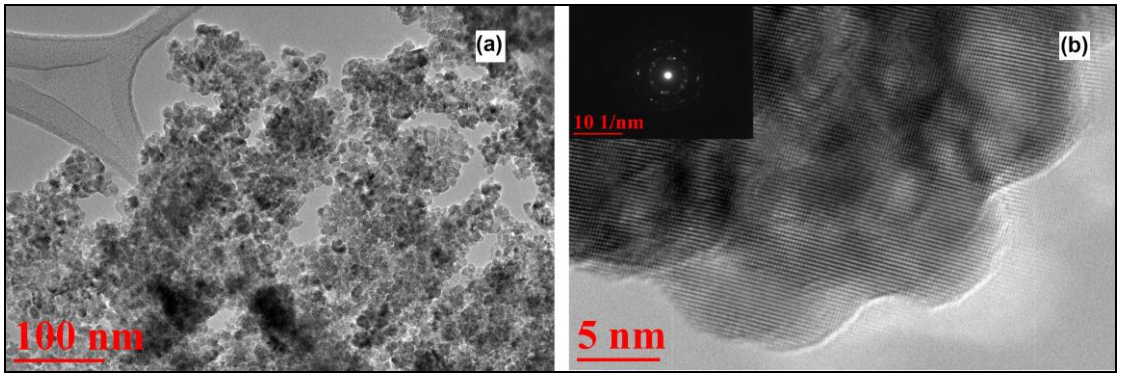


Figure 4. (a) TEM image of g-C_3N_4/ZnO at 100k magnification (b) High resolution image of g-C_3N_4/ZnO and SAED image at (100) plane

Figure 5 represents the UV-Vis reflectance spectra of ZnO, g-C_3N_4, and g-C_3N_4/ZnO. As can be observed, the composite materials exhibit the red shift towards the visible light region. Tauc plot for ZnO, g-C_3N_4, and g-C_3N_4/ZnO calculated based on the equations (2) to (4) [36]. From the reflectance spectra, a tauc plot was drawn, and the values of the band gaps can be obtained.

$$(\alpha h\upsilon) = A(h\upsilon - E_g)^n \qquad (2)$$

where α is the absorption coefficient of the material corresponding to a value of wavelength λ, h is Planck's constant, A is the proportionality constant, n is the frequency of light, E_g is the band energy, and n = ½ (for direct transition mode materials). The absorption coefficient is evaluated using equation (3):

$$\alpha = k \ln\left(\frac{R_{max} - R_{min}}{R - R_{min}}\right) \qquad (3)$$

where k is a constant, R_{max} is the maximum reflectance and R_{min} is the minimum reflectance. Consideration of equations. (2) and (3) gives equation (4),

$$(\alpha h\upsilon)^2 = A'(h\upsilon - E_g) \qquad (4)$$

where A′ is a constant. From Equation (4), a tauc plot can be drawn of $(\alpha h\nu)^2$ versus hν as shown in Figure 6. The point of the extrapolation of the linear part that meets the abscissa gives the value of the band gap energy of the material. It was found that the calculated band gap of ZnO is 3.31 eV. The band gap of g-C_3N_4 prepared is 2.81 eV whereas the band gap of g-C_3N_4/ZnO was observed to be 2.92 eV which is lower than the pristine ZnO. The reduced band gap of composite materials is attributed to the presence of g-C_3N_4 in the crystal lattice. This will cause the shifting of the valence and conduction bands, subsequently narrowing the band gap.

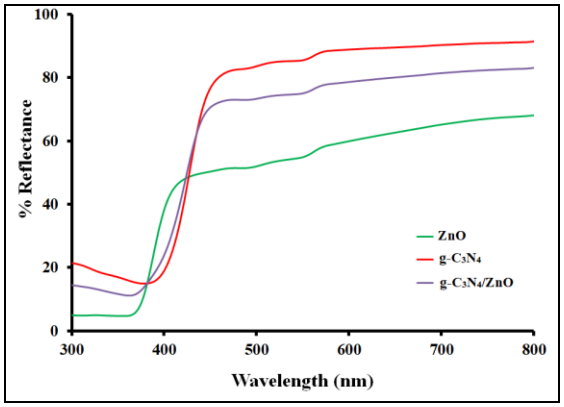


Figure 5. Reflectance spectra of ZnO, g-C_3N_4 and g-C_3N_4/ZnO

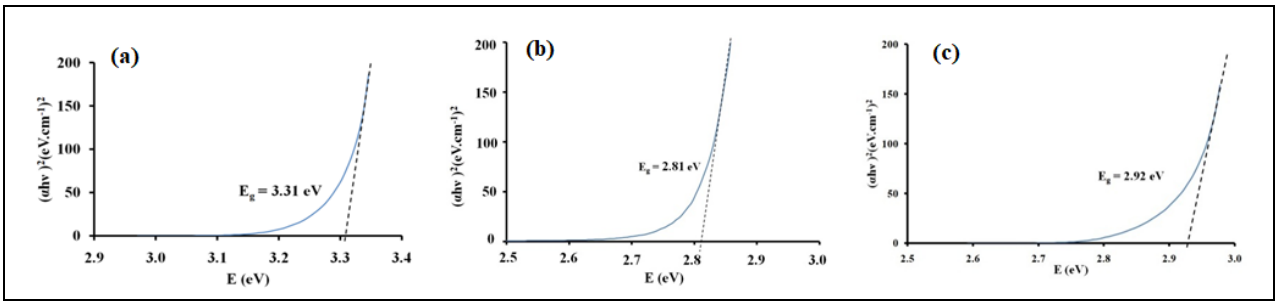


Figure 6. Tauc plot of ZnO, g-C_3N_4 and g-C_3N_4/ZnO

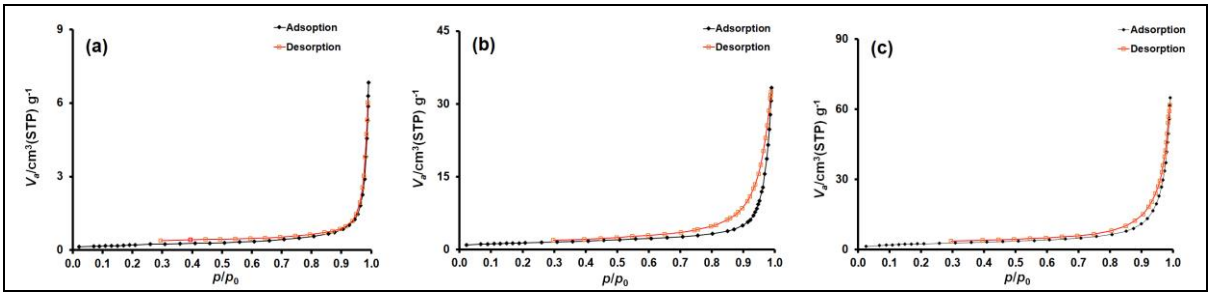


Figure 7. N_2 adsorption-desorption isotherm of (a) ZnO (b) g-C_3N_4 (c) g-C_3N_4/ZnO

Table 1 shows the values of total pore volume, pore diameter, and specific surface area of the sample from the N_2 sorption analysis as well as the percent degradation of OFL. The g-C_3N_4/ZnO had a surface area and pore volume of 8.30 m^2g^{-1} and 0.010 cm^3g^{-1}, respectively, with an average pore diameter of 46.14 nm, which is in the mesoporous range. The surface area of g-C_3N_4/ZnO is higher in comparison with that of pure g-C_3N_4. Specific surface area increases along with lower pore volume, suggesting that ZnO is loaded onto g-C_3N_4, which also enhances the photocatalytic activity [37]. The isotherm plot of g-C_3N_4/ZnO in Figure 7 shows a discerned pattern belongs to type IV and H3 hysteresis loop which represent the existence of mesoporous [38].

The percent degradation of 10 mg/L of OFL was shown in Figure 8 under irradiation of light for 180 min. The optical properties of ZnO may exhibit an absorbance potential that is suitable for the UV spectrum only, which explains the only 5.3% degradation efficiency of ZnO. The photocatalytic performance of g-C_3N_4 shows 47.9% in 180 min higher than ZnO due to the active light response in the visible light. The degradation of g-C_3N_4/ZnO is 63.4% in 180 min, which is 11 times higher than that of pristine ZnO and double than that of pristine g-C_3N_4. The reduced band gap energy of g-C_3N_4/ZnO may result in better absorption of light in the visible region, favoring more electron-hole pair formation and thus improving photocatalytic performance of g-C_3N_4/ZnO. [39]. The photocatalytic performance is influenced by the crystallinity of the photocatalyst and the surface area for both light absorption and molecule adsorption. It is shown that high surface area and pore volume of g-C_3N_4/ZnO can improve photocatalytic degradation due to a larger number of active sites that absorb and mineralize the contaminant through the inter-associated porous structure [40].

Table 1. Surface characteristics analysis and photocatalytic performance of photocatalysts

Sample	Total Pore Volume (cm^3g^{-1})	Mean Pore Diameter (nm)	Surface Area (m^2g^{-1})	Types of Pores	% Degradation
ZnO	0.009	54.10	7.22	Macroporous	5.5
g-C_3N_4	0.005	45.27	4.54	Mesoporous	47.9
g-C_3N_4/ZnO	0.010	46.14	8.30	Mesoporous	63.4

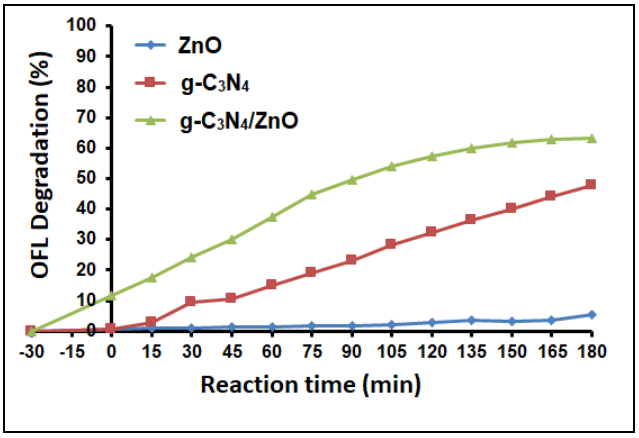


Figure 8. The percentage degradation of OFL under exposure of light at optimized condition in 180 min (Operating parameters: 0.25 g of catalyst loading, 10 mg/L concentration OFL)

Conclusion

In this work, the g-C_3N_4/ZnO photocatalyst was successfully prepared via sol-gel, thermal decomposition, and followed by impregnation methods. The prepared g-C_3N_4/ZnO photocatalyst was successfully characterized with a nanospherical shape, and a higher surface area compared to the pristine. From the band gap analysis, it was found that the band gap of g-C_3N_4/ZnO was reduced from 3.31 eV to 2.92 eV. The reduction of the band gap energy improved the performance of the photocatalytic activity in visible light. The photocatalytic activity of OFL is higher than that of pristine g-C_3N_4 and ZnO, which takes 180 min to degrade 63.4% of the OFL.

Acknowledgement

The authors would like to acknowledge the Institute of Science, Faculty of Applied Sciences, UiTM and the grant Young Talent Researcher (600-RMC/YTR/5/3 (014/2020)) for supporting this research.

References

1. Gupta, G., Kansal, S. K., Umar, A. and Akbar, S. (2023). Visible-light driven excellent photocatalytic degradation of ofloxacin antibiotic using $BiFeO_3$ nanoparticles. *Chemosphere*, 314: 137611.
2. Meng, X., Wang, Z., Li, K., Liu, Y., Zhao, D. and Fu, Y. (2023). Degradation of ofloxacin by lanthanum cerate perovskite activated bisulfite. *Environmental Technology & Innovation*, 32: 103370.
3. Zhou, G., Meng, L., Ning, X., Yin, W., Hou, J., Xu, Q., ... and Wang, X. (2022). Switching charge transfer of g-C_3N_4/$BiVO_4$ heterojunction from type II to Z-scheme via interfacial vacancy engineering for improved photocatalysis. *International Journal of Hydrogen Energy*, 47(14): 8749-8760.
4. Cipagauta-Díaz, S., Estrella-González, A., Navarrete-Magaña, M. and Gómez, R. (2022). N doped-TiO_2 coupled to $BiVO_4$ with high performance in photodegradation of Ofloxacin antibiotic and Rhodamine B dye under visible light. *Catalysis Today*, 394: 445-457.
5. Ding, C., Guo, J., Chen, P., Gan, W., Yin, Z., Qi, S., ... and Sun, Z. (2022). All-solid-state Z-scheme In_2S_3/CQDs/TiO_2 heterojunction for highly efficient degradation of ofloxacin. *Applied Surface Science*, 596: 153629.

6. Su, Q., Li, J., Yuan, H., Wang, B., Wang, Y., Li, Y. and Xing, Y. (2022). Visible-light-driven photocatalytic degradation of ofloxacin by g-C3N4/NH2-MIL-88B (Fe) heterostructure: Mechanisms, DFT calculation, degradation pathway and toxicity evolution. *Chemical Engineering Journal*, 427: 131594.
7. Zhang, M., Xu, J. and Chen, M. (2022). Novel Z-scheme $LaVO_4/Bi_3O_4Cl$ heterojunctions for highly efficient degradation of ofloxacin under visible light irradiation. *Journal of Alloys and Compounds*, 925: 166653.
8. Sharan, S., Khare, P. and Shankar, R. (2023). Electrochemical degradation of ofloxacin using PbO_2/Pb-based lead acid battery electrode: Parametric optimization and kinetics study. *Materials Today: Proceedings*, 78: 128-137.
9. Cai, H., Wang, J., Du, Z., Zhao, Z., Gu, Y., Guo, Z., ... and Fang, Y. (2023). Construction of novel ternary $MoSe_2$/ZnO/p-BN photocatalyst for efficient ofloxacin degradation under visible light. *Colloids and Surfaces A: Physicochemical and Engineering Aspects*, 663: 131050.
10. Radjenović, J., Petrović, M. and Barceló, D. (2009). Fate and distribution of pharmaceuticals in wastewater and sewage sludge of the conventional activated sludge (CAS) and advanced membrane bioreactor (MBR) treatment. *Water Research*, 43(3): 831-841.
11. Zhang, S., Wang, Y., Cao, Z., Xu, J., Hu, J., Huang, Y., ... and Wang, H. (2020). Simultaneous enhancements of light-harvesting and charge transfer in UiO-67/CdS/rGO composites toward ofloxacin photo-degradation. *Chemical Engineering Journal*, 381: 122771.
12. Ding, P., Li, J., Guo, M., Ji, H., Li, P., Liu, W., ... and Chen, S. (2023). Visible light-driven degradation of ofloxacin by graphene oxide-supported titania/zirconia ternary nanocomposites. *Inorganic Chemistry Communications*, 155: 111001.
13. Wen, Y., Wang, Z., Cai, Y., Song, M., Qi, K. and Xie, X. (2022). S-scheme BiVO4/CQDs/β-FeOOH photocatalyst for efficient degradation of ofloxacin: Reactive oxygen species transformation mechanism insight. *Chemosphere*, 295: 133784.
14. He, S., Chen, Q., Chen, G., Shi, G., Ruan, C., Feng, M., ... and Cao, C. (2022). N-doped activated carbon for high-efficiency ofloxacin adsorption. *Microporous and Mesoporous Materials*, 335: 111848.
15. Wang, X., Li, Y., Li, R., Yang, H., Zhou, B., Wang, X. and Xie, Y. (2019). Comparison of chlorination behaviors between norfloxacin and ofloxacin: reaction kinetics, oxidation products and reaction pathways. *Chemosphere*, 215: 124-132.
16. Sun, Q., Sun, Y., Zhou, M., Cheng, H., Chen, H., Dorus, B., ... and Le, T. (2022). A 2D/3D g-C_3N_4/ZnO heterojunction enhanced visible-light driven photocatalytic activity for sulfonamides degradation. *Ceramics International*, 48(5): 7283-7290.
17. Sharma, G., Kumar, A., Kumar, P. S., Alodhayb, A., ALOthman, Z. A., Dhiman, P. and Stadler, F. J. (2022). Carbon quantum dots embedded trimetallic oxide: Characterization and photocatalytic degradation of Ofloxacin. *Journal of Water Process Engineering*, 48: 102853.
18. Singh, R. and Dutta, S. (2019). The role of pH and nitrate concentration in the wet chemical growth of nano-rods shaped ZnO photocatalyst. *Nano-Structures & Nano-Objects*, 18: 100250.
19. Pirhashemi, M., Habibi-Yangjeh, A. and Pouran, S. R. (2018). Review on the criteria anticipated for the fabrication of highly efficient ZnO-based visible-light-driven photocatalysts. *Journal of Industrial and Engineering Chemistry*, 62: 1-25.
20. Sinar Mashuri, S. I., Kasim, M. F., Mohd Kaus, N. H., Yie, H. T., Islam, A., Rashid, U., ... and Ibrahim, M. L. (2023). Photo-response range extension of z-scheme ZnO/Cds for led-light-driven photo-active catalyst. *Renewable Sustainability Energy Review*, 184: 113602.
21. Lu, S., Ma, Y. and Zhao, L. (2022). Production of ZnO-CoOx-CeO_2 nanocomposites and their dye removal performance from wastewater by adsorption-photocatalysis. *Journal of Molecular Liquids*, 364: 119924.
22. Jin, C. Z., Yang, X. A., Zhai, X. M., Wang, S. B. and Zhang, W. B. (2023). ZnO/Sn_3O_4 amorphous-crystalline heterojunctions for Cr (VI) visible photocatalysis: Simple synthesis with excellent

performance. *Applied Surface Science*, 608: 155263.

23. Vo, N. T. T., You, S. J., Pham, M. T. and Van Pham, V. (2023). A green synthesis approach of p-n CuO/ZnO junctions for multifunctional photocatalysis towards the degradation of contaminants. *Environmental Technology & Innovation*, 32: 103285.
24. Akhter, P., Nawaz, S., Shafiq, I., Nazir, A., Shafique, S., Jamil, F., ... and Hussain, M. (2023). Efficient visible light assisted photocatalysis using ZnO/TiO_2 nanocomposites. *Molecular Catalysis*, 535: 112896.
25. Mohamed, M. A., Zain, M. F. M., Minggu, L. J., Kassim, M. B., Jaafar, J., Amin, N. A. S., and Ng, Y. H. (2019). Bio-inspired hierarchical hetero-architectures of in-situ C-doped g-C_3N4 grafted on C, N co-doped ZnO micro-flowers with booming solar photocatalytic activity. *Journal of Industrial and Engineering Chemistry*, 77: 393-407.
26. Wen, J., Xie, J., Chen, X. and Li, X. (2017). A review on g-C_3N_4-based photocatalysts. *Applied Surface Science*, 391: 72-123.
27. Mishra, A., Mehta, A., Basu, S., Shetti, N. P., Reddy, K. R. and Aminabhavi, T. M. (2019). Graphitic carbon nitride (g–C_3N_4)–based metal-free photocatalysts for water splitting: a review. *Carbon*, 149: 693-721.
28. Prasad, C., Tang, H. and Bahadur, I. (2019). Graphitic carbon nitride based ternary nanocomposites: From synthesis to their applications in photocatalysis: A recent review. *Journal of Molecular Liquids*, 281: 634-654.
29. Zhu, J., Xiao, P., Li, H. and Carabineiro, S. A. (2014). Graphitic carbon nitride: synthesis, properties, and applications in catalysis. *ACS Applied Materials & Interfaces*, 6(19): 16449-16465.
30. Naseri, A., Samadi, M., Pourjavadi, A., Ramakrishna, S. and Moshfegh, A. Z. (2021). Enhanced photocatalytic activity of ZnO/g-C_3N_4 nanofibers constituting carbonaceous species under simulated sunlight for organic dye removal. *Ceramics International*, 47(18): 26185-26196.
31. Mohanty, L., Pattanayak, D. S. and Dash, S. K. (2021). An efficient ternary photocatalyst Ag/ZnO/g-C_3N_4 for degradation of RhB and MG under solar radiation. *Journal of the Indian Chemical Society*, 98(11): 100180.
32. Das, D. and Nandi, P. (2022). ZnO/g-C_3N_4 heterostructures: Synthesis, characterization and application as photoanode in dye sensitized solar cells. *Solar Energy Materials and Solar Cells*, 248: 112002.
33. Zhong, Q., Lan, H., Zhang, M., Zhu, H. and Bu, M. (2020). Preparation of heterostructure g-C_3N_4/ZnO nanorods for high photocatalytic activity on different pollutants (MB, RhB, Cr (VI) and eosin). *Ceramics International*, 46(8): 12192-12199.
34. Fallahpour, M., Poursalehi, R. and Yourdkhani, A. (2023). Highly efficient photocatalytic removal of concentrated PEX, PAX and SIPX xanthates collectors by an immobilized nanostructured g-C_3N_4/ZnO low power backlighted module. *Minerals Engineering*, 204: 108416.
35. Tran, D. A., Pham, C. T. N., Ngoc, T. N., Phi, H. N., Ta, Q. T. H., Truong, D. H., and Vo, V. (2021). One-step synthesis of oxygen doped g-C_3N_4 for enhanced visible-light photodegradation of Rhodamine B. *Journal of Physics and Chemistry of Solids*, 151: 109900.
36. Kamarulzaman, N., Kasim, M. F. and Chayed, N. F. (2016). Elucidation of the highest valence band and lowest conduction band shifts using XPS for ZnO and Zn0.99Cu0.01O band gap changes. *Results in Physics*, 6: 217-230.
37. Mao, N., Jiao, Y. and Duan, X. (2022). g-C_3N_4/ZnO heterojunction as Fenton-like catalyst for degradation of organic pollution. *Materials Research Bulletin*, 151: 111818.
38. Garg, R., Gupta, R. and Bansal, A. (2021). Synthesis of g-C_3N_4/ZnO nanocomposite for photocatalytic degradation of a refractory organic endocrine disrupter. *Materials Today: Proceedings*, 44: 855-859.
39. Paul, D. R., Gautam, S., Panchal, P., Nehra, S. P., Choudhary, P. and Sharma, A. (2020). ZnO-modified g-C_3N_4: A potential photocatalyst for environmental application. *ACS Omega*, 5(8): 3828-3838.
40. Portillo-Cortez, K., Romero-Ibarra, J. E., Dominguez, D., Alonso-Nuñez, G. and Caudillo-

Flores, U. (2023). Photodegradation of ceftriaxone using g-C_3N_4-ZnO nanocomposite as an efficient photocatalyst. *Journal of Photochemistry and Photobiology A: Chemistry*, 445: 115090.

Malaysian Journal of Analytical Sciences (MJAS)
Published by Malaysian Analytical Sciences Society

SYNTHESIS, CHARACTERIZATION, DENSITY FUNCTIONAL THEORY AND CYTOTOXICITY OF ISATIN THIOCARBOHYDRAZIDE AND ITS COPPER(II) AND ZINC(II) COMPLEXES

(Sintesis, Pencirian, Teori Fungsi Ketumpatan, dan Sitotoksikiti Isatin Tiokarboidrazida serta Kompleks Kuprum(II) dan Zink(II))

Ummi Liyana Mohamad Rodzi[1], Karimah Kassim[1,2*], Nageswara Rao Meroshine[3], and Nur Azzalia Kamaruzaman[3]

[1]*Faculty of Applied Sciences,*
Universiti Teknologi MARA (UiTM) 40450 Shah Alam, Selangor, Malaysia
[2]*Institute of Science,*
Universiti Teknologi MARA (UiTM) 40450 Shah Alam, Selangor, Malaysia
[3]*National Poison Centre,*
Universiti Sains Malaysia (USM), 11800 Pulau Pinang, Malaysia

[*]*Corresponding author: karimah@uitm.edu.my*

Received: 22 July 2023; Accepted: 3 October 2023; Published: 29 December 2023

Abstract

Isatin and thiocarbohydrazide exhibit a broad spectrum of biological functions including antibacterial, antiviral, antioxidant and antimalarial activities. In this study, copper(II) and zinc(II) complexes derived from isatin thiocarbohydrazide were synthesized and assessed for their potential as antileukemia agents. ^{1}H and ^{13}C NMR, infrared spectroscopy, UV-Vis spectroscopy, thermal and elemental analysis were used to elucidate the structures of the synthesized compounds. The complexation was observed from the shifting frequencies of the *v*(C=N) and the appearance of new peaks assigned as *v*(M-N) and *v*(M-O) at 499 and 583-594 cm^{-1}. The formation of the complexes is also supported by the d-d transition in UV-visible spectra. Using proper DFT functionals and basis sets, the optimized geometries and electronic energies of the complexes were ascertained. Theoretical simulations provide important insights into the stability and electrical structure of the complexes, assisting in understanding their potential biological actions. Cytotoxicity screening was conducted against the human leukemia K562 cell line and low activity was reported, thus indicating minimal toxic profile of the complexes.

Keywords: cytotoxicity, characterization, density functional theory, isatin, thiocarbohydrazide

Abstrak

Isatin dan tiokarboidrazida mempunyai fungsi biologi yang luas seperti aktiviti antibakteria, antivirus, antioksidan dan antimalaria. Dalam kajian ini, kompleks kuprum(II) dan zink(II) telah disintesis daripada isatin tiokarboidrazida dan dinilai potensinya sebagai agen antileukemia. Kaedah spektroskopi iaitu ^{1}H dan ^{13}C NMR, inframerah, UV-Vis, analisis haba dan unsur digunakan untuk menjelaskan struktur sebatian tersintesis. Pengkompleksan diperhatikan daripada frekuensi peralihan *v*(C=N) dan puncak penampilan baharu yang boleh ditetapkan kepada *v*(M-N) dan *v*(M-O) di 499dan 583-594 cm^{-1}. Pembentukan kompleks juga disokong oleh peralihan d-d dalam spektrum UV-Cahaya Nampak. Menggunakan fungsi dan set asas DFT yang sesuai, geometri

molekul dioptimumkan dan tenaga elektronik kompleks telah dikenalpasti. Simulasi teori memberikan gambaran penting tentang kestabilan dan struktur elektrik kompleks, membantu dalam pemahaman potensi tindakan biologi mereka. Saringan sitotoksisiti telah dijalankan terhadap garisan sel leukemia manusia K562 dan sitotoksisiti yang rendah dilaporkan, dengan itu menunjukkan profil toksik kompleks.

Kata kunci: sitotoksisiti, pencirian, teori fungsi ketumpatan, isatin, tiokarboidrazida

Introduction

In contemporary medicinal chemistry, isatin is a privileged scaffold with a wide range of biological activity. Using nitric and chromic acids, Erdmann and Laurent originally isolated it as an indigo oxidation byproduct [1]. Isatin consists of two cyclic rings, which are a six-membered ring with an aromatic character and a five-membered ring possessing an anti-aromatic character [1]. A literature survey reported that isatin is known to have anticancer [2, 3], antiviral [4, 5], antioxidant [6], analgesic [7] and antimicrobial [8, 9] properties. Another important part of the production of the ligand is the higher homologue of thiosemicarbazide, known as thiocarbohydrazide. Thiocarbohydrazide has an extra nitrogen atom that can serve as a metal-coordinating center [10]. Compared to thiosemicarbazide, there are limited studies on the theoretical study and cytotoxicity effects of the thiocarbohydrazide. Therefore, the present work was done to screen for their respective cytotoxicity activity against human leukemia K562 cancer cell lines.

Copper and zinc are chosen as the metal ions to be bound with the isatin-derived thiocarbohydrazide ligand in this work. Formerly, the addition of copper was reported to have increased the antiproliferative activity of salicylaldehyde monothiocarbohydrazide against breast cancer and human prostate adenocarcinoma cell lines [11]. On top of that, zinc(II) complexes also appear to be extremely appealing because zinc is substantially less toxic in larger dosages than other metals [12]. The computational analysis using the B3LYP method with 6-31G+ (d,p) and LANL2DZ basis set has been done on all the compounds to explore their electronic properties. Subsequently, all parameters like the relationships between the highest occupied molecular orbital (HOMO) and lowest unoccupied molecular orbital (LUMO) energies were used to explain the anticancer activity.

Materials and Methods

Materials

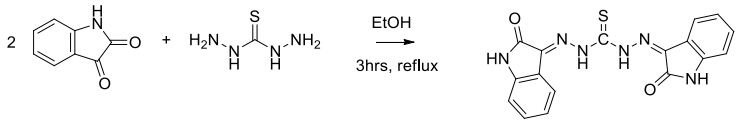
All chemicals used in this study were purchased from Sigma Aldrich Company, St Louis, USA and were used without further purification.

Instrumentation

Elemental analysis (C, H, N and S) for the ligand and complexes were determined using a Thermo Scientific Flash Smart analyzer. The magnetic susceptibility of the complexes was determined using Sherwood Auto Magnetic Susceptibility at room temperature. Molar conductivities were measured using a conductivity standard of 1413 µS/cm. Perkin Elmer 1600 Spectrometer was employed in obtaining the FTIR spectra for ligand and complexes as KBr disc in the region of 400-4000 cm^{-1}. Proton (^{1}H) and carbon (^{13}C) NMR (400 MHz) spectra were recorded using Jeol ECZS spectrometer in DMSO-d_6. The UV-Vis spectra were obtained on Perkin Lambda 365 in acetonitrile at $1x10^{-4}$ M solution using a quartz cuvette in the range of 200-800 nm. Thermal analyses were performed in nitrogen atmosphere using TA Instruments Q50 TGA analyzer with a heating rate of 10 °C/min in a temperature range between 25 and 500 °C. Powder XRD patterns were collected using PANalytical X'pert PRO in Bragg-Brentano reflecting geometry with CuKα (k= 1.5418740 Å). The X-ray tube was utilized for a copper tube operating at 45 kV and 40 mA. Data were collected in 2θ range of 5-90° with 0.0167° and 10 s exposure per step.

Synthesis of ligand

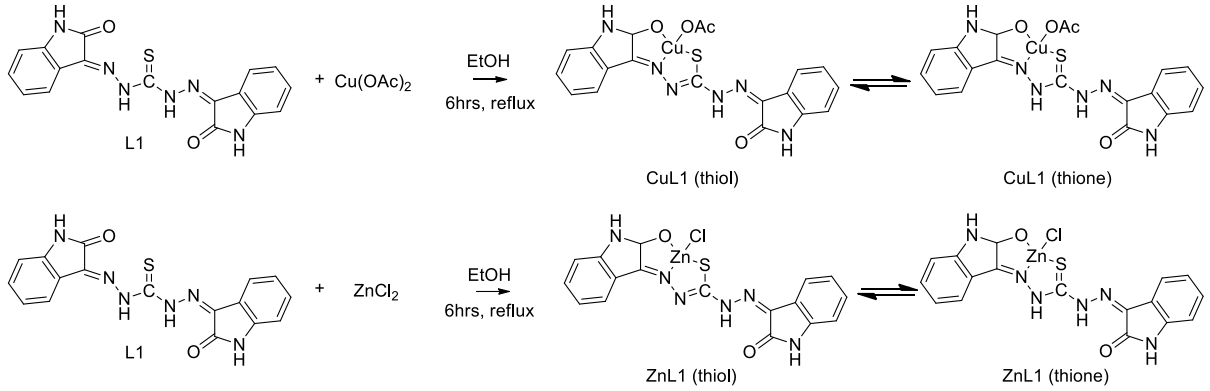
The ligand was prepared with a modification from previous studies [13, 14] by dissolving isatin and thiocarbohydrazide in hot absolute ethanol (30 mL) and the reaction mixture was refluxed for three hours. A yellow precipitate was filtered off, washed with cold ethanol and air-dried overnight. The remaining filtrate was left for recrystallization.



Scheme 1. Synthesis of L1

Synthesis of complexes

Cu(II) and Zn(II) complexes were synthesized by refluxing the ligand with metal salt (copper(II) acetate monohydrate and zinc(II) chloride) with the ratio of 1:1 in a solution of absolute ethanol for six hours. The resulting precipitates were filtered off, washed with cold ethanol and air-dried.



Scheme 2. Synthesis of CuL1 and ZnL1

Computational methods

The structures of the ligand and the complexes were built using Gaussian view 16.0. DFT calculations were then carried out using Gaussian 09 program and B3LYP method [15, 16]. The geometrical optimizations were done against the ligand using the 6-31G+ (d,p) [17] basis set and the complexes using LANL2DZ [18].

Cytotoxicity

A 3-(4,5-dimethylthiazol-2-yl)-2,5-diphenyltetrazolium bromide (MTT) cell proliferation assay described by Mossmann [19] was used to assess the cytotoxicity activity of all the synthesized compounds against human leukemia K562 cell line with slight modification. In a 96-well culture plate, the cells ($5x10^4$ cells/mL) were seeded and incubated for 24 hours. Subsequently, the cells were treated with the compounds at 100, 50, 25, 12.5, 6.25 and 3.125 µM for 48 hours. Each well received 20 µL of MTT solution, which was then incubated for an additional four hours to observe for cell viability. DMSO was used to dilute the purple formazan in the well and the absorbance was measured at 570 and 690 nm. The cytotoxicity activity of the compounds was expressed as IC_{50}. Doxorubicin was used as a positive control against the cancer cell line.

Results and Discussion

The compounds were colored, stable in air and insoluble in most organic solvents except for DMSO and DMA. The elemental analyses for the complexes displayed that they formed in a ratio of 1:1. The analytical findings and the theoretical formula are in good agreement. CuL1 possessed a magnetic moment of 1.71 B.M. which is relatively lower than the regular spin-only value of 1.73 B.M. and showed a square planar geometry, while ZnL1 is diamagnetic affording a tetrahedral geometry [20]. The physical and elemental analysis data are summarized in Table 1.

Table 1. Analytical data of the ligand and its metal complexes

Compounds	Molecular Formula	Color	Yield %	$\mu_{eff.}$ (B.M.)	Λm $\Omega^{-1}mol^{-1}cm^2$	% Found (Calc.)			
						C	H	N	S
L1	$C_{17}H_{12}N_6O_2S$	Yellow	91.46	-	-	56.38 (56.04)	3.58 (3.32)	22.46 (23.06)	8.03 (8.80)
CuL1	$C_{19}H_{20}CuN_6O_6S$	Black	85.78	1.71	0.010	43.73 (43.55)	3.80 (3.85)	16.28 (16.04)	6.10 (6.12)
ZnL1	$C_{17}H_{15}ClN_6O_3SZn$	Red	64.77	Diamagnetic	0.006	42.25 (42.17)	2.92 (3.12)	17.39 (17.36)	6.64 (5.90)

Infrared spectroscopy

The emergence of *v*(C=N) at 1697 cm^{-1} confirmed the formation of Schiff base ligand L1 according to Figure 1, while bands at 499 cm^{-1} and 583-594 cm^{-1} correspond to *v*(M-N) and *v*(M-O) respectively, showing the formation of the proposed complexes, CuL1 and ZnL1 [21, 22]. The strong *v*(C=O) band appeared at 1750 cm^{-1} in the free ligand and shifted in CuL1 and ZnL1. The shifting of the *v*(C=O) band indicates that the carbonyl oxygen participated in coordination with the metal ions [23]. The broad band recorded at 3254 cm^{-1} in the ligand spectrum was attributed to the stretching vibration for *v*(N-H). This band was later shifted to lower frequencies in CuL1 at 3160 cm^{-1} and ZnL1 at 3164 cm^{-1}. The O-H stretching of the water molecules, which are connected by a dense web of hydrogen bonds, results in a strong and broad absorption that is centered at 3474 cm^{-1} in ligand, 3460 cm^{-1} in CuL1 and 3429 cm^{-1} in ZnL1 [24]. The tetrahedral and square planar geometry of ZnL1 and CuL1 was stabilized through coordination with water molecules.

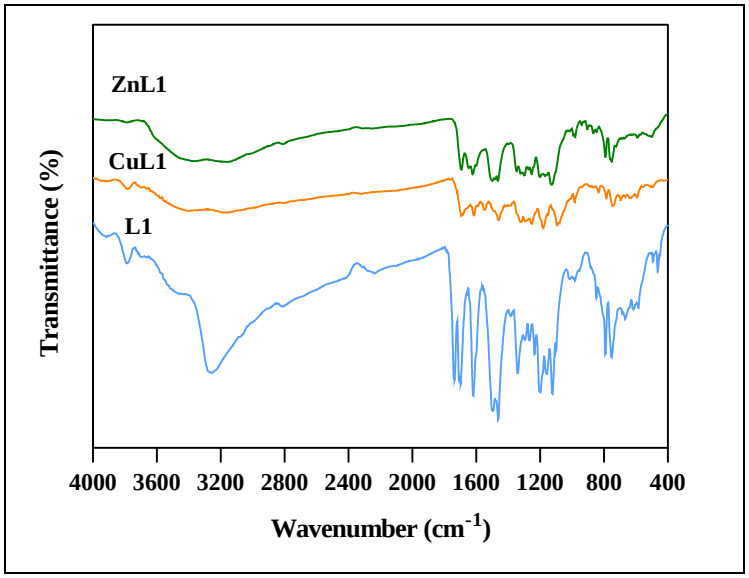


Figure 1. Infrared spectra of the ligand and metal complexes

^{1}H-NMR spectroscopy

The ^{1}H NMR spectra of both ligand and zinc(II) complex were examined to determine each distinct type of hydrogen nuclei. On the contrary, the NMR signal of the copper(II) complex was unable to be examined due to its paramagnetic property. Singlet peaks were found between 12.94 and 11.34 ppm in both spectra, which were attributed to isatin NH and NH thiocarbohydrazide, respectively. The multiplets of the aromatic protons of the isatin ring were recorded at 7.60, 7.42, 7.14, and 6.98 ppm. ZnL1 showed similar aromatic proton peak.

^{13}C-NMR spectroscopy

Based on the ^{13}C NMR spectrum, L1 displays its aromatic carbons between 112.16-138.35 ppm. The signal for thione (C=S) was detected at 175.30 ppm while those for azomethine (C=N) and carbonyl carbon (C=O) were detected at 162.55 and 138.50 ppm, respectively. Thione signal in ZnL1 appeared at a higher range of 178.50 ppm compared to its parent ligand. The peak was seen for azomethine and carbonyl carbon in the range of 164.0 ppm and 144.0 ppm. As a result, it can be inferred that azomethine nitrogen, carbonyl oxygen, and thione sulphur participated in the coordination of complexes, which was further supported by the results from the infrared spectroscopy [25].

UV-visible spectroscopy

The ligand's UV-visible spectrum in Figure 2 showed two absorption peaks that were identified as $\pi \rightarrow \pi^*$ for benzene and $n \rightarrow \pi^*$ transitions for the azomethine group (C=N) at 243 nm and 373 nm, respectively [26]. The two peaks appeared to have bathochromic or red shifting in both copper(II) and zinc(II) complexes. A redshift stipulates that the energy of the π-π^* transition decreases due to metal chelating. The copper(II) and zinc(II) complexes spectra displayed ligand-to-metal transfer (LCMT) peaks 509 and 484 nm [27].

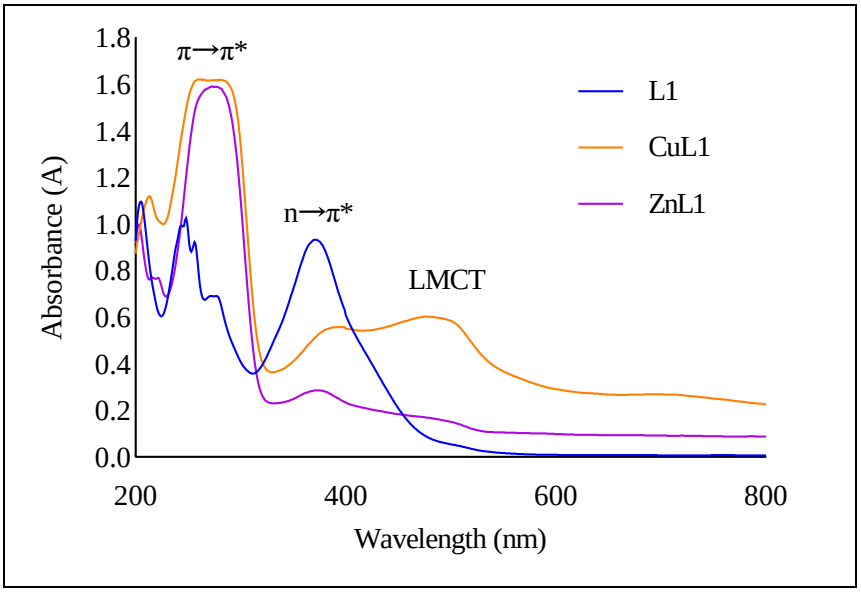


Figure 2. UV-visible spectra of the synthesized compounds

TGA studies

The thermal stability of the copper(II) and zinc(II) complexes was determined using the thermogravimetric (TGA) analysis. TGA aids in separating the coordinated water molecule present in the compound from the lattice water molecule [28]. Based on the curves in Figure 3 and data in Table 2, CuL1 breaks down into two phases, according to the thermogram. Dehydration of the initial lattice water molecule, with a weight loss of 2.30 percent, occurs in the first stage at temperatures between 50 and 125 °C. The second step showed a weight loss of 2.57 % indicating the elimination of the second lattice water molecule. Adversely, ZnL1 revealed a decomposition of water molecules through one stage with a weight loss of 3.10 %.

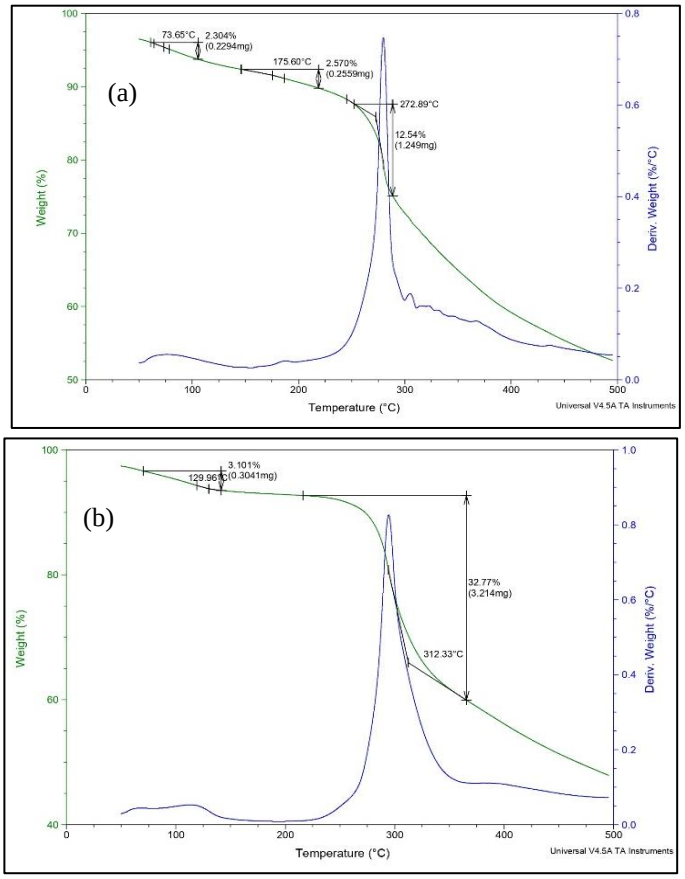


Figure 3. Thermogravimetric curves for (a) CuL1 and (b) ZnL1

Table 2. Decomposition temperature and the percentage weight loss of complexes

Compound	Decomposition Temperature (°C)	Weight Loss (%)		Lost Species
		Found	Calc.	
CuL1	50-125	2.30	3.43	One lattice water molecule
	150-200	2.57	3.43	One lattice water molecule
ZnL1	100-130	3.10	3.72	One lattice water molecule

Powder XRD studies

All compounds were then examined using powder diffraction XRD patterns due to unsuccessful attempts in generating ligand and complexes as single crystals. The 2θ = 5-90 range lattice constants were used to record the powder diffraction patterns. The compounds were found to be crystalline (L1) and semi-crystalline (CuL1 and ZnL1). The X-ray diffractometry patterns for complexes displayed in Figure 4 are entirely distinct from those of the ligands, indicating the discovery of new compounds [29].

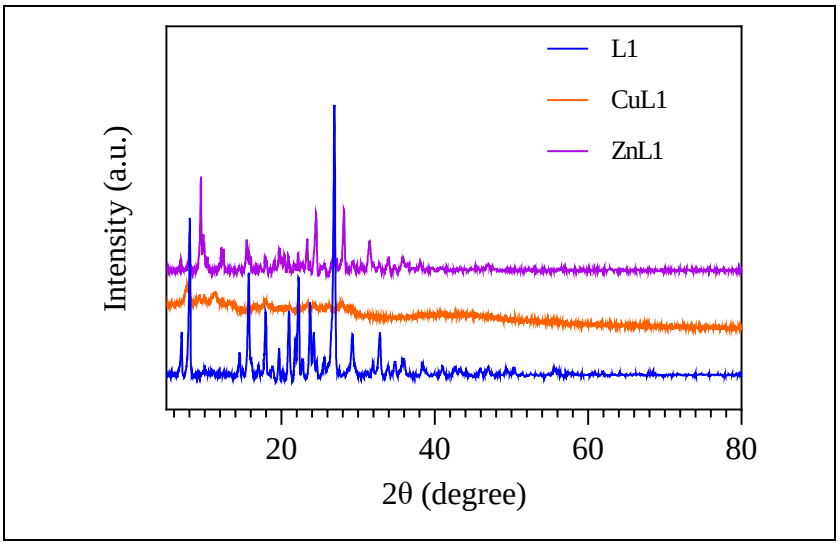


Figure 4. Powder XRD patterns for all synthesized compounds

Computational analysis: Frontier molecular orbitals

The frontier molecular orbitals are used to explore the chemical reactivity of the molecules. The highest occupied molecular orbitals (HOMO) and the lowest unoccupied molecular orbitals (LUMO) are split into molecular orbitals alpha (spin ↑) and beta (spin ↓) because of the doublet multiplicity in the complexes' molecular geometry. The B3LYP/6-31G+ (d,p) and LANDL2DZ level theory's calculations of the molecular orbital energies (E_{HOMO} and E_{LUMO}) reveal that they are all negative, indicating that the ligand and both copper(II) and zinc(II) complexes are stable. The HOMO region of the ligand and complexes are mainly localized around the electronegative sulphur and nitrogen atoms. Both atoms are bonded to the metal ions and are able to attract electrons away from their aromatic rings, thus reducing the HOMO electron density around the rings. This explains why the rings contributed significantly to the LUMO as according to Figure 5. The value of the energy gap between the HOMO and LUMO in Table 3 conveyed the stability and reactivity of each compound. The energy gap of L1 is 3.143 eV, which is considered to be similar to that of a previously reported Schiff base [30]. In comparison, the energy gap of the zinc complex for the alpha spin is the lowest among the ligand and copper complex, indicating that the zinc complex has a greater affinity for receiving electrons [31].

Table 3. The HOMO, LUMO and gap energies of the synthesized compounds

Compounds		**E_{HOMO} (eV)**	**E_{LUMO} (eV)**	**ΔEgap (eV)**
L1		-6.044	-2.901	3.143
CuL1	Alpha	-6.006	-3.085	2.921
	Beta	-6.007	-3.500	2.507
ZnL1	Alpha	-4.987	-3.187	1.800
	Beta	-6.193	-3.434	2.759

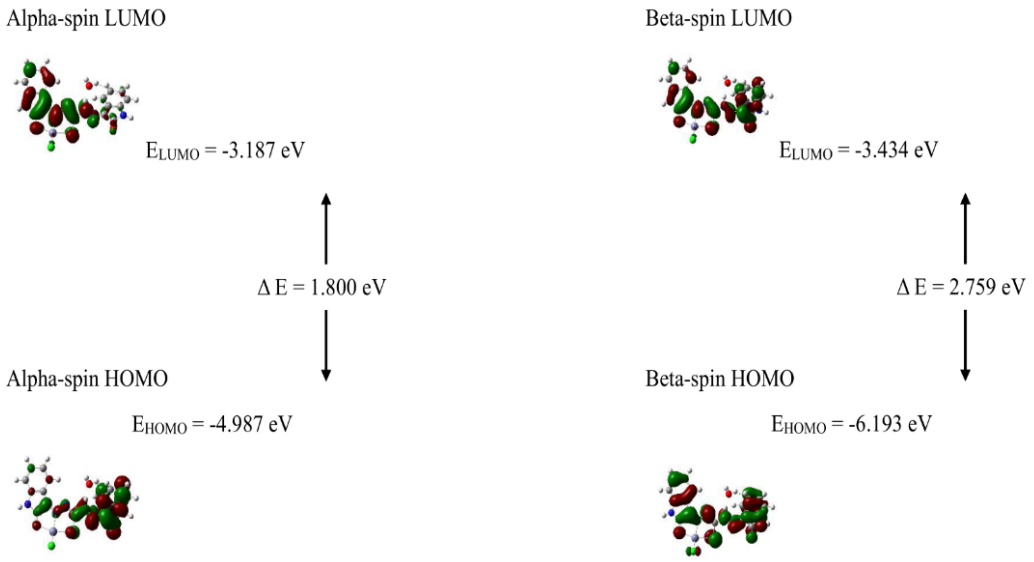


Figure 5. The energy gaps for ZnL1

Global chemical reactivity descriptors (GCRD)

Soft molecules are made of molecular systems with low gap energies and low chemical hardness (η), which in this case is ZnL1 as shown in Table 4. The small energy of ZnL1 indicates that the charge may be transferred easily, and therefore provides an impact on the compounds biological activity [32]. The negative value of chemical potential (μ) indicated that the molecule is capable of accepting electrons from the environment [33] and ZnL1 is considered to have the lowest. Thus, it is suggested that ZnL1 will have the highest chemical reactivity. The dipole moment is one of the parameters responsible for the potential biological activity. The compound with the highest polarity, ZnL1 is expected to display high bio-efficiency [34].

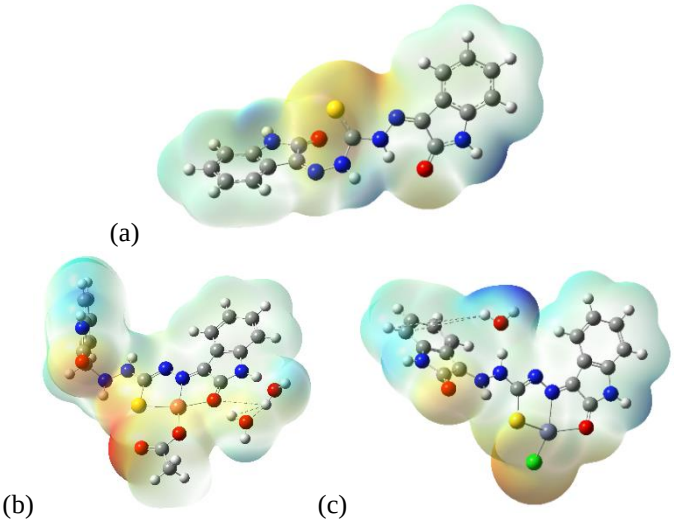
Table 4. The electronic parameters of the ligand and metal complexes

Property	Ligand and Metal Complexes				
	L1	CuL1		ZnL1	
		α	β	α	β
EA (eV)	2.901	3.085	3.500	3.187	3.434
IP (eV)	6.044	6.006	6.007	4.987	6.193
X (eV)	4.473	4.546	4.754	4.087	4.814
η (eV)	1.572	1.461	1.254	0.900	1.380
S (eV^{-1})	0.318	0.342	0.399	0.556	0.362
μ (eV)	-4.473	-4.546	-4.754	-4.087	-4.814
ω	6.363	7.073	9.011	9.280	8.397
Total Energy (Hartree)	-1532.21	-1722.05		-1300.98	
Dipole moment (Debye)	1.885	9.452		14.394	

Molecular electrostatic potential (MEP)

The binding properties of the compounds are presented using the molecular electrostatic potential (MEP) map in Figure 6. The electron density is displayed by the molecular electrostatic potential, which helps to identify the sites of electrophilic and nucleophilic reactions as well as hydrogen bonding interactions [35]. The electronegative potential which is represented by red color is concentrated around the oxygen atoms in the isatin moiety of all the compounds and the acetate ion of the copper complex. The blue color portrays the

electropositive potential, which is centered around the nitrogen atoms and water molecules.



(a) (b) (c)

Figure 6. MEP diagrams of (a) L1, (b) CuL1 and (c) ZnL1

Cytotoxicity

The cytotoxicity of all synthesized compounds was evaluated against human leukemia K562 cell line, whereby three independent studies were conducted and data for each test were reported in triplicates. The anticancer drug, Doxorubicin was used as the positive control. Based on the results shown in Table 5, the ligand and its complexes gave IC_{50} values of more than 100 µM. This indicated that the compounds are poor inhibitors of the human cancer cell line, thus proving to have a low toxicity effect. L1, CuL1 and ZnL1 show low toxicity to human cells due to the presence of the imine group in the structure that may interfere with the cytotoxicity of the compounds [36]. According to Noruzi and co-workers, the toxicity of copper derivate increased as the concentration increased to 200 µg/mL [37].

Table 5. IC_{50} values of the compounds against human leukemia K562 cancer cell line

	IC_{50} values in cancer cells (µM)
Compound	K562
L1	>100
CuL1	>100
ZnL1	>100
Doxorubicin[a]	0.26 ± 0.06

[a]= *reference drug*

Conclusion

Copper(II) and zinc(II) complexes were synthesized through a condensation process with a Schiff base ligand, N,2-bis(2-oxoindolin-3-ylidene)hydrazine carbothioamide resulting in excellent yields. The characterization using spectroscopic techniques confirmed the formation of the desired complexes and ensured their chemical structure. The molar conductivity values for the complexes gave an insight into their non-electrolytic properties. The infrared spectra highlight the shifting of *ν*(C=N) and the appearance of new bands which are *ν*(M-N) and *ν*(M-O) for complexes. Apart from that, ^{1}H and ^{13}C NMR spectra displayed peaks that located the protons and carbon present in each compound. UV-visible spectra confirmed the complexation of metal ions with ligand using the d-d transition. The zinc(II) complex has a better tendency to accept electrons since it has the lowest

energy gap for the alpha spin compared to the ligand and copper(II) complex. From the chemical reactivity descriptors, ZnL1 was predicted to have better cytotoxicity activity compared to the ligand and CuL1. However, low cytotoxicity was reported for all compounds against human leukemia K562 cancer cell line. This indicated a potential development for all compounds due to their minimal toxic profile. In addition, the contradiction between experimental and theoretical results may be due to the solubility of the compounds. Colored compounds may have interfered with the reading of the OD values.

Acknowledgement

The experiments were carried out using the facilities in Universiti Teknologi MARA and Universiti Sains Malaysia. This research was funded by Universiti Teknologi MARA under the grant number 600-RMC/GIP 5/3 (040/2022).

References

1. Kakkar, R. (2019). Isatin and its derivatives: a survey of recent syntheses, reactions, and applications. *Medicinal Chemistry Communication*, 10(3): 351-368.
2. Raju, R., Chidambaram, K., Chandrasekaran, B., Bayan, M. F., Maity, T. K., Alkahtani, A. M. and Chandramoorthy, H. C. (2023). Synthesis, pharmacological evaluation, and molecular modeling studies of novel isatin hybrids as potential anticancer agents. *Journal of Saudi Chemical Society*, 27(2): 101598.
3. Singh, N. K., Shrestha, S., Shahi, N., Choudhary, R., Kumbhar, A., Pokharel, Y. and Yadav, P. (2021). Anticancer potential of N(4) substituted 5-nitroisatin thiosemicarbazones and their copper(II) complexes. *Rasayan Journal Chemistry*, 14: 31788.
4. Elsaman, T., Mohamed, M. S., Eltayib, E. M., Abdel-Aziz, H. A., Abdalla, A. E., Munir, M. U. and Mohamed, M. A. (2022). Isatin derivatives as broad-spectrum antiviral agents: The current landscape. *Medicinal Chemistry Research*, 2022: 1-30.
5. Meleddu, R., Distinto, S., Corona, A., Tramontano, E., Bianco, G., Melis, C., ... and Maccioni, E. (2017). Isatin thiazoline hybrids as dual inhibitors of HIV-1 reverse transcriptase. *Journal of Enzyme Inhibition and Medicinal Chemistry*, 32(1): 130-136.
6. Muğlu, H., Sönmez, F., Çavuş, M. S., Kurt, B. Z. and Yakan, H. (2023). New Schiff bases based on isatin and (thio)/carbohydrazone: preparation, experimental–theoretical spectroscopic characterization, and DFT approach to antioxidant characteristics. *Research on Chemical Intermediates*, 49(4): 1463-1484.
7. Lahari, K. and Sundararajan, R. (2020). Design and synthesis of novel isatin derivatives as potent analgesic, anti-inflammatory and antimicrobial agents. *Journal of Chemical Sciences*, 132: 1-15.
8. Jarrahpour, A., Jowkar, Z., Haghighijoo, Z., Heiran, R., Rad, J. A., Sinou, V., ... and Özdemir, N. (2022). Synthesis, in-vitro biological evaluation, and molecular docking study of novel spiro-β-lactam-isatin hybrids. *Medicinal Chemistry Research*, 31(6): 1026-1034.
9. Hassan, A. S. (2022). Antimicrobial evaluation, in silico ADMET prediction, molecular docking, and molecular electrostatic potential of pyrazole-isatin and pyrazole-indole hybrid molecules. *Journal of the Iranian Chemical Society*, 19(8): 3577-3589.
10. Bonaccorso, C., Marzo, T. and La Mendola, D. (2019). Biological applications of thiocarbohydrazones and their metal complexes: A perspective review. *Pharmaceuticals*, 13(1): 4.
11. Bonaccorso, C., Grasso, G., Musso, N., Barresi, V., Condorelli, D. F., La Mendola, D. and Rizzarelli, E. (2018). Water soluble glucose derivative of thiocarbohydrazone acts as ionophore with cytotoxic effects on tumor cells. *Journal of Inorganic Biochemistry*, 182: 92-102.
12. Pellei, M., Del Bello, F., Porchia, M. and Santini, C. (2021). Zinc coordination complexes as anticancer agents. *Coordination Chemistry Reviews*, 445: 214088.
13. Gangarapu, K., Manda, S., Jallapally, A., Thota, S., Karki, S. S., Balzarini, J., ... and Tokuda, H. (2014). Synthesis of thiocarbohydrazide and carbohydrazide derivatives as possible biologically active agents. *Medicinal Chemistry Research*, 23: 1046-1056.

14. Sathisha, M. P., Revankar, V. K. and Pai, K. S. R. (2008). Synthesis, structure, electrochemistry, and spectral characterization of bis-isatin thiocarbohydrazone metal complexes and their antitumor activity against Ehrlich ascites carcinoma in Swiss albino mice. *Metal-Based Drugs*, 2008: 362105.
15. Lee, C., Yang, W. and Parr, R. G. (1988). Development of the Colle-Salvetti correlation-energy formula into a functional of the electron density. *Physical Review B*, 37(2): 785.
16. Becke, A. D. (1993). A new mixing of Hartree–Fock and local density-functional theories. *The Journal of Chemical Physics*, 98(2): 1372-1377.
17. Casas, J. S., Casanova, N., García-Tasende, M. S., Sánchez, A., Sordo, J., Touceda, Á. and Vázquez, S. (2010). Back to the coordination modes of the thiosemicarbazonate chain: New insights from diorganolead (IV) and lead (II) derivatives of isatin-3-thiosemicarbazone. *European Journal of Inorganic Chemistry*, 31: 4992-5004.
18. Hashem, H. E., Mohamed, E. A., Farag, A. A., Negm, N. A. and Azmy, E. A. (2021). New heterocyclic Schiff base-metal complex: Synthesis, characterization, density functional theory study, and antimicrobial evaluation. *Applied Organometallic Chemistry*, 35(9): e6322.
19. Mossmann, P. B. (1983). Rapid colorimetric assay for cellular growth and survival: application to proliferation and cytotoxicity assays. *Journal Immunology Methods*, 65: 49-53.
20. Cristóvão, B. (2011). Spectral, thermal and magnetic properties of Cu (II) and Ni (II) complexes with Schiff base ligands. *Journal of the Serbian Chemical Society*, 76(12): 1639-1648.
21. Orif, M. I. and Abdel-Rhman, M. H. (2015). Synthesis, spectral and structural studies on some new isonicotinic thiosemicarbazide complexes and its biological activity. *Polyhedron*, 98: 162-179.
22. Mohamed, G. G., Omar, M. M., Moustafa, B. S., AbdEl-Halim, H. F. and Farag, N. A. (2022). Spectroscopic investigation, thermal, molecular structure, antimicrobial and anticancer activity with modelling studies of some metal complexes derived from isatin Schiff base ligand. *Inorganic Chemistry Communications*, 141: 109606.
23. Fernandes, T. S., Melo, W. D., Kalinke, L. H., Rabelo, R., Valdo, A. K., da Silva, C. C., ... and Cangussu, D. (2018). 2D and 3D mixed M II/Cu II metal–organic frameworks (M= Ca and Sr) with N, N′-2, 6-pyridinebis (oxamate) and oxalate: preparation and magneto-structural study. *Dalton Transactions*, 47(33): 11539-11553.
24. Nakamoto, K. (1986). Infrared spectra of inorganic and coordination compounds. 4th edition. New York: Wiley.
25. Kumar, R., Kumar, S. and Bala, M. (2020). Synthesis, characterisation and antibacterial activity of some indole derivatives and their inclusion complexes with β-cyclodextrin. *Oriental Journal of Chemistry*, 36(5): 923.
26. Haribabu, J., Balakrishnan, N., Swaminathan, S., Peter, J., Gayathri, D., Echeverria, C., ... and Karvembu, R. (2021). Synthesis, cytotoxicity and docking studies (with SARS-CoV-2) of water-soluble binuclear Ru-p-cymene complex holding indole thiosemicarbazone ligand. *Inorganic Chemistry Communications*, 134: 109029.
27. Ahmed, A. and Lal, R. A. (2017). Synthesis, characterization and electrochemical studies of copper (II) complexes derived from succinoyl-and adipoyldihydrazones. *Arabian Journal of Chemistry*, 10: S901-S908.
28. Jayakumar, K., Seena, E. B., Kurup, M. P., Kaya, S., Serdaroğlu, G., Suresh, E. and Marzouki, R. (2022). Spectral, thermal and DFT studies of novel nickel (II) complexes of 2-benzoylpyridine-N4-methyl-3-thiosemicarbazone: Crystal structure of a square planar azido-nickel (II) complex. *Journal of Molecular Structure*, 1253: 132257.
29. Sykuła, A., Nowak, A., Garribba, E., Dzeikala, A., Rowińska-Żyrek, M., Czerwińska, J., ... and Łodyga-Chruścińska, E. (2023). Spectroscopic characterization and biological activity of hesperetin Schiff bases and their Cu (II) complexes. *International Journal of Molecular Sciences*, 24(1): 761.
30. Yakan, H., Cavuş, M. S., Kurt, B. Z., Muğlu, H., Sönmez, F. and Güzel, E. (2021). A new series of asymmetric bis-isatin derivatives containing urea/thiourea moiety: Preparation, spectroscopic elucidation, antioxidant properties and theoretical

calculations. *Journal of Molecular Structure*, 1239: 130495.

31. Abdel-Rahman, L. H., Ismail, N. M., Ismael, M., Abu-Dief, A. M. and Ahmed, E. A. H. (2017). Synthesis, characterization, DFT calculations and biological studies of Mn(II), Fe(II), Co(II) and Cd(II) complexes based on a tetradentate ONNO donor Schiff base ligand. *Journal of Molecular Structure*, 1134: 851-862.
32. Fayed, T. A., Gaber, M., Abu El-Reash, G. M. and El-Gamil, M. M. (2020). Structural, DFT/B3LYP and molecular docking studies of binuclear thiosemicarbazide Copper (II) complexes and their biological investigations. *Applied Organometallic Chemistry*, 34(9): e5800.
33. Mahmoud, W. H., Mohamed, G. G. and El-Sayed, O. Y. (2018). Coordination compounds of some transition metal ions with new Schiff base ligand derived from dibenzoyl methane. Structural characterization, thermal behavior, molecular structure, antimicrobial, anticancer activity and molecular docking studies. *Applied Organometallic Chemistry*, 32(2): e4051.
34. El-Ghamry, M. A., Elzawawi, F. M., Aziz, A. A. A., Nassir, K. M. and Abu-El-Wafa, S. M. (2022). New Schiff base ligand and its novel Cr(III), Mn(II), Co(II), Ni(II), Cu(II), Zn(II) complexes: Spectral investigation, biological applications, and semiconducting properties. *Scientific Reports*, 12(1): 17942.
35. Jacob, J. M., Kurup, M. P., Nisha, K., Serdaroğlu, G. and Kaya, S. (2020). Mixed ligand copper(II) chelates derived from an O, N, S-donor tridentate thiosemicarbazone: Synthesis, spectral aspects, FMO, and NBO analysis. *Polyhedron*, 189:114736.
36. Kovala-Demertzi, D., Demertzis, M. A., Miller, J. R., Papadopoulou, C., Dodorou, C. and Filousis, G. (2001). Platinum(II) complexes with 2-acetyl pyridine thiosemicarbazone: synthesis, crystal structure, spectral properties, antimicrobial and antitumour activity. *Journal of Inorganic Biochemistry*, 86(2-3): 555-563.
37. Bahojb Noruzi, E., Shaabani, B., Geremia, S., Hickey, N., Nitti, P. and Kafil, H. S. (2020). Synthesis, crystal structure, and biological activity of a multidentate calix [4] arene ligand doubly functionalized by 2-hydroxybenzeledene-thiosemicarbazone. *Molecules*, 25(2): 370.

Malaysian Journal of Analytical Sciences (MJAS)
Published by Malaysian Analytical Sciences Society

LATENT FINGERPRINTS TECHNIQUES AND THE USE OF STARCH TO IDENTIFY THE PRINTS: A MINI-REVIEW

(Teknik Cap Jari Tidak Kelihatan dan Penggunaan Kanji Sebagai Bahan Asas untuk Mengenal Pasti Cap Jari: Ulasan Ringkas)

Anis Iryani Ahmad Shukri[1], Norlaily Ahmad[2], and NorulNazilah Ab'lah[2*]

[1]*Faculty of Applied Sciences,*
Universiti Teknologi MARA, 40500 Shah Alam, Selangor, Malaysia
[2]*Centre of Foundation Studies,*
Universiti Teknologi MARA, Cawangan Selangor, Kampus Dengkil, 43800 Dengkil,
Selangor, Malaysia

[*]*Corresponding author: nazlila24@uitm.edu.my*

Received: 11 August 2023; Accepted: 24 October 2023; Published: 29 December 2023

Abstract

Early techniques to develop latent fingerprints have shown many drawbacks such as being costly, time-consuming, less stable, highly toxic, low selectivity, low sensitivity, and low contrast. Numerous studies have been introduced to improve the identification of latent fingerprint techniques. The application of starch as a based material or binding agent offers advantages since this biomaterial is nontoxic, easily available, abundant, and cost-saving. Studies show that starch-based materials have good potential in the detection of latent fingerprints. However, studies related to the use of starch-based material in the development of latent fingerprints are still limited. Therefore, this mini-review highlights the techniques used in the detection of latent fingerprints and the potential alternative in detecting latent fingerprints using starch particularly as coating and coated materials.

Keywords: latent fingerprints, powder dusting, quantum dots, carbon nanoparticles, starch

Abstrak

Kajian terdahulu berkaitan kaedah untuk mengesan cap jari tidak kelihatan mempunyai banyak kelemahan seperti mahal, kurang stabil, bertoksid, tahap selektiviti yang rendah, kepekaan yang rendah, serta kontras yang juga rendah. Terdapat banyak penyelidikan yang telah dilakukan bagi mengkaji pelbagai kaedah untuk meningkatkan pengenalpastian cap jari tidak kelihatan. Penggunaan kanji sebagai bahan asas menawarkan beberapa kelebihan seperti tidak bertoksid, mudah didapati, banyak, dan dapat menjimatkan kos. Kajian menunjukkan penggunaan kanji adalah berpotensi dalam pengesanan cap jari tidak kelihatan. Walaubagaimanapun, kajian berkenaan penggunaan kanji sebagai bahan asas dalam teknik pengesanan cap jari tidak kelihatan masih terhad. Sehubungan itu, ulasan ringkas ini memfokuskan kepada kaedah-kaedah yang digunakan dalam mengesan cap jari tidak kelihatan dan kaedah alternatif yang berpotensi dengan menggunakan kanji dalam pengesanan cap jari tidak kelihatan terutamanya sebagai bahan salutan atau bahan bersalut.

Kata kunci: cap jari tidak kelihatan, debu serbuk, titik kuantum, nanopartikel karbon, kanji

Introduction

In forensic analysis, the primary physical evidence that may link to the criminal is fingerprints. This forensic evidence is an imperative method for identifying criminals through examinations at crime scenes. It is also a useful approach for collecting reliable records of evidence against the accused. In the world of law enforcement, fingerprints are regarded as the gold standard for depicting biometric and scientific evidence [1]. Fingerprints are distinctive and easier to verify due to the capillary tube-shaped channels at the fingertips that are connected to the sweat glands and they are unique for each individual, remain permanent, and do not change [2–6]. When a finger contacts a solid object, its secretion leaves a distinctive ridge pattern on the surface. Due to their weak optical contrast with the substrates, these patterns are sometimes referred to as latent fingerprints, which are undetectable to the naked eye [7].

Cyanoacrylate fuming, ninhydrin, 1,8-diazafluoren-9-one method, powder dusting, silver nitrate, silver nanoparticles, and small particle reagent method are among the techniques used to identify latent fingerprints [3, 8, 9] since they are straightforward, effective, and simple to apply [9]. However, these techniques are costly, time-consuming, less stable, high toxicity of the developing reagents, have a low selectivity of the specificity of emerging materials, low sensitivity of the clarity and visibility of the ridge detail due to enormous and irregular particle size, and low contrast due to the non-fluorescence of most powders [3, 8, 9]. Recently, improved latent fingerprint formation has been achieved using novel techniques including nanotechnology such as quantum dots and fluorescent carbon nanoparticles [1]. The latent fingerprints produced by quantum dots have several advantages such as enhanced sensitivity, contrast, and selectivity. However, there are rising concerns about their intrinsic toxicity thus limiting their long-term usage since quantum dots contain heavy metal cores [1].

Fluorescent carbon nanoparticles have been created as an alternative method for the detection of latent fingerprints in substitution of quantum dots since it is biocompatible and non-toxic to nature, people, and the environment [10]. Even so, these fluorescent carbon nanoparticles can lose their luminous properties easily, making it difficult to convert them into brilliant powder. The addition of starch seems able to generate a strong blue fluorescence in its dry solid form and overcome the limitation. The fluorescent powder employed in this process produces distinct images of latent fingerprints on diverse surfaces, and a stain made from carbogenic fluorescent powder is used to disclose the latent fingerprints [1].

The present study aims to review the techniques used in the detection of latent fingerprints and the potential alternative in detecting latent fingerprints using starch particularly as coating and coated materials. Starch is a natural polymer stored in plants. Its major compounds are amylose and amylopectin. Starch is nontoxic, easily available, abundant, and cost savings [5]. Thus, the use of starch in the detection of latent fingerprints is more economical and safer.

An overview of latent fingerprints

Latent fingerprints are invisible to the naked eye. It is skin friction impressions of the fingers left accidentally on surfaces by eccrine sweat and greasy substances such as sebum. The volar pads transfer a small coating of translucent chemical residue [11] known as triglycerides which are composed of hummed, fatty acids, and amino acids in the shape of individual skin ridges, leaving behind latent fingerprints [12]. It can be used as evidence in criminal investigations and may help to identify suspects using three levels of fingerprint recognition.

The different levels of features in a latent fingerprint are divided into three namely Level 1, Level 2, and Level 3. The primary use of Level 1 features (macro-details) is to classify patterns but non-recognizable for fingerprint identification. The arch, tented arch, left loop, right loop, double loop, and whorl, are visible to the naked eye which assists in manual fingerprint matching and visual scrutiny [13]. Level 2 features (minutia points) are recognizable, consistent, and commonly used to verify a fingerprint's uniqueness. Their characteristics consist of hooks, bifurcations, and

ridge ends. However, it may not be retrieved effectively due to the low quality of evidence caused by ridge smudging. The appropriate reconstruction and refinement are necessary to remove false features. The dimension parameters of the ridges known as Level 3 features (pores and ridge contours) provide more precise and reliable details for accurate fingerprint recognition, resulting in a significant performance improvement [14]. There are enduring characteristics that may be identified from a sample, such as pores, line patterns, and scars. Yet, it is difficult to extract such properties due to resolution restrictions. Thus, all of these level features are typically combined to attain the best possible matching results [13].

Latent fingerprints detection techniques

The initial stage of processing latent fingerprints known as latent fingerprint upliftment involves the process of detecting, enhancing, preserving, collecting, and matching the prints from a crime scene [13]. There are various approaches such as cyanoacrylate fuming, ninhydrin, 1,8-diazafluoren-9-one method, powder dusting method, and silver nitrate [3, 8, 9] that commonly used for rendering fingerprint visibility [13].

Cyanoacrylate fuming

Cyanoacrylate fuming which is known as super glue fuming is a chemical technique for detecting latent fingerprints on non-porous surfaces like glass and plastic [15, 16]. Alkyl 2-cyanoacrylate is an ester of the acrylate class that contains cyano or nitrile group. It produces vapours that react with certain of the eccrine elements of the latent finger mark residues, polymerised, and give them a white colour [15]. Tough this fuming technique provides a flexible and successful approach for identifying latent fingerprints on almost all non-porous substrates, particularly rough surfaces, nevertheless, it has a variety of health and safety concerns. Vapours and liquid cyanoacrylate esters are likely to damage mucous membranes, skin, and eyes severely. In addition, the cyanoacrylate fuming method tends to over-fume the fingerprints affecting the fine ridge features to be largely covered by the white polymers, thus reducing the growing sensitivity [9].

Ninhydrin method

Ninhydrin is an amino acid reagent used to develop latent fingerprints on porous surfaces such as paper and cardboard. This reagent exhibits Ruhemann's purple resulting from a reaction with the amino acid (eccrine) component of the finger mark deposit [17, 18]. The complete ninhydrin development may take 24 to 48 hours at room temperature and humidity [9]. Thus, to shorten the process, temperature and humidity shall be increased. A high-humidity environment of 50% to 80% is suggested and the treated fingerprints shall remain cool in the dark since light and oxygen will degrade Ruhemann's purple [9,18]. The use of higher temperatures requires careful monitoring due to its flammable properties [19] and has the potential to significantly discolour the background resulting in reduced contrast and sensitivity [9]. The ninhydrin method also can cause background staining and ink dissolution [18,19].

The 1,8-diazafluoren-9-one method

The 1,8-diazafluoren-9-one method is a ninhydrin analogue which is another amino acid reagent that is used to identify latent fingerprints on porous surfaces, particularly paper [20]. Due to its high sensitivity, high efficiency, and simple operation, this technique is believed to be crucial for fluorescently generating latent fingerprints on porous surfaces. Nevertheless, the method is considered hazardous and causes carcinogenic effects [9]. Contrary to ninhydrin, heat is necessary to elevate the reaction but prolonged exposure to high heat and humidity will affect the luminescence of the treated fingerprints. Thus, employing a heat press at 180 °C for 10 s or heating at 100 °C not exceeding 20 minutes is advisable [18, 21]. It is often recommended to perform ninhydrin treatment after the 1,8-diazafluoren-9-one method since this reagent may not react with some types of amino acids present in the exudate to obtain the best result [22].

Silver nitrate method

The silver nitrate technique is an old method introduced more than 100 years ago to develop latent fingerprints on porous surfaces before ninhydrin. Silver ions that react with chloride ions from the remaining fingerprints remains forming the silver

chloride compound. Upon exposure to light, it will develop black, brown, or violet stain prints. The silver nitrate approach is not recommended as a standard method since the appearance of the prints and the paper background may strongly change with time [9,23].

Powder dusting method

Powder dusting is the simplest and most commonly used technique for developing latent fingerprints. It is also the oldest technique used by fingerprint experts with one of its earlier references dating back to 1891 [5]. The effectiveness with which the powder adheres to the ridges depends on the particle morphology. Small, fine particles adhere more easily than large, coarse particles [5, 24]. Moreover, the thicker coating of micron- or larger-sized powders tends to reduce the little ridge features, particularly the sweat pores thus reducing its sensitivity [9]. Therefore, most formulations consist of either very fine, rounded particles (with a diameter of about 1 μm) or fine flake particles (with a diameter of about 10 μm) [24]. The efficacy of using fingerprint powder also depends on the colour of the fingerprint powder itself to ensure a good contrast, the age of the fingerprint under investigation, temperature, and the nature of surfaces in which the latent fingerprints are deposited either porous or non-porous [5]. Several powder formulations have been terminated due to the hazardous effects of heavy metals and their salts. Numerous studies have suggested that powder formulations pose health risk to experts in fingerprinting [24]. Current research has improved the method such as using non-toxic substances to overcome the issues.

Carbon dots

Carbon dots can be classified as graphene quantum dots, carbon quantum dots, carbon nanodots, and carbonized polymer dots [25]. Carbon dots are smaller-size fluorescent carbon-based nanoparticles that are generally defined as discrete, zero-dimensional carbonaceous materials of less than 10 nm in size with an identical form of surface passivation [26]. The application of carbon dots to develop fingerprints can be divided into two aspects which are carbon dots in a solution phase and a powdered form. However, carbon dots in a solution phase require a long development time (usually an hour or more), which is an obvious obstacle to the rapid development of latent fingerprints at crime scenes. Carbon dots in the solid state still suffer from aggregation-induced luminescence quenching, so only small amounts of carbon dots have been incorporated into some sort of solid to maintain their flowability and fluorescence when used for dusting. This results in weak luminescence intensity, thus giving a low contrast between the fingerprint and the background [3]. Researchers develop new methods based on carbon dots to overcome the limitations. The improved carbon dots exhibited unique features, like aqueous solubility, low toxicity, chemical inertness, functional ability, biocompatibility, photochemical stability, good conductivity, and environmental friendliness. It has been hugely applied in the fields of bio-imaging, therapeutics, diagnosis, chemo-sensing, nanomedicines, drug delivery, fluorescent marker, and optoelectronic devices [27].

Application of starch in latent fingerprints detection

Starch in nano or micro size is a suitable compound for picturing latent fingerprint impressions. The main components of starch are amylose and amylopectin with abundant hydroxyl groups as shown in Figure 1. The combination of amylose from starch-based non-conventional powders such as gram flour, wheat flour, and corn flour with the fat deposits in the fingerprints can produce high-quality fingerprints [5]. Moreover, starch-based particles offer several benefits over other techniques, including affordability, biodegradability, availability, nontoxic, and natural abundance. Despite being highly hygroscopic, starch is capable in detecting latent fingerprints for a very long period [28]. The application of starch in the development of latent fingerprints commonly as coating materials and coated materials is particularly for fluorescent powder to enhance its optical properties. Starch also undergoes a simple grinding process with fluorophore powder to enhance the visibility of the prints.

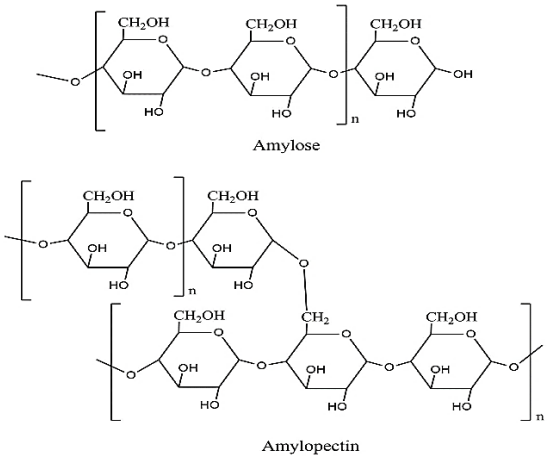


Figure 1. Chemical structure of starch

Starch as coating materials

The adherence of fluorescent powders to fingerprint residue increases after the incorporation of dye into the starch matrix due to the interaction between the matrix and dyes through hydrogen bonding [29, 30]. These powders preserved selectivity and retained sufficient contrast when tested on fingerprints and were effective as commercially available fluorescent powders [30]. This indicates that starch is a good coating material. The optical properties of fluorescent powder increase after incorporation of dye into the starch matrix due to an increase in photostability and fluorescent yield of the dye [29, 31]. Coating of dye with starch prevents photodecomposition since it helps to isolate dye from oxygen and water from the ambient [29].

Starch as coated materials

Starch plays a role as coated materials for research based on starch-fluorescent carbon nanoparticles in the development of latent fingerprints. This fluorescent carbon dots nanoparticle then coating on starch to form phosphors. The process is needed since fluorescent carbon nanoparticles must be combined with hydroxyl groups to emit fluorescence [1]. In one study, malic acid and ammonium oxalate are used as the starting materials for the development of a pyrolysis technique to synthesis N-doped carbon nanoparticles. When the fluorescent carbon nanoparticles are coated on starch (0.1:10 weight ratio) it gives extraordinarily intense blue fluorescence images under UV irradiation on non-porous surfaces in a solid state. Developing latent fingerprints by using this technique on non-porous surfaces [1] is interesting because of their great stability, adjustable fluorescence emission, and luminosity [32]. The author concludes that this fluorescent powder has better sensitivity than iodine vapor [1].

On the other hand, Dong et. al. was the first group of researchers who had studied red fluorescence carbon dots powder for latent fingerprint detection and established an artificial intelligence program to evaluate the similarity of the developed latent fingerprint images quantitatively. The intense red fluorescence of developed phosphors under green light irradiation enhanced the ridge patterns of latent fingerprints without interference from background fluorescence [7].

Carbonized polymer dots have a polymer/carbon hybrid structure rather than the main body carbon structure, which contributes to the predominant properties of carbonized polymer dots. They have unique properties such as high oxygen/nitrogen content, excellent aqueous solubility, and outstanding photoluminescence quantum yield, which are due to the polymer/carbon hybrid structure and the special photoluminescence mechanism [25]. Coating the carbonized polymer dots on the starch surface makes the fingerprints that had been aged for a long period and fingerprints on frequently used substrates are easily

recognised where the created latent fingerprint images reveal the distinct, well-defined ridge features [10].

Starch-based near-infrared organic fluorophores

Near-infrared irradiation has a higher potential over visible light for imaging latent fingerprints. This is due to less interference by the background fluorescence of the bio-tissue and has higher contrast and resolution. The technique is independent of the substrate material and may be used for latent fingerprint formation in a variety of scenarios [33]. Near-infrared radiation is safe for DNA in fingerprint residue during fingerprint development and less harmful to users' skin and eyes than UV light [34]. Ran et. al. developed a new near-infrared-emissive composite material composed of a near-infrared fluorophore, and porous starch via a simple grinding method. The fluorophore powder showed strong near-infrared emission, while the porous starch enabled high adsorption capability for fingerprints. This near-infrared composite offers advantages such as reduced background fluorescence, ease of handling, high photostability, low cost, and low toxicity to developers, indicating its great potential in the field of trace inspection and biological imaging [35].

Future directions

The application of starch in latent fingerprint detection commonly focuses on the role of starch as a coating and coated material. The method is quite simple through the blending of different materials in solvents at a certain time and temperature. The mechanism involved is not clearly mentioned on how starch reacts with fluorescent powders and fat deposits from latent fingerprints. A particular emphasis will be put on the physicochemical principles of latent fingerprint detection and coated/coating principles to enhance the selectivity, sensitivity, and stability of the fluorescent powders.

Conclusion

Amongst other methods in developing latent fingerprints, powder dusting become the one that is most used. Researchers have improvised this method to overcome its limitation. One of the techniques is by incorporating starch forming a fluorescent powder. The friction ridges of the fingerprints using this powder give sharp edges, provide better resolution and offer less background interference. The application of starch has been used quite successfully in the detection of latent fingerprints. Further research is needed as the study on starch powder dusting in the detection of latent fingerprints is still limited.

Acknowledgment

The authors are grateful to Universiti Teknologi MARA for providing Geran Penyelidikan Khas (600-RMC/GPK 5/3 (176/2020) for funding.

References

1. Li, H., Guo, X., Liu, J. and Li, F. (2016). A synthesis of fluorescent starch based on carbon nanoparticles for fingerprints detection. *Optical Materials,* 60: 404-410.
2. Nugroho, D., Oh, W.C., Chanthai, S., and Benchawattananon, R. (2022). Improving minutiae image of latent fingerprint detection on non-porous surface materials under UV light using sulfur doped carbon quantum dots from *Magnolia grandiflora* flower. *Nanomaterials,* 12(19): 3277.
3. Peng, D., Liu, X., Huang, M., Wang, D. and Liu, R. (2018). A novel monodisperse SiO_2@C-dot for the rapid and facile identification of latent fingermarks using self-quenching resistant solid-state fluorescence. *Dalton Transactions,* 47(16): 5823-5830.
4. Prabakaran, E., and Pillay, K. (2021). Nanomaterials for latent fingerprint detection: A review. *Journal of Materials Research and Technology,* 12: 1856-1885.
5. Vadivel, R., Nirmala, M. and Anbukumaran, K. (2021). Commonly available, everyday materials as non-conventional powders for the visualization of latent fingerprints. *Forensic Chemistry,* 24: 100339.
6. Zhao, Y. B., Ma, Y. J., Song, D., Liu, Y., Luo, Y., Lin, S., and Liu, C. Y. (2017). New luminescent nanoparticles based on carbon dots/SiO_2 for the detection of latent fingermarks. *Analytical Methods,* 9 (33): 4770-4775.
7. Dong, X. Y., Niu, X. Q., Zhang, Z. Y., Wei, J. S. and Xiong, H. M. (2020). Red fluorescent carbon

dot powder for accurate latent fingerprint identification using an artificial intelligence program. *ACS Applied Materials and Interfaces,* 12(26): 29549-29555.

8. Prasad, V., Lukose, S., Agarwal, P. and Prasad, L. (2020). Role of nanomaterials for forensic investigation and latent fingerprinting - a review. *Journal of Forensic Sciences,* 65(1): 26-36.
9. Wang, M., Li, M., Yu, A., Zhu, Y., Yang, M., and Mao, C. (2017). Fluorescent nanomaterials for the development of latent fingerprints in forensic sciences. *Advanced Functional Materials,* 27(14): 1606243.
10. Li, F., Wang, X., Liu, W., Wang, L. and Wang, G. (2018). One-step solvothermal synthesis of red emissive carbonized polymer dots for latent fingerprint imaging. *Optical Materials,* 86: 79-86.
11. Friesen, J. B. (2015). Forensic chemistry: The revelation of latent fingerprints. *Journal of Chemical Education,* 92(3): 497-504.
12. Abdollahi, A., Dashti, A., Rahmanidoust, M. and Hanaei, N. (2022). Metal-free and ecofriendly photoluminescent nanoparticles for visualization of latent fingerprints, anticounterfeiting, and information encryption. *Sensors and Actuators B: Chemical,* 372: 132649.
13. Dhaneshwar, R., Kaur, M., and Kaur, M. (2021). An investigation of latent fingerprinting techniques. *Egyptian Journal of Forensic Sciences,* 11(1): 33.
14. Lian, J., Meng, F., Wang, W. and Zhang, Z. (2020). Recent trends in fluorescent organic materials for latent fingerprint imaging. *Frontiers in Chemistry,* 8: 1-8.
15. Bumbrah, G. S. (2017). Cyanoacrylate fuming method for detection of latent fingermarks: A review. *Egyptian Journal of Forensic Sciences,* 7: 1-8.
16. Kanodarwala, F. K., Leśniewski, A., Olszowska-Łoś, I., Spindler, X., Pieta, I. S., Lennard, C., Niedziółka-Jönsson, J., Moret, S. and Roux, C. (2021). Fingermark detection using upconverting nanoparticles and comparison with cyanoacrylate fuming. *Forensic Science International,* 326: 110915.
17. Schulz, M. M., Wehner, H. D., Reichert, W., and Graw, M. (2004). Ninhydrin-dyed latent fingerprints as a DNA source in a murder case. *Journal of Clinical Forensic Medicine,* 11(4): 202-204.
18. Lennard, C. (2013). Forensic sciences: Fingerprint techniques. *Reference Module in Chemistry, Molecular Sciences and Chemical Engineering,* 2013: 1-10.
19. Yang, R. and Lian, J. (2014). Studies on the development of latent fingerprints by the method of solid-medium ninhydrin. *Forensic Science International,* 242: 123-126.
20. Loh, C. N., Chia, W. L. K., Foo, S. C. S., Xu, X. and Tan, W. L. S. (2020). Evaluation of the performance of IND/Zn and DFO on various porous substrates in Singapore context. *Forensic Science International,* 315: 110440.
21. D'Elia, V., Materazzi, S., Iuliano, G. and Niola, L. (2015). Evaluation and comparison of 1,2-indanedione and 1,8-diazafluoren-9-one solutions for the enhancement of latent fingerprints on porous surfaces. *Forensic Science International,* 254: 205-214.
22. Marriott, C., Lee, R., Wilkes, Z., Comber, B., Spindler, X., Roux, C., and Lennard, C. (2014). Evaluation of fingermark detection sequences on paper substrates. *Forensic Science International,* 236: 30-37.
23. Schwarz, L., and Hermanowski, M. L. (2011). Detection of latent fingerprints by the use of silver nitrate. *Archiv Fur Kriminologie,* 227 (3-4): 111-123.
24. Sodhi, G. S. and Kaur, J. (2001). Powder method for detecting latent fingerprints: A review. *Forensic Science International,* 120(3): 172-176.
25. Xia, C., Zhu, S., Feng, T., Yang, M. and Yang, B. (2019). Evolution and synthesis of carbon dots: From carbon dots to carbonized polymer dots. *Advanced Science,* 6(23): 1901316.
26. Shabashini, A., Panja, S. K., and Nandi, G. C. (2021). Applications of carbon dots (CDs) in latent fingerprints imaging. *Chemistry - An Asian Journal,* 16(9): 1057-1072.

27. Xu, L., Li, Y., Wu, S., Liu, X. and Su, B. (2012). Imaging latent fingerprints by electrochemiluminescence. *Angewandte Chemie,* 32(124): 8192-8196.
28. Barros, H. L., Tavares, L. and Stefani, V. (2020). Dye-doped starch microparticles as a novel fluorescent agent for the visualization of latent fingermarks on porous and non-porous substrates. *Forensic Chemistry,* 20: 100264.
29. Barros, H. L. and Stefani, V. (2021). Synthesis and photophysical behavior of fluorescent benzazole dyes and fluorescent microparticles: Their use as fingerprint developer. *Journal of Photochemistry and Photobiology A: Chemistry*, 420:113494.
30. Rajan, R., Zakaria, Y., Shamsuddin, S. and Nik Hassan, N. F. (2019). Fluorescent variant of silica nanoparticle powder synthesised from rice husk for latent fingerprint development. *Egyptian Journal of Forensic Sciences*, 9: 1-9.
31. Valverde-Aguilar, G. (2006). Photostability of laser dyes incorporated in formamide SiO_2 ORMOSILs. *Optical Materials*, 28(10): 1209-1215.
32. Mary, S. K., Koshy, R. R., Arunima, R., Thomas, S. and Pothen, L. A. (2022). A review of recent advances in starch-based materials: bionanocomposites, pH sensitive films, aerogels and carbon dots. *Carbohydrate Polymer Technologies and Applications,* 3: 100190.
33. Lv, Z., Man, Z., Xu, Z., Li, S., Liao, Q. and Fu, H. (2021). Highly emissive near-infrared solid organic fluorophores for visualization of latent fingerprints based on the powder dusting method. *Journal of Materials Chemistry C,* 9(23): 7345-7350.
34. Wang, M., Zhu, Y. and Mao, C. (2015). Synthesis of NIR-Responsive NaYF4:Yb,Er upconversion fluorescent nanoparticles using an optimized solvothermal method and their applications in enhanced development of latent fingerprints on various smooth substrates. *Langmuir,* 31(25): 7084-7090.
35. Ran, C., Xu, Z., He, J., Man, Z., Lv, Z., Wang, P. and Fu, H. (2022). Starch-based near-infrared organic fluorophores for the imaging of latent fingerprints. *Journal of Materials Chemistry C,* 10(43):16347-16352.

Malaysian Journal of Analytical Sciences (MJAS)
Published by Malaysian Analytical Sciences Society

HEAVY METAL DETERMINATION OF SHARK *Scoliodon laticaudus* IN JOHOR WATERS

(Penentuan Logam Berat daripada Ikan Yu *Scoliodon laticaudus* dalam Perairan Johor)

Ng Yenlin Erin[1], Adiana Ghazali[1, 2], Lavannia Ravikumar[1], Yap Chee Kong[3], Noverita Dian Takarina[4], and Ong Meng Chuan[1, 2, 5*]

[1] *Faculty of Science and Marine Environment, Universiti Malaysia Terengganu, 21030 Kuala Nerus, Terengganu, Malaysia*
[2] *Ocean Pollution and Ecotoxicology (OPEC) Research Group, Universiti Malaysia Terengganu, 21030 Kuala Nerus, Terengganu, Malaysia*
[3] *Department of Biology, Faculty of Science, Universiti Putra Malaysia, 43400 Seri Kembangan, Selangor*
[4] *Department of Biology, Faculty of Mathematics and Natural Sciences, Universitas Indonesia, Gedung E, Kampus UI Depok, Depok 16424, Indonesia*
[5] *Institute of Oceanography and Environment, Universiti Malaysia Terengganu, 21030 Kuala Nerus, Terengganu, Malaysia*

[*] *Corresponding author: ong@umt.edu.my*

Received: 22 September 2023; Accepted: 26 October 2023; Published: 29 December 2023

Abstract

The sharks from Johor waters were investigated to evaluate certain heavy metal concentrations and their potential human health concerns. This study obtained 25 *Scoliodon laticaudus* as bycatches from the local fishermen's market in Johor and stored them at a low temperature before further analysis. The sharks were divided into gill, muscle, fin, stomach, and liver samples with oven drying at 60°C. Certain heavy metals (As, Cd, Cr, Cu, Fe, Hg, Pb, and Zn) were then evaluated using an Inductively Coupled Plasma Mass Spectrometer (ICP-MS) after the digestion process using nitric acid (HNO_3). This study presented the ascending metal concentration sequences as Fe > Cd > Hg > Pb > Cr > As > Cu > Zn for livers, Cd > Hg > Fe > Pb > Cr > As > Cu > Zn for stomach linings, Cd < Hg < Pb < Fe < Cr < Cu < As < Zn for fins, Hg < Cd < Fe < Pb < Cr < Cu < As < Zn for gills, and Cd < Hg < Fe < Pb < Cr < Cu < As < Zn for muscles. Therefore, the average pollutant load indexes (PLIs) (contamination levels) for livers, stomach linings, fins, gills, and muscles were 3.31, 2.23, 3.15, 2.47, and 3.35, respectively. Based on the PLI values, this study successfully indicated a moderately polluted contamination level.

Keywords: inductively coupled plasma mass spectrometer, pollution load index, pollution, organisms, Straits of Malacca

Abstrak

Ikan yu dari perairan Johor telah dianalisis untuk menilai jumlah logam berat tertentu dan potensi risiko kesihatan terhadap manusia. Kajian ini memperoleh 25 *Scoliodon laticaudus* sebagai tangkapan sampingan dari pasar nelayan tempatan di Johor dan disimpan pada suhu rendah sebelum dianalisis selanjutnya. Ikan yu dibahagikan kepada sampel insang, otot, sirip, perut, hati, dan dikeringkan di dalam ketuhar pada suhu 60°C. Logam berat tertentu (As, Cd, Cr, Cu, Fe, Hg, Pb, dan Zn) dinilai menggunakan spektrometri jisim plasma gadingan aruhan (ICP-MS) selepas proses pencernaan dengan asid nitrik (HNO_3). Kajian ini menunjukkan kepekatan logam menaik iaitu Fe > Cd > Hg > Pb > Cr > As > Cu > Zn untuk hati, Cd > Hg > Fe > Pb > Cr > As > Cu > Zn untuk perut, Cd < Hg < Pb < Fe < Cr < Cu < As < Zn untuk sirip, Hg < Cd < Fe < Pb < Cr < Cu < As < Zn untuk insang,

dan Cd < Hg < Fe < Pb < Cr < Cu < As < Zn untuk otot. Oleh itu, purata indeks bebanan pencemaran (PLIs) (tahap pencemaran) untuk hati, perut, sirip, insang, dan otot ialah 3.31, 2.23, 3.15, 2.47, dan 3.35. Kajian ini berjaya menunjukkan tahap pencemaran sederhana berdasarkan nilai PLI.

Kata kunci: spektrometri jisim plasma gadingan aruhan, indeks bebanan pencemaran, pencemaran, organisma, Selat Melaka

Introduction

A crucial and significant habitat for sharks is commonly found in the Malaysian waters of Johor. Nonetheless, Johor is an agricultural and industrial state that discharges a substantial amount of ocean waste [1]. This waste includes heavy metals, which are metallic substances with a considerably higher density than water [2]. Since weight and toxicity are related, heavy metals typically include metalloids (arsenic) and are hazardous at low exposure levels. Although numerous natural events (weathering and volcanic eruptions) greatly influence heavy metal poisoning incidents, human activities are primarily responsible for environmental contamination and human exposure concerns [3]. The largest heavy metal concentrations are generally recorded in apex predators at the top of the food chain. Hence, top predators like elasmobranchs (sharks) are more susceptible to environmental pollution.

The biomagnification and bioaccumulation processes absorb the contaminants in the food chain. For example, sharks acquire greater amounts of Hg (particularly monomethyl mercury) than other fish species, which is the most toxic form of metal [4]. Sharks are frequently the “apex” or top predators in their ecosystems as they have few natural predators. Additionally, sharks’ prey on species in the lower food web levels, aiding the regulation and maintenance of the marine ecological equilibrium. Since these predators directly impact their prey populations, the prey populations of the sharks’ prey are also affected. Most top predators consume diverse foods, and the top predators can switch prey species. This switch enables prey species to survive when certain prey populations are depleted [5].

Scoliodon laticaudus, or spade nose shark, is discovered in the Johor markets, one of the smallest tropical carcharhinid sharks inhabiting shallow coastal waters [6]. Generally, these sharks are observed in coastal and estuarine waters at depths ranging from 10 to 75 m (typically less than 50 m), prefer muddy and sandy substrates, and are commonly found around major freshwater outflows. Other spade nose sharks’ characteristics include a yearly litter of 6 to 20 pups, an early maturity age of two years, and a 4.5-year generation time [7]. Nonetheless, shark-based research in Malaysia still requires further investigation. Moreover, the *Scoliodon laticaudus* species are highly demanded as bycatches in the local markets of Johor. This study determined the heavy metal levels in sharks and the correlation between heavy metals and shark weights using statistical analysis.

Materials and Methods

Sample collection and preparation

A total of 25 *Scoliodon laticaudus* were acquired from the local fishermen in Malaysia (see Figure 1). These sharks were purchased from a port or a market in Johor in March 2022 (see Figure 2), which were bycatches from trawls and gillnets while being sold to the locals. The 25 sharks were labelled and stored at a low temperature in a refrigerator until further use. Initially, the sharks were defrosted, dissected, and analysed in a laboratory. The length and weight of the sharks’ whole bodies were also measured. Subsequently, the gender of the sharks was determined using a clasper. A ceramic knife dissected the sharks into muscle, fin, stomach lining, liver, and gill samples. These organs were transferred into a preheated oven at 60 °C until constant dry weights were achieved. Finally, the organs were homogenised into powder form using a pestle and mortar, and the processing equipment was cleaned with ethanol for each sample [8].

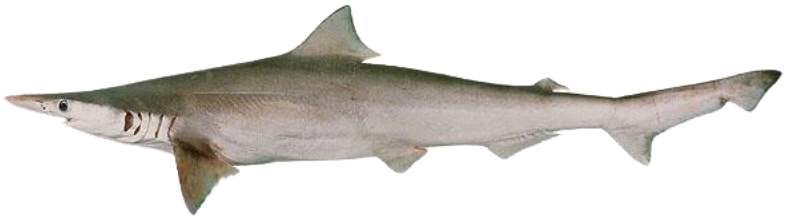


Figure 1. The *Scoliodon laticaudus* or spade nose shark

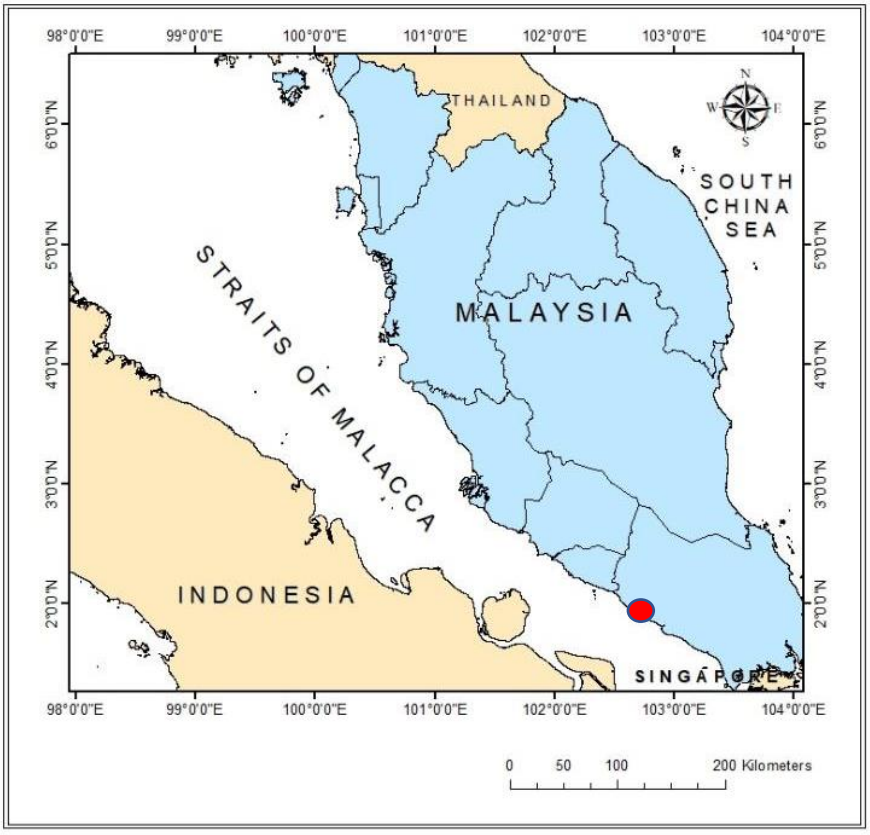


Figure 2. The Johor state map and the Pontian District

Acid digestion technique

The heavy metal contents in the liquid biota samples were measured using the Teflon bomb digestion approach for biological samples. Initially, 0.05 g of the homogenised material was weighed and placed in a 25 mL Teflon beaker containing 1.5 mL of 65% nitric acid (HNO_3) [9]. Since HNO_3 is a strong acid, the approach was conducted within a perchloric fume hood. The Teflon beaker was then tightly sealed to prevent acid leakage throughout the acid digestion process. All Teflon bombs were heated in an oven at 100°C for 8 h to aid digestion [9, 10]. The Teflon bombs were then allowed to cool to room temperature before transferring the solution to separate centrifuge tubes. These tubes were added with deionised water until the 10 mL marks were reached. Simultaneously, the blank and certified

reference material samples (DOLT-4 Dogfish liver) were analysed to assess the accuracy of the procedure. Lastly, the Arsenic (As), Cadmium (Cd), Chromium (Cr), Copper (Cu), Iron (Fe), Lead (Pb), Mercury (Hg), and Zinc (Zn) heavy metal concentrations were evaluated using an Inductively Coupled Plasma Mass Spectrometry (ICP-MS, Elan 6000) [11, 12]. Table 1 lists the detection and quantification limits of the ICP-MS instrument.

Table 1. Summary of the detection and quantification limits of the ICP-MS instrument

Metal	Mass	Detection Limits (µg/L)	Quantification Limits (µg/L)
Ar	075	0.590	1.950
Cd	112	0.003	0.010
Cr	052	0.110	0.380
Cu	063	0.210	0.690
Pb	207	0.020	0.050
Fe	055	8.260	27.54
Hg	200	0.006	0.020
Zn	065	0.260	0.850

Data analysis

The Pearson correlation test was utilised to examine the correlation between heavy metal concentrations and shark weights. All analyses used *p*-values less than 0.05 ($p < 0.05$). Meanwhile, the heavy metal contamination levels were evaluated using the pollutant load index (PLI) [13]. No action was necessary if the PLI value was below 50. Otherwise, monitoring was essential if the PLI value was higher than 50. If the PLI value was greater than 100, extreme pollution was indicated, requiring immediate action [14]. An equation is used to calculate XX as follows:

$$PLI = (CF1 \times CF2 \times CF3 \times \cdots \times CFn)^{1/n} \quad (1)$$

where *n* represents the number of metals.

Results and Discussion

Table 2 tabulates the average length and weight of the *Scoliodon laticaudus*; the maximum weight and length of the shark are 41.3 cm and 295 g, respectively. Meanwhile, the corresponding minimum weight and length were 33 cm and 162 g, respectively. Thus, the shark's average length demonstrated the significant maturity of the sharks [7]. This outcome was supported by Ali and Lim [15] study, which reported that male and female spade nose sharks reached their maturity ranging from 24 to 36 cm and 33 to 35 cm lengths, respectively [15]. When maturity was achieved, an extended survival period for the sharks in the wild was indicated, bioaccumulating a specific number of heavy metals. The weight of the sharks aided in determining the shark's health, which reflected the sharks' condition in their habitat. This factor suggested that the greater the sharks' weight of a certain length, the better their physiological conditions. Consequently, more preys were available for the sharks, which could assess if an ecosystem was healthy or contaminated [16, 17].

Tissue samples reveal the highest Zn and Cu concentrations, which Zn is a required metallic trace element for microbes, plants, animals, and humans. Although Cu and Zn are key minerals offering substantial health benefits and are necessary for metabolic synthesis, they are still potentially toxic metals. For example, Cu is vital as an enzyme cofactor and in Fe consumption [18]. Conversely, excessive Cu in the fish system (particularly in sharks) can harm organs and systems while suppressing the immune system [19]. Another example involves Zn as a crucial inorganic trace element in regulating numerous physiological activities, including defence mechanisms, growth performance, immune system, and radical and free ion resistances [20]. Nonetheless, high Zn concentrations produce deaths in fish by causing damage to the gill tissues. Stress and death are also

induced due to the continuously lethal concentrations [21]. Thus, the World Health Organization (WHO) and the Food and Agriculture Organization (FAO) established the Joint FAO/WHO Expert Committee on Food Additives (JECFA). In JECFA, standards were developed for evaluating the safety of chemicals in foods that were compatible with current risk assessment concepts while considering toxicology advancements and other relevant fields [22].

Table 2. Size parameter summary of the *Scoliodon laticaudus*

Parameter	Length (cm)	Weight (g)
Average	37 ± 2.29	202.9 ± 34.13
Min	33.0	162
Max	41.3	295

Table 3. Summary of the permissible heavy metal limits by WHO

Heavy Metals	WHO (mg/kg)
Cd	0.05
Pb	0.02
Cr	2.00
As	0.12
Zn	0.05
Hg	0.05
Fe	-
Cu	30.0

Significant As concentrations are observed in tissue samples due to pesticides (agricultural, fertiliser, and animal feeding activities) in the captured shark areas [23, 24]. Since As compounds are predominantly soluble, they are more likely to accumulate in seafood [25]. On the contrary, these amounts should not cause a concern considering the As ratio in less organic fishes to pure organic fishes was low [26]. Although As is the third-highest heavy metal concentration and a non-essential element, necessary precautions are still required. As is detrimental to the locals' health if these sharks are consumed. **Tables 4** to **8** summarise the heavy metal concentrations in the gill, muscle, liver, stomach lining, and fin samples, respectively. The mean, minimum, and maximum heavy metal concentrations were recorded, and standard errors or deviations accompanied the mean values. As the sharks were obtained from the same environment, the weight-dependent heavy metal concentrations were most likely determined by the sharks' physical states. Additionally, strong physical conditions with greater lipid tissue contents produced a relative dilution of the stored contaminants in the organs [17, 27].

Table 4. Summary of metal concentrations in spade nose sharks (gills)

Sample	Metal Concentrations in Gills (µg/g dry wt.)							
	Cr	Fe	Cu	Zn	Cd	Pb	As	Hg
Average	5.91 ± 3.53	4.19 ± 2.06	20.02 ± 10.74	193.72 ±74.13	1.45 ± 2.89	4.48 ± 11.67	25.67 ± 56.53	1.35 ± 2.66
Min	1.90	0.16	7.26	98.68	0.43	1.27	14.00	0.48
Max	14.43	7.34	36.87	343.31	2.89	11.67	56.53	2.66

Table 5. Summary of metal concentrations in spade nose sharks (muscles)

Sample	Metal Concentrations in Muscles (µg/g dry wt.)							
	Cr	Fe	Cu	Zn	Cd	Pb	As	Hg
Average	5.47 ± 5.32	2.80 ± 2.02	19.77 ± 10.31	108.02 ± 35.77	0.96 ± 0.27	2.81 ± 1.00	21.68 ± 8.84	1.76 ± 0.63
Min	1.34	0.74	6.17	61.11	0.56	1.40	11.19	0.92
Max	17.64	8.04	42.06	165.17	1.26	4.72	41.22	3.05

Table 6. Summary of metal concentrations in spade nose sharks (fins)

Sample	Metal Concentrations in Fins (µg/g dry wt.)							
	Cr	Fe	Cu	Zn	Cd	Pb	As	Hg
Average	5.97 ± 1.91	5.67 ± 2.01	30.74 ± 21.83	353.54 ± 134.55	1.76 ± 0.85	4.48 ± 2.02	29.45 ± 14.90	2.15 ± 0.99
Min	3.97	2.54	7.80	126.78	0.57	1.73	15.07	0.08
Max	9.38	10.18	70.40	562.20	3.52	8.62	71.12	3.80

Table 7. Summary of metal concentrations in spade nose sharks (stomach linings)

Sample	Metal Concentrations in Stomach Linings (µg/g dry wt.)							
	Cr	Fe	Cu	Zn	Cd	Pb	As	Hg
Average	9.36 ± 3.41	4.37 ± 2.59	71.56 ± 43.19	779.32 ± 291.64	2.72 ± 1.55	6.27 ± 2.22	40.05 ± 13.07	3.77 ± 1.75
Min	3.79	0.38	27.15	446.85	0.96	3.61	21.12	2.17
Max	15.79	10.30	168.13	1428.42	6.51	11.63	64.57	8.16

Table 8. Summary of metal concentrations in spade nose sharks (livers)

Sample	Metal Concentrations in Livers (µg/g dry wt.)							
	Cr	Fe	Cu	Zn	Cd	Pb	As	Hg
Average	13.78 ± 8.29	0.92 ± 0.56	57.42 ± 27.51	1019.62 ± 523.21	3.40 ± 1.81	5.67 ± 2.25	40.04 ± 14.90	5.18 ± 3.12
Min	4.88	0.09	16.70	317.07	0.89	2.35	17.58	1.51
Max	39.12	2.10	107.61	2079.52	6.98	9.75	67.38	12.60

The lowest Hg content was measured in the gill samples, and the heavy metal distributions in the muscles and internal organs were influenced by environmental pollution [28, 29]. The liver sample also absorbed large quantities of ecological pollutants, which was important for pollutant storage, redistribution, detoxification, and transformation [30, 31]. In addition, the liver and stomach samples contained larger heavy metal amounts than other tissue samples. These heavy metal amounts in tissue samples could vary depending on several factors, such as size, gender, dietary habits, and environment. Furthermore, lower metal absorptions were produced due to the decreased free metal ion activities as salinity increased [32]. Table 9 presents the correlation coefficient interpretations from Mukaka's and Schober et al. studies [33, 34]. Meanwhile, Figures 3 to 7 depict the coefficient correlation curves between shark weights and heavy metal concentrations.

The Cu and Pb concentrations were low in gill tissues (see Figure 3), and their concentrations did not vary significantly with body weights. In contrast, the correlations between Cr and Cd concentrations and shark weights were not statistically significant. The correlation coefficients for Zn, As, Hg, and Fe were less than 0.3, indicating a substantial relationship between

shark weights and heavy metal concentrations. In the muscle samples (see Figure 4), a very weak correlation was recorded for all metals between shark weights and heavy metal concentrations. Although the correlation coefficient values for Cr, Fe, Zn, Cd, Pb, As, and Hg were less than -0.2, the values remained in the negative regions (see Figure 5). This outcome suggested that the heavy metal concentrations acquired no significant changes. Likewise, Cu concentration increased slightly with shark weight, which was deemed insignificant.

Table 9. Summary of the correlation coefficient interpretations

Size of Correlation	Interpretation
0.90 to 1.00 (-0.90 to -1.00)	Very high positive (negative) correlation
0.70 to 0.90 (-0.70 to -0.90)	High positive (negative) correlation
0.50 to 0.70 (-0.50 to -0.70)	Moderate positive (negative) correlation
0.30 to 0.50 (-0.30 to -0.50)	Low positive (negative) correlation
0.00 to 0.30 (0.00 to -0.30)	Negligible correlation

In the stomach tissue samples (see Figure 6), the Fe, Cu, Pb, Hg, Zn, and As exhibited significant changes in weight as their concentrations increased. On the contrary, Cr and Cd revealed weak positive and negative significances, respectively. A moderate correlation between Cr and shark weight was also computed in the liver tissue samples (see Figure 7). This result occurred due to the increased sample weight when the Cr concentration decreased. Interestingly, Hg, Cd, and Zn produced corresponding correlation values of -0.32, -0.37, and -0.3, thus indicating significant changes in shark weights and heavy metal concentrations. Lastly, the low Pb, As, and Fe concentrations were deemed insignificant.

The impacts of multiple external aspects (such as the marine environment) and internal factors (fish carcass features) can induce variations in metal accumulations and inter-metal correlations among fish species, locations, and seasons. Generally, the size-age effect on metal content is a well-established study whereby Hg content increase with size and age (particularly in predatory fishes). Nevertheless, this characteristic is not observed in all metals. Certain metals, such as Cr, Cu, Fe, Cd, As, and Pb, have inverse associations with the size or age of the fish. Hence, heavy metal concentrations vary by species, location, and tropic level, generating challenging comparison and interpretation processes [35]. Moreover, negative correlations are more common than positive ones, making it difficult to explain them [36].

All the coefficient values in gills for Cr-Zn, Cu-Cd, Fe-Cd, Fe-Zn, Cu-Cd, Zn-Cd, Cd-As, and Pb-Hg were between 0.5 and 0.7 (see Table 10). Subsequently, all the coefficient values for muscles for Cr-Fe, Cr-Cu, Fe-Zn, Fe-Cd, Fe-Pb, Fe-As, Fe-Hg, and Cu-As were low or negative (see Table 11). Meanwhile, all the coefficient values in fins for Fe-Zn, Fe-Cd, Fe-Hg, Zn-Cd, Cd-Hg, Pb-Hg, and As-Hg were between 0.5 and 0.9 (see Table 12). Alternatively, all the correlation coefficient values for the stomach tissues for Fe-Cu, Fe-Zn, Fe-Pb, Fe-Hg, Cu-Pb, Cu-Hg, Zn-Pb, Zn-Hg, and P-Hg were from 0.5 to 0.9 (see Table 13). Finally, all the correlation coefficient values in liver tissues for Cr-Fe, Cr-Cu, Cr-Zn, Cr-Pb, Cr-As, Cr-Hg, Fe-Cu, and Fe-Cd were low (see Table 14).

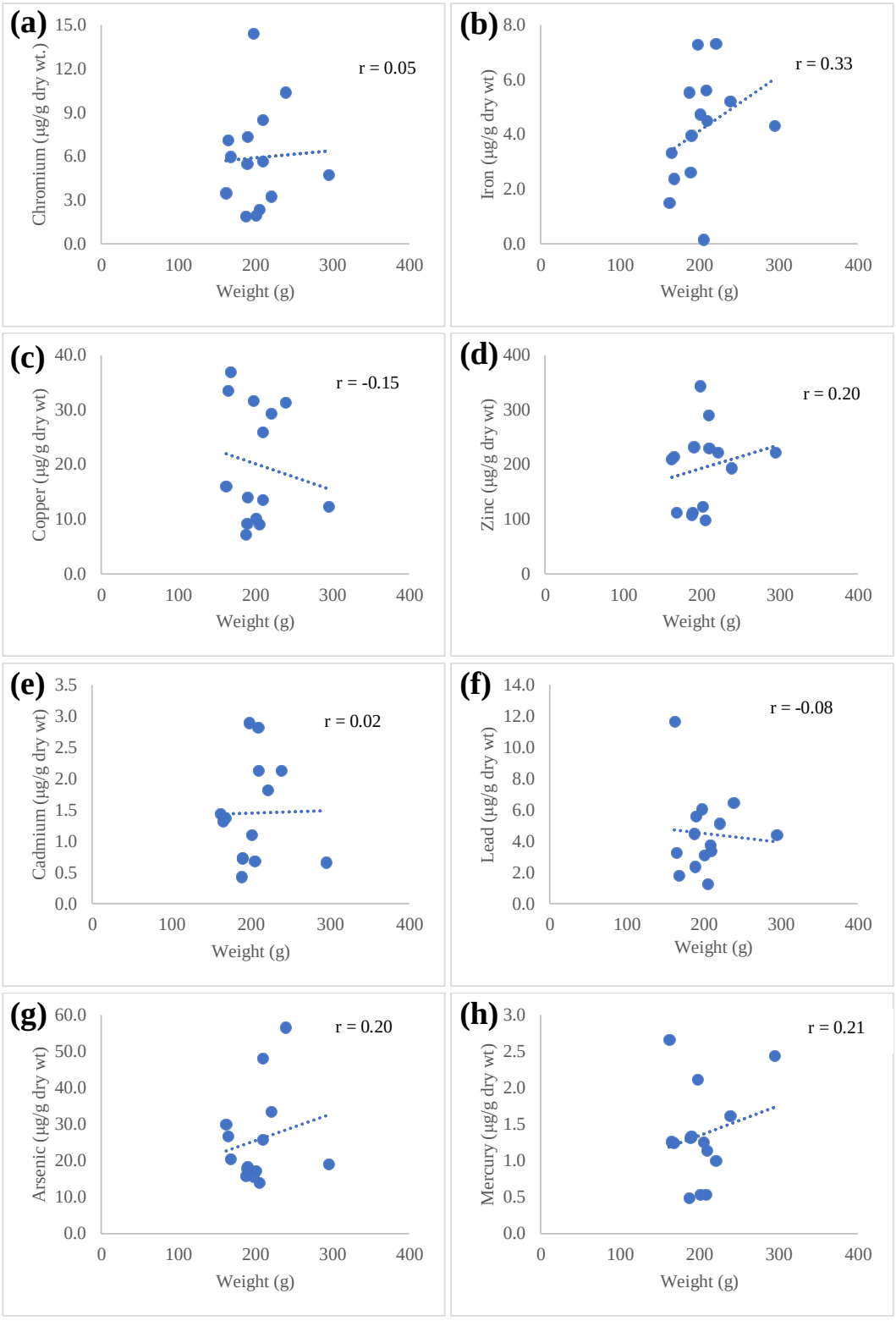


Figure 3. Graphs indicating the correlations (*r*-values) between shark weights (n = 25) with (a) Cr, (b) Fe, (c) Cu, (d) Zn, (e) Cd, (f) Pb, (g) As, and (h) Hg concentrations in gills

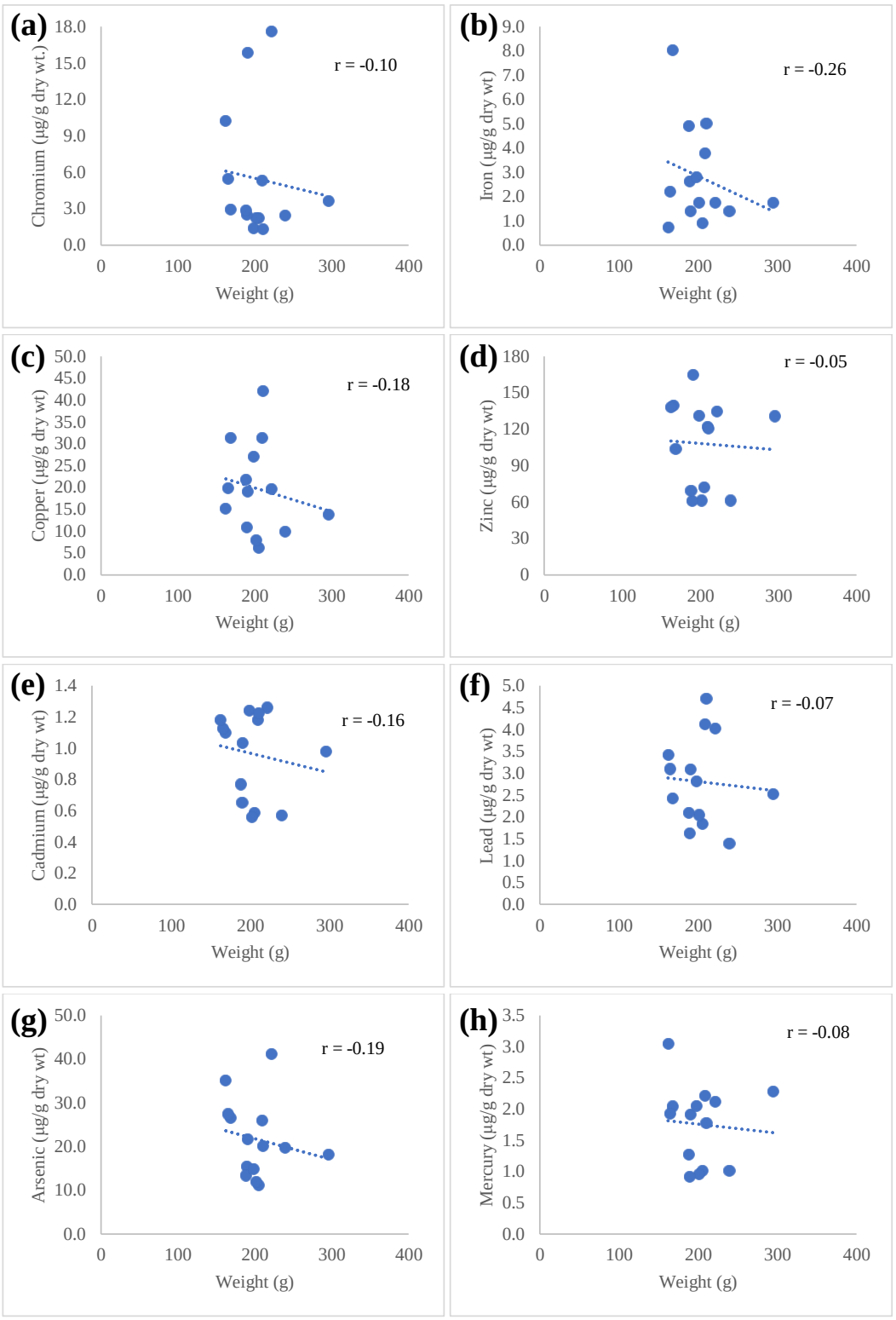


Figure 4. Graphs indicating the correlations (*r*-values) between shark weights (n = 25) with (a) Cr, (b) Fe, (c) Cu, (d) Zn, (e) Cd, (f) Pb, (g) As, and (h) Hg concentrations in muscles

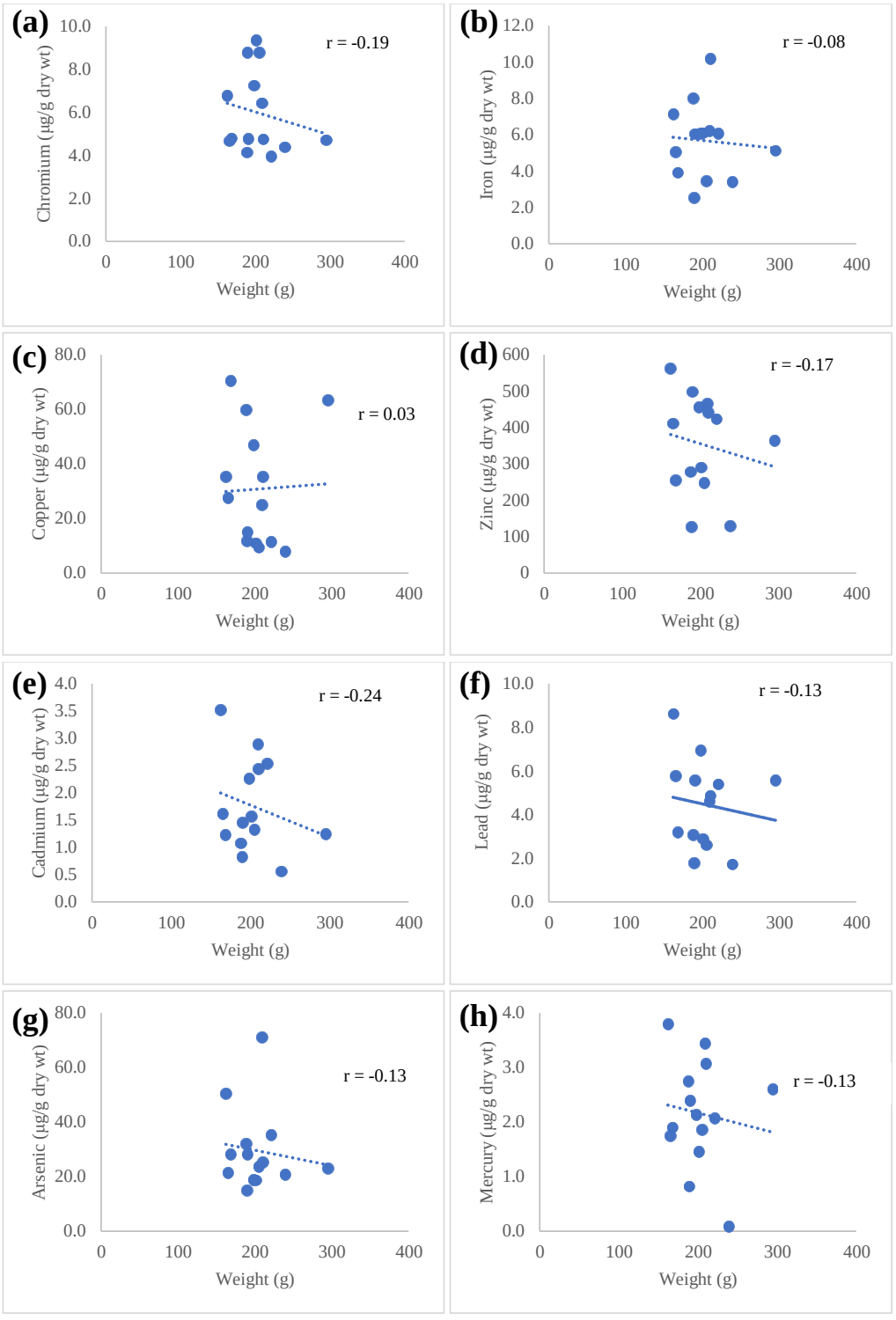


Figure 5. Graphs indicating the correlations (*r*-values) between shark weights (n = 25) with (a) Cr, (b) Fe, (c) Cu, (d) Zn, (e) Cd, (f) Pb, (g) As, and (h) Hg concentrations in fins

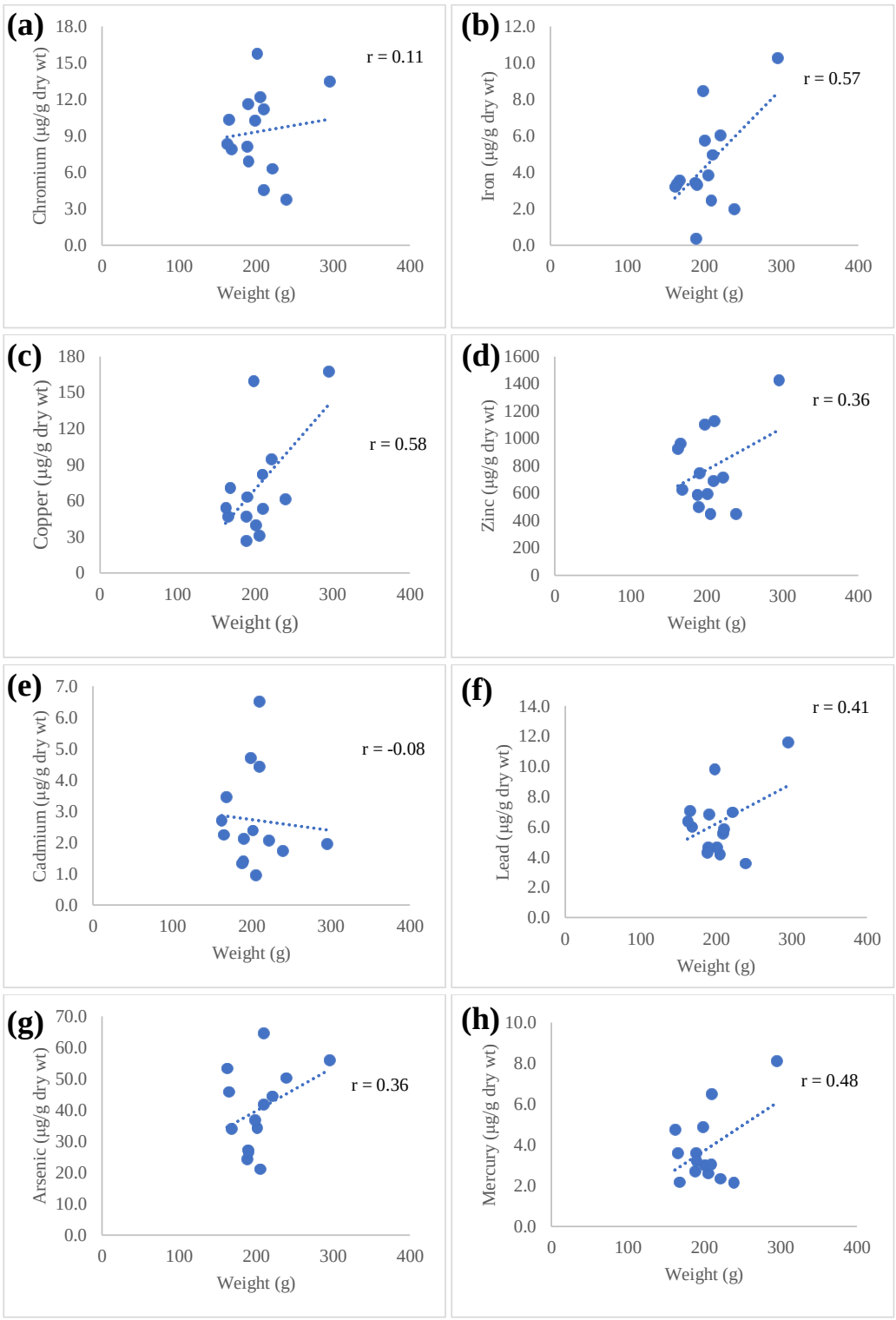


Figure 6. Graphs indicating the correlations (*r*-values) between shark weights (n = 25) with (a) Cr, (b) Fe, (c) Cu, (d) Zn, (e) Cd, (f) Pb, (g) As, and (h) Hg concentrations in stomach linings

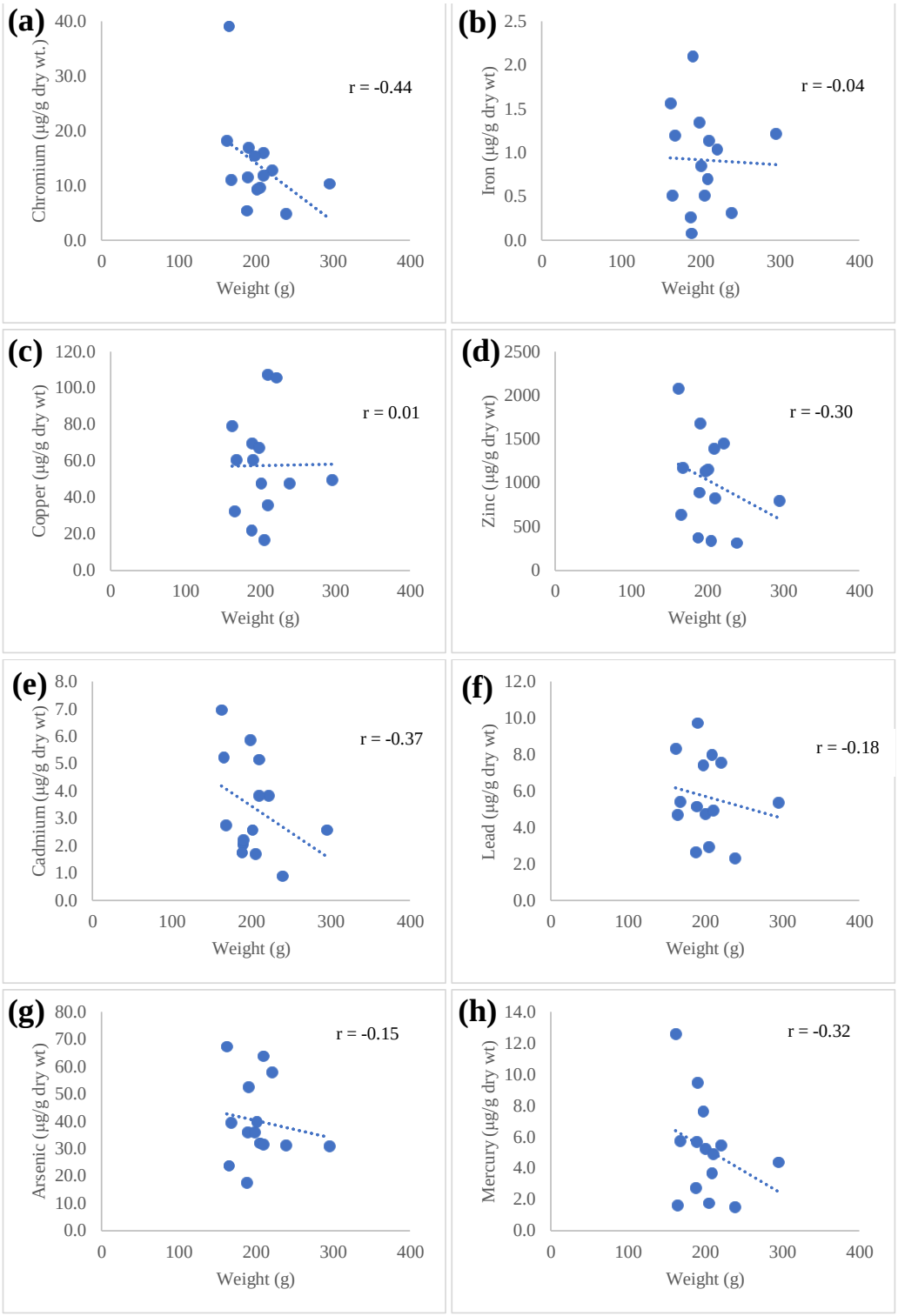


Figure 7. Graphs indicating the correlations (*r*-values) between shark weights (n = 25) with (a) Cr, (b) Fe, (c) Cu, (d) Zn, (e) Cd, (f) Pb, (g) As, and (h) Hg concentrations in livers

Table 10. Summary of the correlation coefficient values of heavy metals in gills

	Cr	Fe	Cu	Zn	Cd	Pb	As
Fe	0.410						
Cu	0.616	0.318					
Zn	0.716	0.576	0.427				
Cd	0.702	0.535	0.636	0.744			
Pb	0.161	0.137	0.066	0.429	0.229		
As	0.335	0.282	0.483	0.333	0.586	0.313	
Hg	0.294	-0.219	0.096	0.344	0.047	0.602	-0.042

Table 11. Summary of the correlation coefficient values of heavy metals in muscles

	Cr	Fe	Cu	Zn	Cd	Pb	As
Fe	-0.350						
Cu	-0.058	0.723					
Zn	0.617	-0.091	0.433				
Cd	0.416	0.257	0.735	0.857			
Pb	0.419	0.153	0.724	0.714	0.851		
As	0.718	-0.023	0.249	0.587	0.670	0.599	
Hg	0.458	0.029	0.418	0.830	0.850	0.660	0.702

Table 12. Summary of the correlation coefficient values of heavy metals in fins

	Cr	Fe	Cu	Zn	Cd	Pb	As
Fe	-0.310						
Cu	-0.383	0.264					
Zn	-0.208	0.645	0.152				
Cd	0.033	0.580	0.018	0.838			
Pb	-0.197	0.481	0.266	0.916	0.769		
As	-0.129	0.312	0.055	0.526	0.686	0.357	
Hg	-0.152	0.709	0.422	0.807	0.768	0.687	0.692

Table 13. Summary of the correlation coefficient values of heavy metals in stomach linings

	Cr	Fe	Cu	Zn	Cd	Pb	As
Fe	0.435						
Cu	0.036	0.777					
Zn	0.298	0.736	0.694				
Cd	-0.053	0.220	0.274	0.474			
Pb	0.231	0.812	0.889	0.877	0.238		
As	-0.328	0.192	0.434	0.451	0.350	0.350	
Hg	0.462	0.628	0.571	0.900	0.389	0.714	0.351

Table 14. Summary of the correlation coefficient values of heavy metals in gills

	Cr	Fe	Cu	Zn	Cd	Pb	As
Fe	0.144						
Cu	0.059	0.284					
Zn	0.223	0.732	0.727				
Cd	0.613	0.380	0.462	0.606			
Pb	0.334	0.770	0.731	0.913	0.598		
As	0.085	0.517	0.836	0.884	0.499	0.804	
Hg	0.073	0.761	0.456	0.878	0.504	0.776	0.655

Positive correlation coefficients implied that the potentially exposed and bioaccumulated tissue samples originated from the same source. Likewise, the Malacca Strait included waste from both terrestrial and marine sources. For example, the vessels in the areas were accompanied by accident-related platform activities. Therefore, the heavy metal contamination of fish in Johor was likely caused by urban activities [37, 24]. The predatory fish in this study acquired a higher trophic level while accumulating more heavy metals. Since carnivorous fish are active swimmers, these fishes mostly ingest fingerlings, shrimps, and zooplankton. These activities can result in large heavy metal accumulations in the body. Furthermore, the surroundings and dietary habits determine the heavy metal accumulations. Another concern lies in fishes with steady growth rates that inhabit contaminated settings, which stabilise the heavy metal accumulations [38].

Based on present data, the livers contained the highest metal concentrations than other tissue samples, and contaminants tend to concentrate in tissues with high lipid content. This outcome suggested that sharks possessed high lipid concentrations in their livers. Similarly, other elasmobranchs also accumulated pollutants [26]. Table 15 lists the results following the calculated average PLI values in Table 14. The overall average results indicated that the samples were moderately contaminated and that no immediate action was necessary for the research region.

Table 15. Summary of the PLI values in this study

Tissue Sample	PLI
Gills	3.31
Muscles	2.23
Fins	3.14
Stomach Linings	2.47
Livers	3.35

Conclusion

This study successfully demonstrated the heavy metal concentrations in tissue samples, which were ascending. The orders were Hg < Cd < Fe < Pb < Cr < Cu < As < Zn for gills, Cd < Hg < Fe< Pb < Cr < Cu < As < Zn for muscles, Cd < Hg < Pb < Fe < Cr < Cu < As < Zn for fins, Cd < Hg < Fe < Pb < Cr < As < Cu < Zn for stomach linings, and Fe < Cd < Hg < Pb < Cr < As < Cu < Zn for livers. The livers acquired the most heavy metals, while Zn was the highest among all tissue samples. Furthermore, shark size was not the only factor determining heavy metal concentrations. Several factors involving eating habits, environment, gender, and species type, could influence heavy metal concentrations. Consequently, this study concluded that no immediate action was required based on the PLI values. Nevertheless, considerable precautions were still needed as most bioaccumulated heavy metals originated from the same source.

Acknowledgements

The Fundamental Research Grant Scheme (FRGS) FRGS/1/2020/WAB05/UMT/02/5, Ministry of Higher Education, Malaysia, funded this study. The authors

would like to thank the Oceanography Laboratory, Faculty of Science and Marine Environment, UMT staff for their significant support and for providing the facilities for this study. The authors also thank Mr. Joseph Bidai of the Institute of Oceanography and Environment, UMT for his assistance in identifying heavy metals with ICP-MS.

References

1. Nordin, R. (2022). Growing agriculture sector for food security, income. Retrieved October 18, 2022, from https://www.thestar.com.my/metro/metro-news/2022/09/06/growing-agriculture-sector-for-food-security-income.
2. Rainbow, P. and Furness, R. (2018). Heavy metals in the marine environment. CRC Press, pp. 2-3.
3. Tchounwou, P., Yedjou, C., Patlolla, A. and Sutton, D. (2012). Heavy metal toxicity and the environment. Springer, Basel: pp. 133-164.
4. Alves, L., Novais, S., Correia, J., Costa, N., Mendes, S., Nunes, M., Marchand, P. and Lemos, M. (2014). Using shark biomarkers as tools for biomonitoring the health of Atlantic Waters. *Frontier Marine Science Conference*, 2014: 105.
5. Sergio, F., Newton, I., Marchesi, L. and Pedrini, P. (2006). Ecologically justified charisma: preservation of top predators delivers biodiversity conservation. *Journal of Applied Ecology*, 43(6): 1049-1055.
6. Devadoss, P. (1989). Observations on the length-weight relationship and food and feeding habits of spade nose shark, *Scoliodon laticaudus* Muller and Henle. *Indian Journal of Fisheries*, 36(2): 169-174.
7. Dulvy, N. K., Simpfendorfer, C., Akhilesh, K. V., Derrick, D., Elhassan, I., Fernando, D., Haque, A. B., Jabado, R. W., Maung, A., Valinassab, T. and VanderWright, W. J. (2022). Scoliodon laticaudus: IUCN red list of threatened species[Access online 15 September 2022].
8. Poong, J., Tee, L., Tan, E., Yip, T., Ramli, M., Rahman Ali Hassan, A., Ali, A., Chen, M., James Lam, C. and Ong, M. (2020). Levels of heavy metals in bamboo sharks (*Chiloscyllium* sp.) in Straits of Malacca, Malaysia. *Malaysia Journal of Analytical Sciences*, 24(4): 546-557.
9. Ong, M. C, Yong, J. C., Khoo, X. Y., Tan, Y. F. and Joseph, B. (2014). Selected heavy metals and polycyclic aromatic hydrogen in commercial fishes caught from UMT enclosed lagoon, Terengganu, Malaysia. *Advances in Environmental Biology*, 8(14): 91-98.
10. Norhazirah, A. A., Adiana, G., Ahmad, N. I., Shamsudin A. A. and Ong, M. C. (2022). Determination of arsenic and mercury in longtail tuna (*Thunnus tonggol*) collected from Terengganu waters: risk assessment of dietary exposure. *Fisheries and Aquatic Sciences* 25(3): 167-174.
11. Ong, M. C., Shazili, N. A. M., Menier, D., Effendy, A. W. M. (2013). Levels of trace elements in tissue of *Ostrea edulis* and *Crassostrea gigas* from Quiberon Bay, Brittany, France. *Journal of Fisheries and Aquatic Science,* 8(2): 378-387.
12. Tengku Nur Alia, T. K. A., Hing, L. S., Sim, S. F., Ahmad, A. and Ong, M. C. (2020). Comparative study of raw and cooked farmed sea bass (*Lates calcarifer*) in relation to metal content and its estimated human health risk. *Marine Pollution Bulletin* 153: 111009.
13. Kowalska, J., Mazurek, R., Gąsiorek, M. and Zaleski, T. (2018). Pollution indices as useful tools for the comprehensive evaluation of the degree of soil contamination–A review. *Environmental Geochemistry and Health*, 40(6): 2395-2420.
14. Angulo, E. (1996). The Tomlinson pollution load index applied to heavy metal, 'mussel-watch' data: a useful index to assess coastal pollution. *Science of the Total Environment*, 187(1): 19-56.
15. Ali, A. and Lim, A. (2012). Field guide to sharks of the Southeast Asian Region. Kuala Terengganu. Yayasan Islam, pp.5-9.
16. Dar, S. A., Thomas, S. N., Chakraborty, S. K. and Jaiswar, A. K. (2022). Length-weight relationships for two commercially important species of Clupeidae (*Sardinellalongiceps, anodontostomachacunda*) from Karachi Fish Harbor, Pakistan. *2nd International Conference on Biological Research and Applied Science,* 51: 291-294.
17. Mansor, M., Mohamad Najamuddin, A., Mohd Zawawi, M., Yahya, K. and Siti-Azizah, M. (2012). Length-weight relationships of some important estuarine fish species from Merbok Estuary, Kedah.

Journal of Natural Sciences Research, 2(2): 8-17.
18. Yap, C. and Al-Mutairi, K. (2022). Copper and zinc levels in commercial marine fish from Setiu, East Coast of Peninsular Malaysia. *Toxics*, 10(2): 52.
19. Yanong, R. P. (2010). Use of copper in marine aquaculture and aquarium systems: FA165/FA165, 12/2009. EDIS, 2010(2).
20. Akram, Z., Fatima, M., Shah, S., Afzal, M., Hussain, S. and Hussain, M. (2019). Dietary zinc requirement of *Labeo rohita* juveniles fed practical diets. *Journal of Applied Animal Research*, 47(1): 223-229.
21. Skidmore, J. (1964). Toxicity of zinc compounds to aquatic animals, with special reference to fish. *The Quarterly Review of Biology*, 39(3): 227-248.
22. FAO (n.d). Food safety and quality: Chemical risks and JECFA. Retrieved from: https://www.fao.org/food/food-safety-quality/scientific-advice/jecfa/en/ [Accessed online 18 November, 2022].
23. Jaishankar, M., Tseten, T., Anbalagan, N., Mathew, B. and Beeregowda, K. (2014). Toxicity, mechanism and health effects of some heavy metals. *Interdisciplinary Toxicology*, 7(2): 60-72.
24. Yap, C., Ismail, A. and Tan, S. (2003). Cd and Zn concentrations in the Straits of Malacca and intertidal sediments of the west coast of Peninsular Malaysia. *Marine Pollution Bulletin*, 46(10): 1349-1353.
25. Wang, M., Chen, C., Chen, C., Tsai, W. and Dong, C. (2022). Assessment of trace metal concentrations in Indian Ocean silky sharks *Carcharhinus falciformis* and their toxicological concerns. *Marine Pollution Bulletin*, 178: 113571.
26. Alves, L., Nunes, M., Marchand, P., Le Bizec, B., Mendes, S. and Correia, J. (2016). Blue sharks (*Prionace glauca*) as bioindicators of pollution and health in the Atlantic Ocean: Contamination levels and biochemical stress responses. *Science of Total Environment*, 563-564 (2016): 282-292.
27. Farkas, A., Salánki, J. and Varanka, I. (2000). Heavy metal concentrations in fish of Lake Balaton. *Lakes & Reservoirs: Science, Policy and Management for Sustainable Use,* 5(4): 271-279.
28. Bełdowska, M., and Falkowska, L. (2016). Mercury in marine fish, mammals, seabirds, and human hair in the coastal zone of the southern Baltic. *Water, Air, Soil Pollution*, 227(2): 52.
29. Suhendrayatna, S., Arahman, N., Sipahutar, L., Rinidar, R. and Elvitriana, E. (2019). Toxicity and organ distribution of mercury in freshwater fish (*Oreochromis niloticus*) after exposure to water contaminated mercury. *Toxics*, *7*(4): 58.
30. Havelková, M., Dušek, L., Némethová, D., Poleszczuk, G. and Svobodová, Z. (2008). Comparison of mercury distribution between liver and muscle – a biomonitoring of fish from lightly and heavily contaminated localities. *Sensors*, *8*(7), 4095-4109.
31. Salam, M., Paul, S., Noor, S., Siddiqua, S., Aka, T. and Aweng, E. (2019). Contamination profile of heavy metals in marine fish and shellfish. *Global Journal of Environmental Science and Management*, 5(2): 225-236.
32. Beiras, R. (2018). Trace metals and organometallic compounds. *Marine Pollution*, Elsevier. pp: 137-164.
33. Mukaka, M. (2012). A guide to appropriate use of Correlation coefficient in medical research. *Malawi Medical Journal*, 24(3): 69-71.
34. Schober, P., Boer, C. and Schwarte, L. A. (2018). Correlation coefficients. *Anesthesia & Analgesia*, 126(5): 1763-1768.
35. Bosch, A., O'Neill, B., Sigge, G., Kerwath, S. and Hoffman, L. (2015). Heavy metals in marine fish meat and consumer health: a review. *Journal of the Science of Food and Agriculture*, 96(1): 32-48.
36. Ansari, T., Marr, I., and Tariq, N. (2003). Heavy metals in marine pollution perspective–a mini review. *Journal of Applied Sciences*, 4(1): 1-20.
37. Ahmad, N., Noh, M., Mahiyuddin, W., Jaafar, H., Ishak, I. and Azmi, W. (2014). Mercury levels of marine fish commonly consumed in Peninsular Malaysia. *Environmental Science and Pollution Research*, 22(5): 3672-3686.
38. Hashim, R., Tan, H., Noor Zuhartini, M. and Tan, P. (2014). Determination of heavy metal levels in fishes from the lower reach of the Kelantan River, Kelantan, Malaysia. *Tropical Life Sciences Research*, 25(2): 21-39.

Malaysian Journal of Analytical Sciences (MJAS)
Published by Malaysian Analytical Sciences Society

METHYLENE BLUE AND METHYL RED FROM PINEAPPLE PEEL–BASED BIOSORBENT FOR MASS TRANSFER SIMULATION AND STATISTICAL APPROACH

(Penggunaan Metilena Biru dan Metil Merah sebagai Biosorben Berbahan Kulit Nanas dalam Simulasi Pemindahan Jisim dan Pendekatan Statistik)

Nur Ayshah Rosli[1*], Mohd Azmier Ahmad[1], and Teh Ubaidah Noh[2]

[1]*School of Chemical Engineering, Engineering Campus, Universiti Sains Malaysia, 14300, Nibong Tebal, Penang, Malaysia*
[2]*Institute of Bioproduct Development, Universiti Teknologi Malaysia, 81310, Skudai, Johor, Malaysia*

[*]*Corresponding author: chnurayshah@usm.my*

Received: 11 August 2023; Accepted: 3 October 2023; Published: 29 December 2023

Abstract

The study focused on the utilization of pineapple peel activated carbon (PineAC) biosorbent, produced through a low–cost and environmentally friendly method, for the adsorption of methylene blue (MB) and methyl red (MR) dyes. PineAC was characterized using various techniques such as surface analysis, scanning electron microscopy (SEM), energy–dispersive X–ray (EDX), and Fourier–transform infrared (FTIR) spectroscopy. ANOVA analysis was conducted to assess the significance of different factors, with *p*–values below 0.05 considered statistically significant. The obtained *F*–values, compared to *F*–crit values, indicated the overall significance of the tests. The kinetic data agreed with the Polymath Mass Transfer (PMT) model, which accurately captured the adsorption behaviour. The PMT model precisely predicted the adsorption surface area (a_m) as 612.60 m^2/g, closely aligning with the actual mesopores surface area of 547.85 m^2/g for the MB dye. Conversely, the PMT model for the MR dye failed to match the actual calculation, suggesting that the MR dye exhibited unfavourable adsorption characteristics towards PineAC. This demonstrated the reliability and robustness of the PMT model in describing the adsorption process. Exploring the potential functionalization of PineAC could offer opportunities for enhanced performance and broader applications in sustainable wastewater treatment.

Keywords: polymath mass transfer, activated carbon, mass transfer, methylene blue, methyl red

Abstrak

Kajian ini memberi tumpuan kepada penggunaan karbon teraktif kulit nanas (PineAC), dihasilkan melalui kaedah yang murah dan mesra alam, untuk penjerapan pewarna metilena biru (MB) dan metil merah (MR). PineAC telah dicirikan menggunakan pelbagai teknik seperti analisis permukaan, mikroskopi imbasan elektron (SEM), sinar–X tersebar tenaga (EDX), dan spektroskopi inframerah transformasi Fourier (FTIR). Analisis ANOVA telah dijalankan untuk menilai kepentingan faktor–faktor berbeza, dengan nilai p yang kurang daripada 0.05 dianggap signifikan secara statistik. Nilai F yang diperoleh, berbanding dengan nilai *F*–kritikal, menunjukkan kepentingan keseluruhan ujian tersebut. Data kinetik selari dengan model pemindahan jisim polimat (PMT), yang menggambarkan dengan tepat tingkah laku penjerapan. Selain itu, model PMT secara tepat meramalkan kawasan permukaan

penjerapan (a_m) sebagai 612.60 m^2/g, hampir seiring dengan kawasan permukaan mesopor sebenar 547.85 m^2/g bagi pewarna MB. Sebaliknya, model PMT bagi pewarna MR gagal sejajar dengan perhitungan sebenar, menunjukkan bahawa pewarna MR menunjukkan ciri–ciri penjerapan yang tidak menguntungkan terhadap PineAC. Ini membuktikan kebolehpercayaan dan ketahanan model PMT dalam menggambarkan proses penjerapan. Meneroka potensi pemekaan PineAC boleh memberi peluang untuk prestasi yang lebih baik dan aplikasi yang lebih luas dalam rawatan air sisa lestari.

Kata kunci: pemindahan jisim polimat, karbon teraktif, pemindahan jisim, metilena biru, metil merah

Introduction

The presence of organic dyes in industrial effluent are responsible for releasing a considerable number of dyes, including substances like methylene blue (MB) and methyl red (MR) dyes, into wastewater during synthesis and processing [1]. MB dye, for example, exhibits remarkable stability to oxidizing agents, light, and heat, due to the high intensity of its amino groups and chromophore's positive ion, making it difficult to degrade or remove from aqueous solutions [2]. The harmful effects of dyes are not limited to the environment but also extend to both human and animal forms, causing various health issues such as respiratory difficulties, nausea, eye irritation, excessive sweating, vomiting, and cognitive confusion [3–5]. Consequently, the removal of MB and MR dyes from wastewater using activated carbon (AC) is of utmost importance to prevent their release into the environment.

Pineapple peels–based AC (PineAC) as an adsorbent offers a practical approach for removing MB and MR dyes from wastewater. PineAC possesses a high surface area and porosity, providing adsorption sites for dye molecules to adhere to its surface through physical interactions such as electrostatic attraction, van der Waals forces, and π–π stacking [6]. These properties make PineAC an ideal choice for the adsorption of MB and MR dyes, facilitating their removal from wastewater prior to its discharge into the environment. The effectiveness of the adsorption process is greatly influenced by variables like temperature, pH, contact duration, and the amount of biosorbent used [7, 8]. Longer contact times and higher biosorbent dosages enhanced the adsorption capacity of AC, while an optimal pH range and temperature can promote favourable dye–biosorbent interactions [9, 8, 10]. Additionally, the mesopores in the PineAC structure can enhance its accessibility and surface area, leading to improved dyes adsorption performance [11].

In this work, mass transfer simulation improved the estimation of mesopores in PineAC structures for dyes adsorption. By employing mass transfer simulation techniques, researchers better understood the intricate processes involved in dyes adsorption within the mesopores [12]. This simulation allowed for a more accurate estimation of the mesopores' effectiveness and their contribution to the overall adsorption capacity of PineAC structures [13]. Based on the reported findings by Mohamad Yusop et al. [14–16], the observed alignment of adsorption kinetics with the mass transfer simulation using the Polymath mass transfer (PMT) model underscored the robustness and reliability in effectively describing the adsorption process. Such optimization endeavours were crucial in ensuring the judicious utilization of resources and achieving the desired level of dye removal efficacy [16]. Moreover, mass transfer simulation enabled the prediction of breakthrough behaviour in dye adsorption systems, contributing to its long–term sustainability and effectiveness [14].

In recent studies conducted by Mohamad Yusop et al. [13–16], the kinetics of dye adsorption were investigated using the PMT model for mass transfer simulation. These investigations' findings suggested that a major factor in the adsorption of dyes was the mass transfer mechanism between the biosorbent and adsorbate. Mohd Ramli et al. [13] observed that the mass transfer coefficient decreased as the initial concentration of MB dye increased when using AC biosorbent derived from the jengkol peel. In the adsorption of the remazol brilliant blue R (RBBR) dye, Mohamad Yusop et al. [14] correctly anticipated the adsorption surface area (a_m) to be 790.04 m^2/g utilizing meranti wood–based AC. This

figure was quite near the 825.58 m^2/g surface area of the mesopores. Similarly, when teak wood–based AC was employed in the adsorption of RBBR dye, the PMT model predicted the a_m value of 940.79 m^2/g, which closely aligned with the actual mesopores surface area of 983.25 m^2/g [15]. Furthermore, the PMT model successfully predicted the a_m of 807.77 m^2/g for jackfruit–based AC in the adsorption of malachite green (MG) dye, which was comparable to the actual mesopores surface area of 714.25 m^2/g with an error of 11.58% [16]. Regarding the kinetics data, the PMT model provided the best fit, and the rate constant (k_{PTM}) was found to increase from 3.96 to 4.34 h^{-1} and 4.84 to 5.22 h^{-1} as the initial RBBR dye concentration increased using meranti wood and teak wood–based AC, respectively. Conversely, jackfruit–based AC exhibited a decrease in K_{PMT} from 1.20 to 0.41 h^{-1} as the MG dye concentration increased from 25 to 300 mg/L. Overall, these studies demonstrated the significance of the PMT model in describing the kinetics of dye adsorption and the influence of various factors, such as dye concentration and biosorbent type, on the mass transfer process.

Meanwhile, ANOVA was employed to evaluate the influence of different factors on dye adsorption. Following ANOVA, post hoc Bonferroni correction analysis was conducted to thoroughly investigate the experimental groups' differences in dye adsorption capacities. This post hoc analysis allowed researchers to perform pairwise comparisons between biosorbents or conditions, identifying cases where significant differences in dye adsorption performance were observed [17]. By employing this analytical framework, valuable insights were gained regarding the relative efficacy of different biosorbents or experimental conditions, aiding in the identification of the most promising candidates for efficient dye removal.

In this study, the MB and MR dyes adsorption using PineAC was done similarly to Rosli et al. [6] work in order to understand the mass transfer simulation and statistic approach studies in adsorption studies. The PineAC was characterized using a surface analyser, Fourier Transform Infrared (FTIR), Energy Dispersive X–ray (EDX), and scanning electron microscopy (SEM). The equilibrium isotherm of PineAC–MB and PineAC–MR dyes adsorption based on different temperatures were also discussed. The study introduced the Polymath mass transfer (PMT) model for the analysis of kinetic data in the PineAC–MB and PineAC–MR dyes adsorption system, representing a novel approach. In comparison to the traditional pseudo–first–order (PFO) and pseudo–second–order (PSO) kinetic models, the PMT model offered distinct advantages, notably its capability to predict the specific surface area implicated in the adsorption process. This characteristic of the PMT model provided researchers with valuable insights, further enriching their comprehension of the underlying adsorption mechanism. By repurposing pineapple peel, disposal costs can be minimized, and the environmental impact of waste accumulation can be reduced.

Materials and Methods

Materials

The studies of the PineAC were determined using 4–dimethylaminoazobenzene–2–carboxylic acid (MR) and 3,7–bis(dimethylamino)phenazathionium chloride (MB) (82%), purchased from Sigma–Aldrich (M) Sdn. Bhd., Malaysia. Potassium hydroxide (KOH) pellets (85%) were procured from Merck in Germany. For pH adjustments during the experiment, hydrochloric acid (HCl)(37%) and sodium hydroxide (NaOH) (99%) were acquired from Merck and Essex, respectively.

Preparation of PineAC and instrumental analysis

The raw material for PineAC, known as pineapple peel, was sourced from Parit Buntar, Perak, Malaysia. To prepare the pineapple peel raw material, it underwent a washing process and was subsequently dried in an oven for two hours, as described by Iamsaard et al. [18] study. The PineAC preparation method employed in this study was a two–step pyrolysis process based on the work conducted by Rosli et al. [6, 8, 10]. The work optimized the conditions for PineAC preparation, and these optimal conditions were used in the current study. The optimal parameters included an impregnation ratio (IR) of 3.0, a carbonization temperature of 732 °C, and a carbonization duration of 1.96 hours, which represented the weight ratio of KOH to char. These specific parameters were chosen based on their ability to yield

PineAC samples with suitable properties and achieved optimal adsorption performance, as demonstrated in the findings of Rosli et al. [6]. Figure 1 illustrates the process of PineAC preparation, which involves the steps mentioned above. PineAC's characteristics were studied using suitable analytical techniques similar to Rosli et al. [6, 8].

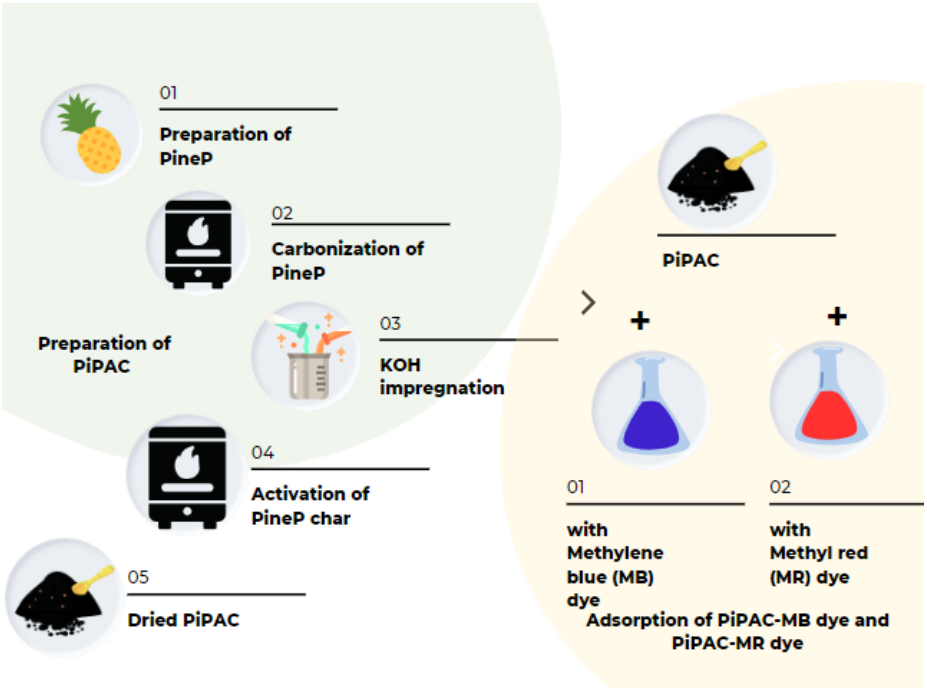


Figure 1. The flowchart for the PineAC preparation process

Adsorption studies

The batch adsorption experiments were conducted based on the methodology described in the works of Rosli et al. [6, 8]. The MB and MR dyes' maximum wavelength was 664 nm and 410 nm, respectively (Figure S1 and S2). In order to investigate the effects of initial adsorbate concentration and contact time on the adsorption process, various initial concentrations ranging from 25 to 300 mg/L for both MB and MR dyes were prepared, and the experiments were conducted over 24 hours. The impact of solution pH on the adsorption process was explored by adjusting the initial pH of the solutions within the range of 2 to 12. Furthermore, the influence of solution temperature on adsorption was investigated by conducting experiments at three different temperatures: 30, 45, and 60 °C.

Results and Discussion

Characterization of PineAC

PineAC exhibited a significant BET surface area of 1160 m^2/g. With an average pore diameter of 2.17 nm and a surface area of 547.85 m^2/g, PineAC's mesoporous character was evident [6]. The increased pore volume and surface area of PineAC were attributed to the removal of volatile matter and moisture content during the carbonization and pyrolysis of pineapple peel raw material (Figure 2(a)) [6–8]. As a result, the overall pore volume of PineAC increased from 0.173 cm^3/g to 0.544 cm^3/g. This is due to the carbonization process effectively enlarging the average pore width in the mesoporous regions [5]. The surface morphology of PineAC is shown in Figure 2(b), which highlights an uneven, sizable pore structure on the surface. The heterogeneous pore structure of PineAC was able to grow thanks to the KOH impregnation. The physiochemical treatment that created porous PineAC

enhanced the adsorption capability of MB and MR dyes [19].

The EDX analysis (Figure 2(c)) showed that the PineAC consisted of 0.14% sulphur, 67.18% carbon, 14.05% oxygen, 12.79% N_2, 4.62% potassium, 0.44% magnesium, and 0.79% calcium, implying that it was a specific sort of AC created by heating carbonaceous materials in the presence of a chemical agent [8]. Figure 2(d) shows the FTIR spectra of PineAC, revealing multiple peaks corresponding to various functional groups. The O–H stretching of the hydroxyl group appeared in the wavelength range of 3865-3610 cm^{-1}. The C≡C stretching of the alkyne group was observed within the range of 2399-2094 cm^{-1}. The presence of the C=O stretching in aldehydes and ketones was indicated by a characteristic peak at approximately 1732 cm^{-1}. Furthermore, the C=C stretching of the aromatic group generated a distinct peak at around 1527 cm^{-1}. Lastly, the =C–H bend of alkenes contributed to the spectrum by exhibiting a peak around 991 cm^{-1}. These specific wavelength ranges provided valuable insights enabling its identification and characterization in MB and MR dye removal [6,16].

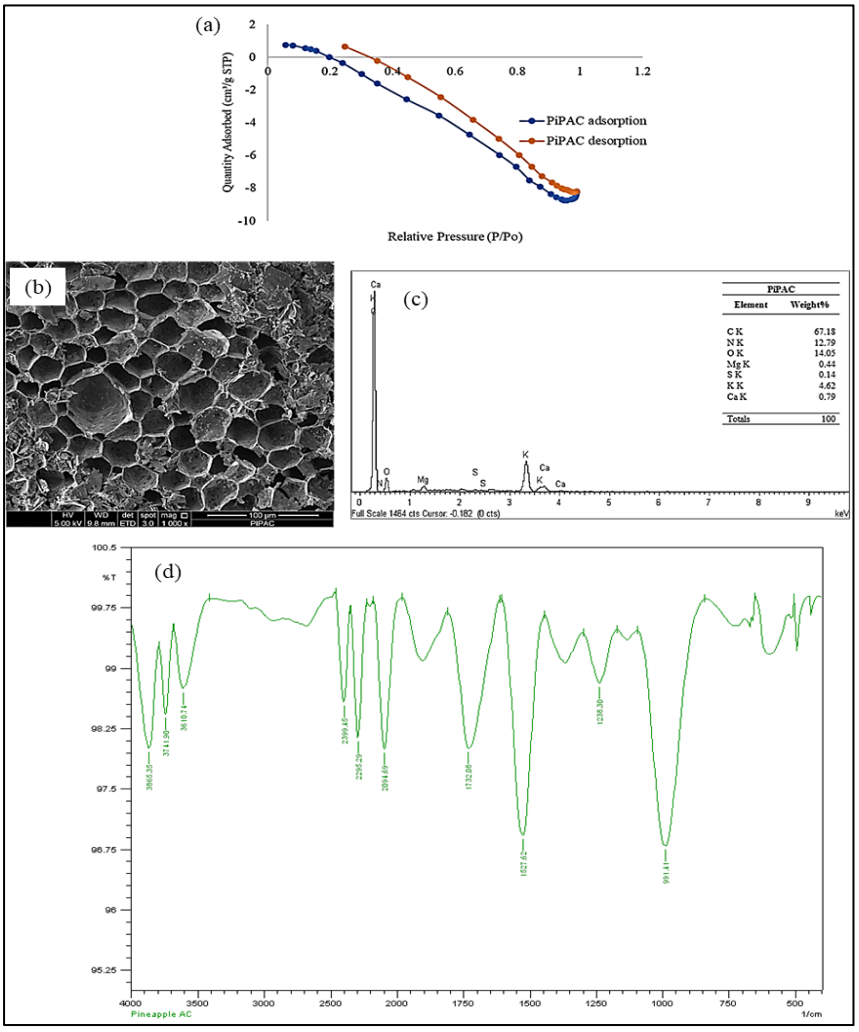


Figure 2. (a) N_2 adsorption/desorption isotherm, (b) SEM image, (c) EDX spectra, and (d) the FTIR spectrums of PineAC

Batch adsorption studies and statistical analysis

The adsorption capacity (q_t) for PineAC–MB dye increased from 23.993 to 165.177 mg/g as the starting concentration increased to 300 mg/L at 60 °C (Figure 3(a)). Initial MB dye concentrations ranging from 25 to 100 mg/L were observed to reach equilibrium more quickly (< 5 hours) compared to between 20 to 24 hours. This can be attributed to a lower ratio of MB dye to available sites, allowing for efficient adsorption at lower concentrations. However, the removal of MB dye (%) decreased at higher concentrations due to the larger ratio of MB dye to accessible sites. This removal efficiency decrease occurred because many PineAC surface sites were initially accessible for adsorption [5, 19]. Similarly, in Figure 3(b), the adsorption uptakes of PineAC–MR dye at equilibrium increased from 14.48 to 94.870 mg/g as the starting concentration was raised from 25 to 300 mg/L. This can be attributed to a stronger mass transfer force driving greater uptake of MR dye at higher concentrations. The presence of other adsorbate species in the solution and the delayed diffusion of solute molecules into the bulk of the biosorbent were additional contributing factors [8]. Furthermore, at 60 °C, the amount of MB dye adsorbed rose from 129.77 mg/g to equilibrium, while the adsorption uptakes of PineAC–MR dye increased from 54.85 mg/g (Figure 3(d)). The rate of adsorbate molecule diffusion into the internal pores of the biosorbent particles and across the external boundary layer was accelerated by the rise in temperature [6, 19].

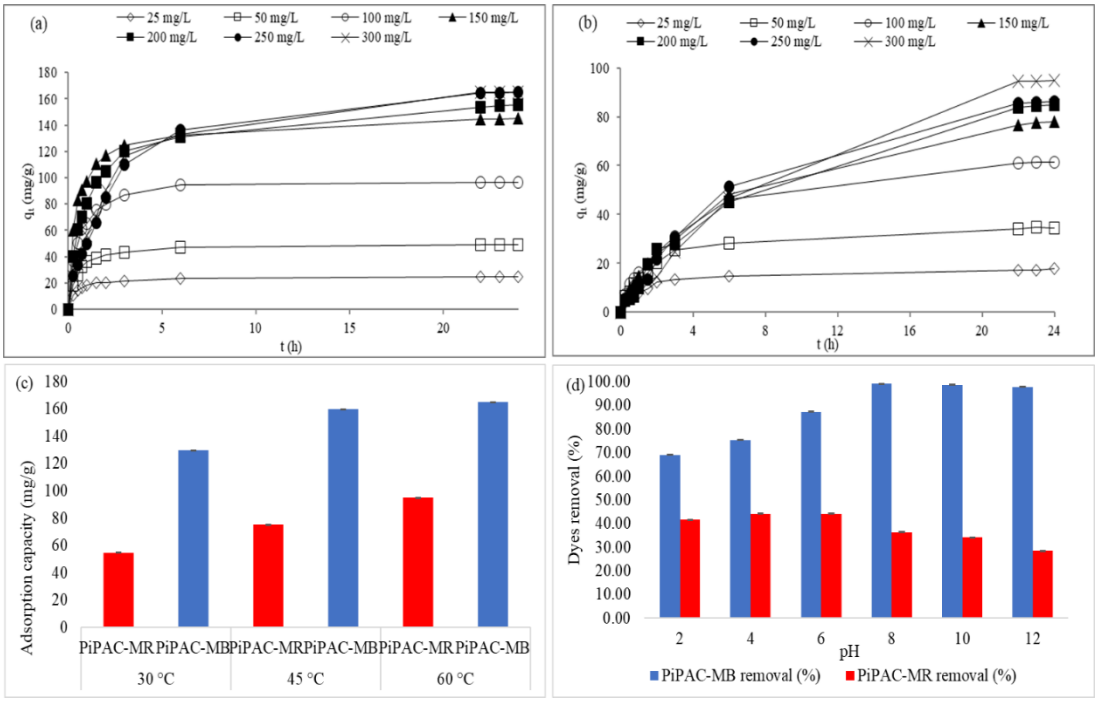


Figure 3. The q_t of (a) PineAC–MB dye and (b) PineAC–MR dye were measured at 60°C within 24 hours (25 to 300 mg/L). The effect of (c) temperature and (d) pH on PineAC–MB and PineAC –MR dyes were also shown

Based on the data presented in Figure 3(d), it was observed that the removal of PineAC–MB dye increased with an increase in pH in the solution. The maximum removal of PineAC–MB dye, reaching 99%, was achieved at pH 8. Moreover, the adsorption of MB dye remained relatively constant above pH 8. At low pH levels, the low adsorption of PineAC–MB dye was attributed to the abundance of H^+ ions competing with the MB dye cation for adsorption sites on the PineAC surface. Conversely, the negatively charged PineAC surface exhibited an attractive electrostatic force at high pH levels, promoting the elevation and adsorption of the positively charged MB dye cation [6]. On the other hand, PineAC–MR dye adsorption displayed a

preference for an acidic environment, with optimal adsorption observed at pH 6. This can be attributed to the abundance of positively charged PineAC sites under acidic conditions, facilitating the adsorption of MR dye. Additionally, as the pH rose above 6, there were more negatively charged sites. The increased adsorption of MR dye with a drop in pH value was explained by the attraction between the azo dye and more H^+ ions in the solution [8, 10].

Because of its azo group–based chemical structure, MR dye had lower adsorption uptakes than PineAC–MB dye. However, MB dye, a basic dye, has cationic properties because of its positive charge, which was frequently dispersed throughout the chromophoric system [20]. Notably, PineAC shared the same hexatomic ring of carbon atoms (Figure 4), enabling it to naturally form π–π interactions with both MB and MR dyes. Due to reduced electrostatic interactions, this showed that van der Waals forces were more important than hydrogen bonding in preserving the stability of the complex [8, 10]. These results suggested that the intensity and frequency of van der Waals interactions within the system affected the binding of PineAC with MB and MR dyes as well as the consequent adsorption capacities and overall stability. These results suggested that the intensity and frequency of van der Waals interactions within the system affected the binding of PineAC with MB and MR dyes as well as the consequent adsorption capacities and overall stability.

The ANOVA test was a statistical tool utilized to assess significant differences among the means of multiple groups in this study. In the context of adsorption studies, ANOVA analysis enabled the investigation of various factors' impacts on the adsorption process and determined their statistical significance [21]. ANOVA tests were conducted to evaluate the significance of four primary adsorption parameters, temperature, initial dye concentration, pH, and contact time, on the PineAC with MB and MR adsorption. The influential factors were identified by examining the statistical significance of these variables, and their effects on the adsorption process were understood. The variables in this study were defined as contact time (24 hours), initial dye concentration (25-300 mg/L), pH (2-12), and temperature (30-60 °C). The summary statistical analysis in Table 1 presented the effects of major interactive variables, including degrees of freedom (df), *F*–values, *F*-crit, sum of squares (SS), mean square (MS), and *p*–values. A *p*–value below 0.05 indicated the significance of the models in the regression analysis considering the independent variables. The analysis of the ANOVA models was conducted by assessing the significance of each term, considering *p*–values below 0.05 as statistically significant. The larger *F*–values compared to *F*-crit values indicated the overall significance of the tests. Consequently, these statistical outcomes supported the acceptance of the alternative hypothesis, suggesting significant differences between the means of the analysed parameters.

However, as the ANOVA test alone does not provide specific information regarding the significant differences between individual parameters, a post–hoc test with Bonferroni correction was conducted to analyse the data further. Table 2 presents a summary of the Post–Hoc Tests (Bonferroni Correction) conducted to assess the effects of temperature, initial dye concentration, and pH on the adsorption of PineAC–MB and PineAC–MR dyes [22]. The *t*–test with adjusted *p*–values were performed for each parameter, and the Bonferroni correction method was employed to account for multiple comparisons. By adjusting the alpha level (0.05) based on the provided data, the likelihood of Type I errors resulting from multiple hypothesis testing was effectively controlled. The analysis yielded significant results, as evidenced by the calculated adjusted *p*–values. Specifically, for PineAC–MB dye, statistically significant differences were observed between contact time and initial dye concentrations of 100-300 mg/L, as well as between pH and dye removal (%). In the case of PineAC–MR dye, all combinations of initial dye concentration, contact time, and pH, with the percentage of dye removal, were found to be statistically significant. These findings further underscore the significance of the analysed parameters and offer more comprehensive insights into their respective effects on the adsorption process.

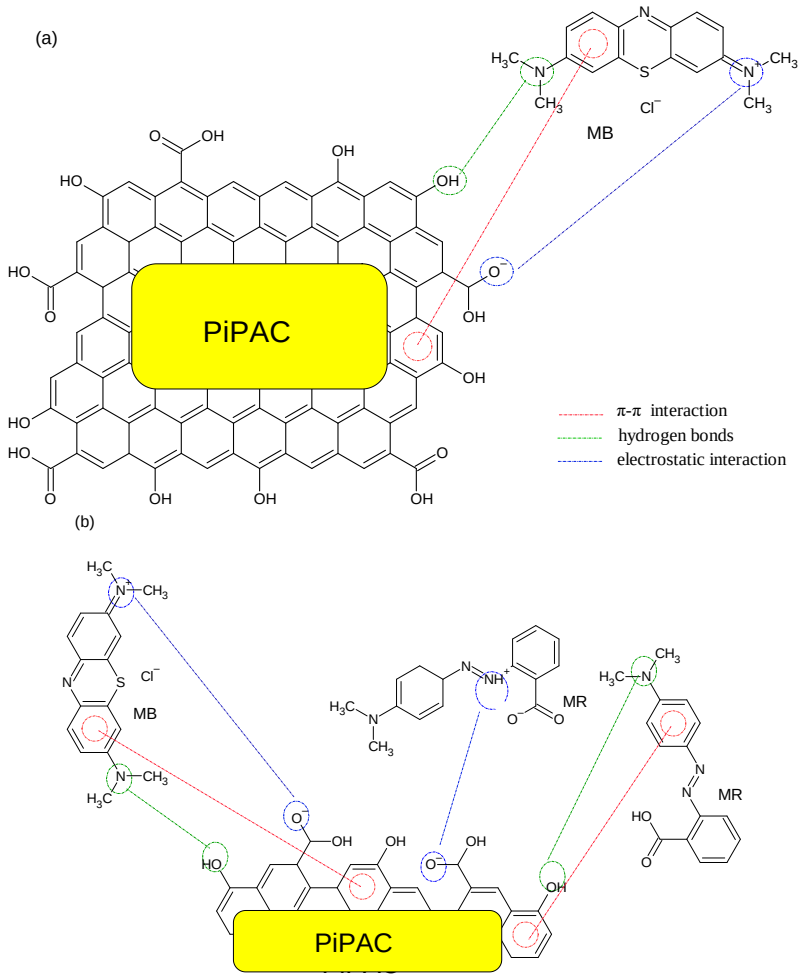


Figure 4. The mechanism of (a) PineAC–MB and (b) PineAC–MR dyes adsorption

Adsorption isotherm studies

In this study, the Langmuir and Freundlich isotherm models were selected to analyse the experimental equilibrium data. Figure S3 illustrates the adsorption equilibrium curves obtained from each isotherm model and compares them with the experimental values for PineAC–MB and PineAC–MR dyes at 30 to 60 °C. The goodness of fit for each model was assessed based on the R^2 values, as shown in Table 3. The Langmuir isotherm model exhibited in agreement with the experimental data ($R^2 > 0.99$) for the adsorption of both PineAC–MB and PineAC–MR dyes at 60 °C. The Langmuir model suggested a monolayer adsorption behaviour, and the maximum adsorption capacities (Q_m) were determined as 168.528 mg/g and 107.798 mg/g for PineAC–MB and PineAC–MR dyes, respectively [6]. On the other hand, the Freundlich isotherm parameters showed that the adsorption process for PineAC–MB and PineAC–MR dyes was favourable at 30 to 45 °C. The Freundlich model describes a physical adsorption process and provides information about the heterogeneity and adsorption intensity of the biosorbent [23]. The results indicated that PineAC demonstrated favourable adsorption characteristics for both PineAC–MB and PineAC–MR dyes. The Langmuir model represented the monolayer adsorption behaviour at 60 °C, while the Freundlich model confirmed the favourable physical adsorption process at lower temperatures.

Table 1. The summary of ANOVA analysis for the effect of temperature, initial dye concentration, and pH for PineAC–MB and PineAC–MR dyes adsorption

PineAC–MB dye							PineAC–MR dye						
Source of Variation	**SS**	**df**	**MS**	**F**	**P–value**	**F crit**	**Source of Variation**	**SS**	**df**	**MS**	**F**	**P–value**	**F crit**
Initial concentration of dye and contact time													
Regression	659482.87	8	82435.36	78.2587	1.9412E–36	2.0467	Regression	796445.72	8	99555.72	145.7884	5.1016E–47	2.0467
Residual	91643.18	87	1053.37				Residual	59410.39	87	682.88			
Effect of temperature													
Regression	120244.13	7	17177.73	10.9740	6.874E–10	2.1155	Regression	10544.06	7	1506.29	2.2321	0.0389	2.1155
Residual	137746.87	88	1565.31				Residual	59385.62	88	674.84			
Effect of pH													
Regression	15704.99	1	15704.99	141.5461	3.1672E–07	4.9646	Regression	5019.404	1	5019.40	178.9319	1.0456E–07	4.9646
Residual	1109.53	10	110.95				Residual	280.5203	10	28.05			

Table 2. The summary of Post–Hoc Tests (Bonferroni Correction) for the effect of initial dye concentration, temperature, and pH for PineAC–MB and PineAC–MR dyes adsorption

PineAC–MB dye				PineAC–MR dye			
Initial concentration of dye and contact time							
Groups (min vs. mg/L)	**t–test (new p–value)**	**Significant**	**Post–Hoc Tests (Bonferroni Correction) alpha**	**Groups (min vs. mg/L)**	**t–test (new p–value)**	**Significant**	**Post–Hoc Tests (Bonferroni Correction) alpha**
time vs. 25	0.4134	NO		time vs. 25	1.0184E–03	YES	
time vs. 50	0.0190	NO		time vs. 50	4.0421E–08	YES	
time vs. 100	0.0002	YES		time vs. 100	4.3543E–13	YES	
time vs. 150	2.701E–07	YES	0.0063	time vs. 150	6.3070E–17	YES	0.0063
time vs. 200	1.678E–10	YES		time vs. 200	2.0634E–19	YES	
time vs. 250	1.056E–12	YES		time vs. 250	2.6235E–20	YES	
time vs. 300	3.289E–14	YES		time vs. 300	1.4000E–21	YES	
Effect of temperature							
Groups	**t–test (new p–value)**	**Significant**	**Post–Hoc Tests (Bonferroni Correction) alpha**	**Groups**	**t–test (new p–value)**	**Significant**	**Post–Hoc Tests (Bonferroni Correction) alpha**
concentration vs. 30°C	0.1721	NO		concentration vs. 30°C	0.0125	YES	
concentration vs. 45°C	0.3257	NO	0.0167	concentration vs. 45°C	0.0222	NO	0.0167
concentration vs. 60°C	0.3968	NO		concentration vs. 60°C	0.0490	NO	
Effect of pH							
Groups	**t–test (new p–value)**	**Significant**	**Post–Hoc Tests (Bonferroni Correction) alpha**	**Groups**	**t–test (new p–value)**	**Significant**	**Post–Hoc Tests (Bonferroni Correction) alpha**
pH vs. removal %	3.1672E–07	YES	0.0250	pH vs. removal %	1.0456E–07	YES	0.0250

Table 3. Isotherm parameters for PineAC–MB and PineAC–MR dyes adsorption

T (°C)	PineAC–MB dye				PineAC–MR dye			
	Langmuir		Freundlich		Langmuir		Freundlich	
30	Q_m	128.529	K_F	46.457	Q_m	58.552	K_F	8.02
	K_L	0.266	n_F	4.747	K_a	0.03	n_F	2.853
	R^2	0.986	R^2	0.991	R^2	0.72	R^2	0.877
	Δq_e (%)	0.72	Δq_e (%)	16.799	Δq_e (%)	0.53	Δq_e (%)	1.561
45	Q_m	160.119	K_F	58.486	Q_m	86.794	K_F	8.153
	K_a	0.287	n_F	4.695	K_a	0.02	n_F	2.451
	R^2	0.885	R^2	0.999	R^2	0.969	R^2	0.997
	Δq_e (%)	2.097	Δq_e (%)	20.549	Δq_e (%)	1.068	Δq_e (%)	1.481
60	Q_m	168.528	K_F	77.152	Q_m	107.798	K_F	13.942
	K_a	0.524	n_F	5.804	K_a	0.032	n_F	2.706
	R^2	0.975	R^2	0.974	R^2	1	R^2	0.948
	Δq_e (%)	15.353	Δq_e (%)	13.522	Δq_e (%)	0.432	Δq_e (%)	7.593

The studies discussed highlighted the diverse applications of pineapple peel and its derivatives as effective biosorbents for pollutant removal. These findings contributed significantly to the field of water and wastewater treatment, showcasing the potential of pineapple–based materials. To further contextualize and add depth to these discussions, a comparative analysis with existing literature and a focus on the novelty of the PineAC biosorbent was elucidated. Comparative studies with existing literature revealed the uniqueness of PineAC in terms of its adsorption capacities. While Ugbe et al. [24] and Chaiyaraksa et al. [25] reported q_{max} values for the removal of Eosin Yellow and Basic Red 9 using untreated pineapple peel, the development of PineAC surpassed these capacities. PineAC achieved a remarkable q_{max} of 165.17 mg/g at pH 8 for the removal of a pollutant, exceeding the reported values in previous studies [22]. This significant enhancement in adsorption capacity could be attributed to the specific activation methods and processing techniques employed in the synthesis of PineAC, setting it apart from traditional pineapple peel–based biosorbents.

The utilization of pineapple peel for hydrogel development, as demonstrated by Dai et al. [26], showcased high adsorption capacities for Congo Red removal. However, PineAC outperformed these hydrogels, achieving a q_{max} of 165.17 mg/g compared to the reported values of 114.940 mg/g for water pineapple peel hydrogels. The alkali and bleaching pineapple peel hydrogels also demonstrated lower q_{max} values of 77.520 mg/g and 138.890 mg/g, respectively. This suggested that the specific formulation and activation process of PineAC contributed to its superior adsorption performance. Activation methods played a crucial role in enhancing the adsorption capacity of biosorbents. While Turkmen et al. [27] activated pineapple peel using $ZnCl_2$ and observed an increased q_{max} for the adsorption of Zn(II), the PineAC biosorbent, activated through a different method, achieved a higher q_{max} at 165.17 mg/g. Similarly, the H_2SO_4–activated pineapple peel showed promise with a q_{max} of 36.99 mg/g, but PineAC surpassed this capacity, indicating the effectiveness of the novel activation method used in its synthesis.

Furthermore, the comparative analysis extended to the temperature–dependent biochar production process explored by Shakya and Agarwal [28]. Pineapple peel biochar exhibited q_{max} values ranging from 23.81 to 33.33 mg/g for Cr(VI) adsorption. In contrast, PineAC demonstrated a significantly higher q_{max} of 165.17 mg/g at pH 8, highlighting the superiority of PineAC for pollutant removal. The investigation of pineapple peel for Cd(II) removal by Yusoff et al. [29] reported a q_{max} of 1.91 mg/g. In comparison, PineAC showcased a substantially higher adsorption capacity of 165.17 mg/g at pH 8. This emphasized the versatility of PineAC across a broad spectrum of pollutants and pH conditions, and its efficacy in comparison to conventional pineapple peel–based biosorbents.

Thus, the presented comparative discussion emphasizes the pioneering nature of the PineAC biosorbent. The innovative approach to activation and processing techniques led to a significant enhancement in adsorption capacities, outperforming existing literature across various pollutants and pH conditions. The development of PineAC opened new avenues for sustainable and efficient solutions in water and wastewater treatment, showcasing its potential as a leading biosorbent in the field. Further research and optimization of PineAC and similar derivatives held promise for advancing the landscape of environmental remediation technologies.

Table 4. Comparative analysis of the adsorption capacity of pineapple peel adsorbate based on different pollutant

Adsorbent Name	q_{max} (mg/g)	pH	Pollutant	Ref.
Pineapple peel as biosorbents	11.76	–	Eosin Yellow	[24]
Pineapple peel activated by $ZnCl_2$	37.23	–	Zn(II)	[27]
Pineapple peel activated by H_2SO_4	36.99	–		
Silver nanoparticles from pineapple peel waste	98.04	9.96	MB	[22]
Pineapple peel biochar	23.81–33.33	2	Cr(VI)	[28]
Pineapple peel	11.389	7	Basic Red 9	[25]
Water pineapple peel hydrogels	114.94	4	Congo Red	[26]
Alkali pineapple peel hydrogels	77.52			
Bleaching pineapple peel hydrogels	138.89			
Pineapple peel	1.91	9	Cd(II)	[29]
PineAC	165.17	8	MB	This work
	94.87	6	MR	

Adsorption kinetic studies and mass transfer simulation

This study utilized three kinetic models: the PFO, PSO, and PMT models. The PFO and PSO models' q_e (mg/g) values showed a rise with increasing starting concentration, from 25 to 300 mg/L at 30 to 60 °C (supplementary data). This trend indicated that as the initial concentrations of MB and MR dyes increased, the adsorption capacity of PineAC also increased, suggesting a stronger affinity between the MB and MR dye molecules and the adsorption sites on PineAC [6]. Comparing the two models, the PSO kinetic model demonstrated higher consistency regarding R^2 and Δq_t values than the PFO model. Additionally, the k^2 value showed a non–linear pattern with increasing initial concentration, suggesting the influence of various mechanisms on the adsorption of PineAC–MB and PineAC–MR dyes.

Table 5 summarizes the kinetic parameters based on different temperatures for PFO, PSO, and PMT, showing relatively high average R^2 values at 30 to 60°C. However, for PineAC–MB dye adsorption, both the PFO and PSO models exhibited relatively high average Δq_t percentages, ranging from 29.01 to 72.59% and 6.55 to 77.12%, respectively, at 30 to 60°C. Similarly, for PineAC–MR dye adsorption, the PFO and PSO models showed relatively low average Δq_t percentages, ranging from 5.50 to 54.11% and 60.82 to 26.96%, respectively, compared to PineAC–MB dye adsorption. These percentages suggested that these models were not able to accurately predict the uptake of PineAC–MB and PineAC–MR dyes at equilibrium, $q_{e,\,cal}$ [13]. In contrast, the PMT model of PineAC–MB and PineAC–MR dyes adsorption demonstrated relatively low average Δq_t percentages of 1.3526 to 1.53% and 0.36 to 1.01%, respectively, at 30 °C to 60 °C, indicating the best fit for the kinetic data.

Moreover, the PMT model (Figures 5 and 6) accurately predicted the highest adsorption surface area to be 612.60 m^2/g (with an error percentage of 1.35%) for the MB dye, closely matching the actual mesopores surface area of 547.85 m^2/g [14]. However, the PMT model for the MR dye showed the highest adsorption surface area of 192.55 m^2/g (with an error percentage of 0.41%) and was unable to correspond to the actual mesopores surface area. This discrepancy was likely due to the low percentage of removal of the MR dye by PineAC, making it less favourable for adsorption. The investigated study explored the relationship between the initial concentrations of MB and MR dyes and mass transfer rates, with a focus on the formation of concentration gradients and the resulting mass transfer driving force [15]. Further analysis revealed that as the initial concentrations of MB and MR dyes increased from 25 mg/L to 300 mg/L, the PMT $q_{e,\ exp}$, and $q_{e\ cal}$ exhibited similar values and increased at 30 to 60°C. Generally, higher initial concentrations of MB and MR dyes resulted in more significant concentration gradients, leading to a more substantial mass transfer driving force. Consequently, this relationship typically led to higher rate constants and increased mass transfer rates [16].

Table 5. The summary of the kinetic model for PFO, PSO, and PMT constant parameters of PineAC–MB and PineAC–MR dyes adsorption at 30 to 60°C

T (°C)	Kinetic Parameters	PineAC–MB Dye			PineAC–MR Dye		
		PFO	PSO	PMT	PFO	PSO	PMT
30	a_{PMT} (m^2/g)	–	–	233.6181	–	–	66.3993
	R^2	0.9609	0.9556	0.9724	0.9414	0.9243	0.9908
	Δq_t (%)	35.3653	10.7867	1.3526	13.3754	26.9687	0.3645
45	a_{PMT} (m^2/g)	–	–	307.4033	–	–	44.1481
	R^2	0.9657	0.9666	0.9695	0.9389	0.8521	0.9453
	Δq_t (%)	72.5954	77.1249	1.5319	54.1171	16.9886	1.0175
60	a_{PMT} (m^2/g)	–	–	612.6089	–	–	192.5528
	R^2	0.9561	0.9366	0.9763	0.9701	0.7047	0.9932
	Δq_t (%)	29.0193	6.5549	1.3528	5.5066	0.8211	0.4190

Conclusion

The physiochemical treatment employed during the production of PineAC resulted in the formation of a porous structure, significantly enhancing its adsorption capacity for MB and MR dyes. The observed surface morphology was consistent with N_2 adsorption isotherm, EDX, and FTIR analysis. The ANOVA models indicated statistically significant differences (*p*–values <0.05), and the larger *F*–values compared to *F*–crit values supported the acceptance of the alternative hypothesis, suggesting significant differences between the means of the analysed parameters. In–depth, kinetic studies revealed that the PMT model provided the best fit for the investigated adsorption system. Notably, the PMT model accurately predicted the MB dye adsorption surface area to be 612.60 m^2/g, closely matching the measured value of PineAC's mesopores surface area. This high level of precision underscores the reliability and accuracy of the PMT model in describing the adsorption process. These findings highlight the potential of PineAC as an efficient and cost–effective adsorption system for the removal of MB and MR dyes. Further research and development in this direction can contribute to the advancement of PineAC–based adsorption systems for effective dye removal.

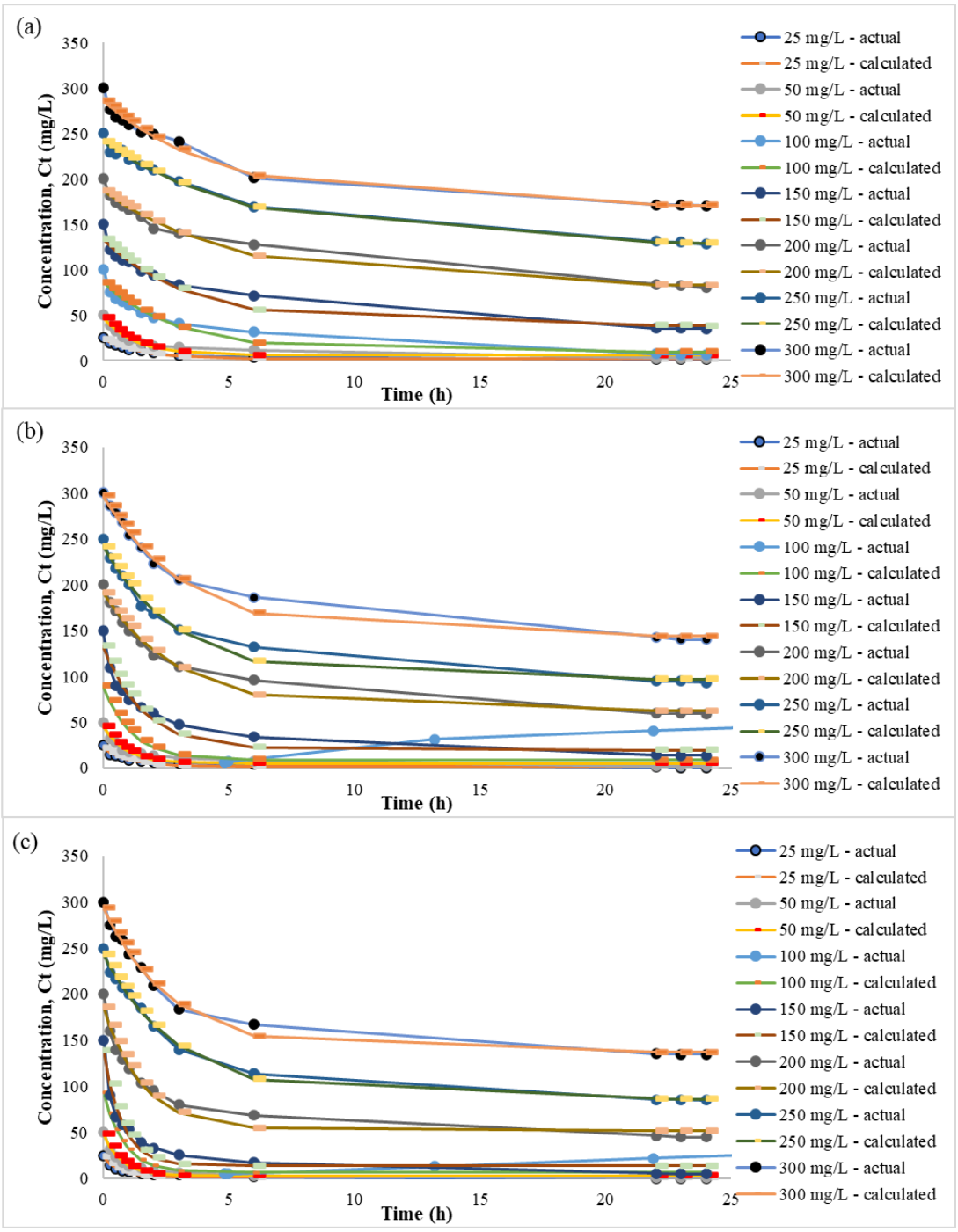


Figure 5. PMT model graphs for adsorption of PineAC–MB dye at (a) 30, (b) 45, and (c) 60°C

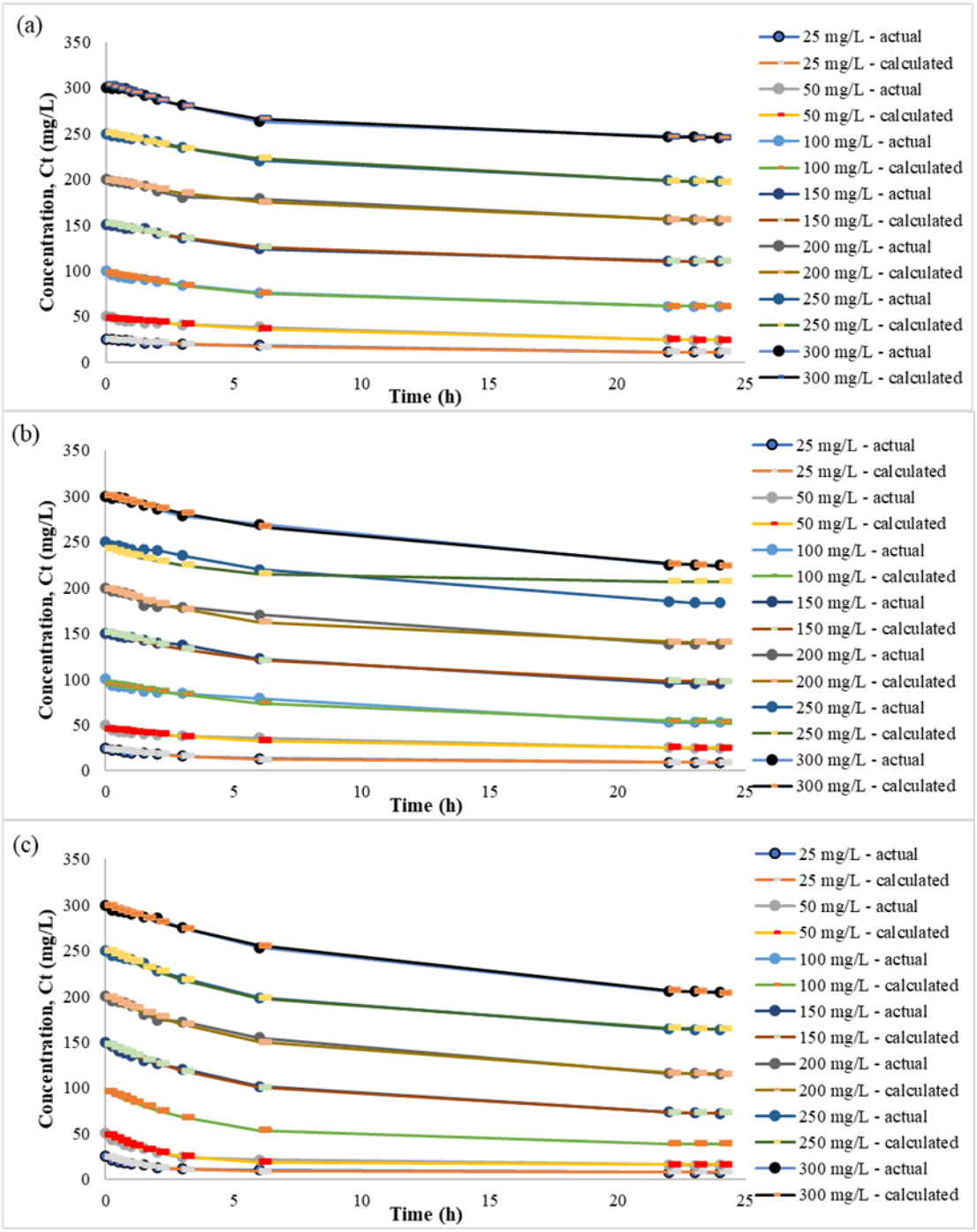


Figure 6. PMT model graphs for adsorption of PineAC–MR dye at (a) 30, (b) 45, and (c) 60°C

Acknowledgements

The authors express their sincere gratitude to Short Term Grant (Grant no. 6315463) from Universiti Sains Malaysia for their support and enabling the advancement of knowledge in this field of study.

References

1. Bilal, M., Ali, J., Bibi, K., Khan, S. B., Saqib, M., Saeed, R., Javeria, R., H. Khan, H., Akhtar, K. and Bakhsh, E. M. (2022). Remediation of different dyes from textile effluent using activated carbon

synthesized from *Buxus Wallichiana*. *Industrial Crops and Products,* 187 (Part A): 115267.

2. Jabar, J. M., Odusote, Y. A., Ayinde, Y. T. and Yılmaz, M. (2022). African almond (*Terminalia catappa L.*) leaves biochar prepared through pyrolysis using H_3PO_4 as chemical activator for sequestration of methylene blue dye. *Results in Engineering,* 14: 100385.
3. Mahmad A., Noh T. U., Khalid N.I. (2023). Eco–friendly water treatment: The role of MIL metal–organic frameworks for the bisphenols adsorption from water. *Inorganic Chemistry Communications,* 152: 110643.
4. Kuśmierek, K., Świątkowski, A., Kotkowski, T., Cherbański, R., Molga, E. (2021). Adsorption on activated carbons from end–of–life tyre pyrolysis for environmental applications. Part II. Adsorption from aqueous phase. *Journal of Analytical and Applied Pyrolysis,* 158: 105206.
5. Ahmad, M. A., Eusoff, M. A., Adegoke, K. A. and Bello, O. S. (2021). Sequestration of methylene blue dye from aqueous solution using microwave assisted dragon fruit peel as adsorbent. *Environmental Technology & Innovation,* 24: 101917.
6. Rosli, N. A., Ahmad, M. A., Noh, T. U. (2023). Unleashing the potential of pineapple peel–based activated carbon: response surface methodology optimization and regeneration for methylene blue and methyl red dyes adsorption. *Inorganic Chemistry Communications,* 2023: 111041.
7. Khasri, A. and Ahmad, M. A. (2018). Adsorption of basic and reactive dyes from aqueous solution onto *Intsia bijuga* sawdust–based activated carbon: batch and column study. *Environmental Science and Pollution Research,* 25: 31508-31519.
8. Rosli, N. A., Ahmad, M. A., Noh, T. U. and Ahmad, N. A. (2023). Pineapple peel–derived carbon for adsorptive removal of dyes. *Materials Chemistry and Physics,* 2023: 128094.
9. Khasri, A., Mohd Jamir, M. R., Ahmad, A. A. and Ahmad, M. A. (2021). Adsorption of Remazol Brilliant Violet 5R dye from aqueous solution onto melunak and rubberwood sawdust based activated carbon: interaction mechanism, isotherm, kinetic and thermodynamic properties. *Desalination and Water Treatment,* 216: 401-411.
10. Rosli, N. A., Ahmad, M. A., Noh, T. U. (2023). Nature's waste turned saviour: Optimizing pineapple peel–based activated carbon for effective Remazol Brilliant Violet dye adsorption using response surface methodology. *Inorganic Chemistry Communications* 153: 110844.
11. Aragaw, T. A. and Bogale, F. M. (2021). Biomass–based adsorbents for removal of dyes from wastewater: A review. *Frontiers in Environmental Science,* 9: 764958.
12. Inglezakis, V. J., Balsamo, M. and Montagnaro, F. (2020). Liquid–solid mass transfer in adsorption systems—an overlooked resistance?. *Industrial & Engineering Chemistry Research,* 59(50): 22007-22016.
13. Mohd Ramli, M. R., Shoparwe, N. F., Ahmad, M. A. (2022). Methylene blue removal using activated carbon adsorbent from Jengkol Peel: Kinetic and mass transfer studies. *Arabian Journal of Science and Engineering,* 48: 8585-8594.
14. Mohamad Yusop, M. F., Tamar Jaya, M. A., Idris, I., Abdullah, A. Z. and Ahmad, M. A. (2023). Optimization and mass transfer simulation of remazol brilliant blue R dye adsorption onto meranti wood based activated carbon. *Arabian Journal of Chemistry,* 16(5): 104683.
15. Mohamad Yusop, M. F., Nasehir Khan, M. N., Zakaria, R., Abdullah, A. Z., Ahmad, M. A. (2023). Mass transfer simulation on Remazol Brilliant Blue R dye adsorption by optimized teak wood based activated carbon. *Arabian Journal of Chemistry,* 16: 104780.
16. Mohamad Yusop, M. F., Abdullah, A. Z. and Ahmad, M. A. (2023). Malachite green dye adsorption by jackfruit based activated carbon: Optimization, mass transfer simulation, and surface area prediction. *Diamond and Related Materials,* 136: 109991.
17. Nandiyanto, A. B. D., Girsanga, G. C. S., Maryanti, R., Ragadhitaa, R., Anggraenia, S., Fauzia, F. M., Sakinaha, P., Astutia, A. P., Usdiyana, D., Fiandinia, M., Dewi, M. W. and Al–Obaidi, A. S. M. (2020). Isotherm adsorption characteristics of carbon microparticles prepared

from pineapple peel waste. *Communications in Science and Technology,* 5(1): 31-39.

18. Iamsaard, K., Weng, C.H., Yen, L.T., Tzeng, J.H., Poonpakdee, C. and Lin, Y.T. (2022). Adsorption of metal on pineapple leaf biochar: Key affecting factors, mechanism identification, and regeneration evaluation. *Bioresource Technology,* 344: 126131.
19. Ahmad, M. A., Eusoff, M. A., Oladoye, P. O., Adegoke, K. A. and Bello, O. S. (2021b). Optimization and batch studies on adsorption of Methylene blue dye using pomegranate fruit peel–based adsorbent. *Chemical Data Collections,* 32: 100676.
20. Thi, H. T., Le Hoang, A., Huu, T. P., Dinh, T. N., Chang, S. W., Chung, W. J., Nguyen, D. D. (2020). Adsorption isotherms and kinetic modeling of methylene blue dye onto a carbonaceous hydrochar adsorbent derived from coffee husk waste. *Science of The Total Environment,* 725:138325.
21. Srivastava, A., Gupta, B., Majumder, A., Gupta, A. K. and Nimbhorkar, S. K. (2021). A comprehensive review on the synthesis, performance, modifications, and regeneration of activated carbon for the adsorptive removal of various water pollutants. *Journal of Environmental Chemical Engineering,* 9(5): 106177.
22. Agnihotri, S., Sillu, D., Sharma, G. and Arya, R. K. (2018). Photocatalytic and antibacterial potential of silver nanoparticles derived from pineapple waste: Process optimization and modelling kinetics for dye removal. *Applied Nanoscience,* 8: 2077-2092.
23. Mahmad, A., Shaharun, M. S., Noh, T. U., Zango, Z. U. and Taha, M. F. (2022). Experimental and molecular modelling approach for rapid adsorption of Bisphenol A using Zr and Fe based metal–organic frameworks. *Inorganic Chemistry Communications,* 142: 109604.
24. Ugbe, F. A., Anebi, P. O. and Ikudayisi, V. A. (2018). Biosorption of an anionic dye, eosin yellow onto pineapple peels: isotherm and thermodynamic study. *International Annals of Science,* 4(1): 14-19.
25. Chaiyaraksa, C., Ruenroeng, C., Buaphuan, B. and Choksakul, S. (2019). Adsorption of cationic and anionic dye using modified pineapple peel. *Songklanakarin Journal of Science and Technology,* 41(1): 199-206.
26. Dai, H., Huang, Y., Zhang, H., Ma, L., Huang, H., Wu, J. and Zhang, Y. (2019). Direct fabrication of hierarchically processed pineapple peel hydrogels for efficient Congo red adsorption. *Carbohydrate Polymers,* 2019: 115599.
27. Turkmen, K. S. N., Kipcak, A. S., Moroydor Derun, E. and Tugrul, N. (2021). Removal of zinc from wastewater using orange, pineapple and pomegranate peels. *International Journal Environmental Science and Technology,* 18: 2781-2792.
28. Shakya, A., T. and Agarwal, T. (2019). Removal of Cr (VI) from water using pineapple peel derived biochars: Adsorption potential and re–usability assessment. *Journal of Molecular Liquids,* 293: 111497.
29. Yusoff, A. H., Mohammad, R., Mohamad, M., Sulaiman, A.Z., Che Zaudin, N. A., Rosmadi, N., Aqsa, F., Yusoff, M. and Teo, P. (2020). Potential of agricultural waste material (*Ananas cosmos*) as biosorbent for heavy metal removal in polluted water. *Material Science Forum,* 1010: 489-494.

Malaysian Journal of Analytical Sciences (MJAS)
Published by Malaysian Analytical Sciences Society

A COMPREHENSIVE REVIEW OF GRAPHENE NANOPLATELETS FOR REMOVAL AND DETECTION OF HEAVY METALS AND ENDOCRINE DISRUPTING COMPOUNDS

(Satu Komprehensif Kajian Semula Berkenaan Nanoplatelet Grafin untuk Penyingkiran dan Pengesanan Logam Berat dan Sebatian yang Mengganggu Endokrin)

Sazlinda Kamaruzaman[1, 2*], Najihah Mohammad Nasir[1], Yugarani Arivalagan[1], Noorfatimah Yahaya[3], Saw Hong Loh[4], Nor Suhaila Mohamad Hanapi[5], Wan Nazihah Wan Ibrahim[5] and Ili Syazana Johari[1]

[1]*Department of Chemistry, Faculty of Science, Universiti Putra Malaysia, Serdang 43400, Selangor, Malaysia*
[2]*Natural Medicines and Product Research Laboratory (NaturMeds), Institute of Bioscience (IBS), Universiti Putra Malaysia, 43400, UPM Serdang Selangor, Malaysia*
[3]*Department of Toxicology, Advanced Medical and Dental Institute (AMDI), Universiti Sains Malaysia, 13200 Bertam Kepala Batas, Penang, Malaysia*
[4]*Faculty of Sciences and Marine Environment, Universiti Malaysia Terengganu, 21030 Kuala Nerus, Terengganu, Malaysia*
[5]*Faculty of Applied Sciences, Universiti Teknologi MARA, Shah Alam 40450, Selangor, Malaysia*

[*]*Corresponding author: sazlinda@upm.edu.my*

Received: 29 August 2023; Accepted: 3 October 2023; Published: 29 December 2023

Abstract

Heavy metals and endocrine disrupting chemicals (EDC) have disruptive effects on an intact organism or its progeny. Due to the widespread presence of heavy metals and EDC in waterways, it is important to determine how effectively these compounds are removed from the environment. Their concentration has attained dangerous levels because of numerous anthropogenic activities such industrial operations, particularly mining, agricultural processes, and the disposal of industrial waste materials. Heavy metals and EDC have been removed using a variety of effective approaches, including chemical oxidation, biodegradation, liquid extraction, membrane techniques, chemical precipitation, ion exchange, reverse osmosis, coagulation, flocculation, etc. These methods have several drawbacks, including a high reagent requirement, unpredictable metal ion removal, the generation of toxic sludge, etc. Adsorption is a method that shows promise because of its simple design, low cost, and high efficiency. Its ability to remove hazardous and micropollutants from wastewater is what makes it the method of choice. The use of graphene nanoplatelets (GNPs) as adsorbents in the treatment of water has been established by research. A wide range of water pollutants, including but not limited to organic molecules and inorganic heavy metals, are reported to be effectively remedied by GNPs. The high surface areas and modifiable functional groups of GNPs can be used to remove various contaminants in water and wastewater treatment processes. More significantly, because GNPs are mainly made up of carbon, this characteristic makes it easier to use these carbon-based materials for adsorbing pollutants in water and wastewater treatment systems. In the present review, the mechanisms of adsorption are demonstrated by investigating the kinetics, isotherms, and thermodynamics of adsorption. Besides that, pH, contact

time, adsorbent dosage, and initial analyte concentration were investigated.

Keywords: graphene nanoplatelets, endocrine disrupting compounds, heavy metals, isotherm, kinetics, thermodynamic

Abstrak

Logam berat dan bahan kimia pengganggu endokrin (EDC) mempunyai kesan yang mengganggu pada organisma yang utuh atau keturunannya. Disebabkan kehadiran meluas logam berat dan EDC dalam laluan air, adalah penting untuk menentukan keberkesanan sebatian ini dikeluarkan dari alam sekitar. Kepekatan mereka telah mencapai tahap berbahaya kerana banyak aktiviti antropogenik seperti operasi perindustrian, terutamanya perlombongan, proses pertanian, dan pelupusan bahan buangan industri. Logam berat dan EDC telah dialih keluar menggunakan pelbagai pendekatan yang berkesan, termasuk pengoksidaan kimia, biodegradasi, pengekstrakan cecair, teknik membran, pemendakan kimia, pertukaran ion, osmosis songsang, pembekuan, pemberbukuan, dll. Kaedah ini mempunyai beberapa kelemahan, termasuk yang tinggi. keperluan reagen, penyingkiran ion logam yang tidak dapat diramalkan, penjanaan enap cemar toksik, dsb. Penjerapan ialah kaedah yang menjanjikan kerana reka bentuknya yang ringkas, kos rendah dan kecekapan tinggi. Keupayaannya untuk membuang bahan pencemar berbahaya dan mikro daripada air sisa adalah yang menjadikannya kaedah pilihan. Penggunaan graphene nanoplatelets (GNPs) sebagai penjerap dalam rawatan air telah ditubuhkan oleh penyelidikan. Pelbagai bahan pencemar air, termasuk tetapi tidak terhad kepada molekul organik dan logam berat bukan organik, dilaporkan akan dipulihkan dengan berkesan oleh KNK. Kawasan permukaan yang tinggi dan kumpulan fungsi GNP yang boleh diubah suai boleh digunakan untuk membuang pelbagai bahan cemar dalam air dan proses rawatan air sisa. Lebih ketara, kerana KNK kebanyakannya terdiri daripada karbon, ciri ini memudahkan penggunaan bahan berasaskan karbon ini untuk menjerap bahan pencemar dalam sistem rawatan air dan air sisa. Dalam kajian ini, mekanisme penjerapan ditunjukkan dengan menyiasat kinetik, isoterma, dan termodinamik penjerapan. Selain itu, pH, masa sentuhan, dos penjerap, dan kepekatan analit awal telah disiasat.

Kata kunci: kepingan nano grafit, sebatian mengendala endokrin, logam berat, isoterma, kinetik, termodinamik

Introduction

Heavy metals are one of the environmental contaminants present in water [1]. In this era, heavy metals have emerged as life-threatening pollutants if left untreated. Heavy metals are one of pollutant that has been thoroughly studied in the research that have worked on the development of graphene applications in the sectors of water and wastewater treatment technologies. Heavy metals include lead, arsenic, cadmium, cobalt, copper, gold, palladium, and zinc, among others. Heavy metals are known for its toxicity and carcinogenicity to human beings. Long term exposure to heavy metals can cause a detrimental to human body. Along with unlimited discharge of wastewater effluents, pollution of heavy metal has become a worldwide concern, which poses a potential threat to human and animals. For instance, lead ion (Pb^{2+}) exists widely in the wastewater, and it could enter human body with food or water, once excessive intake of them for a period, probably leads to some diseases including convulsions, renal failure, even cancer. Besides that, heavy metal ions have non-biodegradable properties which can cause severe health problems in animals and human beings.

Endocrine disrupting chemicals (EDC) are external drug or mixture that may interfere with or modify the functions of the endocrine system, resulting in undesirable health effects in an organism, its offspring, or (sub) populations [2]. The substance may interfere with the synthesis, secretion, transport, binding, action, or elimination of natural hormones in the body, which are responsible for the maintenance of homeostasis, reproduction, development, and/or behaviour, as well as the regulation of developmental processes [3-5]. These two pollutants tend to harm the lives of living organisms, thus a lot of materials have been developed and their effectiveness in the removal of heavy metals is being studied. Nanotechnology is presently reclaiming a significant amount of effort due to their high surface area, small particle size, tremendous potential, excellent inherent reactivity, and capacities as a catalytic reagent of a pollutant through modifying reaction mechanisms. Therefore, due to their high efficacy in a wide range of contaminants – including organic compounds, inorganic compounds, pharmaceutical compounds, chlorinated

compounds, and nitro-groups – nanomaterials have been widely used in environmental applications. These nanomaterials for pollutant removal showed an effective wastewater treatment system under small-scale production; it is anticipated to be less expensive compared to other more traditional methods of removal [1].

Graphene has gained attention as a nanomaterial. Recent studies have been concentrating on the removal of various water pollutants using graphene in its pristine, functionalized, or composite forms [6], due to its flexibility in introducing functional groups and to its easy operation [7-9]. Graphene is composed of carbon atoms organized in a 2D hexagonal array, which gives graphene its characteristic honeycomb structure. Every carbon atom creates three covalent bonds with its closest neighbour as a result of the sp2 hybridized orbitals being coplanar and aligned at 120° to one another, while the remaining 2pz orbital forms a bond with an electron density that is above and below the basal plane. The exceptional electrical and thermal properties of monolayer, bilayer, and few-layer graphene are brought about by the aromatic electron cloud and honeycomb crystal lattice [10]. According to Stoller et al., graphene is suited for adsorption due to its high porosity and exceptional specific surface area of 2600 $m^2.g^{-1}$ [11]. Graphene layer, turbostratic carbon, bilayer graphene, trilayer graphene, multi-layer graphene (MLG), few-layer graphene (FLG), exfoliated graphite (EG), graphene oxide (GO), and reduced graphene oxide (rGO) are all well-known graphene-based materials. This combination of excellent properties has made graphene-based material a promising material for a wide range of applications, such as biological engineering, drug delivery, biosensor [12], biological agents [13], tissue engineering [14], and contaminant sensing [15].

Due to the difficulty and complexity of graphene fabrication, graphene nanoplatelets (GNPs) are also being extensively explored. GNPs are more approachable, have similar characteristics, and can be utilized for the same applications as graphene [16]. GNPs in one of the graphene derivatives consisted of a single to a few layers of sp^2-bonded carbon atoms that interacted to generate nanometre-sized two-dimensional particles. GNPs are composed of single and few layer graphene mixed with thicker graphite; hence, structurally they are in between graphene and graphite [17]. GNPs with a typical thickness of 5–10 nanometres are available in diameters as large as 50 microns. GNPs are cheaper and simpler to create than single-layered graphene and carbon nanotubes, making their utilization appealing [18]. These fascinating nanoparticles consist of 10–30 platelet-shaped graphene sheets identical to those seen in the walls of carbon nanotubes, but in a planar form retaining the single-layer characteristics [19]. Due to their platelet structure, they have a surface area per unit mass that is significantly larger than that of graphite and carbon nanotubes [20]. Considering all these characteristics, GNPs are valuable in numerous domains of research. It can be utilized as a novel and effective analytical adsorbent material [21]. Due to the direct exfoliation of affordable graphite flakes, e.g. by ultrasonics in acid baths, followed by chemical oxidation and reduction of graphite oxide nanoplatelets, GNPs are currently regarded as one of the most remarkable materials [22]. GNPs has recently attracted significant interest as a new and ideal material for the detection of environmental pollution involving water treatment [23], heavy metal ion detection [24], and green technology. Graphene is hydrophobic; therefore, stable dispersions in polar liquids can only be achieved by using the appropriate surfactants [17]. Figure 1 summarizes the chemical properties of graphene-based materials.

The aspect ratios of GNPs can range into the thousands. They exhibit the same thermal and mechanical properties as carbon nanotubes but have greater surface areas or aspect ratios. Considering this, GNPs can be used to improve the properties of a wide range of polymeric materials, including thermoplastic and thermoset composites, natural or synthetic rubber, thermoplastic elastomers, adhesives, paints, and coatings. The GNPs are offered in a granular form that in water, organic solvents and polymers with the right choice of dispersion aids, equipment and techniques [25].

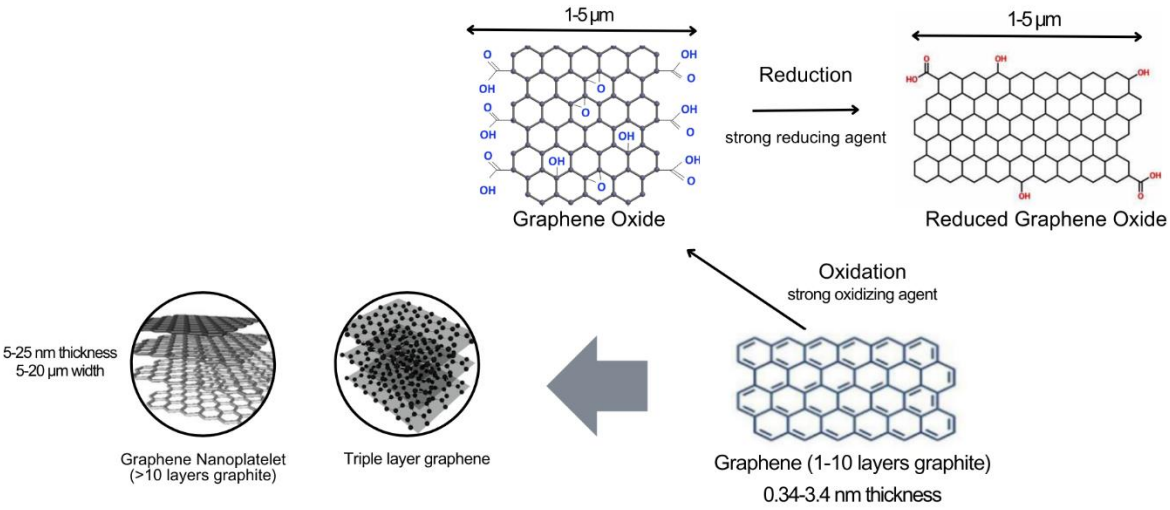


Figure 1. The chemical properties of graphene-based materials

An et al. conducted research on two types of graphene flakes manufactured by the non-oxidative and oxidative routes. In this work, their morphology, crystallographic order, gas adsorption potential, and electrical conductivity were examined [26]. The morphological differences of graphene nanoplatelets produced by oxidative (rGO-NP) and nonoxidative (GIC-NP) processes were compared using several analytical techniques. The adsorptive potential peaks of rGO-NP were found to be significantly more dispersed over the basal and non-basal regions than those of GIC-NP, indicating a heterogeneous surface. Comparing the Raman spectra and transmission electron microscope (TEM) pictures of the rGO-NP and GIC-NP, distinct crystallographic flaws were discovered in the rGO-NP. Compared to the GIC-NP, the R-ratio values evaluated at the edge and basal plane of the rGO-NP were substantially similar. Based on the overall analytical results and characteristics demonstrated in this comparative study, it is believed that GIC-NP is a more advantageous material than rGO-NP for numerous applications, such as conductive inks and conductive additives for batteries, where electric conducting properties are crucial. Consequently, the degree of disagreement in the R-values between the edge and basal plane can be employed as a significant criterion in the quality control of graphite nanoplatelets produced via diverse ways [26].

Exfoliated graphite nanoplatelets (xGnP) are a novel efficient adsorbent material with high adsorption capacity, good stability, and rapid adsorption, with platelet thicknesses in the nanometre range but platelet areas in the micrometre range [27, 28]. In addition, xGnP may be easily extracted from inexpensive, natural graphite in huge quantities, without the requirement for dimension expansion, for water purification applications. These materials are cheaper than carbon nanotubes, can be included into water treatment procedures, and are simple to remove or renew [29].

GNPs exhibit its large surface area, accessible surface, high hydrophobicity, and high mechanical properties, enabling it to be explored and used widely in the removal of heavy metals and EDCs. Moreover, enormous, delocalized π-π electron system that GNPs owe enables the formation of strong bonding with heavy metals and EDCs [30], making the removal process efficient. This article provides a general overview of GNPs being used for the removal of heavy metals. Adsorptive removal of heavy metals is discussed by studying the kinetics, isotherms, and thermodynamics of adsorption. Adsorption parameters which include pH, are also investigated.

Graphene nanoplatelets as adsorbents for the removal of heavy metal ions

According to Briffa et al. [31], heavy metals are defined as naturally occurring elements with high atomic weights and densities greater than 5 g/cm^3 that are

characterised by high stability but low levels of biodegradability, which cause bioaccumulation and biomagnification in living things. According to their toxicological characteristics, heavy metals can either be essential or non-essential for enzymatic activity [32]. The first is crucial for living things and can be present in little amounts; it only becomes harmful at a particular concentration threshold. Disease or abnormalities are caused by an essential heavy metal's excess or deficiency. The most hazardous substances, on the other hand, are non-essential heavy metals since they are difficult to break down through biological and photochemical processes and have harmful effects on both plants and animals, including people. According to Sall et al. [33], heavy metals have a number of negative health impacts, including impaired growth and development, cancer, organ damage, and, in larger amounts, death.

Heavy metals are one of the pollutants that has been thoroughly studied in the development of graphene applications in the sectors of water and wastewater treatment technologies. Heavy metals include lead, arsenic, cadmium, cobalt, copper, gold, palladium, and zinc, among others. Heavy metals have piqued the interest of researchers who are interested in finding a solution to this problem, which can have detrimental impacts on human health and the environment. Bioreactors [34], degradation and photodegradation [35-38], filtration [39], photocatalysis [40, 41], photo-Fenton and Fenton-like [42, 43], coagulation [44] and adsorption [45, 46] are all utilized to remove contaminants from water. Among these technologies, adsorption is the most popular and effective method for treating wastewater. This methodology is superior and considered powerful alternatives to conventional methods [47] because of its low cost, ease of operation, high efficiency, high capacity, simplicity, dependability, and low energy usage [48, 49]. Due to its large specific surface area, delocalized π-electron system, which can form strong interactions with other which is perfect for adsorption, GNP are utilized as an adsorbent to remove the contaminants [30].

The research by Kucherova et al. [50] focused on the adsorption of Pb(II) ions onto graphene materials prepared through the exfoliation of a hydrolysed extended graphite intercalation compound. Few-layered oxidized graphene suspension (FLOGS), multi-layered graphene paste (MLGP), and few-layered graphene paste (FLGP) were employed as adsorbents for the removal of Pb(II) from aqueous solutions. These adsorbents were reported to have maximum experimental Pb(II) adsorption capabilities of 850, 230, and 170 mg/g, respectively. To fit the experimental data, two adsorption isotherm models were applied: Langmuir and Freundlich. The Langmuir model assumes that adsorption occurs at specific homogeneous sites on the adsorbent surface. For non-ideal sorption onto heterogeneous surfaces with multiple layers, the Freundlich model is reported to be more fit. The Type III S-shaped isotherms observed for FLOGS suggest a transitional porous structure of the adsorbent with a complex pore space topology and a wide range of pore sizes. Additionally, the nature of that isotherm's steepness shows that the adsorbent has mostly very small pores. From the origin to the inflection point, the lower portion of the S-shaped curve corresponds to the creation of a monomolecular layer, and the subsequent rise of the curve is explained by the transition from mono- to multi-molecular adsorption. It can be assumed that the adsorption isotherms created for the FLGP and MLGP correspond to L-type curves.

Using functionalized graphite nanoplatelets (FGN) based electrodes, Mishra et al. [51] demonstrated the simultaneous removal of sodium and both pentavalent and trivalent forms of arsenic from an aqueous solution. Furthermore, these electrode-based water filters were employed to extract various metals from seawater. The preparation of graphite nanoplatelets (GNP) involved acid intercalation followed by thermal exfoliation, with additional acid treatment to functionalize the GNP. The performance of a supercapacitor-based water filter was evaluated for removing high concentrations of trivalent and pentavalent arsenic, sodium, and for desalinating seawater, using cyclic voltammetry (CV) and inductively coupled plasma-optical emission spectroscopy (ICP-OES) techniques. The transient behaviour of the metal adsorption process was analysed using the Elovich and intra-particle diffusion kinetic models. Solutions containing sodium arsenate and

sodium arsenite with an initial arsenic concentration of 300 ppm were employed to study the concurrent transient behaviour of sodium and arsenic adsorption. Both the Elovich and intra-particle diffusion kinetic models provided comparable fits for the metallic impurities. The Elovich model pertains to diffusion, while the intra-particle diffusion kinetic model is derived from chemical reaction kinetics. The removal efficiency of the supercapacitor-based water filter was investigated for salt removal, both forms of arsenic, and desalination of seawater. Approximately 72% of arsenic (As) and 75% of sodium (Na) removal efficiency was achieved for sodium arsenate-containing water, while for sodium arsenite-containing water, the removal efficiency was determined to be 73% for arsenic and 76% for sodium. These results were obtained over 20 repeated cycles with 100 mg of FGN loading on each electrode.

Ion et al. [28] conducted an investigation into the sorption behaviour of Pb(II) onto exfoliated graphite nanoplatelets (xGNPs). Among various factors such as specific surface area and solution composition, the presence of surface functional groups emerges as the paramount determinant influencing Pb(II) adsorption on xGNPs. Nitric acid (HNO_3) oxidation plays a crucial role in modifying the ion-exchange capacity, leading to the development of distinct acidic functional groups on the surface, which exhibit dissociation at varying pH levels. Due to the surface functionalization by HNO_3 and additional oxygen-containing groups like hydroxyl, carbonyl, and carboxyl, the adsorption capability of xGNPs treated with concentrated HNO_3 exhibit a substantially enhanced capacity of 13.09 mg/g. The sorption characteristics are profoundly impacted by pH, the presence of active sites and the surface dimensions. The influence of pH was revealing that adsorption percentages reach 100% at pH 6, but rapidly decreased at more acidic pH values. At low pH levels, lead is present as free cations, which is explained by the fact that at these pH levels, the H^+ concentration is large, and protons can compete with lead ions for surface sites. The deprotonation of the sorbent functional groups causes a decrease in positive surface charge as pH rises. The sorption properties of the adsorbent in water were described using the Langmuir and Freundlich isotherm models. Both models displayed excellent agreement with experimental data, as evidenced by correlation coefficient values of 0.9996 and 0.994 for Langmuir and Freundlich, respectively with the optimum initial concentration of 200 ppm at 30 min.

Sheng et al. also conducted an investigation into functionalized graphene nanoplatelets (FGN) by the acidic treatment of graphene nanoplatelets (GNPs) with HNO_3 for removing Pb(II) from solution. Through nitrogen desorption isotherm analysis, BET data revealed FGN's surface area is 714.5 m^2/g, with an average pore size of 4.8502 nm and a pore volume of 0.8598 cm^3/g. These findings indicate FGN's uniform and mesoporous nature. The specific surface area and effective adsorption sites of FGN facilitated Pb(II) adsorption at lower initial concentrations. However, as the initial Pb (II) concentration increased, the percentage removal was decreased due to the electrostatic repulsion among heavy metal ions and increased competition between heavy metal ions for adsorption sites. This study also stated that the capacity for Pb(II) adsorption notably increased as pH shifted from 6 to 7, resulting in approximately 100% removal efficiency of Pb(II) by FGN at pH 7 due to precipitation and adsorption coefficients. The dominant role of monolayer chemical adsorption on FGN's surface was reported while the pseudo-second order kinetic model achieved an R^2 of 0.998, indicating a better fit for the latter. This suggests that valence forces, involving electron exchange or sharing between FGN and Pb(II), may govern the rate-limiting step in the adsorption process [52].

Nandi et al. conducted research on GNPs obtained from human nails and synthesized via a novel *in-situ* synthetic technique involving ferric chloride. This work suggests that the surface of GNPs is mostly positively charged pH < 6 and predominantly negatively charged pH > 6. The highest sorption capacity was reported at pH = 7.0 since the surface of GNPs is almost neutral. However, the sorption capacity of GNPs towards As (III) is decreased at lower or higher pH values than pH = 7.0. The sorption of As(III) on the surface of GNPs happens at pH 7.0 via ion-dipole interaction. The sorption of As(III) fitted the Langmuir model (R^2 = 0.97) can be attributed to the GNPs' high specific surface area and more accessible

opening sites at lower adsorbate concentrations. Notably, the pseudo-second order model provided the best agreement with the experimental data. In addition, thermodynamic analysis offered insight into the reaction's feasibility, nature, and direction. The negative value of ΔG^0 indicated the spontaneous nature of the As(III) adsorption process on GNPs with respect to temperature changes. The positive ΔH^0 value indicated an endothermic reaction, while the increase in entropy ΔS^0 suggested greater randomness at the solid-liquid interface [53].

Zhu et al. have developed magnetic graphene nanoplatelet composites (MGNCs) by synthesizing core-shell Fe-Fe_2O_3 nanoparticles (NPs) through a straightforward one-pot thermal decomposition process. According to this study, MGNCs, comprising GNPs decorated with NPs, showed robust magnetization for magnetic separation and efficiently adsorb arsenic(III) from polluted water. This is due to the magnetic graphene nanoplatelets increasing the adsorption sites. Other than that, the solution pH dominantly affects the surface charge of the adsorbent, and the optimum adsorption capacity of 11.34 mg/g was achieved when the sample solution is at pH 7. Langmuir and Freundlich models fit well (R^2 >0.95), revealing a specific homogenous adsorption mechanism. MGNC's greater surface area (42.1 m^2/g) enhances adsorption capacity. Favourable adsorption is shown by Freundlich parameter (n = 2.79 > 1) and fitted with pseudo-second order kinetics (R^2 = 0.994) and describe the As (III) removal with the chemisorption process [54].

Samaraweera et al. studied the significance of the adsorption method, particularly when dealing with pollutant removal, such as Cu^{2+} ions. In their research, they investigated the potential of using a hybrid material consisting of graphene and pine wood biochar (GPBC) as an adsorbent for Cu^{2+} ions. The study found that biochar, when functionalized with nanomaterials like graphene, can greatly enhance its ability to remove pollutants. This enhancement occurs when both the nanomaterial and the biochar surface act as effective adsorption sites for the target pollutants. Interestingly, the researchers used different types of graphene nanosheets (GNPs) with varying surface areas (G1, G2, and G3) to create GPBCs. They noted that GPBCs with lower surface areas were produced using GNPs with larger surface areas. This counterintuitive observation was attributed to potential pore-filling and pore-blocking effects of the nanomaterials within the biochar. The study focused on GPBC-1, which had the lowest nanophase surface area but the highest Cu^{2+} ion adsorption capacity. This finding challenges the conventional belief that higher surface area always leads to better adsorption. In the case of GPBC-1, Cu^{2+} removal occurred through electrostatic interactions, inner sphere surface complex formation, and other attractive forces with oxygenated functional groups on the GPBC-1 surface. The researchers employed Langmuir and Freundlich isotherm models to understand the interaction between the adsorbate (Cu^{2+}) and the adsorbent (GPBC-1). The Langmuir model, which assumes monolayer adsorption, provided a better fit to the data. Additionally, kinetic models revealed that the adsorption process followed pseudo-second order kinetics, indicating a strong interaction between Cu^{2+} ions and GPBC-1. Thermodynamic studies also showed that Cu^{2+} sorption on GPBC-1 was an endothermic process, requiring energy input. The negative values of ΔG at various temperatures indicated that the adsorption was spontaneous. Positive ΔS^o values suggested an increase in randomness during the adsorption process, controlled by entropy [55].

Rosenzweig et al. investigated Cu^{2+} ion adsorption on various nanomaterials, including carbon nanotubes and different types of graphene nanoparticles (GNPs). They found that functionalized GNPs, such as GNP-COOH and GNP-O^+, exhibited better stability in water, a crucial factor for effective pollutant removal. The study applied these optimized conditions to Cu^{2+} adsorption experiments using GNPs. The adsorption behaviour was analysed using the Freundlich model, revealing that GNPs with 1/n values significantly > 1 had weaker adsorption power, likely due to the formation of irreversible aggregates caused by strong van der Waals forces within multilayer nano-sheets. These aggregates could reduce the adsorption capacity of GNPs by concealing adsorption sites. However, functionalized GNPs maintained high colloidal stability, thanks to oxygen-containing groups at their edges, preventing

excessive aggregation and ensuring a larger accessible surface area for adsorption. This study highlights the importance of nanomaterial properties, especially colloidal stability, in Cu^{2+} ion adsorption, and underscores the impact of functionalization on the effectiveness of GNPs in water treatment applications [56].

Capra et al. examined the removal of Sb(III) from drinking water using oxidized exfoliated graphite nanoplatelets (ox-xGNP). They observed irregularly shaped Sb(III) particles ranging from 50 to 200 nm in TEM images. Notably, the adsorption capacity increased significantly, reaching 16.0 mg/g at a pH of 9.0, a phenomenon influenced by both the composition of metal ions in the solution and alterations in surface functional groups on the adsorbent. Zeta potential measurements confirmed the negative charge on the ox-xGNP surface, which contributed to optimal colloidal stability at pH 9.0 due to electrostatic attractions. Despite the typical drinking water pH range of 6.0 to 8.0, experiments were conducted at pH 7.0 in anticipation of future Sb (III) removal applications. The established optimal removal conditions included a pH of 7.0, 1.0 mg ox-xGNP per 100 mL solution, a temperature of 293 K, 1.0 mg L^{-1} Sb(III), and a 25-minute contact time. Kinetic analysis favoured the pseudo-first order model (R^2 = 0.999), which accurately estimated the adsorption capacity at equilibrium. Furthermore, the Langmuir adsorption isotherm model best described the process, indicating monolayer adsorption on homogeneous ox-xGNP surfaces, emphasizing the favourable Sb(III) adsorption. Thermodynamic analysis unveiled spontaneous and favourable adsorption, potential randomness at the solid-solution interface, and an exothermic process [57].

Smith et al. studied a method for removing Cu(II), Zn(II), and Pb(II) ions from water using single-wall carbon nanotube-graphene nanoplatelet (SWCNT-GNP) aerogels, with varying amounts of carbon nanomaterials (0.2 wt.% and 2.0 wt.%). They tested the pH of metal (II) ion solutions to confirm that metal ion removal was solely due to adsorption and not precipitation, which occurred only at pH > 6.19. The adsorption of Cu(II) onto the aerogel followed a pseudo-second order kinetic model. Initially, there was a rapid adsorption phase for about 75 minutes, after which the adsorption capacity gradually increased, reaching equilibrium at approximately 105 minutes for the 2.0 wt.% aerogel and 90 minutes for the 0.2 wt.% aerogel. The initial rise was attributed to the open valence of Cu(II) ions interacting with the network, saturating the carbon nanomaterial (CNM) aerogel. The sponge-like structure of the aerogel provided more adsorption sites, increasing surface area. The adsorption behaviour for Cu(II) ions was generally similar to that of Zn(II) and Pb(II) ions. However, the uptake capacity for Pb(II) decreased considerably within 120 minutes. This decrease was because Pb(II) has a higher molecular weight and ionic radius compared to Cu(II) and Zn(II), making it more challenging to adsorb as many ions as possible due to the direct association between uptake capacity and these parameters. Interestingly, the equilibrium isotherms for all three metals displayed a largely linear behaviour, unlike the typical Langmuir or Freundlich-type models [58].

Ahmad et al. explored the efficacy of three different adsorbents, namely hybrid graphite nanoflakes/mesoporous silica nanoparticles (GNP-MSN), amine-functionalized mesoporous silica (NH_2-MSN), and graphite nanoflakes (GNP), for the removal of lead from aqueous solutions. The surface area of GNP-MSN was reduced, likely due to the silica coating on GNP surfaces, and the pore size of GNP-MSN was slightly larger than that of GNP, influenced by the presence of ionic template C16PyBr. Furthermore, functionalizing MSNs with amine groups led to a decrease in surface area and pore volume, attributed to the integration of amine groups onto pore surfaces. The maximum lead(II) adsorption for all three adsorbents occurred at pH 4 within 20 minutes. Lower pH hindered adsorption due to hydronium ions surrounding GNP surfaces, obstructing lead(II) ion binding sites. At higher pH, metal cation precipitation occurred. Adsorption kinetics revealed that the pseudo-second order model was the most suitable for describing lead(II) ion adsorption on both GNP and NH2-MSN, suggesting chemisorption. The pseudo-first order and pseudo-second order models yielded lower R^2 values for GNP-MSN, indicating adsorption controlled by physical adsorption or chemical adsorption involving weak

intermolecular forces or strong surface complexation of metal ions with oxygen-containing groups. Langmuir and Freundlich adsorption isotherms were applied, with Langmuir better representing lead(II) ion adsorption by GNP and NH_2-MSN. This suggests monolayer coverage on their surfaces. Conversely, the Freundlich model indicated multilayer adsorption on GNP-MSN's surface, supporting the pseudo-second order kinetic model's suggestion of physisorption involving Van der Waals or dipole-dipole forces [30].

Bogdan et al. investigated the adsorption of ammonium ions from aqueous solutions using exfoliated graphite nanoplatelets (xGNP) as adsorbents. The study examined adsorption characteristics under different conditions, including contact times, initial ammonium ion concentrations, and temperatures. Optimal adsorption parameters were identified as 70 ppm ammonium ions at 25°C with 30 minutes of stirring. The adsorption mechanisms were analysed using pseudo-first order, pseudo-second order, and intra-particle diffusion models. Among these, the pseudo-second order model (R^2 = 0.9831) provided the best fit for describing the adsorption kinetics of ammonium ions onto xGNP. To explain how solutes interacted with the nanostructured carbon-based adsorbents at equilibrium; various isotherm models including Freundlich, Langmuir, Temkin, Halsey, and Harkins-Jura were applied. The data showed that equilibrium data fit well with Freundlich, Langmuir, Harkins-Jura, and Halsey adsorption isotherm models, indicating advantageous, multilayer adsorption, a heterogeneous surface, and pore distribution on xGNP. Thermodynamic parameters were also determined, revealing that the adsorption process was feasible due to the negative value of ΔG^0. The positive value of ΔS^0 suggested ammonium molecules agglomerated at the solid/solution interface, and the endothermic nature of the adsorption process was indicated by the positive value of ΔH^0 [59].

Yin et al. conducted a study on the dispersive magnetic solid-phase extraction (MSPE) of copper and lead in Panax notoginseng using Fe_3O_4/graphene magnetic nanoparticles (Fe_3O_4@G) as adsorbents. They prepared Fe_3O_4/graphene magnetic nanoparticles by adding $FeCl_3.6H_2O$ and $(NH_4)_2Fe(SO_4)_2.6H_2O$ to dispersed graphene nanoparticles. To develop a highly sensitive method for simultaneous determination of Cu(II) and Pb(II) in Panax notoginseng, they optimized various experimental conditions. The optimal sorbent dose for extracting Cu and Pb from samples was found to be 36 mg. pH played a critical role in the MSPE procedure, with the optimal pH at 7. The retention percentage of lead and copper ions on the sorbent decreased at pH values higher than 7, likely due to the precipitation of lead and copper ions in the hydroxide form, reducing the concentration of free ions. An equilibration time of approximately 12 minutes was required for quantitative extraction of the analytes from the solution into the solid phase. The method was validated by applying it to determine the content of Cu^{2+} and Pb^{2+} in Panax notoginseng using standard addition and recovery techniques. The results indicated spiked recoveries for the target metal ions in the range of 96.4% to 102.0%. Furthermore, the concentrations of the two ions were found to be very low in Panax notoginseng samples, demonstrating the effectiveness of the adsorbent in recovering copper and lead as described in the methods [60].

Kucherova et al. examined the adsorption of lead ions (Pb^{2+}) using graphene-based nanocomposites derived from hydrolysed expanded graphite intercalation compound. Three distinct nanocomposites-suspension of graphene nanoplatelets (SGN), paste of multi-layered oxidized graphene (PMOG), and paste of few-layered oxidized graphene (PFOG)-were employed as adsorbents for Pb^{2+} extraction. The adsorption kinetics revealed an initial rapid Pb^{2+} adsorption rate that subsequently slowed, ultimately reaching equilibrium at 30 min. Remarkably, the adsorption capacities achieved were 457 mg/g (SGN), 103 mg/g (PMOG), and 38 mg/g (PFOG). The initial adsorption rate was influenced by the surface area energy of the adsorbents, resulting in a sudden increase in adsorption due to the presence of active adsorption sites. To discern the nature of the adsorption process (diffusion or chemisorption), various kinetic models, including the pseudo-first order, pseudo-second order, Elovich, and intraparticle diffusion models, were applied. Notably, the pseudo-second order model exhibited an excellent fit to the adsorption process, as evidenced by a high correlation coefficient

value ($R^2 = 0.999$) [50].

La et al. highlighted the potential of graphene nanoplatelets (GNPs) as a platform for even distribution of adsorbent nanoparticles to enhance electron exchange and ion transport for heavy-metal adsorption. They employed a thermal decomposition method to create a graphene-supported Fe-Mg oxide composite for efficient arsenic removal from aqueous solutions. The study investigated various factors affecting arsenic adsorption, including different Mg/Fe weight ratios, with initial As(V) concentrations at 10 ppm, an adsorbent dosage of 200 mg/L, pH 7, and room temperature. The addition of GNPs and Fe-Mg oxide significantly improved As(V) adsorption under these optimized conditions. Adsorption isotherms were used to assess arsenic adsorption and calculate the maximum As (V) adsorption capacity of the GNP/FeMg oxide composite. The Freundlich model provided a better fit (correlation coefficient of 0.985) compared to the Langmuir model (correlation coefficient of 0.935) for describing the adsorption behaviour of As(V) by the composite. Additionally, the kinetics of As(V) adsorption on the GNP/FeMg oxide surface were examined using the pseudo-second order model, showing a well-fitted correlation coefficient of 0.957. This suggests electron exchange occurred during the chemical adsorption process between the composite and arsenic. The selectivity of the GNP/FeMg binary oxide adsorbent for arsenic was tested in the presence of common metal ions typically found in drinking water, such as Na^+, K^+, Ca^{2+}, and Mg^{2+}. Notably, only a minimal amount of Na^+, K^+, and Ca^{2+} ions were adsorbed by the composite, whereas over 95% of arsenic was effectively removed. Interestingly, the release of Mg from the adsorbent led to a 10% increase in the concentration of Mg^{2+} in the solution after adsorption [61].

Li et al. conducted research on the adsorption of Pb^{2+} and Cd^{2+} onto GNPs prepared through thermal exfoliation from water. The study investigated the influence of four key factors: pH, adsorption time, temperature, and initial concentration on the adsorption of Pb^{2+} and Cd^{2+} onto GNPs, ultimately determining the maximum adsorption capacities under optimized conditions. The results revealed that the adsorption percentages of Pb^{2+} and Cd^{2+} onto GNPs were 96.27% at pH 5.80 and 76.75% at pH 6.30, respectively. The adsorption process reached equilibrium rapidly, within just 30 minutes, indicating that GNPs have great potential as effective adsorbent materials. Furthermore, the adsorption capacity increased with higher equilibrium concentrations of metal ions, gradually reaching saturation. Notably, Pb^{2+} exhibited a more pronounced adsorption capacity increase with increasing equilibrium concentration compared to Cd^{2+}, suggesting that Pb^{2+} adsorbs more readily onto GNPs. The temperature-adsorption relationship indicated that the adsorption of metal ions onto GNPs is an exothermic reaction, with room temperature being favourable for the adsorption process. Additionally, the study highlighted the inverse relationship between pore size and uptake capacity, with GNPs exhibiting a high content of micro- and mesoporosity, making them excellent candidates for the removal of Pb^{2+} and Cd^{2+} ions [62]

Table 1. Summary of adsorption of heavy metals onto graphene nanoplatelets

Adsorbent	Heavy Metal Ions	Adsorption Conditions	Adsorption Isotherm Model	Adsorption Kinetics Model	Adsorption Thermodynamic	Adsorption Capacity (mg/g) / Removal Efficiency (%)	Additional Remarks	Ref.
Multi-layered graphene paste	Pb(II)	CT=10min, [A]=200-350mg/L	Langmuir and Freundlich	-	-	230	FLGP and MLGP correspond to L-type curves which typical for Type IV isotherms.	[50]
Functionalized graphene nanoplatelets	Pentavalent and trivalent forms of arsenic	CT=40min, AD=100mg [A]=300mg/L	Langmuir and Freundlich	Elovich model (diffusion) Intra-particle diffusion (chemical reaction kinetics)		27mg/g for arsenate, 29mg/g for arsenite / 72%	The adsorption takes place at specific homogeneous sites located on the adsorbent surface.	[51]
Exfoliated graphene nanoplatelets	Pb(II)	CT=30min, pH=6.0, [A]=200mg/L	Langmuir and Freundlich	-	-	13.09	-	[28]
Functionalized graphene nanoplatelets	Pb(II)	CT=12h, pH=6.0, AD=50mg, [A]=30 mg/L	Langmuir	Pseudo-second order	-	57.77	Five cycles of repeated use.	[52]
Graphene nanoplatelets	As(III)	CT=3h, T=300K, pH=6.0, AD=25, [A]=5.0	Langmuir	Pseudo-second order	Endothermic, spontaneous process and reaction has occurred at the solid-liquid interface with increasing randomness	247.22mmol.kg^{-1}	When the sample is at pH <7 the water molecules adsorb on GNPs surfaces more than As (III) species. At higher pH	[53]

							values (>7.0), GNPs surfaces become predominately negative. These both phenomena lead to the less interaction of GNP with As (III).	
Magnetic graphene nanoplatelets composites	As(III)	CT=60min, pH=7.0, [A]=20	Langmuir Freundlich	Pseudo-second order	-	11.34	The larger deviation of the solution pH from the neutral state, the lower adsorption capacity is observed either in acidic or basic solutions.	[54]
Graphene/pine wood biochar hybrid	Cu(II)	CT=24h, pH=6.0, AD=0.05g, [A]= 5mg/L, T=25 ±0.5°C	Langmuir	Pseudo-second order	Endothermic, spontaneous process and increase randomness	4.7 – 10.6	Uses of higher surface area GNPs produced the lower surface areas hybrid adsorbents. This is because biochar loaded with nanomaterials can have a pore filling and pore-blocking effect.	[55]

GNP-COOH, GNP-P, GNP-O^+	Cu(II)	AD=0.1 g, [A]=0.53-0.59mg/L	Freundlich	-	-	16.7	Functionalized GNPs showed good colloidal stability which shows a good adsorbent in water because pollutants must have free and quick access to all adsorptive sites on the adsorbent surface.	[56]
Oxidized exfoliated graphite nanoplatelets (ox-xGnP)	Sb(III)	CT=25min, pH=7.0, AD=1.0mg, [A]=1.0mg/L, T=293K	Langmuir	Pseudo-first order	Exothermic, spontaneous process and increase in randomness	8.91	At range of pH 9.0, a significant increase in the adsorption capacity of Sb (III) on the ox-xGnP surface.	[57]
Single-wall carbon Nanotube-graphene nanoplatelet	Cu(II) Zn(II) Pb(II)	CT=100min, pH=6.1, [A]=0.1mg/L	Langmuir Freundlich	Pseudo-second order	-	-	Pb (II) lower in average uptake capacity compared to Cu (II) and Zn (II) due to larger molecular weight and ionic radius.	[58]
GNP-MSN GNP	Pb(II)	CT=2h, pH=4.0, AD=10mg, [A]=10mg/L	Langmuir	Pseudo-second order	-	23.94 1.11	At lower pH, adsorption was unfavourable due to the	[30]

							surface of the GNP could be surrounded by the hydronium ions (H_3O^+) that hinder lead (II) ions from reaching the binding site on the surface of the GNP.	
Exfoliated graphite nanoplatelets	Ammonium	-	Freundlich, Langmuir, Harkins-Jura and Halsey	Pseudo-second order	Exothermic, feasibility process and increase in randomness	12.04	-	[59]
Fe_3O_4/graphene magnetic nanoparticles	Cu(II) Pb(II)	CT=12min, pH=7.0, AD=36mg	-	-	-	96.4 102.2	Decrease in the percentage of lead and copper ions on the sorbent at pH values higher than 7 is due to precipitation of lead and copper ions in the hydroxide form which leads to decreasing the concentration of free lead and copper ions in the sample.	[60]

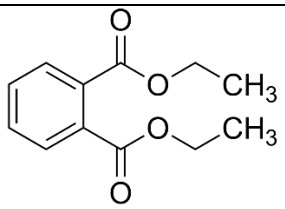
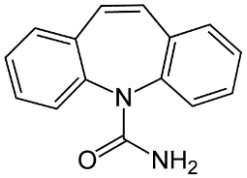
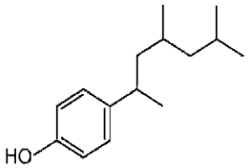
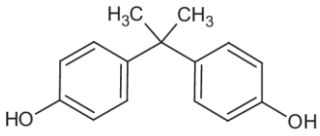
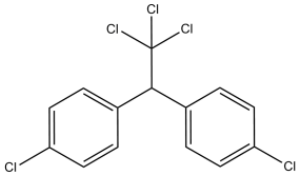
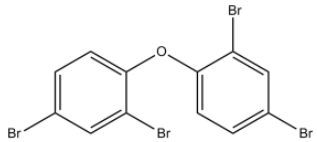
Suspension of graphene nanoplatelets (SGN)	Pb(II)	AD=0.01g, [A]=1,040mg/L	-	Pseudo-second order	-	457	Pb (II) adsorption is initially quite rapid. Then, the adsorption rate gets slower over time and reaches the constant value at 30 min	[63]
GNP/Fe-Mg oxide composite	As(V)	pH=7 AD=200mg/L, [A]=10 mg/L	Freundlich	Pseudo-second order		40.3	-	[61]
Graphene nanoplatelets	Pb(II) Cd(II)	CT=30min, pH=Pb^{2+} 5.80; Cd^{2+} 6.30, AD=15mg, [A]=500mg/L	-	-	-	460.20 72.39	The adsorption capacity increases with increasing equilibrium concentration of metal ions, and reaches saturation progressively.	[62]

Abbreviations: FLOGS = few-layered oxidized graphene suspension; MLGP = multi-layered graphene paste; FLGP = few-layered graphene paste; FGN = functionalized graphite nanoplatelets; GNP-MSN = hybrid graphite nanoflakes/mesoporous silica nanoparticles; NH_2-MSN = amine functionalized mesoporous silica; GNP = graphite nanoflakes; SGN = suspension of graphene nanoplatelets; PMOG = paste of multi-layered oxidized graphene; PFOG = paste of few-layered oxidized graphene; CT = contact time [h], T = temperature [◦C], AD = adsorbent dose [g/L], [IC] = initial concentration [mg/L]

Graphene nanoplatelets as endocrine disrupting chemicals adsorbents

Kumar et al. [64] highlighted growing concerns over the presence of endocrine-disrupting chemicals (EDCs) in aquatic water bodies, especially fresh water environments, and their potential disruptive effects on indigenous fauna. In the past few decades, environmental toxins have interfered with the endocrine systems of humans and animals, leading to deleterious effects, particularly in reproduction and the development of secondary sexual traits [29, 3]. An endocrine disruptor is an external drug or mixture that may interfere with or modify the function(s) of the endocrine system, resulting in undesirable health effects in an intact organism, its offspring, or (sub)populations [2]. The substance may interfere with the synthesis, secretion, transport, binding, action, or elimination of natural hormones in the body, which are responsible for the maintenance of homeostasis, reproduction, development, and/or behaviour, as well as the regulation of developmental processes [3-5]. Table 2 below shows the several examples of EDCs.

Table 2: Some known EDCs molecular structure and their uses

Example EDCs	Category/Use	Molecular Structure	Molecular Weight (g/mol)
Diethyl phthalate	Personal care products		222.24
Carbamazepine	Pharmaceutical		236.269
Nonylphenols	Industrial surfactants		220.35
Bisphenol A	Food contact materials		228.29
Dichlorodiphenyltrichloroethane	Pesticides		354.48
Polybrominated diphenyl ethers	Brominated flame retardants		564.7

According to Ternes et al. [65] and Shi et al. [66] human and animal excretions as inactive polar conjugates such glucuronides and sulphates and their incomplete removal in sewage treatment plants were the main causes of the presence of EDCs in water bodies and sediments. The primary environmental source for these chemicals is the direct discharge of untreated sewage to surface waters. EDCs can also leach from septic tanks or landfills, infiltrate the ecosystem through surface runoff, or enter the water directly by direct discharge from treatment plants [67-73]. Therefore, this emerging class of pollutants need effective treatments. The best approach for removing contaminants is adsorption because no byproducts would be created and water and the adsorbent could both be recycled. As a result, researchers are constantly looking for novel adsorbents and trying to come up with new, effective removal techniques. GNPs are a brand-new, very effective adsorbent material that has a high capacity for adsorption, good stability, and quick adsorption. The platelet thickness is in the nanometer range, but the areas are in the micrometre range [28, 74]. In addition, GNPs may be easily produced in huge quantities from inexpensive natural graphite without the requirement for dimensional enlargement for use in water purification. These materials are less expensive than CNTs, can be used in water treatment procedures, and are simple to remove or regenerate, making them an excellent option for EDC adsorption [29].

Zaka et al. [75] analyzed the diclofenac sodium removal effectiveness of GNPs in water. To figure out the optimal parameters for DCS removal by GNPs, many factors were explored. The different parameters include contact time, adsorbent dosage, the initial concentration of DCS, pH and temperature. At 25°C temperature, 3.5 g/L dosage of GNPs, pH of 5, 5 ppm concentration of DCS, and contact time of 40 minutes, the maximum elimination of 99% was recorded. The interaction of adsorbents with ionizable contaminants has been found to be strongly influenced by electrostatic attractions or repulsions. Under acidic pH conditions, DCS functions as a neutral molecule and is more attracted to the graphene surface. The hydrophobic effects as well as the π–π electron-donor attractions play a significant role in the adsorption process for pH < pKa of DCS since GNPs has a negative charge on the surface for pH values larger than 2.2. The removal effectiveness is shown to diminish at pH levels higher than 4.2 because DCS ionises to produce a negatively charged ion that is electrostatically attracted to the surface of GNPs. Adsorption isotherms were plotted for each model to gain a better knowledge of the adsorption process and insight into the relationships between adsorbent and adsorbate. The adsorption isotherms were obtained under optimal conditions. In addition, the interactions between molecules of adsorbate and adsorbent were investigated using three distinct isotherm models: Langmuir, Freundlich, and Temkin. The data were determined to be best suited by the Langmuir isotherm, which had an R^2 value of 0.9967. The Langmuir isotherm model assumes that there are no lateral interactions between adsorbate molecules on the surface during monolayer adsorption. To comprehend the kinetics of DCS adsorption on GNPs, pseudo-first order and pseudo-second order kinetic models were utilised. With a rate constant of K_2 = 1.8218 g/mg min, it was discovered that the adsorption process followed pseudo-second-order kinetics. The process was confirmed to be exothermic and spontaneous when the thermodynamic properties were computed using Sip's model and indicated the negative value of change in Gibbs free energy and the change in enthalpy was equal to -3.9089 KJ/mol.

Radu et al. [29] utilized exfoliated graphite nanoplatelets (xGnP) as adsorbents for bisphenol A (BPA). This research investigates the possibility of eradicating this endocrine disruptor. The influence of the following parameters on the sorption behaviour of xGnP was investigated: contact time, starting BPA concentration, temperature, ionic strength, and pH. The influence of solution pH on BPA removal was examined. It was found that BPA adsorption decreased when the pH value is below 4, likely as a result of protonation of the xGnP surface's negative charge. The deprotonation of BPA causes a decrease in the hydrophobic interactions between the electrons of the graphite surface and the electrons of the C=C double bonds of BPA above a pH value of 10, and as a result, the adsorption of BPA on the xGnP surface. Between pH 3 and 7, it was seen that BPA adsorption marginally

increased, and between pH 7 and 9, it started to decline. Based on research, the ideal circumstances were (0.1 mg of xGnP and 50 mL of 1-10 mg/L BPA at 298.15 K, pH = 5.5, and contact period 30 minutes). It was also investigated how the ionic strength of the working solutions affected the elimination of organic contaminants. Salts and organic materials from the environment increase the adsorption of BPA on xGnP surfaces. The ideal concentration of NaCl in aqueous solution was determined to be 0.037 M. At low concentrations of NaCl in solution, the adsorption of BPA with a nonplanar and flexible structure greatly increases, and at higher concentrations, it starts to decline. The distribution of the Na+ and Cl- ions among the negatively charged graphite platelets may account for this activity, creating a screening effect that facilitates the adsorption of BPA molecules. BPA is less soluble in solution when NaCl is present, and its ability to bind to xGnP is improved. Because Na^+ and Cl^- ions are present, the "butterfly" or lying-down form of BPA may make it easier for more accessible adsorption sites to be occupied. It was shown that the adsorption capacity reduced at concentrations greater than 0.05 M, most likely as a result of competition amongst the species engaged in the process. In this study, equilibrium adsorption was represented by Langmuir, Freundlich, Harkin-Jura, and Temkin isotherms. When the adsorption process approaches equilibrium, the interactions between the adsorbent and the adsorbate are indicated by the adsorption isotherm models. The adsorption of BPA on xGnP most closely resembles the Langmuir isotherm based on a comparison of R^2 values, indicating a monolayer adsorption system on the surface. The kinetics of the adsorption process were studied using pseudo-first and second order models as well as intraparticle diffusion one. The experimental adsorption capacity, q_e exp (850 mg/g), was in greater agreement with the calculated one based on the pseudo-second order model, according to the results. Due to the large system of graphene, which is a strong electron acceptor, it favours a configuration that allows the interaction with the negatively charged sites of BPA. The physisorption of BPA on graphene is aided by charged controlled interactions in addition to van der Waals interactions; chemisorption is less significant on pure xGnP. The thermodynamic parameters provide insights as to how the internal energy evolves throughout the adsorption process. A process is exothermic when the change in enthalpy value is negative. The absence of normal free energy denotes a spontaneous process.

Al-Khateeb et al. researched the adsorption and removal characteristics of pharmaceutical pollutants such as aspirin (ASA), acetaminophen (APAP), and caffeine (CAF) onto GNPs from aqueous solutions. The TEM characterization analysis reveals that GNPs have many wrinkles and a transparent, layered structure with a smooth surface. Typically, the specific surface area of the solid adsorbent has a significant impact on the adsorption process. The specific surface area of the GNPs must therefore be determined using nitrogen adsorption/desorption isotherms. The obtained adsorption isotherms were categorized as type IV isotherms. The GNPs' specific surface area was discovered to be 635.2 m^2/g. It was studied how the mass of GNPs affected the adsorption patterns of ASA, CAF, and APAP. It found that, when an adsorbent mass of 15.0 mg was used, it was generally observed the percentage of ASA, CAF, and APAP adsorption rose almost linearly with the increase in GNPs mass. This development is mostly attributed to the rise in adsorption surface area brought on by the increased mass of GNPs, which made more active adsorption sites for the molecules ASA, CAF, and APAP molecules available. For the first 10 minutes, the adsorption of these three pharmaceutical pollutants increased over time. At this stage, equilibrium had been reached, with the amounts of ASA and CAF adsorbed being 63.5%, 94.3%, and 87.6%, respectively. The first stage of ASA, CAF, and APAP adsorption took place during the first 10 min of adsorption and was characterized by the high number of active binding sites on the GNPs surface at this time. Adsorption happened fast in this step, which suggests that it was controlled by the process by which the molecules of ASA, CAF, and APAP moved from the bulk phase to the surface of the GNPs. Because there were less active sites available for the ASA, CAF, and APAP molecules on the surface of the GNPs in the second stage, adsorption was probably an attachment-controlled process. It was investigated how pH affected the effectiveness of ASA, CAF, and APAP removal by GNPs. In the case of ASA and CAF,

the pH of the solution did not generally affect the removal of pharmaceutical compounds by GNPs; the percentage of adsorption (70 and 80, respectively) was not considerably affected by changing the pH value. In the case of APAP, raising the pH from 2.0 to 8.0 had no effect on the percentage of adsorption, while raising the pH to 11.0 was linked to a sharp drop in the percentage from 88.7% to 73.8%. The GNPs covered by the negatively charged hydroxide ions and the negatively charged APAP ions, whose pKa value is 9.9, may repel one another due to electrostatic attraction [76].

The electrostatic and hydrophobic interactions between the adsorbate and the solid adsorbent may be influenced by the ionic strength. Therefore, it is essential to research on how ionic strength affects the way that ASA, CAF, and APAP bind to GNPs. Ionic strength has a significant impact on the adsorption of pharmaceutical compounds because it generates a variety of adsorption conditions in which the electrostatic interactions between the pharmaceutical compounds and the surface of the GNPs are either appealing or repellent. An increase in the ionic strength of the solution had no effect on the percentage of ASA adsorption by GNPs. This suggests that the overall adsorption process is not affected by electrostatic contact. Increasing the ionic strength of the solution did, however, significantly increase the percentage of CAF adsorption, which suggests that - stacking between the surface of the GNPs and neutral CAF (pKa = 14.0) has a stronger electrostatic attraction. Pseudo-first-order and pseudo-second-order kinetic models have been proposed in order to understand the mechanisms of adsorption. The pseudo-second-order model was found to have the highest R^2 value for accurately describing the adsorption of ASA, CAF, and APAP by GNPs. The fundamental cause of the adsorption is a contact between the GNPs and the ASA, CAF, and APAP molecules that acts as an electron donor-acceptor. By computing the thermodynamic parameters, the feasibility and spontaneity of the process of ASA, CAF, and APAP adsorption by GNPs were investigated: Changes in enthalpy, entropy, and Gibbs free energy. Enthalpy change values for the adsorption of ASA, CAF, and APAP by GNPs from aqueous solution were negative; 5.42 kJ/mole, 46.6 kJ/mole, and 25.4 kJ/mole, respectively. The negative numbers demonstrate that ASA, CAF, and APAP are adsorbed by GNPs in an exothermic nature which explains for the decrease in adsorption at higher temperatures. The strength of the enthalpy change points to physical adsorption as compared to chemical adsorption as the likely mechanism for the weak bonding between ASA, CAF, and APAP by GNPs. When ASA, CAF, and APAP were adsorbed onto the surface of the GNPs, the negative values of entropy change, 13.1 J/mole K, 123.0 J/mole K, and 67.3 J/mole K, indicated a decrease in randomness at the GNP/solution interface. The decrease in the degree of freedom of the drug molecules may be the cause of the negative entropy of ASA, CAF, and APAP's adsorption and immobilization on the surface of GNPs. As would be expected from a product-favoured and spontaneous reaction, the free energy change was negative. The adsorption of ASA, CAF, and APAP by GNPs from aqueous solution is represented by the negative values of ΔG^o, which are 1.54 kJ/mole, 10.2 kJ/mole, and 5.42 kJ/mole, respectively [76].

Zaka et al. [80] were using a response surface modelling technique to analyse the effect of four distinct parameters on the elimination of levofloxacin (LFX) using GNPs. Extremely acidic and alkaline conditions diminish the effectiveness marginally. It can be noticed that both dosage and time have a positive effect on removal efficiency. If one of the variables is held constant, the trend remains unchanged. This is due to the fact that an increase in dosage will result in a greater number of accessible sites, hence increasing the removal. The change in elimination due to dosage is more important than the change in effect due to time. At any given time, a rise in concentration will result in a decrease in removal efficiency, which could be attributed to active site saturation. Zaka et al. [80] conducted five trials under optimal conditions: contact time = 77 minutes, GNP dosage = 2.1 g/L, pH = 5, and levofloxacin concentration = 10.5 mg/L. These five studies yielded removal efficiencies of 98.29 %, 98.15 %, 98.55 %, 97.97 %, and 98.59 % respectively. To fit the experimental data, three different isotherm models Langmuir, Freundlich, and Temkin were applied. It can be seen that the Langmuir isotherm model, which has an R^2 value of 0.996, best describes

the adsorption of LFX. This shows that the adsorption is monolayer- and homogeneous-based in nature. The experimental model for the removal of LFX using GNPs was fitted using pseudo-first order and pseudo-second order kinetic models. The pseudo-second order model's observed R^2 value of 0.999 was determined to be preferable to the pseudo-first order model's R^2 value of 0.880. Thermodynamic properties including change in Gibbs free energy (ΔG^o), change in enthalpy (ΔH^o), and change in entropy (ΔS^o) were calculated in order to explore the energy changes connected with LFX elimination. It can be shown that the free energy change values vary from -20 to 0 kJ/mol. This leads to the conclusion that LFX is physically adsorbing to GNPs. Additionally, the negative sign shows that the process is spontaneous. Additionally, the rise in Gibbs free energy shows that adsorption is less likely to occur at high temperatures. The process is endothermic, according to the positive sign of enthalpy change (ΔH^o). Additionally, the high affinity of the sorbent for the sorbate is linked to the positive value of entropy, which indicates an increase in randomness at the solid/liquid interface [77].

Kerkez-kuyumcu et al. studied the removal of amoxicillin (AA) from aqueous solution using magnetically modified graphene nanoplatelets (M-GNPs). M-GNPs were produced utilizing a selected GNPs by using a co-precipitation technique. The BET specific surface areas of M-GNPs were measured to be 543.2 m^2/g. The specific surface area of the GNPs (677.5 m^2/g) was significantly higher than that of the M-GNPs, which was decreased upon mixing with the Fe_3O_4 nanoparticles. Up until an adsorbent mass of 5.4 mg was used, the removal % of AA rose almost linearly with increase in M-GNPs mass. According to the study's findings, there was no discernible change in the percentage of amoxicillin removed over the pH range of 3.0 to 5.0, however the percentage clearance decreased when pH rose above 5.0. Amoxicillin is well-known for having three main function groups with different pKa values: -COOH (pK_{a1} 2.69), -NH_2 (pK_{a2} 7.49), and -OH (pK_{a1} 7.49). (pK_{a3} 9.63). At different pH values, these functional groups ionise to create negatively charged amoxicillin. As the pH of the solution rises, a stronger electrostatic attraction forms between the positively charged surface of the M-GNPs and the negatively charged amoxicillin. Additionally, competition for the active sites on the surface of the M-GNPs develops as the pH of the solution rises between the negatively charged -OH ions and positively charged amoxicillin ions. A pH of about 5.0 was selected as the ideal value for amoxicillin adsorption onto M-GNPs. Since there are several adsorption circumstances where the electrostatic interactions between the surface of the M-GNPs and the pharmaceutical compounds are either attracting or repulsive, the influence of ionic strength on the adsorption of pharmaceutical compounds was studied. The results show that an increase in KNO_3 concentration from 0.0001 M to 0.001 M did not significantly alter the percentage of adsorption, but an increase to 0.01 M caused a significant decrease in the percentage of adsorption from 68.3% to 33.9%. This happens as a result of the inhibitory effect of a high concentration of K^+ ions. Last but not least, the ionic strength investigation showed that electrostatic interaction caused by π–π stacking influenced the adsorption behaviour of amoxicillin on M-GNPs solution.

Three different isotherm models—the Langmuir, Freundlich, and Temkin models were used to analyse the adsorption of AA on M-GNPs. The average R^2 values for the Temkin isotherm model and the Langmuir isotherm model were nearly identical (R^2 >0.99). Accordingly, the adsorption mechanism included both monolayer adsorption and electrostatic interaction between the surface and adsorbate through the π–π stacking of electrons, which agreed with the results of the study on ionic strength. The pseudo-second-order model, intraparticle diffusion, and Bangham models were used to analyse the adsorption kinetics. It was determined that the use of M-GNPs for the removal of AA from aqueous solution primarily followed a pseudo-second-order kinetic model, as observed by an excellent correlation coefficient (>0.99), which confirms that the major cause of AA's adsorption on M-GNPs is to π–π electron donor-acceptor interaction, which is the rate-determining step. In this study, the thermodynamic parameters were analysed; the negative value of ΔG^o indicated that the adsorption was spontaneous, the negative value of ΔH^o that the process was exothermic, and the negative value of ΔS^o that the surface

randomness was decreased as AA molecules adsorb on the adsorbents. Investigations on the recovery and reusability of the adsorbent revealed that it had a great ability to remove AA repeatedly without losing stability [78].

Ion et al. published the first data on phenol removal utilizing exfoliated graphitic nanoplatelets (xGnPs) as a sorbent. They studied the influence of contact time on phenol adsorption. The results demonstrated that phenol adsorption is slow, with the majority of adsorption occurring within the first 10 hours. The equilibrium was reached following 30 hours of adsorption. In addition, the results demonstrated that phenol is better adsorbed on as-grown xGnP than on oxidized xGnP, but equilibrium is reached after the same contact time. Hydrogen bonding is one mechanism for the sorption of phenol and other organic compounds on carbon-based sorbents, but from the data suggest that this process may not be relevant between the phenolic and functional groups on the xGnPs. Possible hydrogen bonding between surface-adsorbed phenol and dissolved phenol may contribute to the increased sorption capacity values found for xGnPs with high surface areas. Moreover, the dissociation of –OH groups on the phenols may hinder the formation of hydrogen bonds between the surface adsorbed on oxidized xGnPs relative to as-grown xGnPs, hence reducing sorption. The to π–π electron donor–acceptor interactions have been applied to the adsorption of organic molecules on the graphene surface. As an amphoteric adsorbate, graphene could be extremely polarizable. Hydroxyl is an electron-donating functional group that boosts the π -donating strength of the graphene aromatic ring and the sorption affinity of phenol to the surface of xGnPs. The influence of starting phenol concentration on adsorption efficiency at 400 mg/L xGnP when 72.25 percent phenol removal is accomplished. According to the study, the percentage of phenol adsorption increased as pH rose from 2 to 6 and subsequently reduced as pH approached the phenol pKa. The adsorption of phenol on xGnPs was analysed using Langmuir and Freundlich models. Langmuir sorption isotherm is more applicable to describe phenol adsorption to xGnPs. This is also confirmed by the higher correlation coefficient ($R^2 = 0.985$) in the case of Langmuir model as compared to Freundlich model [74].

Banerjee et al. investigated the potency and effectiveness of graphene oxide nanoplatelets (GONPs) as an adsorbent, as well as its application for the efficient uptake of ibuprofen (IBP) from an aqueous solution. In batch adsorption studies, the various process parameters were investigated in order to determine their effect on the relevant process. Maximum IBP removal (98.17%) was found at an initial IBP concentration of 6 mg/L, adsorbent dosage of 1.00 g/L, solution pH of 6, agitation speed of 180 RPM, and temperature of 308K following 60 minutes of treatment. The adsorbent of GONPs exhibited thin, crinkled, overlapping paper-like structures in intimate association, which represented the distinctive property of single-layer graphene oxide sheets, according to SEM pictures of GONPs. The GONP surface's folded structures gave a larger surface area for more effective adsorption. After being used to adsorb IBP, GONPs' sharp edges notably began to soften. TEM was used to show the surface shape of GONPs before and after IBP adsorption. Images from TEM analysis showed the overlapping GONPs and their stable aqueous phase dispersion, which allows for increased adsorption rates [79].

The adsorption isotherm study was carried out using the Langmuir, Freundlich, Temkin, and Dubinin-Radushkevich isotherm models. $R^2 = 0.994$, the highest correlation coefficient, indicates that the Langmuir model best explains IBP adsorption over GONPs. This indicated the homogeneous nature of the GO and implied that each IBP molecule's binding energy to the surface GO was constant. Thus, it can be inferred that GO molecules did not interact with one another, indicating that IBP molecules formed a monolayer covering on the surface of GO. Intraparticle diffusion, pseudo-first-order, pseudo-second-order, and Elovich models were used to examine the reaction's pathway and any potential rate-limiting phases during the adsorption of IBP by GONPs at various temperatures (293–313 K). The pseudo-second order rate kinetics is thought to best describe IBP adsorption by GONPs based on the highest correlation coefficient values ($R^2 = 0.998$). The Arrhenius equation was used to compute the activation energy (E_a), which was found to be 13.49 kJ/mol. IBP adsorption by GONPs is physisorption in nature because

the E_a value obtained is less than 40 kJ/mol. Furthermore, the endothermic nature of the process was revealed by an increase in the adsorption capacity of GONPs (8.217 - 9.165 mg/g) and a concomitant increase in temperature (293 - 313 K). Adsorption thermodynamics was studied, and the results show that the process reached equilibrium by utilizing energy from the system under consideration. The negative values of ΔG^o indicated that the adsorption was spontaneous, while the positive values of ΔH^o indicated that the process was endothermic in nature. The increased randomness at the solid/solution interface was assumed to be caused by the translational entropy of the displaced water molecules being higher than that of the released IBP ions, which was supported by the positive value of ΔS^o. For the removal and recovery of the IBP compounds for solution, investigation of the GONPs' reusability potential is important. The rate of IBP elimination (%) throughout the course of 10 cycles of adsorption and desorption was practically unchanged for eight cycles and slightly reduced for the final two cycles (97.18 and 95.91%) [79].

Rosli et al. conducted research on the use of GNPs to remove the pharmaceutical pollutants sulfamethoxazole (SMX), an antibiotic, and acetaminophen (ACM), an analgesic, from water. The best adsorbent was chosen from among several different types of GNPs, including C750, C300, M15, and M5, each of which has a different surface area. From this study, it was discovered that C750 (738.44 m^2/g) had the maximum surface area, followed by C300 (390.30 m^2/g), M15 (61.51 m^2/g), and M5 (63.55 m^2/g). As mesopores, the pore diameters of C750, C300, M15, and M5 fall within the range of (2–50 nm). A larger zeta potential may indicate better dispersion. Zeta potential measured the electrostatic repulsion between similarly charged particles and thus indicates a degree of dispersion efficiency thus giving information about the tendency of agglomeration. Among the other three GNPs, GNP C300 had the most stable observed zeta potential (50.80 mV). With an absolute value of 20.87 mV, GNP M5 has the lowest tendency to aggregate because it is below the 30 mV threshold. Although C750 has a bigger surface area, the preliminary adsorption investigation of four different types of GNPs indicated that C300 has the maximum removal effectiveness when compared to other forms of GNPs. Based on zeta potential, C300 has the highest level of stability. Further batch adsorption experiments using C300 were conducted with a number of parameters, including solution pH, GNP concentration, initial SMX concentration, and contact time. The pH of the solution had an impact on GNP C300's capacity to adsorb to both SMX and ACM. The initial pH of the solution rose from 2 to 4, eventually raising the adsorption capacity of SMX onto GNP C300. In contrast, ACM's adsorption capacity and removal efficiency progressively increased from acid to neutral before declining as it increased further. For SMX and ACM, maximum adsorption was found at pH 4 (99.27%) and pH 8 (98.38%), respectively. The removal of SMX molecules was hindered by the rising pH of the solution, which led to a poor adsorption capability at higher pH. Since SMX is a well-known acidic organic chemical with a dissociation constant (pKa) between 1.6 and 5.7, acidic circumstances (pH pKa) were preferable to basic conditions (pH > pKa) for the removal of the target compound. In other words, they are present in aqueous solution as a protonated form when solution pH is lower than their pKa values. The elimination efficiency rose with the increase in GNP C300 dosage from 5 mg to 60 mg, but the adsorption capacity for both medications decreased. Adsorption sites were fully accessible at low adsorbent dosages, increasing adsorption capacity. In comparison to lower adsorbent dosages, the active sites of the adsorbent that were ready to bind with the medicinal compounds were not fully utilised at larger GNP C300 amounts. Adsorbent may aggregate and there may be a chance for solid particle collisions as GNP C300 levels rise. The initial concentration of SMX and ACM rose in a nearly linear fashion. More adsorbate molecules are accessible for adsorption the higher the starting concentration. Adsorption of SMX and ACM by GNP C300 started out pretty rapidly before slowing down as contact time increased. For the purpose of determining the adsorption equilibrium between the pharmaceuticals and GNP C300, the Langmuir and Freundlich isotherm models were used. The Langmuir isotherm model was shown to have R^2 values of 0.9952 for SMX and 0.9946 for ACM, indicating a quite better fit and greater suitability for modelling the adsorption of pharmaceuticals onto GNP

C300. This indicated that SMX and ACM adsorption on GNP C300 occurred in a monolayer on a homogeneous surface without contact between the adsorbate. Adsorption kinetics were investigated, and linear regression was used to obtain the kinetic parameters and the correlation coefficient, R^2. Compared to the pseudo-first-order kinetic models, the pseudo-second-order model fitted the data better. According to the pseudo-second-order model, the correlation coefficients (R^2) for both SMX and ACM were 0.9999, which was higher than the correlation coefficients for the pseudo-first order. Thus, in agreement with chemisorption being the rate-controlling phase, the pseudo-second-order model was better fit for modelling the process of SMX and ACM adsorption on GNP C300. To further describe the diffusion mechanism, the intraparticle diffusion model was used. Data multilinearity suggests that intraparticle diffusion influences the early stages of adsorption but was not the rate-determining step for the entire adsorption process [80].

Badhei et al. worked on adsorption of Metronidazole antibiotic drug (MNAD) onto magnetically modified graphene nanoplatelets (MMGN) from aqueous solution. The MMGNs were prepared by mixing GNPs with freshly prepared magnetite nanoparticles and the new characteristics were further observed during the investigation. The effect of different operational parameters which affect the removal process were explored such as; adsorbent amounts, contact time, initial pH, temperature, and the initial concentration of MNAD. The results showed that the MNAD was removed within 120 min using 9.8 mg adsorbent, at pH 5.0 and 293 K. Adsorption equilibrium data were fitted using both Langmuir and Temkin isotherms, and the Langmuir maximum adsorption capacity was found to be 112.48 mg g^{-1}. Adsorption for MNAD was studied kinetically and thermodynamically, and found to be well fitted by the pseudo second order kinetic model, spontaneous and exothermic in nature. The adsorption behavior of MNAD on MMGN involved π-π stacking and electrostatic interaction, and the rate determining step was the π–π electron donor– acceptor interaction. Recovery, and reusability of the adsorbent was investigated, and the adsorbents showed great ability for the removal of Antibiotic drug for many times without losing its stability. Generally, MMGN could be considered a potential and promising adsorbent for the removal of organic pollutants from polluted water [1].

de Assis et al. the synthesis of graphene oxide (GO) nanosheets, to be used as adsorbent for the removal of textile dyes from wastewater, was optimized by the modified Hummers method. The GO nanosheets produced were compared with commercial GNPs. The surface area (BET model) for commercial GNPs presented a value of 90.08 ± 3.01m^2 g^{-1}. No hysteresis was observed, which was expected since the material is nonporous, formed only by nanosheets, often superposed. The surface area of GO synthesized by the modified Hummers method presented a value of 176.00 ± 2.09 m^2 g^{-1}, which indicates that the oxidation of the material is favoring the free surface area. It is estimated that the application of ultrasound techniques can promote exfoliation of the sheets and increase the specific surface area. The results of removal efficiency for the blue dye (SFGL) on the two sorts of adsorbents studied evidenced the anionic behavior of the direct dye, because there was a tendency to the significant increase of the removal efficiency when at pH <4, especially when adsorbed on graphene oxide, reaching efficiency higher than 90% at pH 1.0. This pattern may be due to the functional groups of the dye adsorbed on the surface of the GO which increase its surface complexing ability. Because of the high functionalization of the graphene oxide by hydroxyl (-OH) and carboxylic groups (-COOH), negatively charged in aqueous solution, the presence of available oxygen groups and the arrangement of the active functional groups of the dye species, it is possible to occur stronger chemical bonds, such as hydrogen bonds, between GO and the dyes. The results of the removal efficiency of the dye Red 81 under the two different adsorbents were quite different. When adsorbed on commercial graphene the dye exhibited exceptional high efficiency at low pH, which rapidly decreased at higher pHs. When adsorbed on graphene oxide, the removal efficiency did not reach values higher than 80% for low pH, however for pHs above 7.5 reached efficiency close to 100%. The presence of large amounts of OH- functional groups in the GO may facilitate interaction with the amine -NH functional groups of the dye at higher pHs, resulting in a greater

adsorption at these levels. It suggested that the negatively charged sulfonate groups (SO_3) of dye molecule neutralize the electrostatic interaction with oxygen-containing groups on the GO surface, so that of the π-π interactions and the hydrogen bonds with the GO surface can play a dominant role in the adsorption process. Hence, a pH of 3.5 was set to evaluate the influence of the initial dye concentration. Best concentration of 50 ppm for the GO and 100 ppm for the commercial graphene were selected as it resulted in a maximum adsorption capacity [24].

The adsorption isotherm of the dyes Indosol SFGL direct blue and Red 81 on graphene oxide (GO) were studied. Langmuir isotherm fitting best suited both data points, with monolayer maximum sorption capacity (q_m) of 128.58 and 190.53 $mg \cdot g^{-1}$ for SFGL and Red 81, respectively, and satisfactory coefficient of determination (R^2) above 0.96. The Freundlich model also showed a satisfactory $R^2 = 0.90$. It were observed that the Red 81 dye is better adsorbed onto GO, when compared to SFGL, showing a higher adsorption capacity for all the concentrations studied. This might be related to strong interactions between the oxygenated function groups of OG and the -NH and -OH groups of the Red 81 dye. The adsorption behavior was best fitted by a pseudo-second order kinetic model. A layer of graphene has a large two-dimensional planar structure; its extended, delocalized π– electron system facilitates interaction with the direct dyes through π–π stacking, low electrostatic interaction, or Van der Waals forces. The simultaneous action of the different adsorption mechanisms present in the interaction between dyes and adsorbents are important for the understanding of the evolution of adsorptive capacity through existing functional groups. The structural properties of GO allow interaction with organic molecules via non-covalent forces such as π-π stacking and hydrogen bonds. The GO surface is negatively charged due to the presence of large numbers of oxygen-containing functional groups, such as epoxy, carboxyl and hydroxyl. With the protonation of the GO surface by acid pH, the number of positively charged sites increases, favoring the adsorption of negatively charged dye ions by attraction forces. Hence, the high removal efficiency at lower pHs for SFGL using this adsorbent. This blue dye has four sulfonic acid groups ($R\text{-}SO_3Na$), which, in aqueous medium has the dissociation of sodium ions (Na^+) and sulfonate ($R\text{-}SO_3$). However, these sulfonic groups have pKa less than zero and therefore exhibit negative charges even at lower pHs, which helps in the interaction with the protonated GO surface. This factor also assists in the removal of red dye 81, since it contains two sulfonic acid groups in its structure. Another crucial factor is the presence of carboxyl and hydroxyl groups on the GO surface, which can promote hydrogen bonds with the -OH groups, quite present in the SFGL blue, contributing to a greater adsorption capacity of these dye. Specifically, for the Red 81 dye, the existence of an amine group and a hydroxyl in its structure also allows hydrogen bonds with the -OH and -COOH groups present on the GO surface. At basic pH's the hydroxyl and carboxylic groups of the GO are deprotonated and form their anionic specimens (-ACOO and -AO), which are believed to interact via dipole-dipole bonds with the -RNaO and -RO groups present in this red dye. This explains the high adsorption of the Red 81 dye onto GO, both in acidic and basic pHs. The Red 81 and SFGL blue dyes have five and seven aromatic rings in one molecule, respectively. Its extended, delocalized π–electron system facilitates interaction with the direct dyes through the π–π stacking interaction. As both dyes exhibit a planar structure, we believe that these π- π stacking are a secondary interaction mechanism between both dyes and GO, and a main interaction mechanism between the dyes and the commercial graphene (as few oxidized functional groups are present). The adsorptive process on the commercial graphene nanosheets surface occurs by low electrostatic interaction or Van der Waals forces. The electrostatic affinity is indicated by the pH through the analysis of the zero-charge point of the adsorbent which consists of the neutral point in the interaction surface. The low adsorptive capacity using commercial graphene as an adsorbent for SFGL can be explained by the absence of functional oxygen groups. It was found that the adsorption mechanism of benzene does not occur through hydrogen bonds, resulting in a lower adsorptive capacity. It is assumed that in acid pH solution, both anionic dyes exhibits repulsion to the liquid medium and consequently a higher affinity to the inert sheets of graphene nanoplatelets, enabling a better fixation of the

dye and consequently higher adsorption capacity [24].

ElHussein et al., studied on removal of carbamazepine (CBZ) from water using UiO-66 and UiO-66/graphene nanoplatelet composite. UiO-66 and graphene nanoplatelet (GNP)/UiO-66 composites were prepared by hydrothermal method. Morphologies of UiO-66 and UiO-66/GNP nanoparticles were investigated by SEM analysis. The images of particles observed to have a shape of crystals are suitable to literature. The crystal shapes are due to ratio of used modulator acid. In this study, particle size distribution of UiO-66 nanoparticles is about 200 nm, UiO-66/GNP nanoparticles is about 700 nm. BET adsorption-desorption isotherms of adsorbents at 77 K were applied, and specific surface area for the UiO-66, and UiO-66/GNP were estimated as 730.6 m^2/g, and 910.5 m^2/g, respectively. The BJH pore volume of UiO-66 is 0.0462 cm^3/g, and pore radius of 1.92 nm. Also, BJH pore volume of UiO-66/GNP is 0.0357 cm^3/g, and pore radius of 1.81 nm. UiO-66 and UiO-66/GNP nanoparticles were prepared for CBZ adsorption. Adsorbent dosage is an important adsorption parameter; 1 mg dosage of UiO-66/GNP and 2.5 mg dosage of UiO-66 was selected as optimum dosage adsorbent. 5 mL of adsorbate solution is more appropriate quantity for UiO-66/GNP. CBZ adsorption capacity reaches to 26.46 mg/g if5 mL of adsorbate solution. 10 mL of solution is better for UiO-66. The pH of CBZ solution was investigated, the results observed that neutral media is better for both of the adsorbents. pKa values of CBZ are 2.3−13.9. Between pH 3 and 10, CBZ protects its neutral form. Acidic and neutral pH values have nearly similar CBZ adsorption capacities on UiO-66. But UiO-66/GNP has very high adsorption capacity at neutral pH value. This result can be connected to GNP surface. Heterogeneity and uncharged surface of GNP is suitable for CBZ adsorption, π-π stacking brings functional addition to GNP. So, UiO-66/GNP nanoparticles is better for CBZ adsorption from water. Non-linear pseudo-first order and pseudo-second order kinetic models were applied. Pseudo-first order R^2 values of CBZ adsorption on UiO-66/GNP and UiO-66 were 0.92 and 0.97, respectively. R^2 values of CBZ adsorption on UiO-66/ GNP and UiO-66 for pseudo-second order were 0.96 and 0.98, respectively. Both of the kinetic model can explain kinetic behaviour of the adsorption systems. The reaction mechanism is directly due to chemical reactions between urea functional group of carbamazepine ($C_{15}H_{16}N_2O_3$) and adsorbents. Non-linear Langmuir and Freundlich isotherms was applied in this study. According to adjusted R^2 values, CBZ adsorption on UiO-66 and UiO-66/GNP are compatible with non-linear Langmuir and Freundlich isotherms. Multilayer adsorption occurs between CBZ and adsorbents. And chemical reaction is the main step of adsorption [81].

Luo et al. investigated the efficiency of GNPs as solid-phase extraction (SPE) sorbent for determination of phthalate esters (PAEs) in aqueous solution. To evaluate the enrichment effect of GNPs sorbent, five PAEs including dimethyl phthalate (DMP), diethyl phthalate (DEP), dipropyl phthalate (DPrP), DBP and dicyclohexyl phthalate (DCHP) were selected as model analytes. The operation parameters affecting the extraction efficiency, including eluent solvent and its volume, and the sample volume were optimized. The eluent solvent for SPE operation has important influence on sample recovery. The choice of eluent solvent is mainly based on the chemical property of the target samples and the chromatographic mode used downstream. Since the separation of five PAEs was performed by reverse phase HPLC (RP-HPLC), the eluent solvent should be compatible with common mobile phase used in RP-HPLC, that is, the eluent solvent should be miscible with the mobile phase. It observed that acetonitrile is the most effective eluent for five PAEs, probably resulting from strong interaction between acetonitrile and GNPs due to its property of aprotic solvent. Thus, acetonitrile was selected as eluent in the following studies. In addition, the pH effect on the extraction was also explored and it was found that the pH had no significant influence on the recoveries. To ensure reliable analytical results and high enrichment factor, the maximal sample loading volume of GNPs-based SPE cartridge was explored. It observed that the peak area of each analyte increased with increase of loading sample volume up to 1000 mL, indicating rich adsorbed sites on the surface of GNPs sorbent. 80-101% of recoveries were achieved for the analytes (except DMP) when the sample loading volume was less than 500 mL [82].

Comparison of GNPs sorbent with other commonly used sorbents, including C_{18} silica, HLB Oasis, Active carbon, and MWCNTs, has been made. To ensure the same level of packing sorbent in the cartridge, different amounts of sorbents were used due to their different densities. C_{18} silica (100 mg), HLB Oasis (100 mg), Active carbon (50 mg), MWCNTs (50 mg) and GN (30 mg) were packed in 1 mL SPE cartridge. These cartridges were loaded with 200 mL of sample solutions spiked at 100 ng mL^{-1} five PAEs. To determine the possible breakthrough of sample, the effluent at different stages of loading, washing, and elution was collected and determined by HPLC. Methanol as the eluent solvent was used for C18 silica and HLB Oasis. Active carbon and MWCNTs were eluted by acetonitrile. It highlighted, GNPs sorbent yielded the highest recoveries (85.6-100.9%) among these tested sorbents, although its amount was the smallest (only 30 mg). By comparison, GNPs sorbent observed the best performance in terms of recoveries and adsorption capacity among several sorbents. This is probably due to its unique structure, which results in strong π-stacking interaction with the benzene ring in the molecule of PAEs. In addition, GNPs have some hydrophilic groups such as hydroxyl and carboxyl groups, which can improve the water-wettability of GNPs and enhance the retention of polar compounds. These features make GN an attractive sorbent for PAEs [82].

Al-Khateeb et al. studied on removal of non-steroidal anti-inflammatory drugs (NSAIDs) from water using high surface area graphene nanoplatelets (HSANGs). The NSAIDs drugs; Ketoprofen (KETO), Naproxen (NAP) and Diclofenac sodium salt (DIC), and Ibuprofen (IBU); were used in this study. Adsorption of pharmaceutical pollutants NSAIDs from aqueous solutions by carbon-based adsorbents such as HSANGs might be occurred through the by π-π stacking due to the presence of the π electrons on both of the organic compounds and the HSANGs surface. However, there are many other factors that may affect this type of interaction and consequently affect the removal process. Therefore, the effect of different factors on the interaction between HSANGs and KETO, NAP, DIC, and IBU was explored and studied. The effect of HSANGs mass on the removal of KETO, NAP, DIC, and IBU was observed. It is found that the increase in the % removal of NSAIDs with the increase of HSANGs mass. 10.0 mg of HSANGs was able to remove most of the NSAIDs compounds. Further increase of HSANGs increased the % removal of NSAIDs using 40.0 mg of the HSANGs. Within 5.0 minutes adsorption of the NSAIDs compounds reached equilibrium. After 5.0 minutes, the removal percentage did not change significantly. It was also observed that the affinity of the NSAIDs compounds towards the HSANGs was different and followed the following order DIC>NAP > KETO> IBU. Also, this observation could be because DIC, NAP, and KETO molecules composed of two benzene rings, whereas IBU composed of one benzene ring, which allowed DIC, NAP, and KETO molecules to interact and adsorbed on the HSANGs through the π-π interaction. Another reason for the affinity of the NSAIDs compounds towards the HSNGs could be due to the molecular weight and consequently the size of the molecule, as the molecular weights of the molecules. The large size of the molecule allowed them to compete effectively for the adsorption on the surface of the HSANGs. The dependence of the removal on the solution pH is a crucial physicochemical factor, which infers the adsorption mechanism at the solid-solution interface. Therefore, the effect of solution pH on the removal of NSAIDs by HSANGs was studied. The results observed the % removal was the highest at pH value of 2.0 NSAIDs and this % removal did not change by raising the solution pH to 4.0 [83].

It is important to study the adsorption process kinetically through the observation of the experimental parameters that may affect the rate of adsorption and, as a result, help attain equilibrium in a fair amount of time in order to comprehend the adsorption and remediation process. The most common and well-known kinetic models, the pseudo-first-order model and the pseudo-second-order model, were used to analyze the adsorption experimental data of KETO, NAP, DIC, and IBU by the HSANGs in order to comprehend the nature of the adsorption process. It observed that, the pseudo-first-order model, was applied to fit the data. However, the adsorption of KETO, NAP, DIC, and IBU by HSANGs was studied using the pseudo-second-order rate equation showed an excellent regression coefficients (R^2 >0.99)

and straight lines were obtained, as well as good fitting to the experimental data. Using two separate models, the liquid film diffusion model and the intra-particle diffusion model, the adsorption rate-controlling mechanism for the adsorption of the KETO, NAP, DIC, and IBU by HSANGs from aqueous solution was studied. Another kinetic model that involves the flow of adsorbate molecules through a liquid film around the solid adsorbent is the liquid film diffusion model. The linear regression coefficients and convergence of the liquid film diffusion model applied to the adsorption data of KETO, NAP, DIC, and IBU by HSANGs were very low. This suggests that the rate-determining stage for the entire adsorption process was not the liquid film diffusion. Only the kinetic data after the first minute of the adsorption were well-converged with respectable linear regression coefficients. The data of KETO, NAP, DIC, and IBU adsorption by HSANGs did not converge, and no straight lines that passed through the origin were found. The intra-particle diffusion is not the rate-determining step, but it is a component of the adsorption mechanism for the adsorption of KETO, NAP, DIC, and IBU by HSANGs, which suggests that the adsorption processes occur in two kinetic steps. NSAIDs under research may have a significant impact on the adsorption process onto HSANGs. Therefore, it is evident that the adsorption processes were regulated by more than one kinetic step, including intra-particle diffusion of the KETO, NAP, DIC, and IBU via HSANGs and liquid film diffusion. The adsorption mechanism is a mixed process because none of the steps is the rate-determining step. Instead, the first linear step within the first minute is the fastest step and is attributed to the diffusion of KETO, NAP, DIC, and IBU molecules to the HSANGs. The second linear portion is a slower process that corresponds to the intra-particle diffusion of the KETO, NAP, DIC, and IBU through the HSANGs. The HSANGs' ability to adsorb the NSAIDs KETO, NAP, DIC, and IBU from an aqueous solution mostly in accordance with the pseudo-second-order kinetic model, as demonstrated by the excellent correlation coefficients (>0.99) and convergence of the experimental data, led to this conclusion. Additionally, the removal process involves several processes, including intra particle diffusion and liquid film diffusion, however none of these steps determine the removal process's rate[83].

The spontaneity of the NSAID adsorption process was studied by thermodynamic analysis. The ΔH^o values for the adsorption of KETO, NAP, DIC, and IBU by HSANGs from the aqueous solution were positive; +39.5 kJ/mole, +42.5 kJ/mole, +47.0 kJ/mole, and +27.5 kJ/mole, respectively. The endothermic character of the adsorption of KETO, NAP, DIC, and IBU by HSANGs is confirmed by the positive enthalpy values, which explains why the rate of adsorption increases as the temperature of the solution rises. Additionally, the amount of ΔH^o points to a substantial affinity between the physical characteristics of the adsorption and KETO, NAP, DIC, and IBU by HSANGs. During the adsorption and immobilisation of KETO, NAP, DIC, and IBU, the positive values of ΔS^o, +144.8 J/mole.K, +159.7 J/mole.K, +184.0 J/mole.K, and +97.1 J/mole.K, revealed a rise in the degree of randomness at the HSANGs/solution interface. According to the negative values of the predicted free energy change, ΔG^o, which were, respectively, -3.38 kJ/mole, -4.79 kJ/mole, -7.45 kJ/mole, and -1.23 kJ/mole for the adsorption of KETO, NAP, DIC, and IBU by HSANGs from aqueous solution, the adsorption of KETO, NAP, and DIC The adsorption of KETO, NAP, DIC, and IBU by HSANG's process is proposed to be an entropy-driven process by the negative values of ΔG^o and the positive values of ΔH^o and ΔS^o. To determine whether the suggested solid adsorbent is practical, the removal of by HSANGs from actual environmental water samples was examined. For this study, two actual samples were chosen: KETO, NAP, DIC, and IBU tap water (TW), as well as wastewater from King Abdulaziz University Wastewater (WW). The initial KETO, NAP, DIC, and IBU concentrations were tested and were below the HPLC's detection limit, showing that these pollutants were not present in the chosen real water samples. It demonstrates that the majority of NSAIDs such KETO, NAP, DIC, and IBU were eliminated from the WW, and TW spiking samples support the usefulness of HSANGs for environmental remediation, particularly in the case of NSAID pollution. Using actual water samples containing KETO, NAP, DIC, and IBU, the applicability of the HSANGs for the removal of NSAIDs was tested, and the findings demonstrated the high removal effectiveness [83].

Bhattacharya et al. investigates the potential of graphene oxide nanoplatelets (GONPs) for removal of a common and extensively used drug, Carbamazepine (CBZ) from aqueous solutions. The surface morphology of GONP as recorded using SEM observed that the SEM images of GONP composed of thin, closely associated and highly overlapping platelet-like carbon sheets. The rough surfaces of these crumpled GONPs reportedly facilitate efficient adsorption. These wrinkled and layered structures of GO are reportedly formed as a result of interactions between oxygen containing functional groups. Batch studies were performed to assess the potential of graphene oxide for adsorption of CBZ under different. A maximum adsorbate removal of 99% was recorded from a solution containing 5 ppm of CBZ under optimized conditions of solution pH (2), adsorbent dosage ($1gL^{-1}$), temperature (35ºC) and contact time (120 min). Different isotherms models such the Langmuir, Freundlich, Temkin, and Dubinin-Radushkevich were fitted to the percentage CBZ removal. The values of $R^2 = 0.815$ suggested that the results from batch experiments were the most closely related to the Temkin isotherm. Therefore, it may be assumed that CBZ was uniformly adsorbable by GONP. Additionally, this implied that the adsorbent moieties' heat of adsorption reduced linearly as the process advanced. For the examination of process kinetics, CBZ removals were fitted to various models. The pseudo-second order kinetic model best fit the results from batch investigations. The Arrhenius equation was used to compute the activation energy (E_a), which was discovered to be 78 kJ/mol for the adsorption of CBZ by GONPS. The CBZ adsorption by GONP was likely chemisorption in nature if the E_a value was greater than 40 kJ/mol. According to the findings of the study on process thermodynamics, negative values observed for $\Delta G°$ suggested the process in question was spontaneous. Additionally, the process' endothermic character was confirmed by the positive figure for enthalpy. Additionally, the positive value for entropy indicated that the translational entropy of the released CBZ ions was lower than that of the water molecules that were displaced, leading to a higher level of unpredictability at the interface between the adsorbent and adsorbate. The CBZ adsorption efficiency of GONP was observed to maintain the same for eight consecutive cycles and fall in the last two cycles (95 and 90% removal efficiency, respectively), according to the study's findings on reusability. This had happened because of handling-related bulk loss or repeated regeneration-related adsorbent surface degradation [84].

Khalil et al., studied on nanostructured porous graphene (PG) for efficient removal of emerging contaminants (ECs) pharmaceutical; atenolol (ATL), carbamazepine (CBZ), ciprofloxacin (CIP), diclofenac (DCF), gemfibrozil (GEM) and ibuprofen (IBP) from water. Detailed batch tests were conducted to investigate the effects of adsorption time, initial EC concentration, PG dosage, solution pH, and temperature. A maximum adsorbate removal of ECs >99.9% was recorded from a solution containing 250 ppm of ECs under optimized conditions of solution pH (2), adsorbent dosage (5 mg), and contact time (60 min).To illustrate the sorption mechanism and the role of surface area and active sites, four kinetic models including pseudo-first order, pseudo-second order, Elovich and intraparticle diffusion reaction models were applied to evaluate the rate of adsorption reaction and its rate controlling step. Of the four suggested models, the pseudo-second order rate model best described the kinetics of ECs adsorption onto graphene oxide (GO) and PG with an excellent fit as indicated by the highest correlation coefficient values ($R^2 = 0.99$ for most ECs). The results indicated further affinity of ECs of hydrophilic nature, such as ATL and CIP towards GO, while the other ECs were more attracted to PG. In general, although the adsorption performance of GO was higher for ATL and CIP removal, but, in terms of super hydrophobicity, ease of separation from water, recyclability and chemical stability, PG is a more attractive candidate for ECs removal in water treatment applications [85].

Seven adsorption isotherm models were compared for their potential to best fit the experimental data in order to better clarify. The Freundlich model might be used to represent the adsorption findings of GO for ATL and CBZ in terms of the best match criterion (R^2). The Freundlich isotherm models plausible for explaining heterogeneous multilayer adsorption. The Langmuir isotherm is used to illustrate the IBP adsorption data for GO and PG. This implied that a monolayer coverage

formed in the event of IBP adsorption onto a graphene-based material (GBM) surface, suggesting that the binding energies of each IBP molecule on the surface GO were uniform. Therefore, it can be said that no interactions between GO molecules occurred during the IBP adsorption. Finally, it was discovered that the Langmuir models fairly produced a better fitting than the other models in the instance of DCF adsorbed by GO and PG. The pseudo-second order model was applied as best to described the kinetics of ECs adsorption onto GO and PG with an excellent fit (R^2 = 0.99 for most ECs). In every situation, the type of adsorption may be predicted based on the principal adsorption energy E (kJ/mol), which is connected to the D-R model. The ECs' adsorption process on GO and PG showed physical properties, as evidenced by the low values of the E parameter that were observed. The exothermic character of the adsorption is confirmed by the negative values of ΔH, which explains why adsorption decreases at increasing temperatures. In contrast to chemical adsorption, which has a range of -400 to -80 kJ/mol, the magnitude of ΔH points to a weak type of bonding between ECs by PG, such as physical adsorption (ΔH range between -20 and -40 kJ/mol). The decrease in degree of freedom of pharmaceutical molecules, as indicated by the negative values of ΔS, is thought to be the cause of the decrease in randomness. The free energy change, ΔG, is negative, indicating an enthalpy-driven process and a product-favorable spontaneous reaction. Finally, after being regenerated and used four times to cure pharmaceutically contaminated solutions, PG showed good promise for recycling[85].

Table 1. Summarize of adsorption of EDCs onto graphene nanoplatelets

Adsorbent	Pollutant	Adsorption Isotherm Model	Adsorption Kinetics Model	Adsorption Thermodynamic	Remarks	Ref.
Graphene Nanoplatelets	DCS	Langmuir	Pseudo-second-order	Exothermic and spontaneous process	At pH conditions greater than 4.2, diclofenac sodium ionizes given a negatively charged ion that is electrostatically repelled by GNP surface causes a decrease in the removal efficiency.	[75]
Exfoliated Graphene Nanoplatelets	BPA	Langmuir Freundlich	Pseudo-second-order	Exothermic and spontaneous process	At pH from 3 to 7, the adsorption of BPA slightly increased, than it begins to decrease between 7 and 9.	[29]
Graphene nanoplatelets	ASA, APAP, CAF	BET	Pseudo-second-order	Exothermic spontaneous process and increase in randomness	The percentage of adsorption of CAF was slightly enhanced by increasing the ionic strength of the solution	[76]
Graphene Nanoplatelets	LFX	Langmuir	Pseudo-second-order	Endothermic, spontaneous process and	The dosage and time have a positive effect on removal efficiency.	[77]

				increase in randomness	If one of the variables is held constant, the trend remains unchanged.	
Magnetically modified graphene nanoplatelets	AA	Langmuir Temkin	Pseudo-second-order	Exothermic and spontaneous process and decrease in randomness	These functional groups in AA ionize at various pH levels to produce negatively charged AA; the electrostatic repulsion increases between amoxicillin and M-GNPs surface as the solution pH rises.	[78]
Exfoliated Graphene Nanoplatelets	Phenol	Langmuir			The hydrogen bonding between surface-adsorbed phenol and dissolved phenol may contribute to the increased sorption capacity values for xGnPs.	[74]
Graphene Oxide Nanoplatelets	IBP	Langmuir	Pseudo-second-order	Endothermic, spontaneous process and increase in randomness	Maximum IBP removal was found at an initial IBP concentration of 6 mg/L, adsorbent dosage of 1.00 g/L, solution pH of 6, agitation speed of 180 RPM, and temperature of 308K following 60 minutes of treatment.	[79]
Graphene Nanoplatelets	ACM, SMX	Langmuir	Pseudo-second-order		Maximum adsorption was observed at pH 4 (99.27%) for SMX and ACM at pH 8 (98.38%).	[80]
Magnetically Modified Graphene Nanoplatelets	MNAD	Langmuir Temkin	Pseudo-second-order	Exothermic and spontaneous process	MNAD was removed within 120 min using 9.8 mg adsorbent, at pH 5.0 and 293 K.	[1]
Graphene Oxide (GO) Nanosheets, Commercial	Dyes	Langmuir Freundlich	Pseudo-second-order		Dye adsorbed on commercial graphene shows high efficiency at low pH, which	[24]

Graphene					rapidly decreased at higher pH.	
UiO-66, UiO-66/graphene nanoplatelet composite	CBZ	Langmuir Freundlich	Pseudo-first-order Pseudo-second-order		Neutral pH of CBZ solution is better for both of the adsorbents.	[81]
Graphene Nanoplatelets	PAEs				GNPs sorbent yielded the highest recoveries (85.6–100.9%), although its amount was the smallest (only 30 mg).	[82]
High Surface Area Graphene Nanoplatelets	NSAIDs		Pseudo-first-order	Endothermic, spontaneous process and increase at randomness	Percentage removal was the highest at pH value of 2.0 NSAIDs and this % removal did not change by raising the solution pH to 4.0.	[83]
Graphene Oxide Nanoplatelets	CBZ	Temkin	Pseudo-second-order	Endothermic, spontaneous process and increase at randomness	A maximum adsorbate removal of 99% was recorded from a solution containing 5 ppm of CBZ under optimized conditions of solution pH (2), adsorbent dosage ($1gL^{-1}$), temperature ($35^{o}C$) and contact time (120min).	[84]
Nanostructured Porous Graphene	ATL, CBZ, CIP, DCF, GEM, IBP	Freundlich (ATL, CBZ) Langmuir (IBP, DCF) Toth (CIP, GEM, DCF)	Pseudo-second-order	Exothermic, spontaneous process and decrease at randomness	A maximum adsorbate removal of these pharmaceuticals > 99.9% was recorded from a solution containing 250 ppm of ECs under optimized conditions of solution pH (2), adsorbent dosage (5 mg), and contact time (60min).	[85]

Abbreviations: DCS: diclofenac sodium; BPA: bisphenol A; ASA: aspirin; APAP: acetaminophen; CAF: caffeine; LFX: levofloxacin; AA: amoxicillin; SMX: sulfamethoxazole; ACM: acetaminophen; MNAD: metronidazole antibiotic drug; PAEs: phthalate esters; NSAIDs: non-steroidal anti-inflammatory drugs; ATL: atenolol; CBZ: carbamazepine; CIP: ciprofloxacin; DCF: diclofenac; GEM: gemfibrozil; IBP: ibuprofen

Over the decades, the research involving the usage of GNPs have progressed in a multitude of directions. The literatures published in area of nanomaterials governing graphene-based materials especially GNPs indicate the intensity of research activities being carried with this material. The properties of GNPs have caused the wide range of application such as sorbent material for wastewater treatment. However, more research is needed to improve the capability of GNPs to adsorb adsorbates at even lower concentrations. It can be done by further fabricating the GNPs with other materials.

Conclusion

The effective use of graphene nanoplatelets as an adsorbent material for the removal of heavy metals and endocrine disruptors in wastewaters is summarized in this review paper. Pollutants become harmful when exposed for a long period of time, endangering not just humans and the environment but also aquatic life. The conventional treatment techniques might not be sufficient to completely remove these pollutants. Adsorption using graphene materials can be thought of as a simple and low-cost technique, especially for treating distinctive wastes like heavy metals and EDCs, which may only be present in very low concentrations and are harmful if not completely removed. The use of graphene nanoplatelets and its modifications for the removal of heavy metal pollutants and EDCs have made recent progress, as shown in this review. It is evident that graphene nanoplatelets offer a promising alternative to other commonly used adsorbent materials. It has been demonstrated that graphene nanoplatelets have the potential to be one of the most reliable and versatile materials for wastewater treatment in the future. It is important to understand that the adsorptive capacity of graphene nanoplatelets depends on the conditions of the experiment. The results of the batch experiments indicated that the adsorption process was affected by adsorbent dose, contact time, initial phosphate concentration, and temperature. The kinetic study indicated adsorption was governed by several mechanisms with various processes dominating different stages of adsorption. Isotherm studies showed the adsorption could be described by Langmuir, Freundlich, Temkin, and Dubinin-Radushkevich isotherms. Based on a comparison of the R^2 values, the adsorption onto GNPs adsorbent mostly closely fit Langmuir isotherm, suggesting a monolayer adsorption system on the surface. The kinetic studies included a pseudo-first order kinetic model of a Lagergren curve, a pseudo-second order model and an intra-particle diffusion model to elucidate the adsorption mechanisms and the adsorption control rates was studied. Besides that, the mechanisms of adsorption include chemical and physical interactions was investigated in this review. The present review investigates the significance of thermodynamic parameters, standard free energy change (ΔG^o), standard enthalpy change (ΔH^o) and standard entropy change (ΔS^o) to predict the spontaneity of adsorption of metals and EDCs onto the surface of adsorbents. On the basis of its chemical and structural stability, the GNPs could become a very good adsorbent with applications for water remediation. More studies should be carried out for low-cost adsorption process to promote large scale use of non-conventional adsorbents. Low-cost adsorbents should be used to minimize cost and maximize heavy metal removal efficiency.

References

1. Badhei, S., & Mitra, J. C. Efficient use of graphene nano platelets for removal of antibiotic drug from aqueous solution.
2. Sarmah, A. K., Northcott, G. L., Leusch, F. D. L. and Tremblay, L. A. (2006). A survey of endocrine disrupting chemicals (EDCs) in municipal sewage and animal waste effluents in the Waikato region of New Zealand. *Science of the Total Environment,* 355(1-3): 135-144.
3. Lyssimachou, A., Bachmann, J. and Porte, C. (2008). Short-term exposure to the organotin compound triphenyltin modulates esterified steroid levels in females of *Marisa cornuarietis*. *Aquatic Toxicology,* 89(2): 129-135.
4. Kavlock, R. J. (1999). Overview of endocrine disruptor research activity in the United States. *Chemosphere,* 39(8): 1227-1236.
5. Rusu, C., Preda, C., Sireteanu, A. and Vulpoi, C. (2015). Risk factors in autism spectrum disorders: the role of genetic, epigenetic, immune and environmental interactions. *Environmental*

Engineering & Management Journal, 14(4): 901-907.

6. Apul, O. G., Wang, Q., Zhou, Y. and Karanfil, T. (2013). Adsorption of aromatic organic contaminants by graphene nanosheets: Comparison with carbon nanotubes and activated carbon. *Water Research,* 47(4): 1648-1654.
7. Ji, L., Chen, W., Duan, L. and Zhu, D. (2009). Mechanisms for strong adsorption of tetracycline to carbon nanotubes: a comparative study using activated carbon and graphite as adsorbents. *Environmental Science & Technology,* 43(7): 2322-2327.
8. Maliyekkal, S. M., Sreeprasad, T. S., Krishnan, D., Kouser, S., Mishra, A. K., Waghmare, U. V. and Pradeep, T. (2013). Graphene: a reusable substrate for unprecedented adsorption of pesticides. *Small,* 9(2): 273-283.
9. Pavagadhi, S., Tang, A. L. L., Sathishkumar, M., Loh, K. P. and Balasubramanian, R. (2013). Removal of microcystin-LR and microcystin-RR by graphene oxide: adsorption and kinetic experiments. *Water Research,* 47(13): 4621-4629.
10. Geim, A. K. and Novoselov, K. S. (2007). The rise of graphene. *Nature Materials,* 6(3): 183-191.
11. Stoller, M. D., Park, S., Zhu, Y., An, J. and Ruoff, R. S. (2008). Graphene-based ultracapacitors. *Nano Letters,* 8(10): 3498-3502.
12. Afsahi, S., Lerner, M. B., Goldstein, J. M., Lee, J., Tang, X., Bagarozzi Jr, D. A., ... and Goldsmith, B. R. (2018). Novel graphene-based biosensor for early detection of Zika virus infection. *Biosensors and Bioelectronics,* 100: 85-88.
13. Nayak, G. S., Zybala, R., Kozinski, R., Woluntarski, M., Telle, R. and Schickle, K. (2018). Immobilization of reduced graphene oxide nano-flakes on inert ceramic surfaces using self-assembled monolayer technique. *Materials Letters,* 225: 109-112.
14. Bai, R. G., Ninan, N., Muthoosamy, K. and Manickam, S. (2018). Graphene: A versatile platform for nanotheranostics and tissue engineering. *Progress in Materials Science,* 91: 24-69.
15. Chan, K. K., Yap, S. H. K. and Yong, K. T. (2018). Biogreen synthesis of carbon dots for biotechnology and nanomedicine applications. *Nano-Micro Letters,* 10: 1-46.
16. Partoens, B. and Peeters, F. M. (2006). From graphene to graphite: Electronic structure around the K point. *Physical Review B*, 74(7): 075404.
17. Wan, Q., Cai, H., Liu, Y., Song, H., Liao, H., Liu, S. and Yang, N. (2013). Graphene nanoplatelets: Electrochemical properties and applications for oxidation of endocrine‐disrupting chemicals. *Chemistry–A European Journal,* 19(10): 3483-3489.
18. Choi, W., Lahiri, I., Seelaboyina, R. and Kang, Y. S. (2010). Synthesis of graphene and its applications: a review. *Critical Reviews in Solid State and Materials Sciences,* 35(1): 52-71.
19. Pumera, M. (2009). Electrochemistry of graphene: New horizons for sensing and energy storage. *The Chemical Record,* 9(4): 211-223.
20. Sadanala, K. C. and Chung, B. C. (2013). Graphene nanoplatelets as a solid phase extraction sorbent for analysis of chlorophenols in water. *Journal of the Korean Society for Applied Biological Chemistry,* 56: 673-678.
21. Geng, Y., Wang, S. J. and Kim, J. K. (2009). Preparation of graphite nanoplatelets and graphene sheets. *Journal of Colloid and Interface Science,* 336(2): 592-598.
22. Kumar, R., Pandey, K. K., Islam, A. and Keshri, A. K. (2019). Graphene nanoplatelets: A promising corrosion inhibitor and toughening inclusion in plasma sprayed cerium oxide coating. *Journal of Alloys and Compounds*, 809: 151819.
23. Liu, J., Dong, J., Zhang, T. and Peng, Q. (2018). Graphene-based nanomaterials and their potentials in advanced drug delivery and cancer therapy. *Journal of Controlled Release,* 286: 64-73.
24. de Assis, L. K., Damasceno, B. S., Carvalho, M. N., Oliveira, E. H. and Ghislandi, M. G. (2019). Adsorption capacity comparison between graphene oxide and graphene nanoplatelets for the removal of coloured textile dyes from wastewater. *Environmental Technology*, 41: 2360-2371.
25. Cataldi, P., Athanassiou, A. and Bayer, I. S. (2018). Graphene nanoplatelets-based advanced materials and recent progress in sustainable applications. *Applied Sciences,* 8(9): 1438.

26. An, J. C., Lee, E. J., Yoon, S. Y., Lee, S. Y. and Kim, Y. J. (2018). Comparative study on the morphological properties of graphene nanoplatelets prepared by an oxidative and non-oxidative route. *Carbon Letters,* 26: 81-87.
27. Huang, Z. H., Zheng, X., Lv, W., Wang, M., Yang, Q. H. and Kang, F. (2011). Adsorption of lead (II) ions from aqueous solution on low-temperature exfoliated graphene nanosheets. *Langmuir,* 27(12): 7558-7562.
28. Ion, A. C., Ion, I. and Culetu, A. (2011). Lead adsorption onto exfoliated graphitic nanoplatelets in aqueous solutions. *Materials Science and Engineering: B*, 176(6): 504-509.
29. Radu, E., Catrinel Ion, A., Sirbu, F. and Ion, I. (2015). Adsorption of endocrine disruptors on exfoliated graphene nanoplatelets. *Environmental Engineering & Management Journal*, 14(3): 551-558.
30. Ahmad, H., Laini, V. V., Qian, T. Z., Jelani, R. M., Rosli, F. A. and Kamaruzaman, S. (2020). Efficient removal of lead from aqueous using hybrid graphite nanoflakes/mesoporous silica nanoparticles, amine functionalized mesoporous silica and graphite nanoflakes as adsorbents. *Malaysian Journal Analytical Sciences,* 24: 236-246.
31. Briffa, J., Sinagra, E. and Blundell, R. (2020). Heavy metal pollution in the environment and their toxicological effects on humans. *Heliyon,* 6(9): 04691.
32. Ali, H., Khan, E. and Ilahi, I. (2019). Environmental chemistry and ecotoxicology of hazardous heavy metals: environmental persistence, toxicity, and bioaccumulation. *Journal of Chemistry,* 2019: 6730305.
33. Sall, M. L., Diaw, A. K. D., Gningue-Sall, D., Efremova Aaron, S. and Aaron, J. J. (2020). Toxic heavy metals: Impact on the environment and human health, and treatment with conducting organic polymers, a review. *Environmental Science and Pollution Research,* 27: 29927-29942.
34. Nguyen, P. Y., Silva, A. F., Reis, A. C., Nunes, O. C., Rodrigues, A. M., Rodrigues, J. E., ... and Carvalho, G. (2019). Bioaugmentation of membrane bioreactor with *Achromobacter denitrificans* strain PR1 for enhanced sulfamethoxazole removal in wastewater. *Science of the Total Environment,* 648: 44-55.
35. Sharma, G., Gupta, V. K., Agarwal, S., Bhogal, S., Naushad, M., Kumar, A. and Stadler, F. J. (2018). Fabrication and characterization of trimetallic nano-photocatalyst for remediation of ampicillin antibiotic. *Journal of Molecular Liquids,* 260: 342-350.
36. Kumar, A., Kumar, A., Sharma, G., Ala'a, H., Naushad, M., Ghfar, A. A. and Stadler, F. J. (2018). Quaternary magnetic BiOCl/g-C_3N_4/Cu_2O/Fe_3O_4 nano-junction for visible light and solar powered degradation of sulfamethoxazole from aqueous environment. *Chemical Engineering Journal,* 334: 462-478.
37. Thakur, A., Kumar, P., Kaur, D., Devunuri, N., Sinha, R. K. and Devi, P. (2020). TiO_2 nanofibres decorated with green-synthesized P Au/Ag@CQDs for the efficient photocatalytic degradation of organic dyes and pharmaceutical drugs. *RSC Advances*, 10(15): 8941-8948.
38. Hemmat, K., Khodabakhshi, M. R. and Zeraatkar Moghaddam, A. (2021). Synthesis of nanoscale zerovalent iron modified graphene oxide nanosheets and its application for removing tetracycline antibiotic: Response surface methodology. *Applied Organometallic Chemistry*, 35(1): e6059.
39. Liu, Q., Li, L., Jin, X., Wang, C. and Wang, T. (2018). Influence of graphene oxide sheets on the pore structure and filtration performance of a novel graphene oxide/silica/polyacrylonitrile mixed matrix membrane. *Journal of Materials Science*, 53(9): 6505-6518.
40. de Matos Rodrigues, M. H., de Sousa, P. A. R., Borges, K. C. M., de Melo Coelho, L., de Fátima Gonçalves, R., Teodoro, M. D., ... and Júnior, M. G. (2019). Enhanced degradation of the antibiotic sulfamethoxazole by heterogeneous photocatalysis using Ce0, 8Gd0, 2O2-δ/TiO*2* particles. *Journal of Alloys and Compounds,* 808: 151711.
41. Hu, L., Zhang, Y., Lu, W., Lu, Y. and Hu, H. (2019). Easily recyclable photocatalyst Bi_2WO_6/MOF/PVDF composite film for efficient degradation of aqueous refractory organic pollutants under visible-light irradiation. *Journal of*

Materials Science, 54: 6238-6257.

42. Tang, J. and Wang, J. (2020). Iron-copper bimetallic metal-organic frameworks for efficient Fenton-like degradation of sulfamethoxazole under mild conditions. *Chemosphere,* 241: 125002.
43. Zhuan, R. and Wang, J. (2020). Enhanced degradation and mineralization of sulfamethoxazole by integrating gamma radiation with Fenton-like processes. *Radiation Physics and Chemistry,* 166: 108457.
44. Xu, J., Xu, W., Wang, D., Sang, G. and Yang, X. (2016). Evaluation of enhanced coagulation coupled with magnetic ion exchange (MIEX) in natural organic matter and sulfamethoxazole removals: the role of Al-based coagulant characteristic. *Separation and Purification Technology,* 167: 70-78.
45. Delgado, N., Capparelli, A., Navarro, A. and Marino, D. (2019). Pharmaceutical emerging pollutants removal from water using powdered activated carbon: study of kinetics and adsorption equilibrium. *Journal of Environmental Management,* 236: 301-308.
46. Xiao, F. Z., Wang, C., Yu, L. M., Pu, Y. Q., Xu, Y. L., Zhang, K., ... and He, S. Y. (2019). Fabrication of magnetic functionalised calix [4] arene composite for highly efficient and selective adsorption towards uranium (VI). *Environmental Chemistry,* 16(8): 577-586.
47. Moghaddam, A. Z., Esmaeilkhanian, E. and Shakourian-Fard, M. (2019). Immobilizing magnetic glutaraldehyde cross-linked chitosan on graphene oxide and nitrogen-doped graphene oxide as well-dispersible adsorbents for chromate removal from aqueous solutions. *International Journal of Biological Macromolecules,* 128: 61-73.
48. Patel, M., Kumar, R., Kishor, K., Mlsna, T., Pittman Jr, C. U. and Mohan, D. (2019). Pharmaceuticals of emerging concern in aquatic systems: chemistry, occurrence, effects, and removal methods. *Chemical Reviews,* 119(6): 3510-3673.
49. Carmalin Sophia, A., Lima, E. C., Allaudeen, N. and Rajan, S. (2016). Application of graphene based materials for adsorption of pharmaceutical traces from water and wastewater-a review. *Desalination and Water Treatment,* 57(57): 27573-27586.
50. Kucherova, A., Burakova, I. and Burakov, A. (2017). Graphene materials for lead(II) extraction: an equilibrium study. *In MATEC Web of Conferences*. EDP Sciences, 129: 06022.
51. Mishra, A. K. and Ramaprabhu, S. (2011). Removal of metals from aqueous solution and sea water by functionalized graphite nanoplatelets based electrodes. *Journal of Hazardous Materials*, 185(1): 322-328.
52. Sheng, Z., Cao, M., Hong, Y., Wang, S., Fan, Z., Xiong, J., ... and Deng, C. (2018). Preparation of functionalized graphene nano-platelets and use for adsorption of Pb^{2+} from solution. *Journal of Wuhan University of Technology-Materials Science Edition*, 33(6): 1395-1401.
53. Nandi, D., Ghosh, S. K., Ghosh, A., Siengchin, S., Roy, A., Gupta, K., ... and Ghosh, U. C. (2021). Arsenic removal from water by graphene nanoplatelets prepared from nail waste: A physicochemical study of adsorption based on process optimization, kinetics, isotherm and thermodynamics. *Environmental Nanotechnology, Monitoring & Management,* 16: 100564.
54. Zhu, J., Sadu, R., Wei, S., Chen, D. H., Haldolaarachchige, N., Luo, Z., ... and Guo, Z. (2012). Magnetic graphene nanoplatelet composites toward arsenic removal. *ECS Journal of Solid State Science and Technology*, 1(1): M1.
55. Samaraweera, H., Pittman Jr, C. U., Thirumalai, R. V. K., Perez, F. and Misna, T. (2021). Characterization of graphene/pine wood biochar hybrids: Potential to remove aqueous Cu^{2+}. *Environmental Research,* 192: 110283.
56. Rosenzweig, S., Sorial, G. A., Sahle-Demessie, E. and McAvoy, D. C. (2014). Optimizing the physical-chemical properties of carbon nanotubes (CNT) and graphene nanoplatelets (GNP) on Cu(II) adsorption. *Journal of Hazardous Materials*, 279: 410-417.
57. Capra, L., Manolache, M., Ion, I., Stoica, R., Stinga, G., Doncea, S. M., ... and Ion, A. C. (2018). Adsorption of Sb(III) on oxidized exfoliated graphite nanoplatelets. *Nanomaterials,* 8(12): 992.
58. Smith, D. M., Hamwi, B. and Rogers, R. E. (2022). Carbon nanomaterial-based aerogels for improved removal of copper(II), zinc(II), and lead(II) ions

from water. *Environmental Science: Advances,* 1(2): 208-215.

59. Bogdan, D., Rizea, G. A., Ion, I. and Ion, A. C. (2016). Ammonium adsorption on exfoliated graphite nanoplatelets. *Revista de Chimie*, 67: 2231-2236.
60. Yin, Q., Zhu, Y., Ju, S., Liao, W. and Yang, Y. (2016). Rapid determination of copper and lead in *Panax notoginseng* by magnetic solid-phase extraction and flame atomic absorption spectrometry. *Research on Chemical Intermediates,* 42: 4985-4998.
61. La, D. D., Patwari, J. M., Jones, L. A., Antolasic, F. and Bhosale, S. V. (2017). Fabrication of a GNP/Fe–Mg binary oxide composite for effective removal of arsenic from aqueous solution. *ACS Omega*, 2(1): 218-226.
62. Li, B.-Q., Yuan, W., and Li, L. (2016). Adsorption of Pb^{2+} and Cd^{2+} on graphene nanosheets prepared using thermal exfoliation. *Acta Physico-Chimica Sinica,* 32: 997-1004.
63. Kucherova, A. E., Romantsova, I. V., Burakov, A. E., Memetov, N. R. and Krasnyansky, M. N. (2017). Graphene-based nanocomposites for enhanced Pb^{2+} adsorption. *Nano Hybrids and Composites*, 13: 323-329.
64. Kumar, A. K., Sarma, P. N. and Mohan, S. V. (2016). Incidence of selected endocrine disrupting estrogens in water bodies of Hyderabad and its relation to water quality parameters. *Environmental Engineering Management Journal,* 15: 315-325.
65. Ternes, T. A., Stumpf, M., Mueller, J., Haberer, K., Wilken, R. D. and Servos, M. (1999). Behavior and occurrence of estrogens in municipal sewage treatment plants—I. Investigations in Germany, Canada and Brazil. *Science of The Total Environment*, 225(1-2): 81-90.
66. Shi, J., Fujisawa, S., Nakai, S. and Hosomi, M. (2004). Biodegradation of natural and synthetic estrogens by nitrifying activated sludge and ammonia-oxidizing bacterium Nitrosomonas europaea. *Water Research,* 38(9): 2323-2330.
67. Auriol, M., Filali-Meknassi, Y., Adams, C. D. and Tyagi, R. D. (2006). Natural and synthetic hormone removal using the horseradish peroxidase enzyme: temperature and pH effects. Water research, 40(15), 2847-2856.
68. Filali-Meknassi, Y., Tyagi, R. D., Surampalli, R. Y., Barata, C. and Riva, M. C. (2004). Endocrine-disrupting compounds in wastewater, sludge-treatment processes, and receiving waters: Overview. *Practice Periodical of Hazardous, Toxic, and Radioactive Waste Management*, 8(1): 39-56.
69. Jobling, S., Nolan, M., Tyler, C. R., Brighty, G. and Sumpter, J. P. (1998). Widespread sexual disruption in wild fish. *Environmental Science & Technology*, 32(17): 2498-2506.
70. Kumar, A. K. and Mohan, S. V. (2012). Removal of natural and synthetic endocrine disrupting estrogens by multi-walled carbon nanotubes (MWCNT) as adsorbent: kinetic and mechanistic evaluation. *Separation and Purification Technology,* 87: 22-30.
71. Pojana, G., Gomiero, A., Jonkers, N. and Marcomini, A. (2007). Natural and synthetic endocrine disrupting compounds (EDCs) in water, sediment and biota of a coastal lagoon. *Environment International,* 33(7): 929-936.
72. Routledge, E. J. and Sumpter, J. P. (1996). Estrogenic activity of surfactants and some of their degradation products assessed using a recombinant yeast screen. *Environmental Toxicology and Chemistry: An International Journal,* 15(3): 241-248.
73. Snyder, S. A., Villeneuve, D. L., Snyder, E. M. and Giesy, J. P. (2001). Identification and quantification of estrogen receptor agonists in wastewater effluents. *Environmental Science & Technology*, 35(18): 3620-3625.
74. Ion, A. C., Alpatova, A., Ion, I. and Culetu, A. (2011). Study on phenol adsorption from aqueous solutions on exfoliated graphitic nanoplatelets. *Materials Science and Engineering: B*, 176(7): 588-595.
75. Zakaa, A., Ibrahima, T. H., Khamisb, M. I. and Samarab, F. (2020). Adsorption characteristics of diclofenac sodium onto graphene nanoplatelets. *Desalination and Water Treatment*, 206: 331-339.
76. Al-Khateeb, L. A., Almotiry, S. and Salam, M. A. (2014). Adsorption of pharmaceutical pollutants onto graphene nanoplatelets. *Chemical Engineering Journal,* 248: 191-199.

77. Zakaa, A., Ibrahima, T. H., Khamisb, M. I. and Jabbara, N. A. (2019). Experimental design modelling and optimization of levofloxacin removal with graphene nanoplatelets using response surface method. *Pharmaceuticals,* 16(18): 19.
78. Kerkez-Kuyumcu, Ö., Bayazit, Ş. S. and Salam, M. A. (2016). Antibiotic amoxicillin removal from aqueous solution using magnetically modified graphene nanoplatelets. *Journal of Industrial and Engineering Chemistry,* 36: 198-205.
79. Banerjee, P., Das, P., Zaman, A. and Das, P. (2016). Application of graphene oxide nanoplatelets for adsorption of ibuprofen from aqueous solutions: evaluation of process kinetics and thermodynamics. *Process Safety and Environmental Protection,* 101: 45-53.
80. Rosli, F. A., Ahmad, H., Jumbri, K., Abdullah, A. H., Kamaruzaman, S. and Fathihah Abdullah, N. A. (2021). Efficient removal of pharmaceuticals from water using graphene nanoplatelets as adsorbent. *Royal Society Open Science,* 8(1): 201076.
81. ElHussein, E. A. A., Şahin, S. and Bayazit, Ş. S. (2020). Removal of carbamazepine using UiO-66 and UiO-66/graphene nanoplatelet composite. *Journal of Environmental Chemical Engineering*, 8(4): 103898.
82. Luo, X., Zhang, F., Ji, S., Yang, B. and Liang, X. (2014). Graphene nanoplatelets as a highly efficient solid-phase extraction sorbent for determination of phthalate esters in aqueous solution. *Talanta,* 120: 71-75.
83. Al-Khateeb, L. A., Hakami, W. and Salam, M. A. (2017). Removal of non-steroidal anti-inflammatory drugs from water using high surface area nanographene: kinetic and thermodynamic studies. *Journal of Molecular Liquids,* 241: 733-741.
84. Bhattacharya, S., Banerjee, P., Das, P., Bhowal, A., Majumder, S. K. and Ghosh, P. (2020). Removal of aqueous carbamazepine using graphene oxide nanoplatelets: Process modelling and optimization. *Sustainable Environment Research,* 30(1): 1-12.
85. Khalil, A. M., Memon, F. A., Tabish, T. A., Salmon, D., Zhang, S. and Butler, D. (2020). Nanostructured porous graphene for efficient removal of emerging contaminants (pharmaceuticals) from water. *Chemical Engineering Journal,* 398: 125440.